TIChE

KHON KAEN UNIVERSITY

TIChE ENKKU ENGINEERING KHON KAEN UNIVERSITY GC

SCGC ptt HMC Polymers GGC GLOBAL GREEN CHEMICALS

The 34th Thai Institution of Chemical Engineering and Applied Chemistry International Conference (TIChE2025)

TIChE2025 PROCEEDINGS

MAY 20-21, 2025
PATTAYA, THAILAND

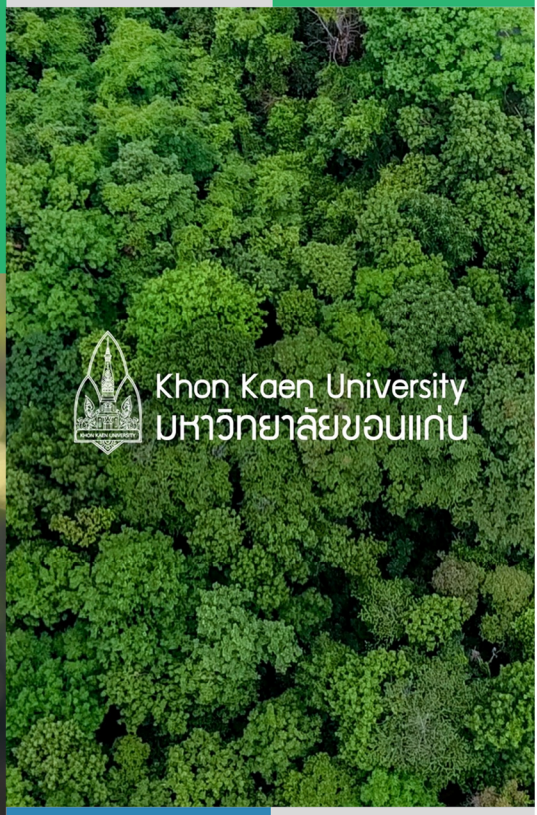

DISCLAIMER

The papers included in the proceeding represent the research and academic work presented at the 34th Thai Institute of Chemical Engineering and Applied Chemistry International Conference (TIChE2025), held in Pattaya, Thailand, from May 20-21, 2025. The conference is organized by the Department of Chemical Engineering, Faculty of Engineering, Khon Kaen University, in collaboration with the Thai Institute of Chemical Engineering and Applied Chemistry (TIChE). Under the theme “Navigating the Future: Challenges and Innovations for Sustainable Green Technologies”, the conference aims to provide a collaborative platform for researchers, educators, and professionals to share knowledge, foster innovation, and address global challenges in chemical engineering and applied chemistry.

These papers reflect the opinions, analyses, and conclusions of the respective authors and are published in their revised form as submitted. While all submissions have undergone a review process to ensure academic quality, the organizing committee does not guarantee the accuracy, completeness, novelty, or applicability of the content. Readers are encouraged to exercise independent judgment and, where appropriate, contact the authors directly for clarification or further information.

The organizing committee shall not be held liable for any errors, omissions, or consequences resulting from the use of any information contained in these manuscripts. Furthermore, unauthorized reproduction, distribution, or use of the content may infringe upon copyright or other intellectual property rights. For permission to reuse or reproduce any part of these manuscripts, please contact the corresponding author(s) listed in each paper.

TIChE2025 Organizing Committee
Department of Chemical Engineering
Faculty of Engineering, Khon Kaen University, Thailand

MASSAGE FROM
Dean of the Faculty of Engineering, Khon Kaen University

Good morning, ladies and gentlemen, and distinguished guests. On behalf of the Faculty of Engineering at Khon Kaen University, it is my distinct honor to welcome you to the 34th Thai Institute of Chemical Engineering and Applied Chemistry International Conference 2025 (TIChE2025). We are truly delighted to host this prestigious international event at the Dusit Thani Pattaya Hotel, Chonburi, Thailand, in collaboration with TNChE Asia 2025. This year, we are pleased to welcome a diverse group of participants from academia, research institutions, and industry, both from Thailand and abroad. Your presence here today reflects our shared commitment to advancing the fields of chemical engineering and applied chemistry. TIChE2025 serves as a vital platform for knowledge exchange, research collaboration, and innovation, especially at a time when sustainable development and technological transformation are crucial to our global future. The themes and sessions of this year's conference cover a wide range of topics, ranging from green technologies, energy and environmental solutions, materials and nanotechnology, to advanced chemical processes and education in engineering. The discussions and insights shared over the next two days will undoubtedly contribute to the development of impactful solutions to address pressing challenges in our world today.

I would like to take this opportunity to express my sincere appreciation to the organizing committee for their unwavering dedication and outstanding coordination in making this event a success. I also extend my heartfelt thanks to our sponsors, collaborators, and institutional partners whose generous support has made TIChE2025 possible.

Most importantly, I wish to thank all of you, our valued participants, for your contributions, enthusiasm, and engagement. Your active participation is what drives the spirit of this conference and ensures its continued success. I hope that over these two days, TIChE2025 will inspire new perspectives, cultivate meaningful partnerships, and spark innovations that will lead us toward a more sustainable and resilient future. Welcome to TIChE2025.

I wish you a productive, enjoyable, and memorable experience.

Assoc. Prof. Dr. Ratchaphon Suntivarakorn
Dean of Faculty of Engineering,
Khon Kaen University, Thailand

MASSAGE FROM
TIChE2025 Organizing Chair

On behalf of the organizing committee, it is my distinct honor to welcome you to the 34th Thai Institution of Chemical Engineering and Applied Chemistry International Conference 2025 (TIChE2025). We are delighted to host this esteemed international event at the Dusit Thani Pattaya Hotel, Chonburi, Thailand, from May 20-21, 2025, in collaboration with TNChE Asia 2025. This year, TIChE2025 brings together a diverse group of researchers, academics, industry professionals, and students from Thailand and around the world. Your participation underscores our collective commitment to advancing the fields of chemical engineering and applied chemistry. The conference serves as a dynamic platform for knowledge exchange, fostering interdisciplinary collaboration and innovation. The conference is held under the theme: "Navigating the Future: Challenges and Innovations for Sustainable Green Technologies", reflecting our shared vision of driving sustainable growth through research, technology, and international collaboration. The technical program of TIChE2025 covers a broad spectrum of topics, particularly in areas such as catalysis and reaction engineering, sustainable and green chemistry, advanced materials and nanotechnology, biochemical and environmental engineering, process engineering and digital technologies, energy and fuels, industrial applications and case studies.

We are honored to welcome our Plenary Lecturer, Dr. Ken-ichi Aika, and our Invited Speakers: Hiroshi Uyama, Ravin Narain, Taketoshi Minato, Nurak Grisdanurak, Tawatchai Charinpanitkul, Katsutoshi Nagaoka, Kieran N. Twaddle, Xiaohong Tan. We also extend our sincere appreciation to Assoc. Prof. Dr. Ratchaphon Suntivarakorn, Dean of the Faculty of Engineering, Khon Kaen University, and Mr. Surachate Chalothorn, President of The Thai Institute of Chemical Engineering and Applied Chemistry, for their continuous support and encouragement throughout the organization of this conference.

I would like to thank the organizing committee, sponsors, and partners whose dedication and contributions have been instrumental in bringing TIChE2025 to fruition. Most importantly, thank you to all participants. Your engagement and enthusiasm are the driving forces behind the success of this conference. We hope that TIChE2025 provides you with valuable insights, fosters meaningful collaborations, and inspires innovative solutions for a sustainable future.

Welcome to TIChE2025

Assoc. Prof. Dr. Kittirote Wantala
Conference Chair of TIChE2025
Faculty of Engineering, Khon Kaen University, Thailand

MASSAGE FROM
President of The Thai Institute of Chemical Engineering and Applied Chemistry

On behalf of The Thai Institute of Chemical Engineering and Applied Chemistry (TIChE), I extend our heartfelt gratitude to each of you for your invaluable contributions to the success of the 34th Annual TIChE Conference, themed "Navigating the Future: Challenges and Innovations for Sustainable Green Technologies." The 34th Annual TIChE Conference (TIChE2025), organized by The Thai Institute of Chemical Engineering and Applied Chemistry (TIChE) in collaboration with the Department of Chemical Engineering, Faculty of Engineering, Khon Kaen University, will be held on May 20-21, 2025, at the beautiful Dusit Thani Pattaya, Chonburi, a vibrant beach city known for its scenic beauty and warm hospitality. This year, TIChE2025 will feature a special joint opening ceremony and plenary lecture with TNChE Asia 2025, a premier regional event that gathers industry professionals and experts in chemical engineering and applied chemistry from across Asia and beyond. By co-locating TIChE2025 with TNChE Asia 2025, participants from both events will have the unique opportunity to join sessions, exhibitions, and networking events across both conferences, enriching their experience and fostering wider collaboration.

In addition to an exciting lineup of technical sessions, keynote speeches, and networking opportunities, TIChE2025 will offer a dynamic platform for exchanging innovative ideas, showcasing cutting-edge research, and building meaningful collaborations. We are confident that this gathering will inspire new approaches to address global challenges and advance sustainable solutions. We also extend our deepest appreciation to our esteemed keynote and plenary speakers, whose expertise and passion will illuminate our discussions and spark innovative thinking, and to our sponsors and supporters, whose generous contributions make this event possible.

As we convene by the serene shores of Pattaya, I am filled with optimism for the transformative conversations, collaborations, and friendships that will emerge. Together, we have the power to shape a brighter, greener future for generations to come. Once again, thank you for your dedication, enthusiasm, and unwavering commitment to environmental sustainability and academic excellence. Your presence enriches our community and strengthens our collective resolve to build a better world.

With deepest gratitude and warm regards

Surachate Chalothorn

Mr. Surachate Chalothorn
President of The Thai Institute of Chemical Engineering and Applied Chemistry

COMMITTEE

ORGANIZERS

Kitirote Wantala (Chair)	Khon Kaen University	Thailand
Sutasinee Neramittagapong (Co-chair)	Khon Kaen University	Thailand
Ratchaphon Suntivarakorn (Patron)	Khon Kaen University	Thailand
Surachate Chalothorn (Patron)	The Thai Institute of Chemical Engineering and Applied Chemistry	Thailand

ORGANIZING COMMITTEE

Arthit Neramittagapong	Khon Kaen University	Thailand
Khanita Kamwilaisak	Khon Kaen University	Thailand
Pornnapa Kasemsiri	Khon Kaen University	Thailand
Duangkanok Tanangteerapong	Khon Kaen University	Thailand
Chaiyaput Kruehong	Khon Kaen University	Thailand
Varinrumpai Seithtanabutara	Khon Kaen University	Thailand
Kaewta Jetsrisuparb	Khon Kaen University	Thailand
Methus Suwannaruang	Khon Kaen University	Thailand
Shawn C. Rood	Khon Kaen University	Thailand

INTERNATIONAL SCIENTIFIC COMMITTEE

Ken-ichi Aika	Tokyo Institute of Technology	Japan
Kazuhiro Takanabe	The University of Tokyo	Japan
Takeshi Furusawa	The University of Osaka	Japan
Katsutoshi Nagaoka	Nagoya University	Japan
Junichi Ryu	Chiba University	Japan
Shogo Kumagai	Tohoku University	Japan
Taketoshi Minato	National Institute of Natural Science	Japan
Yu-Chuan Lin	National Cheng Kung University	Taiwan
Ren-Xuan Yang	National Taipei University of Technology	Taiwan
Chitsan Lin	National Kaohsiung University of Science and Technology	Taiwan
Ravin Narain	University of Alberta	Canada
Keonakhone Khounvilay	National University of Laos	Laos
Behzad Shahmoradi	Kurdistan University of Medical Sciences	Iran
Harikaranahalli Puttaiah Shivaraju	JSS Academy of Higher Education and Research	India
Sumaiya Zainal Abidin	Universiti Malaysia Pahang	Malaysia
Thunyaluk Pojtanabuntoeng	Curtin University	Australia
Giang Le	Duy Tan University	Vietnam

LOCAL SCIENTIFIC COMMITTEE

Kanyarat Holasut	Khon Kaen University	Thailand
Arthit Neramittagapong	Khon Kaen University	Thailand
Apichart Artnaseaw	Khon Kaen University	Thailand
Chaiyaput Kruehong	Khon Kaen University	Thailand
Sutasinee Neramittagapong	Khon Kaen University	Thailand
Yuvarat Ngernyen	Khon Kaen University	Thailand
Khanita Kamwilaisak	Khon Kaen University	Thailand
Kitirote Wantala	Khon Kaen University	Thailand
Pornnapa Kasemsiri	Khon Kaen University	Thailand

Duangkanok Tanangteerapong	Khon Kaen University	Thailand
Panomkorn Kwakhong	Khon Kaen University	Thailand
Tinnakorn Kumsaen	Khon Kaen University	Thailand
Varinrumpai Seithtanabutara	Khon Kaen University	Thailand
Kaewta Jetsrisuparb	Khon Kaen University	Thailand
Oranat Chuchuen	Khon Kaen University	Thailand
Atip Laungphairojana	Khon Kaen University	Thailand
Methus Suwannaruang	Khon Kaen University	Thailand
Shawn C. Rood	Khon Kaen University	Thailand

LOCAL ORGANIZING COMMITTEE

Sutthada Songjorhor	Khon Kaen University	Thailand
Wimonporn Iamamornphanth	Khon Kaen University	Thailand
Pakpoom Athikaphan	Khon Kaen University	Thailand
Tanabodee Leela	Khon Kaen University	Thailand
Plaisuda Janthabut	Khon Kaen University	Thailand
Pimpattra Krongkehung	Khon Kaen University	Thailand
Makhamas Chatkasemwong	Khon Kaen University	Thailand
Sirirat Thammasang	Khon Kaen University	Thailand
Areelak Humarj	Khon Kaen University	Thailand
Natthakrit Montri	Khon Kaen University	Thailand
Natthaphong Lertna	Khon Kaen University	Thailand
Nattapon Banditsean	Khon Kaen University	Thailand
Papol Pimsri	Khon Kaen University	Thailand
Naritsara Suwatsrisakun	Khon Kaen University	Thailand
Nannapat Kaewsaenmaung	Khon Kaen University	Thailand
Pimpisa Pimpaeng	Khon Kaen University	Thailand
Sirikanya Pimsaran	Khon Kaen University	Thailand
Jakkapat Saehkow	Khon Kaen University	Thailand
Noppanan Putdon	Khon Kaen University	Thailand
Wasu Jantapa	Khon Kaen University	Thailand
Waranya Yosburi	Khon Kaen University	Thailand
Siriyakorn Theprat	Khon Kaen University	Thailand
Kritsanan Jareerut	Khon Kaen University	Thailand
Pimchaya Trisong	Khon Kaen University	Thailand
Paemika Pimphatam	Khon Kaen University	Thailand
Kanokwan Panmak	Khon Kaen University	Thailand

PEER REVIEW COMMITTEE

Siriporn Damrongsakkul	Chulalongkorn University	Thailand
Suttichai Assabumrungrat	Chulalongkorn University	Thailand
Tawatchai Charinpanitkul	Chulalongkorn University	Thailand
Apinan Soottitantawat	Chulalongkorn University	Thailand
Paravee Vas-Umnuay	Chulalongkorn University	Thailand
Tharathon Mongkhonsi	Chulalongkorn University	Thailand
Akawat Sirisuk	Chulalongkorn University	Thailand
Chalida Klaysom	Chulalongkorn University	Thailand
Palang Bumroongsakulsawat	Chulalongkorn University	Thailand
Manunya Okhawilai	Chulalongkorn University	Thailand
Benjapon Chalermsinsuwan	Chulalongkorn University	Thailand
Napida Hinchiranan	Chulalongkorn University	Thailand
Nattaya Pongstabodee	Chulalongkorn University	Thailand
Pornpote Piumsomboon	Chulalongkorn University	Thailand

Sirilux Poompradub	Chulalongkorn University	Thailand
Somkiat Ngamprasertsith	Chulalongkorn University	Thailand
Teerawat Sema	Chulalongkorn University	Thailand
Jitti Kasemchainan	Chulalongkorn University	Thailand
Manaswee Suttipong	Chulalongkorn University	Thailand
Anusith Thanapimmetha	Kasetsart University	Thailand
Kandis Sudsakorn	Kasetsart University	Thailand
Manop Charoenchaitrakool	Kasetsart University	Thailand
Maythee Saisriyoot	Kasetsart University	Thailand
Nanthiya Hansupalak	Kasetsart University	Thailand
Paweena Prapainainar	Kasetsart University	Thailand
Waleeporn Donphai	Kasetsart University	Thailand
Supacharee Roddecha	Kasetsart University	Thailand
Khemmathin Lueangwattanapong	Kasetsart University	Thailand
Suthasinee Watmanee	Kasetsart University	Thailand
Thidarat Imyen	Kasetsart University	Thailand
Pornsawan Assawasaengrat	King Mongkut's Institute of Technology Ladkrabang	Thailand
Yaneeporn Patcharavorachot	King Mongkut's Institute of Technology Ladkrabang	Thailand
Pongsert Sriprom	King Mongkut's Institute of Technology Ladkrabang	Thailand
Chaiwat Prapainainar	King Mongkut's University of Technology North Bangkok	Thailand
Patcharin Worathanakul	King Mongkut's University of Technology North Bangkok	Thailand
Santi Chuetor	King Mongkut's University of Technology North Bangkok	Thailand
Supak Tontisirin	King Mongkut's University of Technology North Bangkok	Thailand
Wanwitoo Wanmolee	King Mongkut's University of Technology North Bangkok	Thailand
Anawat Sungpet	King Mongkut's University of Technology Thonburi	Thailand
Somnuk Jarudilokkul	King Mongkut's University of Technology Thonburi	Thailand
Supaporn Therdthianwong	King Mongkut's University of Technology Thonburi	Thailand
Saiwan Nawalertpanya	King Mongkut's University of Technology Thonburi	Thailand
Kantharakorn Macharoen	King Mongkut's University of Technology Thonburi	Thailand
Krittin Korkerd	King Mongkut's University of Technology Thonburi	Thailand
Atthapon Srifa	Mahidol University	Thailand
Chularat Sakdaronnarong	Mahidol University	Thailand
Poomiwat Phadungbut	Mahidol University	Thailand
Wanida Koo-amornpattana	Mahidol University	Thailand
Warangkana Pornputtapitak	Mahidol University	Thailand
Woranart Jonglertjunya	Mahidol University	Thailand
Kulchanat Prasertsit	Prince of Songkla University	Thailand
Pakamas Chetpattananondh	Prince of Songkla University	Thailand
Sininart Chongkhong	Prince of Songkla University	Thailand
Parinya Khongprom	Prince of Songkla University	Thailand

Pornsiri Kaewpradit	Prince of Songkla University	Thailand
Songtham Photaworn	Prince of Songkla University	Thailand
Natacha Phetyim	Rajamangala University of Technology Thanyaburi	Thailand
Thirawat Mueansichai	Rajamangala University of Technology Thanyaburi	Thailand
Weraporn Pivsa-Art	Rajamangala University of Technology Thanyaburi	Thailand
Rinlada Sirisangsawang	Rajamangala University of Technology Thanyaburi	Thailand
Sarawut Jitpinit	Rajamangala University of Technology Thanyaburi	Thailand
Sasiradee Jantasee	Rajamangala University of Technology Thanyaburi	Thailand
Weerinda Mens	Rajamangala University of Technology Thanyaburi	Thailand
Choowong Chaisuk	Silpakorn University	Thailand
Mutsee Termtanun	Silpakorn University	Thailand
Veerayut Lersbamrungsuk	Silpakorn University	Thailand
Weerawat Patthaveekongka	Silpakorn University	Thailand
Wasu Chaitree	Silpakorn University	Thailand
Chanchira Jubsilp	Srinakharinwirot University	Thailand
Atichat Wongkoblap	Suranaree University of Technology	Thailand
Lek Wantha	Suranaree University of Technology	Thailand
Asadullah Baloch	Suranaree University of Technology	Thailand
Terasut Sookkumnerd	Suranaree University of Technology	Thailand
Nurak Grisdanurak	Thammasat University	Thailand
Piyachat Wattanachai	Burapha University	Thailand
Chakkrit Umpuch	Ubon Ratchathani University	Thailand
Chatchai Kunyawut	Ubon Ratchathani University	Thailand
Supatpong Mattaraj	Ubon Ratchathani University	Thailand
Wipada Dechapanya	Ubon Ratchathani University	Thailand
Channarong Puchongkawarin	Ubon Ratchathani University	Thailand
Idtisak Paopo	Ubon Ratchathani University	Thailand
Karnika Ratanapongleka	Ubon Ratchathani University	Thailand
Natthaya Punsuwan	Ubon Ratchathani University	Thailand
Natwat Srikhao	Ubon Ratchathani University	Thailand
Suparat Sasrimuang	Ubon Ratchathani University	Thailand
Rujira Jitrwung	Thailand Institute of Scientific and Technological Research	Thailand
Apichart Artnaseaw	Khon Kaen University	Thailand
Arthit Neramittagapong	Khon Kaen University	Thailand
Chaiyaput Kruehong	Khon Kaen University	Thailand
Duangkanok Tanangteerapong	Khon Kaen University	Thailand
Kanyarat Holasut	Khon Kaen University	Thailand
Khanita Kamwilaisak	Khon Kaen University	Thailand
Kitirote Wantala	Khon Kaen University	Thailand
Pornnapa Kasemsiri	Khon Kaen University	Thailand
Sutasinee Neramittagapong	Khon Kaen University	Thailand
Yuvarat Ngernyen	Khon Kaen University	Thailand
Kaewta Jetsrisuparb	Khon Kaen University	Thailand
Oranat Chuchuen	Khon Kaen University	Thailand
Panomkorn Kwakhong	Khon Kaen University	Thailand
Tinnakorn Kumsaen	Khon Kaen University	Thailand

Varinrumpai Seithtanabutara	Khon Kaen University	Thailand
Atip Laungphairojana	Khon Kaen University	Thailand
Methus Suwannaruang	Khon Kaen University	Thailand
Shawn C. Rood	Khon Kaen University	Thailand

LIST OF CONTENT

Proceeding Code	Title	Page
TIChE-AM-01	Removal of heavy metal ions (Pb^{2+}, Hg^{2+}) from water using N-doped activated carbon derived from bamboo waste: Equilibrium study	1-5
TIChE-AM-02	Enhanced CO_2 photoreduction in synthetic seawater using black TiO_2 nanowires: Synthesis, characterization, and performance	6-10
TIChE-AM-03	Synthesis and characterizations of triethanolamine-copper black titanium photocatalyst for carbon dioxide photoreduction	11-16
TIChE-AM-04	Synthesis, swelling behavior, and niacinamide release of 1,4-butanediol diglycidyl ether-crosslinked levan hydrogels from *Bacillus siamensis*	17-21
TIChE-AM-06	Effects of titanium nitride nanoparticles on the properties of light-responsive polybenzoxazine/epoxidized soybean oil copolymer	22-29
TIChE-AM-07	Antioxidant sugar from co-crystallization of sucrose, erythritol and vitamin C	30-34
TIChE-AM-08	Polybenzoxazine blended with modified natural rubber by graft copolymerization with 2-hydroxyethyl acrylate for shape memory applications	35-40
TIChE-AM-09	Flexible piezoresistive sensor based on natural rubber/chitosan/graphene composites for healthcare applications	41-47
TIChE-AM-10	Development of self-healing polymers from bio-based benzoxazine blended with poly (ethylene glycol)	48-54
TIChE-AM-11	Toughness improvement of polybenzoxazine by blending with glycidyl methacrylate-grafted natural rubber	55-60
TIChE-AM-15	Influence of CaO on the durability of geopolymer in acidic environments	61-66
TIChE-AM-17	Production of graphene from graphite via flash joule heating process	67-71
TIChE-AM-19	Effects of oxygen, nitrogen, and sulfur doped hard carbons derived from longan seed as anode material for sodium-ion batteries	72-77
TIChE-AM-20	Development of shape memory UV curable 3D-print resin based on acrylated epoxidized soybean oil (AESO)	78-83
TIChE-AM-21	Development of a microencapsulation process of phase change materials from palm oil derivatives in a large-scale melamine formaldehyde encapsulation process	84-89

LIST OF CONTENT (Cont.)

Proceeding Code	Title	Page
TIChE-AM-22	Fabrication of polyphenylsulfone (PPSU) electrospun nanofiltration membrane	90-94
TIChE-AM-24	Modification of recycled polyethylene terephthalate membrane by using graphene oxide to enhance antifouling properties for protein separation	95-100
TIChE-AM-25	Development of PVA-PNVCL-Fe_3O_4 composite nanofibrous for drug delivery in cancer treatment	101-107
TIChE-AM-26	Effect of glycerol on xyloglucan-chitosan film preparation and its properties	108-112
TIChE-AM-28	Surface modification of activated carbon from tamarind shell for tartrazine adsorption	113-117
TIChE-AM-36	Biocompatibility of hydrogel film blended jellyfish gelatin	118-122
TIChE-AM-38	Utilization of lignin from agricultural waste for enhancing performance of natural rubber composite	123-127
TIChE-BE-01	Comparative study of methylene blue adsorption using calcium oxide derived from chicken eggshells and standard calcium oxide	128-132
TIChE-BE-02	Removal of Pb(II) and Hg(II) from water on activated carbon: An insight into multicomponent adsorption	133-138
TIChE-BE-03	Development of composite scaffolds derived from palm kernel shell ash with curcumin encapsulation for tissue engineering applications	139-143
TIChE-BE-04	Simultaneous saccharification and fermentation (SSF) of corn cob for bioethanol production using *Saccharomyces cerevisiae* SC 90	144-147
TIChE-BE-05	Optimization of bovine serum albumin concentration and diafiltration via tangential flow filtration	148-152
TIChE-BE-06	Thermo-responsive PVDF-grafted-PVNCL membranes with switchable wettability for efficient oil-water separation	153-158
TIChE-BE-07	Techno-economic analysis of *Ulva spp*. cultivation for capturing CO_2 emissions from natural gas power plants in Thailand	159-166
TIChE-BE-08	*Centella asiatica* active ingredients extraction using ultrasonic-assisted extraction and maceration	167-171

LIST OF CONTENT (Cont.)

Proceeding Code	Title	Page
TIChE-BE-09	*Carthamus tinctorius* L. flower antioxidant extracts from subcritical ethanol extraction	172-176
TIChE-BE-10	Lignin extracted from rice straw and coconut coir	177-181
TIChE-BE-11	The occurrence of polycyclic aromatic hydrocarbons (PAHs) and halogenated PAHs in Chao Praya River in dissolved phase	182-185
TIChE-BE-12	Enhancing absorption under load in alginate-based superabsorbent polymers for sustainable disposable diapers	186-192
TIChE-BE-13	Electrochemical improvement of mangosteen peel extract	193-199
TIChE-BE-15	Effects of cultivation temperature on alpha-amylase production from wild-type rice callus suspensions	200-205
TIChE-BE-16	Lysine production from sugarcane molasses using *Corynebacterium glutamicum*	206-209
TIChE-BE-17	Enhanced extraction of bioactive compounds from *Aloe vera* leaf skin using natural deep eutectic solvents	210-215
TIChE-BE-18	Comparative characterization of microplastics from conventional wastewater treatment plants between inland and island of tourism area in Thailand	216-220
TIChE-BE-19	Reduction of acid usage in chitosan production process from white shrimp shell using electro-chemical activation	221-226
TIChE-BE-21	Pressure vessel for ethanol extraction of Mitragynine from Kratom leaves	227-231
TIChE-BE-26	Study of biomass productivity of phosphate-solubilizing bacteria using rice bran oil as an alternative media	232-236
TIChE-BE-27	Removal of styrene and pyrene in a fixed bed adsorption column using rhamnolipid-modified alumina	237-242
TIChE-BE-36	Valorization of pineapple leaf fiber (PALF) waste: Optimization of alkali pretreatment for fermentable sugar production	243-247
TIChE-BE-37	Residue extraction on artificial knee surfaces using ultrasonic techniques	248-255

LIST OF CONTENT (Cont.)

Proceeding Code	Title	Page
TIChE-CR-01	Autonomous Lorentz force-powered chiral encoded metal rotors for enantioselective synthesis	256-262
TIChE-CR-02	Development of magnesium aluminate supported nickel catalyst in dry reforming of methane reaction	263-268
TIChE-CR-03	Effect of graphene nanoplatelets addition during electroless plating of ABS on the properties of copper-nickel-chromium coated ABS	269-276
TIChE-CR-05	Valorization of biodiesel plant-derived glycerol for 1-propanol synthesis over zeolite-supported iridium and rhenium oxides	277-283
TIChE-CR-06	CO_2 methanation using nickel-based catalysts over alumina-ceria support prepared by sol-gel method	284-291
TIChE-CR-07	Kaolin-based synthesis as an alternative low-cost adsorbent for biodiesel purification	292-296
TIChE-CR-08	A comparative study of commercial- and hydrothermal-synthesized TiO_2 nanoparticles for photocatalytic silver recovery from jewelry plating effluent	297-301
TIChE-CR-09	Photocatalytic silver recovery from cyanide-based plating effluent via TiO_2 nanoparticles synthesized by microwave-assisted method	302-309
TIChE-CR-10	Effect of activation method on biochar supported nickel catalysts performance in steam reforming of biomass-derived tar	310-316
TIChE-CR-11	Double perovskite enhanced with exsolved Ni-Co particles in $Sr_{1.95}TiMo_{1-x}(NiCo)_xO_{6-\delta}$ as anode for direct-fed ammonia solid oxide fuel cell	317-322
TIChE-CR-14	Optimization of biodiesel production from waste cooking oil via transesterification using calcium oxide catalyst	323-327
TIChE-CR-15	Effect of catalyst bed configuration on temperature profile and reactor performance for Fischer-Tropsch synthesis: A computational fluid dynamics simulation	328-337
TIChE-CR-16	Simulation of dry and steam reforming of methane over a nickel-based catalyst in a fixed-bed tube reactor using COMSOL	338-343
TIChE-CR-17	Promotional effect of Fe in the Cu/TiO_2 catalyst on the liquid-phase selective hydrogenation of furfural to furfuryl alcohol	344-349
TIChE-CR-18	Study on epoxidation of vegetable oil using different acidic ion-exchange resins	350-354

LIST OF CONTENT (Cont.)

Proceeding Code	Title	Page
TIChE-CR-19	Photocatalytic activity of N, S-CQDs/TiO_2 composites for the degradation of methylene blue under visible-light irradiation	355-359
TIChE-CR-20	Development of core-shell $LaNi_{0.8}Fe_{0.2}O_3$ catalysts with $CeZrO_2$ shells for carbon-resistant dry reforming of methane	360-365
TIChE-CR-21	Effect of membrane arrangement and operating conditions in electrodialysis system on the performance of the integrated absorption-mineralization process	366-369
TIChE-CR-22	Titania incorporated into magnetite mesoporous silica for removal of ciprofloxacin under UV radiation	370-375
TIChE-CR-23	Electrochemical reduction and regeneration of carbamate	376-382
TIChE-CR-24	Loading iron/manganese/zinc/copper oxide onto TiO_2 for vanillin production from photoconversion of lignin	383-388
TIChE-CR-25	Utilization of biomass from palm oil industry for monoglycerides production	389-396
TIChE-CR-26	Synthesis of biolubricant from waste cooking oil methyl ester by transesterification reaction via ethylene glycol	397-401
TIChE-CR-27	Low-temperature methanol synthesis via ethanol-assisted approach over Cu/ZnO/Al_2O_3 in fixed-bed reactor	402-405
TIChE-CR-28	Hydroconversion of biodiesel over Ni/beta zeolite catalysts prepared by glycine-assisted impregnation for sustainable aviation fuel production	406-411
TIChE-CR-29	Optimization of biodiesel synthesis from waste cooking oil by transesterification reaction	412-420
TIChE-CR-31	Methane dry reforming of calcium carbonate from carbamate mineralization	421-426
TIChE-CR-34	Thermal oxidative reaction of Hydroxymethylfurfural (HMF) to bio-based monomer : 2,5 Furandicarboxylic Acid (FDCA)	427-436
TIChE-EF-03	Feasibility of hydrogen production from crude glycerol via photocatalysis using TiO_2-based photocatalysts	437-442
TIChE-EF-04	Effects of cation types and carrageenan structure on the formation and electrochemical properties of bio-gel electrolytes	443-449

LIST OF CONTENT (Cont.)

Proceeding Code	Title	Page
TIChE-EF-05	Regeneration by electrodialysis of secondary spent monoethanolamine solution obtained after mineralization of captured carbon dioxide with calcium sulphate	450-454
TIChE-EF-06	One-dimensional simulation of an alkaline-acid direct glycerol fuel cell	455-460
TIChE-EF-10	Reduction and capture of chlorine in Napier grass using microwave torrefaction	461-466
TIChE-EF-11	Electrochemical regeneration of spent monoethanolamine solution after carbon dioxide capture and mineralization by calcium sulfate addition	467-471
TIChE-EF-12	The effect of methanol and ethanol-based solvent on enhancing CO_2 absorption efficiency and reducing energy consumption in the desorption process	472-477
TIChE-EF-13	Four-zone modelling of modified downdraft gasifier for performance prediction: Case study of semi-batch operation	478-485
TIChE-EF-14	Improvement of electrocatalytic activities of Ag-based catalysts in oxygen reduction and oxygen evolution reactions	486-490
TIChE-EF-17	Development of low-cost Ag-based ORR electrodes via electrodeposition on carbon cloth for AEM fuel cells	491-495
TIChE-IA-01	Prediction of latent heat of vaporization of binary mixture using COSMO-SAC model	496-505
TIChE-IA-02	Sustainable manufacturing of polycaprolactone films: Effects of processing conditions on film quality	506-510
TIChE-IA-03	Feedforward control of pulsed bed adsorption column for colorant removal in sugar syrup at different flow rates	511-514
TIChE-PE-01	Development of computational fluid dynamics modeling of packed bed membrane reactor for dimethyl ether production from carbon dioxide	515-520
TIChE-PE-02	Analysis of carbon dioxide trapping efficiency in saline aquifer by machine learning	521-525
TIChE-PE-03	Graph neural network for descriptor-free CO_2 solubility prediction in aqueous amines	526-531
TIChE-PE-04	Techno-economic analysis of sequential process to valorization of rambutan seed waste by supercritical CO_2-ethanol and subcritical water extraction	532-536

LIST OF CONTENT (Cont.)

Proceeding Code	Title	Page
TIChE-PE-05	Techno-economic analysis of crude peptides production from defective coffee beans	537-542
TIChE-PE-06	Comparative analysis of machine learning models for predicting operating condition in a pentane-hexane distillation column with limited data	543-548
TIChE-PE-07	Techno-economic analysis of hydrogen production pathways for carbon dioxide to methanol conversion process	549-555
TIChE-PE-08	Performance of combination ESN and LSTM in prediction of temperature in magnetic heating reactor	556-566
TIChE-PE-09	Techno-economic insights and limitation analysis of CO_2 capture via monoethanolamine (MEA) absorption	567-575
TIChE-PE-10	Computational fluid dynamics (CFD) analysis of cooling water temperature profiles in high temperature operation heat exchangers	576-584
TIChE-PE-11	Simulation of desulfurization in natural gas by using ferrous oxide	585-587
TIChE-PE-12	Modification of the syngas production process using fluidized-bed twin reactor system and chemical looping gasifier	588-592
TIChE-PE-13	Reinforcement learning control for optimal ethanol production from microbial fermentation	593-597
TIChE-PE-14	Application of computational fluid dynamics for industrial liquid-liquid mixing tank design	598-603
TIChE-PE-15	Performance evaluation of combined torrefaction and gasification process of lignocellulosic biomass	604-609
TIChE-PE-16	Process simulation of synthetic fuel production from palm oil mill waste	610-617
TIChE-PE-17	Optimal input variables for an artificial neural network to predict evaporation efficiency in detergent production process	618-627
TIChE-PE-18	Effect of ethanol on the crystallization of DL-methionine polymorphs	628-632
TIChE-PE-19	Process simulation of lactic acid esterification in reactive distillation column: Effects of reboiler duty and alcohol	633-637

LIST OF CONTENT (Cont.)

Proceeding Code	Title	Page
TIChE-PE-20	Design and simulation of the coffee drying unit using solar thermal energy and ambient air circulation	638-648
TIChE-PE-21	Production of wood-plastic composite from non-metallic powders recovered from printed circuit board (PCB) waste	649-653
TIChE-PE-23	Machine learning-assisted multi-objective optimization of furfural production from lignocellulosic biomass hydrolysate	654-660
TIChE-PE-24	Optimization of solketal reaction conditions for maximum yield using response surface methodology (RSM) in MATLAB®	661-664
TIChE-PE-25	Enhancing low-carbon hydrogen production from biomass gasification via machine-learning-aided multi-objective optimization with TOPSIS	665-671
TIChE-SG-01	Enhancing non-catalytic biomass pyrolysis yield predictions using machine learning and data augmentation	672-680
TIChE-SG-02	Continuous production of 5-hydroxymethylfurfural using monophasic solvents for pharmaceutical applications	681-688
TIChE-SG-04	Design and development of a sustainable ethylene glycol production process via electrochemical CO_2 reduction	689-693
TIChE-SG-05	Catalytic carbon dioxide desorption from monoethanolamine solvent in fluidized stripper	694-698
TIChE-SG-06	Process simulation of syngas production through glycerol reforming with carbon dioxide and steam for methanol synthesis	699-706
TIChE-SG-08	Preparation of bio-based polyol from soybean meal for polyurethane foam production	707-709
TIChE-SG-10	Off-grade epoxy resin and waste tire composites for CO_2 adsorption	710-715
TIChE-SG-11	A study on the mechanical properties, physical properties and biodegradation of rigid polyurethane foam synthesized from castor and palm oils-based polyol	716-722
TIChE-SG-12	Evaluating the effectiveness of antioxidants in palm oil-based bio-grease	723-727
TIChE-SG-13	Bio-based coating from chitosan and ethyl cellulose for oil- and water-resistant paper packaging	728-732

LIST OF CONTENT (Cont.)

Proceeding Code	Title	Page
TIChE-SG-14	Study of calcium carbonate precipitation from CO_2-rich amine-based solution	733-739
TIChE-SG-15	Development of chitosan-fibroin coating to prolong the shelf life of bananas	740-745
TIChE-SG-16	Synthesis of rigid polyurethane foam from modified castor oil and sugar to enhance thermal insulating properties and degradability	746-751
TIChE-SG-17	Ethanol-assisted CO_2 hydrogenation to methanol in a trickle-bed reactor	752-757
TIChE-SG-19	Sustainable synthesis of monolaurin via glycerol esterification with lauric acid using TPA modified biochar derived from coconut shells	758-763
TIChE-SG-20	Integration of monoethanolamine-based carbon dioxide absorption and mineralization with calcium chloride	764-768
TIChE-SG-21	Enhancement of CO_2 capture performance of alcohols on MEA-IL-based biphasic solvents	769-773
TIChE-SG-22	Accelerated aging testing of three types of transformer oils in 1 phase distribution transformer	774-778
TIChE-SG-23	Development of fibroin-based solid electrolyte for electrochromic windows	779-784
TIChE-SG-24	Development and characterization of bioplastic from banana peel and chitosan: A sustainable alternative for eco-friendly packaging	785-789
TIChE-SG-25	Desalination potential using EDTA modified MOF	790-793
TIChE-SG-27	Synthesis and scale-up of MOF using PET-derived terephthalic acid	794-798
TIChE-SG-28	Effect of co-solvents on the oxidative cleavage of oleic acid under ambient pressure	799-804
TIChE-SG-29	Demonstration of zeolite A produced from coal ash applied to CO_2 capture process for amine regeneration approach	805-810
TIChE-SG-30	Synthesis of monolaurin through glycerol esterification with lauric acid using 12-tungstophosphoric acid	811-815

LIST OF CONTENT (Cont.)

Proceeding Code	Title	Page
TIChE-SG-32	Development of internally circulating fluidized bed reactor performance for enhancing direct air CO_2 capture	816-822
TIChE-SG-33	Valorization of mung bean seed coat through recovery of bioactive compounds with pharmacological properties using percolation extraction	823-828
TIChE-SG-38	Sustainable ethylene synthesis via photocatalytic conversion of succinic acid over metal-TiO2 photocatalysts	829-832

Removal of heavy metal ions (Pb^{2+}, Hg^{2+}) from water using N-doped activated carbon derived from bamboo waste: Equilibrium study

Chaisawat Rattanadon[1], Nikom Klomkliang[1,*]

[1] School of Chemical Engineering, Suranaree University of Technology, Nakhon Ratchasima 30000, Thailand
[*] Corresponding author: nikom.klo@sut.ac.th

ABSTRACT

Water contamination from heavy metals, especially lead (Pb^{2+}) and mercury (Hg^{2+}), is one of the most environmentally harmful issues in water sources. This research examined the removal of Pb^{2+} and Hg^{2+} from aqueous solutions using activated carbon (AC) derived from bamboo and modified with urea and KOH to achieve AC-UK. The original AC was mixed with urea in a 2:1 weight ratio and oxidized with air for 1 hour. The sample was then mixed with KOH in a 2:1 weight ratio and stirred overnight, followed by drying and activation at 650°C under a nitrogen atmosphere. The original AC oxidized with air without urea and KOH was designated as AC-Air. The series of adsorbents were characterized by BET surface area and FTIR, revealing that AC-UK showed a BET surface area of 842 m^2/g, higher than AC-Air (789 m^2/g) and AC (732 m^2/g). FTIR analysis showed that AC-UK had a significant abundance of nitrogen-containing functional groups, including N-H and C-N, compared to the other adsorbents. Pb^{2+} and Hg^{2+} removal from aqueous solutions was conducted using single components in a batch adsorption at 25°C. The results show that AC-UK exhibited high adsorption capacities for both Pb^{2+} and Hg^{2+}, with maximum capacities of 323 and 526 mg/g, respectively. The equilibrium adsorption was best fitted by the Langmuir adsorption isotherm. The modified AC is a promising adsorbent that demonstrated exceptional removal of Pb^{2+} and Hg^{2+} from water.

Keywords: Water treatment; Adsorption; N-doped activated carbon; Surface modification

1. INTRODUCTION

Water pollution caused by heavy metals, resulting from human activities such as fossil fuel combustion, mining, and chlor-alkali production, leads to contamination with lead (Pb^{2+}), mercury (Hg^{2+}), cadmium (Cd^{2+}), and nickel (Ni^{2+}). This is a major environmental and public health concern globally [1]. Heavy metals are non-biodegradable, persistent in nature, and capable of bioaccumulating in living organisms, and making them hazardous, particularly Pb^{2+} and Hg^{2+}. The World Health Organization (WHO) has established maximum permissible limits for Pb^{2+} and Hg^{2+} in drinking water, set at 0.01 mg/L and 0.006 mg/L, respectively. Exceeding these levels can lead to serious ecological consequences [2, 3]. Therefore, effective removal of Pb^{2+} and Hg^{2+} from water is crucial due to their significant health and environmental impacts.

The adsorption process is recognized for its low operating cost and heigh efficiency in removing heavy metals from water. Activated carbons (ACs) are the most widely utilized adsorbent materials due to their large surface area and pollutant-binding capabilities. However, the synthesis of porous carbon typically requires activation and chemical modification processes, which can drive up production costs. Therefore, Agricultural wastes, such as bamboo, coconut shell, and sugar cane offer promising potential for reducing expenses while maintaining high adsorption efficiency [4]. Moreover, modifying ACs with nitrogen, can enhance their adsorption capacity by increasing the binding active sites for interacting with heavy metal ions [5]

Conversely, several studies report the removal of Pb^{2+} and Hg^{2+} from aqueous solutions at concentration ranging from 10-800 mg/L. These studies include the use of AC and modified AC derived from various sources such as rice straw [6], rice husk [7], water hyacinth [8], and cherry kernels [9]. The results indicate that the equilibrium uptake of Pb^{2+} can reach 193.12 mg/g in rice straw, while the adsorption capacity at equilibrium for Hg^{2+} can be 310.35 mg/g in AC derived from water hyacinth. However, there is no research focusing on the removal of Pb^{2+} and Hg^{2+} using bamboo waste.

Accordingly, bamboo was selected as the precursor material. Activated carbon (AC) was first prepared through a carbonization process and subsequently activated with CO_2 to yield the original AC. The N-

doped AC, AC-UK, was then synthesized from the original AC using urea and KOH. A series of adsorbents was evaluated and compared based on their capacity to adsorb Pb^{2+} and Hg^{2+} from aqueous solutions, with concentrations ranging from 10 to 1000 mg/L at 25 °C and natural pH in a batch system. The equilibrium removal efficiencies of Pb^{2+} and Hg^{2+} were assessed and fitted to various adsorption isotherm models

Table 1. Specific surface area (S_{BET}) and their heavy metal ions adsorption capacity.

Adsorbent	Adsorbate	S_{BET} (m^2/g)	Q_e (mg/g) at C_e = 100 (mg/L)	Ref
AC	Pb^{2+}	732	161	This work
	Hg^{2+}		81	
AC-Air	Pb^{2+}	789	190	
	Hg^{2+}		173	
AC-UK	Pb^{2+}	842	270	
	Hg^{2+}		281	
ND-CPC	Pb^{2+}	1135	282	[10]
	Hg^{2+}		188	
	Cr^{5+}		77	
MPAC	Pb^{2+}	424	81	[11]
ATT@PDA-COP	Hg^{2+}	29	307	[12]
TAC	Pb^{2+}	82	194	[13]
	Cu^{2+}		62	
	Zn^{2+}		60	
WS600	Pb^{2+}	156	150	[14]
	Cd^{2+}		101	
	Cu^{2+}		199	

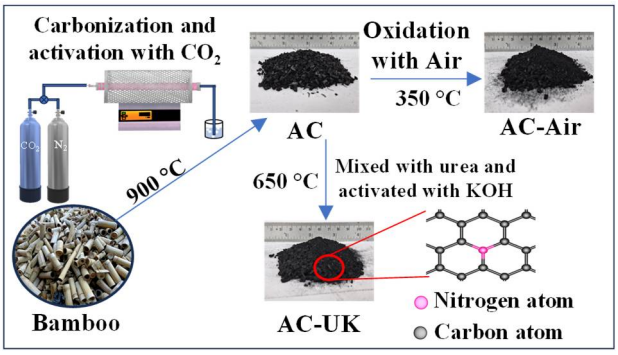

Fig. 1. Synthesis of original and modified AC

2. EXPERIMENTAL

2.1. Synthesis of original and N-doped AC

The original AC was produced from bamboo waste through a two-step thermal treatment process. Initially, the bamboo was cut into small segments (approximately 2–3 cm) and dried at 105 °C for 24 hours to remove moisture. The dried material was then carbonized in a horizontal tube furnace under a N_2 atmosphere (100 mL/min flow rate), where it was heated to 600 °C at a rate of 5 °C/min and held at that temperature for 1 hour. Subsequently, the carbonized product was activated by heating it to 900 °C under a continuous CO_2 flow (100 mL/min), using the same heating rate, and maintaining the temperature for an additional hour. The activated carbon was then cooled to ambient temperature under a N_2 atmosphere to prevent oxidation.

For the surface modification of AC, 5 g of the original AC were mixed with 2.5 g of urea and subjected to oxidation under a continuous air flow of 100 mL/min for 1 hour. Subsequently, the oxidized material (5 g) was mixed with 2.5 g of KOH and stirred overnight. The resulting composite was then dried at 105 °C for 24 hours and thermally activated at 650 °C for 1 hour under a N_2 atmosphere (100 mL/min). The final product was designated as AC-UK. For comparative purposes, a control sample that underwent only air oxidation excluding urea and KOH treatment was prepared under identical conditions and labeled as AC-Air.

2.2. Characterizations

The physical properties, such as the specific surface area (S_{BET}), were calculated using the multipoint Brunauer–Emmett–Teller (BET) method. Pore size distribution was determined using density functional theory (DFT) with a slit-pore model, based on nitrogen adsorption–desorption isotherms measured at –196 °C. All measurements were conducted using a volumetric adsorption analyzer (ASAP 2020 Plus, Micromeritics). We also used Fourier-transform infrared (FTIR) spectroscopy (Tensor 27, Bruker) to examine the surface functional groups of all materials, using the KBr pellet method within the spectral range of 4000–400 cm^{-1}. The concentrations of residual heavy metal ions in solution were measured by inductively coupled plasma optical emission spectrometry (ICP-OES, Optima 8000, PerkinElmer).

2.3. Batch adsorption

For the equilibrium sorption study, 0.05 g of adsorbent (AC, AC-Air, or AC-UK) was added to 18 flasks. Each flask contained 40 mL of heavy metal ions solution, with initial concentrations ranging from 10 to 1,000 mg/L, at a natural pH of approximately 6 and a temperature of 25 °C. The flasks were stirred at a constant speed of 300 rpm. After filtration to remove the adsorbent, the concentrations of Pb^{2+} and Hg^{2+} in each sample at different adsorption times were measured using ICP-OES. The amount of adsorbate retained in the adsorbent at any given time, *t*, denoted as *qt*, was determined by:

$$q_t = \frac{(C_0 - C_t) * V_s}{m}$$

where C_0 and C_t (mg/L) indicated the initial and time-dependent concentrations of Pb^{2+} or Hg^{2+} in solution, respectively. V_s (L) is the volume of the solution; and m (g) is the mass of the adsorbent.

At equilibrium, the adsorption data were analyzed using both the Langmuir and Freundlich isotherm models. The Langmuir isotherm [15], which assumes monolayer adsorption onto a homogeneous surface with a finite number of identical sites, can be expressed in its linearized form as:

$$\frac{C_e}{q_e} = \frac{1}{q_m} C_e + \frac{1}{q_m b}$$

where q_m is the maximum adsorption capacity (mg/g), b is the Langmuir constant related to the affinity of binding sites (L/mg), and C_e is the equilibrium concentration in the bulk phase (mg/L).

The Freundlich isotherms [16] can be formed in logarithmic given by:

$$log(q_e) = log(K_f) + \frac{1}{n} log(C_e)$$

where K_f is the indicators of the adsorption capacity and n is adsorption intensity.

3. RESULTS AND DISCUSSION

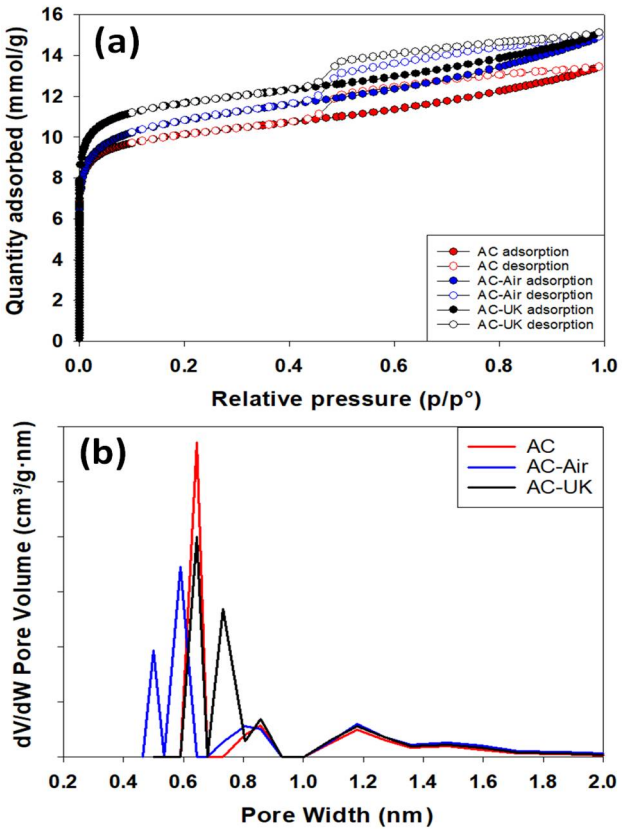

Fig. 2. (a) The Adsorption and desorption isotherm of N_2 and (b) porosity distribution of all adsorbents

The N_2 adsorption isotherms of the synthesized porous carbon are representing in Fig. 2 (a). Based on the IUPAC classification of physisorption isotherms, all AC samples exhibited Type I isotherms accompanied by H4 hysteresis loops. This adsorption behavior is characteristic of materials predominantly composed of micropores, indicating a hierarchical porous structure with a higher proportion of micropores relative to mesopores. This is corroborated by the pore size distribution presented in Fig. 2(b), which shows that all samples exhibit prominent peaks in the range of 0.5 to 1.5 nm, confirming the dominance of micropores. The BET surface areas of AC, AC-Air, and AC-UK are summarized in Table 1.

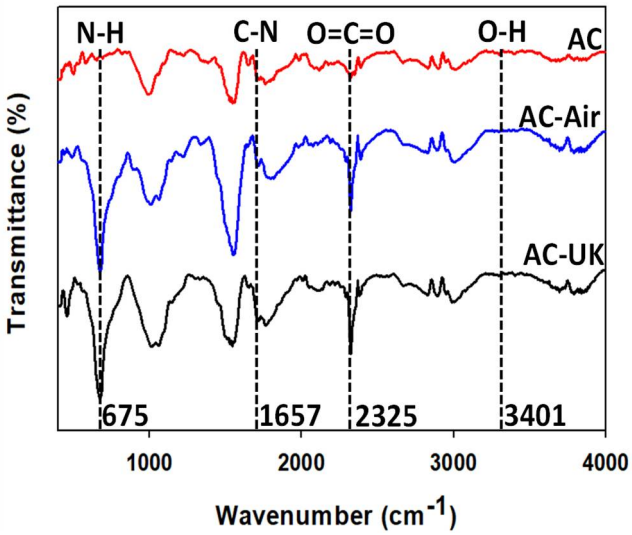

Fig. 3. FTIR spectra of AC samples.

The FTIR spectra revealed characteristic absorption bands at 675, 1657, 2325, and 3401 cm^{-1}, corresponding to N–H wagging, C–N stretching, O=C=O asymmetric stretching, and O–H stretching vibrations, respectively. Notably, the AC-UK sample exhibited a pronounced presence of nitrogen-containing functional groups. The prominent bands associated with N–H and C–N vibrations indicate that the combined use of urea and KOH during activation effectively enhances the incorporation of nitrogen and oxygen functionalities on the activated carbon surface, thereby improving its surface chemistry and potentially increasing its adsorption capacity.

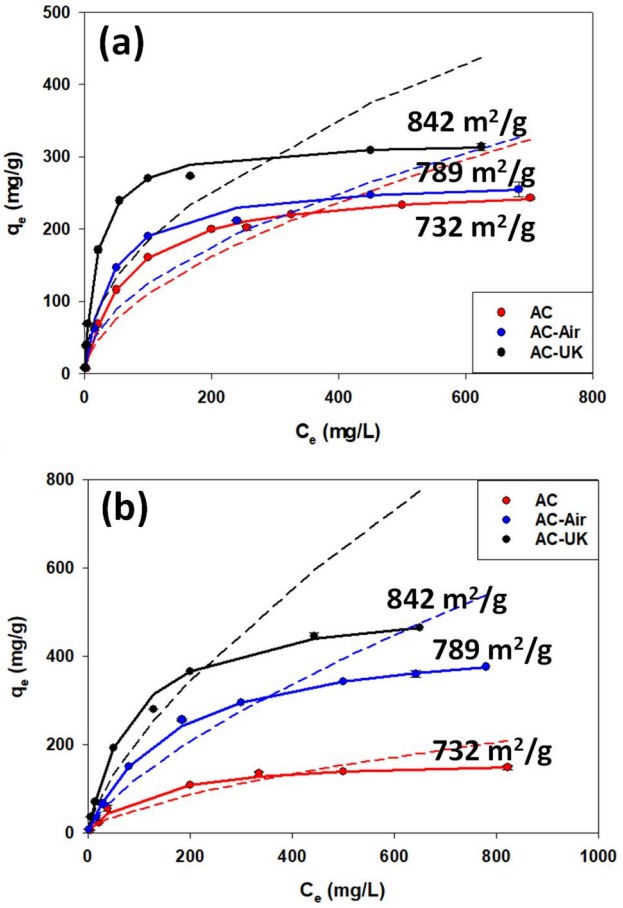

Fig. 4. adsorption equilibrium of Pb^{2+} (a) and Hg^{2+} adsorption (b). The solid lines represent the fitting Langmuir isotherm and dash line represents the fitting Freundlich isotherm.

The adsorption of Pb^{2+} and Hg^{2+} by these porous materials was evaluated at equilibrium concentrations (C_e) ranging from 10 to 1000 mg/L, as illustrated in Fig. 4. The results revealed that the uptake capacity depended on the surface area, total pore volume, and surface functional groups of the adsorbents. AC-UK had the best capacity to adsorb Pb^{2+} and Hg^{2+} from aqueous solutions. Because it was doped with nitrogen and KOH activation, which provided the material with a larger surface area and introduced nitrogen functional groups on the solid surface. Simultaneously, AC-Air had its surface modified to improve both pore size and surface area through air oxidation, thus providing better adsorption efficiency than the original AC. Furthermore, the adsorption data were fitted using the Langmuir and Freundlich models. The results showed that all adsorbents exhibited monolayer adsorption, with the Langmuir model providing a better fit (R^2 > 0.98). AC-UK had maximum capacities for Pb^{2+} and Hg^{2+} of 323 and 526 mg/g, respectively.

4. CONCLUSION

We studied the removal of lead (Pb^{2+}) and mercury (Hg^{2+}) from water through adsorption using activated carbon (AC) derived from bamboo in a single-component batch adsorption system. First, the precursor was synthesized through a thermal treatment process. Subsequently, nitrogen-containing AC (AC-UK) was produced by impregnating the original AC with urea, followed by air oxidation and chemical activation with KOH. All of the adsorbents were characterized, revealing that pore size and surface functional groups developed thoroughly. AC-UK exhibited the highest surface area (842 m^2/g) and the most efficient removal of Pb^{2+} and Hg^{2+}. This is because AC-UK has improved both surface functional groups through nitrogen doping and microporous structure, which enhances its adsorption efficiency compared to other adsorbents. According to the equilibrium isotherm of Pb^{2+} and Hg^{2+} on AC-UK, the Langmuir isotherm was appropriate to discuss the equilibrium uptake, showing that the adsorption process was monolayer adsorption, with maximum capacities for Pb^{2+} and Hg^{2+} being 323 and 526 mg/g, respectively. Overall, the use of AC-UK derived from bamboo presents a sustainable and efficient approach for the removal of heavy metal ions from water, offering a promising solution for environmental pollution control.

ACKNOWLEDGMENTS

This work was supported by Suranaree University of Technology.

REFERENCES

1. Hama Aziz KH, Mustafa FS, Omer KM, Hama S, Hamarawf RF, Rahman KO. Heavy metal pollution in the aquatic environment: efficient and low-cost removal approaches to eliminate their toxicity: a review. *RSC Adv*. 2023;13(26):17595-610.
2. Ihsanullah, Abbas A, Al-Amer AM, Laoui T, Al-Marri MJ, Nasser MS, et al. Heavy metal removal from aqueous solution by advanced carbon nanotubes: Critical review of adsorption applications. *Separation and Purification Technology*. 2016;157:141-61.
3. Mitra S, Chakraborty AJ, Tareq AM, Emran TB, Nainu F, Khusro A, et al. Impact of heavy metals on the environment and human health: Novel therapeutic insights to counter the toxicity. *Journal of King Saud University - Science*. 2022;34(3).
4. Chowdhury IR, Chowdhury S, Mazumder MAJ, Al-Ahmed A. Removal of lead ions (Pb(2+)) from water and wastewater: a review on the low-cost adsorbents. *Appl Water Sci*. 2022;12(8):185.
5. Kasera N, Kolar P, Hall SG. Nitrogen-doped biochars as adsorbents for mitigation of heavy metals and organics from water: a review. *Biochar*. 2022;4(1).
6. Zhang J, Li X, Xu H, Zhang W, Feng X, Yao Y, et al. Removal of Cd2+, Pb2+ and Ni2+ from water by adsorption onto magnetic composites prepared using humic acid from waste biomass. *Journal of Cleaner Production*. 2023;411.
7. Liu Z, Sun Y, Xu X, Qu J, Qu B. Adsorption of Hg(II) in an Aqueous Solution by Activated Carbon Prepared from Rice Husk Using KOH Activation. *ACS Omega*. 2020;5(45):29231-42.

8. El-Wakil AM, Waly SM, Abou El-Maaty WM, Waly MM, Yilmaz M, Awad FS. Triazine-Based Functionalized Activated Carbon Prepared from Water Hyacinth for the Removal of Hg(2+), Pb(2+), and Cd(2+) Ions from Water. *ACS Omega*. 2022;7(7):6058-69.
9. Pap S, Radonic J, Trifunovic S, Adamovic D, Mihajlovic I, Vojinovic Miloradov M, et al. Evaluation of the adsorption potential of eco-friendly activated carbon prepared from cherry kernels for the removal of Pb(2+), Cd(2+) and Ni(2+) from aqueous wastes. *J Environ Manage*. 2016;184(Pt 2):297-306.
10. Bakry AM, Awad FS, Bobb JA, El-Shall MS. Multifunctional Binding Sites on Nitrogen-Doped Carboxylated Porous Carbon for Highly Efficient Adsorption of Pb(II), Hg(II), and Cr(VI) Ions. (2470-1343 (Electronic)).
11. Kongsune P, Rattanapan S, Chanajaree R. The removal of Pb2+ from aqueous solution using mangosteen peel activated carbon: Isotherm, kinetic, thermodynamic and binding energy calculation. *Groundwater for Sustainable Development*. 2021;12:100524.
12. Aliabadi HM, Zargoosh K. Synthesis of 3-amino-1,2,4-triazole-5-thiol functionalized p-phenylenediamine covalent organic polymer as a highly selective adsorbent for Hg2+ ions. *Reactive and Functional Polymers*. 2023;186:105575.
13. Shahrokhi-Shahraki R, Benally C, El-Din MG, Park J. High efficiency removal of heavy metals using tire-derived activated carbon vs commercial activated carbon: Insights into the adsorption mechanisms. (1879-1298 (Electronic)).
14. Qi G, Pan Z, Zhang X, Chang S, Wang H, Wang M, et al. Microwave biochar produced with activated carbon catalyst: Characterization and adsorption of heavy metals. *Environmental Research*. 2023;216:114732.
15. Langmuir I. THE ADSORPTION OF GASES ON PLANE SURFACES OF GLASS, MICA AND PLATINUM. *Journal of the American Chemical Society*. 1918;40(9):1361-403.
16. Freundlich H. Über die Adsorption in Lösungen. 1907;57U(1):385-470.

Enhanced CO_2 photoreduction in synthetic seawater using black TiO_2 nanowires: Synthesis, characterization, and performance

Kongphoom Khumsupa[1], Poomipat Chotngamkham[1], Woranart Jonglertjunya[1,2], Poomiwat Phadungbut[1,2,*], Sira Srinives[1,2]

[1] Department of Chemical Engineering, Faculty of Engineering, Mahidol University, Nakhon Pathom 73170, Thailand
[2] Carbon Conversion Research and Technology Laboratory (CoReTech Lab), Mahidol University, Nakhon Pathom 73170, Thailand
[*] Corresponding author: poomiwat.pha@mahidol.edu

ABSTRACT

Increased ocean CO_2 concentration is vital for ocean acidification, affecting dissolved gas concentration, water temperature, and marine ecosystems. An emerging approach to counter CO_2 removal from seawater relies on, photocatalysts, such as TiO_2, to photoreduce dissolved CO_2 to other substances. A commercial TiO_2 particle (P25) has been employed for wastewater treatment and was demonstrated for CO_2 photoreduction but was considered insufficient due to limited photoactivity. In this work, we promote the photoactivity of TiO_2 by transforming it to TiO_2 nanowires (TiO_2-NWs) for a lowered band gap energy and increased surface-to-volume ratio. The NWs were further converted to black TiO_2 NWs for enhanced photoactivity using thermochemical reduction and studied for CO_2 photoreduction. Preliminary results exhibited promising photoactivity for black TiO_2 NWs facilitating CO_2 conversion to products, including methane, acetaldehyde, ethanol, and acetone at a total carbon consumption of 1,686.77 µmol/g_{cat}.

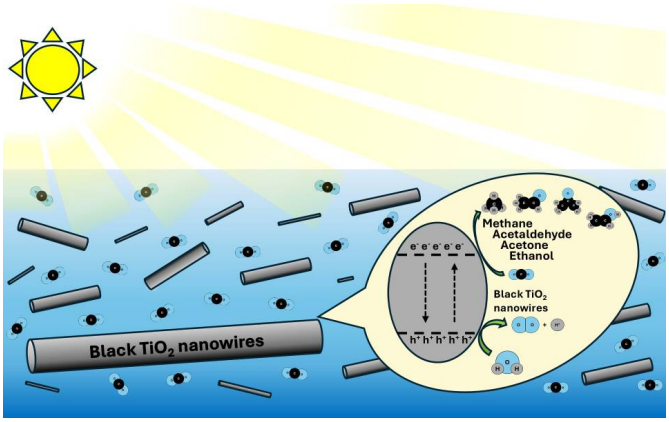

Fig. 1 Black TiO_2-NWs photo-reducing CO_2 in seawater.

Keywords: CO_2 photoreduction; TiO_2 nanowires; Black TiO_2

1. INTRODUCTION

The increase in CO_2 emissions has become a critical global concern, necessitating substantial contributions from industries, governments, and the public to mitigate its impact. Approximately 30% of the 10 billion tons of CO_2 generated annually from human activities is absorbed by the ocean. However, the dissolved CO_2 in oceans causes acidification, adversely affecting marine ecosystems, climate phenomena, and human activities [1]. The amount of CO_2 adsorbed by the sea was determined to have an economic value of more than $3 trillion per year and is crucial for maintaining global warming below 1.5 °C [1]. It is, then, essential to engage the ocean's role in CO_2 capture and study technologies to stabilize seawater quality.

CO_2 conversion is an alternative approach that transforms CO_2 into other valued substances that could be used or sold. The key is to capture CO_2 and partially earn back part of the investment in the form of conversion products. One core technique relies on the photochemical reduction of CO_2 to products such as methane and alcohol in the presence of sunlight; the path is also known as the artificial leaf path [2]. Titanium dioxide (TiO_2) is a popular photocatalyst recognized for its applications in wastewater treatment. It was also demonstrated in CO_2 photoreduction, yielding mainly methane. It is constrained by the

expansive bandgap energy, which leads to rapid recombination of photo-generated electrons and holes, resulting in limited photoactivity. Different approaches have been introduced to promote the photoactivity of TiO_2, including synthesizing TiO_2 into a nanostructure and surface modification, broadening light absorption and reducing its bandgap energy. TiO_2 can be partially reduced to black TiO_2 by replacing Ti^{4+} with Ti^{3+} and creating oxygen vacancy in the structure [3]. The structural defects function as catalytic sites for electron traps, analyte adsorption, and radical accumulation, enhancing photoactivity.

This study focuses on advancing CO_2 photoreduction by synthesizing and testing the black TiO_2 nanowires in synthetic seawater. The aim is to explore the possibility of reducing CO_2 concentrations and converting them into gaseous fuels, thereby reducing CO_2 concentration in seawater and preventing seawater contamination.

2. EXPERIMENTAL

Material and reagent: Titanium dioxide (TiO_2, P25, Sigma-Aldrich, Germany), Sodium hydroxide pellets (NaOH, Ajax Finechem, Australia), L-Ascobic acid (C6H8O6, 99.0% purity, Kemaus, Australia), DI water (type I), Sodium Chloride (NaCl, 99.9% purity, Prung Thip, Thailand), and Hydrochloric acid (HCl, 37%w/v, RCI Labscan, Thailand) were purchased and used as received. Carbon dioxide gas was 99.9% pure and provided by the Lor Ching Tong Oxygen (LCTO), Thailand.

TiO_2 nanowires synthesis: P25 (200 mg) was suspended in 30 ml 10 M NaOH solution and sonicated for 60 mins. The mix was transferred to a Teflon-lined autoclave for hydrothermal treatment at 200 °C for either 24 or 60 h time. The solid powder was filtered and rinsed with 0.1 M HCl solution and DI water to remove residuals before dried at 60 °C for 12 h. The powder was calcined in an oven at 500 °C for 30 mins. The NWs that underwent the hydrothermal treatment for 60 and 24 h were marked as TiO_2 NWs-1 and TiO_2 NWs-2, respectively.

Black TiO_2 NWs synthesis: The as-prepared TiO_2 NWs (100 mg) were suspended in 2.7 ml of 1.325 M L-ascorbic acid and dried at 110 °C for 12 h. The solid power was ground and calcined in a muffle furnace at 500 °C for 30 min, becoming black TiO_2 NWs (B-TiO2 NWs).

The CO_2 photoreduction experiment: A photocatalyst (2 mg) was suspended in 20 ml of DI water (or synthetic seawater) and sonicated for 20 mins. The suspension was poured into a 30-ml quartz reactor with 20 ml CO_2-saturated water. The reactor was mildly stirred inside a closed chamber and introduced to a mercury lamp (160W/220-230V, Philips) for 5 h for Photoreduction. Gas and liquid were collected and analyzed using gas chromatography.

Characterizations: Photocatalyst samples were analyzed using an X-ray diffractometer (XRD, D2 Phaser, Bruker, Germany) for crystallinity, UV-Vis diffuse reflectance spectrometer (UV-2600, Shimadzu, Japan) equipped with an integrating sphere unit (Shimadzu, ISR-2600 Plus) for optical properties. Field emission scanning electron microscopy (FE-SEM, JSM-7610FPlus, JEOL, Japan) was used to observe the surface morphology of the photocatalyst samples. Fourier Transform Infrared Spectroscopy (FT-IR, FT/IR-6800, Jasco, Japan) provide chemical functionality. CO_2 conversion product composition was analyzed using Gas chromatography (GC-FID, Clarus 680, Perkin Elmer, USA) with a DB-Wax column.

3. RESULTS AND DISCUSSION

Physical Morphology: FE-SEM (Fig. 2a and c) revealed the morphology of TiO_2 NWs-1 (60 h) and NWs-2 (24 h). TiO_2 NWs-1 was 1,249.2 ± 826.0 nm long and 125.6 ± 48.4 nm in diameter. The TiO_2 NWs-2 showed a length of 1,006.3 ± 481.2 nm and a diameter of 153.5 ± 65.2 nm. TEM images (Fig. 2b and d) of TiO_2 NWs-1 reveal clear and crystalline structures, while TiO_2 NWs-2 reveal roughness on the surface due to formation of TiO_2 (B) crystal structures [4].

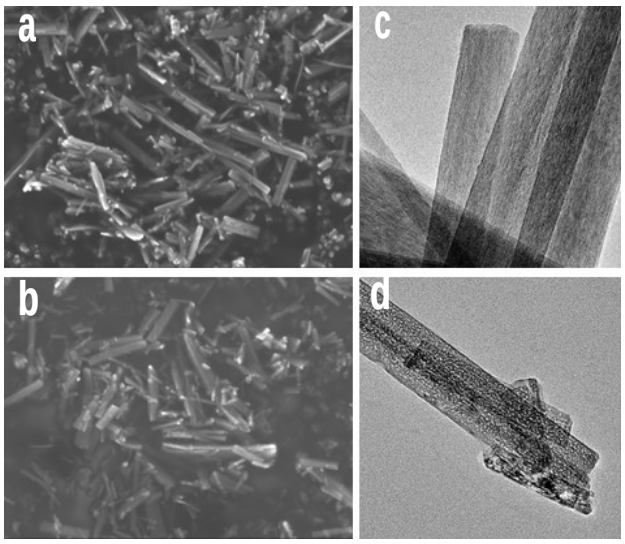

Fig. 2 FE-SEM images of (a) TiO_2 NWs-1, (b) TiO_2 NWs-2 and TEM images of (c) TiO_2 NWs-1, (d) TiO_2 NWs-1.

Crystallinity of the photocatalyst: Crystal structure of TiO_2 NWs-1 and TiO_2 NWs-2 were studied from XRD spectra (Fig. 3). TiO_2 NWs-1 provided characteristic peaks at 38.97°, 48.25 ° and 28.74°, corresponding to {1,1,2}, {2,0,0} planes of TiO_2 anatase (PDF: 01-089-4921), and {1,1,0} planes of TiO_2 rutile (PDF: 01-078-4190). The peaks at 30.98°, 36.51°, 57.89°, 66.74°, and 67.44° were related to {2,1,1}, {1,0,2}, {3,2,2}, {2,3,2}, and {2,2,3} TiO_2 brookite planes (PDF: 03-065-2448). Other XRD peaks at 14.06°, 24.869°, 33.30°, 43.15°, and 44.27° could be ascribed to {2,0,-1}, {4,0,0}, {4,0,2}, {4,0,-4}, and {6,0,2} planes of sodium hexatitanate ($Na_2Ti_6O_{13}$, PDF: 00-014-0277). TiO_2 NWs-2 exhibited characteristic

peaks at 14.15°, 24.95°, 28.69°, 33.23°, 43.57°, 48.50°, 57.47°, 61.55°, 67.25°, and 76.62°, which were associated with {001}, {110}, {002}, {310}, {003}, {020}, {022}, {313}, {023}, and {712} planes of the beta-phase monoclinic polymorph TiO_2 (B) (JCPDS NO.01-74-1940) [4].

For the average crystallize size of the photocatalysts sample, we use Scherer equation (Eq. 1) [5],

$$D_p = \frac{k\lambda}{\beta cos\theta} \quad (1)$$

where D_p represents the crystallite size (nm), k is the Scherer constant (0.9), λ is X-ray wavelength (1.54 Å), β represents the full width at half-maximum (FWHM) of the highest peak, and θ is the diffraction angle at the peak. The average crystallite size is 61.31 nm and 17.29 nm for TiO_2 NWs-1 and TiO_2 NWs-2, respectively, revealing a relatively high crystallinity for TiO_2 NWs-1. The crystallite size was in agreement with SEM images, in which the TiO_2 NWs-1 surface was smoother and longer than the TiO_2 NWs-2.

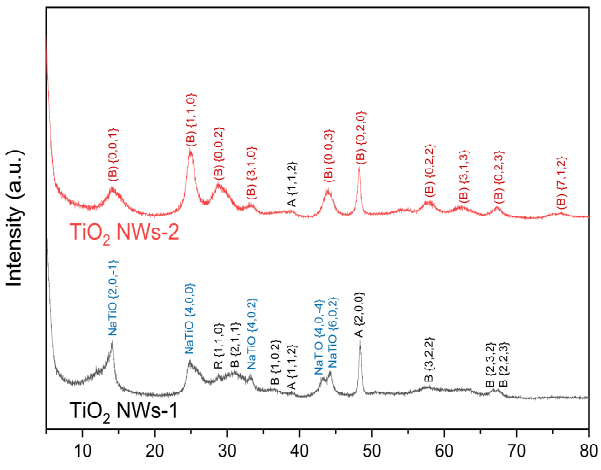

Fig. 3 XRD patterns for TiO_2 NWs-1 (red) and TiO_2 NWs-2 (black)

FTIR: IR transmittance (Fig. 4) revealed a broad peak at 500-800 cm^{-1}, correlating to Ti-O-Ti vibration in TiO_2 (P25), TiO_2 NWs-1, TiO_2 NWs-2, B-TiO_2 NWs-1, and B-TiO_2 NWs-2 [6]. The 600-700 cm^{-1} peak can be assigned to Ti-O and O-Ti-O bonds, which appeared on the transmittances of all the samples [7]. A small peak at 1626 cm^{-1} was associated with the Ti-OH bond and was broader for B-TiO_2 NWs-1 and B-TiO_2 NWs-2 [7]. The Ti-OH bond signal was insignificant in the case of TiO_2 (P25).

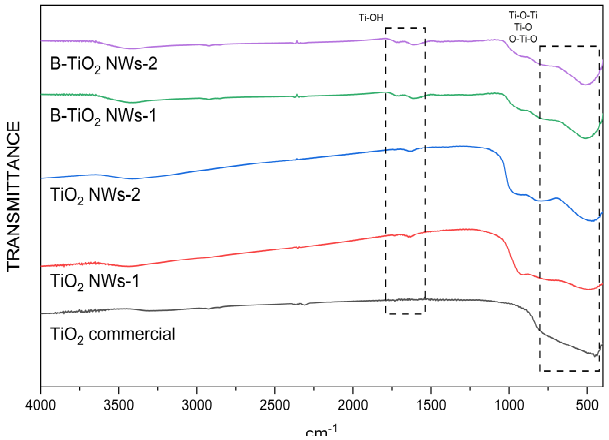

Fig. 4 FT-IR spectra for TiO_2 (P25), TiO_2 NWs-1, TiO_2 NWs-2, B-TiO_2 NWs-1, and B-TiO_2 NWs-2.

Optical properties: UV-vis analyze light reflectance for photocatalyst samples within the 200-800 nm range (Fig. 5a). Each photocatalyst sample has a similar trend, showing UV light adsorption (300 nm), a typical characteristic for TiO_2. The reflective peak occurred at 416, 390, 390, 380, and 371 nm for TiO_2 (P25), TiO_2 NWs-1, TiO_2 NWs-2, B-TiO_2 NWs-1, and B-TiO_2 NWs-2, respectively. The blue shift in reflective peaks indicated improved light adsorption ability in the UV region [4].

Optical band gap energy was determined relying on the Kubelka Munk function (eq 2) and Tauc's correlation equation (eq 3) [5].

$$F(R) = \frac{(1-R)^2}{2R} \quad (2)$$

$$(F(R)hv)^{\frac{1}{2}} = B\,(hv - E_g) \quad (3)$$

in which R represents the reflectance, h is the Planck constant, B is a constant, and Eg is bandgap energy. The power of the left-hand-side term is held at 1/2 for an indirect transition mode electron transfer. Band gaps were 3.19, 3.33, 3.06, 2.98, and 2.89 for TiO_2 (P25), TiO_2 NWs-1, TiO_2 NWs-2, B-TiO_2 NWs-1, and B-TiO_2 NWs-2, respectively. TiO_2 (P25) provided standard band gap value. TiO_2 NWs-1 gave a remarkably higher band gap than the other samples, which could be attributed to overgrowth geometry of the catalyst. Its band gap decreased as TiO_2 NWs-1transformed to B TiO_2 NWs-1. TiO_2 NWs-2 showed the lower band gap than TiO_2 (P25), and went even fewer after being converted to B-TiO_2 NWs-2. The decreased band gap energy after TiO_2 transformation to black titanium is an attribution of Ti^{3+} and oxygen vacancies in black titanium structures that affects light adsorption and electron transfer ability of the material [4].

CO_2 photoreduction: CO_2 conversion is the major key in this work, indicating the photoactivity of the catalysts (Fig. 6). Target products were collected from gas and liquid phases and identified using the GC as methane, acetaldehyde, acetone, methanol, and ethanol.

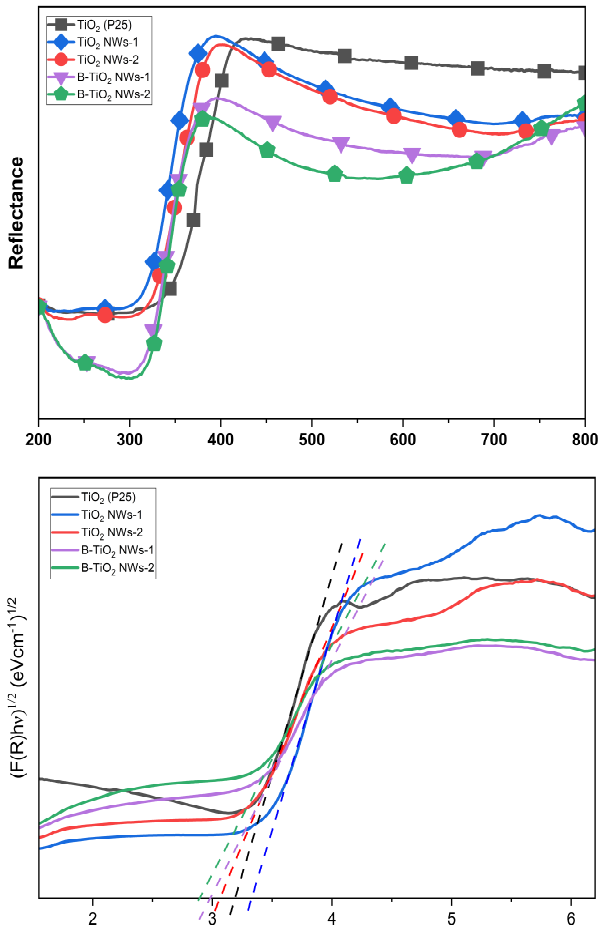

Fig. 5 UV-vis diffuse reflectance spectra (DRS) for (a) TiO_2 (P25), TiO_2 NWs-2, TiO_2 NWs-1, B-TiO_2 NWs-2, and B-TiO_2 NWs-1; (b) A modified Kubelka Munk plot for bandgap determination

To compare the performances of photocatalysts, the total carbon consumption was defined to be

Total carbon consumption (μmol/g_{cat}) = 5 x [(methane generation rate × 1) + (methanol generation rate × 1) + (acetaldehyde generation rate × 2) + (ethanol generation rate × 2) + (acetone generation rate × 3)].

The number inside the parenthesis represents the amount of carbon in the product molecule, and 5 represents the experimental time. The total consumption portrays the amount of carbon from CO_2 that converts into the target products, as determined by the GC. TiO_2 NWs-1 provided the total carbon consumption of 341.46 ± 68.41 μmol/g_{cat}, yielding acetone as the major product at 84.19 μmol/g_{cat}. TiO_2 NWs-2 yielded an increased total carbon consumption of 1,063.52 ± 359.29 μmol/g_{cat} with ethanol as the major product (410.04 μmol/g_{cat}). B-TiO_2 NWs-2 has carbon consumption of 1,686.77 μmol/g_{cat} with ethanol as a major product (684.96 μmol/g_{cat}). It is clear that the B-TiO_2 NWs-2 provides the best photoactivity in photoreducing CO_2 due to excellent light adsorption characteristic and reduced band gap energy [8].

Basic mechanism for CO_2 photoreduction involves photocatalyst being activated in the presence of

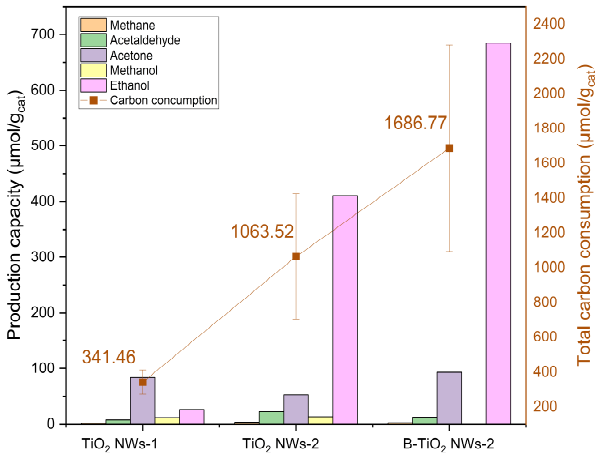

Fig. 6 Total carbon consumption of TiO_2 NWs-1, TiO_2 NWs-2 and B-TiO_2 NWs-2 in DI water

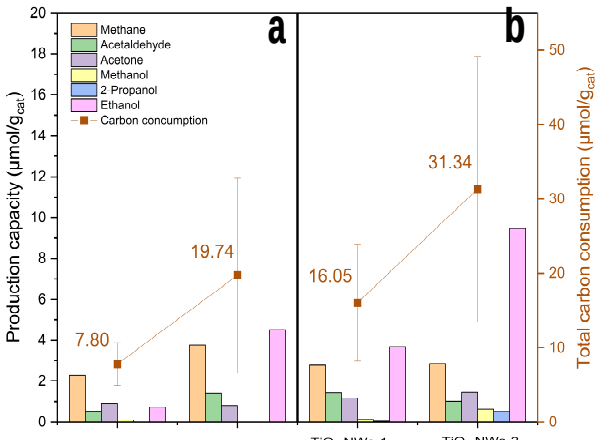

Fig. 7 Total carbon consumption from gas-phase product generations using TiO_2 NWs-1 and TiO_2 NWs-2 in (a) DI water and (b) synthetic seawater.

sunlight, and generation of photo-induced electrons and holes with exceptionally high energy. The photo-induced electrons, or photoelectrons, could couple with CO_2 and become CO_2^- active radical. The radical reacts or interacts with other radicals such as water and other CO_2 to form target product (Fig. 1).

Gas phase from synthetic seawater: CO_2 conversion was conducted in a synthetic seawater with 3.5%wt of NaCl in water, mimicking an actual salt composition in seawater [9]. The plan is to analyze product compositions in both the gas and liquid phases, and we could only provide the gas phase composition for this work (Fig. 7) due to difficulty in product analysis. TiO_2 NWs-1 and TiO_2 NWs-2 yielded a total carbon consumption of 7.80 μmol/g_{cat} and 19.74 μmol/g_{cat} for the water medium, and 16.05 μmol/g_{cat} and 31.34 μmol/g_{cat} for the synthetic seawater. The trend exhibited superior product generation in the synthesis water compared to the water medium, which was attributed to the presence of chloride ion (Cl^-) [10]. The Cl^- could serve as a hole-scavenging substance to the photocatalyst and contribute also to the CO_2 absorption in the medium [9]. Such phenomena result in higher photoactivity for the photocatalyst and higher dissolved CO_2 to be converted to the target products. We expect

the same trend for the liquid composition, in which more product generation will be monitored from the synthetic water than the water. The results from liquid product analysis will be presented in near future.

B-TiO_2 NWs-1 and B-TiO_2 NWs-2 will soon be tested for CO_2 photoreduction in synthetic and actual seawater medium and would be reported elsewhere.

4. CONCLUSION

TiO_2 NWs were synthesized via hydrothermal technique and converted to black titanium (B-TiO_2 NWs) following a dry chemical-thermal oxidation process. The B-TiO_2-NWs-2 performed best as a photocatalyst for CO_2 photoreduction, providing a total carbon consumption of 1,686.77 µmol/g_{cat} with ethanol as a major product (684.96 µmol/g_{cat}). TiO_2 NWs-1 and TiO_2 NWs-2 yielded a gas-phase carbon consumption of 7.80 µmol/g_{cat} and 19.74 µmol/g_{cat} for the water medium and 16.05 µmol/g_{cat} and 31.34 µmol/g_{cat} for the synthetic seawater. In the near future, TiO_2 NWs-1, TiO_2 NWs-2, B-TiO_2 NWs-1, and B-TiO_2 NWs-2 will all be tested for CO_2 photoreduction in synthetic and actual seawater. We trust that our contribution will provide an intriguing alternative and that the artificial photosynthesis approach could be a competitive technology to mitigate CO_2 emissions.

ACKNOWLEDGMENTS

We are grateful for the financial support from the 60th Year Supreme Reign of His Majesty King Bhumibol Adulyadej Scholarship and the Research CESS fund of the Malaysia-Thailand Joint Authority (MTJA). We also thank the Mahidol University Frontier Research Facility (MU-FRF) and the Department of Chemical Engineering Central lab staff for material characterizations and photoreduction product analysis.

REFERENCES

1. Shadwick E, ROHR T, Richardson A. Oceans absorb 30% of our emissions, driven by a huge carbon pump. Tiny marine animals are key to working out its climate impacts: Australia's National Science Agency; 2023.
2. Zhao H, Pan F, Li Y. A review on the effects of TiO_2 surface point defects on CO_2 photoreduction with H_2O. Journal of Materiomics. 2017;3(1): 17-32.
3. Hou X, Li Y, Zhang H, Lund PD, Kwan J, Tsang SCE. Black titanium oxide: synthesis, modification, characterization, physiochemical properties, and emerging applications for energy conversion and storage, and environmental sustainability. Chem Soc Rev. 2024;53(21):10660-708.
4. Makal P, Das D. Self-doped TiO_2 nanowires in TiO_2-B single phase, TiO_2-B/anatase and TiO_2-anatase/rutile heterojunctions demonstrating individual superiority in photocatalytic activity under visible and UV light. Applied Surface Science. 2018;455:1106-15.
5. Karawek A, Kitjanukit N, Neamsung W, Kinkaew C, Phadungbut P, Seeharaj P, et al. Alkanolamine-grafted and copper-doped titanium dioxide nanosheets–graphene composite heterostructure for CO_2 photoreduction. ACS Applied Energy Materials. 2023;6(21):10929-42.
6. Chen S, Fan X, Zhang C, Wei A, Chen W. Synthesis of hierarchical and flower- like TiO_2 nanowire microspheres as biocompatible cell carriers. Materials Science and Engineering: C. 2021;126:112118.
7. Du J, Li X, Li K, Gu X, Qi W, Zhang K. High hydrophilic Si- doped TiO_2 nanowires by chemical vapor deposition. Journal of Alloys and Compounds. 2016;687:893-7.
8. Gao J, Shen Q, Guan R, Xue J, Liu X, Jia H, et al. Oxygen vacancy self-doped black TiO_2 nanotube arrays by aluminothermic reduction for photocatalytic CO_2 reduction under visible light illumination. Journal of CO_2 Utilization. 2020;35:205-15.
9. Chalermthai P, Akkarawatkhoosith N, Kaewchada A, Jaree A. Carbon dioxide removal via absorption using artificial seawater in a microchannel for the case of CO_2-rich gas. Chemical Engineering and Processing - Process Intensification. 2022;175:108928.
10. Iguchi S, Teramura K, Hosokawa S, Tanaka T. Effect of chloride ion as a hole scavenger on the photocatalytic conversion of CO_2 in an aqueous solution over Ni−Al layered double hydroxides. Phys Chem Chem Phys. 2015;17.

Synthesis and characterizations of triethanolamine-copper black titanium photocatalyst for carbon dioxide photoreduction

Poomipat Chotngamkham[1], Kongphoom Khumsupa[1], Somchate Wasantwisut[1,2], Poomiwat Phadungbut[1,2], Woranart Jonglertjunya[1,2,*], Sira Srinives[1,2]

[1] Department of Chemical Engineering, Faculty of Engineering, Mahidol University, Nakhon Pathom 73170, Thailand
[2] Carbon Conversion Research and Technology Laboratory (CoReTech Lab), Mahidol University, Nakhon Pathom 73170, Thailand
[*] Corresponding author: woranart.jon@mahidol.edu

ABSTRACT

CO_2 emission is a leading cause of global warming and has become a prime public concern in recent years. Various methods were explored for CO_2 capture and storage (CCS), including amine scrubbers, solid adsorbents, and underground CO_2 storage, hoping to mitigate the emission incident. An emerging and promising alternative is CO_2 photoreduction, the artificial leaf, which employs photocatalysts to convert CO_2 into valuable products such as methane, acetaldehyde, and methanol. Titanium dioxide (TiO_2) is a notable photocatalyst in surface coating and wastewater treatment industries. In this regard, commercial-grade Degussa P25 TiO_2 was studied for its ability to convert CO_2 into high-value substances with limited photoactivity due to rapid electron-hole recombination and restricted light absorption. In this study, the P25 TiO_2 was transformed to black titanium (BT), dope with copper, and functionalized with triethanolamine (TEA). BT is an amorphous phase of TiO_2 with oxygen vacancy and Ti^{3+} active species, while copper decelerates the electron-hole recombination rate. TEA is a tertiary alkanolamine that can capture CO_2 and release CO_2 to the photocatalyst. Combining BT, copper, and TEA creates TEA-Cu-BT, providing excellent photoactivity for CO_2 photoreduction. Our best result showed TEA-Cu-BT converting CO_2 to target products in both gas and liquid phases, including methane, acetaldehyde, ethanol, and acetone, at a total carbon consumption of 5,760 µmol/g_{CAT}.

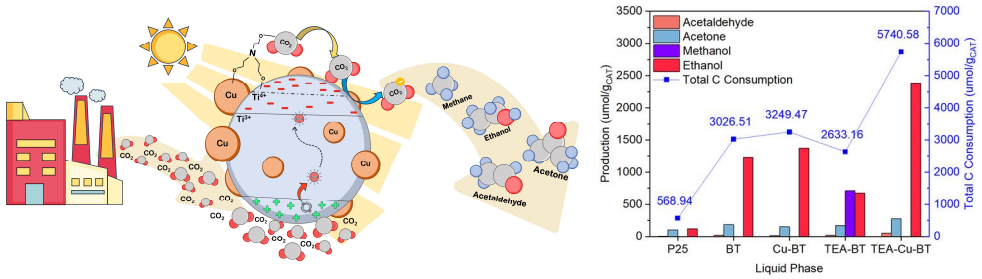

Figure 1 Schematic diagram showing TEA-Cu-BT photo-reducing CO_2 into fuel products (LEFT), and CO_2 photoreduction product generation (RIGHT).

Keywords: CO_2 photoreduction; Titanium dioxide (TiO_2); Triethanolamine (TEA); Black titanium

1. INTRODUCTION

CO_2 emissions are a primary driver of global warming, presenting a critical public challenge worldwide. Numerous strategies for CO_2 capture and storage (CCS) have been developed, including amine scrubbers, solid adsorbents, and underground CO_2 storage. Amine scrubbers are a standard unit in industrial processes that depend on acid-base reactions between CO_2 and amines [5]. The regeneration of CO_2-amine complexes requires thermal energy, which inadvertently leads to additional CO_2 emissions. Solid adsorptions, using minerals like calcium oxide (CaO) and magnesium oxide (MgO), capture CO_2 by forming carbonate compounds (e.g., calcium carbonate ($CaCO_3$) and magnesium carbonate ($MgCO_3$)) [6], which can serve as raw materials for the cement industry or be sequestered in isolated locations. The underground CO_2

storage focuses on capturing and injecting CO_2 into geological formations such as depleted oil reservoirs. The process has undergone practical trials with a promising result.

CO_2 photoreduction is an emerging approach that utilizes photocatalysts to convert CO_2 into valuable products such as methane, acetaldehyde, and methanol. Titanium dioxide (TiO_2) stands out as a widely studied photocatalyst due to its capability to reduce CO_2 into various hydrocarbons and oxygenated compounds. The commercial-grade Degussa P25 TiO_2 nanoparticle, commonly employed in wastewater treatment and surface coatings, was demonstrated in CO_2 photoreduction. Despite its commercial advantages, the photoactivity of TiO_2 is limited by its large band gap, which confines its light absorption to the UV spectrum and causes rapid electron-hole recombination [7].

Various modification techniques were developed to enhance the photoactivity of TiO_2, including Metal Nanoparticle Incorporation: Metal nanoparticles facilitate charge separation and slow down the electron-hole recombination. Metal Doping, introducing metals into TiO_2, induces visible light absorption by narrowing the band gap. Conversion to Black TiO_2, creating black TiO_2 involves removing oxygen from TiO_2's structure under reducing conditions, such as treatment with reducing agents like ascorbic acid or thermal reduction in inert atmospheres. This process generates defects, such as oxygen vacancies and reduced Ti^{3+} sites, which act as active sites for CO_2 photoreduction. And Amines Functionalization, functionalizing TiO_2 with amines improves surface interactions with CO_2. Studies by our group revealed that triethanolamine (TEA), among primary, secondary, and tertiary alkanolamines, exhibited superior photoactivity for CO_2 conversion. TEA-functionalized TiO_2 achieved high yields of methane, acetaldehyde, methanol, ethanol, isopropanol, and acetone [2].

This research synthesizes and tests a TEA-copper black TiO_2 (TEA-Cu-BT) photocatalyst for CO_2 photoreduction. The commercial-grade P25 TiO_2 would be converted into black TiO_2 (BT) nanoparticles and modified with copper metal (Cu) and TEA. The photocatalyst could enhance the conversion of dissolved CO_2 in water into target products, including methane, acetaldehyde, methanol, ethanol, isopropanol, and acetone.

2. EXPERIMENTAL

2.1. CO_2 Photoreduction

A photocatalyst suspension was prepared by suspending 2 mg of photocatalyst in 20 mL DI water under ultrasonication. The suspension was saturated with dissolved CO_2 by passing a CO_2 stream in it for 20 min and was positioned under the mercury lamp (Philips, 160 W) for 5 hours for photoreduction. Products from the gas and liquid phases were collected and analyzed separately for their compositions using Gas chromatography techniques.

2.2. Synthesis of BT

500 mg of P25 TiO_2 Sigma-Aldrich was ground using an analytical-grade mortar and mixed with 4.5 mL of ascorbic acid solution (1.32 M) [1]. The blend was dried and heated at 105 ˚C for 30 mins and ground to ensure uniform powder mixing. The powder was calcined inside a furnace at 500 ˚C for 30 mins with a 10 ˚C/min ramp rate and was lowered to room temperature. The BT powder was obtained and kept in a desiccant for future uses.

2.3. Synthesis of the Cu-BT

500 mg of P25 TiO_2 Sigma-Aldrich was mixed with 5 mL solution of $Cu(NO_3)_2$, containing 97 mg $Cu(NO_3)_2$ (5%w/w of Cu/P25) in DI water. The mix was heated in an oven at 105 ˚C for 30 mins and blended with 4.5 mL of ascorbic acid solution (1.32 M). The mix was heated in the oven at 105 ˚C for 30 mins once again to obtain a dry mixed powder. The powder was ground to ensure uniform particle distribution and calcined at 500 ˚C for 30 min. [1] The Cu-BT was kept in the desiccator for future uses.

2.4. Synthesis of the TEA-BT and TEA-Cu-BT.

A suspension of either BT or Cu-BT was prepared by suspending 200 mg powder in a 3:7 %v/v solution of ethanol and DI water. 10 mmol of TEA was added to the suspension, and the mix was transferred to a hydrothermal reactor. The mix was heated at 180 ˚C for 6 hours before being rinsed with ethanol and DI water. The powder was dried in a vacuum oven at 80˚C for 24 hours.[2]

3. RESULTS AND DISCUSSION

3.1. CO_2 Photoreduction

Our preliminary results on CO_2 photoreduction exhibited photoactivity of the photocatalysts (Figure 1). Photoactivity was studied by monitoring the production of the five target products: methane, acetaldehyde, methanol, ethanol and acetone. The total carbon consumption was determined using the following correlation,

$$\text{Total Carbon Consumption} = [\,(\text{Methane} \times 1) + (\text{Acetaldehyde} \times 2) + (\text{Methanol} \times 1) + (\text{Ethanol} \times 2) + (\text{Acetone} \times 3)\,] \quad (1)$$

Gas and liquid products were collected and analyzed, shown in Figure 2 (a) and (b), respectively. P25 assisted in the CO_2 photoreduction, yielding 3.05, 0.04, 0.1, and 0.93 $\mu mol/g_{CAT}$ of methane, acetaldehyde, acetone, and ethanol in the gas phase.

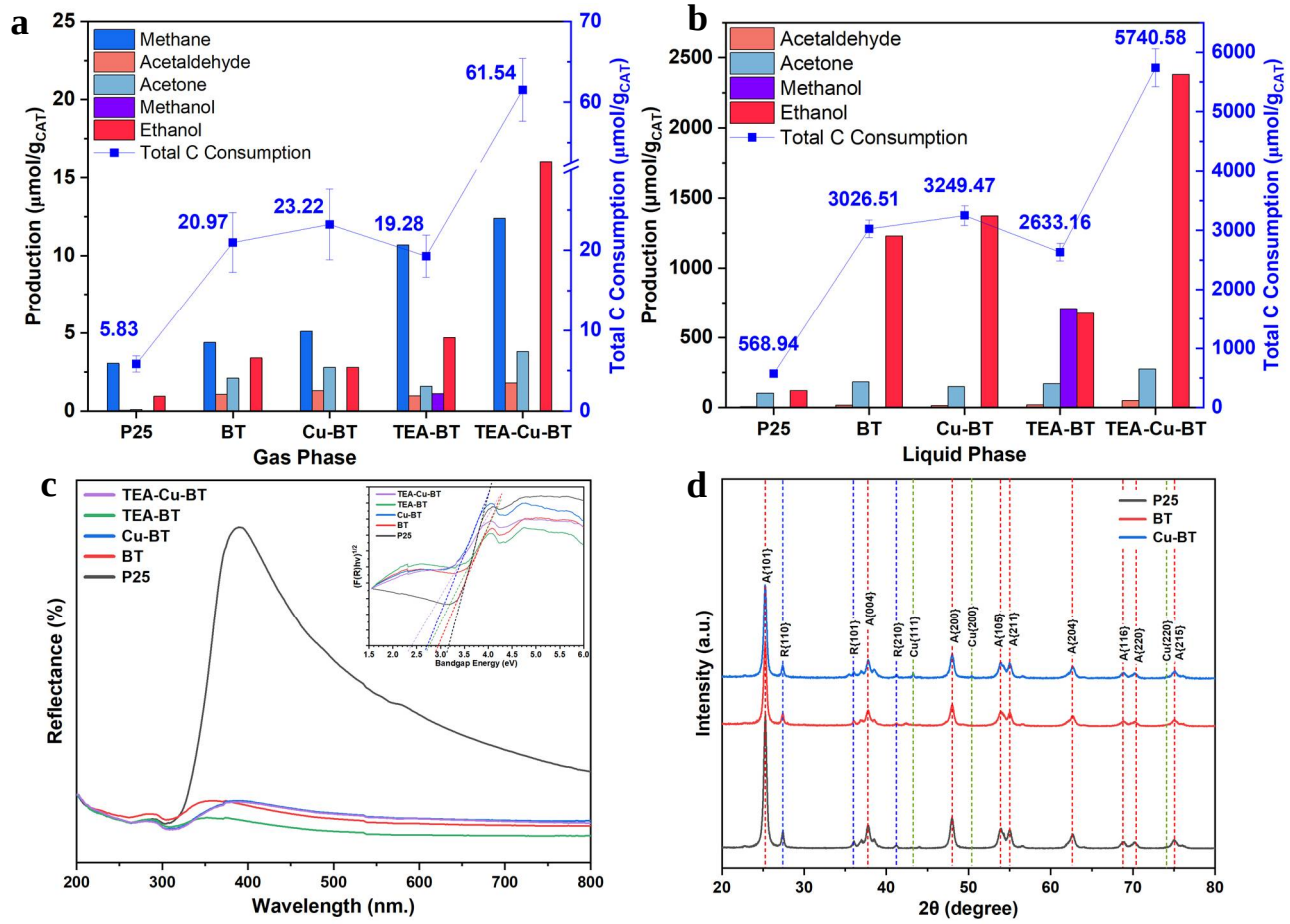

Figure 2 Products from the CO_2 photoreduction in gas phase (a) and liquid phase (b), Photocatalyst analysis using UV-Vis Diffuse Reflectance Spectroscopy (DRS) (c).X-ray diffraction (XRD) result (d).

The total carbon consumption was 5.83±0.99 μmol/g_{CAT}. Liquid phase products from the P25 gave 5.13, 103.24, and 121.89 μmol/g_{CAT} of acetaldehyde, acetone, and ethanol with a total carbon consumption of 568.94±50 μmol/g_{CAT}. BT produced gas products of methane, acetaldehyde, acetone, and ethanol at 4.4, 1.06, 2.1, and 3.4 μmol/g_{CAT} and a total carbon consumption of 20.97±3.7 μmol/g_{CAT}. The BT's liquid products were analyzed as 16.57, 184.12, and 1229.27 μmol/g_{CAT} of acetaldehyde, acetone, and ethanol with a total carbon consumption of 3026.51±150 μmol/g_{CAT}. The Cu-BT provided 5.11, 1.3, 2.8, and 2.8 μmol/g_{CAT} of methane, acetaldehyde, acetone, and ethanol in the gas consumption of 23.22±4.4 μmol/g_{CAT}. Liquid products showed 15.19, 151.76, and 1374.23 μmol/g_{CAT} of acetaldehyde, acetone, and ethanol with a total carbon consumption of 3249.47±167 μmol/g_{CAT}. The TEA-BT produced 10.7, 0.96, 1.58, 4.7, and 1.12 μmol/g_{CAT} of gas-phase methane, acetaldehyde, acetone, ethanol, and methanol. The total carbon consumption was 19.28±2.6 μmol/g_{CAT}. TEA-BT's liquid products, including acetaldehyde, acetone, ethanol, and methanol, were 19.59, 170.72, 676.44, and 709.3 μmol/g_{CAT}, giving a total carbon consumption of 2633.16±147 μmol/g_{CAT}. The TEA-Cu-BT gas-phase products were 12.39, 1.8, 3.8, and 16.03 μmol/g_{CAT} of methane, acetaldehyde, acetone, and ethanol, with a total carbon consumption of 61.54±3.9 μmol/g_{CAT}. Its liquid products were 50.84, 275.12, and 2381.67 μmol/g_{CAT} of acetaldehyde, acetone, and ethanol, which corresponded to a total carbon consumption of 5740.58±320 μmol/g_{CAT}.

3.2. UV-Vis Diffuse Reflectance Spectroscopy (DRS)

Photocatalysts were analyzed using UV-Vis Diffuse Reflectance Spectroscopy (DRS) within the 200 to 800 nm range (Figure 2 (c)). Reflection peaks at 427, 358, 397, 327, and 395 corresponded to P25, BT, Cu-BT, TEA-BT, and TEA-Cu-BT samples. P25 shows light absorbance only in the UV region, while the BT, Cu-BT, TEA-BT, and TEA-Cu-BT present the visible light vacancy) on BT altered the light reflectance within the visible range, causing the reflectance peak to occur at the lowered wavelength. The light reflection balanced well in the visible region for BT, Cu-BT, TEA-BT, and TEA-Cu-BT, which indicated enhanced visible light absorption. Optical band gaps were determined using the Kubelka–Munk function (F(R), Eq 1) and the Tauc's correlation (Eq.2), in which R is the reflectance from the DRS, h is the Planck constant, ν is the photon frequencies, B is a constant, and Eg is bandgap energy. The power is ½, representing an indirect transition mode of electron transfer.

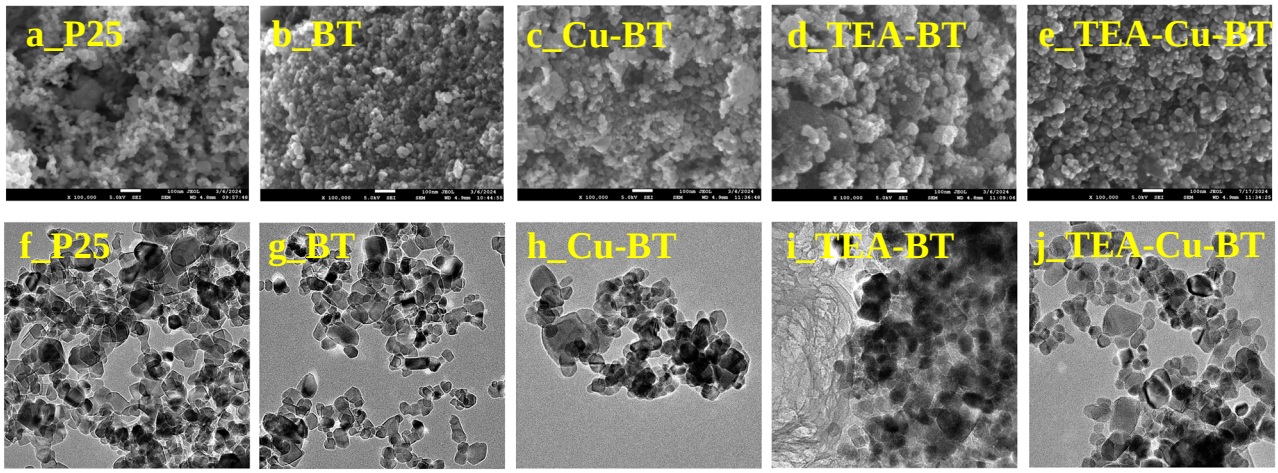

Figure 3 SEM image 100,000×; (a) P25, (b) BT, (c) Cu-BT, (d) TEA-BT, (e) TEA-Cu-BT And TEM image 150,000×; (f) P25, (g) BT, (h) Cu-BT, (i) TEA-BT, (j) TEA-Cu-BT.

$$F(R) = (1-R)^2/2R \quad (2)$$

$$(F(R)h\nu)^{1/2} = B(h\nu - Eg) \quad (3)$$

The bandgaps were 3.16, 2.95, 2.7, 2.75, and 2.39 eV for the P25, BT, Cu-BT, TEA-BT, and TEA-Cu-BT. The band gap indicates the width of the energy barrier between valence and conductive bands, correlated to the number of active electrons involved in the photoreduction. The results supported the idea that TEA-Cu-BT provided outstanding photoactivity and should be an excellent sample for the CO_2 photoreduction test.

3.3. X-ray diffraction (XRD)

XRD analyzed the crystal structure of the photocatalysts (Figure 2 (d)). P25 and BT provide similar XRD spectra, suggesting equivalent crystal structures of anatase and rutile TiO_2. The anatase TiO_2 exhibits peaks at 25.32°, 37.85°, 48.05°, 53.96°, 55.08°, 62.74°, 68.85°, 70.31°, 75.12°, and 82.73° which corresponds to {101}, {004}, {200}, {105}, {211}, {204}, {116}, {220}, {215}, and {224} planes, respectively.

The rutile phase occurs at 27.44°, 36.07°, and 41.24° of XRD spectra, representing {110}, {101}, and {111} planes, respectively. The significant difference between BT and P25 was observed at the A{101} peak, in which the peak signal was significantly lower for BT compared to P25. The result indicates the presence of oxygen vacancies in BT, which reduces the signal from {101} plant of the anatase TiO_2. For Cu-BT, Cu-Ti complex structures were observed at 38.73°, 38.96°, and 68.12°, which corresponds to {110}, {200}, and {220} planes of the Ti-Cu.

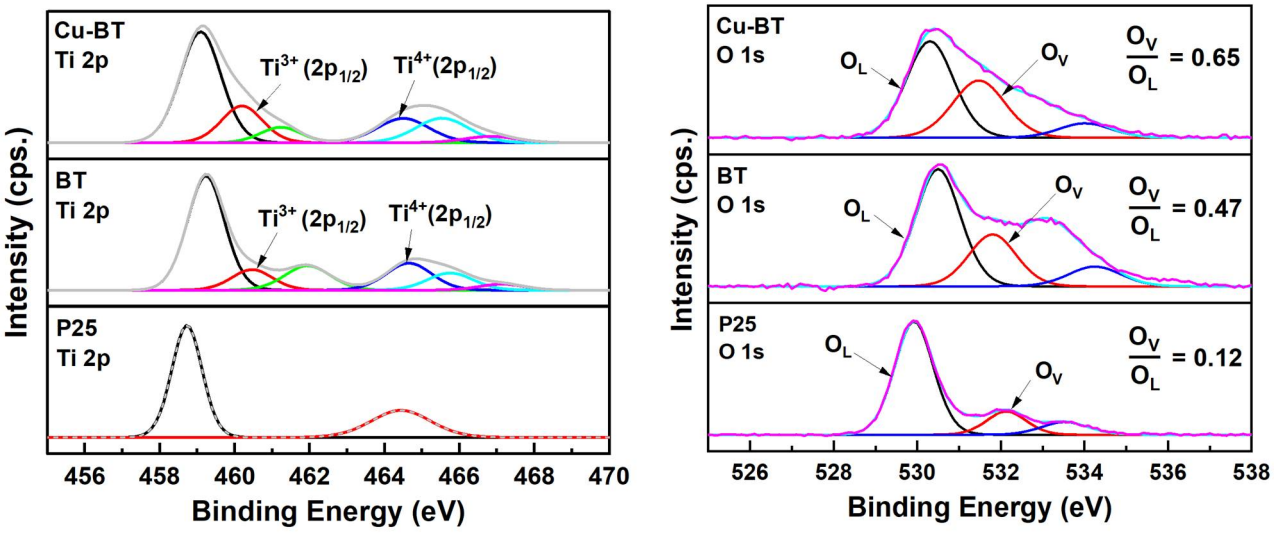

Figure 4 XPS analysis showing deconvoluted spectra of Ti 2p (a), O 1s (b).

Table 1 Summary of CO_2-TPD analysis, showing CO_2 desorption temperature, corresponding to weak (α), medium (β), and strong (γ) basic sites, amounts of basic sites, and total basic sites per triethanolamine.'

				Amount of the basic sites ($umol_{CO2}/g_{CAT}$)				
Catalyst	T_α	T_β	T_γ	α	β	γ	total	total basic site (mol_{CO2}/mol_N)
P25	100	210	420	8.5	15.8	4.8	29.0	-
BT	100	220	540	9.7	18.3	76.3	104.4	-
TEA-BT	110	330	580	12.3	92.1	27.4	131.7	0.090

3.4. Scanning electron microscope (SEM) & Transmission electron microscope (TEM)

The physical structures of the photocatalysts were analyzed using FE-SEM and cryogenic TEM (Figure 3). The photocatalysts were determined to be a rounded-edge square. P25, BT, Cu-BT, TEA-BT, and TEA-Cu-BT have average diameters of 22.25, 20.14, 24.36, 24.64, and 23.64 nm, respectively. The results suggest that not much change happens regarding surface morphology, regardless of critical modification performed on the photocatalysts.

3.5. X-ray Photoelectron Spectroscopy (XPS)

XPS revealed chemical compositions of the photocatalysts. The narrow scan on Ti 2p region of P25 shows a strong signal correlated to Ti^{4+} $2p_{1/2}$ species at 464.4 eV. BT gives new peaks, indicating the presence of Ti^{3+} $2p_{1/2}$ at 461.9 eV (Figure 4 (a)). The Ti^{3+} components partly contribute to structural defects in BT, providing solid evidence for the outstanding photoactivity of the BT over P25. The Cu-BT yields a narrow scan similar to the BT, showing peaks at 464.4 eV for Ti^{4+} $2p_{1/2}$ and 460.2 eV for Ti^{3+} $2p_{1/2}$. We indicate oxygen vacancy in the O 1s orbital (Figure 4 (b)) and analyze the level of the defect using the ratio of Oxygen vacancy (O_V)/Oxygen lattice (O_L). The O_V/O_L ratios for P25, BT, and Cu-BT are 0.12, 0.47, and 0.65, respectively. The O_V contributes as the other part of the structural defect for BT. The P25 conversion to BT causes a significant increase in the O_V/O_L ratio [3], while adding Cu to BT (Cu-BT) reduces the ratio. Adding Cu to BT promotes Ti^{3+} peak intensity and the formation of oxygen vacancies [2], enhancing photocatalytic activity. It is worth noting that the Fermi level of Cu is lower than TiO_2, resulting in electron transfer from TiO_2 to Cu for stability.

3.6. CO_2 temperature-programmed desorption (CO_2-TPD)

CO_2-TPD experiments were conducted to investigate the basicity and functional group on P25, BT, and TEA-BT (**Figure 5**). CO_2 desorption occurs as a function of the temperature, indicating CO_2-photocatalyst weak (α), medium (β), and strong (γ) interactions. The total CO_2 desorption for P25 TiO_2, BT, and TEA-BT were 29, 104.4, and 131.7 $\mu mol_{CO2}/g_{CAT}$. The weak site (α) appeared within the 80-120 °C CO_2 desorption temperature range and can be ascribed to the -OH group for all the photocatalysts. For P25 and BT, medium and strong sites occurred at 150 – 300 °C, representing CO_2 interaction with oxygen vacancies in the samples. For TEA-BT, the influence of the TEA was noticed in the medium basicity interaction at 300 – 450 °C, while a strong basic site was associated with CO_2 interaction with oxygen vacancies and Ti^{3+} in the structure. Results from the CO_2-TPD were analyzed with XPS analysis to summarize basicity sites on the photocatalyst samples (Table 1). Assuming TEA-CO_2 interactions contribute to the medium size (β), adsorption yields the CO_2 adsorption per amine at 0.090 mol_{CO2}/mol_{N2}.

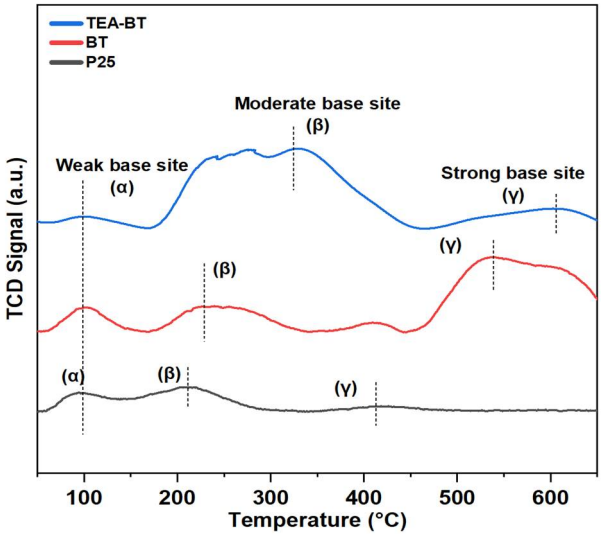

Figure 5 CO_2 temperature program desorption.

4. CONCLUSION

We synthesized and demonstrated outstanding photoactivity of TEA-Cu-BT in CO_2 conversion. The commercial-grade P25 TiO_2 was converted to BT, doped with Cu, and functionalized with TEA to realize more than 10-fold the product generation rate. The best results exhibited CO_2 photoreduction products of methane, acetaldehyde, acetone, and ethanol at a total carbon consumption of 61.54 $\mu mol/g_{CAT}$ and 5,740.58 $\mu mol/g_{CAT}$ for the gas and liquid phase, respectively. This superior performance is the result of the high electron donating ability of the BT, TEA-CO_2 interactions, and enhancement in electron-hole separation due to Cu dopant. Improvement in the photoactivity of the commercial grade P25 would mark

another step closer to a net zero society, in which CO_2 photoreduction was used as an alternative for the CCS technologies.

ACKNOWLEDGMENTS

We are grateful to the financial support from the Research CESS Fund of the Malaysia-Thailand Joint Authority (MTJA). We thank the Mahidol University Frontier Research Facility (MU–FRF), and the Department of Chemical Engineering Central lab for the technical support in material and chemical analysis.

REFERENCES

1. Coto M, Divitini G, Dey A, Krishnamurthy S, Ullah N, Ducati C, et al. Tuning the properties of a black TiO_2-Ag visible light photocatalyst produced by a rapid one-pot chemical reduction. Materials Today Chemistry. 2017;4:142-9.
2. Karawek A, Kitjanukit N, Neamsung W, Kinkaew C, Phadungbut P, Seeharaj P, et al. Alkanolamine-Grafted and Copper-Doped Titanium Dioxide Nanosheets–Graphene Composite Heterostructure for CO_2 Photoreduction. ACS Applied Energy Materials. 2023;6(21):10929-42.
3. Zhao J, Li Y, Zhu Y, Wang Y, Wang C. Enhanced CO_2 photoreduction activity of black TiO_2–coated Cu nanoparticles under visible light irradiation: Role of metallic Cu. Applied Catalysis A: General. 2016;510:34-41.
4. Saensook S, Sirisuk A. A factorial experimental design approach to obtain defect- rich black TiO_2 for photocatalytic dye degradation. Journal of Water Process Engineering. 2022;45.
5. Kapica-Kozar J, Piróg E, Kusiak-Nejman E, Wrobel RJ, Gęsikiewicz-Puchalska A, Morawski AW, et al. Titanium dioxide modified with various amines used as sorbents of carbon dioxide. New Journal of Chemistry. 2017;41(4):1549-57.
6. Chen C, Yang S-T, Ahn W-S. Calcium oxide as high temperature CO_2 sorbent: Effect of textural properties. Materials Letters. 2012;75:140-2.
7. Ni M, Leung MKH, Leung DYC, Sumathy K. A review and recent developments in photocatalytic water-splitting using TiO_2 for hydrogen production. Renewable and Sustainable Energy Reviews. 2007;11(3):401-25.

Synthesis, swelling behavior, and niacinamide release of 1,4-butanediol diglycidyl ether-crosslinked levan hydrogels from *Bacillus siamensis*

Pongtorn Phengnoi[1], Cherdphong Seedao[1], Suphak Nakthongkham[1], Pitchayanin Intarawichai[1], Phumipat Saelao[1], Witawat Jangiam[1,*]

[1] Department of Chemical Engineering, Faculty of Engineering, Burapha University, Chonburi 20131, Thailand
[*] Corresponding author: witawat@eng.buu.ac.th

ABSTRACT

Levan is a fructan polysaccharide used in a broad range of applications, including cosmetics, pharmaceuticals, and medicine. This study focused on the synthesis of hydrogel based on levan produced from *Bacillus siamensis* crosslinked with 1,4-butanediol diglycidyl ether (BDDE) to control niacinamide release. The swelling level of levan hydrogel was observed at different levan concentrations (5, 7, and 10%w/v), pH values (5.5, 7.4, and 9.0), and temperatures (25, 32, 37, and 50 °C). The results showed that levan concentrations affected both the strength of the hydrogel structure and the swelling level, with 10% w/v levan exhibiting the highest swelling level of 2.64. Levan hydrogel (10% w/v levan) demonstrated a higher swelling level in Tris-HCl buffer (pH 9.0) compared to phosphate-buffered saline (pH 7.4) and acetate buffer (pH 5.5). However, temperatures ranging from 25 to 50 °C had a minor effect on the swelling level of the levan hydrogel. In a 10%w/v levan hydrogel, niacinamide entrapment reached 31.27%, and release reached 93.83% within 35 minutes. These results indicate levan has potential in drug delivery applications.

Keywords: Levan; Hydrogel; Niacinamide; *Bacillus siamensis*

1. INTRODUCTION

Niacinamide, also called nicotinamide and vitamin B3, is a water-soluble active ingredient with various applications such as an anti-wrinkle agent, an anti-inflammatory agent, an antioxidant agent, an anti-skin cancer agent, a moisturizer, and a hyperpigmentation reducer [1, 2]. However, high concentrations of niacinamide have shown cytotoxic effects on human keratinocytes [3] and can cause skin irritation, such as flushing [4].

Controlled release systems are an emerging technology in medical applications that can help prevent medicine overdose in therapy [5]. Hydrogels, cross-linked polymer networks with a nano-based matrix, have been used in various medical applications for the delivery and controlled release of drugs to target organelles. Previous research has synthesized hydrogels from levan-based polymers to achieve the controlled release of drugs and active ingredients such as Amphotericin B [6], Aminosalicylate [7], and Hydroxyapatite [8]. Levan, a natural polysaccharide, is composed of repeating D-fructofuranosyl units linked primarily by β-(2, 6) glycosidic bonds, with a D-glucose unit at the terminal end [9]. Levan has been synthesized by many microorganisms, such as *Bacillus licheniformis* [9], *B. subtilis* 168 [10], *Lactobacillus johnsonii*, *L. gasserii*, and *Streptococcus salivarius* [11]. The molecular weight of levan varies depending on the microorganism species and culture conditions. For instance, *Acinetobacter nectaris* produced levan ranging from 1,000 to 6,000 kDa, while *B. atrophaeus* produced levan ranging from 15 to 90 kDa. Furthermore, the sucrose concentration in the culture medium influenced the molecular weight distribution of levan, with higher sucrose concentrations typically resulting in a primary fraction of high molecular weight. Levan is used in many applications because it has various biological properties such as antioxidant, anti-inflammatory, prebiotic activity and biocompatibility [12].

Our previous studies isolated a potentially useful microorganism, *B. siamensis*, from fermented soybeans, a traditional food of northern Thailand. We also successfully synthesized levan using *B. siamensis* levansucrase under various conditions, yielding both high and low molecular weight levan, including 10^6 kDa and 30 kDa, respectively. [13, 14]. Moreover, *B. siamensis* levan exhibited potential prebiotic activity by promoting the proliferation of beneficial gut microorganisms, such as *Lacticaseibacillus casei*. Furthermore, levan demonstrated potential as an additive to improve the water barrier of edible films and increase the shelf life of guava fruit [15].

This research focused on the synthesis and characterization of a hydrogel produced from *B. siamensis* levan cross-linked with 1,4-butanediol diglycidyl ether (BDDE) to control niacinamide release.

2. EXPERIMENTAL

2.1 Bacterial strain

B. siamensis, isolated from fermented soybeans according to our previous study, is a gram-positive, rod-shaped bacterium [13, 14].

2.2 Chemicals and culture media

1,4-butanediol diglycidyl ether (BDDE) (AK Scientific, USA) was used as a cross-linker agent. A pre-growth medium comprised of 50 g/L of sucrose, 5 g/L of yeast extract, 10 g/L of tryptone, and 5 g/L of NaCl and a levan production medium consisting of 20 g/L of sucrose, 3.5 g/L of Na_2HPO_4, 0.8 g/L of NaH_2PO_4, 0.2 g/L of $MgSO_4$, 3.5 g/L of $NaNO_3$, and 5 g/L of yeast extract were prepared. pH was adjusted to 6.0 by 0.1 M HCl or NaOH.

2.3 Levan production

B. siamensis was pre-grown in a 250 mL Erlenmeyer flask containing 100 mL of pre-growth medium using an incubator shaker at 37 °C and 200 rpm for 24 h. Following this pre-growth, *B. siamensis* was cultured in 200 mL of levan production medium with a 10% inoculum, fermenting in an incubator shaker at 37 °C and 200 rpm for 48 h. After fermentation, the culture was centrifuged at 6000 rpm and 4 °C for 1 h to separate the cells. The supernatant was precipitated by adding it to a 2-fold volume of ice-cold ethanol and then stored at 4 °C for 24 hours. The precipitate was washed and resuspended in DI water. Afterward, the resuspended solution was dialyzed using a membrane (MWCO: 12-14 kDa) for 3 days. The dialyzed solution was then dried by lyophilization.

2.4 Levan hydrogel preparation

Levan-based hydrogel was prepared by adding levan and niacinamide to a 10% (w/v) BBDE solution (in 0.25 M NaOH) to achieve final concentrations of levan at 5%, 7%, and 10% (w/v) and niacinamide at 1% (w/v). The mixture was gently stirred for 30 minutes and then stored at 40 °C for 24 h. Afterward, the mixture was dried at 60 °C for 48 h.

2.5 Swelling level test for levan hydrogels

The swelling level of the hydrogels was measured by soaking dried hydrogels in 10 mL of DI water. The hydrogel was blotted to remove excess water and then weighed every 30 seconds for 5 minutes. The swelling level was determined using equation (1)

$$Swelling\ level = \frac{Ws}{Wd} \quad (1)$$

Where W_s is swelled weight of levan hydrogel
W_d is the dried weight of levan hydrogel

The synthesized hydrogel with the levan concentration that resulted in the highest swelling level was observed for its swelling behavior at various pH values (5.5, 7.4, and 9.0) and temperatures (25, 32, 37, and 50 °C).

2.6 Niacinamide entrapment and controlled release

Levan hydrogels were dissolved in 100 mL of DI water and then stirred until completely dissolved. The resulting solution was filtered using a 0.2 µm nylon filter to remove any undissolved particles. The filtrate's optical density was measured at 291 nm to determine the total entrapped niacinamide.

Niacinamide release was measured by soaking the levan hydrogel in 100 mL of DI water. The optical density of the solution was measured at 291 nm every 5 minutes for 35 minutes.

3. RESULTS AND DISCUSSION

3.1 Swelling level of levan hydrogels

The swelling property of levan hydrogels, which involves hydrophilicity, depends on both the properties of levan and the network structure of levan hydrogel (cross-linking). The water uptake of these levan hydrogels was expressed as a swelling level to compare the suitability of hydrogels produced with different levan concentrations.

The morphology of hydrogels made from levan at 5%, 7%, and 10% (w/v), cross-linked with 10% (w/v) BDDE via a reaction between the hydroxyl groups of levan and the epoxide groups of BDDE, is shown in Fig. 1.

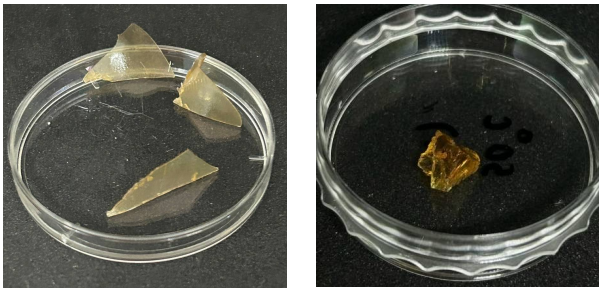

(a) (b)

Figure 1 *B. siamensis* levan hydrogel (a) dried and (b) swollen in water.

According to the swelling levels shown in Fig. 2, levan hydrogels with 5% and 7% (w/v) levan were unstable in DI water, dissolving completely in 30 and 60 seconds, respectively. On the other hand, the levan hydrogel with 10% (w/v) levan exhibited greater stability in DI water, swelling to a level of 2.64. These results suggest that the concentration of levan and the hydroxyl groups of levan contribute to a stronger hydrogel structure [16].

3.2 The effect of pH and temperature on swelling behavior of levan hydrogel

The swelling behavior of the levan hydrogel 10%

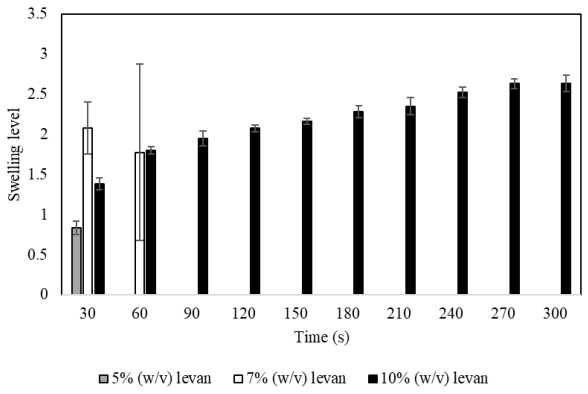

Figure 2 Swelling levels of levan hydrogels with 5%, 7%, and 10% (w/v) levan concentrations in DI water after 5 minutes.

10% (w/v) levan was investigated across a range of pH values, including 5.5 (acetate buffer), 7.4 (phosphate buffered saline, PBS), and 9.0 (Tris-HCl buffer) at room temperature. The resulting swelling levels are depicted in Fig. 3. Notably, the highest swelling level was observed at pH 9.0 in the Tris-HCl buffer, reaching a value of 2.29 after 300 seconds. In contrast, the hydrogel exhibited lower swelling levels of 2.15 and 2.16 at pH 5.5 and 7.4 respectively. These behaviors occurred due to the increased ionization with rising pH, which induced electrostatic repulsion between the negative charges on the levan structure, resulting in matrix expansion [6, 17].

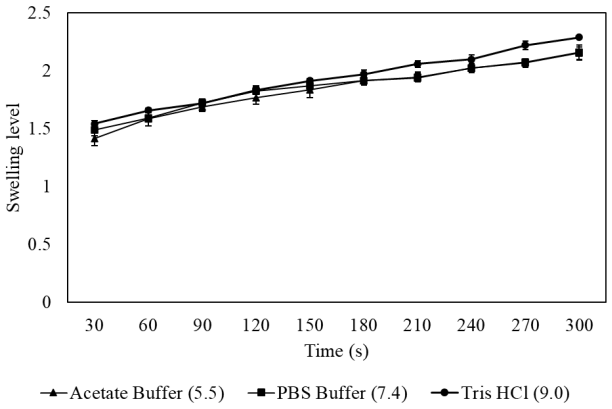

Figure 3 Swelling levels of 10% (w/v) levan hydrogels at pH 5.5, 7.4, and 9.0 after 5 minutes.

The swelling behavior of the levan hydrogel at different temperatures (25, 32, 37, and 50 °C) is illustrated in Fig. 4. The temperature had a slight impact on the swelling level of the levan hydrogel, consistent with a previous report on hydrogel synthesis from *Halomonas* levan cross-linked with BDDE for antifungal drug entrapment [6]. These findings suggest the robust nature of levan hydrogels, enabling their utilization across a spectrum of environmental temperatures. This versatility positions them favorably for applications spanning controlled indoor settings to more variable outdoor environments.

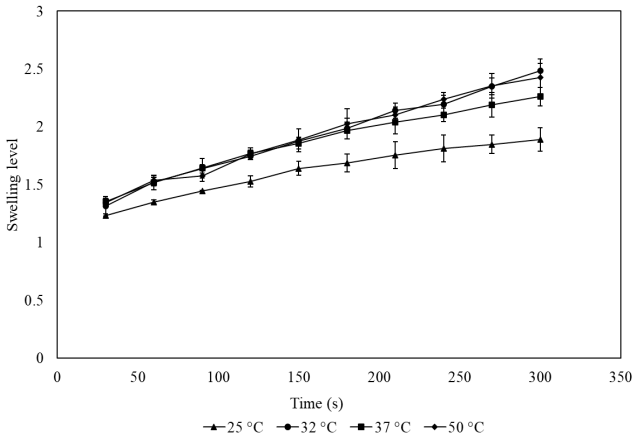

Figure 4 Swelling levels of 10% (w/v) levan hydrogels at different temperatures including 25, 32, 37, and 50 °C 5 minutes.

3.3 Niacinamide entrapment and release

levan hydrogel was dissolved in 10 mL of DI water. After complete dissolution and filtration of the solution, its optical density was measured to determine the niacinamide content. The levan hydrogel was found to contain 31.27% of total niacinamide. Niacinamide release, as shown in Fig. 5, was rapid within the first 5 minutes, reaching 35.65%, and then slightly increased to 93.83% after 35 minutes. According to a previous report, the release of niacinamide depended on the swelling ability and cross-linking degree of the hydrogel. Consistent with this, the *Halomonas* levan hydrogel exhibited an increased release of the active ingredient as the levan concentration increased [16].

These compelling results have clearly demonstrated the controlled active ingredient release capability inherent to the levan hydrogel matrix. This key attribute strongly suggests its promising potential for broad application across diverse fields. These include advanced drug delivery systems with tunable release profiles, pharmaceutical formulations for enhanced therapeutic efficacy, various applications within the realm of medicine, and innovative uses in both cosmetic and cosmeceutical formulations aimed at targeted skin benefits.

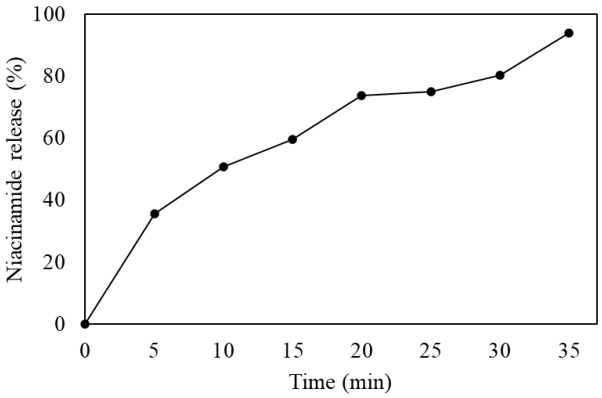

Figure 5 Niacinamide release profile of *B. siamensis* levan hydrogel.

4. CONCLUSION

Levan hydrogels, synthesized using *B. siamensis* levan and cross-linked with BDDE, have shown significant promise as effective nanocarriers for the controlled release of niacinamide. Notably, levan hydrogels formulated with a 10% (w/v) levan concentration demonstrated remarkable stability and sustained functionality across a broad spectrum of pH values and temperatures. This robust performance profile strongly suggests their potential for versatile utilization in a wide array of conditions and diverse applications spanning the pharmaceutical, medical, and cosmetic industries. Furthermore, the levan hydrogel formulation investigated in this study demonstrated a near-complete release of niacinamide within a relatively short timeframe. This characteristic rapid release profile, while potentially advantageous in certain contexts, may not be optimal for applications requiring sustained or prolonged delivery of specific active pharmaceutical ingredients or other beneficial compounds. Therefore, the use of levan hydrogels should consider their properties, such as swelling and release rate, to ensure suitability for specific applications.

ACKNOWLEDGMENTS

This study was funded by the Department of Chemical Engineering, Faculty of Engineering, Burapha University, Thailand. The utilized laboratory facilities provided by the Department of Chemical Engineering, Faculty of Engineering, and the Faculty of Pharmaceutical Sciences, Burapha University, Thailand.

REFERENCES

1. N.F. binti Sukor, R. binti Jusoh, N.S. binti Kamarudin. Controlled release of niacinamide from fibrous silica nanocarrier in face serum formulation. *Materials Today: Proceedings* 2024; 107: 46-52.
2. S.Y. Lee, G. Ahn, S.D. Yoon. Preparation of niacinamide imprinted starch-based biomaterials for treating of hyperpigmentation. *International Journal of Biological Macromolecules* 2023; 232: 123382.
3. A.X. Zhen, M.J. Piao, K.A. Kang, P.D.S.M. Fernando, H.K. Kang, Y.S. Koh, J.M. YI, J.W. Hyun. Niacinamide Protects Skin Cells from Oxidative Stress Induced by Particulate Matter. *Biomol Ther (Seoul)* 2019; 27(6): 562-569.
4. A. Javaid, S.L. Mudavath. Niacin-induced flushing: Mechanism, pathophysiology, and future perspectives. *Archives of Biochemistry and Biophysics* 2024; 761: 110163.
5. G. Xie, S. Lin, F. Wu, J. Liu. Nanomaterial-based ophthalmic drug delivery. *Advanced Drug Delivery Reviews* 2023; 200: 115004.
6. T. Demirci, M.E. Hasköylü, M.S. Eroğlu, J. Hemberger, E.T. Öner. Levan-based hydrogels for controlled release of Amphotericin B for dermal local antifungal therapy of Candidiasis. *European Journal of Pharmaceutical Sciences* 2020; 145: 105255.
7. A. Osman, E.T. Oner, M.S. Eroglu. Novel levan and pNIPA temperature sensitive hydrogels for 5-ASA controlled release. *Carbohydrate Polymers* 2017; 165: 61-70.
8. Y. Hwang, J.S. Lee, H. An, H. Oh, D. Sung, G. Tae, W.I. Choi. Hydroxyapatite-embedded levan composite hydrogel as an injectable dermal filler for considerable enhancement of biological efficacy. *Journal of Industrial and Engineering Chemistry* 2021; 104: 491-499.
9. A. Miranda-Molina, S. Castrejón-Carrillo, G.T. Zavala-Padilla, M. Antúnez-Mojica, L. Alvarez, M.E. Rodríguez-Alegría, A.L. Munguía. Branching and molecular weight in levan: A detailed analysis of structural variability and enzymatic hydrolysis susceptibility. *Carbohydrate Polymers* 2025; 352: 123236.
10. J.R. Porras-Domínguez, Á. Ávila-Fernández, A. Miranda-Molina, M.E. Rodríguez-Alegría, A.L. Munguía. Bacillus subtilis 168 levansucrase (SacB) activity affects average levan molecular weight. *Carbohydrate Polymers* 2015; 132: 338-344.
11. R. Srikanth, C.H.S. Reddy, G. Siddartha, M.J. Ramaiah, K.B. Uppuluri. Review on production, characterization and applications of microbial levan. *Carbohydrate Polymers* 2015; 120: 102-114.
12. G. Mummaleti, C. Sarma, S. Yarrakula, R. Urla, H. Gazula. Production, properties and applications of levan polysaccharide. *Food and Humanity* 2024; 3: 100369.
13. N. Thakham, S. Thaweesak, N. Teerakulkittipong, N. Traiosot, A. Kaikaew, G.A. Lirio, W. Jangiam. Structural Characterization of Functional Ingredient Levan Synthesized by Bacillus siamensis Isolated from Traditional Fermented Food in Thailand. *International Journal of Food Science* 2020; 1: 7352484.
14. P. Phengnoi, N. Thakham, T. Rachphirom, N. Teerakulkittipong, G.A. Lirio, W. Jangiam. Characterization of levansucrase produced by novel Bacillus siamensis and optimization of culture condition for levan biosynthesis. *Heliyon* 2022; 8(12): e12137.
15. P. Phengnoi, S. Sattavanich, C. Charoensup, S. Nuengnoon, K. Janthorn, N. Teerakulkittipong, W. Jangiam. Production and characterization of levan by Bacillus siamensis at flask and bioreactor. *Engineering in Agriculture, Environment and Food* 2023; 16(1): 15-23.

16. S.S. Selvi, M.E. Hasköylü, S. Genç, E. Toksoy Öner. Synthesis and characterization of levan hydrogels and their use for resveratrol release. *Journal of Bioactive and Compatible Polymers* 2021; 36(6): 464-480.
17. J.T. Kim, D.Y. Lee, Y.H. Kim, I.K. Lee, Y.S. Song. Effect of pH on Swelling Property of Hyaluronic Acid Hydrogels for Smart Drug Delivery Systems. *Journal of Sensor Science and Technology* 2012; 21(4): 256-262.

Effects of titanium nitride nanoparticles on the properties of light-responsive polybenzoxazine/epoxidized soybean oil copolymer

Jeremiah Oja[1], Ibrahim Lawan[1], Sarawut Rimdusit[1,*]

[1] Center of Excellence in Polymeric Materials for Medical Practice Devices, Chulalongkorn University, Bangkok 10330, Thailand

[*] Corresponding author: sarawut.r@chula.ac.th

ABSTRACT

This study focused on the effects of titanium nitride nanoparticles (TiN) on the properties of light-responsive shape memory composite. Bisphenol A benzoxazine (BA-a), epoxidized soybean oil (ESO), and TiN ingredients were used to impact rigidity, flexibility, and photothermal effects in the composite, respectively. Different TiN amounts (0, 1, 3, 6, and 9 wt.%) were blended separately in the P(70BA-a/30ESO) copolymer (70/30 wt.%). The blends were heated to ~130^{O}C and stirred until homogenous mixtures were obtained. The mixtures were poured into a silicon mold and cured in an oven at 150°C/hr, 170°C/hr, 180°C/hr, and 200°C/2 hrs. Firstly, the obtained composites were characterized as their flexural properties and viscoelastic properties using a universal testing machine and dynamic mechanical analyzer, respectively. The maximum flexural strength, modulus, and strain values of 176.80 ± 26.5 MPa, 5.58 ± 0.5 GPa, and 4.05 ± 4.0%, respectively, were recorded with the P(70BA-a/30ESO)TiN–(wt.%) composite sample. Also, the glass transition temperature (T_g) of the samples was found to be approximately 179,181,180,174, and 173 ^{o}C for the respective composite samples. Secondly, the obtained T_g values of the composites were used to conduct the shape memory performance experiment with the composite samples using magnified sunlight and infrared (IR) light stimulants. Interestingly, the results achieved reveal that the shape fixity (R_f) and recovery (R_r) ratios and recovery time (T_r) were significantly impacted by the increase in the TiN amounts. Overall, it could be concluded that high-strength and fast light-responsive composite materials have been achieved.

Keywords: Titanium nitride Nanoparticles (TiN); Benzoxazine/Epoxy Copolymer; Shape Memory Property; Light-Responsive Composite; Polymer Composites

1. INTRODUCTION

Shape Memory Polymers (SMPs), a subclass of Shape Memory Materials (SMMs), can recover their original shape upon external stimuli. However, their dependence on temperature, magnetic fields, water-based heating, and Near Infrared Radiation (NIR)[1-4] necessitates more efficient alternatives. While promising in biomedicine, aerospace, and self-healing materials, challenges in reinforcement, functional optimization, and composite development limit their adoption[4, 5]. Enhancing cost-effectiveness, lightweight structures, and deformation capacity is essential for applications in drug delivery, construction, transportation, and textiles[6-11]. Further research is needed to improve SMP performance and expand its practical use.

In recent years, there has been a growing interest in researching light-responsive shape memory effects, primarily because of their potential for applications that entail spatial precision and remote control, particularly at lower operating temperatures. Additionally, this photo-responsive behavior can be easily turned on or off by simply controlling the light source. To enable such photo-induced shape memory functionalities, it is crucial to incorporate specific types of additives, such as organic dyes, nanomaterials like gold nanoparticles and nanorods, and carbon-based materials like carbon nanotubes and graphene nanoplatelets. These additives can convert light energy into heat, thus enabling the photothermal effect within the shape memory [12].

Polybenzoxazine resins exemplify cutting-edge thermosetting phenolic resins synthesized from a mixture of phenol, aniline, and paraformaldehyde via the Mannich condensation reaction. This type of thermosetting resin employs ring-opening polymerization without the need for solvents or the release of by-products [13]. Recognized for its remarkable qualities, polybenzoxazine offers a high glass transition temperature, excellent thermal stability, robust mechanical strength, hydrophobicity, low dielectric constant, good adhesive properties, and strong resistance to fire and chemicals. These resins are divided into monofunctional and bifunctional

benzoxazine monomers, with various chemical structures synthesized to optimize specific characteristics[12].

Epoxy resin is a widely used thermoset known for its low glass transition temperature, high deformability, toughness, mechanical strength, and resistance to heat and electricity. Shape memory epoxies, valued for these properties, have gained significant interest in both industry and academia. They are extensively used in adhesives, electronics, smart devices, textiles, and wearable equipment[4]. Epoxidized soybean oil (ESO), obtained from soybean oil via epoxidation, is a sustainable, environmentally friendly, and economical resource commonly utilized in the synthesis of polymers and the production of plastics[14]. Its reactive epoxy groups render it an advantageous green plasticizer and resin for creating value-added products, supporting sustainability and environmental protection initiatives [15, 16].

Photothermal Shape Memory Polymer Composites (SMPCs) are photo-responsive SMMs that contain a photothermal filler or additives incorporated in a polymer matrix. This polymer matrix is significantly a thermal SMM, and it accomplishes an indirect response to light triggering by combining it with photothermal additives or fillers. Hence, Photothermal SMPs respond excellently to light and thermal triggering. These SMPCs exhibit a transformation of temperature when shape memory functions occur. This type of SMM is of diverse forms, and its shape memory performance changes significantly. Examples of photothermal materials are derived from carbon, metallic, and metal oxide materials. Photothermal materials can convert light energy into heat energy efficiently. As such, the essence of photothermal additives or fillers is to transfer light into heat. The conversion of SMPCs from light to thermal energy is the same.

Recently, petroleum-based shape memory polymers (SMPs) have been widely applied in food packaging, pharmaceuticals, cosmetics, and automotive industries. To provide a more sustainable alternative, our research group previously developed bio-based SMP systems by copolymerizing benzoxazine (BZ) with epoxidized vegetable oils [17]. In that study, titanium nitride (TiN) nanoparticles were incorporated as light-absorbing fillers to enhance the sunlight-responsive shape memory performance of the system. The incorporation of TiN improved the shape recovery ratio (Rr) by approximately 8.2% under normal sunlight and 17% under magnified sunlight, while the recovery time (Tr) was reduced from 130 to 120 seconds under normal sunlight and averaged 38 seconds under magnified sunlight. Despite these promising results, the system exhibited limitations in terms of mechanical properties, incomplete recovery under natural sunlight exposure, and relatively moderate thermal stability, which could restrict its practical applications in more demanding environments.

In this work, we focus on bisphenol A-aniline-based benzoxazine (BA-a) and epoxidized soybean oil (ESO) as our polymer matrix to enhance the material's performance. BA-a is recognized for its exceptional thermal stability, high crosslink density, and impressive mechanical strength, while ESO contributes flexibility and a bio-based origin. By merging BA-a with ESO, we seek to establish an optimized balance of mechanical strength, flexibility, and solar-responsive shape memory behavior. This strategy not only overcomes the limitations identified in our earlier system but also fosters the creation of high-performance, sustainable shape memory polymers (SMPs) suitable for real-world outdoor use.

The focus of this study is to determine the effects of the different weight contents (1, 3, 6, and 9 wt%) of Titanium nitride Nanoparticles (TiN) on the light-responsive shape memory and mechanical properties of the resulting Poly(70BA-a/30ESO) copolymer. The obtained composite samples were characterized to assess shape memory performance as well as flexural and viscoelastic properties. The shape memory evaluation was carried out using Near Infrared Radiation (NIR) and magnified sunlight as stimulants. The flexural properties and viscoelastic properties were obtained using a universal testing machine and dynamic mechanical analyzer, respectively. This research successfully produced a composite exhibiting rapid light-responsive shape memory and outstanding mechanical performance properties.

2. EXPERIMENTAL

2.1 Materials used

Bisphenol-A was supplied by PTT Phenol Co., Ltd. (Thailand), and Epoxidized Soybean Oil by Satya Cashew Products (India). Paraformaldehyde (95%) was sourced from Merck Co., Ltd. (Germany), while Aniline (AR grade) was obtained from Loba Chemie Pvt. Ltd. All chemicals used were of high purity and analytical grade.

2.2 Preparation of shape memory polymers based on BA-a/ESO copolymers

The Benzoxazine monomer was synthesized by reacting Bisphenol-A, Aniline, and Paraformaldehyde in a 1:2:4 molar ratio. The mixture was stirred at 1 rpm in an aluminium pan at 393 K (120°C) for an hour. After removing volatiles under reduced pressure, the light-yellow Benzoxazine monomer (BA-a) was allowed to dry overnight at room temperature.

The obtained BA-a was finely reduced and mixed with ESO at a 70/30 weight ratio. The blend was gently stirred at 120°C for 10 minutes until a homogeneous mixture was achieved. The homogenous mixture was poured into a silicon mold, and before subjecting it to a stepwise thermal curing process in an oven at specific

temperature intervals: 150°C/hour, 170°C/hour, 180°C/hour, and finally 200°C/2 hours. After the curing process was completed, the copolymer was allowed to cool at room temperature. The cured Poly(70BA-a/30ESO) copolymer was then removed from the silicone mold and prepared for subsequent analysis.

2.3 Preparation of photothermally filled light-responsive shape memory composite

The photothermal sunlight-responsive shape memory composites will be prepared by blending the partially heated Poly(70BA-a/30ESO) copolymer with 1, 3, 6, and 9 wt% weight content of the photothermal fillers (TiN) in an aluminium pan to produce four distinct formulations. Furthermore, the four respective well-mixed formulations and a Poly(70BA-a/30ESO) copolymer will be transferred into a silicone mold. The mold containing the separate composite samples will undergo a step-curing process at 150 °C, 170 °C, followed by 180 °C for one hour, and 200 °C/2hours in a convective oven. Subsequently, the composites will be gently removed from the mold and designated.

2.4 Flexural properties of the poly(70BA-a/30ESO)TiN-(wt.%) compositem

The flexural properties of the copolymer and composites will be determined using a Universal Testing Machine (UTM) (INSTRON 5567, Bangkok, Thailand) in the flexural mode. The dimensions of the samples for the analysis will be 50 mm × 12.7 mm × 0.2 mm, using a span-to-length ratio of 16, and a crosshead speed of 8 mm min^{-1} will be utilized for all the prepared samples.

2.5 Viscoelastic properties of the poly(70BA-a/30ESO)TiN-wt% composites

The viscoelastic properties of the samples of the copolymers and composites will be determined using the Dynamic Mechanical Analyzer DMA (model DMA1, Mettler-Toledo, Switzerland) at 1 Hz, a strain amplitude of 5 μm, and 2 °C/min using a tensile mode under a nitrogen atmosphere. This analytical unit operation will be utilized to determine the samples' storage modulus (E') and loss modulus (E''). The dimensions of the samples analyzed will be 50 mm × 10 mm × 0.1 mm. The samples will be analyzed using a dual cantilever mode at a heating rate of 20 °C/min from 30–200 °C.

2.6 Shape memory properties of the poly(70BA-a/30ESO)TiN-wt% composites

The shape memory characteristics of the optimal copolymer and the various composites with different filler weight contents will be evaluated using a folding and deploying method. This process will begin by heating the samples to Tg+20°C, followed by positioning the sample in a fixture at about 90 degrees, and finally allowing it to cool at room temperature while maintaining the applied deformation force. Subsequently, the shape recovery ratio will be determined by reheating the samples to Tg+20°C to restore the original configuration. Also, the shape fixity (Rf) and shape recovery ratio (Rr)[18] will be evaluated by applying the mathematical equations (1) and (2), respectively. While the recovery time is evaluated using a digital stopwatch.

$$R_f = \frac{\theta i}{\theta} \times 100 \quad (1)$$

And

$$R_r = \frac{\theta i - \theta f}{\theta f} \times 100 \quad (2)$$

Where θ_i = the deformation angle after temporary shape fixation. θ = the intended deformation angle.

θ_f = The angle of recovery after deformation.

As shown in Fig. 1, the shape programming process of poly(BA-a/ESO) SMPs involves deforming the material at Tg+20∘C to obtain a temporary shape, followed by recovery to its permanent shape at room temperature

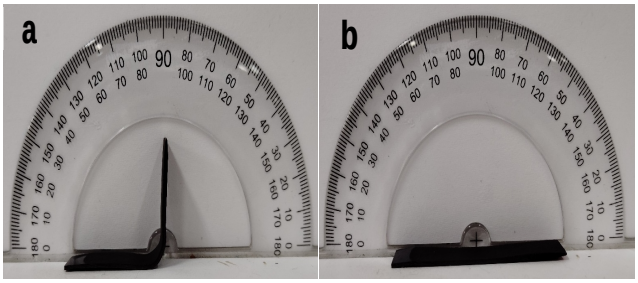

Fig. 1. Shape programming process of poly(BA-a/ESO) SMPs: (a) deformed temporary shape at Tg + 20 °C; (b) permanent shape at room temperature.

3. RESULTS AND DISCUSSION

3.1 Prepared copolymer and poly(70BA-a/30ESO)TiN-wt% composites samples

As illustrated in the diagram, the Benzoxazine resin was initially synthesized and utilized to create the copolymer matrix. Afterward, poly(70BA-a/30ESO) TiN-weight% composite samples were produced by integrating various weight percentages of TiN nanoparticles into the copolymer through in-situ polymerization, leading to the development of reinforced composite materials.

The overall process for synthesizing the benzoxazine resin, forming the copolymer, and preparing the poly(70BA-a/30ESO)/TiN composites is illustrated in Fig. 2.

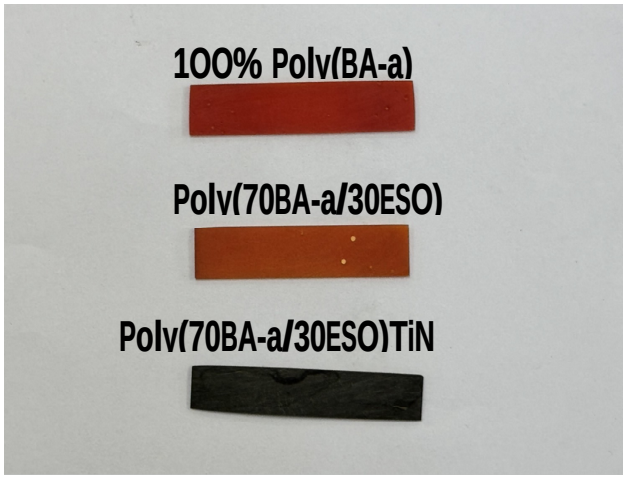

Fig. 2. Visual comparison of (1) neat Poly(BA-a), (2) Poly(70BA-a/30ESO) copolymer, and (3) Poly(70BA-a/30ESO) composite filled with TiN nanoparticles.

3.2 Effects of TiN filler weight content on flexural properties of the copolymer and P(70BA-a/30ESO) TiN-wt% composites

Figure 3 illustrates the relationship between flexural stress and flexural strain on the optimal copolymer and its composites. It shows that increasing the TiN weight content in the polymer matrix from 0 to 3 wt% leads to a notable increase in flexural stress from 144 to 164 MPa. Concurrently, the flexural modulus rises significantly from 3.9 to 5.1 at 1 wt%, then remains stable as the TiN content grows from 3 wt% to 5 wt%. Conversely, the strain at break increases from 3.5 to 5.1 mm−1 before leveling off between 3 and 6 wt%. However, at 9 wt%, both the flexural stress and flexural modulus decrease by 69.8 and 4.8, respectively.

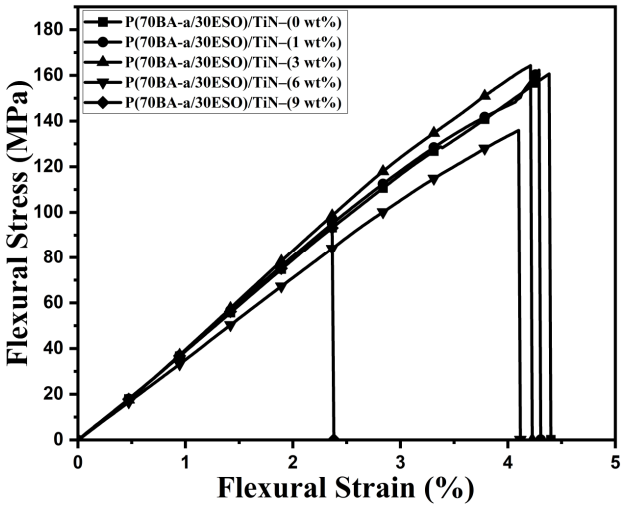

Fig. 3: Flexural properties of P(70BA-a/30ESO)TiN-wt.% composites.

This decline is accompanied by a sharp reduction in strain to 1.8 mm-1. Such a decrease in flexural characteristics may result from the agglomeration of TiN within the copolymer matrix, which disrupts stress distribution

3.3 Viscoelastic properties of poly(70BA-a/30ESO) copolymers reinforced with the TiN filler.

Dynamic Mechanical Analysis (DMA) was used to study the viscoelastic properties of TiN incorporated into poly(70BA-a/30ESO) copolymers. The storage modulus (E') and loss tangent (tan δ) were investigated. The glass transition temperature (T_g) was determined from the maxima of the loss tangent curve.

The results, indicated in Figure 1 and listed in Table 2, TiN incorporated into the polymer matrix impacted the stiffness and strength of the resulting composite as indicated by the increase in storage modulus at the glassy state from 995MPa to 1135.2 MPa. Also, there was a significant increase in the storage modulus at the glassy state from 3 to 9 wt%, This may be a result of the even distribution of TiN in the copolymer matrix, which limits the flexibility of the bonds.

The glass transition temperature increases from 159°C to 180°C as the amount of TiN in the copolymer matrix rises from 0% to 3% by weight, indicating that the incorporation of TiN improves the thermal stability of the composites. However, when the TiN content is increased to between 6% and 9%, the Tg gradually decreases from 174°C to 173°C for the respective composites. This reduction in Tg might be attributed to agglomeration, which undermines the effectiveness of interfacial bonding and the interpenetrating network within the composite structure.

Furthermore, a noted enhancement in storage moduli was seen in the rubbery state as the TiN content rose from 0 to 3 wt%, likely due to the uniform distribution of TiN within the copolymer matrix, which aids in reinforcing the composites. However, a marked decrease in storage moduli occurred from the 3 to 9 wt% range of TiN incorporation, potentially due to the clumping of TiN particles leading to an uneven stress distribution in the copolymer matrix.

3.4 Shape memory properties of the produced composites.

It can be observed that the shape fixity of the composite increases from 0 and peaks at 6wt%. This indicates that the TiN incorporated into the copolymer matrix significantly improves the strength of the composite by hindering the movement of the interpenetrating network, thereby enhancing the fixation of the programmed shape. However, as the weight content of TiN increases to 9 wt%, the shape fixity declines to 79%, which may be caused because of agglomeration in the copolymer matrix.

The shape recovery response to both magnified sunlight and NIR irradiation shows a steady improvement as the TiN content increases, reaching its peak at 6 wt%. At this optimal level, the material exhibited a recovery ratio of 93% under sunlight and an even higher 95% under NIR, with swift recovery times

of 62 seconds and 59 seconds, respectively. This highlights the significant role of TiN nanoparticles in enhancing photothermal conversion, as well-dispersed nanoparticles effectively absorb light energy and transform it into heat, facilitating rapid and complete shape recovery.

However, there was a significant decline in the shape memory performance for both sunlight and NIR actuation, as well as higher recovery time and a drop in recovery ratios. This is attributed to the agglomeration of the TiN, which could cause light scattering and diminish efficient light absorption.

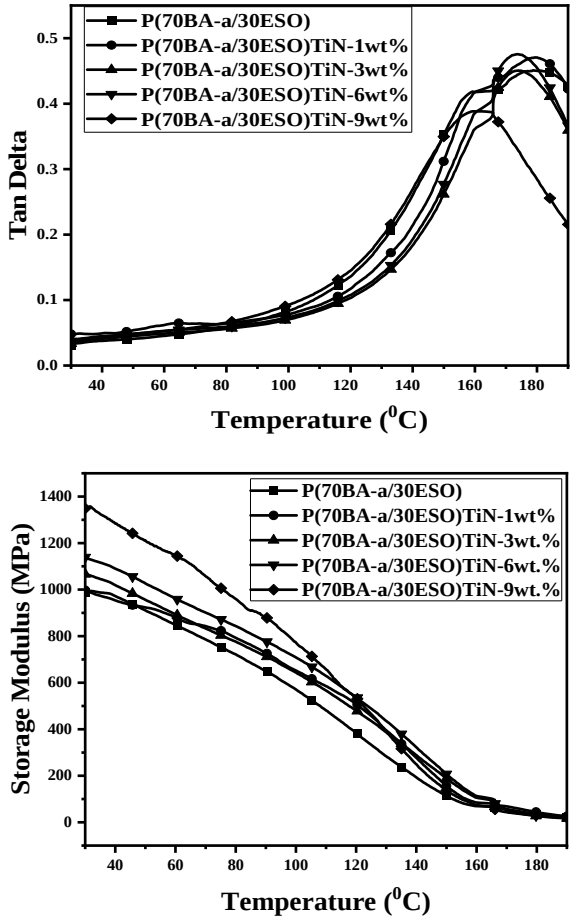

Fig. 4: Storage modulus (a) and loss tangent curves (b) of BA-a/ESO copolymers filled with different contents of TiN

Table 1: Summary of flexural properties of P(70BA-a/30ESO)TiN-wt.% at varying weight ratio.

TiN Weight Content (wt.%) in Optimum Copolymer P(70BA-a/30ESO	Flexural Strength (MPa)	Flexural Modulus (GPa)	Strain at Break (%)
0	143.5 ± 21	3.9 ± 0	3.4 ± 1
1	167.9 ± 6	5.1 ± 0	4.5 ± 0
3	163.9 ± 4	5.0 ± 0	4.1 ± 1
6	136.8 ± 0	5.0 ± 2	4.1 ± 1
9	93.2 ± 29	4.8 ± 0	2.4 ± 1

Table 2: Summary of viscoelastic properties of P(70BA-a/30ESO)TiN-wt.% at varying weight ratio.

TiN Weight Content (wt.%) in Optimum Copolymer P(70BA-a/30ESO	Storage Modulus at Glassy State (MPa)	T_g at Loss Tangent (°C)	Storage Modulus at Rubbery State (MPa)
0	995.4	159.0	11.8
1	996.1	165.6	35.8
3	1003.5	180	19.5
6	1067.9	174	13.2
9	1135.2	173	8.5

Table 3: Shape memory properties of the produced copolymer and composites.

TiN Weight Content (wt.%) in Optimum Copolymer P(70BA-a/30ESO	Shape Fixity R_f (%)	Magnified Sunlight Stimulant		NIR Stimulant	
		R_r (%)	T_r (Sec.)	R_r (%)	T_r (Sec.)
0	82 ± 2.1	72 ± 3.6	135 ±3	79 ± 3.4	125 ± 7
1	90 ± 1.1	86 ± 3.3	100 ± 6	89 ± 2.3	72 ±13
3	93 ± 2.4	91 ± 4.0	76 ± 11	92 ±2.6	73 ± 16
6	95 ± 1.8	93 ± 1.4	62 ±12	95 ±12	59 ± 4.0
9	79 ± 1.8	86 ± 4.8	126 ±39	87±3.2	84 ±15

4. CONCLUSION

From the data collected, analyzed, and discussed, the following conclusions can be made.

I. The Shape memory composite responsive under the actuation of magnified sunlight and near-infrared radiation has been successfully developed by incorporating 1, 3, 6, and 9 (wt%) TiN into the poly(70BA-a/30ESO).

II. The P(70BA-a/30ESO) system, loaded with 1 wt% TiN, seems to be ideal for enhancing the rubbery modulus while preserving the material's elasticity and strength at high temperatures.

III. The evaluation of shape memory performance through shape fixity indicated a noticeable enhancement as the TiN content increased, reaching a maximum of 95% at 6 wt%. This emphasizes the importance of TiN nanoparticles in maintaining the temporary shape by limiting chain mobility.

IV. The enhanced sunlight absorption capability of the SMPCs led to improved photothermal efficiency, which significantly boosted the shape recovery ratio (Rr), with increases of approximately 19.4% and 10.1% under magnified sunlight and near-infrared (NIR) irradiation, respectively. Additionally, the recovery time (Tr) was reduced from 135 to 126 seconds under normal sunlight, and from 125 to 84 seconds under magnified sunlight conditions.

V. The reinforcement of the optimal copolymer with TiN led to a notable improvement in the composite's flexural properties, with an optimal performance achieved at 3 wt%, where flexural properties peaked. This reflects a balance of increased rigidity and flexibility while preserving the material's mechanical integrity.

VI. Overall, this study offers comprehensive insights into how the addition of TiN nanoparticles improves the photothermal performance of composites, facilitating shape memory recovery when exposed to intensified sunlight and near-infrared (NIR) light. Furthermore, it presents the first documented evidence on the stimulation of shape memory behavior in TiN nanoparticle-reinforced copolymers using magnified sunlight and NIR radiation.

ACKNOWLEDGMENTS

The authors gratefully acknowledge the National Research Council of Thailand (NRCT), Chulalongkorn University (Grant No N42A660910), and the Thailand Science Research and Innovation Fund, Chulalongkorn University (BCG_FF_68_206_2100_030), for their generous funding. The authors also appreciate the support provided for research materials and access to unit operation facilities, which were essential to the successful completion of this study.

REFERENCES

[1] B. Atli, F. Gandhi, G. Karst, Thermomechanical characterization of shape memory polymers, Journal of Intelligent Material Systems and Structures, 20 (2009) 87-95.

[2] J. Leng, H. Lv, Y. Liu, S. Du, Electroactivate shape-memory polymer filled with nanocarbon particles and short carbon fibers, Applied Physics Letters, 91 (2007).

[3] H. Lu, Y. Liu, J. Leng, S. Du, Qualitative separation of the effect of the solubility parameter on the recovery behavior ofshape-memory polymer, Smart materials and structures, 18 (2009) 085003.

[4] K. Hamad, M. Kaseem, H. Yang, F. Deri, Y. Ko, Properties and medical applications of polylactic acid: A review, Express polymer letters, 9 (2015).

[5] X. Lan, X. Li, Z. Liu, Z. He, W. Yang, M. Yang, Composition, morphology and properties of poly (lactic acid) and poly (butylene succinate) copolymer system via coupling reaction, Journal of Macromolecular Science, Part A, 50 (2013) 861-870.

[6] X. Song, Y. Chen, Y. Xu, C. Wang, Study on Tough Blends of Polylactide and Acrylic Impact Modifier, BioResources, 9 (2014).

[7] C. Chen, Z. Hou, S. Chen, J. Guo, Z. Chen, J. Hu, L. Yang, Photothermally responsive smart elastomer composites based on aliphatic polycarbonate backbone for biomedical applications, Composites Part B: Engineering, 240 (2022) 109985.

[8] S. Rimdusit, C. Jubsilp, S. Tiptipakorn, Alloys and composites of polybenzoxazines, Springer Singapore, Singapore, 10 (2013) 978-981.

[9] F. Zhao, X. Zheng, S. Zhou, B. Zhou, S. Xue, Y. Zhang, Constitutive model for epoxy shape memory polymer with regulable phase transition temperature, International Journal of Smart and Nano Materials, 12 (2021) 72-87.

[10] M. Zare, M.P. Prabhakaran, N. Parvin, S. Ramakrishna, Thermally-induced two-way shape memory polymers: Mechanisms, structures, and applications, Chemical Engineering Journal, 374 (2019) 706-720.

[11] Y. Xie, D. Lei, S. Wang, Z. Liu, L. Sun, J. Zhang, F.-L. Qing, C. He, Z. You, A biocompatible, biodegradable, and functionalizable copolyester and its application in water-responsive shape memory scaffold, ACS Biomaterials Science & Engineering, 5 (2019) 1668-1676.

[12] H. Ishida, Process for preparation of benzoxazine compounds in solventless systems, Google Patents, 1996.

[13] N. Sahoo, Y. Jung, H. So, J. Cho, Alloys and Composites of Polybenzoxazines: Properties and Applications, Springer: Singapore. doi, 10 (2007) 978-981.

[14] R. Wang, T.P. Schuman, Vegetable oil-derived epoxy monomers and polymer blends: A comparative study with review, Express Polym. Lett, 7 (2013) 272-292.
[15] F.I. Altuna, V. Pettarin, R.J. Williams, Self-healable polymer networks based on the cross-linking of epoxidised soybean oil by an aqueous citric acid solution, Green Chemistry, 15 (2013) 3360-3366.
[16] F. Altuna, L. Espósito, R. Ruseckaite, P. Stefani, Thermal and mechanical properties of anhydride-cured epoxy resins with different contents of biobased epoxidized soybean oil, Journal of Applied Polymer Science, 120 (2011) 789-798.
[17] A. Joseph, I. Lawan, K. Charoensuk, P. Luengrojanakul, P. Mora, C.-H. Ahn, S. Rimdusit, Development of a magnified sunlight responsive shape memory bio-composite: effects of titanium nitride (TiN) nanoparticles on a bio-based benzoxazine/epoxy copolymer, Nanoscale Advances, 6 (2024) 4407-4416.
[18] N. Chen, W. Lien, C. Liu, Y. Huang, Y. Lin, C. Chou, S. Chang, C. Ho, Excitation of surface plasma wave at TiN/air interface in the Kretschmann geometry, Journal of Applied Physics, 109 (2011) 043104-043104-043107.

Antioxidant sugar from co-crystallization of sucrose, erythritol and vitamin C

Norramon Sathanasaowaphak[1], Lek Wantha[1,*]

[1] School of Chemical Engineering, Institute of Engineering, Suranaree University of Technology, Nakhon Ratchasima 30000, Thailand
* Corresponding author: lekwa@sut.ac.th

ABSTRACT

Co-crystallization is a process of producing cocrystals. The co-crystals obtained through co-crystallization exhibited improved properties, such as increased solubility, stability, and flowability. Erythritol is a sugar alcohol used as a low-calorie sweetener. In this study, sucrose, erythritol, and vitamin C (L-ascorbic acid) were co-crystallized to determine a suitable molar ratio between sucrose and erythritol, which can be sweetening and suitable with diabetic patient and delivering vitamin C benefits. The physical properties of the co-crystals were analyzed using XRD, FTIR, and SEM. From FTIR result, all of molar ratio was the same. Therefore, the 2:3 was selected because this ratio is reasonable for daily consumption. Antioxidant activity of co-crystals was determined by DPPH inhibition activity. An antioxidant activity of co-crystals was 86.225%, while that of pure vitamin C was 87.276%. Therefore, Co-crystals can be a sweetener and an antioxidant.

Keywords: Co-crystallization, Vitamin C, Erythritol, Antioxidant.

1. INTRODUCTION

Thailand is the second largest sugar exporter in the world that reported by Shahbandeh [1]. Sugar has another name, “sucrose”. Sugar is used everywhere in food, drink, candy, and more, and is consumed by people every day. Sugar is a sweetener, but excessive consumption can lead to various health issues such as diabetes, obesity, cardiovascular disease, and hyperlipidemia [2].

Co-crystallization is a co-crystal production process which crystals containing two or more molecules in a specific stoichiometric ratio within the lattice. Various molecular species involved in the co-crystal formation is called the coformer. The coformer molecules are primarily bonded by non-covalent interactions such as hydrogen or halogen bonds [3]. Many research used sucrose to co-crystallize with another active pharmaceutical ingredient (API) such as vitamin B12 [4], carotenoid in carrots [5], catechin or curcumin from plant that has antioxidant property [6], etc. In this research co-crystallized sucrose with vitamin C (L-ascorbic acid). Cocrystals obtained from co-crystallization can provide sweetness and the benefit of vitamin C. In diabetes who often lack vitamin C. Vitamin C can help reduce free radicals, inflammation of blood vessels, blood sugar insulin, hormone levels, triglyceride levels, LDL cholesterol and lipid levels. It also helps prevent complications such as heart disease, kidney failure, etc [7]. Vitamin C should be consumed, which is why this research combined erythritol with sucrose to reduce the amount of sucrose. As reported by [8], they co-crystallized sucrose, erythritol, and fibersol-2 for making a sugar that help the digestive system.

Erythritol is a sugar alcohol, also known as polyols, that used to add to sugar free products. Erythritol is about 60-80% as sweet as sugar. Erythritol should be consumed in amounts less than 1000 mg/kg of body weight of erythritol; otherwise, it may cause diarrhea [9]. However, erythritol is generally considered safe in people with diabetes and who want to control their body weight. After cocrystallization obtained co-crystals. Co-crystals can be a sweetening, delivering vitamin C benefits which everyone can consume, also suitable in diabetes.

2. EXPERIMENTAL

2.1 Materials

Food grade sucrose was purchased from Khonburi Sugar Co., Ltd. Erythritol was purchased from Chemiphan Corporation Co., Ltd. L-ascorbic acid was purchased from Kemaus Co., Ltd. DPPH (2,2-diphenyl-1-picrylhydrazyl) was purchased from Chemical Express Co., Ltd.

2.2 Preparation of co-crystals

Sucrose and erythritol were mixed in a jacket crystallizer in a molar ratio of 1:1 and dissolving in distilled water. The ratio between mixed sugar and water was 6:1 g/ml. This was heated at 100oC using a stirring speed of 300 rpm until the solution was clear and then cooled down at 65 ºC. When the slight turbidity occurred, stirring was continued, and 1.5 g of

L-ascorbic acid was added, indicated the beginning of co-crystallization process. The mixture was then immediately cooled by covering the crystallizer with cooling gel until the co-crystals formed. The obtained co-crystals were dried at 40 ºC for 1 day in oven. The co-crystals were packed in amber zip bag and stored at 4-6 ºC in a low-humidity environment for analysis. The experiment was then repeated by varying the variables according to Table 1.

Table 1. Molar ratio of sucrose and erythritol

Sucrose	Erythritol
1	1
1	2
2	1
2	3
3	2

2.3 XRD analysis of co-crystals

The crystalline structure of co-crystals was determined using X-ray diffractometer (D2, PHASER, Bruker). The scanning was conducted at 40kV with a radiation wavelength of 40 mA in the 2θ range between 5º and 60º.

2.4 FTIR analysis of co-crystals

The co-crystals were scanned by using Fourier Transform Infrared Spectroscopy (Tensor 27, Germany). The spectra were recorded in transmission mode from 400-4000 cm-1 at a resolution of 4 cm-1, 64 scans. The obtained spectra were analysed by using Sigma plot.

2.5 Structural morphology of co-crystal

Structural morphology of co-crystal samples was measuring using a scanning electron microscope (SEM JOEL, JSM-6010LV).

2.6 Antioxidant of co-crystals

Preparing 0.1 mmol of DPPH (1,1-diphenyl-2-picrylhydryl) ethanol solution. 1 g of co-crystals was dissolved in 10 ml of distilled water. 2 ml of dissolution was mixed with 2 ml of DPPH ethanol solution. The absorbance of the mixture was measured at 517 nm after incubating for 40 min in dark at room temperature. Antioxidant activity of the co-crystals was expressed as the percentage of radical scavenging activity of DPPH free radical, calculated using the following equation:

$$Antioxidant\ activity\ (\%) = 100 \times \frac{Abs_{conctrol}^{517nm} - Abs_{sample}^{517nm}}{Abs_{control}^{517nm}}$$

where Abscontrol is the absorbance of the control (without the sample) and Abssample is the absorbance of the sample.

3. RESULTS AND DISCUSSION

3.1 X-ray diffractograms (XRD)

Figure 1 shows powder x-ray diffraction (PXRD) pattern of sucrose, erythritol, l-ascorbic acid (vitamin C) and, 2:3 C (co-crystal). PXRD was used to identify a new crystalline phase since characteristic powder pattern arises from its unique internal crystal structure [10]. From this figure presents the difference between diffraction pattern of cocrystal with single compound. Co-crystals displays the characteristic crystalline peak at 11.85º, 25.08º, and 50.82º. This individual peak in the diffractogram could suggest the interaction between sucrose, erythritol and l-ascorbic acid to form co-crystal. From the PXRD result, sucrose has higher intensity peak than co-crystals.

3.2 Fourier transform infrared spectroscopy (FTIR)

FTIR spectroscopy is used to analyze changes in hydrogen bonding because the formation of a solid phase can be directly correlated with changes in the vibrational frequencies of functional groups [9]. Figure 2 displays the FTIR spectra of co-crystals at all ratios. All co-crystal ratios exhibited the same vibrational bands. Therefore, the 2:3 C ratio was selected, as it is considered reasonable for daily consumption.

Figure 3 shows the FTIR spectra of sucrose, erythritol, l-ascorbic acid and co-crystal. It was found that all samples had different change in vibrational frequencies of their functional group. Sucrose, erythritol and l-ascorbic acid showed similar and typical as displayed in the spectral database for organic compounds (SDBS) [11]. FTIR spectra of co-crystal presented appearance C=O and C=C at 1758 cm-1 and 1660 cm-1, respectively. In l-ascorbic acid, the C=O and C=C bonds showed peaks at 1753 cm^{-1} and 1655 cm^{-1}, respectively, in similar areas. This shift occurred due to the formation of hydrogen bonds. In FTIR spectra of co-crystal at 3600-3000 cm-1, several overlapping spectral bands corresponding to sucrose, erythritol, and L-ascorbic acid were observed in all the individual material. This revels that the co-crystallization did not change the chemical structure of the materials [12].

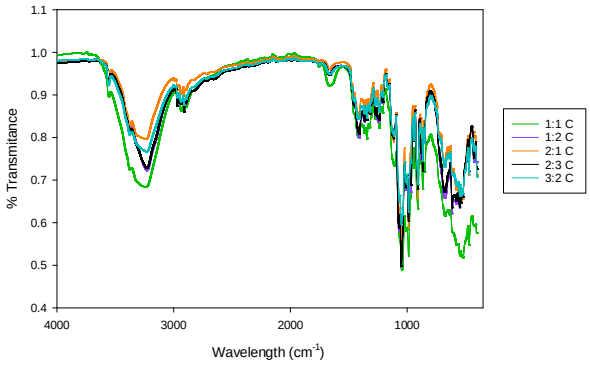

Fig 2. FTIR spectra of all ratios of co-crystals

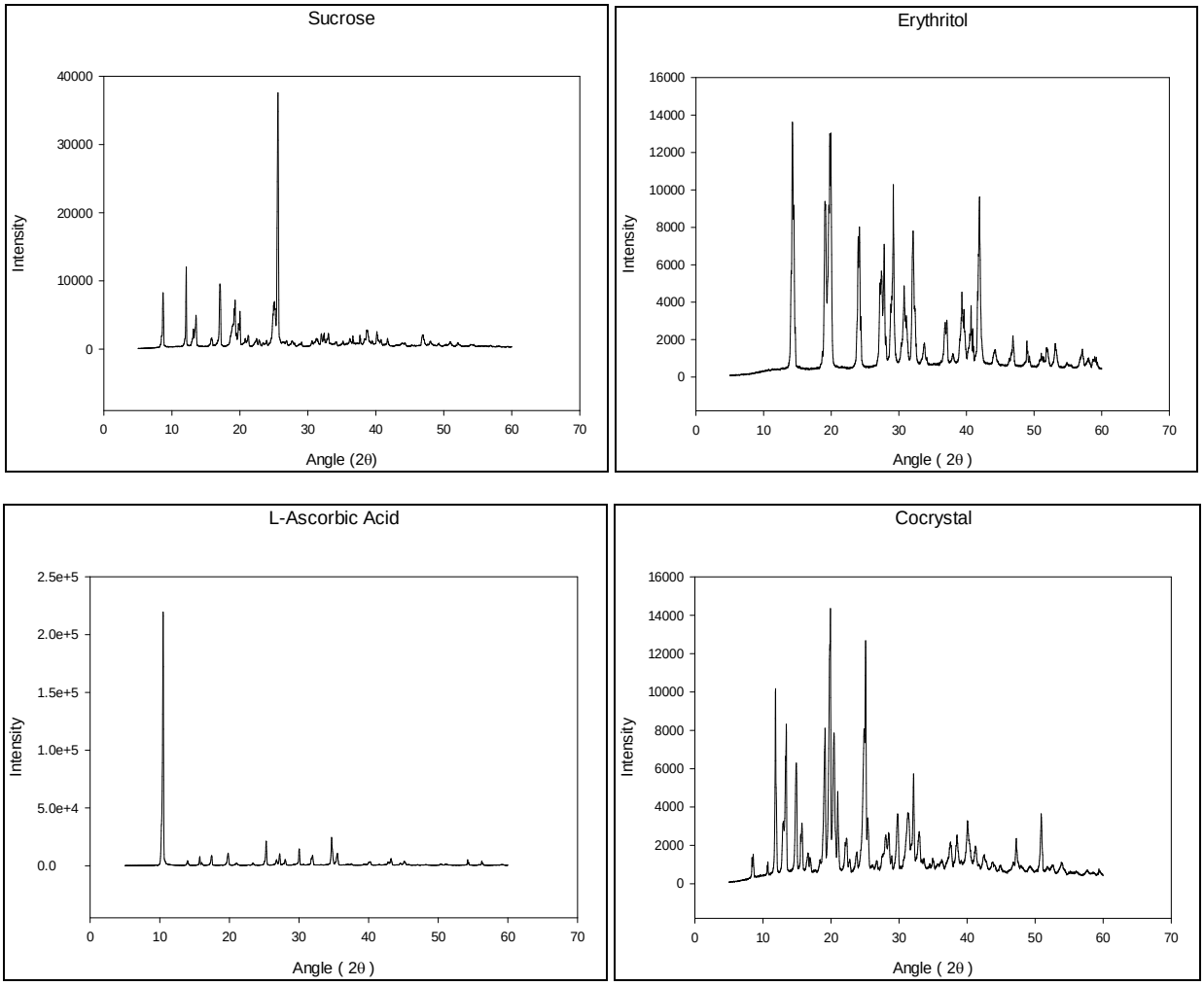

Fig 1. Powder X-ray diffraction pattern of sucrose, erythritol, l-ascorbic acid (vitamin C), and co-crystals

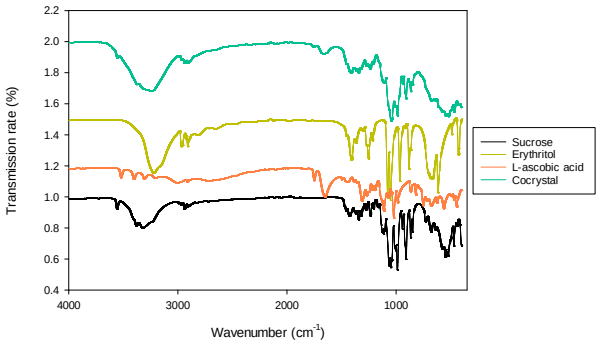

Fig 3. FTIR spectra of sucrose, erythritol, l-ascorbic acid and co-crystal

3.3 Structural morphology

The structural morphology of single components and co-crystals was examined using a scanning electron microscope (SEM) to study their structure. Figure 4 presents SEM micrographs of sucrose, erythritol, l-ascorbic acid and co-crystals. In SEM co-crystals displayed agglomeration on the surface, which was different from that of each individual component. SEM of each single component presented well- defined crystal structures especially sucrose and erythritol as reported by [13] and [14]. L-ascorbic acid showed SEM micrographs similar as reported by [15].

3.4 Antioxidant of cocrystals

Antioxidant of vitamin C were determined by DPPH radical scavenging activity which was used to measure antioxidant activity, as previously reported in [5]. Table 2 presents antioxidant properties of co-crystal, vitamin C and sucrose. Co-crystals exhibited 86.225% radical scavenging activity against free radicals, which was nearly equal to the antioxidant capacity of vitamin C (87.276%). In contrast, pure sucrose showed no antioxidant activity. Therefore, the co-crystals can serve as both a sweetening agent and a carrier for the antioxidant benefits of vitamin C.

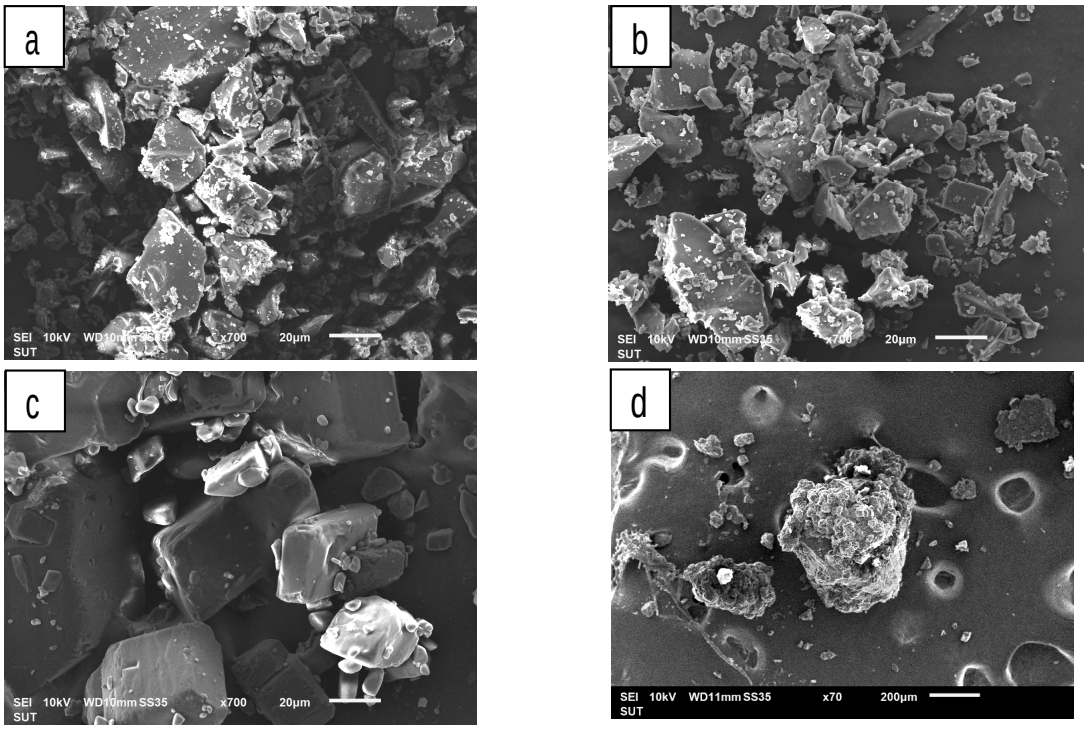

Fig 4. SEM micrographs of (a) sucrose, (b) erythritol, (c) l-ascorbic acid and (d) co-crystal

Table 2. DPPH radical scavenging activity of co-crystal and vitamin C.

Materials	DPPH radical scavenging activity (%)
Co-crystals	86.225 ± 0.0332
Vitamin C	87.276 ± 0.0332

4. CONCLUSION

This study successfully produced co-crystals that can be a sweetening and delivery vitamin C benefits. The FTIR and XRD results confirmed the formation of a new crystalline phase. SEM of co-crystals presented agglomeration on a surface, which was different from each single component. Antioxidant of cocrystals was confirmed by DPPH radical scavenging activity. The co-crystals exhibited 86.225% radical scavenging activity against free radicals.

ACKNOWLEDGMENTS

The authors also acknowledge the research funding from (i) Suranaree University of Technology (SUT), (ii) Thailand Science Research and Innovation (TSRI), and (iii) National Science, Research and Innovation fund (NSRF)-Grant No. 195675 and 204174.

REFERENCES

1. M. Shahbandeh, Principal sugar exporting countries in 2023/2024. Available online: https://www.statista.com/statistics/273437/exported-amount-of-sugar-in-leading-countries/.
2. M. Prada, M. Saraiva, M. V. Garrido, A. Sério, A. Teixeira, D. Lopes, D. A. Silva, D. L. Rodrigues. Perceived Associations between Excessive Sugar Intake and Health Conditions. *Nutrients* 2022; 14, 640: 1-13.
3. N. Pawar, A. Saha, N. Nandan, J. V. Parambil. Solution Cocrystallization: A Scalable Approach for Cocrystal Production. *Crystals* 2021; 11, 303: 1-18.
4. S. R. Bajaj, R. S. Singhal. Enhancement of stability of vitamin B12 by co-crystallization: A convenient and palatable form of fortification. *Journal of Food Engineering* 291 (2021); 110231: 1-9.
5. P. Kaur, A. Elsayed, J. Subramanian, A. Singh. Encapsulation of carotenoids with sucrose by co-crystallization: Physicochemical properties, characterization and thermal stability of pigments. *LWT – Food Science and Technology 140* (2021); 110810: 1-10.
6. H. Wang, S.Gao, D. Zhang, Y. Wang, Y. Zhang, S. Jiang, B. Li, D. Wu, G. Lv , X. Zou, X. Meng. Encapsulation of catechin or curcumin in co-crystallized sucrose: Fabrication, characterization and application in beef meatballs. *LWT – Food Science and Technology 168* (2022); 113911: 1-11.
7. T. Sathienluckana, The medical benefits of vitamin C. *wongkarnpat* 2017: 1-8.
8. M. B. Queiroz, F. R. Sousa, L. B. Silva , R. M. V. Alves, I. D. Alvim. Co-crystallized sucrose-soluble fiber matrix: Physicochemical and structural characterization. *LWT – Food Science and Technology 154* (2022); 112685: 1-9.

9. E. Moriconi, A. Feraco, V. Marzolla, M. Infante, M. Lombardo, A. Fabbri, M. Caprio. Neuroendocrine and Metabolic Effects of Low-Calorie and Non-Calorie Sweeteners. *Frontiers Endocrinology 11* (2020); 444: 1-17.
10. I. Indraa, F. M. Jana, R. Aryani. Enhancing the Solubility of Ketoconazole via Pharmaceutical Cocrystal. *Journal of Physics: Conference Series* (2019); 1179: 012134.
11. S. Matsuyama, S. Kinugasa, K. Tanabe, T. Tamura, Spectral Database for Organic Compounds. SDBS. Available online: https://sdbs.db.aist.go.jp/sdbs/cgi-bin/landingpage?sdbsno=1051.
12. A.L. Cordoba, L. Gallo, V.Bucalá, M. Martino, A. Navarro. Co-Crystallization of zinc sulfate with sucrose: A promissory strategy to render zinc solid dosage forms more palatable. *Journal of Food Engineering* 2016; 170: 100–107.
13. D. Kunkel, Table sugar crystals, SEM. Science Photo Library. Available online: https://www.sciencephoto.com/media/874559/view.
14. M. Yuan, F. Ye, C. Xu. Supercooling study of erythritol/EG composite phase change Materials. Energy Procedia 158 (2019): 4629–4634.
15. J. Burgess, SEM of vitamin C. Science Photo Library. Available online: https://www.sciencephoto.com/media/6699/view/sem-of-vitamin-c.

Polybenzoxazine blended with modified natural rubber by graft copolymerization with 2-hydroxyethyl acrylate for shape memory applications

Chanokkan Buakhlee[1], Nuttinan Boonnao[1], Sarawut Rimdusit[1,*]

[1] Center of Excellence in Polymeric Materials for Medical Practice Devices, Department of Chemical Engineering, Faculty of Engineering, Chulalongkorn University, Bangkok 10330, Thailand

[*] Corresponding author: sarawut.r@chula.ac.th

ABSTRACT

Shape memory polymers (SMPs) consist of rigid and soft molecular segments. Polybenzoxazine-based bisphenol A-aniline (PBA-a) is a thermosetting polymer known for its high mechanical properties and heat resistance. However, its rigidity limits its applicability in shape memory applications. Therefore, incorporating the soft rubber segment with enhanced compatibility through the 2-HEA functional group in the rubber at a suitable amount may provide a twofold benefit to improved toughness of PBA-a as well as endowing PBA-a shape memory capability. This research aims to study the blending of PBA-a with modified natural rubber grafted with 2-Hydroxyethyl Acrylate (NR-g-2-HEA) to develop SMPs. BA-a monomer was melt-blending with NR-g-2-HEA at varying concentrations of 0-20 wt%. The homogeneous mixings were cured in an air-circulated oven before for characterization. The successful grafting of 2-HEA monomer onto the NR backbone was confirmed by grafting efficiency and FTIR spectra. DMA analysis indicates that the rigidity of PBA-a decreases with higher NR-g-2-HEA content, as reflected by a reduced storage modulus in the glassy state. Moreover, the glass transition (T_g) of PBA-a/NR-g-2-HEA increased from 192 to 200 °C with 0-20 wt% of NR-g-2-HEA contents, indicating that possible interaction via H-bonding between hydroxyl groups of PBA-a and NR-g-2-HEA. Regarding shape memory properties, an increase in NR-g-2-HEA content led to significantly faster shape recovery, while shape fixity slightly decreased at higher concentrations. This finding demonstrates the promising potential of NR as a soft segment for shape memory properties.

Keywords: Shape memory polymers; Polybenzoxazine; Modified natural rubber; Grafting copolymerization; 2-Hydroxyethyl acrylate (2-HEA)

1. INTRODUCTION

Shape memory polymers (SMPs) are stimuli-responsive materials that can deform their temporary shape and return their original shape when triggered by external stimuli, such as specific temperature changes, light induction, electricity or magnetic field, and solvent [1-3]. SMPs are widely used in automotive, biomedical, electronic devices, and aerospace applications [1-3]. In general, SMPs possess a stable network or hard segment and a switching unit or soft segment for exhibiting the shape memory effect (SME). The hard segment maintains the permanent shape that prevents the polymers from deforming after undergoing a temporary shape below their transition temperature (T_{trans}), which can be formed through molecular entanglement, crystalline phases, chemical crosslinking, or interfacial network (IPN) [2]. Conversely, the soft segment is controlled by the molecular mobility above T_{trans}, which has the ability to transpose and return to its original shape [2].

Polybenzoxazine is a thermosetting polymer that has been extensively studied for SMPs. Among various types of polybenzoxazine, bisphenol A-aniline-based polybenzoxazine (PBA-a) has gained significantly attention, as it can be utilized as a hard segment in molecular mechanism of SMPs due to its outstanding properties, including an aromatic structure, high thermal stability, high glass transition temperature (T_g), high crosslink density, high storage modulus, and excellent mechanical properties [1-3]. However, only PBA-a is insufficient to be effective SMPs because of their rigid structure and limited soft segment in molecules, which hinders their flexibility and reversible shape transformation. To overcome these limitations, many studies have focused on enhancing flexibility by blending PBA-a with other flexible polymers, such as polyurethane [4, 5] and epoxy prepolymers [6]. Nevertheless, few studies have been conducted on blending PBA-a with natural rubber (NR) to increase the soft segment and improve flexibility.

NR is a biomaterial derived from the Hevea brasiliensis tree. Its unsaturated hydrocarbon structure is known as *cis*-1,4-polyisoprene. NR is commercially available in Thailand, as it is a vital material in the tire industry due to its high elasticity, high abrasion

resistance, high tensile strength, and low heat build-up. In addition, NR has been extensively investigated as an effective modifier for improving the elasticity and toughness of various polymer systems, such as polylactic acid (PLA) [7] and PBA-a [8]. Owing to its intrinsic ability to retain the memory of its unstressed stages and return to its original shape upon release from an external force, NR is considered a promising soft segment in SMPs, contributing to enhanced shape recovery efficiency. Derakhshandeh et al. (2008) [9] reported that grafting NR with a hydrophilic monomer could improve the compatibility before blending with PBA-a. This modification increased the polarity of the NR surface and enhanced interfacial adhesion between PBA-a and NR blends [9, 10]. In addition, Pattulee (2023) [11] studied blending PBA-a with ultrafine vulcanized powdered natural rubber (UFPNR), which was grafted by styrene-methyl methacrylate copolymer (ST/MMA). This ST/MMA-grafted UFPNR enhanced the compatibility between NR and PBA-a.

Moreover, 2-hydroxyethyl acrylate (2-HEA) is another monomer to be used as a compatibilizer between the hydroxyl groups and the carboxyl groups of poly(hydroxyethyl acrylate) (PHEA) on natural rubber grafted with 2-hydroxyethyl acrylate (NR-g-2-HEA). This material increased the polarity of hydrogen bonds and enhanced the compatibilization of rubber-filler interactions, which was widely used in applications requiring adhesion, flexibility, or specific chemical properties [12]. Therefore, blending NR-g-2-HEA with PBA-a can establish hydrogen bonding between the hydroxyl groups of PBA-a and NR-g-2-HEA.

This study aims to develop SMPs from bisphenol A-aniline-based PBA-a blended with NR-g-2-HEA. A variation of NR-g-2-HEA contents ranging from 5 to 20 wt% was investigated. In the underlying molecular mechanism of SMPs, PBA-a and NR-g-2-HEA serve as hard and soft segments, respectively. The PBA-a/NR-g-2-HEA samples with varying NR-g-2-HEA contents were characterized for their mechanical and shape memory properties.

2. EXPERIMENTAL

2.1 Chemicals

Deproteinized natural rubber (DPNR) with 60% dry rubber content was purchased from Unimac Rubber Co., Ltd. (Thailand). Sodium dodecyl sulfate (SDS; 99%), tetramethylene pentaamine (TEPA), tert-butyl hydroperoxide (TBHPO; 70% in water), 2-hydroxyethyl acrylate (2-HEA; 95%), and acetone (99.5%) were obtained from Chemical Express Co., Ltd. (Thailand). Bisphenol A was offered by PTT Phenol Co., Ltd. (Thailand). Aniline was purchased from Panreac Quimica S.A. (Spain). Paraformaldehyde was purchased from Merck Co., Ltd. (Germany). All of the chemicals were used as received.

2.2 Preparation of grafted natural rubber (NR-g-2-HEA)

DPNR latex was diluted with deionized water to achieve a dry rubber content (DRC) of 30%. Then, 300 grams of DPNR with 30% DRC was placed in a 1000 cm^3 glass reactor. An SDS as an emulsifier was added at 0.8 phr. The mixture was purged with N_2 to remove O_2 from the DPNR latex and then stirred at 50°C at a rotation speed of 250 rpm using a homogenizer for 1 h. Next, TEPA and TBHPO with a 1:1 molar ratio were added, along with 2-HEA monomer at 5, 10, 15, 20, and 30 phr. The reaction mixture was then stirred at 50°C at 400 rpm for 3 h. After the reaction was completed, a portion of the mixture was poured into a glass mold and dried for 48 h at 80°C for purification, followed by Soxhlet extraction with acetone as a solvent at 160°C for 24 h. Soxhlet extraction was performed to remove the free 2-HEA from the NR-g-2-HEA mixture.

To determine the grafting efficiency (%GE) of NR-g-2-HEA, Equation (1) was used, as below [13].

$$\%GE = \frac{W_d - W_a}{W_d - W_b} \times 100 \qquad (1)$$

Where W_a is the weight of the dried sample after Soxhlet extraction, W_b is the weight of the dried sample before Soxhlet extraction, and W_d is the weight of dry NR.

2.3 Synthesis of bisphenol A-aniline-based benzoxazine (BA-a)

Bisphenol A-aniline-based benzoxazine resin (BA-a) was synthesized from bisphenol A, paraformaldehyde, and aniline at a 1:4:2 molar ratio. The mixture was heated at 110°C using a hot plate and stirred until the mixture was homogeneous and formed a clear-yellowish resin. The obtained BA-a resin was cooled to a solid at room temperature, then ground into powder, and stored in a refrigerator before use.

2.4 Preparation of PBA-a/NR-g-2-HEA blends

The NR-g-2-HEA with varying contents from 5, 10, 15, and 20 wt% was melt-blended with BA-a powder and stirred thoroughly to ensure the mixture was uniformly distributed. The mixtures were heated at 120°C and stirred using a mechanical stirrer for 3 h to eliminate the water content in NR-g-2-HEA latex. Then, the homogenous BA-a/NR-g-2-HEA blends were obtained and solidified at room temperature, ground into a fine powder, and poured into the mold. Subsequently, the BA-a/NR-g-2-HEA blends underwent thermal curing in the air-circulated oven under the following conditions: 130°C for 3 h, 150°C for 2 h, 180°C for 1 h, and 200°C for 3 h.

2.5 Characterization

The characterization to confirm the successful grafting of the NR-g-2-HEA involves the %GE testing. Fourier transform infrared spectroscopy (FTIR) was employed using a Nicolet iS5 FTIR Spectrometer with an iD7 ATR accessory (Thermo Fisher Scientific Inc., Waltham, MA, USA) to investigate their chemical structures. All spectra were recorded in a range of 400 to 4000 cm^{-1} with 32 scans at a resolution of 4 cm^{-1}.

The cured PBA-a/NR-g-2-HEA samples were analyzed to determine dynamic mechanical properties by using a dynamic mechanical analyzer (DMA, model DMA1) from Mettler-Toledo (Thailand) under a temperature range of 30 to 300 °C at a heating rate of 3 K min^{-1}, with a specimen dimension of 50 × 10 × 1 mm^3. The shape memory properties, including shape fixity (R_f), shape recovery (R_r), and recovery times of these samples, were measured. The samples were heated to their T_g+30°C and bent at a 90° angle, then cooled down to room temperature to maintain a temporary shape for 1 min. The R_f can be calculated using Equation (2).

$$\%R_f = \frac{\theta_1}{90} \times 100 \qquad (2)$$

Where θ_1 is the angle of the temporary shape after cooling and unloading.

The shape recovery process was tested by reheating at T_g+30 °C to allow the samples to recover their original shape. The shape recovery can be calculated using Equation (3).

$$\%R_r = \frac{\theta_1 - \theta_2}{\theta_1} \times 100 \qquad (3)$$

Where θ_1 is the angle of the temporary shape after cooling and unloading, and θ_2 is the final angle after shape recovery.

The recovery time was determined as the time for returning from its temporary shape to its original shape. Each tested sample was repeated three times for accuracy.

3. RESULTS AND DISCUSSION

3.1 Effect of Monomer concentrations on Grafting Efficiency (%GE)

The amount of 2-HEA, which was successfully grafted on the NR backbone, was evaluated using %GE. Figure 1 indicates that the %GE was 73%, 84%, 89%, and 92% for grafting 2-HEA at 5, 10, 15, and 20 phr, respectively. These results revealed that the enhancement of 2-HEA increased the %GE of NR-g-2-HEA. This grafting reaction occurred between macroradical monomers and the free radicals of NR, leading to the formation of the graft copolymer [14]. The %GE of all NR-g-2-HEA was summarized in **Table 1.** The NR-g-2-HEA at 20 phr demonstrated the highest %GE. Therefore, it was selected for further characterization of the mechanical and shape memory properties by blending with PBA-a.

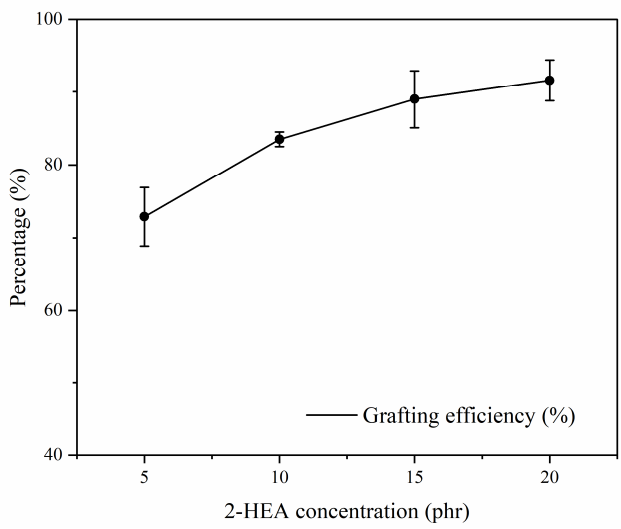

Figure 1 %GE of NR-g-2-HEA at different 2-HEA monomer concentrations.

Table 1 %GE of NR-g-2-HEA at different 2-HEA concentrations.

2-HEA Concentration (phr)	%GE
5	73 ± 4.0
10	84 ± 1.0
15	89 ± 3.9
20	92 ± 2.8

3.2 Molecular characteristics of NR and NR-g-2-HEA

The chemical structures of NR, 2-HEA, and NR-g-2-HEA were characterized using FTIR spectroscopy, as shown in Figure 2. The FTIR spectrum of NR exhibited a peak at 834 cm^{-1}, corresponding to C=H out-of-plane bending. A peak at 1659 cm^{-1} attributed to C=C stretching. The peaks at 1447 and 1375 cm^{-1} were associated with CH_2 blending and CH_3 blending, respectively. The peaks at 2960, 2915, and 2852 cm^{-1} corresponded to C-H stretching in CH_3 and CH_2. The FTIR spectrum of 2-HEA showed a broad peak at 3420 cm^{-1}, corresponding to -OH stretching, while the peak at 1407 cm^{-1} corresponded to -OH blending. The peaks at 1706, 1184, and 1056 cm^{-1} correlated to C=O stretching, C-O stretching of ester, and C-O stretching of primary alcohol, respectively. Moreover, the NR-g-2-HEA showed the shifted peak of -OH stretching to 3354 cm^{-1}. The peaks at 1706 and 1163 cm^{-1} corresponded to C=O stretching and C-O stretching of

primary alcohol, respectively. The characteristic peaks at 2959, 2921, and 2852, which were associated with C-H stretching in CH_3 and CH_2. Additionally, the peaks at 1662, 1447, 1375, and 834 cm^{-1} correspond to C=C stretching, CH_2 blending, CH_3 blending, and C=H out-of-plane bending, respectively. FTIR spectra confirmed that 2-HEA was successfully grafted onto the NR backbone, which was consistent with the report by Chueangchayaphan et al. (2017) [13]. Also, the chemical structure of NR-g-2-HEA is illustrated in Figure 3.

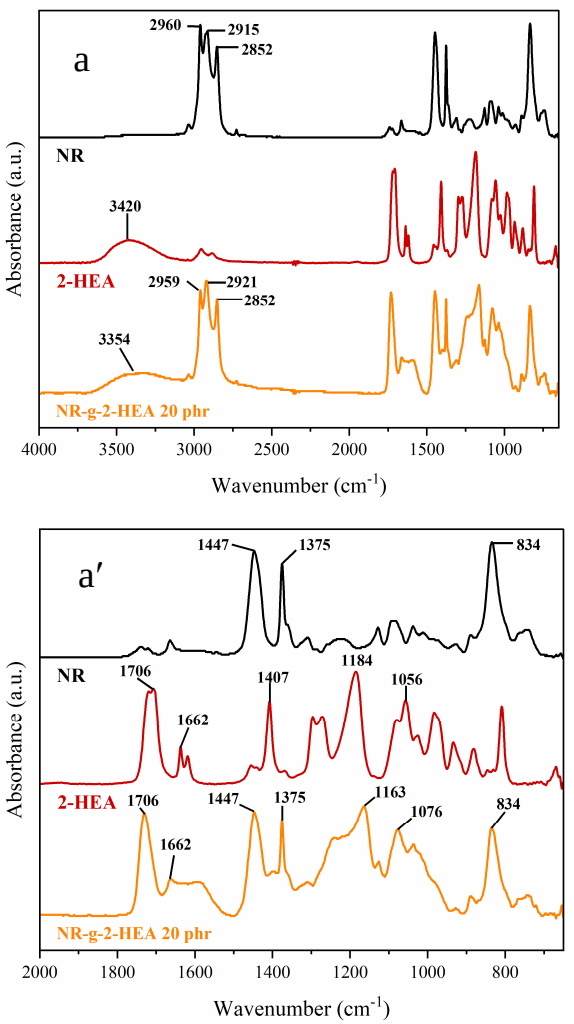

Figure 1 (a, a′) FTIR spectra of the NR, 2-HEA, and NR-g-2-HEA.

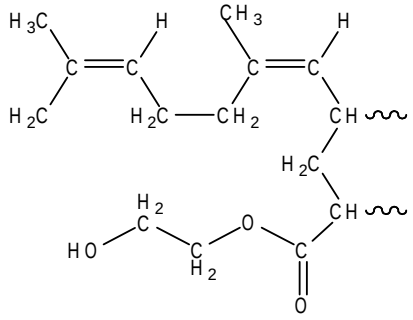

Figure 2 The chemical structure of NR-g-2-HEA.

3.3 Dynamic mechanical properties of PBA-a/NR-g-2-HEA blends

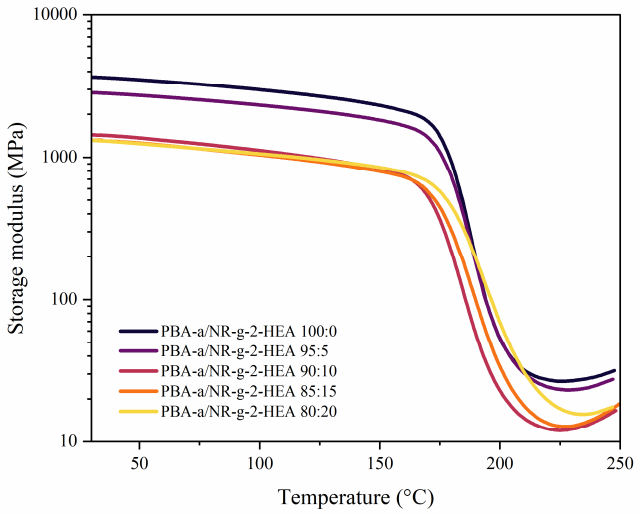

Figure 4 The E' of PBA-a/NR-g-2-HEA blends at various weight ratios.

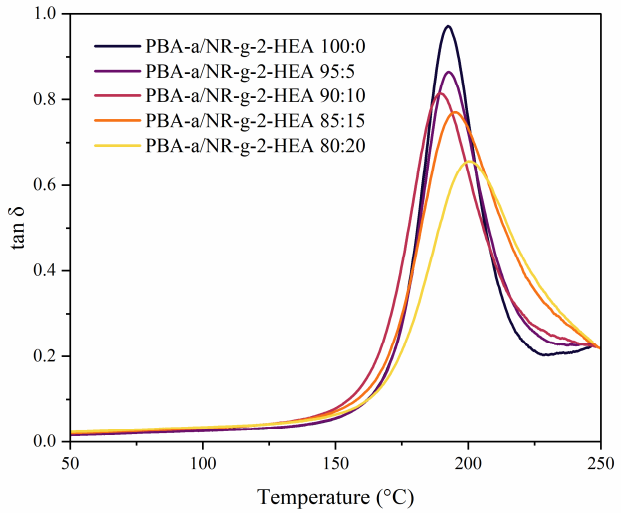

Figure 5 Tan δ curves of PBA-a/NR-g-2-HEA blends at various weight ratios.

Figure 4 illustrates the storage modulus (E') at 30 °C for PBA-a/NR-g-2-HEA blends at different weight ratios of 100/0, 95/5, 90/10, 85/15, and 80/20, which were 3679, 2850, 1437, 1318, and 1326 MPa, respectively. These results indicated that the storage modulus of the samples decreased with increasing NR-g-2-HEA content, owing to the incorporation of a flexible polymer into the high-stiffness PBA-a matrix. Additionally, the T_g of PBA-a/NR-g-2-HEA blends with various weight ratios was determined by the maximum peak of tan delta curves, as shown in Figure 5. The T_g was significantly unchanged for the samples blended with 0 to 10 wt% NR-g-2-HEA, which was approximately 190 to 192 °C. However, the T_g was enhanced when blending NR-g-2-HEA contents of 15 to 20 wt%, which were 195 °C and 200 °C, respectively.

This increase may be attributed to intermolecular hydrogen bonding between hydroxyl functional groups of PBA-a and NR-g-2-HEA, resulting in less polymer mobility. Moreover, the increase in T_g was possibly from the interpenetrating polymer network (IPN) between PBA-a and NR-g-2-HEA, which also restricted the mobility of the polymer chains. The values of dynamic mechanical properties of PBA-a/NR-g-2-HEA blends are summarized in Table 2.

Table 2 Dynamic mechanical properties of PBA-a/NR-g-2-HEA blends at various weight ratios.

PBA-a/ NR-g-2-HEA (wt/wt)	E' at 30 °C (MPa)	T_g (°C)
100/0	3679	192
95/5	2850	192
90/10	1437	190
85/15	1318	195
80/20	1326	200

3.4 Shape memory performance of PBA-a/NR-g-2-HEA blends

Table 3 Shape memory properties of PBA-a/NR-g-2-HEA blends at various weight ratios.

PBA-a / NR-g-2-HEA (wt/wt)	R_f (%)	R_r (%)	Recovery time [min: sec]
100/0	99.9 ± 0.08	86.0 ± 0.04	8:56 ± 0:23
95/5	99.9 ± 0.05	94.4 ± 0.07	5:51 ± 0:32
90/10	99.6 ± 0.59	95.1 ± 0.12	3:52 ± 0:28
85/15	99.3 ± 0.17	96.6 ± 0.06	3:51 ± 0:08
80/20	99.2 ± 0.02	97.6 ± 0.10	3:36 ± 0:15

The shape memory properties of PBA-a/NR-g-2-HEA were investigated. The shape memory properties, as revealed in Table 3, show that all of the tested samples exhibited $\%R_f$ higher than 99%, indicating excellent shape fixity performance regardless of NR-g-2-HEA content. The high $\%R_f$ could be attributed to the intrinsic rigidity of the PBA-a network, which limited the mobility of polymer chains and effectively maintained the temporary shape during the programming process. Regarding the shape recovery performance, the neat PBA-a showed the lowest $\%R_r$ of 86% with a recovery time of 8:56 min: sec. While adding NR-g-2-HEA resulted in an increased $\%R_r$ with increasing NR-g-2 - HEA contents. This behavior was due to the elastomeric nature of the NR-g-2 - HEA, which enhanced the flexibility and elasticity of the polymer network [5, 15]. In addition, the incorporation of 20 wt% NR-g-2-HEA led to the fastest recovery time of 3:36 min: sec.

4. CONCLUSION

The 2-HEA was successfully grafted onto the NR backbone, which was confirmed by its chemical structure using FTIR spectra and %GE. The NR-g-2-HEA at 20 phr, which exhibited the highest %GE, was further utilized in the fabrication of SMPs through blending with PBA-a. The high flexibility of NR-g-2-HEA led to the reduction of storage modulus at 30 °C of PBA-a/NR-g-2-HEA blends, while the T_g of these samples tended to increase at high NR-g-2-HEA contents of 15 and 20 wt%. This increment was preponderantly due to the hydrogen bonding between the hydroxyl groups of PBA-a and NR-g-2-HEA. For shape memory properties, all PBA-a/NR-g-2-HEA blends exhibited an excellent %Rf of 99%. In addition, a significant improvement in %Rr was observed when incorporating NR-g-2-HEA, increasing from 86% for neat PBA-a to 97.6 % for the PBA-a blended with NR-g-2-HEA at 20 wt%. Moreover, the addition of NR-g-2-HEA significantly reduced the shape recovery time. This work successfully indicates the utilization of NR-g-2-HEA as a soft segment in a shape memory PBA-a/ NR-g-2-HEA system, offering a promising option for future industrial and engineering applications.

ACKNOWLEDGMENTS

National Research Council of Thailand (NRCT) and Chulalongkorn University (N42A660910) and Thailand Science Research and Innovation Fund Chulalongkorn University (BCG_FF_68_206_2100_030)

REFERENCES

1. Hu, J., Y. Zhu, H. Huang, and J. Lu, Recent advances in shape–memory polymers: Structure, mechanism, functionality, modeling and applications. Progress in Polymer Science, 2012. **37**(12): p. 1720-1763.
2. Meng, H. and G. Li, A review of stimuli-responsive shape memory polymer composites. Polymer, 2013. **54**(9): p. 2199-2221.
3. Mora, P., et al., Thermosetting Shape Memory Polymers and Composites Based on Polybenzoxazine Blends, Alloys and Copolymers. Chem Asian J, 2019. **14**(23): p. 4129-4139.
4. Gu, S. and S. Jana, Effects of Polybenzoxazine on Shape Memory Properties of Polyurethanes with Amorphous and Crystalline Soft Segments. Polymers, 2014. **6**(4): p. 1008-1025.
5. Prathumrat, P., S. Tiptipakorn, and S. Rimdusit, Multiple-shape memory polymers from benzoxazine–urethane copolymers. Smart Materials and Structures, 2017. **26**(6): p. 065025.

6. Tanpitaksit, T., M. Okhawilai, and S. Rimdusit, Shape fixity and shape recovery characteristics of aliphatic epoxy-benzoxazine shape memory polymer. Journal of Metals, Materials and Minerals, 2014. **24**(1): p. 43-47.
7. Gholami, R., et al., Toughening Polylactic Acid with Ultrafine Fully Vulcanized Powdered Natural Rubber Graft-Copolymerized with Poly(styrene-co-acrylonitrile): Tailoring the Styrene-Acrylonitrile Ratio for Enhanced Interfacial Interactions. Polymers (Basel), 2024. **16**(16): p. 2254.
8. Jubsilp, C., J. Jantaramaha, P. Mora, and S. Rimdusit, Tribological Performance and Thermal Stability of Nanorubber-Modified Polybenzoxazine Composites for Non-Asbestos Friction Materials. Polymers (Basel), 2021. **13**(15): p. 2435.
9. Derakhshandeh, B., A. Shojaei, and M. Faghihi, Effects of rubber curing ingredients and phenolic-resin on mechanical, thermal, and morphological characteristics of rubber/phenolic-resin blends. Journal of Applied Polymer Science, 2008. **108**(6): p. 3808-3821.
10. Salaeh, S., et al., Compatibilization of poly(vinylidene fluoride)/natural rubber blend by poly(methyl methacrylate) modified natural rubber. European Polymer Journal, 2018. **107**: p. 132-142.
11. Pattulee, A., Toughness Enhancement of Polybenzoxazine Composites using Ultrafine Fully Vulcanized Natural Rubber Powder. 2023, Chulalongkorn University.
12. Borapak, W., N. Chueangchayaphan, S. Pichaiyut, and W. Chueangchayaphan, Natural rubber-graft-poly(2-hydroxyethyl acrylate) on cure characteristics and mechanical properties of silica-filled natural rubber composites. Journal of Applied Polymer Science, 2019. **137**(22): p. 48738.
13. Chueangchayaphan, W., et al., Synthesis and thermal properties of natural rubber grafted with poly(2-hydroxyethyl acrylate). Journal of Polymer Research, 2017. **24**(7): p. 107.
14. Rimdusit, N., et al., Radiation Graft-Copolymerization of Ultrafine Fully Vulcanized Powdered Natural Rubber: Effects of Styrene and Acrylonitrile Contents on Thermal Stability. Polymers (Basel), 2021. **13**(19): p. 3447.
15. Salaeh, S., et al., Thermo-responsive programmable shape memory polymer based on amidation cured natural rubber grafted with poly(methyl methacrylate). Polymer, 2022. **262**: p. 125444.

Flexible piezoresistive sensor based on natural rubber/chitosan/graphene composites for healthcare applications

Supakorn Suwanphiphat[1,2], Veerapat Kitsawat[1], Jia-Yu Yang[3], Cheng-Hsin Chuang[3], Ying-Chih Liao[2,*], Muenduen Phisalaphong[1,*]

[1] Bio-Circular-Green economy Technology & Engineering Center, Department of Chemical Engineering, Faculty of Engineering, Chulalongkorn University, Bangkok 10330, Thailand
[2] Precision Printing Technology Laboratory, Department of Chemical Engineering, National Taiwan University, Taipei 10617, Taiwan
[3] Institute of Medical Science and Technology, National Sun Yat-sen University, Kaohsiung 80424, Taiwan
[*] Corresponding author: liaoy@ntu.edu.tw; muenduen.p@chula.ac.th

ABSTRACT

This study presents the development of flexible piezoresistive sensor based on biocomposite film incorporating graphene as a conductive filler, natural rubber as a polymer matrix, and chitosan as a dispersant polymer. The sensor features a uniformly dispersed filler substrate, and a silver electrode fabricated via screen printing, ensuring reinforcement of electrical conductivity, thermal stability and mechanical properties including tensile strength, elastic modulus, and piezoresistivity. The prepared sensor effectively detected directional forces through variations in electrical resistivity and demonstrated high gauge factor. To further assess sensing performance, we systematically evaluated its long-term repeatability under cyclic loading conditions. The sensor maintained stable capability over multiple testing cycles, confirming its robustness for prolonged use. Additionally, the composite films exhibited enhanced antimicrobial activity and chemical resistance against non-polar solvent like toluene. This design optimizes reliable efficacy, offering high sensitivity, durability, biocompatibility, and potential applications in biodegradable wearable electronics such as human motion detectors.

Keywords: Natural Rubber; Chitosan; Graphene; Piezoresistive Sensor; Screen Printing

1. INTRODUCTION

The growing problem of electronic waste has heightened interest in biodegradable materials with enhanced electrical properties as alternatives to non-degradable components. Biopolymers, which are renewable, biodegradable polymers, are increasingly studied to replace petroleum-based plastics that contribute to environmental pollution and microplastic accumulation in ecosystems. Among these, natural rubber (NR) stands out due to its elasticity, biocompatibility, and strong mechanical performance, though it suffers from limited chemical and thermal resistance.

To address these limitations, carbon-based fillers such as graphene are introduced to improve the mechanical, thermal, and electrical properties of NR composites. Graphene, a lightweight, highly conductive two-dimensional material, offers promising reinforcement potential but tends to agglomerate due to its nanoscale size and hydrophobic nature [1]. For enhancing graphene dispersion within the natural rubber latex (NRL), this study introduces chitosan (CHI), which is biodegradable and cationic polysaccharide, as the dispersing agent. In acidic conditions, chitosan becomes protonated, enabling electrostatic stabilization and improved carbon fillers distribution in NRL [2]. Its additional properties including biocompatibility, antimicrobial activity, and environmental friendliness make it a suitable additive for sustainable composite fabrication.

This research investigates the preparation of non-vulcanized NR composite films incorporating graphene fillers, including few-layer graphene nanoplatelets (GNP) and multi-layer graphene commercial-grade (GC). Chitosan-assisted dispersion will be evaluated for its effectiveness in enhancing film properties, with a focus on mechanical strength, thermal stability, water adsorption capacity, antimicrobial activities and electrical conductivity. These composites will be assessed for potential use in flexible sensing devices.

2. EXPERIMENTAL

2.1. Materials

NRL with 60% dry rubber content (DRC) was purchased from the Rubber Research Institute of Thailand (Bangkok, Thailand). Fresh latex underwent treatment with preservatives and centrifugation to

achieve the desired rubber content, alongside the addition of aqueous ammonia to prolong shelf life and preserve NR in its latex state. CHI with food-grade quality, sourced from shrimp shells, possessed a molecular weight 35 kDa, particle size below 1.5 mm, and degree of deacetylation (%DD) of 90% was purchased from Marine Bio Resources Co., Ltd. (Samut Sakhon, Thailand). GNP with few-layer, higher nitrogen and oxygen defects was obtained from XG Sciences (Lansing, USA). GC was obtained from Suzhou Tanfeng Graphene Technology Co., Ltd. (Suzhou, China), presenting as multilayer graphene with higher carbon content and black powder appearance. 25% w/v ammonia solution and anhydrous acetic acid were obtained from Merck (Darmstadt, Germany).

2.2. Preparation of NR-CHI-Graphene Film for Substrate

Composite films of NR-CHI-Graphene were fabricated using the latex aqueous micro-dispersion process, a method previously developed by our research team [2-4]. To prepared the composite films of NR-CHI-GNP15 and NR-CHI-GNP30, the loading quantity of GNP was at 15 and 30 parts per hundred rubbers (phr), respectively. To prepared the composite films of NR-CHI-GC60 and NR-CHI-GC90, the loading quantity of GC was at 60 and 90 phr, respectively. To prepare CHI solution, CHI powder was dissolved in 2% v/v acetic acid, provided by diluting anhydrous acetic acid. The CHI solution was mechanically stirred for 40 minutes until complete dissolution, resulting in a 2% w/v CHI solution. Graphene was then added into 15 mL of 2% w/v CHI and thoroughly mixed the slurry under mechanical stirring at 300 rpm for 20 minutes. Subsequently, 15 mL of 2% v/v ammonia solution was added to neutralize the acid and adjust the optimal pH of the mixture. The slurry was further blended at 500 rpm for an additional 30 minutes and subjected to sonication at 500 Watts for 10 minutes to ensure homogeneous dispersion of filler particles. In the following step, 5 g of NRL was gradually introduced into the slurry while continuously stirring mechanically until homogeneous mixture was attained. Thereafter, the mixture was poured into a glass culture dish and dried at 40 °C for 24 hours in an air circulating oven to obtain NR composite films. After drying, the films were washed with deionized water to eliminate any residual acid and impurities and eventually dried in an oven at 40 °C for 24 hours. The NR composite substrates were stored in an airtight container for subsequent characterization.

2.3. Application for Piezoresistive Sensors

To investigate the strain and pressure sensing performance, the screen-printing technique was employed to fabricate silver ink electrode on the NR composite substrates, enhancing the sensitivity. Human body demonstrations were conducted to evaluate the practical sensing capabilities of the composite. The sensor was connected to a high-sensitivity electrometer to monitor changes in resistance during stretching tests. For repeatability analysis, the sensor was subjected to continuous pressure and strain cycles. The JSV-H1000 vertical stand with an ALGOL force gauge was used to test stretching stability, while a micro-tensile testing machine was utilized for bending stability. To examine the effectiveness of the sensor, double-sided copper tapes were affixed to both ends of the sensing layer, serving as electrodes. These electrodes enabled wire connections and facilitated performance assessments throughout bending tests. Furthermore, a digital multimeter was utilized for real-time resistance monitoring for the whole of various human movement scenarios.

3. RESULTS AND DISCUSSION

3.1. Effect of CHI as dispersant

The investigation into the utilize of CHI as a dispersant for graphene suspension in solution is crucial, because graphene fillers tend to agglomerate within the rubber matrix without CHI, leading to a deterioration in the physical properties of the composites. This study focused on key factors such as concentration, demonstrating the potential of CHI as an effective stabilizing agent to ensure uniform dispersion through electrostatic attractions, hydrogen bonding, and van der Waals force [5, 6]. Due to its hydrophobic nature, graphene does not disperse well in water or hydrophilic polymers. To determine the optimal concentration of CHI solution for preparing biopolymer composites, the aqueous acetic acid concentration was fixed at 2% (v/v), while the CHI concentration was varied between 0.5 wt% and 2 wt%. It was observed that the concentration of CHI used as a dispersing agent significantly influences GNP and GC suspensions; higher CHI concentrations lead to better graphene dispersion and facilitate mass transfer. The maximum CHI concentration is limited to 2% (w/v) to prevent a decrease in the mechanical strength of the films, which can occur due to the increased amorphous phase fraction from excessive CHI incorporation. Furthermore, the prepared composites integrated with CHI were further validated by field-emission scanning electron microscope (FE-SEM) analysis.

The morphology and microstructure of the prepared composite films were initially examined using FE-SEM. As shown in Figure 1, the NR film displays a consistent and smooth appearance. On the other hand, the surfaces of the NR-CHI-Graphene film is noticeably rougher, with surface roughness increasing as the graphene loading is enhanced. Despite this, the composite films consistently demonstrate homogeneity, with graphene fillers well-integrated and uniformly distributed throughout the NR matrix, as observed in both surface and cross-sectional views. This suggests that CHI effectively promotes the dispersion of

graphene fillers. Importantly, the incorporation of graphene fillers into the NR matrix occurs without phase separation or agglomeration, highlighting the potential of CHI as a dispersing agent to improve the suspension and stability of graphene within the NR matrix.

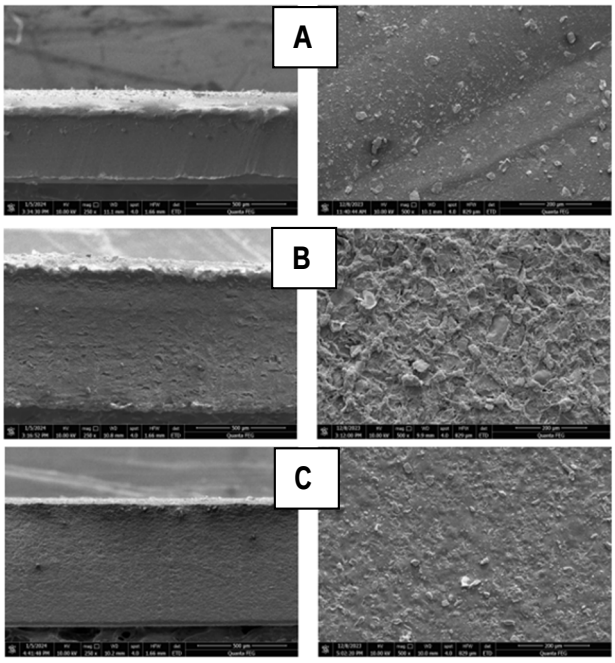

Figure 1 FE-SEM images of cross-sectional (left) and surface (right) of NR (A), NR-CHI-GNP30 (B) and NR-CHI-GC-90 (C).

3.2. Thermal Stability

Thermal stability is a key factor for conductive materials, especially in high-temperature environments. To assess the thermal properties of NR, NR-CHI, NR-CHI-GNP, and NR-CHI-GC films, thermogravimetric analysis (TGA) was performed. The results show that the addition of CHI and graphene fillers improves the thermal stability of the composites. TGA data indicate that both decomposition temperatures and residual mass at 700 °C increase with higher graphene content, due to the shielding effect of crystalline graphene structure, shown in Table 1. This effect is more pronounced with GNP and GC, which have stronger carbon networks and require more energy to degrade [7]. From Figure 2, TGA revealed a two-step degradation process, with the first step occurring around 220 °C and the second between 330 - 480 °C. The remaining weight after degradation was significantly higher for the composites than for pure NR, reflecting stabilizing influence of graphene.

Table 1 Thermal data for NR, NR-CHI, NR-CHI-GNP, and NR-CHI-GC composite films.

Sample	$T_{50\%}$ (°C)	Residual Mass at 700 °C (wt.%)
NR	380.2	0.34
NR-CHI	383.5	1.95
NR-CHI-GNP15	385.3	12.85
NR-CHI-GNP30	388.7	21.72
NR-CHI-GC60	399.5	34.46
NR-CHI-GC90	422.3	44.93

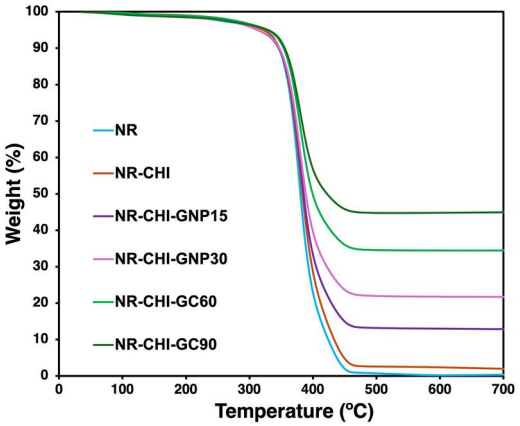

Figure 2 Thermal stability analysis from TGA curves of the NR, NR-CHI, NR-CHI-GNP, and NR-CHI-GC films.

3.3. Thermal Conductivity

The thermal conductivity of the natural rubber-based composites was evaluated at 26 °C to understand the effect of CHI and graphene incorporation. The NR sample exhibited the analysis of 0.145 W/m·K, which is consistent with the values reported in literature for unmodified NR due to its intrinsic low thermal conductivity. Upon integration of CHI (NR-CHI), a decrease in thermal conductivity was observed as shown in Figure 3, with a measured value of 0.088 W/m·K. This phenomenon can be attributed to nanopore construction on composite surface, which may hinder the free movement of molecules [8].

However, CHI has been reported to improve the thermal stability of polymer composites by providing better resistance to thermal degradation [9], thereby contributing to durability under elevated temperatures. Significant enhancement in thermal conductivity was achieved in NR-CHI-GC90 composite, where GC was introduced at 90 phr. The thermal conductivity of this composite film reached values as high as 0.22 W/m·K, corresponding to an increase of approximately 51.7% compared to pristine NR. This substantial improvement is ascribed to the formation of a thermally conductive network through the high aspect ratio graphene sheets embedded within the rubber matrix [10].

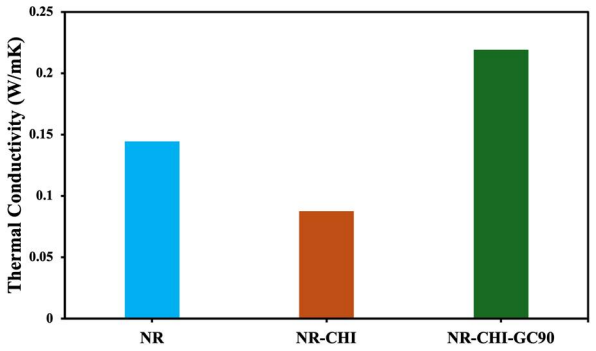

Figure 3 Thermal conductivity of NR, NR-CHI, NR-CHI-GC90 composite films at 26 °C.

3.4. Electrical Conductivity

The electrical conductivity of NR and NR composite films is evaluated using electrochemical impedance spectroscopy (EIS) across a frequency range of 100 kHz to 1 Hz. The Nyquist plots show that electrical conductivity increases with higher graphene loading, as indicated by a reduced semicircle region in the plots, reflecting lower impedance [11].

The film of pure NR displayed the largest semicircle, indicating its insulating properties, with the lowest conductivity measured at 4.12×10^{-12} S/cm. As shown in Table 2, the increase in loading content of GNP and GC resulted in enhanced conductivity. Conductivity values for the highest GNP and GC loadings were 4.75×10^{-4} and 2.36×10^{-4} S/cm, respectively. This improvement is largely due to the crystallinity of GNP and GC, and strong interactions between the graphene fillers and the polymer matrix. The formation of a conductive network within the composite, facilitated by graphene filler, leads to a significant improvement in conductivity, indicating the presence of a tunneling effect as filler content rises [12].

Table 2 Electrical conductivity (σ) for NR, NR-CHI, NR-CHI-GNP, and NR-CHI-GC composite films.

Sample	σ (S/cm)
NR	4.12×10^{-12}
NR-CHI	2.64×10^{-10}
NR-CHI-GNP15	4.12×10^{-6}
NR-CHI-GNP30	4.75×10^{-4}
NR-CHI-GC60	1.80×10^{-5}
NR-CHI-GC90	2.36×10^{-4}

3.5. Water Adsorption Capacity

The water absorption capacity (WAC) profiles of the neat NR and NR composite films incorporated with CHI and GNP/GC are illustrated in Figure 4. The pristine NR sample exhibited a continuous increase in WAC over the 14-day immersion period, indicating a steady diffusion-controlled absorption process. This behavior is attributed to the hydrophobic yet porous nature of NR, which allows water molecules to gradually penetrate and be retained within its polymer matrix. Additionally, the composite films containing CHI and graphene fillers demonstrated significantly different water absorption behaviors. Notably, the NR-CHI-GNP30 film showed a remarkably high initial water uptake (≈34% at day 2), followed by near plateau phase throughout the remainder of this experiment, reaching about 38% at day 14. This indicates that the hydrophilic functional groups of CHI and GNP facilitated rapid water adsorption initially, but became saturated within 2 days, after which water diffusion was restricted that likely due to reduced pore volume and the barrier effect created by stacked GNP layers [4, 13].

Furthermore, The NR-CHI-GC90 composite followed a similar trend but with a lower WAC overall compared to NR-CHI-GNP30. This suggests that although both GNP and GC can enhance water interaction through surface functionality, its high loading or morphology of graphene filler structures may result in a denser network, reducing free volume and thus water permeability. While the NR-CHI composite also absorbed water faster than NR film in the early stage, its WAC values remained consistently lower than those of NR-CHI-GNP30 and NR-CHI-GC90 across all time points. This could be attributed to the lack of extended surface area and layered structure found in graphene, which otherwise promotes initial adsorption.

To conclude, the results demonstrate that the incorporation of both CHI and graphene fillers influences the water affinity of NR composites, where the combination of polar functional groups from CHI and high surface area from graphene contributes to higher water uptake in early immersion periods. However, the structural compaction and barrier effect of graphene tend to limit further water diffusion, leading to an equilibrium state much earlier than that of neat NR.

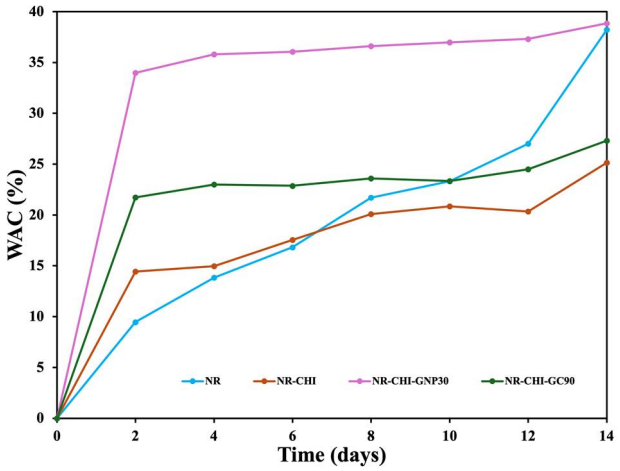

Figure 4 Water adsorption capacity (WAC%) with time of NR, NR-CHI, NR-CHI-GNP30, and NR-CHI-GC90 composite films.

3.6. Antimicrobial Efficacy

To assess antimicrobial activity, *Staphylococcus aureus* (*S. aureus*) and *Escherichia coli* (*E. coli*) were chosen as representative models for gram-positive and gram-negative bacteria, respectively. Meanwhile, *Aspergillus niger* (*A. niger*) was selected to evaluate antifungal ability. The neat NR exhibited moderate antimicrobial properties, showing 44.93% reduction against *S. aureus* and 31.46% against *A. niger*, while no significant effect was observed for *E. coli*. The incorporation of CHI notably improved antibacterial performance, with the NR-CHI composite film achieving 100% efficacy against *S. aureus*. On the other hand, its inhibitory effect on *E. coli* was approximately 50%; whereas, the reduction against *A. niger* was around 6.14%, indicating the restricted antifungal effectiveness of CHI.

The integration of graphene nanoplatelets into NR composite films enhanced antimicrobial activities. The addition of 30 phr GNP (NR-CHI-GNP30) showed some improved antimicrobial activities. Specifically, a reduction of 99.98% in *S. aureus* and 94.31% in *A. niger* was observed. However, no substantial reduction in *E. coli*, highlighting strain-specific differences in response. This can be explicated by the unique role of nitrogen atoms in the structure of graphene. Typically, graphene functions as an electron sink in the bacterial respiratory pathway [14]. Additionally, the film of NR-CHI-GC90 exhibited a wider antimicrobial performance, with reductions of 97.29%, 55.04%, and 93.85% for *S. aureus*, *E. coli*, and *A. niger*, respectively. This demonstrates the combined antimicrobial efficacy of graphene and CHI, which proves effective against both gram-positive and gram-negative bacteria as well as fungal strains.

Furthermore, the number of graphene layers plays a crucial role in determining its antimicrobial activity. A greater number of layers increases the thickness of graphene, which diminishes its "nano-knife" effect, reduces dispersibility, and promotes aggregation [15]. These factors limit the contact between graphene and microorganisms, thus may reduce its antimicrobial effectiveness. Although the increased number of graphene layers enhanced the antimicrobial effect against *E. coli*, likely due to differences in the interaction mechanisms between graphene and gram-negative bacterial membranes.

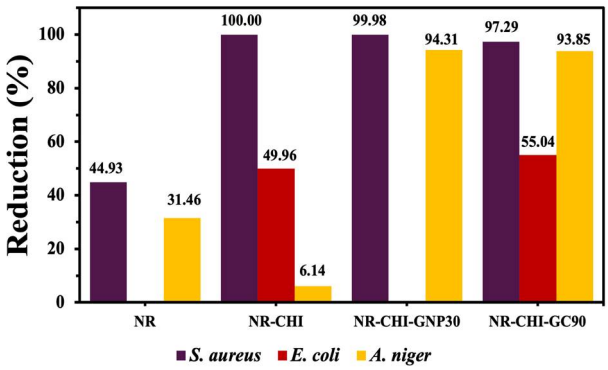

Figure 5 Antimicrobial efficacy by reduction of representative microorganisms in 24 hours.

3.7. Mechanical Properties

The mechanical properties of NR composite films, including tensile strength, Young's modulus, and elongation at break, were significantly influenced by the addition of graphene fillers. The introduction of CHI solution enhanced stability, homogeneity, and filler dispersion in the composites. The addition of graphene fillers significantly improved tensile strength and Young's modulus. For instance, the tensile strength of NR-CHI-GNP15 increased to 8.47 MPa, a 1.6-fold improvement over NR-CHI. The elastic modulus, a measure of stiffness, increased with higher graphene loadings, with the highest value observed at 128.87 MPa for NR-CHI-GC90, about 100 times greater than the neat NR film. The stiff nature of graphene and its effect on restricting chain mobility contributed to this increase [16, 17].

Elongation at break, indicating material toughness, decreased as graphene loading increased due to the rigidity introduced by the fillers. While the neat film's elongation was 563%, NR-CHI-GNP composites ranged from 226% at 15 phr to 88% at 30 phr, and NR-CHI-GC composites ranged from 125% to 90%, depending on loading. This reduction in elongation, combined with increased modulus, reflects the influence of CHI on rubber-filler interactions and filler dispersion, controlling the mechanical properties of NR composites.

Table 3 Mechanical Properties for NR, NR-CHI, NR-CHI-GNP, and NR-CHI-GC composite films.

Sample	Tensile strength (MPa)	Young's modulus (MPa)	Elongation at break (%)
NR	2.512	1.478	562.7
NR-CHI	5.241	11.434	236.8
NR-CHI-GNP15	8.472	34	226.3
NR-CHI-GNP30	7.276	111.83	87.76
NR-CHI-GC60	10.627	124.71	125
NR-CHI-GC90	8.635	128.87	90.48

3.8. Piezoresistive Sensing Performance

To ensure optimal physical performance of the prepared substrate for sensor applications, the geometry of sensor is critical in achieving 2D directional sensing capabilities. In this process, a hairpin-shaped design was employed, characterized by one side being significantly longer than the other. When the sensor was stretched along the direction perpendicular to the longer side, it exhibited a remarkable response to strain. To further assess the performance of the composites in strain sensing, the sensitivity of the sensor was evaluated by calculating the gauge factor (GF) [18].

$$GF = \frac{\Delta R / R_o}{\Delta L / L_o}$$

To study human motion detection ability of the piezoresistive sensor, the typical activity frequency ranges from 1 to 3 Hz. Figure 6 illustrates the electrical response of the prepared sensor across various frequencies. This result demonstrates that the sensor maintains excellent sensitivity and stable response within the applied frequency range of 1 – 6 Hz, indicating that it suitable for wearable motion real-time detection of high frequency without noticeable delay [19]. In addition, the relative resistance changes at different frequency are attributed to the fact that the strain rate has almost no effect on its sensing performance.

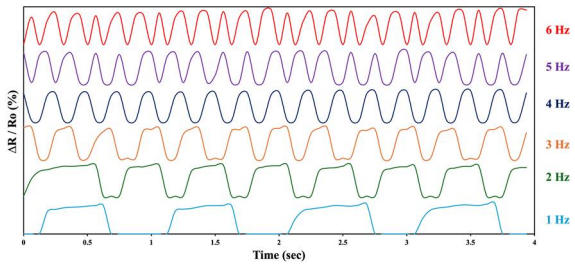

Figure 6 Frequency test showing sensing performance of prepared composite film under 5% strain.

4. CONCLUSION

This study aimed to develop a flexible piezoresistive sensor using a bio-composite film composed of natural rubber (NR), chitosan (CHI), and graphene, targeting applications in wearable healthcare monitoring. The fabricated sensors demonstrated enhanced thermal and electrical conductivity, mechanical robustness, and remarkable piezoresistive sensitivity. Notably, the NR-CHI-GC90 composite exhibited significant thermal conductivity improvement (51.7% increase) and high gauge factor values, validating its effectiveness for real-time strain sensing. Additionally, the composites showed strong antimicrobial activity, particularly when CHI and graphene were synergistically integrated. These findings highlight the promising potential of NR-CHI-Graphene composites in next-generation biodegradable and biocompatible wearable electronics. Overall, this work contributes to the growing field of sustainable smart materials, offering a scalable pathway for eco-friendly, high-performance strain sensors suitable for healthcare and soft robotics applications.

ACKNOWLEDGMENTS

This research was supported by Thailand Science Research and Innovation Fund Chulalongkorn University (BCG_FF_68_146_2100_025). The authors gratefully acknowledge the funding which enabled the successful completion of this work. S.S. would like to thank the Faculty of Engineering, Chulalongkorn University, for providing a scholarship for the dual degree program. The authors also wish to express their appreciation to all individuals and institutions whose support, resources, and guidance contributed to this research.

REFERENCES

1. Hashim, U. R.; Jumahat, A.; Jawaid, M., Mechanical Properties of Hybrid Graphene Nanoplatelet-Nanosilica Filled Unidirectional Basalt Fibre Composites. *Nanomaterials (Basel)* **2021,** *11* (6).
2. Sutipanwihan, N.; Kitsawat, V.; Sintharm, P.; Phisalaphong, M., Natural Rubber Films Reinforced with Cellulose and Chitosan Prepared by Latex Aqueous Microdispersion. *Polymers (Basel)* **2024,** *16* (18).
3. Phomrak, S.; Phisalaphong, M., Lactic Acid Modified Natural Rubber–Bacterial Cellulose Composites. *Applied Sciences* **2020,** *10* (10).
4. Kitsawat, V.; Siri, S.; Phisalaphong, M., Electrically Conductive Natural Rubber Composite Films Reinforced with Graphite Platelets. *Polymers (Basel)* **2024,** *16* (2).
5. Chen, P.; Zhao, C.; Wang, H.; Li, Y.; Tan, G.; Shao, Z.; Nishiyama, Y.; Hu, T.; Wohlert, J., Quantifying the Contribution of the Dispersion Interaction and Hydrogen Bonding to the Anisotropic Elastic Properties of Chitin and Chitosan. *Biomacromolecules* **2022,** *23* (4), 1633-1642.
6. Kim, H.-S.; Lee, S.-H.; Eun, C.-J.; Yoo, J.; Seo, Y.-S., Dispersion of chitosan nanoparticles stable over a wide pH range by adsorption of polyglycerol monostearate. *Nanomaterials and Nanotechnology* **2020,** *10*.
7. Farivar, F.; Lay Yap, P.; Karunagaran, R. U.; Losic, D., Thermogravimetric Analysis (TGA) of Graphene Materials: Effect of Particle Size of Graphene, Graphene Oxide and Graphite on Thermal Parameters. *C* **2021,** *7* (2).
8. George, G.; Sisupal, S. B.; Tomy, T.; Pottammal, B. A.; Kumaran, A.; Suvekbala, V.; Gopimohan, R.; Sivaram, S.; Ragupathy, L., Thermally conductive thin films derived from defect free graphene-natural rubber latex nanocomposite: Preparation and properties. *Carbon N Y* **2017,** *119*, 527-534.

9. Zou, Q.; Xiong, S. W.; Jiang, M. Y.; Chen, L. Y.; Zheng, K.; Fu, P. G.; Gai, J. G., Highly thermally conductive and eco-friendly OH-h-BN/chitosan nanocomposites by constructing a honeycomb thermal network. *Carbohydr Polym* **2021,** *266*, 118127.
10. Chen, H.; Chen, N.; Ma, Q.; He, Y., Experimental study on preparation and properties of carbon nanotubes-, graphene –natural rubber composites. *Journal of Thermoplastic Composite Materials* **2023,** *37* (6), 2013-2034.
11. Barbosa, R.; Gonçalves, R.; Blanco, G. E. d. O.; Saccardo, M. C.; Tozzi, K. A.; Zuquello, A. G.; Scuracchio, C. H., Multi-sensing properties of hybrid filled natural rubber nanocomposites using impedance spectroscopy. *Electrochimica Acta* **2022,** *435*.
12. Lin, G.; Wang, H.; Yu, B.; Liu, S.; Liang, Z.; Liu, F.; Zeng, R.; Chen, S.; Kuang, T.; Yu, K.; Chi, B., Incorporation and optimization of RGO and GO in SSBR/NR composites expands their applicability. *Polymers and Polymer Composites* **2021,** *29* (9_suppl), S411-S421.
13. Raju, G.; Mas Haris, M. R. H.; Azura, A. R.; Ahmed Mohamed Eid, A. M., Chitosan Epoxidized Natural Rubber Biocomposites for Sorption and Biodegradability Studies. *ACS Omega* **2020,** *5* (44), 28760-28766.
14. Elsherbiny, A. S.; Galal, A.; Ghoneem, K. M.; Salahuddin, N. A., Graphene oxide-based nanocomposites for outstanding eco-friendly antifungal potential against tomato phytopathogens. *Biomater Adv* **2024,** *160*, 213863.
15. Mohammed, H.; Kumar, A.; Bekyarova, E.; Al-Hadeethi, Y.; Zhang, X.; Chen, M.; Ansari, M. S.; Cochis, A.; Rimondini, L., Antimicrobial Mechanisms and Effectiveness of Graphene and Graphene-Functionalized Biomaterials. A Scope Review. *Front Bioeng Biotechnol* **2020,** *8*, 465.
16. Mohammad, H.; Stepashkin, A. A.; Laptev, A. I.; Tcherdyntsev, V. V., Mechanical and Conductive Behavior of Graphite Filled Polysulfone-Based Composites. *Applied Sciences* **2022,** *13* (1).
17. Zhang, S.; Xiong, Z.; Zhang, J.; Zhang, X.; Chen, Y.; Chen, Y., Mechanical properties and thermal analysis of graphene nanoplatelets reinforced polyimine composites. *e-Polymers* **2022,** *22* (1), 696-704.
18. Lu, H. C.; Liao, Y. C., Direct Printed Silver Nanowire Strain Sensor for Early Extravasation Detection. *Nanomaterials (Basel)* **2021,** *11* (10).
19. Yang, J. Y.; Kumar, A.; Shaikh, M. O.; Huang, S. H.; Chou, Y. N.; Yang, C. C.; Hsu, C. K.; Kuo, L. C.; Chuang, C. H., Biocompatible, Antibacterial, and Stable Deep Eutectic Solvent-Based Ionic Gel Multimodal Sensors for Healthcare Applications. *ACS Appl Mater Interfaces* **2023,** *15* (48), 55244-55257.

Development of self-healing polymers from bio-based benzoxazine blended with poly (ethylene glycol)

Pharaporn Yodkum[1], Phattarin Mora[2], Krittapas Charoensuk[1], Sarawut Rimdusit[1,*]

[1] Center of Excellence in Polymeric Materials for Medical Practice Devices, Department of Chemical Engineering, Faculty of Engineering, Chulalongkorn University, Bangkok 10330, Thailand
[2] Department of Chemical Engineering, Faculty of Engineering, Srinakharinwirot University, Nakhonnayok 26120, Thailand
[*] Corresponding author: sarawut.r@chula.ac.th

ABSTRACT

Self-healing polymers have recently garnered interest in smart materials because of their ability to prolong material longevity, decrease maintenance expenses, minimize waste creation, and conserve resources. This study presents the development of self-healing polymers utilizing bio-based benzoxazine resin (E-fa resin), sourced from renewable materials, i.e. eugenol as phenolic sources, furfurylamine as amine sources, and paraformaldehyde, combined with poly (ethylene glycol) (PEG) by varying molecular weights (PEG 600, 1500, and 4000 g/mol) (see in Figure. 1). This work focusses on the influences of PEG molecular weights on curing behaviors and self-healing performances of the blended E-fa/PEG polymers. At a constant E-fa/PEG 85/15 wt/wt%, differential scanning calorimetry (DSC) confirmed that the blends were fully cured, with no significant changes in T_{onset} and T_{peak} across different PEG molecular weights compared to that of the neat E-fa (T_{onset} of 194 °C, T_{peak} of 223 °C). In addition, the surface scratching technique was utilized for evaluation of self-healing capability of the blends by observing dimensional scratch change using optical microscopy (OM) before and after thermal healing. The results suggested that increasing PEG molecular weight led to enhance self-healing efficiency, achieving greater than 90% with healing speed of blended E-fa/PEG4000 within 4 minutes. Finally, enhanced hydrophobicity of the blends was exhibited when increasing PEG molecular weights. Hence, a self-healable polybenzoxazine/PEG hybrid systems via a Diels–Alder reaction have successfully been developed in this work, offering a promising approach for sustainable smart materials.

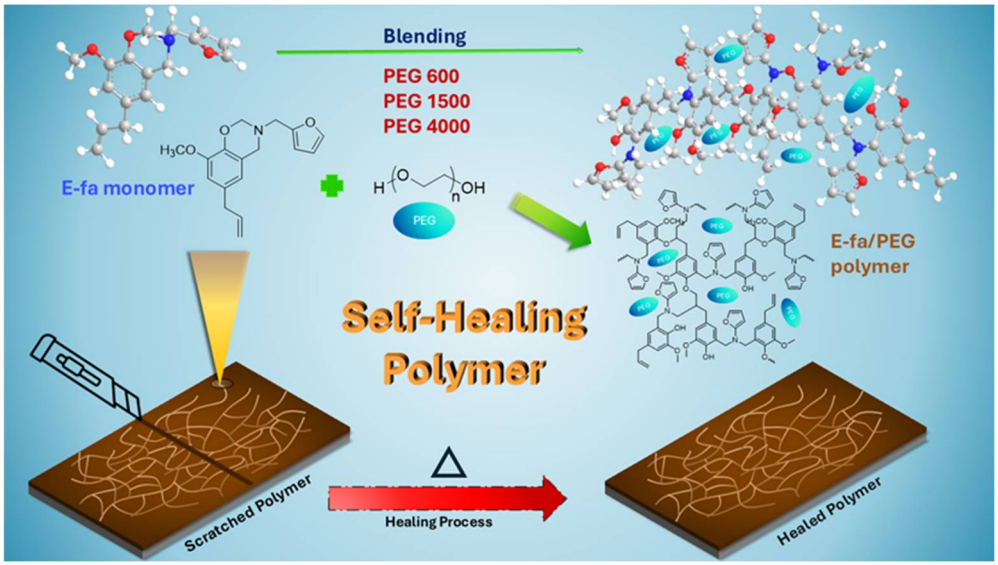

Figure 1. Self-healable polymer based on E-fa/PEG blend.

Keywords: Self-healing Polymer; Bio-based Benzoxazine; Poly (ethylene glycol); Polymer blend.

1. INTRODUCTION

In practice, polymers were used in many fields which have mechanical abrasion, radiation damage, or chemical attack to polymeric products happens as usual due to long-term usability or accidental damage to the products. Thus, damage or fracture within polymers are inevitable and finally results in the failure of polymeric products. In terms of expanding the shelf life of polymer products and the environmental goals which as development of sustainable products. Subsequently, there are increasing interest in the researches of self-healing polymers which possess the recovery ability from actual damage [1, 2]. Self-healing polymers (SHPs) refer to polymers that can partially or fully restore their initial properties including their appearance, shape, mechanical strength, fracture toughness, conductivity, and corrosion resistance [3]. Healing process occurs either autonomically or in response to external stimuli [4]. SHPs are smart materials which are being used in various applications including coatings [5], soft robotics [6], flexible electronics [7], and sensors [8]. SHPs systems can be divided into two systems based on their healing mechanisms: (1) extrinsic system and (2) intrinsic system [1]. The extrinsic system requires the healing agents which contain in microcontainers (e.g., microcapsules or microvascular) and are embedded in polymer matrix to assist in self-healing process. However, microcontainers are unable to be reused after being damaged which is the limitation of this approach. On the contrary, the intrinsic system relies on the molecular interaction between bonds in their structures, reversible chemistry, and those interactions such as Diels-Alder reaction [9], disulfide exchange [10], host-guest interactions [11], supramolecular interactions [12], etc. Moreover, intrinsic self-healing is a repeatable healing process which is outstanding properties of this approach. Intrinsic approach can be accomplished with and without external stimuli including heat [13], light [14], and pH [15].

Polybenzoxazines (PBZs) are thermosetting polymer synthesized from phenolic derivatives, primary amines, and formaldehyde through Mannich condensation reaction [16]. PBZs, commonly known as high-performance thermosetting polymers, provide the attraction with unique properties such as excellent mechanical properties, high thermal stability, low surface free energy, low water absorption, chemical resistance, near-zero shrinkage, and dimensional stability [17]. Those properties render PBZs are used in various applications including advanced coatings, aerospace, electronics, and automotive industries [18]. In addition, PBZs have been utilized in smart materials, especially self-healing polymer [19-21]. However, the conventional benzoxazine components are derived from petroleum-based resources. Currently, petroleum-based benzoxazines are decreasingly used owing to the environmental concerns and increasing energy crisis. Bio-based benzoxazines which derived from renewable resources have become interesting utilization instead of petroleum-based resources [22]. Many researches have been reported on the synthesis of bio-based benzoxazine, such as cardanol-furfurylamine-based benzoxazine [23], eugenol-furfurylamine-based benzoxazine, eugenol-stearylamine-based b/enzoxazine [24], and daidzein-furfurylamine-polyetheramine-based benzoxazine [22]. Among these bio-based benzoxazines, eugenol-furfurylamine-based benzoxazine has an allyl group from eugenol and furan unit from furfurylamine in its molecular structure which provide provide self-healing ability through Diels-Alder reaction. Whereas, others bio-based benzoxazines need to add components that has self-healing ability to create self-healing polymers [13]. Mora et al. (2024) [13] developed a self-healing copolymer from eugenol-furfurylamine-based benzoxazine (E-fa) and epoxidized castor oil (ECO). They investigated the self-healing performance of E-fa as a healing agent in the copolymer. The results revealed that increasing E-fa content enhanced the healing efficiency, reaching up to 93%. Nevertheless, benzoxazine is considered as a brittle material because of its rigid structure, incorporating flexible or long chain polymer networks is essential to improve chain mobility and enhance the self-healing ability of SHPs [25]. Therefore, copolymerization or blending of PBZ with flexible polymer is a promising approach to provide appropriate molecular structure for use in self-healing application.

Poly (ethylene glycol) (PEG) is a thermoplastic, water-soluble, and biocompatible polymer formed from ethylene glycol repeating units [26]. PEG is a flexible, hydrophilic, non-toxic, and non-ionic polymer, widely used in biomedical, food, cosmetics, pharmaceutical products, and coating applications [27]. It has also been studied for copolymerization with thermosetting polymer to enhance toughness Zavareh S. and Samandari G. (2014) [28] used PEG as an epoxy modifier, finding that introducing PEG into epoxy resin improved the impact and fracture properties of the Epoxy/PEG hybrid. The hybrid exhibited an impact strength 5.7 times greater than that of pristine epoxy, while its fracture strength increased by 540%. Due to its flexibility and flowability, PEG offers a strategic pathway to impart both toughness and self-healing capabilities [29]. This synergistic combination aims to create advanced self-healing materials that not only reduce environmental impacts but also meet the demands of advanced engineering applications.

Therefore, this study focuses on developing a self-healing polymer which is prepared from blending bio-based benzoxazine (E-fa resin) derived from eugenol as phenolic sources, furfurylamine as amine sources, and paraformaldehyde with poly (ethylene glycol) (PEG). The influences of PEG molecular weights on curing behavior and self-healing performance of the blended E-fa/PEG polymers.

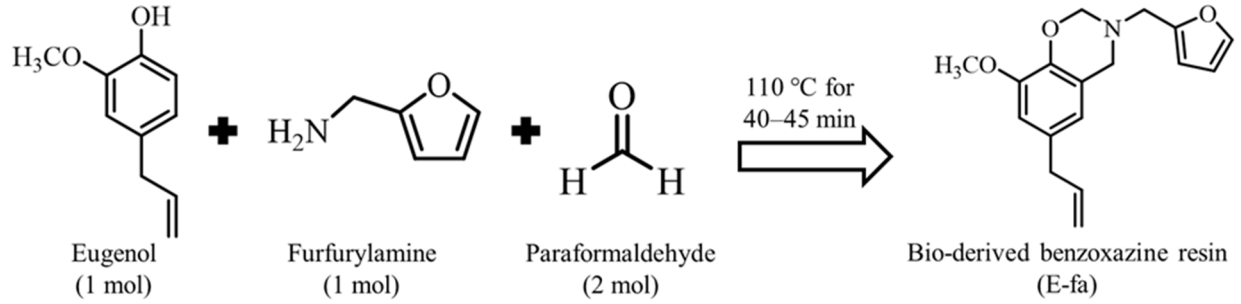

Scheme 1. Preparation of bio-based benzoxazine resin.

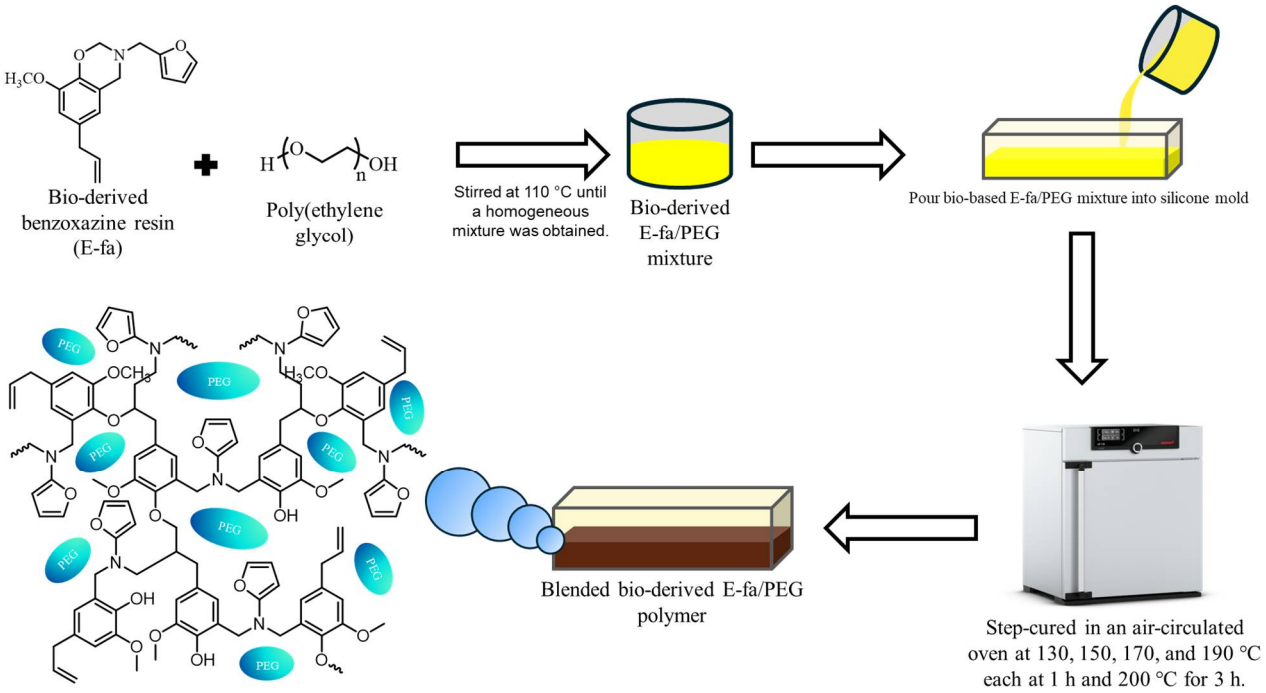

Scheme 2. Preparation of E-fa/PEG blends at a constant ratio of 85/15 wt/wt% with various molecular weights of PEG.

2. EXPERIMENTAL

2.1. Materials

Bio-based benzoxazine resin derived from eugenol, furfurylamine, and paraformaldehyde. Eugenol (>99.0 %) and furfurylamine (98.0 %) were purchased from Tokyo Chemical Industry Co., Ltd., United States. Paraformaldehyde (AR grade) and poly (ethylene glycol) with a molecular weight of 1500 g/mol (PEG1500) were purchased from Sigma-Aldrich Pte. Ltd., United States. Poly (ethylene glycol) with molecular weights of 600 and 4000 g/mol (PEG600 and PEG4000) were purchased from Merck Co., Ltd. (Darmstadt, Germany). All chemicals were used as received.

2.2. Bio-based benzoxazine preparation

Bio-based benzoxazine (E-fa resin) was synthesized from eugenol, furfurylamine, and paraformaldehyde at a molar ratio of 1:1:2 via the solventless synthesis method [15] as shown in Scheme 1. The tree reactants were constantly stirred at 110 °C in an aluminum pan for 40–45 minutes to obtain a homogeneous mixture. Then, the mixture was placed at room temperature, and a transparent yellow resin was obtained.

2.3. E-fa/PEG blends preparation

E-fa/PEG blends were prepared from benzoxazine resin (E-fa) and poly (ethylene glycol) with various molecular weights (PEG600, PEG1500, and PEG4000) at a constant E-fa/PEG 85/15 wt/wt% as depicted in Scheme 2. The E-fa resin was stirred at 110 °C, and then the PEG was added to prepare E-fa/PEG mixtures. The mixture was continuously stirred to achieve a homogeneous mixture. The mixture was poured into a silicone mold. After that, the mixture was step-cured in an air-circulated oven at 130 °C, 150 °C, 170 °C, and 190 °C for 1 h each, followed by curing at 200 °C for 3 h. The sample was cooled down to room temperature for further characterization.

2.4. Curing behavior investigation

The curing behaviors of the mixtures were investigated using a differential scanning calorimeter (DSC) (model DSC1 module from Mettler-Toledo (Thailand) Ltd., Bangkok, Thailand). An aluminum pan with a lid was used to contain a sample mass of 5–10 mg. The sample was dynamically scanned from 25 °C to 300 °C with a heating rate of 10 °C/min while nitrogen gas was purging at a rate of 50 ml/min.

2.5. Thermally triggered surface scratching

The fully cured E-fa/PEG polymer was scratched via a cutter blade (Aroma L-D100, thickness of cutter blade 5 mm), and then the sample was heated at 100 °C on a hot plate stirrer. The scratch width of the samples before and after healing was observed using an optical microscope (OM) in reflection mode (20X magnification, Nikon model ECLIPSE E600 POL from Nikon, Inc., Tokyo, Japan) with a Canon EOS rebel T3 camera, to observe the surface healing behaviors.

2.6. The surface wettability

The surface wettability of the polymers was measured using a contact angle meter (model DMe-210, Kyowa, Japan). The water contact angle was performed using FAMAS software, and each sample was measured five times.

3. RESULTS AND DISCUSSION

3.1. Curing behaviors of E-fa/PEG blends at various molecular weights of PEG.

Table 1 DSC data of the E-fa monomer and E-fa/PEG blends.

Sample	T_{g0} (°C)	T_{onset} (°C)	T_{peak} (°C)	Enthalpy (J/g)
E-fa	74	194	223	24.2
E-fa/PEG 600	83	223	240	17.1
E-fa/PEG 1500	83	222	239	19.7
E-fa/PEG 4000	83	223	240	20.8

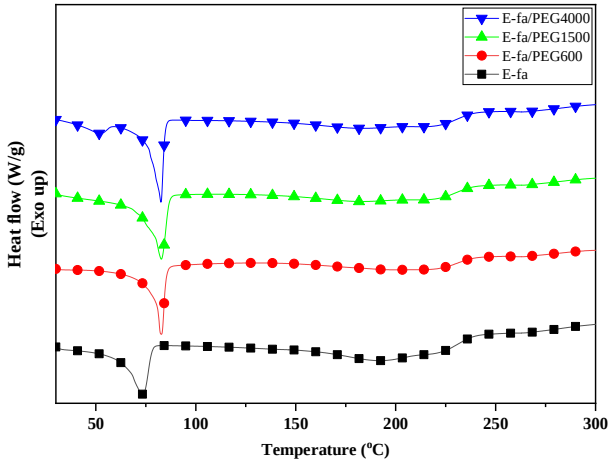

Figure 2. DSC thermograms of E-fa monomer and E-fa/PEG blends with various molecular weights of PEG.

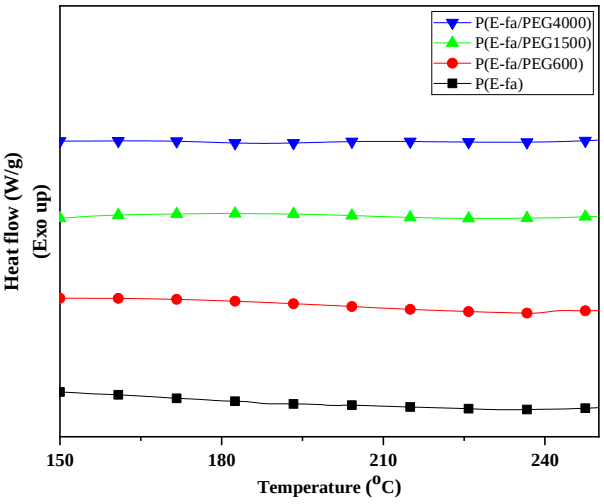

Figure 3. DSC curves of poly (E-fa) and poly (E-fa/PEG) blends with various molecular weights of PEG after the curing process.

DSC thermograms of the E-fa monomer and E-fa/PEG blends with a constant ratio of 85/15 wt/wt% using various molecular weights of PEG are shown in Figure 2 and summarized in Table 1. DSC results display a single endothermic peak refers to T_{g0}, the initial temperature at which the monomer changes state from a glassy to a rubbery state. The T_{peak} represents the exothermic peak associated with ring-opening polymerization of the oxazine rings in benzoxazine, clearly observed in both E-fa monomer and E-fa/PEG blends. A shift in T_{peak} and T_{onset} to higher temperatures for the E-fa/PEG blends compared to the E-fa monomer was due to the dilution effect as reported in previous studies [21, 30, 31]. This effect results from a reduced concentration of the oxazine rings per unit weight, leading to decreased polymerization reactivity and curing enthalpy. In addition, the molecular weights of PEG showed no significant effect on curing behavior of the blends. To confirm complete curing, the cured sample was also evaluated by DSC as presented with

the DSC thermograms in Figure 3. The disappearance of exothermic peaks in the thermograms indicated that the polymerization was completed. Therefore, the curing step that was mentioned for these E-fa/PEG blends in the experimental section could ensure full polymerization.

3.2. Self-healing behaviors of the poly (E-fa/PEG) blends at various molecular weights of PEG

The obtained polymer blends were subjected to microscopic healing process by using thermally triggered scratching techniques as shown in Figure 4. Surface scratches were introduced to the samples which were then heated at 100 °C for 4 minutes, the temperature at which the Diels-Alder reaction is activated [2, 8, 32]. The width of the scratched areas before and after healing was measured, and the results are presented in Table 2. The results revealed that poly (E-fa) exhibited self-healing behavior via Diels-Alder reaction. Moreover, the incorporation of PEG enhanced the healing efficiency, with the healing performance increasing from 90% to 100% as the molecular weights of PEG increased. This improvement was attributed to the enhanced flexibility of the polymer structure [33];higher molecular weight of PEG provides greater chain mobility. Consequently, poly(E-fa/PEG 4000) demonstrated the highest healing capability. In addition to the characteristics of thermoplastics polymer, PEG is flowable to the crack site which is advantageous for the healing process and a key reason for the disappearance of surface cracks after healing [34].

Table 2 Self-healing behaviors of poly (E-fa/PEG) at different molecular weights.

Sample	Initial width (μm)	Final width (μm)	Healing efficiency (%)
E-fa	1	0	100
E-fa/PEG 600	1	0.1	90
E-fa/PEG 1500	2	0.1	95
E-fa/PEG 4000	2	0	100

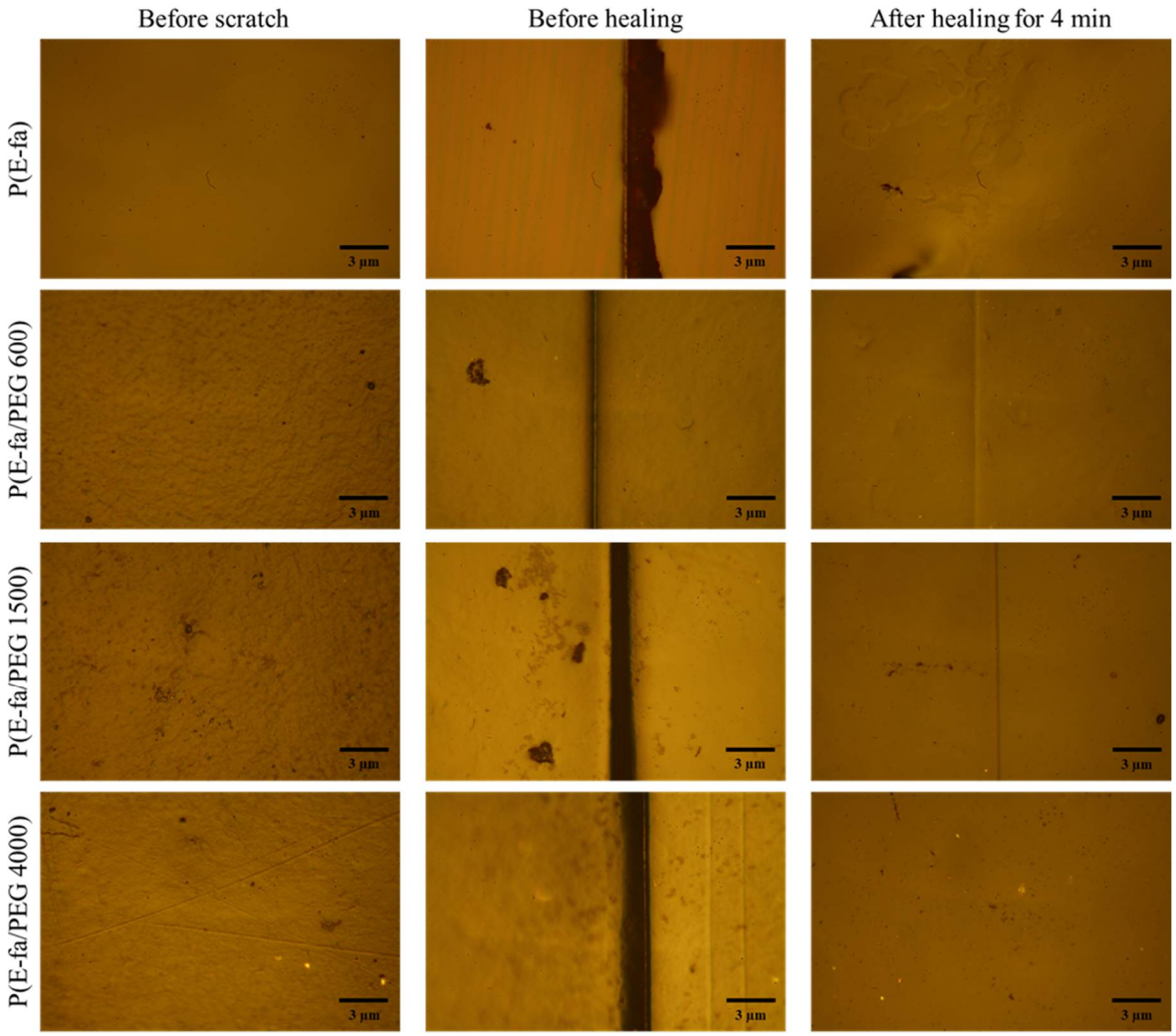

Figure 4. The microscopic healing process of poly (E-fa/PEG) at different molecular weights of PEG.

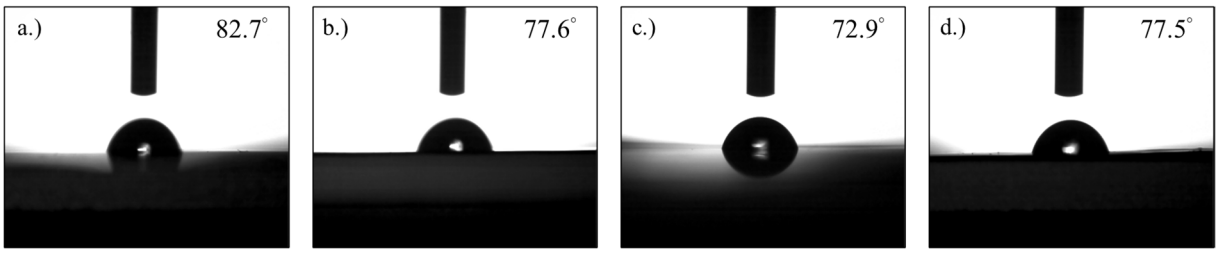

Figure 5. The water contact angle images of a.) poly (E-fa), b.) poly (E-fa/PEG 600), c.) poly (E-fa/PEG 1500), and d.) poly (E-fa/PEG 4000) respectively.

3.3. Surface behaviors of poly (E-fa/PEG) at various molecular weights of PEG.

Figure 5 shows the results of water contact angle measurement of neat poly (E-fa) and poly (E-fa/PEG 600, 1500, and 4000) blends. It was found that incorporating PEG slightly increased hydrophilicity of the blends, as evidenced by a decrease in contact angle from 87.7° to 72.9°. This was attributed to the presence of the hydroxyl group in PEG structure, which can interact with water and reduce the contact angle [35]. However, in the case of poly(E-fa/PEG 4000), the influence of the longer nonpolar chains of PEG4000 became more pronounced, resulting in a slight increase in hydrophobicity, with a contact angle of about 77.5°.

4. CONCLUSION

In this study, self-healing polymers were successful developed using bio-based polybenzoxazines blended with various molecular weights of PEG at a constant E-fa/PEG ratio of 85/15 wt/wt%. The effects of molecular weights of PEG on curing behaviors, self-healing performance, and surface properties were systematically investigated. DSC analysis confirmed complete curing of all samples, with no significant impact of PEG molecular weight on T_{onset} and T_{peak}. The self-healing process, triggered by heating at 100 °C demonstrated that increasing molecular weight of PEG significantly enhanced healing efficiency. Notably, poly (E-fa/PEG 4000) achieved healing efficiency up to approximately 100% within 4 minutes. Moreover, the flowability of PEG facilitated healing capability which enables it to flow into damaged areas leading to fully healed. Additionally, increasing molecular weight of PEG resulted in greater hydrophobicity in the polymer blends. Finally, the obtained self-healable polymers show great potential as smart materials for advanced functional applications.

ACKNOWLEDGMENTS

This research received financial support from the National Research Council of Thailand (NRCT) and Chulalongkorn University (N42A660910) and Thailand Science Research and Innovation Fund Chulalongkorn University (BCG_FF_68_206_2100 _030).

REFERENCES

1. Safaei, A., et al., Fast Self-Healing at Room Temperature in Diels-Alder Elastomers. Polymers (Basel), 2023. **15**(17).
2. Karami, Z., M. Zolghadr, and M.J. Zohuriaan-Mehr, Self-healing Diels–Alder engineered thermosets, in Self-Healing Polymer-Based Systems. 2020. p. 209-233.
3. Joy, J., et al., Applications of self-healing polymeric systems, in Self-Healing Polymer-Based Systems. 2020. p. 495-513.
4. Turkenburg, D.H., Y. Durant, and H.R. Fischer, Bio-based self-healing coatings based on thermo-reversible Diels-Alder reaction. Progress in Organic Coatings, 2017. **111**: p. 38-46.
5. Terryn, S., et al., Self-healing soft pneumatic robots. 2017. **2**(9): p. eaan4268.
6. Tiwari, N., et al., A rapid low temperature self-healable polymeric composite for flexible electronic devices. Journal of Materials Chemistry A, 2018. **6**(43): p. 21428-21434.
7. Han, S., et al., Dual Conductive Network Hydrogel for a Highly Conductive, Self-Healing, Anti-Freezing, and Non-Drying Strain Sensor. ACS Applied Polymer Materials, 2020. **2**(2): p. 996-1005.
8. Du, P., et al., Diels–Alder-based crosslinked self-healing polyurethane/urea from polymeric methylene diphenyl diisocyanate. Journal of Applied Polymer Science, 2013. **131**(9).
9. Ruiz de Luzuriaga, A., et al., Epoxy resin with exchangeable disulfide crosslinks to obtain reprocessable, repairable and recyclable fiber-reinforced thermoset composites. Materials Horizons, 2016. **3**(3): p. 241-247.
10. Zhang, M., et al., Self-healing supramolecular gels formed by crown ether based host-guest interactions. Angew Chem Int Ed Engl, 2012. **51**(28): p. 7011-5.
11. Zhang, A., et al., Self-healing supramolecular elastomers based on the multi-hydrogen bonding of low-molecular polydimethylsiloxanes: Synthesis and characterization. Journal of Applied Polymer Science, 2013. **129**(5): p. 2435-2442.
12. Mora, P., S. Rimdusit, and C. Jubsilp, Fast thermo-responsive thermoset self-healing polymers based on bio-derived Benzoxazine/Epoxidized castor oil

copolymers for coating applications. Arabian Journal of Chemistry, 2024. **17**(11).
13. Amornkitbamrung, L., et al., Effects of glutaric anhydride functionalization on filler-free benzoxazine/epoxy copolymers with shape memory and self-healing properties under near-infrared light actuation. Journal of Science: Advanced Materials and Devices, 2022. **7**(3).
14. Cong, H.-P., P. Wang, and S.-H. Yu, Stretchable and Self-Healing Graphene Oxide–Polymer Composite Hydrogels: A Dual-Network Design. Chemistry of Materials, 2013. **25**(16): p. 3357-3362.
15. Ishida, H., Process for preparation of benzoxazine compounds in solventless systems. 1996, Google Patents.
16. Machado, I., et al., A truly bio-based benzoxazine derived from three natural reactants obtained under environmentally friendly conditions and its polymer properties. Green Chemistry, 2021. **23**(11): p. 4051-4064.
17. Asrafali, S.P., T. Periyasamy, and J. Lee, A Comprehensive Review on Bio-Based Polybenzoxazines Emphasizing Their Antimicrobial Property. Microorganisms, 2025. **13**(1).
18. Zhang, K., et al., A New Benzoxazine Containing Benzoxazole-Functionalized Polyhedral Oligomeric Silsesquioxane and the Corresponding Polybenzoxazine Nanocomposites. Macromolecules, 2013. **46**(7): p. 2696-2704.
19. Zhang, K., X. Yu, and S.-W. Kuo, Outstanding dielectric and thermal properties of main chain-type poly(benzoxazine-co-imide-co-siloxane)-based cross-linked networks. Polymer Chemistry, 2019. **10**(19): p. 2387-2396.
20. Arslan, M., B. Kiskan, and Y. Yagci, Benzoxazine-Based Thermoset with Autonomous Self-Healing and Shape Recovery. Macromolecules, 2018. **51**(24): p. 10095-10103.
21. Lu, G., et al., A New Sight into Bio-Based Polybenzoxazine: From Tunable Thermal and Mechanical Properties to Excellent Marine Antifouling Performance. ACS Omega, 2020. **5**(7): p. 3763-3773.
22. Hariharan, A., et al., Bio-based polybenzoxazine composites for oil-water separation, sound absorption and corrosion resistance applications. Polymer Testing, 2020. **86**.
23. Thirukumaran, P., A. Shakila Parveen, and M. Sarojadevi, Synthesis and Copolymerization of Fully Biobased Benzoxazines from Renewable Resources. ACS Sustainable Chemistry & Engineering, 2014. **2**(12): p. 2790-2801.
24. Anagwu, F.I., V.K. Thakur, and A.A. Skordos, High-Performance Vitrimeric Benzoxazines for Sustainable Advanced Materials: Design, Synthesis, and Applications. Macromolecular Materials and Engineering, 2022. **308**(4).
25. Wang, J. and R. Xu, Preparation and Characterization of Guaiacol-Furfuramine Benzoxazine and Its Modification of Bisphenol A-Aniline Oxazine Resin. Polymers (Basel), 2024. **16**(6).
26. Wang, J., et al., Biomaterials for inflammatory bowel disease: treatment, diagnosis and organoids. Applied Materials Today, 2024. **36**.
27. Parray, Z.A., et al., Amphiphilic nature of polyethylene glycols and their role in medical research. Polymer Testing, 2020. **82**.
28. Zavareh, S. and G. Samandari, Polyethylene glycol as an epoxy modifier with extremely high toughening effect: Formation of nanoblend morphology. Polymer Engineering & Science, 2013. **54**(8): p. 1833-1838.
29. Wang, Z., et al., Tough, Transparent, 3D-Printable, and Self-Healing Poly(ethylene glycol)-Gel (PEGgel). Adv Mater, 2022. **34**(11): p. e2107791.
30. Dai, J., et al., Synthesis of Biobased Benzoxazines Suitable for Vacuum-Assisted Resin Transfer Molding Process via Introduction of Soft Silicon Segment. Industrial & Engineering Chemistry Research, 2018. **57**(8): p. 3091-3102.
31. Agag, T., et al., Low-Viscosity Polyether-Based Main-Chain Benzoxazine Polymers: Precursors for Flexible Thermosetting Polymers. Macromolecules, 2010. **43**(17): p. 7122-7127.
32. Ehrhardt, D., et al., Self-Healing in Mobility-Restricted Conditions Maintaining Mechanical Robustness: Furan-Maleimide Diels-Alder Cycloadditions in Polymer Networks for Ambient Applications. Polymers (Basel), 2020. **12**(11).
33. Van Renterghem, L., et al., Solvent-free coatings based on bio-sourced benzoxazines resins with healing, repair, and recycling capabilities. Progress in Organic Coatings, 2024. **189**.
34. Runqing Ou, K.E., and Ganesh Skandan, PHASE SEPARATED SELF-HEALING POLYMER COATINGS. 2010.
35. Pulikkalparambil, H., et al., Thermally mendable and improved hydrophilic bioepoxy/PEG-PPG-PEG blends for coating application. Materials Research Express, 2018. **6**(2).

Toughness improvement of polybenzoxazine by blending with glycidyl methacrylate-grafted natural rubber

Yadapa Wasikarat[1], Panyawutthi Rimdusit[1], Sarawut Rimdusit[1,*]

[1] Center of Excellence in Polymeric Materials for Medical Practice Devices, Department of Chemical Engineering, Faculty of Engineering, Chulalongkorn University, Bangkok 10330, Thailand
[*] Corresponding author: sarawut.r@chula.ac.th

ABSTRACT

Benzoxazine resin is a thermoset polymer with high thermal stability, high mechanical properties, and no by-products or volatile substances released in the curing process, but its brittleness poses a challenge. This research focuses on improving toughness of polybenzoxazine (PBA-a) using deproteinized natural rubber (DPNR) functionalized with glycidyl methacrylate (GMA). The BA-a was synthesized with bisphenol A, formaldehyde, and aniline. The DPNR grafted with GMA (DPNR-g-GMA) was confirmed by attenuated total reflection Fourier transform infrared spectroscopy and grafting efficiency (%GE) was determined via gravimetric method through Soxhlet extraction. Our preliminary results show that the peak positions at 1080 cm^{-1} were related to the epoxide group, which confirmed the success of GMA grafting onto DPNR, while %GE reached 95% with GMA content at 15 phr. The obtained BA-a blended with DPNR-g-GMA (PBA-a/DPNR-g-GMA) containing different amounts of DPNR-g-GMA of 0-20 wt% were prepared by mechanical mixing at 120 °C at 250 rpm for 30 min, followed by curing steps in an oven at 130 °C for 3 h, 150 °C for 2 h, 180 °C for 1 h, and 200°C for 3 h. The effects of rubber content on the glass transition temperature (Tg) and storage modulus (E') of PBA-a/DPNR-g-GMA were studied using dynamic mechanical analysis. It was found that Tg increased with rubber content, while E' and mechanical strength decreased due to the soft nature of rubber, indicating a trade-off between enhanced flexibility and reduced rigidity. These results highlight the potential of GMA-grafted natural rubber to toughen PBA-a.

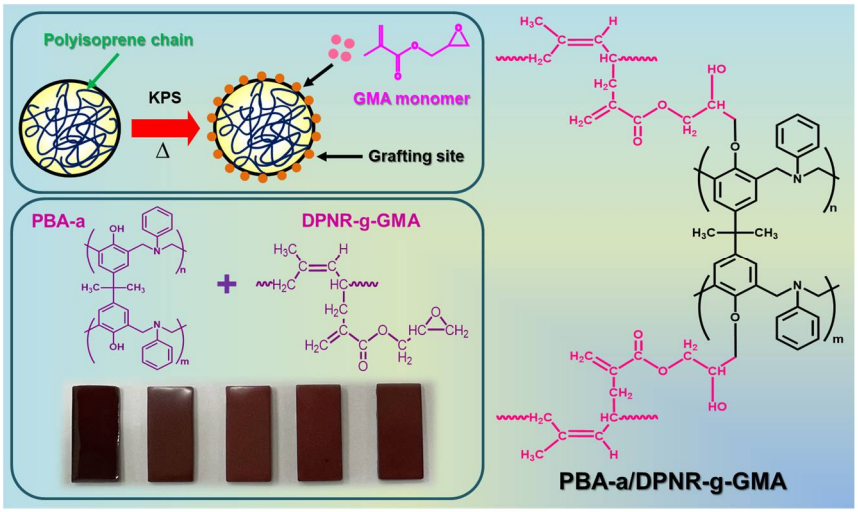

Fig 1: Toughening mechanism of polybenzoxazine blended with GMA-grafted natural rubber.

Keywords: Deproteinized natural rubber; Glycidyl methacrylate; Grafting efficiency; Polybenzoxazine; Graft-copolymerization

1. INTRODUCTION

Benzoxazine resin (BA-a) is a new thermosetting phenolic resin that can be synthesized from phenol, formaldehyde, and amine precursors. These results in high flexibility in molecular design structure. The curing process of BA-a resin is involved in ring-opening polymerization without the use of catalysts and

does not produce any by-products or volatile substances. Poly BA-a (PBA-a) has many outstanding properties, such as high glass transition temperature (T_g), excellent thermal stability, near-zero shrinkage upon curing, low viscosity in melting state, high mechanical properties, and low water absorption. This remarkable property has drawn attention from researchers and utilized it in some applications [1-3]. However, the main limitation of PBA-ais hardness and brittleness [4]. Therefore, it is necessary to improve the toughness of PBA-a to expand the application range in various forms by blending with high-elastic polymers.

Natural rubber (NR) originated from the rubber tree sp. *Hevea brasiliensis*, which is widespread in South and Southeast Asia. It has a chemical structure of *cis*-1,4-polyisoprene and is a natural polymer with high molecular weight and an amorphous material. Due to its distinct characteristics like long and highly flexible molecular chain, it showed excellent abrasion resistance, good heat dissipation, and efficient shock absorption. These properties lead to widely used in many industries, such as transportation, general industry, consumer products, and the medical industry [5-7]. However, to improve the performance of NR, deproteinized natural rubber (DPNR) has been developed and studied. The results indicated low gelation after treating NR which it was suggested as suitable for improving graft copolymerization efficiency than conventional NR [7]. Another concern is the compatibility between natural rubber and benzoxazine, phase separation problems may occur as a result in incompatibility [8]. In the research of Ishida H. and Allen J. D. [9], it was reported that the addition of epoxy to the benzoxazine matrix can form chemical bonds between the phases which results in thermal and mechanical improvement for benzoxazine copolymerized while no phase separation occurred. Therefore, an epoxy-functionalized group is persuaded and presented as selective monomer for rubber modification which can lead to the compatibility and properties enhancement. A study from Ying Li et al. [10] demonstrated grafting glycidyl methacrylate (GMA) onto a natural rubber structure via a graft-copolymerization process. The epoxy functional groups in GMA acted as a mediator between NR and filler, resulting in improving material compatibility. These previous studies suggest that GMA functional group improved compatibility with BA-a and can be functionalized to NR.

In this research, DPNR was modified by graft-copolymerization with GMA using potassium persulfate as an initiator through emulsion polymerization technique. Then, benzoxazine was mixed with DPNR-g-GMA in different proportions to study the effect of DPNR-g-GMA content on the mechanical properties of polybenzoxazine (PBA-a), focusing on the toughness improvement of the material.

2. EXPERIMENTAL

2.1 Raw materials

Deproteinized natural rubber latex (DPNR) with 60 wt% of dry rubber content (DRC) was purchased from the Unimac Rubber Co., Ltd. (Trang, Thailand). Sodium dodecyl sulfate (SDS; >99%) and Glycidyl methacrylate (GMA; 95%) were obtained from Tokyo Chemical Industry Co., Ltd. (Japan). Potassium peroxodisulfate (KPS; 99%) was purchased from Asia Chemie (Thailand) Co., Ltd.. Bisphenol A was obtained from PTT Global Chemical Public Co., Ltd. (Rayong, Thailand). Paraformaldehyde was purchased from Merck Co., Ltd. (Darmstadt, Germany). Aniline (99.5%) was obtained from Loba Chemie Pvt. Ltd. (Mumbai, India).

2.2 Preparation of Deproteinized natural rubber grafted with glycidyl methacrylate (DPNR-g-GMA)

The graft copolymerization of glycidyl methacrylate (GMA) onto natural rubber was performed using the emulsion polymerization technique. Firstly, deproteinized natural rubber latex (DPNR) was diluted with deionized water to 30% of dry rubber content and a total weight of 150 g. Next, adding SDS (1.5 phr) as a surfactant into a 500 cm^3 three-neck glass reactor and purging O_2 using nitrogen gas at room temperature for 30 min at an agitation speed of 250 rpm in the absence of light and elevating temperature to 60 °C. The initiator (KPS) and monomer (GMA) were added into glass reactor prior temperature reached 60°C while the stirring speed was set at 250 rpm and maintain reaction for 1 hour [10]. Finally, the DPNR grafted with GMA (DPNR-g-GMA) was obtained after reaction. The monomer content in this study ranged from 5, 10, 15, and 20 phr and the compositions in the grafting process are summarized in Table 1.

Table 1 The composition of graft-copolymerization onto DPNR.

Monomer content (phr)	DPNR latex (g)	SDS (1.5 phr) (g)	KPS (0.5 phr) (g)	GMA monomer (g)
5	150	4.5	0.4545	4.5
10				9
15				13.5
20				18

After the graft-copolymerization was completed, the samples were casted into a film in Petri dishes and dried in an oven at 80°C to constant weight. The thin film samples were then extracted to remove homopolymers using Soxhlet extraction using acetone as a solvent for 24 h and dried at 80 °C until constant

weight. The grafting efficiency (%GE) of the samples was calculated using the gravimetric method according to Eq 1 [11, 12].

$$\text{Grafting efficiency} = \frac{\text{Weight of GMA graft}}{\text{Weight of GMA graft + Weight of GMA homopolymer}} \times 100 \quad (1)$$

2.3 Synthesis of Benzoxazine resin (BA-a)

Benzoxazine monomer was synthesized from bisphenol A, paraformaldehyde, and aniline in a molar ratio of 1:4:2 by a solventless method and was mixed at 110 ℃ for 40 min. The monomer was obtained as a light-yellow color liquid with low-viscosity and was cooled to room temperature before being ground into a fine powder and stored in the refrigerator for later use [4, 9, 13].

2.4 Preparation of Polybenzoxazine/DPNR-g-GMA copolymer (PBA-a/ DPNR-g-GMA copolymer)

Polybenzoxazine/DPNR-g-GMA was prepared by blending BA-a monomer with DPNR-g-GMA at different weight ratios of 0, 5, 10, 15, and 20 wt%. The mixture was homogenized using a mechanical stirrer at 120 ℃ for 30 min with a rotational speed of 250 rpm. After mixing, the PBA-a/DPNR-g-GMA copolymer was cooled down at room temperature and removed from the mold before grounding into a fine powder. It was then poured into a mold and cured in an oven at 130℃ for 3 h, 150℃ for 2 h, 180℃ for 1 h, and 200℃ for 3 h. The samples were then allowed to cool under room temperature before further testing.

2.5 Characterization

Fourier-transform infrared spectroscopy (FTIR)

The chemical structures of DPNR and DPNR-g-GMA were analyzed using FTIR spectroscopy (model Perkin Elmer 2000) with an attenuated total reflection (ATR) accessory and conducting in the range of 400-4000 cm^{-1} with an average scan of 32 scans at a resolution of 4 cm^{-1}.

Dynamic mechanical analysis (DMA)

Thermo-mechanical properties of PBA-a/DPNR-g-GMA and PBA-a were investigated using a dynamic mechanical analyzer (DMA) (model DMA1, Mettler Toledo, Switzerland). The specimen dimensions were 45 mm × 10 mm × 1.3 mm. The tests were performed using dual cantilever mode at 1 Hz and 2 ℃/min, with scanning temperatures from 30 ℃ to 250 ℃.

Universal testing machine (UTM)

The flexural properties of PBA-a/DPNR-g-GMA and PBA-a were examined under three-point bending mode according to ASTM D790 using an INSTRON 5567 universal testing machine (1 kN load cell, Norwood, USA). The dimensions of the samples were 50 × 12.7 × 2 mm. The measurements were performed in the three-point bending mode with a support span of 51.2 mm. The samples were bent to failure at a speed of 0.853 mm/min. [2, 9]. An average of five specimens are used for calculation.

3. RESULTS AND DISCUSSION

3.1 Grafting Efficiency (%GE) of DPNR-g-GMA.

The grafting efficiency was calculated according to equation (1) to indicate the percentage of monomer that could be successfully bonded to the polyisoprene structure. It was found that the grafting efficiency of DPNR grafted with GMA at monomer contents of 5, 10, 15 and 20 phr were 72%, 86%, 95% and 68%, respectively, as shown in Table 2. From the experimental results, it was found that graft-copolymer of GMA monomer onto DPNR increased as increase monomer content. However, when the monomer content was increased at higher content, specifically at 20 phr, the grafting efficiency was drastically decreased as a result in an increase in homopolymerization reaction of GMA monomer, which dominated over the copolymerization with natural rubber particles [14].

Table 2. Grafting efficiency of the DPNR-g-GMA with various monomer contents.

Monomer content (phr)	Grafting efficiency (%GE)
5	72 ± 0.4
10	86 ± 1.3
15	95 ± 0.4
20	68 ± 0.3

3.2 Chemical structure of DPNR and DPNR-g-GMA.

The chemical compositions of DPNR and DPNR-g-GMA were shown in Fig. 2. From the FTIR spectrum, the absorption bands were observed at positions 841, 1375, and 1446 cm^{-1} related to the stretching vibrations of =C–H, CH_3, and CH_2 groups, respectively, and at position 2960 cm^{-1}, which were consistent with the C-H stretching vibrations of CH_3 groups. In the case of DPNR-g-GMA, the peak was observed at position 1080 cm^{-1}related to the stretching vibrations of epoxy groups, as well as peaks at 1726 and 3293 cm^{-1}, which were assigned to the carbonyl (C=O) and hydroxyl (O–H) groups of GMA, respectively. These results confirmed that the structure of GMA was successfully grafted onto the polyisoprene backbone of natural rubber [11, 15].

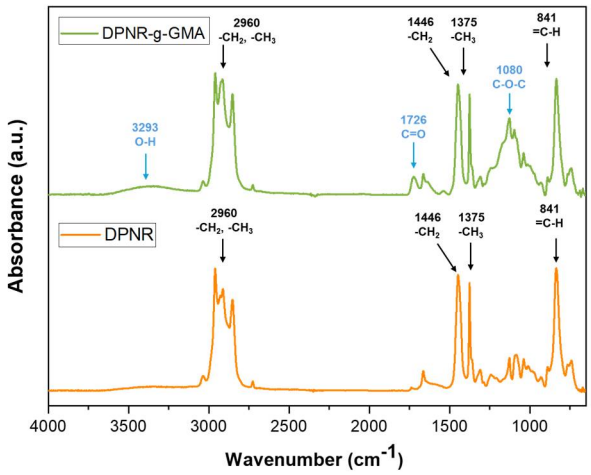

Figure 2: The FTIR spectra of DPNR and DPNR-g-GMA at 15 phr.

3.3 Thermo-mechanical properties of PBA-a/DPNR-g-GMA.

The thermo-mechanical behavior of the materials was analyzed using Dynamic Mechanical Analysis (DMA), focusing on storage modulus (E') and tan δ. The E' represents the material's stiffness and ability to store elastic energy under mechanical stress. A higher E' value indicates better stiffness and resistance to deformation. The specimens include pure BA-a and BA-a blended with grafted natural rubber (DPNR-g-GMA) at 5, 10, 15, and 20 wt%. As shown in Figure 3, increasing the rubber content results in a continuous decrease in E', indicating reduced stiffness due to the inherently low modulus of natural rubber. This implies that adding rubber decreases the system's overall resistance to deformation. From the tan δ vs. temperature graph in Figure 4, the glass transition temperature (T_g) was determined. Pure BA-a exhibited a T_g of 192°C while the addition of DPNR-g-GMA at 5, 10, 15, and 20 wt% increased T_g values to 194°C, 196°C, 199°C, and 210°C, respectively. This trend suggests that although the rubber softens the material, the epoxy functional groups on the modified rubber can chemically react with BA-a, forming covalent bonds and enhancing molecular interactions [16, 17]. This chemical compatibility prevents phase separation and leads to improved thermal property, as evidenced by the higher T_g.

3.4 Mechanical properties of PBA-a/DPNR-g-GMA.

In terms of mechanical performance, the incorporation of DPNR-g-GMA into the BA-a matrix leads to a clear decrease in storage modulus (E') with increasing rubber content. This is attributed to the low intrinsic stiffness and modulus of natural rubber, which diminishes the overall mechanical strength of the blend. The decreased E' indicates improved toughness while decreased stiffness of the resulting material, which is typical behavior soft rubber phases introduced into a rigid polymer matrix. Nonetheless, this trade-off can be strategically leveraged depending on application requirements, such as enhancing flexibility or damping in specific uses. The compatibility between the rubber and the polymer matrix achieved through chemical grafting remains critical to balancing toughness and thermal performance.

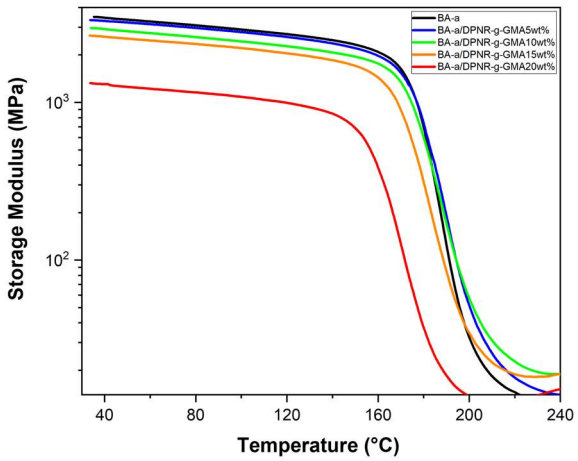

Figure 3: Storage modulus of PBA-a and PBA/DPNR-g-GMA at 5, 10, 15 and 20 wt% rubber content.

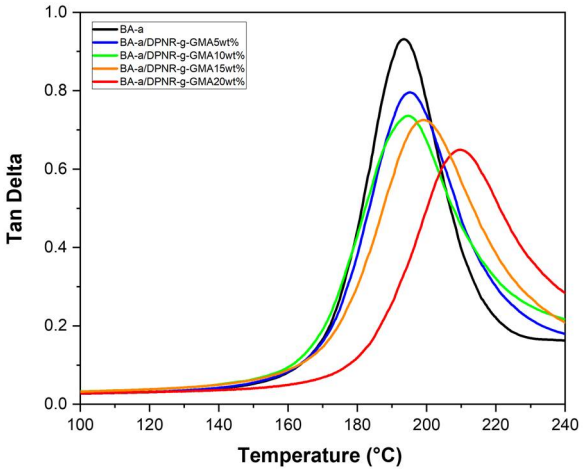

Figure 4: Tan δ of PBA-a and PBA/DPNR-g-GMA at 5, 10, 15 and 20 wt% rubber content.

A comparison of flexural properties between pure BA-a and BA-a/DPNR-g-GMA at 20 wt% is shown in Figure 5. It was found that the addition of rubber to benzoxazine has a significant improvement on the mechanical properties of the materials which can be indicated by a decrease in flexural modulus from 2.3 GPa to 1.2 GPa and flexural strength from 107 MPa to 52 MPa. A decrease in flexural modulus and flexural strength reflects the decrease in stiffness and strength of the materials due to the softening nature of rubber. Addition of rubber tends to increase the toughness of the materials by promoting better energy absorption

during fracture, which is an advantage in increasing the overall fracture resistance of the materials [13].

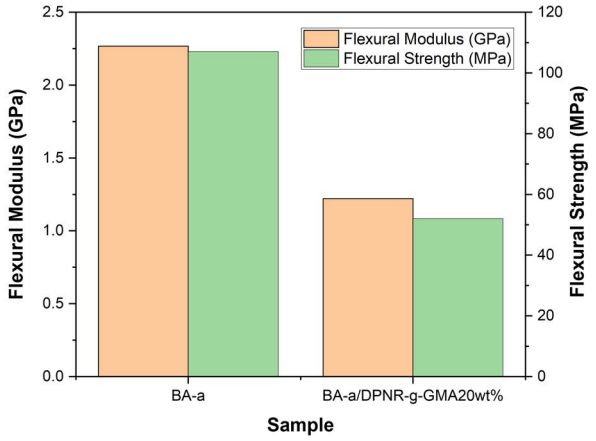

Figure 5: Flexural modulus and flexural strength of PBA-a and PBA/DPNR- g- GMA at 20 wt% rubber content.

4. CONCLUSION

In this research, deproteinized natural rubber was successfully modified with glycidyl methacrylate (DPNR-g-GMA) using graft copolymerization process. The chemical structure of the modified rubber was confirmed by FTIR analysis, which showed specific absorption bands at 1080 cm^{-1} (epoxy group), 1726 cm^{-1} (carbonyl group), and 3293 cm^{-1} (hydroxyl group), indicating the complete grafting of GMA onto polyisoprene structure, with grafting efficiency at 95% after adding 15 phr of GMA monomer. BA-a/DPNR-g-GMA showed a decrease in the storage modulus referring the reduced stiffness due to the presence of the rubber phase. However, the glass transition temperature (Tg) was significantly increased because the modified functional group on rubber surface and benzoxazine are compatible leading to good interaction between two phases. Addition of DPNR-g-GMA decreased the strength and flexural modulus of PBA-a because low modulus and elastic behavior of rubber at high content decrease the overall stiffness.

ACKNOWLEDGMENTS

National Research Council of Thailand (NRCT) and Chulalongkorn University (N42A660910) and Thailand Science Research and Innovation Fund Chulalongkorn University (BCG_FF_68_206_2100_030)

REFERENCES

1. Rimdusit, S., et al., Introduction to commercial benzoxazine and their unique properties. Alloys and Composites of Polybenzoxazines: Properties and Applications, 2013: p. 1-27.
2. Rimdusit, S., P. Kunopast, and I. Dueramae, Thermomechanical properties of arylamine-based benzoxazine resins alloyed with epoxy resin. Polymer Engineering & Science, 2011. 51(9): p. 1797-1807.
3. Sha, X.-L., L. Yuan, G. Liang, and A. Gu, Preparation of high performance bio-based benzoxazine resin through a green solvent-free strategy for shape memory application. Polymer, 2020. 202: p. 122673.
4. Rimdusit, S., S. Pirstpindvong, W. Tanthapanichakoon, and S. Damrongsakkul, Toughening of polybenzoxazine by alloying with urethane prepolymer and flexible epoxy: A comparative study. Polymer Engineering & Science, 2005. 45(3): p. 288-296.
5. James, H.M. and E. Guth, Theory of the elastic properties of rubber. The Journal of Chemical Physics, 1943. 11(10): p. 455-481.
6. Mooibroek, H. and K. Cornish, Alternative sources of natural rubber. Applied microbiology and biotechnology, 2000. 53: p. 355-365.
7. Wongthong, P., et al., Modification of deproteinized natural rubber via grafting polymerization with maleic anhydride. European Polymer Journal, 2013. 49(12): p. 4035-4046.
8. Ravindran, T., M.G. Nayar, and D.J. Francis, Segmented block copolymers based on liquid natural rubber. Journal of applied polymer science, 1991. 42(2): p. 325-333.
9. Ishida, H. and D.J. Allen, Mechanical characterization of copolymers based on benzoxazine and epoxy. Polymer, 1996. 37(20): p. 4487-4495.
10. Li, Y., L. Zhang, and Z. Hou, Preparation and Properties of Graphene oxide/Glycidyl Methacrylate grafted natural rubber nanocomposites. Journal of Polymers and the Environment, 2017. 25: p. 315-322.
11. Juntuek, P., C. Ruksakulpiwat, P. Chumsamrong, and Y. Ruksakulpiwat, Glycidyl methacrylate grafted natural rubber: synthesis, characterization, and mechanical property. Journal of Applied Polymer Science, 2011. 122(5): p. 3152-3159.
12. Nguyen, T.N., et al., Improvement of thermal and mechanical properties of Vietnam deproteinized natural rubber via graft copolymerization with methyl methacrylate. International Journal of Polymer Science, 2020. 2020(1): p. 9037827.
13. Jantaramaha, J., C. Jubsilp, and S. Rimdusit, Thermal and mechanical properties of acrylonitrile-butadiene rubber modified polybenzoxazine as frictional materials. Key Engineering Materials, 2015. 659: p. 511-515.
14. Radabutra, S., et al., Preparation and characterization of wood-to-wood bonding adhesive by glycidyl methacrylate grafting natural rubber. International Journal of Adhesion and Adhesives, 2022. 114: p. 103093.

15. Alfian, Z. and N. Nasution. Addition of divinyl benzene comonomer to glycidyl methacrylate grafting to cyclic natural rubber. in IOP Conference Series: Earth and Environmental Science. 2021. IOP Publishing.
16. Mathew, V.S., S.C. George, J. Parameswaranpillai, and S. Thomas, Epoxidized natural rubber/epoxy blends: Phase morphology and thermomechanical properties. Journal of Applied Polymer Science, 2014. 131(4).
17. Xu, S., X. Song, and Y. Cai, Mechanical properties and morphologies of carboxyl-terminated butadiene acrylonitrile liquid rubber/epoxy blends compatibilized by pre-crosslinking. Materials, 2016. 9(8): p. 640.

Influence of CaO on the durability of geopolymer in acidic environments

Cherdphong Seedao[1,*], Marjorie Valix[2]

[1] Department of Chemical Engineering, Faculty of Engineering, Burapha University, Chonburi 20131, Thailand
[2] Chemical & Biomolecular Engineering, The University of Sydney, NSW 2006, Australia
[*] Corresponding author: cherdphong@eng.buu.ac.th

ABSTRACT

In Australia, the sewer infrastructure includes approximately 122,000 km of concrete sewer pipe networks, known as 'sewer assets'. These assets are vital for urban livability and productivity but are prone to deterioration, primarily due to microbial-induced concrete corrosion (MICC). To extend their service life, alkali-activated binders (AAB), such as geopolymers, are used as protective coatings. While CaO in mortar can enhance early compressive strength, it also increases susceptibility to deterioration in acidic environments due to the formation of expansive corrosion products like gypsum and ettringite. To assess the influence of CaO on the acid resistance of one-part geopolymer mortar (OGPm), four commercial geopolymer samples with varying CaO content and one calcium aluminate cement mortar (CACm) as a reference were immersed in sulfuric acid (H_2SO_4) at pH 1 and 30°C for 28 days. Samples were periodically removed to measure corrosion depth and correlate with CaO content to understand the relationship between depth of corrosion and amount of CaO. The corrosion behavior occurred in two stages: accelerated corrosion stage (R-1) followed by a slower corrosion stage (R-2). The reduction in corrosion rate during R-2 is attributed to increased diffusion resistance, the build-up of the corrosion layer, and pore blocking by gypsum. Thus, the CaO composition in OGPm must be carefully considered to achieve better corrosion resistance.

Keywords: Alkali-activated binders; Geopolymer; Microbial Induced Concrete Corrosion (MICC)

1. INTRODUCTION

In Australia, there are approximately 122,000 km of concrete sewer pipe networks and related infrastructure, collectively referred to as "sewer assets" [1]. These assets are valuable and essential, ensuring our cities and communities remain livable and productive. The primary purpose of sewer assets is to collect, convey, and treat domestic and industrial wastewater. They are constructed from various materials, including bricks, vitrified clays, cement concrete, cast iron, steel pipes, and plastics, depending on operational criteria [2]. However, most assets have been constructed using Ordinary Portland Cement (OPC) known as “concrete”.

The concrete sewer assets are designed to have a service life of approximately 100 years [3]. Unfortunately, sewer assets experience deterioration due to various factors, including operational conditions, microbial-induced concrete corrosion (MICC), and external soil corrosion. Among these, MICC is the most aggressive factor, significantly reducing the service life of concrete sewer assets. MICC is a complex process involving various chemical and biological reactions that convert hydrogen sulfide in wastewater into sulfuric and other biogenic acids. These acids directly react with the concrete material, gradually destroying the sewer assets.

The failure of the sewer asset caused by MICC increasingly triggers high economic expenses and severe health and environmental concerns [4]. For example, the replacement and rehabilitation of sewer assets cost $14 billion annually in the USA, $103 million in the UK, and over $458 million in Germany to maintain the existing infrastructure. [4, 5]. Furthermore, the leakage of sewer gases such as nitrous oxide (N_2O), methane (CH_4) and carbon dioxide (CO_2) into the atmosphere would also contribute to climate change since they consider greenhouse gases formed within sewer assets [6].

Various mitigation strategies have been applied to reduce the impact of MICC. Mitigation strategies for existing concrete sewer assets can target reducing the H_2S generation by chemical dosing and avoiding the development of concrete corrosion by a surface protective coating. However, to reduce the H_2S generation by chemical dosing, injecting the chemical in the various locations along the sewer assets is often required. Furthermore, once the chemical dose is not maintained to the H_2S controllable level, the H_2S will return to the previous production level [7]. From a practical perspective, this mitigation strategy incurs

significant long-term maintenance and operational costs [8]. Using surface protective coating would extend the service life of concrete sewer assets because the surface protective coating acts as a barrier between concrete sewer assets and aggressive environmental conditions under sewer pipe networks. This approach is a highly effective and promising solution for the long-term preservation of concrete sewer assets. Therefore, employing surface protective coatings to mitigate concrete corrosion has emerged as a compelling strategy for safeguarding new or existing sewer assets.

Low-calcium alkali-activated binders (AAB) are recognized as a novel class of binder materials. They are prepared by activating a low-calcium aluminosilicate precursor, such as fly ash (FA) and metakaolin, with an alkali medium, including sodium silicate ($Na_2O{\cdot}mSiO_2{\cdot}xH_2O$), sodium hydroxide (NaOH), and potassium hydroxide (KOH) [9, 10]. The reaction between low-calcium aluminosilicate precursors and an alkali-activated medium results in the formation of a three-dimensional crosslinked poly-sialate amorphous and semi-crystalline structure of sodium aluminosilicate hydrate gel (N-A-S-H), commonly referred to as a "Geopolymer" [11-15]. However, if the aluminosilicate precursor is made with fly ash, slag, or other material, often contains CaO. The reaction between Ca-rich aluminosilicate precursor and high alkali solution can formulate the hydration product as disordered tobermorite-like (C-S-H), which can be partially substituted by aluminum or sodium/potassium to form calcium aluminum silicate hydrate gel (C-A-S-H) or calcium (sodium) aluminum silicate hydrate gel (C-(N)-A-S-H) [16, 17]. Ca-rich phase and sodium aluminosilicate hydrate provide better strength and durability [17]. They offer enhanced durability and resistance to chemical attacks, making them a promising alternative for surface protective coatings [18]. While CaO composition in mortar can enhance early compressive strength by formulating Ca-rich hydration products, it also increases susceptibility to deterioration in acidic environments due to the formation of expansive corrosion products like gypsum and ettringite. There are various commercially available one-part geopolymers on the market. However, they have never been used as protective coating materials for concrete sewer assets due to a lack of corrosion resistance performance data and the impact of CaO composition in the aluminosilicate precursor.

Therefore, the objectives of this study are: (i) to obtain performance data for various commercial one-part geopolymer mortars (OGPm) with different CaO compositions and compare their corrosion resistance to that of high-performing calcium aluminate cement mortars (CACm); and (ii) to correlate the corrosion performance data to understand the influence of CaO composition in the geopolymer precursor.

2. EXPERIMENTAL

This study examined four commercially available one-part geopolymer mortars, each with varying CaO content in their aluminosilicate precursors, alongside one calcium aluminate cement mortar (CACm). The bulk chemical compositions of the OGPm and CACm binders were analyzed using X-ray fluorescence spectroscopy (XRF), as detailed in Table 1.

Table 1 XRF analysis of the chemical composition of OGPm and CACm binder

Components	OGPm-1	OGPm-2	OGPm-3	OGPm-4	CACm
	Binder	Binder	Binder	Binder	Binder
Na_2O	0.37	0.44	0.52	0.54	0.19
MgO	1.35	3.19	2.03	8.69	0.52
Al_2O_3	5.95	27.60	14.41	9.01	43.70
SiO_2	27.55	19.16	48.11	26.18	8.57
SO_3	2.38	1.10	0.77	4.38	0.01
K_2O	0.76	0.17	0.67	0.41	0.22
CaO	53.85	37.43	23.26	44.52	36.97
Fe_2O_3	1.84	8.99	4.92	2.13	6.65
LOI.	5.16	0.27	2.57	5.16	1.2

The OGPm and CACm sample were prepared as 50 mm cube for acid corrosion resistance performance test immersion test. The unhydrated mortar powder was mixed with tap water based on a water and mortar ratio (W/M) from the manufacturer's instruction (2.2-3.6 L/20 kg concrete) (see Table 2).

Table 2 Water and mortar ratio (W/M) by weight

Coating mortar	W/M ratio (w/w)	References
OGPm-1	0.125	Manufacturer
OGPm-2	0.125	Manufacturer
OGPm-3	0.150	Manufacturer
OGPm-4	0.160	Manufacturer
CACm	0.108	Manufacturer

The freshly mixed mortars were poured into 50 x 50 mm prism steel concrete mold and packed with a compactor and a shaker table. Finally, the packed mortar allows for smoothing of the surface with a trowelful. The cast mortars were immediately covered with moisture-woven fabric and allowed to be set in the mold for 24 hours as shown in Figure 1. The mortars were demolded and allowed to cure for another 28 days in a humidity chamber based on ASTM C192/C192M at 23±2 °C and relative humidity (%RH) of not less than 98 %RH [19].

Following a curing period of 28 days in a humidity chamber, the coupons underwent an application of Sika High Strength Epoxy Adhesive Concrete Fix Kit on all four sides of the specimens to force to corrode in two

directions. This adhesive effectively sealed and protected the edges, exposing only the top and bottom surfaces for subsequent testing, as shown in Figure 2

Figure 1 Coupons sample preparation

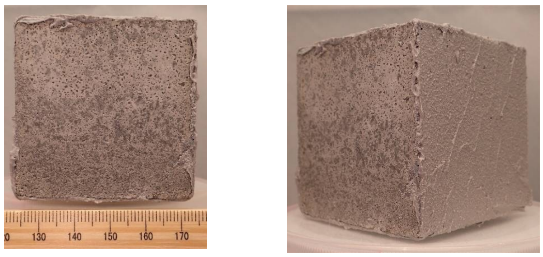

Front view Side view

Figure 2 Example of mortar coupon: (a) Front view and (b) Side view

The acid immersion test was performed in sulphuric acid at pH 1±0.25 and 28±2 °C for up to 28 days (see Figure 3). The pH of the acid solution was monitored through the test with pH-temperature probes with a TPS WP-80D pH meter, and the pH of the solution was adjusted using 98% w/w H_2SO_4 to maintain the pH at 1±0.05. The pH adjustment was made every day for the first week and once a week for the following week.

The mortar sample was periodically removed from the acid up to 28 days. Then, the specimens were immediately rinsed with distilled water to remove the access acid and debris material. The mortar specimens were sliced into sections to analyze the corrosion depth using a universal indicator and optical microscope (if the depth corrosion is less than 5 mm) or calipers (if the depth corrosion is less than 5 mm) as durability performance. This method has been widely used in many studies [20, 21].

Figure 3 acid immersion test

3. RESULTS AND DISCUSSION

During the acid immersion test, both OGPm and CACm exhibited corrosion that initiated from the surface, resulting in visible deterioration. The corrosion depth was determined by examining the cross-section of the coupon mortar. This involved sliding the corroded sample and applying a universal indicator spray, as shown in Figure 4.

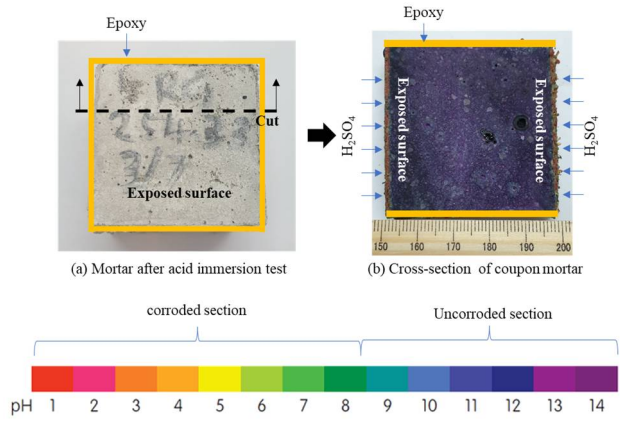

Figure 4 Acid attack on the cross-section of mortar from acid immersion test

The color variations observed in the mortar samples provided indications of their corrosion levels as presented in Figure 5. The purple color represented uncorroded mortar, with a pH range of approximately 9-13. The green to red color indicated the deterioration of the mortar, corresponding to a lower pH range of approximately 1-7. The optical microscope was utilized to help measure the acid permeation less than 5 mm, and the vernier caliper was used when the acid permeation was more than 5 mm.

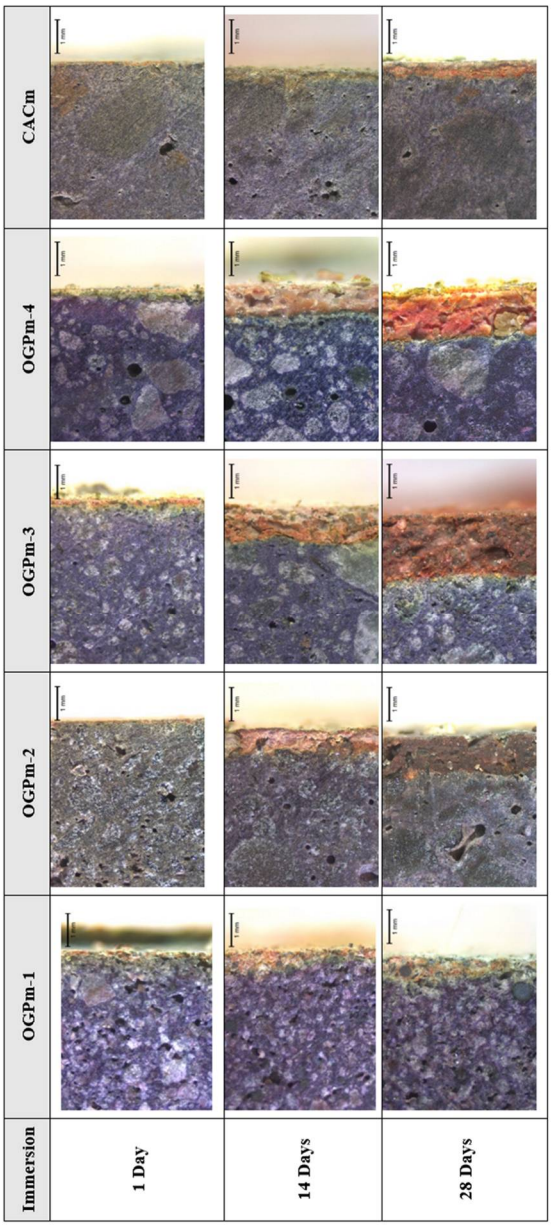

Figure 5 Progression of Corrosion surface for OGPm and CACm after acid immersion up to 28 day

Figure 5 presented microscopic images of OGPm and CACm after acid immersion for up to 28 days after spraying the universal indicator. It visually observed that the acid permeation gradually progressed toward the mortar matrix as a function of time. Moreover, the acid permeation depth was exhibited differently between the coating mortar. This result suggested that corrosion resistance differs depending on the coating mortar type. This suggestion agrees with Dorner [22] that the corrosion resistance of concrete depends on the type and chemical composition of the cement as well as the pH of the attacking acid. Moreover, the porosity was also expected to influence the depth of permeation based on the study by Khan, Castel [20].

In this study, the corrosion resistance performance of the mortar was examined from the depth of corrosion. Figure 6 shows the corresponding plots of the corrosion depths of the four OGPm and CACm as a function of time.

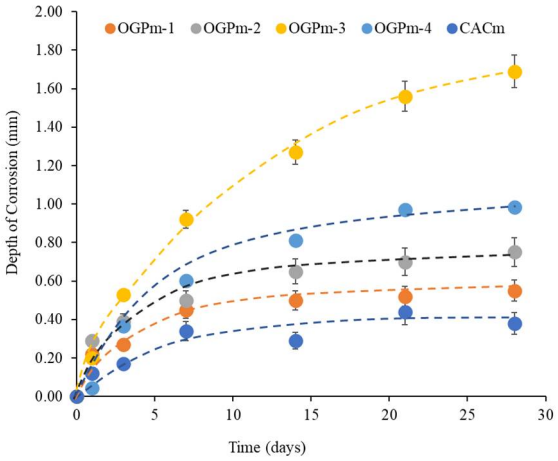

Figure 6 Plot of the depth of corrosion of OGPm and CACm as a function of time of exposure to sulphuric acid (pH 1, 30 °C)

It was observed that the corrosion depth was increased as a function of time. The corrosion behavior was observed to occur in two stages based on the rate of corrosion. The corrosion rates were estimated by fitting the line to the depth of the corrosion plot as presented in Figure 7. The slopes of the fitted line are reported as stage I corrosion rate (R_1) and stage II corrosion rate (R_2). The initial stage exhibited accelerated corrosion, considered stage I corrosion, which persisted for a duration of up to 3 days. This was followed by a subsequent stage characterized by slow corrosion, considered stage II corrosion.

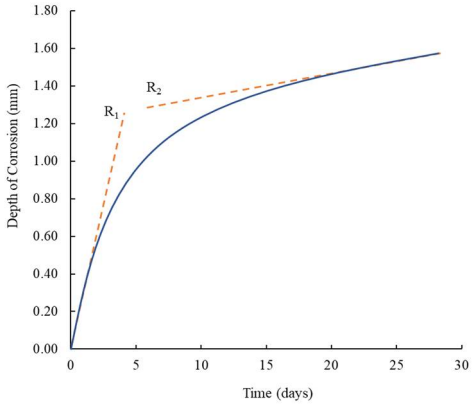

Figure 7 Fitted rates of corrosion

Based on the corrosion depth after 28 days of acid immersion test in Figure 6, the CACm showed the highest resistance to corrosion as expected, followed by OGPm-1, OGPm-2, OGPm-4, and OGPm-3. This result highlighted that the corrosion rates exhibited by the second stage corrosion were an important feature of these protective coating mortar which is reflected by the values of R2. The corrosion rate reduction in the second stage could be attributed to the increased diffusion

resistance for the acid through the build-up of the corrosion layer and to pore blocking by gypsum.

Once the OGPm and CACm were immersed in an acid solution, The dissolution of important elements from hydrates phases such as Na^+, Ca^{2+}, Fe^{3+} and Al^{3+} occurred at lower pH values, resulting in increasing the porosity [20, 22-24]. The increasing porosity provided more H^+ and SO_4^{2-} permeation pathways and reacted further with mortar binder, especially Ca^{2+}. The SO_4^{2-} was reacted with Ca^{2+} formulating expansive corrosion products such as gypsum and ettringite [20, 24-27]. The corrosion products caused the deterioration of the coating mortar by generating more cracks and allowing more acid to penetrate the coating mortar matrix. Therefore, the corrosion resistance performance of the coating mortar depended on the transport mechanism and diffusion of sulphate and proton from the sulphuric acid solution [20, 28]. However, the corrosion products formed along the cracks limited acid diffusion through the pore by acting as a barrier between the sound mortar and acid solution. This phenomenon resulted in reducing the corrosion rate. Additionally, the OH^- that leached out from the coating mortar matrix was reacted with H^+ as a neutralization process, resulting in lower acid permeation. It is important to note that at a lower pH solution than 3.5, the $Al(OH)_3$ was dissolved and neutralized more acid as in this study [27].

As noted, OGPm-1 has the highest calcium (Ca) content and OGPm-3 has the lowest calcium (Ca) content. Figure 8 shows the correlation between the CaO content in the mortar and R_1 and R_2. The Ca content in the coating mortar strongly correlated with R_1 and R_2. These results presented evidence to confirm that the CaO content in OGPm and CACm played an essential role in the corrosion resistance of the mortar. The corrosion rate in stage I and stage II revealed that the corrosion rate decreased when the Ca content in the mortar increased due to the formation of corrosion products such as gypsum and ettringite.

This finding highlighted that the corrosion of coating mortar by acid attacks relied on the transport mechanism and diffusion of sulphate and proton from the sulphuric acid solution. However, the corrosion product, such as gypsum from acid attacks, had an advantage in slowing down the corrosion rate by acting as a barrier to reduce acid diffusion. The formation of gypsum appears to depend on the calcium content of the binders as presented in the correlation between the rate of corrosion and the CaO content in the geopolymer binder in Figure 8. Moreover, if the gypsum is formed excessively, it could accelerate the corrosion rate due to gypsum and ettringite is expansive compounds and one of the most causes of corrosion of coating mortar in sewer environments.

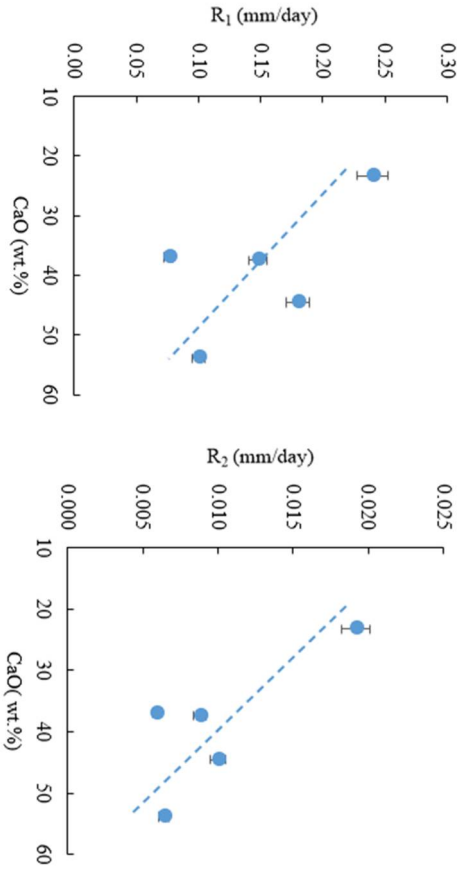

Figure 8 Correlation between stage I (R_1) and stage II (R_2) corrosion rate and CaO content

4. CONCLUSION

Geopolymer mortar samples were exposed to sulphuric acid, simulating the final stage of corrosion impacted by MICC. The corrosion of mortar as a function of time was observed to have a stage I and stage II corrosion rate. The R_2 was an essential feature of these protective coating mortars. These results suggest that the reduction in corrosion rate in the second stage could be attributed to the increased diffusion resistance for the acid through the build-up of the corrosion layer and to pore blocking by gypsum. Therefore, the corrosion resistance performance of mortars was related to the CaO composition.

ACKNOWLEDGMENTS

Acknowledgements are extended to the faculty and staff of the School of Chemical and Biomolecular Engineering at The University of Sydney and Department of Chemical Engineering, Faculty of Engineering, Burapha University for their invaluable assistance and provision of resources, which significantly facilitated the research. Furthermore, appreciation is expressed for the financial support provided by the Australian Government through the Cooperative Research Centre. The successful completion of this project was also made possible by the contributions of our esteemed project partners, who

provided expertise, labor, funding, products, and trial sites.

REFERENCES

1. WSA-201, Manual for selection and application of protective coatings 2017, Water Services Association of Australia Limited: Docklands VIC 3008, Australia.
2. Kim, D., S. Yi, and W. Lee. Life cycle assessment of sewer system: Comparison of pipe materials. in The World Congress on Advances in Civil, Environmental, and Materials Research. 2012.
3. Wu, M., et al., Microbiologically induced corrosion of concrete in sewer structures: A review of the mechanisms and phenomena. Construction and Building Materials, 2020. **239**: p. 117813.
4. Grengg, C., et al., Advances in concrete materials for sewer systems affected by microbial induced concrete corrosion: A review. Water Res, 2018. **134**: p. 341-352.
5. Berger, C., et al., Zustand der Kanalisation in Deutschland. WASSERWIRTSCHAFT WASSERTECHNIK, 2003: p. 10-17.
6. Jensen, H., C.A. Biggs, and E. Karunakaran, The importance of sewer biofilms. WIREs Water, 2016. **3**(4): p. 487-494.
7. Gutierrez, O., et al., Evaluation of oxygen injection as a means of controlling sulfide production in a sewer system. Water research, 2008. **42**(17): p. 4549-4561.
8. Hvitved-Jacobsen, T., Sewer processes: microbial and chemical process engineering of sewer networks. 2001: CRC press.
9. Ibrahim, M. and M. Maslehuddin, An overview of factors influencing the properties of alkali-activated binders. Journal of Cleaner Production, 2021. **286**: p. 124972.
10. Brough, A.R. and A. Atkinson, Sodium silicate-based, alkali-activated slag mortars: Part I. Strength, hydration and microstructure. Cement and Concrete Research, 2002. **32**(6): p. 865-879.
11. Davidovits, J., Geopolymers: inorganic polymeric new materials. Journal of Thermal Analysis and calorimetry, 1991. **37**(8): p. 1633-1656.
12. Liew, Y.-M., et al., Structure and properties of clay-based geopolymer cements: A review. Progress in Materials Science, 2016. **83**: p. 595-629.
13. Majidi, B., Geopolymer technology, from fundamentals to advanced applications: a review. Materials Technology, 2013. **24**(2): p. 79-87.
14. Liguori, B., et al., Geopolymerization Ability of Natural and Secondary Raw Materials by Solubility Test in Alkaline Media. Environments, 2017. **4**(3).
15. Davidovits, J. and S. Cordi, Synthesis of new high temperature geo-polymers for reinforced plastics/composites. Spe Pactec, 1979. **79**: p. 151-154.
16. Provis, J.L. and J.S. Van Deventer, Alkali activated materials: state-of-the-art report, RILEM TC 224-AAM. Vol. 13. 2013: Springer Science & Business Media.
17. Herrmann, A., A. Koenig, and F. Dehn, Structural concrete based on alkali-activated binders: Terminology, reaction mechanisms, mix designs and performance. Structural Concrete, 2018. **19**(3): p. 918-929.
18. Chen, K., et al., Geopolymer concrete durability subjected to aggressive environments – A review of influence factors and comparison with ordinary Portland cement. Construction and Building Materials, 2021. **279**: p. 122496.
19. ASTMC192/C192M, ASTM C192/C192M −19 Standard Practice for Making and Curing Concrete Test Specimens in the Laboratory. 2019, ASTM International: ASTM International.
20. Khan, H.A., A. Castel, and M.S.H. Khan, Corrosion investigation of fly ash based geopolymer mortar in natural sewer environment and sulphuric acid solution. Corrosion Science, 2020. **168**.
21. Sturm, P., et al., Sulfuric acid resistance of one-part alkali-activated mortars. Cement and Concrete Research, 2018. **109**: p. 54-63.
22. Dorner, H. Acid resistance of high performance concrete. in 38th research colloquium, German Committee for Reinforced Concrete (DAfStb), Munich. 2000.
23. Dorner, H. and R. Beddoe. Prognosis of concrete corrosion due to acid attack. in 9th International Conference of Building Materials, Brisbane, Australia. 2002.
24. Yuan, H.F., et al., Degradation modelling of concrete submitted to sulfuric acid attack. Cement and Concrete Research, 2013. **53**: p. 267-277.
25. Beddoe, R.E. and H.W. Dorner, Modelling acid attack on concrete: Part I. The essential mechanisms. Cement and Concrete Research, 2005. **35**(12): p. 2333-2339.
26. Monteny, J., et al., Chemical, microbiological, and in situ test methods for biogenic sulfuric acid corrosion of concrete. Cement and Concrete Research, 2000. **30**(4): p. 623-634.
27. Scrivener, K.L., J.-L. Cabiron, and R. Letourneux, High-performance concretes from calcium aluminate cements. Cement and Concrete Research, 1999. **29**(8): p. 1215-1223.
28. Albitar, M., et al., Durability evaluation of geopolymer and conventional concretes. Construction and Building Materials, 2017. **136**: p. 374-385.

Production of graphene from graphite via flash joule heating process

Siranut Sirathanutworakan[1], Prapan Kuchonthara[1,2], Tharapong Vitidsant[1,2], Napida Hinchiranan[1,2,*]

[1] Department of Chemical Technology, Faculty of Science, Chulalongkorn University, Bangkok 10330, Thailand
[2] Center of Excellence in Catalysis for Bioenergy and Renewable Chemicals (CBRC), Chulalongkorn University, Bangkok 10330, Thailand
[*] Corresponding author: napida.h@chula.ac.th

ABSTRACT

Graphene, a single layer of carbon atoms in a hexagonal lattice, has garnered considerable interest due to its outstanding properties, including high strength, electrical and thermal conductivity. However, conventional production face challenges in scalability, high costs and structural defects, limiting their practical applications. Flash Joule Heating (FJH) is a promising alternative for large-scale with cost-effective graphene production. In this research, graphite is used as a feedstock because of its high carbon purity. By rapidly heating a carbon precursor to high temperatures (>3000 K) using an electric current, FJH enables precise control of graphene layer thickness and quality, which can be identified from the ratios of peak intensity between the D band and G band (I_D/I_G) and the 2D band and G band (I_{2D}/I_G), detected by Raman spectroscopy. The important parameters such as resistance of the system and voltage affected graphene's structural and properties. To consider the resistance in the range of 0.5 to 1.5 Ω, it was found that the increase in the electrical resistance decreased the I_D/I_G ratio and then leveled off when the resistance increased to 2.0 Ω. Furthermore, the I_D/I_G ratio decreased with increasing the I_{2D}/I_G ratio when the voltage was increased from 200 to 240 V. At 240 V, the I_D/I_G and I_{2D}/I_G ratios were 0.53 and 0.01, respectively, suggesing that a few-layer graphene type with minimal defects was formed.

Keywords: Graphene production, Flash joule heating, Graphite

1. INTRODUCTION

Graphene, a two-dimensional carbon allotrope composed of sp^2-bonded atoms arranged in a hexagonal lattice, has attracted considerable interest in both scientific research and industrial applications due to its exceptional electrical conductivity, mechanical strength, thermal stability and surface area [1]. These attributes render graphene a transformative material across various fields, including energy storage, electronics, composite reinforcement and environmental remediation [2–4]. However, the widespread implementation of graphene in commercial applications has been constrained by the limitations of existing production methods, which are often energy-intensive, costly and environmentally detrimental.

Traditional techniques for graphene synthesis include chemical vapor deposition (CVD), mechanical exfoliation, liquid-phase exfoliation and oxidative-reduction processes [5–7]. Although these approaches can yield high-quality graphene under controlled laboratory conditions, their scalability and economic feasibility are challenged by complex procedures, low yield, and the use of hazardous chemicals or high-energy input. In the case of oxidative methods, they introduce structural defects and oxygenated functional groups, which degrade graphene's desirable properties. For the bottom-up methods such as CVD, it typically suffers from limited throughput and substrate constraints [8]. These challenges have driven research into alternative graphene synthesis strategies that are faster, more sustainable, and cost-effective.

In recent years, flash Joule heating (FJH) has emerged as a promising breakthrough in graphene synthesis technology, as shown in Figure 1. First introduced by Luong et al. [9], the FJH method involves discharging a high-voltage capacitor through a carbon-based precursor confined between conductive electrodes. This results in the ultra-rapid heating to temperatures higher than 3000 K within milliseconds, followed by rapid cooling, thereby converting the precursor into turbostratic flash graphene (tFG). This process has many advantages sush as no requirement for solvents, catalysts or controlled atmospheres. This process is also completed in less than one second [10]. Unlike AB-stacked graphite, tFG exhibits rotational misalignment between layers, which enhances its dispersibility in solvents and preserves its two-dimensional properties even in multi-layered forms [11].

The simplicity and scalability of FJH have enabled the valorization of various low-cost carbonaceous

feedstocks, including coal pitch [12], anthracite [13], rubber waste [14] and food or plastic waste [9]. These feedstocks can be rapidly transformed into high-value graphene materials. For example, waste rubber tires were converted to graphene. It does not only mitigate landfill waste and toxic emissions from incineration, but it also produces tFG with reinforcing properties, which are suitable for the use in cementitious composites [14]. Similarly, coal-based feedstocks, abundant and underutilized in many parts of the world, offer an economical and accessible resource for graphene production with minimal preprocessing [12,13].

Among various carbonaceous feedstocks investigated for FJH-based graphene synthesis, graphite stands out due to its inherently high carbon purity, crystalline structure and electrical conductivity. As a naturally occurring layered material, graphite is composed of stacked graphene sheets held together by weak van der Waals forces to make it an ideal precursor for graphene production via rapid thermal and electrical processes. Its excellent electrical conductivity also ensures efficient Joule heating and uniform temperature distribution during the FJH process, facilitating high conversion efficiency. Furthermore, graphite is widely available, cost-effective and requires minimal preprocessing compared to more complex waste-derived sources. This makes it a practical and reproducible option for experimental and industrial applications. The use of graphite as a feedstock thus offers a controlled pathway for producing high-quality turbostratic graphene, and serving as a model system for studying FJH mechanisms under consistent material conditions [15–17].

Despite the apparent advantages, the mechanisms governing the FJH transformation remain complex. Studies have shown that both the electric field and the generation of free radicals play crucial roles in breaking chemical bonds and reassembling carbon atoms into graphitic structures [12]. Molecular dynamics simulations and density functional theory (DFT) analyses suggested that the electric field facilitated molecular ionization and directional alignment of precursors, thereby lowering the energy barrier for graphitization [12]. The process was highly sensitive to system parameters such as pulse voltage, capacitance, and pulse duration. Thus, the optimization of process to maximize graphene yield and purity is required, Liu and Luo [13] demonstrated that a pulse voltage of 190 V produced coal-based tFG with superior crystallinity and interlayer spacing (~0.358 nm), indicating the turbostratic stacking. In the aspect of the environmental and economic concerns, the energy cost for producing one ton of graphene via FJH has been estimated at less than $100, significantly lower than that of conventional methods [14]. Moreover, the process avoids chemical waste and minimizes occupational hazards, making it suitable for industrial adoption, especially for the regions having abundant carbon-rich waste.

Therefore, this research aims to prepare flash graphene (fGp) from graphite using FJH. The effect of FJH parameters on the yield and quality of graphene was investigated. The structural of the resulting fGp were detected by Raman spectroscopy

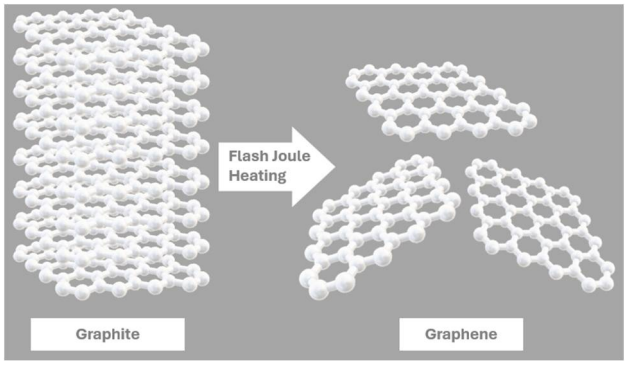

Figure 1 Flash joule heating of graphite to produce graphene.

2. EXPERIMENTAL

2.1 Materials and Sample Preparation

Commercial-grade graphite powder obtained from Repier-Behr Co., Ltd. Was directly used without any chemical or physical pre-treatment. Briefly, 150 mg graphite was manually packed in the borosilicate glass tube (inner diameter = 9 mm; thickness = 1.5 mm; length = 10 cm). The glass tube was then located between two copper mesh electrodes (500 mg each), serving as current collectors and conductive interfaces. The packed sample was squished to achieve the desired electrical resistance (0.5 – 2.0 Ω) before placing in the chamber of the FJH reactor as shown in Figure 2.

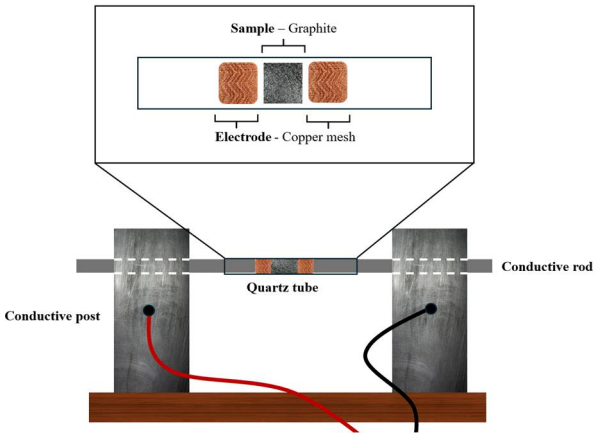

Figure 2 Flash Joule Heating reactor schematic.

2.2 Flash Joule Heating Procedure

The flash Joule heating (FJH) process was performed using a custom-built high-voltage capacitor discharge system. The graphite-loaded quartz tube was mounted within the discharge chamber, and the copper electrodes were connected to the circuit terminals. A capacitor bank was charged to a selected pulse voltage. The estimated peak temperature within the sample

exceeded 3000 K in less than one second, as measured by an oscilloscope (DHO800), initiating thermal decomposition and reassembly of carbon atoms into graphene.

This study was designed to evaluate the effects of electrical parameters on the transformation of graphite to fGp using FJH process. The primary variables manipulated were the pulse voltage (200 and 240 V), and the system resistance (0.5 to 2.0 Ω). Additionally, all FJH reactions were carried out under a controlled low-pressure condition at 50 mbar, maintained using a vacuum pump, to minimize oxidation and thermal dissipation. These controlled conditions allowed for the isolation of the effects of input parameters on graphene quality.

2.4 Characterization Techniques

To evaluate the structural transformation of graphite after FJH, Raman spectroscopy was employed as the primary characterization techniques. Raman spectroscopy (XploRA PLUS) was performed using a 532 nm laser source, focusing on the D (~1,350 cm^{-1}), G (~1,580 cm^{-1}), and 2D (~2,700 cm^{-1}) bands, which are characteristic of graphitic materials. The ratio of the D to G band intensities (I_D/I_G) was used to estimate the degree of structural disorder and defect density, while the shape and intensity of the 2D band (I_{2D}/I_G) provided insight into the number of graphene layers and stacking order. In this study, an I_{2D}/I_G ratio greater than 0.5, when accompanied by a low I_D/I_G ratio, was used as a criterion to indicate a few-layer graphene with high structural quality [18].

3. RESULTS AND DISCUSSION

Two sets of experiments were designed to examine the influence of key electrical parameters: one by varying the system resistance at a constent pulse voltage of 200 V, and another set by varying the pulse voltage with keeping the system resistance constant of 1.5 Ω. Raman spectra of graphite before and after FJH were comparatively shown in Figure 3a and Figure 4a. The intensity ratios of the D to G bands (I_D/I_G) and the 2D to G bands (I_{2D}/I_G) was also exhibited in Figure 3b and Figure 4b. to evaluate the defect density and the development of graphene layers [16].

At a constant pulse voltage of 200 V, the influence of system resistance on graphene structure was evaluated at five representative resistance values: 0.5 Ω, 0.7 Ω, 1.0 Ω, 1.5 Ω and 2.0 Ω.

The analysis of the Raman spectra before and after the FJH process, three main characteristic bands were observed: the D (~1,350 cm^{-1}), G (~1,580 cm^{-1}), and 2D bands (~2,700 cm^{-1}), as shown in Figure 3a and Figure 4a. The results indicate that the system resistance had a significant effect on the D band. As the resistance increased, the intensity of the D band decreased, suggesting a reduction in disordered carbon structures and the formation of higher-quality graphene [12]. Similarly, the pulse voltage also affected the D band. Increasing the pulse voltage results in a reduction of the D band intensity, indicating fewer defects. In addition, the pulse voltage influenced the G band. When the pulse voltage increased, the G band intensity slightly decreased. This might be associated with a reduction in the number of graphene layers at the higher voltages. To better understand these changes, it was necessary to analyze the Raman spectra further using the intensity ratios I_{2D}/I_G and I_D/I_G, which provided clearer insights into graphene quality and structure as presented in Figure 3b and Figure 4b.

For the effect of the system resistance, as shown in Figure 3b, the I_D/I_G ratio was low at 0.10 when the system resistance was 0.5 Ω, indicating the limited defect formation. However, the I_{2D}/I_G ratio (0.33) was lower than that of raw graphite (0.43). This suggested that the resistance was not enough to provide sufficient energy input to complete bond breaking across the carbon lattice. As a result, only partial bond disruption occurred at certain sites within the structure, leading to the formation of disordered carbon domains. This incomplete transformation resulted in the lower graphitic ordering, as reflected by the lower I_{2D}/I_G ratio and slightly higher I_D/I_G ratio than graphite. This indicated the poorer material quality [16, 18].

When the system resistance increased to 0.7 Ω and 1.0 Ω, the I_{2D}/I_G ratio also increased to 0.40 and 0.38, respectively, indicating the initial development of few-layer graphene. However, the I_D/I_G ratio also increased to 0.40 at 0.7 Ω and 0.38 at 1.0 Ω, reflecting a rise in structural disorder. This could be explained that this electrical resistance levels provided the sufficient generated heat to partially break the carbon bonds in the graphite structure. However, the energy was not adequate to complete the bond rearrangement or full structural reorganization. As a result, the partial transformation toward a few-layer graphene was occurred to provide the considerable amount of disorder, which was reflected by the elevated I_D/I_G values.

At the system resistance of 1.5 Ω, the results obtained from Raman spectroscopy showed a significant improvement of graphene quality. The I_D/I_G ratio decreased to 0.16, while the I_{2D}/I_G ratio remained stable at 0.40. This suggested that the electrical energy delivered under this condition was sufficient to break the carbon bonds in graphite, and it also promoted the reorganization to obtain more ordered structures, resulting in the formation of few-layer graphene with fewer defects. At 2.0 Ω, the I_D/I_G and I_{2D}/I_G ratios were similar to those at 1.5 Ω, indicating a comparable structural outcome.

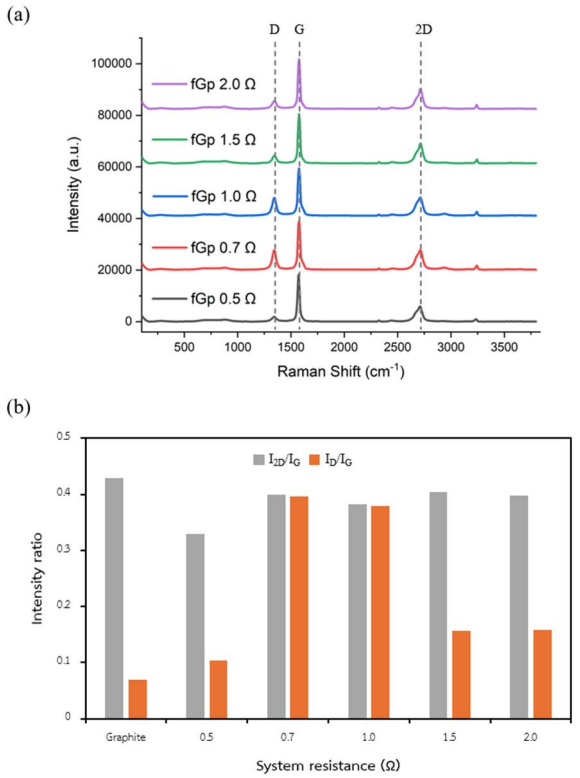

Figure 3 (a) Raman spectra of flash-graphene obtained from the various system resistances, and (b) effect of the system resistance on I_{2D}/I_G and I_D/I_G ratios of produced flash-graphene.

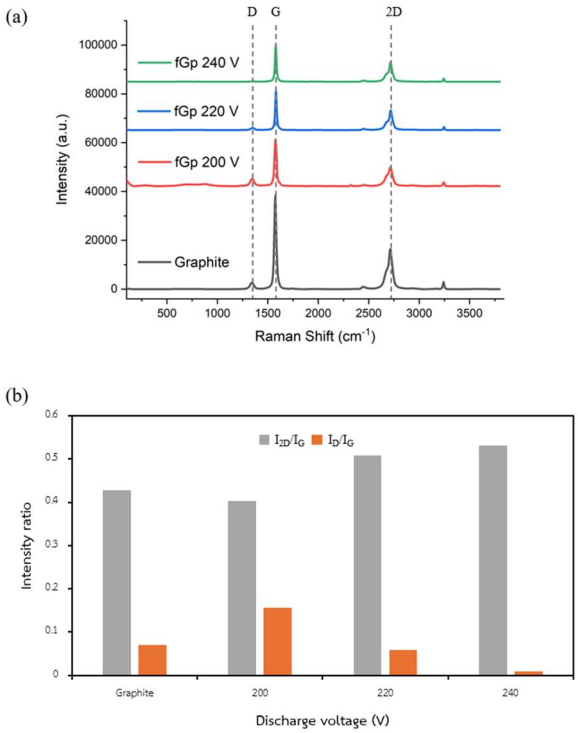

Figure 4 (a) Raman spectra of flash-graphene obtained from the various pulse voltage values, and (b) effect of pulse voltage on I_{2D}/I_G and I_D/I_G ratios of produced flash-graphene.

However, a key observation was that the metal rods used as current conductors exhibited the surface damage at this resistance. Specifically, rod melting occurred at the contact interface between the stainless-steel rod (SS400) and the copper electrode, likely due to excessive and prolonged heating. This localized thermal degradation might influence the duration and consistency of the FJH process, introducing uncertainties in energy delivery and potentially affecting the uniformity and reproducibility of the resulting graphene. Therefore, 1.5 Ω was determined to be the maximum practical system resistance for stable and reliable FJH operation using the current system configuration.

To investigate the effect of pulse voltage under controlled system resistance at 1.5 Ω, the samples were processed at 200 V, 220 V, and 240 V. The I_D/I_G ratio markedly decreased from 0.16 at 200 V to 0.06 at 220 V and reached to 0.01 at 240 V, as shown in Figure 4b, indicating a substantial reduction in defect density with increasing voltage. Concurrently, the I_{2D}/I_G ratio increased from 0.40 to 0.51 and 0.53, respectively, suggesting the improved formation of few-layer graphene. Higher voltages enhanced the thermal energy input, leading to a clearer reduction of the structural defects and improved the layer formation [17]. Thus, the combination of appropriate system resistance and sufficient high voltage is essential to produce high quality graphene via FJH process.

4. CONCLUSION

This study successfully demonstrates the synthesis of graphene from commercial graphite powder using FJH process. The effects of system resistance and pulse voltage on graphene quality were investigated through Raman spectroscopy. At a constant voltage of 200 V, the system resistance of 0.5 Ω could not provide the enough energy to fully break the carbon bonds throughout the graphite structure. The higher system resistance to 0.7 Ω and 1.0 Ω led to the partial formation of few-layer graphene, as indicated by rising I_{2D}/I_G ratios. However, these conditions also introduced higher defect levels, reflected in elevated I_D/I_G values. The optimal condition found at 1.5 Ω cloud provide the efficient thermal energy to from graphene with a low I_D/I_G ratio (0.16) and steady I_{2D}/I_G (0.40), indicating the improved structural order. Although similar results obtained from Raman spectroscopy were observed at 2.0 Ω, the surface melting of the steel rod using as the current condition was occurred due to the excessive heating, potentially disrupting energy delivery and process stability. At the optimized system resistance of 1.5 Ω, increasing the pulse voltage from 200 V to 240 V further improved graphene quality. At 240 V, a minimum I_D/I_G of 0.01 and a peak I_{2D}/I_G of 0.53 were obtained, suggesting the formation of the highly ordered few-layer graphene with minimal defects.

These findings underscore the importance of control over both resistance and voltage in the FJH process.

ACKNOWLEDGMENTS

This research is funded by Repier-Behr Co., Ltd. The author gratefully acknowledges their generous financial support, which was instrumental in facilitating the experimental work and the overall progress of this study.

REFERENCES

1. K.S. Novoselov, A.K. Geim, S.V. Morozov, D. Jiang, Y. Zhang, S.V. Dubonos, I.V. Grigorieva, A.A. Firsov. *Electric field effect in atomically thin carbon films. Science* 2004; 306(5696): 666–669.
2. A.K. Geim, K.S. Novoselov. The rise of graphene. *Nature Materials* 2007; 6: 183–191.
3. Y. Zhu, S. Murali, W. Cai, X. Li, J.W. Suk, J.R. Potts, R.S. Ruoff. Graphene and graphene oxide: Synthesis, properties and applications. *Advanced Materials* 2010; 22(35): 3906–3924.
4. M.J. Allen, V.C. Tung, R.B. Kaner. Honeycomb carbon: A review of graphene. *Chemical Reviews* 2010; 110(1): 132–145.
5. S. Park, R.S. Ruoff. Chemical methods for the production of graphenes. *Nature Nanotechnology* 2009; 4: 217–224.
6. X. Zhang, C. Wang, W. Zhang, Y. Wei, Q. Wang, S. Wang. Transparent, conductive films of graphene and carbon nanotubes. *Science* 2010; 327(5966): 1373.
7. Y. Hernandez, V. Nicolosi, M. Lotya, F.M. Blighe, Z. Sun, S. De, I.T. McGovern, B. Holland, M. Byrne, Y.K. Gun'ko, J.N. Coleman. High-yield production of graphene by liquid-phase exfoliation of graphite. *Nature Nanotechnology* 2008; 3: 563–568.
8. D.R. Dreyer, S. Park, C.W. Bielawski, R.S. Ruoff. The chemistry of graphene oxide. *Chemical Society Reviews* 2010; 39(1): 228–240.
9. D.X. Luong, K. Chen, R. Ghasemi, F. Arai, C. Talapatra, P.M. Ajayan, J.M. Tour. Gram-scale bottom-up flash graphene synthesis. *Nature* 2020; 577: 647–651.
10. P.A. Advincula, S. Gajera, M. Islam, D.X. Luong, C. Talapatra, J.M. Tour. Flash graphene from rubber waste. *Carbon* 2021; 178: 649–656.
11. P. Huang, X. Zhang, L. Yu, Z. Xu, Y. Zhao, H. Liu. Effect of free radicals and electric field on preparation of coal pitch-derived graphene using flash Joule heating. *Chemical Engineering Journal* 2022; 450: 137999.
12. X. Liu, H. Luo. Preparation of coal-based graphene by flash Joule heating. *ACS Omega* 2024; 9(2): 2657–2663.
13. R.T. Zhu, Y. Zhao, Z. Xu, H. Liu. Role of electric fields in graphene synthesis via FJH. *Chemical Engineering Journal* 2022; 450: 137999.
14. R. Shahsavari, S. Gajera, J.M. Tour. Mechanical reinforcement of cement composites using turbostratic flash graphene. *Carbon* 2021; 178: 649–656.
15. K.S. Novoselov, D. Jiang, F. Schedin, T.J. Booth, V.V. Khotkevich, S.V. Morozov, A.K. Geim. Two-dimensional atomic crystals. *Proceedings of the National Academy of Sciences* 2005; 102(30): 10451–10453.
16. A.C. Ferrari, J.C. Meyer, V. Scardaci, C. Casiraghi, M. Lazzeri, F. Mauri, S. Piscanec, D. Jiang, K.S. Novoselov, S. Roth, A.K. Geim. Raman spectrum of graphene and graphene layers. *Physical Review Letters* 2006; 97(18): 187401.
17. W. Lv, W.J. Yu, W. He, F. Kang. Graphite and graphene: From raw materials to sustainable energy devices. *Advanced Materials* 2022; 34(1): 2105172.
18. A. Malekpour, I. Calizo, G. Ghosh, D.L. Nika, A.A. Balandin. Estimation of number of graphene layers using different methods: A comparative study. *Annalen der Physik* 2014; 526(5–6): 347–357.

Effects of oxygen, nitrogen, and sulfur doped hard carbons derived from longan seed as anode material for sodium-ion batteries

Sutida Tammanoi[1], Nikom Klomkliang[1,*], Kajornsak Faungnawakij[2]

[1] School of Chemical Engineering, Suranaree University of Technology, Nakhon Ratchasima 30000, Thailand
[2] National Nanotechnology Center (NANOTEC), National Science and Technology Development Agency (NSTDA), Pathum Thani 12120, Thailand
[*] Corresponding author: nikom.klo@sut.ac.th

ABSTRACT

Sodium-ion batteries (SIBs) have emerged as a promising alternative for sustainable and cost-effective energy storage. Hard carbon, especially from biomass, is a key candidate for anode materials due to its favorable sodium storage capability. In this study, hard carbon was synthesized from longan seed waste through pyrolysis at 900–1200 °C (HCx), and modified via nitrogen (N-HCx) and sulfur (S-HCx) doping using urea and sulfur powder, respectively. The BJH method confirmed a mesoporous structure. Raman spectroscopy revealed increased disorder with higher carbonization temperatures, while TEM showed expanded interlayer spacing: 3.4–3.9 Å for HC1200, 3.4–4.0 Å for N-HC1200, and 3.9–4.1 Å for S-HC1200. Electrochemical testing showed that S-HC1200 delivered the highest reversible capacity (248.43 mAh/g) and good capacity recovery, but exhibited lower early-cycle stability. N-HC1200 showed moderate capacity (173.7 mAh/g), moderate initial stability, and the best capacity recovery. In contrast, HC1200 exhibited the lowest initial capacity (196.5 mAh/g), the lowest capacity recovery, but the most stable cycling behavior. Overall, N-HC1200 presented the most balanced and robust electrochemical performance. This work underscores the importance of precursor selection and highlights the potential of agricultural waste in the development of efficient and sustainable anode materials for sodium-ion batteries.

Keywords: Hard carbon; Sodium ion; Battery; Energy Materials; Anode.

1. INTRODUCTION

The global shift toward sustainable energy systems has highlighted the need for environmentally friendly and cost-effective energy storage technologies. While lithium-ion batteries (LIBs) have dominated the market due to their high energy density and long cycle life, increasing concerns over the limited availability, rising cost, and environmental impact of lithium extraction have driven interest in alternative battery chemistries [1,2]. Sodium-ion batteries (SIBs) have emerged as a promising substitute for LIBs due to the abundance, low cost, and similar electrochemical properties of sodium. Sodium is approximately 1,000 times more abundant in the Earth's crust than lithium, making it a viable option for large-scale energy storage applications [3]. However, the larger ionic radius of Na^+ (0.204 nm vs. 0.152 nm for Li^+) impairs its intercalation into conventional graphite anodes due to the limited interlayer spacing (~0.335 nm) of graphene layers. This presents a key challenge for the development of high-performance sodium-ion anodes [4]. Hard carbon (HC), with its disordered structure and expanded interlayer spacing, has attracted attention as a promising anode for SIBs. Its open framework structure supports reversible Na^+ storage, and it can be synthesized from a variety of low-cost biomass precursors. Biomass-derived hard carbon has additional advantages, including renewability, environmental friendliness, and compatibility with carbon-neutral production processes [5]. In this study, longan seeds—a major agricultural waste product in Thailand—are used as a sustainable precursor for producing hard carbon. Thailand produces over 1.5 million tons of fresh longan annually, generating approximately 20,000 tons of longan seed waste from fruit processing industries. These seeds are rich in lignocellulosic content, making them highly suitable for carbonization. Their availability, low cost, and high fixed carbon content make longan seeds an excellent raw material for hard carbon synthesis, while also contributing to waste valorization and circular economy goals. To enhance sodium storage performance, nitrogen and sulfur doping strategies are applied to modify the hard carbon structure and surface. Nitrogen doping can improve electronic conductivity and introduce active sites for sodium adsorption, while sulfur doping may expand the interlayer spacing and further enhance sodium-ion diffusion [6]. The structural and electrochemical properties of pristine and doped hard carbons are systematically studied through Raman spectroscopy, high-resolution transmission electron microscopy (HR-TEM), and electrochemical analysis

in half-cell configurations. This research aims to explore the influence of pyrolysis temperature and heteroatom doping on the structural characteristics and sodium storage capability of longan seed-derived hard carbon, thereby supporting the development of high-performance, low-cost, and sustainable sodium-ion battery anodes.

2. EXPERIMENTAL

2.1 Synthesis of Hard Carbon and Heteroatom-Doped Hard Carbon

Hard carbon (HC) was synthesized from longan seeds via a two-step pyrolysis process. Initially, the seeds were crushed using a jaw crusher and subjected to pre-carbonization at 450°C for 1 hour under a nitrogen atmosphere (flow rate: 10 mL/min) with a heating rate of 10°C/min. The pre-carbonized material was then further heat-treated at various temperatures (900, 1000, 1100, and 1200°C) for 1 hour under nitrogen flow at a heating rate of 5°C/min to evaluate the effect of pyrolysis temperature on carbon structure. After natural cooling to room temperature, the resulting samples were designated as HCx, where x refers to the treatment temperature. For nitrogen doping, the as-prepared HC was mixed with urea in a 1:1 weight ratio and thermally treated at 350°C for 1 hour in ambient air at a heating rate of 10°C/min to introduce nitrogen-containing functionalities. The resulting HC@Urea was then mixed with 1 M KOH, dried at 100°C for 12 hours, and activated by pyrolysis at 600°C for 1 hour under a CO_2 atmosphere to obtain nitrogen-doped hard carbon (N-HC). For sulfur doping, HC was mixed with elemental sulfur powder in a 1:1 weight ratio and heated at 250°C for 1 hour under an argon atmosphere (heating rate: 10°C/min) to promote sulfur incorporation. The intermediate product (HC@S) was further pyrolyzed at 950°C for 1 hour under argon (heating rate: 5°C/min), followed by washing with diluted hydrochloric acid and deionized water to remove impurities. The final product was dried at 100°C for 16 hours to obtain sulfur-doped hard carbon (S-HC).

2.2 Material Characterization

Various advanced characterization techniques were employed to investigate the structural, morphological, and textural properties of the synthesized hard carbon and doped hard carbon materials. Each technique was selected based on its relevance to specific structural features that directly influence sodium-ion storage performance. To assess the surface area and porosity, nitrogen adsorption–desorption analysis was conducted. The specific surface area was calculated using the Brunauer–Emmett–Teller (BET) method [7], which is based on multilayer adsorption theory. The BET equation is expressed as:

$$\frac{1}{V\left(\frac{P_0}{P}-1\right)} = \frac{C-1}{V_m C}\cdot\frac{P}{P_0} + \frac{1}{V_m C}$$

Where V is the adsorbed gas volume at pressure P, P_0 is the saturation pressure, V_m is the monolayer capacity, and C is the BET constant. This method provides insight into the availability of surface sites for ion interaction and diffusion.

To further analyze the pore structure, the Density Functional Theory (DFT) method [8] was employed to derive pore size distributions from the adsorption isotherms. The DFT model describes the interaction between gas molecules and pore walls, enabling the estimation of pore sizes across the micro-, meso-, and macropore ranges. Unlike classical methods, DFT can accommodate complex pore geometries and assumes local thermodynamic equilibrium, offering a more accurate representation of the porous structure.

Transmission electron microscopy (TEM) was applied to visualize the microstructure and assess the degree of graphitic ordering. In particular, the interlayer distance (d) between carbon planes can be analyzed through diffraction patterns [9] using Bragg's Law:

$$n\lambda = 2d\sin\theta$$

where λ is the wavelength of the electron beam, θ is the diffraction angle, and n is the diffraction order. The interlayer spacing is a critical parameter in determining the ability of sodium ions to intercalate into the carbon structure, especially in hard carbons where expanded interlayer gaps are beneficial.

Raman spectroscopy was utilized to evaluate the degree of disorder and graphitization in the carbon structure. This was achieved by examining the intensity ratio between the D-band (disorder-induced) and G-band (graphitic) in the Raman spectra. The ratio ID /IG is commonly used as a qualitative measure of structural disorder, where a higher ratio indicates a greater presence of defects and amorphous domains within the carbon matrix [10]. These structural imperfections can enhance ion adsorption capacity and electrolyte accessibility. Collectively, these techniques offer a comprehensive understanding of the carbon materials' morphology, pore architecture, and structural features, which are crucial for optimizing electrochemical performance in sodium-ion battery applications.

2.3 Coin cell building

The anode architecture comprised hard carbon (HCx) in powder form, intimately mixed with polyvinylidene fluoride (PVDF) binder and Super P carbon black at a weight ratio of 80:10:10 (HCx: PVDF: Super P) in N-methylpyrrolidone (NMP) solution. The resulting mixture was magnetically stirred for 12 hours to form a homogeneous slurry. This slurry was then uniformly coated onto a copper foil current collector using a doctor blade technique and subsequently dried

at 80°C under vacuum overnight. The dried electrode film was cut into 12 mm round disks. Sodium metal foil served as the counter electrode (cathode) for the half-cell configuration. A Celgard 2400 polyethylene (PP) membrane acted as the separator to physically isolate the anode and cathode. Coin-type cells (CR2032) were assembled in an argon-filled glovebox with oxygen and moisture levels maintained below 0.1 ppm. Subsequently, 50 µL of 1 M sodium perchlorate ($NaClO_4$) electrolyte solution (prepared in a 1:1 (v/v) mixture of ethylene carbonate (EC) and diethyl carbonate (DEC), with 5 wt% fluoroethylene carbonate (FEC) as an additive) was added to each cell. Finally, the cells were hermetically sealed using an ECCCM-160E-A crimping machine at a pressure of 1 ton.

2.4 Electrochemical Measurements

The electrochemical performance of the HC1200, N-HC1200, and S-HC1200 electrodes was evaluated using CR2032-type half coin-cells with sodium metal as the counter/reference electrode. Galvanostatic charge-discharge tests were performed in the voltage range of 0.001–2.5 V (vs. Na^+/Na) using a CT3002A battery testing system (Wuhan Land Electronic Co. Ltd., China). Rate capability tests were conducted at various current densities ranging from 50 to 2000 mA/g to investigate the electrodes' performance under different charge/discharge rates. All measurements were carried out at room temperature (~25°C).

3. RESULTS AND DISCUSSION

3.1 Structural and morphological characterization

To investigate the physical and structural characteristics of hard carbon materials derived from longan seeds, nitrogen adsorption–desorption isotherms (BET), high-resolution transmission electron microscopy (HR-TEM), and Raman spectroscopy were employed. The key data obtained from these techniques are summarized in Table 1.

The pore size distribution curves of HC1200, N-HC1200, and S-HC1200, obtained via DFT analysis based on nitrogen adsorption–desorption at –196°C shown in Fig 1a, reveal distinct differences in porous architecture associated with heteroatom doping. The undoped HC1200 exhibits a relatively broad pore size range dominated by mesopores and macropores, with a lack of microporous contribution. This is consistent with the observed Type III isotherm according to IUPAC classification, which indicates weak interactions between the adsorbate and the carbon surface, typical of nonporous or macroporous materials. In contrast, both N-HC1200 and S-HC1200 exhibit Type IV isotherms with H3 hysteresis loops, characteristic of slit-shaped mesopores often formed between disordered carbon layers. Their pore size distribution profiles further support this:

Table 1 Surface area and Raman ID/IG ratios of pristine and doped hard carbon samples.

Sample	BET Surface Area (m^2/g)	Interlayer Structure (from TEM)	ID/IG ratios
HC900	7.04	-	1.1401
HC1000	10.91	-	1.1347
HC1100	6.10	-	1.1342
HC1200	5.96	Slightly more graphitic (0.382 nm)	1.1770
N-HC1200	34.27	Highly disordered, porous (0.386 nm)	1.8194
S-HC1200	28.67	Highly disordered, porous (0.392 nm)	1.7824

N-HC1200 shows a prominent peak in the microporous region (~1–2 nm) and a secondary distribution in the narrow mesopore range (~2–5 nm), indicating that nitrogen doping induces microporosity and enhances structural disorder. This pore configuration is favorable for sodium-ion storage as it provides abundant active sites and short diffusion paths.

S-HC1200 presents a broader mesopore distribution, with significant volume contributions between 3 and 10 nm. The wider pores are indicative of a more extensive disruption of the carbon framework by sulfur doping. Such porosity facilitates improved electrolyte infiltration and ion transport, while still maintaining sufficient surface area.

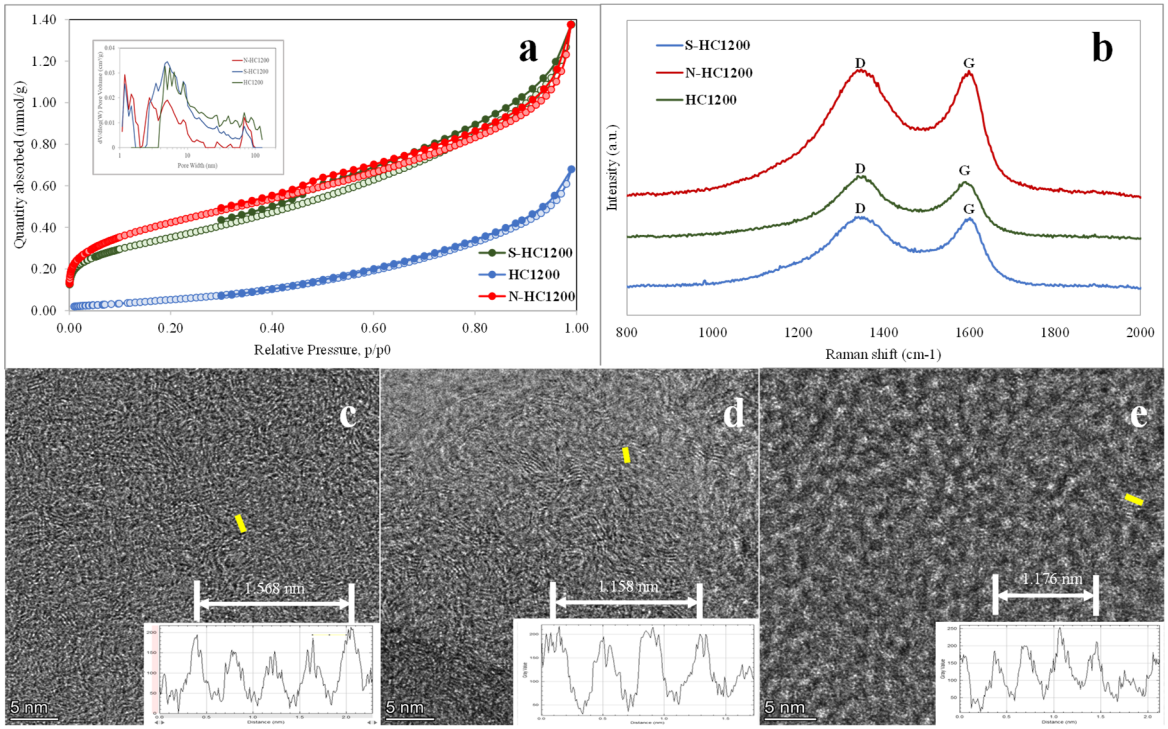

Figure 1 Structure characterization of HC1200, N-Hc1200, and S-HC1200. **a** Nitrogen adsorption-desorption isotherms (inset shows the related pore size distribution. **b** Raman spectra. HRTEM images of HC1200 (**c**), N-H1200 (**d**), and S-HC1200 (**e**)

HR-TEM images confirmed that all carbon materials possessed a turbostratic structure. The graphene layers were randomly stacked and displayed varying degrees of disorder as shown in Fig. 1c to Fig. 1e. The interlayer spacing (d-spacing) of HC900 and HC1200 was approximately 0.379 nm and 0.382 nm, respectively, which is wider than the interlayer spacing of pristine graphite (~0.335 nm), enabling reversible Na^+ intercalation. Notably, the doped samples showed even larger interlayer distances: N-HC1200 exhibited a d-spacing of approximately 0.386 nm, while S-HC1200 showed the highest at around 0.392 nm. These expanded layer distances further promote Na^+ diffusion and storage, aligning with the observed enhancement in BET surface area [5].

The Raman spectra (Fig. 1b) revealed two prominent peaks: the D-band (~1350 cm^{-1}), corresponding to disordered carbon structures, and the G-band (~1590 cm^{-1}), associated with the in-plane vibration of sp^2 carbon atoms in graphitic domains. The ID/IG ratio reflects the degree of structural disorder. Among the undoped samples, HC1100 showed the lowest ID/IG value (1.1342), suggesting a higher graphitization level, while HC1200 displayed a slightly increased ratio (1.1770), indicating a rise in disorder at higher pyrolysis temperatures. In doped samples, the ID/IG ratios were significantly higher—N-HC1200 and S-HC1200 exhibited values of 1.8194 and 1.7824, respectively—demonstrating that heteroatom doping induces more defects and amorphous domains. This increased disorder may introduce additional active sites for Na^+ storage. Interestingly, the N-doped series tended to exhibit a more balanced structure with moderate disorder, whereas S-doped samples displayed more extensive structural defects, which may account for their higher capacity performance [11]. the integration of BET, HR-TEM, and Raman results demonstrates that nitrogen and sulfur doping not only increases structural disorder and porosity but also expands interlayer spacing, all of which are favorable for enhanced Na^+ storage capability in sodium-ion batteries.

3.2 Electrochemical Performance Evaluation

The electrochemical performance of HC1200, N-HC1200, and S-HC1200 electrodes was evaluated through galvanostatic charge–discharge (GCD) testing and rate capability measurements in half-cell configurations using sodium metal as the counter/reference electrode. The GCD voltage profiles for the first five cycles at a current density of 50 mA g^{-1} are illustrated in Figure 2b-d. All samples exhibit the typical two-region behavior of hard carbon anodes: a sloping region above ~0.1 V vs. Na^+/Na, associated with Na^+ adsorption on defect sites and amorphous domains, followed by a plateau region below ~0.1 V, corresponding to Na^+ intercalation between graphene-like layers. The undoped HC1200 shows a first discharge capacity of approximately 196.52 mAh g^{-1} and a charge capacity of 148.17 mAh g^{-1}, yielding an initial Coulombic efficiency (ICE) of ~75.40%. In subsequent cycles, the reversible capacity stabilizes around 66.99 mAh g^{-1}, indicating limited Na^+ storage

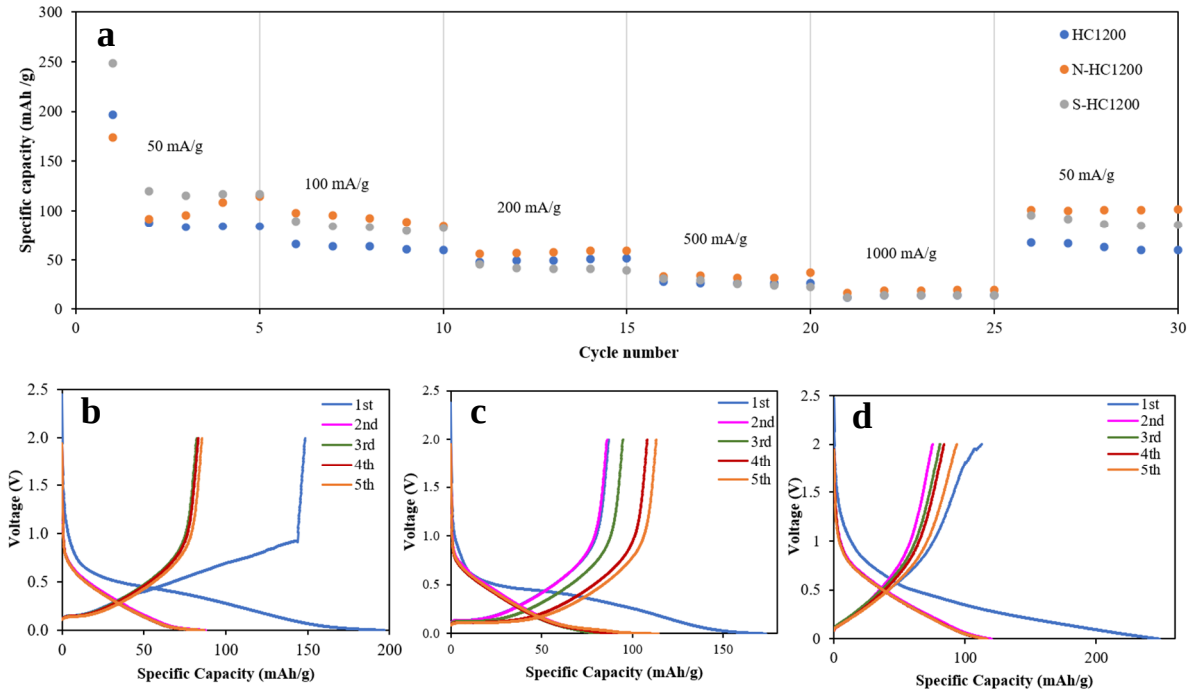

Figure 2 Electrochemical performance of HC1200, N-HC1200, and S-HC1200; (**a**) rate performance of HC1200, N-HC1200, and S-HC1200 at difference current densities from 50 mA/g to 1000 mA/g; Galvanostatic charge–discharge profile of (**b**) HC1200, (**c**) N-HC1200, and (**d**) S-HC1200.

reversibility and sluggish diffusion kinetics. This can be attributed to the low surface area and fewer active sites in undoped carbon. In contrast, N-HC1200 displays a significantly enhanced reversible capacity and a more defined plateau region in cycles 2–5, indicating improved intercalation behavior. The sample delivers a first-cycle discharge and charge capacity of over 173.71 mAh g^{-1} and 86.81 mAh g^{-1}, respectively, resulting in an ICE of ~50%. The reversible capacity increases to approximately 100.6 mAh g^{-1} by the 5th cycle. These improvements are likely due to nitrogen doping, which introduces pyridinic and pyrrolic nitrogen groups that act as additional Na^+ adsorption sites and promote charge transport via defect-induced conduction pathways. S-HC1200 shows the highest initial discharge capacity among all samples (248.26 mAh g^{-1}), although it exhibits a relatively low ICE. Nevertheless, the subsequent cycles reveal notable improvement in capacity retention, with the 5th cycle maintaining a capacity over 95.3 mAh g^{-1}. Sulfur doping is known to increase interlayer spacing and introduce redox-active functionalities, thereby facilitating both intercalation and surface-related pseudocapacitive Na^+ storage mechanisms. The rate performance of the electrodes under varying current densities (50, 100, 200, 500, and 1000 mA g^{-1}) is shown in Figure 2a. All electrodes demonstrate a gradual decrease in capacity with increasing current density, reflecting the intrinsic diffusion limitations of Na^+ in hard carbon structures. However, both heteroatom-doped samples (N-HC1200 and S-HC1200) outperform the undoped HC1200 at every current rate. Although all three materials exhibited low capacities at a high current density of 1000 mA g^{-1}, the current density was reduced back to 50 mA g^{-1} in the final stage (30th cycle) to evaluate capacity recovery. All samples demonstrated partial capacity recovery, with N-HC1200 achieving the highest recovered capacity (100.6 mAh g^{-1}), followed by S-HC1200 (95.3 mAh g^{-1}) and HC1200 (95.3 mAh g^{-1}). This observation indicates that the doped samples possess more flexible structures and exhibit better electrochemical reversibility. The improved rate performance is attributed to enhanced ion transport kinetics and increased electrochemically active surface area resulting from nitrogen and sulfur doping. These results confirm that heteroatom doping plays a crucial role in enhancing sodium storage properties by increasing active sites, reducing diffusion barriers, and improving electronic conductivity, thus enabling better capacity, rate performance, and stability under dynamic cycling conditions.

4. CONCLUSION

Hard carbon materials derived from longan seed were successfully synthesized and modified via heteroatom doping with nitrogen and sulfur. Comprehensive material characterization revealed that heteroatom doping significantly influences the structural features, including increased disorder, expanded interlayer spacing, and enhanced specific surface area and pore volume. Raman spectroscopy indicated a higher defect density in doped samples, while TEM analysis confirmed the presence of disordered and turbostratic domains that favor sodium-

ion intercalation. Nitrogen adsorption–desorption analysis using BET and DFT models showed that doped samples exhibit a hierarchical porous structure with increased micropore and mesopore contributions. Electrochemical testing demonstrated that the doped hard carbons, particularly N-HC1200 and S-HC1200, exhibit improved initial coulombic efficiency and capacity retention compared to undoped samples. The improved electrochemical behavior is attributed to enhanced ion transport kinetics and increased electrochemically active sites provided by the heteroatom-induced structural modifications. These findings suggest that heteroatom-doped hard carbon derived from longan seed is a promising and sustainable anode material for sodium-ion battery applications.

ACKNOWLEDGMENTS

This work was supported by the Thailand Graduate Institute of Science and Technology (TGIST) scholarship, managed by the National Science and Technology Development Agency (NSTDA). (Contract no. SCA-CO-2563-12220-TH).

REFERENCES

1. Tarascon, J. M., & Armand, M. (2001). Issues and challenges facing rechargeable lithium batteries. *Nature*, 414(6861), 359–367.
2. Dunn, B., Kamath, H., & Tarascon, J. M. (2011). Electrical energy storage for the grid: a battery of choices. *Science*, 334(6058), 928–935.
3. Slater, M. D., Kim, D., Lee, E., & Johnson, C. S. (2013). Sodium-ion batteries. *Advanced Functional Materials*, 23(8), 947–958.
4. Stevens, D. A., & Dahn, J. R. (2000). High capacity anode materials for rechargeable sodium-ion batteries. *Journal of The Electrochemical Society*, 147(4), 1271–1273.
5. Xu, Y., Zhang, C., Zhou, M., Fu, Q., Zhao, C., & Wu, M. (2021). *Biomass-derived hard carbon as promising anode materials for sodium-ion batteries: recent progress and perspectives.* Carbon, 184, 226–239.
6. Qie, L., Chen, W., Wang, Z., Shao, Q., Li, X., Yuan, L., & Zhang, W. (2015). Nitrogen-doped porous carbon nanofiber webs as anodes for sodium ion batteries with excellent rate performance. *Energy Environ. Sci.*, 8(3), 1040–1049.
7. Sing, K. S. W., et al. (1985). Reporting physisorption data for gas/solid systems with special reference to the determination of surface area and porosity. *Pure and Applied Chemistry*, 57(4), 603–619.
8. Thommes, M., et al. (2015). Physisorption of gases, with special reference to the evaluation of surface area and pore size distribution (IUPAC Technical Report). *Pure and Applied Chemistry*, 87(9-10), 1051–1069.
9. Ferrari, A. C., & Robertson, J. (2000). Interpretation of Raman spectra of disordered and amorphous carbon. *Physical Review B*, 61(20), 14095.
10. Zhang, L., Chen, L., Zhou, X., & Liu, Z. (2015). Towards high-volumetric energy density lithium-ion batteries: understanding the role of graphite particle size. *Journal of Power Sources*, 273, 1030–1036.
11. Bommier, C., Ji, X. (2015). Electrochemical characteristics of hard carbon anode in sodium-ion batteries. *J. Power Sources*, 288, 518–525.

Development of shape memory UV curable 3D-print resin based on acrylated epoxidized soybean oil (AESO)

Phutthiphong Wongsombun[1], Nuttinan Boonnao[1], Panuwat Luengrojanakul[1], Sarawut Rimdusit [1,*]

[1] Center of Excellence in Polymeric Materials for Medical Practice Devices, Department of Chemical Engineering, Faculty of Engineering, Chulalongkorn University, Bangkok 10330, Thailand
[*] Corresponding author: sarawut.r@chula.ac.th

ABSTRACT

Due to the rapid development of the 3D-printing and increasing concern for eco-friendly environmental practices, renewable vegetable oil (VO)-based materials present an attractive choice for the development of 3D-printing resin. However, to make VO-based material suitable for this application, the incorporation of acrylate groups that can be rapidly solidified upon exposure to UV light into the structure is required. In this present work, we focus on the development of bio-based photoreactive resin from epoxidized soybean oil (ESO) and study its potential use in shape memory applications. Acrylation of epoxidized soybean oil (ESO) with methacrylic acid (MA) was carried out at two different molar ratios, 1:2 and 1:4 (ESO:MA), to produce two types of acrylated epoxidized soybean oil (AESO): A_2ESO (1:2) and A_4ESO (1:4). The curing behavior, mechanical properties, thermal stability, and shape memory properties of cured samples were investigated. FT-IR spectra confirm the successful acrylation of ESO to AESO. The mechanical and dynamic mechanical properties indicate that A_4ESO has higher strength and modulus than A_2ESO, which can be explained by the higher amount of UV-induced crosslinking of acrylate groups. In terms of shape memory capabilities, both cured A_2ESO and A_4ESO exhibit shape memory effects with A_4ESO possessing a higher shape fixity ratio. This work shows the successful development of bio-based-photoreactive resins from sustainable materials with remarkable shape memory properties.

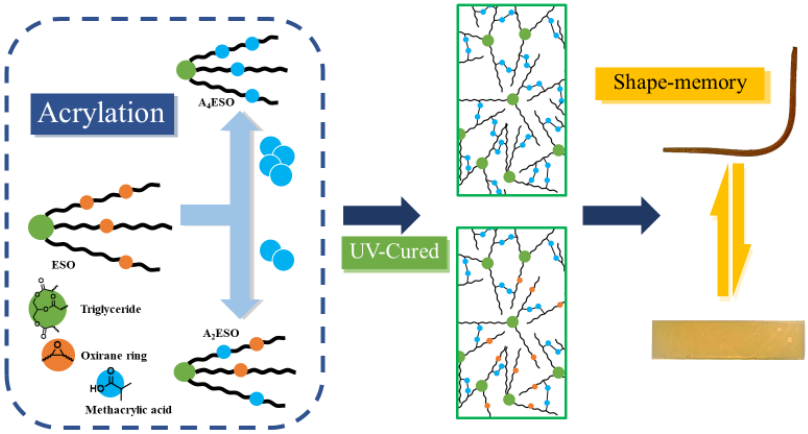

Keywords: Bio-based photoreactive resin; 4D-printing resin; Shape memory polymers; Acrylated epoxidized soybean oil

1. INTRODUCTION

Additive manufacturing (AM), often referred to as 3D-printing, is a process that fabricates complex structures with a high degree of design freedom by building materials layer-by-layer based on a digital 3D model [1]. Typically, 3D-printing methods are divided into seven categories: vat photopolymerization, material extrusion, powder bed fusion, material jetting, binder jetting, directed energy deposition, and sheet lamination [2]. Among these, vat photopolymerization (VP) stands out due to its ability to produce subjects with high resolution and smooth surfaces while requiring short processing times [3]. This technique undergoes polymerization of photopolymer resin by exposing a liquid photopolymer resin to a light source,

either a laser or an LCD projector, at a specific wavelength, initiating photopolymerization and solidifying the material layer-by-layer [4]. For this reason, photopolymer resins used in 3D printing should incorporate highly reactive functional groups, such as acrylates, which are well known for their excellent reactivity in photopolymerization processes [5].

Commercially available photopolymer resins are typically derived from petroleum-based sources, which are associated with low environmental friendliness and poor sustainability [6]. Over the past few decades, sustainable photopolymer resins from vegetable oils (VOs) such as soybean oil, castor oil, and linseed oil have been developed for use in 3D printing applications [7]. To convert VOs into photopolymer resins, high photo-reactive groups must be introduced into the reactive sites of the triglyceride structure, typically by adding acrylate groups through acrylation reactions. Among the various VOs, soybean oil has shown particularly high potential as a raw material for photopolymer resin production, due to its high iodine value, which indicates a high content of unsaturated carbon-carbon double bonds [6].

Nowadays, 3D printing has developed to the next stage, known as 4D printing, which combines 3D printing techniques with smart materials such as shape memory polymers (SMPs). SMPs are a type of smart polymer material that has the capability to memorize their original shape, adopt a temporary deformed shape, and return to their original permanent shape when exposed to specific external stimuli, such as temperature, magnetic fields, light, or humidity [8].

In this study, we explored the utilization of acrylated epoxidized soybean oil (AESO) as a vegetable oil-based photocurable resin for developing shape memory polymers (SMPs). AESO was synthesized by reacting epoxidized soybean oil (ESO) with methacrylic acid (MA) at different epoxide: carboxylic acid ratios. The photocurable resins were then UV-cured in a UV chamber. The UV-curing behavior, thermal stability, mechanical properties, and shape memory performance of the cured AESO samples were evaluated to investigate the effects of the ESO:MA ratio and the potential of AESO as an eco-friendly photocurable resin with shape memory capabilities.

2. EXPERIMENTAL

2.1. Materials

Epoxidized soybean oil (ESO, epoxy value = 6.93%, and molecular weight about 1000 g/mol) was purchased from Srithepthai Chemicals and Products Ltd. (Bangkok, Thailand). Methacrylic acid (MA, 99%), isobornyl methacrylate (IBOMA, 85%), and Hydroquinone (HQ, 99%) were purchased from Tokyo Chemical Industry Co., Ltd. (Tokyo, Japan). Triphenylphosphine (TPP, 98%) was purchased from Sigma-Aldrich Pte. Ltd. (St. Louis, Germany). Phenylbis (2,4,6-trimethylbenzoyl) phosphineoxide (BAPO) was purchased from Ciba Specialty Chemical Inc. (Basel, Switzerland). Sodium chloride (AR grade), paraformaldehyde (AR grade) and ethyl acetate (AR grade) were purchased from Merck Co., Ltd. (Darmstadt, Germany).

2.2. Synthesis of AESO

Tetrafunctional acrylated epoxidized soybean oil (A_4 ESO) was synthesized by reacting ESO with methacrylic acid (MA) at a molar ratio of 1:1 (epoxide: carboxylic acid). ESO (200 g, 0.87 $mol_{epoxide}$), MA (74.58 g, 0.87 $mol_{carboxylic\ acid}$), TPP (1 wt%, 2 g), and HQ (1 wt%, 2 g) were added to the round bottom flask. The mixture was uniformly mixed by mechanical stirrer at 200 rpm and heated to 105 °C. The reaction was maintained for 46 h to complete the acrylation process. The obtained products were then washed several times with 1% NaCl solution via liquid-liquid extraction, using ethyl acetate as the solvent to dissolve the AESO resins. The organic layer was collected and centrifuged at 10,000 rpm for 25 minutes, followed by solvent removal using a rotary evaporator and subsequent drying in a vacuum oven.

Difunctional acrylated epoxidized soybean oil (A_2ESO) was synthesized using the same procedure as A_4ESO, but with a different epoxide: carboxylic acid molar ratios, ESO (200 g, 0.87 $mol_{epoxide}$) and MA (37.29 g, 0.43 $mol_{carboxylic\ acid}$).

2.3. Preparation of UV-curable resins

The UV curable resins were prepared by first dissolving 1 phr of BAPO in acetone. After the solution was homogenous, AESO was added to the solution and sonicated for 30 min. Subsequently, to evaporate the acetone, the resins were placed in a vacuum oven at 70 °C for 1 h. Finally, a reactive diluent, IBOMA, was added to the resins according to the composition shown in Table 1. The photocurable resins were kept in a tightly closed container in a dark room before using.

Table 1. Composition of photocurable resins.

Resins	AESO (wt%)	IBOMA (wt%)	BAPO
A_2ESO	60	40	1 phr
A_4ESO	60	40	

2.4. UV curing process

All photocurable resins were UV-cured in an acrylic mold using a UV chamber (37.73 mW/cm²) for 15 min. Afterward, the cured specimens were washed with isopropyl alcohol to remove residue resin followed by air drying for 15 min.

2.5. Characterizations

The molecular structure of liquid samples was investigated by using Fourier transform infrared (FT-IR). FT-IR spectroscopy was performed in the attenuated total reflection (ATR) mode with a ZnSe HATR accessory on Perkin Elmer Spectrum GX. In total, 32 scans were performed at wavenumber ranging between 4000 to 650 cm^{-1} with a resolution of 4 cm^{-1}.

The thermo-mechanical properties were obtained by using Mettler-Toledo dynamic mechanical analyzer (DMA) model DMA1. In the single cantilever mode with a frequency of 1 Hz and strain amplitude of 5 µm. the sample size was 12.5 mm × 15 mm × 1 mm, heated from 30 to 200 °C with heating rate of 3 °C/min. The glass transition temperature (T_g) was determined from the maximum point on the loss tangent (tan δ) curve. The crosslinked density (υ_e) was calculated from following Equation 1.

$$E' = 3\upsilon_e RT \quad (1)$$

Where E', R, and T stand for the storage modulus in the rubbery plateau region 30 K above T_g, the gas constant, and the temperature 30 K above T_g in K, respectively.

The mechanical properties were characterized by using Instron universal testing machine (UTM) model 5567 with a crosshead speed of 10 mm/min (ASTM D638, type V) at room temperature. The stress-strain curve was plotted to characterize the tensile modulus (E), tensile strength (σ_M), and elongation at break (ε_B). The tested specimen was repeated five times for accuracy.

The thermal stability was analyzed using the Mettler-Toledo thermal gravimetric analyzer (TGA) model TGA1. The testing samples were heated from 30 to 800 °C with a heating rate of 10 °C/min under a nitrogen atmosphere.

The shape memory testing method of all samples is as follows: a) the samples were heated to transition temperature (T_{tran}), T_g + 10 °C, b) the external force was applied to deforming the samples into temporary shape, c) cooling the temperature down while external force still maintained, d) force removal, e) reheating the samples at T_{trans}. The three important parameters were recorded while processing. First is shape fixity ratio (R_f), parameter which present of ability to maintain temporary shape of SMP while shape recovery ratio (R_r) and recovery time (T_r) are recorded as the ability and the duration time for the SMP to return to its original shape. The calculation of R_f and R_r are following Equation 2 and 3.

$$\text{Shape fixity } (R_f, \%) = \frac{\theta_0}{\theta_{max}} \times 100 \quad (2)$$

$$\text{Shape recovery } (R_r, \%) = \frac{\theta_{max}-\theta_t}{\theta_{max}} \times 100 \quad (3)$$

Where θ_{max}, θ_0, and θ_t stand for the maximum bending angle at 90°, the bending angle after the fixing process, and the bending angle after the recovery process, respectively. The tested specimen was repeated five times for accuracy.

3. RESULTS AND DISCUSSION

3.1. Molecular structure and curing behavior

The acrylated epoxidized soybean oil (AESO) was synthesis via acrylation of epoxidized soybean oil (ESO) consisting of methacrylic acid (MA) as ring opener reagent, TPP as catalyst, and HQ as a polymerization inhibitor. The FT-IR spectra, as seen in Figure 1, The reactive site of ESO, oxirane rings, showed an absorption peak at 841 cm^{-1}. Regarding the FT-IR spectra of synthesized resins (A_2ESO and A_4ESO), the peak observed at 1634 cm^{-1} was attributed to the stretching vibration of carbon-carbon double bonds (C=C). Furthermore, characteristic peaks at 1406, 985, and 810 cm^{-1} were associated with the vibrational modes of –C=CH groups on the grafted methacrylate units. absorption peaks at 1634, 1406, 985, and 810 cm^{-1}. These C=C characteristic peaks confirmed the successful conversion of epoxy groups on the ESO backbone into methacrylate groups, indicating effective functionalization. Additionally, the appearance of a broad band around 3450 cm^{-1} corresponds to the stretching vibration of hydroxyl groups (–OH), which were generated as a result of the oxirane ring-opening reaction.

The FT-IR spectra of the A_4ESO showed a complete disappearance of the absorption peak at 841 cm^{-1}, indicating the full conversion of epoxy groups to methacrylate groups. Whereas, the remaining absorption peak at 841 cm^{-1} in the case of A_2ESO revealed the presence of unreacted epoxy groups remaining in the molecular backbone. These results ould confirm the effect of epoxide: carboxylic acid ratios in the acrylation process.

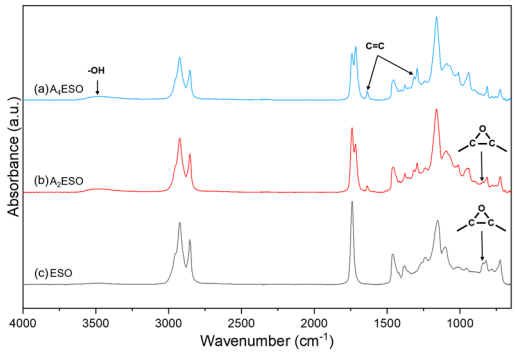

Figure 1. FT-IR spectra of: (a) A_4ESO, (b) A_2ESO, and (c) ESO.

Figure 2 illustrated the FT-IR spectra of the samples before and after UV-light exposure. The absorption peaks at 1634 and 1406 cm^{-1} were used to assess the success of the UV-curing process. The UV-exposed solid sample showed significantly lower absorption at 1634 and 1406 cm^{-1} indicating the effective photopolymerization of photocurable resins.

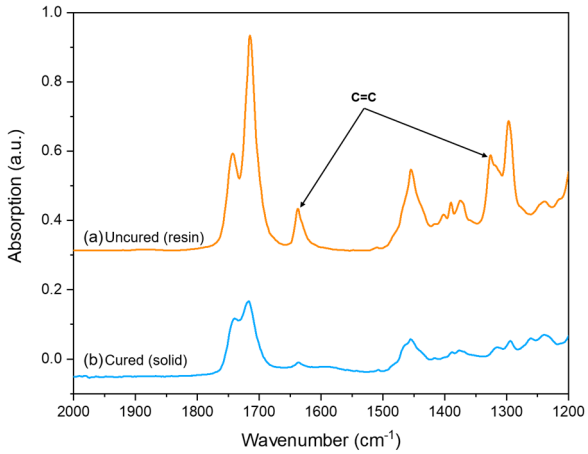

Figure 2. FT-IR spectra of: (a) uncured A_4ESO resin and (b) cured A_4ESO solid sample.

3.2. Thermal stability

The thermogravimetric analysis (TGA) curve in Figure 3 illustrated the thermal stability of the cured AESO samples. The results show a decrease in sample weight as a function of increasing temperature. Both AESO samples exhibit the same two distinct decomposition events: the first decomposition occurs around 330 °C, corresponding to the cleavage of ester bonds resulting from isobornyl fragmentation, while the second decomposition takes place near 380 °C, attributed to the random degradation of carbon-carbon bonds within the polymer backbone [9].

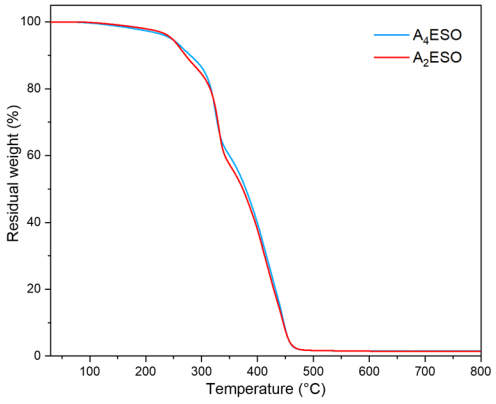

Figure 3. Thermal stability of cured AESO samples.

3.3. Thermo-mechanical properties

The plot of storage modulus as a function of temperature for the AESO samples was shown in Figure 4. The storage modulus at the rubbery plateau was used to determine the crosslink density, as presented in Table 3. The crosslink density of A_2ESO was measured at 303 mol/cm³, while the higher crosslink density of A_4ESO was determined to be 946 mol/cm³. The increase in crosslink density is a consequence of the higher methacrylate content within the molecular structure of A_4ESO, which acts as crosslinking sites between polymer chains during UV-curing. Moreover, the storage modulus in the glassy state for A_4ESO is higher than that of A_2ESO. These findings indicated that A_4ESO exhibited greater stiffness compared to A_2ESO. The higher glassy-state modulus of A_4ESO also suggested higher cohesive energy, which enhances resistance to creep and possibly results in improved shape fixity.

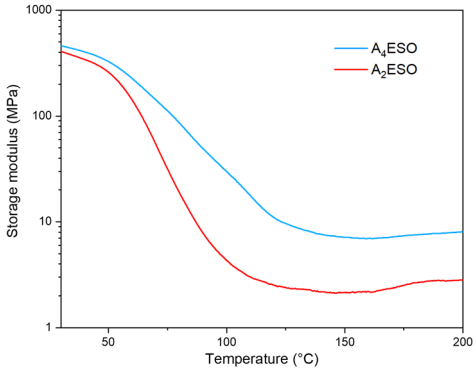

Figure 4. Storage modulus curve of the cured AESO samples.

The tan delta curve was shown in Figure 5, where the glass transition temperature (T_g) was determined at the peak maxima of the curve. The T_g was found at 81 and 96 °C for A_2ESO and A_4ESO, respectively. The increment of T_g of A_4ESO was mainly attributed to the higher crosslink density, which restricts polymer chain mobility. Therefore, more energy was required to transition the polymer structure from the glassy to the rubbery state [10]. The DMA analysis data was summarized in Table 2.

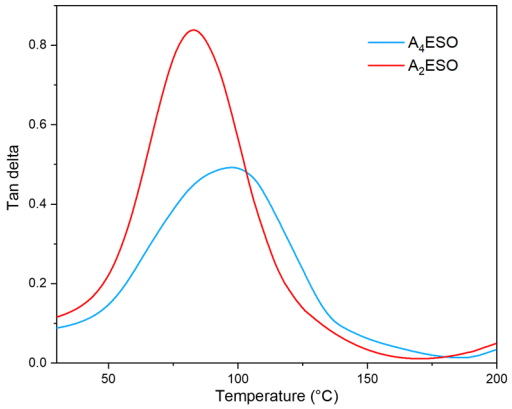

Figure 5. Tan delta curve of cured AESO samples.

Table 2. Summarized thermo-mechanicl properties for the cured AESO samples

Resins	ν_e (mol/cm³)	T_g (°C)
A_2ESO	303	81
A_4ESO	946	96

3.4. Mechanical properties

Figure 6 illustrates the tensile stress-strain curves of the AESO samples. A summary of the tensile strength (σ_M), elongation at break (ε_b), and tensile modulus (E) is presented in Table 3. Comparing the two AESO

samples, the tensile strength of A_2ESO and A_4ESO was measured at 9.1 and 16.8 MPa, while the elongation at break was 6.9 and 4.1%, respectively. The increase in tensile strength is attributed to the higher content of methacrylate functional groups led to greater crosslink density. The higher stiffness of A_4ESO results in the enhancement of tensile modulus with the value of 411.7 and 252.5 for A_4ESO and A_2ESO, respectively. In contrast, A_2ESO exhibits greater elongation at break due to its lower methacrylate functionality, which results in a reduced ability to form crosslinks between polymer chains. Hence, the results indicate that the tensile properties of the AESO-based resin can be tuned by varying the number of methacrylate functional group.

Table 3. Mechanical properties of cured AESO samples

Resins	σ_M (MPa)	ε_b (%)	E (MPa)
A_2ESO	9.1 ± 1.76	6.9 ± 1.42	252.5 ± 38.5
A_4ESO	16.8 ± 2.79	4.1 ± 1.02	411.7 ± 26.9

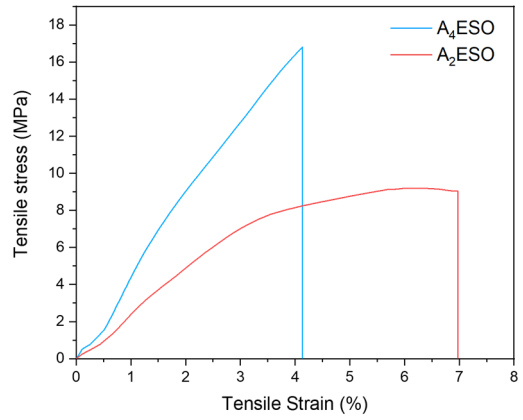

Figure 6. Tensile properties of cured AESO samples.

3.5. Shape memory properties

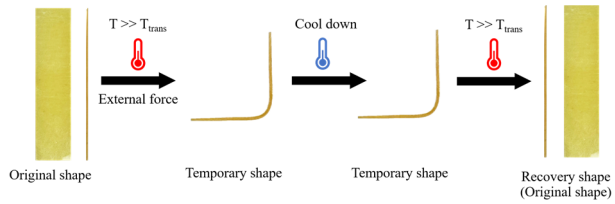

Figure 7. Shape memory process.

The shape memory process of the AESO samples was demonstrated in Figure 7 and the summarized shape memory properties of AESO samples were shown in Table 4. The R_f and R_r of A_4ESO were calculated at 97.23 % and 98.29 %, respectively while A_2ESO showed lower values at 95.17 % and 96.63 %, respectively. The greater shape fixity behavior of A_4ESO was a result of the higher crosslink density, which restricts polymer chain mobility leading to improved fixation. The higher shape recovery of A_4ESO compared to A_2ESO can be explained by the stronger recovery forces which were also attributed to its higher crosslink density [11].

Table 4. Shape memory properties of the cured AESO samples

Resins	R_f (%)	R_r (%)	T_r (s)
A_2ESO	95.17 ± 0.81	96.63 ± 0.81	87 ± 3.0
A_4ESO	97.23 ± 0.37	98.29 ± 0.84	57 ± 2.0

4. CONCLUSION

In this study, acrylated epoxidized soybean oil (AESO) was successfully synthesized using two different molar ratios of epoxide to carboxylic acid: 1:1 and 1:0.5. The different molar ratios in the acrylation process resulted in full epoxy conversion in the case of A_4ESO, while residual epoxy groups were still observed in A_2ESO. The resulting resins have high UV-curing ability and were effectively cured under UV light using a UV chamber. Both AESO UV-cured samples exhibited similar thermal stability. However, the glass transition temperature (T_g), crosslink density, and storage modulus at 30 °C increased with the higher content of methacrylate functional groups. In terms of mechanical properties, a higher degree of functionalization led to increased tensile strength, while a lower functional group content resulted in greater elongation at break. Regarding shape memory properties, both samples demonstrated excellent performance, with shape fixity and shape recovery exceeding 90%. Notably, the sample with a higher number of methacrylate groups showed improved shape fixity, faster recovery, and a recovery time. This work successfully highlighted the utilization of biobased photocurable resin as SMPs.

ACKNOWLEDGMENTS

This work is supported by National Research Council of Thailand (NRCT) and Chulalongkorn University (N42A660910) and Thailand Science Research and Innovation Fund Chulalongkorn University (BCG_FF_68_206_2100_030).

REFERENCES

1. Mendes-Felipe, C., et al., One-step method for direct acrylation of vegetable oils: a biobased material for 3D printing. Polymers, 2023. **15**(14): p. 3136.

2. Al Rashid, A., S.A. Khan, S.G. Al-Ghamdi, and M. Koç, Additive manufacturing: Technology, applications, markets, and opportunities for the built environment. Automation in Construction, 2020. **118**: p. 103268.
3. Colucci, G., F. Sacchi, F. Bondioli, and M. Messori, Fully Bio-Based Polymer Composites: Preparation, Characterization, and LCD 3D Printing. Polymers, 2024. **16**(9): p. 1272.
4. Barkane, A., et al., Uv-light curing of 3d printing inks from vegetable oils for stereolithography. Polymers, 2021. **13**(8): p. 1195.
5. Guit, J., et al., Photopolymer resins with biobased methacrylates based on soybean oil for stereolithography. ACS Applied Polymer Materials, 2020. **2**(2): p. 949-957.
6. Lai, H., J. Zhang, and P. Xiao, Renewable photopolymers: transformation of biomass resources into value-added products under light. ACS Sustainable Chemistry & Engineering, 2023. **11**(46): p. 16365-16406.
7. Briede, S., et al., State-of-the-art UV-assisted 3D printing via a rapid syringe-extrusion approach for photoactive vegetable oil acrylates produced in one-step synthesis. Molecular Systems Design & Engineering, 2022. **7**(11): p. 1434-1448.
8. Pilate, F., A. Toncheva, P. Dubois, and J.-M. Raquez, Shape-memory polymers for multiple applications in the materials world. European Polymer Journal, 2016. **80**: p. 268-294.
9. Huang, S., et al., 4D printing of soybean oil based shape memory polymer and its magnetic-sensitive composite via digital light processing. Polymer-Plastics Technology and Materials, 2022. **61**(9): p. 923-936.
10. Biju, R. and C.R. Nair, High transition temperature shape memory polymer composites based on bismaleimide resin. High performance polymers, 2013. **25**(4): p. 464-474.
11. Hombunma, P., et al., Shape memory polymers from bio-based benzoxazine/epoxidized natural oil copolymers. Smart Materials and Structures, 2019. **29**(1): p. 015036.

Development of a microencapsulation process of phase change materials from palm oil derivatives in a large-scale melamine formaldehyde encapsulation process

Tawatchai Punhapol[1], Rungthiwa Methaapanon[1,2], Apinan Soottitantawat[1,2,*]

[1] Center of Excellence in Particle and Materials Processing Technology, Department of Chemical Engineering, Faculty of Engineering, Chulalongkorn University, Bangkok 10330, Thailand
[2] Bio-Circular-Green-economy Technology & Engineering Center, Department of Chemical Engineering, Faculty of Engineering, Chulalongkorn University, Bangkok 10330, Thailand
[*] Corresponding author: apinan.s@chula.ac.th

ABSTRACT

Global climate change is significantly driven by greenhouse gas (GHG) emissions, with electricity production from fossil fuels being a major contributor. Phase change material (PCM) microencapsulation presents an environmentally friendly alternative as a renewable energy storage. However, large-scale PCM microencapsulation beyond the laboratory scale (150 mL) has not been extensively studied. This study aims to scale up PCM microcapsule synthesis, focusing on reactor design, equipment selection, and process optimization to achieve comparable or improved encapsulation efficiency on a large scale (2 L) relative to the laboratory scale. PCM microcapsules were synthesized by slowly introducing a melamine-formaldehyde pre-polymer solution at pH 8.5 and room temperature into a pH 3.6 oil-in-water emulsion at 70°C. The feed rate was maintained at 9.4 mL/min. The emulsion was prepared using homogenized methyl palmitate as the PCM, deionized (DI) water, and sodium dodecyl benzene sulfonate (SDBS) as a surfactant. The mixture was then stirred for 3.5 hours, followed by drying the microcapsules via spray drying. The results of the scale-up and feed rate variation experiments indicated that increasing the feed rate led to a reduction in microcapsule size distribution from 11.1 µm to 8.64 µm. However, this decrease in size resulted in a lower encapsulation efficiency, dropping from 74.5% to 54.3%. Additionally, increased agglomeration was observed due to higher collision rates between newly introduced and existing pre-polymer droplets, while the microcapsule morphology remained consistently spherical, as shown in Fig. 1. In conclusion, a lower feed rate should be considered to enhance encapsulation efficiency and minimize microcapsule agglomeration.

Keywords: Phase change material (PCM); Microencapsulation; Encapsulation efficiency (EE%)

1. INTRODUCTION

Global climate change was significantly driven by greenhouse gas (GHG) emissions, with electricity production from fossil fuels being one of the contributors. Utilizing renewable energy sources that were less harmful to the environment, such as wind and water, to generate electricity rather than relying on fossil fuels like coal and oil is the alternate solution. However, they were unable to fully replace it because only 10% of the energy was produced from renewable sources in 2020 [1]. Furthermore, the Ministry of Energy's 2023 statistics show that while the industrial sector's trend of electricity usage is expected to decline due to various regulations and inflation, it is still rising from the year before, with 2023's total electricity usage of 203,923 gigawatt hours—a 3.4 percent increase due to hotter weather [2].

As a sustainable energy storage option, phase change material (PCM) microencapsulation offers an eco-friendly substitute [3]. Three steps—emulsion, pre-polymerization, and polymerization—are used to test the use of melamine formaldehyde as a shell material for encapsulated n-eicosane as a PCM. The production of microcapsules is scaled up by increasing the reagents 4, 8, and up to 12 times the base condition [4]. This experiment found that the size distribution, as well as the sphericity, slightly worsened when scaling the process. To increase encapsulation efficiency, microencapsulation was studied on a laboratory scale using initial pH values of 3.7–4.1, reaction temperatures of 40–80 °C, and pre-polymer dropping rates of 0.35–2.5 mL/min prior to microcapsule formation. The

results showed that the most effective conditions for encapsulation efficiency were pH 4.6 at 75 °C and dropping rates of 0.75 mL/min, which produced an encapsulation efficiency of 82.3% [5]. Furthermore, in terms of thermal stability, the melamine formaldehyde shell's durability was confirmed by the minimal property that changed after 2,000 thermal cycles [6].

In order to determine the variable that can produce dry powder in a larger process while maintaining properties like morphology, size distribution, and encapsulation efficiency of the dry powder equivalent to the laboratory-scale process for further scale-up production, this thesis sought to investigate the properties of methyl palmitate dry powder covered with a melamine formaldehyde shell after scaling up a 150 mL laboratory-scale reactor to a 2 L large-scale reactor (up to 13 times the scale-up ratio) by varying initial pH value, reaction temperatures, reaction time, and pre-polymer dropping rate.

2. EXPERIMENTAL

2.1. Materials

Microencapsulation materials used was shown in Table 1.

Table 1 Source of chemicals in experiment

Chemical	Utilization	Supplier
Methyl palmitate 97%	Phase change material Core material	SAFC (US)
Melamine 99%	Monomer Shell material	Sigma Aldrich
Formaldehyde 37%		Loba chemie
Sodium Dodecylbenzene Sulfonate, SDBS	Surfactant Emulsifier	Sigma Aldrich
Triethanolamine, TEA	pH adjustment	Carlo Erba
Citric acid		Loba chemie
Sodium hydroxide		Loba chemie
n-hexane	Rinsing solvent	Kemaus
Deionized water, DI water		-

2.2. Scale-up processing [10-12]

The synthesis of microcapsules consists of 3 steps: preparation of pre-polymer solution, which is a mixture of water-soluble solids and solution; preparation of oil-in-water emulsion solution, which is a mixture of liquid and liquid; and preparation of microcapsules by encapsulation, which is a mixture of emulsion and pre-polymer solution into a slurry. The suitable reactor for such reaction is a mixing tank. Therefore, the scale-up focuses on the condition that allows good mixing, i.e., the energy used for agitation is still sufficient in the system with the same geometric similarity but larger size, as shown in **Error! Reference source not found.**.

$$\frac{P_1}{V_1} = \frac{P_2}{V_2} = \frac{N_p * \rho * N^3 * D^5}{V} \quad (1)$$

by P is agitation power which obtained from agitation power requirement, V is solvent volume, N_p is Power Number based on turbine type (45° pitched blade turbine in baffle Np = 1.27), ρ is solvent density, N is agitation speed, and D is turbine diameter.

2.3. Pre-polymer synthesis

The 1st step of microencapsulation was pre-polymer synthesis. Pre-polymer was produced from melamine and formaldehyde methylolation with material, equipment and condition as shown in Table 2 and Figure 1.

Table 2 Pre-polymer synthesis process condition

	Lab scale	Large scale
Reactor	500 mL two neck flask	2,000 mL two neck flask
Stirring	2 cm magnetic bar at 600 rpm	5 cm impeller at 300 rpm
Chemical		
- Melamine - Formaldehyde - DI water	3 g 5.3 mL 50 mL	40 g 70.6 mL 666.5 mL
pH	Increase pH to 8.5 by triethanolamine before heating	
Reaction temperature	75 degrees Celsius by heater	
Reaction time	After pH adjustment stirred for 20 minutes	After pH adjustment stirred for 40 minutes

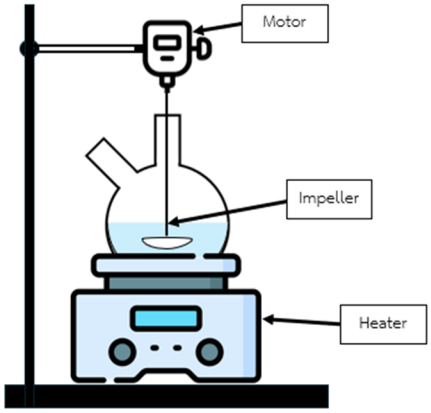

Figure 1 Pre-polymer synthesis in large scale

2.4. Oil in water (O/W) emulsion preparation

The O/W emulsion was created by split the methyl palmitate to be smaller molecule via surfactant that reduce the tension force between water and oil phase for increasing encapsulation surface area with parameter in Table 3.

Table 3 O/W emulsion preparation

	Lab scale	Large scale
Reactor	150 mL beaker	2,000 mL beaker
Stirring	1.8 cm homogenizer diameter at 8,000 rpm	5 cm homogenizer diameter at 4,000 rpm
Reaction time	3 minutes	6 minutes
Chemical		
- Methyl palmitate	10 g	133.3 g
- Sodium dodecyl benzene sulfonate	1 g	13.33 g
- DI water	80 mL	1066.4 mL

2.5. Microencapsulation

This step is feed pre-polymer in acidic condition O/W emulsion to form polymine shell via in-stu polymerization which call condensation reaction as shown in Table 4 and Figure 2 for large scale microencapsulation.

Table 4 Microencapsulation process

	Lab scale	Large scale
Reactor	150 mL beaker	2000 mL standard tank reactor
Stirring	2 cm diameter magnetic bar at 600 rpm	8 cm diameter 45^{O} pitched blade turbine at 500 rpm
Reaction temperature	75 degrees Celsius by heater	75 degrees Celsius by water bath
pH	Decrease pH to 3.6 by citric acid before dropping a pre-polymer solution and increase the pH to 8.5 by sodium hydroxide to terminate the reaction when reaction time reached	
Reaction time	180 minutes	240 minutes
Input method	Dropping pre-polymer solution with 4 mm rubber tube diameter at flow rate 0.6 mL/min (0.8rpm)	Spray with 0.3 mm atomizer nozzle diameter at 14.0 mL/min (63 rpm)

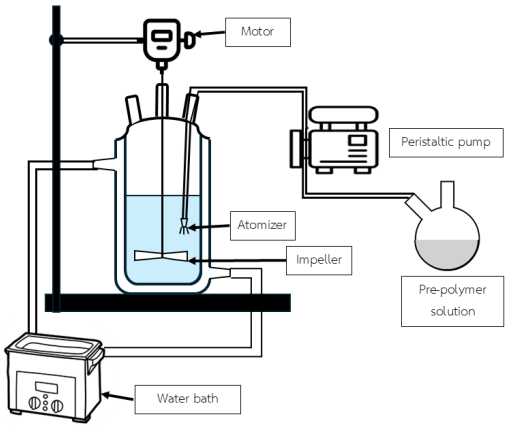

Figure 2 Microencapsulation process in large scale

2.6. Microcapsule rinsing

A slurry solvent that contains microcapsules was filtered by 8-micron filter paper and a vacuum pump. A wet cake from filtration was rinsed with DI water and filtrate again 3 times and n-hexane for the 4th time as shown in Figure 3.

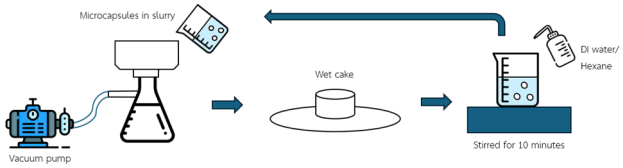

Figure 3 Microcapsule rinsing

2.7. Microcapsule drying

A microcapsule powder was obtained from spray dryer which used heat transfer between microcapsule slurry and hot air for liquid evaporating with parameter in Table 5.

Table 5 Spray dryer parameter

	Lab scale	Large scale
Slurry feed rate (L/min)	0.01	0.1
Hot air flowrates (L/min)	0.04	40
Inlet hot air temperature (°C)	200	200
Environmental temperature (°C)	25.0	33.0*

* In large scale, the equipment is in an open environment, which affects the unstable environmental temperature for drying performance, whereas in lab scale, it is in a closed environment.

2.8. Analytical methods

The microcapsule and emulsion property was investigated its morphology, agglomeration and microcapsule heat to imply the encapsulation efficiency

which indicated the amount of PCM encapsulation in microcapsule as described in Table 6.

Table 6 Analyzing equipment

Analyze	Equipment
Emulsion size distribution and morphology	Microscope and ImageJ program
Microcapsule size distribution	Malvern Mastersizer 3000
Microcapsule morphology and agglomeration	Scanning Electron Microscope, SEM)
Microcapsule enthalpy of melting and crystallization	Differential scanning calorimeter, DSC (DSC3+ module Mettler Toledo)
Encapsulation efficiency*	

***** EE% is encapsulation efficiency which describes how much PCM is encapsulated in microcapsules

$$E = \frac{\Delta H_m,\ \text{MicroPCM} + \Delta H_c,\ \text{MicroPCM}}{\Delta H_m,\ \text{PCM} + \Delta H_c,\ \text{PCM}} \times 100$$

by ΔH_m is enthalpy of PCM melting, ΔH_c is enthalpy of PCM crystallization measured by Differential scanning calorimeter.

3. RESULTS AND DISCUSSION

3.1. Microscopic analysis of O/W emulsion

The microscopic image (Figure 4) shows a dense dispersion of spherical particles, indicating successful formation of oil-in-water emulsion. Moreover, on a larger scale, the emulsion size distribution result from ImageJ remains in the range of 10-20 µm, which proves the mixing stability on a larger scale.

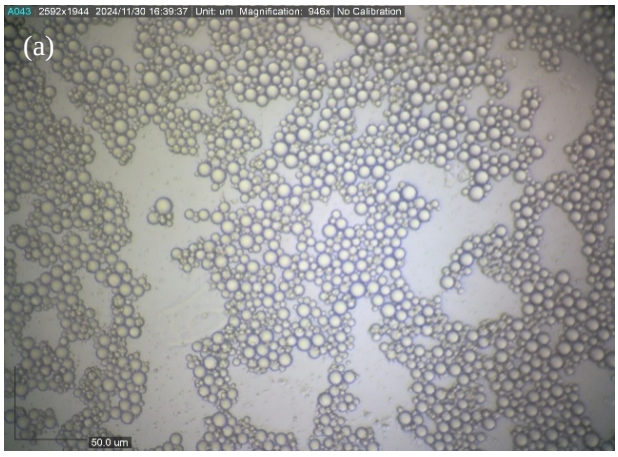

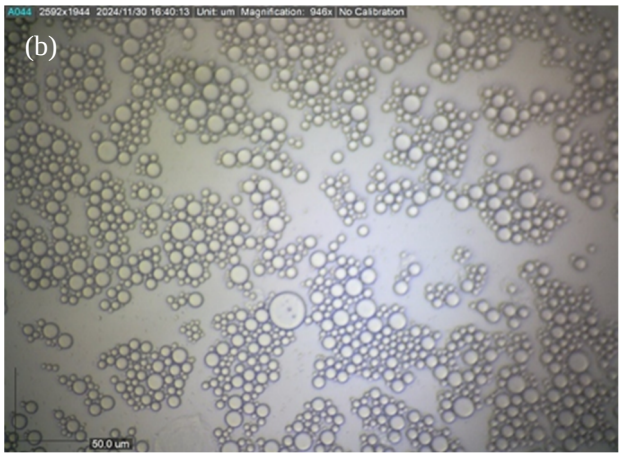

Figure 4 O/W emulsion morphology after homogenized in (a) Lab scale (b) Large scale

3.2. Malvern Mastersizer 3000

Microcapsule size distribution differs slightly in the large-scale microcapsule preparation process due to higher mixing efficiency, such as impeller, reactor baffle, and atomizer nozzle feed. Better agitation results in a well-mixed system, which minimizes the fluctuation of microcapsule size, as demonstrated in Figure 5 (blue line compared to grey line). Similarly, the microcapsule size distribution is larger in large-scale spray dryers, which might occur from higher environment temperatures and longer residence time that affect the smaller microcapsule as shown in Figure 5 (blue line compared to orange line). Microcapsule size distribution is wider, but microcapsule mean particle size (d_{50}) decreases from 11.1 µm in lab-scale reactor to 8.64 µm in large-scale reactor. This is because of improved mixing efficiency and feeder equipment, while in larger spray dryer the mean particle size only decreases from 8.64 µm to 8.26 µm.

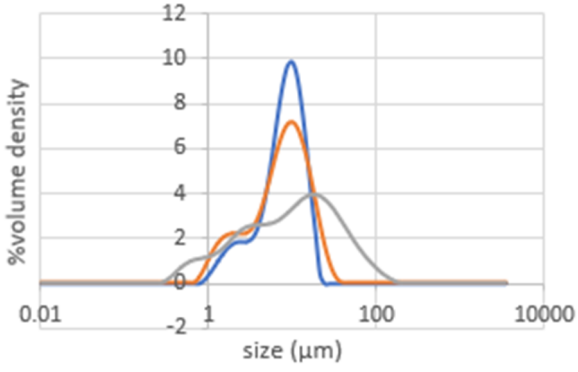

Figure 5 Microcapsule size distribution of lab-scale preparation with lab-scale spray dryer (grey line), large-scale preparation with lab-scale spray dryer (blue line), and large-scale preparation with large-scale spray dryer (orange line)

3.3. Scanning Electron Microscope (SEM)

Figure 6 depicts the morphology of spherical microcapsules, which encapsulate methyl palmitate inside melamine formaldehyde shell. Additionally, the unreacted melamine formaldehyde is likely to deposit on microcapsule shell owing to poor agitation for O/W emulsion encapsulated in lab scale, which supports this notion due to lower unreacted melamine formaldehyde in large scale that improves agitation efficiency. Furthermore, the enhanced microcapsule agglomeration on a large scale was seen because of an excessive pre-polymer feeding rate, which raised the possibility of microcapsule collision.

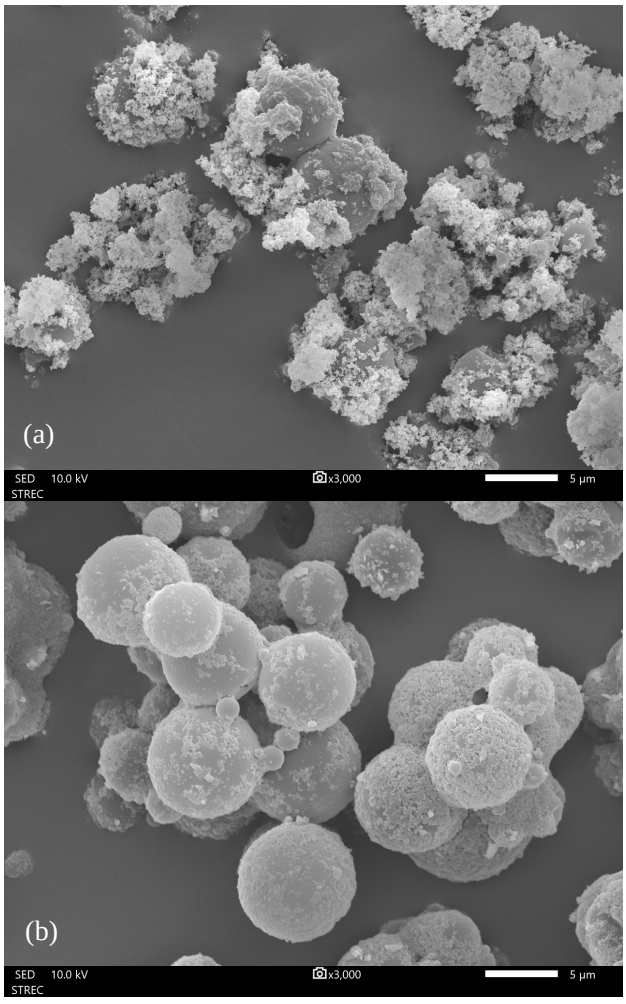

Figure 6 Microcapsule SEM image in different reactors size (a) Lab scale (b) Large scale

3.4. Differential scanning calorimeter (DSC)

The encapsulation efficiency was calculated by integrating the enthalpy of melting and crystallization from DSC curve that heat-cool-heat cycle between 0 – 60 ºC with 4 ºC /min, compared with latent heat of pure phase change material (207 J/g).

Table 7 Latent heat of microcapsule in each condition

Reactor	Spray dryer	Crystallization heat (J/g)	Melting heat (J/g)	EE%
Lab scale	Lab scale	152.74	150.98	73.4
Large scale		111.48	110.23	53.6
	Large scale	99.04	95.99	47.1

As tabulated in

Table **7**, the smaller microcapsule size as describe in Figure 5, the lower PCM encapsulated which result in lower encapsulation efficiency.

4. CONCLUSION

PCM microencapsulation can be scaled up from lab scale to large scale (150 mL to 2000 L) by improving agitation efficiency with impeller and reactor baffles as shown in lower unreacted melamine formaldehyde, but other parameters such as pre-polymer feed rate, initial polymerization pH, polymerization temperature, and polymerization time require additional research to improve encapsulation efficiency and reducing microcapsule agglomerations. Furthermore, the larger spray dryer produces excellent results that differ slightly from the lab scale spray dryer, even though the production rate is increasing.

ACKNOWLEDGMENTS

This research has received funding support from Patum Vegetable Oil Co., Ltd. Whose contribution to the development of a microencapsulation process of phase change materials from palm oil derivatives in large-scale melamine formaldehyde encapsulation process is much appreciated.

REFERENCES

1. Uddin, G.S., et al., Exploring the critical demand drivers of electricity consumption in Thailand. Energy Economics, 2023. 125: p. 106875.
2. Eppo : Energy policy and planning office, M.o.E., Thailand. Energy Situation 2023. 2024; Available from: https://www.eppo.go.th/.
3. Al Shannaq, R. and M.M. Farid, 10 - Microencapsulation of phase change materials (PCMs) for thermal energy storage systems, in Advances in Thermal Energy Storage Systems, L.F. Cabeza, Editor. 2015, *Woodhead Publishing*. p. 247-284.
4. García-Viñuales, S., et al. Study of Melamine-Formaldehyde/Phase Change Material Microcapsules for the Preparation of Polymer Films by Extrusion.

Membranes, 2022. 12, DOI: 10.3390/membranes12030266.
5. Wang, X. and T. Zhao, Effects of parameters of the shell formation process on the performance of microencapsulated phase change materials based on melamine-formaldehyde. *Textile Research Journal*, 2016. 87.
6. Zhang, N. and Y. Yuan, Synthesis and thermal properties of nanoencapsulation of paraffin as phase change material for latent heat thermal energy storage. Energy and Built Environment, 2020. 1(4): p. 410-416.
7. S.Fleischer, A., Thermal Energy Storage Using Phase Change Materials. 1 ed. *SpringerBriefs in Applied Sciences and Technology*. 2015: Springer Cham.
8. Chen, L., et al., Synthesis and properties of methyl palmitate-polyurea phase change microcapsules. *Polymer*, 2025. 319: p. 128073.
9. Maiti, T.K., et al., Advancements in organic and inorganic shell materials for the preparation of microencapsulated phase change materials for thermal energy storage applications. *RSC Sustainability*, 2023. 1(4): p. 665-697.
10. Chapter Seven - Fluid Mixing in Reactors, in Modeling of Chemical Kinetics and Reactor Design, A.K. Coker and C.A. Kayode, Editors. 2001, *Gulf Professional Publishing: Woburn*. p. 552-662.
11. Chapter Thirteen - Scale-Up in Reactor Design, in Modeling of Chemical Kinetics and Reactor Design, A.K. Coker and C.A. Kayode, Editors. 2001, *Gulf Professional Publishing: Woburn*. p. 1034-1081.
12. Chapter Five - Introduction to Reactor Design Fundamentals for Ideal Systems, in Modeling of Chemical Kinetics and Reactor Design, A.K. Coker and C.A. Kayode, Editors. 2001, *Gulf Professional Publishing: Woburn*. p. 260-423.

Fabrication of polyphenylsulfone (PPSU) electrospun nanofiltration membrane

Ornpreeya Pongpan[1], Ratthapol Rangkupan[2], Chalida Klaysom[3,*]

[1] Center of Excellent in Particle and Material Processing Technology, Department of Chemical Engineering, Faculty of Engineering, Chulalongkorn University, Bangkok 10330, Thailand
[2] Metallurgy and Materials Science Research Institute (MMRI), Chulalongkorn University, Bangkok 10330, Thailand
[*] Corresponding author: chalida.kl@chula.ac.th

ABSTRACT

The thin film composite (TFC) membranes were fabricated based on the support layer of polyphenylsulfone (PPSU) waste via an electrospinning process. To improve the support layer of the TFC membrane, the incorporation of a surfactant additive such as Sodium dodecyl sulfate (SDS) and Cetyltrimethylammonium bromide (CTAB) onto the spinning solution will produce nanofibers with a smaller diameter, which helps reduce pore size and improve the adhesion of the selective layer. The results indicated that adding 1 wt.% of CTAB in the spinning solution would reduce the average fiber diameter below 200 nm and increase the $CaSO_4$ rejection from 13.16% to 97.42% compared to the support layer of the TFC membrane without surfactant additive.

Keywords: Polyphenylsulfone; Electro-spun; TFC membrane; Carbon quantum dots

1. INTRODUCTION

The accumulation of plastic waste has escalated dramatically due to global consumption and the inadequate recycling of thermoplastics, leading to significant environmental pollution and resource wastage. Among these plastics, polyphenylsulfone (PPSU) is noted for its high temperature performance and chemical resistance, making it a valuable material for durable applications such as baby bottles. Despite its advantages, the recycling rate of PPSU remains low, and its potential for upcycling into valuable products like membranes for water purification has not been fully explored. This research proposes a novel approach to address plastic waste by upcycling waste or processed PPSU into membrane materials for water purification applications. PPSU's inherent properties, such as mechanical stability and chemical resistance, make it an ideal candidate for this transformation. However, to compete effectively with existing market products, significant enhancements in membrane surface characteristics are necessary.

Currently, there is no research focused on the use of PPSU waste. However, several studies have explored the use of PPSU polymer as a membrane material, with various modifications aimed at enhancing membrane performance [1]. One common method for improving membrane properties involves coating a thin film onto the membrane surface, resulting in the fabrication of a thin film composite (TFC) membrane. TFC membranes typically consist of three layers: a bottom backing layer, a porous support layer (middle layer), and a top selective layer. During fabrication, each layer of a TFC membrane can be optimized independently, allowing for targeted modifications to address specific challenges. This enables a strategic approach to achieve desired membrane properties.

To enhance membrane performance, many studies have focused on improving either the selective layer, the support layer, or both layers. For the support layer, the use of electrospun nanofibers (ENFs) support has shown promising results, particularly in achieving high water flux. ENF-based supports are known for their high specific surface area, high porosity, and low tortuosity, making them suitable for membrane separation applications. However, a key limitation of using ENFs as a support layer for TFC membranes is that their high surface porosity can hinder the adhesion of the thin film selective layer, which negatively impacts membrane performance. To address this issue, several strategies have been proposed, including post-treatment processes and the incorporation of additives into the spinning solution. Notably, Feng Liu et al. [2] reported that introducing surfactants into the spinning solution produces nanofibers with fringed or branched structures, which help reduce pore size, improve the adhesion of the selective layer, and also enhance water permeability of the composite membranes. These benefits show potential in the preparation of the high-performance TFC membranes. Therefore, this research will focus on modifying the electrospun nanofiber (ENF) support layer derived from PPSU waste by incorporating surfactants, aiming to reduce fiber diameter and achieve a more uniform pore size distribution.

2. EXPERIMENTAL

2.1 Materials and chemicals

Polyphenylsulfone (PPSU) waste was received from Pigeon Industries (Thailand) Co., Ltd. n-Methyl-2-pyrrolidone (NMP, ≥ 99%) was purchased from RCI Labscan Company Limited. Acetone (≥ 99%), Cetyltrimethylammonium bromide (CTAB) (≥ 99%), and Calcium sulfate ($CaSO_4$, ≥ 99%) were purchased from Quality Reagent Chemical. Sodium dodecyl sulfate (SDS, ≥ 99%), m-phenylenediamine (MPD, ≥ 99%), Triethylamine (TEA, ≥ 99%), and 1,3,5-benzenetricarbonyl chloride (TMC, ≥ 99.5%) were purchased from Sigma Aldrich Company Limited. n-hexane (≥ 98%) from Anapure, Newzealand.

2.2 Fabrication of ENF support layer

The electrospinning solution, with a concentration of 23 wt.%, was prepared by dissolving PPSU waste pellets in a 1:3 weight ratio mixture of acetone and NMP. A surfactant additive was also incorporated into the solution (SDS as a negative surfactant and CTAB as a positive surfactant). This mixture (as summarized in Table 1) was then stirred continuously at room temperature for 24 hours to ensure it became a homogeneous solution.

Table 1 The conditions for electrospinning solution.

Membrane	Solvent mixture (wt.%)	PPSU (wt.%)	Surfactant additive (wt.%)
ENF support	77	23	0 - 1

The polymer solution was injected into a syringe attached to an electrostatic device as shown in Fig. 1. The solution was electrospun onto a backing support attached to the grounded collector with a diameter of 7.5 cm and a width of 35 cm. The distance between the needle and the collector was fixed at 20 cm. The electrospinning process was carried out at an applied voltage of 14 kV, a flow rate of 1 mL/h, and a spinning duration of 8 h. After electrospinning, the PPSU electrospun substrate was sandwiched between two Teflon papers and heat-pressed at 120°C for 3 min using a commercial, compact fabric screen-printing machine (width 30 cm), equipped with an adjusted pressure knob, digital temperature, and time controls.

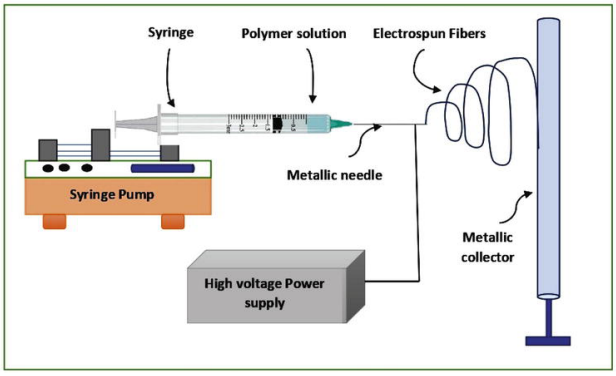

Figure 1 Basic setup of the electrospinning process [3].

2.3 Formation of the thin film selective layer

The polyamide (PA) selective layer was fabricated on the PPSU electrospun support layer via interfacial polymerization (IP) between the MPD and TMC monomers. The aqueous MPD solution was prepared by adding 2 wt.% of MPD flakes, 2 wt.% of TEA, and 0.1 wt.% of SDS into deionized (DI) water under stirring conditions at room temperature. The TMC organic solution was prepared by dissolving 0.15 wt.% of TMC into n-hexane. At room temperature, the well-mixed aqueous MPD solution was poured onto the ENF support (25 cm^2) and kept for 30 min. The excess solution was removed after draining the amine aqueous solution by gently wiping the surface of the electrospun nanofiber support with tissue paper, and it was left to dry partially under a fume hood for 80 seconds at room temperature. The amine-saturated ENF support was mounted on the gasket frame and held with clamps on each edge to deter the solution leakage during the reaction process. Subsequently, a PA thin film was deposited on the ENF support layer after the TMC solution was poured onto the reaction surface area and kept for 80 seconds to carry out the IP reaction. The TMC solution was drained out, and the membrane was rinsed with n-hexane for 5 s and thermally cured in an oven at 60°C for 10 min. The schematic diagram of the fabrication of TFC membranes is depicted in Fig. 2.

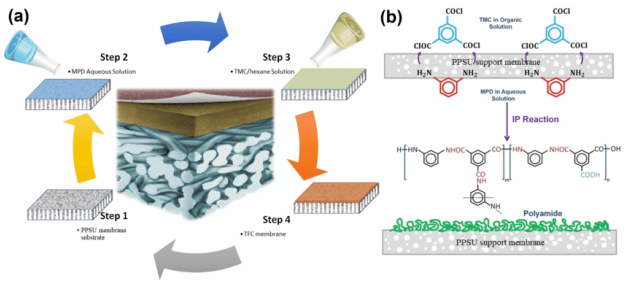

Figure 2 PPSU membrane surface modification schematic diagram: (a) steps in the modification process; (b) interfacial polymerization reaction mechanisms during the formation of the TFC layer [4].

2.4 Characterization of the ENF support layer

The surface morphology of the PPSU electro-spun support and PA TFNC membrane was observed using scanning electron microscopy (SEM, Hitachi S-3400N, Tokyo, Japan) with a secondary electron detector. Observations were conducted at a voltage of 15 kV, achieving a resolution of up to 100 nm. Image-J software (Java 8, National Institutes of Health, Bethesda, MD, USA) was used for analyzing the average fiber diameter and diameter distribution.

2.5 Membrane performance evaluation

The membrane separation performance in terms of water permeance, water flux, and salt rejection were evaluated by crossflow filtration membrane module (Sterlitech CFO16D-CF, Auburn, WA, USA) with 2,000 ppm of salt aqueous solution under pressurization at 5 bar and membrane effective area of 25 cm^2. The salt concentration in the feed and permeate side was measured by a conductivity meter (Metler Toledo, FiveEasyTM FE30, Columbus, OH, USA). The water flux and water permeance were estimated by Equations (1) and (2), respectively.

$$J_w = \frac{V}{(A_m \Delta t)} \quad (1)$$

$$A = \frac{J_w}{(\Delta P - \Delta \pi)} \quad (2)$$

Where J_w is the water flux ($L/m^2 \cdot h$ or LMH), V is the volume of permeated water (L), A_m is the effective area of the membrane (m^2), Δt is the permeation collection time (h), A is the pressure-normalized flux or water permeance ($L \cdot m^{-2} \cdot h^{-1} \cdot bar^{-1}$ or $LMH \cdot bar^{-1}$), ΔP is the transmembrane pressure (bar), and $\Delta \pi$ is the feed osmosis pressure difference (bar).

Salt rejection is a value that indicates how well the solution can retain salts from passing through the membrane, as defined by Equation (3).

$$R = (1 - \frac{C_p}{C_f}) \times 100 \quad (3)$$

Where R is the salt rejection (%), C_p is the salt concentration on the permeated side (ppm), and C_f is the salt concentration on the feed side (ppm).

3. RESULTS AND DISCUSSION

3.1 The effect of surfactant on the ENF support layer

The SEM images in Fig. 3 illustrate the surface morphology of the ENF support layer with varying amounts of the cationic surfactant cetyltrimethylammonium bromide (CTAB) and the anionic surfactant sodium dodecyl sulfate (SDS). The analysis reveals that adding a certain amount of surfactant significantly reduces the average fiber diameter, while both surfactants contribute to a smoother fiber surface. For the PPSU electrospun nanofiber (ENF) support layer, incorporating CTAB surfactant resulted in a substantial reduction in average fiber diameter from 862 nm to approximately 181 nm.

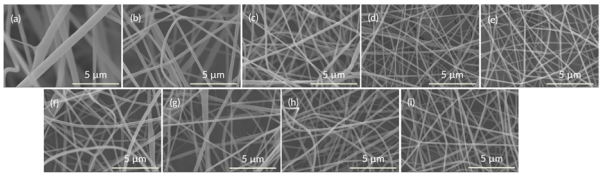

Figure 3 SEM images of PPSU electrospun nanofiber substrate, (a) without surfactant, (b) 0.1wt.%CTAB, (c) 0.2wt.%CTAB, (d) 0.3wt.%CTAB, (e) 0.4wt.%CTAB, (f) 0.1wt.%SDS, (g) 0.2wt.%SDS, (h) 0.3wt.%SDS, and (i) 0.4wt.%SDS.

In contrast, SDS was only able to reduce the fiber diameter to around 203 nm, as shown in Table 2. Since cationic surfactants can improve the electrical conductivity in the high-potential electrospinning process and improve the electrostatic repulsion within the polymer jet, the resulting fibers are finer and easier to control. On the other hand, anionic surfactants, although effective in reducing the surface tension of the polymer, can induce bead formation due to the instability of the polymer jet and also produce uneven nanofibers in the structure.

Table 2 The characteristic information of the ENF support at different surfactant types

ENF support	Surfactant (wt.%)	Average fiber diameter (nm)	SD
pure	0	862	0.19
CTAB (positive surfactant)			
0.1CTAB	0.1	318	0.05
0.2CTAB	0.2	216	0.04
0.3CTAB	0.3	180	0.03
0.4CTAB	0.4	181	0.02
SDS (negative surfactant)			
0.1SDS	0.1	256	0.04
0.2SDS	0.2	247	0.08
0.3SDS	0.3	243	0.07
0.4SDS	0.4	203	0.01

Therefore, the cationic surfactants or CTAB surfactant used in this research are more suitable for applications that require thin and uniform nanofibers for the production of composite thin film membrane support layers. Based on these findings, we further increased the concentration of CTAB surfactant to 1% by weight and observed the morphology again. The results show that a CTAB surfactant concentration of 1 wt.% appears to be the optimal formulation for electrospinning, providing the most desirable fiber morphology and membrane structure.

3.2 The effect of voltages on the ENF support layer

In addition to the addition of surfactant additives in the polymer solution that can help improve the quality of the desired nanofibers, the applied voltage in the electrospinning process is still another important parameter that should be considered. If the applied voltage is too low, it may not be enough to overcome the surface tension of the polymer, causing the polymer jet not to form or become unstable, which may result in thicker fibers. If the voltage is too high, the polymer jet will elongate excessively, resulting in very thin nanofibers. Even though the fibers are as thin as desired, they may be unstable, such as some granulation, or the fibers may agglomerate when in contact with the collector. Therefore, the appropriate voltage in the electrospinning process should balance the surface tension of the polymer and the electric field force.

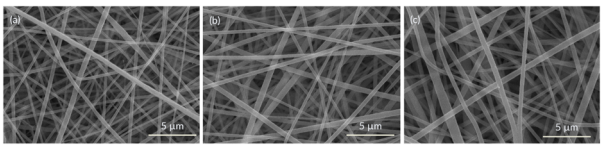

Figure 4 SEM images of PPSU electrospun nanofiber substrate with 1 wt.% of CTAB surfactant at different voltages in the electrospinning process, (a) 14kV, (b) 16kV, and (c) 18kV.

A branched or tree-like nanofibrous structure is desired in this research to overcome the limitation of poor adhesion of electrospun support layers upon deposition of a thin PA film layer. SEM images of the electrospun nanofiber membranes (ENM) at different voltage settings, produced from a PPSU solution containing 1 wt.% CTAB surfactant is shown in Figure 4. Compared to the PPSU electrospun nanofiber support layer without surfactant additive (Fig. 3a), the addition of 1 wt.% CTAB surfactant during electrospinning resulted in the formation of a distinct tree-like structure. At a voltage of 14 kV, sporadic short branches were observed (Fig. 4a). When the voltage was increased to 18 kV (Fig. 4c), the number of branches decreased to a level similar to that observed at 16 kV (Fig. 4b). These findings indicate that the applied voltage significantly influences the formation of the tree-like network. The presence of CTAB or cationic surfactant in the polymer spinning solution notably increased the solution's conductivity, leading to a higher concentration of free-charged ions. These charged ions enhanced the charge-carrying capacity of the solution and the polymer jets under the applied electric field, ultimately affecting the fiber morphology. In addition, increasing the voltage to 18kV results in a 52% larger diameter compared to 14kV. This means that in addition to the voltage affecting the fiber mesh structure, it also affects the fiber size.

Table 3 Characteristic information of the ENF support based on 1 wt.% CTAB at different applied voltages.

ENF support	Applied voltage in electrospinning (kV)	Average fiber diameter (nm)	SD
1wt.%CTAB	14	189	0.06
	16	267	0.08
	18	322	0.12

3.3 Separation performance of the TFC membranes

The experimental results of water permeability, water flow, and solution rejection of the electrospun nanofiber composite membranes fabricated by the interfacial polymerization (IP) process of two main monomers, MPD in aqueous solution and TMC in organic solution, are compiled in Fig. 5 below. From the crossflow model membrane separation efficiency test with calcium sulfate ($CaSO_4$) as the feed material at the concentration of 2,000 ppm, it was found that when no surfactant was added to the ENF support layer of the thin film composite membrane, the cationic salt separation efficiency was very low at 13.16% compared to the addition of 1wt.% CTAB as a cationic surfactant. It can be seen that the rejection of calcium sulfate increased up to 97.42%, indicating that the studied surfactant helped to improve the separation efficiency.

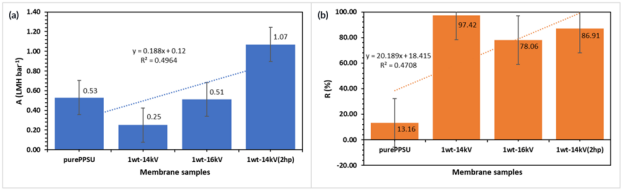

Figure 5 Water permeance (a) and salt rejection (b) of various supports of TFC membranes.

However, when comparing the salt rejection values of TFC membranes with different support layers at different applied voltages in the electrospinning process, it was found that increasing the applied voltages resulted in a 19.36% decrease in salt rejection. This result was due to the larger thickness of the fibers, which caused the gap in the support layer to be wide enough for salt molecules to pass through. Furthermore, when tested between single and double hot pressing before coating the polyamide layer on the support layer, it was found that the post-treatments also resulted in a decrease in salt rejection. This result indicates that the heat during the pressing may cause the fibers of the support layer to relax, resulting in a larger pore size that cannot separate salt.

4. CONCLUSION

This study focuses on the modification of thin film composite (TFC) membranes in part of the support layer from the electrospun technique for their application in the desalination process. Two types of

surfactants, cationic surfactant (CTAB) and anionic surfactant (SDS), were added in different concentrations to improve the quality of nanofibers in the support layer, such as fiber size, fiber distribution, and pore distribution within the structure of the support layer. The optimum electrospinning conditions were also investigated, such as the applied voltage in the spinning process, which also affects the quality of the fibers. Polyphenylsulfone (PPSU) waste was used to fabricate the porous support layer of TFC membranes to demonstrate the potential of upcycling. The thin film composite (TFC) membranes with electrospun nanofibers were successfully fabricated from PPSU waste if the surfactant was added to reduce the size of the nanofibers and create a uniform distribution of fibers and pores. The optimization of the electrospinning parameters to balance the changing polymer composition was also investigated. The modified membranes showed high efficiency in separating multivalent ions such as calcium sulfate ($CaSO_4$) up to 97.42%, despite still having low water permeance and water flux. Meanwhile, if heat-pressed twice, the water permeance and water flux could be increased, but the rejection value was reduced to 86.91%. This research not only proposes an approach to improve the properties of the electrospun nanofiber support layer of TFC membrane but also emphasizes the potential of upcycling PPSU waste into higher value products such as membranes, which can address the issue of making the circular economy more sustainable in resource utilization.

ACKNOWLEDGMENTS

This research study was supported by the Center of Excellence in Particle Technology (CEPT), Department of Chemical Engineering, Faculty of Engineering, Chulalongkorn University, and Material and Metallurgy Research Institute (MMRI), Chulalongkorn University, for providing the experimental facilities for this work.

REFERENCES

[1] Lau, W. J., Ismail, A. F., Misdan, N., & Kassim, M. A. (2012). A recent progress in thin film composite membrane: A review. Desalination, 287, 190-199.

[2] Liu, F., Wang, L., Li, D., Liu, Q., & Deng, B. (2020). Preparation and characterization of novel thin film composite nanofiltration membrane with PVDF tree-like nanofiber membrane as composite scaffold. Materials & Design, 196, 109101.

[3] Sharma, G. K., & James, N. R. (2022). Electrospinning: the technique and applications. In Recent developments in nanofibers research. IntechOpen.

[4] Shukla, A. K., Alam, J., & Alhoshan, M. (2022). Recent advancements in polyphenylsulfone membrane modification methods for separation applications. Membranes, 12(2), 247.

[5] Jambeck, J. R., Geyer, R., Wilcox, C., Siegler, T. R., Perryman, M., Andrady, A., ... & Law, K. L. (2015). Plastic waste inputs from land into the ocean. science, 347(6223), 768-771.

[6] Golpour, M., & Pakizeh, M. (2017). Development of a new nanofiltration membrane for removal of kinetic hydrate inhibitor from water. Separation and Purification Technology, 183, 237-248.

[7] Zhu, S., Zhao, S., Wang, Z., Tian, X., Shi, M., Wang, J., & Wang, S. (2015). Improved performance of polyamide thin-film composite nanofiltration membrane by using polyetersulfone/polyaniline membrane as the substrate. Journal of Membrane Science, 493, 263-274.

[8] Sidney, L., & Srinivasa, S. (1964). U.S. Patent No. 3,133,132. Washington, DC: U.S. Patent and Trademark Office.

[9] Zhang, Q., Zhou, R., Peng, X., Li, N., & Dai, Z. (2023). Development of support layers and their impact on the performance of thin film composite membranes (TFC) for water treatment. Polymers, 15(15), 3290.

[10] Wang, X., & Hsiao, B. S. (2016). Electrospun nanofiber membranes. Current opinion in chemical engineering, 12, 62-81.

[11] Park, S. J., Choi, W., Nam, S. E., Hong, S., Lee, J. S., & Lee, J. H. (2017). Fabrication of polyamide thin film composite reverse osmosis membranes via support-free interfacial polymerization. Journal of Membrane Science, 526, 52-59.

[12] Beigmoradi, R., Samimi, A., & Mohebbi-Kalhori, D. (2021). Controllability of the hydrophilic or hydrophobic behavior of the modified polysulfone electrospun nanofiber mats. Polymer Testing, 93, 106970.

[13] Bui, N. N., Lind, M. L., Hoek, E. M., & McCutcheon, J. R. (2011). Electrospun nanofiber supported thin film composite membranes for engineered osmosis. Journal of membrane science, 385, 10-19.

[14] Meng, L., Niu, F., Deng, P., Li, N., Lv, Y., & Huang, M. (2020). Electrospun nanofiber supports with bio-inspired modification enabled high-performance forward osmosis composite membranes. Composites Communications, 22, 100473.

[15] Augusty, A. C., Rangkupan, R., & Klaysom, C. (2024). Evaluating Post-Treatment Effects on Electrospun Nanofiber as a Support for Polyamide Thin-Film Formation. Polymers, 16(5), 713.

[16] Shokrollahzadeh, S., & Tajik, S. (2018). Fabrication of thin film composite forward osmosis membrane using electrospun polysulfone/polyacrylonitrile blend nanofibers as porous substrate. Desalination, 425, 68-76.

Modification of recycled polyethylene terephthalate membrane by using graphene oxide to enhance antifouling properties for protein separation

Thanapol Meeiam[1], Kiattinatapon Juengchareonpoon[1,*]

[1] Department of Chemical Engineering, Faculty of Engineering, King Mongkut's University of Technology Thonburi, Bangkok 10140, Thailand
[*] Corresponding author: kiattinatapon.juen@kmutt.ac.th

ABSTRACT

Egg white powder protein is commonly found in wastewater from the food industry. This study investigates the synthesis of a nanofibrous membrane from recycled polyethylene terephthalate using electrospinning for egg white powder treatment. Additionally, surface modification with graphene oxide was explored to enhance fouling resistance. The membrane was characterized using SEM and FTIR. Then the Filtration performance was tested using a dead-end stirred cell unit with egg white powder solution to assess protein recovery and membrane fouling. The results showed that the recycled polyethylene terephthalate membrane could recover more than 80 percent of the egg white protein, and the surface modification with graphene oxide could enhance the fouling resistance property.

Keywords: Electrospinning; Graphene oxide; Membrane; Polyethylene terephthalate; Wastewater treatment

1. INTRODUCTION

Wastewater management in the food industry has become critical due to the increasing volume and complexity of waste streams, especially those rich in organic compounds like proteins. Egg white protein is commonly found in wastewater from egg white powder processing and food manufacturing facilities. Improper treatment of such protein-rich wastewater can lead to environmental pollution and increased treatment costs [1][2]. Therefore, the development of effective and sustainable membrane filtration technologies for protein recovery and fouling reduction is of great interest in the field of wastewater treatment.

Nanofibrous membranes produced via electrospinning have gained considerable attention in recent years due to their high surface area, porosity, and tunable properties, making them suitable for advanced filtration applications [3]. Polyethylene terephthalate (PET), a widely used plastic, is a potential raw material for producing such membranes, especially when recycled, offering a promising route for plastic waste valorization and circular economy implementation [4][5]. However, membrane fouling, especially by proteins, remains a major challenge affecting filtration efficiency and operational lifespan. To address this issue, surface modification using nanomaterials like graphene oxide (GO) has been explored. GO possesses hydrophilic properties and functional groups that can improve membrane surface characteristics [6][7], reduce protein adhesion, and enhance fouling resistance [8]. Previous studies have demonstrated the effectiveness of GO in improving membrane performance in various filtration processes.

This study focuses on the fabrication of nanofibrous membranes from recycled PET using electrospinning for the treatment of egg white protein in wastewater. Furthermore, the effect of GO surface modification on fouling resistance was investigated. The membrane properties were characterized using scanning electron microscopy (SEM), Fourier-transform infrared spectroscopy (FTIR), and water contact angle measurements. Filtration performance was evaluated using a dead-end stirred cell to assess protein recovery and fouling behavior.

2. EXPERIMENTAL

2.1. Materials

Polyethylene terephthalate (PET) plastic bottles were collected locally. Trifluoroacetic acid (TFA, 99% w/w) was purchased from Sigma-Aldrich. Graphite powder for graphene oxide synthesis was obtained from QReC, and GO was synthesized using the modified Hummers' method [9]. Glutaraldehyde solution (GA, 25%) and hydrochloric acid (HCl, 37%) were supplied by Merck. Sodium bicarbonate ($NaHCO_3$, analytical grade) was purchased from QReC. Egg white powder was sourced from a local Thai supplier. Deionized water was used in all solution preparations and washing steps.

2.2. PET preparation

Plastic bottle is cut into 1 × 1 cm² pieces, cleaned with deionized water, and dried at 50 °C for 2 hours. Then, 11.92 g of plastic is dissolved in 100 mL of 99% TFA to prepare an 8 wt% PET solution, which is continuously stirred for 6 hours

2.3. Preparation of nanofibrous membrane

The PET solution feed (5 mL) was loaded into a syringe and then electrospun fibers at an injection rate of 0.5 mL/h. The distance from the needle tip to the collector was set to 10 cm, with an applied voltage of 15 kV, and the process was carried out for 10 hours. Finally, the nanofibrous membrane was immersed using 1 M sodium bicarbonate for 6 hours. Next, wash with deionized water, and dry at 70 °C for 2 hours in a hot air oven.

2.4. PET/GO membrane modification

To modify the surface of the PET membrane, GO was dissolved in 25 mLof deionized water at 0.1, and 0.2 g, followed by sonication for 15 minutes to ensure proper dispersion. Subsequently, 0.05 mL of glutaraldehyde (GA) was added as a crosslinking agent, and the pH of the solution was adjusted using 0.1 mL of 1 M hydrochloric acid. The PET membrane was then immersed in this GO-containing solution and shaken at 150 rpm for 3 hours at 60°C to promote uniform coating. Afterward, the membrane was thoroughly rinsed with deionized water to remove loosely bound GO and unreacted reagents [10][11].

2.5. Characterization

2.5.1. SEM analysis

The surface morphology of the electrospun PET nanofibrous membranes was characterized using a field emission scanning electron microscope (FE-SEM), model FEI Nova NanoSEM 450, EDS XFlash 6 series. Before imaging, all samples were sputter-coated with a thin layer of gold to enhance surface conductivity. Imaging was conducted at various magnifications under high vacuum mode.

2.5.2. FTIR analysis

Chemical structures and functional groups on the membrane surfaces were characterized by FTIR spectroscopy (IRTracer-100, Shimadzu) equipped with an ATR accessory. Spectra were collected from 4000 to 600 cm^{-1} with 45 scans per sample to ensure a high signal-to-noise ratio. This analysis confirmed the presence of characteristic PET bonds and verified the successful surface modification with graphene oxide.

2.6. Filtration efficiency test

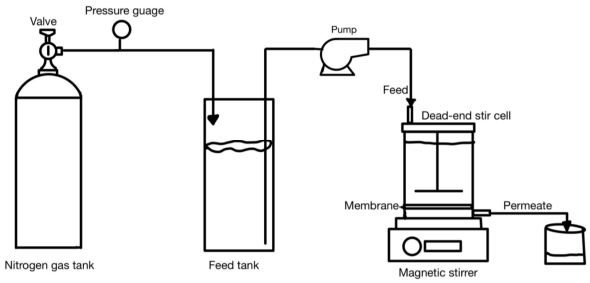

Figure 1 Dead-end-stir cell unit apparatus.

The filtration performance of electrospun PET and GO-modified PET membranes was evaluated using a dead-end stirred cell system (Amicon, 50 mL) operated under a constant pressure of 1 bar. A synthetic protein wastewater solution was prepared by dissolving egg white powder in deionized water at a concentration of 10,000 ppm. Prior to testing, membranes were compacted by filtering deionized water at 1 bar for 30 minutes to stabilize the membrane structure and ensure consistent baseline performance.

During the test, each membrane underwent two consecutive wastewater filtration cycles, with each cycle conducted for 2 hours at a feed of 400 mL under continuous stirring at 600 rpm to minimize concentration polarization. After each wastewater filtration cycle, the membrane was removed and cleaned by rinsing with deionized water under the same stirring condition for 5 minutes, repeated three times, to remove loosely adhered foulants. The permeate was collected during each run, and the filtration flux (J) was calculated using:

$$J = \frac{V}{At} \quad (1)$$

where J is the flux (L/m²·h), V is the permeate volume (L), A is the effective membrane area (m²), and t is the filtration time (h).

To evaluate the antifouling behavior of the membranes, the following parameters were calculated. The flux recovery ratio (FRR) indicates the membrane's ability to recover its permeability after fouling and cleaning.

$$FRR\ (\%) = \frac{J_{w2}}{J_{w1}} \times 100 \quad (2)$$

Where, J_{W1} is the initial pure water flux J_{w2} is the flux after flux after fouling and cleaning.

Reversible fouling ratio (RFR) represents the portion of flux loss due to weakly adhered foulants that can be removed by simple cleaning.

$$RFR\ (\%) = \frac{J_{w1} - J_f}{J_{w2}} \times 100 \quad (3)$$

Where, J_f is the flux of membrane during wastewater filtration.

Irreversible fouling ratio (IFR) quantifies the flux loss that remains after cleaning, typically caused by foulants that are strongly attached or embedded in the membrane pores.

$$IFR\ (\%) = \frac{J_{w1} - J_{W2}}{J_{w1}} \times 100 \quad (4)$$

Protein concentration was measured using UV-Visible spectrophotometry at 280 nm. The filtration efficiency (R) was calculated as:

$$R = (1 - \frac{C_p}{C_f}) \times 100 \quad (5)$$

Where, C_p and C_f are the protein concentrations in the permeate and feed, respectively [12].

3. RESULTS AND DISCUSSION

3.1. Surface morphology of PET and PET/GO

The morphology of electrospun PET and GO-coated PET membranes was analyzed using Scanning Electron Microscopy (SEM). The pure PET membrane exhibited a uniform and continuous nanofibrous structure with smooth surfaces, random fiber orientation, and no observable defects such as beads or fusion as shown in Figure 2.a. The fibers were well-distributed and created a highly porous structure, favorable for membrane filtration due to the ease of water flow and minimal resistance.

Upon coating with 0.1 g of GO, the membrane retained its fibrous morphology with only slight modifications. SEM images showed that GO was evenly distributed across the surface, creating a fine layer that slightly increased fiber roughness. Minimal aggregation was observed, and fiber continuity was preserved as shown in Figure 2.b. The porosity remained open, suggesting that this level of GO loading did not interfere with membrane permeability. The enhanced surface area and oxygen-containing functional groups from GO are expected to improve hydrophilicity and provide antifouling properties.

At a higher GO concentration of 0.2 g, more significant morphological changes were observed. The fiber surfaces became distinctly rougher, and visible GO agglomerates were present. Some fiber fusion and slight pore blockage occurred in localized areas as shown in the Figure 2.c [13].

3.2. FTIR analysis of PET and PET/GO nanofibers

The Fourier-transform infrared (FTIR) spectra of pure PET, PET/GO 0.1, and PET/GO 0.2 are shown in Figure 3. Spectra were recorded from 600 to 4,000 cm^{-1} to investigate the chemical structure and surface interactions of the nanofibrous membranes. The FTIR spectrum of pure PET displays characteristic peaks

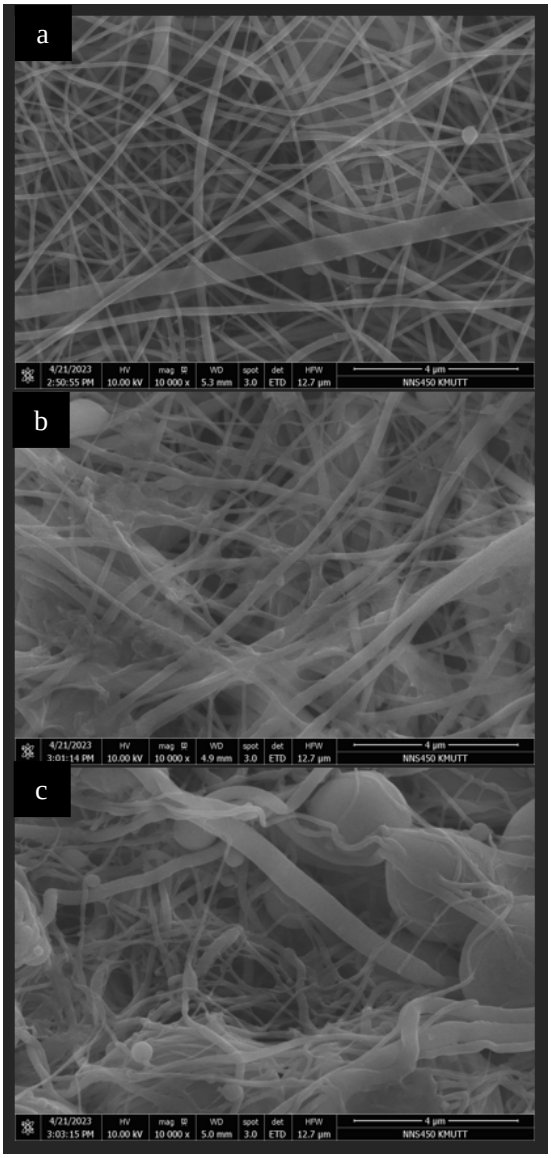

Figure 2 The surface morphology of (a) PET nanofiber membrane (b) PET/GO 0.1 and (c) PET/GO 0.2

corresponding to its functional groups. A strong and sharp absorption band at approximately 1,715 cm^{-1} is assigned to the stretching vibration of the ester carbonyl (C=O) group, a key feature of PET. The C–O–C asymmetric stretching vibration appears near 1,245 cm^{-1}, which is also typical of the ester linkage. Deformation vibrations of the benzene ring are evident around 720 cm^{-1}. Aromatic and aliphatic C–H stretching bands appeared between 2850–3000 cm^{-1}. Additionally, a broad O–H stretching band around 3400 cm^{-1} was observed, likely from moisture adsorption.

In the PET/GO samples, the FTIR spectra retained the major characteristic peaks of PET, indicating that the core chemical structure remained intact. The O–H stretching band around 3,200–3,600 cm^{-1} becomes broader and more intense, especially in the PET/GO

0.2% sample. This enhancement suggests the presence of hydroxyl groups associated with GO and implies possible hydrogen bonding between PET and GO surfaces.

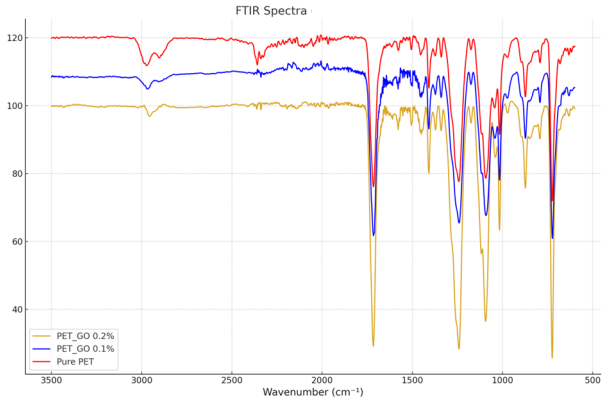

Figure 3 Comparison of FTIR spectra for PET membrane and modified GO at various concentration

Furthermore, a slight broadening of the C=O peak near 1,715 cm^{-1} in the GO-coated samples indicates interaction between the carbonyl group of PET and the oxygen-containing groups of GO. The region around 1100–1150 cm^{-1}, assigned to C–O stretching, also shows a subtle increase in intensity, reflecting the contribution from GO's functionalities. These spectral changes confirm the successful surface modification of PET nanofibers without compromising their structural integrity.

3.3. Membrane antifouling property

The antifouling performance of PET and PET/GO at various concentrations was evaluated through two filtration cycles. The corresponding flux data over time and fouling metrics such as Flux Recovery Ratio (FRR), Reversible Fouling Ratio (RFR), and Irreversible Fouling Ratio (IFR) values are shown in the Table 1.

Table 1 FRR, RFR, IFR, and reducing flux for unmodified and modified PET membrane at various concentration of GO

PET		PET/GO 0.1		PET/GO 0.2	
FRR					
57.85	89.44	49.42	81.01	54.25	92.67
73.645		65.215		73.46	
RFR					
9.26	35.4	19.6	32.07	28.42	61.77
22.33		25.835		45.095	
IFR					
42.15	10.56	50.58	18.99	45.75	7.33
26.355		34.785		26.54	

The flux-time plots clearly show that the PET membrane exhibited the steepest and most consistent decline in flux during both wastewater cycles (Jf1 and Jf2), indicating a high susceptibility to fouling. In contrast, both PET/GO 0.1 and PET/GO 0.2 membranes maintained higher flux values over time, with PET/GO 0.2 displaying the most stable performance as shown in Figure 4. This behavior suggests that surface modification with graphene oxide effectively reduces membrane fouling during operation.

FRR is a key indicator of how well a membrane recovers after fouling. The PET/GO 0.2 membrane demonstrated the highest FRR, reaching 92.67% and 89.44%, signifying excellent fouling reversibility and minimal permanent damage. The PET membrane, on the other hand, showed lower FRRs (54.25% and 57.85%), confirming a large portion of irreversible fouling. The intermediate FRR values of PET/GO 0.1 (81.01% and 49.42%) indicate partial enhancement, though not as effective as the 0.2 wt% GO coating.

The Irreversible Fouling Ratio (IFR) quantifies the fraction of flux loss that could not be recovered, often due to strong foulant adhesion or pore blocking. PET membranes had the highest IFR (42.15% and 45.75%), indicating severe and permanent fouling. In contrast, PET/GO 0.2 membranes had the lowest IFRs (10.56% and 7.33%), attributed to their highly hydrophilic and functional surfaces that resist foulant accumulation. Conversely, the Reversible Fouling Ratio (RFR) was highest for PET/GO 0.2 (35.4% and 61.77%), confirming that most of the fouling could be easily removed by water rinsing.

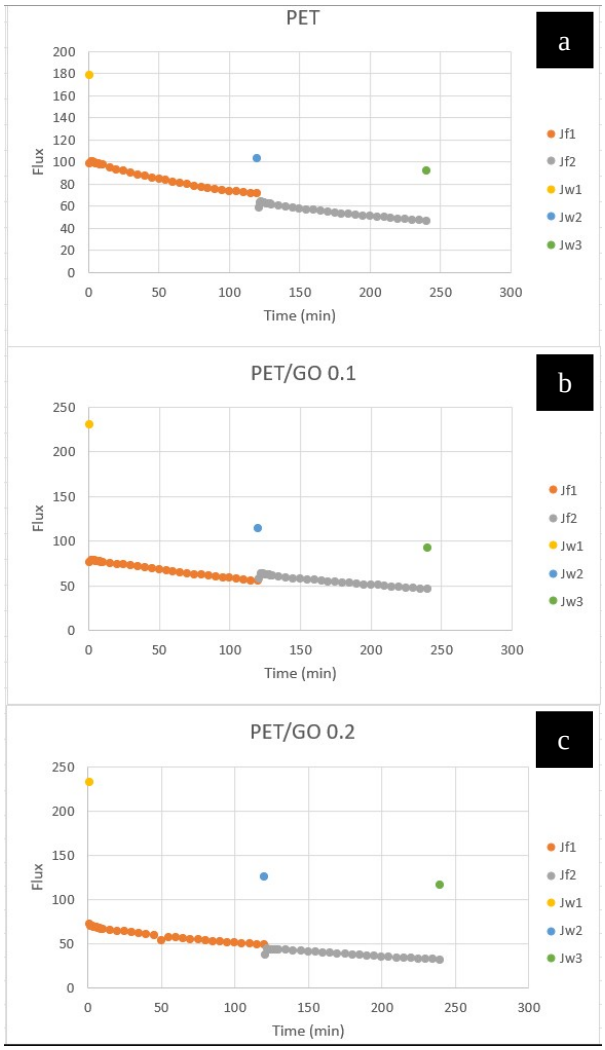

Figure 4 Trend line of flux of the wastewater and water (a) PET (b) PET/GO 0.1 (c) PET/GO 0.2

3.4. Membrane filtration efficiency

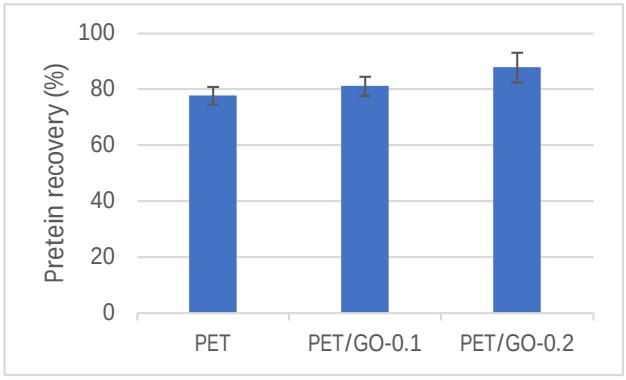

Figure 5 Percent recovery of protein for PET, PET/GO 0.1, and PET/GO 0.2

Filtration efficiency was first evaluated by measuring the PET membrane, PET/GO 0.1, and OET/GO 0.2, respectively. The results showed a notable improvement in recovery as the GO content increased. The PET membrane exhibited a protein recovery of approximately 77%, while the PET/GO 0.1 membrane achieved 81%, and the PET/GO 0.2 membrane reached 88%. This increasing trend highlights the beneficial effect of GO on membrane performance as shown in the Figure 5.

The enhanced protein recovery is primarily attributed to the increased hydrophilicity and functional group density on the membrane surface due to GO coating. Graphene oxide contains a variety of oxygen-rich functional groups, including hydroxyl (–OH), carboxyl (–COOH), and carbonyl (C=O) groups as shown in Figure 3. These functional groups improve the membrane's surface energy and create favorable interactions with water and protein molecules. As a result, the membrane becomes less prone to protein adsorption, allowing more of the target protein to be retained in the feed side rather than being trapped or fouled within the membrane matrix. Further supporting this observation are results from FTIR spectroscopy, which revealed the presence of GO-specific functional groups on the PET/GO membranes. Additionally, SEM imaging illustrated significant changes in the surface morphology of the membranes. While the PET nanofibers were smooth and uniform, the GO-coated membranes displayed rougher textures. This contributed positively to the filtration performance, as evident from the protein recovery of the PET/GO 0.2 membrane [14].

4. CONCLUSION

This study successfully fabricated nanofibrous membranes from recycled polyethylene terephthalate (PET) via electrospinning, with graphene oxide (GO) surface modification to enhance antifouling properties for protein wastewater treatment. SEM and FTIR analyses confirmed uniform fiber morphology and improved surface hydrophilicity. Filtration tests using egg white protein solution demonstrated that GO-modified membranes significantly reduced irreversible fouling and improved protein recovery, with the PET/GO 0.2 membrane achieving 88% recovery and a flux recovery ratio above 90%. These results suggest that GO surface modification is a promising strategy to improve membrane performance in wastewater treatment applications.

ACKNOWLEDGMENTS

This research was supported by King Mongkut's University of Technology Thonburi. Our team also expresses sincere gratitude to the technical staff and supporting laboratories at the Department of Chemical Engineering, KMUTT, for providing essential equipment and assistance. Furthermore, our team thanks our colleagues and collaborators for their valuable discussions and insightful suggestions, which greatly contributed to the quality of this research.

REFERENCES

1. Peydayesh, M., Bagnani, M., Soon, W. L., & Mezzenga, R. Turning food protein waste into sustainable technologies. *Chemical Reviews* 2023; 123: 2112–2154.
2. A sustainable waste-to-protein system to maximise waste resource utilisation for developing food- and feed-grade protein solutions. *Green Chemistry* 2023; 25: 808–832.
3. N. Bhardwaj, S.C. Kundu. Electrospinning: A fascinating fiber fabrication technique. Biotechnology Advances 2010; 28(3): 325–347.
4. M.T. Hossain, M.A. Shahid, A. Ali. Development of nanofibrous membrane from recycled polyethene terephthalate bottle by electrospinning. OpenNano 2022; 8: 100089.
5. A. Baggio, H.N. Doan, P.P. Vo, K. Kinashi, W. Sakai, N. Tsutsumi, Y. Fuse, M. Sangermano. Chitosan-functionalized recycled polyethylene terephthalate nanofibrous membrane for sustainable on-demand oil-water separation. Global Challenges 2021; 5: 2000107.
6. R.K. Joshi, P. Carbone, F.C. Wang, V.G. Kravets, Y. Su, I.V. Grigorieva, H.A. Wu, A.K. Geim, R.R. Nair. Precise and ultrafast molecular sieving through graphene oxide membranes. *Science* 2014; 343(6172): 752–754.
7. G. Zhao, R. Hu, J. Li, H. Zhu. Graphene oxide quantum dots embedded polysulfone membranes with enhanced hydrophilicity, permeability and antifouling performance. *Science China Materials* 2019; 62(8): 1177–1187.
8. Q. Yang, B. Mi. Nanomaterials for membrane fouling control: Accomplishments and challenges. *Advances in Chronic Kidney Disease* 2013; 20(6): 536–551.
9. D.C. Marcano, D.V. Kosynkin, J.M. Berlin, A. Sinitskii, Z. Sun, A. Slesarev, L.B. Alemany, W. Lu, J.M. Tour. Improved synthesis of graphene oxide. *ACS Nano* 2010; 4(8): 4806–4814.
10. J. Wang, P. Zhang, B. Liang, Y. Liu, T. Xu, L. Wang, B. Cao, K. Pan. Graphene oxide as an effective barrier on a porous nanofibrous membrane for water treatment. ACS Applied Materials & Interfaces 2016; 8: 6211–6218.
11. N. Mehranbod, M. Khorram, S. Azizi, N. Khakinezhad. Modification and super hydrophilization of electrospun polyvinylidene fluoride membrane using graphene oxide-chitosan nanostructure and performance evaluation in oil/water separation. Journal of Environmental Chemical Engineering 2021; 9: 106245.
12. A.J. Mazumder, P.H. Raja, A.M. Isloor, M. Usman, S.H. Chowdhury, S.A. Ali, Inamuddin, A. Al-Ahmed. Assessment of sulfonated homo and co-polyimides incorporated polysulfone ultrafiltration blend membranes for effective removal of heavy metals and proteins. Scientific Reports 2020; 10: 7049.
13. T.H. Lin, L.N. Phat, P.M. Tu, T.Q. Thang, B.D.D. Khoa, C.V. Lam, P.T.T. Vy, M.T. Phong, N.H. Hieu. Recycled polyethylene terephthalate fibers aerogels modified with graphene oxide for adsorption of methylene blue and coated with polydimethylsiloxane tetraethyl orthosilicate for oil removal. Journal of Polymers and the Environment 2023; 31: 648–663.
14. J. Li, D. Zhang, T. Yang, S. Yang, X. Yang, H. Zhu. Nanofibrous membrane of graphene oxide-in-polyacrylonitrile composite with low filtration resistance for the effective capture of PM2.5. *Journal of Membrane Science* 2018; 551: 85–92.

Development of PVA-PNVCL-Fe_3O_4 composite nanofibrous for drug delivery in cancer treatment

Sirawit Suknaisilp[1,*], Waritha Janthaporn[1], Saiwan Nawalertpanya[1]

[1] Department of Chemical Engineering, Faculty of Engineering, King Mongkut's University of Technology Thonburi, Bangkok 10140, Thailand
[*] Corresponding author: sirawit.suk23@gmail.com

ABSTRACT

This study investigates the fabrication and morphological tuning of electrospun poly(vinyl alcohol) (PVA) nanofibres incorporating thermo-responsive poly(N-vinylcaprolactam) (PNVCL) and magnetic Fe_3O_4 nanoparticles for potential drug delivery applications. Electrospinning parameters—polymer concentration, flow rate, applied voltage, and tip-to-collector distance—were first optimized using pure PVA to achieve bead-free fibres. Nine composite formulations were then prepared by varying the ratios of PVA, PNVCL, and Fe_3O_4. Macroscopic appearance, scanning electron microscopy (SEM), and fibre diameter analysis were used to evaluate the effects of additive loading. Results showed that both PNVCL and Fe_3O_4 independently increased fibre diameter and surface roughness, while dual incorporation produced the most pronounced morphological changes, with fibre diameters reaching up to 246 ± 33 nm. These findings demonstrate the feasibility of tailoring fibre structure via compositional control, providing a basis for multifunctional nanofibre-based drug delivery systems responsive to thermal and magnetic stimuli.

Keywords: Electrospinning; Poly(vinyl alcohol); PNVCL hydrogel; Fe_3O_4 nanoparticles; Composite nanofibers

1. INTRODUCTION

Stimuli-responsive drug delivery systems have gained considerable attention due to their potential to provide controlled release profiles and improve therapeutic outcomes. These systems allow site-specific or condition-triggered drug release, which can reduce systemic side effects and enhance therapeutic efficiency. Among the many types of delivery platforms, electrospun nanofibrous mats are particularly attractive because of their high surface-area-to-volume ratio, tunable porosity, and ability to incorporate a wide range of therapeutic agents [1]. Their flexible architecture allows for modulation of drug loading and release kinetics, making them suitable for applications such as transdermal patches, wound dressings, and implantable devices.

To achieve responsive functionality, electrospun fibres can be modified with polymers or particles that respond to external stimuli such as temperature, pH, or magnetic fields. Poly(vinyl alcohol) (PVA) is a well-known biocompatible and water-soluble polymer frequently used in electrospinning due to its excellent fibre-forming ability, mechanical strength, and low toxicity [2]. However, PVA by itself does not exhibit stimuli-responsive behaviour. To address this limitation, thermo-responsive polymers can be incorporated. One such polymer is poly(N-vinylcaprolactam) (PNVCL), which exhibits a lower critical solution temperature (LCST) near physiological temperature (~33 °C) [3]. Below its LCST, PNVCL is hydrated and swollen; above it, the polymer collapses, allowing for temperature-triggered drug release. The reversible nature of this transition makes PNVCL an appealing material for temperature-sensitive systems.

In addition to thermal responsiveness, magnetically controlled systems provide the advantage of non-invasive activation through alternating magnetic fields. Magnetic nanoparticles such as magnetite (Fe_3O_4) can generate localized heating through magnetic hyperthermia when exposed to such fields [4]. When incorporated into nanofibres, Fe_3O_4 can facilitate both heating and magnetic targeting. The combination of PNVCL and Fe_3O_4 in a single electrospun fibre matrix opens the possibility for dual-stimuli-responsive systems that respond synergistically to thermal and magnetic cues [5].

While previous research has explored the incorporation of either thermo-responsive or magnetic-responsive components individually, the combination of both in a single nanofibre platform remains underexplored. Moreover, increasing the concentration of such additives can alter fibre morphology, diameter distribution, and mechanical properties — factors that are critical to maintaining a stable and functional drug delivery system. Morphological changes such as bead

formation, fibre fusion, or irregular diameters may negatively impact drug-release behaviour and reproducibility.

In this work, electrospun nanofibres composed of PVA blended with varying concentrations of PNVCL hydrogel and Fe_3O_4 nanoparticles were fabricated and systematically analysed. Electrospinning parameters were first optimised to produce bead-free PVA fibres. Based on this condition, nine additional composite formulations were prepared, incorporating different amounts of single and dual additives. The morphology and diameter of the fibres were characterised using scanning electron microscopy (SEM), and statistical analysis was carried out to examine how additive concentration influences fibre structure. The aim of this study is to gain insight into the relationship between additive composition and fibre morphology, and to identify formulations suitable for further development into dual-stimuli drug delivery platforms. [7]

2. EXPERIMENTAL

2.1 Materials

Poly(vinyl alcohol) (PVA, average molecular weight ≈ 72 kDa, 98–99 % hydrolysed) and N-vinyl-caprolactam monomer (NVCL, ≥ 99 % purity) were used as received. Iron(III) chloride hexahydrate, iron(II) chloride tetrahydrate, ammonium hydroxide solution (25 %), 1-hydroxy-cyclohexyl phenyl ketone (HCPK, photoinitiator), ethanol.

2.2 Preparation of PNVCL hydrogel

A concentrated monomer solution was prepared by dissolving NVCL (0.70 g) and HCPK (1 mg) in de-ionised water (3 mL) under gentle stirring. The homogeneous solution was transferred into a cylindrical glass mould (internal diameter 10 mm) and exposed to 365 nm ultraviolet radiation for 6 h at ambient temperature. After polymerisation, the bulk hydrogel was removed, rinsed thoroughly with water to eliminate unreacted monomer and stored hydrated at 4 °C until use.

2.3 Synthesis of magnetite (Fe_3O_4) nanoparticles

Iron(III) chloride hexahydrate (2.7 g) and iron(II) chloride tetrahydrate (1.0 g) were dissolved in de-ionised water (50 mL) under a nitrogen atmosphere and heated to 80 °C with vigorous stirring. Ammonium hydroxide solution (25 mL) was introduced drop-wise at a rate of 5 mL min^{-1}, causing immediate precipitation of black magnetite. Stirring was continued for 30 min to ensure complete reaction. The solid was magnetically separated, washed repeatedly with water to neutral pH, rinsed twice with ethanol and dried under vacuum at 70 °C for 8 h.

2.4 Optimisation of electrospinning parameters

A PVA solution was prepared by dissolving PVA in hot water (80 °C) and allowing it to cool to room temperature. Optimisation studies were conducted using a single-needle electrospinning set-up equipped with a blunt stainless-steel needle (22 G). 4 independent variables were examined as show in Table 1. And Electrospinning parameter matrix for PVA optimization as show in Table 2.

Table 1. Electrospinning parameters investigated during optimization trials.

Variable	Levels investigated
Concentration (w/w)	6 and 9
Flow rate (mL h^{-1})	0.5 and 1.0
Applied voltage (kV)	10, 15 and 20
Tip-to-collector distance (cm)	10 and 15

Table 2. Electrospinning parameter matrix for PVA optimization.

Sample	PVA conc. (w/v)	Flow rate (ml/hr)	Voltage (kv)	Ttp-to-collector (cm)
PVA 9-0.5-10-10	9	0.5	10	10
PVA 9-0.5-15-10	9	0.5	15	10
PVA 9-0.5-20-10	9	0.5	20	10
PVA 9-1-15-10	9	1	15	10
PVA 9-1-10-10	9	1	10	10
PVA 9-1-20-10	9	1	20	10
PVA6-0.5-10-10	6	0.5	10	10
PVA 6-0.5-15-10	6	0.5	15	10
PVA 6-0.5-20-10	6	0.5	20	10
PVA 6-0.5-10-15	6	0.5	10	15
PVA 6-0.5-15-15	6	0.5	15	15
PVA 6-0.5-20-15	6	0.5	20	15

2.5 Fabrication of composite nanofibers

Nine composite formulations were prepared by adding pre-weighted amounts of PNVCL hydrogel and/or Fe_3O_4 nanoparticles to the 9 wt % PVA solution. The mixtures were stirred for 3 h to ensure homogeneity and then sonicated for 5 min to break up agglomerates. Electrospinning was carried out under the optimised parameters described above. The fibres were collected on aluminium foil as non-woven mats and dried under reduced pressure at 40 °C for 12 h. Table 2 summarises the nominal compositions.

Table 2. Composition of electrospun formulations (mass percentage of total solids).

Run	PVA	PNVCL	Fe_3O_4
PVA	100	–	–
PVA-PNVCL 95-5	95	5	–
PVA-PNVCL 90-10	90	10	–
PVA-PNVCL 85-15	85	15	–
PVA-Fe3O4 95-5	95	–	5
PVA-Fe3O4 90-10	90	–	10
PVA-Fe3O4 85-15	85	–	15
PVA-Fe3O4-PNVCL 90-5-5	90	5	5
PVA-Fe3O4-PNVCL 85-5-10	85	5	10
PVA-Fe3O4-PNVCL 85-10-5	85	10	5

2.6 Characterisation

Surface morphology and fibre dimensions were examined using field-emission SEM operated at 10 kV. Samples were sputter-coated with a thin conductive layer prior to imaging. For each formulation, at least 30 individual fibre diameters were measured from 10 000 × micrographs using ImageJ software; mean values and standard deviations were calculated. No further physicochemical characterisation is reported here, as the focus of this study is the influence of additive content on fibre morphology.

3. RESULTS AND DISCUSSION

3.1 Morphology of pure-PVA fibres

3.1.1 Polymer concentration

Lowering the concentration from 9 wt % to 6 wt % (Fig. 1h–l) produces dense, spindle-shaped beads decorating otherwise thin fibres, whereas all 9 wt % samples (Fig. 1a–g) are bead-free. This confirms that 6 wt % is below the critical chain-entanglement concentration required for defect-free spinning.

3.1.2 Flow rate

At 9 wt % PVA, increasing the flow from 0.5 to 1.0 mL h^{-1} (compare Fig. 1e–g with Fig. 1b–d) approximately doubles bead frequency and introduces occasional fused junctions, indicating that the higher volumetric throughput limits solvent evaporation.

3.1.3 Applied voltage

With concentration and flow fixed (0.5 mL h^{-1}), elevating the electric field from 10 kV to 20 kV (Fig. 1b → 1d) progressively thins the fibres and ultimately removes beads; 20 kV affords the most uniform morphology.

3.1.4 Tip-to-collector distance (TCD)

Extending the gap from 10 cm to 15 cm (compare Fig. 1d with Fig. 1a) eliminates the ribbon-like, flattened segments observed at the shorter distance, confirming that a longer flight path permits complete solvent evaporation and preserves cylindrical geometry.

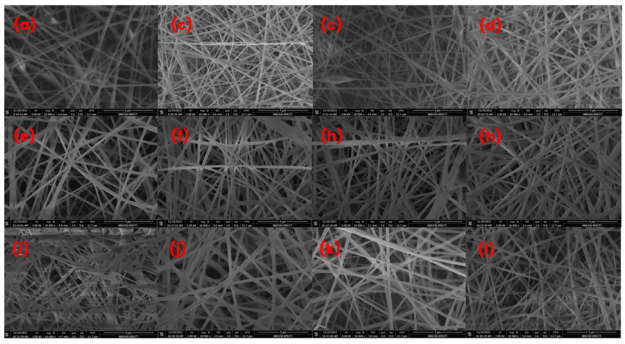

Fig 1. SEM micrographs (10,000 ×) of pure-PVA fibres obtained under the twelve parameter sets in the optimisation matrix: (a) PVA9-0.5-20-15; (b) PVA9-0.5-10-10; (c) PVA9-0.5-15-10; (d) PVA9-0.5-20-10; (e) PVA9-1-15-10; (f) PVA9-1-10-10; (g) PVA9-1-20-10; (h) PVA6-0.5-10-10; (i) PVA6-0.5-15-10; (j) PVA6-0.5-20-10; (k) PVA6-0.5-10-15; and (l) PVA6-0.5-15-15.

3.2. Effect of electrospinning parameters on PVA-fibre diameter

3.2.1 Polymer concentration

Lowering PVA concentration from 9 wt % to 6 wt % increases the mean diameter from 139 ± 19 nm (Fig. 1a) to 150 ± 26 nm (Fig. 1h). This seemingly counter-intuitive thickening has been described by Reneker & Yarin et al [6]: at sub-critical entanglement, the jet breaks into droplets (beads) that drain solvent slowly, leaving the intervening fibre segments swollen when they solidify.

3.2.2 Flow rate

Increasing the volumetric flow from 0.5 to 1.0 mL h^{-1} at 9 wt % (Fig. 1b → 1e) raises the diameter from 119 ± 19 nm to 138 ± 24 nm and doubles the standard

deviation. The trend follows the linear mass-balance model, because the residence time available for solvent evaporation scales inversely with flow Huang et al. [8]. A similar 25–30 % thickening was reported for PVA by Soares et al. [9] when the feed rate exceeded 0.8 mL h^{-1}.

3.2.3 Applied voltage

Raising the field strength from 10 kV to 20 kV produces a monotonic diameter decrease 139 ± 22 nm → 119 ± 21 nm. This inverse relation, predicted by the electro-hydrodynamic stretching model and has been validated for numerous polymer/solvent systems (Li & Xia [10]. Our 15 % reduction between 10 kV and 20 kV matches the 12–18 % reported for aqueous PVA by Nasouri et al. [11].

3.2.4 Tip-to-collector distance

Extending the tip-to-collector distance from 10 cm to 15 cm unexpectedly increases the mean fibre diameter from 150 ± 21 nm to 241 ± 19 nm. This contrasts with the commonly cited trend of diameter reduction at longer distances due to increased flight time for solvent evaporation. However, similar anomalous thickening has been reported when electric field intensity weakens at extended TCD, reducing jet elongation Pham et al. [12]. Moreover, at low flow and moderate voltage, the reduced field strength may dominate over evaporation effects, leading to thicker fibre deposition.

3.3 Visual appearance of electrospun mats

Pure PVA (Fig. 3a) the mat appears bright white and uniformly opaque. No obvious wrinkles or surface speckling are visible, indicating homogeneous fibre packing and negligible bead formation at the macro-scale.

PVA + PNVCL 5–15 wt% (Fig. 3b–d) the colour remains white, but the central window shows a progressively smoother sheen with increasing PNVCL content. PNVCL contains retained water, so the mats exhibit slightly greater flexibility when handled. No dark spots are seen, suggesting that hydrogel domains are well dispersed.

PVA + Fe_3O_4 5–15 wt% (Fig. 3e–g) a faint grey tint develops and becomes more pronounced at higher Fe_3O_4 loadings, reflecting the intrinsic colour of magnetite. Minor surface roughness is visible through the inspection window in Run 6, implying denser packing or possible fibre fusion due to nanoparticle agglomeration.

Dual-additive systems (Fig. 3h–j) the mats show the combined characteristics of earlier sets: a muted grey-white hue and slightly higher opacity. At 10 wt % PNVCL + 5 wt % Fe_3O_4 (Run 9) the central square exhibits small dark speckles, likely exposed clusters of magnetite. These observations support the expectation that simultaneous incorporation of hydrogel and nanoparticles increases fibre diameter variability and local packing density.

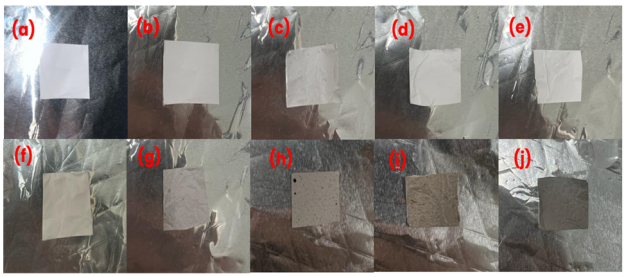

Fig 3. Photographs of the electrospun nanofibre mats deposited on aluminium-foil collectors: (a) Pure PVA; (b) PVA-PNVCL 95-5;(c) PVA-PNVCL 90-10;(d) PVA-PNVCL 85-15; (e) PVA-Fe_3O_4 95-5;(f) PVA-Fe_3O_4 90-10; (g) PVA-Fe_3O_4 85-15; (h) PVA-Fe_3O_4-PNVCL 90-5-5; (i) PVA-Fe_3O_4-PNVCL 95-10-5; (j) PVA-Fe_3O_4-PNVCL 85-5-10

3.4 Morphology of Composite Electrospun Nanofibres

3.4.1. Effect of PNVCL incorporation

The surface morphology of the composite nanofibres is shown in Fig. 4, with each sample representing a specific additive formulation. Compared to the pure PVA benchmark (discussed in Section 3.1), all composite fibres remain bead-free and continuous, confirming that the optimized electrospinning parameters support stable jet formation across all additive combinations.

3.4.1. Effect of PNVCL incorporation

Samples Fig. 4(a–c), corresponding to PVA/PNVCL 95/5, 90/10, and 85/15, show fibres with gradually increasing average diameter and rougher surfaces as PNVCL content increases. This is attributed to partial phase separation of the hydrogel component during solvent evaporation, leading to swelling and surface irregularities. Additionally, the increased polymeric solid content from the hydrogel enhances solution viscosity, which further increases fibre thickness. The changes are clearly visible in the surface texture and fibre thickness progression from Fig. 4(a) to Fig. 4(c).

3.4.2. Effect of Fe_3O_4 incorporation

Samples Fig. 4(d–f), which incorporate 5, 10, and 15 wt % Fe_3O_4 nanoparticles respectively, exhibit more substantial diameter increases than PNVCL alone. SEM images reveal slightly uneven surfaces and occasional signs of nanoparticle clustering at the higher Fe_3O_4 loadings, particularly in Fig. 4(f). These agglomerations may hinder uniform jet stretching and explain the observed fibre thickening. The darker contrast in these images also supports successful nanoparticle retention within the fibre matrix.

3.4.3. Effect of dual-additive loading (PNVCL + Fe_3O_4)

Samples Fig. 4(g–i), which combine both functional additives, show the most significant morphological changes. At low dual loading (PVA/Fe_3O_4/PNVCL 90/5/5, Fig. 4g), fibres appear moderately thickened with minimal disruption. However, at higher dual loading — especially in Fig. 4(i) (85/5/10) — the fibres become substantially thicker, with pronounced surface texture, nodular formations, and non-uniform diameter. This suggests a synergistic effect: hydrogel swelling and nanoparticle crowding jointly disrupt fibre homogeneity and surface smoothness. Nevertheless, fibre continuity is preserved in all cases, indicating that the system tolerates high additive loading without catastrophic phase separation or jet instability.

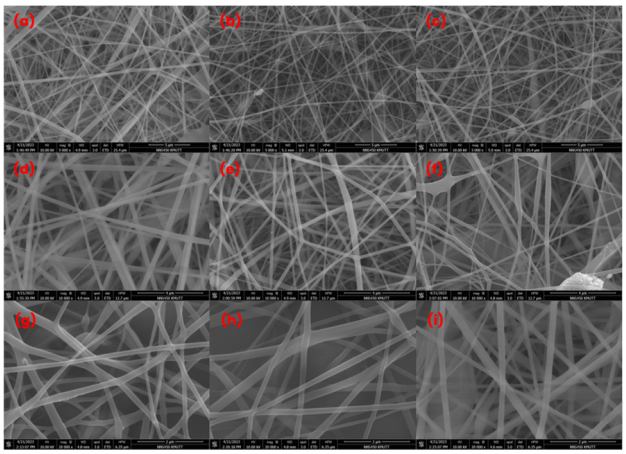

Fig 4.SEM micrographs (10,000×) of electrospun composite nanofibres with various additive compositions: (a) PVA/PNVCL 95/5; (b) PVA/PNVCL 90/10; (c) PVA/PNVCL 85/15; (d) PVA/Fe_3O_4 95/5; (e) PVA/Fe_3O_4 90/10; (f) PVA/Fe_3O_4 85/15; (g) PVA/Fe_3O_4/PNVCL 90/5/5; (h) PVA/Fe_3O_4/PNVCL 95/10/5; (i) PVA/Fe_3O_4/PNVCL 85/5/10.

3.5 Effect of Functional Additives on on PVA-fibre diameter

The influence of additive incorporation on PVA nanofibre diameter was systematically evaluated by comparing composite formulations to the pure PVA reference. Figures 5 to 7 summarize the mean diameters and standard deviations for each group: PNVCL-only, Fe_3O_4-only, and dual-additive systems.

3.5.1. Effect of PNVCL content

As shown in Fig. 5, increasing the PNVCL content from 5 wt% to 15 wt% resulted in a progressive thickening of the nanofibres. The diameter rose from 171 ± 23 nm (PVA/PNVCL 95/5) to 204 ± 27 nm (PVA/PNVCL 85/15). This trend is attributed to the increased viscosity and hydrogel swelling during fibre solidification. The dispersed PNVCL domains likely hinder full electrostatic stretching, leading to a broader fibre profile. This observation aligns with previous findings by Kong et al. [13], who reported similar thickening in thermoresponsive hydrogel-loaded fibres.

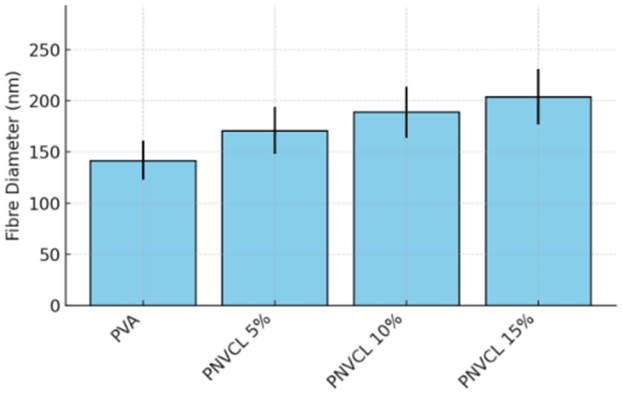

Fig 5. Effect of PNVCL hydrogel content on average fibre diameter. Electrospun fibres were prepared using PVA blended with 5–15 wt% PNVCL.

3.5.2. Effect of Fe_3O_4 nanoparticles

As depicted in Fig. 6, the addition of Fe_3O_4 nanoparticles also increased the average fibre diameter, from 177 ± 22 nm (5 wt%) to 218 ± 30 nm (15 wt%). The effect is slightly more pronounced than with PNVCL, likely due to partial nanoparticle agglomeration disrupting the flow field and inducing non-uniform jet stretching. This agrees with prior findings by Saeed et al. [15], who reported increased fibre thickness and roughness in PVA/Fe_3O_4 composites due to magnetite clustering. SEM micrographs also revealed surface roughness and clustering at higher Fe_3O_4 concentrations, consistent with the mechanical drag imposed by magnetic filler particles during fibre formation, in line with reports from Yang et al. [17].

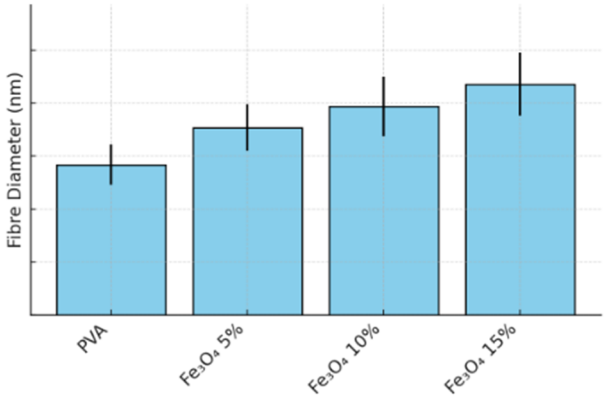

Fig 6. Effect of Fe_3O_4 nanoparticle content on average fibre diameter. Fibre mats containing 5–15 wt% Fe_3O_4

3.5.3. Effect of dual-additive systems

The most significant thickening occurred in dual-additive systems, as shown in Fig. 7. The fibre diameter increased from 226 ± 29 nm (Dual 90/5/5) to 246 ± 33 nm (Dual 85/5/10), confirming a synergistic impact from combining PNVCL and Fe_3O_4. Hydrogel swelling

and magnetic particle crowding together disrupt jet uniformity more severely than either component alone. This agrees with Xu et al. [16], who demonstrated that combining two functional additives exacerbates fibre instability and broadens the diameter distribution. However, no catastrophic jet instability was observed here, indicating the electrospinning process remains robust even under complex loading conditions.

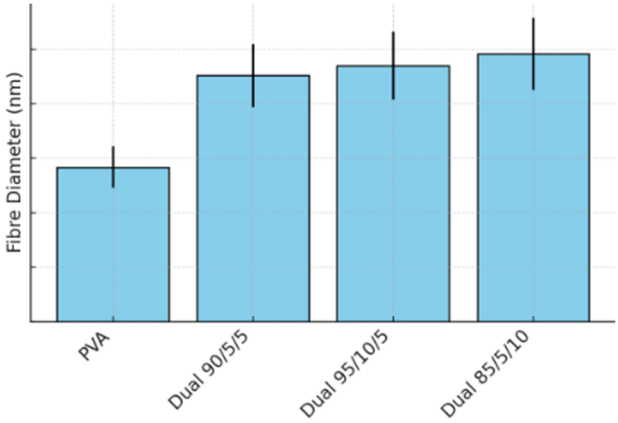

Fig 7. Effect of dual-additive (PNVCL + Fe_3O_4) systems on average fibre diameter.

CONCLUSION

This study successfully demonstrated the fabrication of electrospun nanofibres based on poly(vinyl alcohol) (PVA) incorporating thermo-responsive poly(N-vinylcaprolactam) (PNVCL) hydrogel and magnetic Fe_3O_4 nanoparticles. The electrospinning process was first optimized using pure PVA by systematically varying solution concentration, flow rate, applied voltage, and tip-to-collector distance. The results showed that lower polymer concentration and higher flow rate significantly increased bead formation and fibre diameter, whereas higher voltage and longer flight distance improved fibre uniformity and reduced diameter.

After optimizing the spinning conditions, nine composite formulations were prepared to evaluate the effects of PNVCL, Fe_3O_4, and their combination on fibre morphology and diameter. Macroscopic observations revealed progressive changes in mat colour and texture, with increasing opacity and greyness linked to hydrogel and magnetite content, respectively. SEM analysis confirmed that all composite fibres remained bead-free and continuous. The incorporation of additives led to thicker fibres, with the dual-additive systems showing the highest diameters and most pronounced surface roughness. Quantitative fibre diameter analysis showed clear trends: increasing PNVCL and/or Fe_3O_4 content led to higher mean diameters and greater variability. These effects are attributed to increased solution viscosity, phase separation, and nanoparticle clustering. Among the samples, PVA/Fe_3O_4/PNVCL 85/5/10 exhibited the thickest fibres (246 ± 33 nm), nearly double that of pure PVA (142 ± 19 nm).

Overall, this work highlights the tunability of electrospun fibre properties through compositional modifications and lays a foundation for designing stimuli-responsive nanofibres for future drug delivery or biomedical applications.

ACKNOWLEDGMENTS

The author gratefully acknowledges the invaluable guidance and support of Asst. Prof. Dr. Saiwan Nawalertpanya, thesis advisor, whose expertise and encouragement were instrumental throughout this research. Special thanks are extended to Dr. Waritha Jantaporn, thesis co-advisor, for her insightful advice and thoughtful suggestions. Appreciation is also given to the thesis committee members, Assoc. Prof. Dr. Kwanchanok Pasuwat and Dr. Kiattinatapon Juengchareonpoon, for their constructive feedback and academic contributions that helped shape the final outcome of this work.

REFERENCES

[1] Xue, J., Wu, T., Dai, Y., & Xia, Y. (2019). Electrospinning and Electrospun Nanofibers: Methods, Materials, and Applications. Chemical Reviews, 119(8), 5298–5415.

[2] Huang, Z. M., Zhang, Y. Z., Kotaki, M., & Ramakrishna, S. (2003). A review on polymer nanofibers by electrospinning and their applications in nanocomposites. Composites Science and Technology, 63(15), 2223–2253.

[3] Cortez-Lemus, N. A., & Licea-Claverie, A. (2016). Poly(N-vinylcaprolactam), a comprehensive review on a thermoresponsive polymer becoming popular. Progress in Polymer Science, 53, 1–51.

[4] Revia, R. A., & Zhang, M. (2016). Magnetite nanoparticles for cancer diagnosis, treatment, and treatment monitoring: Recent advances. Materials Today, 19, 157–168.

[5] Echeverria, C., Nisisako, T., & Mijangos, C. (2021). Colloidal electrospinning for hybrid fiber systems: Combining microgels and nanoparticles. Advanced Materials Interfaces, 8(15), 2100405.

[6] Reneker, D. H., & Yarin, A. L. (2008). Electrospinning jets and polymer nanofibers. Polymer, 49(10), 2387–2425.

[8] Huang, Z.M., Zhang, Y.Z., Kotaki, M., & Ramakrishna, S. (2003). A review on polymer nanofibers by electrospinning and their applications in nanocomposites. *Composites Science and Technology*, 63, 2223–2253.

[9] Soares, B. G., et al. (2021). PVA-based nanofibers and flow-rate effects. Journal of Applied Polymer Science, 138(25),

[10] Li, D., & Xia, Y. (2004). Electrospinning of nanofibers: Reinventing the wheel?. Advanced Materials, 16(14), 1151–1170.
[11] Nasouri, K., et al. (2015). Voltage-induced jet elongation in aqueous PVA systems. Journal of Nanoscience and Nanotechnology, 15(2), 1364–1371.
[12] Pham, Q. P., Sharma, U., & Mikos, A. G. (2006). Electrospinning of polymeric nanofibers for tissue engineering applications: A review. Tissue Engineering, 12(5), 1197–1211.
[13] Kong, L., et al. (2020). Thermoresponsive hydrogel composite nanofibres for dual release. Journal of Biomedical Materials Research Part A, 108(10), 2194–2203.
[15] Saeed, M., Ullah, A., Ullah, S., et al., "Advances in wound dressing based on electrospinning nanofibers," *Journal of Applied Polymer Science*, vol. 140, no. 14, e54746, 2023.
[16] Ahmed, A., and Xu, L., "Numerical analysis of the electrospinning process for fabrication of composite fibers," *Thermal Science*, vol. 24, no. 2B, pp. 1377–1386, 2020.
[17] Yang, W., Liu, C., Liu, H., et al., "Electrospun Fe_3O_4-chitosan/polyvinyl alcohol nanofibrous film for improved capture and elimination of foodborne pathogens," *International Journal of Biological Macromolecules*, vol. 248, 126692, 2023.

Effect of glycerol on xyloglucan-chitosan film preparation and its properties

Pornpatu Adair[1], Kanjana Manamoongmongkol[2], Pongsert Sriprom[1,*], Woatthichai Narkrugsa[1], Lamphung Phumjan[1], Pornsawan Assawasaengrat[2]

[1] School of Food Industry, King Mongkut's Institute of Technology Ladkrabang, Bangkok, 10520, Thailand
[2] Department of Chemical Engineering, School of Engineering, King Mongkut's Institute of Technology Ladkrabang, Bangkok 10520, Thailand
[*] Corresponding author: pongsert.sr@kmitl.ac.th

ABSTRACT

This research aims to investigate the influence of glycerol content on the formation of complex compounds between xyloglucan and chitosan in xyloglucan-chitosan films. Xyloglucan was used at 1.00 grams, in combination with 0.25 grams of chitosan, and glycerol was added at concentrations of 25%, 30%, and 35% (w/w of total solids) to act as a plasticizer. The formation of xyloglucan-chitosan complex compounds during the film production process was analyzed using FTIR, which revealed a peak in the wavenumber range of 1635.37 cm^{-1} to 1636.84 cm^{-1}, suggesting the formation of the xyloglucan-chitosan complex. However, the FTIR spectra indicated that the increased amount of glycerol has no effect on the formation of complex compounds between xyloglucan and chitosan during the production process of the films. SEM images revealed that the surface of the xyloglucan-chitosan films was rough, and increasing glycerol content did not affect the formation of the xyloglucan-chitosan complex. The increasing of glycerol content enhanced the elongation of the xyloglucan-chitosan films ($p \leq 0.05$), but did not affect tensile strength ($p > 0.05$). The xyloglucan-chitosan film with 35% glycerol (w/w of total solids) exhibited the highest tensile strength and elongation. Additionally, the addition of glycerol did not significantly affect the water vapor transmission rate ($p > 0.05$).

Keywords: Glycerol; Xyloglucan; Chitosan; Film

1. INTRODUCTION

Glycerol is widely used in polymer science and pharmaceutical formulations due to its excellent compatibility with biopolymers and its function as a plasticizer. As a polyol with three hydroxyl groups, glycerol interacts readily with polymeric chains through hydrogen bonding, thereby disrupting intermolecular forces within the polymer matrix [1]. This action increases the mobility of polymer chains and imparts flexibility to the resulting material. When introduced into film-forming systems, glycerol enhances the pliability and reduces brittleness, which is crucial for applications requiring mechanical resilience, elasticity, and moisture sensitivity. Additionally, glycerol is a non-toxic, biodegradable, and economically viable compound, which makes it particularly attractive for applications in food packaging, medical dressings, and biodegradable films [2].

Xyloglucan is a naturally occurring polysaccharide predominantly found in the primary cell walls of plants [3, 4]. Its structure comprises a β–1,4-D-glucan substituted with xylose residues, and further branching of galactose on the xylose side chains [5-8]. Commercial production of xyloglucan began as early as 1943 in India, primarily for textile applications as a water-resistant agent [7]. Due to its high water retention, solubility, and resistance to thermal, acidic, and shear stresses, xyloglucan has been utilized across a variety of industries [9]. It is applied as a thickener, stabilizer, gelling agent, and fat replacer in products such as ice cream, salad dressings, sauces, etc [10].

Chitosan, a derivative of chitin, is sourced from the exoskeletons of crustaceans such as shrimp and crabs [11]. It is obtained by converting N-acetyl-D-glucosamine units to D-glucosamine through deacetylation [12, 13]. Chitosan, with its primary amino groups at the glucosamine units, is soluble in dilute acids [14] and exhibits biodegradability, biocompatibility, and significant adsorption properties [15]. These attributes make it suitable for applications in biomedical, environmental, and packaging fields [16]. Several studies have focused on improving the performance of biopolymer films through composite formulations. For instance, xyloglucan has been combined with chitosan to form films with enhanced mechanical integrity and barrier properties. However, the rigidity of such films can still pose limitations in practical applications, particularly where flexibility and stretchability are required.

Several studies have investigated the incorporation of glycerol as a plasticizer in film formulations. Tong et

al. [17] incorporated glycerol into films prepared from a composite of pullulan, alginate, and carboxymethylcellulose (CMC). It was found that the addition of glycerol reduced the tensile strength of the films while enhancing their elongation at break. Similarly, Piermaria et al. [18] reported that films prepared from kefiran without glycerol appeared to be brittle and rigid, exhibiting high tensile strength but low elongation. However, the film showed an increase in film flexibility with the addition of glycerol, resulting in elongation values comparable to those of synthetic polymer-based films. Ghasemlou et al. [19] also incorporated glycerol into kefiran-based films and found that tensile strength was reduced, while elongation at break was significantly improved, surpassing that of conventional synthetic films such as polyester and cellophane. Consistent findings were reported by Matta et al. [20], who investigated films derived from mung bean starch blended with xanthan gum. The incorporation of glycerol was found to decrease tensile strength while enhancing the elongation capacity of the films.

This research aimed to study xyloglucan–chitosan films enhanced with glycerol at varying concentrations to improve the mechanical flexibility and structural integrity of the films. This approach was undertaken not only to address the inherent limitations of natural biopolymers such as brittleness and low extensibility but also to contribute to the advancement of sustainable, biodegradable packaging materials.

2. EXPERIMENTAL

2.1 Materials

Xyloglucan from tamarind seed kernels (Pinphet Co., Ltd., Thailand) was extracted using Adair et al. [21] method. Chitosan from shrimp shell (40 mesh pass, molecular weight 1140 kDa, Ta Ming Enterprise Co., Ltd, Thailand). The reagents were acetic acid (CH_3COOH, AR grade, QReC, New Zealand), glycerol ($HOCH_2CH(OH)CH_2OH$, AR grade, Leonid chemicals, India). citric acid (Merck, Germany), peptone (Becton, Dickinson, and Company, USA), tryptone and yeast extract (Biokar diagnostics, France).

2.2 Film preparation

1.00 g of xyloglucan was first dissolved in 10 mL of distilled water at 85 °C and stirred with a glass rod for 15 minutes. Subsequently, 25 mL of 4% (v/v) acetic acid was added, and the resulting solution was stirred using a mixer at 220 rpm for 30 minutes at room temperature. Chitosan solution was prepared by dissolving 0.25 g of chitosan in 25 mL of 4% (v/v) acetic acid using a mixer at 220 rpm for 10 minutes. Homogenization was then carried out using a hand blender operated at maximum speed for 2 minutes at room temperature, followed by additional stirring with a mixer at 220 rpm for 10 minutes. The xyloglucan and chitosan solutions were then combined and mixed at 220 rpm for 2 minutes. Glycerol was subsequently incorporated at concentrations of 25%, 30%, and 35% (w/w based on total solids), and the mixture was stirred for an additional 5 minutes at the same speed and temperature. The final solution was cast onto a 20 × 24 cm acrylic plate and dried in a gel drying oven at 37.5 °C for 6 hours. After drying, the resulting film was stored in desiccator for subsequent analysis.

2.3 Characterization

The influence of glycerol on the formation of a xyloglucan–chitosan film fabrication process was analyzed through various characterization techniques. To identify the functional groups present in the films, Fourier Transform Infrared Spectroscopy (FTIR) analysis was conducted using a spectrometer (Thermo Scientific, Nicolet 6700 model, Germany). The ATR-FTIR technique was utilized for the non-destructive surface analysis of the samples.

The surface morphology of the films was analyzed using Scanning Electron Microscopy (SEM) (LEO, 1455VP model, Germany) at a magnification of 1000x to examine the film surface.

The melting point of the films were evaluated using differential scanning calorimetry (DSC) (Netzsch, DSC 204F1 model, Germany). The DSC was operated under the following analytical conditions: a temperature range from 30°C to 300°C, a heating rate of 10°C/min, a cooling rate of 10°C/min, and nitrogen was used as the purge gas. All measurements were conducted using the first run method to ensure baseline precision.

Mechanical properties, including tensile strength and elongation at break, were evaluated following ASTM D882 standards. Film samples were cut into 2×4 cm rectangles and tested using a Texture Analyzer (TA.XT Plus model) equipped with an A/TG probe.

The water vapor transmission rate (WVTR) of the films was measured using the ASTM E96/E96M–16 method. The test was conducted at a temperature of 38°C and a relative humidity of 90%. During testing, one side of the film was exposed to high humidity while the opposite side was maintained at low humidity.

Antimicrobial activity was evaluated by exposing the films to ambient conditions for 48 hours to allow natural microbial contamination from the environment. Subsequently, the total viable microbial count was determined using a modified method adapted from Simi et al. [22].

The obtained data were statistically analyzed using IBM SPSS Statistics version 21. Analysis of Variance (ANOVA) was performed to determine significant differences among treatments, and the means were compared using Duncan's Multiple Range Test (DMRT) at a 95% confidence level ($P \leq 0.05$). The comparisons of treatment means were conducted based on data obtained from three experimental replications.

3. RESULTS AND DISCUSSION

The effect of glycerol on the formation of complexes between xyloglucan and chitosan during the film fabrication process was investigated using DSC. The presence of endothermic peaks corresponding to the crystalline structures of the films was observed, with variations depending on the film composition. The peak indicated the enthalpy and temperature required to disrupt the crystalline structure and induce a phase transition from solid to liquid. Figure 1 showed the melting peaks of the xyloglucan–chitosan films shifted with increasing glycerol content. It was found that the enthalpy required for the melting of the crystalline regions tended to increase with the addition of glycerol. Moreover, the crystalline structure of the xyloglucan–chitosan films was found to require melting temperatures in the range of 194.3°C to 198.6°C.

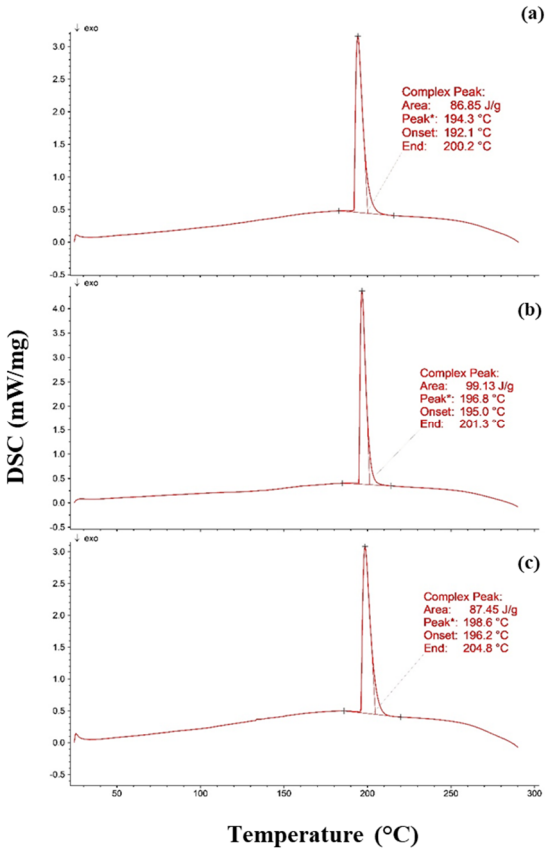

Figure 1 DSC result of xyloglucan-chitosan films with the addition of glycerol at (a) 25%, (b) 30% and (c) 35% (w/w of total solid).

From the FTIR spectra (Figure 2), the xyloglucan–chitosan films exhibited distinct peaks at wavenumbers ranging from 1,550.46 cm^{-1} to 1,553.81 cm^{-1}, which were attributed to primary amine groups (R-NH_2). Peaks observed between 1,632.37 cm^{-1} and 1,635.06 cm^{-1} were assigned to primary amide groups (R-CO-NH_2), while peaks appearing in the range of 1,635.37 cm^{-1} to 1,637.48 cm^{-1} were associated with aliphatic secondary amide groups (R-CO-NH-R'). These observations were consistent with the findings reported by Simi et al. [22] and Adair et al. [21], indicated the formation of complex between aldehyde groups (-CHO) of xyloglucan and the amino groups (-NH_2) of chitosan through covalent bond. Furthermore, it was found that the increasing concentration of glycerol had no significant effect on the complexation between xyloglucan and chitosan during the film fabrication process.

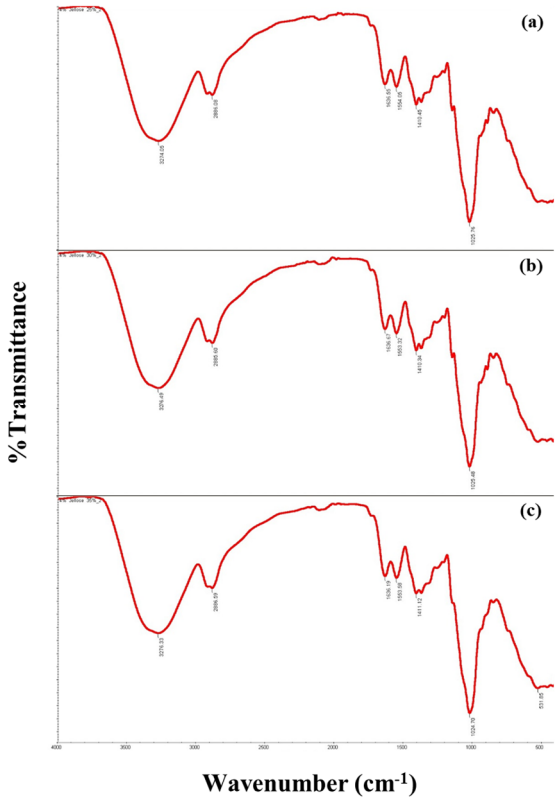

Figure 2 FTIR result of xyloglucan-chitosan films with the addition of glycerol at (a) 25%, (b) 30% and (c) 35% (w/w of total solid).

The surface morphology of the films with varying glycerol contents (25%, 30%, and 35%) was examined by SEM at a magnification of 1000x (Figure 3). It was observed that all three film samples exhibited rough surface textures, with no significant differences among them. The presence of rough surfaces indicated the complex formation between xyloglucan and amino group of chitosan, which was consistent with Simi et al. [23]. Therefore, the increasing concentration of glycerol did not affect the surface morphology of the xyloglucan–chitosan films.

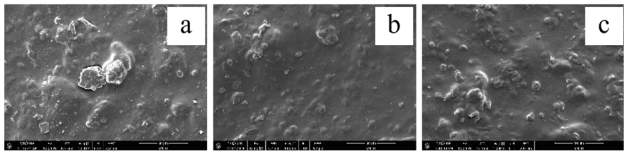

Figure 3 SEM result of xyloglucan-chitosan films with the addition of glycerol at (a) 25%, (b) 30% and (c) 35% (w/w of total solid).

The tensile strength and elongation at break of the xyloglucan–chitosan films containing 25%, 30%, and 35% glycerol were analyzed as shown in Table 1. It was found that variations in glycerol content significantly affected the tensile strength and elongation of the resulting films. There was no statistically significant difference in tensile strength ($p > 0.05$) when the glycerol content was increased. However, a statistically significant difference in elongation was detected ($p \leq 0.05$) when the glycerol content was increased to 25%, 30%, and 35%. The film containing 35% glycerol (w/w of total solids) exhibited the highest tensile strength and elongation. These results indicated that an appropriate ratio between xyloglucan and chitosan, along with an optimal glycerol content, facilitated the formation of a well-structured complex between xyloglucan and chitosan, resulting in films with enhanced mechanical strength and flexibility.

Table 1 Tensile strength and elongation at break of xyloglucan-chitosan films.

Glycerol (%w/w of total solids)	Tensile strength (MPa)	Elongation at break (%)
25	11.55 ± 0.24^{b}	16.20 ± 0.09^{c}
30	12.18 ± 0.67^{a}	22.95 ± 0.41^{b}
35	12.27 ± 0.23^{a}	28.10 ± 0.16^{a}

Note: Different letters (a-c) within the same vertical column indicate statistically significant differences at a 95% confidence level ($p \leq 0.05$).

In Table 2, the water vapor transmission rates of the xyloglucan–chitosan films containing varying amounts of glycerol were analyzed. It was found that the increase in glycerol content did not cause a statistically significant difference in the water vapor transmission rates of the films ($p > 0.05$). The water vapor transmission rates of the films were observed to range from 1230 to 1302 g/m^2.

Table 2 WVTR of xyloglucan-chitosan films.

Glycerol (%w/w of total solids)	WVTR (g/m^2)
25	$1{,}230.00 \pm 32.53^{a}$
30	$1{,}302.00 \pm 4.24^{a}$
35	$1{,}274.00 \pm 42.43^{a}$

Note: Different letters (a-c) within the same vertical column indicate statistically significant differences at a 95% confidence level ($p \leq 0.05$).

In Table 3, the total viable count of the xyloglucan–chitosan films prepared with different glycerol contents (25%, 30%, and 35%) are presented. Microbial growth of less than 30 CFU/g was detected in all samples, indicating that strong antimicrobial activity was exhibited by the films. This antimicrobial property was attributed to the formation of complex between the aldehyde groups of xyloglucan and the amino groups of chitosan, which was suggested to inhibit microbial proliferation. The result is consistent with the findings reported by Simi et al. [22, 23] and Adair et al. [21], who demonstrated that the complexation between xyloglucan and chitosan contributed significantly to the antimicrobial activity of the resulting films.

Table 3 Antimicrobial result of xyloglucan-chitosan films.

Glycerol (%w/w of total solids)	Total viable count (CFU/g)
25	$< 30 \times 10^{1}$
30	$< 30 \times 10^{1}$
35	$< 30 \times 10^{1}$

4. CONCLUSION

The conclusion of a paper should summarize the key findings and their significance, providing a clear and concise wrap-up of the study. Begin by briefly restating the main research question or objectives and summarizing the principal results. Highlight the importance of these findings in the context of the field and their potential impact. Discuss any limitations encountered during the study and suggest directions for future research. Emphasize the overall contribution of the study to the existing body of knowledge and its practical or theoretical implications. Ensure the conclusion is clear, concise, and leaves the reader with a strong understanding of the study's importance and future potential. Ensure the text is in Times New Roman font, 10.5 point, with single row spacing.

ACKNOWLEDGMENTS

This work was supported by School of Engineering from King Mongkut's Institute of Technology Ladkrabang. The authors would like to express their sincere gratitude to all individuals and institutions who supported this research in various ways.

REFERENCES

1. E. Jungermann, N.O. Sonntag, Glycerine: a key cosmetic ingredient, *CRC Press* 1991.
2. M. Ayoub, A.Z. Abdullah, Critical review on the current scenario and significance of crude glycerol resulting from biodiesel industry towards more sustainable renewable energy industry, *Renewable and Sustainable Energy Reviews* 2012; 16(5): 2671-2686.
3. D.R. Nisbet, K.E. Crompton, S.D. Hamilton, S. Shirakawa, R.J. Prankerd, D.I. Finkelstein, M.K. Horne, J.S. Forsythe, Morphology and gelation of thermosensitive xyloglucan hydrogels, *Biophysical Chemistry* 2006; 121(1): 14-20.

4. K. Nishinari, M. Takemasa, H. Zhang, R. Takahashi, 2.19—Storage plant Polysaccharides: Xyloglucans, Galactomannans, Glucomannans, *Comprehensive glycoscience* 2007; 613-652.
5. M. Shirakawa, K. Yamatoya, K. Nishinari, Tailoring of xyloglucan properties using an enzyme, *Food Hydrocolloids* 1998; 12(1): 25-28.
6. S. Yamanaka, Y. Yuguchi, H. Urakawa, K. Kajiwara, M. Shirakawa, K. Yamatoya, Gelation of tamarind seed polysaccharide xyloglucan in the presence of ethanol, *Food Hydrocolloids* 2000; 14(2): 125-128.
7. R.M. Marathe, U.S. Annapure, R.S. Singhal, P.R. Kulkarni, Gelling behaviour of polyose from tamarind kernel polysaccharide, *Food Hydrocolloids* 2002; 16(5): 423-426.
8. P. Goyal, V. Kumar, P. Sharma, Cyanoethylation of Tamarind Kernel Powder, *Starch - Stärke* 2008; 60(1): 41-47.
9. K. El-Siddig, Tamarind: Tamarindus Indica L, *Crops for the Future* 2006.
10. C.S. Kumar, S. and Bhattacharya, Tamarind Seed: Properties, Processing and Utilization, *Critical Reviews in Food Science and Nutrition* 2008; 48(1): 1-20.
11. S. Islam, M.A.R. Bhuiyan, M.N. Islam, Chitin and Chitosan: Structure, Properties and Applications in Biomedical Engineering, *Journal of Polymers and the Environment* 2017; 25(3): 854-866.
12. I. Aranaz, M. Mengibar, R. Harris, I. Paños, B. Miralles, N. Acosta, G. Galed, Á. Heras, Functional characterization of chitin and chitosan, *Current chemical biology* 2009; 3(2): 203-230.
13. P.K. Dutta, J. Dutta, V.S. Tripathi, Chitin and chitosan: Chemistry, properties and applications, *Journal of Scientific & Industrial Research* 2004; 63: 20-31.
14. M.N.V. Ravi Kumar, A review of chitin and chitosan applications, *Reactive and Functional Polymers* 2000; 46(1): 1-27.
15. H. Tan, C.R. Chu, K.A. Payne, K.G. Marra, Injectable in situ forming biodegradable chitosan–hyaluronic acid based hydrogels for cartilage tissue engineering, *Biomaterials* 2009; 30(13): 2499-2506.
16. F. Croisier, C. Jérôme, Chitosan-based biomaterials for tissue engineering, *European Polymer Journal* 2013; 49(4): 780-792.
17. Q. Tong, Q. Xiao, L.-T. Lim, Preparation and properties of pullulan–alginate–carboxymethylcellulose blend films, *Food Research International* 2008; 41(10): 1007-1014.
18. J.A. Piermaria, A. Pinotti, M.A. Garcia, A.G. Abraham, Films based on kefiran, an exopolysaccharide obtained from kefir grain: Development and characterization, *Food Hydrocolloids* 2009; 23(3): 684-690.
19. M. Ghasemlou, F. Khodaiyan, A. Oromiehie, Physical, mechanical, barrier, and thermal properties of polyol-plasticized biodegradable edible film made from kefiran, *Carbohydrate Polymers* 2011; 84(1): 477-483.
20. M.D. da Matta Jr., S.B.S. Sarmento, L.M. de Oliveira, S.S. Zocchi, Mechanical properties of pea starch films associated with xanthan gum and glycerol, *Starch - Stärke* 2011; 63(5): 274-282.
21. P. Adair, P. Sriprom, W. Narkrugsa, L. Phumjan, K. Manamoongmongkol, L. Permana, P. Assawasaengrat, Preparation, characterization, and antimicrobial activity of xyloglucan-chitosan film from tamarind (tamarind indica L.) seed kernel, *Progress in Organic Coatings* 2023; 179: 107486.
22. C.K. Simi, T.E. Abraham, Transparent xyloglucan–chitosan complex hydrogels for different applications, *Food Hydrocolloids* 2010; 24(1): 72-80.
23. C.K. Simi, T.E. Abraham, Physico chemical properties of aminated tamarind xyloglucan, *Colloids and Surfaces B: Biointerfaces* 2010; 81(2): 513-520.

Surface modification of activated carbon from tamarind shell for tartrazine adsorption

Tinutda Phonlam[1], Thanakorn Thammasarn[2], Pongsert Sriprom[2,*], Pornsawan Assawasaengrat[1]

[1] Department of Chemical Engineering, School of Engineering, King Mongkut's Institute of Technology Ladkrabang, Bangkok 10520, Thailand
[2] School of Food Industry, King Mongkut's Institute of Technology Ladkrabang, Bangkok 10520, Thailand
[*] Corresponding author: pongsert.sr@kmitl.ac.th

ABSTRACT

This study proposed the production of activated carbon from tamarind peel for the adsorption of tartrazine food dye. The activated carbon was prepared using a hydrothermal process at 110°C and chemically activated using three different methods: KOH (ATS1), H_2SO_4 (ATS2), and a combination of both (ATS3). The adsorption capacity of the activated carbon was evaluated based on iodine adsorption, where ATS2 exhibited the highest iodine adsorption, indicating a larger surface area. As a result, ATS2 was selected for further investigation in dye adsorption studies. The adsorption process was designed using the Box-Behnken Design and analyzed through Response Surface Methodology (RSM), considering four key factors: activated carbon dosage (g), pH, time (min), and rotation (rpm). The results showed that all factors significantly influenced the tartrazine removal efficiency (R^2 = 93.14). The optimal conditions for tartrazine removal were 2.0 g of activated carbon at pH 2, time of 160 minutes, and rotation of 200 rpm, achieving a removal efficiency of 60.30%. These findings highlight the potential of tamarind peel-derived activated carbon as an effective adsorbent, demonstrating its applicability in reducing water pollution from dye-containing industrial effluents.

Keywords: Tartrazine; Activated carbon; Adsorption; Iodine value

1. INTRODUCTION

Tamarind is an agricultural raw material composed of three main parts: the pulp, seed, and shell. Typically, only the pulp is utilized for cooking and various processing purposes, resulting in large amounts of discarded tamarind shells. Currently, tamarind shells have limited applications, with most being converted into activated carbon to add value [1].

Activated carbon is a highly porous material with a large surface area, giving it excellent adsorption properties. It is widely used in various applications, such as carbon dioxide capture, air filtration in air conditioning systems, pharmaceutical industries, and wastewater treatment [2]. However, traditional methods of producing activated carbon yield relatively low surface area, resulting in limited adsorption efficiency. This has led researchers to explore improved production techniques to enhance its performance.

Previous studies have demonstrated methods to increase the surface area and pore volume of activated carbon. For example, Adetola et al. (2015) used pyrolysis combined with carbon dioxide activation on date seed-derived activated carbon, achieving a surface area of 798 m^2/g and a pore volume of 0.21 cm^3/g [3]. Meanwhile, Akram Alabadi et al. (2015) employed hydrothermal synthesis using gelatin and pre-burned starch with potassium hydroxide as a precursor, producing activated carbon with an increased surface area of 1,957 m^2/g and a pore volume of 0.79 cm^3/g [4]. Furthermore, Kuan Huang et al. (2016) synthesized activated carbon from mesoporous carbon and sodium amide via a hydrothermal process, yielding an exceptionally high surface area of 3,180 m^2/g and a pore volume of 1.86 cm^3/g, making it the most efficient for adsorption applications [5].

In the food industry, tartrazine is a synthetic color additive (Food Additive) commonly used to enhance the visual appeal of products such as beverages, desserts, candies, and chewing gum [6]. However, approximately 10% to 15% of the dye is lost in the effluent during the dyeing process [7]. Tartrazine, an azo dye, is environmentally persistent and hazardous. When ingested, it can metabolize into aromatic amines, which are carcinogenic (Mohammed A. Kassem et al., 2014). Thus, effective treatment methods are necessary to remove tartrazine from wastewater before disposal or reuse [8].

Research by Mohammed A. Kassem et al. (2014) found that activated carbon blended with Belladonna could adsorb tartrazine at a concentration of 100 mg/L

with a maximum efficiency of 60% at 27°C, demonstrating its potential for tartrazine removal [8].

To address these issues, this study focuses on developing activated carbon from tamarind shells using hydrothermal synthesis to enhance tartrazine adsorption efficiency. The Response Surface Methodology (RSM) will be applied to optimize production conditions. This approach not only adds value to tamarind shells but also promotes the sustainable utilization of agricultural waste.

2. EXPERIMENTAL

2.1 Preparation of biochar

The separated tamarind shells (Phinpet company limited) are sun-dried to remove moisture, then pyrolysis carbonization in muffle furnace (Thermo scientific, thermolyne, USA) under N_2 atmosphere at 400°C for 2 hours. The heating rate was maintained at 10 °C/min. The resulting carbon was subjected to hydrothermal treatment with distilled water at 110 °C for 24 hours. After treatment, the carbon was washed with distilled water until a neutral pH (~7) was achieved. Finally, the material was dried and stored in a desiccator.

2.2 Preparation of activated carbon

2.2.1 Activation by KOH (ATS1)

The biochar was subjected to chemical activation using 0.1 M potassium hydroxide (KOH, AR grade, Merck KGaA, Germany) at a weight-to-volume ratio of 1:3 (w/v) for a duration of 3 hours. Following the activation process, the material was thoroughly washed with distilled water until a neutral pH (approximately 7) was attained. Carbonization was subsequently conducted via pyrolysis under a nitrogen (N_2) atmosphere at 500 °C for 1 hour, with a controlled heating rate of 10 °C/min.

2.2.2 Activation by H_2SO_4 (ATS2)

Biochar activation was performed using 0.5 M sulfuric acid (H_2SO_4, AR grade, RCI Labscan Limited, Thailand) at a weight-to-volume ratio of 1:3 (w/v) for 3 hours. After the acid treatment, the material was washed thoroughly with distilled water until the pH of the filtrate reached approximately 7. Subsequently, the tamarind shell was pyrolyzed under a nitrogen (N_2) atmosphere at 500 °C for 1 hour, employing a heating rate of 10 °C/min.

2.2.3 Hybrid activation of H_2SO_4 and KOH (ATS3)

Activated carbon was prepared through a two-step chemical activation process. Initially, biochar was treated with 0.5 M H_2SO_4 using a weight ratio of 1:3 (biochar to acid) and stirred for 3 hours. The material was then subjected to a second activation step using 0.1 M KOH at the same weight ratio of 1:3 (biochar to base), also for 3 hours. After each activation step, the material was thoroughly washed with deionized water until the pH of the filtrate reached neutral (pH ≈ 7). Subsequently, the pre-treated material was carbonized under a nitrogen (N_2) atmosphere at 500 °C for 1 hour, with a controlled heating rate of 10 °C/min.

2.3 Analysis by iodine adsorption technique

The activated carbon powders synthesized from tamarind shell, designated as ATS1, ATS2, and ATS3, were evaluated for their iodine adsorption capacity. Initially, a specific amount of the activated carbon powder was placed into a 250 mL Erlenmeyer flask, followed by the addition of 100 mL of iodine solution (Iodine, AR grade, Merck KGaA, Germany). The mixture was shaken (ZHWY-100B, ZHICHENG, China) for 30 seconds and subsequently filtered to separate the carbon powder from the solution. A 50 mL aliquot of the filtrate was then transferred to another Erlenmeyer flask and titrated with a standardized sodium thiosulfate solution ($Na_2S_2O_3$, AR grade, Merck KGaA, Germany). Titration was continued until the solution changed to a pale yellow color, and then further titrated until the solution became colorless. The volume of sodium thiosulfate solution used was recorded and employed to calculate the iodine adsorption value per gram of carbon, based on the standard equation. The sample exhibiting the highest iodine number was selected for further adsorption studies.

$$\frac{X}{M} = \frac{A-(DFxBxS)}{M} \quad (1)$$

Where X/M is the iodine adsorption value per weight (mg/g), M is the weight of biochar powder (g), A is N_2 x 12693.0, B is N_1 x 126.93, S is the volume of sodium thiosulfate solution ($Na_2S_2O_3.5H_2O$) (mL) and DF is the dilution factor.

2.4 Investigation of the optimal conditions for tartrazine adsorption

Statistical analysis of the experimental results was performed using Response Surface Methodology (RSM). The experimental design was based on the Box–Behnken Design (BBD), incorporating four independent variables: X_1 (activated carbon dosage, g), X_2 (pH), X_3 (contact time, min), and X_4 (rotation speed, rpm). Each variable was evaluated at three levels, as presented in Table 1.

Table 1 Factors and Experimental Levels for Response Surface Methodology (RSM) Analysis.

Factor	Code		Level	
		-1	0	1
AC Dosage (g)	X_1	0.50	1.25	2.00
pH	X_2	2	6.5	11
Time (min)	X_3	10	95	180
Rotate (rpm)	X_4	0	100	200

3. RESULTS AND DISCUSSION

3.1 Analysis of chemical composition of tamarind shell

Proximate analysis revealed that the tamarind shell contains a high proportion of fixed carbon, exhibiting a blackened appearance, with its detailed chemical composition listed in Table 2. The high fixed carbon content and low ash content of tamarind shells suggest their suitability for activated carbon production. This is because a high fixed carbon content enhances the purity and yield of the resulting activated carbon [2].

Table 2 Chemical composition of tamarind shell.

Component	Quantity (%)
Moisture	0.35
Ash	3.66
Volatile substances	3.37
Carbon	92.36

3.2 Determination of iodine number of activated carbon

The iodine numbers of the three activated carbon samples were determined to evaluate their suitability for tartrazine dye adsorption. A higher iodine number indicates a greater surface area and pore volume, which are critical for enhanced adsorption performance [10]. Among the three activated carbon samples ATS1 (KOH), ATS2 (H_2SO_4), and ATS3 (Hybrid) prepared using different activation methods, ATS2 exhibited the highest iodine number, indicating its superior adsorption potential. Consequently, ATS2 was selected for further evaluation of tartrazine dye adsorption efficiency. The corresponding adsorption data are presented in Table 3.

Table 3 Iodine number values of activated carbon samples.

Samples	Iodine number
ATS1	294.48
ATS2	365.56
ATS3	135.39

3.3 Investigation of optimal adsorption conditions for tartrazine dye

3.3.1 Statistical analysis results

The adsorption of tartrazine dye was investigated at an initial concentration of 20 mg/L using a Box-Behnken Design (BBD) [9] to optimize the adsorption conditions. Experimental results revealed a maximum tartrazine removal efficiency of 54.61%, achieved under the following optimal conditions: 2 g of activated carbon dosage, pH of 11, contact time of 95 min, and rotation speed of 100 rpm. The experimental data showed a high correlation coefficient (R^2 = 0.9314), confirming the model's reliability in predicting adsorption performance. These results demonstrate the effectiveness of the BBD approach for evaluating activated carbon's adsorption properties toward tartrazine. Detailed coefficient analysis is provided in Table 4.

Table 4 Regression coefficient analysis.

Term	Coef	SE Coef	T-Value	P-Value
Constant	36.30	1.37	26.41	0.000
AC Dosage	5.768	0.687	8.39	0.000
Time	5.037	0.687	7.33	0.000
pH	3.062	0.687	4.46	0.000
Rotate	4.872	0.687	7.09	0.000
AC Dosage* AC Dosage	-4.95	1.03	-4.80	0.000
Time* Time	-5.66	1.03	-5.49	0.000
pH* pH	10.63	1.03	10.31	0.000
Rotate*Rotate	-5.06	1.03	-4.91	0.000
AC Dosage*Time	-1.93	1.19	-1.62	0.114
AC Dosage*pH	-4.82	1.19	-4.05	0.000
AC Dosage*Rotate	0.64	1.19	0.54	0.592
Time*pH	-2.05	1.19	-1.72	0.093
Time*Rotate	3.38	1.19	2.84	0.007
pH*Rotate	-7.12	1.19	-5.98	0.000

3.3.2 The optimal factor

The Pareto chart analysis (Figure 1) of standardized effects revealed that several factors significantly influenced tartrazine removal efficiency ($p < 0.05$, reference t-value = 2.02). The statistically significant terms included four main effects: (A) adsorbent dosage, (B) contact time, (C) solution pH, and (D) rotation speed; four quadratic effects: (A^2) activated carbon dosage, (B^2) contact time, (C^2) pH, and (D^2) rotation speed; along with two interaction effects: (A*C) activated carbon dosage on pH and (B*C) contact time on rotation speed. All significant terms were retained in the final regression model as they exceeded the critical threshold value, indicating their substantial impact on the adsorption process optimization.

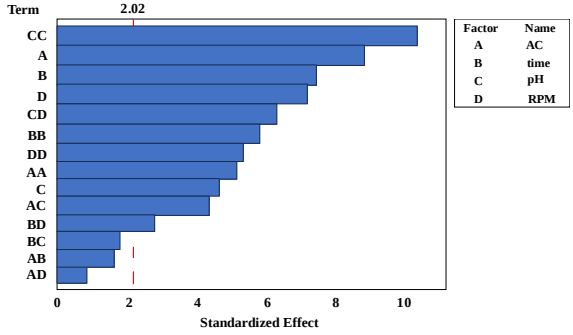

Figure 1 Pareto chart of influence of each factor.

3.3.3 Effect of main factors on tartrazine adsorption

Figure 2 demonstrates that increasing the activated carbon dosage, contact time, pH, and rotation speed enhances tartrazine adsorption efficiency. This improvement can be attributed to several factors: (1) higher adsorbent dosage provides greater active sites for adsorption, (2) prolonged contact time allows more complete interaction between adsorbent and dye molecules, (3) elevated pH (acid or alkaline conditions) promotes H^+ and OH^- ion generation, which enhances dye solubility and modifies adsorption characteristics, and (4) increased rotation speed improves mass transfer by enhancing contact between the adsorbent and target molecules. These synergistic effects collectively optimize the adsorption process. Furthermore, the combined effects of activated carbon dosage (2 g) and pH (2), along with increased rotation speed, demonstrated enhanced tartrazine adsorption efficiency, as illustrated in Figure 3.

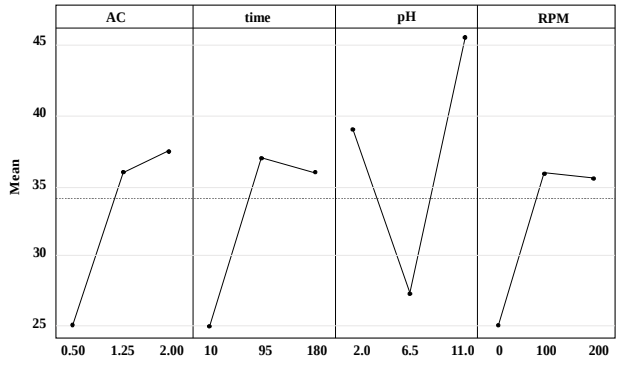

Figure 2 The effect of four main factors on the adsorption efficiency of tartrazine dye.

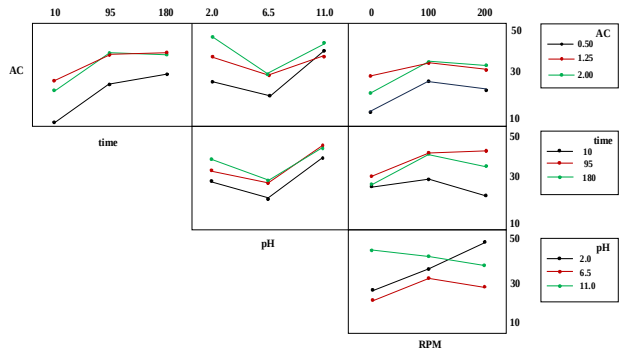

Figure 3 The graph shows the combined impact of four main factors.

3.3.4 Optimum conditions for tartrazine adsorption

Figure 4 presents the optimized conditions for tartrazine removal, which were determined to be: 2 g of activated carbon, 160 min contact time, solution pH of 2, and rotation speed of 200 rpm. Under these conditions, the predicted tartrazine removal efficiency was 60.30%, with a 95% confidence interval ranging from 53.86% to 66.75%. Experimental validation through triplicate testing (Table 5) yielded removal percentages that closely matched the predicted values, all falling within the 95% confidence interval. This agreement between predicted and experimental results confirms the reliability of the optimization model.

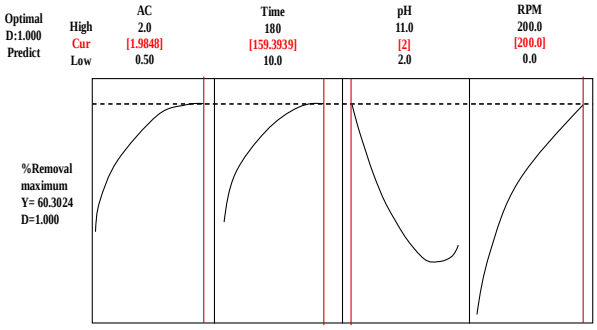

Figure 4 Optimal conditions for tartrazine adsorption process.

Table 5 Verification of optimum conditions in tartrazine adsorption process.

Repeat	**1**	**2**	**3**
Removal (%)	62.68	63.63	66.14

4. CONCLUSION

Activated carbon was synthesized from tamarind shells through hydrothermal treatment followed by chemical activation using sulfuric acid (H_2SO_4), a method known to yield high surface area and pore volume confirm with iodine number. The optimization of tartrazine adsorption was investigated using a Box-Behnken Design (BBD) considering four key parameters: (1) activated carbon dosage (g), (2) contact time (min), (3) solution pH, and (4) rotation speed (rpm). The model predicted optimal conditions of 2 g activated carbon, 160 min contact time, pH 2, and 200 rpm rotation speed (100 mL solution volume), achieving 60.30% tartrazine removal. Statistical analysis confirmed that all four parameters significantly influenced the decolorization efficiency, demonstrating their importance in the adsorption process.

ACKNOWLEDGMENTS

This work was supported by School of Engineering, King Mongkut's Institute of Technology Ladkrabang.

REFERENCES

1. V. Thirumal, K. Dhamodharan, R. Yuvakkumar, G. Ravi, B. Saravanakumar, M. Thambidurai, C. Dang, & D. Velauthapillai. Cleaner production of tamarind fruit shell into bio-mass derived porous 3D-activated carbon nanosheets by CVD technique for supercapacitor applications. *Chemosphere* 2021; 282: 131033.

2. T. Phonlam, B. Weerasuk, P. Sataman, T. Duangmanee, S. Thongphanit, K. Nilgumhang, S. Anantachaisilp, T. Chutimasakul, T. Kwamman, & V. Chobpattana. Ammonia modification of activated carbon derived from biomass via gamma irradiation vs. hydrothermal method for methylene blue removal. *South African Journal of Chemical Engineering* 2023; 43: 67-78.
3. A. E. Ogungbenro, D. V. Quang, K. A. Al-Ali, L. F. Vega, & M. R. M. Abu-Zahra. Physical synthesis and characterization of activated carbon from date seeds for CO2 capture. *Journal of Environmental Chemical Engineering* 2018; 6(4): 4245-4252.
4 A. Alabadi, S. Razzaque, Y. Yang, S. Chen, & B. Tan. Highly porous activated carbon materials from carbonized biomass with high CO_2 capturing capacity. *Chemical Engineering Journal* 2015; 281: 606-612.
5 K. Huang, S.-H. Chai, R. T. Mayes, S. Tan, C. Jones, W., & S. Dai. Significantly increasing porosity of mesoporous carbon by $NaNH_2$ activation for enhanced CO_2 adsorption. *Microporous and Mesoporous Materials* 2016; 230: 100-108.
6 P. Amchova, F. Siska, & J. Ruda-Kucerova. Safety of tartrazine in the food industry and potential protective factors. *Heliyon* 2024; 10(18): e38111.
7 V. K. Gupta, R. Jain, A. Nayak, S. Agarwal, & M. Shrivastava. Removal of the hazardous dye-Tartrazine by photodegradation on titanium dioxide surface. *Materials Science and Engineering: C* 2011; 31(5): 1062-1067.
8 A. Mohammed Kassem and O. Gamal El-Sayed. Adsorption of Tartrazine on Medical Activated Charcoal Tablets under Controlled Conditions. *Journal of Environmental Analytical Chemistry* 2014; 1: 102.
9 M. Assassi, F. Madjene, S. Harchouche, & H. Boulfiza. Modeling and optimization of the photocatalytic degradation of Tartrazine in aqueous solution. *Acta Periodica Technologica* 2021; 52: 133-145.

Biocompatibility of hydrogel film blended jellyfish gelatin

Nongnapas Luecha[1], Sukanya Tastub[2], Pollawat Charoeythornkhajhornchai[3], Santi Phosri[1,*]

[1] Department of Chemical Engineering, Faculty of Engineering, Burapha University, Chonburi 20131, Thailand
[2] Synchrotron Light Research Institute, Nakhon Ratchasima 30000, Thailand
[3] Department of Chemical Engineering, Faculty of Engineering, Srinakharinwirot University, Nakhonnayok 26120, Thailand
[*] Corresponding author: santi.ph@eng.buu.ac.th

ABSTRACT

This study investigates the biocompatibility and functional properties of hydrogel films combining jellyfish-derived gelatin, with the aim of evaluating their potential for biomedical applications, particularly as wound dressing materials. Thermal characterization using differential scanning calorimetry (DSC) revealed that the films exhibited good thermal stability, with melting transitions observed between 150–200 °C. Wettability analysis demonstrated enhanced hydrophilicity, as indicated by a significant decrease in contact angle upon the addition of jellyfish gelatin. Biocompatibility was assessed through in vitro cultivation with Vero, 3T3-L1, and HaCaT cell lines. The results confirmed that the films were non-toxic and supported cell viability, indicating their compatibility with mammalian cells. These findings suggest that jellyfish gelatin-based hydrogel films offer promising potential for biomedical applications such as wound healing and tissue engineering.

Keywords: Hydrogel Film; Carboxymethyl cellulose; Jellyfish Gelatin; Biocompatibility

1. INTRODUCTION

The skin is a vital organ composed of a complex tissue structure that serves as the body's primary barrier against external threats, including harmful chemicals, radiation, and pathogens. Beyond its protective function, the skin plays a crucial role in maintaining physiological homeostasis by regulating body temperature, preventing fluid loss, and supporting immune defense. As the largest organ in the human body, the skin is constantly exposed to environmental factors, making it highly susceptible to damage. Skin injuries such as cuts, burns, pressure ulcers, diabetic wounds, and lesions resulting from chronic diseases can compromise its structural integrity. These wounds may lead to significant pain, disability, or even mortality, thereby negatively impacting patients' quality of life and imposing a considerable economic burden on global healthcare systems [1-3].

Therefore, effective wound treatment is essential. Biomaterials are natural substances with outstanding physical, chemical and biological properties, making them interesting options for the creation of various medical devices, especially wound care [2]. To prevent wounds from infection and re-injury, traditional wound dressings such as gauze may adhere to the regenerating tissue and cause pain, as well as lack antibacterial and wound healing properties [4]. A good wound dressing should have properties to prevent infection, maintain proper moisture and promote new tissue formation. Hydrogels are materials that have gained much attention. Due to its high-water absorption capacity, flexibility and biocompatibility [5].

Carboxymethyl cellulose (CMC) is a very popular wound dressing material due to its outstanding properties such as biocompatibility, non-toxicity, low cost, biodegradability, and the presence of many carboxymethyl functional groups in its structure. It is a chemically crosslink able biopolymer [6], has good water retention, is tissue-like, and does not interfere with the tissue regeneration process, and is easily crosslinked with other materials. Therefore, CMC has been used in various forms such as hydrogels or scaffolds and can be effectively blended with other polymers to create innovative wound dressings. Polyvinyl alcohol (PVA) is a water-soluble polymer that is biocompatible, absorbs water well, and has strong mechanical properties. When blended with CMC and PVA, it increases the water absorption capacity and has natural skin-like properties, maintaining the moisture balance necessary for good wound healing [5,7].

However, further improvement in enhancing the bioactivity of hydrogels to stimulate tissue regeneration is still a matter of great importance. Biomaterials such as gelatin, a natural biopolymer derived from the

hydrolysis of collagen [8], have been used to enhance cell adhesion and promote cell growth [9]. Jellyfish gelatin has attracted much attention as a potential biocompatible and biodegradable natural protein source [10]. Jellyfish biocomponents such as collagen and polysaccharides play an important role in wound healing by stimulating tissue regeneration, reducing inflammation and exhibiting antioxidant activity, which are beneficial for the wound healing process [11].

Therefore, this study aimed to develop and evaluate the biocompatibility of CMC and PVA hydrogel films reinforced with jellyfish gelatin, focusing on their biocompatibility and potential application as high-performance, environmentally friendly, and effective skin regeneration-promoting wound dressings, to meet the demand for sustainable wound dressings with potential medical applications in the future.

2. EXPERIMENTAL

2.1 Preparation of jellyfish gelatin

The extraction of gelatin from salted jellyfish by-products was performed according to the method modified from Charoenchokpanich et al. [12,13] with the following details: The salted jellyfish by-products were washed with tap water to remove salt and impurities. The samples were immersed in 0.05 M 1:3 (w/v) sodium hydroxide (NaOH) solution at 4°C for 1 h. The alkali-treated samples were washed several times with tap water until the pH was neutral (pH 6.5–7.0). The samples were immersed in 0.2 M 1:2 (w/v) hydrochloric acid (HCl) solution at 25°C for 2 h. The acid-treated samples were washed several times with tap water until the pH was neutral. The samples were then extracted with 1:2 (w/v) distilled water at 60°C for 12 h. The resulting gelatin solution was filtered through Whatman No. 4 filter paper to separate the jellyfish flesh. The gelatin solution was then dried in a freeze dryer and the obtained jellyfish gelatin was stored in aluminum foil bags at 4°C until use.

2.2 Preparation of hydrogel film

A 3% (w/v) CMC solution and a 6% (w/v) PVA solution were prepared by mixing them thoroughly. The solution was then heated at 80 °C for 2 h under continuous stirring to obtain a homogeneous solution. After that, 2% (w/v) citric acid was added to the solution to act as a crosslinker and 5% glycerol was added as a plasticizer. The resulting solution was separated into 3 formulas: a solution without jellyfish gelatin (Film), a solution with 1% jellyfish gelatin (Film + Gelatin2), and a solution with 0.5% jellyfish gelatin (Film + Gelatin3). The prepared solution was then poured onto a 25 mL glass plate and dried at 40°C for 3 days to obtain a complete hydrogel film ready for further testing and use.

2.3 Characterization

2.3.1. Differential Scanning Calorimeter (DSC)

The thermal properties of the hydrogel films were studied using the Differential Scanning Calorimetry (DSC) analysis technique using a DSC (DSC 5+, Mettler Toledo, Switzerland). The tested samples consisted of three formulas of hydrogel films: blank film, film containing gelatin type 2 (1%), and film containing gelatin type 3 (0.5%). The samples were cut into small pieces weighing between 3.5–3.9 mg and packed in sealed aluminum pans, using the blank pan as a reference pan. The analysis was carried out under nitrogen atmosphere with a flow rate of 30 mL/min, increasing the temperature from 30 °C to 300 °C at a constant speed of 10°C/min. The heat change data were recorded to evaluate the heat absorption or exothermic values, which reflect the thermal behavior, melting point, and decomposition of the material.

2.3.2 Contact angle

Contact angle was measured by dropping 5 µL of pure distilled water onto the surface of three hydrogel film formulas: blank film, film containing gelatin type 2 (1%) and film containing gelatin type 3 (0.5%). The images of the water droplets were then recorded to analyze the contact angle between the film surface and the edge of the formed water droplets. The obtained contact angle values were used as a representative of the hydrophilicity of the film surface.

2.4 Biocompatibility

2.4.1. Cell viability assay

The cytotoxicity of the hydrogel film was evaluated on African green monkey epithelial cells (Vero), mouse embryonic fibroblasts (3T3-L1), and human keratinocytes (HaCaT) using the MTT assay. Briefly, hydrogel films were sterilized by UV irradiation for 30 minutes. Following sterilization, Dulbecco's Modified Eagle Medium (DMEM) was added to the films, and the samples were incubated at 37 °C in a CO_2 incubator for 24 hours to prepare the extract media. Cells were seeded in 96-well plates at a density of 1×10^4 cells/well and incubated at 37 °C with 5% CO_2 for 24 hours. After incubation, cells were treated with hydrogel extract media at concentrations of 125, 250, 500, and 1,000 µg/mL, and incubated under the same conditions for an additional 24 hours. Following treatment, the media was removed and replaced with MTT solution (0.5 mg/mL in DMEM) for 1 hour. Then, the MTT solution was removed, and 150 µL of 100% DMSO was added to each well to dissolve the formazan crystals. Absorbance was measured at 570 nm using a microplate reader (EnSight, PerkinElmer, USA). Cell viability was calculated and expressed as a percentage relative to the untreated control group, which was defined as 100%.

3. RESULTS AND DISCUSSION

3.1 Physical characteristics of hydrogel films

From the film samples, it was found that the obtained hydrogel films had the characteristics of soft sheets. The blank film was clear, translucent, and had a smooth and uniform surface, indicating good compatibility between CMC and PVA. Meanwhile, the film containing gelatin type 2 (1%) had a light-yellow color and slightly increased turbidity. The film containing gelatin type 3 (0.5%) had similar characteristics to the blank film in terms of both transparency and surface smoothness, reflecting the better gelatin dispersion when used at a lower amount (Figure 1).

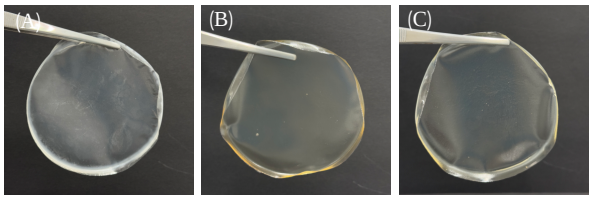

Figure 1 Physical characteristics of hydrogel films: (A) film, (B) film + gelatin2 (1%), and (C) film + gelatin3 (0.5%).

3.2 Differential Scanning Calorimeter (DSC)

The DSC analysis results showed endothermic thermograms of the three film formulations: blank film, film containing gelatin type 2 (1%), and film containing gelatin type 3 (0.5%), with each line representing the thermal behavior of different film formulations (Figure 2).

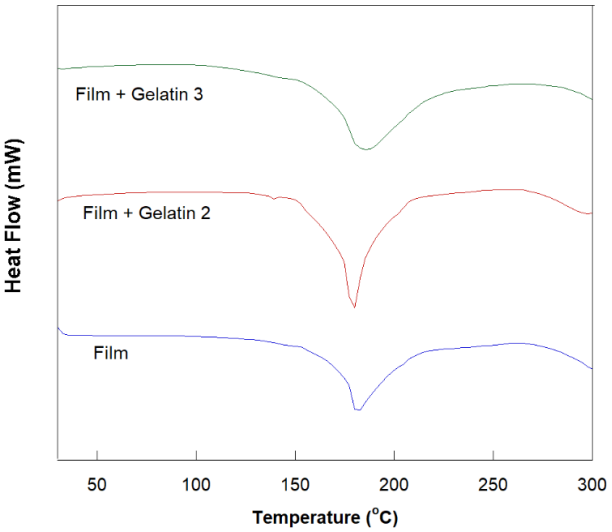

Figure 2 DSC thermograms of the hydrogel films: film, film+gelatin2 (1%), and film+gelatin3 (0.5%).

From the test results, the blank film showed a clear endothermic peak at ~170– 190°C, which was consistent with the melting point of PVA, indicating that the polymer structure maintained high crystallinity. The film containing gelatin type 2 (1%) showed a broader endothermic peak, and the position of the peak shifted slightly from the blank film formula, most clearly at around 180– 210°C, indicating the energy used in melting the polymer structure. The temperature trend was slightly lower than the blank film, and the peak size was clearly deeper, indicating the disruption of the polymer crystal structure by gelatin, which resulted in an increased amorphous internal structure. The film containing gelatin type 3 (0.5%) showed an endothermic peak similar to the film containing gelatin type 2 (1%), but the peak was smaller and the temperature shifted slightly lower than that of the blank film and the film containing gelatin type 2 (1%), indicating that the addition of low amount of gelatin may not be sufficient to significantly change the polymer structure.

3.3 Contact angle

The contact angle measurement results showed that the addition of jellyfish gelatin to the hydrogel film resulted in a significant decrease in the contact angle, indicating that the film had an increased hydrophilicity. The film containing gelatin type 2 (1%), with 1% jellyfish gelatin added, had the lowest contact angle of 36.076°, indicating the best water wettability. The film containing gelatin type 3 (0.5%), with 0.5% jellyfish gelatin added, had a contact angle of 39.054°. Jellyfish gelatin contains polar functional groups such as -OH, -NH_2, and -COOH, which can form hydrogen bonds with water molecules, resulting in higher surface energy and better water adhesion. When compared to the control formula without gelatin, the contact angle was 55. 338°, indicating that the addition of gelatin significantly increased the wettability. In addition, when comparing the formulas containing 0.5% and 1% gelatin, the contact angle tended to decrease with increasing gelatin content, indicating that the concentration of gelatin affects the surface properties of the film. However, the differences between formulations 2 and 3 were not significant, possibly due to saturation of the water-reactive functional groups or limitations in the distribution of gelatin in the film matrix (Figure 3).

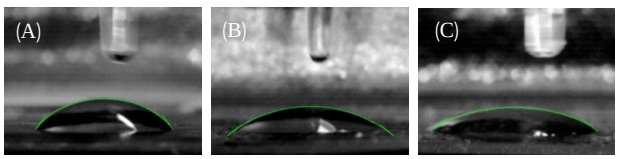

Figure 3 Contact angle measurements of hydrogel films: (A) film, (B) film + gelatin2 (1%), and (C) film + gelatin3 (0.5%).

3.4 Biocompatibility

The effect of hydrogel films on Vero cell viability was evaluated at concentrations of 125, 250, 500, and 1,000 µg/mL. The control film (blank film) showed cell

viability values of 102.81%, 98.67%, 98.28%, and 93.41%, respectively. The film incorporated with Jellyfish Gelatin 2 showed viability values of 98.09%, 95.37%, 95.67%, and 88.23%, respectively. In contrast, the film incorporated with Jellyfish Gelatin 3 demonstrated cell viability values of 105.26%, 109.52%, 110.03%, and 105.66%, respectively compared to the untreated control group, all treatments maintained cell viability above 80%. These results indicate that neither the control film and the films containing jellyfish gelatin 2 or 3 exhibited no cytotoxic effects on Vero kidney epithelial cells (Figure 4).

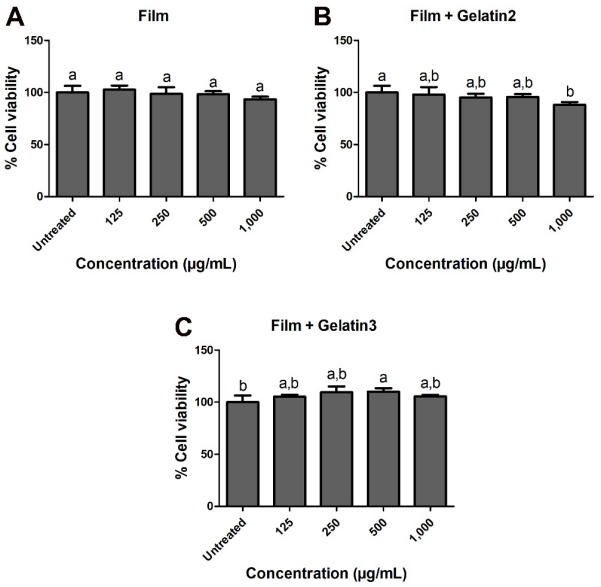

Figure 4 Cell viability of Vero cells following treatment with hydrogel films: (A) Film, (B) Film + Gelatin2 (1%), and (C) Film + Gelatin3 (0.5%). Data are presented as means ± standard deviation (S.D.) from triplicate determinations. Bars labeled with different letters indicate statistically significant differences ($p < 0.05$).

The biocompatibility test of hydrogel films at concentrations of 125, 250, 500, and 1,000 µg/mL on 3T3-L1 cells showed that the blank film had cell viability of 94.71%, 92.34%, 92.01%, and 85.03%, respectively. In comparison, films containing gelatin type 2 (1%) exhibited cell viability ranging from 97.44% to 96.25%, while those containing gelatin type 3 (0.5%) showed viability between 99.58% and 98.75%. These results indicate that all types of hydrogel films are biocompatible with 3T3-L1 cells, as they did not reduce cell viability below 80% compared to the untreated control group (Figure 5).

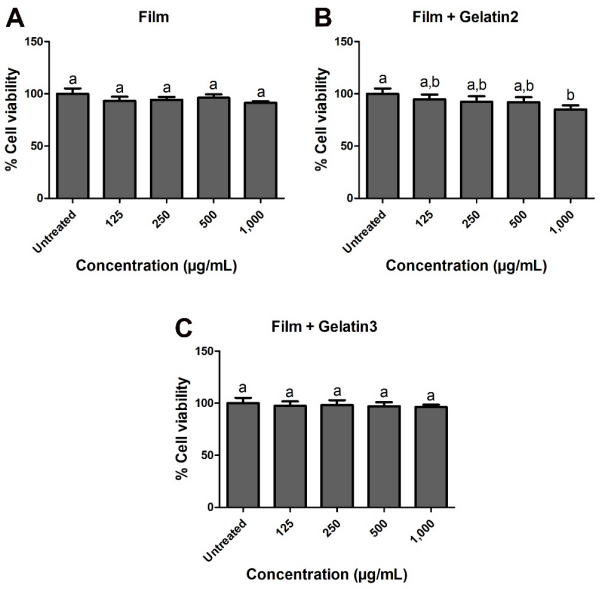

Figure 5 Cell viability of 3T3-L1 cells following treatment with hydrogel films: (A) Film, (B) Film + Gelatin2 (1%), and (C) Film + Gelatin3 (0.5%). Data are presented as means ± standard deviation (S.D.) from triplicate determinations. Bars labeled with different letters indicate statistically significant differences ($p < 0.05$).

Cell viability tests of hydrogel films at concentrations of 125, 250, 500, and 1,000 µg/mL on HaCaT cells revealed that the blank control film maintained cell viability between 96.98% and 105.37%. Films incorporating jellyfish-derived gelatin type 2 (1%) showed viability ranging from 102.49% to 82.75%, while those with gelatin type 3 (0.5%) demonstrated values of 102.81%, 98.67%, 98.28%, and 93.41%, respectively. These findings confirm that all tested films, including the blank control and those containing gelatin types 2 (1%) and 3 (0.5%), did not reduce cell viability below 80%, indicating no cytotoxic effects and demonstrating good (Figure 6).

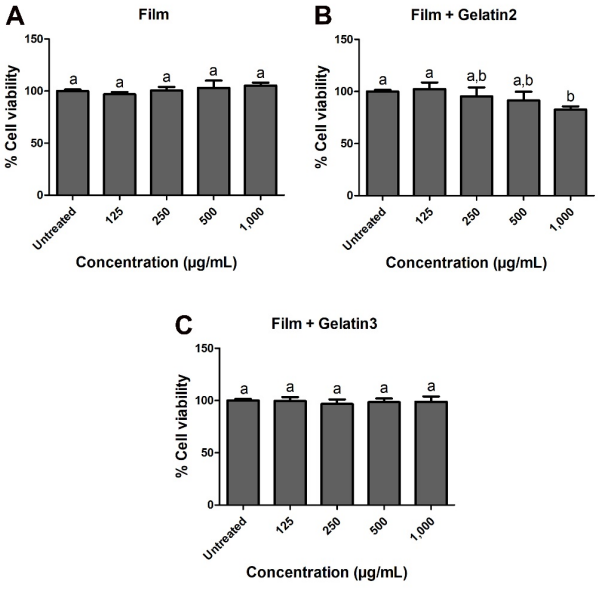

Figure 6 Cell viability of HaCaT cells following treatment with hydrogel films: (A) Film, (B) Film + Gelatin2 (1%), and (C) Film + Gelatin3 (0.5%). Data are presented as means ± standard deviation (S.D.) from triplicate determinations. Bars labeled with different letters indicate statistically significant differences ($p < 0.05$).

4. CONCLUSION

This study explored the biocompatibility of hydrogel films blended with jellyfish gelatin. Thermal analysis using DSC revealed that the combination of jellyfish gelatin influenced the thermal behavior and internal structure of the material, indicating favorable thermal stability. Furthermore, the addition of jellyfish gelatin significantly enhanced the hydrophilicity of the hydrogel films, a key characteristic for biomedical applications such as wound dressings, where a hydrophilic surface supports improved cell adhesion and growth. Biocompatibility tests confirmed that the films were non-toxic and supported the viability of mammalian cells. Overall, these findings demonstrate that jellyfish gelatin-based hydrogel films hold strong potential for applications in wound healing and tissue engineering.

ACKNOWLEDGMENTS

The authors would like to express their sincere gratitude to the Faculty of Engineering, Burapha University, Thailand, for supporting this research under the Project for Promoting and Enhancing the Quality of Graduate Education for the Development of Sustainable Research Assistants (Sc.7/2565).

REFERENCES

1. Mansur, A. A. P., Rodrigues, M. A., Capanema, N. S. V., Carvalho, S. M., Gomes, D. A., & Mansur, H. S. (2023). Functionalized bioadhesion-enhanced carboxymethyl cellulose/polyvinyl alcohol hybrid hydrogels for chronic wound dressing applications. RSC advances, 13(19), 13156-13168.
2. Echavarría, J. O., Vanegas, N. A. G., & Orozco, C. P. O. (2022). Chitosan/carboxymethyl cellulose wound dressings supplemented with biologically synthesized silver nanoparticles from the ligninolytic fungus Anamorphous Bjerkandera sp. R1. Heliyon, 8(9).
3. Capanema, N. S. V., Mansur, A. A. P., Carvalho, I. C., Carvalho, S. M., & Mansur, H. S. (2023). Bioengineered water-responsive carboxymethyl cellulose/poly (vinyl alcohol) hydrogel hybrids for wound dressing and skin tissue engineering applications. Gels, 9(2), 166.
4. Su, J., Li, J., Liang, J., Zhang, K., & Li, J. (2021). Hydrogel preparation methods and biomaterials for wound dressing. Life, 11(10), 1016.
5. Mariello, M., Binetti, E., Todaro, M. T., Qualtieri, A., Brunetti, V., Siciliano, P., ... & Blasi, L. (2024). Eco-Friendly Production of Polyvinyl Alcohol/Carboxymethyl Cellulose Wound Healing Dressing Containing Sericin. Gels, 10(6), 412.
6. De Lima, G. F., de Souza, A. G., & Rosa, D. D. S. (2020, December). Nanocellulose as reinforcement in carboxymethylcellulose superabsorbent nanocomposite hydrogels. In Macromolecular Symposia (Vol. 394, No. 1, p. 2000126).
7. Kanikireddy, V., Varaprasad, K., Jayaramudu, T., Karthikeyan, C., & Sadiku, R. (2020). Carboxymethyl cellulose-based materials for infection control and wound healing: A review. International Journal of Biological Macromolecules, 164, 963-975.
8. Cao, H., Wang, J., Hao, Z., & Zhao, D. (2024). Gelatin-based biomaterials and gelatin as an additive for chronic wound repair. Frontiers in Pharmacology, 15, 1398939.
9. Lukin, I., Erezuma, I., Maeso, L., Zarate, J., Desimone, M. F., Al-Tel, T. H., … & Orive, G. (2022). Progress in gelatin as biomaterial for tissue engineering. Pharmaceutics, 14(6), 1177.
10. Charoenchokpanich, W., Muangrod, P., Roytrakul, S., Rungsardthong, V., Wonganu, B., Charoenlappanit, S., . . . & Thumthanaruk, B. (2024). Exploring the model of cefazolin released from jellyfish gelatin-based hydrogels as affected by glutaraldehyde. Gels, 10(4), 271.
11. Cadar, E., Pesterau, A. M., Sirbu, R., Negreanu-Pirjol, B. S., & Tomescu, C. L. (2023). Jellyfishes— significant marine resources with potential in the wound-healing process: a review. Marine Drugs, 21(4), 201.
12. Charoenchokpanich, W., Muangrod, P., Rungsardthong, V., Vatanyoopaisarn, S., Wonganu, B., Roytrakul, S., & Thumthanaruk, B. (2021). Effect of hydrochloric acid extraction on yield and gel properties of gelatine from salted jellyfish by-products. In E3S Web of Conferences (Vol. 302, p. 02009). EDP Sciences.
13. Charoenchokpanich, W., Muangrod, P., Roytrakul, S., Rungsardthong, V., Vatanyoopaisarn, S., Wonganu, B., & Thumthanaruk, B. (2022). Influence of extraction times on physical and functional properties of gelatin from salted jellyfish by-products. In E3S Web of Conferences (Vol. 355, p. 02014). EDP Sciences.

Utilization of lignin from agricultural waste for enhancing performance of natural rubber composite

Phatcharin Porat[1], Kanisorn Leelasopin[1], Asawin Pratumbud[1], Yeampon Nakaramontri [2], Kiattinatapon Juengchareonpoon[1], Piyabutr Wanichpongpan[1,*]

[1] Department of Chemical Engineering, Faculty of Engineering, King Mongkut's University of Technology Thonburi, Bangkok 10140, Thailand
[2] Sustainable Polymer & Innovative Composite Materials Research Group, Department of Chemistry, Faculty of Science, King Mongkut's University of Technology Thonburi, Bangkok 10140, Thailand
[*] Corresponding author: piyabutr.wan@kmutt.ac.th

ABSTRACT

The growing demand for sustainable materials has driven research into utilizing lignin, a natural polymer derived from agricultural waste, as a reinforcing filler in natural rubber composites. This study investigates lignin extraction from sugarcane bagasse using an alkaline process with varying sodium hydroxide concentrations (10–40% w/v) to optimize yield and purity. The extracted lignin was characterized by Fourier Transform Infrared Spectroscopy (FTIR), confirming the presence of functional groups such as O–H, C=O, and C–H, consistent with commercial lignin. Thermogravimetric Analysis (TGA) was employed to evaluate thermal stability, revealing three main degradation stages: moisture evaporation, structural breakdown, and residual decomposition. Mechanical properties of the lignin-filled natural rubber composites were evaluated through tensile testing following ISO 37. The results were compared with those of rubber composites containing a conventional antioxidant. The findings indicate that lignin derived from sugarcane bagasse can enhance the tensile strength of rubber to a level comparable with conventional antioxidants, highlighting its potential as an eco-friendly reinforcing filler.

Keywords: Lignin; Natural Rubber Composites; Sugarcane Bagasse; Sustainable Materials

1. INTRODUCTION

Thailand's agricultural industry generates a significant amount of biomass waste, particularly sugarcane bagasse approximately 36 million metric tons annually. This fibrous byproduct is one of the most abundant lignocellulosic wastes with cellulose, hemicellulose, and lignin. Lignin constitutes 15–30% of bagasse by weight and is a complex aromatic polymer featuring functional groups such as phenolic and hydroxyl. These groups provide antioxidant capabilities, allowing lignin to neutralize free radicals and stabilize reactive oxygen species (ROS), establishing it as a viable natural antioxidant for sustainable material applications, especially as a substitute for synthetic antioxidants in rubber production [1].

Currently, synthetic antioxidants such as N-(1,3-dimethylbutyl)-N′-phenyl-p-phenylenediamine (6PPD) and Wingstay L are commonly used in rubber products to inhibit oxidative and ozone degradation. However, environmental and health concerns have emerged due to the transformation of 6PPD into 6PPD-quinone, which is a compound toxic to aquatic life. Wingstay L also been associated with potential skin irritation and environmental persistence. These issues have prompted interest in lignin as a safer, eco-friendly alternative [2]. This study aims to extract lignin from sugarcane bagasse using sodium hydroxide at varying concentrations (10%, 20%, 30% and 40% w/v) and to evaluate its potential as a natural antioxidant for application in lignin-reinforced natural rubber composites, with a focus on sustainable sports flooring materials.

2. EXPERIMENTAL

2.1 Lignin Preparation

Lignin extraction from sugarcane bagasse involves multiple steps to obtain a purified product. Initially, fresh bagasse was washed and sun-dried for 24 hours, cut into 1×1 cm pieces, and ground using a centrifugal mill. Next, the bagasse powder was oven-dried at 60°C for 24 hours until reaching a constant weight. Then, 20 grams of bagasse was immersed in 200 mL of 40% sodium hydroxide (NaOH) and 50% ethanol solution (1:1 ratio). The mixture was shaken in a water bath shaker at 90°C and 100 rpm for 4 hours, then cooled naturally to room temperature. After treatment, the lignin solution was separated from the solid fraction

using vacuum filtration. Ethanol was eliminated via rotary evaporation at 40°C. The solution's pH was adjusted to 1.0 with concentrated sulfuric acid (H_2SO_4), inducing lignin precipitation. The precipitate was collected through centrifugation at 3000 rpm for 15 minutes at 25°C, then washed with 0.1 M hydrochloric acid (HCl) until reaching pH 2, and then washed with deionized water twice. Finally, lignin was dried for analysis, with excess moisture removed by centrifugation. It is oven-dried at 65°C for 48 hours to ensure complete dehydration. The dried lignin is then weighed to determine yield and prepared for further characterization.

2.2 Lignin Characterization.

2.2.1. Fourier Transform Infrared Spectroscopy (FTIR) analysis was conducted using an IRTracer-100 (Shimadzu) equipped with the potassium bromide (KBr) technique. This qualitative assessment was utilized to identify the functional groups and chemical composition of lignin. The spectral data were recorded within the range of 4000–400 cm^{-1}, with each sample undergoing 45 scans to ensure detailed characterization.

2.2.2 Thermogravimetric analysis (TGA) was performed using a METTLER TOLEDO TGA/DSC3+ system. The initial temperature was set at 30°C and gradually increased to a maximum of 900°C at a heating rate of 10°C per minute.

2.2.3 Scanning electron microscopy (SEM) was used to examine the morphological features of lignin, utilizing a gold coating to enhance conductivity and image clarity. The analysis was performed at an accelerating voltage of 10 kV under vacuum conditions, allowing for detailed observation of particle size, aggregation, and surface texture.

2.3 Latex Preparation with Lignin

2.3.1 Lignin was treated by using an ultrasonic probe operating at a frequency of 20 kHz. The sonication process was conducted with alternating cycles of 6 seconds of sonication followed by a 4-second pause, repeated continuously for a total duration of 1 hour.

2.3.2 Latex Rubber was prepared by blending natural rubber latex with varying amounts of lignin, as summarized in Table 1. The lignin content ranged from 1 to 10 parts per hundred rubber (phr). A control sample containing only pure latex (without lignin) was also prepared for comparison purposes.

Table 1 Composition of Latex-Lignin Blends.

Sample	Latex/Lignin (phr)
Control Latex	100/0
Latex Lignin 1 phr	100/1
Latex Lignin 3 phr	100/3
Latex Lignin 5 phr	100/5
Latex Lignin 10 phr	100/10

A fixed formulation of additional compounding agents was used across all samples, consisting of zinc oxide (ZnO) at 5.0 phr, stearic acid (SA) at 1.0 phr, sulfur at 1.0 phr, mercaptobenzothiazole disulfide (MBTS) at 2.5 phr, and calcium carbonate ($CaCO_3$) at 40 phr.

The latex-lignin mixtures were poured into molds and pre-cured in an oven for 24 hours. Following the curing stage, the samples underwent melt mixing using a two-roll mill. The mixing process began with rubber mastication for 2 minutes, after which the additives were incorporated sequentially at 1-minute intervals until all components were fully blended. The resulting compounds were then molded by compression at 160 °C to obtain vulcanized rubber sheets. Finally, the mechanical property was evaluated using a universal testing machine.

2.4 Latex Rubber Testing

2.4.1 Vulcanization Characteristics

The vulcanization behavior of the latex rubber samples was evaluated using a Moving Die Rheometer. Specimens measuring 35 × 35 × 2 mm were tested at 160 °C, with torque continuously recorded throughout the curing process. The resulting torque–time curves were used to determine key vulcanization parameters, including scorch time (ts_1), optimum curing time (tc_{90}), and maximum torque, which reflect the rate and extent of vulcanization.

2.4.2 Tensile Strength Testing

Tensile properties were assessed according to ISO 37 standards using a Universal Tensile Testing Machine. Test specimens, sized 150 mm × 35 mm × 2 mm, were securely clamped to prevent slippage. Prior to testing, the machine was calibrated by setting the initial load to zero.

3. RESULTS AND DISCUSSION

3.1 Fourier Transform Infrared Spectroscopy Analysis

The FTIR spectra of lignin extracted from sugarcane bagasse using alkaline treatment with varying NaOH concentrations (10%, 20%, 30%, and 40% w/v) are shown in Figure 1. All samples exhibited characteristic absorption bands corresponding to typical lignin functional groups. A broad band at around 3379–3414 cm^{-1} was attributed to the O–H stretching vibration of hydroxyl groups in phenolic and aliphatic structures. The bands at 1701-1710 and 1589-1600 cm^{-1} correspond to C=O stretching vibrations in unconjugated carbonyl groups and aromatic ring vibrations in guaiacyl/syringyl units. A prominent peak at 1512 cm^{-1} was related to the aromatic skeletal vibrations of lignin, while the peak at 1460 cm^{-1} can be assigned to the C–H deformation in $–CH_3$ and $–CH_2$ groups. Additional peaks at 1423 and 1328 cm^{-1} indicate the presence of syringyl ring breathing and C–O stretching in guaiacyl units, respectively. The region around 1215-1220 cm^{-1} is associated with C–O

stretching in aryl ethers or phenolic hydroxyl groups. Peaks at 1122 cm^{-1} and 1031–1043 cm^{-1} indicate C–H in-plane deformation of syringyl units and C–O stretching in primary alcohols, respectively. Furthermore, bands at 754 and 619 cm^{-1} were observed in all samples, indicating the C–H out-of-plane bending vibrations characteristic of aromatic rings. These results are consistent with previously reported FT-IR spectra of lignin obtained from biomass, confirming that the extracted lignin retains the key structural features of guaiacyl (G) and syringyl (S) units, as well as hydroxyl (OH) and carbonyl functional groups, which are important for antioxidant activity in rubber applications [3].

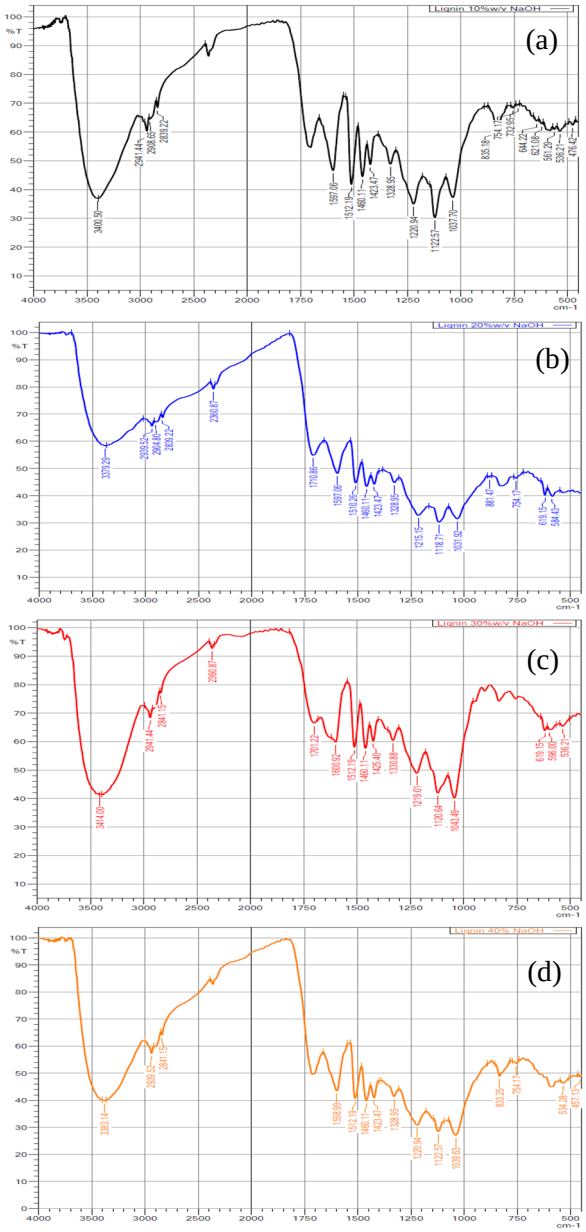

Figure 1 FT-IR spectra of lignin extracted from sugarcane bagasse using varying concentrations of NaOH(a) 10% w/v, (b) 20% w/v, (c) 30% w/v, and (d) 40% w/v.

3.2 Thermogravimetric Analysis

TGA was conducted to evaluate the thermal degradation behavior of lignin extracted using different alkali concentrations. The results revealed notable differences in thermal stability across samples within the temperature range of 40–800 °C (as illustrated in Figure 2). All lignin samples exhibited four distinct stages of thermal degradation. The first stage (40–110 °C) corresponded to moisture evaporation. In the second stage (130–190 °C), low-molecular-weight organic residues were volatilized. The third stage (200–260 °C) involved the breakdown of weak side-chain structures, while the fourth stage (300–480 °C) corresponded to the major decomposition of the lignin matrix, likely involving the degradation of more thermally stable structural components [4]. Lignin extracted at a 10% alkali concentration exhibited broad and multiple degradation transitions, suggesting significant structural heterogeneity and the presence of residual impurities. Samples extracted with 30% and 40% alkali showed higher degradation peaks but also presented greater mass loss in the early stages and higher char residues, indicating potential contamination or over-degradation. In contrast, lignin extracted at a 20% concentration demonstrated a distinct primary degradation peak near 370 °C, closely resembling the behavior of commercial lignin. This sample also showed minimal early-stage mass loss and moderate char residue at high temperatures, reflecting an optimal balance of purity and thermal stability.

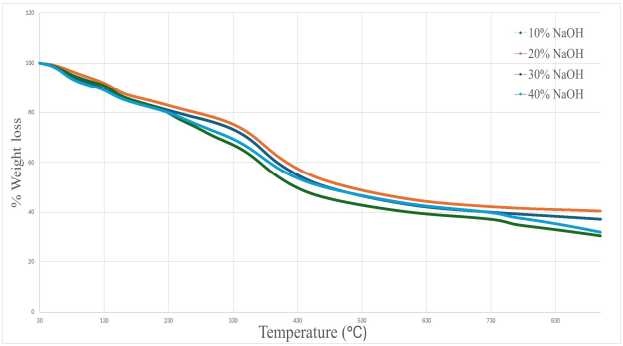

Figure 2 Thermogravimetric analysis thermograms of lignin samples extracted using various alkali concentrations

3.3 Scanning electron microscope

The morphology of lignin extracted from sugarcane bagasse using the alkaline method with varying NaOH concentrations was observed using scanning electron microscopy (SEM) as shown in Figure 3.

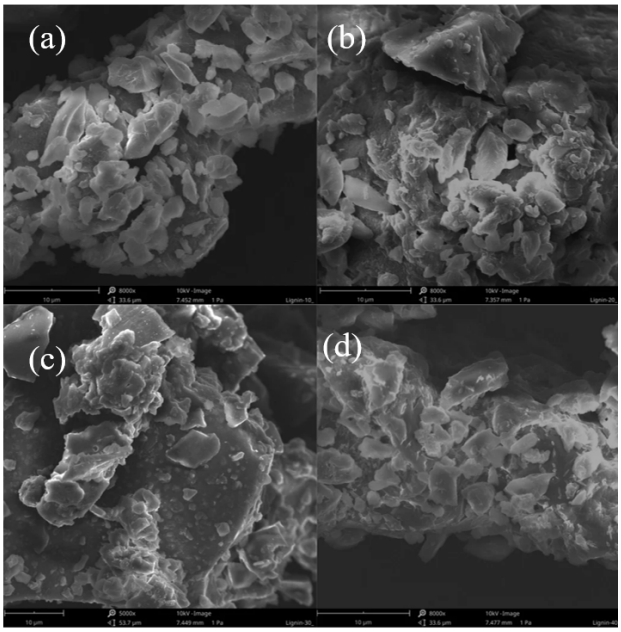

Figure 3 Scanning electron microscopy images of lignin extracted from sugarcane bagasse using varying NaOH concentrations: (a) 10% w/v, (b) 20% w/v, (c) 30% w/v, and (d) 40% w/v.

The samples showed irregular, flake-like particle structures with a tendency to agglomerate. This morphology differs from the spherical shapes often reported in lignin obtained through solvent evaporation methods. To promote the formation of spherical lignin particles, techniques such as fine grinding followed by sieving, or precipitation using ethanol–water systems, are recommended [5]. Spherical particles tend to disperse more effectively in polymer matrices due to their uniformity and lower tendency to aggregate, contributing to better material homogeneity and performance [6].

3.4 Cure Characteristics

The analysis of cure characteristics is a crucial step in evaluating the physical properties of natural rubber after undergoing the vulcanization process, which enhances the strength, elasticity, and durability of rubber. This process involves heating the rubber and adding specific chemicals to promote crosslinking between rubber molecules. According to Figure 4, as the lignin content in the rubber increases, the Maximum Torque tends to decrease. This indicates a reduction in the maximum strength the vulcanized rubber can withstand, implying a deterioration in its properties after crosslinking. Furthermore, the Cure Rate Index (CRI) also decreases with higher lignin content, suggesting that the curing rate of the rubber slows down as more lignin is added [7].

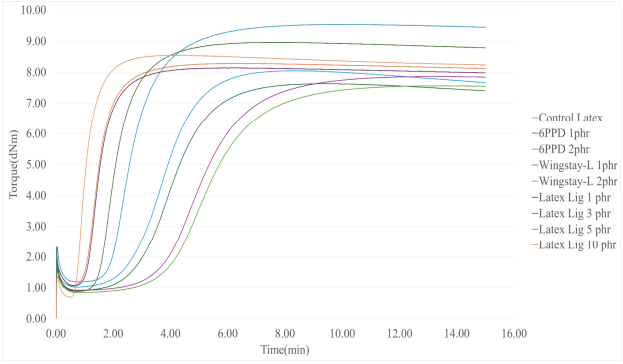

Figure 4 Cure characteristics of composite.

3.5 Tensile Test

The mechanical performance of natural rubber latex filled with lignin, 6PPD, and Wingstay-L was assessed to determine the influence of these additives on tensile strength. As shown in Figure 5, the addition of lignin impacts mechanical properties depending on its concentration. For example, LigninLatex_1 demonstrated a tensile strength of 24.7 MPa. However, increasing the lignin content led to a marked decrease in tensile strength, with LigninLatex_10 recording a reduced value of 14.5 MPa. This reduction in strength is primarily attributed to the agglomeration of lignin particles, which impairs uniform dispersion in the rubber matrix and causes phase separation. Poor interfacial adhesion between lignin and rubber may also result from limited hydrogen bonding, affecting the composite's mechanical integrity. Conversely, synthetic antioxidants such as Wingstay-L and 6PPD create stronger chemical bonding with the rubber, including ionic and hydrogen bonds, which increase dispersion, stability, and mechanical qualities. However, lignin provides mechanical performance approximately on level with 6PPD and Wingstay-L at lower loading levels, such as in LigninLatex_1. Thus, in rubber products, lignin represents a viable substitute for synthetic chemicals, particularly for environmentally sustainable applications. LigninLatex_1 is the best option for substitution where comparable performance is required [8].

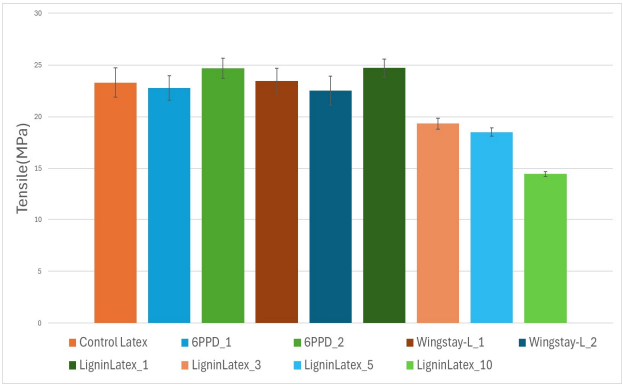

Figure 5 Tensile strength of rubber compounds

4. CONCLUSION

In our study, we explored the use of sugarcane bagasse lignin as a sustainable additive for natural rubber. By extracting lignin from bagasse with different concentrations of sodium hydroxide (10–40 % w/v), this research found that the 20 % w/v solution produced the highest lignin content, making it the most effective for further use. When added to natural rubber at a low loading of just 1 phr (parts per hundred rubber), this lignin significantly boosted tensile strength to 24.7 MPa outperforming conventional antioxidants like 6PPD and Wingstay-L. However, increasing the lignin content to 3 phr or more led to reduced strength due to particle agglomeration, which disrupted the rubber's internal structure. These results highlight that a small amount of lignin (1 phr or less) offers the best mechanical benefits. Moving forward, we aim to study the material's thermal aging and biodegradation to confirm its value as an eco-friendly alternative in rubber production.

ACKNOWLEDGMENTS

The authors would like to express their sincere thanks to the Department of Chemical Engineering and the Sustainable Polymer & Innovative Composite Materials Research Group, Department of Chemistry, Faculty of Science, King Mongkut's University of Technology Thonburi, for their valuable support and contributions to this work.

REFERENCES

1. Li, K., Zhong, W., Li, P., Ren, J., Jiang, K., & Wu, W. (2023). Recent advances in lignin antioxidant: Antioxidant mechanism, evaluation methods, influence factors and various applications. International Journal of Biological Macromolecules, 251, 125992.
2. Demir, E., Gerengi, H., Savcı, K., Altundal, G., Yüksel, C., & Çağıl, D. (2024). Exploration of Green Alternatives to 6PPD (P-Phenylenediamine) Used as Antiozonant and Antioxidant in the Rubber Industry. Materials Sciences and Applications, 15(2), 87–100.
3. Intapun, J.; Rungruang, T.;Suchat, S.; Cherdchim, B.; Hiziroglu,S. The Characteristics of NaturalRubber Composites with KlasonLignin as a Green Reinforcing Filler:Thermal Stability, Mechanical and13, 1109.
4. Oliveira, T. M., Gatti, T. H., & Battistelle, R. A. G. (2020). Characterization of lignin extracted from sugarcane bagasse and its potential use for polyurethane foams. Polímeros, 30(4), e2020044.
5. Tang, P.-D., Du, Q.-S., Li, D.-P., Dai, J., Li, Y.-M., Du, F.-L., Long, S.-Y., Xie, N.-Z., Wang, Q.-Y., & Huang, R.-B. (2018). Fabrication and characterization of graphene microcrystal prepared from lignin refined from sugarcane bagasse. Nanomaterials, 8(8), 565.
6. Pourbaba, R., Abdulkhani, A., Rashidi, A., & Ashori, A. (2020). Lignin nanoparticles as a highly efficient adsorbent for the removal of methylene blue from aqueous media. Scientific Reports, 10(1), 20895.
7. Sirisinha, C., Sakdapipanich, J. T., & Nakason, C. (2021). The characteristics of natural rubber composites with Klason lignin as a green reinforcing filler: Thermal stability, mechanical and dynamical properties. Polymers, 13(7), 1109.
8. Ramaraj, R., & Velayutham, T. S. (2021). Lignin as a sustainable antioxidant for rubber materials: A review. Polymers, 13(7), 1109.

Comparative study of methylene blue adsorption using calcium oxide derived from chicken eggshells and standard calcium oxide

Pinchaphat Poka[1], Woravarun Unkaew[1], Weerawat Clowutimon[1,*], Pornsawan Assawasangrat[2]

[1] Samsenwittayalai School, Bangkok 10400, Thailand
[2] Department of Chemical Engineering, School of Engineering, King Mongkut's Institute of Technology Ladkrabang, Bangkok 10520, Thailand
[*] Corresponding author: t.weerawat@samsenwit.ac.th

ABSTRACT

In this study, a comparative analysis of methylene blue adsorption on chicken eggshell-derived calcium oxide and standard calcium oxide was conducted. Calcium oxide was synthesized from chicken eggshells via calcination at 900 °C for 3 hours and characterized using XRF, XRD, FT-IR, FT-Raman, and BET techniques. The batch adsorption experiment investigated key parameters, including contact time and initial methylene blue concentration. Characterization results indicate that chicken eggshell calcium oxide exhibits similar properties to standard calcium oxide based on XRF, XRD, FT-IR, and FT-Raman analyses. However, BET analysis revealed that chicken eggshell calcium oxide has a slightly larger average pore diameter, with marginally lower total pore volume and surface area, which may influence its adsorption capacity. Adsorption of methylene blue reached equilibrium within 120 minutes for both adsorbents. The adsorption isotherms were modeled using the Langmuir and Freundlich equations. The Langmuir model better describes the adsorption behavior, particularly at high equilibrium concentrations, indicating a homogeneous single-layer adsorption mechanism. In addition, the maximum adsorption capacity of chicken eggshell calcium oxide was approximately 84% of that of standard calcium oxide (32.25 mg/g). However, chicken eggshell calcium oxide presents a significant sustainability advantage, as it is derived from chicken eggshells, a food waste material. Moreover, its preparation does not require the use of chemicals, making it an environmentally friendly and cost-effective alternative.

Keywords: Adsorption; Calcium oxide; Chicken eggshell; Methylene blue

1. INTRODUCTION

Wastewater contamination is a pressing global issue, particularly in water polluted with synthetic dyes. One commonly used dye is methylene blue (MB), a highly water-soluble thiazine dye with the chemical formula $C_{16}H_{18}ClN_3S$. MB contains a positively charged cationic group, which facilitates its adsorption onto negatively charged surfaces. Due to its versatility, MB is widely used in industries such as textiles, pulp mills, leather, and cosmetics [1-3]. However, the discharge of MB-contaminated wastewater into the environment poses significant risks to aquatic ecosystems and human health. Prolonged exposure to MB through contaminated food or water can cause skin and eye irritation and reduce the blood's oxygen-carrying capacity [2,4]. Therefore, effective pretreatment of MB-rich wastewater is essential before discharge into the environment.

Conventional dye removal methods, including sedimentation, coagulation-flocculation, ozonation, and membrane filtration, have been employed to address this issue. Among these, adsorption is widely recognized as one of the most effective and versatile techniques due to its simplicity, cost-efficiency, low energy consumption and high removal rates [1, 5-7]. Recent studies have focused on developing adsorbents from natural, low-cost materials, such as calcium oxide (CaO) derived from chicken eggshells, duck eggshells and oyster shells through high-temperature calcination (700–900 °C) [8,9]. These natural CaO adsorbents have shown great potential for methylene blue removal from wastewater [10,11]. However, the adsorption efficiency of CaO prepared from natural materials have not been reported compared to CaO standard.

This study investigates the adsorption of MB onto CaO prepared from chicken eggshells (CaO-CE) and compares its performance with standard CaO. Key parameters, including initial MB concentration and contact time, were studied to evaluate the adsorption capacity of CaO-CE. The findings aim to demonstrate the viability of CaO-CE as a sustainable and cost-

effective adsorbent for treating dye-contaminated wastewater.

2. EXPERIMENTAL

2.1. Materials

Chicken eggshells were obtained from a local fresh market in Bangkok, Thailand. CaO standard, with 90% purity, and methylene blue were supplied by Kemaus (Australia).

2.2. Preparation of CaO-CE

Chicken eggshells were washed with de-ionized water, dried in an oven (OF-01E, JEIO TECH) at 100 °C overnight, and then ground into fine particles. The ground material was calcinated in a furnace (Thermo Scientific FB1415M, TEquipment) at 900 °C for 3 hours to produce CaO. The obtained CaO was characterized using various techniques: XRF (S8 Tiger, Bruker) to analyze its elemental composition, XRD (D8 Discover, Bruker) to determine its phase and crystallinity, FT-IR (INVENIO S, Bruker) and FT-Raman (XploRA PLUS, Horiba) to identify surface functional groups, and BET (Tristar 3000, Micromeritics Instrument Crop) to measure total surface area, pore volume, and average pore diameter.

2.3. Adsorption experiments

The comparative efficiency of MB on CaO-CE and a CaO standard was investigated using batch adsorption experiments. Initially, equilibrium time for both CaO was determined. A fixed amount of adsorbent (0.25 g) was added to 50 ml of MB solution with initial concentration of 200 mg/l in vials. The vials were then placed in an incubator rotary shaker (ZHWY-100B, Zhicheng) operating at 200 rpm and maintained at 35 °C. Samples were taken at predetermined time intervals (5, 10, 15, 20, 25, 30, 45, 60, 75, 120 and 240 min) for analysis. To separate the adsorbent from the supernatant, the samples were centrifuged using a centrifuge (LC-6S, Joanlab) at 5000 rpm for 2 min. The remaining MB concentration in the supernatant was determined by measuring absorbance at 663 nm using a spectrophotometer (T60 V, PG Instruments). The amount of MB adsorbed per unit mass at time t, denoted as q_t (mg/g), was calculated by equation (1)

$$q_t = \frac{(C_i - C_t)V}{W} \quad (1)$$

where C_i and C_t are the initial concentration and the concentration of MB at time t (mg/L), V is the volume of solution (L) and W is the weight of absorbent (g).

For adsorption isotherm experiments, the same procedure was followed, but the initial MB concentration was varied between 10 and 200 mg/L. The contact time was set at 240 min to ensure equilibrium was achieved.

3. RESULTS AND DISCUSSION

3.1. Characterization of CaO-CE and CaO standard

XRF characterization was employed to determine the composition of calcined chicken eggshell. The results, presented in Table 1, show that the primary element is calcium (Ca), while other elements such as magnesium (Mg), phosphorus (P), and sodium (Na) are present in insignificant amounts.

Table 1 Component of calcined chicken eggshell **.**

Component	Percent
CaO	97.5
MgO	1.37
P_2O_5	0.40
SO_3	0.34
Na_2O	0.22
Other	0.17

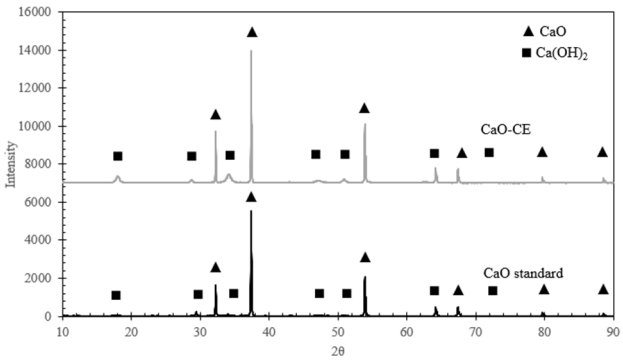

Figure 1 XRD patterns of calcined chicken eggshell and CaO standard

XRD analysis was conducted to examine the phases and crystallinity of calcined chicken eggshell and the CaO standard. The results are displayed in Figure 1. Based on the XRD patterns, Ca in the calcined chicken eggshell is present as CaO and calcium hydroxide ($Ca(OH)_2$). The peaks corresponding to CaO are observed at 2θ = 32°, 37°, 54°, 67°, 80°, and 89°, while the peaks at 2θ = 18°, 29°, 34°, 47°, 51°, 63°, and 72° indicate the presence of $Ca(OH)_2$. The formation of $Ca(OH)_2$ is likely due to the reaction of CaO with moisture during the cooling process, as shown in Equation (2) [9,12].

$$CaO + H_2O \rightarrow Ca(OH)_2 \quad (2)$$

Compared to $Ca(OH)_2$, the intensity of the CaO peaks is significantly higher, indicating that CaO is the dominant phase. Additionally, the XRD pattern of calcined chicken eggshell closely matches that of the CaO standard, suggesting that the calcined chicken eggshell is a high-purity source of CaO.

FT-Raman analysis, an effective technique to determine the present of metal oxide, was conducted to identify the presence of the Ca-O bond, and the results are shown in Figure 2. The spectrum of CaO-CE aligns

closely with the CaO standard, exhibiting three major peaks at 340–350, 670–680, and 1075–1085 cm^{-1}, which are characteristic of the Ca-O bond, confirming the presence of CaO [13]. The impurities in the samples were analyzed using FT-IR, as presented in Figure 3. The absorption band at 3641–3642 cm^{-1} is associated with the hydroxyl group of $Ca(OH)_2$, confirming its presence, as also observed in the XRD characterization. Additionally, peaks in the range of 875–1450 cm^{-1} are attributed to the carboxyl group, likely due to a small residual amount of calcium carbonate ($CaCO_3$) in the sample [9, 14-16]. Overall, the consistent findings from FT-Raman, FT-IR, and prior research validate the successful preparation of CaO-CE, with minor impurities such as $Ca(OH)_2$ and $CaCO_3$.

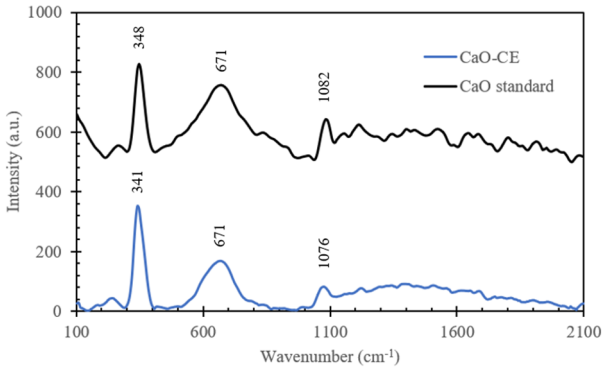

Figure 2 FT-Raman spectrum of CaO-CE and CaO standard

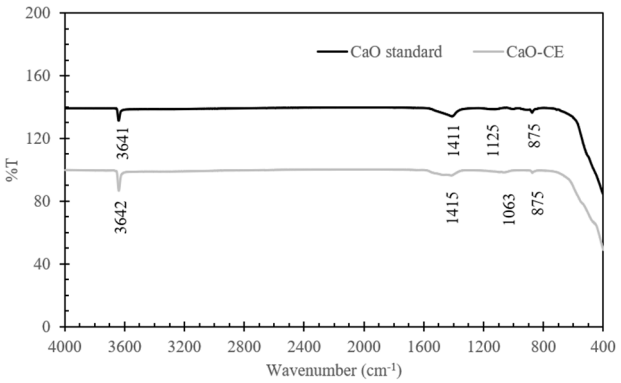

Figure 3 FT-IR spectrum of CaO-CE and CaO standard

Table 2 BET Characterization of CaO standard and CaO-DE.

Adsorbent	Total surface area (m^2/g)	Total pore volume (cm^3/g)	Average pore diameter (nm)
CaO standard	12.23	0.0132	8.54
CaO-CE	9.18	0.0106	9.12

The total surface area, total pore volume, and average pore diameter of both adsorbents were examined by BET characterization, and the results are presented in Table 2. From the table, the average pore diameter of CaO-CE is slightly higher than that of CaO standard, suggesting possible differences in pore structure formation during synthesis. The molecular dimensions of methylene blue (1.7 × 0.76 × 0.33 nm) [17] suggest that it can easily diffuse into the pores of both adsorbents, indicating that the difference in pore diameter may not significantly affect the adsorption capacity. However, the total surface area and total pore volume of CaO-CE are approximately 80% of those of CaO standard, which may indicate a less porous structure or incomplete activation. These differences could affect the adsorption performance, as a lower surface area and pore volume might limit the availability of active sites for dye removal. Overall, the BET results are consistent with those of CaO synthesized from other natural materials [9,18,19], reinforcing the reliability of the preparation method.

3.2. Adsorption experiment results

The equilibrium adsorption time for CaO-CE and CaO standard was preliminarily determined through batch adsorption experiments using an initial MB concentration of 200 mg/L. The results presented in Figure 4 demonstrate that the specific amount of MB adsorbed on both adsorbents increased rapidly within the first 20 minutes. This rapid uptake is attributed to the abundant availability of active sites on the surface of the adsorbents at the beginning of the adsorption process. Subsequently, the adsorption rate slowed as the active sites became increasingly occupied, and equilibrium was achieved at 120 minutes for both materials. To ensure that equilibrium adsorption was fully attained, a contact time of 240 minutes was chosen for the adsorption isotherm determination.

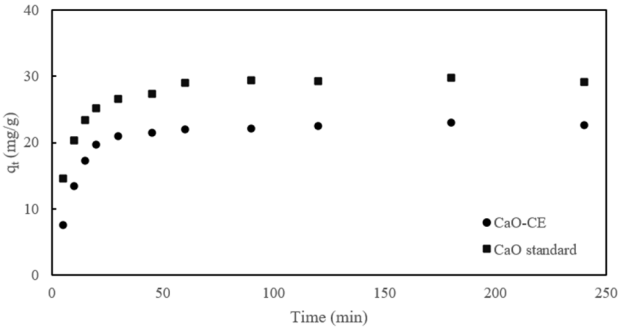

Figure 4 Specific amount adsorbed of MB on CaO-CE and CaO standard at various times (The initial concentration of MB 200 mg/l)

The adsorption isotherm experiments for MB were conducted in a batch process, with the initial MB concentration varying from 10 to 200 mg/L. The results, shown in Figure 5, indicate that the equilibrium adsorption capacity (q_e) of MB on both adsorbents increases linearly with the equilibrium concentration (c_e) up to 20 mg/L. Beyond this point, q_e begins to

plateau, suggesting that most active sites on the adsorbent surfaces are occupied, and the maximum adsorption capacity is reached.

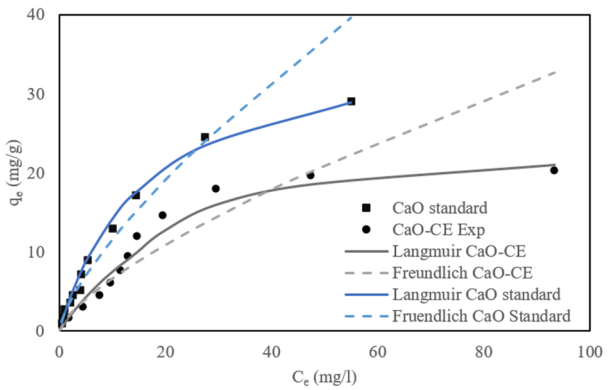

Figure 5 Adsorption isotherm of MB on CaO-CE and CaO standard

Two commonly used models, Langmuir and Freundlich isotherms, were applied to describe the adsorption behavior. Their respective equations are shown below:

$$q_e = \frac{q_{max} K_L c_e}{1 + K_L c_e} \quad (3)$$

$$q_e = K_F c_e^{1/n} \quad (4)$$

where q_{max} is the maximum adsorption capacity, K_L is the Langmuir isotherm constant, and K_F and n are the Freundlich isotherm constants.

The parameters derived from these models, along with the correlation coefficients (R^2), are summarized in Table 3. As indicated by the higher R^2 values, Langmuir model better describes the adsorption behavior of MB on both CaO-CE and CaO standard, particularly at high equilibrium concentrations. This suggests that the adsorption mechanism follows a physical monolayer adsorption, consistent with the adsorption of MB and other dyes onto natural materials [3, 7, 20-22].

Table 3 Langmuir and Fruendlich isotherm parameters

Model	Adsorbent	
	CaO-CE	Calcium oxide standard
Langmuir		
q_{max} (mg/g)	27.03	32.25
K_L(L/mg)	0.0323	0.0680
R^2	0.9835	0.9852
Fruendlich		
K_F (mg/g)	1.28	2.17
n	1.40	1.38
R^2	0.9105	0.9729

In comparison to CaO standard, the maximum adsorption capacity (q_{max}) of CaO-CE is slightly lower, achieving approximately 84% of the standard's capacity. This reduction can be attributed to the lower surface area and total pore volume of CaO-CE, as confirmed by BET characterization. However, CaO-CE provides significant advantages as it is derived from chicken eggshells, a food waste material, through an environmentally friendly preparation process that avoids chemical usage. Future studies should focus on optimizing the preparation process to enhance the surface area and pore volume of CaO-CE, thereby improving its adsorption capacity.

4. CONCLUSION

In this study, CaO-CE was successfully prepared and evaluated for the removal of MB from aqueous solutions. Characterization results showed that while CaO-CE exhibited a relatively larger average pore diameter compared to the CaO standard, its total pore volume and surface area were approximately 75% and 80% of the standard's values, respectively. The adsorption of MB on both adsorbents reached equilibrium within 120 minutes, with the Langmuir model slightly better describing the adsorption behavior than the Freundlich model. The maximum specific amount adsorbed of CaO-CE was slightly lower than that of the standard CaO. Despite this, the results demonstrate that CaO-CE, derived from chicken eggshells, is a sustainable and effective alternative material for the treatment of MB-contaminated wastewater.

ACKNOWLEDGMENTS

The equipment in this research was supported by Department of Chemical Engineering, School of Engineering, King Mongkut's Institute of Technology Ladkrabang and Department of Chemical Engineering, Faculty of Engineering, Chulalongkorn University.

REFERENCES

1. J. Fito, M. Abewaa, A. Mengistu, K. Angassa, A.D. Ambaye, W. Moyo, T. Nkambule. Adsorption of methylene blue from textile industrial wastewater using activated carbon developed from *Rumex abyssinicus* plant. *Scientific reports* 2023; 13: 1-17
2. D. Dimbo, M. Abewaa, E. Adino, A. Mengistu, T. Takele, A. Oro, M. Rangaraju. Methylene blue adsorption from aqueous solution using activated carbon of *spathodea campanulata*. *Results in Engineering* 2024; 21: 1-11.
3. S. Khushnood, J.R. Khan, S. Hussain, H. Khan, F. Wahab, K.C. Ng, M.K. Shahzad. Synthesis and characterization of mesoporous caged silica for efficient adsorption of methylene blue from aqueous solution. *International Communications in Heat and Mass Transfer* 2024; 156: 1-13

4. P. Zou, M. Zhang, C. Li, Y. Guo, W. Zhu, J. Cheng, J. Zhu. Experimental study on dynamic adsorption properties of methylene blue onto coal-based activated carbon using a hydrocyclone. *Chemical Engineering and Processing – Process Intensification* 2024; 203: 1-10.
5. R. Kasirajan, A. Bekele, G. Ermias. Adsorption of lead (Pb-II) using CaO-NPs synthesized by solgel process from hen eggshell: Response surface methodology from modeling, optimization and kinetics studies. *South African Journal of Chemical Engineering* 2022; 40: 209-229.
6. R.S. Brishti, R. Kundu, M.A. Habib, M.H. Ara. Adsorption of iron(III) from aqueous solution onto activated carbon of a natural source: *Bombax ceiba* fruit shell. *Results in Chemistry* 2023; 5: 1-6.
7. Y. Li, Q. Du, T. Liu, J. Sun, Y. Wang, S. Wu, Z. Wang, Q. Xia, L. Xia. Methylene blue adsorption on graphene oxide/calcium alginate composites. *Carbohydrate Polymers* 2013; 95: 501-507.
8. N. Razali, F.N. Musa, N. Jumadi, A.Y. Jalani. Production of Calcium Oxide from Eggshell: Study of Calcination Temperature, Raw Weight and Contact time. *Proceedings of RSU International Research Conference* 2021; 624-637.
9. O. Awogbemi, F. Inambao, E. Onuh. Modification and characterization of chicken eggshell for possible catalytic applications. *Heliyon* 2020; 6: 1-7.
10. H.L. Kelle, E.C. Ogoko, O. Akintola, N.O. Eddy. Quantum and experimental studies on the adsorption efficiency of oyster shell-based CaO nanoparticles (CaONPO) towards the removal of methylene blue dye (MBD) from aqueous solution. *Biomass Conversion and Biorefinery* 2024; 14: 31925-31948
11. U. Tagar, M. Volpe, A. Messineo, R. Volpe. Highly ordered CaO from cuttlefish bone calcination for the efficient adsorption of methylene blue from water. *Frontiers in Chemistry* 2023; 11: 1-15
12. K.R. Nagabhushana, H.S. Lokesha, S. Satyanarayana Reddy, D. Prakash, M. Veerabhadraswamy, H. Bhagyalakshmi, J.R. Jayaramaiah, Thermoluminescence properties of CaO power obtained from chicken eggshells. *Radiation Physics and Chemistry* 2017; 138: 54-59.
13. M. Galvan-Ruiz, L. Banos M.E. Rodriguez-Garcia. Lime characterization as a food additive. *Sensing and Instrumentation for Food Quality and Safety* 2007; 1: 169-175.
14. L. Habte, N. Shiferaw, D. Malatu, T. Thenepalli, R. Chilakala, J.W. Ahn. Synthesis of Nano-Calcium Oxide from Waste Eggshell by Sol-Gel Method. *Sustainability* 2019; 11: 1-10.
15. M.S. Hossain, S.A. Jahan, S. Ahmed. Crystallographic characterization of bio-waste material originated $CaCO_3$, green-synthesized CaO and $Ca(OH)_2$. *Results in Chemistry* 2023; 5: 1-8.
16. R. Mohadi, A. Sueb, K. Anggraini, A. Lesbani, Calcium Oxide Catalyst Based on Quail Eggshell for Biodiesel Synthesis from Waster Palm Oil. *Journal of Pure and Applied Chemistry Research* 2018; 7: 130-139
17. X. Yunxue, Y. Qin, Z. Wei, Z. Yunsong, Z. Maojun. Comparative adsorption of methylene blue by magnetic baker's yeast and EDTAD-modified magnetic baker's yeast: Equilibrium and kinetic study. *Arabian Journal of Chemistry*, 2019; 12: 2448-2456.
18. N. Tangboriboon, R. Kunanuruksapong, A. Sirivat. Preparation and properties of calcium oxide from eggshells via calcination. *Materials Science-Poland* 2012; 30: 313-322.
19. Z. Khoshraftar, A. Ghaemi. Evaluation of CaO derived from *Cerastoderma glaucum* of Caspian beach as a natural sorbent for CO_2 capture. *Current of Research in Green and Sustainable Chemistry* 2023; 6: 1-9.
20. L. Usgodaarachchi, C. Thambiliyagodage, R. Wijesekera, M.G. Bakker. Synthesis of mesoporous silica nanoparticles derived from rice husk and surface-controlled amine functionalization for efficient adsorption of methylene blue from aqueous solution. *Current of Research in Green and Sustainable Chemistry* 2021; 4: 1-11.
21. R. Liu, J. Zhang, H. Fu, L. Yin, Y. Song, G. He. A comparative study of methylene blue adsorption and removal mechanisms by calcium carbonate from different sources. *Bioresource Technology* 2023; 387: 1-8.
22. S. Sudarsan, G. Murugesan, T. Varadavenkatesan, R. Vinayagam, R. Selvaraj. Efficient adsorptive removal of Congo Red dye using activated carbon derived from *Spathodea campulata* flowers. *Scientific Reports* 2025; 15: 1-18.

Removal of Pb(II) and Hg(II) from water on activated carbon: An insight into multicomponent adsorption

Thanyakorn Sangoondee[1], Nikom Klomkliang[1,*]

[1] School of Chemical Engineering, Suranaree University of Technology, Nakhon Ratchasima 30000, Thailand
[*] Corresponding author: nikom.klo@sut.ac.th

ABSTRACT

This study investigates the simultaneous removal of lead (Pb(II)) and mercury (Hg(II)) from aqueous solutions using activated carbon (AC) and nitrogen/oxygen-doped activated carbon (NOAC) derived from coconut shells. The equilibrium adsorption data were obtained with an adsorbent weight of 0.1 g and 40 ml of multi-metal solution and varying initial concentration from 30 to 500 ppm at room temperature. The adsorbents were characterized by using various techniques, including CHN, SEM, and BET analysis. Batch adsorption experiments were conducted to examine the effects of initial concentration and contact time. The adsorption kinetics were found to follow a pseudo-second-order model, indicating chemisorption as the dominant mechanism. The Langmuir isotherm model provided the best fit for both adsorbents, suggesting monolayer adsorption and maximum adsorption capacities on AC of 307.02 $mg \cdot g^{-1}$ for Hg(II) and 104.80 $mg \cdot g^{-1}$ for Pb(II), A NOAC was found to be 272.34 $mg \cdot g^{-1}$for Hg(II) and 111.22 $mg \cdot g^{-1}$ for Pb(II). AC showed superior adsorption capacity for Hg(II), while NOAC showed better efficacy for Pb(II). The study provides insights into the adsorption mechanisms and the potential of modified activated carbons for heavy metal removal from water.

Keywords: Heavy metal; Activated carbon; Batch adsorption

1. INTRODUCTION

Heavy metal contamination in water sources is a critical environmental issue due to its severe impact on human health and ecosystems (Jarup, 2003). Lead (Pb) and mercury (Hg) are particularly concerned due to their high toxicity (Sall et al., 2020). Several technologies, such as chemical precipitation, ion exchange, and membrane filtration, have been widely used (Saleh et al., 2022). However, these techniques often suffer from high operational costs and secondary pollution. Among various treatment approaches, adsorption has gained significant attention due to its cost-effectiveness, high efficiency, and ease of operation. Activated carbon, particularly nitrogen-functionalized activated carbon, has demonstrated enhanced adsorption capabilities for heavy metal removal (Kaźmierczak-Raźna et al., 2021). Recent studies have shown that nitrogen doping introduces additional functional groups, such as pyridinic and pyrrolic nitrogen (Dilokekunakul et al., 2020), which can serve as active sites for metal ion binding.

This study focuses on the synthesis of nitrogen-modified activated carbon (NOAC) derived from coconut shells and its application in the batch adsorption of Pb(II) and Hg(II) from aqueous solutions. Coconut shells are chosen due to their abundance, low cost, and high carbon content, making them a sustainable precursor for activated carbon production. By incorporating nitrogen functionalities, the adsorption efficiency of Pb(II) and Hg(II) is expected to improve due to increased surface reactivity and enhanced binding affinity. The findings from this research will contribute to the development of cost-effective and high-performance adsorbents for heavy metal remediation in water treatment systems.

2. EXPERIMENTAL

2.1. Synthesis and characterization

Biochar derived from coconut shells was synthesized via a carbonization process. In typical preparation, 20 g of coconut shell was placed inside a horizontal ceramic tube furnace under a constant flow of N_2 100 mL/min at 600°C for 1 hour, with a heating rate of 10°C/min. To simplify, the biochar sample was denoted as “Char”. Next, the char was activated at 900°C for 1 hour under a CO_2 underflow of 100 mL/min with a heating rate of 10°C/min to obtain the original activated carbon (AC). In the N/O-doped process, urea was chosen to introduce nitrogen functional groups on the carbon surface due to its ability to decompose into ammonia at high temperatures. The char was mixed with urea (1:1 by weight) and oxidized with air at 350°C for 1 hour with a heating rate of 5°C/min to impregnate nitrogen groups grafting on the solid surface. During this oxidation process, urea decomposes and reacts with the carbon surface, forming various nitrogen functional

groups such as pyridinic, amine/imine, pyrrolic, and quaternary(Sethia & Sayari, 2015). Simultaneously, oxygen in the air reacts with carbon to form oxygen functional groups like carboxyl and phenolic (Zhou et al., 2023). The oxidized char was then mixed with a KOH solution with a mass ratio of sample to KOH of 1:2 (AC 7 g., KOH 14 g.) at room temperature for 24 hours. KOH was selected for its ability to etch and expand the pores of the carbon, thereby increasing surface area and pore volume. The resulting mixture was then dried overnight at 120°C in an oven and placed in a furnace for alkali activation at 900°C for 1 hour under the flow of CO_2 with a heating rate of 10°C/min. The N/O-doped activated carbons are denoted as NOAC.

The determination of structural porous characteristics, such as the total pore volume and Brunnauer-Emmett-Teller surface area (S_{BET}), necessitated determining the N_2 adsorption isotherm at -196°C using the Micromeritics (ASAP 2020 Plus). A scanning electron microscope (SEM) [FE-SEM-JEOL JSM 7800F] was used to analyze the surface morphology of adsorbents. The amount of nitrogen (N), hydrogen (H), and carbon (C) contained was determined using a CHN analyzer) [LECO 628].

2.2. Stock solution preparation

A mixed solution of lead (II) and mercury (II) is directly prepared from the solid salts. Analytical grade $PbCl_2$ (99.99% purity, Sigma Aldrich), and $HgCl_2$ (99.00% purity, Sigma Aldrich), respectively. Weight amounts to obtain a 1:1 molar ratio of Pb(II) and Hg(II). These solid salts were then co-dissolved in ultrapure deionized (DI) water to prepare a stock solution. They are prepared at concentrations ranging from 30 to 500 ppm.

2.3. Heavy metal ion adsorption in batch

Batch adsorption experiments were conducted by adding 0.1 g of activated carbon to 40 mL of a mixed Pb(II) and Hg(II) solution with initial concentrations of 30, 50, 100, 300, and 500 ppm. The mixtures were agitated at 250 rpm in a temperature-controlled orbital shaker at room temperature for varying contact times ranging from 5 minutes to 2 days. After each contact time, the solution was filtered using a 0.45 µm membrane filter, and the remaining Pb(II) and Hg(II) concentrations were analyzed using Inductively Coupled Plasma – Optical Emission Spectroscopy (ICP-OES) [PerkinElmer Optimal8000]. Adsorption capacity (q_t) was calculated using Equations (1).

$$q_t = \frac{(C_o - C_t)V}{W} \quad (1)$$

where C_o and C_t are the concentration at initial condition and at any time, *t*, V is the volume of the solution, and W is the mass of adsorbent.

The kinetics of the adsorption process were evaluated using pseudo-first order (eq. 2) and pseudo-second (eq. 3) (El-Wakil et al., 2022) order models.

$$\ln(q_e - q_t) = \ln q_e - k_1 t \quad (2)$$

$$\frac{t}{q_t} = \frac{1}{q_e} t + \frac{1}{k_2 q_e^2} \quad (3)$$

where q_t is the amount of adsorbate adsorbed at any time t, q_e is the adsorbed amount at equilibrium point, and k_1 and k_2 are the rate constants of pseudo-first order and pseudo-second order, respectively.

Langmuir and Freundlich models (Norsuhailizah et al., 2020) are used for equilibrium adsorption. The Langmuir isotherm can be rewritten in the form of a linear equation.

$$\frac{1}{q_e} = \frac{1}{q_m} + \frac{1}{K_L q_m C_e} \quad (4)$$

where q_m is the maximum adsorption capacity, K_L is constant energy related to the heat of adsorption, and C_e is the equilibrium concentration in the bulk fluid phase.

The Freundlich isotherm model in the logarithmic form is given by,

$$\mathrm{Log}(q_e) = \log(K_f) + \frac{1}{n}\mathrm{Log}(C_e) \quad (5)$$

where K_f and n are the indicators of the adsorption capacity and adsorption intensity, respectively.

3. RESULTS AND DISCUSSION

3.1. Characterization of adsorbents

Figure 1(a) shows the adsorption isotherm of all adsorbents, with the horizontal axis showing the relative pressure (P/P^o) and the vertical axis showing the volume of the adsorbed substance per pore volume (Quantity Adsorbed (mmol/g)). It was found that the NOAC has a type IV isotherm, which is characteristic of mesoporous materials. At a relative pressure of approximately 0.5, adsorption occurs in large amounts. very quickly, which indicates adsorption in mesopores. AC has a Type I isotherm, which is characteristic of microporous materials, with high adsorption at low pressures. Then it will remain constant when approaching saturation pressure. Figure 1(b.) shows the pore size distributions of adsorbents. In the NOAC sample, the peak of pore size has several distributions. The main peak of pore size is in the range of micropores (pore size <2 nm); for mesopores, the size appears as a small peak. On the other hand, for AC showing the pore size distribution in the range of micropores, it indicates microporous material. To further characterize the adsorbents, elemental analysis was performed using a CHN analyzer. Summarizes the chemical composition and porosity properties of both adsorbents. Notably, the BET surface area increased from 532 m^2/g for AC to 652 m^2/g for NOAC. Similarly, the total pore volume

expanded from 0.258 cm^3/g to 0.463 cm^3/g, a significant increase. These improvements in surface area and pore volume for NOAC are likely due to the nitrogen/oxygen doping process and additional activation steps. The elemental analysis reveals the introduction of nitrogen in NOAC (3.828%) compared to AC (0.024%), confirming successful N-doping. The oxygen content also increased in NOAC.

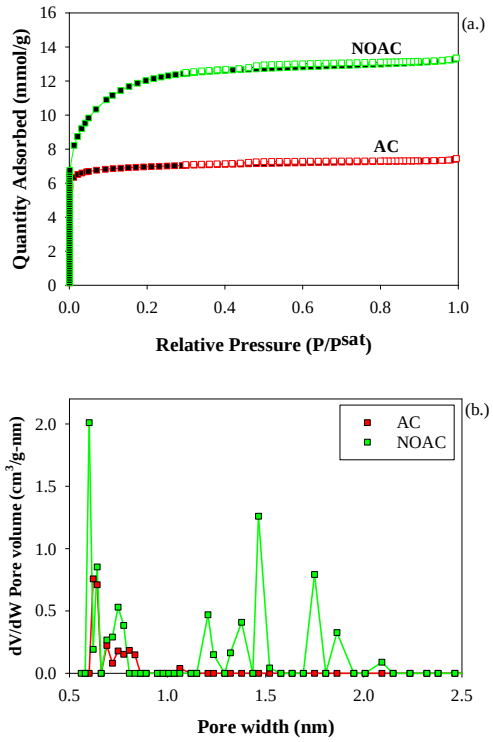

Figure 1 (a) Adsorption/desorption isotherm of N_2 at -196°C and (b) pore size distributions

The morphologies of both adsorbents exhibit distinct characteristics. The NOAC sample, as shown in Figure 2(b), displays a highly porous structure with a sponge-like appearance. The external surface of NOAC reveals a higher degree of porosity compared to AC, with visible surface cracks and well-developed pore networks. These features indicate successful modification and enhanced pore formation during the nitrogen/oxygen doping process. In contrast, Figure 2(a) shows the AC sample with a coral-like structure. While pores are present, they appear less numerous and less defined compared to NOAC. The AC surface exhibits a more compact and less fractured appearance. The stark difference in morphology between NOAC and AC demonstrates the effectiveness of the modification process. The increased porosity and surface area observed in NOAC suggest potential improvements in adsorption capacity and accessibility of adsorption sites. These structural changes are likely to contribute to enhanced performance in heavy metal removal applications. Overall, the SEM analysis confirms the successful synthesis of both activated carbon types, with NOAC showing more pronounced pore development and surface modification. These observations provide visual evidence of the structural changes induced by the nitrogen/oxygen doping process, which are expected to influence the adsorption properties of the materials.

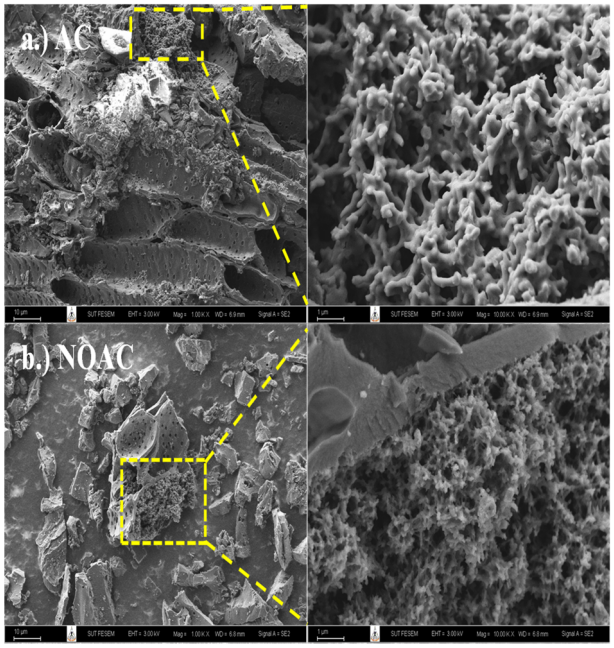

Figure 2 SEM images of a.) AC b.) NOAC

3.2. Batch adsorption study

The influence of multi-metals concentration on its adsorption rate was determined through variation of initial concentration in the solution from 30 to 500 ppm. The equilibrium concentration of heavy metals was evaluated using an adsorbent weight of 0.1 g and 40 ml of multi-metal solution and during time 48 hr. Results from Figure 3. show that both adsorbent and type of ion have a significant impact on adsorption efficiency, with Hg(II) being significantly better adsorbed than Pb(II) on both AC and NOAC materials due to its higher covalent index (4.08 Hg(II), 3.29 Pb(II)) (Zhang et al., 2014), which indicates a stronger tendency to form covalent bonds with functional groups present on the adsorbent surface (Tejada-Tovar et al., 2022). The higher affinity of Hg(II) for adsorption can also be attributed to its slightly smaller ionic radius(1.16 Aº Hg(II) (Luo et al., 2014), 1.20 Aº Pb(II) (Igwe & Augustine, 2007)), allowing better penetration into the adsorbent porous structure and more effective interaction with available active sites (Igwe & Augustine, 2007). Additionally, the approximate free energy hydration of Hg(II) (-1760 kJ/mol) is higher than that of Pb(II) (-1425 kJ/mol) (Kepp, 2019) meaning that Hg(II) ions are more strongly associated with water molecules in solution. This could reduce their mobility, and due to their strong covalent interactions with adsorbent functional groups, their adsorption remains more efficient. In contrast, Pb(II) with lower free energy hydration, may exhibit higher mobility but weaker binding to the adsorbent compared to Hg(II). Furthermore, the difference in

electronegativity (2.00 Hg(II), 2.33 Pb(II)) (Gao et al., 2023) suggests that Pb(II) has a slightly stronger tendency to participate in electrostatic interactions. However, in systems where covalent interactions dominate, such as those involving AC and NOAC with oxygen, nitrogen-containing functional group, Hg(II) is therefore more likely to be adsorbed because it can form stronger bonds with the surface of the adsorbent. When comparing adsorption performance, NOAC exhibited a higher capacity for Pb(II) removal compared to AC. However, at higher Hg(II) concentrations, AC demonstrated superior adsorption efficiency for Hg(II) over NOAC. Nevertheless, at lower Hg(II) concentrations, NOAC outperformed AC in Hg(II) adsorption.

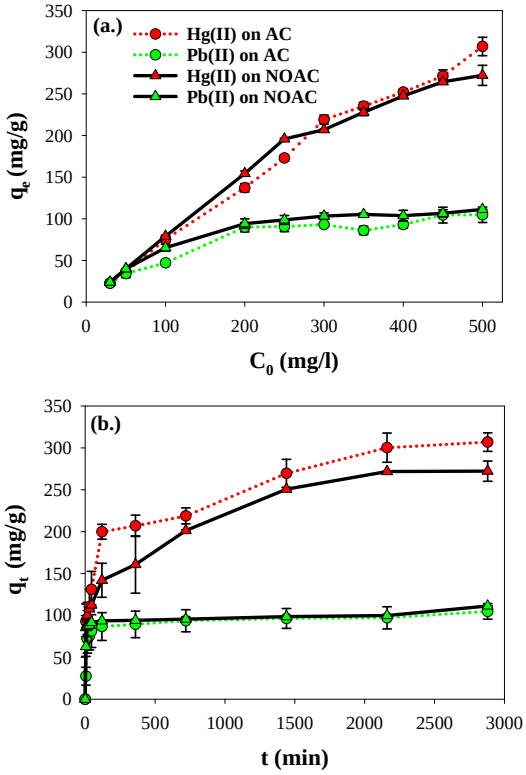

Figure 3 Effects of initial concentration (30-500 ml/min) on heavy metals removal using AC and NOAC (a.), Effects of contact time on difference adsorbents at 500 mg/l (b.).

3.3. Adsorption kinetic

The study found that Pb(II) and Hg(II) adsorption on AC and NOAC, shown in Figure 4, followed the pseudo-second-order more closely than the pseudo-first-order. Table 1-2 presents the fitting parameters. For AC, the pseudo-first-order rate constants (k_1) were 0.00171 min^{-1} for Hg(II) and 0.00155 min^{-1} for Pb(II), both showing poor fits (low R^2) and significant deviations. The pseudo-second-order rate constants (k_2) were 0.000039 g mg^{-1} min^{-1} for Hg(II) and 0.00036 g mg^{-1} min^{-1} for Pb(II), with q_e values matching experimental results and high R^2 values. Similarly, NOAC, k_1 values were 0.00157 min^{-1} for Hg(II) and 0.00173 min^{-1} for Pb(II), with poor fits and calculated q_e values. The k_2 values were 0.0000391 g mg^{-1} min^{-1} for Hg(II) and 0.00033 g mg^{-1} min^{-1} for Pb(II), with q_e values closely matching experimental data. These results confirm that the pseudo-second-order model is a better fit, indicating adsorption is mainly controlled by chemisorption.

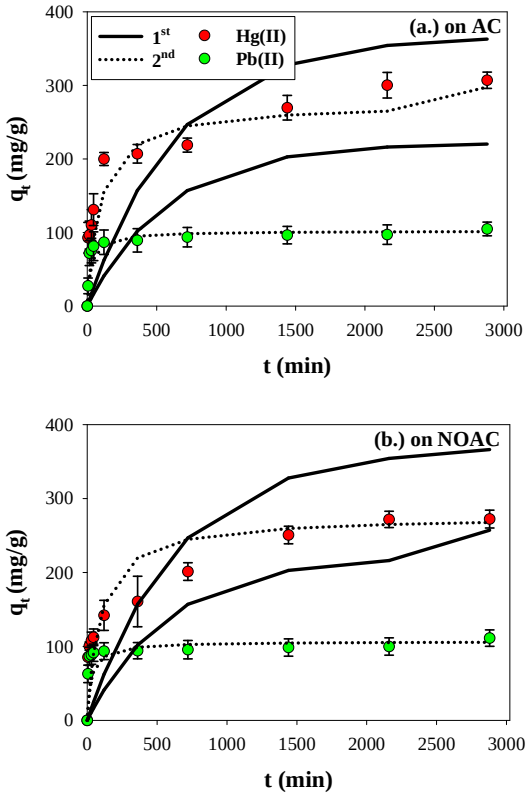

Figure 4 Adsorption kinetics of Hg(II) and Pb(II) on AC (a.) and NOAC (b.)

Table 1 The fitting parameters of the pseudo first order kinetic models on different adsorbents.

Adsorbent	Metal ion	[a]$q_{e,experiment}$	Pseudo first order		
			$q_{e,theory}$	[b]k_1	R^2
AC	Hg(II)	307.016	221.8951	0.001706	0.9586
	Pb(II)	104.8	367.2471	0.00155	0.5391
NOAC	Hg(II)	272.344	260.1726	0.001573	0.8371
	Pb(II)	111.22	368.9352	0.001725	0.5286

[a]q_e unit mg/g, [b]k_1 unit min^{-1}

Table 2 The fitting parameters of the pseudo second order kinetic models on different adsorbents.

Adsorbent	Metal ion	[a]$q_{e,experiment}$	Pseudo second order		
			$q_{e,theory}$	[c]k_2	R^2
AC	Hg(II)	307.0160	306.5621	0.0000390	0.9914
	Pb(II)	104.8000	102.0606	0.0003605	0.9976
NOAC	Hg(II)	272.3440	276.4194	0.0000391	0.9914
	Pb(II)	111.2200	106.6148	0.0003304	0.9951

[c]k_2 unit g•mg^{-1}•min^{-1}

3.4. Adsorption isotherm

Comparing the R^2 values of the Langmuir and Freundlich models shown in Figure 5, it's evident that the Langmuir model provides a better fit for the adsorption isotherms of both Hg(II) and Pb(II) on AC and NOAC adsorbents. The Langmuir model consistently shows higher R^2 values across all systems. The superior fit of the Langmuir model suggests that the adsorption of Hg(II) and Pb(II) on both adsorbents can be considered a monolayer adsorption process. This implies that there is a finite number of adsorption sites on the adsorbent surface, each site can hold only one adsorbate molecule, all sites are energetically equivalent, and there are no interactions between adsorbed molecules on adjacent sites. The Langmuir model parameters in Table 3 provide valuable insights. The maximum adsorption capacity (q_e) shows that AC has a higher capacity for Hg(II) (367.6 mg/g) compared to Pb(II) (106.6 mg/g), while NOAC also exhibits a higher capacity for Hg(II) (273.0 mg/g) than Pb(II) (109.8 mg/g). AC demonstrates superior Hg(II) adsorption compared to NOAC, while their Pb(II) on NOAC has better adsorption capacities. The Langmuir constant (K_L) indicates that NOAC has higher K_L values for both Hg(II) and Pb(II) compared to AC, suggesting a stronger binding affinity. For both adsorbents, K_L values are higher for Pb(II) than for Hg(II), indicating stronger interactions with Pb(II).

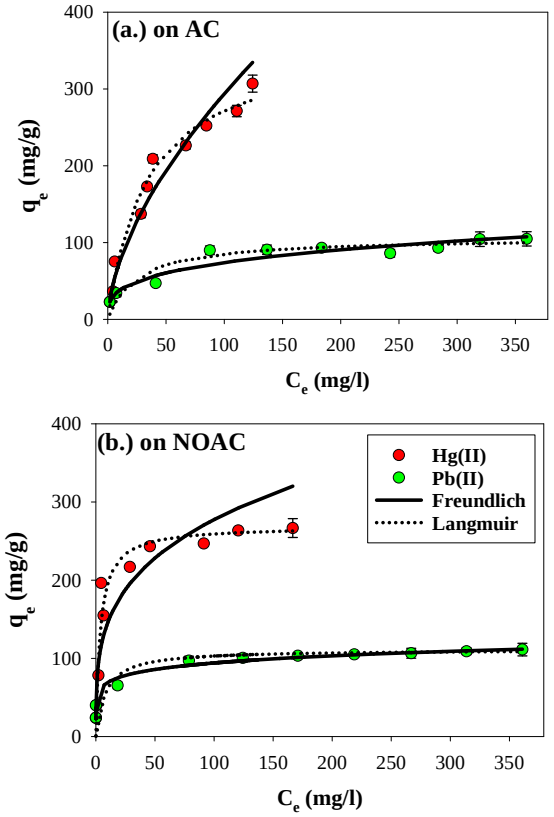

Figure 5 linear fitting curves of Langmuir and Freundlich isotherms on AC (a.) and NOAC. (b.)

Table 3. Fitting parameters of isotherm models.

Adsorbents	Metal ion	Langmuir			Freundlich		
		q_e (mg/g)	K_L (l/mg)	R^2	K_F (l/mg)	n	R^2
AC	Hg(II)	367.55	0.0299	0.967	18.68	1.6711	0.961
	Pb(II)	106.63	0.0394	0.979	19.26	3.4229	0.952
NOAC	Hg(II)	273.04	0.1769	0.994	70.85	3.5137	0.824
	Pb(II)	109.82	0.122	0.998	50.66	7.6061	0.933

4. CONCLUSION

This study confirms that activated carbon (AC) and nitrogen/oxygen-doped activated carbon (NOAC) derived from coconut shells are effective for removing Pb(II) and Hg(II) from aqueous solutions. Adsorption followed the pseudo-second-order kinetic model, indicating a chemisorption-dominated process. The Langmuir model best described the adsorption isotherms, suggesting monolayer adsorption. NOAC exhibited superior Pb(II) adsorption, while AC showed higher Hg(II) removal efficiency at high concentrations. The enhanced performance of NOAC resulted from increased surface area, pore volume, and nitrogen functionalization, improving metal binding affinity. These findings highlight the potential of modified activated carbons for efficient heavy metal removal.

ACKNOWLEDGMENTS

This work was supported by Suranaree University of Technology (SUT).

REFERENCES

[1] Dilokekunakul, W., Teerachawanwong, P., Klomkliang, N., Supasitmongkol, S., & Chaemchuen, S. (2020, 2020/06/01/). Effects of nitrogen and oxygen functional groups and pore width of activated carbon on carbon dioxide capture: Temperature dependence. Chemical Engineering Journal, 389, 124413.

[2] El-Wakil, A. M., Waly, S. M., Abou El-Maaty, W. M., Waly, M. M., Yılmaz, M., & Awad, F. S. (2022,2022/02/22).Triazine-Based Functionalized Activated Carbon Prepared from Water Hyacinth for the Removal of Hg2+, Pb2+, and Cd2+ Ions from Water. ACS Omega, 7(7), 6058-6069.

[3] Gao, Z., Cizdziel, J. V., Wontor, K., & Olubusoye, B. S. (2023, 2023/11/15/). Adsorption/desorption of mercury (II) by artificially weathered microplastics: Kinetics, isotherms, and influencing factors. Environmental Pollution, 337, 122621.

[4] Igwe, J. C., & Augustine, A. (2007, 04/09). Adsorption isotherm studies of Cd (II), Pb (II) and Zn (II) ions bioremediation from aqueous solution using unmodified and EDTA-modified maize cob. Eclética Química, 32(1), 33-42.

[5] Jarup, L. (2003). Hazards of heavy metal contamination. Br Med Bull, 68, 167-182.
[6] Kaźmierczak-Raźna, J., Ziola-Frankowska, A., Nowicki, P., Frankowski, M., Wolski, R., & Pietrzak, R. (2021, 11/20). Removal of Heavy Metal Ions from One- and Two-Component Solutions via Adsorption on N-Doped Activated Carbon. Materials, 14, 7045.
[7] Kepp, K. P. (2019, Aug 1). Free Energies of Hydration for Metal Ions from Heats of Vaporization. J Phys Chem A, 123(30), 6536-6546.
[8] Luo, T., He, M., Gao, C., Liu, J.-H., & Huang, X.-J. (2014, 2014/05/01/). Specific size-matching strategy for electrochemical selective and sensitive detection of mercury(II) based on a three-dimensional-gap-net in a Au–thiol coordination polymer. Electrochemistry Communications, 42, 26-29.
[9] Norsuhailizah, S., Zawati, H., & Norazlianie, S. (2020). A Review on Batch and Column Adsorption of Various Adsorbent Towards the Removal of Heavy Metal. Journal of Advanced Research in Fluid Mechanics and Thermal Sciences, 67(2), 66-68.
[10] Saleh, T. A., Mustaqeem, M., & Khaled, M. (2022, 2022/05/01/). Water treatment technologies in removing heavy metal ions from wastewater: A review. Environmental Nanotechnology, Monitoring & Management, 17, 100617.
[11] Sall, M. L., Diaw, A. K. D., Gningue-Sall, D., Efremova Aaron, S., & Aaron, J. J. (2020, Aug). Toxic heavy metals: impact on the environment and human health, and treatment with conducting organic polymers, a review. Environ Sci Pollut Res Int, 27(24), 29927-29942.
[12] Sethia, G., & Sayari, A. (2015, 2015/11/01/). Comprehensive study of ultra-microporous nitrogen-doped activated carbon for CO2 capture. Carbon, 93, 68-80.
[13] Tejada-Tovar, C., Villabona-Ortiz, A., & Gonzalez-Delgado, A. (2022, Oct 6). Adsorption Study of Continuous Heavy Metal Ions (Pb(2+), Cd(2+), Ni(2+)) Removal Using Cocoa (Theobroma cacao L.) Pod Husks. Materials (Basel), 15(19), 6937.
[14] Zhang, X., Jia, X., Zhang, G., Hu, J., Sheng, W., Ma, Z., Lu, J., & Liu, Z. (2014). Efficient removal and highly selective adsorption of Hg 2+ by polydopamine nanospheres with total recycle capacity. Applied Surface Science, 314, 166-173.
[15] Zhou, J., Yang, P., Kots, P. A., Cohen, M., Chen, Y., Quinn, C. M., de Mello, M. D., Anibal Boscoboinik, J., Shaw, W. J., Caratzoulas, S., Zheng, W., & Vlachos, D. G. (2023, Apr 21). Tuning the reactivity of carbon surfaces with oxygen-containing functional groups. Nat Commun, 14(1), 2293.

Development of composite scaffolds derived from palm kernel shell ash with curcumin encapsulation for tissue engineering applications

Manutchai Eiamniyom[1], Pornchai Bumroongsri[1,*]

[1] Department of Chemical Engineering, Faculty of Engineering, Mahidol University, Nakhon Pathom 73170, Thailand

[*] Corresponding author: pornchai.bum@mahidol.ac.th

ABSTRACT

In Thailand, palm kernel shell ash is the agricultural waste available in large quantities. This research presents a method to produce composite scaffolds from palm kernel shell ash for tissue engineering applications. In the first step, calcium oxide was obtained from palm kernel shell ash. Calcium oxide was then used to synthesize hydroxyapatite via a chemical synthesis method. In the second step, polylactic acid and hydroxyapatite were mixed and extruded into filaments. The composite scaffold was produced from filaments using 3D printing technique. The composite scaffold with the weight ratio between polylactic acid and hydroxyapatite of 60:40 exhibited the best mechanical properties. In the last step, curcumin was encapsulated and coated onto the surface of composite scaffold. The release of curcumin could be prolonged to 5 days. This research paves the way for producing composite scaffolds from palm kernel shell ash for tissue engineering applications.

Keywords: Composite scaffold; Palm kernel shell ash; Curcumin release; Tissue engineering

1. INTRODUCTION

Advancements in biomedical technology have greatly improved approaches to treating damaged or lost bone tissue. Bone scaffolds are now essential in fields like orthopedics and rehabilitation, aiding in the repair and replacement of lost bone. They not only restore bone structure and function but also stimulate new bone growth and help integrate surrounding tissues effectively. Bone scaffolds are crucial in orthopedics and soft tissue repair [1]. Their main purpose is to meet the patient's need for bone reconstruction. They are often used for bone fractures or areas of bone loss, promoting new bone growth and aiding healing. These materials also help maintain stability and movement in the affected region as the new bone regenerates. Additionally, it should be biodegradable, gradually breaking down and being absorbed by the body while maintaining a supportive structure for bone growth. Physical properties like strength, stiffness, and a suitable microstructure also play critical roles in promoting bone regeneration effectively [2].

Bone scaffolds can be crafted from diverse materials like inorganic compounds, metals, and biopolymers to address various orthopedic needs. Notable examples include calcium phosphate-based compounds, such as hydroxyapatite, which mirrors natural bone's chemical composition. Bioactive glasses and glass ceramics are widely used for their ability to promote tissue regeneration. Hydroxyapatite-type ceramics, with their crystal structure resembling bone, are also favored. Metal-ceramic composites merge the strength of metals with the bioactivity of ceramics, enhancing durability and impact resistance. Continuous research aims to develop advanced bone scaffolds, leveraging progress in biotechnology and science to refine their effectiveness.

Subramaniyan et al. [3] developed an optimized biomaterial using polylactic acid (PLA) and hydroxyapatite (HAp) for customized biomedical implants through additive manufacturing. Various weight percentages of HAp were incorporated into PLA and the resulting 3D-printed composites were analyzed for structural, mechanical, thermal, and in-vitro characteristics. Functional groups were identified using FTIR while thermal stability was confirmed through TGA and DSC. The composites showed enhanced mechanical properties with maximum tensile, compressive and flexural strengths observed at specific HAp concentrations. Overall, the results suggested that HAp reinforcement significantly improved the mechanical strength and biocompatibility of PLA, making the composite suitable for biomedical implant applications. In Fitriyana et al. [4], hydroxyapatite (HAp) was synthesized from crab shells which were typically discarded waste rich in calcium carbonate ($CaCO_3$). Using a hydrothermal method at 160 °C with holding times of 14, 16, and 18 hours, precipitated calcium carbonate (PCC) from crab shells was reacted with diammonium hydrogen phosphate ($(NH_4)_2HPO_4$) to produce HAp. The synthesized materials were

characterized using SEM, FTIR, and XRD. Results confirmed successful HAp formation, though traces of $CaCO_3$ remained as impurities. Increasing the hydrothermal holding time improved the crystallinity and reduced impurities. Rodovalho et al. [5] confirmed its ability to enhance cell proliferation, osteoconductive and osteogenic differentiation with in vivo experiments showing effective bone formation after eight weeks. The nanofiber composite demonstrated high tensile strength while HAp-whisker composites improved toughness without compromising bioactivity. The addition of graphene and strontium further enhanced thermal stability, bioactivity and porosity. HAp could increase density, hydrophilicity and interfacial adhesion with PLA while also neutralizing PLA's acidification effect by releasing phosphate ions and calcium. Moreover, carbonated HAp (5–10%) could improve roughness, crystallinity and scaffold porosity. Overall, the PLA/HAp composite stands out as a strong candidate for bone and dental tissue engineering due to its balanced mechanical, biological, and degradation properties.

Ji et al. [6] developed a novel 3D-printed scaffold designed for antibacterial bone repair by combining hydroxyapatite, chitosan, and sodium alginate interconnected using tannic acid to enhance bio-adhesion and mechanical stability. To address the critical issue of implant-related bacterial infections, the scaffold incorporated curcumin-loaded dendritic mesoporous organic silica nanoparticles which provided a controlled release of curcumin with potent antibacterial properties. The resulting scaffold exhibited excellent compressive strength, favorable degradation behavior, efficient mineralization in simulated body fluid and outstanding biocompatibility with bone cells. Antibacterial assays revealed highly effective inhibition against bacteria so this demonstrated a significant improvement in infection resistance. These findings suggested that the scaffold loaded with dendritic mesoporous organic silica nanoparticles gave great promise for application in bone tissue engineering.

Bioactive compounds can be coated onto the surface of scaffolds. Curcumin has a long history in traditional medicine, treating inflammation, respiratory conditions, and diabetic wounds. Its key bioactive compound exhibits anti-inflammatory, antioxidant, antibacterial, antiviral and immunomodulatory properties. However, curcumin's hydrophobic nature and rapid metabolism limit its effectiveness. To overcome this, researchers are exploring biomaterial-based drug delivery systems for localized and controlled release, enhancing curcumin's bioavailability while minimizing side effects. This paper developed composite scaffolds derived from palm kernel shell ash with curcumin encapsulation for tissue engineering applications. This research focused on integrating it into biomaterial platforms for targeted therapeutic delivery.

2. EXPERIMENTAL

Palm kernel shells were washed [7] dried and ground into uniform fine powder (<0.074 mm) using a 200- mesh sieve. The 40 g of powder was heated in a muffle furnace to 900°C at a rate of 10°C/min and maintained for one hour before naturally cooling overnight. The resulting powder was then oven-dried at 120°C for 24 hours and stored for further use. Which used acetic acid (CH_3COOH), produced calcium acetate that was later converted to calcium nitrate and calcined at 950 °C with urea

Hydroxyapatite (HAp) synthesis [8, 9] was carried out using highly pure calcium oxide (CaO) obtained from palm kernel shell ash. CaO 1.5 g was added to 100 ml of deionized water along with an appropriate amount of dipotassium hydrogen phosphate (K_2HPO_4) to maintain a Ca/P ratio of 1.67. The pH was adjusted to 12 by adding more K_2HPO_4. The mixture was stirred for 10 minutes, then placed in a heating chamber at 37°C. The self-reaction was allowed to proceed to complete the formation of HAp.

The synthesized hydroxyapatite (HAp) powder [10] was filtered, washed with distilled water, and dried at 40°C for one day. The dried powder was then calcined at 700, 800, 900 and 1000°C [11] for one hour in an electric furnace. For 3D printing, polylactic acid (PLA) pellets were mixed with HAp at ratios of 60:40, 70:30, 80:20 and 90:10. The mixture was extruded at 55 rpm and 145-151°C to produce filaments. These filaments were 3D printed at 210°C with a diameter set to 1.75 mm to create the final composite scaffold.

A curcumin encapsulation solution [12] was prepared by mixing 3.5 g of curcumin, 25 g of coconut oil, and 100 ml of Tween80, heated at 40°C for 2 hours (Solution 1). Sodium chloride (NaCl) 11.688 g was dissolved in 500 ml of DI water (Solution 2). The two solutions were mixed and cycled between 60°C and 90°C five times until the solution turned milky white. The mixture was filtered and blended with 150 g of maltodextrin for spray drying. The dried encapsulation was dissolved in DI water at 30%, 50% and 70% concentrations and used to coat 3D-printed scaffolds for 24 hours, followed by oven drying at 75°C. The curcumin release was tested by immersing the scaffold in distilled water and analyzing the solution using a UV-Vis instrument. The curcumin encapsulation was dried at 60 °C and then dissolved in DI water at a concentration of 30%, 50%, and 70% (ratio of 3:7, 5:5, 7:3). Then, the scaffold was 3D printed and coated [13] with curcumin encapsulation at the above ratio for 24 hours. It was then dried in an oven at a temperature of 75 °C. The cured scaffold was put into a test tube, 5 ml of distilled water was added, and the incubator shaker was used to suck up 0.5 ml of the solution from the tube. Then, 0.5 ml of distilled water was added. The concentration was measured using a UV-Vis instrument at 425 nm [14]. Measurements were taken every 6 hours for 5 days. The overall experimental steps are summarized in Fig. 1.

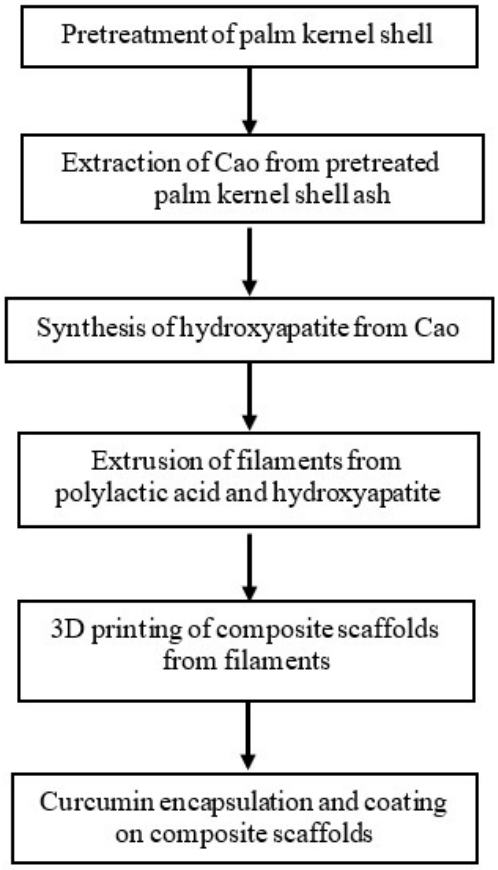

Figure 1 Overall experimental steps.

3. RESULTS AND DISCUSSION

Figure 2 shows an FTIR spectroscopy analysis of synthesized hydroxyapatite (calcium phosphate compound) as the calcination temperature increases from 700°C to 1,000°C. The calcination temperature at 1,000°C was selected because the functional groups of synthesized hydroxyapatite could be clearly identified.

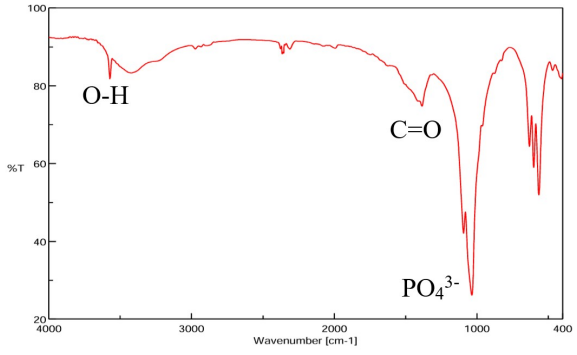

(a) FTIR spectra of HAp calcined at 700 °C

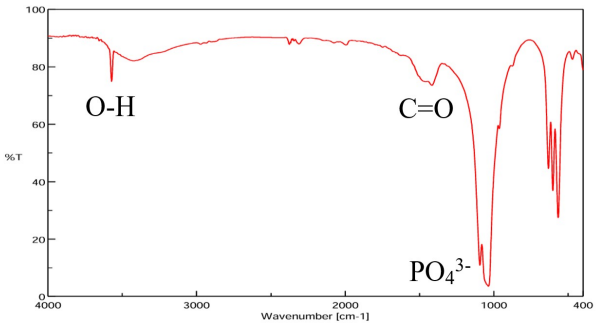

(b) FTIR spectra of HAp calcined at 800 °C

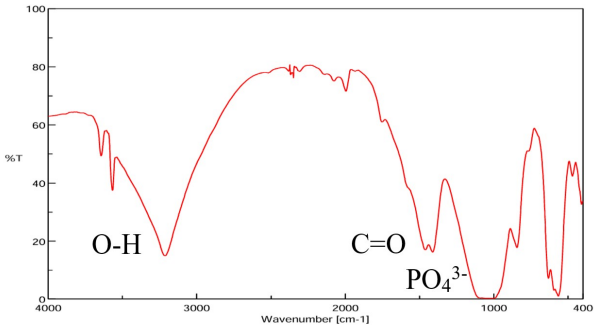

(c) FTIR spectra of HAp calcined at 900 °C

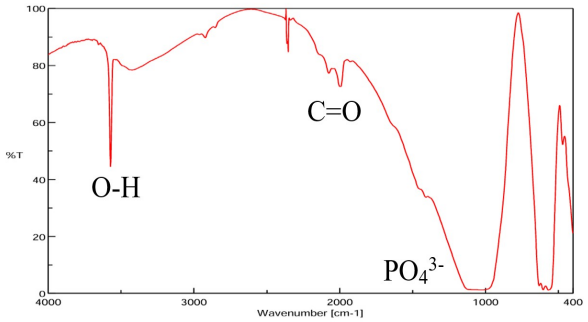

(d) FTIR spectra of HAp calcined at 1,000°C

Figure 2 FTIR spectra of synthesized hydroxyapatite.

Figure 3 shows an SEM image of PLA/HAp filaments. Pure PLA filament exhibited a smooth, uniform surface with minimal roughness, lacking visible particles and intricate surface features. Its edges were clean and sharp. In contrast, PLA filament containing hydroxyapatite displayed significantly rougher and more complex surface.

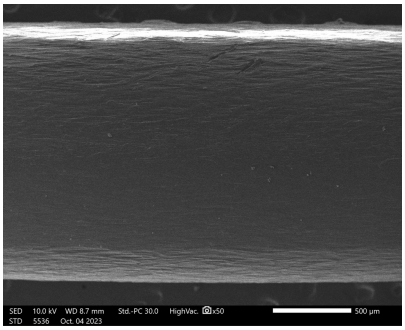

(a) PLA filament

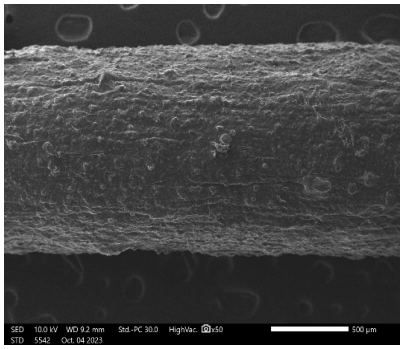

(b) PLA/HAp filament

Figure 3 SEM images of (a) PLA filament and (b) PLA/HAp filament.

The composite scaffold as shown in Fig. 4 was produced from filaments using 3D printing technique. The composite scaffold exhibited mechanical properties such as compressive strength and elastic modulus that were suitable for bone graft applications.

Figure 4 Composite scaffold.

As shown in Table 1, scaffolds with polylactic acid (PLA) and hydroxyapatite (HAp) ratios of 50:50, 60:40, and 70:30 demonstrated compressive strengths of 51 MPa, 58 MPa, and 46 MPa, respectively. The corresponding elastic moduli were 4,397 MPa, 4,416 MPa, and 4,321 MPa. The composite scaffold with the composition of PLA 60%wt and HAp 40%wt exhibited the best mechanical properties.

Table 1 Mechanical properties of composite scaffold.

PLA : HAp (%wt)	Compressive strength (MPa)	Elastic modulus (MPa)
50:50	51	4,397
60:40	58	4,416
70:30	46	4,321

In the last step, curcumin was encapsulated and coated onto the surface of composite scaffold. Figure 5 shows the curcumin release curve. It illustrated an increase in the curcumin concentration over time. The release of curcumin could be prolonged to 5 days as shown in Fig. 5. The curcumin 70% (w/v) exhibited the highest release rate.

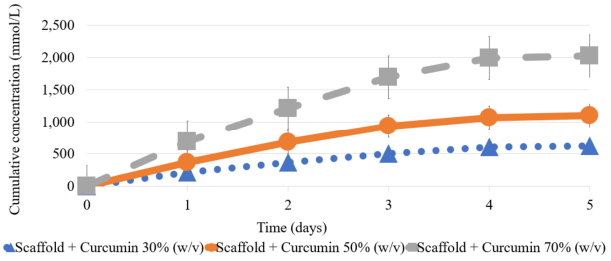

Figure 5 Release of curcumin from composite scaffold.

The FTIR results of released curcumin are shown in Fig. 6. Both spectra exhibited characteristic peaks corresponding to key functional groups. The similarity in these peaks confirmed that main chemical structure of curcumin was preserved after release.

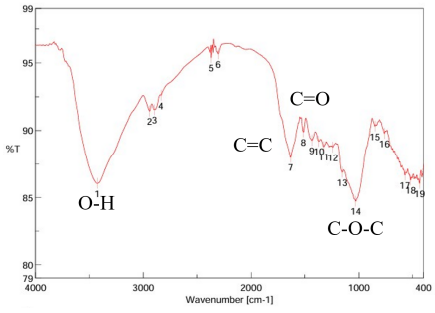

(a) standard curcumin

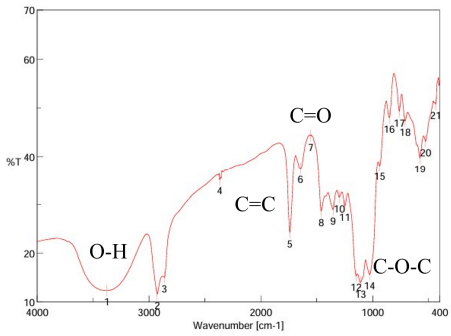

(b) released curcumin

Figure 6 FTIR results showing (a) standard curcumin and (b) released curcumin.

4. CONCLUSION

This study successfully demonstrated the transformation of palm kernel shell ash, an abundant agricultural waste, into value added composite scaffolds for tissue engineering applications. By synthesizing hydroxyapatite from calcium oxide extracted from the palm kernel shell ash and combining it with polylactic acid, the resulting composite scaffolds exhibited mechanical properties particularly at a 60:40 ratio suitable for bone tissue applications. Furthermore, curcumin encapsulation and coating enabled sustained drug release for up to 5 days which offered potential for localized therapeutic delivery. Overall, the developed scaffolds promoted sustainable use of agricultural waste for biomedical applications.

ACKNOWLEDGMENTS

This research project is supported by Mahidol University (Fundamental Fund: fiscal year 2023 by National Science Research and Innovation Fund (NSRF)).

REFERENCES

1. S. Sharma, P. Goyal. Synthesis, characterization and in-vitro study of hydroxyapatite, silver substituted hydroxyapatite and iron substituted hydroxyapatite for bone tissue engineering applications. *Results in Chemistry* 2025; 15: 102167.
2. S. Su, J. Bai, R. Wang, S. Gao, R. Zhou, F. Zhou. A novel strategy for bone defect repair: Stromal cell-derived factor 1α sustained-release acellular fish scale scaffolds combined with injection of bone marrow mesenchymal stem cells promote bone regeneration. *Materials Today Bio* 2025; 32: 101759.
3. M. Subramaniyan, S. Karuppan, S. Helaili, I. Ahmad. Structural, mechanical, and in-vitro characterization of hydroxyapatite loaded PLA composites. *Journal of Molecular Structure* 2024; 1306: 137862.
4. D.F. Fitriyana, R. Ismail, A.P. Bayuseno, J.P. Siregar and T. Cionita. Characterization of hydroxyapatite extracted from crab shell using the hydrothermal method with varying holding Times. *Journal of Renewable Materials* 2024; 12(6): 1145-1163.
5. A.J.R.L. Rodovalho, W.T. Barbosa, J.L. Vieira, C.A.D. Oliva, A.P.B. Gonçalves, P.D.S.M. Cardoso, H.B. Modolon, O.R.K. Montedo, S. Arcaro, K.V.S. Hodel, M.B.P. Soares, P. M. Ajayan, J.D.V. Barbosa. Influence of size and crystallinity of nanohydroxyapatite (nHA) particles on the properties of Polylactic Acid/nHA nanocomposite scaffolds produced by 3D printing. *Journal of Materials Research and Technology* 2024; 30: 3101-3111.
6. C. Ji, C. Zhang, Z. Xu, Y. Chen, Y. Gan, M. Zhou, L. Li, Q. Duan, T. Huang and J. Lin. Mussel-inspired HA@TA-CS/SA biomimetic 3D printed scaffolds with antibacterial activity for bone repair. *Frontiers in Bioengineering and Biotechnology* 2023; 11: 1193605.
7. R. Manurung, S.Z.D.M. Parinduri, R. Hasibuan, B.H. Tarigan, A.G.A. Siregar. Synthesis of nano-CaO catalyst with SiO2 matrix based on palm shell ash as catalyst support for one cycle developed in the palm biodiesel process. *Case Studies in Chemical and Environmental Engineering* 2023; 7: 100345.
8. I. Loughlaimi, Z. Bakher, A. Zouhri. Enhanced heavy metal removal from wastewater produced by chemical analysis laboratory using calcium oxide precipitation: pH improvement and characterization of precipitated phases. *Journal of the Turkish Chemical Society Section A: Chemistry* 2024; 11(1): 83-92.
9. Z. Fu, W. He, Y. Rao, G. Du, N. Wang, S. Wang. A highly selective and low-discharge method for vanadium extraction from vanadium slag: Low-calcification roasting-sodium bicarbonate leaching. *Separation and Purification Technology* 2025; 361: 131584.
10. M.J.A. Mansor, K.W.P. Hieng, S.A. Rosli, N.H. Othman, M.H.M. Yusoff, and S.Z. Abidin. Optimization of calcium oxide extraction from carbide lime via acid leaching a response surface methodology analysis. *Malaysian Journal of Analytical Sciences* 2024; 25(5): 1071-1086.
11. A.M. Castillo-Paza, K.V.G. Vazquez, D.F.C. Davila, M.A.H. Landaverde, L.H..C Chan, R.R. Bon, M.E.R. Garcia. In vitro immersion study and characterization of biomimetic bovine hydroxyapatite scaffolds: Influence of calcination temperature (600 and 1000 ◦C) on apatite formation. *Ceramics international* 2024; 50(15): 26949-26962.
12. J. Lin, Y. Chiang, P. Li and P. Chiang. Structural and release properties of combined curcumin controlled-release tablets formulated with chitosan/sodium alginate/HPMC. *Foods* 2024; 13(13): 2022.
13. R. Chen, J.L. Funnell, G.B. Quinones, M. Bentley, J. R. Capadona, R.J. Gilbert, E.F. Palermo. Poly(pro-curcumin) materials exhibit dual release rates and prolonged antioxidant activity as thin films and self-assembled particles. *Biomacromolecules* 2023; 24(1): 294-307.
14. S. Bose, N. Sarkar, U. Majumdar. Micelle encapsulated curcumin and piperine-laden 3D printed calcium phosphate scaffolds enhance *in vitro* biological properties. *Colloids and Surfaces B: Biointerfaces.* 2023; 231: 113563.

Simultaneous saccharification and fermentation (SSF) of corn cob for bioethanol production using *Saccharomyces cerevisiae* SC 90

Peerawat Suyatar[1], Maythee Saisriyoot[2], Nutchapon Chiarasumran[2], Penjit Srinophakun[2] Anusith Thanapimmetha[2,*]

[1] Department of Chemical Engineering, Faculty of Engineering, Kasetsart University, Bangkok, 10900, Thailand
[2] Bioprocess Engineering Laboratory, Department of Chemical Engineering, Faculty of Engineering, Kasetsart University, Bangkok, 10900, Thailand
[*] Corresponding author: fengjrc@gmail.com

ABSTRACT

The global challenge of air pollution, exacerbated by the emission of fine particulate matter ($PM_{2.5}$), remains the most pressing environmental and public health concerns of the modern era [1]. Among the various sources of such pollution, the field burning of agricultural residues, particularly corn cob, represents a significant contribution. This practice not only degrades air quality but also possess serious health risks, especially in rural area communities. Converting corn cob into a source of energy presents a sustainable and environmentally responsible alternative. As a cost-effective and widely available lignocellulosic material, corn cob can be converted into bioethanol through a series of biochemical processes [2]. Initially, corn cob was treated with 2% (w/v) H_2SO_4, after that it was treated with 2% (w/v) NaOH. This pretreatment step significantly increased its cellulose content from 32.28% to 90.21%. The novel method to discover the optimal temperature for simultaneous saccharification and fermentation (SSF) of pretreated corn cob is proposed. Fermentation at this optimal temperature (35.5 °C) resulted in the highest ethanol concentration of 33.17 g/L. These findings highlight the potential of proposed pretreatment and SSF techniques for different kinds of agricultural residues.

Keywords: Corn cob; Simultaneous saccharification and fermentation; SSF; *Saccharomyces cerevisiae*; Bioethanol;

1. INTRODUCTION

The escalating severity of fine particulate matter $PM_{2.5}$ pollution, comprising particles with an aerodynamic diameter of 2.5 micrometers or less, has become a critical environmental and public health crisis affecting numerous countries worldwide. A major contributor to this harmful air pollutant is the open burning of agricultural residues [3]. This practice directly releases $PM_{2.5}$ into the atmosphere, and due to their minute size, these particles can penetrate deep into the respiratory system and bloodstream, causing a wide range of severe human health impacts, including an increased risk of respiratory illnesses, cardiovascular diseases, and lung cancer [4]. These health consequences not only diminish the quality of life for citizens but also impose substantial burdens on national healthcare systems.

Thailand stands as one of the countries facing this unavoidable challenge, as the open burning of agricultural waste remains a prevalent and traditional disposal method, despite its negative environmental consequences. Statistics from 2023 highlight the gravity of the issue, revealing a significant 28% increase in the average $PM_{2.5}$ concentration in Thailand compared with that from 2022 [5]. This alarming trend underscores the urgent need for the identification and implementation of more sustainable solutions.

Among the vast quantities of agricultural byproducts generated in Thailand, corn cob represents a substantial and potentially valuable biomass resource, estimated at approximately 950,000 tons annually [6]. Regrettably, a significant portion of this corn cob continues to be managed through open burning. This practice not only contributes to the $PM_{2.5}$ air pollution problem but also represents a considerable loss of a potentially valuable economic resource. Consequently, as a crucial and necessary alternative, the research and development of efficient and environmentally benign strategies for the valorization of agricultural residues have emerged. Exploring methods to utilize these materials not only aids in mitigating pollution from burning but also promotes a circular economy and the more efficient use of resources. As a promising technique, the bioconversion of corn cob into bioethanol stands out as a highly effective strategy for the valorization of this agricultural residue.

With its substantial cellulose content, reaching up to 40% [7], corn cob is a valuable substrate for economic conversion into ethanol via fermentation. This bioethanol offers a renewable energy alternative, thereby lessening dependence on non-renewable fossil resources. Among the various ethanol fermentation strategies, Simultaneous Saccharification and Fermentation (SSF) stands out. SSF consolidates the enzymatic hydrolysis of cellulose or starch into fermentable sugars and the microbial fermentation of these sugars to ethanol in a single-step, single-reactor configuration. This integrated approach offers benefits such as reduced processing time and operational costs, alongside a decreased risk of microbial contamination. However, a key challenge associated with SSF is the optimization of the reaction temperature, which must accommodate the differing temperature optima of the enzymatic hydrolysis and microbial fermentation steps. Consequently, determination of a suitable temperature that balances the efficiency of both processes is critical for maximizing the overall performance of the SSF process.

2. EXPERIMENT

Kernels were removed from the corn cob, which were then washed and dry. The dried cob was then ground and sieved to obtain a particle size range of 20–80 mesh. Subsequently, the moisture content was reduced by oven-drying at 105 °C [8].

The corn cob, following size reduction, underwent pretreatment with a 2% (v/v) sulfuric acid solution at a biomass-to-liquid ratio of 0.1 g/mL at 121 °C for 45 minutes [9]. Subsequently, the pretreated biomass was washed with water until the pH of the washing effluent reached that of the water. The washed biomass was then dried in an oven at 105 °C [8] until a constant weight was attained. The pretreated corn cob was further subjected to alkaline pretreatment using a 2% (w/v) sodium hydroxide solution at a biomass-to-liquid ratio of 0.1 g/mL at 121 °C for 30 minutes [10]. The resulting biomass was then washed with water until the pH of the washing effluent was equivalent to that of the water and subsequently dried in an oven at 105 °C [8] until a constant weight was obtained. Finally, the chemical composition of the doubly pretreated corn cob was determined.

Chemical composition analysis of corn cob, including cellulose, hemicellulose, and lignin, was conducted following the analytical procedures of Goering and Van [11].

An investigation into the influence of hydrolysis temperature was conducted utilizing pretreated corn cob for enzymatic hydrolysis with Cellic CTec2 to produce glucose. The reaction was performed using a substrate loading of 10% (w/v) in 250 mL flasks, with an enzyme loading of 10 FPU/g-substrate at pH 5. Hydrolysis was carried out in a temperature-controlled incubator at 30 °C, 37 °C, and 40 °C with agitation at 150 rpm for 24 hours. Samples were collected and heat-inactivated in boiling water for 10 minutes, followed by centrifugation at 5,000 rpm for 15 minutes. The resulting supernatant was then analyzed for glucose concentration.

The influence of incubation temperature on the growth of *Saccharomyces cerevisiae* SC90 was then investigated. Glucose was employed as the carbon source at an initial concentration of 20 g/L, with the culture medium maintained at a pH of 5. Cultivations were conducted in 250 mL Erlenmeyer flasks containing a working volume of 50 mL, inoculated with *S. cerevisiae* SC90 at an initial concentration of 10% (v/v). These cultures were incubated at 30 °C, 37 °C, and 40 °C, under constant agitation at 150 rpm for a period of 24 hours. Aliquots were periodically sampled from each culture to determine the residual glucose concentration.

Subsequently, experiments were conducted under the determined optimal temperature conditions to evaluate the resulting ethanol production and all experiments in this study were repeated five times.

The concentrations of glucose and ethanol were quantified using HPLC with a Rezex ROA-Organic Acid I 00H-0138-K0 column (300 x 7.8 mm). A 0.005 N sulfuric acid solution was employed as the mobile phase at a flow rate of 0.6 mL/min. The eluent was monitored using a refractive index (RI) detector at a column temperature of 60 °C

3. RESULTS AND DISCUSSION

The chemical composition analysis of corn cob after the pretreatment revealed an increase in cellulose content from 32.28% to 90.21% of dry weight. Additionally, the hemicellulose and lignin contents were reduced to 1.33% and 2.34% of dry weight, respectively, as illustrated in Table 1. Following acid pretreatment, which primarily targets hemicellulose hydrolysis and reduction of cellulose crystallinity, the hemicellulose content was significantly decreased from an initial 47.49% to 3.21%. This acid pretreated step also facilitates the partial cleavage of either bonds within the lignin structure, resulting in a decrease in lignin molecular weight and structural complexity [12]. A subsequent alkali pretreatment further reduced the lignin content to 2.34%, attributed to the efficacy of caustic in lignin removal and its ability to induce cellulose swelling, thereby enhancing the accessible surface area for subsequent enzymatic hydrolysis [13].

The results from yeast dry cell weight and residual glucose concentration from the fermentation as well as glucose concentration from the hydrolysis are illustrated in Figure 1. The dry cell weights at 30 °C, 37 °C and 40 °C were 6.26 g/L, 4.14 g/L and 2.50 g/L, respectively. The optimal temperature for yeast proliferation was determined to be 30 °C, as indicated by the maximum dry cell weight achieved under this condition. Although complete glucose consumption

Table 1 The composition of corn cob before and after pretreatment

Chemical Composition	Percentages of dry weight		
	Before pretreatment	After H_2SO_4 pretreatment	After NaOH pretreatment
Cellulose	32.28 ± 0.45	64.92 ± 0.74	90.21 ± 1.82
Hemicellulose	47.94 ± 0.78	3.21 ± 0.93	1.33 ± 0.49
Lignin	5.26 ± 0.66	16.32 ± 0.03	2.34 ± 0.93
Other	14.51 ± 0.79	15.55 ± 0.57	6.12 ± 0.18

was also observed until 37 °C, result dry cell weight at 37 °C was lower than that at 30 °C. This suggests that while 37 °C supported substrate utilization, it likely imposed thermal stress on the yeast cells, diverting metabolic resources from new biomass synthesis towards cellular maintenance and repair, consequently leading to a reduced overall cell yield. Especially, at 40 °C, the dry cell weight was only 2.50 g/L, signifying the least favorable temperature for yeast growth. At this temperature, the yeast consumed very little glucose, resulting in a residual glucose concentration of 13.94 g/L.

Following enzymatic hydrolysis, the resulting glucose concentrations at temperatures of 30 °C, 37 °C, and 40 °C were measured as 21.24 g/L, 31.50 g/L, and 39.80 g/L, respectively. The highest glucose yield was observed at 40 °C, likely due to this temperature being more conducive to optimal enzyme activity, thereby promoting a greater degree of cellulose breakdown into glucose compared to the lower temperatures.

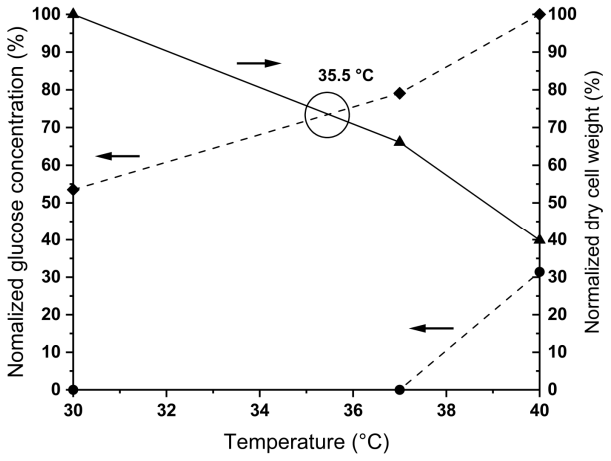

Figure 1 Normalized dry cell weight of *Saccharomyces cerevisiae* SC90 (—▲—) and normalized residual glucose concentration (-●-) from the fermentation, and normalized glucose concentration from the hydrolysis (-◆-)

Considering the optimal temperatures for the growth of yeast and hydrolysis efficiency as two primary variables, their intersection is at 35.5 °C. This temperature is deemed suitable for facilitating a compatible and reasonably efficient operation of both the saccharification and fermentation processes under concurrent conditions.

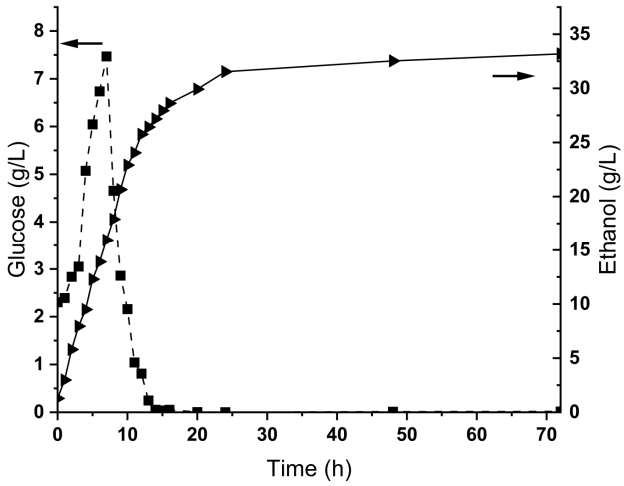

Figure 2 Glucose (-■-) and ethanol (—▶—) concentrations obtained from simultaneous saccharification and fermentation (SSF) of corn cob with *Saccharomyces cerevisiae* SC90 at a yeast concentration of 10% (v/v), at 35.5 °C, with agitation at 150 rpm for 72 hours

SSF at the optimal temperature is illustrated in Figure 2. The initial 0 to 7 hours fermentation period was characterized by a rapid accumulation of glucose, indicating that the enzymatic hydrolysis rate of cellulose to glucose exceeded the yeast's consumption rate. Despite the yeast's initial acclimation phase, glucose production outpaced its utilization, resulting in the highest glucose concentration of 7.46 g/L at the 7 hours. Subsequently, between 7 and 12 hours, the yeast's glucose consumption rate significantly increased to support energy generation and cellular proliferation, leading to a rapid decline in the system's glucose concentration. Concurrently, the ethanol concentration continued to rise. During the 12 to 24 hours interval, a deceleration in the yeast growth rate was observed, likely influenced by the increasingly limited glucose availability and the potentially inhibitory effects of the accumulating ethanol. Nevertheless, the residual glucose, albeit at declining concentrations, continued to be metabolized to ethanol, resulting in a sustained, albeit slower, increase in ethanol concentration. In the terminal phase of fermentation, after 24 hours, the near depletion of glucose and the potential attainment of inhibitory ethanol concentrations led to a cessation of yeast growth and a subsequent reduction in the rate of ethanol production, eventually resulting in a plateau in the ethanol concentration profile. The maximum

ethanol concentration achieved was 33.17 g/L at the culmination of the 72 hours fermentation period.

4. CONCLUSION

Corn cob pretreated with sulfuric acid and sodium hydroxide solutions exhibited an increase in cellulose content up to 90.21%. Subsequently, the optimal temperature for simultaneous saccharification and fermentation (SSF) of the pretreated corn cob was determined to be 35.5 °C. Employing this optimal temperature in the fermentation process yielded a maximum ethanol concentration of 33.17 g/L after 72 hours fermentation period.

ACKNOWLEDGMENTS

The authors thank The Graduate School, Kasetsart University, Thailand, for the scholarship. Faculty of Engineering, Kasetsart University for chance research and experiments. And Department of Chemical Engineering, Kasetsart University for support the location for my experimentation.

REFERENCES

1 Cohen, A.J., Brauer, M., Burnett, R. Estimates and 25-year trends of the global burden of disease attributable to ambient air pollution. *An analysis of data from the Global Burden of Disease Study 2015*. The Lancet 2017; 389(10082): 1907-1918

2 Zhao, B., & Zhang, Q. Agricultural biomass burning and its impact on air quality in China. A review. *Environmental Pollution* 2013; 179; 3-9

3 Pope, C. A., & Dockery, D. W. Health effects of fine particulate air pollution: lines that connect. *Journal of the Air & Waste Management Association* 2006; *56*(6): 709-742.

4 World Health Organization (WHO). *Review of evidence on health aspects of air pollution REVIHAAP Project*. WHO Regional Office for Europe; 2013.

5 IQAir. Thailand's average PM2.5 pollution in 2023 rises 28%. *The Star*; 2023.

6 Department of Alternative Energy Development and Efficiency. *Biomass Database Potential in Thailand*; 2023.

7 Sun, R., & Cheng, L. Chemical Composition and Characteristics of Corncob. *Journal of Agricultural and Food Chemistry* 2002; *50*(10): 2247-2251.

8 AOAC International. *Official Methods of Analysis of AOAC International* (16th ed.). Method 925.10: Moisture in Dried Fruits; 1995.

9 Zhang, M., Wang, F., Su, R., Qi, W., & He, Z. Ethanol production from high dry matter corncob using fed-batch simultaneous saccharification and fermentation after combined pretreatment. *Bioresource Technology* 2010; *101*(13): 4959-4964.

10 Xu, J., Cheng, J. J., Sharma-Shivappa, R. R., & Burns, J. C. Sodium Hydroxide Pretreatment of Switchgrass for Ethanol Production. *Energy Fuels* 2010; *24*: 2113-2119.

11 Goering, H. K., & Van, P. J. *Forage fiber analysis (apparatus, reagents, procedures, and some applications*. Agricultural Research Services. Agriculture Handbook; 1970; *3*(387-59).

12 Modenbach, A.A., Nokes, S.E. Effects of sodium hydroxide pretreatment on structural components of biomass. *Transactions of the ASABE*. 2014; 57(4): 1187-1198. [1]

13 Chaudhary, R., Khullar, S., Manan, A., Kumar, R., & Singh, D. Dilute-Acid Pretreatment of Lignocellulosic Biomass for Biofuels Production: Process Optimization and Techno-Economic Analysis. *Polymers*. 2018; 10(4):

Optimization of bovine serum albumin concentration and diafiltration via tangential flow filtration

Worrawich Boonpan[1], Natthapoom Thadalimawat[1], Pattarathorn Choosakvrrakul[1], Asawin Meechai[1,*]

[1] Department of Chemical Engineering, Faculty of Engineering, King Mongkut's University of Technology Thonburi, Bangkok 10140, Thailand
[*] Corresponding author: asawin.mee@kmutt.ac.th

ABSTRACT

This study aims to optimize process parameters for the concentration and diafiltration of a 100-L bovine serum albumin (BSA) solution, within 3-hour timeframe. The initial solution contained 1 g/L BSA in phosphate buffered saline (PBS) with 250 mM NaCl, and the final target was 5 g/L BSA in PBS with 137 mM NaCl. Given BSA's molecular weight of 66.5 kDa, Merk Millipore's cassettes with Ultracel® 10 kDa membrane were used. Process optimization was first conducted at a small scale using the Pellicon® XL cassettes (50 cm² filtration area), and later validated at larger scale using the Pellicon® 3 cassettes (88 cm²) to confirm process scalability. Transmembrane pressure (TMP) excursions were performed on 1 g/L and 5 g/L BSA solutions at three different feed flow rates (3, 5, and 7 LPM/m²) to determine the optimal TMP and flow rate for protein concentration. The optimal operating conditions were determined to be a TMP of 28 psi and a feed flow rate of 7 LPM/m². Further evaluation revealed that the optimal BSA concentration for diafiltration was 5 g/L. Using these optimal conditions, permeate fluxes obtained from small-scale experiments were used to determine the required volume and filter area for validation and scale-up. At the validated scale with Pellicon® 3, 1.2 L of BSA solution was successfully concentrated and buffer-exchanged within 2 hours and 58 minutes, achieving 81% BSA recovery. Thus, to process 100 L of BSA solution within 3 hours, a minimum area of Ultracel® 10 kDa filter of 0.63 m² is recommended.

Keywords: Tangential flow filtration; Bovine serum albumin; Optimization; Pellicon cassettes

1. INTRODUCTION

Tangential Flow Filtration (TFF) is a widely used technique in bioprocessing for protein concentration and buffer exchange due to its high flux rates, scalability, and efficient separation [1]. One of the most critical parameters for successful filtration is the selection of the appropriate membrane pore size. A membrane with too large a pore size may allow the target protein to pass through, leading to reduced yield, while an overly tight membrane can result in low flux and longer processing times. As a general guideline, a membrane with a molecular weight cut-off (MWCO) three to five times smaller than the molecular weight of the target protein is typically recommended to ensure efficient retention [2]. In addition to membrane pore size, the flux in TFF is also directly influenced by the Transmembrane Pressure (TMP). A low TMP can result in reduced flux, necessitating a larger membrane area and increasing processing time. Conversely, a high TMP may lead to membrane fouling, reducing efficiency. Therefore, optimizing TMP is essential to achieving a balance between maximizing flux and minimizing membrane fouling. In this study, bovine Serum albumin (BSA) was used as a model protein. BSA is widely applied in biochemical and pharmaceutical research due to its stability, solubility, and functional properties. It serves as a standard in protein quantification, a stabilizer in enzyme, vaccine formulations, a carrier molecule in drug delivery systems and cell-culture [3][4]. To retain BSA effectively, an Ultracel® membrane was selected. Ultracel® membranes, made from regenerated cellulose, offer high protein recovery, low fouling, and excellent chemical compatibility, making them highly suitable for sensitive biomolecule processing [5]. The process involves concentrating a 1 g/L BSA solution, followed by diafiltration using six diavolumes (6 DV) [6] to exchange the buffer from PBS containing 250 mM NaCl to PBS containing 137 mM NaCl.

2. EXPERIMENTAL

The Pellicon® XL system (Merck Millipore), installed with a Stand for Pellicon® XL featuring a membrane pore size of 10 kDa and an area of 50 cm²,

was used for the optimization and the Pellicon® 3 system (Merck Millipore), which was installed with a cassette filter holder featuring a membrane pore size of 10 kDa and an area of 88 cm², was used for the validation of a 5× concentration and diafiltration (exchange factor = 6) process for BSA solution.

2.1 Optimization of TMP

To determine the optimal TMP, TMP/flux curves were constructed by conducting filtration at fixed feed flow rates while systematically adjusting the retentate valve to obtain different TMP values. Experiments were conducted at three feed flux rates: 3, 5, and 7 LPM/m². For each experiment, the system was configured in total recirculation mode using a 1 g/L BSA solution as the initial feed. At each feed flux rate, the TMP was gradually adjusted in approximately 5 psi increments (e.g., 15, 20, 25, 30 psi) by regulating the retentate valve. After setting each TMP, the system was allowed to stabilize for 2 minutes before recording feed pressure, retentate pressure, and permeate flow rate. These values were used to calculate TMP and flux (in LMH). The collected data were plotted as TMP vs. Flux curves to identify the critical TMP defined as the point at which increasing TMP no longer results in a significant increase in flux. The optimal TMP was determined as 80% of this critical TMP to prevent membrane fouling. This procedure was repeated using a BSA concentration of 5 g/L, which corresponds to the final concentration after a 5× volume concentration factor. The comparison between 1 and 5 g/L allowed assessment of how protein concentration influences TMP-flux behavior, and helped identify the most suitable operating condition that balances high filtration performance and minimal membrane fouling.

2.2 Concentration Process

The concentration of BSA was carried out using the optimized TMP and feed flow rate obtained from the previous TMP optimization experiment. A 1 g/L BSA solution was used as the initial feed. The TFF system was operated in concentration mode, in which the retentate was continuously recirculated back to the feed tank while the permeate was collected separately. The feed flow rate and TMP were maintained at their optimal values throughout the process using manual valve adjustments. The concentration process was continued until the final retentate volume was reduced to one-fifth of the initial feed volume, resulting in a solution that was five times more concentrated. Permeate volume was measured and recorded every 2 minutes to monitor flux and ensure system stability. Meanwhile, as the filtration progressed, samples from both the permeate and retentate streams were collected every 10 minutes for BSA measurement. After the concentration step was completed, the retentate (concentrated BSA solution) was collected and reserved for use in the subsequent diafiltration step.

2.3 Determination of Optimal BSA Concentration for Diafiltration

The DF optimization parameter serves as a critical metric in determining the optimal protein concentration for performing diafiltration during ultrafiltration/ diafiltration (UF/DF) processes. Defined as the product of protein concentration (g/L) and permeate flux (LMH), this parameter reflects the trade-off between processing efficiency and membrane performance. By plotting the DF optimization parameter against varying concentrations, an optimum point can be identified that maximizes buffer exchange efficiency while minimizing processing time and membrane area.

2.4 Diafiltration Process

Diafiltration was carried out using the concentrated BSA solution (5× concentration) obtained from the previous concentration step. The process was performed using the same TMP and feed flow rate previously optimized for the final product concentration. During diafiltration, the feed tank was filled with the concentrated BSA solution while a buffer reservoir containing PBS Buffer with 137 mM of NaCl was connected to the system. As the permeate was continuously removed, an equal volume of the buffer was simultaneously pumped into the feed tank to maintain a constant working volume. The diafiltration process was continued until six diavolumes (DV = 6) were completed, ensuring that the initial buffer (PBS Buffer with 250 mM of NaCl) was fully exchanged with the final buffer (PBS Buffer with 137 mM of NaCl). At the end of the diafiltration, samples from both the permeate and retentate streams were collected for BSA measurement.

2.5 Measurement of Permeate Flux

Permeate flux was measured during each filtration step to evaluate membrane performance under varying operating conditions. The volume of permeate was collected using a graduated cylinder over a fixed time interval, typically two minutes. Permeate flux was then calculated using the following formula:

$$\text{Flux (LMH)} = \frac{V}{A \times t}$$

where V is the permeate volume (L), A is the membrane surface area (m²), and t is the time (h).

2.6 Measurement of BSA Concentration

The concentration of BSA was determined using UV absorbance at a wavelength of 280 nm. The protein concentration was calculated by comparing the absorbance values to a standard curve prepared from known BSA concentrations. This method provided accurate monitoring of protein concentration and enabled mass balance calculations throughout the concentration and diafiltration processes.

2.7 Calculation of Sample Load for Scale up process

Based on data obtained from the optimization of concentration and diafiltration at small scale, a more accurate calculation of sample load for large-scale filtration was performed. The calculation was based on a 5× concentration (average flux 128.5 LPH/m^2) and diafiltration (exchange factor 6, average flux 127.4 LPH/m^2)

For the calculation, an overall process time of three hours was selected:

$$A = 1.2 \times \left(\frac{V_{con}}{flux_{ave}} + \frac{V_{dia}}{flux_{dia}}\right) / t_{tot}$$

Where:

A = membrane area (m^2)
t_{tot} = total process time (h)
V_{conc} = permeate volume from concentration (L)
V_{dia} = permeate volume from diafiltration (L)
$flux_{ave}$ = average flux during concentration (LPH/m^2)
$flux_{dia}$ = average flux during diafiltration (LPH/m^2)

A safety factor of 20% (1.2 in the equation) was applied in the calculation of membrane area to ensure optimal processing conditions.

To demonstrate scalability, the process was validated using the Pellicon® 3 system, equipped with a Pellicon® 3 cassette (88 cm^2) with a 10 kDa membrane pore size. The process involved a 5× concentration, followed by diafiltration (exchange factor 6) to achieve the desired buffer conditions. The operation was conducted at an optimal TMP and controlled flux conditions. The initial volume of the BSA solution used for the 88 cm^2 cassette was calculated to be 1.2 L. A summary of the process parameters used at both small and validated scales is shown in Table 1.

Table 1 Summary of process parameters

	Pellicon® XL	**Pellicon® 3**
Start volume	500 mL	1200 mL
Final volume	100 mL	250 mL
Start concentration	1 g/L	1 g/L
Target concentration	5 g/L	5 g/L

3. RESULTS AND DISCUSSION

3.1 Process Optimization

Based on the TMP/Flux graph presented in Fig. 1 (a) and (b), the optimal flow rate for the serum albumin solution was determined to be 7 LPM/m^2. This selection was made because the flux values at 7 LPM/m^2 and 5 LPM/m^2 were nearly identical. By choosing 7 LPM/m^2, membrane costs can be minimized for large-scale processes. Additionally, a TMP of 28 psi was selected since increasing TMP beyond this value did not result in a significant flux enhancement. Higher TMP values could also lead to membrane fouling, negatively impacting filtration performance.

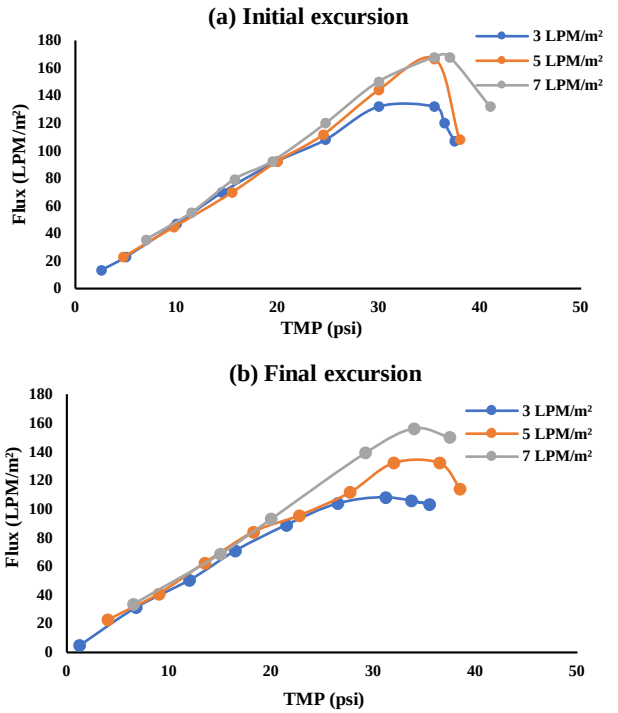

Fig.1 Flux plotted against TMP using (a) 1 g/L (b) 5 g/L BSA solution

To determine the optimal concentration for diafiltration, the relationship between permeate flux and product concentration was analyzed. The goal was to determine the concentration at which the filtration process remains efficient while avoiding excessive flux decline or operational challenges. The first step involved evaluating the flux at different product concentrations to observe how concentration affects membrane performance. As shown in Fig. 2, the permeate flux remains relatively stable across increasing product concentrations, suggesting that the filtration process is not significantly hindered by the concentration range examined. The slight decrease in flux at higher concentrations indicates the beginning of concentration polarization or increased viscosity effects, but no severe fouling is observed within the tested range.

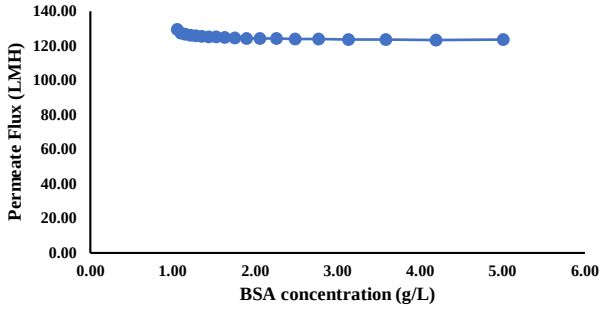

Fig.2 Permeate flux at different BSA concentrations

The second step focused on DF optimization by plotting the relationship between product concentration and the DF optimization parameter. As shown in Fig. 3,

a strong linear correlation is observed, indicating that increasing product concentration directly enhances diafiltration efficiency [6]. Typically, this graph follows an inverted parabolic trend, where the optimization parameter initially increases before reaching a peak, beyond which concentration polarization begins to dominate, leading to a decline in flux. However, in this experiment, the tested concentration range was still below the peak point, meaning that concentration polarization had not yet significantly impacted flux. As a result, the optimization point was chosen as the final concentration of 5 g/L obtained from the experiment, representing the highest tested concentration before reaching the expected polarization threshold. This ensures that the process operates efficiently while avoiding excessive membrane fouling and flux decline.

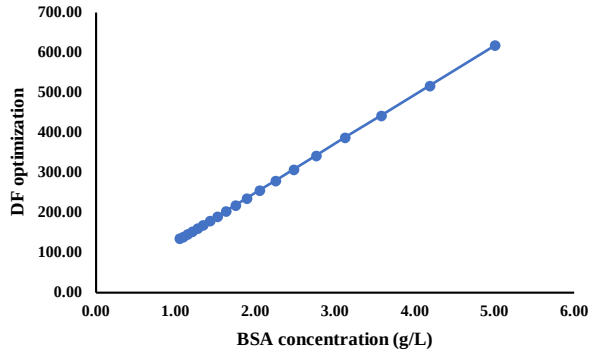

Fig.3 Optimization of BSA concentration for diafiltration

3.1 Process Verification and Scale-up

The performance of the TFF process was evaluated through both small- and validated-scale experiments, with recovery data summarized in Table 2 and Table 3.

Table 2 Recovery of BSA in small scale using Pellicon® XL Cassette

Sample	Volume (mL)	Protein Con. (g/L)	Protein amount (g)	Recovery (%)
Initial feed	500	0.98	0.49	-
Retentate + Flush	98	4.83	0.47	97
Permeate	668	0.09	0.06	12

Table 3 Recovery of BSA in validated scale using Pellicon® 3 Cassette

Sample	Volume (mL)	Protein Con. (g/L)	Protein amount (g)	Recovery (%)
Initial feed	1200	1.01	1.22	-
Retentate + Flush	350	2.83	0.99	81
Permeate	1300	0	0	0

In the small-scale experiment using the Pellicon® XL system, 500 mL of 1 g/L BSA solution was concentrated fivefold, resulting in a final retentate volume of 98 mL with a protein concentration of 4.83 g/L, yielding a protein recovery of 97%. This high recovery reflects minimal protein loss and is likely due to the precise volume handling during the flushing step, in which small beakers were used to gradually refill the retentate and carefully recover the protein with minimal deviation from the target volume. The data obtained from this small-scale experiment were subsequently used to calculate the operation initial volume for the validated scale, ensuring that scale-up parameters remain consistent with the optimized performance achieved at small scale. The outcome of this experiment was suboptimal, as the protein recovery percentage (81%) was lower than expected, suggesting that the process did not perform as efficiently as intended. Specifically, the validated-scale experiment using the Pellicon® 3 system started with 1,200 mL of feed solution and achieved a final retentate volume of 350 mL at a concentration of 2.83 g/L, corresponding to a total protein recovery of 81%. Although the membrane type and operating parameters were kept consistent, the noticeably lower recovery in the validated-scale run was likely due to inaccuracies in sample handling, particularly during the flushing and collection stages. In this case, a larger beaker was used and the final volume was estimated based on volume markings rather than being added incrementally, which may have caused under-collection or unnoticed sample loss. This method lacks precision, and the use of a graduated cylinder instead of a large beaker would have been more appropriate to ensure accurate volume measurement and minimize handling errors. Following the validated-scale experiment, the membrane area required for larger-scale processing was calculated based on the observed filtration performance and time constraints. Therefore, to process 100 L of BSA solution within 3 hours, a minimum membrane area of 0.63 m^2 using an Ultracel® 10 kDa filter is recommended. To further improve recovery during scale-up, enhanced precision in volume measurement and careful retentate collection are also advised.

4. CONCLUSION

An optimized TFF process was developed for the concentration and diafiltration of BSA, aiming to achieve high protein recovery, efficient buffer exchange, and scalability for processing 100 L of solution within a 3-hour timeframe. The optimization focused on key parameters including TMP, feed flow rate, and diafiltration volume to minimize processing time while ensuring high recovery. At the small scale, the process was conducted using Pellicon® XL Ultracel® 10 kDa membranes with a membrane area of 50 cm^2. A starting volume of 500 mL of 1 g/L BSA in phosphate-buffered saline (PBS) containing 250 mM NaCl was processed. The system was operated under

optimized conditions, resulting in a 5× concentration and successful buffer exchange to PBS containing 137 mM NaCl using six diavolumes. The final product volume was 98 mL, and protein recovery reached 97%, with a total processing time of 2 hours and 30 minutes. This indicated minimal fouling, stable flux, and effective retention of the target protein. To evaluate scalability, the same protocol was applied at a validated scale using Pellicon® 3 Ultracel® 10 kDa membranes with a membrane area of 88 cm^2. A 1.2 L batch of BSA solution was processed under identical TMP and feed flow rate conditions. The concentration step and buffer exchange were completed within 2 hours and 58 minutes. The final product volume was 350 mL, and the overall recovery was 81%. The decrease in recovery compared to the small-scale run was attributed to handling losses during sample collection and flushing, rather than inefficiencies in the membrane performance itself. These findings confirm that the optimized TFF process for BSA is robust and scalable. It enables efficient protein concentration and buffer exchange within the timeframe, making it highly suitable for downstream bioprocessing. Furthermore, based on the experimental results, a membrane area of 0.63 m^2 is recommended to process 100 L of BSA solution within 3 hours under the same operating conditions.

ACKNOWLEDGMENTS

This research was made possible through the support of the Biopharmaceutical Training & Educational Center (BTEC) and the Department of Chemical Engineering, KMUTT.

REFERENCES

1. Raghunath **S.** A Review on Tangential Flow Filtration for Separation and Purification of Biomolecules. *JSM Biotechnol Bioeng*. 2015;3(1):1071.
2. Proner MC, Marques IR, Ambrosi A, Rezzadori K, Costa C, Zin G, et al. Impact of MWCO and Dopamine/Polyethyleneimine Concentrations on Surface Properties and Filtration Performance of Modified Membranes. *Membranes*. 2020;10(9):239.
3. Martín-García C, García-Molina IM, Ruiz-Matute B, Moreno MA. Ultrafiltration techniques to obtain and concentrate bioactive compounds from agro-food by-products. *Int J Mol Sci*. 2021;22(16):8411.
4. Tang Y, Zhang J, Zhang Y, Jiang W, Yang X, Zhang L, et al. Applications of human and bovine serum albumins in biomedical engineering. *Int J Biol Macromol*. 2023;246:126914.
5. Aylin Mohammadzadehmarandi , Andrew L. Zydney. Buffer effects on protein sieving losses in ultrafiltration and their relationship to biophysical properties. *Biotechnol Prog*. 2021;37(1):e3481.
6. Van Reis R, Gadam S, Frautschy L, Orlando S, Goodrich E, Saksena S, et al. High performance tangential flow filtration. *Sep Sci Technol*. 1997;32(1-4):709–39.

Thermo-responsive PVDF-grafted-PVNCL membranes with switchable wettability for efficient oil-water separation

Supakorn Janmunee[1,*], Waritha Janthaporn[1], Saiwan Nawalertpanya[1]

[1] Department of Chemical Engineering, Faculty of Engineering, King Mongkut's University of Technology Thonburi, Bangkok 10140, Thailand
[*] Corresponding author: supakorn.janm@kmutt.ac.th

ABSTRACT

Industrial activities in the oil and gas, petrochemical, pharmaceutical, and food and beverage sectors are significant contributors to oily wastewater generation. This environmental concern poses serious threats to drinking water quality, groundwater reservoirs, aquatic ecosystems, and human health [1]. To address these challenges, membrane technology has emerged as an efficient and environmentally friendly solution for oil-water separation, offering high efficiency and exceptional capacity. This study focuses on developing thermo-responsive membranes through alkali pretreatment and UV-induced surface modification of commercial polyvinylidene fluoride (PVDF) membranes. Alkali pretreatment using a sodium hydroxide (NaOH) solution introduces hydroxyl groups onto the PVDF membrane surface. Subsequently, surface modification with 3-methacryloxypropyltrimethoxysilane (MPTS) enhances adhesion for the polymerization step. Poly(N-vinyl caprolactam) (PNVCL) is then successfully grafted onto the PVDF surface via a UV-induced surface modification method, using α-ketoglutaric acid (KGA) as a photo-initiator. The modified membranes were thoroughly characterized by FT-IR, XPS, SEM and water contact angle measurement. The membrane performance tests have shown that the surface membrane modification by PVNCL enhances hydrophilicity while imparting thermo-responsive properties, thus enabling highly efficient oil-water separation [2].

Keywords: Polyvinylidene fluoride; N-vinylcaprolactam; Thermo-responsive; Surface modification; Oil/water separation

1. INTRODUCTION

The rapid industrial development across the oil and gas, petrochemical, pharmaceutical, and food and beverage sectors has resulted in the generation of substantial amounts of oily wastewater. This wastewater poses significant environmental risks, including contamination of drinking water and groundwater resources, adverse effects on aquatic life, and potential harm to human health, in addition to contributing to atmospheric pollution [1, 3]. Conventional oil/water separation methods, such as gravity sedimentation, flocculation, biological treatment, adsorption, and membrane separation, are associated with several limitations, including high costs, excessive energy consumption, large space requirements, the potential for secondary pollution, and low separation efficiency [4, 5]. In recent years, membrane technology has emerged as a promising alternative for oil/water separation due to its environmentally friendly nature, high separation efficiency, low energy consumption, and the absence of the need for additional chemicals. Despite these advantages, practical applications of membrane technology are hindered by issues such as poor long-term stability, fouling, and a short membrane lifespan [5]. Fouling, caused by concentration polarization and pore blocking, significantly degrades membrane performance. This issue can be mitigated by using highly hydrophilic and low-fouling membranes, as well as by optimizing the pretreatment processes [6, 7, 8].

Polyvinylidene fluoride (PVDF) membranes are widely utilized in membrane technology due to their excellent mechanical strength, chemical resistance, thermal stability, and oxidation resistance. These properties make PVDF membranes suitable for a variety of applications, including drinking water treatment, food and beverage processing, gas separation, and wastewater treatment. However, the hydrophobic nature of PVDF membranes leads to fouling, which reduces both membrane performance and permeate flux. To address this issue, surface modification is essential to enhance the membrane's hydrophilicity [9, 10].

N-vinylcaprolactam (NVCL) is a thermo-responsive, water-soluble nonionic amphiphilic polymer. It consists of a seven-membered cyclic amide structure with a polar hydrophilic carboxyl group and an amide group attached to a hydrophobic vinyl chain.

NVCL is soluble in water at ambient temperature, but it undergoes a phase transition and becomes insoluble at a lower critical solution temperature (LCST) in the range of 30–32°C [11]. In this study, PVDF membranes were pretreated with varying concentrations of sodium hydroxide (NaOH) to introduce hydroxyl groups on the membrane surface. The membranes were then modified with 3-Methacryloxypropyltrimethoxysilane (MPTS) and grafted with PNVCL via UV-induced polymerization to enhance hydrophilicity and impart thermo-responsive properties, which are beneficial for efficient oil/water separation. α-Ketoglutaric acid (KGA) was used as a photoinitiator for the polymerization process.

2. EXPERIMENTAL

2.1. Materials

Polyvinylidene fluoride (PVDF) membranes with a pore size of 0.22 μm and a diameter of 47 mm were purchased from Filtrex Technology Pte Ltd, Singapore. N-vinylcaprolactam (NVCL, 98%), 3-Methacryloxy-propyltrimethoxysilane (MPTS, AR grade), α-Ketoglutaric acid ($C_5H_6O_5$, AR grade) were obtained from Merck Pte. Ltd, Singapore. Sodium hydroxide (NaOH, pellets, AR grade), ethanol (C_2H_5OH, AR grade), methanol (CH_3OH, AR grade), and toluene ($C_6H_5CH_3$, AR grade) were supplied by Qrec (Asia) Sdn. Bhd, Malaysia. Tween 80 (Polysorbate 80) was supplied by Labchem Sdn Bhd, Malaysia and soybean oil was purchased from local supermarket (SD Guthrie International Morakot Public Company Limited). All the chemicals were used as received without any further purification.

2.2. Membrane Pretreatment and Surface Modification Procedure

Prior to surface modification, polyvinylidene fluoride (PVDF) membranes were immersed in deionized (DI) water overnight to eliminate surface contaminants. The membranes were then subjected to alkaline pretreatment by immersion in sodium hydroxide (NaOH) solutions of varying concentrations (1-5 M) at 70 °C for 3 h. Following the treatment, the membranes were immediately rinsed with 50% (v/v) ethanol to quench the reaction and subsequently washed with DI water. This step was crucial to neutralize the membrane surface before initiating the subsequent functionalization process.

For surface modification, 3-methacryloxypropyl-trimethoxysilane (MPTS) was employed as a silane coupling agent to facilitate the interaction between hydroxyl groups on the PVDF-OH surface and the initiator used in free radical polymerization. The pretreated PVDF-OH membranes were immersed in a silane solution composed of 1 mL MPTS in 200 mL toluene for 3 h at an ambient temperature. After silanization, the membranes were thoroughly rinsed with methanol and DI water to remove any unreacted MPTS residues.

2.3 Preparation of Thermo-responsive Membranes

Thermo-responsive PVDF-g-PNVCL membranes were prepared via a free radical polymerization technique [17] using α-ketoglutaric acid (KGA) as a photoinitiator. Monomer solutions were first prepared by dissolving 3 g of N-vinylcaprolactam (NVCL), corresponding to a concentration of 0.2 g/mL, in 15 mL of deionized water, along with a fixed amount of 0.0365 g of KGA. The solution was stirred using a magnetic stirrer for approximately 30 minutes until a homogeneous mixture was obtained. Subsequently, the surface-modified PVDF membranes were immersed in the monomer solution and left to soak for 3 hours at room temperature to allow sufficient monomer diffusion and surface interaction. Polymerization was then initiated by exposing the membranes to UV irradiation at 365 nm for 5 minutes, with the membranes placed on the lid of a Petri dish and covered to minimize evaporation during the process. Following polymerization, the membranes were thoroughly rinsed with 50% (v/v) ethanol and deionized water to remove any unreacted poly(N-vinylcaprolactam) (PNVCL) from the surface. Finally, the membranes were neutralized and immersed in deionized water for at least 12 h prior to further use.

2.4 Membrane Characterization

The modified membrane surfaces were characterized using a variety of analytical techniques. Fourier-transform infrared spectroscopy (FT-IR) was employed to identify functional groups present on the membrane surface. X-ray photoelectron spectroscopy (XPS) was used to determine the elemental composition and chemical states on the membrane surface. Scanning electron microscopy (SEM) was utilized for detailed surface morphology characterization. To evaluate surface wettability, a water contact angle meter was used to measure the contact angle of deionized water on the membrane surface at room temperature, providing insight into the hydrophilicity of the membranes.

3. RESULTS AND DISCUSSION

3.1. Effect of NaOH Pretreatment on Membrane Surface

The surface of pristine PVDF membranes was pretreated using sodium hydroxide (NaOH) solutions at 70 °C for 3 h to introduce hydroxyl groups through a dehydrofluorination process. This chemical reaction involves the substitution of fluorine atoms in the PVDF backbone with hydroxide ions (OH^-), thereby enhancing surface reactivity for subsequent modification [12]. A range of NaOH concentrations from 1 to 5 mol/L was explored to determine the optimal conditions for effective surface activation. Following the NaOH treatment, the membranes were

rinsed with 50% ethanol solution and deionized water to neutralize the surface and terminate the reaction. A significant visual transformation was observed in the membranes post-treatment: the surface color changed distinctly from white to brown, indicating successful chemical modification. This color shift, as depicted in Figure 1, becomes more pronounced with increasing NaOH concentration, which is consistent with the progressive removal of fluorine and the formation of conjugated structures on the membrane surface. These findings confirm the effectiveness of NaOH treatment in initiating dehydrofluorination and suggest that surface color change can be used as a qualitative indicator of chemical modification.

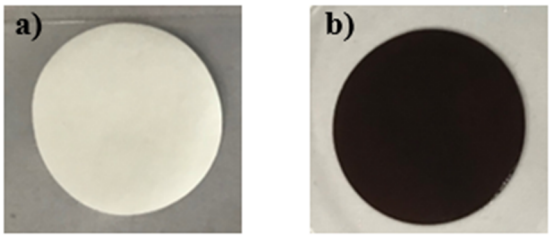

Figure 1 The surface color of a) Pristine PVDF and b) PVDF after pretreated NaOH solution.

A notable visual change was observed after the NaOH treatment: the membrane surface color shifted from white to brown, with increasing intensity at higher NaOH concentrations. As shown in Figure 1, this progressive color change is indicative of successful chemical modification, corresponding to the extent of dehydrofluorination and formation of conjugated structures. These findings align with previous reports by G. Wen et al. [13], who attributed such color change to the formation of C=C bonds in the PVDF backbone due to elimination of fluorine. The reaction mechanism between PVDF and the alkaline solution is described as follows [14].

$$\text{-[CH}_2\text{-CF}_2\text{]- + NaOH} \xrightarrow{\Delta} \text{-[CH=CF]- + NaF + H}_2\text{O} \quad (1)$$

In this reaction, fluorine atoms are eliminated from the carbon backbone, facilitated by the sodium cation acting as a Lewis acid that interacts with fluorine to form NaF. This dehydrofluorination process introduces unsaturation (C=C bonds) into the polymer chain and concurrently allows for the incorporation of hydroxyl groups onto the membrane surface. Notably, this reaction proceeds without the need for a phase transfer catalyst. The introduction of hydroxyl groups significantly enhances membrane hydrophilicity, which in turn improves permeability. As illustrated in Figure 2, membranes pretreated with 1 M and 2 M NaOH exhibited similar and notably increased permeability. However, an unexpected decline in permeability was observed in membranes treated with 1.5 M and 3 M NaOH. This deviation from theoretical predictions may be attributed to structural damage or pore blockage caused by NaF particle deposition, both of which could block fluid transport.

In contrast, Figure 3 shows that membranes treated with 5 M NaOH displayed a marked increase in permeability. This result is likely due to extensive degradation of the membrane matrix caused by the highly concentrated base, which weakened mechanical integrity. During permeability testing, the membrane suffered from tearing, precluding accurate and consistent permeability measurement. These findings highlight the importance of optimizing NaOH concentration to balance surface activation and structural preservation.

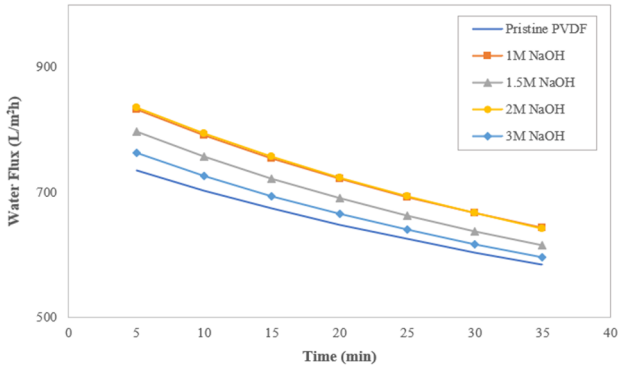

Figure 2 Water permeates flux of pristine PVDF and pretreated with different concentrations of 1, 1.5, 2, and 3 M NaOH.

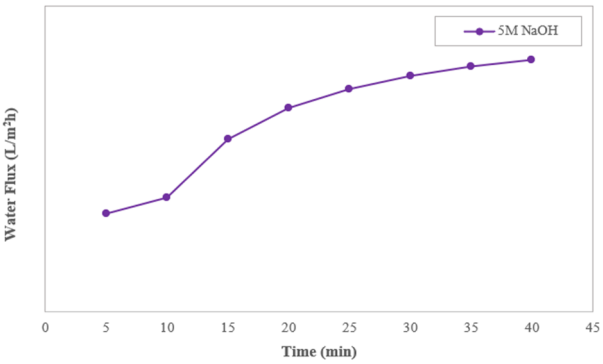

Figure 3 Water permeate flux of PVDF membrane pretreat with 5 M NaOH.

3.2. Characterization of Modified Membranes

3.2.1. Chemical Composition of Membranes

FT-IR spectroscopy was conducted to investigate changes in the surface functional groups of PVDF membranes before and after chemical modification. The spectra are presented in Figure 4. Key characteristic peaks observed in the pristine membrane included the strong absorption at 1179 cm^{-1}, corresponding to the C–F stretching vibration, and a peak at 1382 cm^{-1}, associated with C–H bending. Additionally, a peak around 1655 cm^{-1} was detected and can be attributed to the stretching of C=C groups, which may arise due to the dehydrofluorination process initiated by NaOH pretreatment [13, 14]. Despite these

identifiable bands, significant spectral differences between the pristine and modified membranes were not clearly observed. The similarity in peak positions and intensities suggests that the degree of surface modification might be subtle or that overlapping bands in the FT-IR spectra mask the changes. Particularly, potential new functional groups from grafted NVCL or silane compounds may not be distinguishable due to the dominance of PVDF backbone signals or low grafting density.

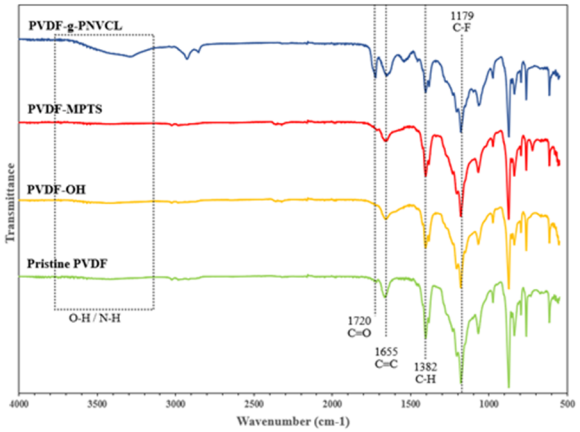

Figure 4 FT-IR spectra of the modified membranes.

Considering the inconclusive findings from FTIR analysis, X-ray Photoelectron Spectroscopy (XPS) was employed to further investigate the surface elemental composition and confirm the successful modification of the PVDF membrane. The XPS survey spectra, as illustrated in Figure 5, revealed distinct binding energy peaks at approximately 284 eV and 685 eV, corresponding to C1s and F1s core levels, respectively, which are characteristic of the PVDF backbone [15, 16]. Following surface modification with 3-methacryloxy-propyltrimethoxysilane (MPTS) and subsequent grafting of poly(N-vinylcaprolactam) (PNVCL), additional peaks appeared in the spectra. Notably, signals at 102 eV and 530 eV were observed, which are assigned to Si2p and O1s, respectively. The appearance of the Si2p signal confirms the successful incorporation of the silane coupling agent, while the O1s peak suggests the presence of oxygen-containing groups derived from both MPTS and PNVCL structures [15, 17]. These findings validate that the surface of the PVDF membrane was effectively modified with MPTS, enabling further functionalization with PNVCL. XPS, being a surface-sensitive technique, provided essential evidence of elemental changes that were not detectable via FT-IR, thereby confirming the success of the surface modification strategy.

3.2.2. Surface Morphology of Membrane

The surface morphology of both pristine and NaOH-pretreated PVDF membranes was analyzed using Scanning Electron Microscopy (SEM), as illustrated in Figure 6-7 at magnifications of 3,000x and 10,000x, respectively.

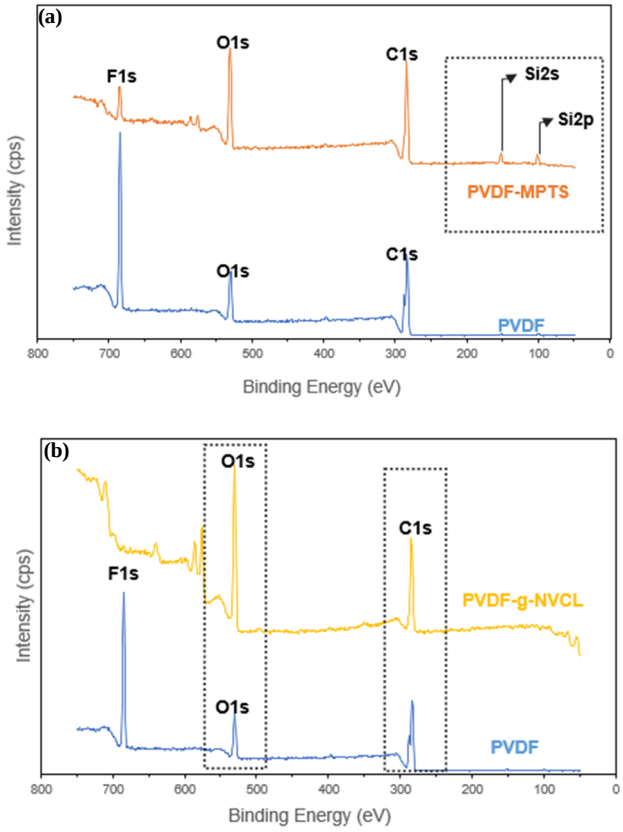

Figure 5 The XPS survey spectra of the modified membranes pristine PVDF, (a) PVDF-MPTS and (b)PVDF-g-PNVCL.

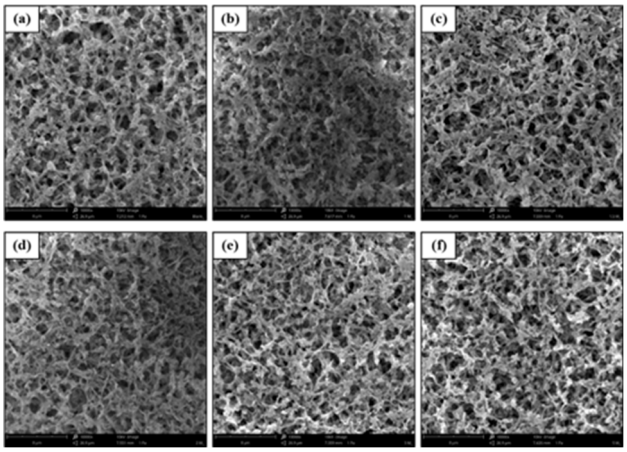

Figure 6 SEM images at magnifications of 10000x of PVDF membranes: (a) pristine PVDF and after pretreatment with NaOH solutions at different concentrations: (b) 1 M, (c) 1.5 M, (d) 2 M, (e) 3 M, and (f) 5 M, respectively.

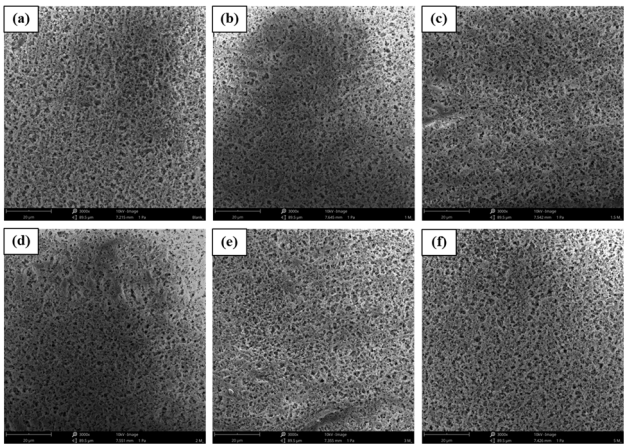

Figure 7 SEM images at magnifications of 3000x of PVDF membranes: (a) pristine PVDF and after pretreatment with NaOH solutions at different concentrations: (b) 1 M, (c) 1.5 M, (d) 2 M, (e) 3 M, and (f) 5 M, respectively.

The SEM image of the pristine PVDF membrane (Figure 6a) exhibits a porous and relatively smooth surface structure, indicating the typical morphology of unmodified PVDF. After pretreatment with NaOH at different concentrations (1 M to 5 M), noticeable morphological changes were observed (Figure 6b-f and 7a-b). At 1 M and 1.5 M NaOH (Figure 6b-7b and 6c-7c), the membrane surface began to show an increase in surface roughness and micro-porous structures, although the changes were still subtle. With higher concentrations of NaOH (2 M, 3 M, and particularly 5 M), the surface became significantly rougher and more heterogeneous. This increasing degree of etching or degradation is likely due to the stronger alkaline conditions attacking the PVDF polymer chains, resulting in enhanced pore formation and altered surface topology. These changes in surface morphology suggest that higher concentrations of NaOH lead to more pronounced chemical modification of the membrane surface. The increased roughness and porosity are expected to improve membrane properties such as hydrophilicity, water permeability, and fouling resistance, making them more suitable for filtration applications [18].

In summary, the SEM analysis confirms that alkaline pretreatment effectively alters the surface structure of PVDF membranes, and the extent of modification correlates with the NaOH concentration used.

3.3. Water Contact Angle Measurement

Water contact angle (WCA) analysis was performed to evaluate the changes in surface wettability of PVDF membranes before and after surface modification. As shown in Figure 8a, the pristine PVDF membrane exhibited a high contact angle of 102.63°, confirming its inherently hydrophobic nature, which is characteristic of the fluorinated polymer backbone. Following chemical pretreatment and grafting with hydrophilic moieties (MPTS and PNVCL), a substantial reduction in contact angle was observed. The modified membrane, as shown in Figure 8b, exhibited a contact angle of 30.50°, corresponding to a decrease of approximately 70%. This significant reduction demonstrates a marked improvement in surface hydrophilicity, attributed to the introduction of polar functional groups, such as hydroxyl, carbonyl, and amide groups, on the membrane surface. The improved wettability is expected to enhance membrane performance by increasing water permeability and reducing fouling tendency. These results further corroborate the successful surface modification, in agreement with XPS and FTIR data.

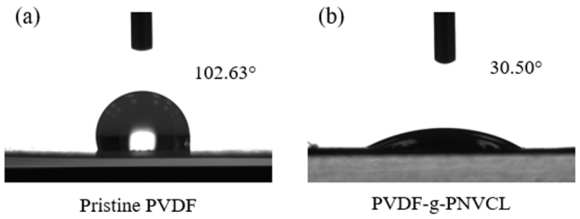

Figure 8 Water contact angle of (a) pristine and modified membrane (b) PVDF-g-PNVCL.

4. CONCLUSION

In this study, thermo-responsive PVDF-grafted-PNVCL membranes were successfully developed through a combination of NaOH pretreatment, silane coupling, and UV-induced graft polymerization. SEM, FT-IR, and XPS analyses confirmed the successful surface modification and incorporation of functional groups. Water contact angle measurements demonstrated a significant enhancement in membrane hydrophilicity, indicating improved wettability. The modified membranes exhibited switchable wettability and enhanced separation performance, making them promising candidates for efficient oil-water separation applications. The results highlight that NaOH concentration plays a crucial role in tuning the surface morphology and wettability, which are critical for membrane functionality. Overall, the proposed modification method offers a simple, effective, and scalable strategy for fabricating smart membranes suitable for practical wastewater treatment.

ACKNOWLEDGMENTS

The authors would like to acknowledge the financial and technical support provided by the Department of Chemical Engineering, Faculty of Engineering, King Mongkut's University of Technology Thonburi (KMUTT). Special thanks are also extended to the Scientific Instrument Center of Standard Industry, Faculty of Science, KMUTT for access to characterization facilities, and to all research team members for their valuable contributions throughout this study.

REFERENCES

1. K. Abuhasel, M. Kchaou, M. Alquraish. Oily Wastewater Treatment: Overview of Conventional and Modern Methods, Challenges, and Future Opportunities. *Water* 2021; 13(7): 980–1015.
2. N.A. Cortez-Lemus and A. Licea-Claverie. Poly(N-vinylcaprolactam), a comprehensive review on a thermoresponsive polymer becoming popular. *Progress in Polymer Science* 2016; 53, 1–51.
3. A.D.M.d. Medeiros, C.J.G.d Silva Junior, J.D.P.d. Amorim. Oily Wastewater and Waste Treatment: Methods, Challenges, and Trends. *Process* 2022; 10, 743.
4. E.O. Ezugbe and S. Rathilal. Membrane Technologies in Wastewater Treatment: A Review, *Membranes* 2020; 10, 89.
5. J. Gao, M. Cai, Z. Nie. Superwetting PVDF membrane prepared by in situ extraction of metal ions for highly efficient oil/water mixture and emulsion separation. *Separation and Purification Technology* 2021; 275, 119174.
6. B.P. Ladewig and M. Al-Shaeli. Fouling in Membrane Bioreactors. *Fundamentals of Membrane Bioreactors* 2017; 39-85.
7. N. Abdullah, M.A. Rahman, J. Jaafar. Membranes and Membrane Processes: Fundamentals. *Current Trends and Future Developments on (Bio-) Membranes* 2018; 45-70.
8. T. Trinh. Fouling in Dairy Processes, *Mineral Scales and Deposits* 2015; 533-556
9. E.S. Dmitrieva, T.S. Anokhina, E.D. Novitsky. Polymeric Membranes for Oil-Water Separation: A Review. *Polymers* 2022; 14(5), 980.
10. R. Dallaev, T. Pisarenko, D. Sobola. Brief Review of PVDF Properties and Applications Potential. *Polymers* 2022; 14, 4793.
11. R. Hoogenboom. Temperature-responsive polymers: properties, synthesis and applications. *Smart Polymers and their Applications* 2014; 15-44.
12. G.S.M.D.P. Sethunga, W. Rongong, R. wang, T.H. Bae. Optimization of hydrophobic modification parameters of microporous polyvinylidene fluoride hollow-fiber membrane for biogas recovery from anaerobic membrane bioreactor effluent. *Journal of Membrane Science* 2018; 548, 510-518.
13. G. Wen, K. Chen, Y. Zhang. Preparation of alkali-resistant PVDF membranes via immobilization of sodium lauryl sulfate (SDS) on surface. *Applied Water Science* 2021. 11, 55.
14. E. Boyraz, F. Yalcinkaya, J. Hruza. Surface-Modified Nanofibrous PVDF Membranes for Liquid Separation Technology. *Materials* 2019; 12(17), 2702.
15. Q. Zhou, S. Xu, C. Zhu. Towards high-performance hybrid hydrophilic membranes: chemical anchoring of hydroxyl-rich nanoparticles on PVDF membranes via a silane coupling agent. *Journal of Materials Science* 2017; 52, 11737-11748.
16. D. Sobola, P. Kaspar, K. Castkova. PVDF Fibers Modification by Nitrate Salts Doping. Polymer 2021; 13,2439.
17. M. Kamaz, A. Sengupta, A. Gutierrez. Surface Modification of PVDF Membranes for Treating Produced Waters by Direct Contact Membrane Distillation. *International Journal of Environmental Research and Public Health* 2019; 16, 685.
18. M.F. Rabuni, N.M. Nik Sulaiman, M.K. Aroua. Effects of Alkaline Environments at Mild Conditions on the Stability of PVDF Membrane: An Experimental Study. Industrial and Engineering Chemistry Research 2013; 52, 15874-15882.

Techno-economic analysis of *Ulva spp.* cultivation for capturing CO_2 emissions from natural gas power plants in Thailand

Kantaphan Punnaanan[1,2], Pichaya In-na[1,2], Kasidit Noothong[1,3], Christopher Dixon[4,*]

[1] Research Unit on Sustainable Algal Cultivation and Applications, Faculty of Engineering, Chulalongkorn University, Bangkok 10330, Thailand
[2] Department of Chemical Technology, Faculty of Science, Chulalongkorn University, Bangkok 10330, Thailand
[3] Department of Chemical Engineering, Faculty of Engineering, Chulalongkorn University, Bangkok 10330, Thailand
[4] Chulalongkorn School of Integrated Innovation, Chulalongkorn University, Bangkok 10330, Thailand
[*] Corresponding author: christopher.d@chula.ac.th

ABSTRACT

The anthropogenic activities are recognised as a primary component contributing to global warming, especially the release of greenhouse gases (GHGs). The emission of carbon dioxide, fossil fuel combustion, is one of the top contributors to GHGs with a continuously increasing energy demand. The natural gas power plant in Thailand currently accounts for up to 38.3% of the energy sector's CO_2 emissions. Carbon capture technologies can contribute to mitigating CO_2 emissions to transition towards a carbon-neutral society. Algal biotechnology is a promising biological carbon capture technology. This study focuses on macroalgae, which have photosynthetic efficiencies up to 16.67% higher than terrestrial tree plantations. *Ulva spp.* is a well-known macroalgae for food production in Thailand, but its cultivation has not been used explicitly for carbon capture. This study conducts a techno-economic analysis of *Ulva spp.* cultivation for CO_2 capture from flue gases emitted from a natural gas power plant based in the city of Rayong, Thailand. SuperPro Designer was applied to simulate the cultivation process with imitation flue gas compositions. The optimal conditions for working volume and biomass yield were determined by varying the residence time of the photosynthesis reaction in the raceway pond. From the simulation, the optimal working volume was 32.18 m^3 and cultivation time was 18 days with the biomass yield was 29.90 ton/L/year and the internal rate of return (IRR) 42.89%. Hence, the cultivation of *Ulva spp.* can potentially be employed as carbon capture technology, contributing to Thailand's carbon sequestration strategy.

Keywords: *Ulva spp.*; Carbon Sequestration; Feasibility Analysis; Algal Decarbonisation

1. INTRODUCTION

Global warming is defined as a gradual and persistent increase in the Earth's average surface temperature. Primary contributors to this phenomenon are human activities, most notably the production of greenhouse gases (GHGs), which include carbon dioxide (CO_2), methane (CH_4), and nitrous oxide (N_2O) [1]. The Intergovernmental Panel on Climate Change (IPCC) reports that atmospheric CO_2 concentrations have increased from approximately 280 parts per million (ppm) prior to the Industrial Revolution to more than 410 ppm in the present day. Fossil fuel combustion is the primary cause of global greenhouse gas emissions [2,3]. The implications of global warming disruptions to ecosystems, all of which pose significant risks to human health, food security, and economic stability [2,3]. Shifting to renewable energy sources, improving energy efficiency, and implementing carbon capture technologies are essential for alleviating these effects and achieving global climate goals set forth in international agreements similar to the Paris Agreement [4]. Reducing CO_2 emissions is crucial for attaining global climate goals, especially those specified in the Paris Agreement, which seeks to cap global warming at well below 2°C above pre-industrial levels, with endeavours to limit the rise to 1.5°C [5].

The energy sector is a major contributor to CO_2 emissions in Thailand, with natural gas comprising a considerable share of electricity production. The Energy Generating Authority of Thailand (EGAT) reported that natural gas-fired power plants accounted for over 65% of total energy generation in 2023, raising worries regarding the environmental ramifications of these emissions [6]. Research demonstrates that although natural gas facilities create lower CO_2

emissions per unit of power generated than coal plants, the total emissions might remain significant due to the large quantity of electricity generated. Thailand is examining multiple strategies to mitigate the challenges associated with CO_2 emissions from natural gas power plants. These strategies include enhancing energy efficiency, incorporating renewable energy sources, and adopting carbon capture and storage (CCS) technologies. These measures are essential for conforming to Thailand's obligations under the Paris Agreement and for realising its long-term climate objectives [7]. The Thai government and several groups are investigating carbon capture utilisation and storage (CCUS) as a component of their climate change efforts. The Thailand Climate Change Master Plan (2015-2050) underscores the nation's dedication to diminishing greenhouse gas emissions, recognising CCUS as an essential technology for accomplishing these objectives [8].

CCUS is an essential technology for reducing greenhouse gas emissions and combating climate change, encompassing post-combustion capture, pre-combustion capture, direct air capture (DAC), and biological carbon capture. Biological carbon capture is a novel method for addressing climate change that utilises natural processes to sequester CO_2 from the atmosphere. This approach employs biological systems, including plants, algae, and microorganisms, to sequester carbon, providing a sustainable and eco-friendly option for mitigating greenhouse gas emissions [9]. The core premise of biological carbon capture is rooted in photosynthesis, wherein plants, algae, and certain microorganisms transform CO_2 into organic matter utilising sunlight [10]. One of the most well-known forms of biological carbon capture is the cultivation of algae. Algae are highly efficient at photosynthesis and can grow rapidly, making them effective at absorbing CO_2 [11]. Algal biomass, especially macroalgae, can be easily harvested and converted into biofuels, animal feed, or other valuable products, creating a circular economy that reduces reliance on fossil fuels while sequestering carbon [12]. Furthermore, algae can be cultivated in various environments, including freshwater, saltwater, and even wastewater, making them a versatile option for carbon capture [13,14]. Macroalgae such as *Ulva spp.* is a promising biological carbon capture approach because Thailand's geological and meteorological advantages facilitate the proliferation of macroalgae. The nation features an extensive coastline with warm, nutrient-dense seas, optimal for producing *Ulva spp.* The tropical climate guarantees a consistent temperature range, facilitating continuous growth throughout the year [15]. Furthermore, Thailand's dedication to sustainable development and marine protection corresponds with the growing of macroalgae [16].

Ulva spp. is a genus of green seaweed distinguished by its exceptional growth rate and considerable capacity for carbon sequestration [17,18]. The cultivation of *Ulva spp.* in Thailand can contribute to carbon sequestration and provide substantial economic advantages. Seaweed cultivation can generate employment opportunities for coastal residents, boosting local economies. The increasing global need for seaweed in food, pharmaceuticals, and biofuels offers Thailand the possibility to establish itself as a leader in the seaweed sector. The quantity of CO_2 that *Ulva spp.* can sequester fluctuates according to several factors, including growth circumstances, biomass composition, and environmental variables. On average, *Ulva spp.* can sequester around 1.8 to 2.5 grams of CO_2 for each gram of biomass generated [12]. Therefore, this study proposes to perform a techno-economic analysis of the cultivation of *Ulva spp.* seaweed for capturing CO_2 emissions from natural gas power plants in Thailand, examining the feasibility, potential advantages, and obstacles associated with this method.

2. EXPERIMENTAL

2.1 Simulation

This simulation study investigates *Ulva spp.* cultivation utilising flue gas from a natural gas power plant in Rayong, Thailand as a carbon dioxide source. SuperPro Designer was used to simulate the overall processes. The whole process followed the process flow diagram illustrated in Figure 1.

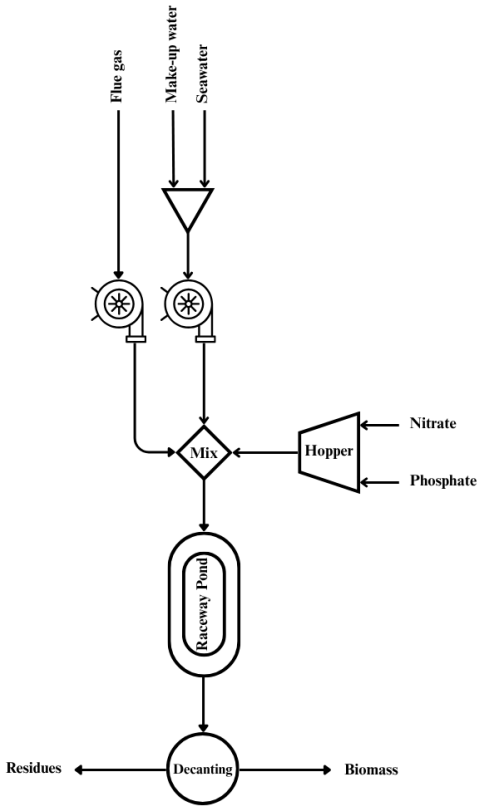

Figure 1: The process flow diagram (PFD) of the simulation for *Ulva spp.* cultivation in Rayong, Thailand.

The experimental protocol initiates with flue gas collection, which undergoes treatment and is subsequently stored under controlled conditions at 25°C and 2 bar pressure. The conditioned gas is then transported via a compressor system to the cultivation pond, where it maintains an operational pressure of 2 atmospheres (approximately 2.068 bar) to enhance carbon dioxide dissolution and bioavailability [19]. Imitation seawater was introduced at a constant flow rate of 50 kg/hr and supplemented with makeup water at a 5% replacement ratio to compensate for evaporative losses, maintain system stability, and ensure appropriate water chemistry parameters [20]. Nutrient streams, consisting of urea and phosphate at equivalent flow rates of 12.5 kg/hr, were homogeneously mixed into the aqueous medium in the mixing unit. The mixed solution was channelled into a raceway pond cultivation system optimised for *Ulva spp.* growth, with operations targeting a biomass density of 37.0 g/L as previously established in the literature [21]. This configuration facilitated the investigation of macroalgal cultivation as a potential carbon sequestration and bioremediation strategy.

Operational expenditures (OPEX) and capital expenditures (CAPEX) were incorporated into the simulation model to assess economic feasibility. Labour costs were calculated at 400 THB/day (approximately 11.2 USD/day), in accordance with the minimum wage regulations established by the Thai government [22]. Additional OPEX components included electrical power consumption and material inputs, primarily nutrient supply for the system. Capital expenditures comprised the necessary equipment investments as itemised in Table 1, although it should be noted that land acquisition costs were excluded from this analysis because of preliminary planning stages. This methodological approach allowed for a comprehensive economic assessment while maintaining clearly defined system boundaries.

Table 1 List of industrial equipment with cost index (2024 fiscal year)

Name	Description	Cost ($)
P-101	Centrifugal Pump	9,000 [23]
P-102	Centrifugal Pump	9,000 [23]
P-103	Compressor	4,000 [24]
RP-101	Raceway Pond	2,000 [24]
V-101	Decanter Tank	30,000 [24]

The biological transformation occurring within the raceway pond is fundamentally governed by the photosynthetic process, which can be expressed through the stoichiometric equation from *Ulloa and Grob (2009)* [25]:

$$106CO_2 + 16HNO_3 + 1H_3PO_4 + 122H_2O \leftrightarrow [(CH_2O)_{106}(NH_3)_{16}(H_3PO_4)] + 138O_2 \quad (1)$$

This reaction can also be simplified as:

$$\textit{carbon dioxide} + \textit{nitrate} + \textit{phosphate} + \textit{water} \leftrightarrow \textit{biomass} + \textit{oxygen} \quad (2)$$

This equation, which can be conceptualised more straightforwardly as the conversion of carbon dioxide, nitrate, phosphate, and water into biomass and oxygen, represents the core mechanism through which the *Ulva spp.* contributes to carbon dioxide mitigation while generating valuable biomass.

2.2 Assumptions

The cultivation parameters were established with several baseline assumptions to standardise growth conditions and facilitate comparative analysis of biomass productivity, including:

- Operational duration was limited to 12 hr/day, corresponding to diurnal photoperiod patterns in Thailand (5°–20°N latitude), characteristic of tropical regions with minimal seasonal photoperiodic variation [26].
- Annual operational frequency established at 183 days/year (50.1% temporal utilisation), derived from photobiological constraints being able to operate 12 hours daily and equatorial proximity considerations in Thailand.
- Cultivation parameters were configured to maintain a standardised biomass concentration equilibrium of 37.0 g/L, a constant derived from established photobioreactor performance metrics in previous systematic investigations from Kristoffer et al., serving as the operational setpoint for metabolic optimisation protocols [21]. Influences of seasonal weather, such as temperature fluctuation, were assumed to be negligible.
- Chemical and microbial contaminations were maintained below detectable threshold levels throughout the cultivation period, attributable to the implementation of aseptic protocols and the system's inherent bio-exclusion properties, eliminating exogenous biological interference as a confounding experimental variable.
- Biomass separation was achieved via decantation technology, functioning as the primary harvesting unit in the downstream processing pathway, facilitating solid-liquid phase separation under controlled operational parameters without subsequent dehydration procedures.

- Non-CO_2 constituents in flue gas emissions were excluded from analytical consideration in carbon capture calculations, with compositional heterogeneity of trace gases deemed statistically negligible for mass transfer and sequestration efficiency determinations.
- Input parameters were maintained as time-invariant continuous variables, establishing steady-state conditions and eliminating temporal fluctuations as confounding factors in system analysis [27].
- Stoichiometrically sufficient nutrient availability facilitated complete biochemical conversion pathways, optimising photosynthetic yield efficiency through the elimination of rate-limiting metabolic bottlenecks in carbon fixation mechanisms.

2.3 Limitations

- Experimental carbon sequestration demonstrated a minimum CO_2 capture removal efficiency threshold of 20%, constrained by the inherent photosynthetic capacity of *Ulva spp.*, which aligns with theoretical quantum yield limitations as established by *Sebök et al.* for marine macroalgal carbon fixation pathways [28].
- Mitochondrial respiratory processes and associated carbon dioxide evolution in *Ulva spp.* were not quantified in this experimental framework, constituting a methodological limitation that potentially affects net carbon flux calculations and warrants consideration in subsequent metabolic modelling of macroalgal carbon sequestration dynamics [29].
- Biomass quantification protocols employed a simplified harvesting methodology that introduced measurement uncertainty, potentially compromising gravimetric precision and yielding approximate biomass values rather than the high-resolution data required for rigorous stoichiometric analysis of carbon partitioning dynamics.
- Comprehensive logistical framework optimisation for carbon dioxide transport networks remains inadequately characterised, necessitating further investigation into multi-objective routing algorithms and infrastructure configuration parameters specifically contextualised within the emerging CCUS hub development in Rayong, Thailand.

2.4 Optimisation

To comprehensively evaluate the system's performance and identify optimal operating conditions, the residence time within the raceway pond was systematically varied across a predetermined range, enabling the quantification of both biomass yield and the percentage of carbon dioxide removal under different temporal constraints. Following the experimental phase, a computational optimisation approach was implemented using MATLAB to identify the ideal operating conditions. This analysis focused specifically on the interrelationship between residence time and working volume as the primary variables influencing system performance. The optimisation procedure employed polynomial surface fitting techniques, particularly utilising the poly23 model expressed below as Equation (3).

$$f(x,y) = p00 + p10x + p01y + p20x^2 + p11xy + p02y^2 + p21x^2y + p12xy^2 + p03y^3 \quad (3)$$

Where:

- x = Residence Time
- y = Working Volume
- pij = Coefficients determined by the fitting algorithm

This allows for the characterisation of complex, non-linear relationships between process variables and performance metrics. This mathematical modelling approach facilitated the systematic identification of the specific combination of residence time and working volume that maximises biomass production, thereby providing valuable insights for the design and operation of large-scale algal cultivation systems aimed at both environmental remediation through carbon sequestration and the sustainable production of algal biomass for various industrial applications.

3. RESULTS AND DISCUSSION

The simulation findings illustrated in Figure 2 are the correlation between CO_2 removal efficiency and cumulative CO_2 absorption rate during the culture of *Ulva spp.* over a 28-day growth period. Initially, the system demonstrates an almost perfect (100%) CO_2 removal capability, which remains stable for around 3 days before undergoing a significant exponential drop. This initial plateau presumably signifies the lag phase during which *Ulva* biomass acclimatises to cultivation conditions while sustaining elevated carbon fixing rates [30]. Simultaneously, the working volume rises linearly from the baseline to around 50 m^3 by day 28, signifying consistent biomass accrual during the cultivation period. The inverse correlation between these parameters indicates a significant cultivation dynamic; as *Ulva* biomass increases, its carbon sequestration efficiency per unit volume diminishes, culminating in around 20% removal by the conclusion of cultivation. This trend indicates that self-shading, nutrient constraint, or alterations in physiological condition become progressively more significant as culture advances. The intersection around day 5 signifies an ideal harvesting period when biomass accumulation and CO_2 fixation efficiency attain equilibrium. The findings offer significant insights for the design of *Ulva* cultivation systems that reconcile carbon mitigation objectives with biomass production targets, indicating that batch cultivation cycles of 12-15 days may elevate

both parameters in comparison to prolonged growth periods.

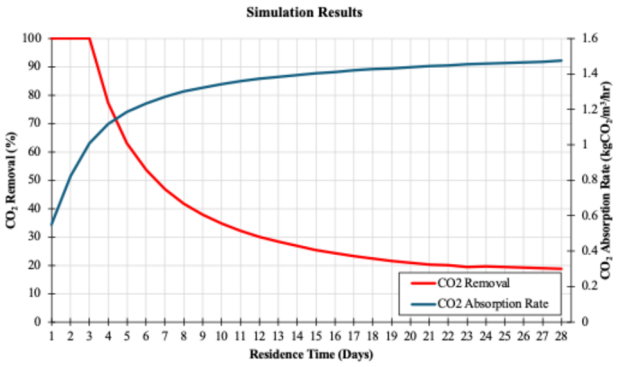

Figure 2: The data results from simulation by using SuperPro Designer

The Figure 3 data illustrate the dynamics of CO_2 absorption by *Ulva spp.* over a 28-day cultivation period. The lower graph demonstrates that CO_2 absorption rates begin at approximately 0.5 kg $CO_2/m^3/hr$ on day 1, followed by a pronounced exponential decline through days 1-7, and eventually stabilise near 0.0037 $kgCO_2/m^3/hr$ by day 28. This pattern likely reflects the physiological adaptation of *Ulva* to cultivation conditions, with initial high metabolic activity transitioning to diminished carbon fixation efficiency as the biomass matures. In contrast, the upper graph depicts cumulative CO_2 absorption rates, which increases rapidly during the initial 10 days before gradually plateauing toward a maximum value of 1.474 $kgCO_2/m^3/hr$ by day 28. This asymptotic behavior indicates that despite continued cultivation, carbon sequestration benefits become marginally incremental after approximately two weeks. The observed absorption kinetics suggest that *Ulva*'s photosynthetic efficiency declines with age, potentially due to progressive physiological transformations. Self-shading, nutrient limitation, and cellular senescence compromise photosynthetic apparatus functionality, resulting in decreased chlorophyll content and reduced quantum yield. The age-related photosynthetic deterioration stems from structural modifications in photosystem complexes and metabolic changes, ultimately diminishing carbon fixation capabilities in senescent thallus regions [28,31]. These findings have significant implications for optimisation of *Ulva* cultivation strategies targeting carbon sequestration, suggesting that harvest cycles of 10-14 days may maximise CO_2 capture efficiency per unit time, as maintaining cultures beyond this period yields diminishing returns for carbon mitigation objectives. Furthermore, these results highlight the importance of harvest timing when balancing carbon sequestration goals with biomass production in *Ulva* cultivation systems.

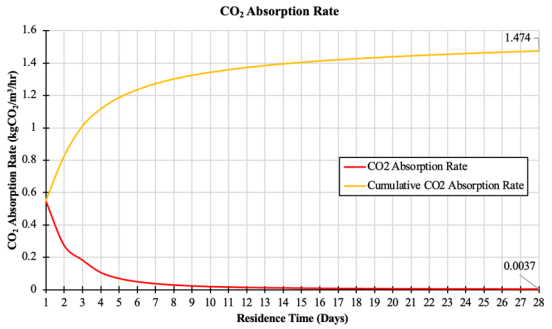

Figure 3: The CO_2 absorption rate and cumulative CO_2 absorption rate

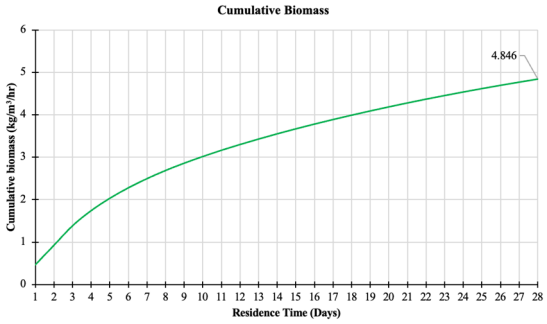

Figure 4 The cumulative biomass of this cultivation

Figure 4 illustrates the cumulative biomass production of *Ulva spp.* during a 28-day cultivation period, reaching a final yield of 4.846 $kg/m^3/hr$. The biomass accumulation curve exhibits a classic sigmoidal pattern characteristic of macroalgal growth dynamics, with three distinct phases. Initially (days 1-5), rapid exponential growth occurs as the vegetative tissue undergoes active cell division with minimal self-shading. This transitions to a linear growth phase (approximately days 6-17) where biomass accumulation proceeds at a relatively constant but slower rate, likely reflecting a balance between photosynthetic capacity and increasing density-dependent limitations [32]. The final phase (days 18-28) demonstrates declining growth rates as the curve begins to plateau, suggesting the onset of cultivation constraints including self-shading, nutrient limitation, and reduced photosynthetic efficiency in physiologically developed fronds [33]. The observed biomass accumulation pattern aligns with the previously noted decline in CO_2 absorption rates, confirming that mature blade tissue contributes proportionally less to both carbon sequestration and biomass production than younger fronds. The final biomass yield of nearly 5 $kg/m^3/hr$ or 0.0438 ton/L/year represents commercially viable productivity for *Ulva* cultivation systems, though staggered harvesting protocols could potentially increase annual productivity by maintaining cultures in their most efficient growth phase. These findings provide valuable parameters for modelling *Ulva* cultivation systems aimed at maximising biomass production for food, feed, or bioremediation applications [21].

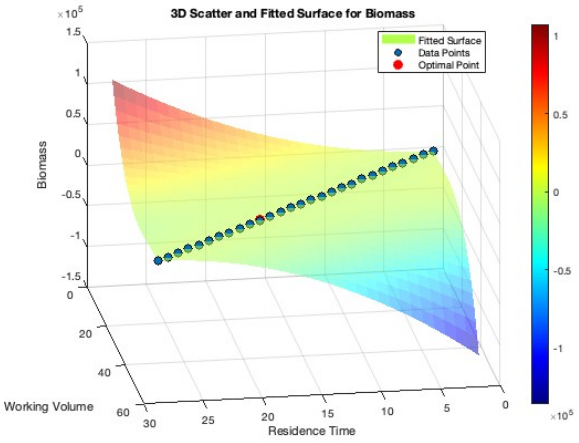

Figure 5 The 3D scatter and fitted surface for optimal biomass cultivation conditions

Figure 5 illustrates a three-dimensional response surface model relating biomass production to residence time and working volume in *Ulva spp.* cultivation systems. The fitted surface demonstrates a clear non-linear relationship between cultivation parameters and biomass yield, with experimental data points (blue circles) validating the model's predictive capability. Statistical optimisation analysis identified optimal cultivation parameters at 17.98, or approximately 18 days residence time and 32.16 m^3 working volume, yielding a maximum predicted biomass of 3.41 $kg/m^3/hr$. The gradient colouration from red (maximum biomass) to blue (minimum biomass) visually emphasises how deviations from optimal conditions substantially reduce cultivation efficiency. This parametric interdependence reveals that shorter residence times, regardless of working volume, consistently produce suboptimal biomass accumulation, while extended cultivation beyond the optimal period results in diminishing returns, likely due to resource limitation and senescent frond dynamics [34]. The surface topology further indicates that working volume exhibits a narrower optimal range than residence time, suggesting that volumetric parameters critically influence light penetration, nutrient availability, and gas exchange in the cultivation matrix. These findings provide quantitative guidance for commercial-scale *Ulva* cultivation, demonstrating that system optimisation requires balanced consideration of both temporal and volumetric parameters rather than maximisation of either variable independently.

Table 2 List of economic evaluation parameters

Parameter	Obtained values
Capital Investment	$253,000
Annual Operating Costs	$549,000
Annual Revenue	$583,000
Unit Production Cost	37.63/kg
Unit Revenue	40.00/kg
ROI	5.92%
Payback Period	7.89 years
IRR	42.89%

The economic evaluation (Table 2) of *Ulva* cultivation reveals important insights into the viability of this venture within the aquaculture sector. The total capital investment is documented at $253,000, an essential amount for initiating the project, which encompasses all infrastructural and operational expenditures necessary to establish the cultivation system. In the operating phase, the annual operating costs have been identified as $549,000, which includes ongoing expenses related to maintenance, labour, and utilities required for effective production management. Analysis indicates that there were no credits applicable to the project, culminating in a net operating cost of $548,823. This high operating cost highlights the extensive ongoing financial commitments required to sustain production levels effectively [35]. On a positive note, the revenues generated from Ulva sales reached $583,000, indicating that the operation successfully produces enough revenue to surpass direct costs, thus achieving profitability. The report further reveals a cost basis annual rate of $14,583, an important metric that benchmarks financial performance against industry standards. The unit production cost stands at $37.63 per kilogram, aligning closely with the net unit production cost, while the unit production revenue, the estimated market value for high-value products, is approximately $40.00 per kilogram [36]. The marginal difference between production costs and revenue signifies a healthy profit margin, essential for the financial sustainability of the cultivation process. Moreover, the gross margin reflects the profitability potential of *Ulva* cultivation, driven by the revenue-cost relationship. The return on investment (ROI) is calculated at 5.92%, indicating a moderate financial return on the capital invested. Additionally, the payback time of 7.89 years signifies the period required to recover initial investments through profit revenues, a critical consideration for investors and stakeholders assessing long-term viability [37]. In conclusion, while *Ulva* cultivation presents a feasible economic opportunity, as evidenced by the robust revenue against costs, there are avenues for enhancing operational efficiencies and cost management. Continuous assessment and strategic planning could augment profitability, thereby making *Ulva* cultivation not only a sustainable agricultural investment but also a resilient model in the face of shifting market dynamics.

4. CONCLUSION

Our simulated study of *Ulva spp.* cultivation dynamics reveals critical insights for optimising both carbon sequestration and biomass production objectives in commercial-scale systems. Integration of CO_2 removal efficiency, absorption kinetics, and biomass accumulation data demonstrates that cultivation performance follows predictable temporal patterns governed by physiological and density-dependent constraints. The identification of distinct growth phases, from initial rapid expansion to eventual

diminishing returns, provides a scientific basis for harvest scheduling optimisation. Mathematical modelling identified that maximum system efficiency occurs at intermediate residence time (18 days) and specific working volumes (32.16 m^3), yielding optimal biomass production of 3.41 kg/m^3/hr or 563.3 ton/year (equivalent to 201.2 tonCO_2/year). These findings explain mechanistically why extended cultivation periods beyond 14-17 days result in suboptimal resource utilisation, as mature fronds contribute proportionally less to both carbon fixation and biomass accumulation. The inverse relationship between biomass density and CO_2 removal efficiency further demonstrates that cultivation management must balance competing objectives rather than maximise individual parameters. For practical implementation, these results support the adoption of staggered harvesting protocols to maintain cultures in their most productive phase, targeting where carbon sequestration and growth rates remain elevated before self-shading and nutrient limitations become significant constraints. This approach would maximise annual productivity while ensuring optimal environmental service provision through sustained CO_2 mitigation efficiency. The study also provides a detailed financial evaluation of commercial-scale *Ulva* cultivation, revealing critical economic parameters. Total capital investment was $253,000, with annual operating costs of $549,000. Despite high operational expenses, the venture demonstrated economic viability, generating $583,000 in revenues. The unit production cost of $37.63/kg compared favourably with a unit revenue of $40.00/kg, yielding a 5.92% return on investment and a payback period of 7.89 years, and the IRR is 42.89%. The analysis underscores the importance of balanced system optimisation, highlighting both the potential and challenges of *Ulva* cultivation as a sustainable aquaculture enterprise. Strategic improvements in operational efficiency could further enhance the economic prospects of this emerging agricultural model.

ACKNOWLEDGEMENTS

I would like to sincerely thank my advisor, Assistant Professor Dr. Pichaya In-na, Principal Investigator (PI), for her invaluable expertise and mentorship throughout my research journey. I am also grateful to Dr. Christopher Dixon, co-PI and optimisation specialist, and Associate Professor Dr. Kasidit Nootong, biochemical engineering expert, for their insightful guidance and unwavering support, which have greatly influenced this work. My heartfelt appreciation goes to my colleagues, Mr. Tanakit Komkhum and Mr. Peradon Phonglamjiakngam, for their collaborative efforts and encouragement that enriched this academic endeavour. This research would not have been possible without the generous support from the Research Unit on Sustainable Algal Cultivation and Applications (RU SACAS), along with the research grant provided by the 72nd Anniversary of His Majesty King Bhumibol Adulyadej Scholarship at Chulalongkorn University, for which I am profoundly thankful. I also acknowledge the collaboration of the Department of Chemical Technology and the Department of Chemical Engineering, both within the Faculty of Science and the Faculty of Engineering at Chulalongkorn University, as well as the Chulalongkorn School of Integrated Innovation (CSII).

REFERENCES

1. Filonchyk M, Peterson MP, Zhang L, Hurynovich V, He Y. Greenhouse gases emissions and global climate change: Examining the influence of CO2, CH4, and N2O. Sci Total Environ. 2024 Jul;935:173359.
2. US EPA O. Climate Change Impacts on Health [Internet]. 2022 [cited 2024 Dec 22]. Available from: https://www.epa.gov/climateimpacts/climate-change-impacts-health
3. Mirzabaev A, Bezner Kerr R, Hasegawa T, Pradhan P, Wreford A, Cristina Tirado Von Der Pahlen M, et al. Severe climate change risks to food security and nutrition. Clim Risk Manag. 2023;39:100473.
4. Gielen D, Boshell F, Saygin D, Bazilian MD, Wagner N, Gorini R. The role of renewable energy in the global energy transformation. Energy Strategy Rev. 2019 Apr;24:38–50.
5. United Nations. The Paris Agreement [Internet]. United Nations. [cited 2024 Dec 22]. Available from: https://www.un.org/en/climatechange/paris-agreement
6. Chandler MHM. Thailand Energy Transition Report - Outlook for 2024 [Internet]. Available from: https://www.chandlermhm.com/content/files/pdf/publications/Thailand%20Energy%20Transition%20Report%20-%20Outlook%20for%202024.pdf
7. Chhay L, Limmeechokchai B. CO_2 Mitigation in the Power Sector of Thailand: Analyses of Cleaner Supply-side Options Beyond the Paris Agreement. Open Environ Res J. 2019 Nov 5;12(1):15–25.
8. The Energy Generating Authority of Thailand. EGAT Sustainability Report 2023 [Internet]. The Energy Generating Authority of Thailand; 2023. Available from: https://www.egat.co.th/home/en/wp-content/uploads/2024/08/EGAT-SR-2023-ENG.pdf
9. Tiwari T, Kaur GA, Singh PK, Balayan S, Mishra A, Tiwari A. Emerging bio-capture strategies for greenhouse gas reduction: Navigating challenges towards carbon neutrality. Sci Total Environ. 2024 Jun;929:172433.
10. Buotte PC, Law BE, Ripple WJ, Berner LT. Carbon sequestration and biodiversity co-benefits of preserving forests in the western UNITED STATES. Ecol Appl. 2020 Mar;30(2):e02039.
11. Yang Y, Tang S, Chen JP. Carbon capture and utilization by algae with high concentration CO2 or bicarbonate as carbon source. Sci Total Environ. 2024 Mar;918:170325.
12. Rehman ZU, Punnaanan K, Nootong K, In-na P. The status of algal decarbonization in Southeast Asian region: a review. Environ Res Lett. 2024 Sep 1;19(9):093004.
13. Li G, Yao J. A Review of Algae-Based Carbon Capture, Utilization, and Storage (Algae-Based CCUS). Gases. 2024 Dec 2;4(4):468–503.

14. Weerakkody WS, Ling KH, Hsieh HH, Abedneko VG, Shyu JF, Lee TM, et al. Carbon capture by macroalgae Sarcodia suae using aquaculture wastewater and solar energy for cooling in subtropical regions. Sci Total Environ. 2023 Jan;855:158850.
15. Pessarrodona A, Franco-Santos RM, Wright LS, Vanderklift MA, Howard J, Pidgeon E, et al. Carbon sequestration and climate change mitigation using macroalgae: a state of knowledge review. Biol Rev. 2023 Dec;98(6):1945–71.
16. Carlson RR, Evans LJ, Foo SA, Grady BW, Li J, Seeley M, et al. Synergistic benefits of conserving land-sea ecosystems. Glob Ecol Conserv. 2021 Aug;28:e01684.
17. Tsubaki S, Nishimura H, Imai T, Onda A, Hiraoka M. Probing rapid carbon fixation in fast-growing seaweed Ulva meridionalis using stable isotope 13C-labelling. Sci Rep. 2020 Nov 23;10(1):20399.
18. Gelashvili R, Chemodanov A, Obolski U, Yakhini Z, Golberg A. Predictive modeling of Ulva sp. growth and chemical composition in an outdoor air-mixed bioreactor under natural environmental conditions: A machine learning approach. Algal Res. 2024 Dec;103832.
19. a YC, a CX. How to narrow the CO2 gap from growth-optimal to flue gas levels by using microalgae for carbon capture and sustainable biomass production. J Clean Prod. 2021 Jan 20;280:124448.
20. Kunz RG. Environmental Calculations: A Multimedia Approach [Internet]. 1st ed. Wiley; 2009 [cited 2025 Apr 27]. Available from: https://onlinelibrary.wiley.com/doi/book/10.1002/9780470925386
21. Stedt K, Gustavsson O, Kollander B, Undeland I, Toth GB, Pavia H. Cultivation of Ulva fenestrata using herring production process waters increases biomass yield and protein content. Front Mar Sci [Internet]. 2022 Sep 13 [cited 2025 Apr 15];9. Available from: https://www.frontiersin.orghttps://www.frontiersin.org/journals/marine-science/articles/10.3389/fmars.2022.988523/full
22. Baker & McKenzie. Thailand: New minimum wage rates now effective [Internet]. 2025 [cited 2025 Apr 25]. Available from: https://insightplus.bakermckenzie.com/bm/employment-compensation/thailand-new-minimum-wage-rates-now-effective
23. Woods DR. Rules of Thumb in Engineering Practice [Internet]. 1st ed. Wiley; 2007 [cited 2025 Jun 26]. Available from: https://onlinelibrary.wiley.com/doi/book/10.1002/9783527611119
24. Loh HP, Lyons J, White CW, EG&G Technical Services, Inc., Morgantown, WV (United States). Process Equipment Cost Estimation, Final Report [Internet]. 2002 Jan [cited 2025 Jun 26] p. DOE/NETL--2002/1169, 797810. Report No.: DOE/NETL--2002/1169, 797810. Available from: http://www.osti.gov/servlets/purl/797810/
25. Ulloa O, Grob C. Marine pelagic ecosystems. In: Le Quéré C, Saltzman ES, editors. Geophysical Monograph Series [Internet]. Washington, D. C.: American Geophysical Union; 2009 [cited 2025 Apr 7]. p. 119–37. Available from: https://onlinelibrary.wiley.com/doi/10.1029/2008GM000867
26. Gadberry BA, Colt J, Maynard D, Boratyn DC, Webb K, Johnson RB, et al. Intensive land-based production of red and green macroalgae for human consumption in the Pacific Northwest: an evaluation of seasonal growth, yield, nutritional composition, and contaminant levels. Algae. 2018 Mar 15;33(1):109–25.
27. Frøysa HG, Skaug HJ, Alendal G. Experimental design for parameter estimation in steady-state linear models of metabolic networks. Math Biosci. 2020 Jan 1;319:108291.
28. Sebök S, Herppich WB, Hanelt D. Outdoor cultivation of Ulva lactuca in a recently developed ring-shaped photobioreactor: effects of elevated CO2 concentration on growth and photosynthetic performance. Bot Mar. 2019 Apr 1;62(2):179–90.
29. Rasmusson LM. Seagrass Respiration : An assessment of oxygen consumption patterns of temperate marine macrophytes. 2015 [cited 2025 Apr 15]; Available from: https://urn.kb.se/resolve?urn=urn:nbn:se:su:diva-120156
30. Gao G, Clare AS, Rose C, Caldwell GS. *Ulva rigida* in the future ocean: potential for carbon capture, bioremediation and biomethane production. GCB Bioenergy. 2018 Jan;10(1):39–51.
31. Ji Y, Jiang Y, Jin P, Xia J. Interactive effects of ocean acidification and nitrate on Ulva lactuca. J Appl Phycol. 2024 Oct 1;36(5):3047–55.
32. Zollmann M, Liberzon A, Golberg A. Modeling of growth of the macroalga *Ulva* sp. in a controlled photobioreactor based on nitrogen accumulation dynamics. Appl Phycol. 2023 Dec 31;4(1):121–40.
33. Robles-Carnero V, Sesmero R, Figueroa FL. Biomass Productivity and Photosynthetic Activity in Ulva compressa (Chlorophyta) in Raceway Photobioreactors Under Stress Conditions. Plants. 2024 Oct 30;13(21):3038.
34. de Mooij T, de Vries G, Latsos C, Wijffels RH, Janssen M. Impact of light color on photobioreactor productivity. Algal Res. 2016 Apr 1;15:32–42.
35. DeAngelo J, Saenz BT, Arzeno-Soltero IB, Frieder CA, Long MC, Hamman J, et al. Economic and biophysical limits to seaweed farming for climate change mitigation. Nat Plants. 2023;9(1):45–57.
36. European Climate, Infrastructure and Environment Executive Agency., ACTeon., Toegepast natuurwetenschappelijk onderzoek., Aarhus University., University of Copenhagen. Algae and climate: final report. [Internet]. LU: Publications Office; 2020 [cited 2025 Apr 30]. Available from: https://data.europa.eu/doi/10.2926/208135
37. El-Gendy NSh, Shaaban Sadek M, Nassar HN, Mustafa A. Eco-Friendly Extraction of Sustainable and Valorized Value-Added Products From *Ulva fasciata* Macroalgae: A Holistic Technoeconomic Analysis. Roy S, editor. Int J Biomater. 2025 Jan;2025(1):5811057.

Centella asiatica active ingredients extraction using ultrasonic-assisted extraction and maceration

Nichapa Areepong[1], Veronica Winoto[1,*]

[1] Department of Chemical Engineering, Faculty of Engineering, Thammasat School of Engineering, Thammasat University, Pathum Thani 12120, Thailand
[*] Corresponding author: wveronic@engr.tu.ac.th

ABSTRACT

Centella asisatica is widely used as an herbal, dietary supplement, and cosmeceutical due to its rich bioactive compounds including total phenolic content. The extraction method is effect in obtaining a high yield of beneficial compounds. In this study, ultrasonic-assisted extraction (UAE) and maceration were evaluated to determine the optimal extraction conditions for maximizing total phenolic content. The three main parameters consisting of the *Centella asisatica* (CAE) concentration, extraction temperature, and extraction time were investigated. The concentration of CAE ranged from 0.5 to 2%w/v, temperature ranged from 40 to 60°C, and time ranged from 1 to 4 h. The antioxidant activity of CAE extracts was analyzed using Total Phenolic Content (TPC) method with Folin-ciocalteu as a reagent and 2,2-diphenyl-1-picrylhydrazyl (DPPH) assay. The absorbance of TPC and DPPH was measured using UV-Vis spectrophotometer at 750 nm and 517 nm, respectively. The results showed that UAE achieved the highest TPC of 33.14 mg GAE/g and DPPH scavenging activity of 91.67% while maceration yielded the highest TPC of 39.56 mg GAE/g and DPPH of 86.34%. Therefore, the optimum condition was 2%w/v of CAE with temperature of 50°C at 2 h using UAE. These findings suggest that UAE provided higher antioxidant activity than maceration due to its ultrasonic vibration, which disrupts the cell walls and enhances the release of bioactive compounds.

Keywords: Antioxidant; *Centella Asiatica*; Maceration; Ultrasonic-assisted extraction

1. INTRODUCTION

Centella asiatica is an herbal plant which is widely used as a medical herb for treatment. It belongs to Apiaceae family, and it is used in part of the green leaves. In Thailand, *Centella asiatica (C. asiatica)* is widely processed into an herbal drink for healing aphthous stomatitis. Moreover, it grows in Asian countries such as Laos, Myanmar, Singapore, China, Indonesia, India, South America, and Africa [1]. In those countries, it is called gotu kola, Thankuni, and pennywort as common names [2, 3]. Additionally, *C. asiatica* usually has medical properties such as anti-ulcer, anti-inflammatory, antimicrobial, anti-cancer, antioxidant [2, 4]. *C. asiatica* is popular as a traditional medicine called Ayurvedic medicine. This traditional medicine is used to treat conditions such as wound healing, bronchitis, asthma, ulcers, anxiety, skin diseases, and high blood pressure [5, 6]. Furthermore, most studies report that *C. asiatica* is rich in bioactive compounds such as polyphenols, flavonoids, and terpenoids [4]. Additionally, phenolic compounds include gallic acid, catechin, and quercetin, which have high antioxidant activity [7]. *C. asiatica* contains several terpenoids, including asiaticoside, madecassoside, asiatic acid, and madecassic acid, which are highly concentrated in *C. asiatica* extract [1, 4].

According to research on the phytochemical and bioactive compounds of *Centella asiatica*, much research focuses on extracting active ingredients from *C. asiatica*. Researchers have studied antioxidant activity using a maceration method. Results confirmed that *C. asiatica* contains antioxidant activity, total phenolic content (TPC), and total flavonoid content (TFC). The highest phenolic content was 2.14 mg GAE/g, a valuable source [8]. Additionally, another study suggested that the methanolic fraction of *C. asiatica* contains asiaticoside, an active ingredient affecting wound healing [9]. Moreover, the extraction of *C. asiatica* is used in powder, so the drying method is an important factor for active ingredients. Other researchers reported that drying methods affected the quality of plants [10]. The basic drying methods, including freeze-drying, hot air-drying, vacuum-drying, and ambient air-drying, were studied, and the results demonstrated that hot air-drying preserved the total phenolic content in *Thunbergia laurifolia* Lindl. better than other methods [11]. However, a higher drying temperature could degrade the quantity of total phenolic content, antioxidant activity, and antimicrobial activity;

thus, the drying temperature should be optimized with appropriate drying time [10]. Additionally, hot air drying is more time-consuming, energy-intensive, and costly compared to other methods [12].

Furthermore, the extraction methods are the most essential processes, e.g., Soxhlet, maceration, ultrasonic-assisted (UAE), microwave-assisted (MAE), subcritical, and supercritical techniques. These techniques would be selected as a suitable method to extract effective bioactive compounds. Most studies reported the extraction of bioactive compounds from lime peel using ultrasonic and microwave-assisted methods. The results showed that a high TPC was extracted using UAE, which was more efficient for extracting TPC and antioxidant activity [13]. Additionally, another study showed that UAE can be used for extracting herbs, such as *Plectranthus amboinicus* leaves. They reported that UAE yielded the highest concentration of thymol due to its capability to break the surface structure [14]. Additionally, the research showed that UAE is a more efficient and economical extraction method [13]. Furthermore, the selection of solvent, which affects bioactive compounds, is considered. Organic solvents such as water, ethanol, methanol, and acetone are widely used [15]. However, ethanol is widely used as an alternative solvent due to its properties, including being non-toxic, a green solvent, and having high efficiency [16].

In this research, *Centella asiatica* powder was extracted using maceration and ultrasonic-assisted extraction with ethanol as the solvent. The effects of extraction temperature, extraction time, and the amount of *C. asiatica* powder were studied to achieve the highest antioxidant activity.

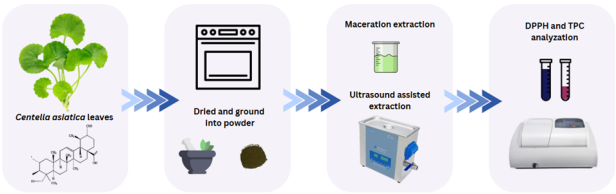

Figure 1 The methodologies of extraction *C. asiatica*

2. EXPERIMENTAL

2.1 Chemicals and materials

Ethanol 99.99% (C_2H_5OH), Folin-Ciocalteu reagent, Gallic acid monohydrate ($C_7H_6O_5 \cdot H_2O$), Sodium carbonate (Na_2CO_3), and 2,2-diphenyl-1-picrylhydrazyl (DPPH) were purchased from QREC Thailand Asia. *Centella asiatica* leaves were purchased from the local market, Pathum Thani, Thailand.

2.2 Preparation of *Centella asiatica* powder

Firstly, *Centella asiatica* fresh leaves were washed until it cleaned. Then, put them on the trays and dried using hot air-drying oven at 80°C for 1.5 h. After that, dried leaves were ground into fine powder using a mortar and pestle and sieved. The powder was kept in the desiccator.

2.3 Maceration extraction

Extraction of antioxidant activity from *Centella asiatica* powder was conducted using a maceration method. Briefly, 50 ml of ethanol (EtOH) was used as the solvent. The weight of *C. asiatica* (CA) powder varied at 0.5, 1, and 2 g. A tea bag containing CA powder was placed in a 50-ml glass bottle of EtOH. Extractions were carried out for 1, 2, 3, and 4 hours at room temperature. The powder was then removed, and the extracts were kept for further analysis.

2.4 Ultrasonic-assisted extraction

Ultrasonic-assisted extraction was performed in an ultrasonic bath. The solvent was fixed at 50 ml of EtOH, like maceration extraction. The CA powder was weighed at 0.5, 1, and 2 g and placed into the tea bag and a glass bottle of EtOH. Then, place it into an ultrasonic bath at 40 kHz frequency with 100% amplitude level. The process was carried out for 1, 2, 3, and 4 h at room temperature, 40, 50, and 60°C. After that, proceed with the same steps as the maceration extraction.

2.5 Total Phenolic Content (TPC) analysis

All samples of the extracts were analyzed using Folin-Ciocalteu reagent. A 1 ml sample was added to a test tube, followed by 1 ml of Folin-Ciocalteu reagent, and the sample was left for 5 min. After that, Na_2CO_3 (7%w/v) of 10 ml was added, and the sample was incubated at room temperature for 30 min. Additionally, gallic acid was used as a standard calibration curve. The concentration of acid was at 0, 5, 10, 20, 40, 60, 80, 100, 200, and 300 µg/ml. Therefore, TPC was expressed as mg gallic acid equivalent per gram of sample (mg GAE/g). The absorbance of the samples and the standard was measured using UV-Vis spectrophotometer at 750 nm.

2.6 DPPH analysis

Briefly describe the DPPH method for determining antioxidant activity. Firstly, the DPPH methanolic solution was mixed with 10 mg of DPPH and 100 ml of methanol in the dark. Next, the extract of 1.5 ml was added to the test tube, followed by DPPH methanolic solution of 1.5 ml. Then, the sample was incubated in the dark for 10 min. Additionally, the blank solution was prepared by mixing DPPH solution equal with methanol. The absorbance was measured using UV-Vis spectrophotometer at 517 nm. Therefore, DPPH (%) was calculated as in equation (1).

$$\text{DPPH (\%)} = \left(1 - \frac{\text{Abs.sample}}{\text{Abs.control}}\right) \times 100 \qquad (1)$$

3. RESULTS AND DISCUSSION

The total phenolic content (TPC) and DPPH scavenging activity (%) were analyzed after the extraction process. The extract sample of UAE at 50ºC is shown in Fig. 2. The color of the extracts was intense with increasing CA powder. The standard calibration curve of gallic acid expressed a significant linear equation at y=0.0036x-0.0057 with a coefficient of determination (R^2) at 0.9997.

3.1 Maceration extraction

3.1.1 Total phenolic content (TPC)

The extracts of each condition were analyzed and showed that the highest TPC was 26.31 mg GAE/g at 3 h of extraction time and CA powder of 0.5 g. It can be seen that the lower the amount of CA powder provided, the higher TPC at room temperature.

3.1.2 DPPH scavenging activity

From Table 1, DPPH (%) ranged from 37.32 to 86.75%. The results were opposite with TPC when the amount of CA powder increased DPPH (%) increased. Additionally, the results indicated that the amount of CA powder was more significant than the extraction time because an excessive extraction time might decrease in antioxidants [17].

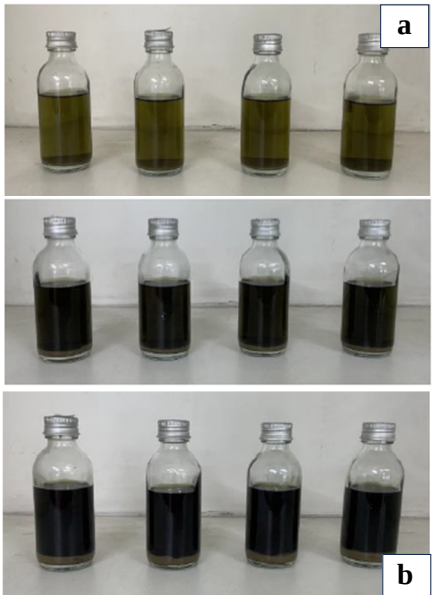

Figure 2 The extracts of *C. asiatica* using UAE at 50ºC by CA powder (a) 0.5 g (b) 1 g (c) 2 g.

Table 1 The conditions of maceration extraction and the results of TPC and DPPH scavenging activity

CA powder (g)	Time (h)	TPC (mg GAE/g)	DPPH (%)
0.5	1	26.14	38.02
	2	19.73	39.56
	3	26.31	41.63
	4	22.23	37.32
1.0	1	11.74	44.59
	2	16.11	57.72
	3	15.24	56.18
	4	13.86	51.03
2.0	1	10.54	82.20
	2	12.49	86.75
	3	9.29	86.34
	4	9.37	86.34

3.2 Ultrasonic-assisted extraction (UAE)

3.2.1 Total phenolic content (TPC)

The results of UAE extracts were demonstrated in Table 2 and 3. At room temperature, the highest TPC was 39.56 mg GAE/g at 3 h, which was higher than in other conditions. Additionally, when extraction temperatures increased from 40 to 60ºC, the highest TPC of each temperature was 24.23, 33.14, and 31.81 mg GAE/g, respectively. While the lowest TPC was 9.58 mg GAE/g at an extraction temperature of 40ºC and 2%w/v of CA. It can be seen that room temperature preserves phenolic compounds better than a high temperature. Supporting this, another research reported that phenolic compounds can be degraded during the thermal process, and they can be oxidized during reaction [10]. Additionally, the researchers studied the extraction of *C. asiatica* at 70ºC for 1 h, the results showed that TPC of ethanolic extract was 2.14±0.29 mg GAE/g. Moreover, the amount of CA powder increased TPC decreased because the volume of solvents was fixed. Hence, phenolic compounds of CA powder couldn't dissolve in the solvent due to their surface contact [15].

3.2.2 DPPH scavenging activity

From Table 2 and 3, DPPH (%) indicated that the highest DPPH (%) was 91.67% at 50ºC of extraction temperature with the highest CA powder. When increasing CA powder, DPPH (%) was slightly increased. On the one hand, the increment of extraction time, DPPH (%), increased. According to the extraction temperature at 40, 50, and 60ºC, DPPH (%) ranged from 52.45 to 86.34%, 45.77 to 91.67%, and 51.80 to 80.13%, respectively. Supporting this, the study of the extraction of *C. asiatica* with ethanol, methanol, and acetone obtained a high DPPH value between 69.8 to 70.6%. Hence, DPPH value had a high antioxidant activity.

Table 2 The conditions of ultrasonic-assisted extraction and the results of TPC and DPPH scavenging activity at room temperature and 40ºC

CA powder (g)	Time (h)	TPC (mg GAE/g)		DPPH (%)	
Temperature (°C)		room	40	room	40
0.5	1	26.64	22.06	66.47	52.45
	2	28.48	23.64	68.18	51.51
	3	39.56	24.23	66.71	51.92
	4	38.89	21.06	65.70	55.23
1.0	1	14.99	12.99	80.90	74.63
	2	23.15	13.90	80.48	75.16
	3	29.20	14.45	79.48	76.52
	4	26.82	13.4	79.30	63.28
2.0	1	11.99	9.58	86.34	83.50
	2	13.49	10.26	86.10	83.32
	3	22.45	11.41	85.04	81.55
	4	18.41	10.33	83.91	81.37

Comparing the extraction methods between maceration and UAE, the results demonstrated that UAE consisted of higher antioxidant activity compared to maceration. Likewise, a lower concentration of CA powder and extraction time, UAE also produced effective antioxidant activity. Supporting this, the ultrasonic used a high frequency of energy which resulted in active ingredients. Additionally, it could improve the solubility and the diffusion of the solvent [18]. Moreover, ultrasonic vibration would disrupt the cell wall and enable solvents to enter the cell plants for the release of bioactive compounds [13, 19].

According to medical properties, *C. asiatica* extract is widely used as a medicine for treatment would healing [9]. There is much research reported that bioactive compounds can be applied with polymer to fabricate nanofibers, which can prevent the infection of wounds and faster healing [20]. Therefore, the highest antioxidant activity of the extracts in this work might be applied in tissue engineering as a dressing.

Table 3 The conditions of ultrasonic-assisted extraction and the results of TPC and DPPH scavenging activity at 50ºC and 60ºC

CA powder (g)	Time (h)	TPC (mg GAE/g)		DPPH (%)	
Temperature (°C)		50	60	50	60
0.5	1	24.31	27.73	45.77	52.33
	2	26.89	31.81	55.80	57.84
	3	33.14	21.06	53.18	51.87
	4	25.23	19.56	50.95	51.80
1.0	1	14.36	19.15	72.33	71.87
	2	21.82	20.57	73.51	72.66
	3	23.15	15.61	73.38	73.64
	4	22.45	15.28	72.00	72.98
2.0	1	11.16	15.10	90.75	78.10
	2	16.33	16.76	91.67	80.13
	3	16.83	15.18	90.16	78.89
	4	15.41	15.14	89.90	78.62

4. CONCLUSION

Extraction of *Centella asiatica* was studied using different extraction methods, and the variables of parameters that affected the antioxidant. The maceration and ultrasonic-assisted extraction were used for investigating total phenolic content (TPC) and DPPH scavenging activity with three variables consisting of the concentration of *C. asiatica* powder, ranging from 0.5 to 2%w/v, extraction temperature 25 to 60°C, and extraction time 1 to 4 h. The ultrasonic-assisted extraction achieved the highest DPPH scavenging activity and TPC at 91.67% and 39.56 mg GAE/g, respectively, whereas maceration yielded the highest TPC of 26.31 mg GAE/g and DPPH scavenging activity of 86.75%. Therefore, the optimum condition, which had the highest DPPH scavenging activity, was 2%w/v of CAE with a temperature of 50°C at 2 h using UAE. In conclusion, a higher concentration of CAE with appropriate extraction temperature and time provided the best antioxidant activity. Hence, the *C. asiatica* extract can be applied in tissue engineering such as wound dressing due to its biological properties.

ACKNOWLEDGMENTS

This research is supported by the Department of Chemical Engineering, Faculty of Engineering, Thammasat School of Engineering, Thammasat University.

REFERENCES

1. Tripathy S, Verma DK, Thakur M, Chakravorty N, Singh S, Srivastav PP. Recent trends in extraction, identification and quantification methods of Centella asiatica phytochemicals with potential applications in food industry and therapeutic relevance: A review. *Food Bioscience*. 2022; 49: 101864.
2. Idris F, Nadzir M. Comparative studies on different extraction methods of Centella asiatica and extracts bioactive compounds effects on antimicrobial activities. Antibiotics, 10, 457. 2021.
3. Rashid MH-O, Akter M, Uddin J, Islam S, Rahman M, Jahan K, et al. Antioxidant, cytotoxic, antibacterial and thrombolytic activities of Centella asiatica L.: possible role of phenolics and flavonoids. Clinical Phytoscience. 2023; 9(1): 1-9.
4. Mohapatra P, Ray A, Jena S, Nayak S, Mohanty S. Influence of extraction methods and solvent system on the chemical composition and antioxidant activity of Centella asiatica L. leaves. Biocatalysis and Agricultural Biotechnology. 2021; 33: 101971.
5. Gunathilake K, Ranaweera K, Rupasinghe H. Response surface optimization for recovery of polyphenols and carotenoids from leaves of Centella asiatica using an ethanol-based solvent system. Food science & nutrition. 2019; 7(2): 528-36.
6. Rattanakom S, Yasurin P. Chemical profiling of Centella asiatica under different extraction solvents and its antibacterial activity, antioxidant activity. Oriental Journal of Chemistry. 2015; 31(4): 2453-9.

7. Eze FN, Tola AJ, Nwabor OF, Jayeoye TJ. Centella asiatica phenolic extract-mediated bio-fabrication of silver nanoparticles: characterization, reduction of industrially relevant dyes in water and antimicrobial activities against foodborne pathogens. Rsc Advances. 2019; 9(65): 37957-70.
8. Quyen N, Quyen N, Quy N, Quan P, editors. Evaluation of total polyphenol content, total flavonoid content, and antioxidant activity of Centella asiatica. IOP Conference Series: Materials Science and Engineering; 2020: IOP Publishing.
9. Azis H, Taher M, Ahmed A, Sulaiman W, Susanti D, Chowdhury S, et al. In vitro and In vivo wound healing studies of methanolic fraction of Centella asiatica extract. South African Journal of Botany. 2017; 108: 163-74.
10. Niamnuy C, Charoenchaitrakool M, Mayachiew P, Devahastin S. Bioactive compounds and bioactivities of Centella asiatica (L.) Urban prepared by different drying methods and conditions. Drying Technology. 2013; 31(16): 2007-15.
11. Oh HKF, Siow LF, Lim YY. Approach to preserve phenolics in Thunbergia laurifolia leaves by different drying treatments. Journal of food biochemistry. 2019; 43(7): e12856.
12. Ho L, Pang W, Tan T, Mustafa K. Effects of drying conditions on the physicochemical and functional properties of red-and yellow-fleshed watermelon rinds flour. Journal of Fundamental and Applied Sciences. 2017; 9(2S): 898-923.
13. Rodsamran P, Sothornvit R. Extraction of phenolic compounds from lime peel waste using ultrasonic-assisted and microwave-assisted extractions. Food bioscience. 2019; 28: 66-73.
14. Zahari NAAR, Chong GH, Abdullah LC, Chua BL. Ultrasonic-assisted extraction (UAE) process on thymol concentration from Plectranthus amboinicus leaves: Kinetic modeling and optimization. Processes. 2020; 8(3): 322.
15. Yoswathana N, Eshtiaghi M. Optimization of subcritical ethanol extraction for xanthone from mangosteen pericarp. International Journal of Chemical Engineering and Applications. 2015; 6(2): 115.
16. Baümler ER, Carrín ME, Carelli AA. Extraction of sunflower oil using ethanol as solvent. Journal of Food Engineering. 2016; 178: 190-7.
17. Rafiee Z, Jafari S, Alami M, Khomeiri M. Microwave-assisted extraction of phenolic compounds from olive leaves; a comparison with maceration. J Anim Plant Sci. 2011; 21(4): 738-45.
18. Seo S, Kim Y. Improving cosmetic activity by optimizing Centella asiatica extraction process. Natural Product Communications. 2019; 14(7): 1934578X19867188.
19. Huang W, Xue A, Niu H, Jia Z, Wang J. Optimised ultrasonic-assisted extraction of flavonoids from Folium eucommiae and evaluation of antioxidant activity in multi-test systems in vitro. Food chemistry. 2009; 114(3): 1147-54.
20. Aruan NM, Sriyanti I, Edikresnha D, Suciati T, Munir MM. Polyvinyl alcohol/soursop leaves extract composite nanofibers synthesized using electrospinning technique and their potential as antibacterial wound dressing. Procedia Engineering. 2017; 170: 31-5.

Carthamus tinctorius L. flower antioxidant extracts from subcritical ethanol extraction

Tanapat Wangsomboonsiri[1], Peerapong Srinukul[1], Veronica Winoto[1,*]

[1] Department of Chemical Engineering, Faculty of Engineering, Thammasat School of Engineering, Thammasat University, Pathum Thani 12120, Thailand

[*] Corresponding author: wveronic@engr.tu.ac.th

ABSTRACT

Carthamus tinctorius L. flower (Safflower) from the Compositae or Asteraceae family was used widely for medicinal applications. The medicinal activities include antifibrosis, antidiabetic, antitumor, anti-inflammatory, anticoagulants, and antioxidant. The flower is rich in bioactive compounds such as phenolics and flavonoids. A suitable extraction method is essential for acquiring antioxidants. Subcritical ethanol extraction is a green extraction technique with high antioxidant extract performance. Optimal extraction is necessary to maximize efficiency. In this work, the three extraction parameters, the *Carthamus tinctorius L.* flower amount, extraction temperature, and extraction duration, were studied. The results illustrate that temperature is the most important parameter affecting antioxidant activity as analyzed using DPPH scavenging method. Higher temperatures extract a higher DPPH percentage up to 87.01% at 200°C; however, above 200°C, the DPPH percentage slightly decreases.

Keywords: Antioxidant; *Carthamus tinctorius L.* flower; subcritical ethanol extraction; DPPH scavenging activity

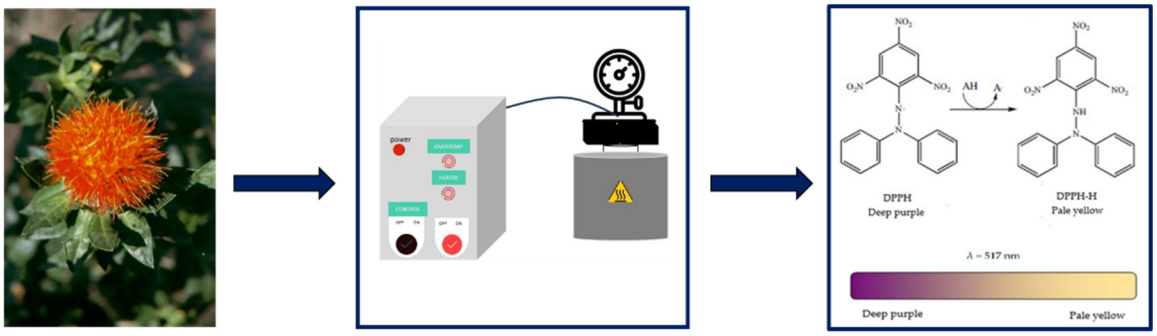

Figure 1. The methodologies of *Carthamus tinctorius L.* flower antioxidant extraction.

1. INTRODUCTION

Safflower (*Carthamus tinctorius L.*) belongs to the Compositae family, the same family as the chrysanthemum. It originated in the Middle East. In Thailand, the main safflower production areas are in the northern region. It is a medicinal plant long used in traditional Thai and Chinese medicine. Common applications include promoting blood circulation, inhibiting tumour development, preventing and treating heart disease, reducing blood lipids, and relieving menstrual pain. Additionally, safflower contains valuable bioactive compounds, such as flavonoids and phenolic compounds, which possess antioxidant properties that help protect cells from oxidative damage caused by free radicals [1–3].

Safflower contains key active compounds in the flavonoid group, such as hispidulin, which exhibits anti-inflammatory and antioxidant properties; luteolin, which helps reduce inflammation and has anticancer effects against certain cancers; and quercetin, a powerful antioxidant that helps lower the risk of heart disease and other chronic illnesses. The extraction of these bioactive compounds from safflower can be achieved through various methods, including solvent extraction, oil extraction, supercritical CO_2 extraction, ultrasound-assisted extraction (UAE), microwave-assisted extraction (MAE), and subcritical ethanol extraction [4–7].

Free radicals are atoms or molecules containing unpaired electrons in their electron shells, making them unstable and needing additional electrons to regain stability. This instability causes free radicals to readily

react with other substances in the body to capture electrons; this process can damage cells and tissues. When free radicals accumulate in large amounts, it can result in oxidative stress, an imbalance between free radical production and the body's antioxidant defense system. This imbalance causes an excess of free radicals beyond the body's ability to neutralize them, potentially damaging cellular components such as proteins, lipids, and DNA. However, free radicals also play important beneficial roles in the body. For instance, they help destroy pathogens and foreign substances, stimulate immune responses to prevent infections, and contribute to the elimination of damaged or malfunctioning cells—a critical process in preventing cancer and other diseases [8–9].

In general, various methods can be used to extract compounds from safflower, such as reflux ethanol extraction. However, this method has certain drawbacks: it requires a long extraction time because the solvent must continuously contact the sample to extract the bioactive compounds, and it also involves high thermal energy consumption due to boiling. The heat may degrade or alter the chemical properties of some sensitive compounds. In contrast, subcritical ethanol extraction requires a shorter processing time. This method utilizes suitable pressure and temperature conditions to accelerate the extraction process and improve extraction efficiency. Subcritical ethanol has enhanced solubility for bioactive compounds due to its elevated pressure and temperature, while the lower temperatures used in this method reduce the risk of thermal degradation of the extracted compounds. Therefore, this research focuses on studying the antioxidant activity of safflower extracts obtained through subcritical ethanol extraction to explore their potential applications in the pharmaceutical industry. [10–11].

In this research, *Carthamus tinctorius L.* was selected as the material for subcritical extraction using ethanol as a solvent. The effects of temperature, time, and the amount of *Carthamus tinctorius L.* powder were varied in this study.

Figure 2. Safflower [14]

2. EXPERIMENTAL

2.1 Chemicals and materials

Ethanol 99. 99% (C_2H_5OH), Folin-Ciocalteu reagent, Gallic acid monohydrate ($C_7H_6O_5 \cdot H_2O$) and Sodium carbonate (Na_2CO_3) were purchased from TPC HERB. Safflower *(Carthamus tinctorius L.)* leaf powder was purchased from India.

2.2 Subcritical fluid extraction

The subcritical extraction was carried out in a stainless-steel reactor, which has a net volume of 100 ml. Then, *Carthamus tinctorius L.* leaves powder ranging from 0.1 to 0.9 g was mixed with 50 ml of ethanol. The reaction temperature was performed at 120, 160, 200, and 240°C with the reaction time being 5, 15, 30, and 45 min (approximately heating-up time 15 min). After the reaction finished, the vessel was cooled down immediately. The extract solution was kept in a glass bottle until further analysis.

Figure 3. Subcritical ethanol extraction

2.3 Total Phenolic Content (TPC) analysis

The total phenolic content was measured by adding 1, 5, and 9 mL of sample to separate test tubes, followed by 1 mL of Folin-Ciocalteu reagent. The samples were left for 5 min. Then, 10 ml of Na_2CO_3 (7% w/v) was added. After mixing, the samples were incubated for 60 min. The absorbance was measured using a UV-VIS spectrophotometer at 750 nm. Gallic acid was used as a standard for a calibration curve with concentration of 0, 5, 10, 20, 40, 60, 80, 100, 200, and 300 µg/ml ($y = 0.0037x + 0.038$, $R^2 = 0.9963$). Therefore, TPC was expressed as mg gallic acid equivalent per gram of sample.

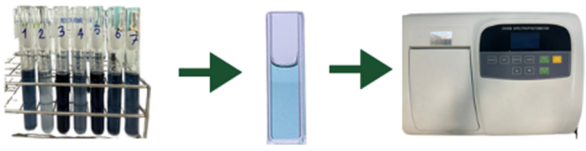

Figure 4. TPC analyzation

2.4 2,2-diphenyl-1-picrylhydrazyl (DPPH) analysis

DPPH solution was prepared by dissolving 10 mg of 2,2-diphenyl-1-picrylhydrazyl (DPPH) in 100 ml of methanol. The solution was mixed in the dark. For the sample analysis, 1 ml of the extract was mixed with 2 ml of the DPPH solution and incubated in the dark for 10 minutes. For the control, 1 ml of methanol was mixed with 2 ml of the DPPH solution and also incubated in the dark for 10 minutes. The absorbance was measured using a UV-VIS spectrophotometer at

517 nm. Total phenolic content (TPC) was expressed as a percentage (%)

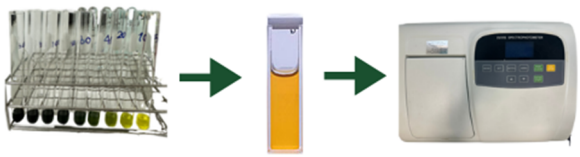

Figure 5. DPPH analyzation

3. RESULTS AND DISCUSSION

Table 1 The preliminary conditions and results of subcritical extraction

Carthamus tinctorius (g/50 ml EtOH)	Temperature (°C)	Time (min)	TPC (mg GAE/g)	DPPH (%)
0.1	160	30	61.49	14.01
0.1	200	30	37.78	15.29
0.5	120	30	29.95	27.04
0.5	160	5	29.02	36.61
0.5	160	15	30.81	55.53
0.5	160	30	36.57	56.22
0.5	160	45	36.41	55.26
0.5	200	30	58.95	78.61
0.5	200	30	58.59	78.26
0.5	240	30	63.65	77.56
0.9	160	30	33.69	62.73
0.9	200	30	99.32	77.51

3.1 Effect of safflower powder content on total phenolic content

From a comparison of experimental results using 0.1, 0.5, and 0.9 g/50 ml ethanol with safflower powder at 160°C for 30 min, the total phenolic content decreased with increasing safflower powder; values were 61.49, 36.57, and 33.69 mg GAE/g, respectively. This happens due to the solvent cannot efficiently extract phenolic compounds at high sample concentrations, resulting in solvent saturation and reduced dissolution of active compounds. Therefore, selecting the appropriate amount of raw material is crucial for efficient extraction. [12].

When considering the experimental results at 160°C and 30 min, comparing antioxidant activity values at 0.1, 0.5, and 0.9 g of safflower powder, the DPPH inhibition values were 14.01%, 46.22%, and 62.73%, respectively. This indicates that increasing the amount of safflower powder increased the antioxidant activity, a trend different from the decrease in phenolic content per gram of sample with increased powder. Increasing the amount of safflower powder may have increased the total active compounds in the extract, thus increasing the total antioxidant activity [12], despite not affecting the average phenolic concentration per gram.

3.2 Effect of temperature on total phenolic content

When considering the effect of extraction temperatures of 120, 160, 200, and 240°C, while controlling the amount of safflower powder at 0.5 g and the extraction time at 30 minutes, it was found that the total phenolic content increased with increasing temperature, with the following values: 29.95, 36.57, 58.95, and 63.65 mg GAE/g, respectively. This is consistent with the principle that increasing temperature increases the solubility of active compounds in the solvent and affects the rate of their diffusion into solution [13]. However, at high temperatures, the stability of phenolic compounds should be considered, as degradation may occur if the temperature exceeds a stability threshold. The experimental results, however, showed that the temperature of 240°C still yielded good extraction results without any decrease in phenolic content.

When controlling the amount of safflower powder at 0.5 g and the time at 30 minutes, the antioxidant activity increased with increasing temperature. Values were 27.04% at 120°C, 46.22% at 160°C, 75.61% at 200°C, and reached a maximum of 77.56% at 240°C. While these differences were not statistically significant, temperature is an important factor enhancing the extraction of antioxidant compounds. Heat likely improves the dissolution and diffusion of these compounds from the cells. However, considering the stability of the active compounds, 200°C may be a more suitable temperature for industrial application.

3.3 Effect of extraction time on total phenolic content

Comparison of extraction times at 5, 15, 30, and 45 minutes under conditions of 0.5 g safflower powder and 160°C showed that phenolic content increased with increasing time initially, with values of 29.02, 30.81, 36.57, and 36.41 mg GAE/g, respectively. However, after 30 minutes, the phenolic content remained relatively constant or increased only slightly, indicating that longer extraction times did not significantly improve efficiency and resulted in unnecessary energy consumption. Therefore, 30 minutes is concluded to be the optimal extraction time under these experimental conditions.

From a comparison of antioxidant activity values at extraction times of 5, 15, 30, and 45 minutes at 160°C and 0.5 g of safflower powder, the DPPH inhibition value increased from 36.61% at 5 minutes to 55.53% at 15 minutes. It peaked at 56.22% at 30 minutes (Experiment 6 from Table 2) and then slightly decreased to 55.26% at 45 minutes. These results indicate that longer initial extraction times significantly increased antioxidant activity. However, after 30 minutes, the antioxidant activity remained constant or slightly decreased, possibly due to degradation of important compounds or oxidation reactions caused by heat accumulation in the extraction system.

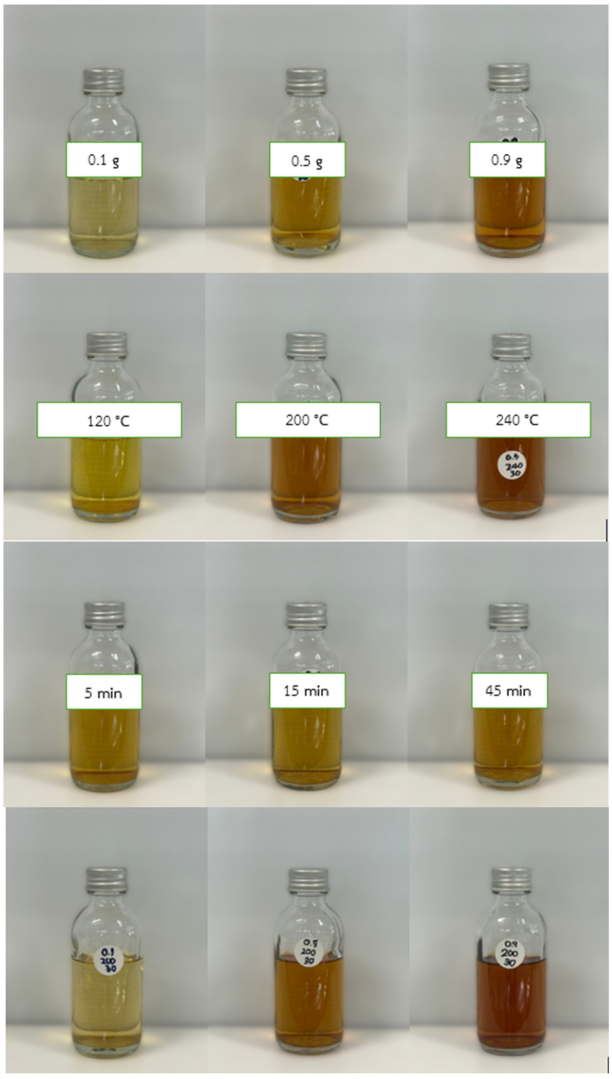

Figure 6. Examples of safflower powder extract.

4. CONCLUSION

Subcritical ethanol extraction was studied using *Carthamus tinctorius L.* powder. The best conditions for antioxidant extraction using a subcritical fluid technique were determined. A study of antioxidant extraction from safflowers using a subcritical fluid technique found the most suitable extraction conditions to obtain the highest antioxidant activity. Using 0.5 g of safflower powder, an extraction temperature of 200°C, and an extraction time of 30 minutes yielded an antioxidant activity of 78.61% with the highest phenolic content of 58.95 mg GAE/g. Three variables affecting antioxidant activity were studied and determined: the amount of safflower powder, temperature, and extraction time. All three variables significantly affected the total phenolic content and antioxidant activity. The amount of safflower powder and the extraction temperature most affected the extract's color and total phenolic content. The higher the amount of safflower powder and the higher the temperature, the greater the antioxidant activity; however, beyond a certain point, antioxidant activity decreased significantly. It can be concluded that the amount of safflower powder is the most significant variable affecting antioxidant activity, followed by temperature and then extraction time.

ACKNOWLEDGMENTS

This research is supported by the Department of Chemical Engineering, Faculty of Engineering, Thammasat School of Engineering, Thammasat University.

REFERENCES

1. A. Aboelsoud, “Herbal medicine in ancient Egypt,” Journal of Medicinal Plants Research*, vol. 4, no. 2, pp. 082–086, 2010.
2. Yu, S.-Y., Lee, Y.-J., Kim, J.-D., Kang, S.-N., Lee, S.-K., Jang, J.-Y., Lee, H.-K., Lim, J.-H., & Lee, O.-H. (2014). Phenolic composition, antioxidant activity and anti-adipogenic effect of hot water extract from safflower (Carthamus tinctorius L.) seed. Journal of Functional Foods, 7, 374-382. Available at: NCBI.
3. Maeonhospital. (2014). Avialable from https:// www.maeonhospital.go.th/?p=1524
4. Zhao, Y., & Lin, Y. (2010). Extraction and analysis of flavonoids from Carthamus tinctorius. Journal of Agricultural and Food Chemistry, 58(12), 7052-7057.
5. Lee, S. Y., & Kim, J. H. (2015). Supercritical CO_2 extraction of bioactive compounds from Carthamus tinctorius. Separation Science and Technology, 50(18), 3425-3432.
6. Disthai.Hispidulin.Avialable from https://www. disthai.com/17323002/
7. Srinagarind Med J. (2013). Anticancer Activities of Flavonoids: Mechanisms of Actions, 28 (4)
8. Tanpaisankit M, Hongsaprabhas C, Charoenlap C, Honsawek S. (2017). High oxidative stressand decrease of mitochondrial DNA copies in musculoskeletal tumors. Chula Med J 61(6): 771 – 82 Avialable from https://digital.car.chula. ac.th/clmjournal/vol61/iss6/8
9. J. Dai and R. J. Mumper, “Plant phenolics: extraction, analysis and their antioxidant and anticancer properties,” *Molecules*, vol. 15, no. 10, pp. 7313–7352, 2010.
10. Yongqiang Wanga, Yujie Gao b, Hui Ding d, Shejiang Liu d, Xu Han d, Jianzhou Guie, Dan Liu e, “Subcritical ethanol extraction of flavonoids from Moringa oleifera leaf and evaluation of antioxidant activity”, *Food Chemistry*, vol. 218, pp. 152-158, 2017.
11. M. Herrero, A. Cifuentes, and E. Ibáñez, “Sub- and supercritical fluid extraction of functional ingredients from different natural sources: Plants, food-by-products, algae and microalgae: A review,” *Food Chemistry*, vol. 98, no. 1, pp. 136-148, 2006.

12. Shalmashi, A., & Khosh-Khui, M. (2014). Supercritical fluid extraction of bioactive compounds: A review.International Journal of Advanced Biological and Biomedical Research, 2(7), 2401-2416.
13. Mokrani, A., & Madani, K. (2016).Effect of solvent, time and temperature on the extraction of phenolic compounds and antioxidant activity of Pomegranate peel.Journal of Food Science and Technology, 53(3), 1077–1085.
14. Dajue, L., & Mündel, H.-H. (1996). Safflower (Carthamus tinctorius L.). Promoting the conservation and use of neglected and underutilized crops. No. 7. IPK and IPGRI, Rome, Italy.

Lignin extracted from rice straw and coconut coir

Supapohn Pohnanothai[1,*], Patcharaporn Wutticharoenmongkol[2]

[1] Department of Chemical Engineering, Faculty of Engineering, Thammasat School of Engineering, Thammasat University, Pathum Thani 12120, Thailand
[*] Corresponding author: supapohn.poh@dome.tu.ac.th

ABSTRACT

Lignin, a complex biopolymer in plant cell walls, has gained significant interest due to its antioxidant and antimicrobial properties. This study focuses on the extraction and characterization of lignin from rice straw and coconut coir using deep eutectic solvents (DES) as a sustainable and environmentally friendly approach. The extracted lignin was analyzed for its chemical structure, functional groups, and antioxidant activity to evaluate its potential applications. The extracted lignin was characterized using Fourier Transform Infrared Spectroscopy (FTIR) analysis, which confirmed the presence of key functional groups, including hydroxyl (-OH), carbonyl (C=O), and aromatic (C=C) bonds, indicating a well-preserved lignin structure. Antioxidant activity was assessed using the DPPH radical scavenging assay, revealing that coconut coir-derived lignin exhibited higher antioxidant potential (up to 91.12% RSA at 1 mg/mL) compared to rice straw-derived lignin. Additionally, the use of recovered DES did not significantly alter lignin's antioxidant properties, demonstrating its feasibility for reuse in extraction processes. This study highlights the effectiveness of DES in lignin extraction while preserving its bioactive properties. The extracted lignin can be further utilized in biomaterials applications. Future research should focus on optimizing lignin recovery and improving its solubility for broader industrial applications.

Keywords: Lignin; Deep Eutectic Solvents (DES); Rice Straw; Coconut Coir; Extraction

1. INTRODUCTION

The sustainable use of agricultural residues has become a critical focus in addressing environmental challenges and promoting resource efficiency. In Thailand, the cultivation of rice and coconuts results in large quantities of agricultural by-products such as rice straw and coconut coir. Traditionally, these residues are either burned or discarded, contributing to significant environmental pollution, including greenhouse gas emissions and degradation of air quality [1,2]. Transforming these residues into high-value products aligns with the principles of the circular economy and supports global sustainability goals. Lignin is the most abundant aromatic biopolymer in nature, made up of phenylpropane units derived from three aromatic alcohol precursors: p-coumaryl, coniferyl, and sinapyl alcohol [3,4]. Its structure comprises phenolic components from these monolignols, classified as p-hydroxyphenyl (H), guaiacyl (G), and syringyl (S) moieties [5]. Lignin, a major structural component of lignocellulosic biomass, plays essential roles in plants by providing mechanical strength, facilitating water transport, and serving as a physical barrier to bacteria [6]. Beyond its natural functions, lignin possesses valuable properties such as ultraviolet (UV) protection [7,8], thermal stability [9], antimicrobial and antioxidant activities [10]. These characteristics make it an attractive candidate for applications in bio-composites, pharmaceuticals, energy storage, and sustainable materials. In addition, a variety of reports have demonstrated that isolated lignin serves as an environmentally sustainable and biocompatible bioactive polymer [11]. However, traditional methods for lignin extraction, such as Kraft and sulfite pulping, involve harsh chemical processes that degrade the polymer's native structure, limiting its potential for advanced applications. In response to these challenges, Deep Eutectic Solvents (DES) have emerged as a promising green technology for the selective and efficient extraction of lignin. DESs are formed by the association of hydrogen bond donors (HBD) and hydrogen bond acceptors (HBA), resulting in mixtures that have melting points significantly lower than that of an ideal liquid mixture [12]. DESs offer notable advantages, including low toxicity, biodegradability, low volatility, and the ability to be tailored for specific biomass processing applications. Their mild extraction conditions help preserve the functional integrity of lignin while facilitating the separation of other lignocellulosic components. Significantly, Kumar et al. demonstrated the successful use of natural deep eutectic solvents (NADES) for the efficient extraction of lignin from rice straw, which is an abundant agricultural residue in Asia.

Their study employed a NADES system composed of lactic acid and choline chloride, achieving over 90% lignin purity under gentle conditions. Furthermore, the structural integrity of the extracted cellulose was largely preserved, and the DES used in the process could be recycled without a significant loss of performance [13]. Their findings highlight the potential of DES as an environmentally friendly and economically viable alternative for lignin extraction, offering a sustainable pathway for biomass valorization and bio-product development. The present study focuses on extracting lignin from rice straw and coconut coir using DESs under optimized conditions. By leveraging the advantages of DESs, this research aims to produce high-quality lignin suitable for incorporation into biopolymer composites, thereby enhancing material properties and adding value to agricultural residues. This approach helps advance the creation of more sustainable and eco-friendly materials, while also aiding the wider shift toward bio-based economies.

2. EXPERIMENTAL

The experimental method was modified from the protocol established by Kumar et al. [13], with changes to incubation conditions tailored to the specific properties of the biomass used in this study.

2.1 Materials

Agricultural residues, including rice straw and coconut coir, were collected from fields in Phetchabun, Thailand. Choline chloride (CC) and lactic acid (LA), used for deep eutectic solvent (DES) preparation, were obtained from LobaChemie Pvt. Ltd. (Thailand). 2,2-Diphenyl-1-picrylhydrazyl (DPPH) was purchased from Sigma–Aldrich Inc. (USA), and *N*, *N*-dimethylformamide (DMF) was sourced from CARLO ERBA Reagents SAS (Italy).

2.2 Methods

2.2.1 Biomass Preparation

Rice straw and coconut coir were prewashed with water to remove surface contaminants and dried under sunlight for 2–3 days. The dried biomass was then cut into small pieces, finely ground, and sieved through a 40-mesh sieve to achieve uniform particle size. The biomass powders were further dried at 80 °C until the moisture content <5% (w/w) and subsequently stored in vacuum-sealed bags at room temperature.

2.2.2 DES Preparation

DES was prepared by combining CC and LA (1:5 molar ratio) in a sealed vessel. The mixture was heated at 60°C under agitation (100 rpm) until complete dissolution (10–15 min), yielding a homogeneous liquid.

2.2.3 Biomass Pretreatment and Lignin Separation

All pretreatment experiments were executed individually at a solid loading of 10%, unless otherwise noted. It is essential to securely close the flask and incubate it in a hot water bath at temperatures of 60 °C, 70 °C, and 80 °C for durations of 8, 12, and 16 hours, with shaking at a speed of 100 rpm. The solution was permitted to return to room temperature after the incubation period. The lignin liquid and the biomass waste were separated using vacuum filtration with 1 µm filter paper. Water was gradually added to the DES solution containing dissolved lignin until the solution became cloudy. The mixture was incubated at 4°C for 12 hours following the onset of cloudiness. The solution was centrifuged at 5000 × g for 20 minutes after incubation. The lignin precipitate was rinsed with distilled water until a pH of 7 was achieved. The separated lignin precipitate was dried in a dryer at 70°C for 12 hours to produce powdered lignin.

2.2.4 DES Recovery

The DES solution was recovered by removing distilled water through evaporation using a rotary evaporator at 60 °C. The recovered DES could be reused in subsequent lignin extraction processes without modification. Distilled water separated during evaporation was stored and reused for future lignin precipitation.

2.2.5 Lignin Yield Determination

The lignin yield (% yield) was calculated based on the initial lignin content in the biomass. The following formula was used as equation (1).

$$\%\text{Yield} = \frac{Weight\ of\ EL\ (g)}{INC\ fraction \times Weight\ of\ DB\ (g)} \times 100 \qquad (1)$$

where DB is dry biomass, INC is initial lignin contents, and EL is extract lignin. Rosado et al. [14] reported a Klason lignin concentration of 12.4% for rice straw, while Rencoret et al. [15] provided the original lignin contents, which reported 32.1% for coconut coir. The Klason lignin method, involving concentrated acid hydrolysis to isolate acid-insoluble lignin, is widely recognized as a standard for quantitative lignin analysis [16].

2.2.6 Antioxidant Activity

The antioxidant activity of lignin was assessed using the DPPH (2,2-diphenyl-1-picrylhydrazyl) radical scavenging assay, following modifications of the methods reported by Wutticharoenmongkol et al. [17] A 0.25 mM DPPH solution in methanol was prepared, and lignin solutions were prepared in DMF at concentrations of 0, 0.1, 0.3, 0.5, 0.7, and 1.0 mg/mL. A volume of 0.08 mL of lignin solution was mixed with 3.0 mL of DPPH solution, and the mixtures were incubated in the dark at room temperature for 30 minutes. Absorbance was measured at 517 nm using a UV/Vis Single Beam Spectrophotometer (Model UV-5100,

Metash, China). Each sample was analyzed in triplicate, and the average value was calculated. The antioxidant activity was determined using the following equation (2).

$$\text{Antioxidant activity (\%)} = \frac{(A_c - A_s)}{A_c} x\ 100 \qquad (2)$$

where A_c and A_s are the absorbance of the control (DPPH + methanol) and the absorbance of the sample (DPPH + lignin solution), respectively.

2.2.7 Fourier Transform Infrared Spectroscopy (FTIR) Analysis

The functional groups present in lignin samples extracted from rice straw and coconut coir were characterized using Fourier transform infrared (FTIR) spectroscopy. The spectra were recorded over a range of 400–4000 cm^{-1} with 16 scans per sample. Samples were pre-dried at 105 °C for 3–5 hours (or overnight) before analysis. Measurements were performed in attenuated total reflectance (ATR) mode for direct solid sample analysis.

3. RESULTS AND DISCUSSION

3.1 Percentage yield of lignin

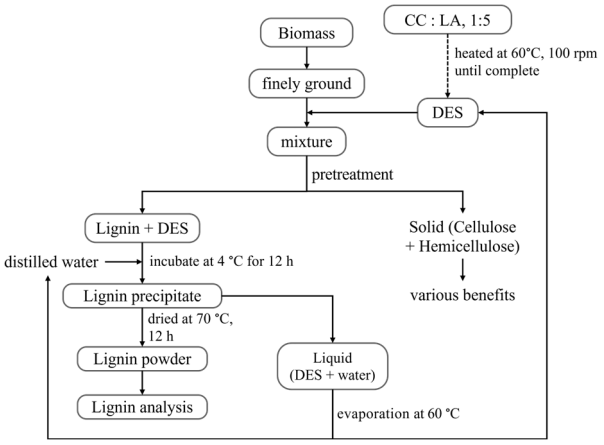

Figure 1 Schematic representation of DES pretreatment of biomass (rice straw and coconut coir)

The lignin yield was calculated based on the initial lignin content in each biomass using literature values. Table 1 shows that rice straw had higher lignin recovery efficiency than coconut coir under both extraction conditions. With fresh DES, rice straw yielded 24.58 ± 0.70%, and this slightly increased to 25.37 ± 0.41% with recovered DES. In contrast, coconut coir yielded 16.26 ± 0.71% with fresh DES and 20.47 ± 0.20% with recovered DES. Despite coconut coir's higher overall lignin content, its fibrous structure may hinder effective extraction. Rice straw has a more porous nature and allows better solvent penetration, enhancing lignin solubilization. Calculating yield based on total dry biomass could misrepresent extraction efficiency, making initial lignin-based yields a more accurate metric for comparison. Additionally, using recovered DES did not compromise extraction performance. This suggests that DES can be a sustainable and reusable medium for lignin extraction.

Table 1 Percentage yield of lignin extracted from rice straw and coconut coir*.

	DES reagent	%Yield lignin**
Rice straw	fresh solution	24.58±0.70
	recovery solution	25.37±0.41
Coconut coir	fresh solution	16.26±0.71
	recovery solution	20.47±0.20

* Condition at 80 °C for 8 h using a DES (CC:LA, 1:5)
**Calculated based on Klason lignin content from literature.

The lignin samples from different biomass sources and extraction conditions show distinct visual differences. In Figure 2, Lignin from rice straw using fresh and recovered DES appears as fine, dark powders, with the recovered DES sample being noticeably darker. Similarly, the lignin from coconut coir extracted with recovered DES is darker and more uniform compared to the lighter, reddish-brown lignin from fresh DES. Despite the color differences, both biomass types produced powdered, non-sticky solids, indicating minimal structural degradation during recycling.

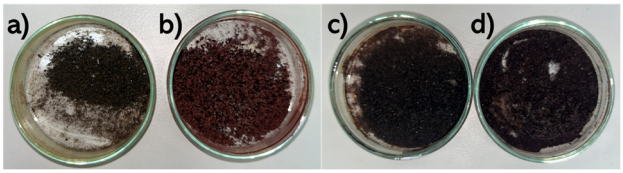

Figure 2 Extracted lignin from: a) rice straw using FS; b) coconut coir using FS; c) rice straw using RS; d) coconut coir using RS.

3.2 Antioxidant Activity of Lignin Extracts

The antioxidant activity of lignin extracted from rice straw and coconut coir was assessed using the DPPH radical scavenging assay. Lignin solutions at concentrations of 0.1–1.0 mg/mL were tested, and the radical scavenging activity (RSA) was calculated based on the reduction in absorbance at 517 nm. Results are presented in Figure 3. Lignin from coconut coir exhibited strong antioxidant activity, with RSA values increasing from 26.53 ± 0.12% to 89.40 ± 0.11% using fresh DES, and from 28.44 ± 0.14% to 91.12 ± 0.11% using recovered DES. The slightly higher RSA observed with recovered DES suggests enhanced extraction or preservation of active phenolic components during reuse. In comparison, rice straw lignin showed a lower RSA, ranging from 12.41 ± 0.10% to 28.40 ± 0.14% with fresh DES, and improving to 50.83 ± 0.27% at 1.0 mg/mL with recovered DES. These results indicate that coconut coir-derived lignin possesses greater antioxidant potential, likely due to higher phenolic

content, and that DES reuse does not negatively affect antioxidant performance.

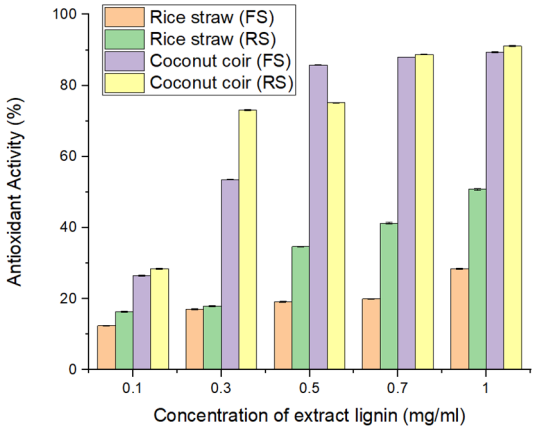

Figure 3 Radical scavenging activity (RSA, %) of lignin extracted from rice straw and coconut coir using fresh (FS) and recovered (RS) DES at various concentrations, measured by the DPPH assay.

3.3 FTIR Analysis of Lignin Extracts

Fourier-transform infrared (FTIR) spectroscopy is a widely utilized, non-destructive technique for identifying functional groups in lignin (mid-IR range: 4000–400 cm^{-1}). FTIR was applied to analyze functional groups in lignin extracted from rice straw and coconut coir using fresh/recovered DES. The spectra in Figure 4 revealed structural features compared to alkali lignin (Sigma-Aldrich, USA), demonstrating DES-extracted lignin's chemical profile and solvent reuse efficacy. All samples showed broad O–H stretching bands at 3460–3410 cm^{-1}, indicating the presence of phenolic and aliphatic structures. The C–H stretching peaks at 2930 and 2840 cm^{-1} corresponded to aromatic, methyl, and methylene methoxy groups, while lignin using fresh solution showed more pronounced peaks than alkali lignin and lignin using recovery solution. Although slight variations were observed in the intensity of the C–H stretching peaks at 2930 and 2840 cm^{-1} among lignin samples, these differences are minor and do not significantly impact the structural integrity or functional properties of the extracted lignin. The weak peak at 1720-1705 cm^{-1}, attributed to C=O stretching of carboxyl and ketone group, Aromatic skeletal vibrations at 1600, 1515, 1426 cm^{-1}, C-H deformation and aromatic ring vibration at 1462 cm^{-1} can be detected as variations in intensity based on S/G ratio. 1400–400 cm^{-1} is the Fingerprint Region Complex region, difficult to analyze due to band complexity with contributions of various vibration modes. This region provides information about monolignol units and linkage peaks attributed at 1369 – 1365 cm^{-1} referred to as aliphatic C-H and O-H stretch, including guaiacyl unit bands at 1269 cm^{-1}, Guaiacyl ring breathing with C-O stretching vibration; 1215 cm^{-1} is C=O stretching vibration of phenolic hydroxyl and phenolic ether; 1157-1139 cm^{-1} is C-H in-plane deformation; 854 and 817 cm^{-1}, CH out-of-plane vibrations of guaiacyl units. At peak 843 cm^{-1} is information on syringyl unit bands, and the examination found that lignin from rice straw showed this peak more clearly than lignin from coconut coir. Some pointed out that the lignin of rice straw has more syringyl units than the lignin of coconut coir. Compared to commercial alkali lignin, the extracted samples displayed similar overall profiles but with stronger absorption in the carboxyl and ketone group regions. This suggests that DES-extracted lignin may retain more native structures or functional diversity, while alkali lignin is processed under harsher conditions. These results confirm that DES is effective in preserving key functional groups in lignin and that solvent recovery does not compromise extract quality.

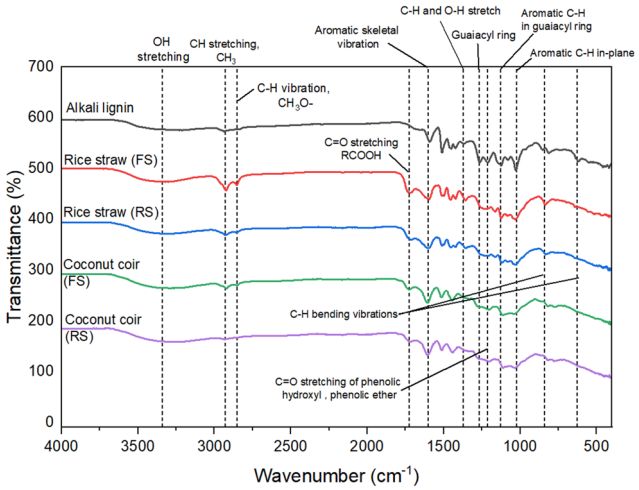

Figure 4 FTIR spectra of lignin extracted from rice straw and coconut coir using fresh solution (FS) and recovered solution (RS), compared with commercial lignin

4. CONCLUSION

In this work, lignin was successfully extracted from rice straw and coconut coir using DES, demonstrating a green, sustainable, and efficient approach for pretreating biomass. The results confirmed that DESs preserved key functional groups of lignin, as evidenced by FTIR spectra, and maintained high antioxidant activity, particularly in coconut coir-derived lignin with radical scavenging activity up to 91.12% at 1 mg/ml. Reuse of DES showed an insignificant impact on extraction efficiency and lignin functionality, supporting the possibility of solvent recycling in lignin extraction. The findings indicate that lignin extracted through the DES method shows significant potential for use in biocomposites and other sustainable materials, contributing to strategies for a circular bioeconomy. Future research should focus on optimizing extraction conditions and enhancing lignin solubility to facilitate its wider industrial application.

ACKNOWLEDGMENTS

The authors acknowledge the funding from the Faculty of Engineering, Thammasat School of

Engineering and the research unit in polymer rheology and processing, Thammasat University.

REFERENCES

1. Singh G, Gupta MK, Chaurasiya S, Sharma VS, Pimenov DY. Rice straw burning: a review on its global prevalence and the sustainable alternatives for its effective mitigation. Environmental Science and Pollution Research. 2021 Jul;28(25):32125-55.
2. Gadde B, Bonnet S, Menke C, Garivait S. Air pollutant emissions from rice straw open field burning in India, Thailand and the Philippines. Environmental Pollution. 2009 May 1;157(5):1554-8.
3. Fengel D, Wegener G, editors. Wood: chemistry, ultrastructure, reactions. Walter de Gruyter; 2011 Aug 2.
4. Ghaffar SH, Fan M. Structural analysis for lignin characteristics in biomass straw. Biomass and bioenergy. 2013 Oct 1;57:264-79.
5. Hu TQ, editor. Chemical modification, properties, and usage of lignin. New York: Kluwer academic/Plenum publishers; 2002 Apr.
6. Vanholme R, De Meester B, Ralph J, Boerjan W. Lignin biosynthesis and its integration into metabolism. Current opinion in biotechnology. 2019 Apr 1;56:230-9.
7. Sadeghifar H, Ragauskas A. Lignin as a UV light blocker—a review. Polymers. 2020 May 15;12(5):1134.
8. Yearla SR, Padmasree K. Preparation and characterisation of lignin nanoparticles: evaluation of their potential as antioxidants and UV protectants. Journal of Experimental Nanoscience. 2016 Mar 3;11(4):289-302.
9. Li Y, Cui D, Tong Y, Xu L. Study on structure and thermal stability properties of lignin during thermostabilization and carbonization. International journal of biological macromolecules. 2013 Nov 1;62:663-9.
10. Dong X, Dong M, Lu Y, Turley A, Jin T, Wu C. Antimicrobial and antioxidant activities of lignin from residue of corn stover to ethanol production. Industrial Crops and Products. 2011 Nov 1;34(3):1629-34.
11. Chen M, Li Y, Liu H, Zhang D, Shi QS, Zhong XQ, Guo Y, Xie XB. High value valorization of lignin as environmental benign antimicrobial. Materials Today Bio. 2023 Feb 1;18:100520.
12. Martins MA, Pinho SP, Coutinho JA. Insights into the nature of eutectic and deep eutectic mixtures. Journal of Solution Chemistry. 2019 Jul 31;48:962-82.
13. Kumar AK, Parikh BS, Pravakar M. Natural deep eutectic solvent mediated pretreatment of rice straw: bioanalytical characterization of lignin extract and enzymatic hydrolysis of pretreated biomass residue. Environmental science and pollution research. 2016 May;23:9265-75.
14. Rosado MJ, Rencoret J, Marques G, Gutiérrez A, Del Río JC. Structural characteristics of the guaiacyl-rich lignins from rice (Oryza sativa L.) husks and straw. Frontiers in Plant Science. 2021 Feb 19;12:640475.
15. Rencoret J, Ralph J, Marques G, Gutiérrez A, Martínez AT, del Río JC. Structural characterization of lignin isolated from coconut (Cocos nucifera) coir fibers. Journal of agricultural and food chemistry. 2013 Mar 13;61(10):2434-45.
16. Carrier M, Loppinet-Serani A, Denux D, Lasnier JM, Ham-Pichavant F, Cansell F, Aymonier C. Thermogravimetric analysis as a new method to determine the lignocellulosic composition of biomass. Biomass and bioenergy. 2011 Jan 1;35(1):298-307.
17. Wutticharoenmongkol P, Laipresert A, Thungrit W. Chitosan/Poly (vinyl alcohol)/Collagen Hydrogel Composites Containing Jackfruit Axis Extract for Wound Dressing Application. Interdisciplinary Research Review. 2022 Dec 29;17(6):1-8.

The occurrence of polycyclic aromatic hydrocarbons (PAHs) and halogenated PAHs in Chao Praya River in dissolved phase

Kanyanat Aunachad[1], Nawatch Surinkul[1,*], Shuhei Tanaka[2]

[1] Department of Environmental and Water Resource Engineering, Faculty of Engineering, Mahidol University, Nakhon Pathom 73170, Thailand
[2] Department of Environmental Engineering, Graduate School of Engineering, Kyoto University, 615-8540, Kyoto, Japan
[*] Corresponding author: nawatch.sur@mahidol.ac.th

ABSTRACT

PAHs are common pollutants found in soil, air, and water. Due to their hydrophobic nature, studies often focus on PAHs in sediments and aerosols, while less is known about their dissolved forms. This study investigated the dissolved PAHs in the Chao Praya River basin, which could affect raw water quality for treatment plants. Water samples were collected from five canals discharging into the river, from upstream to downstream, during the year 2024. Samples were pretreated and extracted using solid-phase extraction (SPE), then analyzed with GC-MS/MS. PAH concentrations ranged from 1,648 to 127,206 ng/L, with higher levels in downstream. Bang-Toei canal showed the highest contamination, followed by Baan-Prao. Two-ring PAHs were most common, making up to 67% of total PAHs in Chiang-Rak canal (upstream) and 83% in Bang-Toei canal (downstream). They were likely due to urban runoff. The source control or bio-retention systems like vegetation buffers could reduce pollution.

Keywords: Polycyclic Aromatic Hydrocarbons (PAHs); Occurrence; Distribution; Chao-Praya River; Dissolved phase

1. INTRODUCTION

PAHs and halogenated PAHs HPAHs) are considered as persistent organic compound which can contribute adverse effect on environment. Surface runoffs tend to be the potential source of PAHs discharging to river bodies. Chao-Praya River is an essential water resource supply for various purposes. However, in the modern era in which pollutants loads could easily contaminated to river without properly managed. Therefore, this study aims to investigate the occurrence and distribution of PAHs and HPAHs in Chao Praya River in dissolved phase.

2. EXPERIMENTAL

The samples were collected at different five points starting from upstream to downstream of Chao-Praya River. After collecting, the samples were immediately stored at cool temperature at least 4 degrees and covered with aluminum foil. The samples can be done by sample preparation which were first filtrated by using Whatmanfilter GF/B. Then filtered samples were extracted target compound by using SPE (Solid-Phase-Extraction) with cartridge InertSep Rp-1 in which properly conditioned with Dichloromethane, methanol and milliQ. The target compounds were eluted with dichloromethane before concentrated volume into 1 mL by using nitrogen purge and final added with acetone before transferring to analytical procedure. The concentrated samples were then analyzed in a form of the quantitative determination in which utilizing gas chromatography-tandem mass spectrometry (GC-MS/MS). GC-MS/MS operated under inlet temperature 350°C. Helium was used as a carrier gas at flow rate 1 mL/min with the injection split less mode at volume 2 µL. In addition, within MS/MS the neutral molecules are first ionized by using Electron ionization (EI) method for ionization and with ion source temperature at 250°C. The mass range ratio (m/z) was between 25-60 and was recorded in MRM (Multiple Reaction Monitoring) mode for ion detection. The peak identification is based on designated retention time. The calibration curve was introduced by using six standard solutions at different concentrations which is within the range 1 to 100 ng/mL. The curve shown in good linearity with R^2 approximately accounts for 0.97. An individual PAH were serial diluted from stock solution with the initial concentration 10 µg/mL by using acetone (purity 99.5%). The instrument detection limit (IDL) and instrument quantitative limit (IQL) were acquired by using a low standard solution at 2 ng/mL with considering repeat measurement 3 times of signal to noise ratio for IDL and 10 times for IQL then the standard deviation was calculated by value given from IDL and IQL.

3. RESULTS AND DISCUSSION

3.1 The occurrence and distribution patterns of PAHs in Chao-Praya River in both seasons

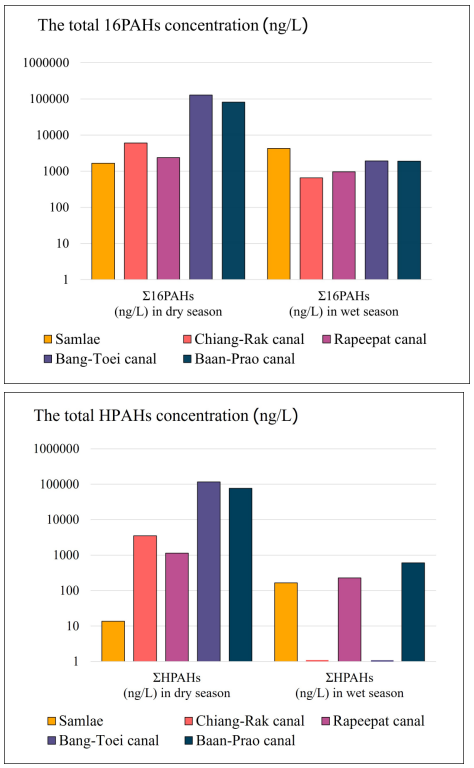

Figure 1 The total concentration of 16PAHs (a) and HPAHs (b) in both dry and wet season.

The total PAH concentrations across the sampled canals ranged from 657 ng/L to 127,206 ng/L, with Bang-Toei canal being the most contaminated. *Naphthalene* (*Nap*) was generally the most prevalent compound across all sites. Notably, halogenated PAHs, particularly *1-Chloronaphthalene* (*1-ClNap*), were found in significantly higher concentrations than the standard 16 PAHs group, especially in Bang-Toei (116,604 ng/L) and Baan-Prao (76,954 ng/L) canals. Samlae and Rapeepat stations showed lower PAH contamination levels, with *Benzo(k)fluoranthene* (*BkF*) being dominant in those areas. The distribution patterns varied by location, indicating their anthropogenic sources or behaviors of PAHs and HPAHs. The PAH concentrations in wet season ranged from 657 ng/L to 4,292 ng/L. The highest concentration was found at Samlae station (4,292 ng/L), while the lowest was at Chiang-Rak canal (657 ng/L). In general, the downstream stations (Samlae, Bang-Toei, and Baan-Prao) had higher PAH levels than the upstream (Rapeepat and Chiang-Rak). At the upstream sites, Chiang-Rak canal had *Ace* as the predominant compound, followed by *BkF*, *Acy*, *Flu*, and *Nap*, HPAHs level were lower than LOD (Lower Detection Limit) which relatively low. Rapeepat canal showed a similar trend but had a higher concentration of *BkF* (372 ng/L), followed by *1-ClNap* (227 ng/L). Downstream, Bang-Toei canal showed the highest concentration of *BkF* (1,128 ng/L), followed by *Ace* (720 ng/L) and *Acy* (73 ng/L), with *1-ClNap* was detected at lower than LOD. Baan-Prao canal represented a similar distribution with *Ace* (690 ng/L) as the major compound, followed by *BkF* (550 ng/L) and *Acy* (61 ng/L), but with a notable presence of *1-ClNap* (605 ng/L). Samlae station had a distinct pattern, with *Nap* (3,227 ng/L) as the most abundant compound, followed by *BkF* (430 ng/L), *Ace* (313 ng/L), and *Acy* (156 ng/L). The concentration of *1-ClNap* was relatively low at this station (166 ng/L). When comparing the results between the dry and wet seasons, it was observed that the distribution of PAHs was generally higher in the dry season than in the wet season. The wet season, influenced by monsoon and rainfall, can transfer PAHs from the earth's surface or atmosphere, leading to their deposition through runoff into rivers. As a result, higher PAH concentrations might be expected during the wet season. However, this study found significant differences, possibly due to the effects of dilution and various hydrological factors such as temperature, salinity, tidal waves, coastal currents, and monsoon patterns. The study also measured basic water quality parameters, finding that the temperature during the dry season was lower than in the wet season, while salinity values were higher in the dry season. Previous studies have suggested that changes in water temperature can directly affect PAH concentrations, with an increase in temperature typically leading to a decrease in PAH levels (Niu et al., 2021). Therefore, the lower temperatures and higher salinity in the dry season could contribute to the elevated PAH levels observed during this period

3.2 The composition ratio of PAHs by ring in both seasons

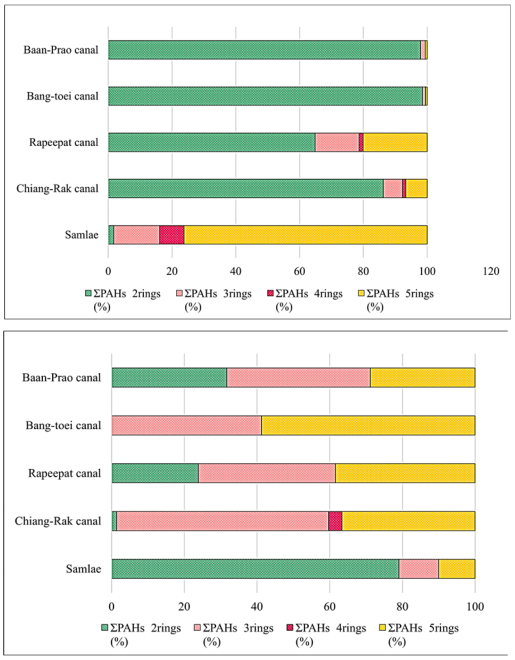

Figure 2 The compositional ratio of PAHs by ring at different canals in dry season (a) and wet season (b)

Figure 2 (a) indicates that low molecular weight (LMW) PAHs were generally more abundant than high

molecular weight (HMW) PAHs. At Bang-Toei and Baan-Prao canals, 2-ring PAHs were predominant, comprising 99% and 98% of total PAHs, respectively. Chiang-Rak station exhibited a similar trend, with 86% of PAHs consisting of 2-ring compounds. In Rapeepat canal, 2-ring PAHs accounted for 65%, followed by 5-ring (20%) and 3-ring (14%) compounds. In contrast, Samlae station showed a distinct profile, with 5-ring PAHs dominating at 76%, and 2-ring PAHs contributing only 2%. In contrast, Figure 2(b) further illustrates the molecular weight distribution. Upstream sites such as Chiang-Rak and Rapeepat were dominated by 3-ring and 5-ring PAHs, whereas downstream sites like Bang-Toei exhibited a higher proportion of 5-ring compounds. Baan-Prao showed a balanced composition of 3-ring (39%), 2-ring (32%), and 5-ring (29%) PAHs. Seasonal comparison shows that in the dry season, both upstream and downstream sites consistently exhibited a dominance of low molecular weight LMW. Conversely, in the wet season, LMW (particularly 2- and 3-ring compounds) were predominant upstream, while high molecular weight HMW were more common downstream. Chiang-Rak and Rapeepat canals were dominated by 3-ring PAHs, indicating a stronger influence from petrogenic sources such as oil spills, urban runoff, and industrial discharge—typical of LMW due to their higher solubility and mobility in water. In contrast, the Bang-Toei canal, located downstream, was rich in 5-ring of HMW, suggesting pyrogenic origins from combustion-related activities. The Baan-Prao canal show a mixed PAH profile, with 3-ring PAHs most prevalent, followed by 2- and 5-ring compounds, indicating inputs from both petrogenic and pyrogenic sources due to residential and industrial areas.

Hence, PAH ring structure patterns varied by location and season: upstream sites were primarily influenced by LMW PAHs, while downstream areas showed greater contributions of HMW PAHs, consistent with pollutant transport and potential point-source discharges. Despite seasonal changes, LMW PAHs remained the most abundant, accounting for 99% in the dry season and 79% in the wet season. These findings align with previous research, such as Liu and Niu (2017), who reported LMW dominance (67%) in both seasons, and Shang et al. (2023), who found LMW proportions of 82% in the dry season and 72% in the wet season.

This research suggests that the concentration of PAHs varies significantly between upstream and downstream sites, with the downstream sites generally exhibiting higher levels of contamination. Samlae station stands out for having the highest total PAH concentration, primarily driven by *Nap*, which suggests a different source or environmental conditions compared to the other sites. *1-ClNap*, a halogenated PAH, was notably present in some sites (e.g., Rapeepat and Baan-Prao) but was absent at others, such as Bang-Toei and Chiang-Rak. The presence of *Nap*, *Ace*, and *BkF* as the major PAHs at most sites suggests that these compounds may be the dominant pollutants in the study area, potentially due to specific local sources such as industrial or vehicular emissions. The lack of halogenated PAHs in some locations may indicate that certain environmental factors or pollution sources do not contribute significantly to these compounds in those areas. The higher concentrations in the downstream sites might indicate accumulation from upstream pollution or increased human activity near those regions, such as industrial discharge or agricultural and urban runoff. Moreover, this study revealed the distribution patterns differently which that LMW were predominant across all sites, especially during the dry season. Upstream areas were mainly influenced by petrogenic sources, while downstream sites showed a greater presence of HMW, indicating pyrogenic contributions. These spatial and seasonal variations reflect differences in pollution sources and hydrological dynamics within the canal system.

4. CONCLUSION

The occurrence of 16PAHs concentrations were observed as 1,648 ng/L to 127,206 ng/L in dry season, and from 657 ng/L to 4,292 ng/L in wet season from five stations. The result represents that the concentrations of PAHs in dry season were higher than in wet season. LMW (2rings, 3-rings) tended to dominate both upstream and downstream, which *Nap, and 1-ClNap* were major compounds during dry season. Whereas in wet season, their distribution pattern showed different trends. LMW were abundant compounds, *Ace*, at upstream, whereas HMW, *BkF*, was the highest compositional ratio downstream.

ACKNOWLEDGMENTS

This research was fully successful, with the support of the Faculty of Graduate Studies at Mahidol University and the Graduate School of Global Environmental Studies (GSGES) at Kyoto University.

REFERENCES

1. Liu, F., Niu, L., Chen, H., Li, P., Tian, F., & Yang, Q. (2017). Seasonal changes of polycyclic aromatic hydrocarbons in response to hydrology and anthropogenic activities in the Pearl River estuary, China. Marine Pollution Bulletin, 117(1–2), 255–263. https://doi.org/10.1016/j.marpolbul.2017.01.061
2. Niu, L., Luo, X., Cai, H., Liu, F., Zhang, T., & Yang, Q. (2021). Seasonal dynamics of polycyclic aromatic hydrocarbons between water and sediment in a tide-dominated estuary and ecological risks for estuary management. Marine Pollution Bulletin, 162. https://doi.org/10.1016/j.marpolbul.2020.111831

3. Shang, N., Wang, C., Kong, J., Yu, H., Li, J., Hao, W., Huang, T., Yang, H., He, H., & Huang, C. (2023). Dissolved polycyclic aromatic hydrocarbons (PAHs-d) in response to hydrology variation and anthropogenic activities in the Yangtze River, China. Journal of Environmental Management, 326. https://doi.org/10.1016/j.jenvman.2022.116673

Enhancing absorption under load in alginate-based superabsorbent polymers for sustainable disposable diapers

Nadiya Abdulroman[1], Paeka Klaitong[2], Nuttawan Arpasopana[1], Suwanna Kitpati Boontanon[1], Nawatch Surinkul[1], Weerawut Chaiwat[2,*]

[1] Department of Civil and Environmental Engineering, Faculty of Engineering, Mahidol University, Nakhon Pathom 73170, Thailand
[2] Department of Chemical Engineering, Faculty of Engineering, Mahidol University, Nakhon Pathom 73170, Thailand
[*] Corresponding author: weerawut.cha@mahidol.ac.th

ABSTRACT

While disposable diapers are convenient and effective, their reliance on non-biodegradable, petroleum-based superabsorbent (SAP) raises environmental concerns, driving interest in environmentally sustainable alternatives. This study aimed to develop biodegradable SAPs based on biopolymer alginate. Alginate-based SAPs were prepared by crosslinking with Ca^{2+} (Ca-Alg) or Ba^{2+} (Ba-Alg), as well as with varying Ca^{2+}:Ba^{2+} weight ratios (CaBa-Alg). Additionally, Ca-Alg SAPs reinforced with sugarcane bagasse ash (SCBAsh) were developed. These SAPs were evaluated for their swelling behavior, water retention capacity, absorbency under load (AUL), as well as re-wet and water holding capacity, in artificial urine. The Ca-Alg exhibited a swelling capacity of 39 g/g, while the CaBa-Alg with varying Ca^{2+}:Ba^{2+} ratios showed higher capacities ranging from 46 to 52 g/g, and the Ba-Alg demonstrated the highest capacity of 56 g/g. For those of the Ca-Alg reinforced with SCBAsh at 25–30 wt%, the swelling capacities were as high as 38 g/g, which was competitive with those of commercial diaper SAPs (cSAPs) obtained at 38–40 g/g. Water retention capacities of the Ca-Alg without ash, Ba-Alg, Ca-Alg with SCBAsh and CaBa-Alg were higher than those of the cSAPs. However, AUL of the alginate-based SAPs remained lower than those of the cSAPs. Under applied pressures ranging from 0.3 to 0.9 psi, their swelling capacities were decreased to approximately 5 g/g, while those of the cSAPs were decreased to around 17 g/g. Nevertheless, the calcium alginate-based SAPs exhibited performance similar to that of cSAPs in their ability to retain water and prevent leakage under load. To further improve the AUL of the alginate-based SAPs, surface crosslinking with Poly (N, N-dimethyl acrylamide) will be investigated.

Keywords: Superabsorbent polymers; Alginate; Sugarcane bagasse ash; Swelling capacity; Absorption under load

1. INTRODUCTION

Disposable diapers (DPDs) are widely used in infant care due to their convenience and effective liquid absorption. However, their primary components, including superabsorbent polymers (SAPs), are made from non-biodegradable, petroleum-based synthetic polymers. Once disposed of, they persist in the environment and landfills for extended periods, becoming significant contributors to global plastic waste and raising serious environmental concerns. Moreover, the materials and production processes involved in DPD manufacturing contribute to global warming, with SAPs accounting for the largest portion of the global warming potential at 34.5% [1]. This highlights the critical need for the development of environmentally sustainable alternative SAPs. Alginate is a natural polysaccharide derived from brown algae, known for excellent water absorption, biodegradability, biocompatibility, and ability to form stable hydrogels [2]. Alginate hydrogels are typically formed through ionic crosslinking involving the interaction between alginate and divalent cations, most commonly calcium ions (Ca^{2+}), as well as barium ion (Ba^{2+}) and zinc ion (Zn^{2+}). Types and ratios of cationic crosslinkers have been shown to significantly affect the properties of alginate hydrogels, such as their mechanical strength, and swelling behavior [3,4]. Alginate-based hydrogels have been developed for a wide range of applications, encompassing biomedical fields such as tissue engineering [5,6], pharmaceutical applications including drug delivery and wound care [3,7], and agricultural uses such as soil conditioning and water-retentive materials [8]. Additionally, they have been employed as supporting matrices for the encapsulation

of functional particles, such as activated carbon, to facilitate the removal of heavy metals, dyes, and uremic toxins [9–12], as well as in the design of colorimetric sensors[13,14]. Alginate-based hydrogels have also been explored for use as SAPs in baby diapers; however, research on this application remains limited. These hydrogels have demonstrated absorption capacities ranging from 24 to 78.4 g/g, but still exhibited limited absorption under load (AUL) [15–17] due to the inherently poor mechanical strength of alginate [18]. Incorporation ash primarily composed of silica (SiO_2) [8,12,19–21] or silica [22–24] has been demonstrated to improve the mechanical strength and overall performance of hydrogels.

In this study, we focused on the development of biodegradable SAPs derived from the biopolymer alginate. Alginate-based SAPs were synthesized through crosslinking with Ca^{2+} (Ca-Alg), Ba^{2+} (Ba-Alg), and combinations of both (CaBa-Alg) at varying Ca^{2+}:Ba^{2+} weight ratios. In addition, Ca-Alg SAPs reinforced with sugarcane bagasse ash (SCBAsh) were formulated. The performance of these SAPs was assessed in terms of swelling capacity, water retention capacity, AUL, including re-wet and water holding efficiency under load properties, in comparison with commercial diaper SAPs (cSAPs).

2. EXPERIMENTAL

2.1 Preparation of Sugarcane bagasse ash (SCBAsh)

The 20-g of sugarcane bagasse ash was leached with 200 mL of 1 M HCl to remove organic impurities. The mixture was heated at 90 °C for 1 h with continuous stirring, then cooled to room temperature. The cooled mixture was then filtered under vacuum, and the pH of the filtrate was adjusted to match the pH of deionized (DI) water. The leached ash residue was dried in a hot-air oven at 110 °C for 24 h.

2.2 Preparation of alginate-based SAPs

A 2% sodium alginate solution was prepared by dissolving 2 g of sodium alginate in 100 mL of DI water. When required, the prepared leached ash was added to the alginate solution (at 5% to 30% relative to alginate weight). The mixture was stirred at room temperature until a homogeneous solution was obtained. The resulting mixture was then loaded into a 20 mL syringe (tip diameter: 1.5–2.0 mm) connected to a syringe pump. The solution was dispensed dropwise into 1% (w/v) $CaCl_2$, $BaCl_2$, or mixed $CaCl_2$/$BaCl_2$ solutions (at $CaCl_2$:$BaCl_2$ weight ratios of 1:1 to 5:1) at a feed rate of 3 mL/min. The formed granules were allowed to crosslink in the solution for 24 h, after which they were washed with DI water to remove any non-crosslinked polymer residues and subsequently freeze-dried. Figure 1 shows the above-mentioned preparation method and physical appearances of the alginate-based SAPs developed in this study.

2.3 Characterization of alginate-based SAPs

2.3.1 Swelling capacity

The swelling capacity of the SAPs was evaluated by immersing 0.2 g of freeze-dried SAPs in artificial urine for 1 h, with a continuous shaking at 120 rpm, at room temperature. The weights of the swollen SAPs were recorded. The swelling capacity was calculated using Eq. 1:

$$Swelling\ capacity\ (g/g) = \frac{W_t - W_0}{W_0} \qquad (1)$$

Where W_t the weight of swollen is gel and W_0 is the initial weight of the freeze-dried gel.

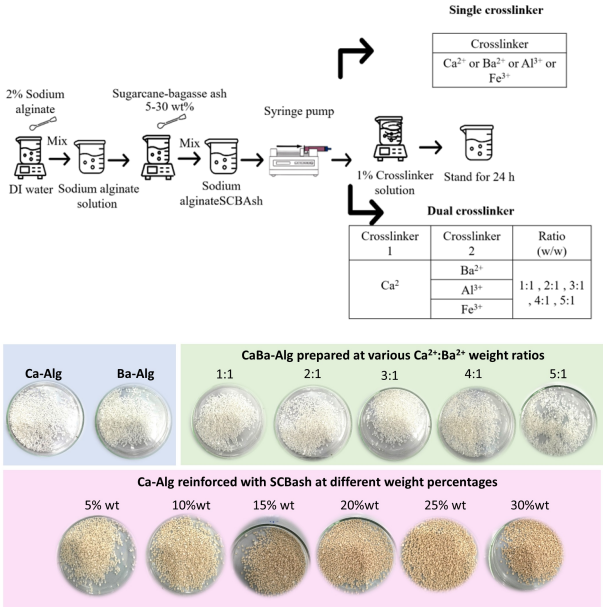

Figure 1. Preparation method and physical appearances of the alginate-based SAPs.

2.3.2 Water retention capacity

The SAPs that had undergone the swelling for 1 h in artificial urine were dried at 60 °C and weighed every 1 h over a 4-h period. Water retention capacity was calculated as a percentage using **Eq. 2.**

$$WR(\%) = \left(\frac{W_t - W_d}{W_{eq} - W_d}\right) x\ 100 \qquad (2)$$

Where W_t is the remaining weight of the gel at indicated time point, W_d is the weight of the freeze-dried gel before swelling and W_{eq} is the initial wet weight of the swollen gel.

2.3.3 Absorption under load (AUL)

To evaluate the AUL of the alginate-based SAPs, freeze-dried samples were placed under a predefined pressure (0.3–0.9 psi) and allowed to absorb artificial urine for 1 h. After the incubation period, the load was

removed, and the swollen SAPs were weighed. The AUL was then calculated using Eq. 3.

$$AUL(g/g) = \frac{W_t - W_0}{W_0} \quad (3)$$

Where W_t is the weight of swollen gel and W_0 is the initial weight of the freeze-dried gel.

2.3.4 Re-wet and water holding efficiency under load

To determine water holding efficiency of the alginate-based SAPs, re-wet test was performed. The SAPs which had been fully swollen in dialysate for 1 h were weighed and placed in a petri dish. Subsequently, 30 pieces of pre-weighed filter papers were placed on the SAPs along with a 0.3 psi load for 2 min to allow the filter to absorb any rewet liquid. Re-wet amount and re-wet value of the SAPs were calculated using Eqs. 4 and 5.

$$RW\ amount\ (g) = W_{p2} - W_{p1} \quad (4)$$

$$RW\ value\ (g/g) = \frac{W_{p2} - W_{p1}}{W_{g1}} \quad (5)$$

Where W_{p1} is the weight of pre-weighed filter papers, W_{p2} is the total weight of the filter papers after re-wetting and W_{g1} is the weight of the fully swollen SAPs.

The water holding efficiency (WH) of the SAPs was also calculated using Eq. 6.

$$WH\ (\%) = \left[\frac{W_{g1} - W_{g0} - RW\ amount}{W_{g1} - W_{g0}}\right] \times 100 \quad (6)$$

Where W_{g0} is the weight of the dried SAPs, W_{g1} is the weight of the fully swollen SAPs and RW amount is the re-wet amount

3. RESULTS AND DISCUSSION

3.1 Swelling capacity of the alginate-based SAPs in artificial urine

To evaluate swelling capacity, 0.2 g of the alginate-based SAPs were swelled in artificial urine for 1 h. The results in **Figure 2** showed that Ba-Alg exhibited the highest swelling capacity at 56 g/g, outperforming Ca-Alg, which showed a lower capacity of 39 g/g. The superior swelling of Ba-Alg can be attributed to the larger ionic radius of Ba^{2+}, as well as the relatively lower concentration of Ba^{2+} ions at the same w/v ratio due to its higher atomic weight, which results in looser crosslinking compared to Ca^{2+}, thus allowing more space for water absorption within the hydrogel network. The CaBa-Alg crosslinked with varying Ca^{2+}:Ba^{2+} ratios, demonstrated intermediate swelling capacities ranging from 46 to 52 g/g. These values were consistently higher than that of Ca-Alg but did not surpass Ba-Alg. This trend suggests that the introduction of Ba^{2+} into a Ca^{2+}-crosslinked network disrupts the tight network structure typically formed by Ca^{2+} alone, resulting in a less dense network that permits greater water uptake. Interestingly, all formulations including Ca-Alg, Ba-Alg, and CaBa-Alg demonstrated swelling capacities competitive with or even higher than those of the cSAPs, which typically exhibit values in the range of 38 to 40 g/g. This indicates that tuning the Ca^{2+}:Ba^{2+} ratio offers a promising strategy for optimizing hydrogel performance, balancing mechanical stability and water uptake. Incorporation of 5% to 20% SCBAsh into the Ca-Alg reduced swelling capacities to 29 g/g. The observed reduction in swelling capacity might suggest an enhancement in the mechanical strength of Ca-Alg hydrogels reinforced with SCBAsh. This mechanical reinforcement is primarily attributed to the presence of silica in the ash which can form additional physical crosslinks via hydrogen bonding, occupy void spaces, and increase the network density, thereby contributing to the enhanced structural stability of the hydrogels [7]. Further increasing the SCBAsh content to 25%–30% led to a rebound in swelling capacity to approximately 38%. This increase may be due to the agglomeration of SCBAsh particles, which could contribute to greater water absorption [25]. Therefore, incorporating 25%–30% SCBAsh may offer an optimal balance between high swelling capacity and improved mechanical strength.

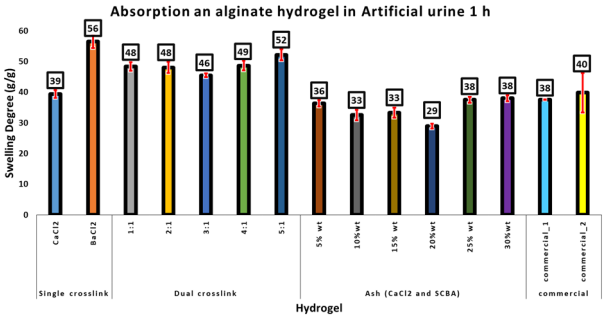

Figure 2. Swelling capacities of the Ca-Alg, Ba-Alg, CaBa-Alg and Ca-Alg reinforced with SCBAsh. (Swelling test condition: 0.2 g of the SAPs in artificial urine for 1 h)

3.2 Water retention capacity of the alginate-based SAPs in artificial urine

For determination of water retention capacity, the SAPs had undergone the swelling for 1 h in artificial urine, then they were dried at 60 °C and weighed every 1 h over a 4-h period. Figures 3a, b revealed that the Ca-Alg, Ba-Alg, CaBa-Alg and Ca-Alg reinforced with SCBAsh exhibited slower water loss at 60 °C compared to the cSAPs, indicating higher water retention capacities. The superior water retention observed in the non-reinforced Ca-Alg, Ba-Alg, and CaBa-Alg might be attributed to their more open, less densely

crosslinked networks, allowing them to absorb and hold more water. The SCBAsh components in the reinforced Ca-Alg may increase network density and form additional crosslinks, which strengthen the hydrogel structure, enhance water retention, and reduce water loss through evaporation. These results also suggest that the alginate-based SAPs have potential for uses beyond diapers, particularly in agriculture, where they could serve as soil conditioners and water-saving materials to enhance moisture retention in soil.

(a)

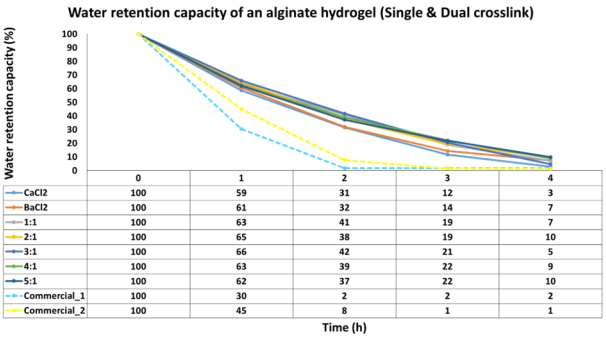

	0	1	2	3	4
CaCl2	100	59	31	12	3
BaCl2	100	61	32	14	7
1:1	100	63	41	19	7
2:1	100	65	38	19	10
3:1	100	66	42	21	5
4:1	100	63	39	22	9
5:1	100	62	37	22	10
Commercial_1	100	30	2	2	2
Commercial_2	100	45	8	1	1

(b)

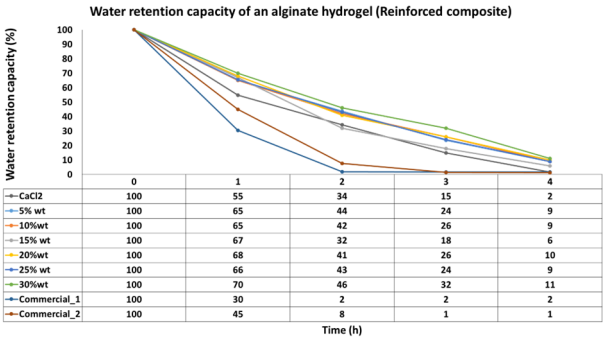

	0	1	2	3	4
CaCl2	100	55	34	15	2
5% wt	100	65	44	24	9
10%wt	100	65	42	26	9
15% wt	100	67	32	18	6
20%wt	100	68	41	26	10
25% wt	100	66	43	24	9
30%wt	100	70	46	32	11
Commercial_1	100	30	2	2	2
Commercial_2	100	45	8	1	1

Figure 3. Water retention capacities of the Ca-Alg, Ba-Alg, CaBa-Alg (a) and Ca-Alg reinforced with SCBAsh (b).

3.3 Absorption under load (AUL) of the alginate-based SAPs in artificial urine

The SAPs were placed under a predefined pressure (0.3–0.9 psi) and allowed to absorb artificial urine for 1 h to determine the AUL property. The results in Figures 4a, b showed that, although the alginate-based SAPs exhibited competitive swelling capacities in the absence of load, AUL remained significantly lower than that of the cSAPs. Under applied pressures ranging from 0.3 to 0.9 psi, the swelling capacities of the alginate-based SAPs decreased to approximately 5 g/g, whereas the cSAPs retained a much higher AUL of around 17 g/g. One of the key factors contributing to the lower AUL of the alginate-based SAPs is the limited mechanical performance of alginate due to its the inherent structural non-uniformity [26]. To further improve the AUL of the alginate-based SAPs, surface crosslinking with Poly (N, N-dimethyl acrylamide) will be further investigated.

(a)

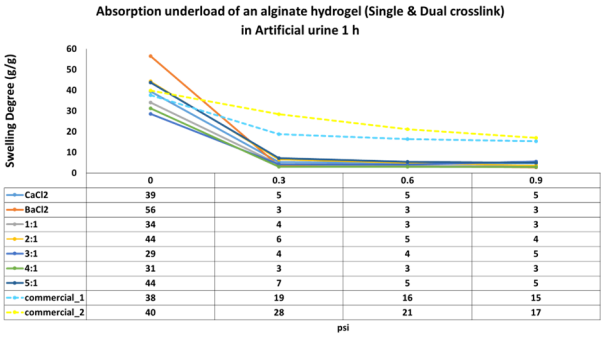

	0	0.3	0.6	0.9
CaCl2	39	5	5	5
BaCl2	56	3	3	3
1:1	34	4	3	3
2:1	44	6	5	4
3:1	29	4	4	5
4:1	31	3	3	3
5:1	44	7	5	5
commercial_1	38	19	16	15
commercial_2	40	28	21	17

(b)

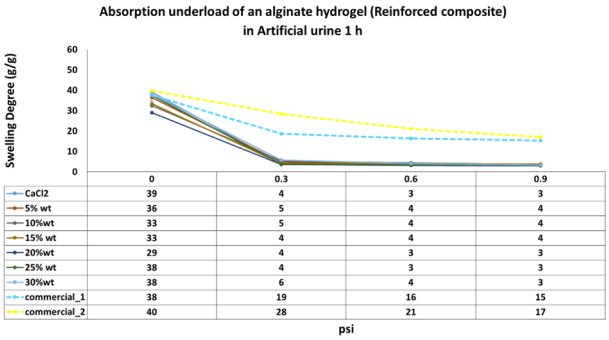

	0	0.3	0.6	0.9
CaCl2	39	4	3	3
5% wt	36	5	4	4
10%wt	33	5	4	4
15% wt	33	4	4	4
20%wt	29	4	3	3
25% wt	38	4	3	3
30%wt	38	6	4	3
commercial_1	38	19	16	15
commercial_2	40	28	21	17

Figure 4. Absorption under load (AUL) of the Ca-Alg, Ba-Alg, CaBa-Alg (a) and Ca-Alg reinforced with SCBAsh (b).

3.4 Re-wet and water holding efficiency under load of the calcium alginate-based SAPs in artificial urine

Re-wet test was performed to assess the ability of the SAPs to re-wet the surface after a simulated load was applied, indicating how well the SAPs retain water under pressure. The results in Figures 5a, b, c show that the calcium alginate-based SAPs exhibited re-wet amounts ranging from 1.4 to 2.4 g, which were slightly lower than the 2.6 g observed for the cSAPs. The re-wet values ranged from 0.2 to 0.3 g/g, and the water holding efficiencies were between 69% and 81%, comparable to those of the cSAPs. The results indicated that the calcium alginate-based SAPs have a comparable performance to cSAPs in terms of their ability to hold water and prevent water leakage under load.

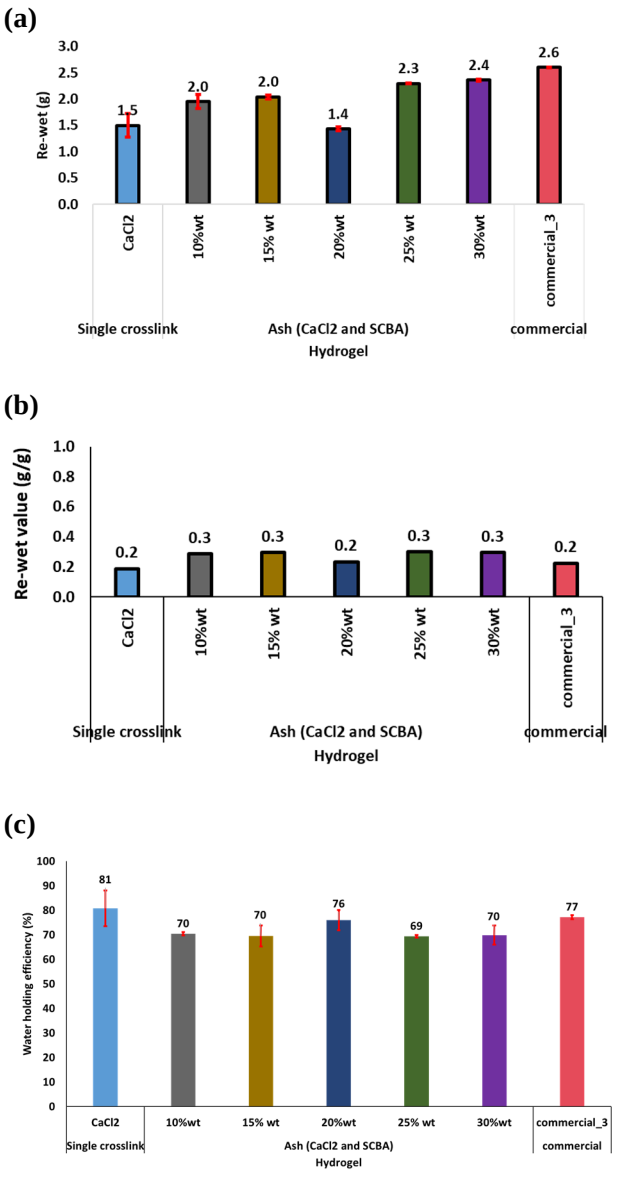

Figure 5. Re-wet amounts (a), re-wet values (b) and water holding efficiencies (c) of the calcium alginate-based SAPs.

4. CONCLUSION

This study developed biodegradable alginate-based SAPs through crosslinking with Ca^{2+}, Ba^{2+}, and varying Ca^{2+}:Ba^{2+} weight ratios. The Ba-Alg showed the highest swelling capacity (56 g/g), followed by the CaBa-Alg (46–52 g/g) and the Ca-Alg (39 g/g), all competitive with the cSAPs (38–40 g/g). The incorporation of SCBAsh into the Ca-Alg reduced swelling capacity (29 g/g), likely enhancing mechanical strength. Water retention was higher in the alginate-based SAPs, as compared to the cSAPs. However, the alginate-based SAPs exhibited lower AUL, with swelling capacities decreasing to 5 g/g under pressures, compared to 17 g/g for the cSAPs. Nevertheless, the calcium alginate-based SAPs demonstrated similar performance in water holding and preventing water leakage under load, as compared to the cSAPs. Future work will explore surface crosslinking with Poly (N,N-dimethyl acrylamide) to improve AUL.

ACKNOWLEDGMENTS

This study is supported by the Faculty of Graduate Studies, Mahidol University. The authors also gratefully acknowledge the Water Quality Research Laboratory, Department of Civil and Environmental Engineering, and Energy and Green Catalysis Laboratory 3 (EGCatLab3), Department of Chemical Engineering, Faculty of Engineering, Mahidol University, for the supports of experimental facilities and equipment.

REFERENCES

[1] M.J. Somers, J.F. Alfaro, G.M. Lewis, Feasibility of superabsorbent polymer recycling and reuse in disposable absorbent hygiene products, J Clean Prod 313 (2021). https://doi.org/10.1016/j.jclepro.2021.127686.

[2] K.Y. Lee, D.J. Mooney, Alginate: Properties and biomedical applications, Progress in Polymer Science (Oxford) 37 (2012) 106–126. https://doi.org/10.1016/j.progpolymsci.2011.06.003.

[3] A. Kumar, D.K. Sah, K. Khanna, Y. Rai, A.K. Yadav, M.S. Ansari, A.N. Bhatt, A calcium and zinc composite alginate hydrogel for pre-hospital hemostasis and wound care, Carbohydr Polym 299 (2023). https://doi.org/10.1016/j.carbpol.2022.120186.

[4] J. Kurowiak, A. Kaczmarek-Pawelska, A.G. Mackiewicz, R. Bedzinski, Analysis of the degradation process of alginate-based hydrogels in artificial urine for use as a bioresorbable material in the treatment of urethral injuries, Processes 8 (2020). https://doi.org/10.3390/pr8030304.

[5] Y. Kusumastuti, N. Rofiqoh Eviana Putri, M. Kobayashi, F. Yohana Purwaningtyas, M. Najmina, H. Tri Bayu Murti Petrus, M. Tanihara, Characterization of three dimensional scaffolds from local chitosan/alginate/geothermal silica for potential tissue engineering applications, 2018. https://www.researchgate.net/publication/330543896.

[6] C.H. Yang, M.X. Wang, H. Haider, J.H. Yang, J.Y. Sun, Y.M. Chen, J. Zhou, Z. Suo, Strengthening alginate/polyacrylamide hydrogels using various multivalent cations, ACS Appl Mater Interfaces 5 (2013) 10418–10422. https://doi.org/10.1021/am403966x.

[7] M.C. Straccia, G.G. D'Ayala, I. Romano, P. Laurienzo, Novel zinc alginate hydrogels prepared by internal setting method with intrinsic antibacterial activity, Carbohydr Polym 125 (2015) 103–112. https://doi.org/10.1016/j.carbpol.2015.03.010.

[8] H. Gharekhani, A. Olad, A. Mirmohseni, A. Bybordi, Superabsorbent hydrogel made of NaAlg-g-poly(AA-co-AAm) and rice husk ash: Synthesis, characterization, and swelling kinetic studies, Carbohydr Polym 168 (2017) 1–13. https://doi.org/10.1016/j.carbpol.2017.03.047.

[9] Y. Na, J. Lee, S.H. Lee, P. Kumar, J.H. Kim, R. Patel, Removal of heavy metals by polysaccharide: a review, Polymer-Plastics Technology and Materials 59 (2020) 1770–1790. https://doi.org/10.1080/25740881.2020.1768545.

[10] Jackson, Christopher, Design and in-vitro characterisation of novel sorbent device for extracorporeal blood filtration and other applications, (2012). https://escholarship.mcgill.ca/concern/theses/4m90dz70v (accessed January 17, 2025).

[11] S. Thakur, S. Pandey, O.A. Arotiba, Development of a sodium alginate-based organic/inorganic superabsorbent composite hydrogel for adsorption of methylene blue, Carbohydr Polym 153 (2016) 34–46. https://doi.org/10.1016/j.carbpol.2016.06.104.

[12] S. Sutthasupa, W. Koo-amornpattana, N. Worasuwannarak, P. Prachakittikul, P. Teachawachirasiri, W. Wanthong, T. Thungthong, P. Inthapat, W. Chanamarn, C. Thawonbundit, A. Srifa, S. Ratchahat, W. Chaiwat, Sugarcane bagasse-derived granular activated carbon hybridized with ash in bio-based alginate/gelatin polymer matrix for methylene blue adsorption, Int J Biol Macromol 253 (2023). https://doi.org/10.1016/j.ijbiomac.2023.127464.

[13] S. Sutthasupa, C. Padungkit, S. Suriyong, Colorimetric ammonia (NH3) sensor based on an alginate-methylcellulose blend hydrogel and the potential opportunity for the development of a minced pork spoilage indicator, Food Chem 362 (2021). https://doi.org/10.1016/j.foodchem.2021.130151.

[14] K. Sattayapanich, W. Chaiwat, S. Boonmark, S. Bureekaew, S. Sutthasupa, Alginate-based hydrogels embedded with ZnO nanoparticles as highly responsive colorimetric oxygen indicators, New Journal of Chemistry 46 (2022) 19322–19334. https://doi.org/10.1039/d2nj04164b.

[15] A. Mignon, N. De Belie, P. Dubruel, S. Van Vlierberghe, Superabsorbent polymers: A review on the characteristics and applications of synthetic, polysaccharide-based, semi-synthetic and 'smart' derivatives, Eur Polym J 117 (2019) 165–178. https://doi.org/10.1016/j.eurpolymj.2019.04.054.

[16] S. Ismaeilimoghadam, B. Azimi, M. Jonoobi, S. Danti, Highly Performing Polysaccharide Hydrogels can Replace Acrylic Acid-Based Superabsorbent Polymers in Sanitary Napkins, Macromol Mater Eng (2024). https://doi.org/10.1002/MAME.202400278.

[17] S. Ismaeilimoghadam, M. Jonoobi, Y. Hamzeh, B. Azimi, A. Mezzetta, L. Guazzelli, P. Cinelli, M. Seggiani, S. Danti, Development and Characterization of Sodium Alginate-Based Bio-hybrid Super Absorbent Polymer with High Retention Capacity Suitable for Baby Diapers, J Polym Environ 32 (2024) 5212–5230. https://doi.org/10.1007/S10924-024-03297-3/METRICS.

[18] X. Yan, H. Huang, A.M. Bakry, W. Wu, X. Liu, F. Liu, Advances in enhancing the mechanical properties of hydrogels through multi-strategic approaches based on biopolymer platforms, Int J Biol Macromol 272 (2024). https://doi.org/10.1016/j.ijbiomac.2024.132583.

[19] K.A.B. Pereira, C.L. Baracho, P.F. Oliveira, L.C.M. Palermo, C.R.E. Mansur, Influence of coal fly ash on the PPG properties and plugging ability in carbonate rocks for conformance control of oil reservoirs, Geoenergy Science and Engineering 231 (2023) 212297. https://doi.org/10.1016/J.GEOEN.2023.212297.

[20] R.H.S. Rodrigues, E.A. de Almeida, F.R. Kruger, E.C. Silva-Filho, E.C. Muniz, Hydrogels Based on Polyacrylamide and Pectin Containing Rice Husk Ash: Preparation, Characterization and Application in Formulation of Cementitious Materials, Materials 2024, Vol. 17, Page 5746 17 (2024) 5746. https://doi.org/10.3390/MA17235746.

[21] B.B. Zhou, W.L. Kang, H. Bin Yang, Z. Li, L.P. Ma, S.T. Wang, J.Q. Wang, A.Q. Xie, B. Sarsenbekuly, Study of the reinforced mechanism of fly ash on amphiphilic polymer gel, Pet Sci 19 (2022) 2175–2184. https://doi.org/10.1016/J.PETSCI.2022.05.019.

[22] C. Zareie, A.R. Bahramian, M.V. Sefti, M.B. Salehi, Network-gel strength relationship and performance improvement of polyacrylamide hydrogel using nano-silica; with regards to application in oil wells conditions, J Mol Liq 278 (2019) 512–520. https://doi.org/10.1016/j.molliq.2019.01.089.

[23] F. Sun, M. Lin, Z. Dong, J. Zhang, C. Wang, S. Wang, F. Song, Nanosilica-induced high mechanical strength of nanocomposite hydrogel for killing fluids, J Colloid Interface Sci 458 (2015) 45–52. https://doi.org/10.1016/j.jcis.2015.07.006.

[24] L. Ye, Y. Tang, D. Qiu, Enhance the mechanical performance of polyacrylamide hydrogel by aluminium-modified colloidal silica, Colloids Surf A Physicochem Eng Asp 447 (2014) 103–110. https://doi.org/10.1016/j.colsurfa.2014.01.072.

[25] T. Jayaramudu, H.U. Ko, H.C. Kim, J.W. Kim, J. Kim, Swelling behavior of polyacrylamide-cellulose nanocrystal hydrogels: Swelling kinetics, temperature, and pH effects, Materials 12 (2019). https://doi.org/10.3390/ma12132080.

[26] X. Yan, H. Huang, A.M. Bakry, W. Wu, X. Liu, F. Liu, Advances in enhancing the mechanical properties of hydrogels through multi-strategic approaches based on biopolymer platforms, Int J Biol Macromol 272 (2024). https://doi.org/10.1016/j.ijbiomac.2024.132583.

Electrochemical Improvement of Mangosteen Peel Extract

Teradon Loypipan[1], Bor-Yann Chen[2], Chung-Chuan Hsueh[2], Penjit Srinophakun[1], Anusith Thanapimmetha[1], Maythee Saisriyoot[1,*]

[1] Department of Chemical Engineering, Faculty of Engineering, Kasetsart University, Bangkok 10900, Thailand
[2] Department of Chemical and Materials Engineering, National I-Lan University, I-Lan 260, Taiwan
[*] Corresponding author: fengmts@ku.ac.th

ABSTRACT

Mangosteen is an important export product of Thailand. The increasing production to meet the high demand has resulted in high waste levels. This study aimed to utilize this agricultural waste for medical purposes. The antioxidant/anti-reductant ratio of mangosteen peel extract (MPE) was improved through the cyclic voltammetry method to increase its electron shuttle property. The magnitude of its electron shuttle property compared with that of dopamine was confirmed by a microbial fuel cell (MFC) system. The compounds found in MPE samples were Polyphenols (57.3493 ± 1.471 mg/g), Flavonoids (20.1373 ± 0.8750 mg/g), Tannins (65.2344 ± 1.221 mg/g), and Xanthones (356.4530 ± 3.530 mg/g). The MPE showed significant bioenergetic properties after cyclic voltammetry treatment. The power density generated from the MFC was increased 2.27-fold when the treated MPE was employed. This electron shuttle property of the MPE comes from its γ-mangostin, major xanthones in mangosteen peel and ranked second in abundance among xanthone compounds. The molecular docking studies were also conducted to investigate the binding affinity of γ-mangostin to the receptors of proteins involved in Parkinson's disease. Results revealed that its binding affinity was higher than that of current reference drugs.

Keywords: Mangosteen peel extract; Xanthones; γ-mangostin

1. INTRODUCTION

Among sources of agricultural waste in Thailand, Mangosteen (*Garcinia mangostana* L.) is a top-rank concern tropical fruit tree in Thailand next to Durian and has a high potential as a fruit for export from Thailand[1]. It is well known in Southeast Asia and the major production comes from Thailand, Malaysia, Indonesia, and the Philippines. Mangosteen fruit has a high economic value. Thus, it has good prospects of being developed into an excellent export commodity. Recently, the Thailand government has placed a high priority on developing mangosteen for export. Statistical data showed that in 2023, mangosteen production in Thailand was 148.36 thousand metric tons [2]. In 2024, the volume of mangosteen fruits exported was approximately 48.83 million kilograms [3].

Mangosteen fruit wastes, particularly peels and other residuals, are often discarded in large quantities by the food processing industry. Due to aforementioned UN criteria, there is an urgent need to reproduce these food wastes, especially fruit peels, which hold significant potential as valuable components in ruminant diets These peels are particularly rich in phytonutrients (PTNs) such as phenolics (15-20% DW), flavonoids (1-3% DW), tannins (5-10% DW), and saponins (1-2% DW), which possess functional properties that make them promising sources of high-value chemicals with antioxidant and antibacterial characteristics [4, 5]. One of PTNs major group, known as polyphenols, is commonly found in fruits and is crucial in animal nutrition and health. Furthermore, mangosteen peel also has xanthone compounds are shown in Table.1 Most of the xanthone compounds are α-mangostin and γ-mangostin. Xanthone compounds are mostly used as antioxidants in various industries such as cosmetics, supplementary foods, and medicine. As a result, xanthones are used in large quantities compared to other compounds found in mangosteen peel. α-mangostin is the most xanthone found in the mangosteen pericarp at 3323.88 ± 82.18 mg/100 g DM (69.02%), followed by γ-mangostin at 860.17 ± 17.46 mg/100 g DM (17.86%). Moreover, the minor compounds (13.13%), including gartanin, 8-deoxygartanin, garcinone E, 1,7-dihydroxy 3-methoxy-

2-(3-methylbut-2-enyl) xanthone, and 1,3,7-tri-hydroxy-2,8-di (3-methylbut-2-enyl) xanthone, are also found in the peel [6].

The target waste of mangostin from xanthone compound to be value-added production is γ-mangostin, as it is the second most abundant compound after α-mangostin.γ-mangostin has the one has pharmaceutical properties similar to α-mangostin, such as antioxidants by reducing oxidative damage in the liver through the activation of NRF2 and SIRT1 [7], have potent to anti-hyaluronidase (IC_{50} 23.85 µg/mL) and anti-tyrosinase (IC_{50} 50.35 µg/mL) by Hyaluronidase and Tyrosinase Inhibitory Activity [8], anti-inflammatory by reducing COX-2, IL-6, IL-1β, and NO production in LPS-induces RAW 264.7 cells [9], anti-neuropathic can attenuate 6-OHDA-induced neuronal cell death by harnessing their antioxidative potential and modulating the apoptotic signaling pathway. among other xanthones, it can be an effective way to prevent neurodegeneration in Parkinson's disease caused by oxidative stress [10], γ-mangostin was able to increase the α-tubulin acetylation in MDA-MD-231 and MCF-7 breast cancer cells. It was also found to possess potent antiproliferative activity against both cell lines. In addition, it was able to induce neurite outgrowth in the N2a cells [11]. and anti-cancer suppresses CRC tumorigenesis and CSC generation via downregulating the GSK3β/β-catenin/CDK6 cancer[12], eradicates murine primary leukemic cells and extends the survival of leukemic mice and restrains primary leukemic cells and CD34+ leukemic progenitor cells from leukemia patients [13]. In addition, due to the lack of widespread studies on α-mangostin, the commercial price of γ-mangostin is quite high, making studies on this substance more difficult.

This study aimed to add value to mangosteen peel by maximizing the production and utilization of xanthones, particularly γ-mangostin as ESs, thereby contributing to the reduction of agricultural waste. Initially, phytochemical analyses were conducted to quantify the phytonutrient content of the mangosteen peel extract. Subsequently, the extract was subjected to cyclic voltammetry (CV) treatment to enhance the electrochemical properties of its bioactive components. Microbial fuel cell (MFC) assays were then employed to compare the γ-mangostin concentration and power density before and after CV treatment. In addition, molecular docking simulations were performed to investigate the binding interactions between γ-mangostin and target proteins associated with Parkinson's disease [10]. The binding affinities of γ-mangostin were compared with those of standard therapeutic drugs to evaluate its potential as a novel treatment option. These integrated approaches collectively highlight the pharmaceutical potential of γ-mangostin and its role in the sustainable valorization of mangosteen peel waste.

2. EXPERIMENTAL

2.1 Mangosteen peel extract

Mangosteen peel extract was purchased from NAP Biotec Co., Ltd. Bangkok, Thailand 2024

2.2 Phytochemical analyses of mangosteen peel

Four spectrophotometric tests were used for the determination of phytochemical contents of mangosteen peel: total polyphenol content (TPC) analysis, total flavonoid content (TFC) analysis, total condensed tannins (TCT) content analysis and total xanthone content (TXC) analysis. These methods were applied for analyses throughout the study.

2.2.1 Total polyphenol content (TPC) analysis

To determine the total polyphenol content present in mangosteen peel the same procedure described by Rejano et al. (2023) was carried out [14]. Gallic Acid 1 mg/mL of DI water is the stock solution. After which, the stock solution was diluted by a fac two to 6 varying concentrations (e.g. 1000, 500, 250, 125, 62.5, and 31.3 µg/mL). For the sample solution, the sample was dissolved in DI water at 10 mg/mL. All the prepared solutions 100 µL per each were treated with 500 µL Folin-Ciocalteu regent (1:1 v/v with DI water) and 400 µL 4 % Na_2CO_3 solution. After that, incubating for 30 mins, 200 µL of each were placed in triplicate in a 96-well plate. The absorbance was measured at 600 nm using an ELISA microplate reader.

2.2.2 Total flavonoid content (TFC) analysis

Rutin 1 mg/mL of DI water is the stock solution. After which, the stock solution was diluted by a fac two to 6 varying concentrations (e.g. 1000, 500, 250, 125, 62.5, and 31.3 µg/mL). For the sample solution, the sample was dissolved in DI water at 10 mg/mL. All the prepared solutions 500 µL per each were treated with 500 µL 2 % $AlCl_3$ solution. After that, incubating for 15 mins, 200 µL of each were placed in triplicate in a 96-well plate. The absorbance was measured at 430 nm using an ELISA microplate reader.

2.2.3 Total condensed tannins (TCT) content analysis

Catechin 1 mg/mL of DI water is the stock solution. After which, the stock solution was diluted to 5 varying concentrations (e.g. 250, 200, 150, 100 and 50 µg/mL). For the sample solution, the sample was dissolved in DI water at 1 mg/mL. All the prepared solutions 300 µL per each were treated with 600 µL Vanillin regent. After that, incubating for 15 mins, 200 µL of each were placed in triplicate in a 96-well plate. The absorbance was measured at 530 nm using an ELISA microplate reader.

2.2.4 Total Xantone content (TXC) analysis

Xanthone 0.1 mg/mL of DI water is the stock solution. After which, the stock solution was diluted to 5 varying concentrations (e.g. 100, 80, 60, 40 and 20 µg/mL). For the sample solution, the sample was

dissolved in DI water at 0.1 mg/mL and filtered using Whatman filter No.1. After that, 100 µL of each were placed in triplicate in a Cuvette Standard Q Quartz Glass. The absorbance was measured at 243 nm using a UV-Vis spectrophotometer.

2.3 Cyclic voltammetry analysis

The electrochemical characteristics of mangosteen peel extract samples were investigated by utilizing a 50-cycle CV scanning on the sample solutions. ZIVE SP1 electrochemical workstation (Won-A-Tech Co. Ltd, South Korea) equipped with a three-electrode system was used for this analysis. A glassy carbon electrode (GCE, ID = 3 mm; model CHI104, CH Instruments Inc., USA) was used as the working electrode polished with aluminum oxide, and rinsed with deionized water multiple times before usage. A standard calomel electrode was used as the reference electrode. Moreover, a platinum electrode with a working area of 6.08 cm^2 was used as the counter electrode for this analysis. Samples are purged with nitrogen gas for 20 minutes before CV measurement. A symmetric scan range of − 1.5 V to +1.5 V was applied for one cycle to avoid water electrolysis. A scan rate of 100 mV/s was employed for this experiment. Redox potential curves in CV loops were described as enclosing regions that served as indications of the electrochemical properties of the extract solutions.

2.4 MFC operation and microbial culture

A dual-chambered MFC setup was employed for this study. The cathodic chamber consisted of an electrolyte solution and the anodic chamber consisted of Aeromonas hydrophilia (NIU01) cell broth with an OD600 of ~2.0. A nutrient rich medium was used for the cell broth (Difco™ Broth, Miller; Luria Bertani). The setup involved carbon rods (Grade: IGS743; Central Carbon Co., Ltd) in each of the chamber soaked in the culture broth and the electrolyte solution. The chambers are separated by a proton exchange membrane (DuPont™ Nafion NR-212) in an immersed area of 0.000452 m^2.

2.5 Power-generating determination

Time courses of electric current (I_{MFC}) and voltage (V_{MFC}) were automatically determined with a D/A system (DAS 5020; Jiehan Tech. Corp., Taiwan). For an identical basis for comparison, 1 KΩ external resistance was applied to MFCs. Power and current densities were determined by the formulae:

$$P_{density} = \frac{V_{MFC} \times I_{MFC}}{A_{anode}}$$

$$I_{density} = \frac{I_{MFC}}{A_{anode}}$$

where I_{MFC} and V_{MFC} could be evaluated with linear sweep voltammetry through a workstation for electrochemical analysis (Jiehan 5600, Jiehan Technology Corp., Taiwan). The parameter A_{anode} was the apparent working area of the graphite anode.

2.6 Molecular Docking

Molecular docking analysis was conducted using the CB-Dock2 web server (https://cadd.labshare.cn/cb-dock2/), which employs an AutoDock Vina-based molecular docking approach. The target proteins for docking were selected based on the hub genes identified in the constructed network. Protein structures were retrieved from the RCSB Protein Data Bank (PDB). The root-mean-square fluctuation (RMSF) plot and the protein-ligand interaction model were generated and obtained from the web server. Additionally, the 2D protein-ligand interactions were visualized using BIOVIA Discovery Studio.

3. RESULTS AND DISCUSSION

3.1 Phytochemical analysis of mangosteen peel extract

To assess the efficiency of Mangosteen Peel Extract antioxidant and anti-viral, the total polyphenol (TPC), total flavonoid (TFC), total condensed tannin (TCT), and total xanthone (TXC) content of MPE were quantitatively evaluated. The TPC of MPE was calculated from the regression equation of the calibration curve ($y = 0.0037x + 0.0034$, $R_{sqrt} = 0.9903$) and expressed in gallic acid equivalents (GAEs). The TFC of MPE was calculated from the regression equation of the calibration curve ($y = 0.0027x + 0.0030$, $R_{sqrt} = 0.9978$) and expressed in rutin equivalents (REs). The TCT of MPE was calculated from the regression equation of the calibration curve ($y = 0.0144x + 0.0455$, $R_{sqrt} = 0.9934$) and expressed in catechin equivalents (CEs). The TXC of MPE was calculated from the regression equation of the calibration curve ($y = 0.0156x + 0.0246$, $R_{sqrt} = 0.9918$) and expressed in xanthone equivalents (XEs). The results are presented in Table. 1

Table 1 Phytochemical Constituent Analysis of Mangosteen Peel Extract.

Phytochemical Content Analysis				
Sample	Total Polyphenol Content (Gallic acid mg/g)	Total Flavonoid Content (Rutin mg/g)	Total Condensed Tannin Content (Catechin mg/g)	Total Xanthone Content (Xanthone mg/g)
MPE	57.35 ± 1.47	20.14 ± 0.88	65.23 ± 1.22	356.45 ± 3.53

This experiment highlights the mechanism and efficacy of MPE by demonstrating its ability to stimulate bioenergy production and electron mediation in microbial fuel cells. To further assess the potential applications of MPE, we conducted phytochemical

content analysis and antioxidant evaluations of its extracts. As shown in the Table.1, MPE contains significant levels of key phytonutrients such as polyphenols, flavonoids, and condensed tannins. Among these, polyphenols and flavonoids are particularly influential in their biological functions.

As can observed in Table.1 MPE contained various phytochemicals in a different concentration as documented by previous studies, Phenolic compounds are believed to have excellent antibacterial as well as anti-microbial properties for decades. They also have been known to encourage protection against infectious diseases and inflammation through protein and enzyme modulation and neutralization mechanisms [15] Flavonoids are a major functional component of many herbal preparations used for medical purposes. They have been used since ancient times and have numerous beneficial effects on human health. Flavonoids can help treat or prevent various human diseases such as cancer, cardiovascular disease, diabetes, and neuronal and anti-viral diseases. They are known to work as antioxidants, enzyme inhibitors, hormones, immune modulators, and have benefits for skin care and wound healing [16]. Condensed tannins can interact with viral proteins, inhibiting viral entry and replication. They can also regulate cytokine synthesis and enhance immune cell activity, impacting the immune system. [14]. and Xanthones and xanthone derivatives have shown potential as pharmacological agents for treating or preventing cardiovascular diseases such as ischemic heart disease, atherosclerosis, and hypertension. The protective effects of xanthones on the cardiovascular system are attributed to their antioxidant, anti-inflammatory, platelet aggregation inhibitory, antithrombotic, and vasorelaxant activities [17]. The most abundant phytochemical compound found in MPE is Xanthone, which means the potential of MPE is mainly related to the potential of xanthone.

3.2 Cyclic voltammetry (CV) analysis

To evaluate the electrochemical stability of the compounds, present in the extracts, serial cycles of cyclic voltammetry (CV) were conducted to simulate repeated oxidation and reduction processes occurring in the test chemicals. Figure 1 illustrates the CV area plotted against the number of cycles for the extract. Electron donor and acceptor species within the extracts underwent irreversible redox reactions, ultimately leaving behind electrochemically stable species (ESs). Notably, the MPE extract exhibited prominent oxidation and reduction peaks, and it remained relatively stable even after 50 CV cycles. This indicates the presence of ESs with stable and reversible redox profiles, suggesting their potential suitability for bioenergy applications. Recent studies have highlighted a strong correlation between the electrochemical properties of traditional Chinese medicine and its efficacy in stimulating bioenergy for disease treatment [18]. The discrepancies observed between the CV profiles and PD amplification may be attributed to an imbalanced ratio of antioxidants to reductants, preventing the complete extraction of all ES-like compounds [19]. Specifically, the MPE extract may contain a higher concentration of antioxidant species compared to ESs. Furthermore, phytochemicals from the previous section support this observation. The MPE extract was found to have significantly higher concentrations of xanthones and demonstrated greater antioxidant activity, indicating a predominance of antioxidant compounds. Ultimately, both ESs and antioxidants play crucial roles in influencing the performance of bioelectricity generation and disease treatment.

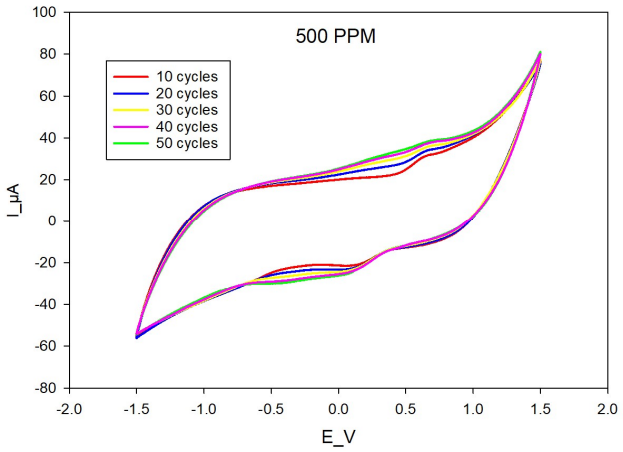

Figure 1 Cyclic voltammograms of MPE.

3.3 Power density (PD) analysis

Power-generating profiles are essential as a pre-screening tool to evaluate the anti-inflammatory potential of herbal extracts, given that bioenergy-stimulating characteristics play a critical role in the therapeutic efficacy of herbal medicines. Figure 2 presents the power density (PD) profiles of the MPE extract, while Table 2 summarizes the amplification factors of dopamine and the MPE extracts at various concentrations, enabling case–control comparisons. In the PD analysis, dopamine was used as the reference standard and positive control.

The ranking of power-generating capacity and amplification factor (denoted by subscript) consistently followed the same order: dopamine > 2000 ppm_MPE > 1500 ppm_MPE > 1000 ppm_MPE > blank. For MPE extracts, a clear trend of increasing amplification factor was observed with rising extract concentration. This saturation in bioelectricity generation may be attributed to the high xanthone content of the MPE extract, which was quantified at 356.4530 ± 3.530 mg/g in the previous phytochemical analysis. Xanthone-rich herbal extracts have been reported to possess therapeutic potential against various diseases, including bacterial infections. In addition to the previously discussed imbalance in antioxidant/anti-reductant ratios, the discrepancies between the CV and PD results may also stem from the antibacterial activity of tannin-rich ethanol extracts,

which could affect microbial electron transfer. These findings suggest that the active compounds in the aqueous MPE extract include electron-shuttling (ES) species that not only facilitate electron transport but also exhibit relatively low biotoxicity, supporting their potential for safe therapeutic applications.

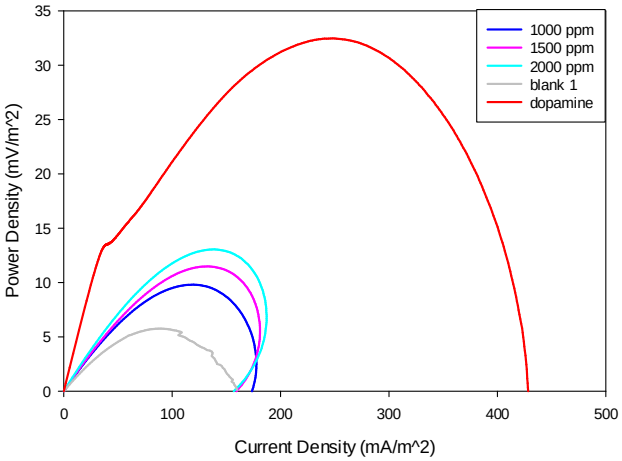

Figure 2 PD profiles of bioenergy generation of MPE extracts.

Table 2 Summary of power density (PD) analysis using different concentrations of MPE extract. Amplification factor is with respect to blank.

Concentration	PD (mW/m2)	Amplification
Blank	5.76 ± 0.61	1.00
1000 ppm	9.80 ± 1.01	1.70
1500 ppm	11.48 ± 0.76	1.99
2000 ppm	13.05 ± 0.82	2.26
Dopamine	32.47 ± 2.80	5.64

3.4 Molecular docking studies

Molecular docking simulations were conducted to evaluate the binding interactions between γ-mangostin, a targeted xanthone compound, and several key Parkinson's disease (PD)-related proteins. The selected target proteins included the adenosine A2A receptor (A2AAR; PDB ID: 3EML), α-synuclein (ASN; PDB ID: 1XQ8), catechol-O-methyltransferase (COMT; PDB ID: 1H1D), and monoamine oxidase B (MAO-B; PDB ID: 2C65). Docking was performed using CBDock2 with Vina scoring, and the results were compared with those obtained for standard reference drugs including dopamine, rasagiline, and selegiline [20]. This study aimed to assess whether γ-mangostin could effectively bind to the target proteins, thereby supporting its therapeutic potential. The docking results indicated that γ-mangostin exhibited the most negative binding affinity values among the tested compounds, as presented in Table 3. A more negative binding affinity score signifies a stronger and more stable interaction between the ligand and the receptor, highlighting γ-mangostin's potential as a promising bioactive compound for PD therapy. The ligand–protein interactions were visualized in two-dimensional formats using Discovery Studio 4.1 software. The 2D interaction diagrams revealed details about the number and types of bonds formed, as well as the specific amino acid residues involved in the interactions between γ-mangostin and the respective protein targets (Figure 3). These results provide additional molecular insight into the mechanism by which γ-mangostin may exert neuroprotective effects relevant to PD.

Table 3 Binding affinity (kcal/mol) interaction of target compounds and conventional drugs against the PD-target protein.

Target Compound	A2AAR (PDB ID: 3EML)	ASN (PDB ID: 1XQ8)	COMT (PDB ID: 1H1D)	MAO_B (PDB ID: 2C65)
γ-mangostin	-8	-6.1	-7.4	-10.5
Dopamine	-5.6	-4.5	-6.4	-6.4
Rasagiline	-5.9	-4.2	-7.1	-8
Selegiline	-5.7	-4	-7	-7.5

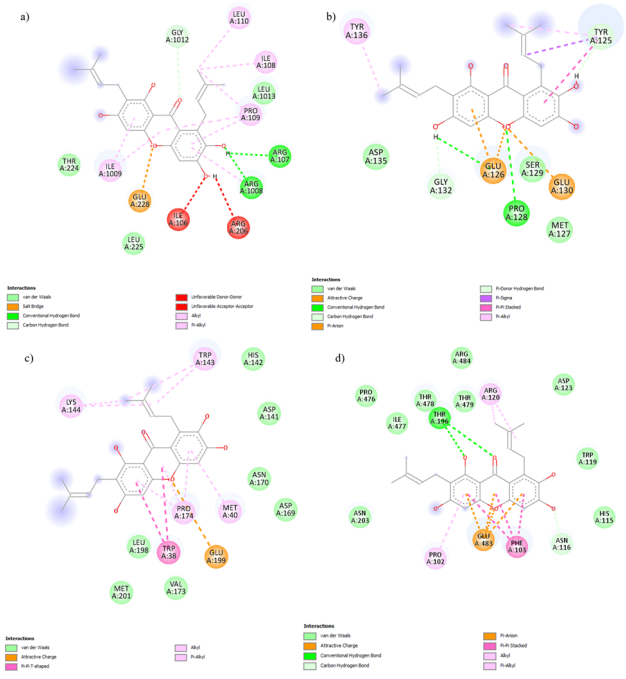

Figure 3 Two dimensional visualization between γ-mangostin with a) A2A receptor, b) α-synuclein, c) catechol-O-methyltransferase and d) monoamine oxidase B

4. CONCLUSION

This study highlights the potential of MPE (Mangosteen Peel Extract) in the prevention and treatment of diseases. The extract exhibits notable bioenergy-stimulating and electron-mediated properties, which contribute to its pharmacological activity. These therapeutic effects are largely attributed to the extract's electron-shuttling capabilities. Among

its key bioactive constituents, γ-mangostin has shown particular promise in addressing neurodegenerative disorders such as Parkinson's disease. These findings support the therapeutic value of MPE and its constituent compounds in the development of novel treatments for Parkinson's disease. However, further research—including follow-up studies and clinical trials—is necessary to validate these effects, assess safety profiles, and explore potential side effects. Future studies should incorporate experimental validation of molecular docking results to determine their translational relevance. Additionally, structure–activity relationship (SAR) analyses, in combination with in 43vitro and in vivo assays, will be essential for elucidating the mechanisms of action and optimizing therapeutic efficacy.

ACKNOWLEDGMENTS

This work was financially supported by the faculty of Engineering, Kasetsart University and TEEP Program from Taiwan's Ministry of Education

REFERENCES

1. Apiratikorn, S., et al., The Impact of Climatic Variability on Phenological Change, Yield and Fruit Quality of Mangosteen in Phatthalung Province, Southern Thailand. Kasetsart Journal - Natural Science, 2012. **46**: p. 1-9.
2. Walderich, A. Production volume of mangosteens in Thailand in 2023, by region. 2024 [cited 2024 3/28/2024]; Available from: https://www.statista.com/statistics/1319833/thailand-mangosteen-production-volume-by-region/#statisticContainer.
3. Ciba, K. Monthly volume of mangosteens exported from Thailand from January 2023 to April 2024. 2024 [cited 2024 6/25/2024]; Available from: https://www.statista.com/statistics/1319725/thailand-monthly-mangosteen-export-volume/.
4. Villacís-Chiriboga, J., et al., Valorization of byproducts from tropical fruits: Extraction methodologies, applications, environmental, and economic assessment: A review (Part 1: General overview of the byproducts, traditional biorefinery practices, and possible applications). Comprehensive Reviews in Food Science and Food Safety, 2020. **19**(2): p. 405-447.
5. Wanapat, M., et al., The recycling of tropical fruit peel waste-products applied in feed additive for ruminants: Food manufacturing industries, phytonutrient properties, mechanisms, and future applications. Journal of Agriculture and Food Research, 2024. **17**: p. 101234.
6. Wittenauer, J., et al., Characterisation and quantification of xanthones from the aril and pericarp of mangosteens (Garcinia mangostana L.) and a mangosteen containing functional beverage by HPLC–DAD–MSn. Food Chemistry, 2012. **134**: p. 445–452.
7. Wang, A., et al., γ-Mangostin, a xanthone from mangosteen, attenuates oxidative injury in liver via NRF2 and SIRT1 induction. Journal of Functional Foods, 2018. **40**: p. 544-553.
8. Widowati, W., et al., Anti-aging Effects of Mangosteen Peel Extract and Its Phytochemical Compounds: Antioxidant Activity, Enzyme Inhibition and Molecular Docking Simulation. Trop Life Sci Res, 2020. **31**(3): p. 127-144.
9. Widowati, W., et al., Anti-inflammatory Effect of Mangosteen (Garcinia mangostana L.) Peel Extract and its Compounds in LPS-induced RAW264.7 Cells. nps, 2016. **22**(3): p. 147-153.
10. Jaisin, Y., et al., Protective effects of γ-mangostin on 6-OHDA-induced toxicity in SH-SY5Y cells. Neuroscience Letters, 2018. **665**: p. 229-235.
11. Yeong, K.Y., et al., Discovery of gamma-mangostin from Garcinia mangostana as a potent and selective natural SIRT2 inhibitor. Bioorganic Chemistry, 2020. **94**: p. 103403.
12. Chang, H.-F. and L.-L. Yang Gamma-Mangostin, a Micronutrient of Mangosteen Fruit, Induces Apoptosis in Human Colon Cancer Cells. Molecules, 2012. **17**, 8010-8021 DOI: 10.3390/molecules17078010.
13. Long, Z.-J., et al., Dietary γ-mangostin triggers immunogenic cell death and activates cGAS signaling in acute myeloid leukemia. Pharmacological Research, 2023. **197**: p. 106973.
14. Rejano, C.J.F., et al., Electrochemical analysis via microbial fuel cells reveals electron-stimulating characteristics, immunomodulation and antiviral properties of Ji Qin Yin. Journal of the Taiwan Institute of Chemical Engineers, 2023. **152**: p. 105193.
15. Prabhu, S., et al., Classifications of polyphenols and their potential application in human health and diseases. International Journal of Physiology, Nutrition and Physical Education, 2021. **6**: p. 293-301.
16. Lee, E.-R., G.-H. Kang, and S.-G. Cho, Effect of Flavonoids on Human Health: Old Subjects but New Challenges. Recent Patents on Biotechnology, 2007. **1**(2): p. 139-150.
17. Jiang, D.-J., Z. Dai, and Y.-J. Li, Pharmacological Effects of Xanthones as Cardiovascular Protective Agents. Cardiovascular Drug Reviews, 2004. **22**(2): p. 91-102.
18. Hsueh, C.-C., C.-C. Wu, and B.-Y. Chen, Polyphenolic compounds as electron shuttles for sustainable energy utilization. Biotechnology for Biofuels, 2019. **12**.
19. Tsai, P.-W., et al., Unraveling the bioenergy production and electron transport characteristics of processed Rheum palmatum L. for antiviral drug development. Industrial Crops and Products, 2023. **195**: p. 116488.

20. Gnanaraj, C., et al. In Silico Molecular Docking Analysis of Karanjin against Alzheimer's and Parkinson's Diseases as a Potential Natural Lead Molecule for New Drug Design, Development and Therapy. Molecules, 2022. **27**, DOI: 10.3390/molecules27092834.

Effects of cultivation temperature on alpha-amylase production from wild-type rice callus suspensions

Worapicha Daungtongcome[1], Kantharakorn Macharoen[1,*]

[1] Department of Chemical Engineering, Faculty of Engineering, King Mongkut's University of Technology Thonburi, Bangkok 10140, Thailand
[*] Corresponding author: kantharakorn.mac@kmutt.ac.th

ABSTRACT

α-Amylase is a key enzyme that hydrolyzes starch into smaller sugars, with applications in food, pharmaceuticals, and biofuels. The objective of this research is to study the effects of cultivation temperature on rice cell growth and the production of α-amylase. Rice callus (*Oryza sativa* subsp. *japonica* cv. Nipponbare) suspensions were cultured for 14 days at 140 rpm in 1-L shake flasks under three different temperatures: 27°C, 32°C, and 37°C. Samples were taken and centrifuged to separate spent media (supernatant) and rice callus pellet on days 0, 2, 4, 6, 8, 10, 12, and 14. The α- amylase activity was measured using the DNS (3,5-dinitrosalicylic acid) method. The results indicated that the amount of α-amylase in the spent media was approximately 4–5 times higher than in the cell extract at all three tested temperatures. The optimal conditions for α-amylase activity were found to be at 37°C and pH 7.0.The highest α-amylase activity in the spent media was found at 37°C (1.02 U/ml), significantly higher than those of 32°C (0.90 U/ml) and 27°C (0.86 U/ml), when one unit of enzyme (U) liberates 1.0 mg of maltose from starch in 3 minutes at pH 7.0 and 37°C. During the final days of cultivation, α-amylase is produced to break down stored starch into sugars, compensating for the decreased sugar levels and maintaining energy balance. This approach has the potential to be applied in industry as an alternative for future production processes.

Keywords: Rice cell cultures, plant callus suspension cultures, amylase enzyme, α-amylase.

1. INTRODUCTION

Plant cell suspension cultures are increasingly recognized as a versatile platform for the sustainable production of high-value compounds, including enzymes, secondary metabolites and biopharmaceuticals [1,2]. Among plant hosts, rice (*Oryza sativa*) callus suspensions offer several advantages, such as fast growth, scalability, and a well-characterized genome, making them suitable for both basic research and applied biotechnology.

α-amylase is a key hydrolytic enzyme responsible for catalyzing the cleavage of α-1,4-glycosidic bonds in starch, yielding smaller sugars such as maltose and glucose. In rice cell cultures, alpha-amylase is a predominant endogenous protein secreted into the culture medium under standard growth conditions, particularly under sugar-depleted or stress-induced states [3]. While traditionally studied for its role in starch mobilization and industrial enzyme applications, alpha-amylase also presents opportunities in pharmaceutical and diagnostic contexts. These include its use in enzymotherapy, controlled digestion systems, and as a model for investigating native secretion mechanisms in plant-based production platforms.

Temperature is a critical parameter that affects plant cell physiology, enzyme expression, and protein folding. Previous studies have shown that cultivation temperature can significantly influence biomass accumulation, metabolic activity, and recombinant protein yield in plant cell systems [1]. However, there remains a lack of systematic data on how temperature modulates the expression and secretion of native proteins, particularly alpha-amylase, in wild-type rice callus suspensions. Therefore, this research aims to develop an alternative for producing amylase enzymes from rice cells because rice cells can produce amylase enzymes and are quite environmentally friendly. Additionally, rice cells are more durable than fungi, which can mutate and become infected during the production process [4].

Rice callus, a type of undifferentiated plant tissue, serves as a promising model for studying enzyme production and characterization. This study aims to investigate the effects of cultivation temperature on alpha-amylase production in rice callus suspensions. By understanding how temperature influences native enzyme expression, we seek to optimize culture conditions for improved enzyme yield and unlock

further potential for pharmaceutical applications of plant-derived α-amylase.

2. EXPERIMENTAL

2.1 Rice calli cultures

Wild-type rice (*Oryza sativa* subsp. *japonica* cv. Nipponbare) calli was cultivated in modified Chu/ Gamborg (NB) basal media pH 5.8 supplemented with 3% sucrose and plant hormones. Suspension cultures were performed in 1-L shake flasks with incubator shaker speed of 140 rpm for 14 days under three different temperatures: 27°C, 32°C, and 37°C. Samples were taken and centrifuged for 15 min at 4000 rpm to separate spent culture media (supernatant) and rice callus pellet on days 0, 2, 4, 6, 8, 10, 12, and 14.

2.2 Cellular metabolic activity

A solution of 2,3,5-triphenyl tetrazolium chloride (TTC) in 0.05 M sodium phosphate buffer pH 7.5 was prepared at a concentration of 0.4% w/v. The rice callus pellet from 2.1 was washed with sodium phosphate buffer and filtered. About 0.04 g of rice callus was transferred to a microtube followed by adding 0.8 ml of TTC solution and incubating in the dark for 24 hours. After incubation, the solution was aspirated, and 1.5 ml of 95% ethanol was added. The microtube was then placed in a dry bath at 60°C for 1 hour. The absorbance of the extracted solution was measured at 485 nm.

2.3 Biomass measurement

Samples were collected in 2.0 ml tubes, with a total of three samples. The fresh weight (FW) and dry weight (DW) of rice callus were measured using 1.6 µm filter paper to filter the samples, leaving only the rice cells. To determine dry weight (DW), the rice cells were dried in an oven at 60°C for 24 hours, and the weighing process was repeated until a constant weight was obtained.

2.4 Analysis of sugar content by Ultra Performance Liquid Chromatography (UPLC)

Three types of sample solutions D-sucrose, D-glucose, and D-fructose were prepared, each at five different concentrations. A volume of 1.5 ml of each sample solution was prepared in vial bottles. An injection volume of 5 µl was used. The Asahipak NH2P-50 4E column (4.6 mm ID × 250 mm L) was employed, with the mobile phase consisting of acetonitrile and water (UPLC grade) at a ratio of 65:35. The flow rate was set at 0.6 ml/min, and the total run time was 15 min.

2.5 Rice α- amylase activity

A 1% w/w starch solution was prepared using 20 mM sodium phosphate buffer (pH 7.0). DNS (3,5-dinitrosalicylic acid) was used as the color reagent. For the assay, 0.5 ml of starch solution was mixed with 0.5 ml of spent media or cell extract, and the mixture was incubated at 37°C for 3 minutes. After incubation, 0.5 ml of DNS reagent was added, and the mixture was heated in a 90°C water bath for 15 minutes. Following heating, 4.5 ml of DI water was added, and the absorbance was measured at 540 nm.

2.6 Optimal conditions for rice α- amylase activity

A 1% w/w starch solution was prepared using 20 mM sodium phosphate buffer adjusted to pH 5, 6, 7, and 8. Each solution was incubated at 37°C for 3 minutes. To evaluate the effect of temperature, the buffer at pH 7 was selected, and the reaction mixtures were incubated at 27°C, 32°C, 37°C, and 42°C for 3 minutes. For each assay, α - amylase activity assay follows section 2.5.

3. RESULTS AND DISCUSSION

3.1 Appearance of rice calli in suspension cultures

Wild-type rice calli grown on semi-solid media plates were transferred and sieved through a pre-sterilized 300-micron screen mesh (No. 50 US mesh) to start suspension cultures with homogenous calli. The cultures were kept in an incubator shaker at 140 rpm and 27°C to obtain sufficient rice calli biomass. After 10 days of cultivation, rice calli suspension cultures were split into several 1-L flasks with 250 mL working volume and kept at 27°C, 32°C, and 37°C, respectively, inside each incubator orbitally shaking at 140 rpm. Each condition was performed in triplicate. A comparison of the appearance of rice calli cultivated at different temperatures over time is shown in Fig 1., with representative images taken on days 0, 6, and 14 to illustrate temperature-dependent changes during cultivation.

From Fig 1., the growth of rice callus in NB medium under different temperatures was evaluated. On day 0, the cell size across all three temperatures (27°C, 32°C, and 37°C) appeared equal, as the experiment was started using rice callus from the same initial culture, ensuring consistent starting conditions. By day 6, which represents the mid-point of the 14-day cultivation period, differences in growth began to emerge. The rice callus at 27°C showed noticeably larger growth compared to that at 37°C. On the final day (day 14), the differences became even more apparent. The rice callus cultured at 27°C exhibited the largest size, while at 37°C, the callus was smaller and more dispersed compared to those grown at 27°C and 32°C. Additionally, the color of the rice callus at 27°C was a deeper yellow than at 32°C and 37°C. It was also observed that, at the same temperature, rice callus on day 14 tended to form larger aggregates than on day 6. When comparing across temperatures, cell aggregation was most clearly seen at 27°C, more so than at 32°C or 37°C. This is likely due to increased cell division, where newly formed cells tend to remain attached to the original cells, resulting in larger clusters of callus tissue [5].

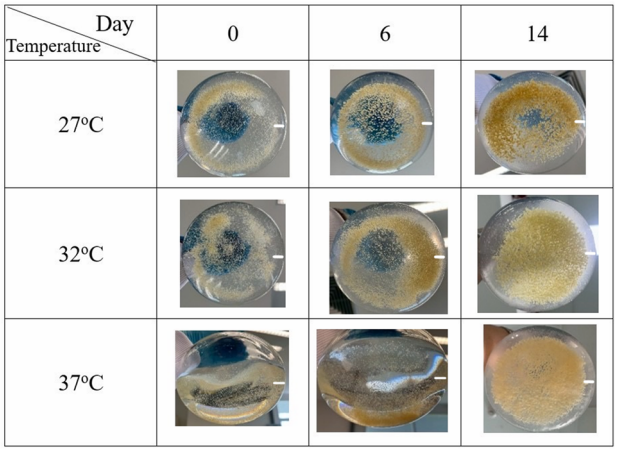

Fig 1. Rice callus suspension cultures grown at temperatures of 27°C, 32°C, and 37°C. The white scale bars are equal to 3 mm.

3.2 Cellular Metabolic Activity with TTC Assay

The analysis of metabolic activity was performed using the TTC assay [6] to evaluate cellular metabolic activity. In this assay, 2,3,5-triphenyltetrazolium chloride (TTC) serves as a redox indicator. Viable, metabolically active cells reduce the colorless TTC to red-colored formazan through the action of dehydrogenase enzymes present in the mitochondria [7]. As a result, rice calli exhibiting metabolic activity changed color from their natural state to red. The red formazan product was then extracted using 95% ethanol at 60°C for 1 hour. The absorbance was measured at 485 nm to quantify the level of metabolic activity. Activity. The results are shown in Fig 2.

From Fig 2, rice calli were cultured at different temperatures (27°C, 32°C, and 37°C) for 14 days to evaluate their metabolic activity. During the initial phase of cultivation, the absorbance values were increasing due to the abundance of nutrients in the medium, which supported rapid cell proliferation and biomass accumulation. As cell density increased, the production of mitochondrial enzymes, such as succinate dehydrogenase, also increased, and hence metabolic activity increased. However, from day 4 to day 6 onward, a decline in absorbance was observed across all temperature conditions. This reduction corresponds to nutrient depletion, particularly the exhaustion of sugars essential for cellular respiration and energy metabolism. As shown in Fig. 3, the sugar content in the culture medium decreased over time, corresponding well with the observed reduction in metabolic activity. When the sugar was nearly exhausted, the growth and metabolic functions of the rice calli slowed down, resulting in lower TTC reduction and absorbance in the later days of culture.

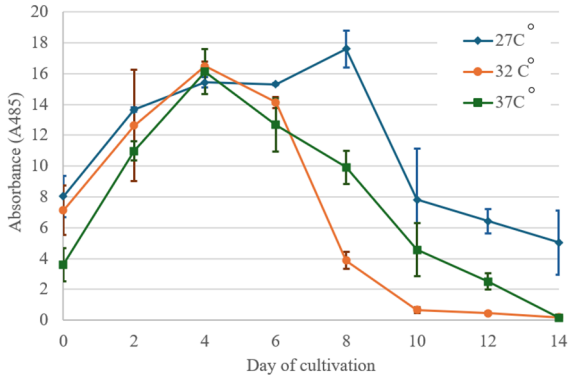

Fig. 2. Effect of cultivation temperatures (27°C, 32°C, and 37°C) on the metabolic activity of rice callus (0.04 g fresh weight each) as determined by TTC assay. Error bars indicate the standard deviation (SD) from three biological samples.

When comparing across cultivation temperatures, rice calli cultured at 37°C showed the lowest absorbance values, indicating significantly lower metabolic activity than those grown at 27°C. This is consistent with previous studies reporting that elevated temperatures can impose thermal stress, impairing mitochondrial function, enzyme activity, and overall cell viability [8].

3.3 Biomass production and sugar consumption

Biomass analysis was performed by collecting three samples from each of the three temperature conditions to evaluate the growth of rice callus. The assessment was based on measuring the cell dry weight. In parallel, the sugar content in the spent media from rice callus cultures grown under different temperatures was analyzed. The cultures were initially grown in an NB medium containing 30 g/L sucrose as the primary carbon source. The analysis of sugar composition was carried out using UPLC and compared against standard sugars including D-sucrose, D-glucose, and D-fructose. The results are shown in Fig.3, which presents a comparison between the growth of rice callus and the changes in sugar content over time.

Fig. 3 shows that the biomass of rice callus initially increased gradually, reaching its peak on day 8. At 27°C, the highest biomass was 5.40 ± 0.27 g DW/L, which subsequently decreased to 4.06 ± 0.68 g DW/L by day 10 (Fig. 3 (a)). At 32°C, the peak biomass reached 4.44 ± 0.37 g DW/L, followed by a decline to 3.68± 0.88 g DW/L on day 10 (Fig. 3 (b)). Similarly, at 37°C, the biomass peaked at 4.65 ± 0.56 g DW/L, and slightly decreased 4.41 ± 0.84 g DW/L by day 10 (Fig. 3 (c)). These results indicate that 27°C provides a more favorable environment for cell proliferation and metabolic activity. The observed decline in biomass after day 8 across all conditions likely reflects nutrient depletion or the accumulation of inhibitory metabolites in the medium. Previous studies have similarly reported 27–28°C as the optimal temperature range for rice callus proliferation and maintenance.

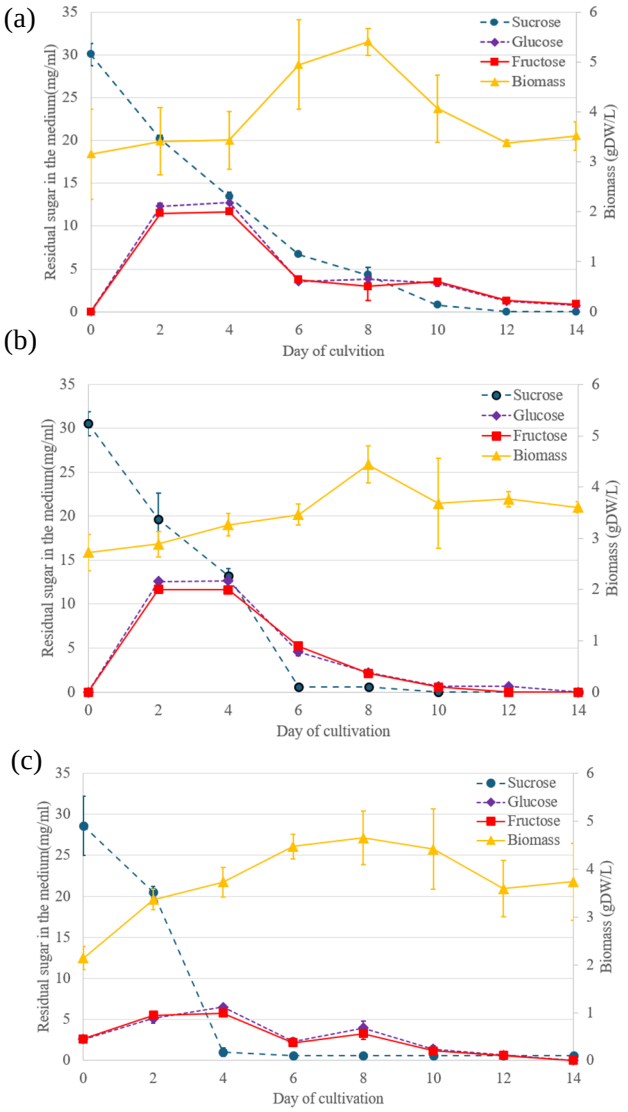

Fig. 3. Growth kinetics and sugar consumption of rice callus cultured at (a) 27ºC, (b) 32ºC, and (c) 37ºC. Error bars indicate SD from three biological samples.

Fig. 3 shows that at day 0 of cultivation at all three temperature cultures. Sucrose levels were slightly lower than 30 mg/mL, while glucose and fructose levels were slightly above 0 mg/mL due to partial sucrose hydrolysis during heat sterilization (autoclaving) of the medium. After that, the concentration of sucrose progressively decreased as it was hydrolyzed into glucose and fructose by cell wall-bound invertase in rice cells [9]. The monosaccharides were then utilized by the plant cells as primary energy substrates for metabolism [10]. A closer look at sucrose consumption rates reveals that sucrose was depleted more rapidly at higher temperatures: by day 10 at 27°C, day 6 at 32°C, and day 4 at 37°C. This trend suggests that higher temperatures may enhance invertase activity and sugar uptake, leading to faster sugar depletion. In the later days of cultivation (days 10, 12, and 14), sugar levels continue to decline, which correlates with a slowdown in biomass accumulation. As energy sources become limited, cell proliferation slows or ceases. Cultures at 27°C show more sustained sugar utilization and higher overall biomass production, leading to more pronounced cell aggregation and larger clusters of rice callus. Thus, the ability of rice callus to grow and maintain biomass is closely linked to the rate of sugar consumption, which is influenced by the cultivation temperature.

3.4 Analysis of α-amylase optimization

The optimal pH and temperature for α-amylase activity were determined by testing buffer solutions at pH 5, 6, 7, and 8, with samples incubated at 37°C for 3 minutes. Once the optimal pH was identified, the temperature varied (27 °C, 32 °C, 37 °C, and 42 °C) to evaluate its effect on enzymatic activity. The dinitro salicylic acid (DNS) method was used to quantify reducing sugars released from starch hydrolysis. Absorbance was measured at 540 nm and then converted to α-amylase activity.

From Figure 4(a), the highest α-amylase activity was found at pH 7, indicating that this pH condition supports optimal α-amylase activity. After that, different temperatures were tested using pH 7 from the first experiment. Based on this result, pH 7 was used for the subsequent temperature optimization. As shown in Fig. 4(b), the highest absorbance occurred at 37°C, suggesting that this temperature is optimal for α-amylase-mediated starch hydrolysis. Therefore, the most suitable conditions for α-amylase activity in this study were pH 7 and 37°C, which is consistent with findings from a previous study [11].

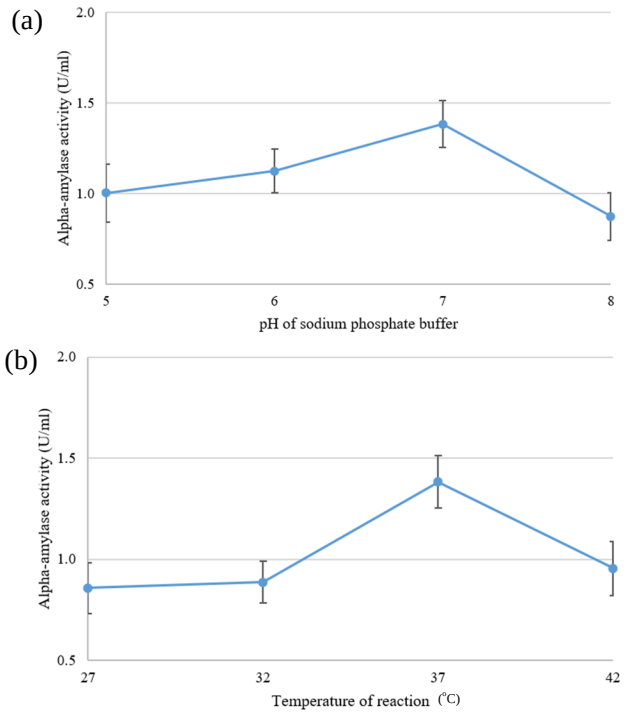

Fig 4. Show the absorbance values of *α*-amylase: a) at pH 5,6,7 and 8, b) at 27ºC, 32ºC, 37ºC, and 42ºC. Error bars indicate SD from triplicate samples.

3.5 Analysis of α-amylase from rice callus suspension cultures

Alpha-amylase activities in the spent media and in the cell extract were analyzed. The results indicated that the amount of α-amylase in the spent media was approximately 4–5 times higher than in the cell extract at all three tested temperatures. In other words, the amount of α-amylase in rice cell extract was negligible. As seen in Fig.5, it was found that the crude α-amylase activity in spent culture media increased after day 8 of cultivation and reached its peak on day 14 of cultivation across all temperature conditions. The maximum activity observed was 0.85 ± 0.02 U/mL at 27°C, 0.90 ± 0.14 U/mL at 32°C, and 1.02± 0.01 U/mL at 37°C. Note that 1 unit of enzyme activity is defined as the amount of enzyme that releases 1.0 mg of maltose from starch in 3 minutes at pH 7.0 and 37°C.

The highest α-amylase activity was observed at 37°C. This elevated activity is likely due to increased sugar depletion at this temperature, which triggers the expression of the *Amy3* genes, known to be activated under carbohydrate starvation, and leads to enhanced α-amylase production to hydrolyze starch and provide sugar for energy sources [12]. As shown in Fig. 3(c), sugar levels in the NB medium began to decline significantly after day 6, with depletion occurring even earlier (day 4) at 37°C. This early sugar depletion corresponds with the earlier and stronger induction of α-amylase activity at higher temperatures. Therefore, when comparing α-amylase production across the three conditions, the highest levels were found at 37°C, while the lowest occurred at 27°C. This is likely because rice callus exhibited the most robust growth at 27°C, reducing its reliance on starch degradation and, consequently, the need for α-amylase induction. In contrast, at 37°C, the faster hydrolysis of sucrose and rapid consumption of glucose and fructose to support callus metabolism led to an earlier depletion of available carbon sources. As a result, carbon starvation occurred sooner, strongly activating *Amy3* gene expression and inducing higher α-amylase production to compensate by converting intracellular starch into sugars for continued growth and survival.

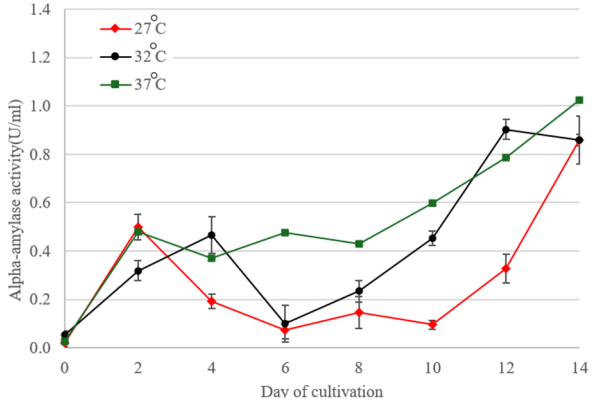

Fig 5. Crude α-amylase activity of spent media of batch 27ºC, 32ºC and 37ºC. Error bars indicate SD from triplicate samples.

The levels of crude α-amylase activity observed in rice callus cultures in this study, ranging from approximately 0.85 U/mL at 27°C to 1.02 U/mL at 37°C, are significantly lower than those typically reported in microbial expression systems. For example, *Bacillus subtilis*, a widely used industrial host for α-amylase production, can yield activity levels exceeding 1,000 U/mL under optimized conditions[11]. Similarly, recombinant *Escherichia coli* strains have been engineered to express α-amylase with activities well above 500 U/mL [13]. However, while microbial platforms offer high volumetric productivity, they often require extensive purification steps to remove endotoxins, host cell proteins, and fermentation by-products, especially for pharmaceutical applications where high purity and safety are critical.

In contrast, plant-based systems such as rice callus suspensions offer several distinct advantages despite their lower enzyme titers. The culture medium from rice callus is relatively simple and contains fewer contaminating proteins, allowing easier downstream purification of secreted enzymes. Previous studies have emphasized the feasibility of using plant cell cultures for producing recombinant proteins with pharmaceutical relevance due to their low risk of human pathogens and scalable production under controlled conditions [14]. Thus, its potential for high purity and safety makes it a promising platform for specialized applications such as diagnostic kits, controlled-release formulations, or as an enzyme supplement in therapeutic contexts.

4. CONCLUSION

This study investigated the production of α-amylase from wild-type rice callus suspension cultures and examined the effects of cultivation temperature on both biomass accumulation and enzyme activity. The findings revealed that while optimal callus growth was achieved at 27°C, the highest α-amylase activity was observed at 37°C. This suggests a trade-off between biomass productivity and enzyme induction, where higher temperatures accelerate sugar depletion and trigger α-amylase expression via stress-responsive pathways. Future research should focus on the purification and biochemical characterization of rice callus-derived α-amylase to assess its suitability for industrial or therapeutic use. Additionally, molecular strategies such as elicitor treatment or genetic engineering may be explored to further enhance α-amylase yield. Investigating the regulatory mechanisms of *Amy3* expression under different stress conditions could also provide insights into optimizing production. Ultimately, this platform holds promise for producing high-purity plant-derived enzymes in a controlled and scalable manner.

ACKNOWLEDGMENTS

We would like to thank Prof. Dr. Supachitra Chadchawan from the Department of Botany, Faculty of Science, Chulalongkorn University, for providing rice seeds used in generating the rice callus. We also gratefully acknowledge the Bioprocess Research and Innovation Center (BRIC) at the National Biopharmaceutical Facility, KMUTT, for providing laboratory facilities for conducting this research. This study was funded by the AHASI Glass Foundation and KMUTT. The tuition fee of Ms. Worapicha Daungtongcome.

REFERENCES

1. Hellwig S., Drossard J., Twyman R. M., & Fischer R. Plant cell cultures for the production of recombinant proteins. *Nature Biotechnology* 2004; 22(11): 1415–1422.
2. Xu J., Ge X., & Dolan M. C. Towards high-yield production of pharmaceutical proteins with plant cell suspension cultures. *Biotechnology Advances* 2011; 29(3): 278–299.
3. Huang T. L., Nguyen H. T., & Fujita M. Roles of OsABA8ox genes in ABA catabolism in rice under normal and stress conditions. *Plant Cell Reports* 2014; 33(3): 385–395.
4. Madhav K., Verma S., & Tanta R. Isolation of amylase producing Bacillus species from soil samples of different regions in Dehradun and evaluation of the effect of pH and temperature on their amylase activity. *Pharmaceutical and Biomedical Sciences* 2011; 12(3).
5. Surachai R., & Anon P. Isolation of thermostable amylase-producing bacteria from soil. *Science and Technology* 2017; 14: 1-8.
6. Mavituna F., & Park J. M. Size distribution of plant cell aggregates in batch culture. *Chemical Engineering* 1987; 35(1): B9–B14.
7. Steponkus P. L., & Lanphear F. O. Refinement of the triphenyl tetrazolium chloride method of determining cold injury. *Plant Physiology* 1967; 42(10): 1423–1426.
8. Wahid A., Gelani S., Ashraf M., & Foolad M. Heat tolerance in plants: An overview. *Environmental and Experimental Botany* 2007; 61(3): 199–223.
9. Shii-ichi A., & Masashi T. Uptake and utilization of sugars in cultured rice cells. *Plant and Cell Physiology* 1988.
10. Macharoen K., McDonald K. A., & Nandi S. Simplified bioreactor processes for recombinant butyrylcholinesterase production in transgenic rice cell suspension cultures. *Biochemical Engineering Journal* 2020; 163: 107751.
11. Chanthai S., Keharom S., Mahachai R., & Chanthai *. The optimization study of α-amylase activity based on central composite design-response surface methodology by dinitrosalicylic acid method. *International Food Research Journal* 2016; 23(1).
12. Damaris R. N., Lin Z., Yang P., & He D. The rice alpha-amylase, conserved the regulator of seed maturation and germination. *International Journal of Molecular Sciences* 2019; 20(2): 450.
13. Souza P. M. de, & Magalhães P. de O. e. Application of microbial α-amylase in industry - A review. *Brazilian Journal of Microbiology* 2010; 41(4): 850–861.
14. Thirumalaivasan N., Gnanasekaran L., Kumar S., Durvasulu R., Sundaram T., Rajendran S., Nangan S., & Kanagaraj K. Utilization of fungal and bacterial bioremediation techniques for the treatment of toxic waste and biowaste. *Frontiers in Materials* 2024; 11.

Lysine production from sugarcane molasses using *Corynebacterium glutamicum*

Phatthariya Phromngulueam[1], Wuttichai Krainok[1], Apinya Janphang[1], Lek Wantha[1,*], Waewdao Dathong[2], Apichat Boontawan[3]

[1] School of Chemical Engineering, Institute of Engineering, Suranaree University of Technology, Nakhon Ratchasima, 30000, Thailand
[2] Biology Program, Faculty of Science and Technology, Nakhon Ratchasima Rajabhat University, Nakhon Ratchasima 30000, Thailand
[3] School of Biotechnology, Institute of Agricultural Technology, Suranaree University of Technology, Nakhon Ratchasima, 30000, Thailand
[*] Corresponding author: lekwa@sut.ac.th

ABSTRACT

One of the essential amino acids for humans and animals is L-lysine. It is helpful to the tissue repairs and the immune system. However, L-lysine can only be obtained through consumption. In general, fermentation is used to produce L-lysine by utilizing glucose as a carbon source. The waste or by-product from agriculture or industry can be used as a carbon source, such as sugarcane molasses, because it contains glucose and sucrose. *Corynebacterium glutamicum* TISTR 461 was selected to produce L-lysine. Firstly, the *C. glutamicum* was cultured on nutrient agar for 2 days. Then, the bacteria were cultured into an seed culture medium, and main medium in an Erlenmeyer flask, respectively. The culture conditions were maintained in a shaker at 200 rpm, a pH of 7.2, a temperature of 30 ˚C for 72 hr. The study investigated the effects of initial sugar concentration, incubated pH, and %inoculum (v/v) in Erlenmeyer flasks with a working volume of 100 ml. For the effect of fermentation time, a parameter was examined in a 5 L fermenter with an agitation speed of 100 rpm, and airflow rate of 1 vvm (volume of air sparged per unit volume of medium per minute). From the results, the optimum initial sugar concentration of 100 g/L, incubated pH of 7.2, and %inoculum of 10 produced the highest L-lysine concentration of 30.6 g/L. In a 5 L Fermenter, the highest L-lysine concentration of 32.6 g/l was achieved at 48 hr.

Keywords: L-lysine; Sugarcane Molasses; *Corynebacterium glutamicum*

1. INTRODUCTION

Molasses is a by-product of sugar production [1]. The price of molasses is inexpensive. It also remains high carbon sources such as glucose and sucrose. This property led to a high potential for raw material, which was used as a carbon source for fermentation such as food, biofuel, organic acid, and amino acid production [2]. This led to an enhancement in the value of molasses and a reduction of waste in the sugar industry.

Amino acids are essential to humans and animals. It helps with tissue repair, hormone system, immune system, and neural system [3]. L-lysine is one of the essential amino acids which cannot be synthesized by the human body. It is only received by consumption. So, it is a component in nutritional supplements, feed additive, and pharmaceutics [4]. Normally, L-lysine is produced by fermentation. Because this method can produce the L-isomer of lysine, which the body can use.

Corynebacterium glutamicum is a widely used bacterium of L-lysine production because of its rapid growth, non-sporulating nature, non-pathogenicity, and ability to utilize inexpensive carbon sources [5]. Thus, this is according to reducing operation costs of L-lysine production, especially raw materials [6].

There are many ways to improve L-lysine production. This research aims to optimize the conditions for fermentation such as initial glucose concentration, incubated pH, and seed inoculum in Erlenmeyer flasks. The fermentation time was examined in a 5 L instead of flasks.

2. EXPERIMENTAL

Sugarcane molasse was obtained from Khonburi Sugar Public Company Limited (KBS), Nakhon Ratchasima, Thailand. The sugarcane molasse consists of glucose (205g/l) and sucrose (263g/l). *Corynebacterium glutamicum* TISTR 461 was purchased from the Thailand Institute of Scientific and Technological Research (TISTR), Bangkok, Thailand.

C.glutamicum TISTR 461 was cultured on nutrient agar at a temperature of 30 ˚C for 48 hr. *C.glutamicum* was collected for two loops full and transferred into 40 mL of seed culture medium. The seed culture was maintained at a temperature of 30 ˚C, pH 7.2, and

agitation speed of 200 rpm for 24 hr. Then, 5 mL of seed culture medium was transferred to 45 mL of the main medium for preparation of 10% v/v inoculum. After that, the main medium was incubated at a temperature of 30 ˚ C, pH 7.2, and agitation speed of 200 rpm for 72 hr using a shaking water bath. During fermentation, the pH of the medium was controlled by adding 5 M of NaOH every 4 hr. The initial glucose concentration, incubated pH, and seed inoculum were investigated in Erlenmeyer flasks. Additionally, fermentation time was examined in a 5 L fermenter with an agitation speed of 50 rpm and airflow rate of 1 vvm.

Nutrient agar was prepared with the following (g/L): beef extract, 3; peptone, 5; agar, 15. This medium was a solid nutrient. Seed culture medium was prepared with the following (g/L): glucose, 20; yeast extract, 5; NaCl, 2.5; thiamine-HCl, $3x10^{-4}$; biotin $4x10^{-4}$. Main medium was included with the following (g/L): glucose, 100; yeast extract, 20; $(NH_4)_2SO_4$, 75; K_2HPO_4, 1; KH_2PO_4, 1; $MgSO_4.7H_2O$, 0.4; $MnSO_4.4H_2O$, 0.01; $FeSO_4.7H_2O$, 0.01; thiamine-HCl, $3x10^{-4}$; biotin, $4x10^{-4}$ [7].

After fermentation, the broth was centrifuged at 8,000 rpm for 10 min. A clear solution was collected for the determination of glucose and L-lysine. The remaining precipitate was determined dry cell weight (DCW) of bacteria.

Sugar concentration (glucose and sucrose) was determined by the HPLC. The Bio-Rad Aminex HPX-87H column was used with RI detectors. The column was controlled at a temperature of 65 ˚C. The mobile phase was 5 mM sulfuric acid with a flow rate of 0.6 mL/min [8]. The injection was prepared by mixing a clear solution and 5 mM sulfuric acid at a ratio of 1:9 (v/v). Cautionary, the mobile phase and injection were filtered by 0.22 µm of membrane filter before through the column.

L-lysine concentration was determined by the Ninhydrin-ferric reagent method [9]. The 20 µL of a clear solution, 660 µL of reagent A (consisting of 373 mL of methylcellosolve, 30 mL of 50 %(w/w) $FeCl_3$ and 600 mL of 0.1 M KCl which was adjusted pH to 1 by 1 N of HCl) and 370 µL of reagent B (consisting of 1 g of ninhydrin, 100 mL of 0.1 M KCl which was adjusted pH to 1 by 1 N of HCl) were mixed in a test tube. The mixture was boiled in boiling water for 20 min and cooled with tap water. Then, 4 mL of Dimethyl sulfoxide (DMSO) and 6 mL of deionized water were added to the mixture. Finally, the mixture was shaken and measured at a wavelength of 470 nm using a UV-visible spectrometer.

The amount of *C. glutamicum* TISTR 461 was determined by DCW [10]. The remaining precipitate was washed twice with distilled water. Then, the precipitate was collected and dried at a temperature of 105 ˚C until the weight of DCW was constant.

3. RESULTS AND DISCUSSION

Figure 1 shows the effect of the initial sugar concentration on L-lysine production at 80 to 120 g/l under incubated pH of 7.2 and %inoculum of 10 for fermentation time of 72 hr. The trend of L-lysine concentration increased while the initial glucose concentration increased. However, the L-lysine slightly decreased after 100 g/l of initial sugar concentration. DCW declined slightly when the initial sugar concentration increased. It was evident that the higher initial sugar concentration could inhibit the growth of bacteria. The product as L-lysine would decrease [11] [1 2]. It leads to a maximum L-lysine concentration of 30.6 g/L. Thus, the optimum initial sugar concentration was 100 g/L.

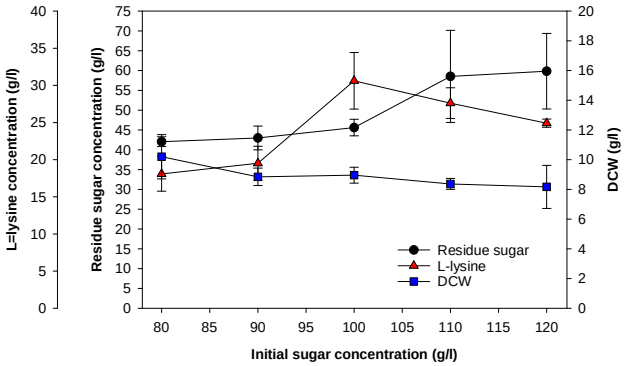

Figure 1 The effect of the initial sugar concentration on L-lysine production under incubated pH of 7.2 and %inoculum of 10 for fermentation time of 72 hr.

Figure 2 shows the effect of the incubated pH on L-lysine production at different incubated pHs of 6.5-8.0 under initial total sugar concentrations of 100 g/L and %inoculum of 10 for fermentation time of 72 hr. When incubated pH increased, DCW also increased but decreased after incubated pH of 7.2. The highest L-Lysine concentration appeared at an incubated pH of 7.2 with 30.6 g/l. These results indicated that pH was a crucial parameter to bacteria because it affected bacteria growth [11]. Moreover, *C. glutamicum* may produce another amino acid when incubated pH was increasing such as L-glutamic [13]. This was observed that total sugar concentration was reduced.

Figure 3 shows the effect of %inoculum on L-lysine production at different %inoculum 6-12% under incubated pH of 7.2, initial sugar concentration of 100 g/l for fermentation time of 72 hr. When the inoculum size was increased, the residual sugar concentration further decreased, but the L-lysine concentration increased to 30.6 g/l and declined after the incubated pH of 7.2. For DCW, this slightly decreased to 9.0 g/l at an incubated pH of 7.2 and then increased. These results indicate that %inoculum had a significant effect on sugar consumption, and lysine production.

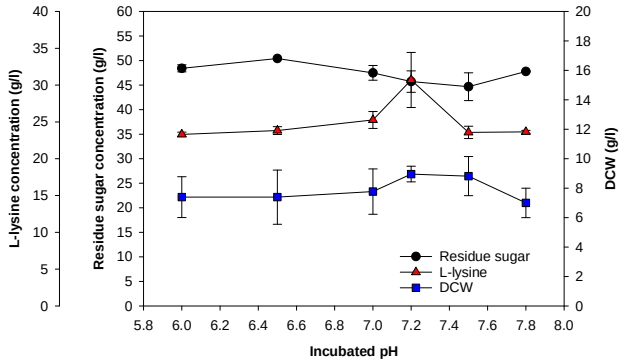

Figure 2 The effect of the incubated pH on L-lysine production under initial sugar concentrations of 100 g/L and %inoculum of 10 for fermentation time of 72 hr.

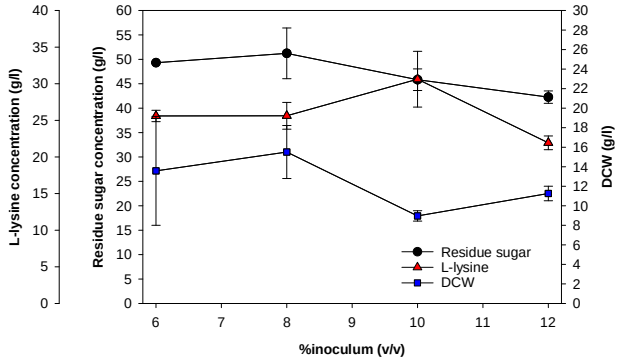

Figure 3 The effect of %inoculum on L-lysine production under incubated pH of 7.2, initial sugar concentration of 100 g/l for fermentation time of 72 hr.

Figure 4 shows the effect of fermentation time on L-lysine production at incubated pH of 7.2, initial sugar concentration of 100 g/l, and %inoculum of 10 in 5 L of fermenter. The L-lysine concentration increased immediately during 0 to 6 hr of fermentation time. Then, L-lysine increased slightly to the maximum concentration of 32.6 g/l at fermentation time of 48 hr. After 48 hr, the L-lysine remained stable. The DCW also increased when fermentation time increased. However, the residue sugar concentration, it further decreased when fermentation time increased. Thus, fermentation time at 48 hr was optimum for L-lysine fermentation.

4. CONCLUSION

This study demonstrates L-Lysine production from sugarcane molasses using *C.glutamicum*. The optimized condition enhances the amount of L-lysine. The optimized conditions included an initial glucose concentration of 100 g/l, incubated pH of 7.2, %inoculum of 10%, and fermentation time of 48 hr, which contributed to the higher L-lysine concentration of 32.6 g/l. Furthermore, there are many ways to improve L-lysine production such as methods of fermentation, downstream process, and genetic modification. It should be examined in the future.

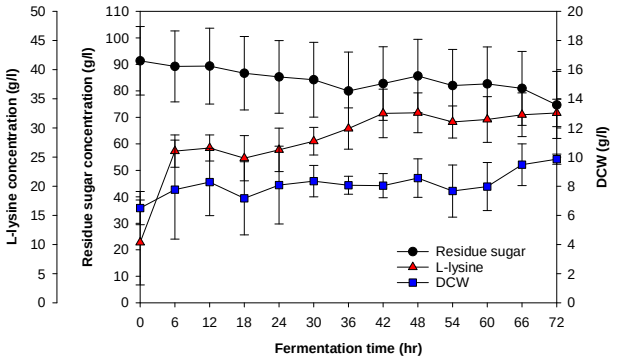

Figure 4 The effect of fermentation time on L-lysine production at incubated pH of 7.2, initial sugar concentration of 100 g/l, and %inoculum of 10 in 5 L fermenter.

ACKNOWLEDGMENTS

This work was supported by (i) Suranaree University of Technology (SUT), (ii) Thailand Science Research and Innovation (TSRI), and (iii) National Science, Research and Innovation Fund (NSRF) - Grant no. 195675.

REFERENCES

1. T. L. T. Nguyen and S. H. Gheewala, Life cycle assessment of fuel ethanol from cane molasses in Thailand. *The International Journal of Life Cycle Assessment*, 2008; 13(4): 301-311.
2. X. He, et al., Enhanced L-lysine production from pretreated beet molasses by engineered Escherichia coli in fed-batch fermentation. *Bioprocess Biosyst Eng*, 2015; 38(8): 1615-22.
3. H. Suzuki, et al., Intake of Seven Essential Amino Acids Improves Cognitive Function and Psychological and Social Function in Middle-Aged and Older Adults: A Double-Blind, Randomized, Placebo-Controlled Trial. *Front Nutr*, 2020; 7: 586166.
4. J. Z. Xu, et al., Metabolic engineering of carbohydrate metabolism systems in Corynebacterium glutamicum for improving the efficiency of L-lysine production from mixed sugar. *Microb Cell Fact*, 2020; 19(1): 39.
5. S. Anastassiadis, L-lysine fermentation. *Recent Pat Biotechnol*, 2007; 1(1): 11-24.
6. J. Xu, et al., Improvement of cell growth and L-lysine production by genetically modified Corynebacterium glutamicum during growth on molasses. *J Ind Microbiol Biotechnol*, 2013; 40(12): 1423-32.
7. M. Jatuponpipat and S. Kiatkittisorn, The Effect of Molasses for Lysine Production by Arthrobacterium citreus NRRL 1258 and Corynebacterium glutamicum ATCC 21475. *CURRENT APPLIED SCIENCE AND TECHNOLOGY*, 2006; 6(2b): 724-728.

8. D. B. Johnston and A. J. Mcaloon, Protease increases fermentation rate and ethanol yield in dry-grind ethanol production. *Bioresour Technol*, 2014; 154: 18-25.
9. C. L. Hsieh, K. P. Hsiung, and J. C. Su, Determination of lysine with ninhydrin-ferric reagent. *Analytical biochemistry*, 1995; 224(1): 187-189.
10. J. Xia, et al., Economical production of poly(epsilon-l-lysine) and poly(l-diaminopropionic acid) using cane molasses and hydrolysate of streptomyces cells by Streptomyces albulus PD-1. *Bioresour Technol*, 2014; 164: 241-7.
11. M. A. Razak and B. Viswanath, Comparative studies for the biotechnological production of L-Lysine by immobilized cells of wild-type Corynebacterium glutamicum ATCC 13032 and mutant MH 20-22 B. *3 Biotech*, 2015; 5(5): 765-774.
12. A. Haleem Sha, et al., Optimization of Culture Conditions for L-Lysine Fermentation by Corynebacterium glutamicum. *Journal of Biological Sciences*, 2002; 2(3): 151-156.
13. J. Xiao, et al., Increasing L-lysine production in Corynebacterium glutamicum by engineering amino acid transporters. *Amino Acids*, 2020; 52(10): 1363-1374.

Enhanced extraction of bioactive compounds from *Aloe vera* leaf skin using natural deep eutectic solvents

Sopita Chanmee[1], Artiwan Shotipruk[1,*]

[1] Bio-Circular-Green-economy Technology & Engineering Center, BCGeTEC, Department of Chemical Engineering, Faculty of Engineering, Chulalongkorn University, Phayathai Road, Patumwan, Bangkok 10330, Thailand

[*] Corresponding author: artiwan.sh@chula.ac.th

ABSTRACT

This study aimed to investigate the extraction efficiency of bioactive compounds, specifically phenolic compounds and anthraquinones, from *Aloe vera* leaf skin (AVLS), a significant by-product of the Aloe vera processing industry. Four environmentally friendly natural deep eutectic solvents (NADESs) were evaluated: choline chloride:lactic acid (ChCl:La), choline chloride:glycerol (ChCl:Gly), choline chloride:propylene glycol (ChCl:Pro), and choline chloride:xylose (ChCl:Xy). These were compared with conventional solvents (water and ethanol) using a magnetic stirring extraction method at room temperature for 30 minutes and a sample to solvent ratio of 1 g: 20 mL. Results demonstrated that ChCl:Xy extracted significantly higher phenolic content (0.43 mg GAE/g AVLS) compared to other solvents. Conversely, ChCl:La yielded the highest anthraquinone extraction among NADES solvents (1.23 mg Alizarin/g AVLS). Antioxidant activity showed strong correlation with anthraquinone content in the AVLS extracts. These findings indicate that specific NADESs offer superior extraction efficiency for phenolic compounds, anthraquinones, and antioxidants compared to conventional solvents. The study suggests the potentials of NADESs for extracting valuable compounds from agricultural waste, offering possible applications in cosmetics, food products, and active food packaging materials.

Keywords: *Aloe vera* leaf skin; Natural deep eutectic solvents (NADESs); Phenolic compound; Antioxidant; Anthraquinone

1. INTRODUCTION

The aloe vera plant, scientifically known as Aloe barbadensis Miller (*Aloe vera*) is a perennial plant in the Liliaceae family and widely recognized medicinal herb that has been used in traditional medicine for centuries due to its various health benefits. The aloe vera leaf consists of three layers: the inner gel, the latex, and the outer green rind. The inner gel is a colorless substance found in the inner part of fresh leaves, and it primarily comprises water (>99%) and the remaining 1% is not aqueous remainder largely consists of minerals, vitamins, polysaccharides, sugars, amino acids, lipid and sterols [1,2].

Aloe vera gel has been traditionally used both topically (for treating wounds, minor burns, and skin irritations) and internally (for conditions like constipation, coughs, ulcers, and diabetes) [3]. Due to its therapeutic properties, *Aloe vera* gel is the most extensively studied and utilized part of the plant in several industries, including pharmaceuticals, food, and cosmetics which have been continuously growing in recent years [4]

In *Aloe vera* processing plants, the inner gel is typically separated from the outer skin, which accounts for over 30% of the total leaf weight, generating large amounts of waste. In most cases, this agricultural waste is not commercially utilized and is commonly discarded, composted, or directly incinerated. Previous studies have reported that the aloe vera rind is a source of bioactive compounds, particularly phenolic compounds. These are key contributors to the antioxidant and antibacterial properties of plant extracts, capable of protecting critical cellular components from oxidative damage by efficiently scavenging free radicals. [4-5].

However, since aloe vera has a complex phytochemical property, consisting of many biocomponents, other components besides phenolic compounds may also have antioxidant and antimicrobial properties. One such interesting compound is aloin, an anthraquinone-c-glycoside found mainly in the latex of aloe vera leaves. According to the MAE, aloe peel contains aloin as high as 10.1 mg/g, which is higher than the phenolic content. Although some studies have reported that aloin may cause side effects when ingested, which limits the research compared to phenolic compounds, the biological potential of aloin remains significant [6-9].

The selective of solvent for extracting these compounds is crucial due to the differing physicochemical properties of each compound, especially their solubility in various solvents, which is dependent on molecular polarity [5]. Polar solvents such as ethanol, methanol, and ethyl acetate are commonly used for polyphenol extraction. However, these organic solvents present limitations in terms of safety, environmental impact, and cost. To address these challenges, natural deep eutectic solvents (NADES) have been developed and studied as sustainable alternatives for bioactive compound extraction [9-10].

NADES represent a novel class of solvents for extracting bioactive compounds from plant-based materials. They are formed from eutectic mixtures comprising two or more natural components: a hydrogen bond acceptor (HBA) and a hydrogen bond donor (HBD). Common HBAs include choline chloride (ChCl) and betaine, while HBDs include sugars, sugar alcohols, amino acids, organic acids, and amines. These mixtures form liquids with unique physicochemical properties through hydrogen bonding interactions, resulting in a eutectic mixture with a melting point lower than that of the individual components. Compared to conventional organic solvents, NADES offer several advantages, including non-toxicity, environmental friendliness, biodegradability, and tunable properties (e.g., polarity). However, one drawback of NADES is their high viscosity, which may hinder extraction efficiency. This limitation can be mitigated by adding water or increasing the extraction temperature. Due to these characteristics, NADES are considered attractive solvents for extracting bioactive compounds [12-15].

However, the use of NADESs solvents for the extraction of polyphenols from Aloe vera leaf skin has been investigated in only one previous study. In that work, Georgia D. et al. [11] examined the selection of NADES formulations that yielded the highest polyphenol extraction efficiency. The results demonstrated that NADES exhibited superior extraction performance compared to conventional solvents. Nevertheless, to date, there has been no study addressing the simultaneous extraction of both polyphenols and anthraquinones from Aloe vera leaf skin using NADES.

Therefore, the objective of this study is to compare the extraction efficiency of polyphenols and anthraquinones from aloe vera leaf skin using various NADES formulations. Choline chloride (ChCl) will be used as the hydrogen bond acceptor (HBA), and four different hydrogen bond donors (HBDs)—lactic acid, glycerol, propylene glycol, and xylose—representing distinct HBD categories, will be evaluated. The performance of these NADES will be compared with conventional solvents (water and aqueous ethanol) to maximize the yield of polyphenols and anthraquinones. Furthermore, the antioxidant activity of the resulting extracts will be assessed.

2. EXPERIMENTAL

2.1 Chemical and reagents

Chloride, cholride, and D-xylose were purchased from Loba Chemie (Mumbai, India). Lactic acid and glycerol were obtained from Ajex-Finechem (Australia). Sodium carbonate and ethanol were supplied by Quer (New Zealand), and propylene glycol was purchased from KemAus (Australia). Folin–Ciocalteu reagent (2N), 2,2-diphenyl-1-picrylhydrazyl (DPPH), sodium acetate, hydrochloric acid, 2,4,6-tripyridyl-s-triazine (TPTZ), ferric chloride hexahydrate, gallic acid, 6-hydroxy-2,5,7,8-tetramethylchroman-2-carboxylic acid (Trolox), and alizarin were obtained from Sigma-Aldrich (Madrid, Spain).

2.2 Plant Material

Aloe vera leaf skin (AVLS) obtained from the farmer in Prachuap Khiri Khan Province, Thailand, and washed with distilled water to remove any residual gel and contaminants. The skin was cut into small pieces and dried in an oven at 65°C for 4 hours. Then pulverized in a blender and seive. The sample were stored in a sealed plastic bag before use.

2.3 Preparation of natural deep eutectic solvents (NADESs)

NADESs were prepared by using Choline chloride as the initial hydrogen bond accepter (HBA) and using four solvents as hydrogen bond donor (HBD) as shown in Table1 with the constant molar ratio. The HBA was mixed with different HBDs using a temperature of 80°C and stirred continuously until a homogeneous and clear liquid was formed. DI water 20 %(v/v) was added to NADES to reduce the viscosity of the solvent. Afterwards, the NADESs were maintained at room temperature in a silica containing desiccator to avoid water absorption [11].

Table 1 Composition and abbreviation of the prepared DESs.

Abbreviation	HBA	HBD	Molar ratio
ChCl:La	Choline chloride	Lactic acid	1:2
ChCl:Gly		Glycerol	1:2
ChCl:Pro		Propylene glycol	1:2
ChCl:Xy		Xylose	1:1

2.4 Preparation of *Aloe vera* leaf skin extracts (AVLSE)

In a beaker glass, 1 g of AVLS powder was dissolved in four different NADESs and 20 mL of conventional solvent (water and ethanol 80%) using magnetic stirring at room temperature for 30 min, then filtered through a vacuum filter to remove any residual

AVLS powder from the extract and stored at 4°C until further analysis.

2.5 Determination of total phenolics content (TPC)

The TPC of AVLSE was determined using the Folin–Ciocalteu spectrophotometric method, as described by García-Roldán et al. [16], with slight modifications. Briefly, 80 µL of each sample extract was diluted and mixed with 3.12 mL of distilled water. Then, a volume of 200 µL of Folin–Ciocalteu reagent 10% (v/v) was added, and a vortex mixer was used for one minute. After 5 min, the mixture was mixed with 600 µL of sodium carbonate solution (20% w/v) and vigorously shaken. A microwell plate spectrophotometer (Thermo Fisher Scientific, Roskilde, Denmark) was used to measure the absorbance of the extracts at a wavelength of 765 nm after 1 h of reaction in the dark and at room temperature. As a standard solution, gallic acid was used, and the quantification of total phenolic content was expressed as the mg of gallic acid equivalents (GAE) per g of AVLS. Quantification was based on calibration curves of gallic acid standard where the equation was $y = 0.0011x + 0.0594$ ($R^2 = 0.9974$). Measurements were carried out in triplicate, and the outcomes were presented as the mean value along with its associated standard deviation.

2.6 Determination of total anthraquinones

The total anthraquinone of AVLSE was determined by a spectrophotometer using alizarin as standard. Briefly, 1 mL of each sample extract was diluted and mixed with 4 mL of distilled water. A microwell plate spectrophotometer (Thermo Fisher Scientific, Roskilde, Denmark) was used to measure the absorbance of the extracts at a wavelength of 435 nm. As a standard solution, alizarin was used, and the quantification of total anthraquinone content was expressed as the mg of Alizarin per g of AVLS. Quantification was based on calibration curves of alizarin standard where the equation was $y = 0.0026x + 0.0105$ ($R^2 = 0.9969$). Measurements were carried out in triplicate, and the outcomes were presented as the mean value along with its associated standard deviation.

2.7 Determination of Radical Scavenging Activity by DPPH

The DPPH radical scavenging activity method was used for antioxidant activity determination as described by Georgia D et al. [11] with slight modifications. Briefly, a 0.1 mM ethanolic solution of DPPH was freshly prepared.. A 3.8 mL DPPH (2,2-diphenyl-1-picrylhydrazyl) solution was mixed with 0.2 mL of sample or Trolox standard in a microwell plate. After incubating for 30 min at room temperature in darkness, absorbance was measured at 517 nm. Measurements were carried out in triplicate and quantification was based on Trolox standard calibration curves where the equation was $y = -0.0027x + 0.8436$ ($R^2 = 0.9931$). Results were reported as Trolox equivalent antioxidant capacity (TE) in mg of Trolox equivalents per g of AVLS.

2.8 Determination of ferric reducing antioxidant power assay (FRAP)

The antioxidant activities of AVLS were evaluated through a reduction in ferric ion (Fe3+) to ferrous ion (Fe2+), according to the FRAP assay method, as outlined by Georgia D. et al. [11]. Firstly, the working solution was prepared by adding 300 mM acetate buffer (pH 3.6), 10 mM TPTZ in 40 mM HCl, and 20 mM FeCl3. 6H2O solutions at a ratio of 10:1:1 were incubated at 37 ◦C for 30 min. Then, a 100 µL aliquot of the sample extract underwent a reaction with 2800 µL FRAP working solution in the dark at room temperature for a duration of 30 min. The absorbance of the blue-colored solution was measured at a wavelength of 593 nm by Microplate reader. Results were expressed as mg TE per g of AVLS using a Trolox as the standard compound. Measurements were carried out in triplicate

2.9 Statistical analysis

Statistical data treatment was performed using SPSS software: namely, IBM SPSS Statistics for Windows, Version 22.0 (Armonk, NY: IBM Corp., released 2013). A one-way analysis of variance (ANOVA) at a 95% confidence level and a Tukey's Honest Significant Difference (HSD) test was subsequently performed to facilitate pairwise comparisons between samples, ensuring rigorous assessment of statistical differences (20). Statistical significant differences were claimed for all analysis at p-value < 0.05.

3. RESULTS AND DISCUSSION

3.1 Comparation of Phenolic Content in Aloe Vera leaf skin Extract

Four types of NADESs, with choline chloride as the primary component, were employed to assess and compare the TPC of AVLSE obtained using NADESs and conventional solvents, as illustrated in Figure 1.

From Figure 1, the experimental results show that among the four NADES tested, ChCl:Xy exhibited the highest TPC (0.434 mg GAE/g powder), followed by ChCl:Gly with a TPC of 0.377 mg GAE/g powder. ChCl:Pro demonstrated a lower extraction efficiency (0.148 mg GAE/g powder), while ChCl:La showed the lowest TPC yield among the NADES tested (0.167 mg GAE/g powder). These findings are consistent with those of a previous study by Georgia D.et al. [11], in which Aloe vera leaf skin was extracted using 11 different NADES formulations and compared with three conventional solvents under ultrasound-assisted extraction (UAE). In that study, ChCl:Citric acid exhibited the highest TPC yield (52.75 mg GAE/g of dried rind), outperforming both water and 80% ethanol,

followed by ChCl:Fructose (45 mg GAE/g of dried rind) and ChCl:Glucose (42 mg GAE/g of dried rind). These results suggest that sugar-based possess high efficiency in extracting phenolic compounds. However, when comparing the TPC values, the previous study reported significantly higher yields than those observed in the present work. This discrepancy may be attributed to differences in solvent ratios and extraction conditions, which may require further optimization.

Similarly, Airouyuwa et al. [17] reported comparable findings, suggesting that the hydroxyl groups in sugar molecules enhance hydrogen bonding and polar interactions with target compounds more effectively than lactic acid, resulting in higher TPC yields. Furthermore, when comparing NADES solvents with conventional solvents, as shown in Figure 1 , ChCl:La and ChCl:Pro produced TPC yields similar to that of water and substantially lower than that of ethanol. In contrast, ChCl:Xy and ChCl:Gly achieved higher TPC yields than both water and ethanol.

These findings indicate that NADES solvents are more effective than conventional solvents in extracting phenolic compounds. This efficiency largely depends on the composition of the hydrogen bond donor (HBD) and hydrogen bond acceptor (HBA), which significantly influence the physicochemical properties of the NADESs particularly their polarity. These characteristics directly affect the ability of NADES to extract polyphenolic compounds from the plant matrix [10].

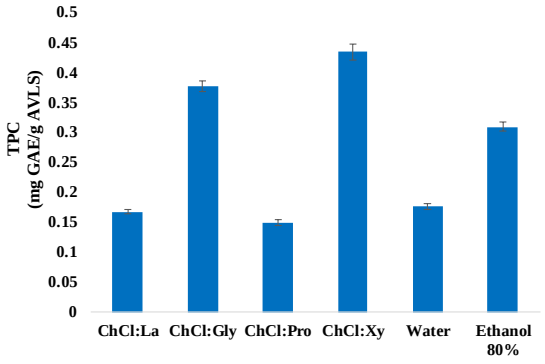

Figure 1 The TPC of AVLS using different green solvents. Error bars indicate SD (n=3)

3.2 Comparation of total Anthraquinones in Aloe Vera leaf skin extract

In addition to the quantification of phenolic compounds, anthraquinones—another significant class of bioactive compounds found in AVLS were further examined. The extracted anthraquinone content was analyzed using alizarin as the standard, with the results presented in Figure 2.

Figure 2 illustrates the extracted anthraquinone content using NADESs based on choline chloride (ChCl) combined with various hydrogen bond donors (HBD), including lactic acid, glycerol, propylene glycol, and xylose. The measured concentrations were 1.234, 0.271, 0.594, and 0.249 mgAlizarin/gAVLS, respectively. Experimental findings indicate that ChCl-LA exhibited a significantly enhanced ability to extract anthraquinone glycosides. Conversely, NADES composed of choline chloride with xylose (ChCl-Xy) and propylene glycol demonstrated extraction efficiency comparable to that of water, when compared to the results obtained using 80% ethanol (1.665 mgAlizarin/gAVLS) and other NADES formulations [21].

Previous studies by Wu et al. [10] reported that ChCl:La effectively extracted anthraquinones from Rheum palmatum L., a compound class sharing structural similarity with those in aloe vera, at higher concentrations than other NADES types. This research has examined extraction processes, demonstrating that both ChCl:LA and ethanol 80% exhibit high efficiency in extracting moderately polar compounds. These findings further affirm that ChCl:La is more suitable for extracting bioactive compounds with moderate polarity [18]. It is reasonable to hypothesize that intermolecular hydrogen bonding, arising from interactions between hydrogen (H) and oxygen (O) atoms in hydroxyl (-OH) or carboxyl (-COOH) functional groups, facilitates the extraction of glycosides with polar characteristics.

Therefore, selecting an appropriate NADESs for bioactive compound extraction depends on multiple factors, such as the structural composition of the plant matrix, diffusion rate of target compounds in the solvent, surface tension, extraction time, and NADESs viscosity [22]. The most significant drawback of using NADES in extraction processes is its viscosity. Even in cases where NADES is formulated with organic acids-based exhibiting a relatively fluid nature at ambient temperature its viscosity remains considerably higher than that of commonly used organic solvents.

However, as this study represents the first quantification of total anthraquinone content, further investigations are required to determine the optimal NADESs composition and solvent system for effective extraction.

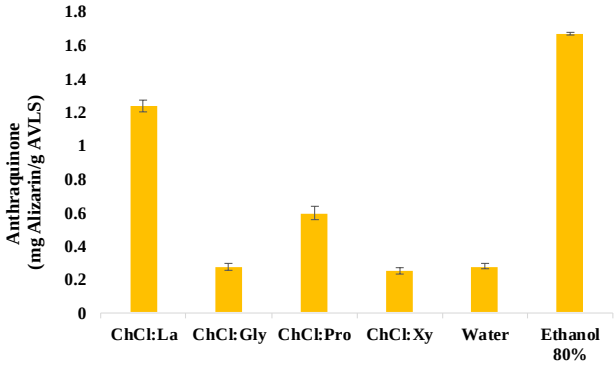

Figure 2 The anthraquinone of AVLS using different NADESs, water and ethanol 89%. Error bars indicate SD (n=3)

3.3 In vitro free radical scavenging power of AVLSE

Polyphenolic compounds and anthraquinones are well known for their potent antioxidant properties and ability to function as effective free radical scavengers. This study focuses on evaluating the antioxidant activity of AVLSE using NADESs as extraction media. The assessment was conducted through in vitro antioxidant assays, specifically DPPH radical scavenging assay and Ferric reducing antioxidant power (FRAP) assay, with results presented in Figure 3.

According to the DPPH assay analysis (Figure 3), ChCl:La (0.221 mgTE/gAVLS) and 80% ethanol (0.201 mgTE/gAVLS) exhibited the highest radical scavenging activity compared to other solvents. Similarly, the FRAP assay demonstrated the extract's ability to reduce ferric ions ($Fe^{3+} \rightarrow Fe^{2+}$) [23], which serves as a key indicator of antioxidant potential. The findings revealed that 80% ethanol (0.9 mgTE/gAVLS) and ChCl:La (0.738 mgTE/gAVLS) had significantly higher antioxidant activity than the other tested solvents.

The observed trend in antioxidant activity aligns with the total anthraquinone content in each solvent (Figure 2), indicating that anthraquinones play a more dominant role in contributing to antioxidant capacity compared to phenolic compounds. Furthermore, ChCl:La, classified as a NADES, demonstrated the highest antioxidant potential, emphasizing the importance of selecting an appropriate NADES for extraction processes in future research.

Thus, subsequent studies should focus on identifying the most suitable NADESs for targeted extraction of bioactive compounds from plants, aiming to enhance the economic value of plant extracts and expand their applications in industries such as food, pharmaceuticals, and cosmetics.

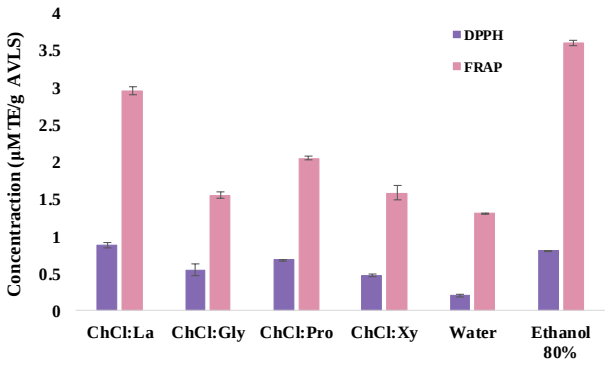

Figure 3 Antioxidant activity (DPPH radical scavenging activity and FRAP) (mM TE g dry powder) of AVLS with NADES, water and 80% ethanol. Different letters on the bars showed significant differences among different samples ($p < 0.05$).

4. CONCLUSION

This study evaluated the extraction efficiency of bioactive compound from aloe vera leaf skin (AVLS) using environmentally friendly natural eutectic solvents (NADESs). The results indicated that the extraction of phenolic compounds using NADESs composed of choline chloride and xylose (ChCl:Xy) have the highest phenolic content (0.434 mg GAE/1 g AVLS) compared to conventional solvents (water and 80% ethanol). For anthraquinone extraction, NADESs consisting of choline chloride and lactic acid (ChCl:La) exhibited the most effective performance, obtaining a maximum yield of 1.234 mg Alizarin/g AVLS, which was comparable to 80% ethanol. Furthermore, analysis of antioxidant activity revealed a strong correlation between anthraquinone content and free radical scavenging potential. Specifically, ChCl:La and 80% ethanol demonstrated the highest antioxidant activities, as assessed by DPPH and FRAP assays. These results highlight the efficacy of NADESs as a sustainable alternative for the extraction of bioactive compounds from AVLS, providing promising applications in cosmetic formulations, functional foods, and bioactive packaging films. Future research should focus on optimizing NADESs compositions and extraction parameters to maximize compound yield and enhance industrial applicability.

ACKNOWLEDGMENTS

This work was financially supported by Department of Chemical Engineering, Faculty of Engineering, Chulalongkorn University

REFERENCES

1. I. Sehgal, WD. Winters, M. Scott, K. Kousoulas . An in vitro and in vivo toxicologic evaluation of a stabilized aloe vera gel supplement drink in mice. Food Chem Toxicol. 2013;55:363–370.
2. S. Sui Chin, F. Han Lyn, Z.A. Nur Hanani. Effect of Aloe vera (Aloe barbadensis Miller) gel on the physical and functional properties of fish gelatin films as active packaging. Food Packaging and Shelf Life 2017; 12:128–134.
3. S. Kumar, S. Kalita, A. Das, P. Kumar, S.B. Singh, V. Katiyar, A. Mukherjee. Aloe vera: A contemporary overview on scope and prospects in food preservation and packaging. Progress in Organic Coatings 2022; 166:106799.
4. S. P. Ramalho, A.F. Silva, M.S. Oliveira. Valorization of Aloe vera skin by-products to obtain bioactive compounds by microwave-assisted extraction: Antioxidant activity and chemical composition. Journal of Agricultural and Food Chemistry 2020; 68(10): 3221-3230.

5. M.M. Hossen, M.L. Hossain, K. Mitra, B. Hossain, U.H. Bithi, M.N. Uddin. Phytochemicals and in-vitro antioxidant activity analysis of Aloe vera by-products (skin) in different solvent extract. J Agric Food Res 2022;10:100460.
6. L. Lucini, M. Pellizzoni, R. Pellegrino, G. Molinari, G. Pietro, G. Colla. Phytochemical constituents and in vitro radical scavenging activity of different Aloe species. Food Chemistry 2015;170: 501–507
7. Q.Q Koh, Y.L. Kua, S. Gan, K.W. Tan, T.Z.E. Lee, H.L.N. Lau, W.K. Cheng. Sugar-based natural deep eutectic solvent (NADES): Physicochemical properties, antimicrobial activity, toxicity, biodegradability and potential use as green extraction media for phytonutrients. Sustainable Chemistry and Pharmacy 2023;35:101218.
8. M.D. Boudreau, F.A. Beland. An evaluation of the biological and toxicological properties of Aloe barbadensis (Miller), Aloe vera. J Environ Sci Health C Environ Carcinog Ecotoxicol Rev 2006;24(1):103–54.
9. S. Kumar, S. Kalita, A. Das, P. Kumar, S.B. Singh, V. Katiyar, A. Mukherjee. Aloe vera: A contemporary overview on scope and prospects in food preservation and packaging. Prog Org Coat 2022;166:106799.
10. Y.C. Wu , P. Wu, Y.B. Li, T.C. Liu, L. Zhang, Y.H. Zhou. Natural deep eutectic solvents as new green solvents to extract anthraquinones from Rheum palmatum L. RSC Adv 2018;8(27):15069–15077.
11. G.D. Ioannou, K.A. Ioannou, A. Christou, I.J. Stavrou, C.P. Kapnissi-Christodoulou. The utilization of an Aloe vera rind by-product: Deep eutectic solvents as eco-friendly and recyclable extraction media of polyphenolic compounds. Antioxidants (Basel) 2024 Jan 26;13(2):162.
12. A. Maimulyanti, I. Nurhidayati, B. Mellisani, F.A. Rachmawati Putri, F. Puspita, A.R. Prihadi. Development of natural deep eutectic solvent (NADES) based on choline chloride as a green solvent to extract phenolic compound from coffee husk waste. Arab J Chem 2023;16(4):104634.
13. E. Simón, M.C. Díaz-Maroto, M.E. Alañón, S. de Pascual-Teresa, M.S. Pérez-Coello. Efficiency of natural deep eutectic solvents to extract phenolic compounds from Agrimonia eupatoria: Experimental study and in silico modelling. Food Chemistry 2023; 405:134973.
14. A.P. Abbott, G. Capper, D.L. Davies, R.K. Rasheed, V. Tambyrajah. Deep eutectic solvents formed between choline chloride and carboxylic acids: Versatile alternatives to ionic liquids. J Am Chem Soc 2003;125(45):11462–3.
15. Chaari M, Elhadef K, Akermi S, Ben Akacha B, Fourati M, Chakchouk Mtibaa A, Ennouri M, Sarkar T, Shariati MA, Rebezov M, Mellouli L, Smaoui S. Novel active food packaging films based on gelatin-sodium alginate containing beetroot peel extract. Antioxidants (Basel) 2022;11(11):2095.
16. A. García-Roldán, L. Piriou, P. Jauregi. Natural deep eutectic solvents as a green extraction of polyphenols from spent coffee ground with enhanced bioactivities. Front Plant Sci 2023;13:1072592.
17. J.O. Airouyuwa, H. Mostafa, A. Riaz, C. Stathopoulos, S. Maqsood. Natural deep eutectic solvents and microwave-assisted green extraction for efficient recovery of bioactive compounds from by-products of date fruit (Phoenix dactylifera L.) processing: Modeling, optimization, and phenolic characterization. Food and Bioprocess Technology 2023;16:823-843.
18. F.M. Fuad, M.M. Nadzir, A.H. Kamaruddin. Hydrophilic natural deep eutectic solvent: A review on physicochemical properties and extractability of bioactive compounds. J Mol Liq 2021t;339:116923.

Comparative characterization of microplastics from conventional wastewater treatment plants between inland and island of tourism area in Thailand

Charintorn Molee[1], Suda Ittisupornrat[1,*], Suthida Theeparaksapan[2]

[1] Climate Change and Environmental Research Center, Pathum Thani, 12120, Thailand
[2] Department of Civil and Environmental Engineering, Faculty of Engineering, Srinakharinwirot University, Nakhon Nayok 26120, Thailand
[*] Corresponding author: suwimolteam@yahoo.com

ABSTRACT

Wastewater treatment plants (WWTPs) are recognized as direct pathways for microplastic (MP) contamination in the environment. Thus, monitoring MP presence in wastewater and evaluating treatment efficiency are essential. This study compares MP characteristics and removal performance between two conventional WWTPs located in inland and island tourism areas of Thailand: one utilizing the activated sludge (AS) process and the other employing an aerated tank system. The occurrence, composition, and removal efficiency of MPs were analyzed using optical microscopy and Fourier Transform Infrared (FTIR) microscopy. The results indicated that polypropylene (PP) and polyethylene (PE) were the predominant MP types in both systems, comprising more than 60% of total MPs, suggesting strong associations with packaging-related plastic waste. Both treatment systems demonstrated high MP removal efficiencies, exceeding 95%, with final effluent MP concentrations ranging from 22 to 75 particles per cubic meter. These findings provide insight into the effectiveness of conventional WWTPs in different geographic contexts and emphasize the need for targeted strategies in tourism-driven regions.

Keywords: Microplastics; Wastewater treatment plant; Activated sludge process; Aerated tank; Tourism area

1. INTRODUCTION

Microplastics (MPs), typically defined as plastic particles smaller than 5 mm, have emerged as pervasive contaminants in aquatic ecosystems and are increasingly recognized for their potential impacts on ecosystems and human health impacts [1, 2]. These particles originate from various sources, including the degradation of larger plastic debris, personal care products, synthetic textiles, and industrial activities. Among the major pathways for MPs to enter the environment, wastewater treatment plants (WWTPs) have been identified as significant, yet often underappreciated, contributors [3].

Although WWTPs play a crucial role in reducing pollutant load from domestic and industrial wastewater, conventional treatment processes such as activated sludge and aerated tanks are not specifically designed to target MPs. Consequently, a substantial proportion of MPs can bypass these systems and be released into receiving water bodies [4]. The removal efficiency of MPs largely depends on the design and operation of the treatment technology, operational parameters, and characteristics of the wastewater.

This issue is particularly relevant in regions with high tourism activities, such as island communities, where the influx of tourists leads to increased generation of plastic waste and pressure on existing wastewater infrastructure [5]. Inadequate waste management and limited treatment capacity in these areas often lead to elevated MP levels in coastal waters, posing risks to marine biodiversity and local livelihoods.

The present study aims to compare the occurrence, types, and quantities of MPs in two conventional WWTPs located in inland and island tourism areas of Thailand specifically, one employing an AS process and the other using an aerated tank. Optical microscopy and Fourier Transform Infrared (FTIR) spectroscopy were used to characterize MPs in influent and effluent samples. The findings contribute to a growing body of research on MP pollution and provide insights into the performance of conventional WWTPs under different environmental and operational conditions [6, 7].

2. EXPERIMENTAL

2.1 Site description of study area

This study was conducted at two community-based wastewater treatment plants (WWTPs) located in tourism-focused regions of Thailand. The first site, located on Samed Island in Rayong Province, utilizes an aerated tank system and treats wastewater from local residents, tourism businesses, and seasonal visitors,

with a treatment capacity of 1000 m^3/day. The second site, operated by the Chonburi Provincial Administrative Organization (PAO), is situated in an inland urban area and employs a conventional Activated Sludge (AS) process with a treatment capacity of 22500 m^3/day. These two sites were selected to represent contrasting geographical settings and to facilitate a comparative assessment of microplastic (MP) removal performance.

2.2 Sampling and collection of water samples

Influent samples (1000 L) were collected after primary screening through a 1 cm screen chamber. Each sample was passed through a cascade of four test stainless steel sieves with a mesh size of 5 mm, 1 mm, 300 µm and 100 µm using water pump. Particles retained on the 5 mm sieve were discarded whereas particles retained on the 1 mm, 300 µm and 100 µm sieves were individually rinsed with distilled water and transferred into separate glass bottle. All equipment was thoroughly rinsed to ensure complete particle recovery. All samples were transferred to the laboratory and stored 4°C in the dark until further analysis.

2.3 Examination and identification of microplastics

Sample preparation followed the method described by Masura et al., 2015 [8], with following minor modifications by Ittisupornrat et al., 2025 [9]. Briefly, the sieved samples were placed in 60 °C drying oven for overnight until almost dry. Then the pretreated samples were digested by wet peroxide oxidation (WPO) to eliminate organic matter. Specifically, 20 mL of 0.05 m Fe (II) solution and 20 mL of 30% hydrogen peroxide (H_2O_2) were added to the dried. The mixture was left to settle down for 5 min at room temperature, and then was agitated on a hotplate with magnetic stirrer at 60 °C by covering with a watch glass. Depending on the organic matter content in sample, perhaps another 20 mL of H_2O_2 were supplemented for complete the oxidative reaction. Density separation was subsequently conducted using saturated sodium chloride (NaCl) solution. settling overnight, the supernatant was filtered through Anodisc filters (0.2 µm pore size). Filtered residues were stored in glass Petri dishes for subsequent analysis. Microplastic identification was performed using an optical microscope and a Fourier Transform Infrared (FTIR) microscope (SP3 DTGS, Perkin Elmer, Germany) in transmittance mode. Each sample was scanned 128 times across the 1200–4000 cm^{-1} spectral range, with a resolution of 4 cm^{-1}. Spectra were compared against reference libraries provided by the manufacturer.

2.4 Quality assurance and quality control (QA/QC)

To prevent sample contamination, cotton clothing and gloves were worn during the experiments, and only non-plastic equipment was used. All glassware and stainless-steel equipment were washed with detergent and rinsed thoroughly with ultrapure water [10]. Blank controls were prepared by filtering ultrapure water through the same sieving and filtration protocols to verify procedural integrity [9].

2.5 Physical and chemical water quality analysis

The pH and dissolved oxygen were measured using appropriate probes (YSI 60, USA). Chemical oxygen demand (COD) was analyzed using Hach methods (HACH, USA). Total nitrogen (TN) was analyzed using a Total Organic Carbon Analyzer (TOC), TOC-L, Shimadzu, Japan. Turbidity was measured using a TN-100 Waterproof Turbidimeter (Thermo Scientific™, USA). A total suspended solids (TSS) was analyzed by standard method [11].

3. RESULTS AND DISCUSSION

3.1 Water quality characterization

In addition to MP analysis, water quality parameters were also monitored at both WWTPs. At the Chonburi PAO facility, influent samples exhibited high turbidity (97 NTU), TSS of 142.7 mg/L, and COD of 290 mg/L were observed. These values significantly decreased in the effluent to 8 NTU, 12.7 mg/L, and 143 mg/L, respectively demonstrating effective removal of particulate matter and organic pollutants. Similarly, at the Koh Samed Island plant, influent values of turbidity, TSS, and COD were 66 NTU, 45.3 mg/L, and 328 mg/L, respectively, which decreased to 2 NTU, 3.3 mg/L, and 33 mg/L after treatment. DO levels also improved substantially, increasing from 0.6 mg/L to 4.5 mg/L in Koh Samed system and from 7.4 mg/L to 8.9 mg/L in the Chonburi system. These results confirm the effective performance of both systems in enhancing water quality prior to effluent discharge. A detailed comparison of key water quality parameters between the two WWTPs is presented in Table 1, highlighting reductions in turbidity, TSS, COD, and improvements in DO concentrations across both systems.

3.2 Microplastic composition and distribution

The analysis of microplastics (MPs) using Fourier Transform Infrared (FTIR) spectroscopy revealed that polypropylene (PP) and polyethylene (PE) were the dominant polymer types detected in both influent and effluent samples collected from the two selected conventional wastewater treatment plants studied one located inland at Chonburi Provincial Administrative Organization (PAO), and the other on Koh Samed Island. These two polymers were consistently detected in nearly all samples, confirming their widespread occurrence in municipal wastewater. Both PP and PE are lightweight, chemically resistant polymers, making them less likely to settle during treatment processes and more prone to persist in aquatic systems. Their prevalence can be attributed to their extensive use in plastic packaging, disposable consumer goods, synthetic textiles, and common household items explains their consistent detection in municipal

wastewater streams. This observation aligns with previous studies reporting PP and PE as the most frequently detected MPs in treated wastewater [1, 10]. As shown in Figure 1, FTIR spectra and microscopic images confirm the presence and morphology of PP and PE particles collected from both sites. These results emphasize the recurring challenge posed by these specific polymers in conventional wastewater treatment systems.

Table 1 Comparison of key water quality parameters between Chonburi PAO (Inland) and Koh Samed (Island) WWTPs

Parameter	Chonburi PAO		Koh Samed	
	Influent	Effluent	Influent	Effluent
pH	6.6	6.4	7.4	8.5
Turbidity (NTU)	97	8	66	2
TSS (mg/L)	142.7	12.7	45.3	3.3
COD (mg/L)	290	143	328	33
DO (mg/L)	7.4	8.9	0.6	4.5
TN (mg/L)	4.8	6.3	4.9	1.1

3.3 Influent Characteristics and Polymer Comparison

In the influent of the Chonburi PAO facility, PP and PE accounted for approximately 40% and 31% of the total detected MPs, respectively. In comparison, the Koh Samed Island system exhibited a slightly different distribution, with PP and PE comprising 44% and 25%, respectively. This variation in polymer composition may reflect differing consumption patterns, waste management practices, and seasonal influences associated with tourism. Figure 2 presents a comparative overview of the polymer composition detected in influent samples from both locations. While PP and PE were predominant in both systems, other secondary polymers such as polyvinyl stearate (PVS), polytetrafluoroethylene (PTFE), and ethylene butyl acrylate (EBA)were also identified in smaller proportions. These secondary polymers may originate from specialized commercial or industrial sources, as well as synthetic textiles commonly associated with tourism activities [6, 12].

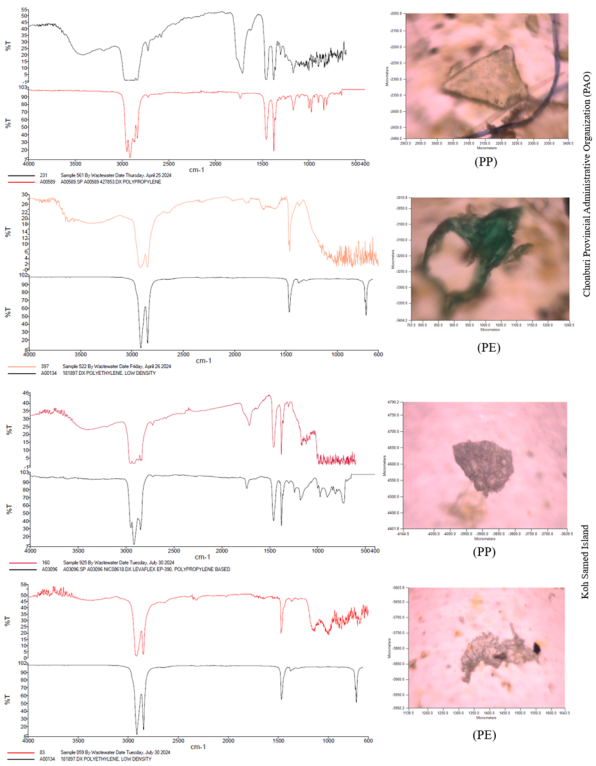

Figure 1 Combined FTIR spectra and microscopic images of polypropylene (PP) and polyethylene (PE) identified in wastewater samples from the treatment systems of Chonburi Provincial Administrative Organization (PAO) and Koh Samed Island.

3.4 Microplastic Removal Efficiency

Both treatment systems demonstrated relatively high MP removal efficiencies, exceeding 95%, indicating that conventional processes are capable of significantly reducing MP concentrations in wastewater [13]. Specifically, the removal efficiency observed at the Chonburi PAO system was 97.8%, while the Koh Samed Island system achieved a slightly higher efficiency of 98.5%. These findings confirm the effectiveness of both systems in reducing MPs prior to discharge into the environment. Such high removal efficiencies are consistent with previous studies reporting over 90% removal in conventional WWTPs, particularly when secondary and tertiary treatment stages are included [3, 4]. The removal of MPs in these systems is typically attributed to mechanisms such as sedimentation and filtration. Nevertheless, certain types of microplastics especially those with low density and high chemical resistance, such as PP and PE were still detected in the treated effluents. Their persistence suggests that although a large fraction of MPs can be removed through conventional processes, complete elimination remains a challenge. This observation is supported by Lares et al. (2018) [14], who noted that small and buoyant MPs are more likely to pass through standard treatment stages.

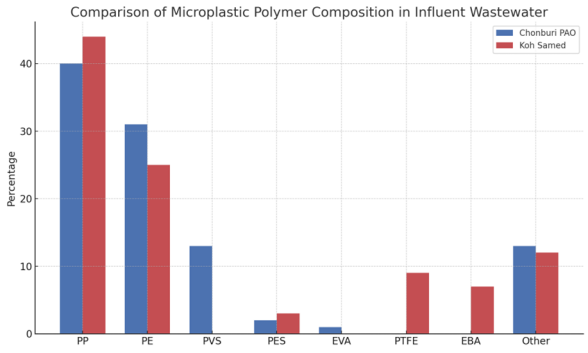

Figure 2 Comparison of microplastic polymer composition in influent wastewater of the two community-based wastewater treatment systems. This chart illustrates the proportion of each polymer type identified in samples from Chonburi PAO and Koh Samed Island WWTPs, highlighting both common and site-specific microplastic distributions.

3.5 Microplastic Discharge to Receiving Waters

A comparison of MP discharge between the two systems revealed distinct differences in input volume and discharge rates, as shown in Table 2. The Chonburi PAO system received approximately 10 million MP/d and discharged about 2.3×10^5 MP/d after treatment. In contrast, the Koh Samed Island system received a lower total input of around 1.5 million MPs but discharged 2.2×10^4 MP/d. However, when normalized by population size, the per capita discharge of MPs on Koh Samed Island was significantly higher estimated at 743 MP/person-d compared to only 7 MP/person-d in the Chonburi PAO system. This stark contrast highlights the influence of tourism-related wastewater generation on microplastic pollution and underlines the importance of developing location-specific management strategies in tourism-intensive areas.

3.6 Implications and Recommendations (Refined)

These findings underscore the necessity for both improved treatment technologies and preventive measures at the source to effectively address microplastic (MP) contamination in wastewater systems. Although both studied WWTPs Chonburi PAO and Koh Samed Island demonstrated high MP removal efficiencies (>95%), trace amounts of MPs, particularly lightweight and chemically resistant polymers such as polypropylene (PP) and polyethylene (PE), were still detected in the treated effluents. The persistence of these polymers highlights a limitation of conventional treatment processes and emphasizes the importance of advanced and complementary technologies. The considerably higher per capita MP discharge observed in the Koh Samed Island system reflects the increased generation of plastic waste associated with seasonal tourism and the pressure it places on existing infrastructure. This finding calls attention to the need for location-specific strategies that account for dynamic population densities and waste characteristics.

Addressing this challenge requires integrated approaches that combine upstream control measures—such as improved waste management and public awareness campaigns—with the adoption of advanced treatment technologies capable of capturing smaller and more buoyant plastic particles. In addition, routine monitoring and the development of regulatory standards for MPs in wastewater would support more informed and targeted interventions. Collaborative efforts among municipalities, environmental agencies, and tourism stakeholders are essential to designing and maintaining resilient infrastructure that can effectively mitigate MP emissions under fluctuating demand conditions.

Overall, the findings support the importance of implementing context-specific solutions to reduce MP pollution and protect water quality in both inland and coastal ecosystems.

Table 2 Summary of microplastic input, discharge, and removal efficiency at both WWTPs

	WWTPs	
	Chonburi PAO	**Koh Samed**
MP Input (MP/d)	10×10^6	1.5×10^6
MP Discharge (MP/d)	2.3×10^5	2.2×10^4
Removal Efficiency (%)	97.8	98.5
Before Treatment (MP/person-d)	7.0	743
After Treatment (MP/person-d)	0.2	10.8

4. CONCLUSION

This study compared the occurrence and removal of microplastics (MPs) in two conventional wastewater treatment systems: an inland activated sludge (AS) system and an island-based aerated tank. Polypropylene (PP) and polyethylene (PE) were identified as the dominant polymer types in both influent and effluent samples. Although both systems achieved high removal efficiencies (>97%), trace amounts of MPs, particularly low-density polymers, remained in the treated effluent. The per capita MP discharge on Koh Samed Island was notably higher, reflecting tourism-driven plastic waste and infrastructure limitations. Additionally, both systems showed substantial improvement in water quality parameters post-treatment.

These findings underscore the need for context-specific wastewater management strategies, particularly in tourism-intensive areas. Integrating upstream plastic reduction measures and advanced treatment technologies are recommended to minimize MP emissions and protect aquatic environments.

ACKNOWLEDGMENTS

The authors thank to the Thailand Science Research and Innovation (Grant no. 180103/2023, 198405/2024) for the financial support. Special thanks are conveyed to municipalities for supporting microplastic sample collection and information of wastewater treatment system.

REFERENCES

[1] Li, J., Liu, H., & Paul Chen, J. (2018). Microplastics in freshwater systems: A review on occurrence, environmental effects, and methods for microplastics detection. Water Research, 137, 362–374.

[2] Wright, S. L., & Kelly, F. J. (2017). Plastic and Human Health: A Micro Issue Environmental Science & Technology, 51(12), 6634–6647.

[3] Carr, S. A., Liu, J., & Tesoro, A. G. (2016). Transport and fate of microplastic particles in wastewater treatment plants. Water Research, 91, 174–182.

[4] Murphy, F., Ewins, C., Carbonnier, F., & Quinn, B. (2016). Wastewater Treatment Works (WwTW) as a source of microplastics in the aquatic environment. Environmental Science & Technology, 50(11), 5800–5808.

[5] Browne, M. A., Crump, P., Niven, S. J., Teuten, E., Tonkin, A., Galloway, T., & Thompson, R. (2011). Accumulation of microplastic on shorelines worldwide: Sources and sinks. Environmental Science & Technology, 45(21), 9175–9179.

[6] Sun, J., Dai, X., Wang, Q., van Loosdrecht, M. C. M., & Ni, B.-J. (2019). Microplastics in wastewater treatment plants: Detection, occurrence and removal. Water Research, 152, 21–37.

[7] Talvitie, J., Mikola, A., Koistinen, A., & Setälä, O. (2017). Solutions to microplastic pollution – Removal of microplastics from wastewater effluent with advanced wastewater treatment technologies. Water Research, 123, 401–407.

[8] Masura, J., Baker, J., Foster, G., & Arthur, C. (2015). Laboratory methods for the analysis of microplastics in the marine environment: Recommendations for quantifying synthetic particles in waters and sediments. In: NOAA Technical Memorandum NOS-OR&R-48, NOAA Marine Debris Program, National Oceanic and Atmospheric Administration, U.S. Department of Commerce, Silver Spring, MD.

[9] [9] Ittisupornrat, S., Namyuang, C., Phetrak, A., Sriromreun, P., & Theepharaksapan, S. (2025). Microplastic contamination and removal efficiency in greywater treatment using a membrane bioreactor. Frontiers in Microbiology, 16, 1519230.

[10] Henry, B., Laitala, K., & Klepp, I. G. (2019). Microfibres from apparel and home textiles: Prospects for including microplastics in environmental sustainability assessment. Science of The Total Environment, 652, 483–494.

[11] APHA. (2017). Standard Methods for the Examination of Water and Wastewater, 23rd Edition (Vol. 53, Issue 9, p. 1699).

[12] Habib, R. Z., Thiemann, T., & Al Kendi, R. (2020). Microplastics and Wastewater Treatment Plants A Review. Journal of Water Resource and Protection, 12(01), 1–35.

[13] Kittipongvises, S., Phetrak, A., Hongprasith, N., & Lohwacharin, J. (2022). Unravelling capability of municipal wastewater treatment plant in Thailand for microplastics: Effects of seasonality on detection, fate and transport. Journal of Environmental Management, 302.

[14] Lares, M., Ncibi, M. C., Sillanpää, M., & Sillanpää, M. (2018). Occurrence, identification and removal of microplastic particles and fibers in conventional activated sludge process and advanced MBR technology. Water Research, 133, 236–246.

Reduction of acid usage in chitosan production process from white shrimp shell using electro-chemical activation

Pat Thongphet[1], Kiattinatapon Juengchareonpoon[1], Piyabutr Wanichpongpan[1,*]

[1] Department of Chemical Engineering, Faculty of Engineering, King Mongkut's University of Technology Thonburi, Bangkok 10140, Thailand
[*] Corresponding author: piyabutr.wan@kmutt.ac.th

ABSTRACT

White shrimp is produced more than 250,000 tons per year in Thailand. This generates a significant amount of waste, primarily from shrimp heads and shells, accounting for 40-50% of the total weight. To enhance the value of this waste, chitosan can be extracted through three main processes: deproteination using an alkaline solution (NaOH), demineralization using an acid solution (HCl) and deacetylation using a strong alkaline solution (NaOH). In this study, white shrimp shell powder was prepared and subjected to various treatments to determine the optimal conditions for chitosan extraction. The effects of concentration, temperature, reaction time, and solid-to-liquid ratio were evaluated using Box-Behnken Design (BBD) in combination with Response Surface Methodology (RSM) to optimize both the demineralization and deproteination processes. Additionally, before the demineralization process, the shrimp shell powder was soaked in demineralized water and stimulated by electro-chemical activation (ECA) to compare the results between ECA treated and untreated samples. Finally, the obtained chitosan was analyzed for purity using UV Spectrophotometer and Atomic Absorption Spectroscopy (AAS). The results showed that ECA pretreatment significantly improved demineralization performance, with all ECA-treated conditions achieving calcium removal efficiencies exceeding 90%, while the untreated group reached a maximum of only 81%.

Keywords: Chitosan; Demineralization; Deproteination; Electro-Chemical Activation; Whtie Shrimp Shell

1. INTRODUCTION

White shrimp (*Litopenaeus vannamei*) is one of the most economically significant aquatic species in Thailand, with an annual production exceeding 250,000 tons [1]. During shrimp processing, large quantities of by-products such as heads and shells are generated, accounting for approximately 40–50% of the total biomass [2]. These shrimp shells are rich in valuable biopolymers, including chitin, which can be converted into chitosan — a versatile and biodegradable material with extensive applications [3].

Chitosan, a deacetylated derivative of chitin, exhibits notable properties such as biocompatibility, non-toxicity, and antimicrobial activity. These attributes make it highly suitable for applications in agriculture, water treatment, biomedical engineering and food packaging [4]. Conventionally, chitosan is extracted from shrimp shells via three main chemical processes: deproteination using sodium hydroxide (NaOH), demineralization using hydrochloric acid (HCl) and deacetylation under concentrated alkaline conditions [5]. However, the demineralization step often requires large volumes of HCl to effectively remove calcium carbonate ($CaCO_3$), raising concerns regarding environmental pollution, safety and production cost [6].

To address this issue, alternative pretreatment methods have been explored to enhance mineral removal efficiency while reducing chemical consumption. One promising approach is electro-chemical activation (ECA), which involves applying a low-voltage electric field to aqueous suspensions. This technique can promote the release of calcium ions (Ca^{2+}) and other minerals from the shrimp shell matrix, thereby potentially lowering the acid demand in subsequent demineralization. ECA has attracted attention for its simplicity, energy efficiency and ability to modify ionic interactions at the solid-liquid interface [7].

This study aims to evaluate the effectiveness of ECA as a pretreatment for shrimp shell powder prior to acid-based demineralization. The impact of ECA on calcium removal efficiency is examined and compared with non-ECA conditions. In addition, Box-Behnken Design (BBD) and Response Surface Methodology (RSM) are employed to identify the optimal conditions for both demineralization and deproteination processes. The objective is to assess whether ECA can enhance

mineral removal and reduce acid usage while maintaining chitosan quality.

2. EXPERIMENTAL

2.1 Collection and Preparation of Shrimp Shells

White shrimp shells were obtained from a local supermarket in Bangkok, Thailand. The collected shells were thoroughly washed with tap water to remove any residual flesh and impurities. After washing, the shells were dried in a hot air oven at 80°C for 24 hours to reduce moisture content. The dried shells were then ground into powder and sieved through a 40–60 mesh stainless steel screen to obtain uniform particle size for subsequent experiments.

2.2 Demineralization of Shrimp Shell Powder

A sample of 5 g of dried shrimp shell powder was immersed in HCl at room temperature. To determine the optimal demineralization conditions, three factors were varied, each at three levels: HCl concentration (1, 2, and 3 M), reaction time (1, 2, and 3 hours), and solid-to-liquid ratio (1:5, 1:10, and 1:15, w/v). After the acid treatment, the samples were washed repeatedly with distilled water until reaching a neutral pH. The solid residues were filtered and dried at 80°C for 12 hours.

2.3 Deproteination of Shrimp Shell Powder

The demineralized shrimp shell powder was subjected to deproteination to remove residual proteins. The sample was treated with NaOH solution by varying three parameters: NaOH concentration (1, 2, and 3 M), temperature (60, 75, and 90°C) and reaction time (1, 2, and 3 hours). A constant solid-to-liquid ratio of 1:10 (w/v) was used in all experiments. After the treatment, the shells were thoroughly washed with distilled water until a neutral pH was achieved. The solid residues were then filtered and dried at 80°C for 12 hours, similar to the previous procedure.

2.4 ECA Pretreatment

ECA was applied as a pretreatment step prior to demineralization to enhance calcium removal efficiency. A sample of 5 g of dried shrimp shell powder was immersed in 100 mL of deionized (DI) water. A direct current (DC) voltage of 4.4 V was applied for 2 hours using copper electrodes as both the anode and cathode, positioned at a distance of 3 cm apart. The immersed electrode surface area was approximately 4 cm^2. Following the ECA treatment, the shrimp shell powder was subjected to the same demineralization and deproteination procedures described previously. The final chitosan products obtained with and without ECA pretreatment were compared in terms of residual calcium content.

2.5 Experimental Design and Statistical Analysis

Table 1 Experimental design matrix of BBD for the demineralization process involving three variables: HCl concentration, reaction time and solid-to-liquid ratio (15 experimental runs).

Run	Time (h)	Conc (M)	Solid to liquid ratio
1	1	1	1 : 10
2	1	2	1 : 5
3	1	2	1 : 15
4	1	3	1 : 10
5	2	1	1 : 5
6	2	1	1 : 15
7	2	2	1 : 10
8	2	2	1 : 10
9	2	2	1 : 10
10	2	3	1 : 5
11	2	3	1 : 15
12	3	1	1 : 10
13	3	2	1 : 5
14	3	2	1 : 15
15	3	3	1 : 10

The optimization of demineralization and deproteination conditions was conducted using a Box-Behnken Design (BBD) combined with Response Surface Methodology (RSM). BBD is an efficient statistical tool for designing experiments, particularly when investigating the interactions between multiple factors and minimizing the number of experimental runs required. RSM was employed to analyze the experimental data obtained from BBD using Minitab software, which facilitated model fitting, statistical testing and graphical visualization. This methodology enables the development of a predictive model that correlates the independent variables with the response variable, which in this case was the residual calcium content after demineralization. The general form of the quadratic model used in RSM can be expressed as [9]:

$$Y = \beta_0 + \Sigma\beta_i X_i + \Sigma\beta_{ii} X_i^2 + \Sigma\beta_{ij} X_i X_j$$

where Y is the predicted response
X_i are the independent variables
β are the regression coefficients for intercept, linear, quadratic and interaction terms, respectively.

A quadratic polynomial model was fitted to the data to evaluate the significance of each variable and their interactions. Analysis of variance (ANOVA) was performed to determine the adequacy of the model. The optimal conditions were then predicted by the model and validated through confirmatory experiments [8]. As an example, the BBD for demineralization involved 15 experimental runs covering all combinations of the three key factors: acid concentration, reaction time, and solid-to-liquid ratio, as shown in Table 1.

2.6 Determination of Calcium Content Using Atomic Absorption Spectroscopy (AAS)

After the demineralization process, the dried shrimp shell powder samples were further subjected to calcium extraction using 6 M HCl at 90°C for 2 h to ensure complete dissolution of residual calcium [5]. 1 ml of the resulting solution was then diluted with DI water to ensure that calcium concentrations fell within the measurable range of the instrument (not exceeding 10 ppm). Calcium content was quantified using AAS at a wavelength of 422.7 nm, which corresponds to the specific absorption line of calcium atoms. A standard calibration curve was constructed using calcium solutions with concentrations of 0, 2, 4, 6, 8, and 10 ppm. A blank solution containing 1% HCl in DI water was used to eliminate background interference. In addition, raw shrimp shell powder (prior to any chemical treatment) was also analyzed using the same acid extraction and AAS procedure to determine the baseline calcium content originally present in the untreated shells.

2.7 Determination of Protein Content Using the Biuret Method

The residual protein content in shrimp shell samples was determined using the Biuret method. After the deproteination step, the treated shrimp shell powder was soaked in phosphate buffer (pH 7.0) for 24 hours at room temperature to ensure complete extraction of residual proteins into the solution [10]. The mixture was then filtered and 1 ml of the filtrate was mixed with 4 ml of Biuret reagent in a test tube. The solution was thoroughly vortexed and allowed to react at room temperature for 30 minutes to allow full color development. Absorbance was measured at 540 nm using a UV-Visible spectrophotometer. A standard calibration curve was constructed using bovine serum albumin (BSA) standards at concentrations ranging from 0 to 10 mg/ml. The protein concentrations in the experimental samples were determined from the calibration curve, and all measurements were performed in triplicate. In addition, raw shrimp shell powder (untreated) was analyzed following the same procedure to determine the baseline protein content naturally present in the shells before any chemical treatment.

3. RESULTS AND DISCUSSION

3.1 Optimization of Demineralization Conditions Using BBD

A standard calibration curve for calcium quantification was established using AAS, yielding a linear equation of $y = 0.0231x + 0.0495$ with an R^2 value of 0.9993, confirming excellent linearity and accuracy over the standard concentration range. This calibration curve served as the basis for determining the residual calcium content under each experimental condition, allowing for the calculation of demineralization efficiency. Preliminary analysis of untreated shrimp shell powder indicated a high initial $CaCO_3$ content of 39.4% by weight.

To optimize the demineralization of shrimp shell powder, the BBD combined with RSM was applied to investigate the effects of reaction time (1–3 h), HCl concentration (1–3 M) and solid-to-liquid ratio (5–15) on the demineralization efficiency of shrimp shell powder. The fitted second-order polynomial model achieved an R^2 of 0.864 and an adjusted R^2 of 0.557, suggesting a moderately good fit. ANOVA results indicated that the quadratic term of reaction time (t^2) was statistically significant ($p = 0.041$), playing the most influential role in the model. The resulting predictive model expressed as a second-order polynomial equation in uncoded variables, is as follows:

$$\%\text{Demin} = 82.07 - 11.18t + 0.70C - 0.41r + 3.07t^2 + 0.50C^2 + 0.03r^2 + 0.20tC - 0.03tr - 0.04rc$$

Where t, C and r represent time, concentration and solid-to-liquid ratio, respectively

The linear term of reaction time (t) also showed a relatively strong effect ($p = 0.057$), suggesting a clear trend even though it did not reach conventional significance. Other factors such as HCl concentration and solid-to-liquid ratio exhibited a positive influence on demineralization efficiency; increasing these variables generally led to higher calcium removal. However, their effects were less statistically significant compared to the quadratic term of time. This indicates that while all variables contributed to improved performance, the curvature effect of reaction time was the most critical factor within the tested range.

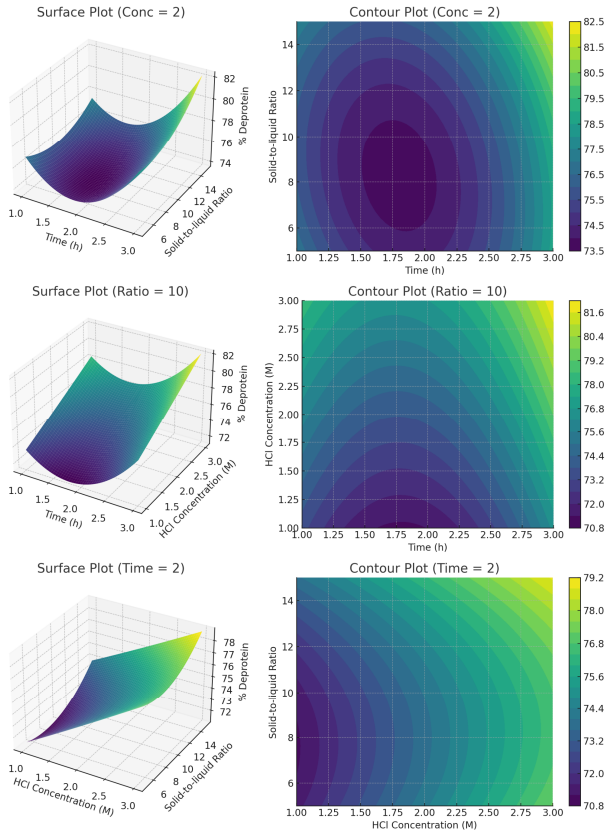

Figure 1 Surface and contour plots showing the effects of HCl concentration, reaction time, and solid-to-liquid ratio on demineralization efficiency.

Each plot is generated by fixing one factor at its center level while varying the other two. The surface and contour plots further illustrate the influential role of reaction time in the demineralization process. From all three pairs of surface and contour plots, it is evident that reaction time consistently influences the efficiency trend, regardless of which variable is fixed—whether HCl concentration, solid-to-liquid ratio, or time itself. This reinforces the conclusion drawn from the statistical analysis that time is the most dominant factor in the model, as shown in Figure 1. As time increased, the calcium removal efficiency initially improved and later plateaued, reflecting the quadratic effect observed in the statistical analysis. Although HCl concentration and solid-to-liquid ratio did not reach statistical significance, both exhibited positive trends, with higher values generally enhancing demineralization performance. This supports the notion that all three factors contributed to the overall efficiency, with time having the most pronounced effect. The highest demineralization efficiency (81.32%) was achieved under the condition of 3 h, 3 M HCl and a 1:10 ratio, while the lowest (70.59%) occurred at 2 h, 1 M HCl and a 1:5 ratio. These findings confirm that optimizing reaction time along with selecting appropriate acid concentration and ratio levels is key to maximizing calcium removal.

3.2 Optimization of Deproteination Conditions Using BBD

Prior to sample analysis, a standard calibration curve was constructed using the Biuret method for protein determination. The resulting linear equation was $y = 0.0512x - 0.0081$ with an R^2 value of 0.9986, confirming excellent linearity across the tested concentration range. This calibration curve was used to determine the residual protein content in each experimental condition. Additionally, analysis of untreated shrimp shell powder revealed that it contained approximately 33% protein by weight.

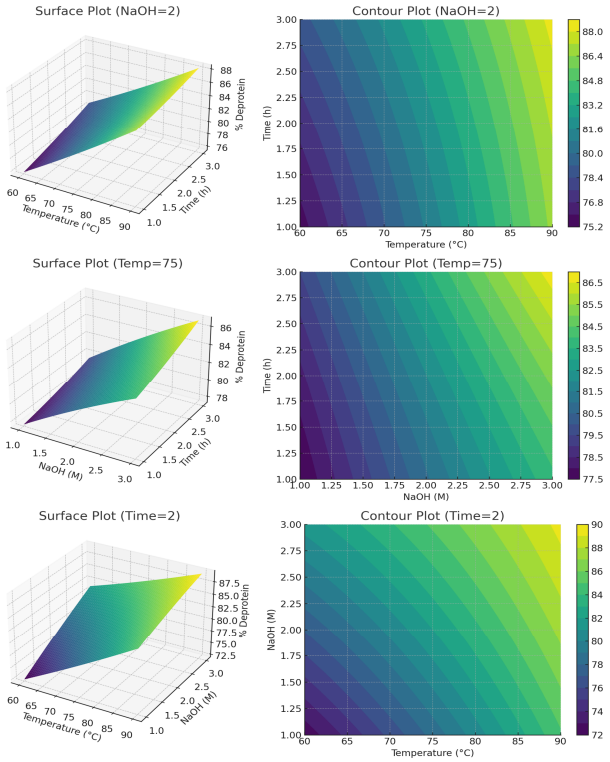

Figure 2 Surface and contour plots showing the effects of NaOH concentration, temperature, and reaction time on deproteination efficiency.

Each plot was generated by fixing one variable at its center level while varying the other two. The BBD combined with RSM was applied to investigate the effects of temperature (60–90°C), NaOH concentration (1–3 M) and reaction time (1–3 h) on the deproteination efficiency of shrimp shell powder. The fitted second-order polynomial model exhibited excellent predictive capability, achieving an R^2 value of 0.988 and an adjusted R^2 of 0.967, indicating a strong fit with the experimental data. The resulting regression model, expressed as a second-order polynomial equation in uncoded variables, is as follows:

$$\%\text{Deprotein} = -41.10 + 0.53T + 23.5C + 0.10t + 0.0005T^2 + 1.54C^2 + 0.47t^2 - 0.321TC + 0.021Tt - 1.22Ct$$

Where T, C and t represent Temperature, Concentration and time respectively

ANOVA results revealed that the interaction between temperature and NaOH concentration (T x C) was statistically significant ($p = 0.0459$), suggesting that their combined effect plays a critical role in enhancing protein removal. While other linear and quadratic terms were not statistically significant, they still exhibited positive trends higher temperatures, stronger alkali concentrations and longer reaction times all generally contributed to increased deproteination efficiency. This aligns with the surface and contour plots, which demonstrate that the response improved across a wide range of conditions. As shown in Figure 2, the highest deproteination efficiency (88.82%) was achieved at 90°C, 2 M NaOH, and 3 h, while the lowest (72.81%) occurred at 60°C, 1 M NaOH, and 2 h. These findings highlight the synergistic role of temperature and alkaline strength and confirm that carefully optimizing these variables can significantly improve protein removal while maintaining practical processing conditions.

3.3 Effect of ECA on Demineralization Efficiency

The application of ECA prior to the acid demineralization step significantly enhanced calcium removal efficiency in all experimental runs. As shown in Figure 3, the demineralization percentage for samples pretreated with ECA consistently exceeded 90%, with several conditions achieving values above 95% and even reaching 99.2%. In contrast, the control group without ECA exhibited lower removal efficiencies, ranging from 70.6% to 81.3%. These results clearly demonstrate the positive effect of ECA on the subsequent acid-based calcium extraction process.

The substantial increase in efficiency across all 15 matched conditions indicates that ECA plays a catalytic role in destabilizing the mineral matrix of the shrimp shell, thereby making calcium ions more readily available for acid solubilization. This observation aligns with the findings of Nowacki et al. (2020) [11], who demonstrated that electrochemically induced environments could enhance the disintegration of biocomposite structures in marine organisms, facilitating the release of chitin and associated minerals. In particular, their work on black coral skeletons showed that in situ electrolysis significantly accelerated the extraction process by altering the physicochemical properties of the matrix and enabling more effective dissolution of calcium compounds.

In our study, the greatest improvement from ECA pretreatment was observed under low-acid conditions, indicating that ECA facilitates efficient calcium removal even with milder acid use. Remarkably, samples treated with ECA achieved more than 90% demineralization using only 1 M HCl for 1 hour at moderate solid-to-liquid ratios. In contrast, the highest efficiency obtained without ECA—despite using 3 M HCl for 3 hours was only 81.3%. These findings underscore the practical advantages of incorporating ECA into chitin extraction workflows, enabling reduced chemical usage while maintaining high efficiency, and supporting more sustainable and cost-effective industrial processing.

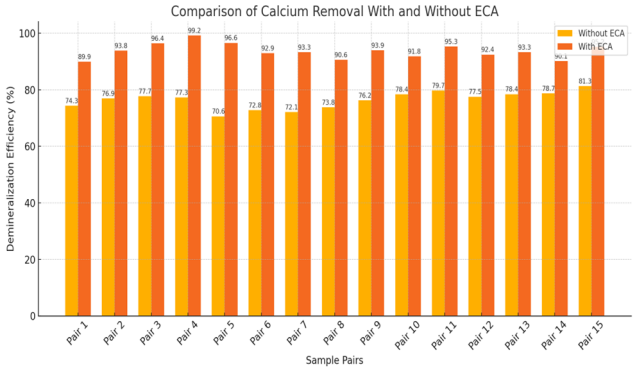

Figure 3 Comparison of demineralization efficiency between shrimp shell samples treated with ECA and untreated controls.

4. CONCLUSION

This study optimized the demineralization and deproteination processes in shrimp shell chitosan production using response surface methodology. The results showed that reaction time significantly influenced calcium removal, while NaOH concentration and its interaction with temperature affected protein extraction. The ECA effectively enhanced demineralization efficiency beyond 90% in all cases, outperforming the non-ECA group and allowing reduced acid usage. The developed models provided strong predictive power and practical insights for improving chitosan extraction in a more sustainable way.

ACKNOWLEDGMENTS

The authors would like to express their gratitude to the Department of Chemical Engineering, Faculty of Engineering, King Mongkut's University of Technology Thonburi, for providing the laboratory facilities, equipment, and chemicals required for this research.

REFERENCES

1. P. Langkapon. Marine shrimp production and trade situation in Thailand during 2018–2022. *Department of Fisheries, Ministry of Agriculture and Cooperatives, Thailand*; 2023. (In Thai)
2. Ridhani M.A., Vidyaningrum I.P., Akmala N.N., Fatihatunisa R., Azzahro S., Aini N. Fortification of shrimp shell flour as a source of calcium on the preference level of bread. *Asian Journal of Fisheries and Aquatic Research*. 2023; 8(3): 61–68.

3. Van Den Broek L.A.M., Boeriu C.G., eds. *Chitin and Chitosan: Properties and Applications*. Chichester, UK: John Wiley & Sons Ltd; 2020.
4. Rinaudo M. Chitin and chitosan: Properties and applications. *Prog. Polym. Sci.* 2006; 31(7): 603–632.
5. Percot A., Viton C., Domard A. Optimization of chitin extraction from shrimp shells. *Biomacromolecules.* 2003; 4(1): 12–18.
6. Ameh A.O., Isa M.T., Abutu D., Danlami A. Kinetic modeling of the demineralization of shrimp exoskeleton using citric acid. *Leonardo Electron. J. Pract. Technol.* 2014; 25: 274–282.
7. W. Piyabutr, J. Kiattinatapon, B. Virote, Electro-Chemical Activation on Shrimp-Shell Chitin Production Process, *Department of Chemical Engineering, Faculty of Engineering, King Mongkut's University of Technology Thonburi*.
8. Cao W., Zhang C., Hong P., Ji H. Response surface methodology for autolysis parameters optimization of shrimp head and amino acids released during autolysis. *Food Chem.* 2008; 109(1): 176–183.
9. W. Cao, C. Zhang, P. Hong, and H. Ji, Response surface methodology for autolysis parameters optimization of shrimp head and amino acids released during autolysis, *Food Chem.*, 2008, 109(1), 176–183.
10. Noor us Saher and S. H. Noor, Evaluation of protein (nutritional property) in some shrimp species found in coastal waters of Pakistan by three different methods, *Pakistan J. Zool., Suppl. Ser.*, 2018, No. 13, 205–211.
11. Nowacki, K., Stępińak, I., Langer, E., Tsurkan, M., Wysokowski, M., Petrenko, I., ... & Ehrlich, H. (2020). Electrochemical Approach for Isolation of Chitin from the Skeleton of the Black Coral Cirrhipathes sp. (Antipatharia). *Marine Drugs*, 18(6), 297.

Pressure vessel for ethanol extraction of Mitragynine from Kratom leaves

Ampai Chanachai[1,*], Ponpailin Lippanon[1], Pansachol Paranundha[1], Pimpisa Techamaunwaiwit[1]

[1] Department of Chemical Engineering, Faculty of Engineering, King Mongkut's University of Technology Thonburi, Bangkok 10140, Thailand
[*] Corresponding author: ampai.cha@kmutt.ac.th

ABSTRACT

Kratom leaves are currently popular among workers because they help increase energy, relieve fatigue, and endure long hours of outdoor work. These properties are due to the mitragynine compound in kratom leaves. The purpose of this research is to design and construct a pressure vessel for mitragynine extraction and determine the most suitable conditions to achieve the highest percentage of extraction efficiency. Ethanol is used as a solvent for safe consumption and to create future medical benefits. A pressure vessel that can withstand a maximum pressure of 11.5 bar at a temperature of 70 °C was designed and built, with a total volume of 1,191 ml. Then, the extraction was tested with an ethanol solvent by using Soxhlet method at 78 °C for 1 hour and using a pressure vessel at 1-2 bar pressure, 50, 60 and 70 °C for 20-60 minutes. It was found that using a pressure vessel gave the highest percentage of mitragynine extraction at 0.147% at 70 °C and 2 bars for 60 minutes with an extraction efficiency when compared to Soxhlet extraction of 105.4%. It can be concluded that increasing temperature, pressure and time resulted in more mitragynine extraction.

Keywords: Kratom leaf; Mitragynine; Pressure vessel; Solvent extraction

1. INTRODUCTION

In ancient Thai medical texts, kratom leaves were used to treat intestinal infections, relieve muscle pain, reduce fever, relieve coughs and diarrhea. Fresh or dried leaves were chewed, smoked or brewed into a tea. Today, workers also use kratom leaves to reduce fatigue, help them endure outdoor work and work longer. It is also used to reduce withdrawal symptoms from other drugs such as opium and morphine because they have fewer side effects when used for a limited period of time. The active ingredient that has a sedative effect in kratom leaves is mitragynine. Because of these properties, researchers are interested in studying the extraction of compounds in kratom leaves to isolate mitragynine, which is safe for consumption and can create medical benefits in the future.

Beng et al. [1] studied the extraction of mitragynine from kratom leaves by Soxhlet extraction technique using petroleum ether as solvent at 60 °C and 8 hours of testing time. It was able to extract 0.88% w/w mitragynine. From the research of Kikura-Hanajiri et al. [2] used ultrasonic method using methanol as solvent which is alcohol and has polarity similar to ethanol. The testing time was 1 hour at room temperature and obtained 0.023% mitragynine.

From the research by Muandao [3], which extracted Mitragynine from kratom leaves using 50% w/w acetic acid solvent for 30 min at 80 °C, the yield was 2.691%, which is high. However, at a high concentration of 50%, acetic acid has a very low pH value which is unsafe for consumers. Sharma et al. [4] extracted mitragynine using ethanol solvent with a 3-day fermentation at room temperature, the mitragynine yield was 0.700%, which is very time-consuming.

Therefore, this research selected ethanol as a safer solvent for the extraction of mitragynine. The approach to increase the extraction efficiency is to use higher temperature. However, ethanol has a low boiling point of about 78.37 °C at 1 atm. Therefore, a pressure vessel that can withstand high pressure is designed and constructed to enable the extraction at high pressure [5] to ensure that the solvent remains in a liquid state if the temperature is increased to increase the extraction efficiency.

2. EXPERIMENTAL

2.1 Preparation of kratom leaves before extraction

Select mature kratom leaves of similar color and free from disease, using the whole leaf including the midrib. Weigh the selected leaves approximately 1.5 kg. Wash the weighed kratom leaves 1-2 times, then wash with DI water for the last time. Then chop to a size of approximately 1 cm x 1 cm and bake in a hot air oven at a temperature of 40 °C for 3 days. Grind the dried kratom leaves finely with a blender and separate the kratom leaves by size using a 35-mesh stainless steel sieve.

2.2 Extraction using pressure vessel

Figure 1 shows the extraction set of the pressure vessel. Put 10 grams of finely ground dried kratom leaves and 400 ml of ethanol into the pressure vessel. Close the pressure vessel lid, put on the gasket, and tighten the nuts. Check if the outlet valve is closed and open the inlet valve to the maximum. Adjust the pressure at the nitrogen cylinder valve to the pressure vessel to the desired pressure. Turn on the heater by setting the temperature control, which will wait until the temperature inside the vessel is equal to the set temperature before starting the timer. When the time is up, turn off the heater and slowly open the outlet valve to release the pressure until the system reaches atmospheric pressure. Cool the pressure vessel using a fan to help cool it. Then open the pressure vessel lid and filter the raw extract with filter paper No. 1 to filter out impurities. The temperature, pressure, and extraction time will vary as shown in Table 1.

The extraction was also performed by Soxhlet method at 78 °C and 1 atmosphere to find the maximum mitragynine in kratom leaves in this research.

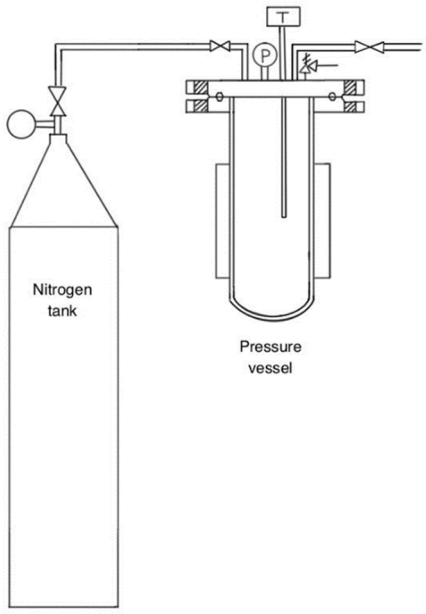

Figure 1 Pressure vessel extraction kit

2.3 Mitragynine measurement

Evaporate the entire crude extract in a filter flask with a rotary evaporator until the volume of the crude extract is reduced to approximately half. Then, start the purification by adding petroleum ether and DI water and shake. When the solution separates, collect the lower solution layer containing mitragynine (called the extracted mitragynine). Repeat the purification step 5 times. Evaporate the extracted mitragynine solution with a rotary evaporator and wait until the extract volume is reduced to dryness. Add 3 mL of ethyl acetate to the rotary evaporator flask to wash the extracted mitragynine. Then, determine the identity of mitragynine by thin-layer chromatography (TLC), and determine the percentage yield of mitragynine and the extraction efficiency.

2.4 Mitragynine Identity Test:

Prepare Ehrlich reagent by dissolving 0.25 g of Dimethylaminobenzaldehyde (DMAB) in 25 mL of ethanol. Stir the solution with a magnetic stirrer, gradually adding 25 mL of hydrochloric acid until completely dissolved. Store in a brown bottle for using in TLC experiments.

Prepare TLC solvent by mixing hexane:ethyl acetate in a ratio of 30:70 (in a hood). Measure 210 mL of the TLC solvent and pour it into the TLC chamber (the height will be 1 cm). Cover and leave for 20 minutes to allow the solution to saturate.

2.5 TLC and Ehrlich test of mitragynine extracted:

Prepare a TLC plate for the experiment by setting the sample drop line at a height of 1.5 cm from the edge. Drop 3 mL of the mitragynine extract solution mixed with ethyl acetate onto the TLC plate along the marked line, leaving a small distance from both edges. Drop lengthwise until the substance disappears. Then immerse the TLC plate in the TLC solvent. Wait until the solution does not move. Then remove the TLC plate from the chamber and place into the UVB box. Turn on the lamp for about 5 minutes to make the color of the band clear. Then take a picture. Drop Ehrlich reagent on each strip of the TLC plate by dropping from the side. If the strip changes from yellow to purple-blue, it indicates that mitragynine has been detected. Calculate the R_f (Retention factor) value by setting the R_f value from the Soxhlet experiment as a standard. For the TLC set of the pressure vessel extract, select the strip with the R_f value equal to the R_f value of mitragynine from Soxhlet.

2.6 Calculation of the percentage of mitragynine yield

The mitragynine band was scraped into a glass lens and filtered through a wheat-lined glass filter funnel, adding 10 mL of ethyl acetate to separate the mitragynine from the silica plate, and then a rotary evaporator was used to evaporate the ethyl acetate completely, and the resulting mitragynine was weighed.

$$\%Yield = \frac{Mitragynine\ weight}{Dry\ kratom\ leave\ weight} \times 100$$

$$\%Extraction\ efficiency = \frac{\%Yield\ by\ pressure\ vessel}{\%Yield\ by\ soxhlet} \times 100$$

3. RESULTS AND DISCUSSION

3.1 Design and construction of extraction pressure vessels

The design of the pressure vessel is in accordance with ASME Boiler & Pressure Vessel (BPV) Code Sect. VIII Div.1. In determining the maximum allowable pressure and the required thickness, consideration must be given to the tank, bottom and flange. When the thickness of both the tank and bottom is 5.5 mm, the pressure vessel can withstand a pressure of 11.5 bar at an operating temperature of 70 °C. The pressure vessel is constructed using 3” sch 40 stainless steel pipe as the shell, using F&D head bases welded to the tank using single point welds and using 3” 150P stainless steel flanges. The tank is 266.70 mm long and has a total volume of 1,191 ml. It can be filled up to 0.6 times the total volume, which is 714 ml, as shown in Figure 1.

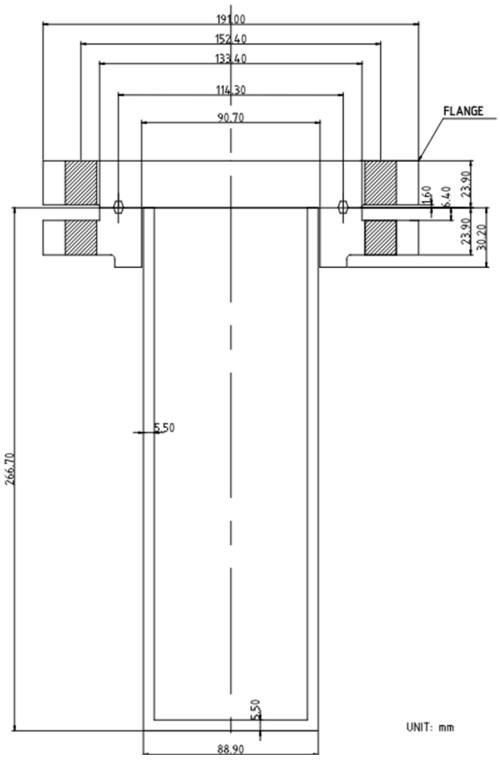

Figure 1 Pressure vessel dimension.

3.2 Results of the examination of mitragynine extracted from kratom leaves

The crude extract obtained from kratom leaves extraction with ethanol solvent was purified of mitragynine by TLC technique and tested for indole alkaloids (e.g. mitragynine) by Ehrlich test before being identified by FT-IR technique.

In the process of purifying mitragynine by TLC technique, the mobile phase used was hexane:ethyl acetate at 30:70, which was found to have R_f value (distance traveled by solution/distance traveled by solvent = 0.602-0.606, which is close to the research of Muandao [3]).

Ehrlich reagent was dropped onto a TLC plate to detect the indole alkaloid of mitragynine. The band predicted to be mitragynine or having an Rf value close to 0.605 and changing color to blue-violet, therefore, the band was confirmed to be mitragynine. The band was scraped off the TLC plate and mitragynine was removed from the silica plate with ethyl acetate. Then, the solution was examined for functional groups using FT-IR technique to identify. The FT-IR result is shown in Figure 2.

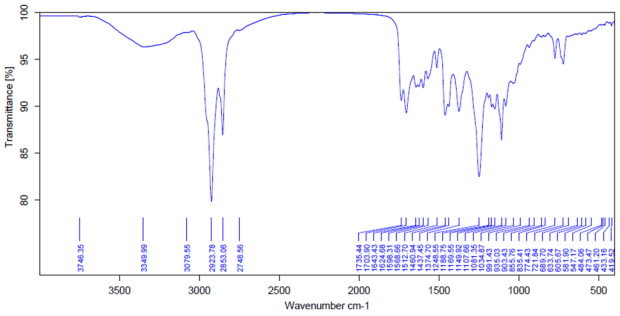

Figure 2 FT-IR Spectrum of mitragynine.

From Figure 2, it was found that the N-H peak appeared at positions more than 3,000 cm^{-1}. The bending and stretching peaks of C-H bond appeared at positions 2,745-2,925 cm^{-1}. The aromatic C-C and C=C peaks appeared at positions 1,435 – 1,465 cm^{-1} and 1,510 – 1,645 cm^{-1}. The bending peak of carbonyl group appeared at positions 1,700 – 1,740 cm^{-1}, and the C-O peak from ether bond appeared at positions 1,249 cm^{-1}. All of which are functional groups consistent with mitragynine.

3.3 Results of mitragynine extraction

Table 1 Percentage yield of mitragynine and extraction efficiency by pressure vessel and Soxhlet method.

Method	Temperature (ºC)	Time (min)	Pressure (Bar)	% Yield	% Extraction Efficiency
Pressure vessel	50	20	1	0.039	28.33
	60	20	1	0.043	30.92
	70	20	1	0.047	33.65
	70	60	1	0.144	103.4
	70	60	2	0.147	105.4
Soxhlet	78	60	-	0.139	100.0

From Table 1, it was found that the extraction of mitragynine by pressure vessel method for 20 min, pressure 1 bar, the percentage of mitragynine yield increased with increasing extraction temperature. This experiment used the highest extraction temperature at 70 °C, resulting in the highest percentage of mitragynine yield of 0.047% or an extraction efficiency of 33.648%. Because the solubility of the solvent and the diffusion rate of the solute will increase with the extraction temperature, resulting in higher extraction

efficiency [6]. However, mitragynine is sensitive to high temperature, so long-term extraction may cause deterioration of the substance [7]. This can be seen from the results of the Soxhlet extraction method at 78 °C. At the same time, but the percentage of mitragynine yield was lower than the extraction using the pressure vessel at 70 °C.

In addition, it was found that the extraction of mitragynine using a pressure vessel, the percentage of mitragynine yield increased with increasing extraction time. In this experiment, the maximum extraction time was 60 min, resulting in the highest percentage of mitragynine yield of 0.144% or the extraction efficiency of 103.4%. This is because the longer the extraction time, the more time the solution has to diffuse, resulting in higher extraction efficiency. Pressure has a slight effect on the extraction. In this experiment, the maximum extraction pressure was 2 bar, resulting in the highest percentage of mitragynine yield of 0.147% or the extraction efficiency of 105.4%. This is because the main reason for increasing the pressure is to keep the solvent in a liquid state at high temperature. However, increasing the pressure increases the ability of the solvent to penetrate the substance to be extracted, resulting in a slightly higher extraction efficiency [6].

From Table 2, it can be seen that the extraction using ethanol is better than that using petroleum ether [1] and methanol [2]. Because the mitragynine molecule contains both polar and non-polar parts, it is less soluble in non-polar petroleum ether than ethanol. And the extraction time of up to 8 hours [1] may cause mitragynine degradation. This may be because the extraction using methanol [2] was carried out at low temperature, i.e. room temperature, so the efficiency is lower than this research.

Although the extraction using this research did not yield as high as that using acetic acid [3], it is safer in terms of safety in use. When compared to the extraction using the same solvent ethanol [4], it was found that using a pressurized vessel can extract at high temperatures, resulting in a 72-fold shorter extraction time and 3-fold less solvent. However, the amount of mitragynine used in various fields is still unclear, but it should not be used in large quantities. Therefore, the extracted mitragynine can definitely be used.

Table 2 Comparison of the results of mitragynine extraction with other research

Method	Solvent	Extraction time (Hours)	Temp. (°C)	Yield (%w/w)	Reference
Soxhlet	Petroleum ether	8	60	0.088	Beng et al. [1]
Ultrasonic	Methanol	1	Room Temp.	0.023	Kikura – Hanajiri et al. [2]
Solvent extraction	Acetic acid 50%	0.5	80	2.691	Muandao, K. [3]
Maceration	Ethanol 95%	72	Room Temp.	0.556	Sharma et al. [4]
Solvent extraction	Ethanol 95%	1	70	0.147	This research

4. CONCLUSION

Design and construction of pressure vessel for mitragynine extraction according to ASME standard. The pressure vessel has a volume of 1,191 mL and can hold up to 714 mL of liquid with a maximum allowable pressure of 11.5 bar at 70 °C by heating via a tubular heater. The constructed pressure vessel series was then studied to examine the effects of temperature, time and pressure using ethanol as the solvent to find the most suitable extraction conditions for the highest percentage yield and efficiency.

The results of TLC purification and identification and Ehrlich reagent for indole alkaloids confirmed that the extracted substance was mitragynine.

It was found that the percentage yield and extraction efficiency increased with time and the extraction efficiency increased. However, mitragynine is sensitive to high temperature, so it should not be used for a long time because the extraction may cause deterioration [7]. The Soxhlet extraction results at 78 °C showed that the percentage yield of mitragynine was lower than that of the pressure vessel extraction at 70 °C. Therefore, the extraction temperature should be around 70 °C. High pressure extraction yields are slightly higher. The optimal conditions for mitragynine extraction using a pressure vessel were 2 bar pressure, 70 °C temperature and 60 min, with a mitragynine yield of 0.147%, with an extraction efficiency of 105.4% compared to the Soxhlet extraction method.

REFERENCES

1. Beng, T., et al., A Simple and cost-effective isolation and purification protocol of mitragynine from mitragyna speciosa korth (Ketum) leaves, The Malaysian Journal of Analytical Sciences 2011; 15(1): 54-60.
2. Kikura – Hanajiri, R., et al., Simultaneous analysis of mitragynine, 7-hydroxymitragynine, and other alkaloids in the psychotropic plant “kratom” (Mitragyna speciosa), LC-ESI-MS. Forensic Toxicol 2009; 2(27): 67-74.

3. Muandao, K., Comparison of mitragynine extraction methods for forensic science and antibacterial activity from kratom, Master of Forensic Science Thesis 2018; Faculty of Science, Silpakorn University.
4. Sharma, A., et al., Simultaneous quantification of ten key Kratom alkaloids in Mitragyna speciosa leaf extracts and commercial products by ultra-performance liquid chromatography−tandem mass spectrometry, Drug Test Anal. 2019; 11(8): 1162–1171.
5. Goh, Y.S., et al., Accelerated solvent extractions (ASE) of Mitragyna speciosa Korth. (Kratom) leaves: Evaluation of its cytotoxicity and antinociceptive activity, Molecules 2021; 26(12): 3704.
6. Viriya Promkong, Food Engineering II. [Online], Available: http://www.agri.ubu.ac.th/mis/evaluate/assess_learn/upload/65913.pdf [1 December 2023].
7. Qiuhong, Z., et al., 2012, Microwave-assisted extraction in combination with capillary electrophoresis for rapid determination of isoquinoline alkaloids in Chelido niummajus L, Talanta 2012; 99: 932–938.

Study of biomass productivity of phosphate-solubilizing bacteria using rice bran oil as an alternative media

Pim-orn Thongpanchang[1], Pichayada Somboon[2,*], Nuttapol Lerkkasemsan[1,*]

[1] Department of Chemical Engineering, School of Engineering, King Mongkut's Institute of Technology Ladkrabang, Bangkok, 10520, Thailand
[2] Program in Fermentation Technology, School of Food Industry, King Mongkut's Institute of Technology Ladkrabang, Bangkok, 10520, Thailand
[*] Corresponding author: pichayada.so@kmitl.ac.th; nuttapol.le@kmitl.ac.th

ABSTRACT

Conventional media are expensive and unsuitable for microorganism cultivation on a large scale. Rice bran oil is abundant in a local of Thailand. Therefore, a challenge for a cost-effective approach to improving bioprocess efficiency is the application of rice bran oil for conventional media. This study aimed to predict kinetic parameters and vary rice bran oil concentration as an alternative media for cultivating a new strain of phosphate-solubilizing bacteria using the Gompertz model. A new strain was isolated from biochar, with a phosphate solubilizing index of 1.116±0.004. The strain was identified as *Bacillus subtilis* (*B. subtilis*)) with 98.37% ANIb similarity by the whole genome sequencing method. It was cultivated with varying rice bran oil concentrations (1% v/v, 3% v/v, and 5% v/v). Optical density at 600 nm (OD600) was measured at various time intervals, and the results were analyzed using the Gompertz model as the primary model. The results indicated that 5% v/v rice bran oil is suitable for bacterial cultivation, based on the predicted kinetic parameters, with a maximum specific growth rate (μ_{max}) of 0.1041 per hour, which was higher than μ_{max} of bacterial cultivation in 1% v/v and 3% v/v rice bran oil of 0.0137 and 0.0096 per hour, respectively. In addition, the growth kinetics of bacteria showed a sigmoid shape, consistent with the Gompertz model. Therefore, future investigations could apply the predicted kinetic parameters to upscaling in alternative media or vegetable oils.

Keywords: Bacterial cultivation; Vegetable oil; Optical density; Gompertz

1. INTRODUCTION

Bioprocessing at a large scale must balance effectiveness with cost competitiveness.[1]. Conventional media is unsuitable on a large scale because it is costly.[2] Therefore, alternative media or low-cost media is used to reduce the cost of microbial cultivation on a large scale, such as agricultural waste[3], and by-products of industry[4] and is readily available locally.[5] Rice bran oil is a widely used resource in Thailand [6] Additionally, rice bran is a by-product of peeling unhusked rice grains and grinding broken rice grains, It is used as a component of animal feed due to its vital nutrients. [7] A previous study, found that rice bran was a component of biofertilizer encapsulation derived from bacteria to provide bacterial nutrients. [8] Consequently, rice bran oil, a derivative of rice bran, presented a notable challenge for microbial cultivation as a potential alternative medium. Mathematical models play a crucial role in bioprocessing by predicting essential parameters of bacterial cultivation conditions.[9] Mathematical models have been divided into two types: empirical model-based and mechanistic-based models. An empirical model is used to describe the number of microbes and time,

In contrast, a mechanistic model describes the mechanism and factors involved in the variance of microbes. For example, in the Monod model, which is an empirical models, there may be limitations for prediction because the number of bacteria depends on the substrate, This model describe a specific exponential phase known as the log phase.[10] Most microbial growth follows a sigmoid function pattern, consisting of four phases: lag phase, exponential phase (log phase), stationary phase, and death phase. [11] The Gompertz model empirical model, also known as the primary model[12], is appropriate because it describes the sigmoid function and the entire microbial growth phase, which are relevant to the number of bacteria and time. [10] The Gompertz model describes the kinetic parameters of microbial growth [13] and predicts essential growth parameters for bioprocessing design. [14] This work aims to study biomass productivity, measured as optical density (OD600), of phosphate-solubilizing bacteria, a novel strain isolated from biochar, and cultivated with various concentrations of

rice bran oil as an alternative media. The Gompertz model was employed to predict the kinetic parameters with OD600 data was μ_{max} and λ.

2. EXPERIMENTAL

2.1 Bacterial strain

Unknown bacteria were isolated from biochar, and the phosphate-solubilizing index (PSI) was tested for screening phosphate-solubilizing bacteria. The bacteria were cultivated using Pikovskaya's agar, which contained 0.5 g/l yeast extract, 10 g/l dextrose, 5 g/l $Ca_3(PO_4)_2$, 0.5 g/l $(NH_4)_2SO_4$, 0.2 g/l KCl, 0.1 g/l $MgSO_4$, 0.0001 g/l $MnSO_4$, 0.0001 g/l $FeSO_4$, and 15 g/l agar powder. They were incubated at 37°C for 20 hours. The measured diameter of the colony and the clear zone formed were used to calculate PSI as shown in Eq. (1) [15]

$$PSI=\frac{Z}{C} \quad (1)$$

Z represents the total diameter (colony + clear zone), in mm, while C denotes the colony diameter in mm as illustrated in Fig.1

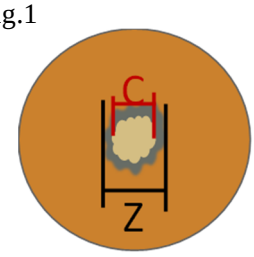

Fig.1 Total diameter (colony + clear zone) and measurement of colony diameter for PSI calculation.

Unknown bacteria were identified using whole-genome sequencing. The bacteria were inoculated in the nutrient broth at 37°C for 20 hours. Next, the prepared cells were centrifuged at 6,000 rpm for 10 minutes. Then, the cell-free supernatant was discarded. The cell were washed with buffered peptone water (BPW) twice. Finally, the unknown bacteria were stored 4-6°C. They were sent for analysis at the Omics Sciences and Bioinformatics Center, Chulalongkorn University, Thailand.

2.2 Medium preparation

Rice bran oil was purchased from a convenience store as an alternative carbon source at concentrations of 1% (v/v), 3% (v/v) and 5% (v/v). It was combined with Mineral salt medium (MSM) prepared using instant media (Hi-media brand), which consisted of 3 g/L KH_2PO_4, 6 g/L Na_2HPO_4, 0.12 g/L $MgSO_4.7H_2O$, 0.5 g/L NaCl, and 0.013 g/L $CaCl_2.2H_2O$. Additionally, the composition included 3 g/L yeast extract and 10 g/L Tween80. The pH of medium was adjusted to 7.00 with 1 M NaOH. The medium was autoclaved at 121°C for 15 minutes and poured into a reagent bottle.

2.3 Bacterial cell preparation for the study of biomass productivity

Identified bacteria were cultivated with MSM, which included D-glucose as a control carbon source. The inoculum of bacteria was centrifuged at 6,000 rpm for 10 minutes. The cell-free supernatant was eliminated, and the bacterial cells were kept. The bacterial cells were twice cleaned with buffered peptone water (BPW). Next, the OD600 of bacteria was adjusted to 0.1.

2.4 Bacterial cultivation for the study of biomass productivity

150 µl of prepared media was pipetted into the 96-well plate at, and 50 µl of bacterial cells was added to the 96-wells plate. Finally, the prepared cells were cultivated in an incubator shaker at 37°C, 200 rpm.

2.5Prediction of kinetic parameter from experimental data

OD600 of bacteria was measured using a microplate reader at specified intervals. The OD600 data were predicted using the Gompertz model, which is employed to forecast bacterial growth[12], as shown in Eq.2

$$y= a.\exp\{-exp[-b(t-m)]\} \quad (2)$$

Where y represents the optical density at a wavelength of 600 nm (OD600), t indicates the time point (hours), a signifies the optical density of the higher asymptote (dimensionless), m denotes the time at which the absolute growth rate is maximum (time at inflection) (in hours) and b represents the relative growth rate determined at that time (per hour) (the slope of tangent). However, a, b, and m parameters were difficult for biological interpretation. The model was revised using a modified Gompertz model[16] as shown in Eq.3

$$y= A\exp\left\{-exp\left[\frac{\mu_{max}e}{A}(\lambda-t)+1\right]\right\} \quad (3)$$

Whereas the maximum specific growth rate (μ_{max}) and the lag time (λ) were derived and are shown in eq.4 and eq.5 respectively.

$$\mu_{max}=\frac{bc}{e} \quad (4)$$

$$\lambda= m-\frac{1}{b} \quad (5)$$

Where c indicates the asymptotic amount of growth as t increases indefinitely and e = 2.781. The experimental data were plotted against time. Gompertz model were used to predict kinetic parameters are μ_{max} and λ. The iteration algorithm were used to predict with Levenberg Marqurdt method.

3. RESULTS AND DISCUSSION

3.1 Bacterial strain

Unknown bacteria were isolated from biochar, which was tested for phosphate solubilizing index (PSI). A strain was inoculated onto Pikovskaya's agar. The total diameter, comprising both the colony and the clear zone, as well as the diameter of the colony, was computed for PSI, resulting in 1.116±0.004, as shown in Fig. 2.

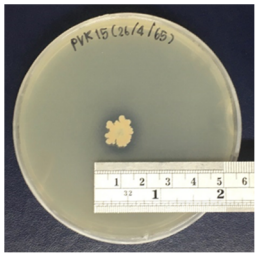

Fig.2 The total diameter (colony + clear zone) and colony diameter measurement on Pikovskaya's agar of unknown bacteria

Unknown bacteria species were identified using with the whole-genome sequencing method. The unknown bacteria were similar to *Bacillus subtilis* E1 (*B. subtilis* E1) with the highest ANIb similarity (98.37%), which suggests that the the unknown bacteria were identified as *B. subtilis* from bacterial species identification, as shown in Table 1.

Table 1. Bacterial species identification

Genome	ANIb[%]	Aligned [%]	Aligned [%]	Total [bp]
Bacillus subtilis E1	98.37	93.89	3797327	4044405
Bacillus subtilis subsp. subtilis str. 168 [T]	98.35	93.32	3774403	4044405
Bacillus subtilis subsp. subtilis DSM 10 [T]	98.35	93.31	3773681	4044405
Bacillus subtilis type strain: N	98.33	93.93	3798932	4044405
Bacillus subtilis B4143	98.33	93.28	3772822	4044405
Bacillus subtilis HJ5	98.02	92.51	3741362	4044405

3.2 Study of biomass productivity

The biomass productivity of phosphate-solubilizing bacteria was measured using a microplate reader for 1% (v/v), 3% (v/v) and 5% (v/v) rice bran oil cultivation. The results for phosphate-solubilizing bacteria were plotted against time. The Gompertz model was employed to predict kinetic parameters from the phosphate-solubilizing bacteria data, as illustrated in Fig.3

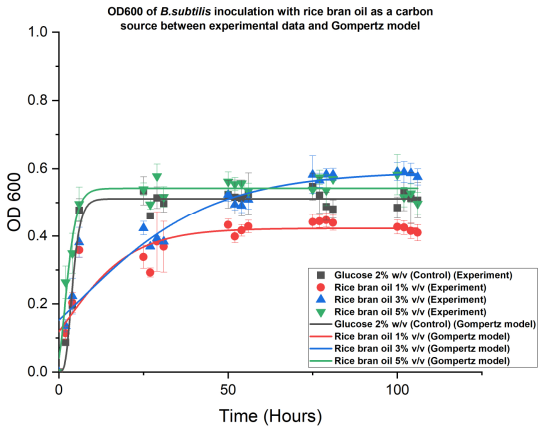

Fig.3 Optical density at 600 nm (OD600) of *B.subtilis* cultivation with rice bran oil as a carbon source in comparison with experimental data and the Gompertz model

3.3 Prediction of kinetic parameters from experimental data

The data for OD600 were predicted using a sigmoidal function and an iterative algorithm based on the Levenberg-Marqurdt method. A specific growth rate (μ_{max}), which is the speed of bacterial growth, and a lag time (λ), which is the initial adaptation of bacteria, were predicted. as shown Table 2.

Table 2. Kinetic parameters were predicted from OD600 measurements of phosphate-solubilizing bacteria.

Carbon source	Asymptote at time (A)	λ (hours)	μ_{max} (per hour)	Adj-R^2
1% (v/v) rice bran oil	0.4230	-8.6485	0.0137	0.7895
3% (v/v) rice bran oil	0.5922	-15.6990	0.0096	0.8670
5% (v/v) rice bran oil	0.5420	-0.0901	0.1041	0.9476

The prediction of μ_{max} reflect the speed of bacterial growth during the exponential phase. Bacteria were cultivated with 5% (v/v) rice bran oil, resulting in the highest prediction of 0.1041 per hour. In contrast,

bacteria cultivated with 1% (v/v) and 3% (v/v) rice bran oil had predictions of 0.0137 and 0.0096 per hour, respectively. The λ prediction, which represents the initial adaptation of bacteria showed that those cultivated with 3% (v/v) rice bran oil exhibited a short λ of -15.6990 hour. In contrast, bacteria cultivated with 1% (v/v) and 5% (v/v) rice bran oil had predictions of -8.6485 and -0.0901 per hour, respectively. The negative value of the λ was adjusted to zero because this parameter was not interpreted, which meant the negative of the time measurement was not meaningful. [17]. Likewise, bacteria immediately grow without lag phase.[13] Furthermore, complex of λ prediction is contingent upon environmental condition, the initial quantity of cells, and various other variable.[17] The λ was a parameter that can probably be further studied to improve conditions for bacterial cultivation. Kinetic parameters, were well predicted and considered based on a high growth rate and low λ. [18] From the adjust R-squared values, bacteria cultivated with 5% (v/v) rice bran oil were well predicted by the Gompertz model, achieving a high adjusted R-squared of 0.9476. The highest adjusted R-squared suggests that the Gompertz model is suitable for the experimental data, pertaining to the cultivation conditions of 5% (v/v) rice bran oil. In contrast, the adjusted R-squared values for bacterial cultivation in 1% (v/v) and 3% (v/v) rice bran oil are 0.8670 and 0.7895, respectively. Furthermore, the growth pattern demonstrated a sigmoid shape, characterized by a non-constant μ_{max}, which increases during the exponential phase (log phase) until it reached a maximum, subsequently followed by a decline during the stationary phase, This behavior is analogius to the exponential growth as defined by the Gompertz model [19]

4. CONCLUSION

In order to investigate the biomass productivity of phosphate solubilizing bacteria, a novel strain was isolated from biochar and cultured using varying concentrations of rice bran oil as an alternative growth medium, replacing conventional media due to economic considerations for bacterial cultivation on a large scale or bacterial cultivation with rice bran components. The results indicated that this new strain possesses characteristics of phosphate solubilizing bacteria, with a PSI of 1.116±0.004. The Gompertz model was used to predict OD600 for the new strain. The 5% (v/v) rice bran oil concentration was well predicted by the Gompertz model, which exhibited a high μ_{max} and short λ, with a μ_{max} of 0.1041 per hour and a λ of -0.091 hours. The growth pattern was sigmoid aligning with the Gompertz model, which indicated that the bacteria grow exponentially. These parameters can be further studied to enhance bacterial cultivation conditions, potentially applying a secondary model such as cultivation at different temperatures, the environmental relevance of cultivation conditions, and additional vegetable oils cultivations.

ACKNOWLEDGMENTS

The authors would like to express gratitude to the Department of Chemical Engineering, School of Engineering, and Program in Fermentation Technology, School of Food Industry, King Mongkut's Institute of Technology Ladkrabang, and Bio Talk Technology (Thailand) Company Limited, which supported the analytical instruments and facilities involved in this research.

REFERENCES

[1] H. Delvigne, Frank; Noorman, "Scale-up/Scale-down of microbial bioprocesses: a modern light on an old issue," *Microb. Biotechnol.*, pp. 685–687, 2017, doi: 10.1111/1751-7915.12732.

[2] S. Basu *et al.*, "Evolution of bacterial and fungal growth media," *Bioinformation*, vol. 11, no. 4, pp. 182–184, 2015, doi: 10.6026/97320630011182.

[3] J. D. Saguibo, R. H. Perez, M. S. S. Brion, and R. A. R. Almazan, "Low-cost Media from Agro-industrial Wastes for the Cultivation and Metabolite Production of Lactic Acid Bacteria," *Philipp. J. Sci.*, vol. 151, no. 6, pp. 2285–2298, 2022, doi: 10.56899/151.6A.20.

[4] E. Tsouko *et al.*, "Bacterial cellulose production from industrial waste and by-product streams," *Int. J. Mol. Sci.*, vol. 16, no. 7, pp. 14832–14849, 2015, doi: 10.3390/ijms160714832.

[5] P. Jadhav, M. Sonne, A. Kadam, and S. Patil, "'Formulation of Cost Effective Alternative Bacterial Culture Media Using Fruit and Vegetables Waste,'" *Int. J. Curr. Res. Rev.*, vol. 10, no. 2, pp. 6–15, 2018, doi: 10.7324/ijcrr.2018.1022.

[6] The Codex Alimentarius Commission, "Discussion paper on the inclusion of quality parameters for crude rice bran oil in the standard for named vegetable oils (CODEX STAN 210-1999)," 2017.

[7] S. H. Dilaga, R. A. Putra, A. N. T. Pratama, O. Yanuarianto, M. Amin, and S. Suhubdy, "Nutritional quality and in vitro digestibility of fermented rice bran based on different types and doses of inoculants," *J. Adv. Vet. Anim. Res.*, vol. 9, no. 4, pp. 625–633, 2022, doi: 10.5455/JAVAR.2022.I632.

[8] R. Kaur, S. Kaur, V. Dwibedi, C. Kaur, N. Akhtar, and A. Alzahrani, "Development and characterization of rice bran-gum Arabic based encapsulated biofertilizer for enhanced shelf life and controlled bacterial release," *Front. Microbiol.*, vol. 14, no. September, pp. 1–13, 2023, doi: 10.3389/fmicb.2023.1267730.

[9] K. Theophel *et al.*, "The importance of growth kinetic analysis in determining bacterial susceptibility against antibiotics and silver nanoparticles," *Front. Microbiol.*, vol. 5, no. NOV, pp. 1–10, 2014, doi: 10.3389/fmicb.2014.00544.

[10] U. Laila, R. Nurhayati, T. Utami, and E. S. Rahayu, "Prediction of Microbial Population in Sorghum Fermentation through Mathematical Models," *Reaktor*, vol. 19, no. 4, pp. 152–161, 2019, doi: 10.14710/reaktor.19.4.152-161.

[11] A. M. Gibson, N. Bratchell, and T. A. Roberts, "Predicting microbial growth: growth responses of salmonellae in a laboratory medium as affected by pH, sodium chloride and storage temperature," *Int. J. Food Microbiol.*, vol. 6, no. 2, pp. 155–178, 1988, doi: 10.1016/0168-1605(88)90051-7.

[12] D. A. Longhi, F. Dalcanton, G. M. F. De Aragão, B. A. M. Carciofi, and J. B. Laurindo, "Microbial growth models: A general mathematical approach to obtain μmax and λ parameters from sigmoidal empirical primary models," *Brazilian J. Chem. Eng.*, vol. 34, no. 2, pp. 369–375, 2017, doi: 10.1590/0104-6632.20170342s20150533.

[13] J. Jiacheng, Shen; Zhu, "Development of General Gompertz Models and Their Simplified Two-Parameter Forms Based on Specific Microbial Growth Rate for Microbial Growth, Bio-Products and Substrate Consumption," *Adv. Biotechnol. Microbiol.*, vol. 4, no. 3, 2017, doi: 10.19080/aibm.2017.04.555640.

[14] V. Kumar, R. Valadez-Blanco, P. Kumar, J. Singh, and P. Kumar, "Effects of treated sugar mill effluent and rice straw on substrate properties under milky mushroom (Calocybe indica P&C) production: Nutrient utilization and growth kinetics studies," *Environ. Technol. Innov.*, vol. 19, p. 101041, 2020, doi: 10.1016/j.eti.2020.101041.

[15] M. Oves, M. S. Khan, and H. A. Qari, "Ensifer adhaerens for heavy metal bioaccumulation, biosorption, and phosphate solubilization under metal stress condition," *J. Taiwan Inst. Chem. Eng.*, vol. 80, pp. 540–552, 2017, doi: 10.1016/j.jtice.2017.08.026.

[16] J. B. J. Njalam'mano and E. M. N. Chirwa, "Determination of Growth Parameters of Butyric Acid-Degrading Bacterium, Achromobacter xylosoxidans, as a Function of Constant Temperatures in Batch System," *Chem. Eng. Trans.*, vol. 76, pp. 1321–1326, 2019, doi: 10.3303/CET1976221.

[17] M. Aalto-Araneda *et al.*, "Strain variability of Listeria monocytogenes under NaCl stress elucidated by a high-throughput microbial growth data," *Appl. Environ. Microbiol.*, vol. 86, no. 6, pp. 1–20, 2020, doi: 10.1128/AEM.02378-19.

[18] L. Solieri, T. C. Dakal, and S. Bicciato, "Quantitative phenotypic analysis of multistress response in Zygosaccharomyces rouxii complex," *FEMS Yeast Res.*, vol. 14, no. 4, pp. 586–600, 2014, doi: 10.1111/1567-1364.12146.

[19] M. H. Zwietering, I. Jongenburger, F. M. Rombouts, and K. Van't Riet, "Modeling of the bacterial growth curve," *Appl. Environ. Microbiol.*, vol. 56, no. 6, pp. 1875–1881, 1990, doi: 10.1128/aem.56.6.1875-1881.1990.

Removal of styrene and pyrene in a fixed bed adsorption column using rhamnolipid-modified alumina

Davone Keomany[1], Emma Asnachinda[1,*]

[1] Department of Chemical Engineering, Faculty of Engineering, Burapha University, Chon Buri 20131, Thailand
[*] Corresponding author: emma@eng.buu.ac.th

ABSTRACT

This study examined the adsolubilization of two organic contaminants, styrene and pyrene, commonly found in soil and groundwater, using a fixed-bed column adsorption process with rhamnolipid-modified alumina. Rhamnolipid biosurfactants produced by Pseudomonas strains were selected to use in this work. In the past research, rhamnolipids were demonstrated to enhance the removal efficiency of oil spills, PAHs, diesel, and heavy metals from contaminated soil and groundwater. The fixed-bed experiment was conducted through a sequential analysis involving tracer studies, surfactant adsorption, and the adsolubilization of organic solutes. The desorption study was also used to determine regeneration capability by distilled water. The primary objectives were to assess the effects of varying organic feeding flow rates, as indicated by the retardation factor and adsolubilization capacity. Results indicated that rhamnolipid significantly enhances the adsolubilization capacity of organic solutes in the column, particularly increasing the retardation rate at lower feed flow rates. Additionally, the molecular weight of organic solutes affects their polarity, which in turn influences their behavior during adsolubilization. As a result, styrene and pyrene are solubilized in different regions of the surfactant admicelle. Styrene, with its lower molecular weight and greater water solubility, is located in the palisade region, while pyrene is found in the core area, representing the higher polar region of the admicelle structure.

Keywords: Rhamnolipid biosurfactant; Adsolubilization; Fixed-bed column; Styrene; Pyrene

1. INTRODUCTION

Petrochemical-based organic hydrocarbons are investigated due to their hazardous and biodegradability characteristics. Styrene and pyrene are organic substances that are widely distributed in the environment [1], [2]. Those have raised much attention because of their low biodegradability, toxic, mutagenic, and carcinogenic properties [3]. They are emitted to the surroundings by leakage from the underground storage tanks, accidental spills in transportation, and released gases from the industrial sector [4]. Currently, styrene and pyrene are contamination issues in soil and groundwater that are the majority concern in an environment [5], [6]. To remove those compounds: precipitation, adsorption, oxidation-reduction, and bioaugmentation are techniques to be applied [7],[8]. In addition, subsurface remediation of petrochemical-based substances using surfactants has been evaluated for many years. Surfactant-modified solid surface has drawn much attention because it was applied to remove heavy metals, petroleum hydrocarbons, and other organic contaminants from aqueous solutions [9]–[12]. Typically, surfactants are chemical-based substances and are not environmentally friendly [13]. Nowadays, biosurfactants produced from bacteria have been reported, such as rhamnolipids [14]. Rhamnolipid biosurfactants produced by Pseudomonas strains were selected to use in this work. In the past research, rhamnolipids were demonstrated to enhance the removal efficiency of oil spills, PAHs,diesel, and heavy metals from contaminated soil and groundwater [11], [15]–[17]. Biosurfactants also have more benefits over conventional surfactants as they are low toxicity and biodegradability [18]. This study aims to develop the removal of styrene and pyrene using rhamnolipid biosurfactant-modified media in a continuous system as a fixed-bed adsorption column. Also, evaluate the adsolubilization of organic solutes in a fixed-bed column.

2. EXPERIMENTAL

2.1 Materials

Biosurfactant used in this work was Rhamnolipid produced from Pseudomonas aeruginosa bacteria and purchased from Jeneil Biosurfactant Co., LLC, USA. Rhamnolipid has a negative charge with mixed 50 w/v% monorhamnolipid and 50 w/v % dirhamnolipid. The formulas of rhamnolipids are presented in Table 1 [19].

Table 1: Formulas of biosurfactants

Surfactant: Rhamnolipid	Mean Mw.	% Active	Molecular Formular
Monorhamnolipids[a]			
R1	504	16.2	$C_{26}H_{28}O_9$
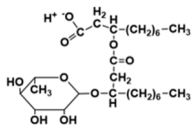			
Dirhamnolipid[a]			
R2	650	16.2	$C_{32}H_{58}O_{13}$
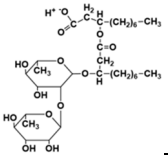			

[a] Adapted from reference [19]

Styrene and pyrene were selected to present nonpolar solutes (dipole moments: 0.13 D and 0 D, respectively) with different aqueous solubilities (310 mg/L and 0.07 mg/L, respectively). Styrene (C_8H_8, 104.15 g/mol with 99% purity) and Pyrene ($C_{16}H_{10}$, 202.3 g/mol with 98% purity) were purchased from Arcos Chemical Company (Belgium). Aluminum oxide (Al_2O_3, alumina ; Aldrich, USA.) is selected to use as an adsorbent. The specific surface area of alumina reported by the manufacturer is 155 m^2/g. The point of zero charges (PZC) of alumina is 9.1 [20].

2.2 Methodology

2.2.1 Column preparation

Fixed-bed experiments were carried out at room temperature in a 15 cm length glass column of 1.3 cm internal diameter. The column was packed with the mixed supporting media of 0.5 g aluminum oxide and 19 g of glass beads, which were used to improve the permeability of the packing media during operation. The schematic diagram of the column study is shown in Figure 1. Sodium nitrate (0.01 M $NaNO_3$) was used as a conservative tracer to estimate the hydrodynamics of the column system. The exhaustion of the tracer test was collected every 5, 10, and 15 min for flow rates of 1, 0.5, and 0.25 mL/min, respectively. Collected samples were observed using a UV/VIS spectrophotometer at a wavelength of 240 nm [21].

2.2.2 Column adsorption study

Adsorption study in a continuous system was carried out by applying the specific rhamnolipid concentration onto alumina-packed media in the up-flow direction as shown in Figure 1. The formation of the rhamnolipid bilayer was achieved by feeding 0.6 mM of rhamnolipid (two-fold concentration greater than CMC) to the column. Samples were collected every 5, 10, and 15 min for the flow rate of 1, 0.5, and 0.25 mL/min. At column exhaustion, the equilibrium concentration was removed for further analysis by using High-Performance Liquid Chromatography (HPLC) coupled with an evaporative light scattering detector (ELSD). Acetonitrile and deionized (DI) water were selected to use as mobile phases and were prepared separately as origin solutions. For analysis with HPLC, a mobile phase mixture was prepared (acetonitrile to DI water ratio = 55:45) and fed as a concentration gradient to the HPLC column (C18 type) at an operating flow rate of 0.5 mL/min. The controlled temperature by the machine was 30°C.

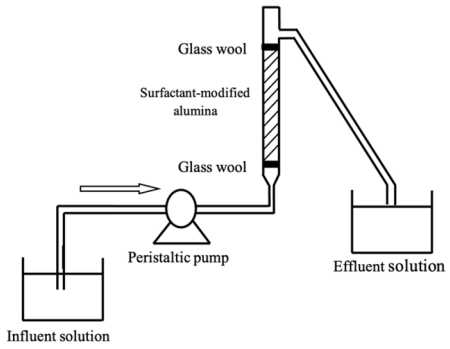

Figure 1. Lab-scale column study in this work.

2.2.3 Column desorption study

In the washing step, a desorption study was conducted to determine the possible amount of rhamnolipid released from the alumina surface. DI water was applied in an up-flow direction with the same flow rate in the column adsorption experiment until it was exhausted. As the concentration of rhamnolipid in an effluent approached zero, the washing process was then terminated. Therefore, rhamnolipid had no longer been detected or desorbed. HPLC with ELSD was used to analyze rhamnolipid exhausting concentration. Acetonitrile and DI water were used as mobile phases at similar conditions and flow rates as performed in the adsorption study.

2.2.4 Column adsolubilization study

In this part, rhamnolipid mixed with organic solutes (styrene and pyrene in each batch) was applied to the fixed-bed column to perform the adsolubilization process. The concentrations of styrene and pyrene were selected below the water solubility to avoid any immiscible phase. The concentration of rhamnolipid biosurfactant was 90% below CMC to prevent micelle formation. Electrolyte (1mM NaCl) was added in feeding during operation to imitate ionic strength in typical water. Solution (pH 8.0-8.5) was applied to the column containing 0.5 g of alumina and 19g of glass bead in the up-flow mode to perform adsolubilization.

Adsolubilization of styrene was applied onto the alumina surface in a continuous system. Styrene (3 mM) and rhamnolipid (0.27 mM) were mixed and applied to the packed column. The prepared solution was fed through the column in up-flow mode with 0.25, 0.5, and 1 mL/min flow rates, respectively. UV-VIS spectrophotometer at 275 nm wavelength was used to

analyze styrene concentration in the effluent. The experiments on pyrene adsolubilization were performed according to the same procedure as for styrene, with an input pyrene concentration of 6.42 µM. The final concentration of pyrene was analyzed by using a UV spectrophotometer at 330 nm wavelength.

3. RESULTS AND DISCUSSION

3.1 Column adsorption study

This section focuses on the adsorption of rhamnolipid biosurfactant onto a positively charged alumina surface in a continuous reactor. Rhamnolipid initially adsorbs onto an alumina surface due to the electrostatic attraction of rhamnolipid (negative charge) and alumina (positive charge) [22], [23]. Breakthrough curves in Figure 2 show that the breakthrough times for the flow rates of 0.25, 0.5, and 1 mL/min are obtained sequentially at 90, 30, and 10 min. The amount of treated water or bed volume (BV) at breakthrough times is 27 mL (0.15 BV), 13.5 mL (0.07 BV), and 9 mL (0.06 BV), respectively. These imply that rhamnolipid has more contact with the alumina surface at a minimum flow rate. Adsorption of rhamnolipid has performed well at the low flow rate of 0.25mL/min. The maximum rhamnolipid adsorption amounts obtained were 0.311, 0.183, and 0.344 µmole/g for 0.25, 0.5, and 1 mL/min, respectively. Similar results found in previous studies reported that short contact time in the adsorption column causes a decrease in adsorption efficiency [24]–[26].

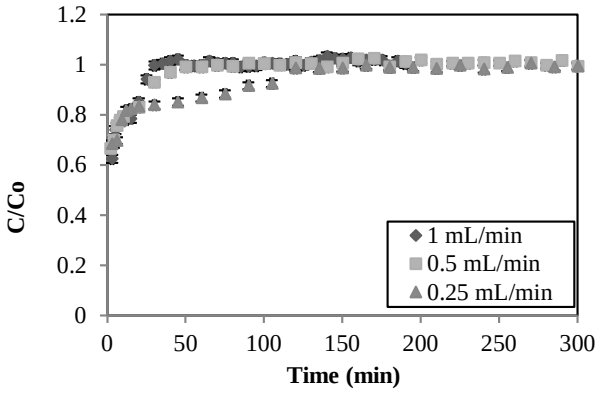

Figure 2 Breakthrough behavior of rhamnolipid biosurfactant at various flow rates (0.25–1.0 mL/min), 1.0 mM NaCl, pH 8.0–8.5, and 28±2°C.

3.2 Column desorption study

Surfactant desorption was investigated by gradually flushing deionized water into the pre-equilibrated column. Results in Figure 3 demonstrate a breakthrough cycle obtained from spent rhamnolipid-modified alumina. Rhamnolipid rapidly desorbs from the surface after 45, 20, and 15 min, and the flushing volumes of DI water are 9 mL (0.04 BV), 13.5 mL (0.07 BV), and 13.5 mL (0.07 BV) with flow rates of 0.25, 0.5, and 1 mL/min, respectively. DI rinsing altered the adsorbed rhamnolipid structure, where surfactant washes off from the alumina adsorbent. However, a slower feed flow rate was more beneficial to rhamnolipid adsorption, as it would prolong the complete desorption in this case.

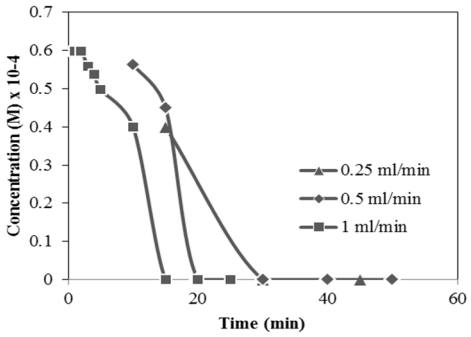

Figure 3 Column desorption of rhamnolipid biosurfactant at varying flow rates (0.25-1.0 mL/min) in 1.0 mM NaCl solution at pH of 8.0-8.5 and 28±2°C.

3.3 Styrene adsolubilization

Summary results of styrene and pyrene adsolubilization in the fixed bed column for flow rates of 0.25, 0.5, and 1 mL/min are shown in Table 2. The adsolubilization of styrene onto the alumina surface reveals that as the flow rates increase, there is a corresponding decrease in the retardation factor, with values of 16.01, 9.04, and 6.24 for flow rates of 0.25, 0.5, and 1 mL/min, respectively. This pattern is likewise observed when styrene adsolubilizes onto rhamnolipid-modified alumina, where the retardation factors are measured as 26.7, 15.21, and 9.82 at the same flow rates. Results also show that retardation of styrene with rhamnolipid is higher than those without for similar flow rates and volumes of water. These findings confirm the presence of rhamnolipid aggregates within the column, which prolongs the adsolubilization of organic solutes and are in close agreement with the previous research [21]. In addition, shortened contact time results in poor liquid distribution inside the column, leading to lower styrene diffusivity through rhamnolipid admicelle. This illustrates that lower feed flow rates lead to a slower movement of solutes, highlighting the critical importance of flow dynamics in optimizing adsolubilization processes. However, retardation of styrene with rhamnolipid is higher than those without for similar flow rates and volumes of water. The formation of rhamnolipid admicelles has promoted the adsolubilization in these structures. Results also show that the enhancement of retardation factors indicates increasing adsolubilization capacities in the system. In the presence of rhamnolipid admicelles, styrene adsolubilization capacities are increased as decreasing flow rates: 167.8, 114.4, and 91.4 µmole/g for 0.25, 0.5, and 1 mL/min feed, respectively.

Table 2 Column study results of styrene and pyrene adsolubilization on various flow rates

	Styrene alone	Styrene with rhamnolipid	Pyrene alone	Pyrene with rhamnolipid
Operating flowrate = 0.25 mL/min				
Retardation Factor	16.01	26.70	32.88	48.08
Adsolubilization capacity (µmole/g)	98.09	167.84	0.154	0.201
Operating flowrate = 0.5 mL/min				
Retardation Factor	9.04	15.21	18.66	19.81
Adsolubilization capacity (µmole/g)	17.07	114.4	0.028	0.254
Operating flowrate = 1 mL/min				
Retardation Factor	6.24	9.82	10.12	15.59
Adsolubilization capacity (µmole/g)	58.50	91.43	0.089	0.118

3.4 Pyrene adsolubilization

Adsolubilization of pyrene was studied under the conditions used for styrene. Results in Table 2 show that rhamnolipid enhances the retardation and adsolubilization of pyrene in fixed-bed columns compare to the system without rhamnolipid. This finding agrees with results in the literature [26], [27]. The effect of feed flow rate on pyrene adsolublization in the column showed a similar trend as observed in the styrene experiments. In pyrene adsolubilization, retardation factors increase with decreasing feed flow rates (retardation factors are 48.08, 19.81, and 15.59 for flow rates of 0.25, 0.5, and 1 mL/min, respectively). The pyrene adsolubilization capacities are 0.201, 0.254, and 0.118 µmol/g for 0.25, 0.5, and 1 mL/min, respectively.

Figure 3 presents a comparison of the breakthrough curves between styrene and pyrene in the rhamnolipid admicelle in fixed-bed columns with the optimum feed flow rate of 0.25 mL/min. Results show that pyrene has a small movement in the columns than in styrene based on the higher retardation factors. This phenomenon can be explained by the larger molecule of pyrene causing a slow movement and prolonging contact time in the column. However, the larger size of the pyrene molecule (MW=202.3 g/mol) than the styrene (MW 104.5 g/mol) may result in less occupation of adsolubilization site or pore clogging within the column.

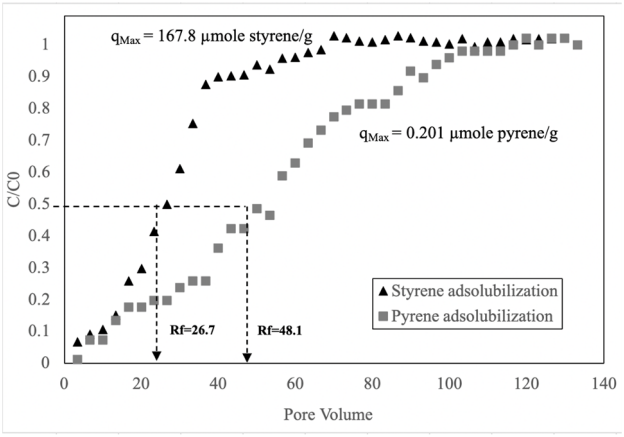

Figure 3. Adsolubilization of styrene and pyrene by rhamnolipid-modified alumina in the fixed-bed column at a flow rate of 0.25 mL/min, initial pH of 8.0-8.5, and temperature of 28±2°C.

In addition, results also showed the very low adsolubilization capacity of pyrene. These findings indicate that the adsolubilization of those two organic solutes is influenced by their aqueous solubilities (styrene: 310 mg/L, pyrene 0.07 mg/L). The greater possibility of contact with the adsorbent in the column of pyrene implied different places for the solutes to adsolubilize in the admicelle. Regarding the unlikeness of the oil-water-like region of the surfactant-modified surface, the polarity of individual organic solutes affects the adsolubilization behavior. Thus, pyrene resides preferably in the hydrophobic part of the admicelle structure (the core region) rather than in the palisade region, as styrene does [10].

4. CONCLUSION

The removal of styrene and pyrene through a fixed-bed column was successfully achieved using a rhamnolipid biosurfactant-modified alumina surface. The effect of flow rate showed that breakthrough time increased with decreasing flow rate for rhamnolipid adsorption. In addition, the rhamnolipid-modified alumina in the column can be regenerated using distilled water. Adsolubilization study demonstrated that pyrene was less adsolubilized in rhamnolipid biosurfactant admicelle compared with styrene, due to the dissimilarity between the hydrophobic properties of the organic solutes.

ACKNOWLEDGMENTS

Authors would like to acknowledge Thailand Research Fund for the grant supported in this work (Grant no.MRG2555). Appreciation would extend to the Faculty of Engineering Burapha University and the Faculty of Environmental Engineering Chulalongkorn University for all their supports in this work.

REFERENCES

1. Lamichhane, S. Krishna, Kc. B. Sarukkalige. P. R. Surfactant-enhanced remediation of polycyclic aromatic hydrocarbons: A review. *Journal of Environmental Management* 2017; 199(1): 46-61.
2. Rodrigues, A. Nogueira, R. Melo, L. F. Brito, A.G. Effect of low concentrations of synthetic surfactants on polycyclic aromatic hydrocarbons (PAH) biodegradation. *International Biodeterioration & Biodegradation* 2013; 83: 48-55.
3. Zhang, Z. Lo, I. M. Yan, D. Y. An integrated bioremediation process for petroleum hydrocarbons removal and odor mitigation from contaminated marine sediment. *Water Research* 2015; 83: 21-30.
4. Mohebbi-Nozar, S. L. Zakaria, M. P. Ismail, W. R. Mortazawi, M. S. Salimizadeh, M. Momeni, M. Akbarzadeh, G. Total petroleum hydrocarbons in sediments from the coastline and mangroves of the northern Persian Gulf. *Marine pollution bulletin* 2015; 95: 407-411.
5. Paria, S. Surfactant-enhanced remediation of organic contaminated soil and water. *Advances in Colloid and Interface Science* 2008; 138(1): 24-58.
6. Yan, Z., Jiang, H., Li, X., Shi, Y. Accelerated removal of pyrene and benzo[a]pyrene in freshwater sediments with amendment of cyanobacteria-derived organic matter. *Journal of Hazardous Materials* 2014; *272*: 66–74.
7. Franco, C. A., Nassar, N. N., Cortes, F. B. Removal of oil from oil-in-saltwater emulsions by adsorption onto nano-alumina functionalized with petroleum vacuum residue. Journal of Colloid and Interface Science 2014; 433: 58–67.
8. Feng, S., Gong, L., Zhang, Y., Tong, Y., Zhang, H., Zhu, D., Huang, X., Yang, H. Bioaugmentation potential evaluation of a bacterial consortium composed of isolated Pseudomonas and Rhodococcus for degrading benzene, toluene and styrene in sludge and sewage. Bioresource Technology 2021; 320(Part A): 124392.
9. Ansari, R., Seyghali, B., Mohammad-khah, A., Zanjanchi, M. A. Application of nano surfactant modified biosorbent as an efficient adsorbent for dye removal. Separation Science and Technology 2012; 47: 1802–1812.
10. Asnachinda, E., Khaodhiar, S., Sabatini, D. A. Styrene and phenylethanol adsolubilization of a polymerizable gemini surfactant. Journal of Surfactants and Detergents 2010; 13: 143–148.
11. Khalladi, R., Benhabiles, O., Bentahar, F., Moulai-Mostefa, N. Surfactant remediation of diesel fuel polluted soil. Journal of Hazardous Materials 2009; 164: 1179–1184.
12. Shen, L. C., Nguyen, X. T., Hankins, N. P. Removal of heavy metal ions from dilute aqueous solutions by polymer–surfactant aggregates: A novel effluent treatment process. *Separation and Purification Technology* 2015; *152*: 101–107.
13. Henkel, M., Muller, M. M., Kugler, J. H., Lovaglio, R. B., Contiero, J., Syldatk, C., Hausmann, R. Rhamnolipids as biosurfactants from renewable resources: Concepts for next-generation rhamnolipid production. *Process Biochemistry* 2012; *47*(8): 1207–1219.
14. Cameotra, S. S., Makkar, R. S., Kaur, J., Mehta, S. K. Synthesis of biosurfactants and their advantages to microorganisms and mankind. *Advances in Experimental Medicine and Biology* 2010; *672*: 261–280.
15. Chen, Q., Bao, M., Fan, X., Liang, S., Sun, P. Rhamnolipids enhance marine oil spill bioremediation in laboratory system. *Marine Pollution Bulletin* 2013; *71*: 269–275.
16. Wang, J., Bao, H., Pan, G., Zhang, H., Li, J., Li, J., Cai, J., Wu, F. Combined application of rhamnolipid and agricultural wastes enhances PAHs degradation via increasing their bioavailability and changing microbial community in contaminated soil. *Journal of Environmental Management* 2021; *294*: 112998.
17. Whang, L. M., Liu, P. W., Ma, C. C., Cheng, S. S. Application of biosurfactants, rhamnolipid, and surfactin, for enhanced biodegradation of diesel-contaminated water and soil. *Journal of Hazardous Materials* 2008; *151*(1): 155–163.
18. Souza, E. C., Vessoni-Penna, T. C., Oliveira, R. P. D. Biosurfactant-enhanced hydrocarbon bioremediation: An overview. *International Biodeterioration & Biodegradation* 2014; *89*: 88–94.
19. Nguyen, T. T., Youssef, N. H., McInerney, M. J., Sabatini, D. A. Rhamnolipid biosurfactant mixtures for environmental remediation. *Water Research* 2008; *42*: 1735–1743.
20. Das, A., Pal, A., Saha, S., Maji, S. K. Behaviour of fixed-bed column for the adsorption of malachite green on surfactant-modified alumina. *Journal of Environmental Science and Health, Part A: Toxic/Hazardous Substances and Environmental Engineering* 2009; *44*(3): 265–272.
21. Fuangswasdi, A., Krajangpan, S., Sabatini, D. A., Acosta, E. J., Osathaphan, K., Tongcumpou, C. Effect of admicellar properties on adsolubilization: column studies and solute transport. *Water Research* 2007; *41*(6): 1343–1349.
22. Asvapathanagul, P., Malakul, P., O'Haver, J. Adsolubilization of toluene and acetophenone as a function of surfactant adsorption. *Journal of Colloid and Interface Science* 2005; *292*(2): 305–311.
23. Esumi, K. Interactions between surfactants and particles: Dispersion, surface modification, and adsolubilization. *Journal of Colloid and Interface Science* 2001; *241*(1): 1–17.
24. Chen, N., Zhang, Z. Y., Feng, C. P., Li, M. A., Chen, R. Z., Sugiura, N. Investigations on the batch and fixed-bed column performance of fluoride adsorption by Kanuma mud. *Desalination* 2011; *268*: 76–82.
25. Mobasherpour, I., Salahi, E., Asjodi, A. Research on the batch and fixed-bed column performance of red mud adsorbents for lead removal. *Canadian Chemical Transactions* 2014; *2*(1): 83–96.

26. Ozdemir, O., Turan, M., Turan, A. Z., Faki, A., Engin, A. B. Feasibility analysis of color removal from textile dyeing wastewater in a fixed-bed column system by surfactant-modified zeolite (SMZ). *Journal of Hazardous Materials* 2009; *166*: 647–654.
27. Ding, C. L., Yang, X., Liu, W., Chang, Y. J., Shang, C. I. Removal of natural organic matter using surfactant-modified iron oxide-coated sand. *Journal of Hazardous Materials* 2010; *174*: 567–572.

Valorization of pineapple leaf fiber (PALF) Waste: Optimization of alkali pretreatment for fermentable sugar production

Khemmathin Lueangwattanapong[1], Kanyarat Thaithonglang[2], Jirapha Koonkonyang[2], Chanya Phromchaloem[2], Laksamee Muensritharam[2,*]

[1] Department of Chemical Engineering, Faculty of Engineering, Kasetsart University, Ladyao, Chatuchuk, Bangkok, 10900, Thailand
[2] Faculty of Science and Technology, Muban Chom Bueng Rajabhat University, Chom Bueng, Ratchaburi, 70150, Thailand
[*] Corresponding author: laksamee_biot@hotmail.com

ABSTRACT

Pineapples are one of the major agricultural exports in Southeast Asia, accounting for a significant portion of the global market. Since a pineapple plant only fruits once or twice in its lifetime, farmers need to clear out the remaining stems and leaves through pruning to return nutrients to soil or utilize the leaf fiber. Pineapple leaf fiber (PALF), consisting primarily of cellulose, can be used for handmade products, packaging, and reinforcing material. However, the process of extracting pineapple leaf fiber generates substantial solid waste which has yet to find promising applications beyond being left to dry on fields (producing greenhouse gases) or used as cattle feed. This study investigated the potential of waste from the pineapple leaf fiber industry for reducing sugar production using alkali pretreatment and enzymatic hydrolysis. The PALF waste was soaked in NaOH solutions of varying concentrations (0.1M, 0.15M, and 0.2M) at 121°C for 0.5 hours. The treated PALF waste was then hydrolyzed for sugar production using cellulase enzyme. Simple characterization was performed to determine total solids and volatile solids, while total sugar determination was conducted using the DNS (3,5-dinitrosalicylic acid) method. Results showed that the highest yield of total sugar was 111.67 g/L, obtained from PALF waste treated with 0.15M NaOH. Sugar was also detected during the pretreatment phase. Changes in volatile solids content could be used as an initial indicator of hemicellulose removal during alkali pretreatment. This work provides an alternative solution for PALF waste valorization through sugar production, offering both environmental and economic benefits to the pineapple industry in Southeast Asia.

Keywords: Pineapple Leaf Fiber; Alkali Pretreatment; Reducing Sugar; Waste Valorization

1. INTRODUCTION

Pineapple (scientific name: *Ananas comosus*) is an important economic crop in Thailand, with cultivation areas distributed throughout all regions of the country, covering approximately 450,000 rai (72,000 hectares). Pineapple is a monocotyledon that can withstand various environmental conditions well. After harvesting the pineapple fruit, there remain significant amounts of pineapple leaves and stems, not less than 10,000 kilograms per rai, which are currently underutilized. These pineapple leaves become a burden for farmers who must manage them before the next planting cycle. The total amount of this biomass nationwide could be equivalent to approximately 1 million tons of carbon dioxide per year.

The composition of pineapple leaves chemically consists of cellulose, hemicellulose, lignin, and certain extractives. Cellulose and hemicellulose together are called holocellulose, which is the main component of plant cell walls. Cellulose is formed by multiple units of cellobiose linked together repeatedly, while hemicellulose is formed by a combination of hexose and pentose units with polymerization levels between 15-14,000. Lignin is formed by three-dimensional cross-linking polymer groups. Pineapple fiber is cellulosic fiber obtained from pineapple leaves, which are agricultural waste materials from pineapple plantations after fruit harvesting. Thailand is one of the world's major pineapple producers. According to reports, the pineapple cultivation area in Thailand is 575,580 rai (92,093 hectares). With 8,000 plants per rai producing 130 kg of fiber per rai, this yields 75,000 tons of fiber, sufficient for annual use in the country's textile and packaging industries. However, the lack of automated fiber extraction machinery to process fibers

from pineapple farms to textile production facilities has limited the full potential utilization of pineapple fibers.

Pineapple leaf residue can also be used as a support material for heavy metal adsorbents in wastewater or as photocatalysts for eliminating organic compounds in water, facilitating easier separation or recycling. Pineapple waste can be fermented to produce biogas for fuel in agro-industrial factories. Additionally, fermented pineapple waste (from factories) that has been processed for up to 8 months can be used to feed dairy cattle when consumed alongside protein supplements. Utilizing this biomass creates value from waste through science and technology, generates employment in communities, and simultaneously helps sequester carbon in various products.

The research began by developing processes to pretreat pineapple leaf residue with alkali and heat. The production of reducing sugars is divided into two main processes: pretreatment to remove lignin compounds that coat or cover the structure of cellulose and hemicellulose, and hydrolysis, which breaks down cellulose to produce reducing sugars as a product. Pretreatment aims to remove lignin and adjust the cellulose structure to be suitable for hydrolysis. Pretreatment helps eliminate lignin, breaks down the crystalline structure of cellulose, and increases the surface area for reactions (Krishna and Chowdary, 2000). Alkaline hydrolysis is a process of digesting cellulose using alkali as a catalyst. This process can be done quickly and with high efficiency, yielding high amounts of reducing sugars because the alkali accelerates the hydrolysis reaction of cellulose. Common solutions used include sodium hydroxide, ethylenediamine, and ammonia. Using alkaline solutions for hydrolysis shortens polysaccharide chains. This reaction occurs at high temperatures around 160-180°C and requires oxygen to participate in the hydrolysis reaction (Niwaswong et. al., 2012). Another study using alkali pretreatment to enhance reducing sugar production from empty fruit bunches found that the NaOH concentration of 15% was deemed suitable for pretreatment of lignocellulosic materials prior to enzymatic hydrolysis. The cellulose content was increased by 14.28%dw while the proportion of lignin was reduced by 3.41%dw (Thanapimmetha et. al., 2018). A study on glucose extraction from sugarcane leaves found that using 125 grams of sugarcane leaves per liter, hydrolyzed with 2% sodium hydroxide by volume at 122°C for 30 minutes, yielded the maximum total sugar amount of 95.63 grams per liter (Sabiha-Hanim & Abd Halim, 2019).

Therefore, this study aimed to investigate the pretreatment of pineapple leaf residue with heat and different concentrations of alkali to find optimal conditions for producing reducing sugars and to study the enzymatic hydrolysis of pineapple leaf residue to determine optimal conditions for reducing sugar production.

2. EXPERIMENTAL METHODS

2.1 Material Preparation

Agricultural waste materials, specifically pineapple leaves, were collected as samples. The pineapple leaves were cut or chopped into small pieces before sun drying. 600 grams of pineapple leaf residue were oven-dried at 105°C for 24 hours or until completely dry (AOAC, 2019). The samples were then ground into fine particles using a grinder and stored in plastic bags. The samples were preserved in dry conditions in a desiccator.

Figure 1 Dried PALF waste

2.2 Alkali Pretreatment

Three concentrations of sodium hydroxide solution were prepared: 0.2 M, 0.15 M, and 0.1 M. Then, 30 grams of dry pineapple leaf residue were mixed into each bottle containing the sodium hydroxide solution at all three concentrations. These were autoclaved at 121°C for 30 minutes, then filtered using a Buchner funnel (vacuum filtration). The filtered liquid was measured for reducing sugar content using a UV-vis Spectrophotometer, and the remaining residue was dried and incinerated to analyze %TS (dry weight), %VS (organic matter weight), and %VS/TS (organic matter weight in dry residue).

2.3 Enzymatic Hydrolysis of PALF Waste

Non-pretreated pineapple leaf residue and pineapple leaf residue pretreated with three different alkali concentrations were used. Three grams each of pretreated pineapple leaf residue at three different alkali concentrations were placed in three flasks, and three grams each of non-pretreated residue were placed in three flasks. Then, 20 milliliters of sodium acetate buffer solution were added to each flask, followed by 3 milliliters of cellulase enzyme. The flasks were incubated in a water bath for 68 hours, then filtered using filter paper, and analyzed for reducing sugar content.

2.4 Reducing Sugar Determination

Two grams of sodium hydroxide were dissolved in 50 milliliters of distilled water. 1.25 grams of 3,5-dinitrosalicylic acid (DNS) were added to 1 M sodium

hydroxide solution (2 grams of sodium hydroxide in 50 milliliters of distilled water) and stirred until dissolved with heat. 37.5 grams of sodium potassium tartrate were dissolved in 62.5 milliliters of distilled water and stirred until dissolved with heat. All solutions were combined in a 250-milliliter volumetric flask, shaken well, and the volume adjusted to 250 milliliters with distilled water. The solution was stored in a 250-milliliter amber bottle.

One milliliter of diluted sample was pipetted into a test tube, then 1 milliliter of DNS solution was added and mixed well. The mixture was boiled in water for 5 minutes with the tube capped and then immediately cooled in ice water for 5 minutes to stop the color reaction. Ten milliliters of distilled water were added and mixed well. The absorbance was measured at a wavelength of 520 nanometers. The absorbance values were compared to a standard glucose curve to determine the reducing sugar content.

3. RESULTS AND DISCUSSION

3.1 Biomass Characteristics

The dry weight analysis (%TS) of pineapple leaf residue before pretreatment with heat and different alkali concentrations had an average value of 92.17%. The organic matter weight analysis (%VS) had an average value of 89.78%. The organic matter weight in dry residue analysis (%VS/TS), repeated for 6 cups, had an average value of 97.41%.

These initial characterisation values indicate that pineapple leaf waste contains a significant proportion of organic matter (89.78%) relative to its dry weight, suggesting it is a promising feedstock for bioconversion processes. The high VS/TS ratio (97.41%) further confirms that the vast majority of the dry matter consists of organic compounds, primarily lignocellulosic materials that could be converted to valuable products through appropriate treatment methods. This composition is comparable to other agricultural residues commonly used in biorefinery applications, such as rice straw and sugarcane bagasse, though pineapple leaf waste appears to have a particularly high organic matter content.

3.2 Effect of Alkali Pretreatment on the Biomass Composition

The analysis of pineapple leaf residue composition after pretreatment with heat (121°C in an autoclave for 30 minutes) and three different alkali concentrations (0.2 M, 0.15 M, and 0.1 M) showed the following results (Table 1). The dry weight analysis (%TS) after pretreatment had average values of 99.62%, 99.54%, and 99.59% for each concentration respectively. The organic matter weight analysis (%VS) after pretreatment had average values of 89.16%, 89.68%, and 91.56% for each concentration respectively. The organic matter weight in dry residue analysis (%VS/TS) after pretreatment had average values of 89.50%, 90.10%, and 91.94% for each concentration respectively.

The pretreatment process appears to have resulted in increased dry matter content across all alkali concentrations (>99% TS compared to the initial 92.17%), which likely indicates the removal of volatile compounds during the high-temperature treatment. The organic matter content (%VS) remained relatively stable after pretreatment with 0.2 M and 0.15 M sodium hydroxide (89.16% and 89.68% respectively), but showed a slight increase with the lowest alkali concentration of 0.1 M (91.56%).

This pattern suggests that higher alkali concentrations may be more effective at removing certain organic components, particularly hemicellulose, which is consistent with the mechanism of alkaline pretreatment reported in the literature. The decrease in VS/TS ratios after pretreatment with higher alkali concentrations (89.50% and 90.10% for 0.2 M and 0.15 M respectively, compared to 91.94% for 0.1 M) further supports this interpretation. This differential effect on biomass composition is a crucial factor in understanding the subsequent enzymatic hydrolysis efficiency.

Table 1 Biomass composition of PALF waste before and after alkali pretreatment

PALF waste sample	%TS	%VS	%TS/VS
Before pretreatment	92.17	89.78	97.41
After pretreatment (1.0 M)	99.59	91.56	91.94
After pretreatment (1.5 M)	99.62	89.68	90.1
After pretreatment (2.0 M)	99.54	89.16	89.5

3.3 Effect of Alkali Pretreatment on the Reducing Sugar Concentration Before Enzymatic Hydrolysis

The study of reducing sugar content after pretreatment with heat (121°C in an autoclave for 30 minutes) and three different alkali concentrations (0.2 M, 0.15 M, and 0.1 M) was measured by absorbance at 520 nanometers using a UV-vis Spectrophotometer. The absorbance values at 520 nanometers for samples after pretreatment were 0.12, 0.13, and 0.12, respectively. These correspond to average sugar concentrations of 1.23, 1.30, and 1.17 mg/ml, respectively.

The reducing sugar concentrations detected immediately after pretreatment were relatively low across all alkali concentrations, ranging from 1.17 to 1.30 mg/ml. This indicates that the alkaline pretreatment alone released only a modest amount of sugars from the biomass structure with the slightly higher sugar concentration observed with 0.15 M NaOH (1.30 mg/ml) compared to both 0.2 M (1.23 mg/ml) and 0.1 M (1.17 mg/ml) treatments.

This phenomenon could be attributed to competing reactions during the pretreatment process—whilst higher alkali concentrations may be more effective at disrupting the lignocellulosic structure, they might also facilitate degradation of released sugars. These results highlight that whilst pretreatment is essential for increasing accessibility of cellulose to subsequent enzymatic attack, it is not primarily a sugar-generating step itself.

3.4 Effect of Alkali Pretreatment on the Reducing Sugar Concentration After Enzymatic Hydrolysis

The sugar concentrations of samples after hydrolysis with cellulase enzyme from pretreated samples at three alkali concentrations (0.2 M, 0.15 M, and 0.1 M) had average values of 111.67, 68.87, and 90.42 mg/ml, respectively. The non-pretreated samples had an average concentration of 66.20 mg/ml. The alkali concentration of 0.2 M was able to produce reducing sugars effectively (Figure 2)

The enzymatic hydrolysis results reveal a dramatic increase in reducing sugar concentrations compared to the pretreatment stage alone, confirming the critical role of enzymatic saccharification in converting the pretreated lignocellulosic material to fermentable sugars. The most striking observation is the substantially higher sugar yield from biomass pretreated with 0.2 M NaOH (111.67 mg/ml), representing a 68.7% increase over the non-pretreated control (66.20 mg/ml).

In this study, the relationship between alkali concentration and sugar yield after enzymatic hydrolysis does not follow a simple linear pattern. The 0.15 M NaOH pretreatment yielded the lowest sugar concentration (68.87 mg/ml), which was only marginally higher than the non-pretreated control, whilst the 0.1 M pretreatment produced an intermediate result (90.42 mg/ml).

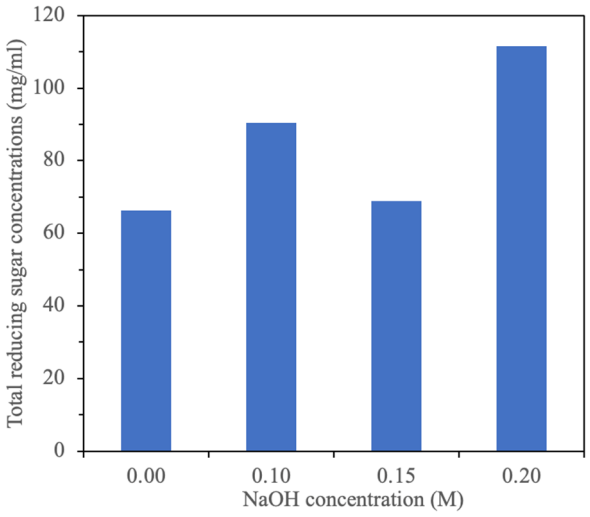

Figure 2 Total reducing sugar concentration obtained from non-treated and alkali-treated PALF waste after enzymatic hydrolysis

The superior performance of the 0.2 M NaOH pretreatment likely stems from its optimal balance between lignin removal and cellulose preservation. Higher alkali concentrations would effectively disrupt the lignin-carbohydrate complexes and reduce cellulose crystallinity, thereby creating more accessible sites for enzymatic attack. The reduced effectiveness of the 0.15 M pretreatment compared to even the 0.1 M condition is unexpected and warrants further investigation—perhaps indicating experimental variability or suggesting that specific structural changes in the biomass occur within narrow parameter ranges.

Overall, these results demonstrate that appropriate alkaline pretreatment significantly enhances the enzymatic digestibility of pineapple leaf waste, with the 0.2 M NaOH concentration emerging as the optimal condition amongst those tested. The nearly 1.7-fold increase in reducing sugar yield compared to non-pretreated biomass underscores the potential economic and environmental benefits of implementing this pretreatment strategy in biorefinery operations utilising pineapple agricultural residues.

4. CONCLUSION

This research demonstrates that pretreatment of pineapple leaf waste with alkaline solution significantly enhances the production of reducing sugars through enzymatic hydrolysis. Among the tested sodium hydroxide concentrations (0.2 M, 0.15 M, and 0.1 M), the 0.2 M concentration proved most effective, yielding the highest reducing sugar concentration of 111.67 mg/ml after enzymatic hydrolysis. This represents a significant improvement compared to non-pretreated samples, which produced only 66.20 mg/ml of reducing sugars. The findings confirm that appropriate pretreatment methods can substantially improve the accessibility of cellulose to enzymatic attack. Future studies should focus on optimizing the enzymatic hydrolysis process and investigating the economic feasibility of this process.

ACKNOWLEDGMENTS

This work was supported by Muban Chombueng Rajabhat University (MCRU) and National Science, Research and Innovation Fund (NSRF)

REFERENCES

1. AOAC. (2019). Official Methods of Analysis of the Association of Official Analytical Chemists: Official Methods of Analysis of AOAC International. 21st Edition, AOAC, Washington DC.
2. Krishna, S. H. & Chowdary, G. V. (2000). Optimization of simultaneous saccharification and fermentation for the production of ethanol from lignocellulosic biomass. Journal of agricultural and food chemistry, 48(5), 1971-1976.

3. Niwaswong, C., Chaiyamate, P., Chotikosaikanon, P., & Ruangviriyachai, C. (2014). Simple and enhanced production of lignocellulosic ethanol by diluted acid hydrolysis process of pineapple peel (Ananas comosus) waste. African Journal of Biotechnology, 13(38).
4. Sabiha-Hanim, S., & Abd Halim, N. A. (2019). Sugarcane Bagasse Pretreatment Methods for Ethanol. Fuel ethanol production from sugarcane, 63.
5. Thanapimmetha, A., Tiyanusorn, S., Srinophakun, P., & Saisriyoot, M. (2018). Reducing sugar production from empty fruit bunches with enzyme Cellic Ctec2®. The Journal of KMUTNB, 28(2), 285–290 (in Thai).

Residue extraction on artificial knee surfaces using ultrasonic techniques

Thitima Naovong[1], Aroonsri Nuchitprasittichai[1], Supunnee Junpirom[1,*]

[1] School of Engineering, Institute of Chemical Engineering, Suranaree University of Technology, Nakhon Ratchasima 30000, Thailand
[*] Corresponding author: supunnee@sut.ac.th

ABSTRACT

The presence of residual contaminants on artificial knee surfaces poses potential risks to implant performance and patient safety. One technique to assess the level of residue on devices is cleaning validation by extracting contaminants from the surfaces. This study investigates the efficiency of residue extraction using ultrasonic techniques on artificial knee components, including the femoral, tibial, and polyethylene inserts. The extraction process was performed using 500 mL of solvent extraction at temperatures ranging from 50°C to 80°C for durations of 10 to 60 minutes, as illustrated in Figure 1. Residual analysis was conducted using Total Organic Carbon (TOC) measurement. The efficiency of extraction was evaluated using the spike recovery method. The optimal condition at each temperature did not exceed 30 minutes, with the femoral component exhibiting the highest level of residual contaminants compared to the tibial and polyethylene inserts. Spike recovery tests confirmed the method's reliability, with recovery rates exceeding between 45 - 90 % at extraction temperature of 50°C. These findings highlight the effectiveness of ultrasonic extraction as a reliable method for residue extraction, providing a foundation for enhancing cleaning validation processes in orthopedic implant manufacturing.

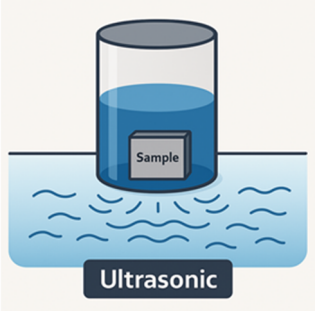

Figure 1 Ultrasonic extraction setup for residue extraction.

Keywords: artificial knee, ultrasonic extraction, cleaning validation, residual, total organic carbon

1. INTRODUCTION

The application of artificial knees has been steadily increasing, driven by the prevalence of arthritis and osteoporosis resulting from the growing proportion of the elderly population [1]. One of challenge in the manufacturing orthopedic implants is cleanliness [2], which is essential to ensure their safety and effectiveness for patient use. Large amounts of residues on artificial knee can pose significant risks to patients when exposed to bodily fluids, potentially leading to toxic reactions. One technique to determine the level of residual is validation of the cleaning process. In the early 1990s, Food and Drug Administration (FDA) started to evaluate cleaning as an action which requires a validation [3]. Additionally, the International Organization for Standardization (ISO) 13485 document that cleaning validation is indeed a critical process to ensure that residues are effectively removed from medical devices during manufacturing [4].

For validation of cleaning methods has various sampling techniques to ensure effective monitoring and control of residues. The swab sampling technique provides information about specific sites selected and swabbed. A limitation of swab sampling is collecting the residue, which manual operation so procedures should establish to develop sampling consistency. On the other hand, the extraction technique is reaches often inaccessible locations on the devices, sing a solvent to contact all surface of a sampled to quantitatively the

residue. It provides an overall of the cleanliness of the devices [5]. The solvent can be water-soluble residues, organic-soluble residues, and non-soluble debris, depending on relative solubility of the residue [6]. Extraction process can be assisted by ultrasonic agitation, reflux, bubbling, or with heat. The residue in the collected solution can be measured using either a specific or non-specific methods [5].

Ultrasonic extraction has become an efficient method for extracting residues from medical devices by utilizing ultrasonic waves to generate microscopic bubbles. The collapse of these bubbles produces high-pressure and high-temperature conditions that aid in detaching residues from device surfaces. Key factors such as temperature and extraction time significantly influence efficiency and must be controlled to optimize the process while preserving material integrity. Shimadzu offers a suitable method to validate the cleanliness of knee implants by using ultrasonic extraction at 70°C for 1 hour, the residue has been purposely applied to the implant's surface. Following by Total Organic Carbon (TOC) analysis, which could detect good precision and evidenced quickly [6]. Furthermore, ASTM International advises the extraction process was not exceeding of 30 minutes for medical devices and most common validation methods utilizes extraction techniques to quantify the residuals that remain on the surfaces is non-specific methods like Total Organic Carbon (TOC), which ensures consistently low residue levels, with offering rapid quantitative analysis [7].

In addition to validating the extraction process is a critical aspect of analytical chemistry, ensuring that methods yield reliable and reproducible results. One widely accepted approach for assessing the efficiency of extraction techniques involves spike recovery test. This method provides a quantifiable measure of an extraction method's accuracy by evaluating its capability to recover a known quantity of analyte to the sample before extraction [8]. ASTM F2459 specifies a minimum extraction efficiency of 75%, with less than 50% generally deemed unacceptable, the efficiency is calculated as the ratio of recovered to doped residue by adjusting contaminants until the desired efficiency is met. This method ensures high specificity but becomes more complex as the number of contaminants, requiring individual doping for each contaminant on each device types [9].

In this study, we aim to investigate of the residual extraction using ultrasonic techniques under different condition 50°C to 80°C for durations of 10 to 60 minutes, with extraction solvents of 250, 500 and 1000 mL from different parts of artificial knee: femoral, tibial, polyethylene inserts as well as test coupon. Along with this, validating the residual extraction by spike recovery. The optimal condition was determined to be at each temperature is not exceed 30 minutes with 500 mL of extraction solvent, which indicated that residual devices has extracted in the highest level.

2. EXPERIMENTAL

2.1 Sample Preparation

The samples used in this work were designed regard to critical artificial knee components features including (1) Femoral, (2) Tibial, (3) polyethylene insert, (4) CoCr test coupon and (5) polyethylene test coupon. Three main components of Artificial knee as shown in Figure 2, which is typically materials used in the manufacturing of artificial knee. For the evaluation of the cleaning procedure, the sample was simulated in worst-case scenario with soaking synthetic oil, which typical contaminations during manufacturing process. Additionally, untreated samples meaning 'unclean device'.

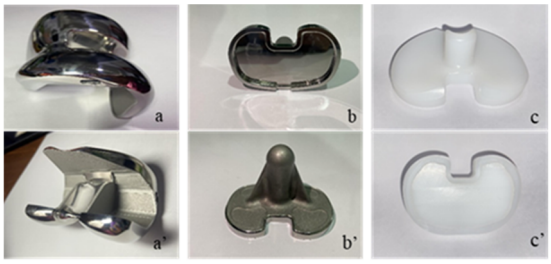

Figure 2 The three main components of Artificial knee including: (a-a') femoral component, (b-b') tibial component, and (c-c') polyethylene insert.

2.2 Cleaning Procedure

The cleaning procedure were carried out in a clean room class 10,000. The procedure consists of four consecutive steps. First, unclean device was emerged in with Liquinox (Alconox Inc, USA) and constantly agitating in ultrasonic cleaner (Ultrasonic system, model GT SONIC-D27) followed by DI-water and isopropyl alcohol. Lastly, the samples were cleaned in an ultrasonic bath in DI-water. The devices were dried with hot air blower for at least 5 min. Finally, the devices were stored in sterile medical packaging until further use. Additionally, treated samples meaning 'clean device'.

2.3 Residue Extraction

Residue on devices is extracted in DI-water was done according to ultrasonic technique (Ultrasonic Cleaner, GT SONIC-D27). First, glass beakers were prepared the solvent with deionized water 500 ml, the cleaned device was placed into beaker. The experimental was carried out in a closed system covered beaker with aluminum foil. Then place them in an ultrasonic. The experiment was performed at temperature of 50, 60, 70, and 80°C of each device. Lastly, fill extraction liquid into sample vessels, the liquids sample were collected at 10, 20, 30, 40, 50 and 60 minutes for each temperature. The experiment was

performed in 5 runs. All handling of the samples was carried out with protection gloves. Subsequently, the devices were dried with hot air blower for at least 5 min. Finally, the devices were stored in sterile medical packaging.

2.4 Extraction solvent volume

To investigate the effect of solvent volume on the efficiency of ultrasonic extraction, three different volumes of extraction solvent: 250 mL, 500 mL, and 1000 mL were evaluated. For each condition, glass beakers were prepared containing the cleaned devices, The beakers were filled with each volume of extraction solvent and placed in an ultrasonic bath. Ultrasonic extraction was carried out under controlled conditions at four different temperatures: 50°C, 60°C, 70°C, and 80°C. For each temperature setting, a range of extraction times (10, 20, 30, 45, and 60 minutes) was applied to evaluate the kinetics of residue extraction.

2.5 Extraction efficiency test

For preparation of standards and controls, the sample is CoCr test was used. The standard consisted of liquinox TOC content of 0.50, 0.100, 0.150, 0.200, 0.250 and 0.300 µg/mL into 500 mL DI-water, 1 µg Liquinox have 224.6 µg/µL of TOC. The volume Liquinox need is equal target liquinox TOC (g/mL) × 500 / 224.6 g/L.

The efficiency tested was that recovery measured using spike recovery. This was tested only select the maximum quantity of residue extraction durations 20-30 min at 50 °C. The quantitative levels of analytes were added with liquinox TOC content of 0.200 µg/mL, then the samples were extracted with deionized water 500 mL. Sample were collected with sample vessel into 40 mL. from each volume. The detected amounts of cleaner residue were determined by total organic carbon analyzer. An unspiked sample was also analyzed to ensure and that the spike and recovery controls were not detected. If the volume of the spike added does increase the sample volume by more than 5% or if a more accurate spike recovery calculation is desired, modify the spike recovery (%) equation as follows [9]:

% Recovery = ((Spiked sample result - Unspiked sample result desired))/ ((Known spike added concentration)) × 100%

2.6 Residue analysis on sample

The amount of organic carbon present in device extracts was measured using Total organic carbon (TOC) for investigate the cleaner residue, select (Hach QBD1200 Plus Laboratory TOC Analyzers). The TOC was measured automatically in liquid samples to determine the organic carbon content. The range of the measurement was between 0.4-100,000 ppb TOC with the accuracy ± 2% error [10]. The cleaner residue was calculated using the following equation [11]:

Cleaner Residue(µg/device) = (TOC Reading (µg TOC/mL) × Device Extraction Volume (mL)/ (Cleaner TOC Content (% TOC w/w))

3. RESULTS AND DISCUSSION

3.1 Exaction of Artificial knee components at each temperature using Total organic carbon (TOC) analysis

3.1.1. Exaction of femoral component at each temperature

This study aimed to identify the optimal extraction conditions temperature and time for maximizing the recovery of cleaner residues from femoral components. Cleaner residue levels were measured at four temperatures (50 °C, 60 °C, 70 °C, and 80 °C) across extraction times ranging from 10 to 60 minutes, with five replicate runs at each condition as shown in Figure 3. At 50 °C, extraction yielded moderate levels of cleaner residue, with most runs peaking at 30 - 40 minutes. The maximum observed residue was approximately 950 µg/device, indicating that moderate heating enables effective desorption.

However, beyond 40 minutes, a notable decline in residue levels was seen, suggesting that extended extraction time may not further enhance recovery at this temperature. When the temperature was increased to 60 °C, a significant improvement in extraction efficiency was observed. The highest residue level exceeded 1100 µg/device at 30 minutes (Run 3), representing the maximum recovery across all tested conditions. Several other runs also showed consistently high residues between 20 - 40 minutes, suggesting that this temperature range enhances the solubility and release of embedded cleaner. However, a high degree of variability was noted between runs, possibly due to inconsistent surface properties or thermal effects during extraction.

At 70 °C, the amount of extracted residue remained high, particularly within the 10 - 30 minute range, reaching up to 850 µg/device. Although the maximum yield was slightly lower than at 60 °C, the data were more consistent across runs, indicating better reproducibility. Interestingly, residue levels tended to decrease steadily after 30 minutes, implying that shorter extraction times may be sufficient, and that prolonged exposure could reduce yield potentially due to degradation or re-adsorption effects. Extraction at 80 °C did not yield higher residue levels than the other temperatures. Most runs fluctuated between 600 - 800 µg/device, with no clear peak or consistent trend. The lack of improvement, combined with increased variability, suggests that excessively high temperatures may not contribute to better recovery and could

introduce noise due to cleaner decomposition or altered surface interactions.

In summary, 60 °C at 30 minutes produced the highest residue recovery, making it the most effective condition for extracting cleaner from femoral components under the tested parameters. However, 70 °C with shorter extraction times (20 - 30 minutes) provided comparably high yields with better reproducibility, which may be advantageous for standardized protocols. Temperatures above 70 °C did not enhance extraction and introduced more variability, while 50 °C showed limited performance compared to higher temperatures.

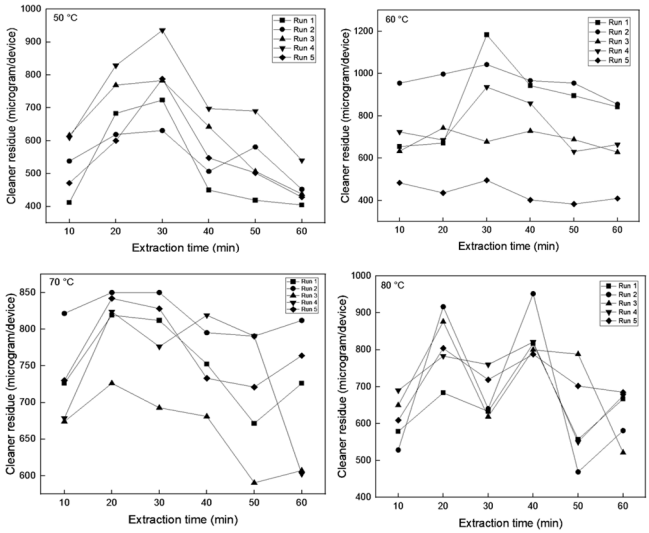

Figure 3 Exaction of femoral component at temperature 50 °C, 60 °C, 70 °C, and 80 °C over varying extraction durations ranging from 10 to 60 minutes.

3.1.2. Exaction of tibial component at each temperature

The extraction of cleaner residues from Tibial components was evaluated across four temperatures 50 °C, 60 °C, 70 °C, and 80 °C with varying extraction durations ranging from 10 to 60 minutes as shown in Figure 4. The goal was to identify the temperature and time combination that yielded the highest residue recovery, indicating the most effective extraction condition.

At 50 °C, residue values ranged mostly between 500 and 750 µg/device, with Run 3 peaking slightly above 800 µg/device at 20 minutes. The trends across most runs showed moderate increases during the early time points, followed by fluctuations with no consistent upward or downward trajectory. While the recovery levels were relatively stable, this condition appears to have limited capacity to extract deeply embedded residues, possibly due to insufficient thermal energy to promote desorption. When the temperature was increased to 60 °C, significant enhancement in extraction efficiency was observed. Run 2 reached a peak of nearly 1000 µg/device at 30 minutes, while other runs such as Runs 1 and 3 showed consistent high recovery between 700 - 900 µg/device across various time points.

This suggests that 60 °C provides adequate thermal activation for effective desorption and diffusion of cleaner residue. However, run 5 exhibited notably lower values (~300 - 400 µg/device), contributing to higher overall variability. Despite this, the average recovery was markedly improved compared to 50 °C, with 30 - 40 minutes appearing to be the optimal extraction duration.

At 70 °C, residue levels were consistently high across all runs, ranging from 700 to over 1100 µg/device. Run 2 notably reached the highest single-point recovery across all temperature conditions, peaking above 1150 µg/device at 20 minutes. Although there were fluctuations in individual runs, most of the data clustered around high values between 800 and 1000 µg/device, particularly within the 20 40-minute extraction window.

This suggests that 70 °C provides both effective and reproducible extraction, likely due to increased cleaner solubility and mobility at this temperature. Extraction at 80 °C yielded relatively high residue recovery as well, but with greater inconsistency. Peak values around 900 µg/device were observed in some runs (e.g., Run 3 at 40 minutes), while others (e.g., Run 5) showed a notable drop at similar times. Although most runs-maintained residues between 600 -800 µg/device, the sharp fluctuations suggest that higher temperatures may induce partial cleaner degradation, re-adsorption, or changes in surface interaction dynamics that could compromise consistent extraction.

In conclusion, 70 °C at 20 - 30 minutes demonstrated the most efficient and consistent extraction of cleaner residue from Tibial components, with high average recovery and minimal outliers. 60 °C at 30–40 minutes also showed strong performance, though with slightly greater variability. While 80 °C did not significantly improve recovery, it introduced erratic patterns, and 50 °C was clearly suboptimal in terms of maximum extraction. These findings indicate that moderate-high temperature (around 70 °C) with a carefully controlled extraction time is preferable for efficient cleaner removal from Tibial implant surfaces.

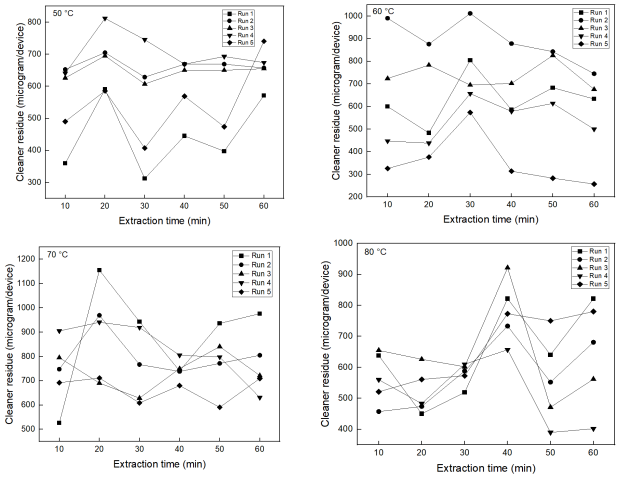

Figure 4 Exaction of tibial component at temperature 50 °C, 60 °C, 70 °C, and 80 °C over varying extraction durations ranging from 10 to 60 minutes.

3.1.3 Exaction of polyethylene insert at each temperature using Total organic carbon (TOC) analysis

The extraction of cleaner residue from polyethylene (PE) inserts showed distinct trends across the temperature range of 50 - 80 °C with varying extraction durations ranging from 10 to 60 minutes as shown in Figure 5. At 50 °C, the maximum residue recovered was slightly above 1000 µg/device (Run 2 at 20 min), but overall values remained below those seen at higher temperatures, indicating limited extraction efficiency at this lower thermal input. At 60 °C, all runs demonstrated a substantial increase in residue recovery, with peak values reaching up to 1700 µg/device. This condition consistently yielded high residues across replicates, particularly at 30 - 40 minutes, suggesting enhanced solubility and release of the cleaner at moderate heat.

The 70 °C extraction yielded similarly high results, with several runs exceeding 1600 µg/device. However, data showed slightly more variability between runs than at 60 °C, although the overall trend remained favorable for effective extraction, especially in the 30 - 50 minute range.

At 80 °C, residue recovery declined slightly compared to 60 and 70 °C, with values mostly under 1300 µg/device. Fluctuations across time points were more prominent, which could indicate thermal degradation of the cleaner or altered interaction with the PE surface at high temperatures.

In summary, 60 - 70 °C at 30 - 40 minutes provided the most efficient and consistent extraction of cleaner residue from PE inserts. Temperatures above 70 °C may not offer additional benefit and could lead to reduced or inconsistent recovery.

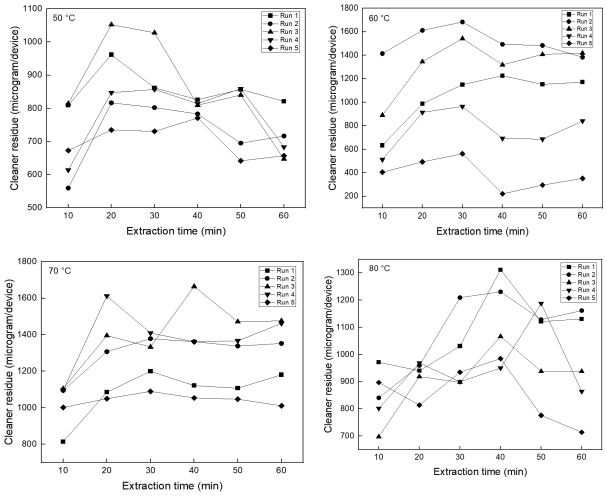

Figure 5 Exaction of polyethylene insert at temperature 50 °C, 60 °C, 70 °C, and 80 °C over varying extraction durations ranging from 10 to 60 minutes.

3.1.4 Exaction of CoCr test coupon at each temperature using Total organic carbon (TOC) analysis

The extraction performance of CoCr (Cobalt-Chromium) test coupons was evaluated at four temperatures 50 °C, 60 °C, 70 °C, and 80 °C with varying extraction durations ranging from 10 to 60 minutes as shown in Figure 6 based on TOC measurements of the extracted residues. The goal was to determine the condition that yields the highest total organic carbon, indicating the most effective extraction of residual cleaner. At 50 °C, the residue recovery was moderate across all runs, ranging between 400 - 700 µg/device. Although Run 3 peaked at around 670 µg/device at 30 minutes, the overall trend showed high variability with no clear peak time, suggesting less efficient or unstable extraction at this lower temperature. When the temperature was increased to 60 °C, a significant improvement was observed. Most runs showed a rising trend, particularly between 20–40 minutes, and Run 1 reached a maximum of ~1150 µg/device at 60 minutes the highest value across all conditions. This indicates enhanced desorption and diffusion of organic residues at moderate heating. At 70 °C, residue levels were consistently high across runs, with the majority falling between 700 - 950 µg/device. A distinct peak appeared around 40 minutes in multiple runs (e.g., Run 2 at ~950 µg/device), suggesting that this condition balances effective residue release with process stability. Variability was also reduced compared to 60 °C. At 80 °C, extraction efficiency did not significantly improve. While some runs (e.g., Run 2 at 40 minutes) reached up to 1000 µg/device, others showed reduced or fluctuating values, particularly beyond 40 minutes. This may indicate thermal degradation of the residue or interference from surface interactions at high temperatures.

In conclusion, 60 - 70 °C for 30 - 40 minutes appeared to be the most effective and consistent condition for extracting cleaner residues from CoCr

coupons using TOC analysis. These conditions provided high residue recovery with moderate variability, while both lower and higher temperatures showed limitations in efficiency or consistency.

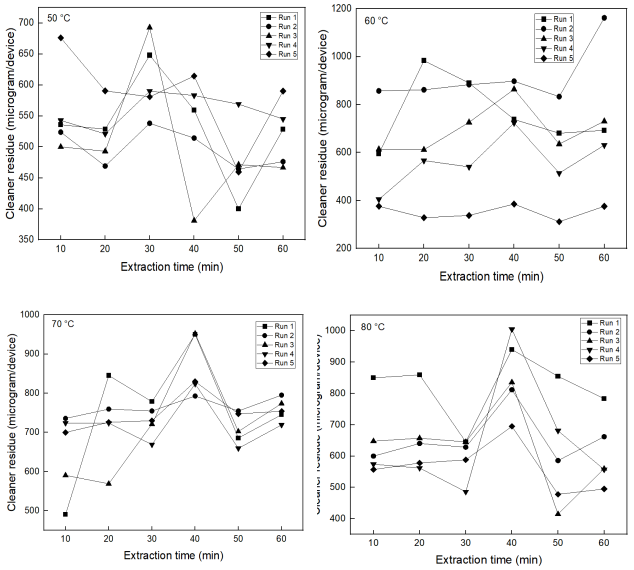

Figure 6 Exaction of CoCr test coupon at temperature 50 °C, 60 °C, 70 °C, and 80 °C over varying extraction durations ranging from 10 to 60 minutes.

3.1.5 Exaction of polyethylene test coupon at each temperature using Total organic carbon (TOC) analysis

The extraction of cleaner residue from polyethylene (PE) test coupons was evaluated across different temperatures (50 °C, 60 °C, 70 °C, and 80 °C), with varying extraction times as shown in Figure 7. The results demonstrate temperature and time dependency in cleaner residue extraction efficiency. At 50 °C, the cleaner residue initially increases with extraction time, peaking at 20 minutes and gradually declining thereafter. This suggests that the extraction process is most efficient at intermediate times, with longer extraction times leading to a decrease in the residue, likely due to saturation or a decrease in solvent efficacy.

At 60 °C, the trend becomes more pronounced, with residue steadily increasing until 40 minutes before plateauing. This suggests that at this temperature, the cleaner's effectiveness remains higher for longer periods of time, supporting the hypothesis that higher temperatures enhance residue extraction efficiency.

At 70 °C, the cleaner residue fluctuates more significantly. A peak is observed at 30 minutes, followed by a sharp decline, indicating that while higher temperatures can enhance initial residue extraction, prolonged exposure may lead to diminishing returns, possibly due to solvent evaporation or breakdown.

Finally, at 80°C, the extraction shows a somewhat stable trend, with cleaner residue remaining relatively consistent across the extraction times, except for a small increase at 40 minutes. This stability indicates that while very high temperatures might provide faster extractions, the total yield may not be substantially higher compared to lower temperatures, suggesting a plateau effect. These results indicate that temperatures between 60°C and 70°C, with extraction times around 20 to 40 minutes, yield the highest cleaner residue, optimizing the extraction process for polyethylene test coupons.

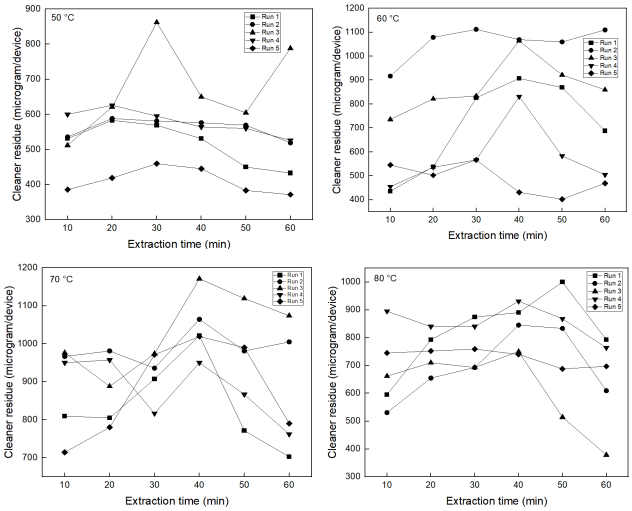

Figure 7 Exaction of polyethylene test coupon at temperature 50 °C, 60 °C, 70 °C, and 80 °C over varying extraction durations ranging from 10 to 60 minutes.

3.2 Spike recovery experiments

The % Recovery data for various test components at a fixed concentration of 0.200 µg/mL as shown in Table 1, extracted under specific conditions under 50 °C, for most components is 30 minutec and 20 minutes for PE. The recovery rates for the components generally range from 60% to 90%, the PE test coupon showing the lowest recovery at approximately 60%. The other materials exhibit slightly higher recovery rates, indicating more efficient extraction under the given conditions. These variations suggest that the extraction process may require optimization for certain materials, such as PE, to achieve better recovery.

Table 1 %Spike recovery for an extraction process to validate the method of standard additions.

Sample ID	Added (µg/mL)	Observed TOC (µg/mL)	Spiked (µg/mL)	%Recovery
Femoral	0.200	0.92	1.136	108
Tibial	0.200	0.36	0.566	103
PE	0.200	0.136	0.226	45
CoCr test	0.200	0.167	0.323	78
PE test	0.200	0.198	0.331	66.5
Standard 1	0.05	0.227	0.262	70
Standard 2	0.10	0.236	0.321	85
Standard 3	0.15	0.213	0.323	78
Standard 4	0.20	0.167	0.343	65
Standard 5	0.25	0.22	0.43	84
Standard 6	0.30	0.276	0.451	58.33

Figure 7 shown the standard curve for Liquinox TOC, which correlates the concentration of Liquinox (ranging from 0.05 to 0.30 µg/mL) with the measured TOC values, The experiments were conducted using CoCr test coupon. The linear trend observed, with an R^2 value of 0.9333, confirms a good relationship between concentration and TOC. This suggests that the method is reliable and effective for quantifying Liquinox at varying concentrations. Notably, as the concentration of Liquinox increases, there is a clear tendency for the TOC values to rise proportionally, indicating that higher concentrations yield higher TOC measurements, which aligns with the expected behavior.

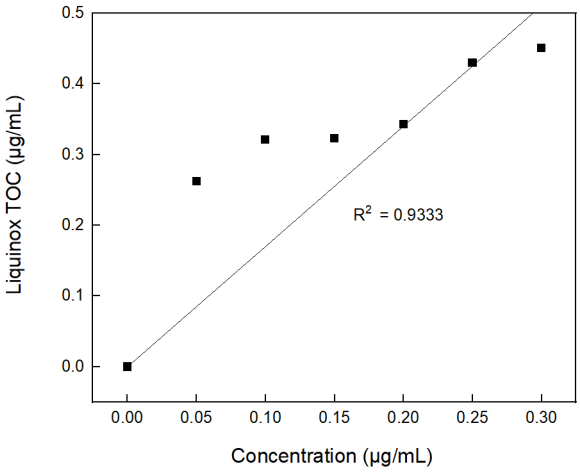

Figure 7 Linearity of the assay investigated by add Liquinox TOC of 0.50, 0.100, 0.150, 0.200, 0.250 and 0.300 µg/mL respectively of CoCr test coupon under 50 °C correlation between observed and expected values for Liquinox TOC showed a linear response with R^2 = 0.9333

Moreover, Figure 8 presents the spike recovery data for different test components, each spiked with a concentration of 0.200 µg/mL. The recovery rates vary across components, with most test coupons recovering between 60% and 90%. The polyethylene (PE) test coupon, extracted at 20 minutes, shows the lowest recovery, which may suggest suboptimal extraction efficiency at this time point. The observed trend indicates that longer extraction times for other materials tend to result in higher recovery rates, though the PE coupon exhibits the most notable deviation. This variability in recovery is likely influenced by factors such as material composition, interaction with Liquinox, and extraction conditions.

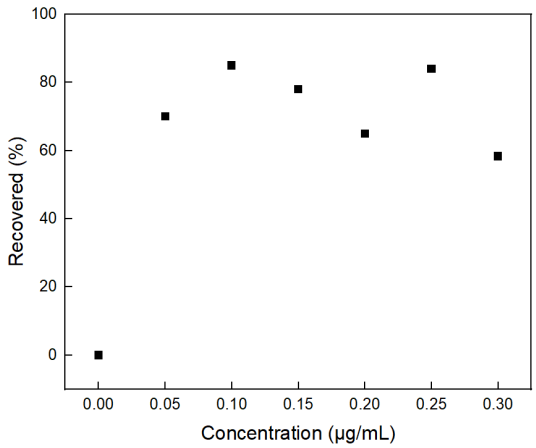

Figure 8 %Spike recovery in CoCr test coupon under 50 °C for Liquinox TOC of 0.50, 0.100, 0.150, 0.200, 0.250 and 0.300 µg/mL respectively.

In summary, the standard curve affirms that Liquinox TOC measurement is concentration-dependent, with higher concentrations yielding higher TOC values. The recovery data underscores differences in extraction efficiency across materials and extraction times, with the PE sample requiring further optimization in extraction conditions for improved recovery.

4. CONCLUSION

This study identified optimal extraction conditions for cleaner residue recovery from femoral, tibial, polyethylene (PE), and CoCr test coupons. For femoral components, the most efficient extraction occurred at 60°C for 30 minutes, providing the highest residue recovery, with 70°C offering good reproducibility at shorter extraction times. For tibial components, 70°C for 20 - 30 minutes was the best condition, ensuring consistent and high recovery. For PE inserts, 60 - 70°C at 30 - 40 minutes yielded the highest cleaner residue, with 60°C providing the most consistent results. Finally, for CoCr coupons, 60 - 70°C for 30 - 40 minutes was the most effective and consistent extraction condition. Overall, moderate temperatures (60 -70°C) with optimized extraction times (20 - 40 minutes) were found to be ideal for maximizing residue recovery across all materials, with higher temperatures (80°C) not significantly improving extraction efficiency. The % Recovery data showed that extraction at 50°C for most components (30 minutes) and PE (20 minutes) resulted in recovery rates between 60% and 90%, with PE exhibiting the lowest recovery (~60%). The standard curve for Liquinox TOC demonstrated a linear relationship between concentration and TOC, confirming the method's reliability for quantification.

ACKNOWLEDGMENTS

We would like to express our sincere gratitude to the Health Systems Research Institute (HSRI) for their generous financial support. This work was also made possible by the Center of Excellence in Biomechanics Medicine, which provided invaluable assistance with critical artificial knee components. Additionally, we extend our thanks to Hach Company for their support in providing the necessary analyzers.

REFERENCES

1 World Health Organization. (n.d.). Osteoarthritis. Retrieved December 27, 2024, from https://www.who.int/news-room/fact-sheets/detail/osteoarthritis
2. International Organization for Standardization. (2018). Implants for surgery - Cleanliness of orthopedic implants - General requirements (ISO Standard No. 19227:2018), Available Online: https://www.iso.org/standard/66817.html
3. U.S. Food and Drug Administration. (1993, July). Guide to inspections validation of cleaning processes. U.S. Food and Drug Administration. https://www.fda.gov/inspections-compliance-enforcement-and-criminal-investigations/inspection-guides/validation-cleaning-processes-793
4. International Organization for Standardization. (2016). ISO 13485:2016 - Medical devices – Quality management systems – Requirements for regulatory purposes. International Organization for Standardization. https://www.iso.org/standard/59752.html
5. ASTM (2016), Standard Guide for Validating Cleaning Processes Used During the Manufacture of Medical Devices. (ASTM F3127-16) Available Online: https://www.astm.org/f3127-16.html
6. FDA. (n.d.). Evaluation of production cleaning processes for electronic medical devices: Part III - Methods. U.S. Food and Drug Administration. Retrieved December 26, 2024, from https://www.fda.gov/inspections-compliance-enforcement-and-criminal-investigations/inspection-technical-guides/evaluation-production-cleaning-processes-electronic-medical-devices-part-iii-methods
7. LeBlanc, D. A. (2005). Analytical Methods and Acceptance Criteria for Cleaning Validation Protocols for Medical Devices. Journal of ASTM International, 3(3), JAI13393. https://doi.org/10.1520/JAI13393
8. Arvanitoyannis, I. S., & Roussis, I. G. (2007). Application of analytical methods for the validation of food extraction techniques. Food Reviews International, 23(2), 115-151. https://doi.org/10.1080/87559120701275522
9. Kanegsberg, B., & Kanegsberg, E. (Eds.). (2012). Handbook for critical cleaning: Applications, processes, and controls (2nd ed.). CRC Press.
10. Hach Company. (n.d.). Hach QBD1200 Plus laboratory TOC analyzer. Retrieved from https://www.adm-adm.com/product/QbD1200
11. Alconox, Inc. (2021). Cleaning validation for medical devices. Retrieved from https://technotes.alconox.com/wp-content/uploads/2021/06/Cleaning-Validation-For-Medical-Device.pdf

Autonomous Lorentz force-powered chiral encoded metal rotors for enantioselective synthesis

Wanmai Srisuwanno[1,2], Gerardo Salinas[2], Chularat Wattanakit[1,*], Alexander Kuhn[1,2,*]

[1] School of Energy Science and Engineering, Vidyasirimedhi Institute of Science and Technology, Rayong 21210, Thailand
[2] University of Bordeaux, CNRS, Bordeaux INP, ISM UMR 5255, 16 Avenue Pey Berland, Pessac 33607, France
[*] Corresponding author: chularat.w@vistec.ac.th; kuhn@enscbp.fr

ABSTRACT

Highly enantioselective synthesis of chiral compounds is enabled by chiral-encoded metals via classic electrochemical approaches. Breakthroughs in the synthesis of various chiral compounds, particularly pharmaceutical products, illustrate the versatility of such tailor-made materials. Nevertheless, the application of chiral-encoded metals as autonomous redox catalysts is still unexplored and is anticipated to further push the boundaries of this field. Herein, Lorentz force-driven chiral rotors are designed by combining chiral metal surfaces with reactive zinc (Zn) as a proof-of-concept experiment for asymmetric synthesis. The spontaneous oxidation of Zn, acting as a sacrificial anode, shuttles a fraction of electrons to the chiral-encoded metal, thus promoting the reduction of a prochiral starting compound at the cathode, leading to the asymmetric formation of a chiral compound. Furthermore, by imposing a magnetic field perpendicular to the ionic charges moving from the anode to the cathode of the rotor, a Lorentz force is induced, which in turn propels the device. This self-propulsion enhances the mass transport from the bulk of the solution to the surface of the mobile electrode, which directly impacts the production rate of the chiral compounds. This indicates promising perspectives in the general frame of heterogeneous redox catalysis.

Keywords: Chiral encoded metals; Enantioselective synthesis; Redox conversion; Autonomous swimmers; Lorentz force

1. INTRODUCTION

Chiral heterogeneous catalysis is a promising alternative for the production of enantiomerically pure compounds (EPCs) [1, 2]. Among the different enantioselective interfaces, molecular-imprinted metals have led to the highly selective synthesis of chiral products *via* electrochemical approaches.[3-7] In this context, molecular-imprinted platinum (Pt)-iridium (Ir) stands out as a heterogeneous catalyst for asymmetric synthesis.[3] The stereoselective properties derived from chiral-imprinted recognition sites allow a very high enantiomeric excess. This opens the door to an efficient pathway for enantioselective synthesis of chiral products from prochiral precursors. However, in the majority of the cases, the low production rate of such a heterogeneous process has been pointed out, in particular, when using them as classic working electrodes for electrosynthesis.[8] This commonly limits the possible scale-up for practical applications. To circumvent this limitation, one specific strategy is to transform the conventional electrocatalytic system into a dynamic heterogeneous catalytic system.

Recently, macro-, micro-, and nano-dynamic systems have been the focus of research efforts due to their different applications, ranging from sensing to environmental remediation and cargo delivery.[9-11] Designing asymmetric devices with highly selective chemical features coupled with spontaneous motion is highly desired.[12-15] Multiple and sophisticated propulsion mechanisms have been developed by including several strategies such as self-electrophoresis[16], diffusiophoresis[17], magnetic [18, 19], light-driven [20], ultrasound [21], and electric field propulsion[22]. Among them, magnetic field-based propulsion is one of the most promising mechanisms. In the presence of an external magnetic field ($\vec{B}$), a ferromagnetic dynamic system can experience an attractive force and torque, which ultimately propels the device.[18] Nonetheless, the use of ferromagnetic components and sophisticated electromagnets limits its applications. Recently, the synergy between the spontaneous ion flux produced by a self-electrophoretic device and an external magnetic field has been proposed.[23] Briefly, the presence of $\vec{B}$ perpendicular to an ion flux generates a horizontal Lorentz force, capable of boosting the motion of the device.[24-27] With this concept, dynamic systems with predictable trajectories have been developed. Most importantly, the impact of the Lorentz force on the electrophoretic motion allows increasing the object's

speed by up to two orders of magnitude. Furthermore, this synergetic effect has been exploited in the field of heterogeneous catalysis, eventually enhancing the conversion rate of the antipodes of phenyl ethanol (PE).[28]

Herein, the design of self-propelled Lorentz force-powered chiral rotors for enantioselective synthesis (Scheme 1) is proposed. The aim of this work is to report a series of proof-of-concept experiments which illustrate the advantage of the dynamic and enantioselective properties of self-propelled chiral-encoded rotors. The chiral-imprinted device has been elaborated by the spontaneous reduction of Pt and Ir salts on the surface of a zinc (Zn) plate in the presence of a non-ionic surfactant and a chiral template, which control the formation of mesoporous channels and chiral-encoded sites, respectively. The enantioselective performance of the bifunctional rotors was evaluated by the reduction of a prochiral compound, acetophenone, into a chiral product, phenylethanol enantiomers, in acidic media. Under these conditions, the oxidation and reduction of Zn and the prochiral molecule, respectively, taking place at opposite extremities of the device, lead to a flux of electrons, which, in the presence of a magnetic field orthogonal to the surface of the rotor, induces a lateral Lorentz force. By introducing an additional break of symmetry, a spontaneous clockwise or anticlockwise rotation at the air-water interface was achieved. Such motion produces a self-mixing of the solution, thus enhancing the conversion rate of the chiral compound, in comparison with a classic static system.

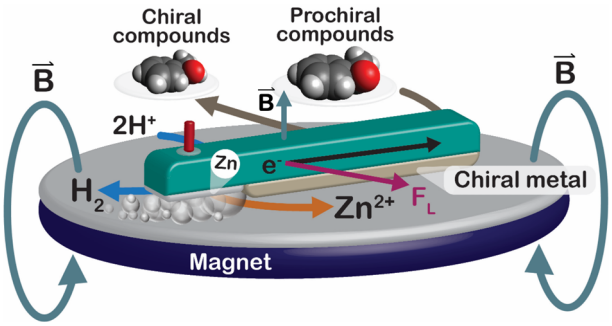

Scheme 1 Illustration of the general concept of the Lorentz force-powered chiral encoded rotor with a representation of the redox reactions, the orientation of the magnetic field, the produced Lorentz force and the flux of electrons.

2. EXPERIMENTAL

2.1. Chemical

Acetophenone (ACP), (R)-(-)-1-phenylethanol ([R]-PE), (S)-(-)-1-phenylethanol ([S]-PE), hexachloroplatinic acid hydrate ($H_2PtCl_6 \cdot xH_2O$), hexachloroiridate acid hydrate ($H_2IrCl_6 \cdot xH_2O$), polyethylene glycol hexadecyl ether (Brij® C10), hydrochloric acid (HCl), and heptanethiol were purchased from Sigma-Aldrich. A zinc foil was purchased from Goodfellow (0.25 mm thick, 10 cm wide, 30 cm long). Ultrapure water (Milli-Q) with 18.2 MΩ·cm was used for all solutions. All chemicals were employed directly without additional purification.

2.2. Preparation of chiral metal-rotors *via* electroless deposition

The chiral-encoded Pt-Ir-Zn-rotor was built following a two-step procedure. First, the Zn foil was cut into rectangular pieces of 1.4 cm in length and 0.2 cm in width, and after this, a hole was drilled into one extremity of the rotor. The resulting Zn support was cleaned by dipping the object in an aqueous 0.5 mM HCl solution for 15 minutes in order to remove ZnO_x species. The direct templated electroless deposition of Pt-Ir alloy was used to coat the majority of one face of the Zn foil. The gel precursor was prepared by mixing 23% (w/w) $H_2PtCl_6 \cdot 6H_2O$, 5% (w/w) $H_2IrCl_6 \cdot 6H_2O$, 40% (w/w) nonionic surfactant (Brij® C10), as mesoporogen, and 4% (w/w) [S]- or [R]-PE, as the chiral template, in water. The resulting gel was heated at 40°C and stirred continuously for 45 minutes, allowing to achieve homogeneity. Subsequently, the mixture was placed on the Zn plate. Upon complete deposition for 1 hour, the resulting Pt-Ir alloy, supported on the Zn plate, was dipped in ultrapure water for at least one day, enabling the removal of the chiral templates and surfactant. Finally, the exposed pristine Zn surface of the as-prepared Pt-Ir-Zn-rotor was coated with varnish, except a window of 0.2 cm × 0.2 cm, which was left without the decorating varnish. To modify the outermost surface of the chiral-imprinted metal, a microcontact printing approach was used in analogy to a previously reported procedure.[29] Briefly, a rubber stamp was used as a support to transfer thiol molecules onto the metal surface. For this, a 50 mM heptanethiol solution was dropped onto the rubber stamp with a density of 1 µl/cm^2. Then, the chiral-imprinted Pt-Ir-Zn-rotor was pressed onto the rubber stamp. Prior to the enantioselective synthesis of chiral compounds, the resulting surface-functionalized plate was dried for at least one day to allow the formation of a self-assembled monolayer of the thiol molecules.

2.3 Characterization

The morphology and composition of the chiral-imprinted rotors were characterized by scanning electron microscopy (SEM) coupled with energy-dispersive X-ray spectroscopy (EDX) using a Vega3 Tescan 20.0 kV equipment. Transmission electron microscopy (TEM) analyses were performed using a JEOL JEM-2100 microscope at 200 kV. A commercial camera (iPhone 14 Pro Max) was used to capture the dynamic behavior and images and videos were processed with Image J software.

2.4 Enantioselective synthesis of chiral compounds

The enantioselective synthesis using the chiral-imprinted Pt-Ir-Zn-rotors was carried out in acidic

media. Solutions containing 30 mM of acetophenone in 0.3 M HCl were prepared and saturated with N_2. The prepared solution was transferred to a reaction chamber, with a FeNdB magnet (B ≈ 200 mT, A = 98 cm^2) placed underneath. The chiral-imprinted Pt-Ir-Zn-rotors were supported at one extremity by a plastic holder at the water-air interface. After the reaction, the resulting product was extracted using heptane as a solvent. A fraction of the organic layer was analyzed using high-performance liquid chromatography (HPLC) equipped with a chiral HPLC column (Chirapak IB-5, 250 × 4.6 mm inner diameter) using a 0.5 % (v/v) i-propanol and 99.5 % (v/v) heptane mixture as a mobile phase, with a flow rate of 0.5 ml/minute at room temperature. The photodiode array (PDA) detector was tuned at 210 nm to analyze all products. Acetophenone conversion was calculated by using the following equation:

$$\% \text{ Acetophenone conversion} = \frac{A_{ACP,\,t_o} - A_{ACP,\,t}}{A_{ACP,\,t_0}} \times 100$$

where $A_{ACP,to}$ and $A_{ACP,t}$ are defined as the area under the HPLC peak of acetophenone at the beginning and after a certain time of reaction, respectively. The enantiomeric excess (ee) was obtained by using the following equation:

$$\% \text{ ee of PE} = \frac{A_{[S]\text{-PE}} - A_{[R]\text{-PE}}}{A_{[S]\text{-PE}} + A_{[R]\text{-PE}}} \times 100$$

where $A_{[S]\text{-PE}}$ and $A_{[R]\text{-PE}}$ are defined as the area under the HPLC peaks of [S]- and [R]-PE, respectively.

3. RESULTS AND DISCUSSION

Commonly the enantioselective reduction of a prochiral molecule on the mesoporous chiral-encoded Pt-Ir alloy was achieved via a conventional electrochemical approach.[3] However, the low production rate of the chiral product represents a limitation of molecular-imprinted metals. In contrast to classic chiral electrocatalysis, one strategy to enhance the prochiral conversion rate is the use of dynamic systems. To demonstrate the proof-of-concept, wireless self-propelled catalysts are proposed for the spontaneous asymmetric synthesis of chiral compounds. For this, a chiral-encoded Pt-Ir-Zn-rotor was designed by chemically modifying one face of a Zn foil with a chiral-imprinted Pt-Ir alloy (Figure 1). A metal plating gel containing metal precursors, a chiral template, and a nonionic surfactant (polyethylene glycol hexadecyl ether, Brij® C10) was prepared at a controlled temperature of 40°C. The presence of the non-ionic surfactant allows the formation of a lyotropic liquid crystal phase.[30] Subsequently, the prepared plating gel was positioned on the Zn surface. Under these conditions, Zn acts as a strong reducing agent, allowing the spontaneous reduction of Pt^{x+} and Ir^{x+}, eventually forming alloy films deposited on the Zn surface in the simultaneous presence of the lyotropic liquid crystal phase. After washing out chiral templates and non-ionic surfactants, chiral-imprinted sites remain within the metal layer. Finally, the pristine Zn surface was covered by varnish leaving exclusively a square of 2 mm × 2 mm exposed to the solution.

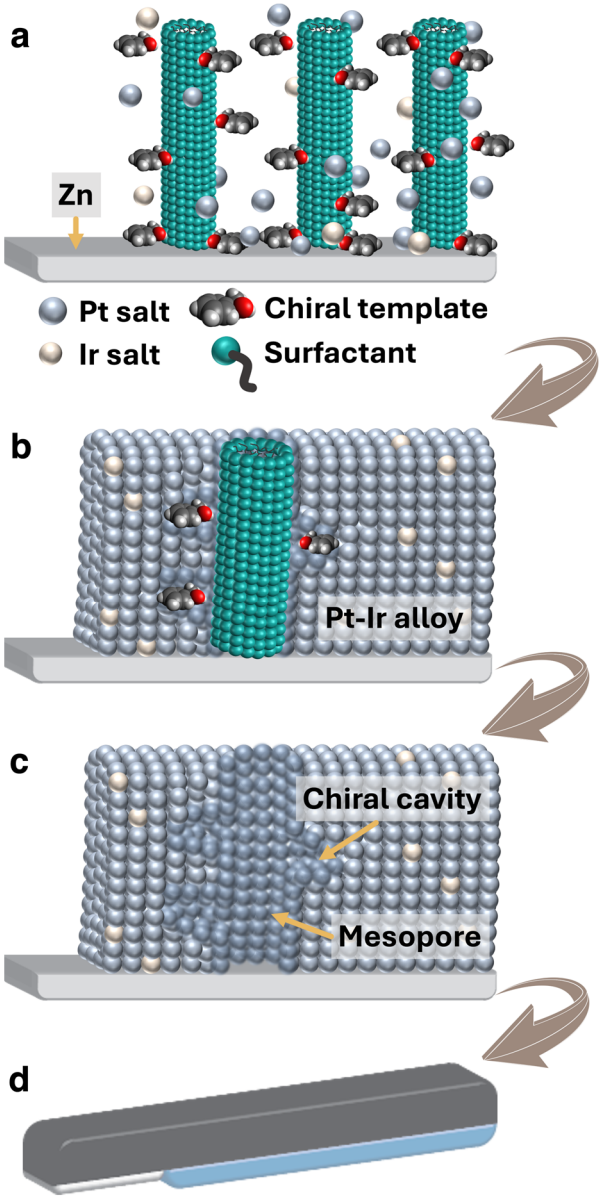

Figure 1 Schematic illustration of the preparation steps of the chiral-imprinted metal-rotors: (a) formation of the self-assembled hexagonal lyotropic liquid crystal phase of non-ionic surfactants on a Zn plate, (b) spontaneous reduction of Pt and Ir salts around the surfactant column and the adsorbed enantiomers, (c) chiral-imprinted mesoporous Pt-Ir film supported on a Zn plate, and (d) final chiral-imprinted Pt-Ir-Zn-rotors.

To corroborate the surface modification and evaluate the morphology of the bimetallic Pt-Ir film, scanning electron microscopy (SEM) analysis coupled with energy-dispersive X-ray spectroscopy (EDX) was carried out. The Pt-Ir film presents a rather homogeneous surface with an atomic ratio of 90:10 for

Pt and Ir, respectively (Figure 2a and c). A rather uniform thickness over the entire area of the Pt-Ir film was observed. In addition, transmission electron microscopy (TEM) and high-resolution transmission electron microscopy (HR-TEM) measurements were performed to reveal the homogeneous porous Pt-Ir film (Figure 2b, left). A highly ordered hexagonal mesoporous structure with a pore size of 1.7 ± 0.1 nm (Figure 2b, right) was observed.

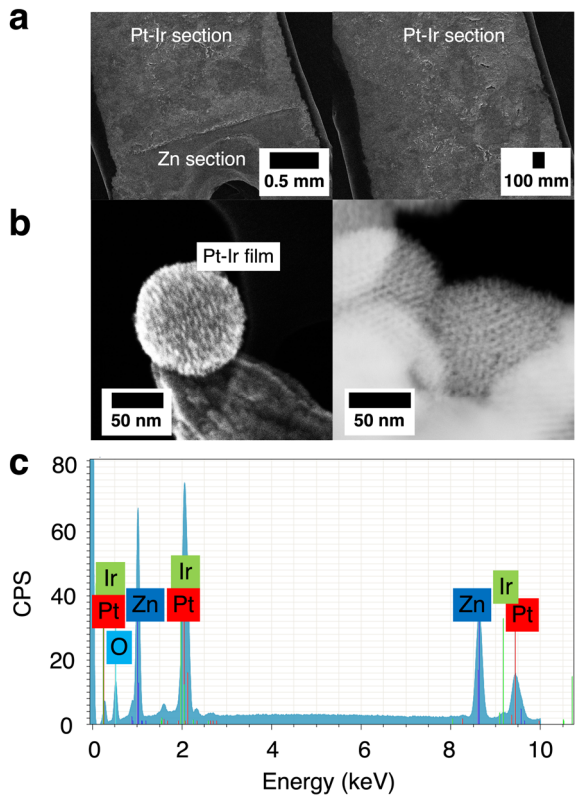

Figure 2 (a) SEM image, (b) TEM and HR-TEM images of the Pt-Ir film, and (c) EDX characterization of the chiral-imprinted Pt-Ir-Zn-rotor.

After the characterization of the metal deposit, we evaluated the dynamic behavior of the device. For this, the designed chiral-imprinted Pt-Ir-Zn-rotor was positioned at the center of the reaction chamber at the water-air interface of a 0.3 M HCl solution. Under these conditions, the thermodynamically spontaneous reduction of protons on the Pt-Ir surface and oxidation of Zn, take place. This produces a flux of charges from the anode (Zn section) to the cathode (Pt-Ir section) of the rotor. In the presence of a magnetic field, placed orthogonal to the surface of the device, a Lorentz force is induced, which deviates the ion flux, leading to the formation of two horizontal macro-magnetohydrodynamic (MHD) flow patterns along the edges of both metallic extremities.[23, 31] Eventually, the overall MHD vortices result in a net amplification of the local hydrodynamics, which powers the motion of the rotor. However, in order to produce a global rotational motion, an additional break of symmetry is required, which is related to the position of the support axis along the device (Figure 3a). Thus, when placing the support axis as close as possible to one extremity of the device, the magnitude of the torque force producing rotational motion is maximized. It is important to point out that by controlling the orientation of the magnetic field, a predictable clockwise or anticlockwise movement is produced. For example, the Lorentz force-powered Pt-Ir-Zn-rotor exhibits a counterclockwise motion, with an average speed of 9 seconds per revolution, in the presence of the north pole facing upwards (Figure 3b). Compared with a static system, this self-induced rotation is expected to mitigate the mass transport limitations of the prochiral compound towards the chiral-imprinted sites, eventually leading to the enhanced production rate of chiral products.

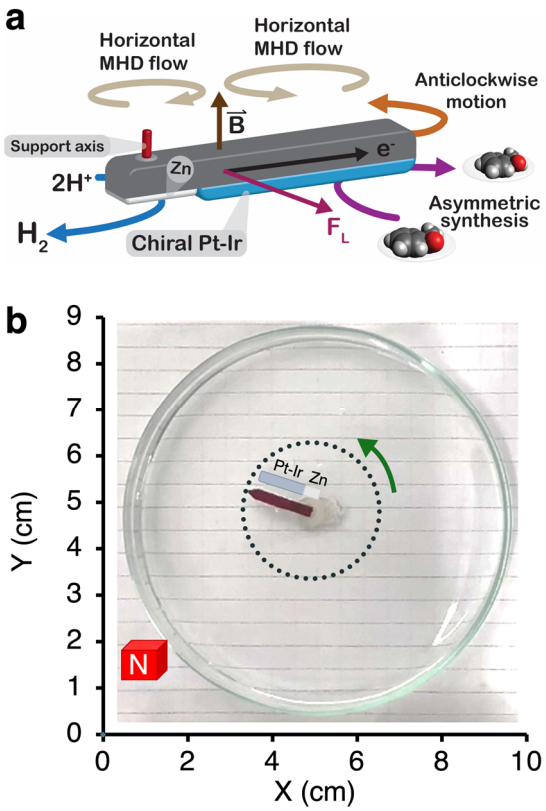

Figure 3 (a) Schematic illustration of the magnetic field-enhanced self-electrophoretic propulsion mechanism with a representation of the redox reactions, the orientation of the magnetic field, and the ion flux. (b) trajectory plot of the Lorentz force-powered chiral-imprinted Pt-Ir-Zn-rotor moving at the water-air interface of a 30 mM acetophenone solution containing 0.3 M HCl.

To confirm this hypothesis, we evaluated the production rate obtained during the dynamic electrosynthesis of the antipodes of phenylethanol (PE). A fraction of the electrons produced during the spontaneous oxidation of Zn is shuttled to the chiral-encoded metal, promoting the reduction of the prochiral compound (Figure 3a). To evaluate the enantioselectivity of the designed rotor, the reduction of acetophenone (ACP) into PE is selected as a model

reaction. Upon completion of the reaction, the product mixture was extracted with heptane and analyzed using enantioselective HPLC with a photodiode array detector. From the obtained chromatograms the ACP conversion was calculated by using the change of the ACP peak area before and after the reaction. Enantioselectivity is estimated using the relative amount of PE products. As it can be seen from the chromatograms, in the presence of an external magnetic field, the ACP conversion increases from 12% to up to 16%, in comparison with the control experiment in the absence of the magnetic field (Figure 4a, red and yellow lines). Moreover, the conversion can be further improved by increasing the reaction time (Figure 4a, blue line), reflecting the benefits of the self-mixing capabilities. However, in all cases the obtained enantiomeric excess (ee%) values are rather low due to dominant unspecific reactions at the bare Zn surface and the non-imprinted outer surface of the Pt-Ir layer. Nonetheless, the spontaneous ACP reduction occurs in a slightly enantiospecific way, leading to an enantiomeric excess of around 3.5%. This also reflects the enhanced mass transport, accelerating the delivery of the prochiral compound towards the chiral recognition sites or *vice versa* and, thus, decreasing undesired side reactions at the non-imprinted outer surface.

After demonstrating the impact of the magnetic field and the electrolysis time on the yield, we further studied in more detail the enantioselectivity of the metal catalyst. For this, three different systems were evaluated; i) non-imprinted, ii) [S]-PE-imprinted, and iii) [R]-PE-imprinted rotors, in acid media under the influence of the magnetic field. In the control experiment with the non-imprinted Pt-Ir-Zn-rotor, ACP was transformed as expected, into the two enantiomers of PE with an ee% around 0.5%, thus, within error bars forming a racemic mixture (Figure 4b, green line). On the contrary, when using the [R]-PE-imprinted rotor, ACP was reduced with a partial preference into the [R]-product, reaching -3.8 %ee (Figure 4b, purple line). The specular results were obtained when using the rotor imprinted with the opposite configuration, slightly favoring the [S]-product (3.5 %ee), estimated using the relative amount of PE products in Figure 4b, red line. This suggests that chiral recognition sites have a certain impact on the enantiospecific synthesis of a chiral compound.

In order to improve the selectivity of the asymmetric synthesis, we decided to suppress the reaction that can occur at the outermost surface of the Pt-Ir film. The chiral-imprinted Pt-Ir-Zn-rotor also contains achiral parts of the surface, in particular the pristine Zn and the outermost surface of the Pt-Ir film. This leads to non-stereoselective reactions, which directly impact the %ee. As it has been demonstrated previously [29, 32], the strong covalent bond between metal and heptanethiol allows the formation of self-assembled monolayers with very high coverage, completely inhibiting the charge transfer. This protects the achiral surface, eventually preventing the ACP reduction. Thus, the chiral-imprinted Pt-Ir-Zn-rotor was decorated with a self-assembled monolayer of thiol molecules via the microcontact printing method. The chiral-imprinted Pt-Ir-Zn-rotor was put in contact with a stamp loaded with 1 µl/cm^2 of a 50 mM heptanethiol solution. After drying, a monolayer of the adsorbed thiol molecules is protecting the surface of the functionalized plate.

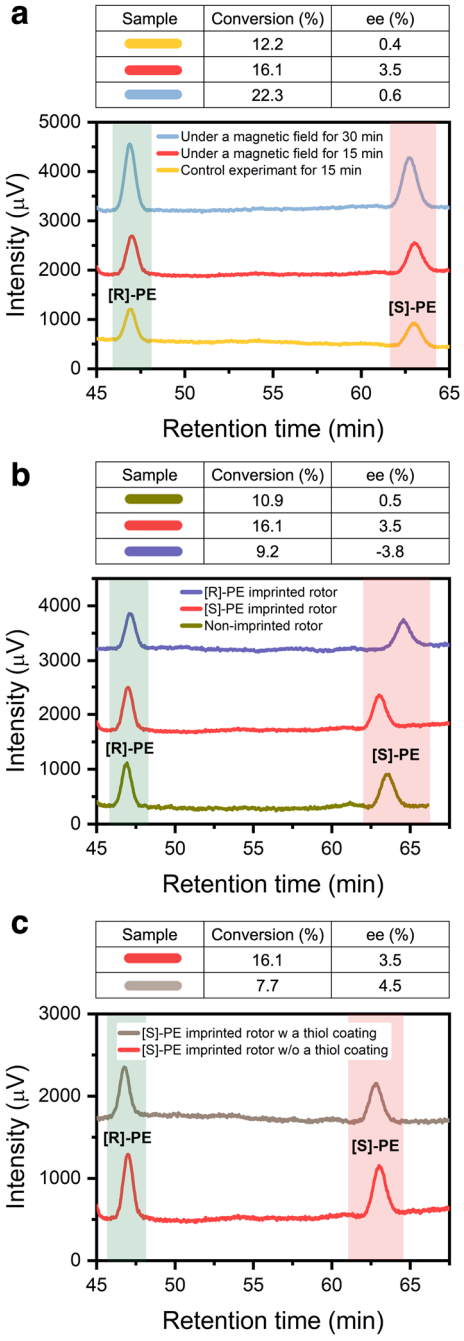

Figure 4 Chromatograms recorded upon complete acetophenone reduction to phenylethanol with different experimental conditions: (a) influence of the reaction time using an [S]-PE rotors, (b) different chiral imprinted molecules, and (c) impact of the presence of a thiol coating during the enantioselective synthesis.

To verify its impact on the performance of the chiral-imprinted Pt-Ir-Zn-rotor, an experiment identical to the previous one has been carried out. Chromatograms in Figure 4c show the ACP conversion and the %ee obtained using the chiral-imprinted Pt-Ir-Zn-rotor with a thiol coating, compared with the thiol-free chiral-imprinted Pt-Ir-Zn-rotor. The thiol coating decreases the ACP conversion at the achiral surface, indicated by a slightly improved enantioselectivity (4.5 %ee), illustrated in Figure 4c, grey line. This suggests that even though the achiral outermost surface of the Pt-Ir film is protected, the low overpotential of Pt for the direct reduction of protons to hydrogen leads to proton-free chiral cavities. This, in turn, facilitates the unspecific reaction of the intermediate species during the transformation of the functional ketone group (C=O) into alcohol (O-H). To circumvent this drawback a replacement of the chiral-imprinted Pt-Ir film by other imprinted metal films can be envisioned, which possess a higher overpotential for the direct reduction of protons to hydrogen.

4. CONCLUSION

We have successfully developed Lorentz force-driven metal rotors containing porous chiral surfaces for the redox synthesis of phenylethanol from acetophenone. The propulsion behavior of these devices is based on a magnetic field-enhanced self-electrophoretic propulsion mechanism. This takes advantage of the synergy between the charge-compensating ion flux produced by the reduction of a prochiral precursor and Zn oxidation, as well as the symmetry breaking of the forces acting on the rotor caused by an asymmetric support axis. These ingredients propel the device in the presence of a magnetic field orthogonal to the surface of the rotor. It is crucial to point out that fine-tuning the reaction time and minimizing the achiral parts of the surface with a self-assembled monolayer of thiol molecules enhances the enantioselectivity. Even though enantiomeric excess is still very low, the design of chiral-imprinted rotors paves the way for scalable redox synthesis of a chiral compound due to adjustable product yield, for example, by multiplying the number of metal rotors in contact with the solution. The obtained results allow us envisioning the further development of chiral-encoded metal rotors for the synthesis of chiral compounds.

ACKNOWLEDGMENTS

This work has been funded by the Vidyasirimedhi Institute of Science and Technology (VISTEC), the National Science and Technology Development Agency (NSTDA), and the Ministry of Science and Technology, Thailand. C.W. acknowledges the cost-sharing research grant between the National Research Council of Thailand and VISTEC (N42A660307), the Program Management Unit for Human Resources & Institutional Development, Research and Innovation (grant number: B41G680026), and the financial support from the Air Force Office of Scientific Research Unit (Awarded R&D grant no. FA2386-23-1-4015). W.S. is indebted to a Ph.D. cotutelle scholarship sponsored by Campus France, the French Embassy in Thailand, and VISTEC. This project was also supported by CNRS through the IRP project ChiraChem.

REFERENCES

1. X. Huang, Q. Zhang, J. Lin, K. Harms, E. Meggers. Electricity-driven asymmetric Lewis acid catalysis. *Nature Catalysis* 2019; 2(1): 34-40.
2. B.M. Trost. Asymmetric catalysis: an enabling science. *Proceedings of the National Academy of Sciences* 2004; 101(5): 5348-5355.
3. S. Butcha, S. Assavapanumat, S. Ittisanronnachai, V. Lapeyre, C. Wattanakit, A. Kuhn. Nanoengineered chiral Pt-Ir alloys for high-performance enantioselective electrosynthesis. *Nature Communications* 2021; 12(1): 1314.
4. S. Somsri, B. Suwankaisorn, K. Yomthong, W. Srisuwanno, S. Klinyod, A. Kuhn, C. Wattanakit. Highly enantioselective synthesis of pharmaceuticals at chiral-encoded metal surfaces. *Chemistry–A European Journal* 2023; 29(61): e202302054.
5. S. Assavapanumat, M. Ketkaew, A. Kuhn, C. Wattanakit. Synthesis, characterization, and electrochemical applications of chiral imprinted mesoporous Ni surfaces. *Journal of the American Chemical Society* 2019; 141(47): 18870-18876.
6. S. Assavapanumat, S. Butcha, S. Ittisanronnachai, A. Kuhn, C. Wattanakit. Heterogeneous enantioselective catalysis with chiral encoded mesoporous Pt–Ir films supported on Ni foam. *Chemistry–An Asian Journal* 2021; 16(21): 3345-3353.
7. C. Wattanakit, Y.B.S. Côme, V. Lapeyre, P.A. Bopp, M. Heim, S. Yadnum, S. Nokbin, C. Warakulwit, J. Limtrakul, A. Kuhn. Enantioselective recognition at mesoporous chiral metal surfaces. *Nature Communications* 2014; 5(1): 3325.
8. G. Salinas, A. Kuhn. Wireless electroorganic synthesis. *Current Opinion in Electrochemistry* 2025; 49: 101612.
9. M. Pacheco, M.Á. López, B. Jurado-Sánchez, A. Escarpa. Self-propelled micromachines for analytical sensing: A critical review. *Analytical and Bioanalytical Chemistry* 2019; 411: 6561-6573.
10. S. Campuzano, B. Esteban-Fernández de Ávila, P. Yáñez-Sedeño, J.M. Pingarrón, J. Wang. Nano/microvehicles for efficient delivery and (bio) sensing at the cellular level. *Chemical Science* 2017; 8(10): 6750-6763.
11. S. Sánchez, L. Soler, J. Katuri. Chemically powered micro- and nanomotors. *Angewandte Chemie International Edition* 2015; 54(5): 1414-1444.
12. J. Wang. Will future microbots be task-specific customized machines or multi-purpose “all in one” vehicles?. *Nature Communications* 2021; 12(1): 7125.
13. M. Urso, M. Ussia, M. Pumera. Smart micro-and nanorobots for water purification. *Nature Reviews Bioengineering* 2023; 1(4): 236-251.

14. J. Bujalance-Fernández, B. Jurado-Sánchez, A. Escarpa. The rise of metal–organic framework based micromotors. *Chemical Communications* 2023; 59(70): 10464-10475.
15. W. Srisuwanno, A. Kuhn, C. Wattanakit. Towards enantioselective synthesis with autonomous chiral encoded metal-swimmers. *ChemCatChem* 2025; e202500243.
16. M. Kuron, P. Kreissl, C. Holm. Toward understanding of self-electrophoretic propulsion under realistic conditions: From bulk reactions to confinement effects. *Accounts of Chemical Research* 2018; 51 (12): 2998-3005.
17. L.F. Valadares, Y.G. Tao, N.S. Zacharia, V. Kitaev, F. Galembeck, R. Kapral, G.A. Ozin. Catalytic nanomotors: Self-propelled sphere dimers. *Small* 2010; 6(4): 565-572.
18. H. Zhou, C.C. Mayorga-Martinez, S. Pané, L. Zhang, M. Pumera. Magnetically driven micro and nanorobots. *Chemical Reviews* 2021; 121(8): 4999-5041.
19. V.M. Kadiri, C. Bussi, A.W. Holle, K. Son, H. Kwon, G. Schütz, M.G. Gutierrez, P. Fischer. Biocompatible magnetic micro- and nanodevices: Fabrication of FePt nanopropellers and cell transfection. *Advanced Materials* 2020; 32(25): 2001114.
20. C. Liu, D. Jiang, G. Zhu, Z. Li, X. Zhang, P. Tian, D. Wang, E. Wang, H. Ouyang, M. Xiao. A light-powered triboelectric nanogenerator based on the photothermal marangoni effect. *ACS Applied Materials & Interfaces* 2022; 14(19): 22206-22215.
21. S. Sabrina, M. Tasinkevych, S. Ahmed, A.M. Brooks, M. Olvera de la Cruz, T.E. Mallouk, K.J. Bishop. Shape-directed microspinners powered by ultrasound. *ACS Nano* 2018; 12(3): 2939-2947.
22. G. Loget, A. Kuhn. Electric field-induced chemical locomotion of conducting objects. *Nature Communications* 2011; 2(1): 535.
23. G. Salinas, K. Tieriekhov, P. Garrigue, N. Sojic, L. Bouffier, A. Kuhn. Lorentz force-driven autonomous Janus swimmers. *Journal of the American Chemical Society* 2021; 143(32): 12708-12714.
24. V. Gatard, J. Deseure, M. Chatenet. Use of magnetic fields in electrochemistry: A selected review. *Current Opinion in Electrochemistry* 2020; 23: 96-105.
25. G. Salinas, C. Lozon, A. Kuhn. Unconventional applications of the magnetohydrodynamic effect in electrochemical systems. *Current Opinion in Electrochemistry* 2023; 38: 101220.
26. I. Mogi, R. Morimoto, R. Aogaki. Surface chirality effects induced by magnetic fields. *Current Opinion in Electrochemistry* 2018; 7: 1-6.
27. K. Tieriekhov, N. Sojic, L. Bouffier, G. Salinas, A. Kuhn. Wireless magnetoelectrochemical induction of rotational motion. *Advanced Science* 2024; 11(9): 2306635.
28. G. Salinas, S. Arnaboldi, P. Garrigue, G. Bonetti, R. Cirilli, T. Benincori, A. Kuhn. Magnetic field-enhanced redox chemistry on-the-fly for enantioselective synthesis. *Faraday Discussions* 2023; 247: 34-44.
29. S. Butcha, V. Lapeyre, C. Wattanakit, A. Kuhn. Self-assembled monolayer protection of chiral-imprinted mesoporous platinum electrodes for highly enantioselective synthesis. *Chemical Science* 2022; 13(8): 2339-2346.
30. T. Yutthalekha, C. Wattanakit, V. Lapeyre, S. Nokbin, C. Warakulwit, J. Limtrakul, A. Kuhn. Asymmetric synthesis using chiral-encoded metal. *Nature Communications* 2016; 7(1): 12678.
31. G. Salinas, A. Kuhn, S. Arnaboldi. Self-sustained rotation of Lorentz force-driven Janus systems. *The Journal of Physical Chemistry C* 2023; 127(30): 14704-14710.
32. L. Jin, B. Liu, S.S. Duay, J. He. Engineering surface ligands of noble metal nanocatalysts in tuning the product selectivity. *Catalysts* 2017; 7(2): 44.

Development of magnesium aluminate supported nickel catalyst in dry reforming of methane reaction

Pongsaporn Poosri[1], Waleeporn Donphai[1,2,*]

[1] KU-Green Catalysts Group, Department of Chemical Engineering, Faculty of Engineering, Kasetsart University, Bangkok 10900, Thailand
[2] Center for Advanced Studies in Nanotechnology for Chemical, Food and Agricultural Industries, KU Institute for Advanced Studies, Kasetsart University, Bangkok 10900, Thailand
[*] Corresponding author: fengwod@ku.ac.th

ABSTRACT

The dry reforming of methane (DRM) represents a highly promising technological approach for the efficient utilization of greenhouse gases, utilizing both methane (CH_4) and carbon dioxide (CO_2) as feedstocks. The resultant products of this reaction are commonly referred to as syngas, a composite of hydrogen and carbon monoxide gases. This research focused on developing a magnesium aluminate-supported nickel catalyst to enhance syngas production in the DRM reaction. It specifically examined the effects of various total molar of magnesium (Mg) combined with alumina (Al) on the structure and properties of magnesium aluminate supports, designated as MA-x (where x = 0.02, 0.04, 0.08, and 0.12). The catalyst support was prepared by the co-precipitation method, with a molar ratio of Mg/Al of 0.50. Then, the nickel metal was loaded on the catalyst support by the impregnation method (Ni/MA-x), and the catalyst was tested in DRM at 700 ^oC. As a result, the Ni/MA-0.04 catalyst exhibited the highest CH_4 and CO_2 conversion compared to the other catalysts. It could be explained that the Ni/MA-0.04 catalyst exhibited good nickel dispersion, which contributed to its effective catalytic performance. Furthermore, this catalyst showed the least carbon deposition, indicating excellent resistance to carbon formation.

Keywords: Magnesium aluminate; Nickel; Dry reforming of methane; Hydrogen; Coke resistance

1. INTRODUCTION

In recent decades, there has been a continuous decline in fossil fuel resources, including coal and natural gas. This trend is fundamentally driven by the rapid growth of the global human population, which has led to a significant increase in resource consumption. Additionally, the transportation and industrial sectors still heavily depend on fossil fuels to support their operations. To address the depletion of these finite resources and to mitigate the adverse effects on the atmosphere resulting from fossil fuel usage, it is essential to implement strategic measures aimed at decelerating their decline and promoting more sustainable energy practices [1,2].

Scientists have increasingly focused on various techniques to manage and utilize greenhouse gases. One of the most promising approaches involves chemical reactions that use greenhouse gases as reactants, such as the dry reforming of methane (DRM). This reaction employs both methane (CH_4) and carbon dioxide (CO_2) as feedstocks, making it an attractive method for greenhouse gas mitigation and resource utilization. The DRM reaction primarily produces synthesis gas, or syngas a mixture of hydrogen (H_2) and carbon monoxide (CO) with the exact ratio depending on the reaction conditions. Syngas can be used directly as a fuel for power generation or as a feedstock for the Fischer-Tropsch process to synthesize a variety of liquid fuels [3,4].

Catalysts are widely utilized in chemical reactions to enhance reaction efficiency by reducing the activation energy, thereby facilitating the progress of reactions under milder conditions. In the context of dry reforming of methane (DRM), numerous studies have investigated the effects of various catalysts to improve reaction performance. Among the commonly studied catalysts, nickel (Ni) has been found to offer high catalytic activity at a relatively low cost [5,6].

Catalyst supports are available in various forms, each possessing distinct physicochemical properties that influence catalytic performance. Numerous studies have explored the effects of different catalyst supports, with magnesium aluminate ($MgAl_2O_4$) emerging as one of the most widely utilized and effective options in the dry reforming of methane (DRM). $MgAl_2O_4$ has been extensively tested and proven to be an excellent support material for DRM due to its high thermal stability,

which contributes to the suppression of carbon deposition on the catalyst surface [7].

In addition, $MgAl_2O_4$ exhibits optimal basic properties and provides enhanced dispersion of active metal particles, which are essential for improving catalyst performance. Notably, its superior ability to adsorb carbon dioxide further contributes to the overall efficiency and long-term stability of the catalytic system, making it a preferred support in DRM applications [8,9].

In this study, nickel-based catalysts supported on magnesium aluminate were synthesized to enhance syngas production via the dry reforming of methane (DRM). The effects of varying total molar amounts of magnesium (Mg), combined with alumina (Al), on the structural and physicochemical properties of the supports were systematically investigated. The resulting support materials were denoted as MA-x, where x = 0.02, 0.04, 0.08, and 0.12. Nickel was subsequently deposited onto the supports to prepare the final catalysts, labeled as Ni/MA-x. The catalytic performance of these materials was then evaluated under DRM conditions.

2. EXPERIMENTAL

2.1. Catalyst preparation

A magnesium aluminate supported Ni catalyst was synthesized in two steps: first by preparing a magnesium aluminate support (MA-x) and then by loading Ni onto this magnesium aluminate support (MA-x) to from the Ni/MA-x.

The MA-x supports were prepared via a co-precipitation method. Magnesium nitrate hexahydrate and aluminum nitrate nonahydrate, with a fixed molar ratio of Mg/Al = 0.50, were dissolved 0.50 M Na_2CO_3 solution under constant stirring at 70 °C. The pH of the mixture was adjusted to 9 using 2 M NaOH. After pH adjustment, the suspension was continuously stirred at 70 °C for 18 hours to allow for proper aging. The resulting precipitate was then filtered and thoroughly washed with deionized water until the filtrate reached neutral pH. The obtained gel was dried overnight at 100 °C, ground into a fine powder, and subsequently calcined at 800 °C for 4 hours. The synthesized supports were denoted as MA-x, where x represents the total molar amount of Mg and Al precursors used (x = 0.02, 0.04, 0.08, and 0.12).

The Ni/MA-x catalysts containing 10 wt% nickel were synthesized via the impregnation method, employing nickel nitrate hexahydrate as the nickel precursor and calcined at 550 °C for 4 hours.

2.2. Characterization techniques

Powder XRD experiments were conducted with a Empyrean, Panalytical, this operated at 45 kV and 40 mA with Cu Kα radiation in 2θ range of 10-80°. To discern the phase composition and all the samples.

The reduction profiles of the catalyst were obtained by temperature programmed reduction. H_2-TPR method (Autochem II Chemisorption analyzer, Micromeritics). Each experiment, the 10% H_2 in Ar gas with a total flow rate of 30 ml/min was fed into the system, and the temperature rose to 1000 °C with 5 °C/min of heating rate. The quantity of H_2 consumption was evaluated by using a thermal conductivity detector (TCD).

The catalyst basicity was investigated by temperature programmed desorption of carbon dioxide with mass spectrometry (CO_2-TPD-MS). CO-TPD-MS uses the same equipment as H_2-TPR, but with an additional mass spectrometer device to assist in analysis. The catalyst was activated under H_2 flow at 700 °C with a heating rate of 5 °C/min for 1 h, after that purging with argon (Ar) gas for 1 h to clean the surface of active metal. Then, the system temperature was cooled down to 50 °C, and the 10% CO_2 in He gas with a flow rate of 50 ml/min was introduced for 1 h to reach adsorption equilibrium. After that, Ar gas was then purged to the catalyst bed to remove physically adsorbed species. The CO_2 desorption profile was investigated with increasing temperature from 50 to 1000 °C with a heating rate of 5 °C/min. The signal intensity of CO_2 (m/z = 44) was measured with an online mass spectrometer (Cirrus™ 3 Powerful and Versatile Atmospheric Gas Analyzer).

The amount of carbon formed on catalyst after reaction was investigated by using thermogravimetric analysis (TGA) technique (TA instrument, SDT2960 Simultaneous DTA-TGA Universal 2000) from 30-900 °C at a heating rate of 5 °C/min in air flow.

2.3. Catalyst test

The catalytic activity tests were performed in a packed-bed reactor of positioned inside the Inconel tube reactor (3/8-in. outside diameter (O.D.)) in which 100 mg of catalyst were loaded for each run. Prior to reaction, all catalysts were in situ reduced in a flow of H_2 at 700 °C for 60 min. The reaction conditions were evaluated at atmospheric pressure passing a flow of 100 ml/min of $CO_2/CH_4/N_2$ (molar ratio of 1:1:3) at 700 °C for 360 min. The conversion and product were determined through the analysis of the thermal conductivity detector gas chromatograph data, with Unibead-C serving as the packed column.

3. RESULTS AND DISCUSSION

The crystalline structures of the Ni/MA-x catalysts, synthesized with varying total molar amounts of magnesium (Mg) and aluminum (Al), were characterized using X-ray diffraction (XRD), as shown in Figure 1. The diffraction peaks observed at 2θ values of 19.0°, 31.3°, 36.8°, 44.8°, 55.7°, 59.4°, 65.2°, and 77.3° correspond to the characteristic planes of magnesium aluminate spinel ($MgAl_2O_4$) (ICDD:00-021-1152). In addition, diffraction peaks associated with nickel oxide (NiO), magnesium oxide (MgO), and magnesium nickel oxide ($MgNiO_2$) phases were also

detected. The diffraction peaks of NiO were identified at 2θ values of 37.2°, 43.3°, 62.9°, 75.4°, and 79.4° (ICDD: 00-047-1049), while MgO peaks appeared at 36.9°, 42.9°, 62.3°, 74.7°, and 78.6° (ICDD: 00-043-1022). Peaks corresponding to $MgNiO_2$ were observed at 37.1°, 43.1°, 62.6°, 75.1°, and 79.1° (ICDD: 00-024-0712), with overlapping positions among the NiO, MgO, and $MgNiO_2$ phases.

The analysis indicates that the variation in total molar amounts of magnesium (Mg) and aluminum (Al) in the $MgAl_2O_4$ support influences both the crystallinity and crystallite size of the NiO phase in the catalysts. This is evident from the differences in peak intensities and sharpness, particularly at $2\theta \approx 43.3°$, the main diffraction peak of NiO. Among the catalysts, Ni/MA-0.08 exhibited the largest NiO crystallite size, while Ni/MA-0.02 showed the smallest. These results suggest that the compositional variation in the support significantly affects the dispersion and crystallinity of the active nickel oxide phase.

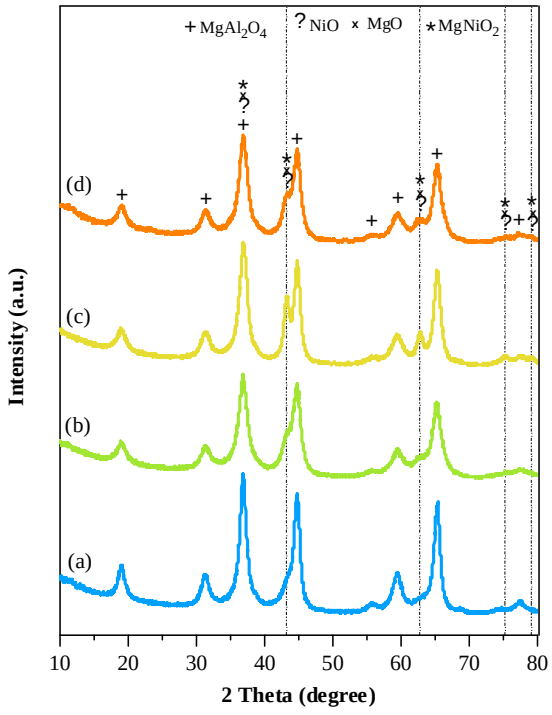

Figure 1 XRD of the fresh Ni/MA-x catalysts. (a) Ni/MA-0.02, (b) Ni/MA-0.04, (c) Ni/MA-0.08 and (d) Ni/MA-0.08

The reducibility and metal-support interactions of the Ni/MA-x catalysts, synthesized with varying total molar amounts of magnesium (Mg) and aluminum (Al), were investigated using H_2-temperature programmed reduction (H_2-TPR), as shown in Figure 2. The profiles revealed a small peak or shoulder in the temperature range of approximately 380-450 °C, which corresponds to the reduction of NiO species weak interaction with the support. A major peak was observed at higher temperatures, approximately 580-700 °C, associated with the reduction of NiO species strong interaction with the support [10]. Typically, stronger metal-support interactions shift the NiO reduction to higher temperatures, while lower-temperature reductions are indicative of weaker interactions and the presence of larger Ni particle sizes [11]. In addition, a shoulder peak at 539 °C was observed in the profile of the Ni/MA-0.08 catalyst, which may be attributed to the reduction of magnesium aluminate ($MgAl_2O_4$) to magnesium oxide (MgO) [12].

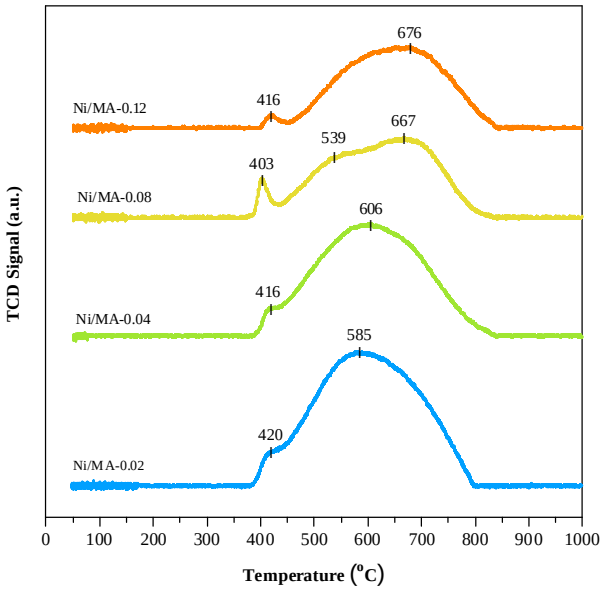

Figure 2 H_2-TPR of the Ni/MA-x catalysts.

CO_2-TPD-MS profiles of the catalysts exhibited three distinct temperature regions, corresponding to different types of basic sites. The low-temperature desorption peak observed below 130 °C is associated with weak basic sites, which are attributed to the desorption of CO_2 adsorbed as bicarbonate species on surface hydroxyl groups. The desorption peak between 130-230 °C corresponds to medium basic sites, indicating the presence of bidentate carbonate species adsorbed on Lewis's acid-base pair sites. Meanwhile, the high-temperature desorption peak above 230 °C reflects strong basic sites, which are associated with surface O^{2-} ions and the desorption of CO_2 in the form of unidentate carbonate species [13] as shown in Figure 3.

Among the catalysts, the Ni/MA-0.08 sample showed significant CO_2 desorption in the strong basic region, in contrast to the other samples. This behavior aligns with the H_2-TPR results, which revealed that this catalyst underwent partial reduction of magnesium aluminate ($MgAl_2O_4$) to magnesium oxide (MgO). The formation of MgO is known to introduce stronger basic sites on the catalyst surface, thereby enhancing CO_2 adsorption and desorption in the high-temperature region.

The catalytic activity and stability of the Ni/MA-x catalysts with varying total molar amounts of magnesium (Mg) and aluminum (Al), were investigated

under dry reforming of methane (DRM) conditions. The reaction was carried out at 700 °C for 360 minutes. Figures 4(a), 4(b) and 4(c) present the time-on-stream methane and carbon dioxide conversion and H_2/CO profiles for the various catalysts.

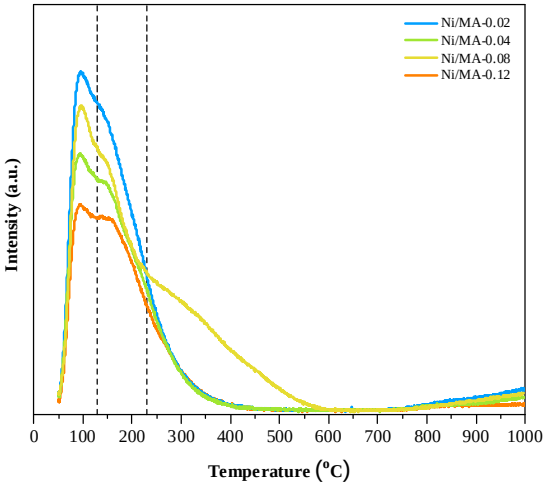

Figure 3 CO_2-TPD-MS of the Ni/MA-x catalysts.

At the reaction temperature of 700 °C, all catalysts exhibited higher CO_2 conversions than CH_4 conversions, which is likely attributed to the occurrence of the reverse water–gas shift (RWGS) reaction ($CO_2 + H_2 \rightarrow CO + H_2O$), a competing side reaction to DRM. This leads to a H_2/CO molar ratio of less than 1

Among the tested catalysts, Ni/MA-0.04 demonstrated the highest catalytic performance. At the initial time point (1 min), CH_4 and CO_2 conversions and H_2/CO were 84.30%, 91.44% and 0.94 respectively. After 360 minutes of reaction, conversions slightly decreased to 81.81% for CH_4, 88.18% for CO_2 and 0.92 for H_2/CO indicating excellent catalytic stability and resistance to deactivation.

The superior performance of Ni/MA-0.04 is mainly attributed to its high nickel dispersion and small Ni particle size, which promote greater availability of active sites for methane activation, even though this catalyst does not exhibit the strongest metal-support interaction among the samples [14]. These characteristics underline the importance of Ni dispersion and particle size in achieving high initial activity and long-term stability under DRM conditions.

The formation of carbon on nickel-based catalysts supported on magnesium aluminate (Ni/MA-x), with varying total molar amounts of magnesium (Mg) and aluminum (Al), was investigated. The carbon formation results from the methane cracking reaction ($CH_4 \rightarrow 2H_2 + C$), a side reaction that occurs during the dry reforming of methane. The amount of carbon deposited on the catalyst surface was analyzed using Thermo-Gravimetric Analysis (TGA), as shown in Figure 5.

It was observed that the temperature range below 100 °C corresponds to the decomposition of moisture present on the catalyst surface. In the range of approximately 100-350 °C, the decomposition of amorphous carbon occurs, while the temperature range of approximately 350-700 °C is associated with the decomposition of filamentous carbon [15]. For the quantification of carbon species, the analysis was initiated at temperatures above 100 °C.

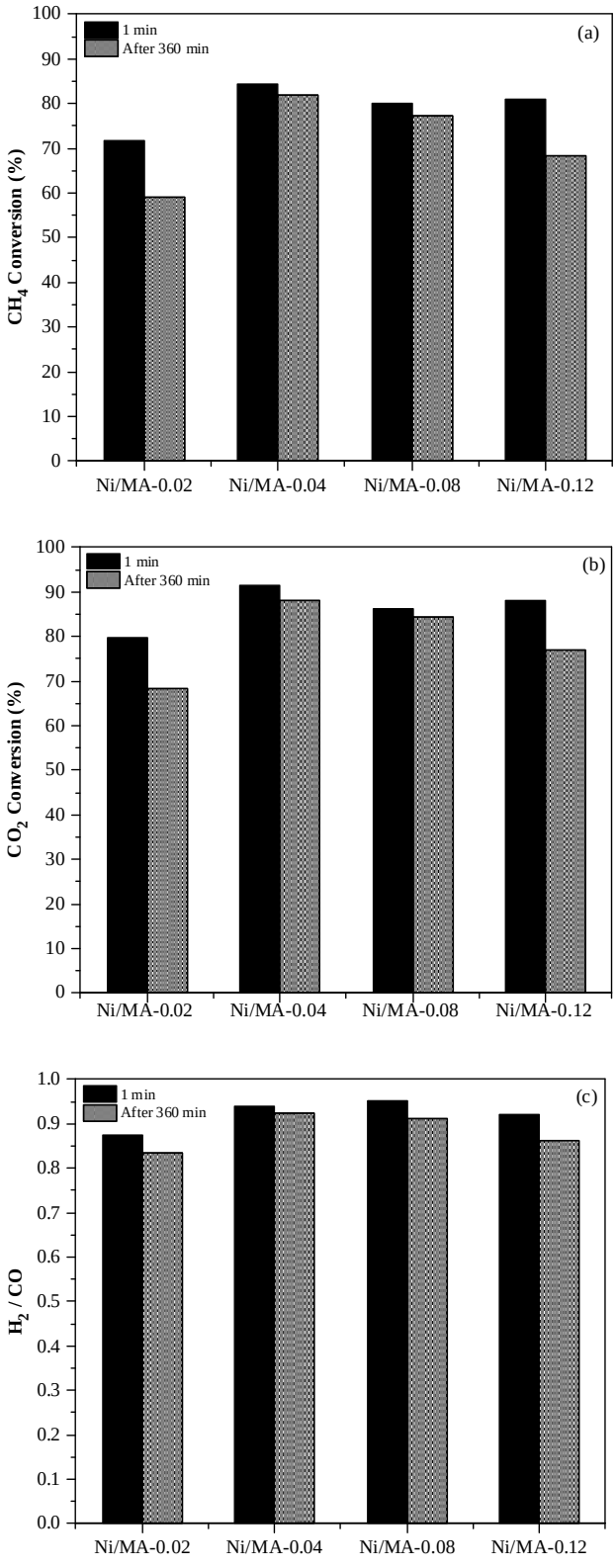

Figure 4 Performance of the Ni/MA-x catalysts with time on stream in DRM reaction at 700 °C for 360 min. (a) CH_4 conversion, (b) CO_2 conversion and (c) H_2/CO.

The results reveal that the Ni/MA-0.04 catalyst exhibited the lowest carbon decomposition at 10.38 wt.%, followed by Ni/MA-0.02 at 16.33 wt.%, Ni/MA-0.12 at 20.71 wt.%, and Ni/MA-0.08 at 33.86 wt.%.

Ni/MA-0.04 < Ni/MA-0.02 < Ni/MA-0.12 < Ni/MA-0.08 Among the studied catalysts, Ni/MA-0.04 exhibited the lowest carbon deposition, indicating superior resistance to carbon formation (coke resistance) under the methane cracking conditions.

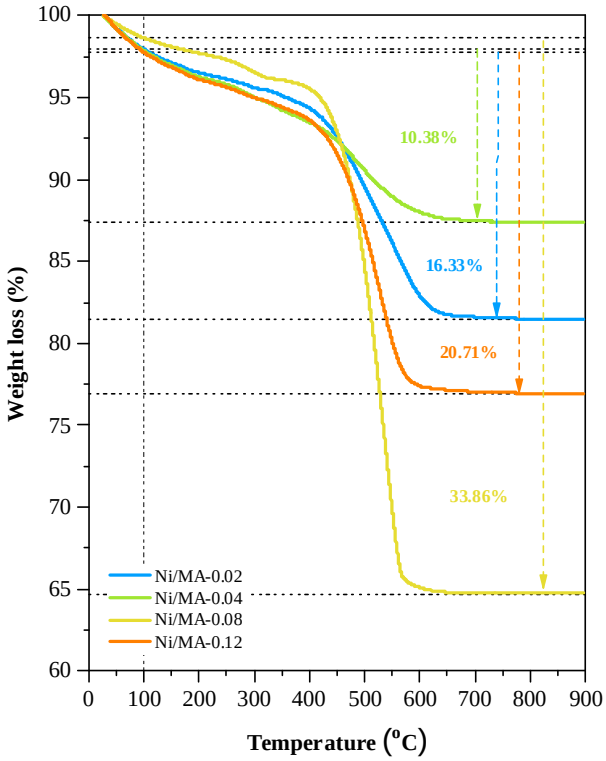

Figure 5 Thermogravimetric curves obtained for the catalysts after the DRM catalytic test.

4. CONCLUSION

In this study, nickel-based catalysts supported on magnesium aluminate with varying total molar amounts of magnesium (Mg) and aluminum (Al), were investigated. The total molar amounts of magnesium (Mg) and aluminum (Al) were found to have a significant impact on the physical and structural properties, reducibility, and basicity of the catalysts. Among the samples, the Ni/MA-0.04 catalyst exhibited the highest catalytic performance and stability. In the DRM reaction at 700 °C for 360 minutes, Ni/MA-0.04 showed superior CH_4 and CO_2 conversion, as well as a higher H_2/CO molar ratio compared to other catalysts. Additionally, it demonstrated lower carbon deposition, indicating improved resistance to carbon formation.

ACKNOWLEDGMENTS

This work was supported by the Fundamental Fund under the Kasetsart University Research and Development Institute (KURDI) (Grant No. FF(KU)51.67).

REFERENCES

1. K. Palanichamy, N. Sasirekha. Dry reforming of methane using bimetallic Pt-Ni/ Ti-SBA-15: Effect of Si/Ti ratio on catalytic activity and stability. *International journal of hydrogen energy* 2023; 48: 31126-31141.
2. L. Qin, Z. Hu, M. Hu, B. Zhao, L. Kong, W. Chen, J. Han. EDTA impregnation assisted synthesis of nickel nanoparticles embedded in activated carbon and its application for dry reforming of methane. *International journal of hydrogen energy* 2023; 48: 13442-13451.
3. C.Q. Pham, A.N.T. Cao, P.T.T. Phuong, L.K.H. Pham, T.T.V. Tran, T.H. Trinh, D.V.N. Vo, T.P.T. Bui, T.M. Nguyen. Enhancement of syngas production from dry reforming of methane over Co/Al_2O_3 catalyst: Insight into the promotional effects of europium and neodymium. *Journal of the Energy Institute* 2022; 105: 314-322.
4. D. Liang, Y. Wang, M. Chen, X. Xie, C. Li, J. Wang, L. Yuan. Dry reforming of methane over Mn-Ni/attapulgite: Effect of Mn content on the active site distribution and catalytic performance. *Fuel* 2022; 321: 124032.
5. B.J. Kim, H.R. Park, Y.L. Lee, S.Y. Ahn, K.J. Kim, G.R. Hong, H.S. Roh. Effect of surface properties of Ni-MgO-Al_2O_3 catalyst for simultaneous H_2 production and CO_2 utilization using dry reforming of coke oven gas. *Catalysis Today* 2023; 411-412: 113855.
6. Q. Song, R. Ran, X. Wua, Z. Si, D. Weng. Dry reforming of methane over Ni catalysts supported on micro- and mesoporous silica. *Journal of CO_2 Utilization* 2023; 68: 102387.
7. E. Akbaria, S. M. Alavia, M. Rezaei. Synthesis gas production over highly active and stable nanostructured Ni-MgO-Al_2O_3 catalysts in dry reforming of methane: Effects of Ni contents. *Fuel* 2017; 194: 171-179.
8. L. Azancot, L.F. Bobadilla, M.A. Centeno, J.A. Odriozola. IR spectroscopic insights into the coking-resistance effect of potassium on nickel-based catalyst during dry reforming of methane. *Applied Catalysis B: Environmental* 2021; 285: 119822.
9. E. Akbaria, S. M. Alavia, M. Rezaei. CeO_2 Promoted Ni-MgO-Al_2O_3 nanocatalysts for carbon dioxide reforming of methane. *Journal of CO_2 Utilization* 2018; 24: 128-138.
10. M. Rezaei, S.M. Alavi. Dry reforming over mesoporous nanocrystalline 5%Ni/M-$MgAl_2O_4$ (M: CeO_2, ZrO_2, La_2O_3) catalysts. *International journal of hydrogen energy* 2019; 44: 16516-16525.

11. L. Azancot, L.F. Bobadilla, J.L. Santos, J.M. Cordoba, M.A. Centeno, J.A. Odriozola. Influence of the preparation method in the metal-support interaction and reducibility of Ni-Mg-Al based catalysts for methane steam reforming. *International journal of hydrogen energy* 2019; 44: 19827-19840.
12. F.V. Maziviero, D.M.A. Melo, R.L.B.A. Medeiros, J.C.A. Silva, T.R. Araújo, A.A.S. Oliveira, Y.K.R.O. Silva, M.A.F. Melo. Influence of Mn, Mg, Ce and P promoters on Ni-X/Al_2O_3 catalysts for dry reforming of methane. *Journal of the Energy Institute* 2024; 113: 101523.
13. A.V.P. Lino, E.M. Assaf, J.M. Assaf. X-ZrO_2 addition (X= Ce, La, Y and Sm) on Ni/$MgAl_2O_4$ applied to methane tri-reforming for syngas production. *Journal of CO_2 Utilization* 2019; 33: 273-283.
14. Y.H. Zhao, J.T. Geng, H.D. Zhu, Q.J. Zhang, H. Wang, X.Q. Feng. Ordered mesoporous Ni-Mg-Al_2O_3 as an effective catalyst for CO_2 reforming of CH_4. *International journal of hydrogen energy* 2023; 48: 7192-7201.
15. P. Song, T. Su. Y. Luo, X. Luo, H. Ji, Z. Qin. Ni-Mg-Al Catalysts for Dry Reforming of Methane: Effect of Surface Properties on Coke Formation and CO_2 Activation. *Industrial & Engineering Chemistry Research* 2024; 63: 10677-16090.

Effect of graphene nanoplatelets addition during electroless plating of ABS on the properties of copper-nickel-chromium coated ABS

Wantana Chuakamhod[1], Weerachon Tolek[1], Wasu Chaitree[2], Joongjai Panpranot[1,*]

[1] Department of Chemical Engineering, Faculty of Engineering, Chulalongkorn University, Bangkok 10330, Thailand

[2] Department of Chemical Engineering, Faculty of Engineering and Industrial Technology, Silpakorn University, Nakorn Pathom 73000, Thailand

[*] Corresponding author: joongjai.p@chula.ac.th

ABSTRACT

Acrylonitrile Butadiene Styrene (ABS) with chromium coating is widely used in applications requiring high strength, durability, and aesthetic appeal, such as automotive parts, electronics, appliances, sanitary fixtures, and decorative consumer goods [1, 2]. Before electroplating, ABS undergoes nickel electroless plating to create a conductive base, traditionally relying on palladium (Pd), a costly material. This research explores reducing Pd usage by incorporating graphene nanoplatelets into the plating bath, which enables a decrease in Pd concentration from the industrial standard of 16–25 ppm to just 6 ppm with the addition of 15 mg/L of graphene nanoplatelets. The Ni-coated ABS achieved an electrical conductivity of 6.1 S/cm, while graphene nanoplatelets enhanced Pd dispersion, reduced agglomeration, and ensured a uniform nickel coating. SEM analysis revealed an optimal etched surface structure with appropriate porosity and grooves, preventing over-etching or insufficient etching, thereby improving Pd adhesion. The findings demonstrate that graphene nanoplatelets increase surface area and Pd uniformity, allowing for significant Pd reduction without compromising plating performance. This study presents a cost-effective and sustainable solution for industrial electroless nickel plating, reducing material costs while maintaining high-quality coatings.

Keywords: ABS plastics; Electrical conductivity; Electroless nickel plating; Graphene oxide

1. INTRODUCTION

Acrylonitrile-butadiene-styrene (ABS) is a highly sought-after plastic due to its outstanding properties: excellent mechanical properties, chemical resistance, easy to process, resistant to abrasion and withstands heat well [1, 2]. Therefore, ABS is widely used in the automotive, electrical appliance, electronics, and office equipment industries, etc. Despite its widespread use, ABS has limitations in the electronics and automotive industries due to its very low electrical conductivity [3, 4]. To address this, past research has focused on improving the electrical conductivity properties of polymers by adding reinforcing substances [5] such as carbon black (CB) [6], carbon fiber (CF) [7], carbon nanotubes (CNT) [8], and graphene [9], etc. While carbon black and carbon nanotubes are commonly used to enhance conductivity, carbon black requires large quantities to achieve the desired conductivity [6], and CNTs, though effective, have relatively high production cost, limiting their use [8]. Graphene, on the other hand, is a promising alternative reinforcing agent, due to its high surface area, aspect ratio, tensile strength, and excellent thermal and electrical conductivity. It also helps to prevent electromagnetic interference (EMI), [10-14]. Currently, graphene is increasingly incorporated into composite materials, which combine graphene with other substances to create materials with improved properties. These composite materials consist of two phases: the matrix and the reinforcer or filler [15-17]. In the electronics and automotive industries, reinforcers are commonly used to make polymers electrically conductive. Conductive polymers that have been widely studied include polyaniline (PAn), polypyrole (PPy), polythiophene (PTh), polyacethylene (PAc) [18, 19], and ABS.

Therefore, this research focuses on the development of GO-ABS composites and examines its influence on the electrical and mechanical properties of ABS polymer. Additionally, our study further explores the methods mentioned above by employing the electroless nickel plating process, a technique that has been traditionally used in industry for a long time. This process enhances the conductivity of ABS by depositing a nickel layer onto the plastic surface without the need for an external electric current. The

primary aim of this research is to reduce the palladium concentration used in the electroless nickel plating process, as palladium is an expensive metal. To achieve this, we use graphene as a palladium enhancer in the catalytic plating bath. Graphene, with its high electrical conductivity, aids in better dispersing palladium, allowing for a reduced amount of palladium while maintaining the optimum efficiency of the nickel plating process [20-23]

2. EXPERIMENTAL

2.1 Materials and equipment

Materials: Acrylonitrile-Butadiene-Styrene (717, ABS) plastic components from Bandai Namco (Thailand) Co., Ltd.

Equipment: 600 ml beaker, OHAUS PR-series digital scale, pipette, OHAUS Guardian™ 5000 hot plate and stirrer, C-Mag HS7 hotplate and magnetic stirrer, rubber bulb, mercury thermometer, chemical spoon, copper wire, shredded paper, magnetic stir bar, litmus paper, graduated cylinder, scissors, ruler, tongs, electrical multimeter.

2.2 Chemicals

Sigma-Aldrich 900411-250G Graphene Nanoplatelets (25 µm particle size, surface area 50-80 m^2/g), Chromium Trioxide (CrO_3), Accelerator and Neutralizer (supplied by MacDermid Co., Ltd.), Boric Acid (H_3BO_3), Palladium (II) Chloride ($PdCl_2$) 99.9% (metals basis), Pd content: 59.0%, Tin (II) Chloride ($SnCl_2$), reagent grade, 98%, Hydrochloric Acid (HCl, 36%), Sulfuric Acid (H_2SO_4, 96%), Ammonia Solution (NH_4OH, 28%), Sodium Citrate Tribasic Dihydrate ($Na_3C_6H_5O_7$), Nickel Sulfate Hexahydrate ($NiSO_4 \cdot 6H_2O$), Sodium Hypophosphite Monohydrate AR Grade ($NaPO_2H_2 \cdot H_2O$).

2.3 Preparation of chemicals for electroless nickel plating process

2.3.1 Conditioner solution

Prepare the conditioner solution by measuring 15 mL of concentrated H_2SO_4 and diluting it with distilled water. Adjust the final volume to 500 mL.

2.3.2 Etching solution

Weigh 200 g of CrO_3 and dissolve it in distilled water. Once fully dissolved, slowly add 100 mL (adjust the volume to the system as the solution forms crystals) of concentrated H_2SO_4 to the solution to avoid the formation of crystalline precipitates. After mixing, add distilled water to adjust the final volume to 500 mL[22].

2.3.3 Neutralizer solution

Measure 10 mL of Adhemax Neutralizer Cr and dissolve it in 10 mL of concentrated HCl. Adjust the final volume to 500 mL with distilled water. [MacDermid (Thailand) Co., LTD]

2.3.4 Catalyst solution

Prepare the catalyst solution using varying concentrations of palladium (Pd) in ppm, as shown in Table 1. Each formulation includes $PdCl_2$, Graphene, $SnCl_2$, and 150 mL of HCl as the base. For all Pd concentrations, 7.5 mg of graphene and 0.75 g of $SnCl_2$ are used, except for the 25 ppm Pd solution, which contains no graphene and uses 1.50 g of $SnCl_2$ instead and adjusts the final volume to 500 mL with distilled water. Each Pd concentration is assigned to a batch number for reference.

Table 1 Preparation of catalyst solution.

No.	Pd (ppm)	$PdCl_2$ (mg)	Graphene (mg)	$SnCl_2$ (g)	HCl (ml)
1	3	2.5	7.5	0.75	150
2	6	5.0	7.5	0.75	150
3	15	12.5	7.5	0.75	150
4	25	21	-	1.50	150

2.3.5 Accelerator solution

Measure 50 mL of the accelerator solution and dilute it with distilled water. Adjust the final volume to 500 mL. [MacDermid (Thailand) Co., LTD]

2.3.6 Electroless nickel plating solution

Weigh the following chemicals:25 g of $Na_3C_6H_5O_7$, 22.5 g of $NiSO_4 \cdot 6H_2O$,20 g of $NaPO_2H_2 \cdot H_2O$. Dissolve all the chemicals in distilled water and mix thoroughly. Add distilled water to adjust the final volume to 500 mL. Adjust the pH of the solution to 4.5–5.0 using NH_4OH, as this pH range is optimal for the electroless nickel plating process in industrial applications. Following these steps will result in the preparation of the appropriate chemical solutions for an effective electroless nickel plating process.

2.4 Experimental method

The ABS plastic samples were cut into dimensions of 1x1 cm and wrapped with copper wire of 1 mm diameter. The following steps were then performed:

2.4.1 Conditioner solution

The ABS samples were cleaned to remove oil and impurities by immersing them in a conditioner solution at 25°C for 3 minutes. Afterward, the samples were rinsed with distilled water.

2.4.2 Etching solution

The ABS samples were etched to create porous surfaces by immersing them in an etching solution at 60-70°C for 10 minutes, with continuous stirring using a magnetic stirrer. After the process, the samples were rinsed with distilled water.

2.4.3 Neutralizer solution

The samples were immersed in a neutralizer solution to reduce Chromium (Cr^{6+}) to Chromium (Cr^{3+})

at 25°C for 3 minutes. Afterward, the samples were rinsed with distilled water [MacDermid (Thailand) Co., LTD].

2.4.4 Catalyst solution

The samples were immersed in a catalyst solution to enhance the adhesion of palladium (Pd) onto the ABS surface. The process was conducted using Pd concentrations of 3,6,15 ppm and 25 ppm at a temperature of 38–42°C for 10 minutes, with continuous stirring using a magnetic stirrer.

For catalyst solutions with Pd concentrations of 3,6,15 ppm, graphene (7.5 mg) and $SnCl_2$ (0.75 g) were added. Graphene, a two-dimensional conductive material, acts as a carrier for palladium, enabling better adhesion of Pd to the porous ABS surface and ensuring uniform distribution.

For the catalyst solution with 25 ppm Pd, no graphene was added. Instead, $SnCl_2$ (1.5 g) was added to enhance the reaction efficiency on the ABS surface.

During this step, palladium (Pd) adheres to the pores of the ABS surface, forming a thin catalytic layer essential for the subsequent electroless nickel plating process. After the treatment, the samples were rinsed with distilled water.

2.4.5 Accelerator solution

The samples were immersed in an accelerator solution to remove any residual tin (Sn) on the ABS surface. Tin could otherwise inhibit the reaction between nickel (Ni) and palladium (Pd). This step was performed at 45–50°C for 3 minutes, with continuous stirring using a magnetic stirrer. Afterward, the samples were rinsed with distilled water.

2.4.6 Electroless nickel plating

The samples were immersed in an electroless nickel solution at 50°C for 10 minutes, with continuous stirring using a magnetic stirrer. During this process, nickel (Ni) reacts with palladium (Pd), forming a thin nickel film on the ABS surface. This nickel layer imparts electrical conductivity to the ABS plastic. After the plating process, the samples were rinsed with distilled water.

Note: Each step was carefully controlled for temperature and duration to optimize the performance of the electroless nickel plating process on ABS plastic surfaces.

2.5 Testing the properties of ABS plastic

2.5.1 Electrical resistance testing

2.5.1.1 Measure the electrical resistance of ABS plastic

After the electroless nickel plating process using a digital multimeter with a measurement range of 0 Ω–40 MΩ. The test is conducted at room temperature. The electrical conductivity of ABS plastic after the Electroless Nickel process varies according to the Pd concentration added in the Catalyst bath. The electrical conductivity (σ) is calculated from the electrical resistivity (ρ) using the equation:

$$\sigma = \frac{1}{\rho} \quad (1)$$

where:

$$\rho = R\,x\,\frac{A}{L} \quad (2)$$

where:

- R is the electrical resistance of the sample (Ω)
- A is the cross-sectional area of the sample (cm^2)
- L is the sample length (cm)

2.5.2 Morphology analysis of ABS plastic

2.5.2.1 Surface morphology examination

Analyze the surface morphology of ABS plastic both before and after the etching process. The sample is cut into dimensions of 1 cm × 5 mm to compare the differences between the original ABS plastic surface and the porous surface of the etched ABS plastic. A scanning electron microscope (SEM) is used for this analysis.

2.5.2.2 Chemical analysis of catalyst solution

Collect chemical samples from the catalyst solution both before and after the immersion process to analyze the absorption of Pd and Sn on the ABS plastic surface. Inductively Coupled Plasma Optical Emission Spectroscopy (ICP-OES) is employed to determine the concentrations of Pd and Sn in the solution. This technique is used for high-sensitivity quantitative analysis of elements in liquid samples.

2.5.2.3 Graphene adsorption analysis

Analyze the adsorption of graphene on the ABS plastic surface after the catalyst process. The sample is cut to 1 cm × 5 mm for scanning electron microscopy-energy dispersive X-ray spectroscopy (SEM-EDX) analysis.

2.5.2.4 Nickel thickness analysis

Examine the distribution, thickness of the nickel coating on the ABS plastic surface after the electroless nickel plating process. The sample is cut to 1 cm × 5 mm for this analysis using a scanning electron microscope (SEM).

3. RESULTS AND DISCUSSION

3.1 Electrical resistance testing

The ABS plastic samples used in this study had dimensions of 1 cm in width, 1 cm in length, and 1 mm (0.1 cm) in thickness, resulting in a cross-sectional area of A = width × thickness = 1 cm × 0.1 cm = 0.1 cm^2. The electrical conductivity of the ABS plastic after

undergoing the electroless nickel process is presented in Table 2, which provides detailed conductivity values for each sample. These findings are further illustrated in Figure 1, which visually represents the conductivity trend, highlighting the improvement in electrical properties because of the metallization process.

Table 2 The electrical conductivity of ABS plastic.

No.	Pd (ppm)	Electrical conductivity (S/cm)
1	3	-
2	6	3.9
3	15	6.1
4	25	11.4

From Table 2 at Pd 3 ppm, no electrical conductivity was observed because the Pd concentration was too low, preventing proper adhesion to the ABS surface. As a result, there was no catalytic activity for the electroless plating process. At 6 ppm, Conductivity increased to 3.9 S/cm as the Pd concentration was sufficient for metal deposition, and the etching process was at an optimal level, allowing Pd and graphene to adhere well. At Pd 15 ppm, the electrical conductivity increased to 6.1 S/cm. Among the samples, at Pd 25 ppm the highest electrical conductivity was observed at 11.4 S/cm. Even though the ABS surface underwent minimal etching, high Pd concentration was sufficient to create a conductive network, even without graphene addition in this case.

From these trends, it can be concluded that Pd concentration directly affects electrical conductivity. However, other factors such as etching level and Pd/graphene adhesion also influence conductivity variation. At 6 ppm and 15 ppm, the ABS surface underwent optimal etching, ensuring a well-structured substrate for Pd and graphene adhesion. However, at 3 ppm, the Pd concentration was too low to sustain catalytic activity, while at 25 ppm, the Pd concentration was high enough to enable significant conductivity, even in the absence of graphene.

However, in the electroless nickel plating process for industrial use, electrical conductivity is not typically measured. Instead, the surface of the ABS plastic piece is observed. If the nickel is evenly coated and the surface of the ABS plastic is completely covered, the electroless nickel plating process is considered successful and can proceed.

3.2 Morphology analysis of ABS plastic

3.2.1 Surface morphology examination

Figure 1 illustrates the ABS plastic surface before and after etching. Figure 1a. shows the normal plastic surface (not etched). The untreated surface is smooth, without obvious grooves or holes. This is because the original ABS plastic structure has not been corroded by the etching agent. This type of surface is not suitable for surface preparation for plating because it lacks a surface for the adhesion of the plated material, such as Palladium (Pd). Figure 1b. and 1e. at Pd concentration of 3 ppm and Pd 25 ppm, show slightly corrosion of the surface with some grooves and pores, but not to a sufficient extent. The etching process does not appear to create a suitable surface for Pd adhesion, resulting in the non-electrical conductivity of Pd 3 ppm sample, and even without graphene added to Pd 25 ppm. The pores formed in the etching are not enough for Pd to properly adhere and disperse. However, the high concentration of Pd 25 ppm, still yields higher conductivity compared to the lower Pd concentrations. Figures 1c. and 1d. at concentrations of Pd 6 ppm and Pd 15 ppm, show a surface with well-formed grooves and pores, uniform, and a structure that allows uniform Pd adhesion. When graphene is added, their enhances dispersion of Pd, improving the efficiency of the coating process.

The results from SEM images show that the etched surface significantly affects Pd dispersion. A well-etched surface, such as those observed at 6 ppm Pd and 15 ppm Pd, provides better Pd adhesion and uniform distribution. However, graphene adhesion is reduced because the pores may not be large enough to accommodate the graphene particle size of 25 µm. This large graphene particle may not be able to penetrate the appropriate erosion level, which is more suitable for Pd dispersion. Graphene acts as a Pd enhancer. The addition of graphene to 3,6 and 15 ppm Pd improves Pd dispersion, leading to more efficient plating and better overall coating performances.

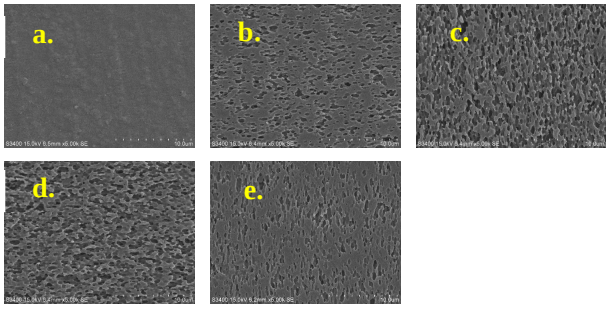

Figure 1 a.) Pure ABS b.) ABS after etching with Pd 3 ppm c.) Pd 6 ppm d.) Pd 15 ppm e.) Pd 25 ppm

3.2.2 Chemical analysis of catalyst solution

This experiment aimed to analyze the adsorption of palladium (Pd) on the surface of ABS using ICP-OES (inductively coupled plasma optical emission spectroscopy). The study focused on understanding the relationship between surface etching conditions, Pd concentration, and the amount of Pd adsorbed onto the ABS surface, particularly in the preparation step for electroless plating. The Pd adsorption values on the ABS surface, before and after the catalyst plating process, are summarized in Table 3. The sample size used for analysis was 1 × 1 cm, corresponding to a surface area of 1 cm^2.

Table 3 Pd adsorption on ABS plastic before and after catalyst plating.

No.	Pd (ppm)	ICP-Pd before Coad(ppm)	ICP-Pd after Coad(ppm)	Diff Pd adsorption (ppm)	Diff Pd adsorption (mg/cm^2)
1	3	0.780	0.646	0.134	0.067
2	6	3.652	3.454	0.198	0.099
3	15	11.640	11.360	0.280	0.140
4	25	20.650	19.890	0.760	0.380

The results of Pd adsorption on ABS plastic are shown in Figure 2. At 3 ppm Pd concentration, the adsorption value was 0.134 ppm, which was the lowest among all measured values. This low adsorption was due to two main factors. First, the ABS surface underwent insufficient etching, resulting in a lack of micropores and the surface roughness necessary for effective Pd adhesion. Without adequate etching, the surface area available for Pd attachment was limited. Second, the low Pd concentration in the solution meant that the number of Pd ions available for adsorption was also limited. The combination of these factors led to the lowest Pd adsorption value in this experiment.

When the Pd concentration increased to 6 ppm, the adsorption value rose to 0.198 ppm, significantly higher than at 3 ppm. At this stage, the ABS surface had undergone optimal etching, creating well-formed micropores that facilitated Pd adhesion. Additionally, the increased Pd concentration in the solution provided more Pd ions for adsorption, further enhancing the adsorption efficiency.

At 15 ppm Pd concentration, the adsorption reached 0.280 ppm, the highest among samples with optimally etched surfaces. This increase was due to two key factors. First, the ABS surface was etched to an ideal level, creating a balanced pore structure that maximized Pd adhesion. Second, the higher Pd concentration in the solution increased the availability of Pd ions, further enhancing the adsorption efficiency. The combination of a well-prepared surface and a higher Pd concentration resulted in the highest adsorption value within the optimally etched range.

However, at 25 ppm Pd concentration, the adsorption value surged to 0.760 ppm, the highest among the samples in this study. Despite the ABS surface being under-etched, the exceptionally high Pd concentration led to significant Pd accumulation on the surface. Although the adhesion efficiency may not have been as high as in the optimally etched samples, the large amount of Pd ions in the solution resulted in excessive Pd deposition, causing a dramatic increase in the adsorption value.

The trend in Pd adsorption showed that both etching conditions and Pd concentration played crucial roles in determining the adsorption efficiency. At 3 ppm, adsorption was the lowest due to insufficient surface etching and low Pd concentration, which limited Pd uptake. At 6 and 15 ppm, adsorption was higher because of optimal etching and increasing Pd concentration, which provided more Pd ions for effective adsorption. At 25 ppm, adsorption increased sharply due to the high Pd concentration, causing excessive Pd accumulation on the surface, even though the surface was under-etched.

Thus, the results highlight the importance of optimizing both etching conditions and Pd concentration to maximize Pd adsorption efficiency, which directly impacts the effectiveness of subsequent electroless plating processes.

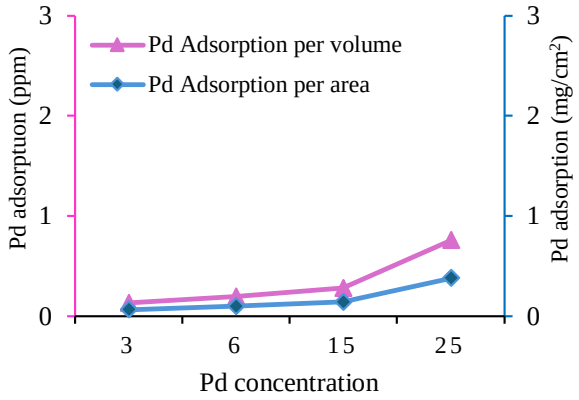

Figure 2 Pd adsorption on ABS plastics.

3.2.3 Graphene adsorption analysis

3.2.3.1 Graphene adsorption after catalyst process analysis

Analysis using the SEM-EDX technique revealed that the percentage of carbon (C), palladium (Pd), tin (Sn), and oxygen (O) varied depending on the concentration of Pd added to the plating bath. The trend in these changes is summarized in Table 4, which presents the atomic percentages of carbon, palladium, tin, and oxygen are presented. A sample size used for analysis was 1 × 1 cm, corresponding to a cross-sectional area of 1 cm^2.

Table 4 Atomic percentage of elements (C,Pd,Sn,O).

No.	Pd (ppm)	%At of C	%At of Pd	%At of Sn	%At of O	C (mg/ L)	C (mg/ cm^2)
1	3	83.340	0.127	0.130	16.400	-	-
2	6	86.030	0.103	0.103	13.770	0.059	0.029
3	15	87.520	0.123	0.103	12.260	0.282	0.141
4	25	-	0.160	0.147	14.050	-	-

The experimental results showed that %C tended to increase with increasing Pd concentration, starting from 83.340% at 3 ppm and increasing to a maximum of 87.520% at 15 ppm.

For the adsorption value of C on the ABS surface, we can calculate it from the carbon atom percentage according to the following equation.

$$\Delta\%C = \%C_{SEM-EDX} - \%C_{STANDARD} = \%C_{SEM-EDX} - 85.64 \quad (3)$$

- Calculate the mass of adsorbed carbon (mg)

$$m_C = \left(\frac{\Delta\%C}{100}\right) x\ Total\ Graphene\ in\ the\ Bath \quad (4)$$

- Calculate the mass of adsorption per volume (mg/L)

$$C_{Adsorption}\left(\frac{mg}{L}\right) = \frac{m_C}{0.5} \quad (5)$$

- Calculate the carbon adsorption per surface area (mg/cm^2)

$$C_{Adsorption}\left(\frac{mg}{cm^2}\right) = \frac{m_C}{1} \quad (6)$$

The ABS plastic piece is 1 x 1 cm in size, square in shape, and 1 mm thick.

Graphene concentration in Catalyst plating pool 7.5 mg/0.5 L

- $\Delta\%C = Carbon\ changes$
- $m_C = Mass\ of\ carbon\ absorbed\ (mg)$
- $C_{Adsorption} = Carbon\ Adsorption$

The result for the graphene adsorption on ABS plastic shown in Figure 3 indicates that the atomic percentages of palladium (%Pd), tin (%Sn) and oxygen (%O) exhibited a decreasing trend within the range of Pd concentration from 3 to 6 ppm. However, at a concentration of Pd 15 ppm, there was an increasing trend. Specifically, as the concentration of Pd increased from 3 ppm to 6 ppm, the values of %Pd, %Sn and %O decreased. The changes were as follows: %Pd decreased from 0.127% at 3 ppm to 0.103% at 6 ppm, %Sn decreased from 0.130% at 3 ppm to 0.103% at 6 ppm. %O decreased from 16.400% at 3 ppm to 13.770% at 6 ppm. This trend may be attributed to poor or uneven dispersion of Pd, Sn, and O in the solution, resulting in lower adsorption on the ABS surface in the range of 3-6 ppm. However, when the concentration of Pd was increased to 15-25 ppm, the atomic percentages of %Pd, %Sn and %O tended to increase, with %Pd increasing from 0.123% at 15 ppm to 0.160% at 25 ppm, %Sn increasing from 0.103% at 15 ppm to 0.147% at 25 ppm, and %O increasing from 12.260% at 15 ppm to 14.050% at 25 ppm. This increasing trend suggests that when Pd concentrations was higher than 6 ppm, more metal was accumulated on the ABS surface. This effect could be due to Pd acting as a catalyst, promoting accumulation of Sn and O on the ABS surface. The increased metal binding caused by the larger among of Pd likely altered the surface structure, enhancing metal binding.

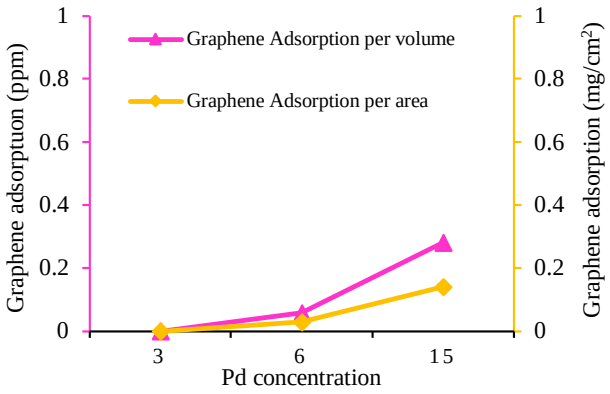

Figure 3 Graphene adsorption on ABS Plastics.

3.2.4 Nickel thickness analysis

The objective of this experiment was to study the effect of palladium (Pd) concentration and graphene addition on the electroless nickel plating process on ABS plastic surfaces. The SEM images were used to analyze the characteristics of the nickel coating layer and the impact of different experimental conditions in detail. The results obtained from this analysis are summarized in Table 5, which shows the thickness and Ni particle size corresponding to various Pd concentrations.

Table 5 Nickel coating thickness and pore size at different Pd concentrations.

No.	Pd (ppm)	Thickness (µm)
1	3	-
2	6	1.95-2.15
3	15	2.00-2.30
4	25	3.30-4.25

Figure 4 shows SEM images of the ABS plastic surface at Pd concentration of 3,6,15 and 25 ppm. At a Pd concentration of 3 ppm, no nickel coating was found on the ABS plastic surface, or it was very thin and nearly invisible. This was due to an insufficient amount of Pd catalyst to initiate the nickel deposition process, leaving the ABS plastic surface bare without any metal coating. In addition, the corrosion process may not be efficient enough, resulting in poor adhesion of Pd to the surface. At a Pd concentration of 6 ppm, the nickel coating thickness was approximately 1.95-2.15 µm. The SEM image showed that a thin nickel layer was attached to the ABS surface, indicating the presence of the Pd catalyst distributed across the ABS surface. However, the coating was not as smooth as desired, likely because the amount of catalyst was still not sufficiently high for optimal deposition. At the Pd concentration 15 ppm, the nickel coating thickness increased slightly to 2.00-2.30 µm. Finally, at a Pd concentration 25 ppm, the nickel layer thickness ranged from 3.30-4.25 µm, which indicated a significant increase in the nickel layer thickness with higher

concentration of Pd. This trend suggests that both the concentration of Pd and the chemicals in the electroless Ni plating bath directly influence the thickness of the deposited nickel layer.

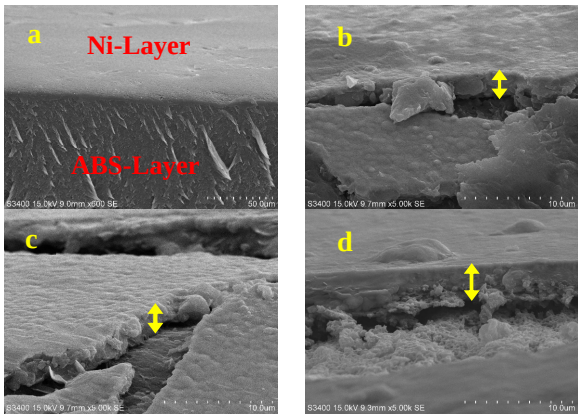

Figure 4 SEM images of the ABS plastic surface. a.) Pd 3 ppm b.) Pd 6 ppm c.) Pd 15 ppm d.) Pd 25 ppm

CONCLUSIONS

The study examines the impact of Pd concentration on the etching, adsorption, and coating properties of ABS plastic. The optimal porosity for Pd adhesion occurs at Pd concentrations of 6 and 15 ppm, while Pd adsorption increases with higher concentrations, peaking at 0.140 mg/cm² at 15 ppm. Graphene adsorption also rises with Pd concentration but decreases beyond 15 ppm, with the highest adsorption at 0.141 mg/cm² at 15 ppm. Nickel coating thickness increases with Pd concentration and graphene adsorption, reaching a maximum of 2.00–2.30 µm at 15 ppm, where surface conditions are ideal for graphene adhesion. Additionally, electrical conductivity improves as Pd concentration increases.

REFERENCES

1. Mohd Alauddin, S., et al., Electrical and Mechanical Properties of Acrylonitrile Butadiene Styrene/Graphene Platelet Nanocomposite. *Materials Today: Proceedings*, 2018. 5: p. S125-S129.
2. Yousefi, M., et al., Polymeric nanocomposite materials: Synthesis and thermal degradation of acrylonitrile–butadiene–styrene/tin sulfide (ABS/SnS). *Inorganica Chimica Acta*, 2011. 371(1): p. 1-5.
3. Lendvai, L., et al., Thermally conductive and electrically resistive acrylonitrile butadiene styrene (ABS)/boron nitride composites: Optimal design using a multi-criteria decision-making approach. *Journal of Materials Research and Technology*, 2023. 26: p. 8776-8788.
4. Arnold, J.C., S. Alston, and A. Holder, Void formation due to gas evolution during the recycling of Acrylonitrile–Butadiene–Styrene copolymer (ABS) from waste electrical and electronic equipment (WEEE). *Polymer Degradation and Stability*, 2009. 94(4): p. 693-700.
5. Kuo,C.-C.,et al., Preparation of starch/acrylonitrile-butadiene-styrene copolymers (ABS) biomass alloys and their feasible evaluation for 3D printing applications. *Composites Part B: Engineering*, 2016. 86: p. 36-39.
6. Jayanth, N., P. Senthil, and B. Mallikarjuna, Experimental investigation on the application of FDM 3D printed conductive ABS-CB composite in EMI shielding. *Radiation Physics and Chemistry*, 2022. 198.
7. Quan, Z., et al., Microstructural design and additive manufacturing and characterization of 3D orthogonal short carbon fiber/acrylonitrile-butadiene-styrene preform and composite. *Composites Science and Technology*, 2016. 126: p. 139-148.
8. Mahmoodi, M., et al., The electrical conductivity and electromagnetic interference shielding of injection molded multi-walled carbon nanotube/polystyrene composites. *Carbon*, 2012. 50(4): p. 1455-1464.
9. Tu, Z., et al., A facile approach for preparation of polystyrene/graphene nanocomposites with ultra-low percolation threshold through an electrostatic assembly process. *Composites Science and Technology*, 2016. 134: p. 49-56.
10. Araby, S., et al., Electrically and thermally conductive elastomer/graphene nanocomposites by solution mixing. *Polymer*, 2014. 55(1): p. 201-210.
11. Kuilla, T., et al., Recent advances in graphene based polymer composites. Progress in Polymer Science, 2010. 35(11): p. 1350-1375.
12. Liang, J., et al., Molecular-Level Dispersion of Graphene into Poly(vinyl alcohol) and Effective Reinforcement of their Nanocomposites. *Advanced Functional Materials*, 2009. 19(14): p. 2297-2302.
13. Iqbal, A.K.M.A., et al., Graphene-based nanocomposites and their fabrication, mechanical properties and applications. *Materialia*, 2020. 12.
14. Rattanapan, C., Green preparation of polymer/reduce graphene oxide electrodes for multicolor electrochromic devices. *Engineering and Industrial Technology*, 2019(10).
15. Naghdi, S., et al., Graphene family, and their hybrid structures for electromagnetic interference shielding applications: Recent trends and prospects. *Journal of Alloys and Compounds*, 2022. 900.

16. Chattong, J., W. Cheewawuttipong, and K. Pantongkum, Thermal and Electrical Properties of Polypropylene/Carbon Fibers Composites. 2015.
17. Pang, H., et al., Conductive polymer composites with segregated structures. *Progress in Polymer Science*, 2014. 39(11): p. 1908-1933.
18. Pornpatkoon, Y., Conducting Polyaniline Produced from Dispersion Polymerization. *KMUTNB*, 2011. 21(1).
19. Li, X., et al., 3D conductive material strategies for modulating and monitoring cells. *Progress in Materials Science*, 2023. 133.
20. Mccaskie, J.E., Plating on plastics : A survey of mechanisms for adhering metal films to plastic surfaces. *Metal Finishing*, 2006. 104(5): p. 31-39.
21. Suman, R., et al., Experimental study of electroless plating on acrylonitrile butadiene styrene polymer for obtaining new eco-friendly chromium-free processes. *Materials Today: Proceedings*, 2020. 28: p. 1575-1579.
22. Boonyongmaneerat, Y., Comparative study of metallization and electrodeposition on acrylonitrile-butadiene-styrene and polylactic acid. *Chulalongkorn University Theses and Dissertations (Chula ETD)*, 2020.
23. Zhan, J., Development of electroless plating processes for low cost plastic-metallization and area-selective metal coating of three-dimensional structures. *School of Mechanical and Aerospace Engineering*, 2020(2020): p. 1-114.

Valorization of biodiesel plant-derived glycerol for 1-propanol synthesis over zeolite-supported iridium and rhenium oxides

Chanoknun Kalvibool[1,2], Supphathee Chaowamalee[1,2], Chawalit Ngamcharussrivichai[1,2,*]

[1] Department of Chemical Technology, Faculty of Science, Chulalongkorn University, Bangkok 10330, Thailand
[2] Center of Excellence in Catalysis for Bioenergy and Renewable Chemicals (CBRC), Faculty of Science, Chulalongkorn University, Bangkok 10330, Thailand
[*] Corresponding author: chawalit.ng@Chula.ac.th

ABSTRACT

Selective hydrogenolysis of bio-based glycerol into 1-propanol (1-PO) as valuable chemical is a promising solution to surplus glycerol from biodiesel production. Hydrogenolysis, involving dehydration and hydrogenation, necessitates a heterogeneous catalyst with well-dispersed active metals, suitable acidity, and glycerol activation ability. In our group, a series of proton-form ultra-stable Y zeolite-supported iridium and rhenium oxides (Ir-ReO_x/HUSY) have been developed for 1-PO synthesis from glycerol. The effects of metal type and HUSY modification on glycerol conversion and 1-PO yield are presented in this communication. Typically, Ir-ReO_x/HUSY was prepared via sequential incipient wetness impregnation, while the acidity modification of HUSY support was carried out through dealumination using mild acid solution. The reaction study revealed that the monometallic Re/HUSY catalyst facilitated only dehydration, leading to incomplete hydrogenolysis process. On the other hand, Ir/HUSY promoted both dehydration and hydrogenation, with insufficient glycerol activation capability, resulting in a low glycerol conversion. The bimetallic Ir-ReO_x/HUSY with a 1:1 Ir: Re atomic ratio exhibited excellent catalytic performance, maximizing a 1-PO yield to 38.4% at 76.8% glycerol conversion. This result was attributed to the synergistic effect of Ir and ReO_x, which provided good dispersion of bimetallic sites and balanced acidity in terms of strength and amount, efficiently facilitating glycerol hydrogenolysis. Furthermore, using modified HUSY as support material significantly affected glycerol hydrogenolysis in which the catalyst performance was determined by concentration of acid solution used in dealumination. These findings emphasize the potential of Ir-ReO_x/HUSY as a promising catalyst for sustainable glycerol valorization.

Keywords: Glycerol hydrogenolysis; 1-propanol; Iridium; Rhenium oxides; USY

1. INTRODUCTION

Currently, fossil fuels significantly contribute to carbon dioxide emissions, exacerbating climate change and environmental issues. The adoption of renewable energy sources to replace fossil fuels is crucial for sustainable development due to their availability and accessibility. Biodiesel, a prominent renewable fuel, is produced from vegetable oils via transesterification, which generates glycerol as a by-product, typically around 10 wt% of the biodiesel produced. With the continuous expansion of biodiesel production, global crude glycerol supply is projected to reach 6 million tons by 2025 [1], leading to fluctuations in glycerol prices. Therefore, the valorization of glycerol into value-added chemicals and fuels is a prospective approach to reduce the problem of the global glycerol community.

A variety of catalytic pathways via heterogeneous catalysis has been explored as an effective strategy for upgrading glycerol, such as oxidation to glyceric acid, dehydration to acrolein, aqueous-phase reforming for hydrogen production, and selective hydrogenolysis to alcohols, such as 1,2-propanediol (1,2-PDO), 1,3-propanediol (1,3-PDO), 1-propanol (1-PO) and 2-propanol (2-PO) [2]. Among various valorization routes, the hydrogenolysis of glycerol to 1-PO is considered as an attractive approach due to its wide range of applications in the pharmaceutical, cosmetic, ink, textile, chemical, and polymer industries [2, 3]. Currently, 1-PO is primarily produced via hydroformylation of ethylene to form propanal, followed by hydrogenation to 1-PO [2]. However, the synthesis of 1-PO from bio-based glycerol offers a more sustainable and environmentally friendly alternative to the conventional petroleum-based method. Although extensive research has been conducted on the conversion of glycerol to 1,2-PDO and 1,3-PDO, the direct synthesis of 1-PO from glycerol has received relatively limited attention.

The selective hydrogenolysis of glycerol into 1-PO involves a complex reaction consisting of sequential

dehydration and hydrogenation steps (Scheme 1), which requires a bifunctional catalyst with both acidic and metallic sites. Previous studies [3] reported the use of bifunctional catalysts to achieve a high yield of 1-PO through a two-step reaction approach. In the first stage, glycerol was converted into 1,2-PDO over Ni/γ-Al_2O_3 at 220°C for 5 h. Subsequently, the Ni/CS–P catalyst was used to transform 1,2-PDO to 1-PO (79.3% selectivity) at 260°C. However, a one-pot hydrogenolysis process is considered a more sustainable alternative, as it simplifies reaction conditions and reduces energy consumption. Generally, an efficient catalyst for 1,3-PDO production via glycerol hydrogenolysis requires noble metals for activation of H_2 molecules and oxophilic promoters for activation of glycerol molecules [4]. Among the reported bimetallic catalysts, Pt-WO_x and Ir-ReO_x have shown a remarkable performance. However, the Pt-WO_x combination exhibited lower 1-PO selectivity than the Ir-ReO_x-based catalysts, as demonstrated by Shi et al. [5]. They reported that Pt-WO_x/SiO_2 achieved high glycerol conversion but led primarily to 1,3-PDO formation rather than 1-PO. In contrast, the Ir-ReO_x-based catalyst exhibits a stronger ability to selectively cleave the C–O bonds, emphasizing it as a plausible alternative for one-step 1-PO synthesis. To further enhance catalytic performance, recent research has explored the optimization of metal composition, acidity, and support materials. Liu et al. [6] demonstrated that Ir-ReO_x/SiO_2 with higher Ir loading level (20%) exhibited enhanced catalyst activity due to ReO_x clusters attached to small metallic Ir crystallites, which led to a uniform dispersion of active Re–OH sites over support, facilitating the adsorption of glycerol molecules. Meanwhile, Nakagawa et al. [7] found that adding sulfuric acid (H_2SO_4) solution as a homogeneous acidic promoter to Ir-ReO_x/SiO_2 increased 1-PO selectivity from 14% to 21%. These findings suggest that incorporating the Ir-ReO_x catalysts with acidic support could enhance 1-PO yield and selectivity. Nevertheless, sulfur leaching raised concerns about catalyst stability and long-term reusability.

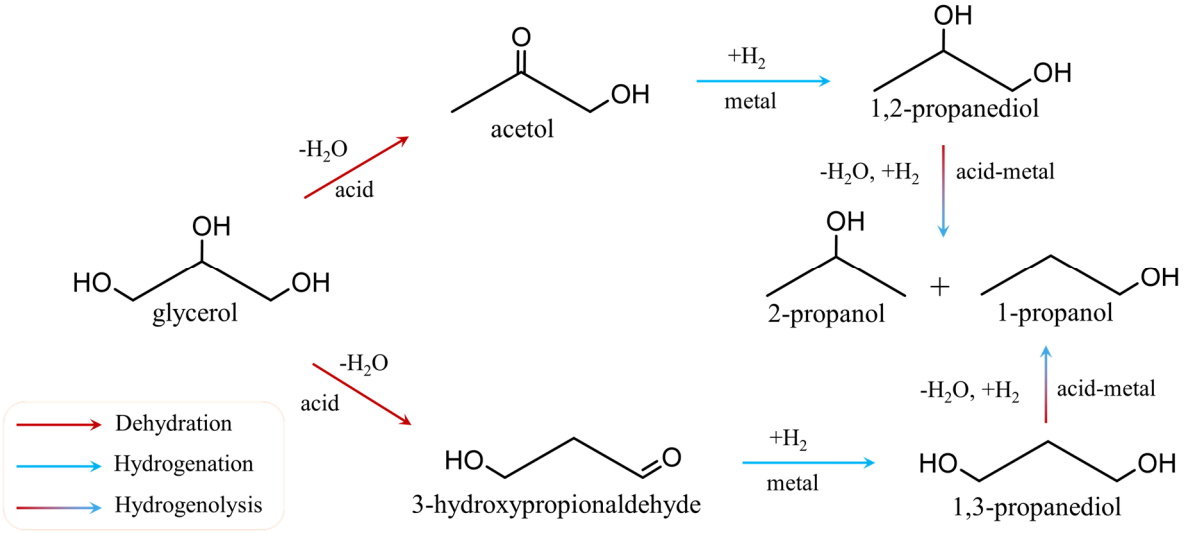

Scheme 1 Glycerol hydrogenolysis reaction pathway to 1-PO.

To overcome these limitations, zeolite-supported catalysts without H_2SO_4 addition have been explored as promising alternatives. Zeolites, a class of microporous aluminosilicate materials, have been widely used as acidic supports due to their tunable acidity, structural and chemical stability, and well-defined pore networks. Their physicochemical properties are influenced by the Si/Al atomic ratio, which directs the distribution and strength of acid sites. Chanklang et al. [8] revealed that Ir-ReO_x supported on H-ZSM5 improved 1-PO yield due to a strong electronic interaction between Ir and Re in the bimetallic catalyst. However, the medium-pore structure of H-ZSM5 imposed diffusion limitations, restricting reactant accessibility and leading to excessive by-product formation. Deng et al. [9] further demonstrated that the dealumination of silica-alumina (ASA) supports improved metal dispersion and Ir–Re interaction, significantly enhancing catalytic activity, since the presence of Al in support hindered the mobility of Re species, limiting Ir–Re interaction. These findings underscore the importance of designing a well-balanced catalyst with optimized acidity and metal–support interactions to achieve high 1-PO yield while minimizing undesired side reactions.

Proton-form ultra-stable Y zeolite (HUSY), a modified form of Y-type zeolite from the faujasite (FAU) family, features a larger micropore structure, higher porosity, and an increased number of external acid sites, facilitating better molecular diffusion and reactant accessibility compared to small and medium-pore structure. Additionally, the content of its extra-framework aluminum (EFAl) provides a balance of Brønsted and Lewis acid sites, which is beneficial for selective dehydration. The acidity of HUSY can be further tailored through dealumination, a process that removes EFAl and framework Al species to adjust the Si/Al ratio. This modification prevented excessive acidity and enhanced specific surface area (S_{BET}) of

ASA supports, resulting in well-dispersed Ir-Re nano-particles [9].

In this study, the development of Ir-ReO_x supported on HUSY zeolite as efficient catalysts for glycerol hydrogenolysis to achieve a high yield of 1-PO has been focused. A series of Ir-ReO_x catalysts were prepared via sequential incipient wetness impregnation on the parent HUSY and the HUSY supports modified through dealumination using mild acid solution with different concentrations. The physicochemical properties of the catalysts obtained were characterized to elucidate the synergistic effect of metal loading and support acidity on 1-PO formation. The findings provide valuable insights for developing efficient bifunctional catalysts for glycerol hydrogenolysis.

2. EXPERIMENTAL

2.1. Preparation of modified HUSY zeolites

The commercial HUSY zeolite (HSZ-330 HUA; Tosoh Corporation) with a Si/Al molar ratio of 3 was pretreated via calcination at 500°C for 6 h before use. The calcined material was denoted as HUSY. The HUSY was dealuminated using 0.1M and 0.3M nitric acid (HNO_3) solution. After mixing HUSY in an acid solution at 80°C for 2 h, the solid product was filtered and thoroughly washed with deionized (DI) water until neutral pH, and the resultant filter cake was dried at 120°C overnight. The dried solid was subsequently calcined in the furnace at 500°C for 6 h to obtain dealuminated HUSY support, labeled as D-HUSY-*x*, where *x* was the HNO_3 concentration.

2.2. Preparation of supported Ir-ReO_x catalysts

HUSY-supported monometallic catalysts with 8 wt% metal loading level, denoted as Ir/HUSY and ReO_x/HUSY, were prepared by incipient wetness impregnation using H_2Cl_6Ir and NH_4ReO_4 as metal precursors, respectively. Bimetallic catalysts supported on HUSY and D-HUSY-*x*, designated as Ir-ReO_x/HUSY and Ir-ReO_x/D-HUSY-*x*, respectively, were prepared via a sequential incipient wetness method in which the calcined HUSY was first loaded with NH_4ReO_4, followed by H_2Cl_6Ir impregnation. The obtained catalyst pastes were dried overnight at 100°C, and then calcined at 500°C for 3 h.

2.3. Catalyst characterization

Powder X-ray diffraction (XRD) was employed to observe the crystalline structure of materials using a Bruker D8 Advanced X-ray diffractometer equipped with a Cu K_α radiation operated at 40 kV and 40 mA. Energy dispersive X-ray fluorescence spectroscopy (ED-XRF) was performed to analyze the elemental composition of the prepared catalysts using a Bruker S_2 PUMA X-ray fluorescence spectrometer.

Nitrogen (N_2) adsorption-desorption measurement was conducted at -196°C using a 3P-Micro300 (3P-Instruments) to determine the textural properties of the prepared catalyst. All samples were degassed at 150 °C for 2 h before the measurement. The S_{BET} was calculated from the adsorption data using the Brunauer-Emmett-Teller (BET) equation.

The temperature-programmed desorption of ammonia (NH_3-TPD) was performed to evaluate the acidity of reduced catalysts using a Micromeritics AutoChemII 2920 chemisorption analyzer. The sample powder was pretreated at 450°C for 60 min under a helium (He) flow, followed by adsorption of NH_3 (10 vol% in He gas) at 50°C. Subsequently, the sample was heated from 50°C to 600°C at a ramp rate of 10°C/min under a He flow to desorb the probe molecules.

The temperature-programmed reduction of hydrogen (H_2-TPR) was used to determine the reduction temperature of dried catalysts. A sample was purged with argon (Ar) flow at 100°C for 60 min to remove the moisture before analysis. The measurement was conducted in the range of 50–600 °C at a heating rate of 10 °C/min under the 10 vol% H_2 in Ar gas.

2.4. Hydrogenolysis of glycerol

Catalytic glycerol hydrogenolysis was performed in a 25-mL stainless-steel autoclave equipped with pressure gauge, thermocouple, and temperature controller. Prior to use, the catalyst was reduced in a tubular reactor under pure H_2 (99.999%) flow at 450°C for 2 h. In a typical experiment, 0.25 g of reduced catalyst and 5 mL of 10 wt% glycerol solution were loaded into the autoclave reactor. The reactor was then purged with 20 bar of H_2 to remove the residual air, and pressurized with H_2 to 40 bar. The reactor temperature was subsequently raised to 250°C under vigorous stirring. Once the reaction was completed, the spent catalyst was separated from product mixture by centrifugation. The sample volume was finally made up by adding dimethylformamide (DMF) as a solvent. The composition of liquid products was analyzed using a gas chromatography. Product yield was quantified using an internal standardization method, with *n*-butanol as the reference standard.

3. RESULTS AND DISCUSSION

3.1. Catalyst characterization

As shown in Figure 1, the XRD pattern of HUSY exhibited characteristic reflections at 2θ = 6.3°, 10.2°, 12.0°, 15.8°, 18.9°, 20.5°, 23.9°, 27.4° and 31.7°, which corresponded to the faujasite (FAU)-type zeolitic framework (JCPDS 00-038-0240) [10]. After metal impregnation, the obtained catalysts retained their FAU structure but exhibited a lower intensity of diffraction patterns than the pristine HUSY, indicating a decrease in relative crystallinity due to the deposition of metal clusters on the zeolite surface. The elemental analysis confirmed that the impregnation of Ir and Re did not affect the Si/Al molar ratio, as shown in Table 1. Interestingly, no reflections corresponding to Ir and Re species were observed, implying that Ir and ReO_x were well dispersed with a nano-crystallite size of <5 nm on

the surface of catalysts [8]. This result indicates that the impregnation procedures used in this work were efficient in loading Ir and ReO_x onto the micropore-confined zeolite support.

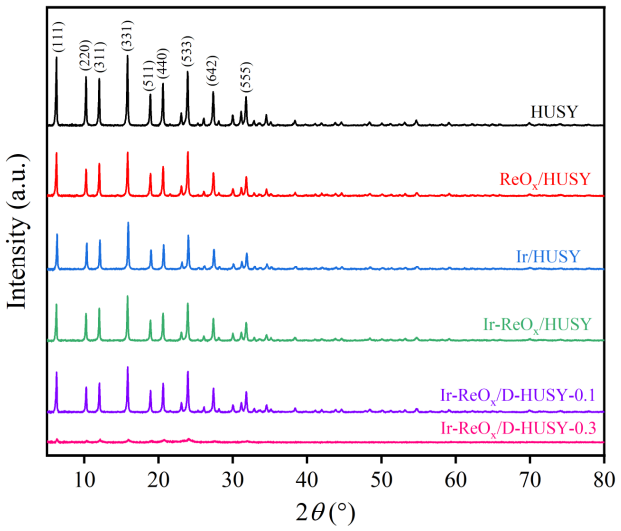

Figure 1 XRD patterns of commercial HUSY and Ir and Re-based catalysts supported on HUSY and D-HUSY-*x*.

Table 1 Chemical properties of obtained catalysts.

Catalysts	Si/Al[a]	Total acidity (mmol/g)[b]	Reducibility (%)[c]	
			< 200°C	> 200°C
HUSY	3.0	1.7	-	-
ReO_x/HUSY	3.0	0.9	0	100
Ir/HUSY	3.1	1.2	100	0
Ir-ReO_x/HUSY	3.0	1.1	100	0
Ir-ReO_x/ D-HUSY-0.1	4.8	1.3	100	0
Ir-ReO_x/ D-HUSY-0.3	34.8	0.4	88	12

[a] Molar ratio of Si/Al was determined by XRF. The content of Ir and Re was different from theoretical value by not exceeding 1%.
[b] Determined by NH_3-TPD
[c] Determined by H_2-TPR

In case of the catalysts prepared using dealuminated zeolites supports, the zeolitic framework of HUSY was preserved after dealumination and metal impregnation, with no detectable phases corresponding to Ir or ReO_x. However, using a high acid concentration in dealumination process (D-HUSY-0.3) was detrimental to the zeolite structure, resulting in significant framework damage due to the severe extraction of framework Al species [11]. This observation was further supported by the dependence of Si/Al ratio of the resulting catalysts on the concentration of HNO_3 solution (Table 1). Treatment with 0.1 M acid solution slightly increased the Si/Al ratio, suggesting that EFAL was mainly removed [12]. However, a large portion of Al was extracted from the zeolite framework when a high concentration of HNO_3 was used, resulting in a substantial increase in the Si/Al ratio.

N_2 physisorption isotherms of various Ir and ReO_x catalysts are compared in Figure 2. All catalyst samples exhibited type I isotherms, representing microporous structure of the zeolite supports [13]. The S_{BET} slightly decreased after metal doping on commercial HUSY, likely due to partial pore blockage by metal clusters [14]. This observation is consistent with the XRD results, which suggest good dispersion of the metals introduced via the impregnation method. Notably, Ir-ReO_x/D-HUSY-0.1 exhibited the highest S_{BET} value among the samples. In contrast, Ir-ReO_x/D-HUSY-0.3 showed a remarkable decreased in S_{BET}, attributed to structural degradation of the zeolite framework caused by excessive removal of framework Al species [12]. The combined XRD and S_{BET} results indicate that 0.1 M HNO_3 was the optimal acid concentration for preparing dealuminated HUSY with high microporosity while preserving the structural integrity of the zeolite, making it a suitable support for Ir and Re-based catalysts.

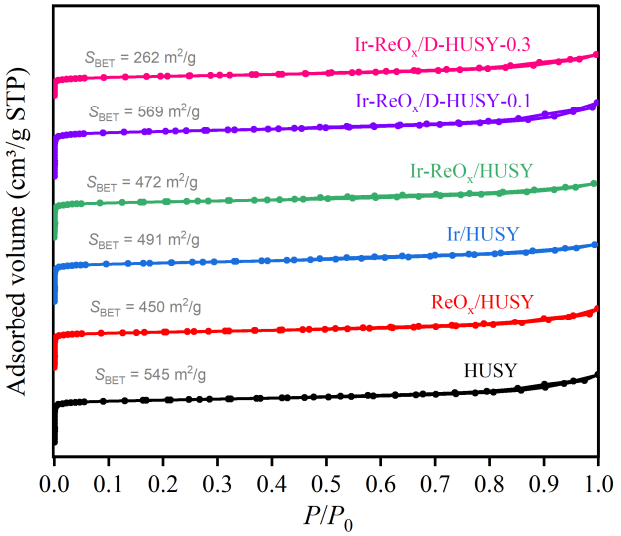

Figure 2 N_2 physisorption isotherms of commercial HUSY and Ir and Re-based catalysts supported on HUSY and D-HUSY-*x*.

Acidity is one of crucial properties of bifunctional catalysts used for one-pot hydrogenolysis of glycerol to 1-PO [2]. The optimal content and strength of acid sites are essential for efficiently promoting the dehydration steps (Scheme 1). The acid properties of the prepared catalysts were measured by NH_3-TPD, as summarized in Table 1. HUSY revealed the highest total acidity, whereas a decrease in the total acidity was observed after metal loading and dealumination. The acidity dropped upon the addition of ReO_x and Ir due to the metal covering on the acidic surface of HUSY [15]. In case of the D-HUSY-supported catalysts, a slight reduction in acidity, compared to the parent HUSY, was observed when using low acid concentration, primarily due to the removal of EFAL species. In contrast, an extensive removal of framework Al and collapse of zeolite structure, caused by treatment with a high acid concentration, rendered a 76% decrease in the total acidity of the resulting catalyst [12].

Based on the H_2-TPR results presented in Table 1, the reduction of the monometallic ReO_x/HUSY catalyst occurred only at temperatures above 200°C, indicating that ReO_x is difficult to reduce on its own. In contrast, the Ir/HUSY sample was fully reduced below 200°C, demonstrating complete reduction of the Ir species. For the bimetallic Ir-ReO_x/HUSY catalyst, reduction also occurred at low temperatures, suggesting the presence of metallic Ir that could facilitate hydrogenation reaction [16]. This behavior was attributed to a synergistic interaction between Ir and ReO_x, which enhanced metal dispersion and promoted easier reduction (<200°C) compared to ReO_x/HUSY. This observation is consistent with the S_{BET} values, which showed that the bimetallic catalyst exhibited a higher surface area than ReO_x/HUSY. For the dealuminated catalysts prepared using low acid concentration, the reducibility of Ir species remained similar to that of Ir-ReO_x/HUSY. However, under more severe acid treatment, the partial reduction peak shifted to higher temperatures (above 200°C), indicating that excessive dealumination impaired the reducibility of the catalyst likely due to enhanced metal–support interactions [15].

3.2. Catalytic hydrogenolysis of glycerol

The commercial HUSY and a series of Ir-ReO_x/HUSY and Ir-ReO_x/D-HUSY-*x* catalysts were systematically evaluated for their catalytic performance in glycerol hydrogenolysis to produce 1-PO. As shown in Figure 3, the bare HUSY support with high acidity showed low glycerol conversion and promoted excessive formation of by-products through side reactions [17]. The monometallic ReO_x/HUSY catalyst exhibited improved activity in glycerol hydrogenolysis; however, only primary intermediates like acetol and 3-hydroxypropionaldehyde (3-HPA) were detected. ReO_x itself is an oxophilic oxide that facilitates the adsorption of glycerol through O–H groups and assists in C–O bond cleavage [18]. Nonetheless, the absence of metallic sites with hydrogenation activity limited the completion of hydrogenolysis pathway. In contrast, the formation of 1-PO was observed over Ir/HUSY, where Ir played a crucial role in the hydrogenation steps, while the acidity of HUSY zeolite promoted dehydration. The presence of Ir nanoclusters reduced the overall acidity of the catalyst and favored C–O bond cleavage over C–C bond cracking [19], enhancing the formation of 1,2-PDO and 1,3-PDO as key intermediates to 1-PO while also minimizing gaseous products. However, Ir/HUSY exhibited lower glycerol conversion due to its weak interaction with glycerol and less efficient substrate activation.

The bimetallic Ir-ReO_x/HUSY catalyst exhibited a substantial improvement in glycerol conversion (76.8%) and 1-PO yield (38.4%). It was attributed to the synergistic effect between Ir and ReO_x, which provided good dispersion of bimetallic sites and balanced level of acidity, thereby efficiently facilitating glycerol anchoring on the catalyst surface, hydrogenolysis, and sequential dehydration to PDO and propanol products.

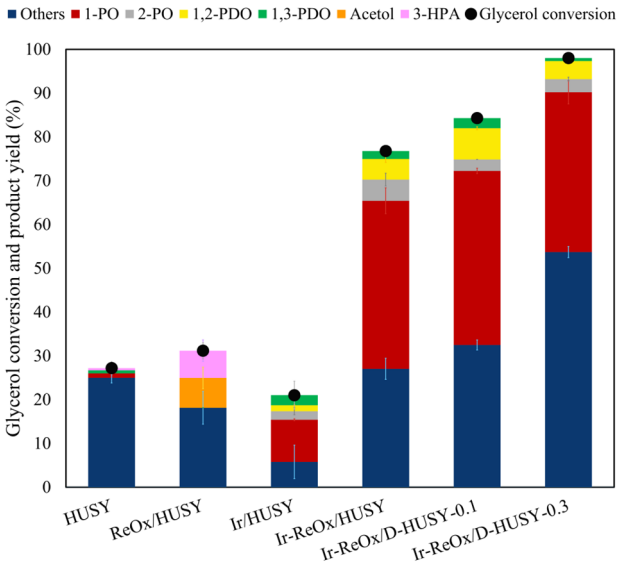

Figure 3 Glycerol conversion and product yield obtained from hydrogenolysis of glycerol over different catalysts. (Reaction conditions: 5 mL of 10 wt% glycerol solution, 0.25 g of catalyst dosage, 250°C, 40 bar H_2, and 4 h)

To further optimize catalytic performance, the dealuminated HUSY samples prepared using 0.1M and 0.3M HNO_3 solutions were employed as support materials for the bimetallic catalysts. The glycerol conversion increased proportionally with concentration of acid solution. However, the highest 1-PO yield (39.8%) was achieved with Ir-ReO_x/D-HUSY-0.1, which was ascribed to the removal of EFAL species from the micropore structure, thereby improving the diffusion of glycerol [12]. This result corresponded to an increase in S_{BET}, leading to better metal dispersion [19]. This finding suggests that moderate dealumination enhanced reactant diffusion and metal–support interactions, thus improving catalytic performance. Despite the increased glycerol conversion, by-product formation was significantly higher for Ir-ReO_x/D-HUSY-0.3. This behavior appeared to correlate with the acidic properties: Ir-ReO_x/D-HUSY-0.1, with a total acidity of 1.3 mmol/g, exhibited lower by-product generation. Moreover, Ir-ReO_x/D-HUSY-0.3 had a marked loss in crystallinity and acidity due to excessive removal of framework Al, which hindered selective hydrogenolysis of glycerol to 1-PO and promoted undesirable side reactions.

4. CONCLUSION

In summary, bimetallic Ir-ReO_x catalysts supported on HUSY and dealuminated HUSY zeolites were successfully synthesized via sequential incipient wetness impregnation, and optimal dealumination conditions were established for the selective hydrogenolysis of glycerol to 1-PO. The Ir-ReO_x/HUSY catalyst demonstrated superior performance compared to its monometallic counterparts, achieving a high 1-PO yield due to the synergistic interaction

between Ir and ReO_x, which provided a balanced combination of acidity and metal dispersion to efficiently facilitate the dehydration–hydrogenation pathway. Furthermore, mild dealumination of HUSY support enhanced catalytic activity by improving metal dispersion and glycerol diffusion, resulting in increased glycerol conversion and 1-PO yield. However, excessive dealumination under harsher conditions caused significant structural degradation and elevated by-product formation, ultimately diminishing catalytic performance. These findings highlight the potential of bimetallic Ir-ReO_x catalysts supported on modified HUSY for efficient glycerol hydrogenolysis and underscore the critical importance of tuning acidity and metal dispersion to achieve high selectivity and yield of 1-PO.

ACKNOWLEDGMENTS

The authors acknowledge Department of Chemical Technology and Center of Excellence in Catalysis for Bioenergy and Renewable Chemicals (CBRC), Faculty of Science, Chulalongkorn University for providing financial supports and research facilities.

REFERENCES

1. R. Ciriminna, C.D. Pina, M. Rossi, M. Pagliaro, Understanding the glycerol market, *European Journal of Lipid Science and Technology* 2014; 116(10): 1432-1439.
2. C.T.Q. Mai, Y. Ye, G.L. Rempel, F.T.T. Ng, A novel one-step synthesis of 1-propanol from hydrogenolysis of glycerol using a Ni-HSiW/Al_2O_3 catalyst – The impact of H_2 pressure on catalyst performance, *Catalysis Today* 2023; 407: 2-10.
3. M.N. Gatti, J.L. Cerioni, F. Pompeo, G.F. Santori, N.N. Nichio, High yield to 1-propanol from crude glycerol using two reaction steps with Ni catalysts, *Catalysts* 2020; 10(6): 615.
4. M.T. Yoshinao Nakagawa, Keiichi Tomishige, Catalytic materials for the hydrogenolysis of glycerol to 1, 3-propanediol, *Journal of materials chemistry A* 2014; 2(19): 6688-6702.
5. G. Shi, Z. Cao, J. Xu, K. Jin, Y. Bao, S. Xu, Effect of WO_x doping into Pt/SiO_2 catalysts for glycerol hydrogenolysis to 1,3-propanediol in liquid phase, *Catalysis Letters* 2018; 148(8): 2304-2314.
6. L. Liu, S. Kawakami, Y. Nakagawa, M. Tamura, K. Tomishige, Highly active iridium–rhenium catalyst condensed on silica support for hydrogenolysis of glycerol to 1,3-propanediol, *Applied Catalysis B: Environmental* 2019; 256.
7. Y. Nakagawa, X. Ning, Y. Amada, K. Tomishige, Solid acid co-catalyst for the hydrogenolysis of glycerol to 1,3-propanediol over Ir-ReO_x/SiO_2, *Applied Catalysis A: General* 2012; 433-434: 128-134.
8. S. Chanklang, W. Mondach, P. Somchuea, T. Witoon, M. Chareonpanich, K. Faungnawakij, A. Seubsai, Hydrogenolysis of glycerol to 1,3-propanediol over H-ZSM-5-supported iridium and rhenium oxide catalysts, *Catalysis Today* 2022; 397-399: 356-364.
9. C. Deng, L. Leng, X. Duan, J. Zhou, X. Zhou, W. Yuan, Support effect on the bimetallic structure of Ir–Re catalysts and their performances in glycerol hydrogenolysis, *Journal of Molecular Catalysis A: Chemical* 2015; 410: 81-88.
10. E.C. Paris, J.O.D. Malafatti, H.C. Musetti, A. Manzoli, A. Zenatti, M.T. Escote, Faujasite zeolite decorated with cobalt ferrite nanoparticles for improving removal and reuse in Pb^{2+} ions adsorption, *Chinese Journal of Chemical Engineering* 2020; 28(7): 1884-1890.
11. Z. Yan, D. Ma, J. Zhuang, X. Liu, X. Liu, X. Han, X. Bao, F. Chang, L. Xu, Z. Liu, On the acid-dealumination of USY zeolite: a solid state NMR investigation, *Journal of Molecular Catalysis A: Chemical* 2003; 194(1-2): 153-167.
12. L. Zhou, H. Zhao, L. Cui, Y. Bai, J. Bian, T. Lu, Y. Su, X. Yang, Promotion effect of mesopore on the conversion of carbohydrates to methyl levulinate over H-USY zeolite, *Catalysis Communications* 2015; 71: 74-78.
13. M. Thommes, K.A. Cychosz, Physical adsorption characterization of nanoporous materials: progress and challenges, *Adsorption* 2014; 20(2-3): 233-250.
14. E.H. Cho, K.-D. Kim, B.S. Yoon, E. Cho, Y.J. Yu, T.N. Phan, S.-G. Jeon, C.H. Ko, Efficient synthesis of nickel-molybdenum/USY-zeolite catalyst for liminating impurities (N, S, and Cl) in the waste plastic pyrolysis oil: dispersion effect of active sites by surfactant-assisted melt-infiltration, *Catalysts* 2023; 13(12): 1476.
15. D. Kubička, N. Kumar, T. Venäläinen, H. Karhu, I. Kubičková, H. Österholm, D.Y. Murzin, Metal−support interactions in zeolite-supported noble metals: Influence of metal crystallites on the support acidity, *The Journal of Physical Chemistry B* 2006; 110(10): 4937-4946.
16. X. Li, B. Zhang, X. Pan, J. Ji, Y. Ren, H. Wang, N. Ji, Q. Liu, C. Li, One-pot conversion of lignin into naphthenes catalyzed by a heterogeneous rhenium oxide-modified iridium compound, *ChemSusChem* 2020; 13(17): 4409-4419.
17. K. Murata, I. Takahara, M. Inaba, Propane formation by aqueous-phase reforming of glycerol over Pt/H-ZSM5 catalysts, *Reaction Kinetics and Catalysis Letters* 2008; 93(1): 59-66.
18. W. Luo, Y. Lyu, L. Gong, H. Du, T. Wang, Y. Ding, Selective hydrogenolysis of glycerol to 1,3-propanediol over egg-shell type Ir–ReO_x catalysts, *RSC Advances* 2016; 6(17): 13600-13608.

19. A.J. Pamphile-Adrián, P.P. Florez-Rodriguez, F.B. Passos, Iridium catalysts for C–C and C–O hydrogenolysis: catalytic consequences of iridium sites, *Journal of the Brazilian Chemical Society* 2016; 27(5): 958-966.

CO_2 methanation using nickel-based catalysts over alumina-ceria support prepared by sol-gel method

Jitsinee Leetrakul[1], Nuttaya Pongstabodee[1,*]

[1] Department of Chemical Technology, Faculty of Science, Chulalongkorn University, Bangkok 10330, Thailand
[*] Corresponding author: sangobtip.p@chula.ac.th

ABSTRACT

Global greenhouse gas emissions, primarily CO_2, have significantly increased since the industrial revolution due to the extensive use of fossil fuels. CO_2 methanation, a process that converts CO_2 and H_2 into CH_4, offers a promising solution for CO_2 recycling. However, low-temperature methanation is hindered by kinetic barriers, and developing a catalyst with high activity and selectivity at low temperatures remains challenging. Nickel-based catalysts are promising due to their high catalytic activity and low cost but suffer from sintering. To address this, Alumina (Al_2O_3) is used as a support to improve nickel dispersion, and ceria (CeO_2) is added to lower the reaction temperature. This study investigates nickel-based catalysts supported on alumina-ceria, synthesized via the sol-gel method, for CO_2 methanation. The optimal nickel loading was determined using wet impregnation on Al_2O_3, and the effect of Al:Ce molar ratio was examined. The catalysts were evaluated in a fixed-bed reactor, and the 50Ni/Al_2O_3-CeO_2 catalyst achieved 82% CO_2 conversion and 99% CH_4 selectivity at 300°C. Characterization of the catalysts was performed using XRD, H_2-TPR, N_2 physisorption, CO_2-TPD and FESEM.

Keywords: CO_2 methanation; Ni catalyst; Sol-gel; Ceria; Alumina

1. INTRODUCTION

Nowadays, combustion of fossil fuels has become a major energy source in many countries since the industrial revolution and contributes to global greenhouse gas emissions, particularly carbon dioxide emissions, which significantly impact the environment and climate change [1, 2]. To address this issue, using carbon dioxide as a feedstock for the CO_2 methanation to produce methane is one of the most interesting research projects because it has the advantage of being easier to store and transport compared to other fuels and also contributes to completing the carbon cycle. Moreover, Methane (CH_4) can be utilized in various applications, such as a source of domestic cooking, high-quality fuel for transportation, and a key raw material for the petrochemical industry [3].

$$CO_2(g) + 4H_2(g) \rightarrow CH_4(g) + 2H_2O(g)$$
$$\Delta H_{298K} = -165 \text{ kJ/mol} \quad (1)$$

From equation (1), the methanation of carbon dioxide is an exothermic reaction including reverse water-gas shift reaction and carbon monoxide methanation [4, 5]. This reaction is suitable for low-temperature conditions, so the kinetic limitations are a big challenge to develop a catalyst with both excellent in catalytic activity and selectivity at low temperatures. By the way, the study has shown that there is a suitable active metal for this reaction. This reaction is catalyzed by both noble metal (Rh, Ru, Pt, Pd etc.) and non-noble metal (Ni, Fe, Co etc.) catalysts. Although the noble catalysts such as Pt and Rh are more active than Ni in the CO_2 methanation but for industrial application nickel-based catalysts are attracted due to their high availability, inexpensive and highly effective in the reaction. However, the activity of this type of catalyst significantly decreases when nickel undergoes sintering. To address this issue, alumina (Al_2O_3) has been used as a support to disperses nickel to reduce sintering issues [6]. However, it is commonly known that Ni/Al_2O_3 has a strong interaction between each other so this issue can inhibit catalytic activity either [7]. In fact, synthesizing alumina as a support has various methods, so this research is interested in sol-gel method because it produces high purity, high pore volume and smaller pore size [8]. Also, anticipating those advantages will decrease interaction between metals and support. Another way to improve catalytic activity is developed catalysts which highly active at low temperature, one of the metals that interesting is ceria (CeO_2) due to its strong redox properties [9]. Moreover, adding CeO_2 to increase basic sites of support that can enhance capacity of CO_2 adsorption which were responsible for enhanced catalytic activity and also favored to dispersion nickel on the support [10, 11]. Therefore, this research aims to study the effect of nickel-based catalysts supported on alumina–ceria prepared by the sol-gel method to the methanation of carbon dioxide.

2. EXPERIMENTAL

2.1. Materials

For preparation of catalysts, Nickel nitrate hexahydrate ($Ni(NO_3)_2$•$6H_2O$, Kemaus, 99%), Aluminum nitrate nonahydrate ($Al(NO_3)_3$•$9H_2O$, Kemaus, 98%), and Cerium nitrate hexahydrate ($Ce(NO_3)_3$•$6H_2O$, Merck, 98%) were used metal precursors respectively. Citric acid ($C_6H_8O_7$, Kemaus, 98%) was also used as a chelating agent. All chemicals were used as received without further treatment.

2.2 Preparation of synthesized Al_2O_3 and Al_2O_3-CeO_2 support

The γ-alumina were synthesized via sol-gel method. Initially, 0.5 M of aluminum nitrate nonahydrate was dissolved in deionized water while the molar ratios of citric acid to metal nitrate (C/N) was 0.5, by citric acid was subsequently added to the solution. Then, this solution was stirred at 80 °C until it became gel. For complete drying, the gels were thermally treated at 110°C overnight. Finally, the dried gels were placed into the furnace for calcined. In the first step, it was heated at 400°C for 1 h. Then in the second step, it was kept at 800°C for 3 h to produce synthesized alumina powders. In the case of Al_2O_3-CeO_2 support, CeO_2 precursor was mixed with aluminum precursor at a designated ratio.

2.3 Preparation of Ni/Al_2O_3

The nickel over synthesized alumina were synthesized via wet impregnation method with different weight of nickel from 30%wt to 60%wt. Firstly, Nickel nitrate hexahydrate was dissolved in deionized water and added this solution into synthesized alumina. Then, this mixture stirred at room temperature for 1 h and used ultrasonic treatment for 30 minutes. The suspension was dried at 110°C and finally calcined at 550°C for 3 h to get xNi/Al_2O_3 (x = 30,40,50 and 60 %wt)

2.4 Material characterizations

All the samples were characterized by various equipment to achieve the results profile to support the catalytic activity and described chemical and physical properties of the catalyst by following equipment:

X-ray diffraction (XRD) patterns were collected in a Bruker D8 ADVANCE diffractometer operating with a Cu Kα radiation source at 40 Kv and 40 mA in the range (2θ) from 5° to 80°. The crystallite size (D) of the samples were calculated by using Scherrer equation (2) [10]:

$$D = \frac{K\lambda}{\beta\cos\theta} \quad (2)$$

where:
K is shape factor (K = 0.9), λ is X-ray wavelength (λ = 1.5406 Å), β is the full-width half maximum of intensity peak and θ is Bragg's diffraction angle.

The reducibility of samples was investigated by H_2-temperature programmed reduction (H_2-TPR) analysis using a Micrometrics AutoChem II 2920 with a thermal conductivity detector (TCD). A 0.06 g of each sample was pretreated under the Ar stream at 550°C for 30 min and then was heated in 10%(v/v) H_2/Ar with flowrate 50 ml/min from 100°C to 700°C at a 10°C/min.

The basicity of samples was investigated by CO_2-temperature programmed desorption (CO_2-TPD) analysis carried out on the same Micrometrics AutoChem II 2920 0.08 g of each sample was first reduced at was pretreated under the He stream at 550°C for 30 min and then was heated in 10% CO_2/He with flowrate 50 ml/min from 50°C to 800°C at a 10°C/min.

The specific surface areas and pore volume were measured with a Surface area and porosity analyzer (ASAP2020). A 0.08 g of each sample using N_2 adsorption-desorption method. The specific surface area and pore size distribution of the samples were calculated by the Brunauer–Emmett–Teller (BET) and Barrett–Joyner–Halenda (BJH) analyses methods.

And the catalyst morphologies and elemental dispersion of the catalysts by using JEOL (JSM-7610F) and X-MaxN 20. And the powder samples sprinkled on a SEM sample stub before analysis.

2.5 Methanation reaction

The CO_2 methanation was performed in a continuous fixed-bed reactor in a quartz tube with an inner diameter of 6 mm at normal pressure but various temperatures from 200°C to 500°C with 50°C step up. Briefly, 0.2 g catalyst was pretreatment at 600°C for 1 h by H_2 stream at 40 ml/min and the temperature was directly measured by a thermocouple. After that, the temperature was reduced to 200°C and the mixture gas containing 40 ml/min of H_2, 10 ml/min of CO_2 (H_2/CO_2 molar ratio of 4/1) and 50 ml/min of He for balancing and a gas hourly space velocity (GHSV) of 30000 ml/g_{cat} h were fed into the reactor. The products were analyzed by on-line gas chromatograph (GC-2014 AT) equipped with a thermal conductive detector. In addition, CO_2 conversion (X_{CO_2}) and CH_4 selectivity (S_{CH_4}) were calculated by the following equations (3) and (4) respectively:

$$\%\ X_{CO_2} = \frac{C^{in}_{CO_2} - C^{out}_{CO_2}}{C^{in}_{CO_2}} \times 100 \quad (3)$$

where:
$C^{in}_{CO_2}$ is the molar concentration of CO_2 at the inlet of the reaction mixture
$C^{out}_{CO_2}$ is the molar concentration of CO_2 at the outlet of the reaction mixture

$$\%\ S_{CH_4} = \frac{C_{CH_4}}{C_{CH_4} + C_{CO}} \times 100 \quad (4)$$

where:
C_{CH_4} is the molar concentrations of CH_4 at the outlet of the post-reaction mixture
C_{CO} is the molar concentrations of CO at the outlet of the post-reaction mixture

3. RESULTS AND DISCUSSION

3.1 Characterization of the catalysts

3.1.1 Effect of Ni Loading

XRD analysis

The variation in the nickel particle phases verified from X-ray diffraction (XRD). As shown in Fig. 1 the characteristic peaks of synthesized Al_2O_3 are located at 2θ = 37.7°, 39.4°, 45.9°, and 66.9° according to PDF 00-056-0457. When loading nickel metals apparent NiO peaks were observed for all samples and the characteristic peaks located at 2θ = 37.2°, 43.3°, 62.8°, 75.4°, and 79.5° according to PDF 00-044-1159. As the nickel loading increased, the intensity of NiO peaks increased while decreasing the peak of Al_2O_3 because NiO covers Al_2O_3 surface. Following by the Scherrer equation in table 1, found that the crystallite size slightly increases when increase nickel loading indicates that nickel does not agglomerate.

Table 1 NiO crystal size of the Ni/Al_2O_3 samples with different Ni loading.

Catalysts	NiO (012) Crystallite size (nm)
$60Ni/Al_2O_3$	27.7
$50Ni/Al_2O_3$	27.9
$40Ni/Al_2O_3$	27.9
$30Ni/Al_2O_3$	27.1

H_2-TPR analysis

The reducibility and the metal–support interactions to identify the nature of Ni species of nickel oxides were investigated with H_2-TPR measurement. As can be seen from Fig. 2, they are usually classified into four types including α is refer to free NiO species out of the support according to first small reduction peak, β_1 is refer to nickel has weak interaction with alumina support according to second main reduction peak, β_2 is refer to nickel has strong interaction with alumina support according to third small broad peak and γ belongs to the much less reducible NiO in nickel aluminate phase with the spinel structure according to forth small broad [6, 12, 13]. In addition, the second peak gradually shifts to the lower temperature when increase Ni loading. By loading $50Ni/Al_2O_3$ is the lowest temperature reducible. And when the increase in nickel loading more than $50Ni/Al_2O_3$ the second peak is shift back to higher temperature.

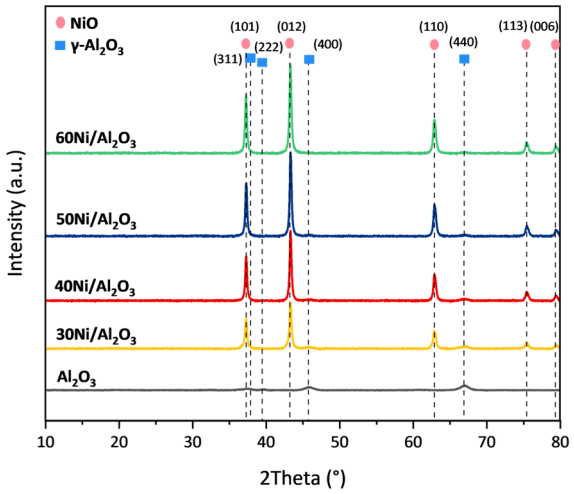

Figure 1 XRD patterns of the Ni/Al_2O_3 samples with different Ni loading.

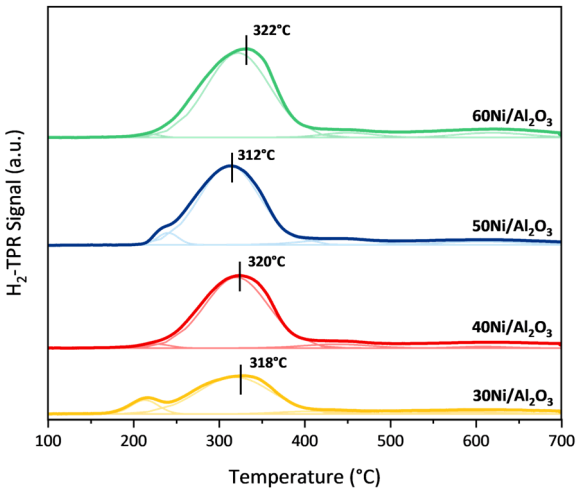

Figure 2 H_2-TPR profiles of the Ni/Al_2O_3 samples with different Ni loading.

N_2 adsorption analysis

As can be seen in Fig. 3(a) shown the N_2 adsorption-desorption isotherms of all the samples type IV, which are typical for the mesoporous structures. Moreover, all samples showed H3 type hysteresis loop that is a non-rigid, flaky aggregate of plate-like particles according to the IUPAC classification [14, 15]. And the surface areas and pore sizes of the catalysts were obtained using the BET and BJH analyses methods and are detailed in Table 2. In addition, when increased nickel loading is found that hysteresis loop becomes narrower than lower nickel loading because nickel fully fills in small pore according to the trend of pore distribution in Fig. 3(b) that shift to be more mesoporous compared with the pore distribution of support which in range of microporous. In addition, $60Ni/Al_2O_3$ would promote larger pore with diameter more than 4.6 nm, these results may be ascribed to $60Ni/Al_2O_3$ decrease catalytic activity because when Ni was fully filled some nickel was concealed in pore that means reactant cannot contact the active site for catalytic activity.

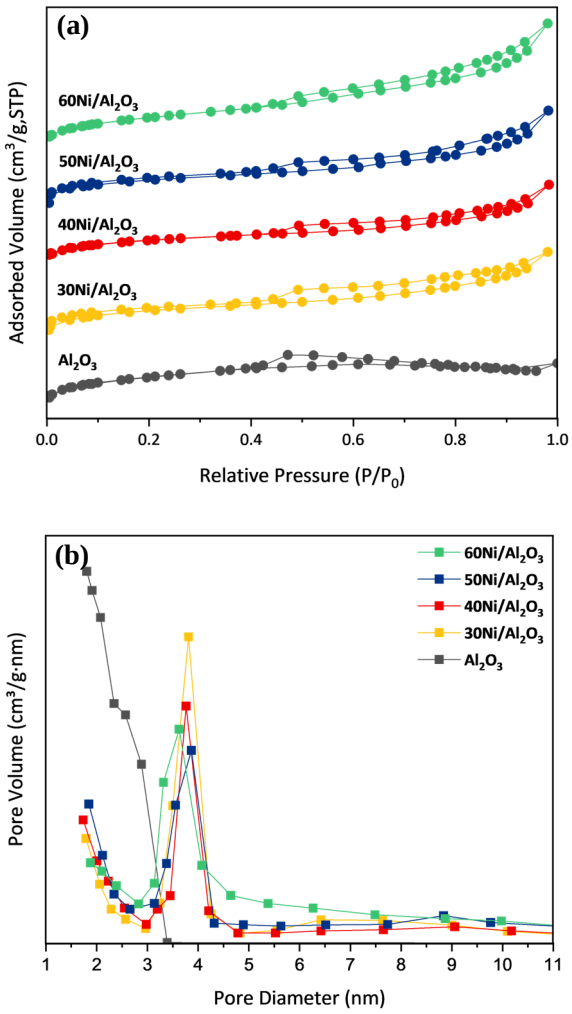

Figure 3 N_2 adsorption-desorption isotherms (a) and pore size distributions (b) of the Ni/Al_2O_3 samples with different Ni loading respectively.

Table 2 Textural properties of Ni/Al_2O_3 samples with different Ni loading.

Catalysts	Surface area (m^2/g)	Pore volume (cm^3/g)	Pore size (nm)
$60Ni/Al_2O_3$	59.526	0.085	6.085
$50Ni/Al_2O_3$	49.692	0.069	5.613
$40Ni/Al_2O_3$	45.504	0.057	5.140
$30Ni/Al_2O_3$	58.781	0.059	5.125
Al_2O_3	63.654	0.048	2.566

3.1.2 Effect of Ce content

XRD analysis

The variation in the ceria and nickel particle phases verified from X-ray diffraction (XRD). As shown in Fig.4 the characteristic peaks of the $50Ni/Al_2O_3$ catalyst could observe a peak at 2θ as the same location. Four new diffraction peaks are located at 2θ = 28.6°, 33.1°, 47.5°, and 56.3° according to PDF 01-083-9465 appeared after the introduction of the Ce species, which corresponded to the characteristic peaks of CeO_2, which more CeO_2 content found that Ni and Al_2O_3 intensity peaks were deceasing while intensity peaks of CeO_2 increased. Furthermore, in Table 3. The CeO_2 promoted crystallite sized nickel became smaller indicated that the Ni species were more dispersed on the support.

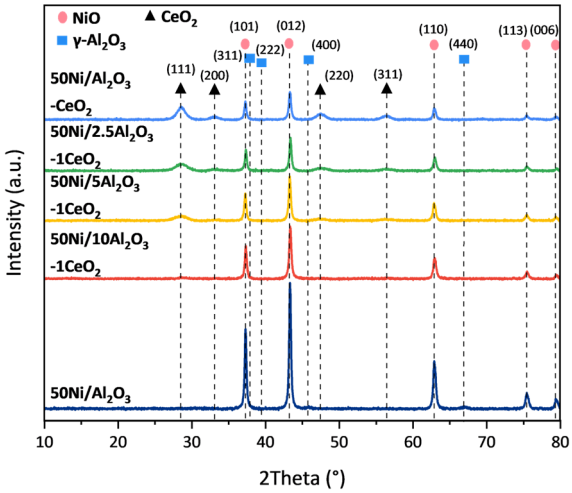

Figure 4 XRD patterns of the $50Ni/xAl_2O_3$-$xCeO_2$ samples with different ceria ratio and $50Ni/Al_2O_3$ samples.

Table 3 NiO crystal size of the $50Ni/xAl_2O_3$-$xCeO_2$ samples with different ceria ratio and $50Ni/Al_2O_3$ samples.

Catalysts	NiO (012) Crystallite size (nm)
$50Ni/Al_2O_3$-CeO_2	25.3
$50Ni/2.5Al_2O_3$-$1CeO_2$	26.5
$50Ni/5Al_2O_3$-$1CeO_2$	26.9
$50Ni/10Al_2O_3$-$1CeO_2$	25.6
$50Ni/Al_2O_3$	27.9

CO_2-TPD

The surface basicity, which was verified with CO_2-TPD characterizations. The results in Fig. 5 showed that there were roughly two separates CO_2 desorption peaks for $50Ni/Al_2O_3$ are related to weak and strong basic sites on the catalyst surface [16]. On the other hand, adding Ce species to modify the support which have a difference ratio between Al:Ce including 10:1, 5:1, 2.5:1 and 1:1 were roughly three separates desorption peaks. By first peak is assigned to weak basic site (< 350°C) associated to the surface OH^-, The second peak is assigned to medium basic site (350-600°C) associated to metal–oxygen pairs, and the last peak is for strong basic site (>600°C) associated to low coordination surface O^{2-} respectively [10]. From the results, it shows that increasing CeO_2 content promoted the medium basic site suitable for CO_2, acid property, to be more adsorption at the support following the H_2 on the Ni can be approachable to hydrogenation CO_2 on the support to produce CH_4.

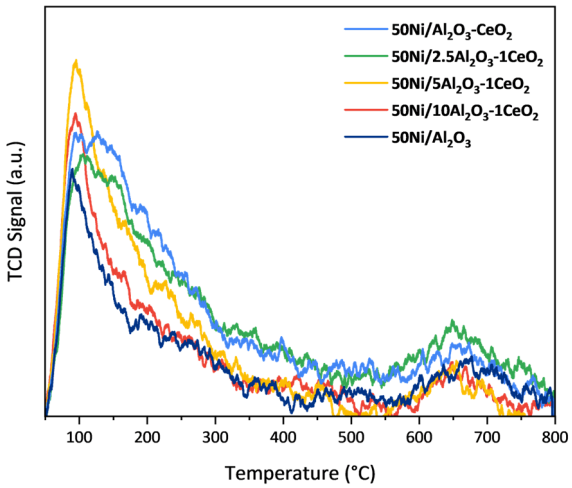

Figure 5 CO_2-TPD profiles of the $50Ni/xAl_2O_3$-$xCeO_2$ with different ceria ratio and $50Ni/Al_2O_3$ samples.

N_2 adsorption analysis

The N_2 adsorption-desorption isotherms of all the samples after the introduction of the Ce species are the same as without CeO_2. Also, the BET and BJH analyses methods and are detailed in Table 4. In addition, Fig. 6(a) increased CeO_2 content found that hysteresis loop becomes wider than lower CeO_2 content. According to the trend of pore distribution in Fig. 6(b) $50Ni/Al_2O_3$-CeO_2 shifted to be more mesoporous compared with the pore distribution of the lower CeO_2 content.

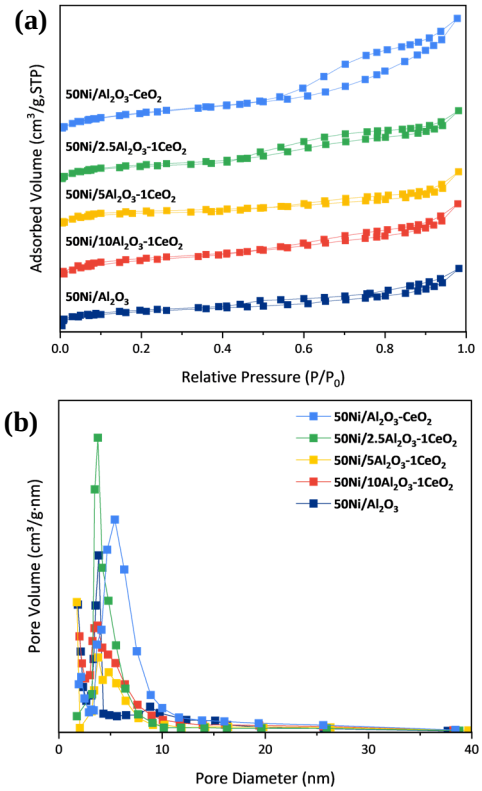

Figure 6 N_2 adsorption-desorption isotherms (a) and pore size distributions (b) of the $50Ni/xAl_2O_3$-$xCeO_2$ samples with different ceria ratio and $50Ni/Al_2O_3$ samples respectively.

Table 4 Textural properties of the Ni/xAl_2O_3-$xCeO_2$ samples with different ceria ratio and $50Ni/Al_2O_3$ samples.

Catalysts	Surface area (m^2/g)	Pore volume (cm^3/g)	Pore size (nm)
$50Ni/Al_2O_3$-CeO_2	85.307	0.137	6.730
$50Ni/2.5Al_2O_3$-$1CeO_2$	75.342	0.091	5.504
$50Ni/5Al_2O_3$-$1CeO_2$	64.746	0.063	6.354
$50Ni/10Al_2O_3$-$1CeO_2$	73.954	0.086	6.117
$50Ni/Al_2O_3$	49.692	0.069	5.613

3.2 FE-SEM images

The morphology of the $50Ni/Al_2O_3$ and $50Ni/Al_2O_3$-CeO_2 catalysts are studied by FE-SEM analysis and the results are presented in Fig7. The $50Ni/Al_2O_3$ shows flaky at the wedge of synthesized Al_2O_3 by one-spot sol-gel method in Fig.7(a) and when impregnate nickel on the synthesized support in Fig.7(b) indicate that nickel-based catalysts are over the surface of synthesized Al_2O_3 and aggregate to from shape by themselves. Moreover, this morphology can support the result from BET analysis (Table 2) about value of pore volume are pore size increase when increase nickel loading. While the $50Ni/Al_2O_3$-CeO_2 catalysts in Fig.7(c) show that the synthesized support which adding CeO_2 the morphology becomes more porous structure. Thus, this structure promotes textural properties of the catalyst including surface area, pore volume and pore sized to be larger according to the BET analysis in Table 4. And when impregnating Ni on the synthesized support in Fig. 7(d) indicate that nickel-based catalysts are fully fill in porous. Furthermore, Ni on synthesized Al_2O_3-CeO_2 can disperse more than Ni on synthesized Al_2O_3 according to Fig.8(a,b), it indicates that CeO_2 can improve the support to be larger and nickel can disperse more than synthesized Al_2O_3.

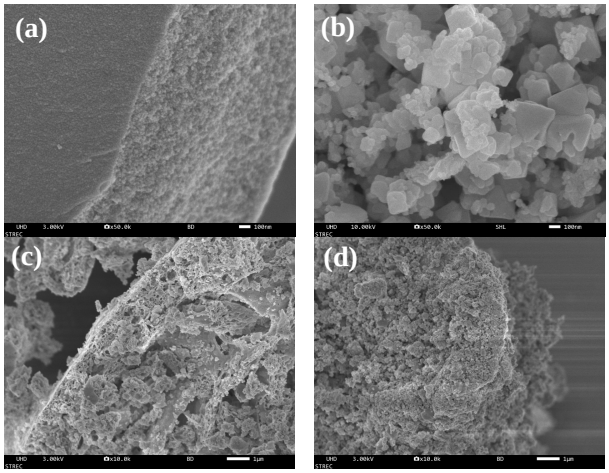

Figure 7 FESEM images of synthesized Al_2O_3 (a), 50Ni/Al_2O_3 (b), synthesized Al_2O_3-CeO_2 (c), and 50Ni/Al_2O_3-CeO_2 (d) samples respectively at the magnification of 50000.

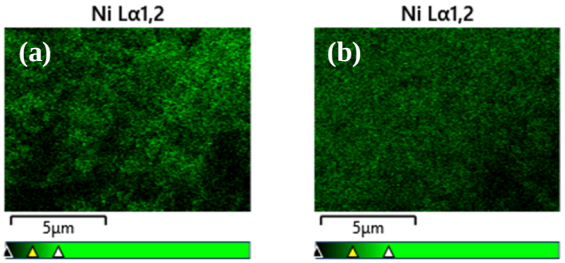

Figure 8 EDS images of synthesized 50Ni/Al_2O_3 (a), 50Ni/Al_2O_3-CeO_2 (b) samples respectively at the magnification of 50000.

3.3 Catalytic activity

The CO_2 methanation using xNi/Al_2O_3 catalysts (x = 30, 40, 50, 60 %wt) showed that increasing Ni loading improves catalytic activity, as nickel acts as an active site for H_2 adsorption. However, when Ni loading exceeds 50 %wt, the catalytic activity gradually decreases due to nickel overload on the support, which reduces the availability of active sites for H_2. This results in lower hydrogenation efficiency for CO_2 and a decline in catalytic performance. When CeO_2 is added to modify the support, it enhances the basicity of the support, favoring CO_2 adsorption and facilitating H_2 uptake from nickel to hydrogenate CO_2, thus improving catalytic activity. Additionally, CeO_2 has redox properties that contribute to better nickel dispersion on the support.

The effect of Ni loading on catalytic activity, shown in Fig. 9(a,b), revealed that increasing the reaction temperature from 200 to 350°C led to higher CO_2 conversion, which reached its optimum at 350°C, with the 50Ni/Al_2O_3 catalyst achieving 80% CO_2 conversion. However, CO_2 conversion began to decrease above 400°C due to the exothermic nature of the reaction and thermodynamic limitations, as well as the promotion of CO formation via the reverse water-gas shift reaction at high temperatures. CH_4 selectivity remained above 90% for all catalysts but decreased significantly above 400°C. The introduction of CeO_2 shifted the reaction to lower temperatures and increased CH_4 production compared to 50Ni/Al_2O_3. As the temperature increased from 200 to 300°C, CO_2 conversion continuously improved, reaching a maximum before decreasing. Among the various Al:Ce ratios, the 50Ni/Al_2O_3-CeO_2 catalyst showed the best performance, achieving 82% CO_2 conversion at 300°C, with CH_4 selectivity exceeding 99%. However, both CO_2 conversion and CH_4 selectivity decreased above 300°C.

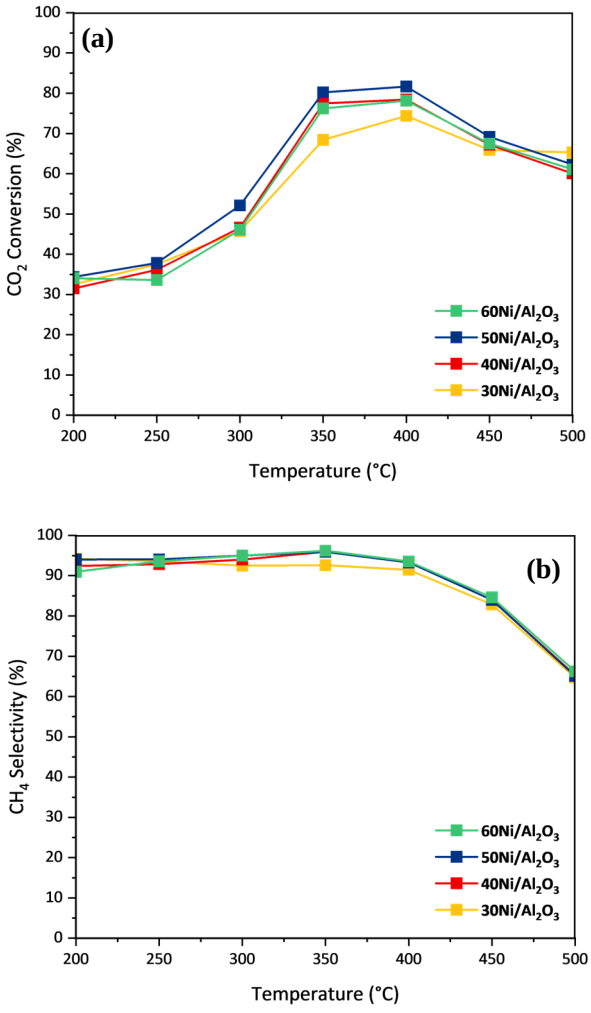

Figure 9 CO_2 conversion (a) and CH_4 selectivity (b) of the Ni/Al_2O_3 samples with different Ni loading.

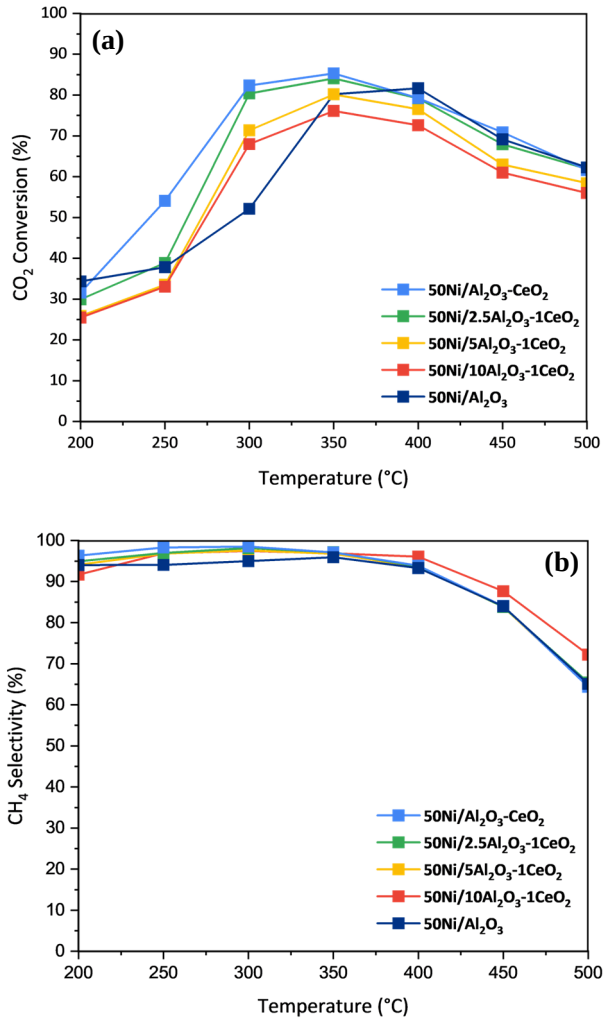

Figure 10 CO_2 conversion (a) and CH_4 selectivity (b) of the 50Ni/xAl_2O_3-xCeO_2 samples with different ceria ratio respectively.

4. CONCLUSION

In summary, the results shown above indicated that the effect of Ni loading is important to find suitable nickel content according to the above results 50Ni/Al_2O_3 reach the highest catalytic activity according to lowest reducible temperature from H_2-TPR. It promotes nickel-based catalysts from Ni^{2+} to Ni^0 easier compared to another Ni loading. And when found appropriate Ni content will be favored H_2 to take more site on nickel-based catalysts which place role for an active site following H_2 hydrogenate CO_2 on the support to convert reactants to CH_4. Beside modified support by introducing CeO_2 into the support to become Al_2O_3-CeO_2 composite catalyst with containing difference Al:Ce ratio which synthesized a one-pot sol–gel route. By comparing the result CeO_2 promotes more Ni dispersion on the support according to crystallite size and EDS results. Moreover, enhanced catalytic activity both CO_2 conversion and CH_4 selectivity also decreases reaction temperature compared to 50Ni/Al_2O_3 due to its strong redox properties and increase medium base on the support for to enhance CO_2 adsorption capacity. The Ni/Al_2O_3 catalyst reaches the highest catalytic activity by 80% CO_2 conversion at 350°C with around 90% CH_4 selectivity. While adding CeO_2 improves the performance by the Ni/Al_2O_3-CeO_2 catalyst reaches the highest catalytic activity by 82% CO_2 conversion with 99% CH_4 selectivity at 300°C.

ACKNOWLEDGMENTS

Firstly, the author would like to express sincere gratitude to Professor Dr. Nuttaya Pongstabodee and the members of her team. Furthermore, heartfelt thanks are extended to all the staff and technicians in the Department of Chemical Technology, Faculty of Science, Chulalongkorn University.

REFERENCES

1. C. Mebrahtu, F. Krebs, S. Abate, S. Perathoner, G. Centi, R. Palkovits. CO_2 methanation: Principles and Challenges. *Studies in Surface Science and Catalysis* 2019; 178: 85-103.
2. Z. Liu, X. Gao, K. Wang, J. Liang, Y. Jiang, Q. Ma, T.S. Zhao, J. Zhang. A short overview of power-to-methane: Coupling preparation of feed gas with CO_2 methanation. *Chemical Engineering Science* 2023; 274: 118692.
3. H. Wang, J. Wu, Y. Bao, H. Feng, J. Liu, H. Wang. CO_2 methanation over Ni/Al_2O_3-ZrO_2 catalysts: Optimizing metal-oxide interfaces by calcinating-induced phase transformation of support. *Journal of Environmental Chemical Engineering* 2023; 11: 109538.
4. P. Frontera, A. Macario, M. Ferraro, P. Antonucci. Supported catalysts for CO_2 methanation: A review. *Catalysts* 2017; 7: 59.
5. W. Gac, W. Zawadzki, M. Rotko, M. Greluk, G. Słowik, G. Kolb. Effects of support composition on the performance of nickel catalysts in CO_2 methanation reaction. *Catalysis Today* 2020; 357: 468-482.
6. L. He, Y. Ren, B. Yue, S.C.E. Tsang, H. He. Tuning metal–support interactions on Ni/Al_2O_3 catalysts to improve catalytic activity and stability for dry reforming of methane. *Processes* 2021; 9: 706.
7. S.V. Moghaddam, M. Rezaei, F. Meshkani, R. Daroughegi. Carbon dioxide methanation over Ni-M/Al_2O_3 (M: Fe, CO, Zr, La and Cu) catalysts synthesized using the one-pot sol-gel synthesis method. *International Journal of Hydrogen Energy* 2018; 43: 16522-16533.
8. S.V. Moghaddam, M. Rezaei, F. Meshkani. Surfactant-free sol–gel synthesis method for the preparation of mesoporous high surface area NiO–Al_2O_3 nanopowder and its application in catalytic CO_2 methanation. *Energy Technology* 2020; 8: 1900778.

9. Y. Wu, J. Lin, G. Ma, Y. Xu, J. Zhang, C. Samart, M. Ding. Ni nanocatalysts supported on mesoporous Al_2O_3-CeO_2 for CO_2 methanation at low temperature. *Royal Society of Chemistry Advance* 2020; 10: 2067-2072.
10. R. Daroughegi, F. Meshkani, M. Rezaei. Enhanced low-temperature activity of CO_2 methanation over ceria-promoted Ni-Al_2O_3 nanocatalyst. *Chemical Engineering Science* 2021; 230: 116194.
11. I. Luisetto, S. Tuti, C. Battocchio, S.L. Mastro, A. Sodo. Ni/CeO_2–Al_2O_3 catalysts for the dry reforming of methane: The effect of $CeAlO_3$ content and nickel crystallite size on catalytic activity and coke resistance. *Applied Catalysis A: General 2015*; 500: 12-22.
12. J. Gao, C. Jia, J. Li, M. Zhang, F. Gu, G. Xu, Z. Zhong, F. Su. Ni/Al_2O_3 catalysts for CO methanation: Effect of Al_2O_3 supports calcined at different temperatures. *Journal of Energy Chemistry* 2013; 22: 919-927.
13. Y. Xue-mei, X. Xian-mei, W. Xu, A. Xia. Catalytic performance of nickel immobilized on organically modified montmorillonite in the steam reforming of ethanol for hydrogen production. *Journal of Fuel Chemistry and Technology* 2016; 44(6): 689-697.
14. S. Yurdakal, C. Garlisi, L. Özcan, M. Bellardita, G. Palmisano. (Photo)catalyst characterization techniques: Adsorption isotherms and BET, SEM, FTIR, UV-Vis, photoluminescence, and electrochemical characterizations. *Heterogeneous Photocatalysis* 2019; 87-152.
15. C. Keluo, Z. Tingshan, C. Xiaohui, H. Yingjie, L. Xing. Model construction of micro-pores in shale: A case study of Silurian Longmaxi Formation shale in Dianqianbei area, SW China. *Petroleum Exploration and Development* 2018; 45(3): 412-421.
16. Q. Pan, J. Peng, T. Sun, S. Wang, S. Wang. Insight into the reaction route of CO_2 methanation: Promotion effect of medium basic sites. *Catalysis Communications* 2014; 45: 74-78.

Kaolin-based synthesis as an alternative low-cost adsorbent for biodiesel purification

Aphirak Tharanuvet[1,*], Kanokwan Ngaosuwan[2,*], Worapon Kiatkittipong[3], Doonyapong Wongsawaeng[4], Weerinda Appamana[5], Merika Chanthanumataporn[1], Suttichai Assabumrungrat[1,6]

[1] Center of Excellence in Catalysis and Catalytic Reaction Engineering, Department of Chemical Engineering, Faculty of Engineering, Chulalongkorn University, Bangkok, 10330, Thailand
[2] Chemical Engineering Division, Engineering Faculty, Rajamangala University of Technology Krungthep, Bangkok, 10120, Thailand
[3] Department of Chemical Engineering, Faculty of Engineering and Industrial Technology, Silpakorn University, Nakhon Pathom, 73000, Thailand
[4] Research Unit on Plasma Technology for High-Performance Materials Development, Department of Nuclear Engineering, Faculty of Engineering, Chulalongkorn University, Bangkok, 10330, Thailand
[5] Departments of Chemical and Materials Engineering, Faculty of Engineering, Rajamangala University of Technology Thanyaburi, Pathum Thani, 12120, Thailand
[6] Bio-Circular-Green-economy Technology & Engineering Center, BCGeTEC, Department of Chemical Engineering, Faculty of Engineering, Chulalongkorn University, Bangkok, 10330, Thailand
[*] Corresponding author: aphirak.th@gmail.com; kanokwan.n@mail.rmutk.ac.th

ABSTRACT

Kaolin-based geopolymer is a low-cost, environmentally friendly adsorbent for biodiesel purification via the dry washing process. This study explores two methods for transforming kaolin into a geopolymer adsorbent: (1) hydrothermal treatment, where kaolin is mixed with sodium hydroxide (NaOH) at 90°C for 24 hours and then calcined at 500°C for 6 hours, and (2) the fusion method, where kaolin is fused with NaOH at a high temperature for 15 hours, followed by dealkalization through washing with deionized water until neutralized. The synthesized geopolymers were characterized using X-ray diffraction (XRD), Fourier-transform infrared spectroscopy (FTIR), Brunauer–Emmett–Teller (BET) surface area analysis, and scanning electron microscopy (SEM). Adsorption performance was evaluated by purifying 100 mL of biodiesel at varying FAME concentrations (30%, 50%, and 70%) using 5 wt.% geopolymer. The mixture was stirred at 60°C, centrifuged, and analyzed via gas chromatography (GC) to determine the increase in biodiesel yield due to glycerol and excess methanol adsorption. Characterization results showed the presence of an amorphous phase in both geopolymers, confirmed by XRD, while FTIR spectra (400–4000 cm^{-1}) validated the formation of geopolymer from kaolin. SEM images revealed rough surface morphologies, and BET analysis showed that the specific surface areas of geopolymers synthesized by the hydrothermal and fusion methods were 6.82 m^2/g and 45.9 m^2/g, respectively. The larger surface area of the fusion-based geopolymer suggests a higher adsorption capacity for glycerol. The comparative performance of these methods in biodiesel purification is still under investigation, with final results to be reported upon completion. However, preliminary findings indicate that kaolin-based geopolymer is a promising adsorbent for biodiesel purification.

Keywords: Biodiesel purification; Kaolin; Geopolymer; Adsorbent; Dry washing.

1. INTRODUCTION

A rising global temperature due to global warming and greenhouse effect in the 21st century pushing a search for an alternative green energy one of which is biodiesel, but the exploding increase of biodiesel production comes with a major problem which are ensuring the quality, reducing cost and time of production. Biofuel is generally generated using transesterification reaction. After reaction, products on the uppermost phase need to be separated and purified to remove remaining free glycerin and contaminants. In purification stage, in order to satisfy biodiesel quality standards such as EN 14214 and the ASTM D6751. The most commonly used purification process is the wet washing method. Despite being an efficient method, it

requires huge amounts of wastewater that have to be treated amounting from 0.2 to 10 L of wastewater per litter of purified biodiesel which added cost between 0.09 and 3.8% of total biodiesel production cost for water treatment. As an alternative to wet washing process, dry washing methods use solid adsorbents or ion exchange resins to purify crude biodiesel. These methods can obtain biodiesel of suitable quality with no wastewater generated. Commercially used adsorbents such as Magnesol™, AmberliteDRY BD10™ and Purolite PD 206™ resins. However, their application at industrial level is still limited due to their high cost, thus the search for alternative sorbents have been investigated. Starch and cellulosic for their natural resin, and silica family such as rice husk ash for their ion exchange possibility. For low-cost alternative adsorbent, kaolin, a universal industrial material, is a promising material due to its mesoporous nature and being an aluminosilicate that can be transformed into geopolymer and have cross-linking framework between tetrahedra, which leads to a 3-dimensional aluminosilicate network, where the negative charge associated with tetrahedral aluminum is balanced by a small alkali metal cation which group which are often ion-exchangeable in covalent bonding. In this study, we compare two different types of synthesis methods. The first is kaolin catalyst which has high porous surface, and the latter one is kaolin geopolymer which has cross-linking framework ion-exchange. This paper is organized as follows. The introduction, The experiment which explains materials and methods including geopolymer synthesis, characterization, application of the synthesized kaolin adsorbent in crude biodiesel purification, The third section presents and discusses the experimental results followed by the investigation of adsorption kinetic and isotherm.

2. EXPERIMENTAL

Commercial kaolin powder (from Krungthepchemi) was used for the synthesis of geopolymer, since it is a rich source of aluminum and silicon. The weight percent of the major chemical ingredients of the kaolin were SiO_2, 45%, Al_2O_3, 35%, Fe_2O_3, 0.5%, MgO, 0.1%, K_2O, 0.1%, TiO_2, 1.5%, Na_2O, 0.5%, CaO, 0.5%, and its loss on ignition (LOI) was 13.92%.

2.1. Geopolymer synthesis

Geopolymer was synthesized in two steps. The first step was fusion of kaolin and sodium hydroxide at elevated temperatures, and the second step consisted of hydration and dealkalization that was performed by washing with distilled water. In this method, there is no need to transform the kaolin into metakaolin. In order to synthesize geopolymer, the kaolin was activated by sodium hydroxide (NaOH, purchased from Merck). NaOH and kaolin were mixed at a 2.2 NaOH/kaolin weight ratio between, by grinding in a mortar. Then, the mixture was placed in a furnace at 800 ºC for 15 h. Subsequently, the fusion product was cooled, ground, and rinsed with distilled water (800 cm^3 distillated water was required for dealkalization and hydration of 1 g of fusion product). This step was carried out till the neutral pH was reached. Finally, the prepared sample was dried at 100 °C for about 24 h and was saved in a desiccator for characterization and application experiments.

2.2. Catalyst synthesis

To synthesis a catalyst we need to calcined kaolin by thermal treatment on raw kaolin (RK) at 800 ºC for 10 h in air with a heating rate at 5 ºC/min. The calcined kaolin is also known as metakaolin, a dehydroxylated form of kaolin. To get the catalyst, calcined kaolin was activating 7 g metakaolin (MK) with 15.4 g NaOH in 500 mL deionized water hydrothermally at 90 ºC, followed by calcination at 500 ºC for 6 h.

2.3. Adsorbent characterization

The synthesized adsorbents were characterized by using X-ray diffraction (XRD) to observe for phase determination by a SIEMENS D5000 X-ray diffractometer using CuKα radiation with Ni filter in the 2θ range of 5-60 degrees with a scanning rate at 4º/min.

Fourier transforms infrared spectroscopy (FT-IR) FT-IR analysis was used to determine the functional group as the chemical structure of synthesis adsorbent structure using a Nicolet 6700 FTIR spectrometer. Scanning Electron Microscopy (SEM) and Energy dispersive X-ray spectroscopy (EDX) Scanning electron microscopy (SEM) and Energy dispersive X-ray spectroscopy (EDX) were used to determine the morphology and elemental distribution of adsorbent. Nitrogen adsorption-desorption isotherm was used to measured specific surface area, pore volume and pore diameter by N2 adsorption-desorption at liquid nitrogen (-196o C) using a Micromeritics ASAP 2000 instrument. The surface area and pore size distribution was calculated by Brunauer-Emmelt-Teller (BET) and BJH method, respectively.

2.3. Crude biodiesel synthesis

The crude biodiesel was synthesized via transesterification of refined palm oil from Morakot Industry Co. Ltd. using a methanol to RPO molar ratio of 6:1, a 1 wt% NaOH catalyst (99% purity from Supelco) based on the oil weight and a rotational speed of 800 rpm in 3-neck bottle. After the reaction the crude biodiesel was separated from the reaction mixture using a separatory funnel, where the methanol was in the upper layer, the crude biodiesel was in the middle layer and glycerin in the lower layer.

2.4. Adsorption test

100 ml of crude biodiesel and the adsorbent at 3-8% weight adsorbent/biodiesel weight at 60°C and stirred with a magnetic stir bar at 600 rpm for 90 mins. Biodiesel purity after adsorption was tested using gas

chromatography in every 15 mins, record %yield and adsorption time. Conclude the optimum condition to use for further experiments.

2.5. Adsorption kinetic and isotherm

100 ml of biodiesel and the adsorbent at optimum% biodiesel weight at 60°C and 40°C and stirred with a magnetic stir bar at 600 rpm for 120 mins. Adsorbed biodiesel was tested using GC, record glycerol weight and adsorption time with temperature.

3. RESULTS AND DISCUSSION

3.1. Geopolymer characterization

Fig. 1 [patterns (a) and (b)] presents the XRD patterns of kaolin and the synthesized phase obtained from fusion of kaolin and NaOH (NaOH/kaolin ratio of 2.2) at 600 °C for 14 h, respectively. The presence of peaks at 13, 20 and 25 diffraction angles (i.e., 2θ) in the kaolin XRD pattern (a) is an indication that the major crystalline phase is kaolinite. The XRD pattern of the synthesized phase (b) contains an amorphous phase in which the kaolin peaks are replaced with a broad peak at 20–40°, indicating geopolymer. Pattern (c) belongs to a semi crystalline geopolymer that will be explained and discussed later. Fig. 2 is the FTIR spectra of kaolin and synthesized geopolymer obtained from fusion of kaolin and NaOH (NaOH/kaolin ratio of 2.2) at 600 °C for 14 h. Kaolin spectra peaks at 468 and 538 cm−1 correspond to Si-O-Si bending and Si-O-Al stretching, respectively. The peak at 698 cm−1 represents quartz Si-O bonds while peaks at 912 and 3694 cm−1 are attributed to the Al-OH bonds. The stretching Si-O peaks are observed at 1006 and 1014 cm−1 . Finally, the peak at 3619 cm−1 could be assigned to OH stretching.

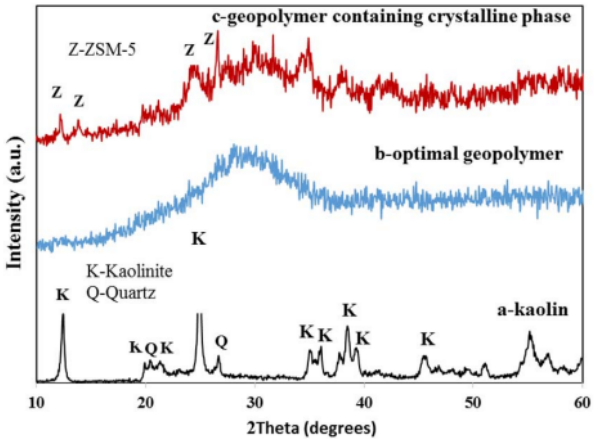

Figure 1 XRD patterns of a) kaolin, b) synthesized phase obtain from fusion of kaolin and NaOH mixture at NaOH/kaolin ratio of 2.2 at 60 °C for 14 h. c) NaOH/kaolin ratio of 2.2 at 800 °C for 14 h. [b) and c) XRD patterns belong to the final geopolymer sample after hydration]

In FTIR spectra of the synthesized geopolymer, the absorption peaks belong to Si-O-Si bending and Si-O-Al stretching can be seen at 440 and 544 cm−1 , respectively. Both of these peaks are shifted because of the microstructure change during geopolymerization. The peak at 703 cm−1 is attributed to the Si-O-Al vibration. The asymmetric stretching vibrations of Si-O-Si or Si-O-Al peak appear at 1005 cm−1 . This indicates geopolymer formation. Finally, the peaks observed at 1652 and 3400 cm−1 are ascribed to OH stretching of water indicates that synthesized phase is hydrated. One concludes that the hydration is performed in the washing and dealkalization stage.

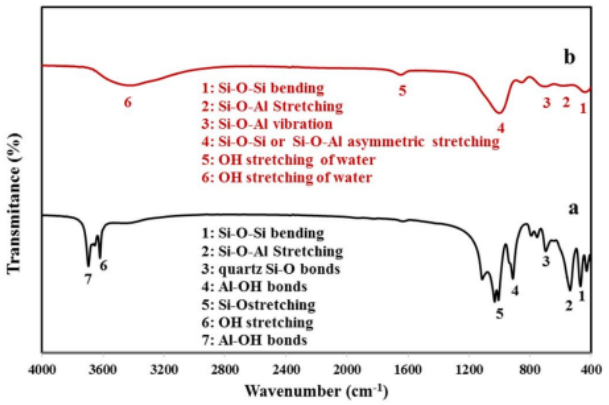

Fig. 2 The FTIR spectra of a) kaolin and b) synthesized geopolymer at NaOH/kaolin ratio of 2.2 at 60 °C for 14 h.

The results of the SEM analysis on the synthesized geopolymer and kaolin are given in Fig. 3. These images vividly show that the morphology of kaolin particles has completely changed in geopolymerization process. In addition, based on these images, the average geopolymer particle size is estimated to be < 1 μm. EDS analysis of the synthesized geopolymer at NaOH/kaolin ratio of 2.2 at 600 °C for 14 h is shown in Fig. 4. The data were obtained from the average of five different areas of the sample. The major elements detected are Si, Al, O and Na. The semiquantitative values of the ratios of Si/Al and Na/Al are 1.66 and 0.65, respectively. Clearly, Na ions are not available in kaolin, as shown by XRF results. However, the presence of Na in geopolymer is necessary for charge balancing. The BET surface area and total pore volume of the synthesized geopolymer were 51.3 m2 ·g−1 and 0.324 cm3 ·g−1 , respectively. The average pore diameter of the synthesized geopolymer was 25.25 nm.

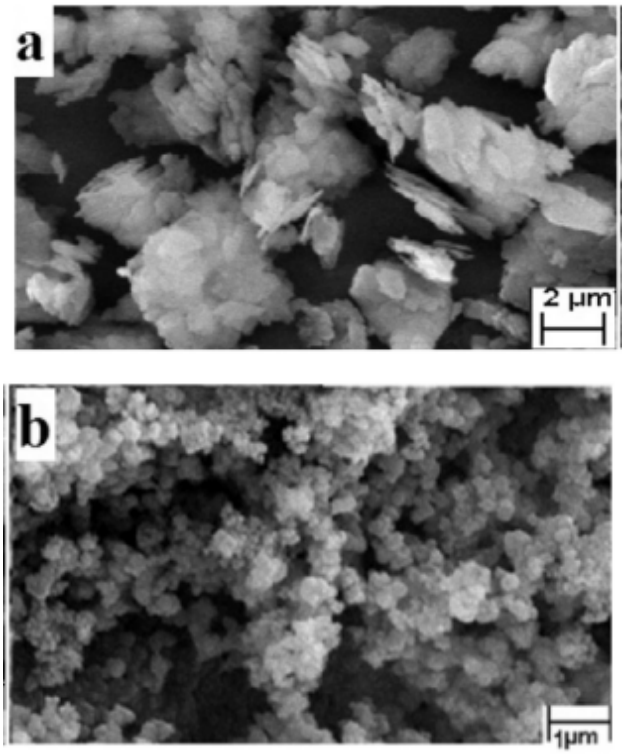

Fig. 3 SEM micrograph of a) kaolin at a magnification of 5000 b) synthesized geopolymer at NaOH/kaolin ratio of 2.2 at 600 °C for 14 h at a magnification of 12,000.

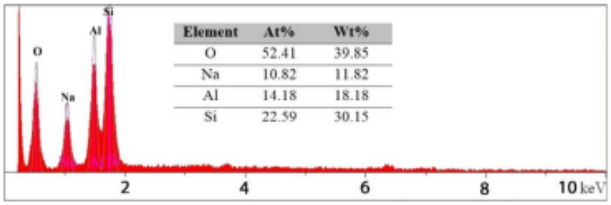

Element	At%	Wt%
O	52.41	39.85
Na	10.82	11.82
Al	14.18	18.18
Si	22.59	30.15

Fig. 4 EDS analysis of the synthesized geopolymer at NaOH/kaolin ratio of 2.2 at 600 °C for 14 h.

3.2. Catalyst characterization

The XRD patterns of RK, CK and TK were provided in Fig 6. The XRD characteristics of RK almost disappeared after thermal treatment leading to formation of CK (aka metakaolin). Explicitly, disordered metakaolin was formed in this work after dehydroxylation of kaolin at 800 °C for 10 h. A new broad band with increasing background in 2 h range from 20–30 θ, which is commonly assigned to amorphous phase of SiO2, could be observed on the XRD pattern of CK. The remaining peaks in this range could be ascribed to traces of mica and quartz in calcined kaolin, and possibly some long-range order due to layer stacking. After NaOH-activation of calcined kaolin (CK), transformed kaolin (TK) with crystallinity is resulted. Coincidently, the XRD characteristics of transformed kaolin catalyst are quite similar to those of zeolite Linde Type A (LTA, dehydrate form).

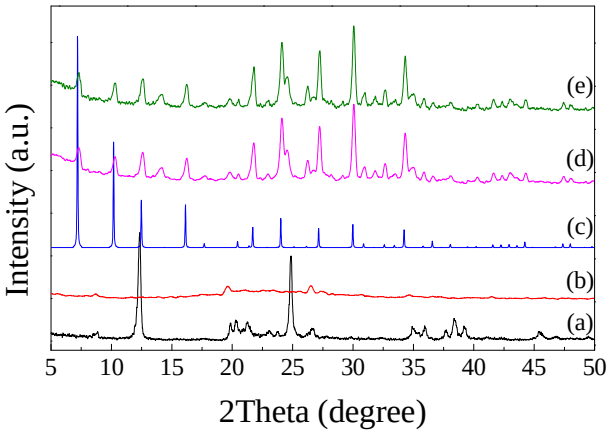

Fig 5 XRD patterns of (a) raw kaolin, (b) calcined kaolin (b), transformed kaolin [(d) fresh, and (e) recycled one], and (c) dehydrated zeolite LTA

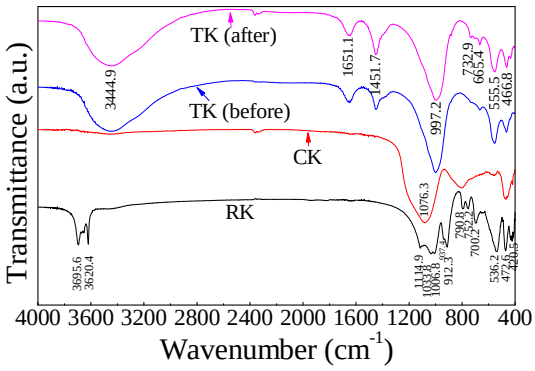

Fig 6 FT-IR spectra of raw (RK), calcined (CK) and transformed kaolin (TK) catalysts

Fourier transform infrared spectroscopy (FT-IR) FT-IR analyses were carried out in the range of 4000–400 cm-1 to investigate the characteristics of surface chemistry, especially functional groups, on raw, calcined and activated kaolin in Fig. 6 . Not only the -OH group (ca. 3659 and 3620 cm-1), but also other feature of raw kaolin (1114.9 cm-1) disappears during calcination at 800 °C for preparation of CK. Once again, significant changes in surface features from CK to TK in the range 1200–400 cm-1 were also observed. For instance, the broad shoulder peak of CK near 1076.3 cm-1 has been shifted to 997.2 cm-1 , corresponding to the characteristics of tetrahedral cations linked by bridging oxygen atoms presented

The morphology of RK, CK and TK was examined with SEM Fig 7. The raw kaolin mainly consists of stacking of flaky particles with rough surface. Despite of being calcined at 800 °C, the morphology of CK is insignificantly different from that of RK. Interestingly, after NaOH-activation treatment, flaky CK turned to cubic TK of ca. 2 lm in size. Again, the observed morphology of TK resembles that of zeolite LTA, consistent with the findings by XRD and FT-IR. Hence, it is rational to conclude that kaolin has been successfully transformed into zeolite LTA after NaOH activation treatment of calcined kaolin. That is,

transformed kaolin (TK) catalyst used in this work is zeolite LTA in dehydrated form

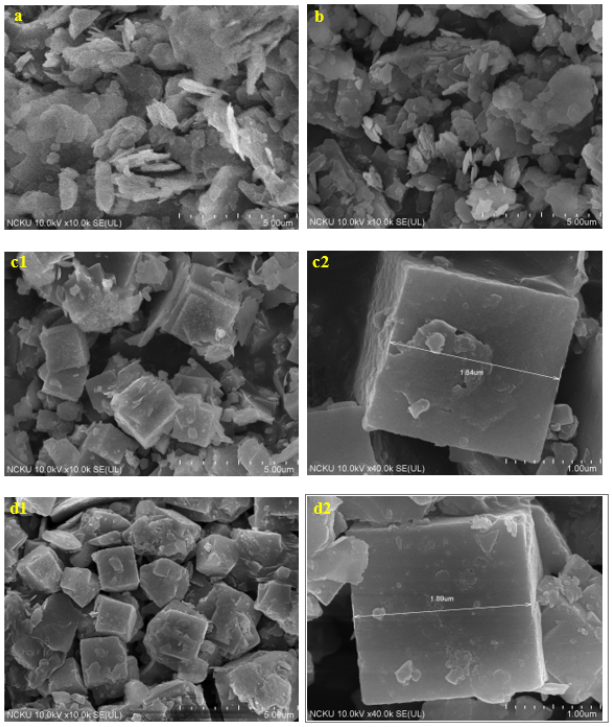

Figure 7: SEM micrographs of (a) raw kaolin, (b) calcined kaolin and (c-d) transformed kaolin before ((c1) 10000×, (c2) 40000×) and after ((d1) 10000×, (d2) 40000×) catalyzing transesterification of vegetable oils in excess ethanol.

3.3. Adsorption test

100 ml of crude biodiesel and the adsorbent at 3-8% weight adsorbent/biodiesel weight at 60°C and stirred with a magnetic stir bar at 600 rpm for 90 mins. Fig 8 and Fig 9 illustrates the percentage of Fatty Acid Methyl Ester (FAME) yield over adsorption time (0–35 min) for three catalyst loadings: 3%wt, 5%wt, and 8%wt. We can observed Initial rapid increase of FAME yield on all adsorbent loadings showed a sharp rise in within the first 5–10 minutes, indicating fast initial adsorption kinetics then follow by a saturation trend at 15–20 minutes, the FAME yield plateaued, suggesting near-completion of the reaction. The 5%wt catalyst and geopolymer seem to have achieved the highest yield around 90-100% later than its 8%wt this can be infer that at lower adsorbent weight can have enough porous to purified biodiesel

Fig 10. illustrates compares FAME yield between two 5%wt adsorbent over the same 100 ml of crude biodiesel and we can conclude that catalyst at 5%wt is the optimal condition to test adsorption kinetic further

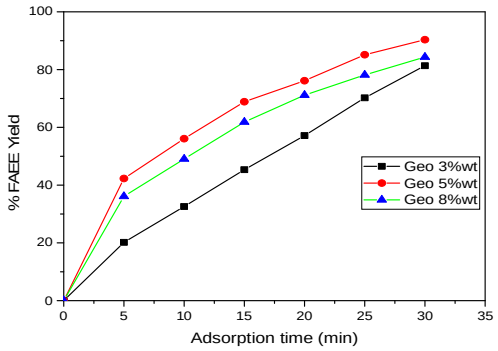

Figure 8: Effect of adsorption time on biodiesel yield for different geopolymer weight.

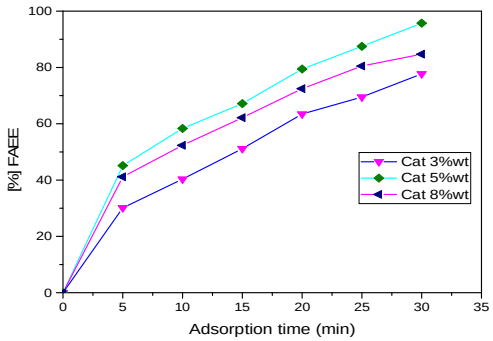

Figure 9: Effect of adsorption time on biodiesel yield for different catalyst weight.

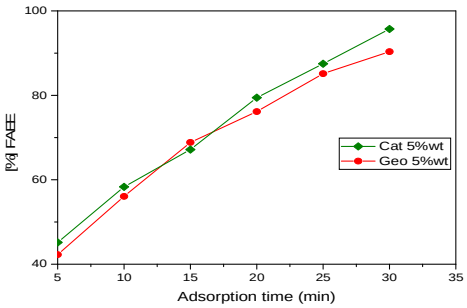

Figure 10: Comparing Biodiesel yield for different adsorbent

4. CONCLUSION

In this work, two low-cost adsorbent for biodiesel purification was produced as an ion-exchange geopolymer and highly porous catalyst which was characterize using various technic then applied to crude biodiesel for adsorption tests. The results revealed that using kaolin catalyst adsorbent for the purification of biodiesel resulted in higher yield compared to using geopolymer adsorbent and water washing method. At the optimal conditions (an adsorbent of <2 µm, 5% wt adsorbent to biodiesel ratio and 30 min contact time) the adsorbent behaves as a nonselective adsorbent with a high capacity of adsorption, which makes it an excellent adsorbent to purify biodiesel.

A comparative study of commercial- and hydrothermal-synthesized TiO_2 nanoparticles for photocatalytic silver recovery from jewelry plating effluent

Midori Tanaka[1], Auttawit Thoumrungroj[1], Pimchanok Longchin[1], Mali Hunsom[1,2,3*]

[1] Department of Chemical Engineering, Faculty of Engineering, Mahidol University, Nakhon Pathom 73170, Thailand
[2] Associate Fellow of Royal Society of Thailand (AFRST), Bangkok 10300 Thailand
[3] Advanced Microfabrication and Biomaterial for Organ-on-chip research unit (AMBiO), Faculty of Engineering, Mahidol University, Nakhon Pathom 73170, Thailand
[*] Corresponding author: mali.hun@mahidol.edu

ABSTRACT

Silver is extensively used in industry and usually discharged in processed effluent. Therefore, an effective process to recover silver is required in order to conserve mineral resources. Silver recovery photocatalysts use light to increase the extraction process efficiency from wastewater. TiO_2 nanoparticles (NPs) are frequently used because of their capacity to produce reactive species when exposed to ultraviolet light. To recover silver ions from jewelry plating effluent using UV light irradiation, TiO_2 NPs were prepared in this work by the hydrothermal process. The morphology and photocatalytic activity were compared with those of commercial TiO_2 NPs. The preliminary results demonstrated that the as-synthesized TiO_2 NPs had a low crystallinity and a small crystallite size with an anatase/brookite mixed phase. In addition, it had superior textural qualities and a lower bandgap value (3.14 eV) than the commercial TiO_2 (3.24 eV). About 100% of the silver was recovered in 3 h using an as-synthesized TiO_2 NPs, which was higher than the photocatalytic activity for silver recovery of the commercial one. Concentrations of hole scavenger and silver ions in effluent importantly affected the photocatalytic performance of as-synthesized TiO_2 NPs.

Keywords: Photocatalyst; Titanium dioxide; Hydrothermal method; Silver recovery; Hole scavenger

1. INTRODUCTION

A precious metal that is widely used in many different industries, such as electronics, jewelry, coinage, photovoltaics, and healthcare is silver (Ag) [1, 2]. Given its special qualities, which include excellent electrical conductivity, corrosion resistance, and antibacterial characteristics, it is applied in many applications. However, the growing demand for silver presents problems with regard to environmental issues and the sustainability of resources. Silver recovery from industrial effluents is crucial, especially from jewelry plating operations. If it is not adequately handled, silver ions found in wastewater can seriously affect the ecosystem and are harmful to aquatic life. Therefore, efficient silver recovery techniques are essential to reduce the environmental impact and recover it.

A potential technique for environmental conservation, particularly in the recovery and degradation of contaminants is the photocatalytic process. Light and photocatalyst are used in photocatalysis to speed up the chemical processes. Electron-hole pairs are produced when light excites electrons from the valence band (VB) to the conduction band (CB). At CB, electrons (e^-) propel the reduction reaction, whereas at VB, holes (h^+) enhance oxidation reaction [3]. Water treatment, in particular metal the recovery (silver cyanide), is the special focus of this effort. Titanium dioxide (TiO_2) has drawn much interest as a potent photocatalyst because of its high oxidizing capability, high chemical stability, and low toxicity [3, 4], its capacity to capture solar energy and ability to produce oxidizing agent [5, 6]. However, some variables, including the synthesis process, the presence of hole scavengers, and the initial concentrations of silver ions, affect the activity TiO_2 photocatalyst.

This study was conducted to synthesize TiO_2 NPs by the hydrothermal method for photocatalytic silver recovery from jewelry plating effluent. Effect of catalyst morphology on the photocatalytic activity was explored. Additionally, effects of hole scavenger concentrations and silver ion concentrations in effluent were also examined.

2. EXPERIMENTAL

2.1 Chemicals and materials

In this research, the utilized effluent was kindly offered from jewelry plating industry. For commercial semiconductors, titanium (IV) oxide (TiO_2 or P25,

Sigma-Aldrich, ≥ 99.5%) was utilized. Also, TiO_2 NPs were synthesized using titanium (IV) isopropoxide ($C_{12}H_{28}O_4Ti$, Sigma-Aldrich, ≥ 97.0%), 2-propanol (C_3H_8O, QReC, AR grade, 99.7%), and hydrochloric acid (HCl, QReC, AR grade, 37%). Ethanol (C_2H_6O, QReC, AR grade, 99.9%) and distilled water were used for the synthesis of materials and photocatalytic experiments.

2.2 Synthesis of TiO_2 photocatalysts

The TiO_2 photocatalyst was synthesized using a hydrothermal method adapted from Zaw et al., 2019 [7]. First, 8.9 mL of titanium (IV) isopropoxide was mixed with 11.5 mL of 2-propanol in a Teflon-lined cylinder and stirred at 400 rpm until the well-mixed solution was obtained. Then, 50 mL of distilled water was added dropwise while maintaining stirring at 400 rpm for 4 h. Subsequently, 1 mL of 3M HCl was introduced into the mixture and stirred for an additional 1 h. The resulting solution was transferred to a stainless-steel autoclave containing the Teflon-lined cylinder and heated at 200°C for 2 h in an oven (Memmert UF55). After the reaction and cooldown overnight, the sample was separated by centrifuge (Allegra X-30R, Beckman Coulter) at 9000 rpm for 15 min, washed three times with ethanol and twice with distilled water, and then dried at 100°C for 12 h.

2.3 Characterizations

The X-ray diffractometer (XRD, Bruker D2 Phaser, Bruker, Switzerland) was used for analyzing the crystallite structures of commercial and synthesized TiO_2 using Cu Kα radiation (λ = 0.15406 Å) using an integrating sphere and barium sulfate as a reference material. Ultraviolet-visible spectrophotometry (UV-Vis, UV-2600, Shimadzu Corporation, Japan) was used to examine the light absorption characteristics of the synthesized catalyst. A photoluminescence spectrometer (AvaSpec-2048TEC-USB2-2, Avantes, Russia) was used to measure the qualitative recombination rate of the electron-hole pair using an excitation wavelength of 255 nm. N_2 adsorption-desorption isotherms were analyzed by TriStar II Plus 3.00, Micromeritics, United States. The surface area was calculated using the Brunauer-Emmett-Teller (BET) theory, and the pore size distribution was calculated using the Barrett-Joyner-Halenda (BJH) theory. The lattice spacing of the synthesized catalyst was examined using high-resolution Transmission Electron Microscopy (HRTEM, JEM-3100F, JEOL Ltd.)

2.4 Photocatalytic activity test

The experiment was conducted in a double-wall cylindrical glass reactor and used ethanol as a hole scavenger. A high-pressure Hg lamp (200-600 nm) was turned on at a light intensity of 5.8 mW/cm^2. The photocatalytic activity of commercial TiO_2 (Com-TiO_2) and synthesized TiO_2 (Syn-TiO_2) catalysts was evaluated for silver ion recovery from effluent using a double-wall cylindrical glass reactor. The experiment involved mixing 163 mL of effluent with distilled water and ethanol, stirring at 400 rpm for 5 min. The required quantity of TiO_2 catalyst was then added, followed by 30 min of stirring in the dark. A high-pressure Hg lamp was then illuminated, and an 5 mL of samples were collected at predetermined intervals up to 120 min. After filtration through a nylon filter, silver ion concentrations were measured using Flame Atomic Absorption Spectroscopy (FAAS, PinAAcle 900T, PerkinElmer). The procedure was repeated by replacing the commercial TiO_2 with the synthesized TiO_2.

3. RESULTS AND DISCUSSION

3.1 Characterization of catalysts

XRD was used to examine the crystal structure of both commercial and synthesized TiO_2 catalysts, as shown in Figure 1(a). According to PDF reference number 01-070-47348, the commercial TiO_2 catalysts showed diffraction peaks at 2θ angles of 25.3°, 37.9°, 48.0°, 53.9°, 55.3°, 62.9°, 68.7°, and 75.0°, which corresponded to the (101), (004), (200), (105), (211), (204), (116), and (215) planes of TiO_2 with an anatase crystal structure. Furthermore, according to PDF 01-079-6029, a peak at 2θ = 27.5° was detected, corresponding to the (110) plane of TiO_2 with a rutile crystal structure. The synthesized TiO_2 catalysts showed diffraction peaks of anatase TiO_2. Additionally, the (211) plane of TiO_2 with a brookite crystal structure, as shown by PDF 03-065-2448, was also appeared at 2θ = 30.8°. By Scherrer equation, the crystallite sizes of TiO_2 photocatalysts were calculated and listed in Table 1. It can be seen that the synthesized TiO_2 exhibited a small crystalline size compared with the commercial TiO_2

UV-Vis spectroscopy was used to determine the light-absorption capacity of commercial and synthesized TiO_2 catalysts over a wide wavelength range of 200 to 800 nm. All photocatalysts exhibited considerable UV light sensitivity, meaning that they can absorb light at wavelengths below 400 nm (λ < 400 nm) and can't absorb light at wavelengths above 400 nm, as shown in Figure 1(b). By Tauc equation [8], the bandgap values were estimated and listed in Table 1. It can be seen that the bandgap of commercial TiO_2 is higher than that of synthesized TiO_2, which affects the light absorption efficiency and performance of the photocatalysts in photocatalytic processes. Commercial TiO_2 may efficiently absorb light in the higher-energy UV range, while synthesized TiO_2 might work well in the UV range with lower-energy range.

Photoluminescence spectroscopy (PL) is then used to visualize the recombination of electrons and holes. As shown in Figure 1(c), the commercial TiO_2 exhibited a high PL intensity, indicating is high charge carrier recombination rate, likely due to the predominant rutile phase present in the samples [9]. In contrast, the synthesized TiO_2 catalyst showed a

slightly lower PL intensity than the commercial TiO_2. This can be attributed to its mixed-phase composition, which helps to reduce recombination rates.

The next section is an analysis of the surface structure characteristics, including BET surface area, pore volume, and pore size. Figure 1(d) shows the N_2 adsorption/desorption isotherms of commercial and synthesized TiO_2. According to the IUPAC classification, the commercial TiO_2 showed the type III isotherms, referring to the non-porous materials. In contrast, the synthesized TiO_2 showed the type IV isotherm, indicating the presence of mesoporous in its structure [10]. The surface area, pore volume, and pore size of the commercial and synthesized TiO_2 catalysts are shown in Table 1. It can be seen that the synthesized TiO_2 has a surface area approximately 3.8 times higher, a pore volume about 4.5 times greater, and a slightly smaller pore size than the commercial TiO_2. The synthesized TiO_2 has significantly more surface area and pore volume, providing more available surface for reactions, which could enhance its photocatalytic efficiency.

The high-resolution TEM image of synthesized TiO_2 catalyst is shown in Figure 2. A clear lattice spacing of anatase and brookite TiO_2 NPs was observed as 0.35 and 0.29 nm, respectively.

Table 1. Physicochemical properties of commercial and synthesized TiO_2 NPs.

Properties	Com-TiO_2	Syn-TiO_2
Anatase phase (%)	90.5	86.6
Brookite phase (%)	-	13.4
Rutile phase (%)	9.5	-
Crystalline size (nm)	20.06	5.94
Bandgap energy (eV)	3.24	3.14
Surface area (m^2/g)	52.38	201.56
Pore volume (cm^3/g)	0.06	0.27
Pore sizes (nm)	5.43	4.45

3.2 Photocatalytic activity test

3.2.1 Effect of catalyst types

Figure 3(a) demonstrates the photocatalytic activity of commercial and synthesized TiO_2 catalysts at ethanol concentration of 20 vol%. It can be seen that the synthesized TiO_2 catalysts exhibited the highest photocatalytic performance for silver recovery, with approximately 97% of silver recovered within 120 min. In contrast, the commercial TiO_2 catalyst showed a much slower rate of silver recovery, achieving only about 67% even after 120 min. The enhanced performance of the synthesized TiO_2 compared with the commercial TiO_2 was attributed to (i) a mixed anatase/brookite phase, which can promote an efficient charge separation and then reduce the charge recombination, (ii) its small bandgap energy, which can effective capture the incident light, and (iii) its high BET surface area, which provides more active sites for the reactions.

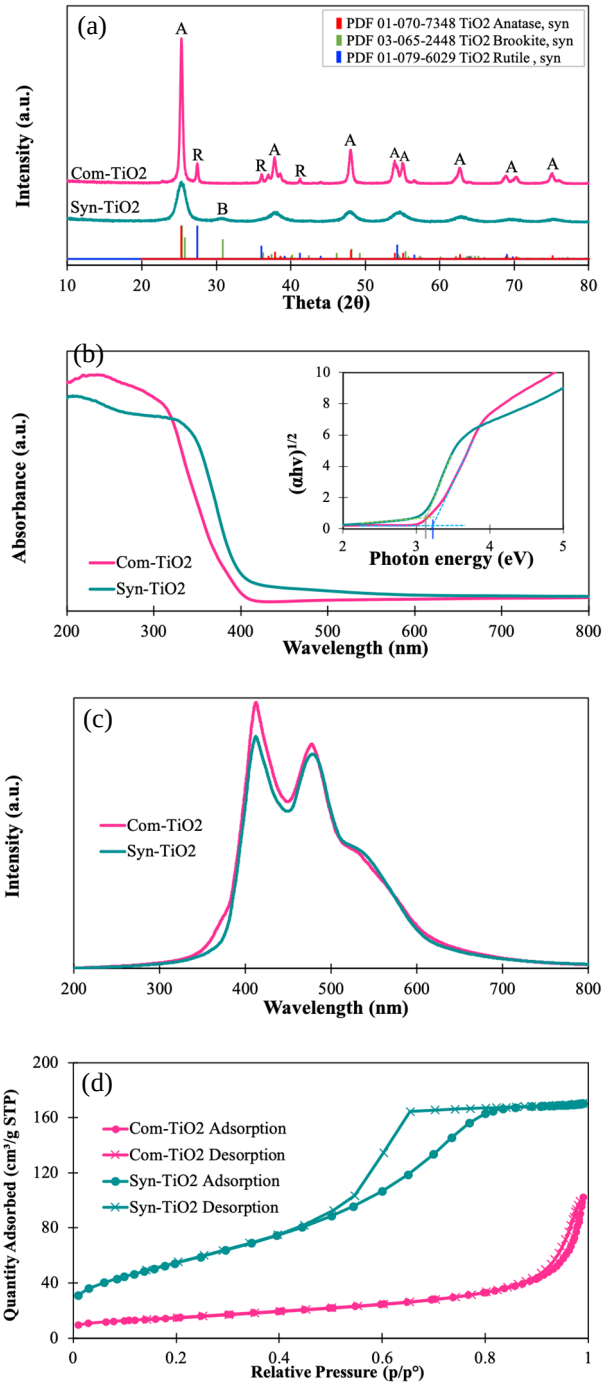

Figure 1. Representative (a) XRD pattern, (b) UV-Vis light absorption, (c) PL emission, and (d) N_2 adsorption/desorption isotherms of commercial and synthesized TiO_2 catalysts.

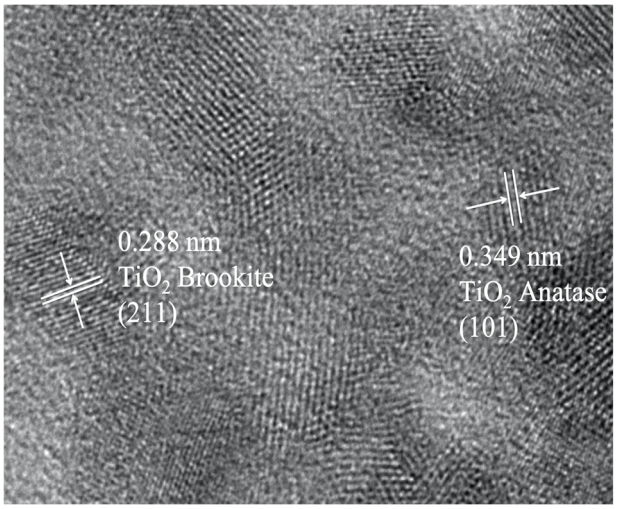

Figure 2. HRTEM of synthesized TiO_2 catalysts.

3.2.2 Effect of concentrations of hole scavenger

Figure 3(b) demonstrates the effect of different ethanol concentrations on the silver recovery percentage of synthesized TiO_2. It can be seen that no silver recovery was observed in the absence of hole scavenger. This is because the photogenerated holes rapidly recombined with electrons, preventing the reduction of silver ions. In the presence of hole scavenger, increasing the ethanol concentration from 10 to 20 vol% increased the silver recovery because ethanol efficiently scavenges photogenerated holes, reducing electron-hole recombination and allowing more electrons to participate in the reduction of silver ions. Further increasing ethanol concentration to 30 vol% decreased the silver recovery percentages. The presence of excessive ethanol inhibits the reaction on the catalyst surface by occupying active sites and interfering with the adsorption of the reactant.

3.2.3 Effect of concentrations of silver ions

Figure 3(c) demonstrates the effect of different initial concentrations of silver ions in effluent on silver recovery by synthesized TiO_2 in the presence of 20 vol% ethanol. It can be seen that, at low concentration (e.g. 40 mg/L), silver recovery rapidly increased within the first 30 min. This is because the low concentration of silver ions allows more efficient interaction between the TiO_2 surface and the photogenerated electrons, leading to a higher reduction rate of silver ion (Ag^+) to metallic silver form (Ag). As the silver ion concentration increased to 160 mg/L, the silver recovery decreased slightly compared to 40 mg/L. This is because, at high concentrations of silver ions, the rate of silver ion reduction was slowed down due to a high probability of ion accumulation on the catalyst surface, which leads to the reduced active sites for further photoreduction. Additionally, high ion concentrations can cause partial blocking of the catalyst surface, resulting in a less efficient reaction. Further increasing the silver ions concentration to 220 mg/L decreased in silver recovery percentages. This is due to the hindrance in light absorption caused by excessive silver deposition on the catalyst surface. The deposited silver can form a shield that blocks incoming light, reducing the efficiency of the photocatalytic process. Additionally, the dense silver layer also interferes the active surface sites of TiO_2, thus limiting the effective interaction between the catalyst and the silver ions.

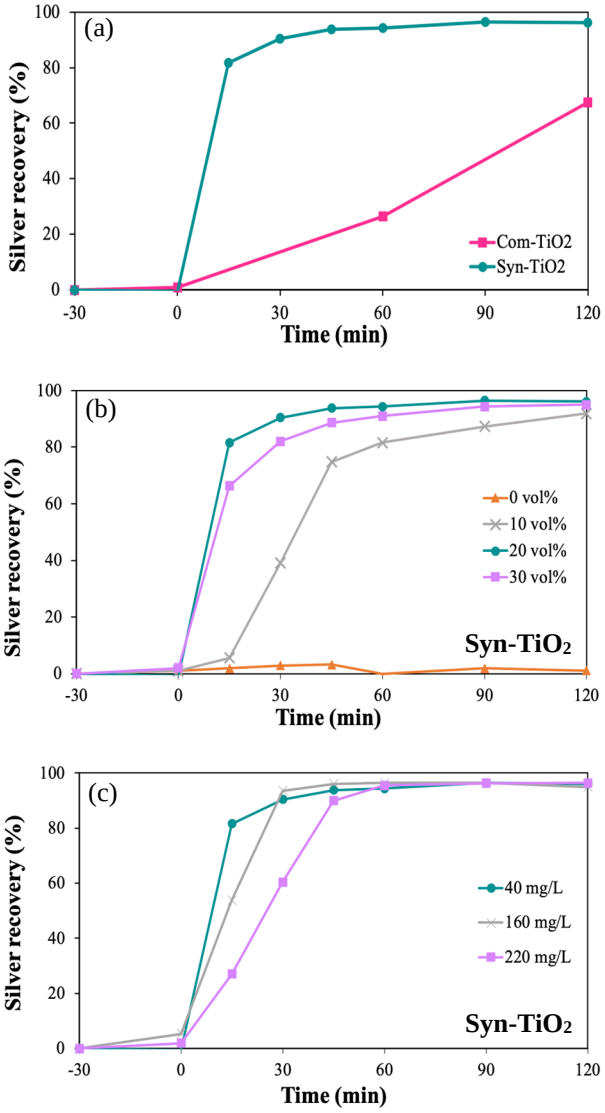

Figure 3. Photocatalytic activity TiO_2 catalysts (a) comparison of commercial and synthesized catalysts, (b) effect of ethanol concentration, and (c) effect of initial silver ion concentration under the UV-vis light intensity of 5.8 mW/cm^2, and photocatalyst loading of 2 g/L.

4. CONCLUSION

The photocatalytic silver recovery was comparatively studied by commercial and synthesized TiO_2 catalysts prepared by the hydrothermal method. It was found that the synthesized TiO_2 catalyst exhibited higher photocatalytic activity than the commercial TiO_2. This enhanced activity was attributed to the presence of anatase brookite mixed phase, its small bandgap value and its good textural property, which can

promote the charge migration, light absorption, and available area to undergo the reactions. An appropriate concentration of hole scavenger significantly improved the photocatalytic silver recovery. However, the photocatalytic activity for silver recovery decreased with the increased concentrations of silver ions in the effluent.

ACKNOWLEDGMENTS

The research project was supported by the Mahidol University (MU's Strategic Research Fund: 2023), Faculty of Graduate Studies, Mahidol University. The author would like to thank the Department of Chemical Engineering, Faculty of Engineering, Mahidol University for equipment and facility supports

REFERENCES

1. Muscetta M, Clarizia L, Race M, Pirozzi F, Marotta R, Andreozzi R, Di Somma I. A novel green approach for silver recovery from chloride leaching solutions through photodeposition on zinc oxide. *J Environ Manage*. 2023; 330: 117075.
2. Ahlatci F, Yazici EY, Yilmaz E, Celep O, Deveci H. A novel method for the recovery of silver from thiosulphate leach solutions using trimercapto-s-triazine (TMT). *Miner Eng*. 2022; 177: 107373.
3. Muhamed AH, Mohamed AE, Marwa RE, Safaa R, Violeta CN, Ahmed EN. Principles of photocatalysts and their different applications: a review. *Top Curr Chem*. 2023; 381(31).
4. Ohama Y, van Gemert D, editors. *Application of titanium dioxide photocatalysis to construction materials: state-of-the-art report of the RILEM Technical Committee 194-TDP*. 2011th ed. Dordrecht, Netherlands: Springer; 2011.
5. Wei Q, Yang D, Fan M, Harris HG. Applications of nanomaterial-based membranes in pollution control. *Crit Rev Environ Sci Technol*. 2013; 43(22): 2389-2438.
6. Nahar S, Zain MFM, Kadhum AAH, Hasan HA, Hasan MR. Advances in photocatalytic CO_2 reduction with water: a review. *Materials (Basel)*. 2017; 10(6): 629.
7. Zaw YIYI. Enhancement of visible-light-driven photocatalytic activity of TiO_2/WO_3 nanocomposite for organic removal [Internet]. Available from: https://nuir.lib.nu.ac.th/dspace/bitstream/123456789/1545/3/YIYIZAW.pdf
8. Makuła P, Pacia M, Macyk W. How to correctly determine the band gap energy of modified semiconductor photocatalysts based on UV–Vis spectra. The Journal of Physical Chemistry Letters. 2018;9(23):6814-7.
9. Anitha B, Khadar MA. Anatase- rutile phase transformation and photocatalysis in peroxide gel route prepared TiO_2 nanocrystals: Role of defect states. Solid State Sciences. 2020;108.
10. Thommes M, Kaneko K, Neimark AV, Olivier JP, Rodriguez-Reinoso F, Rouquerol J, et al. Physisorption of gases, with special reference to the evaluation of surface area and pore size distribution (IUPAC Technical Report). Pure and Applied Chemistry. 2015;87(9-10):1051-69.

Photocatalytic silver recovery from cyanide-based plating effluent via TiO_2 nanoparticles synthesized by microwave-assisted method

Auttawit Thoumrungroj[1], Pimchanok Longchin[1], Mali Hunsom[1,2,3,*]

[1] Department of Chemical Engineering, Faculty of Engineering, Mahidol University, Nakhon Pathom 73170, Thailand
[2] Associate Fellow of Royal Society of Thailand (AFRST), Bangkok 10300 Thailand
[3] Advanced Microfabrication and Biomaterial for Organ-on-chip research unit (AMBiO), Faculty of Engineering, Mahidol University, Nakhon Pathom 73170, Thailand
[*] Corresponding author: mali.hun@mahidol.edu

ABSTRACT

Titanium dioxide (TiO_2) is a common catalyst that is widely used in photocatalytic applications due to its high chemical and thermal resistance, low price and non-toxic. This work was conducted to test the feasibility of silver recovery from the cyanide-based plating effluent of jewelry industry by the photocatalytic process using two types of TiO_2; the commercial TiO_2 (CT) and synthesized TiO_2 by microwave-assisted method (MT). The preliminary results demonstrated that the CT sample illustrated the anatase-rutile mixed phase, while the MT sample possessed the anatase-brookite mixed phase. The MT sample exhibited a comparable bandgap value (~3.06 eV), lower crystallinity, higher BET surface area (~4.4 folds) than the CT sample. The MT sample exhibited a higher silver recovery rate than the CT sample in the presence of a hole scavenger at a low concentration (~10 vol.%) and comparable silver recovery rate in the presence of a high concentration of hole scavenger (~25 vol.%). The presence of $Na_2S_2O_3$ as an additive positively impacted the photocatalytic activity for silver recovery, while the presence of H_2O_2 had a negative impact. Approximately 94.74% of silver was recovered within 30 min in the presence of 0.05 mM $Na_2S_2O_3$. The application of Ag/MT was tested by hydrogen production and decolorization of distillery wastewater.

Keywords: Photocatalyst; Titanium dioxide; Microwave synthesis; Metal recovery; Hole scavenger

1. INTRODUCTION

The silver-plating process, which involves electroplating a base metal with an alkaline cyanide solution, produces wastewater containing heavy metals such as iron, zinc, copper, and silver. Wastewater management presents both environmental and economic concerns, needing effective recovery technologies. Conventional approaches such as chemical precipitation, adsorption and membrane filtration demonstrate high effectiveness but are often costly, generate waste, and require additional treatment [1]. As an alternative, photocatalysis has emerged as a promising technique due to its high efficiency, low energy consumption, and cost-effectiveness, making it an attractive solution for sustainable metal recovery [2]. Photocatalysis is a process where a catalyst is exposed to photon energy that is equal to or greater than its band gap energy. This causes the oxidation of electron, which will transfer from the valence band (VB) to the conduction band (CB). As a result, a hole is created in the VB, acting as an anion, while the electron in the CB acting as a cation. These species can then participate in oxidation and reduction reactions, respectively. Various semiconductor materials such as TiO_2, ZnO, CdS, and PtO have been studied for photocatalytic applications. TiO_2 is popular used due to its low toxicity, high redox potential, stability, and affordability [3]. Various techniques can be used to synthesize a TiO_2 photocatalyst, including hydrothermal, sol-gel, and microwave-assisted hydrothermal (MAH) methods. The MAH method offers several advantages, such as a high reaction rate due to the reduction of the activation energy barrier, high product yield, and high purity since the shorter reaction time minimizes the formation of undesirable products [4]. Additionally, it ensures a homogeneous product by rapidly heating atoms through microwave irradiation, which reduces heat transfer within the molecule. Gilberto et al. [5] investigated a rapid and efficient method for synthesizing high-performance TiO_2 nanoparticles and thin films using colloidal sol-gel and microwave-assisted hydrothermal synthesis. Their results indicated that the synthesized TiO_2 was in the anatase phase, with a crystal size of approximately 7 nm and a specific surface area of 220 m^2/g. Firas et al. [6] synthesized mesoporous TiO_2 hollow spherical nanostructures using a one-step microwave method. The resulting TiO_2 hollow spheres

had the size from 200 to 500 nm, with an average pore diameter of 8 nm, and demonstrated high photocatalytic activity under both ultraviolet and visible light irradiation. TiO_2 has been widely researched for metal recovery, particularly for silver, as its band gap aligns well with the reduction potential of silver cyanide (-0.31 V/NHE), allowing efficient metal deposition. Studies have shown that TiO_2-based photocatalysts can recover up to 99% of silver from simulated wastewater under optimized conditions [7]. Nahyuni et al. [8] successfully recovered silver from radiophotography wastewater containing silver thiosulfate complexes using TiO_2 under UV-A irradiation, further utilizing Ag/TiO_2 nanocomposites for antibacterial applications under visible light, with complete bacterial elimination in contaminated water. López-Munoz et al. [9] explored the photocatalytic degradation of silver cyanide complexes using TiO_2, achieving both cyanide removal and silver recovery under UV light, with oxygen enhancing silver deposition and cyanide oxidation. To enhance silver recovery efficiency, adding a hole scavenger or other additives can improve the reaction. Muscetta et al. [10] investigated the role of ethanol concentration in silver (I) ion photodeposition on ZnO, showing that ethanol acted as a hole scavenger, reducing recombination and enhancing silver recovery. At 1.0 M ethanol, more than 90% silver recovery was achieved within 30 min, compared to 60% recovery in 90 min without ethanol. Han et al. [11] investigated the photolysis of silver–thiosulfate complexes and found that higher thiosulfate concentrations enhanced silver sulfate formation, while lower concentrations minimized Ag_2S formation, crucial for preventing unwanted side reactions.

In this study, TiO_2 was synthesized from titanium (IV) isopropoxide ($C_{12}H_{28}O_4Ti$) using the MAH. Effects of microwave power and microwave treated-cycles were explored. Additionally, different concentrations of ethanol were employed as a hole scavenger to enhance the silver recovery efficiency of the catalyst. The effects of different additives were also investigated by introducing sodium thiosulfate ($Na_2S_2O_3$) and hydrogen peroxide (H_2O_2) into the solution. Furthermore, the performance of the silver-deposited TiO_2 (Ag/MT) catalyst will be evaluated for H_2 production from wastewater.

2. EXPERIMENTAL

2.1 Materials

The chemical utilized in this work were titanium (IV) isopropoxide ($C_{12}H_{28}O_4Ti$, 97%, Sigma Aldrich), commercial TiO_2 (TiO_2, >99.5%, Sigma Aldrich), ethanol (CH_3CH_2OH, 99%, Qrec), sodium thiosulfate ($Na_2S_2O_3$, AR, Kemaus) and argon (UHP, 99.999% Ar, Alternative)

2.2 Synthesis of TiO_2

The synthesis of TiO_2 using a microwave-assisted hydrothermal method began with the preparation of 50 mL of deionized (DI) water, stirred at 700 rpm. Titanium isopropoxide weighed at 8.3388 g, calculated based on a molar ratio of titanium precursor to water of 1:100 was added dropwise into the water to form a white solution, which was stirred for 0.5 h. The solution was then sonicated at a high intensity (D3, GT SONIC) for 1 h before being transferred into a Teflon microwave vessel. The solution was placed in a microwave digestion reactor (Rotor 8 NXF/NXQ, Anton Paar) to initiate the reaction, using 800 W of microwave power for 5 min. This microwave treatment process was repeated three times. The resulting product was washed five times with 35 mL of DI water and centrifuged (5804R, Eppendorf) at 8000 rpm for 5 min each time. The synthesized photocatalyst was then dried at 80°C for 4 h in an oven and labeled as the MT catalyst.

2.3 Photocatalytic silver recovery

The experiment was conducted with silver cyanide complex wastewater with an initial silver concentration of 40 mg/L. A catalyst loading of 2 g/L was dispersed using a stirrer operating at 400 rpm. UV-A irradiation with an intensity of 5.7 mW/cm² was provided by a 400 W high-pressure mercury lamp (RUV 533 BCE). Samples will be collected initially and 30 min before the light source is activated to evaluate the catalyst adsorption. After the light source is turned on, 5 mL of samples will be taken at particular time and filtered using a 0.22 µm nylon filter. The silver concentration was analyzed by flame atomic absorption spectrometry (PerkinElmer, PinAAcle 900T). The MT and commercial TiO_2 (CT) were investigated under different ethanol concentrations of 10 and 25%v/v. After that, the MT photocatalyst was explored with different types of additives including $Na_2S_2O_3$ and H_2O_2 at concentrations of 0.05 mM under the best ethanol concentration. After finding the best condition of additives, the optimal catalyst loading will be explored in the range of 0 – 2 g/L. The used catalyst at an optimum condition will be labelled as Ag/MT.

2.4 Application of resulting Ag/MT

The application of resulting Ag/MT was conducted for simultaneous H_2 production and decolorization of distillery wastewater. H_2 production will be carried out using Ag/MT with a catalyst loading of 1 g/L in 200 mL of distillery effluent wastewater containing 20% v/v of ethanol. The mixture will be stirred at 400 rpm. The experiment began by purging the reactor with Ar at a flow rate of 500 mL/min for 30 min to eliminate air from the reactor. Subsequently, either LED UV or LED full visible light (VIS) will be activated, respectively providing an intensity of 2.3 mW/cm² for LED UV and approximately 200,000 lux for LED VIS at the center of the reactor. The light source was irradiated on for 4 h to activate the catalyst. Finally, a gas sample will be

collected by flushing the reactor with Ar at a flow rate of 500 mL/min for 1 min into a gas bag, followed by analysis of the gas sample using gas chromatography (Shimadzu, GC-2014). The feed solution and final solution will be sampled for 5 mL and filtered by 0.22 µm nylon filter. The absorbance of samples were analyzed using ultraviolet-visible spectrophotometer at 525 nm (UV-2600i Spectrophotometer, Shimadzu Corporation) to obtain the level of decolorization.

2.5 Characterization

Various techniques were employed to characterize the morphology and an optical property of employed catalysts. The phase diffraction analysis was performed at room temperature by XRD analysis using Bruker D2 PHASER instrument (Bruker, Switzerland) with Cu Kα radiation (λ = 0.15406 Å) operated at 40 kV and 50 mA. The light absorption of catalysts was measured using a UV-2600i Spectrophotometer (Shimadzu corporation, Japan). The surface properties were investigated using TriStar II Plus Analyzer (Micromeritics, United States). The measurements were operated based on 99.999% pure N_2 adsorption using Brunauer-Emmett-Teller (BET) process. The morphology and crystallinity of the catalyst, along with the size of the silver deposited on its surface, were analyzed using high-resolution transmission electron microscopy (HRTEM) with a JEM-3100F 300 kV field emission electron microscope (JEOL Ltd., Japan). A photoluminescence (PL) spectrometer (AvaSpec-2048TEC-USB2-2, avantes, Russian) was employed to record the photoluminescence spectra of the powders.

3. RESULTS AND DISCUSSION

The wastewater used in this work was kindly offered from jewelry plating plant. The color of the raw wastewater is yellow brown. Normally, the discharge concentration of silver in wastewater is obtained in the form of silver cyanine complex ($[Ag(CN)]_2^-$) with the few contents of other metal ion as shown in Table 1.

Table 1. Properties of silver wastewater from jewelry plating wastewater.

Parameters	Value
pH	~ 8
Silver ion (Ag^+, mg/L)	~ 40
Copper ion (Cu^{2+}, mg/L)	< 0.210
Iron ion (Fe^{3+}, mg/L)	< 0.030
Zinc ion (Zn^{2+}, mg/L)	< 0.012
Nickel ion (Ni^{2+}, mg/L)	< 0.003

3.1 Property of photocatalyst

The crystal structure and phase of MT and CT photocatalysts were analyzed by the XRD analysis as shown in Figure 1. The CT catalyst shows peaks at 25.4º, 38.1º and 48.0º, relating to the (101), (004) and (200) crystal plane of anatase phase TiO_2 (PDF 01-070-7348) [6] and at 27.33º, 35.90º, and 41.15º, relating to the (110), (101) and (111) crystal planes of the rutile TiO_2 (PDF 01-079-6029) [12]. Its anatase/rutile phase composition was found to be 83.40:16.60. For MT catalyst, it shows the XRD peak at 25.4º, 38.1º and 48.0º, relating to the (101), (004) and (200) crystal plane of anatase phase TiO_2 (PDF 01-070-7348) [6] similar to these of CT catalyst. But, an additional XRD peak at 2θ of 30.8º was detected, corresponding to a brookite TiO_2 (PDF 01-071-6409). The MT sample had an anatase and brookite phase at a ratio of 93.02:6.98. By Scherrer's equation, MT photocatalyst showed a small crystalize size at 5.23 nm compared to that of CT (21.4 nm).

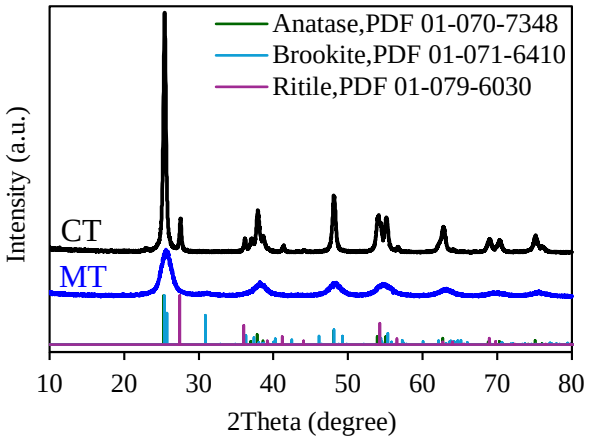

Figure 1. XRD analysis of all photocatalysts.

The light absorption capacity of all catalysts was conducted by the UV-vis analysis as shown in Figure 2. The results indicated that both catalysts were active under the UV irradiation. By a Tauc's equation, the MT and CT sample exhibited a band gap energy around 3.08-3.10 eV.

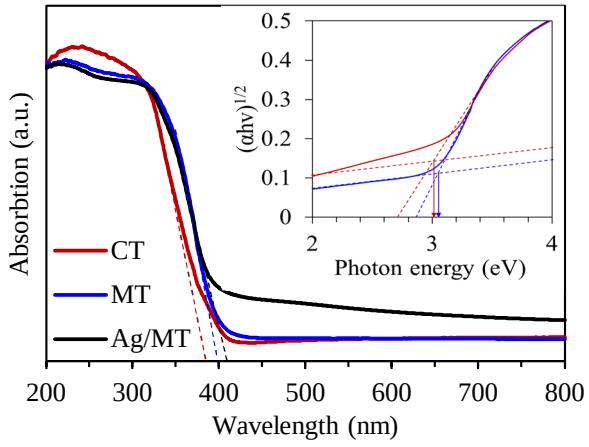

Figure 2. Light absorption capacity of all catalysts.

Figure 3 shows the N_2 adsorption/desorption isotherms of all catalysts. The CT catalyst showed the type IV isotherm, but less pronounced hysteresis

characteristics, indicating a less developed mesoporous structure and low surface area [13]. The MT catalyst also exhibited the type IV isotherm with an H2-type hysteresis loop, identifying as mesoporous materials with narrow necks and wider bodies [6]. The capillary condensation presented as a monolayer formation within the mesopores was demonstrated by the pressure change between P/P_0 of 0.5 and 0.8 [14]. Qualitatively, the MT catalyst had a much larger specific surface area compared to the CT catalyst, with smaller average pore size and higher pore volume as shown in Table 2. These characteristics may provide (MT catalyst) more active sites for photocatalytic reactions and better accessibility for reactants during the silver recovery process [15].

Table 2. BET analysis result of all catalysts.

Samples	Surface area (m^2/g)	Pore size (nm)	Pore volume (cm^3/g)
CT	54.4	12.45	0.1525
MT	239.4	4.17	0.2992
Ag/MT	232.6	4.28	0.2983

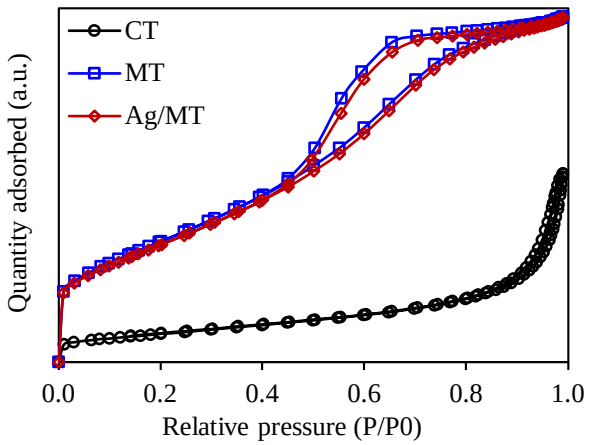

Figure 3. N_2 adsorption/desorption isotherms of all catalysts.

Figure 4 demonstrates the PL analysis of all catalysts with the excitation wavelength of 255 nm. The CT catalyst exhibited a higher PL intensity than MT, indicating its higher electron-hole recombination rate. This is probably due to the presence of the rutile phase in CT, which can induce a faster recombination of charge carriers [12]. A high recombination rate negatively impacts the efficiency of the photocatalytic process, as fewer electrons are available for redox reactions. In comparison, a low PL intensity of MT reflected its ability to suppress the electron-hole recombination. This enhancement is attributed to the presence of high anatase content and mixed-phase composition (anatase and brookite) in MT sample which can promote an efficient charge separation and reduce the recombination rates of charge carries.

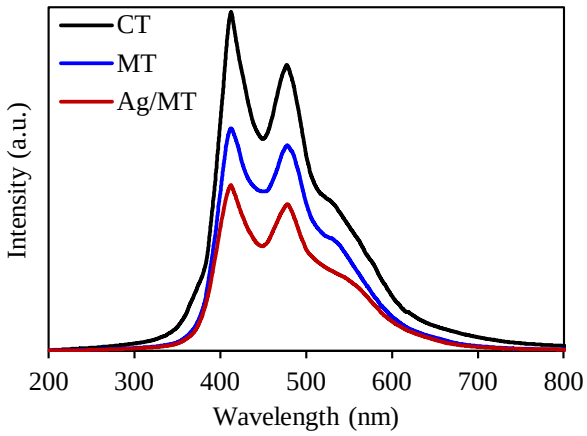

Figure 4. Photoluminescence of all catalysts.

3.2 Photocatalytic silver recovery

The effect of hole scavenger on silver recovery efficiency with different catalysts was first explored using ethanol (EtOH) at concentrations of 10 and 25%v/v. As shown in Figure 5(a), at 10% EtOH, the MT catalyst demonstrated significantly higher silver recovery efficiency (~83%) compared to the CT catalyst under the same conditions. This superior performance of the MT catalyst was attributed to various parameters including a higher charge separation efficiency, the phase junction of anatase and brookite phase, the absence of rutile phase and a small crystallize size [16, 17]. The mixed-phase between anatase and brookite phase composition may promote efficient charge separation at the interfaces between the two phases, reducing electron-hole recombination rate [18]. On the other hand, the presence of rutile phase decrease the efficiency of CT sample. This is because the rutile phase typically exhibits a faster electron-hole recombination than anatase [19]. Also, by the surface properties, the MT catalyst demonstrated a much larger specific surface area compared to CT, along with smaller pore size and higher pore volume. These features provided more active sites for photocatalytic reactions, which is critical for silver recovery [20]. However, both catalysts exhibited slightly low recovery efficiencies at this concentration due to the limited availability of EtOH in the system, which restricted its ability to effectively scavenge holes and promote charge separation. When the EtOH concentration was increased to 25%, both MT and CT catalysts achieved nearly identical silver recovery efficiencies (~98%) within 180 min (Figure 5 (b)). A higher EtOH concentration provided sufficient scavenging capacity to enhance the charge separation for both catalysts, leading to improved photocatalytic performance. This indicated that the limitation at 10% EtOH was primarily due to insufficient scavenger availability rather than intrinsic differences in catalyst properties. However, the MT catalyst offers a significant cost advantage, being approximately 3.5 times cheaper than the CT catalyst (Table 3). Based on these results, the MT catalyst was

selected for further experiments due to its superior performance at lower EtOH concentrations and its economic feasibility.

Table 3. Cost estimation of MT photocatalyst.

Catalysts		Total price (baht/g)	
MT	Raw material	22.99	26.73
	Utility	3.74	
CT	92.02		

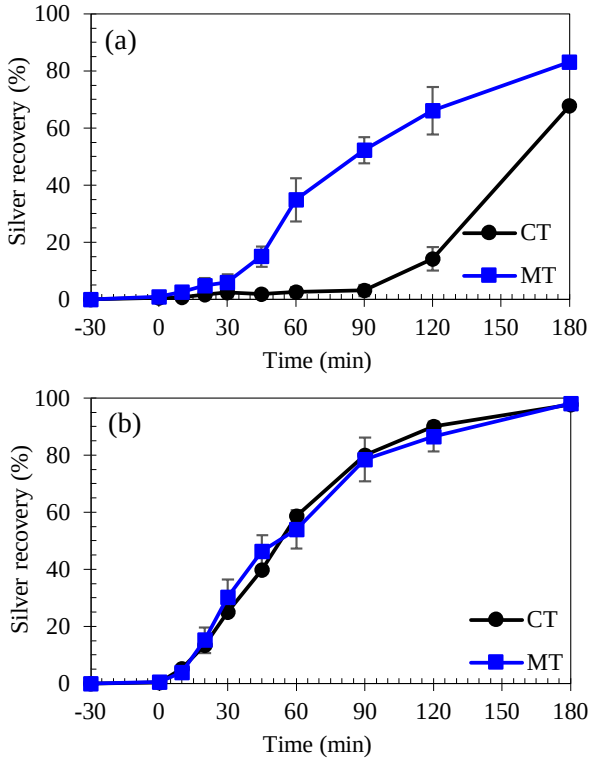

Figure 5. Photocatalytic silver recovery with different catalysts in the present of hole scavenger concentrations of (a) 10 v/v% and (b) 25 v/v%.

The effect of additives on the silver recovery was investigated by using $Na_2S_2O_3$ and H_2O_2. As shown in Figure 6, the present of $Na_2S_2O_3$ significantly enhanced the reaction rate of silver recovery from 30% to 83–95% within 30 min. This improvement is attributed to the ability of $Na_2S_2O_3$ to convert the $[Ag(CN)]_2^-$ complex (+0.373 V/NHE) to silver thiosulfate complex ($[Ag(S_2O_3)_2]^{3-}$, +0.016 V/NHE), which has a more positive reduction potential than the $[Ag(CN)]_2^-$ complex, leading to an improved silver recovery efficiency [21]. However, at excessively high $Na_2S_2O_3$ concentration, the silver recovery rate did not further increase, likely due to the limited availability of active sites on the catalyst surface for the reaction. In contrast, the addition of H_2O_2 as an additive reduced silver recovery efficiency to around 10%. This is because H_2O_2 can react with electrons at conduction band (CB) to produce hydroxyl ions (OH^-), which then compete with silver ions to receive electrons [22, 23].

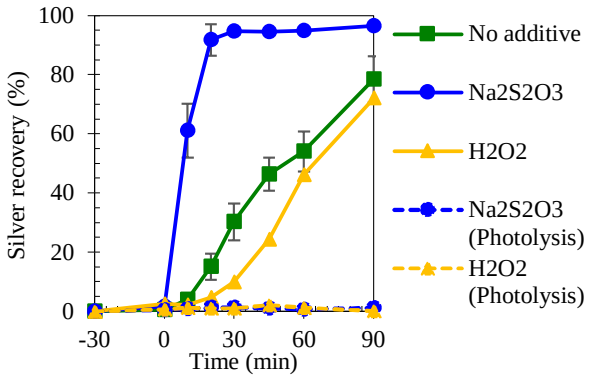

Figure 6. Effect of additives on the photocatalytic silver recovery via MT catalyst.

The effect of catalyst loading on silver recovery efficiency was investigated by varying the catalyst concentration from 0.0 to 2.0 g/L. At high catalyst loading levels (>1.0 g/L), the silver recovery rate reached approximately 95% within 30min (Figure 7), showing no significant improvement beyond this point. This limitation in recovery efficiency was attributed to the limitation of photon availability in the system. That is, excess catalyst did not receive sufficient light to activate the reaction and also induced the light scattering in the reactor [12]. Conversely, at low catalyst loading levels (<1.0 g/L), the silver recovery rate was limited to around 80% within the same timeframe due to the reduced number of active sites available for the reaction [10].

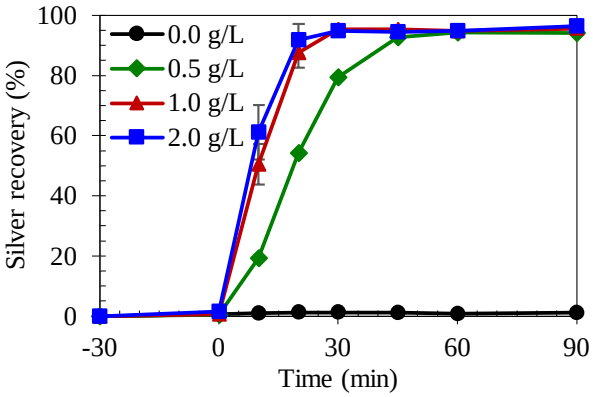

Figure 7. Effect of MT catalyst loading on the photocatalytic silver recovery.

3.3 Properties and possible application of Ag/MTP

The properties of the Ag/MT catalyst were analyzed using various techniques. The BET analysis exhibited slight decrease in surface area approximately 6.8 m^2/g (Table 2) due to the deposition of silver on the catalyst surface. To confirm the deposition of silver on the surface of the MT catalyst, HRTEM analysis was conducted. The results clearly indicated that silver elements were successfully decorated on the catalyst surface as shown in Figure 8. Additionally, the lattice fringes corresponding to the anatase TiO_2 and silver

component were observed at 0.35 nm and 0.22 nm [24]. Furthermore, Ag/MT catalyst possessed a decrease in the PL intensity even further compared to MT. This is because silver nanoparticles can act as electron traps at the CB, effectively holding electrons and reducing their recombination with holes. Moreover, the Ag/MT catalyst exhibited a localized surface plasmon resonance (LSPR) effect, which enhanced the visible-light absorption and facilitated a hot electron generation, thereby improving photocatalytic efficiency under visible light irradiation [25, 26]. The band gap energy of the Ag/MT catalyst was determined to be 3.05 eV, showing a slight decrease compared to the fresh MT catalyst.

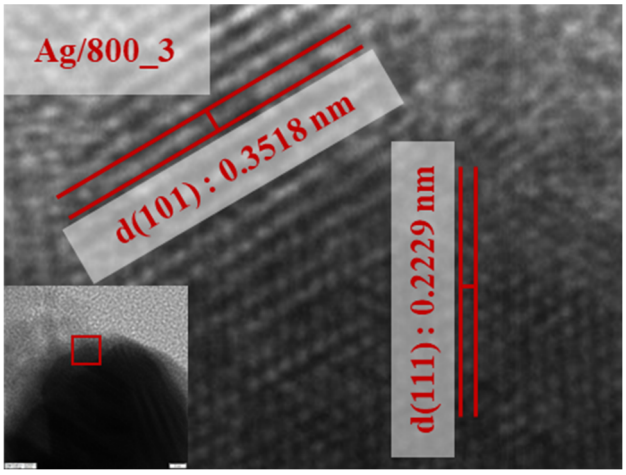

Figure 8. TEM image of Ag/MT catalyst.

The H_2 production and discoloration of real wastewater were studied by the Ag/MT catalyst obtained from the silver recovery process. As shown in Figure 9, the Ag/MT catalyst successfully generated approximately 90 µmol/$g_{catalyst}$ of H_2 under UV light but failed to produce H_2 under visible light (VIS). Despite the lack of H_2 production under VIS, the Ag/MT catalyst demonstrated effective discoloration of real wastewater under both UV and VIS irradiation. This is attributed to dual function of decorated silver as charge separation promotor and light absorption promoter [27]. That is, the doped silver on the catalyst surface effectively retains excited electrons, enhancing their reaction with water to produce H_2 under UV light and promotes degradation reactions by generating reactive oxygen species (ROS) such as hydroxyl radicals ($OH^{\cdot}$) and superoxide anions (O_2^{-}), which are highly effective in breaking down organic pollutants [28]. However, under VIS, the LSPR behavior primarily induces oscillating motions of conduction electrons near the silver surface, which enhances visible-light absorption but does not provide sufficient energy to drive the H_2 evolution reaction [26]. For decolorization of wastewater, the LSPR effect further enhanced the visible-light-driven photocatalytic activity, enabling the catalyst to decolor wastewater by a facilitating small charge separation through the oscillatory motion of silver electrons on the catalyst surface [29].

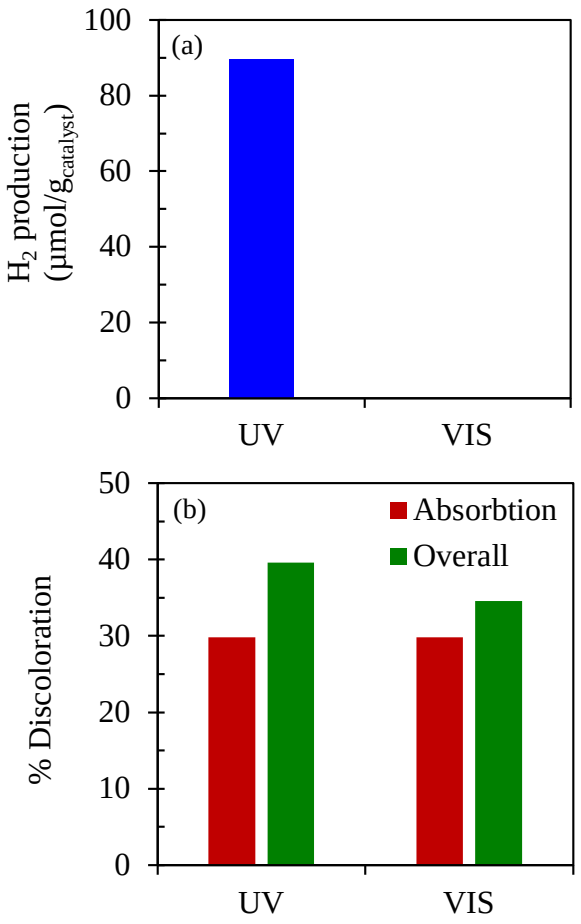

Figure 9. (a) Hydrogen production and (b) decolorization of real wastewater by Ag/MT catalyst.

4. CONCLUSION

The TiO_2 catalyst was synthesized using the MAH technique in the absence of dispersants. The MT catalyst demonstrated a higher performance than CT based on various characteristics, including its mesoporous structure with a high surface area, high charge separation efficiency, anatase-brookite phase combination, and small crystallite size. Silver recovery from a real cyanide-based plating bath was successfully achieved using the MT catalyst with high efficiency under optimal conditions, and low synthesis cost compared to the CT catalyst. Additionally, the Ag/MT catalyst exhibited the photocatalytic activity for simultaneous H_2 production and color reduction in real wastewater under UV light irradiation.

ACKNOWLEDGMENTS

The research project was supported by the Mahidol University (MU's Strategic Research Fund: 2023) and partially supported by The 60th Year Supreme Reign of His Majesty King Bhumibol Adulyadej Academic Year 2023, Faculty of Graduate Studies, Mahidol University. The author would like to thank the Department of Chemical Engineering, Faculty of Engineering, Mahidol University for equipment and facility supports.

REFERENCES

1. B. Van Der Bruggen, C. Vandecasteele. A review of pressure-driven membrane processes in wastewater treatment and drinking water production. *Environmental Progress*. 2003;22(1): 46–56.
2. M. Ding, W. Qiu. Recovery of silver metal from low concentrated wastewater by photocatalysis. *International Journal of Modern Physics B*. 2015;29(15): 1540028.
3. C.-Y. Hsu, W.-H. Lin. Nano titanium oxide (nano-TiO_2): A review of synthesis methods, properties, and applications. *Case Studies in Chemical and Environmental Engineering*. 2024;9: 100626.
4. A. Kumar, H. Mutreja. Microwave chemistry, recent advancements, and eco-friendly microwave-assisted synthesis of nanoarchitectures and their applications: a review. *Materials Today: Nano*. 2020;11: 100076.
5. G. Santalucia, M. Borlaf. Microwave-assisted synthesis of TiO_2 nanoparticles. *Journal of Nanoparticle Research*. 2018;20(2): 42.
6. F.K. Alosfur, B. Omar. One-step formation of TiO_2 hollow spheres via a facile microwave-assisted process for photocatalytic activity. *Nanotechnology*. 2018;29(14):145707.
7. M. Huang, C. Chen. Removal of silver in photographic processing waste by TiO_2-based photocatalysis. *Environmental Science & Technology*. 1996;30(10): 3084–3088.
8. E.T. Wahyuni, M. Rachmawati. Preparation of TiO_2/AgNPs by photodeposition method using Ag(I) present in radiophotography wastewater and their antibacterial activity in visible light illumination. *Journal of Environmental Chemical Engineering*. 2019;7(4): 103226.
9. M.J. López-Muñoz, A. Morcillo. Simultaneous photocatalytic reduction of silver and oxidation of cyanide from dicyanoargentate solutions. *Applied Catalysis B: Environmental*. 2009;86(1): 53–62.
10. M. Muscetta, R. Cipullo. A novel green approach for silver recovery from chloride leaching solutions through photodeposition on zinc oxide. *Journal of Environmental Management*. 2023;330: 117075.
11. C. Han, Y. Zhao. A kinetic and mechanism study of silver-thiosulfate complex photolysis by UV-C irradiation. *Hydrometallurgy*. 2020;191: 105212.
12. N. Posachayanan, M. Sillanpää. Highly-efficient recovery of silver from industrial cyanide-based plating effluent on TiO_2/activated carbon composites. *Chemosphere*. 2024;367: 143614.
13. N. Kunthakudee, A. Jutarosaga. Photocatalytic recovery of gold from a non-cyanide gold plating solution as Au nanoparticle-decorated semiconductors. *ACS Omega*. 2022;7(9):7683–7695.
14. R. Nawaz, A. Rauf. Glycerol-mediated facile synthesis of colored titania nanoparticles for visible light photodegradation of phenolic compounds. *Nanomaterials*. 2019;9(11): 1586.
15. X. Jia, B. Wang. Microwave-assisted synthesis of anatase TiO_2 nanorods with mesopores. *Nanotechnology*. 2007;18(7): 075602.
16. Q. Tay, Z. Chen. Enhanced photocatalytic hydrogen production with synergistic two-phase anatase/brookite TiO_2 nanostructures. *The Journal of Physical Chemistry C*. 2013;117(29): 14973–14982.
17. D.R. Eddy, M. Ikram. Heterophase polymorph of TiO_2 (anatase, rutile, brookite, TiO_2(B)) for efficient photocatalyst: fabrication and activity. *Nanomaterials*. 2023;13(4): 704.
18. P. Du, J. Sun. Constructing anatase–brookite TiO_2 phase junction by thermal topotactic transition to promote charge separation for superior photocatalytic H_2 generation. *The Journal of Physical Chemistry Letters*. 2022;13(19): 4244–4250.
19. J. Zhang, Y. Wu. New understanding of the difference of photocatalytic activity among anatase, rutile and brookite TiO_2. *Physical Chemistry Chemical Physics*. 2014;16(38): 20382–20386.
20. S.R. Damkale, A.M. Mulla. Highly crystalline anatase TiO_2 nanocuboids as an efficient photocatalyst for hydrogen generation. *RSC Advances*. 2021;11(13): 7587–7599.
21. N.A.D. Ho, S. Babel. Electrochemical reduction of different Ag(I)-containing solutions in bioelectrochemical systems for recovery of silver and simultaneous power generation. *RSC Advances*. 2019;9(52): 30259–30268.
22. D. Dvoranová, E. Brezová. EPR investigations of polymeric and H_2O_2-modified C_3N_4-based photocatalysts. *Journal of Photochemistry and Photobiology A: Chemistry*. 2019;375: 100113.
23. E.M. Cuerda-Correa, M.F. Alexandre-Franco. Advanced oxidation processes for the removal of antibiotics from water: An overview. *Water*. 2020;12(1): 102.
24. H. Yang, H. Wang. Preparation and antibacterial activities of $Ag/Ag^{+}/Ag^{3+}$ nanoparticle composites made by pomegranate (*Punica granatum*) rind extract. *Results in Physics*. 2016;6: 299–304.
25. S. Khanam, S.K. Rout. Plasmonic metal/semiconductor heterostructure for visible light-enhanced H_2 production. *ACS Omega*. 2022;7(29): 25466–25475.
26. Z. Ye, Y. Zhang. Exploiting the LSPR effect for an enhanced photocatalytic hydrogen evolution reaction. *Physical Chemistry Chemical Physics*. 2023;25(4): 2706–2716.

27. R. Saravanan, V. Karthikeyan. Mechanothermal synthesis of Ag/TiO_2 for photocatalytic methyl orange degradation and hydrogen production. *Process Safety and Environmental Protection*. 2018;120: 339–347.
28. Y.-K. Park, C. Kim. Characteristics of hydrogen production by photocatalytic water splitting using liquid phase plasma over Ag-doped TiO_2 photocatalysts. *Environmental Research*. 2020;188: 109630.
29. S. Lv, Y. Zhao. Review on LSPR-assisted photocatalysis: effects of physical fields and opportunities in multifield decoupling. *Nanoscale Advances*. 2022;4(12): 2608–2631.

Effect of activation method on biochar supported nickel catalysts performance in steam reforming of biomass-derived tar

Nutcha Jirundorn[1], Prapan Kuchonthara[1,2,3,*]

[1] Department of Chemical Technology, Faculty of Science, Chulalongkorn University, Bangkok 10330, Thailand
[2] Center of Excellence on Petrochemical and Materials Technology, Chulalongkorn University, Bangkok 10330, Thailand
[3] Center of Excellence in Catalysis for Bioenergy and Renewable Chemicals (CBRC), Chulalongkorn University, Bangkok 10330, Thailand
[*] Corresponding author: prapan.k@chula.ac.th

ABSTRACT

Biochar derived from biomass pyrolysis has potential as a support for metal catalysts in tar reforming. However, the limited specific surface area and pore volume of biochar restrict its use as a catalyst support. Activating biochar, particularly through chemical methods, can improve its surface properties. However, using harmful chemicals in the chemical activation raises sustainability concerns. In contrast, physicochemical activation provides a more sustainable approach by minimizing the reliance on harmful chemicals through oxidizing agents. Therefore, this research focuses on the effect of different activation methods (physical, chemical, and physicochemical) on the catalytic performance of biochar-supported nickel catalysts in steam gasification. Additionally, the effect of processing parameters, including the KOH to char ratio and pyrolysis temperature, on gas yield in tar steam reforming. The gasification was carried out in a two-stage fixed-bed reactor. The first stage was the pyrolysis process, which varied the temperature (600, 700, or 800 ^{o}C), while the temperature of the second stage, the tar reforming zone, was kept at 700 ^{o}C. Steam was introduced into the second zone at a flowrate 0.3 mL/min. The mass ratio of biomass feed to catalyst was kept constant at 1:2 (g/g). Activated biochar was characterized using BET, SEM, and FTIR. Ni-loaded biochars were characterized by XRD. Gas products were analyzed by GC. The results indicate that the Ni-loaded physiochemically activated biochar achieved the highest gas yield (20.66 mmol/g of biomass) and maximum hydrogen generation (9.63 mmol/g of biomass) at 700 °C.

Keywords: Activated biochar; Physicochemical activation; Tar reforming; Gasification.

1. INTRODUCTION

Carbon dioxide in the atmosphere acts as a heat trap, with higher concentrations trapping more heat and gradually raising global temperatures. Global carbon emissions from fossil fuels hit a record high in 2024 and are estimated to be 41.6 billion tonnes in 2024, up from 40.6 billion tonnes in 2023. Hydrogen production plays a vital role in mitigating the increasing greenhouse gas emissions and utilizing surplus renewable energy [1]. Producing hydrogen using biomass is considered as a viable source that satisfies those requirements due to being inexpensive, with ready availability. Conversion of biomass to energy can be achieved by either thermochemical (combustion, pyrolysis, and gasification) or biological methods. Thermochemical methods have the potential to accept a wide range of biomass as feedstock, including wastes such as lignocellulosic agricultural residues. Among the thermochemical methods, gasification is favored due to its higher energy efficiency and wider range of applications of the product syngas [2]. However, the tar produced during the biomass pyrolysis and gasification process seriously limits the application of biomass thermal conversion technology because of its complex composition, which is difficult to deal with [3]. Up to now, the existing tar removal technologies mainly include the mechanical (physical) method, thermal chemical method, and catalytic removal method. Due to high removal efficiency and good selectivity, catalytic removal is widely regarded as useful and promising, not only reducing the tar content in fuel gas, but also upgrading the fuel gas quality [4]. Biochar derived from biomass pyrolysis, is cheap and easy to obtain, and can be used as a catalyst or catalyst support , so it was widely used in the process of catalytic cracking of biomass. Meanwhile, it has been found that biochar also has the following advantages : (1) high specific surface area and rich porosity ; (2) abundant O-containing functional groups ; (3) some inherent alkali metals and alkaline earth metals (AAEMs) and inorganic

substances will be retained in the process of biochar formation, so biochar is a potential catalyst for tar removal [5]. However, the limited specific surface area and pore volume of biochar restrict its use as a catalyst support. The process of increasing specific surface are and pore density is called activation. In general, there are two types of activation techniques namely; physical, and chemical are used in activated carbon. Sometimes the two methods can be combined to form a physicochemical activation method [6]. The physical activation of biochar requires the heating of biochar using steam, carbon dioxide, or air, is cheaper and more environmentally friendly than chemical activation, and in a physically activated atmosphere, the carbon atoms bind with the activator and escape in the form of CO + H_2 or CO, leading to the formation of a porous structure [7]. Whereas, chemical activation requires the impregnation with chemical agents such as KOH, H_3PO_4, or $ZnCl_2$, followed by heating. This process effectively improves the porosity and surface area of biochar [8]. However, using harmful chemicals in the chemical activation raises sustainability concerns. In contrast, physicochemical activation provides a more sustainable approach by minimizing the reliance on harmful chemicals through the use of oxidizing agents.

The objective of this study is to evaluate the effect of different activation methods, including physical, chemical and physicochemical, on the catalytic performance of biochar supported nickel (Ni) catalysts in steam gasification. The experimental process used a two-stage fixed-bed reactor. The effects physical, chemical, and physicochemical activations on the physicochemical properties of biochar were characterized using Fourier transform infrared spectroscopy (FTIR), Brunauer-Emmett-Teller (BET) test and scanning electron microscopy (SEM). The catalysts were further characterized using X-ray diffraction (XRD), and the gas products were analyzed using gas chromatography (GC). The effects of the catalyst type and pyrolysis temperature on gas yield in tar steam reforming were studied. This work offers a promising alternative activation method of biochar in tar steam reforming by using lesser chemical and still achieving better gas generation.

2. EXPERIMENTAL

2.1 Material

Palm kernel shell biomass from Saraburi Province was used as the raw material. It was crushed and sieved with particle size 250–600 µm, then dried in an oven at 110 °C overnight.

2.2 Preparation of activated biochars

In the first step, the biochar was prepared from palm kernel shell by conventional pyrolysis at 500 °C under the flow of nitrogen for 1 h. The resulting char was ground into powder form and subjected to the physical activation (PAC) using steam as the activating agent. For steam activation, 4 g of biochar was subjected to heating from room temperature to 700 °C under nitrogen atmosphere at a flow rate of 50 mL/min. After reaching the required temperature, steam was introduced at 0.3 mL/min and nitrogen (50 mL/min) as a carrier gas and maintained at that temperature for 60 min. Chemical activation (CAC) used KOH as the activating agent. The KOH-to-biochar ratio was 1:1 during impregnation. Subsequently, the KOH and char solution were stirred at 70 °C for 4 h. The obtained paste was kept in an oven at 110 °C for 24 h for drying. After drying, the dried biochar was activated by heating from room temperature to 700 °C under nitrogen atmosphere at a flow rate of 80 mL/min and maintained at that temperature for 60 min. For physicochemical activation (PCAC), both chemical (KOH) and steam, were used. The KOH-to-biochar ratio was 0.5:1 during impregnation. Subsequently, following the same procedure as chemical activation, the dried biochar was activated by heating from room temperature to 700 °C under nitrogen atmosphere at a flow rate 80 mL/min for the initial 30 min. Then, steam was introduce at 0.3 mL/min and nitrogen (50 mL/min) as a carrier gas for another 30 min. After 60 min, the temperature was decreased, and the activated char was collected. The resulting activated biochars were called physically activated biochar (PAC), chemically activated biochar (CAC), and physicochemically activated biochar (PCAC). The CAC and PCAC were washed with 0.1 M HCl solution and later with distilled water until a pH of 7.0 was reached, then dried in an oven at 110 °C for 24 h. The PAC, CAC, and PCAC yields were 87 wt%, 83 wt%, and 70 wt%, respectively.

2.3 Preparation of catalyst

After obtaining the activated chars, 10% Ni was loaded using nickel (II) nitrate hexahydrate, $Ni(NO_3)_2.6H_2O$ as a precursor, and activated biochars as a support by the incipient wetness impregnation method. After impregnation, the sample was dried overnight in an oven at 110 °C and calcined at 700 °C under nitrogen atmosphere for 3 h. The catalysts were named Ni/PAC Ni/CAC and Ni/PCAC, respectively.

2.4 Experiment setup and procedure

The steam reforming of biomass-derived tar with catalytic was carried out using a two-stage fixed-bed reactor system. A schematic diagram of the system is shown in Fig. 1. The first stage reactor for the pyrolysis of the biomass was made of quartz and was 65 mm long x 9 mm inner diameter. The catalytic reactor for tar reforming was 88 mm long x 19 mm inner diameter and also made of quartz. Typically, 0.4 g biomass and 0.8 g catalyst were used in an experiment. The carrier gas was N_2 at a flow rate of 50 mL/min and passed through the reactor continuously. During the experiment, when the temperature of the pyrolysis stage rose to the target temperature (600/700/800 °C) and the temperature of catalytic reforming stage rose to 700 °C, the palm kernel

shell was introduced into the pyrolysis stage from the top for rapid pyrolysis. Only the biomass volatiles were allowed to pass through the filter, move to the catalytic reforming stage, and contact with the steam and the catalyst. Then, tar steam reforming occurred under the action of the catalyst. Subsequently, the pyrolysis gas successively passed through the outlet of the reaction tube and entered the condensing bottle. Gas products were finally collected in a 2 L gas bag. The gas collection bag was changed every 5 min during 30 min of reaction time. The gas products generated from the char itself without the biomass feeding were also evaluated in the same procedure and used as the reference data (blank experiment).

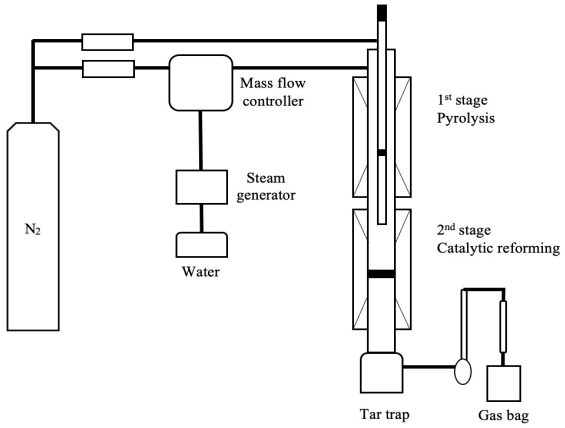

Figure 1. Schematic diagram of a two-stage fixed bed reactor

2.5 Analysis method

2.5.1. Product analysis

The gas product, which mainly comprised four main gases (CO, CH_4, CO_2, and H_2) were quantitatively analyzed by GC using a Shimadzu GC-2014 model with a thermal conductivity detector (TCD) and a Unibeads C column (3.00 mm ID x 200 cm length).

2.5.2 Activated biochars and catalyst characterization

The specific surface area, pore volume and pore size distribution of activated biochars were all determined by the Brunauer-Emmett-Teller (BET) method. The morphology of the activated biochars were characterized using a scaning eletron microscope (SEM, JSM-IT800SHL, JEOL, Japan). The functional groups present in the activated biochars were investigated by Fourier transform infrared spectroscopy (FTIR, Nicolet iS5, USA). The mineral composition of the activated biochars were analyzed by the X-ray fluorescence (XRF, S8 Tiger, Bruker, Germany). The crystal structures of catalysts were characterized by X-ray diffraction (XRD, D8 Discover, Bruker, Germany) in the 2θ range from 10° to 80° with Cu-Kα radiation.

3. RESULTS AND DISCUSSION

3.1 Characterization of activated biochars

3.1.1 Specific surface area and pore structure analysis

Table 1 lists the results of BET analysis for the PAC, CAC and PCAC activated biochar. All activation methods led to a significant increase in the BET surface area of the biochar. The PCAC showed the maximum surface area of 681.66 m^2/g, whereas BC (biomass) showed the minimum surface area of 43.80 m^2/g. In addition, the BET surface areas of PAC and CAC increased to 337.16 and 412.99 m^2/g, respectively, when compared to the original area. The presence of the activator improves the total pore volume and micropore volume to different degrees. During steam (H_2O) activation, amorphous carbon in the biochar reacted with the oxygen in water molecules to generate carbon monoxide or hydrogen, which increased the BET surface area as well as improved the micropore volume. While KOH-activated biochar promoted the formation of biochar micropores through the etching of the carbon skeleton and the removal of tarry products in the pores of the biochar [7]. Moreover, the physicochemical activation is a combination of chemical and steam for the activation, in which KOH has been used for microporosity development, whereas the total amount of pores can be enhanced with the introduction of steam [9], resulting in a maximum total pore volume and micropore volume of 0.38 cm^3/g and 0.32 cm^3/g, respectively. In general, the surface area is an important parameter for catalytic reaction activity. Increasing the surface area not only increases the possibility of contact between the reactants and the active site but also prolongs the reaction time [7].

Table 1 Textural properties of different activated biochars

Sample	BET surface area (m^2/g)	Total pore volume (cm^3/g)	Micropore volume (cm^3/g)	Mean pore diameter (nm)
BC	43.80	0.06	0.02	5.18
PAC	337.16	0.21	0.10	2.48
CAC	412.88	0.24	0.17	2.38
PCAC	681.86	0.38	0.32	2.23

3.1.2 The morphology of activated biochars

Fig. 2 presents the morphology of activated chars using SEM images. The surface morphology of the biochar in Fig. 2(a) consists of irregular pore structure, and random pores are distributed over the matrix. Activation promoted pore formation, leading to the enhancement of pore characteristics of activated biochar. All of the activated biochars have large honeycomb shapes and sponge-like pores. The presence of button-like structure on the surface with the bumps and pores for physically activated biochar (steam) in Fig. 2(b), may be due to the escape of volatile compounds from the surface because of the thermal

decomposition and the steam reforming of volatile as well [10]. Moreover, the chemically activated biochar (KOH) in Fig. 2(c) showed smaller bumps and less roughness with a more regular structure than physically activated biochar. The smaller bumps and regular structure might be due to the higher surface area and the release of minerals from the char. The result was also confirmed by the BET analysis and mineral analysis. Furthermore, the physicochemically activated biochar (KOH+Steam) in Fig. 2(d) showed higher developed porosity inside the mesopores, as compared to the physically and chemically activated biochar (Fig. 2(b-c)). The presence of micropore structure can contribute a larger specific surface area to promote the contact between the tar macromolecules and the active sites in the pores. In contrast, the mesoporous structure can facilitate the diffusion and mass transfer of the tar macromolecules during the adsorption process [9].

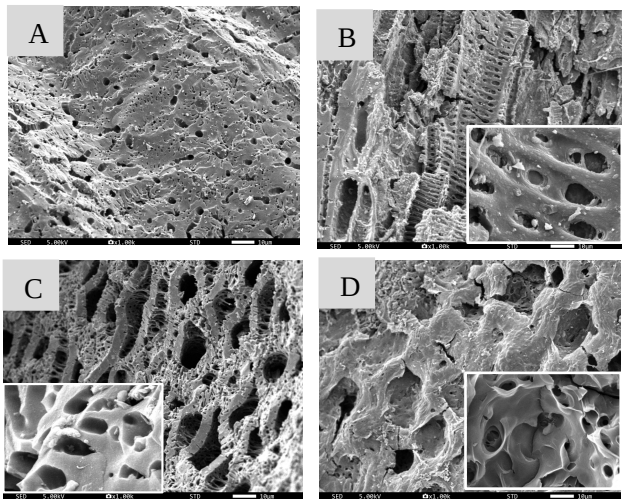

Fig. 2. SEM images of activated biochars (a) Biochar (b)Physically activated biochar (c) Chemically activated biochar (d) Physicochemically activated biochar

3.1.3 FT-IR analysis of activated biochar

The infrared spectrum of the activated biochar is depicted in Fig. 3. The infrared spectra of all the three activated biochars show three main peaks. However, PAC, CAC, and PCAC exhibit characteristic peaks at 1630 cm^{-1} , corresponding to the stretching vibration of C=C aromatic ring skeleton. The results indicate that after activation, new functional groups are formed on the surface of activated biochars, and the degree of aromatization is enhanced. This may be due to the elimination of some unstable carbon atoms on the biochar [5]. As observed, the peak at 3450 cm^{-1} is attributed to the stretching vibration of the hydroxyl (O-H) group, associated with water, alcohol, phenol, and carboxylic acid. In addition, compared to PAC and CAC, the stretching vibration of the C=O carbonyl stretching in Ketone (2070 cm^{-1} and 2010 cm^{-1}) increased in PCAC, indicating that the steam and KOH activation significantly increased the amounts of o-containing functional group in biochars. The o-containing functional groups will provide more acidic sites for the tar removal reaction, which will help to convert tar macromolecules and produce non-condensing gas [5].

3.1.4 The elemental composition of the activated biochars

The XRF analysis of activated biochars were summarized in the Table 2. PAC showed a comparatively larger amount of K and Ca, which are known to increase the rate of the water-gas shift reaction and gas yield [10]. Also, little amount of Mg,Mn and Fe which could further augment the reaction rate and improve gas distribution by cracking tar into lighter hydrocarbons [8]. Although CAC might result in higher surface area to incorporate more nickel species on its surface, it can lead to the removal of minerals from the biochar due to acid washing step [10], resulting in decreases of the K, Ca, and other elements. Moreover, because the steam activated biochar does not include the acid washing, hence the mineral amount stayed intact. Also, the mild oxidation of carbon into CO_2.

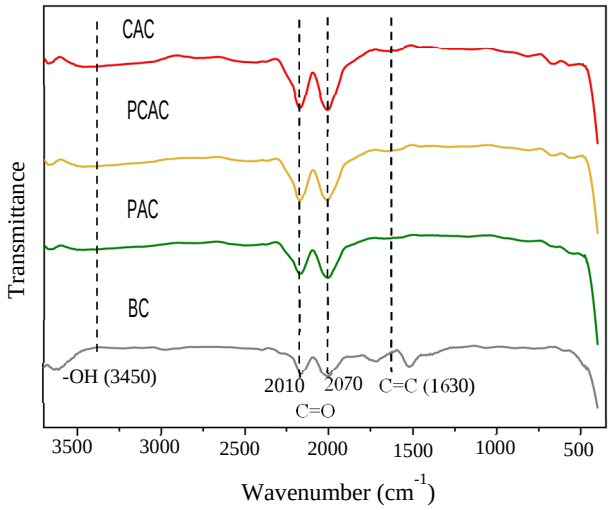

Fig. 3. FT-IR spectrum of activated biochars

Table 2 Relative mineral components in activated biochars by XRF.

Elements	PAC (wt. %)	CAC (wt. %)	PCAC (wt. %)
Mg	0.281	0.087	0.122
Si	0.896	0.348	0.516
P	0.027	0.006	0.005
S	0.020	0.014	0.023
Cl	0.015	0.148	0.185
K	0.670	0.453	0.340
Ca	0.369	0.100	0.150
Mn	0.002	0.002	0.000
Fe	0.041	0.004	0.005
Cu	0.002	0.001	0.002

3.2 Characterization of catalyst

3.2.1 XRD analysis of activated biochar

The XRD patterns of all Ni loaded activated biochars are shown in Fig. 4. The (111), (200), and (220) surfaces of nickel are represented by typical peaks at 44.5º , 51.7º and 76.3º were ascribed to the Niº (active form). The active form of Ni can enhance the cracking of tar and reaction during gasification, such as the water-gas shift, Boudouard, and reforming reactions, resulting in increased H_2 generation [11]. Moreover, the patterns of the activated biochars show broad graphite peaks, indicating a nearly amorphous structure. A broad peak in the range of 20-30º may indicate the early presence of a poor crystalline structure and a carbon-rich phase in these samples. These types of chars are often referred to as turbostratic chars, which are dominated by disordered graphitic crystallites [12].

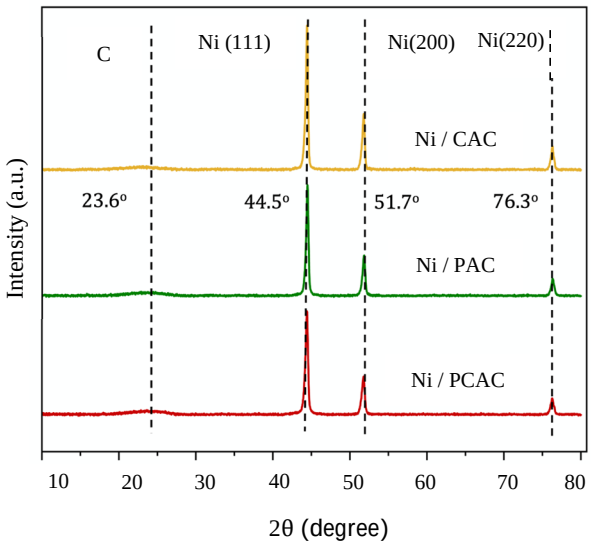

Fig. 4. XRD patterns of activated biochars

3.3 Gas product analysis

3.3.1 Influence of catalyst on gas yield in tar steam reforming

Fig. 5 presents the gas product yield obtained from steam gasification using the Ni/physically activated biochar (Ni/PAC) , Ni/chemically activated biochar (Ni/CAC), Ni/physicochemically activated biochar (Ni/PCAC), and no catalyst (Blank). The gas yield obtained from all Ni-loaded activated biochars showed a higher gas yield than that of no catalyst. This is because Ni has a high activity for breaking C-C and C-H bonds, which is helpful for tar conversion [5]. When comparing the char-based prepared catalysts, Ni/PCAC showed the maximum gas yield is 20.66 mmol/g biomass. H_2 and CO make up the majority of the gas products, with yields of 9.16 and 6.08 mmol/g biomass, respectively. Overall, the gas yield obtained was in the following sequence: Ni/PCAC > Ni/PAC > Ni/CAC > Blank. The gas yield increased when Ni/PCAC was applied as a catalyst, possibly because of the maximum surface area and pore volumes of PCAC (Table 1), which promote the dispersion of active sites for the active metal particle and enhance secondary tar cracking [5,7,11]. In addition, the presence of more oxygen-containing functional groups, such as C=O, on the surface of PCAC, which can provide acidic sites that facilitate the removal of tar molecules [5]. The CAC exhibited lower catalytic activity despite its high surface area. This may be explained by the low content of alkali and alkaline earth metals, such as K and Ca, in CAC, resulting from the acid washing step, which could reduce the overall gas yield. [10].

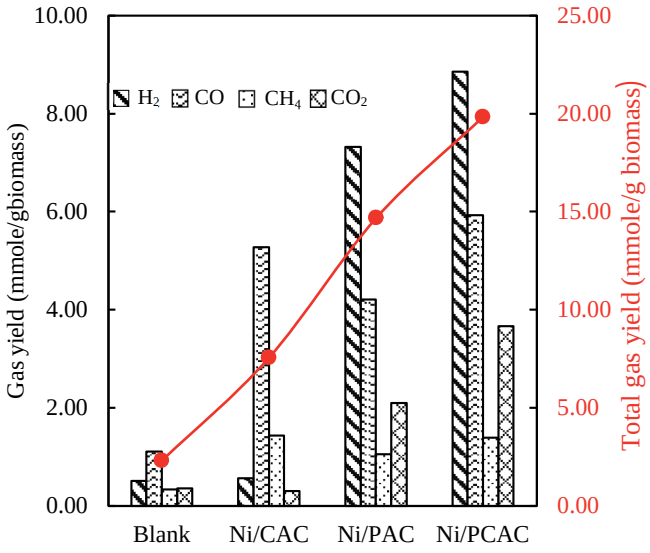

Fig. 5. The gas yield with different catalysts (For all cases : pyrolysis temperature: 700 ºC, tar reforming temperature: 700 ºC)

3.3.2 Influence of pyrolysis temperature on gas yield in tar steam reforming

One of the most crucial factors affecting the catalytic activity of a reaction is temperature. Fig. 6 displays the yield of gas product with different catalysts at different temperatures. It can be seen that when temperature of the pyrolysis reactor was raised from 600 ºC to 700ºC, the gas yield and H_2 yield especially for Ni/PCAC increased significantly, compared to the other catalysts. As the reaction temperature increased, the gas yield and H_2 yield rose from 11.69 and 4.47 mmol/g biomass to 20.68 and 9.16 mmol/g biomass, respectively. This is because tar steam reforming is an endothermic reaction, and high temperature is conducive to steam reforming in the direction of hydrogen production [13]. Additionally, the catalyst's surface undergoes a gasification reaction when the temperature is elevated, which helps to reduce carbon deposits [5]. It is noted that as the pyrolysis temperature increased from 700ºC to 800ºC, the CO yield of Ni/PCAC further increased from 6.08 to 6.58 mmol/g biomass , while the CO_2 yield varied slightly, from 4.06 to 3.64 mmol/g biomass and the content of H_2 yield decrease from 9.16 to 4.88 mmol/g biomass. This occurs because the water-gas shift reaction is an exothermic reaction, and increasing the temperature promotes the reaction toward CO production, thus resulting in the reduction of the yield of CO_2 and H_2 [13].

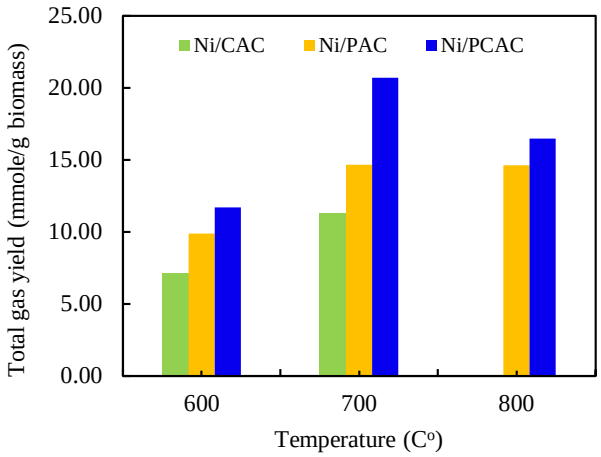

Fig. 6. The gas yield with different catalysts (For all cases : tar reforming temperature: 700 ºC)

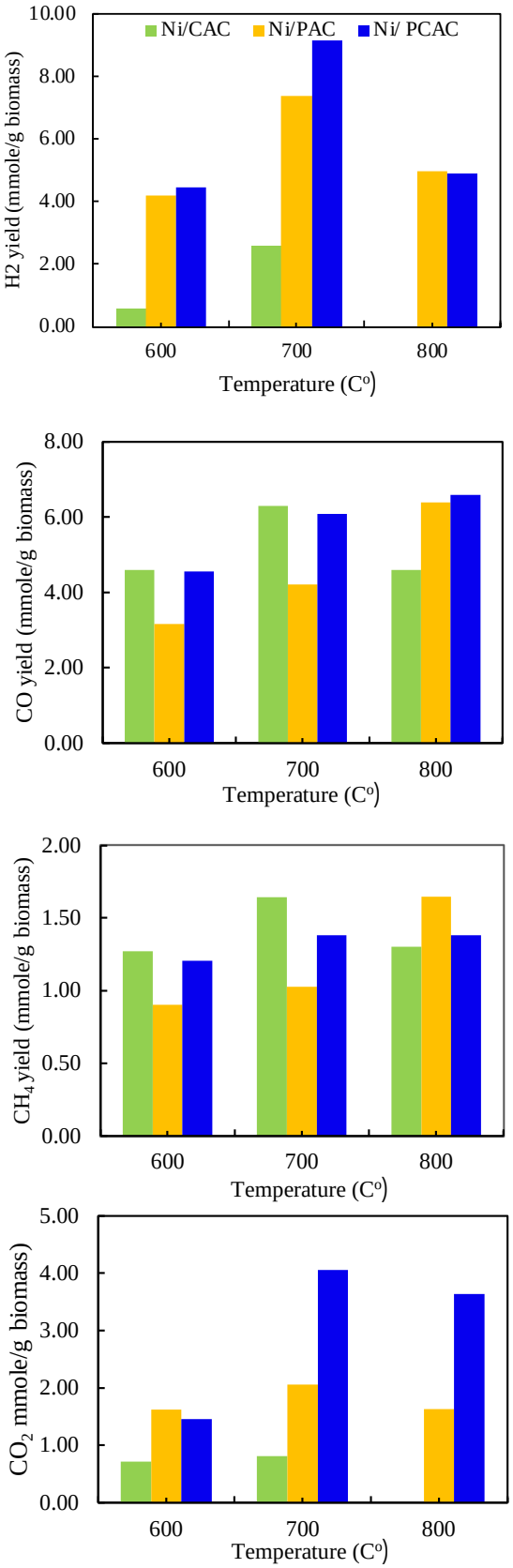

Fig. 7. The gas compositions with different catalysts (For all cases : tar reforming temperature: 700 ºC)

4. CONCLUSION

In summary, physiochemically activated biochar produced by steam and KOH activation of biochar demonstrated the best catalytic performance in tar steam reforming, with a maximum total gas yield and H_2 yield of 20.68 and 9.16 mmol/g biomass, respectively. This is because the catalyst has a higher specific surface area and greater total pore volume, which supplies the active sites for tar removal and gas production. Additionally, more oxygen-containing functional groups, such as C=O, are present on the surface of activated biochar, which can provide acidic sites and facilitate the removal of tar molecules. Moreover, H_2 production was enhanced as the temperature increased from 600 to 700 ^oC due to tar steam reforming can occurs more easily at higher temperature, However, when the temperature was raised to 800 ^oC, the H_2 yield decreased due to the inhibition of the water-gas shift reaction. The maximum H_2 yield was obtained with Ni/physicochemically activated biochar at 700 ^oC. The combination of chemical and steam for the activation is a better alternative for activated biochar preparation with desired gas production, as it reduce the use of harmful chemicals by using an oxidizing agent such as steam.

ACKNOWLEDGMENTS

The author is thankful to Department of Chemical Technology, Faculty of Science, Chulalongkorn University for support of the scholarship.

REFERENCES

1. Khaligh, V., Ghezelbash, A., Akhtar, M. S., Zarei, M., Liu, J., & Won, W. (2023). Optimal integration of a low-carbon energy system – A circular hydrogen economy perspective. *Energy Conversion and Management*, 292.
2. Gao, N., Salisu, J., Quan, C., & Williams, P. (2021). Modified nickel-based catalysts for improved steam reforming of biomass tar: A critical review. *Renewable and Sustainable Energy Reviews*, 145.
3. Li, Y., Di, H., Zhang, T., Hou, J., Yang, J., Li, K., Han, J., & Zhao, R. (2025). Catalytic cracking of tar model compounds over char-based catalysts. *Journal of the Energy Institute*, 119.
4. Zeng, X., Ueki, Y., Yoshiie, R., Naruse, I., Wang, F., Han, Z., & Xu, G. (2020). Recent progress in tar removal by char and the applications: A comprehensive analysis. *Carbon Resources Conversion*, 3, 1–18.
5. Zhang, M., Fan, G., Liu, N., Yang, M., Li, X., & Wu, Y. (2023). Tar removal in pine pyrolysis catalyzed by bio-char supported nickel catalyst. *Journal of Analytical and Applied Pyrolysis*, 169.
6. Jjagwe, J., Olupot, P. W., Menya, E., & Kalibbala, H. M. (2021). Synthesis and Application of Granular Activated Carbon from Biomass Waste Materials for Water Treatment: A Review. *Journal of Bioresources and Bioproducts*, 6(4), 292–322.
7. Zhang, L., Li, Z., Yi, W., Yao, Z., Zhao, L., Jia, J., & Kang, K. (2021). Synthesis and characterization of different activated biochar catalysts for removal of biomass pyrolysis tar. *Energy*, 232.
8. Farooq, A., Rhee, G. H., Lee, I.-H., Khan, M. A., Lee, S. H., Jung, S.-C., Jeon, B.-H., Chen, W.-H., & Park, Y.-K. (2021). Waste furniture gasification using rice husk based char catalysts for enhanced hydrogen generation. *Bioresource Technology*, 341.
9. Adlak, K., Chandra, R., Vijay, V. K., & Pant, K. K. (2021). Physicochemical activation and palletisation of Azadirachta indica wood carbons for increased biomethane adsorbed energy storage. *Journal of Analytical and Applied Pyrolysis*, 155.
10. Farooq, A., Jang, S.-H., Lee, S. H., Jung, S.-C., Rhee, G. H., Jeon, B.-H., & Park, Y.-K. (2021). Catalytic steam gasification of food waste using Ni-loaded rice husk derived biochar for hydrogen production. *Chemosphere*, 280.
11. Jeon, S., Farooq, A., Lee, I. H., Seo, M. W., Choi, Y. J., Park, Y.-K., Lee, D., Jung, S.-C., Hussain, M., Khan, M. A., Jeon, B.-H., Jang, S.-H., & Rhee, G. H. (2024). Green conversion of wood plastic composites: A study on gasification with an activated bio-char catalyst. *International Journal of Hydrogen Energy*, 54, 96–106.
12. Zhang, J., Li, W., Huang, B., Chen, L., Du, J., & Luo, Z. (2018). Pyrolysis kinetics of hulless barley straw using the distributed activation energy model (DAEM) by the TG/DTA technique and SEM/XRD characterizations for hulless barley straw derived biochar. *Brazilian Journal of Chemical Engineering*, 35(3), 1039–1050.
13. Quan, C., Wang, H., & Gao, N. (2020). Development of activated biochar supported Ni catalyst for enhancing toluene steam reforming. *International Journal of Energy Research*, 44(7), 5749–5764.

Double perovskite enhanced with exsolved Ni-Co particles in $Sr_{1.95}TiMo_{1-x}(NiCo)_xO_{6-\delta}$ as anode for direct-fed ammonia solid oxide fuel cell

Solida Oun[1], Pattaraporn Kim-Lohsoontorn[2,*]

[1] Department of Chemical Engineering, Faculty of Engineering, Chulalongkorn University, Bangkok 10330, Thailand
[2] Center of Excellence on Catalysis and Catalytic Reaction Engineering, Department of Chemical Engineering, Faculty of Engineering, Chulalongkorn University, Bangkok 10330, Thailand
[3] Bio-Circular-Green Economy Technology & Engineering Center, BCGeTEC, Faculty of Engineering, Chulalongkorn University, Bangkok, 10330, Thailand
[*] Corresponding author: pattaraporn.k@chula.ac.th

ABSTRACT

Ammonia has gain attention as a promising fuel for solid oxide fuel cell due to its high energy density, carbon-free hydrogen, and easier storage. Herein, an innovative double perovskite $Sr_{1.95}TiMoO_{6-\delta}$ (STM) is designed by integrating the unique properties of $SrTiO_3$ and $SrMoO_3$, with A-site deficiency introduced using the sol-gel method to enhance anode performance. In this study, NiCo particles are in situ exsolved from the parental STM to improve surface active sites, demonstrating the performance of catalytic activity for the ammonia cracking reaction and sintering resistance. This is evaluated by optimizing the NiCo doping amount in $Sr_{1.95}TiMo_x(NiCo)_{1-x}O_{6-\delta}$ (x = 0.1, 0.2 and 0.3) under 5%H_2-95%N_2 at 1000°C for 5 hours, as confirmed by XRD, SEM-EDX, TEM and XPS analyses. The phase transition and the exsolution of the particles are investigated by X-ray diffraction, Transmission electron microscope. Furthermore, The NiCo exsolved surface of $Sr_{1.95}TiMo_{1-x}(NiCo)_{1-x}O_{6-\delta}$ will be further explored as an anode material for evaluating electrochemical performance in a direct ammonia-fed solid oxide fuel cell.

Keywords: $Sr_{1.95}TiMo_{1-x}(NiCo)_xO_{6-\delta}$ anode; Double perovskite; Exsolution; Solid oxide fuel cell

1. INTRODUCTION

Solid oxide fuel cells (SOFCs) are considered a highly promising technology as electrochemical devices that directly convert chemical energy to electricity due to their high efficiency and minimal environmental impact, as well as their adaptability to various fuels, including hydrogen, alcohol and hydrocarbon, making them an attractive key innovation in the development of sustainable energy technologies [1].

Hydrogen is the most frequently used fuel that generates electricity through simple oxidation reaction without producing harmful byproducts. However, ammonia (NH_3) has gained attention as a carbon-free hydrogen carrier because of its high energy density, easier storage and safer handling compared to hydrogen, contributing to a clean and sustainable energy system as it can generate electricity without emission [2]. Consequently, these benefits position ammonia as a strong candidate for renewable energy application in SOFCs.

In order to achieve optimal power output in direct ammonia SOFCs (DA-SOFCs), the anode must demonstrate a strong catalytic activity for both hydrogen oxidation reaction (HOR) and ammonia decomposition reaction (NDR). Although conventional Ni-based cermet anodes have demonstrated satisfactory performance for HOR though they still struggle with low NDR activity and suffer from particles agglomeration (Ni coarsening) which deteriorate microstructure leading to performance degradation [3]. Perovskite oxides have significantly earned attention as alternative anode design on account of their structural stability, high chemical and thermal stability. However, pure perovskite materials may exhibit limited catalytic activity, the in situ exsolution method can enhance their performance by decorating the surface with uniformly dispersed catalytically active nanoparticles (NPs), while the perovskite backbone acts as a stable foundation for anchoring alloy nanoparticles to improve both catalytic performance and stability [4]. So far, double perovskite oxides have been widely used as electrode SOFCs because of their high electric-ionic conductivity, excellent catalytic performance and compatibility with electrolyte. Studies have reported that $Sr_2MgMoO_{6-\delta}$ and Sr_2FeMoO_{6-s} anodes have illustrated superior electrochemical performance and long-term stability, attributed high oxygen vacancy

when operated in H_2 and city gas [5]. A long with various dopants at B-site, namely Ru, Mn, Ni, Co, Fe and Pt, exsolution behavior has been studied with exsolution M (M=Mn, Ni, Co and Fe on $PrBaMn_{0.7}M_{0.3}O_{6-\delta}$ [6]. It was reported that Ni and Co are the most favorable elements due to their co-segregation energy. **Song et al**. revealed that $La_{0.55}Sr_{0.30}TiO_{3-\delta}$ (LST) with exsolved Ni-Co nanoparticles showed highly effectiveness in DA-SOFC compared to undoped LST [7]. Correspondingly, the B-site metal in A site stoichiometric perovskite material is not easily exsolved, as the evidence by a comparative study of A-site deficient $La_{0.52}Sr_{0.28}Ni_{0.06}Ti_{0.94}O_{3-\delta}$ and A-site stoichiometric $La_{0.3}Sr_{0.7}Ni_{0.06}Ti_{0.94}O_{3.09}$ [8].

In this work, we investigated the performance of a composite materials combing simple single perovskite $SrTiO_3$ and $SrMoO_3$ to promote high stability and electrical conductivity. To further improve its potential, Ni-Co was doped into double perovskite material $Sr_{1.95}TiMoO_{6-\delta}$ (STM). The resulting material $Sr_{1.95}TiMo_x(NiCo)_{1-x}O_{6-s}$ with x value 0.1, 0.2 and 0.3, were designed to optimize the exsolution Ni-Co bimetallic nanoparticles.

2. EXPERIMENTAL

2.1 Materials Synthesis

$Sr_{1.95}TiMo_{1-x}(NiCo)_{1-x}O_{6-\delta}$ (STMNC, x=0.1, 0.2, 0.3) were synthesized via sol-gel EDTA/Citrate complexing method. First, amount of high purity $Sr(NO_3)_2$, $Ni(NO_3)_2.6H_2O$, $Co(NO_3)_2.6H_2O$ (purity>98%, all from Sigma Aldrich) and $(NH_4)_6Mo_7O_{24}.4H_2O$ (83%, Sigma Aldrich) were mixed respected to the stoichiometric ratio, then dissolved in diluted nitric acid to form solution A, while solution B was prepared by pouring $C_{16}H_{36}O_4Ti$ ethanol in molar ratio 1:30 with stirring at 80 ℃ for an hour to form stable Ti^{4+}. Next, solution A and solution B were combined, then EDTA and Citric acid were added in sequence by fixing EDTA to citric acid to the total amount of metal ions in molar ratio 1:2:1 and the pH value of solution was adjusted to 8 with ammonia solution. The obtained solution was heated at 80 ℃ until viscous gel was formed. The gel was combusted at 300 ℃ for 4 h and then the fluffy powder was grinded, followed by calcined at 800 ℃ for 6 hours to remove organic residues. Finally, the powder was pressed into a pellet at about 2 MPa followed by sintering 1100 ℃ in air for 5 h to obtain pure phase double perovskite.

2.2 Exsolved samples

The $STMNC_x$ pellets were reduced under 5% H_2/N_2 atmosphere in a quart tube reactor at 1000 ℃ for 5h to form layered double perovskite decorated with Ni-Co particles, as confirmed by XRD and XPS. Thereafter, R-$STMNC_x$ were referred to the exsolved sample (R for reduced).

2.3 Material Characterization

X-Ray diffraction (XRD, BRUCKER D8 ADVANCE) was performed to analyze the phase structure of the sample. The scanning electron microscopy and energy dispersive X-Ray analyzer (SEM, JEOL model S-3400) were used to observe the microstructure of synthesized sample, examine the cell surface morphology and analyze the composition of the samples. Transmission electron microscope (TEM, JEM-2100) was employed to investigate the behavior of metal nanoparticles on the sample surface with respect to exsolution. EDX was also coupled with TEM to identify the composition of exsolved nanoparticles.

X-ray photoelectron spectrometer (XPS, AMICUS) was used to determine the oxidation states of the elements in both the pre-reduced and reduced $STMNC_x$. Thermogravimetric analysis (TGA) was conducted under N_2 atmosphere from room temperature to 1000 ℃ at ramp rate 10 ℃/min to evaluate thermophysical properties.

2.4 Cell fabrication

Dense pellet was fabricated by dry pressing 3 g of commercial LSGM powder (Kceracell, Korea) at 2 Mpa for 30 seconds, following by the sintering disk at 1450 ℃ for 4 h to create high-density electrolyte support. The cathode slurry was prepared by mixture of alpha-terpineol binder with the commercial powder BSCF ($Ba_{0.5}Sr_{0.5}Co_{0.8}Fe_{0.2}O_{3-\delta}$) at mass ratio 1:2, while anode electrode slurries were produced by mixing the same ratio of alpha-terpineol with different $STMNC_x$. Afterward, the anode and cathode slurries were screen-painted both faces of dense LSGM, then sintered at 1150 ℃ for 2 h to create porous electrodes. Finally, the electrolyte support-supported cell was completely obtained $STMNC_x$/LSGM/BSCF. Pt paste and Pt wire were employed as the current collector and current lead respectively.

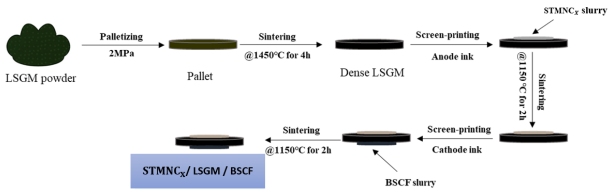

Figure 1 Cell fabrication process

3. RESULTS AND DISCUSSION

3.1 Theoretical prediction

The Goldsmidt's tolerance factor (t) was used to predict the structure of $Sr_{1.95}TiMo_{1-x}(NiCo)_xO_{6-\delta}$ ($STMNC_X$) double perovskite structure, based on the equation for ABX_3 simple perovskite. This equation was further modified for the double perovskite structure $A_2B(B'_{1-x}M_x)O_{6-\delta}$, where Mo at the B′ is partially substituted by dopants M (NiCo). Thus, the modified

equation for tolerance factor is expressed by the following equation: $t = \frac{r_A + r_o}{\sqrt{2}\left(\frac{r_B + x r_{B'} + (1-x) r_M}{2} + r_o\right)}$.

The value of tolerance factor (t) falls within the range between 0.825< t < 1.059 result in the classification as the stability of the perovskite structure [9]. The calculated tolerance factor of $STMNC_X$ with various Ni-Co doping levels (x=0, 0.1, 0.2, 0.3) were t=1.005, 1.003, 1.001 and 0.999 respectively. These t values existed in theoretical stability range, thereby confirming the structural stability perovskite for all compositions. The measured tolerance factor(t) demonstrated that the perovskite structure is maintained without distortion upon Ni-Co doping.

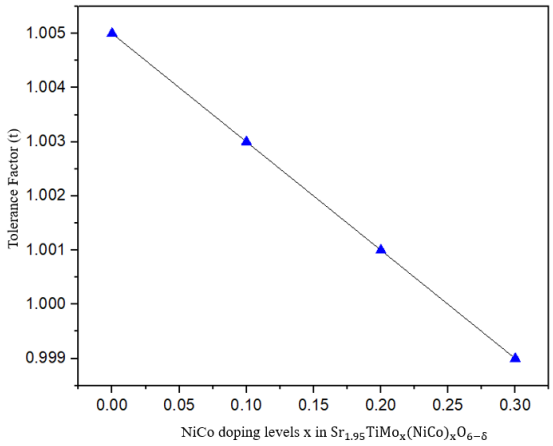

Figure 2. Tolerance factor of $STMNC_X$ ($0 \leq x \leq 0.3$)

The predictive tolerance factor serves as an additional parameter to offer new insight into prediction of double perovskite oxide. The formula for τ extends the concept of t by including not only ionic radii but also the oxidation state of the A-site ion (Sr^{2+}ion), which is written in the form $\tau = \frac{r_x}{r_B} - n_A\left(n_A - \frac{\frac{r_A}{r_B}}{\ln\left(\frac{r_A}{r_B}\right)}\right)$ where τ<4.18 is used for pointing out perovskite structure. The predictive tolerance factor τ, remained consistently below the critical threshold of 4.18, suggesting that all levels of Ni-Co doping at the B-site favor the formation and stability of double perovskite structure [10].

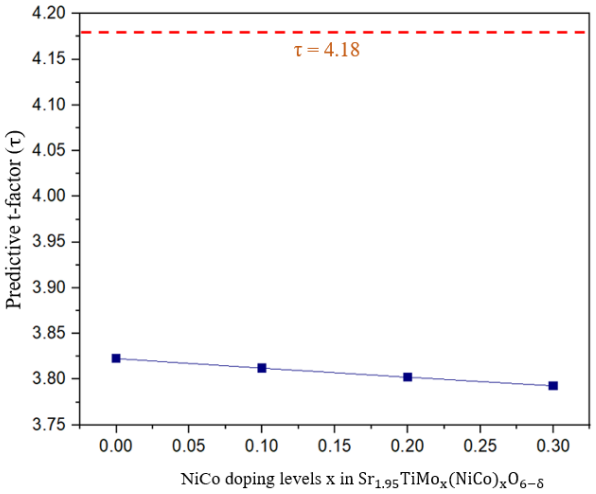

Figure 3 Predictive tolerance factor τ of $STMNC_X$

3.2 Structural and Microstructural analysis

A phase analysis of undoped $Sr_{1.95}TiMoO_{6-s}$ (STM) parent is shown in Fig 4. The XRD pattern reveals that pure STM double perovskite was obtained, while a significant amount of $SrMoO_4$(JCPDS#00-008-0482) was detected as a secondary phase. Clearly, a pure STM-based perovskite in air is challenging to synthesis due to the high oxidation state of Mo^{6+}under oxidizing atmosphere [11]. The formation of $SrMoO_4$which is not a perovskite structure, suggests that Mo is more stable with +6 oxidation state, whereas the single-phase double perovskite is required Mo in the +4 oxidation state [12]. The attempt to sinter the STM-based perovskite in reducing atmosphere ($5\%H_2$-N_2) at 1000 ℃ for 5 h resulted in the diminishing of the distinct peaks of $SrMoO_4$ as depicted in Figure 4. This suggests that the reducing in condition 5% H_2 assist in promoting the formation of STM-based pure phase double perovskite (JCPDS#01-082-9192).

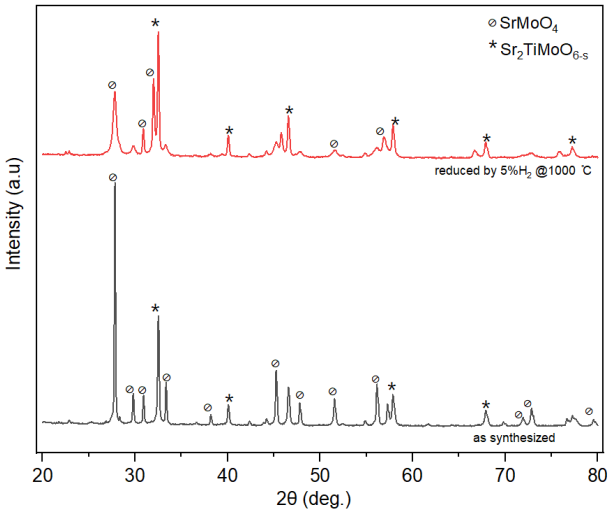

Figure 4 XRD patterns of STM material before and after treating in 5% H_2/N_2 at 1000℃ for 5 h

The X-ray photoelectron spectroscopy (XPS) analysis of the Mo 3d region reveals multiple deconvoluted peaks in Fig 5, indicating the coexistence of Mo in various oxidation states. Notably, distinct peaks at binding energies of 230.1 eV and 230.5 eV are assigned to the Mo^{4+}, in agreement with the formation of STM based perovskite. These peaks confirm the formation of Mo^{4+} species, which is direct evidence of reduction from the higher Mo^{6+} state (typically found at 233.0–233.5 eV in $SrMoO_4$) [13]. The presence of Mo^{4+} is attributed to the treatment in a reducing atmosphere (5% H_2/N_2 at 1000 °C for 5 h). Thus, the XPS results provide clear and direct confirmation that reduction processing successfully converts Mo^{6+} into Mo^{4+} in the sample.

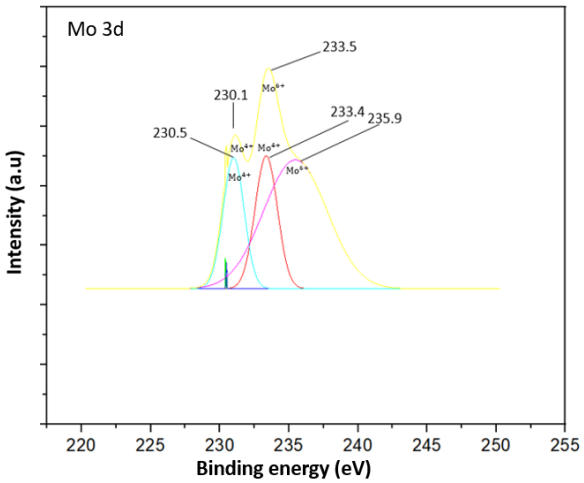

Fig 5 XPS deconvoluted peak of Mo 3d

Fig 6 summarizes the effect of different NiCo doping amounts on the parent perovskite STM. The substitution elements of Ni and Co for Mo in $Sr_{1.95}TiMo_{1-x}(NiCO)_xO_{6-\delta}$ ($STMNC_x$ x= 0.1, 0.2, 0.3) maintained the main phase along with the secondary phase $SrMoO_4$, which is consistent with the phase observed without NiCo doping. It can be inferred that Sr site deficiencies and partial substitution of Mo by Ni and Co did not affect the perovskite phase formation. According to Fig 6, the amount of $SrMoO_4$ was diminished which indicated that replacing Mo with low-valence Ni and Co can stabilize the single-phase perovskite structure in air [14]. The shift of XRD peak was left-shifted to smaller 2θ angle, likely attributed to a lattice expansion resulting from the successful incorporation of larger ions Ni^{2+} (0.069 nm) and Co^{2+}(0.075 nm) into smaller ions Mo^{6+} (0.059 nm) site. Co substitution may also partly occur in Ni site [15].

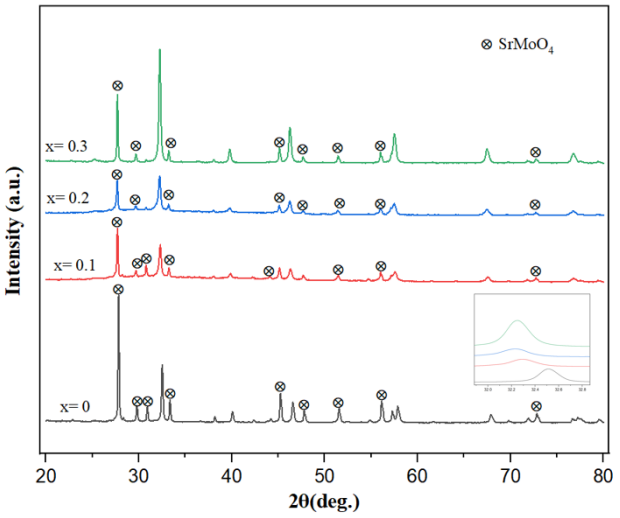

Figure 6 (a) XRD pattern of $STMNC_x$ (x=0.1, 0.2, 0.3)

Following sintering at 1100 °C for 5 h, the morphology and elemental compositions of the $STMNC_x$ samples were investigated using SEM-EDX. SEM observations revealed that the samples exhibited an agglomerated structure with relatively homogeneous morphology. The elemental analysis confirmed that the compositions of most samples were close to the targeted stoichiometry. However, a significant deviation was observed for $STMNC_x$ with x=0.3, where the Mo content was notably elevated and the Ti content substantially reduced compared to the nominal values. This deviation may be attributed to the surface segregation of Mo, which could obscure the Ti signal in the EDX analysis (Fig 7).

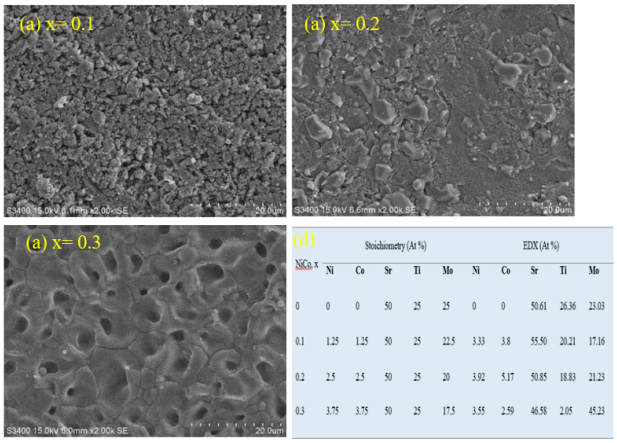

Figure 7 SEM image of $STMNC_x$ at x (a) 0.01, (b) 0.02, (c) 0.03 and (d) EDX (At%)

The exsolution behavior of $STMNC_x$ (x = 0.1) treated in 5% H_2/N_2 atmosphere at 1000 °C for 5 h revealed the absence of the pure perovskite phase (STM). Instead, phase separation was observed in Fig 8(b) with the formation of Co, $SrTiO_3$, and $SrMo_{0.9}Co_{0.1}O_{2.95}$, as identified by the standard JCPDS cards #00-015-0806, #01-088-2325, and #01-090-0696, respectively. SEM was also conducted to investigate the exsolution of $STMNC_x$ (x= 0.1), as mentioned in Fig

8(a), no nanoparticles appear on the surface of R-STMNC$_x$ (x= 0.1), except for small particles aggregated together. This result suggests that processing at elevated temperatures 1000 ℃ induces phase decomposition and inhibits the formation of the desired bimetallic NiCo nanoparticles, with only metallic Co being exsolved. However, the metallic Co phase detected by XRD was not consistent with the XPS results, as the XPS spectra showed Co in the satellite state at a binding energy of 789 eV (Figure 8(c)). This discrepancy suggests that the Co phase is predominantly present in the bulk rather than at the surface.

TGA analysis was carried out to determine the weight losses of STMNC$_x$ (x = 0.1) under reducing N_2 atmosphere while heating from 20 ℃ to 1000 ℃ at a heat rate of 10 ℃/min. In Figure 8(d), the result was illustrated the initial weight loss 250 ℃ due to either evaporation of water or other species. Between 250 °C and 650 °C, mass loss was detected, which is attributed to the release of lattice oxygen. This promotes the formation of oxygen vacancies, thereby enhancing oxygen ion conductivity within the bulk material. The significant weight loss observed above 650 ℃ is linked to a phase transition to a double perovskite structure. The phase shift is accompanied by the exsolution of nanoparticles, which are believed to separate out from the bulk material during process [16]. Therefore, 850 °C was identified as the critical temperature for exsolution according to the TGA results, aligning with findings reported in previous studies.

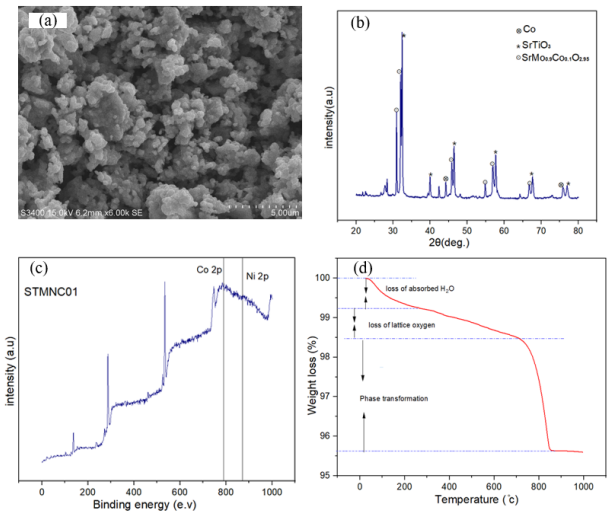

Figure 8 R-STMNC$_x$ (x = 0.1) (a) SEM image, (b) XRD pattern, (c) XPS spectra and (d) TGA analysis of STMNC$_x$ (x = 0.1)

4. CONCLUSION

In summary, inspired by theoretical understanding, double perovskite anode $Sr_{1.95}TiMo_{1-x}(NiCo)_xO_{6-\delta}$ x= 0.1, 0.2, 0.3) have been synthesized, with secondary phase detected $SrMoO_4$. Structural characterization reveals that the formation of a single-phase perovskite is promoted under reducing atmosphere $5\%H_2/N_2$ at elevated temperature 1000 ℃. However, Ni–Co doping was found to enhance the stability of the perovskite phase, enabling its formation even in air without the need for a reducing atmosphere. This indicates that Ni–Co substitution is an effective strategy for simplifying synthesis. At 1000 °C, the exsolution of bimetallic Ni–Co from the perovskite surface was not observed, and the elevated temperature instead promoted phase separation, disrupting the double perovskite structure. To overcome this limitation and enable controlled exsolution of surface bimetallic Ni–Co particles, further investigation is conducted at a lower temperature of 850 °C along with TEM analysis. The exsolution behavior of Ni–Co under H_2/N_2 should be investigated at 850 °C. Additionally, electrochemical impedance spectroscopy (EIS) should be conducted as the next step to evaluate the electrochemical performance of the cell performance with direct-fed ammonia gas.

ACKNOWLEDGMENTS

This research was funded by Research Cess Fund, Malaysia-Thailand Joint Authority (MTJA) and the NSRF via the Program Management Unit for Human Resources & Institutional Development, Research and Innovation [grant number grant number B16F640164]. Kim-Lohsoontorn also would like to acknowledge Thailand Science research and Innovation Fund Chulalongkorn University (BCG66210021).

OUN would like to acknowledge the financial support from the NON-ASEAN and ASEAN scholarship program and Chulalongkorn University research fund and technical support from scientists at the Center of Excellence on Catalysis and Reaction Engineering (CECC) for their unwavering contributions.

REFERENCES

1. M.K. Singla, P. Nijhawan, and A.S. Oberoi, Hydrogen fuel and fuel cell technology for cleaner future: a review. Environ Sci Pollut Res Int, 2021; 28(13): 15607-15626.
2. M. Bertagni, B., Socolow, R. H. Martirez, J. M. P., Carter, E. A., Greig, C., Ju, Y., Lieuwen, T., Mueller, M. E., Sundaresan, S., Wang, R., Zondlo, M. A., & A. Porporato. Minimizing the impacts of the ammonia economy on the nitrogen cycle and climate. Proc Natl Acad Sci U S A, 2023; **120**(46): p. e2311728120.
3. Y. Li, H. S Pillai, T. Wang, S. Hwang, Y. Zhao, Z. Qiao, Q. Mu, S. Karakalos, M. Chen, J. Yang, D. Su, H. Xin, Y. Yan & G. Wu. High-performance ammonia oxidation catalysts for anion-exchange membrane direct ammonia fuel cells. Energy & Environmental Science, 2021; **14**(3): 1449-1460.
4. Y. H. Kim, H. Jeong, B. Won, H. Jeon, C. H. Park, D. Park, Y. Kim, S. Lee & J. H. Myung. Nanoparticle Exsolution on Perovskite Oxides: Insights into Mechanism, Characteristics and Novel Strategies. Nanomicro Lett, 2023; **16**(1): 33.

5. L. Jiang, G. Liang, J. Han& Y. Huang. Effects of Sr-site deficiency on structure and electrochemical performance in Sr 2 MgMoO 6 for solid-oxide fuel cell. Journal of Power Sources, 2014; **270**: 441-448.
6. O. Kwon, S. Sengodan, K. Kim, G. Kim, H. Y. Jeong, J. Shin, Y. W. Ju, J. W. Han & G. Kim. Exsolution trends and co-segregation aspects of self-grown catalyst nanoparticles in perovskites. Nat Commun, 2017; **8**: 15967.
7. Y. Song, H. Li, M. Xu, G. Yang, W. Wang, R. Ran, W. Zhou & Z. A.-O. Shao. Infiltrated NiCo Alloy Nanoparticle Decorated Perovskite Oxide: A Highly Active, Stable, and Antisintering Anode for Direct-Ammonia Solid Oxide Fuel Cells. Small, 2020; **16**(28): e2001859.
8. N. Yu, G. Jiang, T. Liu, X. Chen, M. Miao, Y. Zhang & Y. Wang. Understanding the A-site non-stoichiometry in perovskites: promotion of exsolution of metallic nanoparticles and the hydrogen oxidation reaction in solid oxide fuel cells. Sustainable Energy & Fuels, 2021; **5**(2): 401-411.
9. T. Sato, S. Takagi, S. Deledda, B. C. Hauback & S.-i. Orimo. Extending the applicability of the Goldschmidt tolerance factor to arbitrary ionic compounds. Sci Rep, 2016; **6**: 23592.
10. C. J. Bartel, C. Sutton, B. R. Goldsmith, R. Ouyang, C. B. Musgrave, L. M. Ghiringhelli & M. Scheffler. New tolerance factor to predict the stability of perovskite oxides and halides. Science Advances, 2019; **5**(2): eaav0693.
11. Y. A.-O. Yang, W. A.-O. Li, S. Yang, X. A.-O. Shen, Z. A.-O. Han, H. Yu, M. A.-O. Gao, K. Wang & Z. A.-O. Yang. Ni-Substituted Sr(2)FeMoO(6-delta) as an Electrode Material for Symmetrical and Reversible Solid-Oxide Cells. ACS Appl Mater Interfaces, 2024; **16**(17): 21790-21798.
12. M. Saxena, K. Tanwar, and T. Maiti, Environmental friendly Sr2TiMoO6 double perovskite for high temperature thermoelectric applications. Scripta Materialia, 2017; **130**: 205-209.
13. Wang, X., Yu, M., Lv, C., Wang, L., Kan, W., Xu, G., Sun, L., & B. Zhao. Mo-doped NiCoP nanoplates with amorphous/crystalline heterostructure for efficient alkaline overall water splitting. FlatChem, 2024; **45**.
14. Z. Du, H. Zhao, S. Yi, Q. Xia, Y. Gong, Y. X. Zhang. Y. Cheng, L. Li, L. Gu & K. Świerczek. High-Performance Anode Material Sr2FeMo0.65Ni0.35O6-delta with In Situ Exsolved Nanoparticle Catalyst. ACS Nano, 2016; **10**(9): 8660-9.
15. C. Li, Y. Deng, L. Yang, B. Liu, D. Yan, L. Fan, Li, J., & Jia, L. An active and stable hydrogen electrode of solid oxide cells with exsolved Fe–Co–Ni nanoparticles from Sr2FeCo0.2Ni0.2Mo0.6O6-δ double-perovskite. Advanced Powder Materials, 2023; **2**(4).
16. Y. Tan, J. Tang, C. Yang, Y. Tian, Z. Wang, J. Pu, & B. Chi. Double perovskite decorated with in situ exsolved Fe nanoparticles as active catalyst for CO2 electrolysis. Ceramics International, 2023; **49**(24): 40797-40803.

Optimization of biodiesel production from waste cooking oil via transesterification using calcium oxide catalyst

Pornsawan Assawasaengrat[1,*], Natthapol Nakbun[1], Atipong Paikamnam[1], Phusit Prasom[1], Wasan Chokelarb[1], Woatthichai Narkrugsa[2], Pongsert Sriprom[2]

[1] Department of Chemical Engineering, School of Engineering, King Mongkut's Institute of Technology Ladkrabang, Bangkok 10520, Thailand
[2] Program of Food Process Engineering, School of Food Industry, King Mongkut's Institute of Technology Ladkrabang, Bangkok 10520, Thailand
[*] Corresponding author: pornsawan.as@kmitl.ac.th

ABSTRACT

Biodiesel is primarily derived from vegetable oils, animal fats, and cooking oils. When these materials react with methanol and use acids, bases, or enzymes as catalysts, biodiesel are produced. Base-catalyzed transesterification is the most widely used method due to its cost-effectiveness and simplicity. This research aims to study the optimization of biodiesel synthesis from waste cooking oil via transesterification using calcium oxide catalyst. The experiment was created by a Box-Behnken design. The variables affecting the transesterification reaction included temperature (60-70 °C), methanol percentage (30-50% v/v), calcium oxide catalyst (0.856-1.712% wt./v), and reaction time (120-240 min). After that, the chemical and physical properties were analyzed. The optimum reaction condition was a temperature of 70 °C, a reaction time of 240 min, methanol of 50% v/v, and calcium oxide catalyst of 1.712 %wt./v. In this condition, the highest yield of biodiesel was 99.20%. The functional groups of the biodiesel structure were analyzed by FTIR. The results showed that the C=O (Stretching) of the ester in triglyceride was found at a peak of 1743 cm^{-1}. The presence of the C-H (Bending) bond of the methylene group (CH_2) and the methyl group (CH_3) were found at peak 1466 cm^{-1} and peak 1438 cm^{-1}, respectively, indicating that the product was actual biodiesel. The physical properties of biodiesel were analyzed and found that the viscosity at 40°C was 5.78 cSt, the acidity was 0.22 mg KOH/g, the water content was 0.0745% wt., the density at 15°C was 0.891 g/cm^3, and the flashpoint was at 170 °C.

Keywords: Biodiesel; Transesterification; Waste cooking oil; Calcium oxide.

1. INTRODUCTION

Waste cooking oil (WCO) is vegetable oil or animal fat that has formerly been used in the heating process. In Thailand, most of the cooking process use palm oil (90%). There are many ways to dispose of WCO; one interesting method is to produce biodiesel. It is also a way to convert waste into fuel for use in machines. Nowadays, the research for new energy alternatives to fossil fuels has received attention from all over the world due to the limited reserves of fossil fuels and the increasing price of fuel, and there are also concerns about greenhouse gas emissions. Therefore, biodiesel is considered another interesting alternative to solve the problem because it can be used in place of diesel fuel for industrial machines and automobiles, and it is also environmentally friendly [1]. Biodiesel is primarily derived from vegetable oils, animal fats, and cooking oils. When these materials react with methanol and use acids, bases, or enzymes as catalysts, biodiesel is produced by two main reactions: esterification and transesterification [2]. Among these, acid- or base-catalyzed transesterification is the most used technique because it is cost-effective and easy to implement [3]. Transesterification is the reaction to locate the ester group between triglycerides in oil and alcohol to form a new ester and glycerol using excess alcohol. To move the reaction forward, most of the catalysts used in biodiesel production, such as homogeneous alkaline bases, for example, NaOH and KOH, require washing of the product to remove the catalyst, which results in higher costs, and the methods used to eliminate the catalyst from the product in a homogeneous phase are difficult [4]. Solid alkaline earth oxides, such as calcium oxide (CaO), are used as highly efficient catalysts for biodiesel production. Many advantages of CaO catalysts include durability, easy separation from products, high recyclability, non-corrosion, environmental friendliness, and the fact that calcium oxide is found in nature, such as in eggshells and seashells [4],[5].

Therefore, this research studied the synthesis of biodiesel from used palm oil via the transesterification

process using a calcium oxide catalyst. Various factors, including methanol content, catalyst amount, time, and temperature, are considered to find the optimal conditions for biodiesel production.

2. EXPERIMENTAL

2.1 Material

Prepare a sample of used palm oil by filtering food waste sludge or various impurities with a filter fabric cloth, then heat-treatment by boiling at 110°C to remove moisture from the oil. Commercial calcium oxide (Loba) was used in this experiment.

2.2 Esterification Reaction

250 ml. of used palm oil was added to methanol 30, 40, and 50 percent by volume per volume of used palm oil and calcium oxide catalyst 0.856, 1.284, and 1.712 percent by weight per volume of used oil into a glass reactor. Vary the temperature at 60, 65, and 70°C and the reaction time at 120, 180, and 240 min. Then, the obtained mixture from the transesterification reaction was transferred into a separating funnel and allowed to stand for approximately 12 hours. until layer separation occurs between biodiesel, glycerol, and catalyst.

2.3 Experimental design

In this study, the optimization of biodiesel production was applied by the Box-Behnken design (BBD) technique with the Minitab program for designing experiments, building models, and evaluating the effects of factors. The complete model is based on the simultaneous variation of 4 factors at 3 levels with 27 experiments shown in Table 1.

2.4 Characterization of synthesis biodiesel

The functional groups of biodiesels were analyzed by a Fourier transform infrared (FT-IR) spectrometer (Spectrum G.X., PerkinElmer Ltd., United Kingdom) using the standard method ASTME2412. Viscosity was analyzed by a viscometer (SNB-1, Protronics Co., Ltd., Thailand) using the ASTM D445 standard method. Determination of density according to the ASTMD1298 standard method. The acidity value was measured according to the ASTMD974 standard method by titration, which was measured in mg KOH/g oil units as well as the alkalinity value. Represents the total amount of acid present in the oil. The value of the measured acidity indicates the rate of deterioration of the oil. The flash point according to the ASTM D93 standard method (PM-93 Pensky-Martens, stanhope-seta Ltd., United Kingdom). Moisture content is measured using titration with iodine (OMNIS, Metrohm AG, Switzerland).

3. RESULTS AND DISCUSSION

3.1 Response Surface Methodology of synthetic biodiesel from used palm oil by using calcium oxide catalyst

Percentages of yield's biodiesel from different conditions by Box-Benhken design (BBD) are shown in table 1. The result shows a yield of biodiesel between 77.60 and 98.00%.

Table 1 % yield of biodiesel obtains from experiment by Box-Benhken design.

Run order	Factors				
	CaO:WCO (%wt./v)	CH_3OH:WCO (%v/v)	Temp (°C)	Time (min)	% yield
1	1.284	50	65	240	91.2
2	1.284	40	65	180	92
3	0.856	50	65	180	84
4	0.856	40	60	180	90.4
5	1.712	50	65	180	87.2
6	0.856	30	65	180	90.8
7	1.712	40	70	180	89.6
8	1.284	40	60	240	94
9	1.284	40	65	180	89.2
10	1.284	30	70	180	93.2
11	1.712	40	65	240	98
12	0.856	40	65	240	91.6
13	1.284	50	65	120	77.6
14	1.284	40	60	120	81.2
15	1.284	40	70	120	90.8
16	1.284	40	65	180	86
17	0.856	40	70	180	92
18	1.712	30	65	180	85.6
19	1.712	40	65	120	83.2
20	1.284	30	60	180	91.2
21	0.856	40	65	120	86.8
22	1.284	50	60	180	85.2
23	1.284	40	70	240	96.4
24	1.284	30	65	240	90.8
25	1.284	50	70	180	91.6
26	1.284	30	65	120	86.8
27	1.712	40	60	180	90.8

A polynomial equation 1 was developed to describe the approximate regression model of synthetic biodiesel from used palm oil by using calcium oxide catalyst:

$$\%Yield = 422 - 14.4X_1 - 1.52X_2 - 9.95X_3 + 0.197X_4 + 0.20X_1^2 - 0.018X_2^2 + 0.084X_3^2 - 0.000042X_4^2 + 0.42X_1X_2 - 0.28X_1X_3 + 0.0833X_1X_4 + 0.022X_2X_3 + 0.004X_2X_4 - 0.006X_3X_4 \quad (1)$$

In equation 1, X_1 is %wt./v of catalyst to oil ratio, X_2 is %v/v of methanol to oil ratio, X_3 is temperature (°C), and X_4 is the reaction time (min).

The coefficient of determination (R^2) value means a good agreement between the experimental and predicted values of the fitted model. From the results, R^2 implies that 90.19% of the total variation in the response was justified by the model.

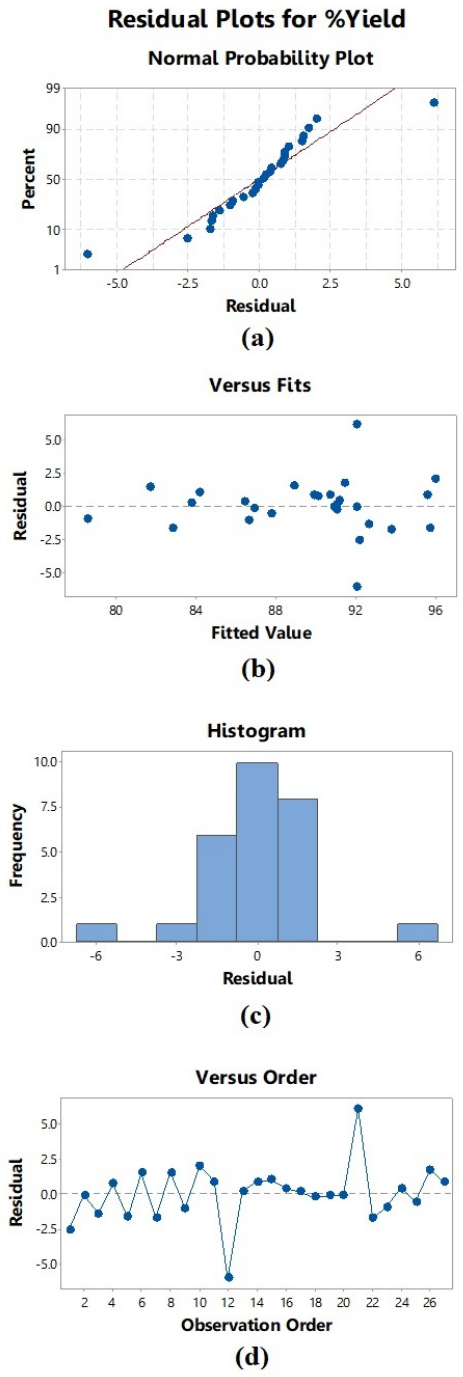

Figure 1 (a) Normal probability vs. residual, (b) residual vs. fitted values, (c) residual histogram, and (d) residual vs. observation order.

A comparison between the predicted and observed biodiesel product yields is presented in Figure 1. From the Figure 1(a), the error values, which are a scatter plot paired with the estimated values, on the regression line from the Normal Probability Plot graph have a graph like a straight line, indicating that the errors are normally distributed. Because the linear distribution of the biodiesel yield percentage did not show any abnormalities or the independence of residual values by graphing the relationship between residual and fitted values. The distribution of biodiesel yield percentages was found to exhibit an uncertain pattern(Figure 1(b)), as indicated by the distribution of independent samples. This demonstrates a high degree of information freedom. The residual histogram displays a bell-shaped curve, suggesting a linear distribution of the data, as shown in Figure 1(c). Additionally, the scatter plots show that the variance is stable. Furthermore, Figure 1(d) was observed that the percentage yield of biodiesel remained consistent on both the positive and negative sides, indicating stability in the variance of the data. Based on these findings, it can be concluded that the data obtained from this series of experiments are reliable and suitable for decision coefficient analysis and variance analysis applications.

3.2 Factors influencing of synthetic biodiesel

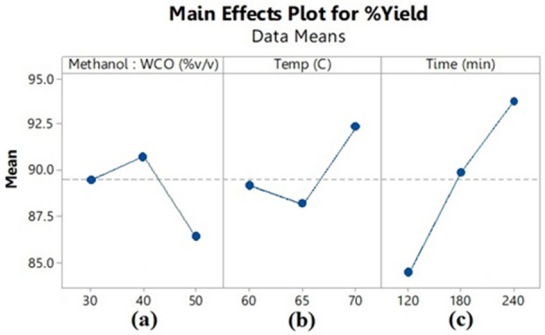

Figure 2 Main Effects Plot of %yield of synthesis biodiesel.

The P value of 0.011 shows that the %v/v of methanol : WCO was significant. When the amount of methanol is greater than 40 percent, the average percentage of biodiesel yield will decrease, as shown in Figure 2(a). Theoretically, it is found that 3 moles of methanol must be used per 1 mole of triglyceride to get 3 moles of methyl ester and 1 mole of glycerol. When an increase in the amount of alcohol is used, a reaction will occur. faster and more complete. From Figure 2(b), temperature has a significant effect on the percentage yield of biodiesel with a P value of 0.014, showing that temperature influences the transesterification reaction. The figure shows that the temperature is higher than 65°C and the graph becomes steeper. Because the temperature accelerates the transesterification reaction of oil and methanol by changing out the glycerol group and replacing it with the CH_3 group of methanol. The efficiency of the catalyst depends on the temperature at

which the biodiesel conversion system is made. It has been found that as the temperature increases, production also increases. Figure 2(c) shows that the reaction time has a most significant effect on the transesterification reaction, corresponding to a P-value of 0.000. The figure shows that the distribution of the data is linear. It can be concluded that the longer the reaction time, the higher the percentage of biodiesel yield will be. This is because the specific surface area and mass transfer are directly affected by the reaction time. With increased reaction time, productivity will increase until equilibrium is reached, before decreasing again due to the reversible nature of the reaction, but the temperature used is related.

However, it is clear that interaction between CaO:WCO ratio and time (X_1X_4), and Methanol:WCO and time (X_2X_4) were significantly effects on %biodiesel yield, when time is decreased, CaO and methanol were decreased with increasing %biodiesel yield as shown in Figure 3(a),(b). These results show that CaO can accelerate the reaction to produce the biodiesel and methanol can react with WCO complete.

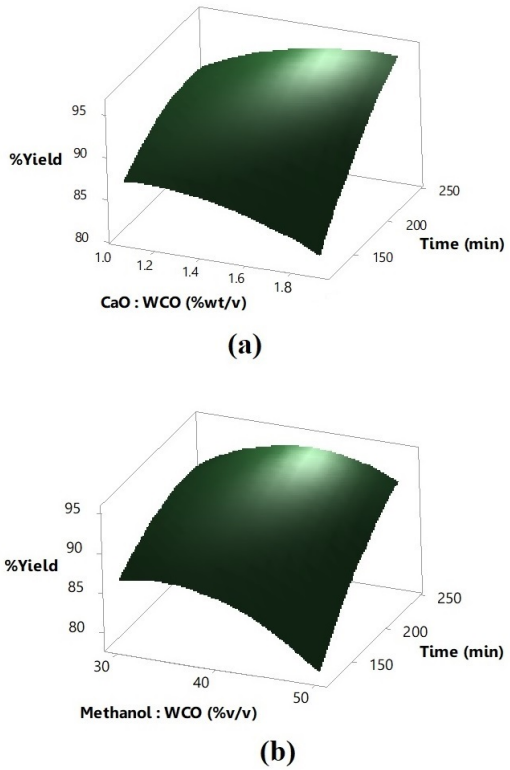

Figure 3 Response surface plots for the interaction of (a) CaO : WCO to time and (b) Methanol : WCO to time.

3.3 The Optimum Condition and Model Verification

The performance of finding the most suitable factors to obtain the highest percentage of biodiesel yield using the Response Optimizer function in the statistical package (Minitab). It was concluded that the most suitable conditions for producing biodiesel from vegetable oils are a reaction temperature of 70 °C, a reaction time of 240 minutes, and 50%v/v of methanol : WCO and 1.712%wt./v CaO :WCO, which yielded 99.33 percent biodiesel. When the experiment was repeated 5 times to prove the optimal condition, an average biodiesel yield of 99.20%. The value was close to the response optimizer's prediction of 99.33%. The obtained biodiesel was then further analyzed for its physical and chemical properties.

3.4 Characterization of synthesis biodiesel

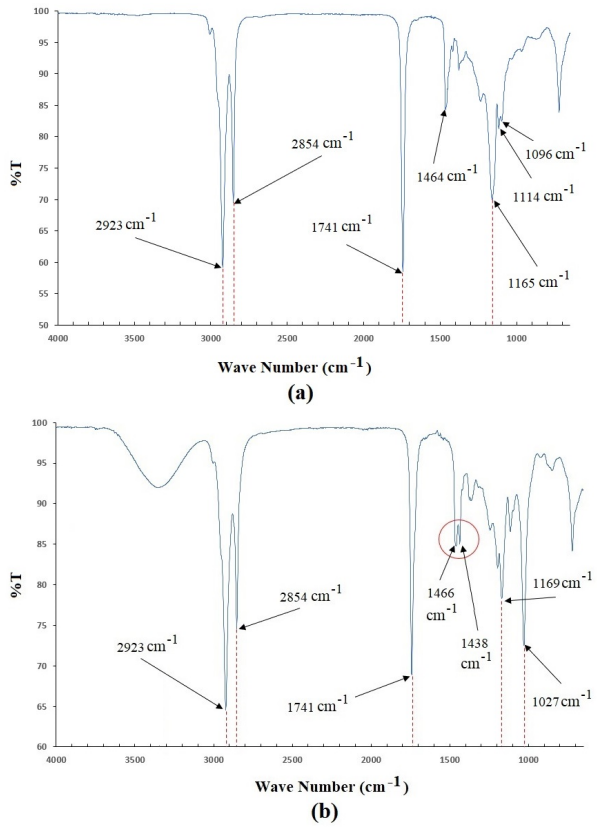

Figure 4 FT-IR spectrum of (a) Waste cooking oil (WCO) and (b) synthesis biodiesel.

The functional group of synthesis biodiesel was operated on by FT-IR techniques. The FTIR spectrum of waste cooking oil is shown in Figure 4(a). The peaks at 2923 cm^{-1} and 2854 cm^{-1} indicated the presence of C-H (Stretching) bonds of the methyl group (CH_3) and methylene group (CH_2). The peak at 1741 cm^{-1} and 1165 cm^{-1} corresponded to the C=O (Stretching) group and C-O (Stretching) of the ester, respectively. Furthermore, the band at 1464 cm^{-1} is due to C-H (Bending) of methylene group. The appearance of absorption frequencies at 1114 cm^{-1} and 1096 cm^{-1} reflected the C-O bonds of primary alcohol and secondary alcohol that were found in triglycerides. Figure 4(b) shows the FT-IR spectrum of biodiesel that was synthesized from the transesterification reaction of used palm oil at optimum condition. The peaks at 1466 cm^{-1} and 1438 cm^{-1} indicate the presence of C-H (Bending) bonds of methylene group (CH_2) and methyl group (CH_3), which is different from FT-IR. The

spectrum of waste palm oil found only a single peak at 1464 cm^{-1} of the methylene group (CH_2). The FT-IR result shows that the methyl group (CH_3) was produced by waste palm oil reacting with methanol under a calcium oxide catalyst. The resulting product is methyl ester (biodiesel), of which the FT-IR spectrum has the same characteristics as commercial biodiesel on the market [6].

The acidity value is 0.22 mg KOH/g which is acceptable according to standard biodiesel. Higher acidity directly affects engine corrosion, which reduces the service life of the filter and engine. The density and viscosity of synthesized biodiesel are 0.891 g/cm^3, and 5.78 cSt, respectively. Density is a one of the factors in properties of biodiesel; when the density of fuel is higher, more heat energy is required. Viscosity is an important biodiesel property because fuels with too high viscosity result in poor atomization characteristics of the injector in the combustion chamber, causing incomplete combustion. A water content of 0.0745 %wt. is higher than the standard value of biodiesel, according to the announcement from ASTM D6751-12. Water left over from the biodiesel production process results in poor combustion and causes a hydrolytic reaction between water and esters to form wax, which results in corrosion in the engine. The flash point of biodiesel is 170°C, which is higher than standard biodiesel.

4. CONCLUSION

This study investigated the transesterification reaction of used palm oil with methanol using calcium oxide as a catalyst. The optimum condition for the synthesis of biodiesel was studied via the Box-Behnken design, in which temperature, time, methanol, and calcium oxide catalyst were chosen as the important parameters. Based on the results, the highest yield of biodiesel synthesis (99.20%) was investigated at a temperature of 70°C, a reaction time of 240 min., 50% v/v of methanol, and 1.712% wt./v of calcium oxide catalyst. Upon analyzing the synthesized biodiesel with FT-IR, the C-H (Bending) bands of the methyl (CH_3) and methylene (CH_2) groups were observed at peaks of 1466 cm^{-1} and 1438 cm^{-1}, respectively. These peaks signify the characteristics of biodiesel, which are closely consistent with standard biodiesel. The chemical and physical properties of the produced biodiesel were examined and found that the viscosity at 40°C is 5.78 cSt, the acidity is 0.22 mg KOH/g, the water content is 0.0745 %wt., the density at 15°C is 0.891 g/cm^3, and the flash point is at 170°C. It was found that the acidity, density, viscosity, and flash point values are within standard biodiesel, while the water content is slightly higher than the standard.

ACKNOWLEDGMENTS

This work is supported by the School of Engineering, King Mongkut's Institute of Technology Ladkrabang. Focus lab Ltd. support oil analysis and instruments.

REFERENCES

1. S. V. Lakshmi, A. M. Aparna, and R. Baskaran Production of Biodiesel from Waste Cooking Oil. *5th Int. Conf. Sci. Technol. Eng. Math. ICONSTEM* 2019: 270-274.
2. S. M. Pavlović, et al. A CaO/zeolite-based catalyst obtained from waste chicken eggshell and coal fly ash for biodiesel production. *Fuel* 2020; 267(1): 117-171.
3. D. M. Marinković, et al. Calcium oxide as a promising heterogeneous catalyst for biodiesel production: Current state and perspectives. *Renew. Sustain. Energy Rev* 2016; 56: 1387–1408.
4 H. Mazaheri, et al. An overview of biodiesel production via calcium oxide based catalysts: Current state and perspective. *Energies* 2021; 14(13): 1–23.
5 R. Thaoklua, J. Janjaroen, and K. Tedsree. The study of activity and selectivity of calcium oxide nanocatalyst for transesterification of high free fatty acid crude palm oil. *Chiang Mai J. Sci.* 2018; 45(2): 973–983.
6 R. Naureen, M. Tariq, I. Yusoff, A. J. K. Chowdhury, and M. Ashraf. Synthesis, spectroscopic and chromatographic studies of sunflower oil biodiesel using optimized base catalyzed methanolysis. *Saudi J. Biol. Sci.* 2014; 22(3): 332–339.

Effect of catalyst bed configuration on temperature profile and reactor performance for Fischer-Tropsch synthesis: A computational fluid dynamics simulation

Natthasit Khawyen[1], Lida Simasatitkul[2,*], Suwimol Wongsakulphasatch[3], Sakhon Ratchahat[4], Suttichai Assabumrungrat[1,5]

[1] Center of Excellence in Catalysis and Catalytic Reaction Engineering, Department of Chemical Engineering, Faculty of Engineering, Chulalongkorn University, Bangkok 10330, Thailand
[2] Department of Industrial Chemistry, Faculty of Applied Science, King Mongkut's University of Technology North Bangkok, Bangkok 10800, Thailand
[3] Department of Chemical Engineering, Faculty of Engineering, King Mongkut's University of Technology North Bangkok, Bangkok 10800, Thailand
[4] Department of Chemical Engineering, Faculty of Engineering, Mahidol University, Nakhon Pathom 73170, Thailand
[5] Bio-Circular-Green-economy Technology & Engineering Center (BCGeTEC), Faculty of Engineering, Chulalongkorn University, Bangkok 10330, Thailand
[*] Corresponding author: lida.s@sci.kmutnb.ac.th

ABSTRACT

Reactor performance and catalyst stability are significantly impacted by the extremely exothermic reaction of Fischer-Tropsch synthesis (FTS) that results in hot spot formation. In this regard, the arrangement of catalyst could change a temperature profile within the reactor and reduce hot spot effect. This study investigates the performance analysis of a single-layer (i.e., 15%, 20%, and 30% loading) and multilayers (varying at 1% to 30% loading) of the catalytic fixed-bed reactor for the Fischer-Tropsch synthesis (FTS) by using a spiral-structured Co/SiO_2 catalyst. A simulation model of a fixed-bed reactor with a 1 cm of diameter and a 25 cm of catalyst zone is developed using COMSOL Multiphysics. The inlet temperature and pressure are operated at 220°C and 20 bar, respectively. The results showed that the use of spiral-structured Co/SiO_2 catalyst could offer advantages in heat distribution and removal. The single-layer catalytic bed with 15%, 20%, and 30% catalyst loadings showed the hot spot temperatures of 233°C, 235°C, and 237°C, respectively. Different arrangements of a multilayered catalytic bed reactor are proposed (Model A, increasing catalyst loading from 1% to 30%, and Model B decreasing from 30% to 1%). The results showed that the multilayered catalytic bed arrangement in Model B can significantly enhance FTS reactor performance by reducing the hotspot to 230°C and improving a CO conversion efficiency to 80.9%

Keywords: Fischer-Tropsch synthesis (FTS); CFD simulation; Cobalt structured catalyst; Hot spot; Multilayer catalytic bed

1. INTRODUCTION

Fischer-Tropsch synthesis (FTS) is a well-established catalytic process that converts synthesis gas (CO and H_2) into long-chain hydrocarbons, offering a sustainable route to produce clean synthetic fuels and chemicals. As global demand for cleaner energy increases, the relevance of FTS has grown, particularly due to its compatibility with alternative carbon sources such as biomass, natural gas, and industrial CO_2 emissions. FTS produces a range of hydrocarbons, including n-paraffins, olefins, and waxes, which are highly dependent on operating conditions and catalyst design. These products follow the Anderson-Schulz-Flory (ASF) distribution, where product selectivity is dictated by chain growth probability (α) [1].

The FTS operates under moderate temperatures (200–350 °C) and pressures (2–5 MPa), with the operating temperature playing a crucial role in determining product selectivity. High-temperature FTS, typically conducted with iron-based catalysts, favors the production of gasoline-range and low molecular weight olefins. Conversely, low-temperature FTS using cobalt-based catalysts is more suited to producing heavier hydrocarbons and waxes [2]. However, the high exothermicity of the reaction (ΔH_{298} = –160 kJ/mol CO) poses significant challenges, for example, the formation of hot spots within fixed-bed reactors can easily form on the catalyst surface,

impacting the performance of FTS reactor and causing the production of lighter hydrocarbon products instead [3].

Various methods have been employed to mitigate the exothermicity of the FTS reaction. One approach is to reduce a reactor tube diameter, as seen in Shell's narrower Co-based multi-tubular reactors compared to Sasolburg's Fe-based designs to control heat release [2, 4,5]. Another method involves using milli-fixed bed reactors, where a 2.5 mm tube diameter was shown to lower radial temperatures and hot spot formation by 10°C, improving selectivity and minimizing light hydrocarbons production [6]. Additionally, optimizing internal reactor designs by adjusting neck diameter and frustum cavity height have been shown to suppress hot spots and enhance product selectivity [7].

The development and design of catalysts for FTS are extensively studied to enhance heat transfer and manage the exothermic heat. Common FTS catalysts are based on transition metals such as cobalt, iron, nickel, and ruthenium, with selection depending on temperature regime and feedstock type [8,9].

Pellet catalysts, typically spherical or cylindrical and composed of porous materials, are widely used for syngas conversion. However, their performance is often limited by poor heat and mass transfer. One major challenge is the uneven heat distribution within the granules, which can lead to localized overheating of active sites, potentially degrading catalyst performance and reaction efficiency. Moreover, this unequal heat distribution may result in thermal runaway conditions, in which the temperature in the center of the granule rises noticeably above the surface, further impairing stability and selectivity [10].

Improving heat transfer is a critical challenge in FTS due to the highly exothermic reaction. Two main strategies have been proposed: (I) incorporating high thermal conductivity materials into the Co/SiO_2 catalyst systems, and (II) using structured reactors with well-designed structured of Co/SiO_2. Adding materials such as silicon carbide (SiC) and aluminum chips improves heat transfer during Fischer-Tropsch synthesis (FTS). Notably, SiC has a thermal conductivity of 490 W/m·K, while aluminum has 237 W/m·K, both of which facilitate effective heat dissipation from the reaction zone [11].

Structured Co/SiO_2 catalyst, particularly in spiral-type configurations, offers enhanced heat and mass transfer over packed beds with added materials and plate-type structures. Its geometry ensures uniform temperature distribution, minimizes hot spot formation, and improves catalyst performance. Compared to systems like aluminum foams [12], honeycomb monoliths [13], and 3D-printed AlSiMg monoliths [14], despite their effectiveness, they are more costly, need more complicated preparation and are more difficult to scale up. In contrast, spiral catalysts are relatively low-cost, easy to prepare, and improve reactant distribution, leading to higher reaction rates and enhanced selectivity, especially valuable for green diesel production [11].

Enhancing catalytic bed utilization and ensuring a uniform temperature profile along the axial direction of the reactor are important factors in managing the highly exothermic FTS reaction. To control temperature, catalyst activity can be reduced by diluting the catalyst with inert materials or by using catalysts with different activities along the reactor length [15, 16, 17]. In addition, investigations of multilayer catalyst beds have shown positive effects on the temperature profile by optimizing catalyst layer utilization and promoting more uniform heat distribution. This method can effectively reduce the adiabatic temperature rise, lower the maximum temperature in the reactor, and decrease catalyst deactivation due to high heat, thereby improving overall catalyst efficiency. Furthermore, studies using a dual-tube reactor system have examined changes in product distribution caused by adjusting catalyst layers, highlighting the importance of optimizing reaction parameters and controlling temperature to ensure uniform catalytic activity across all reactor tubes [5].

Computational Fluid Dynamics (CFD) has proven to be an essential tool for analyzing and optimizing reactor performance in Fischer-Tropsch synthesis. CFD simulations enable a detailed understanding of the complex interactions between fluid flow, heat transfer, mass transfer, and reaction kinetics, which are difficult to study experimentally. Therefore, CFD simulation studies are of great interest. While Moazami et al. (2015) presented a numerical pseudo-homogeneous one-dimensional (1D) mathematical model to simulate a mini-scale laboratory fixed-bed reactor for FTS, the model focused on the conversion of N_2-rich syngas (17% CO, 33% H_2, and 50% N_2) over a Co/SiO_2 catalyst, aiming to predict reactant conversion rates and product selectivity, particularly hydrocarbons. Additionally, it calculated the kinetic parameters essential for the proposed model. The study also examined the impact of various operating conditions, including temperature, pressure, and gas hourly space velocity (GHSV), on conversion efficiency and product distribution [18]. Jianqi Shen and Xinying Liu (2022) presented a study using Computational Fluid Dynamics (CFD) and a two-dimensional (2D) pseudo-homogeneous model to investigate the effect of thermal conductivity in the Co/SiO_2 catalyst bed on FTS within a fixed-bed reactor. The primary objective of the study was to explore how variations in the thermal conductivity of the Co/SiO_2 catalyst bed influence the overall FTS process. The researchers aimed to optimize key reactor parameters, such as catalyst activity and space velocity (SV), to maximize productivity [18]. Meanwhile, Arzamendi et al. (2010) conducted a Computational Fluid Dynamics (CFD) study on heat transfer in a microchannel reactor for FTS, coupling the exothermic reaction with efficient heat removal. Three-dimensional (3D) simulations were performed using

ANSYS CFX software to analyze heat transfer characteristics within the microreactor. The study aimed to evaluate the effectiveness of heat removal during the FTS process and to identify optimal design parameters, such as channel geometry and grid characteristics, to enhance overall reactor performance [19].

One-dimensional (1D) modeling in FTS offers benefits such as computational efficiency, simplicity, and faster calculations. However, it often assumes uniform flow profiles and neglects axial dispersion, which can lead to inaccuracies in predicting reactor performance. Two-dimensional (2D) models strike a balance between computational cost and accuracy by capturing key heat transfer, mass transfer, and fluid flow behaviors, making them suitable for studying thermal conductivity and temperature profiles in catalyst beds. In contrast, three-dimensional (3D) models provide the most detailed reactor representation but demand significant computational resources, longer simulation times, and involve complex meshing and boundary condition settings. Moreover, 3D models can become overfitted to specific operating conditions, reducing their generalizability.

Fischer-Tropsch Synthesis (FTS) has been extensively studied using Computational Fluid Dynamics (CFD), primarily with pellet catalysts, while structured catalyst designs remain underexplored. Although spiral-type structured catalysts have demonstrated improved heat transfer performance, they may not fully eliminate hot spots within the reactor. Catalyst arrangement such as multilayer configurations has been investigated as a potential solution to enhance thermal management. However, the complexity and high cost of fabricating spiral-type structured catalysts pose significant challenges for experimental validation.

To overcome these constraints, this study proposes an innovative approach by integrating spiral-type structured catalysts with multilayer catalytic bed arrangements to improve heat dissipation and minimize hot spot formation during FTS. The optimal reactor configuration and operating conditions are evaluated in terms of CO conversion, hydrocarbons yield, and product selectivity. A two-dimensional pseudo-homogeneous model is employed to investigate key transport phenomena such as temperature distribution, flow behavior, and catalyst performance—through Computational Fluid Dynamics (CFD) simulations using COMSOL Multiphysics 6.1.

This study aims to evaluate and optimize the temperature profile and catalytic performance of a fixed-bed reactor with a Co/SiO_2 spiral structured catalyst. The primary focus is on analyzing heat distribution efficiency and mitigating hot spot formation by comparing single-layered catalyst bed with uniform loadings of 15%, 20%, and 30% to multilayered catalyst beds with graded loadings of 1%, 3%, 5%, 10%, 15%, 20%, and 30%. Two multilayered configurations are investigated: Model A, in which catalyst loading increases from 1% to 30% from top to bottom, and Model B, where the loading decreases from 30% to 1% from top to bottom. The performance of these configurations is assessed to identify the optimal design for improved thermal management and catalytic efficiency in Fischer–Tropsch Synthesis.

2. MODELING AND SIMULATION

The Fischer-Tropsch Synthesis was simulated using COMSOL Multiphysics Version 6.1 software, a software that use a Finite Element Method (FEM) solver for engineering applications. The heterogeneous catalytic process was simulated in a two-dimensional fixed-bed reactor model with a spiral-structured catalyst for investigate transport phenomena.

An asymmetric 2D fixed-bed reactor model based on the assumption of uniformly distributed catalyst is introduced in the geometry to present the symmetric cylindrical properties of a typical reactor regardless of any changes in the angular direction shown in Figure 1. All the spiral catalysts are loaded in a fixed-bed reactor with the catalytic zone length and diameter of 25 cm and 1 cm shown in Figure 2

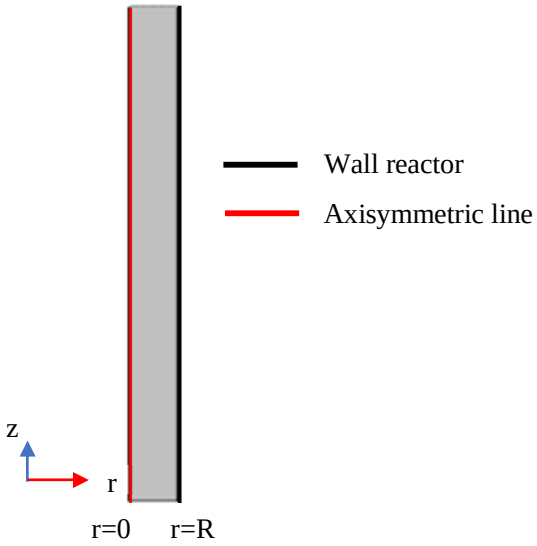

Figure 1 The schematic of fixed-bed reactor

Table 1 The dimension of catalyst

Loading (%)	1%	3%	5%	10%	15%	20%	30%
Bed length, h (mm)	50	50	50	50	50	50	50
Bed width, w (mm)	7	7	7	7	7	7	7
ρ_{be} (kg/m^3)	53.8	161.5	269.2	538.4	807.5	1076.7	1615.1
ρ_b (kg/m^3)	18.8	56.5	94.2	188.4	282.6	376.9	565.3
Porosity, ε	0.65	0.65	0.65	0.65	0.65	0.65	0.65

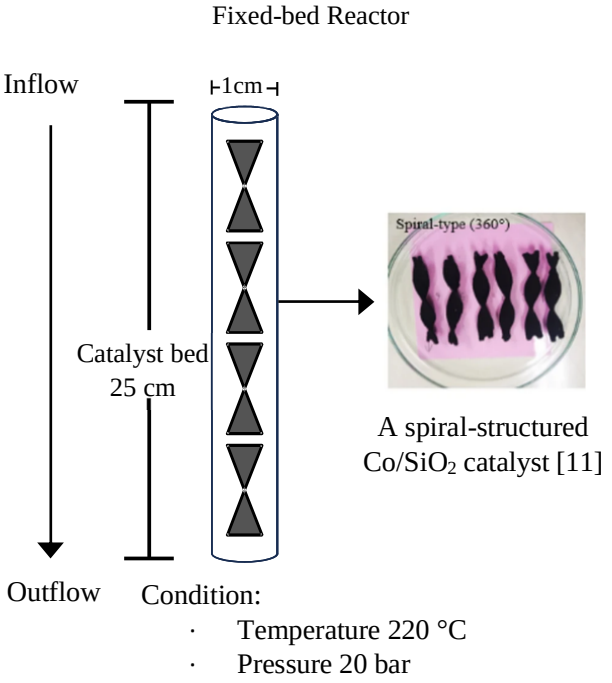

Figure 2 The schematic of fixed-bed reactor

The following assumptions were made to develop the governing equations:

- The simulation is conducted under steady-state and non-isothermal conditions.
- A pseudo-homogeneous model is used to describe momentum transfer, heat transfer, mass transfer, and chemical reactions in the fixed-bed reactor.
- The gas mixture behaves as an ideal gas at the operating conditions of 220 °C and 20 bar.
- Viscosity and density of syngas are assumed to be constant throughout the reactor [21].
- Liquid-phase flow is neglected in the simulation [21].
- The catalyst bed is assumed to be homogeneous, with uniform distribution and constant porosity throughout the reactor.
- The model includes only paraffin formation, excluding olefins and other hydrocarbon products
- The formation of oxygenates and water-gas shift (WGS) reactions are neglected due to their low occurrence with Co-based catalysts [6].

2.1 Catalyst geometrical characterization

The correlations of the characteristic and dimension of spiral catalyst are expressed in Table 1, The result of The Spiral-type catalyst S_{BET} of 143.6 m^2/g, Total pore volume of 0.636 cm^3/g and Pore diameter of 18.9 nm. A theoretical correlation for predicting the correlations of the characteristics of spiral catalyst was given by Aurud et al, (2024). The spiral structured catalyst (SCS) is designed with a twist angle of 360° shown in Figure 2.3, which enhances the flow dynamics of reactant gases. This unique shape allows for improved contact between the gases and the catalyst surface, facilitating better heat and mass transfer during the Fischer-Tropsch synthesis (FTS) process. The preparation involves a coating method where the Co/SiO_2 catalyst powder is mixed with an alumina sol-gel binder. This slurry is then applied to an aluminum substrate, which is shaped into a spiral form. The use of aluminum as a substrate is crucial for achieving the desired structural properties and thermal conductivity [11].

Figure 3 The spiral structured catalyst (SCS) [22]

2.2 Governing equations

The equation of mass was used to investigate the fluid flow within a fixed-bed reactor, characterizing the rate of fluid inflow and output within the boundary. The followings are the differential forms, Eqs. 1 – 3

$$\nabla \cdot J_i + u \cdot \nabla C_i = R_i \qquad \text{(Eq. 1)}$$

$$J_i = -(D_{D,i} + D_{e,i}) \nabla C_i \qquad \text{(Eq. 2)}$$

$$\nabla \cdot [-(D_{D,i} + D_{e,i}) \nabla Ci] + u \cdot \nabla Ci = Ri \qquad \text{(Eq. 3)}$$

Where J_i is mass flux of species i [mol/(m²·s)], u is fluid velocity [m/s], C_i is concentration of species i [mol/m³], Ri is reaction rate of species iii [mol/(m³·s)], $D_{D,i}$ is molecular diffusion coefficient [m²/s], De,i is effective dispersion coefficient [m²/s].

The transport of gaseous reactants such as CO and H_2 through the porous catalyst structure is governed by the effective diffusivity De,j accounting for the

complex nature of diffusion within porous media. The effective diffusivity is expressed in Eq. 4:

$$D_{e,j} = \frac{\varepsilon_p}{\tau_{F,j}} D_{F,j} \qquad \text{(Eq. 4)}$$

where $D_{e,j}$ is the bulk/molecular diffusivity [m²/s], $D_{F,j}$ is the effective diffusivity [m²/s], ε_p is the porosity of the medium, and $\tau_{F,j}$ is the tortuosity factor, accounting for the complexity of diffusion paths in the porous structure.

The equation of energy was used to describe the average temperature distribution of the fluid in the reactor. The differential forms of the energy equation is as follows as Eqs. 5 – 7

$$\rho_f C_p u \cdot \nabla T + \nabla \cdot q = Q \qquad \text{(Eq. 5)}$$

Conductive Heat Transfer:

$$\nabla \cdot q \qquad \text{(Eq. 6)}$$

This term models heat transfer through conduction, governed by Fourier's law

$$q = -k_{eff} \nabla T \qquad \text{(Eq. 7)}$$

where ρ_f is the fluid density [kg/m³], C_p is the specific heat capacity [J/(kg·K)], u is the velocity vector [m/s], T is the temperature [K], q is the heat flux [W/m²], and Q is the heat source term [W/m³].

The mass conservation (Continuity) equation ensures that mass is conserved within a flow system by stating that the rate of mass accumulation in a control volume is equal to the net mass flux across its boundaries. This principle is fundamental for accurately modeling the transport of reactants and products within Fischer-Tropsch catalyst beds. Additionally, Darcy's Law describes the flow of fluids through porous media, asserting that the fluid velocity is directly proportional to the pressure gradient and permeability, and inversely proportional to the fluid's viscosity. This relationship is critical in modeling gas transport through the porous catalyst structure in Fischer-Tropsch synthesis.

The governing equations are represented as follows in Eqs. 8–9.

$$\nabla \cdot (\rho u) = Q_m \qquad \text{(Eq. 8)}$$

$$u = -\frac{\kappa}{\mu} \nabla P \qquad \text{(Eq. 9)}$$

Where ρ is the fluid density [kg/m³], u is the velocity vector [m/s], Q_m is the mass source term [kg/(m³·s)] representing mass generation or consumption (e.g., from chemical reactions), κ is the permeability of the porous medium [m²], μ is the dynamic viscosity of the fluid [Pa·s], and ∇P is the pressure gradient [Pa/m].

Boundary conditions are constraints that determine the behavior of the physical system at the boundary, important for accurately solving the mathematical equations of the reactor model. The feed parameters, namely temperature, pressure and reactant concentration, are set as boundary conditions as listed in Table 2

Table 2 The boundary conditions

Location	Mass Equations	Energy Equations	Momentum Equation
Reactor Inlet	C_i (0, r) = $C_{i,in}$	T (0, r) = Tin	$P(0,r) = P_{in}$ $u(0,r) = u_{in}$
Reactor Outlet	J_i (L, r) = J_i	q_i (L, r) = 0	$P(L,r) = P_{in}$
Reactor wall	J_i (0, R) = 0	T (0, R) = T_W = T_{in}	$P(z, R) = 0$ $u(z, R) = 0$

2.3 Reaction kinetic model

The Fischer-Tropsch reaction and CO-methanation as shown in Eqs. 10-11 consist of a paraffin reaction and methane, with the enthalpy of reaction ΔH_{298K} of -160 kJ/mol and -41 kJ/mol, respectively. In this reaction carbon monoxide and hydrogen are fed in a ratio of 1:2 at a temperature of 220 °C and a pressure of 20 bar. Thus, the water-gas shift reaction could be neglected when using FTS cobalt-based catalyst [6]

Paraffins reaction

$$nCO\,(g) + (2n+1)\,H_2\,(g) \longrightarrow C_nH_{2n+2} + H_2O \qquad \text{(Eq. 10)}$$

CO-methanation

$$CO\,(g) + 3H_2\,(g) \longrightarrow CH_4\,(g) + H_2O\,(g) \qquad \text{(Eq. 11)}$$

The reactor model developed in this study incorporates CO-methanation kinetics proposed by Iglesia et al. [23] and Fischer-Tropsch (FT) reaction kinetics from Yates and Satterfield [24]. The reaction stoichiometry is based on the work of Hillestad et al. [25], which applies the Anderson-Schulz-Flory (ASF) distribution. The ASF model statistically represents the distribution of FT products according to the chain growth probability (α). Hillestad's approach simplifies the overall reaction network by considering only the methanation reaction occurring in parallel with the FT reaction, focusing solely on the formation of linear paraffins as FT products [26].

This kinetic model depends on both carbon monoxides and hydrogen partial pressures and Temperature. Co/SiO_2 Catalyst was applied to the simulation because of the extensive studies of the kinetic modeling in two main equilibrium reactions of the FTS process. The kinetic rate expressions and

kinetic parameters are shown in Tables 3 and 4, respectively.

Table 3 The kinetic rate expression [22,23,24]

Kinetics reaction rate	Expression	
CO methanation	$R_{CH4} = \frac{k_1 P_{H_2} P_{CO}^{\beta}}{1+K_3 P_{CO}}$	(Eq. 12)
Fischer-Tropsch Reaction	$R_{FT} = \frac{k_2 P_{H_2} P_{CO}}{(1+K_4 P_{CO})^2}$	(Eq. 13)
Stoichiometry	$\nu_{i,p} = \frac{\alpha^{i-1}\cdot(1-\alpha)^2}{1 + e^{-0.3}}$	(Eq. 14)
Paraffins Reaction	$R_p = \frac{R_{FT} - R_{CH4}}{1-\nu_{i,p}}$	(Eq. 15)

Table 4 The kinetic rate parameters [22,23,24]

Parameter		Value
Order of reaction	β	0.05
Alpha parameter	α	0.9
Pre-exponential factor of reaction j	k_1 ($kmol_{CH4}/(m^3 \cdot s \cdot bar^{1.005})$)	Table 5
	k_2 ($kmol_{FT}/(m^3 \cdot s \cdot bar^2)$)	Table 5
Adsorption constant for species	K_3 (1/Pa)	3.31×10^{-5}
	K_4 (1/Pa)	3.61×10^{-6}

Table 5 The kinetic parameters of a spiral structured Co/SiO_2 catalyst

%loading of Co	Kinetic parameters	
	k_1 ($kmol_{CH4}/(m^3 \cdot s \cdot bar^{1.005})$)	k_2 ($kmol_{FT}/(m^3 \cdot s \cdot bar^2)$)
1	4.67×10^{-11}	1.00×10^{-7}
3	1.40×10^{-10}	2.74×10^{-7}
5	2.33×10^{-10}	1.27×10^{-6}
10	4.67×10^{-10}	1.01×10^{-5}
15	7.00×10^{-10}	3.42×10^{-7}
20	9.34×10^{-10}	8.11×10^{-5}
30	1.40×10^{-9}	9.58×10^{-5}

2.4 Mesh geometry

The mesh grid resolution plays a crucial role in the accuracy of CFD simulations. An insufficient number of elements may result in non-convergent or inaccurate solutions, whereas overly fine meshes improve precision at the expense of computational time. Therefore, performing a mesh independence study is essential to balance solution accuracy and computational efficiency.

In this study, the computational domain was discretized using mapped rectangular elements generated with COMSOL's built-in meshing tools, which provide resolution settings ranging from extremely coarse to extremely fine. A series of mesh densities were tested, ranging from 100 to 3000 elements, including intermediate values such as 500, 1015, 1890, and 2520, to evaluate the sensitivity of the results to mesh refinement and ensure numerical stability and accuracy.

The mapped mesh structure yielded an average mesh quality of 1.0, indicating excellent suitability for the reactor geometry. During the grid independence analysis, CO conversion values stabilized at finer mesh resolutions, particularly beyond 1600 elements. As shown in Figure 4, further refinement had negligible impact on the results. Therefore, a mesh size of 1600 elements was selected as the optimal configuration, providing a balance between computational efficiency and simulation accuracy.

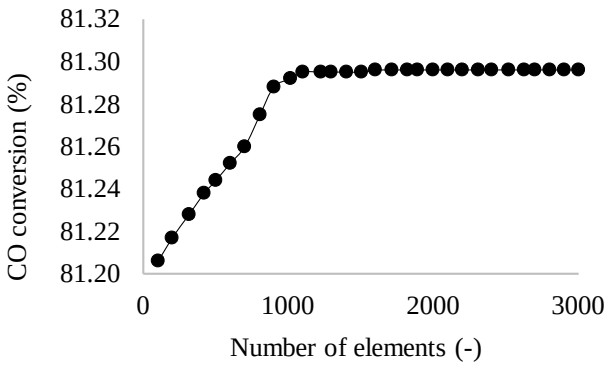

Figure 4 Mesh analysis

3. Results and discussion

3.1 Model Verification and Validation

The fixed-bed reactor model packed with a Co/SiO_2 spiral structured catalyst was validated with the experimental data reported by Aurud et al. [11] under adiabatic conditions. As shown in Table 6, the model predicted CO conversion with a low relative error of 1.9%. Product selectivity for CH_4, C_2H_6, and C_5^+ was accurately predicted, with errors of 7.3%, 2.1%, and 3.7%, respectively. Oil selectivity in the C_5–C_{11} and C_{12}–C_{20} ranges consistent with experimental data within 4% error. A higher deviation of 4.3% was noted for the C_{21}^+ fraction, likely due to limitations in the kinetic model for heavier hydrocarbons. Overall, the model demonstrated strong predictive accuracy and reliability for Fischer–Tropsch synthesis under the specified conditions, supporting its use in further design its use in further parametric and catalyst configuration studies.

Table 6 Comparison of CO Conversion, Product and Oil selectivity between experiment and simulation.

Parameter	Experiment (%)	Simulation (%)	Error (%)
CO Conversion	79.4	80.5	1.9
Product selectivity (%)			
CH_4	7.7	7.1	7.3
C_2H_6	0.96	0.98	2.1
C_{5+}	87.8	91.1	3.7
Oil selectivity (%)			
C_5-C_{11}	35.4	36.5	3.1
C_{12}-C_{20}	63.7	62.2	2.4
C_{21+}	0.92	0.88	4.3

3.2 Temperature profile

A comparison between experimental and simulation results of the temperature profile along the length of a 25 cm catalyst bed in a fixed-bed reactor with a Co/SiO_2 spiral-structured catalyst was shown in Figure 5. The temperature in the reactor initially rises near the inlet due to the exothermic nature of the Fischer–Tropsch synthesis reaction, peaking within the first few centimeters. Thereafter, the temperature gradually declines along the bed length. The simulation closely follows the trend of the experimental data, with a relative error of only 2.46%, indicating that the model provides a reliable prediction of the thermal behavior within the reactor. The small discrepancy observed near the reactor outlet may be attributed to limitations in experimental temperature control.

Figure 6 illustrates the simulated temperature profiles along a 25 cm catalyst bed for three catalyst loadings (15%, 20%, and 30%), showing an initial sharp temperature rise near the reactor inlet due to the exothermic Fischer–Tropsch reaction, with the 30% loading exhibiting the highest peak indicating intensified reaction activity and heat generation followed by a gradual decline in temperature along the bed as reactants are consumed; higher loadings lead to steeper thermal gradients and potential hot spot formation, whereas lower loading offers improved thermal management but potentially lower CO conversion efficiency.

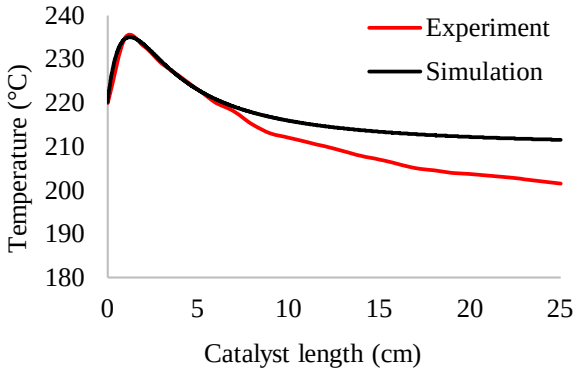

Figure 5 Comparison of experimental and simulation temperature profiles along the catalyst bed length.

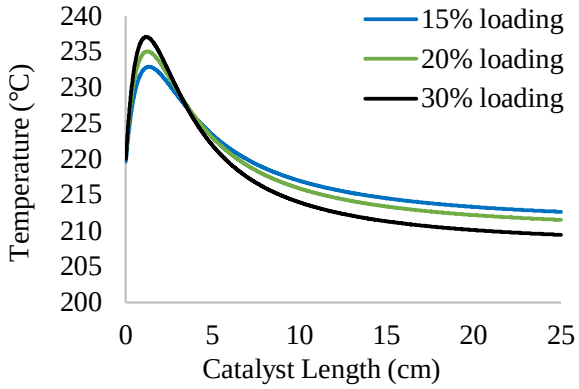

Figure 6 Temperature contours of the 2D axisymmetric fixed-bed reactor for different catalyst loading

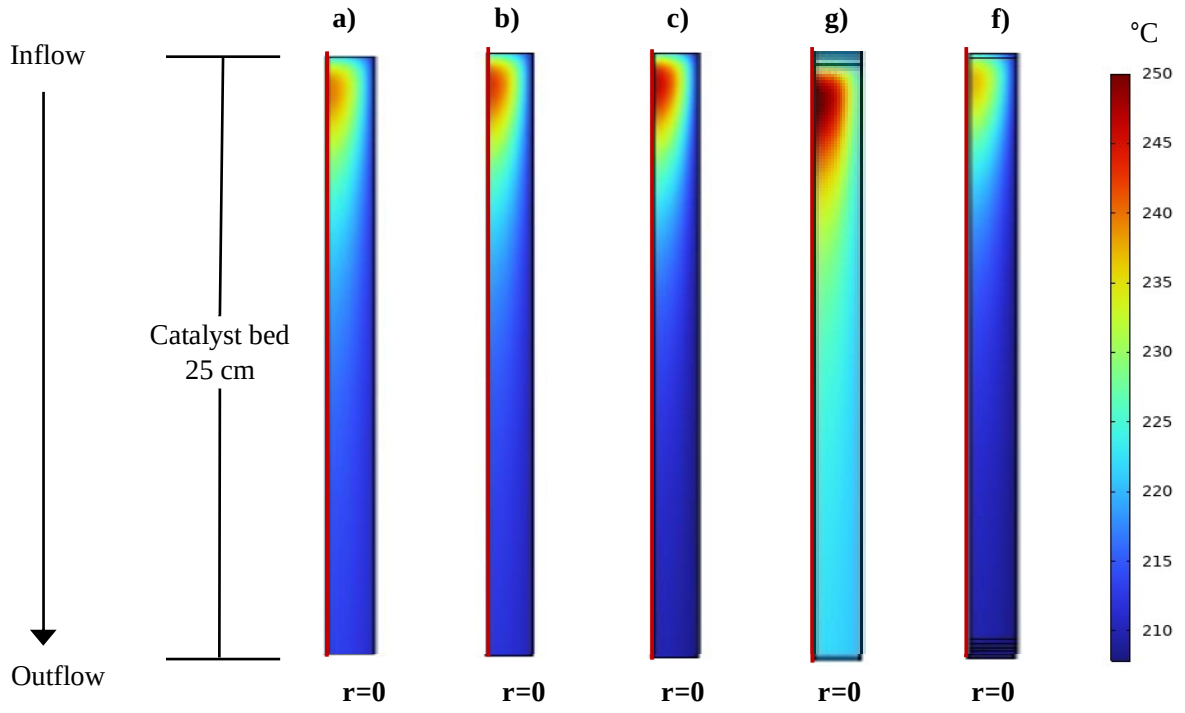

Figure 7 Temperature contours of the 2D-axisymmetric reactor with a 25 cm catalyst bed under various catalyst loading configurations: (a) single-layer with 15% loading, (b) single-layer with 20% loading, (c) single-layer with 30% loading, (g) Model A: multilayered catalytic bed arrangement with increasing loading from 1% to 30% (top to bottom), (f) Model B: multilayered catalytic bed arrangement with decreasing loading from 30% to 1% (top to bottom).

3.3 Effect of catalyst bed configurations

Table 7 Comparison of CO conversion and hydrocarbon product selectivity in Fischer–Tropsch Synthesis with different catalyst bed configurations

Catalyst Configuration	CO conversion (%)	Product selectivity (%)			Oil selectivity (%)		
		CH_4	C_2H_6	C_{5+}	C_5-C_{11}	C_{12}-C_{20}	C_{21+}
15% loading	78.6	3.1	0.48	95.4	62.9	36.9	0.26
20% loading	80.5	7.1	0.98	91.1	36.5	62.2	0.88
30% loading	81.4	6.0	0.45	92.5	43.9	55.3	0.67
Model A	81.3	7.6	0.92	90.8	61.2	39.0	0.22
Model B	80.9	7.2	0.92	91.0	36.4	62.8	0.82

In Figures 7 (a)–(c), representing the single-layered catalyst, the temperature peak occurs near the reactor inlet due to the exothermic nature of the Fischer–Tropsch reaction. As catalyst loading increases, the maximum temperature rises, with the 30% loading in (c) exhibiting the most pronounced hot spot formation, indicating intensified reaction rates and increased heat generation.

In Figures 7 (d)–(f), representing multilayer catalytic bed arrangements, the temperature profiles show improved temperature compared to the single-layer catalyst, effectively limiting excessive hot spot formation near the reactor inlet. Configurations (d) and (e), with a catalyst loading increasing from 1% to 30%, exhibits a higher maximum hot spot temperature of 243 °C, indicating intensified reaction zones and gradual heat accumulation due to increasing %loading of catalyst. In contrast, configuration (f), with a catalyst loading decreasing from 1% to 30%, further reduces the temperature hot spot to 230 °C. This significant improvement in thermal management is attributed to enhanced heat dissipation and more efficient utilization of the catalyst zones. These results highlight the potential of multilayered catalytic bed in achieving more stable thermal behavior and improving overall reactor performance.

Table 7 highlights the effect of catalyst bed configurations on Fischer–Tropsch synthesis performance, showing that CO conversion increases with catalyst loading in single-layered catalyst bed, reaching a maximum of 82.4% at 30% loading. However, Model B multilayered catalytic beds arrangements, achieving a high conversion of 81.3%, close to the best single-layered catalyst case. In terms

of product selectivity, single-layer configurations yield the highest C_5^+ selectivity to 95.4% at 15% loading and the lowest methane formation of 3.1%, indicating favorable chain growth under consistent temperature distribution. In contrast, Model B multilayered catalytic bed maintains high C_5^+ selectivity 91.0% while significantly enhancing diesel-range C_{12}–C_{20} selectivity to 62.8% and promoting heavier hydrocarbon fractions C_{21}^+ selectivity to 0.82%, which is advantageous for production. Overall, the modified multilayered catalytic bed configuration provides an optimal balance between conversion efficiency, effective temperature control, and product selectivity towards valuable longer-chain hydrocarbons.

4. CONCLUSION

This study addresses the challenge of managing heat distribution in Fischer–Tropsch synthesis (FTS), a highly exothermic of reaction where excessive hot spot formation can lead to reactor performance and poor product selectivity. To overcome this, the research focuses on optimizing the design and performance of a fixed-bed reactor with Co/SiO_2 spiral structured catalysts through computational fluid dynamics (CFD) simulations using a two-dimensional pseudo-homogeneous model in COMSOL Multiphysics 6.1. The objectives include analyzing temperature profiles and catalytic performance under different catalyst bed configurations specifically single-layered catalyst with uniform catalyst loading (15%, 20%, 30%) and multilayered catalytic bed with gradient loadings (1%–30% and 30%–1%). The model integrates reaction kinetics from Iglesia et al. for CO methanation and from Yates and Satterfield for the Fischer–Tropsch reaction, along with Hillestad's stoichiometric approach based on the Anderson–Schulz–Flory distribution. Validation against experimental data reported by Aurud et al. shows excellent agreement, with a CO conversion error of just 0.9%. Results reveal that while single-layer beds achieve high C_5^+ selectivity to 95.4%, they suffer from more intense hot spots to 237 °C. In contrast, the multilayered catalytic bed arrangement with Model B a decreasing catalyst loading from top to bottom significantly reduces the hot spot to 230 °C, while maintaining high CO conversion 80.9% and enhancing diesel-range selectivity C_{12}–C_{20} 62.8%. This demonstrates the effectiveness of the proposed multilayer strategy in improving heat management, conversion efficiency, and selectivity toward longer-chain hydrocarbons, making it a promising design for industrial-scale FTS reactors.

ACKNOWLEDGMENTS

The authors would like to acknowledge the supports from the Office of National Higher Education Science Research and Innovation Policy Council - PMU C, PTT EXPLORATION AND PRODUCTION PUBLIC Co., Ltd., CHERDCHAI CORPORATION Co., Ltd., POLAWAT ENGINE Co., Ltd., and VERASUWAN Co., Ltd., (C04F660060), and from Thailand Science Research and Innovation Fund Chulalongkorn University (BCG_FF_68_056_2100_010).

REFERENCES

[1] Nowicki, L., & Bukur, D. B. (2001). Kinetic modeling of the slurry phase Fischer-Tropsch synthesis on iron catalysts. In E. Iglesia, J. J. Spivey, & T. H. Fleisch (Eds.), Studies in Surface Science and Catalysis (Vol. 136, pp. 123-128). Elsevier.

[2] Dry, M. E. (2002). The Fischer–Tropsch process: 1950–2000. Catalysis Today, 71(3), 227-241.

[3] de Klerk, A. (2014). Chapter 12 - Transport Fuel: Biomass-, Coal-, Gas- and Waste-to-Liquids Processes. In T. M. Letcher (Ed.), Future Energy (Second Edition) (pp. 245-270).

[4] Sie, S. T., & Krishna, R. (1999). Fundamentals and selection of advanced Fischer–Tropsch reactors. Applied Catalysis A: General, 186(1), 55-70.

[5] Gholami, Z., Tišler, Z., & Šimek, J. (2023). Effect of multilayered catalytic bed on temperature profiles and catalytic performance for Fischer–Tropsch synthesis over Co/Al2O3 catalyst in a multitubular fixed-bed reactor. Chemical Engineering Research and Design, 197, 274-291.

[6] Chabot, G., Guilet, R., Cognet, P., & Gourdon, C. (2015). A mathematical modeling of catalytic milli-fixed bed reactor for Fischer–Tropsch synthesis: Influence of tube diameter on Fischer Tropsch selectivity and thermal behavior. Chemical Engineering Science, 127, 72-83

[7] Shen, J., Ho, W. H., Liu, X., & Hildebrandt, D. (2021). Tubular reactor internals for suppressing hot spot formation applied to the Fischer-Tropsch reaction. Chemical Engineering and Processing - Process Intensification, 161, 108309.

[8] Glasser, D., Hildebrandt, D., Liu, X., Lu, X., & Masuku, C. M. (2012). Recent advances in understanding the Fischer–Tropsch synthesis (FTS) reaction. Current Opinion in Chemical Engineering, 1(3), 296-302.

[9] Luque, R., de la Osa, A. R., Campelo, J. M., Romero, A. A., Valverde, J. L., & Sanchez, P. (2012). Design and development of catalysts for Biomass-To-Liquid-Fischer–Tropsch (BTL-FT) processes for biofuels production. Energy & Environmental Science, 5(1), 5186-5202.

[10] Derevich, I. V., Ermolaev, V. S., Mordkovich, V. Z., Solomonik, I. G., & Fokina, A. Y. (2018). Heat and mass transfer in Fischer–Tropsch catalytic granule with localized cobalt microparticles. International Journal of Heat and Mass Transfer, 121, 1335-1349.

[11] Aurud, P., Srifa, A., Koo-Amornpattana, W., Assabumrungrat, S., Wongsakulphasatch, S., Fukuhara, C., & Ratchahat, S. (2024). The improvement of heat transfer using Co/SiO2 spiral structured catalyst for green diesel production by Fischer–Tropsch synthesis. Scientific Reports, 14(1), 19782.

[12] Fratalocchi, L., Visconti, C. G., Groppi, G., Lietti, L., & Tronconi, E. (2018). Intensifying heat transfer in Fischer-Tropsch tubular reactors through the adoption of conductive packed foams. Chemical Engineering Journal, 349, 829-837.
[13] Visconti, C. G., Tronconi, E., Groppi, G., Lietti, L., Iovane, M., Rossini, S., & Zennaro, R. (2011). Monolithic catalysts with high thermal conductivity for the Fischer–Tropsch synthesis in tubular reactors. Chemical Engineering Journal, 171(3), 1294-1307.
[14] Wang, X., Ren, Y., Liu, H., Lu, L., & Zhang, L.(2023). Heat management of Fischer-Tropsch synthesis by designing the catalyst activity and thermal conductivity. Chemical Engineering Science, 280, 119045.
[15] Sadhukhan, P. and Petersen, E.E. (1976), Oxidation of naphthalene in packed-bed reactor with catalyst activity profile: A design scheme for improved reactor stability and higher product yield. AIChE J., 22: 808-810.
[16] Nie, Y., Witt, P. M., Agarwal, A., & Biegler, L. T. (2013). Optimal Active Catalyst and Inert Distribution in Catalytic Packed Bed Reactors: ortho-Xylene Oxidation. Industrial & Engineering Chemistry Research, 52(44), 15311-15320.
[17] Hong, G. H., Noh, Y. S., Park, J. I., Shin, S. A.,& Moon, D. J. (2018). Effect of catalytic reactor bed dilution on product distribution for Fischer-Tropsch synthesis over Ru/Co/Al2O3 catalyst. Catalysis Today, 303, 136-142.
[18] Moazami, N., Wyszynski, M. L., Mahmoudi, H., Tsolakis, A., Zou, Z., Panahifar, P., & Rahbar, K. (2015). Modelling of a fixed bed reactor for Fischer–Tropsch synthesis of simulated N2-rich syngas over Co/SiO2: Hydrocarbon production. Fuel, 154, 140-151.
[19] Shen, J., & Liu, X. (2022). A CFD Simulation Study of the Effect of Thermal Conductivity of the Catalyst Bed on Fischer-tropsch Synthesis. Chemical Engineering Transactions, 96, 187-192.
[20] Arzamendi, G., Diéguez, P. M., Montes, M., Odriozola, J. A., Falabella Sousa-Aguiar, E., & Gandía, L. M. (2010). Computational fluid dynamics study of heat transfer in a microchannel reactor for low-temperature Fischer–Tropsch synthesis. Chemical Engineering Journal, 160(3), 915-922.
[21] Teimouri, Z., Borugadda, V. B., Dalai, A. K., & Abatzoglou, N. (2022). Application of computational fluid dynamics for modeling of Fischer-Tropsch synthesis as a sustainable energy resource in different reactor configurations: A review. Renewable and Sustainable Energy Reviews, 160, 112287.
[22] Huynh, H. L., & Yu, Z. (2020). CO2 Methanation on Hydrotalcite-Derived Catalysts and Structured Reactors: A Review. Energy Technology, 8(5), 1901475.
[23] Iglesia, E., Reyes, S. C., Madon, R. J. and Soled, S. L. (1993), 'Selectivity Control and Catalyst Design in the Fischer-Tropsch Synthesis: Sites, Pellets, and Reactors', Advances in Catalysis 39.
[24] Hillestad, M. (2015), 'Modeling the Fischer-Tropsch Product Distribution and Model Implementation', Chemical Product and Process Modeling 10, 147–159.
[25] Yates, I. C., & Satterfield, C. N. (1991). Intrinsic kinetics of the Fischer-Tropsch synthesis on a cobalt catalyst. Energy & Fuels, 5(1), 168-173. doi.org/10.1021/ef00025a029
[26] Morales, A., & Leonard, G. (2022). Simulation of a Fischer-Tropsch reactor for jet fuel production using Aspen Custom Modeler. In L. Montastruc & S. Negny (Eds.), Computer Aided Chemical Engineering (Vol. 51, pp. 301-306). Elsevier.

Simulation of dry and steam reforming of methane over a nickel-based catalyst in a fixed-bed tube reactor using COMSOL

Krissadang Khamma[1], Asawin Meechai[1], Suwimol Wongsakulphasatch[2], Paritta Prayoonyong[1,*]

[1] Department of Chemical Engineering, Faculty of Engineering, King Mongkut's University of Technology Thonburi, Bangkok 10140, Thailand
[2] Department of Chemical Engineering, Faculty of Engineering, King Mongkut's University of Technology North Bangkok, Bangkok 10800, Thailand
[*] Corresponding author: paritta.boom@gmail.com

ABSTRACT

At present, most of the world's synthesis gas (syngas), composed of carbon monoxide (CO) and hydrogen (H_2), originates from methane reforming. Syngas is a crucial feedstock in the chemical industry for producing various chemicals. In this study, we developed mathematical models of methane steam reforming and methane dry reforming in COMSOL Multiphysics. These models were employed to investigate the effects of operating conditions on product yield, composition, and temperature and concentration profiles, as well as to determine the optimal temperature and pressure conditions for maximizing the product yield. The inlet temperature was set from 700 to1000 K, with pressures ranging from 1 to 50 bar. The results indicated that steam reforming primarily produced hydrogen, whereas dry reforming predominantly yield carbon monoxide. Both reactions exhibited high efficiency at high temperatures and low pressures due to their endothermic nature and the characteristics of gas expansion. The 3D flow behavior analysis, as illustrated by the flux direction and concentration distribution, revealed that the flow flux is predominantly aligned parallel to the reactor length. For the concentration profiles, the reactant concentration was lowest at the reactor center and increased toward the near-wall region (Fig. 3 and Fig. 5), while the opposite trend was observed for product concentration due to enhanced reaction efficiency at high temperatures in the middle of the reactor. The optimal conditions for steam reforming were found to be 900 K at 1 atm, achieving a conversion of 95.26%, while for dry reforming, the optimal conditions were 1000 K at 1 atm, with a conversion of 88.77%.

1. INTRODUCTION

Currently, approximately 90% of global hydrogen (H_2) production is derived from fossil fuels, with steam methane reforming (SMR) of natural gas being the predominant method. However, the rapid increase in global energy demand, driven by population growth, has intensified concerns about the environmental impact of fossil fuel consumption [1]. This dependency has led to a significant rise in anthropogenic greenhouse gas emissions, particularly carbon dioxide (CO_2) and methane (CH_4), which are the two most influential greenhouse gases contributing to climate change [2].

Although CH_4 is present in the atmosphere at much lower concentrations than CO_2, it has a global warming potential approximately 25 times greater, making its mitigation and utilization increasingly important [3]. One promising and renewable source of both CH_4 and CO_2 is biogas, which is generated through the anaerobic digestion of organic waste materials. Biogas is widely produced in landfill sites, wastewater treatment plants, and commercial digesters, with CH_4 concentrations ranging from 25–75% and CO_2 from 7–60%, depending on the feedstock. Due to its renewable nature and wide availability, biogas represents a sustainable feedstock for reforming technologies aimed at converting greenhouse gases into useful products [4].

Dry reforming of methane (DMR) has gained attention as a promising method for simultaneously utilizing CH_4 and CO_2 to produce syngas (CO and H_2) with a near-unity H_2/CO ratio [2]. The resulting syngas serves as a key feedstock for chemicals like methanol, Fischer–Tropsch fuels, and dimethyl ether. Compared to conventional SMR, DMR eliminates the need for water and simplifies gas separation, making it a more efficient and environmentally friendly approach for upgrading biogas [5].

2. EXPERIMENTAL

In this work, mathematical models for the steam and dry reforming process were developed based on a previously reported model of packed-bed steam reforming of propane [6]. The reactor was modeled as

adiabatic and non-isothermal. Both dry reforming and steam reforming of methane were assumed to occur within the pores of a Ni/Al_2O_3 catalyst. The system was treated as ideal gas, and thus ideal gas thermodynamics were applied throughout the model. The details of the reactor model are presented in Figure 1.

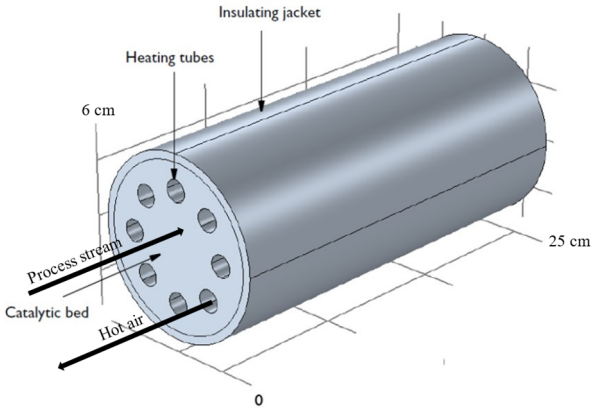

Figure 1 Geometry of the reformer unit.

The reactor geometry was a 25 cm nickel-based catalytic fixed-bed tubular reactor, which is equipped with a counterflow air heat exchanger housed in a small tube within the reactor. The process gas flows through the catalytic bed on the shell side, while the heating medium flows through the tubes on the tube side. A counter-current flow configuration was employed between the process stream and the hot air to enhance heat exchange efficiency [7]. The reactor data used in the simulation, along with the feed and operating conditions for both dry and steam reforming of methane, are presented in Table 1.

Table 1 Reactor configuration and operating conditions for the steam and dry reforming processes.

Data		
Reactor length	25 cm	
Tube diameter (hot air)	0.8 cm	
Shell diameter (process stream)	6 cm	
Feed temperature	700 - 1000 K	
Hot air temperature	800 - 1100 K	
Process pressure	1 – 50 bars	
Feed mole fraction	**Steam reforming**	**Dry reforming**
CH_4	0.267	0.490
H_2O	0.533	0.007
H_2	0.180	0.007
CO	0.010	0.490
CO_2	0.010	0.007

2.1 Steam methane reaction scheme

This study considered only three reactions in the steam methane reforming process, as listed below [1]:

$CH_4(g)+H_2O(g) \rightleftharpoons CO(g)+3H_2(g)$ ΔH_{298K}= 206 kJ/mol Eq.1

$CO(g)+H_2O(g) \rightleftharpoons CO_2(g)+H_2(g)$ ΔH_{298K}= -42 kJ/mol Eq.2

$CH_4(g)+2H_2O(g) \rightleftharpoons CO_2+4H_2(g)$ ΔH_{298K}= 165 kJ/mol Eq.3

The kinetic, thermodynamic, and equilibrium parameters, as well as the rate constants, were adopted from previous studies [8].

2.2 Dry methane reaction scheme

This study considered only two reactions in the dry methane reforming process, as listed below [6]:

$CH_4(g)+CO_2(g) \rightleftharpoons 2CO(g)+2H_2(g)$ ΔH_{298K}= 247 kJ/mol Eq.4

$CO_2(g)+H_2(g) \rightleftharpoons CO(g)+2H_2O(g)$ ΔH_{298K}= 42 kJ/mol Eq.5

The kinetic, thermodynamic, and equilibrium parameters, as well as the rate constants, were adopted from previous studies [9].

2.3 Mathematical modeling

The simulations of steam and dry methane reforming in this study were carried out using COMSOL Multiphysics 6.1. The mathematical model employed is a heterogeneous catalytic reaction model, developed based on the following assumptions:

- The system operates under steady-state conditions.
- The gas phase follows ideal gas behavior.
- The bed porosity is assumed to be constant.
- The pressure drop across the reactor is considered constant.

2.4 Process optimization

The process optimization of dry and steam methane reforming was first conducted by fixing the pressure at 1 bar and varying the temperature to determine the optimal temperature. CH_4, as the reaction-controlling reactant, was used to evaluate conversion. Temperature was optimized first because both the reaction rate and the reaction equilibrium are strongly temperature-dependent, making it the most influential factor. Once the optimal temperature was identified, it was then held constant while the pressure was varied to determine the optimal pressure. The optimization was based on the observation of the maximum CH_4 conversion, which reflects the most favorable operating conditions.

3. RESULTS AND DISCUSSION

3.1 Steam methane reforming

SMR at 700 K and 1 bar was simulated to observe the concentration profiles of each chemical species along the reactor length (

Figure ***2***). The simulation results clearly show that the concentrations of the reactants, H_2O and CH_4, continuously decrease along the reactor length, while the concentrations of the main product H_2 increase. However, the concentration of CO does not increase. This behavior can be attributed to the Water-Gas Shift (WGS) Eq. 2, which consumes CO and converts it into CO_2 and H_2. The presence of steam (H_2O) in the reactor promotes the WGS reaction, particularly in regions with higher steam concentration. Consequently, the CO concentration decreases as it is being converted into CO_2 and H_2 [10]. A sharp change in concentrations is observed before the reactor length reaches 0.2 m, indicating that most of the reaction occurs in this region. Beyond this point, the concentration changes become more gradual, suggesting that the reaction is approaching equilibrium.

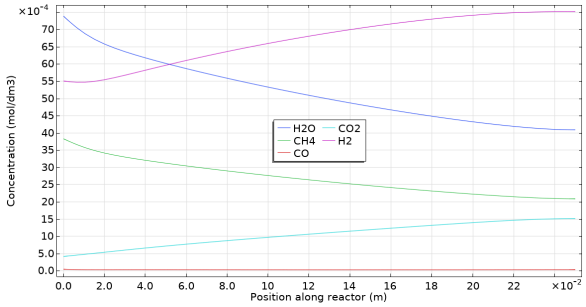

Figure 2 Concentration profiles of each component in the SMR process along the reactor length at 700 K and 1 bar.

Furthermore, a three-dimensional (3D) model of SMR is considered in this work, as illustrated in Figure **3**.

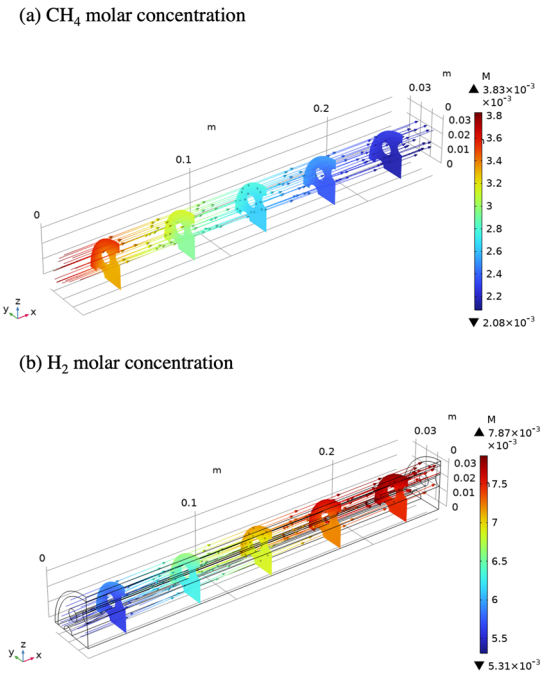

Figure 3 Molar concentration profiles of (a) CH_4 (b) H_2 of SMR along the fixed bed tube reactor at 1 bar and 700 K

Figure **3**a shows that the concentration of CH_4 in SMR decreases along the reactor length, as CH_4 serves as a primary reactant in the process, as shown in Eq.1 and Eq.3. Moreover, the CH_4 concentration is not uniformly distributed across the same cross-sectional plane of the reactor due to the temperature gradient within the reactor, where the central region tends to exhibit higher temperatures compared to the outer regions. The elevated temperature in the core zone accelerates the rate of endothermic reactions, especially the steam reforming reaction. As a result, the CH_4 concentration is lower near the reactor center and higher near the periphery, where the temperature is relatively lower.

For Figure **3**b, the concentration of hydrogen (H_2) in the SMR process increases along the reactor, particularly in the early and middle sections, as H_2 is a primary product formed via the reactions described in Eq.1, Eq.2 and Eq.3 for the reasons previously discussed. The increase in H_2 concentration correlates with the consumption of CH_4 and the progression of endothermic reforming reactions facilitated by the elevated temperatures in these regions.

Furthermore, when considering the y–z plane of the reactor model, the distribution of H_2 is not uniform across the cross-section. This non-uniformity is attributed to the same factors affecting CH_4 concentration, namely the temperature gradient and localized reaction rates. Within the middle section of the reactor, the reactions have not yet reached thermodynamic equilibrium, leading to spatial differences in H_2 concentration. This highlights the role of reactor geometry and heat distribution in influencing local reaction kinetics and product formation.

3.2 Dry methane reforming

DMR at 700 K and 1 bar was also simulated to observe the concentration profiles of each chemical species along the reactor length (Figure 4).

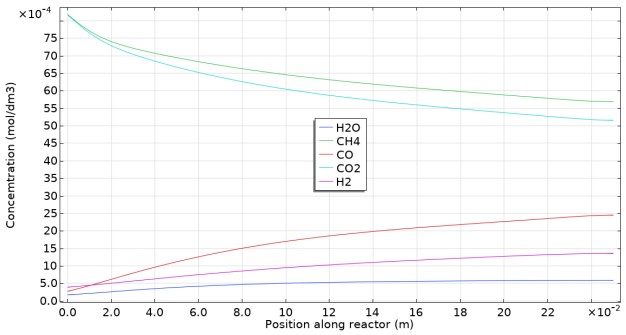

Figure 4 Concentration profiles of each component in the DMR process along the reactor length at 700 K and 1 bar.

As shown in Figure 4, the concentrations of the reactants, CO_2 and CH_4, continuously decrease along the reactor length due to their consumption in the reforming reactions. In contrast, the concentrations of the main products, carbon monoxide (CO) and hydrogen (H_2), increase significantly in the initial section of the reactor and then gradually level off. This behavior is attributed to the decreasing concentration of reactants and the approach to thermodynamic equilibrium as the reaction progresses.

The concentration of CO is higher than that of H_2 because CO is produced from both Eq.4 and Eq.5, while H_2 is only produced in Eq.4 and consumed in Eq.5 to form CO and H_2O, results in a relatively lower concentration of H_2. Furthermore, a three-dimensional (3D) model of DMR is considered in this work, as illustrated in Figure 5.

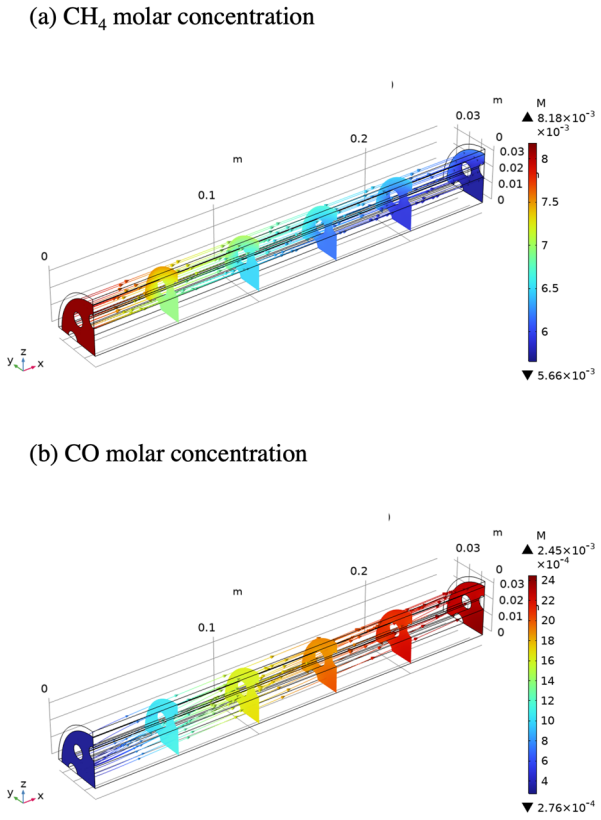

Figure 5 Molar concentration profiles of (a) CH_4 (b) CO of dry methane reforming along the fixed bed tube reactor at 1 bar and 700 K

From Figure 5a, the concentration of CH_4 in DMR exhibits a behavior similar to that observed in SMR, where it decreases along the reactor, especially in the initial half of the reactor. This decrease is attributed to both the consumption of the reactants and the equilibrium constraints of the reaction. Additionally, in the cross-section, the concentration of CH_4 is not uniform due to the non-uniform rate of reaction in the reactor. The rate of reaction is temperature-dependent, following the Arrhenius equation, with the center of the reactor having a higher temperature. As a result, the reaction rate is faster in this region, and since the reaction is endothermic, it proceeds in the forward direction. Consequently, the concentration of CH_4 in the center is lower than at other positions along the same length of the reactor.

As shown Figure 5b, the concentration of CO in DMR follows a trend similar to the H_2 product in SMR, as both are primary products of their respective process.

3.3 Process optimization for steam methane reforming

In this section, the developed model was used to determine the optimal temperature and pressure for the SMR process, and the results are shown in Figure ***6***.

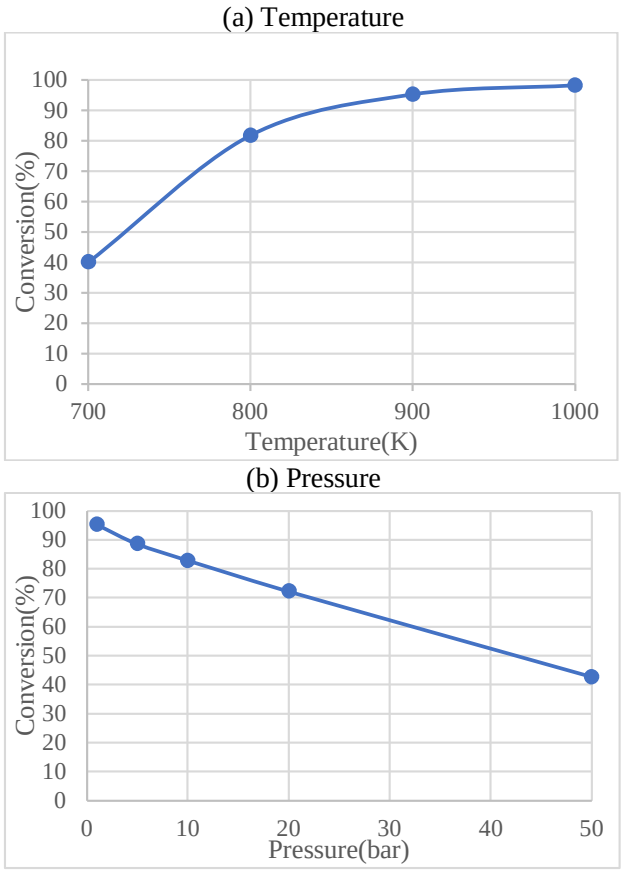

Figure 6 CH_4 conversion of SMR under varying (a) Temperature (b) Pressure

From Figure ***6***a, the temperature of steam methane reforming process was varied from 700 to 1,000 K while maintaining a constant pressure of 1 bar. The results show that CH_4 conversion increases significantly between 700 and 900 K; however, beyond 900 K, the increase becomes marginal. These findings suggest that the optimal temperature for achieving the highest CH_4 conversion in the steam reforming process is approximately 900 K, at which the CH_4 conversion reaches 95.26%. Based on this result, a temperature of 900 K was selected to investigate the effect of pressure, which was varied from 1 bar to 50 bar, as shown in

Figure 6b. The results indicate that the highest CH_4 conversion occurs at 1 bar and decreases with increasing pressure. This trend is because SMR is a gas-expansion reaction; therefore, lower pressure favors the forward reaction and enhances CH_4 conversion.

3.4 Process optimization for dry methane reforming

In this section, the developed model was used to determine the optimal temperature and pressure of the DMR process, and the results are shown in Figure 7.

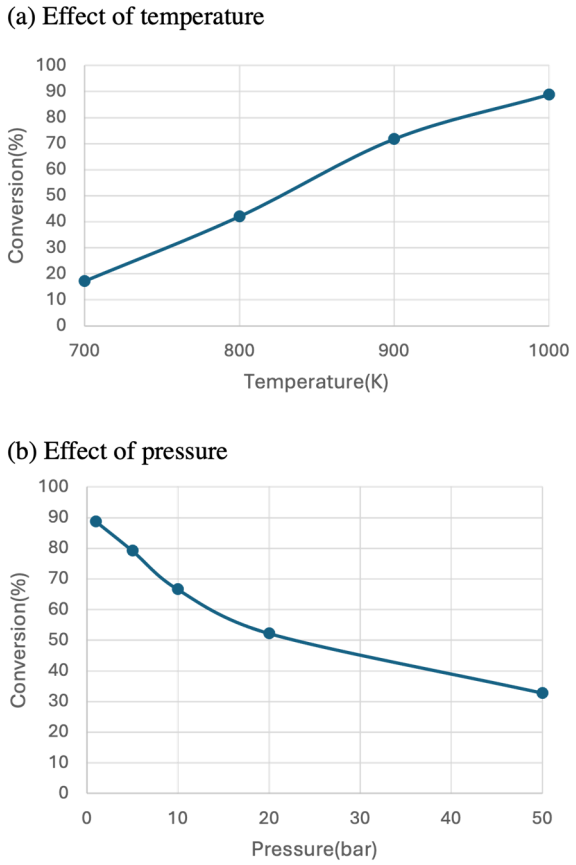

Figure 7 CH_4 conversion of DMR under varying (a) Temperature (b) Pressure

The optimization of the DMR process begins by varying the temperature from 700 to 1,000 K while maintaining a constant pressure of 1 bar. Figure 7a shows that the highest CH_4 conversion is observed at 1,000 K, which is 88.77%. This is because DMR is an endothermic reaction, and therefore higher temperatures favor the forward reaction. Based on this result, a temperature of 1,000 K was selected for the next step, in which the pressure was varied from 1 to 50 bar. Additionally, Figure 7b indicates that the highest CH_4 conversion occurs at 1 bar. This behavior is because DMR is a gas expansion process, similarly to SMR, and thus lower pressure promotes the forward reaction.

4. CONCLUSION

A study of steam and dry methane reforming revealed that operating steam methane reforming with a high CH_4:H_2O ratio results in a significant formation of the primary product H_2, while CO formation is minimal, approaching zero. On the other hand, in dry methane reforming, CO is the dominant primary product, whereas H_2 is produced in lower amounts.

When considering the 3D model results, it is observed that both steam and dry methane reforming exhibit similar characteristics. The reaction primarily occurs in the initial and middle sections of the reactor, leading to a rapid decrease in reactant concentrations and a simultaneous increase in the product concentrations. Additionally, when examining the y-z cross-sectional plane, it is evident that the concentrations of both reactants and products in the steam and dry methane reforming are non-uniform in the early and middle parts of the reactor. This is due to the higher temperatures at the center of the reactor tube, which enhance reaction rates according to the Arrhenius law. However, toward the end of the reactor, the concentrations tend to become more uniform because the reactions are increasingly governed by chemical equilibrium.

For the optimization, it is evident that both dry and steam methane reforming perform better at high temperatures due to their endothermic nature, and under low-pressure conditions as both are gas expansion processes. From the optimization results, the optimal conditions for steam methane reforming were found to be 900 K and 1 bar, achieving a CH_4 conversion of 95.26%. Meanwhile, the optimal conditions for dry methane reforming were 1,000 K and 1 bar, with a CH_4 conversion of 88.77%.

ACKNOWLEDGMENTS

Krissadang Khamma gratefully acknowledged the Department of Chemical Engineering at King Mongkut's University of Technology Thonburi for providing the Graduate Scholarship throughout his studies.

REFERENCES

1. Abbas, S.Z., Dupont, V., and Mahmud, T., 2017, "Kinetics Study and Modelling of Steam Methane Reforming Process over a NiO/Al_2O_3 Catalyst in an Adiabatic Packed Bed Reactor", *International Journal of Hydrogen Energy*, Vol. 42, No. 5, pp. 2889-2903.
2. Hussien, A. and Polychronopoulou, K., 2022, "A Review on the Different Aspects and Challenges of the Dry Reforming of Methane (Drm) Reaction", *Nanomaterials*, Vol. 12, No., p. 3400.
3. Muraza, O. and Galadima, A., 2015, "A Review on Coke Management during Dry Reforming of Methane", *International Journal of Energy Research*, Vol. 39

4. Zhao, X., Joseph, B., Kuhn, J., and Ozcan, S., 2020, "Biogas Reforming to Syngas: A Review", *iScience*, Vol. 23, No. 5, p. 101082.
5. San-José-Alonso, D., Juan-Juan, J., Illán-Gómez, M.J., and Román-Martínez, M.C., 2009, "Ni, Co and Bimetallic Ni–Co Catalysts for the Dry Reforming of Methane", *Applied Catalysis A: General*, Vol. 371, No. 1, pp. 54-59.
6. Abbasi, M., Farniaei, M., Rahimpour, M.R., and Shariati, A., 2015, "Simultaneous Syngas Production with Different H_2/CO Ratio in a Multi-Tubular Methane Steam and Dry Reformer by Utilizing of Clc", *Journal of Energy Chemistry*, Vol. 24, No. 1, pp. 54-64.
7. Rostrup-Nielsen, J. and Christiansen, L.J., 2011, Concepts in Syngas Manufacture, *Imperial College Press*, 392 Pages.
8. Neni, A., Benguerba, Y., Balsamo, M., Erto, A., Ernst, B., and Benachour, D., 2021, "Numerical Study of Sorption-Enhanced Methane Steam Reforming over Ni/Al_2O_3 Catalyst in a Fixed-Bed Reactor", *International Journal of Heat and Mass Transfer*, Vol. 165, p. 120635.
9. Benguerba, Y., Dehimi, L., Virginie, M., Dumas, C., and Ernst, B., 2015, "Modelling of Methane Dry Reforming over Ni/Al_2O_3 Catalyst in a Fixed-Bed Catalytic Reactor", *Reaction Kinetics, Mechanisms and Catalysis*, Vol. 114, No. 1, pp. 109-119.
10. Ahmed, S., Lee, S.H.D., and Ferrandon, M.S., 2015, "Catalytic Steam Reforming of Biogas – Effects of Feed Composition and Operating Conditions", *International Journal of Hydrogen Energy*, Vol. 40, No. 2, pp. 1005-1015.

Promotional effect of Fe in the Cu/TiO_2 catalyst on the liquid-phase selective hydrogenation of furfural to furfuryl alcohol

Jenjeera Sathukan[1], Luksiga Noomsalee[1], Chadaporn Jirawantanasakun[1], Menisa Choochuen[1], Choowong Chaisuk[1,*]

[1] Department of Chemical Engineering, Faculty of Engineering and Industrial Technology, Silpakorn University, Nakhon Pathom 73000, Thailand

[*] Corresponding author: chaisuk_c@su.ac.th

ABSTRACT

Copper chromite is a commercially used catalyst for producing furfuryl alcohol through the selective hydrogenation of furfural, but it is highly toxic to the environment. The development of Cu-based catalysts without Cr has been investigated. Fe was an interesting promoter due to the synergistic effect between Fe sites with a strong oxophilic nature and Cu sites with a high ability for hydrogen activation. In this work, Fe with varying contents was impregnated onto a 10 wt% Cu/TiO_2 catalyst, and the Cu content was subsequently varied to 5 - 20 wt%, while maintaining a suitable ratio of Fe to Cu. The catalysts were characterized using the X-ray diffraction, N_2 physisorption, temperature-programmed reduction and N_2O decomposition. The furfural hydrogenation was conducted under 20 bar of hydrogen at 160 °C for 2 h in isopropanol solvent. The BET surface area was decreased by about 30% when Fe was added at high loadings (1, 2, and 5 wt%). The presence of Fe had little effect on the pore characteristics of the catalysts and the crystalline sizes of the CuO particles. The reduction temperature of the catalysts shifted to higher temperatures with increasing the Fe loadings. The 2 wt% Fe content was optimal for achieving a high yield of furfuryl alcohol, which is consistent with the high Cu active sites measured by N_2O decomposition. By fixing the Fe to Cu ratio at 1:5 and varying the Cu content, the 10 wt% Cu - 2 wt% Fe/TiO_2 catalyst was promising.

Keywords: Furfural hydrogenation; Furfuryl alcohol; Cu/TiO_2 catalyst; Fe promoter

1. INTRODUCTION

Furfural (FAL) is a key bio-based chemical derived from lignocellulosic biomass, particularly from hemicellulose-rich agricultural residues such as corn cobs, oat hulls, and sugarcane bagasse. It is selectively hydrogenated to furfuryl alcohol (FOL), a valuable intermediate used in the production of resins, plastics, and pharmaceuticals [1]. The hydrogenation of furfural typically employs metal-based catalysts such as copper, cobalt, nickel, or noble metals under hydrogen atmosphere [2, 3]. Commercially, the most widely used catalyst for this reaction is copper chromite. However, copper chromite reacts with substances that are highly toxic to the environment and generate undesirable by-products. As a result, the development of chromium-free catalysts has been actively pursued [4]. Copper-based catalysts are favored for their inherent selectivity toward the carbonyl group in furfural; however, they often exhibit moderate activity [5], limited hydrogen activation capability [6], and rapid deactivation over time [7]. To address these challenges, research has focused on incorporating promoter metals to enhance catalytic performance. Among various promoters, iron (Fe) has emerged as a promising candidate due to the synergistic interaction between Fe sites, which possess strong oxophilic properties, and Cu sites, which exhibit high hydrogen activation ability [8]. In this work, the effect of Fe as a promoter in the Cu/TiO_2 catalyst on the catalytic performance for the liquid-phase selective hydrogenation of furfural to furfuryl alcohol was investigated.

2. EXPERIMENTAL

The Cu-Fe/TiO_2 catalysts were prepared using the impregnation method. First, commercial P25 TiO_2 powder was mixed with an aqueous solution of copper (II) nitrate trihydrate. The resulting slurry was stirred at 70 °C for 6 h. The material was then dried in an oven at 110 °C for 12 h, crushed into a fine powder, and calcined in an air flow of 30 mL/min at 400 °C for 3 h. After calcination, 2 mL of an aqueous solution of iron (III) nitrate nonahydrate was impregnated onto the Cu/TiO_2 powder and left at room temperature for 6 h. The resulting material was again dried at 110 °C for 12 h, crushed, and calcined under the same conditions. The final product was the Cu-Fe/TiO_2 catalyst. The copper content was initially fixed at 10 wt%, while the iron content was varied at 0.1, 0.5, 1, 2, and 5 wt%.

Following catalytic testing, the Cu content was subsequently varied between 5 and 20 wt%, while maintaining an appropriate Fe-to-Cu ratio. In this work, the notation *x*Cu-*y*Fe/TiO_2 refers to catalysts prepared by sequential impregnation-first of Cu and then Fe-on commercial P25 TiO_2, with *x* and *y* denoting the respective weight percentages of Cu and Fe.

The catalysts were characterized using X-ray diffraction (XRD), N_2 physisorption, temperature-programmed reduction (TPR), and N_2O decomposition techniques. The bulk crystalline phases were identified by XRD using a Bruker AXS Model D8 Discover instrument, operated in the 2θ range of 20°-80° with Cu Kα radiation. Crystallite sizes were estimated using the Scherrer equation. The specific surface area was determined by N_2 physisorption using a Micromeritics ASAP 2010 analyzer. Prior to measurement, the catalysts were pretreated under a helium flow (50 mL/min) at 180 °C for 3 h to remove surface-bound water. After pretreatment, the sample cell was placed in a dewar containing liquid nitrogen, and N_2 adsorption was measured at -196 °C over a range of partial pressures. The bulk reduction behavior of the catalysts was investigated by TPR using a Micromeritics AutoChem 2910 instrument. Samples were pretreated under N_2 flow at 150 °C for 1 h to eliminate adsorbed moisture. Reduction was carried out in a 10% H_2/N_2 mixture (30 mL/min) with a temperature ramp from 100 °C to 800 °C at 10 °C/min, followed by a 1-hour hold at 800 °C. Water formed during the reduction was trapped using liquid nitrogen. N_2O decomposition was performed to determine the number of accessible Cu active sites, using the same AutoChem 2910 instrument. Before the measurement, catalysts were reduced in H_2 flow (25 mL/min) at 300 °C for 3 h. The measurement was carried out at 90 °C using N_2O pulse injections until saturation was reached.

The catalytic performance was evaluated via the liquid-phase hydrogenation of furfural to furfuryl alcohol. Reactions were conducted in a 25 mL stainless-steel batch reactor equipped with a magnetic stirrer to ensure uniform mixing. Prior to testing, 0.05 g of the catalyst was reduced ex situ under a flow of hydrogen gas at 300 °C for 3 h. The reduced catalyst was then introduced into a liquid mixture containing 0.1 mL of furfural (reactant) and 10 mL of isopropanol (solvent). The reaction was performed under 20 bar of H_2 pressure at a temperature of 160 °C for a fixed duration of 2 h. Upon completion, the reactor was cooled, and the liquid product was collected and analyzed using gas chromatography with a flame ionization detector (GC-FID).

3. RESULTS AND DISCUSSION

The XRD patterns of the 10Cu-*y*Fe/TiO_2 catalysts are presented in Figure 1. The commercial P25 TiO_2 support exhibits characteristic diffraction peaks corresponding to anatase and rutile phases, in agreement with literature data [9]. All modified catalysts show distinct peaks associated with CuO, consistent with previous studies [10-13]. The CuO crystallite sizes were estimated using the Scherrer equation and are summarized in table 1. The incorporation of Fe had minimal influence on the crystallite size of CuO. Furthermore, no diffraction peaks corresponding to iron oxide phases such as Fe_2O_3 or Fe_3O_4, as reported in the literature [14, 15], were observed in any of the samples, suggesting that iron species may be highly dispersed or present in an amorphous form.

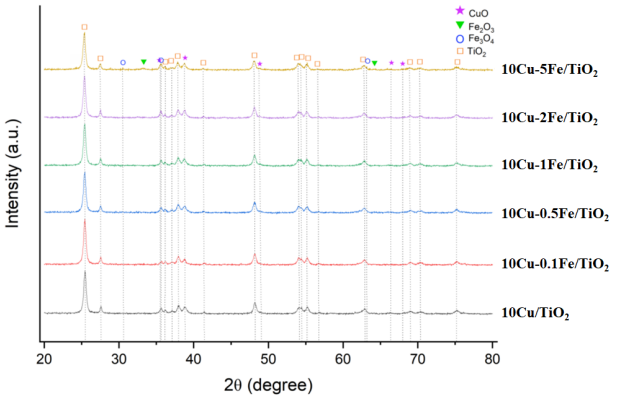

Figure 1 X-ray diffraction (XRD) patterns of the 10Cu-*y*Fe/TiO_2 catalysts.

Table 1 CuO crystallite size, BET surface area and total reducibility of the 10Cu-*y*Fe/TiO_2 catalysts determined by XRD, N_2 physisorption and H_2-TPR, respectively.

Catalyst	CuO crystallite size (nm)	BET surface area (m^2/g)	Total reducibility (%)
10Cu/TiO_2	29.1	49	84.7
10Cu-0.1Fe/TiO_2	35.7	47	21.3
10Cu-0.5Fe/TiO_2	29.5	48	71.6
10Cu-1Fe/TiO_2	31.6	35	97.1
10Cu-2Fe/TiO_2	28.7	35	97.7
10Cu-5Fe/TiO_2	33.0	34	86.2

The textural properties of the 10Cu-*y*Fe/TiO_2 catalysts were investigated using N_2 adsorption-desorption measurements, and the results are summarized in table 1. The specific surface area was calculated using the Brunauer-Emmett-Teller (BET) method. A slight decrease in BET surface area was observed with the incorporation of Fe above 1 wt%, likely due to partial pore blockage or changes in particle agglomeration during synthesis. Although the isotherms are not shown here, all samples exhibited type IV physisorption isotherms with noticeable hysteresis loops, characteristic of mesoporous materials with pore diameters ranging from 2 to 50 nm. Based on

IUPAC classification [16], the hysteresis loops were identified as type H2, typically associated with ink-bottle-shaped pores featuring narrow necks and wider cavities.

Figure 2 presents the TPR profiles of the 10Cu-*y*Fe/TiO_2 catalysts. All samples exhibited reduction peaks between 120-350 °C, attributed to the reduction of CuO species dispersed on the TiO_2 support. According to literature [17], bulk CuO was typically reduced between 200-325 °C. The introduction of Fe as a promoter resulted in a noticeable shift of the TPR peaks toward higher temperatures. This shift was associated with changes in metal oxide particle size, as larger particles generally exhibited higher reduction temperatures. Previous work [18] reported that supported CuO reduces in the range of 130-260 °C, suggesting that Fe promoted the growth of CuO particles, thereby increasing their reduction temperature. Iron oxides also underwent reduction within the 150-500 °C range. Specifically, Fe_2O_3 was reduced to Fe_3O_4 and FeO between 150-350 °C, followed by the reduction of FeO and Fe_3O_4 to metallic Fe between 250-500 °C [19]. Accordingly, catalysts with Fe loadings exceeding 1 wt% showed additional peaks above 250 °C. It was noted that the total reducibility values reported in table 1 were calculated under the assumption that only CuO species underwent reduction.

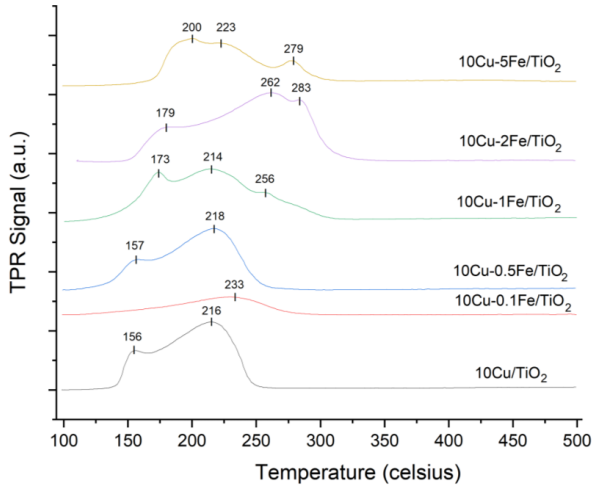

Figure 2 TPR profiles of the 10Cu-*y*Fe/TiO_2 catalysts.

The concentration of Cu active sites on the 10Cu-*y*Fe/TiO_2 catalysts was determined by N_2O decomposition. This approach relied on the decomposition of N_2O to N_2, which occurred exclusively on metallic Cu sites. It was important to emphasize that N_2O did not decompose on metallic Fe, ensuring that the measurement reflected only the accessible Cu surface area. The results, shown in Figure 3, indicate that the catalyst containing 2 wt% Fe exhibited the highest concentration of Cu active sites. This finding suggested that Fe, when present at an optimal concentration, promoted the redispersion of CuO species during the reduction process. These findings were consistent with previous reports highlighting the role of Fe in facilitating Cu redispersion [20]. At lower Fe contents, this promotion effect may be insufficient, while at higher Fe contents, excessive Fe could potentially block active Cu sites that were less reducible under the applied conditions.

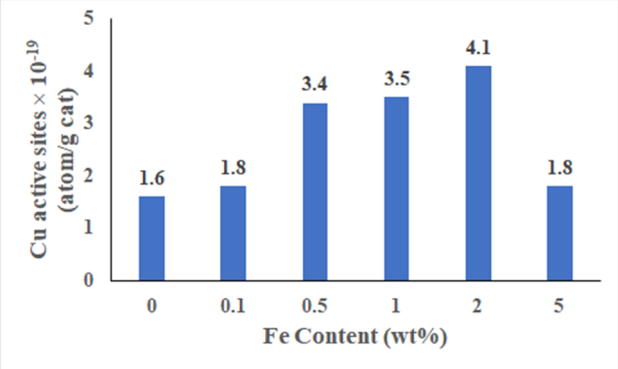

Figure 3 N_2O decomposition results for the 10Cu-*y*Fe/TiO_2 catalysts.

Figure 4 presents the yield of furfuryl alcohol from the selective hydrogenation of furfural over the 10Cu-*y*Fe/TiO_2 catalysts. It was remarked that the selectivity toward furfuryl alcohol remained close to 100% for all catalysts, suggesting that the addition of Fe had little impact on the reaction pathway but significantly influenced the conversion of furfural. This implied that Fe acted primarily as a structural promoter, enhancing the dispersion of Cu species rather than altering the hydrogenation mechanism itself. An optimal Fe content of 2 wt% in the 10 wt% Cu/TiO_2 catalyst resulted in the highest furfural conversion, which correlated with the maximum number of Cu active sites as measured by N_2O decomposition. This indicated that Fe facilitated the formation of highly dispersed Cu^0 particles, which were known to be the active phase in furfural hydrogenation. The trend observed here was in line with previous studies on Cu/Al_2O_3 catalysts, where an appropriate amount of Fe also enhanced catalytic activity for this reaction [8, 21].

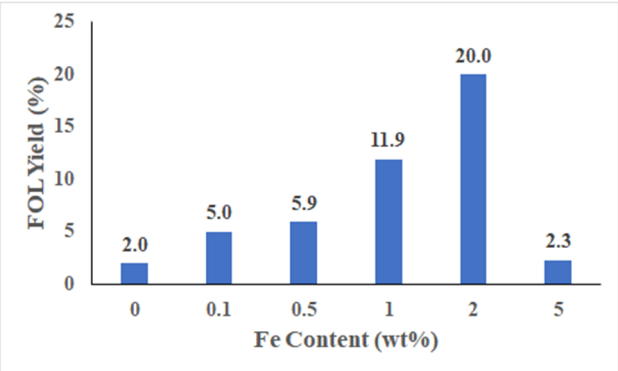

Figure 4 Effect of Fe content in 10 wt% Cu/TiO_2 catalyst on the selective hydrogenation of FAL to FOL.

Based on the high performance observed for the 10Cu-2Fe/TiO_2 catalyst in the selective hydrogenation of furfural, a fixed Fe-to-Cu weight ratio of 1:5 was selected for further optimization. To investigate the influence of Cu loading on the catalyst structure and performance, a series of *x*Cu-*y*Fe/TiO_2 catalysts was prepared with Cu contents of 5, 10, 15, and 20 wt%, while maintaining the Fe content proportionally at 1, 2, 3, and 4 wt%, respectively. These samples were subsequently characterized and evaluated in catalytic tests. Figure 5 presents the XRD patterns of the synthesized *x*Cu-*y*Fe/TiO_2 catalysts. As expected, diffraction peaks corresponding to TiO_2 and CuO were observed in all samples. However, no distinct peaks associated with iron oxides were detected, likely due to the high dispersion or amorphous nature of the Fe species. Table 2 summarizes the CuO crystallite sizes estimated using the Scherrer equation, as well as the BET surface areas determined from N_2 physisorption measurements. No clear trend was observed for either parameter.

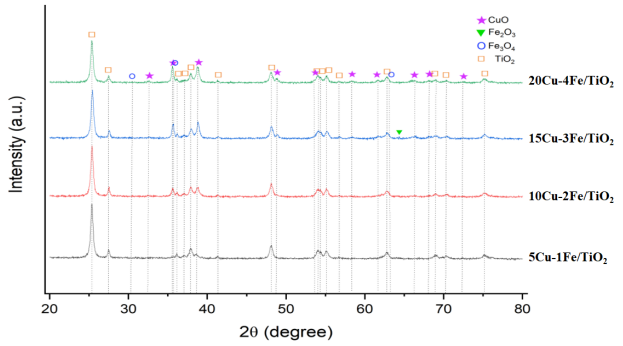

Figure 5 X-ray diffraction (XRD) patterns of the *x*Cu-*y*Fe/TiO_2 catalysts (*x*:*y* = 5).

Table 2 CuO crystallite size, BET surface area and total reducibility of the *x*Cu-*y*Fe/TiO_2 catalysts (*x*:*y* = 5) determined by XRD, N_2 physisorption and H_2-TPR, respectively.

Catalyst	CuO crystallite size (nm)	BET surface area (m^2/g)	Total reducibility (%)
5Cu-1Fe/TiO_2	34.5	45	48.8
10Cu-2Fe/TiO_2	28.7	35	97.7
15Cu-3Fe/TiO_2	38.2	41	95.5
20Cu-4Fe/TiO_2	35.2	36	92.9

Figure 6 shows the TPR profiles of the *x*Cu-*y*Fe/TiO_2 catalysts. The total reducibility, based on CuO reduction, is presented in table 2. The reduction characteristics of the four catalysts were similar. Increasing the Cu loading while maintaining a fixed Fe-to-Cu ratio had little effect on the reduction temperature. This suggested that the Fe promoter had a consistent ability to facilitate the redispersion of CuO on the catalyst surface. Only the 5Cu–1Fe/TiO_2 catalyst exhibited low reducibility, possibly due to strong interactions between small CuO particles and the TiO_2 support [22].

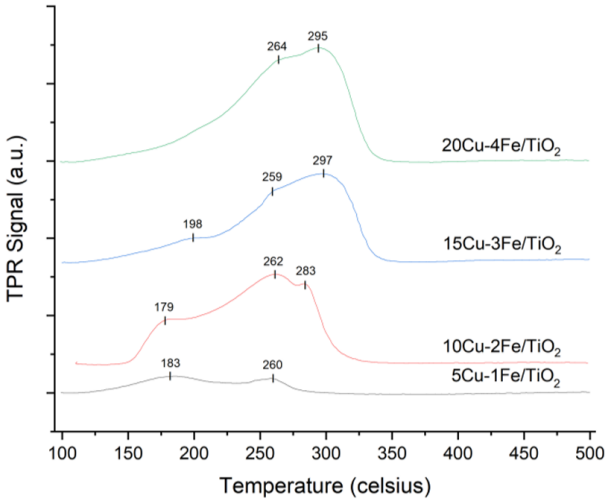

Figure 6 TPR profiles of the *x*Cu-*y*Fe/TiO_2 catalysts (*x*:*y* = 5).

Figure 7 presents the results of N_2O decomposition experiments. The number of accessible Cu sites increased with increasing Cu content; however, the relationship was not linear. Interestingly, the catalyst with 10 wt% Cu exhibited high number of active sites, suggesting that this loading provides an optimal balance between dispersion and surface accessibility. At higher Cu loadings (15 and 20 wt%), a decline in surface-exposed Cu sites was observed, likely due to particle agglomeration.

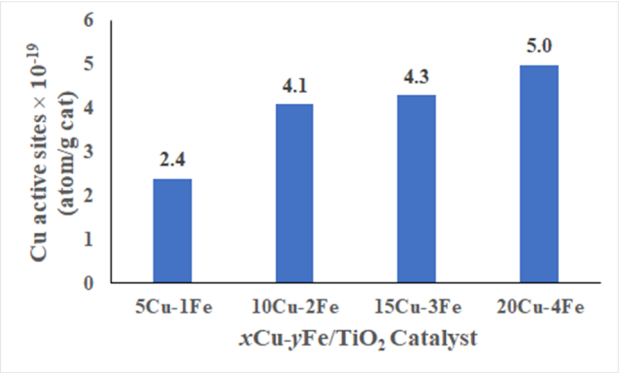

Figure 7 N_2O decomposition results for the *x*Cu-*y*Fe/TiO_2 catalysts (*x*:*y* = 5).

A non-linear trend of Cu active sites correlated well with catalytic performance results shown in Figure 8, where the 10Cu-2Fe/TiO_2 catalyst achieved the highest furfuryl alcohol yield, approaching nearly 100% selectivity. The superior performance at this composition indicated that both the Cu loading and the Fe promoter content are critical in optimizing catalyst

structure and function. While Fe served as a structural promoter to enhance Cu dispersion, excessive Fe content appeared to negatively affect the hydrogenation activity. This may be due to excessive Fe species covering active Cu sites or altering the electronic environment unfavorably, thus hindering the adsorption or activation of furfural molecules.

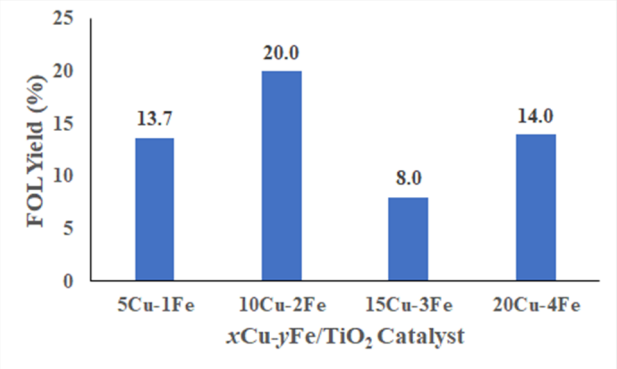

Figure 8 Yield of furfuryl alcohol for the selective hydrogenation of furfural on the *x*Cu-*y*Fe/TiO_2 catalysts (*x*:*y* = 5).

4. CONCLUSION

This study systematically explored the effects of Fe promoter on the structural, redox, and catalytic properties of Cu-Fe/TiO_2 catalysts in the selective hydrogenation of furfural. XRD analysis confirmed the formation of CuO phases and the absence of crystalline iron oxides, indicating that Fe species were likely highly dispersed or amorphous. BET surface area measurements showed a slight decrease with increasing Fe content, attributed to pore blockage or agglomeration. Temperature-programmed reduction (TPR) and N_2O decomposition experiments revealed that Fe acted as an effective structural promoter, enhancing the dispersion of Cu species and facilitating the formation of surface-exposed Cu^0 active sites. An optimal Fe content of 2 wt% in the 10Cu-2Fe/TiO_2 catalyst resulted in the highest concentration of active Cu sites and the best catalytic performance, yielding nearly 100% furfuryl alcohol. When the Cu content was varied while maintaining a fixed Fe-to-Cu ratio (1:5), the relationship between Cu loading and catalytic activity was non-linear. The 10 wt% Cu catalyst again exhibited the optimal balance between active site availability and dispersion. Higher Cu loadings led to decreased performance, likely due to particle agglomeration, while excessive Fe hindered activity by blocking Cu sites or modifying the surface electronic environment. Overall, these findings demonstrate that tuning the Cu and Fe composition is crucial for optimizing metal dispersion and catalytic activity, offering valuable insights for the design of efficient bimetallic catalysts for biomass-derived platform molecule upgrading.

ACKNOWLEDGMENTS

This work was financially supported by Department of Chemical Engineering, Faculty of Engineering and Industrial Technology, Silpakorn University.

REFERENCES

1. X. Li, P. Jai, T. Wang. Furfural: A promising platform compound for sustainable production of C_4 and C_5 chemicals. *ACS Catalysis* 2016; 6: 7621-7640.
2. A. Racha, C. Samanta, S. Sreekantan, B. Marimuthu. Review on catalytic hydrogenation of biomass-derived furfural to furfuryl alcohol: Recent advances and future trends. *Energy & Fuels* 2023; 37(16): 11475-11496.
3. Y. Wang, D. Zhao, D. Rodríguez-Padrón, C. Len. Recent advances in catalytic hydrogenation of furfural. *Catalysts* 2019; 9(10): 796.
4. M.M. Villaverde, N.M. Bertero, T.F. Garetto, A.J. Marchi. Selective liquid-phase hydrogenation of furfural to furfuryl alcohol over Cu-based catalysts. *Catalysis Today* 2013; 213: 87-92.
5. C.P. Jiménez- Gómez, J.A. Cecilia, F.I. Franco-Duro, M. Pozo, R. Moreno-Tost, P. Maireles-Torres. Promotion effect of Ce or Zn oxides for improving furfuryl alcohol yield in the furfural hydrogenation using inexpensive Cu- Based catalysts. *Molecular Catalysis* 2018; 455: 121-131.
6. S. Liu, N. Govindarajan, K. Chan. Understanding activity trends in furfural hydrogenation on transition metal surfaces. *ACS Catalysis* 2022; 12: 12902-12910.
7. Y. Dong-Dong, Y. Xin-Rui, Z. Ya-Jing, W. Kang-Jun. Deactivation mechanism of Cu/SiO_2 catalyst in gas phase hydrogenation of furfural to furfuryl alcohol. *Journal of Fuel Chemistry and Technology* 2023; 51(12): 1751-1760.
8. M. Manikandan, A.K. Venugopal, A.S. Nagpure, S. Chilukuri, T. Raja. Promotional effect of Fe on performance of supported Cu catalyst for ambient pressure hydrogenation of furfural. *RCS Advances* 2016; 5: 3888-3898.
9. L.A. González-Burciaga, C.M. Núñez-Núñez, M.M. Morones-Esquivel, M. Avila-Santos, A. Lemus-Santana, J.B. Proal-Nájera. Characterization and comparative performance of TiO_2 photocatalysts on 6-mercaptopurine degradation by solar heterogeneous photocatalysis. *Catalysts* 2020; 10 (1): 118.
10. R. Etefagh, E. Azhir, N. Shahtahmasebi. Synthesis of CuO nanoparticles and fabrication of nanostructural layer biosensors for detecting Aspergillus niger fungi. *Scientia Iran* 2013; 20(3): 1055-1058.
11. D. Santos-Cruz, S.A. Mayén-Hernández, F. de Moure-Flores, J. Campos-Álvarez, M. Pal, J. Santos-Cruz. CuO_x thin films by direct oxidation of Cu films deposited by physical vapor deposition. *Results in Physics* 2017; 7: 4140-4144.

12. A.A. Kabure, S.R. Mane, B.S. Shirke. The lpg gas-sensing performance of CeO_2-CuO nanocomposite film synthesized by microwave assisted sol- gel method. *International Journal of Recent Scientific Research* 2020; 11(5): 38560-38567.
13. C.P. Jiménez-Gómez, J.A. Cecilia, I. Márquez-Rodríguez, R. Moreno-Tost, J. Santamaría-González, J. Mérida-Robles, P. Maireles-Torres. Gas-phase hydrogenation of furfural over Cu/CeO_2 catalysts. *Catalysis Today* 2017; 279: 327-338.
14. S. Nasiri, M. Rabiei, A. Palevicius, G. Janusas, A. Vilkauskas, V. Nutalapati, A. Monshi. Modified Scherrer equation to calculate crystal size by XRD with high accuracy, examples Fe_2O_3, TiO_2 and V_2O_5. *Nano Trends* 2023; 3: 100015.
15. R. Hatel, S. El Majdoub, A. Bakour, M. Khenfouch, M Baitoul. Graphene oxide/Fe_3O_4 nanorods composite: structural and Raman investigation. *Journal of Physics (Conf. Series)* 2018; 1081: 012006.
16. Q. Xiang, J. Yu, W. Wang, M. Jaroniec. Nitrogen self-doped nanosized TiO_2 sheets with exposed {001} facets for enhanced visible-light photocatalytic activity. *Chemical Communications* 2011; 47(24): 6906-6908.
17. G. Fierro, M. Lojacono, M. Inversi, P. Porta, R. Lavecchia, F. Cioci. A study of anomalous temperature-programmed reduction profiles of Cu_2O, CuO, and CuO-ZnO catalysts. *Journal of Catalysis* 1994; 148(2): 709-721.
18. F. Boccuzzi, A. Chiorino, G. Martra, M. Gargano, N. Ravasio, B. Carrozzini. Preparation, characterization, and activity of Cu/TiO_2 catalysts. I. Influence of the preparation method on the dispersion of copper in Cu/TiO_2. *Journal of Catalysis* 1997; 165(2): 129-139.
19. K. Keyvanloo, B. Huang, T. Okeson, H.H. Hamdeh, W.C. Hecker. Effect of support pretreatment temperature on the performance of an iron Fischer-Tropsch catalyst supported on silica-stabilized alumina. *Catalysts* 2018; 8(2): 77.
20. L. Dong, Z. Liu, Y. Hu, B. Xu, Y. Chen. Dispersion and reduction behavior of CuO/α-Fe_2O_3 systems. *Journal of the Chemical Society, Faraday Transactions* 1998; 94: 3033-3038,
21. S.A. Selishcheva, A.A. Smirnov, A.V. Fedorov, D.Y. Ermakov, Y.K. Gulyaeva, V.A. Yakovlev. Production of furfuryl alcohol in the presence of copper-containing catalysts in the selective hydrogenation of furfural. Catalysis in Industry 2019; 11(3): 216-223.
22. C. Zhang, L. Wang, U.J. Etim, Y. Song, O.M. Gazit, Z. Zhong. Oxygen vacancies in Cu/TiO_2 boost strong metal-support interaction and CO_2 hydrogenation to methanol. Journal of Catalysis 2022; 413: 284-296.

Study on epoxidation of vegetable oil using different acidic ion-exchange resins

Patiphan Palachote[1], Ornsiripim Siriphat[1], Naseerat Khunmathurot[1], Anusorn Seubsai[1,*]

[1] Department of Chemical Engineering, Faculty of Engineering, Kasetsart University, Bangkok 10900, Thailand
[*] Corresponding author: fengasn@ku.ac.th

ABSTRACT

The increasing demand for plastics has raised concerns about the depletion of limited resources. Vegetable oils are interesting as an alternative resource, as their unsaturated fatty acids, such as oleic acid, linoleic acid, and linolenic acid, contain double bonds that can be oxidized to epoxy groups. This work explores the epoxidation reaction through the Prilezhaev epoxidation, the most widely used in industrial applications. This study investigates the epoxidation process using canola oil as a representative of vegetable oil. Various acidic ion-exchange resins with different ion-exchange capacities, including Amberlite IRC120, Amberlyst 15, and NKC-9, were used as catalysts in the epoxidation process. The highest epoxy value achieved was 4.5 h using Amberlyst-15 0.368 mol/100 g of canola oil as determined by titration. The kinetic study showed that the reaction follows a pseudo-first-order model. Thermodynamic values are presented, including enthalpy, entropy, and Gibbs free energy. This study shows an alternative approach to preparing monomers for preparing epoxy resin, one of the essential components in many applications.

Keywords: Vegetable oils; Ion-exchange resin; Epoxidation; Epoxy value

1. INTRODUCTION

Vegetable oils (VOs) are composed of fatty acids, which can be classified based on the length of their carbon chains and their degree of saturation. Saturated fatty acids have no double bonds, while monounsaturated fatty acids have one double bond. Polyunsaturated fatty acids have several double bonds. Due to these structural characteristics, especially oleic acid, linoleic acid, and linolenic acid, vegetable oils can serve as alternative precursors for various chemical reactions, such as epoxidation, hydroxylation, and carboxylation, when combined with appropriate catalysts. Among all vegetable oils, soybean and sunflower are the main vegetable oils produced globally. Canola oil and rice bran oil are also excellent alternatives for oxidation processes due to their high oleic and linoleic acid content.

Different routes have explored the epoxidation reaction, but the most widely used in industries is commonly Prilezhaev epoxidation [1]. This process consists of the formation of performic and peracetic acid form action between hydrogen peroxide and the corresponding carboxylic acid in the presence of a strong acid (H_2SO_4). However, the strong acid leads to the corrosion of chemical equipment, low selectivity, and difficulty in separating product and catalyst so that ion exchange resin can replace the strong acid [2].

In this study, the epoxidation of canola oil and rice bran oil was carried out using different acidic ion-exchange resins as catalysts, including Amberlite IRC120, Amberlyst 15, and NKC-9, each possessing distinct ion-exchange capacities. The objective was to investigate the effect of catalyst type on the epoxy value and to study the kinetic and thermodynamic behavior of the epoxidation reaction under various conditions. The findings contribute to a deeper understanding of catalyst efficiency and support optimizing reaction parameters for improved epoxidation performance.

2. EXPERIMENTAL

2.1 Materials

Glacial acetic, hydrochloric acid (37%), glycerol (99.5%), and hydrogen peroxide (35%) were purchased from Qrec. Ion-exchange resin Amberlite IRC120 and Amberlyst 15 were purchased from Thermo Scientific. Ion-exchange resin NKC9 was purchased from Tianjin Yunkai. For the titration process, sodium hydroxide and 1,4 Dioxane were purchased from Fisher Scientific, cresol red was purchased from Loba Chemie, and methanol was purchased from Qrec.

2.2 Epoxidation of canola oil

The epoxidation of canola oil was carried out by placing 50 g of canola oil, 7.5 g of catalyst and acetic acid 3 g in a 500 ml triple-neck round bottom flask equipped with a reflux condenser, thermometer and magnetic stirrer. The flask was placed in oil bath on top of hot plate to control temperature. The mixture was stirred 500 rpm with three difference temperature at 30, 50 and 70°C respectively. After desired temperature is reached, hydrogen peroxide was slowly added to prevent a temperature decrease caused by its low

storage temperature. The sample was taken from various reaction times (3, 4.5, 6, 7.5, and 9 h)

2.3 Epoxidation of rice bran oil

The epoxidation of rice bran oil was carried out by placing 50 g of rice bean oil, 7.5 g of catalyst, and acetic acid 3 g in a 500 ml triple-neck round bottom flask equipped with a thermometer and magnetic stirrer. The flask was placed in an oil bath on top of a hotplate stirrer to control temperature. The mixture was stirred at 500 rpm until the temperature reached 65°C, and hydrogen peroxide was slowly added to prevent a temperature decrease caused by its low storage temperature. The sample was taken from various reaction times (30, 60, 90, 120, 150, and 180 min)

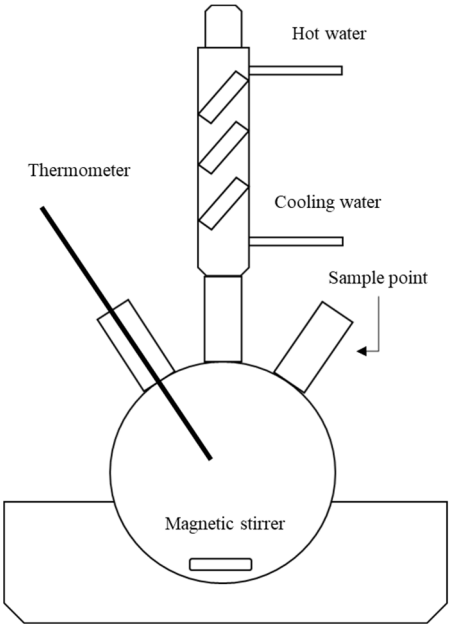

Figure 1 Experimental setup for the epoxidation process

2.4 Characterization of epoxide oils

The epoxy value (Ev) was determined using a titration method. Before titration, the sample was cooled for 15 minutes and washed with distilled water to prevent hydrolysis. A 0.1 M sodium hydroxide solution was prepared by mixing sodium hydroxide with methanol and stirring until homogeneous. Hydrochloric acid was diluted with 1,4-dioxane to obtain a concentration of 0.2 M. Then, 10 mL of the hydrochloric acid solution and 10 drops of cresol red indicator were added to the sample. The titration was stopped when the color of the solution changed from pink to yellow. The epoxy value was calculated using equation (1).

$$E_v = \frac{V_b - V_s \cdot C_{NaOH} \cdot 100}{m_s \cdot 1000} mol/100g \quad (1)$$

Where: V_b = the volume of sodium hydroxide solution consumed in the blank test, V_s = the volume of sodium hydroxide solution consumed during the titration with the sample, and M_s = the mass of the sample.

3. RESULTS AND DISCUSSION

3.1 Epoxidation of canola oil

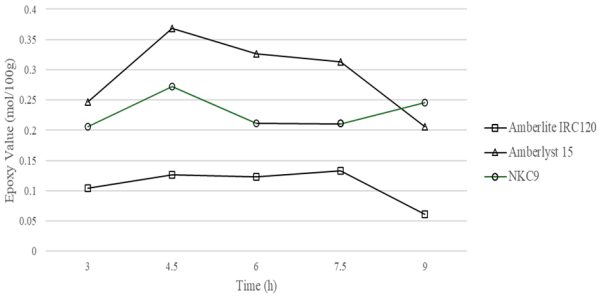

Figure 2 Comparison of epoxy values of canola oil using three different catalysts: Amberlite IRC120, Amberlyst 15, and NKC-9

Figure 2 shows that at 4.5 hours of reaction time, the epoxy value using Amberlyst 15 as a catalyst reached its highest value of 0.368 mol/100 g. After 4.5 hours, all catalysts showed a decreasing trend in epoxy value. This decline is likely due to the increased formation of by-products and the opening of the epoxy rings, which can occur under prolonged reaction conditions or in the presence of excess water or acid.

3.2 Kinetic study of epoxidation reaction of canola oil

The epoxidation reaction usually occurs in two steps: (i) the reaction between acetic acid and hydrogen peroxide, which leads to the formation of peracetic acid, and (ii) the reaction of peracetic acid with unsaturated fatty acids (UFA) of canola oil [2].

$$AA + H_2O_2 \rightarrow PAA + H_2O \quad (2)$$

$$UFA + PAA \rightarrow \text{Epoxidized oil} + AA \quad (3)$$

Where:
AA = Acetic acid
PAA = Peracetic acid
UFA = Unsaturated fatty acid

$$-r_{CO} = \frac{-dC_{CO}}{dt} = k' C_{CO} C_{PAA} \quad (4)$$

The reaction rate can be written as equation (4), assuming that the concentration of peracetic acid remains constant during the reaction because the catalyst produces it in excess. Hence, the epoxidation rate is expressed as shown in equation (5).

$$\frac{-dC_{CO}}{dt} = kC_{CO} \quad (5)$$

Where $k=k'C_{PAA;}$ a term of fractional conversion of canola oil (X_{CO}) as shown in equation (6).

$$\frac{-dC_0(1-X_{CO})}{dt} = kC_0(1 - X_{0)} \quad (6)$$

Where C_0 is the initial concentration of the canola oil. Since, $C_0=(1-X_0)$

$$\frac{-dX_{CO}}{dt} = k(1 - X_{CO}) \quad (7)$$

The rate of reaction can be written as integral from equation (8) with $X_0=0$, t=0, and $X=X_{CO}$ at t=t.

$$\int_0^{X_{CO}} \frac{-dX_{CO}}{1-X_{CO}} = k \int_0^t dt \quad (8)$$

Then, after the integration of equation (8), the final equation can be written as equation (9).

$$\ln(1 - X_{Co}) = kt \quad (9)$$

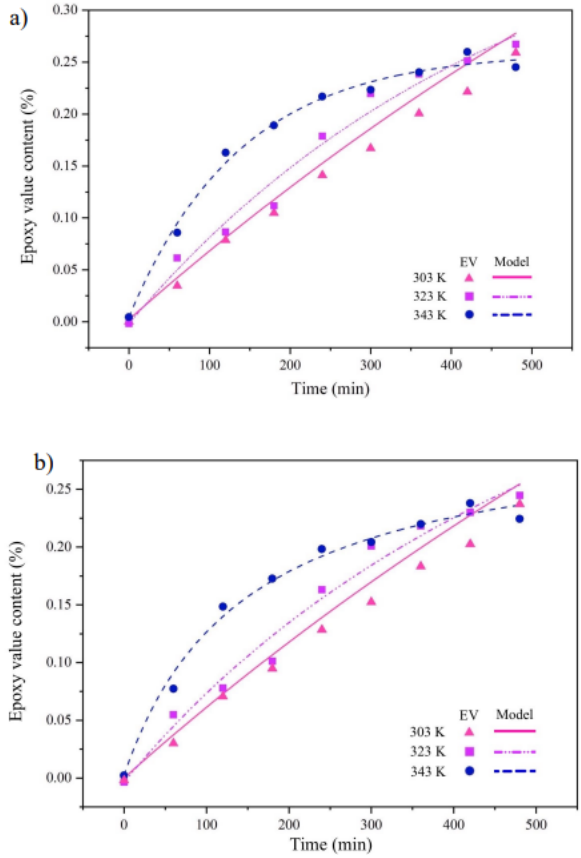

Figure 3 Plots of epoxy value versus time (a) pseudo-first-order (b) pseudo-second-order.

3.3 Activation energy and thermodynamic study of epoxidation reaction of canola oil

For the pseudo-first-order, the reaction rate is relatively constant and increases with temperature. Thus, it can be described by the Arrhenius Law in (10)

$$K = A \cdot exp\left(\frac{-E_a}{RT}\right) \quad (10)$$

Where:
K = extraction rate constant ($L \cdot g^{-1}min^{-1}$)
A = temperature independent factor ($L \cdot g^{-1}min^{-1}$)
E_a = activation energy ($J \cdot mol^{-1}K^{-1}$).
R = gas constant (8.314 $J \cdot mol^{-1}K^{-1}$)
T = absolute suspension temperature (K)

Table 1 Rate constant (k) value for epoxidation of canola oil at various temperature.

	Temp. (°C)	1/T(1/K)	k(min^{-1})	-lnk
Pseudo 1st Order	30	0.003300	7.710×10^{-4}	7.1678
	50	0.003096	0.0021	6.1658
	70	0.002915	0.0073	4.9200
Pseudo 2nd Order	30	0.003300	2.805×10^{-4}	8.1789
	50	0.003096	8.299×10^{-4}	7.0942
	70	0.002915	0.0061	5.0994

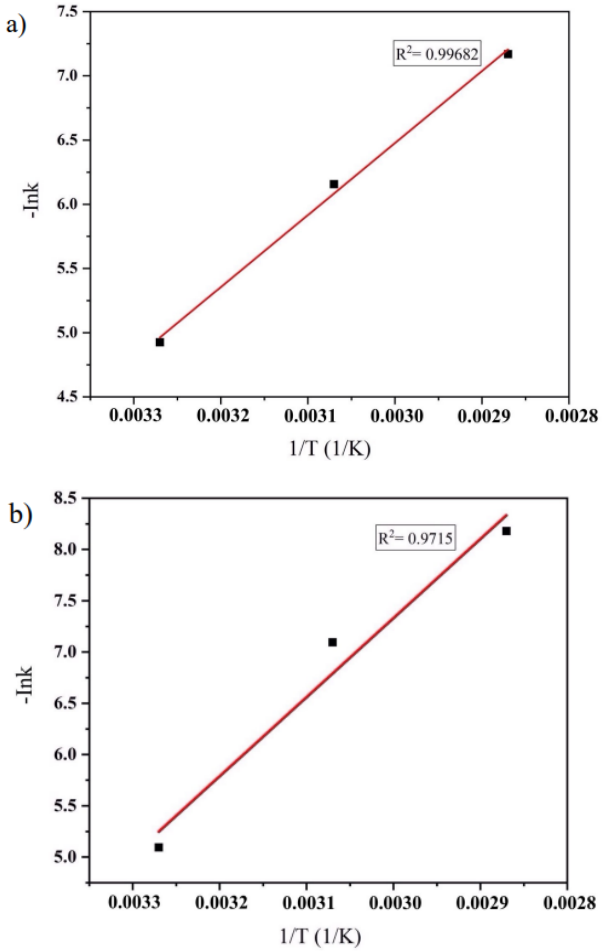

Figure 4 Plots of -lnk verses 1/T(1/K) for the epoxidation of canola oil by using Arrhenius equation (a) pseudo-first-order (b) pseudo-second-order models.

In the epoxidation of canola oil, the average enthalpy of activation ΔH of the reaction was study by using equation (11).

$$\Delta H = E_a - RT \quad (11)$$

Where E_a denotes the activation energy calculated from the Arrhenius plot, T denotes the temperature, and R denotes the gas constant

$$k = \frac{RT}{Nh} \cdot e^{\Delta S/R} \cdot e^{-E_a/RT} \quad (12)$$

$$\Delta G = \Delta H - T\Delta S \quad (13)$$

The average entropy of activation energy ΔS and Gibbs free energy of activation ΔG can be obtained using equations (12) and (13), respectively [4], as shown in Table 2.

Table 2 Thermodynamic parameter for epoxidation of canola oil.

	Temp. (°C)	E_a (kJ/mol)	ΔH (kJ/mol)	ΔS (kJ/mol)	ΔG (kJ/mol·K)
Pseudo 1st Order	30	48.38	45.86	-145.0	89.79
	50		45.69	-147.1	93.19
	70		45.53	-145.9	95.58
Pseudo 2nd Order	30	66.03	63.51	-27.12	71.73
	50		63.35	-41.14	76.64
	70		63.18	-53.56	81.55

3.4 Effect of ion-exchange capacity on the epoxidation process

The effect of reaction time on the epoxy value of epoxidized oil has been investigated. The epoxy value increased with reaction time for all reactions. Figure 5 shows the epoxy value of rice bran oil using Amberlite IRC120 as a catalyst. The results indicate a continuous increase in epoxy value over time, with the highest value achieved being 0.136 mol/100 g at 180 min.

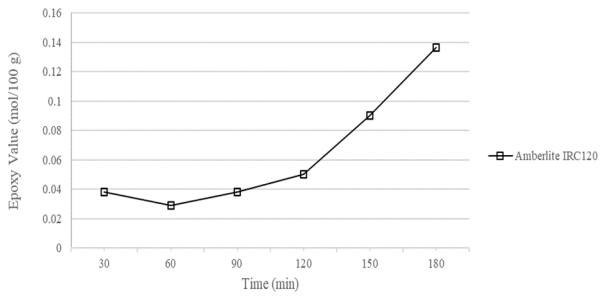

Figure 5 Epoxy value of epoxidized rice bran oil with Amberlite IRC120.

Figure 6 shows the epoxy value of rice bran oil using Amberlyst 15. The epoxy value increased rapidly during the first 60 minutes, followed by a slower, more gradual increase until 150 min.

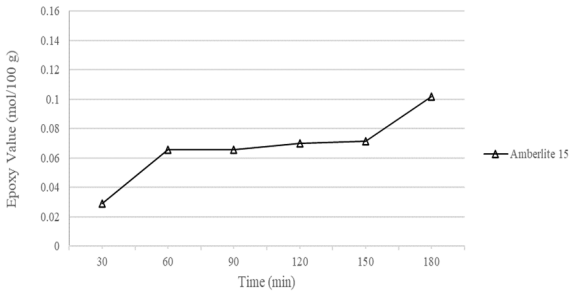

Figure 6 Epoxy value of epoxidized rice bran oil with Amberlyst 15 as catalyst.

The epoxy value of rice bran oil using NKC-9 rapidly increased, reaching 0.12 mol/100g at 150 min. However, after this point, the epoxy value decreases to 0.11 mol/100g, as shown in Figure 7.

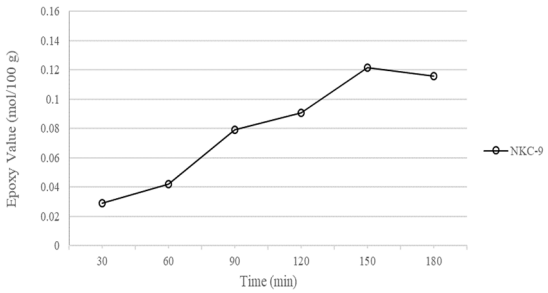

Figure 7 Epoxy value of epoxidized rice bran oil with NKC9.

Table 3 Ion-exchange capacity of acidic resin

Ion-exchange resin	Ion-exchange Capacity (IEC)
Amberlite IRC120	1.8 eq/L
Amberlyst 15	2.9 eq/L
NKC-9	3.3 eq/L

Table 3 demonstrates that differences in the ion exchange capacity of the catalysts significantly affect the epoxy value of rice bran oil. This is because the catalyst enhances the formation rate of peracetic acid during the reaction. However, when the ion exchange capacity is excessively high, as in the case of NKC-9, the rapid generation of peracetic acid also leads to the formation of excessive by-products [5]. These by-products interfere with the epoxy groups, causing ring opening and ultimately decreasing the epoxy value.

4. CONCLUSION

This study investigated various acidic ion-exchange resins: Amberlite IRC120, Amberlyst 15, and NKC9 as catalysts in the epoxidation reaction of canola and rice bran oil. The first phase of the study focused on the kinetic and thermodynamics of the epoxidation reaction of canola oil. Three reaction temperatures were considered: 30, 50 and 70°C. The kinetic model results showed that as the reaction temperature increases, the reaction rate also tends to increase—the second phase

aimed to investigate the effect of ion exchange capacity. The results showed that a higher ion exchange capacity led to an increased reaction rate. However, excess water was generated at higher reaction rates, which disrupted the epoxy rings and caused ring opening.

ACKNOWLEDGMENTS

This work was financially supported by the Fundamental Fund, Thailand (FF(KU)1.68), the Kasetsart University Research and Development Institute (KURDI), Bangkok, Thailand.

REFERENCES

1. Ibrahima BALDE, C.K., Abdou K.D. DIME, Samba BALDE, Khady NDIAYE, *Vegetable Oils Epoxidation Mechanisms.* World Journal of Analytical Chemistry, 2022.
2. Mungroo, R., Pradhan, N. C., Goud, V. V., & Dalai, A. K. (2008). Epoxidation of Canola Oil with Hydrogen Peroxide Catalyzed by Acidic Ion Exchange Resin. Journal of the American Oil Chemists' Society, 85(9), 887-896.
3. Danial Nuruddin Azlan Raofuddin, Intan Suhada Azmi, and M.J. Jalil, *Catalytic Epoxidation of Oleic Acid Derived from Waste Cooking Oil by In Situ Peracids.* Journal of Polymers and the Environment, 2024. 32: p. 803–814.
4. Agu, C. M., Agulanna, A. C., Kadurumba, C. H., Nnaji, P. C., Udokporo, E. L., & Menkiti, M. C. (2022). Characterization, kinetics and thermodynamics of epoxidation-esterification of Irvingia gabonensis kernel oil methyl ester. Heliyon, 8(5), 9520.
5. Kurańska, M., & Niemiec, M. (2020). Cleaner Production of Epoxidized Cooking Oil Using A Heterogeneous Catalyst. Catalysts, 10(11).

Photocatalytic activity of N, S-CQDs/TiO_2 composites for the degradation of methylene blue under visible-light irradiation

Thanyapak Akkharaamnuay[1], Okorn Mekasuwandumrong[2], Joongjai Panpranot[1,*]

[1] Center of Excellence on Catalysis and Catalytic Reaction Engineering, Department of Chemical Engineering, Faculty of Engineering, Chulalongkorn University, Bangkok 10330, Thailand
[2] Department of Chemical Engineering, Faculty of Engineering and Industrial Technology, Silpakorn University, Nakorn Pathom 73000, Thailand
[*] Corresponding author: joongjai.p@chula.ac.th

ABSTRACT

Water pollution occurs when harmful substances contaminate water environments. Among the prominent contributors to this issue are dyes, originating predominantly from industrial sectors such as textiles, using complex compounds like methylene blue (MB). In this work, N and S co-doped carbon quantum dots (N, S-CQDs)/titanium dioxide (TiO_2) were used to eliminate MB from water via photodegradation reaction under visible light. N, S-CQDs were synthesized via hydrothermal reaction using glycine as a precursor and ammonium sulfate as N and S source. TiO_2 was synthesized via a sol-gel method using titanium tetra-isopropoxide (TTIP). The SEM-EDX analysis confirmed the presence of C, O, S, N, and Ti as the primary elements in the composites. Moreover, TEM shows the lattice space of both N, S-CQDs and TiO_2 at 0.21 nm and 0.33 nm, corresponding to (100) planes of graphite and (110) plane of TiO_2, respectively. Incorporating N, S-CQDs into TiO_2 boosts the photodegradation efficiency under visible-light for 150 min from 41% to 70%. The optimum amount of N, S-CQDs was determined to be around 1 wt%.

Keywords: Methylene blue; Titanium dioxide; Carbon quantum dots; Photodegradation

1. INTRODUCTION

Water pollution occurs when harmful chemicals or substances enter natural water bodies like rivers, lakes, and oceans. These contaminants may dissolve in the water, float on the surface, or settle at the bottom, all of which reduce the overall quality of the water. There are several causes of water pollution, and one major source is the discharge of dyes. These dyes mainly come from industries such as textiles, paper production, and plastics [1].

Methylene blue (MB) is a heterocyclic dye widely used in various industries, but it poses significant environmental risks due to its high toxicity and tendency to accumulate in environment. Over the years, numerous methods have been explored to eliminate MB from water [2, 3].

Titanium dioxide (TiO_2) is one of the most commonly used photocatalysts due to its strong oxidizing power, excellent chemical stability, and non-toxicity. However, its practical applications are limited by its wide bandgap energy (3.2 eV for anatase), which restricts its photocatalytic activity to the ultraviolet (UV) region. Since UV light constitutes only a small fraction (~5%) of the solar spectrum, the low efficiency of TiO_2 under visible light significantly hinders its environmental applications [4, 5]. To overcome this limitation, various strategies have been employed to enhance the visible-light responsiveness of TiO_2, including metal and non-metal doping, surface modification, heterojunction formation, and coupling with carbon-based nanomaterials [6, 7]. Among these, the incorporation of carbon quantum dots (CQDs) has emerged as a promising approach due to their unique electronic and optical properties.

Carbon quantum dots (CQDs), a newly identified quasi-zero-dimensional material, have drawn significant interest due to their broad absorption spectrum, high light absorption coefficient, and exceptional chemical stability. Recent studies have demonstrated that CQDs exhibit unique up-conversion luminescence properties, where they absorb long-wavelength, low-frequency light and subsequently emit short-wavelength, high-frequency light. Additionally, CQDs can function as electron acceptors, reducing the recombination rate of photogenerated electron-hole pairs, thereby enhancing the photocatalytic degradation efficiency of semiconductors [8-10]. In recent years, beyond their integration with various nanomaterials, researchers have also introduced nonmetallic element doping—such as nitrogen (N), phosphorus (P), sulfur (S), and chlorine (Cl)—to enhance CQDs' adsorption and photocatalytic performance. For instance, nitrogen-doped CQDs exhibit unusual photoluminescence beyond the visible spectrum and can modify the local

electronic structure, increasing capacitance and improving charge separation to boost photocatalytic activity. Similarly, sulfur doping influences the surface functional groups and conjugation system of CQDs, thereby enhancing their optical properties [11-13]. These features make CQDs highly effective in improving charge separation and extending the light absorption range of TiO_2.

In this study, we investigate the photocatalytic activity of N, S-CQDs/TiO_2 composites for the degradation of methylene blue under visible-light irradiation. N, S-CQDs were synthesized via hydrothermal reaction using glycine as a precursor and ammonium sulfate as N and S source. TiO_2 was synthesized via a sol-gel method using titanium tetra-isopropoxide (TTIP) as a titanium precursor. The composites have been characterized using XRD, TEM, SEM, PL, and UV techniques.

2. EXPERIMENTAL

2.1. Chemicals

Glycine, the starting material for CQDs synthesis, was purchased from Krungthepchemi Co. Ltd. Ammonium sulfate ($(NH_4)_2SO_4$), and concentrated hydrochloric acid (HCl, 36%) were purchased from Kemaus. Hydrogen peroxide (H_2O_2) was purchased from Nippon Intertrade Co. Ltd. Titanium isopropoxide (TTIP) was purchased from Thermo Fisher Scientific. Methylene blue was purchased from Sigma-Aldrich. Deionized water (DI) used in the preparation was from local sources.

2.2. Synthesis of N, S-CQDs

N, S-CQDs were synthesized by using glycine as a precursor and ammonium sulfate as nitrogen and sulfur source. Initially, 2.64 g of ammonium sulfate and 5.63 g of glycine were dissolved in a mixture of 36.5 ml of deionized water and 13.5 ml of hydrogen peroxide. Then, the mixture was stirred at 300 °C with a stirring rate of 390 rpm for 40 minutes. After cooling to room temperature, it was dried in a Carbolite oven at 270 °C for 720 minutes overnight to obtain a black powder. The final product was washed several times with deionized water and dried in an oven at 110 °C overnight.

2.3. Synthesis of N-GQDs/TiO2 composites

Titanium tetraisopropoxide (TTIP) of 98% purity served as the titanium precursor, while 36% hydrochloric acid (HCl) of analytical grade, acted as a catalyst for peptization. Deionized water was utilized as the dispersing medium. 35 ml of deionized water was heated to 70 °C with a stirring rate of 40 rpm. Then, 5 ml of TTIP and 1 ml of 36% HCl were added, forming a thick white precipitation. Different amounts (0, 0.2, 0.5, 1, 2.5, and 5 wt%) of N, S-CQDs in 15 ml of deionized water were added to this mixture to obtain various N, S-CQDs/TiO_2 suspensions, which were continuously stirred for 24 hours. After that, the suspension was transferred into an autoclave and treated by hydrothermal process at 230 °C for 8 hours, then dried in an oven at 110 °C overnight to obtain N, S-CQDs/TiO_2 powder. The resulting composites were further calcined under N2, heated the powder at a rate of 2 °C/h to 400 °C, and held the powder at 400 °C for 1 hour.

2.4. Photocatalytic test

The photocatalytic activity of all composite samples was evaluated through the photodegradation of methylene blue under visible-light irradiation. Initially, 0.05 g of photocatalyst was dispersed in 50 ml of a 10 ppm methylene blue solution at room temperature. A 35 W, 12 V of xenon lamp was used for visible-light irradiation. The suspension was stirred in a dark condition at a stirring rate of 400 rpm for 30 minutes to establish adsorption/desorption equilibrium. Then, the suspension was stirred under visible light for 120 minutes, 5 ml sample was taken out every 30 minutes to determine the methylene blue concentration via UV-visible spectrophotometry. The degradation of methylene blue in the suspension was measured of the decay of absorbance at λ_{max} = 664 nm. The dye degradation percentage was calculated using the following equation:

$$\% \text{ Degradation} = \frac{C_0 - C_t}{C_o} \times 100 \quad (1)$$

where C_0 and C_t represent the dye concentration at the initial time and at a certain time, respectively.

2.5 Characterization

For characterization of all composites, X-ray diffraction (XRD) patterns were recorded using a Siemens D5000 diffractometer equipped with CuK_α radiation (λ = 1.5418 Å) at scanning range of $5<2\theta<80$. Scanning electron microscopy and energy dispersive X-ray spectroscopy (SEM-EDX) images were obtained on Hitachi S-3400N SEM with Edex 2371 series 300 software. Transmission electron microscopy (TEM) images were obtained on a Talos F200X at STREC, Chulalongkorn University. UV-vis spectroscopy was analyzed using a Varian Cary 5000 UV-Vis-NIR UV-visible spectrophotometer. PL spectra were analyzed using a Horiba 4P-Fluoromax spectrofluorometer with a Xenon lamp as the excitation source, using an excitation wavelength of 320 nm at room temperature.

3. RESULTS AND DISCUSSION

XRD analysis was performed to examine the phase composition of the composites. As seen in Fig. 1, the XRD patterns of TiO_2 and N, S-CQDs/TiO_2 composites show that the characteristic peak positions (2θ) remain largely unchanged across different N, S-CQDs contents, aligning closely with those of pure TiO_2. Since TiO_2 particles were synthesized using the sol–gel

method with 36% hydrochloric acid, where the pH is typically below 1. Preparation of TiO_2 under such strongly acidic conditions can hinder the development of anatase crystals, leading to a poor crystalline arrangement or an amorphous-like structure, particularly when the pH is below 4.5. Moreover, TiO_2 tends to form the rutile phase under acidic conditions, whereas the anatase phase is more likely to form under alkaline conditions (pH above 7) [14, 15]. In the XRD patterns of TiO_2 and N, S-CQDs/TiO_2 composites, a rutile peak was observed at $2\theta = 26.67°$, corresponding to the (110) plane. Meanwhile, the XRD patterns of the 5% N, S-CQDs/TiO_2 composite also showed an anatase peak at $2\theta = 25.21°$, corresponding to the (101) plane.

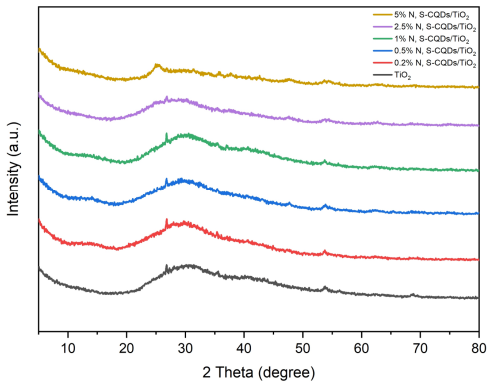

Figure 1 XRD patterns of TiO_2 and N, S-CQDs/TiO_2 composites.

The morphology and microstructure of 1% N, S-CQDs/TiO_2 composites were determined by TEM analysis as shown in Fig. 2. Fig. 2a shows the TEM image of TiO_2, revealing that it has an almost spherical morphology. Fig. 2b shows the TEM image of 1% N, S-CQDs/TiO_2, the lattice space of both N, S-CQDs and TiO_2 at 0.21 nm and 0.33 nm, corresponding to (100) planes of graphite and (110) plane of TiO_2, respectively. Fig. 2b also demonstrates that the N, S-CQDs in the 1% N, S-CQDs/TiO_2 composite are successfully loaded and evenly distributed across the TiO_2 surface.

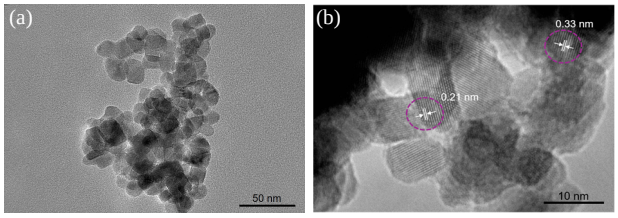

Figure 2 TEM images of (a) TiO_2 and (b) 1% N, S-CQDs/TiO_2 composites.

The SEM image of 1% N, S-CQDs/TiO_2 are shown in Fig. 3a, revealing that the N, S-CQDs are uniformly distributed over the TiO_2 particles and are closely attached, forming a coating-like N, S-CQDs/TiO_2 heterojunction structure. The EDX elemental mapping (Fig. 3b–f) confirmed the presence of C, O, S, N, and Ti as the primary elements in the composites, indicating a consistent distribution of N, S-CQDs on the TiO_2 particles. Additionally, the TEM image in Fig. 2b further verifies the incorporation of N, S-CQDs in the composite, as evidenced by the observed 0.21 nm lattice spacing corresponding to the (100) planes of graphite.

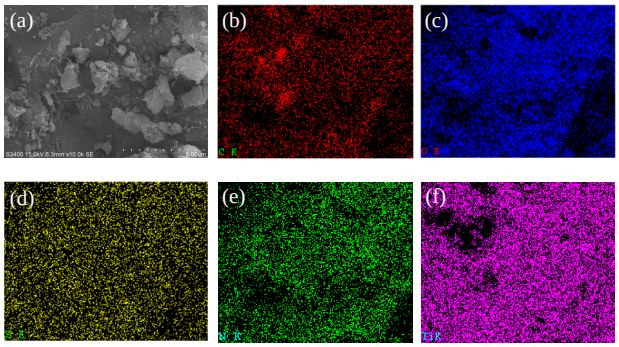

Figure 3 SEM image of (a) 1% N, S-CQDs/TiO_2; EDX mapping of 1% N, S-CQDs/TiO_2: (b) C, (c) O, (d) S, (e) N, and (f) Ti.

Fig. 4 presents the UV-vis spectrum, which was recorded to examine the optical characteristics of all the photocatalysts within the wavelength range of 200 to 800 nm. TiO_2 shows strong absorption in the UV region, with an absorption edge around 400 nm. When N, S-CNQDs are loaded onto the surface of TiO_2, the absorption edge extends into the visible-light range. Moreover, as the amount of N, S-CNQDs in the composite increases, the absorption in the visible region becomes more pronounced compared to pure TiO_2. This enhancement is attributed to the superior visible-light response of the N, S-CNQDs. In the case of 5% N, S-CQDs/TiO_2 composites, two prominent absorption regions are observed in the UV range, specifically between 200–250 nm and 300–400 nm. These absorption bands are attributed to the π–π^* electronic transitions occurring within the aromatic sp^2 carbon structures present in the N, S-CQDs [16]. At higher doping levels, the formation of a thicker N, S-CQDs layer within the heterojunctions or the clustering of N, S-CQDs without direct contact with the TiO_2 particles results in the appearance of two prominent absorption peaks associated with the N, S-CQDs [17].

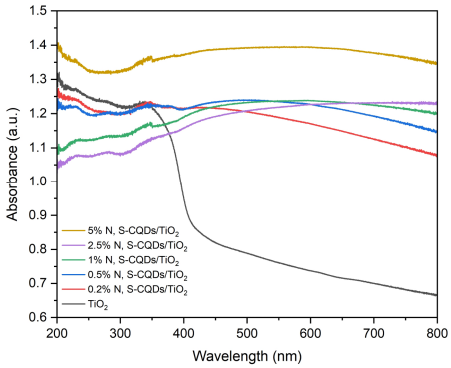

Figure 4 The UV-vis spectra of TiO_2 and N, S-CQDs/TiO_2 composites.

Photoluminescence (PL) spectroscopy was used to investigate the recombination behavior of photogenerated charge carriers. As shown in Fig. 5, TiO_2 exhibited fluorescence emission peak at 467 nm and had the highest luminescence intensity among the samples. In contrast, the 1% N, S-CQDs/TiO_2 composite exhibited the lowest emission intensity. The luminescence intensity followed the sequence: TiO_2 > 0.5% N, S-CQDs/TiO_2 > 2.5% N, S-CQDs/TiO_2 > 0.2% N, S-CQDs/TiO_2 > 5% N, S-CQDs/TiO_2 > 1% N, S-CQDs/TiO_2. High fluorescence intensity indicates efficient recombination of photogenerated electrons and holes, while lower intensity suggests better charge separation. Modifying the TiO_2 surface with suitable amount of N, S-CQDs enhances the separation of charge carriers, thereby improving photocatalytic activity [18, 19].

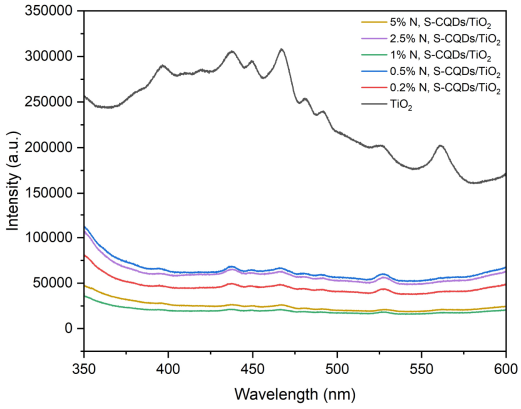

Figure 5 The PL spectra of TiO_2 and N, S-CQDs/TiO_2 composites.

Fig. 6 shows the degradation results of methylene blue (MB) under visible light for N, S-CQDs/TiO_2 composites with varying N, S-CQDs weight percentages. The catalytic degradation efficiency of the N, S-CQDs/TiO_2 composites increases initially and then decreases as the N, S-CQDs content rises. It is evident that the visible-light catalytic efficiency of pure TiO_2 is 41%. When the N, S-CQDs content is 1%, the degradation efficiency of the composites reaches its highest point at 70%, which is 1.7 times greater than that of TiO_2. When the N, S-CQDs content is below 1%, the visible-light catalytic efficiency of the composites gradually increases with higher N, S-CQDs content, indicating that a moderate amount of N, S-CQDs positively impacts the photocatalytic performance of the composites [20]. A small amount of N, S-CQDs help create crystal defects during TiO_2 crystallization, which enhances the separation of photogenerated electrons and holes during photocatalysis. However, further increasing the N, S-CQDs content significantly reduces photocatalytic activity. Excessive amounts of N, S-CQDs can hinder the formation of anatase and rutile crystal structures, likely due to reduced catalytic active sites, increased charge carrier recombination, and decreased efficiency in separating photo-induced electron-hole pairs, which is caused by the excessive loading of N, S-CQDs on the TiO_2 surface [21-23].

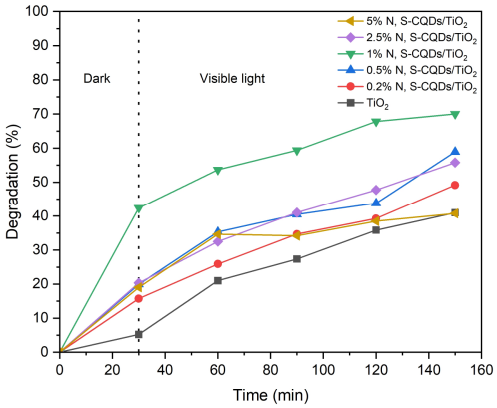

Figure 6 Photodegradation activity of MB using N, S-CQDs/TiO_2 composites.

4. CONCLUSION

In this study, N, S-CQDs were synthesized through a hydrothermal process using glycine as the carbon source and ammonium sulfate as the nitrogen and sulfur source. TiO_2 was prepared via the sol-gel method using titanium tetra-isopropoxide (TTIP) as the precursor. SEM-EDX analysis confirmed that the primary elements in the composites are C, O, S, N, and Ti. TEM imaging revealed lattice spacings of 0.21 nm for N, S-CQDs and 0.33 nm for TiO_2, corresponding to the (100) plane of graphite and the (110) plane of TiO_2, respectively. N, S-CQDs were successfully coupled with TiO_2 to form stable N, S-CQDs/ TiO_2 composites. This coupling enhanced visible-light absorption and suppressed the recombination of charge carriers. As a result, the photocatalytic activity of the composites is significantly higher than that of TiO_2.

ACKNOWLEDGMENTS

The authors gratefully acknowledge the support provided by the Center of Excellence in Catalysis and Catalytic reaction Engineering (CECC) and CrystalLyte Co., Ltd. in the conduct of this research.

REFERENCES

1. Periyasamy, A.P., Recent advances in the remediation of textile-dye-containing wastewater: prioritizing human health and sustainable wastewater treatment. *Sustainability*, 2024. 16(2): p. 495.
2. Albayati, T.M., A.A. Sabri, and R.A. Alazawi, Separation of methylene blue as pollutant of water by SBA-15 in a fixed-bed column. *Arabian Journal for Science and Engineering*, 2016. 41: p. 2409-2415.
3. Derakhshan, Z., et al., Adsorption of methylene blue dye from aqueous solutions by modified pumice stone: kinetics and equilibrium studies. 2013.
4. Pelaez, M., et al., A review on the visible light active titanium dioxide photocatalysts for environmental applications. *Applied Catalysis B: Environmental*, 2012. 125: p. 331-349.

5. Zhang, J., et al., New understanding of the difference of photocatalytic activity among anatase, rutile and brookite TiO 2. *Physical Chemistry Chemical Physics*, 2014. 16(38): p. 20382-20386.
6. Patil, S.B., et al., Recent advances in non-metals-doped TiO2 nanostructured photocatalysts for visible-light driven hydrogen production, CO2 reduction and air purification. *International Journal of Hydrogen Energy*, 2019. 44(26): p. 13022-13039.
7. Truppi, A., et al., Visible-light-active TiO2-based hybrid nanocatalysts for environmental applications. *Catalysts*, 2017. 7(4): p. 100.
8. Jin, T., et al., Synthesis of g-C3N4/CQDs composite and its photocatalytic degradation property for Rhodamine B. *Carbon Letters*, 2022. 32(6): p. 1451-1462.
9. Di, J., et al., Novel visible-light-driven CQDs/Bi2WO6 hybrid materials with enhanced photocatalytic activity toward organic pollutants degradation and mechanism insight. *Applied Catalysis B: Environmental*, 2015. 168: p. 51-61.
10. Gao, H., et al., Construction of a CQDs/Ag3PO4/BiPO4 heterostructure photocatalyst with enhanced photocatalytic degradation of rhodamine B under simulated solar irradiation. *Micromachines*, 2019. 10(9): p. 557.
11. Zhao, F., et al., Photocatalytic degradation of tetracycline by N-CQDs modified Sg-C3N4 nanotubes and its product toxicity evaluation. *Separation and Purification Technology*, 2023. 314: p. 123533.
12. Yu, H., et al., Enhanced photocatalytic tetracycline degradation using N-CQDs/OV-BiOBr composites: Unraveling the complementary effects between N-CQDs and oxygen vacancy. *Chemical Engineering Journal*, 2020. 402: p. 126187.
13. Chang, L., N, S-doped carbon quantum dots/TiO_2 nanocomposites for visible-light-driven photocatalytic degradation of water pollutants. 2022, Memorial University of Newfoundland.
14. Yalcin, M., The effect of pH on the physical and structural properties of TiO2 nanoparticles. *Journal of Crystal Growth*, 2022. 585.
15. Tsega, M. and F.B. Dejene, Influence of acidic pH on the formulation of TiO(2) nanocrystalline powders with enhanced photoluminescence property. *Heliyon*, 2017. 3(2): p. e00246.
16. Huang, S., et al., Red emission nitrogen, boron, sulfur co-doped carbon dots for “on-off-on” fluorescent mode detection of Ag+ ions and L-cysteine in complex biological fluids and living cells. *Analytica Chimica Acta*, 2018. 1035: p. 192-202.
17. Pan, D., et al., Efficient separation of electron–hole pairs in graphene quantum dots by TiO2 heterojunctions for dye degradation. *ACS Sustainable Chemistry & Engineering*, 2015. 3(10): p. 2405-2413.
18. Avciata, O., et al., Ag doped TiO2 nanoparticles prepared by hydrothermal method and coating of the nanoparticles on the ceramic pellets for photocatalytic study: Surface properties and photoactivity. *Journal of Engineering Technology and Applied Sciences*, 2016. 1(1): p. 34-50.
19. Ju, Y., et al., Novel strategy for enhanced visible light-responsive photoactivity of ZnFe2O4 with a single-mode microwave combustion process: Primary parameters. *Chemical Engineering Journal*, 2022. 440: p. 135551.
20. Yang, H., et al., MOFs-derived fusiform In2O3 mesoporous nanorods anchored with ultrafine CdZnS nanoparticles for boosting visible-light photocatalytic hydrogen evolution. *Small*, 2021. 17(36): p. 2102307.
21. Li, Y., et al., RETRACTED: LncRNA myocardial infarction-associated transcript (MIAT) contributed to cardiac hypertrophy by regulating TLR4 via miR-93. 2018, Elsevier.
22. Chen, L., et al., The enhancement of photocatalytic CO 2 reduction by the in situ growth of TiO 2 on Ti 3 C 2 MXene. *Catalysis Science & Technology*, 2021. 11(4): p. 1602-1614.
23. Ke, J., et al., Upconversion carbon quantum dots as visible light responsive component for efficient enhancement of photocatalytic performance. *Journal of colloid and interface science*, 2017. 496: p. 425-433.

Development of core-shell $LaNi_{0.8}Fe_{0.2}O_3$ catalysts with $CeZrO_2$ shells for carbon-resistant dry reforming of methane

Suchayamon Kaewprasert[1], Merika Chanthanumataporn[1,2,*]

[1] Department of Chemical Engineering, Faculty of Engineering, Chulalongkorn University, Bangkok 10330, Thailand
[2] Center of Excellence in Catalysis and Catalytic Reaction Engineering, Department of Chemical Engineering, Faculty of Engineering, Chulalongkorn University, Bangkok 10330, Thailand
[*] Corresponding author: merika.c@chula.ac.th

ABSTRACT

The dry reforming of methane (DRM) often faces challenges due to Ni-based catalyst deactivation caused by carbon deposition and metal sintering. This study investigates the performance of core-shell $LaNi_{0.8}Fe_{0.2}O_3@CeO_2$ (LNFO@CeO_2) and $LaNi_{0.8}Fe_{0.2}O_3@Ce_{0.95}Zr_{0.05}O_2$ (LNFO@$CeZrO_2$) catalysts, synthesized via sol-gel and precipitation methods. The catalysts were reduced in situ under 50% H_2-N_2 at 700 °C and tested for DRM reaction at 600 °C using CH_4/CO_2 (3:2) with a WHSV of 7.5 $L \cdot h^{-1} \cdot g_{cat}^{-1}$. LNFO@$CeZrO_2$ exhibited a higher surface area and porosity than those for CeO_2 coated LNFO. Although both catalysts exhibited catalytic activity over 360 minutes, the CH_4 and CO_2 conversions, particularly for LNFO@$CeZrO_2$, were not entirely stable. The CH_4 conversion of LNFO@$CeZrO_2$ fluctuated noticeably during the reaction, with a sudden increase around 220 minutes that was followed by a decline, suggesting possible experimental disturbance. The average CH_4 conversion was approximately 21.0% for LNFO@$CeZrO_2$ and 23.5% for LNFO@CeO_2, while the average CO_2 conversion was 50.8% and 55.0%, respectively. TG analysis revealed lower weight loss (~3%) for LNFO@$CeZrO_2$ versus ~6% for LNFO@CeO_2, suggesting reduced carbon formation. However, due to its lower conversion, this cannot be conclusively attributed to enhanced carbon resistance. Further testing is required to validate these trends and better elucidate the role of Ce-Zr interactions in improving catalyst durability and resistance to coke deposition in DRM.

Keywords: Core-shell catalyst; Perovskite; Dry reforming of methane; Oxygen mobility; Carbon deposition inhibition

1. INTRODUCTION

The increasing global demand for energy has raised significant environmental concerns, particularly due to the emission of greenhouse gases such as CO_2 and CH_4 [1]. While steam reforming is a widely adopted method for hydrogen production [2,3,4], the dry reforming of methane (DRM) presents a promising alternative by simultaneously utilizing CH_4 and CO_2 to produce syngas (H_2 and CO), as illustrated in Eq. (1). However, the endothermic nature of DRM ($\Delta H° = 247$ kJ/mol) necessitates high operating temperatures, which often accelerate catalyst deactivation through sintering and coke formation. These conditions also favor undesired side reactions, including reverse water-gas shift (RWGS) (Eq. (2)), decomposition of CH_4 (Eq. (3)), the Boudouard reaction or decomposition of CO (Eq.(4)) [11], and hydrogenation of CO_2 and CO, respectively [12].

$$CH_4 + CO_2 \rightarrow 2CO + 2H_2 \quad \Delta H° = 247.3 \text{ kJ mol}^{-1} \quad (1)$$
$$H_2 + CO_2 \leftrightarrow CO + H_2O \quad \Delta H° = 41 \text{ kJ mol}^{-1} \quad (2)$$
$$CH_4 \rightarrow C + 2H_2 \quad \Delta H° = 75 \text{ kJ mol}^{-1} \quad (3)$$
$$2CO \leftrightarrow C + CO_2 \quad \Delta H° = -172 \text{ kJ mol}^{-1} \quad (4)$$
$$CO_2 + 2H_2 \rightleftharpoons C + 2H_2O \quad \Delta H° = -90 \text{ kJ mol}^{-1} \quad (5)$$
$$H_2 + CO \rightleftharpoons C + H_2O \quad \Delta H° = -131.3 \text{ kJ mol}^{-1} \quad (6)$$

A wide range of oxygen carriers, including noble and transition metals, have been explored to enhance catalyst performance in reforming reactions. Among them, low-cost transition metals such as Ni, Fe, Co, and Mn have attracted attention for their redox activity, carbon resistance, and capacity for oxygen transfer, all of which contribute to improved catalyst stability and syngas yield. Notably, Ni- and Fe-based materials exhibit high activity for hydrogen-rich gas production and demonstrate excellent stability under DRM conditions [6,7].

Bimetallic catalysts often exhibit superior dispersion, enhanced resistance to sintering, and higher intrinsic activity compared to their monometallic

counterparts [8]. In particular, perovskite oxide catalysts have emerged as effective supports due to their structural stability and tunable redox properties. For example, Lanthanum nickel oxide ($LaNiO_3$ or LNO) perovskites have demonstrated high catalytic performance in steam reforming of tar and other hydrocarbons [9,10].

LNO has attracted substantial interest due to its thermal stability and catalytic activity in reforming reactions. Nevertheless, its long-term performance is hindered by Ni particle sintering and carbon deposition [5]. Recent studies suggest that partial substitution of Ni with Fe at the B-site of LNO enhances the catalyst's redox properties and oxygen mobility. Fe doping modulates the cationic environment and strengthens metal-support interactions, which in turn facilitates the oxidation of carbon intermediates and suppresses coke formation.[5]

Liu et al. [5] reported that Lanthanum Nickel Iron Oxide ($LaNi_{0.8}Fe_{0.2}O_3$ or LNFO) exhibited enhanced catalytic stability at 600 °C under chemical looping steam reforming conditions. LNFO also delivered the highest H_2/CO ratio. However, studies on the performance of bimetallic perovskite catalysts, particularly those involving partial substitution of Ni with Fe at the B-site of LNO under DRM conditions a reaction that requires high temperatures and suffers more severely from sintering and coke formation compared to chemical looping steam reforming have not received sufficient attention to date.[5]

In addition to compositional tuning, structural design strategies such as the development of core-shell structure have gained attention for enhancing catalytic durability [11]. Encapsulation of active metal sites helps minimize coke formation and prevent Ni particle agglomeration. Cerium oxide (CeO_2) has been widely employed as a shell material due to its high oxygen storage capacity, redox properties, and abundant oxygen vacancies, which promote CO_2 activation and reduce carbon accumulation on Ni sites [11]. The incorporation of zirconium into the ceria lattice further improves its thermal stability and oxygen mobility. Zr^{4+}doping induces lattice distortion, facilitates the partial reduction of Ce^{4+} to Ce^{3+}, and increases the concentration of oxygen vacancies [11].

Sonali Das [11] reported that doping ceria with Zr (x = 0.05-0.1) significantly enhances DRM activity. Among the tested catalysts, $Ce_{0.95}Zr_{0.05}O_2$ demonstrated the highest oxygen storage capacity and H_2/CO ratio under CH_4/CO_2 = 1:1 at 600 °C. Extensive characterizations, including HRTEM, XRD, TPR, O_2-TPD, XPS, EXAFS, and CO pulse chemisorption, revealed that Zr incorporation improves lattice oxygen mobility and strengthens metal support interactions. Moreover, mechanistic analysis indicated that lattice oxygen actively participates in CH_4 activation via an oxygen-mediated pathway, contributing to the overall increase in DRM activity.

Based on these findings, this study proposes the synthesis and evaluation of a core-shell structured LNFO@$Ce_{0.95}Zr_{0.05}O_2$(LNFO@CeZrO2) catalyst. The catalyst will be tested under DRM conditions (CH_4/CO_2 = 3:2 at 600 °C) compared with LNFO@CeO_2 to assess its coke resistance and catalytic performance. X-ray diffraction (XRD) was employed for phase analysis, while surface area and porosity was determined by N_2 adsorption-desorption analysis. Thermogravimetric analysis (TGA) was conducted to quantify carbon deposition on spent catalysts.

2. EXPERIMENTAL

2.1 Catalyst preparation

LNFO perovskite as a core material was synthesized by sol-gel method using $La(NO_3)_3{\cdot}6H_2O$, Ni $(NO_3)_2{\cdot}6H_2O$ and Fe $(NO_3)_3{\cdot}9H_2O$ as raw materials. Metal ions and critic acid with molar ratio of 1:1.2 were first mixed in 100 mL DI water , also with the addition of a certain amount of glycol at a molar ratio of 1:1 relative to citric acid to reduce segregation of the metal ions. The mixed solution was continuously stirred at 80 °C until it started to form wet gel. Then, the wet gel was dried at 100 °C for 24 h to obtain the dry gel. The dry gel was subsequently calcined at 500 °C for 5 h and 800 °C for 2 h in air condition with a heating rate of 5 °C/min.

In addition, CeO_2 and $Ce_{0.95}Zr_{0.05}O_2$ as a shell material were synthesized by a (co-)precipitation method. The LNFO powder was dispersed in ethanol and sonicated, followed by the dissolution of cerium nitrate hexahydrate ($Ce(NO_3)_3{\cdot}6H_2O$) at a ratio of 1.302 g per 1 g of the LNFO powder material into the solution. For $Ce_{0.95}Zr_{0.05}O_2$, cerium nitrate hexahydrate (1.237 g) and zirconyl(IV) nitrate hydrate ($ZrO(NO_3)_2 \cdot 6H_2O$) (0.0346 g) were added per 1 g of the LNFO powder. The mixed solution was continuously stirred at room temperature for 2 h, followed by the addition of hexamethylenetetramine 20 g in water. The mixture was then heated at 70 °C under magnetic stirring for 5 h. The solid catalyst was collected by centrifugation at 4500 rpm, washed with distilled water and ethanol, dried at 100 °C for 24 h, and finally calcined at 850 °C for 4 h.

2.2 Catalyst characterization

Crystal phases of the fresh and reduced perovskite were analyzed by X-ray diffraction using Cu Ka radiation operated at 40 kV and 40 mA. The samples were scanned with 2θ angle from 20° to 80° at a scanning rate of 2°/min.

The specific surface area and pore size were measured by N_2-isotherm adsorption and calculated by using the Brunauer-Emmett-Teller (BET) method.

TGA was used to measure the carbon residue on the spent catalyst after testing in a dry reforming reaction.

2.3 Catalyst evaluation

Dry reforming of methane (DRM) was conducted in a quartz tube reactor under atmospheric pressure. Before testing in the DRM reaction, the 2 types of prepared catalysts were reduced in-situ in 50%H_2-N_2 atmosphere with a total flow rate of 60 ml/min at a temperature of 700 °C for 1 h. The reaction temperature was set at 600 °C. A gas mixture was used with a composition of CH_4/CO_2 = 3:2. The WHSV of dry reforming reaction was performed at 7.5 $L{\cdot}h^{-1}{\cdot}g_{cat}^{-1}$.WHSV = 7.5 $L{\cdot}h^{-1}{\cdot}g_{cat}^{-1}$ uses each type of catalyst 0.2 g, CH_4 flow rate 15 ml/min, CO_2 flow rate 10 ml/min.

The composition of CO_2, CH_4, H_2, CO in the outlet gas was analyzed using a gas chromatography (GC) to calculate reactant conversion and product selectivity of the catalysts.

CO_2, CH_4 conversion and H_2/CO of the catalysts were calculated using the following equations:

$$CH_4 \text{ conversion} = \frac{CH4(mol/min)in - CH4(mol/min)out}{CH4(mol/min)in} \text{ x100} \quad (5)$$

$$CO_2 \text{ conversion} = \frac{CO2(mol/min)in - CO2(mol/min)out}{CO2(mol/min)in} \text{ x100} \quad (6)$$

$$H_2/CO = \frac{H2(mol/min)out}{CO(mol/min)out} \quad (7)$$

3. RESULTS AND DISCUSSION

3.1 Fresh catalyst characterization

3.1.1 Crystal structure of fresh catalyst

The X-ray diffraction (XRD) patterns of the two synthesized catalysts, LNFO@CeO_2 and LNFO@$CeZrO_2$, were analyzed over a wide 2θ range, as illustrated in Figure 1.

Figure1(a), the XRD pattern of LNFO coated with a CeO_2 shell aligns well with the hexagonal structure of LNFO, as evidenced by diffraction peaks at 2θ values of 22.913°, 32.43°, 32.824°, 40.08°, 46.812°, 53.002°, 57.849°, 58.1°, 58.848°, 67.901°, and 68.816°(ICDD 04-006-1883).[13] Additionally, two minor peaks corresponding to NiO are observed at 2θ values of 37.2° and 43.2°.[5] The CeO_2 shell contributes additional diffraction peaks at 2θ values of 28.6°, 33.1°, 47.5°, 56.4°, 59.4°, 69.6°, 76.7°, and 79.2°, indicative of the fluorite-type cubic structure of CeO_2[14].

Similarly, Figure1(b), the XRD pattern of LNFO with a $Ce_{0.95}Zr_{0.05}O_2$ shell exhibits the hexagonal structure characteristic of LNFO, along with additional peaks attributable to the CeO_2 phase. Notably, despite the incorporation of Zr^{4+} into the ceria lattice, no distinct peaks corresponding to ZrO_2 are detected. This observation is consistent with findings reported by Sonali Das et al.[11], where ZrO_2 peaks emerged only at a zirconium content of x = 0.2. The absence of ZrO_2 peaks in this study suggests the formation of a homogeneous ceria-zirconia solid solution, typically observed at lower Zr concentrations (x = 0.05, 0.1). Higher Zr contents tend to result in phase separation and the formation of crystalline ZrO_2 phases.

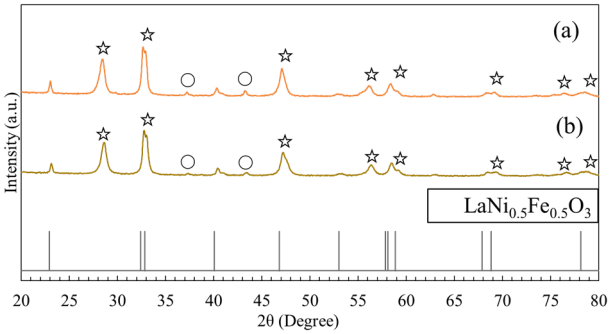

Figure 1 XRD patterns of the prepared catalysts:(a) LNFO@CeO_2 (b) LNFO@$CeZrO_2$
(☆ represents CeO_2, ○ represents NiO)

3.1.2 Surface area and porosity analysis (N_2 adsorption–desorption analysis)

Table 1 : BET surface area and pore volume for the prepared LNFO@CeO_2 and LNFO@$CeZrO_2$ catalysts.

Samples	S_{BET} (m^2/g)	Pore size (Å)	Pore volume (cm^3/g)
LNFO@CeO_2	7.0185	143.8558	0.025241
LNFO@$CeZrO_2$	9.3562	179.6177	0.042013

The surface characteristics of the synthesized core-shell catalysts are presented in Table 1. It is evident that LNFO@$CeZrO_2$ exhibits superior surface properties compared to LNFO@CeO_2. Specifically, the BET surface area of LNFO@$CeZrO_2$ is 9.36 m^2/g, which is higher than that of LNFO@CeO_2 (7.02 m^2/g). Moreover, the average pore size and total pore volume of LNFO@$CeZrO_2$ (179.62 Å and 0.0420 cm^3/g, respectively) are also greater than those of LNFO@CeO_2 (143.86 Å and 0.0252 cm^3/g, respectively). These enhancements suggest that the incorporation of zirconium into the ceria shell leads to a more porous and accessible structure. The increased surface area and pore volume may facilitate better dispersion of active sites and improve gas diffusion during the dry reforming reaction. Consequently, these structural advantages are likely to contribute to enhanced catalytic performance and resistance to carbon deposition.

3.1.3 Crystal structure of reduced catalyst (XRD)

The XRD patterns of reduced LNFO@CeO_2 and LNFO@$CeZrO_2$ (Figure 2) reveal the presence of metallic Ni^0, Fe^0 La_2O_3, and CeO_2 related phases. Three prominent peaks at 2θ ≈ 44.5°, 51.8°, and 76.4° of FCC Ni^0 (Cubic Ni or metallic nickel) (JCPDS No. 04-0850), indicating successful reduction of Ni species. The absence of peaks at 37.2° and 43.3° confirms that NiO

was completely reduced and peaks at 2θ ≈ 44.7° of BCC Fe^0 (α-Fe or Metallic Iron) (ICDD PDF#0696).

Hexagonal La2O3 is identified at 27.2°, 28.3°, 39.5°, 44.7°, 53.2°, 66.3°, and 75.5° (JCPDS No. 05-0602), resulting from the reduction of LaNiO3 under reducing conditions [15]. CeO2 fluorite-type peaks are observed at 28.6°, 33.1°, 47.5°, 56.4°, 59.4°, 69.6° and 76.7° (PDF# 34-0394), suggesting that the shell structure remained stable during reduction.

In the Zr-doped sample, no separate ZrO2 peaks were detected, indicating the formation of a Ce-Zr solid solution. A slight shift to higher 2θ in CeO2 related peaks supports the substitution of Ce4+ by smaller Zr4+ ions, resulting in lattice contraction. This confirms homogeneous Ce0.95Zr0.05O2 formation with improved structural and redox properties [11].

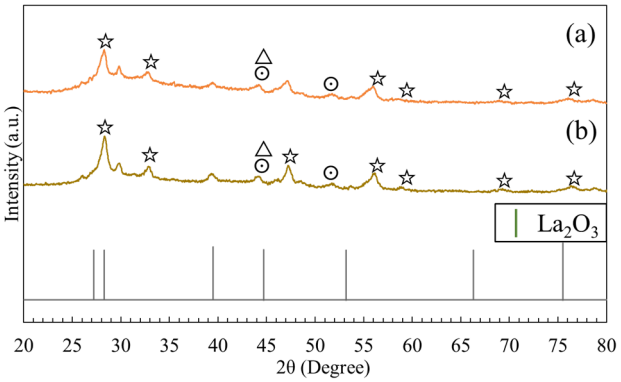

Figure 2 XRD patterns of the reduced catalysts:(a) LNFO@CeO_2(b) LNFO@$CeZrO_2$
(☆ represents CeO_2, ⊙ represents Ni, △ represents Fe)

3.3 Catalytic evaluation

Figures 3 illustrate the catalytic performance of LNFO@CeO_2 and LNFO@$CeZrO_2$ catalysts during 360 minutes of dry reforming of methane (DRM), including CH_4 and CO_2 conversions and the H_2/CO ratio. As shown in Figure 3(a), CH_4 conversion of LNFO@CeO_2 remained higher throughout the reaction compared to LNFO@$CeZrO_2$, with average values of 23.5% and 21.0%, respectively, indicating a performance gap of 2.5 percentage points. throughout the reaction period. Surprisingly, LNFO@$CeZrO_2$ shows a sharp peak in CH_4 conversion at approximately 220 minutes, followed by a rapid decline. This irregular trend suggests that the observed increase is likely due to a fluctuation during the operation, possibly resulting from experimental disturbance such as momentary flow rate or temperature instability.

Figure 3(b) shows that the CO_2 conversion remained relatively stable throughout the reaction for both catalysts. LNFO@CeO_2 showed slightly higher average conversion at 55.0%, while LNFO@$CeZrO_2$ achieved 50.8%, indicating a modest difference of 4.2 percentage points. Despite the inclusion of Zr in the CeO_2 lattice previously reported to enhance oxygen mobility and structural stability [16] the expected catalytic improvement was not clearly observed in this case. The H_2/CO ratio of both catalysts remains stable throughout the reaction, as shown in Figure 3(c). LNFO@$CeZrO_2$ exhibits a slightly lower H_2/CO ratio than LNFO@CeO_2 , with average values of approximately 0.61 and 0.68, respectively, consistent with its lower CH_4 conversion performance.

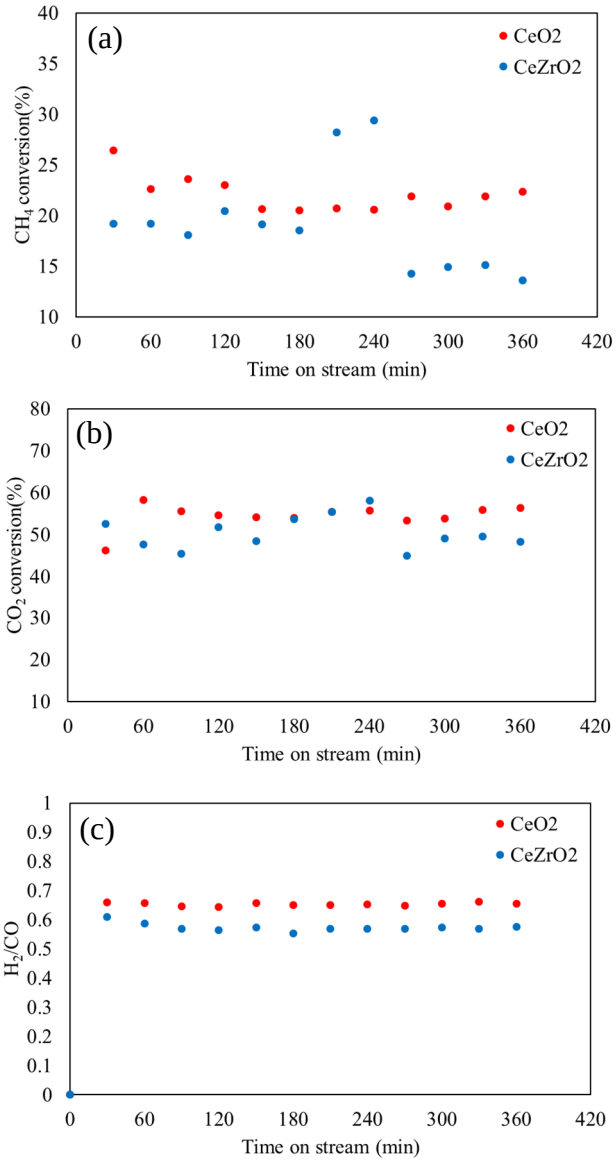

Figure 3 Catalytic performance of LNFO@CeO_2 and LNFO@$CeZrO_2$ for dry reforming at 600 °C testing with CH_4:CO_2 = 3:2, WHSV = 7.5 $L \cdot h^{-1} \cdot g_{cat}^{-1}$: (a) Conversion of CH_4, (b) Conversion of CO_2, and (c) H_2/CO ratio

3.4 Spent catalyst characterization

3.4.1 Amount of carbon deposition TG analysis

Figure 4 presents the TGA profiles of the spent LNFO@CeO_2 and LNFO@$CeZrO_2$ catalysts after dry reforming of methane (DRM). Both catalysts exhibit a gradual weight gain between 400-600 °C, which is commonly attributed to the reoxidation of reduced Ni species back to NiO in an oxidative atmosphere.

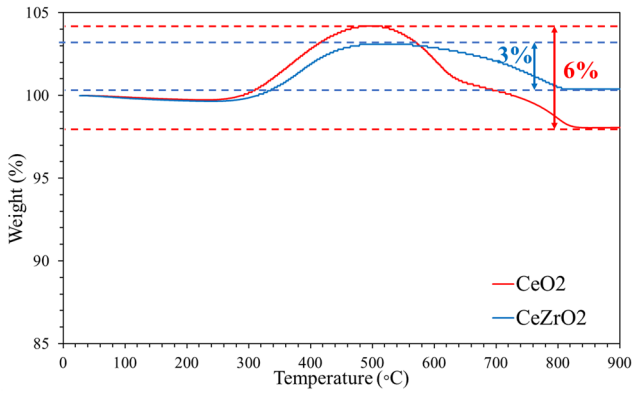

Figure 4 TG analysis of spent catalysts: LNFO@CeO_2 and LNFO@$CeZrO_2$ after 6 h of dry reforming of methane at 600 °C, WHSV = 7.5 $L \cdot h^{-1} \cdot g_{cat}^{-1}$

Subsequently, a weight loss is observed in the range of 650-850 °C, corresponding to the oxidation of carbon species accumulated during the DRM reaction. Based on the TGA results, LNFO@$CeZrO_2$ shows a weight loss of approximately 3%, whereas LNFO@CeO_2 exhibits a greater loss of around 6%, indicating a smaller amount of deposited carbon in the Zr doped sample. However, it is important to note that LNFO@$CeZrO_2$ also demonstrated lower CH_4 conversion throughout the reaction, as discussed earlier. Therefore, while the TGA data visually suggest less carbon formation on the $CeZrO_2$ based catalyst, this may partly result from its lower catalytic activity. As such, it cannot be conclusively stated that LNFO@$CeZrO_2$ possesses inherently superior carbon resistance based on these results alone.

4. CONCLUSION

In this study, core-shell structured $LaNi_{0.8}Fe_{0.2}O_3$ (LNFO) catalysts coated with CeO_2 and $Ce_{0.95}Zr_{0.05}O_2$ shells were successfully synthesized and evaluated for the dry reforming of methane (DRM) at 600 °C. Structural characterization confirmed the formation of a homogeneous core-shell architecture, where the incorporation of Zr into the CeO_2 lattice was achieved without the appearance of separate ZrO_2 phases.

BET analysis revealed that LNFO@$Ce_{0.95}Zr_{0.05}O_2$ (LNFO@$CeZrO_2$) possessed a higher surface area, larger pore size, and greater pore volume compared to LNFO@CeO_2, which are beneficial for enhanced gas diffusion and active site accessibility. Catalytic performance tests revealed that although both catalysts remained active throughout the 360 minutes reaction, their CH_4 and CO_2 conversions particularly for LNFO@$CeZrO_2$ were not entirely stable. The average CH_4 conversions were approximately 23.5% for LNFO@CeO_2 and 21.0% for LNFO@$CeZrO_2$, while the CO_2 conversions averaged 55.0% and 50.8%, respectively. However, LNFO@$CeZrO_2$ exhibited slightly lower CH_4 conversion compared to LNFO@CeO_2, along with an unexpected temporary increase in conversion during the mid-reaction period. This fluctuation suggests a possible experimental disturbance or instability during the operation, which warrants further investigation. TG analysis of the spent catalysts showed that LNFO@$CeZrO_2$ exhibited a lower weight loss (~3%) than LNFO@CeO_2 (~6%), suggesting lower carbon accumulation. Nonetheless, due to the lower catalytic activity of the Zr-doped sample, it cannot be conclusively determined whether the reduced carbon formation is a result of improved coke resistance or simply a consequence of lower CH_4 conversion.

ACKNOWLEDGMENTS

This Research is funded by Thailand Science research and Innovation Fund Chulalongkorn University (BCG_FF_68_277_2100_038). The authors would also like to express their sincere gratitude to the Department of Chemical Engineering, Faculty of Engineering, Chulalongkorn University, for providing essential facilities and research support.

REFERENCES

[1] Institute, E.a.E.S.; Available from: https://www.eesi.org/topics/fossil-fuels/description.

[2] Goicoechea S, Kraleva E, Sokolov S, Schneider M, Pohl MM, Kockmann N, et al. Support effect on structure and performance of Co and Ni catalysts for steam reforming of acetic acid. Appl Catal Gen 2016;514:182-91.

[3] Trane R, Dahl S, Skjøth-Rasmussen MS, Jensen AD. Catalytic steam reforming of bio-oil. Int J Hydrogen Energy 2012;37:6447-72.

[4] Medrano JA, Oliva M, Ruiz J, Garcı´a L, Arauzo J. Hydrogen from aqueous fraction of biomass pyrolysis liquids by catalytic steam reforming in fluidized bed. Energy 2011;36:2215-24.

[5] Liu C, Li S, Chen D, Xiao Y, Li T, Wang W. Hydrogen-rich syngas production by chemical looping steam reforming of acetic acid as bio-oil model compound over Fe-doped $LaNiO_3$ oxygen carriers. International Journal of Hydrogen Energy 2019; 44(37): 17732-17744.

[6] Chen G, Tao J, Liu C, Yan B, Li W, Li X. Hydrogen production via acetic acid steam reforming: a critical review on catalysts. Renew Sustain Energy Rev 2017;79:1091-8.

[7] Luo M, Yi Y, Wang S, Wang Z, Du M, Pan J, et al. Review of hydrogen production using chemical-looping technology. Renew Sustain Energy Rev 2018;81:3186-214.

[8] Theofanidis SA, Galvita VV, Sabbe M, Poelman H, Detavernier C, Marin GB. Controlling the stability of a Fe-Ni reforming catalyst: structural organization of the active components. Appl Catal B Environ 2017;209:405-16.

[9] Theofanidis SA, Galvita VV, Poelman H, Marin GB. Enhanced carbon-resistant dry reforming Fe-Ni catalyst: role of Fe. ACS Catal 2015;5:3028-39.

[10] Zou X, Ma Z, Liu H, Chen D, Wang C, Zhang P, et al. Green synthesis of Ni supported hematite catalysts for syngas production from catalytic cracking of toluene as a model compound of biomass tar. Fuel 2018;217:343-51.

[11] Das S, Jangam A, Jayaprakash S, Xi S, Hidajat K, Tomishige K, Kawi S. Role of lattice oxygen in methane activation on Ni-phyllosilicate@$Ce_{1-x}Zr_xO_2$ core-shell catalyst for methane dry reforming: Zr doping effect, mechanism, and kinetic study. Applied Catalysis B: Environmental 2021; 282: 119998.

[12] Torrez-Herrera, J. J., Korili, S. A., & Gil, A. (2021). Recent progress in the application of Ni-based catalysts for the dry reforming of methane. Retrieved fromhttps://www.tandfonline.com/doi/full/10.1080/01614940.2021.2006891

[13] Savchenko, V. F. Synthesis of Solid Solutions in the $LaNi_{0.5}Fe_{0.5}O_3$ System. Inorganic Materials (English Translation), 1983, 19, 1346. (Referenced by ICDD PDF# 04-006-1883)

[14] S. Dasa, et al., Silica-Ceria sandwiched Ni core–shell catalyst for low temperature dry reforming of biogas: Coke resistance and mechanistic insights. Applied Catalysis B: Environmental, 2018. 230: p. 220-236.

[15] Die Kristallstruktur der A-Modifikation von den Sesquioxyden seltenen Erdmetalle. (La_2O_3, Ce_2O_3, PrO_3, Nd_2O_3). Zeitschrift fuer Physikalische Chemie (Leipzig), 1926. 123: p. 134-150.

[16] Sun, C., Li, H., & Chen, L. (2012). Nanostructured ceria-based materials: synthesis, properties, and applications. Energy & Environmental Science, 5(9), 8475–8505.

[17] Trovarelli, A. (1996). Catalytic properties of ceria and CeO_2-containing materials. Catalysis Reviews, 38(4), 439–520.

Effect of membrane arrangement and operating conditions in electrodialysis system on the performance of the integrated absorption-mineralization process

Wannida Lilathanakiad[1], Palang Bumroongsakulsawat[2], Chalida Klaysom[1,*]

[1] Center of Excellence in Particle and Material Processing Technology, Department of Chemical Engineering, Faculty of Engineering, Chulalongkorn University, Bangkok 10330, Thailand
[2] Center of Excellence on Catalysis and Catalytic Reaction Engineering, Department of Chemical Engineering, Faculty of Engineering, Chulalongkorn University, Bangkok 10330, Thailand
[*] Corresponding author: chalida.klaysom@gmail.com

ABSTRACT

This work is a new and exciting technology that aims to capture and convert CO_2 into stable minerals that can be easily stored or become valuable minerals used in other industries. It can also return the adsorbent to the system, thereby reducing the amount of chemical addition and providing a new alternative for adsorbent recovery that doesn't require the use of heat energy. This study used an electrodialysis system for carbon dioxide capture and carbonate mineral crystallization. A membrane process was used to separate calcium ions from the salt chamber. The calcium ions then moved to the alkaline chamber, reacted with CO_3^{2-}, and formed $CaCO_3$ in the alkaline chamber. Still, no precipitation could occur in the salt chamber. It is considered a potential option due to its slightly alkaline, higher Ca^{2+} and Mg^{2+} content, as well as lower cost than distilled water and chemical solvents. The study is mainly about the steps that were taken in this research project, which aims to recover amine-based absorbents that are usually used to capture CO_2 in factories by combining the process of turning CO_2 into stable minerals.

Keywords: CO_2 capture; Electrodialysis system; Amine regeneration

1. INTRODUCTION

Excessive carbon dioxide emissions due to increasing energy demand are the most critical contributor to the greenhouse effect [1]. Carbon capture, utilization, and storage technologies are essential for creating low-carbon and efficient energy systems [2].

CO_2 adsorption with solvent is one of the popular methods for capturing CO_2 released from the industrial sector because it is low-cost and can capture gas efficiently. The solvents commonly used for capturing CO_2 are substances with a carbonyl group. However, the process of separating CO_2 from the solvent to utilize CO_2 or store and reuse the solvent requires heat at a temperature of approximately 120 °C, which increases the cost of the operation because the high temperature causes the oxidation reaction of amines and causes the response of acid solution to occur in the reaction, resulting in more acid solution, thus increasing the cost. In addition, the CO_2 gas separated from the solvent must be compressed for storage, resulting in increased energy consumption and potential safety problems from the risk of CO_2 leakage during storage [3-6]. Mineralization is an important route in CO_2 sequestration for reducing carbon emissions permanently and safely. It is a simulated process of natural rock weathering, where carbonic acid from the dissolved CO_2 is neutralized with noncarbonate minerals to form geologically and thermodynamically stable carbonates. As natural alkaline minerals containing calcium and magnesium, such as wollastonite, olivine, and serpentine, are widely available and inexpensive, the economy of mineralization is considered promising. However, because of the slow reaction rate of mineralization, raw materials always need mechanical activation or acid leaching as pretreatment. The reaction conditions are at high temperature and CO_2 partial pressure, which increases the cost of CO_2 sequestration [9-11].

The integrated absorption-mineralization (IAM) process combines the absorption and mineralization processes, which take advantage of the rapid absorption of CO_2 by solvents and can convert CO_2 into minerals, a low-energy and safe CO_2 capture method. It can convert CO_2 into stable and valuable solid carbonate. However, the problem of the IAM process lies in the stability of the expensive amine and calcium solvents. Kang et al. [7] found that the 2-amine-2- methyl-1-propanol solution reacted with calcium chloride cannot be reused for CO_2 capture, while calcium oxide can recover the amine solution well and is stable for multiple reuses. To reduce the cost of calcium sources, Ji et al. [8] used fly ash for solvent recovery and mineral crystallization. However, fly ash contains relatively low calcium oxide content, so it cannot efficiently precipitate and recover solvents. The electrochemical method, which is regarded as a sustainable and energy-

saving technique, is one of the most promising research trends. Two main electrochemical methods for mineral carbonation were investigated. One is membrane electrolysis, and the other is BPED. The concept of this field is basically using an electrochemical method to transport the target ions and adjust the pH of the solution [12].

2. EXPERIMENTAL

2.1 Reagents and materials

All of the reagents were of analytical grade, and deionized water was used. anion exchange membrane (AEM) were purchased from Asahi Glass Co., Japan. Cation exchange membrane (CEM) were purchased from Selemion AGC Engineering Limited and Bipolar membrane (BPM) were purchased from YDS EnvironmentalEquipment Co., Ltd. The main characteristics of the membranes are listed in Table 1.

The solution used in the experiment is 99% MEA, 99% $CaCl_2 \cdot 2H_2O$, 35% HCl, 99% NaOH, and 99% $NaNO_3$.

2.2 Membrane arrangement

The membrane stack was arranged as a cathode. BPM-CEM-AEM-anode. The alkaline chamber was positioned between the BPM and CEM, while the salt chamber was located between the CEM and AEM. The schematic diagram of electrodialysis system is shown in Fig. 1.

2.3 Experimental Setup

In this paper, we study the effect of membrane arrangement and operation conditions of the electrodialysis system on the efficiency of the integration process between absorption and mineralization. The MEA solution was prepared by pipetting 75.2 mL of the solution and adjusting it with deionized water in a 250 mL volumetric flask. The adjusted solution was then placed in a Duran flask for CO_2 capture using a flow rate of 180 L/h, and the pH of the solution was measured at 7-8 for two hours. The MEA solution, which had been treated for CO_2 capture, is shown in the schematic diagram of the preparation method for CO_2 capture of the MEA solution in Fig. 2. It was placed in the alkaline chamber. In contrast, 1 M $CaCl_2$ solution was added to the salt chamber, and a 0.2 M $NaNO_3$ solution was introduced into the polar chamber. In each chamber, the flow rates were set at 50, 75, and 100 ml/min, and the electric current varied at 5, 10, 15, and 20 volts. The pH and conductivity were measured every 15 minutes in the alkaline and salt chambers. The experimental system was operated for 3 hours. After this period, the white precipitate was filtered using deionized water for 2-3 rounds. The filtered precipitate was then dried in an oven at 80 °C overnight, and its weight was recorded to calculate the percent yield and efficiency. The figure shows the arrangement of the membrane and the exchange of salt ions, as shown in Figure 1.

2.4 Experimental analysis

To obtain the effect of the electrodialysis reaction process, a Fourier transform infrared spectrometer (FT-IR) was used to analyze the components and functional groups of solid products. Scanning Electron Microscopy (SEM) and X-ray powder diffraction (XRD) were used to analyze the composition and crystal structure of carbonation products.

Table 1 The main characteristics of the membranes.

Materials	initials	Characteristics
Anion exchange membrane	AEM	-IEC (mmol/g) : 1.68 ± 0.06 -l_{dry} (μm) : 100
Cation exchange membrane	CEM	-Thickness (μm) : 100 -Electrical resistance (Ωcm2) : 2 -Transport number : >0.97
Bipolar membrane	BPM	-Thickness (mm) : 0.15–0.18 -Capacity (meq dry/g) : 1.6–1.8

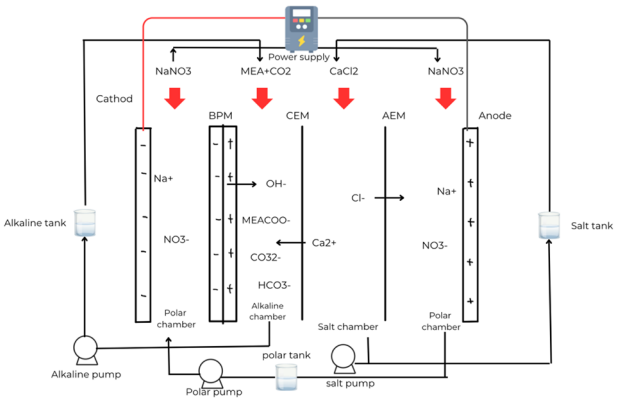

Figure 1 The schematic diagram of the electrodialysis system.

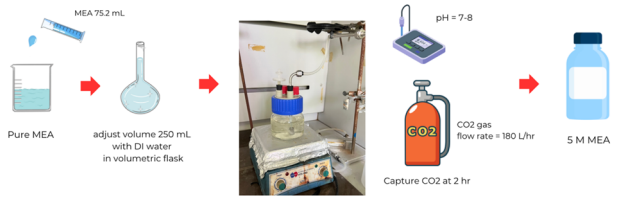

Figure 2 The schematic diagram of the preparation method for CO_2 capture of the MEA solution.

3. RESULTS AND DISCUSSION

This study evaluates the effect of membrane arrangement and operation conditions of the electrodialysis system on the efficiency of the integration process between absorption and mineralization.

Table 2 The conditions of the experiment.

Chemical	Concentration (Molar)	Volume (mL)
$CaCl_2$	1 M	250 ml
MEA + CO_2	5 M	250 ml
$NaNO_3$	0.2 M	250 ml

According to the schedule, 1 M $CaCl_2$ was used in 250 mL in the salt chamber, 5 M MEA in 250 mL in the alkaline chamber, and 0.2 M $NaNO_3$ in 250 mL in the polar chamber. The membrane arrangement was started from this paper [13] and kept changing until it was as shown in Figure 1.

Table 3 The parameters of the experiment.

Flow rate (mL/min)	Voltage (V)	Time (min)
30,50,75,100	5,10,15,20	0 -180 Check pH and conductivity every 15 min

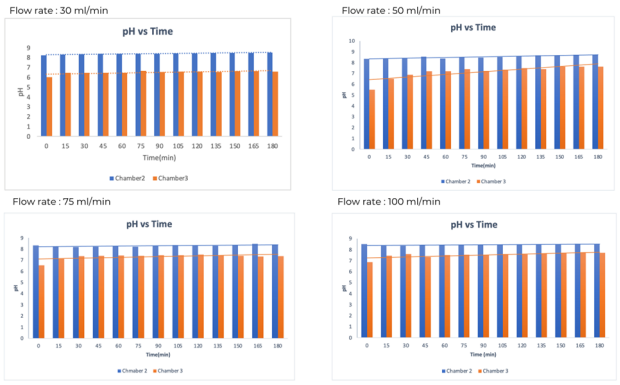

Figure 3 The performance of the 5 M MEA solution under different times.

The experiment will arrange the membrane as shown in Figure 1, where Chamber 2 is the solution of 5 M MEA and Chamber 3 is the $CaCl_2$. The flow rate of the solution varies at 30, 50, 75, and 100 ml/min, and the electric current is 5, 10, 15, and 20 volts. The pH and conductivity are measured every 15 minutes in the alkaline and salt chamber. The experimental system is tested for 3 hours. From Figure 3, it can be seen that at different flow rates, Chamber 2 will start at around pH 8, and as time goes by, the pH value will start to change and increase slightly, and gradually become constant. Chamber 3 will begin at around pH 5, and as time goes by, the pH value will change, increase slightly, and gradually become constant. Since in the system, there may be an exchange of $Ca2+$ in solution that occurs in the salt chamber that moves through the membrane to bind with the Co_3^{2-} to the alkaline chamber, causing a reaction that occurs to form a white calcium carbonate precipitate in the system, therefore causing the pH of the solution to increase and the yield of calcium carbonate to increase [14], which from varying the flow rate, the result that gives the highest white calcium carbonate precipitate is 50 ml/min and the electric current is 20 volts.

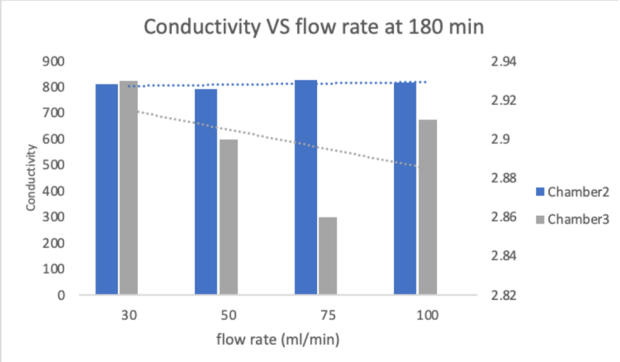

Figure 4 The conductivity performance of the 5 M MEA solution under different times.

Figure 4 shows that the conductivity value at 180 minutes, chamber 2, is at 800 µs/cm. As time goes by, the conductivity value starts to change, increases slightly, and gradually becomes constant, and chamber 3 is at 2.9 µs/cm. As time goes by, the conductivity value starts to change, increases slightly, and gradually becomes constant, which only looks at the ability of the solution to conductivity. The results are not much different, so there is no effect on the ion exchange.

4. CONCLUSION

In the experiment on Integrated CO_2 Absorption and Mineralization (IAM), we aimed to study the effects of membrane arrangement and operating conditions of the electrodialysis system on the efficiency of the integrated absorption and mineralization process. A solution from 5 MEA, which had captured CO_2, was placed in the alkaline chamber. A 1 M $CaCl_2$ solution was added to the salt chamber, and a 0.2 M $NaNO_3$ solution was added to the polar chamber. The flow rates for each chamber were set at 30, 50, 75, and 100 ml/min, while the electric current varied at 5, 10, 15, and 20 volts. The pH and conductivity were measured every 15 minutes in both the alkaline and salt chambers. The experimental system operated for a total of 3 hours. Under these conditions, the optimal setup was found to be a flow rate of 50 ml/min and an electric current of 20 volts, which produced the highest amount of white precipitate. The 1 M $CaCl_2$ solution dissociated into Ca^{2+} ions, which migrated through the cation exchange membrane (CEM) into the alkaline chamber, where they combined with CO_3^{2-} to form a calcium carbonate precipitate. This allowed us to calculate both the percent yield and percent efficiency of the process. The test by Fourier transform infrared spectrometer (FT-IR) was used to analyze the components and functional groups of solid products. Scanning Electron Microscopy (SEM), and X-ray powder diffraction (XRD) was used to analyze the composition and crystal structure of carbonation

products. In future experiments, the concentration of monoethanolamide (MEA) will be adjusted to 1 molar, and the lowest flow rate will be tested. This electrodialysis system involves ion migration, membrane fouling control, and crystallization. Thus, this newly proposed process represents a promising technology. While salt is abundant, the potential application, value, and market demand for carbonated products may limit the development of this technology. It can effectively address environmental pollution issues and reduce energy consumption associated with traditional chemical reagents, ultimately contributing to CO_2 emissions reduction through this innovative approach.

ACKNOWLEDGMENTS

The author supports the research, who would also like to acknowledge the Center of Excellence in Particle and Material Processing Technology, Department of Chemical Engineering, Faculty of Engineering, Chulalongkorn University, for financial interest and for providing the experimental facilities for this work.

REFERENCES

1. Lee, G., et al., Electrochemical upgrade of CO_2 from amine capture solution. Nat. Energy 2020, 6, 46−53.
2. Li, X., et al., The application of trans-1,4-diaminocyclohexane as a bicarbonate formation rate promoter in CO_2 capture. Fuel 2018, 226, 479−489.
3. Lv, B., et al., Mechanisms of CO_2 Capture into Monoethanolamine Solution with Different CO_2 Loading during the Absorption/Desorption Processes. Environ. Sci. Technol. 2015, 49, 10728−10735.
4. Yang, Q., et al., Toward Intelligent CO_2 Capture Solvent Design through Experimental Solvent Development and Amine Synthesis. Energy Fuels 2016, 30, 7503−7510.
5. Akachuku, A., et al., Experimental and kinetic study of the catalytic desorption of CO_2 from CO_2-loaded monoethanol- amine (MEA) and blended monoethanolamine − Methyl-diethanol- amine (MEA-MDEA) solutions. Energy 2019, 179, 475−489.
6. Liu, M., et al., Novel aqueous amine looping approach for the direct capture, conversion, and storage of CO_2 to produce magnesium carbonate. Sustainable Energy Fuels 2020, 4, 1265−1275.
7. Kang, J. M., et al., Energy- efficient chemical regeneration of AMP using calcium hydroxide for operating carbon dioxide capture process. Chem. Eng. J. 2018, 335, 338−344.
8. Ji, L., et al., Integrated absorption-mineralisation for low-energy CO_2 capture and sequestration. Appl. Energy 2018, 225, 356−366.
9. Wang, F., et al., Quantifying kinetics of mineralization of carbon dioxide by olivine under moderate conditions. Chem. Eng. J. 2019, 360, 452−463.
10. Zhou, Z., et al., Modeling of the carbonation kinetics of a synthetic CaO-based sorbent. Chem. Eng. Sci. 2013, 95, 283−290.
11. Bhardwaj, R., et al., Accelerating Natural CO2 Mineralization in a Fluidized Bed. Ind. Eng. Chem. Res. 2016, 55, 2946−2951.
12. Ho, H.-J. and A. Iizuka, Mineral carbonation using seawater for CO2 sequestration and utilization: A review. Separation and Purification Technology, 2023. 307: p. 122855.
13. Zhao, Y., et al., A novel technology of carbon dioxide adsorption and mineralization via seawater decalcification by bipolar membrane electrodialysis system with a crystallizer, Chemical Engineering Journal, 2020. 381: p. 122542.
14. Wang, Z.-h., et al., Study on CO2 absorption-mineralization characteristics of mixed amine solution coupled with CaO and key influencing factors in mineralization process. Journal of Fuel Chemistry and Technology, 2022. 50(10): p. 1371-1380.

Titania incorporated into magnetite mesoporous silica for removal of ciprofloxacin under UV radiation

Dwita Widyawati[1], Numpon Insin[1,2,*]

[1] Department of Chemistry, Faculty of Science, Chulalongkorn University, Bangkok 10330, Thailand
[2] Photocatalysts for Clean Environment and Energy Research Unit, Faculty of Science, Chulalongkorn University, Bangkok 10330, Thailand
[*] Corresponding author: numpon.i@chula.ac.th

ABSTRACT

Ciprofloxacin (CIP) is a widely used antibiotic, but its poor absorption leads to its release into the environment. CIP accumulation in surface waters raises concerns about antibiotic resistance. Photodegradation can break down pollutants in the environment through the action of light. This study presents a magnetite-silica-titania photocatalyst that can be magnetically extracted after degrading organic compounds in water. Magnetite was successfully coated with MCM-48 mesoporous silica, creating a large surface area for the attachment of TiO_2. The catalyst was characterized using XRD, SEM-EDX, FTIR and BET. Magnetite MCM-48 mesoporous silica (MSI) possesses a surface area of 1,115.24 m²/g. The incorporation of titania altered the surface area while maintaining the mesoporous structure. As a result, titania-modified magnetite MCM-48 mesoporous silica (T-MSI) exhibited a reduced surface area of 489.44 m²/g. T-MSI achieved 95.99% photocatalytic degradation of 20 ppm CIP under UV radiation within 2 hours. This experimental result demonstrates the efficiency of T-MSI in degrading high concentrations of CIP within a short time, reinforcing its potential for environmental remediation applications.

Keywords: Magnetite; Mesoporous silica; Titania; Ciprofloxacin

1. INTRODUCTION

Antibiotics have been a major medical breakthrough, helping to control infections effectively. However, their widespread use has led to the release of antibiotic residues into the environment, affecting bacterial communities and ecosystems [1]. Ciprofloxacin (CIP) is a type of antibiotics that is commonly used in pharmaceutical practice. The German Environment Agency's database indicates that ciprofloxacin is one of the antibiotics with the highest levels of residue across 47 countries. The accumulation of these residues in wastewater has emerged as a serious and persistent problem. In a previous report, industrial wastewater specifically contained disproportionately high average concentrations of ciprofloxacin (3548.6 µg/L) [2].

Various treatment methods, including ion exchange, adsorption, and membrane separation, have been implemented to address wastewater contamination. Despite these efforts, several challenges remain including low adsorption capacity, secondary pollutant and rapid deactivation [3]. Semiconductor photocatalysis helps solve water pollution and energy shortages by using sunlight to produce hydrogen. Titanium dioxide (TiO_2) is a well-known n-type semiconductor used as a photocatalyst, owing to it is non-toxic, stable, efficient, and affordable. Its potent pollutant degradation ability makes it valuable for environmental applications [4]. Recently, Abdulrahman, S.A. *et al.* was done the photodegradation of Ciprofloxacin antibiotic using TiO_2 and achieved the efficiency 87.87% in 2 hours under UV radiation [5].

Considering to the tendency of aggregation, support materials with high porosity and large pore sizes have drawn significant attention to overcome this drawback. Mesoporous Silica Nanoparticles (MSNs) are promising material due to their large surface area, adjustable surface properties, and good biocompatibility. However, the next challenge is the separation of materials after photodegradation. To address this problem, the catalyst's magnetic response provides a simple method for separating it from the water after treatment. Magnetic nanoparticles such as magnetite (Fe_3O_4) offer an efficient separation using an external magnet and recovery of the materials. Magnetic nanoparticles dispersed within the pores of mesoporous materials can lead to pore blockage, resulting in enhanced mass transfer resistance. Recent developments have produced magnetic mesoporous microspheres, which comprise a magnetic core surrounded by a mesoporous shell, which potentially enhancing efficiency in various applications [6].

In this study, titania incorporated into core-shell magnetite mesoporous silica was synthesized. The magnetite mesoporous silica can provide high surface area with magnetic properties for separation. The photocatalytic activities of magnetite MCM-48 mesoporous silica (MSI) and titania-modified magnetite MCM-48 mesoporous silica (T-MSI) were investigated for degradation of ciprofloxacin under UV radiation.

2. EXPERIMENTAL

2.1 Materials

D-Glucose (Merck), Iron (II) sulfate heptahydrate, Iron (III) chloride, tetraethyl orthosilicate (TEOS), hexadecyltrimethylammonium bromide (CTAB), Tertbutyl orthotitanate (TBOT), Urea, and Ciprofloxacin•HCl were purchased from Sigma-Aldrich. All chemical reagents were analytical grade.

2.2 Material Characterization

Powder X-ray diffraction (XRD, Rigaku DMAX2200/Ultima+) with Cu-K_α radiation (λ = 1.541862 Å) was used to determine the structure of the products. Scanning electron microscopy (SEM, Hitachi SU3500-Horiba X-maxN) was used to study the morphology of material. A surface characterization analyzer (Micromeritics 3Flex) was employed to measure the BET surface area. Fourier-Transform Infrared Spectrometer (FT-IR, Nicolet iS50) was used to determine the functional group of materials. HPLC (Agilent 1290) was used to identify and quantify CIP components in samples.

2.3 Methods

2.3.1 Synthesis of Fe_3O_4

The magnetite (Fe_3O_4) was prepared by co-precipitation method. Briefly, 0.54 g of $FeSO_4.7H_2O$ and 0.31 g of $FeCl_3$ were dissolved in 150 mL of MiliQ water and sonicated for 10 minutes. Then, 1M of NaOH solution was added dropwise into the mixture solution (pH = 10) and followed by refluxing for 2.5 h with the temperature of 70 ˚C. After that, the mixture was washed with MiliQ water 3 times and ethanol solution 3 times. Finally, the mixture was dried in the oven overnight at 60 ˚C.

2.3.2. Synthesis of Fe_3O_4@SiO_2 microsphere

The magnetite silica microspheres were prepared by microemulsion method. In this part, 0.1 g of Fe_3O_4 was dissolved into the mixture of 20 mL of MiliQ water and 70 of ethanol solution and sonicated for 10 minutes. Then, 2 mL of TEOS and 1 mL of $NH_3.H_2O$ were added dropwise and stirred for 24 h at room temperature. Finally, the mixture was dried in the oven overnight at 60 ˚C.

2.3.3. Synthesis of Fe_3O_4@SiO_2@MCM-48 (MSI)

The magnetite mesoporous silica was prepared by hydrothermal method. In this part, 0.3 g of Fe_3O_4, 1 mL of ammonia solution and 3 mL of MiliQ water were mixed and sonicated for 5 minutes. Then 2 mL of Tetraethyl orthosilicate was added dropwise, followed with the addition of 0.18 g of NaOH and 0.038 g of NaF. The mixture was stirred for 2 h at room temperature. After that, 1.4 g of Cetyltrimethylammonium bromide (CTAB) was dissolved with 6 mL of MiliQ water and was stirred for 2 h at room temperature. The whole mixture was poured in a Teflon lined stainless-steel autoclave, transferred to an oven and heated at 120 ˚C for 48 h. Finally, the obtained powder samples were calcined at 550 ˚C for 5 h.

2.3.4. Synthesis of Fe_3O_4@SiO_2@MCM-48/TiO_2 (T-MSI)

The TiO_2 incorporated into the magnetite mesoporous silica was prepared by sol-gel method. In this part, a certain amount of Tetrabutyl titanate (TBOT) was mixed with the 40 mL of ethanol solution. Then, 20 mL of MiliQ was added dropwise to the mixing solution. Afterward, 1 g of MSI was introduced to the mixture, and the mixture was stirred for 2 h at room temperature. Next, the mixture was aged for 6 h and heated in an oven at 80 ˚C for 24 h. Finally, the obtained powder samples were calcined at 350 ˚C for 4 h.

2.3.5. Photocatalytic Experiment

Photodegradation activity test was performed using 20 ppm Ciprofloxacin solution. The reaction took place in a black box reactor, with 30 mg of photocatalyst added and UV light provided by two 45 W black lamps, while the mixture was stirred continuously. Initially, the reaction was conducted in the dark for 30 minutes, followed by exposure to light for 2 hours, with sampling conducted every 15 minutes. The test involved comparing the antibiotic solution with MSI and T-MSI and the antibiotic solution without catalyst. The results were analyzed using HPLC.

3. RESULTS AND DISCUSSION

3.1. Characterization of catalysts

X-Ray Diffractometer (XRD) was used to determine the crystallinity level of the samples and identification of phase composition contained inside it. XRD patterns of magnetite core and magnetite mesoporous silica (MSI) core-shell were shown in Figure 1. The blue asterisks signs are the characteristic of magnetite phase based on the JCPDS No. 19-0629. Magnetite (Fe_3O_4) core and magnetite mesoporous silica (MSI) core-shell shows five prominent diffraction peaks at 2θ values of 30.2°, 35.5°, 43.2°, 57.1°, and 62.9°, which correspond to the (220), (311), (400), (511), and (440) crystalline planes of the magnetite phase [7]. However, MSI spectra lack sharp peaks,

indicating that it has a lower degree of crystallinity compared to magnetite, which is typical of silica materials with mesoporous structures.

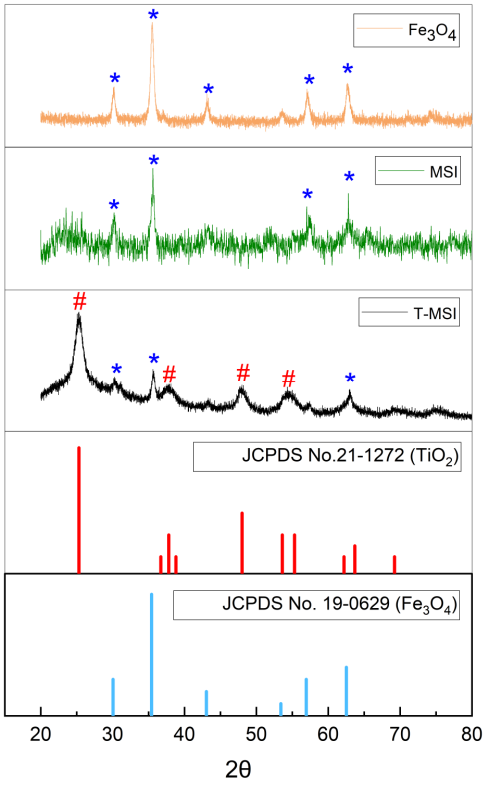

Figure 1 Wide-Angle XRD Patterns of magnetite, magnetite mesoporous silica (MSI) and TiO_2-MSI (T-MSI)

The red hash (#) symbols represent the characteristic peaks of the anatase phase, according to JCPDS No. 21-1272, which are detected at 2θ values of 24.8°, 37.3°, 47.6°, 53.5°, 55.1°, and 62.2° [8]. The incorporation of TiO_2 into MSI can further influence the crystallinity, contributing to the broadening of the peaks. As shown in the Figure 1, T-MSI has a broader peak rather than the others. T-MSI displayed the characteristics of the anatase phase, while the Fe_3O_4 phase still remains.

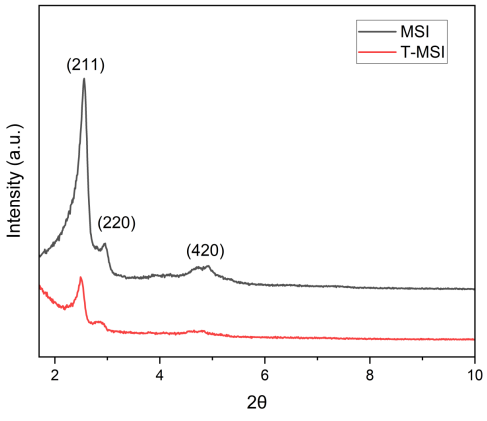

Figure 2 Low-Angle XRD Pattern of magnetite mesoporous silica (MSI) and TiO_2-MSI (T-MSI)

The Low-Angle XRD patterns indicated an Ia3d bicontinuous cubic phase for MCM-48. As shown in the Figure 3, the XRD pattern of MCM-48 displays a cubic mesophase with prominent peaks below 2θ = 3°, corresponding to the (211) and (220) reflections, along with a diffuse pattern in the 3–4° (2θ) range, which is attributed to the (420) reflections [9]. A comparison of the X-ray diffraction profiles of MSI and T-MSI suggests that the mesoporous structure remains unchanged after the incorporation of titania into the mesoporous silica. However, a decrease in the intensity of the peaks was observed. The incorporation of titania into mesoporous silica led to the disappearance of (420) diffraction peak, suggesting that titania is present as highly dispersed species.

In order to investigate the functional groups, present on the materials, Fourier Transform InfraRed (FTIR) was used. The Fe_3O_4 core spectrum in Figure 3 was shown a broad band in the range of 550–650 cm^{-1} corresponding to the Fe-O vibration modes from magnetite phase [10]. The sharp peak in the region of 1000–1200 cm^{-1} were observed after the silica coating. This peak corresponds to Si-O-Si stretching, characteristic of mesoporous silica materials, as shown in the magnetite mesoporous silica core-shell (MSI) spectrum. A broad band around 3400 cm^{-1}, which is associated with O-H stretching vibrations of surface hydroxyl groups [11] . An absorption band at 678 cm^{-1} is associated with the stretching vibrations of the O–Ti–O bond, while the vibration of the ≡Ti–O– bond was observed at 505 cm^{-1}. The interaction between the stretching vibrations of the Ti-O-Ti bond and the Fe-O bond at 590 cm^{-1} contribute to the formation of a broad band within the range of 500 cm^{-1} - 700 cm^{-1} [12]. The absorption bands at 960–910 cm^{-1} and 1650–1620 cm^{-1} correspond to the stretching vibration of Ti–O–Si and the bending vibration of OH groups, respectively. The band at 930 cm^{-1} indicates the successful covalent interaction of titanium and the silica framework. The absorption band at 2361 cm^{-1} showed the characteristic O=C=O stretching vibration [13].

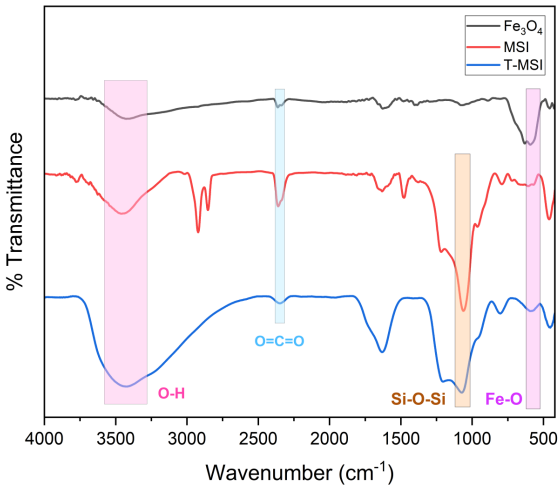

Figure 3 The FTIR spectra of Fe_3O_4, magnetite mesoporous silica (MSI) and TiO_2-MSI (T-MSI)

The nitrogen adsorption-desorption isotherms of the samples, as presented in Figure 4, exhibited a Type IV isotherm according to the IUPAC classification, accompanied by an H1 hysteresis loop. This specific isotherm type suggests that the samples possess a uniform mesoporous structure, characterized by a regular pore size distribution. The BET surface areas of MSI and T-MSI were determined to be 1,115.24 m^2/g and 489.44 m^2/g, respectively. MSI has a higher surface area than T-MSI, which can be attributed to the incorporation of titania into the mesoporous silica. Additionally, the pore size distribution of MSI and T-MSI were found to be 2.5 nm, indicating both of them have mesoporous structure.

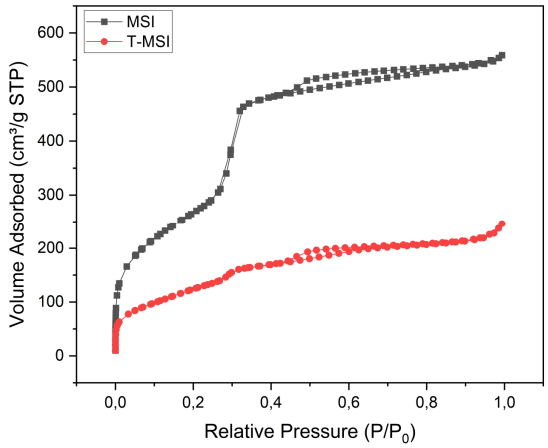

Figure 4 BET adsorption desorption isotherm

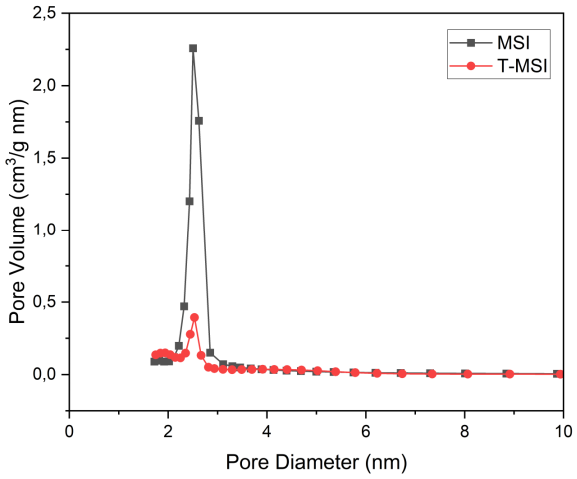

Figure 5 Pore size distribution

As shown in the Table 1 below, MSI has a significantly higher surface area (1,115.24 m^2/g) and pore volume (0.841944 cm^3/g) compared to T-MSI, which has 489.44 m^2/g and 0.340948 cm^3/g, respectively. Additionally, MSI has a larger pore diameter of 3.02 nm, while pore diameter of T-MSI is slightly smaller at 2.78 nm. These results indicate that the incorporation of titania into MSI reduces its surface area, pore volume, and pore diameter, suggesting that titania altered the mesoporous structure, potentially affecting its properties for applications such as photocatalysis or adsorption.

Table 1 Textural properties of mesoporous silica

Catalyst	S_{BET} ($m^2\ g^{-1}$)	V_p (cm^3/g^{-1})	D_p(nm)
MSI	1,115.24	0.841944	3.02
T-MSI	489.44	0.340948	2.78

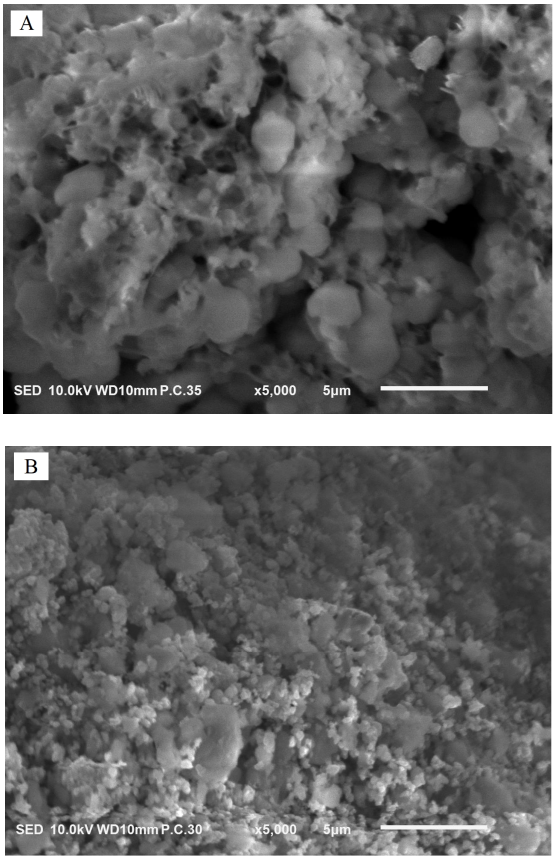

Figure 6 SEM images of (a) MSI and (b) T-MSI

Figure 6 illustrated the morphological properties of MSI and T-MSI. MSI exhibits an irregular, mesoporous structure, characterized by spherical particles with rough surfaces and interconnected pores. The rough surface is indicative of a heterogeneous structure that offers a large number of active sites. The interconnected pores create a highly accessible network for molecules to interact with. The mesoporous network, with its highly interconnected pores, facilitates high adsorption capacities and catalytic activities due to the large surface area. In contrast, T-MSI shows a similar porous structure, but the incorporation of titania results in a modification of the surface morphology. The addition of titania makes the structure denser, which partially fills the mesopores and reduces the surface area and porosity of the material compared to MSI. This alteration in morphology impacts the material's properties and performance in adsorption capacity and stability.

Table 2 SEM-EDX mesoporous silica

Catalyst					
	C	Si	O	Fe	Ti
MSI	11.49	28.96	53.12	6.42	-
T-MSI	18.16	14.72	54.94	4.44	7.74

As shown in Table 2, both materials have high silica and oxygen atom. The reduction in silica content observed in T-MSI compared to MSI is attributed to the incorporation of titania (TiO_2) into the mesoporous silica framework. During the synthesis of T-MSI, titania nanoparticles are introduced, leading to the partial replacement of silica within the structure. As expected, T-MSI contains 7.74% titanium, which confirms the successful incorporation of titania into the mesoporous silica structure. The presence of titanium is crucial for enhancing the photocatalytic properties of the materials under UV light. However, the content of iron atom was slight decrease, titania might modify the pore structure, making it less favorable for iron to be trapped or bound within the pores of the silica.

3.2. Photocatalytic activity

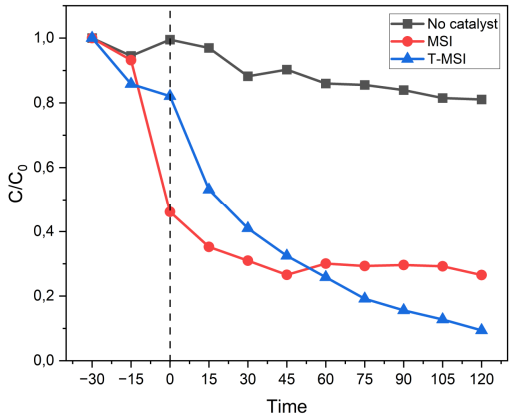

Figure 5 The photocatalytic degradation of CIP 20 ppm under UV radiation

The photocatalytic degradation data shown in the figure were obtained under UV light exposure, where the degradation of CIP at 20 ppm, mesoporous silica (MSI), and titania-doped mesoporous silica (T-MSI) were compared. In the absence of a catalyst (CIP 20 ppm), the degradation rate is minimal, as indicated by the stable C/C_0 ratio over time. It showed only 21% photocatalytic activity under UV radiation in 2 hours. This suggests that UV radiation does not significantly degrade the CIP without a catalyst. When MSI was used, there is a noticeable decrease in the C/C_0 ratio, mainly due to adsorption of CIP. Due to MSI having high surface area, it showed significance decreasing concentration in dark condition and at the beginning of UV radiation. Upon UV radiation, CIP photodegradation occurred at a similar rate with the CIP without catalyst. However, after 45 minutes, desorption CIP could be observed, likely due to the adsorption sites on the surface may become saturated. On the other hand, T-MSI exhibits the most significant photocatalytic activity, with a significance decline in the C/C_0 ratio shortly after UV light exposure begins. This enhanced degradation rate in T-MSI can be attributed to the presence of titania, which acts as a photocatalyst under UV, accelerating the breakdown of CIP. The UV radiation likely excites the titania particles, generating radical species, which in turn enhance the degradation of CIP. T-MSI was achieved the best photocatalytic activity with 95.99% photocatalytic degradation of CIP in 2 hours. Thus, T-MSI has good performance and more efficient photocatalytic degradation of CIP solution compared to MSI and the absence of a catalyst.

4. CONCLUSION

Core-shell magnetite mesoporous silica was successfully synthesized by the hydrothermal method. It has a high surface area of 1,115.24 m^2/g. TiO_2 was incorporated into the magnetite mesoporous silica to lessen the surface area to 489.44 m^2/g. Based on the removal of 20 ppm ciprofloxacin, MSI and T-MSI achieve 75% and 95.99% removal efficiency, respectively. TiO_2 can enhance CIP removal efficiency owing to its photocatalytic properties under UV radiation, which are attributed to its appropriate band gap that activates photocatalytic processes. Due to its extensive surface area and effective light absorption characteristics, T-MSI demonstrates significant potential for water remediation. This study requires further optimization and modification of its features to enhance photocatalytic performance.

ACKNOWLEDGMENTS

This research is funded by the Thailand Science Research and Innovation Fund Chulalongkorn University (DIS66230004). The authors gratefully acknowledge the financial support by ASEAN-NON ASEAN Scholarship-Chulalongkorn University.

REFERENCES

1. Kümmerer, K., Antibiotics in the aquatic environment–a review–part I. Chemosphere, 2009. 75(4): p. 417-434.
2. Booth, A., D.S. Aga, and A.L. Wester, Retrospective analysis of the global antibiotic residues that exceed the predicted no effect concentration for antimicrobial resistance in various environmental matrices. Environment International, 2020. 141: p. 105796.
3. Onkani, S.P., et al., Enhanced Aqueous Photo-Degradation of Ciprofloxacin and Tetracycline Using Ag-Decorated ZnO Plasmonic Catalyst. ACS Sustainable Resource Management, 2024. 1(10): p. 2294-2303.

4. Li, J., et al., Preparation and characterization of ternary Cu/Cu2O/C composite: An extraordinary adsorbent for removing anionic organic dyes from water. Chemical Engineering Journal, 2021. 404: p. 127091.
5. Abdulrahman, S.A., et al., Photocatalytic degradation of ciprofloxacin by UV light using N-doped TiO2 in suspension and coated forms. Catalysts, 2022. 12(12): p. 1663.
6. Wang, S., et al., Adsorption of Pb2+ on amino-functionalized core–shell magnetic mesoporous SBA-15 silica composite. Chemical Engineering Journal, 2015. 262: p. 897-903.
7. Ouyang, Z.-W., E.-C. Chen, and T.-M. Wu, Thermal stability and magnetic properties of polyvinylidene fluoride/magnetite nanocomposites. Materials, 2015. 8(7): p. 4553-4564.
8. Li, W., et al., Generation of oxygen vacancies in visible light activated one-dimensional iodine TiO 2 photocatalysts. RSC advances, 2014. 4(70): p. 36959-36966.
9. Bhagiyalakshmi, M., et al., Synthesis of chloropropylamine grafted mesoporous MCM-41, MCM-48 and SBA-15 from rice husk ash: their application to CO 2 chemisorption. Journal of Porous Materials, 2010. 17: p. 475-484.
10. Bini, R.A., et al., Synthesis and functionalization of magnetite nanoparticles with different amino-functional alkoxysilanes. Journal of magnetism and magnetic materials, 2012. 324(4): p. 534-539.
11. Dabagh, S., et al., Silver-decorated and silica-capped magnetite nanoparticles with effective antibacterial activity and reusability. ACS Applied Bio Materials, 2023. 6(6): p. 2266-2276.
12. Dagher, S., et al., Photocatalytic removal of methylene blue using titania-and silica-coated magnetic nanoparticles. Materials Research Express, 2018. 5(6): p. 065518.
13. Sabir, M., et al., Effect of nanocrystalline cellulose/silica-based fillers on mechanical properties *of experimental dental adhesive.* Polymer Bulletin, 2023. **80**(8): p. 9131-9148.

Electrochemical reduction and regeneration of carbamate

Nattiya Jumpadib[1], Parivat Phiphatbunyabhorn[1], Varong Pavarajarn[1,*]

[1] Center of Excellence in Particle and Materials Processing Technology, Department of Chemical Engineering, Faculty of Engineering, Chulalongkorn University, Bangkok 10330, Thailand
[*] Corresponding author: varong.p@chula.ac.th

ABSTRACT

A reliable method for removing carbon dioxide (CO_2) gas from industrial emissions involves CO_2 absorption into monoethanolamine (MEA) solution to achieve carbon neutrality. However, the regeneration of MEA is costly and still requires heat to release the CO_2 that was captured. In our research, integrating CO_2 capture with electrochemical CO_2 conversion is demonstrated to lower energy consumption. The electrochemical reduction and regeneration of MEA-CO_2 adduct were investigated simultaneously by using copper pulse-electrodeposited on different metal sheets as a cathode in Bipolar Membrane (BPM) cell and H-cell reactor. The gas products were analyzed by gas chromatography, and several C_1 products, e.g., CO and CH_4, were revealed. While the liquid was examined through ^{13}C nuclear magnetic resonance spectroscopy, revealing the conversion of MEA-CO_2 adduct back to MEA after the reaction. The result indicated that the electrochemical reduction of CO_2 captured in the MEA solution reaction competes with the hydrogen evolution reaction (HER). A high negative potential tends to favor HER over electrochemical reduction of MEA-CO_2 adduct. The result also showed that different metal substrates produce different amount of gas products. Additionally, CO_2 was released from MEA solution through the electrochemical reduction at the same time as the MEA-CO_2 adduct was electrochemically converted into gas products. In conclusion, the electrochemical reduction of MEA-CO_2 adduct presents an alternative approach for producing value-added products while regenerating MEA with low energy consumption.

Keywords: Electrochemical reduction of MEA-CO_2; Amine regeneration for carbon capture; Monoethanolamine (MEA)

1. INTRODUCTION

At present, the average global temperature is increasing every year. Since 1981, the annual global temperature has increased with the rate more than double compared to before the 1980s [1], affecting the ocean temperature even more—impacting humans, wildlife, sea life, and all creatures in the world due to greenhouse gases, climate change, and global warming [2, 3]. Initiating the Paris Agreement aims to limit temperature increase and greenhouse gas emissions [4]. Thailand aims to reach carbon neutrality by 2050 and net zero greenhouse gas emissions by 2065 [5]. Carbon capture utilization and storage (CCUS) is one of the solutions, which is a technique of removing carbon dioxide (CO_2) gas from air and industrial emissions [6].

The amine-based solution, monoethanolamine (MEA), is commonly used as a capturing agent in the industry due to its high absorption capacity of CO_2, and the reaction is reversible [7]. The mechanism by which MEA absorbs CO_2 involves a two-step reaction. First, the amine group (-NH_2) in MEA acts as a nucleophile, attacking the electrophilic carbon in CO_2 to form a zwitterion intermediate (MEA^+COO^-) as shown in Eq (1). This intermediate is unstable and quickly loses a proton (H^+) to form a carbamate ion ($MEACOO^-$) as shown in Eq (2) [8, 9]

$$CO_2 + MEA \leftrightarrow MEA^+COO^- \quad (1)$$
$$MEA^+COO^- + MEA \leftrightarrow MEACOO^- + MEAH^+ \quad (2)$$

While MEA primarily reacts with CO_2 to form carbamate, side reactions can lead to the formation of additional byproducts. Initially, CO_2 reacts with water to form carbonic acid, a weak acid that partially dissociates into bicarbonate and a proton as shown in Eq (3) and (4) [10]. Bicarbonate can further dissociate into carbonate and another proton through Eq (5). The relative concentrations of these species depend on the pH of the solution. At low pH (acidic conditions), CO_2 and carbonic acid dominate. At neutral pH, bicarbonate is the primary species, while at high pH (alkaline conditions), carbonate becomes more prevalent [11].

$$CO_2 + H_2O \leftrightarrow H_2CO_3 \quad (3)$$
$$H_2CO_3 \leftrightarrow HCO_3^- + H^+ \quad (4)$$
$$HCO_3^- \leftrightarrow CO_3^{2-} + H^+ \quad (5)$$

Thermal regeneration which is traditional method of MEA-CO_2 regeneration is the most widely used method for regenerating MEA after it has absorbed CO_2 [12-14]. In this process, the CO_2-rich MEA solution is heated to temperatures between 100°C and 120°C in a stripper or regenerator column [15]. The heat breaks the chemical bonds between MEA and CO_2, releasing CO_2 gas and regenerating the MEA for reuse [16], as shown in Eq (6). Additionally, the high temperatures can lead to MEA degradation, producing byproducts that reduce the efficiency of MEA [17], such as oxazolidinones [15] and formamide compounds [18], and decrease the solvent operational lifetime [17].

$$MEACOO^- + MEAH^+ \xrightarrow{Heat} 2MEA + CO_2 \quad (6)$$

After the CO_2 gas was released from the MEA-CO_2 during the regeneration process, CO_2 gas is typically handled in one of several ways, depending on the carbon capture and storage (CCS) goals or carbon capture and utilization (CCU) project [19]. For CCU, electrochemical CO_2 reduction reaction (CO_2RR) is one of effective ways which directly converts CO_2 into fuels and chemicals using electricity and catalysts at ambient temperature and pressure [20]. This method enables the production of carbon monoxide, methane, formic acid, methanol, ethanol, and even hydrocarbons [21]. However, electrochemical studies are conducted effectively in liquid phase due to improved ion mobility and the capacity to establish and sustain a stable electrochemical interface, which can be challenging in gas phase.

Electrochemical CO_2 reduction reaction (CO_2RR) and regeneration of amine-captured CO_2 offer several advantages. Especially, the electrochemical reduction of MEA-CO_2 can pass over the CO_2 regeneration step and the conversion process of CO_2 to beneficial products as shown in Figure 1. Additionally, a CO_2-loaded capture agent can be used as the reactant instead of CO_2 gas in electrochemical conversions. Many researches have been studied about electrochemical reduction of CO_2-loaded capture medium by using various of metal electrode. For example, Copper metal is commonly used in CO_2RR, but in the MEA-CO_2 system, copper as a working electrode did not give a good result in the Faradaic efficiency (FE) of CO_2RR products (9% FE of CO) [22]. Additionally, copper metal electrode provides high 73% FE for formic production in alcohol amine (n(ethanolamine): n (diethanol amine) = 2:3) system [23]. Moreover, by using silver as the cathode, 72±8% FE for CO was demonstrated in 1 M AMP aqueous solution system at -1.1 V vs RHE applied condition [24], while in 30 wt% MEA solution system showed limited CO production (on the order of 10-30% FE) with high FE of hydrogen gas from competing hydrogen evolution reaction (HER) [22]. For Zinc metal cathode in CO_2-captured into 30% MEA solution system, a zinc cathode produced 3% FE of CO at -0.8 V vs RHE applied condition [22]. In addition, Xu et al. stated that single-atom zinc catalysts (ZnN_4/C) enhanced CO_2RR to yield CO, achieving high FE of 95% for CO at -0.43 V vs RHE in a 0.5 M aqueous potassium bicarbonate solution ($KHCO_3$) [25]. Furthermore, challenges of electrochemical MEA-captured CO_2 reduction were found. The protonated amine ($MEAH^+$) affects to the difficulty of CO_2RR. The $MEAH^+$ forms a primary electrochemical double layer (EDL) on the cathode because of negative bias conditions on cathode side, and according to $MEAH^+$ is the only cation in the MEA-CO_2 solution which blocked electron transfer to carbamate due to the length of the molecular chain [26]. Also, competing between CO_2RR and hydrogen evolution reaction [22].

In this study, range of potential and current affected to electrochemical reduction and regeneration of carbamate, metal substrate cathode, and different supporting electrolyte will be investigated along with Faradaic efficiency and power consumption of MEA-CO_2 regeneration.

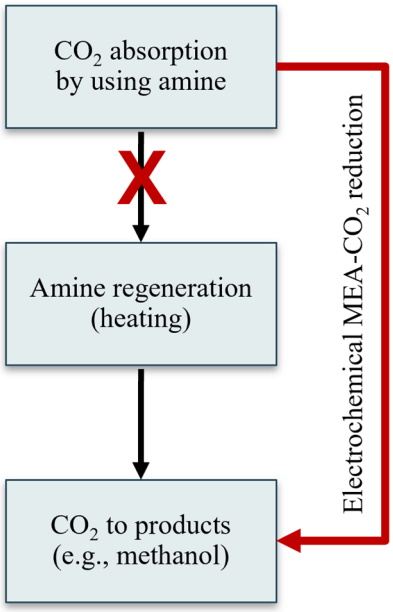

Figure 1. The schematic diagram of electrochemical CO_2 reduction reaction and regeneration of amine-captured CO_2.

2. EXPERIMENTAL

2.1 Materials

Monoethanolamine (MEA; 99.99%) and potassium bromide (KBr; 99.5%) was purchased from Loba Chemie. Carbon dioxide gas (CO2; ≥ 99.5%) was supplied by Linde (Thailand). Helium gas (He; 99.999%) was supplied by S.I. Technology. Copper mesh (width 100 mm) was purchased from Xiamen TOB New energy technology. Silver/Silver Chloride reference electrode (Ag/AgCl) was purchased from Ossila. Copper (II) sulfate ($CuSO_4$; 98.0%) was purchased from CARLO ERBA Reagents srl. Sulfuric acid (H_2SO_4; 50%) and potassium chloride (KCl;

99.5%) were purchased from QRëC. Potassium hydrogen carbonate ($KHCO_3$; 99.5%) was purchased from KEMAUS Chemicals. Deionized water (≥18.2 MΩ·cm) was used in all the experiments. All materials possessed high purity and were utilized without additional purification.

2.2 Carbon dioxide captured into Monoethanolamine solution

The absorption experiments were carried out in the laboratory bottle at ambient temperature and pressure. During the absorption, CO_2 was continuously supplied to the absorber with a flow rate of 180 mL/min and the initial concentration of MEA solution was 5 M. During absorption process, a magnetic stirrer was employed to disperse the CO_2 bubbles uniformly throughout the solution. The absorption experiment was assumed to be complete when pH value of the system stayed unchanged.

2.3 Copper electrodeposition

2.3.1 On Gas Diffusion Electrode (GDE) and copper sheet (BPM cell)

GDE, DSA, and silver/silver chloride were used as working, counter, and reference electrodes, respectively. Electrical potential -0.65 V was applied for 450 seconds. The solutions used for copper electrodeposition were 0.01 M $CuSO_4$ mixed with 0.1 M H_2SO_4.

2.3.2 On metal sheet (H-cell)

Metal sheet (e.g., copper or silver commercial grade) was used as the substrate for copper (Cu) electrodeposition, and subsequently used as the cathode for electrochemical reduction and regeneration of carbamate. Before electrodeposition, the metal sheet was cleaned using commercial grade acetone and ethyl alcohol. A silver/silver chloride (Ag/AgCl) and copper mesh were used as reference and counter electrodes, respectively. The copper electrodeposition electrolyte included 0.64 M $CuSO_4$, 1.1 M H_2SO_4, and 0.684 mM KBr. The working copper electrode was coded by pulse-electrodeposition (Cu-PED). The applied reduction current density (Ir) was -360 mA for 300 ms, the oxidation current density (Io) was 80 mA for 100 ms and then applied open-circuit voltage (OCV) for 400 ms per one cycle as shown in Figure 2. The iteration for the Cu-PED electrode was 4500 cycles. Total time was 60 minutes. After the electrodeposition, the Cu-PED electrode was cleaned with deionized water and dried with N_2 gas.

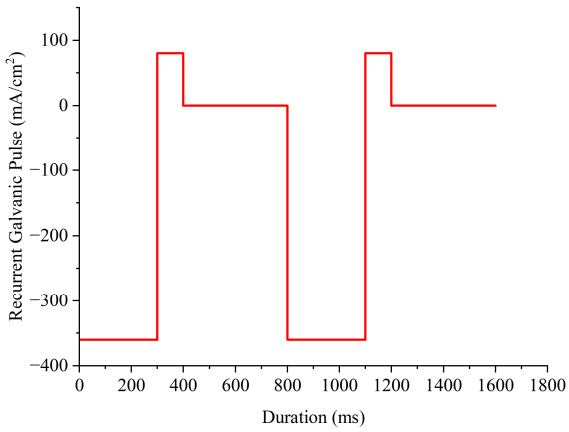

Figure 2. Diagram of Pulse Electrodeposition on metal sheet

2.4 Electrochemical regeneration and reduction of carbamate

2.4.1 Bipolar membrane (BPM) cell

The BPM cell was assembled as shown in Figure 3. For the anode side, deionized (DI) water was fed in, and protons were produced when passing the Pt/Ti mesh. After that, the proton transferred to the central part while carbamate was fed into the central part. The CO_2 reduction reaction occurred with the cathode, which is a GDE deposited copper on the surface. Argon, carrier gas, was fed in the cathode side to let the gas product out. A constant current density was applied to the cathode side by Autolab PGSTAT302N potentiostat to conduct the reduction reaction.

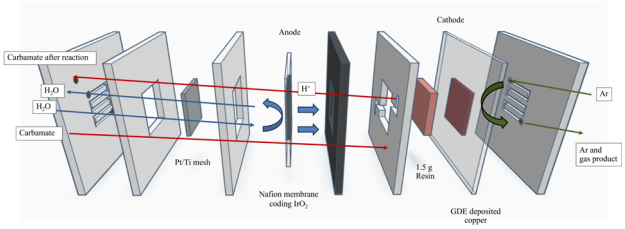

Figure 3. BPM Cell configuration

2.4.2 H-cell

CO_2 reduction reaction was conducted in the H-cell reactor, in which anode and cathode were separated by cation exchange membrane. The electrodeposited metal sheet and stainless-steel sheet were used as cathode and anode electrodes, respectively. The Ag/AgCl electrode was used as a reference electrode. Carbamate solution with/without addition of supporting electrolyte was fed in at the cathodic side, while 1 M H_2SO_4 solution was fed in anode side as an electrolyte. A constant current was applied to the cathode side by Autolab PGSTAT302N potentiostat to conduct the reduction reaction for 60 minutes.

2.5 Characterizations

In order to calculate the amount of carbon dioxide absorbed into MEA solution, applying Chittick method can provide the data. Chittick method involved acid titration. Acid released carbon dioxide from sample. Then, the volume of carbon dioxide gas was used to calculate CO_2 loading (mol/L) following the Eq 7.

$$CO_2 \text{ loading (mol/L)} = \frac{P(V_{gas,f} - V_{gas,i} - V_{acid})}{RTV_{sample}} \quad (7)$$

where P is pressure (atm), $V_{gas,f}$ is final volume of gas released in burette, $V_{gas,i}$ is initial volume of gas released in burette (ml), Vacid is volume of acid used for titration (ml), V_{sample} is volume of the sample (ml), R is gas constant (0.082 L atm K^{-1} mol^{-1}), and T is ambient temperature (K). In addition, to characterize chemical structure of MEA-CO_2 system, ^{13}C nuclear magnetic resonance (NMR, Bruker 500 MHz) was applied with an internal standard of 0.1 mL D_2O for the deuterium lock. While gas and liquid products were analyzed by gas chromatography (GC) (Agilent Technologies 6890N Network GC System) equipped with a thermal conductivity detector (TCD) and a flame ionization detector (FID). Helium carrier gas was used for all systems. For gas product analysis, the column selection was the HayeSep column. For a split injection ratio of 2.5:1, the initial oven temperature was 40°C and held for 3 minutes. Then, the first ramp rate was 8 °C/min until the temperature reached 90°C, and the second ramp rate was 75°C/min until the temperature reached 110°C and held for 1 minute. For liquid products analysis, the column selection was the HP-INNOWax column. For a split injection ratio of 10:1, the initial oven temperature was 40°C and hdld for one minute. Then, the first ramp rate was 20°C/min until the temperature reached 100 °C, and the second ramp rate was 40°C/min until the temperature reached 180 °C and held for 5 minutes. Moreover, the amount of energy consumed to regenerate carbamate per mol (kWh/mol CO_2 released) was calculated by specific power consumption (SPC) following Eq 8.

$$SPC \text{ (kWh/mol)} = \frac{E_{cell} It}{(\Delta C)V} \quad (8)$$

Where SPC is specific power consumption (kWh/mol), E_{cell} is the cell voltage (V), I is applied current (A), t is resident time (h), ΔC is the concentration of CO_2 released by electrochemical reaction (mol/L), and V is the reaction volume (L). Furthermore, Faradic efficiency (FE) is defined as the ratio of the empirically measured quantity of target gas to the theoretically produced quantity of gas following Eq 9.

$$FE\ (\%) = \frac{n_e FCP\upsilon}{RTI} \times 100 \quad (9)$$

Where n_e is the number of moles of electrons required to get one product molecule, F is the Faraday constant (96485 C/mol), C is the concentration of gas product (ppm), P is ambient pressure (101.325 kPa), υ is gas flow rate (mL/s), R is gas constant (8.314 L kPa K^{-1} mol^{-1}), T is ambient temperature (K), and I is average current (mA).

3. RESULTS AND DISCUSSION

The electrochemical reduction of MEA-absorbed CO_2 was investigated using copper (Cu) catalysts electrodeposited onto different metal substrates. The experiments were conducted in carbamate solution in two different cell type (BPM cell and H-cell), under constant current conditions, and the performance was assessed by evaluating Faradaic efficiencies (FE%), along with the calculation of specific power consumption for MEA-CO_2 regeneration.

3.1 BPM cell

3.1.1 Effect of current density

60, 100, 200, and 300 mA/cm^2 current density were applied in this reaction. The results showed that 60-100 mA/cm^2 current densities were found to be optimal for CO_2 reduction to CO, as evidenced by the initial rise in Faradaic efficiency (FE). Conversely, excessively high current densities induce significant overpotentials that favor the hydrogen evolution reaction (HER) over CO_2 reduction as shown in Figure 4. This transition is attributed to the competitive consumption of electrons by water reduction, which occurs more readily under high overpotential conditions due to abundant proton availability in the electrolyte. These findings underscore the necessity of optimizing current density to maximize CO_2RR selectivity. Furthermore, the SPC amount increased with higher applied current densities due to the elevated electric input at the cathode as a result of the constant feed flow rate of the MEA solution limited the contact between carbamate molecules and the catalyst surface which was shown in Figure 4.

3.1.2 Effect of substrate cathode (GDE vs copper sheet)

The gas diffusion electrode (GDE) substrate showed superior performance compared to the flat copper sheet as shown in Figure 5. GDE creates a triple-phase boundary where gas, liquid, and solid meet, drastically enhancing CO_2 accessibility to catalytic sites. This allows a steady supply of CO_2 molecules, avoiding mass transport limitations. In contrast, flat copper sheet relies on CO_2 dissolved in the liquid phase only, which is slower and less efficient. Moreover, these two cathodes used roughly the same amount of SPC to release CO_2 gas from the MEA solution due to the limit contact between carbamate molecules and the catalyst surface.

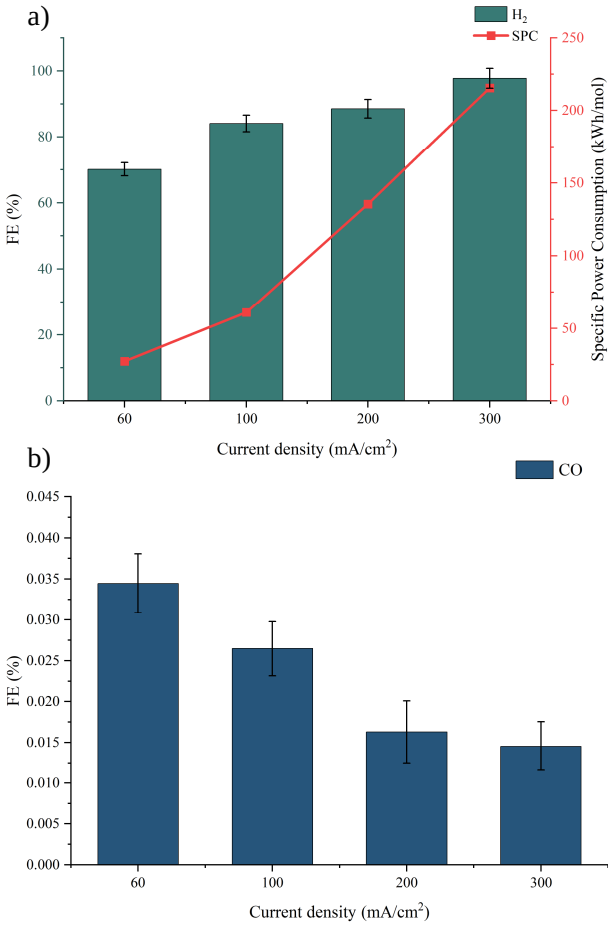

Figure 4. (a) Faradaic efficiency of MEA-CO_2 conversion to H_2 at carbamate flow rate of 5.5 mL/min and at different applied current density, and specific power consumption (SPC) in BPM cell. **(b)** Faradaic efficiency of MEA-CO_2 conversion to CO at 2 M carbamate: 2 M KCl flow rate of 5.5 mL/min and at different applied current density in BPM cell.

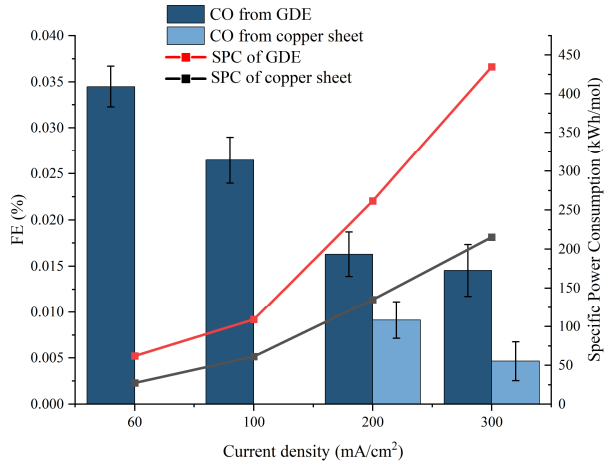

Figure 5. Faradaic efficiency of MEA-CO_2 conversion to CO of GDE and copper sheet electrode at carbamate flow rate of 5.5 mL/min and specific power consumption (SPC) at different applied current density in BPM cell.

3.2 H-cell

3.2.1 Effect of current

The result demonstrated that low constant current condition (0.2 A per 17.5 cm^2) gave greater FE of product as shown in Figure 6 which followed the same trend with the reaction in BPM cell. In addition, at low constant current also gave low SPC. According to sample collection with every 10 minutes, the trend suggested that as the reaction proceeded, the HER became increasingly dominant, reducing the selectivity toward carbon dioxide reduction. This behavior observed when copper catalysts are used under high current densities or prolonged operation.

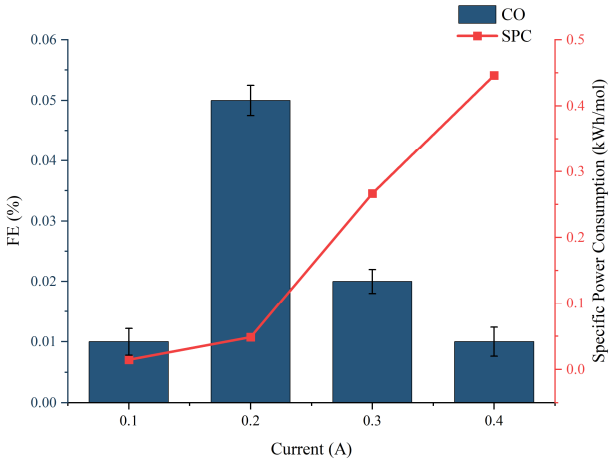

Figure 6. Faradaic efficiency of MEA-CO_2 conversion to CO of Cu deposited on Cu sheet by using 2M carbamate: 2M $KHCO_3$ as a reactant at different applied current density in H-cell.

3.2.2 Effect of substrate cathode (copper sheet vs silver foam)

Silver foam outperformed copper sheet as a substrate in the H-cell reactor as shown in Figure 7. Silver is well-known for its intrinsic catalytic properties favoring CO formation. Moreover, the high surface area and porosity of silver foam promote superior CO_2 adsorption and activation, enhancing both kinetics and selectivity toward CO production. In comparison, copper exhibits stronger binding of intermediates, often resulting in side reactions or favoring HER under similar conditions. However, the SPC of CO_2RR using a copper sheet as the cathode substrate was lower compared to that of silver foam, according to high surface area. As a result, CO_2 released from carbamate had a greater opportunity to undergo reduction to CO at the silver foam cathode, whereas the copper sheet cathode offered fewer active sites for this conversion.

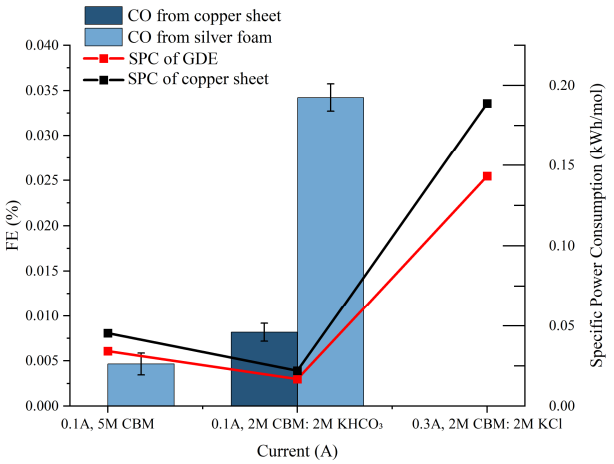

Figure 7. Faradaic efficiency of MEA-CO_2 conversion to CO of Cu deposited on Cu sheet and silver foam by adding different supporting electrolyte at -0.1 A applied condition in H-cell.

3.2.3 Effect of supporting electrolyte

KCl, and $KHCO_3$ as supporting electrolyte were added into carbamate solution. The results showed that KCl did not affect to SPC of regeneration and CO_2 conversion to gas and liquid products as shown in Figure 7. While $KHCO_3$ not only affected to CO_2 conversion to CO, but also affected to SPC of CO_2 regeneration which under this condition CO_2 could be regenerated in high concentration. Although the SPC of adding $KHCO_3$ supporting electrolyte was low, it could be the result of CO_2 which released from $KHCO_3$ combined with CO_2 released from carbamate. However, electrolytes still enhanced ionic conductivity and reduced solution resistance, facilitating better reaction kinetics compared to non-supporting electrolyte. Therefore, a balance between electrolyte conductivity and chemical stability must be maintained to optimize performance.

4. CONCLUSION

In summary, this study systematically evaluated the effects of current density, metal substrate, and electrolyte conditions on the electrochemical reduction of monoethanolamine (MEA)-captured CO_2 using copper-based and silver-based cathodes under both BPM and H-cell configurations. The results demonstrate that moderate current densities, the use of gas diffusion electrodes (GDE) or high-surface-area silver foams, and optimized flow rates significantly enhance CO_2 conversion selectivity and minimize competing hydrogen evolution. Furthermore, while supporting electrolytes improve ionic conductivity. These findings emphasize the critical interplay between electrode design, operating conditions, and electrolyte chemistry in optimizing MEA-CO_2 electroreduction performance. The insights gained here provide important guidelines for designing more efficient CO_2 capture and conversion systems, offering a promising pathway toward sustainable carbon utilization technologies.

REFERENCES

1. Marcott, S.A., J.D. Shakun, P.U. Clark, and A.C. Mix, A Reconstruction of Regional and Global Temperature for the Past 11,300 Years. Science, 2013. **339**(6124): p. 1198-1201.
2. Sorenson, L.G., R. Goldberg, T.L. Root, and M.G. Anderson, Potential Effects of Global Warming on Waterfowl Populations Breeding in the Northern Great Plains. Climatic Change, 1998. **40**(2): p. 343-369.
3. Rossati, A., Global Warming and Its Health Impact. Int J Occup Environ Med, 2017. **8**(1): p. 7-20.
4. Rogelj, J., et al., Paris Agreement climate proposals need a boost to keep warming well below 2 °C. Nature, 2016. **534**(7609): p. 631-639.
5. Rajbhandari, S. and B. Limmeechokchai, Assessment of greenhouse gas mitigation pathways for Thailand towards achievement of the 2°C and 1.5°C Paris Agreement targets. Climate Policy, 2021. **21**(4): p. 492-513.
6. Zhang, Z., et al., Advances in carbon capture, utilization and storage. Applied Energy, 2020. **278**: p. 115627.
7. Putta, K.R., D.D.D. Pinto, H.F. Svendsen, and H.K. Knuutila, CO2 absorption into loaded aqueous MEA solutions: Kinetics assessment using penetration theory. International Journal of Greenhouse Gas Control, 2016. **53**: p. 338-353.
8. Danckwerts, P.V., The reaction of CO2 with ethanolamines. Chemical Engineering Science, 1979. **34**(4): p. 443-446.
9. Caplow, M., Kinetics of carbamate formation and breakdown. Journal of the American Chemical Society, 1968. **90**(24): p. 6795-6803.
10. Meng, F., et al., Research progress of aqueous amine solution for CO2 capture: A review. Renewable and Sustainable Energy Reviews, 2022. **168**: p. 112902.
11. Lv, B., B. Guo, Z. Zhou, and G. Jing, Mechanisms of CO2 Capture into Monoethanolamine Solution with Different CO2 Loading during the Absorption/Desorption Processes. Environmental Science & Technology, 2015. **49**(17): p. 10728-10735.
12. Rochelle, G.T., Amine Scrubbing for CO2 Capture. Science, 2009. **325**(5948): p. 1652-1654.
13. Markewitz, P., et al., Worldwide innovations in the development of carbon capture technologies and the utilization of CO2. Energy & Environmental Science, 2012. **5**(6): p. 7281-7305.
14. Bui, M., et al., Carbon capture and storage (CCS): the way forward. Energy & Environmental Science, 2018. **11**(5): p. 1062-1176.
15. Rochelle, G.T., Thermal degradation of amines for CO2 capture. Current Opinion in Chemical Engineering, 2012. **1**(2): p. 183-190.

16. Borhani, T.N., E. Oko, and M. Wang, Process modelling, validation and analysis of rotating packed bed stripper in the context of intensified CO2 capture with MEA. Journal of Industrial and Engineering Chemistry, 2019. **75**: p. 285-295.
17. Zoannou, K.-S., D.J. Sapsford, and A.J. Griffiths, Thermal degradation of monoethanolamine and its effect on CO2 capture capacity. International Journal of Greenhouse Gas Control, 2013. **17**: p. 423-430.
18. Freeman, S.A., Thermal degradation and oxidation of aqueous piperazine for carbon dioxide capture. 2011.
19. Gulzar, A., et al., Carbon dioxide utilization: A paradigm shift with CO2 economy. Chemical Engineering Journal Advances, 2020. **3**: p. 100013.
20. Zong, S., et al., Effect of temperature and pressure on electrochemical CO2 reduction: A mini review. Carbon Capture Science & Technology, 2023. **8**: p. 100133.
21. Jones, J.-P., G.K.S. Prakash, and G.A. Olah, Electrochemical CO2 Reduction: Recent Advances and Current Trends. Israel Journal of Chemistry, 2014. **54**(10): p. 1451-1466.
22. Chen, L., et al., Electrochemical Reduction of Carbon Dioxide in a Monoethanolamine Capture Medium. ChemSusChem, 2017. **10**(20): p. 4109-4118.
23. Li, L., et al., Electrolytic reduction of CO2 in KHCO3 and alkanolamine solutions with layered double hydroxides intercalated with gold or copper. Electrochimica Acta, 2022. **402**: p. 139523.
24. Ahmad, N., et al., Electrochemical CO2 reduction to CO facilitated by MDEA-based deep eutectic solvent in aqueous solution. Renewable Energy, 2021. **177**: p. 23-33.
25. Yang, F., et al., Highly Efficient CO2 Electroreduction on ZnN4-based Single-Atom Catalyst. Angewandte Chemie International Edition, 2018. **57**(38): p. 12303-12307.
26. Lee, G., et al., Electrochemical upgrade of CO2 from amine capture solution. Nature Energy, 2021. **6**(1): p. 46-53.

Loading iron/manganese/zinc/copper oxide onto TiO_2 for vanillin production from photoconversion of lignin

Pornpimol Kritasumpun[1], Chatkun Puakpong[1], Saranya Ngaopitakkul[1], Artittaya Suksri[1], Paksanan Rattanachunnoppohn[1], Varaporn Paradamit[2], Paul Egwuonwu Dim[3], Mutsee Termtanun[1,*]

[1] Department of Chemical Engineering, Faculty of Engineering and Industrial Technology, Silpakorn University, Nakhon Pathom 73000, Thailand
[2] Department of Chemistry, Faculty of Science, Silpakorn University, Nakhon Pathom 73000, Thailand
[3] Department of Chemical Engineering, School of Infrastructure, Process Engineering and Technology, Minna, Nigeria
[*] Corresponding author: termtanun_m@su.ac.th

ABSTRACT

In general, large amount of lignin is disposed from the pulp and paper manufacturing process. Considerable efforts have been made to convert lignin into value-added chemicals using photocatalysis. Titanium dioxide is one of the most potential and widely investigated photocatalysts due to its high efficiency in decomposition of many organic pollutants under ultra-violet light, but with the 3.2 eV bandgap energy seems to be a drawback. Therefore, titanium dioxide has been developed for many years to extend the absorption spectrum into visible light region by loading titanium dioxide with various transition and precious metals. To improve the potential of titanium dioxide, this research added the transition metals on to the titanium dioxide and applied to photocatalytic conversion of lignin under visible light. 1%, 3%, and 5% by weight of iron, copper, manganese, zinc oxide on P-25 titanium dioxide were prepared by incipient wetness impregnation. Four hours photocatalytic conversion of Kraft based lignin using prepared titanium dioxide was performed at room temperature and atmosphere pressure in lithium hydroxide aqueous under visible light. Vanillin was confirmed as a main product and its yield was evaluated using ultra violet visible spectroscopy. Among all promotors, 5% copper oxide on titanium dioxide provides the highest vanillin yield at 6.14% with the highest vanillin production rate at 1.17 ppm·min^{-1} compared with other metal loaded-TiO_2.

Keywords: Photocatalyst; Lignin conversion; Vanillin production

1. INTRODUCTION

Lignin is a waste product from papermaking industry. Each year a large amount of lignin is eliminated from the pulp and paper manufacturing process, both in the form of lignosulphonates (world annual production of 500,000 tons) and kraft lignin (under 100,000 tons p.a.). Considerable efforts have been made to convert lignin into value-added chemicals using photocatalysis. Since lignin is a three-dimensional polymer that is composed of p-hydroxyphenyl- (H), guaiacyl- (G), and syringyl-propane (S) type monomeric units [1], aromatic compounds are achieved as products such as, vanillin, phenol, syringaldehyde and guaiacol [2-7]. Titanium dioxide is one of the most potential and widely investigated photocatalysts due to its optical and electronic properties, low cost, easy availability, chemical stability, non-toxicity and high efficiency in decomposition of many organic pollutants under UV light. However, its wide band gap of TiO_2 of 3.2 eV allowing only UV light absorption is still be the drawback. According to the fact, there is only 3-4%UV radiation domain in solar energy when compared to the visible region, containing approximately 45%. Therefore, TiO_2 has been developed for many years to extend the absorption spectrum into visible light region by loading TiO_2 with various transition and precious metals [6-12]. Loading TiO_2 with transition metals assists in modification of hetero-nanostructures and electronic structure of TiO_2 to improve the photocatalytic activity for degradation of organic compounds. In general, the most popular transition metals used for TiO_2 loading to improve the optical properties include Cr, Co, Cd, Mn, Mo, Fe, Ni, V, Mn, Zn, W, V and Cu. Among these transition metals, Fe, Cu, Zn and Mn seem to be the potential promotors according to higher photocatalytic activity reported from previous researches [8-12]. In this work, TiO_2 will be modified with different percent by weight of Fe, Cu,

Zn and Mn as photocatalysts for lignin conversion to vanillin as a high valuable product in pharmaceutical industry. The influence of amount and types for metal oxide loading (Fe, Cu, Zn and Mn) in lignin conversion were investigated based on crystal structure, surface structure, and optical properties of photocatalysts.

2. EXPERIMENTAL

Kraft based lignin (95% purity) was purchased from Sigma-Aldrich (Singapore) as a reactant, Lithium hydroxide (99.5 % purity) from was used as a solvent in photocatalytic conversion. Kraft based lignin can completely dissolve in LiOH and their pH are within the same range. P-25 TiO_2 (99.9 % purity), ferric (III) nitrate (98% purity), copper (II) chloride (99% purity) zinc (II) chloride (99% purity) and manganese (II) chloride (99% purity) from Sigma-Aldrich (Singapore) were used in catalyst preparation.

2.1 Catalysts preparation

P-25 TiO_2 loading with Fe, Cu, Zn, Mn oxides were prepared by incipient impregnation wetness using ferric nitrate, copper chloride, zinc chloride and manganese chloride as precursors with different loading at 1%, 3wt% and 5wt%. The solution was fully dissolved in DI water by rigorously stirring and dried in the oven at 110^{o}C for 12 hours. The prepared catalysts were calcined at 400 ^{o}C for 3 h with a heating rate 10 ^{o}C/min.

2.2 Catalysts characterization

BET was applied to measure catalysts surface area, pore diameter, and pore volume. XRD was applied to determine phase composition of catalysts using CuK_{α} radiation with Ni filter in the 2-theta range of 20-90 degrees with resolution 2 radian per sec. The average crystalline size and phase compositions of TiO_2 will be calculated according to Debye-Scherrer equation [13] and Squrr-Myers equation [14], respectively. Photoluminescence spectrophotometry was used to measure recombination rate of electrons and holes pair. UV-Vis was used in investigation of band gap energy of metals doped TiO_2 which will be calculated based on Kubelka – Munk relationship [15].

2.3 Photocatalytic conversion of lignin

In each experiment, 0.3 g doped- TiO_2 photocatalysts were added to 300 ml of lignin solution with the lithium hydroxide as a solvent. The experimental rig was set up for photocatalytic conversion of lignin in closed-black box. The mixture was vigorously stirred for 30 min in dark condition to confirm no influence from catalyst surface adsorption and then continued the reaction under visible light. Four compact 45 W fluorescent lamps were applied as visible light sources and the product samples were collected until end of 4 h. Afterward, photocatalysts were then removed using microcentrifuge and microfilter. Finally, % yield of vanillin was determined using UV-vis spectroscopy at the wavelength of 352 nm. High performance liquid chromatography was applied to confirm vanillin as a photocatalytic conversion product of lignin. Using C-18 column with the dimension of 4.6 mm ID & 25 cm length and 5 um particle size, HPLC peaks from product sample were further compare with the vanillin standard to check whether the same footprint of vanillin under lithium hydroxide aqueous as a solvent. Before operating HPLC, the samples were pass through 0.45-micron microfilter to remove catalyst. Then, sample was diluted with 5 times of ultrapure water prior to fed into C-18 HPLC column with 20 ul injection volume. The mobile phase used in HPLC was methanol HPLC grade with MeOH to H_2O ratio = 50: 50 at the wavelength of 280 nm-350nm, 5 min runtime, using isocratic pump and single wavelength UV visible detector.

3. RESULTS AND DISCUSSION

3.1 XRD results

XRD pattern of commercial P-25 TiO_2 and metal loading on TiO_2. TiO_2 (P-25) contains two phases including with anatase and rutile that can observe the main peak of anatase TiO_2 phase at 2-Theta = 25^{o} and rutile phase at 2-Theta = 27^{o} were indicated in all samples. In the cases of this study low metal percentage loading (1%, 3% and 5% by weight), the XRD pattens did not show the peaks of metal loading due to small doped metal oxide content and good dispersion on TiO_2. According to Table 1, when crystallite size of rutile phase decrease, there is a tendency to more photocatalytic activity which will be related to the lignin photodegradation and yield of vanillin results. This can be seen from 5 wt% Fe-doped TiO_2, extension loading amount of metal oxide leads to enlarging crystalline size of rutile phase could bring about lower degradation rate of lignin and decrease in vanillin yield when compared with 3 wt% Fe-doped TiO_2, respectively.

As related to the recent research carried out by Fu et al. , in 2021 loading Mn assists in minimizing crystalline size of rutile phase, reducing rutile portion, also facilitating electron transfer from valence band of anatase to valence band of rutile and conduction band of rutile to conduction band of anatase [16] . These results are corresponding with the photocatalytic conversion of lignin that Mn oxide has better photocatalytic activity than Zn oxide. However, the extension of loading amount of metal oxide leads to enlarging crystalline size of rutile phase could bring about lower degradation rate of lignin and decrease in vanillin yield as it can be seen in case of Fe-doping that from 1 wt% to 5 wt% the larger the crystallite size of rutile phase.

Table 1 Results of crystallite size and anatase to rutile ratio of different metal oxide doped- TiO_2 compared with P-25 TiO_2.

Catalysts	Crystallite size (nm)		% Phase ratio	
	Anatase	Rutile	Anatase	Rutile
P-25 TiO_2	21	149	85	15
1wt% Fe-doped TiO_2	23	97	84	16
3wt% Fe-doped TiO_2	23	135	85	15
5wt% Fe-doped TiO_2	22	192	85	15
1wt% Cu-doped TiO_2	27	97	84	16
3wt% Cu-doped TiO_2	23	105	86	14
5wt% Cu-doped TiO_2	33	110	85	15
1wt% Mn-doped TiO_2	15	105	84	16
3wt% Mn-doped TiO_2	15	85	82	18
5wt% Mn-doped TiO_2	17	54	80	20
1wt% Zn-doped TiO_2	14	86	83	17
3wt% Zn-doped TiO_2	15	68	82	18
5wt% Zn-doped TiO_2	17	67	81	19

3.2 BET surface area

All doped TiO_2 has an average pore size ranging between 10-16 nm, which is within the mesopore size structure based on IUPAC pore size classification. This is relating to the fact that the mesoporous is the most active pore structure for photocatalytic degradation. When comparing at the same loading amount, BET surface area of Zn oxide doped TiO_2 and Mn oxide doped-TiO_2 were insignificant different with P-25 TiO_2. Also, the pore volume and pore size were none significant difference between Zn loaded-TiO2 and Mn loaded-TiO_2. These results are in corresponding with the results of Sakee and Wanchanthuek research that loading 0.5-20% of Zn onto TiO_2 showed similar surface areas and pore structures. There were none of any specific trend with the amount of Zn loading influence on surface area [17].

Table 2 Results of surface and pore size analysis of P-25 TiO_2 and different metal oxide-doped TiO_2

Catalysts	S_{BET} (m^2/g)	Pore volume (cm^3/g)	Average pore size (nm)
P-25 TiO_2	42.18	0.16	13.88
1wt% Fe-doped TiO_2	49.40	0.19	15.37
3wt% Fe-doped TiO_2	47.86	0.18	15.08
5wt% Fe-doped TiO_2	47.85	0.18	15.28
1wt% Cu-doped TiO_2	47.05	0.17	14.35
3wt% Cu-doped TiO_2	43.23	0.14	13.06
5wt% Cu-doped TiO_2	43.43	0.16	14.76
1wt% Mn-doped TiO_2	52.2	0.15	12.06
3wt% Mn-doped TiO_2	40.6	0.16	14.85
5wt% Mn-doped TiO_2	45.0	0.16	14.17
1wt% Zn-doped TiO_2	37.0	0.12	12.02
3wt% Zn-doped TiO_2	44.7	0.15	14.08
5wt% Zn-doped TiO_2	46.5	0.16	13.99

3.3 Results of UV-Vis spectroscopy

From Table 3, the results of Kubelka-Munk calculation showed that the band gap energy of Fe-doped catalyst was smallest at the same percent loading. The different types of metal doping leads to different light absorption with the magnitude order of bandgap energy: Zn> Mn> Cu> Fe. Fe oxide- TiO_2 provides the most shift to visible wavelengths when compared to others metal doping. In addition, increasing the loading amount of wt% of all types of doped metal from 1 wt% to 5 wt%, it appeared that the band gap energy decreased. A smaller bandgap energy means that less energy is required to excite an electron across the bandgap, leading to increased absorption of lower-energy photons which enhancing photocatalytic reaction under visible light irradiation.

Table 3 Bandgap energy of P-25 TiO_2 and different metal oxide-doped TiO_2.

Catalysts	Band gap energy (eV)
P-25 TiO_2	3.2
1wt% Fe-doped TiO_2	2.82
3wt% Fe-doped TiO_2	2.72
5wt% Fe-doped TiO_2	2.6
1wt% Cu-doped TiO_2	2.92
3wt% Cu-doped TiO_2	2.78
5wt% Cu-doped TiO_2	2.62
1wt% Mn-doped TiO_2	3.05
3wt% Mn-doped TiO_2	2.80
5wt% Mn-doped TiO_2	2.70
1wt% Zn-doped TiO_2	3.1
3wt% Zn-doped TiO_2	3.02
5wt% Zn-doped TiO_2	2.8

3.4 Results of Photoluminescence Spectrophotometry

According to Figure 1, there is a major peak at 425 nm represented to the electrons-holes recombination phenomena. The unloaded TiO_2 has the highest peak intensity of Photoluminescence, referring to fast electron recombination rate. However, after adding transition metals into TiO_2, the peak intensity of loaded catalyst decreases, the electron recombination rate of metal loading is slow than unloading metal thus increasing their lifetime. With more amount of metal loading, the less electrons-holes recombination rate occurs.

At every loading content, Fe doping had lower peak intensity than Cu, Mn and Zn doping, respectively. Therefore, the PL results exhibited the similar tendency as the bandgap energy in UV-Vis results. The smaller the bandgap energy, the slower the recombination rate of electrons and holes pair. It is also apparent the lowest peak intensity occurred with 5 wt% Fe so that it has the slowest electrons and holes recombination rate when compared with other metal oxide doped TiO_2 since it generates the lowest PL spectrum curve. These results are also in agreement with bandgap energy calculation and XRD results already discussed in the previous section that loading Fe oxide on TiO_2 enhances the crystalline defect in TiO_2 phase and leads to lowest electrons -holes recombination rate and smallest bandgap energy.

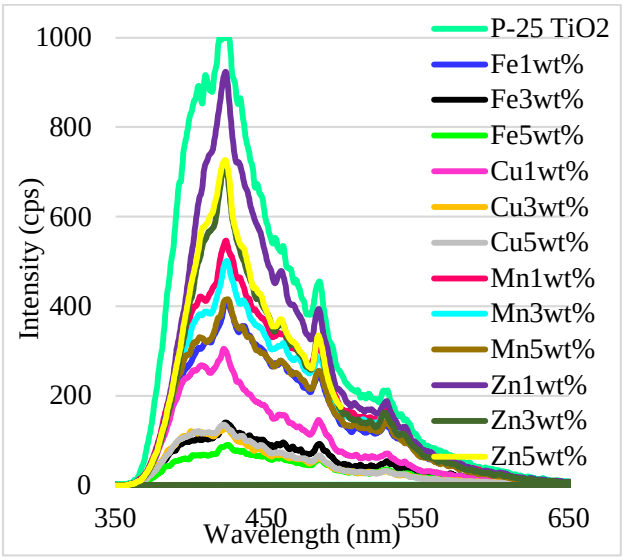

Figure 1 PL spectra of various metal doped TiO_2 photocatalysts compared with that of P-25 TiO_2.

3.5 Vanillin identification

To confirm that vanillin produced in the experiment, HPLC-DAD (high performance liquid chromatography-diode array detector) was utilized.

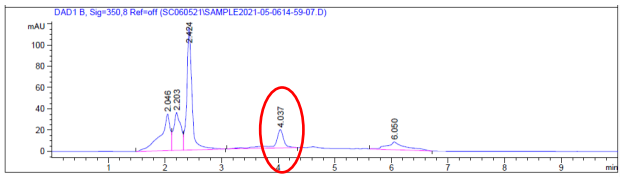

Figure 2 HPLC chromatogram of product sample in LiOH aqueous solvent from lignin photodegradation 4 hours under visible light using 1 wt% Cu-doped TiO_2

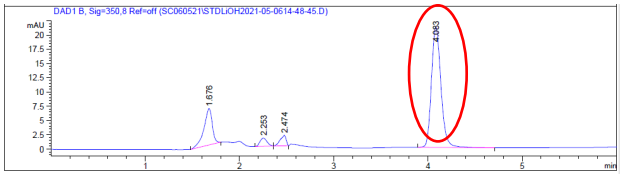

Figure 3 HPLC chromatogram of vanillin standard in LiOH aqueous solvent

The red rounded shape in Figure 2and 3 stands for reference peak of vanillin with the retention time at about 4 minutes. Though from Figure 1, it seems to be also other products achieved from lignin degradation, this research mainly focused on vanillin as a valuable product. As seen from Figure 2, the vanillin peak also appeared in HPLC- DAD chromatogram of product samples, corresponding with the appearance peak in vanillin standard.

The results of this work corresponding with previous researches, vanillin has evidenced as one of major products when using Cu, Mn and Zn oxide photocatalyst. From Jeon et al. research, Cu-Mn mixed oxide catalysts exhibited better redox properties and a higher catalytic performance for lignin oxidation to

vanillin as a major product [18]. In the experimental work performed by Mazarji et al. when using graphene -based zinc oxide as a photocatalyst under UV, they found that the derived compounds from lignin-rich residue biomass depolymerization were syringaldehyde and vanillin [19].

3.6 Vanillin yield

The lignin conversion to vanillin follows pseudo-first order reaction with the highest rate at the initial 20 minutes. Table 4 showed the calculated %vanillin yield and the initial vanillin production rate when using different photocatalysts. The vanillin production after using metal oxide doped TiO_2 was then calculated as percentage from calculated vanillin moles divided by initial moles of lignin.

$$\%\text{vanillin yield} = \frac{\text{Concentration of product at 240min(mol)}}{\text{Concentration of reactant (mol)}} \times 100$$

According to the characterization results, the influence of the bandgap energy and the possibility of electrons-holes recombination are more crucial than surface area and pore size. The lower the bandgap energy, the lower the recombination rate of electrons-hole pair lead to enhance vanillin yield and vanillin production rate. Considering the effect of metal loading content, it was appeared that the bandgap energy decreases after increasing loading amount wt% of Fe, Cu, Mn, Zn. This finding occurs as the same for all doped metal oxide. Among three doped metal oxides, Fe possesses the highest light absorption activity in visible wavelength region. This is corresponding with its lowest calculated bandgap energy and the lowest electrons- and holes recombination rate. However, when comparing between types of doped metal, the vanillin yield and vanillin production rate from doped TiO_2 are aligned in the order of Cu> Fe> Mn> Zn. Though all doped metals accelerate the emerging of vanillin after lignin conversion, some research in 2017 proposed phenol as the dominant product using Fe_2O_3 with Al_2O_3 supported [20], corresponding with this research finding why Fe_2O_3 doped TiO_2 provides lower %yield of vanillin than CuO doped TiO_2. It can be concluded that comparison with various photocatalysts after 4 h reaction passed, 5wt%Cu-TiO_2 produce the highest amount of vanillin at about 28.01 ppm brings about the highest %vanillin yield. The optimum loading amount for each doped TiO_2 is different which relies on type of metal oxide doped.

Table 4 Vanillin production rate and %vanillin yield using P-25 TiO_2 and different metal oxide-doped TiO_2.

Catalysts	Vanillin yield (%)	Vanillin production rate (ppm·min^{-1})
P-25 TiO_2	0.49	0.13
1wt% Fe-doped TiO_2	3.83	0.72
3wt% Fe-doped TiO_2	4.96	0.93
5wt% Fe-doped TiO_2	4.39	0.84
1wt% Cu-doped TiO_2	3.84	0.78
3wt% Cu-doped TiO_2	5.01	0.95
5wt% Cu-doped TiO_2	6.14	1.17
1wt% Mn-doped TiO_2	0.87	0.39
3wt% Mn-doped TiO_2	1.52	0.62
5wt% Mn-doped TiO_2	2.35	1.14
1wt% Zn-doped TiO_2	1.16	0.45
3wt% Zn-doped TiO_2	1.41	0.68
5wt% Zn-doped TiO_2	1.85	0.91

4. CONCLUSION

Lignin was successfully photocatalytic converted to vanillin using metal oxide doped TiO_2, as confirmed from HPLC chromatogram. Loading Fe, Cu, Mn and Zn on TiO_2 leads to narrow the bandgap energy, enlarge the catalyst surface area, reduce electrons-holes recombination possibility and smaller crystalline size of rutile TiO_2. Among four doped metal oxides, Fe possesses the highest light absorption activity in visible wavelength region. This is corresponding with its lowest calculated bandgap energy and the lowest electrons- and holes recombination rate. However, the measurement of vanillin production rate indicates that Cu oxide is the most efficiency promotor in catalyzing for vanillin production when compared with Fe oxide. This is possible that copper oxide functions well in catalyzing into vanillin product, whereas iron oxide works as promotor in other conversion products such as

phenol, which can be generated through different pathway. According to the results, adding copper oxide on titanium dioxide at 5% by weight had the best vanillin production rate at 1.17 ppm·min^{-1} and provides the highest vanillin yield (6.14%) when compared with other metal oxide doped-TiO_2 photocatalysts.

ACKNOWLEDGMENTS

This research was financially supported by "Silpakorn University Research, Innovation and Creative Fund".

REFERENCES

1. Y. Song, Z. Wang, N. Yan, R. Zhang and J. Li. Demethylation of Wheat Straw Alkali Lignin for Application in Phenol Formaldehyde Adhesives, *Polymers*, 2016; 8: 209.
2. M. Ksibi, S. B. Amor, S. Cherif, E. Elaloui, A. Houas, M. Elaloui. Photodegradation of lignin from black liquor using a UV/TiO_2 system, *Journal of Photochemistry and Photobiology A: Chemistry*, 2002; 154: 211–218.
3. K. Kamwilaisak, and P. C. Wright. Investigating Laccase and Titanium Dioxide for Lignin Degradation, *Energy Fuels*, 2012; 26(4): 2400−2406.
4. R. Prado, X. Erdocia, J. Labidi. Effect of the photocatalytic activity of TiO_2 on lignin depolymerization, *Chemosphere*, 2013; 91: 1355-1361.
5. N. Srisasiwimon, S. Chuangchote, N. Laosiripojana, T. Sagawa. TiO_2/Lignin-Based Carbon Composited Photocatalysts for Enhanced Photocatalytic Conversion of Lignin to High Value Chemicals, *ACS Sustainable Chemical Eng*ineering, 2018; 6: 13968−13976.
6. Z. Xie, Y. Wang, P. Wang, L. Zhang. W-doped TiO_2 Preparation and Photocatalytic Degradation of guaiacol, *Applied Mechanics and Material*, 2014; 513-517: 33-36.
7. W. Li, M. Zhang, Z. Du, Q. Ma, H. Jameel, H.-M. Chang. Photocatalytic Degradation of Lignin Model Compounds and Kraft Pine Lignin by CdS/TiO_2 under Visible Light Irradiation, *BioResources*, 2015; 10(1): 1245-1259.
8. G. Colo´n, M. Maicu, M.C. Hidalgo, J.A. Navı´o. Cu-doped TiO_2 systems with improved photocatalytic activity, *Applied Catalysis B: Environmental*, 2016; 67: 41–51.
9. Y. Yakob, K. Naknun, P. Hirunmas, P. E. Dim, M. Termtanun. Mo and Mn co-doping for isoproturon degradation under visible light *Engineering journal*, 2021; 25(2): 277-283.
10. P. Yodsomnuk, K. Junjeam, M. Termtanun. Photoactivity of Fe and Zn-doped TiO_2 in phenol degradation under visible light, *MATEC Web of Conferences* 2018; 192(1-2): 03047
11. S. Somayeh and A. Faranak. The Effect of Fe-Loading and Calcination Temperature on the Activity of Fe/TiO_2 in Phenol Degradation, *Iran Journal of Chemical Engineering*, 2016; 35(2): 43-50.
12. T. Ali, P. Tripathi, A. Azam, W. Raza, S. A. Ahmed, A. Ahmed and M. Muneer. Photocatalytic performance of Fe-doped TiO_2 nanoparticles under visible-light irradiation, *Material Research Express*, 2017; 4: 1-11.
13. K. M. Reddy, S. V. Manorama, A. R. Reddy. Bandgap studies on anatase titanium dioxide nanoparticles, *Materials Chemistry and Physics*, 2003; 78(1): 239-245.
14. D. A. Torres, F. Gordillo-Delgado, J. Plazas-Saldaña, Formation of TiO_2 nanostructure by plasma electrolytic oxidation for Cr(VI) reduction, *Journal of Physics: Conference Series*, , 2017; 786: 012046.
15. J. S. Lee, K. H. You, C. B. Park. Highly photoactive, low bandgap TiO_2 nanoparticles wrapped by graphene, *Advance Materials Communication*, 2012; 24(8): 1084-1088.
16. F. Fu, Y. Zhang, Y. Zhang and Y. Chen Synthesis of Mn-doped and anatase/rutile mixed-phase TiO_2 nanofibers for high photoactivity performance, *Catalysis Science & Technology*, 2021; 12: 4181-4195.
17. U. Sakee and R. Wanchanthuek, The catalytic activity of bimetallic Zn/TiO_2 catalyst for herbicide paraquat degradation: Synthesis and characterization, *Materials research express*, 2017; 4(11): 115504.
18. W. Joen, I. Choi, J.-Y. Park, J.-S. Lee, and R-K. Hwang, Alkaline wet oxidation of lignin over Cu-Mn mixed oxide catalysts for production of vanillin, *Catalysis today*, 2020; 352: 95-103.
19. M. Mazarjia, M. Alvarado-Morales, P. Tsapekos, G. Nabi-Bidhendi, N. M. Mahmoodi, I. Angelidaki, Graphene based ZnO nanoparticles to depolymerize lignin-rich residues via UV/iodide process, *Environment International*, 2019; 125: 172–183.
20. D. Wu, Z. Hu, X. Zhang, C. Zhang, K. Sun and S. Lu. Remarkable lignin degradation in paper wastewaters over Fe_2O_3/g-Al_2O_3 catalysts using the catalytic wet peroxide oxidation method, *RCS Advances*, 2017; 7: 37487-37494.

Utilization of biomass from palm oil industry for monoglycerides production

Sutthiphong Rangauthok[1], Suttichai Assabumrungrat[1,2], Kanokwan Ngaosuwan[3,*]

[1] Center of Excellence on Catalysis and Catalytic Reaction Engineering, Department of Chemical Engineering, Faculty of Engineering, Chulalongkorn University, Bangkok 10330, Thailand
[2] Bio-Circular-Green economy Technology & Engineering Center (BCGeTEC), Faculty of Engineering, Chulalongkorn University, Bangkok 10330, Thailand
[3] Chemical Engineering Division, Faculty of Engineering, Rajamangala University of Technology Krungthep, Bangkok,10120, Thailand
[*] Corresponding author: kanokwan.n@mail.rmutk.ac.th

ABSTRACT

As the third-largest global palm oil producer, Thailand has abundance of waste materials such palm kernel shell (PKS) and palm fatty acid distillate (PFAD). This research aims to utilize biomass as a feedstock and a catalyst to produce high-value chemicals of monoglycerides (MGs) and diglycerides (DGs). They are useful as an emulsifier and stabilizer in the food and pharmaceutical industries, supporting the concept of bio-circular-green economy. Biochar derived from PKS was pyrolyzed under N_2 gas at 600°C for 2 h. Then, 30 wt.% of tungstophosphoric acid (TPA) was further modified on the biochar to produce TPA/PKS catalyst. NH_3-TPD revealed that a high acid site density of 2.402 mmol/g was observed from TPA/PKS. The TPA/PKS catalyst was further used to catalyze glycerolysis of PFAD to produce MGs and DGs using a glycerol to PFAD molar ratio of 3:1, a catalyst loading of 3 wt.%, and a reaction temperature of 130°C for 240 min. The PFAD conversion was increased along the reaction time. The maximum PFAD conversion of 48% and MGs selectivity of 67.0% were found at 210 min. The high catalytic activity of TPA/PKS catalyst was due to its abundant of acid site density. However, the optimum condition for TPA/PKS catalyzed glycerolysis of PFAD should be further investigated to achieve high conversion and high MGs and DGs selectivities by varying the reaction temperature, glycerol to PFAD molar ratio and catalyst loading.

Keywords: Palm kernel shell (PSK); Palm fatty acid distillate (PFAD); Tungstophosphoric acid (TPA); Monolgyceride (MGs), Glycerolysis; Biochar

1. INTRODUCTION

Currently, palm oil has become the largest source of vegetable oil production in the world. Globally, the production of palm oil in 2024-2025 is expected to be 79.53 million tonnes, especially in Southeast Asia. Thailand was ranked as the third-largest producer of palm oil in the world, producing as much as 3.7 million tonnes, accounting for 5% of the global palm oil production, with a steady annual increase. However, the rapid expansion of the palm oil industry has led to an increase in biomass waste [1], resulting in challenges both environmental and economic issues. Palm oil fruits are red and about the size of a large plum but grow in large bunches. Typically, each bunch approximately weighs 10 to 40 kg. Each fruit consists of a single seed (palm kernel) covered by soft pulp, from which oil is extracted [2]. 90% of the biomass was discarded, and only 10% of the palm kernel oil was obtained. This leads to a large amount of waste material. The solid biomass from fresh fruit bunches consists of empty fruit bunches (EFB) at 22%, palm mesocarp fiber (MF) at 13.5%, and palm kernel shell (PKS) at 5.5% [3]. Especially, biomass from the PKS was reported as 4.56 million tonnes per year [4]. Additionally, there is palm fatty acid distillate (PFAD), a by-product from the refining process of crude palm oil (CPO). 3.66 tonnes of PFAD is generated for every 100 tonnes of CPO [5]. 80% of free fatty acids (FFAs) was consisted in PFAD as an important resource to be a starting material for high-value chemicals.

The palm oil industry also raises environmental concerns, contributing 55 tonnes of biomass waste per hectare annually [6]. The decomposition and burning of this biomass release greenhouse gases. In order to achieve carbon neutrality by 2050 [7], there is a growing awareness of the need to reduce biomass waste in the palm oil industry, as the vast amount of biomass produced each year would otherwise be considered waste if not properly utilized, especially in Thailand. This research aims to achieve sustainability by using biomass as a raw material and a catalyst in the production of high-value chemicals such as monoglycerides (MGs) and diglycerides (DGs), which are beneficial as emulsifiers and stabilizers in the food and pharmaceutical industries.

MGs can be synthesized through the process of glycerol esterification or glycerolysis by esterifying PFAD with glycerol, offering a general option for catalysts. However, the traditional MGs production method typically required homogeneous acid catalyst such as phosphoric acid, sulfuric acid, and *p*-toluene sulfonic acid [8] to promote high reaction rate and high conversion efficiency. Nevertheless, homogeneous acid catalysts face environmental limitation [5], corrosion issues, side reaction, and the use of toxic solvent. Moreover, these catalysts have limited recyclability, involving the complicated processes, and are highly sensitive to water [9]. Enzyme catalyst, such as lipase, also face the limitation due to the formation of non-polar residues around the active sites and the factors influencing their specificity in reacting with ester bonds of the triglycerides (TGs) [10, 11]. Additionally, the cost and stability of these catalysts remain significant limitation for large-scale use. The enzyme catalyzed glycerolysis can achieve high selectivity but often face challenges in the enzyme reusability [12]. This issue could limit their practical application in esterification processes [9]. Therefore, solid acid catalyst have been proposed as a sustainable alternative due to their ease of operation, recyclability, and environmental sustainability [13]. Solid acid catalysts include Bronsted acid catalysts [14-17] and Lewis acid catalysts [18]. An ideal solid acid catalyst for glycerolysis or glycerol esterification should have a hydrophobic surface to avoid deactivation of water, a well-connected large porous network to reduce diffusion limitation, and a medium to high density of acidic sites to achieve significant reaction rates and enhance MGs selectivity under mind condition. However, these catalysts often suffer from drawbacks such as a low surface area, poor catalytic activity and rapid deactivation [19]. Consequently, there is a need for more cost-effective and environmentally friendly alternatives to replace the traditional catalyst [9].

Biochar has been proposed as a green supporting catalyst which can be prepared from biomass subjected to pyrolysis. PKS was promising raw material due to its high carbon content (approximately 72.5%), compared to EFB (41.7%) [20]. Dehkhoda et al. [19]. reported that sulfonated biochar based solid acid catalyst significantly improved the catalytic performance and reusability for both esterification and transesterification to produce biodiesel. The idea solid acid catalyst for the esterification to produce biodiesel was in analogy with the glycerol esterification in this study [24]. The impregnation with strong acid site such as tungstophosphoric acid (TPA), a type of heteropoly acid can promote the catalytic activity of biochar [21, 22]. TPA has been used for various catalytic applications, including esterification and transesterification. For instance, da Costa et al. [21] synthesized the biochar modified with TPA as a solid acid catalyst. The high catalytic performance and selectivity in the oxidative conversion of isoeugenol to vanillin were achieved, demonstrating the potential of TPA impregnated biochar as an effective solid acid catalyst for the related esterification [21]. Likewise, Zhang et al. [23], reported that TPA supported on bimetallic MOF derived carbon material significantly enhanced the catalytic activity and the stability in the esterification of oleic acid and methanol for biodiesel production, achieving a high biodiesel yield and excellent reusability.

Therefore, this research focus on the utilization of waste materials of PKS and PFAD from palm oil industry to produced high-value MGs. PKS was used to synthesize biochar as a catalyst support. TPA was modified on the PKS biochar to enhance catalytic activity. PFAD was used as a reactant to promote the sustainability for MGs production via glycerolysis.

2. EXPERIMENTAL

2.1 Material

The biochar used in this study was produced from palm kernel shell (PKS) which was sourced from Asia Biomass Public Co., Ltd. TPA was purchased from Tokyo Chemical Industry Co., Ltd. Glycerol (99.5%) was supplied by KemAus (Australia) Co., Ltd., PFAD was obtained from Pratum Vegetable Oil Co., Ltd. Additionally, acetonitrile, tetrahydrofuran, methanol (HPLC grade), and acetone (AR grade) were provided by Honeywell International and ACI Labscan. Trifluoroacetic acid (TFA, 99% HPLC grade) was sourced from Sigma-Aldrich.

2.2 PKS biochar Synthesis

The PKS was first rinsed with running water and then dried in an oven at 110°C for 12 h and ground using a knife mill and sieved to obtain particles between 150–425 µm. The calcination process was carried out at 600°C for 2 h, with a heating rate of 10°C/min under a N_2 atmosphere[21]. The PKS was coded of biochar derived from palm kernel shells.

2.3 Impregnation of TPA onto PKS biochar

To synthesize the catalyst, 1 g of PKS biochar was placed in a beaker along with 50 mL of distilled water. The mixture was subjected to ultrasonic treatment in a bath at 35°C for 2 h. Then, 0.56 g of TPA as equivalent to 30 wt.% was added to the resulting mixture [24], and was stirred for 1 h. The mixture was then dried in an oven at 110°C for 12 h and subsequently calcined in a muffle furnace at 200°C for 2 h. The final product was designated as TPA/PKS catalyst.

2.4 Glycerolysis of PFAD

Glycerol (58.99 g) was mixed with PFAD at a molar ratio of glycerol to PFAD of 3:1 ratio in a 250 mL round-bottom flask. Then, 1 wt.% of the catalyst based on the total mixture was added. The system was continuously stirred at 1,200 rpm and heated to 130°C for 240 min. Samples were collected every 30 min, and

the reaction was stopped using an ice bath. After the reaction, the catalyst was separated from the reaction mixture by centrifugation.

2.5 Catalysts Characterization

X-ray diffraction technique (XRD) was used on a D8 Advance, Bruker equipped with a long, fine-focus Cu K X ray source, to determine the phases and crystallite sizes of catalyst powder. The XRD patterns were taken at $10° < 2\theta < 80°$ using a 0.04° step, 1.54056 nm wavelength, and 0.5 s/step scan speed. The SEM image of catalyst was recorded using a field emission scanning electron microscope (Hitachi, S3400N) with operating condition at 15 kV were used to examine the surface morphology. ATR-FT-IR (Thermo Electron Corporation, Nicolet 6700) with 64 scans at a resolution of 4 cm^{-1} was used to characterize the functional groups of the catalyst. The specific surface area of the catalyst was investigated using the Brunauer-Emmett-Teller (BET) method with a QuantaChrome AutoSorb-1-MP (Micromeritics Chemisorp 2750) to measure N_2 adsorption/desorption at -196°C. The average pore size diameter and pore volume were determined using the Barrett-Joyner-Halender (BJH) method. Thermogravimetric analysis (TGA) was used to determine the stability of catalyst in the temperature range of 25-1000°C with a ramp rate of 10°C/ min under N_2 gas (TGA/DSC 1 model, Mettlor Toledo).

2.6 HPLC analysis and product quantification

High-performance liquid chromatography (HPLC) analysis of the reaction mixture was conducted using a refractive index detector (RID). The separation was achieved with a Shim-pack GIST C18 column (5 µm, 4.0 mm I.D. × 250 mm, P/N: 227-30016-08) under isocratic conditions. The HPLC system used consisted of a Shimadzu CBM-20A system controller, LC-20AD solvent pump, SIL-2 0 A autosampler, CTO-2 0 A column oven, and an RID-2 0 A refractive index detector.

100 mg of solid obtained from the reaction was dissolved in acetone to a final volume of 5 mL, and approximately 40 µL of the resulting solution was injected into the HPLC system at a flow rate of 1 mL/min. The column and detector temperatures were maintained at 40°C throughout the analysis process. Since, oleic acid was considered as model compound in PFAD. To identify oleic acid and monoolein, a mobile phase consisting of acetonitrile and water in a 90:10 volume ratio with 0.1% trifluoroacetic acid (TFA) was used. The retention time for oleic acid and monoolein were approximately 8.1 and 6.5 min, respectively, following the previously reported [25]. The longer retention time of oleic acid was attributed to its higher hydrophobicity, while the more polar monoolein elutes faster due to stronger interactions with the mobile phase highlighting the importance of molecular polarity in HPLC separation [26, 27].

For the detection of diolein and triolein, the mobile phase was a mixture of acetonitrile, methanol, and tetrahydrofuran (ACN/MeOH/THF) in a 40:40:20 volume ratio. The retention time for diolein and triolein were around 5.3 and 17.0 min, respectively.

3. RESULTS AND DISCUSSION

3.1 X-ray Diffraction

The XRD pattern of PKS shows in Figure 1. The diffraction pattern revealed a dominant broad peak around 23°, along with a smaller hump near 43°, corresponding to the (002) and (100) planes of the aromatic carbon framework. The low intensity of the peak at 43.2° across this sample clearly suggested that the graphitic structure within the biochar catalyst remained poorly developed [28]. Additionally, the XRD pattern of TPA/PKS gave the similar XRD pattern with two broad peaks at identical 2θ position which could be refer to the TPA loading on PKS biochar. Hence, the TPA was more likely to be an amorphous phase as well as a well dispersed on the PKS surface which was in agreement to the previous works [29].

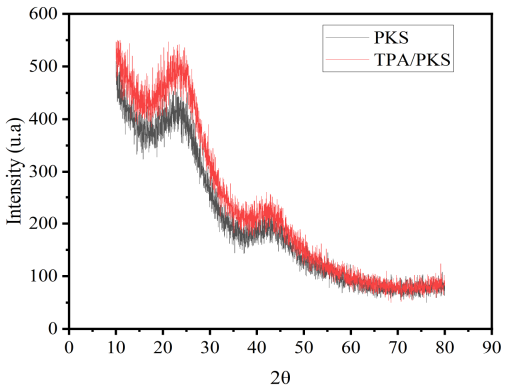

Figure 1 XRD patterns of the PKS and TPA/PKS.

3.2 Scanning Electron Microscopy

Scanning electron microscopy (SEM) was employed to investigate the surface morphology of PKS and TPA/PKS. During the pyrolysis of lignocellulosic biomass, volatile compounds were released and interacted each other, causing partial surface melting and the formation of vesicle-like structures. Additionally, the high lignin and low cellulose content of PKS contributed to the strengthened structure of the biomass cell walls [30].

Figures 2C and 2D reveal the SEM images of TPA/PKS with different magnitude. The irregular rough surface with a continuous network of small pores were observed which was corresponding to the previous work [31]. TPA/PKS catalyst exhibited a more porous and rougher surface as compared to the PKS biochar. The structural change could enhance the surface area to expose more active sites for catalysis. The porous structure is particularly favorable for enhancing the diffusion of reactants and contact with acid sites as consistent with previous report [31]. They found that

the TPA impregnated onto biochar can enhance the catalytic efficiency, particularly in biodiesel production and the synthesis of high-value chemicals from biomass, such as 5-ethoxymethyl furfural (EMF).

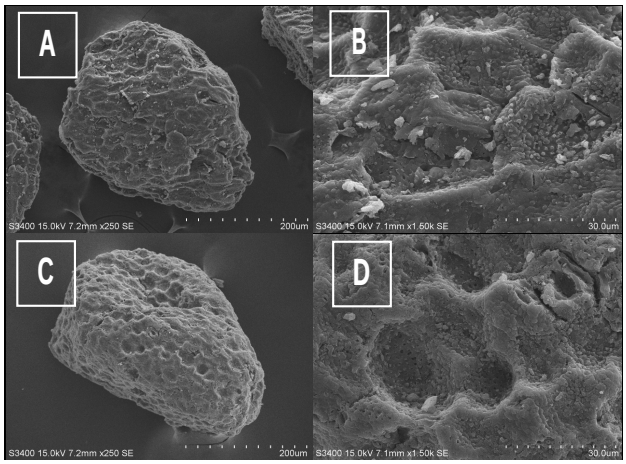

Figure 2 SEM micrographs of the PKS biochar at A) 250x and B) 1500x magnification, the micropgraph of TPA/PKS catalyst at C) 250x and D) 1500x magnification

3.4 Fourier Transform Infrared Spectrometer

Figure 3 illustrates the FTIR spectra of PKS and TPA/PSK. The oxygen-containing functional groups including of hydrogen-bonded O-H stretching, S-H/acid O-H stretching, carbonyl ester C=O stretching, phenolic and alkoxy C-O stretching vibrations were observed at 3759.6, 2282.8, 1707.5, 1105.2, 876.6 cm^{-1} and 809.1 cm^{-1}, respectively. The appearance of intense bands at 1500-1600 cm^{-1} (aromatic C=C stretching), 1380-1450 cm^{-1} (=C-H_2 bending), 1105.2 cm^{-1} (≡C-H bending) at 563.7 cm^{-1} (aromatic C-H bending) and at 750 cm^{-1} (aromatic C-H out-of-plane) which could be due to the increasing degree of condensation and aromatization of the PKS biochar organic compounds [[32], 38, 39]. In contrast to, the two bands at 2927–2850 cm^{-1} representing aliphatic C-H and O=C-H stretching of cellulose and hemicellulose nearly disappeared due to the degradation and dehydration (volatilization) of cellulosic and ligneous components.

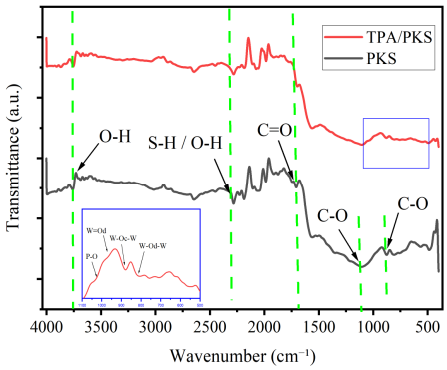

Figure 3 FTIR spectra of PKS and TPA/PKS.

In addition, the FTIR spectrum of TPA/PKS reveals four oxygen-related bands of the TPA, located at 1039 cm^{-1} for P-O and 961 cm^{-1} for W=O_d), along with peaks associated with W-O_c-W (881 cm^{-1}) and W-O_d-W (815 cm^{-1}) to confirm the presence of Kigging structure on the biochar surface [33]. Since, the Keggin anion of TPA ($PW_{12}O_{40}^{3-}$) modified on the PKS biochar surface consists of a PO_4 tetrahedron surrounded by four W_3O_{13} groups arranged in octahedral structures [34, 35].

3.3 BET adsorption analysis

The N_2 adsorption-desorption analysis summarizes in Table 1. BET surface area, BJH pore volume and BJH average pore size of TPA/PKS were 3.91 m^2/g, 0.0084 cm^3/g and 10.41 nm, respectively indicating as mesoporous material [36].This characteristic makes the catalyst a promising candidate for glycerol esterification. The low BET surface area can be attributed to the obstruction of pores by inorganic ash residues as corresponding to the SEM image presented in Figure 2. In addition, the accumulation of disintegrated and amorphous products could be derived from condensed volatiles contributed to this effect. Divyangkumar and Panwar [37] stated that the specific surface area of biochar was declined with increasing concentrations of inorganic constituents. The presence of molten ash can infiltrate and occlude the pore structures of the resulting to reduce their surface area of biochar.

Table 1 N_2 adsorption and desorption of TPA/PKS.

Catalyst	Total surface area (m^2/g)	Total pore volume (cm^3/g)	Average pore diameter (nm)
TPA/PKS	3.91	0.0084	10.41

3.5 Thermogravimetric Analysis

TGA result demonstrates the similar thermal degradation pattern for both PKS and TPA/PKS as can be seen from Figures 4 and 5. The initial weight loss below 150°C was attributed to the loss of physiosorbed moisture. The subsequent weight loss between 200–500°C was likely due to decomposition of hemicellulose, cellulose, and lignin-derived structures and functional groups. The significant decomposition from 500 to 800°C was due to the degradation of lignin. Then, the weight loss tended to stabilize in presence of carbon-rich structures[38]. his should be noted that the TGA result confirmed the thermal stability of this TPA/PKS catalyst making them viable to catalyzed glycerolysis conditions (typically <250°C). This catalyst gave higher thermal stability as compared to the other reports on biochar catalysts derived from PKS. Dandamudi et al. [39] reported that over 60% of their mass was retained over 60% of their mass was retained at 600°C.

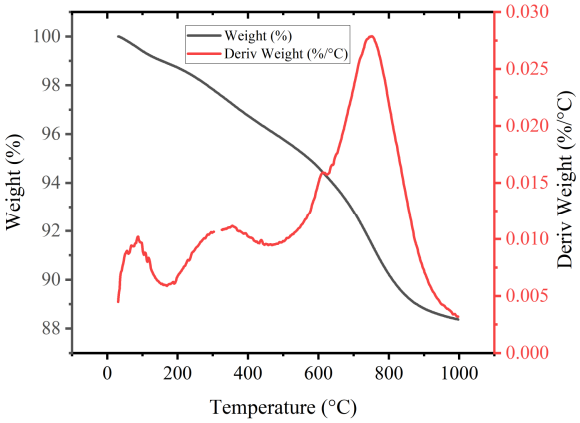

Figure 4 TGA analysis of the synthesized PKS

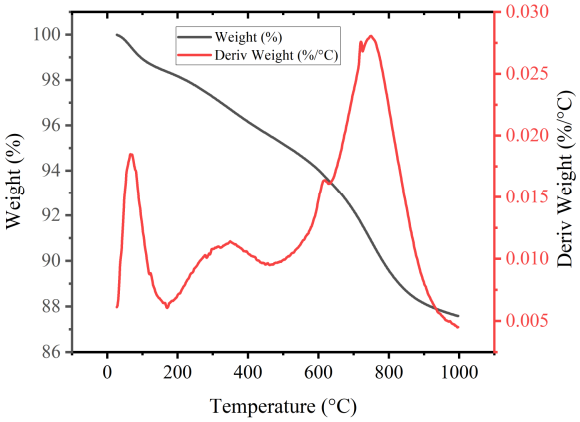

Figure 5 TGA analysis of the synthesized TPA/PKS catalyst

3.6 NH_3-TPD Analysis of TPA/PKS catalyst

The NH_3-temperature programmed desorption (NH_3-TPD) profile of the TPA/PKS biochar catalyst in Figure 6 displays distinct desorption peaks in the temperature range of approximately 100–750°C. This result indicated the presence of multiple types of acid sites distributed across the catalyst surface. The desorption peak centered around 180–250°C corresponds to weak acid sites, likely due to physiosorbed ammonia or surface hydroxyl groups on catalyst surface. The broad and more intense peak observed between 400 and 700°C suggesting the presence of medium to strong acid sites, which are associated with the incorporation of TPA onto the PKS porous carbon surface.

The maximum desorption temperature (~747.8°C) was indicative of strong acid sites with high thermal stability. This reflected the strong interaction between TPA and the support, forming stable acidic functionalities. Such strong acidity is favorable for acid catalyzed reaction such as glycerolysis of PFAD. Strong acid strength could favor high proton availability which is necessary to activate carboxylic acid groups for ester bond formation.

Moreover, the broad distribution of acid strength suggested a good balance between different acid strengths, which can help in minimizing side reactions and improving selectivity [40].

To quantify the total acidity, the area under the NH_3-TPD curves was integrated. The TPA/PKS catalyst demonstrated a total acidity of approximately 2.402 mmol/g. High acidity was attributed to the successful incorporation of TPA onto the PKS biochar surface, introducing the additional Brønsted acid sites essential for catalytic activity for glycerolysis.

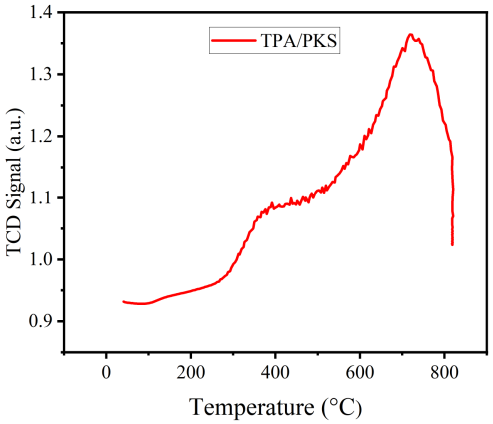

Figure 6 NH_3-TPD profile of TPA/PKS catalyst

3.7 Catalytic Performance of TPA/PKS for Glycerolysis of PFAD

The TPA/PKS catalyst was further employed to catalyze the glycerolysis of PFAD as illustrated in Figure 7. A glycerol to PFAD molar ratio of 3:1, catalyst loading of 3 wt.%, and a reaction temperature of 130°C were employed to produce MGs. The maximum PFAD conversion of 48% was observed at 210 min. At this same reaction time, the selectivity for the MGs was determined to be 67.0%, resulting in an MGs yield of 33%, while the DGs exhibited a selectivity of 33.0% with a corresponding DGs yield of 16%. As the glycerolysis is a stepwise mechanism—initially PFAD reacts with glycerol to form MGs, followed by partial conversion of MGs into DGs. However, the final product of TGs did not observe under this test. The reaction appears to reach a dynamic equilibrium around 210 min, The further increases in reaction time (up to 240 min) did not significantly improve conversion or selectivity. Similarly, Weerachanchai, et al. [41] observed that the extension of reaction time beyond the optimal window did not lead to significant improvements in conversion or selectivity for esterification using acid catalyst with a maximum conversion of 86.87%. These observations substantiated the optimization of reaction time (210 minutes in this case) as a key factor in maximizing product yield. Further, the optimization of reaction parameters and catalyst reusability studies are recommended to enhance the economic feasibility and practical application of the catalyst system in industrial-scale glycerolysis processes

The catalytic activity was compared to the previous works. For instance, Kong et al.[40] reported that the mesoporous zirconia-silica heterogeneous acid catalyst required the equimolar of oleic acid to glycerol ratio, 160°C reaction temperature, 5 wt.% catalyst to achieve 80% of oleic acid conversion with a 59.4 and 34.6% for MGs and DGs selectivities at 4 h. Although, this catalyst had high surface area of 79.75 m^2/g but the lower acidity of only 0.62 mmol/g was observed. They also used Amberlyst-15 to catalyze this reaction under similar condition. The oleic acid conversion of 90% with the MGs and DGs selectivities of 22 and 65%, respectively were observed. Since, the acidity of Amberlyt-15 was 4.7 mequiv./g which was 7.5 times higher than that of the mesoporous zirconia-silica heterogeneous acid catalyst. This can be concluded that the high acidity can favor glycerolysis rate in term oleic acid conversion. However, the balance in acidity can favor the MGs selectivity achieve high MGs yield.

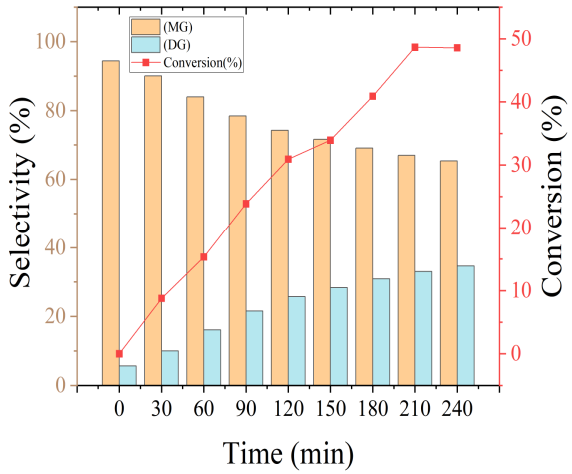

Figure 7 Conversion and selectivity for glycerolysis of PFAD

4. CONCLUSION

In this study, the TPA/PKS catalyst was successfully synthesized and applied for the glycerolysis of PFAD under mild reaction conditions. The catalyst exhibited satisfactory performance, achieving a maximum PFAD conversion of 48% and MG selectivity of 67.0% at 210 min of reaction time. The findings demonstrated that the TPA/PKS catalyst provided the good balance in acidity to facilitate the formation of MGs. The results highlighted the potential of using biochar-supported heteropoly acid catalysts for sustainable and efficient glycerolysis processes, offering a promising route for the valorization of low-cost industrial by-products like PFAD into high-value MGs. Further optimization of reaction parameters and catalyst reusability studies are recommended to enhance the economic feasibility and practical application of the catalyst system in industrial-scale glycerolysis processes.

ACKNOWLEDGMENTS

This research was funded by the NSRF through the Program Management Unit for Human Resources & Institutional Development, Research, and Innovation (Grant number B05F640085). Appreciation is also extended to the Center of Excellence on Catalysis and Catalytic Reaction Engineering for providing laboratory facilities and technical support.

REFERENCES

1. United States Department of Agriculture, F.A.S. Production - Palm Oil. 2025 March 26,2025; Available from: https://www.fas.usda.gov/data/production/commodity/4243000.
2. Shuit, S.H., et al., Oil palm biomass as a sustainable energy source: A Malaysian casestudy. *Energy*, 2009. 34(9): p. 1225-1235.
3. Liew, W.L., et al., Agro-industrial Waste Sustainable Management – A Potential Source of Economic Benefits to Palm Oil Mills in Malaysia. *Journal of Urban and Environmental Engineering* ,2017. 11: p. 108-118.
4. Cheah, W.Y., et al., Circular bioeconomy in palm oil industry: Current practices and future perspectives. *Environmental Technology & Innovation*, 2023. 30: p. 103050.
5. Sudibyo, H., et al., Kinetic Study of Palm Fatty Acid Distillate Esterification with Glycerol over Strong Acidic Cation Exchanger Tulsion 42SM. *Engineering Journal*, 2017. 21: p. 45-61.
6. Abdullah, M.A., et al., New perspectives on biomass conversion and circular economy based on Integrated Algal-Oil Palm Biorefinery frame work for sustainable energy and bioproducts co-generation. *Industrial Crops and Products*, 2024. 213: p. 118452.
7. Jamaludin, N.F., et al., A holistic mitigation model for net zero emissions in the palm oil industry. *Heliyon*, 2024. 10(6): p. e27265.
8. Montes D'Oca, M.G., et al., Sulfamic acid: An efficient acid catalyst for esterification of FFA. *Fuel*, 2012. 97: p. 884-886.
9. Ngaosuwan, K., et al., A green sulfonated carbon-based catalyst derived from coffee residue for esterifica
tion. *Renewable Energy*, 2016. 86: p. 262-269.
10. Stergiou, P.-Y., et al., Advances in lipase-catalyzed esterification reactions. *Biotechnology Advances*, 2013. 31(8): p. 1846-1859.
11. Fojan, P., et al., What distinguishes an esterase from a lipase: A novel structural approach. *Biochimie*, 2000. 82(11): p. 1033-1041.
12. Checa-Gómez, M., et al., Recent Advances in Glycerol Catalytic Valorization: A Review. *Catalysts*, 2020. 10: p. 1279.

13. Mardhiah, H.H., et al., A review on latest developments and future prospects of heterogeneous catalyst in biodiesel production from non-edible oils. *Renewable and Sustainable Energy Reviews*, 2017. 67: p. 1225-1236.
14. de Godói Silva, V.W., et al, Novel $H_3PW_{12}O_{40}$: Catalysed Esterification Reactions of Fatty Acids at Room Temperature for Biodiesel Production. *Catalysis Letters*, 2010. 135(3): p. 207-211.
15. Baig, A. ,F.T.T. et al., A Single-Step Solid Acid-Catalyzed Process for the Production of Biodiesel from High Free Fatty Acid Feedstocks. *Energy & Fuels*, 2010. 24(9): p. 4712-4720.
16. Suwannakarn, K., et al., Simultaneous Free Fatty Acid Esterification and Triglyceride Transesterification Using a Solid Acid Catalyst with in Situ Removal of Water and Unreacted Methanol. *Industrial & Engineering Chemistry Research*, 2009. 48(6): p. 2810-2818.
17. Ngaosuwan, K., et al., Reaction Kinetics and Mechanisms for Hydrolysis and Transesterification of Triglycerides on Tungstated Zirconia. *Topics in Catalysis*, 2010. 53(11): p. 783-794.
18. Chen, S.-Y., et al., Ti-incorporated SBA-15 mesoporous silica as an efficient and robust Lewis solid acid catalyst for the production of high-quality biodiesel fuels. *Applied Catalysis B: Environmental*, 2014. 148-149: p. 344-356.
19. Dehkhoda, A.M., et al., Biochar based solid acid catalyst for biodiesel production. *Applied Catalysis A: General*, 2010. 382(2): p. 197-204.
20. Faiz Norrrahim, M.N., et al., Emerging technologies for value-added use of oil palm biomass. *Environmental Science Advances*, 2022. 1(3): p. 259-275.
21. da Costa, A.A.F., et al., Synthesis of biochar modified with 12-tungstophosphoric acid for the selective conversion of isoeugenol to vanillin. *Arabian Journal of Chemistry*, 2023. 16(12): p. 105313.
22. Baroi, C., A.K. et al., Review on Biodiesel Production from Various Feedstocks Using 12-Tungstophosphoric Acid (TPA) as a Solid Acid Catalyst Precursor. *Industrial & Engineering Chemistry Research*, 2014. 53(49): p. 18611-18624.
23. Zhang, Q., et al., Facile Preparation of Bimetallic MOF-derived Supported Tungstophosphoric Acid Composites for Biodiesel Production. *Periodica Polytechnica Chemical Engineering*, 2023. 67.
24. Yu, H., et al., Microwave-assisted preparation of coal-based heterogeneous acid catalyst and its catalytic performance in esterification. *Journal of Cleaner Production*, 2018. 183: p. 67-76.
25. Lee, K.W.Y., C.J.H. Porter, and B.J. Boyd, A Simple Quantitative Approach for the Determination of Long and Medium Chain Lipids in Bio-relevant Matrices by High Performance Liquid Chromatography with Refractive Index Detection. *AAPS PharmSciTech*, 2013. 14(3): p. 927-934.
26. Al Musaimi, O., O.M.M. Valenzo, and D.R. Williams, Prediction of peptides retention behavior in reversed-phase liquid chromatography based on their hydrophobicity. *J Sep Sci*, 2023. 46(2): p. e2200743.
27. Tripet, B., et al., Requirements for prediction of peptide retention time in reversed-phase high-performance liquid chromatography: hydrophilicity/hydrophobicity of side-chains at the N- and C-termini of peptides are dramatically affected by the end-groups and location. *J Chromatogr A*, 2007. 1141(2): p. 212-25.
28. Jagadish, T., et al., Synthesis of sustainable biochar acid catalyst by utilization of palmyra palm fruit shell waste biomass and application to glycerol esterification. *Journal of Molecular Liquids*, 2025. 424: p. 127039.
29. Ning, Y., et al., Catalytic capability of phosphotungstic acid supported on bamboo activated carbon in esterification for biodiesel production with density functional theory. *Biomass and Bioenergy*, 2020. 143: p. 105873.
30. Prabakaran, E. et al., Synthesis of palm kernel shells-biochar adsorbent for removal of methylene blue and then reused for latent fingerprint detection using spent adsorbent. *Green Analytical Chemistry*, 2025. 13: p. 100259.
31. Babu, S., et al., Metal-based catalysis for biomass and renewables valorization- current status. *Tetrahedron Green Chem*, 2023. 2: p. 100018.
32. Uttran, A., et al., Adsorption of NPK fertilizer and humic acid on palm kernel shell biochar. *Journal of oil palm research*, 2018. 30: p. 472-484.
33. Ooi, S.Y., et al., Magnesium stabilized 12-tungstophosphoric acid impregnated SBA-15 for selective monolaurin production. *South African Journal of Chemical Engineering*, 2022. 41: p. 51-64.
34. Almeida, R.P.d., et al., Residue-based activated carbon from passion fruit seed as support to $H_3PW_{12}O_{40}$ for the esterification of oleic acid. *Journal of Cleaner Production*, 2021. 282: p. 124477.
35. Caliman, E., et al., Solvent effect on the preparation of $H_3PW_{12}O_{40}$ supported on alumina. *Catalysis Today*, 2005. 107-108: p. 816-825.
36. Babatunde, E.O., et al., Novel-activated carbon from waste green coconut husks for the synthesis of biodiesel from pig fat oil blends with tallow seed oil. *Case Studies in Chemical and Environmental Engineering*, 2025. 11: p. 101058.

37. Divyangkumar, N. et al., Optimizing high perfor mance biochar from sugarcane bagasse and corncob via vacuum pyrolysis. *Energy 360*, 2025. 3: p. 100014.
38. Li, S. and G. Chen, Thermogravimetric, thermochemical, and infrared spectral characteriza tion of feedstocks and biochar derived at different pyrolysis temperatures. *Waste Management*, 2018.78: p. 198-207.
39. Dandamudi, K.P.R., et al., Production of functionalized carbon from synergistic hydrother mal liquefaction of microalgae and swine manure. *Resources, Conservation and Recycling*, 2021. 170: p. 105564.
40. Kong, P.S., et al., Esterification of Glycerol With Oleic Acid Over Hydrophobic Zirconia-Silica Acid Catalyst and Commercial Acid Catalyst: Optimization and Influence of Catalyst Acidity. *Front Chem*, 2019. 7: p. 205.
41. Weerachanchai, P., et al., Effect of reaction conditions on the catalytic esterification of bio-oil. *Korean Journal of Chemical Engineering*, 2012. 29(2): p. 182-189.

Synthesis of biolubricant from waste cooking oil methyl ester by transesterification reaction via ethylene glycol

Atipong Paikamnam[1], Thanakorn Whangchang[2], Worawut Thongpradit[2], Anuphan Submee[2], Wasan Chokelarb[1], Woatthichai Narkrugsa[2], Pongsert Sriprom[2], Pornsawan Assawasaengrat[1,*]

[1] Department of Chemical Engineering, School of Engineering, King Mongkut's Institute of Technology Ladkrabang, Bangkok 10520, Thailand
[2] School of Food Industry, King Mongkut's Institute of Technology Ladkrabang, Bangkok 10520, Thailand
[*] Corresponding author: pornsawan.as@kmitl.ac.th

ABSTRACT

This research aimed to present the Box-Behnken experimental design for the determination of optimal conditions for biolubricant production from waste cooking oil by double transesterification via ethylene glycol with three factors such as FAMEs:EG ratio (1:1 to 3:1), temperature (from 110 to 130 ºC) and reaction time (from 120 to 240 min). This study found that the optimal condition for biolubricant synthesis from methyl esters of waste cooking oil by transesterification with ethylene glycol was FAMEs: EG molar ratio of 2:1, the reaction temperature 110 ºC, and reaction time 135 min, using 1%w/w K_2CO_3 as a catalyst, under these conditions, an 80% biolubricant yield was achieved. For this reason, a molar ratio of 2:1 ensured an adequate supply of ethylene glycol while maintaining an excess of FAME, which assisted shift the equilibrium toward biolubricant formation. A temperature of 110 ºC was optimal for promoting transesterification while avoiding the negative effects of excessive heat and prolonged reaction time on conversion. Regarding reaction time, the yield of biolubricant production tends to decrease due to methanol which can promote the reverse reaction, converting biolubricant back into FAME. It can be that biolubricant is synthesized by transesterification of methyl esters derived from waste cooking oil in the presence of ethylene glycol.

Keywords: A Biolubricant; Transesterification; Biodiesel; Waste cooking oil; Ethylene glycol.

1. INTRODUCTION

Nowadays, waste cooking oil (WCO) from households and industrial production is approximately 16.5 million tons per year [1]. In Thailand, there is high potential of waste cooking oil generation. however, clear regulations regarding its disposal are currently lacking [2]. Improper disposal of waste oil impacts the environment; therefore, improving the properties of biodiesel from waste cooking oil is one of the methods to add value to waste cooking oil and eliminate the disposal problems [3]. Then, the biodiesel can be used to produce biolubricant, which can be used in industrial plants. Normally, synthesized lubricant is quite expensive and impacts food processing. Thus, to abolish the limitation of petroleum lubricant, biolubricant is an alternative in food grade for the food industry as biodegradability and no toxic residues in the environment. It can also reduce the production cost [4,5,6].

Transesterification is one of the modifying reactions to synthesize the biolubricant. N.A. Zainal et al. study a comprehensive overview of bio-based lubricants, covering the different types of vegetable oils used as feedstocks, the physicochemical characteristics of biolubricants, and the chemical modification processes applied to enhance their performance. It also examines the lubrication properties of bio-based lubricants and explores the various additives employed to improve the properties of bio-based lubricants [7]. B. Angulo et al. reported that 84% conversion resulted for synthesized biolubricant from fish oil with trimethylolpropane. The biolubricant properties were measured of 5.81 cSt of viscosity at 100 °C, viscosity index 211, -6 °C of pour point, and 204 °C of flash point [8]. Varnish-related problems are found in the deposits inside lubricated systems in terms of soluble and insoluble varnish by increasing the coefficient of friction and decreasing performance rating index of the lubricant [9,10, 11]. However, Ethylene glycol and its derivatives are widely used as solvents in cleaning products and highlight their effectiveness in various cleaning scenarios. [12]. N.K. Attia et al. studied ethylene glycol di-esters (EGDEs) as biolubricants were produced by transesterification of the obtained FAMEs and ethylene glycol as di-alcohol.

Physicochemical properties: density and pour point agree with ASTM standards [13].

The main purpose of this research is to study the production of biolubricant from waste cooking oil using potassium carbonate (K_2CO_3) as the catalyst and optimizing the major factors of transesterification, such as FAMEs:EG (Ethylene glycol) ratio, temperature, and reaction time. In this study, the optimization and factors were observed.

2. EXPERIMENTAL

The Waste Cooking Oil (WCO) sample was obtained from the Program of Food Process Engineering's Laboratory in School of Food Industry, King's Mongkut Institute of Technology Ladkrabang (KMITL), Bangkok, Thailand. It was filtered through the filter paper and then pretreated at 110°C for 1 h to remove sludges and moisture contents before being used in the biodiesel production by transesterification reaction. Additional reagents were methanol (99.5%, AR grade, I.C.P Chemicals, Thailand), Ethylene glycol (99.9%, KenAusTM, Australia), Potassium Carbonated (99.5%, KenAusTM, Australia), and Sodium hydroxide pellets (99%, AR grade, Qrec, New Zealand). Sulfuric acid (97%, AR grade, Merck, Germany) was applied as a catalyst remover.

The 1st transesterification reaction was carried out in a 500 mL batch reactor. The pretreated WCO was replaced into the batch reactor, adding the amount of methanol and catalyst (sodium hydroxide), heating to the desired temperature, and stirring at 300 rpm. The reaction was carried out at 33%v/v of methanol to WCO, 1% wt. of catalyst concentration, 65ºC, and 120 min. Afterward, the obtained product was separated by glycerol through decantation in the separating funnel. Then, the attained biodiesel was purified with 1%v/v of sulfuric acid and distilled water to remove the catalyst and impurities. Finally, the treated biodiesel was dried at 110°C to eliminate the possible moisture. The biodiesel was stored in opaque containers in a desiccator to maintain the properties of biodiesel for further characterization or application.

The 2nd transesterification was proceeded by reacting biodiesel (product from 1st transesterification) with ethylene glycol (EG). The reaction was carried out in a 500 ml 3-neck round flask which was connected to a condenser and thermometer. The Box-Behnken Design (BBD) was applied to determine the effect of parameters such as FAME:EG ratio (1:1 to 3:1), temperature (from 110 to 130 ºC), and reaction time (from 120 to 240 min). 1% wt. of K_3CO_3 was fixed as a catalyst. Subsequently, the obtained product (Biolubricant) was separated through decantation in the separating funnel and purified with 1%v/v of sulfuric acid and distilled water at 80 ºC to remove the catalyst and impurities. In the end, the treated biolubricant was dried at 110°C to eliminate the possible moisture. The biolubricant was stored in opaque containers into desiccator to maintain the properties of biolubricant for further characterization or application.

The yield of produced biolubricant from 2nd transesterification of FAME was calculated as follows:

$$\%yield = \frac{(Volume\ of\ Produced\ Biolubricant\ )}{(Volume\ of\ FAME)} \times 100\%$$

In this study, the optimization of experimental conditions for biolubricant yield by transesterification with ethylene glycol was designed using Box–Behnken design (BBD) technique under response surface methodology (RSM). The software MINITAB version 18.0 was used for the experimental design, data analysis, quadratic model building, and graph plotting. The independent variables, including FAMEs:EG ratio, temperature, and reaction time, were coded with low levels as -1 and high levels as +1 in BBD as shown in Table 1.

Table 1 Factors and levels of Box-Behnken design.

Factor	Unit	Level	
		-1	1
FAMEs:EG ratio	-	1	2
Temperature	°C	110	120
Time	min	120	180

3. RESULTS AND DISCUSSION

BBD analysis was considered design for three independent parameters such as FAMEs:EG ratio, temperature, and reaction time to respond to yield of biolubricant production. The experiment was run 30 runs, and the yields were obtained as shown in Table 2. The result of Response Surface Methodology (RMS) is shown in Table 3, with the 95.58% R-sq for the estimated regression coefficient for biolubricant production, indicating that the quadratic regression model can accurately predict biolubricant yield based on the selected process variables.

$$Biolubricant\ Yeild\ (Coded\ units) = 74.67 + 4.37X_1 - 10.38X_2 + 2.38X_3 - 13.27X_1^2 + 10.23X_2^2 - 9.27X_3^2 + 9.13X_1X_2 - 23.63X_1X_3 + 0.37X_2X_3$$

where X_1 is temperature (°C), X_2 is reaction time (min), and X_3 is FAMEs:EG ratio.

Main effect for biolubricant production was significant parameters to production yield as Figure 1. The effect of FAMEs:EG ratio expresses the highest of yield at 2:1 ratio. Exceed FAME leads to reaction to be shifted to biolubricant product due to transesterification is a reverse reaction.

Table 2 Percentage of yield for biolubricant production according to Box-Behnken design.

No.	FAMEs:EG Ratio	Temp. (°C)	Time (min.)	%Yeild
1	2	110	120	83
2	2	130	120	72
3	2	110	240	52
4	2	130	240	73
5	1	110	180	18
6	1	130	180	81
7	3	110	180	72
8	3	130	180	40
9	1	120	120	83
10	1	120	240	61
11	3	120	120	89
12	3	120	240	66
13	2	120	180	66
14	2	120	180	69
15	2	120	180	80
16	2	110	120	95
17	2	130	120	75
18	2	110	240	51
19	2	130	240	72
20	1	110	180	18
21	1	130	180	79
22	3	110	180	71
23	3	130	180	38
24	1	120	120	88
25	1	120	240	64
26	3	120	120	87
27	3	120	240	67
28	2	120	180	82
29	2	120	180	78
30	2	120	180	73

Temperature played a crucial role in yield optimization. Temperature of 110 °C was identified as optimal for promoting the transesterification process by facilitating the cleavage of the methyl group from FAME, allowing substitution by the CH_2 group of ethylene glycol. However, transesterification is one of the exothermic and reversible reactions. Then, excess temperature can push equilibrium into reactant side.

In the case of reaction time, yield of biolubricant production tends to decrease because of reversible process. Methanol is a by-product from biolubricant production which can react to reverse biolubricant to FAME. Therefore, maintaining an appropriate reaction time is essential to prevent reverse conversion and to ensure optimal yield.

Table 3 Quadratic regression model evaluating the effect of temperature, reaction time, and FAMEs:EG ratio on biolubricant yield by RSM.

Source	DF	Adj SS	Adj MS	F-Value	P-Value
Model	9	10103.9	1122.65	48.10	0.000
Linear	3	2118.7	706.25	30.26	0.000
Temp (°C)	1	306.3	306.25	13.12	0.002
Time (min)	1	1722.2	1722.25	73.78	0.000
Ratio	1	90.3	90.25	3.87	0.063
Square	3	2852.7	950.91	40.74	0.000
Temp (°C)*Temp (°C)	1	1300.5	1300.54	55.72	0.000
Time (min)*Time (min)	1	772.7	772.70	33.10	0.000
Ratio*Ratio	1	634.7	634.70	27.19	0.000
2-Way Interaction	3	5132.4	1710.79	73.29	0.000
Temp (°C)*Time (min)	1	666.1	666.13	28.54	0.000
Temp (°C)*Ratio	1	4465.1	4465.13	191.29	0.000
Time (min)*Ratio	1	1.1	1.12	0.05	0.828
Error	20	466.8	23.34		
Lack-of-Fit	3	162.0	54.00	3.01	0.059
Pure Error	17	304.8	17.93		
Total	29	10570.7			
S		R-sq	R-sq (adj)	R-sq (pred)	
4.83132		95.58%	93.60%	90.85 %	

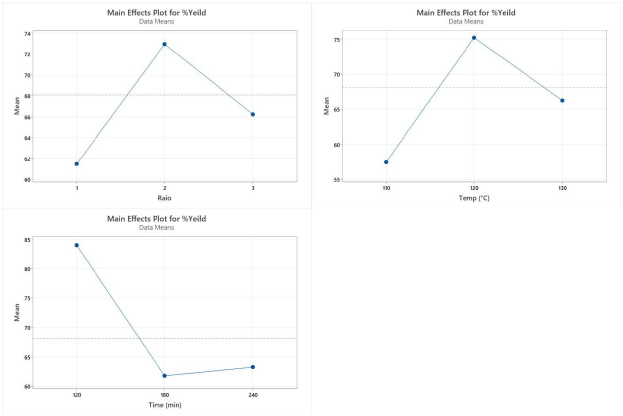

Figure 1 Main effect of parameters to respond to yield of biolubricant.

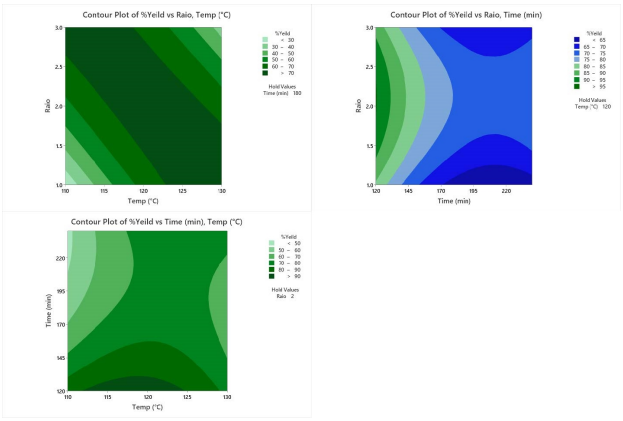

Figure 2 The contour plots of interaction effect of parameters to response to yield of biolubricant.

The contour plots show the interactions between parameters as Figure 2. The interaction effect of FAMEs:EG ratio and temperature express that yield to be achieved either by increasing of FAME:EG ratio or increasing temperature. The reaction can be interrupted by excess FAME or reversible process from temperature. In terms of FAME:EG ratio and time, it is obvious that 2:1 ratio is suitable to achieve biolubricant in 120 to 140 minutes. Moreover, the interaction between temperature and time indicates that yield decreases while increasing reaction time at same temperature.

The optimization is performed for response optimizer function of suitable parameters to obtain yield of biolubricant production. The composite desirability (D) expresses 1, which means the setting parameters seem to achieve favorable results for all responses. The optimal condition is 2:1 (FAMEs:EG) ratio, 110 °C, and 135 minutes to achieve 80% of yield. The optimal condition was investigated 3 times. Mean percentage yield was 80, which is close to predicted value from response optimizer. Consequently, this result can predict biolubricant production from parameters.

4. CONCLUSION

This study demonstrated Box-Behnken design to optimize the biolubricant production from waste cooking oil through double transesterification with ethylene glycol. Main effects of biolubricant yield were FAMEs ratio, Temperature, and reaction time. The optimal FAMEs:EG ratio of 2:1 was obtained as the highest yield due to the reaction was shifted toward biolubricant formation. At 110ºC, the reaction was assisted by promoting the substitution of methyl group from FAMEs with CH_2 of ethylene glycol. Moreover, prolonged reaction time led to a decrease in yield mainly due to the reversibility of the process and methanol formation, which promotes the reverse reaction. Contour plot analysis further confirmed the interaction effects between these parameters. Therefore, the results indicated that the optimal condition: FAMEs:EG molar ratio of 2:1, temperature of 110 ºC, and reaction time of 135 minutes with the presence of 1% w/w K_2CO_3 as catalyst. biolubricant yield of 80% was achieved and close to the value predicted from the response optimizer. This means that the model is reliable to predict biolubricant production based on these reaction parameters.

ACKNOWLEDGMENTS

This work is supported by School of Engineering, King Mongkut's Institute of Technology Ladkrabang, Bangkok, Thailand. Finally, thanks to all individuals and institutions who supported this research in various ways.

REFERENCES

1. Khodadadi M.R., Malpartida I, Tsang C.W, Lin C.S.K, Len C. Recent advances on the catalytic conversion of waste cooking oil. *Molecular Catalysis. 2020*; 494:111128.
2. Indika Thushari, Sandhya Babel. Comparative study of the environmental impacts of used cooking oil valorization options in Thailand. *Journal of Environmental Management. 2022*; 310: 114810.
3. Monika, Banga S, Pathak V.V. Biodiesel production from waste cooking oil: A comprehensive review on the application of heterogenous catalysts. Energy Nexus. 2023; 10:100209.
4. Amenaghawon, A.N., Obahiagbon, K., Isesele, V. and Usman, F. Optimized biodiesel production from waste cooking oil using a functionalized bio-based heterogeneous catalyst. *Cleaner Engineering and Technology. 2022*; 8:100501.
5. Suzihaque M.U.H, Syazwina N, Alwi H, Ibrahim U.K, Abdullah S, Haron N. A sustainability study of the processing of kitchen waste as a potential source of biofuel: Biodiesel production from waste cooking oil (WCO). *Materials Today: Proceedings. 2022*; 63:484-489.
6. Encinar J.M, Nogales-Delgado S, Pinilla A. Biolubricant Production through Double Transesterification: Reactor Design for the Implementation of a Biorefinery Based on Rapeseed. *Processes. 2021*; 9: 1224.
7. Zainal N.A, Zulkifli N.W.M, Gulzar M, Masjuki H.H. A review on the chemistry, production, and technological potential of bio-based lubricants. *Renewable and Sustainable Energy Reviews. 2018*; 82: 80-102.
8. Angulo B, Fraile J.M, Gil L, Herrerias C.I. Bio-lubricants production from fish oil residue by transesterification with trimethylolpropane. *Journal of Cleaner Production. 2018*; 202:81-87.
9. Hong S-H, Jang E.K. Varnish Formation and Removal in Lubrication Systems: *A review. Materials (Basel). 2023*; 16(10): 3737.
10. Chokelarb W, Assawasaengrat P, Sitton A, Sirisithichote T, Sriprom P. Soluble and Insoluble Varnish Test Methods for Trending Varnish Buildup in Mineral Turbine Oil. *Journal of the Japan Institute of Energy. 2022*; 101: 242-250.

11. Chokelarb W, Sriprom P, Permana L, Assawasaengrat P. Assessment of overall remaining useful life of lubricants by integrating oil quality and performance. *Heliyon. 2024*; 10: e37486.
12. Ibrahim R.K, Hayyan M, AlSaadi M.A, Ibrahim S, Hayyan A, Hashim M.A. Physical properties of ethylene glycol-based deep eutectic solvents. *Journal of Molecular Liquids. 2019*; 276: 794-800.
13. Attia N.K, El-Mekkawi S.A, Elardy O.A, Abdelkader E.A. Chemical and rheological assessment of produced biolubricants from different vegetable oils. *Fuel. 2020*; 271: 117578.
14. Thailand Institute of Scientific and Technological Research (TISTR). Preliminary of production and inspection of biodiesel standards [Internet]. 2019 [cite 2023 Mar 30]. Available from http://www.ksp108.com/private_folder/bio200712.pdf.
15. Ali C.H, Asif A.H, Iqbal T, Qureshi A.S, Kazmi M.A, Yasin S, Danish M, Mu B.Z. Improved transesterification of waste cooking oil into biodiesel using calcined goat bone as a catalyst. E*nergy Sources, Part A: Recovery, Utilization, and Environmental Effects. 2018*; 40: 1076-1083.

Low-temperature methanol synthesis via ethanol-assisted approach over $Cu/ZnO/Al_2O_3$ in fixed-bed reactor.

Panisara Kampaeng[1], Pattaraporn Kim[2,*]

[1] Department of Chemical Engineering, Faculty of Engineering, Chulalongkorn University, Bangkok 10330, Thailand
[2] Center of Excellence on Catalysis and Catalytic Reaction Engineering (CECC), Chulalongkorn University, Bangkok 10330, Thailand
[*] Corresponding author: pattaraporn.k@chula.ac.th

ABSTRACT

Our world is facing many crises. One of the biggest problems that needs to be addressed is global warming, which is caused by human activities such as wildfire, fossil fuel, and industry. These activities emit greenhouse gases, especially carbon dioxide (CO_2), a major factor in global warming. Many research projects have focused on the CO_2 utilization by converting it into high-value substances. One approach is the synthesis of methanol from CO_2 and hydrogen via an ethanol-assisted. The conventional methanol production process is energy intensive due to the increased reaction temperature and pressure. However, the ethanol-assisted method presented in this research altered the reaction pathway and allowed the reaction to occur at a relatively lower temperature. In this research, $Cu/ZnO/Al_2O_3$ catalyst was used because ZnO helps disperse the reduced Cu, resulting in more active sites. In addition, Cu^+ is also stable on the ZnO surface, and ZnO facilitates Cu^{2+} to be reduced easily while Al_2O_3 enhances the stability of the catalyst and reduces the sintering. This research studied the effect of temperature on the reaction. The results found that the reaction temperature increased from 130-170 °C. The CO_2 conversion and methanol yield increased. However, the selectivity of methanol decreased. CO selectivity increased as increasing temperature facilitated reverse water gas shift reaction. Ethyl acetate which was an unwanted by-product was also increased with increasing temperature.

Keywords: CO_2 utilization; Ethanol-assisted; methanol synthesis; $Cu/ZnO/Al_2O_3$ catalyst

1. INTRODUCTION

Nowadays, the world is facing a serious global warming problem. One method of decreasing carbon dioxide (CO2) currently receiving more attention is the thermocatalytic conversion of valueless carbon dioxide into high-value products [1]. This method uses green hydrogen (H2) from sustainable energy to convert wasteful carbon dioxide into valuable substances [1]. High-value chemicals including formaldehyde, amines, acetic acid, esters, ethylene, and propylene can be produced using methanol, an important industrial chemical, as a fuel, solvent, and intermediary. Furthermore, methanol can be readily transported and stored, which makes it suitable for a range of uses [2]. Commercial-scale methanol synthesis proceeds via CO2 hydrogenation with Cu/ZnO/Al2O3 catalysts. Le Chatelier's thermodynamic principle still governs this process since the reaction is exothermic, meaning it performs better at low temperatures. However, methanol synthesis necessitates strong pressure to move the reaction along and high temperature to get the proper reaction rate [3]. Some researchers have discovered a new technique of methanol synthesis known as alcohol-assisted methanol synthesis. By using alcohol as a solvent, this technique decreases the temperature needed for the chemical reaction and modifies the reaction pathway to esterification [4-6]. Additionally, some research can also reduce the energy consumption in the reactor section compared to the conventional method by using Aspen Plus simulation to investigate preliminary studies [7]. This research focuses on methanol synthesis via ethanol assisted by Cu/ZnO/Al2O3 as a catalyst. This research finds the effect of temperature (130, 150 and 170°C). The results found that the reaction temperature increased from 130, 150, and 170°C respectively. The CO_2 conversion and methanol yield increased but also the selectivity of methanol is decreased, which shows that the methanol synthesis via ethanol-assisted approach can convert CO_2 into methanol effectively.

2. EXPERIMENTAL

A commercial $Cu/ZnO/Al_2O_3$ catalyst (045776, Alfa Aesar) was prepared by grinding and sieving through a mesh40 screen.

2.1 Characterization

The catalyst surface properties and chemical structure were studied using Scanning Electron Microscopy (SEM, Hitachi, S3400) with energy-dispersive X-ray analysis (EDX, EDAX, Apollo x). Brunauer-Emmett-Teller was used to calculate the pore size, pore volume, and surface area (BET, Micromeritics, ASAP 2020).

2.2 Fixed-Bed reactor

The fixed-bed reactor is constructed from stainless steel that is 78 cm in height and 10 mm in inner diameter which can be shown in Figure 1.

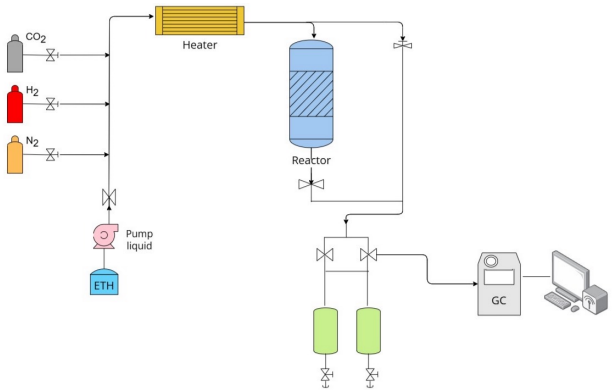

Figure 1 P&ID process.

2.3 Catalyst packing

The catalysts were positioned at the tip of the thermocouple for temperature analysis. The catalysts were ground and sieved to particle sizes between 180 and 425 microns, with a total weight of 20 g for the experiment. Additionally, 2 g of aluminum oxide and 0.2 g of quartz wool were placed at the bottom of the reactor. The thermocouple was first wrapped tightly with quartz wool, followed by the addition of the catalysts. Finally, another layer of 2 g of aluminum oxide and 0.2 g of quartz wool was added to the top of the reactor.

2.4 Pressure testing leak

Nitrogen gas was introduced into the reactor at a flow rate of 450 mL/min. The pressure was increased to 50 bar, after which the nitrogen supply was stopped. The system was maintained under these conditions for 1 hour. In the event of a continuous pressure drop, all valves in the reactor system were inspected for possible leaks. Leak detection was performed by spraying the valves with a leak-detection solution and observing for bubble formation, which would indicate the presence of gas leaks.

2.5 Catalyst reduction

A N_2:H_2 gas mixture with a 1:1 ratio was used for catalyst reduction. Nitrogen and hydrogen gases were each introduced at a flow rate of 30 mL/min under a pressure of 5 bar, while the reactor temperature was maintained at 300 °C. The temperature was controlled to remain below 310 °C throughout the process. The reduction was carried out for 3 hours or until the target temperature was achieved and stabilized.

2.6 Reaction testing

The reaction testing was used to study the influence of various temperatures. Ethanol was introduced into the system by a pump to regulate the flow rate, maintaining an ETH:CO_2 molar ratio of 1:1. The experiments were performed using 20 g of $Cu/ZnO/Al_2O_3$ catalyst. The system temperature was controlled with a heater and set at 130, 150, and 170 °C, respectively, under a CO_2:H_2 molar ratio of 1:5 and a pressure of 50 bar. Samples from both the gas and liquid phases were collected during the reaction. Sampling was performed at three different time points each 3 hours. For gas-phase sampling, the gas phase was directed into a gas chromatograph by rotating a valve, allowing concentration analysis. The gas flow rate was measured three times to determine the average flow rate. For liquid phase sampling, the liquid product was collected from a liquid trap, weighed to calculate its density, and subsequently analyzed for concentration using gas chromatography.

2.7 Calculation of results

This research was evaluated through three key factors: CO_2 conversion, CH_3OH yield, and CH_3OH methanol selectivity. These parameters were calculated according to Equations (1-3).

$$\%\ CO_2\ \text{conversion} = \frac{CO_2\ \text{react in reaction}}{CO_2\ \text{in feed}} \times 100 \quad (1)$$

$$\%\ CH_3OH\ \text{yield} = \frac{CH_3OH}{CO_2\ \text{in feed}} \times 100 \quad (2)$$

$$\%\ CH_3OH\ \text{selectivity} = \frac{CH_3OH}{\text{Total product}} \times 100 \quad (3)$$

3. RESULTS AND DISCUSSION

3.1 Characterization

This research investigated the characterization of $Cu/ZnO/Al_2O_3$ catalyst to study surface properties and chemical structure which can be shown in Figure 2, Table 1 and 2.

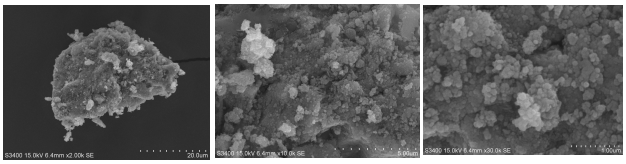

Figure 2 SEM-EDX of $Cu/ZnO/Al_2O_3$.

Scanning Electron Microscopy (SEM) analysis reveals that the commercial catalyst exhibits a spherical-like morphology with finely shaped crystallites. The particles are uniformly distributed, indicating good dispersion and structural consistency.

Table 1 Chemical composition of $Cu/ZnO/Al_2O_3$.

Element	%wt
Cu	65.99
Zn	24.53
Al	9.48

Table 2 BET of $Cu/ZnO/ Al_2O_3$.

BET surface area (m^2/g)	Pore volume (cm^3/g)	Pore size (nm)
80.34	0.18	8.92

Figure 3 shows that the BET surface area, pore volume, and average pore diameter of the catalyst are 80.34 m^2/g, 0.18 cm^3/g, and 8.92 nm, respectively, indicating a mesoporous structure suitable for catalytic applications.

3.2 Methanol synthesis via ethanol-assisted reaction

Some researchers introduced a new mechanism of alcohol-assisted methanol synthesis, which adjusts the methanol synthesis pathway via esterification, enabling the reaction to occur at lower operating temperatures. The reaction mechanism is shown by Equations (4–8) [6].

$$CO_2 + 0.5H_2 + Cu \leftrightarrow HCOOCu \quad (4)$$
$$HCOOCu + ROH \leftrightarrow HCOOR + CuOH \quad (5)$$
$$HCOOR + 2H_2 \leftrightarrow CH_3OH + ROH \quad (6)$$
$$CuOH + 0.5H_2 \leftrightarrow H_2O + Cu \quad (7)$$
$$CO_2 + H_2 \leftrightarrow CO + H_2O \quad (8)$$

The occurrence of the esterification pathway in this system is supported by the data presented in Figures 4 and 5, where the formation of ethyl acetate and ethyl formate was detected as by-products. These findings strongly indicate the presence of additional reaction pathways beyond conventional CO and CO_2 hydrogenation. In equation (5), a surface-bound formate species (HCOOCu) reacts with an alcohol (ROH, in this case ethanol), forming an ester (HCOOR) and regenerating a hydroxylated copper site (CuOH). The formed ester can subsequently undergo hydrogenation (Eq. 6) to yield methanol (CH_3OH) and regenerate the alcohol co-feed (ROH), completing a catalytic cycle. This reaction is exothermic, with an estimated standard enthalpy change ($\Delta H°$) of approximately –51.7 kJ/mol [8]. Such a negative enthalpy value indicates that the process releases heat, thereby thermodynamically favoring the forward reaction at lower operating temperatures, providing a more energy-efficient process [7].

3.3 Effect of reaction temperature

The reaction pathway for methanol production from carbon dioxide hydrogenation in the ethanol-assisted. This research investigates the role of ethanol in assisting the reaction pathway for CO_2 hydrogenation to methanol. The study of the reaction pathway was evaluated in terms of CO_2 conversion, CH_3OH yield, and CH_3OH selectivity, based on the reaction mechanisms described in the Equations (4-7).

The result of the hydrogenation of CO_2 via ethanol-assisted under a pressure of 50 bar and temperatures of 130°C, 150°C, and 170°C are shown in Figures 3, 4, and 5.

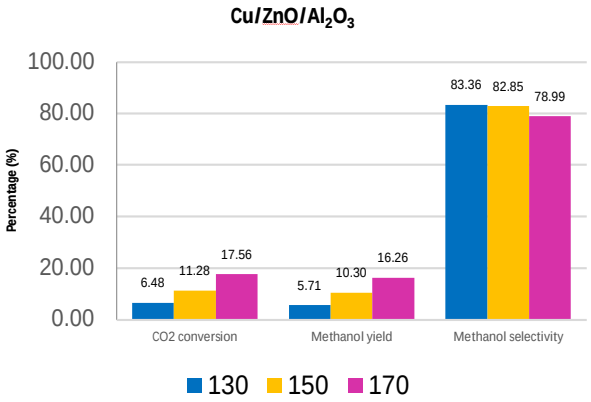

Figure 3 CO_2 conversion, CH_3OH yield and selectivity.

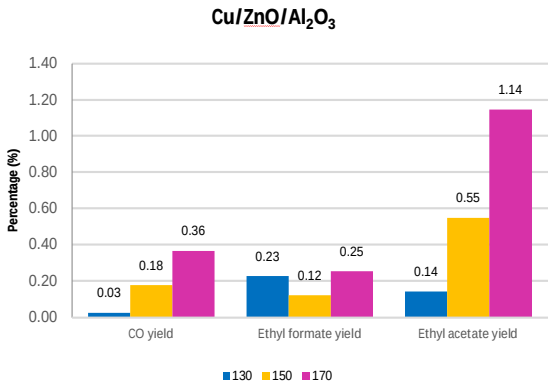

Figure 4 Yield of by-products.

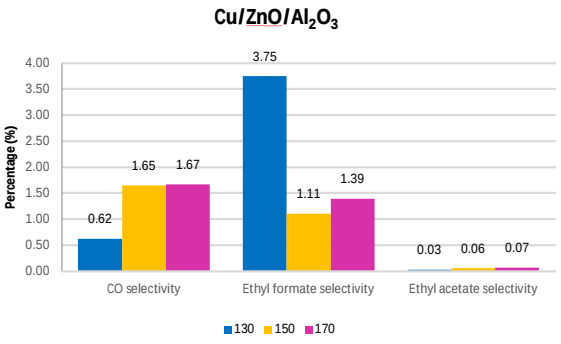

Figure 5 Selectivity of by-products.

Figure 3 shows that $\%CO_2$ conversion and $\%CH_3OH$ yield increase, but on the contrary, $\%CH_3OH$ selectivity decreases due to the increase of CO, ethyl formate and ethyl acetate. This can be observed as shown in Figures 4 and 5. It can be seen that when the temperature increases, CH_3OH, CO, ethyl formate and ethyl acetate also increase. This behavior is explained by the enhanced activity of the reverse water gas shift reaction as in equation 8 can react better, which promotes CO formation and consequently reduces methanol selectivity. Ethyl acetate and ethyl formate are identified as by-products formed during the hydrogenation step in ethanol-assisted methanol synthesis.

4. CONCLUSION

This study explores the catalytic conversion of CO_2 into methanol via an ethanol-assisted pathway. Conventional methods require high operating temperatures, leading to substantial energy consumption. The ethanol-assisted pathway offers a modified reaction mechanism through esterification intermediates, thereby facilitating methanol synthesis at significantly lower temperatures and reduced energy in the reactor section. $Cu/ZnO/Al_2O_3$ catalyst was employed. Where ZnO promoted the dispersion of Cu nanoparticles, stabilized Cu^+ species, and enhanced the reducibility of Cu^{2+}, while Al_2O_3 provided structural support and resistance to sintering. The effect of reaction temperature studies revealed that increasing the reaction temperature from 130 °C to 170 °C resulted in enhanced CO_2 conversion and methanol yield, but also methanol selectivity was decreased because when the temperature increases, the reverse water gas shift reaction dominated, resulting in an increase in CO and a decrease in CH3OH selectivity. Ethyl acetate and ethyl formate were detected as by-products of the hydrogenation reaction of methanol synthesis via ethanol-assisted. The by-product increased as increasing temperature.

ACKNOWLEDGMENTS

This research was funded by Research Cess Fund, Malaysia-Thailand Joint Authority (MTJA) and the NSRF via the Program Management Unit for Human Resources & Institutional Development, Research and Innovation [grant number grant number B16F640164]. Kim-Lohsoontorn also would like to acknowledge Thailand Science research and Innovation Fund Chulalongkorn University (BCG66210021).

Panisara Kampaeng also deeply thankful to my family for their support and understanding during this journey and would like to express my heartfelt appreciation to my partner for always standing by my side with constant encouragement and love.

REFERENCES

[1] Azhari, N.J., et al., *Methanol synthesis from CO2: A mechanistic overview.* Results in Engineering, 2022. **16**: p. 100711.

[2] Denise, B., R. Sneeden, and C. Hamon, *Hydrocondensation of carbon dioxide: IV.* Journal of Molecular Catalysis, 1982. **17**(2-3): p. 359-366.

[3] Meesattham, S. and P. Kim-Lohsoontorn, *Low-temperature alcohol-assisted methanol synthesis from CO2 and H2: The effect of alcohol type.* International Journal of Hydrogen Energy, 2022. **47**(54): p. 22691-22703.

[4] Tsubaki, N., M. Ito, and K. Fujimoto, *A new method of low-temperature methanol synthesis.* Journal of Catalysis, 2001. **197**(1): p. 224-227.

[5] Nieminen, H., et al., *Alcohol promoted methanol synthesis enhanced by adsorption of water and dual catalysts.* Journal of CO2 Utilization, 2018. **24**: p. 180-189.

[6] Jeong, Y., et al., *Effect of the aging time of the precipitate on the activity of Cu/ZnO catalysts for alcohol-assisted low temperature methanol synthesis.* Journal of Molecular Catalysis A: Chemical, 2016. **418**: p. 168-174.

[7] Khunathorncharoenwong, N., et al., *Techno-economic analysis of alternative processes for alcohol-assisted methanol synthesis from carbon dioxide and hydrogen.* International Journal of Hydrogen Energy, 2021. **46**(48): p. 24591-24606.

[8] Lide, D. R. (Ed.). *CRC Handbook of Chemistry and Physics*, 87th Edition, CRC Press, Boca Raton, FL, 2006.

Hydroconversion of biodiesel over Ni/beta zeolite catalysts prepared by glycine-assisted impregnation for sustainable aviation fuel production

Witchakorn Jankool[1], Napida Hinchiranan[1,2,3,*]

[1] Department of Chemical Technology, Faculty of Science, Chulalongkorn University, Bangkok 10330, Thailand
[2] Center of Excellence on Petrochemical and Materials Technology (PETROMAT), Chulalongkorn University, Bangkok 10330, Thailand
[3] Center of Excellence in Catalysis for Bioenergy and Renewable Chemicals (CBRC), Chulalongkorn University, Bangkok 10330, Thailand
[*] Corresponding author: napida.h@chula.ac.th

ABSTRACT

According to a measure to reduce carbon dioxide emissions from aviation sector announced by International Civil Aviation Organization (ICAO), hydroprocessed esters and fatty acids (HEFA) is a promising process to commercially produce sustainable aviation fuel (SAF). Nickel (Ni) is attractive for using as a metal site for bi-functional catalysts in hydroconversion due to its high activity and cost effectiveness. However, Ni-based catalysts are suffered from metal agglomeration resulting in the poor metal dispersion and weak metal-support interaction, which could affect catalyst activity and stability. Hence, the objective of this research was to emphasize the improvement of Ni-based catalysts using glycine-assisted impregnation method for hydroconversion of biodiesel derived from palm oil. The hydroconversion was conducted in a fixed-bed reactor operated under 30 bar H_2 pressure at 380 °C and WHSV of 1.6 h^{-1}. Product selectivity was analyzed by gas chromatography-mass spectrometer (GC-MS). It was found that liquid yield increased from 66.6 wt% to 67.6 wt% when the system was operated by Ni0.4Gly/beta catalyst (10 wt% Ni loading, glycine:Ni molar ratio = 0.4) compared to Ni/beta catalyst with bio-jet (C_9-C_{14}) yield increased from 10 wt% to 13.6 wt%. Moreover, glycine-assisted impregnation could promote hydrodeoxygenation of biodiesel to decrease the selectivity of oxygenated compounds from 21.2% to 9.2%.

Keywords: Hydroconversion; Bio-jet; Nickel; Glycine

1. INTRODUCTION

Nowadays, the aviation industry has been growing faster in recent decades, especially for civil aviation. This rapid growth results in an increase of carbon dioxide (CO_2) emission into the atmosphere [1]. The CO_2 emission from the aviation industry is accounted for 2% of all CO_2 emissions generated from human activity or accounted for 12% of all emissions released from transportation sector [2]. The International Civil Aviation Organization (ICAO) predicted that CO_2 emission from civil aviation will reach 2700 Mt in 2050. Therefore, ICAO has announced a measure for using sustainable aviation fuel (SAF) to decrease the CO_2 emission approximately 63% in 2050 [3].

There are several pathways to produce SAF, but only 8 pathways are certified by ASTM D7566 standards. Hydroprocessed esters and fatty acids (HEFA) process, one of the certified methods, is mostly applied to commercially produce SAF for blending with the fossil aviation fuel at the maximum ratio of 50% (v/v) [4]. Moreover, this process is suitable for agricultural countries, which have high amounts of lipid products such as vegetable oil or biodiesel.

Recently, the consumption of biodiesel in some regions has declined due to the rise of renewable diesel [5]. Therefore, to maintain the market price and add value for biodiesel, producing SAF via HEFA process of biodiesel could be the solution. Normally, biodiesel has a large molecular structure (C_{17}-C_{19}) [6] which is higher than jet fuel range (C_9-C_{14}) [7]. Moreover, unsaturated bonds and oxygenated compounds in biodiesel structure negatively affect fuel properties. Therefore, hydroconversion process involving hydrodeoxygenation, hydrogenation, hydroisomerization, and hydrocracking, is crucial to produce bio-jet fuel having comparative properties to Jet A-1 according to ASTM D1655 [3].

Bi-functional catalysts consisting of metal sites and acid sites play an important role in the hydroconversion process. The precious noble metals such as platinum (Pt) or palladium (Pd) are normally used as the metal sites for hydroisomerization in oil refinery due to their high stability and hydro/dehydrogenation activity [8]. To minimize the operation cost, the non-noble metal like nickel (Ni) is attractive to be used as the active metal instead of Pt and Pd. According to the lower

hydro/dehydrogenation activity of Ni-based catalyst than that of the noble metals, the higher amount of Ni in the applied catalyst is required. Since Ni based-catalysts normally exhibit the weak metal-support interaction, resulting in the lower metal dispersion and consequently reducing the number of metal active sites [9].

Solution combustion synthesis (SCS) is a method to prepare metal oxide in nanoscale. It involves the reaction between metal nitrate and organic compound, acting as an oxidizer and fuel, respectively [10]. Recently, glycine, as a fuel in SCS method, has been used as a chelating agent for metal impregnation to prepare catalysts. Xu et al. [11] prepared Ni/SiO_2-Gly catalysts via combustion-impregnation method for CO_2 methanation. It was found that 6 nm Ni particle size was obtained. Yang et al. [12] prepared Ni/SiO_2 catalysts with different glycine to nitrate molar ratio by glycine-assisted incipient wetness impregnation method for dry reforming of methane reaction. It was found that Ni dispersion and metal-support interaction were improved when the proper glycine to nitrate ratio was added. Moreover Yang et al. [13] prepared Ni/beta zeolite catalysts using ligand assisted method for n-hexane hydroisomerization. It was found that 5.1 nm Ni particle size was obtained with the improvement of iso-hexane yield from 61.5% to 72.8% compared to normally prepared Ni/beta catalysts.

According to the advantages of the addition of glycine, this research aims to prepare Ni-based catalysts using glycine-assisted impregnation method for hydroconversion of biodiesel to produce bio-jet fuel in a fixed-bed reactor. The effect of glycine:Ni molar ratio to the properties of the catalyst were evaluated. Moreover, product distribution and compositions in the liquid products obtained from hydroconversion were also investigated.

2. EXPERIMENTAL

2.1. Materials

Biodiesel was obtained from Bangchak Corporation Public Co., Ltd. (Thailand). Analytical grade Ni (II) nitrate hexahydrate ($Ni(NO_3)_2{\cdot}6H_2O$) and glycine were obtained from Sigma-Aldrich Co., Ltd. (Singapore) and KemAus (Australia), respectively. Commercial grade H-beta zeolite extrudates (931HOD1A) was purchased from TOSOH Co., Ltd. (Japan). The H_2 gas (99.99% purity) was supplied by Bangkok Industrial Gas Co., Ltd. (Thailand). Analytical grade ethyl acetate for gas chromatography-mass spectrometer (GC-MS) was purchased from QRëC (New Zealand).

2.2. Catalyst preparation

The Ni0.4Gly/beta catalysts (10 wt% Ni loading and glycine:Ni molar ratio of 0.4) were prepared by wetness impregnation. Briefly, 3.30 g $Ni(NO_3)_2{\cdot}6H_2O$ and 0.34 g glycine were dissolved in 4.00 g deionized (DI) water. Then, 6 g H-beta zeolite extrudates were immersed in the above prepared solution at room temperature for 24 h. The excess water was removed by rotary vacuum evaporator at 60 °C for 1 h and then dried in an oven at 110 °C for 24 h followed by calcination at 500 °C for 2 h with a heating rate of 10 °C/min. The calcined catalysts were then ex-situ reduced in a horizontal tubular furnace at 600 °C for 2 h with a heating rate of 10 °C/min under a H_2 atmosphere at a flow rate of 10 mL/min. The reduced catalysts were passivated under O_2:N_2 5:95 (v/v) mixed gas at room temperature overnight. The catalysts having other glycine:Ni ratios were prepared by the same procedure.

2.3. Catalyst characterization

The textural properties of the H-beta zeolite support and calcined catalysts were determined from nitrogen (N_2) adsorption-desorption isotherms analyzed by 3P micro 300 model (3P Instrument). The samples were degassed at 300 °C (10 °C/min) for 3 h before the measurement. The specific surface (S_{BET}) area and total pore volume (V_p) were calculated from Brunauer–Emmett–Teller (BET) and Barrett–Joyner–Halenda (BJH) method, respectively.

The X-ray diffraction (XRD) patterns of H-beta zeolite and calcined catalysts were detected by X-ray diffractometer (Bruker D8 advance) using Cu-Kα (λ = 0.154 nm) operated at 40 kV and 40 mA with scanning range from 5-80° (10°/min).

The reduction temperature of the catalysts was also determined from hydrogen temperature-programed reduction (H_2-TPR) by chemisorption analyzer (MicrotracBEL, BELCAT II). The samples were pretreated under 50 mL/min of argon (Ar) at 110 °C for 30 min. The pretreated samples were heated from 110 to 900 °C with the heating rate of 10 °C/min under 5/95 (v/v) H_2/Ar gas at a flow rate of 30 mL/min.

2.4. Hydroconversion of biodiesel

The reaction was performed in a stainless steel fixed-bed reactor (L = 300 mm, ϕ = 10 mm) operated under 30 bar H_2 pressure with flow rate of 100 sccm at 380 °C and WHSV of 1.6 h^{-1}. First, 4 g glass beads (ϕ = 3 mm) were packed in the reactor column to keep the catalysts bed located at the middle of the reactor, followed by 3 g reduced catalysts and then heated to 380 °C and waited for 30 min before releasing the biodiesel by high-performance liquid chromatography (HPLC) pump. After 3 h time on stream, the HPLC pump was stopped, and the system was left for 1 h to minimize the liquid residue trapped inside the reactor. The liquid product was collected at the bottom of the reactor. The schematic diagram of hydroconversion process was shown in Figure 1.

2.5. Product analysis

The chemical compositions in the liquid product classified as n-alkane, iso-alkane, cyclics, aromatics, oxygenated compounds and unsaturated compounds

and product distribution categorized following the carbon number as bio-gasoline, bio-jet and green diesel were identified by gas chromatography–mass spectrometry (GC–MS, Shimadzu QP2020NX) equipped with DB-5HT column (ϕ = 0.25 mm, L = 30 m) using helium (He) as a carrier gas at a flow rate of 53 mL/min. The liquid sample was diluted with ethyl acetate to reach a concentration of 10,000 ppm. The diluted sample was then injected into the column with a split ratio of 25. The initial column temperature was held at 40 °C before increasing to 280 °C with a heating rate of 5 °C/min and held at this temperature for 10 min.

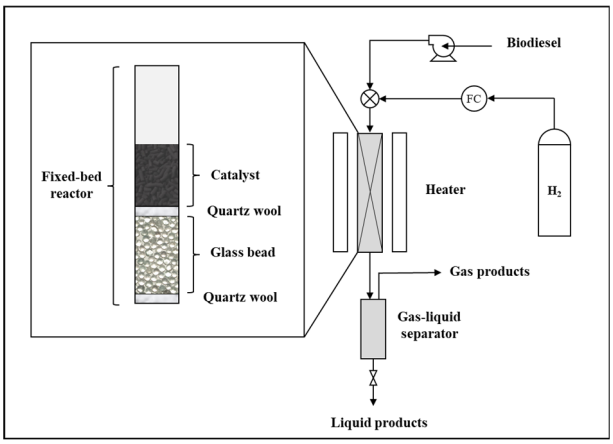

Figure 1 Schematic diagram of biodiesel hydroconversion in a fixed-bed reactor.

3. RESULTS AND DISCUSSION

3.1. Characterization of prepared catalysts

Table 1 shows the physical appearance of calcined catalysts with and without using glycine-assisted impregnation. The particle size of the catalysts decreased from 1.5 mm to 0.5 mm, when the glycine:Ni ratio of 0.8 was applied (Ni0.8Gly/beta). This resulted the higher bulk density from 0.75 to 0.79 g/cm^3 due to the effect of higher flame temperature occurring during the combustion synthesis when the glycine:Ni ratio increased [10]. This phenomenon could possibly damage the structure of the catalysts.

Table 1 Physical appearance of calcined Ni-based catalysts with and without using glycine-assisted impregnation.

Catalysts	Ni/beta	Ni0.4Gly	Ni0.8Gly
Physical appearance			
Particle size (mm)	1.5*	1.5*	0.5
Bulk density (g/cm^3)	0.75	0.75	0.79

* Same size as the H-beta zeolite extrudates (ϕ = 1.5 mm, L = 2-3 mm)

Textural properties of H-beta zeolite extrudates and calcined Ni-based catalysts with and without using glycine-assisted impregnation method were also comparatively shown in Table 2. BET surface area (S_{BET}), pore volume, and average pore diameter (D_{avg}) decreased when Ni metal was loaded onto the H-beta zeolite due to the partial blocking of Ni metal in the pores of zeolite. However, the D_{avg} of Ni0.4Gly/beta (3.17 nm) and Ni0.8Gly/beta (3.24 nm) was wider than that of Ni/beta catalyst (3.11 nm). However, the total volume (V_{total}) and external surface area (S_{ext}) of all prepared catalysts were remained.

Figure 2 shows XRD patterns of H-beta zeolite and Ni-based catalysts with different glycine:Ni molar ratio. Diffraction peaks at 7.8° and 22.7° of H-beta zeolite [13] were remained for all catalysts, suggesting that there was no change in H-beta structure after combustion synthesis. The NiO crystalline size at of Ni0.4Gly/beta decreased from 8.6 nm to 7.0 nm compared with Ni/beta as shown in Table 2. Moreover, the low intensity of diffraction peaks of NiO at 2θ of 37.2° (111) and 43.3° (200) [12, 13] was observed for Ni0.8Gly/H-beta. The results indicated the small crystal size with high dispersion of NiO particles on the beta zeolite support.

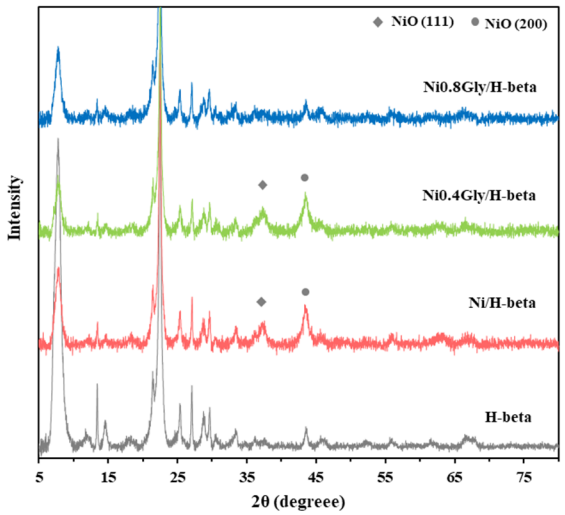

Figure 2 XRD patterns of H-beta zeolite and calcined Ni-based catalysts.

H_2-TPR profiles in Figure 3 indicated a reduction temperature of all catalysts. For Ni/beta catalyst, there were three main peaks at 458, 507, and 580 °C, attributed to the NiO particles located in α cavity, sodalite cavity, and hexagonal prisms, respectively [14]. Moreover, a peak at 725 °C corresponded to a strong interaction of Ni species and aluminium (Al) in the H-beta zeolite structure was appeared [15]. The reduction peaks were shifted to the lower temperature for Ni0.4Gly/beta and Ni0.8Gly/beta catalysts, indicating an easier to be reduced than Ni/beta catalyst.

Table 2 Textural properties of H-beta zeolite and calcined Ni-based catalysts

Samples	Surface area (m^2/g)			Pore volume (cm^3/g)			D_{avg} (nm)	NiO crystalline size[a] (nm)
	S_{micro}	S_{ext}	S_{BET}	V_{micro}	V_{meso}	V_{total}		
H-beta	353	116	469	0.17	0.20	0.37	3.14	-
Ni/beta	288	99	387	0.14	0.16	0.30	3.11	8.6
Ni0.4Gly/beta	273	98	371	0.13	0.16	0.29	3.17	7.0
Ni0.8Gly/beta	263	98	361	0.13	0.17	0.29	3.24	n.d.[b]

[a] Calculated by Scherrer equation from XRD pattern of NiO (111)
[b] Could not be detected

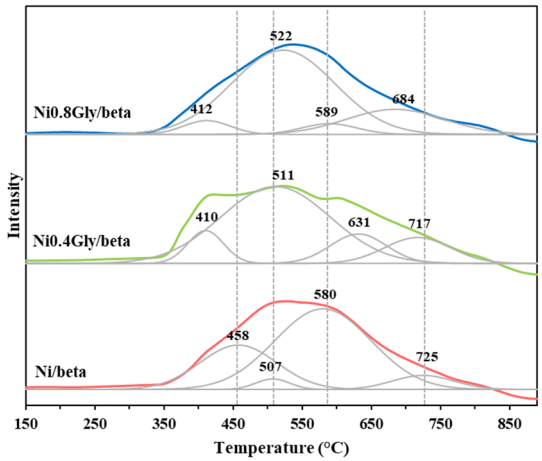

Figure 3 H_2-TPR profiles of Ni-based catalyst with and without using glycine-assisted impregnation.

3.2. Hydroconversion of biodiesel

GC-MS chromatograms (Figure 4a) showed three main components in biodiesel, consisting of methyl palmitate ($C_{17}H_{34}O_2$), methyl oleate ($C_{19}H_{36}O_2$), and methyl stearate ($C_{19}H_{38}O_2$). After hydroconversion over Ni/beta catalyst, the three peaks of biodiesel dramatically decreased with the formation of hydrocarbons with the smaller molecules (Figure 4b), indicating a superior conversion of biodiesel. Two mains peaks of n-C_{15} and n-C_{17} were generated from the hydrodeoxygenation (HDO), whereas the n-C_{16} and n-C_{18} molecules were obtained from the hydrodecarbonization (HDC) of $C_{17}H_{34}O_2$ and $C_{19}H_{36}O_2$, respectively [16]. Additionally, a peak of palmitic acid, the product from the hydrogenolysis of biodiesel [17], was also occurred. However, the overall peaks intensity for the liquid product obtained from Ni0.4Gly/beta catalyst increased with the peak reduction of palmitic acid (Figure 4c). These results showed the higher hydrodeoxygenation and hydrocracking performance of glycine-assisted catalysts.

Product distribution and chemical compositions of obtained liquid were also summarized in Table 3 and Table 4, respectively. The liquid product was consisted of organic phase and aqueous phase. The presence of aqueous phase confirmed the hydrodeoxygenation of biodiesel to release H_2O as a by-product in the hydroconversion process [16]. For Ni0.4Gly/beta catalyst, the liquid yield increased from 66.6 wt% to 67.6 wt% and bio-jet fraction increased from 10.0% to 13.4% with an increase in the iso-alkane components from 11.0% to 12.3% compared with the system using Ni/beta catalyst. Moreover, Ni0.4Gly/beta catalyst exhibited the better performance in hydrodeoxygenation to significantly decrease oxygenated compounds from 21.2% to 9.0% than the system using Ni/beta catalyst. The decrease in the oxygenated compounds also related to an increase in the n-alkane compositions, which increased from 49.7% to 62.2%. This could be due to the wider pore size of the glycine-assisted Ni/beta catalysts that could promote the higher bio-jet fraction. Moreover, the smaller size of Ni particles resulted in the higher active metal surface area to promote hydroisomerization and hydrodeoxygenation. For Ni0.8Gly/beta catalyst with smaller size of Ni particle compared to Ni0.4Gly/beta, the liquid yield increased to 70.1 wt%. However, the bio-jet fraction decreased to 11.8% with the higher formation of n-alkanes and iso-alkanes to 70.9% and 14.7%, respectively. The results showed that the Ni0.8Gly/beta catalyst had the better hydrodeoxygenation performance to achieve only 2.9% oxygenated compounds than Ni0.4Gly/beta catalyst, which provided the liquid product contained 9.0% oxygenated compounds.

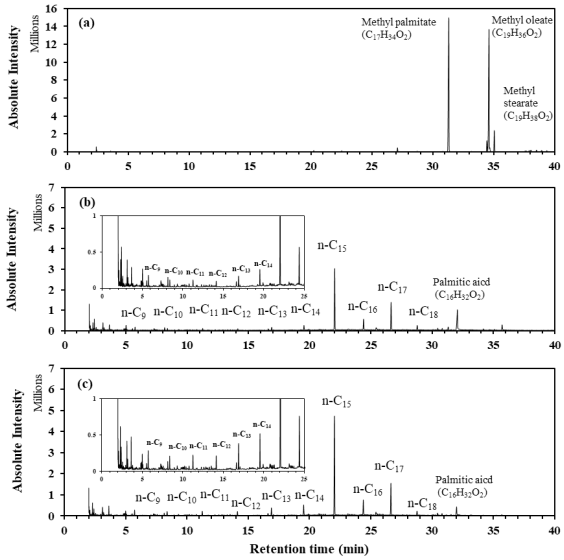

Figure 4 GC-MS chromatograms of (a) biodiesel and organic phase obtained from hydroconversion of biodiesel over (b) Ni/beta and (c) Ni0.4Gly/beta.

Table 3 Product distribution obtained from hydroconversion of biodiesel over different catalysts

Catalysts	Liquid yield (wt%)	Selectivity (%)			
		Bio-gasoline ($<C_9$)	Bio-jet (C_9-C_{14})	Green diesel ($>C_{14}$)	Aqueous
Ni/beta	66.6	6.4	10.0	38.0	12.2
Ni0.4Gly/beta	67.6	5.9	13.4	37.4	10.9
Ni0.8Gly/beta	70.1	6.0	11.8	39.5	12.9

Table 4 Chemical compositions of organic phase obtained from hydroconversion of biodiesel over different catalysts

Catalysts	Selectivity (%)					
	n-alkane	iso-alkane	Cyclics	Aromatics	Oxygenated compounds	Unsaturated compounds
Ni/beta	49.7	11.0	3.9	11.8	21.2	2.5
Ni0.4Gly/beta	62.2	12.4	3.6	10.8	9.0	2.2
Ni0.8Gly/beta	70.9	14.7	1.9	7.0	2.9	2.6

4. CONCLUSION

This research enhanced Ni-based catalysts performace for bio-jet fuel production form hydroconversion of biodiesel operated in fixed-bed reactor by using glycine-assisted impregnation method. The effect of glycine:Ni molar ratio on the liquid yield and its compositions were also evaluated. The study showed that the size of the catalysts changed after increased glycine:Ni molar ratio to 0.8 (Ni0.8Gly/beta) because of the effect of flame temperature from combustion synthesis, which could affect the textural properties of the catalysts. The increase in D_{avg} and the decrease in the Ni particle size of glycine-assisted catalysts could enhance catalytic performance for hydroconversion of biodiesel; especially, in hydrodeoxygenation. For Ni0.4Gly/beta catalyst, oxygenated compounds decreased from 21.2% to 9.0%, which was higher than the system using Ni/beta catalyst. Moreover, bio-jet yield increased from 10.0% to 13.4 %. Moreover, the Ni0.8Gly/beta catalyst showed the better performance on hydrodeoxygenation, where oxygenated compounds decreased to 2.9% with 11.8% of bio-jet fuel.

ACKNOWLEDGMENTS

This research is funded by National Research Council of Thailand (NRCT, N42A670605) and Chulalongkorn University.

REFERENCES

1. I. Abrantes, A.F. Ferreira, A. Silva, M. Costa. Sustainable aviation fuels and imminent technologies - CO_2 emissions evolution towards 2050. *Journal of Cleaner Production* 2021; 313; 127937.
2. A.F.D. Center, Sustainable Aviation Fuel. https://afdc.energy.gov/ fuels/sustainable-aviation-fuel#:~:text=SAF%20can%20be%20produced%20from,%2Foils%2C%20and%20other%20feedstocks (accessed 5 Apr. 2025).
3. ICAO, Sustainable Aviation Fuels Guide, The International Civil Aviation Organization, 2018. https://www.icao.int/environmental-protection/knowledge-sharing/Docs/Sustainable%20Aviation%20Fuels%20Guide_vf.pdf (accessed 5 Apr. 2025).
4. J. Soone, Sustainable aviation fuels European Parliamentary Research Service, 2020. https://www.europarl.europa.eu/RegData/etudes/BRIE/2020/659361/EPRS_BRI(2020)659361_EN.pdf (accessed 5 Apr. 2025).
5. EIA, Biofuels are displacing petroleum-based distillate fuel oil consumption on the West Coast, 2023. https://www.eia.gov/todayinenergy/detail.php?id=57040 (accessed 29 Apr. 2025).
6. X. Li, Y. Wu, Q. Wang, S. Li, Y. Ye, D. Wang, Z. Zheng. Effect of preparation method of NiMo/γ-Al_2O_3 on the FAME hydrotreatment to produce C15–C18 alkanes. *Renewable Energy* 2022; 193; 1-12.
7. P. Chintakanan, T. Vitidsant, P. Reubroycharoen, P. Kuchonthara, T. Kida, N. Hinchiranan. Bio-jet fuel range in biofuels derived from hydroconversion of palm olein over Ni/zeolite catalysts and freezing point of biofuels/Jet A-1 blends. *Fuel* 2021; 293; 120472.
8. H. Deldari. Suitable catalysts for hydroisomerization of long-chain normal paraffins. *Applied Catalysis A: General* 2005; 293; 1-10.
9. Y. Tan, W. Hu, Y. Du, J. Li. Species and impacts of metal sites over bifunctional catalyst on long chain n-alkane hydroisomerization: A review. *Applied Catalysis A: General* 2021; 611; 117916.
10. N. Amirkhanyan, S. Kharatyan, K. Manukyan, A. Aprahamian. Thermodynamics and kinetics of solution combustion synthesis: $Ni(NO_3)_2$ + fuels systems. *Combustion and Flame* 2020; 221; 110-119.
11. Y. Xu, Y. Wu, J. Li, S. Wei, X. Gao, P. Wang. Combustion-impregnation preparation of Ni/SiO_2 catalyst with improved low-temperature activity for CO_2 methanation. *International Journal of Hydrogen Energy* 2021; 46; 20919-20929.

12. J. Yang, X. Lu, C. Han, H. Liu, D. Gong, L. Mo, Q. Wei, H. Tao, S. Cui, L. Wang. Glycine-assisted preparation of highly dispersed Ni/SiO_2 catalyst for low-temperature dry reforming of methane. *International Journal of Hydrogen Energy* 2022; 47; 32071-32080.
13. Y. Yang, Y. Lyu, L. Zhao, W. Zhan, L. Fan, F. Li, X. Liu. Ligand assistance via solid-state coordination for promoting nickel dispersion over the Ni/Beta hydroisomerization catalyst. *Fuel* 2022; 318; 123568.
14. M.H. Jordão, V. Simões, D. Cardoso. Zeolite supported Pt-Ni catalysts in n-hexane isomerization. *Applied Catalysis A: General* 2007; 319; 1-6.
15. A. Penkova, S. Dzwigaj, R. Kefirov, K. Hadjiivanov, M. Che. Effect of the Preparation Method on the State of Nickel Ions in BEA Zeolites. A Study by Fourier Transform Infrared Spectroscopy of Adsorbed CO and NO, Temperature-Programmed Reduction, and X-Ray Diffraction. *The Journal of Physical Chemistry C* 2007; 111; 8623-8631.
16. W. Zhang, T. Wang, Y. Gao, Y. Xue, F. Li, C. Pang, J. Fu, X. Liu, Y. Lyu. Highly efficient Ni/Beta catalyst for one-step hydrodeoxygenation-isomerization of fatty acid ester to bio-jet fuel. *Fuel* 2025; 381; 133586.
17. Z. Zhang, J. Cheng, Y. Qiu, X. Zhang, J. Zhou, K. Cen. Competitive conversion pathways of methyl palmitate to produce jet biofuel over Ni/desilicated meso-Y zeolite catalyst. *Fuel* 2019; 244; 472-478.

Optimization of biodiesel synthesis from waste cooking oil by transesterification reaction

Sarun Phonpho[1], Sutthirat Wilaisai[1], Sanchai Pomunruan[1], Chariyaporn Thanyathippipat[2], Wasan Chokelarb[2], Pongsert Sriprom[1,*], Pornsawan Assawasaengrat[2]

[1] School of Food Industry, King Mongkut's Institute of Technology Ladkrabang, Bangkok 10520, Thailand
[2] Department of Chemical Engineering, School of Engineering, King Mongkut's Institute of Technology Ladkrabang, Bangkok 10520, Thailand
* Corresponding author: pongsert.sr@kmitl.ac.th

ABSTRACT

The optimum conditions for biodiesel production from waste cooking oil by transesterification reaction was investigated the four-factors determination by using the Box-Behnken experimental design were: Reaction temperature (45 to 65°C), Reaction time (60 to 120 min), Volume of methanol (15 to 45% by volume), and the amount of catalyst (1.0 to 1.5% by weight). The waste cooking oil used in this study had oleic acid as the major fatty acid and a free fatty acid (FFA) content of 2.81%. The optimum reaction condition was a temperature at 65°C, a reaction time of 120 min, the methanol of 33% by volume, and amount of catalyst of 1.0% by weight. The highest yield of 94.82% was obtained under the optimal condition. The biodiesel structure was characterized by Fourier Transform Infra-Red (FT-IR), and the biodiesel properties were measured viscosity at 40°C is 4.52 cSt, total acid number is 0.25 mg KOH/g, water content is 0.06% by weight, density at 15°C is 0.877 g/cm^3, and flash point is 180°C. The obtained properties were comparable to those of biodiesel standards an announcement from the Department of Energy Business. Therefore, it can be concluded that the conditions used for biodiesel synthesis from waste cooking oil in this study were optimal.

Keywords: Biodiesel; Transesterification reaction; Waste cooking oil

1. INTRODUCTION

The widespread use of vegetable oils for cooking, both in households and the food industry, has led to the generation of large amounts of waste cooking oil. In Thailand, waste cooking oil production is estimated at approximately 74 million liters per year [1], with the quantity expected to continue increasing alongside the expansion of the food service sector. Improper disposal methods, such as discharging waste cooking oil into drainage systems, can cause environmental problems including sewage blockages and water contamination, leading to long-term ecological impacts [2].

A sustainable solution for managing waste cooking oil is to convert it into biodiesel, a renewable and biodegradable energy source that produces lower emissions compared to conventional diesel. Biodiesel is typically produced through a transesterification reaction between triglycerides in the oil and a short-chain alcohol [3, 4], usually methanol, in the presence of a catalyst. This reaction produces fatty acid methyl esters (FAME), which constitute biodiesel, and glycerol as a by-product. Among various types of catalysts, sodium hydroxide (NaOH) is commonly used due to its low cost and high efficiency under mild operating conditions [5], [6].

However, producing biodiesel from waste cooking oil presents challenges due to the presence of high levels of free fatty acids (FFA) and moisture. These impurities can lead to saponification when using a base catalyst, resulting in lower biodiesel yields and complications in product separation and purification. Therefore, careful control and optimization of process parameters are essential to maximize yield and ensure product quality [7], [8], [9].

The production efficiency of biodiesel is influenced by several process variables, including reaction temperature, reaction time, volume of methanol, and the amount of catalyst. While many studies have traditionally focused on varying one factor at a time, this approach limits the understanding of interaction effects between variables [7], [8], [9].

This study investigates the combined effects of reaction temperature, reaction time, volume of methanol, and catalyst amount on biodiesel yield from waste cooking oil. The Box-Behnken Design (BBD), a type of Response Surface Methodology (RSM), was employed to systematically evaluate the individual and

interaction effects of these variables and to determine the optimal production conditions.

2. EXPERIMENTAL

2.1 Materials

Waste cooking oil obtained from school of food industry, KMITL, Thailand. Methanol (AR Grade, I.C.P. Chemicals, Thailand), Sodium Hydroxide (European distribution center, Belgium), and Sulfuric acid (Merck KGaA, 64271 Darmstadt, Germany).

2.2 Analytical methods

The synthesized biodiesel from waste cooking oil (WCO) was analyzed to determine its physicochemical properties and confirm the presence of functional groups. The following analytical techniques and instruments were used according to standardized methods:

2.2.1 Functional Group Analysis

Fourier Transform Infrared Spectroscopy (FTIR) was employed to identify the functional groups present in the biodiesel samples. The spectra were recorded using a Perkin Elmer FTIR spectrometer according to ASTM E412 standard. Samples were analyzed in the range of 4000–400 cm^{-1} with an appropriate resolution.

2.2.2 Viscosity

The kinematic viscosity of biodiesel was measured using a Cannon viscometer according to ASTM D445.

2.2.3 Density

Density was determined using a Metrohm digital density meter according to ASTM D1298.

2.2.4 Total Acid Number (TAN)

The acid value, which indicates the amount of free fatty acids in the biodiesel, was evaluated through titration according to ASTM D974.

2.2.5 Flash Point

Flash point was measured using a Petrotest flash point tester according to ASTM D93. The closed cup method was employed to determine the temperature at which the biodiesel vapor ignites upon exposure to a flame.

2.2.6 Moisture Content

Moisture content was analyzed using Karl Fischer titration with a Mettler Toledo moisture analyzer in compliance according to ASTM D6304. The method provided accurate quantification of water content in the biodiesel samples.

2.3 Experimental procedure

2.3.1 Waste cooking oil preparation

Waste cooking oil which has been used for food frying. The waste cooking oil was filtered by sieves to remove any suspended food particles and inorganic residues and followed by heating at 110 °C for water removal.

2.3.2 Biodiesel synthesis

A total of 250 mL of waste cooking oil was transesterified with methanol using NaOH as the catalyst. The amount of NaOH catalyst was added in the range of 1.0 to 1.5% by weight relative to the mass of the waste cooking oil. The reaction time was set between 60 and 120 min, while the reaction temperature was maintained within the range of 45 to 65°C. The volume of methanol was added in the range of 15 to 45% by volume relative to the volume of the waste cooking oil.

Following the reaction, the purification of biodiesel was carried out by separating the glycerol using a separating funnel. The biodiesel product was then washed with 1 wt.% sulfuric acid to remove the catalyst, followed by successive washing with distilled water until the washing water reached a neutral pH. After purification, the sample was heated at 110°C to remove any remaining water. Finally, the biodiesel yield was determined using Eq. (1) [10].

$$\text{Biodiesel yield (\%)} = \left(\frac{\text{Volume of biodiesel product}}{\text{Volume of waste cooking oil}}\right) \times 100 \quad (1)$$

2.4 Statistical analysis

The statistical design was selected to develop and optimize biodiesel production from waste cooking oil was the Box-Behnken Design (BBD) implemented using Minitab Statistical Software. This method was employed to evaluate the effects of four factors: reaction temperature, reaction time, volume of methanol, and amount of catalyst. Biodiesel yield was chosen as the response variable. The ranges and levels of the investigated variables are presented in Table 1.

The method was used to assess the influence of various factors within specified limit points (maximum and minimum values) for application purposes. Table 2 presents the results obtained from the different run orders and evaluated factors.

Table 1 Box-Behnken Design conditions for the operating factors.

Factors	Symbol code	Level	
		minimum	maximum
Temperature (°C)	X_1	45	65
Time (min)	X_2	60	120
The amount of catalysts (wt.%)	X_3	1	1.5
Volume of methanol (%v/v)	X_4	15	45

Table 2 Run Order of Box-Behnken Design for four-factors obtained from Minitab Statistical Software.

Run order	Factors			
	Temperature (°C)	Time (min)	The amount of catalysts (wt.%)	Volume of methanol (%v/v)
1	45	60	1.25	30
2	65	60	1.25	30
3	45	120	1.25	30
4	65	120	1.25	30
5	55	90	1.00	15
6	55	90	1.00	45
7	55	90	1.50	15
8	55	90	1.50	45
9	45	90	1.00	30
10	65	90	1.00	30
11	45	90	1.50	30
12	65	90	1.50	30
13	55	60	1.25	15
14	55	120	1.25	15
15	55	60	1.25	45
16	55	120	1.25	45
17	45	90	1.25	15
18	65	90	1.25	15
19	45	90	1.25	45
20	65	90	1.25	45
21	55	60	1.00	30
22	55	120	1.00	30
23	55	60	1.50	30
24	55	120	1.50	30
25	55	90	1.25	30
26	55	90	1.25	30
27	55	90	1.25	30

3. RESULTS AND DISCUSSION

3.1 Biodiesel production

The biodiesel was synthesized under conditions designed based on a Box-Behnken experimental design comprising a total of 27 runs. The process variables selected for biodiesel production included: reaction temperature in the range of 45 to 65°C, reaction time in the range of 60 to 120 min, Volume of methanol in the range of 15 to 45% by volume with respect to volume of the waste cooking oil, and the amount of catalyst in the range of 1.0 to 1.5% by weight with respect to mass of the waste cooking oil. The biodiesel yields, as shown in Table 3, ranged from 73% to 91%.

Table 3 Biodiesel yield from Box-Behnken Design.

Run order	Factors				Biodiesel yield
	Temperature (°C)	Time (min)	The amount of catalysts (wt.%)	Volume of methanol (%v/v)	
1	45	60	1.25	30	83
2	65	60	1.25	30	86
3	45	120	1.25	30	87
4	65	120	1.25	30	91
5	55	90	1.00	15	84
6	55	90	1.00	45	86
7	55	90	1.50	15	73
8	55	90	1.50	45	74
9	45	90	1.00	30	87
10	65	90	1.00	30	91
11	45	90	1.50	30	76
12	65	90	1.50	30	76
13	55	60	1.25	15	80
14	55	120	1.25	15	84
15	55	60	1.25	45	82
16	55	120	1.25	45	85
17	45	90	1.25	15	80
18	65	90	1.25	15	85
19	45	90	1.25	45	82
20	65	90	1.25	45	87
21	55	60	1.00	30	88
22	55	120	1.00	30	91
23	55	60	1.50	30	74
24	55	120	1.50	30	76
25	55	90	1.25	30	86
26	55	90	1.25	30	85
27	55	90	1.25	30	85

From the experimental data presented in Table 3, a regression model was developed to describe the relationship between the process variables and the biodiesel yield. The regression coefficients and their standard errors for the linear, quadratic, and interaction terms are summarized in Table 4. The analysis shows that several terms in the model exhibit statistically significant effects on biodiesel yield, as indicated by p-values less than 0.05 at a 95% confidence level.

The resulting quadratic regression model, expressed in coded units, is shown in Eq. (2):

$$\text{Biodiesel Yield (\%)} = 85.33 + 1.75X_1 + 1.75X_2 - 6.50X_3 + 0.833X_4 + 0.88X_1^2 + 0.38X_2^2 - 3.50X_3^2 - 2.75X_4^2 + 0.25X_1X_2 - 1.00X_1X_3 - 0.25X_2X_4 - 0.25X_2X_3 - 0.25X_3X_4 \quad (2)$$

where X_1 is the reaction temperature (°C), X_2 is the reaction time (min), X_3 is the amount of catalyst (NaOH, wt.%), and X_4 is the volume of methanol (%v/v).

The quality of the model was evaluated using statistical parameters. The R-squared (R^2) value was 98.32%, and the adjusted R-squared (Adj-R^2) was 96.36%, indicating that the model provides an excellent fit to the experimental data and is reliable for describing the biodiesel production process within the studied range.

Table 4 Regression Coefficient for Response Surface Analysis.

Term	Coefficients	Standard errors	T-Value	P-Value
Constant	85.333	0.587	145.30	0.000
X_1	1.750	0.294	5.96	0.000
X_2	1.750	0.294	5.96	0.000
X_3	0.833	0.294	2.84	0.015
X_4	-6.500	0.294	-22.14	0.000
X_1^2	0.875	0.440	1.99	0.070
X_2^2	0.375	0.440	0.85	0.411
X_3^2	-2.750	0.440	-6.24	0.000
X_4^2	-3.500	0.440	-7.95	0.000
X_{12}	0.250	0.509	0.49	0.632
X_{13}	-1.000	0.509	-1.97	0.073
X_{23}	-0.250	0.509	-0.49	0.632
X_{24}	-0.250	0.509	-0.49	0.632
X_{34}	-0.250	0.509	-0.49	0.632

S=1.01721, R^2=98.32%, Adj.R^2=96.36%

The two-dimensional contour plots were used to graphically represent the regression equation and analyze the interaction effects between variables on the biodiesel yield. As shown in Fig. 1A, the interaction between reaction temperature and time revealed that increasing both parameters simultaneously led to higher biodiesel yields, with the maximum yield achieved near 65 °C and 120 min. In Fig. 1B, the interaction between the volume of methanol and reaction temperature showed that a methanol volume around 30–35% v/v, combined with a high temperature, promoted higher yields; however, excessive methanol slightly decreased the yield due to the reverse reaction between methyl esters and glycerol. Fig. 1C demonstrates the interaction between reaction temperature and the amount of catalyst, where a moderate catalyst loading (approximately 1.0 wt.%) combined with elevated temperatures improved biodiesel production, while an excessive amount of catalyst led to soap formation, negatively affecting the yield. Finally, Fig. 1D shows the interaction between the volume of methanol and the amount of catalyst, indicating that balanced levels of methanol (30–35% v/v) and catalyst (1.0–1.25 wt.%) achieved the highest yields, whereas excessive amounts of both factors reduced the overall biodiesel yield. These findings emphasize the importance of optimizing key parameters to maximize biodiesel production efficiency.

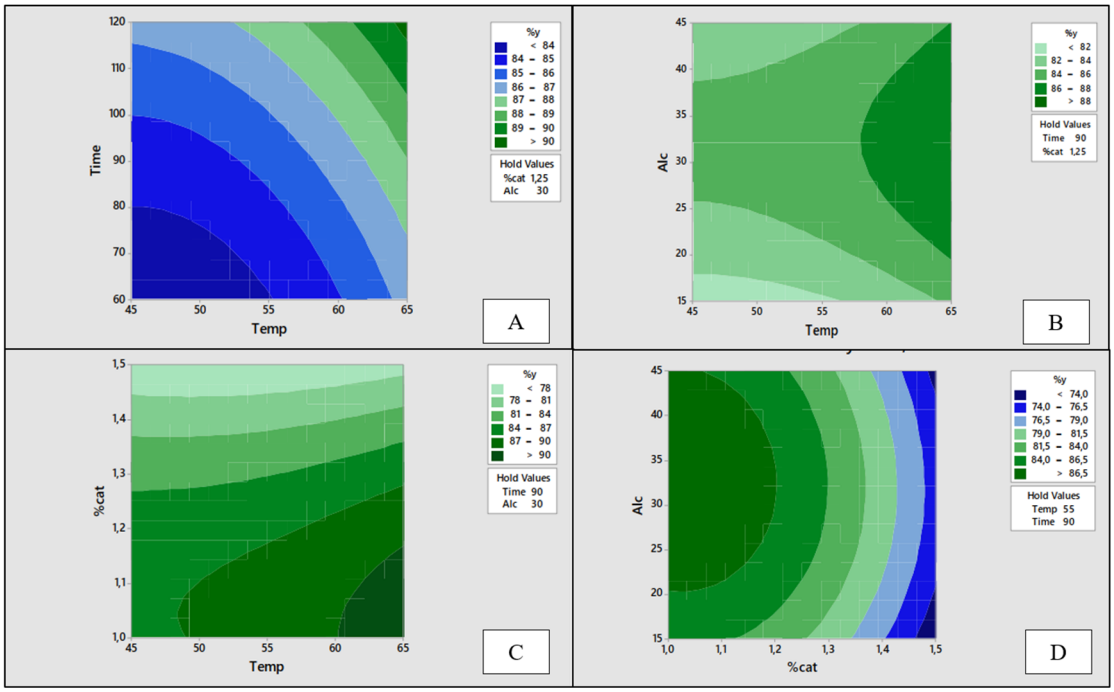

Figure 1A–D Contour plots showing the interaction effects of the four studied factors on biodiesel yield: (A) reaction temperature and time, (B) volume of methanol and reaction temperature, (C) reaction temperature and the amount of catalyst, and (D) volume of methanol and the amount of catalyst.

Fig. 2 shows the response optimizer analysis used to identify the optimal conditions for maximizing biodiesel yield from waste cooking oil. The optimal conditions were determined to be a reaction temperature of 65 °C, a reaction time of 120 min, a volume of methanol of 33% (v/v), and an amount of catalyst of 1 wt.%. Under these conditions, the model predicted a biodiesel yield of approximately 94.64%.

To validate the predicted result, five replicate experiments were conducted under the identified optimal conditions. As summarized in Table 5, the biodiesel yields obtained ranged from 93.5% to 96.0%, with an average yield of 94.82%, which closely matched the predicted value of 94.64%. This close agreement demonstrates the accuracy of the model prediction and confirms that the selected conditions effectively maximize the biodiesel yield.

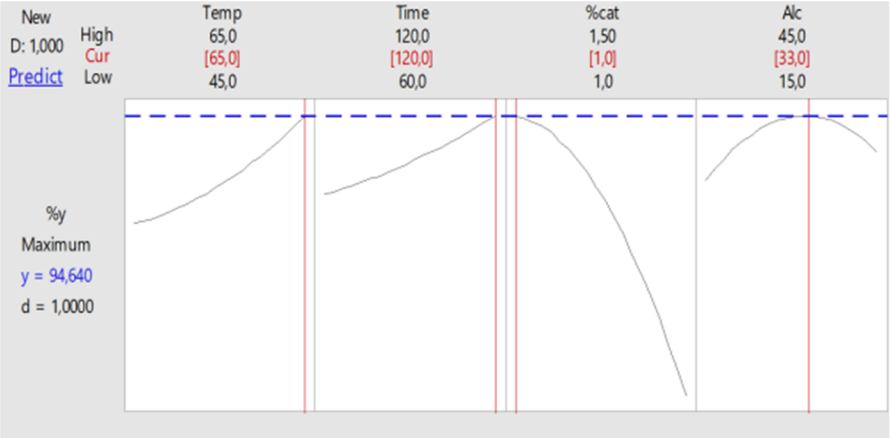

Figure 2 Response optimizer plot showing the optimal transesterification conditions for maximizing biodiesel yield from waste cooking oil.

Table 5 Experimental validation results for biodiesel yield under the optimized transesterification conditions.

Repeat	Temperature (°C)	Time (min)	The amount of catalysts (wt.%)	Volume of methanol (%v/v)	Biodiesel yield (%)
1	65	120	1	33	96
2	65	120	1	33	93.5
3	65	120	1	33	94
4	65	120	1	33	95.6
5	65	120	1	33	95
Average of Biodiesel yield					94.82

3.2 Biodiesel characterization

3.2.1 FTIR analysis

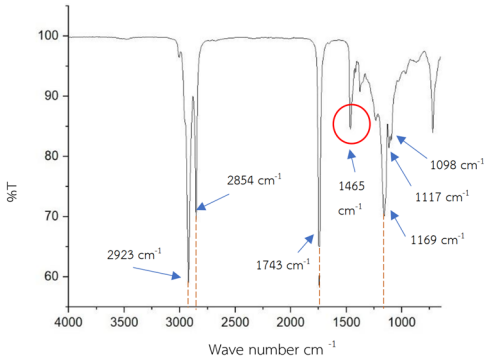

Figure 3 FTIR spectrum of waste cooking oil.

Fig. 3 shows the IR spectrum of waste cooking oil, where two main absorption bands were observed at 1743 and 1465 cm^{-1}, corresponding to carbonyl group (C=O stretching) and methylene group (CH_2 bending), respectively. In addition, a peak at around 1169 cm^{-1} was obtained, related to the antisymmetric and asymmetric axial stretching of C–O bond from ester group [11]. Finally, a band appeared at 1117 cm^{-1} and 1098 cm^{-1} can be attributed to C–O stretching of alcohol functional groups, which are typically found in the triglyceride structure of waste cooking oil.

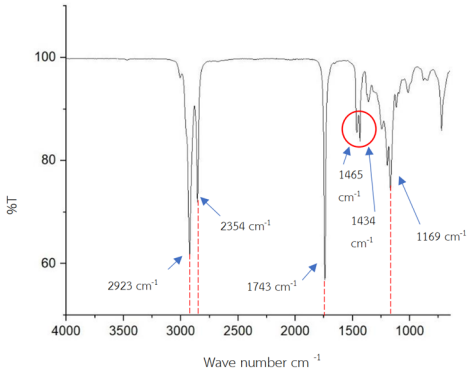

Figure 4 FTIR spectrum of biodiesel products.

Fig. 4 shows the IR spectrum of biodiesel produced from waste cooking oil. A strong absorption band was observed at 1743 cm^{-1}, corresponding to the carbonyl group (C=O stretching) of the ester functional group. A peak at 1169 cm^{-1} is associated with the antisymmetric and asymmetric axial stretching of the C–O bond, also attributed to the ester group. Moreover, two absorption bands appeared at 1465 cm^{-1} and 1434 cm^{-1}, which are assigned to the bending vibrations of the C–H bond from methylene (CH_2) and methyl (CH_3) groups, respectively. Compared to the IR spectrum of waste cooking oil, which showed only a single band at 1465 cm^{-1}, the additional peak at 1434 cm^{-1} suggests the formation of methyl groups. These methyl groups are formed through the transesterification reaction between triglycerides and methanol, indicating the successful production of methyl esters (biodiesel).

Table 6 Comparing the Chemical and Physical Properties of Biodiesel with the Biodiesel Standard according to the announcement from the Department of Energy Business.

Properties	Product-Biodiesel	Standard-Biodiesel [12]
Density at 15 °C (g/cm^3)	0.877	0.86-0.90
Viscosity @40°C, cSt	4.52	3.50-5.00
Water content (wt.%)	0.06	< 0.05
Total acid number, mg KOH/g	0.25	<0.5
Flash Point (°C)	180	>120

3.2.2 Viscosity

Viscosity plays an important role in the atomization and injection of fuel into the combustion chamber. The viscosity of the biodiesel sample at 40°C was measured using a Viscometer following ASTM D445. The results from Table 6 indicated a viscosity of 4.52 cSt, which lies within the standard range of 3.50-5.00 cSt for biodiesel. Adequate viscosity is essential to ensure efficient spray and combustion; excessively high viscosity can lead to incomplete atomization, while excessively low viscosity can result in fuel leakage and insufficient lubrication within the engine.

3.2.3 Density

Density is a critical property for evaluating the combustion characteristics of biodiesel in engines. The density of the biodiesel sample was measured using a Density Meter following ASTM D1298. According to the results shown in Table 6, the density at 15°C was found to be 0.877 g/cm^3, which falls within the acceptable range of 0.8600–0.9000 g/cm^3 for

commercial biodiesel. Proper density ensures optimal energy content per unit volume and affects engine performance during combustion.

3.2.4 Total Acid Number (TAN)

The total acid number of biodiesel indicates the amount of free fatty acids present in the sample, which arise from the degradation of triglycerides during the production process. The TAN was measured by titration following Table 6, the TAN of the biodiesel sample was found to be 0.25 mg KOH/g. According to biodiesel quality standards, the total acid number should not exceed 0.5 mg KOH/g to ensure oxidative stability during storage. In addition, a high TAN value indicates an increased concentration of free fatty acids, which can lead to corrosion of engine components during fuel use. Therefore, controlling the TAN within acceptable limits is essential for maintaining both the chemical stability of biodiesel and the durability of engine parts.

3.2.5 Flash Point

The flash point of biodiesel was measured using the Pensky-Martens Closed Cup method according to ASTM D93. The results in Table 6 indicated a flash point of 180°C, exceeding the minimum standard requirement of 120°C. Flash point is a critical safety parameter for storage and transportation. A low flash point could indicate residual methanol in biodiesel, which can reduce safety levels. To meet commercial standards, biodiesel should have a flash point greater than 100°C with residual methanol content below 0.2% by weight.

3.2.6 Moisture Content

The moisture content in biodiesel was determined using a Karl Fischer titrator according to ASTM D6304. As shown in Table 6, the moisture content was measured at 0.06%, which is slightly higher than the standard but still considered acceptable. Excessive moisture can promote hydrolysis reactions leading to the formation of free fatty acids and soap, causing degradation of biodiesel quality. It can also encourage microbial growth in the fuel system, negatively affecting fuel stability during storage.

4. CONCLUSION

In this study, biodiesel was successfully produced from waste cooking oil through a transesterification reaction using sodium hydroxide (NaOH) as a catalyst. The effects of four key process variables: reaction temperature, reaction time, volume of methanol, and amount of catalyst on biodiesel yield were systematically investigated using the Box-Behnken Design (BBD), and the analysis revealed that all four variables significantly influenced the biodiesel yield. Optimization using response surface methodology identified the optimal conditions as a reaction temperature of 65 °C, a reaction time of 120 min, a volume of methanol of 33% (v/v), and an amount of catalyst of 1 wt.%, with a predicted biodiesel yield of 94.64%. Experimental validation under these optimized conditions resulted in an average biodiesel yield of 94.82%, closely matching the predicted value and confirming the accuracy of the developed model.

The produced biodiesel was characterized using Fourier Transform Infrared (FTIR) spectroscopy, which confirmed the formation of fatty acid methyl esters through the appearance of characteristic functional groups. Additionally, the physicochemical properties of the biodiesel, including viscosity, density, acid value, moisture content, and flash point, were found to comply with ASTM standards, indicating that the biodiesel produced from waste cooking oil possesses suitable quality for use in diesel engines. Overall, this study demonstrates the feasibility of utilizing waste cooking oil as a raw material for biodiesel production and highlights the importance of process optimization in achieving both high yields and ensuring the structural and quality integrity of the product.

ACKNOWLEDGMENTS

This work was supported by the School of Engineering, King Mongkut's Institute of Technology Ladkrabang (KMITL), which provided essential facilities, equipment, and technical support throughout the course of this research. Their contribution was instrumental in ensuring the successful completion of this project.

REFERENCES

[1] Energy Policy and Planning Office, Ministry of Energy, Thailand. "Biodiesel: Energy for Sustainable Life" 2007. [Online] Available: https://www.eppo.go.th/images/Infromation_service/Publication/Book/Biodiesel.pdf.

[2] Naruemon Intarat. Ethyl ester production from high free fatty acid mixed crude palm oil by two-stage circulation process using static mixer. M.Eng. thesis, Faculty of Engineering, Prince of Songkla University, Songkhla, Thailand, 2016.

[3] Encinar, J. M., Nogales, S., and González, J. F. Biodiesel and biolubricant production from different vegetable oils through transesterification. *Engineering Reports* 2020; 2(12): e12190.

[4] Freedman B. E. H. P. Pryde, E. H. & Mounts T. L. Variables affecting the yields of fatty esters from transesterified vegetable oils. *Journal of the American Oil Chemists Society* 1984; 61(10): 1638-1643.

[5] M.U.H. Suzihaque, Nur Syazwina, Habsah Alwi, Ummi Kalthum Ibrahim, Sureena Abdullah, Normah Haron. A sustainability study of the processing of kitchen waste as a potential source of biofuel: Biodiesel production from waste cooking oil (WCO). *Materials Today: Proceedings* 2022; 63(1): S484-S489.

[6] Kedir D. Mekonnen and Zenamarkos B. Sendekie. NaOH-Catalyzed Methanolysis Optimization of Biodiesel Synthesis from Desert Date Seed Kernel Oil. *ACS Omega* 2021; 6: 24082−24091.

[7] Francis J. Sprules, Arlington, N.J. and Donald Price, New York, N.Y. Production of fatty acids. *US Patent* 1950.

[8] B. Freedman, E. H. Pryde, and T. L. Mounts. Variables affecting the yields of fatty esters from transesterified vegetable oils. *Journal of the American Oil Chemists Society* 1984; 6: 1638-1643.

[9] A.S. Ramadhas, S. Jayaraj, and C. Muraleedharan. Production from high FFA rubber seed oil. *Fuel* 2005; 84 (4): 335-340.

[10] Negasa Tesfaye Tefera, Ramesh Babu Nallamothu, Getachew Alemayehu Lakew, Teshome Kumsa Kurse. Optimization of biodiesel production from cotton-seed oil using response surface methodology and artificial neural network techniques. *Scientific African* 2025; 28: e02665.

[11] Sergio Nogales-Delgado, Jos´e María Encinar, Alvaro ´ Gonzalez ´ Cort´es. High oleic safflower oil as a feedstock for stable biodiesel and biolubricant production. *Industrial Crops & Products* 2021; 170.

[12] Department of Energy Business. “Notification on quality specification of biodiesel” 2019. [Online] Available: https://www.ratchakitcha.soc.go.th/DATA/PDF/2562/E/264/T_0004.PDF.

Methane dry reforming of calcium carbonate from carbamate mineralization

Nattanan Watcharasawat[1], Varong Pavarajarn[1,*]

[1] Center of Excellence in Particle and Materials Processing Technology, Department of Chemical Engineering, Faculty of Engineering, Chulalongkorn University, Bangkok 10330, Thailand
[*] Corresponding author: varong.p@chula.ac.th

ABSTRACT

To address the dual challenges of carbon dioxide (CO_2) emissions and efficient utilization of captured CO_2, this study investigates the integration of chemical absorption-mineralization with dry reforming of methane (DRM) using a Ni-$CaCO_3$ catalyst. CO_2 was first captured using a monoethanolamine (MEA) solution and subsequently mineralized with $CaCl_2$ to form $CaCO_3$. The resulting $CaCO_3$ was impregnated with nickel nitrate to synthesize a DRM catalyst. Upon exposure to CH_4, the Ni-$CaCO_3$ catalyst was converted to Ni-CaO and generating syngas (H_2 and CO). The spent Ni-CaO was then reused in a subsequent mineralization cycle, completing a closed-loop process. Each cycle demonstrated effective CO_2 sequestration and syngas production, with minor reductions in CO_2 removal capacity likely due to carbon deposition. Structural analyses using TEM and XRD confirmed reversible transformations between $CaCO_3$ and CaO, as well as stable dispersion of Ni particles. The integration of absorption-mineralization and DRM offers a promising route for carbon capture, utilization, and hydrogen-rich fuel production with potential for energy and cost savings.

Keywords: Integrated absorption-mineralization (IAM); Dry reforming of methane (DRM); Nickel-calcium carbonate (Ni-$CaCO_3$) catalyst; Looping of calcium carbonate

1. INTRODUCTION

One of the primary global environmental concerns today is the reduction of carbon dioxide (CO_2) emissions. According to the 2023 IPCC report [1], CO_2 emissions have already contributed to a 1.1°C rise in global surface temperatures compared to pre-industrial levels (1850-1900), with the rate of increasing temperature accelerating. This has caused significant changes in the atmosphere, oceans, cryosphere, and biosphere, leading to considerable damage to both nature and human populations. In response to climate change and global warming, members of the United Nations Framework Convention on Climate Change (UNFCCC) agreed to the Paris Agreement, which was further reinforced at COP26 in Glasgow, where 200 countries committed to achieving carbon neutrality and net-zero emissions by 2050 and 2060, respectively [2].

To meet these targets, Carbon Capture, Utilization, and Storage (CCUS) technologies have emerged as a key strategy for mitigating CO_2 emissions [3]. CCUS technologies directly capture CO_2 from emission sources, which can then be stored in deep geological formations or utilized in various applications such as chemical production or enhanced oil recovery. As CCUS presents significant economic potential by converting CO_2 waste into valuable products, many studies have focused on improving its efficiency and cost-effectiveness [4].

Among the various CCUS technologies, chemical absorption is one of the most mature and widely used methods. It has been employed in industries such as fertilizer production, cement manufacturing, and power generation. The most used chemical absorption methods are based on ethanolamine (MEA), diethanolamine (DEA), and N-methyl-diethanolamine (MDEA) [5]. The interaction between primary and secondary amines with CO_2 is widely acknowledged to follow the "zwitterionic" mechanism. This process involves the initial formation of a zwitterion as the amine reacts with CO_2, which subsequently interacts with another amine molecule to generate protonated amines and carbamate ions [20].

$$R\text{-}NH_2 + CO_2 \leftrightarrow R\text{-}NH_2^+COO^- \quad (1)$$

$$R\text{-}NH_2 + R\text{-}NH_2^+COO^- \leftrightarrow R\text{-}NH^+COO^- + R\text{-}NH_3^+ \quad (2)$$

$$2R\text{-}NH_2 + CO_2 \leftrightarrow R\text{-}NH_2^+COO^- + R\text{-}NH_3^+ \quad (3)$$

The mechanism shows that theoretically the CO_2 absorption of primary and secondary amine solutions should be 0.5 mol CO_2/mol amine, but because hydrolysis reactions of some of the carbamates will occur at higher CO_2 absorptions, as shown in Eq. 4, free amines and bicarbonates are produced. Therefore, the CO_2 absorption of primary and secondary amines can sometimes be slightly higher.

$$R\text{-}NH^{+}COO^{-} + H_2O \leftrightarrow R\text{-}NH_2 + HCO_3^{-} \quad (4)$$

While these methods offer advantages such as technological maturity, high CO_2 selectivity, rapid absorption rates, and ability to regenerate [6], they also have significant drawbacks. Specifically, the desorption process requires high temperature (around 120°C), which is energy-intensive, costly, and also results in CO_2 emissions contradicting environmental goals. High temperature can also cause corrosion of equipment and degradation of amines, further increasing costs [7]. Moreover, compressing and transporting the captured CO_2 for storage is energy-consuming and raises safety concerns. To address these challenges, mineralization technology has been proposed as a solution to reduce both costs and energy consumption [8].

Mineralization mimics the natural rock weathering process, where carbonic acid from dissolved CO_2 neutralizes noncarbonate minerals to form stable carbonates [9]. Carbonation reactions can occur at moderate temperature and release significant amount of heat. By integrating the amine scrubbing process with mineralization, the Integrated Absorption–Mineralization (IAM) process has been developed. This process leverages the rapid CO_2 absorption capabilities of amine solvents and the low energy requirements of CO_2 sequestration, converting CO_2 into stable carbonate solids [10]. As recent studies have been on using $CaCl_2$ as noncarbonate minerals, the precipitation of $CaCO_3$ via addition of $CaCl_2$ in primary and secondary amine was achieved by the following reactions.

$$R\text{-}NHCOO^{-} + H^{+} + H_2O \leftrightarrow HCO_3^{-} + R\text{-}NH_3^{+} \quad (6)$$

$$2HCO_3^{-} + 2R\text{-}NH_3^{+} + CaCl_2 \leftrightarrow Ca(HCO_3)_2 + 2R\text{-}NH_3Cl \quad (7)$$

$$Ca(HCO_3)_2 \leftrightarrow CaCO_3 + CO_2 + H_2O \quad (8)$$

However, the IAM process faces challenges relating to the calcium source. Previous studies have shown that the mineralization with calcium chloride ($CaCl_2$) fails to regenerate the amine for recapturing of CO_2 [11]. The calcium carbonate ($CaCO_3$) produced using MEA, DEA, and MDEA is typically in the calcite phase [12], which is low-value. However, $CaCl_2$ is more expensive than $CaCO_3$ [13, 14], making this process economically unfeasible.

Recently, the combination of calcium looping (CaL) and DRM, termed calcium-looping dry reforming of methane (CaLDRM), was proposed [15]. The CO_2 is captured by CaO forming $CaCO_3$ in the first step, followed by the regeneration of CaO by a CH_4 stream, while the released CO_2 is converted by CH_4 into syngas as shown in Eq. 9, 10.

$$CaO + CO \leftrightarrow CaCO_3 \quad (9)$$

$$CaCO_3 + CH_4 \leftrightarrow CaO + 2H_2 + 2CO \quad (10)$$

The process has been studied by employing either a physical mixture of a CaO-based sorbent and a Ni-based catalyst or a bifunctional CaO-Ni material, however, the synthesized of Ni and CeO_2 nanoparticles co-loaded on ZrO_2-coated $CaCO_3$ instead of CaO has successfully drive CaLDRM cycles [16] indicating the possibility of using $CaCO_3$ as a support for Ni catalyst in DRM process.

The purpose of this research is to propose the looping of calcium carbonate in IAM and DRM. By combining the IAM process with the dry reforming of methane (DRM) using a Nickel-calcium carbonate (Ni-$CaCO_3$) catalyst. Using the $CaCO_3$ produced with IAM process, the $CaCO_3$ can then be regenerated to CaO, which can then be recycled as a calcium source for the mineralization process. Moreover, the H_2 and CO produced from DRM can serve as versatile raw materials for various chemicals, addressing the cost-efficiency issue of the IAM process demonstrating the feasibility of this integrated approach and its potential for further development.

2. EXPERIMENTAL

2.1 Materials

Monoethanolamine (MEA) solution was prepared using Ethanolamine (>99.5%; QReC Chemical Co., Ltd., Auckland, New Zealand). Calcium chloride dihydrate (>99%; KemAus, New South Wales, Australia) and Calcium hydroxide (>96%; QReC Chemical Co., Ltd., Auckland, New Zealand) were utilized as calcium source for the mineralization process. Nickel (II) nitrate hexahydrate (>97%; QReC Chemical Co., Ltd., Auckland, New Zealand) was used as the nickel precursor.

2.2 Materials characterization

The morphologies of catalyst as-prepared and spent were examined using a Transmission Electron Microscope (TEM; Talos F200X, Thermo Fisher Scientific, Massachusetts, USA), and the elemental distribution was analyzed by energy-dispersive spectroscopy (EDS). X-ray diffraction (XRD) analysis was performed on the materials using a powder X-ray diffractometer (D8 Discover; Bruker, Karlsruhe, Germany) equipped with Cu-Kα radiation, operating at 40 kV and 40 mA.

2.3 CO_2 absorption using MEA

A 99.5% CO_2 gas was introduced at a flow rate of 180 mL/min using a mass flow meter and pressure of 2 bar with a sparger into a 250 mL laboratory bottle that contained 5M MEA solution under constant stirring. The pH and temperature changes during the absorption were constantly monitored. The absorption was assumed to be complete when the pH and temperature monitored were stable. The outlet was connected to a

2.5 micrometer filter to prevent the vaporized solution from escaping the bottle.

2.4 Measurement of CO_2 loading in MEA solution

The CO_2 loading measurement was conducted by using 50 mL of deionized (DI) water mixed with 0.5 mL of CO_2-saturated amine solution in laboratory bottle, which was placed on a magnetic stirrer. With methyl orange as an indicator, the HCl solution with a concentration of 1M was added to the liquid sample from a burette until the solution turned red color. During the titration, CO_2 gas was released from the solution and displaced the colored fluid in the reservoir. The titrant volume and CO_2 gas displaced volume of color liquid was noted down and it is further used for calculating the CO_2 loading in Eq. 11.

$$\alpha = \frac{\frac{P(V_{gas} - V_{acid})}{RT}}{mol_{amine}} \quad (11)$$

where α is CO_2 loading (%), P is ambient pressure (Pa), V_{gas} is displaced volume of the colored fluid in the reservoir (L), V_{acid} is volume of HCl used during the titration (L), R is gas constant; 8,314 ($L \cdot Pa \cdot K^{-1} \cdot mol^{-1}$), T is temperature during the titration (K) and mol_{amine} is amine concentration (mol).

2.5 Mineralization of CO_2 using $CaCl_2$

The CO_2-absorbed MEA solution and a 5 M $CaCl_2$ solution were mixed at a 1:2 volume ratio and stirred continuously for 3 hours. The suspension was then centrifuged to separate the solid phase from the liquid. The CO_2 loading of liquid phase was measured the CO_2 loading by Chittick apparatus, and the remaining solid was collected and dried in an oven at 60 °C overnight to obtain the final product.

2.6 Dry Methane Reforming using Nickel-calcium carbonate (Ni-$CaCO_3$) catalyst

2.6.1 Ni-$CaCO_3$ catalyst preparation

Ni-$CaCO_3$ was prepared via Wet Impregnation method by dropping dissolved $Ni(NO_3)_2$ in DI water on $CaCO_3$ from mineralization process in ratio of 1:1 by mass and let dried in the oven overnight, achieving a $CaCO_3$:Ni weight ratio of 1:0.2, then grinded before using it as catalyst in methane reforming process.

2.6.2 Dry methane reforming process

Ni-$CaCO_3$ 0.15 g was used as catalyst in a fixed bed reactor with 95% N_2 and 5% CH_4 gas with flow rate of 200 ml/min using mass flow rate controller. The tube furnace was programmed to run a temperature-programmed test until 800° C. The outlet concentrations of reactants and products were quantified using a series of analyzers, including a CO_2 non-destructive infrared spectrometer (ND-IR; CI-IR 20; Chang-Ai, Shanghai, China), a CH4 ND-IR (CI-IR 10; Chang-Ai), a CO ND-IR (CI-IR 10; Chang-Ai), and a H2 thermal conductivity detector (TCD) analyzer (CI-TC 90; Chang-Ai).

2.7 Integrated Absorption–Mineralization and Dry Methane Reforming looping

After DRM reaction, the Ni-CaO product was used as calcium source to react with CO_2-saturated amine solution in 1:2 ratio by mol. Then, the solid and the solution were separated using centrifuge. The solid was characterized by using XRD and TEM to confirm the Ni-$CaCO_3$ formation. While the solution was measured of CO_2 loading using Chittick apparatus. Next, the solution was run in another cycle of absorption-mineralization and tested for CO_2 loading using Chittick apparatus, while the solid was used again in DRM then the gas and solid product were observed using ND-IR, TCD, XRD and TEM respectively to demonstrate the feasibility of the looping process.

3. RESULTS AND DISCUSSION

3.1 CO_2 absorption and mineralization

5M MEA solution with volume of 250 mL is saturated with CO_2 after 2 hours with pH of 7.96 and 57% CO_2 loading. The solid after mineralization is then characterized as calcite-phase calcium carbonate.

3.2 Dry Methane Reforming using Nickel-calcium carbonate (Ni-$CaCO_3$) catalyst

Temperature-programmed scanning tests to evaluate the catalytic performance of the mineralized material resulting from an integrated absorption-mineralization and dry reforming of methane loop is shown in Figure 1, Ni precursor decomposed to metallic Ni as the temperature increased, without requiring calcination to avoid decomposition of $CaCO_3$ at high temperatures. CO_2 started to be released from the material at ~630 °C, while methane dry reforming was initiated at ~670 °C as CH_4 concentration decreased while syngas concentration increased. The higher H_2 concentration to CO was due to methane cracking (Eq. 12).

$$CH_4 \rightarrow C + 2H_2 \quad (12)$$

CO_2 was directly released from the material without being converted due to weak interface of Ni in precursor form. Overall, the result showed the possibility of using mineralized material in DRM reaction.

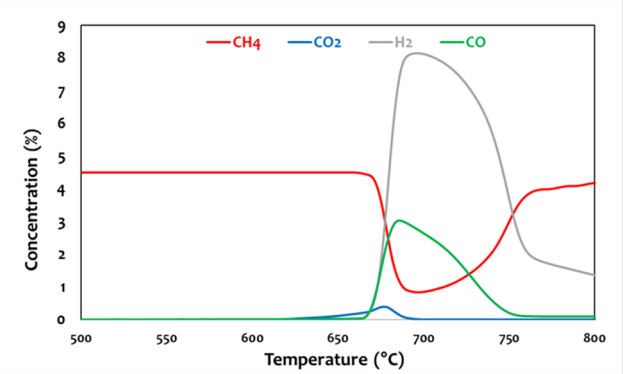

Figure 1 Gaseous concentration profiles during temperature-programmed catalytic performance test on first DRM step.

3.3 Integrated Absorption–Mineralization and Dry Methane Reforming looping

After the DRM process, the Ni-CaO was turned into Ni-$CaCO_3$ through mineralization. As per the CO_2 loading measurement method, the CO_2 removed from the CO_2-absorbed MEA solution is 4.8 $mmol_{CO2}/g_{catalyst}$ indicated that Ni-CaO from the DRM process can be used as a calcium source in an integrated absorption-mineralization and dry reforming of methane looping. Then, the Ni-$CaCO_3$ was subjected to another DRM cycle. The DRM initiated at ~550 °C, and no CO_2 was released from the catalyst as shown in Figure 2. As the Ni was already activated during the previous cycle, the initiated reaction temperature was lower than that in the previous cycle. However, methane cracking still occurred.

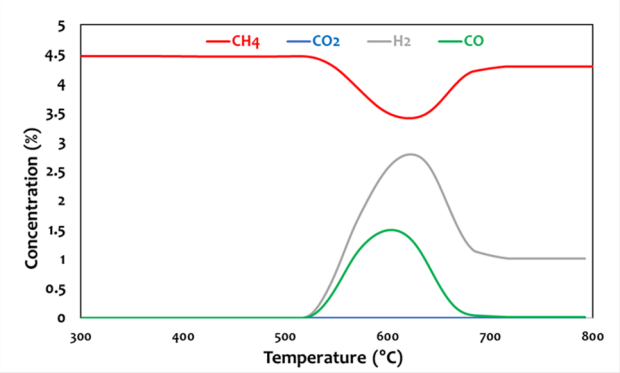

Figure 2 Gaseous concentration profiles during temperature-programmed catalytic performance test on second DRM step.

Mineralization was conducted again using Ni-CaO from the second DRM cycle. The CO_2 removed from the CO_2-absorbed MEA solution is 4.3 $mmol_{CO2}/g_{catalyst}$ which is lower than previous cycle likely due to the coke deposition from methane cracking.

The TEM image of the Ni-$CaCO_3$ after the first DRM step is shown in Figure 3a. The irregularity in morphology is due to the transformation of $CaCO_3$ into CaO with the incorporation of Ni and Ni sintering, while the presence of carbon existed due to methane cracking. After mineralization (Figure 3b), CaO was reconverted into $CaCO_3$ making Ni more distributed which caused the reaction temperature in the second DRM step to be lowered. After the second DRM step, the structural changes became more pronounced, with the CaO and carbon, while Ni sintering occurred again due to exposure to high temperature (Figure 3c).

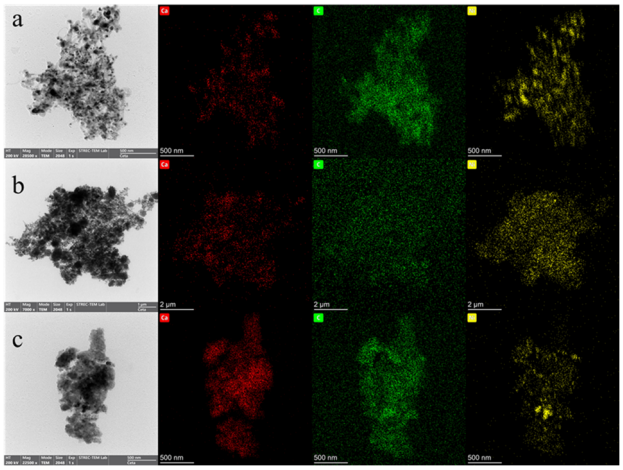

Figure 3 TEM-EDS images of the dual-functional material before and after temperature-programmed activity test. (a) Ni-CaO after first DRM step. (b) Ni-CaCO3 after mineralization. (c) Ni-CaO after the second DRM step.

As shown in Figure 4. The $CaCO_3$ from mineralization peaks was characterized as calcite phase ($d_{c,CaCO3}$ = 36.7 nm) and after DRM, the peak indicated the occurrence of CaO though $CaCO_3$ was not fully converted. $Ca(OH)_2$ ($d_{c,Ca(OH)2}$ = 8.6 nm), Ni ($d_{c,Ni}$ = 18.7 nm) and crystallize carbon peaks were also found. The presence of $Ca(OH)_2$ was due to the exposure of CaO to moisture, while the Ni peak confirmed the transformation of precursor to metallic form of Ni and carbon from methane cracking. After mineralization using CaO, all $Ca(OH)_2$ and CaO converted back to $CaCO_3$. After the second DRM step, $CaCO_3$ partially decomposed into CaO and $Ca(OH)_2$, while Ni still had same crystallites size of $d_{c,Ni}$ = 18.2 nm. Then, in the second mineralization step all of the catalysts convert to $CaCO_3$, however, vaterite phase has form which may be due to Ni metal induce on CaO.

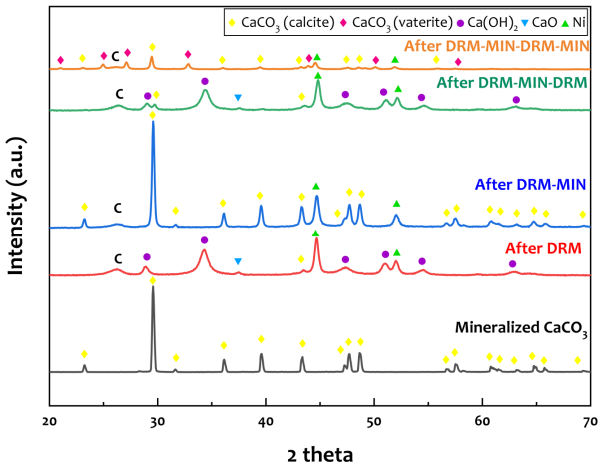

Figure 4 XRD pattern of the dual-functional material before and after temperature-programmed activity test.

4. CONCLUSION

This research demonstrates the feasibility and potential of combining integrated absorption–mineralization and dry reforming of methane (IAM-DRM) process for carbon capture and utilization. Using MEA for CO_2 absorption and $CaCl_2$ for mineralization effectively converted captured CO_2 into $CaCO_3$, which was then used to prepare a Ni-$CaCO_3$ catalyst for DRM. The catalyst enabled syngas generation at elevated temperatures (~670 °C) during the first DRM cycle, with H_2 production enhanced by methane cracking. Post-reaction Ni-CaO was successfully used in mineralization, confirming the recyclability of the calcium source. Notably, the second DRM cycle exhibited a lower initiation temperature (~550 °C), indicating effective Ni activation. Although a slight reduction in CO_2 absorption (from 4.8 to 4.3 $mmolCO_2/g_{catalyst}$) was observed in the second cycle, likely due to coke formation, the system remained operational with consistent catalyst structure and function. TEM and XRD analyses revealed the transformation between $CaCO_3$ and CaO phases, the formation of intermediate $Ca(OH)_2$ due to moisture exposure, and stable Ni dispersion with minor sintering. These findings highlight the potential of this looping strategy to reduce operational costs, minimize external resource inputs, and enhance CO_2 utilization efficiency. Future work should aim to optimize coke management and assess the long-term durability of the system under continuous looping conditions.

ACKNOWLEDGMENTS

The authors gratefully acknowledge the financial support provided by Center of Excellence in Particle Technology (CEPT), Chulalongkorn University. Special thanks are extended to the Department of Chemical Engineering, National Tsing Hua University, Hsinchu, Taiwan, R.O.C. for providing the analytical instruments and facilities used in this study.

REFERENCES

1. C. Méndez, N. Simpson, F. Johnson, and A. Birt, Climate Change 2023: Synthesis Report (Full Volume) Contribution of Working Groups I, II and III to the Sixth Assessment Report of the Intergovernmental Panel on Climate Change. 2023.
2. L. Chen, G. Msigwa, M. Yang, A. I. Osman, S. Fawzy, D. W. Rooney, and P.-S. Yap, "Strategies to achieve a carbon neutral society: a review," Environmental Chemistry Letters, vol. 20, no. 4, pp. 2277-2310, 2022/08/01 2022.
3. E. Hanson, C. Nwakile, and V. O. Hammed, "Carbon capture, utilization, and storage (CCUS) technologies: Evaluating the effectiveness of advanced CCUS solutions for reducing CO2 emissions," Results in Surfaces and Interfaces, vol. 18, p. 100381, 2025/01/01/ 2025.
4. Y. A. Alli et al., "Transforming waste to wealth: Harnessing carbon dioxide for sustainable solutions," Results in Surfaces and Interfaces, vol. 17, p. 100321, 2024/10/01/2024.
5. S. Davoodi, M. Al-Shargabi, D. A. Wood, V. S. Rukavishnikov, and K. M. Minaev, "Review of technological progress in carbon dioxide capture, storage, and utilization," Gas Science and Engineering, vol. 117, p. 205070, 2023/09/01/ 2023.
6. F. Meng, Y. Meng, T. Ju, S. Han, L. Lin, and J. Jiang, "Research progress of aqueous amine solution for CO2 capture: A review," Renewable and Sustainable Energy Reviews, vol. 168, p. 112902, 2022/10/01/ 2022.
7. B. Lv, B. Guo, Z. Zhou, and G. Jing, "Mechanisms of CO2 Capture into Monoethanolamine Solution with Different CO2 Loading during the Absorption/Desorption Processes," Environmental Science & Technology, vol. 49, no. 17, pp. 10728-10735, 2015/09/01 2015.
8. Y. Wang et al., "An Integrated Absorption–Mineralization Process for CO2 Capture and Sequestration: Reaction Mechanism, Recycling Stability, and Energy Evaluation," ACS Sustainable Chemistry & Engineering, vol. 9, no. 49, pp. 16577-16587, 2021/12/13 2021.
9. J. Li and M. Hitch, "Mechanical activation of magnesium silicates for mineral carbonation, a review," Minerals Engineering, vol. 128, pp. 69-83, 2018/11/01/ 2018.
10. M. Liu, H. Asgar, S. Seifert, and G. Gadikota, "Novel aqueous amine looping approach for the direct capture, conversion and storage of CO2 to produce magnesium carbonate," Sustainable Energy & Fuels, 10.1039/C9SE00316A vol. 4, no. 3, pp. 1265-1275, 2020.
11. J. M. Kang et al., "Energy-efficient chemical regeneration of AMP using calcium hydroxide for operating carbon dioxide capture process," Chemical Engineering Journal, vol. 335, pp. 338-344, 2018/03/01/ 2018.

12. M. Arti, M. H. Youn, K. T. Park, H. J. Kim, Y. E. Kim, and S. K. Jeong, "Single Process for CO2 Capture and Mineralization in Various Alkanolamines Using Calcium Chloride," Energy & Fuels, vol. 31, no. 1, pp. 763-769, 2017/01/19 2017.
13. Chemanalyst. "Calcium Chloride Price Trend and Forecast." https://www.chemanalyst.com/Pricing-data/calcium-chloride-1297 (accessed 10 January, 2025).
14. Chemanalyst. "Calcium Carbonate Price Trend and Forecast." https://www.chemanalyst.com/Pricing-data/calcium-carbonate-1158 (accessed 10 January, 2025).
15. S. Tian, F. Yan, Z. Zhang, and J. Jiang, "Calcium-looping reforming of methane realizes in situ CO2 utilization with improved energy efficiency," Science Advances, vol. 5, no. 4, p. eaav5077.
16. J. Hu, P. Hongmanorom, V. V. Galvita, Z. Li, and S. Kawi, "Bifunctional Ni-Ca based material for integrated CO2 capture and conversion via calcium-looping dry reforming," Applied Catalysis B: Environmental, vol. 284, p. 119734, 2021/05/05/ 2021.

Thermal oxidative reaction of Hydroxymethylfurfural (HMF) to bio-based monomer : 2,5 Furandicarboxylic Acid (FDCA)

Settakorn Upasen[1], Dang Saebea[1], Piyasan Praserthdam[2], Joongjai Panpranot[2], Piyachat Wattanachai[3], Patipan Boonruam[1], Pailin Ngaotrakanwiwat[1], Karaked Tedsree[4], Chaiwat Kanhari[3], Soipatta Soisuwan[1,*]

[1] Research Unit of Developing Technology and Innovation of Alternative Energy for Industries, Department of Chemical Engineering, Faculty of Engineering, Burapha University, Chonburi 20131, Thailand
[2] Center of Excellence in Catalysis and Catalytic Reaction Engineering, Department of Chemical Engineering, Faculty of Engineering, Chulalongkorn University, Patumwan District, Bangkok 10330, Thailand
[3] Department of Chemical Engineering, Faculty of Engineering, Burapha University, Chonburi 20131, Thailand
[4] Department of Inorganic Chemistry, Faculty of Science, Burapha University, Chonburi 20131, Thailand
[*] Corresponding author: soipatta@eng.buu.ac.th

ABSTRACT

Our experiment aims to use titanium dioxide alternatively under thermal excitation to apply an oxidative catalyst. A behavior of HMF (hydroxymethylfurfural) oxidation over three different titanium oxide-based catalysts, i.e., commercial titanium dioxide, black titanium dioxide, and black titanium dioxide modified with copper oxide, were investigated in a range of temperature (70 to 180 °C). According to the observation, the Power Law Model of HMF oxidation to FDCA(2,5 Furandicarboxylic acid) was proposed, and the activation energy for all catalysts was reported at 62.0, 28.4, and 12.3 kJ/mole. The black titanium dioxide modified with copper oxide catalyst was the most active at 70 °C, and it possessed the lowest activation energy and was selective to FFCA (5-Formyl-2-Furancarboxylic acid) (>90%), which approached the desired FDCA product.

Keywords: Titanium dioxide; Black titanium dioxide; Copper oxide doped titanium dioxide; HMF and FDCA

1. INTRODUCTION

Plastics are a material consisting of a wide range of organic compounds that were derived from the petrochemical industry, where processing and implementation can cause severe issues of global energy consumption, leading to consecutive problems, i.e., carbon dioxide emissions, which are highly impacted by the incrementation of greenhouse gases, global warming, and climate change. Since the era of fossil fuel depletion is due soon, the exploitation of biomass to develop alternative renewable energy and materials is of interest. Bio-based plastic is a significant material of the era. A fossil-fuel derived monomer of polyethylene terephthalate (PET) is terephthalic acid (TPA: $C_6H_4(COOH)_2$), consisting of aromatic ring and delocalization of electrons inside, of which crystalline structures in polymer metrics are well-refined due to highly symmetric and planar structure which has π - π stacking, resulting in mechanical property and chemical stability sufficiently for practical applications so that it is popular worldwide and has been widely used; however, PET plastic takes a long period to decompose in an ecosystem and can cause plenty of waste and plastic pollution after utilization and disposal in landfills [1, 2], while as polyethylene furanoate (PEF) and polybutylene furanoate (PBF) are bio-based plastics of which monomer are 2,5 furan dicarboxylic acid (FDCA); the most potential substitute to fossil-fuel derived monomer (TPA) due to similarity of their structural, physical and chemical properties. The FDCA structure engages with one furan ring (4 carbon atoms aligned with one oxygen atom inside) and two carboxylic groups, as shown in Figure 1, compared to TPA. The structural alignment of FDCA is a loss of molecular packing due to the inherent angle of 129.4° between the carboxylates [3], contributing to an increase in flexible polymeric chain packing and improvement of elastic properties.

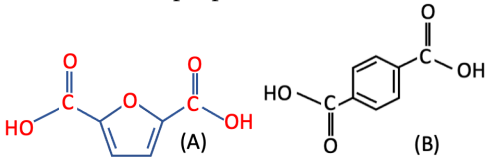

Figure 1: A comparative molecular structure of (A) 2,5

Furan dicarboxylic acid and (B) Terephthalic Acid Homogeneous and heterogeneous systems for FDCA production were reported in many publications. The investigation of homogeneous Co/Mn/Br in acetic medium, free-base system, with oxygen revealed that the starting period of oxidation was governed by reaction temperature. The step of oxidation FFCA to FDCA was a rate-determining step, while the first two oxidation steps were dependent on gas-liquid mass transfer limitation [4, 5]. The FDCA yields acquired from other heterogeneous systems were comparable to homogeneous systems; however, separating, purifying, and recycling were easy [6]. Noble metals, e.g., Pt [7], Pd [8, 9], Au [10-14], Ru [15-18], and bimetallic alloy [19-21] immobilized on various supports, tested at several conditions [22], i.e., differences in medium, temperature, and oxidizing agents, altered FDCA yields ranging from 30 to 99% including its derivatives; DFF (2,5 Diformylfuran), HMFCA, and FFCA. The development of non-noble metal catalysts, i.e., transition metals and transition metal compounds, has been researched for industrial applications [23-25]. Titanium dioxide has a good reputation as a catalyst for oxidation photocatalysis, which gives powerful superoxide oxygen or hydroxyl radical under UV to visible light radiation to oxidize organic compounds or elements, i.e., mercury [26-31], and it has been currently used for photocatalytic oxidation of HMF to FDCA or DFF. The home-prepared, single-phase titanium dioxide samples, i.e. anatase, rutile and brookite, which are predominantly amorphous, are selective toward FDCA more twice than that of commercial P25, which is well-crystallized catalyst under UV irradiation and the home prepared rutile catalyst is mostly selective to FDCA 25% [32]. The photocatalytic reaction is based on the creation of electron and hole pairs. The titanium-based catalysts were modified by gold and metal oxide (MO_x), i.e. Fe, Co, Ni, which can promote electron transfer and generate dual-active sites ($Au^{\delta-}$-O- Ti^{3+}) that facilitate hydroxyl group oxidation by superoxide radical species, yielded FDCA up to 71.2% under pressurized oxygen 2 MPa at 90°C [42], while the high selective oxidation of 5-hydroxymethyl furfural to 5-hydroxymethyl-2-furan carboxylic acid (HMFCA) using Ag-TiO_2 catalyst (96 % HMFCA yield) according to strong synergetic interaction between Ag+ and metallic Ag and TiO_2 for oxygen activation at 80°C [43]. The most outstanding up to date for photocatalytic reaction under sunlight irradiation is 64.5 mg $g_{catalyst}^{-1}$ h^{-1} of DFF over $(Cu_2O)_x||TiO_2$ in oxygen and water and without any additive and the selectivity of DFF was impacted by content of Cu_2O and crystalline phase of TiO_2, i.e. anatase and rutile, it was due to optimum strong interaction between Cu_2O and TiO_2 that can promote a generation of $^1O_2$ species on Cu_2O by O_2 activation to drive a reaction to DFF more selectively than HMF oxidation via holes which was able to destroy the furan ring in HMF molecule into CO_2 and H_2O [35, 36]. Recently, many types of photocatalytic reactions have been tested with titanium-based materials to evaluate the role of external energy [37-39]. The excessive temperature can cause heat loss and break chemical bond in the reaction system. This work aimed to identify appropriate temperature that requires for HMF oxidation in acetonitrile solution with TBHP (tert-butyl hydroperoxide) over three types of titanium-based catalysts, i.e. titanium dioxide Degussa P25, black titanium dioxide and black titanium dioxide modified with copper oxide. The main products of HMF oxidation were HMF, FFCA, HMFCA and FDCA.

2. EXPERIMENTAL

2.1 Chemicals

Commercial titanium dioxide Degussa P25 (78%, analytical purity) was purchased from AEROXIDE and was employed as a starting chemical for a preparation of black titanium dioxide. Sodium borohydride (98% analytical purity) was purchased from Fisher Scientific U.K. Limited, Copper (II) nitrate trihydrate, Sodium Carbonate (Na_2CO_3) and Tetrahydrofuran were purchased from Ajax Finechem Pty Ltd. 5-(Hydroxymethyl)furfural (5-HMF), Tert-butyl hydroperoxide (70% analytical purity) (TBHP), 5-hydroxymethyl-2-furancarboxylic acid (HMFCA), 2,5-Furandicarboxaldehyde (DFF), 5-Formyl-2-furoic acid (FFCA) and 2,5-Furandicarboxylic acid (FDCA) were purchased from Sigma-Aldrich Corporation. Acetonitrile (99% analytical purity) and Ammonium Acetate (98% analytical purity) were purchased from Daejung Chemical & Metal Co., Ltd. Oxygen (99.9%) and Nitrogen (99.9%) were supplied by Thai Industrial Gas.

2.2 Preparation of black titanium dioxide and black titanium dioxide modified with copper oxide.

Titanium dioxide Degussa P25 and sodium borohydride was physically mixed at a weight ratio of TiO_2:$NaBH_4$ equal to 0.5:2.5 [44] and the mixture was mounted into tubular in-house furnace under nitrogen gas continuously flowing at 30 ml/min. To decompose $NaBH_4$, gradually release H_2 for reduction white titanium dioxide, the temperature was ramped to 400°C and held for 6 hours. After cooled down to room temperature, black solid mixed oxide was removed from the furnace and mixed with deionized water 10 ml. The resulting black solid was washed by de-ionized water to remove hydroxide until a pH of supernatant solution was constant approximately at 8. The resulting black solid was dried at 100°C for 24 hours and it was renamed as Black TiO_{2-x}. Copper (II) nitrate trihydrate was 0.0872 gram was dissolved in 10-ml de-ionized water and then slightly mixed with 2.2659 gram of Black TiO_{2-x} powder to obtain 1.25 wt% loaded on Black TiO_{2-x}. The resulting powder was dried at 100oC for 12 hours and then calcined at 650°C for 6 hours.

2.3 Oxidation of HMF

The HMF oxidation was carried out in a batch reactor, a 100-ml Teflon reactor fixed in a closed stainless-steel autoclave putting in a sand bath on a hot plate stirrer. Temperature of the system was controllable and tunable in a range of 70 to 180°C. Acetonitrile was employed as a solvent in the reaction. The initial HMF concentration was started at 100 mM and 20-ml solution was added in the Teflon reactor. Since three oxidizing agents were used in our experiments, i.e., tert-butyl hydroperoxide. Tert-butyl hydroperoxide aqueous solution (70% wt) was added into the HMF solution. The molar ratio of TBHP and HMF was at 6:1. The catalyst 200 mg and sodium carbonate 40 mg were directly added into the solution per one batch. After well fitted Teflon reactor into stainless-steel autoclave, 4 bar of nitrogen gas was pressurized into the system in order to raise up the reaction temperature higher than the boiling points of solvents. The reaction was carried out for 2 hours. After the reaction ended, the supernatant was separated from the solid catalyst. The products and reactants in the resulting liquid were detected by High Performance Liquid Chromatography. Reactant (HMF) and products (FDCA and others) was determined by High Performance Liquid Chromatography (HPLC) system, Agilent Technology model 1260 Infinite II. Products were separated by a reversed-phase C18 column (Cosmosil, 5C18-AR-II, 4.6 ID x 250 mm) and detected by Photodiode array (PDA) at wavelength of 260 nm. The temperature of the reversed-phase column was maintained at 20°C. A buffer solution of ammonium acetate 50 mM adjusted pH to 5 by acetic acid mixed with acetonitrile (HPLC Grade) were employed as a mobile phase for gradient elution. Times of elution for gradient mobility of FDCA, HMFCA, FFCA, HMF, and DFF were located at 4.7, 5.3, 5.9, 9.4, and 10.3 minutes, respectively.

3. RESULTS AND DISCUSSION

3.1 Power Law Model of the oxidation of HMF to FDCA in Acetonitrile solution

Power Law Model of the oxidation of HMF to FDCA catalyzed by black titanium dioxide (Black TiO_{2-x})

$$\text{HMF} \xrightarrow{[TBHP]} \text{HMFCA} \xrightarrow{[TBHP]} \text{FFCA} \xrightarrow{[TBHP]} \text{FDCA} \quad (1)$$

$$3\,\text{HMF} + 6\,\text{TBHP} \rightarrow \text{HMFCA} + \text{FFCA} + \text{FDCA} \quad (2)$$

$$\text{Rate of reaction} = k\,[\text{HMF}]^n[\text{TBHP}]^m \quad (3)$$

$$\log(\text{Rate of reaction}) = n \log[\text{HMF}] + \log k.\,[\text{TBHP}]^m \quad (4)$$

$$\log(\text{Rate of reaction}) = m \log[\text{TBHP}] + \log k\,[\text{HMF}]^n \quad (5)$$

Power Law Models was chosen to simplify a prediction of the reaction rate of HMF oxidation on species concentration of reactants, i.e. [HMF]: HMF concentration and [TBHP]: TBHP concentration as shown in Equation (3). This algebraic equation relates the rate of reaction to species concentration called the kinetics expression or rate law. The exponents of concentrations are the reaction order which refers to the powers of concentration to raise the kinetic rate law. The reaction is an *n* order with respect to reactant HMF and *m* order with respect to reactant TBHP. The overall order of the reaction is *n* + *m*. The functional dependence on concentration may be postulated from theory, however; experiments are necessary to confirmed. The Power Law Model is dependent on concentration of reactant species; however, the catalytic reaction occurs at fluid-solid interface which is large interfacial area and steps of molecular adsorption and desorption on surface are almost always essential in significant reaction rate and surface reaction rate law is involved with either single- or dual-site mechanism and the surface reaction rate law is more complicated [46]. The k stands for rate constant at certain temperature, [HMF] is concentration of HMF (mM), [TBHP] is concentration of TBHP (mM), n and m parameters are the orders of HMF oxidation to FDCA corresponding to concentration of reactants, i.e., HMF and TBHP. The rate of reaction is in a molar change of HMF to HMFCA, FFCA and FDCA per one-minute and one-gram of catalyst. The oxidation of HMF to FDCA was taken a place in 3 steps of consecutive oxidations as shown in equation (1), i.e., the oxidation starts at a position of aldehyde group in HMF to HMFCA, and it subsequently oxidizes HMFCA to FFCA and ends with oxidation of FFCA to FDCA. The rate of reaction was calculated in corresponding with %total product yield of HMFCA, FFCA and FDCA. Table 1 exhibits data acquisition for prediction of parameters of Power Law Model of HMF oxidation to FDCA as shown in equation (2) and (3). The reaction was taken a place in magnetically stirred batch reactor under 4 bar nitrogen atmosphere and at temperature 120°C. The linear fitting lines in Figures 2(A) and 2(B) gave two valuable parameters of *n* and *m*. The valuable *n* parameter obtained from linear fitting line in Figure 2(A) is equal to 1.6212, while as the *m* parameter in Figure 2(B) is equal to 0.6985. The y-axis intersection in Figure 2(A) gave a solution of the rate constant equal to 9.61×10^{-5} $mM^{-1.3}\ h^{-1}$ kg $catalyst^{-1}$ and a solution of rate constant was obtained from the y-Axis intersection in Figure 2(B) is 12.9×10^{-5} $mM^{-1.3}\ h^{-1}$ kg $catalyst^{-1}$ which is approach to the rate from Figure 2(A) and the average rate constant is 11.26×10^{-5} $mM^{-1.3}\ h^{-1}$ kg $catalyst^{-1}$. All parameters were placed in the equation (3) shown as follows.

$$\text{Rate of reaction} = 11.26 \times 10^{-5}\,[\text{HMF}]^{1.6212}\,[\text{TBHP}]^{0.6985} \quad (6)$$

Whereas the rate of reaction is a change of HMF concentration in mM to the products per hour per kg catalyst, the rate constant = 11.26 x 10^{-5} $mM^{-1.3}$ h^{-1} kg $catalyst^{-1}$, the concentration of [HMF] and [TBHP] are in term of millimole per liter (mM).

3.2 Activation energy of titanium dioxide, black titanium dioxide and modified black titanium dioxide with copper oxide

The oxidation of HMF to FDCA and its derivative was carried out in systems of chosen-3 titanium oxide-based catalysts, i.e., Commercial titanium dioxide Degussa P25 (TiO_2), in house prepared black titanium dioxide (Black TiO_{2-x}) and modification of the in-house titanium dioxide catalyst coated with copper oxide 1.25% wt (Black TiO_{2-x} CuO). The experiment was set at an interval of temperature ranging from 70 to 180°C. The calculation of reaction rate was obtained from a yield of HMF oxidation to HMFCA, FFCA and FDCA and subsequently the Power Law Model was introduced to determine a rate constant at each temperature. Experimental data and calculations were determined in Table 2 and illustrated in Figures 3 to Figure 5. The yield of HMF oxidized to total products over TiO_2 and selectivity were independent on temperature in the range of temperature from 120 to 180°C as shown in Figure 3 and products were mostly selective towards HMFCA. The selectivity of FDCA was found only at 3-4%. At 180°C, the selectivity to HMFCA was the most dominated and there was no trace of FFCA, however, at this temperature, HMF was mostly found to decompose to other by-products more than 50% compared with the yield of HMF oxidation to FDCA and derivative. The behavior of HMF oxidation to FDCA by Black TiO_{2-x} and Black TiO_{2-x}_CuO were similar as shown in Figure 4(left) and 5(left). Neither trace of oxidation product nor others was found at temperature lower than 70°C where the oxidation was initially accelerated. Trace of other products, such as levulinic acid, 2-ketoglutalic acid, succinic acid, melaic acid, formic acid and fumaric acid were found, revealed the thermal oxidation of HMF to FDCA coincidently occurred with other different pathways and other route of reaction, possibly a cleavage of furan ring to other products or over oxidation [47, 48]. As demonstrated in Figure 3(left), 4(left) and 5(left), it was distinctive on Black TiO_{2-x} and Black TiO_{2-x} CuO, especially at temperature higher than > 120°C, while as TiO_2 gave the other products high up to 53% only at 180°C. The relation of rate constant and temperature as mentioned in the *Arrhenius Equation*. The equation, $k_A(T)=A\, e^{-E/RT}$, where A is the pre-exponential factor or frequency factor, E is activation energy (J/mol), R = gas constant = 8.314 J/(mol.K), and T is absolute temperature (K). The equation gives the temperature behavior of reaction rate constants, which is derived from *Collision Theory*. For atoms and molecules undergoing reaction, the molecules need energy to distort or stretch the bond to break and form a new bond or to overcome the steric and electron repulsion forces for reacting molecules to come close together. The overcome energy, which is identified as an energy barrier for a transfer of reacting molecules to products, is activation energy. According to postulation of Arrhenius equation, the experimental reactions which take a place at several different temperatures are used to determine the activation energy after taking the natural logarithm of the Arrhenius Equation as $\ln k_A = \ln A - \frac{E}{R}(\frac{1}{T})$. The activation energy becomes lower by a catalyst to differ reaction pathway and produce possible product. The activation energies of HMF oxidation to FDCA and its derivatives in a temperature range from 70 to 150°C or 180°C were derived from linear algebraic equations illustrated in Figure 6. The reactions were catalyzed by TiO_2 P25 Degussa, Black TiO_{2-x} and Black TiO_{2-x} CuO catalysts and differed in the activation energy at 62.0, 28.4 and 12.3 kJ/mol, respectively as shown in Table 2.

The TiO_2 P25 Degussa was inactive at low temperature, and it was more active at temperature ≥ 120°C, while Black TiO_{2-x} and Black TiO_{2-x} CuO catalysts were active at a lower temperature ≥ 100°C, leading TiO_2 to exhibit the highest activation energy at 62.0 kJ/mol. The Black TiO_{2-x} CuO catalyst was the most attractive since it considerably accelerated HMF to FFCA while as TiO_2 and Black TiO_{2-x} gave HMFCA largely, a first step of HMF oxidation product. Note that the more increase in temperature took a place, the more increased in products of oxygen ring cleavage, which was dominated extremely at high temperature, and has overcome the rate of HMF oxidation to FDCA, especially at 180°C as shown in Figures 3(left), 4(left) and 5(left).

Table 1 Data acquisition for prediction the parameters of Power Law Model of HMF oxidation to FDCA.

Concentration of HMF [HMF], mM	Concentration of TBHP [TBHP], mM	% Total yield	Rate of reaction (mM h^{-1} g $catalyst^{-1}$)	log (Rate of reaction)	log [HMF]
9.921	730	0	0	-	0.996
25.040	730	13.81	8.65	0.9369	1.399
50.000	730	59.80	74.76	1.8736	1.699
99.206	730	55.38	137.34	2.1378	1.999
158.730	730	48.00	190.48	2.2798	2.201
Concentration of TBHP [TBHP], mM	Concentration of HMF [HMF], mM	% Total yield	Rate of reaction (mM h^{-1} g $catalyst^{-1}$)	log (Rate of reaction)	log [TBHP]
730	99.206	8.75	21.71	1.3365	2.863
3651	99.206	26.25	65.09	1.8135	3.562
7301	99.206	58.23	144.42	2.1596	3.863
12734	99.206	55.38	137.34	2.1378	4.105

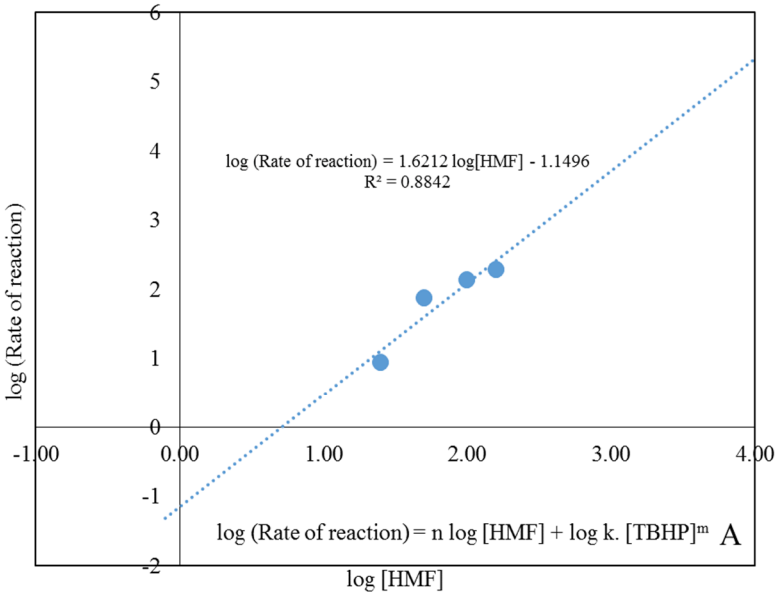

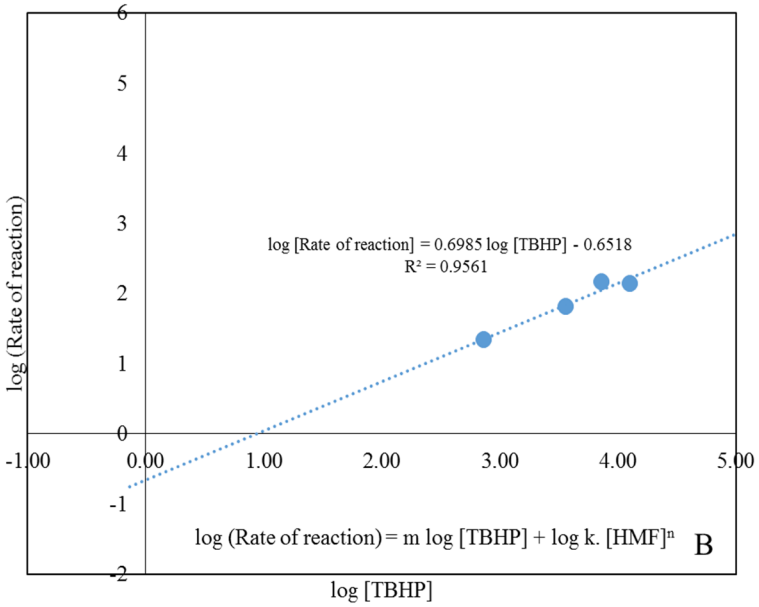

Figure 2(A) and **2(B)** demonstrates data fitting of the rate of oxidation reaction and starting concentration of reactants i.e. [HMF] and [TBHP]; concentration of TBHP for equation (4) and (5)

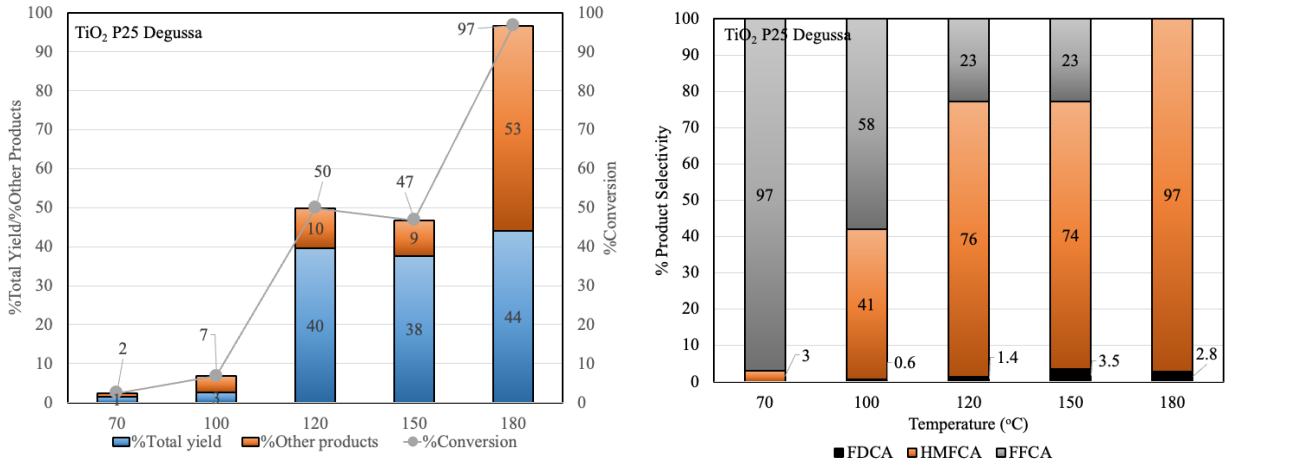

Figure 3 The oxidation yield to FDCA, FFCA, HMFCA and other products and %HMF Conversion (left) and % selectivity to HMF oxidation products (right) on TiO_2.

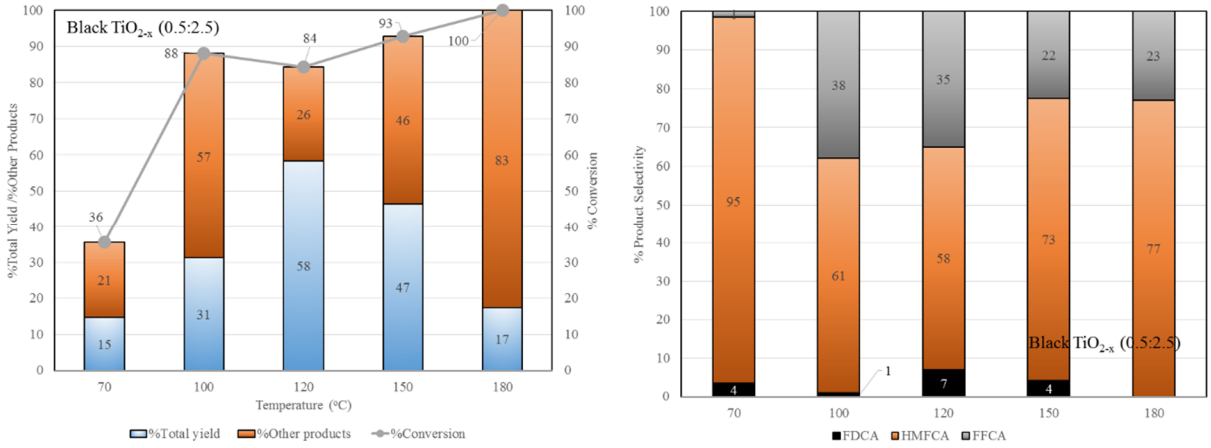

Figure 4 The oxidation yield to FDCA, FFCA, HMFCA and other products and %HMF Conversion (left) and % selectivity to HMF oxidation products (right) on Black TiO_{2-x} .

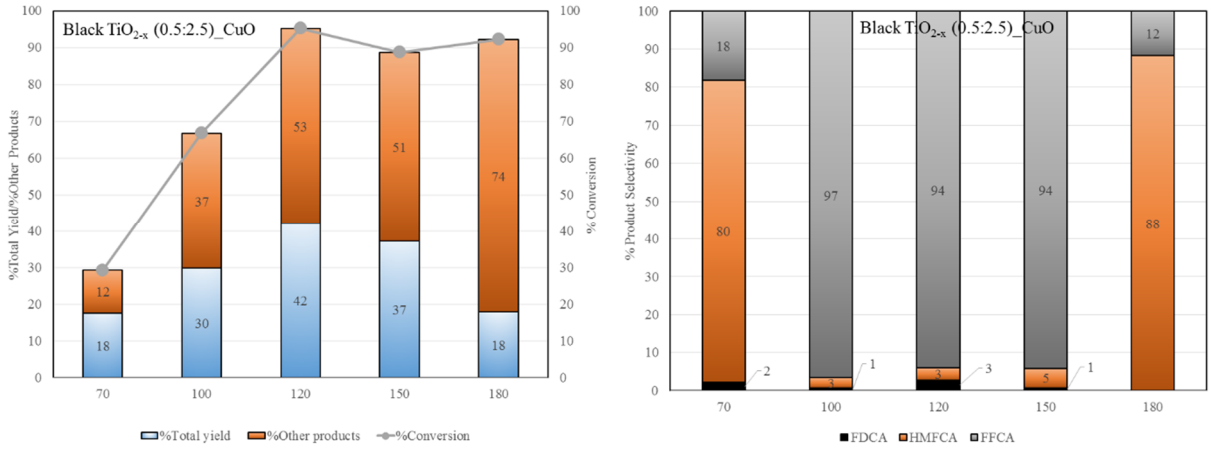

Figure 5 The oxidation yield to FDCA, FFCA, HMFCA and other products and %HMF Conversion (left) and % selectivity to HMF oxidation products (right) on Black TiO_{2-x} CuO.

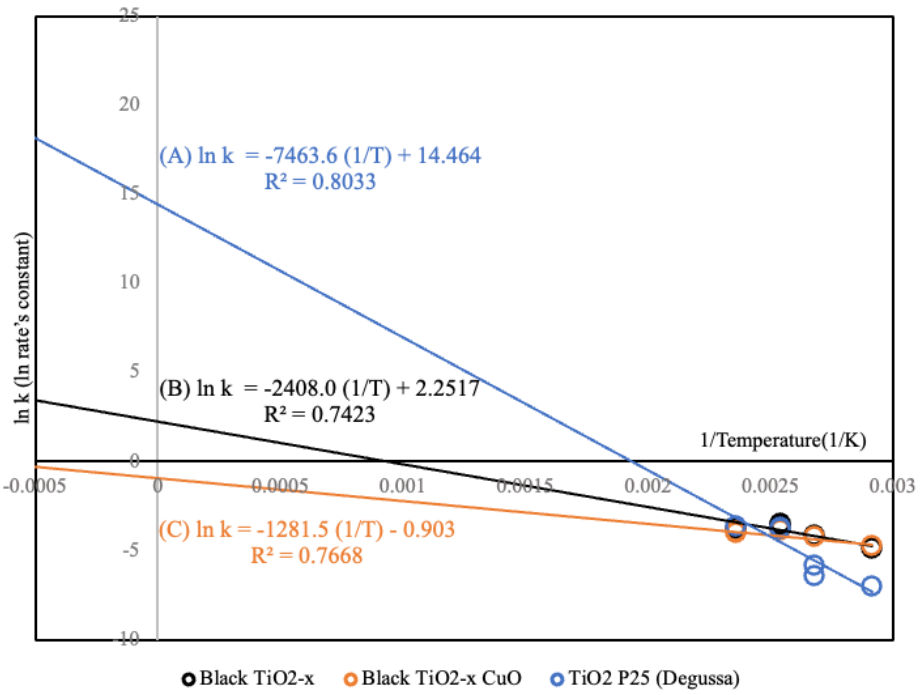

Figure 6 The temperature behaviors and the rate constant of (A) TiO_2, (B) Black TiO_{2-x} and (C) Black TiO_{2-x} CuO.

Table 2 Rate of reaction and rate's constant of oxidation of HMF to FDCA (initial concentration of HMF = 100 mM) and activation energy (kJ/mol)

Catalysts	Temperature (°C)	Rate of reaction (mM h^{-1} g $catalyst^{-1}$)	Rate's constant k = [rate of reaction]/ $[100\ mM]^{1.6}$	ln k	Activation Energy (Ea)(kJ/mol)
TiO_2(Degussa P25)	70	1.4	0.0008	-7.0582	62.0 (70 -180°C)
	100	3.4	0.0021	-6.1402	
	120	37.1	0.0234	-3.7547	
	150	35.3	0.0222	-3.8052	
	180	41.3	0.0260	-3.6479	
Black TiO_{2-x}	70	13.7	0.0071	-4.9479	28.4 (70-150°C)
	100	29.3	0.0148	-4.2133	
	120	54.6	0.0254	-3.5935	
	150	43.5	0.0220	-3.8164	
	180	16.3	0.0080	-4.8227	
Black TiO_{2-x}_CuO	8	0.0	-	-	12.3 (70-150°C)
	50	0.0	-	-	
	70	16.5	0.0085	-4.7655	
	100	27.8	0.0141	-4.2612	
	120	39.5	0.0199	-3.9127	
	150	34.8	0.0177	-4.0333	
	180	16.8	0.0085	-4.7656	

4. CONCLUSION

Power Law Model of HMF oxidation to FDCA was proposed and activation energy for all catalysts were calculated at 62.0, 28.4 and 12.3 kJ/mole. The thermal catalytic activity over three titanium-based catalysts may possibly relay on oxygen vacancy existing and reaction temperature. No trace of oxygen vacancy sites on titanium oxide Degussa P25, while black titanium dioxide consisted of oxygen vacancy with one electron and copper-modified black titanium dioxide consisted of doubly ionized oxygen vacancy. The HMF oxidation occurred on the catalysts composed of oxygen vacancy with one or two electrons existing are superior because the reaction initially activated at 70°C whereas titanium oxide Degussa P25 was inactive until the reaction temperature reaches to 120°C. The copper-modified black titanium dioxide catalyst was the most selective to FFCA (>90%), which is an approach to FDCA.

ACKNOWLEDGMENTS

The authors would like to give their gratitude to Burapha University, Thailand Science Research and Innovation, National Science Research and Innovation Fund (NSRF) (Fundamental Fund grant No.

43.2/2566), and the Research Promotion Team of Prof. Dr. Joongjai Panpranot. We thank the Research and Innovation Administration Division, Burapha University, for the Research Unit of Developing Technology and Innovation of Alternative Energy for Industries and our undergraduate students.

REFERENCES

[1] M. N. Miranda, M. J. Sampaio, P. B. Tavares, A. M. T. Silva, and M. F. R. Pereira, "Aging assessment of microplastics (LDPE, PET and uPVC) under urban environment stressors," *Science of The Total Environment*, vol. 796, p. 148914, 2021/11/20/ 2021, doi:

[2] F. Silvianti, D. Maniar, L. Boetje, and K. Loos, "Green Pathways for the Enzymatic Synthesis of Furan-Based Polyesters and Polyamides," in *Sustainability & Green Polymer Chemistry Volume 2: Biocatalysis and Biobased Polymers*, vol. 1373, (ACS Symposium Series, no. 1373): American Chemical Society, 2020, ch. 1, pp. 3-29.

[3] H. Kim *et al.*, "Remarkable elasticity and enzymatic degradation of bio-based poly(butylene adipate-co-furanoate): replacing terephthalate," *Green Chemistry*, 10.1039/D0GC01688H vol. 22, no. 22, pp. 7778-7787, 2020, doi: 10.1039/D0GC01688H.

[4] X. Zuo *et al.*, "Kinetics of homogeneous 5-hydroxymethylfurfural oxidation to 2,5-furandicarboxylic acid with Co/Mn/Br catalyst," *AIChE Journal*, vol. 63, no. 1, pp. 162-171, 2017/01/01 2017,

[5] K.-T. Li and S.-W. Li, "CoBr2-MnBr2 containing catalysts for catalytic oxidation of p-xylene to terephthalic acid," *Applied Catalysis A: General*, vol. 340, no. 2, pp. 271-277, 2008/06/01/ 2008

[6] M. Sajid, X. Zhao, and D. Liu, "Production of 2,5-furandicarboxylic acid (FDCA) from 5-hydroxymethylfurfural (HMF): recent progress focusing on the chemical-catalytic routes," *Green Chemistry*, 10.1039/C8GC02680G vol. 20, no. 24, pp. 5427-5453, 2018

[7] S. E. Davis, L. R. Houk, E. C. Tamargo, A. K. Datye, and R. J. Davis, "Oxidation of 5-hydroxymethylfurfural over supported Pt, Pd and Au catalysts," *Catalysis Today*, vol. 160, no. 1, pp. 55-60, 2011/02/02/ 2011.

[8] B. Siyo, M. Schneider, J. Radnik, M.-M. Pohl, P. Langer, and N. Steinfeldt, "Influence of support on the aerobic oxidation of HMF into FDCA over preformed Pd nanoparticle based materials," *Applied Catalysis A: General*, vol. 478, pp. 107-116, 2014/05/20/ 2014.

[9] S. Upasen, P. Boonruam, J. Panpranot, S. Soisuwan, and P. Praserthdam, "CATALYTIC ACTIVITY OF VANADIUM OXIDE DOPED WITH PALLADIUM NANOPARTICLES ON OXIDATION OF 5-HYDROXYMETHYLFURFURAL," 2021. ASEAN Engineering Journal, 10.2, 2020

[10] C. Megías-Sayago, A. Lolli, S. Ivanova, S. Albonetti, F. Cavani, and J. A. Odriozola, "Au/Al2O3 – Efficient catalyst for 5-hydroxymethylfurfural oxidation to 2,5-furandicarboxylic acid," *Catalysis Today*, vol. 333, pp. 169-175, 2019/08/01/ 2019

[11] L. Ardemani *et al.*, "Solid base catalysed 5-HMF oxidation to 2,5-FDCA over Au/hydrotalcites: fact or fiction?," *Chemical Science*, 10.1039/C5SC00854A vol. 6, no. 8, pp. 4940-4945, 2015

[12] T. Gao, T. Gao, W. Fang, and Q. Cao, "Base-free aerobic oxidation of 5-hydroxymethylfurfural to 2,5-furandicarboxylic acid in water by hydrotalcite-activated carbon composite supported gold catalyst," *Molecular Catalysis*, vol. 439, pp. 171-179, 2017/10/01/ 2017.

[13] N. K. Gupta, S. Nishimura, A. Takagaki, and K. Ebitani, "Hydrotalcite-supported gold-nanoparticle-catalyzed highly efficient base-free aqueous oxidation of 5-hydroxymethylfurfural into 2,5-furandicarboxylic acid under atmospheric oxygen pressure," *Green Chemistry*, 10.1039/C0GC00911C vol. 13, no. 4, pp. 824-827, 2011

[14] B. Sang, J. Li, X. Tian, F. Yuan, and Y. Zhu, "Selective aerobic oxidation of the 5-hydroxymethylfurfural to 2,5-furandicarboxylic acid over gold nanoparticles supported on graphitized carbon: Study on reaction pathways," *Molecular Catalysis*, vol. 470, pp. 67-74, 2019/06/01/ 2019.

[15] G. Yi, S. P. Teong, and Y. Zhang, "Base-free conversion of 5-hydroxymethylfurfural to 2,5-furandicarboxylic acid over a Ru/C catalyst," *Green Chemistry*, 10.1039/C5GC01584G vol. 18, no. 4, pp. 979-983, 2016.

[16] T. Gao, Y. Yin, W. Fang, and Q. Cao, "Highly dispersed ruthenium nanoparticles on hydroxyapatite as selective and reusable catalyst for aerobic oxidation of 5-hydroxymethylfurfural to 2,5-furandicarboxylic acid under base-free conditions," *Molecular Catalysis*, vol. 450, pp. 55-64, 2018/05/01/ 2018.

[17] F. Kerdi *et al.*, "Evaluation of surface properties and pore structure of carbon on the activity of supported Ru catalysts in the aqueous-phase aerobic oxidation of HMF to FDCA," *Applied Catalysis A: General*, vol. 506, pp. 206-219, 2015/10/05/ 2015

[18] F. Wang, Z. Yuan, B. Liu, S. Chen, and Z. Zhang, "Catalytic oxidation of biomass derived 5-hydroxymethylfurfural (HMF) over RuIII-incorporated zirconium phosphate catalyst," *Journal of Industrial and Engineering Chemistry*, vol. 38, pp. 181-185, 2016/06/25/ 2016, doi:

[19] A. Lolli *et al.*, "Insights into the reaction mechanism for 5-hydroxymethylfurfural oxidation to FDCA on bimetallic Pd–Au nanoparticles," *Applied Catalysis A: General*, vol. 504, pp. 408-419, 2015/09/05/ 2015

[20] H. Xia, J. An, M. Hong, S. Xu, L. Zhang, and S. Zuo, "Aerobic oxidation of 5-hydroxymethylfurfural to 2,5-difurancarboxylic acid over Pd-Au nanoparticles supported on Mg-Al hydrotalcite," *Catalysis Today*, vol. 319, pp. 113-120, 2019/01/01/ 2019

[21] T. Pasini *et al.*, "Selective oxidation of 5-hydroxymethyl-2-furfural using supported gold–copper nanoparticles," *Green Chemistry*, 10.1039/C1GC15355B vol. 13, no. 8, pp. 2091-2099, 2011.

[22] Z. Zhang and K. Deng, "Recent Advances in the Catalytic Synthesis of 2,5-Furandicarboxylic Acid and Its Derivatives," *ACS Catalysis*, vol. 5, no. 11, pp. 6529-6544, 2015/11/06 2015.

[23] E. Hayashi *et al.*, "Effect of MnO2 Crystal Structure on Aerobic Oxidation of 5-Hydroxymethylfurfural to 2,5-Furandicarboxylic Acid," *Journal of the American Chemical Society*, vol. 141, no. 2, pp. 890-900, 2019/01/16 2019.

[24] S. Soisuwan *et al.*, "Capability of single and double elements doped perovskite oxide catalysts in 5-hydroxymethyl furfural oxidation," *Biomass Conversion and Biorefinery*, 2022/12/23 2022.

[25] F. Neațu, R. S. Marin, M. Florea, N. Petrea, O. D. Pavel, and V. I. Pârvulescu, "Selective oxidation of 5-hydroxymethyl furfural over non-precious metal heterogeneous catalysts," *Applied Catalysis B: Environmental*, vol. 180, pp. 751-757, 2016/01/01/ 2016.

[26] A. H. Navidpour, S. Abbasi, D. Li, A. Mojiri, and J. L. Zhou, "Investigation of Advanced Oxidation Process in the Presence of TiO2 Semiconductor as Photocatalyst: Property, Principle, Kinetic Analysis, and Photocatalytic Activity," *Catalysts*, vol. 13, no. 2.

[27] J. Wang, J. Yu, X. Zhu, and X. Z. Kong, "Preparation of hollow TiO_2 nanoparticles through TiO2 deposition on polystyrene latex particles and characterizations of their structure and photocatalytic activity," *Nanoscale Research Letters*, vol. 7, no. 1, p. 646, 2012/11/24 2012.

[28] G. Snider and P. Ariya, "Photo-catalytic oxidation reaction of gaseous mercury over titanium dioxide nanoparticle surfaces," *Chemical Physics Letters*, vol. 491, no. 1, pp. 23-28, 2010/05/07/ 2010.

[29] E. Galata, E. A. Georgakopoulou, M.-E. Kassalia, N. Papadopoulou-Fermeli, and E. A. Pavlatou, "Development of Smart Composites Based on Doped-TiO_2 Nanoparticles with Visible Light Anticancer Properties," *Materials*, vol. 12, no. 16.

[30] D. A. Giannakoudakis *et al.*, "Ultrasound-assisted decoration of CuOx nanoclusters on TiO2 nanoparticles for additives free photocatalytic hydrogen production and biomass valorization by selective oxidation," *Molecular Catalysis*, vol. 514, p. 111664, 2021/09/01/ 2021.

[31] I. Krivtsov *et al.*, "Consequences of Nitrogen Doping and Oxygen Enrichment on Titanium Local Order and Photocatalytic Performance of TiO2 Anatase," *The Journal of Physical Chemistry C*, vol. 121, no. 12, pp. 6770-6780, 2017/03/30 2017.

[32] S. Yurdakal *et al.*, "Photocatalytic Selective Oxidation of 5-(Hydroxymethyl)-2-furaldehyde to 2,5-Furandicarbaldehyde in Water by Using Anatase, Rutile, and Brookite TiO2 Nanoparticles," *ACS Sustainable Chemistry & Engineering*, vol. 1, no. 5, pp. 456-461, 2013/05/06 2013.

[33] V. Augugliaro, M. Bellardita, V. Loddo, G. Palmisano, L. Palmisano, and S. Yurdakal, "Overview on oxidation mechanisms of organic compounds by TiO2 in heterogeneous photocatalysis," *Journal of Photochemistry and Photobiology C: Photochemistry Reviews*, vol. 13, no. 3, pp. 224-245, 2012/09/01/ 2012..

[34] A. Allegri *et al.*, "Photocatalytic Oxidation of HMF under Solar Irradiation: Coupling of Microemulsion and Lyophilization to Obtain Innovative TiO2-Based Materials," *Molecules*, vol. 25, no. 22.

[35] Q. Zhang, H. Zhang, B. Gu, Q. Tang, Q. Cao, and W. Fang, "Sunlight-driven photocatalytic oxidation of 5-hydroxymethylfurfural over a cuprous oxide-anatase heterostructure in aqueous phase," *Applied Catalysis B: Environmental*, vol. 320, p. 122006, 2023/01/01/ 2023.

[36] L. Luo, T. Zhang, M. Wang, R. Yun, and X. Xiang, "Recent Advances in Heterogeneous Photo-Driven Oxidation of Organic Molecules by Reactive Oxygen Species," *ChemSusChem*, vol. 13, no. 19, pp. 5173-5184, 2020/10/07 2020.

[37] C. K. N. Peh, M. Gao, and G. W. Ho, "Harvesting broadband absorption of the solar spectrum for enhanced photocatalytic H2 generation," *Journal of Materials Chemistry A*, 10.1039/C5TA05042A vol. 3, no. 38, pp. 19360-19367, 2015.

[38] L. Ren, M. Mao, Y. Li, L. Lan, Z. Zhang, and X. Zhao, "Novel photothermocatalytic synergetic effect leads to high catalytic activity and excellent durability of anatase TiO2 nanosheets with dominant {001} facets for benzene abatement," *Applied Catalysis B: Environmental*, vol. 198, pp. 303-310, 2016/12/05/ 2016.

[39] T. H. Tan, J. Scott, Y. H. Ng, R. A. Taylor, K.-F. Aguey-Zinsou, and R. Amal, "Understanding Plasmon and Band Gap Photoexcitation Effects on the Thermal-Catalytic Oxidation of Ethanol by TiO2-Supported Gold," *ACS Catalysis*, vol. 6, no. 3, pp. 1870-1879, 2016/03/04 2016.

[40] Z. Sun, X. Huang, and G. Zhang, "TiO2-based catalysts for photothermal catalysis: Mechanisms, materials and applications," *Journal of Cleaner Production*, vol. 381, p. 135156, 2022/12/25/ 2022.

[41] M. Przydacz, M. Jędrzejczyk, M. Brzezińska, J. Rogowski, N. Keller, and A. M. Ruppert, "Solvothermal hydrodeoxygenation of hydroxymethylfurfural derived from biomass towards added value chemicals on Ni/TiO2 catalysts," *The Journal of Supercritical Fluids*, vol. 163, p. 104827, 2020/09/01/ 2020.

[42] W. Yang, M. Fu, C. Yang, Y. Zhang, and C. Shen, "Auδ−–Ov–Ti3+: Active site of MOx-Au/TiO_2 catalysts for the aerobic oxidation of 5-hydroxymethylfurfural," *Green Energy & Environment*, vol. 8, no. 3, pp. 785-797, 2023/06/01/ 2023.

[43] T. Xie *et al.*, "High selective oxidation of 5-hydroxymethyl furfural to 5-hydroxymethyl-2-furan carboxylic acid using Ag-TiO2," *Molecular Catalysis*, vol. 525, p. 112353, 2022/06/01/ 2022.

[44] Y. Liu, L. Tian, X. Tan, X. Li, and X. Chen, "Synthesis, properties, and applications of black titanium dioxide nanomaterials," *Science Bulletin*, vol. 62, no. 6, pp. 431-441, 2017/03/30/ 2017.

[45] J. Wu *et al.*, "Photocatalytic oxidation of gas-phase Hg0 by CuO/TiO2," *Applied Catalysis B: Environmental*, vol. 176-177, pp. 559-569, 2015/10/01/ 2015.

[46] P. Geng, J. Zheng, C. Li, and Y. Zhang, "Normalization of the power-law rate equation for determining the kinetic parameters of the char-CO2 reaction," *Thermochimica Acta*, vol. 700, p. 178933, 2021/06/01/ 2021.

[47] S. Zhang and L. Zhang, "A facile and effective method for preparation of 2.5-furandicarboxylic acid via hydrogen peroxide direct oxidation of 5-hydroxymethylfurfural," *Polish Journal of Chemical Technology*, vol. 19, no. 1, pp. 11-16, 2017.

[48] S. Li, K. Su, Z. Li, and B. Cheng, "Selective oxidation of 5-hydroxymethylfurfural with H_2O_2 catalyzed by a molybdenum complex, *GreenChemistry*, vol. 18, no. 7, pp. 2122-2128, 2016.

Feasibility of hydrogen production from crude glycerol via photocatalysis using TiO_2-based photocatalysts

Thanapol Sutthiphong[1], Auttawit Thoumrungroj[1], Pimchanok Longchin[1], Mali Hunsom[1,2,3,*]

[1] Department of Chemical Engineering, Faculty of Engineering, Mahidol University, Nakhon Pathom 73170, Thailand
[2] Associate Fellow of Royal Society of Thailand (AFRST), Bangkok 10300 Thailand
[3] Advanced Microfabrication and Biomaterial for Organ-on-chip research unit (AMBiO), Faculty of Engineering, Mahidol University, Nakhon Pathom 73170, Thailand
[*] Corresponding author: mali.hun@mahidol.edu

ABSTRACT

In this work, the feasibility of hydrogen (H_2) production from commercial- and crude glycerol was conducted the by photocatalytic process with TiO_2 and gold-doped TiO_2 (Au/TiO_2) photocatalysts. The preliminary results demonstrated that both photocatalysts possessed similar crystallinity and textural property. However, the Au/TiO_2 displayed a higher visible light absorption, a longer lifetime of electron-hole pairs as well as a higher photocatalytic H_2 production. Besides, it was found that the glycerol purity and content significantly affected the H_2 production rate. Via the commercial glycerol, approximately 313 µmol/g·h of H_2 was produced with Au/TiO_2, which is about 28 times higher than the yield with TiO_2 sample. By the Au/TiO_2 photocatalysts, approximately 71 µmol/g·h of H_2 was generated in the presence of 5 vol.% crude glycerol, which was lower than that of commercial glycerol of around 4.41 times. Additionally, the operating cost of H_2 production from crude glycerol solution was 4.17 times higher than that of commercial glycerol. The improvement of H_2 production from crude glycerol will be explored. It is expected that the results obtained from this work may widen the horizon on the conversion of by-product of biodiesel process to a versatile energy carrier.

Keywords: Crude glycerol; Photocatalysis; Hydrogen production; Au/TiO_2; Water splitting

1. INTRODUCTION

The escalating global demand for energy, driven by industrial development, population growth, and technological advancements, has resulted in a fuel crisis predominantly reliant on fossil fuels, which currently account for 80% of energy generation. These finite resources contribute significantly to environmental issues, including climate change, due to greenhouse gas emissions [1]. Consequently, the transition to renewable energy sources such as hydropower, wind, solar, and hydrogen has gained momentum. Hydrogen (H_2), with its clean combustion producing only water, stands out as a highly efficient and sustainable alternative fuel [2]. However, most hydrogen production technologies today depend on hydrocarbon-based methods that release CO_2, underscoring the need for environmentally friendly production techniques [3].

Photocatalytic water splitting, a promising green H_2 production method, employs light energy to drive reactions on a semiconductor photocatalyst under ambient conditions. The photocatalytic generation of H_2 is influenced by the specific catalyst employed, the potential difference between its valence band and conduction band, and the reaction potential. Oxygen evolution occurs when the valence band potential exceeds the oxidation potential of water (O_2/H_2O) at 1.23 V. Conversely, H_2 evolution takes place when the conduction band potential of the photocatalyst is lower than the reduction potential of protons (H^+/H_2) at 0 V. Photocatalysts such as TiO_2, ZnO, and CdS, which possess a wide energy bandgap encompassing the redox potentials of water splitting, can effectively facilitate this process [4]. Titanium dioxide (TiO_2) is mostly used as a photocatalyst due to its stability and cost-effectiveness, making it a widely investigated material for this application. However, its high bandgap energy (~3.2 eV) and limited absorption in the visible light spectrum restrict its overall efficiency. The incorporation of Au nanoparticles (Au NPs) enhances TiO_2 performance by improving the light absorption capacity through surface plasmon resonance and suppressing electron-hole recombination, thereby improving its photocatalytic activity. The addition of sacrificial agents, such as alcohol or biomass-derived compounds like glycerol, can further improve H_2 production efficiency. Glycerol, a by-product of biodiesel production generated in significant quantities, offers a sustainable approach to repurpose industrial

waste for higher-value applications. Utilizing crude or purified glycerol as a hole scavenger in photocatalytic processes provides a dual benefit: supporting green H_2 production and reducing excess glycerol waste [5].

Bajpai et al. investigated Au-TiO_2 photocatalysts for solar-driven H_2 production using biomass-derived sacrificial agents. The study found that TiO_2 with 0.5% Au achieved the highest H_2 yield (18 mmol/h·g) due to an enhanced visible light absorption from surface plasmon resonance. Optimal conditions included a neutral pH and a 5% glycerol solution, which outperformed other sacrificial agents [6]. Reddy et al. found that $Ni(OH)_2$-loaded titanate nanotubes (TNT) significantly enhanced H_2 production using crude glycerol. The optimal 2 wt% $Ni(OH)_2$ (NT-3) achieved 4719 μmol/h·g, 12 times higher than pristine TNT. $Ni(OH)_2$ quantum dots improved electron trapping and reduced recombination. Using pure glycerol (5% v/v), NT-3 reached 45571 μmol/h·g, 9 times higher than crude glycerol [7]. Ribao et al. studied rGO/Pt/TiO_2 for H_2 production, finding optimal conditions at pH 7 with 20% pure glycerol (70.8 mmol/h·g) and 1% crude glycerol (12.7 mmol/h·g). Crude glycerol required more catalyst due to impurities deactivating active sites. At 20%, crude glycerol nearly stopped H_2 production, highlighting impurity effects [8].

This research focused on the H_2 production via photocatalytic water splitting using Au-doped TiO_2 and glycerol was used as a sacrificial agent. It aimed to optimize the process and demonstrated its potential for sustainable energy and waste management, aligning with global efforts toward cleaner energy solutions.

2. EXPERIMENTAL

2.1. Chemicals and materials

In this research, various chemicals were employed. Crude glycerol was obtained from a local biodiesel plant in Thailand, which utilizes palm oil as the raw material for biodiesel production via a transesterification process. Commercial glycerol ($C_3H_8O_3$, AR grade, 99.5%) was purchased from Kemaus.

Titanium (IV) isopropoxide ($C_{12}H_{28}O_4Ti$, ≥ 97.0%), gold (III) chloride trihydrate ($HAuCl_4 \cdot 3H_2O$, 99.9%) and standard solution of gold (Au, AR grade) were procured from Sigma Aldrich. Additionally, 2-propanol (C_3H_8O, AR grade, 99.7%), ethanol (C_2H_5OH, AR grade, 99.9%) and hydrochloric acid (HCl, AR grade, 37%) were obtained from Quality Reagent Chemical (QRec). Acetone (AR grade) was sourced from Merck. Distilled water was used for synthesis of materials and photocatalytic experiments.

2.2. Synthesis of TiO_2 photocatalysts

The TiO_2 photocatalyst was synthesized using a hydrothermal method. Initially, 8.9 mL of titanium (IV) isopropoxide was mixed with 11.5 mL of 2-propanol in a Teflon-lined stainless-steel autoclave and stirred at 400 rpm until the solution was well-mixed and turned a pale-yellow color. Subsequently, 50 mL of distilled water was incrementally added to the mixture while maintaining stirring at 400 rpm, which led to the formation of a white precipitate. The stirring continued for 4 h before adding 1 mL of 3 M HCl to the precipitate solution, followed by further stirring at 400 rpm for 1 h. The mixture was then transferred to the autoclave and heated at 200°C for 2 h in an oven (Memmert-UF55). Afterward, the autoclave was allowed to cool down overnight. The precipitate was separated by centrifugation at 8500 rpm for 15 min using a centrifuge (5804R, Eppendorf), washed three times with ethanol and twice with distilled water, dried at 100°C for 12 h, and ground using a mortar. Finally, the samples were calcined in a furnace at 500°C for 2 h.

2.3. Synthesis of Au/TiO_2 photocatalyst

The Au/TiO_2 photocatalyst was synthesized by photo-deposition using $HAuCl_4 \cdot 3H_2O$ as the gold precursor. First, an $HAuCl_4$ solution at a concentration of 50 mg/L was prepared for Au deposition. Approximately, 90 mL of the $HAuCl_4$ solution was mixed with 150 mL of distilled water, followed by the addition of 60 mL of ethanol. The mixture was stirred thoroughly at 400 rpm for 2 min until well-mixed. Then, 0.6 g of TiO_2 catalyst (from section 2.2) was added to the solution. Afterwards, the solution was carried out under UV irradiation generated by UV-LED 365 nm at the light intensity of 2.3 mW/cm^2 for 20 min. After the reaction, the precipitate was separated by centrifugation at 8500 rpm for 3 min, washed twice with distilled water, and dried at 80°C for 4 h. The final product was a titanium dioxide photocatalyst containing 0.75% Au by weight, as so-called Au/TiO_2 for further use.

2.4. Characterizations

The crystallite structures of Au/TiO_2 were analyzed by x-ray diffractometer (Bruker D2 PHASER, Bruker, Switzerland) with Cu Kα radiation (λ = 0.15406 Å). The light absorption properties of the synthesized catalyst were investigated by UV visible spectrometer, carried out with a UV-2600i Spectrophotometer (Shimadzu Corporation, Japan) equipped with an integration sphere and using barium sulphate as a reference material. The optical bandgaps were estimated with with the Kubelka– Munk equation. The morphology and elemental distribution of the synthesized catalyst were examined using a Field Emission Scanning Electron Microscope equipped with Energy Dispersive Spectroscopy (FESEM-EDS, JSM-7610FPlus, Leica Microsystems, Germany). The textural properties of the samples were analyzed by N_2 adsorption–desorption isotherms, carried out with a TriStar II Plus Analyzer (Micromeritics, United States). The Braunauer–Emmet-Teller (BET) theory, for the determination of the surface area, and the Barret–Joyner– Halenda (BJH) theory, for the determination of pore size distribution,

were applied. The recombination rate of the electron-hole pair were recorded using a photoluminescence spectrometer (AvaSpec-2048TEC-USB2-2, Avantes, Russia) at 25°C with an excitation wavelength of 255 nm. The photoluminescence spectra were collected over a range of 200–800 nm.

2.5. Photocatalytic H_2 production

The photocatalytic H_2 production using the Au/TiO_2 photocatalyst, with crude glycerol was conducted in a homemade photocatalytic reactor under UV light irradiation (Philips TUV PL-S 11W) at a light intensity of 0.16 mW/cm^2. In the glass reactor, 190 mL of distilled water was mixed with 10 mL of glycerol, followed by the addition of 0.4 g of Au/TiO_2 catalyst. The reactor was then sealed tightly to prevent the gas leakage. The glass reactor was placed inside the reactor chamber, and the gas inlet was connected to gas line. The mixture was stirred at 400 rpm while Ar gas (UHP Ar, 99.999%, Alternative Chemical) flowed into the reactor at a rate of 100 mL/min under dark conditions for 1 h to remove dissolved oxygen. Subsequently, the UV light was turned on, and the photocatalytic reaction proceeded under UV irradiation for 3 hours. Gas samples were collected at time intervals and the H_2 concentration was analyzed by gas chromatograph (Shimadzu, GC-2014C) using a Shincarbon column at 100°C with an Ar gas flow rate of 30 mL/min.

3. RESULTS AND DISCUSSION

3.1. Characterization of catalysts

The crystal structure of TiO_2 and Au/TiO_2 catalysts was analyzed using XRD, as shown in Figure 1(a). The TiO_2 sample exhibited diffraction peaks at 2θ angles of 25.3°, 37.9°, 48.0°, 54.0°, 55.1°, 62.7°, 68.8°, 70.3°, and 75.1°, corresponding to the (101), (004), (200), (105), (211), (204), (116), (220), and (215) planes of TiO_2 with an anatase crystal structure, according to PDF reference number 01-071-4943. Additionally, a peak at 2θ = 30.9° was observed, corresponding to the (211) plane of TiO_2 with a brookite crystal structure, as referenced by PDF 01-071-4943.

For the Au/TiO_2 catalyst, diffraction peaks at the same positions for both the anatase and brookite phases were observed, similar to the TiO_2. The XRD patterns of Au/TiO_2 catalyst showed no new diffraction peaks associated with Au, indicating that the Au NPs were well-dispersed or presence in small quantities. By Scherrer equation, the crystallite sizes of TiO_2 and Au/TiO_2 were found to be 12.05 nm and 11.81 nm, respectively. The crystallite size of TiO_2 in Au/TiO_2 was similar to that of pristine TiO_2, suggesting that the deposition of Au on the TiO_2 surface by the photo-deposition method did not affect the crystallite size of TiO_2.

Figure 1(b) shows UV-Vis spectroscopy of TiO_2 and Au/ TiO_2 catalysts over a wavelength range of 200–800 nm. The TiO_2 sample absorbed light only at wavelengths below 400 nm, indicating its exclusive absorption in the ultraviolet region. In contrast, the Au/ TiO_2 catalyst exhibited absorption in the visible light region, specifically around 540–570 nm, which results from localized surface plasmon resonance (LSPR) of deposited Au NPs. The bandgap energies, estimated from the Kubelka-Munk equation, were 3.29 eV for TiO_2 and 3.30 eV for Au/ TiO_2.

Photoluminescence (PL) spectroscopy was conducted to study the qualitative rate of charge recombination. From Figure 1(c), it can be observed that the pure TiO_2 sample exhibited the highest PL intensity, indicating a high level of electron-hole recombination. However, upon the addition of Au NPs, the PL intensity decreased. This is because the Au NPs help to create a Schottky barrier at the interface between Au and TiO_2, which can serve as an electron trap to suppress charge carrier recombination.

The quantitative properties of the surface structure, including BET surface area, pore size, and pore volume, were analyzed as follows. The Au/TiO_2 sample exhibited a BET surface area similar to that of TiO_2, with the surface area of around 76 m^2/g. The average pore size of TiO_2 was 9.44 nm. After the addition of Au, the pore size slightly decreased to approximately 9.35 nm. The pore volume of TiO_2 was 0.2153 cm^3/g, while the Au-loaded sample exhibited a comparable pore volume of approximately 0.21 cm^3/g. This suggests that the addition of Au had negligible effects on the surface property material. The N_2 adsorption/desorption isotherm of TiO_2 and Au/TiO_2 catalyst are shown in Figure 1(d).

As shown in Figure 2(a), SEM–EDS analysis confirmed the presence of titanium (Ti), oxygen (O), and gold (Au) on the surface of the material, which a well dispersion across the catalyst surface Figure 2(b).

3.2. Photocatalytic activity test

3.2.1. Effect of photocatalyst types

Figure 3 illustrates the effect of different types of photocatalysts including synthesized TiO_2, Au/TiO_2 and Au/TiO_2 (P25) on the amount and rate of H_2 production, using photocatalysts loading of 2 g/L and 5 vol% of commercial glycerol. As shown in Figure 3(a), during the first 30 min, all photocatalysts exhibited low H_2 production, which gradually increased as the reaction progressed. However, TiO_2 still exhibited a consistently low level of H_2 production throughout the entire experiment, possibly due to the rapid recombination of e^--h^+ pairs. In terms of H_2 production rate, the TiO_2, Au/TiO_2 (P25), and Au/TiO_2 exhibited the H_2 production rates of 11, 227, and 313 μmol/g·h, respectively. Notably, Au/TiO_2 (P25) and Au/TiO_2 gave the H_2 production rates approximately 21 and 28 times higher than of TiO_2. These results indicated that the incorporation of Au NPs significantly enhances H_2 production by reducing overpotential and suppressing electron–hole recombination. Au NPs are particularly

effective due to their unique light-absorbing properties, which improved the charge separation and boosted photocatalytic activity. Among all the tested photocatalysts, Au/TiO_2, synthesized via a hydrothermal method, demonstrated the highest H_2 production performance. This is attributed to its smaller crystallite size, which enhances the surface area and provides more active sites for photocatalytic reactions [9].

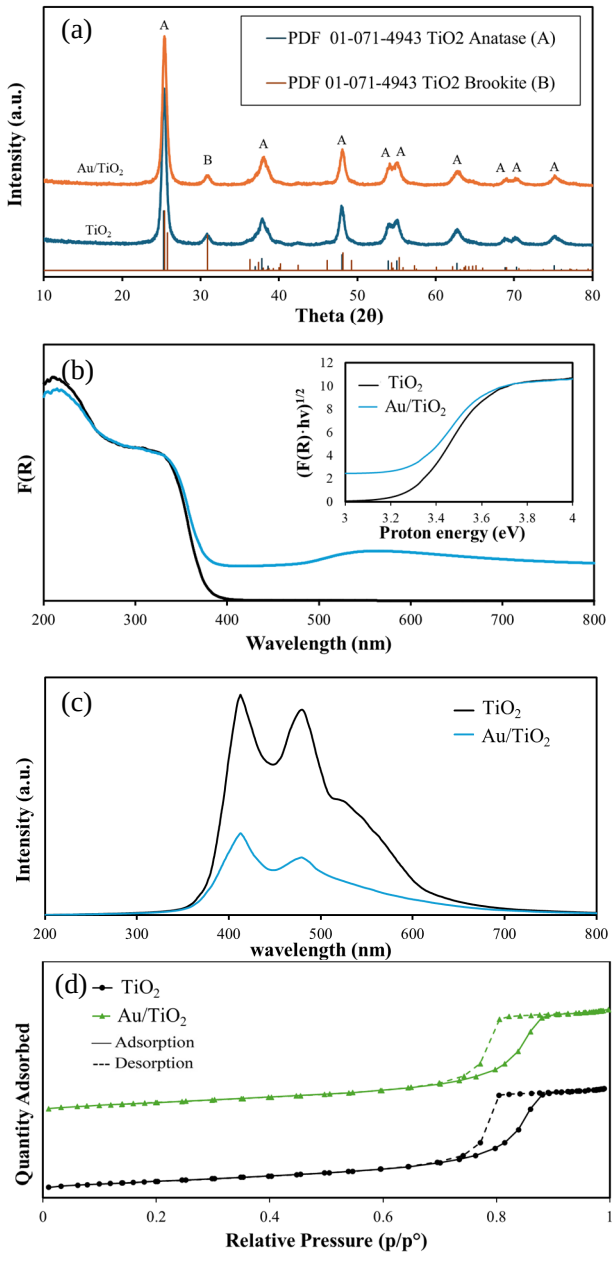

Figure 1. Representative (a) XRD spectra, (b) UV–Vis spectra, (c) PL spectra, and (d) N_2 adsorption/desorption isotherms of TiO_2 and Au/TiO_2 photocatalysts.

3.2.2. Effect of glycerol types

Figure 4 shows the effects of glycerol types, including commercial- and crude glycerol, on the photocatalytic H_2 production via the Au/TiO_2 photocatalyst at glycerol concentration of 5 vol%. It can be seen that a relatively low H_2 was produced in the absence of glycerol. In the presence of glycerol, commercial glycerol exhibited the highest H_2 production, reaching approximately 313 µmol/h·g at 60 min before saturation. In contrast, crude glycerol gave the H_2 production rate of around 71 µmol/h·g. The H_2 production efficiency using commercial glycerol was 4.41 times higher than that of crude glycerol, which was likely due to its higher purity and the absence of impurities. Typically, impurities in glycerol negatively affected the H_2 production rates, as they could have interfered with the catalytic active sites required for efficient hydrogen generation from glycerol [8].

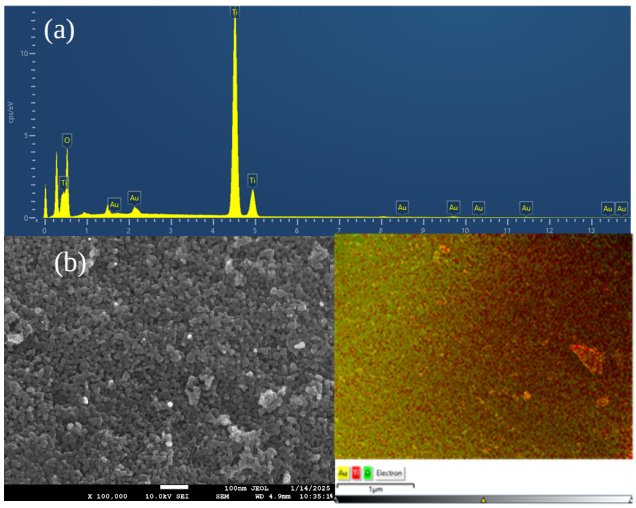

Figure 2. Representative of SEM-EDX images and element mapping.

3.2.3. Effect of crude glycerol concentration

Figure 5(a) shows the effect of crude glycerol concentration on the amount of H_2 produced. During the first 30 min, all photocatalysts exhibited low H_2 production, which gradually increased as the reaction progressed. After 3 h, the H_2 production at crude glycerol concentrations of 0, 3, 5, and 7 vol% were 4.03, 50.68, 79.33, and 45.42 µmol, respectively. These results indicated that 5 vol% of crude glycerol was the optimal concentration for H_2 production. As presented in Figure 5(b), the H_2 production rates for crude glycerol concentrations at 0, 3, 5, and 7 vol% were 3.57, 43.07, 68.39, and 38.43 µmol/h·g, respectively. The results indicated that a glycerol concentration of 5 vol% was the optimal condition, yielding the highest H_2 production rate of 68.39 µmol/h·g. At low crude glycerol concentrations, such as 3 vol%, H_2 production decreased, likely due to the insufficient amount of glycerol available to effectively facilitate catalytic reaction. Conversely, increasing the crude glycerol concentration to 7 vol% resulted in a decline in H_2 production. This reduction may be attributed to the increased impurities, which can reduce the catalyst active sites, and indue a higher solution turbidity, which

limited the light penetration and reduced photocatalytic efficiency.

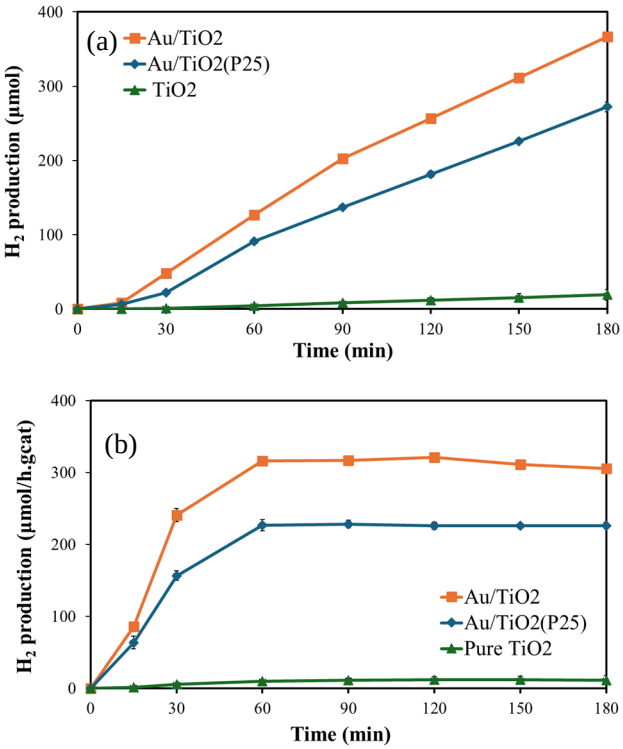

Figure 3. Effect of different types of photocatalysts on (a) the amount and (b) rate of hydrogen production.

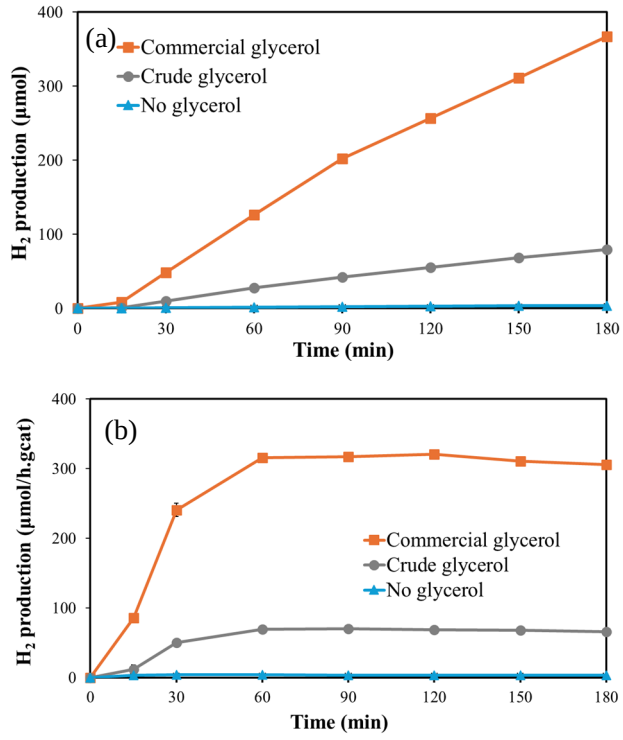

Figure 4. Effect of glycerol types on (a) the amount and (b) rate of hydrogen production.

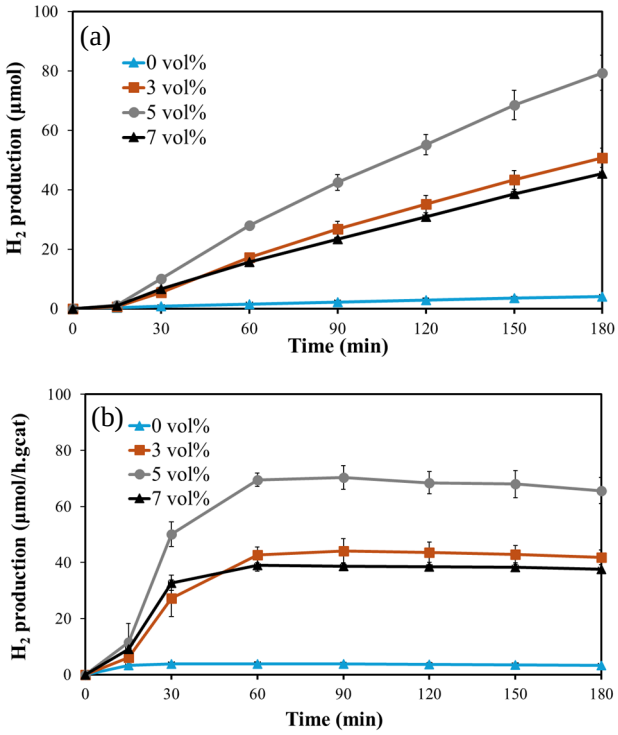

Figure 5. Effect of crude glycerol concentration on (a) the amount and (b) rate of hydrogen production.

From the cost analysis, it was found that the H_2 production cost using commercial glycerol was 0.0097 USD/µmol (exchange rate: 1 USD = 33.68 THB as of April 16, 2025). In contrast, the production cost using crude glycerol was 0.0402 USD/µmol. This indicated that using crude glycerol incurred approximately 4.14 times higher costs than commercial glycerol, primarily because crude glycerol produced a lower amount of H_2 under the same conditions. To reduce costs and improve the H_2 production efficiency, additional process is required to pretreat or purify crude glycerol before using. However, it is essential to balance between the purification cost and the H_2 production cost to get the most cost-effective process.

4. CONCLUSION

This work was conducted to evaluate the feasibility of hydrogen production from crude glycerol via photocatalysis using TiO_2-based photocatalysts. The results indicated that pristine TiO_2 exhibited limited photocatalytic activity due to the rapid recombination of photogenerated electron–hole pairs. The incorporation of Au NPs significantly enhanced the photocatalytic performance by facilitating charge separation and suppressing recombination. Among the prepared photocatalysts, Au/TiO_2 synthesized by hydrothermal and photo-deposition a higher H_2 production rate than TiO_2 and $Au/TiO_2(P25)$. The presence of glycerol as a hole scavenger played a critical role in promoting hydrogen generation, while water alone resulted in negligible H_2 production. Additionally, a crude glycerol concentration of 5 vol%

was found to be optimal. Too low concentrations provided insufficient sacrificial agents, while too high concentrations introduced more impurities and turbidity, both of which reduced the photocatalytic performance.

ACKNOWLEDGMENTS

The research project has been supported by Mahidol University (Fundamental Fund: fiscal year 2025 by National Science Research and Innovation Fund (NSRF)). The author would like to thank the Department of Chemical Engineering, Faculty of Engineering, Mahidol University, for equipment and facility support. Special thanks are also extended to the Faculty of Graduate Studies, Mahidol University, for the financial support for conference participation.

REFERENCES

1. J.O. Abe, A.P.I. Popoola, E. Ajenifuja, O.M. Popoola. Hydrogen energy, economy and storage: Review and recommendation. *International Journal of Hydrogen Energy* 2019; 44(29): 15072–15086.
2. A.J. Bard, M.A. Fox. Artificial photosynthesis: solar splitting of water to hydrogen and oxygen. *Accounts of Chemical Research* 1995; 28(3): 141–145.
3. P. Afanasev, A. Askarova, T. Alekhina, E. Popov, S. Markovic, A. Mukhametdinova. An overview of hydrogen production methods: Focus on hydrocarbon feedstock. *International Journal of Hydrogen Energy* 2024; 78: 805–828.
4. C.Y. Toe, C. Tsounis, J. Zhang, H. Masood, D. Gunawan, J. Scott. Advancing photoreforming of organics: highlights on photocatalyst and system designs for selective oxidation reactions. *Energy & Environmental Science* 2021;14(3):1140-75.
5. S. Abad, X. Turon. Valorization of biodiesel derived glycerol as a carbon source to obtain added-value metabolites: Focus on polyunsaturated fatty acids. *Biotechnology Advances* 2012; 30(3): 733–741.
6. H. Bajpai, I. Chauhan, K. N. Salgaonkar, N. B. Mhamane, C. S. Gopinath. Biomass components toward H_2 and value-added products by sunlight-driven photocatalysis with electronically integrated $Au\delta^-$–TiO_2: concurrent utilization of electrons and holes. *RSC Sustainability* 2023; 1(3): 481–493.
7. N.L. Reddy, K. K. Cheralathan, V. Durga Kumari, B. Neppolian, S. Muthukonda Venkatakrishnan. Photocatalytic reforming of biomass derived crude glycerol in water: A sustainable approach for improved hydrogen generation using $Ni(OH)_2$ decorated TiO_2 nanotubes under solar light irradiation. *ACS Sustainable Chemistry & Engineering* 2018; 6(3): 3754–3764.
8. P. Ribao, M. Alexandra Esteves, V. R. Fernandes, M. J. Rivero, C. M. Rangel, I. Ortiz. Challenges arising from the use of TiO_2/rGO/Pt photocatalysts to produce hydrogen from crude glycerol compared to synthetic glycerol. *International Journal of Hydrogen Energy* 2019; 44(3): 28494-28506.
9. N. Kunthakudee, T. Puangpetch, P. Ramakul, K. Serivalsatit, M. Hunsom. Light-assisted synthesis of Au/TiO_2 nanoparticles for H_2 production by photocatalytic water splitting. *International Journal of Hydrogen Energy* 2022; 47(56): 23570–23582.

Effects of cation types and carrageenan structure on the formation and electrochemical properties of bio-gel electrolytes

Dedy Firmansyah[1], Peerasak Paoprasert[2], Phongphot Sakulaue[3], Khanin Nueangnoraj[1,*]

[1] School of Bio-Chemical Engineering and Technology, Sirindhorn International Institute of Technology, Thammasat University, Pathum Thani 12120, Thailand
[2] Department of Chemistry, Faculty of Science and Technology, Thammasat University, Pathum Thani 12120, Thailand
[3] Division of Chemical Engineering, Faculty of Engineering, Rajamangala University of Technology Krungthep, Bangkok 10120, Thailand
[*] Corresponding author: khanin@siit.tu.ac.th

ABSTRACT

Bio-gel electrolytes have gained significant attention due to their potential applications in energy storage devices. This study investigates the effects of cation types (Li^+, Na^+, K^+) from their respective chloride salts (LiCl, NaCl, KCl) and carrageenan variants (kappa, iota, and lambda) on the maximum salt concentration for gel formation, electrochemical stability window, and ionic conductivity. Dissolving different chloride salts in carrageenan-based matrices produced gel electrolytes, followed by an analysis of their electrochemical properties. Cyclic voltammetry determined the electrochemical stability window, while electrochemical impedance spectroscopy analyzed ionic conductivity and charge transfer resistance. The results indicate that lithium chloride can form stable gels up to 5 M in all three carrageenan types, while sodium chloride and potassium chloride exhibit lower solubility limits. Cyclic voltammetry measurements show that at 5 M concentration, kappa-carrageenan achieves the most expansive electrochemical stability window of 2.0 V, compared to iota and lambda, which both reach 1.8 V. Electrochemical impedance spectroscopy analysis reveals that ionic conductivity increases with salt concentration, with lithium chloride-based gels demonstrating the lowest resistance. These findings highlight the importance of selecting optimal cation-carrageenan combinations for enhanced electrochemical performance in bio-gel electrolytes, paving the way for their potential application in sustainable energy storage systems.

Keywords: Gel electrolyte; Carrageenan; Electrochemical stability window; Energy storage

1. INTRODUCTION

The demand for high-performance energy storage systems has led to extensive research in improving battery and supercapacitor technologies. These devices are essential for portable electronics, electric vehicles, and grid storage [1], [2], [3]. One of the key challenges is enhancing energy density while maintaining safety and long-term stability. Since the electrolyte governs ion transport, charge storage efficiency, and operating voltage, its optimization is crucial for advancing next-generation energy storage systems [4], [5].

Improving energy density includes developing high-capacity electrodes, increasing the operating voltage, and optimizing electrolyte composition. While liquid electrolytes provide high ionic conductivity, they pose leakage and safety risks [6]. On the other hand, solid-state electrolytes enhance safety and stability but often suffer from lower ionic conductivity [7]. Gel electrolytes offer a promising alternative by combining the advantages of both liquid and solid electrolytes, ensuring improved ionic transport, flexibility, and reduced leakage risks [8], [9].

Recent studies have explored bio-based gel electrolytes using natural polymers such as carrageenan, which offers biocompatibility and cost-effectiveness. Carrageenan-based gels exhibit tunable ionic conductivity depending on the type of carrageenan (kappa, iota, and lambda) and the salt used [10], [11]. However, optimizing their electrochemical properties remains challenging, particularly in achieving a wide stability window, enhancing ionic conductivity, and ensuring long-term durability. While previous research has investigated the individual roles of cation type and polymer structure, their combined influence on gel formation and electrochemical properties has not been thoroughly explored. Understanding these interactions is essential for optimizing bio-gel electrolytes for energy storage applications.

This study investigates the effects of different cation species (Li^+, Na^+, and K^+) and carrageenan types on bio-gel electrolytes' formation and electrochemical properties. The maximum salt concentration required for gel formation is determined, followed by electrochemical stability window analysis using cyclic voltammetry. Electrochemical impedance spectroscopy (EIS) evaluates ionic conductivity and charge transfer resistance. Special attention is given to the electrochemical stability window, as it directly impacts operational voltage and energy density. These findings contribute to advancing bio-based gel electrolytes with improved electrochemical performance and stability.

2. EXPERIMENTAL

2.1. Materials

The carrageenan variants used in this study, kappa, iota, and lambda, were obtained in analytical-grade quality from Tokyo Chemical Industry Co., Ltd. The salts employed as electrolyte components include lithium chloride (LiCl) and potassium chloride (KCl) from Elago Enterprises Pty. Ltd. (Kemaus) and sodium chloride (NaCl) from Loba Chemie Pvt. Ltd. The electrode composite material consisted of activated carbon (YEC), carbon black, and polytetrafluoroethylene (PTFE), which was used as a binder for preparing carbon electrodes.

2.2. Preparation of Gel Electrolyte

The bio-gel electrolytes were synthesized using carrageenan (kappa, iota, and lambda), salts, and water. The salts were introduced at varying concentrations (0.5 M, 1 M, 3 M, 5 M, 7 M, and 9 M) to determine the maximum concentration capable of forming a stable gel structure.

The preparation process involved dissolving 2 g of carrageenan in 55 mL of deionized water, then heating it in a water bath at 80 °C under continuous stirring for 2 minutes. Once fully dissolved, the designated salt was added and stirred until complete dissolution. The solution was mixed for another 2 minutes to ensure homogeneity before being removed from the water bath and cooled at room temperature for 24 hours to form the gel electrolyte.

2.3. Preparation of carbon electrode

The carbon electrode was fabricated by blending activated carbon, carbon black, and PTFE in a weight ratio of 9:0.5:0.5. The mixture was thoroughly ground using an agate mortar and pestle until a uniform paste-like consistency was achieved. The electrode was then molded into a 1×1 cm^2 square, and its initial mass was recorded. The electrode was mounted onto a titanium mesh current collector to establish efficient electrical contact. Before electrochemical testing, the electrode was immersed in the gel electrolyte for 24 hours to ensure optimal electrolyte absorption.

2.4. Electrochemical investigations

The electrochemical performance of the gel electrolytes was evaluated using cyclic voltammetry (CV) and electrochemical impedance spectroscopy (EIS), focusing on determining the electrochemical stability window, ionic conductivity, and charge transfer characteristics.

2.4.1. Determination of electrochemical stability window

The electrochemical stability window was identified through a two-step potential determination process; (1) Maximum Negative Potential Determination: To establish the onset of reduction reactions, the system was subjected to incrementally negative potential while monitoring the current response, and (2) Maximum Positive Potential Determination: Similarly, progressively positive potentials were applied to determine the onset of oxidation reactions.

2.4.2. Cyclic voltammetry analysis

Cyclic voltammetry (CV) was performed within the identified potential window to evaluate the gel electrolyte's redox behavior, electrochemical reversibility, and stability. The potential was cycled between the maximum reduction and oxidation limits, and the resulting current response was recorded to assess charge storage capability and electrolyte decomposition limits.

2.4.3. Electrochemical impedance spectroscopy analysis

Electrochemical impedance spectroscopy (EIS) was conducted to analyze the gel electrolytes' ionic conductivity and resistance properties. The impedance spectra were used to extract key electrochemical parameters: (1) Solution resistance (R_s): Representing intrinsic ionic resistance of the gel electrolyte, (2) Charge transfer resistance (R_p): Associated with interfacial charge transfer at the electrode-electrolyte interface, and (3) Warburg impedance (W): Indicating ion diffusion characteristics within the electrolyte.

The ionic conductivity of the gel electrolytes was further verified using a conductivity meter, which applied a known voltage across the electrolyte sample and measured the resulting current.

By integrating CV and EIS techniques, this study provides a comprehensive evaluation of the electrochemical properties of carrageenan-based bio-gel electrolytes, focusing on their stability, ionic conductivity, and suitability for energy storage applications.

3. RESULTS AND DISCUSSION

3.1. Maximum concentration of gel electrolytes

An experiment was conducted to determine the maximum salt concentration that could be incorporated

into a well-structured gel using kappa carrageenan. The salt concentrations ranged from 0.5 M to 9 M, and the study involved three different salts: LiCl, NaCl, and KCl. Various preparation methods were explored, including mixing carrageenan powder with deionized (DI) water, directly adding salt, and combining carrageenan with DI water and salt. Dissolving carrageenan in a water bath at 80 °C most effectively produced a dense and stable gel.

The results identified the maximum concentration of salts that could be incorporated into the gel electrolyte without compromising the gel structure. Table 1 summarizes the maximum concentrations for each salt in the kappa, iota, and lambda carrageenan gel.

Table 1. Maximum concentration of slats in gel electrolyte.

Type of Carrageenan	Type of salts		
	LiCl	NaCl	KCl
Kappa	5 M	2 M	1 M
Iota	5 M	2 M	1 M
Lambda	5 M	2 M	1 M

The investigation classified the salts based on their cation types: Li^+, Na^+, and K^+. The results showed that chloride-based salts required higher concentrations to form stable electrolyte gels. Notably, LiCl could form stable gels at higher concentrations than NaCl and KCl. The size of the cations can explain this difference; smaller cations like Li^+ can occupy more space within the carrageenan matrix, which allows for greater incorporation of these salts into the gel.

This observation aligns with the gel formation mechanism of carrageenan, which creates a helical structure during gelation [12]. The cations fill the gaps within the helix, and smaller cations fit more effectively, enhancing the gel's overall stability and ionic conductivity.

In contrast, salts with larger cations, such as K^+, require lower concentrations to form stable gels because these larger cations take up significant space in the carrageenan helix, which limits the number of cations that can be accommodated. This is consistent with the gel formation mechanism of carrageenan, which forms a helical structure during gelation. The cations fill the spaces within the helix, and smaller cations can fit more effectively, enhancing the gel's overall stability and ionic conductivity [13].

Conversely, salts with larger cations, such as K^+, require a lower concentration to form stable gels, as the larger cations occupy significant space within the carrageenan helix, limiting the number of cations that can fit.

3.2. Electrochemical stability window

The electrochemical stability window of the gel electrolytes was determined by analysing the electrochemical system's maximum positive and negative potentials under a constant current. The potential range for the electrochemical scan was set between 0.6 V and 2.0 V with a scan rate of 1 mV/s. The maximum positive and negative potential values were identified by analyzing the CV curves.

Table 2 summarizes the potential window values for the different gel electrolytes prepared using three types of carrageenan (kappa, iota, and lambda) and three different salts (LiCl, NaCl, and KCl). The data reveals distinct differences in the potential window across various gel formulations.

Table 2. Electrochemical stability window of gel electrolytes.

Type of salts	Conc. (M)	Electrochemical Stability Window (V)		
		Kappa	Iota	Lambda
LiCl	0.5	1.4	1.4	1.4
	1	1.6	1.5	1.5
	3	1.7	1.6	1.5
	5	2.0	1.8	1.8
NaCl	0.5	1.4	1.4	1.4
	1	1.6	1.5	1.5
	2	1.6	1.5	1.6
KCl	0.5	1.5	1.5	1.4
	1	1.6	1.5	1.5

The differences in the electrochemical stability window across various carrageenan types (kappa, iota, and lambda) can be attributed to the distinct chemical structures and properties of carrageenan. These variations significantly influence the gel structure, ion diffusion rates, and interactions between the electrolyte and electrodes, all of which impact electrochemical performance, including the electrochemical stability window [14].

The presence of sulfate groups in the carrageenan matrix may also contribute to the observed differences. Sulfate groups, which are present in varying amounts across different types of carrageenan, can enhance the redox stability of the electrolyte gel [15], [16]. This improved stability helps prevent unwanted side reactions and degradation during electrochemical testing, thus enabling a wider potential range for the electrolyte. With one sulfate group per disaccharide unit, kappa-carrageenan exhibits a more flexible helical structure, which can enhance ionic conductivity, contributing to a wider electrochemical stability window. This suggests that kappa-carrageenan gels exhibit superior performance, allowing for a broader electrochemical stability window than iota and lambda carrageenan gels.

Furthermore, the type of salt used in the electrolyte gels influences the electrochemical stability window as well. Salts containing smaller cations like Li^+ tend to create more compact interactions within the gel matrix, potentially limiting ion mobility. Conversely, salts with larger cations, such as K^+, result in more efficient ion transport due to weaker interactions with the gel matrix,

allowing for a broader electrochemical stability window. This effect is particularly notable for gels containing KCl, where the larger K^+ ion facilitates greater ion mobility, leading to an expanded potential window compared to NaCl and LiCl.

3.3. Effect of salt concentration

Electrochemical impedance spectroscopy (EIS) analysis revealed that increasing salt concentration significantly affects the resistance and conductivity of gel electrolytes. As shown in Figure 1(a), the series resistance (R_s) of LiCl-based kappa-carrageenan gels decreases from 8.06 Ω at 0.5 M to 2.50 Ω at 5 M, indicating improved ion mobility due to the greater availability of free ions. This trend is consistent in NaCl and KCl-based gels, where R_s decreases with increasing concentration, as seen in Figures 1(b) and 1(c). The decrease in R_s across all salt types signifies enhanced charge transport.

Similarly, the polarization resistance (R_p) also declines with increasing salt concentration. For instance, in LiCl-kappa gels, R_p drops from 3.31 Ω at 0.5 M to 2.07 Ω at 5 M, suggesting more efficient charge transfer and improved ionic conductivity. These reductions in R_s and R_p confirm that higher salt concentrations reduce internal resistance within the gel matrix.

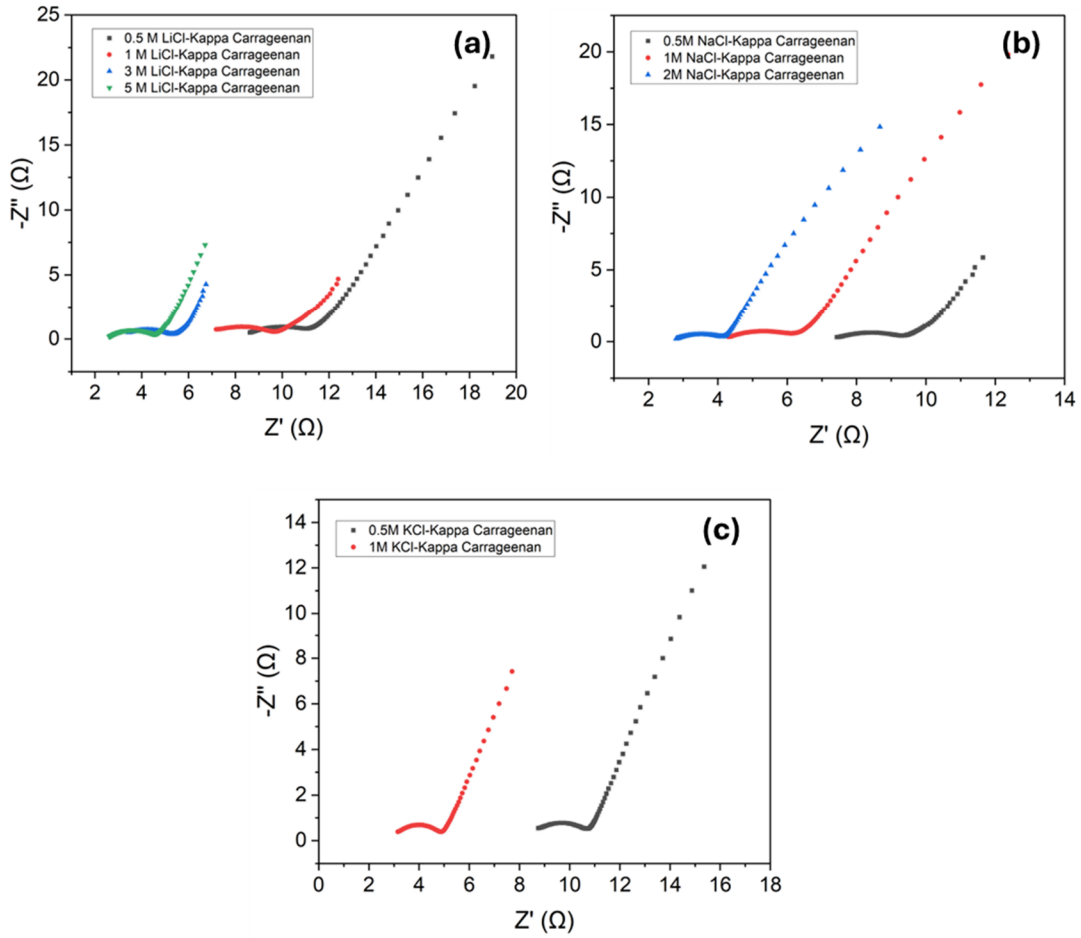

Figure 1 EIS curves of kappa carrageenan gel electrolytes: (a) 0.5 M - 5 M LiCl, (b) 0.5 M - 2 M NaCl, and (c) 0.5 M - 1 M KCl.

Warburg impedance (W), related to ion diffusion, slightly increases with salt concentration. In LiCl-kappa gels, W increases from 430 mMho at 0.5 M to 520 mMho at 5 M. It may indicate that while ion mobility improves, denser ion environments create more restricted diffusion pathways, adding complexity to ion transport.

The ionic conductivity, which is inversely related to resistance, consistently increases with higher salt concentrations. For example, as shown in Figure 2, in kappa-carrageenan LiCl gels, conductivity rises from 41.2 mS/cm at 0.5 M to 130.9 mS/cm at 5 M. These observations confirm that salt concentration plays a vital role in improving the electrochemical performance of gel electrolytes.

3.4. Effect of cation types

The type of cation in the salt also influences the gel electrolyte's electrochemical characteristics and physical integrity. Each cation interacts differently with the carrageenan matrix, affecting gelation behaviour and ionic transport properties. For instance, K^+ ions,

with their larger ionic radius and lower hydration energy, tend to exhibit higher mobility in polymeric systems, contributing to favourable ionic conductivity, especially at lower concentrations.

However, the ability of each salt to form a homogeneous and solid gel differs significantly. As shown in Figures 1(a–c), LiCl-based gels can be prepared up to a concentration of 5 M, while NaCl-based gels are limited to 2 M and KCl-based gels only up to 1 M. These differences are attributed to the solubility of each salt and the nature of its interaction with the carrageenan network. While K^+ may offer higher mobility, its practical application is restricted due to the limited concentration range in which a stable gel structure can be achieved.

3.5. Effect of carrageenan types

The type of carrageenan used as a polymer matrix is a pivotal factor in shaping the electrochemical behaviour of gel electrolytes. Even when the salt type and concentration remain constant, the differences in molecular structure, such as the number of sulfate groups, lead to variations in ion mobility, ionic conductivity, and diffusion characteristics within the gel. These findings underscore the critical role of carrageenan type in the performance of gel electrolytes.

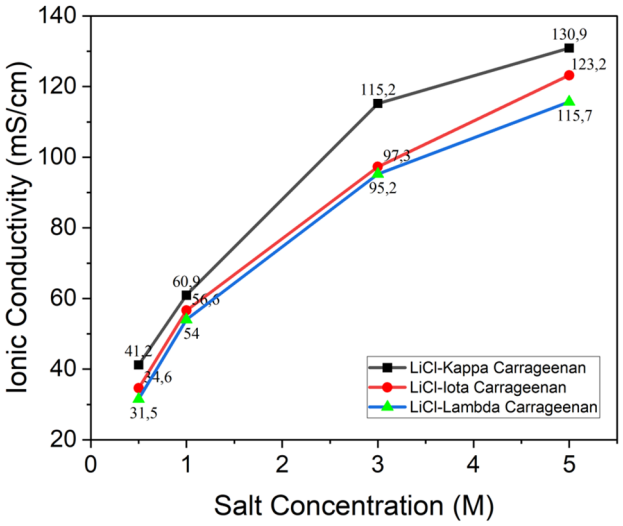

Figure 2. Ionic conductivity of gel electrolyte for LiCl with different types of Carrageenan.

Among the three types studied, kappa carrageenan exhibits superior performance in terms of ionic transport. It is reflected in the ionic conductivity values of LiCl-based gels, as shown in Figure 2, where kappa consistently shows the highest conductivity across all concentrations. At 5 M LiCl, the conductivity reaches 130.9 mS/cm in kappa gels, compared to 123.2 mS/cm in iota and 115.7 mS/cm in lambda gels. The lower conductivity in lambda is attributed to its higher sulfate content and more disordered structure, which creates additional barriers to ion movement.

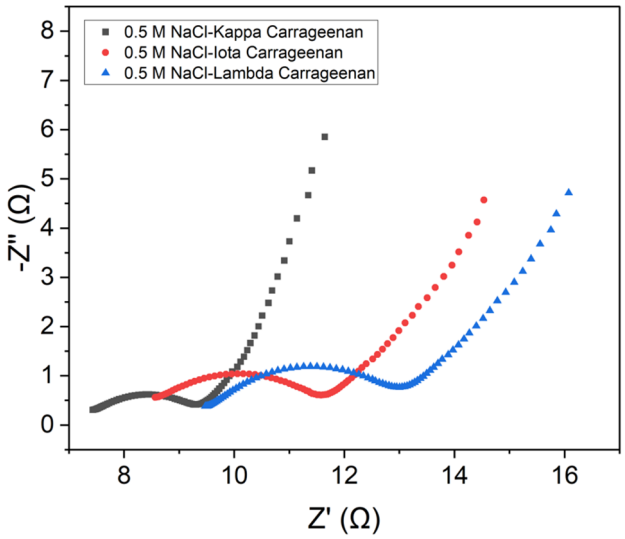

Figure 3. EIS curve of 0.5 M NaCl in different types of Carrageenan gel electrolyte.

Further evidence is provided by EIS analysis using 0.5 M NaCl, as shown in Figure 3, where kappa gels demonstrate the lowest resistance values R_s = 7.27 Ω and R_p = 2.10 Ω, indicating efficient ion transport and charge transfer. In contrast, iota and lambda gels exhibit higher resistances, with lambda showing the highest R_s = 9.37 Ω and R_p = 3.57 Ω, consistent with its lower ionic conductivity 41.0 mS/cm compared to kappa 44.1 mS/cm.

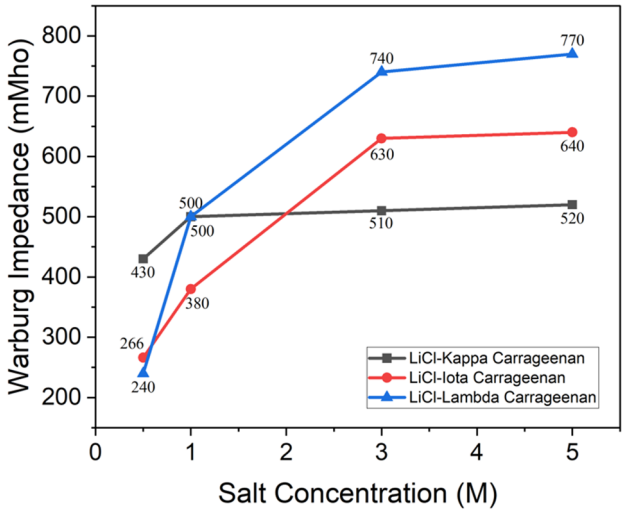

Figure 4. Warburg impedance of gel electrolyte for LiCl with different types of Carrageenan.

The Warburg impedance, which characterizes ion diffusion behavior, increases with higher LiCl concentrations across all carrageenan types, indicating more restricted diffusion pathways at elevated salt concentrations, as shown in Figure 4. In kappa carrageenan, *W* rises from 430 mMho at 0.5 M to 520 mMho at 5 M, suggesting that while ion mobility improves with increased free ion availability, intensified ion-ion interactions create additional resistance to diffusion. Iota carrageenan exhibits a more

significant increase in *W*, from 266 mMho at 0.5 M to 640 mMho at 5 M, highlighting stronger polymer-ion interactions that influence charge transport. Lambda carrageenan demonstrates the highest *W* values, increasing from 240 mMho at 0.5 M to 770 mMho at 5 M. This confirms that its higher sulfate group content leads to stronger electrostatic interactions and a more constrained diffusion process. The increasing *W* trend across all gels establishes that higher salt concentrations enhance ionic conductivity but simultaneously contribute to more complex ion transport mechanisms due to intensified interactions within the gel matrix. The higher resistance and lower conductivity observed in lambda gels result from their more rigid structure, which limits ion mobility and reduces overall performance. This comparison underscores the critical role of carrageenan structure in optimizing gel electrolyte properties, with kappa gels demonstrating the most favorable characteristics for high-performance electrochemical applications.

4. CONCLUSION

This study investigated the electrochemical properties of gel electrolytes composed of salts (LiCl, NaCl, and KCl) and carrageenan (kappa, iota, and lambda) using electrochemical impedance spectroscopy (EIS) and cyclic voltammetry (CV). Results indicated that increasing salt concentration enhanced the electrochemical stability window, ionic conductivity, and ion mobility but also increased Warburg impedance, suggesting more complex ion diffusion pathways.

Cation type also played a role in gel formation and performance. Li^+ enabled the highest salt concentration (5 M) in a stable gel matrix. In comparison, Na^+ and K^+ were limited to 2 M and 1 M, respectively, indicating better compatibility of Li^+ with the carrageenan network.

Among the carrageenan types, kappa carrageenan consistently exhibited the highest ionic conductivity and lowest resistance. Structural differences between carrageenan types significantly influenced ion transport and electrochemical performance.

These findings highlight the importance of optimizing the salt concentration and polymer type in developing gel electrolytes, with kappa carrageenan–LiCl systems offering promising potential for high-performance electrochemical applications.

ACKNOWLEDGMENTS

This research was supported by Thailand Science Research and Innovation (TSRI) Fundamental Fund, fiscal year 2025. D.F. acknowledges the graduate scholarship from Sirindhorn International Institute of Technology (under the EFS Program).

REFERENCES

[1] G. G. Njema, R. B. O. Ouma, and J. K. Kibet, “A Review on the Recent Advances in Battery Development and Energy Storage Technologies,” *Journal of Renewable Energy*, vol. 2024, pp. 1–35, May 2024, doi: 10.1155/2024/2329261.

[2] C. V. V. Muralee Gopi, S. Alzahmi, V. Narayanaswamy, R. Vinodh, B. Issa, and I. M. Obaidat, “Supercapacitors: A promising solution for sustainable energy storage and diverse applications,” Apr. 01, 2025, *Elsevier Ltd.* doi: 10.1016/j.est.2025.115729.

[3] R. T. Yadlapalli, R. K. R. Alla, R. Kandipati, and A. Kotapati, “Super capacitors for energy storage: Progress, applications and challenges,” May 01, 2022, *Elsevier Ltd.* doi: 10.1016/j.est.2022.104194.

[4] R. Tiwari *et al.*, “Fundamental chemical and physical properties of electrolytes in energy storage devices: A review,” Mar. 15, 2024, *Elsevier Ltd.* doi: 10.1016/j.est.2023.110361.

[5] S. Awasthi, “A review on the optimization of electrolytes to enhance lithium-ion batteries’ safety and performance under abuse conditions,” Oct. 15, 2024, *Elsevier Ltd.* doi: 10.1016/j.est.2024.113439.

[6] P. U. Nzereogu *et al.*, “Solid-State lithium-ion battery electrolytes: Revolutionizing energy density and safety,” Mar. 01, 2025, *Elsevier B.V.* doi: 10.1016/j.hybadv.2024.100339.

[7] N. Sarfraz *et al.*, “Materials advancements in solid-state inorganic electrolytes for highly anticipated all solid Li-ion batteries,” Aug. 01, 2024, *Elsevier B.V.* doi: 10.1016/j.ensm.2024.103619.

[8] F. Ahmad *et al.*, “Gel polymer electrolyte composites in sodium-ion batteries: Synthesis methods, electrolyte formulations, and performance analysis,” Nov. 01, 2024, *Elsevier B.V.* doi: 10.1016/j.jpowsour.2024.235221.

[9] K. Aruchamy, S. Ramasundaram, S. Divya, M. Chandran, K. Yun, and T. H. Oh, “Gel Polymer Electrolytes: Advancing Solid-State Batteries for High-Performance Applications,” Jul. 01, 2023, *Multidisciplinary Digital Publishing Institute (MDPI)*. doi: 10.3390/gels9070585.

[10] J. P. Serra *et al.*, “Carrageenan-Based Hybrid Materials with Ionic Liquids for Sustainable and Recyclable Printable Pressure Sensors,” *ACS Sustain Chem Eng*, vol. 10, no. 26, pp. 8631–8640, Jul. 2022, doi: 10.1021/acssuschemeng.2c02374.

[11] M. S. Elfaruk, C. Wen, C. Chi, X. Li, and S. Janaswamy, “Effect of salt addition on iota-carrageenan solution properties,” *Food Hydrocoll*, vol. 113, Apr. 2021, doi: 10.1016/j.foodhyd.2020.106491.

[12] T. Fenton, K. Kanyuck, T. Mills, and E. Pelan, “Formulation and characterisation of kappa-carrageenan gels with non-ionic surfactant for melting-triggered controlled release,” *Carbohydrate Polymer Technologies and Applications*, vol. 2, Dec. 2021, doi: 10.1016/j.carpta.2021.100060.

[13] J. Li *et al.*, "Hydrogel polymer electrolytes toward better zinc-ion batteries: a comprehensive review," *eScience*, p. 100294, Jul. 2024, doi: 10.1016/j.esci.2024.100294.
[14] G. Guzmán-González, "A Brief Review of the Role of Polymers in Fifferent Lithium-Ion Conducting Electrolytes for LIBs," Sep. 19, 2023, *Sociedad Quimica de Mexico A.C.* doi: 10.29356/jmcs.v67i4.1959.
[15] S. Elmarhoum, S. Mathieu, K. Ako, and W. Helbert, "Sulfate groups position determines the ionic selectivity and syneresis properties of carrageenan systems," *Carbohydr Polym*, vol. 299, Jan. 2023, doi: 10.1016/j.carbpol.2022.120166.
[16] H. Mokhtari *et al.*, "Recent advances in chemically-modified and hybrid carrageenan-based platforms for drug delivery, wound healing, and tissue engineering," Jun. 01, 2021, *MDPI AG*. doi: 10.3390/polym13111744.
[17] L. S. Kremer *et al.*, "Influence of the Electrolyte Salt Concentration on the Rate Capability of Ultra-Thick NCM 622 Electrodes," *Batter Supercaps*, vol. 3, no. 11, pp. 1172–1182, Nov. 2020, doi: 10.1002/batt.202000098.

Regeneration by electrodialysis of secondary spent monoethanolamine solution obtained after mineralization of captured carbon dioxide with calcium sulphate

Ketwarang Nimnualrat[1], Nathaporn Kenbubpha[1], Kittiporn Laitha[1], Palang Bumroongsakulsawat[1,*]

[1] Department of Chemical Engineering, Faculty of Engineering, Chulalongkorn University, Bangkok 10330, Thailand
[*] Corresponding author: palang.b@chula.ac.th

ABSTRACT

The greenhouse effect has been impacting our planet further than we even realized. In recent years, the earth's atmosphere has rapidly changed at a faster pace than ever. The main villain, mostly released from industry, is carbon dioxide (CO_2), which contributes about 79.7 percent of total greenhouse gases. Consequently, Carbon Capture, Utilization and Storage (CCUS) has now become an important role to mitigate this problem. A widely used industrial medium for capturing CO_2 is aqueous solution of monoethanolamine (MEA), which is capable of capturing CO_2 from fossil fuel-fired processes. However, current MEA regeneration by stripping has high energy requirements for boiling the solution. In this study, mineralization followed by electrodialysis was examined as an alternative method to recover MEA. $CaSO_4$ was added to CO_2-rich MEA solution to precipitate CO_2 out as $CaCO_3$. This mineralization process produced protonated MEA ($MEAH^+$) and left sulphate in the solution. Electrodialysis was performed to deprotonate $MEAH^+$ and remove sulphate. The main energy requirement of this coupled process lay in the electrical energy for electrodialysis and did not involve the energy-intensive boiling of solution. Preliminary results showed that a higher flow rate resulted in a higher faradaic efficiency for sulfate removal. Experimental results also hinted at currently unknown processes hindering sulfate removal.

Keywords: Carbon dioxide; CCUS; MEA; Electrodialysis; Regeneration

1. INTRODUCTION

The greenhouse effect has been impacting our planet further than we even realized. In recent years, the earth's atmosphere has rapidly changed at a faster pace than ever. Carbon dioxide (CO_2) is a primary factor contributing to global warming, accounting for more than 70% of greenhouse gas emissions worldwide. As CO_2 emission levels rise, the effects of climate change become more serious and dangerous, thus resulting in major environmental challenges such as rising in sea levels, melting glaciers, and ocean acidification [1].

Carbon capture, utilization and storage (CCUS), the process concepts of capturing CO_2 from relevant emission sources, can apply to reduce CO_2 emissions [1]. The CCUS has become a main crucial technology that is significantly reducing environmental impact.

The use of organic amine solutions as an absorbent in CO_2 absorption process is widely used in industry due to its strong absorptive capacity and effectiveness [1]. One generally used absorbent is monoethanolamine (MEA) which is effective in absorbing CO_2 gas from fossil fuel-fired processes [2] by forming carbamate solution according to the following net reactions:

Carbamate formation reaction:

$$RNH_2 + CO_2 + H_2O \leftrightarrow RNHCOO^- + H_3O^+ \quad (1)$$

Amine protonation reaction:

$$RNH_2 + H_3O_+ \leftrightarrow RNH_3^+ + H_2O \quad (2)$$

Overall, roughly two moles of MEA can capture one mole of CO_2.

Although MEA-based CO_2 capture has a remarkable efficacy to absorb CO_2, the conventional stripping regenerator technology requires high energy usage to reproduce lean MEA solution with 4.0 GJ/t-CO_2 of heat requirement [3], which is about 70-80% of the total energy consumption for this process. The high sensible heat and latent heat of MEA have been a serious difficulty for improving the required energy usage [1]. The large amount of heat duty can contribute to increasing operating temperature, which subsequently causes absorbent degradation. Moreover, amines such as MEA are highly corrosive, so higher concentrations require chemical additives or higher cost in appropriate materials of construction to prevent

corrosion [4]. Thus, mitigating the energy consumption problem of desorption of organic amine solution is a crucial part in the growth of CO_2 capture technology in the future.

CO_2 may be removed from carbamate by spontaneous precipitation as $CaCO_3$ with $CaSO_4$ according to the following reaction.

$$RNHCOO^- + RNH_3^+ + CaSO_4 + H_2O \leftrightarrow 2RNH_3^+ + SO_4 + CaCO_3 \quad (3)$$

It can be seen that the carbamate ion is converted into RNH_3^+ and SO_4^{2-} is added to the solution. RNH_3^+ must be deprotonated to MEA and SO_4^{2-} must be removed so that the solution can be reused for CO_2 capture. Electrodialysis may be used for this purpose. In a related regeneration process, only 0.87 GJ/t-CO_2 was required with a low resistance membrane [3] compared to the conventional process which requires high energy usage around 4.0 GJ/t-CO_2.

We present in this work our preliminary investigation of the use of the proposed mineralization-electrodialysis process for the regeneration of spent MEA solution.

2. EXPERIMENTAL

2.1 Materials and chemicals

MEA was purchased from Sigma Aldrich with 99% purity. Carbon dioxide (CO_2) was obtained from Linde Inc., Thailand. Calcium sulphate ($CaSO_4$) and sodium sulphate (Na_2SO_4) were locally sourced. The anion exchange membrane and bipolar membrane used in the electrodialysis cell were Fumasep FAB-PK-130 and Fumasep FBM-PK, respectively.

2.2 Experiment procedures

2.2.1 Carbon dioxide capture

250 mL of 1 M MEA in water was prepared and loaded into a Duran bottle. A dispersion tube was inserted into the bottle to add CO_2 into the solution. CO_2 was dispersed into the MEA solution until the pH trend of the solution became stable around 8.

2.2.2 Mineralization

250 mL of the carbamate solution (1 M MEA saturated with CO_2), which was obtained after saturation with CO_2, was reacted with calcium sulphate ($CaSO_4$) in a batch stirred-tank reactor. The reaction was carried out at ambient conditions for 180 minutes. To ensure that all carbamate was reacted, an excess amount of calcium sulphate was added.

2.2.3 Supernatant and precipitate separation

The slurry from the mineralization reaction was filtered by filter paper to separate the liquid solution and the precipitate. The precipitate was dried at 110 °C for 20 minutes for TGA analysis.

2.2.4 Regeneration of solution after mineralization by electrodialysis

The electrodialysis cell (Figure 1) consisted of in-house designed rigid end plates and flexible flow channels. The parts were fabricated by additive manufacturing (3D printing) provided by Septillion Co., Ltd. The rigid end plates and the flexible flow channels were printed with Formlabs' Form 3 from Formlabs' Clear resin and Elastic 50A resin, respectively by Print my design Co., Ltd. Both end plates each have an electrode slot. One of the two end plates has 6 solution ports. The thickness of the flow channels was 2 mm. The cell was configured with 3 chambers. The solution to be generated was pumped through the middle chamber. A bipolar membrane was placed on the cathode side with the anion exchange layer (AEL) facing away from the cathode. An anion exchange membrane was placed on the anode side. This assembly was placed between two 3 mm thick stainless-steel plates and compressed with two c-clamps.

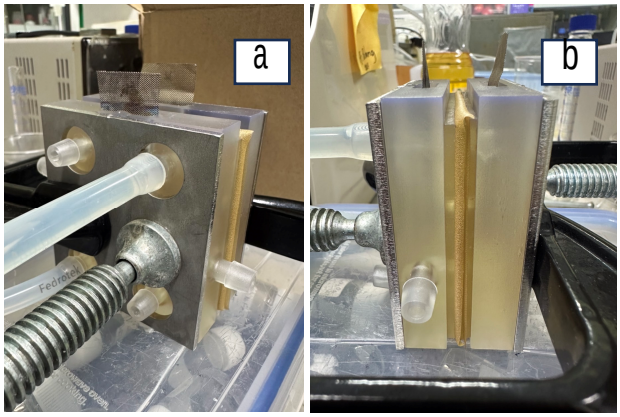

Figure 1 Photograph of the electrodialysis cell: ports (a) and layers (b).

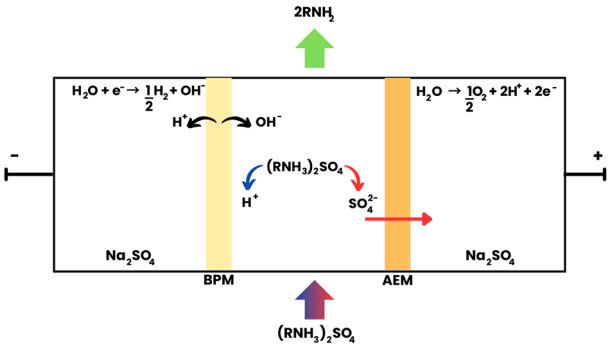

Figure 2 Schematic of electrodialysis apparatus for MEA regeneration

Figure 2 shows the configuration of the electrodialysis cell. With a voltage applied in the direction indicated, sulfate ions were expected to be transported through the AEM towards the anode, eventually removed from the $(RNH_3)_2SO_4$ solution. Simultaneously, the bipolar membrane (BPM), which consisted of an anion-exchange layer and a cation-

exchange layer adhering to one another and hence would not allow transport of any ions between adjacent chambers, allowed the splitting of water into protons and hydroxide ions between the two layers when the potential drop across the membrane was above a threshold. The generated protons and hydroxide ions would then migrate to the cathode chamber and the $(RNH_3)_2SO_4$ solution. The hydroxide ions would neutralize RNH_3^+ to MEA and water. In the anode chamber, water would be oxidized into oxygen and protons. With the sulfate ions from the AEM, the process would essentially be the addition of sulfuric acid to the anode solution. On the cathode side, water would be reduced into hydrogen and hydroxide ions, the latter of which was expected to be neutralized by the protons from the bipolar membrane.

Electrodialysis was performed at ambient conditions with a current of 0.3 A. 20 mL of the supernatant, which was obtained from the step described in section 2.2.3, was circulated with a peristaltic pump at 5.9 mL/min and 24.0 mL/min through the middle chamber. Into each of the cathode and anode chamber was added 8 mL of 0.5 M Na_2SO_4. Platinized titanium mesh was used as an electrode. The experiments were carried out for 5.5 h with a flow rate of 5.9 ml/min and 2.0 h with a flow rate of 24.0 ml/min.

2.3 Characterization and Product analysis

The components of the precipitate were analyzed by thermogravimetric analysis (TGA) (TA Instrument). The sample was heated from 50-1000 °C at a heating rate of 10 °C/min with air zero flowing at 400 mL/min.

The pH of the $(RNH_3)_2SO_4$ solution was measured by a pH meter (Mettler-Toledo, SevenDirect SD20) during the carbon dioxide capture process and after the electrodialysis process.

The amount of sulphate remaining in the regenerated solution from the electrodialysis process was analyzed by precipitation. $BaCl_2$ in excess was added to 2 mL of the solution. Precipitates were filter out with filter paper, washed with DI water, dried at 110 °C for 20 minutes, and weighed. The amount of sulphate was calculated with an assumption that the precipitates were purely $BaSO_4$.

2.4 Faradaic efficiency (FE)

Faradaic efficiency (FE) explains the overall selectivity of a desirable process in an electrochemical process. The faradaic efficiency is the ratio of the equivalent charge effecting a desirable process that actually occurs to the total charge passed during electrodialysis. In this work, the desirable process was the transport of sulfate ions across the AEM. FE was defined in this work according to the following equation:

$$(FE) = \frac{nZF}{Q} = \frac{nZF}{It} \quad (8)$$

Where n is the amount of sulfate transported across the AEM (mole); F is the Faraday constant (96485 C mol^{-1}); Z is the charge number of the sulfate ion; I is the current passed (A); *Q* is the total charge passed through the system; t is time (second) [6, 7].

3. RESULTS AND DISCUSSION

3.1 Thermogravimetric analysis (TGA) of precipitates from mineralization

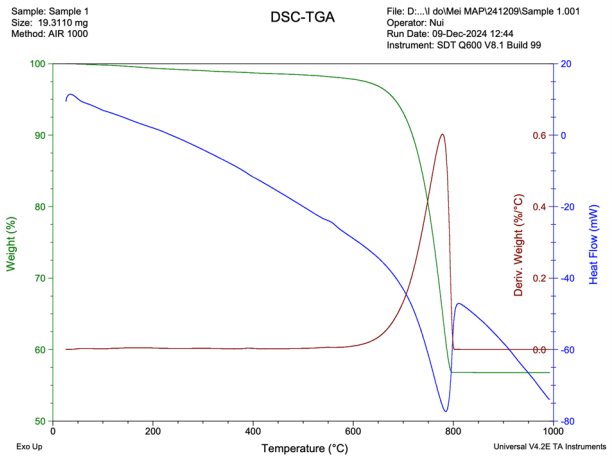

Figure 3 Thermogravimetric curves of precipitates from mineralization

From figure 3, the results indicated percent weight loss with respect to temperature. The decomposition of calcium carbonate into calcium oxide and CO_2 begins around 700 ℃ while the decomposition of calcium sulfate into calcium oxide and SO_3 is higher than 1000 ℃ and this was consistent with the peak beginning at around the same temperature. Due to the amount of released CO_2 shown in the TGA graph, this precipitate was apparently mostly $CaCO_3$ and it was inferred that using $CaSO_4$ could separate almost all CO_2 out of MEA.

3.2 Electrodialysis

Table 1 Remaining sulfate and pH after electrodialysis.

Sample	Flowrate (mL/min)	Time (h)	Remaining SO_4	pH of MEA
1	5.9	5.5	50.64%	12.67
2	5.9	5.5	24.22%	13.02
3	24.0	2.0	79.27%	11.86
4	24.0	2.0	56.35%	12.29

Table 2 Faradaic efficiency after electrodialysis.

Sample	Flowrate (mL/min)	Time (h)	FE
1	5.9	5.5	16.04%
2	5.9	5.5	24.62%
3	24.0	2.0	18.52%
4	24.0	2.0	39.00%

Table 1 shows that sulfate could be partially removed from the $(RNH_3)_2SO_4$ solution. Our preliminary results exhibited high levels of uncertainty. Nevertheless, Table 2 shows that the faradaic efficiencies seemed to be dependent on the flow rates. A higher flow rate resulted in higher faradaic efficiencies. The improvement was plausibly brought about by faster mass transfer associated with high flow rates. As the electrodialysis was conducted at a fixed current of 0.3 A, anions had to be transported across the AEM at a rate that was equivalent to the current passed. Ideally, only sulfate ions would be transported. However, if the mass transfer of this ion is insufficient, other anions will be transported along and the faradaic efficiency will be decreased. The source of other anions could be the splitting of water into protons and hydroxide ions at the surface of the AEM. This process would be similar to what commonly happens inside a bipolar membrane and hence could also happen on an AEM when the potential drop across the membrane is sufficiently large following poor transfer of the intended ions.

In addition, we have recently found that ethanol-o-sulfate (EOS), an inorganic acid ester, could form from MEA and sulfuric acid. As the main precursors of this species already existed in the solution in this work, we suspected that EOS might form and bind MEA and sulfate together. If this happens, the transport of sulfate across the AEM will be even more difficult and the faradaic efficiency will be decreased. We are investigating whether EOS forms in our system.

Despite the low sulfate removal, the pH of the $(RNH_3)_2SO_4$ solution after treatment was restored to the usual range of fresh MEA solution of about 12-13; this was consistent with the pH-CO_2 loading presented in Figure 5.

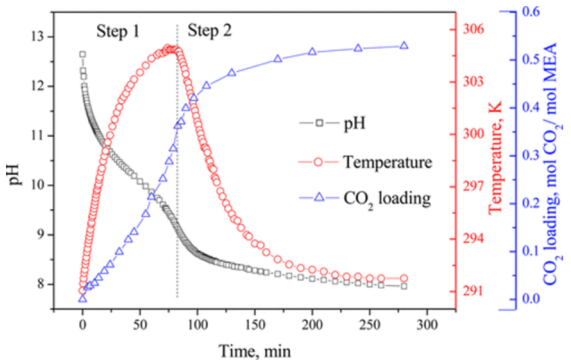

Figure 5 pH-CO_2-temperature relation in CO_2 absorption by MEA solution [5]

From figure 5, in the first stage, the formation of carbamate was the main reaction between CO_2 and MEA. Once the pH dropped below 8.5, both pH and the maximum intensity of the carbamate concentration were reduced in contrast with CO_2 loading. Therefore, bicarbonate/carbonate (HCO_3^-/CO_3^{2-}) species were detected in the solution. These results can be suggested that some of carbamate began to decompose to bicarbonate/carbonate (HCO_3^-/CO_3^{2-}) species during this period, and the decomposition rate nearly equal to the formation rate.

Figure 5 also shows that after saturation with CO_2 and the reaction equilibrium, the pH of MEA solution approached 8. This was consistently observed in our experiments.

4. CONCLUSION

The feasibility of the proposed mineralization-electrodialysis as a process for the regeneration of MEA solution was reported. Experimental results showed that $CaSO_4$ could be used to separate CO_2 from the solution in the form of $CaCO_3$ precipitates. Electrodialysis could be used to partially remove sulfate. Despite the high uncertainty in the preliminary results, the faradaic efficiencies seemed to increase with increasing flow rates. Experimental results also hinted at currently unknown processes hindering sulfate removal.

ACKNOWLEDGMENTS

I would like to express my gratitude to everyone who supported me along with this project. Firstly, this research was supported by the Department of Chemical Engineering, Faculty of Engineering, Chulalongkorn university for providing financial support, essential materials and technical support which made this study possible. I am also deeply thankful to my advisor, Professor Dr. Palang Bumroongsakulsawat, for their invaluable guidance and continuous support throughout this project. Their expertise and insightful feedback were significant in leading this work. Additionally, I am grateful to my colleague, Miss Nathaporn Kenbubpha and Mr.Kittiporn Laitha, for their helpful collaboration, insightful discussions, and significant assistance with data collection and analysis, all of which contributed greatly to the success of this study.

This research has received funding support from the NSRF via the Program Management Unit for Human Resources & Institutional Development, Research and Innovation [grant number B42G670036].

REFERENCES

1. Fu, L., et al., Research progress on CO2 capture and utilization technology. Journal of CO2 Utilization, 2022. 66: p. 102260.
2. dos Santos, T.C., et al., Supramolecular dimers drive the reaction between CO2 and alkanolamines towards carbonate formation. Journal of CO2 Utilization, 2022. 61: p. 102054.
3. Taniguchi, I. and T. Yamada, Low energy CO2 capture by electrodialysis. Energy Procedia, 2017. 114: p. 1615-1620.
4. Rubin, E.S., et al., The outlook for improved carbon capture technology. Progress in Energy and Combustion Science, 2012. 38(5): p. 630-671.

5. Lv, B., et al., Mechanisms of CO_2 capture into monoethanolamine solution with different CO2 loading during the absorption/desorption processes. Environmental science & technology, 2015. 49(17): p. 10728-10735.
6. Kempler, P.A. and A.C. Nielander, *Reliable reporting of Faradaic efficiencies for electrocatalysis research.* Nature Communications, 2023. **14**(1): p. 1158.
7. Zhao, J., et al., *An overview of Cu-based heterogeneous electrocatalysts for CO 2 reduction.* Journal of Materials Chemistry A, 2020. **8**(9): p. 4700-4734.

One-dimensional simulation of an alkaline-acid direct glycerol fuel cell

Papitchaya Chaloeypanit[1], Supaporn Therdthianwong[1], Apichai Therdthianwong[2,*]

[1] Department of Chemical Engineering, Faculty of Engineering, King Mongkut's University of Technology Thonburi, Bangkok 10140, Thailand
[2] Fuel Cells and Hydrogen Research and Engineering Center, Pilot Plant Development and Training Institute, King Mongkut's University of Technology Thonburi, Bangkok 10140, Thailand
[*] Corresponding author: apichai.the@kmutt.ac.th

ABSTRACT

A one-dimensional numerical model of an alkaline-acid direct glycerol fuel cell (AA-DGFC) was developed to investigate the influences of the operating parameters such as glycerol to sodium hydroxide ratio ($C_3H_8O_3$:NaOH) and glycerol concentration on the AA-DGFC performance. A model of AA-DGFC was created by using computational software. In setting up the model, mass transport and charge transport, and ionic charge transport equations were coupled under steady state assumptions. Fick's law was used to describe species diffusion, while Butler-Volmer kinetic governed electro-chemical charge transfer at electrode-electrolyte interfaces. Concentration-dependent diffusivity formulation of Sodium ion (Na^+) transport in membrane was used. The simulation results show good agreement with experimental data under steady-state conditions, yielding a MAE of 0.03 V, and RMSE of 0.0330 V as shown in Table 6. The model not only captures both electrochemical and transport phenomena but also can be extended to analyze various operating conditions and support design optimization for AA-DGFC systems.

Keywords: Alkaline-acid direct glycerol fuel cell (AA-DGFC); Mass transport; Charge transport; Steady-state conditions; Butler-Volmer kinetic

1. INTRODUCTION

The growing concerns over climate change and fossil fuel depletion have intensified the global pursuit of clean and sustainable energy technologies. Among these, fuel cells have emerged as promising devices due to their high efficiency, modularity, and environmentally friendly operation [1]. Direct alcohol fuel cells (DAFCs) offer the advantage of liquid fuel usage, room temperature operation, and potential cogeneration of value-added chemicals [2].

Glycerol, a byproduct of biodiesel production, has attracted increasing interest as a low-cost, renewable feedstock for DAFCs. Its high hydrogen content, low toxicity, and water solubility make it a promising candidate for direct conversion in electrochemical systems [2, 3]. The alkaline-acid direct glycerol fuel cell (AA-DGFC) utilizes an alkaline environment at the anode and an acidic cathode, leveraging favorable kinetics for both glycerol oxidation and hydrogen peroxide reduction, respectively [4].

Previous experimental studies, including those by Banjong et al. [4] and Sangkheaw et al. [5], demonstrated that the AA-DGFC configuration can achieve high performance under appropriate electrolyte and catalyst conditions. However, most existing models have either simplified the electrochemical kinetics or neglected the effect of sodium ion (Na^+) transport across the membrane. Moreover, predictive models have been limited to single-condition simulations without systematic comparison against multi-condition experimental data.

This study presents a one-dimensional numerical model of an AA-DGFC developed under steady-state and isothermal conditions. The model incorporates species transport, ionic conductivity, electrochemical charge transfer, and concentration-dependent diffusivity of Na^+ through the Nafion membrane. Simulation results were validated against experimental polarization data under various operating scenarios. The objective is to evaluate the predictive capability of the model and provide mechanistic insight into performance-limiting phenomena in AA-DGFCs.

2. Numerical Modeling

2.1 Model formulation and assumptions

The alkaline-acid direct glycerol fuel cell (AA-DGFC) system was modeled under one-dimensional steady-state assumptions. The computational domain consists of five primary regions: the anode diffusion layer (ADL), anode catalyst layer (ACL), Nafion 115 membrane (MEM), cathode catalyst layer (CCL), and cathode diffusion layer (CDL). These layers were arranged sequentially in the x-direction to simulate mass and charge transport across the cell. The

corresponding schematic and domain are illustrated in Figure 1.

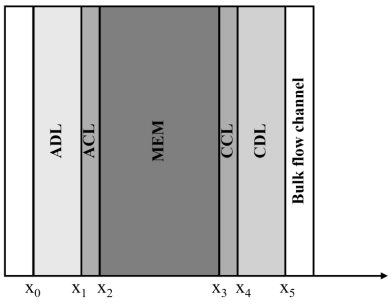

Figure 1. One-dimensional schematic of the AA-DGFC structure, consisting of anode and cathode diffusion layers (ADL and CDL), catalyst layers (ACL and CCL), and a Nafion 115 membrane (MEM). The x-axis indicates spatial used in the 1D model.

The geometric dimensions and porosity values of each domain in the AA-DGFC model are summarized in Table 1. All values were assigned based on representative structures reported in the literature for direct alcohol fuel cells. No porosity or thickness optimization was performed in this study. The selected parameters are consistent with prior modeling approaches, including Banjong et al. [4], where porosity values were adopted from experimentally typical ranges for porous carbon-based layers and Nafion membranes under compression.

Table 1 Geometric and physical parameters of each domain in the AA-DGFC model.

Domain	Symbol	Value	Unit	Ref.
Anode diffusion layer, ADL	l_{ADL}, ε_{ADL}	200, 0.7	μm, -	[4]
Anode catalyst layer, ACL	l_{ACL}, ε_{ACL}	20, 0.3	μm, -	[4]
Membrane, MEM	L_{MEM}, ε_{MEM}	127, 0.3	m, -	data sheet
Cathode diffusion layer, CDL	l_{CDL}, ε_{CDL}	20, 0.3	μm, -	[4]
Cathode catalyst layer, CCL	l_{CCL}, ε_{CCL}	200, 0.7	μm, -	[4]

To simplify the glycerol oxidation reaction (GOR), glycerate acid (GA) was assumed as the main product in this model. This assumption is based on previous experimental where GA was identified as the major product under alkaline conditions[6]. (1) The numerical one-dimensional model was developed under the steady-state and isothermal conditions. An operating temperature of 80°C was used, consistent with experimental data [5]. (2) The model does not account for transient behavior. (3) The ion transport across the Nafion 115 membrane occurred via Na^+. (4) No fuel crossover through membrane.

The electrochemical reactions in alkaline-acid direct glycerol fuel cell (AA-DGFC) are assumed to produce glycerate acid (GA) for GOR in anode and hydrogen peroxide (H_2O_2) reduction at the cathode. The overall reaction reflects the net electron transfer through the external circuit, while sodium ion (Na^+) act as charge carriers through the membrane. The half-cell and overall reaction are as follows [5]:

Anode (GOR):
$C_3H_8O_3 + 5OH^- \rightarrow C_3H_5O_4^- + 4H_2O + 4e^-$
Standard potential: $E_0^a = -0.74$ V vs. SHE

Cathode (H_2O_2 reduction):
$H_2O_2 + 2H^+ + 2e^- \rightarrow 2H_2O$
Standard potential: $E_0^c = 1.78$ V vs. SHE

Overall reaction:
$C_3H_8O_3 + 5OH^- + H_2O_2 + 2H^+ \rightarrow C_3H_5O_4^- + 4H_2O$
Theoretical cell voltage: $E_0 = 2.52$ V

2.2 Governing Equations and Electrochemical Kinetics

The AA-DGFC model incorporates mass transport and electrochemical kinetics under steady-state and isothermal conditions. Species transport in each domain is governed by Fick's second law:

$$\frac{dC_i}{dt} = \nabla\cdot\left(D_{eff,i}\nabla C_i\right) + R_i \qquad (2.1)$$

where C_i is the local concentration of species i, $D_{eff,i}$ is the effective diffusivity, and R_i is the local reaction derived from electrochemical reactions. The effective diffusivity in porous electrodes was estimated using the Bruggeman correlation:

$$D_{eff,i} = D_i\cdot\varepsilon^{1.5} \qquad (2.2)$$

Electrochemical reactions at the anode and cathode catalyst layers follow the Butler–Volmer formulation. In this model, the cell current density is set as a known input and is assumed to equal the local current densities in both electrodes: $I_{cell} = j_a = j_c$. The anodic current density is expressed as:

$$j_a = j_{0,a}\left[\exp\left(\frac{\alpha_a F\eta_a}{RT}\right) - \exp\left(\frac{-\alpha_c F\eta_a}{RT}\right)\right] \qquad (2.3)$$

Instead of computing η_a from the electrode potentials, it is numerically obtained from the above equation given I_{cell}. The exchange current density j_0 is expressed as a function of local concentrations, adapted from Han et al. [2]:

$$j_{0,a} = j_{0,a,ref}\left(\frac{C_{GLY}}{C_{GLY,ref}}\right)^{\gamma_{GLY}}\left(\frac{C_{OH}}{C_{OH,ref}}\right)^{\gamma_{OH}} \qquad (2.4)$$

In this study, $\gamma_{GLY} = \gamma_{OH} = 1$ was assumed for all cases. At the cathode, hydrogen peroxide reduction occurs under acidic conditions. The reaction kinetics were also described using the Butler–Volmer equation:

$$j_c = j_{0,c}\left[\exp\left(\frac{\alpha_a F \eta_c}{RT}\right) - \exp\left(\frac{-\alpha_c F \eta_c}{RT}\right)\right] \quad (2.5)$$

The local cathodic current density j_c was assumed to equal the applied cell current I_{cell}. The cathodic overpotential η_c was calculated from this expression. The exchange current density at the cathode was defined as:

$$j_{0,c} = j_{0,c,ref}\left(\frac{C_{H2O2}}{C_{H2O2,ref}}\right)^{\gamma_{H2O2}} \quad (2.6)$$

In this study, γ_{H2O2} was set to 1 for simplification, and C_{H2O2} was the local concentration at the cathode–membrane (CCL-MEM) interface.

In the numerical model, species transport was described by Fick's law with source terms added to account for electrochemical reactions at the corresponding domains. The source term R_i for each species i was formulated based on the overall electron balance and stoichiometric coefficients in the half-cell reactions. The following table summarizes the domain, and the corresponding source term used in the governing equations for species transport:

Table 2 Source term R_i is used in the mass transport equations for each species.

Species	Domain	Source term, R_i
Glycerol	ACL	$\frac{-I_{cell}}{n_a F}$
OH^-	ACL	$\frac{-5I_{cell}}{n_a F}$
H_2O_2	CCL	$\frac{-I_{cell}}{n_c F}$
Na^+	MEM	0

These source terms reflect the stoichiometric consumption of reactants according to the half-cell reactions. In the anode catalyst layer (ACL), glycerol and OH^- are consumed in the glycerol oxidation reaction (GOR), while hydrogen peroxide is reduced in the cathode catalyst layer (CCL). Sodium ions are not produced or consumed chemically but are transported through the membrane to maintain charge neutrality. Here, $n_a = 4$ and $n_c = 2$ denote the number of electrons involved in the anode and cathode reactions, respectively.

The boundary conditions in this model were specified to represent the feed concentrations and electrochemical transport characteristics at relevant interfaces. At the inlet boundaries of the anode and cathode, Dirichlet conditions were applied to fix the concentrations of species based on the experimental feed composition. Additionally, flux boundary conditions for sodium ions were implemented at the membrane interfaces to account for ionic transport driven by the external current, with the direction determined by the assumed Na^+ transference number. The applied boundary conditions are summarized in Tables 3 and 4.

Table 3 Dirichlet boundary conditions for species at inlet boundaries.

Species	Location, x	Value	Unit
C_{GLY}	$x = x_0$	$C_{GLY,in}$	mol m^{-3}
C_{OH}	$x = x_0$	$C_{OH,in}$	mol m^{-3}
C_{H2O2}	$x = x_5$	$C_{H2O2,in}$	mol m^{-3}

Table 4 Flux boundary conditions for Na^+ transport in the membrane.

Interface location, x	BC	Unit
$x = x_2$ (ACL-MEM)	$\frac{I_{cell} t_{Na}}{F}$	mol m^{-2} s^{-1}
$x = x_3$ (MEM-CCL)	$\frac{-I_{cell} t_{Na}}{F}$	mol m^{-2} s^{-1}

The electrochemical kinetic parameters used in the Butler–Volmer equations were obtained by fitting the model to experimental polarization data under the base-case condition. The anode and cathode exchange current densities, as well as the anodic charge transfer coefficient, were calibrated to achieve the best match with observed steady-state performance. The cathodic charge transfer coefficient was assumed, as variation of this parameter showed minimal influence on the overall result.

Table 5 Electrochemical kinetic parameters used in the AA-DGFC model.

Parameter	Symbol	Value	Unit	Ref.
Anode exchange current density	$j_{0,a,ref}$	0.4	A m^{-2}	Fitted
Cathode exchange current density	$j_{0,c,ref}$	31	A m^{-2}	Fitted
Anode transfer coefficient	α_a	0.7	-	Fitted
Cathode transfer coefficient	α_c	0.5	-	Assumed

The electrochemical kinetic parameters used in the Butler–Volmer equations are summarized in Table Z. The anode exchange current density ($j_{0,a,ref} = 0.4$ A m^{-2}) was significantly lower than that of the cathode ($j_{0,c,ref} = 31$ A m^{-2}), reflecting the sluggish kinetics of the glycerol oxidation reaction (GOR) compared to the

H_2O_2 reduction reaction. This large kinetic difference is consistent with previous studies on Pt/C electrodes, which report that GOR proceeds through multiple adsorbed intermediates and complex electron transfer steps, while H_2O_2 reduction exhibits fast kinetics under acidic conditions [2, 4].

For charge transfer coefficient, the anodic charge transfer coefficient (α_a=0.7) was fitted from experimental data, while the cathodic value (α_c=0.5) was assumed. The number of electrons transferred in each half-cell reaction was determined from the reaction stoichiometry: four electrons for GOR and two electrons for H_2O_2 reduction.

2.3 Cell Voltage Calculation

The cell voltage (V_{cell}) was determined by accounting for the activation overpotentials and the ohmic loss in the membrane, as expressed in Eq. (2.7):

$$V_{cell}=E_{OCV}-\eta_a-\eta_c-I_{cell}\left(\frac{l_{MEM}}{\sigma_{MEM}}\right) \quad (2.7)$$

2.4 Numerical implementation

Following the formulation of physical properties and electrochemical kinetics, the complete system of partial differential equations was implemented in COMSOL Multiphysics®. A finite element approach was employed to discretize the one-dimensional domain consisting of five layers. The mesh was constructed using 100 uniformly distributed elements, providing sufficient resolution to capture gradients in concentration and potential. Steady-state simulations were conducted under isothermal conditions (80 °C) using parametric sweeps of the cell current density (I_{cell}). A fully coupled solution method with a direct linear solver was adopted to enhance numerical stability.

3. RESULTS AND DISCUSSION

3.1 Base-case Validation

The experimental and model-predicted polarization curve at the base case (1 M glycerol with 5 M NaOH) is shown in Figure 2. This case was used to calibrate kinetic and transport parameters, particularly the anode and cathode reference exchange current densities ($j_{0,a,ref}$ = 0.4 A/m^2, $j_{0,c,ref}$ = 31 A/m^2) and the anode charge transfer coefficient (α_a=0.7), while the cathode coefficient (α_c) was assumed to be 0.5. The model showed excellent agreement with experimental data, accurately reproducing the voltage drop across the full range of current densities. The Root Mean Square Error (RMSE) and Mean Absolute Error (MAE) values are summarized in Table 6, confirming the predictive capability of model under this condition.

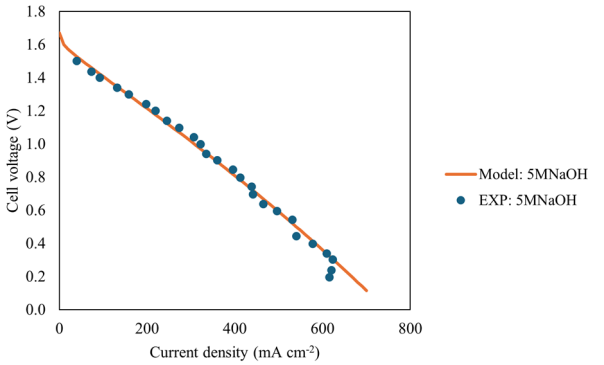

Figure 2 Polarization curve comparison between experiment and model prediction at 1 M glycerol with 5 M NaOH.

Table 6 MAE and RMSE simulation between experimental polarization curves after excluding transient regions.

Case (GLY:NaOH)	MAE (V)	RMSE (V)
0.5M:2.5M	0.06	0.0660
1.0M:3.0M	0.05	0.0619
1.0M:5.0M	0.03	0.0330
1.0M:8.0M	0.02	0.0250
1.0M:10.0M	0.01	0.0110
1.5M:7.5M	0.03	0.0376

To investigate the effect of electrolyte concentration on the performance of AA-DGFC, simulations were conducted at a fixed glycerol concentration of 1 M, while the NaOH concentration varied from 3 M to 10 M. Figure 5 shows the comparison between model predictions and experimental data for all four cases. The simulation used the same electrochemical and transport parameters calibrated from the base-case (1 M GLY : 5 M NaOH), with no further parameter adjustments.

3.2 Effect of NaOH Concentration on Cell Performance

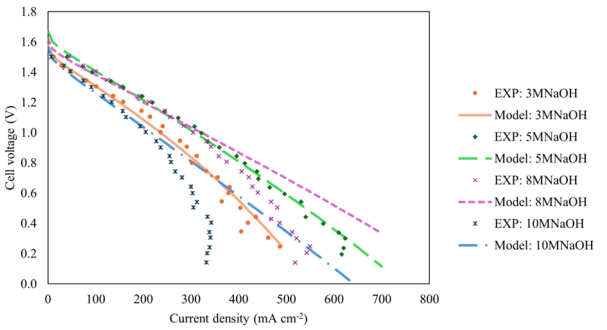

Figure 3 Comparison of experimental and model-predicted polarization curves at 1 M glycerol with varying NaOH concentrations (3 M, 5 M, 8 M, and 10 M).

Overall, the cell performance improved with increasing NaOH concentration from 3 M to 8 M, as shown by the upward shift of the polarization curves. This trend can be attributed to enhanced ionic conductivity in the membrane due to higher Na^+ ion concentration, which reduced ohmic resistance and improved charge transport across the cell. However, further increase to 10 M NaOH did not result in significant voltage gain, particularly at high current densities. This suggests that a saturation point in conductivity enhancement was reached, or that mass transport limitations became more dominant at very high electrolyte concentrations.

In all cases, the model was able to capture the trend of performance enhancement with increasing NaOH concentration. Slight deviations at high current densities may stem from transient effects, water management, or side phenomena not accounted for in the steady state 1D model, consistent with observations previously reported by Ponkaranan et al. [5].

These results suggest that increasing NaOH concentration enhances ionic conductivity and reduces ohmic losses, up to an optimal point around 8 M. Beyond this point, further improvement is limited, likely due to emerging mass transport resistances or water management effects. Overall, the model demonstrates robustness in predicting the performance trend across a range of electrolyte concentrations.

To further evaluate the model's predictive capability, additional case studies were conducted to examine the effect of varying glycerol-to-NaOH molar ratios on fuel cell performance.

3.3 Effect of Glycerol-to-NaOH Ratio

Figure 4 shows the polarization curves comparing experimental and simulated results under varying glycerol-to-NaOH molar ratios (0.5:2.5, 1.0:5.0, and 1.5:7.5). All cases were evaluated at a constant Glycerol-to-NaOH molar ratio of 1:5.

It can be observed that increasing the glycerol concentration (from 0.5 M to 1.0 M) significantly improved the maximum current density and cell voltage. This is likely due to the greater availability of glycerol molecules at the anode, enhancing the oxidation reaction rate. However, further increase to 1.5M glycerol led to a minor gain in current density, suggesting a limiting effect possibly caused by increased viscosity, diffusion limitations, or oxygen transport resistance at the cathode.

The model captures the performance trend well in all three cases, with good agreement in both shape and magnitude of the polarization curves. Predictive capability confirms the model's robustness in simulating the effects of reactant concentration variation.

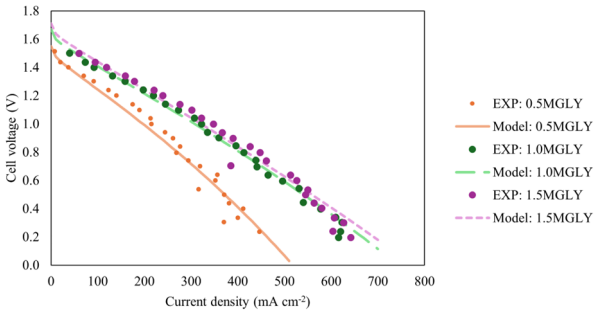

Figure 4 Comparison of experimental and model-predicted V–I curves at varying glycerol concentrations (0.5 M, 1.0 M, and 1.5 M) with fixed Glycerol-to-NaOH molar ratio of 1:5.

3.4 Overpotential Contributions under Base-Case Condition

To desccribe the origins of cell voltage loss, the contributions from anode overpotential, cathode overpotential, and ohmic overpotential were analyzed under the base-case condition (1 M glycerol : 5 M NaOH). Figure 5 displays the simulated overpotential values as a function of current density. The results reveal that the ohmic overpotential, primarily governed by ionic resistance across the membrane, increases linearly with current density and becomes the dominant contributor to the total voltage loss.

In contrast, both anode and cathode overpotentials exhibit logarithmic growth with current density, in line with typical Butler-Volmer behavior. The anode overpotential is slightly higher than the cathode counterpart, which reflects the relatively sluggish kinetics of glycerol electrooxidation. Nonetheless, the magnitude of kinetic losses remains relatively small compared to the ohmic loss throughout the current density range studied, indicating that further performance improvement may be achieved through reduction in internal resistance, particularly in the membrane domain.

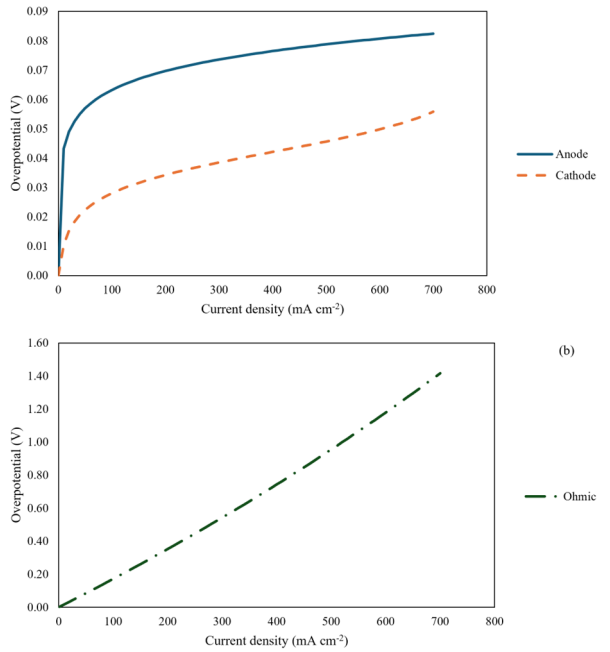

Figure 5 Simulated overpotentials under the base-case condition (1 M glycerol : 5 M NaOH): (a) anode and cathode overpotentials, (b) ohmic overpotential.

These results confirm that the cell performance in the base-case condition is predominantly governed by ohmic resistance, while activation losses at both electrodes contribute modestly. The model thus highlights the potential benefit of reducing membrane resistance to enhance overall performance.

4. CONCLUSION

A one-dimensional steady-state model of an alkaline-acid direct glycerol fuel cell (AA-DGFC) was developed and validated against experimental data. The model successfully captured the electrochemical behavior and mass transport phenomena across multiple operating conditions, including variations in sodium hydroxide concentration and glycerol-to-NaOH molar ratio. Simulation results showed good agreement with experimental polarization curves, with RMSE values as low as 0.0110 V in optimal cases.

Although some deviation was observed at high current densities, particularly in conditions where experimental voltage dropped sharply, these regions are likely associated with transient phenomena and water management effects that were not considered in the steady-state model. Despite this limitation, the model was able to predict the overall performance trend with reasonable accuracy.

Parametric studies revealed that ohmic loss, primarily due to ionic resistance in the membrane, was the dominant factor limiting cell performance. Activation losses at both electrodes were comparatively small, especially at higher electrolyte concentrations. The model's ability to replicate these trends highlights its robustness and suitability for future use in AA-DGFC system design and performance optimization. Further work may involve extension to transient operation and incorporation of product selectivity modeling.

ACKNOWLEDGMENTS

The authors would like to acknowledge the Fuel Cells and Hydrogen Research and Engineering Center, King Mongkut's University of Technology Thonburi, for providing experimental facilities and technical support. The first author gratefully acknowledges the academic support provided by Department of Chemical Engineering, KMUTT.

REFERENCES

1. Larminie, J. and A. Dicks, Fuel Cell Systems Explained. 2003.
2. Han, X., et al., Numerical analysis of anion-exchange membrane direct glycerol fuel cells under steady state and dynamic operations. International Journal of Hydrogen Energy, 2014. 39(34): p. 19767-19779.
3. Yahya, N., S.K. Kamarudin, and N.A. Karim, Direct glycerol fuel cells (DGFCs), in Direct Liquid Fuel Cells. 2021. p. 115-136.
4. Banjong, J., et al., High performance alkaline-acid direct glycerol fuel cells for portable power supplies via electrode structure design. International Journal of Hydrogen Energy, 2020. 45(3): p. 2244-2256.
5. Sangkheaw, P., et al., Enhancement of anode performance for alkaline-acid direct glycerol fuel cells. Renewable Energy, 2020. 161: p. 395-407.
6. Zhang, Z., L. Xin, and W. Li, Electrocatalytic oxidation of glycerol on Pt/C in anion-exchange membrane fuel cell: Cogeneration of electricity and valuable chemicals. Applied Catalysis B: Environmental, 2012. 119-120: p. 40-48.

Reduction and capture of chlorine in Napier grass using microwave torrefaction

Prodpran Siritheerasas[1,*], Roong Sirinuntavitaya[1], Phakjira Sangcharoenwathana[1]

[1] Department of Chemical Engineering, Thammasat School of Engineering, Thammasat University, Pathum Thani 12120, Thailand
[*] Corresponding author: sprod@tu.ac.th

ABSTRACT

The purpose of this study was to reduce and capture chlorine (Cl) from Napier grass using microwave torrefaction with the microwave power of 300 or 600 W for 5 min. A microwave absorber (MA), either silicon carbide (SiC) or activated carbon (AC), in the amount of 10 or 20 wt.% of the mass of Napier grass, was added to Napier grass to simultaneously absorb microwave irradiation and capture Cl during torrefaction. It was found that microwave torrefaction could reduce Cl by ~69-95 wt.% of the initial amount of Cl in Napier grass. Increases in both microwave power and amount of MA led to an increase in the Cl reduction percentage. When considering the Cl capture percentage of each MA, it was discovered that SiC could barely capture Cl, whereas AC was able to capture Cl in the amount of ~3-93 wt.% of the amount of Cl released into the atmosphere. Increases in both microwave power and amount of AC resulted in an increase in the Cl capture percentage.

Keywords: Chlorine capture; Chlorine reduction; Microwave absorber; Napier grass; Torrefaction

1. INTRODUCTION

It is reported that, in 2023, the global consumption of fossil fuels reaches a record high; the combined consumption of coal, oil (or liquid petroleum products), and natural gas is accounted for ~82% of the global energy consumption [1]. In 2023, The global fossil fuel consumption is reported as 140,231 TW-h, with the consumption of coal of 45,565 TW-h, of oil of 54,564 TW-h, and of natural gas of 40,102 TW-h [1].

It is clear that the combustion of these fossil fuels leads to the emissions of greenhouse gases (GHGs), which, in turn, result in the phenomenon called the global warming effect [2-3]. Several attempts have been made to mitigate this calamity. One of which is to transition from the uses of fossil fuels to renewable energy or such non-fossil fuels as biomass, as biomass is considered a CO_2-neutral fuel [4-5], on the ground that the amount of CO_2 emitted from the burning of this non-fossil fuel is equivalent to that absorbed by the plants, which are the source of biomass, for their photosynthesis [5].

Problematically, however, biomass possesses such drawbacks as a low heating value (*i.e.* the amount of energy *per* unit mass) and a low energy density (*i.e.* the amount of energy *per* unit volume), high moisture and volatile matter (VM) contents, and a hydrophilic nature [6-7]. Additionally, certain types of biomass contain chlorine (Cl) whose emission leads to such operating problems as deposition, fouling, and corrosion in thermal conversion systems of these fuels [8-10].

Torrefaction, a thermochemical process in an inert environment, with the temperature range of 200-300 °C [11], can be employed to overcome these technical difficulties. Recent studies reveal that torrefaction can improve the fuel properties of biomass such that the moisture is nearly completely reduced and the VM content is decreased, thus increasing the portion of fixed carbon (FC), which, in turn, results in an increase in the heating value of biomass [12-14].

The torrefied biomass is also of hydrophobic nature because of the loss of the hydroxyl (OH) groups, thus reducing the ability to induce water or moisture to its surface [11]. In addition, torrefaction can lead to a reduction in the Cl content, which, in turn, lower the technical problems caused by the emission of Cl [12-14]. The released Cl from biomass torrefaction can be captured by such absorbents as sodium carbonate (Na_2CO_3), potassium carbonate (K_2CO_3) [14], and calcium-based sorbents [15]. Biochar (*i.e.* solid char obtained from biomass) or activated carbon (AC) is reported to also have an ability to capture chlorinated compounds [16].

It is reported that microwave irradiation is a favourable heating technique for torrefaction as it consumes a low amount of energy and provides a rapid and uniform heating [17-18]. However, raw biomass poorly absorbs microwave irradiation [19-20]. Thus, the addition of a microwave absorber (MA), such as silicon carbide (SiC) or carbon black [21-23], is required to enhance the ability of biomass to absorb microwave irradiation. Char or AC produced from biomass itself can also be used as the MA. [21-23]

In the present study, the effects of torrefaction *via* microwave irradiation on the solid yield (Y), defined as

$$\mathrm{Y} = \frac{(m_{\mathrm{NG}})_a}{(m_{\mathrm{NG}})_b} \times 100 \qquad (1)$$

where $(m_{\mathrm{NG}})_b$ and $(m_{\mathrm{NG}})_a$ are the mass of Napier grass before and after torrefaction, respectively, and the reduction of Cl from Napier grass, which contains a considerable amount of Cl, were investigated. In addition, the possibility of utilising SiC or AC to simultaneously absorb microwave irradiation and capture Cl during torrefaction was examined.

2. EXPERIMENTAL

Napier grass used in this study was obtained from the province of Phetchaburi. The proximate analysis of Napier grass was analysed following ASTM E871, E872, E1755 for moisture, volatile matter (VM), and ash contents, respectively. The percentage of fixed carbon (FC) was obtained by subtracting 100 by the combined moisture, VM, and ash contents. Napier grass was chopped to the size of ~4-5 mm, as depicted in Figure 1, using a knife.

Figure 1 Napier grass used in the present study.

Microwave absorbers employed in the present study included silicon carbide (SiC), as shown in Figure 2, which was purchased from Cernic International and has an average size of ~0.15 mm; and activated carbon (AC), as displayed in Figure 3, which was a commercial AC available at a local hardware store and has an average size of ~1.7 mm.

Figure 2 Silicon carbide (SiC) used in this study.

Figure 3 Activated carbon (AC) used in this study

The amounts (in percentage) of chlorine (Cl) in Napier grass and in both microwave absorbers (*i.e.* SiC and AC) were analysed using an X-ray fluorescence (XRF) spectrometer (Rigaku, ZSX Primus).

In each experiment, the chopped Napier grass was weighed for ~20 g, using a 2-decimal electric balance (AND, FX2000i), and put into a 250-mL porcelain crucible. Occasionally, either SiC or AC, with the mass of 10 or 20 wt.% of the mass of Napier grass, also weighed by the 2-decimal electric balance (AND, FX-2000i), was added as a microwave absorber (MA) into the same porcelain crucible as Napier grass. The crucible containing the sample (either Napier grass or the mixture of Napier grass and the MA) was covered by a lid (to prevent air from entering into the crucible to burn with the sample during torrefaction) and then placed in a household microwave oven (Samsung, MS23T-5018A) operated at 300 or 600 W for 5 min.

The torrefied Napier grass and MA samples (either SiC or AC) were separated using a sieve with the size of ~2 mm, weighed separately, and subsequently calculated for the solid yield using Eq. (1). The percentage of Cl in the torrefied Napier grass and MA samples were also analysed using the same XRF spectrometer as the samples before torrefaction.

The mass of Cl in the Napier grass sample $\left(m_{\mathrm{Cl_{NG}}}\right)$ and in the MA sample $\left(m_{\mathrm{Cl_{MA}}}\right)$ were:

$$m_{\mathrm{Cl_{NG}}} = m_{\mathrm{NG}} \times \%\mathrm{Cl} \qquad (2)$$

and

$$m_{\mathrm{Cl_{MA}}} = m_{\mathrm{MA}} \times \%\mathrm{Cl} \qquad (3)$$

where m_{NG} and m_{MA} were the mass of the Napier grass and MA samples, respectively, and %Cl was the percentage of Cl analysed using the XRF spectrometer.

The reduction percentage of Cl (%Cl reduction), defined as the mass of Cl reduced by torrefaction with respect to the initial mass of Cl in the Napier grass sample (*i.e.* before torrefaction), was calculated using the following equation:

$$\%\mathrm{Cl\ reduction} = \frac{\left(m_{\mathrm{Cl_{NG}}}\right)_b - \left(m_{\mathrm{Cl_{NG}}}\right)_a}{\left(m_{\mathrm{Cl_{NG}}}\right)_b} \times 100 \qquad (4)$$

Note that this was the percentage of Cl emitted into the atmosphere.

The capture percentage of Cl (%Cl capture), defined as the mass of Cl captured by the MA sample during torrefaction with respect to the mass of Cl in the Napier grass sample released into the atmosphere also during torrefaction, was computed using the following equation:

$$\%\text{Cl capture} = \frac{\left(m_{\text{Cl}_{\text{MA}}}\right)_a - \left(m_{\text{Cl}_{\text{MA}}}\right)_b}{\left(m_{\text{Cl}_{\text{NG}}}\right)_b - \left(m_{\text{Cl}_{\text{NG}}}\right)_a} \times 100 \qquad (5)$$

where $\left(m_{\text{Cl}_{\text{MA}}}\right)_b$ and $\left(m_{\text{Cl}_{\text{MA}}}\right)_a$ were the mass of Cl in the MA sample (either SiC or AC) before and after torrefaction, respectively.

3. RESULTS AND DISCUSSION

The proximate analysis (on dry basis) of the raw Napier grass sample was as summarised in Table 1

Table 1 Proximate analysis (on dry basis) of the raw Napier grass sample.

Proximate analysis	Amount (wt.%)
• Ash	11.83
• Volatile matter (VM)	81.72
• Fixed carbon (FC)	6.45

It was evident that Napier grass contained a high amount of VM, while its FC content was low. The total amount of combustibles, comprising VM and FC, was ~88%, in which VM was accounted for ~93% of the combustibles.

For the torrefaction of Napier grass, with and without the addition of the microwave absorber (MA), either silicon carbide (SiC) or activated carbon (AC), the notations used in the present study were as follows

- T-300 = Napier grass torrefied at 300 W without the MA
- T-600 = Napier grass torrefied at 600 W without the MA
- GS300-10 = Napier grass torrefied at 300 W with 10 wt.% SiC as the MA
- GS600-10 = Napier grass torrefied at 600 W with 10 wt.% SiC as the MA
- GC300-10 = Napier grass torrefied at 300 W with 10 wt.% AC as the MA
- GC600-10 = Napier grass torrefied at 600 W with 10 wt.% AC as the MA
- GS300-20 = Napier grass torrefied at 300 W with 20 wt.% SiC as the MA
- GS600-20 = Napier grass torrefied at 600 W with 20 wt.% SiC as the MA
- GC300-20 = Napier grass torrefied at 300 W with 20 wt.% AC as the MA
- GC600-20 = Napier grass torrefied at 600 W with 20 wt.% AC as the MA
- SiC-300-10 = Silicon carbide with 10 wt.% torrefied at 300 W
- SiC-600-10 = Silicon carbide with 10 wt.% torrefied at 600 W
- AC-300-10 = Activated carbon with 10 wt.% torrefied at 300 W
- AC-600-10 = Activated carbon with 10 wt.% torrefied at 600 W
- SiC-300-20 = Silicon carbide with 20 wt.% torrefied at 300 W
- SiC-600-20 = Silicon carbide with 20 wt.% torrefied at 600 W
- AC-300-20 = Activated carbon with 20 wt.% torrefied at 300 W
- AC-600-20 = Activated carbon with 20 wt.% torrefied at 600 W

The solid yields of the torrefied Napier grass samples *via* microwave torrefaction at 300 or 600 W for 5 min, with and without the addition of the MA, were as shown in Figure 4

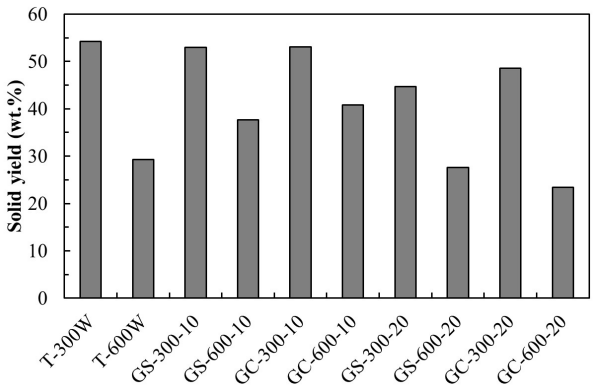

Figure 4 Solid yields of the Napier grass samples torrefied using microwave irradition at 300 or 600 W for 5 min with the addition of either SiC (GS) or AC (GC) as a microwave absorber for either 10 or 20 wt.% of the mass of the Napier grass sample

Figure 4 revealed that an increase in microwave power (MP) led to a dramatic decrease in solid yield, from ~45-55 wt.% when torrefied at 300 W to ~24-41 wt.% when torrefied at 600 W. An increase in MP resulted in an increase in the amount of energy required to drive off both moisture and VM from the Napier grass sample, thus reducing the total mass and solid yield of the torrefied Napier grass sample.

An increase in the amount of MA also led to a decrease in solid yield, but with a lesser degree when comparing to an increase in MP. The addition of the MA also resulted in an increase in the amount of energy needed to drive off both moisture and VM from the sample, which, in turn, lowered the mass and solid yield of the sample as *per* an increase in MP.

The percentage of chlorine (Cl) in the raw Napier grass, SiC, and AC samples; in the torrefied MA samples; and in the torrefied Napier grass samples, with

and without the addition of the MA, at various MPs and MA amounts, were summarised in Table 2.

Table 2 Chlorine contents of the raw Napier grass, silicon carbide (SiC), and activated carbon (AC) samples; of the torrefied SiC or AC sample; and of the torrefied Napier grass samples, with and without the addition of the microwave absorber (MA), at various microwave powers and MA amounts.

Sample	Chlorine content (wt.%)
• Raw Napier grass	6.2208
• SiC	0
• AC	0.0488
• SiC-300-10	0.0900
• SiC-600-10	0.0780
• AC-300-10	1.6950
• AC-600-10	6.9210
• SiC-300-20	0.1350
• SiC-600-20	0.0400
• AC-300-20	12.221
• AC-600-20	27.128
• T-300	3.5595
• T-600	2.0006
• GS-300-10	2.9382
• GS-600-10	1.9223
• GC-300-10	3.1883
• GC-600-10	2.5909
• GS-300-20	2.1476
• GS-600-20	1.1232
• GC-300-20	2.7939
• GC-600-20	1.6566

The percentage of Cl in the raw Napier grass sample was found to be higher than 6 wt.%, which could be considered relatively high, comparing to those found in the literature (*e.g.*, Refs. 8, 9, 10, 13, and 14).

From the percentage of Cl appeared in Table 2 and the solid yield in Figure 1, the reduction percentage of Cl by torrefaction and the capture percentage of Cl by each MA (either SiC or AC) could be calculated and subsequently exhibited in Figures 5 and 6, respectively.

The reduction percentages of Cl of the torrefied Napier grass samples, with and without the addition of the MA, at various MP and MA amounts, were found to be within the range of 69-95 wt.% of the initial amount of Cl in the Napier grass sample.

It was found, from Figure 5, that an increase in MP caused the Cl reduction percentage to increase (*i.e.* a higher amount of Cl was removed from the Napier grass sample) from ~69-85 wt.% for the MP of 300 W to ~83-95 wt.%. for the MP of 600 W. The possible explanation was similar to that for the reduction of VM due to an increase in MP described previously in the present study. As discussed previously, an increase in MP led to an increase in the amount of VM removed from the Napier grass sample. It is reported [10] that the release of Cl mainly occurs during the devolatilisation (*i.e.* the release of VM from the sample) and that torrefaction can lead to a reduction in the chlorine content in biomass [9, 13-14].

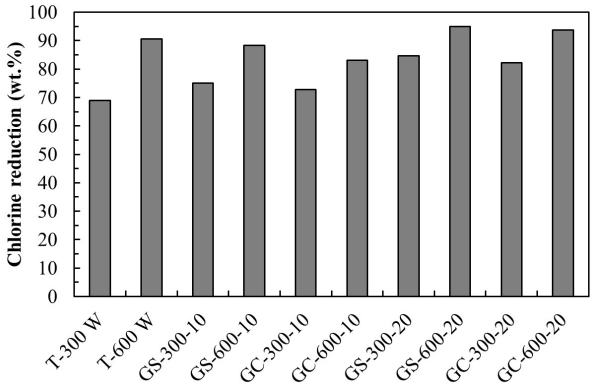

Figure 5 Percentages of chlorine reduction of the torrefied Napier grass using microwave torrefaction at 300 or 600 W for 5 min with the addition of either SiC (GS) or AC (GC) as a microwave absorber for either 10 or 20 wt.% of the mass of the Napier grass sample

The Cl reduction percentages found in this study (~69-95 wt.%) were higher those that found in the work of Kajina and Rousset, which is ~44-56 %, and was comparable to those found in the work of Ramao *et al*, which is ~88-95 % [12], and of Ren *et al*, which is ~74% [14].

It was also discovered, from Figure 5, that the Cl reduction percentages of the Napier grass sample with the amount of the MA of 10 wt.% were in the range of ~73-88 wt.%, while those with the amount of the MA of 20 wt.% were ~82-95 wt.%, indicating that an increase in the amount of the MA resulted in an increase in the reduction percentage of Cl. Once again, since reduction of Cl was directly related to the reduction of VM, the explanation was in the similar manner to that for the reduction of VM because of an increase in the amount of the MA.

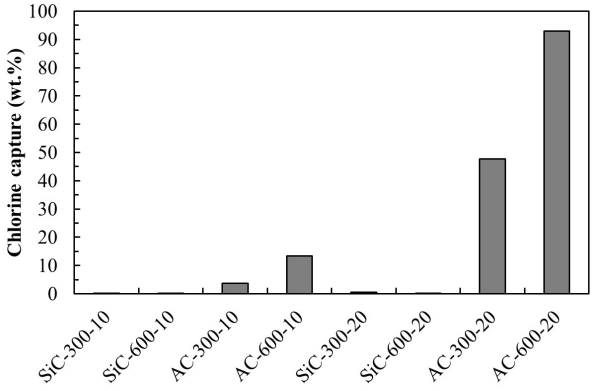

Figure 6 Percentages of chlorine capture using silicon carbide (SiC) and activated carbon (AC) in the amount of 10 or 20 wt.% with the microwave power of 300 or 600 W for 5 min.

For the capture percentage of Cl of either SiC or AC appeared in Figure 6, it was evident that SiC could barely capture Cl; the percentages of Cl captured by SiC were only ~0.1-0.5 wt.%. of the amount of Cl emitted into the atmosphere. This meant almost all of Cl released during torrefaction directly emitted into the atmosphere.

The Cl capture percentages of AC were within the range of ~3-93 wt.% of the amount of Cl emitted into the atmosphere. Increases in both MP and amount of MA led to an increase in the capture percentage of Cl. The possible explanation was that an increase in MP resulted in a higher amount of Cl removed from the sample, thus enhancing the possibility of Cl to be captured by AC, and that an increase in the amount of AC also increased the area onto which Cl could be deposited and eventually captured.

The capture percentages of Cl, which represented the ability of the MA to capture Cl, found in this study were comparable to those found in the work of Ren *et al* [14], in which Cl in the form of HCl can be captured by ~26-80% for the $CaCO_3$, Na_2CO_3, and K_2CO_3 sorbents, and Cl in the form of CH_3Cl can be captured by ~12-22% for $CaCO_3$, Na_2CO_3, and K_2CO_3 sorbents.

4. CONCLUSION

The overall results obtained in the present study indicated that microwave torrefaction at the microwave power (MP) of 300 or 600 W with the addition of silicon carbide (SiC) or activated carbon (AC) as the microwave absorber (MA) in the amount of 10 or 20 wt.% could lead to the reduction of chlorine (Cl) in Napier grass by ~69-95 wt.% of the initial amount of Cl in the Napier grass sample. An increase in both MP and amount of MA led to an increase in the Cl reduction percentage. For the Cl capture percentage of the MA, which indicated the ability of the MA to capture Cl, it was discovered that SiC could barely capture Cl, whereas AC could capture Cl in the range of ~3-93 wt.% of the amount of Cl released into the atmoshere. An increase in both MP and amount of AC resulted in an increase in the Cl capture percentage.

ACKNOWLEDGMENTS

The research stipend provided by the Department of Chemical Engineering at Thammasat School of Engineering was greatly acknowledged. The staff of the Department of Chemical Engineering and those at the Office of Advanced Science and Technology (OAST) at Thammasat University for providing counsel on the analysis of chlorine were also thankfully appreciated.

REFERENCES

1. Energy Institute. 2024 Statistical Review of World Energy, 73rd ed. UK. 2024.
2. M.A. Siddik, M.T. Islam, A.K.M.M. Zaman, M.M. Hasan. Current Status of Correlation of Fossil Fuels Consumption and Greenhouse Gas Emissions. *International Journal of Energy, Environment, and Economics* 2021; 28(2): 103-119.
3. A.K. Karmaker, M.M. Rahman, M.A. Hossain, M.R. Ahmed. Exploration and corrective measures of greenhouse gas emissions from fossil fuel stations in Bangladesh. *Journal of Cleaner Production* 2020; 244: Paper No. 118645.
4. M. Baldelli, L. Bartolucci, S. Cordiner, E.D. Maina, V. Mulone. Toward carbon neutral fuels: Process analysis of integrated biomass conversion routes for sustainable biofuels production. *Energy* 2025; 324: Paper No. 136077.
5. I. Sebos. Fossil fraction of CO_2 emissions of biofuels. *Carbon Management* 2022; 13(1): 154-163.
6. W.H. Chen, B.J. Lin, Y.Y. Lin, Y.S. Chu, A.T. Ubando, P.L. Show, H.C. Ong, J.S. Chang, S.H. Ho, A.B. Culaba, A. Petrissans, M. Petrissans. Progress in biomass torrefaction: Principles, applications and challenges. *Progress in Energy and Combustion Science* 2021; 82; Paper No. 100887.
7. Y. Niu, Y. Lv, Y. Lei, S. Liu, Y. Liang, D. Wang, S. S. Hui. Biomass torrefaction: properties, applications, challenges, and economy. *Renewable and Sustainable Energy Reviews* 2019; 115: Paper No. 109395.
8. Y. Liu, S. Liu, Y. Li, J. He. Influence of Operating Parameters on Chlorine Release and Pollutant Emission Characteristics of a 130 t/h BCFB Combustion System. *ACS Omega* 2121; 6: 12530-12540.
9. W. Kajina, P. Rousset. Couple effect of torrefaction and blending on chlorine removal. 7th National Conference on Sustainable Energy and Environment (SEE 2018): Technology & Innovation for Global Energy Revolution, 28-30 November 2018, Bangkok, Thailand: 48-51.
10. J.M. Johansen, J.G. Jakobsen, F.J. Frandsen, P. Glarborg. Release of K, Cl, and S during Pyrolysis and Combustion of High-Chlorine Biomass. *Energy & Fuels* 2011; 25: 4961-4971.
11. P. Basu. Biomass Gasification, Pyrolysis, and Torrefaction: Practical Design and Theory, 3rd ed. Academic Press, 2018.
12. E.L. Romao, J.M. da Silva, N.V. dos Santos Luz, R.A. Conte. Torrefaction as a Chlorine Reduction Process of Brazilian *Eucalyptus* sp. for Use as a Biofuel. *BioEnergy Research* 2023; 16: 448-456.
13. L.C.R. Sa, L.M.E.F. Loureiro, L.J.R. Nunes, A.M.M. Mendes. Torrefaction as a Pretreatment Technology for Chlorine Elimination from Biomass: A Case Study Using *Eucalyptus globulus* Labill. *Resources* 2020; 9: Paper No. 54.
14. X. Ren, E. Rokni, L. Zhang, Z. Wang, Y. Liu, Y.A. Levendis. Use of Alkaline Carbonate Sorbents for Capturing Chlorine-Bearing Gases from Corn Straw Torrefaction. *Energy & Fuels* 2018; 32: 11843-11851.
15. B. Shemwell, Y.A. Levendis, G.A. Simons. Laboratory study on the high-temperature capture of HCl gas by dry-injection of calcium-based sorbents. *Chemosphere* 2001; 42: 785-796.

16. Q. Song, F. Kong, B.F. Liu, X. Song, H.Y. Ren. Biochar-based composites for removing chlorinated organic pollutants: Applications, mechanisms, and perspectives. *Environmental Science and Ecotechnology* 2024; 21: Paper No. 100420.
17. P. N. Y. Yek, S.H. Kong, M.C. Law, C. Xia, R.K. Liew, T.S. Sie, J.W. Lim, S.S. Lam. Microwave torrefaction of empty fruit bunch pellet: Simulation and validation of electric field and temperature distribution. *Journal of Bioresources and Bioproducts* 2022; 7: 270-277.
18. M. A. H. M. Fuad, M.F. Hasana, F.N. Ani. Microwave torrefaction for viable fuel production: A review on theory, affecting factors, potential, and challenges. *Fuel* 2019; 253: 512-526.
19. B. Li, X. Fan, S. Yu, H. Xia, Y. Nong, J. Bian, M. Sun, W. Zi. Microwave heating of biomass waste residues for sustainable bioenergy and biomass materials preparation: A parametric simulation study. *Energy* 2023; 274: Paper No. 127347.
20. X. Ren, M.S. Ghazani, H. Zhu, W. Ao, H. Zhang, E. Moreside, J. Zhu, P. Yang, N. Zhong, X. Bi. Challenges and opportunities in microwave-assisted catalytic pyrolysis of biomass: A review. *Applied Energy* 2022; 315: Paper No. 118970.
21. S. Mao, R. Shu, F. Guo, J. Bai, L. Xu, K. Dong, H. Wei, L. Qian. Fuel gas production from microwave-induced biomass pyrolysis using char-supported metal composites as both catalysts and microwave absorber. *International Journal of Hydrogen Energy* 2022; 47: 25309-25321.
22. W. Zuo, Y. Tian, N. Ren. The important role of micro-wave receptors in bio-fuel production by microwave-induced pyrolysis of sewage sludge, *Waste Management* 2011; 31: 1321-1326.
23. X. Liu X, Z. Zhang, Y. Wu. Absorption properties of carbon black/silicon carbide microwave absorbers, *Composites Part B: Engineering* 2011; 42: 326-329.

Electrochemical regeneration of spent monoethanolamine solution after carbon dioxide capture and mineralization by calcium sulfate addition

Nathaporn Kenbubpha[1], Ketwarang Nimnualrat[1], Palang Bumroongsakulsawat[1,*]

[1] Department of Chemical Engineering, Faculty of Engineering, Chulalongkorn University, Bangkok 10330, Thailand

[*] Corresponding author: palang.b@chula.ac.th

ABSTRACT

Carbon dioxide (CO_2) is widely recognized as the primary greenhouse gas (GHG) driving global warming. Since the onset of the Industrial Revolution around 1850, the average atmospheric concentration of CO_2 has risen from 280 ppm to 370 ppm [1]. As a result, Carbon Capture, Utilization, and Storage (CCUS) have become a critical approach to mitigate this issue. Monoethanolamine (MEA) solution is widely used in various industries to capture CO_2; however, the regeneration of MEA remains a challenge due to the high energy demands associated with the conventional stripping method, which requires boiling the solution. This research proposes a novel method for MEA recovery through a mineralization process, wherein $CaSO_4$ was added to an MEA solution with high CO_2 concentration to precipitate CO_2 as $CaCO_3$. The resulting solution was then subjected to electrolysis to be converted back into MEA solution for reuse. This method utilizes electrical energy for electrolysis, thereby having a possibility of reducing the need for high energy consumption required for boiling the solution in traditional methods.

Keywords: Carbon dioxide; CCUS; MEA; Electrolysis; Electrochemical; Regeneration.

1. INTRODUCTION

Carbon dioxide (CO_2) is widely recognized as the primary greenhouse gas (GHG) driving global warming. Since the onset of the Industrial Revolution around 1850, the average atmospheric concentration of CO_2 has risen from 280 ppm to 370 ppm. This increase has contributed to a corresponding rise in global average temperatures. If greenhouse gas emissions continue to rise uncontrollably, they may lead to higher sea levels and the potential extinction of various species [1].

To reduce CO_2 emissions into the atmosphere, several strategies have been proposed. These include reducing energy consumption by increasing the efficiency of energy conversion, transitioning to fuels with lower carbon intensity, and increasing the use of renewable energy sources. However, these measures may not be sufficient to fully mitigate global warming in the long term. As a result, Carbon Capture, Storage, and Utilization (CCUS) technology offers a viable mid-term solution to mitigate environmental impacts [1].

Among the various CCUS approaches, chemical absorption is widely regarded as one of the most effective technologies for capturing CO_2. Monoethanolamine (MEA) is a commonly used absorbent, known for its high reactivity with CO_2 and superior absorption capacity compared to other amines of similar mass concentrations, owing to its smaller molecular weight. MEA has been employed extensively in industrial processes for CO_2 capture through the formation of carbamate species [2], as represented by the following reactions:

Carbamate formation reaction:

$$RNH_2 + CO_2 + H_2O \leftrightarrow RNHCOO^- + H_3O^+ \quad (1)$$

Amine protonation reaction:

$$RNH_2 + H_3O^+ \leftrightarrow RNH_3^+ + H_2O \quad (2)$$

During CO_2 absorption by MEA, a carbamate ($RNHCOO^-$) is formed. This compound can be thermally decomposed, releasing CO_2 and regenerating MEA for subsequent reuse. The reversibility of this reaction is fundamental to the economic feasibility and long-term sustainability of the CO_2 capture process [3].

While absorption technology is widely employed for CO_2 capture, it suffers from high energy requirements for amine solvent regeneration, typically ranging from 2.5 to 3.5 GJ per ton of CO_2 captured. Elevated regeneration temperatures also promote solvent degradation, leading to increased operational costs, solvent loss, and corrosion within absorption systems. Reducing the energy demand for desorption remains essential for improving the efficiency and sustainability of CO_2 capture technologies [3,4].

Electrochemical methods for CO_2 capture and solvent regeneration have recently gained significant attention. In this study, electrolysis was employed to regenerate a CO_2-rich MEA solution. The process

involves passing an electric current through the electrolyte, promoting the decomposition of compounds and the recovery of MEA. To facilitate regeneration and prevent fouling of the anion exchange membrane (AEM), the carbamate solution was first reacted with calcium sulfate ($CaSO_4$) in a batch stirred-tank reactor, forming MEA sulfate. The resulting solution was subsequently subjected to electrolysis to remove sulfate ions and deprotonate RNH_3^+. In this setup, a Na_2SO_4 solution served as the anolyte. Electrolysis enables the regeneration of lean amine, with the reaction proceeding as follows:

$$RNHCOO^- + RNH_3^+ + CaSO_4 + H_2O \leftrightarrow (RNH_3)_2SO_4 + CaCO_3 \quad (3)$$

At the anode, water is oxidized to produce oxygen gas, protons, and electrons through the oxygen evolution reaction (OER). This reaction gradually increases the proton concentration on the anode side. Meanwhile, sulfate ions (SO_4^{2-}) migrate through the anion exchange membrane (AEM) to maintain charge neutrality and is also removed from the MEA solution.

Oxidation reaction:

$$H_2O \rightarrow 1/2O_2 + 2H^+ + 2e^- \quad (4)$$

At the cathode, water is reduced to generate hydrogen gas and hydroxide ions (OH^-)

Reduction reaction:

$$H_2O + e^- \rightarrow 1/2H^2 + OH^- \quad (5.1)$$

The produced hydroxide ions deprotonate protonated amines (RNH_3^+) to form MEA (RNH_2)

Deprotonation reaction:

$$RNH_3^+ + OH^- \rightarrow RNH_2 + H_2O \quad (5.2)$$

This integrated mineralization–electrolysis approach significantly could reduce the energy requirements associated with traditional thermal regeneration methods. Furthermore, it could enhance the sustainability of the CO_2 capture process by extending the lifespan of the MEA solvent, providing a more energy-efficient and environmentally friendly alternative to conventional practices.

Therefore, this study aims to investigate the feasibility and key characteristics of using electrolysis for regenerating monoethanolamine (MEA) solutions.

2. EXPERIMENTAL

2.1 Materials

All materials and chemicals utilized in this study are listed in Table 1.

Table 1. Materials and chemicals used in this experiment.

Name	Purity	Source
Monoethanolamine (MEA)	99.5%	QReC
Carbon dioxide (CO_2)	99.5%	Linde
Calcium sulfate ($CaSO_4$)	99.0%	Kemaus
Sodium sulfate (Na_2SO_4)	99.0%	Kemaus
Anion Exchange Membrane (AEM)	-	FuMA-Tech
Platinized titanium Mesh (Pt-Ti mesh)	-	Fuel Cell Store

2.2 Preparation of carbamate Solution

A 250 mL solution of 5 M MEA in DI water was prepared and transferred into a Duran bottle. A dispersion tube was inserted into the bottle to introduce CO_2 into the solution. CO_2 was bubbled through until the pH of the solution stabilized around 8.

2.3 Mineralization

A 20 mL sample of a carbamate solution (5 M MEA saturated with CO_2) was diluted with DI water to increase the total volume to 100 mL. The resulting solution was then reacted with calcium sulfate ($CaSO_4$) in a batch stirred-tank reactor at ambient conditions for a duration of 3 hours. To ensure complete reaction of the carbamate, an excess amount of calcium sulfate was used.

After the reaction, the resulting slurry was filtered using filter paper to separate the liquid phase from the solid precipitates (primarily $CaCO_3$). The collected liquid was subsequently introduced into the electrolysis cell for further processing, while the solid residue was washed with DI water and dried to prepare for thermogravimetric analysis (TGA).

2.4 Anion Exchange Membrane Preparation

Prior to use, the anion exchange membrane (AEM) was activated to ensure optimal ionic conductivity. The membrane was first soaked in a 1 M sodium sulfate (Na_2SO_4) solution at 25 °C overnight to facilitate ion exchange and to remove any residual additives. During this process, the counterions originally present in the membrane were replaced with sulfate ions (SO_4^{2-}). Care was taken to prevent the membrane from drying at any stage, as shrinkage-induced microcracks could occur. Following ion exchange, the membrane was thoroughly rinsed by soaking in deionized (DI) water for 15 minutes and subsequently spraying with additional DI water to eliminate any remaining Na_2SO_4. The membrane was then dried until fully dry and subsequently utilized in the electrolysis cell.

2.5 MEA Regeneration by Electrolysis

The electrolysis cell was fabricated using stereolithography (SLA) and consisted of 3D-printed rigid end plates (Formlabs' Clear resin) and elastic gaskets (Formlabs' Elastic 50A resin), manufactured by PRINT MY DESIGN Co., Ltd. Each end plate had a slot to hold the electrodes. The gaskets had a thickness of 2 mm, and the active electrolysis area was 20 × 20 mm². An anion exchange membrane (AEM) was placed between two gaskets and assembled between the rigid end plates. This assembly was then positioned between two stainless-steel plates (3 mm thick) and compressed using two C-clamps. Platinized titanium mesh was employed as both the cathode and the anode.

Figure 1 Illustration of electrolysis cell.

To investigate the influence of applied current on the MEA regeneration process, electrolysis experiments were conducted at three different current levels: 0.1 A, 0.2 A, and 0.3 A. The electrolysis durations were 127 minutes, 64 minutes, and 43 minutes, respectively. These durations included a 13% time

The MEA regeneration was carried out in an electrolysis cell under ambient conditions. 7 mL of the MEA sulfate solution was introduced into the cathode compartment, while 7 mL of 0.5 M sodium sulfate (Na_2SO_4) solution was added to the anode compartment. The two compartments were separated by an anion exchange membrane (AEM). Electrolysis was performed using a DC power supply (Tenma 72-2700), with a constant current applied across the electrodes.

For each current setting, all other experimental conditions were kept constant. After the specified electrolysis time elapsed, the power supply was turned off, and the solutions from the cathode and anode compartments were collected for further analysis.

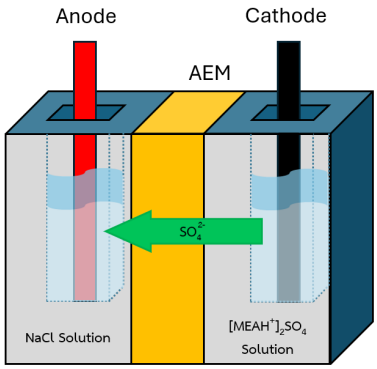

Figure 2 Schematic of electrolysis apparatus for MEA regeneration.

3. RESULTS AND DISCUSSION

The study investigated the effects of varying the current (0.1 A, 0.2 A, 0.3 A) on the electrochemical regeneration of a MEA-based CO_2 capture solution.

3.1 Effects of Currents on Sulfate Removal

Table 2 Effects of applied currents on sulfate removal performance (0.1, 0.2, and 0.3 A).

Current (A)	SO^{2-}_4 Removal (%)
0.1	61.62
0.1	70.56
0.2	76.15
0.2	72.26
0.3	76.72
0.3	78.05

The results showed that increasing the applied current generally enhanced sulfate removal up to a certain point. At 0.1 A, sulfate removal ranged from approximately 61.6% to 70.6%. At 0.2 A, removal improved to 72.3%–76.1%, and at 0.3 A, removal increased to 76.1%–78.0%. This trend was consistent with Faraday's law, Q = It. A higher current supplied more electrons per unit time, thus accelerating the regeneration process.

Nevertheless, at 0.3 A, although the applied current was increased, the improvement in sulfate removal efficiency was only marginal compared to 0.2 A. This indicated that simply increasing the current did not continuously enhance performance in a linear manner, as other competing factors came into play and affected the process.

3.2 Effects of currents on cell voltages

Table 3 Initial and final voltages during electrolysis at varying currents (0.1, 0.2, and 0.3 A).

Current (A)	Initial V (V)	Final V (V)
0.1	4	6.5
0.1	3.98	5.59
0.2	5	12.5
0.2	5	7
0.3	5.86	12.61
0.3	6	12

The initial and final voltages during electrolysis increased substantially with higher applied currents. For instance, at 0.2 A, voltages ranged between 5–12.5 V, whereas at 0.3 A, the voltages rose further to approximately 6–12.6 V. As current density increased, the reaction rates also increased and required higher overpotentials. The need for greater overpotential to drive faster electrochemical reactions resulted in additional energy losses. On the other hand, the rise in the voltage from the initial to final value during the same electrodialysis operation could be attributed to the diminishing ionic species, which contributed to electrolyte conductivity, in the MEA sulfate solution. This situation could be improved by adding supporting electrolyte.

3.3 Effects of currents on pH of catholytes and anolytes

Table 4 pH at cathode and anode under different applied currents (0.1, 0.2, and 0.3 A).

Current (A)	pH at Cathode	pH at Anode
0.1	11.51	0.94
0.1	12.18	0.96
0.2	12.42	0.86
0.2	11.32	0.95
0.3	11.48	0.84
0.3	11.12	0.94

These observations are consistent with expected electrochemical reactions, wherein OH^- ions are generated at the cathode and H^+ ions accumulate at the anode.

Notably, the alkaline (pH 11–12) pH at the cathode facilitates the deprotonation of protonated MEA species (RNH_3^+), promoting the regeneration of free MEA. Meanwhile, the acidic (pH 0.8–0.9) conditions at the anode confirm proton accumulation, which is a byproduct of water oxidation. These pH profiles thus align with the underlying chemical environment required for effective MEA regeneration.

3.4 Hypothesis on Formation of Large Anionic Complexes

Table 5 Faradaic efficiency under varying applied currents (0.1, 0.2, and 0.3 A).

Current (A)	Faradaic efficiency (%)
0.1	54.4
0.1	62.3
0.2	67.2
0.2	63.8
0.3	67.7
0.3	68.9

As the current increased, the faradaic efficiencies of sulfate removal increased. This was considered unusual for this kind of operation where ionic mass transport usually could not keep up with the required ion transport at high currents. When this scenario occurred, water splitting would occur on the surface of the AEM, supplying hydroxide ions across the membrane along with sulfate ions and injecting protons back into the MEA sulfate solution. Water splitting would result in decreases in the faradaic efficiencies. The observed increase in the faradaic efficiency when the current was increased was plausibly caused by secondary phenomena such as stronger agitation from more rising hydrogen bubbles at higher currents.

Additionally, we have recently known that ethanolamine-o-sulfate (EOS), an inorganic acid ester, could be formed from MEA and sulfuric acid. As the main precursors were already in the MEA sulfate solution, EOS might form and bind MEA and sulfate together, limiting or inhibiting sulfate transport across the AEM. This hypothesis is currently under investigation.

4. CONCLUSION

In this study, an integrated mineralization–electrolysis process was developed for the regeneration of CO_2-rich monoethanolamine (MEA) solutions. By reacting the spent MEA with calcium sulfate ($CaSO_4$), carbon dioxide was effectively mineralized into calcium carbonate ($CaCO_3$), and the resulting MEA sulfate solution was subjected to electrochemical regeneration. The experiments demonstrated that increasing the applied current enhanced sulfate removal efficiency, achieving up to 78% removal at 0.3 A. The faradaic efficiencies increased with increasing currents.

Overall, the electrochemical approach showed promise for improving the sustainability of MEA-based carbon capture systems.

ACKNOWLEDGMENTS

This project would not have been possible without the support and encouragement of many individuals and organizations. I would like to sincerely thank the Department of Chemical Engineering, Faculty of Engineering, Chulalongkorn University, for providing

the funding, research facilities, and technical resources essential for carrying out this study. My deepest appreciation goes to Professor Dr. Palang Bumroongsakulsawat, my advisor, whose expert advice, thoughtful guidance, and continual encouragement were invaluable at every stage of the research. I am also thankful to my colleagues, Miss Ketwarang Nimnualrat and Mr. Kittiporn Laitha, for their generous help, stimulating discussions, and constant support throughout the experimentation and data analysis processes. Their contributions have been crucial to the successful completion of this work.

This research has received funding support from the NSRF via the Program Management Unit for Human Resources & Institutional Development, Research and Innovation [grant number B42G670036].

REFERENCES

1. Li, L., Zhao, N., Wei, W., & Sun, Y. (2013). A review of research progress on CO_2 capture, storage, and utilization in Chinese Academy of Sciences. Fuel, 108, 112–130.
2. Liu, Y., Fan, W., Wang, K., & Wang, J. (2016). Studies of CO_2 absorption/regeneration performances of novel aqueous monothanlamine (MEA)-based solutions. Journal of Cleaner Production, 112, 4012–4021.
3. Kühn, F., & Wessling, M. (2021). A compact review of current technologies for carbon capture as well as storing and utilizing the captured CO_2. Processes, 13(1), 283.
4. Zoannou, K.-S., Sapsford, D. J., & Griffiths, A. J.(2013). Thermal degradation of monoethanolamine and its effect on CO_2 capture capacity. International Journal of Greenhouse Gas Control, 17, 423–430.

The effect of methanol and ethanol-based solvent on enhancing CO_2 absorption efficiency and reducing energy consumption in the desorption process

Sasiphan Deenan[1], Weerawat Patthaveekongka[1,*], Kuntima Krekkeitsakul[2], Parinya Thongyindee[2], Penpan Pedsawang[2], Sunisa Luadlai[2], Rujira Jitrwung[3]

[1] Department of Chemical Engineering, Faculty of Engineering and Industrial Technology, Silpakorn University, Sanam Chandra Palace Campus, Muang, Nakhon Pathom 73000, Thailand
[2] Expert Center of Innovative Clean Energy and Environment Thailand Institute of Scientific and Technological Research (TISTR), Pathum Thani 12120, Thailand
[3] Research and Development Group for Sustainable Development, Thailand Institute of Scientific and Technological Research (TISTR), Pathum Thani 12120, Thailand
[*] Corresponding author: patthaveekongka_w@silpakorn.edu

ABSTRACT

This research focuses on investigating the effects of using methanol and ethanol as solvents in amine solutions, specifically MEA (monoethanolamine) and DEA (diethanolamine), for CO_2 absorption. The study investigates six different solutions: MEA+H_2O, MEA+MeOH, MEA+EtOH, DEA+H_2O, DEA+MeOH, and DEA+EtOH, in the CO_2 absorption process and their impact on CO_2 capture efficiency from flue gas, which consists of 12% CO_2, 5% O_2, and 83% N_2 and the energy consumption of the process, in comparison to conventional water-based amine absorption. Various process parameters were examined, including the amine solution flow rate (0.6–1.2 L/min), gas mixture flow rate (15–25 L/min), and reboiler temperature (85–100°C). Previous research indicates that incorporating alcohols into amine solutions can enhance CO_2 absorption performance. [1] demonstrated that alcohol-amine mixtures reduce regeneration energy by 10–15%. [2] reported a 5–8% increase in absorption efficiency when ethanol was introduced into MEA solutions. The findings of this study reveal that DEA-ethanol solutions exhibit superior CO_2 absorption (95.04%) and desorption efficiency (94.52%) compared to conventional MEA-H_2O systems (85–90%) [3]. Furthermore, ethanol-based DEA solutions outperformed methanol-based counterparts by 6–10% [4]. The optimal DEA-ethanol system, operating at a solution flow rate of 1 L/min, achieved an energy consumption of 24.46 MJ/kg CO_2, representing a reduction of over 50% relative to traditional water-based absorption (48–50 MJ/kg CO_2) [1]. These findings suggest that the use of alcohol as a solvent in amine-based CO_2 absorption could be a promising approach to improving process efficiency and reducing energy costs, which are critical factors in the sustainable development of CO_2 capture technology.

Keywords: Alcohol-based solvents; Amine absorption; CO_2 capture; Desorption Process; energy consumption

1. INTRODUCTION

The intensifying issue of climate change in the present era is primarily driven by the accumulation of greenhouse gases, particularly carbon dioxide (CO_2). CO_2 is a greenhouse gas predominantly emitted through anthropogenic activities such as fossil fuel combustion in power plants, industrial production, transportation, and even cement manufacturing. Due to its ability to absorb infrared radiation from sunlight and re-emit it back into the atmosphere, CO_2 contributes to the greenhouse effect, resulting in a continuous rise in the Earth's average temperature. The impacts of global warming are increasingly evident, with more frequent occurrences of natural disasters such as floods, droughts, and extreme heatwaves [5].

Nevertheless, CO_2 is not solely a harmful byproduct; with proper management, it can be utilized beneficially in a variety of applications. These include urea production, pressure enhancement in oil reservoirs, agricultural productivity improvement in greenhouses, and as a raw material for synthetic fuels and novel construction materials. Therefore, the appropriate capture and utilization of CO_2 represents a crucial strategy for simultaneously addressing environmental challenges and advancing the principles of a circular economy [6,7].

Various CO_2 capture technologies have been developed, such as solid adsorption, membrane separation, and chemical absorption. Among these, amine-based chemical absorption using solvents such as monoethanolamine (MEA) and diethanolamine (DEA) is one of the most widely adopted methods. These systems are highly efficient at separating CO_2, even at low concentrations, and are well-demonstrated at an industrial scale. However, a major drawback lies in the energy-intensive regeneration process, especially when water is used as the primary solvent. The high boiling point of water requires significant thermal input to separate CO_2 from the amine solution and to evaporate the solvent [8,9].

Table 1: Properties of Amine Compounds for CO_2 Capture.

Chemical name	Formula	Source	CAS Number
Monoethanolamine (MEA)	C_2H_7NO	Petronas Chemicals Derivatives Sdn. Bhd.	141-43-5
Diethanolamine (DEA)	$C_4H_{13}NO_2$	Petronas Chemicals Derivatives Sdn. Bhd.	111-42-2

To reduce the energy burden associated with solvent regeneration, several studies have proposed the use of alcohols, such as methanol and ethanol, as alternative solvents to water. These alcohols possess lower boiling points, reduced surface tension, and greater CO_2 diffusivity, thereby offering a more energy-efficient desorption process and making them promising alternatives.

Table 2: Properties of solvents used in amine systems.

Chemical name	Density (g/m^3)	Boiling Point (°C)	Purity (%)	CAS Number
Deionized Water	1.00	100.00		7732-18-5
Methanol	0.79	64.70	99.90	67-56-1
Ethanol	0.79	78.40	95.00	64-17-5

Accordingly, this study aims to investigate the effects of methanol and ethanol as alternative solvents in amine-based CO_2 capture systems using MEA and DEA. The objective is to compare the absorption and desorption performance of each system, along with energy consumption, to establish a more sustainable and energy-efficient CO_2 capture process suitable for future application.

2. EXPERIMENTAL

2.1 Raw Materials

2.1.1 Simulated gas mixture

A synthetic gas composition containing 12% CO_2, 5% O_2, and 83% N_2 was supplied by Thai Special Gas Co., Ltd.

2.1.2 Amine solvents

Monoethanolamine (MEA) and Diethanolamine (DEA) were obtained from Petronas Chemicals Derivatives Sdn. Bhd.

2.1.3 Methanol and ethanol

Commercial-grade methanol and ethanol were procured from Srithanaperfect and Trimongkol Thurakit Co., Ltd.

2.2 Experimental Procedure

This experiment aimed to investigate the absorption performance of carbon dioxide (CO_2) using a monoethanolamine (MEA) solution under various operating conditions in a packed column system. The detailed procedure is as follows:

2.2.1 Solution preparation

Amine solutions with concentrations of 20 wt% and 30 wt% were prepared separately for the following solvent systems: MEA–water, MEA–methanol, MEA–ethanol, DEA–water, DEA–methanol, and DEA–ethanol.

2.2.2 CO_2 Absorption and Stripping Process Using Amine Solution

The process begins with feeding in the amine solution to the reboiler located at the bottom of the stripper column using a pump. The solution is then passed through a heat exchanger to reduce its temperature before being sent to the top section of the absorption column. Simultaneously, a simulated flue gas containing carbon dioxide is introduced at the bottom of the absorption column.

Within the absorption column, contact between the gas and liquid phases occurs, allowing carbon dioxide to be absorbed into the amine solution. Upon completion of the absorption process, the carbon dioxide-rich amine solution (rich amine) is transferred to a storage tank before being pumped into the stripper column for heating. This heating process facilitates the separation of carbon dioxide from the solution.

The separated carbon dioxide is released from the top of the stripper column, while the regenerated amine solution (lean amine) is recycled back to the absorption column for reuse. This constitutes a cyclic process.

2.2.3 Operating Conditions

The experiments were carried out under the following conditions:

- Gas flow rates: 15, 20 and 25 L/min
- Liquid flow rates: 0.6, 0.8,1.0 and 1.2 L/min
- Inlet gas concentrations: 12% CO_2, 5% O_2, and 83% N_2
- Operating temperature: absorption constant at 25°C

2.2.4 Measurement and Data Collection

The concentrations of CO_2 at both the inlet and outlet of the column were measured using a CO_2 gas analyzer. The absorption efficiency was calculated using the following equation:

$$\text{Efficiency} = \left(\frac{C_{in}-C_{out}}{C_{in}}\right)x100$$

where C_{in} and C_{out} represent the CO_2 concentrations at the inlet and outlet, respectively.

2.2.5 Data Reliability

Each experimental condition was repeated three times to ensure data reliability. The average values and standard deviations were calculated and analyzed to determine the influence of each parameter on the CO_2 absorption efficiency.

All data points were recorded at 30-minute intervals to capture any variations and trends throughout the 16-hour experimental period. This allowed for a comprehensive understanding of the system's performance under varying operational conditions, and facilitated the analysis of cycle stability and potential improvements for CO_2 capture efficiency.

2.3 Experimental Conditions

2.3.1 Lean amine flow rate

Absorption was carried out at 25 °C, while desorption was performed at 85 °C for MEA and 100 °C for DEA. The lean amine flow rate was varied from 0.6 to 1.2 L/min.

2.3.2 Solvent base variation

DEA solutions with 30 wt% concentration were tested using both aqueous and methanol solvents. The gas flow rate was adjusted between 15 and 25 L/min.

2.3.3 Temperature optimization

Absorption temperatures were varied from 25 to 30 °C, while desorption temperatures were set at either 85 °C or 100 °C.

2.3.4 Comparison of methanol types

The performance in terms of CO_2 capture efficiency and energy consumption was compared between commercial-grade methanol and commercial-grade ethanol.

2.3.5 Measurement under flue gas conditions

A 30 wt% DEA solution mixed with 70 wt% waste methanol (30DEA70WMET) was tested under simulated flue gas conditions with a composition of 12% CO_2, 5% O_2, and 83% N_2.

In order to illustrate the experimental setup and provide a clear overview of the CO_2 absorption and desorption process using amine-based solvents, the process flow diagram (PFD) is presented in Fig 1. This diagram outlines the major equipment units, flow directions, and interconnections within the system. The schematic serves as a foundation for understanding the configuration prior to introducing the actual experimental apparatus.

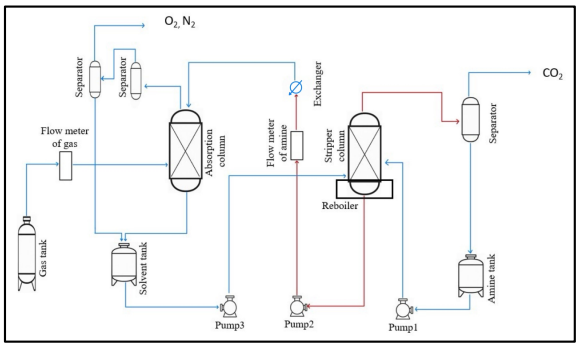

Fig 1. Process flow diagram of the CO_2 absorption–desorption system using amine-based solvent.

The actual experimental apparatus corresponding to the PFD is shown in Fig 2, which demonstrates the physical layout of the system in the laboratory, including the absorption column, stripper unit, and associated tanks and pumps.

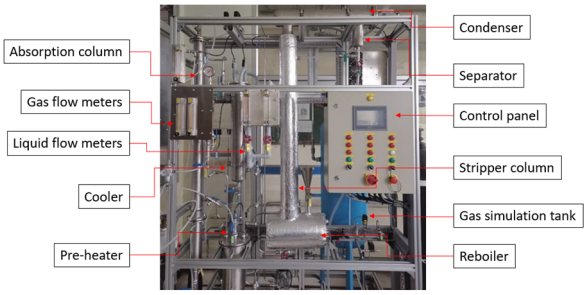

Fig 2 . Amine-Based CO_2 Capture Unit: Pilot-scale setup

3. RESULTS AND DISCUSSION

3.1 Effect of Amine Flow Rate on CO_2 Absorption and Desorption

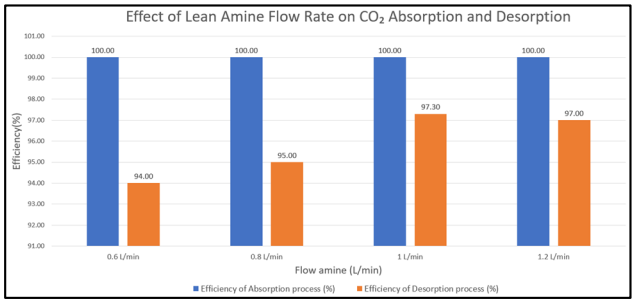

Fig 3. Effect of Amine Flow Rate on CO_2 Absorption and Desorption

The experiment investigated the effect of lean amine solution flow rates ranging from 0.6 to 1.2 L/min. In the DEA–water system, an increase in flow rate from 0.6 to 1.0 L/min resulted in a rise in CO_2 absorption efficiency from 68.2% to 82.5%. This trend suggests that higher flow rates enhance mass transfer by

delivering more solvent to the system, thus improving gas-liquid contact efficiency.

However, when the flow rate was further increased to 1.2 L/min, the absorption efficiency slightly decreased to 79.8%. This could be attributed to reduced contact time between the gas and liquid phases within the absorption column, leading to incomplete mass transfer. On the other hand, desorption efficiency rose from 60.4% at 0.6 L/min to 75.1% at 1.2 L/min. Despite this improvement, the thermal energy requirement also increased by approximately 8–12% at higher flow rates due to the need for additional heating.

3.2 Influence of Solvent Type on CO_2 Capture Efficiency

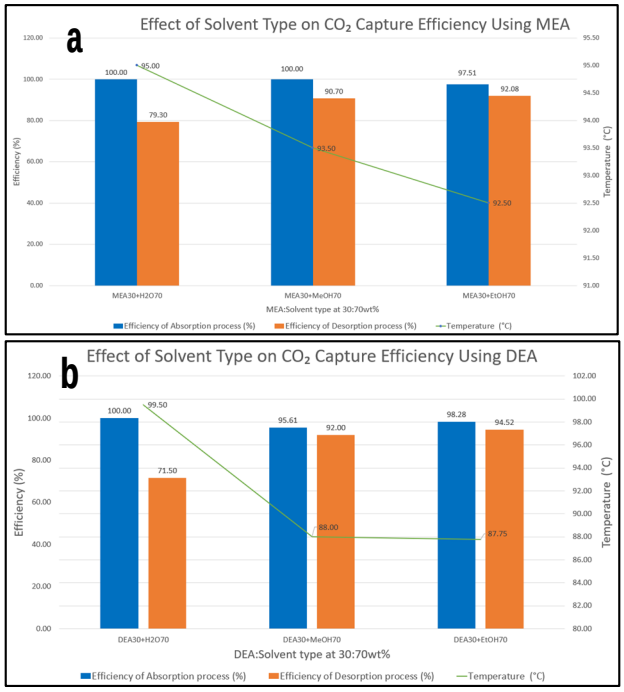

Fig 4. Effect of solvent type on CO_2 capture efficiency using MEA (a), Effect of solvent type on CO_2 capture efficiency using DEA (b)

The impact of different solvents water, methanol, and ethanol on CO_2 capture performance was assessed using MEA and DEA at a concentration of 30 wt%. The results were as follows:

Table 3: Effect of Solvent Type on CO_2 Capture Performance of MEA and DEA Solutions.

Type of Amine–Solvent Mixture	Efficiency of absorption process (%)	Efficiency of desorption process (%)
MEA–Water	100.00	79.30
MEA–Methanol	100.00	90.70
MEA–Ethanol	97.51	92.08
DEA–Water	100.00	71.50
DEA–Methanol	95.61	92.00
DEA–Ethanol	98.28	94.52

These findings indicate that both methanol and ethanol enhance absorption and desorption efficiencies compared to water. Ethanol exhibited the best performance in the DEA system. This is likely due to ethanol's ability to reduce surface tension, increase CO_2 diffusivity, and lower the system's boiling point, which collectively improve mass transfer and regeneration performance.

3.3 Temperature Optimization for Absorption and Desorption

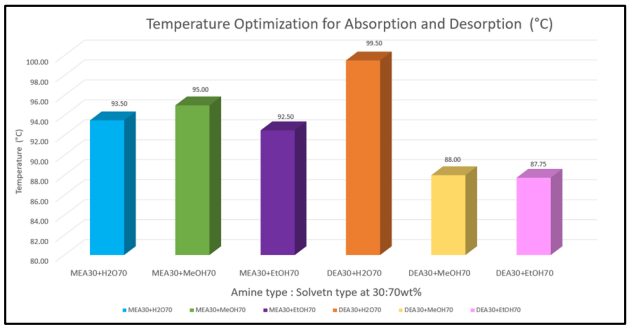

Fig 5. Temperature Optimization for Absorption and Desorption

Temperature played a critical role in the performance of CO_2 capture. The optimum absorption temperature was identified as 25 °C. Increasing the absorption temperature beyond this point did not significantly enhance the CO_2 absorption efficiency and, in some cases, resulted in a slight decline. This is consistent with the principle that higher temperatures reduce the solubility of gases in liquids, thereby impairing CO_2 capture.

Conversely, desorption was most effective at temperatures between 85 and 100 °C, depending on the amine used (85 °C for MEA and 100 °C for DEA). Elevated temperatures facilitated the release of CO_2 from the amine solution. Nevertheless, energy consumption must also be considered, as higher temperatures demand more heat input. Therefore, optimizing the desorption temperature is essential to balancing energy efficiency with separation performance.

3.4 Comparison Between Methanol and Ethanol Systems

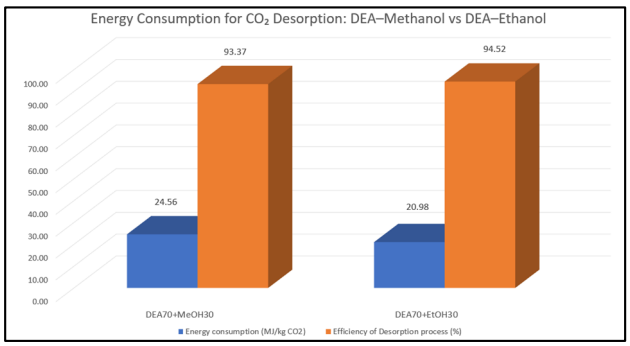

Fig 6. Energy consumption for CO_2 desorption: DEA-Methanol vs DEA-Ethanol

A comparison between DEA-based systems using 30 wt% methanol and ethanol as solvents revealed the following:

- **DEA–Methanol:** Absorption = 95.14%, Desorption = 93.37%, Energy consumption = 24.56 MJ/kg CO_2
- **DEA–Ethanol:** Absorption = 98.28%, Desorption = 94.52%, Energy consumption = 20.98 MJ/kg CO_2

Although methanol has a lower boiling point (64.7 °C) than ethanol (78.4 °C), the ethanol-based system demonstrated superior overall performance. Ethanol achieved higher absorption and desorption efficiencies while consuming less energy per unit of CO_2 captured. This may be attributed to ethanol's better system stability and lower evaporation loss, which collectively contribute to greater process efficiency and reduced operational costs.

4. CONCLUSION

This research investigates the effects of using methanol and ethanol as co-solvents with amine-based absorbents, namely Monoethanolamine (MEA) and Diethanolamine (DEA), on the efficiency of carbon dioxide (CO_2) absorption and the energy consumption during the desorption process. The experiments were conducted using a pilot-scale CO_2 absorption system to ensure that the results closely reflect conditions applicable to industrial operations.

The experimental results revealed that DEA exhibited superior CO_2 absorption performance compared to MEA in terms of both capture efficiency and energy consumption. Notably, the combination of DEA with ethanol as a solvent provided the most favorable outcome, achieving the highest CO_2 absorption efficiency while significantly reducing energy consumption during the desorption process. Specifically, this condition required only 20.98 MJ per kilogram of CO_2, which was lower than that observed with methanol and deionized water.

Based on the findings, it can be concluded that the use of DEA in combination with ethanol is a highly promising approach for improving CO_2 capture performance and reducing energy consumption in the regeneration process. This combination holds strong potential for further development in industrial CO_2 separation applications, particularly in contexts where both operational efficiency and energy sustainability are of paramount importance.

ACKNOWLEDGMENTS

The authors would like to express their sincere gratitude to the Thailand Institute of Scientific and Technological Research (TISTR) for providing essential research facilities and technical support throughout the experimental work. Special thanks are also extended to Silpakorn University for academic guidance and research collaboration. Additionally, the authors would like to thank Assoc. Prof. Dr. Weerawat Pattawikonkha, Dr. Rujira Jitwang, and Dr. Kantima Kerdkiattisakoon for their valuable advice and support throughout all stages of this research. The authors would also like to acknowledge all colleagues for their assistance and valuable suggestions, which were crucial for the successful completion of the experiments.

REFERENCES

[1] Fu D, Xie J, Wang F; Wang S. Investigation of surface tension and viscosity for aqueous solutions of MEA-MeOH and DEA-MeOH. *J. Chem. Thermodynamics* 2018;116:197–205.

[2] Hanna K, Rennemo R, Arlinda F. New solvent blends for post-combustion CO_2 capture. *Green Energy & Environment* 2019;4:439–452.

[3] Harbou I, Hoch S, Mangalapally H, Notz R, Sieder G, Garcia G, Spuhl O, Hasse H. Removal of carbon dioxide from flue gases with aqueous MEA solution containing ethanol. *Chem. Eng. Process: Process Intensification* 2014;75:81–89.

[4] Lai Q, Kong L, Gong W, Russell A, Fan M. Low-energy-consumption and environmentally friendly CO_2 capture via blending alcohols into amine solution. *Applied Energy* 2019;245:113696.

[5] Pandey D, Agrawal M, Pandey JS. Carbon footprint: current methods of estimation. *Environ. Monit. Assess.* 2011;178:135–160.

[6] Aresta M, Dibenedetto A, Angelini A. Utilisation of CO_2 as a raw material in organic chemistry: a challenge for sustainable development. *J. CO_2 Util.* 2013;3–4:65–73.

[7] Artz J, Müller TE, Thenert K, Kleinekorte J, Meys R, Sternberg A, Bardow A. Sustainable conversion of carbon dioxide: an integrated review of catalysis and life cycle assessment. *Chem. Rev.* 2018;118(2):434–504.

[8] Rochelle GT. Amine scrubbing for CO_2 capture. *Science* 2009;325(5948):1652–1654.

[9] Zhao B, Su Y, Wang Y, Xu G, Liu H, Tan Y, Chen C. A review of post-combustion CO_2 capture technologies from industrial flue gases. *J. Environ. Chem. Eng.* 2021;9(5):105302.

[10] Abroodi M, Bagheri A, Razavizadeh B. Investigation of surface tension and surface properties of alkanolamine–alcohol mixtures at T = 313.15 K and P = 90.6 kPa. J. Mol. Liq. 2019;287:110924.

[11] Aghel B, Maleki M, Sahraie S, Heidaryan E. Desorption of carbon dioxide from a mixture of monoethanolamine with alcoholic solvents in a microreactor. Fuel 2021;306:121636.

[12] Fu K, Rongwong W, Liang Z, Na Y, Idem R, Tontiwachwuthikul P. Experimental analyses of mass transfer and heat transfer of post-combustion CO_2 absorption using hybrid solvent MEA–MeOH in an absorber. Chem. Eng. J. 2015;260:11–19.

[13] Gao J, Yin J, Zhu F, Chen X, Tong M, Kang W, Zhou Y, Lu J. Experimental study of regeneration performance for CO_2 desorption from a hybrid solvent MEA–methanol in a stripper column packed with three different packing: Sulzer BX500, Mellapale Y500 and Pall Rings 16x16. Environ. Prog. Sustainable Energy 2016;12516.
[14] Gómez-Díaz D, López M, Navaza J, Villarquide L. Influence of organic co-solvents upon carbon dioxide chemical absorption. J. Taiwan Inst. Chem. Eng. 2018;91:413–419.
[15] Guo H, Li C, Shi X, Li H, Shen S. Nonaqueous amine-based absorbents for energy efficient CO_2 capture. Appl. Energy 2019;239:725–734.
[16] Kaewchada A, Tongsamaur S, Jaree A. Carbon dioxide capture using monoethanolamine in a microchannel. J. Appl. Sci. 2016;1:1–12.
[17] Kim Y, Park J, Yun S, Nam S, Jeong S, Yoon Y. Carbon dioxide absorption using a phase transitional alkanolamine–alcohol mixture. J. Ind. Eng. Chem. 2014;20:1486–1492.
[18] Li X, Fan G, Zhang Z, Wang Y, Lu Y. Density and viscosity for binary mixtures of diethylene glycol monobutyl ether with monoethanolamine, diethanolamine, and triethanolamine from (293.15 to 333.15) K. J. Chem. Eng. Data 2013;58:1229–1235.
[19] Mehrabi K, Javanmardi J, Rasoolzadeh A, Mohammadi A. Effects of diethanolamine and ethylene glycol + diethanolamine aqueous solutions on methane hydrate stability conditions: Experimental measurements and thermodynamic modeling. J. Mol. Liq. 2021;328:115472.
[20] Pandey D, Agrawal M, Pandey J. Carbon footprint: current methods of estimation. Environ. Monit. Assess. 2011;178:135–160.
[21] Rashidi H, Sheyda P, Sahraie S. A multiobjective experimental based optimization to the CO_2 capture process using hybrid solvents of MEA–MeOH and MEA–water. Energy 2020;190:116430.
[22] Yang F, Wang X, Liu Z. Volumetric properties of binary and ternary mixtures of bis(2-hydroxyethyl) amine with water, methanol, ethanol from (278.15 to 353.15) K. Thermochim. Acta 2012;533:1–9.
[23] Yin L, Li X, Zhang L, Li J. Characteristics of carbon dioxide desorption from MEA-based organic solvent absorbents. Int. J. Greenh. Gas Control 2021;104:103224.

Four-zone modelling of modified downdraft gasifier for performance prediction: Case study of semi-batch operation

Kantapat Palawat[1,*], Phavanee Narataruksa[1,2], Piyapong Hunpinyo[1,2], Nuwong Chollacoop[3], Apichart Meechai[4]

[1] Department of Chemical Engineering, Faculty of Engineering, King Mongkut's University of Technology North Bangkok, Bangkok 10800, Thailand
[2] Research Center for Chemical Engineering Unit Operation and Catalyst Design (RCC), King Mongkut's University of Technology North Bangkok, Bangkok 10800, Thailand
[3] National Energy Technology Center (ENTEC), Klong Luang, Pathum Thani 12120, Thailand
[4] Phra Nakhon Energy Co., Ltd, Ban Phae, Mueang Rayong, Rayong 21000, Thailand
[*] Corresponding author: kantapat.pt@gmail.com

ABSTRACT

This study presents a simulation investigation of a four-zone downdraft gasifier model for semi-batch operation by using Aspen Plus®. The model incorporates condensing, drying, combustion, and reduction zones, along with units such as a gas collection box and a downstream buffer tank. The simulation is designed to reflect the practical concepts of batch feeding and internal gas feedback. Internal flow (R) is assumed to range from 0 to 0.3, affecting gas composition and thermal behavior. A dataset of 54 simulation cases was generated under various feed rates and residence times. Linear regression was used to correlate operating conditions with syngas performance indicators, including the H_2/CO ratio and the lower heating value. The model was validated against data from the literature and offers a user-oriented approach to downdraft gasifier operation under semi-batch conditions.

Keywords: Downdraft gasifier; Aspen Plus; Semi-batch operation; Syngas; Linear regression

1. INTRODUCTION

Downdraft gasifiers are widely recognized for their ability to produce low-tar syngas, making them suitable for small-scale energy production. However, practical gasifier operation is often influenced by fluctuating air supply, batch feeding, and thermal losses, all of which cause deviations from ideal performance. To address these issues, this study proposes a refined four-zone model for a downdraft gasifier operating under semi-batch conditions. The model used the kinetic reactions, internal flow (R) effects, and process control elements. Unlike continuous models, the semi-batch configuration simulates both solid- and vapor-phase reactions under different feed conditions. The internal flow is introduced as a conceptual parameter reflecting thermal feedback from the combustion to the drying zones. The model is built in Aspen Plus® using component blocks for condensing, drying, gasification, and reduction. The resulting syngas quality is evaluated through mole fractions, hydrogen/carbon monoxide (H_2/CO) ratio, and lower heating value (LHV) [1,3].

2. EXPERIMENTAL

The experimental framework of this study is divided into two core phases to 1. investigate and predict the performance of a 150 cm (H) × 50 cm (D) downdraft gasifier under semi-batch operation, as illustrated in Figure 1, and 2. to develop a predictive database for syngas quality using simulation results combined with a linear regression model.

Figure 1 The modified downdraft gasifier [4]

2.1 Simulation Procedures

This phase focuses on the refinement of a four-zone, downdraft-gasifier model grounded in theoretical principles. A process simulation is developed in Aspen Plus® to represent both continuous and semi-batch operations. The model includes the four primary

thermochemical zones—condensing, drying, combustion, and reduction—and integrates units such as a gas collection box, a gas cleanup system, and a downstream buffer tank where syngas is temporarily stored prior to the blowdown process.

2.1.1 Refinement of Four-zone Modelling Concept

The downdraft gasifier was divided into four zones based on height from top to bottom of gasifier sown in Figure 2.

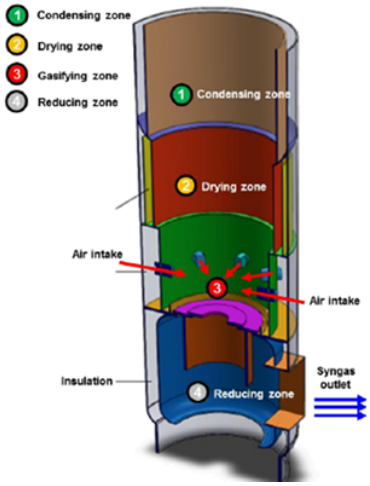

Figure 2 Four-zone model of downdraft gasifier [4]

• Condensing zone – where moisture from the biomass is released.

• Drying/pyrolysis zone – where volatile matter is removed and thermal decomposition begins.

• Gasifying zone – where air is injected and partial oxidation of char generates heat.

• Reduction zone – where the remaining char reacts with CO_2 and H_2O to produce syngas.

This four-zone concept was used as a foundation for simulation modelling and internal flow analysis in the following sections

2.1.2 Internal Flow Analysis

The simulation was adjusted to show the internal gas flow characteristics of the downdraft gasifier, with particular attention to pressure behavior. According to Danışmaz and Demirtaş (2024), the pressure inside a downdraft gasifier follows the trend:

$$P_{condesing} > P_{drying} > P_{combustion} > P_{reduction}$$

that supports gas naturally flowing downward, from high to low-pressure zones. However, near the air inlets in the gasifying zone, a local pressure peak is observed due to air injection. This causes a localized increase in pressure within the combustion zone. Although the overall gas flow remains downward, these pressure peaks can disturb the flow and cause a portion of the gas to move upward toward the drying zone.

To explain this phenomenon, the study introduces the concept of R, which represents internal gas or heat flow recirculating from the heat source back to the primary heat sink—the drying zone. Although R is not directly measured, it is inferred from pressure changes observed in the CFD results. The effect of R is to raise the temperature in the drying zone and alter gas composition—particularly by increasing hydrogen production and enhancing tar cracking.

Therefore, in this study, particularly under continuous process conditions. the internal flow (R) was examined within the range $0 < R < 0.3$. This analysis led to the creation of the box flow diagram shown in Figure 3, which illustrates how gas circulate through the four thermochemical zones, including the impact of internal flow (R) on overall gas dynamics and system performance.

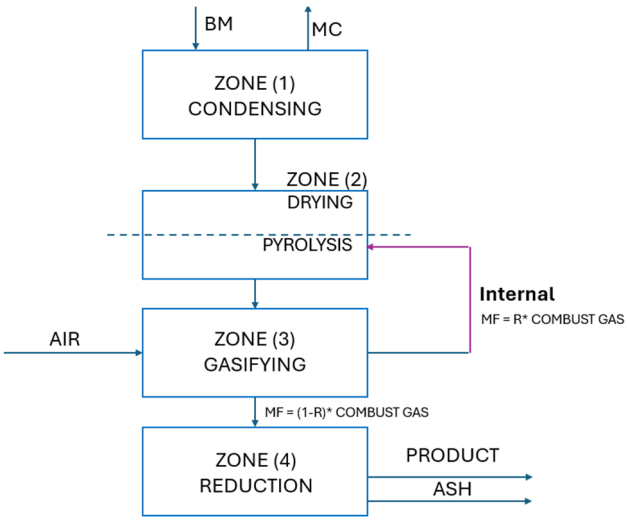

Figure 3 Box flow diagram of downdraft gasifier.

2.1.3 Model Development

Following the refined four-zone concept and internal flow analysis presented in the previous sections, a complete downdraft gasifier system was developed in Aspen Plus®, which consists of a downdraft gasifier, a gas collection box, a cleaning system, and a buffer tank, as shown in Figure 4.

It is important to note that Aspen Plus® was not used in this study to simulate pressure gradients or perform detailed fluid dynamics analyses. Instead, the focus was placed on material and energy balances, reaction tracking, and the flow paths of individual components throughout the gasifier. Additionally, a gas collection box was integrated at the outlet of the reduction zone to enable pressure-driven suction and to ensure that syngas flows into the upper section of the gas collection box before proceeding to the next process. The following sections provide detailed descriptions of each individual sub-model, covering the four gasification zones, the gas collection unit, and the cleaning section.

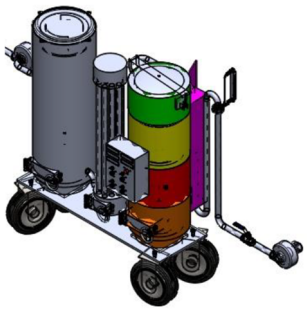

Figure 4 Downdraft gasifier system [4].

(1) Condensing Zone

This zone represents the first section of the gasifier model, labeled as “DRY-ZONE” in the main flowsheet in the upcoming section. The details of the hierarchical sub-model are shown in Figure 5., where moisture from the biomass is released. Heat transfer in this zone is primarily dominated by conduction, with a minor effect from radiation, which is neglected in this model. To represent this behavior, the “ZONE-1” contact dryer model was used to simulate moisture removal from the biomass. The vaporized moisture moves upward and condenses at the top of the gasifier, following a concept analogous to domestic steam condensation, where vapor rises and condenses on cooler surfaces such as the lid or walls. This phenomenon is represented using a “COND-MC” FLASH block, which separates the vapor and liquid phases. The remaining biomass, with reduced moisture content, flows downward into the drying/pyrolysis zone for further thermal decomposition.

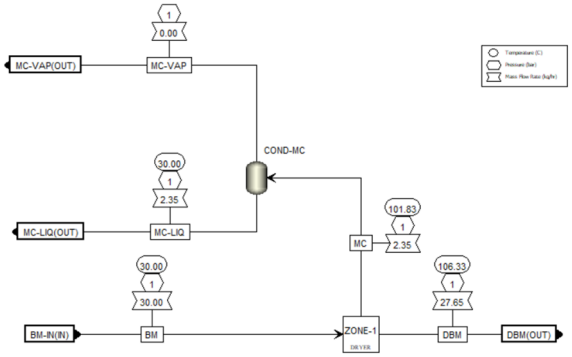

Figure 5 Condensing zone modelling

(2) Pyrolysis zone

This zone represents the first section of the gasifier model, labeled as “PY-ZONE” in the main flowsheet in the upcoming section. The details of the hierarchical sub-model are shown in Figure 5. The remaining biomass from the condensing zone enters the “DECOMP” (decomposition) block, where Fortran code is used to decompose the biomass into elemental components, based on the ultimate analysis and estimated tar content, with tar components represented as methane.

An ideal separator block (“IDL-SEP1”) is then used to show how each phase of the decomposed material proceeds through the system. This step ensures that tar components are not reprocessed in the following reactor. The stream then enters the “2ND-PYRO” block, an RGIBBS reactor, which simulates the equilibrium distribution of the remaining products in the pyrolysis zone. All outputs from this zone are combined in the “MX-PY” mixer block and routed through the stream labeled “PY-TOT,” which is then directed to the next zone.

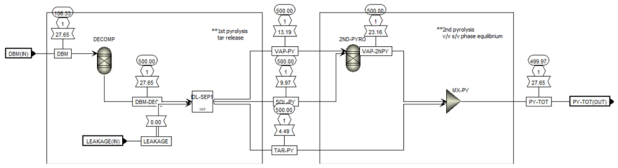

Figure 6 Combustion zone modelling

(3) Gasifying Zone

This zone represents the third section of the gasifier model and is labeled as “COM-ZONE” “DRY-ZONE” in the main flowsheet in the upcoming section; It is considered the most complex section within the overall gasification framework. As the initial zone where oxidation reactions occur, the design of this gasifying section must be approached carefully. For the overall modeling, all reactions were consisting into two types based on phase reaction:

1. Heterogeneous Reaction

Represented by the “COM-HET” block, this simulates vapor–solid (gas–char) reactions where air is injected into the system.

• For the continuous process, the kinetic approach for heterogeneous reactions from Martínez et al. (2012) is followed, using RCSTR modeling. Approximately 70% of the combustion zone volume is used for kinetic reaction modeling, as illustrated in Figure 7.

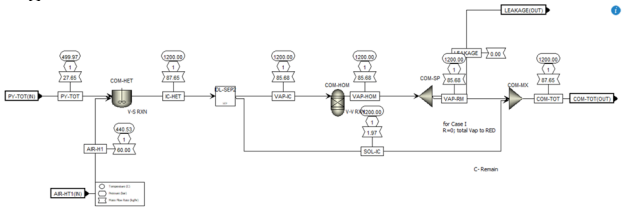

Figure 7 Gasifying modelling for continuous process

• For the semi-batch process (shown in blue in the main flowsheet), the same kinetic set used in the continuous model is applied. However, the RBATCH model is used to simulate semi-batch biomass feeding while maintaining continuous air injection, as illustrated in Figure 8, to represent real gasifier operation. Two main parameters must be defined: the batch feed time and the batch discharge time, which together determine the biomass fed per batch. Since the biomass input is now adjusted, the air flow must be

recalibrated accordingly to maintain the desired air/biomass (A/B) ratio of 0.5, which mainly target for producing high-quality syngas in downdraft gasifiers (Basu, 2010; Puig-Arnavat et al., 2010). In the simulation flowsheet, the air feed rate is automatically updated based on the biomass feed and user-defined parameters within the RBATCH block.

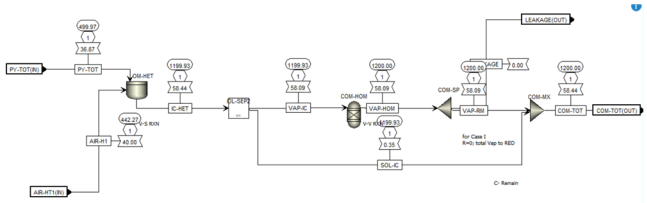

Figure 8 Gasifying modelling for semi-batch process

2. Homogeneous reaction

The remaining vapor-phase components, excluding char—which is separated via the "IDL-SEP2" block—are routed to the "COM-HOM" reactor. This reactor is modeled using RGIBBS to estimate the equilibrium composition of the remaining vapor species with remain oxygen, where vapor–vapor equilibrium reactions take place. This separation step ensures that gas-phase species are not double-counted in gas–solid reactions. As previously discussed in the flow analysis, internal gas leakage (referred to as the R effect) is assumed to occur after vapor-vapor reaction ended in the combustion. This represents thermal feedback from the combustion zone (heat source) to the reduction zone (heat sink). The remaining vapor and solid components are merged into the stream labeled "SOL-IC," which is directed into the reduction zone, as shown in Figures 7 and 8, following the "COM-HET" model in both the continuous and semi-batch processes.

(4) Reduction Zone

This zone represents the fourth section of the gasifier model and is labeled as the "RED-ZONE," in the main flow sheet, where the remaining char reacts and all major gas-phase reactions—including the Boudouard reaction, water–gas reaction, and water–gas shift reaction—take place. A kinetic modeling approach based on Martínez et al. (2012), the same as in the gasifying zone, is applied.

For the continuous process, the reduction zone is modeled using an RCSTR block, as shown in Figure 9, with the total reactor volume specified in the modified gasifier design. After all reactions are completed, the syngas flows into the gas collection zone.

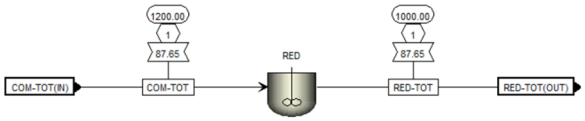

Figure 9 Reduction modelling for continuous process.

For the semi-batch process, the same kinetic set used in the continuous model is also applied. However, the RBATCH model is used to represent batch operation, as shown in Figure 10. Attention must be given to how the batch feed time and batch discharge time are defined. Since the gas flow has already been scaled based on biomass input per batch (kg/batch) in the upstream gasifying zone, it is assumed in this zone that the batch feed time equals the batch discharge time, denoted as t minutes. This assumption implies that all syngas entering the reduction zone exits after t minutes. Therefore, t also serves as the gas collection time in the final zone. Under this condition, syngas is considered to be within the reduction zone for the full duration of the batch reduction cycle. Only after this cycle is complete does it become practical to initiate suction, drawing syngas upward from the bottom of the gasifier into the gas collection system.

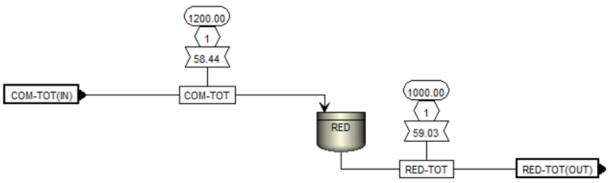

Figure 10 Reduction modelling for semi-batch process

(5) Gas Collecting Box

As discussed in the reduction zone modeling, the suction valve is activated after *t* minutes, corresponding to the batch residence time which syngas is generated. At this point, suction is applied at the top of the gas collection box, drawing syngas upward through the outlet system which driven by the pressure gradient, the condition:

$$P_{reduction} > P_{top,box}$$

Importantly, the syngas flows upward past the air inlet pipe which feed air into the gasifying zone. This creates a natural heat exchange effect: the hot syngas transfers heat to the incoming air, beneficial as it preheats the combustion air while cooling the syngas led to improving overall thermal efficiency. After continued suction, the temperature in the reduction zone begins to drop, typically to around 300–400 °C. Signal that most of the combustible gases have been depleted. If suction is continued beyond this point, only air (or low-quality residual gas) would be drawn into the collection gas box, lead to poor syngas quality at the end of tank. therefore, suction should be end after the reduction zone temperature falls below 400 °C, ensuring that only high-quality syngas is collected as shown in Figure 11

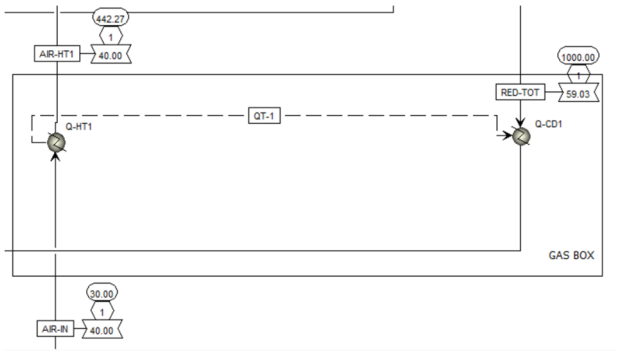

Figure 11 Gas collecting box process

(6) Syngas Cleaning and Buffer tank

After syngas exits the gas collection box, it goes into a cleaning before storage and utilization in tank. this section includes four key steps: cooling, impurity removal, and buffering.

The raw syngas is first cooled by heat exchange against the outlet air flow; this process reduces the syngas temperature from approximately 800 °C to around 150 °C to condense tars and reduce the thermal load on downstream cleaning equipment. Next, the cooled gas enters a separator system (SV-SEP and V-SEP) designed to remove unwanted condensable tars, heavy hydrocarbons, and fine particulates. It is noted that this was modeled under an ideal SEP separation model, to improve the process simulation in future studies, potentially using a column separator model was recommend for heat integration. A portion of volatile, high-molecular-weight gases is removed through purge streams (V-PURGE and S-PURGE). These purges prevent degradation of the final gas quality. After cleaning, the purified syngas is routed into a buffer tank, represented by the TANK block in the model, as shown in Figure 12. This tank temporarily stores the gas and smooths out flow fluctuations. The syngas exits the tank at a stabilized flow rate and reduced temperature (approximately 35 °C), ready for end use in engines, flare systems, or further processing

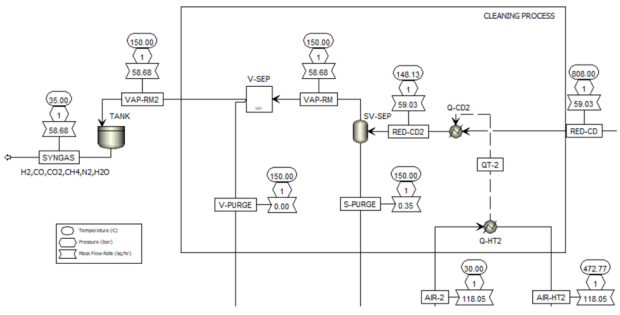

Figure 12 Syngas Cleaning and Buffer tank.

(7) Integration of Sub-Models into Complete Gasifier Systems

After all investigations from Sections 2.1.3.1 to 2.1.3.6, all models were integrated into the Complete Gasifier System. As shown in Figure 4,

For the continuous process, designed for steady-state operation, this configuration uses RCSTR reactors to simulate reaction kinetics in the combustion and reduction zones. Biomass and air are continuously fed, with syngas flowing continuously into the gas collection and cleaning sections, as shown in Figure 13.

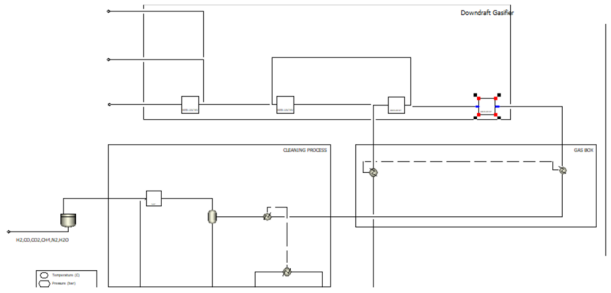

Figure 13 Full downdraft gasifier modelling for continuous process.

For the semi-batch process, the configuration uses the RBATCH model with the same kinetic reactions as the continuous model to simulate batch biomass feeding while maintaining continuous air input. Batch feed time and discharge time are set to track syngas residence time, as shown in Figure 14. The suction operation is controlled to begin after a full batch cycle (t minutes), with syngas drawn upward by pressure differential.

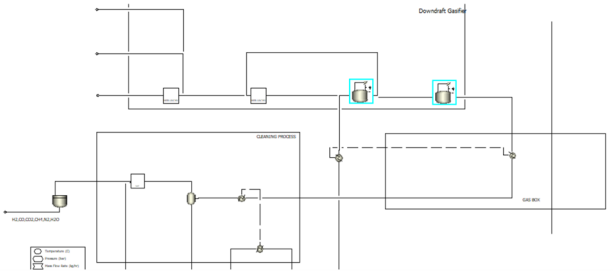

Figure 14 Full downdraft gasifier modelling for semi-batch process

2.2 Simulation Database with Machine Learning Concept: Linear Regression

In this study, a semi-batch downdraft gasifier model was developed and implemented in Aspen Plus® to perform simulations under various biomass input conditions, as illustrated in Figure 14. The objective was to create a simulation database and apply a linear regression approach to analyze the effect of process timings on syngas quality, with a primary focus on the Lower Heating Value (LHV) and the Hydrogen/Carbon Monoxide ratio (H_2/CO).

2.2.1 Input Configuration and Range

A simulation database was created with same torrified rubberwood with three different biomass feed rates: 15 kg, 30 kg, and 45 kg. For each feed rate, batch feed times of 0.25, 0.5, and 1 hour were used to represent different operational batch durations. Five gas

collection times were selected for each batch configuration: 0.333, 0.416, 0.5, 0.75, and 1.0 hour. This led to a total of 54 simulated conditions, calculated as 3 × 3 × 6 = 54.

2.2.2 Feature Generation and Regression Design

To develop regression models, the following independent variables were set from the simulation inputs:

- R: residence time in the reduction zone
- C: batch feed time in the combustion feed
- R + C (Total time)
- R/C (Time ratio)
- R×C (Time interaction)

The main concern for linear regression is to show the equation support that have acceptable R^2 and focus on different differences in batch time configurations with Filtering criteria were applied to remove unstable or unphysical results:

- LHV > 4.6 MJ/Nm^3 (for steady electricity generate)
- R ≥ 0.333 hr (collected time more than 20 min)

2.2.3 Data Filtering and Case Selection

Out of the 54 simulated conditions, 38 valid cases passed the quality check. These were further grouped by biomass input:

- 15 kg: 11 valid cases
- 30 kg: 13 valid cases
- 45 kg: 14 valid cases

Separate linear regression models were created for each biomass flow rate to better reflect the behavior of each case.

3. RESULTS AND DISCUSSION

The results are presented in three parts: (1) model validation (2) internal recycle (R) effect to gasifier and (3) database-driven performance; analysis discussed in the following section.

3.1 Model Validation

The primary focus of this session is to validation of the continuous model, which serves as the foundational basis for developing the semi-batch gasifier configuration. This is achieved by replacing the RCSTR with an RBATCH reactor in the kinetic reaction zone model, leading to specific assumptions and boundary conditions applied in the batch-time simulations.

Several approaches exist for validating gasifier models, including comparison of temperature profiles, syngas compositions, and carbon conversion efficiency. In this report, we focus on the comparison of syngas composition trends under varying Air-to-Biomass (A/B) ratios, which serve as indicators of the model's predictive accuracy under different oxidizing conditions, as presented in Figure 15.

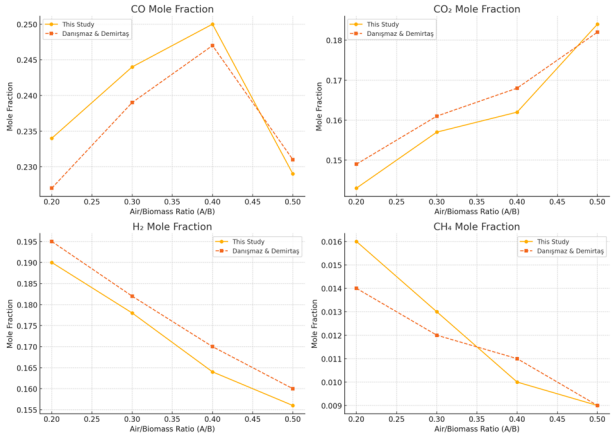

Figure 15 Vapor mole fraction of our study compare to Danışmaz & Demirtaş [2]

Across all components (CO, CO_2, H_2, CH_4), the simulated results trends consistent with reported in the literature under varying Air-to-Biomass (A/B) ratios. The CO mole fraction increased and peaked at approximately A/B = 0.4, followed by a decline at higher air flow rates. In contrast, H_2 and CH_4 showed decreasing trends, attributed to gas-phase reactions and the cracking of hydrocarbons under oxygen-rich conditions. These observed trends validate the model's reliability in predicting syngas composition behavior under different oxidizing environments.

3.2 Effect of Internal Recycle Ratio (R)

This section focuses on the case where the Air/Biomass (A/B) ratio is fixed at 0.5, in order to examine the impact of the internal recycle ratio (R) on gasifier performance. Two key performance indicators are considered: the H_2/CO ratio and residual carbon content. With increase in the recycle ratio enhances char conversion due to improved heat and gas feedback, but slightly decreases the H_2/CO ratio as gas-phase equilibria shift as shown in Figure 16. This trade-off highlights the balance between conversion efficiency and syngas composition. An optimal recycle ratio in the range of 0.15–0.18 yields improved thermal utilization while maintaining syngas quality. However, in practical systems, the recycle ratio is typically maintained only for short intervals due to dynamic flow variations, as discussed in the flow analysis section. Therefore, a limited R range is adopted for this investigation amd for the semi-batch configuration, the recycle ratio is set to zero, since the biomass remains stationary in discrete zones until the complete cycle is finished.

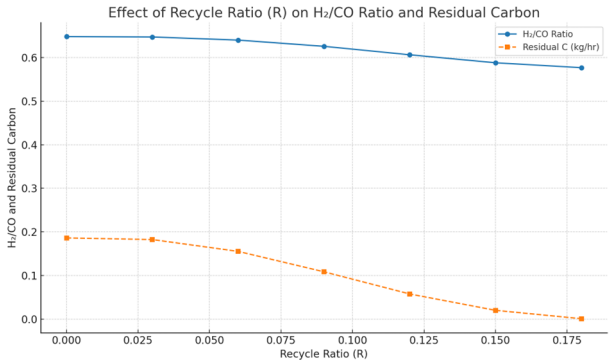

Figure 16 Effect of recycle ratio on H_2/CO and Residual Carbon

3.3 Database-Driven Performance Analysis

This section presents the performance analysis of the semi-batch downdraft gasifier based on the simulation database, utilizing linear regression techniques. The analysis focuses on two primary indicators: the Lower Heating Value (LHV) and the H_2/CO ratio.

For each biomass feed rate, separate linear regression models were developed, and their predictive accuracy was evaluated using the coefficient of determination (R^2). This metric quantifies how well the regression model explains the variability in the target outputs, thereby providing insight into the reliability of the simulation-based performance predictions.

3.3.1 Model Performance Prediction

The regression models show a varying level of predictive accuracy depending on biomass input show as subscript 15,30,40 kg

- For input biomass flowrate 15 kg

$LHV_{15} = 2.15 + 0.78 \cdot R - 0.45 \cdot C + 1.22 \cdot (R/C) + 0.94 \cdot (R \times C)$ $[R^2 = 0.995]$

$(H_2/CO)_{15} = 0.84 + 0.91 \cdot R - 0.47 \cdot C + 1.68 \cdot (R/C) + 1.05 \cdot (R \times C)$ $[R^2 = 0.999]$

- For input biomass flowrate 30 kg

$LHV_{30} = 2.88 + 0.42 \cdot R - 0.21 \cdot C + 0.54 \cdot (R/C) + 0.67 \cdot (R \times C)$ $[R^2 = 0.680]$

$(H_2/CO)_{30} = 0.96 + 0.87 \cdot R - 0.41 \cdot C + 1.44 \cdot (R/C) + 0.89 \cdot (R \times C)$ $[R^2 = 0.998]$

- For input biomass flowrate 40 kg

$LHV_{40} = 1.76 + 0.63 \cdot R - 0.33 \cdot C + 1.01 \cdot (R/C) + 0.78 \cdot (R \times C)$ $[R^2 = 0.984]$

$(H_2/CO)_{40} = 0.77 + 0.79 \cdot R - 0.39 \cdot C + 1.56 \cdot (R/C) + 1.02 \cdot (R \times C)$ $[R^2 = 0.998]$

All of these linear regression equations serve as a foundational basis for future studies investigating the influence of varying batch durations in semi-batch operations on gasifier performance and syngas quality

3.3.2 High-Quality Output Conditions

Top LHV Conditions: High residence time ($R \geq 0.75$ hr) combined with low combustion time ($C \leq 0.25$ hr)

Top H_2/CO Conditions: Residence time (R) between 0.75 and 1.0 hr, with a time ratio ($R/C \geq 3$

This analysis will support future development efforts aimed at creating a user-friendly operational guideline for the semi-batch operation of downdraft gasifiers. It will assist in identifying optimal operational batch for biomass feeding under varying batch durations, based on key syngas quality indicators such as LHV and the H_2/CO ratio.

4. CONCLUSION

A semi-batch downdraft gasifier model was successfully developed using Aspen Plus® with the four thermochemical zones: condensation, drying, gasifying, and reduction. The model also discusses about the thermal feedback through an internal flow parameter (R), in ranges from 0 to 0.3 to simulate realistic gas recirculation effects. Detailed kinetic modeling was implemented for both continuous and semi-batch operations, based on established literature sources [1][3].

Simulation results, validated against reference trends, also show that increasing internal recirculation (R) improves char conversion but may slightly decrease the H_2/CO ratio due to gas-phase equilibrium shifts.

Regression models developed from 54 simulation cases with various biomass feed rates and residence times with a high predictive accuracy ($R^2 > 0.98$ in most cases) for key syngas quality indicators, including the Lower Heating Value (LHV) and H_2/CO ratio.

The resulting regression equations show a practical foundation for the operation of batch-mode downdraft gasifiers, with decision-making; $R \geq 0.75$ hr and $C \leq 0.25$ hr for top LHV quality and $0.75 \leq R \leq 1$ hr, $R/C \geq 3$ for top H_2/CO quality under 3 batch feed 15,30,40 kg.

Future work should focus on experimental validation using laboratory-scale units, incorporating a range of biomass types, and integrating CFD-based modeling to capture transient heating effects with real-time feedback control, where feasible.

ACKNOWLEDGMENTS

This research was funded by King Mongkut's University of Technology North Bangkok and National Science and Technology Development Agency, Thailand. The project entitled "Testing of bio-syngas to electricity generator for household application" has been granted by contract number ๖.009/2563.

REFERENCES

[1] Martínez, J.D., Mahkamov, K., Andrade, R.V., and Lora, E.E.S. (2012). Syngas production in downdraft biomass gasifiers and its application using internal combustion engines. *Renewable Energy*, 38(1), 1–9.

[2] Danışmaz, İ.M., and Demirtaş, M. (2024). CFD analysis of pressure distribution in downdraft biomass gasifiers. *Biomass and Bioenergy*, 181, 107–118.

[3] Basu, P. (2010). *Biomass Gasification and Pyrolysis: Practical Design and Theory*. Academic Press.
[4] Apichart Meechai. (2023). Laboratory-scale demonstration units for biomass-to-liquid (BTL) systems. Internal documentation, Biomass Energy Lab, Thailand.

Improvement of electrocatalytic activities of Ag-based catalysts in oxygen reduction and oxygen evolution reactions

Phatcharanan Pipatnawakit[1], Jatupon Chaiwasu[1], Apichai Therdthianwong[2], Montree Ob-choey[1,*], Sarayut Yongprapat[2,*], Supaporn Therdthianwong[1,]**

[1] Department of Chemical Engineering, Faculty of Engineering, King Mongkut's University of Technology Thonburi, Bangkok 10140, Thailand
[2] Fuel Cell and Hydrogen Research and Engineering Center, Pilot Plant Development and Training Institute, King Mongkut's University of Technology Thonburi, Bangkok 10140, Thailand
[*] Corresponding author: sarayut.yon@kmutt.ac.th
[**] Co-corresponding author: supaporn.the@kmutt.ac.th

ABSTRACT

The electrocatalytic performances in oxygen reduction and oxygen evolution reactions (ORR/OER) are critical for advancing regenerative fuel cells (RFCs). In this work, silver-based catalysts were developed by incorporating cerium-doped cobalt oxide (Ce-Co_3O_4) through a precipitation method to enhance bifunctional activity in alkaline media. Structural analysis confirmed the presence of CeO_2 and Co_3O_4 phases in the synthesized catalysts. Electrochemical evaluation using cyclic voltammetry (CV) and linear sweep voltammetry (LSV) demonstrated that the integration of cobalt-based oxides with AgNWs improved OER performance by lowering the onset potential and increasing current density, while also enhancing ORR kinetics and oxygen transport behavior. These results indicated that AgNWs-supported CeO_2-Co_3O_4 composites are promising candidates for cost-effective bifunctional electrocatalysts in alkaline energy conversion systems.

Keywords: Oxygen reduction reaction; Oxygen evolution reaction; Ag-based catalysts; CeO_2-Co_3O_4; Regenerative fuel cell

1. INTRODUCTION

The development of efficient electrocatalysts for the oxygen reduction reaction (ORR) and oxygen evolution reaction (OER) plays a vital role in advancing electrochemical energy systems such as regenerative fuel cells (RFCs). These reactions are crucial to the performance and efficiency of devices that rely on reversible oxygen electrode processes. Given the importance of these reactions, the search for cost-efficient and high-performance bifunctional catalysts has become a major focus in recent years.

In general, the most effective catalyst for ORR is platinum (Pt), but inefficient in OER[1]. However, the most efficient catalysts in OER are iridium (Ir)[2] which is inefficient for ORR. Several researchers have studied the ratio between Pt and Ir for the bifunctional catalyst. Silva (2018) [3] indicated that the best ratio of Pt: Ir that balance the OER and ORR activities in the form of Pt/IrO_2 was 1:9. However, due to the high cost of Pt and Ir, researchers have explored the alternative low-cost catalysts. Ghosh (2021) [4] found that CeO_2/NiO has better performance in OER than IrO_2. It was also discovered that CeO_2 has the best performance in ORR compared to CeO_2/IrO_2 and commercial CeO_2. Xu et al. (2019) [5] discovered that cerium-doped cobalt oxide (CoO_x (Ce)) has the outstanding performance in OER due to the low overpotential and comparable current density with the commercial grade of ruthenium oxide (RuO_2). Khan et al. (2016) [6] discover that the CeO_2/Co_3O_4 is the most active catalyst in the water splitting reaction with the lowest overpotential and high current density indicated through the linear sweep voltammogram (LSV) method.

Silver (Ag)-based catalysts are known for their moderate catalytic activities and cost-effectiveness, but their performances remain limited compared to precious metal catalysts. The incorporation of transition metals and rare earth elements has been widely explored to enhance their bifunctional catalytic activity. Ashok et al. (2018) [7] synthesized a bifunctional Ag/Co_3O_4 catalyst via solution combustion synthesis for ORR and OER in alkaline media. Their study demonstrated that the synergistic interaction between Ag and Co enhances the electrocatalytic performance by facilitating O-O bond cleavage and improving oxygen adsorption and transport. Alia et al (2012) [8] synthesized supportless silver nanowires (AgNWs) with controlled diameters as oxygen reduction catalysts for hydroxide-exchange membrane fuel cells (HEMFCs). Their study demonstrated that the synergistic effect of Ag morphology and facet exposure

enhances ORR activity by promoting a four-electron transfer with minimal peroxide formation, highlighting the superior performance of 25 nm AgNWs compared to both bulk Ag and Ag nanoparticles.

The goal of this study was to identify a cost-effective bifunctional catalyst with improved performance for future energy conversion applications. In this work, we explored the effects of incorporating cobalt oxide (Co_3O_4) and cerium oxide (CeO_2) into Ag nanowires (AgNWs) to enhance the ORR and OER performance in alkaline media. We aimed to investigate the synergistic interactions between Ag, Co, and Ce, and their influence on electrocatalytic behavior. The catalysts were synthesized and characterized, and their electrochemical activity measurements were evaluated using cyclic voltammetry (CV) and linear sweep voltammetry (LSV) techniques.

2. EXPERIMENTAL

Ag-based catalysts were developed by combining cobalt oxide and cerium oxide (CeO_2-Co_3O_4) with commercial silver nanowires (AgNWs) to improve bifunctional activity toward oxygen reduction and evolution reactions (ORR/OER). The commercial silver nanowires have a length of approximately 4.104 microns and a diameter of 0.06 µm, resulting in an aspect ratio of 67.13.

2.1 Synthesis of Co_3O_4, CeO_2, and CeO_2-Co_3O_4

The catalysts were synthesized via a urea precipitation method using nitrate salts as metal precursors. For the synthesis of pure oxides, pure Co_3O_4 was prepared using $Co(NO_3)_2{\cdot}6H_2O$ as the sole metal precursor, while pure CeO_2 was obtained using only $Ce(NO_3)_3{\cdot}6H_2O$. In both cases, the solutions were heated at 120 °C for 6 h and subsequently calcined at 400 °C for 2 h in air.

For the synthesis of mixed CeO_2-Co_3O_4, both $Co(NO_3)_2{\cdot}6H_2O$ and $Ce(NO_3)_3{\cdot}6H_2O$ were used as metal precursors. In the case of Co95Ce5, the required amount of $Co(NO_3)_2{\cdot}6H_2O$ and $Ce(NO_3)_3{\cdot}6H_2O$ were used to obtain an atomic ratio of 95:5 (Co: Ce). The same procedure was followed as described above.

2.2 Catalyst Ink Preparation

The synthesized oxide was individually and physically mixed with 10 wt% AgNWs. Each mixture (2 mg total) was dispersed in isopropanol and ionomer solution, ultrasonicated for 30 min, and dropped-cast onto a glassy carbon disk electrode before drying at room temperature.

2.3 Electrochemical Measurements

Electrocatalytic activity was evaluated in 0.1 M NaOH using cyclic voltammetry (CV) and linear sweep voltammetry (LSV) with a rotating ring-disk electrode (RRDE) setup. A mercury/mercury oxide (MMO) was used as the reference electrode, and a 1cm^2 platinum (Pt) gauze was used as the counter electrode. All reported potentials were converted and are presented versus the standard hydrogen electrode (SHE).

CV tests were conducted under both argon-purged and oxygen-saturated conditions, while LSV was performed at a fixed rotation speed of 1600 rpm. Electrochemical parameters such as onset potential, current density, and stability were analyzed to compare catalytic performance.

The half-wave potential ($E_{1/2}$) is defined as the potential at which the current reaches half of the limiting current. It serves as an indicator of catalytic activity, with a more positive $E_{1/2}$ generally reflecting better activity in ORR, as it reflects a lower energy barrier for the reaction. Higher current density at a given potential also indicates higher catalytic activity, while better stability was characterized by minimal changes in performance over time during continuous operation.

3. RESULTS AND DISCUSSION

3.1 Physical Characterization

The X-ray diffraction (XRD) results (not shown here) confirmed that Ce exists predominantly as CeO_2, while Co is present in the form of Co_3O_4. For the Co sample, diffraction peaks were observed at 2θ values of approximately 19.0°, 31.3°, 36.9°, 38.6°, 44.8°, 55.7°, 59.3°, and 65.3°, which can be indexed as (111), (220), (311), (222), and (511) planes of the Co_3O_4 phase, matching well with the standard JCPDS card No. 42-1467 [9].

For the Ce sample, characteristic diffraction peaks at around 28.42°, 32.95°, and 47.30° correspond to the (111), (220), and (311) planes of the cubic fluorite structure of CeO_2, consistent with JCPDS card No. 34-0394 [10].

In the Co-Ce composite samples, Co95Ce5, both Co_3O_4 and CeO_2 peaks were detected, indicating that Ce is predominantly present as CeO_2 while Co exists mainly as Co_3O_4. No additional impurity phases were observed, suggesting high phase purity of the synthesized materials.

3.2 Cyclic Voltammetry (CV) for Oxygen Evolution Reaction (OER) and Oxygen Reduction Reaction (ORR)

Cyclic voltammetry (CV) was conducted in 0.1 M NaOH solution to investigate the bifunctional electrocatalytic performance of AgNWs-supported oxide catalysts. The CV curves obtained under Ar-purged conditions as shown in Figure 1 were used to analyze the baseline capacitive behavior and initial electrochemical activity.

The ORR and OER performance in O_2-saturated conditions is illustrated in Figure 2. The key electrochemical parameters extracted from the CV curves are summarized in Table 1.

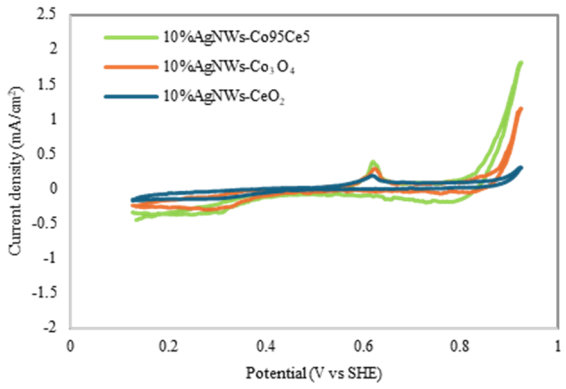

Figure 1: Cyclic voltammograms of 10%AgNWs mixed with CeO_2, Co_3O_4, and Ce-Co_3O_4 in Ar-purged 0.1 M NaOH solution

Among the tested samples, 10%AgNWs-Co_3O_4 and 10%AgNWs-Co95Ce5 exhibited the highest current peak densities for OER at 21 mA/cm² and 17.5 mA/cm², respectively, indicating enhanced electrocatalytic activity. Both samples shared a comparable lower OER onset potential ($E_{on, OER}$) of 0.79 V, suggesting similar reaction initiation characteristics.

On the other hand, 10%AgNWs-CeO_2 exhibited the least favorable performance at the lowest peak current (12.2 mA/cm²), with a relatively high onset potential of 0.80 V. This result indicates that CeO_2 alone, without the presence of cobalt oxide, may exhibit limited intrinsic activity for oxygen evolution under the tested conditions.

For the oxygen reduction reaction (ORR), both 10%AgNWs-Co_3O_4 and 10%AgNWs-Co95Ce5 showed ORR onset potentials of 0.34 V, while 10%AgNWs-CeO_2 exhibited an intermediate value of 0.33 V. These results suggest that catalyst compositions containing transition metal oxides are generally active for ORR in alkaline condition.

Overall, the CV results indicate that cobalt oxide-based systems integrated with AgNWs provide promising bifunctional catalytic performance. The balance between onset potential and current density highlights the role of catalyst structure and conductivity in governing electrochemical activity.

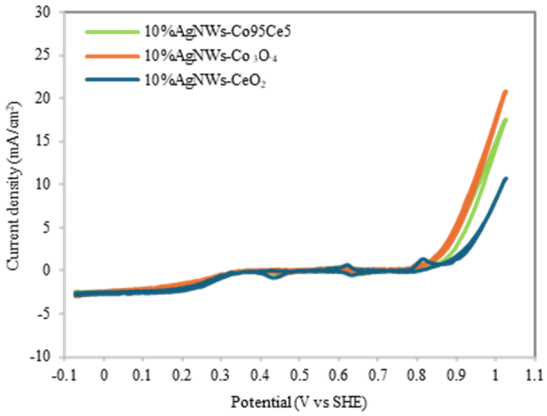

Figure 2: Cyclic voltammograms of 10%AgNWs mixed with CeO_2, Co_3O_4, and Ce-Co_3O_4 saturated with oxygen, 0.1 M NaOH solution at a rotating speed of 1600 rpm

Table 1: Onset potential (E_{on}), and maximum current density of 10% AgNWs-supported catalysts for OER

Catalysts	$E_{on, ORR}$ (V)	$E_{on, OER}$ (V)	Maximum Current density (mA/cm²)
10%AgNWs-Co95Ce5	0.34	0.79	17.5
10%AgNWs-Co_3O_4	0.34	0.79	21.0
10%AgNWs-CeO_2	0.33	0.80	12.2

3.3 Linear Sweep Voltammetry (LSV) for Oxygen Reduction Reaction (ORR)

The oxygen reduction activity of the AgNWs-supported oxide catalysts was further evaluated via linear sweep voltammetry (LSV) in O_2-saturated 0.1 M NaOH electrolyte using a rotating ring-disk electrode (RRDE) setup. The polarization curves and corresponding electrochemical parameters are shown in Figure 3 and Table 2, respectively.

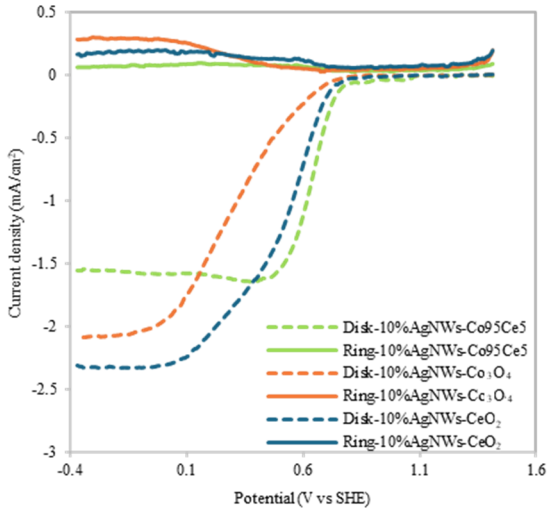

Figure 3: LSV polarization curves of AgNWs-supported Co-Ce oxide catalysts in saturated oxygen, 0.1 M NaOH solution at a rotating rate of 1600 rpm, with ring signal amplification by a factor of 10

Among the catalysts studied, 10%AgNWs-Co95Ce5 exhibited the most favorable ORR performance, with the highest onset potential (E_{on}) of 0.75V and a high $E_{1/2}$ value of 0.64V, indicating excellent ORR kinetic. This sample also delivered a reasonably high limiting current density of 1.64 mA/cm^2, suggesting good oxygen transport and electron transfer efficiency. Notably, based on the Ring current data, it was found that the catalytic process for all the catalysts proceeded via a 4-electron mechanism, confirming the high efficiency of electron transfer in these reactions.

10%AgNWs-Co_3O_4, a well-known ORR catalyst in alkaline media, also demonstrated high activity, with E_{on} and $E_{1/2}$ values of 0.74 V and 0.67 V, respectively. Interestingly, it exhibited the second-highest limiting current density (2.09 mA/cm^2). This reflects the material's strong capability to sustain high ORR rates under mass transport-limited conditions.

On the other hand, 10%AgNWs-CeO_2, although showing a slightly lower E_{on} of 0.72 V and moderate $E_{1/2}$ (0.52 V), recorded the highest limiting current density of 2.33 mA/cm^2 among all the samples. This indicates that while its surface may support excellent oxygen diffusion and transport, its kinetic performance for ORR is relatively limited.

These results reinforce the suitability of silver nanowire-supported cobalt oxide systems as bifunctional catalysts for oxygen electrode reactions, providing a foundation for future optimization based on morphology, dispersion, and conductivity improvements.

Table 2: Onset potential (E_{on}), half-wave potential ($E_{1/2}$), and limiting current density of 10% AgNWs-supported catalysts for ORR

Catalysts	$E_{on, ORR}$ (V)	$E_{1/2}$ (V)	Limiting current density (mA/cm^2)
10%AgNWs-Co95Ce5	0.75	0.64	1.64
10%AgNWs-Co3O4	0.74	0.67	2.09
10%AgNWs-CeO2	0.72	0.52	2.33

4. CONCLUSION

This study focused on evaluating the electrocatalytic performance for both the Oxygen Evolution Reaction (OER) and the Oxygen Reduction Reaction (ORR) in alkaline media. The results revealed distinct differences in catalytic activity depending on oxide composition, with particular emphasis on Co_3O_4-based and AgNWs-based systems.

The results demonstrated that the catalyst containing 95% cobalt oxide (Co_3O_4) and 5% cerium oxide (CeO_2), 10%AgNWs-Co95Ce5, exhibited superior bifunctional behavior, achieving both high current density and low overpotential in OER, as well as the highest onset potential and a favorable half-wave potential in ORR. These outcomes indicate that a small addition of cerium into cobalt oxide can enhance both catalytic processes due to the synergistic interaction between the metal oxides.

In the ORR evaluation, 10%AgNWs-Co95Ce5 showed the most promising activity, with the highest onset and half-wave potential and a high limiting current density, suggesting excellent reaction kinetics and efficient electron transfer. 10%AgNWs-Co_3O_4 demonstrated strong ORR performance as well, with high onset potential and limiting current density. 10%AgNWs-CeO_2, while exhibiting the highest limiting current density, had relatively lower ORR kinetics, indicating that it supports mass transport but may not be as efficient in electron transfer.

The comparative analysis of the mixed Co Ce oxide suggested that 10%AgNWs-Co95Ce5 strikes an optimal balance between high catalytic activity and structural stability, making it a promising candidate for cost-effective, AgNWs-based bifunctional catalysts. These findings align with the initial research objective and provide a strong foundation for future development of advanced electrocatalysts in energy conversion devices such as rechargeable metal-air batteries and fuel cells.

ACKNOWLEDGMENTS

This research project is supported by King Mongkut's University of Technology Thonburi (KMUTT), Thailand Science Research and Innovation (TSRI), and National Science, Research and Innovation Fund (NSRF) Fiscal year 2024. The first author would like to acknowledge an academic scholarship provided by the Department of Chemical Engineering, KMUTT.

REFERENCES

[1] M. Hunsom, D. Kaewsai, and A. M. Kannan, 'Recent developments in bifunctional air electrodes for unitized regenerative proton exchange membrane fuel cells – A review', Nov. 15, 2018, *Elsevier Ltd*. doi: 10.1016/j.ijhydene.2018.09.152.

[2] S. Cherevko, A. R. Zeradjanin, A. A. Topalov, N. Kulyk, I. Katsounaros, and K. J. J. Mayrhofer, 'Dissolution of noble metals during oxygen evolution in acidic media', *ChemCatChem*, vol. 6, no. 8, pp. 2219–2223, 2014, doi: 10.1002/cctc.201402194.

[3] A. Catalysis, G. C. Da Silva, M. R. Fernandes, and E. A. Ticianelli, 'Subscriber access provided by READING UNIV Activity and stability of Pt/IrO_2 bifunctional materials as catalysts for the oxygen evolution/reduction reactions Activity and stability of Pt/IrO_2 bifunctional materials as catalysts for the oxygen evolution/reduction reactions', 2018. [Online]. Available: http://pubs.acs.org

[4] D. Ghosh, M. Manikanta Kumar, C. R. Raj, and D. Pradhan, 'Bifunctional Catalytic Activity of Solvothermally Synthesized CeO_2Nanosphere/NiO Nanoflake Nanocomposites', *ACS Appl Energy Mater*, 2021, doi: 10.1021/acsaem.1c04036.

[5] S. Xu, C. Lv, T. He, Z. Huang, and C. Zhang, 'Amorphous film of cerium doped cobalt oxide as a highly efficient electrocatalyst for oxygen evolution reaction', *J Mater Chem A Mater*, vol. 7, no. 13, pp. 7526–7532, 2019, doi: 10.1039/C9TA00061E.

[6] S. A. Khan, S. B. Khan, and A. M. Asiri, 'Electro-catalyst based on cerium doped cobalt oxide for oxygen evolution reaction in electrochemical water splitting', *Journal of Materials Science: Materials in Electronics*, vol. 27, no. 5, pp. 5294–5302, May 2016, doi: 10.1007/s10854-016-4427-3.

[7] A. Ashok, A. Kumar, M. A. Matin, and F. Tarlochan, 'Synthesis of Highly Efficient Bifunctional Ag/Co_3O_4 Catalyst for Oxygen Reduction and Oxygen Evolution Reactions in Alkaline Medium', *ACS Omega*, vol. 3, no. 7, pp. 7745–7756, Jul. 2018, doi: 10.1021/acsomega.8b00799.

[8] S. M. Alia, K. Duong, T. Liu, K. Jensen, and Y. Yan, 'Supportless silver nanowires as oxygen reduction reaction catalysts for hydroxide-exchange membrane fuel cells', *ChemSusChem*, vol. 5, no. 8, pp. 1619–1624, 2012, doi: 10.1002/cssc.201100684.

[9] J. Sun, H. Wang, Y. Li, and M. Zhao, 'Porous Co3O4 column as a high-performance Lithium anode material', *Journal of Porous Materials*, vol. 28, no. 3, pp. 889–894, Jun. 2021, doi: 10.1007/s10934-021-01041-z.

[10] P. Shanmugam, G. P. Kuppuswamy, K. Pushparaj, B. Arumugam, A. Sundaramurthy, and Y. Sivalingam, 'CeO_2 nanoparticles based extended gate field effect transistor for enzyme free detection of glucose', *Journal of Materials Science: Materials in Electronics*, vol. 33, no. 12, pp. 9483–9489, Apr. 2022, doi: 10.1007/s10854-021-07441-w.

Development of low-cost Ag-based ORR electrodes via electrodeposition on carbon cloth for AEM fuel cells

Parinrat Chitsaart[1], Nutthaphon Sirireak[1], Mongkon Thongom[1], Jatupon Chaiwasu[1,*], Sarayut Yongprapat[2], Supaporn Therdthianwong[1], Apichai Therdthianwong[2]

[1] Department of Chemical Engineering, Faculty of Engineering, King Mongkut's University of Technology Thonburi, Bangkok 10140, Thailand
[2] Fuel Cell and Hydrogen Research and Engineering Center, Pilot Plant Development and Training Center, King Mongkut's University of Technology Thonburi, Bangkok, 10140, Thailand
[*] Corresponding author: jatupon.chai@kmutt.ac.th

ABSTRACT

This project aims to develop a low-cost silver-based catalyst layer on carbon cloth for the oxygen reduction reaction (ORR) in anion exchange membrane fuel cells (AEMFCs). Silver was electrodeposited onto a carbon cloth using a simple electrochemical method. A three-electrode setup was used, and cyclic voltammetry (CV) helped identify a suitable deposition potential. Silver nitrate ($AgNO_3$) in a Sodium nitrate ($NaNO_3$) electrolyte was used as the plating solution, and Ag was deposited at a constant potential of –0.1 V (vs Hg/Hg_2SO_4 reference) for 30 minutes. Scanning electron microscopy (SEM) confirmed that silver particles were successfully deposited across the carbon cloth fibers. Energy-dispersive X-ray spectroscopy (EDX) verified the presence of Ag on the cloth. A preliminary test of the Ag-deposited carbon cloth as an AEM fuel cell cathode showed measurable current and clear ORR activity under operating conditions. These results demonstrate a straightforward and cost-effective route to fabricate silver catalyst electrodes on porous carbon supports, which could help reduce the reliance on expensive platinum catalysts in fuel cells.

Keywords: Silver catalyst; Electrodeposition; Carbon cloth; Oxygen reduction reaction (ORR); Anion exchange membrane fuel cell (AEMFC)

1. INTRODUCTION

Anion exchange membrane fuel cells (AEMFCs) are attractive for sustainable energy because they can use inexpensive catalysts in alkaline conditions [4]. In AEMFCs, the oxygen reduction reaction (ORR) occurs at the cathode, traditionally using platinum (Pt) as the catalyst [5]. However, Pt is expensive and scarce, which drives up the cost of fuel cells [6 -7]. Silver (Ag) is a promising cathode catalyst for AEMFCs because it has good ORR activity in alkaline media and is significantly cheaper than Pt [4-5]. Prior studies have shown that the ORR performance of Ag in high-pH environments can approach that of Pt, making Ag a viable alternative in alkaline fuel cells [4-5]. In addition, silver is about one to two orders of magnitude less expensive than platinum, which can greatly reduce catalyst cost [4].

Various methods have been explored to prepare Ag-based ORR catalysts for fuel cells. For example, chemical reduction and impregnation methods have been used to synthesize silver on carbon supports (Ag/C) for AEMFC cathodes [8]. Another effective approach is electrochemical deposition of Ag onto conductive substrates. Electrodeposition allows the catalyst to be formed directly on the gas diffusion layer, potentially improving utilization. Notably, electrodeposition is a simple and "green" synthesis route that can produce well-dispersed Ag nanoparticles at low loading levels. This makes electrodeposited Ag catalysts attractive for ORR in alkaline fuel cells [9]. In this study, silver catalyst was electrodeposited onto carbon cloth (a typical gas diffusion electrode material) using a concentration of 20 mM Ag NO_3 in 0.1 M $NaNO_3$ as the depositing solution. The deposited Ag catalyst was characterized by SEM and EDX to evaluate its morphology and composition. Furthermore, the performance of the Ag electrodeposited carbon cloth was tested in a real lab-scale AEM fuel cell. A chronoamperometry experiment was conducted in the fuel cell to assess the catalyst's ORR activity and stability under operating conditions. The objective was to demonstrate that the electrodeposited silver catalyst can provide efficient ORR activity as an AEMFC cathode.

2. EXPERIMENTAL

2.1 Preparation of Carbon Cloth

Commercially carbon cloth (ELAT Hydrophilic) was purchased from FuelCell Store, to serve as a catalyst backing. Firstly, the 2.3 × 3.5 cm^2 of carbon cloth was treated with conc. H_2SO_4/HNO_3 in ratio 3:1 %v/v at 70 °C for 5 h. Then the carbon cloth was rinsed with deionized water and dried in a vacuum oven at 80 °C for 1 h [1].

2.2 Electrodeposition of Silver

An aqueous solution of 20 mM $AgNO_3$ in 0.1 M $NaNO_3$ was prepared and purged with argon (Ar) for 30 minutes prior to electrodeposition, cyclic voltammetry (CV) was performed to determine a suitable reduction potential for silver ion (Ag^+) deposition. The CV measurement was carried out using a three-electrode setup consisting of a carbon cloth (2.3 × 3.5 cm^2) with the electrodeposit area of 2.3 × 2.3 cm^2as the working electrode, an Hg/Hg_2SO_4 (saturated K_2SO_4) as the reference electrode, and a platinum mesh as the counter electrode. The potential was swept over -1.0 to 0.3 V. Based on the CV result, a constant potential of –0.10 V vs Hg/ Hg_2SO_4 was selected for electrodeposition. For the chronoamperometric deposition, the working electrode was immersed in the $AgNO_3$/$NaNO_3$ solution and held at –0.10 V for 30 minutes. During this process, the current was recorded over time, and a steady cathodic current confirmed the continuous reduction of Ag^+ ions to silver metal on the carbon cloth. After deposition, the electrode was carefully removed, rinsed thoroughly with deionized water, and dried in a vacuum oven at 80 °C for 1h.

2.3 Characterization (SEM and EDX)

The morphology and distribution of the deposited silver on the carbon cloth were examined using scanning electron microscopy. Nova NanoSEM 450,XFlash 6 Series operated at an accelerating voltage of 10.00 kV and magnifications of 50× and 250×. The SEM micrographs of the Ag-electrodeposited carbon cloth were used to observe the presence of silver particles on the carbon fibers. Energy-dispersive X-ray spectroscopy (EDX) was carried out with an EDX detector attached to the SEM to confirm the elemental composition of the electrodeposited layer.

2.4 Fuel Cell Assembly and Testing

A 5.0 cm^2 AEM fuel cell was assembled to evaluate the electrochemical performance of the Ag-electrodeposited cathode. The cathode consisted of silver-electrodeposited carbon cloth (Ag/CC), while a commercial Pt/C was used as the anode for hydrogen oxidation. An anion exchange membrane (Fumasep FAA-3-50) was placed between the anode and cathode to serve as the solid electrolyte. The cathode and anode (Commercial Pt electrode 2 mg cm^{-2} on Carbon Cloth) were pressed onto either side of the membrane to form a membrane-electrode assembly (MEA). Hydrogen gas was supplied to the anode at 40 mL min^{-1}, and oxygen was supplied to the cathode at 20 mL min^{-1}. Both gases were supplied in humidified condition. The cell temperature was maintained at 60 °C. The performance of the cell with the Ag-electrodeposited cathode was measured and presented as polarization and current stability. The fuel cell was connected to a potentiostat; the polarization measurement was performed with a scan rate of 5 mV s^{-1} from 0 to 1 V. The current stability was performed by applying a constant cell voltage of 0.4 V while recording the current response over time. This test at 0.4 V was used to evaluate the stability of the cathode catalyst under a constant load. The test was conducted for 1 h.

3. RESULTS AND DISCUSSION

3.1 Mass loading of Silver

The mass loading of silver electrodeposited onto the carbon cloth was determined by a gravimetric method. The mass of the carbon cloth was measured before and after electrodeposition using an analytical balance. The difference between the two measurements was attributed to the mass of silver deposited. Based on this method, the mass loading of silver was found to be approximately 2.54 mg cm^{-2}. This confirms that a significant amount of silver was successfully deposited.

3.2 SEM and EDX Analysis

The surface morphology of the Ag electrodeposited carbon cloth prepared using 20 mM $AgNO_3$ was observed using scanning electron microscopy (SEM) as shown in Figure 1. The SEM image reveals a woven structure of smooth carbon fibers, typical of commercial carbon cloth. After electrodeposition, numerous bright, faceted particles are clearly visible on the fiber surfaces. These particles are identified as electrodeposited silver based on their morphology and confirmed by EDX analysis, as shown in Fig. 2. The silver particles appear as discrete, well-defined crystals, suggesting a nucleation-and-growth mechanism typical of electrochemical metal deposition. Most particles exhibit polyhedral shape, characteristic of crystalline silver growth commonly observed in electrochemical metal deposition processes [2]. The distribution of Ag was moderately uniform; some areas displayed dense clusters of silver particles, while others appeared more sparsely covered. This non-uniformity is consistent with earlier studies reporting surface-dependent nucleation behavior during electrodeposition of metals on carbon materials [3]. The Ag particle size ranges from 8 to 12 µm.

To confirm the elemental composition of the electrodeposited particles, energy-dispersive X-ray spectroscopy (EDX) was performed as shown in Fig. 2. The EDX spectrum showed strong peaks corresponding to silver (Ag), along with minor oxygen (O) likely due

to surface oxidation or moisture. The EDX spectrum also revealed the presence of sodium (Na) and nitrogen (N) signals in addition to the dominant silver (Ag) peaks. The detection of Na and N is attributed to residual adsorption from the 0.1 M of $NaNO_3$ supporting electrolyte used during the electrodeposition process. Despite rinsing, small amounts of Na^+ ions and nitrate-related species may remain adsorbed on the carbon cloth surface. No other metallic impurities were detected, verifying the high purity of the electrodeposited silver.

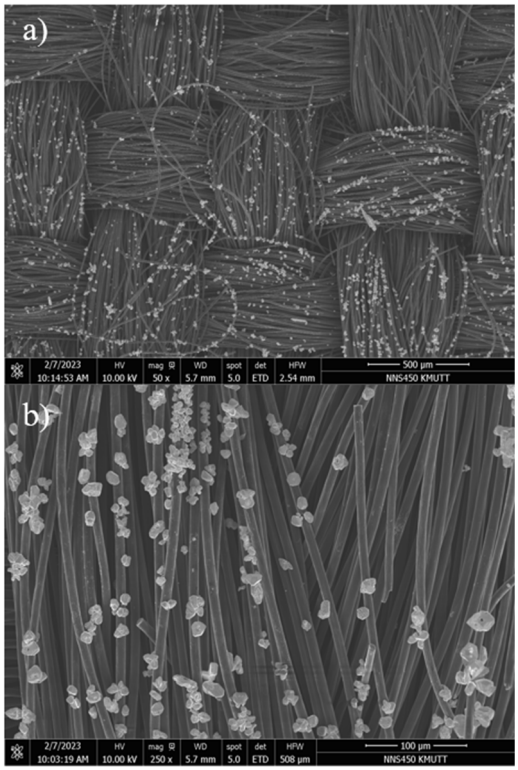

Fig. 1 SEM images of Ag electrodeposited onto carbon cloth (a) (b)

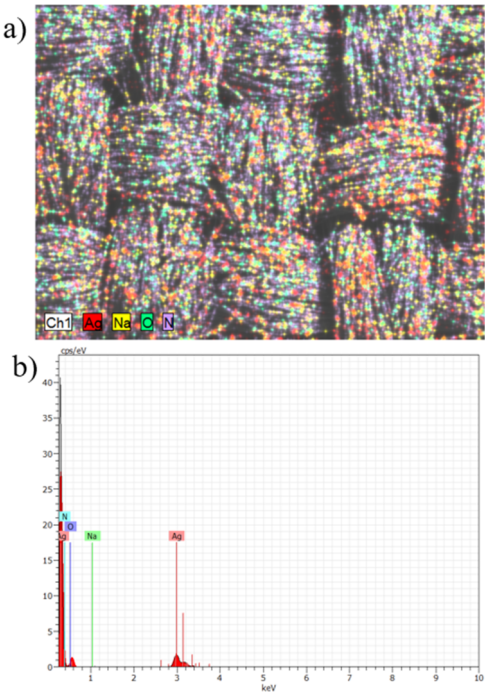

Fig. 2 EDX analysis of Ag electrodeposited onto carbon cloth (a) (b)

3.3 Fuel Cell Performance

The Ag-electrodeposited carbon cloth was assembled as the cathode in a lab-scale anion exchange membrane fuel cell (AEMFC) and evaluated using polarization and current stability test.

Fig. 3 Shows the polarization curve of Ag electrodeposited on carbon cloth in our AEMFC setup. This typical polarization shows a current density range of 0–80 mA cm^{-2} with the open circuit potential of 0.86 V. The peak power density of 11.80 mW cm^{-2} was observed at 0.33 V. These values are lower than those reported for advanced Ag-based and Fe-N-C cathodes in AEMFCs, which can exceed 200 mW cm^{-2} under optimized conditions [10-12]. This performance gap may be attributed to factors such as suboptimal catalyst loading, limited active surface area, or insufficient ionomer distribution. Future work will focus on optimizing electrodeposition parameters, increasing catalyst loading, and improving electrode assembly to enhance ORR activity and overall fuel cell performance. Attention will be given to modifying the electrode structure. The current cathode consists of only a thin carbon cloth without a gas diffusion layer (GDL), which limits its water management capability. This simple structure lacks both hydrophobic channels for gas diffusion and porous media to support water transport. Incorporating a GDL or using a composite electrode with controlled pore structure could help maintaining oxygen access, preventing local flooding, and improving catalyst utilization during extended fuel cell operation.

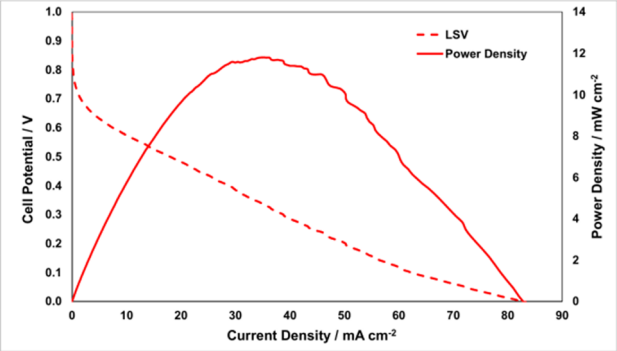

Fig. 3 Polarization and power density curves of anion exchange membrane fuel cells using Ag/CC as the cathode catalyst.

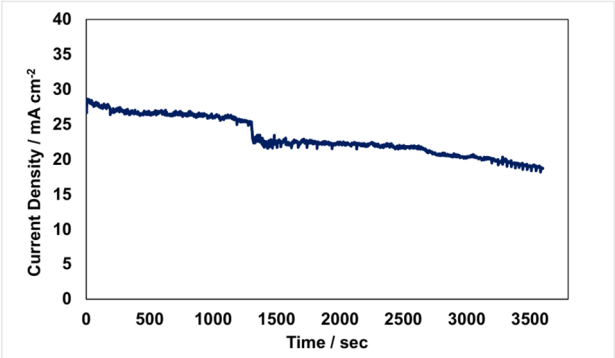

Fig. 4 Chronoamperometric test of anion exchange membrane fuel cells using Ag/CC as the cathode catalyst at 0.4 V at 60 °C for 1 h

Fig. 4 shows The CA test at 0.4 V reveals a 28% current density loss (from 26 to 18.7 mA cm^{-2}) over 1 h. This degradation may be attributed to water management issues and limited KOH concentration inside the cell. Water accumulation at the cathode could have caused local flooding, hindering oxygen transport to the catalyst surface. Additionally, the small amount of KOH used might have resulted in insufficient hydroxide ion availability, reducing ionic conductivity and ORR kinetics. These observations suggest that optimizing water balance and maintaining adequate electrolyte concentration may be important for prolonging AEMFC operation. Despite H_2SO_4/HNO_3 pretreatment, SEM shows clusters of Ag particles (8–12 µm) with uneven adhesion, indicating incomplete surface functionalization. Residual $NaNO_3$ (EDX-detected Na/N) further exacerbates degradation by blocking active sites. Future work will optimize pretreatment parameters (e.g., 6M HNO_3, 6 hours) and employ pulsed electrodeposition to achieve smaller, uniformly distributed Ag particles (1–5 µm) with stronger carbon support adhesion.

4. CONCLUSIONS

This study demonstrates that silver can be effectively electrodeposited onto carbon cloth using a simple, low-cost electrochemical method, producing a catalyst with-oxygen reduction reaction (ORR) activity for AEMFCs. SEM and EDX confirm uniform Ag deposition across the fibers, and preliminary fuel cell tests show promising current and oxygen reduction performance, making silver a potential alternative to platinum-based catalysts. However, further optimization of particle size, distribution, and electrode assembly is needed to improve performance and stability. The Ag electrodeposited on acid-treated carbon cloth forms crystalline 8–12 µm particles, achieving a peak power density of 11.80 mW cm^{-2}, but with a 28% current density loss due to particle detachment. Future work will focus on optimizing pretreatment, pulsed electrodeposition for smaller particles, and electrode assembly to enhance AEMFC efficiency and durability.

ACKNOWLEDGMENTS

This research project is supported by King Mongkut's University of Technology Thonburi (KMUTT), Thailand Science Research and Innovation (TSRI), and National Science, Research and Innovation Fund (NSRF) Fiscal year 2025.

REFERENCES

1. H. Qingshui, L. Huimin. In-situ Electrodeposition of Highly Active Silver Catalyst on Carbon Fiber Papers as Binder Free Cathodes for Aluminum-air Battery. *Scientific Reports* **2017**; 7: 3378.
2. J. M. Linge, H. Erikson, M. Merisalu, V. Sammelselg, K. Tammeveski. Oxygen reduction on silver catalysts electrodeposited on various nanocarbon supports. *SN Applied Sciences* **2021**; 3(2): 263.
3. A. T. S. C. Brandão, S. Rosoiu, R. Costa, O. A. Lazar, A. F. Silva, L. Anicai, C. M. Pereira, M. Enachescu. Characterization and electrochemical studies of MWCNTs decorated with Ag nanoparticles through pulse reversed current electrodeposition using a deep eutectic solvent for energy storage applications. *Journal of Materials Research and Technology* **2021**; 15: 342–359.
4. H. Erikson, A. Sarapuu, K. Tammeveski. Oxygen reduction reaction on silver catalysts in alkaline media: a minireview. *ChemElectroChem* **2019**; 6(1): 73–86.
5. M. Chatenet, L. Genies-Bultel, M. Aurousseau, R. Durand, F. Andolfatto. Oxygen reduction on silver catalysts in solutions containing various concentrations of sodium hydroxide – comparison with platinum. *Journal of Applied Electrochemistry* **2002**; 32(10): 1131–1140.

6. A. Sarapuu, E. Kibena-Põldsepp, M. Borghei, K. Tammeveski. Electrocatalysis of oxygen reduction on heteroatom-doped nanocarbons and transition metal–nitrogen–carbon catalysts for alkaline membrane fuel cells. *Journal of Materials Chemistry A* **2018**; 6(3): 776–804.
7. Q. G. He, E. J. Cairns. Review—Recent progress in electrocatalysts for oxygen reduction suitable for alkaline anion exchange membrane fuel cells. *Journal of The Electrochemical Society* **2015**; 162(14): F1504–F1539.
8. R. Vinodh, D. Sangeetha. *C*arbon supported silver (Ag/C) electrocatalysts for alkaline membrane fuel cells. *Journal of Materials Science* **2012**; 47(2): 852–859.
9. S. Salomé, R. Rego, M. C. Oliveira. Development of silver-gas diffusion electrodes for the oxygen reduction reaction by electrodeposition. *Materials Chemistry and Physics* **2013**; 143(1): 109–115.
10. Peng, X., Kashyap, V., Ng, B., Kurungot, S., Wang, L., Varcoe, J. R., Mustain, W. E. High-Performing PGM-Free AEMFC Cathodes from Carbon-Supported Cobalt Ferrite Nanoparticles. *Catalysts* **2019**, *9*(3): 264.
11. Li, Q., Pollock, C. J., Soto, J., Villarino, A. M., Shi, Z., Krumov, M. R., Muller, D. A., & Abruña, H. D. Operando X-ray absorption spectroscopic investigation of electrocatalysts state in anion exchange membrane fuel cells. *Nature Communications* **2025**, *16*, 3008.
12. Omasta, T. J., Park, A. M., LaManna, J. M., Zhang, Y., Peng, X., Wang, L., Jacobson, D. L., Varcoe, J. R., Hussey, D. S., Pivovar, B. S., & Mustain, W. E. Beyond catalysis and membranes: visualizing and solving the challenge of electrode water accumulation and flooding in AEMFCs. *Energy & Environmental Science* **2018**, *11*, 551-558.

Prediction of latent heat of vaporization of binary mixture using COSMO-SAC model

Natamorn Kamlue[1], Surat Areerat[1,*]

[1] Department of Chemical Engineering, School of Engineering, King Mongkut's Institute of Technology Ladkrabang, Bangkok 10520, Thailand
[*] Corresponding author: surat.ar@kmitl.ac.th

ABSTRACT

The accurate prediction of the latent heat of vaporization (ΔH_{vap}) is crucial in various industrial applications, for example chemical process design, energy optimization, and refrigeration system. Traditional models such as UNIFAC require extensive experimental data for parameterization, whereas the COSMO-SAC model presents a promising alternative with minimal empirical input. This study evaluates the performance of the COSMO-SAC model in predicting ΔH_{vap} of binary mixtures and compares its accuracy against UNIFAC model. Four binary mixtures were investigated: Ethyl acetate/Benzene, Ethyl acetate/Toluene, Ethanol/Isooctane, and R152A/Dimethyl ether. The methodology involved utilizing quantum chemistry-based sigma profiles to determine activity coefficients, which were then applied in the Clausius-Clapeyron equation and modified Raoult's law to estimate ΔH_{vap}. The results indicate that COSMO-SAC provided superior accuracy for Ethyl acetate/Benzene and Ethyl acetate/Toluene mixtures, with mean absolute deviations (MAD) of 1.73% and 9.86%, respectively, compared to 13.46% and 16.37% for UNIFAC. In contrast, UNIFAC demonstrated higher accuracy for Ethanol/Isooctane and R152A/Dimethyl ether mixtures, achieving MAD of 8.79% and 3.32%, while COSMO-SAC show deviations of 13.90% and 6.47%, respectively. These findings suggest that COSMO-SAC is more reliable for non-hydrogen bonding systems but struggles with mixtures exhibiting strong hydrogen bonding interactions. Overall, COSMO-SAC outperformed UNIFAC across all mixtures, achieving an average deviation of 7.99% compared to 10.48% for UNIFAC. This research highlights the potential of COSMO-SAC in thermodynamic property prediction and its implications for improving energy efficiency in industrial applications.

Keywords: COSMO-SAC; UNIFAC; Latent heat of vaporization; Sigma-profile; Activity coefficients

1. INTRODUCTION

The latent heat of vaporization is of great importance for industrial processes and refrigeration systems, as it plays a crucial role in the design and control of processes involving the phase transition of substances, which aids in the analysis and design of separation processes. Additionally, it serves as an indicator of the cooling capability of refrigerants. Therefore, the accuracy in predicting the latent heat of vaporization is crucial for precise energy calculations, leading to more efficient production processes and reduced energy consumption. Currently, the UNIFAC model (Universal Quasi-Chemical Functional Group Activity Coefficients) is widely used to predict thermodynamic properties, such as the activity coefficients of mixtures. However, this model requires a significant amount of experimental data for matrix parameter determination, which can pose challenges in cases where sufficient experimental data is unavailable. In contrast, the COSMO model (Conductor-like Screening Model) is a later alternative that uses fewer parameters to predict thermodynamic properties of mixtures. From the research of R. P. Gerber and R. P. Soares [1] employed the COSMO-SAC model to predict activity coefficients of molecules with multiple functional groups in comparison to UNIFAC. It was found that UNIFAC had a deviation of 0.44 from experimental results, while COSMO-SAC exhibited a deviation of 0.2, demonstrating that COSMO-SAC provides higher accuracy for predicting properties of complex molecules than the UNIFAC model.

In thermodynamic property prediction using the COSMO-SAC model, sigma-profile datasets derived from quantum chemistry calculations are utilized. In this research, the datasets from F. Ferrarini's study [2] are applied to predict the thermodynamic properties of mixtures.

In this research, the prediction of latent heat of vaporization of binary mixtures using the UNIFAC and COSMO-SAC models are compared with experimental results. Four binary mixtures will be analyzed: ethyl acetate/benzene [3], ethyl acetate/toluene [3], ethanol/iso-octane [4], and 1,1-difluoroethane (R152A)/dimethyl ether (DME) [5]. The objective is to evaluate the accuracy and reliability of each model in predicting the latent heat of vaporization.

2. THEORY

2.1. COSMO-SAC model

COSMO-RS was first proposed by Klamt in 1995 [6], focusing on modeling dielectric continuum solvation for liquid phase thermodynamics. While COSMO-SAC is a modified version of COSMO-RS, proposed by Lin and Sandler [7]. In this study, the improved COSMO-SAC model developed by Soares [8] will be utilized, which operates similarly to the UNIFAC model. The activity coefficient is calculated as the sum of a combinatorial and a residual part:

$$ln\gamma_i = ln\gamma_i^C + ln\gamma_i^R \quad (1)$$

where γ_i^C is activity coefficient based on differences in the size and shape of the molecules and γ_i^R is activity coefficient based on the effects that arise from differences in the free energy interactions

$$ln\,\gamma_i^C = ln\left(\frac{\phi_i}{x_i}\right) + \frac{z}{2} q_i ln\left(\frac{\theta_i}{\phi_i}\right) + l_i - \frac{\phi_i}{x_i}\sum_j x_j l_j \quad (2)$$

$$\theta_i = \frac{x_i q_i}{\sum_j x_j q_j} \quad (3)$$

$$\varphi_i = \frac{x_i r_i}{\sum_j x_j r_j} \quad (4)$$

$$l_j = \frac{z}{2}(r_i - q_i) - (r_i - 1) \quad (5)$$

$$r_i = V_i / r_0 \quad (6)$$

φ_i is the volume fraction; θ_i is the normalized surface-area fraction; z is the coordination number; x_i is the mole fraction; r_i is the normalized volume; V_i is the cavity volume; r_0 is a universal parameter of the model and q_i normalized surface area.

$$ln\,\gamma_i^R = n_i \sum_{m\in i} p_i\left[ln(\Gamma_m^s) - ln\,(\Gamma_m^i)\right] \quad (7)$$

$$\ln \Gamma_m = -ln\left[\sum_n p_n \Gamma_n exp\left(-\frac{E_{m,n}}{RT}\right)\right] \quad (8)$$

n_i is the number of segments; p_i is the probability of finding charge density σ on surface; Γ_m^s is the segment activity coefficient of solution; Γ_m^i is the segment activity coefficient of pure substance; $E_{m,n}$ is the interaction energy for contact between segments m and n.

2.2. Clausius-Clapeyron equation [9]

The Clausius–Clapeyron equation is used to describe the relationship between pressure and temperature during the phase transition of a substance, such as evaporation or condensation. It applies to liquids or solids transitioning to vapor, or vapor transitioning to liquid. This equation illustrates how pressure changes as the system's temperature changes and is expressed in the following form:

$$\frac{dlnP}{dT} = \frac{\Delta H}{RT^2} \quad (9)$$

P is the pressure (bar); T is the temperature (K); ΔH is the latent heat of phase transition (J/mol)

It is considered an important thermodynamic relationship as it aids in calculating the latent heat of vaporization (ΔH_{vap}) or the change in pressure with temperature at the saturated conditions by integrating equation (13) at two saturated points as follows:

$$ln\left(\frac{P_2}{P_1}\right)_{sat} = \frac{\Delta H_{vap}}{R}\left(\frac{1}{T_1} - \frac{1}{T_2}\right)_{sat} \quad (10)$$

2.3. Raoult's law [10]

Raoult's law is a fundamental law used to calculate the vapor-liquid equilibrium (VLE) of a solution. This law is applied to calculate the vapor pressure of a component in a solution, assuming that the solution behaves similarly to an ideal solution.

2.3.1. Simple Raoult's Law [10]

The simple Raoult's law states that the partial vapor pressure of each component in an ideal solution is directly proportional to the mole fraction of that component in the liquid and the vapor pressure of the pure component at the same temperature in the gas phase and ideal solution conditions. This law can be expressed in the following equation:

$$P_i = x_i P_i^{sat} \quad (11)$$

P_i is the partial pressure of component i; x_i is the mole fraction; P_i^{sat} is the saturation pressure of component i

2.3.2. Modified Raoult's Law

In cases where the solution behavior deviates from ideality, the equation (15) is modified by using the activity coefficient to account for deviations from ideal solutions. The modified Raoult's law can be written as follows:

$$P_i = \gamma_i x_i P_i^{sat} \quad (12)$$

For saturated liquid system:

$$P_1 = \gamma_1 x_1 P_1^{sat} + \gamma_2 x_2 P_2^{sat} \quad (13)$$

For saturated vapor system:

$$P_2 = \frac{1}{\left(\frac{y_1}{\gamma_1 P_1^{sat}} + \frac{y_2}{\gamma_2 P_2^{sat}}\right)} \quad (14)$$

2.4. Antoine Equation [10]

The Antoine equation is derived from the Clausius-Clapeyron equation and expresses the relationship between the vapor pressure and temperature of pure substances.

$$\log(P_i^{sat}) = A - \frac{B}{C + T_i} \quad (15)$$

2.5. UNIFAC Model [10]

Beyond having coefficients that explain deviations in the vapor phase, the behavior of solutions that deviate from ideal solutions has also been extensively studied. The activity coefficient can be used to describe the behavior of solutions in a system, illustrating the deviations of substances in the liquid phase of the system. The UNIFAC (Universal Quasi-Chemical Functional Group Activity Coefficients) model, which uses activity coefficients, is represented by the following equation:

$$ln\gamma_i = ln\gamma_i^C + ln\gamma_i^R \quad (16)$$

$$ln\,\gamma_i^C = 1 - J_i + lnJ_i - 5q_i\left(1 - \frac{J_i}{L_i} + ln\frac{J_i}{L_i}\right) \quad (17)$$

$$ln\,\gamma_i^R = q_i\left[1 - \sum_k \left(\theta_k \frac{\beta_{ik}}{s_k} - e_{ki} ln\frac{\beta_{ik}}{s_k}\right)\right] \quad (18)$$

$$r_i = \sum_k v_k^{(i)} R_k \quad (19)$$

$$q_i = \sum_k v_k^{(i)} R_k \quad (20)$$

$$e_{ki} = \frac{v_k^{(i)} Q_k}{q_i} \quad (21)$$

$$\beta_{ik} = \sum_m e_{mi}\tau_{mk} \quad (22)$$

$$\theta_k = \frac{\sum_m x_i q_i e_{ki}}{\sum_m x_i q_i} \quad (23)$$

$$s_k = \sum_m \theta_m \tau_{mk} \quad (24)$$

$$\tau_{mk} = exp\frac{-a_{mk}}{T} \quad (25)$$

a_{mk} is the group interaction parameters; R_k is the relative volume; Q_k is the relative surface area; v_k is the number of subgroups

3. EXPERIMENTAL

3.1. Predicting the Latent Heat of Vaporization using UNIFAC Model

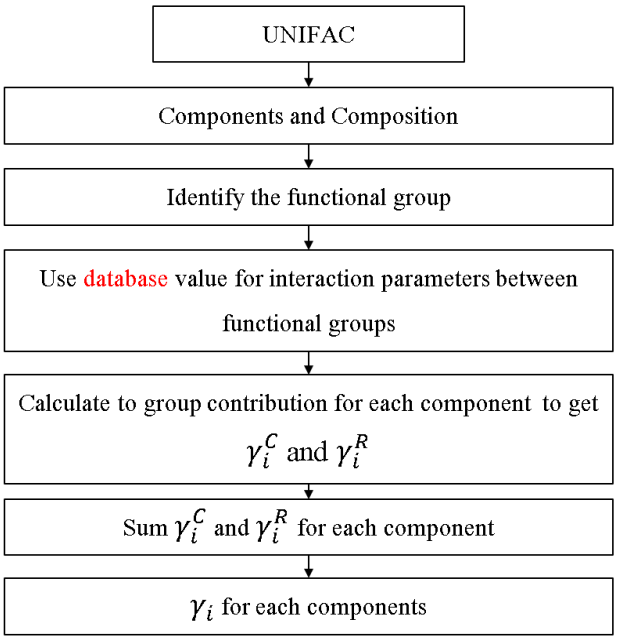

Figure 1 Flowchart of latent heat predictions using UNIFAC model

3.2. Predicting the Latent Heat of Vaporization using COSMO-SAC Model

(1) Create the molecular structure of each component for generating sigma-profile in **Avogadro software**

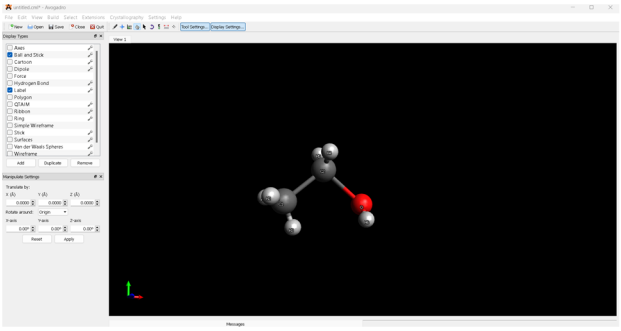

Figure 2 Avogadro software.

(2) Optimize and Export GAMESS Input file (.inp)

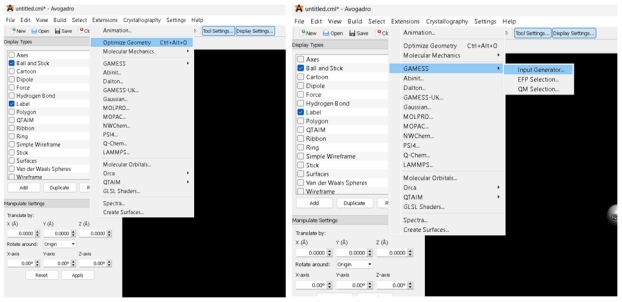

Figure 3 Optimize geometry of molecules and export GAMESS Input

(3) Modify the (.inp) file to be ready for use in GAMESS for sigma-profile calculations

```
!   File created by the GAMESS Input Deck Generator Plugin for Avogadro
 $BASIS GBASIS=STO NGAUSS=3 $END
 $CONTRL SCFTYP=RHF RUNTYP=ENERGY $END

 $DATA
Title
C1
C      6.0    -6.23342     0.15201     0.01027
C      6.0    -4.92088     0.90302    -0.07521
H      1.0    -6.25548    -0.66998    -0.71271
H      1.0    -7.07777     0.81884    -0.18533
H      1.0    -6.35965    -0.29330     1.00263
O      8.0    -3.83636     0.01061     0.13540
H      1.0    -4.87360     1.69721     0.67603
H      1.0    -4.80247     1.35585    -1.06388
H      1.0    -3.95357    -0.39213     1.01270
 $END
```

Figure 4 GAMESS Input .inp original file.

```
! SELECT RESTRICTED HARTREE-FOCK AS DEFAULT
 $contrl scftyp=rhf $end

! THEORY: HF OR DFT
 $contrl mplevl=0 $end

 $system timlim=10000 mwords=20 $end
 $SCF DIRSCF=.TRUE. $end

! BASIS SETS
! KTZVP
 $contrl ISPHER=1 $END
 $BASIS GBASIS=KTZVP $END

! One of the following
 $guess guess=HUCKEL $end

 $statpt projct=.FALSE. $end
! $STATPT IFREEZ(1)=1,2,3 $END

! Run COSMO on perfect conductor
 $COSGMS PRFCND=.TRUE. $end

! Specifying RSOLV
 $COSGMS COSRAD = 1.4 $end

! available memory
 $SYSTEM MWORDS=500 $END

! Optimize the geometry
 $statpt opttol=0.0005 nstep=50 $end
 $contrl runtyp=OPTIMIZE maxit=200 $end

! Internal Coordinates, for faster convergence
! See http://molecularmodelingbasics.blogspot.com/2009/07/some-gamess-input-basics_24.html
 $CONTRL nzvar=1 $END
 $zmat dlc=.t. auto=.t. $END

 $DATA

C1
C      6.0    -6.23342     0.15201     0.01027
C      6.0    -4.92088     0.90302    -0.07521
H      1.0    -6.25548    -0.66998    -0.71271
H      1.0    -7.07777     0.81884    -0.18533
H      1.0    -6.35965    -0.29330     1.00263
O      8.0    -3.83636     0.01061     0.13540
H      1.0    -4.87360     1.69721     0.67603
H      1.0    -4.80247     1.35585    -1.06388
H      1.0    -3.95357    -0.39213     1.01270
 $END
```

Figure 5 GAMESS Input .inp modify file.

(4) Run **Command Prompt** in GAMESS folder to generate sigma-profile as (.gout) file

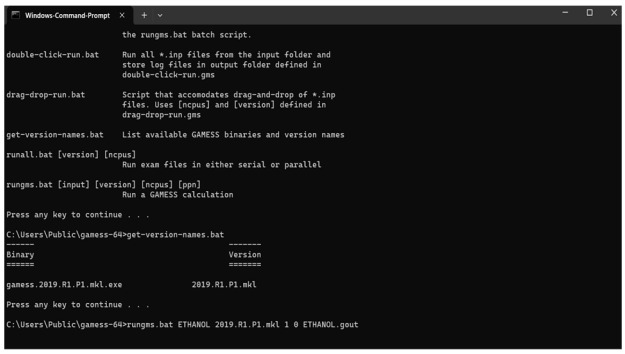

Figure 6 Command Prompt in GAMESS software.

```
          GAMESS/COSab RESULTS
 ================================================

  Dielectric Constant                = INFTY
  Basic Grid Size                    =                1082
  Number of Segments                 =                  92
  Number of Segments located on spheres=                163
  Number of Segments of the cavity   =                362
  Solvent Radius (rsolv)             = 1.40
  Outlying Charge Error Method       = double cavity

 ================================================

  Total solvated Energy (a.u.)       =  -154.1496971807
  Total Energy corrected (a.u.)      =  -154.1498312121

  Outlying charge effect (a.u.)      =    -0.0001340314
  Outlying charge effect (kcal/mol)  =    -0.0841060460

  Dielectric Energy (a.u.)           =    -0.0113527450
  Dielectric energy corr. (a.u.)     =    -0.0114867764

  Sum of polarization charges        =     0.0197434912
  Sum of polarization charges(cor.)  =    -0.0197434912

  Total surface area of cavity (A**2)  =   87.39
  Total volume of cavity (A**3)        =   69.21

 ================================================
 NPS=                 362
NR.  ATOM  (X, Y, Z)(a.u.)                    CHARGE(e)  AREA(A**2) SIGMA(e/A**2)
   1    1   0.620029   1.758630  -1.632974   0.000886   0.232280   0.003815
   2    1   0.029959  -1.317990   0.974090   0.000674   0.371649   0.001813
   3    1  -0.341224   0.307334   4.327834   0.001456   0.371649   0.003917
   4    1   5.251773  -0.161392   0.811611   0.000536   0.139368   0.003843
   5    1   4.762685  -0.798831   0.797531   0.000622   0.185824   0.003348
   6    1   4.928000  -0.808224   2.185284   0.000491   0.139368   0.003524
   7    1  -0.971143   0.728394   3.761153   0.000904   0.278737   0.003243
   8    1  -0.797020  -0.541323   1.010074   0.000838   0.418105   0.002005
   9    1  -0.018669   2.150530  -1.246408   0.001348   0.371649   0.003626
```

Figure 7 GAMESS Output.gout

(5) Add compounds that generate before in **JCOSMO** folder to calculate activity coefficient (γ)

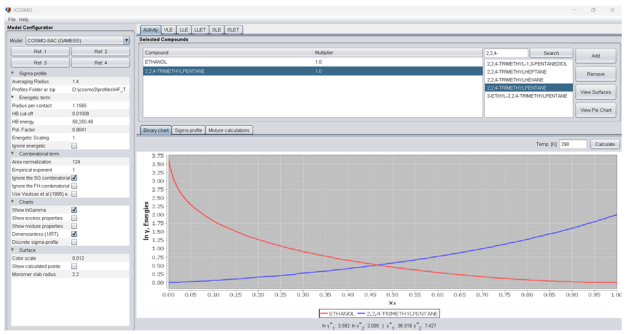

Figure 8 JCOSMO Program

(6) Use the activity coefficient to calculate temperature (T_2) and pressure (P_1) at saturated conditions through Modified Raoult's Law for each composition.

(7) Use the temperature (T_2) and pressure (P_1) obtained from section (6) to calculate the Heat of vaporization through the Clausius–Clapeyron equation.

4. RESULTS AND DISCUSSION

4.1. Comparison of experimental and predicted ΔH_{vap} using UNIFAC and COSMO-SAC

Table 1 shows the comparison of experimental and predicted latent heat of vaporization (ΔH_{vap}) for the Ethyl acetate/Benzene mixture using UNIFAC and COSMO-SAC models. COSMO-SAC predictions are significantly more accurate, with a much lower mean absolute deviation (MAD%) compared to UNIFAC as shown in Table 5. The UNIFAC model consistently overestimates ΔH_{vap}, with MAD% reaching up to 16.82%, whereas COSMO-SAC remains within 1.73%. This suggests that COSMO-SAC provides a more reliable prediction for this nonpolar system.

Table 2 compares the result for Ethyl acetate/Toluene system, where COSMO-SAC still performs better than UNIFAC. The UNIFAC model overestimates ΔH_{vap} more severely, with MAD% exceeding 16.37%, while COSMO-SAC has a lower but still significant deviation at MAD% = 9.86%. The accuracy of COSMO-SAC decreases as Ethyl acetate concentration increases, indicating limitations in handling strong molecular interactions.

Table 3 compares ΔH_{vap} predictions for the Ethanol/Isooctane mixture, where UNIFAC outperforms COSMO-SAC. At low ethanol concentrations, both models predict values close to the experimental data, but as ethanol content increases, COSMO-SAC significantly underestimates ΔH_{vap}, leading to a higher MAD% of 13.90%. The UNIFAC model remains more consistent, but both models struggle at higher ethanol fractions, highlighting the challenge of modeling polar-nonpolar interactions.

Table 4 compares ΔH_{vap} for the R152A/DME system, where UNIFAC again provides better predictions than COSMO-SAC. The deviation for COSMO-SAC increases with mole fraction, reaching an MAD of 6.47%, while UNIFAC remains more accurate at 3.32%. COSMO-SAC consistently overestimates ΔH_{vap} across all compositions, indicating that it may not fully capture the intermolecular interactions between R152A and DME. For the histogram graphs:

For the Ethyl acetate/Benzene system, as illustrated in Figure 9(a), the COSMO-SAC model outperforms UNIFAC, showing a much lower absolute deviation (AD%), especially at higher mole fractions. The histogram confirms this trend, with UNIFAC consistently overpredicting ΔH_{vap}, while COSMO-SAC remains closer to experimental values.

For the Ethyl acetate/Toluene system, as illustrated in Figure 9(b), both models exhibit higher deviations than in the benzene case, but UNIFAC consistently has larger errors. The histogram reveals that %AD of COSMO-SAC remains lower across all mole fractions, though the deviations increase at higher concentrations.

For the Ethanol/Iso-octane system, which can be seen from Figure 9(c), UNIFAC initially performs well at low ethanol concentrations but diverges significantly at higher mole fractions. COSMO-SAC, however, shows higher deviations throughout. The histogram illustrates UNIFAC better accuracy in the low-to-mid concentration range, while COSMO-SAC remains consistently above.

For the R152A/DME system, which can be seen from Figure 9(d), both models perform relatively well, but UNIFAC has slightly lower deviations than COSMO-SAC. The histogram confirms this, showing a generally lower AD% for UNIFAC, though COSMO-SAC remains close.

The overall trend from the histograms supports the conclusion that COSMO-SAC generally provides better predictions for polar-nonpolar systems (e.g., Ethyl acetate/Benzene), while UNIFAC performs better for systems with stronger deviations from ideality (e.g., Ethanol/Iso-octane)

Table 1 Comparison of Experimental and Predicted ΔH_{vap} using UNIFAC and COSMO-SAC Models for Ethyl acetate (1)/Benzene (2).

X_1 (mol fraction)	ΔH_{vap_exp} (kJ/mol)	ΔH_{vap_UNIFAC} (kJ/mol)	$\Delta H_{vap_COSMO-SAC}$ (kJ/mol)	AD%$_{UNIFAC}$	AD%$_{COSMO-SAC}$
0.00	30.68	33.87	29.41	10.42%	4.13%
0.02	30.67	33.90	29.44	10.52%	4.02%
0.03	30.67	33.92	29.47	10.59%	3.94%
0.06	30.67	33.98	29.53	10.79%	3.73%
0.14	30.67	34.12	29.68	11.25%	3.24%
0.16	30.67	34.17	29.73	11.40%	3.07%
0.23	30.66	34.29	29.85	11.83%	2.65%
0.30	30.66	34.42	29.98	12.27%	2.21%
0.36	30.65	34.52	30.09	12.64%	1.83%
0.42	30.64	34.64	30.15	13.04%	1.62%
0.44	30.64	34.67	30.25	13.16%	1.28%
0.53	30.63	34.83	30.33	13.71%	0.98%
0.59	30.62	34.93	30.36	14.10%	0.83%
0.70	30.60	35.13	30.51	14.82%	0.30%
0.77	30.58	35.27	30.58	15.32%	0.02%
0.83	30.57	35.37	30.64	15.72%	0.24%
0.84	30.57	35.39	30.64	15.77%	0.25%
0.86	30.56	35.42	30.65	15.87%	0.27%
0.91	30.55	35.51	30.69	16.24%	0.46%
0.95	30.54	35.58	30.72	16.49%	0.57%
1.00	30.53	35.66	30.74	16.82%	0.70%

*%Absolute Deviation (%AD) = $\left|\frac{X_{exp}-X_{cal}}{X_{exp}}\right|$

Table 2 Comparison of Experimental and Predicted ΔH_{vap} using UNIFAC and COSMO-SAC Models for Ethyl acetate (1)/Toluene (2).

X_1 (mol fraction)	ΔH_{vap_exp} (kJ/mol)	ΔH_{vap_UNIFAC} (kJ/mol)	$\Delta H_{vap_COSMO-SAC}$ (kJ/mol)	AD%$_{UNIFAC}$	AD%$_{COSMO-SAC}$
0.00	33.87	37.93	36.52	11.99%	7.83%
0.02	33.78	38.01	36.38	12.51%	7.69%
0.03	33.73	38.04	36.31	12.78%	7.63%
0.05	33.66	38.10	36.21	13.16%	7.57%
0.11	33.43	38.26	35.84	14.45%	7.21%
0.18	33.18	38.39	35.69	15.70%	7.56%
0.27	32.86	38.47	35.47	17.04%	7.93%
0.28	32.82	38.47	35.44	17.19%	7.98%
0.37	32.58	38.41	35.31	17.93%	8.39%
0.45	32.33	38.27	35.20	18.38%	8.91%
0.60	31.91	37.82	34.99	18.51%	9.64%
0.66	31.74	37.58	34.96	18.40%	10.13%
0.72	31.56	37.31	34.87	18.20%	10.47%
0.77	31.38	37.01	34.83	17.95%	11.01%
0.84	31.16	36.66	34.80	17.63%	11.67%
0.89	30.95	36.32	34.78	17.33%	12.35%
0.92	30.83	36.13	34.76	17.18%	12.76%
0.95	30.70	35.93	34.75	17.05%	13.20%
0.97	30.63	35.84	34.75	17.00%	13.43%
1.00	30.50	35.66	34.74	16.93%	13.91%

*%Absolute Deviation (%AD) = $\left|\frac{X_{exp}-X_{cal}}{X_{exp}}\right|$

Table 3 Comparison of Experimental and Predicted ΔH_{vap} using UNIFAC and COSMO-SAC Models for Ethanol (1)/Iso-octane (2).

X_1 (mol fraction)	ΔH_{vap_exp} (kJ/mol)	ΔH_{vap_UNIFAC} (kJ/mol)	$\Delta H_{vap_COSMO-SAC}$ (kJ/mol)	$AD\%_{UNIFAC}$	$AD\%_{COSMO-SAC}$
0.00	35.08	35.23	34.00	0.41%	3.09%
0.11	38.21	37.62	34.66	1.54%	9.29%
0.24	39.61	37.73	36.19	4.74%	8.63%
0.41	43.99	38.03	37.08	13.57%	15.71%
0.60	47.43	39.18	37.20	17.40%	21.56%
0.74	48.93	40.62	37.13	17.00%	24.12%
0.87	48.39	41.81	37.54	13.59%	22.42%
0.93	47.28	42.27	38.37	10.60%	18.84%
1.00	42.45	42.56	41.83	0.27%	1.45%

*%Absolute Deviation (%AD) = $\left|\frac{X_{exp}-X_{cal}}{X_{exp}}\right|$

Table 4 Comparison of Experimental and Predicted ΔH_{vap} using UNIFAC and COSMO-SAC Models for R152A (1)/DME (2).

X_1 (mol fraction)	ΔH_{vap_exp} (kJ/mol)	ΔH_{vap_UNIFAC} (kJ/mol)	$\Delta H_{vap_COSMO-SAC}$ (kJ/mol)	$AD\%_{UNIFAC}$	$AD\%_{COSMO-SAC}$
0.00	21.07	22.08	22.39	4.76%	6.23%
0.07	21.36	22.11	22.51	3.51%	5.37%
0.15	21.42	22.15	22.68	3.43%	5.88%
0.23	21.50	22.19	22.85	3.23%	6.30%
0.32	21.62	22.24	22.98	2.84%	6.29%
0.41	21.70	22.29	23.10	2.72%	6.48%
0.51	21.83	22.34	23.21	2.35%	6.36%
0.62	21.80	22.40	23.25	2.74%	6.68%
0.74	21.72	22.46	23.29	3.39%	7.25%
0.86	21.70	22.52	23.31	3.76%	7.38%
1.00	21.77	22.59	23.30	3.76%	7.00%

*%Absolute Deviation (%AD) = $\left|\frac{X_{exp}-X_{cal}}{X_{exp}}\right|$

Table 5 Comparison of Mean Absolute Deviation (MAD) between of Predicted ΔH_{vap} between UNIFAC and COSMO-SAC Models.

Binary Mixtures	$\%MAD_{UNIFAC}$	$\%MAD_{COSMO-SAC}$
Ethyl acetate (1)/Benzene (2)	13.46%	1.73%
Ethyl acetate (1)/Toluene (2)	16.37%	9.86%
Ethanol (1)/Iso-octane (2)	8.79%	13.90%
R152A (1)/DME (2)	3.32%	6.47%

*%Mean Absolute Deviation (%MAD) = $\frac{\Sigma|X_{exp}-X_{cal}|}{n}$

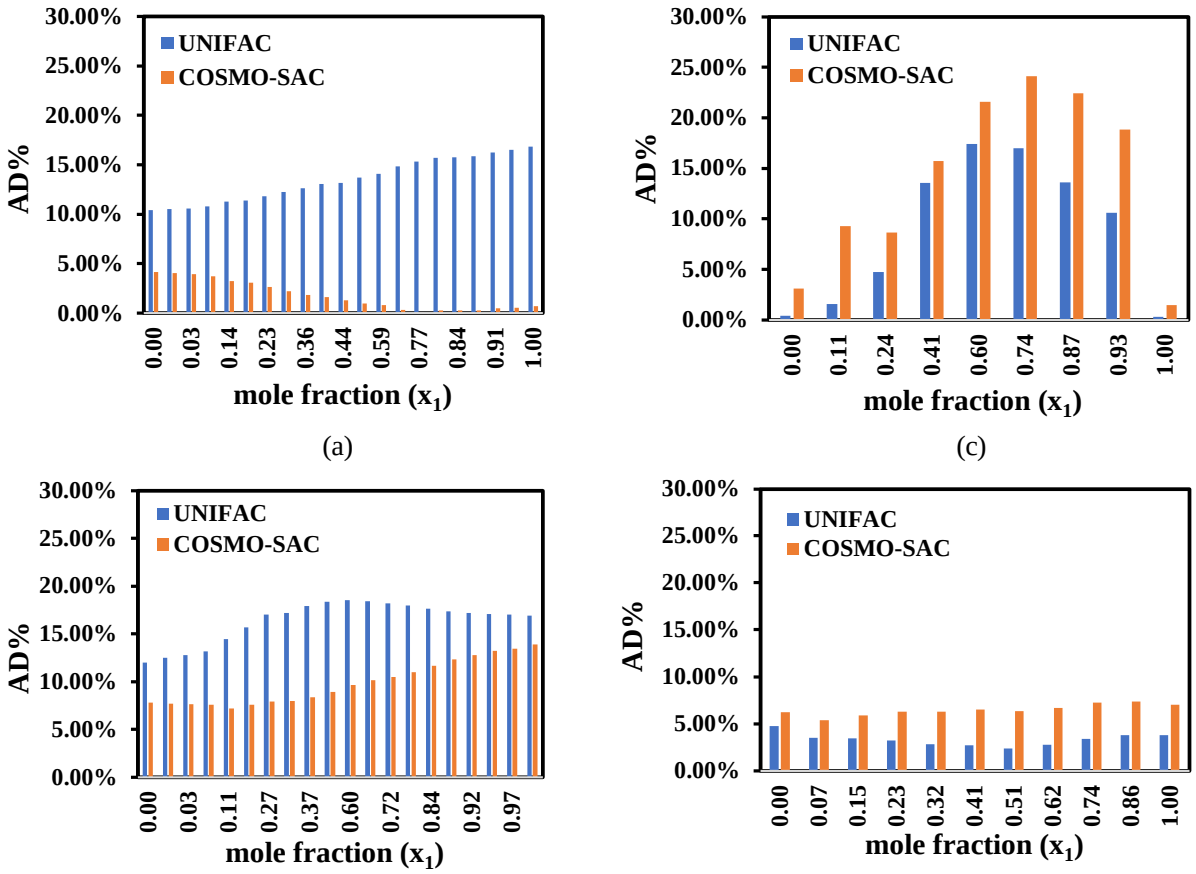

Figure 9 Absolute deviation between experimental and prediction UNIFAC and COSMO-SAC for (a) Ethyl acetate (1)/benzene (2), (b) Ethyl acetate (1)/Toluene (2), (c) Ethanol (1)/Iso-octane (2), (d) R152A (1)/DME (2)

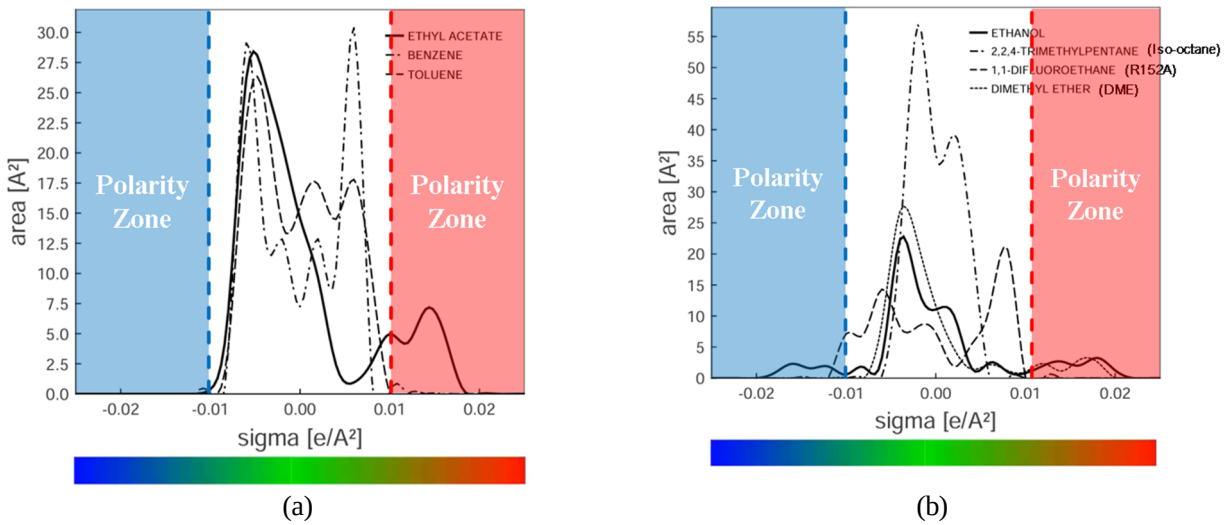

Figure 10 Sigma-profile of (a) Ethyl acetate/Benzene/Toluene, (b) Ethanol/Iso-octane /R154A/DME

The deviation analysis from Figure 9 indicates that the COSMO-SAC model generally provides higher accuracy than UNIFAC, particularly for systems without strong hydrogen bonding, such as ethyl acetate/benzene and ethyl acetate/toluene. However, for hydrogen-bonding systems like ethanol/iso-octane and R152A/DME, this can be observed in Figure 10(b), where ethanol and R152A are distributed within the blue polarity zone, indicating their hydrogen-bonding nature. As a result, the COSMO-SAC model exhibits a higher deviation, particularly for the ethanol/iso-octane mixture, where ethanol forms strong hydrogen bonds. This leads to the highest MAD% among all four binary systems, reaching 13.90%, due to the less refined hydrogen-bonding parameters in COSMO-SAC. And for ethyl acetate, which is distributed within the red polarity zone as shown in Figure 10(a), this indicates its high polarity. However, the distributions of ethyl acetate/benzene and ethyl acetate/toluene do not extend into the blue polarity zone, suggesting that these are polar + non-polar binary mixtures where hydrogen bonding does not occur. As a result, the COSMO-SAC model maintains better predictive accuracy than UNIFAC for these systems. For the R152A and DME pair that exhibits both hydrogen-bonding characteristics and polarity, but to a lesser extent compared to ethyl acetate and ethanol mixtures. Additionally, the smaller molecular size of R152A and DME results in lower structural complexity, making their intermolecular interactions easier to model. As a result, both COSMO-SAC and UNIFAC provide more accurate predictions, with MAD% values of 6.47% and 3.32%, respectively, which are the lowest among all binary mixtures studied.

4. CONCLUSION

From the study comparing on the accuracy of UNIFAC and COSMO-SAC in predicting the latent heat of vaporization (ΔH_{vap}) for four binary mixtures revealed that COSMO-SAC performed better for ethyl acetate/benzene and ethyl acetate/toluene, with lower MAD% of 1.73% and 9.86%, compared to UNIFAC at 13.46% and 16.37%, respectively. However, UNIFAC was more accurate for ethanol/iso-octane and R152A/dimethyl ether, with MAD% of 8.79% and 3.32%, compared to COSMO-SAC at 13.9% and 6.47%. These results indicate that COSMO-SAC may be less suitable for highly polar systems involving hydrogen bonding. Overall, COSMO-SAC demonstrated slightly better accuracy than UNIFAC, with average MAD% values of 7.99% and 10.48%, respectively, though both models require further refinement for improved predictive reliability in engineering applications and more data improve prediction accuracy and better align with experimental results.

REFERENCES

1. R. P. Gerber and R. P. Soares, “ASSESSING THE RELIABILITY OF PREDICTIVE ACTIVITY COEFFICIENT MODELS FOR MOLECULES CONSISTING OF SEVERAL FUNCTIONAL GROUPS”, Brazilian Journal of Chemical Engineering, Vol. 30, No. 01, January – March 2013, pp. 1 – 11.
2. F. Ferrarini, G. B. Flˆ ores, A. R. Muniz, and R. de P. Soares, “An open and extensible sigma-profile database for COSMO-based models”, Thermodynamics and Molecular-Scale Phenomena, Volume64, Issue9, September 2018, Pages 3443-3455.
3. K. L. Shivabasappa, P. Nirguna Babu and Y. Jagannadha Rao, “ENTHALPY OF MIXING AND HEAT OF VAPORIZATION OF ETHYL ACETATE WITH BENZENE AND TOLUENE AT 298.15 K AND 308.15 K”, Brazilian Journal of Chemical Engineering, Brazilian Journal of Chemical Engineering, Vol. 25, No. 01, January - March 2008, pp. 167 – 174.
4. Longfei Chen and Richard Stone, “Measurement of Enthalpies of Vaporization of Isooctane and Ethanol Blends and Their Effects on PM Emissions from a GDI Engine”, Energy Fuels, 25, 2011, 1254–1259.
5. Ayyalusamy Baskarana and Koshy Mathews, “Thermodynamic Analysis of R152a and Dimethylether Refrigerant Mixtures in Refrigeration System”, JJMIE, Vol. 9, N0. 4, August 2015, ISSN 1995-6665, Pages 289 – 296.
6. Andzelm, J., Kölmel, C. and Klamt, A., Incorporation of solvent effects into density functional calculations of molecular energies and geometries. The Journal of Chemical Physics, 103, (21), 9312 9321 (1995).
7. Lin, S.-T. and Sandler, S. I., A priori phase equilibrium prediction from a segment contribution solvation model. Industrial & Engineering Chemistry Research, 41, (5), 899-913 (2002).
8. Soares, R. D. P., The Combinatorial term for COSMO based activity coefficient models. Industrial & Engineering Chemistry Research, 50, (5), 3060 3063 (2011).
9. Çengel, Yunus A. Boles, Michael A. Kanoğlu, Mehmet, “Thermodynamics An Engineering Approach”, Ninth Edition, McGraw- Hill Education (2019).
10. J.M. Smith, Hendrick Van Ness, Michael Abbott, Mark Swihart, “Introduction to Chemical Engineering Thermodynamics”, Eighth Edition. McGraw-Hill Education (2018).
11. Ian H. Bell, Erik Mickoleit, Chieh-Ming Hsieh, Shiang-Tai Lin, Jadran Vrabec, Cornelia Breitkopf, and Andreas Jäger, “A Benchmark Open-Source Implementation of COSMO-SAC”, J. Chem. Theory Comput. 2020, 16, 4, 2635–2646.

12. Ruichang Xiong, Stanley I. Sandler, and Russell I. Burnett, “An Improvement to COSMO-SAC for Predicting Thermodynamic Properties”, Ind. Eng. Chem. Res. 2014, 53, 19, 8265–8278.
13. Qilei Liu, Kun Tang, Jinyuan Zhang, Yixuan Feng, Chenyang Xu, Linlin Liu, Jian Du, Lei Zhang, “QMaC: A Quantum Mechanics/Machine Learning-based Computational Tool for Chemical Product Design”, Computer Aided Chemical Engineering, Volume 48, 2020, Pages 1807-1812.
14. Daniela F. Borghia, Charlles R. A. Abreub, Reginaldo Guirardello, “Use of COSMO-SAC to Determine the Activity Coefficient and Predict Phase Equilibrium of Binary Systems Involving Methanol, Glycerol and Water”, Chemical Engineering Transactions, 43, May 2015, 1879-1884.
15. lvpp/sigma: LVPP sigma-profile database (Version 20.06) [Online]. Available: https://doi.org/10.5281/zenodo.3924076
16. lvpp/sigma: LVPP sigma-profile database (Version 20.06) [Online]. Available: https://doi.org/10.5281/zenodo.3613786

Sustainable manufacturing of polycaprolactone films: Effects of processing conditions on film quality

Kitthanya Ritthichai[1], Sirilux Poompradub[2,3,4*]

[1] Petrochemistry and Polymer Science Program, Faculty of Science, Chulalongkorn University, Bangkok 10330, Thailand
[2] Department of Chemical Technology, Faculty of Science, Chulalongkorn University, Bangkok 10330, Thailand
[3] Center of Excellence on Petrochemical and Materials Technology Chulalongkorn University, Bangkok 10330, Thailand
[4] Center of Excellence in Green Materials for Industrial Application, Chulalongkorn University, Bangkok 10330, Thailand
[*] Corresponding author: sirilux.p@chula.ac.th

ABSTRACT

Polycaprolactone (PCL) is a biodegradable polymer with a low melting point and excellent biocompatibility, making it widely used in medical applications such as tissue engineering, drug delivery, and sutures. It is synthesized from ε- caprolactone through ring- opening polymerization and can be dissolved in organic solvents such as chloroform, dichloromethane, and acetone. However, conventional solvent- based processing raises environmental concerns and presents challenges in process control. To develop a more sustainable and continuous manufacturing process, cast film extrusion is a promising alternative. Despite its advantages, PCL film extrusion presents challenges related to gel formation, which negatively impacts film quality and mechanical properties. The gel formation is influenced by multiple factors, including temperature, shear rate, and residence time within the extruder. This study aims to investigate the effect of extrusion processing conditions on the mechanical properties of PCL films, focusing on temperature variations and their impact on film properties. The results demonstrate that higher extrusion temperatures significantly promote gel formation on the film surface, leading to defects such as uneven thickness and reduced mechanical performance. In contrast, optimized processing conditions help minimize gel formation and improve film uniformity. Understanding these relationships is critical for enhancing the quality of PCL films and expanding their potential applications in biomedical and industrial fields. This study provides insights into the optimization of PCL film extrusion, offering a pathway to more efficient and environmentally friendly processing methods.

Keywords: Polycaprolactone; Extrusion; Film quality; Processing optimization; Gel formation.

1. INTRODUCTION

Environmental pollution, particularly from single-use plastics, has become one of the most pressing global challenges [1]. Conventional plastics, while versatile and cost-effective, are resistant to degradation, resulting in long-term accumulation in landfills and natural ecosystems. This has intensified the search for sustainable alternatives, leading to the increased use of biodegradable materials in everyday products [2]. These materials, capable of breaking down under natural or industrial composting conditions, are now seen in applications ranging from food packaging films and shopping bags to agricultural mulch and disposable medical items. Among biodegradable polymers, polycaprolactone (PCL) has gained significant attention due to its unique combination of properties.

PCL is a semi-crystalline aliphatic polyester derived from the ring-opening polymerization of ε-caprolactone. Although it is not bio-based and synthesized from fossil-derived monomers, it is fully biodegradable and compostable. It can degrade in various environments, including soil, compost, and even in the human body, making it suitable for both environmental and biomedical applications [3]. Its biocompatibility and low melting point (~60 °C) make it attractive for use in tissue engineering, drug delivery systems, and temporary implants [4], where it safely degrades without releasing toxic residues. In addition to biomedical uses, PCL is increasingly explored for packaging and agricultural films due to its flexibility,

low glass transition temperature, and ease of blending with other biodegradable polymers.

Despite its many advantages, PCL presents challenges in large-scale processing. Its low thermal resistance and relatively high melt viscosity limit to the processability using conventional methods. Moreover, PCL is sensitive to prolonged exposure to heat, resulting in the degradation and loss of mechanical performance. The most common technique for producing PCL films is solvent casting using organic solvents such as chloroform, acetone, or dichloromethane. While this method can yield uniform and transparent films, it raises concerns related to solvent toxicity, environmental hazards, and scalability. The use of volatile organic compounds (VOCs) poses health and safety risks and contributes to environmental pollution. These factors limit the industrial applicability of solvent casting, especially in applications requiring continuous or large-scale production.

To overcome these limitations, the melt extrusion presents a promising alternative. As a solvent-free, continuous, and scalable method, this technique is widely used in the plastic and polymer industry to produce films, sheets, and various molded products. Among the available extrusion techniques, cast film extrusion and blown film extrusion are the most common methods for manufacturing thin polymer films. However, blown film extrusion is not well-suited for low-melt-strength materials because it requires precise control of bubble stability and air pressure, which can be difficult to maintain when processing thermally sensitive or low-viscosity polymers. Additionally, setup and adjustment times are relatively long, which leads to material waste and cost issues that are particularly problematic when working with expensive biopolymers. In contrast, cast film extrusion offers a more stable and user-friendly method for processing biodegradable materials. It provides excellent control over film thickness and width, faster setup, and compatibility with a broader range of materials, including those with low-melt-strength. Moreover, cast film extrusion produces less waste and avoids the use of solvents, aligning well with sustainability goals.

Despite its advantages, challenges in processing thin PCL films via cast film extrusion remain, such as gel formation, surface roughness, and film opacity, which still need to be addressed to improve the quality of the final product. A detailed understanding of the relationship between processing conditions and material properties is crucial to overcome these limitations. Specifically, factors such as processing temperature, screw speed, and die design have been shown to significantly affect the properties of PCL films, including film thickness, transparency, and mechanical strength [5].

The effect of temperature on polymer processing is particularly important, as temperature influences the melt flow behavior, molecular weight distribution, and crystallization behavior of PCL. Higher temperatures often lead to improve flow properties, resulting in films with good uniformity. However, excessively high temperatures can also lead to thermal degradation, which compromises the mechanical properties of the polymer. This highlights the need for careful control of processing conditions to achieve the desired balance between flow and stability during extrusion. While studies have examined the effect of processing parameters on the mechanical properties of various polymers, the specific impact of temperature on PCL remains less explored.

This study focuses on producing PCL thin films using a cast film extrusion process, with a particular emphasis on the effect of processing temperature on film quality. Mechanical properties such as tensile strength and elongation at break are evaluated to assess the impact of temperature variations. The goal is to identify suitable processing windows that optimize film performance while maintaining the thermal stability of PCL. By investigating these relationships, the study contributes to the development of more sustainable and efficient methods for producing biodegradable films, particularly for applications where environmental impact, material safety, and product quality are critical. The following sections present the materials and methods used in this study, followed by a result and discussion of the film thickness and mechanical testing result of Young's modulus, tensile strength and elongation at break. Finally, conclusions are drawn based on the findings and their implications for the future processing of biodegradable films.

2. EXPERIMENTAL

2.1 Material

PCL grade CAPA 6800 manufactured by Ingevity was used for the production of thin films. The material has a molecular weight of 80,000 and a melting point of 58-60 °C. PCL is synthesized through ring-opening polymerization of ε-caprolactone, resulting in a biodegradable linear polyester with excellent biocompatibility. The PCL pellets were used as received without further purification. Prior to processing, the PCL pellets were pre-dried at 40 °C to minimize moisture absorption and avoid hydrolytic degradation during extrusion.

2.2 Production of polymer films

Thin PCL films were produced using a cast film extrusion process from Labtech Engineering as shown in Figure 1. The machine configuration included a 25 mm single-screw extruder with a length-to-diameter (L/D) ratio of 30:1, a die, and a casting unit. The extruder had four heating zones with all heating zones set equally to ensure uniform thermal profiles. The screw speed was fixed at 25 rpm to maintain a constant output rate. The die width was 200 mm with two heating zone which were also set equal to the extruder barrel

temperature. The target film thickness of 40 µm. The sample labeling is based on the extrusion temperature, as detailed in Table 1.

Figure 1 Cast film extrusion line used for the production of thin PCL films.

Table 1 Processing temperature and screw speeds for PCL film extrusion.

Sample code	Processing temperature (°C)	Controlled screw speed (rpm)	Actual screw speed (rpm)
PCL80	80	25	10
PCL90	90	25	16
PCL100	100	25	25
PCL110	110	25	25
PCL120	120	25	25

During extrusion to produce the film thickness of 40 µm, the barrel temperature of the extruder and the die was kept constant at 80°C, 90°C, 100°C, 110°C, and 120°C. No additive, solvent, or filler was used.

2.3 Film thickness measurement

The film thickness of PCL films was measured using a digital thickness gauge. Thickness measurements were performed along both the machine direction (MD) and transverse direction (TD) of the film to assess the uniformity and consistency of the PCL film throughout the sample.

2.4 Study of polymer film mechanical properties

The mechanical properties of the PCL films were evaluated using a universal testing machine (UTM) equipped with a load cell capacity of 1 ton. The testing followed the standards outlined in ASTM D882-E, which is specifically designed for testing the mechanical properties of thin plastic films, such as tensile strength, Young's modulus, and elongation at break. Specimens were prepared by cutting the PCL films into rectangular strips with dimensions of 20 mm × 100 mm. The strips were then mounted on the testing machine, with the initial grip separation set to 50 mm. The testing speed was set to 25 mm/min, in line with the standard recommendations for a 50 mm gauge length. Young's modulus, tensile strength, and elongation at break were measured. Each test was repeated for five times to ensure reliability and statistical significance.

3. RESULTS AND DISCUSSION

3.1 Effect of processing temperature on motor current and melted pressure

The results from this study demonstrate the significant influence of processing temperature on the motor current and melt pressure during the extrusion of PCL films. Figure 2 shows the relationship between motor current or melt pressure and processing temperature. Usually, the lower the processing temperature of the polymer, the higher the motor current requires to melt the polymer. PCL80 showed the highest motor current. Due to the limitation of motor capacity, the controlled screw speed of 25 rpm was not achievable at the processing temperatures of 80 °C. The similar behavior was also observed in the case of processing temperature at 90°C. Therefore, the screw speed needed to be adjusted lower, as shown in the actual speeds (Table 1). This result indicates that a low processing temperature resulted the difficult polymer melt flow and required more energy input for processing. This result was in agreement with a previous study [6]. In addition, at low processing temperatures, the viscosity of the polymer material was increased, resulting in the increased motor current to drive the extruder screw and to completely melt the polymer. At the same actual screw speed (25 rpm), the motor current tended to decrease with the increase of processing temperature. This result indicated that the low motor current was used to drive the rotating screw.

In the case of melted pressure under the actual screw speed, higher processing temperatures resulted in lower melted pressure. This is because the melt viscosity of the polymer decreased at high processing temperatures. Unfortunately, this behavior could not be compared to the processing temperatures at 80 °C and 90 °C because the actual screw speed was not equal. Accordingly, the processing temperature is a main factor affecting motor current and melt pressure, and it must be carefully considered and controlled in a cast film extrusion line.

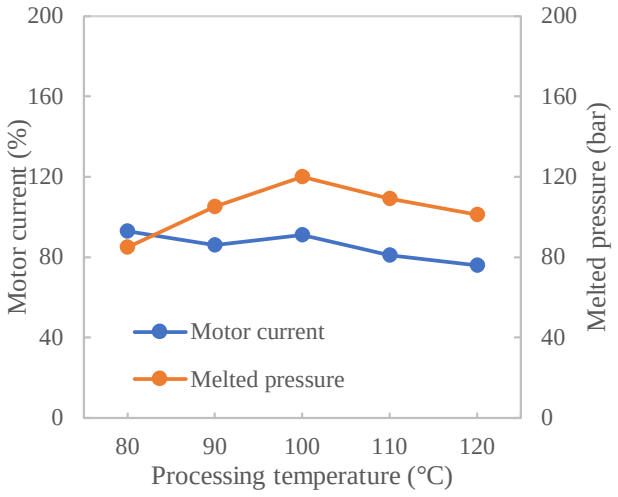

Figure 2 Melted pressure and motor current of PCL film extrusion.

3.2 Effect of processing temperature on film thickness

The relationship between film thickness and processing temperature was presented in Figure 3. It was clearly seen that different temperatures under the actual screw speed did not show the difference of film thickness. Therefore, the processing temperature was independent on film thickness.

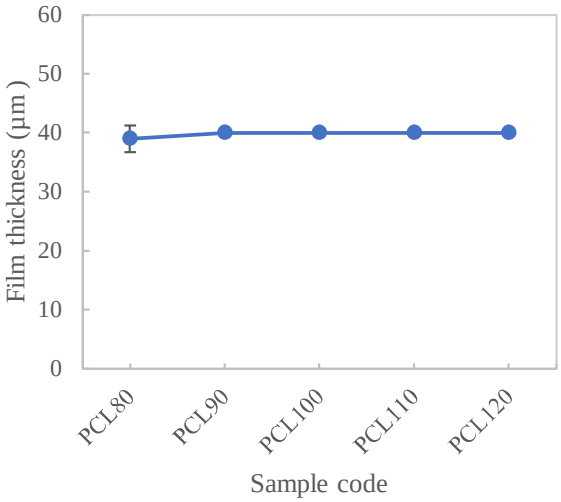

Figure 3 Thickness of PCL films obtained from different process temperature.

Additionally, when the film come out of the flat die after extrusion, the neck-in phenomenon can be observed. It is a common issue where the edges of the film are thicker than the central portion. However, the film edges can be trimmed, and there is no effect on the central area. Accordingly, by using cast film extrusion, the film thickness can be easily controlled, offering consistent and uniform thickness along both the machine direction (MD) and transverse direction (TD).

3.3 Mechanical properties of PCL films

Figure 4 shows the mechanical properties of PCL films. The PCL films were processed under the actual screw speed given in Table 1. It was clearly seen that the Young's modulus tended to decrease with the increase of processing temperature. The decrease of modulus at higher process temperatures might be due to the presence of gels or defects on the film surface or the chain scission of the polymer, causing lower resistance and stiffness of the film [7]. Considering the result of tensile strength and elongation at break. It is interesting to note that the tensile strength and elongation at break for all samples did not show a significant change. The processing temperature affects the mechanical properties of PCL film in terms of only the Young's modulus. Accordingly, the optimal condition of casting film was obtained under the processing temperature of 100 °C and controlled screw speed of 25 rpm.

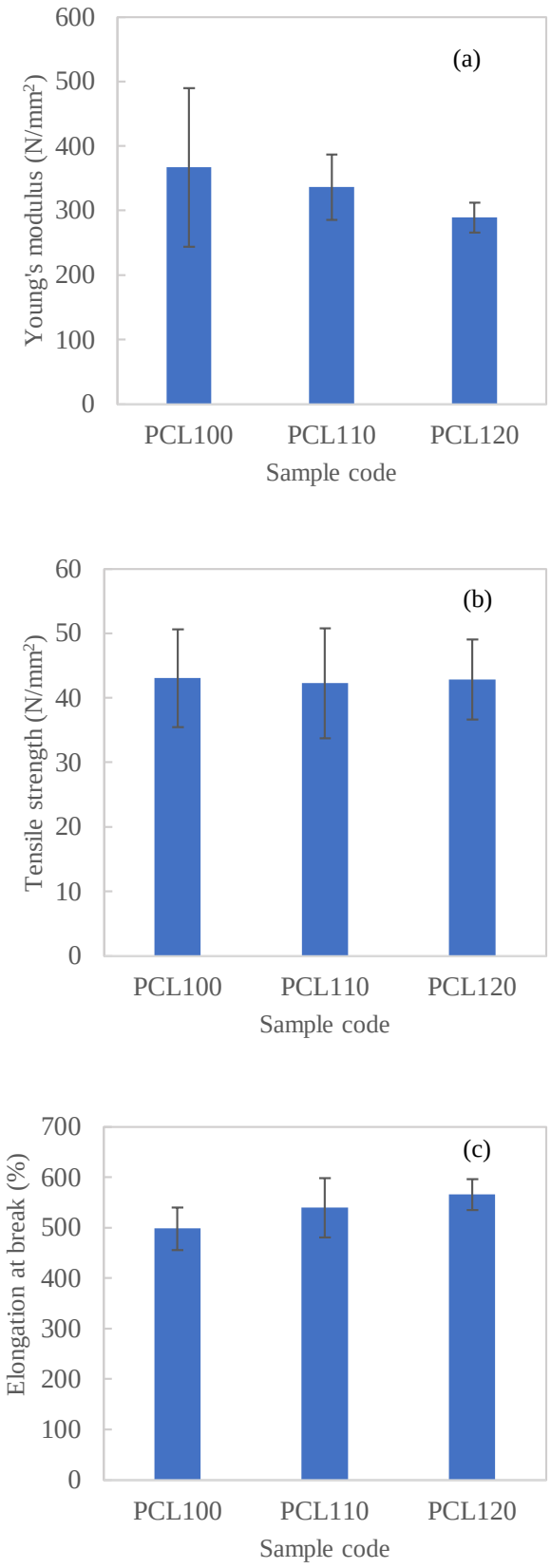

Figure 4 Mechanical properties of PCL film where (a) Young's modulus, (b) tensile strength and (c) elongation at break.

3.4 Implications for industrial applications

The findings from this study have significant implications for the industrial-scale processing of PCL films. Cast film extrusion has been shown to be a viable method for producing biodegradable PCL films with good control over film thickness, mechanical properties, and film consistency. The ability to adjust processing temperature allows for optimization of the film's mechanical performance, making cast film extrusion a suitable choice for applications in sustainable packaging and biomedical devices.

However, challenges remain in further optimizing processing conditions to ensure high-quality films with consistent mechanical properties. For instance, the tendency for polymer degradation at temperatures higher than 100°C necessitates careful control of temperature profiles to avoid thermal damage. Additionally, the neck-in phenomenon in the films suggests that further research is needed to improve the die design or flow channels to minimize this issue and reduce material waste during extrusion.

4. CONCLUSION

This study aimed to investigate the effect of processing temperature on the quality and mechanical properties of PCL films produced by cast film extrusion. The principal findings demonstrated that processing temperature significantly influenced the motor current, melt pressure, and Young's modulus of the films. Lower temperatures resulted in higher motor load and melted pressure due to the high melted viscosity of the polymer. PCL polymer which was extruded under the processing temperature of 100°C and controlled screw speed of 25 rpm provided the optimal performance. The results highlight the importance of carefully controlling processing conditions to ensure uniform film thickness, enhanced mechanical properties, and overall production efficiency.

ACKNOWLEDGMENTS

The authors would like to express their sincere gratitude to Labtech Engineering for providing the cast film extrusion equipment and technical support essential to the experimental work. Thanks, are also extended to the Petrochemistry and Polymer Science Program, Faculty of Science, Chulalongkorn University for financial support.

REFERENCES

1. Geyer, R., Jambeck, J. R., & Law, K. L. (2017). Production, use, and fate of all plastics ever made. *Science Advances*, 3(7), e1700782.
2. Emadian, S. M., Onay, T. T., & Demirel, B. (2017). Biodegradation of bioplastics in natural environments. *Waste Management*, 59, 526–536.
3. Woodruff, M. A., & Hutmacher, D. W. (2010). The return of a forgotten polymer—Polycaprolactone in the 21st century. *Progress in Polymer Science*, 35(10), 1217–1256.
4. Dash, T. K., & Konkimalla, V. B. (2012). Poly-ε-caprolactone based formulations for drug delivery and tissue engineering: A review. *Journal of Controlled Release*, 158(1), 15–33.
5. Osswald, T. A., & Hernández-Ortiz, J. P. (2006). *Polymer Processing: Modeling and Simulation*. Hanser Publishers.
6. Vlachopoulos, J., & Strutt, D. (2003). The role of rheology in polymer extrusion. *Journal of Plastic Film & Sheeting*, 19(3), 191–215. https://doi.org/10.1177/8756087903038895
7. Cai, W., Zhang, X., Zhang, L., & Liu, Z. (2018). Effects of processing conditions on the melt flow behavior and energy consumption of polypropylene in a twin-screw extruder. *Journal of Applied Polymer Science*, 135(29), 46598. https://doi.org/10.1002/app.46598

Feedforward control of pulsed bed adsorption column for colorant removal in sugar syrup at different flow rates

Chanya Plangklang[1], Terasut Sookkumnerd[1,*]

[1] School of Chemical Engineering, Institute of Engineering, Suranaree University of Technology, Nakhon Ratchasima 30000, Thailand
[*] Corresponding author: terasut@sut.ac.th

ABSTRACT

To minimize the environmental impact of colorant removal in sugar syrup, pulsed bed adsorption columns present a promising alternative to conventional ion exchange resin processes. Despite their environmental advantages, these columns pose new challenges in operation due to their cyclic steady-state nature. In this study, the numerical method of lines was applied to investigate the dynamic behavior of pulsed bed adsorption columns under various conditions. Specifically, the effectiveness of feedforward control when the inlet colorant concentration in syrup fluctuates periodically at flow rates between 4 and 8 ml/min was investigated. From the study, it was confirmed that feedforward control successfully regulated the outlet colorant concentration. These findings support the adoption of feedforward control to improve the practicality and efficiency of pulsed bed adsorption columns in sugar refining processes.

1. INTRODUCTION

The sugar industry is a significant agro-industrial sector in Thailand, as the country ranks as the world's second-largest exporter of sugar [1]. With more than 400,000 farmers and over 50 sugar factories nationwide, the industry plays a vital role in Thailand's economy [2]. Due to intense competition, value-added products—such as refined sugar with extremely low color or ICUMSA value—are increasingly preferred over white sugar. However, conventional methods for colorant removal in sugar refining primarily rely on acrylic and styrene-based ion exchange resins, which require brine solution for regeneration. The disposal of spent brine poses environmental risks and challenges, particularly if accidentally released into surrounding areas.

Consequently, the use of granulated activated carbon (GAC) for colorant removal in sugar refining presents a promising approach, as spent GAC can be reactivated on-site with minimal losses—approximately 5% [3]. To optimize adsorption efficiency, the process utilizes pulsed-bed adsorption columns, where the counterflow movement of fluid and adsorbent is simulated. While this system, along with on-site GAC reactivation, offers an environmentally friendly alternative to conventional methods, the cyclic steady-state nature of pulsed-bed adsorption presents operational and control challenges [4]. Significant lag time arises due to feed disturbances and the inherently unsteady-state dynamics of the process.

To investigate the application of simple feedforward control in pulsed-bed adsorption columns, Plangklang and Sookkumnerd applied the numerical method of lines, using the cycle time of the pulsed-bed as the manipulated variable [5]. Their results indicated that simple feedforward control could successfully regulate pulsed-bed adsorption. However, the study was limited by a narrow range of flow rates. Therefore, this paper extends the analysis by examining a broader range of disturbances.

The mathematical models and numerical method of lines used in the study are first discussed in the Experimental Section. Subsequently, the results of applying feedforward control to pulsed-bed adsorption columns are presented, along with key findings—particularly regarding the practical implementation of feedforward control in real-world refining processes. Finally, the paper concludes with a summary of significant insights and recommendations for future research.

2. EXPERIMENTAL

2.1 Mathematical model for pulsed-bed adsorption column

Assuming a linear adsorption isotherm, a linear driving force model and plug flow conditions, the mathematical model of the adsorption column is presented in Eq. (1) and (2) [5]

$$\frac{\partial C}{\partial t} = -v\frac{\partial C}{\partial z} - \frac{q_0}{C_0}\left(\frac{1-\varepsilon}{\varepsilon}\right)\frac{\partial q}{\partial t} \quad (1)$$

$$\frac{\partial q}{\partial t} = k(C - C_{eq}) \quad (2)$$

The boundary conditions of adsorption column is

$$C(z = 0, t) = C_0 \quad (3)$$

The initial conditions at the first cycle of pulsed bed are

$$C(z, t = 0) = 0 \text{ and } q(z, t = 0) = 0 \quad (4)$$

At the start of the (N+1)th cycle, the system underdoes a 10% replacement process (pulse), where in granular activated carbon (GAC) is removed from the bottom of the column and an equivalent amount of GAC is introduced at the top. The initial condition for this cycle are as follows:

$$C = \begin{cases} 0 \; when \; Z \geq (1 - 0.1)L \\ C(t = N t\tau_{cycle}, Z - 0.1L) \; if \; Z \leq (1 - 0.1)L \end{cases} \quad (5)$$

$$q = \begin{cases} 0 \; when \; Z \geq (1 - 0.1)L \\ q(t = N t\tau_{cycle}, Z - 0.1L) \; if \; Z \leq (1 - 0.1)L \end{cases} \quad (6)$$

The numerical method of lines (NMOL) [6] was applied to solve Eq. (1) and (2) with spatial derivative terms approximated using a five-point biased up-winding approximation and a step sizes of 0.01 m. The resulting ODEs were then solved using the 4th-order Runge-Kutta algorithm in SCILAB [7]. The accuracy of the mathematical model was validated by comparing the numerical results with different step sizes.

The mass transfer coefficient (k) and the equilibrium constant of adsorption (K) were directly adopted from Plangklang and Sookkumnerd [5] which obtained these parameters by fitting them to the breakthrough curve as listed in Table 1.

Table 1. Equilibrium constant of adsorption (K) can mass transfer coefficient (k).

Flowrate [ml/min]	K [-]	k [1/s]
4	1.58	2.35×10^{-4}
6		8.08×10^{-4}
8		8.09×10^{-4}

2.2 Simple feedforward Control of pulsed-bed adsorption column

Plangklang and Sookkumnerd demonstrated that a simple feedforward control with the relationship between the cycle time and the colorant concentration of feed syrup [5] as described by Eq. (7) to (9) effectively maintained the colorants in product syrup within its specification at the flow rate of 6 ml/min

$$\tau_{cycle} = -2.06 \ln(C_0 - 100) + 20.9 \; at \; 4 \; ml/min \quad (7)$$

$$\tau_{cycle} = -1.91 \ln(C_0 - 100) + 19.9 \; at \; 6 ml/min \quad (8)$$

$$\tau_{cycle} = -1.53 \ln(C_0 - 100) + 15.0 \; at \; 8 \; ml/min \quad (9)$$

A similar approach was applied to cases where the flow rate was 4 and 8 mL/min to evaluate the effectiveness of this simple feedforward control across a wider range of flow rates.

3. RESULTS AND DISCUSSION

Figures 1 and 2 illustrate the results of an uncontrolled pulsed-bed adsorption column under colorant disturbances in the feed syrup. As shown in these figures, the syrup exiting the columns exceeded its specified color requirements, demonstrating that manual control of the pulsed-bed adsorption column is challenging.

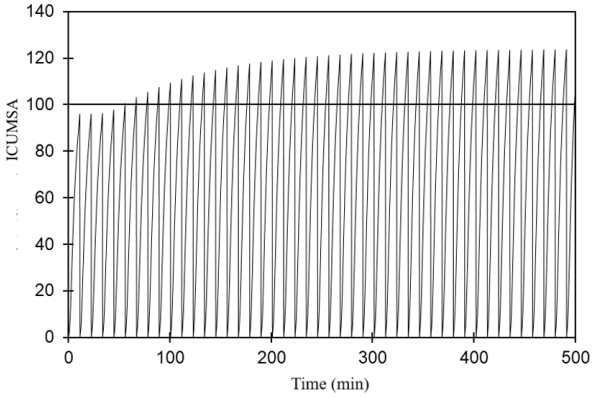

Figure 1. Uncontrolled pulsed-bed adsorption column at flow rate of 4 ml/min when the colorants in feed syrup increased from 700 to 900 ICUMSA.

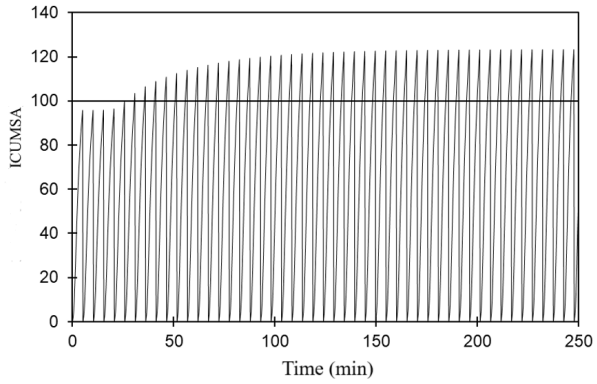

Figure 2. Uncontrolled pulsed-bed adsorption column at flow rate of 8 ml/min when the colorants in feed syrup increased from 700 to 900 ICUMSA.

Figures 3 and 4 present the results of the simple feedforward control applied to the pulsed-bed adsorption column. To ensure smoother controller action, a delay of five periods was implemented. As shown in Figures 4 and 5, this control strategy was successfully applied to colorant removal in sugar refining.

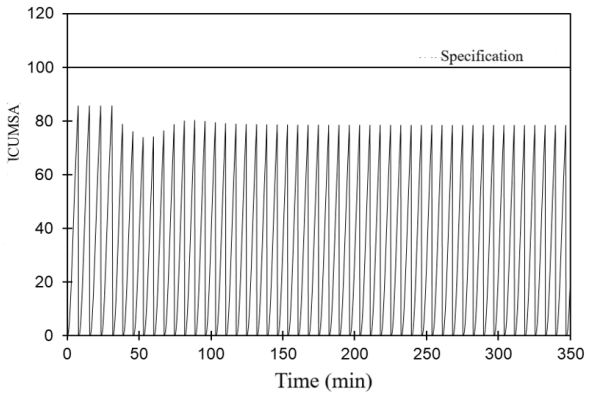

Figure 3. Feedforward controlled pulsed-bed adsorption column at flow rate of 4 ml/min when the colorants in feed syrup increased from 700 to 900 ICUMSA.

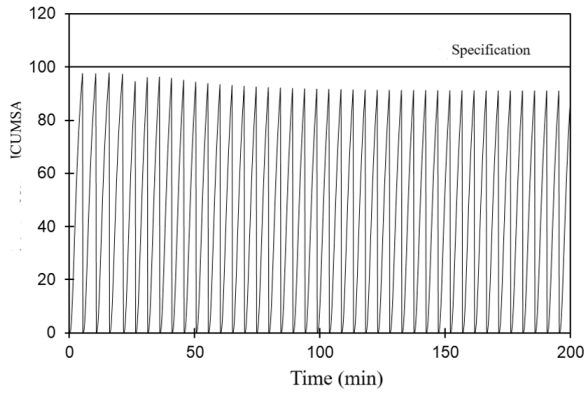

Figure 4. Feedforward controlled pulsed-bed adsorption column at flow rate of 8 ml/min when the colorants in feed syrup increased from 700 to 900 ICUMSA.

The feedforward control was systematically evaluated by analyzing the response time and ICUMSA value of the product syrup after achieving cyclic steady state, as shown in Table 2. It was observed that higher flow rates generally resulted in longer response times. Nevertheless, the product syrup consistently adhered to its colorant specifications.

Table 2. Response time and ICUMSA after reaching the cyclic steady state.

Flowrate [ml/min]	Response time (cycle)	ICUMSA after cyclic steady state
4	10	92.58
6	13	95.01
8	17.15	86.15

To evaluate the effectiveness of feedforward control in a pulsed-bed adsorption column under conditions where the colorants in the feed syrup vary continuously, the system's response was studied. Specifically, the feed syrup's colorant concentration was modeled as a cosine function with a maximum value of 900 ICUMSA, a minimum of 700 ICUMSA, and a period of 4 hours. The results are presented in Figures 5 and 6.

Figures 5 and 6 clearly illustrate that the feedforward control of the pulsed-bed adsorption column effectively maintained the colorant concentration in the product syrup within the specification of 100 ICUMSA, even when the feed syrup's colorant variation was modeled as a cosine function. These findings highlight the potential application of feedforward control in pulsed-bed operations for sugar refining processes, offering a promising approach to optimize performance and enhance efficiency.

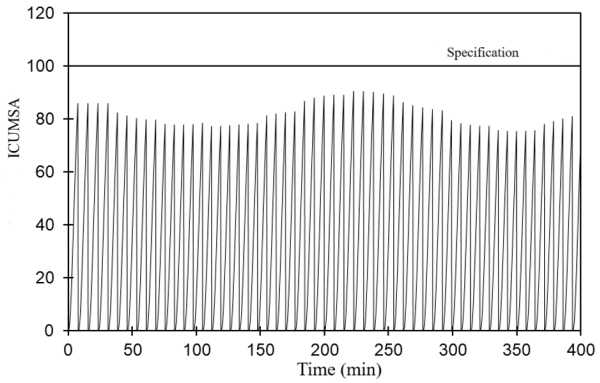

Figure 5. Feedforward controlled pulsed-bed adsorption column at flow rate of 4 ml/min when the colorants in feed syrup was modeled as cosine function.

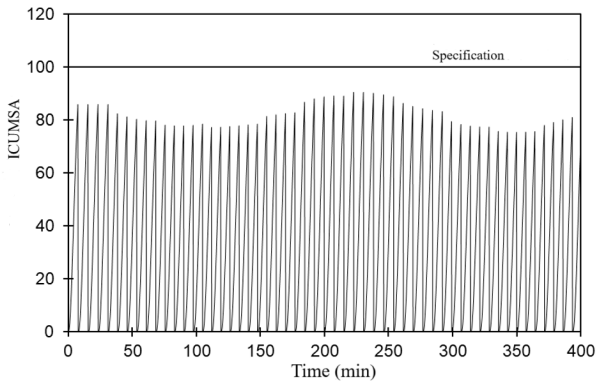

Figure 6. Feedforward controlled pulsed-bed adsorption column at flow rate of 8 ml/min when the colorants in feed syrup was modeled as cosine function.

4. CONCLUSION

In conclusion, the feedforward control of the pulsed bed was successfully implemented, demonstrating that cycle time can serve as the manipulated variable when disturbances were caused by colorants in the feed syrup. In real sugar refining processes, disturbances may also arise from factors such as feed flow rate fluctuations and the efficiency of granular activated carbon reactivation. Therefore, future research should focus on addressing these disturbances to optimize the application of pulsed-bed adsorption columns in sugar refining processes. This would ultimately minimize the environmental impact of sugar refining operations.

ACKNOWLEDGMENTS

Chanya Plangklang is grateful for the financial support by Suranaree University of Technology.

REFERENCES

1. P. Thaweekan. Analysis of Thai Sugar Export Competitiveness in ASEAN Market. *Journal of Education and Social Development* 2020; 15(2): 72-80.
2. Office of the Cane and Sugar Board. Report sugarcane plantations and sugarcane production [Internet] 2024. Available from: https://www.ocsb.go.th/2024/reports-articles/area-yield/27524/
3. J.-H.Liang, Pulsed-Bed Moving-Granular Activated Carbon System, in: C.C. Chou (Ed.) Handbook of sugar refining: a manual for the design and operation of sugar refining facilities, John Wiley & Sons, New York, USA, 2000.
4. J.K. Conlee, A Pulse Bed Granular Carbon System for Refining Glucose, *Starch - Stärke*, 1971; 23, 366-369.
5. C. Plangklang and T. Sookkumnerd, Modelling and Feedforward Control of Pulsed Bed Adsorption Column for Colorant Removal in Sugar Syrup 2023; *Eng. J.*, 27(1), 29-38.
6. W.E. Schisser, The Numerical Method of Lines. Integration of Partial Differential Equations, Elsevier, 1991.
7. A.V. Wouwer, P.Saucer and C. Vilas, Simulation of ODE/PDE Models with Matlab, Octave and Scilab. Scientific and Engineering Applications, Springer Charm, 2014.

Development of computational fluid dynamics modeling of packed bed membrane reactor for dimethyl ether production from carbon dioxide

Kannika Lhongbangplee[1], Pornchai Bumroongsri[1,*]

[1] Department of Chemical Engineering, Faculty of Engineering, Mahidol University, Nakhon Pathom 73170, Thailand

[*] Corresponding author: pornchai.bum@mahidol.ac.th

ABSTRACT

Dimethyl ether (DME) is a valuable chemical synthesized from syngas. This research investigated the DME production in a catalytic membrane reactor and a water-selective membrane. Computational fluid dynamics modeling was applied to study key parameters including velocity profile, pressure profile and DME concentration. The results indicated that the axial flow behavior observed in the packed bed membrane reactor implied minimal back-mixing and supported the efficient progression of the reaction along the reactor length. The concentration increased progressively from the catalytic bed inlet to the outlet indicating that the methanol dehydration reaction proceeded as the reactant mixture flowed downstream. The selective removal of water significantly enhanced the equilibrium shifted toward DME formation. The study confirmed that an efficient catalytic membrane reactor design could provide a scalable and sustainable solution for DME production.

Keywords: Dimethyl ether; Carbon dioxide; Computational fluid dynamics; Catalytic membrane reactor

1. INTRODUCTION

The scientific consensus on climate change has been well-established: human activities were identified as the primary cause, as affirmed by the Intergovernmental Panel on Climate Change (IPCC). According to the IPCC, the concentration of greenhouse gases in the atmosphere correlated directly with the Earth's rising average global temperature. Since the Industrial Revolution, both greenhouse gas concentrations and global temperatures have steadily increased. Carbon dioxide (CO_2), the most prevalent greenhouse gas, primarily originated from the combustion of fossil fuels. Methane, a major component of natural gas, contributed over 25% to recent warming trends. Its potency as a greenhouse gas—with a global warming potential more than 80 times that of CO_2 over a 20 years period, was emphasized in the Methane Emissions fact sheet by the United Nations Environment Program (UNEP) [1].

Dimethyl ether (DME) stood out among the array of products derivable from CO_2 due to its appeal as an alternative clean fuel, capable of substituting diesel or LPG with minimal engine modifications [2]. Two distinct pathways for DME production were identified: the indirect route, involving methanol production followed by dehydration, and the direct route, a more efficient process combining methanol synthesis and dehydration in a single reactor [2]. At the time, the primary feedstock for methanol production was syngas, generated through steam reforming of natural gas or gasification of crude oil, coal, biomass, or municipal solid waste [3, 4]. Consequently, the prevailing DME production process was predominantly fossil-based, with a CO_2 footprint typically ranging from 89 to 98 g CO_2/MJ DME [5, 6]. Furthermore, the estimated production cost of DME from natural gas ranged between 0.12 and 0.16 USD/kg DME, indicating relatively modest production expenses [7].

Given these considerations, the production of DME from captured CO_2 and renewable H_2 emerged not only as a viable pathway for CO_2 valorization and H_2 storage, but also as a means of enhancing process sustainability [8, 9]. Poto et al. [7] developed a Langmuir–Hinshelwood (L–H) kinetic model intended for reliably scaling up industrial and decentralized reactors for the direct hydrogenation of pure CO_2 to methanol. In their kinetic model, Li et al. [3] assumed methanol production to occur solely from CO_2, with water generated as a co-product that participated in the water–gas shift (WGS) reaction. The model was based on a single-site Langmuir–Hinshelwood mechanism, which included discrete elementary reaction steps. This reaction scheme effectively represented a redox process, where CO_2 acted as the oxidizing agent. It oxidized the metallic copper active site, resulting in CO formation, which subsequently underwent the reverse WGS reaction. The oxidized site was then reduced by adsorbed hydrogen, releasing a water molecule.

In an earlier study, Poto et al. [8] developed a one-dimensional phenomenological model of a membrane reactor to investigate how membrane characteristics, such as permeability and selectivity, influenced reaction outcomes. They designed and optimized a reactor in which a sweep gas, mixed with CO_2 and H_2, flowed in a co-current configuration to enhance selective water removal from the reaction zone. In a subsequent study, they refined the reactor further by introducing boiling water circulation in an external jacket to improve thermal management. The membrane reactor was eventually scaled up and integrated into a process flowsheet to evaluate its efficiency and cost-effectiveness [9].

To utilize carbon dioxide from carbon capture and storage (CCS) plants and advance scientific knowledge while applying innovative technologies, it is essential to achieve maximum CO_2 and H_2 conversion rates, optimize reactant selectivity, and maximize product yield under optimal operating conditions.

2. MODELING AND SIMULATION

2.1. Reactions for dimethyl ether production

This study developed a computational fluid dynamics (CFD) model for direct dimethyl ether (DME) production from carbon dioxide (CO_2) and hydrogen (H_2) using a CuO-ZnO-Al_2O_3/HZSM-5 catalyst and a water-selective Linde type A (LTA) zeolite-based membranes. The simulations were conducted using computational fluid dynamics technique to analyze the effects of operating parameters such as temperature, pressure, and sweep gas ratio. The following reversible reactions are taken into account in this research work.

CO hydrogenation:

$$CO + 2H_2 \leftrightarrow CH_3OH;\ \Delta H^0_{295K} = -90.5\ kJ/mol \quad (1)$$

Reverse water gas shift:

$$CO_2 + H_2 \leftrightarrow CO + H_2O;\ \Delta H^0_{295K} = 41.1\ kJ/mol \quad (2)$$

CO_2 hydrogenation:

$$CO_2 + 3H_2 \leftrightarrow CH_3OH + H_2O;\ \Delta H^0_{295K} = -49.4\ kJ/mol \quad (3)$$

Methanol dehydration:

$$2CH_3OH \leftrightarrow CH_3OCH_3 + H_2O;\ \Delta H^0_{295K} = -23.4\ kJ/mol \quad (4)$$

2.2. Packed bed membrane reactor model

This section presented the development of a three-dimensional (3D) isothermal model of the packed bed membrane reactor (PBMR), focused on assessing concentration polarization effects along the membrane surface. The reactor was modeled as pseudo-homogeneous and incorporated a modified Thiele modulus approach to evaluate internal diffusion resistance and mass transfer behavior within a microporous carbon membrane, with permeability effects integrated into the model assumptions.

In practice, the flow rate on the permeate side of the membrane was often equal to or greater than that within the reaction zone (i.e., sweep ratio SW $\geq$ 1), even though the permeate region typically had a significantly narrower cross-sectional area ($L_m/D_m \gg 50$). Under these conditions, significant radial gradients in physical quantities were unlikely to develop. However, due to the membrane's permeation flux, a non-zero radial velocity component could still exist within the reaction zone. Although this radial component was commonly neglected in modeling studies, it could influence simulation accuracy. In this model, a radial dispersion term was included to partially account for this effect, and the radial pressure gradient was omitted, in line with standard practice reported in the literature [43,51].

Furthermore, when the reactor-to-particle diameter ratio (D_r/D_p) exceeded 15, it was acceptable to treat bed porosity as radially constant, resulting in a nearly uniform axial velocity profile across the radius [52]. To simplify the application of the 2D formulation, a single membrane positioned at the center of the reactor was assumed, allowing for axisymmetric modeling. This assumption removed the need to account for angular velocity components and enabled further simplification of the equations.

Given the availability of well-established correlations for estimating heat transfer, these were used directly in the model. Additionally, heat exchange with the reactor wall and heat transfer to/from the membrane in the radial direction were considered negligible. The governing mass balance equations for both the reaction and permeation zones, along with their respective boundary conditions, were summarized in Eqs. (5)-(9). In the reaction zone, mass conservation was expressed through Eq. (5) which did not explicitly include the permeation flux. Instead, species transfer due to permeation was accounted for via a boundary condition at the membrane interface ($r = R_{mo}$). Another boundary condition in the radial direction set the species flux at the reactor wall ($r = R_{ri}$) to zero representing the absence of mass transfer across the reactor boundary. The mass transport in the permeation zone was modeled using Eq. (8) with concentration as the boundaries. The heat balance equation is shown in Eq. (10).

Governing equations for mass and heat conservation.

Mass balance-Reaction zone:

$$\frac{\partial(v^R C_i^R)}{\partial z} - \frac{1}{r}\frac{\partial}{\partial r}\left(r D_{rad,i}\frac{\partial C_i^R}{\partial r}\right) = R_i \quad (5)$$

Boundary conditions:

$$z = 0,\ C_i^R = C_i^{R,IN},\ r = R_{ri},\ \frac{\partial C_i^R}{\partial r} = 0 \quad (6)$$

$$r = R_{mo},\ D_{rad,i}\frac{\partial C_i{}^R}{\partial r} = \delta_i(P^R{}_i - P^P{}_i) \quad (7)$$

Mass balance-Permeation zone:

$$\frac{\partial(v^P C_i{}^P)}{\partial z} = a_{memb} * J_{perm,i} \quad (8)$$

Boundary conditions:

$$C_{i,b}{}^P = C_{i,b}{}^{P,IN} \quad (9)$$

Heat balance:

$$\frac{1}{r^2}\frac{\partial}{\partial r}\left(\lambda_{eff} * r^2\frac{\partial T}{\partial r}\right) + \Sigma_{j=1}^{N_r} r''_j(-\Delta H_r) = 0 \quad (10)$$

The study compared the packed bed membrane reactor (PBMR) and the packed bed reactor (PBR) to evaluate their performance under various conditions. The traditional catalytic reactor without a membrane was the packed bed reactor (PBR), while the packed bed membrane reactor (PBMR) incorporated an LTA zeolite membrane for selective water removal, thereby enhancing equilibrium conversion.

2.3. Modeling of reaction kinetics and membrane characteristics

Reactions (11) to (13) were considered to proceed over a CuO-ZnO-Al_2O_3 catalyst, employing the kinetic expressions proposed by Poto et al. [9]. In contrast, reaction (14) was catalyzed by HZSM-5 and followed the kinetic model described by Ortega et al. [6].

$$r_1 = k_1 b_{co}\left(\frac{P_{co}P^{\frac{3}{2}}_{H_2} - \frac{P_{CH_3OH}}{P^{\frac{1}{2}}_{H_2}K_1}}{(1 + b_{co}P_{co} + b_{CO_2}P_{co_2})\left(P^{\frac{1}{2}}_{H_2} + \left(\frac{b_{H_2O}}{b^{\frac{1}{2}}_{H_2}}\right)P_{H_2O}\right)}\right) \quad (11)$$

$$r_2 = k_2 b_{co_2}\left(\frac{P_{co}P_{H_2} - \frac{P_{co}P_{H_2O}}{K_2}}{(1 + b_{co}P_{co} + b_{CO_2}P_{co_2})\left(P^{\frac{1}{2}}_{H_2} + \left(\frac{b_{H_2O}}{b^{\frac{1}{2}}_{H_2}}\right)P_{H_2O}\right)}\right) \quad (12)$$

$$r_3 = k_3 b_{co}\left(\frac{P_{co_2}P^{\frac{3}{2}}_{H_2} - \frac{P_{CH_3OH}P_{H_2O}}{P^{\frac{3}{2}}_{H_2}K_3}}{(1 + b_{co}P_{co} + b_{CO_2}P_{co_2})\left(P^{\frac{1}{2}}_{H_2} + \left(\frac{b_{H_2O}}{b^{\frac{1}{2}}_{H_2}}\right)P_{H_2O}\right)}\right) \quad (13)$$

$$r_4 = k_4\left(\frac{(b_{CH_3OH}P_{CH_3OH})^2(1-\frac{P_{H_2O}P_{DME}}{P_{CH_3OH}{}^2K_4})}{(1+b_{CH_3OH}P_{CH_3OH}+b_{H_2O}P_{H_2O})^2}\right) \quad (14)$$

The carbonate species was initially formed from the reaction between adsorbed CO_2 and surface hydroxyl groups. This intermediate was quickly hydrogenated into format, which further transformed into formaldehyde and methoxy species before ultimately yielding methanol. Within this mechanism, the hydrogenation of format was considered the rate-determining step (RDS) [3, 4]. In this work, the single-site mechanisms were focused. Rates of reactions are given as follows.

Methanol formation:

$$r_{CH_3OH} = \frac{k_1 P_{CO_2}P_{H_2}*(1-\frac{P_{CH_3OH}*P_{H_2O}}{k_1*P_{H_2}{}^3*P_{CO_2}})}{(1+K_a*\sqrt{P_{H_2}}+K_b*P_{H_2O}+K_c*\frac{P_{H_2O}}{P_{H_2}})^3} \quad (15)$$

Water gas shift reaction:

$$r_{rWGS} = \frac{k_2 P_{CO_2}*(1-\frac{P_{CO}*P_{H_2O}}{k_2*P_{H_2}*P_{CO_2}})}{(1+K_a*\sqrt{P_{H_2}}+K_b*P_{H_2O}+K_c*\frac{P_{H_2O}}{P_{H_2}})} \quad (16)$$

Methanol dehydration:

$$r_{DME} = k_3\left(\frac{P_{CH_3OH}{}^2}{P_{H_2O}} - \frac{P_{CH_3OCH_3}}{K_{p,3}}\right) \quad (17)$$

Equilibrium constants:

$$K_1 = \frac{3066}{T} - 10.592 \quad (18)$$

$$K_2 = \frac{-2073}{T} + 2.029 \quad (19)$$

$$K_3 = 8.2894 * 10^4 \exp\left(\frac{-5.2940*10^4}{RT}\right) \quad (20)$$

General rate constant expression:

$$k_i = A_i \exp\left(-\frac{B_i}{R}\left(\frac{1}{T} - \frac{1}{473.15}\right)\right), i = 1, 2 \quad (21)$$

2.4. Geometry design and configuration

3D reactor geometries were designed for both reactors type PBMR and PBR. The geometry was meshed using tetrahedral elements, with finer meshes used near the catalyst bed and membrane interface to capture mass and heat transfer phenomena. The feed reactants at the X-axis are CO_2 and N_2. The feed reactant at Y-axis is H_2. The meshing element size is 4 × 10^{-4} m and the total number of nodes is 108,104. The geometries of packed bed membrane reactor and packed bed reactor are shown in Figs. 1(a) and 1(b), respectively.

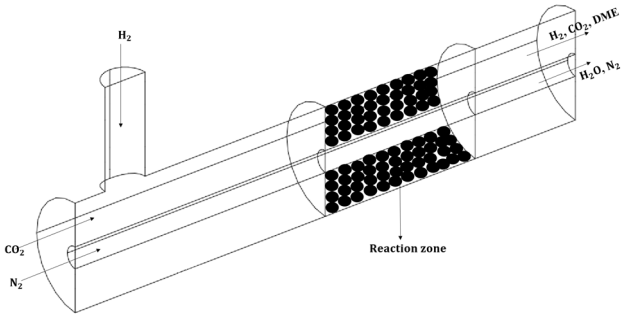

(a) Packed bed membrane reactor

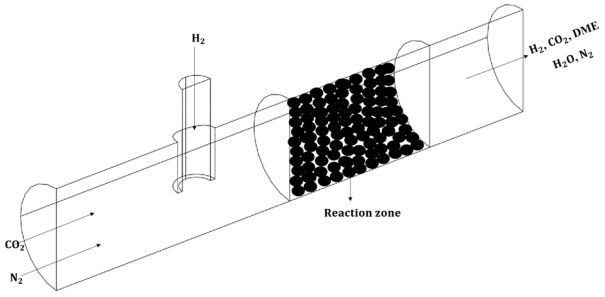

(b) Packed bed reactor

Figure 1 Geometries of packed bed membrane reactor and packed bed reactor

3. RESULTS AND DISCUSSION

The computational fluid dynamics (CFD) simulation of the packed bed membrane reactor (PBMR) was carried out to gain a comprehensive understanding of the flow characteristics, species transport, and reaction behavior under the specified operating conditions. The results obtained from the CFD simulation provided valuable insights into the reactor performance, particularly in terms of velocity distribution, dimethyl ether (DME) production, and flow regime.

3.1. Velocity profile in packed membrane reactor

The velocity profile obtained from the simulation as shown in Fig. 2 revealed a predominantly axial flow behavior as expected in tubular packed bed reactor configurations. The velocity magnitude was high in the axial direction indicating the development of the velocity field as the gas mixture flowed through the reactor. The profile was relatively uniform in the axial direction supporting the assumption of plug-flow behavior. This finding was particularly important as it validated the simplification applied in the model where convection was considered in the axial direction. Additionally, the observed velocity magnitude, approximately 2 m/s aligned well with the calculated value based on the gas hourly space velocity (GHSV) and reactor cross-sectional area. This reinforced the physical realism of the model and supported the accuracy of the velocity input value used in the simulation.

The clear axial flow behavior observed in the velocity distribution implied minimal back-mixing and supported the efficient progression of the reaction along the reactor length. Such characteristics were desirable for achieving high conversion and selectivity in catalytic processes especially when integrated with a membrane for selective species removal.

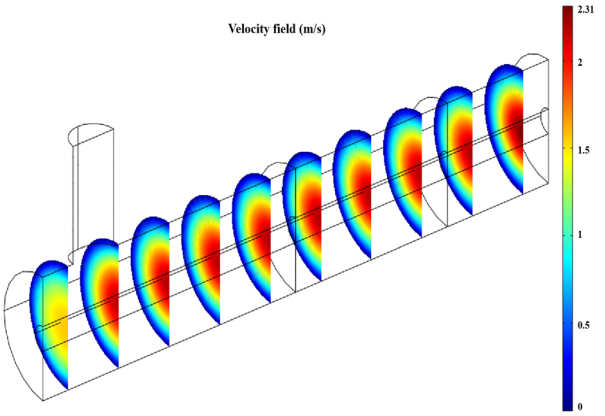

Figure 2 Velocity profile in packed membrane reactor.

3.2 Pressure profile in packed membrane reactor

The pressure distribution within the reactor was simulated and is presented in Fig. 3. The pressure field clearly showed a high-pressure region near the gas inlet, where the maximum pressure reached approximately 1.989×10^5 Pa. This was indicated by the red zone at the top of the inlet pipe. As the gas flowed into the main reactor body, a gradual decrease in pressure along the axial direction was observed, transitioning from yellow and green near the inlet to light blue and finally dark blue toward the outlet.

The pressure gradient demonstrated that the flow experienced a significant pressure drop along the reactor length. This behavior was consistent with expectations for a system under laminar flow conditions within a packed bed or membrane reactor structure. The pressure became almost uniform near the reactor outlet, suggesting that the major pressure loss occurred within the first portion of the reactor.

Moreover, a small region of negative pressure (as indicated by the minimum value of approximately 3131 Pa) was detected. This could have resulted from numerical effects at the boundary conditions, particularly if a backflow or reverse flow was present near the outlet or permeate side. Nevertheless, the overall pressure profile confirmed that the majority of the pressure drop took place in the initial part of the reactor and stabilized as the flow progressed downstream.

This pressure behavior was in good agreement with typical trends observed in packed bed membrane reactors, validating the model assumptions and boundary conditions applied during the simulation.

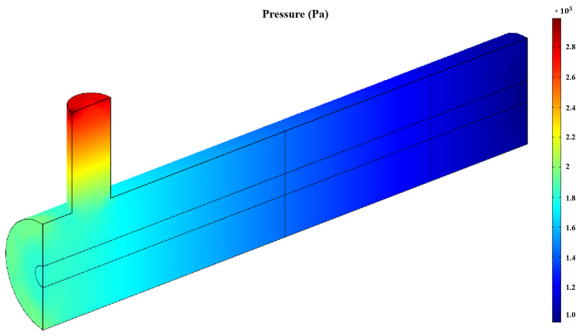

Figure 3 Pressure profile in packed membrane reactor.

3.3. Dimethyl ether concentration

Figure 4 illustrates the simulated concentration distribution of dimethyl ether (DME) (in mol/m³) along the length of the packed bed membrane reactor. The concentration field revealed a clear gradient where DME production progressively increased along the reactor axis. Near the reactor inlet, the DME concentration remained close to zero indicating minimal reaction progress at the early stage of flow. As the reactants (CO_2 and H_2) moved downstream, the DME concentration increased steadily and reached its maximum value of approximately 350 mol/m³ near the reactor outlet. This trend reflected the catalytic activity within the packed bed where the syngas components continuously reacted to form DME as they traveled through the catalyst bed. The concentration distribution also showed a relatively smooth and continuous increase without sharp local fluctuations suggesting efficient mass transport and reaction kinetics. The uniformity of the gradient implied that the reactor operated under favorable reaction and diffusion conditions that promoted the desired DME formation throughout the catalyst zone. These results validated the reactor design and operating conditions chosen for the study, providing insight into the system's potential for effective DME production from carbon dioxide hydrogenation.

The formation pattern was typical for plug-flow behavior in a pseudo-homogeneous reactor, where reactants were continuously consumed and products formed along the flow direction. Overall, the simulation results confirmed that the reactor configuration effectively supported the gradual production of DME, with the highest concentrations achieved near the outlet. The observed trend was in agreement with expected behavior for DME synthesis under steady-state operating conditions.

The progressive increase in DME concentration also reflected the effectiveness of the catalytic system employed which in this case included the bifunctional CuO-ZnO-Al_2O_3/HZSM-5 catalyst. The data suggested that the reactor was well-optimized for the dehydration of methanol under the studied temperature and pressure conditions confirming the feasibility of using PBMR for intensified DME production.

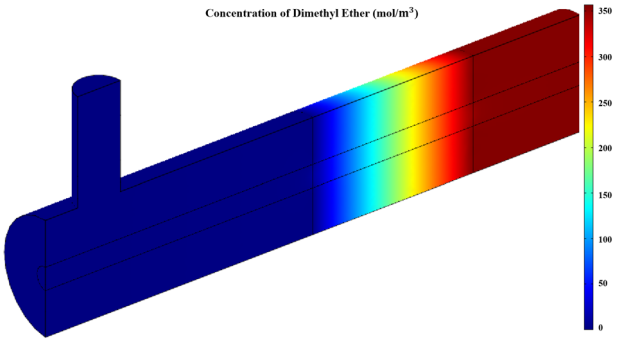

Figure 4 Concentration profile of dimethyl ether in packed bed membrane reactor.

3.4. Comparison with packed bed reactor

The simulation results indicated a significant enhancement in Dimethyl Ether (DME) production within the packed bed membrane reactor compared to the conventional packed bed reactor. In the packed bed membrane reactor as shown in Fig. 4, the DME concentration increased steadily along the reactor length, reaching values as high as 350 mol/m³ near the outlet. This substantial increase in product concentration suggested that the selective removal of water through the membrane facilitated the forward progression of the methanol dehydration equilibrium, thereby promoting DME formation. Conversely, in the packed bed reactor without a membrane as shown in Fig. 5, the maximum DME concentration only reached approximately 342 mol/m³. These findings demonstrated that the integration of a membrane notably improved product yield by enhancing the reaction-driving force and reducing product inhibition effects.

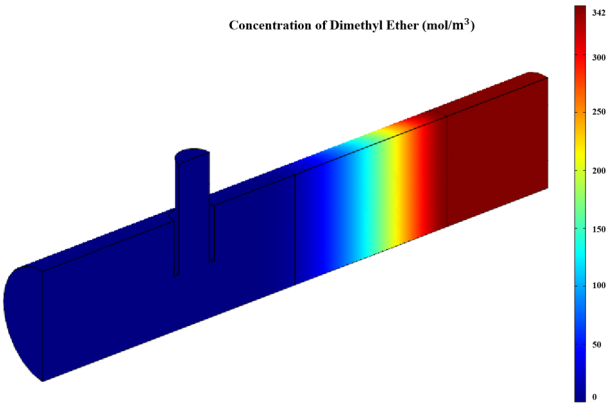

Figure 5 Concentration profile of dimethyl ether in packed bed reactor.

3.5. Integrated interpretation and design implications

The combined analysis of the velocity profile, DME concentration, and pressure profile provided a holistic understanding of the PBMR performance. The results demonstrated that the reactor geometry, flow conditions and catalytic system worked synergistically to support efficient DME synthesis. The use of a membrane added further enhancement by potentially shifting the equilibrium in favor of product formation through selective water removal.

These findings not only validated the simulation setup but also provided a strong foundation for scaling up the reactor design. The ability to predict and visualize species distribution and flow behavior allowed for targeted optimization of parameters such as membrane position, reactor length and catalyst loading. Future work can build upon these insights by exploring the effects of sweep gas composition, membrane selectivity and temperature gradients on reactor performance.

3.6. Limitations and future work

While the results were promising, certain limitations should be acknowledged. The study was conducted under specific operational conditions and further investigations across a broader range of parameters were necessary. Additionally, the long-term stability of the membrane and catalyst performance required further evaluation. Future research could explore advanced membrane materials and reactor designs to optimize DME production.

4. CONCLUSION

In conclusion, the simulation results confirmed that the packed bed membrane reactor configuration under study was highly effective for dimethyl ether production with clear benefits derived from its plug-flow-like hydrodynamics and integrated membrane functionality. These observations contributed significantly to the ongoing research in process intensification and provided valuable design guidelines for the development of next-generation catalytic membrane reactors.

ACKNOWLEDGMENTS

This research project is supported by Mahidol University.

REFERENCES

[1] H. Yuanyuan & Zhang, Y. Weiyong, F. Dingye. Modeling and simulation of production process on dimethyl ether synthesized from coal-based syngas by one-step method. *Chinese Journal of Chemical Engineering* 2009; 17(1): 108–112.

[2] S. Poto, M. A. L. Tanco, D. A. P. Tanaka, M. Fernanda, Neira d′Angelo, F. Gallucci. Experimental investigation of a packed bed membrane reactor for the direct conversion of CO_2 to dimethyl ether. *Journal of CO_2 Utilization* 2023; 72: 102513.

[3] L. Hou-Xing & Y. Liuqingqing & C. Z. & Zhang, Y.L Li, X.G & H. Yulian & R. Reina, T. & X., Wende. CO_2 Hydrogenation to methanol over $Cu/ZnO/Al_2O_3$ catalyst: kinetic modeling based on either single-or dual active site mechanism. *Catalysis Letters* 2022; 152: 10.1007/s10562-021-03913-0.

[4] G.H. Graaf, P.J.J.M. Sijtsema, E.J. Stamhuis, G.E.H. Joosten. Chemical equilibria in methanol synthesis. *Chemical Engineering Science* 1986; 41: 2883–2890.

[5] S. & S. Ghosh, J. Olsson, L. & C. Derek. Experimental and kinetic modeling studies of methanol synthesis from CO_2 hydrogenation using In_2O_3 catalyst. *Chemical Engineering Journal* 2021;416:129120.

[6] C. Ortega, M. Rezaei, V. Hessel, G. Kolb. Methanol to dimethyl ether conversion over a ZSM-5 catalyst: Intrinsic kinetic study on external recycle reactor. *Chemical Engineering Journal* 2018;347:741-53.

[7] S. Poto, H. Bogaard, F. Gallucci, M.F.N. Angelo, F. Gallucci. Evaluation of the relevant mass and heat transfer phenomena in a packed bed membrane reactor for the direct conversion of CO_2 to dimethyl ether. *Fuel, Volume* 350, 128783 2023;350:128783.

[8] S. Poto, F. Gallucci, M.F.N. Angelo. Direct conversion of CO_2 to dimethyl ether in a fixed bed membrane reactor: Influence of membrane properties and process conditions. *Fuel*. 2021;302:121080.

[9] S. Poto, Vink T, Oliver P, F. Gallucci, M.F.N. Angelo. Techno-economic assessment of the one-step CO_2 conversion to dimethyl ether in a membrane-assisted process. *Journal of CO_2 Utilization* 2023;69:102419.

Analysis of carbon dioxide trapping efficiency in saline aquifer by machine learning

Jakkai Jitkoolsamphan[1], Suparit Tangparitkul[2], Teerawat Sema[1,*]

[1] Department of Chemical Technology, Faculty of Science, Chulalongkorn University, Bangkok 10330, Thailand
[2] Department of Mining and Petroleum Engineering, Faculty of Engineering, Chiang Mai University, Chiang Mai 50200, Thailand
[*] Corresponding author: teerawat.se@chula.ac.th

ABSTRACT

With growing climate change concerns, carbon capture and storage (CCS) plays a key role in reducing carbon dioxide (CO_2) emissions. Saline aquifers are a promising option for long-term CO_2 storage [1], where Residual Trapping Index (RTI) and Solubility Trapping Index (STI) indicate storage efficiency [2]. Accurate estimation of RTI and STI is crucial for CCS projects, yet conventional numerical simulations are computationally expensive. This work proposes an Extreme Gradient Boosting (XGBoost) model to predict RTI and STI due to its efficiency and predictive power. The model was trained and validated on a simulation-generated dataset (5,790 data collected from 35 articles) incorporating geological attributes and reservoir characteristics from various saline aquifers. Inputs include physical properties, i.e., permeability, thickness, porosity, depth, and salinity, along with operational conditions (time elapsed and injection rate). Hyperparameter tuning was performed for key parameters, including the number of estimators, regularization terms, maximum tree depth, learning rate, subsample ratio, and minimum child weight. The optimized XGBoost model achieved high predictive accuracy, with R^2 of 0.9961 and RMSE of 0.0077 on the test set. SHapley Additive exPlanations (SHAP) analysis reveals that injection rate, porosity, and thickness are the most influential factors on storage efficiency. RTI is primarily affected by injection rate, porosity, and depth, while STI is influenced by time elapsed and thickness. This method provides a reliable tool for assessing CCS feasibility, supporting carbon reduction efforts, and paving the way for more efficient, data-driven climate solutions.

Keywords: CO_2 storage; Saline aquifer; Machine Learning; Extreme gradient boosting

1. INTRODUCTION

The impact of climate change on global ecosystems has become an urgent issue, necessitating swift actions to mitigate greenhouse gas emissions, particularly carbon dioxide (CO_2). Among various strategies being explored to address this global challenge, Carbon Capture and Storage (CCS) has garnered significant attention as a key solution. CCS involves capturing CO_2 from large point sources such as power plants and industrial processes, and storing it in deep geological formations to prevent its release into the atmosphere. This method is considered essential for achieving long-term climate stabilization targets, particularly for industries that are difficult to decarbonize.

Saline aquifers, a type of deep underground reservoir, have emerged as a promising option for CO_2 storage due to their widespread distribution and significant storage potential. These aquifers are typically located deep beneath the Earth's surface and consist of porous rock formations saturated with saline water, providing a natural storage medium for CO_2. The effectiveness of CO_2 storage in saline aquifers depends on various trapping mechanisms, including structural, residual, solubility, and mineral trapping [1]. Among these, the Residual Trapping Index (RTI) and Solubility Trapping Index (STI) are particularly useful for assessing CO_2 storage efficiency and long-term stability [2].

However, traditional methods for estimating RTI and STI, which rely on computationally expensive numerical simulations, often face challenges in terms of time, cost, and computational resources. These methods require detailed geological data and are sensitive to site-specific variability. Therefore, alternative approaches that offer faster, more efficient predictions are needed to enhance the feasibility of large-scale CCS deployment.

There are many applications of machine learning (ML) in CCS projects [3], particularly for improving the efficiency of CO_2 storage estimation. Recent studies have applied ML to predict RTI and STI for more efficient CO_2 storage estimation. However, these models often lack interpretability. The present study

addresses this gap by using SHapley Additive exPlanations (SHAP) to predict CO_2 trapping efficiency and reveal how each parameter impacts RTI and STI. By applying SHAP, this research provides a clearer understanding of the relationships between geological and operational factors in CO_2 storage.

Using Extreme Gradient Boosting (XGBoost), the model is trained on 5,790 data points from saline aquifer simulations, incorporating features like permeability, porosity, depth, and injection rate. The aim is to create a predictive model that not only estimates CO_2 storage efficiency but also explains the factors driving these predictions, enhancing decision-making in CCS planning.

2. METHOD

2.1. Data Collection

A comprehensive dataset of 5,790 data points was curated from 35 published studies [4] and simulation results focused on CO_2 storage in saline aquifers. The dataset includes key geological and operational parameters that influence CO_2 trapping efficiency, specifically permeability, thickness, porosity, depth, and salinity, as well as operational factors such as injection rate and time elapsed. The range (min-max) for each parameter is provided in Table 1. Data preprocessing involved cleaning, normalization, and outlier removal to ensure consistency and suitability for machine learning model training.

Table 1 Ranges of the inputs and outputs for ML model.

		Min	Max
Output	RTI	0.01653	0.90163
	STI	0.06871	0.89298
Input	Injection rate (ton/day)	0.000	54,794.521
	Time elapsed (year)	10	1,977
	Permeability (mD)	5.62	1,013.25
	Thickness (m)	0.5	360.0
	Porosity	0.093	0.300
	Salinity (ppm)	0	100,000
	Depth (m)	704.69	2,612.00

RTI refers to a ratio of CO_2 volume trapped by residual mechanisms compared to the total injected CO_2 volume. It reflects how well CO_2 is retained in the reservoir due to capillary forces, with a higher RTI indicating more efficient residual trapping. STI is considered as a fraction of CO_2 that dissolves into the brine over time, indicating the efficiency of solubility trapping. A higher STI reflects better CO_2 dissolution and retention in the saline aquifer. RTI and STI can be calculated using the following formulas:

$$RTI = \frac{Total\ mass\ of\ CO_2\ trapped\ as\ residual\ (kg)}{Total\ mass\ of\ CO_2\ injected\ (kg)}$$

$$STI = \frac{Total\ mass\ of\ CO_2\ dissolved\ in\ brine\ (kg)}{Total\ mass\ of\ CO_2\ injected\ (kg)}$$

2.2. Machine Learning Model

XGBoost is a powerful and efficient machine learning algorithm widely used for supervised learning tasks such as regression and classification. It is based on the gradient boosting framework, which builds an ensemble of decision trees, where each new tree corrects the errors made by the previous trees. XGBoost is highly effective for large datasets and high-dimensional data because of its ability to handle missing values, its regularization capabilities, and its optimization for both speed and accuracy.

XGBoost works by sequentially adding decision trees that predict the residual errors of the ensemble, focusing on hard-to-predict instances. This approach reduces bias and variance, improving the model's accuracy. Additionally, XGBoost implements regularization (L1 and L2) to prevent overfitting, making it highly suitable for real-world applications where model generalization is crucial.

2.3. Hyperparameter Tuning

To optimize the performance of the XGBoost model, a hyperparameter tuning process was conducted using grid search and cross-validation. Key hyperparameters, including n_estimators, learning rate, max_depth, subsample, min_child_weight, reg_alpha, and reg_lambda, were systematically adjusted to identify the optimal settings for maximizing model accuracy while preventing overfitting. Preventing overfitting is crucial to ensure that the model generalizes well to new, unseen data, rather than fitting too closely to the training data and capturing noise or irrelevant patterns. This process ensured that the model produced reliable and generalizable predictions for RTI and STI. The ranges of the hyperparameters and their optimized values, as given in Table 2, were selected to balance the model's complexity and performance.

n_estimators (Number of Trees): The total number of decision trees in the model. More trees typically improve accuracy, but excessive trees can lead to overfitting.

learning_rate (Step size): Controls the contribution of each tree. A smaller rate requires more trees, balancing accuracy and overfitting.

max_depth (Tree Depth): Limits the depth of each tree. Deeper trees capture more complexity but may overfit, while shallow trees reduce overfitting but may underfit.

subsample (Subsample ratio): Defines the fraction of training data used for each tree. Values less than 1.0 reduce overfitting by adding randomness.

min_child_weight (Minimum child weight): Specifies the minimum weight in a child node. Larger values help prevent the model from overfitting by making it more conservative.

reg_alpha (L1 regularization): Controls L1 regularization (sparsity) to prevent overfitting by penalizing large weights.

reg_lambda (L2 regularization): Applies L2 regularization to penalize large weights, helping reduce overfitting.

Table 2 Control parameters for tuning ML model.

Hyperparameter	Tuned Range	Optimal Value
n_estimators	100 - 5,000	2,160
learning_rate	0.001 - 1	0.1
max_depth	3 - 7	5
subsample	0.5 - 1.0	0.8
min_child_weight	1 - 10	1
reg_alpha	0.001 - 1	0.01
reg_lambda	0.01 - 200	140

2.4. Model Interpretation

Following the model training, SHAP was applied to interpret the contributions of individual features to the model's predictions. SHAP values provide a transparent means of understanding how each input parameter affects the model's output, quantifying the influence of each feature on the predicted CO_2 trapping efficiency. This interpretability tool was crucial for identifying the most significant parameters, such as injection rate, porosity, and depth, and understanding their respective roles in determining RTI and STI. The use of SHAP not only enhances model transparency but also supports deeper insights into the mechanisms driving CO_2 storage in saline aquifers.

3. RESULTS AND DISCUSSION

3.1. Model Performance

The XGBoost model demonstrated excellent performance in predicting CO_2 trapping efficiency, achieving R^2 values of 0.9993 and RMSE of 0.0042 for RTI, and R^2 of 0.9991 and RMSE of 0.0024 for STI on the training dataset. These results indicate that the model can accurately predict RTI and STI, confirming its potential as a reliable tool for CO_2 storage prediction. For the test dataset, the model achieved R^2 = 0.9961 and RMSE = 0.0077 for RTI, and R^2 = 0.9973 and RMSE = 0.0046 for STI, demonstrating good generalization. In comparison to previous studies, our model's performance is on par with other XGBoost-based models. For example, a recent study using XGBoost reported RTI with R^2 = 0.9981 and RMSE = 0.010, and STI with R^2 = 0.9993 and RMSE = 0.0113, which is comparable to the performance observed in this study [4]. Additionally, in comparison with an Artificial Neural Network (ANN) model from another study, which reported RTI R^2 = 0.9933 and RMSE = 0.0197, and STI R^2 = 0.9442 and RMSE = 0.0082 [2], the XGBoost model in this study shows similarly high performance and robustness in predicting both RTI and STI.

These results demonstrate that the XGBoost model used in this study is competitive with other machine learning approaches for predicting CO_2 trapping efficiency, offering reliable predictions while maintaining efficiency in training and testing.

3.2. SHAP Analysis: Feature Importance and Interpretation

SHAP analysis provides valuable insights into the contributions of different parameters to the model's predictions of RTI and STI. By evaluating the mean absolute SHAP values, we identified the parameters that most strongly influence CO_2 storage efficiency. Figure 1 presents the mean SHAP value plot, which shows the relative importance of each feature in predicting CO_2 trapping efficiency. Parameters with longer bars have a greater impact on the model's predictions. The most influential parameters, in order, are injection rate, porosity, thickness, depth, time elapsed, salinity, and permeability. Among these, the top five parameters (injection rate, porosity, thickness, depth, and time elapsed) contribute to over 80% of the model's prediction impact for both RTI and STI, as shown in the plot. Since they are critical for understanding CO_2 trapping efficiency, their impacts on RTI and STI, respectively, should be further individually analyzed.

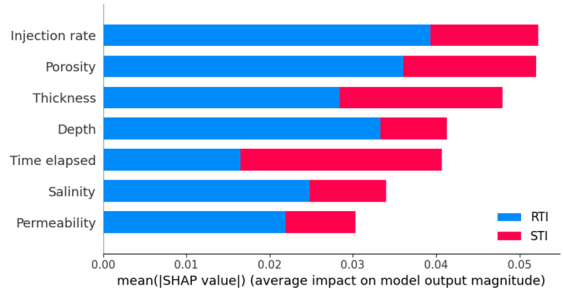

Figure 1 Mean SHAP Values for RTI and STI.

3.2.1. Feature Importance on RTI

To interpret the importances of the prior mentioned top five features on RTI, SHAP beeswarm plot for RTI (Figure 2) was applied. This plot illustrates the distribution and influence of each parameter on the interested feature, which is RTI in this case.

As presented in Figure 2, injection rate is the most influential factor for RTI. A higher injection rate increases the capillary pressure within the aquifer, improving residual CO_2 trapping. This pressure forces CO_2 into smaller pore spaces, preventing its migration and resulting in higher RTI values, indicating more efficient CO_2 storage.

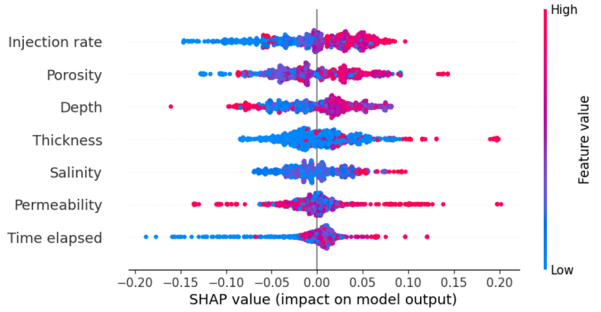

Figure 2 Beeswarm plot for RTI.

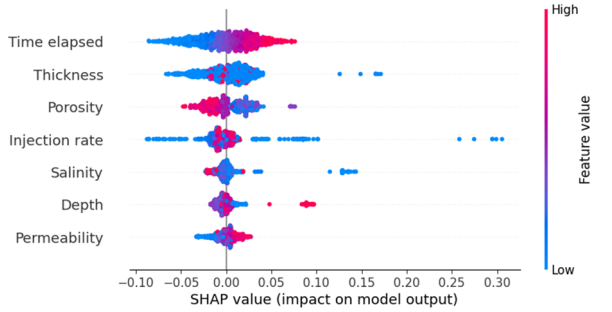

Figure 3 Beeswarm plot for STI.

Porosity also has a significant positive impact on RTI. Lower porosity leads to higher pressure buildup, which promotes the transition of CO_2 from residual trapping to solubility trapping, enhancing CO_2 retention and improving residual trapping. The beeswarm plot for porosity (Figure 2) illustrates this trend, showing a clear positive correlation between porosity and RTI.

Thickness influences RTI by providing more vertical space for CO_2 to travel. CO_2 rises due to buoyancy forces, and as it moves toward the top of thicker aquifers, it becomes trapped along the way, enhancing residual trapping. The beeswarm plot for RTI shows that thicker aquifers tend to have higher RTI values.

Depth impacts RTI due to temperature effects. As depth increases, the temperature also increases, making it harder for CO_2 to dissolve into the brine. This limits the transition from residual trapping to solubility trapping, thereby improving residual trapping efficiency and leading to higher RTI values.

Time elapsed has a small but still notable impact on RTI. Over time, structural trapping gradually shifts to residual trapping, and residual trapping itself can transition to solubility trapping as CO_2 dissolves into the brine. These changes enhance CO_2 retention, slightly improving RTI as time progresses.

3.2.2. Feature Importance on STI

Even though the features of interest (i.e., injection rate, porosity, thickness, depth, and time elapsed) are not the top five features affecting the STI (see Figures 1 and 3), this work considers analyzing their importances on the STI through the beeswarm plot. This is because they highly affect the storage efficiency of both RTI and STI.

The SHAP beeswarm plot for STI (Figure 3) illustrates how these factors influence solubility trapping efficiency. Injection rate influences STI, but the impact is relatively small. The beeswarm plot for injection rate shows that most data points are concentrated around the center, indicating that changes in injection rate result in only slight variations in STI values. While injection rate does influence solubility trapping, its effect on STI is less significant compared to other key parameters.

Porosity influences STI, with low porosity generally leading to higher STI. Lower porosity results in higher pressure within the aquifer, which enhances CO_2 dissolution into the brine, facilitating the shift from residual trapping to solubility trapping. The beeswarm plot for porosity shows that low porosity aquifers tend to have higher solubility trapping efficiency, leading to higher STI values.

Thickness is a key parameter for STI. While the SHAP beeswarm plot for STI (Figure 3) indicates some variability in the impact of thickness, the data does not provide a clear, consistent pattern to fully understand how it influences solubility trapping. Although thicker aquifers are generally expected to provide more space for CO_2 to dissolve into the brine, the spread of SHAP values across the thickness range in the plot suggests that the relationship between thickness and STI requires further investigation. Additional data or further analysis could help clarify the exact role thickness plays in solubility trapping efficiency.

Depth has a relatively minor impact on STI, but temperature increases with depth, making it more difficult for CO_2 to dissolve into the brine. This higher temperature limits the transition from residual trapping to solubility trapping, reducing the efficiency of solubility trapping at greater depths.

Time elapsed has a significant impact on STI. As time progresses, all CO_2 trapping mechanisms gradually shift toward solubility trapping. Over time, CO_2 starts to dissolve into the brine, enhancing solubility trapping. This transition increases the efficiency of CO_2 storage, leading to higher STI values as the duration of storage increases. Longer time elapsed promotes greater solubility trapping, improving overall CO_2 storage efficiency [5].

3.3. Implications for CO_2 Storage in Saline Aquifers

The model's high accuracy and interpretability provide several key advantages for CO_2 storage assessments. First, it offers a faster and more resource-efficient alternative to traditional simulation methods, making it a valuable tool for initial site evaluations and large-scale assessments. Second, the SHAP analysis allows for a deeper understanding of the factors driving CO_2 storage efficiency, enabling better decision-making in selecting and optimizing storage sites. By

identifying the most influential geological and operational parameters, the model can help prioritize the characteristics that need to be optimized to maximize CO_2 trapping efficiency.

3.4. Limitations and Future Work

Although the current model performs well, there are some limitations. The model relies on historical simulation data, which may not capture all potential site-specific factors affecting CO_2 storage. Additionally, the study primarily focuses on RTI and STI, but further research could extend the model to predict other trapping mechanisms, such as mineral trapping, and incorporate real-world experimental data for further validation.

A key limitation of this model is that it can only predict CO_2 trapping efficiency within the range of the data it was trained on. Extrapolating predictions beyond this range could lead to unreliable results, as the model has not been tested on data outside the parameter space it was trained on.

However, it is important to note that while the model provides valuable insights, it is limited by the scope of the dataset, which may not cover all possible variations in saline aquifer characteristics. Future work could involve expanding the dataset to include more diverse geological formations and operational conditions, as well as incorporating dynamic parameters such as CO_2 plume migration and post-injection effects. Additionally, integrating more complex features like pressure and temperature variations over time could simulate a more dynamic CO_2 storage process. The application of transfer learning techniques could also allow the model to generalize to new, unseen sites with limited data, further enhancing its practical applicability.

4. CONCLUSION

This study presents a machine learning-based approach for predicting CO_2 storage efficiency in saline aquifers using XGBoost. The model was trained on a comprehensive dataset of 5,790 data points and demonstrated excellent performance, with $R^2 = 0.9961$ and RMSE = 0.0077. These results highlight the potential of XGBoost as a reliable and efficient tool for predicting the RTI and STI, outperforming traditional simulation methods that are often computationally expensive and time-consuming.

Additionally, SHAP were applied to interpret the model's predictions, offering valuable insights into how geological and operational parameters, such as injection rate, porosity, thickness, depth, and time elapsed, influence CO_2 trapping efficiency. SHAP analysis revealed the interactions between these parameters and their roles in determining CO_2 storage capacity, providing a deeper understanding of the mechanisms involved in CO_2 sequestration.

The model's high accuracy and interpretability make it a powerful tool for initial site evaluations and large-scale CCS deployment. By identifying the most impactful parameters, the model can assist in optimizing CO_2 storage site selection and contribute to more effective and efficient CO_2 storage strategies. However, the model is limited by the scope of the dataset, which may not encompass all possible variations in saline aquifer characteristics. Future work could involve expanding the dataset to include more diverse geological formations, integrating dynamic features like pressure and temperature variations, and validating the model with real-world experimental data. Additionally, the application of transfer learning could allow the model to generalize to new, unseen sites, further enhancing its practical applicability for real-world CCS operations.

This study's contributions to the field of CO_2 storage and machine learning provide valuable insights into future research and practical applications in CCS, advancing efforts to mitigate climate change through efficient CO_2 sequestration strategies.

ACKNOWLEDGMENTS

The authors would like to express my sincere gratitude to Prof. Dr. Benjapon Chalermsinsuwan for providing invaluable assistance throughout this study. His support in offering access to the on-cloud Jupyter notebook for machine learning model development was crucial in enabling the successful implementation of the XGBoost model. The acknowledgment also extends to Dr. Phuwadej Pornaroontham for his advice on coding and the implementation of SHAP analysis.

Additionally, the first author would like to thank the Department of Chemical Technology, Faculty of Science, Chulalongkorn University for their financial support, which made this research possible.

REFERENCES

1. A. Luo, Y. Li, X. Chen, Z. Zhu, Y. Peng. Review of CO_2 sequestration mechanism in saline aquifers. *Natural Gas Industry B* 2022; 9(4): 383–93.
2. Y. Song, W. Sung, Y. Jang, W. Jung. Application of an artificial neural network in predicting the effectiveness of trapping mechanisms on CO_2 sequestration in saline aquifers. *International Journal of Greenhouse Gas Control* 2020; 98: 103042.
3. P. Yao, Z. Yu, Y. Zhang, T. Xu. Application of machine learning in carbon capture and storage: An in-depth insight from the perspective of geoscience. *Fuel* 2023; 333: 126296.
4. H. Vo Thanh, Q. Yasin, W.J. Al-Mudhafar, K.K. Lee. Knowledge-based machine learning techniques for accurate prediction of CO_2 storage performance in underground saline aquifers. *Applied Energy* 2022; 314: 118985.
5. A. Khanal, Md. Irfan Khan, Md. Fahim Shahriar. Comprehensive parametric study of CO_2 sequestration in deep saline aquifers. *Chemical Engineering Science* 2024; 287: 119734.

Graph neural network for descriptor-free CO_2 solubility prediction in aqueous amines

Apri Wahyudi[1], Natthapong Sueviriyapan[1,*], Uthaiporn Suriyapraphadilok[1,2]

[1] The Petroleum and Petrochemical College, Chulalongkorn University, Bangkok 10330, Thailand
[2] Centre of Excellence on Petrochemical and Materials Technology, Bangkok 10330, Thailand
[*] Corresponding author: natthapong.su@chula.ac.th

ABSTRACT

The development of an effective carbon capture unit via chemical absorption depends on the knowledge of CO_2 solubility in amine solutions. Conventional modeling methods lack flexibility in solvent representation by relying on predetermined molecular descriptors, such as the COSMO σ-profile, which requires computationally expensive quantum chemistry calculations. This study presents a graph neural network (GNN) for learning molecular representations directly from SMILES notations, thereby removing the reliance on predefined descriptors. Our approach offers flexible and reliable solubility prediction for 61 species of single amine systems over wide ranges of concentrations, temperatures, and CO_2 partial pressures, achieving equivalent accuracy for the training and validation sets compared to descriptor-based approaches ($R^2 > 0.97$, RMSE < 0.07 mol CO_2/mol amine). Under industrially relevant conditions, the model effectively predicted the CO_2 solubility for different amines, including well-known amines such as Monoethanolamine (MEA), Piperazine (PZ), and 2-(ethylamino)ethanol (EMEA). Our proposed method allows for the rapid screening of new amine structures without relying on feature engineering. This enables inverse molecular design, that is, identifying ideal amine structures for certain operating conditions, potentially accelerating the development of better solvents. This study demonstrates how graph-based machine learning can overcome the constraints of conventional descriptor-based models, thereby offering a more flexible approach to rational solvent design for carbon-capture applications.

Keywords: Amine; Carbon capture; Graph neural network; Machine learning; Solubility

1. INTRODUCTION

Amine-based chemical absorption is a widely adopted method for CO_2 capture owing to its high selectivity, efficiency, and scalability. It remains a leading industrial choice for capturing CO_2 from gas streams due to its proven effectiveness [1]. However, the selection of the most suitable amine solvent is highly dependent on understanding the solubility of CO_2 in amine solutions at varying concentrations, temperatures, and partial pressures. The ability to accurately and quickly predict CO_2 solubility can significantly reduce the experimental overhead involved in screening potential solvents and help identify optimal conditions for carbon capture processes, which is critical for improving the economic feasibility and environmental impact of carbon-capture technologies.

The accurate prediction of the CO_2 equilibrium solubility in amine solutions remains a complex task because of the intricate interactions that can occur within the reactive amine–H_2O–CO_2 system. These interactions are influenced by the operating conditions and the specific amines used. Traditional approaches, which often rely on empirical correlations or thermodynamic models, struggle to generalize across different amines and operating conditions, thus limiting their scalability [2].

In recent years, machine learning techniques have been employed to predict the CO_2 equilibrium solubility in amine solutions. A previous study applied XGBoost to predict CO_2 solubility using fingerprint-based descriptors [3]. Similarly, another study employed Artificial Neural Networks (ANNs) with quantum chemistry-derived descriptors to model CO_2 solubility in amine solutions [4]. Although these methods have shown promise based on their performance metrics, their reliance on predefined descriptors can result in rigid models.

Graph Neural Networks (GNNs) have emerged as a promising approach for modelling complex molecular systems, as reported in a previous study on the prediction of CO_2 solubility in Deep Eutectic Solvents (DES) [5]. Unlike traditional methods, which rely on predefined descriptors, GNNs leverage the underlying graph structure of molecules, allowing for the dynamic learning of molecular representations. This flexibility

enables GNNs to capture intricate atomic and bonding relationships, which can be critical for accurately predicting molecular properties, such as CO_2 solubility. The primary advantage of GNNs over previous frameworks is their ability to learn directly from molecular graphs, bypassing the need for predefined features or domain-specific assumptions.

The objective of this study was to explore GNN-based applications using Graph Convolutional Networks (GCNs) to predict the CO_2 equilibrium solubility in amine solutions. By utilizing a graph-based approach, we aim to enhance the prediction accuracy, reduce the computational complexity, and eliminate the reliance on fixed descriptors, thereby providing a more accurate, flexible, and scalable model.

2. COMPUTATIONAL DETAILS

2.1. Molecular graph representation

A graph is a data structure that represents pairwise relationships between objects using nodes and edges [6]. These nodes and edges are an exact analogy of the molecules, where they correspond to atoms and bonds, respectively. Each node can be represented by a vector of features; similarly, edges can also have their own feature vectors. This representation allows the graph to encode both topological and geometrical information regarding molecules [7]. Topological information refers to the connectivity between atoms, that is, the bonding between atoms. In contrast, geometrical information concerns the spatial arrangement of atoms, including bond lengths, bond angles, and bond torsions. Figure 1 illustrates this concept using ethylamine as an example of a typical amine. The node feature matrix (**X**) encodes atomic-level properties, with each column representing a specific feature (Table 1) and each row corresponding to an atom in the molecule. The edge connectivity matrix (**id**) defines which atoms are bonded by referencing their respective indices, whereas the bond feature matrix (**e**) encodes additional information regarding the properties of the connections.

Table 1 Defined features for the molecular graph.

Feature	Level	Description
Atomic number	Node	Element identifier
Ring membership	Node	Identifier for atom in ring
Degree	Node	Number of direct neighbors
H-neighbors	Node	# of bonded hydrogen atoms
C-neighbors	Node	# of bonded carbon atoms
1° nitrogen	Node	Primary nitrogen identifier
2° nitrogen	Node	Secondary nitrogen identifier
3° nitrogen	Node	Tertiary nitrogen identifier
Connectivity	Edge	Bonds representation

In this study, we focused solely on utilizing topological information from graph representations. Although this choice may limit the potential for a more accurate model that could have been achieved by including geometrical details, it can still provide valuable insights into the molecular behavior. The decision to prioritize topological information allowed us to simplify the model and reduce the computational complexity without compromising the essential structural features. The graphs generated in this study are in the format shown in Table 1 and were generated using open-source libraries such as RDKit and Torch Geometric.

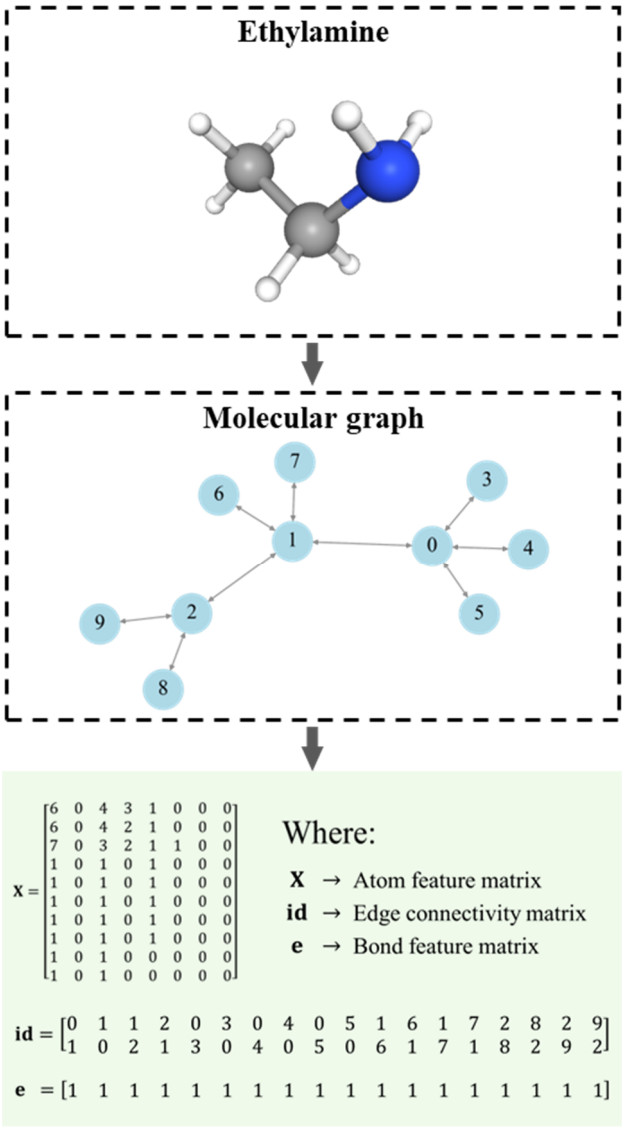

Figure 1. Graph-structured data of ethylamine.

2.2. Graph neural networks

GNNs are a class of neural network architectures specifically designed for processing graph-structured data. Unlike traditional neural networks that operate with grid-like structures, such as images or sequences, GNNs can capture pairwise relationships between nodes through their edges, making them ideal for tasks involving interrelated data. A GNN learns to map each node feature into a high-dimensional vector that encodes both the local and global information of the graph. The learning process involves iteratively passing messages between neighboring nodes in a graph, where each node aggregates information from its neighbors and updates its feature vector [8]. This allows the

network to learn the complex relational dependencies between atoms based on their connectivity.

Here, we applied GCNs to molecular graphs to obtain the learned feature vectors and used them with the operating condition vectors in fully connected layers to predict the equilibrium solubility. GCN was chosen for its computational efficiency and ability to aggregate full-neighborhood information, which effectively captures the molecular structures. Unlike Graph Attention Networks (GATs), GCN avoids a computationally costly attention mechanism. Compared with GraphSAGE, GCN ensures that all atomic interactions contribute to feature updates [9]. Initial experiments confirmed the strong predictive performance of the GCN with lower training complexity. Unlike traditional methods that rely on fixed descriptors, such as fingerprint-based or quantum chemistry descriptors, which are independent of the model training process, graph-based approaches allow for more flexible learning and generalization. The GCN enables the upstream part of the pipeline to participate in the gradient descent process, as the gradients computed during backpropagation flow through the fully connected and GCN layers. This allows the GCN to learn task-specific feature representations directly from molecular graphs and optimize them for downstream prediction tasks [9]. An illustration of the proposed model pipeline is shown in Figure 2.

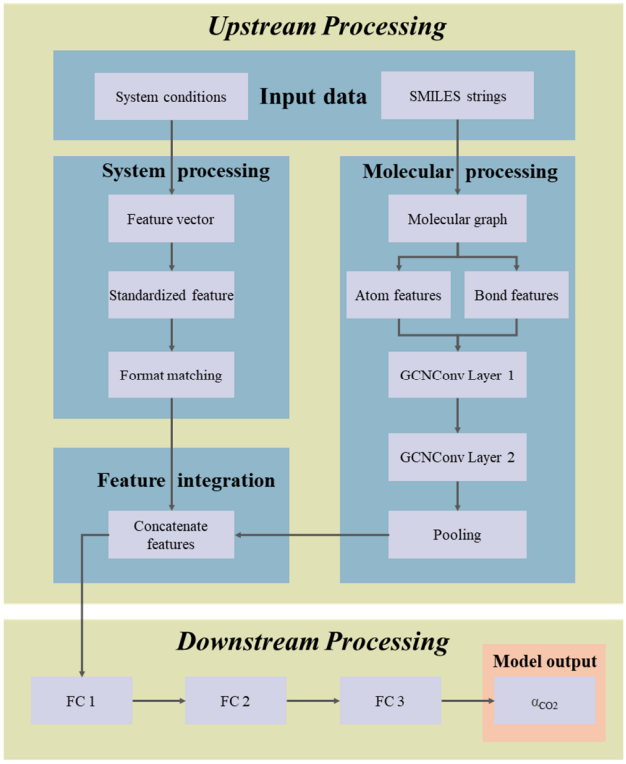

Figure 2 Model pipeline proposed in this study.

2.3. Dataset and data processing

The dataset was compiled from the literature and included SMILES representations of amines, along with their concentrations, temperature, CO_2 partial pressure, and equilibrium loadings. It includes various amines, including primary, secondary, tertiary, and polyamines. The concentration ranges from 0.2 to 8.0 M, temperature from 293.15 to 313.15 K, and CO_2 partial pressure from 1.6×10^{-3} to 6135 kPa. This dataset is based on a previous study [4], but with heavy outliers and noise removed, reducing the total number of data points from 3096 to 3003. In the final version, 2912 data points from 57 amines were used for training (80%) and validation (20%), and 91 data points from four amines were set aside for testing purposes. The concentration, temperature, and partial pressure of the validation and test sets were standardized with respect to the standard deviation and mean values of the training set. To ensure a fair evaluation, the test set contained only amines that were not included in the training or validation sets. The distribution of data points in the final dataset is shown in Figure 3.

Since class imbalance was apparent, we ensured that the underrepresented amines were included in the training set and that the overrepresented amines were distributed between the training and validation sets. The median of the dataset was 35 occurrences of diglycolamine (DGA). To address class imbalance, we defined two classes based on the occurrence frequency, namely, high and low occurrence with respect to the median. We ensured that low-occurrence data were always in the training set, whereas high-occurrence data were distributed on both the training and validation sets.

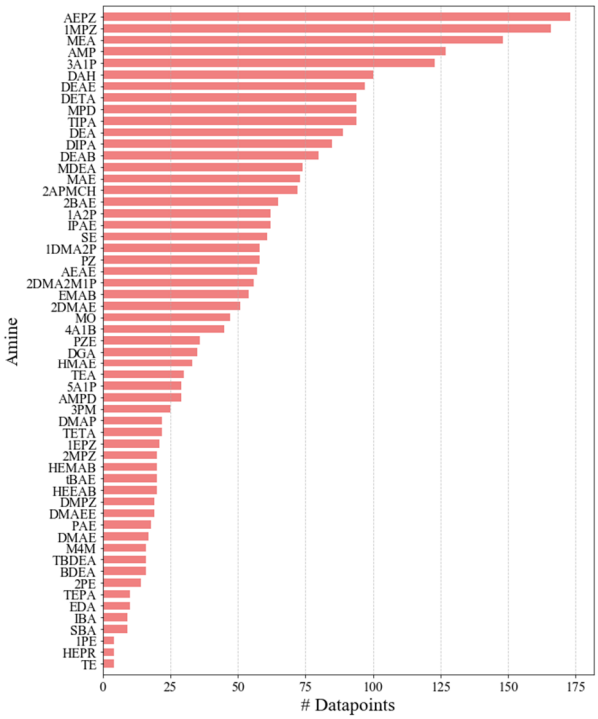

Figure 3 Number of data points across different amines.

2.4. Model architecture and training

The model architecture is summarized in Table 2 and consists of two GCN layers followed by three fully connected (FC) layers. In the "shape" column, N and B represent the number of nodes in one graph and batch size, respectively. After processing the molecular graph through the GCN layers, a global pooling operation aggregates the node features into a graph-level representation. This representation was then concatenated with additional features, such as amine concentration, temperature, and CO_2 partial pressure, and was passed through fully connected layers. The Swish activation function was used across all neurons in all hidden layers because of its higher resistance to the dying neuron problem, as demonstrated in a previous study [4], whereas the ReLU activation function was employed in the last prediction layer to prevent the model from providing physical impossibility (negative solubility).

Table 2 Overview of the model architecture

Layer	Shape	Activation
Molecular layer	(N,8)	-
GCNConv1	(N,8)→(N,64)	Swish
GCNConv2	(N,64)→(N,64)	Swish
Global Mean Pooling	(N,64)→(B,64)	-
Condition layer	(B,3)	-
Concatenation	(B,3)+(B,64)→(B,67)	-
FC 1	(B,67)→(B,64)	Swish
FC 2	(B,64)→(B,32)	Swish
FC 3	(B,32)→(B,1)	ReLU

The model was trained using the hyperparameter settings listed in Table 3. We employed an early stopping mechanism in the training process by monitoring the validation loss; if the validation loss stagnated, the training ended prematurely to prevent massive overfitting in the model. In the current stage of our study, we did not attempt to fine-tune the model systematically using a grid hyperparameter or Bayesian search.

Table 3 Hyperparameter settings.

Hyperparameters	Value or Type
Loss function	Mean Squared Error Loss
Optimizer	Adam optimizer
Learning rate	1 x 10^{-4}
Batch size	32
Max epochs	10000
Patience	100

3. RESULTS AND DISCUSSION

The performance of the proposed model was evaluated using key metrics, such as the root mean squared error (RMSE) and r-score (R^2), as shown in Figure 4. The parity plot illustrates the consistency between the predicted and actual CO_2 solubility values, indicating the model's capability to capture the underlying trends in the data points. These values demonstrate the robustness and generalizability of the model. The performance on the test set was consistent with those of the training and validation sets, confirming that the model did not suffer from overfitting.

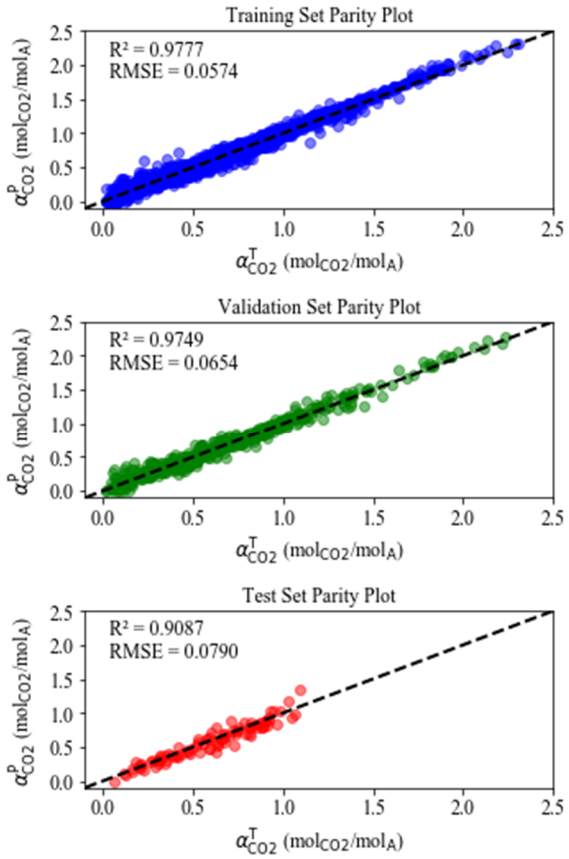

Figure 4 Parity plot of the training, validation, and test results.

An interesting observation in the training instance is that the early stopping mechanism implemented during training was not triggered, resulting in the model being trained for a maximum of 10,000 epochs. This suggests consistent improvements in the validation metrics every 100 epochs, as evidenced by the minimal difference between the training and validation performances in the parity plot (Figure 4). This behavior can likely be attributed to the relatively low learning rate (1×10^{-4}) and high patience threshold (100 epochs), which together might promote slow convergence at the expense of computational efficiency. Although this training scheme appears superficially promising—implying that extending the maximum epochs could suffice while relying on early stopping—it risks suboptimal resource utilization. Prolonged training demands significant computational resources without guaranteeing proportional performance gains. A more systematic approach, such as hyperparameter tuning (e.g., optimizing the learning rate, adjusting patience, dropout layer, regularization, or increasing the batch size), would better balance the convergence speed, model performance, and resource efficiency.

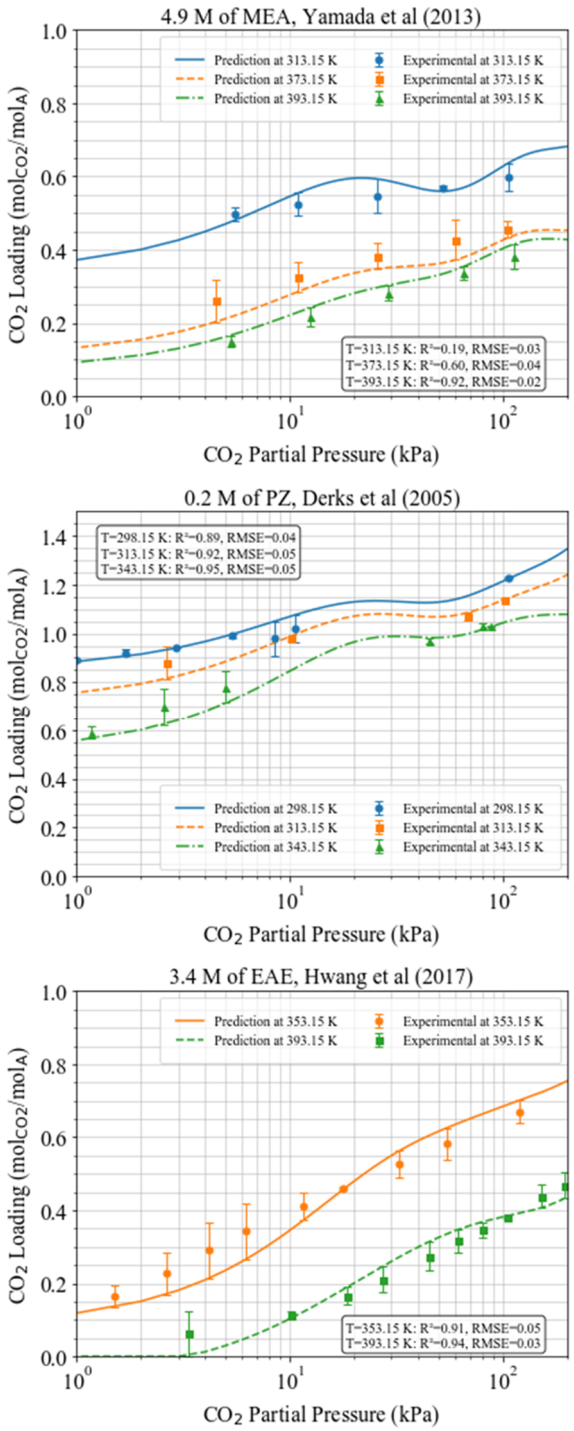

Figure 5 Equilibrium plot of P_{CO2} vs α_{CO2} a). Monoethanolamine [10] (MEA), b). Piperazine [11] (PZ), c). 2-(ethylamino)ethanol (EAE) [12]

To illustrate the applicability of the model, we generated an equilibrium plot of P_{CO2} vs. α_{CO2} for some sampled amines in the training set (MEA and PZ) and one amine from the testing set (EMEA) and compared it with the experimental values (Figure 5). It can be inferred that the model learns well, considering the shape of the equilibrium plot, which is similar to the trend in the knowledge domain. Most importantly, in amine-based carbon capture, this curve can be used to calculate the cyclic capacity, another important parameter that is directly related to process efficiency. Cyclic capacity is defined as the difference between two equilibrium solubilities at two temperatures, and usually corresponds to the absorber and stripper operating conditions.

Despite the apparent usefulness of the model, the decision not to fine-tune it resulted in certain limitations. Specifically, the model demonstrated suboptimal performance in the low-pressure region of the curve. Although this outcome is partially attributable to the imposition of ReLU activations in the final output layer, which restricts values to strictly positive or zero, it is evident that even if the activation function is changed to an identity function, the prediction would remain negative. This suggests that the model architecture or training process may require further refinement to accurately capture the behavior in the low-pressure regime. Future studies could explore alternative activation functions or network structures that better accommodate the full range of pressure values. Additionally, incorporating domain-specific knowledge or constraints into the model design could potentially improve its performance across all pressure regions.

On a related note, the model in the current stage of our investigation can be described by the following relationship:

$$\alpha_{CO2} = \theta_{NN}(\mathbf{h}, C_A, T, P_{CO2}) \qquad (1)$$

Equilibrium loading can be calculated by feeding amine structure $(\mathbf{h})$, concentration (C_A), temperature (T), and partial pressure (P_{CO2}) into a neural network θ_{NN}. However, the reverse (e.g., predicting the partial pressure at constant equilibrium loading, concentration, temperature, and constant amine) is not yet possible. Most neural networks do not inherently guarantee bijectivity, which is a two-way mapping between the input and output. To ensure bijectivity, a specialized architecture called an Invertible Neural Network (INN) can be employed along with the appropriate training scheme [13].

In our case, additional insights could be gained if our model was invertible to some extent. The most practical example is the calculation of the heat of absorption, which is directly correlated to the energy requirement in the stripping process. The heat of absorption for amine–CO_2 absorption can be calculated using the Van't Hoff equation, which is derived from the fundamental thermodynamic relation known as the Gibbs–Helmholtz equation. Based on many reported studies [14, 15], the Van't Hoff equation can provide slight inaccuracies. However, this drawback is outweighed by its practicality; the calculation is quite straightforward, and the required data to compute the equation are easily obtained.

$$\left[\frac{\partial \ln(P_{CO2})}{\partial\left(\frac{1}{T}\right)}\right]_{\alpha_{CO2}} = \frac{\Delta H_{abs}}{R} \qquad (2)$$

Calculating ΔH_{abs} from the Van't Hoff equation requires us to compute the gradient of the natural logarithm of the partial pressure with respect to the inverse temperature. Computing this gradient requires the following relation

$$P_{CO2} = \theta_{NN}^{T}(\mathbf{h}, C_A, T, \alpha_{CO2}) \quad (3)$$

If our model is capable of bijective mapping between $\alpha_{CO2} \leftrightarrow P_{CO2}$, and then the calculation of ΔH_{abs} can be performed in a straightforward manner. However, it should be noted that the quality of the calculated ΔH_{abs} will be highly sensitive to the model's performance. An even more promising yet challenging opportunity is to implement the Van't Hoff equation directly in the neural network as a thermodynamics-based loss function to enforce physical realism.

4. CONCLUSION

This study demonstrated the effectiveness of a GCN in predicting the CO_2 equilibrium solubility in amine solutions by learning molecular representations directly from SMILES without relying on predefined descriptors. The model performed well, capturing the key trends in the data, as indicated by the strong performance metrics and consistent results across the training, validation, and testing sets. While the model showed promise, it struggled with low-pressure predictions, indicating room for improvement.

Future studies will prioritize optimizing the model by integrating geometrical features, such as three-dimensional coordinates, bond angles, and bond torsions, to capture 3D molecular effects more effectively. In addition, systematic hyperparameter tuning will be employed to enhance the model generalization, particularly under low-pressure conditions. The incorporation of this model into process simulation tools could bridge molecular-scale predictions with process-level carbon capture efficiency, thereby improving its applicability in real-world scenarios. Expanding the model to cover multi-amine blends could also provide greater relevance to industrial applications.

By addressing these limitations and expanding their capabilities, this study contributes to the development of more efficient solvent formulations for carbon capture. This enhanced model could accelerate the discovery of novel amines, ultimately supporting the design of more effective carbon capture processes.

ACKNOWLEDGMENTS

The authors would like to express gratitude to The Petroleum and Petrochemical College, Chulalongkorn University, and the Graduate Scholarship Program for ASEAN or Non – ASEAN countries, Chulalongkorn University, for scholarship support. This research was funded by the Thailand Science Research and Innovation Fund, Chulalongkorn University (DISF67630023).

REFERENCES

1. Nakao, S.-i., et al., Advanced CO_2 Capture Technologies Absorption, Adsorption, and Membrane Separation Methods. 2019.
2. Law, J.H., et al., A systematic review on the application of machine learning in carbon dioxide absorption in amine-related solvents. *Reviews in Chemical Engineering*, 2025. 41(2): p. 147-178.
3. Liu, B., et al., Prediction of CO_2 solubility in aqueous amine solutions using machine learning method. *Separation and Purification Technology*, 2025. 354.
4. Wahyudi, A. and U. Suriyapraphadilok, Predicting CO_2 equilibrium solubility in various amine-CO_2 systems using an artificial neural network model. *Energy and AI*, 2024. 18.
5. Hernández Morales, G., et al., Graph neural networks for CO_2 solubility predictions in Deep Eutectic Solvents. *Computers & Chemical Engineering*, 2024. 187.
6. Bondy, J.A. and U.S.R. Murty, Graph Theory. 1 ed. Graduate Text in Mathematics. 2010, London: Springer London. XII, 663.
7. Leite, L.S.G., et al., Modern chemical graph theory. *WIREs Computational Molecular Science*, 2024. 14(5).
8. Liu, Z. and J. Zhou, Introduction to Graph Neural Networks. 2020: Springer.
9. Reiser, P., et al., Graph neural networks for materials science and chemistry. *Commun Mater*, 2022. 3(1): p. 93.
10. Yamada, H., et al., CO_2 solubility and species distribution in aqueous solutions of 2-(isopropylamino)ethanol and its structural isomers. *International Journal of Greenhouse Gas Control*, 2013. 17: p. 99-105.
11. Derks, P.W.J., et al., Solubility of carbon dioxide in aqueous piperazine solutions. *AIChE Journal*, 2005. 51(8): p. 2311-2327.
12. Hwang, S.J., et al., Solubility of Carbon Dioxide in Aqueous Solutions of Three Secondary Amines: 2-(Butylamino)ethanol, 2-(Isopropylamino)ethanol, and 2-(Ethylamino)ethanol Secondary Alkanolamine Solutions. *Journal of Chemical & Engineering Data*, 2017. 62(8): p. 2428-2435.
13. Ardizzone, L., et al., Analyzing Inverse Problems with Invertible Neural Networks, in *The International Conference on Learning Representations (ICLR)*. 2019: New Orleans, US.
14. Narku-Tetteh, J., et al., Selection of components for formulation of amine blends for post combustion CO 2 capture based on the side chain structure of primary, secondary and tertiary amines. *Chemical Engineering Science*, 2017. 170: p. 542-560.
15. Liu, H., et al., Analysis of CO_2 solubility and absorption heat into 1-dimethylamino-2-propanol solution. *Chemical Engineering Science*, 2017. 170: p. 3-15.

Techno-economic analysis of sequential process to valorization of rambutan seed waste by supercritical CO_2-ethanol and subcritical water extraction

Kassama Utthachat[1], Ruengwit Sawangkeaw[2], Somkiat Ngamprasertsith[1,3,*]

[1] Department of Chemical Technology, Faculty of Science, Chulalongkorn University, Bangkok 10330, Thailand
[2] Institute of Biotechnology and Genetic Engineering, Chulalongkorn University, Bangkok 10330, Thailand
[3] Center of Excellence on Petrochemical and Materials Technology, Chulalongkorn University, Bangkok 10330, Thailand
[*] Corresponding author: somkiat.n@chula.ac.th

ABSTRACT

Rambutan is an agricultural fruit widely cultivated in Thailand, generating approximately 270,000 tons annually. During industrial processing, rambutan seeds are typically discarded as waste. This study presents a techno-economic analysis (TEA) of a sequential process for valorizing rambutan seeds, aiming to extract valuable compounds for using in food and pharmaceutical applications. The process involves screw pressing, supercritical carbon dioxide (CO_2) extraction with ethanol as a co-solvent, and subcritical water extraction. Due to the high fat content of rambutan seeds, oil removal is necessary prior to polysaccharide extraction. Supercritical CO_2 extraction is selected as a non-toxic method for oil removal, while subcritical water extraction is applied to obtain polysaccharides with functional biological properties. Screw pressing was used to enhance the overall extraction efficiency and reduce solvent consumption. The process was simulated using Aspen Plus to assess mass and energy balances, as well as electricity consumption. In addition, a comparative scenario using supercritical CO_2 without ethanol was considered, which achieved an oil yield of 7.32% by weight. The TEA evaluates the feasibility of supercritical CO_2 with co-solvent process configuration by analyzing factors such as product selling price, raw material cost, and operating costs at an industrial scale. The findings demonstrate the economic viability and sustainability of a value-added extraction approach for rambutan seed utilization.

Keywords: Supercritical; Subcritical water; Polysaccharide; Techno-economic analysis

1. INTRODUCTION

Currently, agricultural waste management has received growing attention due to increasing environmental concerns and global efforts toward sustainable development. As agricultural production expands, large volumes of waste are generated, often causing environmental problems if not properly managed. Converting this waste into value-added products offers both environmental and economic benefits. Among various types of agricultural residues, fruit seeds are often discarded despite their potential value still remained. Rambutan (*Nephelium lappaceum L.*) is a tropical fruit widely cultivated in Southeast Asia, particularly in Thailand, and generates a substantial amount of seed waste during industrial processing. With an annual production of approximately 270,000 tons in Thailand [1], the resulting seed waste presents both environmental and economic challenges.

Rambutan seeds are rich in bioactive compounds such as oils and polysaccharides, which have potential for applications in the food, cosmetic and pharmaceutical industries. However, efficient and sustainable extraction methods are essential to extract these compounds effectively. Subcritical water extraction has proven to be an effective technique for isolating high-purity polysaccharides from rambutan seeds. Nevertheless, the high fat content of the seeds, ranging from 33.40% to 39.13% [2], can significantly reduce polysaccharide extraction efficiency, making prior fat removal a necessary step.

Supercritical extraction was selected as a non-toxic and environmentally friendly method for oil removal. To improve the overall extraction efficiency and reduce solvent usage, screw pressing was applied as a preliminary step. This approach achieved oil yields of 6.29 and 11.69 g per 100 of feed with screw pressing and supercritical CO_2 with ethanol as a co-solvent, respectively [3]. Following defatting, rambutan seeds were subjected to subcritical water extraction, resulting in polysaccharide (POLS) yields ranging from 52.33 to 55.63 g per 100 g of feedstock, and total sugar contents between 83.37 and 87.45 g per 100 g of POLS [4].

However, the integration of these techniques into a continuous, efficient, and cost-effective process remains limited in literature. This study aims to add

value to rambutan seed waste through a sequential extraction process comprising screw pressing, supercritical CO_2 extraction with ethanol as a co-solvent, and subcritical water extraction. The objective is to assess the feasibility of implementing this value-added extraction approach at an industrial scale. A techno-economic analysis (TEA) was conducted using Aspen Plus simulations to model the process at a commercial production scale, based on extraction conditions derived from lab-scale experiments reported in the literature.

2. EXPERIMENTAL

2.1 Rambutan Seed Component Estimation

In this study, proximate and ultimate analysis were performed to determine the composition of rambutan seeds, which are considered non-conventional materials in Aspen Plus simulations. The results are presented in Table 1.

Table 1 Proximate and ultimate analyses of rambutan seed

Proximate analysis (%wt, dry basis)	
Moisture	2.23±0.19
Volatile matter	79.89±0.60
Fixed carbon	15.87±0.94
Ash	2.01±0.15
Ultimate analysis (%wt, dry basis)	
Carbon	48.19±0.39
Hydrogen	7.99±0.17
Nitrogen	2.02±0.04
Sulfur	1.62±0.16
Oxygen *	40.18±0.76

* By difference

2.2 Supercritical CO_2 Extraction Without Co-Solvent

In the supercritical CO_2 extraction experiment, 20 g of rambutan seed cake obtained from the screw press process was loaded into a supercritical extractor. The extraction was carried out at a temperature of 50 ± 5 °C and a pressure of 300 bar for 90 minutes, following the procedure described in [3]. The process flow diagram is shown in Figure 1.

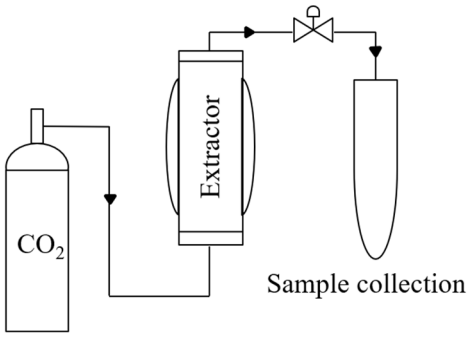

Figure 1 Process flow diagram of the supercritical CO_2 extraction experiment

2.3 Process modeling and simulation

In the process simulation, the feed stream of rambutan seeds was set at 100 kg/day, equivalent to 576 tons per year based on an operational period of 240 days annually, reflecting seasonal availability. These conditions were used as the base case for the analysis. The solvent-to-solid ratios, extraction conditions, and corresponding extraction yields for each process were sourced from selected literature, as summarized in Table 2. The UNIQUAC thermodynamic model was applied throughout the simulation to represent the phase behavior of the system. This model was selected due to its capability to handle non-ideal phase interactions, which are characteristic of supercritical and subcritical extraction systems.

Table 2 Extraction conditions based on selected literature and experimental results.

Extraction technique	Condition	Ref.
$SCCO_2$-EtOH	Solid to CO_2 to EtOH ratio 1:3:1, 50°C, 300 bar, 90 min.	[3]
SWE	Liquid to solid ratio 10:1, 150°C, 20 bar, 15 min.	[4]

$SCCO_2$-EtOH: supercritical CO_2 extraction with ethanol as a co solvent
SWE: subcritical water extraction.

2.3.1 Sequential Process of Supercritical CO_2–Ethanol and Subcritical Water Extraction

The process flow diagram for the sequential extraction is shown in Figure 2. Initially, rambutan seeds were dried at 60 °C for 8 hours to remove moisture. The oil extraction process was divided into two stages. In the first stage, screw pressing (B3) was employed, with an oil yield set at 6.29%, based on values reported in the literature [3]. In the second stage, supercritical CO_2 extraction with ethanol as a co-solvent (B9) was carried out under the conditions summarized in Table 2, with an oil yield of 11.69%. The resulting mixture was passed through a filter unit (B6) to separate the defatted seed cake (SCCO2C) from the extracted mixture. The extracted oil (SCCO2OIL) was then separated using a separator (B14), defined as a cartridge filter, and the recovered ethanol (ETOH-RE) was recycled back into the supercritical extraction process. The defatted seed cake was subsequently subjected to polysaccharide extraction using subcritical water extraction (B15). The extraction conditions were adopted from the literature, and the yield was assumed to be 53.98%, based on average reported values. Ethanol was used to precipitate the polysaccharides (POLYSAC) from the extract, which were then separated using a decanter (B13), while the remaining residue was filtered to isolate hydrochar (HYDROCHAR).

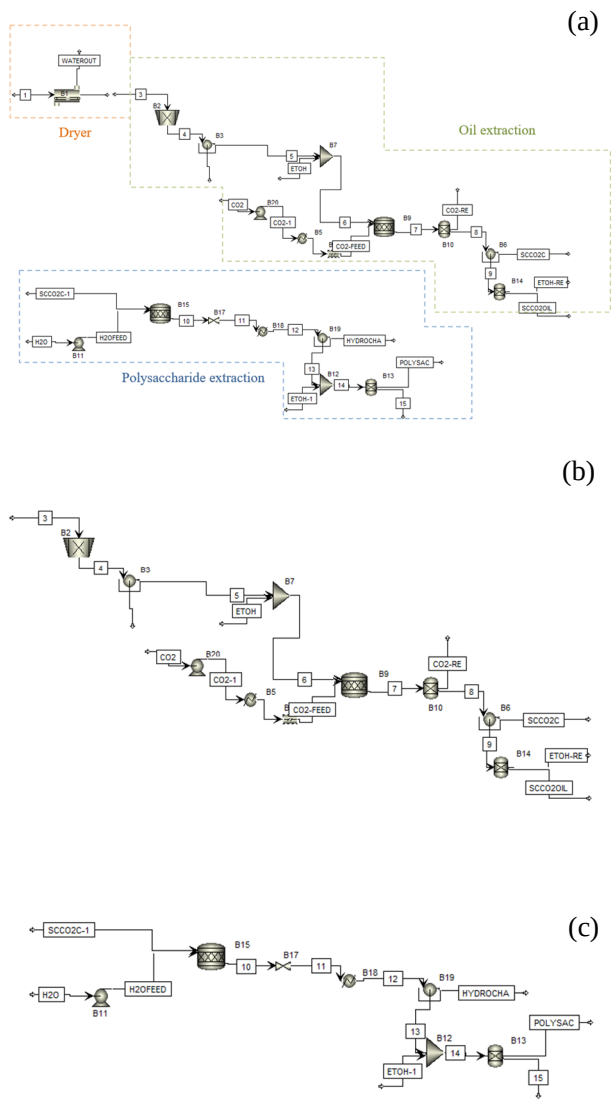

Figure 2 Process flow diagram of the sequential extraction process using Supercritical CO_2–Ethanol and Subcritical Water Extraction: (a) overall process, (b) oil extraction process, and (c) polysaccharide extraction process

Solvents of each extraction process are transported as liquid phase and stored in a storage vessel. Pumps were assumed to have an isentropic efficiency of 80% to reflect realistic energy consumption.

2.4 Economic assessment

In this study, the plant is assumed to operate 240 days per year, reflecting the seasonal availability of rambutan seeds. The economic performance was evaluated based on Fixed Capital Investment (FCI), Cost of Manufacturing (COM), utility costs (CUT), and labor costs (COL). The profitability analysis considered the Net Present Value (NPV) over a 20-year plant lifespan. The input prices of raw materials, solvents, products, and utilities used in the assessment are summarized in Table 3.

Table 3 Summary of raw materials, solvent, product and utility costs.

Item	Price	Units	Ref.
Raw materials			
Rambutan seed	57.75	US$/ton	[5]
Solvents			
Ethanol	626.91	US$/ton	[6]
CO_2	620.85	US$/ton	[7]
DI Water	503.90	US$/ton	[8]
Utility			
Electricity	0.12	US$/kWh	[9]
Product			
SPE oil	12994.51	US$/ton	[10]
$SCCO_2$ oil	101068.40	US$/ton	[11]
Polysaccharide	31764.37	US$/ton	[12]
Hydrochar	866.30	US$/ton	[13]
Diluted ethanol *	144.38	US$/ton	

* An assumed value used solely for the purpose of economic analysis
SPE oil: screw press extracted oil

To avoid additional ethanol recovery costs, the ethanol used in the polysaccharide extraction process was not recycled, as it was added specifically to induce polysaccharide precipitation from the subcritical water extract, resulting in a diluted ethanol mixture. This mixture, consisting of 76.89% ethanol and 23.11% water by weight, was designated as a secondary product and assumed to be sold to a purification company. The selling price, which varies with ethanol concentration, was assumed to be 5 baht/kg (equivalent to 144.38 USD/ton) for economic assessment purposes.

3. RESULTS AND DISCUSSION

3.1 Experimental Result

The supercritical CO_2 extraction without co-solvent method achieved an oil yield of 7.32%, which was lower than that obtained using supercritical CO_2 with ethanol as a co-solvent. This lower oil recovery led to a subsequent reduction in polysaccharide yield during the subcritical water extraction stage. However, the solvent-free supercritical CO_2 method offers the advantage of reducing ethanol consumption during the oil extraction process which will study in the further work.

3.2 Simulated Results of the Sequential Process Using Aspen Plus

The results of the overall material balance and energy consumption are presented in Table 4. The flow rate of rambutan seed was set at 100 kg/h, based on the initial assumption, while the amount of solvent used in each extraction stage was determined by the solid-to-liquid ratios adopted from relevant literature. The simulation was conducted based on the target conversion efficiency specified for each extraction step.

Table 4 Mass balance results for sequential process using Supercritical CO_2–Ethanol and Subcritical Water Extraction.

Material flow input (kg/h)	
Rambutan seed	100
Ethanol	1721.10
CO_2	169.98
Water	500.38
Product and waste (kg/h)	
SPE oil	3.80
$SCCO_2$ oil	6.62
Polysaccharide	27.01
Hydrochar	23.03
Diluted ethanol	2164.83

3.3 Economic assessment

The economic assessment of the sequential process is summarized in Table 5. The total Fixed Capital Investment (FCI) and Cost of Manufacturing (COM) were estimated at 2.09×10^6 USD and 10.00×10^6 USD, respectively. An analysis of the COM indicated that the Cost of Raw Materials (CRM) accounted for 8.31×10^6 USD, or 83.05% of the total COM. The majority of this cost resulted from ethanol consumption, which alone made up 74.80% of the CRM. However, this expense could be partially offset by the sale of diluted ethanol as a by-product, leading to a 16.37% cost reduction based on the by-product's sales value. This approach presents a potential strategy for improving the overall economic feasibility of the process.

Table 5 Economic assessment of the sequential process using Supercritical CO_2–Ethanol and Subcritical Water Extraction.

Item	Unit	Price
Fixed Capital	US$	2,094,666
Raw materials	US$/year	8,308,441
Utilities	US$/year	127,413
Labor	US$/year	302,825
Cost of manufacturing	US$/year	10,003,671
Product sale	US$/year	10,997,932

3.4 Feasibility analysis

The cumulative cash flow estimation is illustrated in Figure 3 The sequential process for valorizing rambutan seed waste demonstrated economic feasibility, with a payback period of 4.95 years to recover the initial investment. Additionally, the Net Present Value (NPV) over a 20-year operational period was estimated at 2.61×10^6 USD, with an Internal Rate of Return (IRR) of 13.75%, confirming that the process is economically viable and presents a promising investment opportunity.

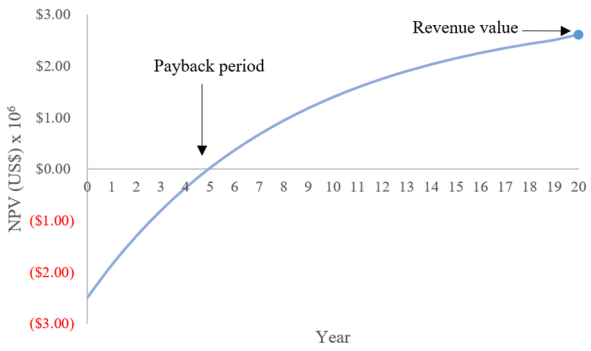

Figure 3 Cumulative cash flow over project life of the sequential extraction process

3.5 sensitivity analysis

Sensitivity analysis was conducted to assess the impact of key uncertain variables on the Net Present Value (NPV) of the sequential process over a 20-year plant lifetime. The analysis focused on variations in the product prices of SPE oil, $SCCO_2$–EtOH oil, polysaccharides, hydrochar, and diluted ethanol. Each parameter was varied within a range of ±50% from its baseline value. Figure 4 illustrates how changes in the prices of these products affect the NPV. The NPV was found to be highly sensitive to the polysaccharide price, increasing by approximately $3.65 million for every 10% price increase. Similarly, a 10% rise in the prices of $SCCO_2$–EtOH oil and diluted ethanol led to NPV increases of about $2.84 million and $0.95 million, respectively. In contrast, changes in the prices of SPE oil and hydrochar had relatively minor effects on the overall NPV.

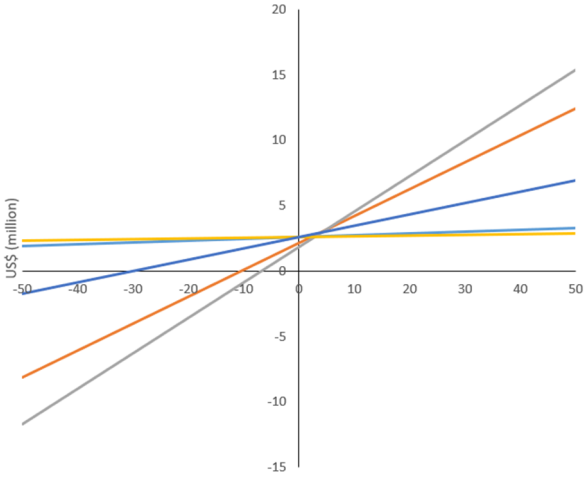

Figure 4 Sensitivity analysis of the variation in the product prices on the NPV (●) SPE oil, (●) $SCCO_2$ oil, (●) Polysaccharide, (●) Hydrochar, (●) Diluted ethanol

The effects of changes in the raw material price on the NPV values of each process are shown in Fig. 5. It can be clearly seen that ethanol price had the greatest impact on the economic performance across all scenarios. A 10% increase in ethanol price resulted in a decrease in NPV of approximately $2.98 million. Water

and CO_2 prices followed, with NPV reductions of around $0.69 million and $0.29 million, respectively. In contrast, changes in the price of fresh rambutan seeds (FS) had a minimal effect on the overall NPV.

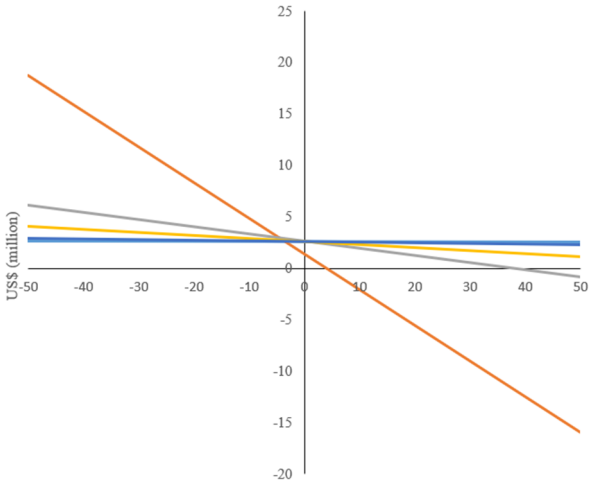

Figure 5 Sensitivity analysis of the variation in the raw material prices on the NPV (●) Rambutan seed, (●) Ethanol, (●) Water, (●) CO_2, (●) Operating labor cost

4. CONCLUSION

The techno-economic analysis (TEA) of the sequential process for the valorization of rambutan seed waste using supercritical CO_2–ethanol and subcritical water extraction was successfully conducted, based on a processing capacity of 100 kg/h (equivalent to 576 tons per year). The results indicated that this approach represents a promising zero-waste alternative for the valorization of rambutan seed waste, as confirmed by the positive Net Present Value (NPV) and Internal Rate of Return (IRR). However, ethanol usage remains a significant contributor to the overall cost, highlighting the need for further development in this area. As part of future work, a techno-economic analysis of the sequential process using supercritical CO_2 without ethanol and subcritical water extraction will be conducted to compare the economic feasibility of both processes.

ACKNOWLEDGMENTS

This work was financially supported by the Department of Chemical Technology, Faculty of Science, Chulalongkorn University. The authors gratefully acknowledge the department's support and resources throughout the course of this study.

REFERENCES

1. Torgbo, S., Rugthaworn, P., Sukatta, U., Sukyai, P. Biological characterization and quantification of rambutan (Nephelium lappaceum L.) peel extract as a potential source of valuable minerals and ellagitannins for industrial applications, *ACS Omega* 2022; 7: 34647-34656
2. Jahurul, M.H.A., Azzatul, F.S., Sharifudin, M.S., Norliza, M.J., Hasmadi, M., Lee, J.S., Patricia, M., Jinap, S., Ramlah George, M.R., Firoz Khan, M., Zaidul, I.S.M. Functional and nutritional properties of rambutan (Nephelium lappaceum L.) seed and its industrial application: A review. *Trends in Food Science & Technology* 2020; 99: 367-374.
3. Nilmat, K., Ngamprasertsith, S., Sakdasri, W., Karnchanatat, A., Sawangkeaw, R. Sequential process to valorisation of rambutan seed waste by supercritical CO2 -ethanol and subcritical water extractions. *Chemical Engineering Transactions* 2024; 109: 313-318.
4 Nilmat, K., Hunsub, P., Ngamprasertsith, S., Sakdasri, W., Karnchanatat, A., Sawangkeaw, R. Effects of defatting pretreatment on polysaccharide extraction from rambutan seeds using subcritical water: optimization using the desirability approach. *Foods* 2024; 13: 1967.
5 Rambutan seed price. 2025, 13 January; Available from: https://www.nanagarden.com/subcat/s01800
6 Ethanol price. 2025, 13 January; Available from: https://www.globalpetrolprices.com/Thailand/ethanol_prices/
7 Carbon dioxide price. 2025, 13 January; Available from: https://www.sn-oxygen.com/17150184/%E0%B8%96%E0%B8%B1%E0%B8%87-6-%E0%B8%84%E0%B8%B4%E0%B8%A7
8 DI water price. 2025, 13 January; Available from: https://www.ttytech.com/product-page/%E0%B8%99-%E0%B8%B3%E0%B8%81%E0%B8%A5-%E0%B8%99%E0%B8%9A%E0%B8%A3-%E0%B8%AA-%E0%B8%97%E0%B8%98-de-ionized-water
9 Metropolitan Electricity Authority. 2025, 13 January; Available from: https://www.mea.or.th/our-services/tariff-calculation/other/vauexlKUw
10 Screw press extracted oil price. 2025, 13 January; https://www.chocolasia.com/product/cocoa-butter/
11 Supercritical extracted oil price. 2025, 13 January; Available from: https://thai.alibaba.com/product-detail/1 0 0 - Pure-Rambutan-Peel-Extract-Cosmetic-1600388196304.html
12 Polysaccharide price. 2025, 13 January; Available from: https://www.myskinrecipes.com/shop/th/healthy-digestion/33353-soluble-soybean-polysaccharide-ssps.html
13 Hydrochar price. 2025, 13 January; Available from: http://www.alungkarngarden.com/product/756/%E0%B8%96%E0%B9%88%E0%B8%B2%E0%B8%99%E0%B9%84%E0%B8%9A%E0%B9%82%E0%B8%AD%E0%B8%8A%E0%B8%B2%E0%B8%A3%E0%B9%8C-%E0%B9%81%E0%B8%9A%E0%B8%9A%E0%B8%81%E0%B9%89%E0%B8%AD%E0%B8%99-biochar

Techno-economic analysis of crude peptides production from defective coffee beans

Chatchaphong Nakphadungsuk[1], Ruengwit Sawangkeaw[2], Somkiat Ngamprasertsith[1,3,*]

[1] Department of Chemical Technology, Faculty of Science, Chulalongkorn University, Bangkok 10330, Thailand
[2] Institute of Biotechnology and Genetic Engineering, Chulalongkorn University, Bangkok 10330, Thailand
[3] Center of Excellence on Petrochemical and Materials Technology, Chulalongkorn University , Bangkok 10330, Thailand
[*] Corresponding author: somkiat.n@chula.ac.th

ABSTRACT

Coffee is one of the world's most significant economic crops, serving as a primary source of income for millions globally. In Thailand alone, approximately 9,510 tons of Arabica coffee beans are produced annually, contributing to the country's agro-economic sector. However, during the grading process, 15–20% of green coffee beans (GCB) are classified as defective and discarded, resulting in about 1,900 tons of underutilized biomass per year. These defective beans, though unsuitable for brewing, retain high levels of proteins and bioactive compounds. To enhance the value of GCB waste, this study proposes a comprehensive approach to convert them into crude peptides, a value-added product with potential use in food, pharmaceutical, and nutraceutical industries. The process involves several stages: drying and crushing of GCB, supercritical CO_2 ($SCCO_2$) extraction of coffee oil using ethanol as a co-solvent, enzymatic hydrolysis using papain to break down proteins into peptides, and encapsulation of peptides via spray drying. This encapsulation is conducted with and without maltodextrin to evaluate its influence on peptide stability and cost. Three oil extraction methods, Soxhlet, solvent, and $SCCO_2$, were compared, yielding 23.36%, 6.86%, and 7.80%, respectively. Although Soxhlet yielded the most oil, $SCCO_2$ was preferred due to lower environmental impact and solvent safety. Additionally, $SCCO_2$ extraction is better suited for large-scale industrial applications because it can operate as a continuous process with relatively short extraction times, making it more efficient for high-throughput production environments. The entire process was modeled using Aspen Plus to simulate mass and energy balances, and to design the process flowsheet. A techno-economic analysis (TEA) was then conducted to assess capital investment, operating costs, revenue generation, and financial viability under various market conditions. Sensitivity analysis identified product price and labor cost as critical variables affecting economic outcomes. The encapsulation with maltodextrin enhanced product quality but increased costs. Conversely, omitting maltodextrin reduced cost but introduced risks related to powder stability and shelf life. These findings suggest that crude peptide production from GCB is not only technically viable but also economically attractive under optimal conditions.

Keywords: Green coffee beans; Supercritical CO_2 extraction; Techno-economic analysis; Enzymatic hydrolysis; Spray drying

1. INTRODUCTION

Green coffee beans (GCB) are rich in proteins and bioactive compounds, yet around 15–20% of GCB are rejected during grading due to physical defects such as discoloration, insect damage, or irregular shape, despite being nutritionally comparable to high-grade beans.[1] These defective beans—classified based on physical imperfections rather than chemical composition—are often discarded or relegated to low-value applications like animal feed or compost. Such underutilization neglects their potential as a sustainable raw material for producing high-value bioproducts. As sustainability and circular economy concepts gain traction in the agro-industrial sector, valorizing these agricultural byproducts presents both economic and environmental opportunities.

Thailand, ranked among the top coffee producers in Asia, generates approximately 9,510 tons of Arabica coffee annually, mostly from the northern region [2,3]. Despite their undesirable appearance, these beans retain high levels of proteins (15–17%), lipids (9–10%), and carbohydrates (60–62%), indicating strong potential for alternative valorization [4]. Notably, previous studies have demonstrated the successful extraction of high-

quality oil and bioactive peptides from GCB, with suitable characteristics for functional food and pharmaceutical applications [5].

Supercritical CO_2 ($SCCO_2$) extraction has emerged as a promising method for oil recovery from coffee beans, especially in industrial contexts. Operating under high pressure and temperature beyond the critical point of CO_2, the method enables efficient solubilization and separation of oil without the use of toxic organic solvents. $SCCO_2$ is inherently continuous, energy-efficient, and yields products of high purity and safety. When ethanol is used as a co-solvent, extraction efficiency improves, particularly for polar or semi-polar compounds like polyphenols [6]. The scalability and environmental compatibility of $SCCO_2$ make it an attractive choice for large-scale operations.

Defatted GCB are going to enzymatic hydrolysis using papain to break down proteins into peptides, and encapsulation of peptides via spray drying. The crude peptide powder will be encapsulated with maltodextrin to enhance stability, improve solubility, and protect the peptides from degradation, making them more suitable for commercial use. [7,8].

This study aims to investigate a holistic process for producing crude peptides from defective GCB through a series of unit operations—drying, grinding, oil extraction, enzymatic hydrolysis, and spray drying—integrated with simulation and techno-economic analysis (TEA). By incorporating process modeling in Aspen Plus and evaluating capital and operating expenditures, revenue potential, and sensitivity to key economic factors, this research provides a data-driven foundation for industrial-scale implementation. The scalability of the process, particularly the suitability of continuous supercritical CO_2 extraction for large-scale operations, is emphasized, aiming to bridge laboratory-scale innovation with commercial feasibility.

2. EXPERIMENTAL

2.1 Materials

Defective Arabica GCB were obtained from northern Thailand. Ethanol (95%) and CO_2 (food grade) were used for experimental extraction and simulation. The proximate and ultimate compositions of the GCB were analyzed to inform process modeling. The results are summarized in Table 1.

Table 1. Proximate and Ultimate Analysis of Green Coffee Beans (Dry basis).

Parameter	Value (%)
Moisture (M)	1.14 ± 0.16
Ash (ASH)	2.61 ± 0.08
Volatile Matter (VM)	78.36 ± 0.45
Fixed Carbon (FC)	17.89 ± 0.37
Carbon (C)	43.90 ± 2.12
Hydrogen (H)	6.96 ± 0.48
Nitrogen (N)	2.54 ± 0.14
Sulfur (S)	1.38 ± 0.11

These values were obtained using ASTM D3172–3175 for proximate analysis and CHNS/O elemental analysis for ultimate analysis.

2.2 Oil Extraction

Oil extraction from defective GCB was carried out using four methods: Soxhlet extraction, solvent extraction, supercritical CO_2 ($SCCO_2$) and supercritical CO_2 extraction with ethanol as a co-solvent ($SCCO_2$-EtOH). Prior to extraction, the beans were oven-dried at 60°C for 3 hours and ground into fine powder.

- Soxhlet Extraction: Approximately 2 g of GCB powder was placed in a Buchi fat extractor (E-500) using ethanol as the solvent. The extraction was carried out at 85°C for 6 hours (~30 cycles).
- Solvent Extraction: 50 g of GCB powder was mixed with 100 mL of ethanol (95% v/v) and soaked at 50°C for 1.5 hours.
- $SCCO_2$ Extraction: 20 g of GCB powder was subjected to supercritical CO_2 extraction at 50°C and 20 MPa for 1.5 hours.
- $SCCO_2$-EtOH Extraction: 1 kg of GCB powder was subjected to supercritical CO_2 extraction at 50°C and 20 MPa for 1.5 hours, with ethanol used as a co-solvent with ratio 1:2. [10]

Oil yields from each method were recorded and compared. These experimental data were used as input for subsequent process simulation in Aspen Plus.

2.3 Process Simulation

In the simulation, the feed stream for the extraction process was set at 200 kg/h of defective GCB, reflecting the processing scale and the operational period of 8,304 hours per year. This feed rate was derived from the estimated annual availability of defective green coffee beans in the northern region of Thailand. These parameters were used as the base case for the simulation. The material streams for the process, including CO_2, ethanol, and water, were set according to the simulation model. CO_2 was used as the primary solvent for supercritical CO_2 extraction, with ethanol (95% v/v) added as a co-solvent to enhance extraction efficiency. The phase behavior of the system was represented using the UNIQUAC thermodynamic model, selected for its ability to handle non-ideal phase

interactions that are typical of supercritical extraction systems. This model allowed the accurate prediction of the material flow through the system, including the extraction of coffee oil and the production of crude peptide.

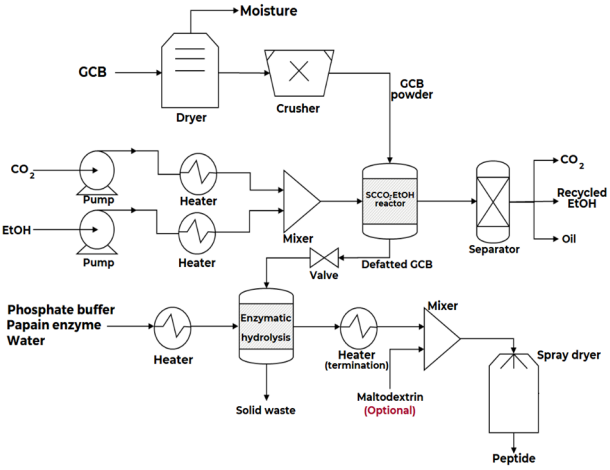

Figure 1. Process flow diagram for crude peptide production from defective coffee beans simulated in Aspen Plus.

The process includes drying, grinding, $SCCO_2$ extraction, separation, and spray drying (with maltodextrin) as shown in Figure 1.

2.3.1 Drying and Grinding.

Before entering the extraction system, the GCB was first subjected to drying and grinding. Drying was carried out at 60°C for 1.5 hours to reduce the moisture content and prepare the beans for further processing. After drying, the beans were ground into powder to increase surface area, thereby enhancing extraction efficiency. This powder served as the feedstock for all subsequent simulations.

2.3.2 Supercritical CO_2 Extraction with ethanol as a co-solvent.

The $SCCO_2$-EtOH extraction process was then modeled using a reactor block in Aspen Plus, operated at 50°C and 20 MPa with ethanol (95% v/v) as a co-solvent. The reactor simulated the solubilization of coffee oil into the supercritical phase. GCB at a feed rate of 200 kg/h, CO_2 at 2,310 kg/h, and ethanol at 400 kg/h were used as input materials. The main outputs were coffee oil and defatted GCB solids. In this simulation, CO_2 and ethanol were modeled as once-through streams and not recycled.

2.3.3 Enzymatic Hydrolysis.

Following oil removal, the defatted GCB solids were subjected to enzymatic hydrolysis in the simulation. Although not conducted experimentally, this process was represented using a stoichiometric reactor block in Aspen Plus to estimate peptide yield. Input components included defatted coffee solids, water, and papain enzyme. The resulting output stream was a peptide-rich slurry, which also contained residual solids and excess water. The efficiency of the enzymatic reaction was assumed based on literature-reported values.

2.3.4 Spray Drying.

The peptide slurry from the hydrolysis stage was processed using a spray dryer in Aspen Plus, operated at 60°C and 1 bar. Base case scenarios was simulated which maltodextrin was added to the crude peptide solution to drying. In this case, spray dryer reduced the moisture content and produced a dried crude peptide powder. The inclusion of maltodextrin improved the powder's stability and flowability, while its absence resulted in a more hygroscopic product prone to clumping and degradation.

2.4 Economic Assessment

In this study, the plant was designed to operate 346 working days per year, equivalent to 8,304 hours annually. The economic analysis was based on simulation outputs. Fixed Capital Investment (FCI) was estimated using CapCost software, with cost indexes updated using CEPCI (2024). The FCI for the entire process—including drying, grinding, $SCCO_2$-EtOH extraction, enzymatic hydrolysis, and spray drying.

The Cost of Manufacturing (COM) included the cost of raw materials (CRM), utilities (CUT), and labor (COL). Major cost contributors were GCB, CO_2, ethanol, and maltodextrin, along with water and energy inputs. Utility consumption rates and prices were taken directly from Aspen Plus outputs and mass balance calculations recorded in the Excel file, are summarized in Table 2. These values served as the core input for financial evaluation.

Profitability indicators—Net Present Value (NPV), Internal Rate of Return (IRR), Payback Period, and Return on Investment (ROI)—were calculated using a project lifetime of 20 years and a corporate tax rate of 35%. A sensitivity analysis was conducted to evaluate economic robustness under variations in raw material price and product pricing.

Table 2. Raw Material, Product, and Cost of Utilities in base case scenario.

Items	Value	Cost per Unit	Ref
GCB	213	US$/ton	Farm
Carbon dioxide	637	US$/ton	[11]
Ethanol	761	US$/ton	[12]
Maltodextrin	1,333	US$/ton	[13]
Water	503	US$/ton	[14]
GCB Oil	59,259	US$/ton	[15]
Crude peptide	48,889	US$/ton	[16]
Electricity	0.0921	US$/kWh	[17]

3. RESULTS AND DISCUSSION

3.1 Experimental Results

The oil extraction experiments yielded varying results depending on the extraction method used. The oil yields from the different methods are shown in Table 3.

Table 3. Oil Yield Comparison for Different Extraction Methods

Extraction	%yield
Soxhlet Extraction	23.36
Solvent Extraction	6.86
$SCCO_2$ Extraction	7.80
$SCCO_2$-EtOH Extraction	3*

*From research data [10]

Soxhlet Extraction: This method was the most efficient, with an oil yield of 23.36%. However, it was not suitable for large-scale production because it was complicated to recover the solvent and has safety concerns when handling large amounts of ethanol. The process is also time-consuming, and solvent recycling makes it less efficient for large-scale operations.

Solvent Extraction: This method was less efficient, with an oil yield of 6.86%. While it was easier to set up and operate than Soxhlet extraction, it produces a much lower yield. It also depends heavily on the amount of solvent and the extraction time, making it less effective for large-scale applications.

Supercritical CO_2 ($SCCO_2$) Extraction: The oil yield from this method was 7.80%, higher than solvent extraction but lower than Soxhlet. Despite the lower yield, $SCCO_2$ extraction offers several advantages for industrial-scale production. It is more eco-friendly since it does not use harmful solvents and works at low temperatures, preserving bioactive compounds in the coffee oil. It is also more efficient and scalable for industrial. To enhance oil yield, the operating pressure may be applied.

$SCCO_2$-EtOH Extraction: This method resulted in the lowest yield at 3%. The lower yield is due to some oil being trapped in the equipment, particularly in the pipes and joints, which reduces the efficiency of the extraction process. While this method has a lower yield, it combines supercritical CO_2 with ethanol to enhance extraction under certain conditions, making it safer and more environmentally friendly for scaling up.

3.2 Process Simulation Results

The process simulation in Aspen Plus provided mass balance data for crude peptide production. The simulation calculates material balance and energy consumption based on a feed of 200 kg/h of GCB. The simulation results for these processes are summarized in Table 4.

Table 4: Material Flow and Product Outputs of Crude Peptide Production.

Materials Flow inputs	Units (tons/year)
GCB	1,659
Carbon dioxide	19,175
Ethanol	3,318
Maltodextrin	2,526
Water	38,889
Product & Waste	**Units (tons/year)**
Crude peptide	848
GCB Oil	50
Solid waste	760.71

The mass balance data from the Aspen Plus simulation reflects the required material flows and product outputs based on the feed of 1,659 tons/year of GCB. The high water usage in this process can be attributed to the enzymatic hydrolysis stage, where water is crucial for breaking down the defatted coffee solids. Additionally, the spray drying process requires significant amounts of energy for moisture removal. This high water demand results in high energy consumption, especially in the spray drying unit, which is the most energy-intensive step. As shown in Table 5, the drying process requires a large amount of energy to evaporate the water, making it a key factor in the overall energy consumption of the process.

Table 5: Energy Consumption for Crude Peptide Production.

Unit Operation	Energy Consumption (kWh/year)
Supercritical CO_2 Extraction	468,801
Enzymatic Hydrolysis	1,784,612
Spray Drying	6,767,353

The highest energy consumption occurred in spray drying, followed by enzymatic hydrolysis. The process requires a large amount of water, especially during spray drying for moisture removal. The hydrolysis stage also demands heat to activate the enzyme and stop its action, contributing to high energy usage. Despite supercritical CO_2 extraction being more energy-efficient, the overall process still consumes significant energy, emphasizing the need for energy optimization to improve cost-efficiency and sustainability at a large scale.

3.3 Economic Assessment

The key financial figures from the economic assessment of crude peptide production are summarized in Table 6. These include capital investment, operating costs, manufacturing costs, and projected revenue, which are essential for evaluating the project's economic feasibility. In addition, performance indicators such as the IRR and payback period are also provided to support investment decision-making.

Table 6: Economic Assessment of Crude Peptide Production

Cost	Unit	
Fixed Capital Investment	US$	2,688,624
Utilities	US$/year	832,659
Labor	US$/year	263,431
Cost of Manufacturing	US$/year	39,535,539
Product Sale	US$/year	44,420,530
Raw Materials	US$/year	38,052,959
Internal Rate of return	%	10.08
Payback Period	Years	6.14

The economic assessment of the crude peptide production process was based on the Fixed Capital Investment (FCI), Operating Costs (OPEX), and COM. The FCI for the plant was estimated at 2.7 x 10^6 US$. OPEX, including utilities and labor, was calculated to be 8.3 x 10^5 US$/year and 2.6 x 10^5 US$/year, respectively. Major cost factor is the high electricity demand for spray drying, which is the most energy-intensive step. The substantial energy required to evaporate water from the peptide slurry leads to significant electricity costs. The revenue from the sale of crude peptides was projected at 4.4 x 10^7 US$/year, based on the market price of the product. This revenue is crucial for covering production costs and ensuring the project's financial feasibility. Meanwhile, COM, which includes raw materials, utilities, labor, and overhead, amounted to 3.9 x 10^7 US$/year. This high cost underscores the complexity of the process, which demands significant raw materials like green coffee beans, ethanol, and CO_2. The combination of these inputs leads to high overall production costs. These cost factors were used to calculate key profitability indicators, such as the IRR and Payback Period. The calculated IRR of 10.08% indicates a positive return on investment, while the Payback Period of 6.14 years suggests that the initial investment would be recouped in just over six years, demonstrating the financial feasibility of the project.

3.4 Sensitivity Analysis

The sensitivity analysis was conducted to evaluate how changes in key parameters, such as product prices, raw material costs, and utility costs, affect the project's financial viability. Key variables, including ethanol cost, CO_2 cost, water usage cost, and electricity cost, were varied by ±50% from their baseline values to observe the impact on the NPV.

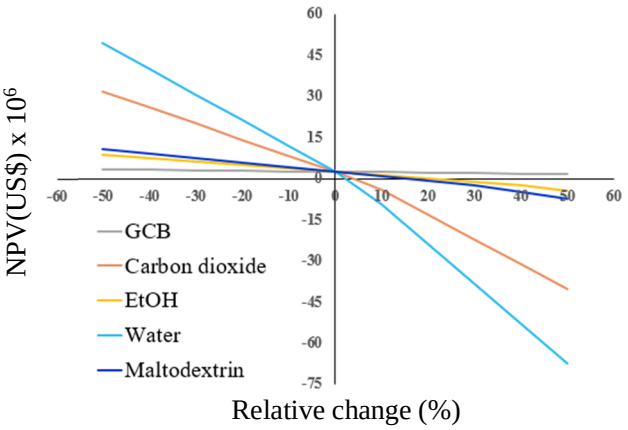

Figure 2. Sensitivity Analysis of Raw Material Prices on NPV

In Figure 2, the analysis indicates that the NPV is most sensitive to fluctuations in the prices of water, CO_2, ethanol, maltodextrin, and GCB, respectively. A 10% increase from baseline in the price of water leads to a significant drop in NPV, decreasing from approximately 2.46 x 10^6 US$ to -9.53 x 10^6 US$. This is primarily due to the large quantities of water required in the process, particularly during hydrolysis stages.

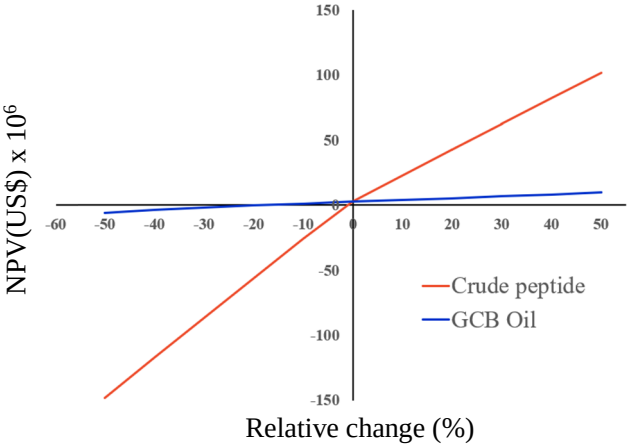

Figure 3. Sensitivity Analysis of Product Prices on NPV

The sensitivity analysis for the crude peptide production process in Figure 3 shows that product price has a significant impact on the NPV. A 10% increase in the price of crude peptide results in a substantial rise in NPV, from approximately 2.46 x 10^6 USD to 22.34 x 10^6 USD. In contrast, a 10% increase in the price of crude peptide oil has a smaller effect on NPV. These results suggest that the financial viability of the project is more sensitive to changes in the price of crude peptide, as it makes a larger contribution to the revenue compared to crude oil.

4. CONCLUSION

The techno-economic analysis of crude peptide production from defective green coffee beans using $SCCO_2$-EtOH extraction, enzymatic hydrolysis, and spray drying confirmed its financial viability, with a positive NPV and IRR. However, the process is sensitive to changes in raw material costs, especially water. Additionally, fluctuations in the price of crude peptides also significantly affect profitability. The sensitivity analysis shows that managing raw material costs and optimizing water usage are critical to improving profitability. Furthermore, reducing energy consumption, particularly during spray drying, could lower costs and improve efficiency. The results support the feasibility of large-scale crude peptide production from defective green coffee beans. Moreover, obtaining more reliable experimental data on the $SCCO_2$-EtOH extraction process will further enhance the accuracy of the TEA, providing a more precise evaluation of its economic viability.

ACKNOWLEDGMENTS

This work was supported by the Department of Chemical Technology, Faculty of Science, Chulalongkorn University, whose financial support and resources were invaluable throughout the course of this study. The department's continuous assistance is deeply appreciated.

REFERENCES

1. A guide to visually spotting green coffee defects. (2022). *MTPak Coffee*. Available at: http://mtpak.coffee/22022/07/a-guide-to-visually-spotting-green-coffee-defects. Accessed on: September 30, 2024.
2. Coffee species. (2024). *Delong Coffee Mix*. Available at: https://delongcoffeemix.com /content/22814. Accessed on: September 3, 2024.
3. Coffee production in Thailand. (2024). *Chaodoi*. Available at: https://chaodoi.co.th/coffee-bean-thailand. Accessed on: September 30, 2024.
4. Oliveira, L. S., Franca, A. S., Mendonça, J. C. F., & Barros-Júnior, M. C. (2006). Proximate composition and fatty acids profile of green and roasted defective coffee beans. *Journal of Food Science and Technology*, 39(3), 235–239.
5. Karmee, S. K. (2018). A spent coffee grounds based biorefinery for the production of biofuels, biopolymers, antioxidants and biocomposites. *Waste Management*, 72, 240–254.
6. Barajas-Álvarez, P., Castillo-Herrera, G. A., Guatemala-Morales, G. M., Corona-González, R. I., Arriola-Guevara, E., & Espinosa-Andrews, H. (2021). Supercritical CO_2-ethanol extraction of oil from green coffee beans: optimization conditions and bioactive compound identification. *Journal of Food Science and Technology*, 58(12), 4514–4523.
7. Encapsulation technique. (2024). *RDI, KU*. Available at: https://rdi.ku.ac.th/cl/knowledge /2565/Encapsulation.pdf. Accessed on: September 30, 2024.
8. Akbarbaglu, Z., Jafari, S. M., Sarabandi, K., Mohammadi, M., Heshmati, M. K., & Pezeshki, A. (2019). Influence of spray drying encapsulation on the retention of antioxidant properties and microstructure of flaxseed protein hydrolysates. *Colloids and Surfaces B: Biointerfaces*, 178, 421–429.
9. Thoppil, Y., & Zein, S. H. (2021). Techno-economic analysis and feasibility of industrial-scale biodiesel production from spent coffee grounds. *Journal of Cleaner Production*, 307(127113), 127113.
10. Hunsub, P., Ngamprasertsith, S., Prichapan, N., Sakdasri, W., Karnchanatat, A., & Sawangkeaw, R. (2024). Life cycle assessment of spray-drying encapsulation of crude peptides produced from defective green coffee beans. *Clean Technologies and Environmental Policy*.
11. Green coffee beans oil price. (2025). *Nature in Bottle*. Available at: https://www.natureinbottle. com/product/green_coffee_oil. Accessed on: January 13, 2025.
12. CO_2 price. (2025). *SN Oxygen*. Available at: https://www.sn-oxygen.com/17150184/%E0% Accessed on: January 13, 2025.
13. Ethanol price. (2025). *Global Petrol Prices*. Available at: https://www.globalpetrolprices.com/ Thailand/ethanol_prices/. Accessed on: January 13, 2025.
14. Maltodextrin price. (2025). *Chemecosmetics*. Available at: https://chemecosmetics.com/shop/ maltodextrin/?srsltid=AfmBOor-p-z42ylQMUprteTnkNzVQspCIrmxPK7SDKEtEpm _gfvIP8IT. Accessed on: January 13, 2025.
15. Water price. (2025). *Mitr Water*. Available at: https://mitrwater.com/product-category/filter-water-industry. Accessed on: January 13, 2025.
16. Crude peptide price. (2025). *Bulk Supplements*. Available at: https://www.bulksupplements. com/th-TH/products. Accessed on: January 13, 2025.
17. Metropolitan Electricity Authority. (2025). *Tariff Calculation*. Available at: https://www.mea.or.th/ our-services/tariff-calculation / other / vauexlKUw. Accessed on: January 13, 2025.

Comparative analysis of machine learning models for predicting operating condition in a pentane-hexane distillation column with limited data

Jirapat Romkaew[1], Kritchart Wongwailikhit[1*]

[1] Department of Chemical Engineering, Faculty of Engineering, Chulalongkorn University, Bangkok 10330, Thailand

[*] Corresponding author: kritchart.w@chula.ac.th

ABSTRACT

Distillation process is a energy intensive separation process. Many researchers have been implemented machine learning models to its optimize operating condition to reduce costs. In contrary, few study different models' performance on distillation. This study was done to find suitable model for distillation process and minimum amount of data samples to develop accurate model. The study was done in the following procedure (1) data acquisition and validation (2) data preparation (3) model development and evaluation. Among all studied models, feedforward neural network outperforms other models with mean squared error and mean absolute percentage error of 0.0010 and 0.15% which was considered accurate using 10 train samples to train the model.

Keywords: Binary distillation column; Machine learning; Optimization; Prediction model

1. INTRODUCTION

Distillation is a widely used process of separating homogenous liquid mixture in the chemical industry due to its vast application of substances. Despite its long usage and development, distillation process accounts for 50% of operation cost [1] and 40% of total energy consumption in the production plant [2]. Cost of operating distillation column can be varied depending on many factors. The most crucial factor in operating distillation column without having to change the column is operating condition. By changing the operating condition, the cost from distillation can change significantly. To reduce the cost and maximize profit in the production process, the operating condition must be tuned while keeping products quality and quantity to meet demands.

Nowadays, operating conditions of distillation column can be predicted by thermodynamics model that use mass and energy balance or use commercially available simulations. In this research will be called conventional model. Capability of conventional model in predicting operating conditions depends on complexity of interaction between substances within mixture. With more complexity, less accuracy can be achieved from conventional model.

To address this problem, empirical model emerges. Empirical model observes and studies real data from experiment to find correlations between each variables, creating the model. At the present, computation power is used to aid in finding correlations which can be defined as machine learning model. Machine learning model's performance is varied on the applicable between data correlations and model's characteristics. To apply machine learning model with distillation process, a noticeable disadvantage is there must be real data from real distillation process first before using the obtained data for creating machine learning model to be able to predict operating conditions.

Prediction of operating conditions and products using machine learning model has been studied and applied in chemical processes, Berkey et al. developed a control scheme of complex reaction in rotating cylinder electrode reactor using recurrent neural network (RNN) [3]. Machine learning model prediction in thermochemical process was studied by Sison et al., three machine learning models were used to develop model to predict yields during chemical looping gasification process [4]. There are many researchers studied application of machine learning model in distillation process, Kwon et al. developed machine learning-based prediction model and optimized process using the model [2] while Plehiers et al. developed four deep learning artificial neural networks to predict detailed characterization of a naphtha from steam cracking for a real-time optimization [5].

In the contrary, machine learning models in the previous section were never studied the applicable of various model types and the minimum amount of data used to develop model. Due to the disadvantage of machine learning model being required significant amount of data for developing model, the study of minimum required data would contribute in further development of machine learning model application in chemical industry. This study aims to study the suitable model for distillation process and the minimum amount of data to develop accurate machine learning model.

2. EXPERIMENTAL

2.1 Data source and validation

Data used in this study was obtained from an operator training simulation of binary distillation column separating n-pentane from n-hexane. The column is seven-tray tower providing fractionation with boil-up from kettle-type reboiler using steam as heat source. Overhead system includes a total condenser and an overhead receiver using cooling water as coolant. Cooling water will be kept flow rate as constant throughout this study. The simulation can designate ranges of input variables bounded with equipment limitation which facilitates the goal of this study to find effective amount of data with great distribution.

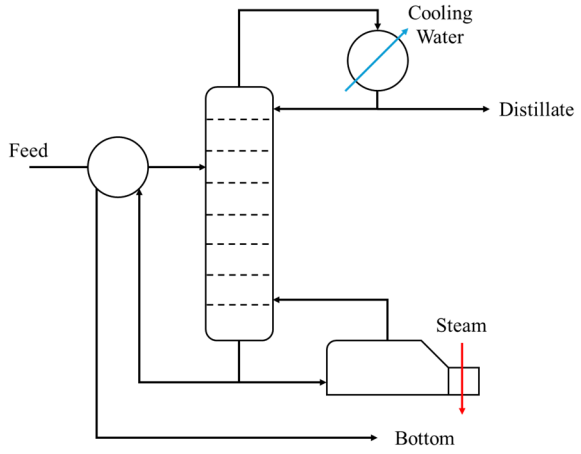

Figure 1 Process flow diagram of distillation column

25 samples of steady-state data were collected from the simulation within predefined range of operating conditions in the simulation. The collected data was proved thermodynamics credibility by Peng-Robinson equation of states with same temperature and pressure then compared composition of overhead and bottom product if the collected data samples follow with thermodynamics model. The six input variables are volumetric feed flow rate, feed temperature, overhead temperature, overhead pressure, bottom temperature, and column pressure drop. The five output variables are distillate volumetric flow rate, n-pentane composition in distillate, bottom volumetric flow rate, n-hexane composition in bottom, and reboiler duty.

Table 1 Name and ranges of input variables obtained.

Variable	Unit	Lower bound	Upper bound
Volumetric feed flow rate	m^3/h	26.89	40.33
Feed temperature	°C	33.00	36.37
Overhead temperature	°C	37.90	41.90
Overhead pressure	kPa	97.70	102.70
Bottom temperature	°C	65.80	69.80
Column pressure drop	kPa	11.52	21.45

2.2 Data preparation

The variables of data were gone through Pearson correlation analysis (R) to study their relationship and identify any collinearity in data. According to Eq.1, n is n^{th} sample. x_i, y_i are values of variable in data samples. $\bar{x}$, $\bar{y}$ are mean of values of variable in data samples.

$$R = \frac{\sum_{i=1}^{n}(x_i - \bar{x})\,(y_i - \bar{y})}{\sqrt{\sum_{i=1}^{n}(x_i - \bar{x})^2\,(y_i - \bar{y})^2}} \qquad \text{Eq. 1}$$

Unrelated variables were removed, and the data was undergone feature engineering to remove collinearity resulting in variables mentioned in section 2.1 which helps in improving performance of machine learning model. This step was done using seaborn V0.13.2 and iapws V1.5.4 libraries in Python programming language V3.12.5. In this study, the data samples were not normalized due to worsening result with normalized data.

The data samples were split into train and test set. Train set is the data samples used in train and improve the model accuracy. Test set is unseen data to test if the model is applicable to other data that were not used in training process. Ratio of train to test was 80:20 with train set be 80% (20 samples) and test set be 20% (5 samples). The splitting used train_test_split function from scikit-learn V1.5.1 library in Python.

2.3 Model development and evaluation

There are many machine learning models can be used depending on types and relationships of using data. In this study, regression machine learning models were selected and implemented due to nature of data and target of predicting outcomes from input. The selected regression models included kernel ridge (KR), k-nearest neighbor (kNN), decision tree (DT), and feedforward neural network (FNN). Each model algorithm was developed as one multi-input multi-output (MIMO) and five multi-input single-output (MISO) following each output variable, results in total of six model for each algorithm. These models were adopted from scikit-learn library in Python.

$$MSE = \frac{1}{n}\sum_{i=1}^{n}\left(Y_i - \hat{Y}_i\right)^2 \qquad \text{Eq. 2}$$

$$MAPE = \frac{1}{n}\sum_{i=1}^{n}\left|\frac{Y_i - \hat{Y}_i}{Y_i}\right| \qquad \text{Eq. 3}$$

Metrics used for model evaluation are mean squared error (MSE) and mean absolute percentage error (MAPE). MSE was used in optimizing model hyperparameters to improve accuracy of each model to most suit with train set before evaluating which generally used in regression problems [6]. While MAPE was used to identify the error of prediction. According to Eq.2 and 3, n is n^{th} sample. Y_i is real value of a variable and $\hat{Y}_i$ is prediction value of a variable.

Each regression machine learning model (MIMO and MISO of every model) was hyperparameters optimized to improve accuracy with the train set. This step was done by GridseachCV function from scikit-learn library. GridsearchCV uses ranges of defined hyperparameters grouping into every possible combination to find which group of hyperparameters yield best performance, which in this study is the lowest MSE.

The optimized models were then compared performance by plotting learning curve. Learning curve helps in identifying performance of machine learning models if there is any underfit or overfit in the model and how each model performs with different number of train samples. There were two plots of learning curve, first learning curves were plotted with train set compare with validate set which accounts for 20% of train set to study amount of data samples used to train the model, this was done to minimize effects of limited amount of data samples causing underfitting. Second learning curves were comparison between train set and test set to identify overfitting and performance of the model. Both curve uses KFold cross-validation with 5 folds.

Most suitable model was decided based on two factors, (1) minimum amount of data samples used to train the model to achieve stable plateau and (2) performance of the model at 20 train samples. Then, the most suitable model's predictions would be plotted in parity plot to identify if great performance of the model came from high variance low value mean prediction.

Table 2 Hyperparameter values of models used in GridsearchCV.

Model algorithm name	Name and bound of hyperparameters

Kernel ridge	alpha = [0.2 - 3.0];
	degree = [2 - 5];
	kernel =
	['linear', 'chi2', 'poly', 'rbf',
	'laplacian', 'sigmoid', 'cosine']

k-Nearest neighbor	n_neighbors = [1 - 8];
	weights = ['uniform', 'distance'];
	algorithm = ['auto', 'kd_tree'];
	leaf_size = [5 - 50];
	p = [1.0 - 2.0]

Decision tree	random_state = 0;
	criterion =
	['squared_error', 'friedman_mse',
	'absolute_error'];
	splitter = ['best', 'random'];
	max_depth = [none, 3 - 9];
	min_samples_split = [2, 4, 6]

Feedforward neural network	max_iter = 100000;
	random_state = 0;
	early_stopping = True;
	validation_fraction = 0.25;
	solver = 'lbfgs';
	alpha = 0.0001;
	hidden_layer_sizes =
	[(20), (50), (100),
	(20,20), (20,50), (20,100),
	(50,20), (50,50), (50,100),
	(100,20), (100,50), (100,100)];
	activation = ['identity', 'logistic',
	'tanh', 'relu'];
	learning_rate =
	['constant', 'invscaling', 'adaptive']

3. RESULTS AND DISCUSSION

3.1 Data validation

25 data samples were validated with Peng-Robinson equation of state. Using temperature and pressure from data samples in equation of state, giving composition of n-pentane and n-hexane at specified conditions. Compare composition between obtained data samples and equation of state using MAPE, resulting in 0.22% average MAPE of n-pentane composition in distillate and 3.33% average MAPE of n-hexane in bottom. The results show indifference in thermodynamics model between operator training simulation and Peng-Robinson equation of state proving the thermodynamics credibility of data samples.

3.2 Data preparation

Variables in data samples were studied their correlation and collinearity through Pearson correlation analysis. According to figure 2, Reflux volumetric flow rate (Reflux Flow), Distillate temperature (DIS Temp) show no significant correlation (> 0.5 or < - 0.5) with most input variables except column pressure drop (Pres Drop) and they provide no valuable outputs for models to be trained for since this column-controlled distillate purity by cascade control of first tray or overhead temperature (OVH Temp). Furthermore, steam mass flow rate (Steam Flow) and steam pressure (Steam Pres) are collinear variables because they were used to adjust bottom temperature (BTM Temp). They were merged into one variable called Reboiler Duty to reduce noise that can do to models.

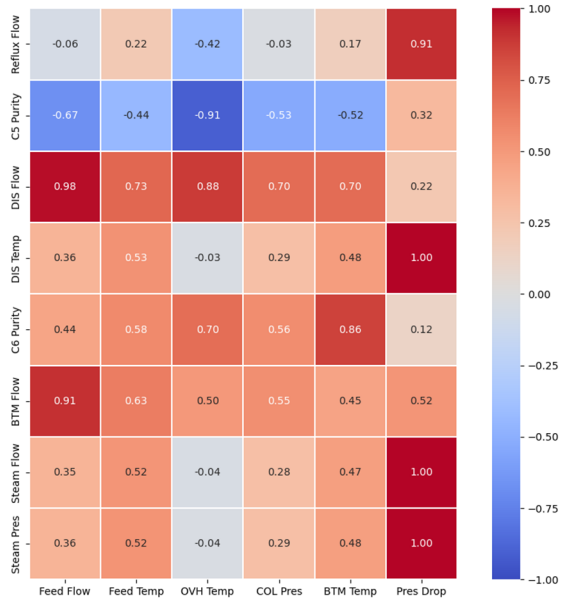

Figure 2 Variables correlation heatmap

After feature engineering with data samples, the data samples were gone through Pearson correlation analysis once again with no collinear appearance. The data samples were then split into train and test set at 20 and 5 samples respectively.

3.3 Model development and validation

3.3.1 GridsearchCV results of models

All the regression models were developed and hyperparameters optimized. Table 3 shows the hyperparameters of each model and their evaluation metrics with train dataset, both MIMO and MISO of each algorithm. Most algorithms show better performance with MISO model, with FNN having best performance. Model with single output has lower complexity in relationship between input and output variables causing less "noise" for the model to learn [7], by developing multiple MISO model results in better performance of model with every algorithm implemented in this study. This show model generally performs better with less complexity or less output variables, which supports different developed models with at most two outputs in the model [2], [3], [4], [8].

Table 3 Optimized regression algorithm models

Model algorithm name	MIMO		MISO	
	MSE	MAPE	MSE	MAPE
Kernel ridge	0.0108	0.22%	0.0108	0.11%
k-Nearest neighbor	0.6182	2.49%	0.3077	2.57%
Decision tree	1.5548	5.54%	1.0887	3.36%
Feedforward neural network	0.9018	5.22%	0.0009	0.10%

FNN MISO model showed higher performance than other MISO models, this was caused by many factors being that FNN in scikit-learn library hyperparameters was more diverse than other model algorithms used within same library causing hyperparameters optimization of FNN model suited dataset better than other models. Another factor was FNN has validation and early stopping built within function which helps in preventing overfitting model [6], [7]. With these factors considered, FNN was the best performing model with train dataset due to its unique mechanism and adaptable hyperparameters to characteristic of dataset.

3.3.2 Learning curve of model algorithms

Only KR MISO and NN MISO model were selected to done learning curve analysis due to their outperformance to other models. Learning curve was plotted comparing train-validate and train-test dataset evaluation results to study minimum amount of train data samples to develop regression model which determined by graph reaching stable plateau and performance of the model at 20 train samples to identify which model truly most suitable for distillation process. Validate and test line should approach to and parallel with train line to indicate great performance of model algorithms learning.

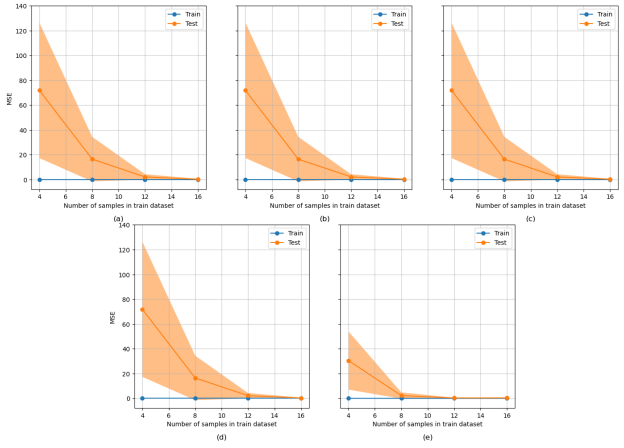

Figure 3 KR MISO learning curve (train-validate): (a) n-pentane composition in distillate (C5 Purity), (b) distillate volumetric flowrate (DIS Flow), (c) n-hexane composition in bottom (C6 Purity), (d) bottom volumetric flowrate (BTM Flow), (e) reboiler duty

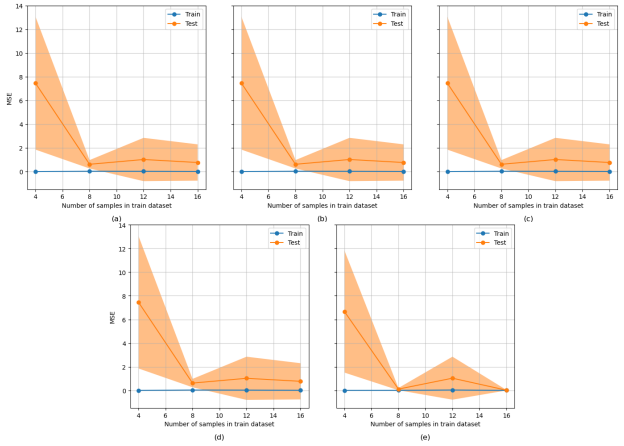

Figure 4 FNN MISO learning curve (train-validate): (a) n-pentane composition in distillate (C5 Purity), (b) distillate volumetric flowrate (DIS Flow), (c) n-hexane composition in bottom (C6 Purity), (d) bottom volumetric flowrate (BTM Flow), (e) reboiler duty

According to figure 3 and 4, KR MISO model performed worse compared to KNN MISO model at 4 and 8 train samples due to characteristics of hyperparameters of KR MISO models that might be overfitting to 20 train samples while FNN MISO model has overfitting prevention mechanisms like early stopping [7]. With increasing amounts of train samples, KR MISO model performed as well as FNN MISO model due to the model was optimized to fit well with 20 train samples, with KR MISO model's average MSE and MAPE was 0.0121 and 0.19% respectively while FNN MISO model's average MSE and MAPE was 0.0010 and 0.15%. The results indicate that FNN MISO model outperformed KR MISO model in train and validate dataset.

KR MISO model required 20 total samples (16 train and 4 validate) to reach stable plateau while FNN MISO model reached stable plateau at 10 total samples (8 train and 2 validate), indicating different required train samples with FNN MISO model used the least samples.

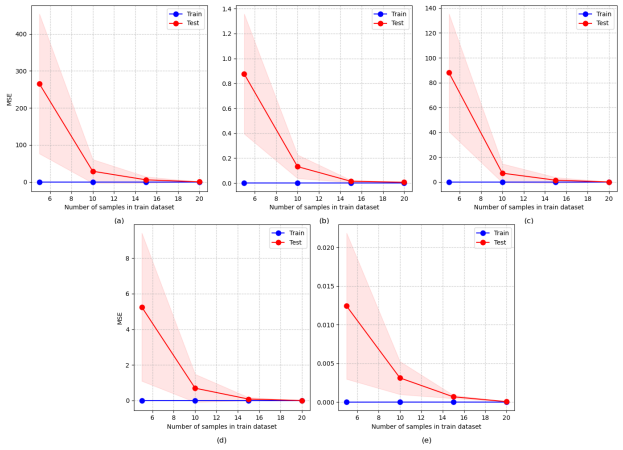

Figure 5 KR MISO learning curve (train-test): (a) n-pentane composition in distillate (C5 Purity), (b) distillate volumetric flowrate (DIS Flow), (c) n-hexane composition in bottom (C6 Purity), (d) bottom volumetric flowrate (BTM Flow), (e) reboiler duty

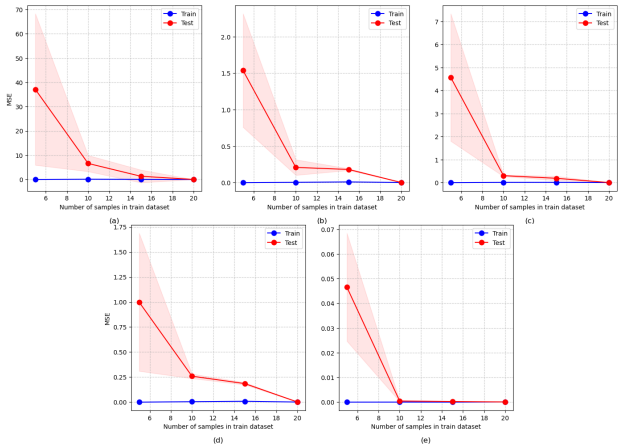

Figure 6 FNN MISO learning curve (train-test): (a) n-pentane composition in distillate (C5 Purity), (b) distillate volumetric flowrate (DIS Flow), (c) n-hexane composition in bottom (C6 Purity), (d) bottom volumetric flowrate (BTM Flow), (e) reboiler duty

Considering prediction accuracy by each output variables, KR MISO model slightly outperformed FNN MISO model on (b) distillate volumetric flowrate (DIS Flow) and (e) reboiler duty while in other variables FNN MISO model significantly outperformed KR MISO model. Due to complex physical properties of distillation column and nature of each algorithm that can fit into different relationship of variables, both model outperform other model in some variables. Contrary to limitations of low amount of data samples, both model shows no overfitting at 20 train samples which can be observed from test and train line were close and parallel.

At 5 train samples, average MSE and MAPE of KR MISO model were 71.8494 and 8.49% respectively while average MSE and MAPE of FNN MISO model were 8.8494 and 4.76%. As train samples increased to 20, average MSE and MAPE of KR MISO model lowered to 0.0317 and 0.19% while FNN MISO model were 0.0010 and 0.15%, indicating FNN MISO model performance was overall better.

3.3.3 Parity plot of FNN MISO model

FNN MISO model's predictions were used to plot parity plot to identify if the predictions were high variance. According to figure 7, all predicted values were on the line which indicates great accuracy of the model.

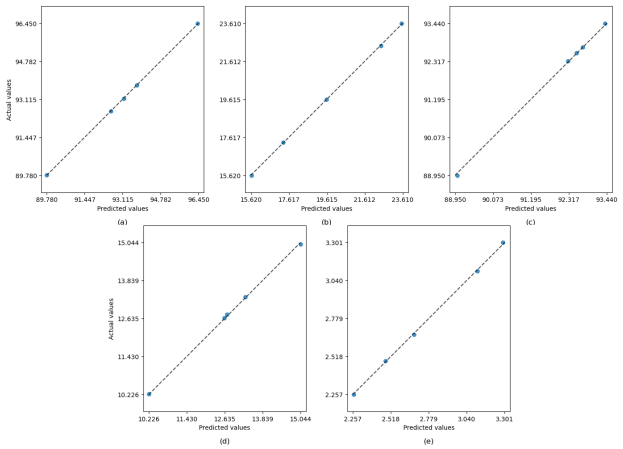

Figure 7 FNN MISO parity plot: (a) n-pentane composition in distillate (C5 Purity), (b) distillate volumetric flowrate (DIS Flow), (c) n-hexane composition in bottom (C6 Purity), (d) bottom volumetric flowrate (BTM Flow), (e) reboiler duty

4. CONCLUSION

This study was done to identify the suitable machine learning regression model for distillation process and the minimum required amount of data samples to develop accurate model. Feedforward neural network (FNN) outperforms other models (kernel ridge, k-nearest neighbor, decision tree) using multi-input single-output (MISO) model with MSE and MAPE of 0.0010 and 0.15% which was considered accurate. With the minimum required amount of data samples to train accurate model for FNN was 10 train samples. The results of this study proposes supporting information for future development of machine learning regression models to be applied with process engineering field with minimum data samples required for training models with sufficient hyperparameter optimization. Nevertheless, this study was done within limit amount of data samples. Broader and more diverse range of data samples would improve the understanding of model algorithms further.

ACKNOWLEDGMENTS

Authors acknowledge the financial support provided by Faculty of Engineering at Chulalongkorn University. The authors would like to thank the Department of Chemical Engineering at Chulalongkorn University for providing operator training simulation used for data samples. Appreciation to Sirawit Ploymuang for his data science expertise.

REFERENCES

[1] A. A. Kiss, S. J. Flores Landaeta, and C. A. Infante Ferreira, "Towards energy efficient distillation technologies – Making the right choice," *Energy*, vol. 47, no. 1, pp. 531–542, Nov. 2012, doi: 10.1016/j.energy.2012.09.038.

[2] H. Kwon, K. C. Oh, Y. Choi, Y. G. Chung, and J. Kim, "Development and application of machine learning-based prediction model for distillation column," *International Journal of Intelligent Systems*, vol. 36, no. 5, pp. 1970–1997, 2021, doi: 10.1002/int.22368.

[3] B. Çıtmacı, J. Luo, J. B. Jang, C. G. Morales-Guio, and P. D. Christofides, "Machine learning-based ethylene and carbon monoxide estimation, real-time optimization, and multivariable feedback control of an experimental electrochemical reactor," *Chemical Engineering Research and Design*, vol. 191, pp. 658–681, Mar. 2023, doi: 10.1016/j.cherd.2023.02.003.

[4] A. E. Sison, S. A. Etchieson, F. Güleç, E. I. Epelle, and J. A. Okolie, "Process modelling integrated with interpretable machine learning for predicting hydrogen and char yield during chemical looping gasification," *Journal of Cleaner Production*, vol. 414, p. 137579, Aug. 2023, doi: 10.1016/j.jclepro.2023.137579.

[5] P. P. Plehiers, S. H. Symoens, I. Amghizar, G. B. Marin, C. V. Stevens, and K. M. Van Geem, "Artificial Intelligence in Steam Cracking Modeling: A Deep Learning Algorithm for Detailed Effluent Prediction," *Engineering*, vol. 5, no. 6, pp. 1027–1040, Dec. 2019, doi: 10.1016/j.eng.2019.02.013.

[6] K. C. Oh, H. Kwon, S. Y. Park, S. J. Kim, J. Kim, and D. Kim, "Hyperparameter Optimization of the Machine Learning Model for Distillation Processes," *International Journal of Intelligent Systems*, vol. 2024, no. 1, p. 5564380, Jan. 2024, doi: 10.1155/2024/5564380.

[7] B. Sabiri, B. El Asri, and M. Rhanoui, "Mechanism of Overfitting Avoidance Techniques for Training Deep Neural Networks:," in *Proceedings of the 24th International Conference on Enterprise Information Systems*, Online Streaming, --- Select a Country ---: SCITEPRESS - Science and Technology Publications, 2022, pp. 418–427. doi: 10.5220/0011114900003179.

[8] A. H. Elsheikh, E. M. S. El-Said, M. Abd Elaziz, M. Fujii, and H. R. El-Tahan, "Water distillation tower: Experimental investigation, economic assessment, and performance prediction using optimized machine-learning model," *Journal of Cleaner Production*, vol. 388, p. 135896, Feb. 2023, doi: 10.1016/j.jclepro.2023.135896.

Techno-economic analysis of hydrogen production pathways for carbon dioxide to methanol conversion process

Gantaphon Manimon[1], Kritchart Wongwailikhit[1,*]

[1] Center of Excellence in Particle and Material Processing Technology Department of Chemical Engineering, Faculty of Engineering, Chulalongkorn university, Bangkok 10330, Thailand
[*] Corresponding author: kritchart.w@chula.ac.th

ABSTRACT

The petrochemical industry significantly contributor to global carbon dioxide (CO_2) emissions. Specifically, from the steam naphtha crackers process. Carbon capture and utilization (CCU) has been introduced as an effective approach to reducing CO_2 emissions. One promising pathway involves the hydrogenation of CO_2 for methanol synthesis. Given the crucial role of hydrogen as a raw material in CCU, this study evaluates three primary hydrogen production methods: grey, blue, and green hydrogen. Grey hydrogen production was studied using Steam Methane Reforming (SMR), Autothermal Reforming (ATR), and a combined SMR-ATR process. Blue hydrogen follows the same processes as grey hydrogen with the CO_2 capture process, while for green hydrogen, Alkaline Electrolysis (AEL) was analyzed. Process simulations were conducted in Aspen Plus, with economic feasibility is assessed by the levelized cost of hydrogen (LCOH), considering capital expenditures (CAPEX) and operating expenses (OPEX) including raw material, utility and other related costs. Environmental impact is assessed via CO_2 emissions. The results indicate that the most economical H_2 production pathway is grey hydrogen via the ATR process achieves the lowest LCOH at 2.38 USD/kg with relatively high CO_2 emissions at 9.83 kg CO_2 per kg H_2. Blue hydrogen has an LCOH of 2.38 USD/kg with a lower emissions of 2.72 kg CO_2 per kg H_2. Green hydrogen, which has CO_2 emissions 2.74 kg CO_2 per kg H, achieves the highest LCOH of 8.11 USD/kg. These findings provide insights into H_2 production strategies for methanol synthesis and MTO process.

Keywords: Hydrogen production; Carbon capture and utilization; Techno-economic analysis

1. INTRODUCTION

The petrochemical industry is a major contributor to global emissions, accounting for approximately 6.1% of total GHG emissions [1]. A key process in this industry is the steam cracking of naphtha, which emits 1.5–2 tons of CO_2 per ton of ethylene produced [2]. To reduce these emissions, Carbon Capture and Utilization (CCU) have been developed to capture CO_2 from industrial sources for reuse in chemical processes, one promising way is methanol synthesis via CO_2 hydrogenation. Methanol can then serve as a precursor for olefin production in the Methanol-to-Olefins (MTO) process [3].

Hydrogen (H_2) as a raw material in CO_2 hydrogenation, and its source significantly impacts both economic feasibility and environmental sustainability. Hydrogen production is classified into three main types: grey, blue, and green hydrogen. Grey and blue hydrogen, produced via Steam Methane Reforming (SMR) and Autothermal Reforming (ATR), remain the dominant methods but contribute significantly to CO_2 emissions. Green hydrogen, produced via water electrolysis using renewable energy, offers low CO_2 emissions but remains costly due to high electricity consumption [4].

Previous research has studied on the CO_2 utilization for converting it into value-added products such as olefins using methanol intermediate by CO_2 hydrogenation but there is still lack of comprehensive analysis of the cost and environmental impact of different hydrogen production methods This study aims to evaluate the economic feasibility and environmental impact via CO_2 emission of grey, blue, and green hydrogen production for CO_2 to methanol conversion process via hydrogenation. By assessing these pathways, this research seeks to identify a low-carbon and economically pathway for CO_2 utilization process applications.

2. EXPERIMENTAL

In this study, has primary CO_2 emission source came from steam naphtha cracker process 500,000 tons/year. Cost of CO2 capture from the process was assume equivalent to 100 USD/ton. Three hydrogen production pathways are considered in this study include grey hydrogen, blue hydrogen, and green hydrogen. Process simulations were conducted in Aspen Plus. Assessment framework of hydrogen production for pathways was analyzed. Economic feasibility is assessed by the levelized cost of hydrogen (LCOH), considering capital expenditures (CAPEX) and operating expenses (OPEX) including raw material, utility, operating labor, maintenance and other related costs. Environmental impact is assessed via CO_2 emissions per hydrogen production including direct emissions from process and indirect emissions from feedstock or Utility.

2.1 Simulation model development

Thermodynamic properties were selected based on suitability for the components involved in each process to ensure accurate system representation.

Grey and blue hydrogen were produced via steam methane reforming (SMR) and autothermal reforming (ATR) reactions. Both processes operate at high temperatures and pressures. The Peng-Robinson (PENG-ROB) equation of state was selected, as it is well-suited for non-polar mixtures under high-pressure conditions. The SMR reaction was modeled using an RPlug reactor with a Generalized Langmuir-Hinshelwood-Hougen-Watson (GLHHW) kinetic model to accurately represent the chemical reactions occurring on the catalyst surface. In contrast, the ATR reactor was modeled using an RGibbs reactor, where chemical equilibrium was assumed by minimizing the system's Gibbs free energy.

Green hydrogen was produced via alkaline electrolysis (AEL), which operates at low pressure and involves both liquid and vapor phases. The NRTL-RK property method was selected to accurately represent the electrolyte system and vapor–liquid equilibrium. The AEL process was simulated using Aspen Custom Modeler (ACM), which is capable of predicting the electrochemical behavior of an alkaline water electrolysis stack under various operating conditions.

2.2 Hydrogen Production process

This section investigates grey, blue, and green hydrogen production methods, were evaluated to meet the required feedstock demand for the methanol synthesis via CO_2 hydrogenation process.

2.2.1 Grey hydrogen

Grey hydrogen production was investigated using three process configurations: SMR, ATR and combined SMR-ATR processes. Reactions were simulated in Rplug reactor. Each system was evaluated under the following operating conditions: Temperature: 700, 800, 900, and 1000 °C, Steam-to-methane (S/C) Ratio:1, 2, 3, and 4 for SMR, Oxygen-to-methane (O/C) Ratio: 0.5 for ATR, all at a pressure at 50 bars.

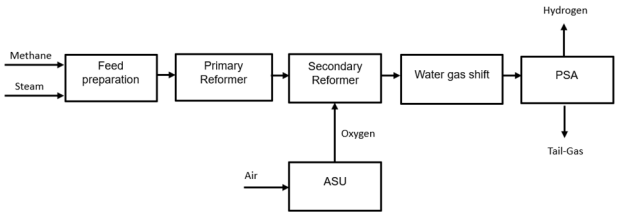

Figure 1 Block flow diagram of grey hydrogen production via methane reforming

2.2.2 Blue hydrogen

Blue hydrogen production conducts the same process configurations and operating conditions as grey hydrogen. Operating condition were also conducted with the same range of temperatures and S/C and O/C ratios. In blue hydrogen included an additional CO_2 capture process to reduce emissions. The captured CO_2 used as a feedstock in the methanol synthesis via CO_2 hydrogenation process.

CO_2 Capture and emissions accounting. For blue hydrogen, a CO_2 capture rate of 70% was assumed from the process gas stream (i.e., Tail gas). CO_2 emissions from combustion flue gases were excluded according to the real-world practice.

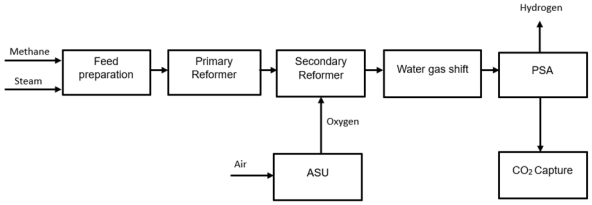

Figure 2 Block flow diagram of blue hydrogen production via methane reforming following with CO_2 capture process

2.2.3 Green hydrogen

Green hydrogen production was investigated using the Alkaline Electrolysis (AEL) process. The simulation was conducted under the following operating conditions: temperature: 70 to 100 °C, pressure at 7 bar, and current densities between 1000 and 5000 A/m² and other input variable, number of cells (N_{cell}) and active area of the electrode (A_{cell}) were defined according to the design scale to meet hydrogen demand.

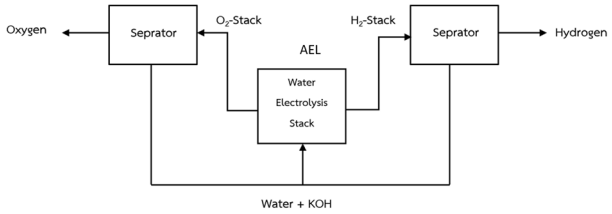

Figure 3 Block flow diagram of green hydrogen production via AEL

2.3 Processes Assessment

To comprehensively evaluate the feasibility of each hydrogen production pathway, three key criteria were assessed: energy consumption, environmental impact, and economic.

2.3.1. Process performance

To determine the optimal operating conditions for grey and blue hydrogen production, methane conversion and hydrogen yield were used to evaluate process performance.

$$CH_4 \text{ conversion } (\%) = \frac{CH_{4,Inlet} - CH_{4,Outlet}}{CH_{4,Inlet}} \quad (1)$$

$$H_2 \text{ Yield} = \frac{H_{2,Produced}}{CH_{4,Inlet}} \times 100 \quad (2)$$

In green hydrogen, performance was evaluated based on stack efficiency and hydrogen production

$$\text{Stack efficiency} = \frac{H_{2,Produced} \cdot LHV_{H_2}}{W_{stack}} \quad (3)$$

$$H_2 \text{ production} = \eta_F \cdot \frac{I}{z \cdot F} \cdot N \quad (4)$$

2.3.2 Energy consumption

Energy consumption for each hydrogen production pathway was determined, based on total energy require in processes compare with hydrogen produce.

$$\text{Energy consumption} = \frac{Q_{Total}}{H_{2,Produced}} \quad (5)$$

2.3.3 Environmental impact

Environmental aspect was evaluated by calculating via the CO_2 emissions from direct and indirect source compare with hydrogen produce.

$$CO_2 \text{emission} = \frac{CO_{2,Emission}}{H_{2,Produced}} \quad (6)$$

2.3.4 Economic analysis

Economic analysis of each hydrogen production pathways was assessed using the Levelized Cost of Hydrogen (LCOH), total cost of producing hydrogen over its entire lifecycle. The LCOH includes both Capital Expenditures (CAPEX) and Operating Expenses (OPEX).

$$LCOH = \frac{\text{Total Annualized Cost (CAPEX + OPEX)}}{H_{2,Produced}} \quad (7)$$

3. RESULTS AND DISCUSSION

3.1 Model and Validation

The simulation model was validated with experimental data, its accuracy and reliability were assessed by comparing results using the root mean square (RMS) error. For grey and blue hydrogen production, the SMR and ATR reactions were validated based on methane conversion under varying conditions of temperature, pressure, and steam-to-carbon (S/C) ratio.

Table 1 The validation result for SMR and ATR models.

Model	Condition	RMS
SMR	Temperature = 400 to 900 °C Pressure = 1.01 bar S/C = 1 – 4	CH_4 conversion = 0.998
ATR	Temperature = 400 – 900 °C Pressure = 1.01 bar S/C = 1	CH_4 conversion = 0.991

Green hydrogen, AEL reaction, was validation using voltage per cell (Vcell), faraday efficiency (η_F) and HTO

Table 2 The validation result for AEL model.

Model	Condition	RMS
AEL	Temperature = 75 Pressure = 7 bar A = 2.5 m^2 Cell = 1 Current density = 1 - 3 A/cm^2	Vcell = 0.980 η_F = 0.995 HTO = 0.913

The RMS values obtained indicate good agreement between the simulation models and experimental data, confirming the models' reliability for further performance simulation and economic evaluations.

3.2 Process performance analysis

3.2.1 Grey and blue hydrogen

This section shows the effect of operating condition on methane conversion and hydrogen yield for three systems, SMR, ATR and SMR+ATR.

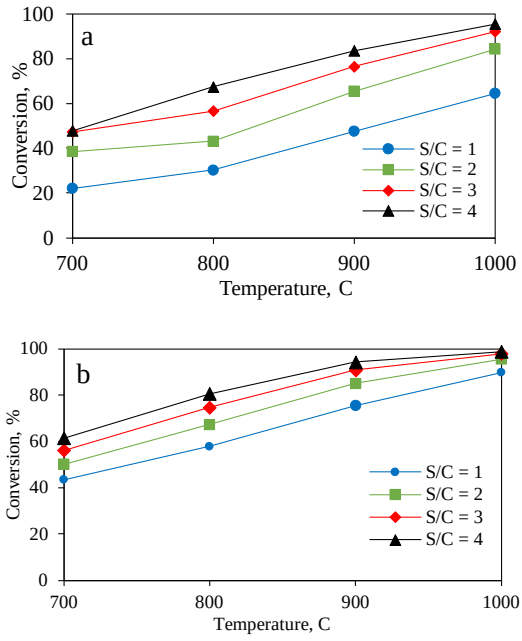

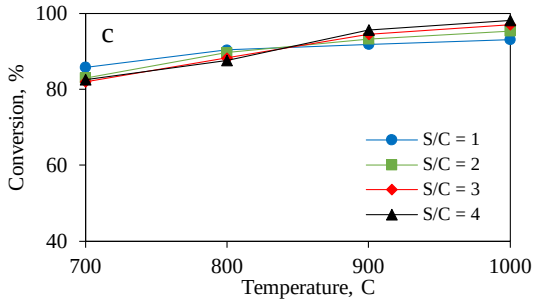

Figure 4 Methane conversion in SMR (a), ATR (b) and SMR+ATR (C) at temperature range 700 – 1000 C, pressure of 50 bar: S/C ratios of 1, 2, 3 and 4 by blue, green, red and black lines respectively.

From figure 4 the results reveal that methane conversion increases with an increase in steam-to-carbon (S/C) ratio and temperature.

For the SMR process, methane conversion improves significantly from 64.61% at S/C = 1 to 95.51% at S/C = 4 at 1000 °C. In the ATR process, conversion rises from 61.43% at S/C = 1 to 98.80% at S/C = 4 at 1000°C, achieving the highest conversion among the systems studied. Similarly, the SMR+ATR system shows an improvement from 82.52 % at S/C = 1 to 98.07% at S/C = 4 at 1000°C.

SMR+ATR consistently achieves the highest methane conversion, demonstrating the synergistic effect of combining endothermic steam reforming with exothermic partial oxidation reactions in the autothermal reformer. It's enhancing overall process efficiency and enables more complete methane utilization for hydrogen production, while requiring less raw material and energy input to achieve high conversion compared to standalone SMR and ATR processes

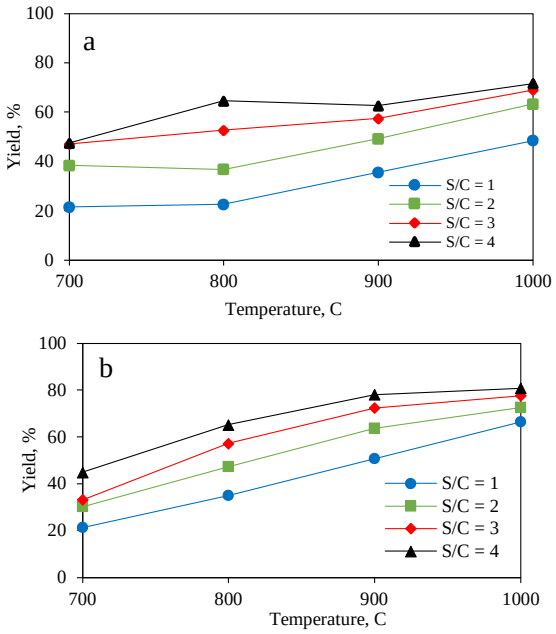

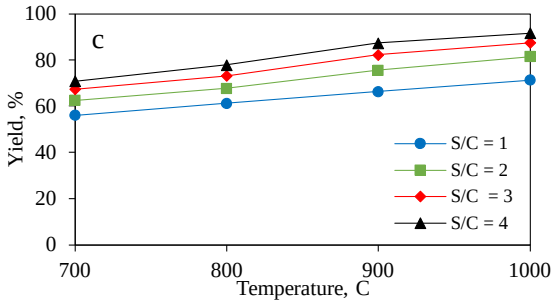

Figure 5 Hydrogen yield in SMR (a), ATR (b) and SMR+ATR (c) at temperature range 700 – 1000 C, pressure of 50 bar and S/C = 1, 2, 3 and 4 by blue, green, red and black lines respectively.

Figure 5 reveal that hydrogen yield increases more favorable operating conditions, higher S/C and higher temperature). The SMR+ATR system achieves the highest hydrogen yield of 91.64%, while ATR and SMR achieve yields of 80.93% and 71.63%, respectively, under similar conditions.

These results confirm that the SMR+ATR system provides superior process performance for hydrogen production, benefiting from two reforming reactions that work synergistically to convert methane into hydrogen more efficiently. The findings indicate that optimizing the S/C ratio and reaction temperature is crucial for maximizing hydrogen production efficiency across all reforming processes.

3.2.2 Green hydrogen

The performance of green hydrogen production via Alkaline Electrolysis (AEL) was assessed under varying conditions evaluated include stack efficiency and hydrogen production rate.

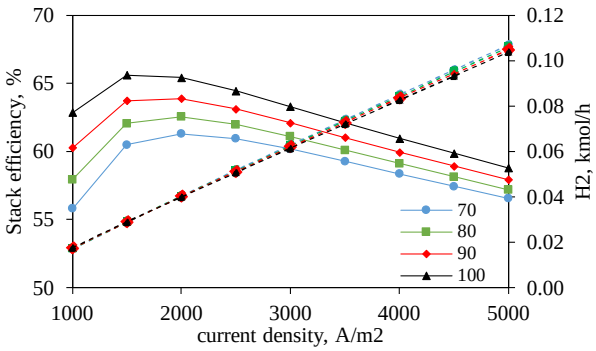

Figure 6 Effect of current density and temperature on AEL at pressure of 7 bar. Temperature range 700 – 1000 °C in blue, green, red and black lines respectively. Stack efficiency and hydrogen production rate represented in solid and dashed lines respectively.

From figure 6 shows an effect of current density and temperature on stack efficiency and hydrogen production rate. It reveals that stack efficiency peaks at around 1500 A/m² and decreases at higher current densities. The highest stack efficiency of 65.6% was

achieved at 100 °C, indicating that higher operating temperatures improve reaction kinetics and electrochemical performance.

The hydrogen production rate increases linearly with current density, following Faraday's law. However, higher current densities and elevated temperatures also lead to hydrogen gas crossover, which causes losses in the stack efficiency of the system.

3.3 Energy Consumption and Environmental impact

3.3.1 Grey and blue hydrogen

The energy consumption and environmental impact of grey and blue hydrogen pathways were analyzed under varying steam-to-carbon (S/C) ratios to evaluate their influence on process efficiency and CO_2 emissions.

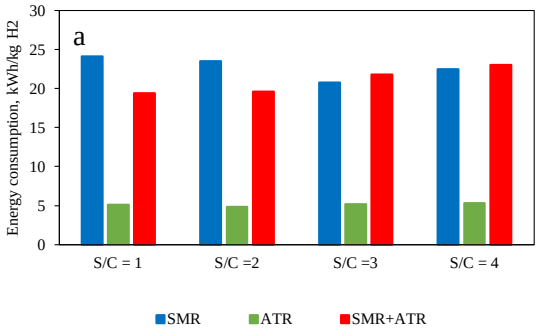

Compare Grey and Blue hydrogen

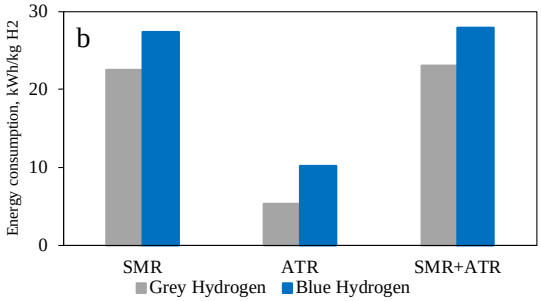

Figure 7 The energy consumption results of SMR, ATR and SMR+ ATR at temperature 1000 °C pressure of 50 bar. S/C ratio of 1, 2, 3 and 4 graph (a). A comparison between grey and blue hydrogen pathways on energy consumption at S/C at 4 and 1000 °C graph (b).

From figure 7a, show A reduction in energy demand is observed for the SMR process as the S/C ratio increases, due to the utilization of waste heat for steam generation. In contrast, the SMR+ATR system requires more energy at higher S/C ratios, owing to increased steam requirements and the additional cooling water demand needed to manage the high-temperature steam. The ATR process, however, consistently exhibits lower energy consumption across all S/C ratios. Among the three systems, SMR shows the highest energy demand due to its reliance on external heat supply. In comparison, ATR benefits from internal heat generation through partial oxidation reactions, resulting in significantly lower overall energy requirements.

A comparison between grey and blue hydrogen pathways is shown in figure 7b, the introduction of CO_2 capture slightly increases the overall energy demand, particularly for SMR and SMR+ATR processes. Nevertheless, ATR remains the most energy-efficient configuration, even with the integration of CO_2 capture. This is because the majority of energy consumption in these systems came from the reforming reactions rather than the CO_2 capture process.

3.3.2 Green hydrogen

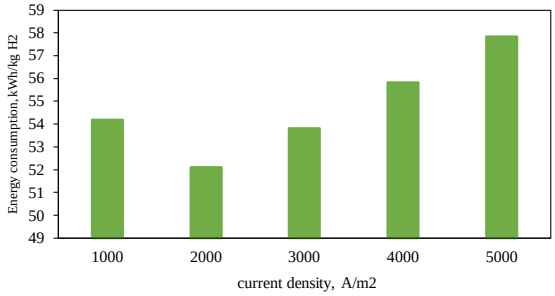

Figure 8 The energy consumption result of AEL at temperature 100 °C pressure of 7 bar. Current density in range 1000 – 5000 A/m^2.

The lowest energy consumption is 52.1 kWh/kg H_2 at current density 2000 A/ m^2. However, beyond 3000 A/m², energy demand increases significantly, reaching about 58 kWh/kg H_2 at 5000 A/m². This sharp rise is attributed to overpotential losses at higher current densities.

These findings highlight that green hydrogen production requires substantially higher specific energy consumption compared to grey and blue hydrogen.

3.4 Environmental and economic impacts

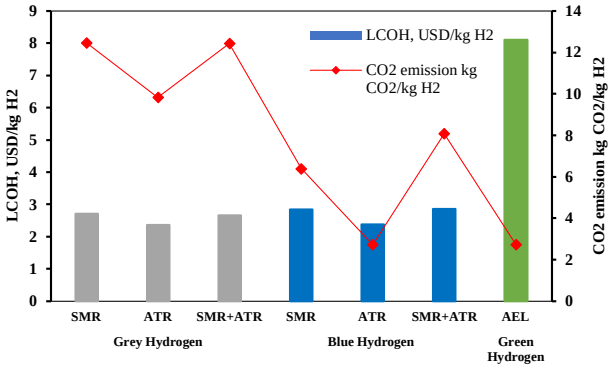

Figure 9 shows the environmental and economic impacts of various hydrogen production pathways based on CO_2 emissions and levelized cost of hydrogen (LCOH).

Among grey hydrogen routes, ATR exhibits the lowest LCOH at approximately 2.38 USD/kg H_2, while SMR and SMR+ATR system shows slightly higher costs due to additional process complexity. However, all grey hydrogen systems result in high CO_2 emissions, ranging from 9 - 12 kg CO_2/kg H_2, making them less environmentally favorable.

Blue hydrogen, CO_2 emissions are significantly reduced due to the incorporation of carbon capture. ATR with CO_2 capture achieves the lowest emissions around 2.72 kg CO_2/kg H_2 and remains the most cost-effective option at 2.39 USD/kg H_2. While SMR and SMR+ATR system with capture shows the same trend at grey hydrogen with slightly higher emissions and cost.

Green hydrogen produced has a near-zero CO_2 emissions, quantified at 2.74 kg CO_2 per kg H_2. However, this benefit comes at a significant economic cost, with the highest LCOH at 8.11 USD/kg H_2, primarily driven by demand in
Electricity from renewable energy, this emphasizes the trade-off between environmental sustainability and economic feasibility.

3.4.1 Sensitivity analysis

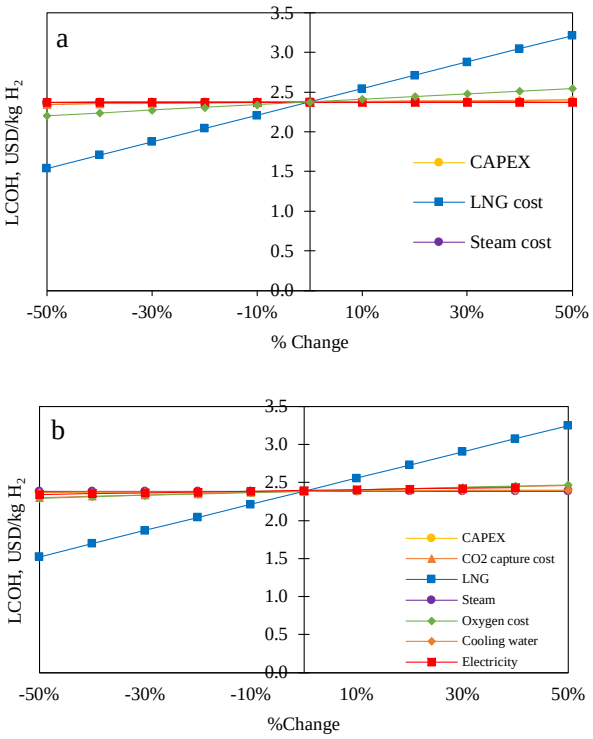

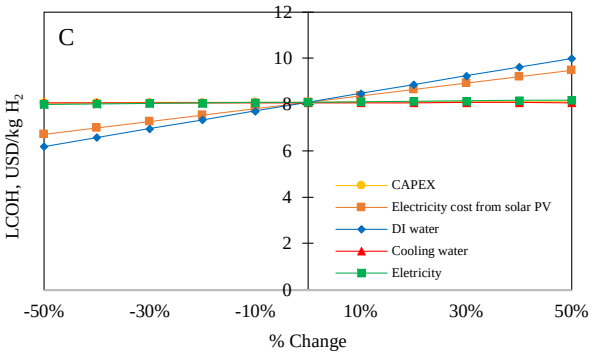

Figure 10 show the sensitivity analysis of the Levelized Cost of Hydrogen (LCOH) for three hydrogen production pathways: grey hydrogen (a), blue hydrogen (b) and green hydrogen (c).

In Figure 10a, the LCOH for grey hydrogen is most sensitive to fluctuations in LNG cost, with a 50% increase resulting in a rise from approximately 2.3 to 3.2 USD/kg H_2, and a 50% reduction decreasing it to 1.5 USD/kg H_2. Other variables, including CAPEX, steam, and utility costs (cooling water and electricity), have comparatively minor effects on the LCOH, indicating that grey hydrogen economics are primarily driven by feedstock prices.

Blue hydrogen in Figure 10b, LNG cost has a critical influencer. A similar sensitivity trend is observed with LNG, while CO_2 capture costs show moderate impact. CAPEX, steam, oxygen, and utility costs exhibit relatively flat responses across the tested variation range.

Green hydrogen in Figure 10c, the sensitivity analysis indicates that the LCOH is primarily affected by the costs of deionized (DI) water and solar PV electricity. A 50% increase in DI water raises the LCOH from approximately 8.1 to 10.7 USD/kg H_2, while a 50% reduction lowers it to around 6.2 USD/kg H_2. Other variables, such as utility costs (cooling water and electricity), exhibit minimal impact on LCOH.

4. CONCLUSION

This study aimed to evaluate the techno-economic of grey, blue, and green hydrogen production pathways for methanol synthesis via CO_2 hydrogenation. Grey hydrogen, produced from SMR, ATR, and SMR+ATR processes, result demonstrated the lowest LCOH in ATR system, with the SMR+ATR system achieving the best process performance in terms of methane conversion and H_2 yield across all operating condition range. Blue hydrogen, incorporating CO_2 capture, effectively reduced emissions to as low as 2.32 kg CO_2/kg H_2, particularly in the ATR system, while maintaining competitive LCOH values. Green hydrogen, produced via AEL, reach near-zero direct CO_2 emissions 2.74 kg CO_2/kg H_2 but with the highest LCOH, 8.11 USD/kg H_2, primarily due to its high electricity demand.

The results highlight a trade-off between LCOH and environmental impact. While grey hydrogen is the most economically favorable option, blue hydrogen offers a reasonable economics and low environmental impact. Green hydrogen presents the most sustainable option, but with significantly higher economic cost, emphasizing the need for further improvements in electrolyze efficiency and renewable sourcing.

A key challenge of this study is to fairly compare the three hydrogen production pathways grey, blue, and green hydrogen under consistent and realistic assumptions. In particular, the integration of CO_2 capture in blue hydrogen introduces an additional CO_2 stream that must be utilized for upstream methanol synthesis, thereby requiring higher hydrogen production than grey and green pathways, which complicates fair comparison

Future work is to explore heat integration to optimize energy within the hydrogen production processes to optimize overall energy efficiency. Incorporating techno-economic optimization and life cycle assessment (LCA) could provide deeper insights into the environmental and economic trade-offs of each hydrogen pathway.

ACKNOWLEDGMENTS

The authors gratefully acknowledge the support of the Department of Chemical Engineering, Faculty of Engineering, Chulalongkorn University, and sincere appreciation to the advisors who provided critical technical support and validation data for this study.

REFERENCES

1. Gabrielli, P., et al., Net-zero emissions chemical industry in a world of limited resources. One Earth, 2023. 6(6): p. 682-704.
2. Liu, J., et al., Conceptual carbon-reduction process design and quantitative sustainable assessment for concentrating high purity ethylene from wasted refinery gas. Chinese Journal of Chemical Engineering, 2023. **57**: p. 290-308.
3. Cordero-Lanzac, T., et al., A CO2 valorization plant to produce light hydrocarbons: Kinetic model, process design and life cycle assessment. Journal of CO2 Utilization, 2023. **67**: p. 102337.
4. Cordero-Lanzac, T., et al., A techno-economic and life cycle assessment for the production of green methanol from CO2: catalyst and process bottlenecks. Journal of Energy Chemistry, 2022. 68: p. 255-266.

Performance of combination ESN and LSTM in prediction of temperature in magnetic heating reactor

Rasiq Dipta Alkindi[1,*], Paisan Kittisupakorn[1]

[1] Department of Chemical Engineering, Faculty of Engineering, Chulalongkorn University, Bangkok 10330, Thailand
[*] Corresponding author: rasiqdipta@gmail.com

ABSTRACT

Hydrogen is critical to numerous industrial applications, yet its efficient production remains challenging due to the complex and often unpredictable dynamics of reactor systems. In this study, we address this challenge by employing a neural network (NN) approach to emulate a reactor model in cases where traditional mathematical modeling struggles with unknown factors. We propose a hybrid neural network model that integrates an Echo State Network (ESN) with a Long Short-Term Memory (LSTM) network in series. The ESN processes complex systems and high-dimensional input data by transforming them into a simplified state while preserving essential nonlinear dynamics. The LSTM then captures both rapid fluctuations and long-term trends through its gating mechanisms. These experiments rely on input and output datasets derived from a simulated reactor model. By combining these two methods, our approach enhances prediction accuracy and reliability in modeling dynamic, complex systems. The experiments revealed that increasing the number of reservoir nodes from 10 to 20 reduced the ESN's training mean absolute error (MAE) by over 90%, and the optimal configuration with 30 reservoir nodes, a spectral radius of 0.5, 0.9 connectivity, a batch size of 4, 50 LSTM units, and 60 epochs, achieved training MAE values ranging from 9.15 to 6.33, testing MAE of 8.74 to 8.06, and validation MAE of 14.88 to 14.96, with R^2 consistently exceeding 0.998 across 7N, 9N, and 17N winding coils. Simulation experiments demonstrate that the ESN-LSTM model achieves better prediction accuracy and overall model fitness.

Keywords: Artificial Neural Network; Echo State Network; Long-Short Term Memory; series ESN-LSTM.

1. INTRODUCTION

Hydrogen is increasingly recognized as the future of energy systems and a valuable industrial raw material, given its significant potential to support a cleaner and more sustainable planet. [1]. In recent studies, alternative approaches have been explored to optimize hydrogen production, including research on steam methane reforming (SMR) using Joule heating, which resulted in a temperature profile that increased continuously along the reactor, and temperature distribution control via induction heating. SMR reactors play a crucial role in this evolving energy landscape by converting steam and methane into hydrogen through Ni-Co catalytic processes [2, 3].

Meanwhile, the complex dynamics of chemical process reactors often exhibit significant nonlinearity, requiring advanced control techniques. Artificial Neural Networks (ANNs) have emerged as a powerful tool in this context, offering impressive predictive abilities through their structured design comprising an input layer, one or more hidden layers, and an output layer [4]. These networks learn from datasets using various training methods and validation techniques, effectively mimicking physical processes to develop dynamic models of complex systems. Different types of ANNs have been employed to address the challenges of modeling nonlinear systems [5].

One approach involves Recurrent Neural Networks (RNNs), such as the echo state network (ESN) and simplified dual network (SDN), which are designed to identify unknown nonlinear dynamical systems with multi-input, multi-output configurations [6]. In addition, Long Short-Term Memory (LSTM) networks have been introduced to overcome issues like the vanishing gradient problem by incorporating memory cells that retain information over time. This capability enables LSTMs to capture long-term dependencies that are critical for accurate future predictions. Research has shown that combining these architectures enhances

performance by leveraging their complementary strengths [7, 8].

For example, E. López developed a neural network model for forecasting wind power over a 48-hour horizon by integrating LSTM memory blocks within a framework that also employs an ESN architecture. His approach utilized gradient descent methods to train the hidden layer and applied regularized quantile regression to the output layer [9]. Similarly, Y. Yang proposed a Deep Memory Echo State Network (DMESN) that combines the echo state mechanism with hidden state formation, using gating functions to stabilize information flow and high-dimensional mapping to extract relevant features, as demonstrated through exhaust gas temperature prediction experiments [10].

Building on these advances, the proposed hybrid architecture integrates an ESN with an LSTM in series to model the nonlinear dynamics of a magnetic heating reactor. In this configuration, the ESN, with its randomly initialized recurrent reservoir, rapidly transforms complex, high-dimensional input signals into a richer state space that effectively captures immediate nonlinearities and transient behaviors. The resulting state representations are then refined by the LSTM, which learns both short-term fluctuations and long-term dependencies through its gating mechanisms. This integrated approach enhances prediction accuracy and improves robustness in dynamic complex systems. In the future, the ESN-LSTM model will be used in Model Predictive Control (MPC) instead of directly modeling the reactor.

2. EXPERIMENTAL

2.1 Model Reactor

The model used in this study, based on López's paper [11], involves a quartz tube reactor with a catalyst inside and a magnetic coil as the heat source. The reactor dimensions are 1 m in length, with an inside diameter of 6.5 mm and an outside diameter of 12.5 mm. It contains 11 grams of catalyst at a height of 9.5 cm. The induction coil consists of 17 turns, with a coil diameter of 3.25 mm and a height of 13.5 cm. The model is insulated with Promasil 1000 L to prevent heat leakage. The feed temperature is 300°C, with an S/C ratio of 2, a flow rate of 30 NL/h CH_4, yH_2 = 10.7 mol%, and pressure of 1 bar. The reactor illustration is provided in [11] :

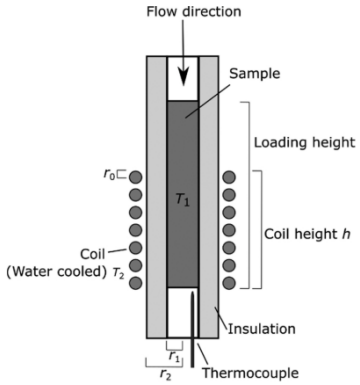

Figure 1 Cross-sectional sketch of the reactor setup with a sample (catalyst), insulation, and coil.

Efficient modeling and control are vital for power systems, as mathematical models and process control ensure optimal performance [12]. Reactor systems, governed by nonlinear PDEs derived from reaction kinetics and physical properties, require nonlinear controllers. The primary challenge lies in developing a simplified yet accurate model [11, 13]. In an induction-heated reactor, power losses can be expressed as follows:

$$P_{in} = P_{reaction} + P_{coil} + P_{iso} + P_{rest} \quad \textbf{Eq 1.}$$

Here, hysteresis-induced loss (P_{hys}) contributes partially to the SMR reaction while also dissipating through insulation. Thus, $P_{reaction} = P_{hys} + P_{iso}$, with P_{rest} measured at 200 ± 10 W and 290 W, leading to the following equation:

$$P_{reaction} = P_{hys} + P_{iso} \quad \textbf{Eq 2}$$

$$P_{in} = P_{hys} + P_{coil} + P_{rest} \quad \textbf{Eq 3}$$

The hysteresis heating power in a magnetic sample of mass m_s under an alternating magnetic field (amplitude B_{app} with B_{max} and frequency f) is given by:

$$P_{hys} = A_{hys}\,(B_{max}, T)\; f\; m_s \quad \textbf{Eq 4}$$

Where the area of the hysteresis loop $A_{hys}\,(B_{max}, T)$ is given as:

$$A_{hys}\,(B_{max}, T) = \oint_{-Bmax}^{Bmax} \sigma(B_{max}, T)\, dB_{app} \quad \textbf{Eq 5}$$

and σ is the mass-specific magnetization; for small B_{max}, A_{hys} increases proportionally B_{max}^2. For simplicity, the magnetic field inside a coil (height h with N turns) carrying

$$I(t) = I_0 \cos(2\pi f t) \quad \textbf{Eq 6}$$

is assumed homogeneous with winding density $n = N/h$, so

$$B_{app} = \mu_0\, n\, I(t) \quad \textbf{Eq 7}$$

In a solenoid, a current I produce a uniform magnetic field

$$H = NI/L \quad \textbf{Eq 8}$$

where L is its length. The catalyst's magnetization derived from synthesized precursors is described by the Brillouin function, crucial due to the dynamic, oscillatory nature of B_{app} [14, 15]. Specifically

$$B_j(y) = \frac{2J+1}{2J} \coth\left(\frac{2J+1}{2J} y\right) - \frac{1}{2J}\coth\left(\frac{1}{2J} y\right) \quad \text{Eq 9}$$

with,

$$y = x J = {gJ \mu BJ B}/{kB T} \quad \text{Eq 10}$$

and magnetization is

$$M = M_s B_j(y) \quad \text{Eq 11}$$

with

$$M_s = n gJ \mu B J \quad \text{Eq 12}$$

The dynamic B field influences M as shown by the hysteresis loop (approximating a trapezoidal shape). Heat loss through insulation is modeled by Fourier's law in cylindrical coordinates:

$$P_{iso} = \frac{2\pi h_{iso}\lambda}{ln\left(\frac{r_2}{r_1}\right)}(T_1 - T_2) \quad \text{Eq 13}$$

Where λ is the thermal conductivity, h_{iso} is the height cylinder, r_1 and r_2 are the inner and outer radii of insulation, T_1 and T_2 are the inner and outer temperatures, respectively [11]. Coil losses (P_{coil}) arise from Joule heating and are affected by both the skin effect, where current concentrates near the surface

$$d = \sqrt{\frac{\rho}{\pi f \mu}} \quad \text{Eq 14}$$

and the proximity effect, which induces eddy currents.

The AC resistance is approximated by

$$R_{coil} = R_{DC}\xi\left[\frac{sinh(2\xi)+sin(2\xi)}{cosh(2\xi)-cos(2\xi)}\right] \quad \text{Eq 15}$$

Where $R_{DC} = L\rho/A$ and the proximity factor ξ

$$\xi = \sqrt{\frac{N\sqrt{\pi}r_0}{h_{coil}}}\frac{\sqrt{\pi}r_0}{d} \quad \text{Eq 16}$$

leading to

$$P_{coil} = I_{rms}^2 L \frac{\pi r_0}{A}\sqrt{\frac{N\sqrt{\pi}r_0\rho\mu}{h_{coil}}}\sqrt{f} \quad \text{Eq 17}$$

Temperature is mainly affected by the current amplitude I_o and frequency f. Higher I_o boosts H and P_{in}, while higher f increases P_{hys} can raising T. Since dH/dt, dB/dt, and dM/dt depend on I_o and f, adjusting these parameters enables dynamic temperature control to ensure optimal reaction conditions [11].

Overall, P_{in} depends on both P_{coil} and P_{hys}, as I_o and f increase, so do these losses, which, according to the energy balance, raise T. The first law of thermodynamics states that the energy entering equals the energy leaving plus energy stored, so energy balances (Q_{in}, Q_{out}, Q_{gen}, Q_{acc}) are governed by

$$Q_{in} - Q_{out} + Q_{gen} = Q_{acc} \quad \text{Eq 18}$$

with

$$Q_i = m_i C_{pi} dT_i \quad \text{Eq 19}$$

Moreover,

$$Q_{gen} = P_{in} t \quad \text{Eq 20}$$

and combining these yields

$$Q_{in} - Q_{out} + Q_{gen} = m_i C_{pi} \frac{dT}{dt} \quad \text{Eq 21}$$

or

$$\frac{dT}{dt} = \frac{Q_{in} - Q_{out} + Q_{gen}}{m_i C_{pi}} \quad \text{Eq 22}$$

manipulating I_o precisely controls P_{in}, Q, and T, ensuring efficient, optimal operation.

2.2 Echo State Network

When using ANNs for MPC modeling, several types are employed. One project utilizes a Recurrent Neural Network (RNN), specifically an Echo State Network (ESN) and a Simplified Dual Network (SDN), to identify unknown nonlinear dynamical systems with multi-input, multi-output (MIMO) configurations [6]. In an Echo State Network (ESN), the reservoir state $x_{ESN}(k) \in \mathbb{R}^N$ at time k evolves according to

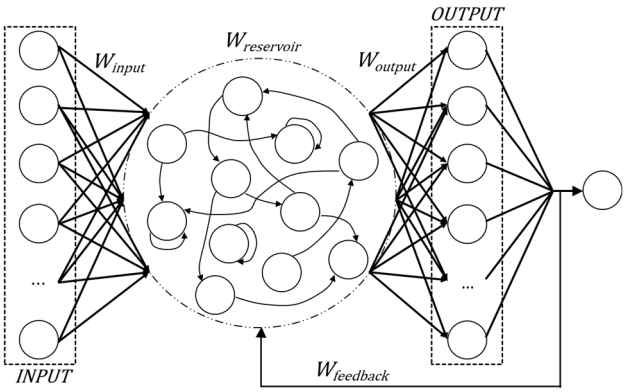

Figure 2 Architecture of ESN

$$x_{ESN}(k+1) = f(W_{in}\, u(k+1) + W_{res}\, x(k) + W_{fb}\, y_{ref}(k) + b) \quad \text{Eq 23}$$

$$\hat{y}_{ESN}(k+1) = W_{out}\, x(k+1) \quad \text{Eq 24}$$

where $u(k) \in \mathbb{R}^M$ is the input at time k, Win is the input weight matrix (typically drawn from a uniform distribution such as W_{in}~Uniform(−1,1), and $b \in \mathbb{R}^N$ is a bias vector. The recurrent reservoir weight matrix $W_{res} \in \mathbb{R}^{N\times N}$ is structured to be sparse, meaning that only a fraction of its N^2 elements is nonzero. The number of nonzero elements is given by

$$W_{res\ non-zero} = N^2 \times connectivity \quad \text{Eq 25}$$

These nonzero entries are then scaled so that the largest absolute eigenvalue (spectral radius) of W_{res} is equal to a prescribed value [10, 16]. Denoting the

spectral radius of the unscaled matrix by λ_{max} the scaling is performed as:

$$W_{res} = W_{res\ non-zero} \times \left(\frac{spectral\ radius}{\lambda_{max}}\right) \quad \text{Eq 26}$$

This ensures that the reservoir exhibits the echo state property, meaning that the influence of initial conditions decays over time while maintaining dynamic richness. An optional feedback term, $W_{out}\, y_{ref}\,(k-1)$ (with $y_{ref}(k-1) \in \mathbb{R}^L$ denotes the previous target output), is also added before applying the nonlinear activation function $f(\cdot)$, which is often chosen as tanh. The network output is then obtained through a simple linear readout:

$$\hat{y}_{ESN}(k) = W_{out}\, X(k) \quad \text{Eq 27}$$

where $\hat{y}_{ESN}(k) \in \mathbb{R}^L$ and $W_{out} \in \mathbb{R}^{L\times N}$ is the readout weight matrix. Training in ESNs focuses solely on determining the readout weights W_{out}. During a training period of length T, the reservoir states are collected in the matrix $S(k) = [x(k)^T, u(k)^T, b]^T$ then collected state X=[*S(1),S(2),…,S(T)*] and the corresponding reference outputs in the matrix $Y = [y_{ref}(1), y_{ref}(2), \ldots, y_{ref}(T)]$. The standard approach involves solving a ridge regression problem that minimizes the sum of squared errors, combined with an *L2* regularization term:

$$\min_{W_{out}} \sum_{k=1}^{T} \left\| y_{ref} - W_{out}\, S(t) \right\|_2^2 + \alpha \|W_{out}\|_F^2 \quad \text{Eq 28}$$

where $\boldsymbol{\alpha} \geq 0$ is the regularization parameter and $\|\cdot\|_F$ denotes the Frobenius norm. This minimization has a closed-form solution given by:

$$W_{out} = Y^T \cdot X(X^T \cdot X + \alpha I)^{-1} \quad \text{Eq 29}$$

While the readout weights W_{out} are typically computed via an efficient closed-form solution during training, the performance of the network is often evaluated using the Mean Absolute Error (MAE) [16, 17]. MAE is defined as

$$MAE = \frac{1}{T} \sum_{k=1}^{T} \left| y_{ref}(k) - \hat{y}_{ESN}(k) \right| \quad \text{Eq 30}$$

This metric provides a direct measure of the average magnitude of errors between the network's predictions and the target outputs. Emphasizing MAE in the evaluation provides an intuitive understanding of the typical prediction error, making it particularly useful in applications where robust performance is essential and large deviations must be minimized. This combination of a fixed, sparsely connected reservoir with controlled spectral properties and a readout layer, trained and evaluated using MAE, enables ESNs to efficiently capture complex temporal dynamics while providing clear insight into predictive accuracy.

2.3 Long-Sort Term Memory

Long Short-Term Memory (LSTM) networks, introduced by Hochreiter and Schmidhuber [18] in 1997, are a type of recurrent neural network designed to capture long-range dependencies in sequential data. An LSTM cell consists of a cell state, a hidden state, and three gates: the input gate, which regulates how much new information is added; the forget gate, which decides what previous information to discard; and the output gate, which controls how much of the cell state affects the hidden state. The candidate cell state, denoted by (*gt*), is computed using the tanh function on a weighted sum of the current input and the previous hidden state. This candidate is then combined with the previous cell state to form the updated cell state (*ct*), and the hidden state (*ht*) is updated by applying tanh to ct and filtering it through the output gate. This structure enables LSTMs to effectively manage long sequences, overcoming the limitations of standard RNNs [19, 20].

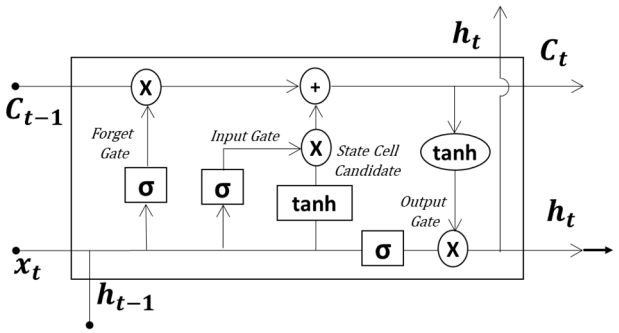

Figure 3 Architecture of LSTM

Before presenting the formulas, we define the following notation: *H* denotes the dimensionality of the hidden state (and cell state), *D* denotes the dimensionality of the input vector, and *O* denotes the dimensionality of the final output.

At each time step, the LSTM cell computes the candidate state using the equation:

$$g_k = tanh(W_{gx} \cdot x_k + W_{gh} \cdot h_{k-1} + b_g) \quad \text{Eq 31}$$

In this formula, $g_k \in \mathbb{R}^H$ is the candidate cell state that represents the potential new information to be added to the cell state. The function tanh compresses values into the range between -1 and 1. Here, $x_k \in \mathbb{R}^D$ is the current input vector, $h_{t-1} \in \mathbb{R}^H$ is the previous hidden state, $W_{gx} \in \mathbb{R}^{H\times D}$ is the weight matrix applied to the input, $W_{gh} \in \mathbb{R}^{H\times H}$ scales the previous hidden state, and $b_g \in \mathbb{R}^H$ is the bias vector.

$$i_k = \sigma(W_{ix} \cdot x_k + W_{ih} \cdot h_{k-1} + b_i) \quad \text{Eq 32}$$

The input gate equation defines $i_k \in \mathbb{R}^H$, which represents the input gate's activation, determining the proportion of the candidate state (g_k) that should be added to the cell state. The sigmoid function $\boldsymbol{\sigma}$ outputs values between 0 and 1. Here, $x_k \in \mathbb{R}^D$ is the current input, $h_{k-1} \in \mathbb{R}^H$ is the previous hidden state, $W_{ix} \in \mathbb{R}^{H\times D}$

and $W_{ih} \in \mathbb{R}^{H\times H}$ are the weight matrices applied to the input and the previous hidden state respectively, and $b_i \in \mathbb{R}^H$ is the bias for the input gate.

$$f_k = \sigma(W_{fx} \cdot x_k + W_{fh} \cdot h_{k-1} + b_f) \quad \text{Eq 33}$$

The forget gate equation defines $f_k \in \mathbb{R}^H$, which represents the forget gate activation and determines the fraction of the previous cell state (c_{k-1}) to retain. Here, $W_{fx} \in \mathbb{R}^{H\times D}$ scales the current input, $W_{fh} \in \mathbb{R}^{H\times H}$ scales the previous hidden state, and $b_f \in \mathbb{R}^H$ is the bias vector.

$$c_k = f_k \odot c_{k-1} + i_k \odot g_k \quad \text{Eq 34}$$

The updated cell state formula defines $c_k \in \mathbb{R}^H$ as the new cell state and $c_{t-1} \in \mathbb{R}^H$ as the previous cell state. The operator $\odot$ denotes element-wise multiplication. The term $f_k \odot c_{k-1}$ retains a portion of the previous cell state as determined by the forget gate f_k, while $i_k \odot g_k$ adds the new candidate state, scaled by the input gate it. After updating the cell state, the output gate activation $o_k \in \mathbb{R}^H$ determines how much of the updated cell state contributes to the new hidden state. The weight matrices $W_{ox} \in \mathbb{R}^{H\times D}$ and $W_{oh} \in \mathbb{R}^{H\times H}$ scale the current input and the previous hidden state, respectively, while $b_o \in \mathbb{R}^H$ is the bias term.

$$o_k = \sigma(W_{ox} \cdot x_k + W_{oh} \cdot h_{k-1} + b_o) \quad \text{Eq 35}$$

Finally, the new hidden state $h_k \in \mathbb{R}^H$ is computed using this equation. It serves both as the output for the current time step and as the input for the next time step.

$$h_k = o_k \odot tanh(c_k) \quad \text{Eq 36}$$

The tanh function normalizes the updated cell state $c_k \in \mathbb{R}^H$ by the output gate o_k through element-wise multiplication [21, 22]. To generate the final output, the hidden state is transformed using:

$$\hat{y}_{LSTM}(k) = g(W_y \cdot h_t + b_y) \quad \text{Eq 37}$$

In this transformation, $\hat{y}_{LSTM}(k) \in \mathbb{R}^O$ represents the final output at time step k, where g is activation function and O is the output dimension. The weight matrix $W_y \in \mathbb{R}^{O\times H}$ maps the hidden state h_k to the output space, and $b_y \in \mathbb{R}^O$ is the corresponding bias vector. These dimensions and operations align with standard LSTM formulations commonly used in major deep learning frameworks and literature.

Several hyperparameters influence the performance and architecture of LSTM systems, including the number of layers, hidden units, and batch size. Increasing the number of layers allows the model to capture more complex patterns but also increases computational complexity. Similarly, using more hidden units enhances learning but requires greater computational resources. Batch size affects training speed and generalization. Larger batches accelerate training but may cause overfitting, whereas smaller batches can hinder performance [23, 24]. Additionally, the activation function like commonly "tanh", "linear," "sigmoid," or "ReLU" [25], the number of epochs, the choice of optimizer, the timestep parameter, and the unit count all play crucial roles. Too few units may result in underfitting, while too many can prolong training and increase the risk of converging to local minima [24].

An approach to error control methods for enhancing prediction accuracy in LSTMs involves using the mean absolute error (MAE), which computes the average absolute difference between predicted and actual values. The coefficient of determination R^2 measures the proportion of variance in the dependent variable that can be explained by the independent variables, providing insight into the model's explanatory power. MAE and R^2 quantify prediction error magnitude and assess the overall fit of the model. This dual evaluation provides a more comprehensive assessment of LSTM performance.

2.4 Combination of ESN and LSTM

In this subchapter, we introduce a novel hybrid architecture that leverages the complementary strengths of Echo State Networks (ESNs) and Long Short-Term Memory (LSTM) networks for modeling complex temporal dynamics. The proposed method integrates these two recurrent structures in series: the ESN serves as a dynamic feature extractor, while the LSTM refines these features by capturing long-term dependencies.

The overall architecture consists of two main stages: (1) an ESN layer for feature extraction, and (2)

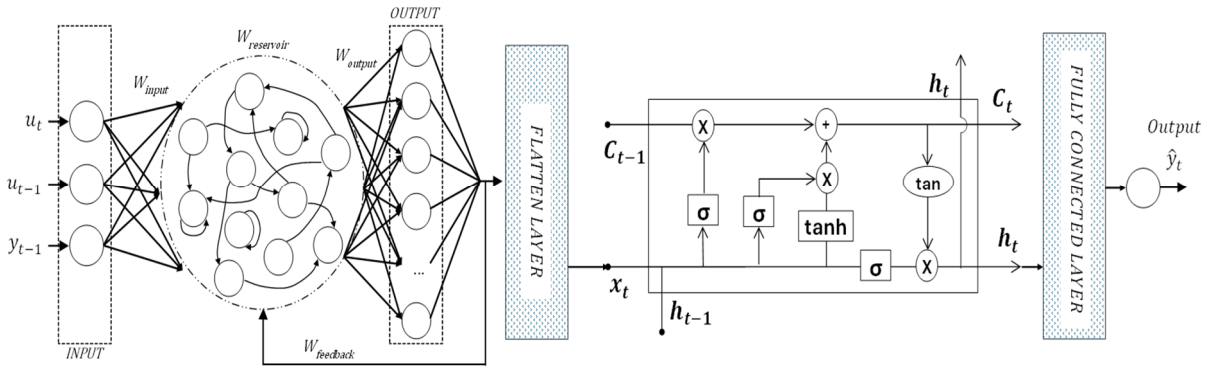

Figure 4 Architecture of Echo State Network with Long-Short Memory Term in series combination

an LSTM layer for sequence modeling. n intermediate flattening (or reshaping) step ensures that the ESN outputs are properly formatted for the LSTM. Figure 4 illustrates the data flow. In our approach, raw time series data $u(k)$, where $k=0,1,\ldots, N$, are first preprocessed through normalization to stabilize the learning process. As shown in Figure 5, the system consists of three consecutive stages: the ESN layer, a flattening (or reshaping) layer, and the LSTM layer.

Initially, we set the ESN hyperparameters, including the reservoir size, the sparsity of the recurrent weight matrix W_{res}, the spectral radius, and the input scaling factor, which controls how strongly the external input $u(k)$ drives the reservoir.

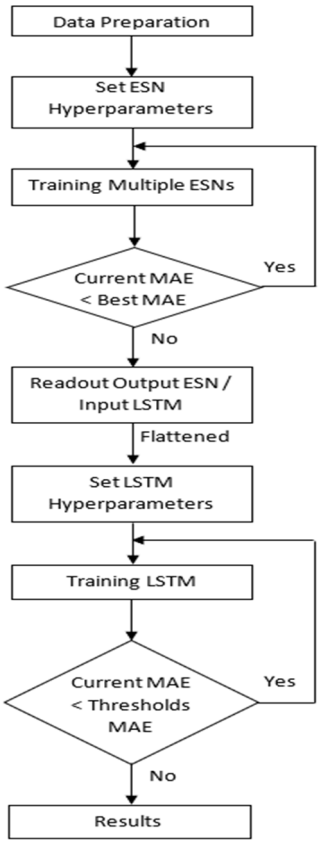

Figure 5 Procedure Obtaining Prediction in Combination in series ESN and LSTM

Using these hyperparameters, we train multiple ESNs by varying the reservoir size and random seeds to identify the configuration that yields the lowest validation error. In each trial, the ESN updates its reservoir state $x_{ESN}(k)$ according to equation (23).

Here $\phi(\cdot)$ is typically the tanh function, W_{in} projects inputs into the reservoir, and W_{fb} optionally feeds back past outputs. The ESN's output is then given by equation (24) with W_{out} often learned via ridge regression by equation (28). The hyperparameters for the ESN (reservoir size, sparsity, spectral radius, and input scaling) are essential for determining the network's ability to capture short-term dynamics.

Once we identify the best ESN, its outputs become the input to an LSTM network. We flatten or reshape the sequence $[\hat{y}_{ESN}(1),\ldots, \hat{y}_{ESN}(T)]$ into the [batch, time, features] format so that the LSTM can process it sequentially. At this stage, we configure the LSTM hyperparameters, including the number of hidden units d_h, the number of LSTM layers, and the dropout rate to mitigate overfitting. The LSTM employs gating mechanisms to maintain and update its hidden state h_t and cell state c_t. At each time step t, the LSTM computes using equation (31-36).

After passing through all T time steps, the final hidden state h_t is typically fed into a dense output layer for prediction, given by $\hat{y}_{LSTM}(k) = g(W_y \cdot h_t + b_y)$ for prediction. During training, the LSTM uses backpropagation through time (BPTT) to update both its own parameters and those of the dense output layer, while the ESN's reservoir weights remain fixed. After each training cycle, we monitor the current MAE and compare it to a predefined threshold. If the error falls below the threshold or stabilizes sufficiently, the process terminates. Otherwise, we may further refine the LSTM hyperparameters or adjust the ESN–LSTM interface.

This iterative and modular workflow (Figure 4) ensures that each stage reaches an optimal or near-optimal configuration. The ESN efficiently captures short-term dynamics, while the LSTM models extended temporal dependencies. By systematically testing multiple ESNs and fine-tuning the LSTM, we minimize the risk of underfitting or overfitting while maintaining control over the total number of trainable parameters. As a result, the ESN–LSTM series approach achieves strong predictive performance in tasks such as time series forecasting, anomaly detection, and signal processing, especially when the data exhibit both rapid transient patterns and gradual long-term trends.

3. RESULTS AND DISCUSSION

The study investigated the performance of a hybrid series model combining Echo State Networks (ESNs) with Long Short-Term Memory (LSTM) networks to characterize the dynamical behavior of a magnetic heat reactor. The reactor's data was obtained from coils with configurations of 7N, 9N, and 17N windings. For model training, the input features included the maximum current $I_0(k)$, the previous current $I_0(k-1)$, and the previous temperature $T(k-1)$, while the target output was the current temperature $T(k)$.

Hyperparameters were manually tuned by exploring various settings for the ESN's reservoir nodes, spectral radius, and connectivity, as well as the LSTM's batch size, number of units, and epochs. A default configuration was set with 10 reservoir nodes, a spectral radius of 0.1, a connectivity of 0.1, a batch size of 4, 10 LSTM units, and 20 epochs.

3.1 Reservoir Nodes

Varying the number of reservoir nodes demonstrated a significant reduction in the Mean Absolute Error (MAE) as the nodes increased from 10 to 20. Beyond this threshold, increasing the number of nodes up to 50 did not yield substantial improvements in error metrics.

Table 1 Reservoir Nodes effect to the model ESN-LSTM

	Reservoir Nodes				
	10	20	30	40	50
	ESN Mean Absolute Error				
Train	2.3107E-04	1.7923E-05	8.7167E-06	7.7968E-06	4.1015E-06
Test	2.3794E-03	9.4498E-04	8.0846E-04	9.1003E-04	9.0228E-04
Val	5.1199E-03	1.9108E-03	1.6431E-03	1.8351E-03	1.7962E-03
	LSTM Mean Absolute Error				
Train	1.2826E+01	1.1005E+01	1.4771E+01	1.2821E+01	1.4630E+01
Test	1.8026E+01	1.5659E+01	1.8578E+01	1.7036E+01	1.9052E+01
Val	2.5677E+01	2.1956E+01	2.2879E+01	2.2225E+01	2.4893E+01
Overall	1.5145E+01	1.3025E+01	1.6338E+01	1.4599E+01	1.6535E+01
	LSTM R^2				
Train	9.9941E-01	9.9952E-01	9.9905E-01	9.9933E-01	9.9924E-01
Test	9.9868E-01	9.9883E-01	9.9847E-01	9.9865E-01	9.9852E-01
Val	9.9574E-01	9.9633E-01	9.9642E-01	9.9629E-01	9.9603E-01
Overall	9.9893E-01	9.9909E-01	9.9869E-01	9.9892E-01	9.9880E-01
	Average Loss				
Test	4.3045E-02	3.4081E-02	3.5390E-02	4.3683E-02	3.4394E-02
Train	5.4069E-02	4.5541E-02	4.7301E-02	5.5206E-02	4.5404E-02
Val	4.3096E-02	3.5868E-02	3.5743E-02	4.2705E-02	3.5207E-02
	Training Time per Seconds				
	1.2806E+01	1.3114E+01	1.2205E+01	1.1779E+01	1.2780E+01
	Average Throughput per Sample				
	1.7088E+03	1.7504E+03	1.8020E+03	1.8649E+03	1.9061E+03

Notably, the configuration with 30 nodes exhibited minimal disparities across training, testing, and validation metrics, indicating robust learning and minimal overfitting. Additionally, models with 40 nodes trained faster than those with 20 nodes, and throughput consistently improved as the number of nodes increased. The configuration with 30 nodes emerged as the optimal balance for model performance.

3.2 Spectral Radius

Experiments on the spectral radius revealed a relatively uniform impact across different node configurations. Although errors remained similar when the number of nodes varied from 10 to 50, a spectral radius of 0.1 delivered better performance compared to other values. While the R2 values remained consistent between 0.1 and 0.7, a spectral radius of 0.5 resulted in a close alignment of MAE across training, testing, and validation sets, indicating stable model behavior.

Interestingly, increasing the spectral radius led to a decrease in overall loss. However, the widening gap between training and validation metrics suggested the onset of underfitting. Moreover, the spectral radius influenced training time and throughput. A value of 0.3 reduced training time and increased throughput, while a spectral radius of 0.5 ultimately provided the best overall performance.

Table 2 Spectral Radius effect to the model ESN-LSTM.

	Spectral Radius				
	0.1	0.3	0.5	0.7	0.9
	ESN Mean Absolute Error				
Train	2.3107E-04	2.0383E-04	2.1529E-04	2.1738E-04	2.1654E-04
Test	2.3794E-03	2.4797E-03	2.5905E-03	2.5789E-03	2.5636E-03
Val	5.1199E-03	5.4075E-03	5.5850E-03	5.5478E-03	5.4991E-03
	LSTM Mean Absolute Error				
Train	1.2826E+01	1.3403E+01	1.5310E+01	1.2147E+01	1.0510E+01
Test	1.8026E+01	1.8269E+01	1.8563E+01	1.6440E+01	1.6448E+01
Val	2.5677E+01	2.4704E+01	2.5172E+01	2.2577E+01	2.4469E+01
Overall	1.5145E+01	1.5500E+01	1.6943E+01	1.4043E+01	1.3086E+01
	LSTM R^2				
Train	9.9941E-01	9.9923E-01	9.9927E-01	9.9946E-01	9.9951E-01
Test	9.9868E-01	9.9837E-01	9.9847E-01	9.9861E-01	9.9840E-01
Val	9.9574E-01	9.9539E-01	9.9546E-01	9.9561E-01	9.9498E-01
Overall	9.9893E-01	9.9870E-01	9.9876E-01	9.9894E-01	9.9887E-01
	Average Loss				
Test	4.3045E-02	3.4324E-02	3.2243E-02	3.0521E-02	2.7062E-02
Train	5.4069E-02	4.3806E-02	4.2971E-02	4.1021E-02	3.6451E-02
Val	4.3096E-02	3.5984E-02	3.4894E-02	3.3413E-02	3.1097E-02
	Training Time per Seconds				
	1.2806E+01	1.2180E+01	1.2319E+01	1.2274E+01	1.2201E+01
	Average Throughput per Sample				
	1.7088E+03	1.7967E+03	1.7980E+03	1.7697E+03	1.7843E+03

3.3 Connectivity

Connectivity within the ESN framework was another critical hyperparameter. A connectivity value of 0.9 delivered the most balanced and optimal performance, as indicated by the lowest MAE and minimal differences between training, testing, and validation metrics. Although a connectivity of 0.3 provided a favorable balance between training and validation loss, the overall performance in terms of Mean Absolute Error was superior at 0.9 connectivity. This parameter also affected the LSTM's training time and throughput, where a connectivity of 0.3 proved beneficial for faster training and higher throughput, but the ESN's performance in terms of MAE was best at 0.9.

Table 3 Connectivity effect to the model ESN-LSTM

	Connectivity				
	0.1	0.3	0.5	0.7	0.9
	ESN Mean Absolute Error				
Train	2.3107E-04	4.5488E-05	2.0269E-04	1.0328E-04	5.1100E-04
Test	2.3794E-03	1.6089E-03	2.1275E-03	2.2296E-03	3.9179E-04
Val	5.1199E-03	3.2801E-03	4.4555E-03	4.4852E-03	4.1456E-04
	LSTM Mean Absolute Error				
Train	1.2826E+01	1.4351E+01	1.3430E+01	1.1272E+01	1.4282E+01
Test	1.8026E+01	1.8707E+01	1.9387E+01	1.7813E+01	1.8254E+01
Val	2.5677E+01	2.3560E+01	2.5289E+01	2.5177E+01	2.2436E+01
Overall	1.5145E+01	1.6137E+01	1.5799E+01	1.3962E+01	1.5886E+01
	LSTM R^2				
Train	9.9941E-01	9.9910E-01	9.9920E-01	9.9949E-01	9.9898E-01
Test	9.9868E-01	9.9819E-01	9.9803E-01	9.9799E-01	9.9850E-01
Val	9.9574E-01	9.9556E-01	9.9486E-01	9.9426E-01	9.9655E-01
Overall	9.9893E-01	9.9859E-01	9.9856E-01	9.9870E-01	9.9866E-01
	Average Loss				
Test	4.3045E-02	4.0367E-02	3.9702E-02	4.0891E-02	4.1141E-02
Train	5.4069E-02	5.1380E-02	5.1494E-02	5.2149E-02	5.3559E-02
Val	4.3096E-02	4.0647E-02	4.0730E-02	4.2285E-02	3.9644E-02
	Training Time per Seconds				
	1.2806E+01	1.1482E+01	1.2086E+01	1.3923E+01	1.2402E+01
	Average Throughput per Sample				
	1.7088E+03	1.8894E+03	1.8187E+03	1.8406E+03	1.8115E+03

Table 4 Batch Size effect to the model ESN-LSTM

	Batch Size				
	4	9	16	25	36
	ESN Mean Absolute Error				
Train	2.3107E-04	2.3107E-04	2.3107E-04	2.3107E-04	2.3107E-04
Test	2.3794E-03	2.3794E-03	2.3794E-03	2.3794E-03	2.3794E-03
Val	5.1199E-03	5.1199E-03	5.1199E-03	5.1199E-03	5.1199E-03
	LSTM Mean Absolute Error				
Train	1.2826E+01	1.7273E+01	2.3015E+01	3.0430E+01	5.4877E+01
Test	1.8026E+01	2.2892E+01	2.8863E+01	3.6827E+01	6.8947E+01
Val	2.5677E+01	2.7282E+01	3.1298E+01	3.4362E+01	5.7661E+01
Overall	1.5145E+01	1.9390E+01	2.5004E+01	3.2092E+01	5.7945E+01
	LSTM R^2				
Train	9.9941E-01	9.9864E-01	9.9573E-01	9.8801E-01	9.6028E-01
Test	9.9868E-01	9.9765E-01	9.9425E-01	9.8573E-01	9.5581E-01
Val	9.9574E-01	9.9503E-01	9.9282E-01	9.8655E-01	9.6380E-01
Overall	9.9893E-01	9.9811E-01	9.9515E-01	9.8740E-01	9.5967E-01
	Average Loss				
Test	4.3045E-02	7.4782E-02	1.7165E-01	2.3238E-01	2.5720E-01
Train	5.4069E-02	8.2687E-02	1.8147E-01	2.3814E-01	2.6038E-01
Val	4.3096E-02	7.0456E-02	1.6254E-01	2.1790E-01	2.3867E-01
	Training Time per Seconds				
	1.2806E+01	7.1157E+00	6.7072E+00	5.1951E+00	4.9634E+00
	Average Throughput per Sample				
	1.7088E+03	3.4551E+03	4.0301E+03	5.5203E+03	6.0591E+03

3.4 LSTM Batch Size

Regarding batch size in the LSTM, smaller batch sizes, particularly a batch size of 4, were found to be most effective. This configuration led to more frequent parameter updates, allowing for finer adjustments and improved predictive accuracy, as reflected in the highest R^2 and lowest MAE across training, testing, and validation. Larger batch sizes led to fewer weight updates per epoch, hindering fine-tuning and increasing both training loss and MAE. Moreover, batch sizes between 4 and 36 provided shorter training times and higher throughput due to more efficient matrix operations. However, a batch size of 4 consistently outperformed the others in key metrics.

3.5 LSTM Units

The number of LSTM units had a nuanced effect on performance. Although changes in LSTM units did not affect the ESN's MAE, within the LSTM itself, configurations with 20 and 50 units yielded the best R2 and MAE. Performance remained consistent across training, testing, and validation when the number of units ranged between 30 and 50. This range represents the "sweet spot," balancing the risk of overfitting with the need for adequate model complexity. Notably, although 50 units led to longer training times, they also delivered higher throughput, making this configuration the most effective overall despite the increased computational cost.

Table 5 LSTM Units effect to the model ESN-LSTM

	LSTM Units				
	10	20	30	40	50
	ESN Mean Absolute Error				
Train	2.3107E-04	2.3107E-04	2.3107E-04	2.3107E-04	2.3107E-04
Test	2.3794E-03	2.3794E-03	2.3794E-03	2.3794E-03	2.3794E-03
Val	5.1199E-03	5.1199E-03	5.1199E-03	5.1199E-03	5.1199E-03
	LSTM Mean Absolute Error				
Train	1.2826E+01	1.1209E+01	7.1484E+00	1.3535E+01	9.9785E+00
Test	1.8026E+01	1.4670E+01	1.5579E+01	2.1848E+01	1.2231E+01
Val	2.5677E+01	2.1998E+01	2.5917E+01	3.2401E+01	2.1158E+01
Overall	1.5145E+01	1.2976E+01	1.0700E+01	1.7073E+01	1.1545E+01
	LSTM R^2				
Train	9.9941E-01	9.9957E-01	9.9975E-01	9.9950E-01	9.9975E-01
Test	9.9868E-01	9.9905E-01	9.9872E-01	9.9835E-01	9.9919E-01
Val	9.9574E-01	9.9637E-01	9.9506E-01	9.9430E-01	9.9632E-01
Overall	9.9893E-01	9.9917E-01	9.9911E-01	9.9879E-01	9.9932E-01
	Average Loss				
Test	4.3045E-02	1.5931E-01	1.9621E-02	1.9438E-02	1.8104E-02
Train	5.4069E-02	3.9544E-01	2.8094E-02	2.6480E-02	2.4609E-02
Val	4.3096E-02	1.4053E-01	2.5719E-02	2.5944E-02	2.4992E-02
	Training Time per Seconds				
	1.2806E+01	1.2368E+01	1.2251E+01	1.2223E+01	1.2656E+01
	Average Throughput per Sample				
	1.7088E+03	1.8042E+03	1.7821E+03	1.7928E+03	1.8170E+03

Table 6 Epochs effect to the model ESN-LSTM

	Epochs				
	20	40	60	80	100
	ESN Mean Absolute Error				
Train	2.3107E-04	2.3107E-04	2.3107E-04	2.3107E-04	2.3107E-04
Test	2.3794E-03	2.3794E-03	2.3794E-03	2.3794E-03	2.3794E-03
Val	5.1199E-03	5.1199E-03	5.1199E-03	5.1199E-03	5.1199E-03
	LSTM Mean Absolute Error				
Train	1.2826E+01	6.0250E+00	8.5800E+00	3.0842E+00	1.8218E+00
Test	1.8026E+01	1.2076E+01	1.3795E+01	1.1818E+01	1.0815E+01
Val	2.5677E+01	2.2378E+01	2.1772E+01	2.3587E+01	2.2567E+01
Overall	1.5145E+01	8.8634E+00	1.0936E+01	6.8701E+00	5.6834E+00
	LSTM R^2				
Train	9.9941E-01	9.9987E-01	9.9973E-01	9.9997E-01	9.9998E-01
Test	9.9868E-01	9.9915E-01	9.9904E-01	9.9911E-01	9.9914E-01
Val	9.9574E-01	9.9601E-01	9.9612E-01	9.9566E-01	9.9573E-01
Overall	9.9893E-01	9.9937E-01	9.9926E-01	9.9940E-01	9.9942E-01
	Average Loss				
Test	4.3045E-02	2.6428E-02	2.1775E-02	1.9394E-02	1.9186E-02
Train	5.4069E-02	3.0028E-02	2.2771E-02	1.7737E-02	1.6872E-02
Val	4.3096E-02	3.1421E-02	2.6782E-02	2.6236E-02	2.5807E-02
	Training Time per Seconds				
	1.2806E+01	2.2330E+01	3.4911E+01	4.4676E+01	5.5710E+01
	Average Throughput per Sample				
	1.7088E+03	1.8573E+03	1.8419E+03	1.8174E+03	1.7788E+03

3.6 LSTM Epochs

The number of epochs in LSTM training affected both model convergence and accuracy. Optimal performance was achieved at 60 epochs, where the LSTM attained the highest R2 and lowest MAE, with minimal discrepancies across training, testing, and validation metrics. Although increasing the number of epochs can further refine the weights and reduce error, it also raises the risk of overfitting, as indicated by a growing divergence between training and validation losses at higher epoch counts. Additionally, training time increased steadily with more epochs, whereas throughput peaked at around 40 epochs before declining. Thus, 60 epochs represented the best trade-off between performance and computational efficiency.

3.7 Performance

Based on the incremental selection of optimal hyperparameters, the best overall configuration identified from the experiments consists of 30 reservoir nodes, a spectral radius of 0.5, 0.9 connectivity, a batch size of 4, 50 LSTM units, and 60 epochs. This combination consistently delivers the lowest Mean Absolute Error and highest Coefficient of Determination across the training, testing, and validation datasets for all coil configurations (7N, 9N, and 17N). The superior performance under these settings underscores the model's robust generalization capabilities, indicating that it can effectively capture and predict the underlying dynamics of the magnetic heat reactor.

Table 7 Performance at the best option each hyperparameters

	7N		**9N**		**17N**	
	MAE	**R^2**	**MAE**	**R^2**	**MAE**	**R^2**
Train	9.1479	0.9997	7.8645	0.9998	6.3318	0.9997
Test	8.7376	0.9998	8.2303	0.9998	8.0625	0.9997
Validation	14.8820	0.9982	14.7771	0.9981	14.9685	0.9980

Table 8 Loss value in training, testing, validating to the model

	7N			**9N**			**17N**		
Epoch	**Testing Loss**	**Training Loss**	**Validation Loss**	**Testing Loss**	**Training Loss**	**Validation Loss**	**Testing Loss**	**Training Loss**	**Validation Loss**
1	0.1040	0.2892	0.0922	0.1227	0.3405	0.1077	0.1064	0.2988	0.0948
2	0.0159	0.0361	0.0165	0.0167	0.0450	0.0184	0.0186	0.0336	0.0205
3	0.0088	0.0119	0.0144	0.0107	0.0096	0.0171	0.0094	0.0103	0.0156
4	0.0095	0.0071	0.0163	0.0074	0.0064	0.0129	0.0094	0.0067	0.0153
…	…	…	…	…	…	…	…	…	…
60	0.0075	0.0048	0.0127	0.0070	0.0060	0.0126	0.0069	0.0050	0.0128

a

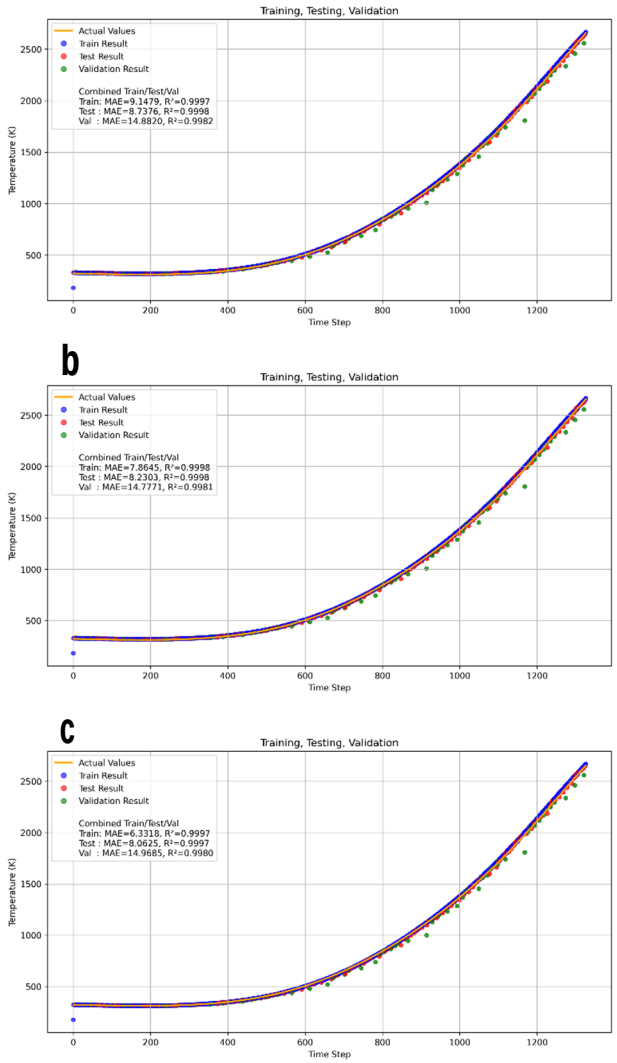

Figure 6 Prediction ESN-LSTM Vs Reference at: a) 7N winding coil, b) 9N winding coil, c) 17N winding coil

4. CONCLUSION

The hybrid combination in series ESN–LSTM approach demonstrates the experiments impact regarding of hyperparameter tuning on model performance in predicting the dynamics of a magnetic heat reactor. For instance, increasing the number of reservoir nodes from 10 to 20 led to a significant reduction in the ESN's Mean Absolute Error (MAE), with training MAE dropping from 2.31×10^{-4} to 1.79×10^{-5} and testing MAE decreasing from 2.38×10^{-3} to 9.45×10^{-4}. However, further increasing the nodes to 50 produced minimal gains, as test MAE stabilized around 9.02×10^{-4}. Similarly, experiments on the spectral radius showed that while a value of 0.1 produced a lower ESN MAE, a spectral radius of 0.5 resulted in consistent MAE values across training, testing, and validation.

Additionally, overall loss decreased with higher spectral radii, as indicated by a growing gap between training and validation metrics. For connectivity, a value of 0.9 yielded the lowest ESN test MAE (3.92×10^{-4}) compared to lower connectivity levels. However, a connectivity of 0.3 provided faster training times and higher throughput for the LSTM component. Moreover, a smaller batch size, particularly 4, proved most effective. It delivered the lowest overall MAE (1.51×10^{1}) and highest R^2, with throughput reaching up to 6.06×10^{3} per sample for the LSTM. In contrast, larger batch sizes hindered fine-tuning due to fewer weight updates per epoch. For LSTM units, configurations between 30 and 50 emerged as the 'sweet spot,' with 50 units achieving a test MAE of 1.22×10^{1} and a test R^2 of 0.999. However, this configuration required longer training times but provided improved throughput. Training for 60 epochs provided the best compromise between convergence and overfitting, achieving an overall MAE of 1.09×10^{1} with minimal discrepancies across training, testing, and validation.

However, additional epochs increased the risk of overfitting. The optimal configuration—30 reservoir nodes, a spectral radius of 0.5, 0.9 connectivity, a batch size of 4, 50 LSTM units, and 60 epochs—consistently delivered the lowest MAE and highest R^2 across various coil configurations (7N, 9N, and 17N), with MAE values of 9.15, 7.86, and 6.33 and R^2 values above 0.998. The key advantages include low ESN MAE, high LSTM R^2 scores, and consistent reductions in training, testing, and validation losses, which together indicate excellent predictive accuracy and strong fit. However, the model's complexity introduces several trade-offs as increasing reservoir nodes, LSTM units, and epochs can raise computational costs and potentially lead to overfitting, as seen in slightly higher validation loss relative to training and testing losses. Additionally, the necessity of tuning multiple hyperparameters can prolong experimentation and complicate the optimization process. Overall, while the combination in series ESN–LSTM hybrid delivers robust results, users should balance the benefits of improved accuracy against the added complexity and potential overfitting risk.

ACKNOWLEDGMENTS

I would like to express my sincere gratitude to all those who supported me throughout the course of this research. First and foremost, I am deeply indebted to my advisor, Prof. Paisan Kittisupakorn, Ph.D., whose expert guidance, constructive feedback, and continuous encouragement were invaluable in shaping this work. I extend my appreciation to my colleagues and peers at Department of Chemical Engineering, Chulalongkorn University for their stimulating discussions and moral support. Finally, I am grateful to my family and friends for their unwavering encouragement throughout this journey.

REFERENCES

1. Rasul, M.G., et al., The future of hydrogen: Challenges on production, storage and applications. Energy Conversion and Management, 2022. **272**.
2. Lu, Y.R. and P.A. Nikrityuk, Steam methane reforming driven by the Joule heating. Chemical Engineering Science, 2022. **251**.
3. Mortensen, P.M., et al., Direct Hysteresis Heating of Catalytically Active Ni–Co Nanoparticles as Steam Reforming Catalyst. Industrial & Engineering Chemistry Research, 2017. **56**(47): p. 14006-14013.
4. Bestwick, T. and K.V. Camarda, Artificial Neural Network-Based Real-Time PID Controller Tuning, in 33rd European Symposium on Computer Aided Process Engineering. 2023. p. 1609-1614.
5. Carvalho, C.B., E.P. Carvalho, and M.A.S.S. Ravagnani, Implementation of a neural network MPC for heat exchanger network temperature control. Brazilian Journal of Chemical Engineering, 2020. **37**(4): p. 729-744.
6. Pan, Y. and J. Wang, Model Predictive Control of Unknown Nonlinear Dynamical Systems Based on Recurrent Neural Networks. IEEE Transactions on Industrial Electronics, 2012. **59**(8): p. 3089-3101.
7. Malashin, I., et al. Applications of Long Short-Term Memory (LSTM) Networks in Polymeric Sciences: A Review. Polymers, 2024. **16**, DOI: 10.3390/polym16182607.
8. Al-Selwi, S.M., et al., RNN-LSTM: From applications to modeling techniques and beyond—Systematic review. Journal of King Saud University - Computer and Information Sciences, 2024. **36**(5): p. 102068.
9. López, E., et al. Wind Power Forecasting Based on Echo State Networks and Long Short-Term Memory. Energies, 2018. **11**, DOI: 10.3390/en11030526.
10. Yang, Y., X. Zhao, and X. Liu, A Novel Echo State Network and Its Application in Temperature Prediction of Exhaust Gas From Hot Blast Stove. IEEE Transactions on Instrumentation and Measurement, 2020. **69**(12): p. 9465-9476.
11. Almind, M.R., et al., Improving performance of induction-heated steam methane reforming. Catalysis Today, 2020. **342**: p. 13-20.
12. Kemjariya, S., et al., Designing MPC Controller for a Heat Exchanger Equipped with Thermoelectric Generators. Journal of Physics: Conference Series, 2022. **2261**(1): p. 012007.
13. Vasičkaninová, A., et al. Model Predictive Control of a Tubular Chemical Reactor. in 2019 22nd International Conference on Process Control (PC19). 2019.
14. Vinum, M.G., et al., Dual-Function Cobalt-Nickel Nanoparticles Tailored for High-Temperature Induction-Heated Steam Methane Reforming. Angew Chem Int Ed Engl, 2018. **57**(33): p. 10569-10573.
15. Stephen, B., Magnetism in Condensed Matter. Oxford Master Series in Condensed Matter Physics. 2001, Oxford: OUP Oxford.
16. Jaeger, H., The “echo state” approach to analysing and training recurrent neural networks-with an erratum note. Bonn, Germany: German National Research Center for Information Technology GMD Technical Report, 2001. **148**(34): p. 13.
17. Nguyen, H.M., et al. A Novel Echo State Network Model Using Bayesian Ridge Regression and Independent Component Analysis. in Artificial Neural Networks and Machine Learning – ICANN 2018. 2018. Cham: Springer International Publishing.
18. Hochreiter, S., Long Short-term Memory. Neural Computation MIT-Press, 1997.
19. Selvin, S., et al. Stock price prediction using LSTM, RNN and CNN-sliding window model. in 2017 International Conference on Advances in Computing, Communications and Informatics (ICACCI). 2017.
20. Ghojogh, B. and A. Ghodsi, Recurrent neural networks and long short-term memory networks: Tutorial and survey. arXiv preprint arXiv:2304.11461, 2023.
21. Pulver, A. and S. Lyu. LSTM with working memory. in 2017 International Joint Conference on Neural Networks (IJCNN). 2017.
22. Landi, F., et al., Working Memory Connections for LSTM. Neural Networks, 2021. **144**: p. 334-341.
23. Dokuz, Y. and Z. Tüfekci, Investigation of the Effect of LSTM Hyperparameters on Speech Recognition Performance. Avrupa Bilim ve Teknoloji Dergisi, 2020: p. 161-168.
24. Wang, S., et al., A Hyperparameter Optimization Algorithm for the LSTM Temperature Prediction Model in Data Center. Scientific Programming, 2022. **2022**(1): p. 6519909.
25. Rasamoelina, A.D., F. Adjailia, and P. Sinčák. A Review of Activation Function for Artificial Neural Network. in 2020 IEEE 18th World Symposium on Applied Machine Intelligence and Informatics (SAMI). 2020.

Techno-economic insights and limitation analysis of CO_2 capture via monoethanolamine (MEA) absorption

Manisa Mahahing[1], Kritchart Wongwailikhit[1,*]

[1] Center of Excellence in Particle and Materials Processing Technology, Department of Chemical Engineering, Faculty of Engineering, Chulalongkorn University, Bangkok 10330, Thailand
[*] Corresponding author: kritchart.w@chula.ac.th

ABSTRACT

Carbon dioxide (CO_2) capture is crucial for reducing greenhouse gas emissions, which not only drive climate change but also negatively impact the environment and human health. This study focuses on a techno-economic analysis and limitation study of CO_2 absorption using monoethanolamine (MEA). Although chemical absorption offers high capture efficiency, it faces challenges with solvent regeneration and degradation. Therefore, this study analyzes key parameters affecting the performance of this technology, including factors influencing carbon capture costs and CO_2 emissions. The simulation results show that at the same recovery, as the CO_2 inlet concentration increases, the levelized cost of carbon capture decreases. Moreover, as the percentage of CO_2 recovery increases within a CO_2 inlet concentration range of 5–16%, the levelized cost of carbon capture rises because higher capital and operating costs are required. In contrast, beyond a CO_2 inlet concentration of 17%, the levelized cost of carbon capture decreases due to enhanced mass transfer at higher concentrations. The findings provide valuable insights for selecting suitable technologies for different industries and offer guidance for developing future innovations to improve the efficiency and sustainability of carbon capture processes.

Keywords: CO_2 capture; Chemical absorption; Monoethanolamine; Process simulation

1. INTRODUCTION

In recent years, carbon dioxide (CO_2) emissions have continued to rise, leading to global warming and climate change. According to the International Energy Agency (IEA), global CO_2 emissions in 2023 were reported to reach 37.7 billion tons [1]. Carbon Capture, Utilization, and Storage (CCUS) technologies have been implemented to reduce greenhouse gas emissions and mitigate their effects.

Among the most widely used methods for CO_2 capture is chemical absorption with monoethanolamine (MEA). This method is especially effective in post-combustion processes, as MEA can efficiently react with CO_2, even in exhaust gases with low CO_2 concentrations. MEA's high sensitivity and CO_2 inlet capture capacity make it a suitable approach for the industry, as it does not require major process modifications [2].

In recent years, various studies have analyzed CO_2 capture efficiency, economics, and emission reductions. For example, Huertas et al. examined CO_2 inlet concentration profiles in the range of 0 to 30 mol% during CO_2 absorption by MEA, revealing the correlation between adsorption efficiency and process configuration [3]. Jaffar et al. conducted a technical and economic analysis on MEA-based post-combustion technologies, assessing key performance indicators such as emission reductions, energy efficiency, and capture costs [4].

Despite significant attention given to MEA-based post-combustion CO_2 capture, comprehensive research on the effects of variables such as CO_2 inlet concentration at the inlet and CO_2 recovery percentage on capture efficiency, capture costs, and total greenhouse gas emissions remains limited.

This study aims to focus on this gap by thoroughly investigating the techno-economic aspects and limitations of CO_2 capture via MEA absorption. Specifically, the study examines the impact of variables such as CO_2 inlet concentration and recovery percentage on capture efficiency, cost, and emissions, providing critical insights into potential process optimizations.

2. EXPERIMENTAL

2.1 Process Description and Modeling

2.1.1 Exhaust Gas Sources

In industrial applications, exhaust gas is mainly generated from combustion and production processes such as cement plants, power plants, steel industries, and ethylene plants [5]. The composition of exhaust gas varies depending on the fuel type and process used. A

summary of exhaust gas sources and their characteristics is provided in Table 1.

Table 1 The table captions should be placed above the table as shown in this example.

Parameter	Cement plant	Power plant	Steel plant	Ethylene plant
Mole fraction				
N_2	0.59	0.73	0.42	0.73
O_2	0.12	0.13	0.12	0.04
CO_2	0.18	0.05	0.08	0.08
H_2O	0.11	0.09	0.08	0.16

In this study, the exhaust gas composition from a cement plant was used. To investigate the effects of varying inlet CO_2 concentrations ranging from 5 to 70 mol%, the gas composition was systematically modified. Specifically, the proportion of inert nitrogen (N_2), which does not participate in the CO_2 capture process and has no significant impact on its efficiency, was reduced. Subsequently, the proportions of all gas components were uniformly adjusted, either increased or decreased proportionally, to achieve the desired CO_2 inlet concentration range for analysis.

2.1.2 Operating and Design Constraints

Operating and design constraints were specified to guide the proper sizing and operation of the absorption column. The flooding percentage, defined as the ratio of actual liquid holdup to the maximum liquid holdup, was maintained within the range of 50–80% to prevent excessive liquid accumulation that could impede gas flow and lead to operational instability [6]. The maximum column height was set at 50 meters to avoid the need for specialized structural designs and to limit construction and maintenance costs [6]. The column diameter was constrained between 0.2 and 15 meters to promote uniform gas–liquid contact and maintain operational efficiency [7]. Furthermore, the height-to-diameter (H/D) ratio was required to be greater than or equal to 1.5 to ensure proper hydrodynamic performance [8]. A summary of these constraints is provided in Table 2.

Table 2 Design constraints for MEA CO_2 capture.

Parameter	Value
Flooding percentage (%)	50-80
Maximum column height (m)	≤50
Column diameter (m)	0.2-15
Height-to-diameter (H/D) ratio	≥1.5

2.1.3 CO_2 Capture Section

An overview of the chemical absorption process for carbon capture from exhaust gas at a rate of 14,400 kmol/hr using MEA was developed based on Reactor and Process Design in Sustainable Energy Technology [9] and is illustrated in Figure 1. The process simulation was performed in Aspen Plus V14 using the ENRTL-RK model. The absorber and stripper columns were modeled using a rate-based distillation model. The exhaust gas entering the system has a temperature of 97°C and a pressure of 1.02 bar. This configuration serves as the baseline for more complex process design, optimization, debottlenecking, and equipment sizing.

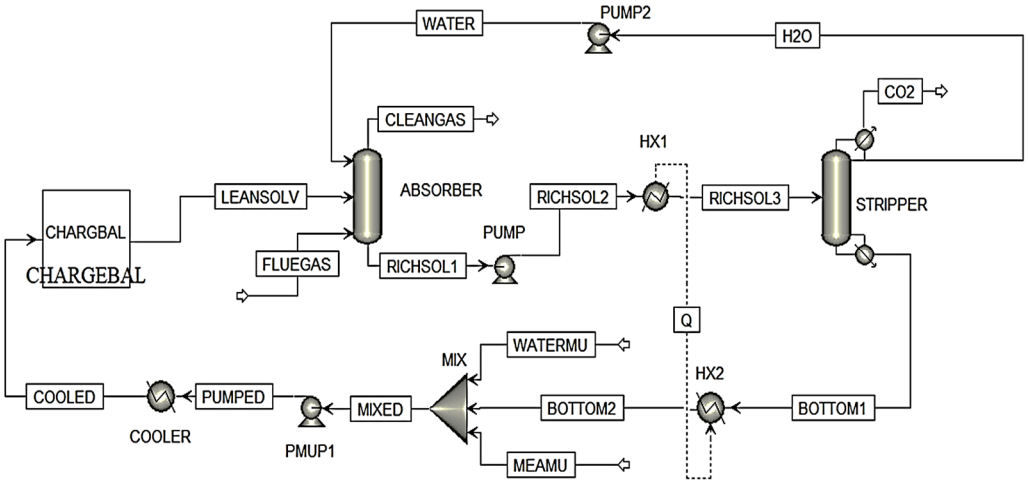

Figure 1 The simulation of the chemical absorption carbon capture using MEA process.

The inlet exhaust gas, primarily composed of nitrogen, oxygen, carbon dioxide, and water vapor, is pretreated to remove impurities such as nitrogen oxides (NOx) and sulfur oxides (SOx) before entering the CO_2 capture process. This pretreatment step helps to protect the solvent and enhance the overall efficiency of the system. After pretreatment, the gas enters the absorber column from the bottom, where CO_2 is captured. In the simulation, the packed absorber column is modeled with 30 stages. A lean MEA solution (30 wt% MEA) is introduced into the column at stage 6 under operating conditions of 60ºC and 1.08 bar.

Within the absorber, CO_2 in the exhaust gas reacts with MEA in a counter-current flow, undergoing gas-liquid mass and heat transfer that results in the formation of unstable amine salts [10]. Water is

introduced at the top of the column to wash MEA from the gas stream, thereby minimizing solvent loss. Clean gas exits at the top of the absorber, while rich solvent is withdrawn from the bottom and directed to the stripper.

Before entering the stripper, the rich solvent is preheated via a heat exchanger to approximately 70ºC. The stripper column is modeled with 20 stages. Rich solvent enters at stage 2, where CO_2 is desorbed and MEA is regenerated. Lean MEA from the bottom of the stripper is recycled back to the absorber along with makeup solvent. The desorbed gas stream is passed through a condenser to remove water vapor, yielding a CO_2 product with 94% purity [11].

2.1.4 Monoethanolamine Technology

Two main types of reactions occurred in the absorption of CO_2 by MEA. The first was the reaction of MEA with CO_2 to form carbamate:

$$MEA + CO_2 + H_2O \rightarrow MEACOO^- + H_3O^+ \quad (1)$$

The second type was a protonation reaction. First, the CO_2 dissolved in water dissociated into bicarbonate (HCO_3^-), carbonate (CO_3^{2-}), and hydronium (H_3O^+) ions, which included the ionization reaction of water:

$$CO_2 + OH^- \rightarrow HCO_3^- \quad (2)$$

$$2H_2O \leftrightarrow H_3O^+ + OH^- \quad (3)$$

$$HCO_3^- + H_2O \leftrightarrow H_3O^+ + CO_3^{2-} \quad (4)$$

Then, MEA is combined with (H_3O^+) to produce the protonated salt $MEAH^+$:

$$MEA + H_3O^+ \leftrightarrow MEAH^+ + H_2O \quad (5)$$

Both reactions aim to enhance CO_2 dissolution in the absorbent, with desorption being the reverse of absorption [12]. Reactions (1) and (2) are kinetic reactions, with rate constants in Table 3.

Table 3 Kinetic parameters for MEA-based CO_2 absorption reactions

Reaction	k	E (cal/mol)
(1)	3.02×10^{14}	9,855.81
(2)	1.33×10^{17}	13,249.00

Reactions (3) to (5) are equilibrium-based, and their equilibrium constants (K_eq) can be calculated using the Gibbs free energy relation:

$$\Delta G^\circ = -RT\ln K_{eq} \quad (6)$$

Where ΔG^o is the standard Gibbs free energy change, R is the universal gas constant (8.314 J/mol·K), and T is the absolute temperature in Kelvin. The reverse of these reactions governs the CO_2 desorption process in the regeneration unit [12].

2.2 Characterization and Evaluation

The outputs of the simulation were used to perform an economic and environmental analysis, evaluating capital cost (Capex), operating cost (Opex), levelized cost of carbon capture (LCOC), and specific net CO_2 emissions. The CO_2 inlet concentration in the exhaust gas was varied between 5% and 70%, and the CO_2 recovery was set between 90% and 99% to determine optimal operational conditions.

2.2.1. Total capital investment cost

Total Capital Investment (TCI) is an important indicator for evaluating the total investment cost of a project, and it can be classified into two main components: Fixed Capital Investment (FCI) and Working Capital (WC), which can be expressed in the following equation [13].

$$TCI = FCI + WC \quad (7)$$

$$WC = 0.15 \times TCI \quad (8)$$

The fixed capital investment (FCI) comprises the costs of equipment purchase, installation, piping, electrical systems, and civil construction. Working capital (WC) represents the operational buffer required for materials, utilities, and labor. Equipment investment (EI) is a major contributor that significantly influences both FCI and total capital investment (TCI).

2.2.2. Cost of Manufacturing

The cost of manufacturing (COM_d) incorporates raw materials, utilities, labor, and waste treatment, expressed as [13]:

$$COM_d = 0.180FCI + 1.23 \times (C_{RM}+C_{WT}+C_{UT}) + 2.73C_{OL} \quad (9)$$

Where C_{OL} is operating labor, C_{RM} is the cost of raw materials, C_{WT} is the cost of waste treatment, and C_{UT} is the cost of utilities.

2.2.3. Levelized Cost of Carbon Capture

Levelized Cost of Carbon Capture (LCOC) refers to the average cost per unit of CO_2 captured over the lifetime of a project. Its purpose is to help compare the cost-effectiveness of different projects in reducing CO_2 emissions over the long term. Which can be expressed in the following equation [14].

$$LCOC = \frac{TCI + \sum_t^n \frac{COM_d}{(1+i)^t}}{\sum_t^n \frac{M_{t,CO_2}}{(1+i)^t}} \quad (10)$$

Where i is the interest rate in percentage, n is the economic lifetime in years, t is the year of the lifetime, and $M_{t,\ CO2}$ represents the amount of carbon dioxide captured in year t.

2.2.4. Specific Net CO_2 Emissions

Specific net CO_2 emissions (SNCE) refer to the net amount of carbon dioxide per unit of production remaining after carbon capture and storage (CCS). Which can be expressed in the following equation [15].

$$SNCE=\left(\frac{CO_2 \text{ outlet}-CO_2 \text{ inlet}}{CO_2 \text{ inlet}}\right)\times 100 \quad (11)$$

3. RESULTS AND DISCUSSION

3.1 Simulation results and validation

The reliability of the CO_2 capture model using a monoethanolamine (MEA) solvent was validated to ensure its suitability for subsequent techno-economic and environmental analyses. The validation was conducted over a wide range of CO_2 inlet concentrations (5–70 mol%) to represent various industrial exhaust gas conditions. In particular, the model was benchmarked against literature data representative of post-combustion exhaust gas from a coal-fired power plant, which typically contains 14.1 mol% CO_2 and a total exhaust gas flow rate of approximately 600,000 kg/h. The simulation results were in good agreement with the reference data in terms of energy consumption, solvent circulation rate, CO_2 loading, reboiler temperature, amount of CO_2 captured, and CO_2 purity. Detailed values for these parameters are presented in Table 3. These results demonstrate the capability of the MEA-based absorption process to achieve high-purity CO_2 suitable for downstream conversion applications. Overall, these findings confirm that the developed MEA absorption model can accurately predict system performance under varying operating conditions.

Table 3 Comparison of the simulation and reported results.

Key parameters	Value	Ref.
MEA make-up (kg/t-CO_2)	0.09	0.09
MEA circulation (t/h)	369.22	369.22
Lean CO_2 loading (mol/mol)	0.35	0.35
Reboiler temperature (°C)	104.59	104.59
CO_2 captured (t/h)	126.97	126.96
Captured CO2 purity (%)	96.74	96.73

3.2 Comparison of Economic Performance

3.2.1 Total Capital Investment (TCI) Analysis

In the MEA absorption CO_2 capture process, with an CO_2 inlet concentration of 18 mol% (typical for a cement plant) and a CO_2 recovery of 90%, the absorber accounts for 46.06% of the total equipment cost, while the stripper makes up 51.73% of the total cost. The pump and heat exchanger contribute 0.31% and 1.90%, respectively. These data show that most of the equipment costs are concentrated in the absorber and stripper, as both need to be large-sized and designed to withstand high-performance conditions, corrosion, and large gas and solvent flow rates. As a result, the production and installation costs are significantly higher compared to other equipment. Figure 2 shows the distribution of equipment costs in a pie chart.

In the study of the impact of CO_2 inlet concentration (ranging from 5% to 70%) and CO_2 recovery (ranging from 90% to 99%) on the total capital investment (TCI) for the MEA absorption CO_2 capture process, it was found that overall, TCI tends to increase as the CO_2 inlet concentration and CO_2 recovery increase. The analysis, represented by a contour plot in Figure 3, shows the change in TCI (in MMUSD) as CO_2 inlet concentration and CO_2 recovery vary.

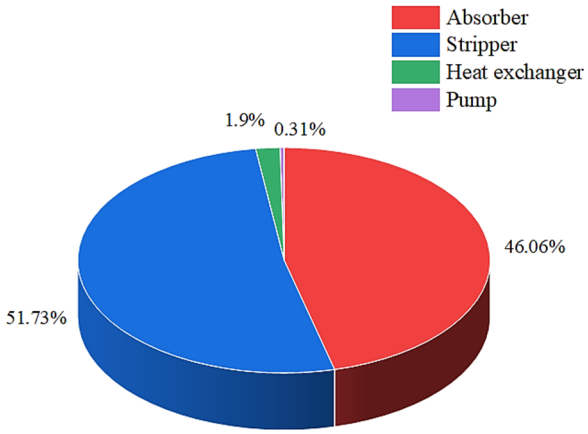

Figure 2 Equipment Cost Distribution for MEA Absorption CO_2 Capture Process (18 mol% CO_2, 90% CO_2 Recovery)

Particularly, as the CO_2 inlet concentration in the exhaust gas increases from 5–70 mol%, the total capital investment continuously rises. This is because higher CO_2 concentrations require handling larger volumes of gas per unit time, necessitating an expansion of the process size to accommodate the increased gas absorption. This requires larger equipment, including absorbers, strippers, heat exchangers, pumps, and other components, resulting in higher total investment costs.

In terms of CO_2 recovery increasing from 90% to 99%, the total capital investment rises rapidly, especially as the CO_2 recovery approaches 99%. This increase in cost arises from the need to add more absorbent material and significantly higher energy requirements for regenerating the absorbent, as well as expanding the process size to maintain high performance continuously.

For instance, simulation results at 90% CO_2 recovery show that a power plant exhaust gas stream with 5 mol% CO_2 results in a TCI of 15.25 MMUSD. For a steel plant and ethylene plant, where the inlet CO_2 inlet concentration is approximately 8 mol%, the TCI is 16.71 MMUSD. Meanwhile, a cement plant with an 18 mol% CO_2 inlet concentration results in a TCI of 24.54 MMUSD. These values, obtained through process simulations, are also shown in the contour plot.

These results show that both higher CO_2 inlet concentrations and CO_2 recovery directly impact the increase in total capital investment (TCI). Therefore, the design of the MEA absorption CO_2 capture process must consider finding a balance between the desired CO_2 recovery level and the acceptable cost, ensuring that the project remains economically viable.

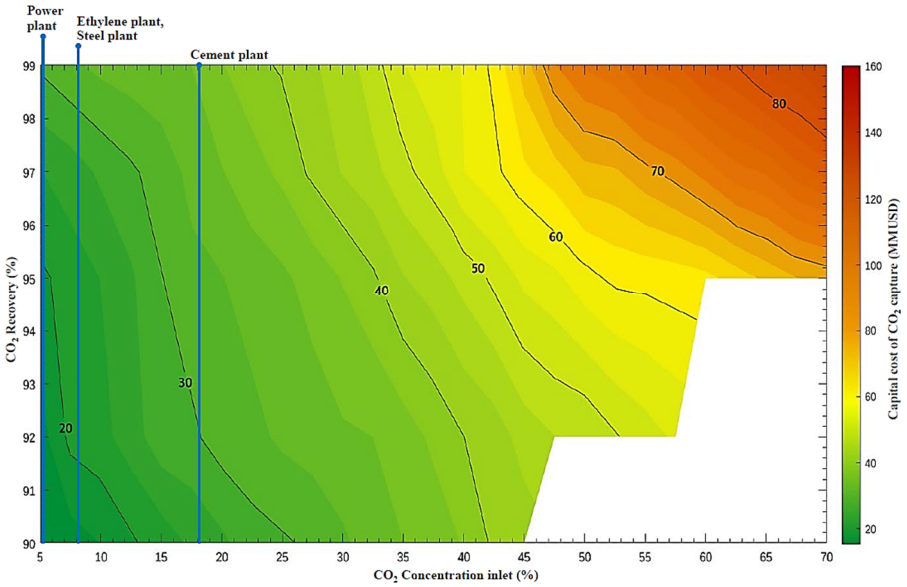

Figure 3 Total capital cost of MEA carbon capture at MEA-to-CO_2 ratio equal to 2.

3.2.2 Cost of Manufacturing (COM_d) Analysis

In the MEA absorption CO_2 capture process, with a CO_2 inlet concentration of 18 mol% (typical for a cement plant) and a CO_2 recovery of 90%, the cost of manufacturing (COM_d) is distributed with utility cost accounting for 76.39%, raw material cost at 0.17%, fixed capital investment representing 20.64%, and operating labor cost contributing 2.79%. This data highlights that utility costs are the most significant component of the overall manufacturing cost, reflecting the substantial energy requirements associated with the process.

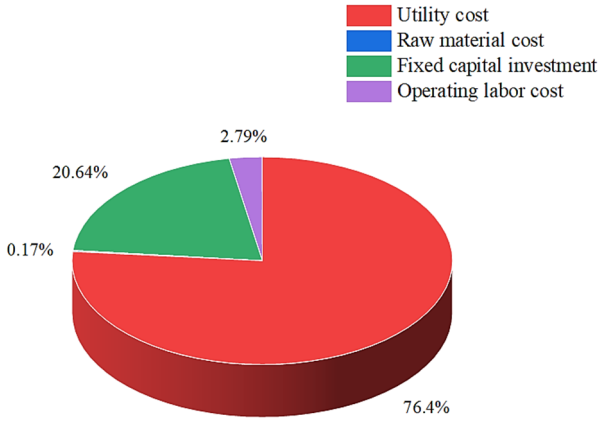

Figure 4 Cost of Manufacturing (COM_d) Distribution for MEA Absorption CO_2 Capture Process (18 mol% CO_2, 90% CO_2 Recovery)

The effects of varying CO_2 inlet concentration (5–70%) and CO_2 recovery (90–99%) on the cost of manufacturing (COM_d) for the MEA absorption CO_2 capture process were investigated. Overall, it was found that COM_d tends to increase as both the CO_2 inlet concentration and recovery increase. The analysis, represented by a contour plot in Figure 5, illustrates the change in COM_d (in MMUSD/year) as CO_2 inlet concentration and CO_2 recovery vary.

An increase in the CO_2 inlet concentration in the exhaust gas from 5 to 70 mol% results in a continuous rise in the cost of manufacturing (COM_d). This is due to higher CO_2 concentrations requiring larger volumes of gas to be handled within a unit time, necessitating a larger process size to accommodate the increased gas absorption. As a result, additional energy is required for the process, contributing to an increase in utility costs, which is the largest portion of COM_d. In addition, larger equipment such as absorbers, strippers, heat exchangers, pumps, and other components are required, driving up the total manufacturing costs.

In terms of CO_2 recovery increasing from 90% to 99%, the cost of manufacturing (COM_d) rises significantly, especially as the CO_2 recovery approaches 99%. This increase in cost is mainly driven by the higher energy demands for regenerating the absorbent and the need to add more absorbent material, as well as expanding the process size to maintain continuous high performance.

At 90% CO_2 recovery, simulation results show that a power plant exhaust gas stream with 5 mol% CO_2 results in a COM_d of 11.97 million USD/year, whereas a steel plant and an ethylene plant with approximately 8 mol% CO_2 yield a COM_d of 16.96 million USD/year. Meanwhile, a cement plant with an 18 mol% CO_2 inlet concentration results in a COM_d of 38.30 million USD/year. These values, obtained through process simulations, are also shown in the contour plot.

These results demonstrate that both higher CO_2 inlet concentrations and recovery directly affect the increase in cost of manufacturing (COM_d), primarily through increased utility costs. Therefore, the design of the MEA absorption CO_2 capture process must balance the desired CO_2 recovery level with the acceptable manufacturing costs to ensure economic viability

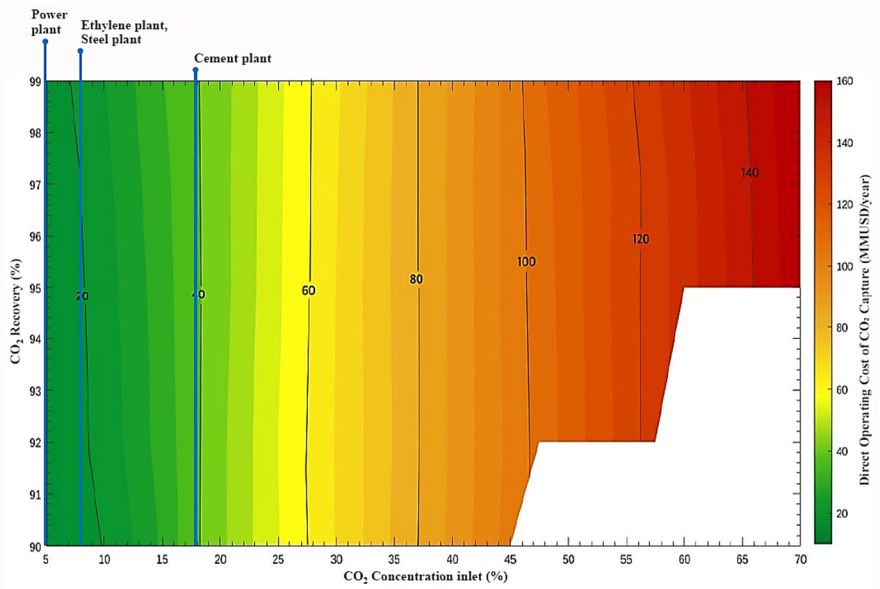

Figure 5 Direct operating cost of MEA carbon capture at MEA-to-CO_2 ratio equal to 2.

3.2.3 Levelized Cost of Carbon Capture (LCOC) Analysis

The Levelized Cost of Carbon Capture (LCOC) is calculated by considering both the total capital investment (TCI) and the manufacturing cost (COM_d), with an interest rate of 12% and an economic lifetime of 12 years. The total cost is divided by the amount of CO_2 captured annually. The results are presented in the contour plot shown in Figure 6.

As the CO_2 inlet concentration in the exhaust gas increases, the LCOC exhibits a decreasing trend, which is primarily attributed to improved process efficiencies at higher CO_2 inlet concentrations. Elevated concentrations enhance mass transfer rates , thus reduce the specific energy requirements for CO_2 separation and compression. Additionally, capital equipment such as absorbers and compressors, which contribute significantly to fixed costs, can be utilized more effectively when processing gases with higher CO_2 content. Consequently, the overall cost per tonne of captured CO_2 decreases, making the carbon capture process more economically favorable at higher CO_2 inlet concentrations.

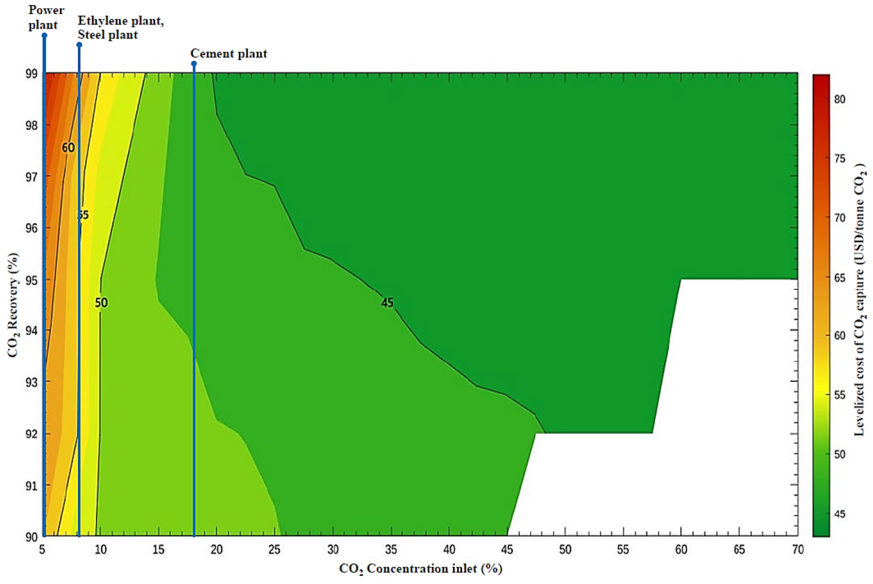

Figure 6 Levelized cost of MEA carbon capture at MEA-to-CO_2 ratio equal to 2.

The simulation results show that, at the same CO_2 recovery, the LCOC decreases as the CO_2 inlet concentration increases. Moreover, within the CO_2 inlet concentration range of 5–16 mol%, increasing the CO_2 recovery percentage leads to a rise in the LCOC, because higher capital investments and operating expenditures are required to achieve greater capture efficiencies. In contrast, when the CO_2 inlet concentration exceeds 17 mol%, the LCOC continues to decline, even as recovery increases, due to enhanced mass transfer and improved cost distribution across a larger mass of captured CO_2.

For specific cases at 90% CO_2 recovery, the LCOC values for different industrial plants are as follows. A power plant with a 5 mol% CO_2 inlet concentration has an LCOC of 57.74 USD/tonne CO_2, steel and ethylene plants with an 8 mol% CO_2 inlet concentration have an LCOC of 52.42 USD/tonne CO_2, and a cement plant with an 18 mol% CO_2 inlet concentration has an LCOC of 48.30 USD/tonne CO_2.

These findings are crucial for optimizing carbon capture processes , as they highlight the importance of balancing CO_2 recovery with associated capital and operating expenditures. By simultaneously considering the CO_2 inlet concentration and the CO_2 recovery level, it is possible to optimize the LCOC and enhance the economic viability of carbon capture systems.

3.3 Comparison of Environmental Performance

3.3.1 Specific net CO_2 emission (SNCE) Analysis

Specific Net CO_2 Emission (SNCE) is an indicator used to measure the efficiency of CO_2 capture processes by calculating the net CO_2 emissions released per unit of CO_2 captured. When the SNCE value is negative, it indicates that the CO_2 capture process is effectively reducing the overall CO_2 emissions. Conversely, a positive SNCE value suggests that the process results in higher CO_2 emissions compared to the amount of CO_2 captured. A lower (or more negative) SNCE value represents better performance in reducing CO_2 emissions.

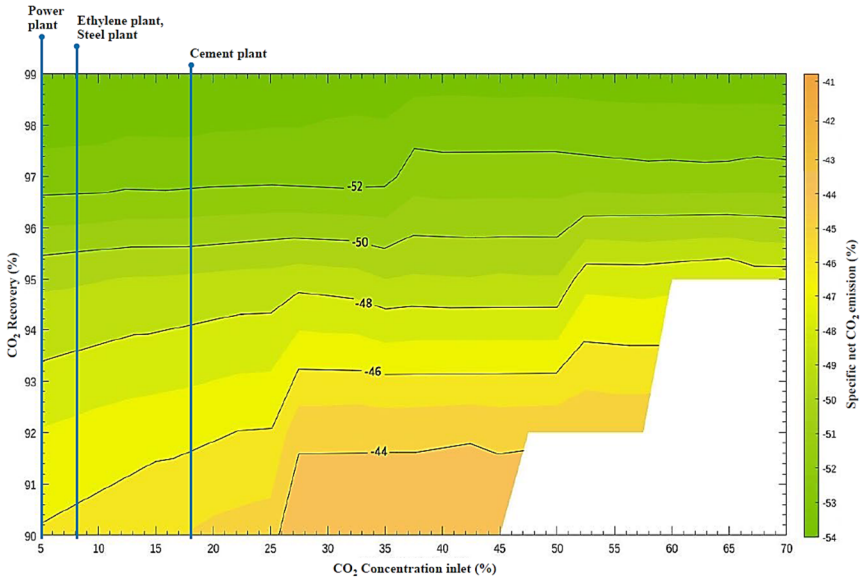

Figure 7 Specific net CO_2 emission of MEA carbon capture at MEA-to-CO_2 ratio equal to 2.

In the contour plot shown in Figure 7, it can be observed that as the CO_2 inlet concentration increases, the SNCE value becomes less negative. This means that as the CO_2 inlet concentration at the inlet increases, the amount of CO_2 captured increases, but the efficiency of reducing CO_2 emissions may not increase proportionally. The higher CO_2 inlet concentration leads to a larger amount of CO_2 entering the system, thus the reduction in CO_2 emissions is less effective, resulting in a smaller negative SNCE value.

On the other hand, as the CO_2 recovery increases, the SNCE value becomes more negative, indicating a higher reduction in CO_2 emissions. An increase in CO_2 recovery means that more CO_2 is being captured, which results in a greater reduction in CO2 emissions from the system, making the SNCE value more negative and showing better performance in CO_2 emission reduction.

For example, at 90% CO_2 recovery, a power plant with a 5 mol% CO_2 inlet concentration has an SNCE of -45.87%. For a steel plant and ethylene plant with an 8 mol% CO_2 inlet concentration, the SNCE is -45.69%, while for a cement plant with an 18 mol% CO_2 inlet concentration, the SNCE is -45.09%. These values show that the SNCE changes based on both the CO2 inlet concentration and CO_2 recovery, which, in turn affects the ability to reduce CO_2 emissions in each type of plant.

3.4 Effect of Exhaust Gas Flow Rate on Capital Cost, Utility Cost, and LCOC Analysis

The effect of exhaust gas flow rate was also evaluated at a CO_2 recovery of 90% and a CO_2 inlet concentration of 18 mol%. Increasing the exhaust gas flow rate leads to notable changes in both capital and operational expenditures. Specifically, the total capital

investment (TCI) and utility costs increase with higher exhaust gas throughput. The larger flow requires larger equipment sizes, such as absorbers, compressors, and associated utilities, thus driving up the capital and energy costs.

However, despite these increases, the Levelized Cost of Carbon Capture (LCOC) continues to decrease. This is because the higher gas flow results in a proportionally greater amount of CO_2 being captured annually. The larger captured volume distributes the total costs more effectively, thereby reducing the cost per tonne of captured CO_2. Consequently, even though the absolute expenses rise, the enhanced throughput improves overall cost efficiency, further emphasizing the economic advantage of capturing CO_2 at higher processing rates under favorable inlet concentration conditions.

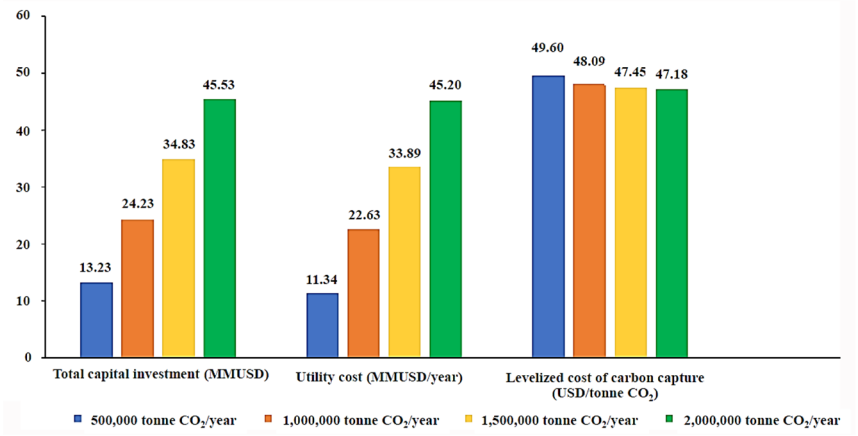

Figure 8 Effect of Exhaust Gas Flow Rate at 18 mol% CO_2, 90% CO_2 recovery on Capital Cost, Utility Cost, and LCOC.

4. CONCLUSION

This study presented a comprehensive technical and economic evaluation of CO_2 capture using monoethanolamine (MEA) absorption. The findings indicated that both total capital investment (TCI) and direct operating cost (COM_d) increased with rising CO_2 inlet concentration and CO_2 recovery, due to the need for larger equipment and greater energy consumption. The Levelized Cost of CO_2 Capture (LCOC) decreased with increasing CO_2 inlet concentration as a result of enhanced mass transfer efficiency and improved cost distribution. However, within the range of 5–16 mol% CO_2, increasing recovery led to higher LCOC owing to the significant additional investment required. Beyond 17 mol% CO_2, the efficiencies gained substantially reduced LCOC.

Specific net CO_2 emissions (SNCE) analysis revealed that although higher inlet concentrations captured more CO_2, the proportionate increase in CO_2 entering the system resulted in a smaller negative SNCE, indicating a relative decline in net emissions reduction performance.

The study further demonstrated that increasing exhaust gas flow rate under optimal inlet conditions improved the economy by lowering LCOC, despite higher capital and operating costs. This underscores the importance of process scale-up to enhance cost efficiency.

Overall, these results highlight the necessity of balancing investment, operational costs, and capture efficiency to optimize CO_2 capture economics. The contour plots generated provide practical tools for estimating capture costs and SNCE across a range of operating conditions, supporting informed design and optimization of industrial CO_2 capture systems.

ACKNOWLEDGMENTS

The author gratefully acknowledges Chulalongkorn University for providing the essential resources, including access to Aspen Plus V14 and MATLAB, which were vital to the technical aspects of this research. This research was conducted under the guidance of Asst. Prof. Kritchart Wongwailikhit, whose expert advice, constructive feedback, and continued support were instrumental in the successful completion of the project. Appreciation is also extended to family, friends, and all individuals whose encouragement and support contributed to the progress and completion of this work.

REFERENCES

1. Agency. IE. World Energy Outlook 2024. Paris, France (for IEA reports). 2024. Contract No.: 22 February.
2. Kanniche M, Gros-Bonnivard R, Jaud P, Valle-Marcos J, Amann J-M, Bouallou C. Pre-combustion, post-combustion and oxy-combustion in thermal power plant for CO2 capture. Applied Thermal Engineering. 2010;30(1):53-62.
3. Huertas, J. and J. Garzon (2015). "CO2 Absorbing Capacity of MEA." Journal of Chemistry 2015: 1-7.

4. Jaffar, M. M., et al. (2023). "Comparative techno-economic analysis of the integration of MEA-based scrubbing and silica PEI adsorbent-based CO2 capture processes into cement plants." Journal of Cleaner Production 414: 137666.
5. Hu, G., et al. (2023). "Techno-economic evaluation of post- combustion carbon capture based on chemical absorption for the thermal cracking furnace in ethylene manufacturing. " Fuel **331**: 125604.
6. Seader JD, Henley EJ, Roper DK. Separation Process Principles, 3rd Edition: John Wiley Incorporated; 2010.
7. Chemtech s. Structured Packings for Distillation, Absorption and Reactive Distillation. Winterthur, Switzerland.
8. Team TIECM. IECM Technical Documentation: Amine-based Post-Combustion CO_2 Capture. Carnegie Mellon University, Department of Engineering and Public Policy; 2018.
9. Shi, F., Reactor and Process Design in Sustainable Energy Technology. 1st ed. Elsevier, 2014
10. Soltani SM, Fennell PS, Dowell NM. A parametric study of CO2 capture from gas-fired power plants using monoethanolamine (MEA). Int J Greenhouse Gas Control 2017;63:321–8.
11. Oh S, Binns M, Cho H, Kim J. Energy minimization of MEA-based CO2 capture process. Appl Energy 2016;169:353–62.
12. Li K, Leigh W, Feron P, Yu H, Tade M. Systematic study of aqueous monoethanolamine (MEA)-based CO2 capture process: Techno-economic assessment of the MEA process and its improvements. Applied Energy. 2016;165:648-59.9. Shi, F., Reactor and Process Design in Sustainable Energy Technology. 1st ed. Elsevier, 2014
13. Turton R., shaeiwitz A. Analysis, Synthesis, and design of chemical process.5th ed. Elsevier, 2018
14. Short, W., D. Packey and T. Holt (1995). "A Manual for the Economic Evaluation of Energy Efficiency and Renewable Energy Technologies." NASA STI/Recon Technical Report N **95**.
15. Pramulya R, Bantacut T, Noor E, Yani M, Zulfajrin M, Setiawan Y, et al. Carbon Footprint Calculation of Net CO2 in Agroforestry and Agroindustry of Gayo Arabica Coffee, Indonesia. Jordan Journal of Biological Sciences. 2023;16:335-43.

Computational fluid dynamics (CFD) analysis of cooling water temperature profiles in high temperature operation heat exchangers

Suwapat Thiaranatron[1], Kritchart Wongwailikhit[1,*]

[1] Center of Excellence in Particle and Material Processing Technology, Department of Chemical Engineering, Faculty of Engineering, Chulalongkorn University, Bangkok 10330, Thailand
[*] Corresponding author: kritchart.w@chula.ac.th

ABSTRACT

Cooling water plays a crucial role in various industrial processes, particularly in petrochemical plants and power plants, where it serves to dissipate excess heat from machinery and heat exchangers. One common heat exchanger type is the double-pipe heat exchanger, where heat is transferred between hot and cold fluids through conduction and convection mechanisms. This study investigates the temperature profiles of cooling water in a double-pipe heat exchanger operating under high-temperature of hot fluid in order to avoid boiling in the pipe. Computational Fluid Dynamics (CFD) is employed to analyze the effect of cooling water Reynolds number on its temperature profiles inside the pipe. The research focuses on the relationship between the Reynolds number and the thermal boundary layer thickness on the inner surface of the pipe, as well as temperature variations. For the simulation scope, two pipe sizes: 30 mm and 25 mm, are used. The Re is set between 500 to 240000, and the hot fluid temperature ranges from 100°C to 250°C. From the simulation results, it can be observed that the larger tube (30 mm) exhibits a thicker thermal boundary layer and a significantly higher wall temperature (Twall) than the smaller tube (25 mm). As the Reynolds number increases, the Temperature wall/ Temperature bulk Ratio increases while the thermal boundary layer thickness decreases, indicating enhanced convective heat transfer. Tube size affects flow dynamics, but both diameters in this study exhibit similar trends in improving heat transfer efficiency.

Keywords: Cooling Water; Double Pipe Heat Exchanger; Computational Fluid Dynamics (CFD); Boundary Layer

1. INTRODUCTION

Cooling water is an essential medium used to dissipate heat from various industrial systems, particularly in petrochemical plants and power generation facilities. It plays a crucial role in maintaining system efficiency and safety by transferring excess heat through heat exchangers, such as double-pipe configurations. As cooling water passes through a heat exchanger, heat is transferred from the high-temperature process fluid to the relatively cooler water. This heat transfer raises the temperature of the cooling water, which is subsequently directed to a cooling tower for temperature reduction via evaporative cooling. The cooled water is then recycled back into the system.

In Thailand, the typical inlet temperature of cooling water is regulated to be around 30°C, with the outlet not exceeding 40°C [7]. For cooling towers, the inlet is commonly set at 52°C [9]. Excessive cooling water temperature can compromise heat exchanger performance, with surface temperatures ideally maintained below 60°C to avoid equipment degradation, scaling, and reduced thermal efficiency

To address these concerns, proper design of the heat exchanger is essential, particularly with regard to pipe diameter and length. These parameters directly influence heat transfer efficiency. Undersized pipes may lead to high flow velocity, causing significant pressure drop and potential erosion, whereas oversized pipes can reduce heat transfer rates. Engineering calculations involving Reynolds number and Nusselt number are commonly employed to optimize these geometrical parameters for balanced thermal performance.

Moreover, the coolant flow rate must be carefully selected. Low flow rates lead to thicker thermal boundary layers and decreased heat transfer, while excessive flow rates increase the risk of corrosion and pump energy consumption. Other influencing factors include the material composition of the heat exchanger.

Although conventional design calculations can estimate overall heat transfer rates, they lack the spatial resolution necessary to visualize temperature gradients. This limitation is addressed by Computational Fluid Dynamics (CFD), which allows for detailed analysis of temperature profiles, turbulence, and flow structures

such as vortices. These insights enable the optimization of heat exchanger designs under high-temperature operating conditions.

In 2017, Basim O. Hasan et al. [2] investigated the effect of heat transfer enhancement on crystallization fouling in a double-pipe heat exchanger. Their study reported a 150%–180% increase in heat transfer rates, depending on the Reynolds numbers of both hot and cold streams. In 2019, Ojaniemi et al. [5] applied CFD using the SST k–ω turbulence model to examine calcium phosphate fouling in a plate heat exchanger. Their results demonstrated that SST k–ω effectively captured near-wall flow behavior, critical for analyzing fouling initiation at the boundary layer. The model showed excellent agreement with experimental data for predicting wall temperatures and fouling-prone regions.

Further, in 2022, Chow et al. [10] studied the effect of Reynolds number and baffle design on shell-and-tube heat exchanger performance using the SST k–ω model. Their results indicated that higher Reynolds numbers significantly improved heat transfer via increased Nusselt numbers, while SST k–ω provided superior prediction accuracy compared to other turbulence models.

Despite these advancements, previous studies have not yet addressed the temperature profiles of cooling water under extreme thermal conditions. This research therefore utilizes CFD to analyze the temperature profiles of cooling water in a high-temperature double-pipe heat exchanger, with the coolant flowing through the inner pipe. The study aims to evaluate heat transfer performance and pinpoint potential thermal hotspots, ultimately supporting the development of more robust and efficient exchanger designs for industrial applications.

2. EXPERIMENTAL

2.1 Overview of Operations

A double-pipe heat exchanger model was developed using ANSYS Fluent to investigate the thermal behavior of cooling water under high-temperature operating conditions. To ensure the accuracy of the simulation, a model validation process was conducted. This involved evaluating the variation in results based on three key parameters: Reynolds number, wall temperature, and heat transfer coefficient.

These parameters were obtained using empirical correlations commonly employed in actual heat exchanger design. By comparing the simulation outcomes against these benchmark values, the model with the highest level of accuracy was identified. The validated model was then employed to analyze the temperature profiles within the heat exchanger, which directly influences the cooling water performance and overall system reliability.

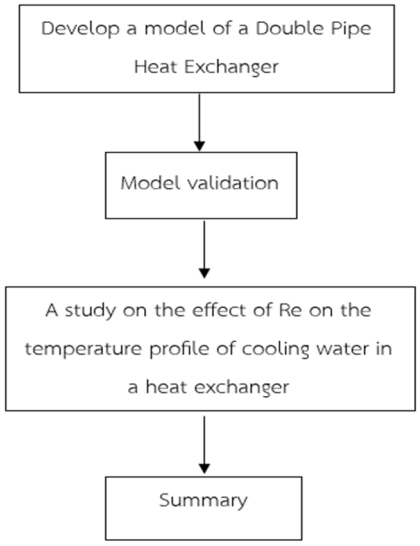

Figure 1 Schematic workflow of the operational procedure

2.2 Thermophysical Properties of Fluids and Solids Used in the Simulation

In a double-pipe heat exchanger, the system consists of an outer pipe and an inner pipe. The fluid properties listed in Table 1 were used for the CFD calculations. Additionally, the material properties of the pipes, which were made of stainless steel, such as density, thermal conductivity, and specific heat capacity, are also presented in Table 2 and were applied during the simulation setup. The overall details of the operating fluids are summarized in Table 1

Table 1 Thermophysical Properties of Fluids Used in the Simulation.

Fluid	Density (kg/m^3)	Viscosity (kg/ms)	Thermal Conductivity (W/m/K)	Specific Heat Capacity (J/kg/k)
Cooling Water	998.2	0.001003	0.6	4182
Ethanol	789	0.001074	0.167	2570

Table 2 Thermophysical Properties of Solid Materials Used in the Simulation.

Material	Density (kg/m^3)	Thermal Conductivity ($W/m^2/K$)	Specific Heat Capacity (J/kgk)
Stainless Steel	7900	15	515

2.3 Control Volume Generation

The control volume in this study was constructed using ANSYS Fluent, where the geometry was discretized into smaller sub-volumes known as a mesh. This meshing process enables the numerical calculation of energy transfer across interconnected control volumes.

To ensure simulation accuracy, the number and size of these sub-volumes must be appropriately defined. A Grid Independence Study was conducted to evaluate the effect of mesh resolution on the simulation results. The mesh density that provided an optimal balance between computational cost and accuracy was selected for subsequent simulations.

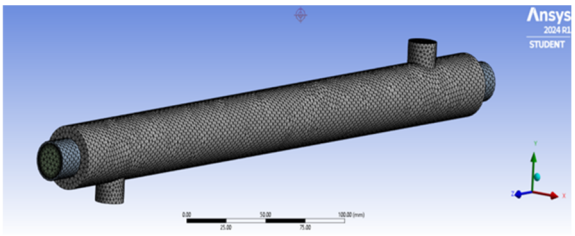

Figure 2 Internal mesh control volumes of the simulated system.

2.4 Model Validation

To evaluate model variation and ensure its accuracy, a counter-flow configuration was used in the simulation. In this setup, the hot fluid flows through the outer pipe, while the cooling water flows in the opposite direction through the inner pipe. Several thermal boundary conditions were defined to reflect realistic industrial operations.

The inlet temperatures of the hot fluid were set at 120°C, 150°C, 200°C, and 250°C, with the outlet temperature constrained to not exceed 100°C. For the cooling water, the inlet temperature was fixed at 30°C, with a maximum outlet temperature of 40°C. The mass flow rate of the cooling water was set at 1000 kg/hr.

Based on these parameters, the flow rates of both fluids were calculated and adjusted to fit the pipe dimensions, aiming to determine the most appropriate operating conditions. The optimal pipe length for each operating case was then estimated, depending on the overall heat transfer coefficient, which was derived from standard correlation equations used in engineering design.

The validation process was divided into two main steps:

(1) Theoretical calculation : Theoretical equations were used to independently compute the wall temperature and heat transfer performance based on the same set of conditions.

(2) Numerical simulation : The calculated pipe length was applied in a CFD simulation to evaluate the resulting pipe wall temperature under each operating condition.

The results from theoretical and the simulation approaches were then compared to assess the model's accuracy. This validation ensured that the CFD model could reliably predict the temperature profiles and heat transfer characteristics for further analysis.

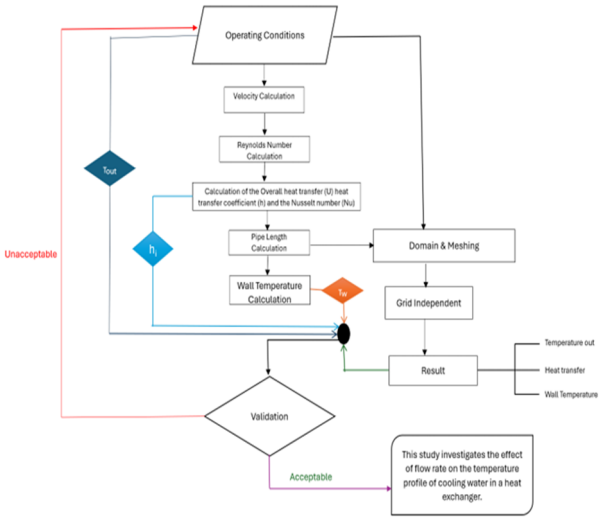

Figure 3 Workflow diagram of the operational procedure.

2.4.1 Theoretical calculation

Theoretical equations were employed to calculate the pipe wall temperature and evaluate heat transfer performance under the same boundary conditions as used in the CFD simulation. The heat transfer coefficients on both hot and cold sides were determined using empirical correlations, and a thermal resistance model was applied to estimate the wall temperature. This result served as a reference for comparison with simulation data to validate the accuracy of the CFD model.

Determination of Optimal Flow Velocity

$$M_{hot}C_{p,hot}\Delta T_{hot} = M_{cold}C_{p,cold}\Delta T_{cold} \quad (1)$$

$$Velocity = \frac{V}{\rho} \quad (2)$$

Estimation of Reynolds Number Using Empirical Correlations

$$Re_{in} = \frac{\rho u d_e}{\mu} \quad (3)$$

$$Re_{annulus} = \frac{\rho u (D - d_e)}{\mu} \quad (4)$$

Estimation of the Nusselt Number Using Prandtl-Based Correlations

$$Pr = \frac{Cp\mu}{k} \quad (5)$$

Estimation of the Nusselt Number Using Empirical Correlations

$$Nu = 1.86(RePr)^{0.33}\left(\frac{de}{L}\right)^{0.33}\left(\frac{\mu}{\mu w}\right)^{0.14} \quad ; \text{Re} < 2100 \quad (6)$$

$$Nu = 0.116(Re^{\frac{2}{3}} - 125)Pr^{\frac{1}{3}}\left(\frac{\mu}{\mu w}\right)^{0.14}\left(1 + \frac{de^{\frac{2}{3}}}{L}\right) \quad (7)$$

$$; 2100 < \text{Re} < 4000$$

$$Nu = CRe^{0.88}Pr^{0.33}(\frac{\mu}{\mu w})^{0.14} \quad ; \text{Re} > 4000 \quad (8)$$

Determination of Heat Transfer Coefficient Using Empirical Correlations

$$h = \frac{Nuk}{D} \quad (9)$$

Estimation of Temperature as a Function of Pipe Length

$$\frac{1}{U_o} = \frac{d_o}{h_i d_i} + \frac{d_o R_{f,i}}{d_i} + \frac{d_o \ln(\frac{d_o}{d_i})}{2k} + R_{f,o} + \frac{1}{ho} \quad (10)$$

$$\Delta T_{lm} = \frac{(\Delta T_{in} - \Delta T_{out})}{ln\frac{\Delta T_{in}}{\Delta T_{out}}} \quad (11)$$

$$Q = UA\Delta T_{lm} \quad (12)$$

$$L = \frac{A}{\pi d_o N} \quad (13)$$

Estimation of Pipe Wall Temperature

$$Tw = \frac{h_i T_{i,avg} + h_o(\frac{D_o}{D_i})T_{o,avg}}{h_i + h_o(\frac{D_o}{D_i})} \quad (14)$$

2.4.2 Numerical simulation

The calculated pipe length for each operating condition was implemented in the CFD model to simulate heat transfer within the double-pipe heat exchanger. The simulation focused on evaluating the pipe wall temperature, allowing visualization of thermal behavior along the pipe. This step provided detailed insight into how well the theoretical design performs under realistic flow and temperature conditions.

2.4.2.1 Specifications of the Double-Pipe Heat Exchanger

In this study, the physical dimensions of the double-pipe heat exchanger used in the Computational Fluid Dynamics (CFD) simulation were carefully defined to ensure accurate and realistic results. The specifications were selected to reflect practical equipment dimensions, enhancing the relevance of the model validation. The key geometric parameters of the heat exchanger are summarized in Table 3 below

Table 3 Specifications of the double-pipe heat exchanger used for model validation

Pipe specification	Input parameters
Pipe size (diameter)	30 mm
Outer diameter of the pipe	10 mm
Inner diameter of the pipe	18 mm
Pipe wall thickness	2 mm

2.4.2.2 CFD Model Used in the Study

Several turbulence models are available in CFD simulations, including Large Eddy Simulation (LES), Spalart–Allmaras, k–ω, and k–ε models. However, recent developments have introduced more robust models that improve prediction accuracy near wall regions. One such model is the Shear Stress Transport (SST) k–ω model, developed by Menter (1994). The SST k–ω model was designed to address the sensitivity of the standard k–ω model to free-stream conditions and to enhance its capability in predicting flows with adverse pressure gradients. It combines the strengths of both the k–ω and k–ε models: it uses the k–ω formulation in the near-wall region for improved resolution of boundary layer behavior, and the k–ε model in the far-field for better free-stream stability. Due to its accuracy and versatility, the SST k–ω model is widely adopted for simulating turbulent flows in complex geometries and engineering applications, including heat exchangers, where accurate prediction of near-wall turbulence and thermal behavior is critical.

2.5 Temperature Profiles Analysis

In this study, the temperature profiles within a double-pipe heat exchanger was investigated to analyze the effects of fluid temperature and Reynolds number on heat transfer behavior.

The independent variables were defined as the radial position within the pipe and the flow velocity of the fluids. The dependent variables included the temperature profiles within the pipe, the wall temperature, and the bulk fluid temperature.

The study conditions involved setting the hot fluid inlet temperatures at 100°C, 150°C, 200°C, and 250°C, as summarized in Table 4 and Two pipe sizes were considered, with inner diameters of 25 mm and 30 mm.

The flow configuration was arranged in a counter-flow setup, where the cooling water flowed through the inner pipe and the hot fluid flowed through the outer pipe.

2.5.1 Specifications of the Double-Pipe Heat Exchanger and Operating Conditions

In this study, two pipe sizes, 30 mm and 25 mm in diameter, were investigated to analyze the effect of pipe size on the temperature profiles within the double-pipe heat exchanger.

Four operating conditions were considered, with each case corresponding to different Reynolds numbers of the cooling water. The simulations aimed to evaluate how variations in pipe diameter and flow conditions influence the thermal behavior and heat transfer performance within the system.

Table 4 Operating Conditions of the Double-Pipe Heat Exchanger

Boundary Conditions	Parameter Description
Outer Pipe Inlet	100,150,200,250 °C
Inner Pipe Inlet	30 °C
Outer Pipe Flow Velocity	0.957 m/s
Re of Inner Pipe (Velocity)	500 - 230000 (0.005 m/s – 3 m/s)

Table 5 Specifications of the Double-Pipe Heat Exchanger

Pipe specification	Input parameters
Pipe size (diameter)	25 mm and 30 mm
Outer diameter of the pipe	10 mm
Inner diameter of the pipe	18 mm
Pipe wall thickness	2 mm

2.5.2 Thermal Boundary Layer Thickness at the Inner Pipe Wall

In this study, the thermal boundary layer thickness at the inner surface of the pipe was evaluated using Equation 15. This equation is based on the fundamental theory of boundary layer development, which describes the behavior of the thermal boundary layer in internal flow. The thickness of the boundary layer is related to both the flow distance along the pipe and the Reynolds number of the fluid. Understanding this relationship provides critical insights into heat transfer characteristics and flow development within the heat exchanger.

$$Boundary\ Layer\ Thickness = \frac{X}{D_{inner}} \quad (15)$$

2.5.3 Relationship Between Temperature and Reynolds Number

For the study of the relationship between temperature and Reynolds number, the wall temperature (Twall) and the bulk fluid temperature (Tbulk) were analyzed and compared against the Reynolds number. The Ratio of Temperature wall/ Temperature bulk was used as an indicator of convective heat transfer performance. The analysis focused on observing the trend of Temperature wall/ Temperature bulk as the Reynolds number increased, and on investigating the effect of pipe size on Reynolds number behavior and heat transfer efficiency.

$$Wall - Bulk\ Temperature\ Ratio = \frac{T_{wall}}{T_{bulk}} \quad (16)$$

3. RESULTS AND DISCUSSION

3.1 Contour of Temperature Profiles

In a double-pipe heat exchanger, counter-flow configuration is commonly used due to its higher thermal efficiency compared to parallel flow arrangements. In this setup, the hot fluid and the coolant flow in opposite directions, which maintains a larger average temperature difference along the length of the exchanger, thus enhancing the heat transfer process [3].

Figure 4 illustrates the temperature distribution at three axial positions along the pipe under the condition where ethanol enters at 200°C and the coolant flows at a Reynolds number of 15,000. This case was selected as a representative example from several simulated conditions to visualize the typical thermal behavior along the exchanger. It can be observed that the outer layer (hot ethanol) gradually loses heat as it flows downward, while the inner coolant progressively gains temperature. This is evident from the change in color of the central region from green at the top to blue at the bottom, indicating a drop in the hot fluid's temperature and a successful heat transfer into the coolant flow. The sharp temperature gradient near the pipe wall reflects the formation of the thermal boundary layer and confirms the effectiveness of the counter-current operation.

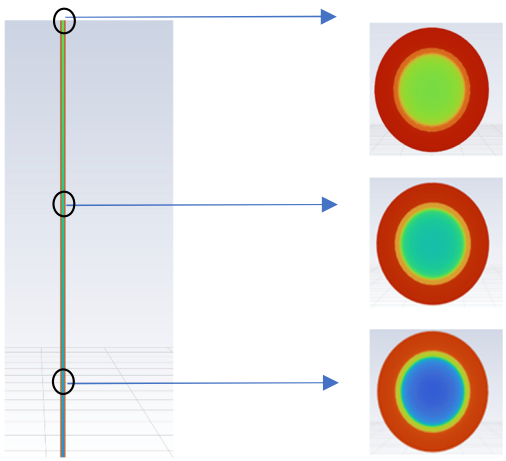

Figure 4 Temperature profiles across three axial sections of the double-pipe heat exchanger.

3.2 Model Validation

3.2.1 Pipe Length

Figure 5 illustrates the relationship between the required pipe length and the inlet temperature of the hot fluid (ethanol) under specified outlet conditions. In this study, the outlet temperature of the hot fluid (ethanol) was maintained at 100°C, while the cooling water entered at 30°C and exited at 40°C, ensuring consistent boundary conditions across all cases.It is observed that the required pipe length for effective heat exchange increases linearly with an increase in the inlet

temperature of the hot fluid, which was varied from 120°C to 160°C.

This behavior can be explained by the fact that a higher inlet temperature results in a larger temperature difference at the inlet, requiring a longer heat transfer surface to bring the hot fluid down to the fixed outlet temperature of 100°C while simultaneously maintaining the desired cooling water outlet temperature.

This trend is consistent with fundamental heat exchanger design principles, where the increase in thermal load at higher inlet temperatures necessitates either an increase in heat transfer area or an extension of the exchanger length to achieve the targeted thermal performance.

These findings reinforce the importance of carefully considering inlet temperature variations in the design and optimization of high-temperature heat exchangers to ensure stable operation and performance.

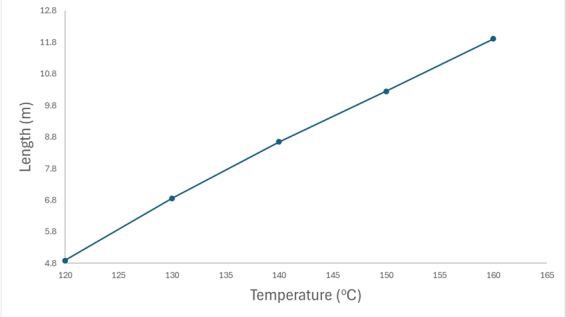

Figure 5 Relationship between Required Pipe Length and Hot Fluid Inlet Temperature.

3.2.2 Temperature Variation

The validation process compares numerical simulation results with theoretical calculations to ensure accuracy and reliability of the CFD model. After determining the appropriate pipe length based on the specified outlet conditions with the hot fluid (ethanol) Inlet temperature fixed at 120–160°C outlet temperature fixed at 100°C and the cooling water temperatures controlled between 30°C (inlet) and 40°C (outlet) the validated pipe length was subsequently used as the geometric basis for detailed CFD simulations.

This approach ensures that the subsequent heat transfer analyses were performed under realistic and practically achievable design configurations, thereby enhancing the reliability and applicability of the results for real-world heat exchanger systems.

Figures 6 and 7 illustrate the validation of wall temperature as influenced by fluid temperature and Reynolds number, respectively. The numerical simulation closely aligns with theoretical values, demonstrating minimal discrepancies.

In Figure 6, the comparison of wall temperature against varying fluid temperatures (120°C to 160°C) shows strong agreement between numerical and theoretical results. A slight deviation observed at lower temperatures may be attributed to simplifying assumptions in theoretical calculations or minor numerical errors inherent in computational simulations

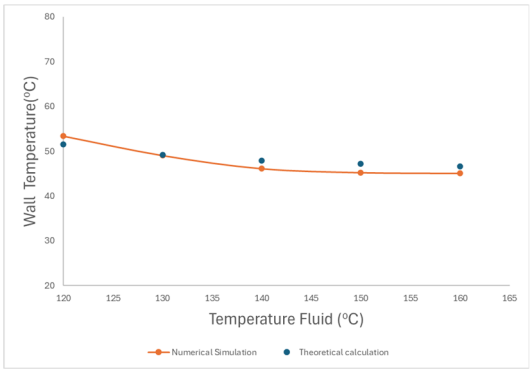

Figure 6 Comparison of Average Wall Temperature Between Numerical Simulation and Theoretical Calculation at Different Fluid Temperatures.

Similarly, Figure 7 indicates the variation of wall temperature with increasing Reynolds number, covering a range from approximately 26,000 to 81,000. Consistent agreement further confirms the model's effectiveness in capturing complex heat transfer phenomena,.

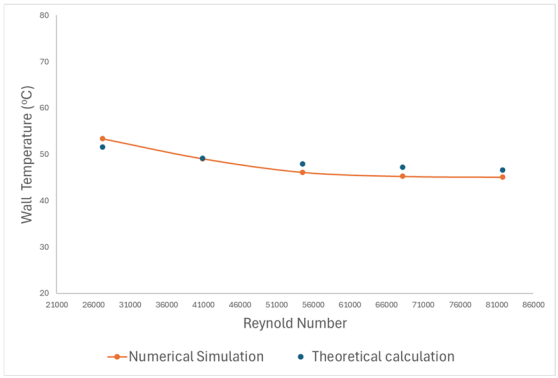

Figure 7 Comparison of Average Wall Temperature Between Numerical Simulation and Theoretical Calculation at Different Reynolds Numbers.

These results substantiate the validity of the numerical model, suggesting that it accurately predicts wall temperatures for the given operational conditions. However, minor variations highlight the sensitivity of computational predictions to boundary conditions and numerical parameters, indicating areas for future refinement.

3.2.3 Heat Transfer Coefficient

Figure 8 illustrates the validation of the Heat Transfer Coefficient (HTC) by comparing numerical simulation results against theoretical calculations. Four computational methods were evaluated: Surface Heat Transfer Coefficient, Wall Adjacent Heat Transfer Coefficient, Y-plus Based Heat Transfer Coefficient, and Wall Function Heat Transfer Coefficient. Among these, the Y-plus Based method consistently demonstrated the highest accuracy, with deviations maintained within ±20% of theoretical values.

The reliability of the Y-plus Based method can be further supported by the work of Menter (2009) [4], who emphasized the critical role of accurate near-wall modeling in turbulent flow simulations. Menter's study introduced the SST k-ω turbulence model, which highlighted that resolving the near-wall region through appropriate Y-plus treatment significantly improves predictions of both flow behavior and convective heat transfer. According to Menter, maintaining an appropriate Y-plus range ensures that the viscous sublayer is correctly captured, leading to more reliable heat transfer coefficient estimations, particularly in high Reynolds number regimes.

These validation results confirm that the present CFD model accurately captures convective heat transfer characteristics, especially in turbulent flow regimes. The superior performance of the Y-plus Based Heat Transfer Coefficient not only reflects its ability to resolve near-wall phenomena but also aligns with established best practices for turbulence modeling in heat exchanger applications.

Minor discrepancies observed beyond the ±20% range could stem from mesh limitations or idealized assumptions in the theoretical models. Future improvements may involve adaptive meshing strategies and more detailed wall treatment algorithms to further refine simulation accuracy.

Overall, the validation process establishes the CFD model as a reliable predictive tool for heat transfer performance evaluation, supporting its application in the design and optimization of advanced thermal systems.

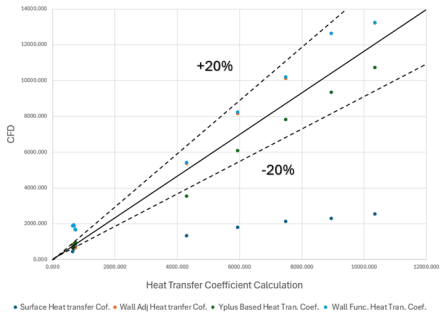

Figure 8 Comparison Between Numerical Simulation and Theoretical Calculation of Heat Transfer Coefficient.

3.3 Temperature Profiles Analysis

Temperature Profiles Analysis present the averaged thermal profiles obtained from simulations at ethanol inlet temperatures of 100°C, 150°C, 200°C, and 250°C, with a fixed cooling water inlet temperature of 30°C. These results reflect the natural thermal and flow development without imposing outlet temperature constraints, thus providing a genuine depiction of the system's thermal behavior under varying Reynolds numbers.

Due to the numerous conditions simulated in this study, only selected representative results are presented to illustrate the temperature distribution within the heat exchanger. Figure 9 shows a Simulated Temperature Profiles at an ethanol inlet temperature of 100°C for Reynolds numbers ranging from 2100 to 3900.The method used to determine the thermal boundary layer involves identifying the point at which the temperature changes by more than 90% of the difference between the pipe wall temperature and the bulk temperature of the coolant fluid. From this threshold, the thermal boundary layer thickness and the Temperature Wall / Temperature Bulk ratio can subsequently be obtained.

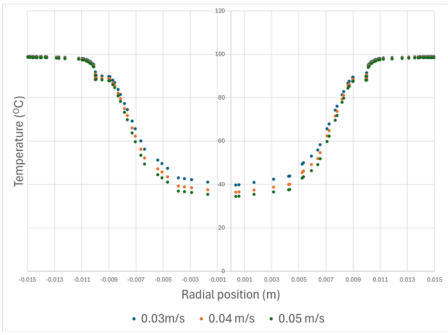

Figure 9 Simulated Temperature Profiles at an ethanol inlet temperature of 100°C.

In Figure 10, the normalized thermal boundary layer thickness (δ/Do) generally exhibits a decreasing trend with increasing Reynolds number, consistent with classical boundary layer theory [8]. As Re increases, inertial forces dominate over viscous forces, thinning the boundary layer and enhancing convective heat transfer.

However, noticeable oscillations or "swings" occur particularly in the transitional flow regime (Re ≈ 4000 – 8000). These fluctuations can be attributed to the interplay between laminar and turbulent structures during transition [6] In this regime, minor disturbances in flow momentum and thermal gradients lead to instabilities, causing local variations in boundary layer thickness.

Moreover, the imposed high thermal load from the hot ethanol intensifies thermal gradients at the wall, promoting buoyancy effects[1] This natural convection component superimposes onto the forced convection, creating transient thickening and thinning of the thermal boundary layer, especially evident in the transitional Re range.

When analyzing pipe size effects, the curves for 30 mm and 25 mm pipes initially overlap closely at low Re, indicating negligible size influence in the laminar regime. However, as Re increases beyond 4000, the 30 mm pipe (blue line) consistently exhibits a slightly thicker boundary layer than the 25 mm pipe (orange line). This observation aligns with White (2006) [12] , who noted that larger hydraulic diameters reduce near-wall shear rates, leading to thicker thermal boundary layers. The slight divergence confirms that pipe size has a measurable but secondary influence under higher turbulence intensities.

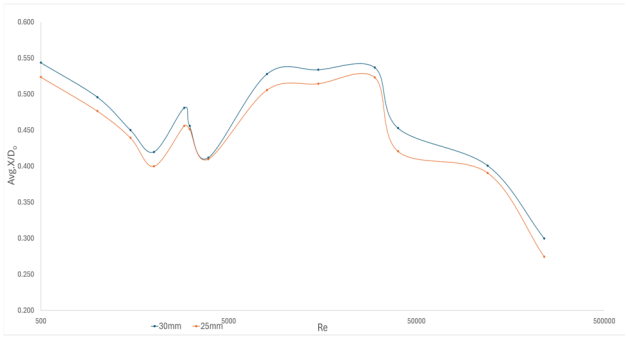

Figure 10 Variation of Average Thermal Boundary Layer Thickness at the Inner Pipe Wall with Reynolds Number.

The partial separation of curves at higher Re suggests that pipe diameter affects the fine structure of heat transfer but becomes less critical as the flow fully transitions to turbulence (Re > 50,000), where turbulence homogenizes the flow field.

In Figure 11, the Temperature wall/ Temperature bulk Ratio exhibits an overall increasing trend with Reynolds number, contrasting traditional expectations where Temperature wall approaches Temperature bulk at high Re due to enhanced mixing [3]. This behavior can be attributed to the high inlet temperature of the ethanol (100–250°C), which generates a substantial heat flux across the pipe wall. Despite thinner boundary layers at higher Re, the intense thermal load causes the wall temperature to remain significantly elevated relative to the cooling water bulk temperature, thereby increasing the Temperature wall/ Temperature bulk Ratio.

Similar to δ/Do, the Temperaturewall/ Temperature bulk Ratio curve shows oscillations in the transitional regime (Re ≈ 4000–8000). These fluctuations are caused by unstable thermal boundary layer development, where variations in turbulence intensity affect the ability of the bulk fluid to absorb heat from the wall effectively. As Re increases further and turbulence becomes fully developed, the Temperature wall/ Temperature bulk trend stabilizes, reflecting more uniform convective heat transfer performance.

Regarding pipe size, the 30 mm pipe consistently shows higher Temperature wall/ Temperature bulk values compared to the 25 mm pipe throughout the entire Re range. This difference results from the larger hydraulic diameter and lower wall shear stress in the bigger pipe, leading to slightly reduced convective heat transfer rates from the wall to the fluid [12].

The separation of the curves indicates that pipe size influences near-wall temperature gradients and hence affects the apparent heat transfer efficiency.

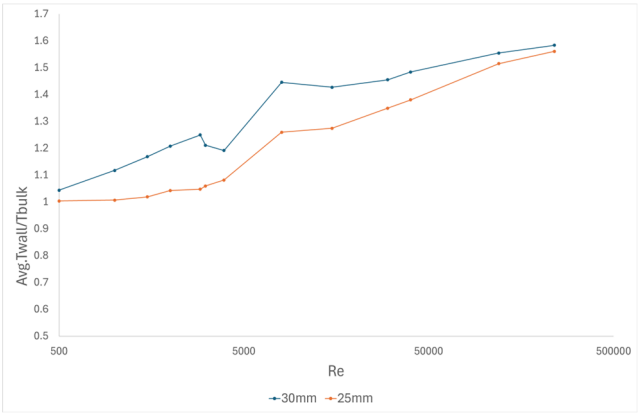

Figure 11 Variation of Average Temperature wall/ Temperature bulk Ratio at the Inner Pipe Wall with Reynolds Number.

Unlike δ/Do, where the curves converge at high Re, Temperature wall/ Temperature bulk Ratio maintains a consistent gap between the 30 mm and 25 mm cases. This persistence suggests that pipe size continues to affect wall temperature behavior even under fully turbulent conditions

The observed swings in both δ/Do and Temperature wall/ Temperature bulk Ratio around Re ≈ 4000–8000 highlight the system's sensitivity to transitional instabilities and heat loading. The high thermal gradients induced by elevated ethanol inlet temperatures exacerbate flow and thermal instability, leading to non-monotonic behavior.

The comparison between pipe sizes further reveals that while boundary layer thickness differences diminish at high Re, wall temperature disparities persist, underlining the complex interaction between geometry, turbulence, and heat transfer performance.

These results are consistent with theoretical predictions and previous studies on turbulent heat transfer confirming the CFD model's validity for capturing intricate thermal behaviors in high-temperature heat exchangers.

However, minor deviations and fluctuations suggest that future improvements could focus on incorporating transition models or enhanced near-wall treatments to capture transitional phenomena more accurately.

4. CONCLUSION

This study investigated the influence of Reynolds number and pipe geometry on the cooling water temperature profiles in high-temperature operation heat exchangers using Computational Fluid Dynamics (CFD) simulations. The main findings reveal that as the Reynolds number increases, the convective heat transfer improves significantly, demonstrated by a decrease in the boundary layer thickness and a increases, in the temperature wall/ temperature bulk Ratio. Temperature profiles analysis showed initial fluctuations during the transition from laminar to turbulent flow, which subsequently stabilized at higher

Reynolds numbers, indicating more efficient heat transfer conditions. These results are significant as they confirm the strong dependence of heat transfer efficiency on flow regime characteristics, contributing valuable insights for the design and optimization of double-pipe heat exchangers operating under extreme thermal conditions. The study highlights the critical role of increasing Reynolds number to enhance cooling performance, aligning with classical heat transfer theory. Some limitations were encountered, such as the assumption of constant fluid properties and the exclusion of detailed transition models, which may influence the accuracy of the simulations, especially within the transitional flow regime. Future research should aim to integrate variable property models and turbulence-transition models to further improve prediction fidelity. Overall, the findings contribute meaningfully to the field by providing CFD-based evidence supporting strategies for improving the thermal performance of cooling systems under high-temperature operations, offering both theoretical insights and practical guidelines for future heat exchanger designs.

ACKNOWLEDGMENTS

The author would like to express sincere gratitude to the Center of Excellence in Particle and Material Processing Technology for providing computational facilities that supported the research activities. Special thanks are extended to Advisor for dedicated supervision, valuable advice, and continuous encouragement throughout the study.

REFERENCES

1. Bejan, A. (2013). Convection Heat Transfer (4th Edition). Wiley.
2. Hasan, B. O., Jwair, E. A., & Craig, R. A. (2017). The effect of heat transfer enhancement on the crystallization fouling in a double pipe heat exchanger. Experimental Thermal and Fluid Science, 86, 272-280.
3. Incropera, F. P., & DeWitt, D. P. (2007). Fundamentals of heat and mass transfer (6th ed.). John Wiley & Sons.
4. Menter, F. R. (2009). Review of the shear-stress transport turbulence model experience from an industrial perspective. International Journal of Computational Fluid Dynamics, 23(4), 305–316.
5. Ojaniemi, U., Pättikangas, T. P., Jäsberg, A., Puhakka, E., & Koponen, A. (2019). CFD simulation of fouling of plate heat exchanger by phosphate calcium. In Proceedings of International Conference on Heat Exchanger Fouling and Cleaning–2019 (pp. 45-52).
6. Pope, S. B. (2000). Turbulent Flows. Cambridge University Press.
7. Ricado. (n.d.). Practical advice: Keep the pH between 7 and 9. SWEP Refrigerant Handbook. Retrieved April 20, 2025, from https://www.swep.net/refrigerant-handbook
8. Schlichting, H., & Gersten, K. (2016). Boundary-layer theory. springer.
9. Sloley, A. (2020, October 21). Choose the correct cooling medium. Chemical Processing. https://www.chemicalprocessing.com/processing-equipment/heat exchangers
10. Teck, C. K., Ming, K. W., Anuar, M. S. S., Sham, H. H. N., Soundrapaman, A., Didane, D. H., & Manshoor, B. (2022). Simulation of Shell and Tube Heat Exchanger: Influence of the Lower Flows and the Baffles on a Fluid Dynamics. Journal of Design for Sustainable and Environment, 4(1), 9-15.
11. Teck, C. K., Ming, K. W., Anuar, M. S. S., Sham, H. H. N., Soundrapaman, A., Didane, D. H., & Manshoor, B. (2022). Simulation of Shell and Tube Heat Exchanger: Influence of the Lower Flows and the Baffles on a Fluid Dynamics. Journal of Design for Sustainable and Environment, 4(1), 9-15.
12. White, f. m. (2006) . fluid mechanics 6th edition . mcgraw-hill.

Simulation of desulfurization in natural gas by using ferrous oxide

Satok Chaikunchuensakun[1,*], Kanokwan Kammongkhun[1], Pronpranate Jenhud[1]

[1] Department of Chemical Engineering, Faculty of Engineering, Thammasat School of Engineering, Thammasat University, Pathum Thani 12120, Thailand
[*] Corresponding author: csatok@engr.tu.ac.th

ABSTRACT

This study investigated the desulfurization process in natural gas by examining the reaction between hydrogen sulfide (H_2S) and ferrous oxide (FeO) using Gibbs free energy minimization. The simulation aimed to analyze the effects of varying temperatures, pressures, and the amount of ferrous oxide in the reactor. The inlet gas mainly contained methane with a flowrate of 4.685 kmol/hr (3000 ppm) hydrogen sulfide at 40°C and 35.5 bar. The solid feed consisted of ferrous oxide at a flowrate of 5.3928 kmol/hr. The outlet gas contained a trace amount of hydrogen sulfide at 2.67×10^{-14} kmol/hr (equivalent to 4.65×10^{-12} ppm). The flowrate of hydrogen sulfide in the outlet gas remained constant with pressure variations between 0.1 and 100 bar. However, when the temperature varied between 25°C and 500°C, the flowrate of hydrogen sulfide in the outlet increased from 6.5×10^{-33} to 4.3×10^{-9} kmol/hr (equivalent to 1.21×10^{-30} to 8.01×10^{-7} ppm). Sensitivity analysis revealed that a minimum of 4.7 kmol/hr of ferrous oxide was required for efficient desulfurization, with a hydrogen sulfide flowrate below 1×10^{-12} kmol/hr (equivalent to 1.86×10^{-10} ppm).

Keywords: Desulfurization; Ferrous oxide; Simulation

1. INTRODUCTION

Natural gas may contain hydrogen sulfide (H_2S), which can be harmful to humans, (NIOSH, OHSA, ACGIH) and can poison process catalysts due to corrosion caused by acid gases [1]. Therefore, the removal hydrogen sulfide from gas is crucial for industrial processes. Traditional equipment used for separating H_2S includes wet and dry absorber, scrubber, absorber, cryogenic, and membrane [2].

Aspen Plus simulations have been used by many researchers, including M. Mofarahi *et al.*, who simulated the absorption of CO_2 from fuel gas turbines [3], W. Ruengsri [4] and later, L. O. Carneiro [5], who simulated the absorption of H_2S using diethanolaine (DEA) monoethanol-amine (MEA) and Methyldiethanolamine (MDEA) respectively.

2. EXPERIMENTAL

Ferrous oxide (FeO) is used in desulfurizing solid-gas reactions because of its high reactivity with sulfur. The desulfurization reaction uses the RGibb block in Aspen Plus V12. The RGibb block is a minimization of the Gibb free energy of the substances in the reactor, eliminating the need for specified reaction stoichiometry in the calculations [6]. Additionally, material and heat balances are also calculated to predict chemical and phase equilibria for substance distribution.

The inlet natural gas mainly consists of methane, as shown in Table 1. The inlet gas flows to the heater1 block, where the temperature is raised to 100°C to prevent the formation of dew points. The HEATOUT stream flows to the expander block, where the pressure is decreased to 1.0325 bar, and then flows to the heater2, where the temperature is decreased to 300°C. The FeO stream, at 5.939 kmol/hr at 300°C and 1.0325 bar specified as CIPSD and is combined with the GASFEED stream, both entering the reactor under the same conditions of 300°C and 1.0325 bar (see Figure 1).

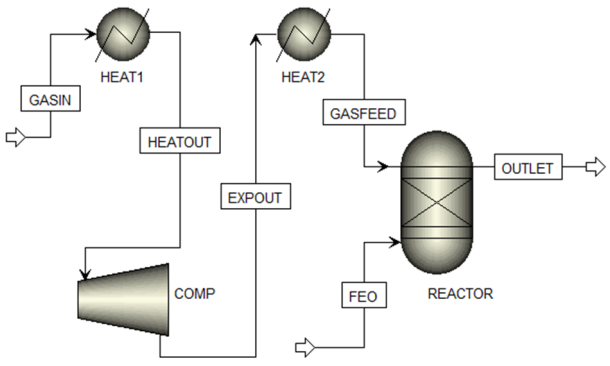

Figure 1 Desulfurization in natural gas using ferrous oxide.

Table 1 Inlet and Outlet streams composition (kmol/hr).

substance	GASIN	FEO	OUTLET
Temp. (°C)	40	300	300
Press. (bar)	35.5	1.01325	1.01325
H2O	12.330346		17.015346
METHANE	3840.6347		3840.6347
ETHANE	838.99962		838.99962
PROPANE	324.87781		324.87781
I-BUTANE	82.023605		82.023605
N-BUTANE	147.96415		147.96415
I-PENTAN	61.115627		61.115627
N-PENTAN	44.5		44.5
N-HEXANE	6.9693259		6.9693259
H2S	4.685		2.67E-14
NITROGEN	1.072204		1.072204
FEO	0	5.3928	0
FEO-CONV	0		0.7078
FES	0		4.685

This assumption is supported by the work of Gonzalez-Vazquez *et al.* [7]. The enthalpy of formation for FeS is -99.998 kJ/kmol and, while for FeO is -271.96 kJ/kmol [8]. Other thermodynamic properties are obtained from the default data in Aspen Plus.

3. RESULTS AND DISCUSSION

The simulation results for the outlet gas (OUTLET) indicate that the flowrate of H_2S is $2.67x10^{-14}$ kmol/hr (equivalent to 4.65×10^{-12} ppm), while the flowrate of FeS is 4.685 kmol/hr at 300°C and 1.0325 bar. The flowrates of other substances are presented in Table 1. A sensitivity analysis was conducted to evaluate the effects of variations in pressure, temperature, and FeO flowrate on the H_2S outlet flowrate.

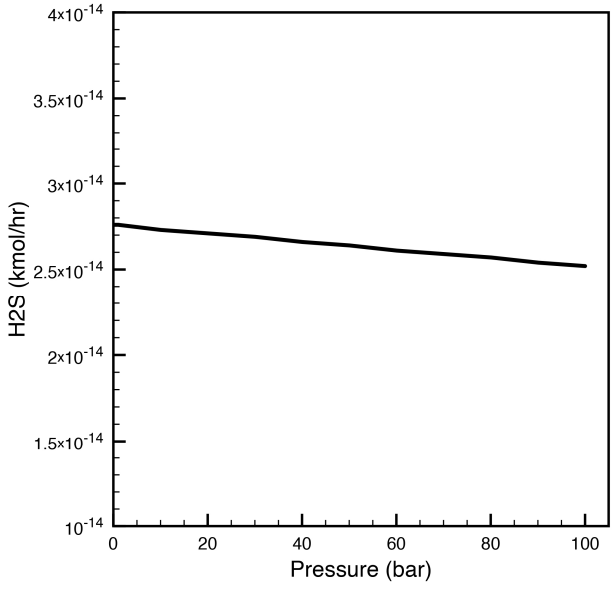

Figure 2 H_2S in outlet gas when vary pressure between 0.1-100 bar.

The pressure varies from 0.1 to 100 bar. The inlet flowrates of H_2S and FeO are 4.685 and 5.3928 kmol/hr, respectively. The flowrate of H_2S in OUTLET is slightly decreases or can be assumed to remain constant as the pressure increases, as shown in Figure 2. The simulation results of the desulfurization process are consistent with those of a previous study conducted by J. B. Mutabazi and J. Chidamoio [9].

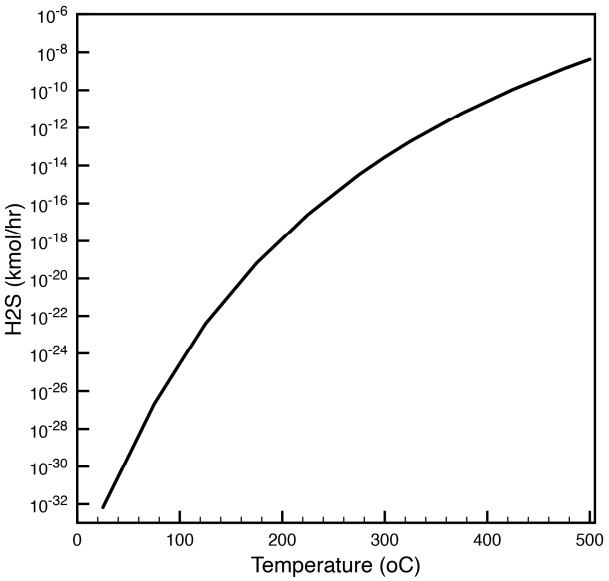

Figure 3 H_2S in outlet gas when vary temperature 25-500°C

Figure 3 shows the effect of temperature on the flowrate of H_2S in OUTLET. The inlet flowrates of H_2S and FeO are 4.685 and 5.3928 kmol/hr respectively. The flowrate of H_2S in OUTLET increased from 6.5×10^{-33} to 4.3×10^{-9} kmol/hr (equivalent to 1.21×10^{-30} to 8.01×10^{-7} ppm) as the temperature was increased from 25 to 500°C. This indicates that desulfurization is highly effective at low temperatures.

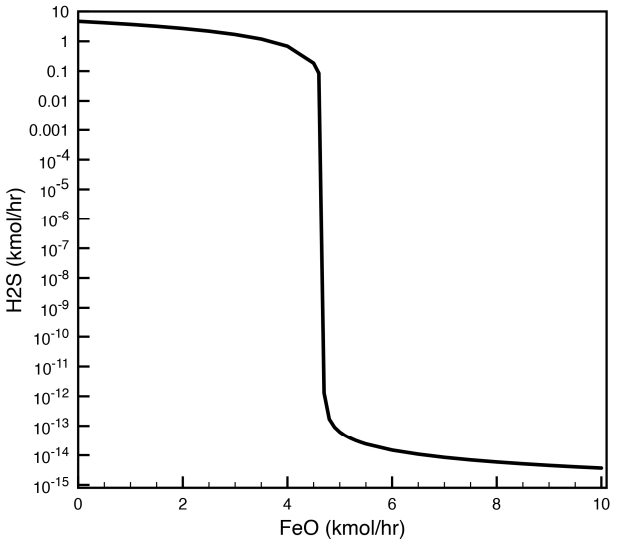

Figure 4 H_2S in outlet gas when vary FeO between 0-10 kmol/hr

The flowrate of H_2S in OUTLET is decreased from 4.685 to 3.67×10^{-15} kmol/hr when the FeO flowrate is between 0.01 to 10 kmol/hr, as shown in Figure 4. The flowrate of H_2S in OUTLET slightly decreass with a low FeO inlet flowrate. When, the FeO flowrate exceeds 4.7 kmol/hr, the flowrate of H_2S in the outlet gas decreases dramatically. However, when the FeO flowrate exceeds 8 kmol/hr, the flowrate of H_2S in OUTLET remains nearly constant.

4. CONCLUSION

This simulation demonstrates that the reaction between H_2S and FeO can serve as an alternative method for desulfurization. The process is effective at low temperatures and low pressures, with a ratio $1.003< FeO/H_2S <1.7076$.

REFERENCES

1. A. Mohebbi. CFD Simulation of a Wetted-Wall Column for Natural Gas Sweetening using DEA Solution. *Gas Processing J.* 2017; 5(2): 13-32.
2. M. Rezakazemi, Z. Niazi, M. Mirfendereski, S. Shirazian, T. Mohammadi, A. Pak. DFD Simulation of Natural gas in a gas-liquid hollow-fiber membrane contractor. *Chem. Eng. J.* 2011; 168(3): 1217-1226.
3. M. Mofarahi, Y. Khojasteh, H. Khaledi, A. Farahnak. Design of CO_2 absorption plant for recovery of CO_2 from flue gases of gas turbine. *Energy.* 2008; 33(9):1311-1319.
4. W. Ruengsri. Simulation of hydrogen sulfide and methyl methyl mercaptan removal by alkanolamine absorption using ASPEN HYSYS program. Maser thesis, Chulalongkorn University. 2010.
5. L. O. Carneiro, S. F. Vasconcelos, V. W. Farias Neto, R. P. Brito, K. D. Brito. Improving H_2S removal in the coke oven gas purification process. *Sep Purif Technol*. 2021; 257:117862.
6. R. Schefflan Tech Yourself the Basics of Aspen Plus. AIChE-Wiley & Sons, 2016; 181-183.
7. M.P. Gonzalez-Vazquez, F. Rubiera, C. Pevida, D. T. Pio, A. C. Tarelho. Thermodynamic analysis of biomass gasification using Apen plus: Comparison of stoichiometric and non-stoichiometric models. Energies 2021; 14(189): 1-17.
8. F. Fronvold, S. Stolen. Heat capacities of the wustites $Fe_{0.9329}O$ and $Fe_{0.9254}O$ at temperatures T from 5 K to 350 K. Thermodynamics of the reaction: $xFe(s)+(1/4)Fe_3O_4(s)=Fe_{0.7500+x}O(s)=Fe_{1-y}O(s)$ at T~850 K, and properties of $Fe_{1-y}O(s)$ to T= 1000K. Thermodynamics of formation of wustite. *J. Chem. Thermodynamics* 1993; 25: 1089-1117.
9. J.B. Mutabazi, J. Chidamoio. Simulation on performance of Metal Oxide for H2S removal in Natural gas under influence of CO2. *Global Scientific J.* 2023; 10(6): 1392-1407.

Modification of the syngas production process using fluidized-bed twin reactor system and chemical looping gasifier

Sutanon Krataipo[1], Monsicha Sitta[1], Ratchaphon Chaloemkamonsit[1], Bunyaphat Yimsanguan[1], Choowong Chaisuk[1,*]

[1] Department of Chemical Engineering, Faculty of Engineering and Industrial Technology, Silpakorn University, Nakhon Pathom 73000, Thailand
[*] Corresponding author: chaisuk_c@su.ac.th

ABSTRACT

Currently, biomass is widely used as a replacement for fossil fuels to produce syngas. One of the processes for producing syngas is downdraft technology, which consists of four main stages: pyrolysis, combustion, gasification and CO_2 separation. The major problems are the formation of coke in downdraft gasifiers, as well as the dilution of the syngas product by other gases. It is interesting to address these issues using fluidized-bed gasifiers, such as twin reactors and chemical looping. In this work, the economic indicators and energy usage of two modified processes were evaluated using Aspen Plus program, version 14. The prototype process was referenced from the work of Adnan and Hossain. The twin reactors replaced the reaction zone, while the chemical looping, containing calcium oxides to remove CO_2 from the syngas, replaced both reaction and separation zones. From the simulation results, both modified processes showed high purity of the syngas product on a dry basis: 88.2 mol% for twin reactors and 94.6 mol% for chemical looping, compared to 87.1% for the prototype process. The CO_2 in the syngas was effectively removed through chemical looping. Its composition was 1.8 mol%, compared to 7.1 mol% in the prototype process. The economic indicators, including CAPEX, OPEX, NPV, IRR, and DPP, showed positive results after modification. The energy cost for chemical looping was decreased by 31.6% but that for twin reactors was increased by 14.7%. Hence, the chemical looping proved to be a promising process for producing the syngas.

Keywords: Syngas production; Fluidized-bed; Twin reactors; Chemical looping; Aspen Plus

1. INTRODUCTION

In recent years, biomass has emerged as a promising alternative to fossil fuels due to its renewable nature and widespread availability. One of the key energy carriers derived from biomass is synthesis gas (syngas), which is produced by thermochemical conversion of organic waste [1, 2]. Syngas not only serves as a renewable energy source but also acts as a versatile chemical intermediate in the production of fuels and industrial chemicals such as methanol, ethanol, and ammonia. Among the various syngas production technologies, downdraft gasifiers are commonly employed due to their simplicity and cost-effectiveness [3]. However, conventional downdraft gasification faces several critical challenges: (1) dilution of the product gas when using air as the gasifying agent, (2) bed coking that impedes the gasification process, and (3) excessive tar formation, which leads to fouling of downstream equipment and degradation of gas quality [4, 5]. To overcome these limitations, process enhancements are essential. Strategies such as bitumen cracking, coke suppression, and selective gas separation can significantly improve syngas quality. Advanced gasification technologies-particularly fluidized-bed systems including twin-reactor configurations and chemical looping-offer promising solutions for cleaner and more efficient syngas production [6-9]. In this study, two modified gasification processes based on fluidized-bed technology were evaluated. Process simulations were conducted using Aspen Plus (version 14) to assess energy efficiency and economic performance.

2. EXPERIMENTAL

Process simulation was conducted using Aspen Plus (version 14) to evaluate the performance and feasibility of biomass gasification configurations. Initially, a baseline (prototype) process was developed, comprising four main sections: pyrolysis, combustion, gasification, and CO_2 separation. This configuration was constructed and validated based on the methodology proposed by Adnan and Hossain [10]. Following successful validation, two modified configurations were developed to enhance system

performance: twin reactors and chemical looping, both incorporating fluidized-bed gasifiers. In the twin reactor configuration, the gasification reaction zone was redesigned to separate combustion and reduction processes. The chemical looping system introduced calcium oxide (CaO) as an oxygen carrier and in-situ CO_2 sorbent, thereby modifying both the reaction and gas separation zones to achieve improved syngas purity. After implementing these configurations, mass and energy balance analyses were performed for each process. Additionally, a comprehensive techno-economic assessment was conducted. Key economic indicators evaluated included capital expenditure (CAPEX), operational expenditure (OPEX), net present value (NPV), internal rate of return (IRR), and discounted payback period (DPP).

3. RESULTS AND DISCUSSION

Figure 1 illustrates the prototype process, adapted from the work of Adnan and Hossain [10]. Our simulation results showed an error of approximately 5% under the same feed stream and operating conditions. After validation, the feed composition of pine sawdust, as presented in Table 1, was used. The mass flowrate was fixed as 1000 kg/h.

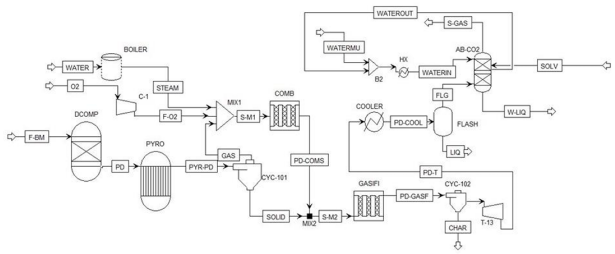

Figure 1 The prototype process flowsheet.

Table 1 The feed composition of pine sawdust.

Proximate, wt%	Moisture	13.43
	Fixed carbon	11.11
	Volatile matters	73.45
	Ash	2.01
Ultimate, wt%	C	56.16
	H	6.11
	N	0.14
	S	0.70
	O	34.88
	Ash	2.01

Biomass was fed into the decomposition reactor (DCOMP: RYield model) to adjust the conditions before entering the pyrolysis reactor (PYRO: RGibbs model). The pyrolysis products were separated into solid and gas phases using a cyclone (CYC-101). The gas was mixed with O_2 to increase the pressure and combined with steam, which was preheated before being fed into the combustion reactor (COMB: RPlug model). The combustion products were then mixed with the solid residue from the pyrolysis process and converted in the gasification reactor (GASIFI: RPlug model), regardless of the composition of the gasification output. The solid particles were separated from the gas stream using another cyclone (CYC-102). After condensing the gas, the resulting streams were split into a liquid stream (LIQ) and a remaining gas stream (FLG) using a knock-out drum (FLASH). The gas, containing CO_2, was directed to an absorption tower. At times, the feed water was preheated before preparing the solvent mixture. The syngas was collected in the S-GAS stream, while the W-LIQ stream contained the solvent used for CO_2 absorption.

After simulating the prototype process, the process flowsheets of the fluidized-bed twin reactors and the fluidized-bed chemical looping gasifier were generated as shown in Figures 2 and 3. According to the process flowsheet of the fluidized-bed twin reactor system, the feed stream entering the unit originated from the output of the pyrolysis reactor used in the prototype process. This feed was combined with two recycle streams (COAL and SOLID-RE) to form a mixed stream. The combined stream was then passed through a cyclone separator (CYC-F) to remove solids before being introduced into the first fluidized-bed reactor (FLUIDIZD: FluidBed model). The outlet stream from the FLUIDIZD reactor was separated into two streams: the PD-GAS stream, consisting of gas products and considered the main output of the process, and the PD-SOD stream, containing partially reacted solids. The PD-SOD stream was fed into a secondary fluidized-bed reactor (COMBUS: FluidBed model) where combustion occurs in the presence of an air feed. The products of the combustion process included a gas stream (GAS-COM) and a solid stream (COAL), which contained unreacted material. The GAS-COM stream was passed through another cyclone (CYC-RE) to separate solids from the gas. The resulting solid stream (SOLID-RE) was recycled and combined again with the fresh feed and COAL stream, completing the loop.

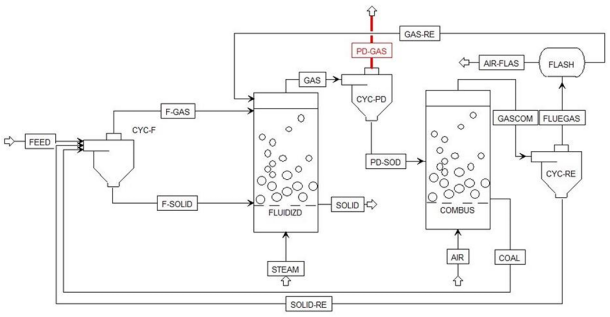

Figure 2 The process flowsheet of the fluidized-bed twin reactors.

The process of the fluidized-bed chemical looping gasifier began with feedstock generated via pyrolysis in a prototype system, analogous to a twin fluidized-bed configuration. This feed was first routed through a cyclone separator (CYC) to remove solids before

entering the main fluidized-bed reactor (FLUIDIZD: FluidBed model). The reactor output stream (FLUID-G) underwent further separation in a second cyclone (CYC2) to yield two distinct product streams: a solid stream (CHAR) and a gas stream (GAS). The GAS stream was mixed with calcium oxide (CaO) and directed into the AD-CO2 reactor, where CO_2 reacts with CaO to form calcium carbonate ($CaCO_3$). The resulting CO_2-free gas stream (P-GAS) was separated from $CaCO_3$ in a third cyclone (CYC-CACO). The separated $CaCO_3$ was subsequently transferred to the regenerator (REGEN: FluidBed model), where it was thermally decomposed back into CaO and CO_2, completing the chemical looping cycle.

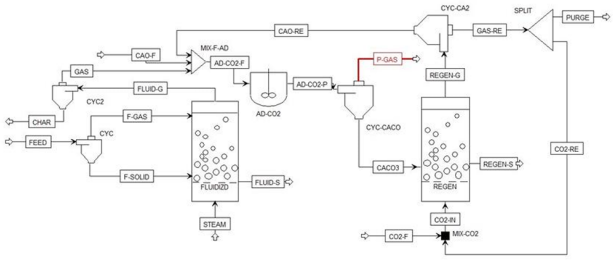

Figure 3 The process flowsheet of the fluidized-bed chemical looping gasifier.

After simulating the two modified processes, the resulting syngas products were compared with the syngas obtained from the prototype process, as shown in table 2. Using the same feed conditions (table 1), both modified processes demonstrated a higher syngas production rate; however, the moisture content was significantly elevated. An adsorption unit was therefore required to remove excess water. The H_2-to-CO ratio remained relatively consistent across all processes. Notably, SO_2 was detected in the product gas stream when using the fluidized-bed twin reactor system. Meanwhile, CO_2 in the syngas was effectively removed through the chemical looping process. Its composition was 1.8 mol%, compared to 7.1 mol% in the prototype process.

Table 2 The resulting syngas product obtained by simulating three processes.

Product	Prototype	Twin reactor	Chemical looping
Molar flow rate (kmol/h)	69.14	88.39	83.74
Syngas purity (mol% wet basis)	78.6	68.4	72.2
Syngas purity (mol% dry basis)	87.1	88.2	94.6
Ratio of H_2-to-CO	1.79	1.76	1.76

Energy consumption across the three evaluated processes was classified into three categories: hot utilities, cold utilities, and electricity, as illustrated in Figure 4. The cold utility requirement consisted exclusively of cooling water, whereas the hot utilities comprised fuel oil and low-pressure (LP) steam, with fuel oil representing the predominant energy source. Among the three configurations, the chemical looping process demonstrated the most favorable energy performance, exhibiting notably lower demands for both cold utilities and electrical power. It was noted that the additional heat supply required in the second fluidized-bed reactor of the twin reactor process led to increased usage of hot utilities.

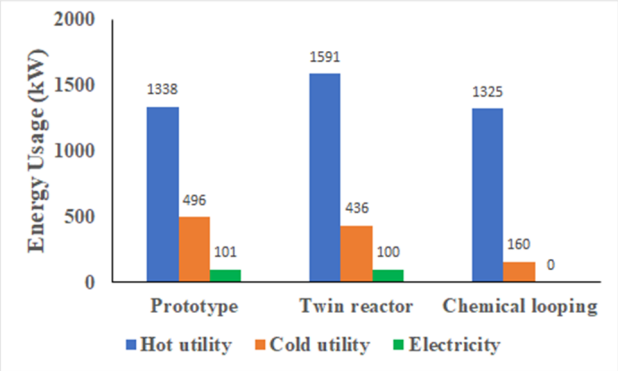

Figure 4 Energy consumption for three processes.

Figures 5 and 6 present a comparative analysis of capital expenditure (CAPEX) and operational expenditure (OPEX) for the three process configurations. Both modified processes incurred lower capital investments compared to the prototype configuration. This reduction was primarily attributed to high equipment costs of the prototype's combustion and gasification reactors, which were significantly minimized or redesigned in the modified systems.

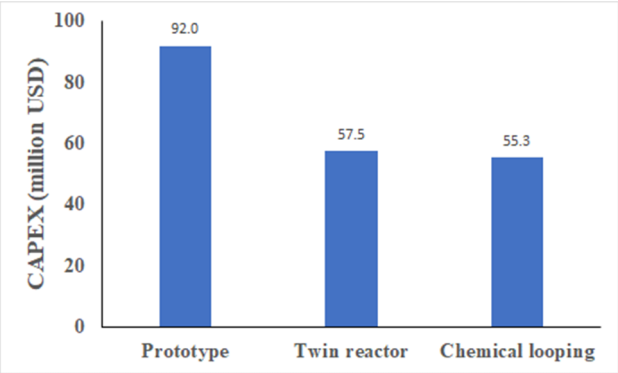

Figure 5 Capital expenditure for three processes.

Operational expenditures followed a similar pattern. However, a closer examination of energy-related operating costs revealed distinct trends. The chemical looping gasifier demonstrated a 31.6% reduction in total energy costs. This improvement was largely due to its enhanced thermal efficiency and effective heat integration, which reduce the dependency on external utilities. On the other hand, the twin reactor

process experienced a 14.7% increase in energy costs. This increase stemmed from the additional heat requirement in the second fluidized-bed reactor, resulting in greater consumption of fuel oil. These findings suggested that while both modified processes offered capital cost advantages, only the chemical looping configuration provides a net benefit in terms of overall energy efficiency and cost savings.

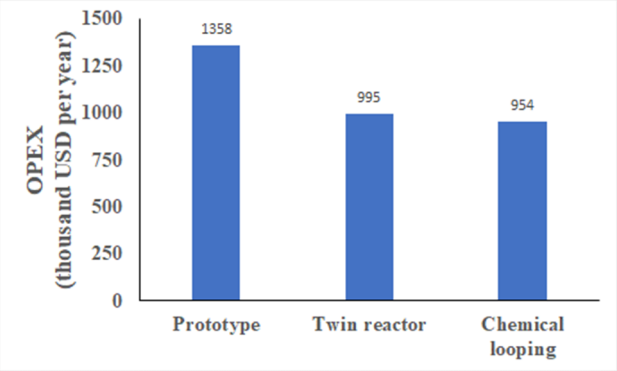

Figure 6 Operational expenditure for three processes.

Economic performance was assessed for the three process configurations using key financial indicators: net present value (NPV), internal rate of return (IRR), and discounted payback period (DPP), as illustrated in Figures 7 - 9. All evaluations were conducted based on a 10-year project lifespan and a discount rate of 7%. The prototype process involved the highest capital investment due to more complex and costly equipment. In contrast, the twin reactor and chemical looping configurations required significantly lower capital outlays. Despite the lower investment, both modified processes yielded higher NPVs than the prototype, driven primarily by their improved product output. Among these, the chemical looping process achieved the highest NPV, attributed to both reduced capital expenditure and enhanced energy efficiency. These advantages collectively render the chemical looping configuration the most economically favorable option.

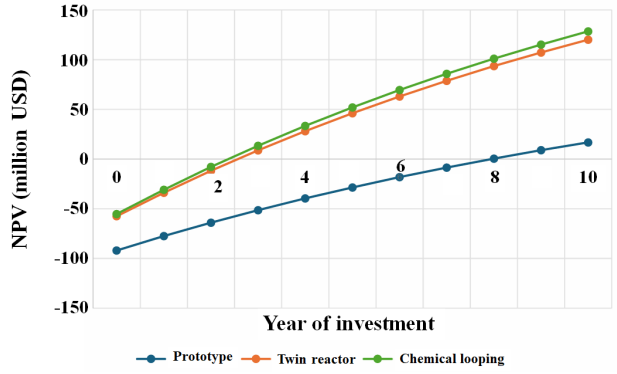

Figure 7 Net present value for three processes.

The IRR analysis, under identical project conditions, reinforced this conclusion. The prototype process recorded the lowest IRR at 11%, while the twin reactor and chemical looping processes achieved 41% and 46%, respectively. The markedly higher IRR of the chemical looping system indicated superior profitability and investment attractiveness over the project duration.

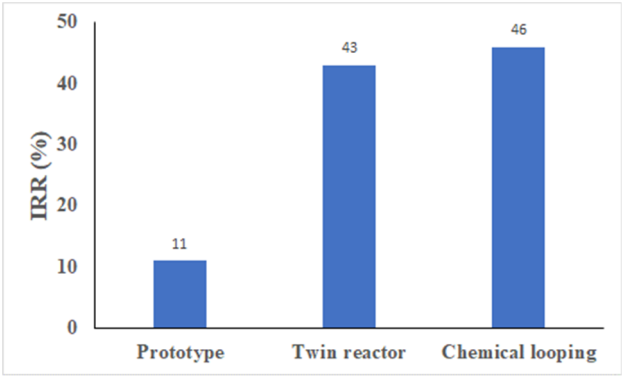

Figure 8 Internal rate of return for three processes.

Similarly, the discounted payback period analysis highlighted the rapid return on investment of the chemical looping configuration. With a payback period of only 3.4 years, it significantly outperformed the twin reactor and prototype systems. This short payback time, coupled with the highest NPV and IRR, positioned the chemical looping process as the most economically viable configuration among those evaluated.

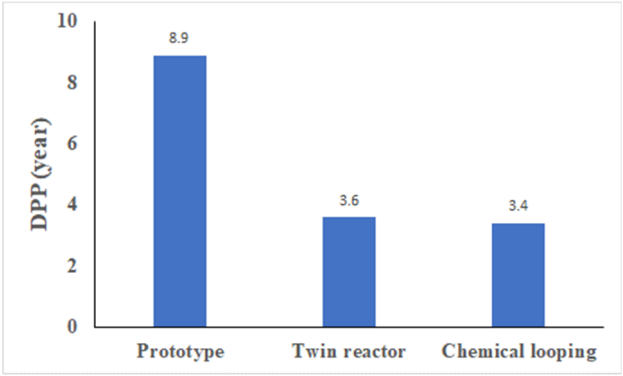

Figure 9 Discounted payback period for three processes.

4. CONCLUSION

This study evaluated and compared the prototype gasification process with two modified configurations: a fluidized-bed twin reactor system and a fluidized-bed chemical looping gasifier. All three systems were modeled under identical feed and operating conditions to ensure a consistent basis for performance comparison. The simulation of the prototype process was validated with reference data, showing an acceptable deviation of approximately 5%. Both modified systems demonstrated improved syngas production rates compared to the prototype, although the moisture content in the product gas was

significantly higher, necessitating an additional drying or adsorption unit. Importantly, the chemical looping process achieved effective in-situ CO_2 removal, reducing CO_2 content in the product gas to 1.8 mol%, compared to 7.1 mol% in the prototype. In contrast, the twin reactor configuration produced trace amounts of SO_2 in the syngas, requiring further gas cleanup. From an energy perspective, the chemical looping configuration exhibited the lowest consumption of hot utilities, cold utilities, and electricity, attributed to better heat integration and reduced dependence on external energy inputs. The twin reactor system, however, showed increased hot utility usage due to additional heating requirements in the secondary reactor. Economic analysis confirmed the technical advantages of the chemical looping configuration. It not only required lower capital investment than the prototype but also delivered the highest net present value (NPV) and internal rate of return (IRR), alongside the shortest discounted payback period (3.4 years). While both modified systems reduced overall CAPEX and OPEX, only the chemical looping gasifier offered significant energy cost savings-reducing total energy expenses by 31.6%. These findings underscored its superior economic performance. In conclusion, the fluidized-bed chemical looping gasifier emerged as the most promising configuration among those studied, offering enhanced syngas quality, improved energy efficiency, and strong economic viability. It presented a compelling option for future biomass gasification applications aimed at sustainable and cost-effective syngas production.

ACKNOWLEDGMENTS

This work was financially supported by Department of Chemical Engineering, Faculty of Engineering and Industrial Technology, Silpakorn University.

REFERENCES

1. Q. Liu, S.C. Chmely, N. Abdoulmoumine. Biomass treatment strategies for thermochemical conversion. *Energy & Fuels* 2017; 31(4): 3525-3536.
2. H. Wang, S. Liu, J. Chao. Thermochemical conversion of biomass to fuels and chemicals: A review of catalysts, catalyst stability, and reaction mechanisms. *Catalysis Reviews* 2023; 67(1): 57-129.
3. J.D. Martínez, K. Mahkamov, R.V. Andrade. Syngas production in downdraft biomass gasifiers and its application using internal combustion engines. *Renewable Energy* 2012; 38(1): 1-9.
4. P.R. Havilah, A.K. Sharma, G. Govindasamy, L. Matsakas, A. Patel. Biomass gasification in downdraft gasifiers: A technical review on production, up-gradation and application of synthesis gas. *Energies* 2022; 15(11): 3938.
5. A.V. Cong, H. Enomoto, R. Naryyanto, K. Fukadu, Z. Zong, C. Chunti, R. Noda. Major tar compounds in raw producer gas and deposits from a small downdraft gasifier: Analysis and comparison. *BioResources* 2020; 15(1): 1773-1790.
6. M. Siedlecki, W. de Jong, A.H.M. Verkooijen. Fluidized bed gasification as a mature and reliable technology for the production of bio-syngas and applied in the production of liquid transportation fuels - A review. *Energies* 2011; 4(3): 389-434.
7. Y.P. Chyou, D.M. Chang, P.C. Chen, H.Y. Chien, K.T. Wu, R.Y. Chein. Development of biomass gasification technology with fluidized-bed reactors for enhancing hydrogen generation: Part I, hydrodynamic characterization of dual fluidized-bed gasifiers. *Applied Sciences* 2020; 10(1): 2.
8. J. Zeng, R. Xiao, D. Zeng, Y. Zhao, H. Zhang, D. Shen. High H_2/CO ratio syngas production from chemical looping gasification of sawdust in a dual fluidized bed gasifier. *Energy & Fuels* 2016; 30(3): 1764-1770.
9. T. Shen, J. Wu, L. Shen, J. Yan, S. Jiang. Chemical looping gasification of coal in a 5 kW_{th} interconnected fluidized bed with a two-stage fuel reactor. *Energy & Fuels* 2018; 32(4): 4291-4299.
10. M.A. Adnan, M.M. Hossain. Gasification performance of various microalgae biomass - A thermodynamic study by considering tar formation using Aspen plus. *Energy Conversion and Management* 2018; 165: 783-793.

Reinforcement learning control for optimal ethanol production from microbial fermentation

Khanisorn Thanutwuttikorn[1], Suttirak Pairoj[2], Pornpimon Kavansu[3], Bundit Boonkhao[4,*], Rujapa Nanthapodej[4]

[1] Division of Mechanical Engineering, Faculty of Engineering, Nakhon Phanom University, Nakhon Phanom 48000, Thailand
[2] Division of Applied Foundation, Faculty of Industrial Technology, Nakhon Phanom University, Nakhon Phanom 48000, Thailand
[3] Research and Development Institute, Nakhon Phanom University, Nakhon Phanom 48000, Thailand
[4] Division of Industrial Engineering, Faculty of Engineering, Nakhon Phanom University, Nakhon Phanom 48000, Thailand
[*] Corresponding author: bundit@npu.ac.th

ABSTRACT

Ethanol serves as a renewable alternative energy source that can be synthesised through microbial fermentation. However, the efficiency of this production process is inherently challenged by the variability in microbial growth, which is influenced by key process parameters such as temperature, pH, and substrate concentration, among others. Consequently, the effectiveness of model-based control strategies may be compromised due to the inherent uncertainties associated with these dynamic biological factors. Reinforcement Learning (RL) has recently been introduced as a control strategy, leveraging its capability for optimal control to determine the most effective control trajectory under process variability. In this context, the Deep Deterministic Policy Gradient (DDPG) algorithm has been implemented as a control strategy for ethanol fermentation, specifically regulating temperature and pH to enhance process performance. By including temperature and pH as biological model, then applying DDPG algorithm to find the optimal path of fermentation and to maximise the alcohol yield. The result found that DDPG can maintain the process to optimal alcohol yield with random noise. This control strategy may further be applied for real process.

Keywords: Reinforcement learning; Deep deterministic policy gradient; Fermentation; Ethanol production

1. INTRODUCTION

The microbial fermentation process, recognised as one of the oldest chemical and biological processes, continues to play a crucial role in the production of green chemical products [1]. Alcohol is an example product from the fermentation process. It involves the conversion of a substrate (sugar) to ethanol, where the reaction occurs inside the cell of a microorganism. Since this process is environmentally friendly, the ethanol produced from fermentation is considered a green chemical. Moreover, ethanol is accounted as alternative energy and if the ethanol produced from fermentation, this chemical is accounted as green alternative energy.

Currently, environmentally friendly processes are considered a key priority in chemical production. Ethanol production through fermentation is a promising method that addresses this concern. However, the variability in the growth rates of microorganisms makes the fermentation process challenging to control and economically unviable. To overcome these limitations, reinforcement learning (RL) has emerged as a promising control strategy [2], offering model-free adaptive control by learning optimal policies directly from interaction with the process.

Deep deterministic policy gradient (DDPG) is one RL algorithm which is favourably applied for continuous process [3] such as chemical and biological processes [4, 5, 6, 7]. DDPG is an actor-critic reinforcement learning algorithm designed for continuous action spaces, combining deterministic policy gradients with deep neural networks to learn optimal control policies. Its ability to handle nonlinear dynamics and continuous variables makes it particularly suitable for complex bioprocesses such as fermentation. With these advantages, in this article, DDPG is proposed as a tool for control of temperature and pH to maximise ethanol product from microbial fermentation.

2. FERMENTATION MODEL

2.1 Mathematical Model

The production of ethanol from microbial fermentation is the conversion of substrate by cell to ethanol product. For material balance, it should be started from the reaction of the cell

$$r_X = \frac{dC_X}{dt} = \mu C_X \quad (1)$$

where r_X – reaction rate of cell (kg/m^3 h) and C_X – dry cell mass (kg/m^3). The reaction rate of the cell depends on the specific growth rate (μ; 1/h) which is specific to species of the microorganism. The product of the reaction, in case of yeast, the rate of product generation (ethanol) is

$$\frac{dC_P}{dt} = \nu C_X \quad (2)$$

where C_P – ethanol product (kg/m^3) and ν - product yield coefficient on biomass (1/h). The substrate consumed by the cell and converted to product is modelled as

$$-\frac{dC_S}{dt} = \frac{1}{Y'_{\frac{X}{S}}}\frac{dC_X}{dt} + \frac{1}{Y'_{\frac{P}{S}}}\frac{dC_P}{dt} + K_{CM}C_X \quad (3)$$

where C_S – substrate (kg/m^3), $Y'_{X/S}$ - the cell yield respect to substrate, $Y'_{P/S}$ - product yield respect to substrate and K_{CM} – maintenance coefficient (kg substrate/kg cell/h) which represents the amount of substrate consumed per unit biomass per unit time that is not used for growth or product formation.

As mentioned earlier, the efficiency of the fermentation process depends on the growth rate. If the growth rate is maximised, the fermentation performance can also be improved. The growth rate is influenced by environmental variables such as temperature and pH, which are controllable in the fermentation process. Therefore, modelling the growth rate as a function of temperature and pH can be applied using a cardinal model.

$$f(T) = \mu_{opt}\frac{(T-T_{min})(T-T_{max})}{(T-T_{min})(T-T_{max}) - (T-T_{opt})^2} \quad (4)$$

and

$$f(pH) = \mu_{opt} \times \frac{(pH-pH_{min})(pH-pH_{max})}{(pH-pH_{min})(pH-pH_{max}) - (pH-pH_{opt})^2} \quad (5)$$

Then, the growth rate model is

$$\mu(T,pH) = \mu_{max}\cdot f(T)\cdot f(pH) \quad (6)$$

Table 1 Parameters for fermentation model.

Parameter	Value	Unit
μ_{max}	0.35 – 0.45	1/h
ν	0.8 – 2.5	1/h
$Y'_{\frac{X}{S}}$	0.10 – 0.15	-
$Y'_{\frac{P}{S}}$	0.45 – 0.51	-
K_{CM}	0.02 – 0.05	1/h

For simulation, the material balance equations are solved using ODEINIT library in Python program. Table 1 represents the parameters using for solving fermentation model. The solutions from the material balance equations will be used as an environment of reinforcement learning that will described in the next section.

3. REINFORCEMENT LEARNING

3.1 Reinforcement learning

Reinforcement learning (RL) is one class of machine learning (ML) beside supervised and unsupervised learning. RL is also derived from optimal control theory, which applies dynamic programming to solve decision-making problems over time. The fundamental framework of RL is the Markov Decision Process (MDP), which describes the environment in terms of states (*S*), actions (*A*), transition probabilities (*P*), and rewards (*R*). Fig. 1 represents schematic diagram of RL. When the agent at state S_t takes action A_t, the agent will move to new state S_{t+1} and obtain reward R_t.

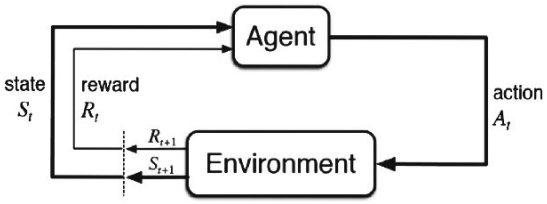

Figure 1 Schematic diagram of reinforcement learning.

The main task of RL is to find the series of action that maximises an expectation discount reward

$$\arg\max_A \mathbb{E}\left[R_t := \sum_{k=0}^{\infty}\gamma^k r_{t+k}\right] \quad (7)$$

where $\gamma \in (0,1)$ is a discount factor, $\mathbb{E}[\cdot]$ – expectation of discount reward R_t, r – reward corresponding to time t and k – time step. For solving this, Q-learning algorithm is introduced

$$Q_\pi(s_t, a_t) = \mathbb{E}_\pi\left[\sum_{k=0}^{\infty} \gamma^k r_{t+k} | s_t = s, a_t = a\right] \quad (8)$$

The objective of Q-learning is to find the optimal policy by learning the optimal Q-value, $Q^*(s_t, a_t)$

$$Q^*(s_t, a_t) = \mathbb{E}\left[r_t + \gamma \max_{a_{t+1}} Q^*(s_{t+1}, a_{t+1} | s_t = s, a_t = a)\right] \quad (9)$$

The Q-learning algorithm update iteratively until converges to the optimal Q-function. The update iteration is

$$Q(s_t, a_t) \leftarrow Q(s_t, a_t) + \alpha\left(r_t + \gamma \max_{a_{t+1}} Q^*(s_{t+1}, a_{t+1}) - Q(s_t, a_t)\right) \quad (10)$$

where α – learning rate.

Q-learning is limited to problems with finite and discrete state-action spaces because it relies on tabular updates, making it unsuitable for high-dimensional or continuous systems. In fermentation processes, key variables like temperature, pH, and concentration change continuously over time, meaning Q-learning cannot be directly applied. To address this, DDPG has been developed [3], combining deep learning with policy gradients to handle continuous action spaces effectively. Next section will introduce DDPG and how to apply for optimising fermentation process

3.2 Deep deterministic policy gradient

In reinforcement learning, algorithms can be broadly categorised into value-based methods, which learn the value of actions (e.g., Q-learning), and policy-based methods, which learn a direct mapping from states to actions [2]. While value-based methods are suitable for discrete action spaces, policy-based approaches are more effective in continuous domains. The actor-critic framework combines both approaches by using an actor to represent the policy and a critic to estimate the value function. Building on this, the Deterministic Policy Gradient (DPG) method [8] improves learning efficiency in continuous spaces by learning a deterministic policy rather than a stochastic one. DDPG extends DPG by incorporating deep neural networks, allowing it to scale to high-dimensional, continuous control problems such as those found in fermentation process optimisation.

The optimisation should begin by applying policy-based methods that use the gradient of the objective function with respect to the parameterised stochastic policy, π_θ

$$\nabla_\theta(J(\pi_\theta)) = \mathbb{E}\left[\left(\sum_{t=0}^{T} \nabla_\theta \log \pi_\theta(a_t|s_t)\right) R(\tau)\right] \quad (11)$$

where $R(\tau)$ – the return obtained from the trajectory $\tau = \{s_0, a_0, s_1, a_1, \dots\}$. In DPG, the expected gradient of the Q-value function is used to compute the gradient of the objective function with respect to the parameter θ in order to optimise the policy

$$\nabla_\theta(J(\mu_\theta)) = \mathbb{E}[\nabla_\theta Q_\mu(s, a)|_{a=\mu_\theta(s)}] \quad (12)$$

where μ – deterministic policy. However, DPG uses linear function approximators to evaluate Q-values. Therefore, DDPG is extended DPG by using non-linear function approximators for estimating Q-values. DDPG also applies experience replay and target networks to enhance the stability and robustness of Q-value learning. Instead of directly copying the weights from the critic and policy networks, DDPG updates the target networks gradually to softly follow the learned network parameters, which helps improve training stability. The algorithm of DDPG is shown in Fig. 2.

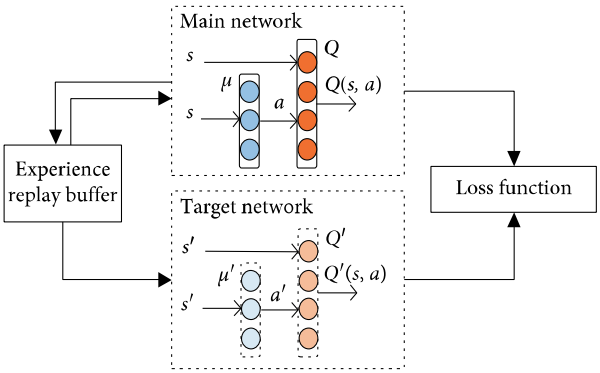

Figure 2 Schematic diagram of DDPG. (Source: [9])

Algorithm DDPG

1. Randomly initialise critic network $Q(s_t, a_t|\theta^Q)$ and actor $\mu(s|\theta^\mu)$ with weight θ^Q and θ^μ.
2. Initialise target network Q' and μ' with weight $\theta^{Q'} \leftarrow \theta^Q$ and $\theta^{\mu'} \leftarrow \theta^\mu$.
3. Initialise replay buffer.
4. **For** episode = 1, M **do**
   4.1 Initialise a random process $\mathcal{N}$ for action exploration.
   4.2 Receive initial observation state s_1
   4.3 **For** t = 1, T **do**
   4.3.1 Select action $a_t = \mu(s_t|\theta^\mu) + \mathcal{N}_t$ according to current policy and exploration noise.
   4.3.2 Execute action a_t and observe reward r_t and observe new state s_{t+1}.
   4.3.3 Store transition (s_t, a_t, r_t, s_{t+1}) in replay buffer.
   4.3.4 Sample a random minibatch of $\mathcal{N}$ transitions (s_i, a_i, r_i, s_{i+1}) from replay buffer.

4.3.5 Set
$Q^*(s_i, a_i) = r_i + \gamma Q'(s_{i+1}, \mu'(s_{i+1}|\theta^{\mu'})|Q')$.
4.3.6 Update critic by minimising the loss: $\mathbb{E}\left[\left(Q^*(s_i, a_i) - Q(s_i, a_i)\right)^2\right]$.
4.3.7 Update actor policy using the sample policy gradient: $\mathbb{E}[\nabla_\theta Q_\mu(s, a)]$.
4.3.8 Update the target networks:
$\theta^{Q'} \leftarrow \tau\theta^{Q} + (1-\tau)\theta^{Q'}$
$\theta^{\mu'} \leftarrow \tau\theta^{\mu} + (1-\tau)\theta^{\mu'}$
End for loop 4.3
End for loop 4.

4. RESULTS AND DISCUSSION

For the simulation of RL to optimise the production of ethanol from fermentation process, the agents are selected as substrate, temperature, pH and ethanol. These parameters are chosen because, in practice, they can be directly measured. The initial condition for all agents is as shown in Table 2. The time step for simulation is 1 hr and the end time is 336 hr (14 days). The reward is set to be $r = C_P - 0.1 * C_s$. This reward is designed to force the process consuming substrate and converting to alcohol. It is found that if reward designed as only C_P, the simulation would not force to consume the substrate. Therefore, the second term is added.

Table 2 Initial condition for material balance equations.

Parameter	Value	Unit
C_X	0.05	kg/m^3
C_P	0.0	kg/m^3
C_S	25.0	kg/m^3
T	27.0	℃
T_{opt}	30.0	℃
pH	7.0	-
pH_{opt}	7.0	-

For the first case, RL is applied for the model with no noise. Fig. 3. shows the simulation with no noise. The yield of alcohol reached at 13.88% and the substrate remained of 0.14 kg/m^3. As without noise, the temperature and pH were adjusted with ideal perfect controller to maximise the alcohol yield.

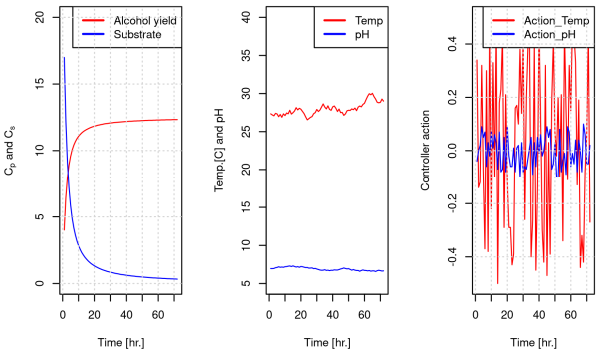

Figure 3 The simulation of DDPG for optimisation with no noise.

In case of adding noise to temperature and pH, the RL can also maintain the process to optimal yield. Fig. 4 shows the simulation results of the fermentation process with adding noise to temperature and pH.

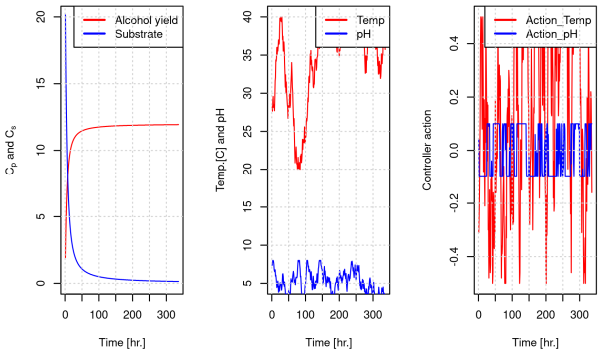

Figure 4 The simulation of DDPG for optimisation with adding noises to temperature and pH.

The final case is with the variation of initial conditions. Concentration of substrate, temperature and pH were set to be random at the initial state. Then, the simulation shows that DDPG can also maintain the yield to the optimal point. Fig. 5 shows the simulation in random initial condition cases.

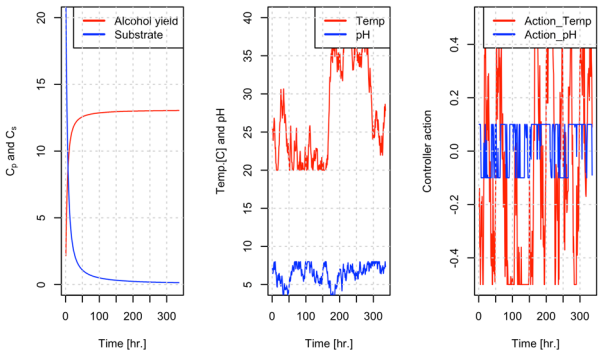

Figure 5 The simulation of DDPG for optimisation with random initial conditions.

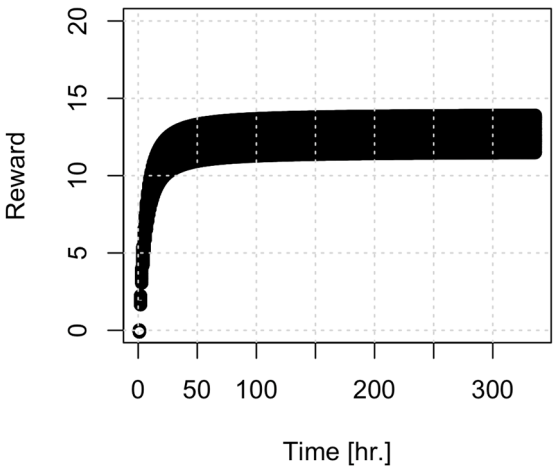

Figure 6 The simulation reward with 100 episodes along time step.

Fig. 6 represents the simulation of RL to fermentation process. The result shows that the maximum yield is not over 13.88% and not less than 11.22%. This can be concluded that DDPG can be applied for fermentation process and can drive the process to the optimal process.

5. CONCLUSION

This study demonstrates the application of Deep Deterministic Policy Gradient (DDPG) reinforcement learning to optimise ethanol production from a fermentation process. By selecting substrate concentration, temperature, pH, and ethanol concentration as controllable agent variables, and defining a reward function that promotes substrate consumption and alcohol generation, the RL model was able to effectively learn optimal control strategies. Under different scenarios—including ideal conditions, the presence of measurement noise, and varying initial states—DDPG consistently guided the process toward high ethanol yield, achieving a maximum of 13.88% and a minimum of 11.22%. These results confirm the robustness and potential of DDPG as a viable model-free control approach for complex bioprocesses such as ethanol fermentation.

ACKNOWLEDGMENTS

This research was financially supported by Fundamental Fund 2567 Nakhon Phanom University.

REFERENCES

1. S. Katoh, J. Horiuchi, F. Yoshida. *Biochemial Engineering* 2nd 2015, Wiley-VCH.
2. R.S. Sutton, A.G. Barto. *Reinforcement Learning: An Introduction* 2nd 2020; The MIT Press.
3. T.P. Lillicrap, J.J. Hunt, A. Pritzel, N. Heess, T. Erez, Y. Tassa, D. Silver, D. Wierstra. Continuous control with deep reinforcement learning. *International Conference on Learning Representations (ICLR)* 2016. https://arxiv.org/abs/1509.02971.
4. D. Li, L. Qian, Q. Jin, T. Tan. Reinforcement learning control with adaptive gain for a *Saccharomyces cerevisiae* fermentation process. *Applied Soft Computing* 2011; 11(8): 4488-4495.
5. P. Petsagkourakis, I.O. Sandoval, E. Bradford, D. Zhang, E.A. del Rio-Chanona. Reinforcement Learning for Batch-to-Batch Bioprocess Optimisation. *Computer Aided Chemical Engineering* 2019; 46: 919-924.
6. Q. Meng, P.D. Anandan, C.D. Rielly, B. Benyahia. Multi-agent reinforcement learning and RL-based adaptive PID control of crystallization. *Computer Aided Chemical Engineering* 2023; 52: 1667-1672.
7. N. Rajasekhar, T.K. Radhakrishan, N. Samsudeen. Deep deterministic policy gradient reinforcement learning based temperature control of a fermentation bioreactor for ethanol production. *Journal of the Indian Chemical Society* 2025; 102: 101575.
8. D. Silver, G. Lever, N. Heess, T. Degris, D. Wierstra, M. Riedmiller. Deterministic policy gradient algorithm. *Proceedings of the 31st International Conference on Machine Learning, PMLR* 2014; 387 – 395.
9 J. Wu, H. Li. Deep ensemble reinforcement learning with multiple deep deterministic policy gradient algorithm. *Mathematical Problems in Engineering* 2020; 4275623.

Application of computational fluid dynamics for industrial liquid-liquid mixing tank design

Patiphon Klongyut[1], Ratchanon Piemjaiswang[2], Benjapon Chalermsinsuwan[3,*]

[1] Program in Science for Industry, Faculty of Science, Chulalongkorn University, Bangkok 10330, Thailand
[2] Sustainable Environment Research Institute, Chulalongkorn University, Bangkok 10330, Thailand
[3] Department of Chemical Technology, Faculty of Science, Chulalongkorn University, Bangkok 10330, Thailand
[*] Corresponding author: benjapon.c@chula.ac.th

ABSTRACT

Industrial mixing tank is a common process used in various industries. Agitator tanks are widely used as fundamental operations in multiphase flow mixing. The applications of agitators encounter long blending times due to dead zones within the tank while increasing agitation turbulence is insufficient without proper dimensional design considerations. This research focuses on liquid-to-liquid batch mixing using a commercial blade (Viscoprop) with comparative simulation data augmentation. The objective is to determine the effects of important factors, including mechanical design and liquid material properties that affect mixing time. Computational fluid dynamics (CFD) simulations are numerical methods used to investigate mixing performance by studying the effect of agitator tank design parameters on 95% homogeneity of liquid in a period. A turbulent model with the large eddy simulation (LES) is successfully validated by analyzing velocity data from literature research study to ensure the correctness of flow phenomena. The ten parameters are investigated, selecting optimal levels depending on real case application. The analysis of variance (ANOVA) indicates that revolution speed has a highly significant effect ($p = 0.0026$), followed by number of impeller stages ($p = 0.0223$) as the most influential factors. Other parameters including number of baffles, specific gravity, viscosity, tank diameter, impeller diameter, liquid level, impeller clearance, and number of blades were found to have lesser or statistically insignificant effects ($p > 0.05$). These results suggest the importance of proper agitator tank design for improving mixing homogeneity.

Keywords: Industrial mixing tank; Agitator; Liquid to liquid mixing; Computational fluid dynamics

1. INTRODUCTION

As an important process that may significantly impact the efficiency and quality of the final product, industrial liquid to liquid phase mixing mainly depends on mixing tanks and agitators as essential components of equipment. However, poor performance may result from dead zones within the tank. Increased turbulent flow could not be enough if the proper mechanical parameters and dimensions are not present. Inappropriate blade form, agitator location, and rotating rates can also result in early equipment failure, higher operating expenses, and increased energy usage. Poor mixing can also cause variable mass and heat transfer, which can affect process reliability, reaction times, and product quality.

Computational fluid dynamics (CFD) is a numerical method for solving the governing equations of fluid mechanics, particularly the Navier-Stokes (RANS) or Large Eddy Simulation (LES) equations that characterize the conservation of mass, momentum, and energy. By discretizing continuous equations across a predefined computational domain, CFD methods convert them into algebraic forms that can be solved numerically. Finite volume, finite difference, or finite element methods are typically used. In order to efficiently simulate flow properties such as temperature distributions, pressure, turbulence, and velocity within detailed geometry, the computational domain can be divided into small control volumes or cells that form a grid (mesh). For studying the mixing issues, analysis and visualization of the complex fluid dynamics within mixing tanks are summarized. Without the need for costly experimental studies, researchers can apply CFD to predict flow patterns, identify areas of poor mixing, and evaluate the impacts of various agitator designs and operating conditions. The turbulence intensity, velocity distribution, shear rate, and mixing time data obtained from CFD simulations contribute to the optimization of agitator design and operation parameters. Using accurate CFD modeling based on experimental data is necessary to represent fluid dynamics precisely and improve mixing efficiency.

Mixing homogeneity is generally measured by measuring mixing time, which is the amount of time needed to achieve uniformity or the degree of concentration uniformity within the mixing tank. It is common practice to employ measurement methods such as tracer injection and concentration monitoring at different locations within the tank. This study uses a commercially available Viscoprop impeller [1], as shown in Fig. 1, to investigate mixing performance by impeller dimensions. This impeller was created to produce axial flow patterns, improve fluid circulation, and reduce energy loss. These blades are similar to hydrofoil derived designs. The similar hydrofoil blades design efficiently reduces dead zones and enhances homogeneity while also reducing axial pumping, shear stress, and fluid motion in the tank.

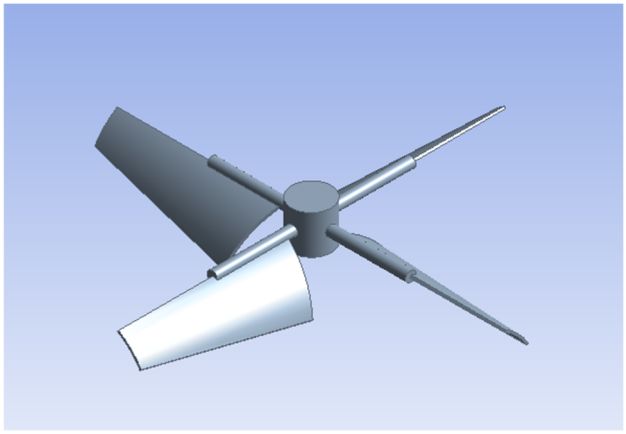

Figure 1 Viscoprop impeller

2. EXPERIMENTAL

2.1 Computational Models Setup

The commercial CFD program ANSYS Fluent 2024 R1 was used to discretize and solve the governing equations numerically of mixing tank using a finite volume method. The linear equations were solved algebraically, and the computations were based on the finite volume approach of unstructured grids. The sliding mesh model for unstructured grids was used to simulate the motion of the impeller. The momentum equations were spatially discretized using the center differencing scheme, while time advancement was done using the second order accurate implicit method. The pressure implicit with splitting of operators (PISO) algorithm was used to achieve the connection between the continuity and momentum equations. A pre-calculated quasi-steady state flow field from an early RANS simulation was used to establish the LES model. In all cases, the simulation assumption was converged when all variables were as low as 10^{-4}. The general geometry of mixing tank domain is shown as Fig. 2 with containing agitator, tank vessel, baffles and rotation zone of impeller.

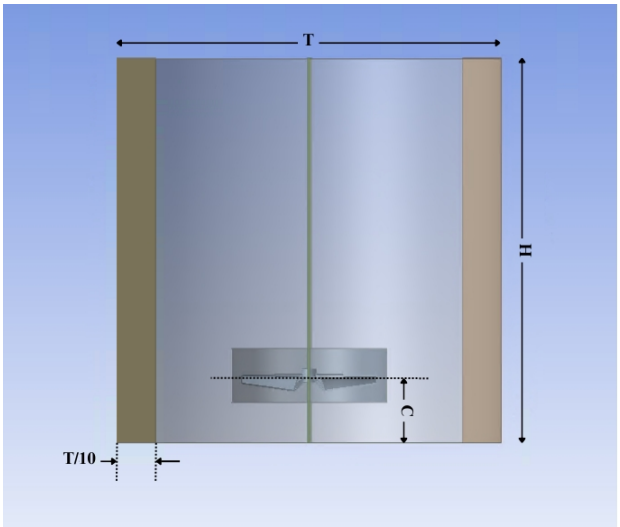

Figure 2 Schematic side view of mixing tank

From Fig. 2, T is the mixing tank internal diameter, H is the mixing tank height and C is the bottom clearance of the impeller.

2.2 Grid Independence

Grid independence verifying that numerical simulation results, such as those obtained from computational fluid dynamics (CFD), are not significantly affected by the size or density of the computational grid or mesh. The main idea behind grid independence is that numerical solutions should stabilize and become consistent as the grid is progressively refined (cell size decreases or the number of cells increases). Grid independence is achieved by simulations using finer grids. If, despite further refinement, the changes in major outcomes including velocities, pressures, flow rates, or related quantities become negligible, the solution is considered grid independent and ensures accuracy and reliability and minimizes errors caused by inaccurate grid selection. This makes it crucial before conducting numerical investigations or drawing conclusions.

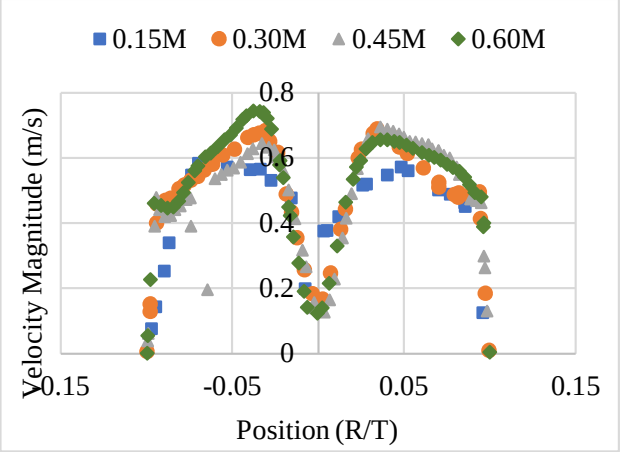

Figure 3 Grid independence test result at C = 0.84 m where R = mixing tank radius.

In this study, unstructured tetrahedron mesh sizes of 0.15, 0.30, 0.45, and 0.60 million (M) cells were used to assess grid independence. The simulation was based on a lab-scale mixing tank that was 0.32 m height (H) and had an internal diameter (T) of 0.20 m and the bottom clearance of the impeller (C) was set to 0.084 m. The working fluid was water. The impeller diameter was approximately 0.12 m, four baffles plate with 0.02 m width (T/10) which is compatible with the geometric ratios commonly observed in laboratory mixing tanks. A Viscoprop impeller was used in the simulation. The rotation zone was set up with a width of half the tank diameter and a height 50% more than the impeller height to ensure that the impeller motion was contained within the moving mesh region. The mixing tank was operated at a rotational speed of 150 rpm. The no-slip boundary conditions were applied to all solid surfaces including the impeller blades, hub, and tank walls. The grid independence results are illustrated in Fig. 3, which shows the velocity magnitude profiles at different mesh sizes. After mesh refinement, the simulation results showed no significant differences in the velocity profile beyond 0.45 million cells. Therefore, the mesh with 0.45 million cells was selected for subsequent simulations.

2.2 Validation of CFD Model

The Large Eddy Simulation (LES) turbulence model's accuracy was confirmed its accuracy by comparing simulation results with experimental data [2] from a laboratory scale stirred tank powered by a Rushton turbine impeller. The tank included four evenly spaced baffles, each one tenth of the tank's diameter (T/10), with an internal diameter of 0.476 m. The liquid height (H) was set equal to the tank diameter. The impeller was positioned at a fixed clearance from the bottom tank, equal to 0.15T. The observation point was located at the midpoint between two baffles. The Rushton turbine used in the experiment had detailed geometric characteristics as shown in Table 1 and Fig. 4. The fluid used was tap water. The velocity field was measured using the Particle Image Velocimetry (PIV) technique, which records the movement of tracer particles in the fluid. Phase averaged velocity data were gathered for an impeller rotational speed of 97 rpm, which corresponds to a Reynolds number of approximately 40,000. In this numerical simulation, the LES model was applied. After the flow had reached a statistically steady state, the simulation was continued for an additional 40 revolutions of the impeller. The time averaged velocity field was then sliced out and used for comparison to the experimental PIV data.

Table 1 Geometric of Ruston turbine impeller [2].

Parameter	Value	Unit
Impeller Diameter (D)	158	mm
Disk diameter (D_{disk})	118	mm
Hub diameter (D_{hub})	35	mm
Blade width (W_{imp})	40	mm
Blade height (H_{imp})	32	mm
Disk thickness (t_{disk})	4	mm
Blade thickness (t_{imp})	3	mm
Rotational speed (N)	97	rpm
Tip velocity (V_{tip})	0.80	m/s
Reynolds number (Re)	40,000	-

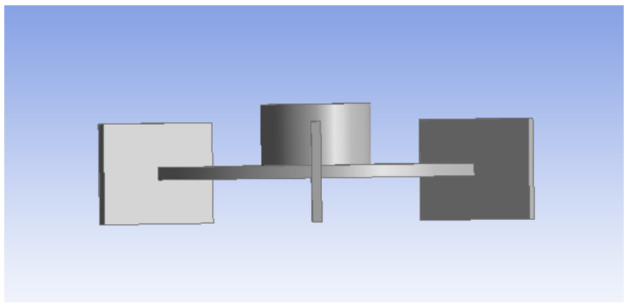

(A)

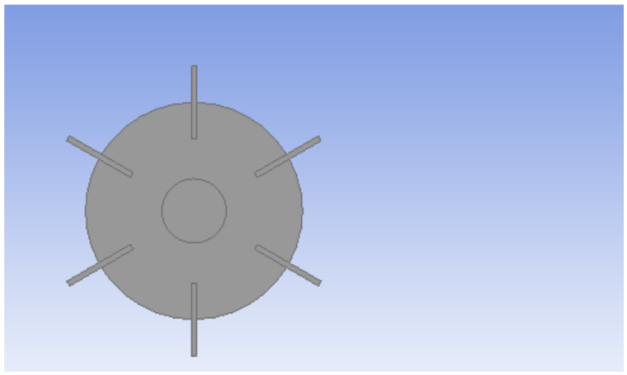

(B)

Figure 4 Schematic (A) side view, (B) top view of Ruston turbine impeller.

The validation test showed at the mid of impeller level (C=0.150), the horizontal velocity profile in Fig. 5 illustrates that the two curves follow a similar trend, although the simulation predicts a lower peak velocity than the PIV measurements. Likewise, the vertical velocity profile in Fig. 6 has a comparable shape, but the simulation again underestimates the maximum velocity relative to the PIV data.

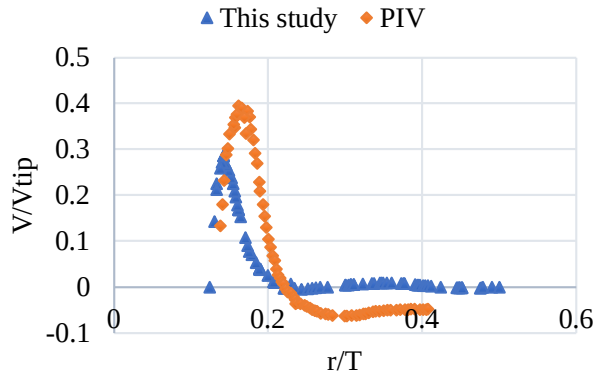

Figure 5 Graph of averaged radial velocity compared to the PIV data at z/T = 0.150.

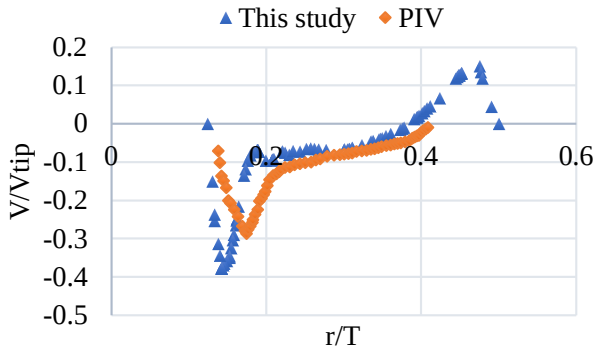

Figure 6 Graph of averaged vertical velocity compared to the PIV data at z/T = 0.150.

2.3 Design of Experiments

In this research, the Taguchi Design method was utilized to identify the optimal levels of various input parameters that significantly impact the output variables. By employing orthogonal arrays, this Taguchi's robust design framework offers a systematic route to maximize performance while trimming the experimental workload. By arranging trials in an orthogonal array, every control factors are examined independently of the others, so their individual influences can be isolated without resorting to a full factorial design.

An orthogonal array (OA) is a carefully selected subset of a full factorial design in which the combinations of factor levels are arranged through a design matrix, ensuring that every level of each control factor is represented the same number of times and in a statistically balanced manner. In Taguchi's framework, an OA is specified by three quantities including the total number of experimental trials (La), the number of levels per factor (b), and the total number of factors (c). The array is therefore written $La(b^c)$. By definition, for every level of any single factor, all b levels of each of the remaining $c-1$ factors appear at least once within the experimental matrix [3].

In this study, a full factorial plan becomes prohibitively large as the number of factors and levels increase. For the present study we analyzed ten control factors ($c = 10$). One of these factors, the number of impeller stages was examined at two levels, whereas the remaining nine factors were each studied at four levels to capture possible non-linear effects. Factor names together with their corresponding level values are listed in Table 2 and Table 3, bounded by the operating limits of the pilot scale mixing tank. Several of these factors were selected based on precedent in the literature, ensuring that our design reflects both established findings and practical operating constraints [4,5,6,7]. The minimum number of experimental runs required for an appropriate orthogonal array is obtained from the degrees of freedom [8] expression by equation (1).

$$N_{taguchi} = 1 + \sum_{i=1}^{c} b_i - 1 \qquad (1)$$

where b_i denotes the number of levels for factor i. Substituting $b_1 = 2$ for the two level factor and b_2 to $b_{10} = 4$ for the nine four level factors. Accordingly, an L32′ mixed level orthogonal array comprising 32 experimental trials was adopted, fully satisfying the minimum 29 degrees of freedom requirement while preserving statistical balance. By contrast, a full factorial design would necessitate $2 \times 4^9 = 524{,}288$ runs. The chosen OA reduces the experimental burden by more than four orders of magnitude.

Table 2 A control factor with two study levels.

Control Factor	Level	
	1	**2**
Number of Impeller Stages	1	2

Table 3 Nine control factors with four study levels

Control Factors	Level			
	1	**2**	**3**	**4**
Number of baffles	0	2	4	6
Specific gravity	0.6	1	1.4	1.8
Viscosity (Pa s)	0.001	0.004	0.007	0.01
Revolution speed (rpm)	50	100	150	200
Tank diameter (m)	1	1.5	2	2.5
Impeller diameter (m)	0.5	0.6	0.7	0.8
Liquid level (m)	1	1.5	2	2.5
Impeller clearance (m)	0.25	0.3	0.35	0.4
Number of blades	2	3	4	5

2.4 Homogeneity and Mixing Time Measurement

The mixing time was evaluated by monitoring the convergence of the time averaged tracer-concentration signals registered at a network of six measurement points (probes). In the numerical model, an additional passive scalar was defined as a tracer species

chemically inert, with the sole purpose of visualizing the dispersion process and a pulse of this tracer was injected into the liquid phase. Six virtual probes were then placed inside the vessel exactly at the positions indicated in Fig. 7, ensuring that the sensor captured the major hydrodynamic regions created by the impeller with two probes near the top of the tank, two at mid-height and two closed to the bottom.

During the transient simulation, the instantaneous tracer mass fraction recorded at each probe was continuously averaged to smooth out high frequency fluctuations caused by turbulent eddies. The resulting average concentration curves were compared against their respective final steady state values. The mixing time t_{95} was then defined as the instant when the normalized residual error of every signal computed with respect to its final steady state value below 10^{-2} and continued to converge at that threshold. Using this residual based criterion confirmed that the concentration field has practically reached equilibrium. In other words, the system can be considered > 95 % [9] homogeneous throughout the entire vessel.

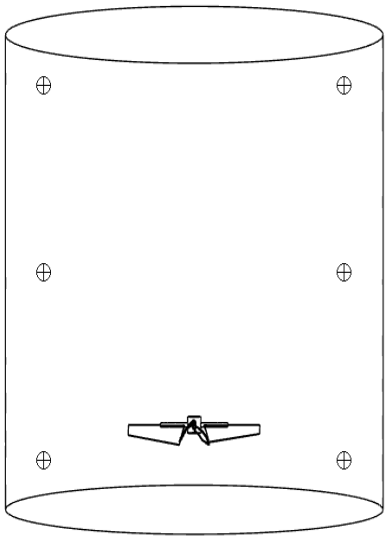

Figure 7 Schematic side view of six virtual probes in mixing tank

3. RESULTS AND DISCUSSION

From the obtained results, the analysis of variance was performed and demonstrated that the fitted model is statistically significant (F = 9.49, p = 0.0437) and explains about 98.9 percent of the total variability in the response (SS_{model} / SS_{total} ≈ 0.989). Among the ten factors studied, revolution speed is by far the most influential, contributing roughly 84 percent of the model sum of squares with a very high F value of 74.09 and a highly significant p value of 0.0026. The number of impeller stages is the second most important factor, responsible for about 7 percent of the model sum of squares and statistically significant (F = 18.99, p = 0.0223). In contrast, the remaining geometric variables tank diameter, impeller diameter, impeller clearance, number of baffles, and number of blades and the fluid-property variables specific gravity and viscosity did not show statistically significant effects under the conditions tested (all p values greater than 0.05). These findings indicate that impeller rotational speed is the primary factor for process optimization, while altering the number of impeller stages offers a secondary but meaningful adjustment. Although the residual sum of squares was low (SS = 658.16), the residual degrees of freedom were limited to three.

Table 3 The ANOVA analysis.

Source	Sum of Squares	DF	Mean Square	F-Value	p- Value
Model	58322.75	28	2082.96	9.49	0.0437
Number of Impeller Stages	4166.25	1	4166.25	18.99	0.0223
Number of baffles	213.58	3	71.19	0.32	0.81
Specific gravity	1562.62	3	520.87	2.37	0.2481
Viscosity	1072.61	3	357.54	1.63	0.349
Revolution speed	48764.8	3	16254.93	74.09	0.0026
Tank diameter	203.17	3	67.72	0.31	0.8199
Impeller diameter	484.24	3	161.41	0.74	0.5965
Liquid level	555.46	3	185.15	0.84	0.5538
Impeller clearance	1187.23	3	395.74	1.8	0.32
Number of blades	112.8	3	37.6	0.17	0.9093
Residual	658.16	3	219.39		
Cor Total	58980.91	31			

The two most influential factors on mixing time were the number of impeller stages (Factor A) and the impeller rotational speed (Factor E). As shown in Fig. 8, increasing the number of stages from one to two lengthened the predicted mixing time from approximately 93 to 128 s. This effect is attributed to the formation of additional recirculation loops and dead

zones, which impede rapid homogenization. In contrast, raising the impeller speed from 50 to 200 rpm sharply reduced mixing time (from approximately 93 s down to 12 s), owing to enhanced turbulence and higher energy dissipation rates.

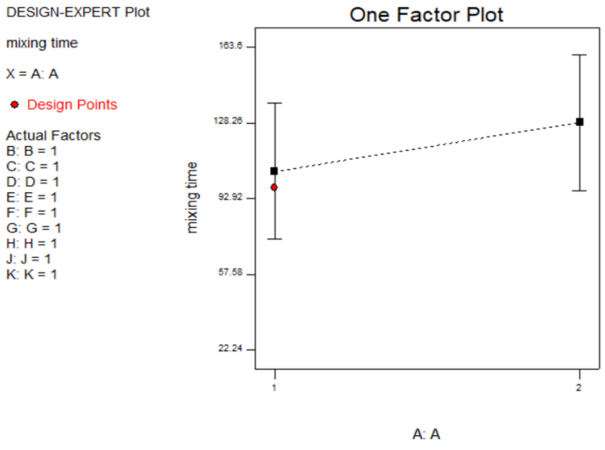

(A)

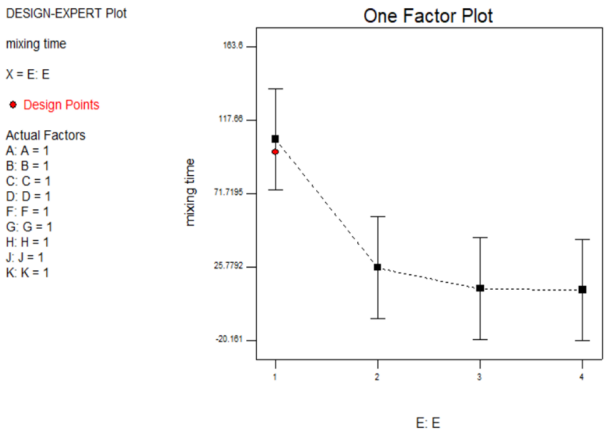

(B)

Figure 8 one factor plots of (A) number of impeller stages (Factor A) and (B) impeller rotational speed (Factor E).

4. CONCLUSION

This study successfully combined LES–CFD simulations with a Taguchi L32 orthogonal array to investigate the effects of ten mechanical and fluid-property factors on mixing homogeneity in an industrial-scale stirred tank. The results highlighted impeller rotational speed as the overwhelmingly dominant parameter, contributing about 84 % of the explained model variance, followed by the number of impeller stages with approximately 7 %. Other variables including tank diameter, impeller diameter, baffle count, clearance, blade number, specific gravity, and viscosity were statistically insignificant under the tested conditions. While the residual error was low, the limited residual degrees of freedom point to the importance of including replicated runs and interaction studies in future research. Overall, this work emphasizes that operational adjustments, particularly to impeller speed, are more effective for improving mixing performance than geometric modifications, providing a valuable framework for process optimization and future experimental validation.

ACKNOWLEDGMENTS

This study was made possible through the generous financial support of the Higher Education for Industry Consortium (HiFI-Consortium) and the Science for Industry Program (Sci-FI), Faculty of Science, Chulalongkorn University. Their funding under research initiative provided both resources and motivation for pursuing the computational investigation reported here. Additional thanks are extended to the Sci-Fi Program's administrative team for their efficient logistical support throughout the project.

REFERENCES

1. EKATO. Viscoprop impellers significantly reduce energy consumption and process time at coatings facility. PlantAutomation.com News 2011 (Jan 27).
2. Z. Li, Y. Bao, Z. Gao. PIV experiments and large eddy simulations of single-loop flow fields in Rushton turbine stirred tanks. *Chemical Engineering Science* 2011; 66: 1219-1231.
3. G. Taguchi, S. Chowdhury, Y. Wu. *Taguchi's Quality Engineering Handbook*. John Wiley & Sons, Hoboken; 2005.
4. M. Foukrach, H. Ameur. Effect of baffles shape on the flow patterns and power consumption in stirred vessels. *SN Applied Sciences* 2019; 1:1503. DOI:10.1007/s42452-019-1550-9
5. P.A. Mahakal, A.W. Patwardhan. CFD Modeling of Liquid–Liquid Batch-Stirred Tank at High Organic to Aqueous Phase Ratios. Industrial & Engineering Chemistry Research 2023; 62: 19323-19340.
6. J. Stelmach. Mixing power and hydrodynamics for different clearances of the flat blade turbine impeller. *Chemical and Process Engineering: New Frontiers* 2023; 44(2): e7. DOI:10.24425/cpe.2023.144693.
7. W. M. Haynes. CRC Handbook of Chemistry and Physics. 95th ed. Boca Raton (FL): CRC Press; 2014. 2704 pp. DOI:10.1201/b17118.
8. P. Satjaritanun, J.R. Regalbuto, J.A. Regalbuto, N. Tippayawong, S. Shimpalee. Mixing optimization with inward flow configuration. *Alexandria Engineering Journal* 2021; 60: 3759–3779.
9. L. Liangchao, B. Xu. CFD Simulation of Local and Global Mixing Time in an Agitated Tank. *Chinese Journal of Mechanical Engineering* 2017; 30(1): 118–125.

Performance evaluation of combined torrefaction and gasification process of lignocellulosic biomass

Aphiwat Lakkhanasombat[1], Supachai Jadsadajerm[1], Jindarat Pimsamarn[2], Awat Wisetsai[1], Lida Simasatitkul[1,*]

[1] Department of Industrial Chemistry, Faculty of Applied Science King Mongkut's University of Technology North Bangkok, Bangkok 10800, Thailand
[2] Department of Chemical Engineering, Faculty of Engineering, King Mongkut's University of Technology Thonburi, Bangkok 10140, Thailand.
* Corresponding author: lida.s@sci.kmutnb.ac.th

ABSTRACT

Durian peels, commonly classified as agricultural waste, present significant challenges in terms of disposal and associated costs. This study explores the potential of utilizing durian peel in a torrefaction process, supported by machine learning techniques to predict key fuel properties. The predictive models consider variables such as residence time, temperature, oxygen concentration, and elemental composition. Outputs from these models are subsequently integrated into Aspen Plus simulations to model the torrefaction and gasification processes for hydrogen production. The simulation investigates a torrefaction temperature of 260 °C and evaluates various operational parameters, including the steam-to-durian peel ratio, air-to-durian peel ratio, combined steam–air-to-durian peel ratio (ranging from 1.0 to 1.5), and gasification temperatures between 700 °C and 900 °C. Results indicate that optimal hydrogen production occurs at 750 °C with a steam-to-durian peel ratio of 1.2, achieving a hydrogen yield of 46.67 %. Furthermore, the incorporation of a palladium membrane in the separation process enhances hydrogen purity to 99%. These findings underscore the potential of converting agricultural waste into clean hydrogen fuel, contributing to environmental sustainability and waste valorization. The overall simulation model is illustrated in Figure 1

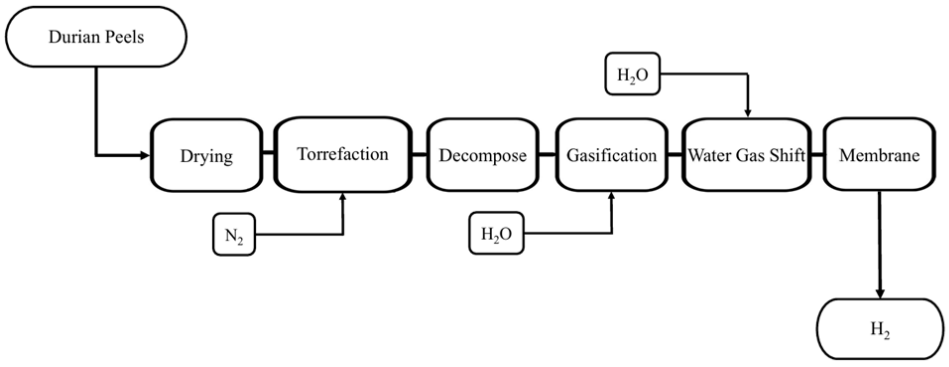

Figure 1 Simulation model of torrefaction and gasification process

Keywords: Durian peels; Gasification; Hydrogen; Torrefaction; Simulation

1. INTRODUCTION

Lignocellulose is a renewable energy source derived from plant biomass or agricultural residues, such as durian peels, rice husks, sugarcane bagasse, Napier grass, and other naturally occurring materials. The primary components of this type of biomass include cellulose, hemicellulose, and lignin. Thailand's fertile soil and favorable climate conditions are highly suitable for agriculture, resulting in an abundance of lignocellulosic biomass and agricultural waste. This availability offers significant potential for the country to convert such biomass into energy or fuel. The conversion of lignocellulosic biomass into energy can be achieved through various thermochemical processes. These include combustion for heat production, pyrolysis for generating bio-oil or bio-char, torrefaction for solid fuel production, and gasification for producing bio-gas. (Wang & Wu, 2023)

Torrefaction is one of the processes that has attracted significant attention in recent years from

both researchers and various industries. This growing interest is due to its potential as a thermal pretreatment method aimed at improving the characteristics of biomass to resemble those of coal (Onsree & Tippayawong, 2021) The torrefaction process is typically conducted at temperatures ranging from 200 to 300 °C, with residence times between 0 and 120 minutes. It is generally carried out in an inert atmosphere, using gases such as nitrogen (N_2), helium (He), or argon (Ar), with oxygen concentrations ranging from 0 to 21% vol. The process results in a solid fuel product, which can subsequently be utilized for hydrogen production.

Hydrogen can be produced through gasification. The process begins with torrefaction, which thermochemically converts biomass into gas and char through pyrolysis at temperatures ranging from 300 to 900 °C. The resulting char is then subjected to the gasification process to produce carbon dioxide (CO_2), carbon monoxide (CO), hydrogen (H_2), and methane (CH_4), which are collectively referred to as synthesis gas or syngas. This stage is conducted at temperatures between 700 and 900 °C (Basu, 2 0 1 0) , utilizing different steam-to-biomass, air-to-biomass, and steam-to-air ratios, typically ranging from 1 to 1.5, The syngas produced from the gasification process is subsequently subjected to a Water-Gas Shift (WGS) reaction in order to increase hydrogen production. In this step, carbon monoxide (CO) reacts with steam (H_2O) to produce additional hydrogen (H_2) and carbon dioxide (CO_2), thereby enhancing the overall hydrogen yield.

According to literature reviews, types of biomass is an interesting issue using as raw materials such as eucalyptus, which has been subjected to torrefaction under inert gas atmospheres at temperatures of 240, 260, and 280 °C to improve its fuel properties. Through this process, the biomass exhibited enhanced characteristics, including increased energy density, reduced moisture content, and improved grindability, making it more suitable for subsequent energy applications. (Arias et al., 2008)

Bamboo favorable fuel properties is considered a potential energy crop for fuel production. In this study, bamboo was subjected to torrefaction under inert gas atmospheres at temperatures of 220, 250, and 280 °C. The results revealed that the torrefied bamboo exhibited fuel characteristics comparable to those of coal. (Rousset, Aguiar, Labbé, & Commandré, 2011)

Pine sawdust, wood chips, and wood residues were selected as biomass feedstocks for the simulation. A gasification model for syngas production with steam as the gasifying agent and subsequent syngas adjustment was developed using Aspen Plus, based on Gibbs free energy minimization via the restricted equilibrium method. The model was used to study the effects of gasification temperature, steam-to-biomass ratio, and shift reaction temperature on hydrogen concentration, CO concentration, CO conversion, CO_2 conversion, and the H_2/CO molar ratio. Simulation results aimed to adjust the H_2/CO molar ratio to approximately 2.15, as required for Fischer–Tropsch synthesis. The results revealed that hydrogen concentration remained almost constant with increasing gasification temperature, while CO concentration increased, leading to a decrease in the H_2/CO molar ratio. Increasing the steam-to-biomass ratio resulted in higher hydrogen and CO_2 concentrations and lower CO and CH_4 concentrations, thereby enhancing the H_2/CO molar ratio. Furthermore, the model indicated that syngas derived from pine sawdust, wood chips, and wood residues required further adjustment via the water-gas shift reaction to achieve the desired H_2/CO molar ratio, confirming the need for subsequent syngas conditioning for these biomass types.(Pala, Wang, Kolb, & Hessel, 2017)

Therefore, this research employs torrefied durian peel as the feedstock, due to durian peels with high potential for use as a solid fuel in energy production. (Chua, Pen, Poi, Ooi, & Yee, 2023) The torrefied material is utilized for hydrogen production through the gasification process. The combination of different operating conditions, such as the temperature and ratio (steam, air and steam-air) were studied to stablish the best ones for to increase the hydrogen yield production of either chemical via water-gas shift reaction is employed to increase the hydrogen yield in the final product by using Aspen Plus.

2. Modeling

2.1 Model assumptions

- The Torrefaction and gasification process is under a steady state condition.
- The Peng Robinson-Boston Mathias (PR-BM) Equation of State is employed to evaluate the thermodynamic properties of various substances, especially in vapor-liquid equilibrium systems. (Carlassara, 2024)
- Durian peel is processed through torrefaction, it will decompose and produce various substances such as CO, CO_2, CH_3OH, CH_3COOH, lactic acid and torrefied durian peels (Carlassara, 2024)
- Torrefied durian peels devolatilization takes place instantaneously and volatile products mainly consist of H_2, CO, CO_2, CH_4, and H_2O
- Ash is not considered in the model.

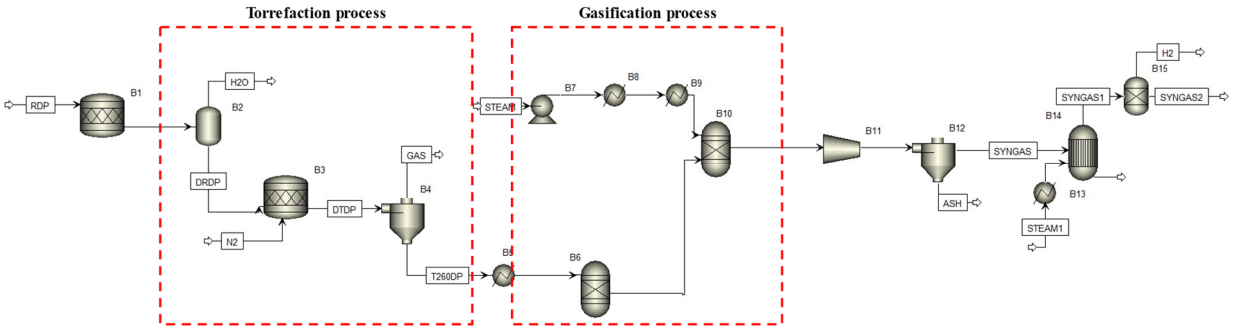

Figure 1 Process of torrefaction and gasification model

2.2 Model description

In this study, Aspen Plus is utilized to model the torrefaction and gasification processes, along with the subsequent water-gas shift reaction following gasification. Durain Peels (DP) size less than 250 µm. Table.1 shows the ultimate, proximate analysis and high heating value of raw DP and Table.2 shows the ultimate, proximate analysis and high heating value of torrefied DP which separates water from the dried durian peels. The dried peels exit via the DRDP stream and are subsequently introduced into the torrefaction process via another Stoichiometric reactor (B3). In this reactor, nitrogen gas is supplied as the inert carrier gas.

Table 1. Properties of raw DP

Ultimate analysis (wt.%) d.a.f. [a]		Proximate analysis (wt.%) d.b. [a]		HHV (MJ/kg) [a]
C	47.51	M	20.00	19.02
H	6.42	VM	52.41	
N	1.26	FC	20.82	
O	44.81	ASH	6.78	

Table 2. Properties of torrefied DP

Ultimate analysis (wt.%) d.a.f. [a]		Proximate analysis (wt.%) d.b. [a]		HHV (MJ/kg) [a]
C	55.65	M	10.00	23.02
H	5.75	VM	60.10	
N	1.45	FC	23.02	
O	37.14	ASH	6.86	

[a] d.a.f. = Dry ash free basis; d.b. = Dry basis; M = moisture; VM = Volatile matter; FC = Fixed carbon; HHV = High heating value.

The simulation begins by setting the enthalpy and density calculation methods to HCOALGEN and DCOALIGT, respectively. Durian peels are fed 1250 kg/hr. from the RDP stream into Stoichiometric reactor (B1) to remove their moisture content. The output stream from B1 is then sent to a Flash separator (B2),

In this unit, the fraction of solids to the solid outlet and the fraction of vapor to the vapor outlet are both set to 1. Within the Yield reactor, the yield basis is defined in terms of elemental composition, including carbon, hydrogen, oxygen, nitrogen, water, and ash. The gaseous products exit through the T260DP stream, which is then directed to Yield reactor (B6). Prior to entering Yield (B6), the gas stream is preheated in a heater (B5) to ensure temperature consistency with the Yield operating conditions. A calculator block is employed to assist in determining the appropriate distribution of yield. The output from Yield reactor (B6) is then fed into the gasification unit, modeled as Gibbs reactor (B10), along with steam, air, and steam–air. The reactor operates at a pressure of 3 bar. The syngas produced from Gibb reactor (B10) is subsequently compressed or expanded in a compressor (B11) to reduce the pressure from 3 bar to 1 bar. Afterward, the stream enters a splitter unit (SSplit, B12) to remove ash from the product gas. The ash-free gas stream is then introduced into Equilibrium reactor (B14) together with additional steam to perform the Water-Gas Shift (WGS) reaction, aimed at increasing the hydrogen yield. Finally, the shifted gas stream enters a separator unit (Sep, B15), which is assumed to represent a palladium membrane module. This unit selectively separates hydrogen with a purity of 99.99 wt.%, effectively completing the hydrogen enrichment process. (Marcantonio et al., 2019)

Within Stoichiometric reactor (B3), the torrefaction reactions are modeled by specifying fractional conversions function as follows:

$$M_{i,volatile} = A \times T^{B}_{torrefied} \quad (1)$$

where T = temperature of torrefaction process
A, B = parameters for volatiles fraction conversion equation (Carlassara, 2024)

Following the torrefaction process, the resulting products are separated using a cyclone separator (B4) to isolate gaseous components.

3. RESULTS AND DISCUSSION

3.1 Model validation

To check the accuracy of the torrefaction process, by using the root mean square error (RMSE) function as follows:

$$RMSE = \sqrt{\frac{\sum (Prediction\text{-}Simulation)^2}{N}} \quad (2)$$

where N represents the number of data sets.

The result model validation torrefaction process is presented table 3. The model validation results, which compared the predicted mass yield percentage from the machine learning model with the simulation results, revealed a Root Mean Square Error (RMSE) of 9.93. This indicates that the torrefaction process model is capable of accurately predicting the mass yield percentage, confirming the reliability of the developed predictive framework.

Table 3. Model validation torrefaction process between prediction vs simulation data

Prediction data (wt.%)	Simulation data (wt.%)	RMSE
69.49	74.08	9.93

3.2 Effect of Temperature

The profile of the product gas composition at steam/biomass (S/B) ratio of 1.4 over different temperatures is shown in Figure 2(a, b, c, d) the gasifier temperature was varied from 700 ºC to 900 ºC. As the operating temperature increases, the production of carbon monoxide (CO) tends to increase, whereas the productions of carbon dioxide (CO_2) and methane (CH_4) tend to decrease, respectively. The production of hydrogen (H_2) initially increases with rising temperature but subsequently decreases after reaching an optimal point.

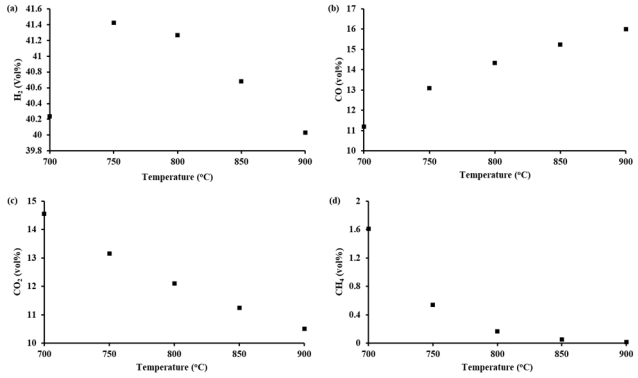

Figure 2 (a) Effect of Temperature on the hydrogen (b) Effect of Temperature on the carbon monoxide (c) Effect of Temperature on the carbon dioxide (d) Effect of Temperature on the methane

Figure 3 illustrates the H_2 yield at S/B ratio of 1.4 with varying temperatures from 700 ºC to 900 ºC. The result presented in Figure 3, It was observed that the H_2 yield increased as the temperature rose from 700 °C to 800°C, reaching approximately 121 g/kg total biomass. However, further increases in temperature led to a decline in H_2 yield because, at temperatures above 800 °C, CO formation became dominant due to the Boudouard reaction (Lv et al., 2004), resulting in a sequential decrease in H_2 production.

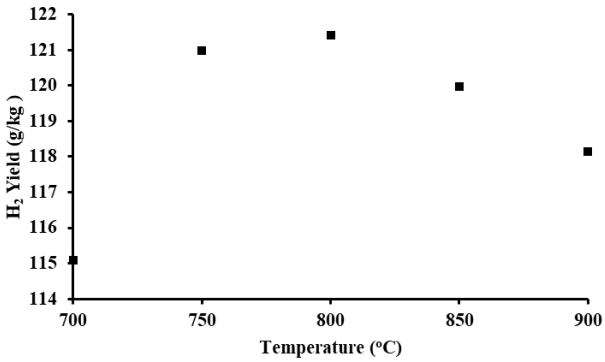

Figure 3 Effect of temperature on the hydrogen yield

3.3 Effect of steam/biomass (S/B) ratio

The steam/biomass ratio was varied from 1 to 1.5 at 800 ºC is shown in Figure 4 (a, b, c, d) The production of H_2 and CH_4 decreased with increasing steam-to-biomass (S/B) ratio, while the production of CO slightly decreased and the production of CO_2 increased. These results indicate that the addition of steam promotes oxidation reactions, as reflected by the increased CO_2 production and decreased H_2 production.

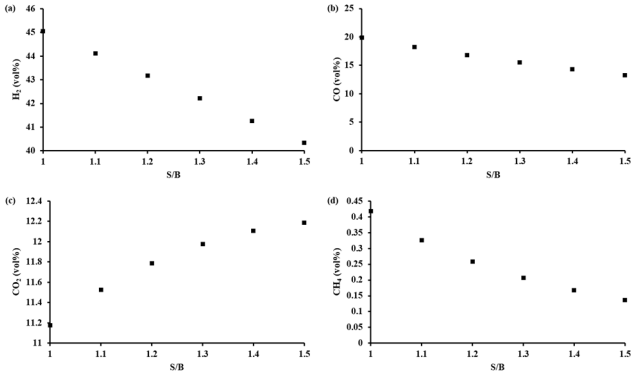

Figure 4 (a) Effect of S/B on the hydrogen (b) Effect of S/B on the carbon monoxide (c) Effect of S/B on the carbon dioxide (d) Effect of S/B on the methane

Figure 5 illustrates the H_2 yield with varying steam-to-biomass (S/B) ratios from 1.0 to 1.5 at 800°C. The results demonstrated that increasing the steam-to-biomass ratio led to a continuous enhancement in hydrogen production. In the initial stage, the hydrogen yield increased sharply, indicating that steam addition effectively promoted hydrogen generation. However, as the steam-to-biomass ratio further increased, the hydrogen yield continued to rise but at a slower rate, suggesting a diminishing enhancement effect of steam addition on hydrogen production. The increase in hydrogen production can be attributed to the steam reforming reaction of CH_4, whose amount showed a decreasing trend with higher S/B ratios.

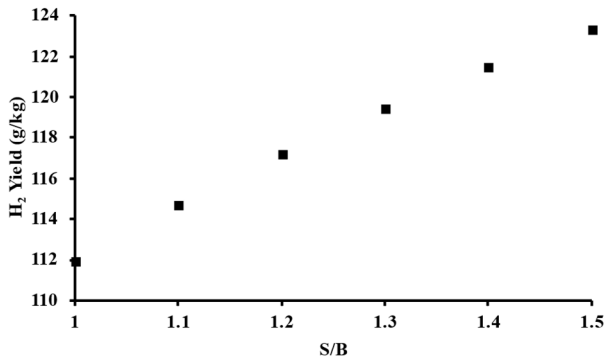

Figure 5 Effect of S/B on the hydrogen yield

3.4 Effect of water gas shift (WGS)

Figure 6 illustrates the effect of the H_2O/CO molar ratio on gas composition and hydrogen yield at a reaction temperature of 350°C. (Phan, Minh, Espitalier, Nzihou, & Grouset, 2022) In this study, the H_2O/CO ratio was varied from 1.5 to 2.2 by introducing additional steam into the water-gas shift reaction in order to enhance hydrogen production efficiently without adversely affecting the gasification process. As shown in the figure, increasing the H_2O/CO ratio led to a significant increase in the hydrogen production yield, while the amount of CO exhibited a decreasing trend. Meanwhile, the amount of H_2O increased, and the amount of CO_2 showed a slight decrease. The addition of steam facilitated the conversion of CO and H_2O into CO_2 and H_2 through the forward progression of the water-gas shift reaction. However, as the H_2O/CO ratio increased further, the rate of hydrogen production enhancement slowed down. From the results, it can be observed that the hydrogen yield improved from 122 g/kg total biomass at 800°C with an S/B ratio of 1.4 to 130 g/kg at an H_2O/CO ratio of 1.8.

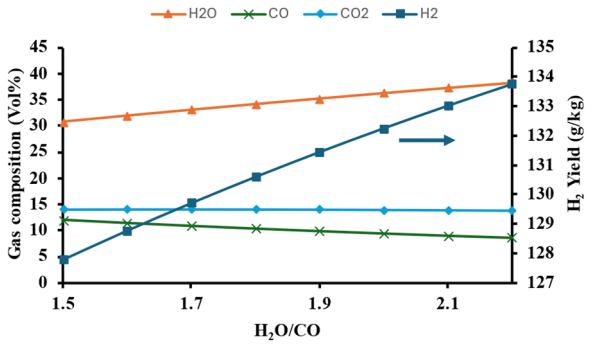

Figure 6 Effect of water gas shift on the product gas

4. CONCLUSION

In this study, the accuracy of the torrefaction process model was evaluated by comparing the predicted data with the simulated process data. The obtained RMSE value of 9.93 indicates that the model is reliable for predicting the solid yield. Subsequently, the effects of temperature during the gasification process were investigated. The results showed that the H_2 production increased as the temperature rose from 700 °C to 800 °C, but decreased when the temperature exceeded 800 °C, which was attributed to the Boudouard reaction leading to increased CO_2 production. The effects of the S/B ratio were also studied, revealing that a higher S/B ratio led to a decrease in H_2 production, an increase in CO_2 production, and a slight decrease in CO production. Moreover, the water-gas shift reaction was found to enhance the H_2 yield at higher H_2O/CO ratios, where the hydrogen yield increased from 122 g/kg total biomass to 132 g/kg total biomass as the H_2O/CO ratio was optimized. However, excessive steam addition resulted in a slower rate of increase in H_2 production. To further purify the hydrogen, a palladium membrane separation unit was applied, achieving a hydrogen purity of 99.99 wt%.

ACKNOWLEDGMENTS

This research budget was allocated by National Science, Research and Innovation Fund (NSRF), and King Mongkut's University of Technology North Bangkok (Project no. KMUTNB-FF-68-B-34).

REFERENCES

Arias, B., Pevida, C., Fermoso, J., Plaza, M. G., Rubiera, F., & Pis, J. J. (2008). Influence of torrefaction on the grindability and reactivity of woody biomass. Fuel Processing Technology, 89(2), 169-175.

Basu, P. (2010). Biomass gasification and pyrolysis: practical design and theory: Academic press.

Carlassara, T. (2024). Simulation of a biomass treatment process for the production of biofuels with pressurized torrefaction and plasma gasification on Aspen Plus. Politecnico di Torino,

Chua, J. Y., Pen, K. M., Poi, J. V., Ooi, K. M., & Yee, K. F. (2023). Upcycling of biomass waste from durian industry for green and sustainable applications: An analysis review in the Malaysia context. Energy Nexus, 10, 100203.

Lv, P. M., Xiong, Z. H., Chang, J., Wu, C. Z., Chen, Y., & Zhu, J. X. (2004). An experimental study on biomass air–steam gasification in a fluidized bed. Bioresource Technology, 95(1), 95-101.

Marcantonio, V., De Falco, M., Capocelli, M., Bocci, E., Colantoni, A., & Villarini, M. (2019). Process analysis of hydrogen production from biomass gasification in fluidized bed reactor with different separation systems. International Journal of Hydrogen Energy, 44(21), 10350-10360.

Onsree, T., & Tippayawong, N. (2021). Machine learning application to predict yields of solid products from biomass torrefaction. Renewable Energy, 167, 425-432.

Pala, L. P. R., Wang, Q., Kolb, G., & Hessel, V. J. R. e. (2017). Steam gasification of biomass with subsequent syngas adjustment using shift reaction for syngas production: An Aspen Plus model. 101, 484-492.

Phan, T. S., Minh, D. P., Espitalier, F., Nzihou, A., & Grouset, D. (2022). Hydrogen production from biogas: Process optimization using ASPEN Plus®. 47(100), p. 42027-42039. doi:10.1016/j.ijhydene.2022.01.100

Wang, Y., & Wu, J. J. (2023). Thermochemical conversion of biomass: Potential future prospects. Renewable and Sustainable Energy Reviews, 187, 113754.

Process simulation of synthetic fuel production from palm oil mill waste

Worawit Morin[1], Suksun Amornraksa[2], Amata Anantpinijwatna[3], Suttichai Assabumrungrat[4,5], Lida Simasatitkul[1,*]

[1] Department of Industrial Chemistry, Faculty of Applied Science King Mongkut' s University of Technology North Bangkok, Bangkok, 10800, Thailand
[2] Chemical Engineering and Management Program, The Sirindhorn International Thai German Graduate School of Engineering, King Mongkut's University of Technology North Bangkok, Thailand
[3] Department of Chemical Engineering, School of Engineering, King Mongkut's Institute of Technology Ladkrabang, Bangkok 10520, Thailand
[4] Center of Excellence in Catalysis and Catalytic Reaction Engineering, Department of Chemical Engineering, Faculty of Engineering, Chulalongkorn University, Bangkok 10330, Thailand
[5] Bio-Circular-Green-Economy Technology & Engineering Center (BCGeTEC), Faculty of Engineering, Chulalongkorn University, Bangkok 10330, Thailand
[*] Corresponding author: lida.s@sci.kmutnb.ac.th

ABSTRACT

This research focuses on the simulation of biofuel production from oil palm wastes using the Fischer-Tropsch (FT) process. The waste, consisting of empty fruit bunches (EFB) 12.15 tons/hr. and palm kernel shells (PKS) 5.4 tons/hr., are fed into a gasification process followed by the FT process. This study employs process simulation using Aspen Plus software to investigate the optimal operating conditions for maximizing biofuel yield. The suitable operating conditions are a temperature of 900 °C and a pressure of 2 bars, with a steam-to-carbon ratio of 0.8, to produce synthesis gas (syngas). The produced syngas, primarily composed of hydrogen (H_2), carbon monoxide (CO), and carbon dioxide (CO_2), is then introduced into the Fischer-Tropsch (FT) process, which is conducted at 230 °C and 25 bar, to produce synthetic fuels. The resulting distillate yields include 819.28 kg/hr. of gasoline, 469 kg/hr. of kerosene, 1,091.42 kg/hr. of diesel, and 1,131.74 kg/hr. of wax. The overall simulation model is shown in Figure 1.

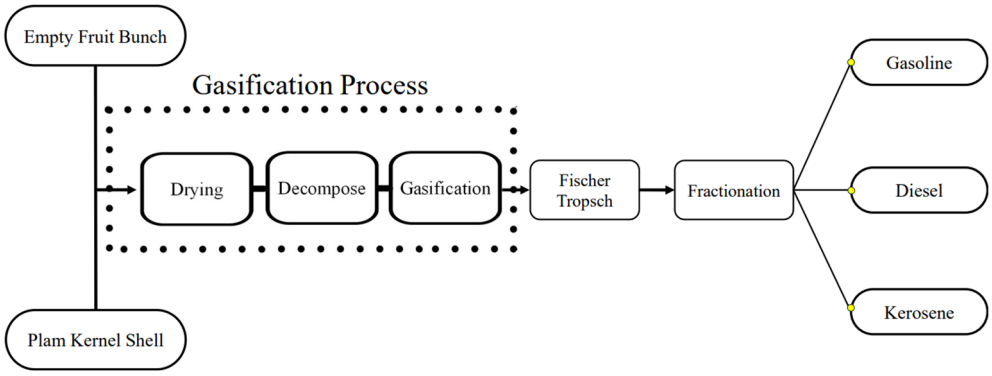

Figure 1 Simulation model of Gasification and Fischer-Tropsch

Keywords: Empty fruit bunches; Palm kernel shells; Gasification; Fischer-Tropsch; Process simulation; Synthetic fuels

1. INTRODUCTION

Oil palm residues such as empty fruit bunches (EFB) and palm kernel shells (PKS) are abundant lignocellulosic biomass sources in Southeast Asia. These materials are rich in cellulose, hemicellulose, and lignin, and have shown strong potential as feedstocks for renewable fuel production through thermochemical conversion(Acevedo, Posso, Durán, & Arenas, 2018)With the growing need to reduce dependency on fossil fuels and mitigate greenhouse gas emissions, the utilization of biomass residues has gained substantial interest in both research and industrial applications.

Gasification is a high-temperature thermochemical process typically performed at temperatures between

700°C and 1000°C, pressures ranging from atmospheric pressure up to 10 bars, and steam-to-carbon (S/C) ratios between 0.3 and 1.5, depending on the desired syngas quality (Basu, 2010). Palm kernel shells (PKS) and empty fruit bunches (EFB) have been shown to produce high-quality syngas with a relatively high concentration of hydrogen (H_2) and carbon monoxide (CO) — typically in the range of 40–60 vol% for H_2 and 15–25 vol% for CO — and lower amounts of tar (less than 1 g/Nm³) and ash (below 5 wt%) compared to other biomass feedstocks. (Lv et al., 2004)Such favorable gas composition makes PKS- and EFB-derived syngas particularly suitable for direct integration into catalytic synthesis processes, notably Fischer–Tropsch (FT) synthesis. This integration enhances process efficiency, enabling the production of high-value synthetic fuels such as gasoline, diesel, and wax.

The Fischer–Tropsch (FT) synthesis is a well-established catalytic process that converts synthesis gas (syngas), composed primarily of hydrogen (H_2) and carbon monoxide (CO), into a broad spectrum of hydrocarbons. The resulting products include light gases (C_1–C_4), liquid fuels such as gasoline (C_5–C_{12}), kerosene (C_{13}–C_{16}), diesel (C_{15}–C_{20}), and heavy waxes (C_{21}+). Among these, diesel and wax are typically dominant in low-temperature Fischer–Tropsch synthesis (LTFT), which operates at 220–250 °C and 20–30 bar (Dry, 2002; Rytter & (Rytter, Tsakoumis, & Holmen, 2016). Operating conditions significantly influence product distribution. Under optimal LTFT conditions (T = 220–250 °C, P = 20–30 bar), chain growth is favored, leading to a high yield of diesel and wax fractions (C_{15}–C_{20} and C_{21}+). However, deviations from these parameters shift the product spectrum. For instance, at higher temperatures (T > 270 °C) but similar pressures, the process transitions to high-temperature Fischer–Tropsch synthesis (HTFT), favoring the formation of light gaseous products such as CH_4, C_2H_6, C_3H_8, and C_4H_{10}. Similarly, operating at lower pressures (P < 10 bar) within the LTFT temperature range also results in increased production of lighter hydrocarbons due to reduced chain propagation efficiency (Dry; Iglesia, 1997)These findings underscore the importance of maintaining tightly controlled FT synthesis conditions to ensure maximum yield of desired middle distillates while minimizing undesirable light gas formation. Cobalt-based catalysts are commonly employed in LTFT due to their high activity and selectivity toward linear paraffinic hydrocarbons, making them particularly effective for producing high-quality diesel and wax (Selvatico, Lanzini, & Santarelli, 2016). Biomass-derived syngas, with its moderate H_2/CO ratio (typically close to 2:1) and low inert gas content, is highly compatible with LTFT conditions, reducing the need for extensive gas purification prior to synthesis (van der Laan & Beenackers, 1999).

Several studies have confirmed the feasibility and performance of Fischer–Tropsch (FT) synthesis using syngas derived from biomass gasification wax (Selvatico et al., 2016) demonstrated favorable selectivity toward long-chain hydrocarbons when cobalt-based catalysts were applied to syngas obtained from gasified wood biomass under low-temperature Fischer–Tropsch (LTFT) conditions. In their study, an H_2/CO ratio close to 2.0 was found to be optimal for maximizing the yield of long-chain hydrocarbons such as diesel-range alkanes. Similarly, Dry (2002) emphasized the thermodynamic advantages of LTFT in promoting hydrocarbon chain growth at moderate temperatures (220–250 °C) and pressures (20–30 bar). Under these conditions, the primary products are high-molecular-weight hydrocarbons, predominantly waxes and diesel-range liquids, which can subsequently be upgraded into transportation fuels through hydrocracking and other refining processes.

The integration of FT synthesis with biomass gasification forms the foundation of biomass-to-liquid (BTL) pathways, which enable the sustainable production of synthetic fuels such as gasoline, diesel, and wax. These pathways have been successfully demonstrated in several configurations, including the conversion of switchgrass (Li, Hao, Sheng, & Xu, 2008)and wood pellets (Van der Drift, Boerrigter, Coda, Cieplik, & Hemmes, 2004)into liquid fuels. Such integration not only contributes to fossil fuel displacement but also offers a viable route for carbon-neutral fuel production.

Despite extensive studies on single biomass feedstocks, including investigations using palm kernel shells (PKS) (Basha, Sulaiman, & Uemura, 2020) and empty fruit bunches (EFB) (Wan Ismail & Rasid, 2017) individually, comprehensive research on the combined utilization of multiple oil palm residues within an integrated gasification–Fischer–Tropsch (FT) framework remains limited. Previous studies have primarily focused on the characterization, gasification behavior, and syngas production efficiency of either PKS or EFB as isolated feedstocks, often emphasizing the favorable syngas composition—high hydrogen (H_2) and carbon monoxide (CO) concentrations with minimal tar and ash formation—achieved during gasification at 700–1000 °C and up to 10 bar (Basu, 2010; Lv et al., 2004) Such syngas quality is particularly suitable for direct catalytic conversion via FT synthesis, especially under low-temperature Fischer–Tropsch (LTFT) conditions (220–250 °C, 20–30 bar) that favor chain growth toward diesel (C_{15}–C_{20}) and heavy waxes (C_{21}+) (Dry, 2002; Rytter & (Rytter et al., 2016).

However, the potential synergistic benefits of co-processing EFB and PKS—such as balancing reactivity, optimizing thermochemical properties, and enhancing overall system robustness—have not been thoroughly explored. Integrating both EFB and PKS as feedstocks is expected to enhance process flexibility by accommodating variations in biomass availability and quality while improving system efficiency through

blended feedstock characteristics (e.g., moisture content, volatile matter, and ash composition). Addressing these integration aspects is critical for the development of scalable, resilient, and economically viable biomass-to-liquid (BTL) pathways in palm oil–producing regions, where multiple types of oil palm residues are abundantly available and can be efficiently utilized within the gasification–FT synthesis chain.

In this study, torrefied EFB and PKS are used as feedstocks for gasification, followed directly by Fischer-Tropsch synthesis without intermediate shift conversion. Process simulation is conducted using Aspen Plus® to evaluate optimal process configurations and product yields. The simulation aims to maximize the production of gasoline, kerosene, diesel, and wax under conditions relevant to industrial applications.

2. Modeling

The simulation of the integrated gasification and Fischer-Tropsch process was conducted using Aspen Plus software. Biomass (EFB and PKS) were defined as non-conventional components and decomposed via an RYIELD reactor. The resulting volatiles entered a RGIBBS reactor to simulate equilibrium gasification. Syngas produced were then conditioned and fed into a plug flow reactor (RPlug) to simulate low-temperature Fischer-Tropsch synthesis. A distillation train was used to separate FT products into gasoline, kerosene, diesel, and wax.

2.1 Model assumptions

- The entire gasification and Fischer-Tropsch process is simulated under steady-state conditions.
- The Peng-Robinson (PR) equation of state is applied for thermodynamic property estimation throughout the simulation.
- Oil palm residues (EFB and PKS) are modeled as non-conventional components and decomposed via RYIELD block based on ultimate and proximate analysis.
- The gasification process assumes equilibrium conditions, and syngas is produced primarily consisting of H_2, CO, and CO_2.
- The Fischer-Tropsch synthesis is modeled using a plug flow reactor (PFR) at 230 °C and 25 bar, assuming cobalt-based wax (Selvatico et al., 2016)
- No catalyst deactivation, coke formation, or heat loss is considered in the simulation.
- Distillation columns are assumed to operate with ideal separation and no pressure drop unless otherwise specified.
- The number of stages include condenser and reboiler.

2.2 Model description

The ultimate and proximate analyses of EFB and PKS, shown in Table 1 and Table 2, provide essential data for biomass characterization and process simulation.

Table 1. Properties of raw EFB (Emami Taba, Irfan, Wan Daud, & Chakrabarti, 2012)

Ultimate analysis (wt.%)		Proximate analysis (wt.%)	
C	46.62	M^{ad}	5.18
H	6.45	VM^{ad}	82.58
N	1.21	FC^{ad}	8.79
O	42.235	ASH^{d}	3.45
S	0.035		

Table 2. Properties of raw PKS (Acevedo et al., 2018)

Ultimate analysis (wt.%)		Proximate analysis (wt.%)	
C	46.05	M	7.52
H	5.14	VM	69.35
N	0.62	FC	20.46
O	45.38	ASH	2.67
S	0.14		

[a]d: on dry basis, ad: on air dried basis

The process begins with the preparation of empty fruit bunches (EFB) at a feed rate of 12.15 tons/hr. EFB undergoes mechanical crushing to reduce particle size, followed by drying at 110 °C to lower its moisture content, with excess water removed via a flash separator (FLASH). After drying, the EFB is heated to 500 °C in HEATER1 and fed into an RYIELD reactor (RYIELD1), where it decomposes into volatile gases and solid char based on experimental yield data. The volatile fraction is subsequently introduced into a GASIFIER unit, modeled as an RGibbs reactor, operating at 900 °C and 2 bar with a steam-to-biomass

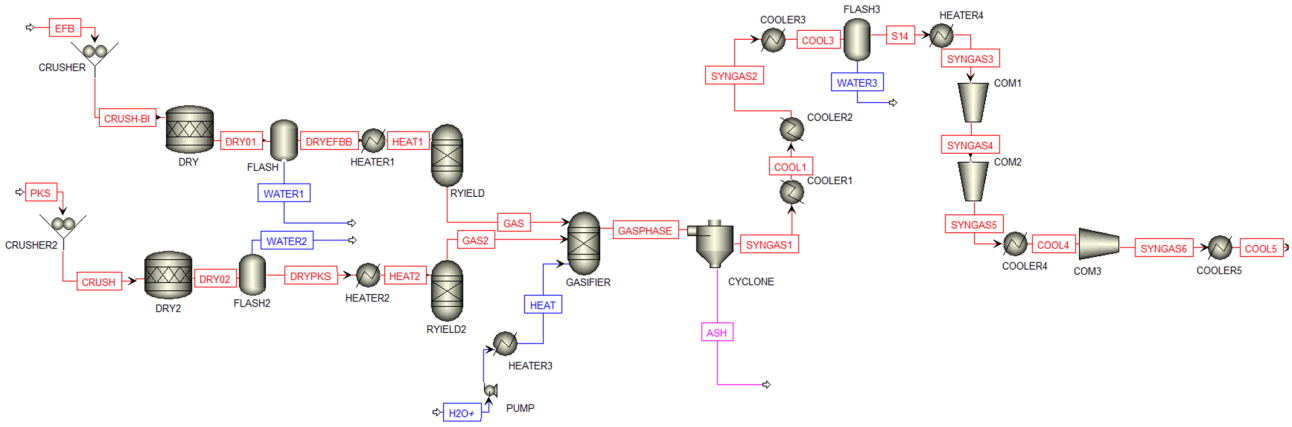

Figure 1 Process of Gasification

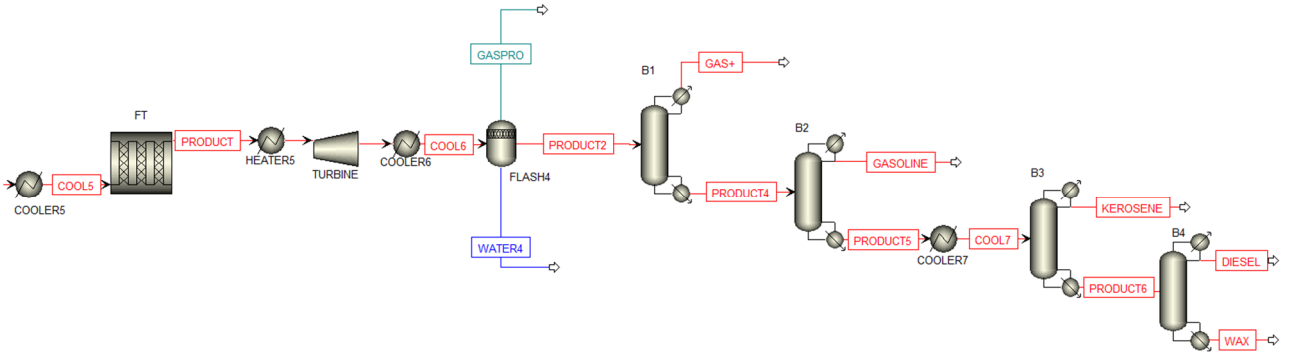

Figure 2 Fischer–Tropsch Synthesis and Downstream Product Separation

ratio (S/B) of 0.8 to facilitate partial oxidation and reforming reactions. This results in the generation of synthesis gas (syngas) predominantly composed of hydrogen (H_2), carbon monoxide (CO), and carbon dioxide (CO_2). Palm kernel shells (PKS), fed at 5.4 tons/hr, follow an identical pretreatment and conversion pathway as EFB, involving drying, thermal decomposition, and gasification under the same operating conditions, before being merged into the syngas stream. Following gasification, the syngas undergoes purification steps including ash removal via a cyclone separator, sequential cooling in COOLER1–COOLER3, and moisture removal in FLASH3. The dried syngas is preheated in HEATER4 and compressed in a three-stage compression system (COM1–COM3) to elevate the pressure from 2 bar to 25 bar is approximately:

$$\frac{P_{out}}{P_{in}} = \frac{25}{2} = 12.5$$

Thus, for three stages, the individual stage pressure ratio becomes:

$$r = (12.5)^{\frac{1}{3}} = 2.36$$

with each stage achieving a pressure ratio of approximately 2.36 to ensure mechanical and thermal efficiency. Intercooling between stages minimizes temperature rises and enhances compressor performance. (Towler & Sinnott, 2012)

The conditioned syngas is subsequently fed into the Fischer–Tropsch (FT) reactor, operating at 230 °C and 25 bar under low-temperature FT (LTFT) conditions. Catalytic conversion, employing a cobalt-based catalyst, promotes chain growth reactions, favoring the formation of heavier hydrocarbons such as diesel and wax, given the moderate H_2/CO ratio derived from biomass gasification.

After synthesis, the FT product stream is cooled in COOLER6 and separated into gas and liquid phases via FLASH4. The liquid hydrocarbon stream (PRODUCT2) is fractionated through a series of distillation columns (B1–B4) with integrated heat exchangers (HEATER5 and COOLER7), resulting in the sequential recovery of gasoline, kerosene, diesel, and wax in a single continuous distillation train, thereby ensuring high product purity and efficient energy utilization.

All unit operations are connected in a continuous process simulated in Aspen Plus, with thermodynamic properties evaluated using the PR-BM equation of state. Enthalpy and density calculations for biomass are handled using the HCOALGEN and DCOALIGT models.

3. RESULTS AND DISCUSSION

3.1 Model Validation

The percentage error (%Error) was calculated using the following equation:

$$\%\text{Error} = \frac{|\text{Measured} - \text{Simulated}|}{\text{Measured}} \times 100$$

where Measured refers to the experimental values and Simulated refers to the model prediction results obtained from simulation.

The calculated Abs.Error (%) values are summarized in Table 3. for syngas from EFB gasification and in Table 4. for syngas from PKS gasification. The low error percentages observed confirm that the simulation results are in good agreement with experimental data.

As shown in Figure 3, the simulated Fischer–Tropsch product distribution matches closely with experimental results of wax (Selvatico et al., 2016) indicating that the model can accurately predict hydrocarbon yields across a wide range of carbon numbers.

Table 3. Comparison between simulated and experimental results for syngas from EFB gasification.

Type of gas	Simulation (%Vol)	Experiment (%Vol) (Emami Taba et al., 2012)	Abs. Error (%)
H_2	59.20	59.00	0.00
CO	28.22	27.00	0.01
CO_2	12.57	14.00	0.01

Table 4. Comparison between simulated and experimental results for syngas from PKS gasification

Type of gas	Simulation (%Vol)	Experiment (%Vol) (Acevedo et al., 2018)	Abs. Error (%)
H_2	55.90	58.80	1.10
CO	17.14	21.10	4.00
CO_2	22.92	19.80	3.10
CH_4	0.01	0.30	0.30

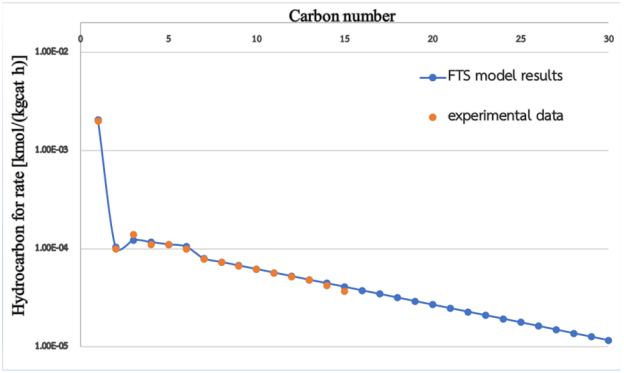

Figure 3 FT product distribution: FTS model results in comparison to literature data

3.2 Effect of Temperature

The variation in syngas composition with respect to gasification temperature is illustrated in Figure 4(a–d). The operating temperature varied from 800 °C to 1000 °C. As the gasifier temperature increases, the concentration of carbon monoxide (CO) gradually rises, while the concentrations of carbon dioxide (CO_2) and methane (CH_4) tend to decrease. The hydrogen (H_2) content initially increases with temperature but shows a slight decline after reaching a peak point. This behavior is attributed to the endothermic nature of the gasification and reforming reactions, where higher temperatures promote the formation of CO and H_2 while reducing CO_2 and CH_4 formation through enhanced Boudouard and reforming reactions.

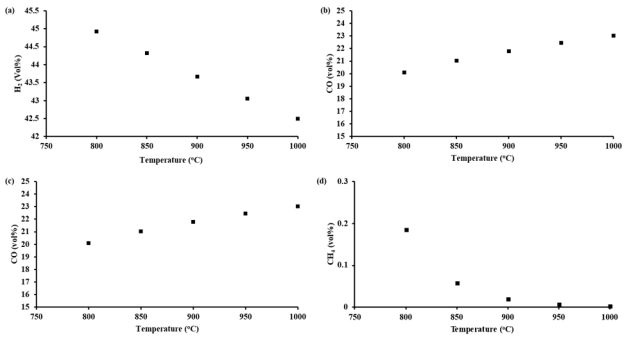

Figure 4 (a) Effect of gasification temperature on hydrogen yield, (b) Effect of gasification temperature on carbon monoxide yield, (c) Effect of gasification temperature on carbon dioxide yield, and (d) Effect of gasification temperature on methane yield, at a constant steam-to-biomass (S/B) ratio of 0.8

Based on the results shown in Figure 5, although the highest hydrogen yield (~88.95 g/kg) was achieved at 800 °C, the temperature of 900 °C was selected as the optimal gasification condition. This selection was made to maintain a balanced syngas composition, particularly targeting a H_2/CO molar ratio of approximately 2:1, which is essential for efficient Fischer–Tropsch synthesis. Operating at 900 °C offers a compromise between hydrogen production and carbon monoxide availability, ensuring an optimal feedstock for

downstream catalytic conversion. Similar considerations have been emphasized in previous gasification studies aiming to optimize syngas quality for synthetic fuel production (Lv et al., 2004); (Zhang, Li, & Wu, 2013)

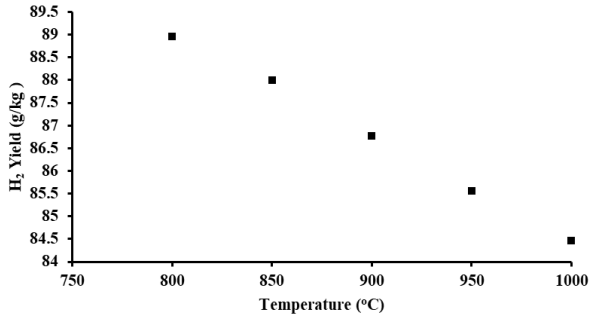

Figure 5 Effect of temperature on the hydrogen yield

3.3 Effect of steam/biomass (S/B) ratio

At 900 °C and 2 bar, increasing the steam-to-biomass (S/B) ratio from 0.1 to 1.0 led to a gradual decrease in H_2 and CO concentrations, while CO_2 concentration increased significantly (Figure 6a–d). This indicates that higher steam ratios promote oxidation reactions, favoring CO_2 formation over H_2 and CO production. CH_4 content rapidly declined to near zero as steam input increased. These trends align with observations reported by (Lv et al., 2004) and (Basu, 2010)

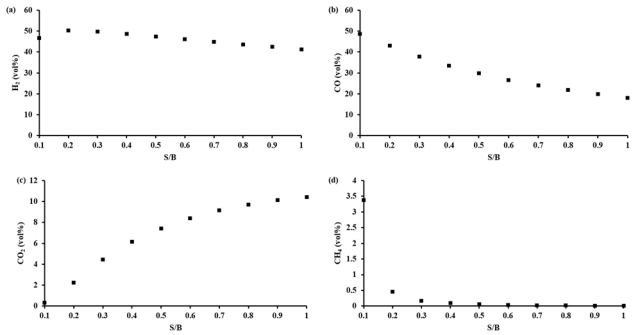

Figure 6 (a) Effect of S/B on the hydrogen (b) Effect of S/B on the carbon monoxide (c) Effect of S/B on the carbon dioxide (d) Effect of S/B on the methane under a constant gasification temperature of 900 °C.

At a temperature of 900 °C and a pressure of 2 bar, the hydrogen yield increased consistently with the rising steam-to-biomass (S/B) ratio, as shown in Figure 7 Initially, hydrogen production rose sharply due to the promotion of steam gasification and steam reforming reactions, enhancing the conversion of carbonaceous materials into hydrogen-rich syngas. However, when the S/B ratio exceeded 0.6, the hydrogen yield increment became marginal. This trend is attributed to the saturation of reactive sites and the dilution effect caused by excess steam in the reactor. Similar behaviors have been reported in previous studies (Lv et al., 2004)

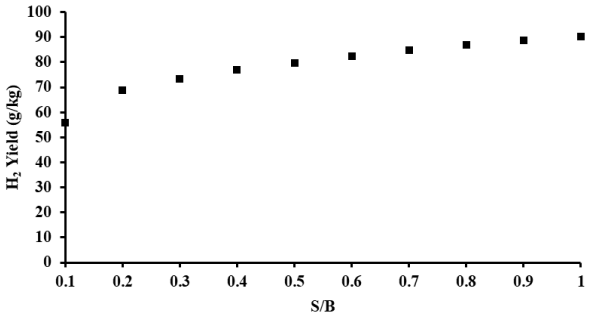

Figure 7 Effect of S/B on the hydrogen yield

3.3 Fischer–Tropsch Product Distribution

Table. 5 Optimum Design Parameters for Distillation Column Configurations (B1–B4).

Parameter	B1	B2	B3	B4
Number of stages	15	30	30	30
Reflux ratio (Mole)	4	4	2	4
Distillate-to-feed ratio	0.27	0.42	0.26	0.59
Above feed stage	8	14	16	16
Condenser heat duty (MW)	-0.23	-0.44	-0.09	-0.36
Reboiler heat duty (MW)	0.75	0.69	0.34	0.34

As shown in Table 5, the number of stages, reflux ratios, and feed locations for each distillation column (B1–B4) were designed to optimize both separation efficiency and energy utilization.

Initially, column B1 was configured with 15 stages, a lower number compared to the others, because it was responsible for separating lighter hydrocarbons and off-gas with relatively narrow boiling ranges below 200 °C. The lighter nature of the separated fractions reduced the need for a high number of stages. A reflux ratio of 4 was applied to enhance vapor-liquid equilibrium and achieve the required product purity, while the feed was introduced at stage 8, just above the midpoint of the column, to promote effective separation.

However, B1 exhibited the highest reboiler duty (0.75 MW) among the columns, attributed to the greater energy demand for vaporizing lighter components with high latent heats.

In contrast, columns B2, B3, and B4 were each designed with 30 stages to enable effective separation of heavier components with overlapping boiling points. Diesel typically boils between 200–360 °C, while wax fractions extend beyond 360 °C, necessitating greater separation precision. The clearly defined cut points

between these boiling ranges allowed for efficient recovery of distinct product streams — gasoline, kerosene, diesel, and wax — minimizing contamination between fractions.

Feed locations in B3 and B4 were positioned at stage 16 to optimize phase equilibrium and minimize remixing losses during separation.

Energy analysis indicated that B3 and B4 achieved lower reboiler duties (0.34 MW each) and relatively moderate condenser duties, with B3 demonstrating the most energy-efficient condenser duty (−0.09 MW), owing to optimized vapor-liquid distribution across the column stages.

These findings highlight the trade-off between stage number, reflux ratio, and energy consumption, consistent with classical distillation design guidelines (Seader, Henley, & Roper, 2011; Towler & Sinnott, 2012) Overall, the integrated design achieves a balanced performance between separation efficiency, product quality, and operational cost in Fischer–Tropsch product recovery.

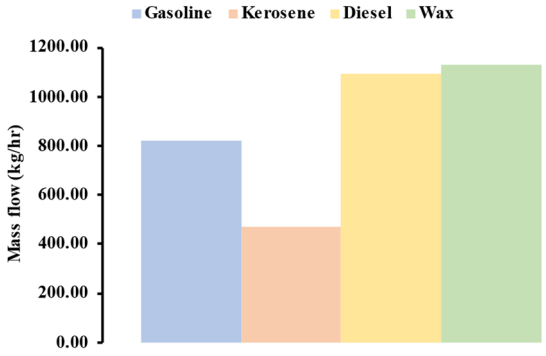

Figure 8 Mass flow rate of Fischer–Tropsch products

The Fischer–Tropsch (FT) synthesis was conducted at a pressure of 25 bar and a temperature of 230 °C. The feed syngas, primarily composed of hydrogen (H_2) and carbon monoxide (CO), was supplied with a H_2/CO ratio of 2:1 to optimize hydrocarbon chain growth. The syngas was subsequently converted into various hydrocarbon products.

The simulation results, illustrated in Figure 8, show the mass flow rates of the major FT products, including gasoline, kerosene, diesel, and wax. Figure 8 presents the distribution of these liquid fuels and wax in terms of mass flow rate (kg/hr). Wax exhibited the highest production rate at 1,131.74 kg/hr, followed by diesel (1,091.42 kg/hr), gasoline (819.28 kg/hr), and kerosene (469.00 kg/hr).

The simulation results demonstrated a high yield of diesel, consistent with the objectives of this study. The high production of heavy hydrocarbons, particularly diesel and wax, is a characteristic feature of low-temperature Fischer–Tropsch synthesis (LTFT). LTFT conditions, typically operated at lower temperatures (220–240°C) and moderate to high pressures (20–30 bar), favor extensive chain growth, resulting in the formation of long-chain paraffinic hydrocarbons wax (Selvatico et al., 2016). The operating conditions applied in this study (230°C and 25 bar) fall within the LTFT regime, thereby promoting the synthesis of heavier hydrocarbon products such as diesel. This outcome aligns with the findings reported wax (Selvatico et al., 2016), who demonstrated that LTFT processes using biomass-derived syngas led to a higher selectivity toward diesel and wax fractions under optimized reaction conditions.

4. CONCLUSION

This study successfully demonstrated the conversion of oil palm residues, namely empty fruit bunches (EFB) and palm kernel shells (PKS), into synthetic fuels through an integrated gasification and Fischer–Tropsch (FT) synthesis process. The gasification stage was operated at 900 °C and 2 bar, with a controlled steam-to-biomass (S/B) ratio of 0.8, corresponding to a feed rate of approximately 14.04 tons/hr. The S/B ratio was specifically adjusted to produce a syngas with an optimal H_2/CO molar ratio of 2:1, suitable for direct FT synthesis without requiring intermediate gas conditioning steps.

The generated syngas, enriched in hydrogen and carbon monoxide, was then fed into a low-temperature FT reactor that operated at 230 °C and 25 bar. Under these conditions, the FT process effectively converted syngas into a spectrum of hydrocarbon products, with wax and diesel being the dominant fractions, followed by gasoline and kerosene.

The results validate the feasibility of directly utilizing EFB and PKS as feedstocks for synthetic fuel production under optimized conditions, highlighting the potential of oil palm biomass as a sustainable and scalable resource for renewable fuel generation.

ACKNOWLEDGMENTS

This research budget was allocated by National Science, Research and Innovation Fund (NSRF), and King Mongkut's University of Technology North Bangkok (Project no. KMUTNB-FF-68-B-42).

REFERENCES

Acevedo, J., Posso, F., Durán, J., & Arenas, E. (2018). Simulation of the gasification process of palm kernel shell using Aspen PLUS. Paper presented at the Journal of Physics: Conference Series.

Basha, M. H., Sulaiman, S. A., & Uemura, Y. (2020). Co-gasification of palm kernel shell and polystyrene plastic: Effect of different operating conditions. Journal of the Energy Institute, 93(3), 1045-1052.

Basu, P. (2010). Biomass gasification and pyrolysis: practical design and theory: Academic press.

Dry, M. E. The Fischer–Tropsch (FT) Synthesis Processes. In Handbook of Heterogeneous Catalysis.

Emami Taba, L., Irfan, M. F., Wan Daud, W. A. M., & Chakrabarti, M. H. (2012). The effect of temperature on various parameters in coal, biomass and CO-gasification: A review. Renewable and Sustainable Energy Reviews, 16(8), 5584-5596.

Iglesia, E. (1997). Design, synthesis, and use of cobalt-based Fischer-Tropsch synthesis catalysts. Applied Catalysis A: General, 161(1), 59-78.

Li, M. T., Hao, L. L., Sheng, L. X., & Xu, J. B. (2008). Identification and degradation characterization of hexachlorobutadiene degrading strain Serratia marcescens HL1. Bioresource Technology, 99(15), 6878-6884.

Lv, P. M., Xiong, Z. H., Chang, J., Wu, C. Z., Chen, Y., & Zhu, J. X. (2004). An experimental study on biomass air–steam gasification in a fluidized bed. Bioresource Technology, 95(1), 95-101.

Rytter, E., Tsakoumis, N. E., & Holmen, A. (2016). On the selectivity to higher hydrocarbons in Co-based Fischer–Tropsch synthesis. Catalysis Today, 261, 3-16.

Seader, J. D., Henley, E. J., & Roper, D. K. (2011). Separation Process Principles: Chemical and Biochemical Operations (3 ed.). Hoboken, NJ: John Wiley & Sons.

Selvatico, D., Lanzini, A., & Santarelli, M. (2016). Low Temperature Fischer-Tropsch fuels from syngas: Kinetic modeling and process simulation of different plant configurations. Fuel, 186, 544-560.

Towler, G., & Sinnott, R. (2012). Chemical Engineering Design: Principles, Practice and Economics of Plant and Process Design (2 ed.). Oxford: Butterworth-Heinemann.

Van der Drift, A., Boerrigter, H., Coda, B., Cieplik, M. K., & Hemmes, K. (2004). Entrained flow gasification of biomass. Ash behaviour, feeding issues, system analyses. Retrieved from Netherlands:

Wan Ismail, W. M. S., & Rasid, R. A. (2017). Empty fruit bunch (EFB) gasification in an entrained flow gasification system. Chemical Engineering Research Bulletin, 19(0), 43-49. doi:10.3329/cerb.v19i0.33775

Zhang, J., Li, Y., & Wu, C. (2013). The Influence of Individual and Team Cognitive Ability on Operators' Task and Safety Performance: A Multilevel Field Study in Nuclear Power Plants. PLoS ONE, 8(12), e84528. doi:10.1371/journal.pone.0084528

Optimal input variables for an artificial neural network to predict evaporation efficiency in detergent production process

Baramee Imsin[1], Pailin Ngaotrakanwiwat[1,3], Chalermpan Fongsamut[2,3,*]

[1] Department of Chemical Engineering, Faculty of Engineering, Burapha University, Chonburi 20131, Thailand
[2] Department of Electrical Engineering, Faculty of Engineering, Burapha University, Chonburi 20131, Thailand
[3] Interdisciplinary Center for Decarbonisation and Green Energy, Faculty of Engineering, Burapha University, Chonburi 20131, Thailand
[*] Corresponding author: chalerm@eng.buu.ac.th

ABSTRACT

The spray drying process is the most energy-intensive unit in detergent production; therefore, the operation parameters must be controlled to achieve lower energy consumption per unit of dried detergent powder production, which is defined as evaporation efficiency. Unfortunately, evaporation efficiency cannot be measured directly by sensors; however, it must be calculated using the multiple data monitored in the process, using mass and energy balance. [14] Therefore, this research focuses on developing a soft sensor using data obtained from the actual production process, starting from the beginning of production, reaching a steady state, and ending the production, with an artificial neural network (ANN) model to predict evaporation efficiency by optimizing various configurations, i.e., activation functions, and neurons per layer. In particular, the effect of the number of input variables on the predicted evaporation efficiency was investigated to achieve an optimal model with a simple structure and high prediction accuracy. The results showed that the ANN (4-34-1) model with four input variables, i.e., rate of natural gas consumption, inlet hot air temperature, Feed rate of slurry detergent and moisture content in dried detergent powder achieved a root mean squared error (RMSE) of 0.0403 and a coefficient of determination (R^2) of 0.9969. This high level of accuracy in predicting evaporation efficiency can be directly applied to optimize detergent production processes, reducing energy consumption and improving product quality.

Keywords: Soft sensor; Evaporation efficiency; Spray drying process; Detergent production

1. INTRODUCTION

Spray drying is a process that transforms liquid materials into powder form and is widely utilized in various industries, including food, pharmaceuticals, and chemicals [1]. Notably, detergent powder, a primary product in the cleaning agent category, is projected to reach a global market value of USD 93 billion by 2027 [2]. In the spray drying process of detergent, heat and mass are transferred between the detergent slurry, which is atomized into fine droplets through nozzles, and hot air. This rapid evaporation of water from the slurry leads to in the formation of detergent powder [3].

Several factors influence the spray drying process, such as the temperature and flow rate of hot air, droplet size, and the feed rate of the liquid. Although these parameters can be well-controlled, real-world operations still encounter challenges due to uncontrollable variables. One such variable is the humidity of the intake air used to generate hot air, which can lead to variability in the moisture content of the drying air and result in increased fuel consumption. Moreover, the viscosity of the detergent slurry may vary due to raw material differences, affecting the feed consistency. Proper control of these variables enhances product quality and improves drying efficiency.

The efficiency of the drying process can be evaluated through various metrics, such as the ratio of consumed exergy to input exergy in mushroom drying [4], or the ratio of evaporated water mass to input energy in celery drying [5]. These indicators relate to energy usage within the drying chamber, which isn't directly measured by physical sensors. Therefore, the development of soft sensors, which are data-driven models that estimate unmeasurable process variables using measurable input data, provides an accurate and efficient means for evaluating process performance.

Soft sensors have been developed for predicting outputs in complex processes, such as butane concentration in debutanizer columns and tail gas composition in sulfur recovery units [6]. They are also useful in scenarios where real-time measurement is not feasible, such as

assessing steel quality post-production, which typically requires laboratory analysis [7]. In drying processes, soft sensors have been used to predict the quality of pharmaceutical products in fluidized bed drying [8] and estimate drying time for slurries with varying compositions [9].

The development of soft sensors relies on machine learning (ML) models, including multiple linear regression (MLR), suitable for linear relationships [10]; support vector regression (SVR), which is effective for complex, nonlinear patterns when combined with kernel functions [11]; and artificial neural networks (ANNs), which offer highly flexible architectures and tunable parameters, enabling accurate learning from complex data. However, ANNs require large datasets to achieve high prediction accuracy [12]. In previous studies, ANNs were trained using experimental input variables such as hot air temperature and flow rate, spray rate, and concentration of calcium chloride solution. These models were developed to predict the moisture content of calcium chloride powder and the temperature of exhaust air. The models achieved mean absolute errors (MAE) of 7% for moisture content and 4 % for exhaust air temperature, respectively [13].

Currently, the development of soft sensors for detergent spray drying is still limited, particularly those trained with real-world production data, which is more variable than experimental data. The research team previously developed models to predict the energy efficiency of detergent spray drying using limited real-world data supplemented by simulation data. Seven input variables were used: temperature of intake air, natural gas consumption, detergent slurry temperature, slurry feed rate, exhaust air temperature, chamber pressure, and moisture content of dried detergent. The effect of varying the ratio of real to simulated data on model performance was investigated. A long short-term memory-based transfer learning (TL-LSTM) model yielded high prediction accuracy with a coefficient of determination (R^2) of 0.938 [14]. Furthermore, an adaptive version of this model, capable of online learning during sensor failures without requiring offline retraining, achieved an R^2 of 0.9859 [15]. However, complex models often require a large number of input variables, necessitating multiple physical sensors, which increases operational costs, data collection time, and computational effort.

This study, therefore, aims to investigate the impact of reducing the number of input variables in the development of a soft sensor for detergent spray drying using an ANN-based technique to evaluate the drying process efficiency. The data used for model development are obtained from real industrial production and stored in a database system.

2. EXPERIMENTAL

2.1 Spray Drying Process for Detergent Powder

The spray drying process for detergent powder begins with the intake of fresh air, where its temperature (Sensor No. 1, T_{amb}) and relative humidity (Sensor No. 2, RH_{amb}) are measured. These values vary depending on daily weather conditions. The fresh air is then passed through a heat exchanger to increase its temperature. The preheated air is subsequently directed to the furnace and divided into two streams: combustion air and quench air. Combustion air is used to burn with natural gas, whose flow rate is measured (Sensor No. 3, FR_{NG}), while quench air is supplied from the bottom of the furnace to raise its temperature, resulting in the production of hot air. The temperature of the hot air is monitored and controlled (Sensor No. 4, T_{HA}) before being directed to the side of the drying chamber. Meanwhile, detergent slurry is stored in a tank, where its temperature is controlled and measured (Sensor No. 5, T_S) to maintain appropriate viscosity. The slurry is then atomized from the top of the drying chamber through a nozzle using a high-pressure pump, forming fine liquid droplets. The slurry feed rate is monitored (Sensor No. 6, FR_S). During the drying process, heat and mass are exchanged between the hot air and the atomized droplets, causing rapid evaporation of water. The resulting vapor exits the top of the chamber along with the exhaust air, whose temperature is measured (Sensor No. 7, T_{EA}). The dried detergent powder, referred to as base powder, falls to the bottom of the chamber for collection. The moisture content of the dried powder is analyzed using a moisture analyzer (Sensor No. 8), as illustrated in Figure 1.

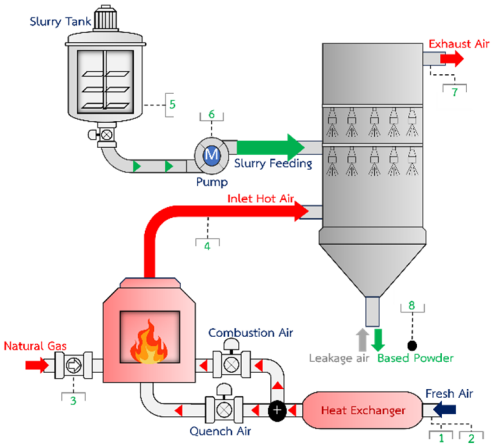

Figure 1 Detergent spray drying process.

2.2 Calculation of Water Evaporation Efficiency

In this study, the energy efficiency of the spray drying process is evaluated based on the ratio between the heat input rate delivered to the drying chamber via hot air ($\dot{Q}_{input}$) and the mass flow rate of the dried detergent powder ($\dot{m}_{BP}$). This ratio is referred to as the water evaporation efficiency (E_{eff}), as shown in Equation (1). The evaluation of this energy efficiency

can serve as a guideline for process control and is also useful for assessing production costs and potential profit margins.

$$E_{eff} = \frac{\dot{Q}_{input}}{\dot{m}_{BP}} \quad (1)$$

The calculation of the heat input rate delivered to the drying chamber via hot air ($\dot{Q}_{input}$) is shown in Equation (2). This is determined by analyzing the total enthalpy of the hot air and the water vapor entering the chamber. The hot air supplied to the drying chamber is composed of combustion gases generated in the furnace. Therefore, the calculation of the flow rate and composition of these combustion gases is carried out using a mass balance around the furnace. This requires information on the composition of the natural gas and its flow rate—measured by sensors—as well as the flow rate of fresh air, whose temperature and humidity vary daily with ambient conditions. These values are used to estimate the amount of moisture carried with the incoming air. The combustion reaction is assumed to proceed with 100% conversion efficiency, resulting in combustion gases composed of nitrogen, oxygen, carbon dioxide, and water vapor.

$$\dot{Q}_{input} = \dot{Q}_{DA,HA} + \dot{Q}_{H_2O,HA} \quad (2)$$

Where:

$\dot{Q}_{input}$ is the total heat input rate into the drying chamber. $\dot{Q}_{DA,HA}$ is the heat input rate of the dry combustion gases, which include nitrogen, oxygen, and carbon dioxide, at the temperature of the hot air entering the drying chamber.

$\dot{Q}_{H_2O,HA}$ is the heat input rate of the water vapor at the temperature of the hot air entering the drying chamber.

To calculate the mass flow rate of dried detergent powder ($\dot{m}_{BP}$), a mass balance is performed based on the solid content in the detergent slurry ($\dot{m}_{RM(s),SL}$), which is assumed to be equal to the solid content in the dried detergent powder ($\dot{m}_{RM(s),BP}$), as shown in Equation (3). The process includes a sensor that measures the volumetric flow rate of the detergent slurry, along with known values of the slurry's density and the weight fraction of water in the slurry ($x_{mc,SL}$), which is a constant value defined by the process. This allows the mass flow rate of the detergent slurry ($\dot{m}_{SL}$) to be calculated using Equation (4). Meanwhile, the moisture content in the dried detergent powder ($x_{mc,BP}$) is measured by a sensor installed in the actual production process, enabling the calculation of the mass flow rate of dried detergent powder ($\dot{m}_{BP}$) according to Equation (5).

$$\dot{m}_{RM(s),BP} = \dot{m}_{RM(s),SL} \quad (3)$$

$$\dot{m}_{RM(s),SL} = (1 - x_{mc,SL})\dot{m}_{SL} \quad (4)$$

$$\dot{m}_{BP} = \frac{\dot{m}_{RM(s),BP}}{(1 - x_{mc,BP})} \quad (5)$$

2.3 Mathematical Modeling and Model Performance Evaluation

2.3.1 Artificial Neural Network (ANN)

The Artificial Neural Network (ANN) is a machine learning and deep learning technique capable of efficiently processing and analyzing complex data. An ANN consists of small processing units called "neurons," which work together in a layered structure. Generally, an ANN is composed of three main layers: the input layer, the hidden layer(s), and the output layer.

The operation of an ANN begins when data is fed into the input layer and then passed through the hidden layers via connections, each assigned a weight that determines the importance of the input from each neuron. The data is then processed through an activation function, which determines whether a neuron should transmit the signal forward. Common activation functions include Sigmoid, Tanh, and ELU. Once the data passes through all layers, the final result is produced in the output layer [16].

2.3.2 Model Performance Evaluation

The performance of the model is evaluated using the Root Mean Squared Error (RMSE), as defined in Equation (6), and the Coefficient of Determination (R^2), as shown in Equation (7). RMSE measures the deviation between the model's predicted values and the actual values in the dataset. A lower RMSE, approaching zero, indicates higher predictive accuracy. R^2, on the other hand, reflects the degree of linear correlation between the predicted values and the actual values. An R^2 value close to one indicates a strong linear relationship. Relying solely on RMSE for model evaluation may lead to overfitting, where the model performs well on training data but poorly on new, unseen data. Therefore, it is essential to consider R^2 alongside RMSE. Together, these two indicators provide a comprehensive assessment of model performance and support effective identification and correction of modeling issues.

$$RMSE = \sqrt{\frac{1}{n}\sum_{i=1}^{n}(y_i - \hat{y}_i)^2} \quad (6)$$

$$R^2 = 1 - \frac{\sum_{i=1}^{n}(y_i - \hat{y}_i)^2}{\sum_{i=1}^{n}(y_i - \bar{y}_i)^2} \quad (7)$$

2.4 Development and Performance Evaluation of the Virtual Sensor

The development of the virtual sensor in this study consists of three main stages: data preparation, artificial neural network (ANN) modeling, and prediction using a test dataset.

2.4.1 Data Preparation

The data collected from the production process are in the form of continuous data, which often contain a considerable number of outliers. These outliers typically reflect changes in process conditions under specific control settings. Therefore, raw data must undergo a data cleansing process [17], which involves filtering and removing incomplete data segments as well as eliminating outliers that fall outside the acceptable range. This step is essential to improve the consistency of the dataset and minimize the influence of anomalies.

In this study, eight input variables were selected based on their relevance to the energy efficiency of the detergent spray drying process. These include: Temperature of fresh air (T_{amb}), Relative humidity of fresh air (RH_{amb}), Flow rate of natural gas (FR_{NG}), Temperature of hot air (T_{HA}), Temperature of detergent slurry (T_S), Flow rate of detergent slurry (FR_S), Temperature of exhaust air (T_{EA}) and Moisture content of dried detergent (FMC) The output variable for the model is the evaporation efficiency (E_{eff}), which is calculated based on mass and energy balances in the drying process. The dataset used in this research consists of a total of 21,416 data samples, which were divided into three subsets: Training Dataset: 12,520 samples, Validation Dataset: 8,096 samples and Test Dataset: 800 samples

Normalization of data is essential for model development since the variables naturally differ in magnitude and variance, which can affect the learning process of the model [18]. This study employed Z-score normalization, as shown in Equation (8).

$$X_{norm} = \frac{x - \mu(x)}{\delta(x)} \quad (8)$$

Where: X_{norm} is the normalized value of the data, x is the actual data value, $\mu(x)$ is the mean of the data, ann $\delta(x)$ is the standard deviation of the data.

2.4.2 Soft Sensor Creation

The basic structure of the ANN model in this study consists of: 1) the Input layer, which has the same number of neurons as the number of input variables; 2) the Hidden layer, which has a variable number of layers and neurons in each layer, adjustable depending on the complexity of the data; and 3) the Output layer, which has one neuron corresponding to the number of output variables, as shown in Figure 2.

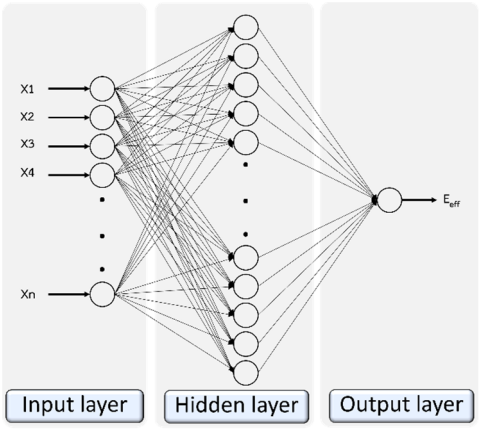

Figure 2 The basic structure of the ANN model.

Defining the appropriate structure and parameters is a crucial step in enhancing the performance of an Artificial Neural Network (ANN). In this study, hyperparameter tuning was performed to find the optimal model structure that yields the best results. The process began with experiments to adjust the number of training epochs and the model structure, initially setting up a single hidden layer and varying the number of neurons in the hidden layer from 1 to 50. Additionally, the effect of adding more hidden layers (Deep Neural Network) was studied to assess the impact of a deeper structure on model performance. The resulting models were evaluated using the test dataset, with performance assessed through the Root Mean Square Error (RMSE) and the Coefficient of Determination (R^2) as metrics. Models that demonstrated adequate performance were required to have an RMSE value of less than 0.5 and an R^2 value greater than 0.9. [19] Furthermore, results from different activation functions—Elu, Tanh, and Sigmoid—were compared to identify the most suitable structure. Although increasing the number of input variables can provide the model with more comprehensive data, including variables that do not have significant relationships with the output may lead to overfitting and increase computational burden. As a result, Shapley Values were used to analyze and select only those variables that significantly impact the evaporation efficiency (E_{eff}). This technique assesses the importance of variables based on their cumulative impact across all possible consideration sequences, averaging the results to rank the importance of each variable. [20]

3. RESULTS AND DISCUSSION

Data from eight input variables were collected throughout the entire process, including the initial phase (when the dryer temperature was raised to the set point before slurry feeding), the steady-state operational phase, and the final phase (the cooldown stage).

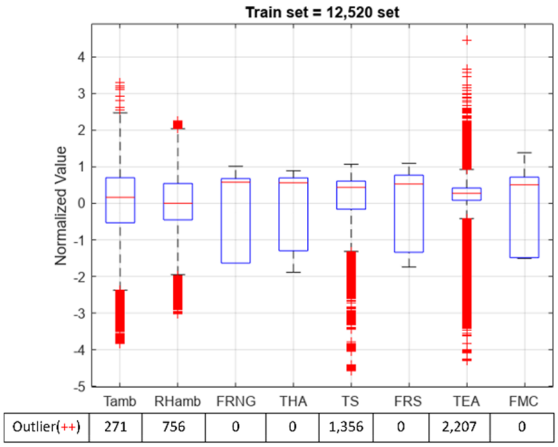

Figure 3 Distribution characteristics of raw data.

The majority of the data falls within the interquartile range (IQR), indicating a relatively narrow distribution as shown in Figure 3, which corresponds to the steady-state phase of the spray drying operation and reflects overall process stability. However, several variables, including ambient air temperature (T_{amb}), ambient air humidity (RH_{amb}), slurry temperature (T_S), and exhaust air temperature (T_{EA}), exhibit a substantial number of outliers, with 271, 756, 1356, and 2207 data points, respectively.

The presence of outliers in T_{amb} and RH_{amb} can be attributed to fluctuations in ambient conditions throughout the day and across different seasons. The high variability observed in T_S is primarily due to the limited capacity of the slurry tank, which necessitates frequent refilling from a storage tank during the drying process. This intermittent refilling disrupts thermal equilibrium, resulting in fluctuations in slurry temperature. The variability in T_{EA} can be attributed to inconsistencies in the slurry feed rate, primarily caused by partial nozzle blockages, which disrupt the uniformity of heat and mass transfer during the drying process.

The analysis of the Violin Plot of Shapley values reveals that T_{HA} (hot air temperature) and FR_S (liquid detergent feed rate) exhibit a broad distribution of values, highlighting their strong explanatory influence on variations in water evaporation efficiency (E_{eff}). When FR_S is low, the mass flow rate of dry detergent produced decreases, while the thermal energy input via hot air remains constant. This results in a higher E_{eff}, as the same amount of energy is used to evaporate water from a smaller quantity of material. Conversely, an increase in T_{HA} raises the thermal energy input while FR_S remains unchanged, also leading to an increase in E_{eff}. In this scenario, more energy is supplied to process the same quantity of material, thereby enhancing the efficiency of water evaporation. In both cases, the elevated E_{eff} values reflect inefficient energy utilization, where thermal energy input exceeds the amount required for optimal output. This phenomenon is captured by the consistently positive Shapley values observed for T_{HA} and FR_S in Figure 4, indicating their significant contribution to the model's prediction of E_{eff}.

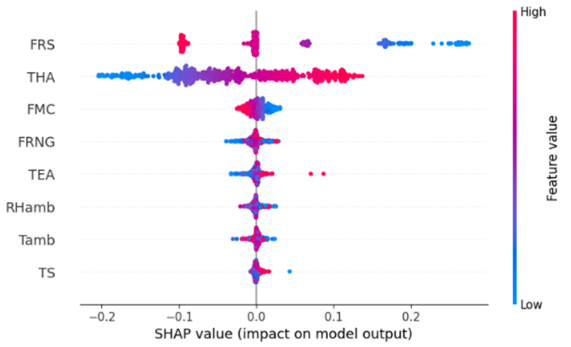

Figure 4 The effect of variables on model prediction using Shapley values method.

The remaining variables can be ranked according to their mean Shapley values as follows: T_{HA} (0.083), FR_S (0.081), FMC (0.007), FR_{NG} (0.005), T_{amb} (0.005), RH_{amb} (0.005), T_{EA} (0.004), and T_S (0.004). A higher Shapley value indicates greater importance in influencing evaporation efficiency.

The natural gas consumption rate (FR_{NG}), ambient air temperature (T_{amb}), and ambient air humidity (RH_{amb}) have an equal Shapley value of 0.005, indicating a similar level of influence on the prediction. Moreover, these variables are interrelated: when T_{amb} increases, less natural gas is required to heat the fresh air to meet the setpoint temperature. In contrast, higher RH_{amb} raises the energy demand [21]. Therefore, FR_{NG} was chosen as a representative of these three variables as it exhibited no outliers. Meanwhile, the temperature of the slurry (T_S) and the exhaust air temperature (T_{EA}) exhibited highly fluctuating values, with the lowest Shapley value at 0.004, leading to their exclusion.

Therefore, the number of input variables was reduced from 8 to 4 variables (T_{HA}, FR_S, FMC, and FR_{NG}), which is expected to improve the model's prediction performance and reduce its complexity. However, the exhaust air was recycled to preheat the fresh air in the heat exchange before being fed to the furnace, and this variable may affect energy efficiency. Consequently, T_{EA} was included as a fifth input variable in the model, as shown in Table 1.

Table 1 Selection of input variables for model development.

Group	Variable	Input Structure		
		8	5	4
Input	1. T_{amb}	✓	×	×
	2. RH_{amb}	✓	×	×
	3. FR_{NG}	✓	✓	✓
	4. T_{HA}	✓	✓	✓
	5. T_S	✓	×	×
	6. FR_S	✓	✓	✓
	7.T_{EA}	✓	✓	×
	8. FMC	✓	✓	✓
Output	9. E_{eff}	✓	✓	✓

In the development of a soft sensor using Artificial Neural Networks (ANN), determining the model's structure and parameters accurately is a crucial factor that directly impacts the model's accuracy and performance.

Hyperparameter tuning was performed to find a suitable structure through multi-dimensional experiments. The ADAM optimizer was selected for its ability to combine the advantages of Momentum and RMSProp. Momentum accelerates convergence by using the moving average of gradients to smooth parameter updates, while RMSProp improves stability by adapting the learning rate based on the variance of past gradients.

The learning rate (Lr) is a critical parameter in training artificial neural network (ANN) models as it controls the size of parameter updates (weights) in each training epoch. Selecting an appropriate learning rate has a direct impact on the model's learning performance. An appropriate learning rate allows the model to learn quickly and stably. On the other hand, if the learning rate is too high, it may cause overshooting, where the model updates parameters too drastically, preventing it from converging to the optimal solution. A too-low learning rate may cause the model to become stuck in a local minimum, rather than reaching the global minimum, thereby hindering the model's performance. In this study, the initial learning rate was set to 0.2, which is relatively high compared to the standard default values used in artificial intelligence applications (e.g., 0.001). This higher value was intended to allow the model to learn quickly in the early stages. The study also applied a learning rate scheduling technique called step decay, which reduces the learning rate at specific intervals, ensuring more precise weight updates as training progresses. Specifically, after 100 epochs, the learning rate was decreased to 0.025 and kept constant until the training process finished at 300 epochs, as shown in Figure 5.

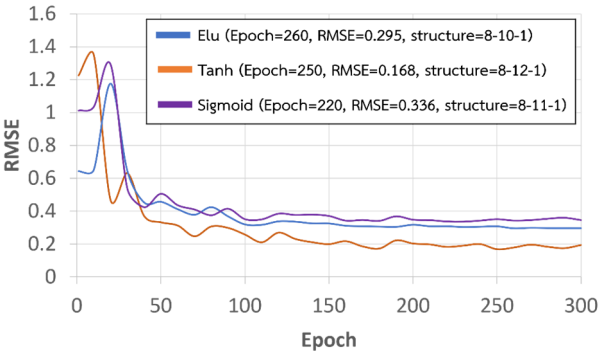

Figure 5 Comparison of the number of epochs in an ANN with different activation functions.

The number of training epochs was initially set to 300 for the models with different activation functions: Exponential Linear Unit (Elu), Hyperbolic Tangent (Tanh), and Sigmoid to learn the characteristics of the entire process (including the start-up, steady-state operation, and the end of the process). The resulting RMSE values from testing the model with different activation functions were 0.295, 0.168, and 0.336, respectively, with epoch values of 260, 250, and 220, as shown in Figure 5. Therefore, 300 epochs were sufficient to achieve adequate learning and model accuracy.

Therefore, those hyperparameters were selected to conduct experiments in three scenarios: using 8, 5, and 4 input variables. Each scenario was tested with three activation functions: Elu, Tanh, and Sigmoid. Additionally, the models were evaluated using RMSE and R^2 as shown in Table 2.

For the model with 8 input variables, the optimal structures were identified as 8-41-1 for ELU, 8-43-1 for Tanh, and 8-28-1 for Sigmoid activation functions, yielding RMSE values of 0.0537, 0.0534, and 0.0544, respectively, and corresponding R^2 values of 0.9945, 0.9945, and 0.9943.

For the model with 5 input variables, the optimal structures were identified as 5-35-1 for ELU, 5-38-1 for Tanh, and 5-20-1 for Sigmoid activation functions, yielding RMSE values of 0.0861, 0.0539, and 0.0569, respectively, and corresponding R^2 values of 0.9858, 0.9942, and 0.9938.

For the model with 4 input variables, the optimal structures were identified as 4-12-1 for ELU, 4-34-1 for Tanh, and 4-30-1 for Sigmoid activation functions, yielding RMSE values of 0.0710, 0.0403, and 0.0699, respectively, and corresponding R^2 values of 0.9903, 0.9969, and 0.9906.

From those results, the ANN model using the Tanh activation function with the 4-34-1 structure, which consists of 4 input variables, yielded the lowest RMSE of 0.0403 and the highest R^2 of 0.9969 compared to the Elu and Sigmoid activation functions, under the optimal number of input variables and model structure for each case.

Furthermore, those models with different input variables (8, 5, and 4 input variables) and different activation functions (Elu, Tanh, and Sigmoid) were tested with unseen data as shown in Figure 6.

For the model using 8 input variables (Figure 6a), the model using the Tanh activation function provided the highest accuracy (RMSE = 0.0534, R^2 = 0.9945). While, the ELU activation function demonstrated good trend-tracking capability but showed signs of overfitting in specific data ranges. In contrast, the Sigmoid function produced values close to the target but failed to capture the overall trend, indicating underfitting accurately.

For the model using 5 input variables (Figure 6b), the model with the Tanh function still showed the best performance (RMSE = 0.0537, R^2 = 0.9945), maintaining its ability to track the target data trend with high accuracy, even as the number of input variables decreased.

For the model using only 4 input variables (Figure 6c), the model using the Tanh function again showed the best results (RMSE = 0.0403, R^2 = 0.9969), demonstrating the most accurate predictions and best trend tracking, reflecting the potential of the Tanh activation function to enhance the learning and processing capability of the ANN model, even with fewer input variables.

Table 2 Results of the ANN model design experiments for predicting water evaporation efficiency

Model	Feed Forward Neural Network (FFNN)			Performance model					
	Transfer Function	Structure (input-hidden-output)	Time (sec)	Train		Validation		Test	
				RMSE	R^2	RMSE	R^2	RMSE	R^2
1	Elu-Purelin	8-41-1	28.71	0.0924	0.9930	0.0541	0.9982	0.0537	0.9945
2	Tanh-Purelin	8-43-1	24.48	0.092	0.9931	0.0484	0.9986	0.0534	0.9945
3	Sigmoid-Purelin	8-28-1	23.06	0.1062	0.9908	0.0549	0.9981	0.0544	0.9943
4	Elu-Purelin	5-35-1	26.01	0.1070	0.9906	0.0701	0.9970	0.0861	0.9858
5	Tanh-Purelin	5-38-1	21.86	0.0933	0.9929	0.0538	0.9982	0.0539	0.9942
6	Sigmoid-Purelin	5-20-1	23.09	0.1022	0.9915	0.0608	0.9977	0.0569	0.9938
7	Elu-Purelin	4-12-1	25.98	0.1108	0.9900	0.0672	0.9972	0.0710	0.9903
8	Tanh-Purelin	4-34-1	22.66	0.0813	0.9946	0.0501	0.9985	0.0403	0.9969
9	Sigmoid-Purelin	4-30-1	22.07	0.1089	0.9903	0.0708	0.9969	0.0699	0.9906

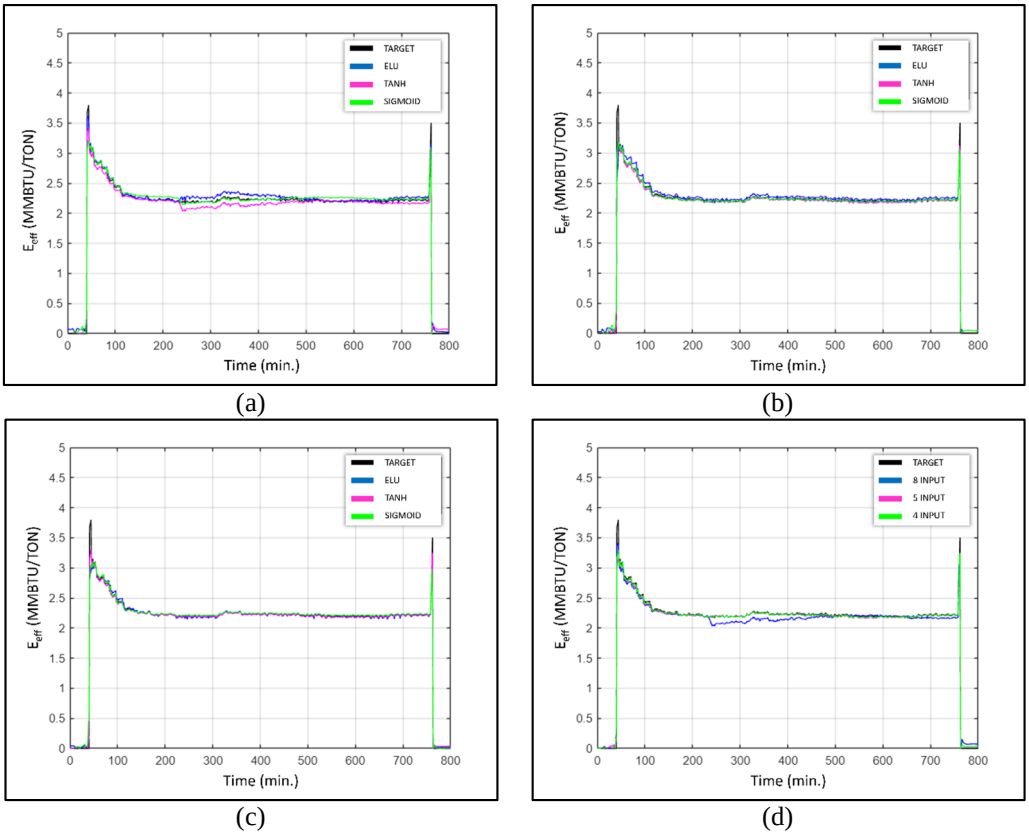

Figure 6 Results of the water evaporation efficiency prediction experiments: Prediction with an ANN model having (a) 8 input variables, (b) 5 input variables, (c) 4 input variables with different activation functions, and (d) Comparison of ANN models using the "Tanh" activation function with different input variables.

Furthermore, the effect of the number of input variables using the same activation function (Tanh) is illustrated in Figure 6d. The model with four input variables demonstrated the best performance, achieving lower RMSE and higher R^2 values. It also effectively captured the overall trend, particularly during periods of rapid data variation, where the model remained responsive and aligned closely with the actual values.

The results indicate that the Tanh activation function effectively captures the nonlinear relationships among variables in the drying process. This performance is attributed to the use of Z-score normalization, which scales the input data to approximately the range of −1 to 1, closely matching the output range of the Tanh function. This alignment ensures a balanced data distribution, enabling the model to efficiently handle variations in both positive and negative directions, which is characteristic of the detergent powder drying process. Although the RMSE and R^2 values from the ELU function were comparable to those of Tanh, ELU's focus on positive outputs can lead to slower and less stable learning during significant positive changes. In contrast, the Sigmoid function

suffers from the vanishing gradient problem and limited output range, making it less suitable for capturing complex patterns.

Thus, selecting only the input variables that have a significant influence on water evaporation efficiency (E_{eff}) enables a reduction in the number of inputs without compromising accuracy. This, in turn, decreases computational time and minimizes the need for multiple sensors in real-world applications.

Notably, the model developed in this research, characterized by lower complexity and fewer input variables, proved suitable for processes involving large datasets (e.g., 12,500 training data points). However, when the training dataset is limited (e.g., 2,000 data points), a more complex model with additional input variables is required. In such cases, a Transfer Learning-based Long Short-Term Memory (TL-LSTM) model using seven input variables, including hot air temperature, natural gas consumption rate, liquid detergent temperature, liquid detergent feed rate, exhaust air temperature, internal pressure in the drying tower, and moisture content of dry detergent, demonstrated effective performance despite the smaller dataset [14].

4. CONCLUSION

This research presents an approach for developing a soft sensor using Artificial Neural Networks (ANNs) to predict evaporation efficiency in the energy-intensive spray drying process of detergent. Eight process variables, including ambient air temperature (T_{amb}), ambient air humidity (RH_{amb}), natural gas consumption rate (FR_{NG}), hot air temperature (T_{HA}), liquid detergent temperature (T_S), liquid detergent feed rate (FR_S), exhaust air temperature (TEA), and dry detergent moisture content (FMC) were considered as influential factors affecting the evaporation efficiency in the drying process. The prediction of evaporation efficiency using four input variables (T_{HA}, FR_S, FMC, and FR_{NG}), identified through Shapley value analysis and validated using a box plot along with the Tanh activation function, resulted in improved model performance. The optimized model achieved a lower Root Mean Squared Error (RMSE) of 0.0403 and a higher Coefficient of Determination (R^2) of 0.9969, compared to the model using all eight input variables, which yielded an RMSE of 0.0534 and an R^2 of 0.9945.

ACKNOWLEDGMENTS

This work was financially supported by the Faculty of Engineering, Burapha University. We also would like to express our sincere gratitude to Assoc. Prof. Dr. Chanin Panjapornpon for his valuable suggestions and insightful discussions.

REFERENCES

[1] A.K. Patil. A review: Spray dryer design and control system. *Journal of Pharmaceutical Negative Results* 2022; 13(S02): 321.

[2] S. Tonkhum, P. Ngaotrakanwiwat. The recovery of linear alkylbenzene sulfonic acid from the waste sulfonation process. *The Journal of KMUTNB* 2024; 34(1): 1–16.

[3] M. Aghbashlo, H. Mobli, S. Rafiee, A. Madadlou. The use of artificial neural network to predict exergetic performance of spray drying process: A preliminary study. *Computers and Electronics in Agriculture* 2012; 88: 32–43.

[4] Z.L. Liu, D. Sun, S. Wu, J. Sun, W. Yang, Z. Wang. Prediction of energy and exergy of mushroom slices drying in hot air impingement dryer by artificial neural network. *Drying Technology* 2019; 37(12): 1561-1573.

[5] U. Baysan, A.I. Harun, M. Koç. Evaluation of innovative drying approaches in celery drying considering product quality and drying energy efficiency. *Innovative Food Science and Emerging Technologies* 2024; 88: 103636.

[6] H.K. Mohanta, A.K. Pani. Adaptive non-linear soft sensor for quality monitoring in refineries using Just-in-Time Learning-Generalized regression neural network approach. *Applied Soft Computing* 2022; 119: 108546.

[7] Y.A. Shardt, K. Brooks, X. Yang, S. Kim. Advanced soft-sensor systems for process monitoring, control, optimisation, and fault diagnosis. *IFAC PapersOnLine* 2023; 56(2): 11768–11777.

[8] M.O. Roseberry, F. Gagnon, A. Desbiens, J. Bouchard, P.P. Lapointe-Garant. Monitoring the moisture content in pharmaceutical batch fluidized bed dryers using observer-based soft sensors. *IFAC PapersOnLine* 2020; 53(2): 12056–12061.

[9] M. Gyürkés, B. Nagy, Z.K. Nagy, L. Szabó, G. Marosi. Soft sensor for content prediction in an integrated continuous pharmaceutical formulation line based on the residence time distribution of unit operations. *International Journal of Pharmaceutics* 2022; 624: 121950.

[10] X. Wang, K. Kvaal, H. Ratnaweera. Explicit and interpretable nonlinear soft sensor models for influent surveillance at a full-scale wastewater treatment plant. *Journal of Process Control* 2019; 77: 1–6.

[11] S. Taheri, G. Brodie, D. Gupta. Optimised ANN and SVR models for online prediction of moisture content and temperature of lentil seeds in a microwave fluidised bed dryer. *Computers and Electronics in Agriculture* 2021; 182: 106003.

[12] B. Demirbay, D.B. Kara, Ş. Uğur. Multivariate regression (MVR) and different artificial neural network (ANN) models developed for optical transparency of conductive polymer nanocomposite films. *Expert Systems with Applications* 2022; 207: 117937.

[13] L. Chen, C. Chen, J. Yu, S. Jin. Study on the heat and mass transfer characteristics of spray separation tower at low temperature and normal pressure. *International Journal of Heat and Mass Transfer* 2020; 153: 119662.

[14] S. Bardeeniz, C. Panjapornpon, C. Fongsamut, P. Ngaotrakanwiwat, M.A. Hussain. Digital twin-aided transfer learning for energy efficiency optimization of thermal spray dryers: Leveraging shared drying characteristics across chemicals with limited data. *Applied Thermal Engineering* 2024; 242: 122431.
[15] C. Panjapornpon, S. Bardeeniz, M.A. Hussain. Deep learning approach for energy efficiency prediction with signal monitoring reliability for a vinyl chloride monomer process. *Reliability Engineering and System Safety* 2023; 231: 109008.
[16] B.P. Adedeji, G. Kabir. A feedforward deep neural network for predicting the state-of-charge of lithium-ion battery in electric vehicles. *Decision Analytics Journal* 2023; 6: 100255.
[17] F. Ridzuan, W.M.N.W. Zainon. A review on data cleansing methods for big data. *Procedia Computer Science* 2019; 161: 731–738.
[18] A. Meola, M. Winkler, S. Weinrich. Metaheuristic optimization of data preparation and machine learning hyperparameters for prediction of dynamic methane production. *Bioresource Technology* 2023; 372: 128604.
[19] S. Francik, B. Łapczyńska-Kordon, M. Hajos, G. Basista, A. Zawiślak, R. Francik. Modeling the drying process of onion slices using artificial neural networks. *Energies* 2024; 17(13): 3199.
[20] S. Sebastián, C.E. González-Guillén. A feature selection method based on Shapley values robust for concept shift in regression. *Neural Computing and Applications* 2024; 36(23): 14575–14597.
[21] P.S. Bisht, B. Gopalakrishnan, R. Dahal, H. Li, Z. Liu. Parametric energy efficiency impact analysis for industrial process heating furnaces using the manufacturing energy assessment software for utility reduction. *Processes* 2024; 12(4): 737.

Effect of ethanol on the crystallization of DL-methionine polymorphs

Lamphoun Inthavideth[1], Lek Wantha[1,*]

[1] School of Chemical Engineering, Institute of Engineering, Suranaree University of Technology, Nakhon Ratchasima 30000, Thailand
[*] Corresponding author: lekwa@g.sut.ac.th

ABSTRACT

DL-methionine (DL-met) plays a crucial role in maintaining health and is utilized in various fields such as pharmaceuticals, dietary supplements, animal feed, and chemical synthesis. When crystallized, DL-methionine can exist in three forms: α-, β- and γ-form. In this study, an antisolvent crystallization process was conducted to induce nucleation, with a focus on obtaining the pure α-form crystals in order to estimate its nucleation rate. Raman spectroscopy and microscopy were employed to identify the crystal polymorph. Additionally, the nucleation rate of the α-form was assessed using Focus Beam Reflectance Measurement (FBRM). Nucleation rate (J) of the α-form was increasing with increasing the volume fraction of ethanol (x). Furthermore, the transformation of polymorph α- into β-form was also carried out by an offline-Raman spectroscopy. Therefore, this work illustrated the nucleation and transformation stage of DL-met polymorph in the antisolvent crystallization, and the nucleation rate of pure α-form was included.

Keywords: Nucleation; Transformation; Antisolvent; Polymorph

1. INTRODUCTION

Polymorphism refers to a solid compound's capability to form crystals in multiple crystalline forms. Various polymorphs exhibit distinct shapes and possess different characteristics like solubility, dissolution rate, and density [1]. The antisolvent crystallization is effective, time-independent, and readily adjustable. Significantly, altering the initial supersaturation ratio and the fraction of antisolvent can notably change the nucleation rate. Supersaturation arises from the introduction of antisolvent into the mother solution, resulting in a reduction of the solute's equilibrium solubility in the solution and leading to create the level of supersaturation that produces the crystallization [2-5].

DL-methionine (DL-met) is crucial amino acid in the case of health maintenance and is used widely in edible supplements and pharmaceutical industries, especially, their solid-state properties and structures have been thoroughly inspected under a variety of conditions. DL-met crystallizes from saturated aqueous solutions, normally that both α- and β-polymorphs nucleate concomitantly and occur together in aqueous solutions during harvest. This happens during most of the crystallization experiments where the physical separation of these two forms is found always difficult and challenging.

Previously, Suresh et al. [4, 6-8] studied the concomitant α- and β-polymorphs of DL-met in the nucleation in the water-ethanol solution which was reported that a pure α-polymorph obtained at ethanol fraction higher than 0.10 and also investigated the crystal structure of both forms in a cooling crystallization and with the effect of additive, which were success obtained the crystal shape and packing for α- and β-polymorphs. Matsuoka et al. [9] reported DL-met polymorphic transformation in aqueous solution that resulted α-form was transformed into γ-form in the step of solution-mediated transformation while γ-form transformed back to α-form in the solid-state transformation. Wantha et al. [5] investigated the influence of solvent in the solution-mediated transformation of L-histidine polymorphs which reported that water-acetonitrile solution was shortest the transformation compared to methanol and acetone. The lower antisolvent volume fraction was given higher the transformation of metastable into stable form. Moreover, Wang et al. [10] studied the selective crystallization of racemic polymorph via native enantiomer inhibition in DL-met crystallization which resulted a unique chiral self-positioning mechanism, affording selective crystallization of only one polymorph of DL-met.

Therefore, this work studies the effect of ethanol in the nucleation, and transformation of DL-met polymorphs in an antisolvent crystallization.

2. EXPERIMENTAL

Antisolvent crystallization of DL-met was carried out to investigate the nucleation of its polymorphs and to examine how the transformation between the two

forms was influenced by different ethanol volume fractions.

2.1 Materials

Pure powder of DL-met (> 99 %, ACROS Organics), ethanol (> 99 %, DUKSAN Reagent), and deionized water for the experiments were used without further purification.

DL-met could be crystallized into three polymorphs of crystals, however, we interested for two forms: α- and β-form, thus, the preparation of pure polymorph was carried out in the study. A pure α-form was produced by antisolvent crystallization at 25 °C and 250 rpm, with a volume ratio of ethanol to water of 9:1 [2, 5, 11]. The crystals of pure α-form were collected at the initial stage of the crystallization in a batch crystallizer within a minute count. All crystals were characterized by microscopy, and Raman spectroscopy. A pure β-form was prepared in cooling crystallization at 60 °C to 10 °C [12] with mixing speed of 250 rpm and hold for 24 h. After that, the suspension was filtered, and dried, then confirmed by microscopy and Raman spectroscopy.

2.2 Nucleation of Polymorph

A saturated solution of amino acid crystals was prepared at the desired temperature of 35 °C and stirred speed of 250 rpm in a batch crystallizer for an hour, then the antisolvent i.e., ethanol was added into the mother solution to observed the nucleation of DL-met polymorph. FBRM was used observed the nucleation and induction time of crystals [13]. The volume fraction of the antisolvent, x, in each of the solutions corresponding to the known volume of water is calculated as Eq. (1):

$$x = \frac{V_A}{V_A + V_W + V_M} \qquad Eq.(1)$$

where V_A is the volume of the antisolvent, V_W is the volume of the solvent water, V_M is the volume of the solute.

The number of crystals detected by the FBRM can be transformed to the total number of crystals in the solution, based on the correlation equation defined in [13, 14]. Therefore, the number by FBRM converted to the total number of crystals is found as Eq. (2):

$$N_{actual} = f_x N_{FBRM} \qquad Eq.(2)$$

where N_{actual} is the actual number of particles present in the solution, N_{FBRM} is the number of particles detected by the FBRM and f_x is a conversion fraction. The interested form was α-form, which in a monoclinic crystal ($P2_1/c$) [6, 9, 15], as similar as a monoclinic ($P2_1$) B-form L-histidine in [3, 16-18], thus, f_x was used according to the literature [13] reported with the value of 2.0886×10^7 #/m^3.

Therefore, the nucleation rate (J) is calculated as Eq. (3):

$$J = \frac{dN}{dt} V^{-1} \qquad Eq.(3)$$

where N is the number of crystals in the solution (the actual present), t is the time of crystals in the solution. V is the volume of solution.

2.3 Transformation of polymorph

DL-met crystals were introduced into saturated solutions under isothermal conditions for the operation in the antisolvent crystallization. The transformation of DL-met was monitored by measuring the fraction of the one-form in the crystals (by offline-Raman spectroscopy). During the experiment, a small volume of suspension was taken with a syringe, filtration, and dry in silica gel. The DL-met crystals were then identified polymorph via Raman spectroscopy.

The curve of α-DL-met polymorph fraction was estimated. The characteristic peaks of two forms were selected to reference via Raman spectroscopy [5, 19]. The fraction of α-form to β-form (x_a) was calculated from the intensity of the characteristic peaks of Raman spectra of form α-form (I_a) and β-form (I_b) as Eq. (4):

$$x_a = \frac{I_a}{I_a + I_b} \qquad Eq.(4)$$

3. RESULTS AND DISCUSSION

The results and discussion present the influence of ethanol on the crystallization of DL-met polymorphs, which relate to the step of nucleation and transformation.

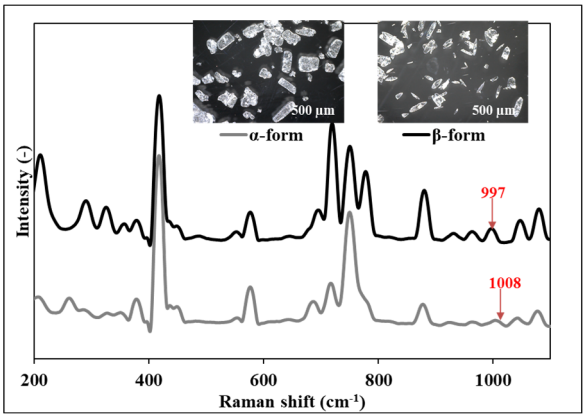

Figure 1 Raman spectra of DL-met polymorphs.

3.1 Nucleation of polymorph

Nucleation of DL-met polymorph(s) in the antisolvent crystallization is presented by Raman and microscope results as shown in Figures 2 and 3, respectively. The characteristics peak of α- and β-form were reported from previous works [6, 10], α-form is Raman wavelength of 1008 and 1040 cm^{-1}, while β-form 997 and 1048 cm^{-1}. Figure 1 shows the pure polymorph α- and β-form, thus, both forms observed the peak of 1008 and 997 cm^{-1} for α- and β-form, respectively. Moreover, the microphotograph of two forms were also detected. The results showed α-form

was a bit wider in width while β-form was a bit smaller in width. Thus, we could say α-form looked a plate-like crystal, and β-form seemed a rod-like crystal [7, 9].

Figure 2 is reported the Raman spectra of the samples collecting from the product of the nucleation in each ethanol fraction varying for 6 fractions (0.11-0.60). the initial obtained crystals from antisolvent was the pure α-form for all fraction (where DL-met normally nucleated concomitant polymorphs in an aqueous solution), which this is agreement with literature said at ethanol higher than 0.10 produced a pure form of α-Dl-met [4]. Microphotographs of nucleated DL-met were also supported the Raman results that it looked like α-form crystal-shape for almost fractions (Figure 3). Additionally, the smaller particle size of crystals was obtained with increasing the amount of ethanol, this occurred due to higher driving force at higher ethanol fraction. However, we notice the mixture of two forms at ethanol of 0.23 fraction, this might cause by the formation of molecules in the H-bonding interaction which occurred the reversible of molecules (form) [20, 21]. Another possible may be said that the sensitive of DL-met nucleation shall be very careful in the process at this ethanol fraction.

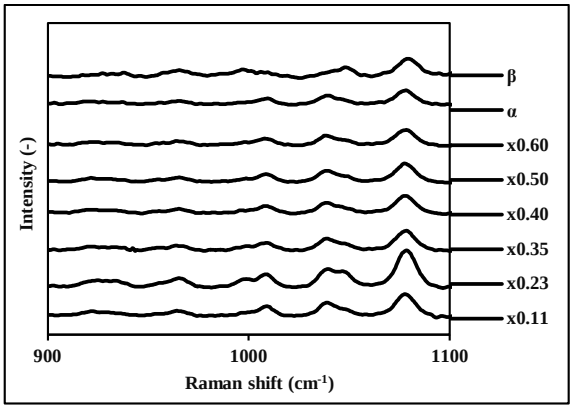

Figure 2 Raman spectra of DL-met crystals obtained from various ethanol fraction (x).

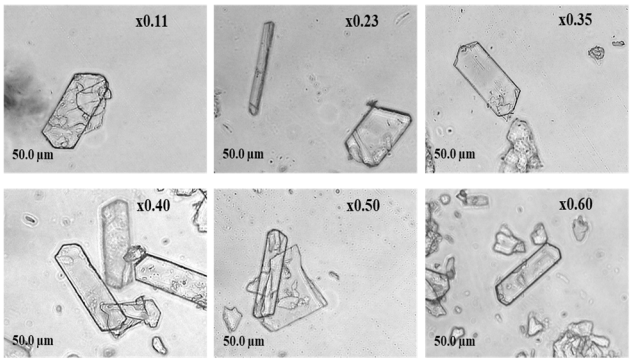

Figure 3 Microphotograph of DL-met polymorphs obtained from various fraction of ethanol.

The number density of DL-met nucleated in real solution was correlated from the FBRM count total number function for each ethanol fraction as results shown in Figure 4 and the repeated three experiments (Figure 5). Nucleation rate of pure α-form was further calculated. From Raman and microphotograph results, number at ethanol of 0.23 fraction was not considered due to its mixture. Nucleation rates of α-form along with its induction time at various ethanol fraction are shown in Figure 6. Results show that the nucleation rate was increased with ethanol amount, but the induction time was opposite. This because the higher ethanol gives higher in the driving force to crystal nucleate then faster of nucleation occurred. It agrees with above explain that a smaller size of crystal obtained with higher ethanol addition because of the rate of nucleated was enhanced.

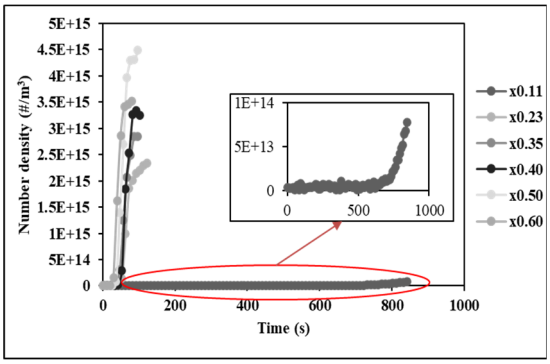

Figure 4 Number density of DL-met crystals nucleated in the solution over time in different ethanol fraction.

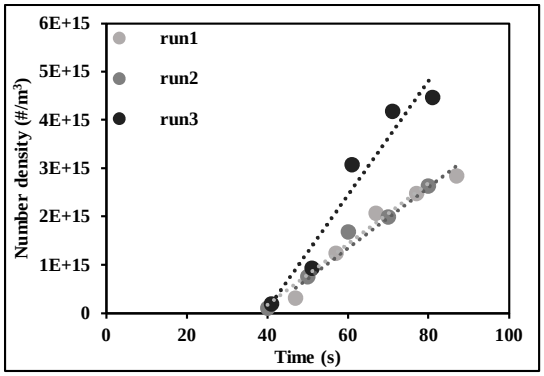

Figure 5 Number density of DL-met crystals nucleated in the solution over time at ethanol of 0.40 fraction in three runs.

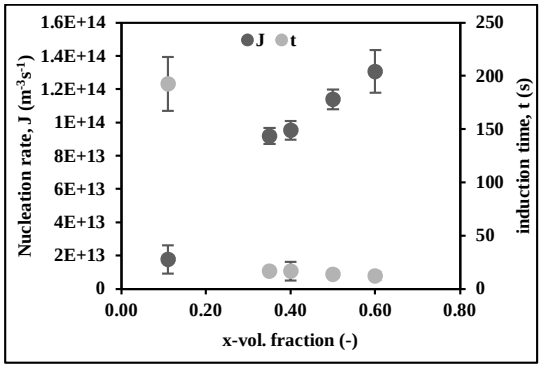

Figure 6 Nucleation rate and induction time of α-form DL-met as function of ethanol fraction.

3.2 Transformation of polymorph

Effect of ethanol in the transformation of DL-met from α-form (metastable) into β-form (stable) in the solution was carried out. Raman spectroscopy was utilized to quantify the polymorphic fraction during crystallization using an offline approach. The characteristics peak of two forms is selected (see Figure 1), and approximately calculation for α-form fraction between the height of two peas as equation describe (see Eq. (4)). Figure 7 shows Raman spectra of DL-met under two days of the crystallization for three different ethanol fractions, from 0.11, 0.23, 0.35 are shown in Figure 7a), 7b), 7c), respectively.

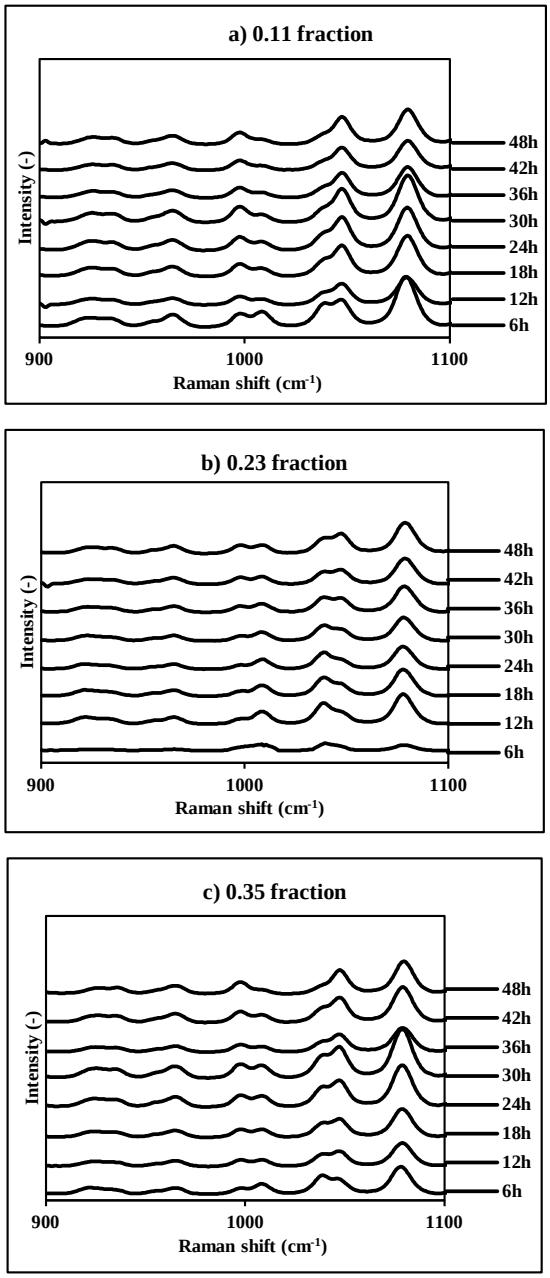

Figure 7 Raman spectra of DL-met crystals as function of time in ethanol fraction of a) 0.11, b) 0.23 and c) 0.35.

For low ethanol fraction was given faster transformed than the other two higher fractions (Figure 8). There is an explain that the transformation is depended on the fraction of stable form initial nucleate [5]. However, we supposed to start with α-form for the nucleation stage, except for ethanol of 0.23 fraction. Nevertheless, these results may due to nucleation rate, high nucleation would require more times to transform. This is based on the preparation of DL-met pure β-form was obtained in 48 h crystallization [8, 12, 22]. Moreover, for 0.23 ethanol fraction, it still displayed the unstable in α-form fraction which means its sensitive behavior in the solution crystallization was remained (not only in nucleation but also in transformation stage). Therefore, we can conclude that ethanol slows the transformation of DL-met polymorphs in the solution crystallization.

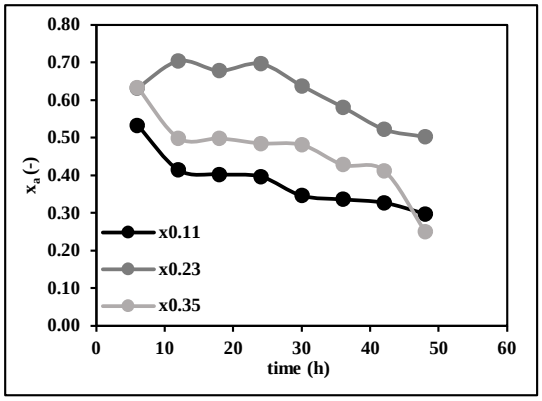

Figure 8 The α-form fraction (x_a) in the binary polymorphs as function of time with various ethanol fraction (x).

4. CONCLUSION

Effect of ethanol on the crystallization of DL-met polymorphs for the nucleation and transformation stages was reported in this work. The addition of ethanol enhanced the purity of α-DL-met polymorph and also significantly increased its nucleation rate with increasing ethanol fraction (0.11-0.60). However, the mixture of polymorphs was displayed at ethanol of 0.23 fraction, which could be concluded as its critical careful for crystallization process for this work. The transformation of DL-met polymorphs was also influence by ethanol, in which higher ethanol amount, it was lower the transformation, result the α-form fraction slowly decreased.

ACKNOWLEDGMENTS

This research was financially supported by Suranaree University of Technology (SUT) scholarship for SUT Graduate International Students. Authors would be very thankful to our Bachelor senior students at the School of Chemical Engineering to partly assisted doing some experiments. The authors also acknowledge the research funding from (i) Suranaree University of Technology (SUT), (ii) Thailand Science Research and

Innovation (TSRI), and (iii) National Science, Research and Innovation fund (NSRF)-Grant No. 195675 and 204174.

REFERENCES

1. Al Rahal, O., et al., Polymorphism of l-Tryptophan. Angew Chem Int Ed Engl, 2019. **58**(52): p. 18788-18792.
2. Punmalee, N., L. Wantha, and A.E. Flood, Antisolvent Crystallization of Polymorphs of L-Histidine. Chemical Engineering & Technology, 2018. **41**(6): p. 1132-1138.
3. Mark Roelands, C.P., et al., Antisolvent Crystallization of the Polymorphs of L-Histidine as a Function of Supersaturation Ratio and of Solvent Composition. Journal of Crystal Growth & Design, 2005. **Vol. 6 No. 4**: p. 955-963.
4. Suresh, M. and K. Srinivasan, Concomitant Polymorphism and Nucleation Control of DL-Methionine Through Antisolvent Crystallization. Chemical Engineering & Technology, 2021. **44**(4): p. 614-621.
5. Wantha, L., N. Punmalee, and A.E. Flood, Influence of Solvents on Solution-Mediated Polymorphic Transformation of the Polymorphs of L-Histidine. Chemical Engineering & Technology, 2019. **42**(7): p. 1505-1511.
6. Suresh, M. and K. Srinivasan, Crystal structure and Hirshfeld surface analysis of dl-methionine polymorphs (α and β). Journal of Molecular Structure, 2022. **1250**.
7. Manivel, S. and S. Karuppannan, Crystallization ofdl-methionine polymorphs in the presence of structurally compatible additives. Molecular Crystals and Liquid Crystals, 2022. **745**(1): p. 68-83.
8. Suresh, M. and K. Srinivasan, Polymorphic Control of α and β dl-Methionine through Swift Cooling Crystallization Process. Crystal Research and Technology, 2021. **56**(5).
9. Matsuoka, M., et al., Polymorphism, morphologies and bulk densities of DL-methionine agglomerate crystals. Journal of Crystal Growth, 1999. **198/199**: p. 1299-1306.
10. Wang, Y., et al., Selective Crystallization of Racemic Polymorph via Native Enantiomer Inhibition: dl-Methionine. Crystal Growth & Design, 2023. **23**(3): p. 1370-1377.
11. KITAMURA, M., Crystallization behavior and transformation kinetics of L-histidine polymorphs. Journal of Chemical Engineering of Japan, 1993. **26(3)**.
12. Shi, G., et al., Distinct pathways of solid-to-solid phase transitions induced by defects: the case of dl-me-thio-nine. IUCrJ, 2021. **8**(Pt 4): p. 584-594.
13. Kongsamai, P., et al., In-situ measurement of the primary nucleation rate of the metastable polymorph B of L-histidine in antisolvent crystallization. Journal of Crystal Growth, 2019. **525**.
14. Maosoongnern, S. and A.E. Flood, Validation of Models Predicting Nucleation Rates from Induction Times and Metastable Zone Widths. Chemical Engineering & Technology, 2018. **41**(10): p. 2066-2076.
15. McL Mathieson, A., The crystal structures of the dimorphs of DL-methionine. Acta Crystallographica, 1952. **5**(3): p. 332-341.
16. MADDI:N, J.J., et al., The Crystal Structure of the Monodinie Form of L-Histidine. Acta Cryst., 1972. **B28**.
17. Park, S. and W.-S. Kim, Influence of Fluid Motions on Polymorphic Crystallization of l-Histidine: Taylor Vortex Flow and Turbulent Eddy Flow. Crystal Growth & Design, 2018. **18**(2): p. 710-722.
18. Shibata, F., M. Yokota, and N. Doki, Thermodynamic characteristics of L-histidine polymorphs and effect of ethanol on the crystallization. Journal of Crystal Growth, 2021. **564**.
19. Maiko, Y., T. Hiroshi, and M. Masakuni, Polymorphic transformation of dl-methionine crystals in aqueous solutions. Journal of Crystal Growth, 2002. **237-239**: p. 2221-2226.
20. Zborowski, K.K., H. Szatyłowicz, and T.M. Krygowski, Solvent influence on intramolecular interactions and aromaticity in meta and para nitroanilines. Structural Chemistry, 2020. **31**(5): p. 1717-1728.
21. Feskov, S.V., et al., Symmetry-breaking charge transfer in an excited acridine-dione derivative: Effects of hydrogen bonding, clustering, and cooperativity in mixtures of methanol and dimethylformamide. Journal of Molecular Liquids, 2023. **385**: p. 122386.
22. Li, S., et al., Mechanism and kinetic modeling study on the crystallization of concomitant polymorphs. AIChE Journal, 2024. **70**(9).

Process simulation of lactic acid esterification in reactive distillation column: Effects of reboiler duty and alcohol

Satakhun Imsomboon[1], Phongsatorn Tatiyaboworchai[1], Apinya Silamas [1], Jatupon Chaiwasu[1], Anawat Sungpet[1,*]

[1] Department of Chemical Engineering, Faculty of Engineering, King Mongkut's University of Technology Thonburi, Bangkok 10140, Thailand
[*] Corresponding author: anawat.sun@kmutt.ac.th

ABSTRACT

This study investigates the effects of reboiler duty on the esterification of lactic acid using three alcohols: methanol, ethanol, and butanol in a reactive distillation column. The main objective was to evaluate how variations in reboiler duty and alcohol type influence reaction and separation. The results showed that methanol and ethanol achieved high conversion rates, with methanol demonstrating the highest conversion rate. While butanol provided the highest product purity, it also required the least reboiler duty compared to the reboiler duty range for methanol and ethanol. From the result, the reboiler duty did not significantly affect the reaction, as the conversion rates for each alcohol showed almost no difference. These findings are critical for optimizing reactive distillation columns in bio-based chemical production, particularly in lactic acid esterification. The study contributes to the design of more energy-efficient and sustainable processes for green chemical manufacturing, particularly in producing biodegradable esters like polylactic acid.

Keywords: Lactic acid; Reactive distillation; Esterification; Reboiler duty

1. INTRODUCTION

With increasing global focus on sustainability and environmentally friendly technologies, bio-based chemical production has become a major area of interest in chemical engineering. Lactic acid, a key bio-derived compound, can be produced through fermentation using agricultural waste from crops such as sugarcane, cassava, and corn. It is widely used in the food, pharmaceutical, and polymer industries, especially in the production of polylactic acid. However, purifying and converting lactic acid remains challenging due to the high cost, energy consumption, and environmental impact of traditional separation methods such as crystallization, solvent extraction, and precipitation. Reactive distillation offers a more efficient and sustainable alternative by integrating chemical reactions and separation into a single step, making it particularly suitable for equilibrium-limited reactions like externalization. Previous studies have shown that reactive distillation using alcohols such as ethanol, methanol, and butanol can improve ester yield and reduce energy requirements. Despite these advancements, limited work has systematically examined how key operating parameters, especially reboiler duty, affect conversion and separation performance across different alcohols. This study used ASPEN Plus V.14 to simulate lactic acid esterification with methanol, ethanol, and butanol, focusing on the effects of reboiler duty on lactic acid separation. The results could support the development of more efficient and sustainable process designs for bio-based chemical production.

2. EXPERIMENTAL

This study uses ASPEN Plus V.14 to simulate the esterification of lactic acid with three alcohols: methanol, ethanol, and butanol in a reactive distillation column. The objective is to investigate the impact of reboiler duty on the esterification reactions and the separations. The feed composition in the simulation includes water (0.905 mol fraction), lactic acid (0.084 mol fraction), and acetic acid (0.011 mol fraction), representing a typical fermentation composition. The alcohol to lactic acid molar ratio was fixed at 5:1 in all cases to ensure consistent comparison across different alcohol systems. Simulations were performed using the RadFrac model in ASPEN Plus under steady-state conditions. The UNIQUAC-HOC model was used to calculate activity coefficients, while the Hayden-O'Connell model accounted for non-ideal vapor behavior. Binary interaction parameters were estimated using the UNIFAC method when necessary. The process was divided into two units: pre-concentration (to remove water) and esterification (reactive distillation). This study specifically focused on the esterification column, where alcohol was introduced below the reactive zone. The operating pressures of the

esterification columns were 0.2 atm for the methanol and ethanol, and 0.3 atm for butanol. The reboiler duty varied within specific ranges for each alcohol: 330 to 350 kW for methanol, 425 to 445 kW for ethanol, and 205 to 225 kW for butanol. The reboiler duty range of 425 to 445 kW for ethanol used in this study is higher than that in reference research, where the reboiler duty was lower and resulted in a lower conversion rate. By increasing the reboiler duty in our study, the conversion rate was improved. Only the reboiler duty was adjusted, while all other variables, including feed conditions, composition, and column configuration, remained constant. This approach ensured that any observed performance differences were directly attributed to variations in reboiler duty. Simulation results were exported to Microsoft Excel for analysis of conversion percentage, product conversion, purity, and ester distribution. These results were compared with reference data from previous studies to validate the model's trends and accuracy. In this study, there were 2 side reactions in the esterification process as shown below.

$$C_3H_6O_3 + C_3H_6O_3 \leftrightarrow C_6H_{10}O_5 + H_2O \quad (1)$$

$$C_6H_{10}O_5 + H_2O \leftrightarrow C_3H_6O_3 + C_3H_6O_3 \quad (2)$$

These side reactions are typically undesirable because they not only reduce the product yield but also introduce water into the system. The presence of water can shift the reaction equilibrium and reduce the overall performance of the esterification process. These reactions occur when the temperature in the esterification column exceeds 80°C. However, in this study, the occurrence of side reactions was minimal, resulting in a negligible impact on the overall process. This study includes the reaction kinetics for each alcohol, as well as the kinetics for the side reactions, which were used in the simulations [1].

3. RESULTS AND DISCUSSION

A simulation model of a reactive distillation column for lactic acid esterification with methanol, ethanol, and butanol was successfully developed using ASPEN Plus V.14. To ensure model accuracy, key simulation results were validated against reference research data, as presented in Tables 1-3. Following successful validation, the ASPEN Plus V.14 program was employed to investigate the influence of varying the reboiler duty. The results of these simulations, demonstrating the effect of reboiler duty adjustments for esterification processes using methanol, ethanol, and butanol, are summarized in Tables 4-9. The principal aim of this particular investigation was to analyze how changes in reboiler duty impact important performance metrics such as conversion rate, separation, and product purity within the reactive distillation process.

Table 1 Comparison with reference research using data and results from the simulation of methyl lactate production.

Feed	This research		Reference research [1]	
	Lactic acid	Methanol	Lactic acid	Methanol
Stage	2	20	2	20
Temperature (°C)	75.0	30	72.5	30
Pressure (atm)	2	2	2	2
Flow rate (kmol/h)	10.165	16.850	10.165	16.695
Lactic acid (kmol/h)	4.174	-	4.174	-
Methanol (kmol/h)	-	16.850	-	16.695
Water (kmol/h)	5.460	-	5.460	-
Acetic acid (kmol/h)	0.531	-	0.531	-
Reflux ratio	0.08		N/A	
Reboiler duty (kW)	330.000		330.098	
Methyl lactate reaction: $C_3H_6O_3 + CH_4O \leftrightarrow C_4H_8O_3 + H_2O$				
Result				
Distillate rate (kmol/h)	26.614		26.298	
Bottom rate (kmol/h)	0.400		0.564	
Condenser duty (kW)	-344.09		-333.16	
Distillate product				
Lactic acid (kmol/h)	0.0013		0	
Dilactic acid (kmol/h)	0		0	
Trilactic acid (kmol/h)	0		0	
Methanol (kmol/h)	12.679		12.597	
Methyl lactate (kmol/h)	3.864		4.076	
Water (kmol/h)	9.629		9.572	
Acetic acid (kmol/h)	0.439		0	
Bottom product				
Lactic acid (kmol/h)	0		0.005	
Dilactic acid (kmol/h)	0.0031		0.021	
Trilactic acid (kmol/h)	0		0	
Methanol (kmol/h)	0.004		0	
Methyl lactate (kmol/h)	0.302		0.008	
Water (kmol/h)	0		0	
Acetic acid (kmol/h)	0.092		0.531	

Table 2 Comparison with reference research using data and results from the simulation of ethyl lactate production.

Feed	This research		Reference research [1]	
	Lactic acid	Ethanol	Lactic acid	Ethanol
Stage	2	28	2	28
Temperature (°C)	75.0	30	72.5	30
Pressure (atm)	2	2	2	2
Flow rate (kmol/h)	10.165	16.850	10.165	16.688
Lactic acid (kmol/h)	4.174	-	4.174	-
Ethanol (kmol/h)	-	16.850	-	16.688
Water (kmol/h)	5.460	-	5.460	-
Acetic acid (kmol/h)	0.531	-	0.531	-
Reflux ratio	0.0002		N/A	
Reboiler duty (kW)	385.477		385.477	
Esterification reaction: $C_3H_6O_3 + C_2H_6O \leftrightarrow C_5H_{10}O_3 + H_2O$				
Result				
Distillate rate (kmol/h)	26.594		26.275	
Bottom rate (kmol/h)	0.421		0.594	
Condenser duty (kW)	-343.94		-406.74	

Table 2 Comparison with reference research using data and results from the simulation of ethyl lactate production. (Cont.)

Distillate product		
	This research	Reference research [1]
Lactic acid (kmol/h)	0.079	0.053
Dilactic acid (kmol/h)	2.2634E-05	0
Trilactic acid (kmol/h)	0	0
Ethanol (kmol/h)	12.8439	12.665
Ethyl lactate (kmol/h)	3.646	4.020
Water (kmol/h)	9.508	9.538
Acetic acid (kmol/h)	0.516	0
Bottom product		
Lactic acid (kmol/h)	0.421	0.001
Dilactic acid (kmol/h)	0.0462	0.053
Trilactic acid (kmol/h)	0	0
Ethanol (kmol/h)	0.004	0
Ethyl lactate (kmol/h)	0.355	0.008
Water (kmol/h)	0	0
Acetic acid (kmol/h)	0.015	0.531

Table 3 Comparison with reference research using data and results from the simulation of butyl lactate production.

Feed	This research		Reference research [1]	
	Lactic acid	Butanol	Lactic acid	Butanol
Stage	2	17	2	17
Temperature (°C)	75.0	30	72.5	30
Pressure (atm)	2	2	2	2
Flow rate (kmol/h)	10.165	5.831	10.165	5.831
Lactic acid (kmol/h)	4.174	-	4.174	-
Butanol (kmol/h)	-	5.831	-	5.831
Water (kmol/h)	5.460	-	5.460	-
Acetic acid (kmol/h)	0.531	-	0.531	-
Reflux ratio	0.001		N/A	
Reboiler duty (kW)	202.133		202.133	
Esterification reaction: $C_3H_6O_3 + C_4H_{10}O \leftrightarrow C_7H_{14}O_3 + H_2O$				
Result				
Distillate rate (kmol/h)	9.873		9.692	
Bottom rate (kmol/h)	6.123		6.317	
Condenser duty (kW)	-116.56		-148.74	
Distillate product				
	This research		Reference research [1]	
Lactic acid (kmol/h)	0.012		0	
Dilactic acid (kmol/h)	0		0	
Trilactic acid (kmol/h)	0		0	
Butanol (kmol/h)	5.271×10^{-5}		0.033	
Butyl lactate (kmol/h)	0		0	
Water (kmol/h)	9.430		2.980	
Acetic acid (kmol/h)	0.430		0	
Bottom product				
Lactic acid (kmol/h)	0.0006		0.038	
Dilactic acid (kmol/h)	0.189		0.013	
Trilactic acid (kmol/h)	0.0001		0	
Butanol (kmol/h)	2.049		1.623	
Butyl lactate (kmol/h)	3.782		4.112	
Water (kmol/h)	0.001		0	
Acetic acid (kmol/h)	0.100		0.531	

Table 4 Conversion and product purity obtained from the simulation of the esterification column using methanol.

Reboiler duty (kW)	Temperature range (°C)	Conversion (%)	Conversion to methyl lactate (%)
330	35.88-112.05	99.989	99.911
335	36.16-112.54	99.987	99.902
340	36.43-112.88	99.984	99.895
345	36.70-113.20	99.981	99.890
350	36.97-113.60	99.978	99.884

Table 5 Separation results with different reboiler duty using methanol.

Reboiler duty (kW)	Product (kmol/h) Methyl lactate		Methyl lactate purity (%)	
	Distillate	Bottom	Distillate	Bottom
330	2.5803	1.5900	20.8046	82.2814
335	2.9655	1.2044	23.1515	78.9647
340	3.3190	0.8507	25.1018	76.5038
345	3.6410	0.5284	26.6902	76.3662
350	3.9665	0.2027	28.1981	75.9743

The effect of reboiler duty on the esterification of lactic acid with methanol is presented in Tables 4 and 5. As shown in Table 4, increasing reboiler duty from 330 kW to 350 kW resulted in a steady conversion rate of 99.98%, indicating that reboiler duty had little impact on the overall conversion and the conversion to product or methyl lactate. As the reboiler duty increases, the temperature in the column also rises. The temperature at the top stages, where methyl lactate was generated between stage 2 and stage 5 out of a total of 21 stages, with a temperature range from 64°C to 73°C. The separation results shown in Table 5 reveal that as reboiler duty increased, the distillate flow rate of methyl lactate increased from 2.58 kmol/h at 330 kW to 3.97 kmol/h at 350 kW, which suggests that increasing the temperature by increasing the reboiler duty improved separation for methanol esterification. The bottom flow rate decreased from 1.59 kmol/h to 0.20 kmol/h, suggesting improved separation. The purity of methyl lactate in the distillate also increased from 20.80% to 28.20%. Conversely, the percentage of methyl lactate in the bottom stream decreased from 82.28% to 75.97%, which implies that higher reboiler duty enhances the recovery of the desired ester in the distillate.

Table 6 Conversion and product purity obtained from the simulation of the esterification column using ethanol.

Reboiler duty (kW)	Temperature range (°C)	Conversion (%)	Conversion to ethyl lactate (%)
425	45.15-121.49	98.723	97.638
430	45.41-121.84	98.570	97.434
435	45.67-122.32	98.415	97.231
440	45.93-123.35	98.256	97.028
445	46.19-151.81	98.097	96.828

Table 7 Separation results with different reboiler duty using ethanol.

Reboiler duty (kW)	Product (kmol/h) Ethyl lactate		Ethyl lactate purity (%)	
	Distillate	Bottom	Distillate	Bottom
425	2.5894	1.4860	20.5412	93.9875
430	2.9457	1.1212	22.7036	93.6077
435	3.3058	0.7526	24.7709	92.7203
440	3.6692	0.3807	26.7454	89.9708
445	4.0307	0.0109	28.6080	28.8373

For ethanol, as shown in Table 6, increasing reboiler duty from 425 kW to 445 kW had a minimal effect on the overall conversion rate, 98.72% to 98.10%, and the conversion to ethyl lactate slightly decreased from 97.64% to 96.83%. These results suggest that ethanol esterification benefits from increased reboiler duty, although the effect on conversion is less pronounced compared to methanol. As the reboiler duty increases, the temperature in the column rises. At the top stages, where ethyl lactate was generated between stage 3 and stage 8 out of a total of 29 stages, the temperature range was between 83°C and 88°C. The distillate flow rate of ethyl lactate as shown in Table 7 increased from 2.59 kmol/h at 425 kW to 4.03 kmol/h at 445 kW. The increase in reboiler duty and temperature allowed the ethyl lactate ester to vaporize more effectively, resulting in improved separation. The bottom flow rate decreased sharply, from 1.49 kmol/h to 0.01 kmol/h. Additionally, the percentage of ethyl lactate in the distillate increased from 20.54% to 28.61%, while by-products in the distillate decreased, suggesting that higher reboiler duty optimizes both purity and yield.

Table 8 Conversion and product purity obtained from the simulation of the esterification column using butanol.

Reboiler duty (kW)	Temperature range (°C)	Conversion (%)	Conversion to butyl lactate (%)
205	56.09-91.87	99.573	99.410
210	56.06-91.95	99.537	99.396
215	56.03-92.03	99.498	99.374
220	56.01-92.13	99.458	99.346
225	56.00-92.20	99.417	99.314

Table 9 Separation results with different reboiler duty using butanol.

Reboiler duty (kW)	Product (kmol/h) Butyl lactate		Butyl lactate purity (%)	
	Distillate	Bottom	Distillate	Bottom
205	0.07592	4.0735	0.7559	95.7795
210	0.09239	4.0564	0.9173	96.0821
215	0.10979	4.0381	1.0868	96.3774
220	0.12797	4.0187	1.2631	96.6605
225	0.14683	3.9985	1.4450	96.9295

In the case of butanol, Table 8 shows that the conversion rate remained relatively stable from 99.57% at 205 kW to 99.42% at 225 kW, indicating minimal impact of reboiler duty on overall conversion. The temperature at the top stages, where butyl lactate was generated, was between stage 3 and stage 5 out of a total of 18 stages, with a temperature range from 75°C to 88°C. This temperature was higher than the boiling point of butanol, which was 87°C at 0.3 atm. The temperature range indicated that butanol might vaporize in some stages, but butyl lactate did not vaporize at these temperatures. The temperature decreases from 79 °C at stage 2 to 75 °C at stage 3, which was the stage responsible for the highest amount of butyl lactate formation. Butanol remained mostly in the liquid phase, allowing more reaction between butanol and lactic acid. Notably, stage 3 contributed to 87% of the total butyl lactate generation. As a result, the column for butanol esterification required fewer stages compared to methanol and ethanol. Despite having fewer stages, it still achieved a high conversion similar to methanol and ethanol. The conversion to butyl lactate decreased from 99.41% to 99.31%. However, product purity improved significantly from 95.78% to 96.93%, as observed in Table 8. This suggests that while butanol esterification is less sensitive to reboiler duty changes in terms of conversion, the separation, as reflected in product purity, is greatly enhanced by increasing reboiler duty. As butyl lactate had a lower volatility compared to methyl lactate and ethyl lactate, meaning it required more heat to vaporize and be separated into the distillate. As a result, its higher boiling point made it flow down to the bottom of the column as a bottom product. As shown in Table 9, the bottom flow rate slightly decreased from 4.07 kmol/h at 205 kW to 3.99 kmol/h at 225 kW, while the distillate flow rate of butyl lactate increased from 0.076 kmol/h at 205 kW to 0.147 kmol/h at 225 kW. The purity of butyl lactate in the bottom rose from 95.78% to 96.93%, confirming that higher reboiler duty helped vaporize other components to the top of the column, thus improving the overall recovery.

Comparing the three alcohols, methanol showed the highest conversion, followed by ethanol, while butanol exhibited the highest purity in the product. Butanol esterification showed significant benefits in terms of product purity, which is essential for processes requiring high-quality products, such as in pharmaceutical applications. These findings align with previous research, which indicated that methanol is highly effective for maximizing conversion, while butanol excels in achieving high purity. The ethanol esterification process, on the other hand, strikes a balance between these two extremes.

4. CONCLUSION

This study investigated the effects of reboiler duty on the esterification of lactic acid using three alcohols: methanol, ethanol, and butanol in a reactive distillation column. The objective was to evaluate how reboiler duty and alcohol type influence separation. The results showed that methanol and ethanol achieved high conversion and product rate in distillate, with methanol showing the highest conversion rate and ethanol balancing product rate in distillate and purity. Butanol, while offering the highest product purity. Unlike the lactates produced from methanol and ethanol, because of its lower volatility, butyl lactate is obtained as the bottom product.

Increasing reboiler duty improved product purity and separation, especially for methanol and ethanol, while butanol exhibited improved purity without a significant increase in product rate in the distillate. These findings are critical for optimizing reactive distillation columns in bio-based chemical production, particularly in lactic acid esterification. By examining the impact of reboiler duty on yield and purity, this

study contributes to the design of more energy-efficient and sustainable processes for green chemical manufacturing, especially in the production of biodegradable esters like polylactic acid. However, the study has limitations, including the use of steady-state simulations, which may not fully reflect real-time industrial dynamics. It also did not account for variations in catalyst efficiency, which could affect reaction rates and overall conversion. Future research should focus on dynamic simulation models and experimental validation to confirm the findings. Further studies could explore the economic feasibility of optimizing reboiler duty in large-scale operations and investigate the effects of different catalysts on the esterification process. These insights lay the foundation for further innovations in sustainable chemical production.

ACKNOWLEDGMENTS

Mr. Satakhun Imsomboon, Mr. Phongsatorn Tatiyabowornchai, and Ms. Apinya Silamas are grateful to the parents, family, and friends for their steadfast support and continuous encouragement, which proved instrumental in the completion of this undertaking.

Furthermore, the authors accept responsibility for any deficiencies that may be present in this work and would welcome constructive suggestions from readers toward future refinement.

REFERENCES

1. Cheien-Yuan Su et al, 2013, "Plant-Wide Economic Comparison of Lactic Acid Recovery Processes by Reactive Distillation with Different Alcohols", *Industrial & Engineering Chemistry Research*, Vol. 52, No.32.
2. Hu, J., Lin, Y., Zhang, Z., Xiang, T., Mei, Y., Zhao, S., Liang, Y., and Peng, N., 2016, "High-Titer Lactic Acid Production by Lactobacillus Pentosus Fl0421 from Corn Stover Using Fed-Batch Simultaneous Saccharification and Fermentation", *Bioresource Technology*, Vol. 214, pp. 74-80.
3. Foster Agblevor and Timothy Evans, 2004, Method for production of lactic acid [Online], Available: https://patents.google.com/patent/US20040229327A1/en
4. Kumar, A., Thakur, A., and Panesar, P.S., 2019, "Lactic Acid and Its Separation and Purification Techniques: A Review", *Reviews in Environmental Science and Bio/Technology*, Vol. 18, No. 4, pp. 823-853.

Design and simulation of the coffee drying unit using solar thermal energy and ambient air circulation

Rittichai Preungchana[1], Passapong Sangthong[1], Pongsapak Rattanachai[1], Wipada Sonsiri[1], Krittin Korkerd[1], Kiattinatapon Juengchareonpoon[1], Wimolsiri Pridasawas[1,*]

[1] Department of Chemical Engineering, Faculty of Engineering, King Mongkut's University of Technology Thonburi, Bangkok 10140, Thailand
[*] Corresponding author: wimolsiri.pri@kmutt.ac.th

ABSTRACT

Sun drying is one of the most crucial and widely used techniques in coffee processing due to its effectiveness in inhibiting microbial spoilage and slowing enzymatic activity. However, several drawbacks exist, such as the prolonged too high surface temperature, and strong dependence on weather conditions. Despite these limitations, sun drying is preferred over mechanical drying because of its low cost and availability. High temperature drying can degrade the structure of green bean coffee and its overall quality. This study focuses on the design and simulation of a coffee drying greenhouse using a three-dimensional model developed in COMSOL Multiphysics and an experimental solar drying unit. The research aims to analyze airflow characteristics and temperature distribution within the greenhouse. Simulations examine airflow through inlets of varying areas (0.010, 0.025, and 0.050 m^2) and different exhaust fan sizes (6-, 8-, and 10-inch), each with different volumetric flow rates (270, 540, and 900 m^3/h), with sunlight transmitted only through the greenhouse roof. Results indicate that narrower inlet openings, together with larger ventilation fans, resulted in higher inlet air velocity. For larger fans, airflow recirculation became more noticeable due to the increased flow rate, leading to the formation of larger vortex zones, especially at the center of the drying house. Additionally, narrower inlet openings consistently resulted in higher internal temperatures for the same fan size. Simulation results show that with a 0.050 m^2 inlet area, the drying house maintained internal temperatures of 38.7–41.0 °C. Reducing the inlet area to 0.025 m^2 and 0.010 m^2 raised these temperatures to 39.9–43.2 °C and 42.4–45.3 °C, respectively. The smaller inlet area limited airflow and thus reduced convective heat transfer, causing more heat to be retained within the drying house. Consequently, the overall interior temperature increased. Moreover, different coffee processing stages require different temperature ranges, suggesting that operators should adjust the inlet area accordingly to maintain optimal conditions throughout the drying process.

Keywords: Coffee drying unit; Solar drying

1. INTRODUCTION

Coffee is one of the most commercially consumed and widely popular beverages in the world [1]. The International Coffee Organization (ICO) reported that the global annual coffee consumption is approximately 148 million cups [2]. The quality of coffee depends on several factors, such as the quality of green beans, post-harvest handling, extraction process, and the type of water used during brewing [3]. Arabica and Robusta are the two most economically important coffee species [4]. Arabica is renowned worldwide for its pleasant aroma, sweet flavor, bright acidity, and wide-ranging taste profile. In contrast, Robusta is generally considered to have less desirable sensory characteristics, such as bitterness due to high caffeine content, lower sweetness, and reduced acidity [5].

The coffee production process begins with harvesting and drying [6]. Drying is an essential step that effectively inhibits microbial spoilage, slows down enzymatic activity, prevents chemical degradation, and extends shelf life [7]. Coffee drying can be done by sun drying or by using various mechanical drying techniques [8].

Sun drying is commonly used in the coffee industry. However, it has some drawbacks, including long drying times and high labor costs [9]. In addition, weather conditions significantly affect the drying duration [6], [10]. Despite these limitations, sun drying remains more widely adopted than mechanical drying, as it tends to result in roasted coffee with better sensory qualities [9]. This is partly due to the increased sugar content caused by the pre-germination of embryos

during sun drying. In contrast, high temperatures during mechanical drying may damage the structure of fresh beans and reduce the final quality of coffee [11], [12].

To produce high-quality coffee, it is important to control temperature and moisture in phases during the drying process. Moisture must be removed quickly at certain stages, while at other times it should be removed more slowly to support fermentation. Additionally, increasing the drying temperature at the final stage helps to evenly distribute moisture within the coffee beans. This careful process ensures the production of high-quality coffee [11].

Simulation plays a vital role in the development of efficient coffee drying systems, as it allows researchers to visualize and predict airflow patterns, and temperature distribution. By utilizing computational tools, potential issues such as uneven drying or excessive heat exposure can be identified and addressed before constructing the actual drying unit. Therefore, this study focuses on the design and simulation of a coffee drying house using COMSOL Multiphysics to investigate airflow patterns and temperature distribution within a three-dimensional model of the drying house.

2. EXPERIMENTAL

2.1 Design of three-dimensional modeling of the coffee drying unit

In this study, a three-dimensional model of a coffee drying unit was created using COMSOL Multiphysics and later used for computational fluid dynamics (CFD) analysis.

The drying house model has dimensions of 310 cm in width, 370 cm in length, and 235 cm in height. At the front side, there are two air inlet openings, each with a length of 50 cm. These inlets are positioned 10 cm above the ground and 12.5 cm from the side walls. At the back side, two exhaust fans are installed. The center of each fan is located 217.5 cm above the ground and 37.5 cm from the centerline of the drying house.

Inside the drying unit, four drying racks are installed. Each rack has dimensions of 45 cm in width, 120 cm in length, and 160 cm in height. Each rack holds twelve baskets for containing coffee beans, with each basket measuring 31 cm in width, 40 cm in length, and 8 cm in height. The racks are positioned 40 cm away from both the front and rear walls and 15 cm away from the side walls.

The schematic diagrams of the coffee drying unit model are shown in Figures 1 to 3, and the three-dimensional model of the coffee drying unit created in COMSOL Multiphysics is presented in Figure 4, respectively.

In addition, this study analyzes the effects of variations in key design parameters, including different air inlet widths of 2, 5, and 10 cm, which correspond to inlet areas of 0.010, 0.025, and 0.050 m², respectively. These inlet sizes are paired with ventilation fans of different diameters, namely 6-, 8-, and 10-inch fans, each providing different volumetric flow rates of 270, 540, and 900 m³/h, respectively [13]. These parameters are evaluated in COMSOL Multiphysics to assess their effects on airflow characteristics and temperature distribution inside the coffee drying unit.

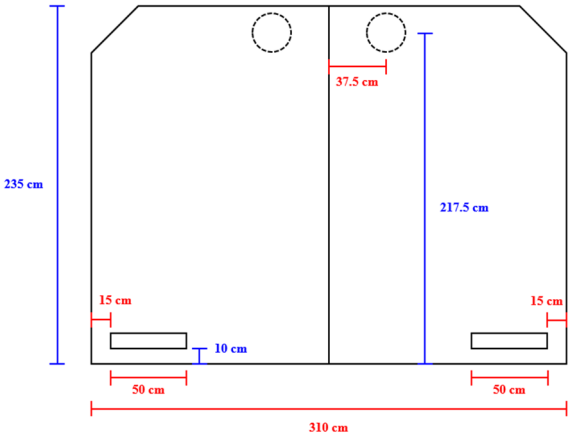

Figure 1 Front view layout of the coffee drying unit model.

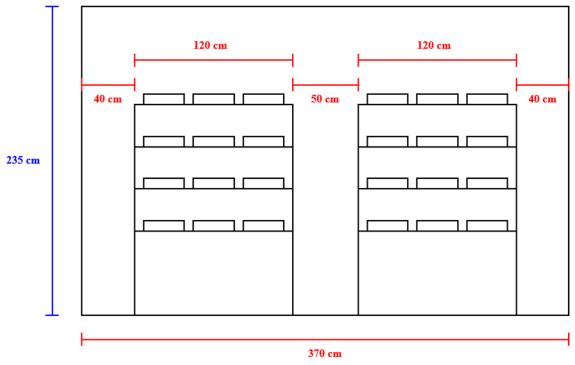

Figure 2 Side view layout of the coffee drying unit model.

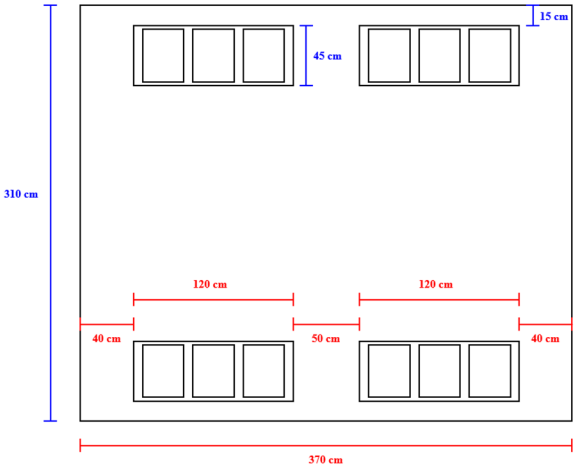

Figure 3 Top view layout of the coffee drying unit model.

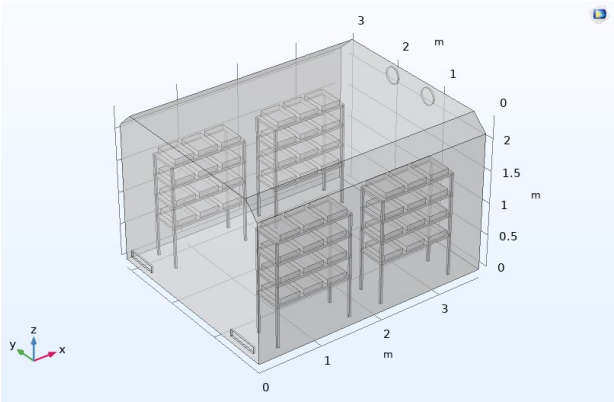

Figure 4 Three-dimensional model of the coffee drying unit created in COMSOL Multiphysics.

2.2 Assumptions used in the simulation with COMSOL Multiphysics

In the simulation of airflow characteristics and temperature distribution inside the coffee drying unit using COMSOL Multiphysics, the following assumptions were made:

1. The airflow inside the system is treated as a Newtonian fluid and is assumed to be incompressible.
2. Air enters through the front inlet of the coffee drying unit and exits only through the ventilation fan. No backflow is allowed at the outlet boundary (suppress backflow).
3. The airflow is considered turbulent, with the Turbulent Flow, Realizable k-ε physics model selected for the simulation.
4. Solar radiation is assumed to penetrate only through the roof area of the coffee drying unit.
5. The Heat Transfer in Fluids physics model is used to simulate heat transfer within the system.
6. Ambient properties around the coffee drying unit are set in COMSOL Multiphysics based on meteorological data from the software database
7. The floor of the coffee drying unit is considered an adiabatic boundary, and heat transfer through the floor is neglected.

2.3 Initial values and boundary conditions

The boundaries of each domain in the simulation are defined with appropriate initial values and boundary conditions. In this model, there are two air inlets located at the front and two ventilation fans equipped with specified static pressure curves. The details of the initial values and boundary conditions are described as follows.

1. The airflow at the inlet is assigned to the boundary condition of the Inlet, with the inlet pressure set equal to the atmospheric pressure.
2. The airflow at the outlet through the ventilation fans is assigned to a boundary condition of Fan, with the outlet pressure set equal to the atmospheric pressure. A static pressure curve is defined with the static pressure at no flow set to 100 Pa. The free delivery flow rates for the 6-, 8-, and 10-inch ventilation fans are set to 270, 540, and 900 m³/h, respectively.
3. The initial temperature of the air inside the coffee drying unit is set to 30°C.
4. The air entering through the inlets is assigned a boundary condition of Inflow, with the inlet air temperature set equal to the ambient temperature.
5. The air exiting through the ventilation fans is assigned a boundary condition of Outflow.
6. Solar radiation penetrating only through the roof is simulated using a Heat Flux boundary condition, defined as General Inward Heat Flux, with a time-dependent heat flux function (heat_flux(t)) to represent the variation of solar radiation over time [14], as illustrated in Figure 5.

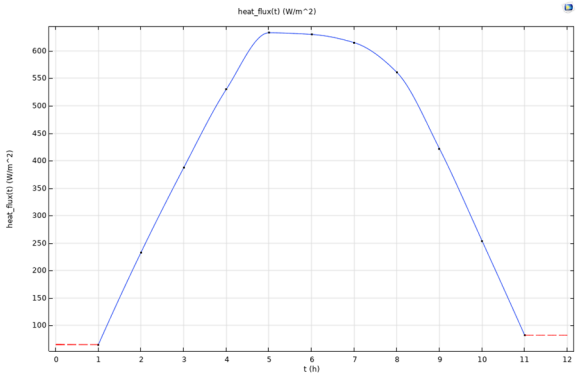

Figure 5 Variation of Solar Radiation Over Time.

7. Heat transfer at the walls of the coffee drying unit is simulated using a Heat Flux boundary condition, specified as External Natural Convection, Vertical Wall. The heights of the front and rear walls are set to 235 cm, while the heights of the side walls are set to 212 cm. The ambient pressure and temperature are assigned based on ambient conditions.

The simulation steps in COMSOL Multiphysics are illustrated in Figure 6.

2.4 Construction of the coffee drying unit prototype

The prototype of the coffee drying unit was designed to be easily assembled, disassembled, and stored, with a focus on low construction cost. The design was based on accommodating approximately 100 kg of coffee cherries and was dimensioned according to hygienic standards and operational convenience within the prototype. Commercially available materials, such as standard baskets and shelving units, were selected for ease of sourcing. The dimensions of the baskets and shelving units used are shown in Figures 7 and 8, respectively.

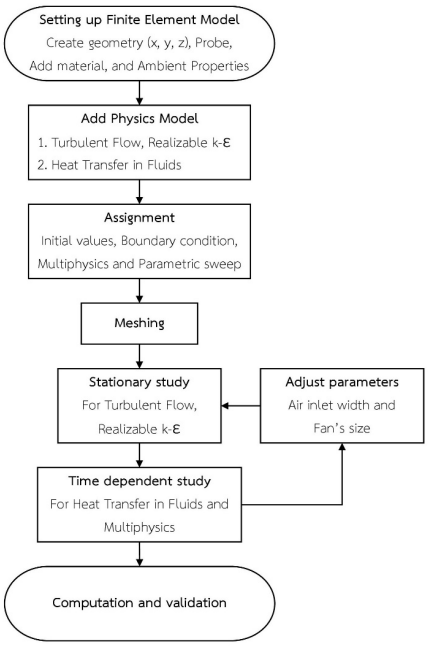

Figure 6 Procedure followed during the simulation of the coffee drying unit using COMSOL Multiphysics.

Inside the prototype, four shelving units are installed, each measuring 45 cm in width, 120 cm in length, and 160 cm in height. Each shelving unit holds twelve baskets for containing coffee beans, with each basket measuring 35 cm in width and 54 cm in length. The shelving units are arranged in two rows on each side of the greenhouse. 15 cm is maintained between the shelving units and the side walls. The depth of coffee cherries in each basket is set at 4 cm.

Figure 7 Dimensions of the baskets used in the prototype.

Figure 8 Dimensions of the shelving units used in the prototype.

The materials used for constructing the prototype include a main structure made of lightweight, easy-to-assemble PVC pipes. The roof is covered with transparent PVC plastic sheets to allow sunlight to penetrate into the drying space, while the side walls are made of opaque polypropylene plastic sheets. Two air inlet openings were created at the front of the greenhouse, each with a width of 10 cm and a length of 50 cm. Two ventilation fans with a diameter of 10 inches are installed at the rear of the greenhouse to assist in extracting air from the system. The prototype structure is shown in Figures 9 to 11.

Figure 9 Structure of the coffee drying unit prototype.

Figure 10 Front view of the coffee drying unit prototype.

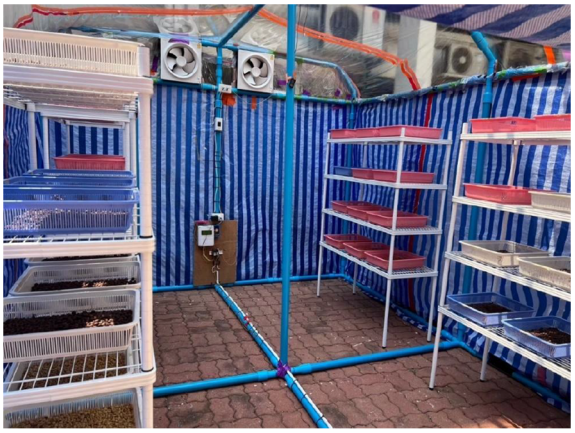

Figure 11 Interior view of the coffee drying unit prototype.

3. RESULTS AND DISCUSSION

3.1 Analysis of airflow characteristics inside the coffee drying unit

The simulation results of airflow characteristics inside the coffee drying unit indicate that smaller air inlet sizes combined with larger ventilation fans lead to higher air inflow velocities within the greenhouse. The simulated air inlet velocities for various model configurations are summarized in Table 1.

Table 1 Simulated air inlet velocities (m/s) for different model configurations.

Ventilation fan size	Air inlet area		
	0.010 m²	**0.025 m²**	**0.050 m²**
6-inch	3.6250	2.4208	1.0122
8-inch	4.5372	4.1375	1.7517
10-inch	4.7540	5.3871	2.9504

From Table 1, it can be observed that the general trend of air inflow velocity inside the coffee drying unit increases with the use of larger ventilation fans and decreases in air inlet area. In the case of the coffee drying unit with a 6-inch ventilation fan, the simulated air inlet velocities were 3.6250, 2.4208, and 1.0122 m/s for air inlet areas of 0.010, 0.025, and 0.050 m², respectively. For the greenhouse with an 8-inch ventilation fan, the corresponding air inlet velocities were 4.5372, 4.1375, and 1.7517 m/s, respectively. It is evident that for both 6-inch and 8-inch fans, the highest air inlet velocities occurred when combined with the smallest air inlet area of 0.010 m², which aligns with the principle of the continuity equation, stating that a reduction in the flow cross-sectional area results in an increase in flow velocity when the volumetric flow rate remains constant [15].

However, for the greenhouse with a 10-inch ventilation fan, the simulated air inlet velocities were 4.7540, 5.3871, and 2.9504 m/s for inlet areas of 0.010, 0.025, and 0.050 m², respectively. It can be seen that the trend is not consistent in this case, as the smallest inlet area of 0.010 m² resulted in a lower air inlet velocity than the 0.025 m² inlet area. This deviation may be attributed to complex flow interactions that cannot be fully explained by the linear assumptions of the continuity equation alone.

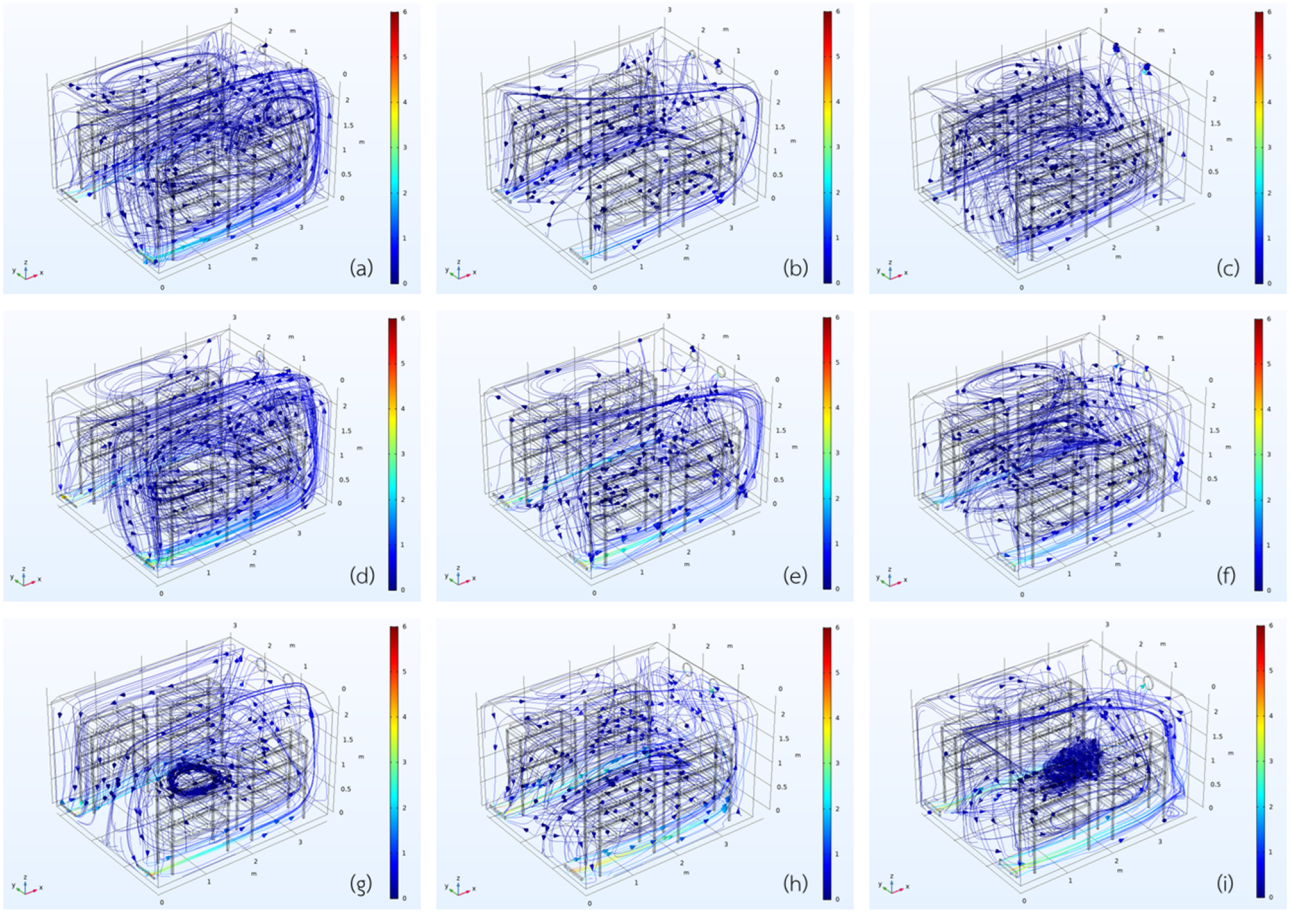

Figure 12 Streamline simulation results of airflow inside the coffee drying unit.
(a) 6-inch ventilation fan with 0.010 m² inlet area (b) 6-inch ventilation fan with 0.025 m² inlet area
(c) 6-inch ventilation fan with 0.050 m² inlet area (d) 8-inch ventilation fan with 0.010 m² inlet area
(e) 8-inch ventilation fan with 0.025 m² inlet area (f) 8-inch ventilation fan with 0.050 m² inlet area
(g) 10-inch ventilation fan with 0.010 m² inlet area (h) 10-inch ventilation fan with 0.025 m² inlet area
(i) 10-inch ventilation fan with 0.050 m² inlet area

When a large fan with a high volumetric flow rate is paired with a small air inlet, significant back pressure may develop at the inlet, potentially causing the fan to operate outside its optimal performance range and reducing the actual airflow rate, thus leading to a decrease in air velocity [16]. Additionally, the pressure buildup at the small inlet may induce unstable flow phenomena such as turbulence, vortex flow, or even reverse flow, all of which can negatively impact the airflow efficiency [17]. The consistent behavior of the 6-inch and 8-inch ventilation fans, which do not deviate from the trend predicted by the continuity equation, may be attributed to their relatively low airflow power. As a result, the resistance caused by the small inlet area is not yet high enough to significantly reduce fan performance. Under these conditions, the system is still capable of maintaining stable flow conditions effectively [18].

The simulation results of airflow streamlines inside the coffee drying unit, shown in Figure 12, illustrate the airflow patterns for each configuration. It was found that in cases with 6-inch and 8-inch ventilation fans, no vortex formation was observed—even when combined with the smallest inlet area of 0.010 m². This reflects the fact that the airflow strength was not sufficient to trigger flow instability. Small fans were able to maintain a stable flow regime under low to moderate inlet resistance conditions [18].

However, in the greenhouse configurations with 10-inch ventilation fans combined with inlet areas of 0.010 and 0.050 m², vortex formation was clearly observed. This was a result of high airflow force encountering inlets of improper size. Specifically, too narrow an inlet caused pressure build-up and flow separation, while too wide an inlet reduced directional control of the airflow, leading to increased shear and flow instability. These conditions contributed to the formation of vortices and recirculation zones. In contrast, when the 10-inch fan was used with an inlet area of 0.025 m², no vortex was observed. The streamline pattern remained continuous and stable, indicating that the inlet size matched well with the fan's airflow strength—demonstrating a balanced matching condition [17].

3.2 Analysis of temperature distribution inside the coffee drying unit

The simulation results of temperature distribution inside the coffee drying unit indicate that smaller air inlet sizes result in higher internal temperatures compared to larger inlet sizes, under the same fan configuration. The simulated temperature distributions at the front and rear sections of the greenhouse equipped with a 6-inch ventilation fan are shown in Figures 13 and 14, respectively.

It was found that the size of the air inlet directly influences the level of temperature accumulation throughout the day. The smallest air inlet area of 0.010 m² resulted in the highest internal temperatures, especially during the peak period from 12:00 to 15:00, where the temperature rose to 42.75–44.46 °C. In comparison, inlet areas of 0.025 m² and 0.050 m² produced lower internal temperatures at the same time period, reaching 40.74–43.17 °C and 38.49–40.49 °C, respectively. Smaller air inlets reduce the airflow rate due to increased flow resistance encountered by the fan. This resistance arises from higher air velocity and frictional losses within the narrow inlet passage. Since the fan operates under limitations defined by its performance curve, it cannot maintain the same airflow rate when resistance increases [19].

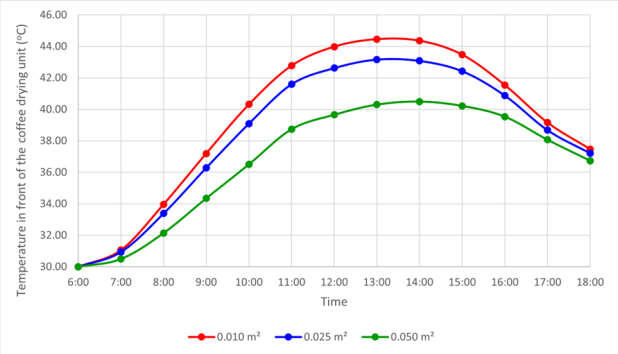

Figure 13 Simulated temperature distribution at the front section of the coffee drying unit equipped with 6-inch ventilation fan.

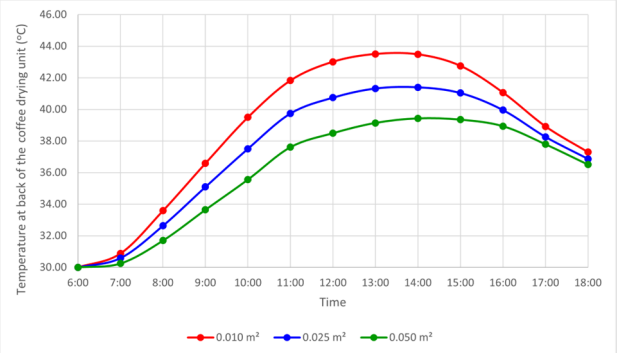

Figure 14 Simulated temperature distribution at the rear section of the coffee drying unit equipped with 6-inch ventilation fan

These results directly affect the convective heat transfer mechanism. Specifically, even if the air velocity at the inlet is high, a reduction in the total airflow entering the system will decrease the capacity to convect heat away from the greenhouse. As a result, heat accumulates inside the system faster than it can be removed, leading to an overall increase in internal temperature [20].

The simulated temperature distributions at the front and rear sections of the greenhouse equipped with an 8-inch ventilation fan are shown in Figures 15 and 16, respectively. For the configuration with a 10-inch ventilation fan, the corresponding results are presented in Figures 17 and 18, respectively.

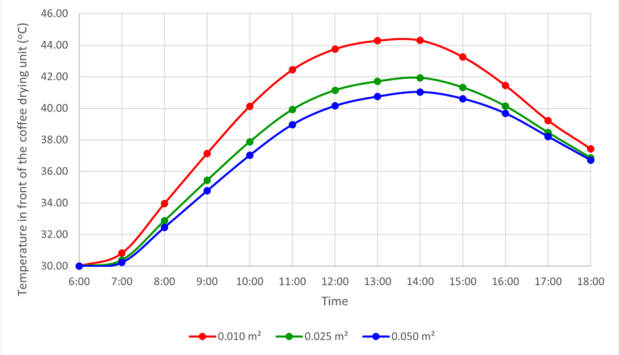

Figure 15 Simulated temperature distribution at the front section of the coffee drying unit equipped with 8-inch ventilation fan.

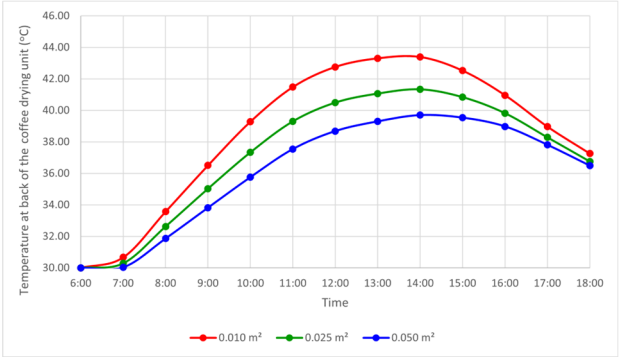

Figure 16 Simulated temperature distribution at the rear section of the coffee drying unit equipped with 8-inch ventilation fan

From Figures 15 to 18, it can be observed that the temperature distribution inside the coffee drying unit equipped with 8-inch and 10-inch ventilation fans exhibits the same trend as in the case of the 6-inch fan. That is, smaller air inlet areas result in higher internal temperatures compared to larger inlet areas, under the same fan size [21].

For the 8-inch fan configuration, the internal temperatures ranged from 42.52–44.30 °C, 40.49–41.93 °C, and 38.68–41.03 °C for inlet areas of 0.010, 0.025, and 0.050 m², respectively. In the case of the 10-inch fan, the corresponding temperature ranges were 43.11–45.29 °C, 40.47–42.03 °C, and 38.60–40.59 °C, respectively, for the same inlet area sizes. The simulated temperature distribution for the coffee drying unit with a 10-inch ventilation fan is shown in Figure 19.

As each stage of the coffee processing requires different temperature conditions, from the early phase, which focuses on the evaporation of surface moisture, to the later phase, which emphasizes slow and uniform internal moisture removal, temperature control within the coffee drying unit should not be based on a single fixed value. Instead, it should be flexible and adjustable according to the requirements of each drying stage. Therefore, the design of an adjustable air inlet system plays a crucial role in enabling operators to manage the internal environment of the greenhouse with greater precision [22]. Maintaining temperatures within the optimal range for each drying phase directly contributes to the final quality of the dried coffee beans [23].

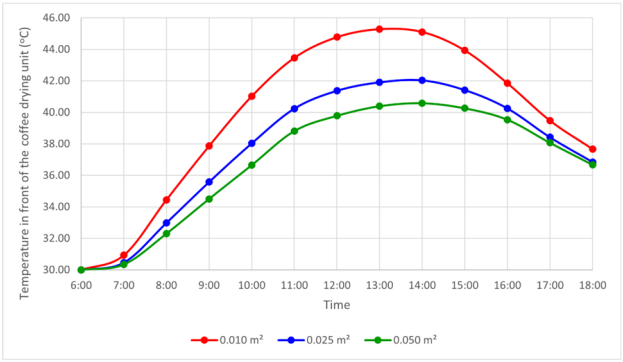

Figure 17 Simulated temperature distribution at the front section of the coffee drying unit equipped with 10-inch ventilation fan.

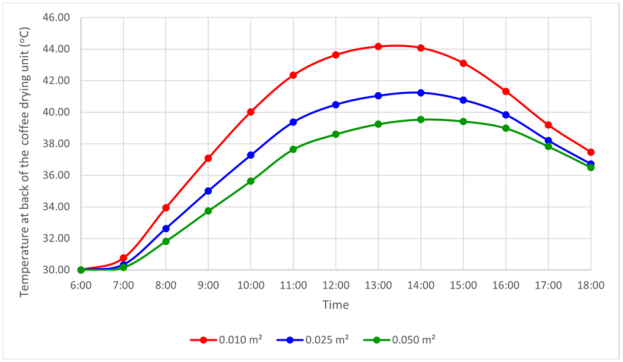

Figure 18 Simulated temperature distribution at the rear section of the coffee drying unit equipped with 10-inch ventilation fan

3.3 Comparison of Simulated and Experimental Air Velocity and Temperature

A comparison was conducted between the simulation results obtained from COMSOL Multiphysics and the experimental data from the prototype coffee drying unit equipped with a 10-inch ventilation fan and an air inlet area of 0.050 m². The air velocity values obtained from the COMSOL simulation and those measured in the prototype are summarized in Table 2.

Table 2 Comparison of air velocity values obtained from COMSOL Multiphysics simulation and prototype measurements.

Position	Air velocity (m/s)	
	Simulation	Prototype
Air inlet	2.950	2.443
Greenhouse corner	0.445	0.200
Greenhouse center	0.325	0.257
Front-side shelf	0.137	0.187
Rear-side shelf	0.199	0.189

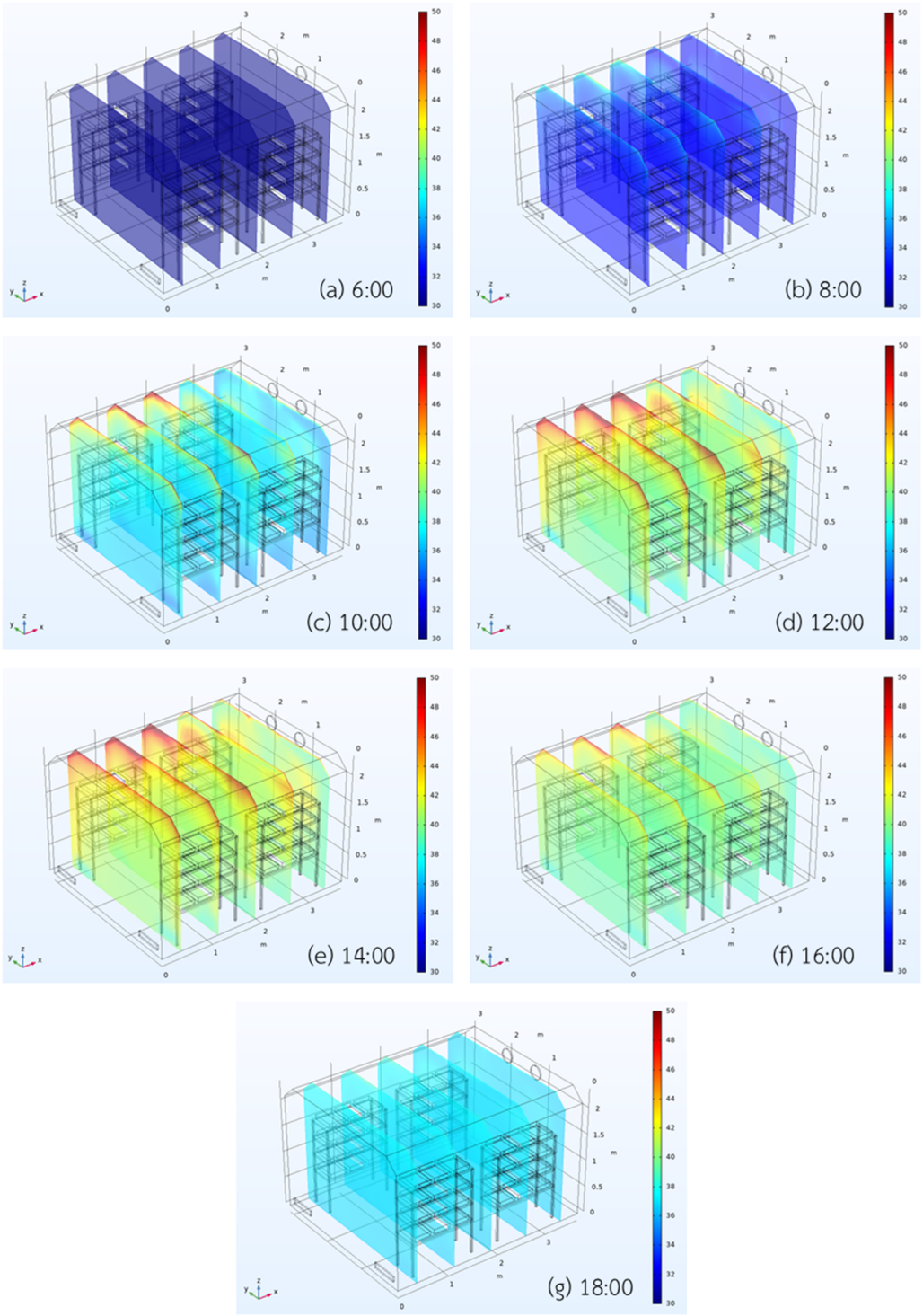

Figure 19 Simulated temperature distribution inside the coffee drying unit equipped with a 10-inch ventilation fan with 0.050 m² inlet area (a) 6:00, (b) 8:00, (c) 10:00, (d) 12:00, (e) 14:00, (f) 16:00, and (g) 18:00.

It can be observed that the simulation results from COMSOL Multiphysics yielded higher air velocity values at all measurement points compared to the prototype. This discrepancy is particularly evident at the air inlet, where the simulated velocity was 2.950 m/s, while the measured value from the prototype was only 2.443 m/s. A similar trend was observed at the corner and central positions of the greenhouse.

This difference can be explained by technical limitations in the simulation, particularly the mesh size settings. In this study, the mesh was set to an Extra Coarse level to accommodate the computational capacity of the available hardware. Using such a coarse mesh tends to reduce the resolution of small-scale flow features, such as shear layers and airflow through narrow gaps, resulting in less accurate representations. Consequently, the overall velocity values obtained from the simulation tend to be higher than the actual measurements [24], [25].

Another factor to consider is air leakage in the prototype greenhouse, which may occur at structural joints, edges, or imperfect assembly connections. This

unintended air loss is not included in the simulation, which assumes a fully enclosed system. As a result, the simulated model may overestimate airflow compared to the real system [26]. The simulated and measured temperature distributions at the front and rear sections of the greenhouse are shown in Figures 20 and 21, respectively.

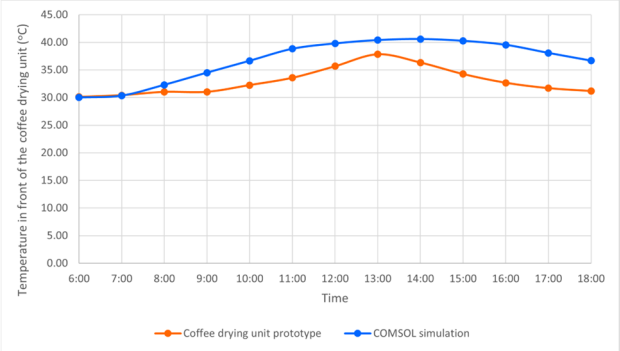

Figure 20 Temperature at the front section of the coffee drying unit obtained from COMSOL Multiphysics simulation and prototype measurements.

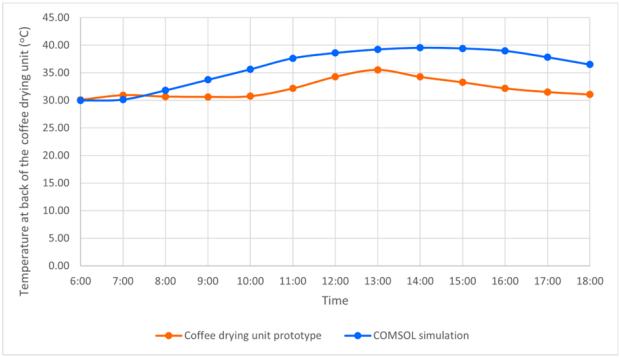

Figure 21 Temperature at the rear section of the coffee drying unit obtained from COMSOL Multiphysics simulation and prototype measurements.

Figures 4.9 and 4.10 show that the simulated temperatures obtained from COMSOL Multiphysics were higher than those measured in the prototype coffee drying unit. Between 12:00 and 15:00, the simulated internal temperatures ranged from 38.49 to 40.49 °C, while the measured values in the prototype ranged from 33.28 to 37.84 °C.

This difference can be explained by the idealized nature of the simulation model. Specifically, the simulation did not account for air leakage through material joints, energy exchange through non-perfect insulation materials, or environmental factors such as external wind and shading from surrounding objects. In practice, these factors contribute to more effective heat dissipation from the greenhouse [27].

Based on the above findings, it can be concluded that the discrepancy between the COMSOL Multiphysics simulation and the prototype experiment is primarily due to the simulation resolution chosen to match computational constraints, as well as simplified boundary conditions that do not fully reflect real-world complexity. Understanding these limitations allows the simulation model to be applied more effectively within an engineering design framework, particularly for improving coffee drying systems in practical contexts [28], [29].

4. CONCLUSION

This study aimed to investigate the airflow characteristics and temperature distribution inside a coffee drying unit using COMSOL Multiphysics, with a focus on the relationship between the size of ventilation fans and the air inlet area. The simulation results revealed that both fan size and inlet area had a direct influence on the air velocity entering the greenhouse. Generally, using a larger ventilation fan with a smaller air inlet area resulted in higher air velocity, consistent with the principle of the continuity equation. However, in cases where an excessively large fan was combined with a narrow air inlet, the system experienced back pressure and flow instability, which led to a reduction in actual air velocity and, in some cases, vortex formation inside the greenhouse. These findings indicate that the relationship between fan size and inlet area is nonlinear and subject to mechanical constraints. Therefore, the ventilation system should be designed with careful consideration of the appropriate pairing between these two parameters to ensure that the fan operates within its optimal performance range, avoiding excessive resistance that could reduce airflow efficiency.

The simulation also showed that the air inlet area significantly affected the internal temperature of the greenhouse. Smaller inlets resulted in higher internal temperatures due to reduced airflow rates and diminished convective cooling efficiency. The appropriate temperature range for coffee drying varies by drying stage. In the early phase, effective ventilation is necessary to accelerate surface moisture evaporation, while in the later phase, a higher and more stable temperature is preferred to promote internal moisture migration. Therefore, the design of adjustable air inlet systems holds strong potential for temperature control tailored to each stage of the drying process.

When comparing the simulation results with experimental data from the prototype greenhouse, some discrepancies in air velocity and temperature were observed. The simulation tended to produce higher values than the actual measurements at several points. These differences can be attributed to simulation settings, such as the use of an Extra Coarse mesh and simplified boundary conditions that do not fully reflect real-world complexities. Additionally, air leakage through structural joints, which commonly occurs in field systems, was not considered in the simulation.

In summary, the simulation model developed in this study was able to effectively represent the airflow and temperature distribution inside the coffee drying unit. Despite some limitations, the model proves valuable for

engineering analysis and can be applied to improve system-level design of coffee drying facilities, particularly in selecting appropriate fan sizes, inlet dimensions, and managing drying conditions suitable for each stage of the drying process.

ACKNOWLEDGMENTS

1. The mesh resolution should be increased in future simulations, particularly in areas with high flow gradients such as the air inlet, greenhouse corners, and around internal structures. A finer mesh in these regions would allow for more accurate representation of shear forces, flow separation, and vortex behavior.
2. Further studies should evaluate the energy efficiency of different greenhouse configurations under varying airflow and temperature conditions. This would help reduce energy costs and minimize environmental impacts.
3. Additional research should be conducted on the arrangement and positioning of the drying racks. The layout of these internal structures may significantly influence airflow distribution, potentially causing flow obstruction, recirculation zones, or uneven temperature profiles inside the greenhouse. Understanding this relationship could support the design of more effective drying systems.

REFERENCES

1. Malinovsky D, Dunn PJH, Rooke P, Goenaga-Infante H. The effect of roasting on boron isotope ratio in coffee beans: Implications for provenance studies of roasted coffee. *Food Chem* 2024; 439:138128.
2. Lee H, Yim J, Lee Y, Lee KG. Effect of organic acid-soaking and sonication on the formation of volatile compounds and α-dicarbonyl compounds in Robusta coffee. *Ultrason Sonochem* 2023; 99:106580.
3. Clarke R, Vitzthum OG. Coffee: recent developments. Chichester: John Wiley & Sons; 2008.
4. Gunning Y, Defernez M, Watson AD, Beadman N, Colquhoun IJ, Le Gall G, et al. 16-O-methylcafestol is present in ground roast Arabica coffees: Implications for authenticity testing. *Food Chem* 2018; 248:52–60.
5. de Azevedo Mendes G, de Oliveira MAL, Rodarte MP, dos Anjos VDC, Bell MJV. Determination of Arabica and Robusta species in blends of roasted coffee by Mid Infrared spectroscopy in association with mixture design. *Food Chem Adv* 2024; 4:100592.
6. Shofinita D, Lestari D, Aliwarga L, Sumampouw GA, Ambarwati SA, Gunawan KC, et al. Drying methods of coffee extracts and their effects on physicochemical properties: A review. *Food Bioproc Technol* 2024;17(1):47–72.
7. Zhang K, Cheng J, Hong Q, Dong W, Chen X, Wu G, et al. Identification of changes in the volatile compounds of Robusta coffee beans during drying based on HS-SPME/GC-MS and E-nose analyses with the aid of chemometrics. *LWT* 2022;161:113317.
8. de Melo Pereira GV, de Carvalho Neto DP, Júnior AIM, Vásquez ZS, Medeiros AB, Vandenberghe LP, et al. Exploring the impacts of postharvest processing on the aroma formation of coffee beans – A review. *Food Chem* 2019; 272:441–452.
9. Kulapichitr F, Borompichaichartkul C, Suppavorasatit I, Cadwallader KR. Impact of drying process on chemical composition and key aroma components of Arabica coffee. *Food Chem* 2019; 291:49–58.
10. Susana IGB, Alit IB, Okariawan IDK. Rice husk energy rotary dryer experiment for improved solar drying thermal performance on cherry coffee. *Case Stud Therm Eng* 2023; 41:102616.
11. Dong W, Hu R, Chu Z, Zhao J, Tan L. Effect of different drying techniques on bioactive components, fatty acid composition, and volatile profile of Robusta coffee beans. *Food Chem* 2017; 234:121–130.
12. Borém FM, Marques ER, Alves E. Ultrastructural analysis of drying damage in parchment Arabica coffee endosperm cells. *Biosyst Eng* 2008;99(1):62–66.
13. Hatari Electric Co., Ltd. Ventilating Fan. 2023 [cited 2023 Nov 7]. Available from: https:// s3-ap-southeast-1.amazonaws.com / hatari – media / cms / wp-content/ uploads /2017/04/12145910/ven-fan.pdf
14. TuTiempo.net. Solar radiation in Bangkok. 2024 [cited 2024 Nov 2]. Available from: https://en.tutiempo.net/solar-radiation/bangkok.html
15. Ibrahim M, Abdllatif O, Khalil E. Modelling of heat distribution and air turbulent flow inside a greenhouse at different air flow rates. In: *46th AIAA Aerospace Sciences Meeting and Exhibit*; 2008; Reno, NV. p. 1176.
16. Ibuki R, Behnia M. Optimization of air flow circulation with branching perforating duct and fan system. In: *1st International Symposium on CFD Applications in Agriculture*; 2012 Jul; p. 241–247.
17. Cao Z, Wang Y, Zhai C, Wang M. Performance evaluation of different air distribution systems for removal of concentrated emission contaminants using vortex flow ventilation system. *Build Environ* 2018;142:211–220.
18. Liu Y, Lin Z, Lin P, Jin Y, Setoguchi T, Kim HD. Effect of inlet guide vanes on the performance of small axial flow fan. *J Therm Sci* 2017;26:504–513.
19. Kim SY, Webb RL. Analysis of convective thermal resistance in ducted fan-heat sinks. *IEEE Trans Compon Packag Technol* 2006;29(3):439–448.
20. Wen J, Fu Y, Bao X, Liu Y, Xu G. Flow resistance and convective heat transfer performances of airflow through helical-tube bundles. *Int J Heat Mass Transf* 2019;130:778–786.
21. Moey LK, Sing YH, Tai VC, Go TF, Ng JY. Numerical investigation of inlet opening size on wind-driven cross ventilation. *J Mech Eng Sci* 2022;16(1):8662–8672.
22. Berbert PA, Queiroz DM, Silva JS, Pinheiro Filho JB. Drying of coffee (Coffea arabica L.) in a fixed bed with a simulated periodic airflow reversal. *J Agric Eng Res* 1994;59(3):195–202.

23. Alves GE, Borém FM, Andrade ET, Isquierdo ÉP, Siqueira VC, Dias CDA. Influence of different temperatures and airflows on drying of natural and pulped coffee. *Eng Agríc* 2020;40:192–200.
24. Rosminahar SN, Mat MNH, Yusup EM. Mesh refinement for dynamic airflow in healthcare. *Int J Integr Eng* 2024;16(6):90–99.
25. Liu Y, Long Z, Liu W. A semi-empirical mesh strategy for CFD simulation of indoor airflow. *Indoor Built Environ* 2022;31(9):2240–2256.
26. Babu AK, Kumaresan G, Aroul Raj VA, Vishal Surya SB. Numerical simulation of heat pump thin layer drying of Amaranth leaves. *Energy Sources A Recover Util Environ Eff* 2023;45(3):9383–9395.
27. Pasaribu H, Lumbangaol P, Napitupulu RA, Siagian P, Siagian HS, Setyawan EY. Simulasi CFD distribusi temperatur pada pengering biji kopi dengan sistem konveksi paksa. *Sprocket J Mech Eng* 2023;5(1):14–23.
28. Cebulski D, Cyklis P. Application of CFD simulation to the design of an innovative drying chamber. *Energies* 2024;17(13):3338.
29. Oberkampf WL, Blottner FG. Issues in computational fluid dynamics code verification and validation. *AIAA J* 1998;36(5):687–695.

Production of wood-plastic composite from non-metallic powders recovered from printed circuit board (PCB) waste

Ampai Chanachai[1,*], Preechaya Sanguansai[1], Watcharapon Wimonratpanya[1], Mewika Norachai[1], Waraporn Kidkarn[1]

[1] Department of Chemical Engineering, Faculty of Engineering, King Mongkut's University of Technology Thonburi, Bangkok 10140, Thailand
[*] Corresponding author: ampai.cha@kmutt.ac.th

ABSTRACT

This research studied the recovery of nonmetallic powders (NMPs) from waste printed circuit board (PCB) to produce a wood plastic composite. The NMPs was blended with polymers including: recycled high density polyethylene (rHDPE), wood flour, ethylene vinyl acetate (EVA) and linear low-density of polyethylene grafted with maleic anhydride (LLDPE - g - MAH) as compatibilizer. NMPs was prepared by grinding PCB to 0.106 mm size. Copper in PCB powders was extracted by ammoniacal alkaline solution in the ratio of PCB powder to solvent is 1 g : 10 ml Then, all compositions were blended in various ratios through twin-screw extruder to produce the wood-plastic composite and molded by hot compressor. The mechanical properties such as tensile strength, %elongation at break and flexural strength of polymer composites were tested. Morphological characteristics were studied by scanning electron microscope. All polymer composites, which contained wood flour, had mechanical properties pass Thai industry standard of composite wood (TIS.178 – 2549) i.e., Flexural strength > 34 Pa and Elastic Modulus > 4,500 Pa. Thus, all composites could be produced as composite wood. It was found from the SEM results that the composite that had the ratio of rHDPE : NMPs : Wood flour equal to 50 : 30 : 20 were well dispersed of NMPs. It also had the highest tensile strength, which was 20.34 MPa and Flexural strength and Elastic Modulus were 16.68 MPa and 2.54 MPa, respectively. This research enables the utilization of NMPs from electronic waste (PCB), which helps create sustainability and protect the environment.

Keywords: Nonmetallic powders; Polymer composite; Printed circuit board; TIS.178-2549

1. INTRODUCTION

Currently, technology is developing rapidly, resulting in the increased use of electronic devices such as mobile phones, computers and various electronic devices, resulting in an increase in the amount of electronic waste. Currently, the problem of electronic waste has increased by three times the rate of municipal solid waste. In addition, Thailand is also a destination for electronic waste from around the world, which is hidden in the form of computers and mobile phones imported from abroad, which have a short lifespan [1]. This electronic waste is considered a major environmental problem.

The components of printed circuit boards (PCBs) are composed of 30.6% heavy metals and 69.4% non-metallic powders (NMPs), which are composed of 31.8% epoxy resin and 37.6% glass fiber. Currently, there are studies on the removal of metals from electronic circuit boards, which are mostly copper, with a maximum content of 20% [2]. This results in a large amount of residual NMPs. If disposed of in landfills, it will have an environmental impact due to the presence of heavy metals. Therefore, NMPs should be recycled.

There have been studies using NMPs from PCB as an adsorbent [3] to adsorb heavy metals from paper industry and treat wastewater before releasing into the environment. However, the preparation process of the adsorbent involves the use of hazardous chemicals. NMPs has been used in the production of composite materials [4], using NMPs as an alternative material in concrete production. It was found that the composite materials could not withstand fire at high temperatures because NMPs contains epoxy resin. In addition, NMPs was mixed with polyester and styrene monomers [5], and the flexural strength and flexural modulus were increased, but the materials were hard but brittle and had high production costs.

NMPs was blended with polyvinyl chloride (PVC) [6] to be used as a reinforcement for composite materials, resulting in increased tensile strength. It was found that the tensile strength value increased as a result of using small size NMPs, which made it compatible

with PVC. However, since PVC is originally a thermoplastic plastic, the overall properties of the material were hard but brittle. When NMPs were blended with polypropylene [7], the material was found to be much stronger. However, since polypropylene is commonly used as a raw material for the production of consumer goods, when blended with NMPs, heavy metals are still mixed, so they cannot be used further, as heavy metals can be harmful to living things. In addition, NMPs were blended with high-density polyethylene (HDPE) because HDPE has good physical properties, namely, higher tensile strength and percentage of elongation at break. Therefore, it is possible that the resulting composite material could be used in practice.

Research has found that NMPs and HDPE were blended and the separation efficiency of NMPs was improved using a triboelectric device [8]. The mechanical properties test results of the material showed that it had high tensile strength, but lower than the tensile strength of pure HDPE. Since HDPE is expensive, the production cost is high. This experiment was conducted by blending NMPs with recycled high-density polyethylene (rHDPE) and using ethylene vinyl acetate (EVA) and polyethylene grafted with maleic anhydride (PE-g-MAH) [9, 10]. It was found that the material had higher tensile strength and percentage elongation at break due to the conditioning of NMPs using PE-g-MAH, which provided rHDPE with functional groups that could better bond with NMPs. EVA is a substance that can increase percentage elongation at break of the material. In addition, the production cost of raw materials is low because rHDPE is cheap, and from the overall properties of the raw materials, it can be further applied.

This research aimed to study the application of NMPs recovered from PCBs mixed with rHDPE and wood flour using EVA and linear low density polyethylene grafted with maleic anhydride (LLDPE-g-MAH) as compatibilizer in the production of wood-plastic composites. It is expected that the composite materials will have properties in accordance with the industrial product standards for plywood (TIS 178-2006) [11].

2. EXPERIMENTAL

2.1 PCB powder preparation

Cut the PCB board into 5 cm × 5 cm size, weighing 5 kg, and grind it to a smaller size in sequence. 1) Coarse grinder, use 60 rpm until the size is about 1 - 1.5 cm. 2) Fine grinder, use 60 rpm until the size is about 3 - 5 mm. and 3) Rod mill vessels, use 15 - 20 rpm for 12 hours, 2 rounds until the size is about 0.106 - 0.180 mm. Sieve the PCB powder to get a size of 0.106 mm.

2.2 Wood flour preparation

Prepare the wood flour by using a sieve to separate the grain size to 0.106 mm.

2.3 Extracting copper from PCB powder with ammonia solvent/ Preparation of NMPs

Ammonia solvent was prepared by mixing 7.37 L of 5 M NH4OH, 1.25 and 1.32 kg of 0.5 M CuSO4 and 1 M (NH4)2SO4, respectively, with water to a volume of 3 L. The 140 mesh (0.106 mm) PCBs were immersed in 1 g:10 mL of ammonia solvent for 24 h, and then filtered with 0.7 μm pore size GF/C filter paper to separate NMPs from the ammonia solvent. The solution was washed with distilled water until the pH was approximately 8. The NMPs were dried at 95 °C for 24 h and weighed.

2.4 Forming wood-plastic composite

NMPs, rHDPE, EVA, LLDPE-g-MAH and wood flour were preheated at 80 °C for 4 h. The preheated mixture was mixed with NMP using a high-speed mixer at 1000 rpm for 2 min in the proportions according to Table 1. The mixture was then preheated into pellets using a Rheomex CTW 100 OS twin-screw extruder (Fig. 1) from HAAKE, using a melt temperature of 150 °C at the feed section and 160 °C at the end of the head-die section, and a screw speed of 50 rpm. The mixture was discharged from the head-die through a cooling bath, and then pelletized with a COPERION pelletizing machine.

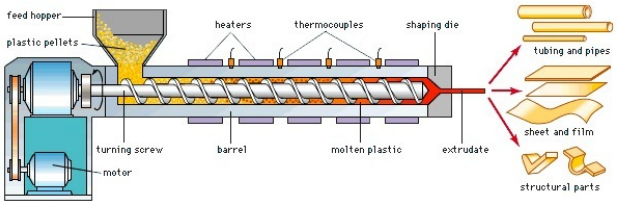

Feed section	Screw section	Header die section
150 °C	50 rpm	160 °C

Figure 1 Screw extruder [12].

2.5 Morphological and Mechanical property testing of wood plastic pellets

The 8 formulas of wood-plastic pellets were put into a hot press to form dumbbells by heating the mold at 200 degrees Celsius for 10 minutes. Then, the plastic pellets were put into the mold and heated for 15 minutes using a pressure of 150 pounds per square inch. Then, they were cooled down using a coolant for 5 minutes. Then, the formed dumbbells were analyzed for morphological structure using a Scanning Electron Microscope (SEM, JSM-5410 LV) of JEOL Company and tested for tensile strength, elongation at break, and bending strength using a universal testing machine (HUT-300) of BAIROE Company.

3. RESULTS AND DISCUSSION

3.1 Morphological properties of polymer composite materials

Morphological analysis of Wood-Plastic Composite blended with rHDPE: EVA: NMPs: Wood flour at different proportions with LLDPE - g - MAH as a compatibilizer are shown in Figure 2.

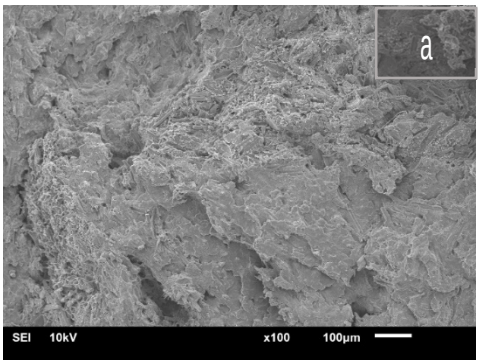

(a) Composite 1 (50 rHDPE : 10 EVA : 30 NMPs : 20 WF)

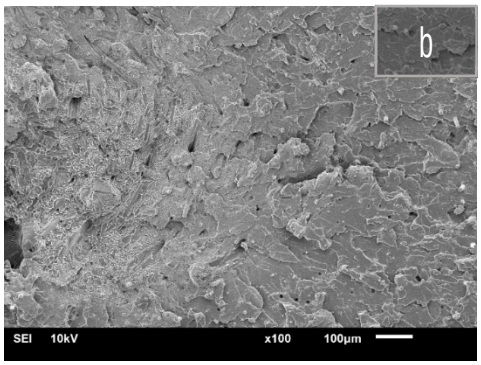

(b) Composite 2 (50 rHDPE : 20 EVA : 20 NMPs : 10 WF)

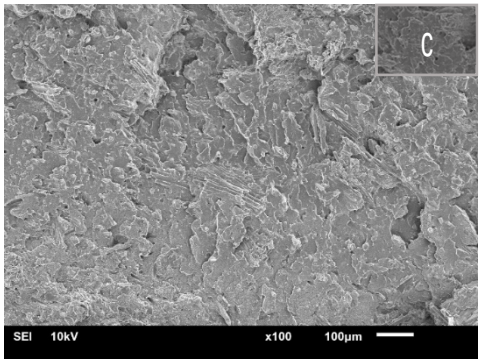

(c) Composite 3 (50 rHDPE : 0 EVA : 30 NMPs : 20 WF)

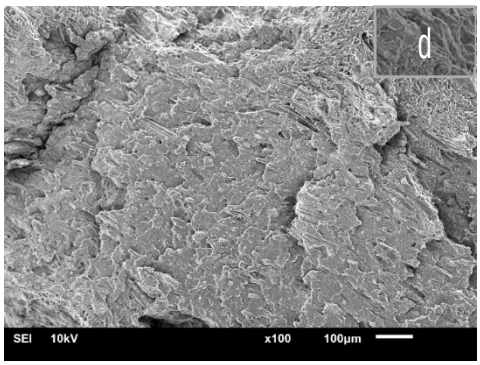

(d) Composite 4 (50 rHDPE : 0 EVA : 40 NMPs : 10 WF)

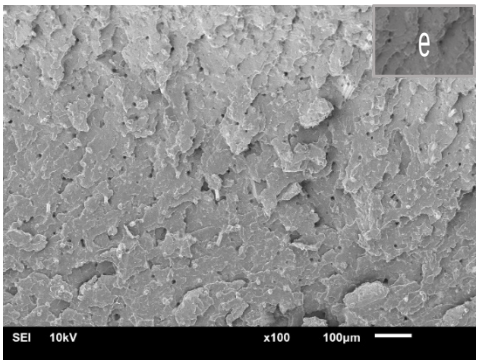

(e) Composite 5 (50 rHDPE : 10 EVA : 40 NMPs : 0 WF)

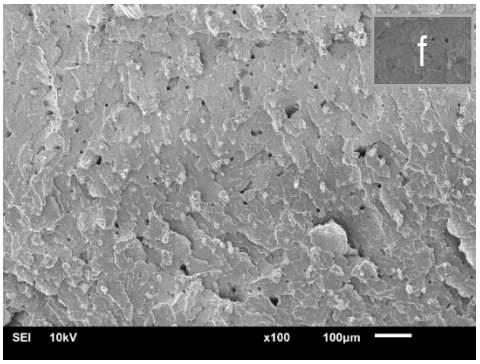

(f) Composite 6 (50 rHDPE : 20 EVA : 30 NMPs : 0 WF)

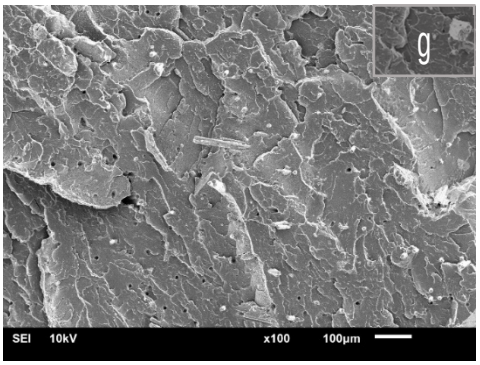

(g) Composite 7 (50 rHDPE : 30 EVA : 20 NMPs : 0 WF)

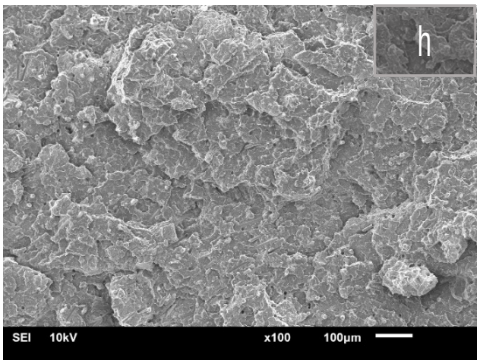

(h) Composite 8 (50 HDPE : 0 EVA : 50 NMPs : 0 WF)

Figure 2 Comparison of SEM images of wood-plastic composite materials at different proportions, Magnification 100 times.

From Figure 2 (a and b), it can be seen that the polymer phase was divided into two parts: the NMPs part, which is in the form of a rod, combined with the wood flour, which was in the form of wood pulp, and

the polymer part, which was smooth. This is because EVA has vinyl acetate, which is a substance with a very high polarity. NMPs and wood flour have hydroxyl groups, which are also polar substances, but the polarity is lower than that of EVA, while rHDPE is non-polar, but the polarity is increased with maleic anhydride graphene LLDPE. This makes rHDPE more polar, so it can be mixed together. However, wood flour and EVA are substances with different characteristics. Wood flour is a solid, while EVA is a rubber, so it cannot be mixed together. When the amount of EVA increases from 10% to 20%, the polarity will increase even more, pushing some of the rHDPE, NMPs, and wood flour together.

Meanwhile, if the amount of NMPs increased from 20% to 30% as shown in Figure 2 (a – c) respectively, it can be seen that the amount of NMPs distributed in the polymer increased, but the distribution was disordered and undirected. However, if there was too much NMPs, they will agglomerate. (Agglomeration) of NMPs as shown in Figure 2 (d), which has 40% NMPs in the polymer composite material. In case the amount of wood flour is reduced from 20% to 10%, the proportion of NMPs was more than the wood flour, resulting in less adhesion between them. Therefore, some NMPs were released from the material as shown in Figure 2 (a and b), respectively. However, in the case where the wood flour content was reduced from 20% to 10% but no EVA was added, it can be seen that there was more dispersion of NMP and wood flour. Since EVA is a polar substance, the absence of EVA does not cause the other substances to disperse, as shown in Figure 2(c - d). From the morphology of components 1 - 4, it can be seen that component 3 was the most homogeneous, with NMPs and wood powder dispersed and not agglomerated.

Table 1 Mechanical properties of wood-plastic composites in various compositions.

No.	rHD-PE (%)	EVA (%)	NMPs (%)	WF (%)	HD PE (%)	TS (MPa)	EB (%)	FS (MPa)
1	50	10	20	20	0	11.99	10.20	8.68
2	50	20	20	10	0	11.75	16.23	5.67
3	50	0	30	20	0	20.34	10.48	16.68
4	50	0	40	10	0	12.88	6.96	14.18
5	50	10	40	0	0	14.52	14.25	10.01
6	50	20	30	0	0	11.24	26.57	7.37
7	50	30	20	0	0	10.71	71.08	4.74
8	0	0	50	0	50	17.40	10.85	14.45

* WF = Wood Flour TS = Tensile strength
EB = Elongation at break FS = Flexural strength

From Table 1, it was found that Composite 1, which had a higher amount of wood flour, had a higher tensile strength value, while Composite 2, which had a higher amount of EVA, resulted in a higher % Elongation at break value. When considering Composite 2 and 4 with the same amount of wood flour, it was found that Composite 2 mixed with EVA had a higher % Elongation at break value than Composite 4, which did not have any EVA. Because EVA is a material with a high % Elongation at break, when mixed with polymer composite materials, the elongation will increase.

In addition, Composites 5, 6, 7 with reduced NMP content, added EVA and no Wood Flour, found that when EVA content increased, the percentage of elongation at break increased. Composite 7 had the highest percentage of elongation at break at 71.08%. When NMP content decreased, the Tensile Strength value decreased. From the morphological structure, it was found that Composite 5 NMP was compatible with the Matrix phase, resulting in high Tensile Strength value.

While Composite 7 has a higher proportion of EVA, resulting in a higher %Elongation at break value, while Composite 8, which has 50% NMPs and 50% HDPE, when studying the morphology, found that NMPs were well distributed in HDPE plastic, resulting in the material being able to withstand force better, resulting in a higher tensile strength value than general HDPE, but a lower %Elongation at break value. The production guidelines for composite wood found that Composite 1, 2, 3, and 4 have tensile strength values that pass the values specified in the plywood industry product standard (TIS 178-2549).

4. CONCLUSION

The results of the mechanical properties test of the 8 Wood-Plastic Composite were consistent with the results of the morphology analysis, that is, when the amount of NMPs increases, it will be well distributed in the polymer, resulting in a higher tensile strength. When the amount of EVA increases, the EVA particles will be agglomerated, making them larger, resulting in more phase separation between the polymers, resulting in a lower tensile strength but a higher %Elongation at break. The proportion that gave the best mechanical properties was Composite 5, which has a ratio of rHDPE: EVA: NMPs of 50: 10: 40, with a tensile strength of 14.52 MPa. In addition, in the composition containing Wood flour, it was found that when the amount of Wood flour increased, it was better distributed, resulting in a higher tensile strength. The proportion that gave the best mechanical properties was Composite 3, which has a ratio of rHDPE: NMPs: Wood flour of 50: 30: 20, with a tensile strength of 20.34 MPa.

Polymer composites containing Wood Flour had values that pass the industrial product standards for plywood (TIS 178-2549) in all proportions. Therefore, they can be produced as wood-plastic composite. However, the most suitable proportion for producing wood-plastic composite was Composite 4 because it has the lowest cost and the highest amount of NMPs used, and it also has the standard properties of plywood.

REFERENCES

1 Electronic waste, environmental problems from technological society [online], retrieved from: http: // www .oknation.net/blog/mena/2007/06/20/ entry-1 [19 October 2017].

2. Jirang Cui and Lifeng Zhang, Metallurgical recovery of metals from electronic waste: A review, Journal of Hazardous Materials 2008; 158: 228-256.

3. Yujiao Kan, Qinyan Yue, Baoyu Gao and Qian Li, Preparation of epoxy resin-based activated carbons from waste printed circuit boards by steam activation, Material Letters 2015; 159: 443-446.

4. Peng Mou, Dong Xiang and Guanghong Duan, Products Made from Nonmetallic Materials Reclaimed from Waste Printed Circuit Boards, Tsinghua Science & Technology 2007; 12(3): 276-283.

5. Premrudee Kanchanapiya, Sawanya Jareemit, Suphaphat Kwonpongsagoon and Waraporn Pinyo, Recycling of non - metallic powder from printed circuit board waste as a filler material in a fiber reinforced polymer, Environment Protection. Engineering 2015; 41(4): 151-166.

6 Xinjie Wang, Yuwen Guo, Jingyang Liu, Qi Qiao and Jijun Liang, PVC-based composite material containing recycled non-metallic printed circuit board (PCB) powders, Journal of Environmental Management 2010; 91: 2505-2510.

7 Yanhong Zheng, Zhigang Shen, Chujiang Cai, Shulin Ma and Yushan Xing, The reuse of nonmetals recycled from waste printed circuit boards as reinforcing fillers in the polypropylene composites, Journal of Hazardous Materials 2009; 163: 600-606.

8 Guangwen Zhang, Yaqun He, Haifeng Wang, Tao Zhang, Xing Yang, Shuai Wang and Wen Chen, 2016, “Application of triboelectric separation to improve the usability of nonmetallic fractions of waste printed circuit boards: Removing inorganics, Journal of Cleaner Production 2016; 142: 1911-1917.

9 Shantha Muniyandi, Johan Sohaili, Azman Hassan and Siti Suhaila Mohamad, 2013, “Converting non-metallic printed circuit boards waste into a value added product”, Journal of Environmental Health Science and Engineering 2013; 11(2): 1-9.

10 Fatimah Abd Rajak Hamim, Supri Abdul Ghani and Firuz Zainudin, Properties of Recycled High Density Polyethylene (RHDPE)/Ethylene Vinyl Acetate (EVA) Blends : the Effect of Blends Composition and Compatibilisers, Journal of Physical Science 2016; 27(2): 23–39.

11 Thai Industrial Standards Institute, Ministry of Industry, TIS.178 – 2006: Industrial Product Standards for Plywood, the Government Gazette, Announcement and General Affairs Edition 2007; 124 (Special Section 28D): 10.

12 Screw Barrel [online], retrieved from: http://www.jnha.com/P_19/ [30 April 2017].

Machine learning-assisted multi-objective optimization of furfural production from lignocellulosic biomass hydrolysate

Patcharapuek Pattaramanon[1,*], Choowong Chaisuk[1], Nutchapon Chotigkrai[1]

[1] Department of Chemical Engineering, Faculty of Engineering and Industrial Technology, Silpakorn University, Nakhon Pathom 73000, Thailand

[*] Corresponding author: pattaramanon_p@su.ac.th

ABSTRACT

The conventional process for furfural production from lignocellulosic biomass has disadvantages due to low furfural yield and high operating costs. Therefore, the reactive distillation (RD) process can mitigate these drawbacks by continuously separating furfural from the reaction medium, preventing its degradation. In this study, the process of furfural production via RD from three biomass hydrolysates was simulated using Aspen Plus V14. and optimized using machine learning (ML). The dataset (1,406 datapoints) consisting of 9 input features and 4 output variables was generated using Latin hypercube sampling by integrating Python code with Aspen Plus. Multi-layer perceptron (MLP) models were developed to predict each output separately, including furfural revenue, CO_2 emissions, furfural purity, and total annual cost (TAC). For multi-objective optimization (MOO), non-dominated sorting genetic algorithm II and technique for order preference by similarity to ideal solution were employed for maximizing profit while minimizing CO_2 emissions. The MLP models demonstrated high predictive performance, with R^2 scores exceeding 0.94 for all outputs. The MOO results showed that optimizing for 2-objectives reduced CO_2 emissions by 68.63% and increased gross profit margin by 7.18% compared to the 1-objective optimization for maximum profit. SHapley Additive exPlanations revealed that hydrolysate feed rate and RD reboiler duty significantly influenced TAC, CO_2 emissions, and revenue. Additionally, acetic acid concentration had a substantial impact on TAC due to acetic acid cost, while biomass type influenced revenue based on xylose content. To improve economic feasibility, biomass hydrolysates should have high xylose content with optimal acetic acid levels and feed rate optimization is essential for efficiency.

Keywords: Furfural production; Reactive distillation; Machine learning; Multi-objective optimization

1. INTRODUCTION

Biomass is a versatile feedstock that can be used to produce fuels, generate electricity, and manufacture materials traditionally made from fossil resources. Transitioning to biomass energy offers a significant opportunity to reduce greenhouse gas emissions. While burning biomass releases carbon dioxide at rates similar to fossil fuels, this emission is largely balanced by the carbon absorbed during the biomass's growth, making the process nearly carbon-neutral [1].

Furfural is a highly selective and reactive solvent widely used in industrial applications like fuel refining and abrasive production, and it serves as a crucial platform chemical for creating valuable compounds and advanced biofuels [2]. Furfural is produced from lignocellulosic biomass through acid-catalyzed hydrolysis of hemicellulose, dehydration of pentosans into furfural, and subsequent recovery and purification using heterogeneous azeotropic distillation [2]. The biomass pretreatment method significantly influences both the energy consumption and environmental impact of furfural production [3]. Moreover, the composition of the biomass hydrolysate significantly affects the yield of furfural [4]. Traditional xylose dehydration is carried out using mineral acids like sulfuric or phosphoric acid at temperatures ranging from 160 to 240 °C [2]. In the furfural recovery and purification stage, the furfural solution is introduced into an azeotropic distillation column to concentrate the furfural near its azeotropic composition in the distillate. The resulting distillate is then cooled and directed to a decanter, where it is separated into aqueous and organic phases. The aqueous phase is recycled back to the initial column, while the organic phase is sent to a subsequent distillation column to further purify the furfural product [5]. The conventional furfural production process has drawbacks, including low product yield and high operating costs [2]. To address these issues, existing research has focused on increasing furfural yield and enhancing the overall efficiency of the production process. L. Liu et al. [6] investigated a vapor-releasing

reactor system for producing and separating furfural from biomass hydrolysate, achieving a high furfural yield (73%) without the need for additional catalysts. G. Contreras-Zarazúa et al. [3] explored furfural production using various types of biomass feedstocks under different intensified separation and pretreatment methods. Their findings reveal that dilute acid pretreatment, when combined with a thermally coupled distillation system, offers the most cost-effective and environmentally friendly solution across all biomass types, with wheat straw demonstrating the lowest production cost and environmental impact. L.C. Nhien et al. [7] investigated an innovative hybrid process combining RD with extraction for furfural production. The study demonstrated that using butyl chloride as the extracting solvent in this hybrid system significantly enhanced performance, resulting in savings of up to 51.8% in total investment costs and 57.4% in TAC compared to the conventional method, along with a 58.9% reduction in total annual CO_2 emissions. Moreover, K. Wiranarongkorn et al. [8] investigated a sustainable furfural production process from lignocellulosic biomass using RD, employing exergy and exergoeconomic analyses to assess its performance. The study involved designing and optimizing the RD system, identifying the RD column as the main source of exergy destruction. It also found that reducing the reboiler duty and feedstock costs can significantly decrease the overall production cost. As a result, methods that enable simultaneous reaction and separation of furfural can significantly enhance production performance, particularly through process intensification.

In MOO, ML can address the limitations of first-principles modeling tools such as Aspen Plus, which often struggle to explore infeasible regions due to convergence rate challenges [9]. Moreover, ML significantly reduces computation time. T. Shi et al. [10] developed a novel ML-based optimization framework that combines artificial neural network (ANN) with mixed-integer linear programming to improve biohydrogen production from waste co-gasification, resulting in enhanced sustainability and significantly lower computational time compared to traditional approaches. J. Zhang et al. [11] explored an innovative solar-powered integrated multi-generation system designed to simultaneously produce electricity, cooling, and freshwater. This system combines a supercritical CO_2 Brayton cycle with an organic Rankine cycle. To enhance performance prediction and reduce computational time during MOO, the study employs ML techniques, specifically an ANN. The results highlight the effectiveness of this approach for analyzing complex energy systems. The optimized configuration delivers a total output of 2.486 MW, achieves a thermal efficiency of 26.16%, and results in a levelized cost of energy of $0.105/kWh. Z. Liu et al. [9] investigated a novel ML proxy method based on XGBoost is proposed to optimize low-carbon hydrogen production. This approach simultaneously minimizes economic cost, exergy destruction, and CO_2 emissions, while maximizing hydrogen output. Serving as an efficient surrogate for first-principles modeling, the ML proxy significantly outperforms first-principles modeling by thoroughly exploring both feasible and infeasible solution spaces. Moreover, The ML can used for interpret complex model by SHapley Additive exPlanations (SHAP) analysis [12]. Consequently, the ML model significantly reduces optimization time and expands the search space to the infeasible domain, enabling more comprehensive and efficient exploration.

The aim of this study is to perform multi-objective optimization to enhance the efficiency of furfural production from biomass hydrolysate using a machine learning model.

2. EXPERIMENTAL

This study comprises four sections: (1) Aspen Plus model simulation, (2) development of machine learning model, (3) multi-objective optimization, and (4) SHAP analysis.

2.1. Aspen Plus model simulation section

In this section, Aspen Plus version 14 was used to simulate furfural production through reactive distillation. The non-random two-liquid model was chosen to predict thermodynamic properties [8]. The biomass hydrolysate served as the feedstock for this process. Table 1 shows composition of biomass hydrolysate.

Table 1 The composition of each biomass hydrolysate

Component	Sugarcane Bagasse	Wheat Straw	Corn Stover
Xylose	0.0215	0.0100	0.0692
Furfural	0.0005	0.0005	0.0025
Acetic acid	0.0036	0.0012	0.0072
Water	0.9743	0.9883	0.9212

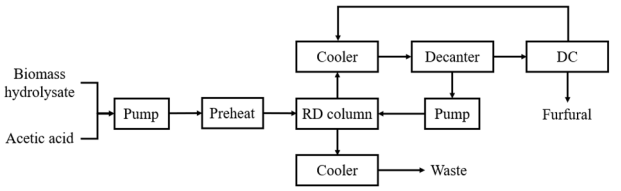

Figure 1 Block flow diagram for furfural production

Figure 1 shows furfural production via RD. This model's simulation was adapted from previous work [8]. First, the biomass hydrolysate was mixed with additional acetic acid, pressurized, preheated to 150 °C, and then fed into the RD column. In the RD column, furfural was produced and separated. Furfural and water were separated in near azeotrope composition at top of the column. The heavy components such as unreacted xylose, water, acetic acid, and humins were removed at the bottom of the column and cooled to 30 °C. The top product of RD column was cooled to 90 °C and fed into decanter. In a decanter, the product was separated into

organic and aqueous phases. The aqueous phase was fed into pump and sent into RD column while organic phase was fed into distillation column (DC). In DC, furfural was concentrated to produce high purity of furfural at bottom product and cooled to 30 °C while the top product was mixed with top product of RD column. Moreover, Reaction and kinetic model for RD column are shown in (1)-(6)

$$\text{Xylose} \xrightarrow{R1} \text{Furfural} + 3\text{Water} \quad (1)$$

$$\text{Furfural} \xrightarrow{R2} \text{Humins} \quad (2)$$

$$\text{Xylose} + \text{Furfural} \xrightarrow{R3} \text{Humins} \quad (3)$$

$$R1 = 4.189\times10^{10}[A]^{0.1676}\exp\left(-\frac{108.6}{RT}\right)[C_X] \quad (4)$$

$$R2 = 1.271\times10^{4}[A]^{0.1375}\exp\left(-\frac{63.413}{RT}\right)[C_F] \quad (5)$$

$$R3 = 3.4051\times10^{10}[A]^{0.1676}\exp\left(-\frac{104.99}{RT}\right)[C_X][C_F] \quad (6)$$

Where [A], [C_X], and [C_F] are acetic acid concentration in mol/L, Xylose concentration in mol/L, and Furfural concentration in mol/L, respectively. This kinetic model was reported by Z. Chen et al. [4].

2.2. Development of machine learning model section

The dataset for training and testing ML model was generated by integrated Python and Aspen Plus model. The Latin hypercube sampling (LHS) was employed to generate dataset. The LHS sampling 500 times for each type of biomass. Table 2 shows list of features and range of each feature.

Table 2 List of feature and range

Feature	Value	Unit
Type of biomass	1-3	-
[A]	0.17-1.5	mol/L
RD Pressure	8-18	bar
RD Reflux ratio	1-20	mole
RD Reboiler duty	5000-30000	kW
RD residence time	0.1-3	min
DC Reflux ratio	0.01-5	mole
DC Reboiler duty	50-500	kW
Feed Hydrolysate	5000-35000	kg/hr

Abnormal data points were removed from the generated dataset to prevent inaccurate predictions [9]. The generated dataset initially contained 1,500 data points, of which 1,406 remained after removing abnormal datapoints. The outputs of ML model consist: revenue of furfural, purity of furfural, TAC, and CO_2 emissions. The MLP model was chosen to predict each output individually. The dataset was split into training dataset (80%) and testing dataset (20%). The MLP model was trained on the training dataset, and hyperparameter optimization was conducted to achieve optimal performance. The MLP model consist: input layer, one or more hidden layer, and output layer. Each layer contains neurons, with each neuron fully connected to those in the subsequent layer. The number of hidden layers and the number of neurons per layer are hyperparameters to be optimized. The Optuna library was employed to hyperparameter optimization. Moreover, 5-folds cross validation (5-CV) method was selected to prevent overfitting. The training dataset was split into 5 folds. The model was trained using four folds for training and tested on the remaining fold, repeating this process five times so that each fold served as the test set once. The model performance was calculated as the average of the five test results. The optimal hyperparameters were selected based on the highest cross-validation score. The model performance indicators are shown in (7)-(9).

$$R^2 = 1 - \frac{\sum(\hat{y}_i - y_i)^2}{\sum(y_i - \bar{y})^2} \quad (7)$$

$$RMSE = \sqrt{\frac{\sum(\hat{y}_i - y_i)^2}{\text{Number of observations}}} \quad (8)$$

$$MAPE = \frac{100}{\text{Number of observations}} \sum \frac{|y_i - \hat{y}_i|}{|y_i|} \quad (9)$$

Where y_i is the real value, $\hat{y}_i$ is the predicted value, and $\bar{y}$ is is the average of the real values.

2.3. Multi-objective optimization section

The ML model was integrated with the Non-dominated Sorting Genetic Algorithm II (NSGA-II) to identify the optimal Pareto front. The ML models were predicting objective values and constraints. The objective values for multi-objective optimization including maximize profit and minimize CO_2 emissions. Moreover, purity of furfural was use as constraints for multi-objective optimization. Technique for order preference by similarity to ideal solution (TOPSIS) was selected for captured optimal solution.

The profit was calculated from equation (10)-(11). Where TIC is total investment cost, and TOC is total operating cost. Payback period was assumed to be 10 years [7]. Moreover, the CO_2 emissions were calculated based on the utilities consumed in the process.

$$\text{Profit} = \text{Revenue} - \text{TAC} \quad (10)$$

$$\text{TAC} = \frac{\text{TIC}}{\text{Payback period}} + \text{TOC} \quad (11)$$

NSGA-II is an optimization algorithm in which an initial population is generated, followed by tournament selection based on objective quality, and then crossover and mutation are applied to create a new population [13]. TOPSIS is multi-criteria decision-making method.

TOPSIS chooses optimal solution by rank alternatives based on their closeness to an ideal solution and distance from a negative ideal solution [11].

2.4. SHAP analysis section

Explainable Artificial Intelligence focuses on interpreting ML predictions, and the SHAP value method employs game-theoretic concepts to quantify both the magnitude and direction of each feature impact, thereby enhancing our understanding of the model decision-making process [12].

3. RESULTS AND DISCUSSION

3.1. Model validation

The model for predicting the furfural yield was validated by compared with experimental results from Z. Chen et al. [4]. The acetic acid concentration is 0.5 mol/L and xylose concentration of 80 g/L were used as initial feed to validation. The results demonstrated good performance, as shown in Table 3.

Table 3 Comparison of yield of furfural from simulation and experimental

Temperature (°C)	Yield of furfural (%)		Error (%)
	Simulation	Experimental	
210	55	54	1.61
190	37	35	6.33
180	25	23	8.67

3.2. Hyperparameter optimization

The ML model was optimized based on 5-CV score, as shown in Table 4. The results demonstrated ML can explained variance of each output with R^2 close to 1. The optimized hyperparameters for revenue, purity of furfural, CO_2 emissions, and TAC were (257, 211, 82), (211, 57, 231), (258, 263, 65), and (298, 110, 54, 286), respectively. For example, the ML model of revenue had 3 hidden layers and 257, 211, and 82 nodes in hidden layer 1, 2, and 3, respectively. The optimal model demonstrates high predictive performance for each output, as shown in Figure 2-Figure 5. The R^2 of testing set was close to 1. Moreover, The RMSE and MAPE values for all models indicate a high level of accuracy and are considered acceptable.

Table 4 5-CV score of each machine learning model

Model	5-CV score via R^2
Revenue	0.9954
Purity of furfural	0.9275
CO_2 emissions	0.9995
TAC	0.9981

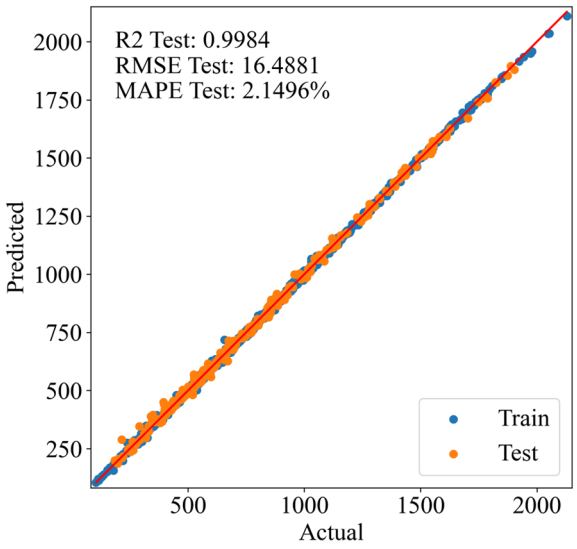

Figure 2 Model performance on TAC ($/hr)

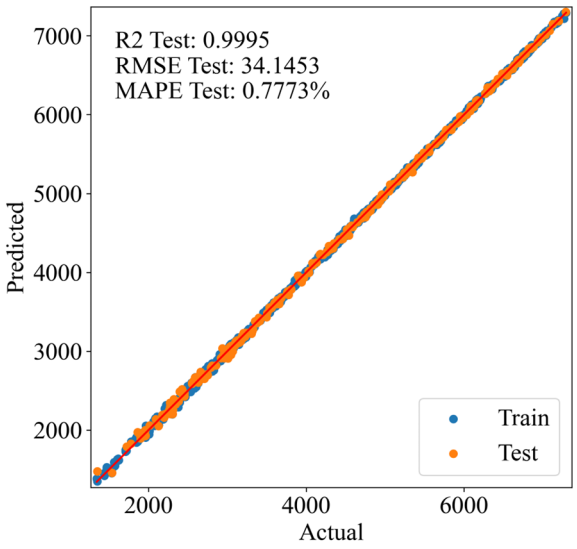

Figure 3 Model performance on CO_2 emissions (kg/hr)

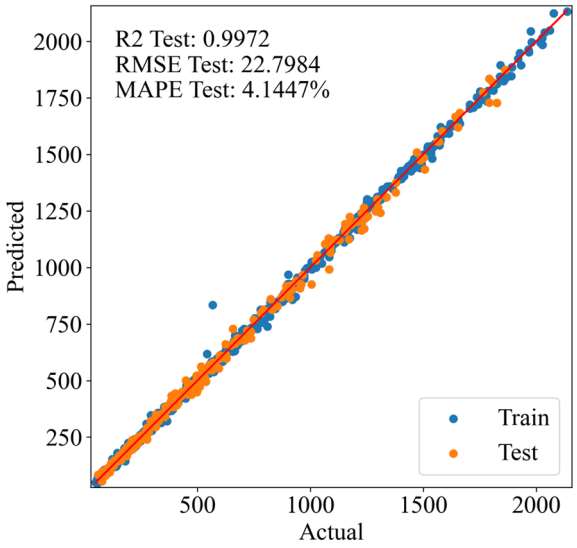

Figure 4 Model performance on Revenue ($/hr)

Table 5 Optimal solution of multi-objective and single objective optimization

Parameter	Multi-objective	Single-objective	Unit
Input			
Type of biomass	Corn Stover	Corn Stover	-
[A]	0.17	0.17	mol/L
RD Pressure	8.42	8.24	bar
RD Reflux ratio	3.67	1.86	mole
RD Reboiler duty	5110	27713	kW
RD residence time	1.64	1.02	min
DC Reflux ratio	2.28	2.41	mole
DC Reboiler duty	210	226	kW
Feed Hydrolysate	34228	33904	kg/hr
Result			
Revenue	1583	2261	$/hr
TAC	193	408	$/hr
Profit	1391	1852	$/hr
CO_2 emissions	2198	7006	kg/hr
Gross profit margin	0.8782	0.8193	
CO_2 Reduction	68.63	-	%
TAC Reduction	52.77	-	%
Gross profit margin improvement	7.18	-	%

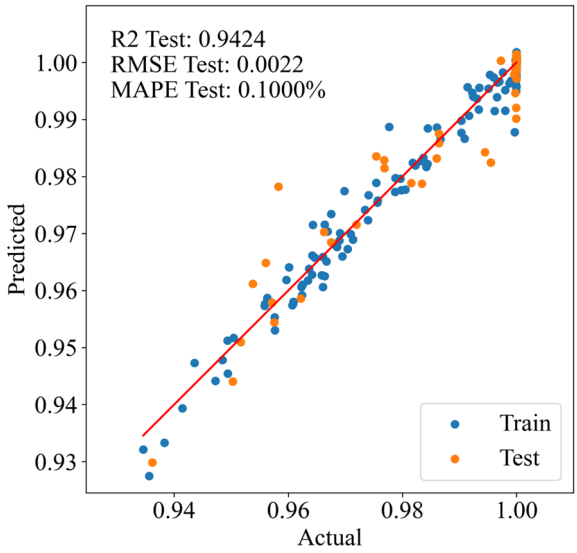

Figure 5 Model performance on purity of furfural

3.3. Multi-objective optimization

The optimal solution from the multi-objective optimization was determined using the TOPSIS method, with each objective assigned an equal weight. Moreover, single-objective optimization to maximize profit was performed by assigning a weight of 1 to the profit objective. The results of optimization show in Table 5. Corn stover was identified as a suitable biomass hydrolysate for furfural production due to high xylose concentration. A high plant capacity was found to be favorable for obtained high profit. However, the reboiler of RD in multi-objective optimization was lower than in the single-objective case due to the CO_2 emissions associated with high-pressure steam. Therefore, operating cost of multi-objective was decreased. Consequently, TAC and CO_2 of multi-objective was lower than single-objective about 52.77% and 68.63%, respectively. Moreover, gross profit margin defined as the ratio of profit to revenue can be improved through multi-objective optimization compared to single-objective optimization, as incorporating CO_2 emissions as an objective helps reduce utility consumption.

3.4. SHAP analysis

Feature importance analysis was conducted in this section based on SHAP analysis. The SHAP values for revenue, TAC, and CO_2 emissions were visualized using beeswarm plots, as shown in Figure 6-Figure 8. Type of biomass hydrolysate was highest effect on revenue and rank 4 in TAC, where the composition of biomass hydrolysate direct effect on yield of furfural [4]. The feed flow rate of biomass hydrolysate (Factor) had a significant impact on all outputs, as increasing the flow rate led to higher furfural production, capital costs, and utility consumption.

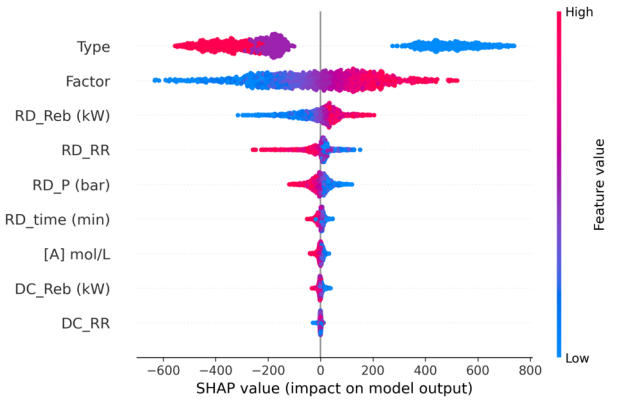

Figure 6 Beeswarm plot of revenue

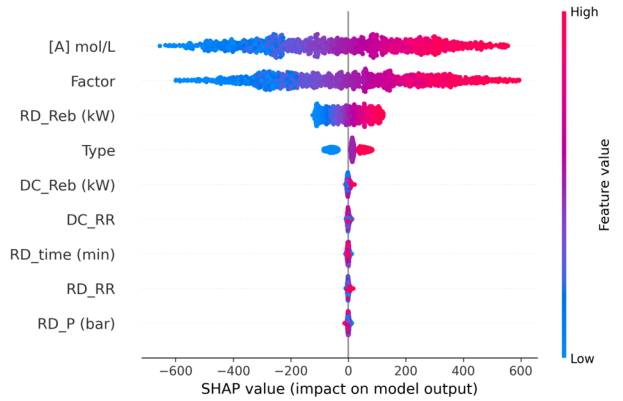

Figure 7 Beeswarm plot of TAC

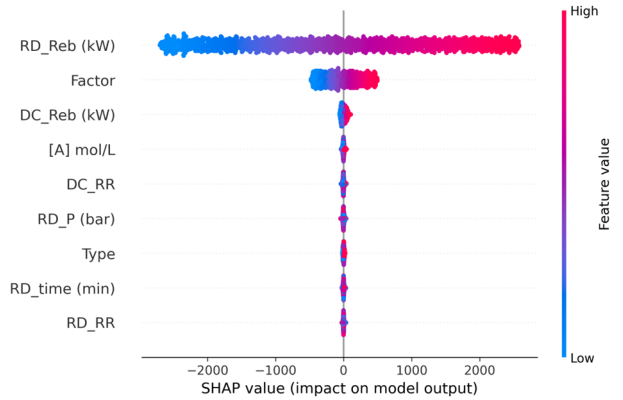

Figure 8 Beeswarm plot of CO_2 emissions

The reboiler duty of the RD column had a significant impact on all outputs, an increase in reboiler duty led to higher revenue, TAC, and CO_2 emissions. Moreover, the concentration of acetic acid had a significant impact on TAC due to cost of acetic acid, while concentration of acetic acid had a minimal effect on revenue. Consequently, in the reactive system, no additional catalyst is required [6]. Therefore, the type of biomass hydrolysate, plant capacity, and reboiler duty be optimized to achieve high profit and low CO_2 emissions without the need for an additional catalyst.

4. CONCLUSION

The multi-objective optimization of furfural production from various biomass hydrolysates via ML was presented. The proposed system was simulated and optimized using Aspen Plus and Python programs. A MLP models including TAC, revenue, purity of furfural, and CO_2 emissions were developed using a dataset from the Aspen Plus model, which demonstrates high performance in predicting the output. The R^2 of the testing set for the four output predictions exceeds 0.94, with a maximum MAPE of 4.2%. The optimal solution was obtained by integrating ML with NSGA-II and using TOPSIS for selecting the optimal point. The results of the multi-objective and single-objective optimizations demonstrated that the multi-objective optimization reduced TAC and CO_2 emissions by 52.77% and 68.63%, respectively, while increasing gross profit margin by 7.18% compared to the single-objective optimization. In addition, the SHAP value analysis indicated that the type of biomass hydrolysate, feed flow rate of biomass hydrolysate, and reboiler duty of the RD column had a significant impact on revenue, TAC, and CO_2 emissions. The concentration of acetic acid had a high impact on TAC but a low impact on revenue. Consequently, the multi-objective optimization of this process should focus on optimizing the type of biomass hydrolysate, the feed flow rate of biomass hydrolysate, and the reboiler duty of the RD column, without the use of an additional catalyst to maximize profit and minimize CO_2 emissions.

ACKNOWLEDGMENTS

The authors sincerely acknowledge the financial support provided by the Department of Chemical Engineering at Silpakorn University.

REFERENCES

1. Biomass Energy Basics. NREL. Available from: https://www2.nrel.gov/research/re-biomass (accessed 08/04/2025).
2. K.J. Yong, T.Y. Wu, C.B.T.L. Lee, Z.J. Lee, Q. Liu, J.M. Jahim, et al. Furfural production from biomass residues: Current technologies, challenges and future prospects. *Biomass and Bioenergy* 2022; 161: p. 106458.
3. G. Contreras-Zarazúa, M. Martin-Martin, E. Sánchez-Ramirez and J.G. Segovia-Hernández. Furfural production from agricultural residues using different intensified separation and pretreatment alternatives. Economic and environmental assessment. *Chemical Engineering and Processing - Process Intensification* 2022; 171: p. 108569.
4. Z. Chen, W. Zhang, J. Xu and P. Li. Kinetics of xylose dehydration into furfural in acetic acid. *Chinese Journal of Chemical Engineering* 2015; 23(4): p. 659-666.
5. J.F.L. Silva, M.A. Selicani, T.L. Junqueira, B.C. Klein, S. Vaz and A. Bonomi. Integrated furfural and first generation bioethanol production: Process simulation and technoeconomic analysis. *Brazilian Journal of Chemical Engineering* 2017; 34(3): p. 623-634.
6. L. Liu, H.-m. Chang, H. Jameel and S. Park. Furfural production from biomass pretreatment hydrolysate using vapor-releasing reactor system. *Bioresource Technology* 2018; 252: p. 165-171.
7. L.C. Nhien, N.V. Long and M.Lee. Novel Hybrid Reactive Distillation with Extraction and Distillation Processes for Furfural Production from an Actual Xylose Solution. *Energies* 2021; vol. 14: no. 4.
8. K. Wiranarongkorn, K. Im-orb, J. Panpranot, F. Maréchal and A. Arpornwichanop. Exergy and exergoeconomic analyses of sustainable furfural production via reactive distillation. *Energy* 2021; 226: p. 120339.
9. Z. Liu, Z. Cui, M. Wang, B. Liu and W. Tian. A machine learning proxy based multi-objective optimization method for low-carbon hydrogen production. *Journal of Cleaner Production* 2024; 445: p. 141377.

10. T. Shi, J. Zhou, Y. Ayub, S. Toniolo and J. Ren. Novel process optimization based on machine learning: A study on biohydrogen production from waste resources. *Biomass and Bioenergy* 2024; 185: p. 107222.
11. J. Zhang, J. Wang, W. Liu, B. Hu, J. Lou and P. Zhao. Multi-objective optimization design of a solar-powered integrated multi-generation system based on combined SCO_2 Brayton cycle and ORC using machine learning approach. *Applied Thermal Engineering* 2024; 252: p. 123684.
12. K. Aliyon, F. Rajaee and J. Ritvanen. Use of artificial intelligence in reducing energy costs of a post-combustion carbon capture plant. *Energy* 2023; 278: p. 127834.
13. N. Khani, M.H. Khoshgoftar Manesh and V.C. Onishi. Optimal 6E design of an integrated solar energy-driven polygeneration and CO_2 capture system: A machine learning approach. *Thermal Science and Engineering Progress* 2023; 38: p. 101669.

Optimization of solketal reaction conditions for maximum yield using response surface methodology (RSM) in MATLAB®

Sittinut Damnoensawat[1], Paisan Kittisupakorn[1,*]

[1] Department of Chemical Engineering, Faculty of Engineering, Chulalongkorn University, Bangkok 10330, Thailand
[*] Corresponding author: paisan.k@chula.ac.th

ABSTRACT

Due to its desirable physicochemical properties, Solketal is widely used in medications, solvents, and biofuels. Therefore, solketal's demand is increasing. Because of its demand, the reaction condition parameters needed to predict and optimize solketal synthesis, MATLAB® R2022b is used to analyze important reaction condition parameters such as temperature, pressure, and molar ratio. Solketal yield is predicted under various situations using a nonlinear regression model created from simulation data with temperature between 298K and 323K, pressure between 1 and 10 bar, and acetone and glycerol molar ratio between 0.1 and 1, which is validated. Under the circumstances, the best conditions for maximum yield are found using optimization algorithms, such as response surface methodology (RSM) and restricted optimization techniques using root mean square error (RMSE) and R-squared to approve the optimization. Optimal conditions are 298K, 5.5 bar, and the molar ratio of 1:10 with a yield of 99.18, R-squared of 0.9968, and RMSE of 0.4004.

Keywords: Optimization; Simulation; Solketal; Yield

1. INTRODUCTION

A glycerol derivative called solketal has garnered considerable interest from various industries due to its numerous applications and the global trend toward sustainable practices. Solketal (2,2-dimethyl-1,3-dioxolane-4-methanol) is an acetal glycerol derivative formed by acetone and glycerol.[1] Solketal is widely used in various industries, including the pharmaceutical and petrochemical sectors. The solketal reaction is shown in Figure 1 [2].

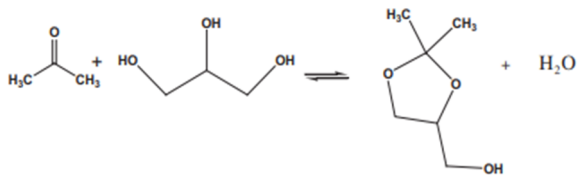

Figure 1: Solketal reaction with acetone and glycerol as reactants

Efficient optimization of reaction conditions is critical for increasing solketal yield while minimizing resource consumption and environmental impact. Traditional experimental approaches to optimization are often time-consuming and costly. In contrast, statistical and computational techniques such as Response Surface Methodology (RSM) offer a systematic and efficient framework for modeling and optimizing complex chemical processes.

Several process variables influence the ketalization reaction, such as reaction temperature and, acetone-to-glycerol molar ratio. Optimizing these variables using traditional one-variable-at-a-time approaches is not only time-consuming, but it also fails to capture the complex interactions between variables. As a result, Response Surface Methodology (RSM) has been used as a sophisticated statistical and mathematical tool for systematically modeling and optimizing reaction conditions. RSM allows you to investigate the relationships between multiple input factors and the desired output—in this case, solketal yield—by fitting a second-order polynomial model and analyzing the response surfaces.

To improve the optimization process, this study combines RSM with simulation capabilities in MATLAB®, a high-level computing environment commonly used in engineering, chemical process modeling, and optimization tasks. MATLAB®, with its built-in functions and toolboxes such as the Statistics and Machine Learning Toolbox and the Optimization Toolbox, provides a powerful platform for executing statistical computations, visualizing multidimensional data, and simulating complex systems. This study uses MATLAB® to perform not only the RSM analysis but also predictive simulations to evaluate the effect of variable combinations across a large design space, significantly reducing the need for extensive physical experimentation.

The purpose of this study is to provide a computationally driven and experimentally validated framework for maximizing solketal production. This approach not only helps to develop cleaner, more efficient biofuel additives but also demonstrates how

modern computational tools can be combined with chemical engineering principles to improve process design and optimization.

2. EXPERIMENTAL

2.1. Modeling and simulation

The solketal reaction reactants are acetone and glycerol. Solketal reaction data is simulated using ASPEN PLUS® under the various conditions of temperature (298 to 323K), pressure (1 to 10 bar), and molar ratio (A/G 1 to 10). The Solketal simulation model is represented in Figure 2 [3]

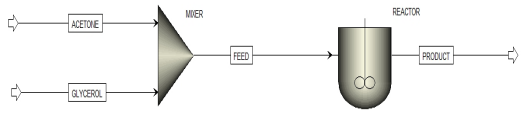

Figure 2: Solketal simulation model using ASPEN PLUS®.

2.2. Kinetic model

A kinetic model and kinetic parameters are proposed [3] in equation (1) and Table 1:

$$r = k\frac{C_G C_A - C_S C_W / K c C_G}{(1+K_W C_W + K_G C_G + K_A C_A)^2} \qquad (1)$$

The equation C_G , C_A , C_S , C_W Represents the concentrations of glycerol, acetone, solketal, and water. The parameters k, K_W, K_G, K_A, and K_C Represent the kinetic constant of the overall ketalization reaction, the equilibrium constant for water, glycerol, and acetone adsorption on the catalyst surface, and the equilibrium constant for glycerol and acetone.

Table 1: The kinetic parameter value for the solketal reaction.

k	k_0	14.094
	E	7479.06
K_W	A	-12.103
	B	3632.11
K_G	A	-24.451
	B	6670.7
K_A	A	-10.276
	B	2327.2
K_C	A	-5.852
	B	308.2

2.3. Optimization

After validating and collecting data, MATLAB® is used to optimize for maximum yield. Optimization is a fundamental concept in engineering and scientific research that seeks to identify the best solution from a set of feasible alternatives given certain constraints.[4] In this research, optimization refers to determining the input conditions, including temperature (298 to 323 K), pressure (1 to 10 bar), and the acetone to glycerol molar ratio (A/G 0.1 to 1) that maximize a solketal yield. Response Surface Methodology (RSM) to represent the maximum yield condition, followed by restricted optimization techniques such as root mean square error and R-squared to validate the optimization.

2.4. Root mean square error (RMSE) and R-squared

The root mean square error (RMSE) is the average difference between a statistical model's predicted values and actual results. It is mathematically defined as the standard deviation. The residuals represent the distance between the regression line and the data points.[3] The formula for the RMSE is as follows (2):

$$RMSE = \sqrt{\frac{\sum (y_i - \hat{y}_i)^2}{N - P}} \qquad (2)$$

y_i is the actual value for the i^{th} observation. $\hat{y}_i$ is the predicted value for the i^{th} observation. N is the number of observations. P is the number of estimation parameters, including the constant.

R-squared (R2) is a statistical measure that indicates how much of the variance in the dependent variable can be explained by the independent variables in a regression equation. It is commonly referred to as the coefficient of determination. [4] The formula for the R-squared is as follows (3):

$$R^2 = 1 - \frac{\text{sum of square residual}}{\text{total sum of square}} \qquad (3)$$

The model's ability to explain variability in the dependent variable improves as the squared value approaches 1. However, examining other metrics and features of model evaluation is critical, especially when dealing with complicated datasets and models**.**

3. RESULTS AND DISCUSSION

3.1 Validating the process simulation

This study's modeling and simulation were designed to relate to experimental data; nonetheless, the model has to be confirmed. While the mathematical model developed using Response Surface Methodology (RSM) provides a theoretical basis for estimating solketal yield under various reaction conditions, it is vital to ensure that the model accurately represents the actual chemical system. Model validation is a key step in this process since it assesses the model's predictive capability and robustness when applied to experimental data.[5] As a result, the experimental data [6] were utilized to validate the simulation model. Figures 3 and 4 show validation using solketal yield as a function of molar ratio and temperature.

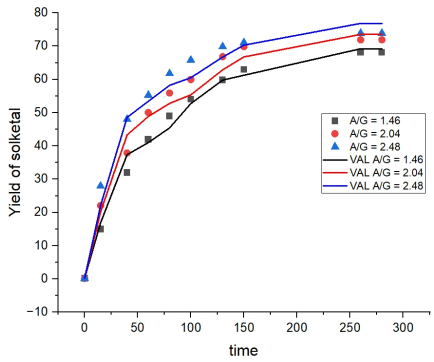

Figure 3: Validation graph of the simulation model compared with experiment data using various molar ratios.

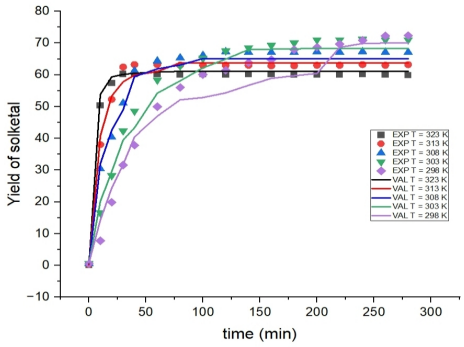

Figure 4: Validation of the simulation model compared with experiment data using various temperatures.

Figures 3 and 4 show that the simulation model agrees strongly with the actual results over a range of reaction circumstances. When compared to actual experimental results, the simulation model achieves an accuracy level of more than 95%. As a result, the created simulation model is valid, robust, and dependable for estimating solketal yield under process parameters. This validated model can be utilized with confidence for future simulations, sensitivity analysis, and MATLAB® optimization tasks. After validating the process, the optimization is created by using MATLAB®.

3.2. Optimization of the process condition

The solketal synthesis procedure was optimized using MATLAB®, which included dispersed interpolation, response surface modeling, and nonlinear optimization. Experimental data were first used to develop a prediction surface using a dispersed interpolant function, allowing continuous estimation of solketal yield based on three critical variables: reaction temperature (298 – 323 K), pressure (1 – 10 bar), and the acetone-to-glycerol molar ratio (A/G 0.1 - 1). The optimization algorithm (fmincon) was used to maximize the anticipated yield within the experimental constraints.

Figure 5 provides RSM, which is a complete picture of how the solketal yield responds to changes in three essential process parameters: temperature (K) on the X-axis, pressure (bar) on the Y-axis, and molar ratio on the Z-axis. The color gradient given to the data points, which ranges from dark blue (lower yield) to bright yellow (greater yield), depicts the distribution and intensity of yield values across various input variable combinations. This surface representation aids in identifying trends and locations in the reaction space where solketal yield is highest or minimized.

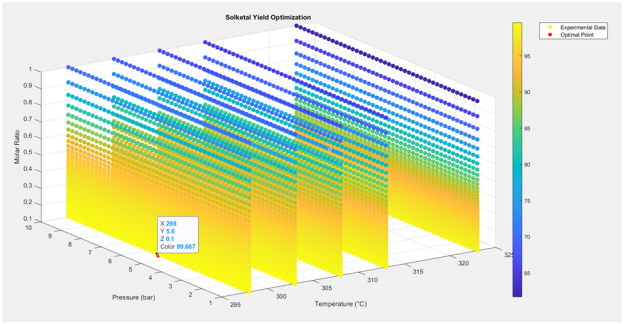

Figure 5: The solketal reaction optimization using response surface methodology (RSM).

Each point on this 3D graph represents an experimental or simulated data point, with the color indicating the matching solketal yield percentage. The red point stands out from the others and represents the optimal condition determined by the MATLAB® optimization method (fmincon). This ideal point is the exact combination of temperature 298 K, pressure 5.6 bar, and molar ratio A/G 0.1 that results in the highest projected yield, which is around 99.61%, as indicated by the color legend and tooltip.

Furthermore, the figure acts as a validation tool for the simulation model, demonstrating that the anticipated best point is well inside the highly populated experimental region, eliminating concerns about extrapolation. It also supplements numerical outputs like root mean square error (RMSE) and correlation coefficients by giving a visual cross-check of model performance. In conclusion, this figure is useful not only for explaining optimization results but also for illustrating the reliability and precision of the built model and optimization framework in MATLAB®.

In Figure 6, this graph shows the accuracy of the created model in simulating solketal yield using experimental data. The depicted data points (blue markers) are closely aligned with the red dashed line, indicating an excellent 1:1 correlation between experimental and projected values. This strong alignment implies that the model performs extraordinarily well, with little variance from actual data. The model's predictions are highly accurate and reliable, as evidenced by their close clustering around the ideal line. Such behavior indicates that the modeling strategy, whether based on interpolation, response surface methods, or regression techniques, can accurately reflect the underlying link between reaction conditions and yield. As a result, the predictive model has been validated and is acceptable for use in future

optimization studies of solketal production. The excellent agreement between experimental and anticipated results confirms the applicability of the modeling approach used in this study, which could incorporate techniques like scattered data interpolation, Gaussian process regression, or response surface methodology (RSM).

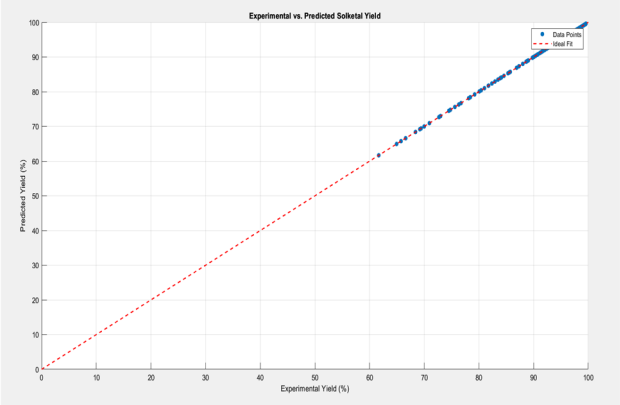

Figure 6: Regression graph of experimental and predicted yield data

It also improves the accuracy of the optimization approach utilized to discover the ideal reaction conditions. The model's capacity to generalize across various input parameters makes it useful in real-world optimization and scale-up applications. Overall, this graph demonstrates that the model fits the available data well and can accurately estimate solketal yield for untested situations inside the stated parameter space.

The solketal yield prediction model's statistical indicators, including R^2 = 0.9968 and RMSE = 0.4004, show outstanding accuracy and dependability. With a R^2 value of 0.9968, the model explains 99.68% of the variation in experimental yield data, indicating a nearly-perfect fit between predicted and actual values. This shows that the model accurately represents the underlying relationships between the essential process factors (temperature, pressure, and molar ratio) and their effect on solketal yield.

The RMSE value of 0.4004%, which represents the average variation between projected and experimental yields, is quite low. This small error margin indicates that the model's predictions are close to the measured values, with low dispersion. In practice, a low RMSE increases confidence in utilizing the model for both optimization and process management, implying that any predictions made are precise and reliable. these metrics support the model's stability and validate its applicability for simulating, analyzing, and optimizing solketal output. MATLAB®'s response surface methodology (RSM) effectively optimizes reaction conditions for maximum yield, as seen by high R^2 and low RMSE in experimental chemical data.

4. CONCLUSION

In this investigation, the solketal synthesis reaction was simulated using ASPEN PLUS® at various temperatures (298-323 K), pressures (1-10 bar), and acetone-to-glycerol molar ratios (A/G 0.1-10). The model was evaluated with experimental data and optimized in MATLAB® using Response Surface Methodology. The best reaction conditions were determined to be 298 K, 5.6 bar, and an A/G ratio of 0.1, resulting in a maximum anticipated solketal yield of 99.61%. The prediction model performed well with R^2 = 0.9968 and RMSE = 0.4004, indicating good accuracy and dependability for process optimization.

ACKNOWLEDGMENTS

The researcher would like to give gratitude to the Department of Chemical Engineering, Faculty of Engineering, Chulalongkorn University, for supplying the necessary information to complete this article.

REFERENCES

[1] Saikia, K., et al., Sulphonated biomass-based catalyst for solketal synthesis by acetalization of glycerol – A byproduct of biodiesel production. Fuel Processing Technology, 2022. **238**: p. 107482.

[2] Nanda, M.R., et al., Thermodynamic and kinetic studies of a catalytic process to convert glycerol into solketal as an oxygenated fuel additive. Fuel, 2014. **117**: p. 470-477.

[3] Yu, B.-Y., et al., Evaluation on the solketal production processes: Rigorous design, optimization, environmental analysis, and control. Process Safety and Environmental Protection, 2022. **157**: p. 140-155.

[4] Waga, M., D. Valladão, and A. Street, Robust portfolio optimization meets Arbitrage Pricing Theory. European Journal of Operational Research, 2025.

[5] Ribeiro, M.B., R.M. Cavalcante, and A.F. Young, Simulation and economic evaluation of fuel additives production from glycerol. Renewable Energy, 2022. 181: p. 1081-1099.

[6] Malaya R. Nanda a, Z.Y.a., Wensheng Qin b, Hassan S. Ghaziaskar c, Marc-Andre Poirier d, Chunbao Charles Xu a,⇑, Thermodynamic and kinetic studies of a catalytic process to convert glycerol into solketal as an oxygenated fuel additive. Fuel 2014.

Enhancing low-carbon hydrogen production from biomass gasification via machine-learning-aided multi-objective optimization with TOPSIS

Kitti Kamolram[1], Phantisa Limlaemthong[1,*]

1 Department of Chemical Engineering, Faculty of Engineering, Kasetsart University, Bangkok 10900, Thailand
* Corresponding author: phantisa.l@ku.th

ABSTRACT

Biomass gasification is one of the most promising technologies to produce bioenergy, i.e., hydrogen. The modeling and optimization of this process usually struggles from the complication of conventional calculation using thermodynamics and kinetics. Machine learning has emerged and gained momentum recently as a valuable tool regarding modeling and optimization problems. This study proposes Machine-Learning-aided Multi-Objective Optimization and Multi-Criteria Decision Making (ML-aided MOO & MCDM) framework to model and optimize the biomass gasification process to obtain the most suitable operating condition aiming at achieving low-carbon hydrogen production. Several machine learning models were trained and evaluated for predictive models of syngas from biomass gasification, including hydrogen. Gradient Boosting Regressor was selected for further study as it is able to achieve the highest average R^2 score of around 0.89. The selected model was then implemented with multi-objective optimization as an objective function to maximize hydrogen yield and minimize carbon dioxide. The bi-objective optimization result suggests that gasification occurs at around 1,000 degrees Celsius with steam as gasifying agent in fluidized bed reactor could result in the desired optimization objectives. TOPSIS technique, one of commonly used MCDM techniques, was utilized as a tool to rank pareto optimal solutions from MOO, which can finally prioritize the most suitable decision-option for further implementation. These optimal solutions can serve as a useful guideline and, particularly, the refined scope for further detailed process study and optimization.

Keywords: Biomass gasification; Machine learning; Multi-objective optimization; Multi-criteria decision-making

1. INTRODUCTION

As non-renewable energy sources like coal, oil, and gas face eventual depletion and contribute heavily to greenhouse gas emissions, global interest is shifting towards renewable alternatives. These include solar, wind, hydro, geothermal, and biomass—resources that are more sustainable and environmentally friendly. However, some renewables like solar and wind are weather-dependent and often inconsistent.

Biomass, derived from organic plant and animal waste, is a promising renewable resource, especially in agricultural countries like Thailand, where nearly 40% of the land is used for farming [1]. Utilizing agricultural waste for energy not only addresses waste management but also offers a sustainable energy solution.

Among various biomass conversion methods, gasification stands out for its ability to produce clean fuels like hydrogen, which offers high energy output and minimal environmental impact. Although hydrogen can be produced from several sources, biomass gasification is one of the most eco-friendly options, attracting significant research interest.

Accurate modeling of the gasification process is essential for scale-up and optimization. Traditional models, such as thermodynamic or kinetic approaches, often struggle with the complexity of interacting variables. Recently, machine learning (ML) has emerged as a powerful alternative for modeling non-linear relationships and predicting process outcomes with high accuracy.

Machine learning enables data-driven modeling without the need for predefined equations, making it well-suited for complex systems like gasification. Despite its potential, many existing ML models are limited in scope, often trained on small datasets or specific conditions. For example, studies by Baruah [2], Kargbo [3], and Li [4] developed models with limited generalizability due to narrow datasets and specific reactor-feedstock combinations. To address this gap, Ascher et al [5]. introduced a more comprehensive model using a broader dataset. Yet, with only 312 data points, predictive performance could still be improved.

In this research, we developed and compared multiple ML models—including Extra Trees (ETR), Gradient Boosting (GBR), XGBoost (XGB),

ADABoost (ADA), K-Nearest Neighbors (KNN), and Multi-Layer Perceptron (MLP)—using a larger dataset of 408 gasification experiments. Bayesian optimization was applied with cross-validation to fine-tune each model's hyperparameters. The best-performing model was identified for further application and study. To enhance interpretability, SHapley Additive exPlanations (SHAP) was used to identify the most influential input features. Building on this, we adopt a machine-learning-aided multi-objective optimization and decision-making (ML-aided MOO-MCDM) framework—previously proposed by Wang et al. [6]—to optimize the gasification process for high H_2 yield and low CO_2 emissions. The resulting Pareto-optimal conditions were presented and discussed for future process design and improvement.

2. METHODOLOGY

2.1 Data Collection and description of the data set

A dataset comprising 408 samples was gathered from various literature sources to train and evaluate the machine learning models. The input variables represent information about the feedstock and operating conditions. The output variables consist of the percentage volume of syngas. Table 1 presents the predictor or input data consisting of 8 categorical predictors and 18 continuous predictors, while Table 2 displays the target variables or outputs, comprising 12 continuous target variables.

2.2 Data preprocessing

In the machine learning procedure, data pretreatment is the most time-consuming process to meticulously prepare a completed and high-quality data set for model development. There are various steps needed to be conducted as follows:

2.2.1 Feature selection

Using an excessive number of predictors in model training can lead to overfitting, thereby reducing the model's generalizability. To address this issue, it is often necessary to exclude some variables, particularly when a large number of features have been collected. One effective approach is to draw upon domain knowledge and existing literature to identify relationships or dependencies among variables. This information can help in determining which variables are redundant, allowing researchers to retain only the most relevant predictors for the analysis.

Another effective way to gain insight into the relationships among input variables is to utilize the Pearson correlation coefficient (PCC). PCC measures the strength and direction of linear relationships between two variables. However, it is important to note that PCC only captures linear correlations and may not fully capture other types of relationships. Eq. (1) was used to calculate PCC:

$$PCC = \frac{\sum (x_i - \overline{x})(y_i - \overline{y})}{\sqrt{\sum (x_i - \overline{x})^2 \sum (y_i - \overline{y})^2}} \quad (1)$$

Where *PCC* is the Pearson Correlation Coefficient. x_i and y_i are data points of two observed variables. $\overline{x}$ and $\overline{y}$ are the average value of the two variables.

Table 1. Summary of input variables.

	Max	Min	Mean	SD*	No. of samples
Feedstock Information					
Type	Woody biomass, Herbaceous biomass, Sewage sludge, Municipal solid waste, Plastics, and Other				408
Shape	Chips, Dust, Fibers, Particles, Pellets, Other				408
Particle Size [mm]	70.00	0.25	4.52	6.29	346
LHV [MJ/kg wb]	45.10	11.50	19.27	8.11	408
Ultimate Analysis					
C [% daf]	70.00	40.07	53.16	10.91	408
H [% daf]	14.23	3.79	7.12	2.30	408
O [% daf]	53.40	0.00	37.99	12.80	408
N [% daf]	7.32	0.00	1.05	1.82	408
S [% daf]	1.90	0.00	0.34	0.49	408
Proximate Analysis					
Ash [% db]	44.00	0.27	8.76	12.48	408
Moisture [% db]	51.02	0.00	7.64	5.99	408
Volatile matter [% db]	99.00	52.03	77.11	10.57	380
Fixed carbon [% db]	31.80	0.00	14.23	5.62	318
Lignocellulosic Composition					
Cellulose [% db]	46.20	29.60	39.42	5.08	28
Hemicellulose [% db]	29.60	14.00	20.91	4.67	28
Lignin [% db]	24.99	14.00	20.91	5.39	28
Gasifier Conditions and Information					
Temperature [◦C]	1050	553	805	71.77	408
Operation Mode	Batch, Continuous				398
Residence Time [min]	403	6.00	89.98	94.17	156
Steam/Biomass [wt/wt]	4.04	0.00	1.00	0.70	132
ER	0.87	0.09	0.29	0.01	355
Gasifying Agent	Air, Air + Steam, Air + Oxygen, Steam, Oxygen, Other				383
Reactor Type	Fixed bed, fluidized bed, Other				374
Bed Material	Silica, Sand, Alumina, Dolomite, Olivine, Y-alumina, Calcium oxide				381
Catalyst	Present, Not present				308
Scale	Lab, Pilot				108

Table 2 Summary of output variables.

	Max	Min	Mean	SD*	No. of sample
Syngas Composition					
N_2 [vol.% db]	74.90	0.00	39.27	25.02	408
H_2 [vol.% db]	71.50	3.10	20.83	14.93	405
CO [vol.% db]	50.00	2.20	18.84	8.98	405
CO_2 [vol.% db]	38.25	0.90	14.90	6.46	405
CH_4 [vol.% db]	16.00	0.04	4.6	3.41	405
C_2H_n [vol.% db]	9.50	0	1.58	47.85	193
Syngas LHV [MJ/Nm3 db]	15.60	1.30	7.14	3.29	408
Tar content [g/Nm3 db]	364.0	0.00	29.89	47.85	193
Yield and Process Efficiency					
Syngas yield [Nm3 /kg wb]	6.19	0.49	1.93	1.15	292
Char yield [g/kg wb]	301.5	3.60	97.43	77.08	83
CGE [%]	122.9	16.70	61.47	20.11	299
CCE [%]	126.9	24.03	71.30	15.91	295

A PCC of 0 indicates that the two interested variables are not correlated. On the other hand, a PCC closer to +1 or -1 represents a strong positive and negative correlation, respectively, between the two variables. In this work, a value of |PCC| more than or equal to 0.6 is considered as a criterion for feature removal before model training to help reduce the model complexity and the chance of model overfitting.

Feedstock type, feedstock shape, LHV, volatile matter, and fixed carbon were excluded as it is relevant and dependent on other variables [5].

2.2.2 Missing data imputation

Before using the data for model training and testing, it is crucial to handle any missing information. In this study, missing data was addressed by replacing it with the median as the collected data did not follow a normal distribution.

In this step, missing data was imputed using group-specific median values based on related categorical variables. For instance, since the particle size of feedstock is closely associated with its shape and type, the missing values were not filled using the overall median. Instead, the median particle size was calculated separately for each combination of feedstock shape and type.

However, not all variables require imputation through this method. Some missing values can be inferred or calculated based on domain knowledge. For example, missing sulfur content may be estimated from the values of other related components, while a missing steam-to-biomass ratio could be reasonably assumed to be zero in cases where steam was not used as a gasifying agent.

2.2.3 One-hot encoding

Categorical variables were included as predictor variables, as they can contribute to improving the model's performance and generalization. However, unlike models such as Random Forest that can handle categorical variables directly, the machine learning algorithms used in this study require numerical input. Therefore, one-hot encoding was employed to convert categorical variables into a numerical format. In this method, a categorical variable with *n* unique categories is transformed into *n* binary variables, each indicating the presence (1) or absence (0) of a specific category. Table 3 provides an example of this transformation, illustrating how the reactor type variable was encoded using one-hot encoding.

Some categorical variables can only take on two categorical values, including catalyst use (present/not present), operation mode (batch/continuous), and experiment scale (lab/pilot). The categorical values of these variables were encoded into a binary value.

Table 3 One-hot encoded reactor type data.

Observation	Reactor type	Fixed bed	Fluidized bed
1	Fixed bed	1	0
2	Fluidized bed	0	1

2.2.4 Min-max normalization

Normalization of numeric variables is crucial to ensure consistency in scale and facilitate model training. Min-max scaling was employed in this research to normalize the data, bringing all variables within a standardized range of 0 to 1. This step enhances model stability and convergence during training. Eq. (2) has been used to normalize the data set:

$$x_{norm} = l + \frac{x - x_{min}}{x_{max} - x_{min}}(u - l) \qquad (2)$$

Where $\boldsymbol{x}$ is the observed value and $\boldsymbol{x_{norm}}$ is the normalized value. $\boldsymbol{x_{min}}$ and $\boldsymbol{x_{max}}$ represent the minimum and maximum values of the observed variable, respectively. While l and u are lower and upper values of the normalized range, which are 0 and 1, as mentioned.

2.3 Model Development and Evaluation

Several machine learning models, including Extra trees regressor, Gradient boosting regressor, K-Nearest Neighbors regressor, and Multi-layer perceptron, were developed to predict H_2 and CO_2 production. The dataset was split into training and testing sets in a 70:30 ratio. A training set containing 70% of the overall data set was used to train these models. Hyperparameters of every model were optimized using a Bayesian optimization algorithm to find the best model configuration and enhance model performance. These models underwent training with 10-fold cross-validation

The other 30% of the data set, namely the testing set, was used to test and evaluate the performance of each model for the comparison and selection of the best model for this problem. The model performance

assessment was done using evaluation metrics including coefficient of determination (R^2), mean squared error (MSE), and mean absolute error (MAE). Eq. (3) – (5) demonstrate the calculation of three performance indicators used:

$$R^2 = \frac{SSR}{SST} = \frac{\sum(\hat{y}_i - \bar{y})^2}{\sum(y_i - \bar{y})^2} \quad (3)$$

$$MSE = \frac{1}{n}\sum(\hat{y}_i - y_i)^2 \quad (4)$$

$$MAE = \frac{1}{n}\sum|\hat{y}_i - y_i| \quad (5)$$

Where SSR stands for the Sum of Squared Regression and SST stands for the Sum of Squared Total. y_i , $\hat{y}_i$ and $\bar{y}$ refer to the observed value, predicted value, and average value of the data set, respectively. n is the number of data points in the data set.

2.4 Feature Importance Analysis

The selected H_2 and CO_2 prediction models will go through Shapley Additive exPlanation (SHAP) analysis to analyze and indicate influential factors affecting the prediction of the models, interpretable as H_2 and CO_2 production in the Biomass gasification process.

The fundamental idea underpinning SHAP is the assignment of a score to each feature in each data point that quantifies the degree to which that feature contributed to the model's prediction. These scores are based on the Shapley values from cooperative game theory, which is an approach to attributing the value of a collective effort to each participant.

2.5 Multi-objective Optimization

In biomass gasification, variations in feedstock and operating conditions result in a range of product gases, including desirable and undesirable. In this study, H_2 is the desired product, and CO_2 is the undesired. Multi-objective optimization (MOO) is vital for pinpointing conditions to maximize desired products like H_2 while minimizing undesired ones such as CO_2.

To begin with, the optimization problem needs to be formulated. Objective functions and constraint functions were required for the multi-objective optimization as follows:

$$\min F(x) = \{-f_{H_2}(x_{m,norm}, y_k); f_{CO_2}(x_{m,norm}, y_k)\}$$

$$\sum_k y_k = 1, \forall k \in K$$

$$\sum_m x_m = 100, \forall m \in L$$

$$x_m \geq x_{m,min}, \forall m \in M$$

$$x_m \leq x_{m,max}, \forall m \in M$$

$$x_{m,norm} = \left[\frac{x_m - x_{m,min}}{x_{m,max} - x_{m,min}}\right]$$

$$x_m \in X, y_k \in \{0,1\}, L \subseteq M$$

The objective function f_{H2} seeks to maximize the hydrogen content percentage in syngas. The multiplication with -1 was applied to convert the function into a minimization problem. On the other hand, f_{CO2} is the objective function aiming to minimize the carbon dioxide content in syngas percentage. The previously trained machine learning models were utilized as the representative of both objective functions.

x_m is the continuous decision variable representing the continuous process variables. M is a set of all continuous variables while L is a set of variables belonging to the group of feedstock composition content and L is a subset of M. The equation $\sum_m x_m = 100$ is introduced to restrict the summation of feedstock composition content, including the percentage of C, H, N, S, O, ash, and moisture, which is equal to 100. All x_m is bounded between the minimum and the maximum values of the raw data. The normalization equation is introduced to represent the interrelationship between x_m and $x_{m,norm}$ which the latter will be used as inputs for the machine learning models.

y_k is the binary decision variable to restrict the selection of categorical variables. K represents each set of variables. The equation $\sum_k y_k = 1$ is introduced to enforce the selection of only one type per each group of categorical variables.

Non-dominated sorting genetic algorithm II (NSGA-II) method is widely used for MOO application in chemical engineering [7]. The method consists of two main steps, creating child solutions from the current population and choosing the new population by non-dominated sorting of parent and child solutions. Through the execution of NSGA-II, the Pareto front is to be obtained. The Pareto front, as shown in Figure. 1, consists of the curve representing the trade-offs between the two objectives of the minimizing problem in the MOO.

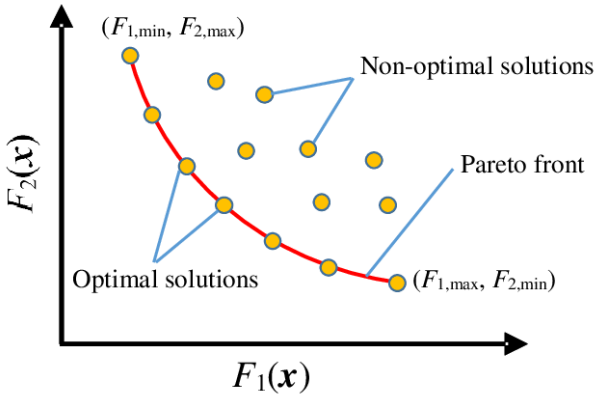

Figure. 1 Pareto Front diagram

Where each axis of the plot represents each objective function. Optimal solutions, which are the points considered to be the nearest to the desired solution according to the objectives, can be found on the Pareto front curve.

2.6 Technique for Order of Preference by Similarity to Ideal Solution

The Technique for Order of Preference by Similarity to Ideal Solution (TOPSIS) is a widely used method in multi-criteria decision-making (MCDM) [8]. It is designed to identify the optimal alternative from a set of options based on the principle of a compromise solution. The method selects the alternative that is closest to the positive ideal solution (PIS) and farthest from the negative ideal solution (NIS) in terms of Euclidean distance.

Let $A = \{A_k \mid k = 1, \dots, n\}$ represent the set of alternatives, and $C = \{C_j \mid j = 1, \dots, m\}$ denote the set of criteria. The performance ratings matrix is given by $X = \{x_{kj}\}$ is the performance score of alternatives A_k with respect to criterion C_j, and $w = \{w_j\}$ is the set of criterion weights.

Step 1: Normalize the Decision Matrix
Normalization ensures that all criteria are placed on a comparable scale, facilitating fair comparison and integration in the decision-making process. The normalized value r_{kj} is calculated using Eq. (6):

$$r_{kj}(x) = \frac{x_{kj}}{\sqrt{\sum_{k=1}^{n} x_{kj}^2}} \quad (6)$$

Step 2: Calculate Weighted Normalized Decision Matrix
Each normalized rating is multiplied by its corresponding weight to reflect the importance of each criterion:

$$v_{kj}(x) = w_j \cdot r_{kj}(x) \quad (7)$$

Step 3: Determine Positive Ideal Solution (PIS) and Negative Ideal Solution (NIS)
The PIS and NIS are determined by identifying the best and worst values across alternatives for each criterion:

$$A^+ = \{v_j^+\} = \{\max v_{kj} | j \in J_1; min\ v_{kj} | j \in J_2 \quad (8.1)$$

$$A^- = \{v_j^-\} = \{\min v_{kj} | j \in J_1; max\ v_{kj} | j \in J_2 \quad (8.2)$$

where J_1 and J_2 are the sets of benefit and cost criteria, respectively.

Step 4: Calculate Separation Measures
The Euclidean distance of each alternative from the PIS and NIS is calculated as:

$$D_k^* = \sqrt{\sum_{j=1}^{m} (v_{kj} - v_j^+)^2} \quad (9.1)$$

$$D_k^- = \sqrt{\sum_{j=1}^{m} (v_{kj} - v_j^-)^2} \quad (9.2)$$

Step 5: Calculate the Relative Closeness to the Ideal Solution
The relative closeness coefficient C_k^* is calculated as:

$$C_k^* = \frac{D_k^-}{D_k^* + D_k^-}, 0 \le C_k^* \le 1 \quad (10)$$

Step 6: Rank the Alternatives
Alternatives are ranked in descending order of C_k^*, with the highest value indicating the best compromise solution.

3. RESULTS AND DISCUSSION

3.1 Model Development and Evaluation

Using the testing set to evaluate tuned-and-trained models, performance indicators were received and shown in Table 4

Table 4 Summary of performance evaluation of a test set of all models for syngas H_2.

	R^2 (MAE)					
	ETR	GBR	XGB	ADA	KNN	MLP
H_2	0.96 (1.99)	0.95 (2.08)	0.94 (2.28)	0.92 (2.65)	0.93 (1.99)	0.95 (2.37)
CO_2	0.97 (0.83)	0.96 (1.13)	0.96 (1.09)	0.96 (1.02)	0.97 (0.83)	0.91 (1.57)
CO	0.95 (1.34)	0.93 (1.69)	0.92 (1.74)	0.94 (1.56)	0.95 (1.34)	0.81 (2.31)
Tar	0.61 (8.85)	0.71 (7.83)	0.58 (9.66)	0.47 (12.88)	0.61 (8.85)	0.75 (7.56)
Avg.	0.87 (3.25)	0.89 (3.18)	0.85 (3.69)	0.82 (4.53)	0.86 (3.25)	0.86 (3.45)

Among the evaluated models, Gradient Boosting Regressor (GBR) demonstrated the most robust overall performance, achieving the highest average coefficient of determination (R^2 = 0.89) and the lowest average prediction error (MAE = 3.18). While GBR slightly underperforms compared to Extremely Randomized Trees (ETR) in predicting specific outputs such as H_2 and CO_2, it significantly outperforms other models in predicting the remaining target variables. This highlights GBR's superior generalization ability across diverse outputs.

Both XGBoost (XGB) and AdaBoost (ADA) also showed competitive performance, closely following GBR in terms of predictive accuracy. Their comparable results can be attributed to the shared foundation of boosting ensemble techniques, which iteratively improve weak learners to enhance overall model performance

In contrast, models based on clustering algorithms like K-Nearest Neighbors (KNN) and neural network-based approaches such as Multi-Layer Perceptron (MLP) yielded comparatively lower predictive accuracy. Although these methods exhibit potential in capturing complex patterns within the dataset, their performance suggests limitations in handling the

nonlinearities and interactions present in the process data when compared to ensemble-based tree models. These observations reaffirm the effectiveness of boosting algorithms, particularly GBR, in modeling complex process systems with multiple correlated outputs.

3.2 Feature Importance Analysis

From studying the factors contributing to H_2 and CO_2 production in the process, based on SHAP analysis results, the most impactful variables for generating CO_2 and H_2 are the gasifying-agents-related variables and temperature. Additionally, oxygen content in feedstock also impacts CO_2 production, as observed in Figure. 2 and Figure 3

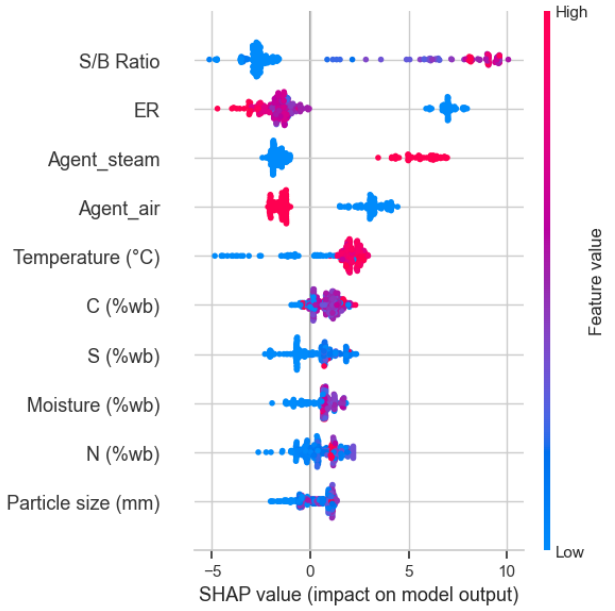

Figure. 2 The results of SHAP analysis of the H_2 prediction model.

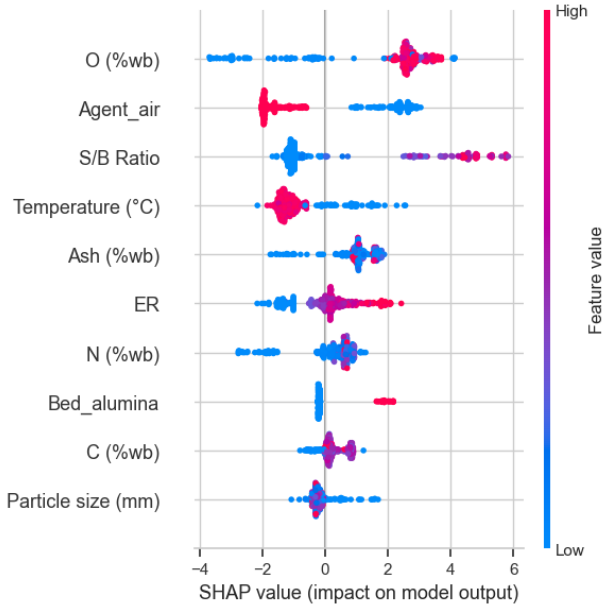

Figure. 3 The results of SHAP analysis of the CO_2 prediction model.

3.3 Multi-Objective Optimization

After formulating the multi-objective optimization problem, the NSGA-II algorithm was employed to solve it under varying configurations, including different population sizes, numbers of generations, and random seeds. This process was repeated multiple times to ensure robustness and explore a wide solution space. Following each optimization run, non-dominated sorting was applied to identify the true Pareto front, resulting in a total of 85 Pareto-optimal solutions. To further narrow down the best compromise solutions, the Technique for Order Preference by Similarity to Ideal Solution (TOPSIS) method was applied to rank the 85 Pareto-optimal solutions. Pareto plot with rank distribution is illustrated in Figure 4.

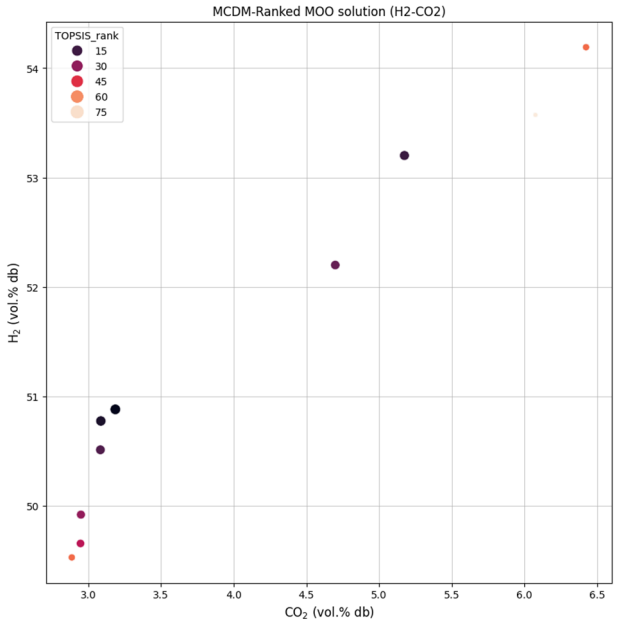

Figure. 4 Pareto curve of non-dominated solutions for the solved problem of maximizing H_2 and minimizing CO_2 from biomass gasification with rank distribution.

Based on the obtained Pareto-optimal set, a recommended operational configuration can be proposed to achieve the desired outcomes. The discrete decision variables suggest the process in a batch-operated fluidized-bed gasifier. Olivine is recommended as the bed material, with steam employed as the gasifying agent, and the presence of a catalyst further enhances the reaction environment. The continuous decision variables, in contrast, exhibit a range of optimal values, as detailed in Table 6, reflecting flexibility within operational boundaries.

Table 6 summarizes the continuous decision variables corresponding to these top-ranked solutions. The analysis suggests prioritizing feedstocks with inherently high hydrogen content, which directly contributes to enhanced H_2 production. Additionally, using biomass with smaller particle size is recommended to promote better gas-solid interaction, thereby increasing reaction efficiency, leading to higher

H_2 yield and reduced CO_2 formation. Feedstocks with low ash content are also favored, as they minimize the risks of slagging and fouling within the gasifier, thereby supporting more stable and efficient operations.

Table 6 Summary of suggested ranges of the optimal continuous variables**.**

Input variables		**Range**
Particle Size	mm	0.51-2.69
Carbon	%wb	45.47-47.87
Hydrogen	%wb	9.65-10.73
Nitrogen	%wb	0.06-2.83
Sulfur	%wb	0.69-3.60
Oxygen	%wb	7.96-21.30
Ash	%wb	0.55-10.26
Moisture	%wb	9.60-29.93
Temperature	°C	998.56-1040.18
Steam-to-biomass Ratio	wt/wt	0.13-1.61
ER		0.09 – 0.30
Output variables		**Range**
Syngas H_2	vol.% db	49.53-54.19
Syngas CO_2	vol.% db	2.89-6.42

Regarding the operating conditions, while high temperatures and elevated steam-to-biomass ratios both typically favor the formation of H_2 products, higher steam-to-biomass ratios also trends to elevate CO_2. the presence of CO_2 as an undesired byproduct leads to a preference for moderate to lower values of steam-to-biomass ratios in the top-ranked solutions from TOPSIS ranking, while higher temperature is still be suggested. These settings strike a balance between maximizing H_2 production and minimizing CO_2 output, in alignment with the objectives of the optimization.

4. CONCLUSION

This study compared several machine learning models—Extra Trees (ETR), Gradient Boosting (GBR), XG Boost (XGB), ADA Boost (ADA), K-Nearest Neighbors (KNN), and Multi-Layer Perceptron (MLP)—for predicting key products in biomass gasification. GBR outperformed other models, achieving the highest overall accuracy (R^2 = 0.89). SHAP analysis identified gasifying-agent-related variables and temperature as influential features affecting H_2 and CO_2 prediction.

Multi-objective optimization using NSGA-II produced Pareto-optimal solutions with H_2 ranging from 49.53 to 54.19 vol.% (db) and CO_2 from 2.89 to 6.42 vol.% (db). TOPSIS was applied to rank these solutions, identifying optimal operating conditions involving a batch-operated fluidized-bed gasifier, olivine bed material, steam as the gasifying agent, and a catalyst. Key process parameters include high steam-to-biomass ratio, low equivalence ratio, high temperatures, and small particle size. These trends, however, should be adapted to practical constraints during implementation.

ACKNOWLEDGMENTS

The authors gratefully acknowledge the Faculty of Engineering, Kasetsart University, Bangkok, Thailand, for providing both financial support and research facilities for this study.

REFERENCES

[1] B. Sajjakulnukit and P. Verapong, “Sustainable biomass production for energy in Thailand,” *Biomass and Bioenergy*, vol. 25, no. 5, pp. 557–570, 2003.

[2] D. Baruah, D. C. Baruah, and M. K. Hazarika, “Artificial neural network based modeling of biomass gasification in fixed bed downdraft gasifiers,” *Biomass and Bioenergy*, vol. 98, pp. 264–271, 2017.

[3] H. O. Kargbo, J. Zhang, and A. N. Phan, “Optimisation of two-stage biomass gasification for hydrogen production via artificial neural network,” *Appl. Energy*, vol. 302, no. April, p. 117567, 2021.

[4] J. Li, M. Suvarna, L. Pan, Y. Zhao, and X. Wang, “A hybrid data-driven and mechanistic modelling approach for hydrothermal gasification,” *Appl. Energy*, vol. 304, no. April, p. 117674, 2021.

[5] S. Ascher, X. Wang, I. Watson, W. Sloan, and S. You, “Interpretable machine learning to model biomass and waste gasification,” *Bioresour. Technol.*, vol. 364, no. September, 2022.

[6] Z. Wang, J. Li, G. P. Rangaiah, and Z. Wu, “Machine learning aided multi-objective optimization and multi-criteria decision making: Framework and two applications in chemical engineering,” *Comput. Chem. Eng.*, vol. 165, no. June, 2022.

[7] K. Deb, A. Pratap, S. Agarwal, and T. Meyarivan, “A fast and elitist multiobjective genetic algorithm: NSGA-II,” *IEEE Trans. Evol. Comput.*, vol. 6, no. 2, pp. 182–197, 2002.

[8] M. Behzadian, S. Khanmohammadi Otaghsara, M. Yazdani, and J. Ignatius, “A state-of the-art survey of TOPSIS applications,” *Expert Syst. Appl.*, vol. 39, no. 17, pp. 13051–13069, 2012.

Enhancing non-catalytic biomass pyrolysis yield predictions using machine learning and data augmentation

Anchalee Chaichanavongsaroj[1], Dasakorn Rungrampan[1], Phantisa Limleamthong[1,*]

[1] Department of Chemical Engineering, Faculty of Engineering, Kasetsart University, Bangkok 10900, Thailand
[*] Corresponding author: phantisa.l@ku.th

ABSTRACT

Predicting product yields from biomass pyrolysis is challenging due to the complexity of chemical reactions and the wide variety of influential factors. Machine learning offers an alternative modelling solution by capturing complicated patterns and handling high-dimensional data. However, a deficiency in the number of datasets, particularly the experimental-based dataset, potentially hinders the prediction accuracy of the machine learning models. This study aims to enhance machine learning prediction performance by exploring different algorithms and incorporating data augmentation under non-catalytic fixed-bed pyrolysis reactor condition. Three ensemble models, containing Random Forest (RF), Extra Trees (ET), and Extreme Gradient Boosting (XGBoost), were evaluated. Augmented data was generated using Aspen Plus process simulator, with the dataset sizes varied at 5%, 10%, and 15% of the original dataset. Input features include lignocellulosic biomass characteristics (proximate and ultimate analyses), biomass category (e.g., hardwood, softwood) and pyrolysis operating conditions (e.g., particle size, final temperature), while outputs were solid, liquid, and gas yields. Results indicated that XGBoost achieved the highest accuracy, with R^2 score enhancing by the data augmentation from 0.68 to 0.72 for the solid-phase yields, slightly increasing from 0.85 to 0.86 for the liquid-phase yield, and remaining stable at 0.86 for the gas-phase yield predictions. The optimal augmented dataset size varied depending on the output predicted. This research demonstrates the potential of machine learning applications in achieving high-accuracy predictions in sustainable process design, providing a strong foundation for further practical process optimization.

Keywords: Biomass pyrolysis; Machine learning; Data augmentation; Process simulation; Prediction model

1. INTRODUCTION

An exponential growth of the global population has substantially increased the demand for energy, leading to the rapid depletion of primary energy sources, i.e., fossil fuels. However, this continuous reliance on fossil fuels has led to higher greenhouse gas emissions, significantly contributing to global warming. To mitigate these environmental concerns, extensive efforts have been made to develop greener and renewable energy alternatives. Among these, bioenergy derived from renewable resources, such as biomass, has stood out as a sustainable solution.

Biomass originates from diverse sources, including agricultural residues, energy crops, woody biomass, forest residues, animal wastes, organic municipal solid waste, and algae [1]. Notably, lignocellulosic biomass is particularly attractive due to its low cost and abundant availability. This renewable resource, primarily composed of lignin, cellulose, and hemicellulose, is generally found in agricultural waste or residual, micro algae, and forestry. To produce bioenergy, several approaches exist, such as the direct combustion of biomass or the conversion of biomass into biofuel through various processes. The latter approach has recently gained much attention due to fuel quality improvements, reduced environmental impact, and low greenhouse gas emissions. The great potential for biofuel production renders lignocellulosic biomass a highly promising renewable resource [2].

Biomass can be converted into fuels through various methods, including chemical conversion (producing liquid fuels), biological conversion (producing liquid and gaseous fuels), and thermochemical conversion (producing solid, liquid, and gaseous fuels). The broad range of products obtained from thermochemical conversion enhances its appeal as a versatile and valuable technological pathway. Thermochemical conversion, a process involving thermal decomposition, encompasses combustion, gasification, hydrothermal liquefaction, and pyrolysis. The specific method employed depends on the availability of oxygen during the conversion process and the desired type of end product [3]. Among these, pyrolysis is unique in its capability to produce all three-single phases products,

i.e., biochar (solid), bio-oil (liquid), and biogas. Biomass pyrolysis is generally conducted at high temperatures in the absence of oxygen [4]. The accurate prediction of product yields from biomass pyrolysis is challenging due to the complex interactions between biomass characteristics and operating conditions. Traditional thermodynamic and conservation laws often fail to provide highly accurate predictions due to numerous factors affecting the yields. These factors include the characteristics of biomass, which are generally categorized into proximate and ultimate analysis. Proximate analysis refers to properties such as moisture, volatile matter, fixed carbon, and ash, while the ultimate analysis focuses on the basic elemental composition (i.e., carbon, hydrogen, nitrogen, and oxygen). Other influencing factors are the pyrolysis operating conditions, such as operating temperature, particle size of biomass, residence time in the reacting chamber [5], and its complicated chemical reactions mechanism [6].

Machine learning, a form of data-driven artificial intelligence, has become a modern alternative for predicting product yields from biomass pyrolysis, replacing unattainable traditional methods which rely on thermodynamic and conservation laws. Numerous studies have demonstrated the high accuracy of yield prediction using machine learning models that use biomass characteristics and pyrolysis conditions as input features [7]. For the task of predicting product yields, a supervised regression machine learning model is usually selected. Previous studies indicated that the type of machine learning algorithm significantly affects prediction accuracy. When comparing bagging models like Random Forests (RF) with boosting models such as Extreme Gradient Boosting (XGBoost), Gradient Boosting Decision Tree (GBDT), and AdaBoost, bagging models generally exhibit the higher prediction accuracy [8].

Enhancing the predictive accuracy of the model continues to be a significant challenge. Techniques such as k-fold cross-validation are crucial for such a task through hyperparameters tuning [11]. This technique helps to avoid overfitting by providing a more robust estimation of model performance through averaging results across multiple folds. The procedure of this technique involves four steps: (1) randomly shuffling observations, (2) splitting the dataset into k groups, (3) evaluating the model in each unique group, and (4) summarizing using evaluation scores. In practical, configuring the k value for validating must be carefully selected, as an inappropriate k value can result in high variance or high bias models [12]. Another significant factor directly impacting the predictive efficiency is the size of the dataset. Too small dataset hardly captures all underlying patterns and variations. A larger size of the dataset can reduce overfitting during the model evaluation step, as it enhances the model's evaluation efficiency [13]. With the scarcity of the experimental dataset, obtaining more datasets can be complemented by data augmentation through the assistance of process simulation. This was supported by previous literature which demonstrated that the models trained by the augmented data can achieve higher accuracy in predicting bio-char yield [14].

Therefore, this research aims to enhance the accuracy of machine learning models in predicting the yields of three-phase products through the data augmentation technique. Five different models were applied and compared: two bagging models—Random Forest (RF) and Extra Trees (ET)— included to further investigate findings from the reviewed literature regarding superior performance of bagging model, a boosting model (XGBoost), a traditional nonparametric and lazy learning model like k-nearest neighbors (kNN) [9], and neural networks using Multi-Layer Perceptron (MLP), a commonly used supervised feedforward neural network [10]. The k value was also optimized during the cross-validation step. These models were tested and compared on both the experimental data and the augmented data, where the latter was constructed from the experimental data and the additional data obtaining through the process simulation. The model inputs comprised essential numerical variables, including biomass characteristics, containing proximate analysis and ultimate analysis, and pyrolysis conditions, alongside biomass type, treated as a categorical variable. The model outputs were single-phase product yields. In addition, feature importance analysis using SHAP was also performed to assess the influence of input variables on product yield predictions.

2. METHODOLOGY

2.1 Data Collection and Pre-processing

The experimental dataset was collected from the literature [8], which was gathered from the studies using fixed-bed pyrolysis reactors. The dataset comprises 751 observations, including biomass names and all necessary variables. Input variables include biomass characteristics, proximate analysis (i.e., moisture content (M), ash content (Ash), volatile matter (VM), and fixed carbon content (FC)) and ultimate analysis (i.e., contents of carbon (C), hydrogen (H), oxygen (O), nitrogen (N)), and pyrolysis operation conditions (i.e., particle size (PS), final temperature (FT), heating rate (HR), and inert gas flow rate (FR)). The outputs are the yields of single-phase products: solid, liquid, and gas phases.

After compiling the dataset, the data conformity was rechecked again by revisiting the original sources and noticed a significant variety of biomass types that could influence the outputs. Therefore, biomass was grouped into categories, starting with references to the typical classifications of lignocellulosic biomass and establishing criteria that cover all biomass types in the dataset. These categories include Agricultural waste, Algae, Grass, Hardwood, Softwood, and Other.

Cleaning the verified dataset was necessary before training the machine learning models. Missing data were detected and treated using various methods, including data imputation and deletion. Missing feature values were primarily substituted with the average values for the same biomass type. If no such values existed, the median value was used. The observations with more than one missing variable in each input category (i.e., proximate analysis, ultimate analysis, and pyrolysis conditions) were removed. Moreover, outliers were handled by applying box plot visualization and defining trimming boundaries. After preprocessing, 625 effective observations remained, with 13 input variables, including 12 numerical variables and a categorical variable, and 3 output variables.

To prevent feature dominance, numerical variables were normalized by using Min-max scaling technique as computed by the equation below:

$$x' = \frac{x - min(x)}{max(x) - min(x)} \quad (1)$$

Where x is the value to be normalized, x' is the normalized value, which falls within the range of 0 and 1, *max(x)* is the maximum value of the variable to which x belongs, and *min(x)* is the minimum value.

In addition, one-hot encoding technique was applied to the categorical variable, converting categorical data into numerical vectors. Each unique category was exhibited as a binary column, with a value of 1 indicating its presence and 0 indicating its absence.

2.2 Exploratory Data Analysis (EDA)

The dataset for developing a machine learning model includes diverse input variables with intricate interrelationships. Exploratory Data Analysis (EDA) and Pearson correlation coefficients (PCC) analyses are utilized to gain deeper insights into these complexities. The EDA involves the analysis and visualization of data to understand data structure, identify patterns and relationships, and detect anomalies or outliers. The PCC measures the degree of linear association between two variables. It is the most used method for numerical variables, assigning a value between -1 and 1, where 0 indicates no correlation, 1 represents a perfect positive correlation, and -1 represents a perfect negative correlation. The PCC is normally utilized to evaluate the relationships between input and output variables, reducing overfitting caused by non-essential input variables. The corresponding equation is shown below:

$$r = \frac{\sum(x - m_x)(y - m_y)}{\sqrt{\sum(x - m_x)^2 \times \sum(y - m_y)^2}} \quad (2)$$

Where x and y are vectors of length n, m_x and m_y correspond to means of x and y, respectively.

2.3 Data Splitting

The dataset is split into training and testing subsets in an 80:20 ratio, using a random state of 42, implemented with a function from Scikit-learn library. The training dataset is used exclusively for augmentation and the testing dataset is used to evaluate model performance.

2.4 Data Augmentation

The synthetic data was generated from process simulation performed in Aspen Plus. In this simulation, Peng-Robinson was used as a property method. RYIELD block was chosen to decompose biomass, provided with a Fortran subroutine in a calculator block to determine the product yield based on biomass properties before feeding to a pyrolysis process. The Fortran subroutines were shown in the equations below:

$$Y_{H_2O} = \frac{Moisture}{100} \quad (3)$$

$$Y_{CHAR} = \frac{Carbon}{100} \times (1 - Y_{H_2O}) \quad (4)$$

$$Y_{H_2} = \frac{Hydrogen}{100} \times (1 - Y_{H_2O}) \quad (5)$$

$$Y_{O_2} = \frac{Oxygen}{100} \times (1 - Y_{H_2O}) \quad (6)$$

$$Y_{N_2} = \frac{Nitrogen}{100} \times (1 - Y_{H_2O}) \quad (7)$$

Where Y_a represents yield value of component a.

RGIBBS block was selected to simulate the pyrolysis reactor. After the reaction was completed, the biochar was separated, and the resulting syngas were cooled to 20°C using a HEATER block, before separating the biogas and the bio-oil at SEP block. The biomass pyrolysis simulation was developed under the procedure described in [15], as shown in Figure 1. Once the process simulation model was completed, the input variables from the train dataset of the experimental data were then entered as the inputs of the process simulation and the calculated output or the synthetic outputs was collected by using MATLAB. This synthetic dataset is then combined with the experimental dataset to create an augmented dataset. The size of the synthetic dataset affects the accuracy of machine learning model predictions. In this study, we compare the impact of increasing the size of the synthetic dataset by 5%, 10%, and 15% of the experimental dataset.

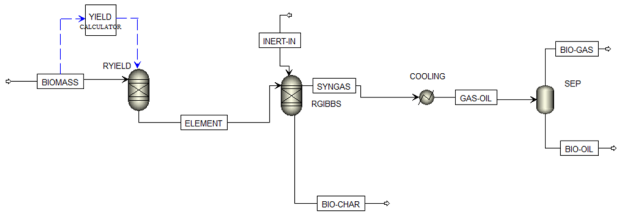

Figure 1 Process flow diagram of biomass pyrolysis

2.5 Developing Machine Learning Models

Machine learning (ML) models, including Random Forests (RF), Extra Trees (ET), Extreme Gradient Boosting (XGBoost), k-Nearest Neighbors (kNN), and Multi-Layer Perceptron (MLP), were developed to predict single-phases product yields. These models were chosen as a representative of their types, except for bagging models. Bagging and boosting models are ensembled models that combine multiple models to predict an output by modeling different analytical models and then synthesizing the results into an output. However, boosting is a technique where the errors of one model are corrected by subsequent models in an iterative process, while bagging does not rely on previous iterations [16]. Lazy learning algorithms operate by storing the training data and generating predictions when a new query is received. Upon receiving a query, the algorithm retrieves similar instances from the training set and uses them to make predictions [17]. Neural networks are designed to process data by mimicking the structure and function of the human brain [18].

To optimize the hyperparameters of these models, the hyperparameters were tuned under various k-fold cross-validation condition, including no fold, 5-fold, and 10-fold, using the Sequential Model-Based Optimization (SMBO) method.

The model performance was assessed using R^2 score, Mean Absolute Error (MAE), and Mean Squared Error (MSE), as expressed in the equations below.

$$R^2 = 1 - \frac{SSR}{TSS} \tag{8}$$

$$MAE = \frac{1}{n}\sum_{i=1}^{n}\left|y_{a,i} - y_{p,i}\right| \tag{9}$$

$$MSE = \frac{1}{n}\sum_{i=1}^{n}\left(y_{a,i} - y_{p,i}\right)^2 \tag{10}$$

Where SSR represents the sum of squares of residuals, TSS is the total sum of squares, n is the number of predictions, $y_{a,i}$ denotes actual values, and $y_{p,i}$ represents predicted values.

The R^2 score is used to determine the accuracy of a model. It ranges from 0 to 1, where a value closer to 1 indicates higher accuracy in performance. The MAE measures the average absolute values. It treats all errors equally, making it less sensitive to the outliers. For the high prediction accuracy of the models, MAE should approach 0. Additionally, The MSE measures the average squared values. It helps evaluate how well the line of best fit matches the data points. The closer the MSE is to 0, the more accurate the prediction [19].

2.6 Feature Importance Analysis

Due to the complex relationships between input and output variables, this study employs SHapley Additive exPlanations (SHAP) to analyses how input variables affect output variables. These methods are used to identify the strong effect of input variables on output variables.

SHAP values, derived from game theory, are calculated to attribute φ_i values to each feature [20]:

$$\varphi_i = \sum_{S \in F \setminus \{i\}} \frac{|S|!\,(M - |S| - 1)!}{M_i}\left[f_x(S \cup \{i\}) - f_x(S)\right] \tag{11}$$

Where F is a non-zero set of inputs in z, S represents subset of F excluding the i-th feature, and φ_i denotes unified measure of additive feature attributions or SHAP value.

However, positive SHAP values positively impact the prediction, while those with negative values have a negative impact. The magnitude of the SHAP value is a measure of how strong the effect is. This study describes the SHAP values using bar plots and Beeswarm plots.

The research methodology is illustrated in Figure 2, which includes data collection, data augmentation, developing machine learning models, and feature importance analysis.

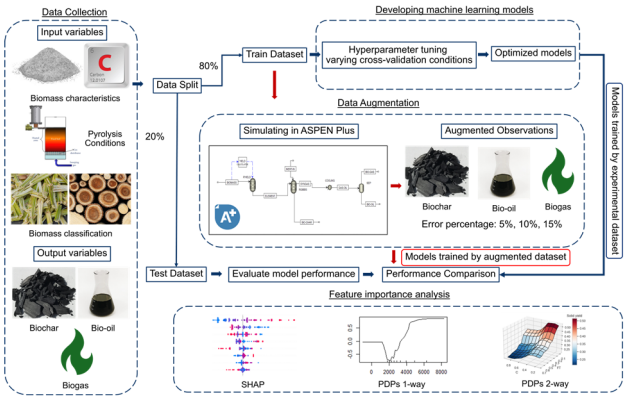

Figure 2 The schematic view of the research methodology

3. RESULTS AND DISCUSSION

3.1 Statistical analysis and feature reduction of data

625 cleaned observations were visualized using box plot distributions, as shown in Figure 3, which provides a description for each numerical variable, including lower and upper boundaries, outliers, average values, and standard deviations. The proximate analysis indicates the ranges for moisture, ash, volatile matter, and fixed carbon contents ranges, which are 0.00-15.76%, 0.24-23.01%, 51.46-89.23%, and 0.20-31.13% by weight, respectively. The ultimate analysis consists of contents of C, H, O, and N, with 37.92-62.10%, 3.00-13.25%, 24.90-55.31%, and 0.00-10.66% by weight, respectively. Pyrolysis conditions, including, PS, FT, HR, and FR are in the ranges of 0.10-7.00 mm (PS), 300.00-900.00 °C (FT), 0.00-700.00 °C/min (HR), 0.00-10000.00 mL/min (FR), respectively. Lastly, the product yields, for the solid, liquid, and gas phases fall

within ranges of 8.22-72.36%, 10.47-74.22%, and 6.48-60.57%, respectively. In addition, as shown in the categorical distribution in Figure 4, the biomass categories include 427 agricultural waste, 97 hardwood, 63 grass, 25 algae, 9 softwood, and 4 others.

A Pearson correlation coefficients (PCCs) heatmap, depicted in Figure 5 explains the linear relationships among the numerical features. While most input features demonstrate notably non-linear relationships, with PCC values in the range of -0.5 to 0.5, a few pairs display moderate correlation, with PCC values lower than -0.5 or greater than 0.5, such as the pairs of VM and FC, VM and Ash, C and H, and C and O. VM shows a strong negative correlation with both Ash and FC, which is confirmed by the estimation equation of VM = 100% - (M + Ash + FC). However, a weak negative correlation between Ash and FC indicates that there is no significant relationship among proximate analysis inputs. Similarly, within the ultimate analysis, variables like C, H, and O show strong correlations with each other, as indicated by their PCC values. Especially, O has a strong negative linear relationship with other elements, as indicated by the high PCC value of -0.71 and -0.93 when paired with C and H, respectively. This can be explained by the formula O = 100% - (C + H + N). Based on this analysis, feature reduction was performed. O was removed from the dataset before training the model to improve model's ability and prevent overfitting caused by inessential repeated variables that convey the same information [21].

Furthermore, no strong correlations were observed between input and output features, except for a strong positive correlation between C and the solid-phase product yield, which is consistent with this literature [22]. However, the correlation coefficient value alone is not sufficient to imply that there is a significant linear relationship between these variables. The PCC analysis results also justify the choice of discarding variables using linear regression machine learning models prediction.

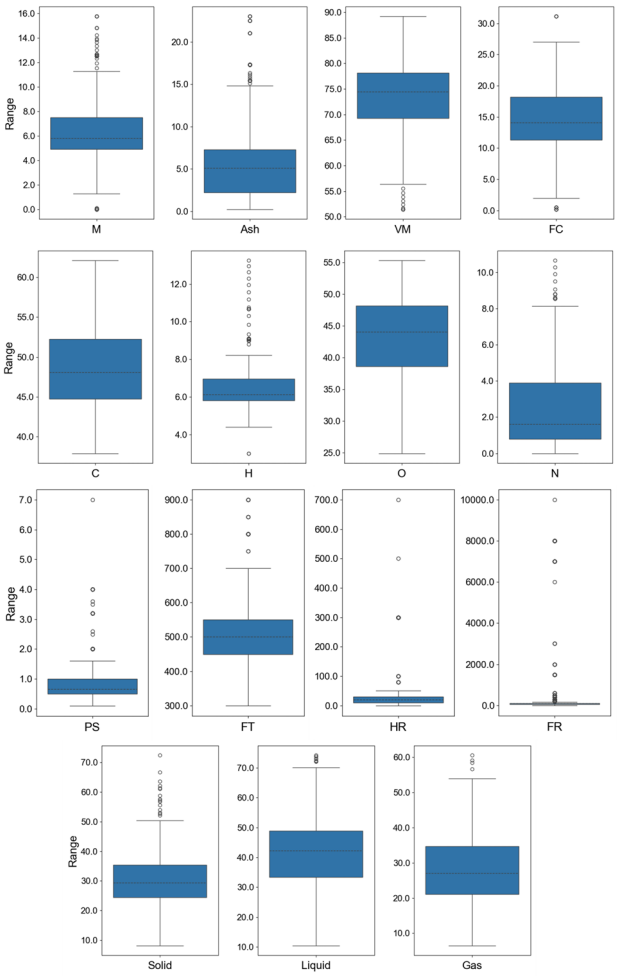

Figure 3 Box plot distribution diagram

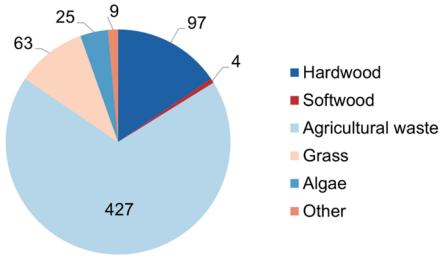

Figure 4 Distribution of Biomass Category

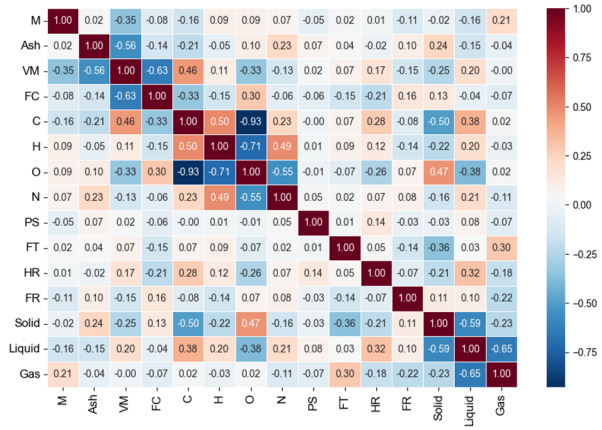

Figure 5 A Pearson Correlation Coefficients Matrix

3.2 Performance of machine learning models on the Experimental Dataset

After feature selection, five ML models were constructed with various k-fold cross-validation. The performance were evaluated and depicted in term of R^2 score in Table 1 and Figure 6.

Table 1 R^2 score comparison of five machine learning algorithms for predicting single-phases product yields trained by the experimental dataset.

Model	Cross-validation condition	Solid	Liquid	Gas
RF	Without CV	0.656	0.848	0.805
	5-fold CV	0.660	0.825	0.810
	10-fold CV	0.650	0.826	0.811
ET	Without CV	0.625	0.854	0.774
	5-fold CV	0.623	0.847	0.778
	10-fold CV	0.620	0.846	0.775
XGBoost	Without CV	0.621	0.833	0.826
	5-fold CV	0.668	0.847	0.857
	10-fold CV	0.678	0.848	0.854
kNN	Without CV	0.456	0.771	0.694
	5-fold CV	0.511	0.771	0.673
	10-fold CV	0.511	0.774	0.678
MLP	Without CV	0.444	0.604	0.648
	5-fold CV	0.482	0.577	0.651
	10-fold CV	0.453	0.644	0.654

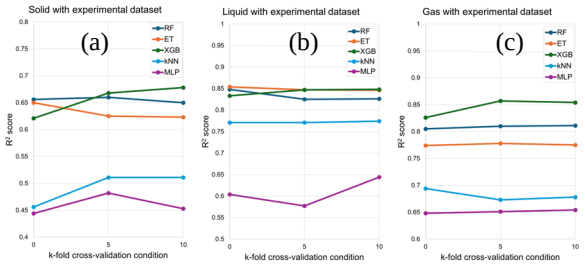

Figure 6 R^2 score comparison of models under various cross-validation conditions: (a) Solid (b) Liquid (c) Gas.

The results showed that the ensembled models, including RF, ET, and XGBoost, outperformed kNN and MLP. This might be due to the fact that the outliers were still included in the dataset. The outliers were not handled by using Interquartile Range (IQR) or Z-distribution methods concerning that the size of the dataset would become too small after trimming. In addition, ensembled models are usually robust to outliers, while kNN and MLP are sensitive to them [23]. The size of the dataset that is less than a thousand might be too small for an effective training of the neural network models [24].

Furthermore, our analysis indicated that 10-fold cross-validation condition yielded the best performance, closely followed by 5-fold, as a higher k-value generally enhances predictive performance. This marginal improvement observed in the 10-fold case was likely attributed to a greater reduction in overfitting to the training dataset, which could degrade the model's generalization capability on unseen test data [25]. However, as clearly demonstrated in Figure 7, the computational time increased sharply with higher k-values. Considering this significant trade-off between the slight performance gain and the substantial increase in computational time, 5-fold cross-validation was determined to be the optimal condition. Therefore, ensemble models with 5-fold cross-validation were chosen for further study with augmented dataset.

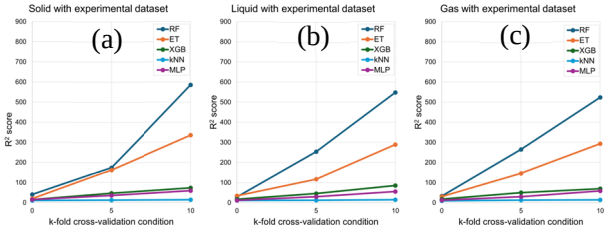

Figure 7 Computational time comparison of models under various cross-validation conditions: (a) Solid (b) Liquid (c) Gas

3.3 Performance of machine learning models on the Augmented Dataset using ASPEN Plus

The number of synthetic data points for the 5%, 10%, and 15% scenarios is 32, 63, and 94, respectively, resulting in augmented dataset sizes of 657, 688, and 719, respectively. The variation in the number of synthetic datasets resulted in a higher proportion of agricultural waste categories and led to differences in the percentage error of the synthetic datasets, However, this change did not significantly impact the descriptive statistics of the augmented dataset. The highest percentage error observed among the synthetic datasets is shown in Table 2. The percentage error represents the difference between the product yields from the synthetic and experimental data, calculated using the following equation:

$$\%error = \frac{Y_{exp} - Y_{syn}}{Y_{exp}} \times 100\% \qquad (12)$$

Where Y_{exp} is the product yield of the experimental dataset and Y_{syn} is the product yield of the synthetic dataset.

In this study, selecting a synthetic dataset based on the lowest percentage error ensures that the descriptive statistics of the augmented dataset closely approximate those of the experimental dataset.

Table 2 The highest percentage error of the synthetic datasets.

Synthetic dataset	Product phase		
	Solid	Liquid	Gas
5%	3.85%	9.83%	11.84%
10%	5.89%	18.41%	23.58%
15%	9.31%	25.25%	30.30%

After building an augmented dataset, the tree-based models with 5-fold cross-validation were used for training and then validated using the test dataset. The model performance for predicting solid-phase, liquid-phase, and gas-phase are presented in Figure 8(a), Figure 8(b), Figure 8(c), respectively. The best performed models for predicting solid-phase, liquid-phase, and gas-phase are XGBoost with 15% synthetic data, XGBoost with 10% synthetic data, and XGBoost with 5% synthetic data, respectively. When considering the percentage error, the best performed models typically showed a percentage error of approximately 5 percent. These results demonstrated that the variation in the amount of synthetic data influences the performance of the machine learning models, which aligns with the results from the existing literature [26] and adding the synthetic data, with a percentage error of around 5 percent compared to the experimental dataset contributes to improved model efficiency.

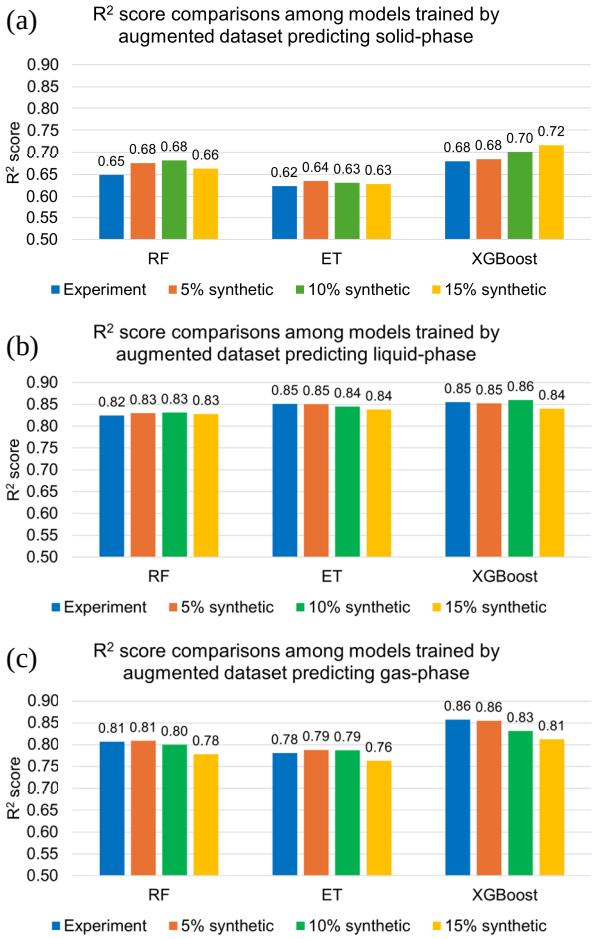

Figure 8 R^2 score: (a) Solid (b) Liquid (c) Gas

3.4 SHapley Additive exPlanations (SHAP)

After creating the machine learning models for predicting products from biomass pyrolysis process, the models with the highest R^2 score for the prediction of each output phase were summarized in Table **3**. These models were further used for the SHAP analysis to study the effect of input variables on output variables.

Table 3 The machine learning model has the highest R^2 score.

Phase prediction	Dataset	Machine learning model	Cross-validation condition
Solid	15% synthetic	XGBoost	5-fold cross-validation
Liquid	10% synthetic		
Gas	Experimental		

The SHAP results of solid-phase, liquid-phase, and gas-phase are presented in Figure 9, Figure 10, and Figure 11, respectively. The Beeswarm and bar plots used in the SHAP analysis illustrate the magnitude of each input variable's effect on product yield in each phase. However, these plots can be challenging to interpret regarding the precise direction of influence. Therefore, the top three input variables affecting

product yield in solid-phase yield are FT, C, and Ash. For liquid-phase, the top three are C, N, and FT, while for gas-phase yield, the top three are M, FT, and PS. The research showed that FT has a strong effect on the product yield across all phases, which is consistent with findings from research [27]. FT is a pyrolysis condition that can be adjusted and applied to all types of biomasses, unlike intrinsic biomass characteristics that cannot be modified.

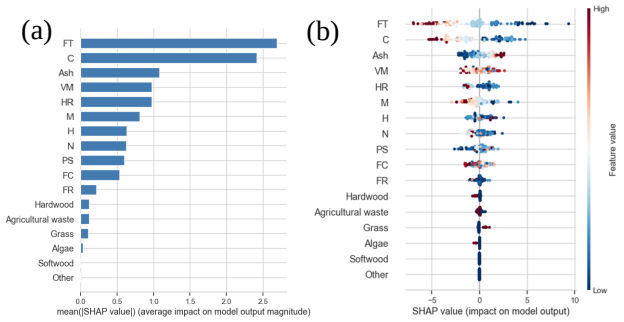

Figure 9 Input variables effect on solid-phase yield: (a) Bar plots (b) Beeswarm plots

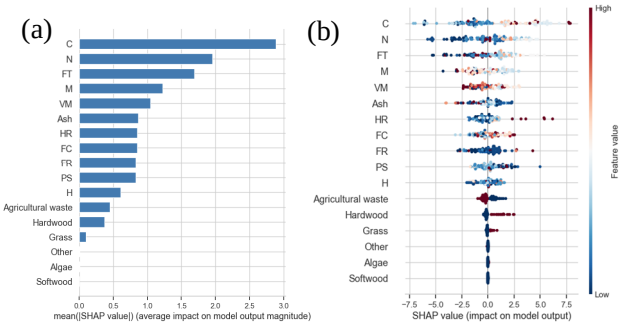

Figure 10 Input variables effect on liquid-phase yield: (a) Bar plots (b) Beeswarm plots

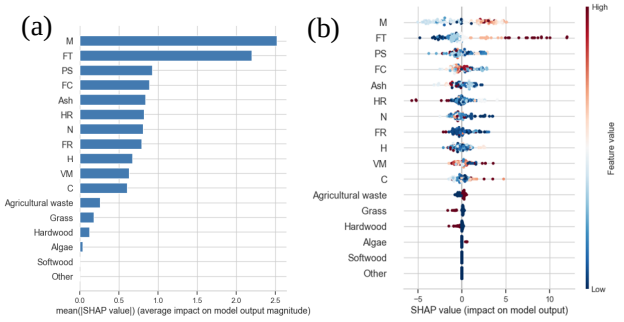

Figure 11 Input variables effect on gas-phase yield: (a) Bar plots (b) Beeswarm plots.

4. CONCLUSION

Five machine learning models, including Random Forest, Extra Trees, Extreme Gradient Boosting (XGBoost), k-Nearest Neighbors (kNN), and Multi-layer Perceptron (MLP), were developed to predict biochar (solid), bio-oil (liquid), and biogas (gas) yields from biomass pyrolysis process. Ensemble models trained by experimental dataset like RF, ET, and XGBoost outperformed the others, with the XGBoost achieving the highest R^2 scores of 0.68, 0.85, and 0.86 for solid, liquid, gas-phase product yields prediction, respectively. The 5-fold cross-validation condition was found to be optimal for hyperparameter tuning. Data augmentation using process simulation via ASPEN Plus moderately improved the performance of machine learning models, particularly for solid and liquid-phase product yield predictions. Notably, the XGBoost's performance increased to 0.72 for solid-phase and slightly improved to 0.86 for liquid-phase predictions. SHAP analysis across all output predictions identified final temperature as the most crucial feature. These findings suggested that ensembled models, especially XGBoost, are highly effective in predicting biomass pyrolysis yields, and that dataset augmentation plays a critical role in enhancing the prediction accuracy of the machine learning models, underscoring the potential for optimizing biomass pyrolysis studies.

ACKNOWLEDGMENTS

The authors sincerely acknowledge the support of the Faculty of Engineering, Kasetsart University, Bangkok, Thailand.

REFERENCES

[1] J. N. Rogers *et al.*, "An assessment of the potential products and economic and environmental impacts resulting from a billion ton bioeconomy," *Biofuels, Bioproducts and Biorefining*, vol. 11, no. 1, pp. 110–128, 2017.

[2] A. Zoghlami and G. Paës, "Lignocellulosic Biomass: Understanding Recalcitrance and Predicting Hydrolysis," *Front. Chem.*, vol. 7, Dec. 2019.

[3] eia, "Biomass explained - U.S. Energy Information Administration (EIA)," eia.gov. Accessed: Oct. 06, 2024. [Online]. Available: https://www.eia.gov/ energyexplained/biomass/

[4] AR, "Biomass Pyrolysis," Chemical and Process Engineering. Accessed: Jul. 01, 2024. [Online]. Available: https://www.arhse.com/biomass-pyrolysis

[5] R. Arisanti, M. Yusuf, and M. Faizal, "Study of the Effect of Proximate, Ultimate, and Calorific Value Analysis on Methane Gas Emission (CH4) on Combustion of Coal for Sustainable Environment," *Science and Technology Indonesia*, vol. 3, no. 2, Art. no. 2, Apr. 2018.

[6] V. Dhyani and T. Bhaskar, "Chapter 9 - Pyrolysis of Biomass," in *Biofuels: Alternative Feedstocks and Conversion Processes for the Production of Liquid and Gaseous Biofuels (Second Edition)*, A. Pandey, C. Larroche, C.-G. Dussap, E. Gnansounou, S. K. Khanal, and S. Ricke, Eds., in Biomass, Biofuels, Biochemicals. , Academic Press, 2019, pp. 217–244.

[7] H. Lee, I.-H. Choi, and K.-R. Hwang, "Machine learning prediction of bio-oil production from the pyrolysis of lignocellulosic biomass: Recent advances and future perspectives," *Journal of Analytical and Applied Pyrolysis*, vol. 179, p. 106486, May 2024.

[8] Z. Dong, X. Bai, D. Xu, and W. Li, "Machine learning prediction of pyrolytic products of lignocellulosic biomass based on physicochemical characteristics and pyrolysis conditions," *Bioresource Technology*, vol. 367, p. 128182, Jan. 2023.

[9] Y. Shi, K. Yang, Z. Yang, and Y. Zhou, "Chapter Two - Primer on artificial intelligence," in *Mobile Edge Artificial Intelligence*, Y. Shi, K. Yang, Z. Yang, and Y. Zhou, Eds., Academic Press, 2022, pp. 7–36.

[10] T. Kotsiopoulos, P. Sarigiannidis, D. Ioannidis, and D. Tzovaras, "Machine Learning and Deep Learning in smart manufacturing: The Smart Grid paradigm," *Computer Science Review*, vol. 40, p. 100341, May 2021.

[11] S. Hrvoje, "Cross-Validation." Accessed: Oct. 06, 2024. [Online]. Available: https://graphite-note.com/the-importance-of-cross-validation-in-machine-learning/

[12] J. Brownlee, "How to Develop Multi-Output Regression Models with Python," MachineLearningMastery.com. Accessed: Aug. 01, 2024. [Online]. Available: https://machinelearningmastery.com/multi-output-regression-models-with-python/

[13] H. Gunasekaran, "Is it correct that if dataset is large one needs less of evaluation, which means that the fraction of the dataset used for evaluation can be decreased with increased size of the dataset?," EITCA Academy. Accessed: Oct. 06, 2024. [Online]. Available: https://eitca.org/artificial-intelligence/eitc-ai-gcml-google-cloud-machine-learning/first-steps-in-machine-learning/deep-neural-networks-and-estimators/is-it-correct-that-if-dataset-is-large-one-needs-less-of-evaluation-which-means-that-the-fraction-of-the-dataset-used-for-evaluation-can-be-decreased-with-increased-size-of-the-dataset/

[14] P. Jiang *et al.*, "A hybrid approach combining mechanism-guided data augmentation and machine learning for biomass pyrolysis," *Chemical Engineering Science*, vol. 296, p. 120227, Aug. 2024.

[15] P. Lestinsky and A. Palit, "Wood Pyrolysis Using Aspen Plus Simulation and Industrially Applicable Model," *GeoScience Engineering*, vol. 62, no. 1, pp. 11–16, 2016.

[16] B. Gauri, "Comparison of Boosting algorithms | Kaggle." Accessed: Oct. 14, 2024. [Online]. Available: https://www.kaggle.com/discussions/general/a

[17] A. A. Awan, "What is Lazy Learning?" Accessed: Apr. 17, 2025. [Online]. Available: https://www.datacamp.com/blog/what-is-lazy-learning

[18] A. A. Awan, "What are Neural Networks?" Accessed: Apr. 17, 2025. [Online]. Available: https://www.datacamp.com/blog/what-are-neural-networks

[19] A. V. Tatachar, "Comparative Assessment of Regression Models Based On Model Evaluation Metrics," vol. 08, no. 09, 2021.

[20] S. M. Lundberg, G. G. Erion, and S.-I. Lee, "Consistent Individualized Feature Attribution for Tree Ensembles," Mar. 06, 2019, *arXiv*: arXiv:1802.03888. Accessed: Oct. 06, 2024. [Online]. Available: http://arxiv.org/abs/1802.03888

[21] A. Ashraf, "Correlation in machine learning — All you need to know," Medium. Accessed: Oct. 07, 2024. [Online]. Available: https://medium.com/@abdallahashraf90x/all-you-need-to-know-about-correlation-for-machine-learning-e249fec292e9

[22] Q. Xu, L. Du, and R. Deng, "Using machine learning to predict biochar yield and carbon content: Enhancing efficiency and sustainability in biomass conversion :: BioResources." Accessed: Oct. 07, 2024. [Online]. Available: https://bioresources.cnr.ncsu.edu/

[23] ruhong, "Answer to 'Are deep neural networks robust to outliers?,'" Cross Validated. Accessed: Oct. 11, 2024. [Online]. Available: https://stats.stackexchange.com/a/500220

[24] V. Veenstra, "Are there any obvious reasons for why a NN regressor performs worse than a Xgboost regression on my dataset (about 5k data points)?," Quora. Accessed: Oct. 12, 2024. [Online]. Available: https://www.quora.com/Are-there-any-obvious-reasons-for-why-a-NN-regressor-performs-worse-than-a-Xgboost-regression-on-my-dataset-about-5k-data-points

[25] J. Brownlee, "A Gentle Introduction to k-fold Cross-Validation," MachineLearningMastery.com. Accessed: Oct. 06, 2024. [Online]. Available: https://machinelearningmastery.com/k-fold-cross-validation/

[26] C. Zhou, Y. Zhang, H. Xin, X. Li, and X. Chen, "Complex multiphase predicting of additive manufactured high entropy alloys based on data augmentation deep learning," *Journal of Materials Research and Technology*, vol. 28, pp. 2388–2401, Jan. 2024.

[27] S. Cheng *et al.*, "Pyrolysis of Crofton weed for the production of aldehyde rich bio-oil and combustible matter rich bio-gas," *Applied Thermal Engineering*, vol. 148, pp. 1164–1170, Feb. 2019.

Continuous production of 5-hydroxymethylfurfural using monophasic solvents for pharmaceutical applications

Kritsanalak Thongkan[1], Nattee Akkarawatkhoosith[1], Tiprawee Tongtummachat[1,*]

[1] Department of Chemical Engineering, Faculty of Engineering, Mahidol University, Nakhon Pathom 73170, Thailand

[*] Corresponding author: tiprawee.ton@mahidol.edu

ABSTRACT

5-Hydroxymethylfurfural (5-HMF) is a bio-based compound with pharmaceutical applications due to its antioxidant, anti-cancer, and anti-sickling properties, along with its potential use as a dietary supplement. However, production processes designed explicitly for pharmaceutical-grade 5-HMF remain underexplored, with most studies concentrating on maximizing yields using solvents and catalysts unsuitable for pharmaceutical purposes. This study aims to develop a safe, cost-effective, and efficient method for producing 5-HMF by utilizing sugarcane syrup as a low-cost feedstock and citric acid as a catalyst within a microreactor system. Monophasic solvents with low boiling points, including deionized water, acetone, 1-propanol, 2-propanol, and tetrahydrofuran, were selected to facilitate easy solvent removal by evaporation, ensuring minimal residual solvent contamination in the final product. Analysis of reaction outcomes revealed that all solvents achieved relatively high syrup conversion rates. Tetrahydrofuran showed the highest selectivity (41.21%) at a residence time of 40 min. Nevertheless, cost analysis identified acetone as the most cost-effective solvent. Acetone's low boiling point facilitated easier solvent removal, enhancing process efficiency and safety. At an 80-min residence time, acetone achieved a 5-HMF yield of 32.02% and a selectivity of 34.46%. These results indicate acetone as the optimal solvent for further process optimization, offering a balanced combination of cost-effectiveness, efficiency, and pharmaceutical compliance suitable for large-scale 5-HMF production.

Keywords: 5-hydroxymethylfurfural; Syrup; Microreactor; Monophasic system; Pharmaceutical applications

1. INTRODUCTION

Recently, interest in utilizing biomass as a feedstock for producing organic chemicals has significantly increased. Efficient utilization of biomass resources offers a promising approach to reducing dependence on fossil hydrocarbons such as oil, coal, and natural gas. 5-Hydroxymethylfurfural (5-HMF) was recognized by the US Department of Energy in 2010 as one of the top 10 most valuable bio-based chemicals [1]. Derived from biomass, 5-HMF exhibits significant potential across various industries, including biofuels, bio-based polymers, chemical precursors, and pharmaceuticals [2-9]. In pharmaceutical applications specifically, 5-HMF demonstrates antioxidant properties capable of protecting the liver from alcohol-induced damage [10], extending survival rates in rats with cerebral ischemia [11], and potential anti-cancer [12], anti-sickling [13], and anti-allergenic effects [14]. Additionally, studies suggest that 5-HMF may enhance physical performance and improve recovery following surgery when utilized as a dietary supplement [15,16]. Despite these promising applications, producing pharmaceutical-grade 5-HMF remains challenging, primarily due to solvent toxicity and product purity concerns.

Most existing research on 5-HMF synthesis prioritizes yield maximization using solvents and catalysts unsuitable for pharmaceutical applications. Biphasic systems, known for their high yields [17], typically employ solvents like methyl isobutyl ketone (MIBK) [18-21], which pose significant environmental and health risks due to their high boiling points and potential residual contamination. The US Food and Drug Administration recommends that solvent residues in pharmaceutical products not exceed 4500 ppm [22]. Consequently, there is a growing necessity to explore safer alternative solvents that can be easily removed from the final product. Monophasic systems offer a homogeneous reaction medium, enhancing efficiency through uniform mixing and improved mass transfer. Studies have compared monophasic and biphasic solvent systems; for instance, Sayed et al. (2020) demonstrated the effectiveness of tetrahydrofuran and 2-propanol, yielding 5-HMF at 51.5% and 67.1%, respectively [24]. Furthermore, Chen et al. (2023) explored continuous 5-HMF production via fructose

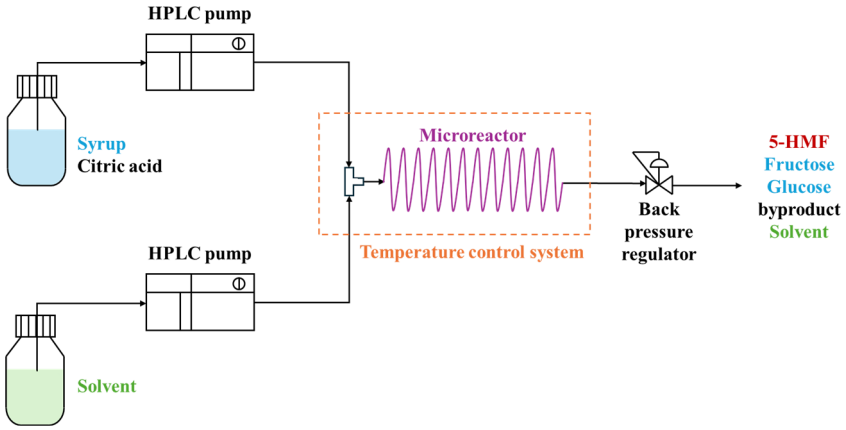

Figure 1 Continuous production of 5-HMF from syrup using a monophasic system.

dehydration using various polar aprotic cosolvents, reporting acetone achieving the highest dehydration rate. In contrast, tetrahydrofuran provided stable 5-HMF formation with fewer byproducts [25].

Selecting suitable feedstocks impacts 5-HMF synthesis efficiency significantly. While fructose is the most effective C6 carbohydrate for 5-HMF production [26], its high cost has directed research toward more economical alternatives, such as syrups. This is especially relevant in countries like Thailand, where sugarcane-based syrups are readily available and cost-effective due to the robust sugarcane industry [27]. Research investigating high-fructose corn syrup as a feedstock has demonstrated its feasibility for industrial-scale production of 5-HMF [28,29].

Citric acid has been investigated as a catalyst for enhancing 5-HMF production due to its environmental friendliness and effectiveness compared to conventional strong acids. Its weak acidity helps mitigate the undesirable rehydration of 5-HMF into byproducts, a common issue when stronger acids are used [30]. Previous studies have successfully demonstrated the catalytic potential of citric acid in efficient 5-HMF synthesis [31].

Microreactors represent a promising continuous processing technology for optimizing 5-HMF production. Microreactors offer rapid heating, efficient mixing, and enhanced mass transfer than traditional batch reactors, resulting in shorter reaction times and higher yields [32,33].

This study proposes a continuous, safe, and economically viable production process for pharmaceutical-grade 5-HMF from sugarcane syrup, focusing on monophasic solvent systems. The research investigates the effectiveness of organic solvents such as acetone (ACT), 2-propanol (IPA), and tetrahydrofuran (THF)—previously reported as efficient for 5-HMF production—and further evaluates the performance of 1-propanol (PrOH). The impact of these solvents on syrup conversion (%), 5-HMF yield (%), 5-HMF selectivity (%), cost per mass flow rate (Million baht per kg/hr), and mass flow rate per cost (kg/hr per Million baht) is analyzed and compared with deionized water (DI). Additionally, the role of citric acid in enhancing 5-HMF production efficiency is examined, aiming to establish an optimized, safe, and cost-effective continuous production method suitable for pharmaceutical applications.

2. EXPERIMENTAL

2.1. Materials

Sugarcane syrup, consisting of 24% sucrose, 37% glucose, and 38% fructose, was purchased from Mitr Phol Group (Bangkok, Thailand). The 5-HMF standard was obtained from Sigma-Aldrich (USA). Solvents used in this study, including AC, PrOH, IPA, and THF, were acquired from ACI Labscan (Thailand). Deionized water and acetonitrile, utilized for preparing the mobile phase in HPLC analysis, were also purchased from ACI Labscan. Citric acid, employed as the catalyst, was obtained from Kemaus (Australia).

2.2. 5-HMF production

The experiment begins by feeding sugarcane syrup at a concentration of 20 g/L, along with 15 wt.% citric acid, into a T-micromixer (0.020-inch thru-hole diameter) using an HPLC pump. Simultaneously, another HPLC pump delivers the selected solvent at an organic-to-aqueous (O:A) ratio of 0.5:1. The resulting mixture enters a microreactor with a 1/16-inch diameter and a 4 mL volume maintained at 190°C using an oven. Upon exiting the reactor, pressure is regulated at 1000 psi using a backpressure regulator, and the final product is collected for further analysis, as illustrated in Fig. 1. The syrup conversion (%C, syrup), 5-HMF yield (%Y, 5-HMF), and 5-HMF selectivity (%S, 5-HMF) are calculated using Equations (1)–(3).

$$C_{syrup}\,(\%) = \left(1 - \frac{\text{Moles of monosaccharide remaining}}{\text{Initial mole of monosaccharides}}\right) \times 100 \quad (1)$$

$$Y_{5\text{-HMF}}\,(\%) = \left(\frac{\text{Moles of 5-HMF produced}}{\text{Initial mole of monosaccharides}}\right) \times 100 \quad (2)$$

$$S_{5\text{-HMF}}\,(\%) = \left(\frac{Y_{5\text{-HMF}}}{C_{syrup}}\right) \times 100 \quad (3)$$

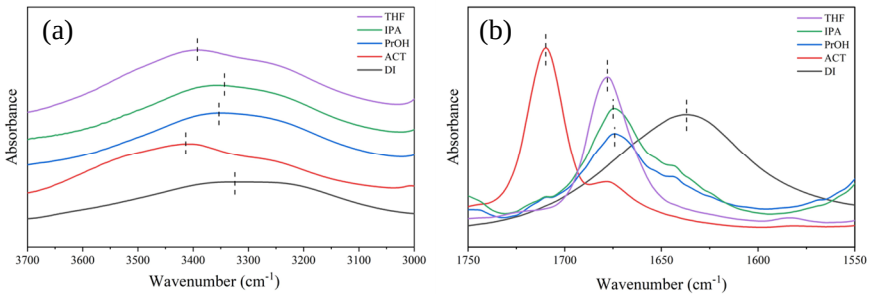

Figure 2 ATR-FTIR spectra of (a) O-H stretching regions in the mixture of syrup with organic solvents, (b) C=O stretching regions in the mixture of 5-HMF with organic solvent.

2.3. Product analysis

The quantities of 5-HMF and byproducts, including formic acid and levulinic acid, were analyzed using High-Performance Liquid Chromatography (HPLC) equipped with a Photodiode Array Detector (PDA). An ACE Excel Super C18 column (250 mm length × 4.6 mm diameter, 5 µm particle size; Advanced Chromatography Technologies) was employed. The mobile phase consisted of deionized water (DI) and acetonitrile in a 90:10 volumetric ratio, delivered at a 1 mL/min flow rate. The column temperature was maintained at 40°C. Detection of 5-HMF was performed at a wavelength of 320 nm, while formic acid and levulinic acid were analyzed at 280 nm. The sample concentrations (g/L) were quantified using standard calibration curves for each compound.

The concentrations of fructose, glucose, and sucrose were also determined by HPLC, this time using a Refractive Index Detector (RID). An ACE Excel Super NH_2 column (250 mm length × 4.6 mm diameter, 5 µm particle size; Advanced Chromatography Technologies) was used. The mobile phase comprised DI and acetonitrile in an 18:82 volumetric ratio, with a 1 mL/min flow rate. The column temperature was set at 40°C, and concentrations (g/L) were calculated based on individual standard calibration curves.

To investigate the interactions between syrup or 5-HMF and the solvents, Attenuated Total Reflectance-Fourier Transform Infrared (ATR-FTIR) spectroscopy was conducted using a Thermo Nicolet Nexus 470 spectrometer. The analysis focused on identifying shifts in peak positions corresponding to hydroxyl stretching vibrations (O–H stretch: 3000–3500 cm^{-1}) and carbonyl stretching vibrations (C=O stretch: 1600–1700 cm^{-1}). Spectra were collected over the 500–4000 cm^{-1} range at a resolution of 2 cm^{-1}, with 32 scans per sample.

3. RESULTS AND DISCUSSION

3.1. Solvent effects on dehydration in 5-HMF production

Selecting an appropriate solvent system is pivotal in influencing the efficiency, selectivity, and safety of 5-HMF production. This study focuses on developing a non-toxic and pharmaceutically compliant synthesis process for 5-HMF. To this end, monophasic solvents with low boiling points were selected to facilitate easy removal through evaporation, thereby minimizing the risk of residual solvent contamination in the final product. The solvents investigated in this study include DI, ACT, PrOH, IPA, and THF. To evaluate their impact on the dehydration process, a key step in efficient 5-HMF production, the interactions between these solvents and either syrup or 5-HMF were examined using ATR-FTIR.

The ATR-FTIR spectra in Fig. 2a focus on the O–H stretching region (3000–3700 cm^{-1}) for syrup dissolved in different solvents. The O–H stretching peak in DI appeared at the lowest wavenumber (3325 cm^{-1}), indicating strong hydrogen bonding. When organic solvents were used, however, the O–H stretching bands exhibited a blueshift (i.e., shift to higher wavenumbers), increasing progressively from IPA to PrOH and THF, with the most pronounced shift observed for ACT at 3414 cm^{-1}. This blueshift reflects a weakening of hydrogen bonding interactions, suggesting that syrup molecules interact weaklier with organic solvents than water. Weaker hydrogen bonding facilitates the dehydration reaction, which is critical for effective 5-HMF production [25].

Similarly, Fig. 2b presents the ATR-FTIR spectra of 5-HMF in various organic solvents, focusing on the C=O stretching region (1550–1750 cm^{-1}). Compared to DI water, the C=O stretching bands in organic solvents appear at higher wavenumbers, indicating a blueshift. This effect is most pronounced in ACT, where the band shifts to 1709 cm^{-1}. This shift suggests a stronger carbonyl bond resulting from reduced hydrogen-bonding interactions [35,36]. Acetone, being a polar aprotic solvent with low hydrogen-bond donating ability, interacts minimally with the carbonyl group of 5-HMF. This reduced hydrogen bonding not only strengthens the carbonyl bond but also contributes to greater product stability by decreasing susceptibility to side reactions such as rehydration.

In summary, ATR-FTIR spectroscopy was employed to investigate the influence of various monophasic solvents on hydrogen bonding interactions in the dehydration process. Shifts in the O–H and C=O stretching bands indicate that organic solvents weaken hydrogen bonding interactions, promoting more

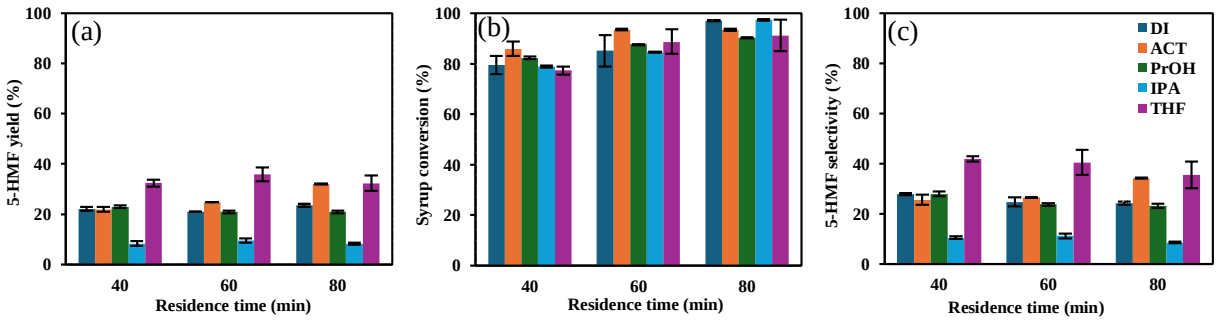

Figure 3 Effect of solvent system for 5-HMF synthesis: (a) 5-HMF yield, (b) syrup conversion, and (c) 5-HMF selectivity.

effective dehydration. This insight underscores the role of solvent selection in designing a safer, more efficient route for producing 5-HMF suitable for pharmaceutical applications.

3.2. Optimal solvent system for 5-HMF production

3.2.1. Solvent Effects on 5-HMF synthesis efficiency

Organic solvents, including DI, ACT, PrOH, IPA, and THF, were evaluated for their suitability in 5-HMF production for pharmaceutical applications. The ideal solvent should offer both high production efficiency and cost-effectiveness. In this study, 5-HMF selectivity (%) was used as the primary indicator of production efficiency, while cost-effectiveness was assessed using two metrics: cost per mass flow rate (Million baht per kg/hr) and mass flow rate per cost (kg/hr per Million baht).

The experimental setup employed a syrup concentration of 20 g/L as the feedstock and 15 wt.% citric acid as the catalyst. This mixture was introduced into a continuous microreactor system operating at 190°C with the O:A phase ratio of 0.5:1. Reactions were carried out at residence times of 40, 60, and 80 min, and the products were collected for analysis.

Figure 3 presents the results for syrup conversion, 5-HMF yield, and 5-HMF selectivity across the different solvents. At 40 min, THF yielded the highest 5-HMF output (31.41%), followed by ACT, PrOH, and DI, while IPA showed the lowest performance. A similar trend was observed at 60 min, with THF maintaining the highest yield (33.87%). However, at 80 min, ACT surpassed THF, achieving a yield of 32.02%, while THF declined to 30.23% (Fig. 3a). All solvents exhibited relatively high syrup conversion across all residence times (Fig. 3b). ACT showed the highest conversion at both 40 and 60 min (85.88% and 93.63%, respectively). By 80 min, conversion rates for all solvents converged to approximately 90%.

The trend in 5-HMF selectivity closely mirrored that of the yield (Fig. 3c). At 40 min, THF showed the highest selectivity at 41.21%—the highest value recorded across all solvents and residence times. ACT, PrOH, and DI followed with similar selectivity values around 26%, while IPA remained the lowest. At 60 min, THF retained the highest selectivity (36.93%), though slightly reduced from 40 min. By 80 min, ACT outperformed THF, reaching 34.46%, while THF continued to decline to 31.99%, followed by PrOH, DI, and IPA, and for DI, PrOH, and IPA, residence time had a limited effect on 5-HMF yield and selectivity. In contrast, ACT exhibited improved performance with longer residence time, while THF demonstrated a reverse trend with declining efficiency. These findings align with the report by Vasishta et al. (2023) [34], which indicated that prolonged residence time may lead to reduced 5-HMF yield and selectivity due to the formation of byproducts such as levulinic acid and humins.

Comparisons with DI revealed that most organic solvents, particularly THF and ACT, outperformed in terms of 5-HMF yield and selectivity. PrOH delivered similar values, while IPA consistently showed low performance. This is likely due to increased byproduct formation, as shown in Fig. 4, which shows a darker product color when IPA was used, indicating greater byproduct content compared to other solvents. The selection of the solvent system plays a crucial role in determining the efficiency, selectivity, and safety of 5-HMF production.

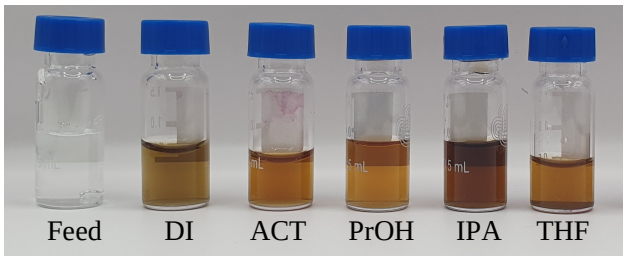

Figure 4 5-HMF solutions obtained from different solvents.

3.2.2. Solvent Effects on 5-HMF synthesis cost-effectiveness

The cost-effectiveness of the 5-HMF production process was evaluated using different organic solvents. The analysis employed two key indicators: cost per mass flow rate (Million baht per kg/hr), representing the cost of producing one unit of 5-HMF mass per hour (where a lower value indicates greater cost-efficiency), and mass flow rate per cost (kg/hr per Million baht), indicating the amount of 5-HMF that can be produced

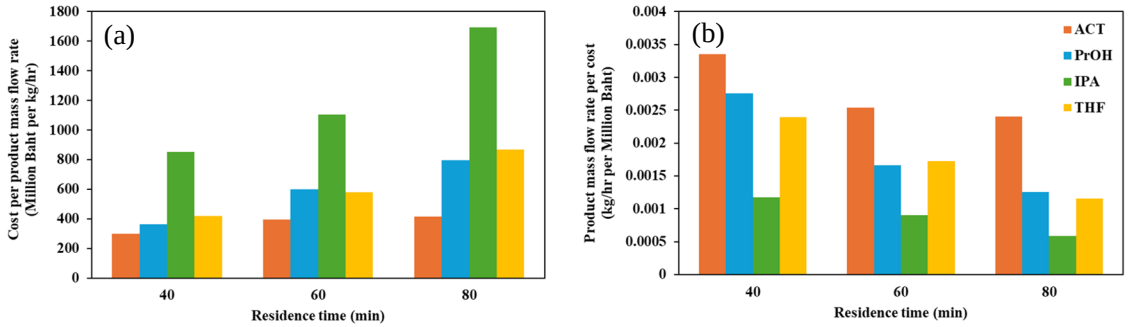

Figure 5 Comparison of (a) Cost per unit product mass flow rate and (b) Product mass flow rate per unit cost for various solvents.

per one million baht (where a higher value reflects better economic performance).

As discussed in Section 3.2.1, THF exhibited the highest selectivity at 41.21% at a residence time of 40 min. However, cost-effectiveness calculations revealed that ACT is the most economically viable solvent, offering both the lowest cost per unit product mass flow rate and the highest product mass flow rate per unit cost, as shown in Fig. 5. In addition to its favorable economic profile, ACT demonstrated high 5-HMF yield, and selectivity compared to other solvents.

Notably, while ACT delivered strong cost-efficiency at a residence time of 40 min, its performance further improved at 80 min, achieving a 5-HMF yield of 32.02%, a selectivity of 34.46%, and excellent economic value. Furthermore, ACT's low boiling point (56.2°C) facilitates easy removal from the final product, enhancing both process efficiency and safety, especially critical factors in pharmaceutical applications.

These advantages position ACT as the most promising solvent for further process optimization, offering an optimal balance of cost-effectiveness, production efficiency, and pharmaceutical suitability for large-scale 5-HMF manufacturing.

3.3. Effect of citric acid on 5-HMF production

Citric acid has emerged as a promising catalyst in the synthesis of 5-HMF, primarily due to its non-toxic and environmentally friendly characteristics. Its mild acidity reduces the likelihood of 5-HMF undergoing rehydration into undesired byproducts, thus improving product selectivity [30]. Several studies have reported the effective use of citric acid in optimizing 5-HMF production, highlighting its role in facilitating efficient and cleaner reaction pathways [31].

In this study, a 20 g/L syrup solution was used as the feedstock, with ACT serving as the solvent. The reaction mixture was introduced into a continuous microreactor system maintained at 190°C and operated with an O:A ratio of 0.5:1. Reactions were conducted at residence times of 40, 60, and 80 minutes. To evaluate the role of citric acid, experiments were carried out both in the presence and absence of the catalyst. When applied, citric acid was used at a concentration of 15 wt%. The resulting products were analyzed using HPLC.

The results demonstrated that the addition of citric acid significantly improved the overall reaction performance. Specifically, the presence of citric acid enhanced 5-HMF yield, syrup conversion, and 5-HMF selectivity across all tested residence times. These improvements suggest that citric acid plays a crucial role in promoting dehydration, thereby increasing the efficiency and selectivity of 5-HMF synthesis. The performance comparison is illustrated in Fig. 6.

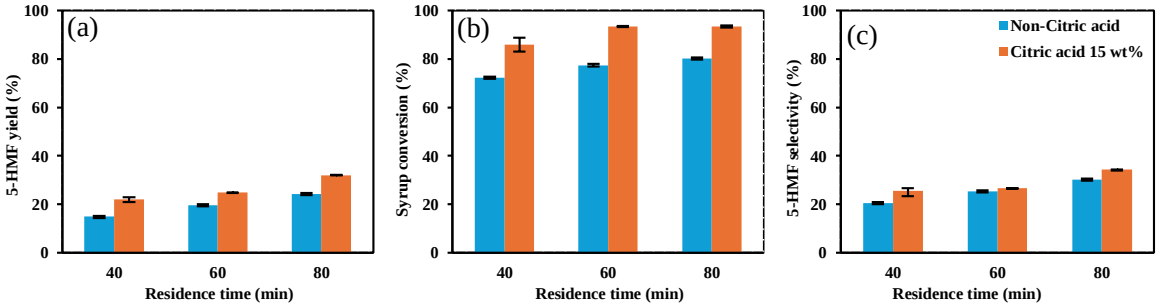

Figure 6 Effect of citric acid for 5-HMF synthesis: (a) 5-HMF yield, (b) syrup conversion, and (c) 5-HMF selectivity.

4. CONCLUSION

This study presents the development of a continuous 5-HMF production process from sugarcane syrup for pharmaceutical applications, focusing on a monophasic reaction system. The objective was to

explore safe, non-toxic, and economically viable methods by comparing various organic solvents and evaluating the role of citric acid as a catalyst in enhancing reaction efficiency. ATR-FTIR analysis and experimental results confirmed the superior performance of organic solvents over DI, with ACT and THF showing the most significant improvements. While PrOH demonstrated performance comparable to DI, IPA exhibited reduced efficiency due to increased byproduct formation.

Among the solvents studied, THF achieved the highest 5-HMF selectivity (41.21%) at a residence time of 40 min. However, from an economic standpoint, ACT emerged as the most cost-effective solvent, providing the lowest cost per unit product mass flow rate and the highest mass flow rate per unit cost at the same residence time. At an extended residence time of 80 min, ACT improved efficiency and economic performance, achieving a 5-HMF yield of 32.02% and a selectivity of 34.46%. Additionally, using citric acid at 15 wt.% as a catalyst significantly enhanced performance, increasing the 5-HMF yield from 24.57% (without catalyst) to 32.02%.

Therefore, the optimal conditions for 5-HMF production in this study were identified as using ACT as the solvent and 15 wt.% citric acid as the catalyst, with a residence time of 80 min—offering a balanced combination of cost-effectiveness and high production efficiency suitable for pharmaceutical applications. Future work should optimize additional parameters such as reaction temperature, O:A phase ratio, syrup concentration, and catalyst loading, along with refining the purification process to achieve higher 5-HMF purity and ensure product safety for pharmaceutical use.

ACKNOWLEDGMENTS

This work was partially supported by The 60th Year Supreme Reign of His Majesty King Bhumibol Adulyadej Academic Year 2023, Faculty of Graduate Studies, Mahidol University. Additional support for the presentation was kindly provided by the Faculty of Graduate Studies, Mahidol University.

REFERENCES

1. Bozell, J. J., & Petersen, G. R. (2010). Technology development for the production of biobased products from biorefinery carbohydrates—the US Department of Energy's "Top 10" revisited [10.1039/B922014C]. Green Chemistry, 12(4), 539-554.
2. Hou, Q., Qi, X., Zhen, M., Qian, H., Nie, Y., Bai, C., Zhang, S., Bai, X., & Ju, M. (2021). Biorefinery roadmap based on catalytic production and upgrading 5-hydroxymethylfurfural [10.1039/D0GC02770G]. Green Chemistry, 23(1), 119-231.
3. Chauhan, A. S., Kumar, A., Bains, R., Kumar, M., & Das, P. (2024). A comprehensive study of palladium-based catalysts on different supports for the hydrogenolysis of 5-hydroxymethylfurfural (HMF) to 2,5-dimethylfuran (DMF) biofuel. Biomass and Bioenergy, 185, 107209.
4. Zuo, M., Lin, L., & Zeng, X. (2023). The synthesis of potential biofuel 5-ethoxymethylfurfural: A review. Fuel, 343, 127863.
5. Kim, M., Su, Y., Aoshima, T., Fukuoka, A., Hensen, E. J. M., & Nakajima, K. (2019). Effective Strategy for High-Yield Furan Dicarboxylate Production for Biobased Polyester Applications. ACS Catalysis, 9(5), 4277-4285.
6. Yan, D., Xin, J., Zhao, Q., Gao, K., Lu, X., Wang, G., & Zhang, S.. (2018). Fe–Zr–O catalyzed base-free aerobic oxidation of 5-HMF to 2,5-FDCA as a bio-based polyester monomer. Catalysis Science & Technology, 8(1), 164–175.
7. Dorn, L., Thirion, A., Ghorbani, M., Olaechea, L. M., & Mayer, I.. (2023). Exploring Fully Biobased Adhesives: Sustainable Kraft Lignin and 5-HMF Adhesive for Particleboards. Polymers, 15(12), 2668.
8. Jiang, Z., Zeng, Y., Hu, D., Guo, R., Yan, K., & Luque, R. (2023). Chemical transformations of 5-hydroxymethylfurfural into highly added value products: present and future [10.1039/D2GC03444A]. Green Chemistry, 25(3), 871-892.
9. Kong, Q.-S., Li, X.-L., Xu, H.-J., & Fu, Y. (2020). Conversion of 5-hydroxymethylfurfural to chemicals: A review of catalytic routes and product applications. Fuel Processing Technology, 209, 106528.
10. Li, W., Qu, X. N., Han, Y., Zheng, S. W., Wang, J., & Wang, Y. P. (2015). Ameliorative effects of 5-hydroxymethyl-2-furfural (5-HMF) from Schisandra chinensis on alcoholic liver oxidative injury in mice. International journal of molecular sciences, 16(2), 2446–2457.
11. Ya, B., Zhang, L., Zhang, L., Li, Y., & Li, L. (2012). 5-hydroxymethyl-2-furfural prolongs survival and inhibits oxidative stress in a mouse model of forebrain ischemia. Neural regeneration research, 7(22), 1722–1728.
12. Michail, K., Matzi, V., Maier, A., Herwig, R., Greilberger, J., Juan, H., Kunert, O., & Wintersteiger, R. (2007). Hydroxymethylfurfural: an enemy or a friendly xenobiotic? A bioanalytical approach. Analytical and bioanalytical chemistry, 387(8), 2801–2814.
13. Abdulmalik, O., Safo, M. K., Chen, Q., Yang, J., Brugnara, C., Ohene-Frempong, K., Abraham, D. J., & Asakura, T. (2005). 5-hydroxymethyl-2-furfural modifies intracellular sickle haemoglobin and inhibits sickling of red blood cells. British journal of haematology, 128(4), 552–561.

14. Yamada, P., Nemoto, M., Shigemori, H., Yokota, S., & Isoda, H. (2011). Isolation of 5-(hydroxymethyl)furfural from Lycium chinense and its inhibitory effect on the chemical mediator release by basophilic cells. Planta medica, 77(5), 434–440.
15. Gatterer, H., Böcksteiner, T., Müller, A., Simi, H., Krasser, C., Djukic, R., Schroth, R., & Wallner, D. (2020). 5-Hydroxymethylfurfural and Alpha-Ketoglutaric Acid as an Ergogenic Aid During Intensified Soccer Training: A Placebo Controlled Randomized Study. Journal of dietary supplements, 17(2), 161–172.
16. Matzi, V., Lindenmann, J., Muench, A., Greilberger, J., Juan, H., Wintersteiger, R., Maier, A., & Smolle-Juettner, F. M. (2007). The impact of preoperative micronutrient supplementation in lung surgery. A prospective randomized trial of oral supplementation of combined alpha-ketoglutaric acid and 5-hydroxymethylfurfural. European journal of cardio-thoracic surgery : official journal of the European Association for Cardio-thoracic Surgery, 32(5), 776–782.
17. Chen, T.-Y., Hsiao, Y. W., Baker-Fales, M., Cameli, F., Dimitrakellis, P., & Vlachos, D. G.. (2022). Microflow chemistry and its electrification for sustainable chemical manufacturing. Chemical Science, 13(36), 10644–10685.
18. Martina, A., van de Bovenkamp, H. H., Winkelman, J. G. M., Noordergraaf, I. W., Picchioni, F., & Heeres, H. J. (2024). Biobased Chemicals from d-Galactose: An Efficient Route to 5-Hydroxymethylfurfural Using a Water/MIBK System in Combination with an HCl/AlCl3 Catalyst. ACS Omega, 9(39), 40378-40393.
19. Tongtummachat, T., Thongkan, K., Chuphueak, W., Jaree, A., & Akkarawatkhoosith, N. (2024). Efficient continuous-flow separation and purification processes of 5-hydroxymethylfurfural. Chemical Engineering Journal Advances, 20, 100641.
20. Souzanchi, S., Nazari, L., Rao, K. T. V., Yuan, Z., Tan, Z., & Xu, C. (2023). 5-HMF production from industrial grade sugar syrups derived from corn and wood using niobium phosphate catalyst in a biphasic continuous-flow tubular reactor. Catalysis Today, 407, 274-280.
21. Bounoukta, C. E., Megías-Sayago, C., Rendón, N., Ammari, F., Centeno, M. A., & Ivanova, S.. (2024). Finely Tunable Carbon Nanofiber Catalysts for the Efficient Production of HMF in Biphasic MIBK/H2O Systems. Nanomaterials, 14(15), 1293.
22. Office of the Commissioner. (n.d.). US Food and Drug Administration. US Food And Drug Administration.
23. Rosenfeld, C., Konnerth, J., Sailer-Kronlachner, W., Solt, P., Rosenau, T., & Van Herwijnen, H. W. G.. (2020). Current Situation of the Challenging Scale-Up Development of Hydroxymethylfurfural Production. Chemsuschem, 13(14), 3544–3564.
24. Sayed, M., Warlin, N., Hulteberg, C., Munslow, I., Lundmark, S., Pajalic, O., Tunå, P., Zhang, B., Pyo, S.-H., & Hatti-Kaul, R.. (2020). 5-Hydroxymethylfurfural from fructose: an efficient continuous process in a water-dimethyl carbonate biphasic system with high yield product recovery. Green Chemistry, 22(16), 5402–5413.
25. Chen, P., Yamaguchi, A., Hiyoshi, N., & Mimura, N. (2023). Efficient continuous dehydration of fructose to 5-hydroxymethylfurfural in ternary solvent system. Fuel, 334, 126632.
26. Wang, T., Nolte, M. W., & Shanks, B. H.. (2014). Catalytic dehydration of C6carbohydrates for the production of hydroxymethylfurfural (HMF) as a versatile platform chemical. *Green Chemistry*, *16*(2), 548–572.
27. Prasara-A, J., & Gheewala, S. H. (2021). An assessment of social sustainability of sugarcane and cassava cultivation in Thailand. Sustainable Production and Consumption, 27, 372-382.
28. Chang, H., Bajaj, I., Motagamwala, A. H., Somasundaram, A., Huber, G. W., Maravelias, C. T., & Dumesic, J. A. (2021). Sustainable production of 5-hydroxymethyl furfural from glucose for process integration with high fructose corn syrup infrastructure. Green Chemistry, 23(9), 3277-3288.
29. Rao, K., Hu, T., Yuan, Z., Zhang, Y., & Xu, C. (2021). Nitrogen-doped carbon: A metal-free catalyst for selective oxidation of crude 5-hydroxymethylfurfural obtained from high fructose corn syrup (HFCS-90) to 2,5-furandicarboxylic acid (FDCA). Chemical Engineering Journal, 404, 127063.
30. Songtawee, S., Kraithong, W., Klaysom, C., & Faungnawakij, K. (2021). The efficient conversion of D-Fructose to 5-Hydroxymethylfurfural using organic acids as catalytic promoters. Biomass Conversion and Biorefinery, 13.
31. Morais, E. S., Freire, M. G., Freire, C. S. R., & Silvestre, A. J. D. (2022). Improved Production of 5-Hydroxymethylfurfural in Acidic Deep Eutectic Solvents Using Microwave-Assisted Reactions. International Journal of Molecular Sciences, 23(4), 1959.
32. Zhang, H., Yu, Z., Gu, T., Xiang, L., Shang, M., Shen, C., & Su, Y. (2020). Continuous synthesis of 5-hydroxymethylfurfural using deep eutectic solvents and its kinetic study in microreactors. Chemical Engineering Journal, 391, 123580.

33. Muranaka, Y., Nakagawa, H., Masaki, R., Maki, T., & Mae, K. (2017). Continuous 5-Hydroxymethylfurfural Production from Monosaccharides in a Microreactor. Industrial & Engineering Chemistry Research, 56(39), 10998-11005.
34. Vasishta, A., & Pawar, H. S. (2023). PolyE-IL Is an Efficient and Recyclable Homogeneous Catalyst for the Synthesis of 5-Hydroxymethyl Furfural in a Green Solvent. ACS Omega, 8(1), 1047-1059.
35. George, W. O., Jones, B. F., Lewis, R., & Price, J. M. (2000). Computations of medium strength hydrogen bonds–complexes of mono- and bi-functional carbonyl and nitrile compounds with hydrogen chloride [10.1039/B006028N]. Physical Chemistry Chemical Physics, 2(21), 4910-4917.
36. Wang, H., Wang, L., Shen, S., Zhang, W., Li, M., Du, L., Zheng, X., & Phillips, D. L. (2012). Effects of hydrogen bond and solvent polarity on the C=O stretching of bis(2-thienyl)ketone in solution. *The Journal of chemical physics*, *136*(12), 124509.

Design and development of a sustainable ethylene glycol production process via electrochemical CO_2 reduction

Nichapat Leelalertwong[1,*], Phuet Prasertcharoensuk[1]

[1] Department of Chemical Engineering, Faculty of Engineering, Chulalongkorn University, Bangkok 10330, Thailand
[*] Corresponding author: 6670089121@student.chula.ac.th

ABSTRACT

Addressing the critical issue of rising atmospheric CO_2 concentrations and their impact on global climate change requires innovative technological solutions. This study introduced a novel and sustainable method for the production of ethylene glycol, commonly used in antifreeze, polyester manufacturing, and various industrial applications. Unlike conventional methods relying on coal or biomass-derived resources, our proposed method employed electrochemical CO_2 reduction, significantly decreasing environmental impacts. Central to this process was the innovative "OCEAN" technique, which strategically utilized oxalic acid as a key intermediate, enhancing overall conversion efficiency and minimizing undesirable byproducts. The proposed methodology involved a sequential procedure comprising electrochemical CO_2 reduction followed by catalytic hydrogenation steps. Initially, CO_2 was electrochemically converted into oxalic acid with a conversion efficiency of approximately 74.663%. Subsequently, oxalic acid was hydrogenated to glycolic acid, achieving around 56.715% conversion efficiency. In the final stage, glycolic acid underwent hydrogenation to produce ethylene glycol, attaining a high conversion efficiency of 84.878% and a product purity of 96.011%. Compared to conventional methods for ethylene glycol production, such as coal-based synthesis or biomass conversion, the "OCEAN" technique demonstrated superior conversion efficiencies and reduced environmental impact. Furthermore, this method achieved a 93.716% ethylene glycol yield, outperforming several previously reported methods with typically lower efficiencies. Collectively, this integrated approach enabled a substantial reduction of CO_2 emissions by approximately 62.631%, providing a cleaner, sustainable, and economically viable alternative for industrial chemical manufacturing.

Keywords: Ethylene glycol; Process modeling; Electrochemical CO_2 reduction

1. INTRODUCTION

Carbon dioxide (CO_2) is the primary driver of the greenhouse effect, accounting for over 75% of the observed global warming and climate change over the past century. In 2023, atmospheric CO_2 concentrations reached 419.3 ppm, representing a 2.8 ppm increase from the previous year and marking a level more than 50% higher than preindustrial times. CO_2 emissions continue to rise due to human activities, such as fossil fuel combustion [1], with a global rate of emissions growth predicted to increase by 0.6% to 0.7% per year. The urgent need to mitigate these emissions has become a worldwide focus in recent years.

To combat the rise in CO_2 levels, many countries have revised their Nationally Determined Contributions (NDCs), aligning with the global goal of limiting temperature increases to 1.5°C. These revised NDCs include targets for 2035 and update goals for 2030, pushing for significant emissions reductions across key sectors like energy, industry, and agriculture. Achieving these reductions is essential for the global ambition of net-zero emissions by 2050. This will require strong national policies, substantial investment in clean technologies, and international cooperation to succeed [2].

In this study, CO_2 is not only seen as a pollutant but also as a valuable raw material to produce high value chemicals and fuels. For instance, CO_2 can be converted into methanol, urea, or oxalic acid. Oxalic acid is crucial in industries such as metal processing, textile cleaning, and chemical synthesis, where its high solubility and metal binding capacity make it an efficient chelating agent. Moreover, oxalic acid plays a key role as a precursor in green chemistry, promoting ecofriendly processes and reducing reliance on traditional petrochemical routes. One innovative method for utilizing CO_2 in the production of oxalic acid is through electrochemical CO_2 reduction. This process not only offers high current efficiency (over 90%) but also minimizes the formation of unwanted

byproducts and reduces the need for precious metals [3, 4]. This technology, known as OCEAN, represents a significant step forward in CO_2 utilization, offering industries a sustainable solution for reducing greenhouse gas emissions while meeting industrial demands.

On the other hand, coal remains a dominant feedstock in global chemical production due to its availability and energy density. However, the environmental concerns associated with coal have prompted the search for more sustainable alternatives. For example, biomass offers a promising feedstock to produce chemicals like ethylene glycol. While the conversion of biomass to ethylene glycol process (BtEG) reduces emissions to 1.69 tons of CO_2 per ton of product substantially less than the coal to ethylene glycol process (CtEG) [5] it still results in some emissions. As such, further technological improvements are necessary to fully minimize the carbon footprint of these processes.

Ethylene glycol, a colorless, odorless liquid, has wide applications across various industries. It is primarily used as an antifreeze and coolant in automotive and industrial systems. Additionally, ethylene glycol is a key raw material for producing polyester fibers and resins, including polyethylene terephthalate (PET) [5]. The CtEG and BtEG production methods, both of which use dimethyl oxalate (DMO), are among the most widely used industrial processes. However, this study focuses on the production of ethylene glycol using oxalic acid [6], with CO_2 as the raw material. Utilizing CO_2 in chemical processes not only helps reduce atmospheric carbon emissions but also provides sustainable feedstock for chemical synthesis.

2. EXPERIMENTAL

The block flow diagram of the electrochemical CO_2 reduction reaction and hydrogenation process is illustrated in Fig. 1. The CO_2 feedstock is first fed into the electrochemical CO_2 reduction reaction unit using water as a reactant. This process converts CO_2 into oxalic acid (OA). The oxalic acid then undergoes a hydrogenation reaction to form glycolic acid (GA). Subsequently, Glycolic acid is further hydrogenated to produce ethylene glycol (EG) as the final product.

2.1 Steady-state modeling and simulation method

To facilitate the modeling and simulation of the process, it is divided into three distinct process units: the electrochemical CO_2 reduction reaction unit, hydrogenation to glycolic acid, and hydrogenation to ethylene glycol units, as illustrated in Fig. 1. In this study, the widely used and commercially available steady-state process simulator, Aspen Plus, is adopted to build and simulate the process model, as shown in Fig. 2.

Given that technology involves a highly complex process with numerous chemical reactions and heat and mass transfer steps, several simplifying assumptions have been made. These assumptions are necessary to make the modeling and simulation process more manageable while still providing reliable results. It should be noted that these simplifications help balance between accuracy and computational efficiency, ensuring the model remains practical for industrial applications [3-4, 6].

2.2 Electrochemical CO_2 reduction reaction

The electrochemical CO_2 reduction reaction (CO_2RR) unit mainly processes the transformation of carbon dioxide gas (CO_2) into value-added chemicals using electrical energy. Among various products, oxalic acid ($C_2H_2O_4$) stands out as a valuable C_2 compound that can be selectively synthesized under controlled electrochemical conditions. In this process, CO_2 is continuously introduced into an electrochemical cell and reduced at the cathode. The formation of oxalic acid typically involves the coupling of two CO_2 molecules via a two-electron transfer, forming oxalate ($C_2O_4^{2-}$) [3,7], which is then protonated:

$$2CO_2 + 2e^- \rightarrow C_2O_4^{2-} \quad (1)$$

$$Pb \rightarrow Pb^{2+} + 2e^- \quad (2)$$

$$2CO_2 + Pb \rightarrow PbC_2O_4^{2-} \quad (3)$$

$$PbC_2O_4 + H_2SO_4 \rightarrow PbSO_4 + C_2H_2O_4 \quad (4)$$

$$PbSO_4 + H_2O \rightarrow Pb + H_2SO_4 + 1/2O_2 \quad (5)$$

$$2CO_2 + H_2O \rightarrow 1/2O_2 + C_2H_2O_4 \quad (6)$$

Thus, oxalic acid (OA) is formed through a stepwise reduction and protonation pathway. After OA from electrolysis sent to the OA column to get purity oxalic acid that shows in Fig 3.

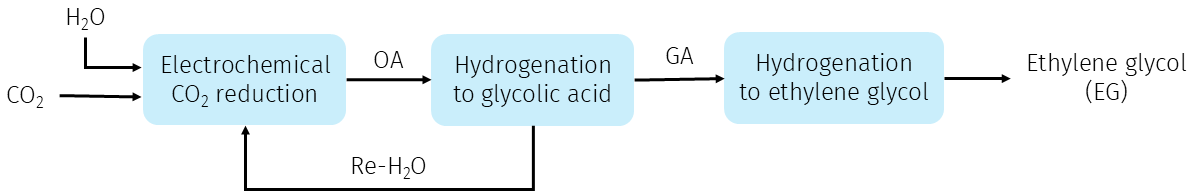

Fig. 1. Block flow diagram of the electrochemical CO_2 reduction reaction and hydrogenation process.

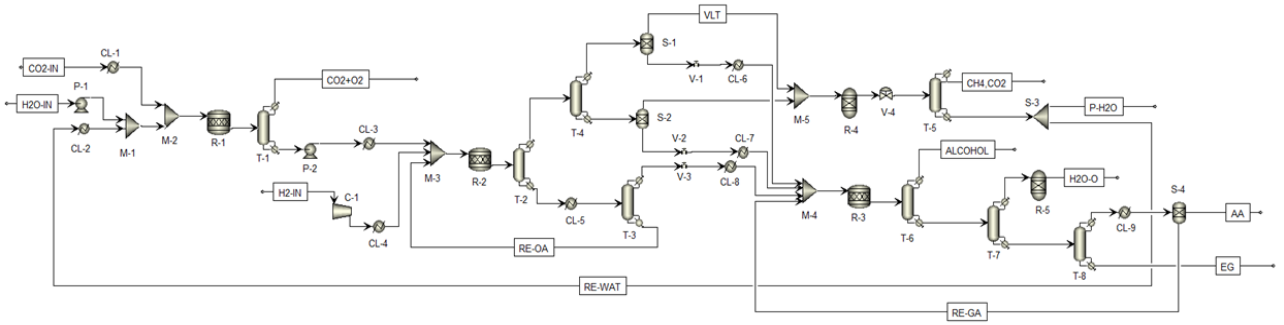

Fig. 2. Overall process flowsheet simulated in Aspen Plus

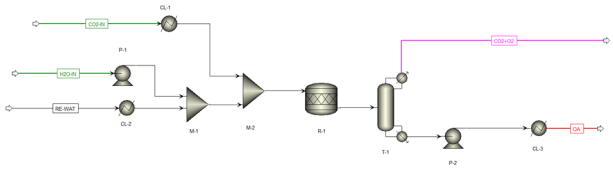

Fig. 3. Process flow of Electrochemical CO_2 reduction reaction process.

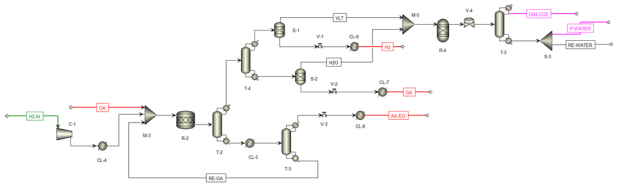

Fig. 4. Process flow of Hydrogenation to Glycolic acid process.

2.3 Hydrogenation to Glycolic acid

In this study, the hydrogenation of oxalic acid to glycolic acid ($C_2H_4O_3$) was carried out using hydrogen in the presence of a Ru-based catalyst [4], following the reaction:

$$C_2H_2O_4 + 2H_2 \rightarrow C_2H_4O_3 + H_2O \quad (7)$$
$$C_2H_2O_4 + 3H_2 \rightarrow C_2H_4O_2 + 2H_2O \quad (8)$$
$$C_2H_2O_4 + 4H_2 \rightarrow C_2H_6O_2 + 2H_2O \quad (9)$$

Byproducts of this reaction include acetic acid, ethylene glycol, and various volatile low-boiling compounds (VLTs), which are formed as a result of side reactions during the catalytic hydrogenation processes. These byproducts are typically present in smaller quantities but can still affect overall efficiency and product purity. The reaction is generally carried out in the liquid phase under controlled conditions, where the pressure is maintained at 80 bar and the temperature is kept within the range of 120 - 150 °C [4, 8-9]. These parameters ensure the efficient conversion of reactants and minimize the formation of unwanted byproducts, thereby optimizing the process for maximum yield.

The outlet stream from the glycolic acid (GA) reactor, which contains the desired product, is directed to the GA product column for further separation and purification. The overhead stream from this column, which includes water and lighter components, is sent to the dehydration column to remove excess moisture. Meanwhile, another portion of the stream is cooled and recycled back to the oxalic acid column for further processing. This recycling step not only improves process efficiency but also reduces the consumption of raw materials, making the process more sustainable in the long term. The process is shown in Fig. 4.

2.4 Hydrogenation to ethylene glycol

The high purity of glycolic acid mixed with hydrogen then enters to EG reactor, the overall reaction can be represented as:

$$C_2H_4O_3 + 2H_2 \rightarrow C_2H_6O_2 + H_2O \quad (10)$$
$$C_2H_4O_3 + H_2 \rightarrow C_2H_4O_2 + H_2O \quad (11)$$
$$C_2H_4O_3 + 3H_2 \rightarrow C_2H_6O + 2H_2O \quad (12)$$
$$C_2H_4O_3 + 3H_2 \rightarrow 2CH_4O + H_2O \quad (13)$$

In the reactor, glycolic acid hydrogenation in the resented of a ruthenium-based catalyst (Ru/C), facilitates the conversion of glycolic acid into ethylene glycol. This reaction typically occurs under moderate to high hydrogen pressures, ranging from 40 - 80 bars, and at temperatures between 100 - 150°C [6, 10]. These operating conditions are essential for achieving optimal reaction rates and high selectivity. The choice of Ru/C catalyst is particularly important, as it significantly affects both the selectivity and overall efficiency of the process. The catalyst ensures that the reaction proceeds with minimal formation of unwanted byproducts, thus enhancing the yield of ethylene glycol.

After the reaction is completed, the output from the ethylene glycol (EG) reactor is a mixture containing ethylene glycol, unreacted hydrogen, water, and various byproducts. This mixture is immediately directed to the separation system, which consists of three distinct columns: the first column is used for alcohol removal, the second is a dehydration column, and the third is dedicated to separating and purifying the ethylene glycol product. After passing through these columns, the final product is high-purity ethylene glycol, which has been effectively separated and purified from the remaining impurities and byproducts. These separation and purification steps are crucial for obtaining the

desired product in its pure form while minimizing the presence of any unwanted substances that may result from side reactions or incomplete conversion. The process is shown in Fig. 5.

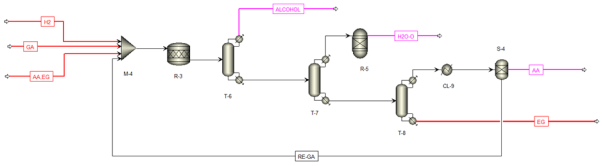

Fig. 5. Process flow of Hydrogenation to ethylene glycol process.

3. RESULTS AND DISCUSSION

3.1 Process description

The process flowsheet simulated in Aspen Plus was presented in Fig. 2. As mentioned earlier, the studied process consisted of three main steps: the first step was the production of oxalic acid via electrochemical CO_2 reduction; the second step involved the catalytic hydrogenation of oxalic acid to glycolic acid; and the final step was the hydrogenation of glycolic acid to ethylene glycol.

The feed gas supplied to the CO_2 reduction reactor consisted of carbon dioxide (71.6 mol%) and water vapor (27.3 mol%). The outlet from the electrolysis cell, containing oxalic acid with a conversion efficiency of approximately 74.663%, unreacted CO_2, and water, was conditioned before being sent to the hydrogenation reactor. In this step, oxalic acid was converted into glycolic acid using hydrogen and a Ru-based catalyst achieving around 56.719% conversion efficiency. During the hydrogenation of oxalic acid to glycolic acid, about 72.5% of the water produced was recovered and recycled into the electrochemical CO_2 reduction unit to enhance overall process efficiency. The produced glycolic acid was then sent to the second hydrogenation reactor to be converted into ethylene glycol. This step achieved a high conversion efficiency of 84.878%. The product stream was subsequently processed in a purification system, and high-purity ethylene glycol (96.011%) was obtained as the main product. Overall, the process achieved a significant reduction in CO_2 emissions by approximately 62.63%. Various byproducts were also formed during the conversion reactions, including acetic acid, ethanol, methanol, unreacted oxygen, CO_2, and steam. The simulation accounted for all relevant chemical transformations of CO_2, oxalic acid, and glycolic acid in the model.

3.2 Process energy consumption

The energy consumption of the overall process was evaluated based on a carbon dioxide feed rate of 123 tons per hour. This rate is considerably lower than the annual CO_2 emissions of a typical industrial facility, which range from 1 to 1.5 million tons per year. Under these conditions, the process achieved an ethylene glycol (EG) production rate of 38.18 tons per hour.

Table 1 summarizes the specific energy consumption per kilogram of ethylene glycol for each major process unit. As illustrated, the total thermal energy requirement for EG production was found to be 5.84 MJ/kg. In addition, the electricity consumption was 0.01 MJ/kg, while mechanical energy in the form of horsepower accounted for 0.27 MJ/kg. Among all units, the electrolysis system was identified as the most energy intensive component. Enhancing the energy efficiency of the electrolysis cell primarily influenced by current density and cell voltage [3] offers a promising opportunity for reducing overall energy demand. Additionally, the distillation units also contributed significantly to energy consumption. Implementing advanced separation techniques such as extractive distillation has the potential to reduce energy usage in these stages further [10].

Table 1 Total process energy consumption of ethylene glycol.

Process unit	Thermal energy (MJ)	Electricity & Horsepower (MJ)
Electrolysis cell	2.06	
Pump		0.01
Compressors		0.27
Distillation unit	3.55	
Separation unit	0.22	
Total Energy	5.84	0.28

In Table 2, we present a global mass balance of the studied process. We note that effectively this process recycles an important amount of stream. Producing 38.18 tons of ethylene glycol, 122.89 tons of CO_2, 19.18 tons of H_2O, and 70.56 tons of H_2 are consumed. 72.5% of the stream produced is recycled to the process, and the remaining 27.5% is purged. In Table 2, a global mass balance of the studied process was presented. It was observed that a substantial amount of carbon dioxide and hydrogen was consumed during the reaction. Approximately 76,965.03 kg/hr of CO_2 was converted into various high-value products such as ethylene glycol, acetic acid, glycolic acid, methanol, and ethanol. In this process, hydrogen was also a significant factor, with approximately 7,139.47 kg/hr consumed mainly as a reducing agent. Ethylene glycol is the main product with an output of 38,182.49 kg/hr, followed by acetic acid and glycolic acid. In contrast, water was generated in significant quantities, increasing from 7,042.85 kg/hr to 22,818.47 kg/hr, suggesting it was formed as a byproduct of several conversion pathways.

Table 2 Global mass balance of the process

	Inlet (kg/hr)	Outlet (kg/hr)
CO_2	122,885.85	45,920.82
H_2O	7,042.85	22,818.47
OA		0.01
O_2		16,677.42
CH_4	5.49	2,637.61
H_2	7,139.47	169.01
MEA	0.19	0.19
GA		947.83
AA		7,454.14
EG		38,773.79
ETOH		812.82
MEOH		861.37
CO		0.05

4. CONCLUSION

The objective of this research was to investigate a novel, innovative, and ecofriendly route for the production of ethylene glycol using carbon dioxide as a key raw material in the "OCEAN" process, combining electrochemical CO_2 reduction with sequential catalytic hydrogenation. The main results showed that oxalic acid could be effectively produced from CO_2 with a conversion efficiency of 74.663%, followed by hydrogenation of oxalic acid into glycolic acid at a conversion efficiency of 56.719%, before finally yielding ethylene glycol with a conversion efficiency of as high as 84.878% along with a product purity of 96.011%. This process was more efficient in terms of yield and lower in environmental impact compared with traditional methods involving the use of coal or biomass, resulting in around 62.631% CO_2 emission reduction. The significance of these results is in their ability to address global needs in climate change mitigation by converting CO_2, a greenhouse gas, into valuable chemicals. Despite these encouraging results, limitations were noted in terms of the energy requirements of the electrolysis and separation sections. Future studies should aim at improving the energy efficiency of these sections as well as introducing advanced purification processes involving extractive distillation and hydrogen recovery processes. Overall, this study adds a new dimension to the subject of green chemical manufacturing by introducing a new CO2 utilization path. The "OCEAN" process has environmental, as well as economic, merits, setting a platform for the future use of CO_2- based chemical production.

ACKNOWLEDGMENTS

The researcher would also like to convey earnest thanks to Asst. Prof. Phuet Prasertcharoensuk for his instructive guidance and constructive criticisms throughout this study. The researcher would also like to acknowledge the Department of Chemical Engineering, Faculty of Engineering, Chulalongkorn University, for allowing the use of its facilities and for the support extended during this research.

REFERENCES

1. Administration, N.O.a.A. No sign of greenhouse gases increases slowing in 2023. 1 November 2024; Available from: https://research.noaa.gov/2024/04/05/no-sign-of-greenhouse-gases-increases-slowing-in-2023/.
2. Institute, W.R. The Next NDCs: A 5-Point Plan. 1 November 2024; Available from: https://www.wri.org/insights/next-ndcs-5-point-plan.
3. Sale, H., G.R. Ubbara, and M.D. Symes, Optimising the electrochemical reduction of CO_2 to oxalic acid in propylene carbonate. *Sustainable Energy & Fuels*, 2023. 7(20): p. 5093-5100.
4. Schuler, E., M. Demetriou, N.R. Shiju, and G.J.M. Gruter, Towards sustainable oxalic acid from CO2 and biomass. *ChemSusChem*, 2021. 14(18): p. 3636-3664.
5. Yang, Q., et al., Optimal design and exergy analysis of biomass-to-ethylene glycol process. *Bioresource Technology*, 2020. 316: p. 123972.
6. Schuler, E., et al., Oxalic acid hydrogenation to glycolic acid: heterogeneous catalysts screening. *Green Chemistry*, 2023. 25(6): p. 2409-2426.
7. Mohammadi, E., et al., Oxalate and oxalic acid production from CO_2. Carbon Dioxide Conversion to Chemicals and Energy, 2023. p.331-348.
8. Schuler, E.; Grooten, L.; Kasireddy, M.; More, S.; Shiju, N. R.; Tanielyan, S. K.; Augustine, R. L.; Gruter, G.-J. M. Oxalic Acid Hydrogenation to Glycolic Acid: Heterogeneous Catalysts Screening. *Green Chem.* 2023, 25, 2310–2322.
9. Santos, J.H., et al., Selective hydrogenation of oxalic acid to glycolic acid and ethylene glycol with a ruthenium catalyst. Reaction Kinetics, Mechanisms and Catalysis, 2020. 131: p. 139-151.
10 Harth, F.M., Goepel, M., and Gläser, R., Selective hydrogenation of glycolic acid to renewable ethylene glycol over supported ruthenium catalysts. *ChemCatChem*, 2022. 14(1): p. 1–10.
11 Gil ID, Uyazan AM, Aguilar JL, Rodriguez G, Caicedo LA. Separation of ethanol and water by extractive distillation with salt and solvent as entrainer: Process simulation. *Brazilian Journal of Chemical Engineering* 2008;25:207-215.

Catalytic carbon dioxide desorption from monoethanolamine solvent in fluidized stripper

Sathida Doungsri[1], Rattanaporn Apaiyakul[2], Teerawat Sema[1,*]

[1] Department of Chemical Technology, Faculty of Science, Chulalongkorn University, Bangkok 10330, Thailand
[2] Petrochemistry and Polymer Science Program, Faculty of Science, Chulalongkorn University, Bangkok 10330, Thailand
[*] Corresponding author: teerawat.se@chula.ac.th

ABSTRACT

Amine-based absorption, particularly using monoethanolamine (MEA) solvent, is widely employed in an industrial CO_2 capture. However, conventional thermal desorption is energy-intensive and inefficient. To solve this problem, catalytic desorption by acid catalyst (e.g., HZSM-5) has been applied, mostly in batchwise operation. Since the actual operation is a continuous process, both catalytic packed and fluidized bed strippers are found to be more promising than the conventional batchwise system. This study investigated a transition from a packed bed to a fluidized bed catalytic HZSM-5 desorption in comparison with the non-catalytic system and evaluated the key operating conditions to optimize the performance of the CO_2 desorption. The fluidized stripper (0.022 m diameter and 0.6 m height) was employed, with CO_2-rich MEA solution preheated to 90 °C. Fixed experimental parameters covered MEA concentration (5 M), initial CO_2 loading (0.5 mol CO_2/mol MEA), and HZSM-5 Si/Al ratio of 38. Preliminary results showed that the catalytic fluidized stripper achieved a CO_2 desorption efficiency of 3.8 %, compared to 2.1 % in the non-catalytic system and 4.5 % in the packed-bed stripper. The fluidized bed operation demonstrated faster and more stable CO_2 loading reduction than the non-catalytic system. Interestingly, the packed bed system exhibited slightly higher desorption efficiency due to a longer catalyst-MEA contact time. Despite this, the fluidized stripper offers potential advantages in terms of enhanced mass transfer and easier catalyst replacement. Further optimization is required to maximize its feasibility for continuous CO_2 capture applications.

Keywords: CO_2 desorption; Amine regeneration; Fluidization; Solid Acid- Catalyst; HZSM-5

1. INTRODUCTION

Global climate change has become one of the most pressing environmental concerns in the modern era, primarily driven by the greenhouse effect. Among greenhouse gases, carbon dioxide (CO_2) is a major contributor due to its large-scale emissions into the atmosphere, which have continued to rise steadily [1]. In 2023, global CO_2 emissions reached a record high of 37.4 gigatons [2]. Significant sources of these emissions include industrial sectors such as steel, cement, ammonia, and fertilizer production, where CO_2 is inherently generated as part of chemical reactions. Furthermore, the combustion of fossil fuels—including coal, natural gas, and petroleum—remains a critical driver of CO_2 release .

To mitigate global warming, reducing anthropogenic CO_2 emissions is essential. Carbon capture and storage (CCS) has been proposed as a key strategy, particularly in hard-to-abate industrial processes. Among the available capture technologies, post-combustion capture has gained wide acceptance due to its compatibility with existing infrastructure [3]. This method includes several techniques such as adsorption, absorption, and membrane separation. However, chemical absorption using amine-based solvents is the most widely adopted due to its high CO_2 loading capacity, fast absorption rate, and reversibility of the absorption reaction—allowing the solvent to be regenerated and reused. One of the most used amines in industry is monoethanolamine (MEA), selected for its simple synthesis and high reactivity with CO_2 [1].

Despite its advantages, the regeneration of MEA—typically achieved through thermal desorption—poses significant challenges. Thermal regeneration is energy–intensive, operates at high temperatures, and often results in solvent loss due to evaporation and long cycle time. To overcome these drawbacks, catalytic regeneration using solid acid catalysts has been investigated. Studies have shown that such catalysts can significantly lower the desorption temperature, reduce solvent evaporation, decrease energy requirements, and shorten the regeneration time.

In addition, solid acid catalysts are reusable and compatible with various types of amine solvents [3].

Among the solid acid catalysts, HZSM–5 has emerged as a promising material due to its high surface area and a wide range of available Brønsted/Lewis acid site ratios. The silica-to-alumina ratio (Si/Al) in HZSM–5 strongly influences both the CO_2 desorption rate and the heat duty associated with regeneration. Prior research suggests that a Si/Al ratio of 38 offers the best performance in terms of catalytic efficiency and thermal balance [1].

Although numerous studies have investigated catalytic CO_2 desorption using HZSM–5 in different reactor types—such as batch reactors [4], packed-bed reactors [5], and continuous stirred tank reactors (CSTR) [6]—these systems often present limitations. Batch reactors do not reflect continuous industrial operations; packed–bed systems are complex when it comes to catalyst replacement; and CSTRs may cause mechanical abrasion of the solid catalyst due to impeller agitation.

To address these challenges, this study explores catalytic CO_2 desorption from MEA using HZSM–5 in a fluidized bed column, which offers several advantages. Fluidized bed reactors enable continuous operation, improve contact between the liquid and catalyst surfaces, and simplify catalyst handling or replacement. Due to these features, this configuration holds significant promise for real-world industrial applications [6].

Therefore, the primary objectives of this research are to compare the percentage of catalytic CO_2 desorption from MEA solvent between packed bed and fluidized bed columns, and to study the effects of operating parameters on the percentage of catalytic CO_2 desorption from MEA solvent in a fluidized bed column.

2. EXPERIMENTAL

2.1 Materials

MEA (98 % purity) was purchased from Chemipan Co., Ltd., Thailand. HZSM–5 (Si/Al ratio of 38) was supplied from Zr Catalyst Co., Ltd., China. MEA was prepared as a 5 M aqueous solution with CO_2 loading of 0.5 mol CO_2/mol MEA by continuously bubbling with gaseous CO_2.

2.2 Material Physical Properties

The physical properties of HZSM–5, including true density and particle size distribution, were measured to determine key parameters necessary for the fluidization process. True density was determined by a pycnometer (Anton Paar model Ultrapyc 5000). Particle size distribution was measured using a laser particle size distribution analyzer (Horiba Model LA960 V2). The two data were used in the particle classification according to Geldart's diagram and in the calculation of minimum fluidization velocity (U_{mf}).

2.3 Particle Classification and Velocity Calculation

The HZSM–5 particles were classified according to the Geldart diagram based on their size and density relative to properties. The U_{mf} was estimated theoretically using the Ergun equation [7]. Additionally, the terminal velocity of the particles was calculated using the Pinchbeck and Popper equation [7] to provide essential data for the design of the experimental apparatus.

2.4 Experimental Apparatus

The experimental system consisted of three primary components: a preheater unit, a fluidized bed reactor, and a condenser, as shown in Figure 1**.** The preheater incorporated a heat exchanger to elevate the temperature of the CO_2-loaded MEA solution to 85–90 °C. Temperature was measured before entry into the reactor to ensure thermal consistency. The main reactor was constructed from glass, featuring a height of 0.6 m and an internal diameter of 0.022 m. At the reactor outlet, three channels were installed, with one specifically designated for sample collection. Downstream, a condenser was used to recover evaporated MEA and water vapor, using cooling water as the medium, maintaining the solvent concentration at 5 M throughout the experimental operation.

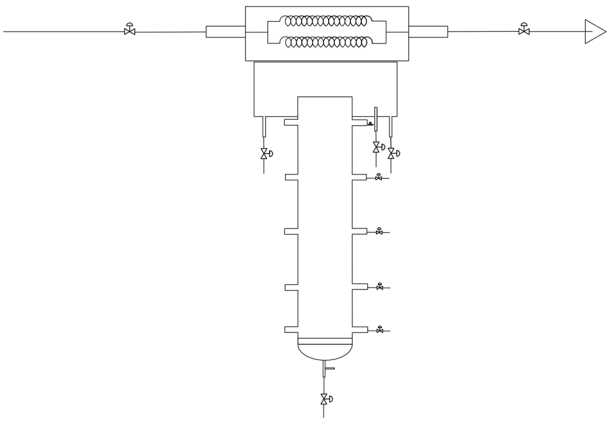

Figure 1 Schematic of the experimental apparatus including inlet reactor, fluidized bed reactor, and condenser.

2.5 Experimental Design and Procedure

The experiment was designed to evaluate the effect of catalyst presence and rich solvent flow rate on CO_2 desorption percentage. Three experimental conditions were studied, as summarized in Table 1. In the first setup, a flow rate of 100 mL/min was employed without the addition of a catalyst, serving as the blank experiment to assess the contribution of the catalyst to CO_2 desorption performance. In the second one, the flow rate was maintained at 100 mL/min, but HZSM–5 catalyst was packed to a bed height of 10 cm within the reactor. Lastly, the flow rate was increased to 500 mL/min while maintaining the catalyst bed height at 10 cm.

In both runs involving catalyst, HZSM–5 particles with a size range of 1–2 mm were used. This particle size was chosen for its suitability in achieving stable fluidization and efficient liquid–solid interactions during the desorption process. The experiments with 100 mL/min and 500 mL/min flow rates under catalytic conditions were specifically designed to compare the performance between packed bed and fluidized bed operations.

The primary response variable was the percentage of CO_2 desorption, determined based on the difference in CO_2 concentration between the inlet and outlet streams. The percentage of CO_2 desorption was calculated according to the following equation:

$$\text{Percentage of } CO_2 \text{ desorption} = \frac{Rich\ CO_2\ loading - lean\ CO_2\ loading}{Rich\ CO_2\ loading} \times 100$$

where rich CO_2 loading and lean CO_2 loading are the CO_2 concentrations at the reactor inlet and outlet, respectively.

This experimental design enabled a comparative evaluation of the impact of both catalyst presence and reactor hydrodynamics on CO_2 desorption performance.

Table 1 Summary of experimental conditions for CO_2 desorption study.

Run	Flow Rate (mL/min)	Catalyst	Bed Height (cm)	Regime
1	100	None	0	-
2	100	HZSM–5	10	Packed bed
3	500	HZSM–5	10	Fluidization

3. RESULTS AND DISCUSSION

3.1 Material Physical Properties

The true density and particle size distribution of the HZSM–5 catalyst were measured and summarized in Table 2.

Table 2 True density and particle size of HZSM–5 samples.

Sample	True density (g/cm³)	d_p (mm)
HZSM–5; d_p 1–2 mm	2.5794 ± 0.0011	1.8932

3.2 Classification of Solid Particles

The classification of HZSM–5 particles was performed using Geldart's diagram. Noted that the density of the MEA solution at 30 °C was 1.0008 g/cm³ [8]. For particle sizes (1–2 mm), the classification fell into Geldart Group D (Spoutable particles), as shown in Figure 2. This classification implies that the HZSM–5 particles are suitable for operation in fluidized bed systems with a high velocity regime, where stable spoutable fluidization behavior can be expected.

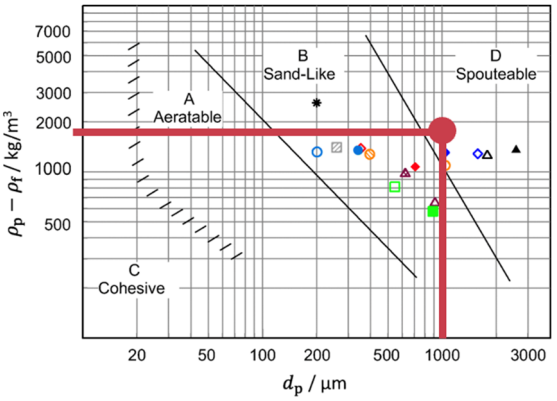

Figure 2 Position of HZSM–5 particles on Geldart's diagram.

3.3 Minimum Fluidization Velocity (U_{mf})

The experimental measurement of the U_{mf} in water at 30 °C for HZSM–5 particles (1–2 mm) was 0.00804 m/s. This value showed good agreement with the theoretically calculated U_{mf} values for close random packing, which ranged from 0.00787 to 0.00868 m/s depending on the packing condition (Table 3). In these calculations, the density of the MEA 5 M solution at 30 °C was 1.0008 g/cm³ [8].

Table 3 Theoretical and experimental minimum fluidization velocities of HZSM–5 particles in water at 30 °C.

Sample	Loose random packing U_{mf} (m/s)	Dense random packing U_{mf} (m/s)	Close random packing U_{mf} (m/s)	Experimental U_{mf} (m/s)
HZSM–5 ; d_p 1–2 mm	0.01151–0.01379	0.00868–0.01050	0.00787–0.00868	0.00804

When operating in 5 M MEA solution at 90 °C, the U_{mf} further decreased due to a reduction in solvent's viscosity and density. Based on the experimental results in 5 M MEA solution at 30 °C, where the measured U_{mf} value fell within the range for close random packing, the U_{mf} value at 90°C was calculated accordingly. For HZSM–5 particles (1–2 mm), the estimated U_{mf} at 90 °C ranged between 0.00363–0.00450 m/s.

3.4 Terminal Velocity (U_t)

The terminal velocity or U_t of HZSM–5 particles was calculated and compared with the U_{mf} values to ensure stable fluidization without particle entrainment. The U_t (0.41464 m/s) were much higher than the corresponding U_{mf} values (0.00363–0.00450 m/s). The high U_t/U_{mf} ratio (114.23) supports efficient fluidization operation under the selected experimental conditions.

3.5 CO_2 Desorption Performance

The CO_2 desorption performance under varying experimental conditions is summarized in Table 4. The CO_2 loading, expressed in terms of mol CO_2/mol MEA, was monitored at 0, 20, and 40 minutes for three distinct experimental setups: (i) 100 mL/min (0.00438 m/s) without catalyst (blank condition), (ii) 100 mL/min (0.00438 m/s) with HZSM–5 catalyst packed to a bed height of 10 cm (packed bed configuration), and (iii) 500 mL/min (0.02193 m/s) with HZSM–5 catalyst at a bed height of 10 cm (fluidized bed configuration). The percentage of CO_2 desorption was then calculated based on the reduction between the initial value at 0 min and the final value at 40 min.

Under the blank condition (Run 1), a modest desorption of 1.581% was observed, indicating limited natural CO_2 release without catalytic assistance. In contrast, the catalytic experiments (Run 2 and Run 3) exhibited significantly higher percentages of CO_2 desorption, approximately 8%, highlighting the enhanced desorption performance facilitated by the presence of the HZSM–5 catalyst. Notably, Run 3 (fluidized bed operation) demonstrated a slightly superior desorption performance compared to Run 2 (packed bed operation), attributed to improved solid–liquid interactions arising from bed expansion and particle fluidization.

The temporal evolution of CO_2 loading for all three experimental conditions is depicted in Figure 3. This figure consolidates the desorption profiles of Run 1, Run 2, and Run 3, facilitating a direct comparison of desorption trends. At the initial stage (0 min), all setups exhibited similar CO_2 loading values of approximately 0.500 mol CO_2/mol MEA, confirming the consistency of the initial conditions. Over time, a steady decline in CO_2 loading was observed under all conditions; however, the desorption rates varied markedly depending on the catalyst presence and the hydrodynamic regime.

Under the blank condition (Run 1), only a slight decrease in CO_2 loading was recorded, reflecting the inherently slow natural desorption process. In the packed bed setup (Run 2), a greater decline was achieved due to catalytic activity, though limitations associated with the static bed structure were still apparent. The fluidized bed setup (Run 3) exhibited the most significant enhancement in desorption performance, as dynamic particle movement and improved mass transfer contributed to the lowest final CO_2 loading among all experimental conditions.

Nevertheless, it should be noted that during the fluidized bed operation, the system temperature did not consistently reach the target of 90 °C, unlike the packed bed operation. This incomplete temperature control may have attenuated the observable differences in desorption efficiency between the two catalytic conditions. Future investigations should prioritize temperature stabilization during fluidized bed operation to enable a more definitive assessment of catalytic effects on CO_2 desorption performance.

Table 4 CO_2 loading and the percentage of CO_2 desorption under different experimental conditions.

Run	CO_2 loading (mol CO_2/mol MEA)			Percentage of CO_2 desorption (%)
	Operating time			
	0 min.	20 min.	40 min.	
1	0.504	0.497	0.496	1.581
2	0.504	0.472	0.464	8.016
3	0.503	0.470	0.463	8.019

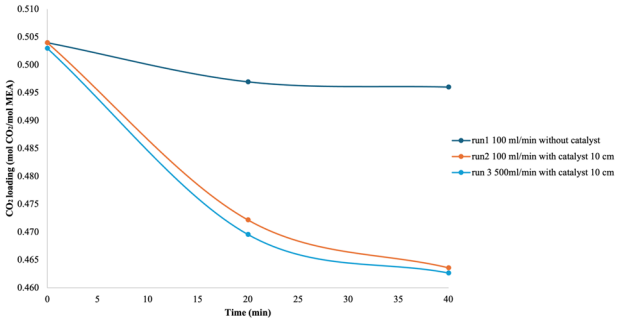

Figure 3 CO_2 desorption profiles under different experimental conditions: Run 1 (100 mL/min without catalyst, blank condition), Run 2 (100 mL/min with HZSM–5 catalyst, packed bed configuration), and Run 3 (500 mL/min with HZSM–5 catalyst, fluidized bed configuration).

The visual appearances of the reactor during the three experimental runs are shown in Figures 4. In the blank run, Figure 4(a), the liquid phase remained mostly clear with sparse bubble generation and no solid catalyst present. In the packed bed operation, Figure 4(b), the catalyst particles were tightly packed and stationary, with gas channeling observed but limited interaction between solid and liquid phases. In the fluidized bed operation (Figure 4(c)), significant bed expansion and vigorous mixing were observed, indicating efficient fluidization of the catalyst particles. These visual observations supported the conclusion that fluidized bed operation enhanced mass transfer and catalytic desorption efficiency compared to packed bed operation. Overall, the combination of HZSM–5 catalyst and fluidized bed operation demonstrated superior CO_2 desorption performance, providing a promising strategy for energy–efficient carbon capture processes.

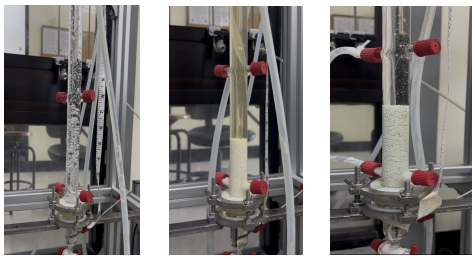

(a) (b) (c)

Figure 4 Reactor during (a) Run 1: 100 mL/min, no catalyst (blank operation), (b) Run 2: 100 mL/min, with catalyst, packed bed operation, and (c) Run 3: 500 mL/min, with catalyst, fluidized bed operation.

4. CONCLUSION

This study aimed to investigate the catalytic desorption of CO_2 from MEA solution using HZSM–5 as a solid acid catalyst under different reactor hydrodynamic conditions, specifically comparing packed bed and fluidized bed operations.

The experimental results demonstrated that the presence of the HZSM–5 catalyst significantly enhanced the CO_2 desorption rate compared to the blank condition without catalyst. Furthermore, transitioning from a packed bed to a fluidized bed configuration, by increasing the flow rate, led to even greater desorption efficiency due to improved solid–liquid interactions and enhanced mass transfer.

Visual observations supported these findings, revealing distinct differences in reactor behavior between the packed and fluidized bed operations. The fluidized bed exhibited vigorous particle movement and expanded bed structure, which contributed to the accelerated CO_2 desorption process.

The U_{mf} was validated experimentally and matched well with theoretical predictions, confirming that stable fluidization conditions were achieved for HZSM–5 particles in MEA solution.

The significance of these findings lies in the demonstration that combining catalytic effects with optimized fluidization enhances the desorption performance of CO_2 from amine-based solvents. This approach offers a promising pathway toward developing more energy–efficient carbon capture systems, with potential applications in reducing greenhouse gas emissions in industrial processes.

However, limitations such as slight fluctuations in CO_2 loading during prolonged operation and minor experimental variability were observed. These issues highlight the need for improved system stability, real–time monitoring of CO_2 concentrations, and precise temperature control in future work.

In conclusion, this study contributes valuable insights into the design and operation of catalytic fluidized bed reactors for CO_2 desorption, providing a foundation for scaling up and integrating such systems into commercial CCS technologies. Future research should explore long–term catalyst stability, dynamic system behavior, and techno–economic analysis to further advance the practical deployment of catalytic fluidized bed processes for carbon capture applications.

ACKNOWLEDGMENTS

The first author gratefully acknowledges the financial support provided by the Department of Chemical Technology, Faculty of Science, Chulalongkorn University, which made this research possible.

The authors would also like to express their sincere gratitude to the Department of Chemical Technology, Faculty of Science, Chulalongkorn University, for providing essential facilities and resources throughout the study.

Appreciation is further extended to the Carbon Capture and Utilization Research Laboratory and the Multiphase Flow Research Laboratory, Department of Chemical Technology, for providing equipment, laboratory facilities, and technical support crucial to the experimental work.

REFERENCES

[1] M. Waseem, M. Al-Marzouqi, N. Ghasem. A review of catalytically enhanced CO_2-rich amine solutions regeneration. *Journal of Environmental Chemical Engineering* 2023; 11(4): 110188.

[2] IEA, CO_2 Emissions in 2023. 3/11/2024; Available from: https://www.iea.org/reports/co2-emissions-in-2023

[3] S. An, et al. Recent progress and prospects in solid acid-catalyzed CO_2 desorption from amine-rich liquid. *Gas Science and Engineering* 2023; 120: 205152.

[4] H. Shi, A. Naami, R. Idem, P. Tontiwachwuthikul. Catalytic and non catalytic solvent regeneration during absorption-based CO_2 capture with single and blended reactive amine solvents. *International Journal of Greenhouse Gas Control* 2014; 26: 39-50.

[5] P. Natewong, N. Prasongthum, P. Reubroycharoen, R. Idem. Evaluating the CO_2 capture performance using a BEA-AMP biblend amine solvent with novel high-performing absorber and desorber catanovel CO_2 desorption process integrated with highly turbulent catalytic heat exchanger. *Fuel* 2019; 359: 130028.

[6] C. Yang, T. Li, T. Sema, C. Chan, P. Tontiwachwuthikul. Performance assessment of novel catalytic spouted-bed vapor jet flow heat exchanger in amine-based carbon capture process. *Separation and Purification Technology* 2025; 353: 128393.

[7] D. Kunii, L. Octave., Fluidization Engineering (2nd ed.). *Butterworth-Heinemann*. 1991; 1-13.

[8] A. Hartono, E. O. Mba, H. F. Svendsen. Physical properties of partially CO_2 loaded aqueous monoethanolamine (MEA). *Journal of Chemical & Engineering Data* 2014; 59(6): 1808–1816.

Process simulation of syngas production through glycerol reforming with carbon dioxide and steam for methanol synthesis

Patcharapol Chaladthunyakij[1], Sarochinee Mitnoom[1], Suttapa Thadsoun[1], Yaneeporn Patcharavorachot[1,*]

[1] Department of Chemical Engineering, School of Engineering, King Mongkut's Institute of Technology Ladkrabang, Bangkok 10520, Thailand
[*] Corresponding author: yaneeporn.pa@kmitl.ac.th

ABSTRACT

This study focuses on the production of synthesis gas from glycerol through a combined reforming process using carbon dioxide and steam. The goal is to produce synthesis gas suitable for methanol synthesis. The process is simulated using Aspen Plus™ software to determine optimal operating conditions. The research evaluates the molar ratio of synthesis gas components ($H_2/(2CO+3CO_2)$) to ensure suitability for methanol production. Three reforming processes are investigated: carbon dioxide reforming, steam reforming, and combined carbon dioxide-steam reforming. The effects of temperature (600-1000°C) and pressure (1-50 bar) are analyzed. The simulation results indicate that the optimal reforming temperature of all processes is 900°C at a pressure of 1 bar. For carbon dioxide reforming, adjusting the CO_2 to glycerol feed ratio between 1 and 3 reveals an optimal range. In steam reforming, the optimal steam-to-glycerol feed ratio is found to be 3. However, for the combined reforming process, the synthesis gas molar ratio remains below the target value of 1.05 at temperatures between 600 and 1000°C. To address this, a water-gas shift reactor and gas separation adjustments should be implemented to achieve the desired molar ratio. Energy analysis indicates that selecting an operating temperature of 900°C is optimal in terms of product gas composition and thermal efficiency. These findings contribute to the development of an efficient synthesis gas production process for methanol synthesis from glycerol.

Keywords: Synthesis gas; Reforming; Methanol; Glycerol; Carbon dioxide

1. INTRODUCTION

The rapid growth of the biodiesel industry aims to replace fossil fuels, which are costly and major contributors to CO_2 emissions and global warming. Both the public and private sectors are focusing on sustainable CO_2 reduction, leading to an increased use of renewable biomass energy for fuel and chemical production. Glycerol, a byproduct of biodiesel production, has accumulated in large quantities, resulting in market oversaturation [1]. To be used in industry, glycerol must undergo purification, which incurs high costs and increases production expenses. Therefore, there is a need for research to add value to crude glycerol to enhance its utilization efficiency. Producing synthesis gas (syngas) from glycerol is of interest, as syngas is widely used in chemical industries, including hydrogen [2], ammonia [3], and methanol production [4]. Various methods exist for producing syngas from glycerol, such as steam reforming, autothermal reforming, partial oxidation, aqueous phase reforming [5], and dry reforming [6]. Each method involves different catalysts and operating conditions, leading to distinct advantages and disadvantages. Dry reforming is a promising method for syngas production from glycerol, as it utilizes carbon dioxide, a greenhouse gas as a reactant, which addresses environmental concerns. However, this process typically results in a low hydrogen yield. To address this, the combined use of CO_2 and steam as reagents in the reforming process is expected to enhance hydrogen yield. The resulting syngas is intended for subsequent use in methanol synthesis.

Therefore, the objective of this research is to study the operational conditions of glycerol reforming to generate syngas suitable for methanol production, thereby enhancing product value, reducing CO_2 emissions, lowering energy consumption, and efficiently utilizing renewable energy for maximum benefit. A model for syngas production from the glycerol reforming process, utilizing three types of reagents—carbon dioxide, steam, and a combination of both—is designed and developed using Aspen Plus™ simulation software. This model is employed to investigate the effects of key operational conditions (i.e., reactor temperature and reagent-to-glycerol feed ratio) on syngas production. Not only mole fraction of gas product but also the mole ratio of the syngas component ($H_2/(2CO+3CO_2)$) that is suitable for

methanol synthesis are considered. Finally, the energy consumption associated with each process is evaluated.

2. PROCESS DESCRIPTION

Figure 1 presents the model of syngas production from glycerol reforming processes that are developed and designed through AspenPlus™ software. The flowsheet can be divided into two main parts: syngas production and adjustment of syngas composition. For the part of syngas production, glycerol (GLYCEROL stream) and reagent (AGENT stream), as carbon dioxide or steam or both, are firstly mixed in the mixer (MIXER model) before delivering to heater (HEATER model) to increase temperature as desired values. Then, the preheated stream (FEEDHOT stream) is sent to reformer (REFORMER model) where the reforming reactions occur as follows:

Steam Reforming Reaction:
$C_3H_8O_3+3H_2O \rightarrow 3CO_2+7H_2$ $\Delta H = 128$ kJ/mol (1)
Dry Reforming Reaction:
$C_3H_8O_3+CO_2 \rightarrow 3H_2+4CO+H_2O$ $\Delta H = 292$ kJ/mol (2)
Water-Gas Shift Reaction (WGS):
$CO+H_2O \rightarrow CO_2+H_2$ $\Delta H = -41$ kJ/mol (3)
Methanation Reaction:
$CO + 3H_2 \leftrightarrow CH_4 + H_2O$ $\Delta H = -206$ kJ/mol (4)
$CO_2 + 4H_2 \leftrightarrow CH_4 + 2H_2O$ $\Delta H = -165$ kJ/mol (5)
Methane Dry Reforming Reaction:
$CH_4 + CO_2 \leftrightarrow 2CO + 2H_2$ $\Delta H = 261$ kJ/mol (6)
Glycerol Decomposition Reaction:
$C_3H_8O_3 \leftrightarrow 4H_2 + 3CO$ $\Delta H = 250$ kJ/mol (7)
Boudouard Reaction:
$C + CO_2 \leftrightarrow 2CO$ $\Delta H = 172$ kJ/mol (8)
Methane Decomposition Reaction:
$CH_4 \leftrightarrow 2H_2 + C$ $\Delta H = 75$ kJ/mol (9)
Carbon Gasification Reaction:
$C \leftrightarrow 2H_2O + CO_2 + 2H_2$ $\Delta H = 90$ kJ/mol (10)
$C + H_2O \leftrightarrow CO + H_2$ $\Delta H = 131$ kJ/mol (11)

The product gas (PROD1 stream) obtained from glycerol reforming, consisting of hydrogen, carbon monoxide, carbon dioxide, methane and steam, is considered with a wider range of reagent types, reformer temperatures and agent-to-glycerol feed ratio.

Next, the mole ratio of the syngas component is calculated according to $H_2/(2CO+3CO_2)$. If the mole ratio is below 1.05 that is target for methanol synthesis, the syngas composition must be adjusted. Firstly, the PROD1 stream is depressurized using a turbine (TURBINE model) and cooled down using a cooler (COOLER-1 model) before entering the reactor where the water-gas shift reaction occurs (WGS model). The resulting product gas (PROD2 stream) is further cooled using another cooler (COOLER-2 model), then passed through a flash separator (FLASH model) to separate water from the gas. Finally, methane is separated and the syngas composition, consisting of hydrogen, carbon monoxide and carbon dioxide, is adjusted in a separator (SEP model) to obtain the appropriate ratio for methanol production.

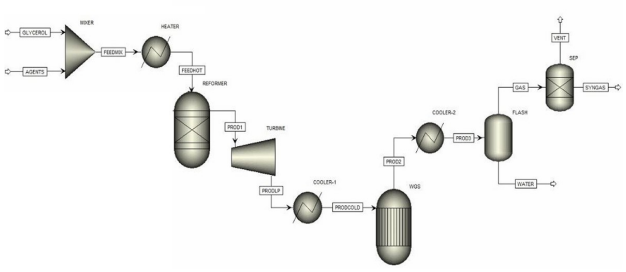

Figure 1 The model of syngas production from glycerol reforming processes designed through AspenPlus™ software.

3. METHODOLOGY

In this work, thermodynamic calculation of syngas production process from glycerol reforming is performed through Aspen Plus V10 simulation software. The Soave-Redlich-Kwong Model (SRK) is selected as thermodynamic method. In the simulation, glycerol is set at 100% purity with a feed rate of 1 kmol/h, temperature 25°C, and pressure 1 bar. In the case where the glycerol reforming process is studied using either steam or carbon dioxide as the sole reactant, the initial flow rate of steam or carbon dioxide is set at 1 kmol/h, while the flow rate of glycerol is also maintained at 1 kmol/h. Therefore, the molar ratio of steam or carbon dioxide to glycerol is equal to 1.

When the operating conditions of all unit operations (Table 1) are given, the equilibrium compositions from glycerol reforming process can be calculated by the minimization of the Gibbs free energy. Subsequently, the molar ratio of the synthesis gas is calculated and adjusted to be greater than or equal to 1.05. This is achieved by enhancing the hydrogen content through the water-gas shift reaction. Additionally, the molar ratio of the syngas is further refined using the Design Specification tool to calculate and achieve a composition suitable for subsequent methanol synthesis.

In this work, the effects of key parameters—including reformer temperature and reagent-to-glycerol feed ratio—on syngas production for methanol synthesis are investigated to determine the optimal conditions for the glycerol reforming process, utilizing three types of reagents: carbon dioxide, steam, and a combination of both. In addition to syngas production, the energy consumption of each process is also evaluated.

Table 1 Models and operating condition of each unit operation used in the simulation.

Units Name	Model	Operating Condition
MIXER	Mixer	-
HEATER	Heater	Temperature: 600 °C
REFORMER	RGibbs	Temperature: 600 °C Pressure: 1 bar
TURBINE	Compr	Pressure: 1 bar
COOLER-1	Heater	Temperature: 250 °C
WGS	REquil	Temperature: 250 °C Pressure: 1 bar
COOLER-2	Heater	Temperature: 25 °C
FLASH	Flash2	Temperature: 250 °C Pressure: 1 bar
SEP	Sep	The molar ratio of H_2:CO:CO_2 is 1 : 1 : 1.

4. RESULTS AND DISCUSSION

4.1 Glycerol Reforming using Carbon Dioxide

Figure 2 presents the effect of reformer temperature on the mole fraction of gas components when the reformer pressure is set at 1 bar and the CO_2 to glycerol feed ratio is fixed at 1. It is found that as the reformer temperature increases, the production of hydrogen and carbon monoxide increases. This is because the carbon dioxide reforming reaction is endothermic and proceeds more efficiently at higher temperatures, shifting the reaction equilibrium toward the product side and thereby reducing the mole fraction of carbon dioxide. Additionally, the methane content decreases due to methane reforming (Equation (6)) and methane decomposition reactions (Equation (9)). However, it is observed that increasing the temperature above 900°C results in a slight decrease in the hydrogen. This is because the reforming reaction begins to reach equilibrium. Therefore, a temperature of 900°C is selected as optimal temperature [10].

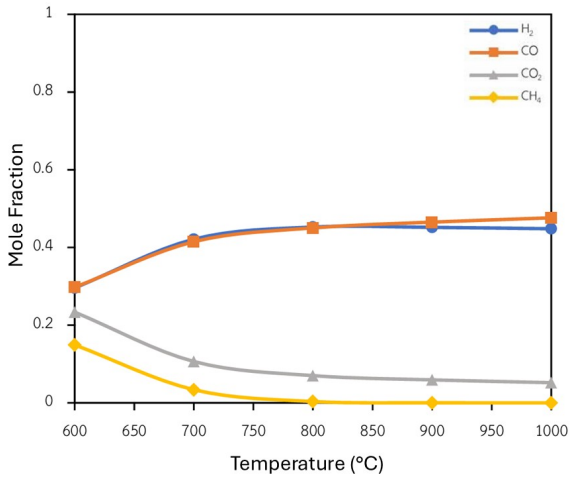

Figure 2 Effect of reformer temperature on the mole fraction of gas product at a pressure of 1 bar and a carbon dioxide to glycerol feed ratio of 1.

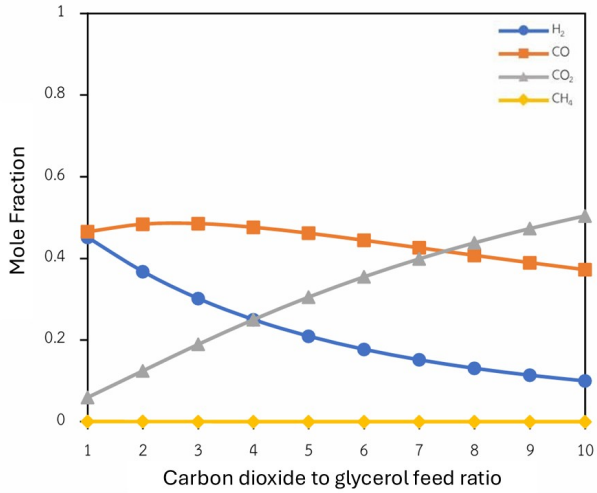

Figure 3 Effect of the CO_2-to-glycerol feed ratio on mole fraction of gas product at 900°C and a pressure of 1 bar.

Figure 3 illustrates the effect of the CO_2-to-glycerol feed ratio, ranging from 1 to 10, on the mole fractions of the gas products. The simulation results show that increasing the amount of carbon dioxide in the reforming process leads to a decrease in both the mole fraction and molar flow rate of hydrogen, primarily due to the occurrence of the reverse water-gas shift reaction [10]. While the mole fraction of carbon monoxide decreases, its molar flow rate increases as a result of the higher carbon dioxide input. Additionally, the methanation reaction, as represented by Equation (4), consumes both hydrogen and carbon monoxide. The graph indicates that the feed ratio strongly influences product composition between the ratios of 1 and 3, beyond which the changes stabilize. Increasing the feed ratio above 3 results in reduced production of both hydrogen and carbon monoxide. Therefore, an optimal CO_2-to-glycerol ratio lies between 1 and 3 for efficient reforming.

3.2 Glycerol Reforming using Steam

Figure 4 illustrates the effect of reformer temperature, ranging from 600 to 1,000°C at a pressure of 1 bar, with a steam-to-glycerol feed ratio of 1. It is found that the mole fraction of hydrogen and carbon monoxide increases with an increase in reformer temperature because the steam reforming reaction is endothermic and occurs more efficiently at high temperatures. Meanwhile, the mole fractions of carbon dioxide, methane, and water decrease. This is due to the water gas shift reaction and the Boudouard Reaction, which are reversible and endothermic. From the simulation, it is observed that at a temperature of 900°C, the optimal composition of syngas, consisting of hydrogen, carbon monoxide, and carbon dioxide, can be achieved [7].

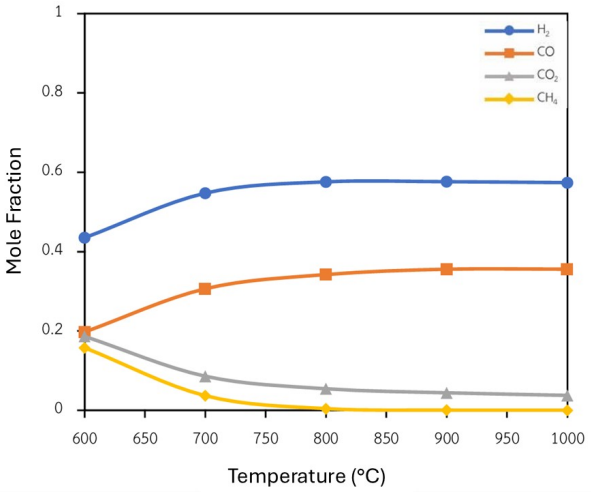

Figure 4 Effect of temperature on the molar ratio of components in the product gas at a pressure of 1 bar and a steam to glycerol feed ratio of 1.

The effect of steam-to-glycerol feed ratio, adjusting from 1 to 10, on the mole fraction of the gas product is shown in Figure 5. The simulation results indicate that increasing the steam-to-glycerol feed ratio increases the mole fraction and molar flow rate of hydrogen and carbon dioxide, while the mole fraction and molar flow rate of carbon monoxide decrease. This is due to steam reforming reaction and water gas shift reaction. Increasing the steam feed disturbs the chemical equilibrium and shifts it toward the product side, enhancing the production of hydrogen and carbon dioxide. Simultaneously, the reverse methanation reaction contributes to additional hydrogen and carbon monoxide formation. The carbon monoxide generated is subsequently converted to carbon dioxide via the water-gas shift reaction [8].

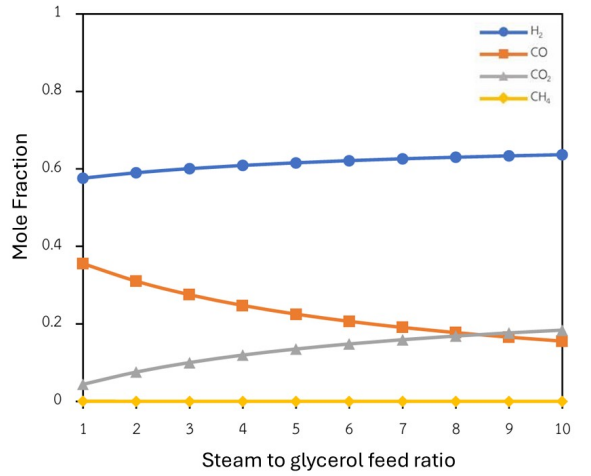

Figure 5 Effect of the steam to glycerol feed ratio on the molar ratio of components in the product at a temperature of 900°C and a pressure of 1 bar.

The simulation result also indicates that the steam-to-glycerol feed ratio significantly affects the product mole fractions, particularly between ratios of 1 and 3, after which the values begin to stabilize. Increasing the feed ratio beyond 3 leads to only marginal increases in hydrogen and carbon dioxide production. Although a steam-to-glycerol ratio above 3 may provide a more favorable syngas composition for downstream methanol synthesis [7], it also results in higher production costs and requires a larger reactor size. Therefore, the optimal feed ratio should be selected based on a balance between syngas quality, production cost, and reactor design constraints.

The optimal operating conditions and results obtained from glycerol reforming using carbon dioxide and steam are summarized in Table 2. It is found a comparison of hydrogen production that steam reforming yields higher hydrogen output than carbon dioxide reforming, as steam promotes the forward direction of the water-gas shift reaction. When the molar ratio of syngas component is considered, the results show that the molar ratio of syngas component obtained from CO_2 reforming is lower than that from steam reforming. However, the molar ratio of syngas component obtained both reforming processes cannot achieve 1.05 that is target for methanol synthesis.

Table 2 The optimal operating conditions and results obtained from glycerol reforming using carbon dioxide and steam.

	CO_2 reforming	**Steam reforming**
Operating condition		
Temperature	900 °C	900 °C
CO_2-to-glycerol ratio	1	-
Steam-to-glycerol ratio	-	3
Gas product (%mol)		
Hydrogen	0.45	0.60
Carbon monoxide	0.47	0.28
Carbon dioxide	5.9×10^{-3}	0.10
Methane	3.7×10^{-3}	9.4×10^{-5}
Molar ratio of syngas	0.47	0.70

3.3 Glycerol Reforming using a Combined CO_2 and Steam

This section involves simulating the production of syngas through a combined process of carbon dioxide and steam reforming of glycerol. The aim is to study the effects of optimal operating conditions on syngas production. Not only mole fraction of gas product but also the mole ratio of the syngas component are considered.

Figure 6 shows the effect of CO_2 feed percentage (0 -100%) and the reformer temperature (600 - 1,000°C) at a pressure of 1 bar and a steam-to-glycerol feed ratio of 1. The simulation results indicate that as more carbon dioxide is added into the reformer, the mole fraction of hydrogen decreases. In contrast, increasing the reformer temperature increases the mole fraction of hydrogen, as shown in Figure 6(a). While, the mole fraction of

carbon monoxide increases with increasing CO_2 feed percentage and reformer temperature (Figure 7(b)).

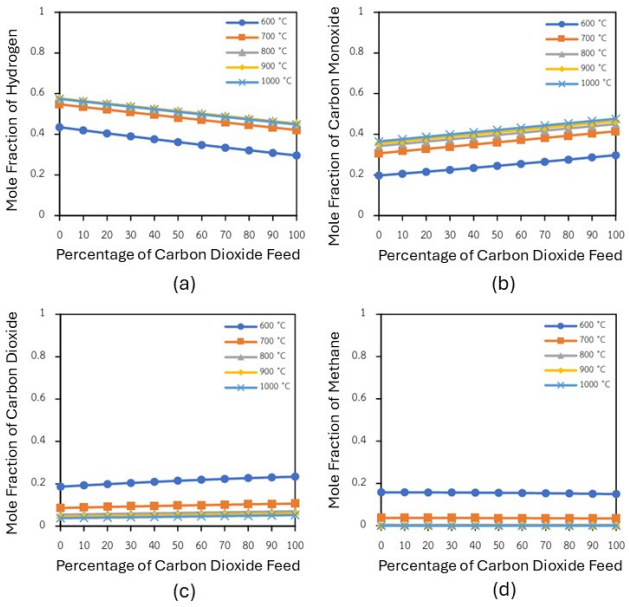

Figure 6 Effects of CO_2 feed percentage and reformer temperature on the molar composition of (a) hydrogen, (b) carbon monoxide, (c) carbon dioxide, and (d) methane at a pressure of 1 bar and a steam-to-glycerol molar feed ratio of 1.

When a higher percentage of carbon dioxide is introduced into the process, the water-gas shift reaction proceeds in the reverse direction, leading to a reduction in hydrogen production and an increase in carbon monoxide formation. As the reformer temperature increases, the production of both hydrogen and carbon monoxide also rises. This is attributed to the endothermic nature of both the dry reforming reaction (Equation (1)) and the steam reforming reaction (Equation (2)), which are thermodynamically favored at elevated temperatures, thereby driving the reactions forward.

In contrast, the mole fractions of carbon dioxide and methane decrease with increasing reformer temperature. Although increasing the carbon dioxide feed percentage results in a slight increase in the mole fraction of carbon dioxide, the mole fraction of methane remains relatively unchanged, as illustrated in Figures 7(c) and 7(d). This behavior is primarily due to the enhancement of methanation reactions (Equations (4) and (5)) at higher temperatures. Since these reactions are exothermic, elevated temperatures promote their reverse direction, contributing to methane decomposition and the subsequent formation of hydrogen, carbon monoxide, and carbon dioxide, while maintaining a nearly constant methane concentration. Simultaneously, the reverse water-gas shift reaction (Equation (3)) further reduces the net production of carbon dioxide [11].

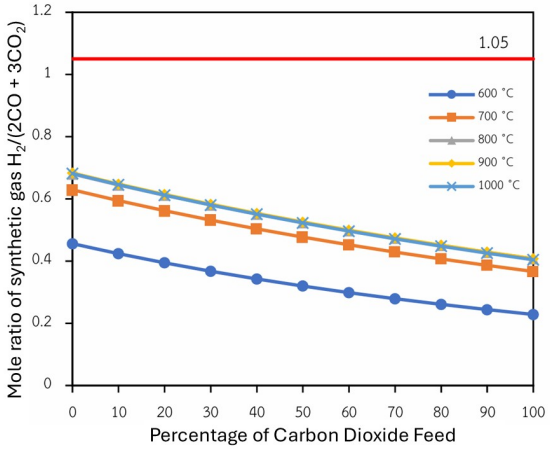

Figure 7 Effect of the percentage of carbon dioxide feed and the reformer temperature on the mole ratio of synthesis gas.

The mole fractions of hydrogen, carbon monoxide, and carbon dioxide obtained at various carbon dioxide feed percentages (ranging from 0% to 100%) were used to calculate the mole ratio of synthesis gas, defined as $H_2 / (2CO + 3CO_2)$, at different reformer temperatures. The resulting trends are illustrated in Figure 7. As the reformer temperature increases, the syngas mole ratio also increases. However, beyond 900 °C, a slight decline in the ratio is observed. This decrease is attributed to the suppression of hydrogen production at elevated temperatures due to the exothermic nature of the water-gas shift reaction (Equation (3)), which is thermodynamically disfavored at higher temperatures.

Additionally, increasing the carbon dioxide content in the feed leads to a reduction in the syngas mole ratio. This is primarily due to the enhanced reverse water-gas shift reaction under high CO_2 conditions, which reduces hydrogen formation and thus lowers the overall mole ratio. Consequently, the highest synthesis gas mole ratio is achieved in the absence of carbon dioxide (0% CO_2 feed), corresponding to a scenario where steam reforming occurs exclusively at a reformer temperature of 900 °C.

Despite this optimal condition, simulation results indicate that the syngas mole ratio remains below the target value of 1.05—required for efficient methanol synthesis—across all reformer temperatures investigated. Therefore, to meet the desired stoichiometric ratio for methanol production, it is necessary to either enhance hydrogen yield or selectively remove carbon monoxide from the synthesis gas stream.

3.4 Adjustment of the Syngas Mole Ratio

To achieve syngas mole ratio closely to 1.05, the installation of a water gas shift reactor which undergoes the reaction shown in Equation (3), is proposed to improve hydrogen content and reduce carbon monoxide in syngas. The WGS reactor is designed to operate at a temperature of 250°C and a pressure of 1 bar.

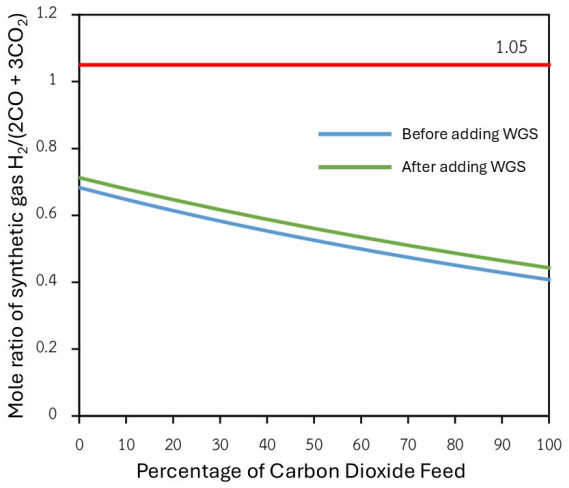

Figure 8 Comparison of the effect of CO_2 feed percentage on the syngas mole ratio at 900 °C, 1 bar pressure, and a steam-to-glycerol feed ratio of 1, before and after the addition of the water-gas shift reactor.

When the reformer is operated at 900 °C, pressure of 1 bar with a steam-to-glycerol feed ratio of 1, a comparison of the effect of CO_2 feed percentage on the syngas mole ratio, before and after the addition of the WGS reactor is shown in Figure 8. The results indicate that the addition of the WGS reactor increases the mole ratio of syngas. This improvement occurs because when the syngas produced from the reforming process is fed into the WGS reactor, the water gas shift reaction takes place, which increases the mole fractions of hydrogen and carbon dioxide while reduces the mole fraction of carbon monoxide. As a result, the mole ratio of syngas increases. However, the syngas mole ratio is still below 1.05, which does not meet the target requirement, further adjustments are necessary.

To achieve a syngas mole ratio of 1.05, a gas separator (SEP) is employed to selectively remove either carbon monoxide or carbon dioxide. The operating conditions of the gas separator are determined using the design specification tool available in Aspen Plus software. The separation ratio of carbon monoxide or carbon dioxide is adjusted accordingly to ensure that the syngas exiting the separator attains the target mole ratio of 1.05.

Table 3 summarizes the results of syngas composition obtained from the gas separator to achieve a syngas mole ratio of 1.05 at varying CO_2 feed percentages. The results indicate that, across the full range of CO_2 feed ratios (0% to 100%), the desired mole ratio can be attained by selectively reducing the mole fraction of carbon monoxide in the syngas. This adjustment leads to an increased removal of carbon monoxide from the system. As shown in Figure 9, the rate of carbon monoxide removal rises with increasing CO_2 feed percentage. The separated carbon monoxide may be recycled into the process, either as a reactant in the water-gas shift reaction or for use in other downstream applications.

Table 3 The results of syngas composition obtained from the gas separator to achieve a syngas mole ratio of 1.05 at varying CO_2 feed percentages.

CO_2 feed Percentage	Syngas Composition		
	H_2	CO	CO_2
0	0.726	0.131	0.143
10	0.727	0.127	0.146
20	0.728	0.122	0.150
30	0.729	0.118	0.153
40	0.731	0.112	0.157
50	0.732	0.107	0.161
60	0.733	0.102	0.165
70	0.735	0.096	0.169
80	0.736	0.090	0.174
90	0.738	0.083	0.179
100	0.740	0.077	0.184

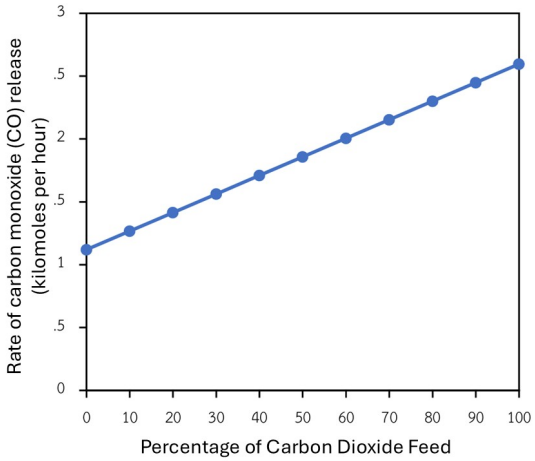

Figure 9 The rate of carbon monoxide removal at different CO_2 feed percentages, ranging from 0% to 100%.

3.5 Energy consumption in the process.

This section examines the energy consumption of the heater and reformer as functions of CO_2 feed percentage and reformer temperature. As shown in Figure 10, the heater's heat duty decreases with increasing CO_2 feed percentage. This trend is attributed to a reduction in the steam content of the system, which lowers the energy required to heat the steam, thereby decreasing the overall heat duty of the heater. In contrast, the heat duty increases with rising heater temperature, as more energy is needed to elevate the temperature of the reactants within the range of 600 °C to 1,000 °C to facilitate the reforming reactions.

The heat duty analysis indicates that operating conditions involving higher steam ratios and excessively elevated heater temperatures may result in reduced process efficiency. These conditions contribute to increased energy consumption and, consequently, higher production costs.

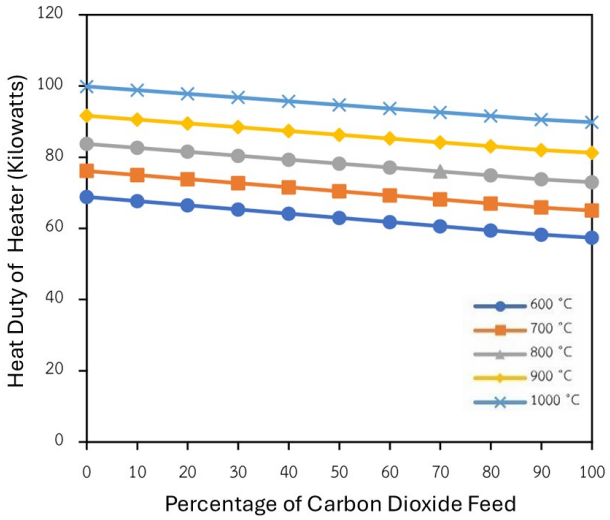

Figure 10 Effect of the CO_2 feed percentage and heater temperature on the heat duty of the heater.

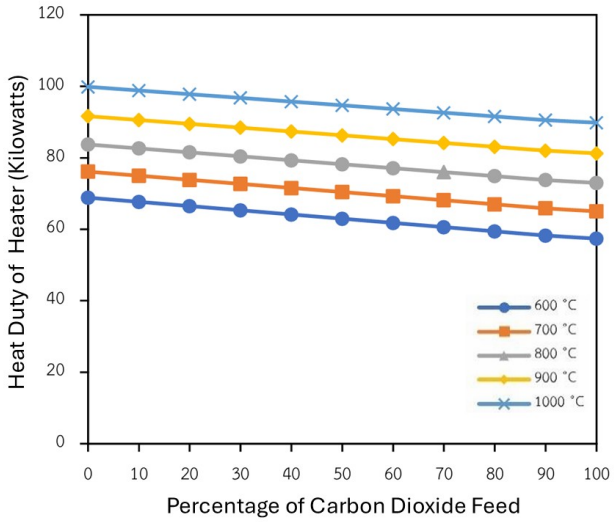

Figure 11 Effect of the CO_2 feed percentage and reformer temperature on the heat duty of reformer.

Figure 11 illustrates that the reformer's heat duty increases with both the CO_2 feed percentage and reformer temperature. This trend is attributed to the additional energy required to heat the reactants to the operating temperature, particularly due to the endothermic nature of the reforming reactions. As discussed in Section 3.3, within the temperature range of 700 °C to 900 °C, the composition of the product gas remains relatively stable, and the reformer's heat duty shows minimal variation—except at 700 °C, where increased methane formation is observed. At temperatures above 900 °C, a decline in hydrogen yield occurs. Based on the analyses in Sections 3.1 and 3.2, a reformer temperature of 900 °C yields the most favorable synthesis gas composition. Therefore, 900 °C is identified as the optimal operating temperature, balancing both syngas quality and energy efficiency.

4. CONCLUSION

This study focuses on the syngas production from glycerol reforming process. There were three types of reagents utilized that include carbon dioxide, steam, and a combination of both. This study was performed through Aspen Plus™ simulation software. The model of syngas production from glycerol reforming process was developed and employed to identify the favorable operating conditions for syngas production. Not only mole fraction of gas product but also the syngas mole ratio as $H_2/(2CO+3CO_2)$ that is suitable for methanol synthesis were considered.

The simulation results indicated that the optimal reformer temperature for both CO_2 and steam reforming processes was 900 °C, as this temperature provides the most favorable composition of hydrogen, carbon monoxide, and carbon dioxide—the primary components of synthesis gas. For the CO_2 reforming process, the optimal CO_2-to-glycerol feed ratio for achieving the desired syngas composition lies within the range of 1 to 3. In contrast, a steam-to-glycerol feed ratio of approximately 3 is identified as the optimal value, balancing syngas quality, production cost, and reactor size. Furthermore, the simulation results demonstrated that the hydrogen mole fraction produced via steam reforming is higher than that obtained from the CO_2 reforming process.

Next, the combined CO_2 and steam reforming process was investigated. The simulation results revealed that, within the temperature range of 600 to 1,000°C and CO_2 feed percentage between 0% and 100%, the syngas molar ratio could not achieve the desired value of 1.05. However, when the WGS reactor and gas separator was included in the process, it was found that the syngas molar ratio of 1.05 can be provided by CO removal.

Finally, the energy consumption of the combined CO_2 and steam reforming process was evaluated. The results show that increasing the CO_2 feed percentage leads to a reduction in the heater's heat duty, whereas increasing the reformer temperature results in higher heat duty for the heater. In contrast, the heat duty of the reformer increases with both higher CO_2 feed percentages and elevated operating temperatures, due to the endothermic nature of the reforming reactions. Among the temperatures studied, 900 °C was found to produce the most favorable syngas composition. Therefore, 900 °C is identified as the optimal operating temperature, offering a balance between desirable product gas composition and energy efficiency. Moreover, the heat duty analysis suggests that excessively high reaction temperatures and elevated steam ratios can reduce process efficiency, leading to increased energy consumption and higher production costs.

ACKNOWLEDGMENTS

This work was supported by the School of Engineering, King Mongkut's Institute of Technology Ladkrabang Thailand.

REFERENCES

1. D. M, "Crude glycerol potential described," Feedstuffs, vol. 79, 2007.
2. R. Tayebe, A. Mitra, M. A. Mohammad and R. R. Mohammad. Chapter 2- Hydrogen production from syngas. *Syngas Production and Usages* 2023; 3: 27-43.
3. E.M. Golet, I. Xifra. Environmental exposure assessment of fluoroquinolone antibacterial agents from sewage to soil. *Environmental Science & Technology* 2023; 37: 3243-3249.
4. B. Anicic, P. Trop and D. Goricanec. Comparison between two methods of methanol production from carbon dioxide. *Energy* 2024; 1-11.
5. R. A. Nural, A. Z. Sumaiya, I. Asmida and V. N. Dai-Viet. A review on glycerol reforming process over Ni-based catalyst for hydrogen and syngas productions. *International journal of hydrogen energy* 2019; 45: 18466-18489.
6. S. A. Carine, A. J. Helton, S. A. Rodolfo, d. S. A. Fernando, S. Rodrigo and B. R. Vanessa. Overview of glycerol reforming for hydrogen production. *Renewable and sustainable energy reviews* 2016; 58: 259-266.
7. B. V. Andre and O. M. d. Mona Lisa. Glycerol steam reforming in bench scale continuous flow heat recovery. *International journal of hydrogen energy* 2013; 38: 399-400.
8. V. Pranas, T. Andrius, G. Dovile, V. Vitas and J. Mejdi. Glycerol steam reforming for hydrogen and synthesis gas production. *International journal of hydrogen energy* 2017; 1-9.
9. X. Wang, S. Li, H. Wang, B. Liu and X. Ma. Thermodynamic analysis of glycerin steam reforming. *Energy and Fuels* 2008; 22: 4285-4291.
10. K. W. Siew, H. C. Lee, G. Jolius, S. Y. Chin, R. K. Makusudur, H. T.-Y. Yun and C. K. Cheng. Syngas production from glycerol-dry (CO_2) reforming over La-promoted Ni/Al_2O_3 caralyst. *Renewable energy* 2015; 74: 441-447.
11. C. Zhang, G. Kwak, J. Yun, H.-G. Park and K.-W. Jun. Efficient utilization of carbon dioxide in a gas-to-methanol process composed of CO_2/steam-mixed reforming and methanol synthesis. *Journal of CO_2 utilization* 2016; 16: 1-7.

Preparation of bio-based polyol from soybean meal for polyurethane foam production

Jidapa Klinputt[1], Chanatip Samart[1,2], Suwadee Kongparakul[1,2*]

[1] Department of Chemistry, Faculty of Science and Technology, Thammasat University, Pathum Thani 12120, Thailand
[2] Research Unit in Bioenergy and Catalysis, Thammasat University, Pathum Thani 12120, Thailand
[*] Corresponding author: ksuwadee@tu.ac.th

ABSTRACT

This study investigated the utilization of soybean meal, a cost-effective agricultural byproduct, as a precursor for bio-based polyurethane (PU) foam. Soybean meal was converted into polyols via acid hydrolysis and transesterification, utilizing the amine groups in soybean protein to create urethane-based polyols [1, 2], then reacted with isocyanate to produce PU foam. The chemical structure of bio-based polyols was characterized using nuclear magnetic resonance (NMR) and Fourier-transform infrared spectroscopy (FTIR). The amount of acid value after hydrolysis, amine value after transamidation, and hydroxyl value of polyols were determined by acid-base titration. A comparison of amine value from transamidation (soy hydrolyzate reacted with ethanolamine) and amination (soy hydrolyzate reacted with ethylene diamine) processes have been studied. The results show transamidation process achieved a higher amine value about 3 times than amination process which led higher hydroxyl value in polyol products for ring opening of amine with propylene carbonate. From the process, bio-based polyol contains a hydroxyl value of 111.3 mg KOH/g which can compete with polyether polyol 975 has a hydroxyl value of approximately 100-110 mg KOH/g, a commercially available polyol. The obtained polyol was further used for bio-based polyurethane applications such as PU foam or PU coating.

Keywords: Soybean meal; Bio-based polyols; Polyurethane foam; Transamidation; Aminolysis

1. INTRODUCTION

Polyurethane (PU) foams are widely used in various fields such as construction, automotive, and packaging industries due to their mechanical strength and insulating properties. However, conventional PU foams use petroleum-based polyols, which harm the environment, contributing to carbon emissions and resource depletion. Soybean meals are a promising raw material due to their excellent properties. Soybean meals are rich in functional groups, especially amines, which are found in the protein structure. These amine groups, along with other reactive sites, facilitate the chemical reactions necessary for the conversion of soybean meal to bio-polyols. This study aimed to develop bio-polyols from soybean meals via hydrolysis, transamidation, and ring-opening reactions and to evaluate their efficiency in producing PU foams. This research focused on optimizing the ratio of polyols to isocyanates to improve the foam structure and mechanical properties.

2. EXPERIMENTAL

2.1 Synthesis of Soymeal Polyols

The soybean meal was dried using an oven to remove moisture content at 60 °C for 48 h. After the soybean meal is dried, then sieved using a vibratory sieve shaker with mesh sizes of 1400 µm, 1000 µm, and 750 µm, soybean meal particles under 750 µm are selected for subsequent chemical processing, due to their larger surface area and consistency.

2.2 Hydrolysis of Soybean Meal

Soymeal sieve size under 750 µm, 62.5 g of pre-treated soybean meal was mixed with 250 mL of 3.0 M HCl in a three-neck round-bottom flask equipped with a mechanical stirrer and reflux condenser. The mixture was heated to 100 °C and stirred for 45 h. After hydrolysis, the solution was neutralized to pH 5.0–5.5 using 36% NaOH solution. The neutralized mixture was filtered, and the filtrate was concentrated via vacuum distillation at 80 °C for 2 h to remove water.

2.3 Comparative study of transamidation and amination Transamidation Reaction

Soybean hydrolyzate was reacted with ethanolamine at mass ratios of 1:1, 1:2, 1:3 and 1:5. The reaction was carried out under nitrogen atmosphere at 100–105 °C for 2 h using a magnetic stirrer at 400 rpm for mixing.

2.4 Aminolysis Reaction

Soybean hydrolyzate 59.45 g was reacted with excess ethylenediamine 22.24 g under constant stirring at 110 °C for 6 h. After completion, the mixture was distilled under vacuum to remove excess ethylenediamine and water.

2.5 Ring-opening Reaction

Propylene carbonate was added to the transamidation and aminolysis step in a molar ratio of 1:1.1. The mixture was stirred at 70–75°C for 2 h using a magnetic stirrer at 400 rpm for mixing.

2.6 Bio-based Rigid polyurethane (PU) foam production

PU foams are prepared by mixing the components in two plastic cups. Cup A consists of soy polyol, oil-based polyol, glycerol, water, Polycat® 77, and DABCO® 33LV. And cup B consists of 4,4'-MDI, cup B is added to Cup A and stirred by hand for 30–60 seconds in a plastic cup. The foam is cured at 50°C for 12 hours. The mixing ratios of the components are as shown in Table 1 below:

Table1. Formulation ratios for synthesis soymeal polyurethane foam production

Ingredient	Parts by weight (wt%)
Oil-based polyols (OHV = 170 mgKOH/g)	28-35
Soybeanmeal polyols (OHV = 111.3 mgKOH/g)	14-16
Glycerol (Crosslink reagent)	14-16
Water (Blowing agent)	14-16
Polycat® 77 (Gelling catalyst)	2
DABCO® 33 LV (Tertiary amine catalyst)	2
Ethanol (Solvent)	11
4,4-MDI (Monomer)	14

3. RESULTS AND DISCUSSION

The hydrolysis and transamidation reactions successfully modified soybean meal into amine-rich intermediates, as confirmed by titration results showing increased amine value. Following ring-opening reactions with propylene carbonate, the synthesized polyols showed hydroxyl values in the range of 105–115 mgKOH/g, which are suitable for polyurethane (PU) foam applications, as shown in **Table 2.**

Table2. End group analysis of intermediates synthesizes from soymeal.

	Amine value (mgKOH/g)	Acid value (mgKOH/g)	Hydroxyl value (mgKOH/g)
Exp.	ASTM D 2074– 92	ASTM D 1980 - 87	ASTM E 1899 - 97
	Aminolysis Reaction		
Soyhydrolyzate	15.44	78.52	-
Soy : ED	369.26	68.74	-
Soy polyol ED	28.01	30.93	34.88
	Transamidation Reaction		
Soyhydrolyzate	15.44	78.52	-
Soy : EA	798.04	-	-
Soy polyol EA	31.10	-	111.30

Note1: EA refers to ethanolamine; ED refers to ethylenediamine.

The hydrolysis process extracted functional components from soybean meals, resulting in an increased presence of amine groups. This was especially obvious after the transamidation reaction, where the amine value increased significantly with the rise in ethanolamine reacting with soymeal, as shown in Figure 1. In this process, the maximum amine value reached 789.04 mg KOH/g. When compared to the amination reaction, as shown in Figure 2, which yielded a maximum amine value of 369.26 mg KOH/g, the transamidation process achieved approximately three times higher amine content. This clearly indicates the superior efficiency of the transamidation reaction in functionalizing soymeal derived intermediates for polyol synthesis.

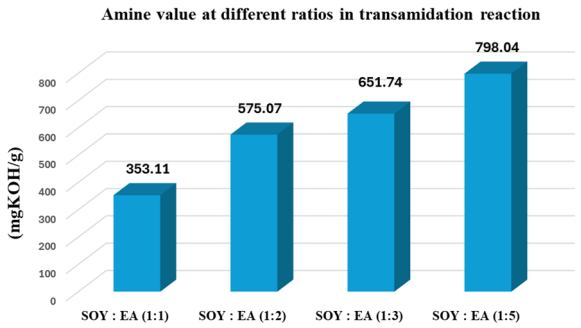

Figure 1. Amine value comparison in soy hydrolyzate: ethanolamine mixtures (ratios 1:1, 1:2, 1:3, 1:5)

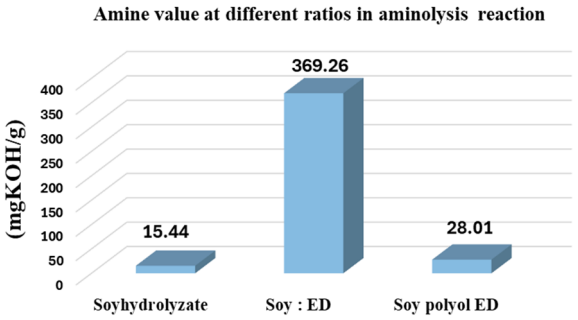

Figure 2 Amine value comparison of soy hydrolyzate, Soy: ED, and Soy polyol ED

From Figure 3. The hydroxyl values of the synthesized soymeal-based polyols from the transamidation reaction ranged from 105.2 to 111.3 mgKOH/g, depending on the transamidation conditions. In stark contrast, the polyol derived from the amination process with ethylenediamine showed a much lower hydroxyl value of 28.01 mg KOH/g, as shown in Figure 2. This noticeable difference shows that transamidation effectively transforms amine groups into hydroxyl-containing polyols that are suitable for polyurethane applications.

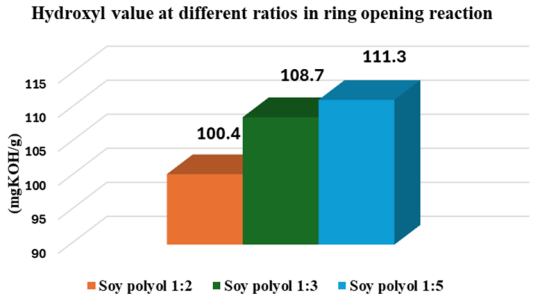

Figure 3. Hydroxyl value trends in Soy Hydrolyzate: Ethanolamine mixtures (ratios 1:2, 1:3, 1:5)

From Figure 4, foams made from oil-based polyols are generally hydrophobic, but water still partially adheres to the surface. In contrast, soy-based polyol foams exhibit particularly hydrophobic properties, with a high water contact angle (θA) of 148° due to their micro/nano surface roughness and bio-based surface chemistry, which makes them more water-resistant and more suitable for moisture-sensitive applications than conventional oil-based foams.

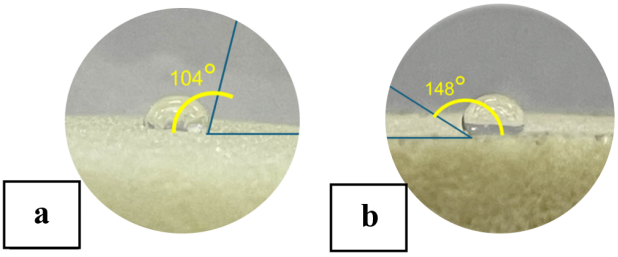

Figure 4. Contact angle of (a) Oil-Based PU Foams, (b) Soy-Based PU Foams

From Figure 5, the bio-based rigid polyurethane foam shows irregular cell sizes and partial wall breakage, indicating poor cell stability likely caused by the high viscosity of soymeal-based polyols.

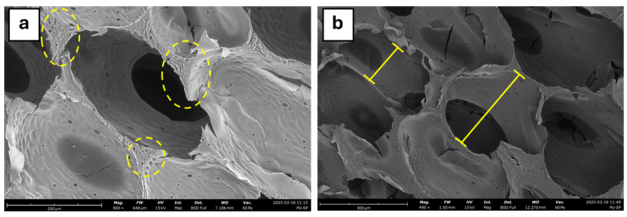

Figure 5. SEM images of (a) Soymeal Polyols and Oil Base Polyols Foam (1:1 Ratio) at 800X Magnification, (b) Soymeal Polyols and Oil Base Polyols Foam (1:1 Ratio) at 490X Magnification

4. CONCLUSION

Bio-based polyols were successfully synthesized from soybean meals through hydrolysis, transamidation, and ring-opening reactions. Among the two modification methods, transamidation yielded higher amine values than amination, leading to polyols with better reactivity. The resulting polyols were suitable for rigid PU foam production, producing foams with uniform structure and superhydrophobic properties.

ACKNOWLEDGMENTS

This work was supported by Thammasat University Thailand and Research Unit in Bioenergy and Catalysis.

REFERENCES

1. S. Zhu, K. Chen, J. Xu, J. Li, L. Mo. Bio-based polyurethane foam preparation employing lignin from corn stalk enzymatic hydrolysis residues. *RSC Advances* 2018; 8: 15754–15761.
2. H. Lim, S. H. Kim, B. K. Kim. Effects of the hydroxyl value of polyol in rigid polyurethane foams. *Polymers for Advanced Technologies* 2008; 19: 1729–1734
3. J. H. Lee, S. H. Kim, K. W. Oh. Bio-Based Polyurethane Foams with Castor Oil Based Multifunctional Polyols for Improved Compressive Properties. *Polymers* 2021; 13(4): 576.
4. S. D. Bote, R. Narayan. Synthesis of Biobased Polyols from Soybean Meal for Application in Rigid Polyurethane Foams. *Industrial & Engineering Chemistry Research* 2021; 60(16): 5733–5743.
5. Y. Guo, J. H. Hardesty, V. M. Mannari, J. L. Massingill Jr. Hydrolysis of Epoxidized Soybean Oil in the Presence of Phosphoric Acid. *J Am Oil Chem Soc* 2007; 84: 929–935.

Off-grade epoxy resin and waste tire composites for CO_2 adsorption

Teerapat Inudom[1], Sirilux Poompradub[1,2,3,*]

[1] Department of Chemical Technology, Faculty of Science, Chulalongkorn University, Bangkok 10330, Thailand
[2] Center of Excellence on Petrochemical and Materials Technology Chulalongkorn University, Bangkok 10330, Thailand
[3] Center of Excellence in Green Materials for Industrial Application, Chulalongkorn University, Bangkok 10330, Thailand
[*] Corresponding author: sirilux.p@chula.ac.th

ABSTRACT

Global warming is a major environmental concern, driven by the continuous rise of carbon dioxide (CO_2) in the atmosphere. Among the available technologies, adsorption using solid adsorbents stands out for its lower energy requirements and lower corrosion risk. Recently, the epoxy resin (EP) has been successfully prepared into activated carbon by carbonization process. However, this method requires high energy consumption and long preparation time. Waste tire (WT) is another interesting polymer waste material for CO_2 adsorption. It contains carbon black, silica and zinc oxide as components. The oxygen from silica and zinc oxide enhances CO_2 physisorption through electrostatic interactions between oxygen atoms and carbon atoms of CO_2. Additionally, the oxygen in silica and zinc oxide can act as Lewis bases, bonding with CO_2 to form carboxylate ions. Therefore, this research aims to propose a new method for preparing the polymeric adsorbents using WT mixed with the off-grade EP at various mass ratios of EP:WT (1:1, 1:2, 1:3 and 1:4). It was found that the composite of EP:WT at the mass ratio of 1:3 (EPWT13) exhibited the highest CO_2 adsorption capacity (7.12 $mg_{CO2}/g_{adsorbent}$) under the ambient temperature and atmospheric pressure using 12% v/v CO_2 in nitrogen and the inlet flow rate of 100 mL/min. Furthermore, the kinetic study of EPTW13 fitted well with Avrami's model indicating both CO_2 physisorption and chemisorption. Moreover, the EPWT13 showed 8.40% decrease in CO_2 adsorption capacity after five adsorption-desorption cycles.

Keywords: Off-grade epoxy resin; Waste tire; CO_2 adsorption; Kinetic adsorption

1. INTRODUCTION

Global warming is a major environmental concern, largely driven by the carbon dioxide (CO_2) emissions from burning fossil fuels in the industrial processes. The most widely used CO_2 capture process is amine-based absorption. However, this process has several disadvantages, including high energy requirements, corrosiveness, and maintenance costs [1]. In contrast, the adsorption process using solid adsorbents has gained attention due to its lower energy consumption, lower corrosion, and cost-effectiveness [2]. Developing the polymeric adsorbents from the waste polymers is interesting, as it not only reduces production costs compared to commercial adsorbents but also provides a sustainable solution for managing the large volumes of polymer waste generated globally [3]. Tiwari et al. demonstrated the successful preparation of epoxy resin (EP) into an oxygen-enriched carbon adsorbent by mixing the EP with zeolite in the mass ratio of 1:4, followed by carbonization at 700°C for 1 h and subsequent treatment with sodium hydroxide for 48 h. Although this method achieved a maximum CO_2 adsorption capacity of 40.04 mg/g under 100% v/v of CO_2, its high energy demand and many preparation steps caused limitations for practical application [4]. To address these issues, this study proposed a new approach for preparing composite materials without the carbonization process by mixing EP with waste tire powder (WT). WT was expected to enhance the CO_2 adsorption capacity of the composite materials because the presence of natural rubber and synthetic rubber could promote the CO_2 physisorption on the material's surface [5]. In addition, the additives in WT including carbon black, silica, and zinc oxide could enhance both CO_2 physisorption and chemisorption which involves stronger chemical interactions [6, 7]. This study was expected to develop a more sustainable method to prepare the CO_2 adsorbent material. The utilization of waste materials aligned with circular economic principles, contributing to environmental and economic benefits [8]. Moreover, the kinetic adsorption and regeneration process are also investigated to evaluate the adsorption mechanism and reusability of adsorbent.

2. EXPERIMENTAL

2.1 Materials

The EP supported by Aditya Birla Chemicals Ltd. (Advanced Materials) (Thailand). The WT with the particle size of 60 mesh supported by Union Commercial Development Co., Ltd. (Thailand). The nitrogen gas (N_2) (99.995% v/v) was purchased from Labgaz Co., Ltd. (Thailand). The CO_2 (12% v/v in N_2) was purchased from Thai-Japan Gas Co., Ltd. (Thailand).

2.2 Adsorbent preparation

The dried EP and WT were mixed by the grinder at different mass ratio, as seen in Table 1, for 5 min using the rotational speed of 5,000 rounds per min. Each composite was labeled as EPWTxy, where x and y represent the mass ratio of EP and WT, respectively.

Table 1 The composition of each composite material.

Sample	Mass (g)		
	EP	WT	Total
EPWT11	15.0	15.0	30
EPWT12	10.0	20.0	30
EPWT13	7.5	22.5	30
EPWT14	6.0	24.0	30

2.3 Characterization

The functional groups of each adsorbent material were analyzed using Fourier-transform infrared spectroscopy (FTIR) technique. The analysis was conducted using a Thermo Fisher Nicolet iS5 spectrometer (USA) with a resolution of 4 cm^{-1} and 64 scans.

The elemental composition including carbon (C), hydrogen (H) , nitrogen (N) and oxygen (O) was determined using a Perkin Elmer EA 2400 Series II elemental analyzer (USA) with the combustion temperature of 925°C. The combustion gases were analyzed using a chromatographic column with helium as the carrier gas.

2.4 CO_2 adsorption measurement

Figure 1 shows the CO_2 adsorption experimental setup. Each adsorbent was placed inside a stainless-steel reactor under ambient temperature (~35°C) and atmospheric pressure. Initially, the reactor was pre-treated by heating at 60°C under vacuum for 20 min to remove any adsorbed gases. Then, the reactor was cooled to the ambient temperature under N_2 flow. Subsequently, the mixed gas stream with the CO_2 concentration of 12% v/v in N_2 was introduced into the reactor until the outlet CO_2 concentration reached equilibrium. The outlet CO_2 concentration was monitored using CO_2 sensor (CM-40401, USA). The EP and WT were used to test the CO_2 adsorption performance using different gas inlet flow rates of 50, 70, 100 and 130 mL/min to find the optimal flow rate for CO_2 adsorption.

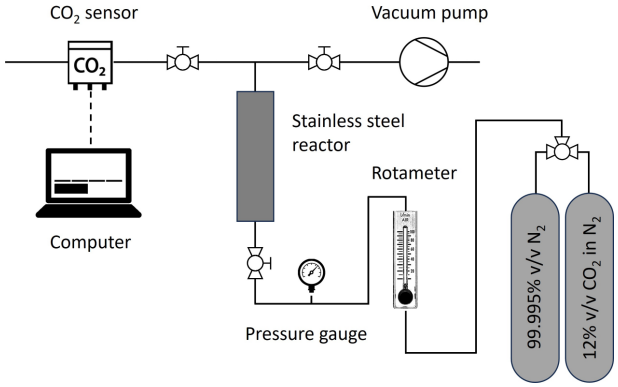

Figure 1 CO_2 adsorption experimental setup.

Once the optimal flow rate was identified, it was used to evaluate the CO_2 adsorption capacity of the composites. The CO_2 adsorption capacity was determined by calculating the difference between the adsorption capacity of the sample and the blank, following Eq. (1) [5],

$$q = \frac{1}{M}\left[\int_0^t Q(C_0 - C)dt\right]\frac{P}{RT} \quad (1)$$

where q is the CO_2 adsorption capacity (mmol/g), M is the mass of adsorbent (g), Q is the gas flow rate (mL/min), C_0 is the outlet CO_2 concentration (% v/v), C is the CO_2 concentration (% v/v), t is the denoted time (min), P is the gas pressure (atm), R is the gas constant (82.0573 cm^3 atm/K·mol) and T is the gas temperature (K).

2.5 Kinetic adsorption

The kinetic study was used to confirm the adsorption mechanism of the adsorbent that demonstrated the highest CO_2 adsorption capacity. The CO_2 adsorption experimental data were then fitted to the pseudo-1st order model, the pseudo-2nd order model, and the Avrami's model, as shown in Eq. (2), (3) and (4), respectively [5],

$$q_t = q_e[1 - exp(-k_1 t)] \quad (2)$$

$$q_t = \frac{k_2 q_e^2 t}{1 + k_2 q_e t} \quad (3)$$

$$q_t = q_e\{1 - exp[\ -(k_A t)^{n_A}]\} \quad (4)$$

where q_e is the adsorption capacity at equilibrium (mg/g), q_t is the adsorption capacity in a specifc time t (min), k_1 is the pseudo-1st order rate constant (1/min), k_2 is the pseudo-2nd order rate constant (g/(mg·min)), k_A is the avrami's rate constant (1/min) and n_A is the kinetic order of the Avrami's model.

2.6 Regeneration process

The regeneration of the adsorbent was evaluated using the pressure and temperature swing with N_2 flow process. After CO_2 adsorption, the adsorbent was heated to 60°C under reduced pressure with the N_2 flow rate of 100 mL/min for 20 min, then cooled down to

ambient temperature and repeated the CO_2 adsorption measurement for five adsorption-desorption cycles

3. RESULTS AND DISCUSSION

3.1 Characterization of adsorbent materials

Table 2 illustrates the elemental composition of each adsorbent. EP consisted of C, H and O because it is hydrocarbon compound with O functional group in the chemical structure. Similarly, WT contained C, H, N, and O originated from rubber molecules and additives. A little N content of WT obtained from nylon textile which was used as reinforcing material for the tire production [9]. The C and H contents of all samples increased with the increase of WT loading. It is interesting to note that the O content for all samples tended to decrease due to the lower EP content. Moreover, the N content in the composite materials showed no significant change due to its very low nylon textile content.

Table 2 Elemental composition of adsorbents.

Sample	Elemental composition (%)			
	C	H	N	O[a]
EP	74.95	6.97	-	18.08
WT	78.31	7.14	0.59	13.96
EPWT11	65.42	5.90	0.23	28.45
EPWT12	76.37	7.04	0.40	16.19
EPWT13	78.41	7.31	0.37	13.91
EPWT14	80.31	7.52	0.44	11.73

[a] Calculated by difference.

FTIR spectra were used to confirm the functional groups of each adsorbent as shown in Fig. 2. The EP exhibited the C–O–C stretching of the epoxy ring at 823, 870, 915, 1010, 1100, and 1232 cm^{-1} [10-14]. The C–O stretching and O–H stretching appeared at 1036 cm^{-1} and 3500 cm^{-1}, respectively [15, 16]. The peaks at 2848 and 2915 cm^{-1} were related to the C-H stretching [17] while the asymmetric CH_3 bending and stretching were detected at 1456 cm^{-1} and 2964 cm^{-1}, respectively. [18, 19]. Additionally, the aromatic C–O stretching at 1180 cm^{-1} [20], aromatic C–C stretching at 557 and 1512 cm^{-1} [20, 21] and aromatic C=C stretching at 1612 cm^{-1} [20] were associated with the aromatic ring structures in the EP molecules and also indicated the presence of styrene-butadiene rubber as the synthesis rubber, which contained aromatic ring in the molecule, as seen in Fig. 3. The C–S stretching at 1538 cm^{-1} [22], indicated the presence of crosslinked structures from tire manufacturing. Furthermore, the symmetric Si–O stretching was detected at 810 cm^{-1} [23], confirming the presence of silica additives in the WT. When considering the composite materials, it was found that the peak intensity of the C–O–C stretching decreased with the increased mass ratio of WT (highlighted in the orange box). This was in agreed with the reduction of epoxy rings in the composite material due to the decrease of EP and O content.

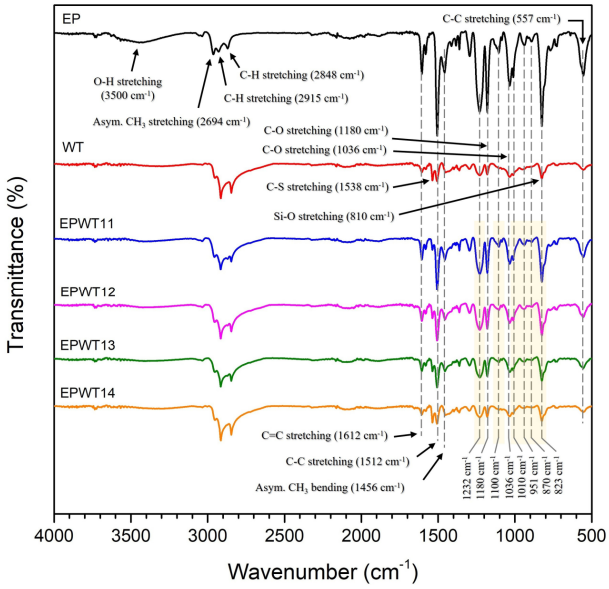

Figure 2 FTIR spectra of each absorbent.

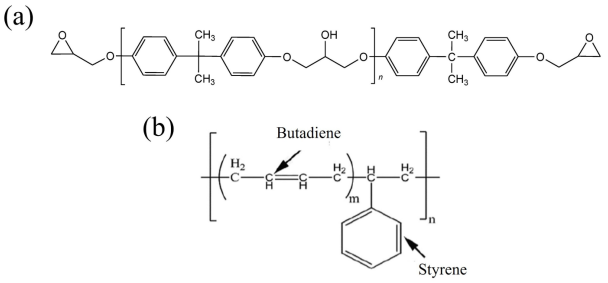

Figure 3 Structure of (a) EP and (b) styrene-butadiene rubber [24, 25].

3.2 CO_2 adsorption performance

Figure 4 shows the CO_2 adsorption capacity of EP and WT at different gas inlet flow rates under ambient temperature and atmospheric pressure. The CO_2 adsorption capacity of EP and WT increased as the gas inlet flow rate increased, reaching the maximum at 6.50 $mg_{CO2}/g_{adsorbent}$ and 4.00 $mg_{CO2}/g_{adsorbent}$, respectively, at the flow rate of 100 mL/min. However, the CO_2 adsorption capacity of both adsorbents decreased at the flow rate of 130 mL/min due to the excessively high flow rate. This allowed CO_2 to pass through adsorbent too rapidly which reduced the residence time for CO_2 adsorption. [26]. Therefore, the gas flow rate of 100 mL/min was selected as the optimal condition for testing the CO_2 adsorption capacity of the composites as seen in Fig. 5. It was found that the CO_2 adsorption capacity increased with the increased mass ratio of WT due to the presence of not only rubber molecules but also additives which enhanced both CO_2 physisorption and chemisorption [6, 7]. EPWT13 exhibited the highest CO_2 adsorption capacity of 7.12 $mg_{CO2}/g_{adsorbent}$. The CO_2 adsorption capacity tended to decrease in case of EPWT14 due to the excessive WT content, which reduced the proportion of EP. Since EP contained O functional groups which served as active sites for electrostatic interactions with

CO_2, the reduction in EP led to the low interaction between lone pair electron of O-molecules and CO_2. Although EPWT14 showed a higher C content, its CO_2 adsorption capacity was lower, suggesting that the O content performed a more important role than C content for CO_2 adsorption.

3.3 Kinetic adsorption

For the kinetic model, the pseudo-1st order model describes physisorption interactions between CO_2 and the adsorbent's surface [27], the pseudo-2nd order model characterizes chemisorption as the rate-controlling step [28]. In contrast, Avrami's model accounts for both physisorption and chemisorption mechanisms [5]. It was found that Avrami's model fitted well with the CO_2 adsorption experimental data of EPTW13 (Fig. 6) with the highest coefficient of determination (R^2) of 0.9954, as seen in Table 3. This suggested that CO_2 adsorption mechanism in EPTW13 occurred through physisorption and chemisorption.

Table 3 Kinetic parameters of each kinetic model for CO_2 adsorption by EPTW13 at ambient conditions.

Model	Parameter	EPTW13
Pseudo-first	R^2 [a]	0.9919
	k_1 [b]	1.1925
	$q_{e,(exp)}$ [c]	7.11
	$q_{e,(cal)}$ [d]	7.12
Pseudo-second	R^2 [a]	0.9622
	k_2 [b]	0.0856
	$q_{e,(exp)}$ [c]	9.26
	$q_{e,(cal)}$ [d]	7.12
Avrami's	R^2 [a]	0.9954
	k_A [b]	0.9160
	$q_{e,(exp)}$ [c]	7.12
	$q_{e,(cal)}$ [d]	7.12

[a]Coefficient of determination, [b]Kinetic coefficient of pseudo-1st order (1/min), [c]CO_2 adsorption capacity from experiment (mg/g), [d]CO_2 adsorption capacity from kinetic model (mg/g), [e]Kinetic coefficient of pseudo-2nd order (g/mg·min), [f]Kinetic coefficient of Avrami (1/min) and [g]Avrami's model order.

3.4 Regeneration

The long-term performance of EPWT13 was evaluated through five cycles of CO_2 adsorption-desorption using a pressure and temperature swing with N_2 flow process as shown in Fig. 7. The CO_2 adsorption capacity of EPWT13 gradually decreased after 3 cycles from 7.14 $mg_{CO2}/g_{adsorbent}$ to 6.53 $mg_{CO2}/g_{adsorbent}$. After that, it appeared to be constant up to 5 cycles. This demonstrated that EPWT13 exhibited good reusability for long-term operation.

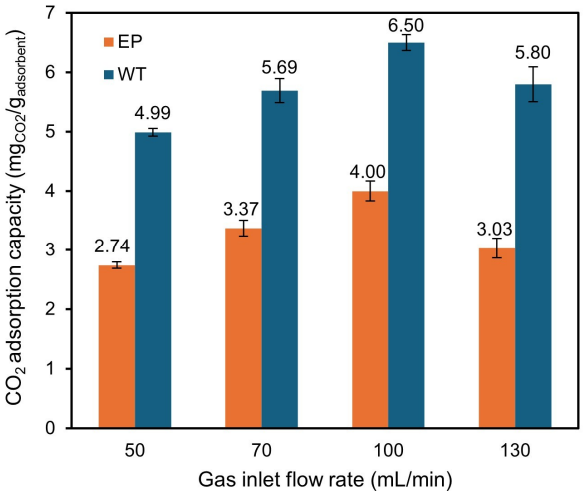

Figure 4 CO_2 adsorption capacity of EP and WT at different gas inlet flow rates under ambient temperature and atmospheric pressure.

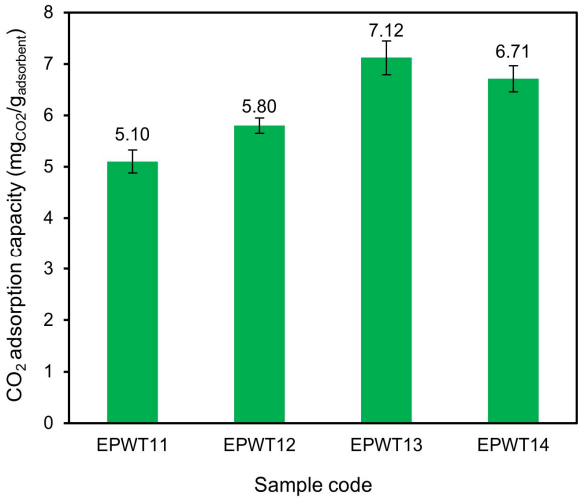

Figure 5 CO_2 adsorption capacity of EPWT composites under ambient temperature and atmospheric pressure.

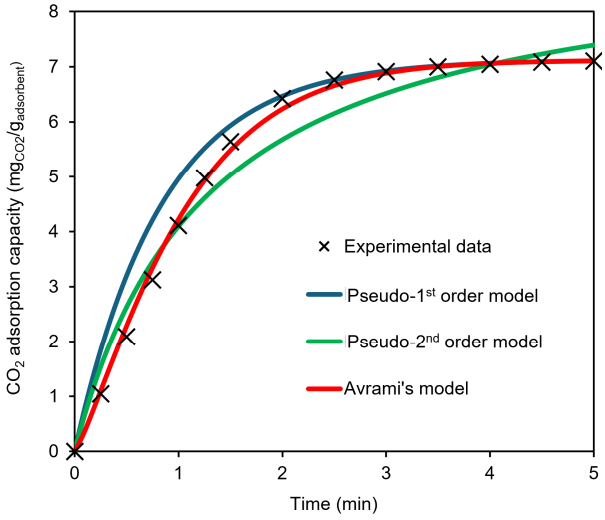

Figure 6 Fitting curve of the kinetic model for CO_2 adsorption of EPTW13.

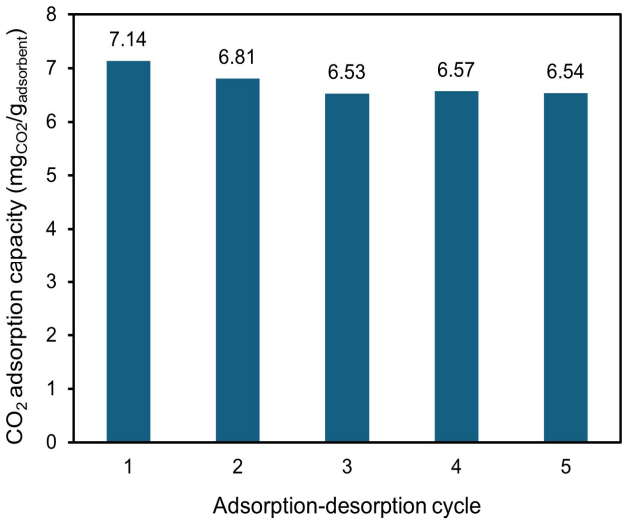

Figure 7 CO_2 adsorption capacity of each adsorption-desorption cycle.

Table 4 summarizes the comparison of CO_2 adsorption capacity between EPWT13 and EP-derived carbon prepared by carbonization process at 700 °C (EZ-700) [29]. Under ambient temperature and atmospheric pressure, EPWT13 exhibited a lower CO_2 adsorption capacity than EZ-700. However, the adsorption time of EPWT13 (5 min) was significantly shorter than EZ-700 (37 min). As a result, EPWT13 demonstrated a higher CO_2 adsorption rate than EZ-700 indicating that EPWT13 offered more CO_2 adsorption performance for continuous process.

Table 4 Comparison of CO_2 adsorption capacity of EPWT13 and EZ-700.

Data	EPWT13	EZ-700
CO_2 adsorption capacity ($mg_{CO2}/g_{adsorbent}$)	7.12	28.6
Adsorption time (min)	5	37
CO_2 adsorption capacity rate ($mg_{CO2}/g_{adsorbent}$·min)	1.42	0.77
CO_2 concentration (% v/v)	12	12.5
Adsorption temperature (°C)	35	30
Reference	This work	[29]

4. CONCLUSION

This study demonstrated an efficient approach to prepare the composite materials for CO_2 adsorption. EPWT13 exhibited the highest CO_2 adsorption capacity (7.12 $mg_{CO2}/g_{adsorbent}$) under the ambient temperature and atmospheric pressure using 12% v/v CO_2 in nitrogen at the gas inlet flow rate of 100 mL/min. The kinetic model of EPWT13 fitted well with the Avrami's model, confirming a combination of CO_2 physisorption and chemisorption mechanisms. Furthermore, EPWT13 illustrated the higher CO_2 adsorption rate and required significantly lower energy for preparation compared to carbonization process. Moreover, the CO_2 adsorption decreased by 8.40% after 5 adsorption-desorption cycles using the pressure and temperature swing with N_2 flow process. These advantages made EPWT13 not only environmentally friendly but also a promising alternative green adsorbent aligned with circular economic principle for CO_2 capture.

ACKNOWLEDGMENTS

The authors gratefully acknowledge the funding support from Department of Chemical Technology, Faculty of Science, Chulalongkorn University, the Center of Excellence on Petrochemical and Materials Technology, Chulalongkorn University and the Center of Excellence in Green Materials for Industrial Application, Chulalongkorn University. Special thanks are extended to Aditya Birla Chemicals (Thailand) Ltd. (Advanced Materials) for providing the EP and Union Commercial Development Co., Ltd. (Thailand) for supplying WT.

REFERENCES

1. Y. Gao, C. Ning, L. Liu, Y. Ye, S. Tian, X. Zhao. Research progress of CO_2 absorbent in postcombustion capture process. *Asia-Pacific Journal of Chemical Engineering* 2025; 20(2): e3172.
2. H. Zentou, B. Hoque, M.A. Abdalla, A.F. Saber, O.Y. Abdelaziz, M. Aliyu, A.M. Alkhedhair, A.J. Alabduly, M.M. Abdelnaby. Recent advances and challenges in solid sorbents for CO_2 capture. *Carbon Capture Science & Technology* 2025; 15: 100386.
3. J. Rubel, X. Guo, D. Madhav, S. Verslype, J. Zhang, Y. Ji, P. Eliášová, V. Vandeginste. Modified porous carbon from waste printed circuit boards for enhanced adsorption of carbon dioxide in abandoned mines. *Journal of Environmental Chemical Engineering* 2025; 13(2): 115790.
4. D. Tiwari, H. Bhunia, P.K. Bajpai. Epoxy based oxygen enriched porous carbons for CO_2 capture. *Applied Surface Science* 2017; 414: 380-389.
5. K. Panploo, B. Chalermsinsuwan, S.Poompradub, Effect of amine types and temperature of a natural rubber based composite material on the carbon dioxide capture. *Chemical Engineering Journal* 2020; 402: 125332.
6. D.B. Culver, A. Venkatesh, W. Huynh, A.J. Rossini, M.P. Conley. $Al(OR^F)_3(R^F=C(CF_3)_3)$ activated silica: A well-defined weakly coordinating surface anion. *Chemical Science* 2020; 11: 1510-1517.
7. S.A.S. Farias, E. Longo, R. Gargano, J.B.L. Martins. CO_2 adsorption on polar surfaces of ZnO. *Journal of Molecular Modeling* 2013; 19: 2069-2078.
8. I. Aiguobarueghian, U.M. Adanma, E.O. Ogunbiyi, N.O. Solomon. Waste management and circular economy: A review of sustainable practices and economic benefits. *World Journal of Advanced Research and Reviews* 2024; 22(2): 1708-1719.

9. N. Choosang, W. Smitthipong. Study of nylon textile-reinforced natural rubber composite. *IOP Conference Series: Materials Science and Engineering* 2022; 1234: 012012.
10. D. Nandhini, M.H. Nandakrishnan, R. Viswanatha. Optimization analysis of epoxidation of silkworm pupae oil with citric acid and eco-friendly oil coating on mild steel for corrosion protection. *Journal of the American Oil Chemists' Society* 2025; 1: 1-16.
11. M. Li, N. Liu, J. Chen, K. Shi, Q. Li. Development of reprocessable novel sulfur-containing epoxy based on thermal treatment. *RSC Advances* 2018; 8: 28386-28394.
12. J. Liu , J. Tang , X. Wang, D. Wu. Synthesis, characterization and curing properties of a novel cyclolinear phosphazene-based epoxy resin for halogen-free flame retardancy and high performance. *RSC Advances* 2012; 2: 5789-5799.
13. M. Azogagh, C. Hejjaj, R. Hsissou, A.E. Magri, R. Lachhab, K.P. Katin, E. Berdimurodov, M. Rbaa, M. Galai, S.E. Hegazi, M. Rafik. Synthesis and characterization of diglycidyl bisphenol A aryl ether sulfone epoxy resin as a corrosion inhibitor for mild steel in 1 M HCl solution: DFT, MC, and MD studies. *Polymer Bulletin* 2025; 82: 2571-2592.
14. K. Baglo, L. Remy, K. Mundsinger, J. Torgersen, C. Barner-Kowollik. α-methoxy benzaldehyde based photopolymers as a promising toolbox for architected carbon. *Macromolecular Rapid Communications* 2025; 1: 2500175.
15. S. Thakor, A. Joshi, P. Jain, M. Tannarana, C.R. Vaja, B. Shingala, P. Panchal, P. Sharma. Characterization of polymethyl methacrylate-multi-walled carbon nanotubes doped epoxy resins through infrared, ultraviolet and machine learning-enhanced dielectric spectroscopy. *Journal of Macromolecular Science* 2025; Part B: 1-14.
16. A.A. Amusa, N.I.M. Razali, F. Ali, T.N.M.T. Ismail, A.S. Azmi, J. Jamaluddin. Optimization of microwave-assisted polycondensation for flexible biodegradable polyurethane in sustainable packaging applications. *Materials Today Communications* 2025; 44: 111878.
17. R. Lima, L. Amorim, J. Nunes-Pereira, C.R. Tubio, S. Lanceros-Mendez, P. Costa. Development of thermo- and piezoresistive responses in epoxy resin-based adhesives. *Polymer Composites* 2025; 1: 1-16.
18. M. Asemani, A.R. Rabbani. Detailed FTIR spectroscopy characterization of crude oil extracted asphaltenes: Curve resolve of overlapping bands. *Journal of Petroleum Science and Engineering* 2020; 185: 106618.
19. M. Dworschak, M. Müller, T. Tjardts, L. Kienle, J. Benedikt. Surface passivation of silicon nanoparticles monitored by in situ FTIR. *Plasma Processes and Polymers* 2025; 22(4): e2400206.
20. C.A. Ramírez-Herrera, I. Cruz-Cruz, I.H. Jiménez-Cedeño, O. Martínez-Romero, A. Elías-Zúñiga. Influence of the epoxy resin process parameters on the mechanical properties of produced bidirectional [±45°] carbon/epoxy woven composites. *Polymers* 2021; 13: 1273.
21. S. Moussa, F. Namouchia, H. Guermazi. Elaboration, structural and optical investigations of ZnO/epoxy nanocomposites. *The European Physical Journal-Plus* 2013; 130: 152.
22. F. Karabork, E. Pehlivan, A. Akdemir. Characterization of styrene butadiene rubber and microwave devulcanized ground tire rubber composites. *Journal of Polymer Engineering* 2014; 34(6): 543-554.
23. I.F.S.D. Bosque, S. Martínez-Ramírez, M.T. Blanco-Varela. FTIR study of the effect of temperature and nanosilica on the nano structure of C–S–H gel formed by hydrating tricalcium silicate. *Construction and Building Materials* 2014; 52: 314-323.
24. T.V. Jinitha, K.P.S. Hussan, T.M. Shahin, E. Purushothaman. The interplay between the fragility and mechanical properties of styrene–butadiene rubber composites with unmodified and modified sago seed shell powder. *Journal of Applied Polymer Science* 2020; 137(39): 49180.
25. H. Jeong, K.S. Jang. Catalysis of silver and bismuth in various epoxy resins. *Polymers* 2024; 16(3): 439.
26. C. Wang, M. Liu, H. Liu, Q. Yang, C. Zhou, L. Song, K. Ma, H. Yue. Numerical analysis of CO_2 absorption characteristics in industrial flue gas mineralization spray tower reactor. *Separation and Purification Technology* 2025; 354: 129051.
27. G. Durán-Jiménez, J. Rodriguez, E.T. Kostas, L.A. Stevens, L. Lozada-Rodríguez, E. Binner, C. Dodds. Simultaneous conventional and microwave heating for the synthesis of adsorbents for CO_2 capture: Comparative study to pristine technologies. *Chemical Engineering Journal* 2022; 438: 135549.
28. S. Wang, Y. Lee, Y. Won, H. Kim, S. Jeong, B.W. Hwang, A.R. Cho, J. Kim, Y.C. Park, H. Nam, D. Lee, H. Kim, S. Jo. Development of high-performance adsorbent using KOH-impregnated rice husk-based activated carbon for indoor CO_2 adsorption, *Chemical Engineering Journal* 2022; 437: 135378
29. D. Tiwari, C. Goel, H. Bhunia, P.K. Bajpai. Novel nanostructured carbons derived from epoxy resin and their adsorption characteristics for CO_2 capture. *RSC Advances* 2016; 6: 97728.

A study on the mechanical properties, physical properties and biodegradation of rigid polyurethane foam synthesized from castor and palm oils-based polyol

Panchan Sricharoon[1,*], Atjima Khachon[1], Thinnapong Dorbutr[1], Narubet Sriprung[1], Nutthapart Nithiyasotharanon[1]

[1] Department of Chemical Engineering, Faculty of Engineering, King Mongkut's University of Technology Thonburi, Bangkok 10140, Thailand
[*] Corresponding author: panchan.sri@kmutt.ac.th

ABSTRACT

This study aimed to synthesize rigid polyurethane foam as an insulating material using castor oil and palm oil to improve biodegradability and replace petroleum-based polyols. Both oils were modified to increase their hydroxyl values before being polymerized with polymeric diphenylmethane diisocyanate (PMDI). The research varied the weight ratios of castor oil and palm oil and examined their effects on the mechanical and physical properties of the synthesized foam, including microstructure, bulk density, compressive strength, thermal conductivity, and biodegradability through hydrolysis. The foam exhibited a predominantly spherical, closed-cell structure. An increased proportion of palm oil-based polyol led to higher bulk density and compressive strength, which can be attributed to its higher hydroxyl value of 437.2 as compared to 414.8 for castor oil polyol, as well as the smaller foam cell size associated with higher palm oil content. However, ANOVA analysis indicated no significant change in thermal conductivity at a 95% confidence level, with values remaining within the range of 0.0512–0.0542 W/m·K. All measured properties exceeded the standard values for commercial foam. Additionally, biodegradability in the phosphate buffer solution decreased as the palm oil polyol content increased. Further optimization of synthesis conditions or renewable raw materials is necessary to achieve properties comparable to commercial foam.

Keywords: Renewable material; Rigid polyurethan foam; Vegetable oils; Insulation; Biodegradability

1. INTRODUCTION

Nowadays, products from the petroleum industry are widely used as precursors in the production of many petrochemical products related to daily life due to their distinctive characteristics, such as versatility, suitability for industrial production, and, in some cases, superior properties compared to natural materials. However, the issue of incineration and the poor degradability of petrochemical products, which are difficult to decompose naturally or take a long time to do so, has had a lasting impact on humans, animals, plants, and the environment. This has remained an unsolved problem for decades. As a result, many researchers have become aware of this issue and are seeking solutions by using biodegradable and environmentally friendly natural substitutes.

Polyurethane foam is one such product derived from the petrochemical industry. It can be mainly classified based on its physical characteristics into two types: flexible foam and rigid foam [1]. Among these, rigid polyurethane foam is widely used in various applications, such as insulation in building materials, furniture, and automotive components. Polyurethane is a polymer containing the functional group -NHCOO-, derived from a polymerization reaction between isocyanate and polyol. The most commonly used isocyanates are toluene diisocyanate (TDI) and diphenylmethane diisocyanate (MDI), depending on the type of polyurethane foam. The preferred polyols for industrial polyurethane production are polyether and polyester polyols [2], which are typically derived from petrochemicals. Due to declining petroleum reserves and the thermosetting nature of polyurethane making it non-recyclable, natural raw materials that are low-cost and have comparable properties to petrochemical polyols have been studied and used as biopolyols.

Thailand's geography is favorable for agriculture, making it a major source of raw agricultural products such as rice, palm oil, and sugar, which are exported worldwide. These products are low-cost and may contain naturally biodegradable polymers such as starch, pectin, and cellulose. One way to add value to these resources is by modifying them into polyols to replace petrochemical raw materials, which are key components in the production of rigid polyurethane foams. However, the use of vegetable oils as polyols requires a suitable hydroxyl content to successfully react with diisocyanates. When three or more hydroxyl

groups are available for reaction, a cross-linked polymer structure forms, resulting in rigid polyurethane foam [3].

Previous research on the synthesis of rigid polyurethane foam using bio-based polyols modified from vegetable oils has included the use of palm oil, castor oil, rapeseed oil, and soybean oil [4–8]. These studies show that different types of vegetable oils and synthesis conditions lead to variations in the properties of the resulting foams. For example, modified castor oil can produce a high hydroxyl value due to its high content of unsaturated fatty acid (ricinoleic acid) which contains a hydroxyl group in its structure [9]. The resulting foams exhibited low thermal conductivity and high mechanical strength, suitable for insulation applications. However, the foam also had a slightly high density and came with a high raw material cost [10]. In contrast, palm oil-based polyols have a lower hydroxyl value but can produce foams with comparable strength to commercial products at a lower cost [5]. The modification of soybean oil polyols involves a more complex process. Therefore, blending palm oil and castor oil polyols presents a promising alternative in Thailand. This approach may help reduce the cost associated with castor oil while maintaining the desired foam properties. Palm oil in Thailand is affordable, widely available, and contains polyunsaturated fatty acids that can be easily modified to increase hydroxyl content.

Therefore, this research focuses on studying the effect of different weight ratios of castor oil and palm oil polyols on the properties of synthesized rigid polyurethane foams. Vegetable oils are natural and biodegradable raw materials. If used in foam synthesis, they may also contribute to enhancing the degradability of polyurethane foams.

2. EXPERIMENTAL

Castor oil and palm oil were modified based on transesterification using triethanolamine (TEA) and pentaerythritol, respectively. They were later polymerized with polymeric diisocyanates (PMDI) to obtain rigid polyurethane foam. Details description of each preparation steps are as follows.

2.1 Preparation of Castor Oil Polyol [6, 11, 12]

Castor oil (supplied by South City) was mixed with Triethanolamine (TEA, 99.7%wt, Ajax Finechem) at the mole ratio of 1: 3, with the addition of 2% by the weight $Ca(OH)_2$ as a catalyst (99% wt Ajax Finechem). All were added into a 4-necked round bottom bottle purged with nitrogen gas and equipped with a thermometer and glass trap connected to the condenser. The mixture was mixed using magnetic stirrer at a speed of 700 rpm. The mixture temperature was kept constant at 150°C for 2 hours using a heating mantle. The castor oil polyol would then be obtained.

2.2 Preparation of Palm Oil Polyol [5]

Edible Palm oil (Morakot Industries) was added into a 4-necked round bottom bottle purged with nitrogen gas and equipped with a thermometer and a glass trap connected to the condenser. The mixture was mixed using magnetic stirrer at a speed of 700 rpm. The palm oil was heated up in a heating mantle until the temperature reached 150°C. Then pentaerythritol (98% wt, Sigma Aldrich) was added into the palm oil at the weight ratio between palm oil and pentaerythritol of 2.25 to 1. After the temperature reached 200°C, small amount of calcium oxide using as a catalyst was added and the temperature was increased to 245°C and held constant for 90 minutes. The palm oil polyol would then be obtained.

2.3 Synthesis of Rigid Polyurethane Foam

Castor oil and palm oil polyols of 0 to 100 weight ratio (100:0, 75:25, 50:50, 25:75 and 0:100, respectively) were studied in this work. 100 php of polyols with different polyol weight ratio was premixed with 3 php water, 1 php TEDA (Thai Mitsui specialty chemicals) and 2.5 php silicone oil, using a stirrer at the speed of 2,500 rpm. The polymeric methylene diphenyl isocyanate (PMDI, supplied by Thai Mitsui specialty chemicals), with an isocyanate index of 110 was then rapidly added into the premix to polymerize the rigid polyurethane foam in an open mold using water as a blowing agent. The foam was kept for 24 hour before it was cut into pieces and characterization, including the cell foam morphology (scanning electron microscope, SEM, JEOL Model JSM-6610 LV), density (ASTM D-1622-98), mechanical properties (Universal testing machine, Lloyd-Instruments - Ametek Test Model LD, ASTM D-1621), thermal conductivity (Thermal Conductivity Analyzer) and biodegradability by hydrolysis in 0.1 M phosphate buffer of pH 7.4 for 7 days at a controlled temperature of 60°C.

3. RESULTS AND DISCUSSION

Polyol is a key precursor in the synthesis of polyurethane foams. To ensure suitability for this application, the polyol must possess appropriate properties, which are commonly assessed by its hydroxyl (OH) value. In this study, hydroxyl values were determined in accordance with ASTM D-1957. The as-received castor oil and palm oil, used as precursors, exhibited hydroxyl values of 152.9 and 11.2 mgKOH/g, respectively. Although castor oil generally has a higher hydroxyl value than most vegetable oils, the value obtained was still below the optimal range for rigid polyurethane foam production, typically 250-1000 mgKOH/g [13]. Consequently, both castor oil and palm oil required modification, which was carried out via transesterification.

Castor oil was transesterified with triethanolamine at a molar ratio of 1:3 to increase its hydroxyl value. Due to its inherently low hydroxyl value in the raw

state, palm oil also required modification, which was achieved through transesterification with pentaerythritol [5]. After transesterification, the modified castor oil polyol appeared as a clear, dark yellow liquid, while the polyol derived from palm oil was a dark brown, viscous liquid. The hydroxyl values of the castor oil and palm oil polyols increased to 414.8 and 437.2 mgKOH/g, respectively, indicating significant improvement.

Castor oil primarily contains ricinoleic acid, which inherently possesses hydroxyl groups [9]. Transesterification with triethanolamine, a tri-functional alcohol, further enhanced the hydroxyl content of the castor oil-based polyol. In contrast, palm oil lacks fatty acids with hydroxyl groups; however, transesterification with pentaerythritol, which contains four hydroxyl groups per molecule, effectively raised the hydroxyl value of the palm oil polyol. Therefore, blending polyols derived from castor oil and palm oil is expected to yield a hydroxyl value within the optimal range for rigid polyurethane foam synthesis (250–1000 mgKOH/g) [13].

To further confirm the presence of functional groups in the modified polyols, FTIR analysis was conducted on both castor oil and palm oil polyols. An example FTIR spectrum for castor oil polyol is shown in Figure 1. The spectrum exhibited transmission peaks in the range of 3625–3200 cm^{-1}, characteristic of hydroxyl-containing compounds. Additional peaks at 1036.69 and 1072.31 cm^{-1} correspond to C–O stretching vibrations associated with triethanolamine (TEA) [14]. Notably, the castor oil polyol spectrum showed reduced % transmittance in the hydroxyl region compared to the as-received castor oil, indicating an increase in hydroxyl content. This enhancement is attributed to the conversion of triglycerides in the vegetable oils into diglycerides and monoglycerides, resulting in a higher number of hydroxyl groups. Similar FTIR results and trends were observed for the palm oil polyol.

Based on the hydroxyl values and FTIR analysis, the polyols derived from castor oil and palm oil were considered suitable for the synthesis of rigid polyurethane foams. Due to their high hydroxyl values, each modified polyol could potentially be used independently for foam production. However, the distinct chemical compositions of the two polyols may influence the properties of the resulting foams. Therefore, blending the polyols offers an opportunity to balance these differences and optimize the final foam formulation. The effects of varying the weight ratio of castor oil and palm oil polyols are discussed in the following section.

From the SEM micrographs of the rigid PU foams synthesized at different weight ratios of polyols, as shown in Figure 2 (a) - (e), it was found that most

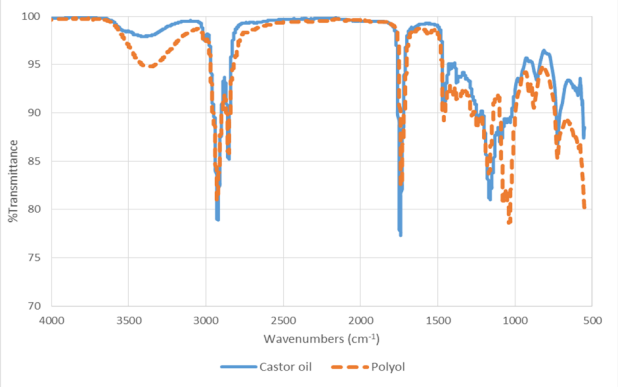

Figure 1 FTIR Spectra of the Castor Oil and Castor Oil Polyol.

foam cells were closed and round shaped. When the weight ratio of castor oil to palm oil polyol was changed from 100:0 to 25:75 (i.e., with an increasing percentage of palm oil in the polyol mixture), the foam cell size decreased. This was confirmed by the cell size measurements and calculations shown in Figure 3.

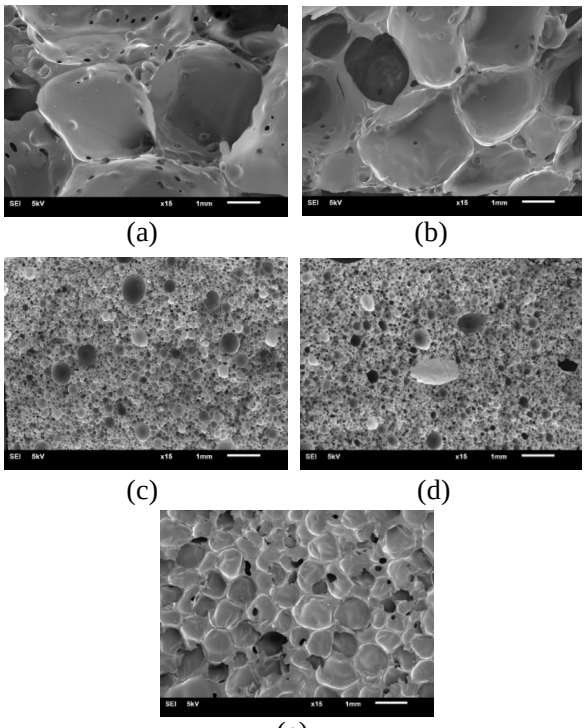

Figure 2 SEM Micrographs of the rigid polyurethane foam synthesized from different weight ratio of castor oil to palm oil polyols: (a) 100:0, (b) 75:25, (c) 50:50, (d) 25:75 and (e) 0:100.

However, the foam with a weight ratio of 0:100 (containing 100% palm oil polyol) showed an increase in cell size, as seen in Figure 2(e) and Figure 3. This may be attributed to the viscosity of the polyol, which can affect foam cell expansion. Since the polyol from palm oil is more viscous than that from castor oil, the overall foam mixture becomes more viscous, hindering gas bubble expansion and resulting in smaller, more evenly distributed foam cells. Nevertheless, excessive

viscosity can hinder foam expansion by restricting bubble mobility, causing gas bubbles to remain in close proximity and eventually coalesce into larger cells.

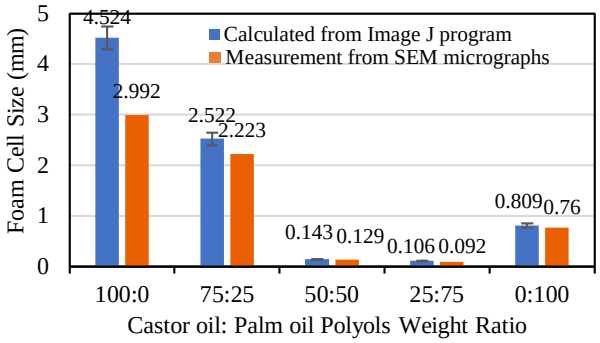

Figure 3 Foam cell size of the rigid polyurethane foam synthesized from different weight ratio of castor oil to palm oil polyols.

Bulk density measurement of the synthesized rigid polyurethane foams was performed by cutting foam samples to a size of 3 × 3 × 3 cm^3 using a vernier caliper, then weighing them and calculating the volume based on their dimensions. The bulk density of the foams synthesized using various polyol ratios is shown in Figure 4. It was observed that as the proportion of palm oil polyol increased, the bulk density also increased. As previously mentioned, the higher viscosity of palm oil polyol interferes with gas bubble expansion, resulting in smaller and more closely packed foam cells. This increased the likelihood of the polymer matrix bonding more tightly, thereby increasing the foam's density. Nonetheless, the slightly higher density of the foam made with 100% palm oil polyol, despite its larger average cell size, is consistent with findings from previous studies [15-16], which reported that foam cell size and density are not necessarily inversely related. This may be due to other influencing factors, such as additives, viscosity, or gas bubble coalescence. Additionally, the increase in foam density with palm oil polyol content was expected, as higher viscosity reduces foam rise height, resulting in a more compact structure with less expansion, thereby leading to higher density.

In comparison, it was seen that the synthesized foams had a higher bulk density than those of the previous works [5, 10], including commercial foam and TISI standard of cellular plastic used for insulation (TIS no. 1859-2562), which should be in the range of 30 - 35 kg/m^3, respectively. Therefore, further improvement in foam density is necessary for its potential application as a lightweight material in the future.

In this research, thermal conductivity tests were performed on foam samples with dimensions of 7 × 7 × 1.5 cm^3 using a thermal conductivity analyzer (ANACON model 88). In closed-cell foams, thermal conductivity typically results from heat transfer through the solid and gaseous phases, primarily via conduction and radiation mechanisms. According to Figure 5,

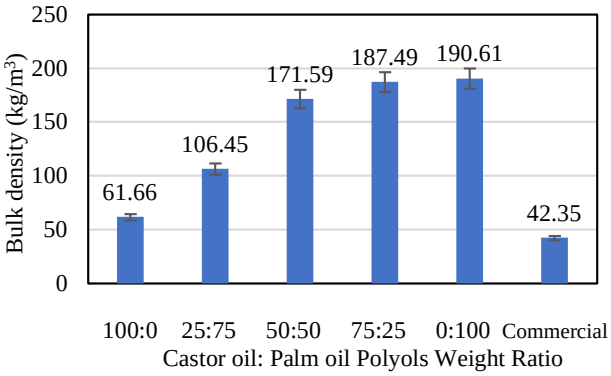

Figure 4 The bulk density of the rigid polyurethane foam synthesized from different weight ratio of castor oil to palm oil polyols, as compared with the commercial foam [10].

the rigid polyurethane foams synthesized with varying weight ratios of castor oil to palm oil polyols (from 100:0 to 0:100) exhibited thermal conductivity values in the range of 0.0512–0.0542 W/m·K. No clear correlation or trend was observed between the polyol weight ratio and thermal conductivity as the palm oil polyol content increased. Statistical analysis using one-way analysis of variance (ANOVA) confirmed that the differences in thermal conductivity among the foams were not statistically significant at a 95% confidence level. Therefore, it can be concluded that thermal conductivity was not influenced by the increasing palm oil polyol content or the resulting changes in foam density.

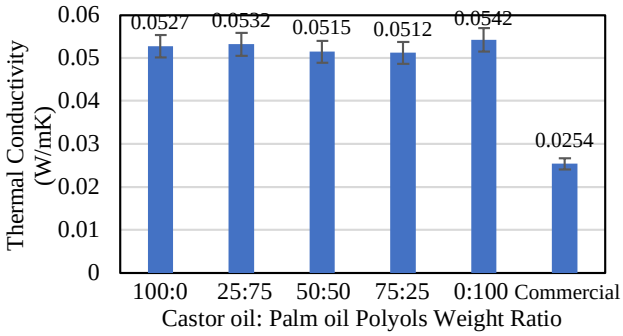

Figure 5 The thermal conductivity of the rigid polyurethane foam synthesized from different weight ratio of castor oil to palm oil polyols, as compared with commercial foam [10].

In addition, when compared with commercial foams that have a thermal conductivity of 0.0254 W/m·K [10], the polyurethane foams synthesized in this work, across various polyol ratios, exhibited higher thermal conductivity values. These values also exceeded the standard range specified by the Thai Industrial Standards Institute (TISI) (TIS No. 1859-2562), which is 0.024–0.029 W/m·K. This discrepancy is likely due to the higher foam density observed in this study, which increases the proportion of the solid matrix phase and consequently enhances heat transfer

through the solid structure. However, thermal conductivity in foam cells can also be influenced by several other factors, such as hydroxyl value, isocyanate index, foam porosity, cell wall thickness, and the carbon dioxide content within the pores.

Compressive strength is a fundamental mechanical property required for rigid polymeric materials to maintain structural integrity under load. In this study, compression tests were conducted using a universal testing machine at a constant speed of 3 mm/min, and the compressive force at 10% strain was recorded. The compressive strength of rigid polyurethane foams synthesized with varying polyol ratios is presented in Figure 6. It was observed that increasing the proportion of palm oil polyol led to higher compressive strength. This correlated with the increased foam density, which was attributed to enhanced polyurethane bond linkages, allowing the material to better withstand compressive stress and loading. Additionally, at higher palm oil content, the formation of closed and smaller foam cells helped distribute the applied force more evenly across the structure. However, for the foam produced with 100% palm oil polyol, a larger cell size was observed, which likely reduced the ability to effectively distribute the force, resulting in lower resistance to compression. These findings are consistent with the previous work [16], which reported higher compressive strength in foams with smaller cell sizes and greater crosslink density.

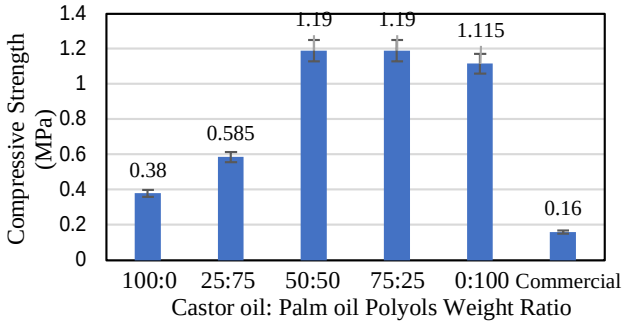

Figure 6 The compressive strength of the rigid polyurethane foam synthesized from different weight ratio of castor oil to palm oil polyols, as compared with commercial foam [10].

Moreover, when compared with commercial foam, the rigid polyurethane foams synthesized in this work exhibited compressive strength values ranging from 0.38 to 1.19 MPa, which were significantly higher than those of commercial polyurethane foams (0.16 MPa) [10], and exceeded the standard compressive strength requirement for solid foams used as thermal insulators according to the TISI standard (TIS No. 1859-2542), which ranges from 0.10 to 0.15 MPa. Compared with the previous work [17], which also utilized castor oil-derived polyol for rigid polyurethane foam synthesis, the compressive strength values were found to be comparable. On the other hand, the study of other works [5], which used pure palm oil as the polyol, reported a wider variation in compressive strength values. This discrepancy may be attributed to several factors, including hydroxyl value, isocyanate index, and synthesis conditions, all of which strongly influence foam density. As foam density increases, compressive strength generally improves. The hydroxyl value of the castor oil polyol in this study was similar to that reported in [17], resulting in comparable compressive strength. In contrast, the hydroxyl value reported by [5] was 273.23 mgKOH/g, which differs significantly from the values in this study and likely contributed to the differences observed in foam density and, consequently, compressive strength.

Due to their resistance to decomposition, rigid polyurethane foams synthesized from petrochemical precursors can pose environmental concerns. Therefore, this research aimed to reduce the use of petrochemical-based substances by incorporating renewable, natural materials. In this study, polyols derived from vegetable oils, castor oil and palm oil, were prepared through a transesterification process and used as substitutes in the foam synthesis. The resulting foams contained soft segments from vegetable oils, which are more susceptible to biodegradation. The biodegradability of the synthesized foams was evaluated via hydrolysis in a phosphate buffer solution, which promoted the cleavage of ester bonds and urethane linkages in the polymer chains [18]. Upon hydrolysis, the ester bonds within the polyurethane structure were broken, leading to the degradation of the foam into polyols and smaller polymer fragments [12]. The released polyols dissolved into the buffer solution, resulting in a measurable weight loss of the polyurethane foam.

In the biodegradability test via hydrolysis, the foam samples were cut into small pieces ($15 \times 15 \times 10$ mm^3), oven-dried at 60 °C for 12 hours, and then immersed in a 0.1 M phosphate buffer solution at pH 7.4 for 24 hours. After soaking, the specimens were rinsed with distilled water, oven-dried again at 60 °C for 12 hours, and weighed to determine the weight loss. This cycle of immersion, drying, and weighing was repeated until the end of the specified testing period. The cumulative weight loss of the rigid polyurethane foams after soaking for up to 144 hours is shown in Figure 7.

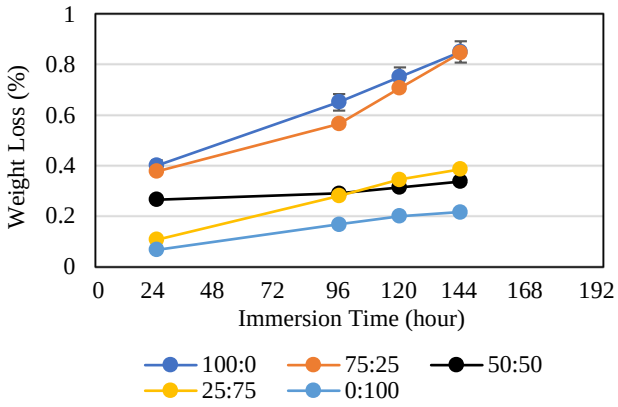

Figure 7 Weight Loss of the rigid polyurethane foam synthesized from different weight ratio of castor oil to palm oil polyols.

As shown in Figure 7, increasing the proportion of palm oil-based polyol from 0% to 100% resulted in a decrease in the percentage weight loss of the synthesized foams, indicating lower degradability. This trend can be attributed to the higher hydroxyl value of palm oil polyol compared to castor oil polyol, which allowed for more urethane linkages to form during the reaction with PMDI. The increased crosslinking led to a denser and more robust molecular structure, consistent with the observed increase in foam density at higher palm oil content. Upon immersion in the buffer solution, polyurethane bonds underwent hydrolysis; however, foams synthesized with higher palm oil content were more resistant to degradation due to their stronger crosslinked networks.

Moreover, the foam cell structures also influenced biodegradability. Foams with polyol weight ratios of 100:0 and 75:25 exhibited larger cell sizes and greater pore volumes, providing more surface area for contact with the buffer solution and facilitating hydrolysis. This contributed to their relatively higher weight loss compared to other formulations.

When compared to previous studies that synthesized rigid polyurethane foams from 100% castor oil polyol (hydroxyl value = 338 mg KOH/g) [10] and 100% palm oil polyol (hydroxyl value = 273.23 mg KOH/g) [5], which reported weight losses of 4.5% and 2.5% after six days of soaking, respectively, the foams in this study exhibited lower weight loss under the same conditions. This may be due to the higher hydroxyl values of both polyols used in this work, resulting in more extensive crosslinking and stronger molecular structures, thereby reducing the rate of degradation.

4. CONCLUSION

Rigid polyurethane foams were successfully synthesized from modified castor oil and palm oil polyols at different weight ratios. The surface morphologies, foam cell size, bulk density, compressive strength, and biodegradability (based on hydrolysis) of the synthesized foams were found to correlate with the increasing weight ratio of palm oil polyol, while no statistically significant difference in thermal conductivity was observed. Based on the characterization of the synthesized foams, both the bulk density and thermal conductivity were higher than the standard values specified by TISI. Therefore, it is important to consider exploring alternative precursors or additives to reduce the foam density while enhancing thermal insulation performance.

ACKNOWLEDGMENTS

Thank you to Siam Chemical Industries Co., Ltd., Thai Mitsui Specialty Chemicals Co. Ltd., South City Group and the laboratory staff of the Chemical Engineering Department at King Mongkut's University of Technology Thonburi for their support in chemicals, testing various properties and experimental set up.

REFERENCES

1. D. Randal, I. Steve. The polyurethane book. *UK: John Wiley & Sons*, 2002; 13.
2. K. Ashida. Polyurethane and Related Foams: Chemistry and Technology. *CRC Press: Taylor and Francis* 2006; 6.
3. J. Lazonby, D. Waddington. Polyurethanes. [Online URL: *http://www.essentialchemicalindustry.org/polymers/polyurethane.html*] accessed on January 15, 2023.
4. V.J. Dave, H.S. Patel. Synthesis and characterization of interpenetrating polymer networks from transesterified castor oil-based polyurethane and polystyrene. *Journal of Saudi Chemical Society* 2013; 21(1): 18-24.
5. P. Sricharoon, S. Piboonsilp. A Study on the Effect of tapioca addition on the physical properties and biodegradability of rigid polyurethane, *NPRU Journal of Science and Technology* 2010; 1: 6-13.
6. M. Z. Arniza, S. S. Hoong, Z. Idris, S. K. Yeong, H. A. Hassan, A. K. Din, Y.M. Choo. Synthesis of Transesterified Palm Olein-Based Polyol and Rigid Polyurethanes from this Polyol. *Journal of American Oil Chemical Society* 2015; 92: 243-255.
7. A. Guo, D. Demydov, W. Zhang, Z.S. Petrovic. Polyols and Polyurethanes from Hydroformylation of Soybean Oil. *Journal of Polymers and the Environment* 2002; 10: 49 – 52.
8. Y.H. Hu, Y. Gao, D.N. Wang, C.P. Hu, S. Zu, L. Vanoverloop, and D. Randall. Rigid Polyurethane Foam Prepared from a Rape Seed Oil Based Polyol. *Polymer Science* 2002; 84: 591-597.
9. V.B. Veronese, R.K. Menger, M.M. Forte, and C.L. Petzhold. Rigid Polyurethane Foam Based on Modified Vegetable Oil. *Polymer Science* 2010; 120: 530-537.

10. P. Sricharoon, N. Srisuphinanon, S. Kittisarnun, S. Santichavalit, and S. Yensatid. Biodegradation of Rigid Polyurethane Foam from Castor Oil with Polylactic Acid Addition. In *Proceedings of the 30th Thai Institute of Chemical Engineering and Applied Chemistry (TICHE 2021) "Sustainable Development for Better Lives"* 2021, Nakhon Ratchasima, Thailand.
11. M. Zhang, H. Pan, L. Zhang, L. Hu, Y. Zhou. Study of the mechanical, thermal properties and flame retardancy of rigid polyurethane foams prepared from modified castor-oil-based polyols. *Industrial Crops and Products* 2014; 59: 35-143.
12. U. Stirna, B. Lazdin, D. Vilsone, , M.J. Lopez, M.C. Vargas-Garcia, F. Sua´rez-Estrella, J. Moreno. Structure and properties of the polyurethane and polyurethane foam synthesized from castor oil polyols. *Journal of Cellular Plastics* 2012: 48: 476-488.
13. D. Simón, J.F. Rodríguez, M. Carmona, A. Serrano, A.M. Borreguero. Glycolysis of advanced polyurethanes composites containing thermoregulating microcapsules. *Chemical Engineering Journal* 2018; 350: 300-311.
14. M. A. Mosiewicki, , G. A. Dell'Arciprete, M. I. Aranguren, N. E. Marcovich. Polyurethane Foams Obtained from Castor Oil-based Polyol and Filled with Wood Flour. *Journal of Applied Polymer Science* 2009; 113(1): 1–10.
15. H. Demir, M. Sipahioglu, D. Balkose, S. Ulku. Effect of additives on flexible PVC foam formation. *Journal of materials processing technology* 2008; 195: 144-153.
16. D. Ji, Z. Feng, W. He, X. Jiang, T. Wang, K. Guo. Polyurethane rigid foams from different soy - based polyols by the ring opening of epoxidised soybean oil with methanol, phenol and cyclohexanol. *Industrial Crops and Products* 2015; 74: 76-82.
17. Omark, K., Jiranugrom, P., Boonmak, S and Narod, N. Effect of cellulose nanocrystal on the properties of rigid polyurethane foam synthesized from castor oil, palm oil and soybean oil. [Online URL:https://opac.lib.kmutt.ac.th/vufind/Search/Results?type=AllFields&lookfor=Effect+of+cellulose+nanocrystal&submit=Search] accessed on January 15, 2023.
18. P.S. Sathiskumar, G. Madras. Synthesis, characterization, degradation of biodegradable castor oil based polyesters. *Polymer Degradation and Stability* 2011; 96(9): 1695-1704.

Evaluating the effectiveness of antioxidants in palm oil-based bio-grease

Eumporn Buarod[1], Pornpasson Sanenopakul[1], Sitthichai Watthanalao[1], Parncheewa Udomsap[1,*], Suparoek Henpraserttae[1], Boonyawan Yoosuk[1]

[1] National Energy Technology Center, National Science and Technology Development Agency, Pathum Thani 12120, Thailand
[*] Corresponding author: parncheewa.udo@entec.or.th

ABSTRACT

Bio-grease is a renewable, non-toxic, and environmentally friendly lubricant. Unlike traditional petroleum-based greases, it is formulated using plant-based oils that degrade more easily, reducing harm to ecosystems and wildlife if leaked or disposed of. The characteristics of our in-house made palm oil-based bio-grease comply with the Thai Industrial Standard (TIS) number 713-2541, making it suitable for general use. It is a lithium grease, with palm oil as the main component. Palm oil, containing about 50% unsaturated fatty acids, is more prone to oxidation than mineral or synthetic oils with higher saturated hydrocarbon content. Oxidation degrades the grease, forming acids, sludge, and contaminants that reduce lubrication efficiency. To improve the oxidation resistance of bio-greases, antioxidants are added to delay the oxidation process and extend the service life of grease. The 2,2'-Methylenebis(6-tert-butyl-4-methylphenol) (MBMP) and N, N´-Diphenyl-1,4-phenylenediamine (DPPD) were studied for their effectiveness in bio-grease by measuring Onset Oxidation Temperature (OOT) using Differential Scanning Calorimetry. The OOT results for grease blends showed: DPPD (202°C) > MBMP (184°C) > No antioxidant (156°C), indicating better performance from the amine antioxidant. The addition of antioxidants slightly altered grease consistency, measured by the spread method using the SKF grease test kit. The spread diameter of the grease with DPPD was 20.3 mm, compared to 18.5 mm for the greases with MBMP and no antioxidants, indicating that DPPD softened the grease. While antioxidants improve oxidation resistance. Balancing their effects on other properties is crucial to ensure the grease performs optimally in its intended application.

Keywords: Bio-grease; Palm oil-based grease; lithium grease; Oxidation stability; Antioxidant

1. INTRODUCTION

Grease is a semi-solid lubricant composed of three main components: a base oil (75–90%), a soap-based thickener (5–20%), and additives (0–10%) that enhance specific properties [1]. Most greases currently use petroleum-based oil as the primary base component. However, in cases of leakage or improper disposal, these greases can pose significant environmental risks due to their non-biodegradable nature and potential to contaminate soil and water resources. To address these environmental concerns, natural esters, particularly vegetable oils, have received increasing attention as alternative base components in grease formulations [2].

Palm oil is an economically significant and abundant crop in Thailand. The conversion of palm oil into bio-grease promotes alternative utilization, adds value to palm oil, and helps address issues of price instability and surplus stock. The ester functional groups in the triglyceride structure of vegetable oils impart excellent lubricity by facilitating strong boundary film formation and reducing friction between contacting metal surfaces [3]. In contrast, the presence of double bonds in the fatty acid chains adversely affects the oxidative stability of these bio-based lubricants [4]. The allylic positions adjacent to the double bonds are highly susceptible to free radical attack, leading to the formation of peroxides and subsequent degradation products [5]. The oxidation process occurs in three stages: initiation, propagation, and termination. The initiation involves the formation of free radicals through the cleavage of unsaturated fatty acids triggered by external factors such as heat, light, or metal ions. In propagation, radicals react with oxygen to form hydroperoxides, which decompose into aldehydes and ketones. Termination happens when radicals combine into stable products, ending the chain reaction and often forming high-molecular-weight compounds [6]. This oxidation tendency limits the thermal and oxidative performance of vegetable oil-based greases, especially under high-temperature or extended-use conditions.

The addition of antioxidants has proven to be one of the most effective, simple, and cost-effective

solutions to delay the onset of oxidation. These compounds function by scavenging free radicals and interrupting the oxidative chain reactions that lead to the degradation of oil quality [7, 8]. Despite their established utility, the performance of different antioxidant types can vary significantly depending on the base oil and formulation matrix. Therefore, this research focuses on producing general-use bio-grease from palm oil that meets the requirements of Thai Industrial Standard 713-2541. Additionally, the study investigates the performance of 2,2'-Methylenebis(6-tert-butyl-4-methylphenol) as a hindered phenolic antioxidant and N, N′-diphenyl-1,4-phenylenediamine as an aromatic amine antioxidant in palm oil–based bio-grease, along with the effects of antioxidant addition on other key grease properties. The goal is to develop a bio-grease with oxidative stability comparable to that of commercial greases.

2. EXPERIMENTAL

2.1 Material

Refined palm olein oil (ROL), purchased as commercial cooking oil from local supermarkets, was used as the base oil for bio-grease formulation. The thickener, lithium soap, was synthesized through the reaction between 12-hydroxystearic acid (melting point: 77.5 °C; acid value: 155 mg KOH/g; saponification value: 188 mg KOH/g) and lithium hydroxide monohydrate ($LiOH \cdot H_2O$, purity: 98.0%). Two antioxidants supplied by Tokyo Chemical Industry were employed in this study: 2,2'-Methylenebis(6-tert-butyl-4-methylphenol) (MBMP, purity >99.0%) and N,N′-Diphenyl-1,4-phenylenediamine (DPPD, purity >95.0%).

2.2 Bio-grease preparation

Grease is typically produced through four main stages of processing: saponification, soap dissolution, recrystallization, and homogenization. The palm oil-based bio-grease was formulated using 15% lithium soap thickener and 85% base oil by weight of the total product. A mixture of 12-hydroxystearic acid (in a 1:1.10 molar ratio with lithium hydroxide) and approximately 50% of the total ROL base oil was uniformly mixed using a mechanical stirrer at 90-95°C. The lithium hydroxide solution was gradually added to the mixture until soap formation was observed. The temperature was then gradually increased to 165 °C and maintained for 3 hours under continuous stirring. Heating continued until the soap melted completely at a temperature between 200-220°C. The mixture was then recrystallized by immediately cooling to 100-110°C, followed by the addition of the remaining portion of ROL base oil. Finally, the mixture was allowed to cool to room temperature. To stabilize the structure of the grease, the mixture was homogenized using a three-roll mill until a uniform consistency was achieved.

The incorporation of antioxidants into the grease was carried out during the recrystallization step. The antioxidants were first dissolved in the remaining portion of the base oil and then mixed with the grease using mechanical stirring. The resulting mixture was subsequently homogenized using a three-roll mill to ensure uniform dispersion and consistency. The procedure for incorporating the antioxidant into the grease is illustrated in Figure 1.

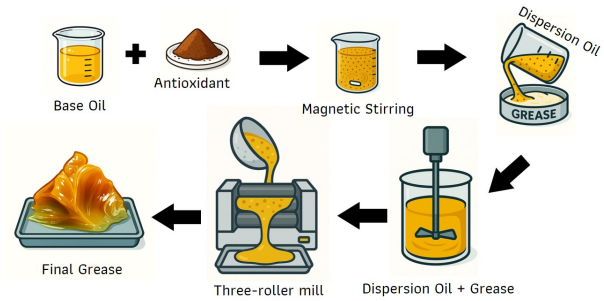

Figure 1 The procedure for incorporating the antioxidant into the grease.

2.3 Characterizations

The produced bio-grease was characterized as a general-purpose grease according to TIS 713-2541 standards, as presented in Table 1.

Table 1 Characteristics for general-purpose grease following TIS 713-2541.

Properties	ASTM	Specification
1. Penetration worked 60 strokes, dmm	D217	265-295 (NLGI 2) 220-250 (NLGI 3)
2. Dropping point, °C	D2265	180 Min.
3. Copper corrosion, class	D4048	2b Max.
4. Evaporation loss at 105°C, 8 hrs, wt.%	D6375	1.0 Max.
5. Water Washout at 38°C, 1 hr, wt.%	D1264	20 Max.
6. Worked stability, dmm	D217	375 Max.

The oxidation stability of the grease is evaluated by measuring the Oxidation Onset Temperature (OOT) using Differential Scanning Calorimetry (DSC). This temperature indicates the onset of oxidation when the grease is heated. The test, following ASTM E2009, is conducted at an oxygen flow rate of 50 mL/min under atmospheric pressure, with a heating rate of 10°C/min from room temperature to the temperature at which exothermic heat is released due to the chemical reaction. The change in consistency of the bio-grease before and after adding antioxidants is measured using the spread method with an SKF test kit. A specified amount of grease is placed between two glass plates and compressed for 15 seconds under a standard weight. The resulting spread is then compared to a calibrated measuring scale to evaluate consistency, and its diameter is measured. Furthermore, the acidity of grease is determined using a titration method based on ASTM D128-98.

3. RESULTS AND DISCUSSION

3.1 Properties of palm oil-based bio-grease

The palm oil-based grease product exhibited a smooth, paste-like texture, as illustrated in Figure 2, and its properties are represented in Table 2.

Figure 2 Texture of palm oil-based bio-grease.

Table 2 Properties of palm oil-based bio-grease following TIS 713-2541 compared with petroleum-based grease.

Properties	Bio-grease	Petroleum-based grease
1. Penetration worked 60 strokes, dmm	247	244
2. Dropping point, °C	197	201
3. Copper corrosion, class	1a	1a
4. Evaporation loss at 105°C, 8 hrs, wt.%	0.2	0.0
5. Water Washout at 38°C, 1 hr, wt.%	0.3	0.0
6. Worked stability, dmm	305	265

The palm oil-based bio-grease showed a worked penetration of 247 dmm, corresponding to NLGI grade 3 consistency based on the National Lubricating Grease Institute (NLGI) classification. Reducing the thickener concentration allows adjustment of the grease to a softer consistency, corresponding to a lower NLGI grade, such as grade 2. Its dropping point exceeded 185 °C, indicating good thermal stability and representing the temperature at which the grease loses its semi-solid structure. While this reflects the upper limit of heat resistance, it does not define the maximum operating temperature. A copper strip corrosion rating of 1a, indicating that the copper strip remained bright and shiny with no signs of corrosion. Evaporation loss and water washout of grease depend on the type of base oil and the strength of the grease structure. The palm oil-based bio-grease met the standard requirements for both properties. Worked stability refers to the penetration value after the grease is worked for 10,000 strokes. However, after testing at 100,000 strokes, the penetration increased but remained below the 375 dmm limit specified by the standard. The palm oil-based bio-grease met the requirements of TIS 713-2541, making it suitable for use as a general-purpose grease. Its properties are comparable to those of petroleum-based grease without additives. Moreover, the bio-grease is biodegradable, achieving over 90% degradation within 28 days when analyzed according to OECD 301B standards.

3.2 Performance of antioxidant

The effectiveness of antioxidants in the bio-grease was tested by adding antioxidants at a concentration of 0.5 wt.% and analyzing the oxidation onset temperature (OOT) using DSC. The DSC results of the bio-grease, both without and with antioxidants at a concentration of 0.5 wt.%, are shown in Figure 3.

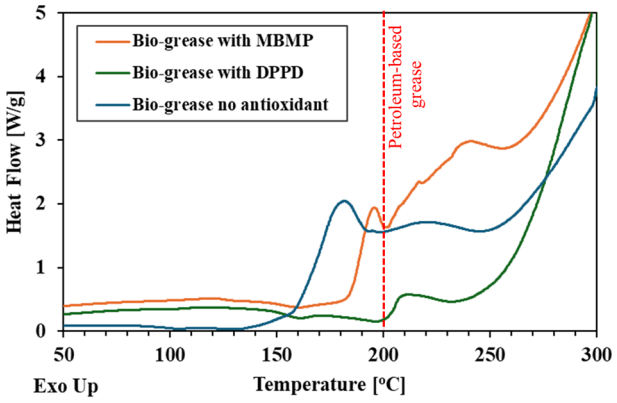

Figure 3 DSC profiles of bio-grease without and with an antioxidant at a concentration of 0.5 wt.%.

A sharp rise in the DSC graph indicates an exothermic reaction resulting from the oxidation of the material, which corresponds to the oxidation onset temperature. The bio-grease without antioxidants exhibited an OOT of 156 °C, which is notably lower than that of petroleum-based grease (200 °C). This difference is attributed to the higher oxidative susceptibility of palm oil, which ROL base oil contains approximately 56% of total unsaturated fatty acids, including 10-12% of polyunsaturated fatty acids. In contrast, mineral oil is composed primarily of saturated hydrocarbons, offering greater oxidative stability. The antioxidants enhanced the oxidative stability of the bio-grease, with effectiveness ranked as follows: DPPD (256 °C) > MBMP (184 °C) > no antioxidant (156 °C). The effectiveness of an antioxidant is often correlated with its chemical structure, as illustrated in Figure 4.

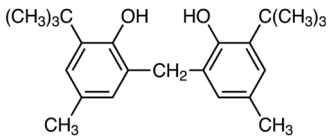

Hindered phenolic antioxidant; MBMP

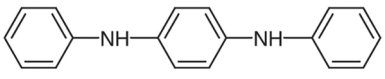

Aromatic amine antioxidant; DPPD

Figure 4 Chemical structure of the MBMP and DPPD antioxidants.

The mechanisms of both antioxidants were investigated, revealing that the hindered phenolic antioxidant (MBMP) functions as a primary antioxidant

by donating hydrogen from its phenolic –OH group to neutralize free radicals during the initiation stage of oxidation. The presence of a methyl group (–CH_3) at the para-position slightly donates electrons through hyperconjugation, enhancing the reactivity of the antioxidant. The resulting phenoxyl radical is stabilized via resonance across the benzene ring, preventing further radical propagation. While DPPD acts as a secondary antioxidant by donating hydrogen from its –NH– groups to stabilize existing free radicals in the grease. It is highly reactive toward peroxyl (ROO•) and alkyl (R•) radicals during the propagation phase, effectively terminating radical chains. The resulting radical is stabilized through electron delocalization across the aromatic rings, preventing further radical coupling [9]. Both antioxidants exhibit similar thermal stability, solubility in bio-grease, and cost; however, DPPD often causes color darkening.

Based on the OOT test results, DPPD demonstrated superior performance to MBMP in enhancing oxidative stability. This suggests that the grease production process, which is conducted at high temperatures and under oxygen exposure, induces significant oxidation during the initiation stage, resulting in a high concentration of free radicals within the grease matrix. When evaluated by DSC under an oxygen atmosphere, the propagation phase of oxidation is promoted. DPPD is more reactive toward peroxyl radicals (ROO•) than hindered phenolic antioxidants; therefore, it exhibits better effectiveness in delaying the oxidation process. On the other hand, MBMP may have already reacted with a portion of the existing free radicals in the grease, leaving fewer active antioxidants to respond during the DSC test, which results in comparatively lower performance under the same conditions.

The addition of DPPD significantly softens the grease, enhancing its spreadability compared to both the base grease and those with MBMP antioxidant, as presented in Figure 5.

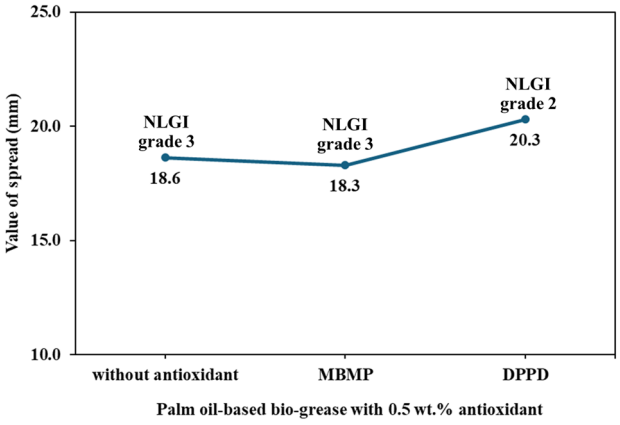

Figure 5 Spread diameter (mm) of palm oil-based bio-grease without and with 0.5 wt.% antioxidant addition.

DPPD has a small, planar molecular structure with low steric hindrance, allowing it to integrate easily into the lithium soap and disrupt the thickener network more effectively, resulting in softer grease. In contrast, MBMP contains bulky tert-butyl groups that hinder its ability to penetrate the thickener structure, thereby preserving the grease's structure and causing minimal change in spreadability.

Both antioxidants did not significantly affect the acid value of the grease, as shown in Figure 6. Hindered phenolic antioxidants contain phenol groups with very weak acidity and typically do not significantly increase the acid value of grease. The acid value of bio-grease with MBMP was 1.25 ± 0.04 mg KOH/g, comparable to the base grease (1.31 ± 0.16 mg KOH/g). Alternatively, DPPD, with weak basicity, may potentially reduce the existing acid content. However, the acid value after adding DPPD was 1.37 ± 0.05 mg KOH/g, comparable to that of the base bio-grease. The slight increase may result from interfacial reactions between the antioxidant and other grease components. In addition, all antioxidant-added bio-greases exhibited a copper strip corrosion rating of 1a, indicating that acid values in the range of 1.2-1.5 mg KOH/g do not induce corrosive effects.

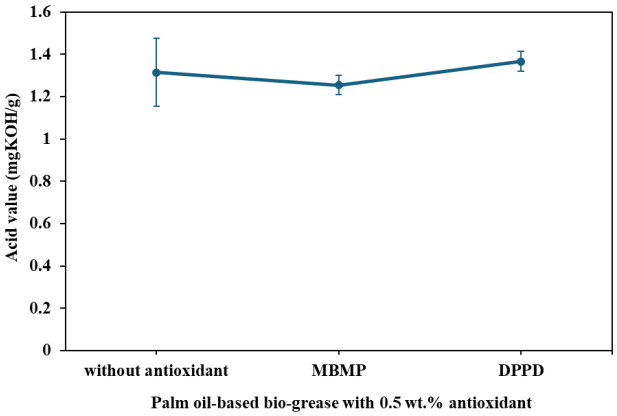

Figure 6 Acid value of palm oil-based bio-grease without and with 0.5 wt.% antioxidant addition.

MBMP and DPPD were added to the bio-grease at concentrations of 0.1, 0.5, and 1 wt.%, and the OOT values are presented in Figure 7. The addition of antioxidants at increasing concentrations (0.1, 0.5, and 1 wt.%), both MBMP and DPPD significantly enhance the oxidative stability of the grease, as indicated by the rise in OOT values. DPPD consistently outperforms MBMP across all concentrations. At 1 wt.%, DPPD raises the OOT to 268 °C, which is substantially higher than the petroleum-based grease benchmark (~200 °C), indicating superior thermal-oxidative resistance. In comparison, MBMP reaches only 194 °C, remaining below the reference threshold. However, high antioxidant concentrations may adversely affect the grease's consistency and acid value, as well as increase production costs.

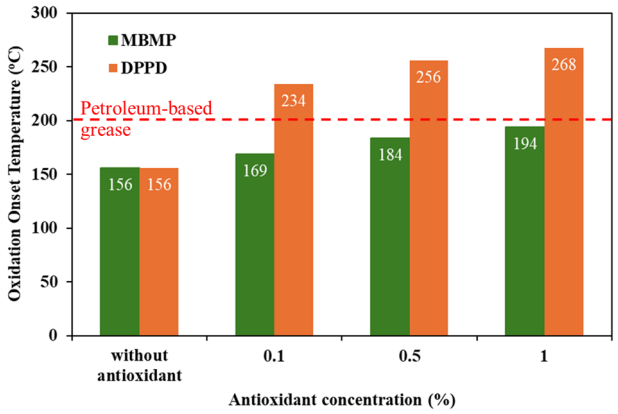

Figure 7 Oxidation onset temperature of palm oil-based bio-grease without and with MBMP and DPPD antioxidants at concentrations of 0.1, 0.5, and 1 wt.%.

DPPD increased the OOT to 234 °C, 257 °C, and 268 °C at concentrations of 0.1, 0.5, and 1 wt.%, corresponding to improvements of 50.0%, 64.7%, and 71.8%, respectively. While the efficiency per unit concentration tended to decline with increasing dosage, it followed a decreasing trend of 780 > 202 > 112 °C/% for 0.1, 0.5, and 1 wt.%, respectively, suggesting a saturation effect in antioxidant performance. Therefore, the optimal concentration range for antioxidant applications is recommended to be 0.1-0.5 wt.%.

In terms of physical stability, the changes in consistency and acid value remained within acceptable limits across all DPPD concentrations, with lower variation observed at 0.1 wt.% compared to 0.5 wt.%. This further supports the suitability of low to moderate concentrations of DPPD for improving both oxidative and physicochemical stability of the palm oil-based bio-grease formulation.

4. CONCLUSION

A general-purpose bio-grease was successfully developed using palm olein oil and lithium 12-hydroxystearate soap, meeting the requirements of TIS 713-2541 and demonstrating readily biodegradable properties.

The incorporation of antioxidants significantly improved the oxidative stability of the biobased grease. Among the tested antioxidants, DPPD, an aromatic amine, provided the greatest enhancement in oxidation onset temperature. The optimal concentration range for antioxidant application was identified as 0.1-0.5 wt.%, balancing oxidative performance and physical property stability. The potential synergistic interaction between hindered phenolic and aromatic amine antioxidants also warrants further investigation to optimize antioxidant systems in biobased grease formulations.

ACKNOWLEDGMENTS

The authors would like to acknowledge the Thailand Science Research and Innovation (TSRI) for funding this research through the Fundamental Fund (FF68) under the fiscal year 2025. The authors gratefully acknowledge the National Energy Technology Center for providing research facilities and technical support.

REFERENCES

1. L. R. Rudnick. Synthetic greases, Synthetics, Mineral Oils, and Bio- based lubricants. *Chemistry and Technology 2nd Edition, CRC Press Taylor & Francis Group, England* 2013.
2. A.Z. Syahir, N.W.M. Zulkifli, H.H. Masjuki, M.A. Kalam, A. Alabdulkarem, M. Gulzar, L.S. Khuong, M.H. Harith. A review on bio-based lubricants and their applications. *Journal of Cleaner Production* 2017; 168: 997-1016.
3. C. T. Lee, M. B. Lee, W. W. F. Chong, J. H. Ng, K. J. Wong, & C. T. Chong. Boundary lubricity of vegetable-oil-derived trimethylolpropane (TMP) ester. *Lubricants* 2022; 10(12): 346.
4. C. Murru, R. Badía-Laíño, & M. E. Díaz-García. Oxidative stability of vegetal oil-based lubricants. *ACS Sustainable Chemistry & Engineering* 2021; *9*(4): 1459-1476.
5. G. Verghese, K. Saeed. Advances in the measurements of the biodiesel oxidative stability. *Biofuels* 2025; *16*(3): 307-332.
6. W. Krasodomski, A. Skibińska, M. Żółty. Thermal Oxidation Stability of Lubricating Greases, Advances in Science and Technology Research Journal, Vol. 14(3), 2020, pp. 75–82.
7. D. Xia, Y. Wang, H. Liu, J. Yan, H. Lin, S. Han. Research progress of antioxidant additives for lubricating oils. *Lubricants* 2024; 12(4): 115.
8. M. A. Jedrzejczyk, S. Van den Bosch, J. Van Aelst, K. Van Aelst, P. D. Kouris, M. Moalin, K. V. Bernaerts. Lignin-based additives for improved thermo-oxidative stability of biolubricants. *ACS Sustainable Chemistry & Engineering* 2021; *9*(37): 12548-12559.
9. M. Soleimani, L. Dehabadi, L.D. Wilson, L.G. Tabil. Antioxidants classification and applications in lubricants, Chapter 2 in Lubrication - Tribology, Lubricants and Additives, InTechOpen, 2018.

Bio-based coating from chitosan and ethyl cellulose for oil- and water-resistant paper packaging

Oraya Sraphaengnoi[1], Lunjakorn Amornkitbamrung[2], Sanong Ekgasit[3], Sarawut Rimdusit[1,*]

[1] Center of Excellence in Polymeric Materials for Medical Practice Devices, Department of Chemical Engineering, Faculty of Engineering, Chulalongkorn University, Bangkok 10330, Thailand
[2] Department of Chemical Engineering, Faculty of Engineering, Srinakharinwirot University, Nakhon Nayok 26120, Thailand
[3] Department of Chemistry, Faculty of Science, Chulalongkorn University, Bangkok 10330, Thailand
[*] Corresponding author: sarawut.r@chula.ac.th

ABSTRACT

Plastic pollution is a growing global issue, with disposable food packaging as a major contributor. Limited recyclability and poor waste management allow plastics to accumulate in ecosystems. While paper packaging offers better recyclability and biodegradability, its poor oil-water resistance often requires a plastic coating. This coating hinders recyclability, slows decomposition, and exacerbates environmental challenges. Therefore, using a biopolymer coating on paper packaging is a promising solution for improving oil and water resistance while supporting environmental sustainability. In this work, we developed a new biobased, bi-layer coating for paper packaging. The first layer, hydrophilic chitosan, provided oil resistance, while the second layer, hydrophobic ethyl cellulose, enhanced water resistance. This combination created a synergistic effect on the paper's barrier properties. Infrared spectroscopy confirmed the coating's presence, and its composition was optimized to achieve strong oil-water resistance (Kit value of 12, Cobb 60 < 5 g/m²) with minimal material use. Scanning electron microscopy revealed that the coating fully sealed the paper's porous structure. Overall, this system offers a promising eco-friendly solution for oil- and water-resistant paper packaging.

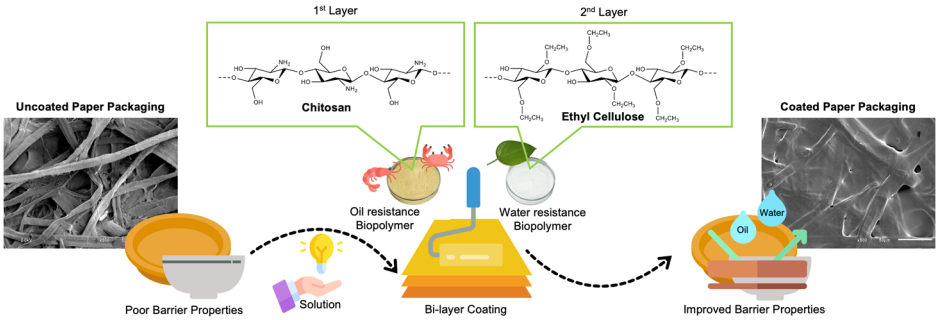

Figure 1 Illustration of the process for the oil- and water-resistant chitosan/ethyl cellulose bi-layer coating.

Keywords: Paper; Packaging; Coating; Oil-resistance; Water-resistance

1. INTRODUCTION

Plastic pollution represents an intensifying global environmental crisis, with an estimated 19–23 million tons of plastic waste entering aquatic ecosystems each year. This extensive contamination poses substantial threats to biodiversity, ecological function, and the security of global food systems [1]. In response, there is growing interest among consumers and industries in transitioning toward sustainable alternatives, particularly biodegradable and recyclable materials such as paper-based packaging. However, the inherent hydrophilicity and porous microstructure of cellulose-based paper result in inadequate water and oil resistance, thereby restricting its broader applicability in packaging applications [2].

Conventional polymer coatings including polyethylene (PE), polypropylene (PP), polyamide (PA), polyvinyl chloride (PVC), polyethylene terephthalate (PET), and ethylene vinyl acetate (EVA) can provide effective moisture and oil barriers. Nevertheless, their use compromises the biodegradability and recyclability of the paper substrate [3]. Moreover, while poly(fluoroalkyl) substances

(PFAS) offer enhanced barrier properties, their persistence and toxicity have led to increasing regulatory restrictions, particularly within the food packaging sector [4]. These challenges underscore the urgent need for the development of environmentally benign, non-toxic, and biodegradable coating systems that deliver both mechanical robustness and effective barrier performance.

In 2020, Kanzal et al. developed paper-based food packaging using chitosan and zein. The study showed that a single-layer coating of either chitosan or zein was ineffective in blocking both water and oil permeation. Chitosan blocked oil but allowed water to pass, while zein prevented water permeability but allowed oil to penetrate. However, a bilayer coating combining both chitosan and zein successfully prevented both water and oil penetration. This bilayer achieved a Kit No value of 12, indicating the highest level of oil barrier effectiveness, and a Cobb value of 4.88 g/m² [5]. This study proposes a bi-layer coating system for paper packaging that utilizes sustainable, bio-based materials. Chitosan, a natural polysaccharide derived from the deacetylation of chitin, exhibits significant potential as an oil barrier material when applied as a coating on porous substrates such as paper. The oil resistance of chitosan is primarily attributed to its excellent film-forming ability, its capacity for hydrogen bonding [6].

Among bio-based polymers, ethyl cellulose (EC) is a particularly notable and commercially available derivative of cellulose, in which ethyl ether groups replace a portion of the hydroxyl groups along the cellulose backbone. This chemical modification imparts EC with enhanced hydrophobicity and improved solubility in organic solvents, distinguishing it from its unmodified parent compound. In the food industry, EC plays a multifaceted role due to its excellent film-forming ability, thermal stability, and inertness. It is widely employed as a moisture barrier to extend shelf life, an oleogelator for structuring edible oils, and an emulsifier for stabilizing food emulsions [7].

This research contributes to the advancement of sustainable packaging technologies by integrating biodegradable barrier materials and supporting circular economy strategies. a bi-layer coating was applied to the surface of paper packaging. Chitosan is the first layer to create an oil-resistant coating, while ethyl cellulose modified from cellulose derivative with hydrophobic functionality is to develop water resistance at the second layer coating. The proposed approach offers a promising solution to mitigate the environmental impact of plastic waste, aligning with broader goals of environmental preservation and resource efficiency.

2. EXPERIMENTAL

2.1 Raw materials

Chitosan (50,000 Dalton, 90% DAC) was sourced from Chanjao Longevity Co., Ltd., Bangkok, Thailand. Ethyl cellulose powder (viscosity 100 cP) was obtained from Sigma Aldrich and distributed by Merck (Thailand). Ethanol (99.9%) was procured from V.S. Chem House Co., Ltd., Bangkok, Thailand. Acetic acid (100%) was purchased from Merck, Germany, and Merck (Thailand).

2.2 Preparation of chitosan and ethyl cellulose solution for paper coating

To prepare the chitosan stock solution, 6 grams of chitosan were added to a beaker containing 100 mL of 2% (v/v) acetic acid solution. The mixture was then stirred thoroughly using a magnetic stirrer at room temperature for approximately 2 hours to ensure complete dissolution of the chitosan. This process resulted in a 6% (w/v) chitosan stock solution with a final volume adjusted to 100 mL.

For the ethyl cellulose stock solution, 6 grams of ethyl cellulose were dissolved in 100 mL of ethanol. The mixture was stirred continuously at a controlled temperature of 50 °C for 2 hours to facilitate full dissolution of the polymer. This process resulted in a 6% (w/v) ethyl cellulose stock solution.

2.3 Preparation of coated paper

filter paper (Whatman 93, CAT NO.1093-125) was coated layer by using a Lab Customized Film Coating Machine with a velocity of 70 mm s^{-1}. The coating weight was controlled by adjusting the gap size between bar coater and coating bed. The first layer of chitosan was applied as a solution and dried for 2 h at room temperature before applying the ethyl cellulose solution. And then applying the ethyl cellulose solution, the bilayer-coated paper was dried at room temperature for 10 min to obtain coated papers.

2.4 Oil-resistance test

The oil resistance of coated papers was evaluated following the TAPPI T 559 pm-96 standard procedures. Solutions with varying ratios of castor oil, heptane, and toluene, ranging from number 1 to 12, were applied to the samples for 15 seconds. The results were recorded as a kit rating number, with lower numbers indicating weaker oil resistance and higher numbers indicating stronger oil resistance of the paper substrate.

2.5 Water-resistance test

The water absorptivity of paper samples was assessed using the Cobb tester, following TAPPI T441 standards. The paper samples, cut into 12.5 cm² circles, were placed in 100 ml of water inside the Cobb cylinder. The samples were clamped between the top ridge and bottom cylinder, then rotated 180° to allow the samples to absorb water for 60 seconds. Excess water was quickly removed from the paper surface using a metal roller, and the sample's weight was measured. The Cobb value was calculated by determining the weight difference of the paper before and after the test, as shown in the equation below.

$$\text{Cobb value } (g/m^2) = (m_2 - m_1) \times 100 \quad (1)$$

Where m_1 is mass before test and m_2 is mass after test.

2.6 Material Characterization

2.6.1 Fourier transform infrared spectroscopy

The chemical structure of paper samples was studied by a Nicolet iS5 FT-IR Spectrometer with iD7 ATR accessory (Thermo Fisher Scientific Inc., Waltham, MA, USA). All spectra were taken as a function of time with 64 scans at a resolution of 4 cm^{-1} and wavenumber ranging from 4000-400 cm^{-1}.

2.6.2 Scanning electron microscopy (SEM)

Morphology of paper samples was investigated by scanning electron microscope (SEM, model JSM-6510A from JEOL Ltd. (Tokyo Japan)). All specimens were coated with a thin layer of gold using a JEOL ion sputtering device (model JFC- 1200).

3. RESULTS AND DISCUSSION

3.1 Effect of Chitosan Coating Weight on the Oil Resistance of Paper

Paper substrates were coated with chitosan at varying amounts (5–25 g/m²), followed by a constant 7 g/m² layer of ethyl cellulose. Oil resistance was evaluated using the Kit Test (TAPPI T559, scale 0–12). According to the results, the Kit number increased as the chitosan content increased. The highest Kit number (No. 12) was observed at 15 g/m² of chitosan, and it remained constant at higher concentrations (20 and 25 g/m² of chitosan), as shown in Table 1. The increase in Kit number can be attributed to the enhanced ability of chitosan to form a more uniform and continuous film as the coating weight increases. The chitosan layer effectively seals the pores on the paper surface, as shown in Figure 2(a-d). This physical barrier restricts the diffusion pathways available for oil molecules to penetrate through the substrate[6]. Moreover, chitosan contains functional amino (–NH_2) and hydroxyl (–OH) groups that enable extensive hydrogen bonding both within the chitosan matrix and with the substrate surface. This hydrogen-bonded network increases the film density, reducing free volume.

Table 1 Oil Resistance of Paper Coated with Chitosan and Ethyl Cellulose.

1st layer chitosan (g/m²)	2nd layer ethyl cellulose (g/m²)	Kit No.
5	7	0
10	7	4
15	7	12
20	7	12
25	7	12

The hydrogen-bonding of the material promotes hydrophilic interactions, which in turn restricts the diffusion and mobility of non-polar substances such as oils [8]. These features hinder the absorption and transmission of oils through the coated layer, especially when chitosan is applied in combination with a hydrophobic overlayer such as ethyl cellulose. The ethyl cellulose layer enhances the sealing performance, as shown in Figure 2(e-g). The ethyl cellulose film that tightly adheres to the chitosan and paper substrate, further minimizing pathways for oil permeation. Thus, the oil resistance of chitosan-coated paper is attributed to a combination of physical sealing and molecular interactions. A synergistic effect between chitosan and ethyl cellulose further enhances the oil barrier, providing robust protection.

3.2 Effect of Ethyl Cellulose Coating Weight on the Water Resistance of Paper

Paper substrates were coated with a fixed chitosan layer at 15 g/m² in the previous section as the most effective for oil resistance, followed by ethyl cellulose coatings at varying weights (2, 4, 5, 6, and 7 g/m²),as show Table2.

Table 2 Water Resistance of Paper Coated with Chitosan and Ethyl Cellulose.

1st layer chitosan (g/m²)	2nd layer ethyl cellulose (g/m²)	Cobb values (g/m²)	Kit No.
15	2	35.1 ± 2.65	6
15	4	23.1 ± 2.52	7
15	5	4.94 ± 0.04	12
15	6	4.88 ± 0.03	12
15	7	4.38 ± 0.07	12

We explored the impact of ethyl cellulose coating weight on the water resistance of paper, aiming to identify the minimum effective dosage for optimal barrier performance. Water resistance was evaluated using the Cobb60 test, which measures water absorption at 60 seconds. A Cobb value of less than 10 g/m² indicates acceptable water resistance. The results showed a significant decrease in Cobb value as the ethyl cellulose coating weight increased from 2 to 5 g/m², indicating enhanced water resistance.

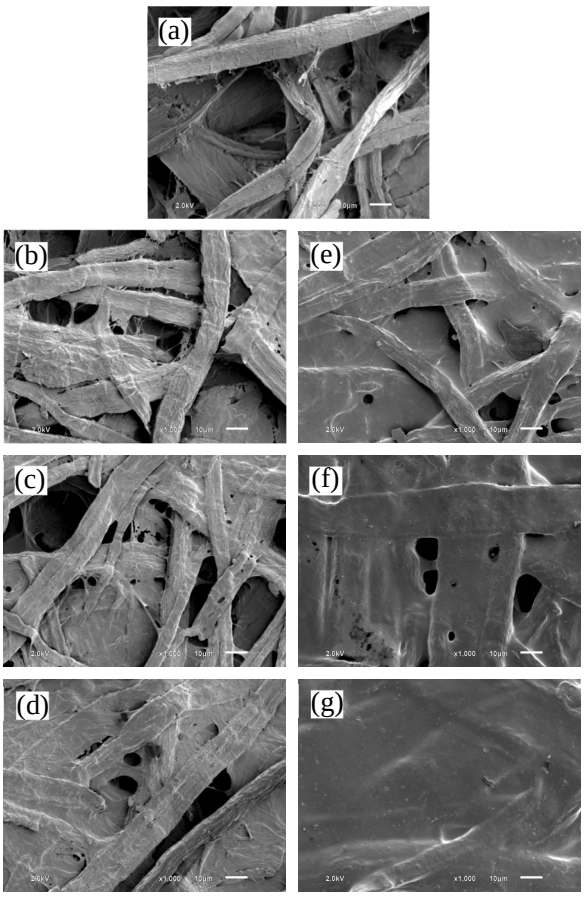

Figure 2 SEM images of (a) uncoated paper, (b-d) single-layer: 5, 10, and 15 g/m² of Chitosan coated paper, and (e-g) bi-layer: 5, 10, and 15 g/m² of Chitosan/ 7 g/m² of Ethyl Cellulose coated paper.

This improvement is attributed to the hydrophobic nature of ethyl cellulose, which forms a continuous, dense film that effectively seals the paper surface and restricts water penetration. At the molecular level, ethyl cellulose molecules consist of hydrophobic hydrocarbon chains, promoting film formation and creating a barrier that prevents water from diffusing into the paper substrate [5]. An increase in coating weight beyond 5 g/m² (e.g., at 6 and 7 g/m²) resulted in only marginal reductions in the Cobb value, indicating a saturation threshold for water resistance enhancement. The molecular packing and film density reached a level sufficient to achieve complete sealing of the paper surface.

3.3 Fourier transform infrared (FT-IR) spectroscopy

The coated paper substrates were characterized at various stages of the fabrication process using ATR-FTIR spectroscopy, As shown in Figure 3. The uncoated paper showed peak at 1029 $cm^{-1}$and 2898 cm^{-1} corresponding to C–O and C-H stretching vibration of cellulose in paper [9]. The absorption peak at 3345 cm^{-1} corresponded to the –OH stretching vibration.

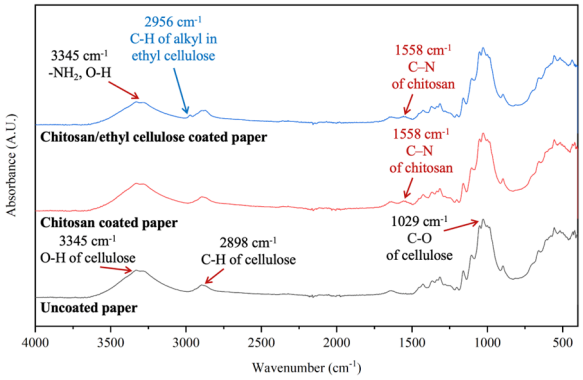

Figure 3. FTIR spectra of uncoated and coated paper substrates.

For coated paper, the spectra showed main characteristic of cellulose in paper. The FTIR-ATR spectra were used to verify the existence and relationship of uncoated paper, chitosan-coated paper and chiosan/ethyl cellulose-coated paper through different characteristic peaks. The absorption peak at 1558 cm^{-1} corresponds to the C–N stretching vibration which can confirm the existence of chitosan, as shown in Figure 3 [10-11]. The absorption peak at 2956 cm^{-1} corresponds to the C–H stretching vibration of CH_2CH_3 in ethyl cellulose(EC) which can confirm the existence of EC, as shown in Figure 3 [12].

4. CONCLUSION

The use of chitosan and ethyl cellulose coatings to enhance the barrier properties of paper substrates was optimized. Chitosan coating at 15 g/m² was identified as the optimal level for oil resistance, achieving the maximum Kit value of 12. At this coating weight, chitosan forms a dense, uniform film that effectively seals surface pores and limits oil penetration through both physical blocking and molecular interactions such as hydrogen bonding. For water resistance, ethyl cellulose demonstrated excellent performance due to its hydrophobic nature and ability to form a compact, continuous film. A coating weight of 5 g/m² was found to be the minimum effective dosage for significantly reducing water absorption, as indicated by Cobb values 4.89 g/m². The combination of 15 g/m² chitosan and 5 g/m² ethyl cellulose was found to be optimal. The synergistic use of these materials offers strong potential for developing biodegradable, sustainable, and oil- and water-resistant paper-based materials.

ACKNOWLEDGMENTS

This research was supported by the National Research Council of Thailand (NRCT) and Chulalongkorn University under Grant No. N42A660910. Additional support was provided by the Thailand Science Research and Innovation Fund through Chulalongkorn University (Grant No. BCG_FF_68_206_2100_030). The authors gratefully acknowledge the financial support that made this study possible.

REFERENCES

[1] UNEP. Plastic Pollution. *United Nations Environment Programme*; 2024 [cited 2024 Oct 9]. Available from: https://www.unep.org/plastic-pollution.

[2] Tan, J., et al., Recyclable, UV-shielding, and biodegradable chitosan-based cardanol glycidyl ether as excellent water and oil resistance as well as gas barrier coating for paper. International Journal of Biological Macromolecules, 2023. 227: p. 1305-1316.

[3] Trinh, B.-M., B.P. Chang, and T. Mekonnen, The Barrier Properties of Sustainable Multiphase and Multicomponent Packaging Materials: A review. Progress in Materials Science, 2023. 133: p. 101071.

[4] Zhang, X., et al., Fabrication of durable fluorine-free superhydrophobic polyethersulfone (PES) composite coating enhanced by assembled MMT-SiO2 nanoparticles. Applied Surface Science, 2017. 396: p. 1580-1588.

[5] Kansal, D., et al., Food-Safe Chitosan–Zein Dual-Layer Coating for Water- and Oil-Repellent Paper Substrates. ACS Sustainable Chemistry & Engineering, 2020. 8(17): p. 6887-6897.

[6] J.W. Rhim, A. Gennadios, C.L. Weller, M.A. Hanna. Chitosan-based biodegradable films and coatings: Physicochemical properties and applications. Food Science and Biotechnology 2006; 15(2): 185-192.

[7] W.H. Lee, H.R. Park, W.J. Cho. Characterization and application of ethyl cellulose-based coatings for barrier properties in food packaging. Food Hydrocolloids 2016; 56: 290–298.

[8] K. Khwaldia, E. Arab-Tehrany, S. Desobry. Biopolymer coatings on paper packaging materials. Comprehensive Reviews in Food Science and Food Safety 2010; 9(1): 82-91.

[9] Y. Kim, D. Jeong, K.H. Park, J. Yu, S. Jung. Efficient adsorption on benzoyl and stearoyl cellulose to remove phenanthrene and pyrene from aqueous solution. Polymers 2018; 10(9): 1042.

[10] A. Drabczyk, S. Kudłacik-Kramarczyk, M. Głąb, M. Kędzierska, A. Jaromin, D. Mierzwiński, B. Tyliszczak. Physicochemical investigations of chitosan-based hydrogels containing aloe vera designed for biomedical use. Materials 2020; 13(14): 3073.

[11] W. Kwon, E. Jeong. Detoxification properties of guanidinylated chitosan against chemical warfare agents and its application to military protective clothing. Polymers 2020; 12(7): 1461.

[12] M. Shandilya, S. Thakur, S. Thakur. Magnetic amendment in the fabrication of environment friendly and biodegradable iron oxide/ethyl cellulose nanocomposite membrane via electrospinning. Cellulose 2020; 27(17): 10007–10017.

Study of calcium carbonate precipitation from CO_2-rich amine-based solution

Kannika Jongauksorn[1], Pattaraporn Kim[1,*]

[1] Center of Excellence on Catalysis and Catalytic Reaction Engineering, Department of Chemical Engineering, Faculty of Engineering, Chulalongkorn University, Bangkok 10330, Thailand
* Corresponding author: pattaraporn.k@chula.ac.th

ABSTRACT

The precipitation of calcium carbonate ($CaCO_3$) from CO_2-rich amine solutions is a novel and promising approach to carbon capture and utilization. This process reduces atmospheric CO_2 while producing valuable $CaCO_3$ for industrial use. Compared to traditional CO_2 capture and utilization methods, which require high energy for CO_2 separation and chemical conversion, $CaCO_3$ precipitation is a low-energy alternative. It occurs under near-ambient conditions and permanently stores CO_2 in solid form, making it a sustainable and cost-effective approach. This study investigates the use of polyethylene glycol (PEG)-modified monoethanolamine (MEA) absorbents to enhance CO_2 absorption and promote $CaCO_3$ precipitation. Absorbent formulations with different MEA concentrations were tested in three systems: MEA/H_2O, MEA/PEG200, and MEA/PEG200+H_2O. To precipitate $CaCO_3$, $Ca(OH)_2$ was added Ca^{2+} source to the CO_2-rich solution after the absorption. The results indicate that both the MEA/H_2O and MEA/PEG200+H_2O systems successfully facilitated $CaCO_3$ precipitation. However, the MEA/PEG200 system, which lacked water, did not produce $CaCO_3$ due to the absence of CO_3^{2-} formation. As the MEA concentration decreased in the MEA/H_2O system, the dominant phase of $CaCO_3$ shifted to calcite, while the MEA/PEG200+H_2O system consistently produced the vaterite phase, even at lower MEA concentrations. This indicates that the presence of PEG in the system helped control the phase formation. The vaterite phase is rarer and more expensive than calcite, offering distinct advantages in certain applications. SEM and XRD analyses revealed clear differences in the crystallinity and morphology of the precipitates, with vaterite displaying spherical particles and calcite showing well-defined rhombohedral crystals.

Keywords: Carbon capture and storage; Calcium carbonate precipitation; Polyethylene glycol; Monoethanolamine; Vaterite

1. INTRODUCTION

Global warming is one of the most significant threats to human survival, primarily caused by the rise in global carbon emissions from human activities such as fossil fuel consumption in industry, transport, and energy production. These activities are the main contributors to rising carbon dioxide (CO_2) concentrations [1-3]. Carbon capture, utilization, and storage (CCUS) is a significant technology for lowering greenhouse gas emissions and achieving carbon neutrality [2]. The technologies for CO_2 capture include direct air capture (DAC), pre-combustion (efficient and low-cost), post-combustion (widely used and highly selective), and oxyfuel combustion (direct CO_2 extraction using pure oxygen) [1,4]. Common separation techniques include adsorption on a solid, absorption into a liquid, and membrane systems [5]. Absorption in a solvent at temperatures and pressures close to ambient is a common approach for carbon capture. Although current amine-based solvents have been the most popular, offering several advantages for carbon capture, such as low operating temperatures, high efficiency, low viscosity, and low cost, they also come with significant challenges. The major disadvantages are the high energy requirements for solvent regeneration and the risk of corrosion [2, 6-7]. Wen Tian et al. found that the inclusion of PEG in the absorbent reduced the corrosion of equipment. They studied the combination of polyethylene glycol (PEG) with monoethanolamine (MEA) for CO_2 capture. The MEA/PEG200 absorbent demonstrated superior performance compared to MEA/H_2O, showing higher CO_2 desorption rates, better stability for reuse, and a 33% reduction in energy required for CO_2 regeneration at the same concentration. Additionally, the MEA/PEG200 absorbent exhibited notable corrosion resistance [8]. The solubility of CO_2 in PEG depends on its molecular weight and structure. PEG-600, which has a longer carbon chain than PEG-200 and PEG-300, shows reduced CO_2 solubility due to its lower density of –OH groups available for CO_2 binding and increased viscosity, which hinders CO_2 diffusion. Therefore, as the molecular weight of PEG increases, the CO_2

solubility decreases due to higher viscosity and a reduced density of functional groups [6]. Current efforts to capture CO_2 from flue gas and store it in underground reservoirs face several challenges, including limited mineral trapping, slow mineralization processes, and the risk of CO_2 migration [1]. However, there is a growing focus on recycling CO_2 through chemical processes to produce valuable products. Therefore, technologies such as absorption in solvents and in situ mineral carbonation are key to the success of CO_2 capture and storage. In situ mineral carbonation offers a long-term solution by converting CO_2 into stable carbonates, ensuring its safe storage. Compared to traditional CO_2 capture and utilization methods, such as methanol synthesis, which require high energy for CO_2 separation and chemical conversion, calcium carbonate ($CaCO_3$) precipitation is a low-energy alternative [6]. Utilizing $CaCO_3$ to store CO_2 prevents its return to the environment by combining carbon storage with utilization [9]. Converting CO_2 into $CaCO_3$ for products such as cement, additives, and construction materials enhances the economic value of CO_2 [10, 11]. $CaCO_3$ is a versatile inorganic material that can exist in several crystalline forms, such as calcite, vaterite, and aragonite. Several factors influence the production of these crystalline polymorphs, including temperature, pH, reaction time, aging time, absorbents, and chemical additives [12-15]. $CaCO_3$ in the vaterite phase is of particular interest for this work because it offers considerable potential in various synthetic applications, especially in the field of medicine. Its advantages, including cost-effectiveness, biocompatibility, and the ability to customize its properties, make it a promising material for future innovations compared to calcite and aragonite [16, 17].

This study focuses on exploring the effectiveness of different absorbent solutions in capturing CO_2, while aiming to reduce energy consumption in the regeneration process of the absorbent by employing a precipitation method to form $CaCO_3$ from CO_2-saturated solutions. Absorbent formulations with different MEA concentrations (1, 3, and 5 M) were tested in three systems: MEA/H_2O, MEA/PEG200, and MEA/PEG200+H_2O, with Calcium hydroxide ($Ca(OH)_2$) added to provide Ca^{2+} source after CO_2 absorption under near-ambient conditions. The study was limited to laboratory-scale evaluation of CO_2 absorption capacity of different absorbent mixtures, and the $CaCO_3$ phase obtained from the precipitation.

2. EXPERIMENTAL

2.1. Materials

Analytical reagents of monoethanolamine (MEA) and Hydrochloric acid (HCl) were supplied by QReC, Polyethylene Glycol 200 (PEG200) was purchased from the Chanjao Longevity Co., Ltd., Methyl orange 0.1% was supplied by Lab valley. Calcium hydroxide ($Ca(OH)_2$), Ethanol were supplied by Sigma-Aldrich. Carbon dioxide (CO_2) and nitrogen (N_2) were supplied by Linde (Thailand) Public Company Limited. Deionized (DI) water was used in all the experiments.

2.2. Apparatus and Procedures

2.2.1. Carbon dioxide capture process

Absorbents consisting of MEA/H_2O, MEA/PEG200, and MEA/PEG200+H_2O were prepared with MEA molar concentrations of 1, 3, and 5 M. The MEA/PEG200+ H_2O absorbent was made at a 1:1 volume ratio of PEG200 to H_2O. As shown in Figure 10, a mixed gas stream containing 20% CO_2 and 80% N_2 at a constant flow rate of 100 mL/min was bubbled through 20 mL of the absorbent solution in a 50 mL Duran bottle. This was maintained at 30 °C in a water bath with magnetic stirring at 300 rpm. The CO_2 concentration in the off gas was measured using an infrared CO_2 analyzer until it stabilized. The pH of the absorbents was measured before and after absorption until the solution reached CO_2 saturation, at which point the pH became constant. CO_2 loading in the solution was determined by titration analysis.

2.2.2. Precipitation process

As shown in Figure 1, $CaCO_3$ was synthesized by a precipitation reaction between $Ca(OH)_2$ and CO_2 saturated solutions at a 1:2 molar ratio of $Ca(OH)_2$ to CO_2 in beaker. The solution was continuously mixed under ambient temperature and pressure with a fixed stirring speed of 800 rpm and 15 minutes reaction times. Afterward, the $CaCO_3$ precipitate was aged until the solvent was clearly separated from the precipitate and then centrifuged at 4500 rpm for 10 minutes to further separate the precipitated $CaCO_3$ from the solvent. The resulting powder was rinsed with ethanol to remove any residual impurities, as shown by the powder's white color. The powder was then dried overnight in a vacuum drying oven. The solution obtained after centrifugation will be used for the regeneration of the solution in the CO_2 desorption process.

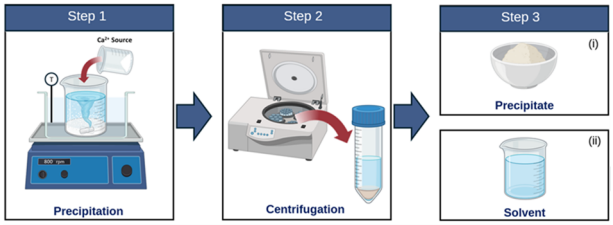

Figure 1. $CaCO_3$ Precipitation Setup.

2.3. Calculation and Analysis Methods.

2.3.1 CO_2 content calculation from Chittick method.

The CO_2 contents in the solutions before and after desorption were also determined by titration and calculated, as shown in Eqs. 1 – 3.

$$CO_2\ loading\ (\alpha) = \frac{mol\ absorbed\ CO_2}{solvent} \quad (1)$$

$$= \frac{P(V_{gas,f} - V_{gas,i} - V_{acid})}{RT} / V_{sample} \quad (2)$$

$$= \frac{P(V_{gas,f} - V_{gas,i} - V_{acid})}{RTV_{sample}} \quad (3)$$

2.3.2. Analysis Method

2.3.2.1 Measured pH during CO_2 absorption. pH meter (Mettler-Toledo, Seven Direct SD20).

2.3.2.2 The morphology of the $CaCO_3$ precipitate. Scanning electron microscopy coupled with energy dispersive X-ray spectroscopy (SEM-EDX) on a Hitachi S-3400N.

2.3.2.3 The crystallinity and phase composition of the $CaCO_3$ precipitate. X-ray diffraction (XRD), with patterns recorded in the 2-theta range of 20–60° on a SIEMENS D5000 X-ray diffractometer equipped with CuKα radiation (40 kV, 30 mA, λ = 1.5406 Å) at a step size of 0.021°.

3. RESULTS AND DISCUSSION

3.1. Carbon dioxide capture process

3.1.1. Measurement of pH during CO_2 absorption with varying MEA concentrations and absorbents

As shown in Figure 2(a-c), the pH of the absorbent tended to decrease over time due to the acidic nature of CO_2. As CO_2 was continuously introduced into the absorption system, the amount of dissolved CO_2 in the solution increased, leading to a drop in pH.

This decrease was particularly rapid during the first 30 minutes (pH dropped from ~12.3 to ~9.5), reflecting efficient CO_2 absorption and active chemical reactions occurring within the solution. During the initial stage, CO_2 reacted with MEA to form carbamate, as shown in Eqs. 4 and 5. In aqueous solution, $RHNCOO^-$ underwent hydrolysis to form HCO_3^-, as shown in Eqs. 6 and 7 [18].

$$RNH_2 + CO_2 \leftrightarrow RNH_2^+COO^- \ (zwitterion) \quad (4)$$

$$RNH_2 + RNH_2^+COO^- \leftrightarrow RHNH_2^+ + RHNCOO^- \quad (5)$$

$$RHNCOO^- + H_2O \leftrightarrow RNH_2 + HCO_3^- \quad (6)$$

$$CO_2 + RNH_2 + H_2O \leftrightarrow RHNH_2^+ + HCO_3^- \quad (7)$$

After the initial stage, the rate of pH gradually declined and tended to stabilize toward the end of the experiment, indicating that the solution begins to reach saturation in terms of CO_2 absorption capacity. As the pH decreased, the chemical reactions with MEA were weakened, while the hydration reaction of CO_2 in the aqueous solution became more dominant, as shown in Eqs. 8 and 9 [8].

$$CO_2 + H_2O \leftrightarrow H^+ + HCO_3^- \quad (8)$$

$$CO_2 + H_2O \leftrightarrow 2H^+ + CO_3^{2-} \quad (9)$$

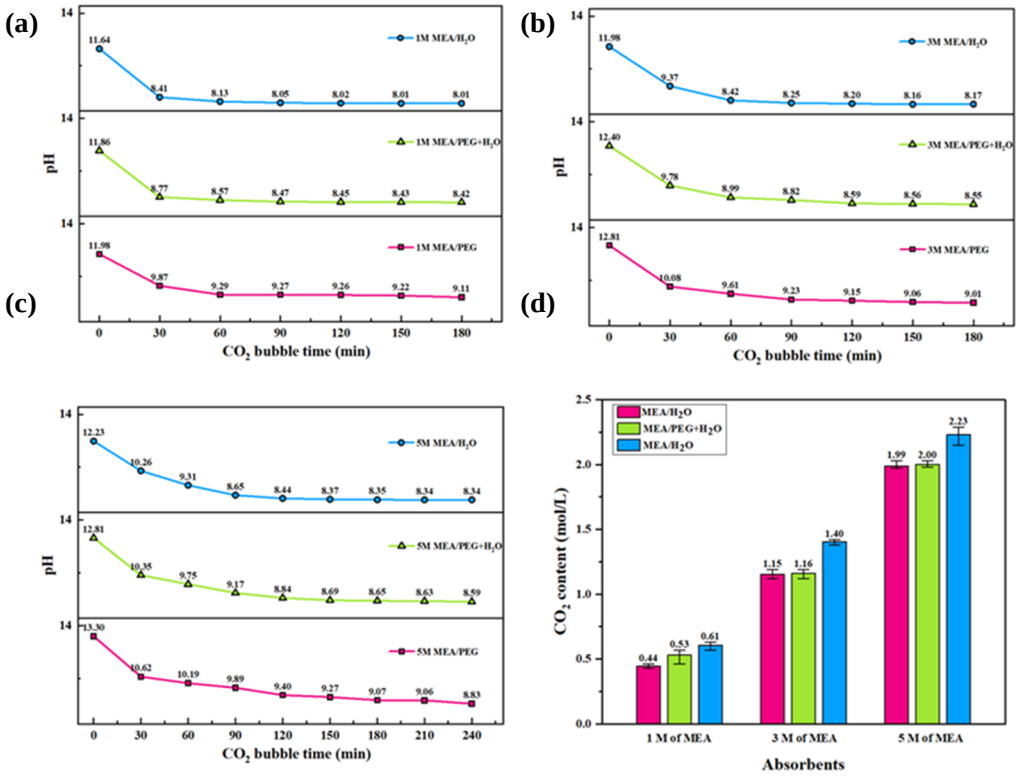

Figure 2 Measured pH during CO_2 absorption (a) 1 M, (b) 3 M, (c) 5 M of MEA concentrations, and (d) CO_2 content of CO_2-rich solvents with varying MEA concentrations and absorbents.

Specifically, with nonaqueous solvents, the amine-to-CO_2 stoichiometric ratio is 2:1, as shown in Eqs. 10-12 [8]. The solubility of CO_2 in PEG is primarily driven by interactions between the polar C–O bonds in CO_2 and the hydroxyl (–OH) groups in PEG. Although CO_2 is a non-polar molecule overall, it can act as a Lewis acid or base and form hydrogen bonds with polar functional groups. PEG molecules with a high density of terminal –OH groups exhibit enhanced CO_2 absorption due to strong polar interactions and hydrogen bonding [6].

$$RNH_2 + CO_2 \leftrightarrow RNH_2^+COO^- \ (zwitterion) \quad (10)$$

$$RNH_2 + RNH_2^+COO^- \leftrightarrow RHNH_2^+ + RHNCOO^- \quad (11)$$

$$2RNH_2 + CO_2 \leftrightarrow RHNH_2^+ + RHNCOO^- \quad (12)$$

Additionally, the solution concentration was found to affect the rate of pH decrease. Higher concentrations (from 1 M to 3 M and 5 M) were able to maintain the pH for a longer duration, possibly due to the enhanced CO_2 absorption capacity of more concentrated solutions. When comparing different solvent systems, MEA/PEG200 demonstrated a better ability to maintain alkalinity than MEA in water (MEA/H_2O). MEA/H_2O exhibited the fastest pH decline, suggesting rapid CO_2 absorption but a quicker loss of absorption efficiency. Additionally, the addition of water to the MEA/PEG200 system (MEA/PEG200+H_2O) resulted in a faster pH drop compared to MEA/PEG200 alone, possibly because the presence of water enhanced CO_2 solubility and accelerated the absorption process.

3.1.2. CO_2 content of CO_2-rich solvents with varying MEA concentrations and absorbents

The amount of CO_2 absorbed was found to depend on both the type and concentration of the solution. Solutions with higher concentrations exhibited greater CO_2 absorption capacity, as shown in Figure 2(d). Experimental results showed that MEA in water (MEA/H_2O) demonstrated the highest CO_2 absorption efficiency across all concentration levels (1 M, 3 M, and 5 M). This observation was consistent with the rapid pH drop, indicating that the absorption reaction occurred quickly and efficiently due to favorable reaction kinetics. Increasing the solution concentration enhanced CO_2 absorption in all systems, with MEA/H_2O consistently exhibiting superior performance. Although MEA/PEG200 solutions were able to maintain a higher pH for a longer duration, they exhibited slower CO_2 absorption kinetics, leading to a lower overall CO_2 uptake compared to MEA/H_2O. The slower pH decline observed in MEA/PEG200 systems suggested that the reaction rate between CO_2 and MEA was reduced, possibly due to the higher viscosity of PEG, which could hinder mass transfer. Furthermore, considering the stoichiometric ratio of amine to CO_2 (2:1) in nonaqueous solvents, as shown in Eqs. 12, MEA/H_2O is theoretically expected to exhibit higher CO_2 absorption than MEA/PEG200, aligning with the experimental findings [8]. However, the addition of water to the MEA/PEG200+H_2O system slightly improved CO_2 absorption by reducing viscosity, enhancing CO_2 solubility, and promoting faster reaction kinetics within the solution.

3.2. Precipitation process

3.2.1 Effect of water presence in absorbent systems on $CaCO_3$ precipitation

According to the XRD results, as shown in Figure 3, distinct diffraction peaks corresponding to $CaCO_3$ phases, specifically calcite and vaterite, were observed in both the MEA/H_2O and MEA/PEG200+H_2O systems at all MEA concentrations. This indicated that the crystallization of $CaCO_3$ readily occurred under conditions where water was present. The crystallization process was facilitated through the reaction of CO_2 with water, catalyzed by the enzyme carbonic anhydrase, leading to the formation of carbonic acid (H_2CO_3). The carbonic acid subsequently dissociated into bicarbonate ions (HCO_3^-) and carbonate ions (CO_3^{2-}), which then reacted with calcium ions (Ca^{2+}) in solution to precipitate $CaCO_3$, as depicted in Eqs. 13–16 [19].

$$CO_2(aq) + H_2O \leftrightarrow H_2CO_3 \quad (13)$$

$$H_2CO_3 \leftrightarrow H^+ + HCO_3^- \quad (14)$$

$$HCO_3^- + OH^- \leftrightarrow CO_3^{2-} + H_2O \quad (15)$$

$$Ca^{2+} + CO_3^{2-} \leftrightarrow CaCO_3 \quad (16)$$

In contrast, in the MEA/PEG200 system without water, only diffraction peaks corresponding to $Ca(OH)_2$ were detected, with no evidence of calcite or vaterite formation. This observation suggested that $CaCO_3$ crystallization did not occur under these conditions. In the absence of water, the carbamate formed from the reaction between MEA and CO_2 could not further convert into bicarbonate or carbonate ions, thereby eliminating the essential precursors required for $CaCO_3$ precipitation.

3.2.2 Effect of PEG on the formation and phase composition of $CaCO_3$ precipitation

The XRD analysis revealed that in the MEA/H_2O system with 1 M MEA concentration shown in Figure 3(a), a clear peak corresponding to calcite, the stable phase of $CaCO_3$, was observed. However, in the MEA/PEG200+H_2O system, a distinct peak for vaterite was detected. As the MEA concentration increased to 3 M and 5 M, the XRD patterns (shown in Figures 3(b) and 3(c), respectively) indicated that at 3 M, both calcite and vaterite peaks were present in the MEA/H_2O system. At 5 M, a clear peak for vaterite appeared, with only a small peak for calcite remaining. These XRD observations were consistent with the SEM results,

where an increase in MEA concentration led to the formation of more spherical crystals, particularly in the MEA/PEG200+H_2O system, where vaterite was the dominant phase.

A comparison of the three systems through SEM analysis revealed that the presence of PEG significantly affected the crystal morphology and phase of $CaCO_3$ formed in the system, as shown in Figure 4. In the MEA/H_2O system, as the MEA concentration increased from 1 M to 5 M, the crystal morphology changed from angular crystals (calcite) to more spherical crystals (vaterite). This indicated that a higher concentration of MEA promoted the formation of the less stable vaterite phase, although a small of calcite remained even at 5 M.

In the MEA/PEG200+H_2O system, spherical crystals were observed starting from 1 M MEA concentration. As the concentration increased, the crystal size continuously decreased, reflecting the role of PEG in controlling crystal size and crystallization processes by promoting the formation of vaterite, which has a higher surface energy than calcite. PEG contains numerous hydroxyl groups (-OH) that can interact with Ca^{2+} ions on the surface of $CaCO_3$ crystals via electrostatic attraction. This interaction caused PEG to absorb onto the crystal surface during the early stages of crystallization.

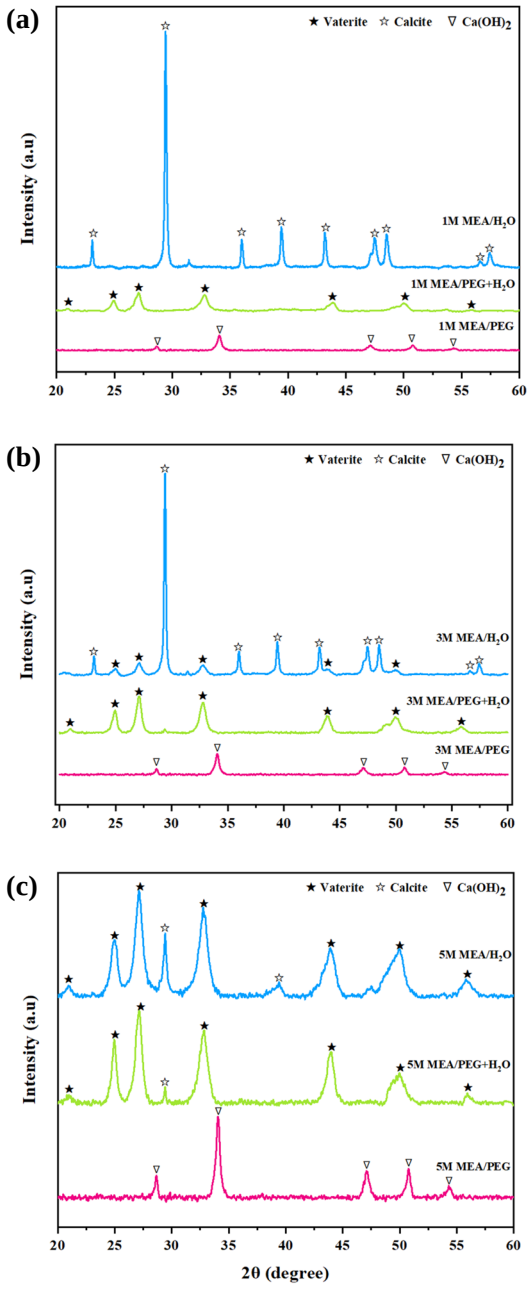

Figure 3 XRD images of synthesized $CaCO_3$ particles (a) 1 M, (b) 3 M, (c) 5 M of MEA concentrations.

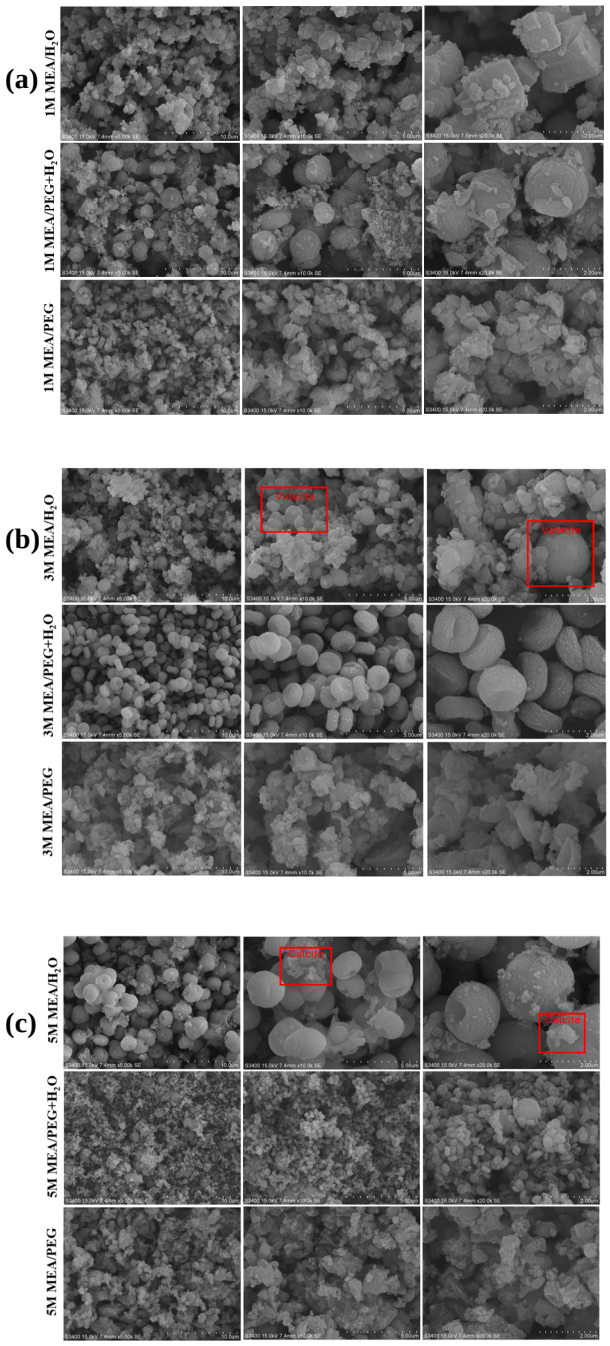

Figure 4 SEM images of synthesized $CaCO_3$ particles (a) 1 M, (b) 3 M, (c) 5 M of MEA concentrations.

Once PEG was absorbed on the crystal surface, it hindered the attachment of Ca^{2+} and CO_3^{2-} ions in specific directions, leading to irregular or anisotropic crystal growth. This resulted in a shift from angular shapes (characteristic of calcite) to spherical shapes (typical of vaterite). The directional growth inhibition promoted by PEG also supported the formation of high-energy phases, such as vaterite and aragonite. These phases, which typically reverted to calcite over time, remained stable in the system due to the presence of PEG. Thus, PEG played a significant role in controlling the morphology and polymorphic form of $CaCO_3$ crystals, stabilizing less stable phases that would otherwise transform into calcite [20-21]. In the MEA/PEG200 system without water, the crystals formed were very small and lacked a defined shape, resembling $Ca(OH)_2$ crystals. This suggested that in the absence of water, the crystallization of $CaCO_3$ was significantly hindered in the presence of only MEA and PEG.

4. CONCLUSION

This study demonstrates the performance of various absorbent solutions for CO_2 capture, focusing on reducing energy consumption by utilizing a precipitation method to form $CaCO_3$. The results showed that MEA/H_2O had the highest CO_2 loading, while MEA/PEG200 systems were slower but maintained the better pH stability. The presence of water was crucial for $CaCO_3$ crystallization, with PEG influencing the formation of spherical vaterite crystals. PEG also played a key role in stabilizing the less-stable phases like vaterite and aragonite.

Further research should focus on optimizing the regeneration process to enhance energy efficiency, investigate the long-term stability of $CaCO_3$ phases, and explore the scalability of the system for industrial applications. Additionally, the role of PEG in controlling crystal size and morphology could be refined to improve overall CO_2 capture performance.

ACKNOWLEDGMENTS

This research was funded by Research Cess Fund, Malaysia-Thailand Joint Authority (MTJA) and the NSRF via the Program Management Unit for Human Resources & Institutional Development, Research and Innovation [grant number grant number B42G670036] and B16F640164]. Kim-Lohsoontorn also would like to acknowledge Thailand Science research and Innovation Fund Chulalongkorn University (BCG66210021). Kannika Jongauksorn would like to acknowledge a scholarship from Department of Chemical Engineering, Chulalongkorn University.

REFERENCES

1. Huisingh, D., et al., Recent advances in carbon emissions reduction: policies, technologies, monitoring, assessment and modeling. Journal of Cleaner Production, 2015. 103: p. 1-12.
2. Allangawi, A., et al., Carbon Capture Materials in Post-Combustion: Adsorption and Absorption-Based Processes. C, 2023. 9(1): p. 17.
3. Snæbjörnsdóttir, S.Ó., et al., Carbon dioxide storage through mineral carbonation. Nature Reviews Earth & Environment, 2020. 1(2): p. 90-102.
4. Chen, S., et al., A critical review on deployment planning and risk analysis of carbon capture, utilization, and storage (CCUS) toward carbon neutrality. Renewable and Sustainable Energy Reviews, 2022. 167: p. 112537.
5. Figueroa, J.D., et al., Advances in CO2 capture technology—The U.S. Department of Energy's Carbon Sequestration Program. International Journal of Greenhouse Gas Control, 2008. 2(1): p. 9-20.
6. Aschenbrenner, O. and P. Styring, Comparative study of solvent properties for carbon dioxide absorption. Energy & Environmental Science, 2010. 3(8): p. 1106-1113
7. Tian, W., et al., Nonaqueous MEA/PEG200 Absorbent with High Efficiency and Low Energy Consumption for CO2 Capture. Industrial & Engineering Chemistry Research, 2021. 60(10): p. 3871-3880.
8. Vadillo, J.M., et al., Non-dispersive CO2 separation process using vacuum desorption and ionic liquids as carbon capture and utilization innovative technology. Separation and Purification Technology, 2022. 301: p. 121923.
9. Hills, C.D., N. Tripathi, and P.J. Carey, Mineralization Technology for Carbon Capture, Utilization, and Storage. Frontiers in Energy Research, 2020. 8.
10. Chang, R., et al., Calcium Carbonate Precipitation for CO2 Storage and Utilization: A Review of the Carbonate Crystallization and Polymorphism. Frontiers in Energy Research, 2017. 5.
11. Eloneva, S., et al., Fixation of CO2 by carbonating calcium derived from blast furnace slag. Energy, 2008. 33(9): p. 1461-1467.
12. Jimoh, O.A., et al., Synthesis of precipitated calcium carbonate: a review. Carbonates and Evaporites, 2018. 33(2): p. 331-346.
13. Clarà Saracho, A., et al., Characterisation of CaCO3 phases during strain-specific ureolytic precipitation. Scientific Reports, 2020. 10(1): p. 10168.
14. Tan, W.-L., et al., A critical review to bridge the gaps between carbon capture, storage and use of CaCO3. Journal of CO2 Utilization, 2020. 42: p. 101333.
15. Yuan, X., R.A. Mayanovic, and G. Zhang, Phase transitions in CaCO3 under hydrous and anhydrous conditions: Implications for the structural transformations of CaCO3 during subduction processes. American Mineralogist, 2021. 106(11): p. 1780-1788.

16. Konopacka-Łyskawa, D., Synthesis Methods and Favorable Conditions for Spherical Vaterite Precipitation: A Review. Crystals, 2019. 9(4): p. 223.
17. Febrida, R., et al., Structure and phase analysis of calcium carbonate powder prepared by a simple solution method. Heliyon, 2021. 7(11): p. e08344.
18. Lv, B., et al., Mechanisms of CO2 Capture into Monoethanolamine Solution with Different CO2 Loading during the Absorption/Desorption Processes. Environmental Science & Technology, 2015. 49(17): p. 10728-10735.
19. Zheng, T. and C. Qian, Influencing factors and formation mechanism of CaCO3 precipitation induced by microbial carbonic anhydrase. Process Biochemistry, 2020. 91: p. 271-281.
20. Siva, T., et al., Enhanced Polymer Induced Precipitation of Polymorphous in Calcium Carbonate: Calcite Aragonite Vaterite Phases. Journal of Inorganic and Organometallic Polymers and Materials, 2017. 27.
21. Xu, X., et al., Effect of Polyethylene Glycol on Phase and Morphology of Calcium Carbonate. Journal of Applied Polymer Science, 2011. 119.

Development of chitosan-fibroin coating to prolong the shelf life of bananas

Wannida Sawangarunporn[1], Pailin Ngaotrakanwiwat[1,2,*]

[1] Department of Chemical Engineering, Faculty of Engineering, Burapha University, Chonburi 20131, Thailand
[2] Interdisciplinary Center for Decarbonisation and Green Energy, Faculty of Engineering, Burapha University, Chonburi 20131, Thailand
[*] Corresponding author: pailin@eng.buu.ac.th

ABSTRACT

The synergistic properties of silk-based fibroin from cocoons, which possess excellent water barrier properties, and chitosan, with low oxygen permeability, were utilized to develop coating solutions that prolong the shelf life of Namwa bananas. The coating solutions were prepared by blending fibroin (SF) and chitosan (CS) in various weight ratios: SF 100, SF 80, SF 70, SF 60, and CS 100. The effects of composition and the number of coating layers (single and double coating) were investigated in terms of weight loss and ethylene release, a key hormone involved in fruit ripening. The results demonstrated that the coatings effectively reduced weight loss and ethylene release by limiting exposure to atmospheric oxygen and reducing respiration. The SF80 formulation was the most effective, resulting in a superior low water vapor transmission rate (WVTR) of approximately 46 $g \cdot m^{-2} \cdot day^{-1}$, comparable to that of pure SF film, and a moderate oxygen transmission rate (OTR) of 607 $cc/m^2 \cdot day$. Moreover, the Namwa bananas, single-coated with the SF80 film, exhibited a weight loss of 14.8%, compared to 19% in uncoated bananas after 7 days at 25 °C. Furthermore, the ethylene release rates were significantly reduced to 3 µL $C_2H_4 \cdot g^{-1} \cdot h^{-1}$ compared to 13 µL $C_2H_4 \cdot g^{-1} \cdot h^{-1}$ in uncoated bananas after storage for 1 day. Therefore, the SF80 coating formulation effectively delayed ripening and helped maintain banana freshness for up to 7 days.

Keywords: Fibroin; Chitosan; Weight loss; Ethylene; Bananas

1. INTRODUCTION

Climacteric fruits (e.g., durian, mango, and banana) can ripen after harvest. This ripening process is accelerated by ethylene, a hormone produced during respiration, which is influenced by factors such as the fruit's maturity and the concentration of oxygen in the handling atmosphere. During respiration, energy is produced along with the release of carbon dioxide (CO_2), water vapor through transpiration, and ethylene. The rate of ethylene production, which is associated with the fruit's physiological age, plays a crucial role in the progression of ripening and eventual spoilage. For instance, durian exhibits a respiration rate of approximately 80-250 mg $CO_2 \cdot kg^{-1} \cdot h^{-1}$, and an ethylene release rate of 1-20 µL $C_2H_4 \cdot kg^{-1} \cdot h^{-1}$ at 25 °C [1]. Similarly, bananas have a respiration rate of 40–280 mg $CO_2 \cdot kg^{-1} \cdot h^{-1}$, comparable to that of durian. However, their ethylene release rate is lower, ranging from 0.3 to 10 µL $C_2H_4 \cdot kg^{-1} \cdot h^{-1}$ at 20 °C [2]. In addition to ethylene-induced ripening, transpiration also contributes to fruit spoilage. Transpiration results from respiration and the difference in water vapor pressure between the fruit's internal moisture and the ambient environment, leading to moisture loss and textural degradation [3]. Therefore, bananas were selected in this study as a representative climacteric fruit to explore shelf-life extension strategies that can enhance post-harvest quality and export potential.

Coating solutions derived from natural resources, including lipids, polysaccharides, and proteins, have been demonstrated to extend the shelf life of fruits effectively. Lipid-based coatings exhibit excellent water barrier properties due to their hydrophobic nature, effectively reducing transpiration [4]. Despite their excellent moisture barrier properties, lipid-based coatings have several drawbacks. They often exhibit poor gas permeability, leading to anaerobic respiration and off-flavors. Additionally, their opaque or greasy appearance may negatively affect the visual quality and consumer acceptance of coated fruits. They sometimes cause skin browning in fruits, such as lychee [5].

Polysaccharide-based coatings, such as chitosan, alginate, and cellulose, exhibit excellent gas barrier properties, which help slow respiration and delay ripening. Unfortunately, due to their hydrophilic nature, they provide poor barriers to water vapor, leading to increased moisture loss. A coating solution derived from chitosan with a molecular weight of 540 kDa, when applied to "Hom Thong" bananas, was reported to reduce the respiration rate from 175 to 140 mg $CO_2 \cdot kg^{-1} \cdot h^{-1}$ by day 12 and decrease ethylene release from 12 to 3 µL $C_2H_4 \cdot kg^{-1} \cdot h^{-1}$ at 25 ± 2 °C, owing to its high oxygen barrier property (3.9 ± 0.3 $mL \cdot m^{-2} \cdot day^{-1}$) [6].

Meanwhile, protein-based coatings, such as silk fibroin, whey protein, and soy protein, exhibit good resistance to water permeability but generally have lower gas barrier properties than polysaccharides. For example, strawberries coated with fibroin containing 58% β-sheet structure retained 80% of the initial fruit weight after 14 days of storage, while the uncoated strawberries retained only 30% of the initial fruit weight. This effect was attributed to a significant decrease in the oxygen permeability coefficient from 83.2×10^{-11} cm²·s to 1.1×10^{-11} cm²·s, indicating improved barrier performance [7].

As discussed in the literature above, individual components used in coating solutions may exhibit certain disadvantages and may not efficiently prolong shelf life. Therefore, combining materials derived from natural sources offers a promising strategy to overcome the limitations associated with each component. To date, a chitosan-based coating solution incorporating silk nanodisks at concentrations ranging from 0.5 to 1.5wt% has been developed and applied to bananas. Notably, bananas coated with the solution containing 1.5wt% silk nanodisc retained 79% of their original weight after 7 days of storage, compared to only 65% retention in uncoated bananas [8]. Recently, a composite coating composed of silk fibroin (SP), chitosan (CH), and Aloe vera gel (AVG) was applied to ghost chili (a non-climacteric fruit). The chili coated with the SP/CH/AVG-2 formulation showed only 12.9% weight loss, whereas the uncoated chili experienced 19.1% weight loss during storage for 7 days [9].

Therefore, this study investigated coating formulations composed of silk fibroin and chitosan solutions to achieve a suitable oxygen transmission rate (OTR) and water vapor transmission rate (WVTR) for Namwa bananas, which serve as a representative climacteric fruit. Additionally, the film structures of various coating formulations were examined to identify the factors influencing these properties. Furthermore, the ethylene release and weight loss of bananas coated with these solutions were evaluated to assess their effectiveness in extending shelf life.

2. EXPERIMENTAL

The fibroin solution (SF) was prepared by degumming Thai native yellow silk cocoons (Nang Noi Srisaket-1; NN) in 0.02 M Na_2CO_3 solution to remove sericin. The extracted fibroin was then dissolved in 9.4 M LiBr solution, and the resulting solution was dialyzed to remove LiBr. Subsequent water dialysis was performed to concentrate the fibroin solution to 18-20 wt%. Meanwhile, the chitosan solution (CS) was prepared by dissolving 2 g of chitosan in 100 mL of 1 vol% acetic acid and stirring for 3 hours. The pH was then adjusted to 5.5 by adding KOH solution [10]. Various coating formulations were prepared by varying the weight ratio between fibroin (SF) and chitosan (CS) as follows: SF 100, SF 80/CS 20 (SF80), SF 70/CS 30 (SF70), SF 60/CS 40 (SF60), and CS 100. Then, films of uniform thickness were prepared by casting varying volumes of each coating solution onto 13 × 13 cm² acrylic sheets, allowed to dry at 30 °C and 50% RH.

Film characterizations were conducted as follows: the water vapor transmission rate (WVTR) was measured using a water vapor permeability tester (Labthink Instruments Co., Ltd., Model C360M), and the oxygen transmission rate (OTR) was determined using an oxygen transmission rate analyzer (MOCON OX-TRAN® 2/12 (R)) at 23°C and 50% RH. The structural characteristics of the films were analyzed using an attenuated total reflectance Fourier-transform infrared spectroscopy (ATR-FTIR; Nicolet iS50 FT-IR) in the range of 800-1800 cm^{-1}. The secondary structure of fibroin was further analyzed by deconvolution of the Amide I region using Origin 2024 software. The fraction of each secondary structure component (e.g., side chain, β-sheet, random coil, α-helix, and turn) was calculated as the ratio of the corresponding peak area to the total area of the Amide I region [11].

Bananas were dip-coated with different coating formulations once or twice, namely D1 and D2, and allowed to dry at 25 °C and 50% RH for 1 hour. Since both coated and uncoated bananas continued to lose moisture over time, the weight of the coating film was determined by subtracting the weight of the uncoated banana (after 1 hour of drying) from the weight of the coated banana after 1 hour under the same conditions (25-28 °C and 50-60% RH). Weight loss was determined gravimetrically using the following formula:

Weight loss (%) = [(Initial weight − Weight after storage) / Initial weight] × 100.

The thickness of the films coated on bananas was estimated based on the ratio of the film weight to the surface area of the banana, using the calibration curve of thickness from a known weight of the coating solution applied to a defined area (13 × 13 cm²).

Furthermore, to determine the ethylene release, the bananas were placed in a sealed container for 1–3 hours to allow ethylene accumulation after being stored for 1 day under the same conditions (25-28 °C, 50-60% RH). The accumulated ethylene in the container was then analyzed using gas chromatography.

3. RESULTS AND DISCUSSION

The structure of silk fibroin (SF)-based films containing various chitosan contents, with a thickness of 30 ± 3 µm, was analyzed using attenuated total reflectance Fourier transform infrared (ATR-FTIR) spectroscopy, as shown in Figure 1(A). The pure fibroin film (SF100) exhibited characteristic absorption peaks in three regions: Amide I (1596-1685 cm^{-1}), Amide II (1477-1587 cm^{-1}), and Amide III (1187-1288 cm^{-1}) [12]. Among them, the Amide I region is most commonly used to evaluate the secondary structure of fibroin, including β-sheets, random coils, α-helices, turns, and side chains. Notably, β-sheet conformations form

highly ordered, crystalline domains that impede water diffusion, in contrast to amorphous structures such as random coils and α-helices, which facilitate greater water permeability. Therefore, the secondary structures of the films were determined by deconvoluting the peaks within the Amide I region, as presented in Figure 1(B). While the FTIR spectrum of the pure chitosan film (CS100) exhibited characteristic peaks at 1558, 1406, and 1027 cm^{-1}, corresponding to N-H bonding, antisymmetric stretching of C-O-C, and C-O stretching vibrations [13].

The FTIR spectrum of the film containing 20 wt% chitosan (SF80) revealed characteristic peaks of both silk fibroin (SF) and chitosan. Notable shifts in the SF-related peaks to lower wavenumbers in the Amide I and higher wavenumbers in the Amide III bands were observed. Additionally, the appearance of characteristic chitosan peaks at 1406 and 1027 cm^{-1}, along with the migration of the amine peak (1558 cm^{-1}) into the Amide II region of SF, is observed. These spectral changes indicated strong molecular interactions between chitosan and SF, likely through hydrogen bonding between the amine groups of chitosan and the carbonyl or hydroxyl groups of SF [13,14]. However, when the chitosan content exceeded 20 wt%, the amine peak at 1558 cm^{-1} gradually shifted back toward its original position, resembling that of pure chitosan. This behavior suggests that the available interaction sites on the SF matrix became saturated, reducing the extent of chitosan-SF interactions [10].

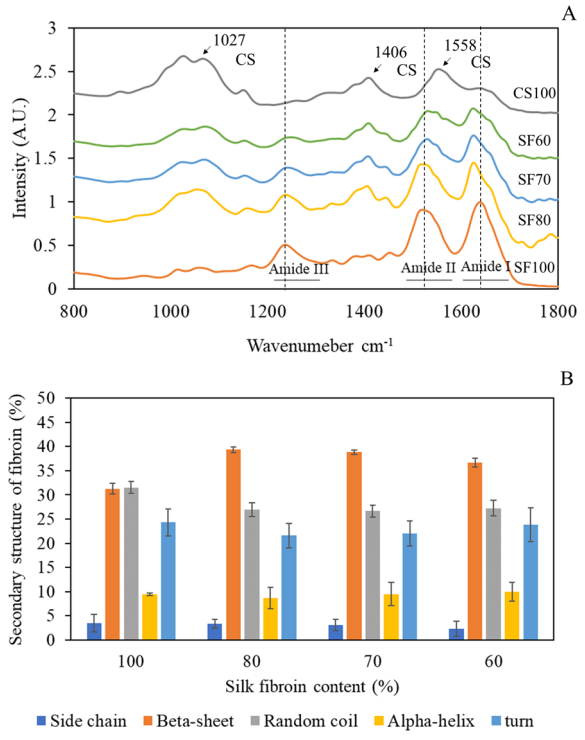

Figure 1 (A) ATR/FTIR spectra and (B) percentage of secondary structure of SF-based films containing various chitosan contents.

The secondary structures of fibroin in the SF-based films were determined by deconvoluting the Amide I region, as shown in Figure 1(B). Incorporating chitosan into the SF matrix promoted the transition from random coil structures to β-sheet conformations, resulting in a higher β-sheet content in the SF–CS composite films than the pure SF film [14]. Notably, the addition of 20 wt% chitosan yielded the highest β-sheet content, attributed to hydrogen bonding interactions between fibroin and chitosan. This phenomenon is consistent with previous studies, although the optimal chitosan content reported in other works varies, ranging from 25 wt% to 40 wt%, depending on the preparation conditions and processing techniques [10]. However, further addition of chitosan beyond 20 wt% led to a slight decrease in β-sheet content, likely due to the disruption of the ordered fibroin structure by excess chitosan, which may interfere with β-sheet formation through steric hindrance and restricted chain mobility [15].

3.1 Water Vapor Transmission Rate (WVTR)

Films prepared from various coating formulations were analyzed for their water vapor transmission rate (WVTR), as shown in Figure 2. The film made from chitosan exhibited a high WVTR of 321.59 ± 16.07 $g \cdot m^{-2} \cdot day^{-1}$, attributed to its poor water vapor barrier properties. In contrast, the film made from silk fibroin showed a significantly lower WVTR of 46.15 ± 14.34 $g \cdot m^{-2} \cdot day^{-1}$, indicating its superior resistance to water vapor permeability [13]. An increasing chitosan content in fibroin-based films (20, 30, and 40 wt%) resulted in progressively higher WVTR values of 42.26 ± 2.26, 64.64 ± 16.93, and 230.58 ± 36.20 $g \cdot m^{-2} \cdot day^{-1}$, respectively. Although the SF film containing 20 wt% chitosan (SF80) exhibited a higher β-sheet content than the pure fibroin film, its water vapor transmission rate (WVTR) was comparable to that of the pure SF film. This observation can be attributed to the hydrophilic nature of chitosan, which offsets the barrier-enhancing effect of the increased β-sheet content. On the other hand, increasing the chitosan content beyond 20 wt% resulted in a slight decrease in β-sheet content compared to the SF film containing 20 wt% chitosan. The excess unbound chitosan in the matrix likely contributed to a significant increase in WVTR, as the hydrophilic nature of free chitosan facilitated water absorption and diffusion through the film.

3.2 Oxygen Transmission Rate (OTR)

The effect of chitosan incorporation into SF-based films on the oxygen transmission rate (OTR) was evaluated, as shown in Figure 3. The pure silk fibroin film (SF100) exhibited a high oxygen permeability of 939 ± 118.49 $cc \cdot m^{-2} \cdot day^{-1}$. In contrast, the pure chitosan film (CS100) exhibited significantly lower oxygen permeability, at 59 ± 21.06 $cc \cdot m^{-2} \cdot day^{-1}$. This reduction in OTR is attributed to the high crystallinity of chitosan, resulting from a high degree of deacetylation (%DD) of 99.08% [16]. SF-based composite films containing

various chitosan contents exhibited lower OTR values than pure SF films. As the chitosan content increased, a further reduction in OTR was observed. This observation can be attributed to the combined effects of enhanced β-sheet formation in the fibroin matrix and unbound chitosan domains, which contribute to a more compact and oxygen-resistant structure.

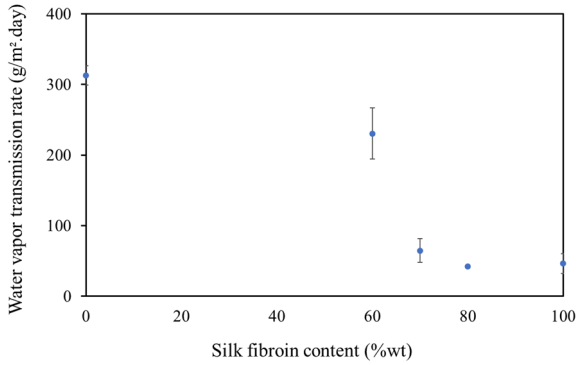

Figure 2 Water vapor transmission rate (WVTR) of SF-based films containing various chitosan contents.

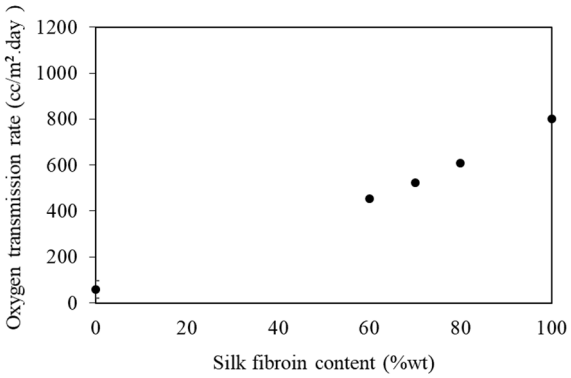

Figure 3 Oxygen transmission rate (OTR) of SF-based films containing various chitosan contents.

3.3 Weight loss of Namwa bananas

To evaluate the coating efficiency, Namwa bananas were coated using a dip-coating method with either a single layer (single coating) or two layers (double coating) of SF-based films containing various chitosan contents, resulting in film thicknesses of 6-10 µm and 16-22 µm, respectively. Due to the limited number of bananas in each bunch, the experimental sets for single and double coating were each compared with uncoated bananas within the same group.

After 7 days of storage, bananas coated with chitosan, either with a single coating (D1) or a double coating (D2), exhibited a weight loss of approximately 19-21%, comparable to that of uncoated bananas, as shown in Figure 4. This observation is likely due to the high water vapor transmission rate (WVTR) of chitosan. In contrast, bananas double-coated with pure fibroin films showed a significantly lower weight loss of around 12%, compared to uncoated bananas (21%). However, single-coated fibroin films have insufficient thickness to act as a moisture barrier; therefor, their weight loss was similar to that of the uncoated control.

Interestingly, single-coated SF-based films containing 20-40 wt% chitosan exhibited lower weight loss than pure fibroin and pure chitosan films of similar thickness. In particular, the single coating of the SF-based film with 20 wt% chitosan exhibited the lowest weight loss per unit thickness, at 1.48%·µm^{-1}. In comparison, those with 30 wt% and 40 wt% chitosan exhibited values of 1.75 and 2.24 %· µm^{-1}, respectively, as shown in Figure 5(A). Although the SF-based film containing 20 wt% chitosan has a WVTR comparable to that of the pure SF film, its weight loss per unit thickness (1.48%·µm^{-1}) was significantly lower than that of the pure SF film (2.74%·µm^{-1}). This phenomenon highlights the synergistic effect of improved water vapor resistance and reduced oxygen transmission rate (OTR), which is critical in controlling fruit transpiration. However, the weight loss per unit thickness for the double-coated SF-based films with various chitosan contents was nearly identical, suggesting that the increased film thickness may have exceeded the optimal barrier threshold, thereby minimizing the influence of compositional differences, as shown in Figure 5(B).

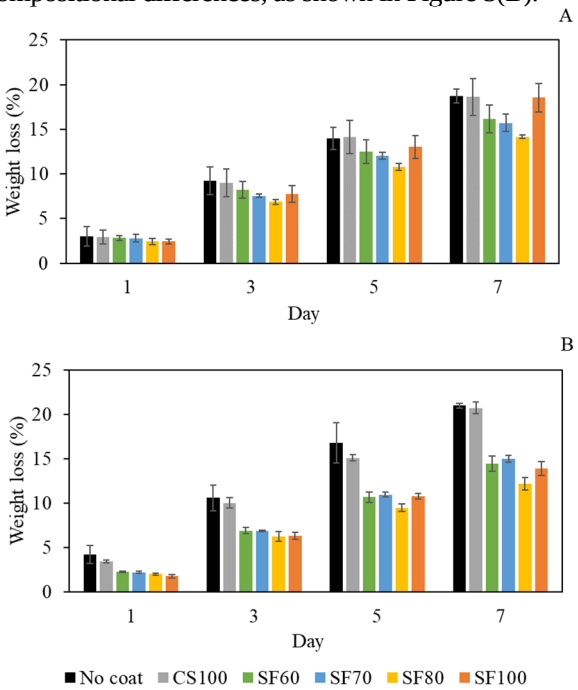

Figure 4 Weight loss of Namwa bananas coated with SF-based films containing various chitosan contents during 7 days of storage: (A) single-coated with fibroin-based film and (B) double-coated with fibroin-based film.

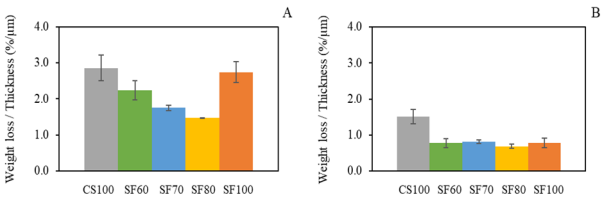

Figure 5 Weight loss per unit film thickness of Namwa bananas coated with SF-based films containing various chitosan contents after 7 days of storage: (A) single coating with fibroin-based film and (B) double coating with fibroin-based film.

3.4 Ethylene release of Namwa bananas

The rate of ethylene release from bananas coated with SF-based films containing different chitosan contents (single and double coatings) during a 7-day storage period is shown in Figure 6. Bananas coated with both single- and double-coating chitosan films exhibited high ethylene release rates, comparable to those of uncoated bananas, despite the low OTR value of the chitosan film (59 cc·m^{-2}·day^{-1}). The elevated ethylene production may be attributed to a stress response triggered by the low-oxygen environment, which can lead to the regulation of 1-aminocyclopropane-1-carboxylic acid (ACC) synthase and ACC oxidase (ACO), the key enzymes involved in ethylene biosynthesis [17]. Furthermore, the appearance of bananas coated with chitosan films turned brown after just one day of storage, compared to the uncoated bananas, as shown in Figure 8. This discoloration may indicate the onset of anaerobic respiration in the chitosan-coated bananas.

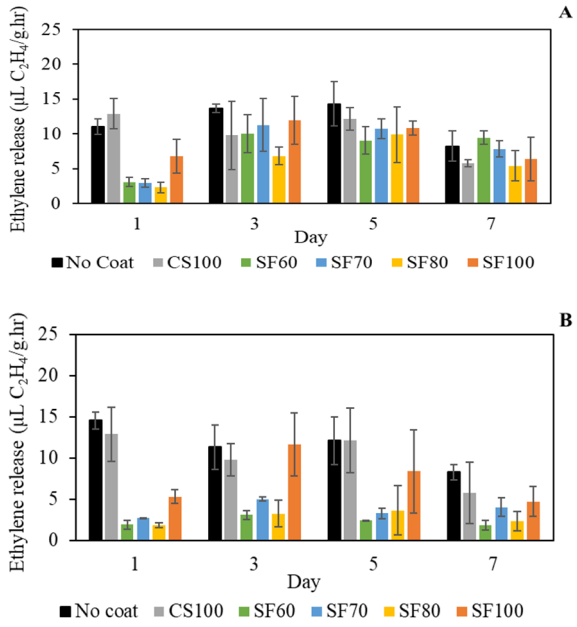

Figure 6 Ethylene release rate of Namwa bananas coated with SF-based films containing various chitosan contents during 7 days of storage: (A) single-coated with fibroin-based film and (B) double-coated with fibroin-based film.

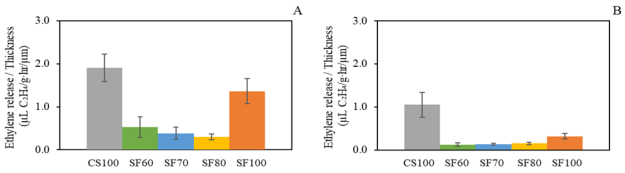

Figure 7 Ethylene release rate per unit film thickness of Namwa bananas coated with SF-based films containing various chitosan contents after 1 day of storage: (A) single coating with fibroin-based film and (B) double coating with fibroin-based film.

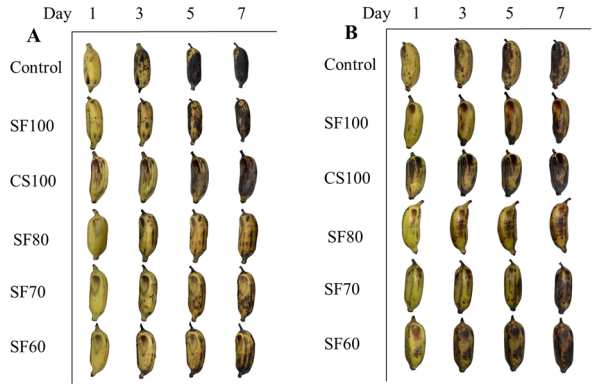

Figure 8 Appearance of Namwa bananas coated with SF-based films containing various chitosan contents during 7 days of storage: (A) single-coated with fibroin-based film and (B) double-coated with fibroin-based film.

Conversely, bananas coated with pure fibroin (SF100) exhibited a lower rate of ethylene release than uncoated bananas, which may be attributed to the moderate oxygen permeability of the film (939 cc/m^2·day). This allowed a controlled respiration rate, resulting in reduced ethylene production. Additionally, the color change from yellow to brown occurred more gradually over the storage period.

The ethylene release rates of bananas single-coated with SF-based films containing different chitosan contents (SF60, SF70, and SF80) were measured after 1 day of storage, as shown in Figure 7(A). The reduced ethylene release observed in these samples highlights the ability of the films to delay ripening, likely due to their reduced oxygen transmission rate (OTR). Notably, the SF-based film with 20 wt% chitosan (SF80) exhibited the lowest ethylene release per unit thickness of 0.30 µL C_2H_4·g^{-1}·h^{-1}·µm^{-1}, compared to 0.38 and 0.53 µL C_2H_4·g^{-1}·h^{-1}·µm^{-1} for films containing 30 wt% and 40 wt% chitosan, respectively. This suggests that the optimal ratio of fibroin and chitosan (SF80) contributes to a lower water vapor transmission rate (WVTR) and moderate OTR, providing favorable conditions for extending shelf life.

4. CONCLUSION

Silk fibroin (SF)-based films incorporating various chitosan contents were successfully developed to prolong fruit shelf life. ATR-FTIR analysis confirmed the formation of β-sheet structures in SF-based films with 20 wt% chitosan (SF80), resulting in the highest β-sheet conformation due to optimal hydrogen bonding between the two biopolymers. Despite having a WVTR comparable to pure SF film, SF80 exhibited superior performance in reducing weight loss and ethylene release, indicating a synergistic effect of enhanced crystallinity and reduced OTR. Furthermore, Namwa bananas coated with SF80 exhibited the lowest weight loss per unit film thickness and delayed ethylene emission, resulting in slower ripening compared to

uncoated or coated bananas with other films. These findings emphasize that an appropriate ratio of fibroin and chitosan (SF80) improves both water and gas barrier properties, making it a promising candidate for sustainable postharvest coatings to extend the shelf life of climacteric fruits, such as bananas.

ACKNOWLEDGMENTS

This work was financially supported by the Agricultural Research Development Agency (Public Organization), Thailand (Grant No. PRP6605030540) and the Faculty of Engineering, Burapha University.

REFERENCES

[1] Wisutiamonkul, A., Ketsa, S., & van Doorn, W. G. Endogenous ethylene regulates accumulation of α-and β-carotene in the pulp of harvested durian fruit. *Postharvest Biology and Technology* 2015; 110, 18-23.

[2] Al-Dairi, M., Pathare, P. B., Al-Yahyai, R., Jayasuriya, H., & Al-Attabi, Z. Postharvest quality, technologies, and strategies to reduce losses along the supply chain of banana: A review. *Trends in Food Science & Technology* 2023; 134, 177-191.

[3] Nor, S. M., & Ding, P. Trends and advances in edible biopolymer coating for tropical fruit: A review. *Food Research International* 2020; 134, 109208.

[4] Ahmed, A., Ali, S. W., Imran, A., Afzaal, M., Arshad, M. S., Nadeem, M., Ikram, A. Formulation of date pit oil-based edible wax coating for extending the storage stability of guava fruit. *Journal of Food Processing and Preservation* 2020; 44(2), e14336.

[5] Mota, W. F. d., Salomão, L. C. C., Cecon, P. R., & Finger, F. L. Waxes and plastic film in relation to the shelf life of yellow passion fruit. *Scientia Agricola* 2003; 60, 51-57.

[6] Wantat, A., Rojsitthisak, P., & Seraypheap, K. Inhibitory effects of high molecular weight chitosan coating on 'Hom Thong'banana fruit softening. *Food Packaging and Shelf Life* 2021; 29, 100731.

[7] Marelli, B., Brenckle, M., Kaplan, D. L., & Omenetto, F. G. Silk fibroin as edible coating for perishable food preservation. *Scientific reports* 2016; 6(1), 25263.

[8] Ghosh, T., Mondal, K., Giri, B. S., & Katiyar, V. Silk nanodisc based edible chitosan nanocomposite coating for fresh produces: A candidate with superior thermal, hydrophobic, optical, mechanical and food properties. *Food Chemistry* 2021; 360, 130048.

[9] Kalita, S., Kumar, S., & Mukherjee, A. Composite coatings containing silk protein, chitosan, and Aloe vera for prolonging postharvest shelf-life of ghost chilli (Capsicum chinense). *Food and Humanity* 2024; 2, 100290.

[10] de Moraes, M. A., Nogueira, G. M., Weska, R. F., & Beppu, M. Preparation and characterization of insoluble silk fibroin/chitosan blend films. *Polymers* 2010; 2(4), 719-727.

[11] Kaewpirom, S., & Boonsang, S. Influence of alcohol treatments on properties of silk-fibroin-based films for highly optically transparent coating applications. *RSC advances* 2020; 10(27), 15913-15923.

[12] Geminiani, L., Campione, F. P., Corti, C., Giussani, B., Gorla, G., Luraschi, M., Recchia, S., & Rampazzi, L. Historical silks: A novel method to evaluate their condition with ATR-FTIR spectroscopy and Principal Component Analysis. *Journal of Cultural Heritage* 2024; *67*, 9-22.

[13] Chen, X., Hu, X., & Zhang, J. Properties of an active film based on chitosan/silk fibroin loaded with an essential oil microemulsion and its application in preservation of strawberries. *Food Packaging and Shelf Life* 2024; 43, 101270.

[14] Luangbudnark, W., Viyoch, J., Laupattarakasem, W., Surakunprapha, P., & Laupattarakasem, P. Properties and biocompatibility of chitosan and silk fibroin blend films for application in skin tissue engineering. *The Scientific World Journal* 2012; 2012(1), 697201.

[15] Chen, X., Li, W., & Yu, T. Conformation transition of silk fibroin induced by blending chitosan. *Journal of Polymer Science Part B: Polymer Physics* 1997; 35(14), 2293-2296.

[16] Ibrahim, M. A., Alhalafi, M. H., Emam, E.-A. M., Ibrahim, H., & Mosaad, R. M. A review of chitosan and chitosan nanofiber: Preparation, characterization, and its potential applications. *Polymers* 2023; 15(13), 2820.

[17] Leeggangers, H. A., Rodriguez-Granados, N. Y., Macias-Honti, M. G., & Sasidharan, R. A helping hand when drowning: The versatile role of ethylene in root flooding resilience. *Environmental and Experimental Botany* 2023; 213, 105422.

Synthesis of rigid polyurethane foam from modified castor oil and sugar to enhance thermal insulating properties and degradability

Panchan Sricharoon[1,*], Kwanjira Janrueang[1], Yossawadee Jitsukha[1], Wanicha Suphap[1]

[1] Department of Chemical Engineering, Faculty of Engineering, King Mongkut's University of Technology Thonburi, Bangkok 10140, Thailand
[*] Corresponding author: panchan.sri@kmutt.ac.th

ABSTRACT

In this study, rigid polyurethane foams were synthesized using modified castor oil polyol and varying amounts of sugar to enhance thermal insulating properties and degradability. Castor oil was first converted into polyol and subsequently polymerized with polymeric diphenyl methane diisocyanate (PMDI). The weight ratio of castor oil polyol to sugar was systematically varied to assess its effect on foam properties. The experimental results showed that the 1:3 ratio yielded the highest hydroxyl value of 905.75 mg KOH/g, providing more reactive sites for cross-linking. However, the foam synthesized with a 1:1 weight ratio exhibited the most suitable overall properties, including a thermal conductivity of 0.0356 W/m·K, a bulk density of 44.84 kg/m³, and a compressive strength of 0.1528 MPa. Although the addition of sugar contributed to improved degradability, it also increased thermal conductivity, bulk density, and compressive strength, exceeding typical industrial and production standards. Group 1 foams (ratios 1:0 and 1:1) had smaller, closed-cell structures that limited heat transfer, while Group 2 foams (ratios 1:2 and 1:3) exhibited larger cell size, leading to increased heat conduction. These findings suggest that while sugar enhances biodegradability, excessive amounts may compromise thermal performance and mechanical stability.

Keywords: Renewable material; Rigid polyurethan foam; Sugar; Insulation; Biodegradility

1. INTRODUCTION

Polyurethane is a widely used thermosetting polymer, particularly in foam applications, due to its versatile properties ranging from flexible to rigid. Rigid polyurethane foam is especially valued for its excellent thermal insulation, dimensional stability, low water absorption, and high compressive strength, making it suitable for use in construction, automotive, and aerospace industries. However, its long degradation time and reliance on petrochemical-based raw materials pose significant environmental challenges [1].

To address these concerns, recent research has explored bio-based alternatives to conventional polyols, including palm oil and modified soybean oil. Castor oil, a renewable plant-derived oil, is considered particularly promising due to its inherent hydroxyl group [2,3], which can be chemically modified to achieve suitable reactivity for polyurethane synthesis. Sugar has also gained attention as a bio-based polyol because of its abundance and hydroxyl-rich molecular structure, which supports polymerization. Additionally, sugar's biodegradability and susceptibility to enzymatic degradation offer potential for creating more environmentally friendly and recyclable polyurethane materials [4].

Previous studies using castor oil in rigid polyurethane foams have demonstrated promising thermal insulation properties; however, their biodegradability remains limited. This study, therefore, focuses on synthesizing rigid polyurethane foams from a combination of castor oil and sugar to enhance biodegradability while maintaining key functional properties. The effects of varying castor oil-to-sugar weight ratios on the thermal, mechanical, and degradation characteristics of the foam are investigated.

2. EXPERIMENTAL

The experiment was divided into three parts: (1) preparation of castor oil polyol, (2) synthesis of rigid polyurethane foams from castor oil polyol and sugar, and (3) characterization of the resulting foams. The details are as follows:

2.1 Preparation of Castor Oil Polyol

Castor oil (as received) was mixed with triethanolamine at a molar ratio of 1:3. Calcium hydroxide, at 2% by weight of the mixture, was added as a catalyst [5,6]. The mixture was transferred to a three-neck round-bottom flask placed on a heating magnetic stirrer equipped with a thermometer, nitrogen gas inlet, and condenser. Stirring was carried out at

1,200 rpm while heating at 150 °C for 2 hours. After the reaction, the resulting castor oil polyol was cooled to room temperature and blended with granulated sugar (sucrose) at weight ratios of 1:0, 1:1, 1:2, and 1:3. The polyol blends were characterized for hydroxyl value according to ASTM D4274-99 Method C. Fourier-transform infrared (FTIR) spectroscopy was performed to confirm the presence of hydroxyl functional groups.

2.2 Preparation of Rigid Polyurethane Foam

To synthesize rigid polyurethane foams, the prepared polyol blend was used as the resin premix base. The premix contained the polyol blend, distilled water, triethylenediamine (TEDA), and silicone oil, as shown in Table 1. These components were added to a beaker and mixed using a mechanical stirrer equipped with a marine-type impeller at 1,500 rpm for 15 minutes at room temperature to ensure homogeneity. After mixing, stirring was stopped.

Table 1 Composition of components used in the formulation of rigid polyurethane foam.

No.	Weight ratio of Castor oil polyol to sugar	Polyol blend (php)	Silicone oil (php)	Distilled water (php)	TEDA (php)
1	1:0	100	2.5	4	1
2	1:1				
3	1:2				
4	1:3				

Polymeric methylene diphenyl diisocyanate (PMDI) was weighed based on an isocyanate index of 120 and transferred to a 32-ounce plastic cup. It was stirred at 1,500 rpm for 1 minute at room temperature. The resin premix was then added to the PMDI under continuous stirring. Foam expansion, indicating the onset of the polymerization reaction, was observed shortly after. At this stage, the stirrer blade was carefully removed to avoid interfering with foam rise. The foam was allowed to fully expand and cure at room temperature for at least 24 hours prior to further characterization.

2.3 Characterization of Rigid Polyurethane Foam

The cured foam samples were cut and analyzed for cellular morphology and physical properties. Cell morphology was examined using scanning electron microscopy (SEM). Bulk density was measured according to ASTM D3576, compressive strength according to ASTM D1621, and thermal conductivity using a Thermal Conductivity Analyzer (TCA, INSEIS). Biodegradability was assessed through hydrolytic degradation in a 0.1 M phosphate buffer solution (pH 7.4) prepared from 0.2 M monosodium phosphate (NaH_2PO_4) and 0.2 M disodium phosphate (Na_2HPO_4) in a fixed volume ratio. Foam samples were immersed for 24 hours, then washed, dried, and re-immersed. Weight loss was monitored over 7 days and reported as the percentage of initial mass loss.

3. RESULTS AND DISCUSSION

Castor oil is a triglyceride primarily composed of approximately 90% ricinoleic acid, an unsaturated C18 fatty acid with a hydroxyl group at the 12th carbon position [7]. In this study, the hydroxyl value of raw castor oil was measured at 162.13 mg KOH/g, which is relatively low for use as a polyol in rigid polyurethane foam. Rigid foams typically require hydroxyl values ranging from 250 to 1000 mg KOH/g [8]. To meet this requirement, the hydroxyl value was increased through a transesterification reaction with triethanolamine (TEA), using calcium hydroxide ($Ca(OH)_2$) as a catalyst. Following the modification, the physical appearance of the castor oil changed from a clear liquid to a yellowish, opaque liquid, with an increase in viscosity, indicating a successful chemical modification.

Fourier-transform infrared spectroscopy (FT-IR) was employed to identify functional groups in the raw and modified castor oil. Figures 1(a) and 1(b) present the FT-IR spectra of the unmodified and modified castor oil polyol, respectively. In Figure 1(a), the raw castor oil exhibits characteristic peaks at 3335.22 cm^{-1} for O–H stretching vibration, 2850–2950 cm^{-1} for C–H symmetric and asymmetric stretching, 1742.99 cm^{-1} for C=O stretching of ester groups, and 1162.15 cm^{-1} for C–O stretching associated with the ester linkages in the triglyceride structure. In contrast, Figure 1(b) shows corresponding peaks for the modified polyol at 3326.57 cm^{-1} (O–H stretching) and 1736.81 cm^{-1} (C=O stretching). Additional peaks at 1036.4 and 1068.81 cm^{-1} are attributed to C–O stretching vibrations associated with triethanolamine (TEA) [9].

The increased intensity of the O–H stretching band in the modified polyol indicates a higher hydroxyl content, confirming the effectiveness of the transesterification process. The incorporation of TEA introduced additional primary hydroxyl groups, resulting in the formation of mono- and diglycerides. This transformation is further supported by the disappearance of the 1162.15 cm^{-1} peak in the modified polyol spectrum, indicating a reduction in ester linkages due to the breakdown of triglycerides. The formation of hydroxyl-rich structures in the polyol led to enhanced infrared absorption in the O–H region and a corresponding decrease in % transmittance at the relevant wavelengths [9].

The functional groups of the sugar-blended castor oil polyol were also analyzed using FT-IR, as shown in Figure 2(a), and compared with those of pure sugar in Figure 2(b). The spectra reveal differences in the peak positions between the two substances. In Figure 2 (a), the FT-IR spectrum of the sugar-blended castor oil polyol exhibits peaks at 3332.76 cm^{-1} for O–H stretching, 1069.16 cm^{-1} for C–O stretching, and 2924.44 cm^{-1} for C–H stretching. In contrast, the

FT-IR spectrum of pure sugar is consistent with literature reports, showing prominent O–H stretching vibrations in the 3329.02–3560.24 cm^{-1} range. Strong and characteristic peaks observed in the 900–1250 cm^{-1} region are attributed to C–O stretching vibrations in both C–O–H groups and C–O–C ether linkages, which are commonly present in sugar structures [10].

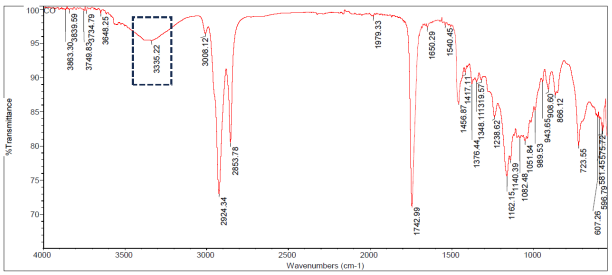

(a)

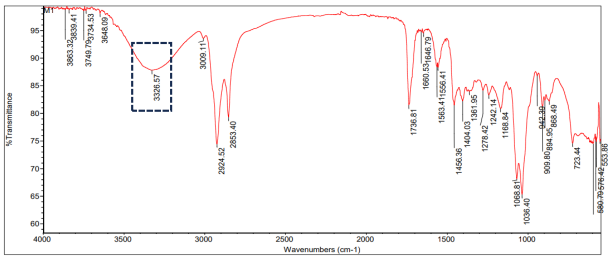

(b)

Figure 1 FTIR Spectra of (a) raw castor oil and (b) castor oil polyol after transesterification.

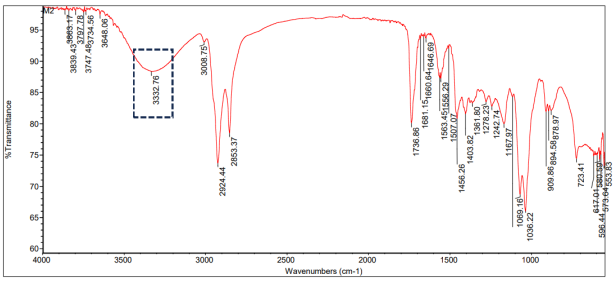

(a)

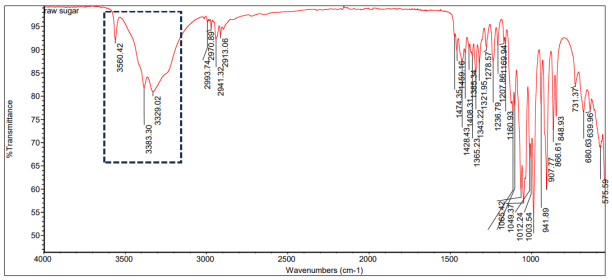

(b)

Figure 2 FTIR Spectra of (a) castor oil polyol after transesterification and blended with sugar at the weight ratio of 1:1 and (b) sugar.

The comparison between the sugar-blended polyol and pure sugar spectra shows that while some peak positions appear similar, the overall intensity and spectral pattern differ significantly. Pure sugar exhibits sharper and more intense O–H and C–O peaks, reflecting its high concentration of hydroxyl and ether groups. In contrast, the sugar-blended polyol displays broader O–H absorption and slightly shifted peaks, likely due to hydrogen bonding interactions between the sugar and polyol matrix.

Additionally, when comparing the FT-IR spectrum of the sugar-blended polyol (Figure 2(a)) with that of the modified castor oil polyol (Figure 1(b)), the peak positions and % transmittance values are nearly identical. This similarity suggests that the small amount of sugar added does not significantly alter the overall FT-IR spectra of the polyol. However, as presented in Table 2, the hydroxyl values of the sugar-blended polyols increase with higher sugar content, likely due to the high density of hydroxyl (–OH) groups in sugar, as expected, even though this change is not clearly reflected in the FT-IR spectra.

Table 2 Hydroxyl value of the sugar-blended polyol.

Weight ratio of castor oil polyol to sugar (w/w)	Hydroxyl value (mg KOH/g)
1 : 0	473.46
1 : 1	492.68
1 : 2	592.58
1 : 3	905.75

The morphology and cell size of rigid polyurethane foams synthesized at varying castor oil polyol-to-sugar weight ratios were analyzed using scanning electron microscopy (SEM) at 30x magnification, as shown in Figure 3 (a)–(d). The SEM micrographs reveal predominantly closed-cell structures, composed of both polygonal and spherical cells. These morphological characteristics were consistently observed across all samples.

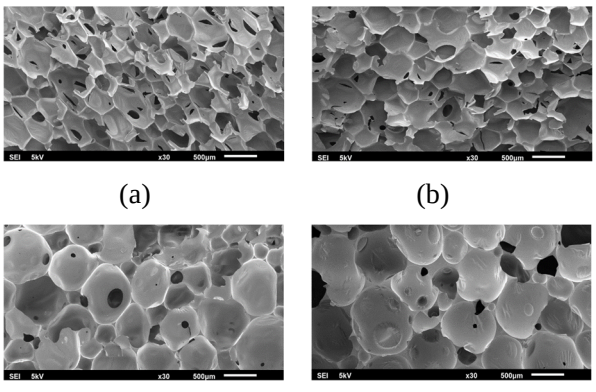

(a) (b)

(c) (d)

Figure 3 SEM Micrographs of rigid polyurethane foam synthesized at the weight ratio of castor oil polyol to sugar of: (a) 1:0, (b) 1:1, (c) 1:2 and (d) 1:3.

As the sugar content increased, the average cell size also increased. Specifically, average cell sizes of 485.89, 489.35, 676.07, and 721.19 μm were recorded for castor oil polyol-to-sugar weight ratios of 1:0, 1:1,

1:2, and 1:3, respectively. In the absence of sugar (1:0), the castor oil polyol underwent polymerization with other reactants to form relatively small and well-defined closed cells. When sugar was added at a 1:1 ratio, the resulting foam displayed a similar morphology and average cell size. This observation suggests that, at this ratio, sugar did not significantly participate in the reaction with other foam components, such as water and isocyanate, and thus had a minimal impact on the foaming process.

At higher sugar contents (1:2 and 1:3), the foams exhibited noticeably larger closed-cell structures. This increase in cell size is likely due to the presence of excess sugar that did not fully react, which contributed to a higher viscosity of the polyol mixture. The increased viscosity may have caused gas bubbles to be packed more closely together, leading to cell coalescence and the formation of larger foam structures. Additionally, the unreacted sugar may have remained dispersed within the foam matrix, further influencing the internal cell arrangement.

The resulting bulk density values of the synthesized rigid polyurethane foam for each weight ratio of castor oil-based polyol to sugar are shown in Figure 4. It can be observed that the bulk density of the rigid polyurethane foam increases with increasing weight ratios of castor oil-based polyol to sugar. This increase in density is due to the greater amount of sugar used both as a filler and as a co-polyol with castor oil-based polyol, resulting in a higher overall polyol content. When this mixture reacts with other components, such as isocyanate, the combined polyol content (from both castor oil and sugar) is more than sufficient to fully react with the available isocyanate and form polyurethane foam. Consequently, the increased polymer content per unit volume leads to a higher bulk density in the synthesized foam.

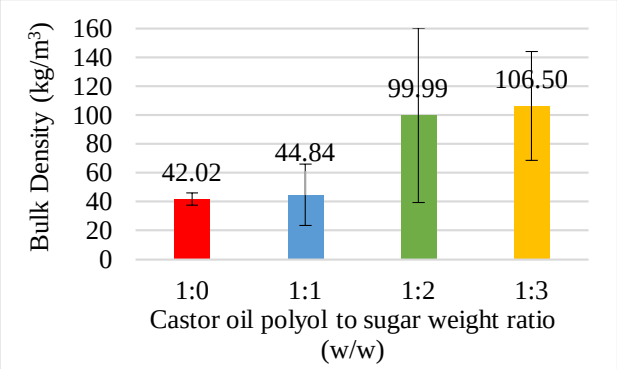

Figure 4 Bulk density of rigid polyurethane foam synthesized at various weight ratio of castor oil polyol to sugar.

Furthermore, when considering the relationship with the cell size of the synthesized rigid polyurethane foam at each weight ratio of castor oil polyol to sugar, a consistent trend is observed. The increase in sugar content raises the viscosity of the polyol, which promotes cell coalescence and the formation of larger cells in the resulting rigid polyurethane foam. This may also lead to an increase in the solid content of the foam, contributing to higher bulk density.

At mass ratios of castor oil-based polyol to sugar of 1:2 and 1:3, the bulk densities are significantly higher than standard values. This is attributed to the excessive amount of sugar added, which raises the hydroxyl (OH) value of the polyol and promotes extensive crosslinking with isocyanate, resulting in overly dense foams that exceed typical industrial specifications. The optimal bulk density for rigid polyurethane foam in practical applications is typically between 30 and 35 kg/m^3, whereas the lowest bulk density observed in this study was 42.02 kg/m^3, indicating that all synthesized foams surpassed the acceptable range.

Figure 5 illustrates that increasing the weight ratio of castor oil polyol to sugar enhances the compressive strength of the resulting rigid polyurethane foams. For clarity, the results can be categorized into two groups based on formulation behavior. The first group (ratios 1:0 and 1:1) shows a moderate increase in compressive strength with higher sugar content. This correlates with increased foam density and cell size, particularly at the 1:1 ratio, where the addition of sugar promotes greater foam formation and improved mechanical properties compared to the sugar-free formulation. The second group (ratios 1:2 and 1:3) exhibits a significant rise in compressive strength and density. This is likely due to partial incorporation of unreacted sugar into the foam matrix under the given synthesis conditions, leading to a denser, more rigid structure.

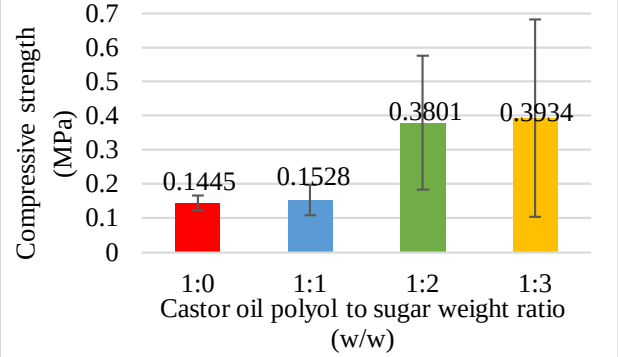

Figure 5 Compressive strength of rigid polyurethane foam synthesized at various weight ratio of castor oil polyol to sugar.

At higher sugar levels (ratios of 1:2 and 1:3), the compressive strength of the foams reaches a plateau, despite the increasing sugar content. This could be due to the fact that, at these higher ratios, the excess sugar may hinder the effective crosslinking between polyol and isocyanate. While sugar does contribute to the initial strength enhancement, its higher concentration beyond a certain point may lead to a saturation effect in the polymer network. This saturation results in diminishing returns in terms of compressive strength, causing the strength to level off even with additional

sugar incorporation. Nevertheless, all foam samples prepared in this work exceed the minimum standard compressive strength of 0.1 MPa, confirming their suitability for structural applications.

Figure 6 presents the thermal conductivity values of foams prepared with varying sugar content in the castor oil polyol/sugar system. Again, the samples can be grouped into Group 1 (1:0 and 1:1 polyol-to-sugar ratios) and Group 2 (1:2 and 1:3 ratios). For insulation applications, lower thermal conductivity is desirable, and Group 1 foams showed better performance in this regard, with values of 0.036 and 0.035 W/m·K, compared to 0.040 and 0.039 W/m·K for Group 2. The observed trend is consistent with expectations, as Group 2 foams exhibited significantly higher density (99–106 vs. 42–44 kg/m³) and compressive strength (0.38–0.39 vs. 0.14–0.15 MPa), both of which are typically associated with increased thermal conductivity due to a higher proportion of solid-phase material. Additionally, the increase in cell size from approximately 486 µm in Group 1 to over 700 µm in Group 2 likely contributed to the higher thermal conductivity by facilitating greater gas-phase conduction.

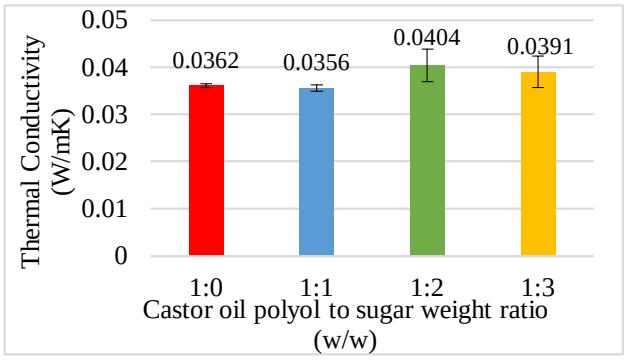

Figure 6 Thermal conductivity of rigid polyurethane foam synthesized at various weight ratio of castor oil polyol to sugar.

Therefore, while the higher sugar formulations (Group 2) produced mechanically stronger and denser foams, the lower-sugar formulations (Group 1) demonstrated better thermal insulation performance, making them more suitable for insulation applications. Despite these variations, all synthesized foams exhibited thermal conductivities above the typical commercial insulation range of 0.024–0.026 W/m·K, with the lowest value observed at 0.0356 W/m·K for the 1:1 ratio.

The degradation of rigid polyurethane foams synthesized from castor oil-based polyol was evaluated by weight loss in phosphate buffer solution over 7 days, as shown in Figure 7. In Group 1 (low sugar content), weight loss slightly increased from 1.203% (1:0) to 1.214% (1:1), likely due to hydrolysis of ester bonds in the castor oil-based polyol [11-13]. Although sugar forms glycosidic linkages and lacks hydrolysable ester linkages, its water solubility may contribute to weight loss through dissolution during washing and degradation.

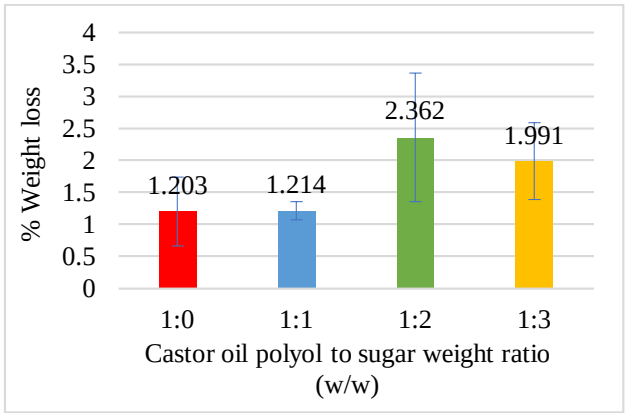

Figure 7 % Weight loss in phosphate buffer solution of rigid polyurethane foam synthesized at various weight ratio of castor oil polyol to sugar.

In Group 2 (polyol-to-sugar ratios of 1:2 and 1:3), weight loss increased more noticeably to around 2%, compared to approximately 1.2% in Group 1. This trend suggests that higher sugar content enhances degradation, possibly due to structural changes such as larger cell sizes that promote buffer penetration and hydrolysis at broken cell walls [14]. However, the slight decrease at 1:3 may result from increased foam density and stronger cell walls, which limit buffer access to internal polymer chains despite the larger cells.

4. CONCLUSION

In this study, the synthesis of rigid polyurethane foams from castor oil-based polyol and sugar was investigated to assess the effects of varying polyol-to-sugar weight ratios on foam properties. The results demonstrated that increasing the sugar content improved foam density and compressive strength. The highest compressive strength was observed in the 1:2 and 1:3 ratios, but the optimal balance of properties (combining manageable foam density, compressive strength, and enhanced insulation performance) was achieved at the 1:1 ratio. This formulation exhibited the best thermal insulation properties while maintaining mechanical properties that exceeded the minimum standard, along with low foam density and improved degradation compared to the non-sugar case. These characteristics confirm its suitability for structural applications, making it the most practical choice for rigid polyurethane foam production in this study.

ACKNOWLEDGMENTS

Thank you to Siam Chemical Industries Co., Ltd., the head of the PENTEC research group at the Faculty of Energy, Environment, and Materials, and the laboratory staff of the Chemical Engineering Department at King Mongkut's University of Technology Thonburi for their support in testing various properties and experimental set up.

REFERENCES

1. G.T. Howard. Biodegradation of polyurethane: A review. *International Biodeterioration & Biodegradation 2002;* 49(4): 245–252.
2. S. Das, P. Pandey, S. Mohanty, S.K. Nayak. Insight on Castor Oil Based Polyurethane and Nanocomposites: Recent Trends and Development. *Polymer-Plastics Technology And Engineering* 2017; 56(14): 1556–1585.
3. Y.L.U. Maldonado, L.E.D. Barrera, M.F.V. Valdivieso, E. Coy-Barre. Synthesis and characterization of polyurethane films based on castor oil-derived polyols with heparin and low molecular weight chitosan for cardiovascular implants. *Journal of Materials Research* 2023; 38(13): 3349-3361.
4. J. Jeong, Y. Hong, M.W. Lee, M. Goh. Synthesis and enzymatic recycling of sugar-based bio-polyurethane foam. *European Polymer Journal* 2022; 171: 111188.
5. M. Zhang, , H. Pan, , L. Zhang, , L. Hu, Y. Zhou. Study of the mechanical, thermal properties and flame retardancy of rigid polyurethane foams prepared from modified castor- oil- based polyols. *Industrial Crops and Products* 2014; 59: 135-143.
6. M. Sánchez-Cantú, L.M. Pérez-Díaz, I. Pala-Rosas, E. Cadena-Torres, L. Juárez-Amador, E. Rubio-Rosas, M. Rodríguez-Acosta, J.S. Valente. Hydrated lime as an effective heterogeneous catalyst for the transesterification of castor oil and methanol. *Fuel* 2013; 110: 54-62.
7. S. Ibrahim, A. Ahmad, N.S. Mohamed. Characterization of Novel Castor Oil-Based Polyurethane Polymer Electrolytes. *Polymers* 2015; 7: 747-759.
8. D. Simón, J.F. Rodríguez, M. Carmona, A. Serrano, A.M. Borreguero. Glycolysis of advanced polyurethanes composites containing thermoregulating microcapsules. *Chemical Engineering Journal* 2018; 350: 300-311.
9. M. A. Mosiewicki, , G. A. Dell'Arciprete, M. I. Aranguren, N. E. Marcovich. Polyurethane Foams Obtained from Castor Oil-based Polyol and Filled with Wood Flour. *Journal of Applied Polymer Science* 2009; 113(1): 1–10.
10. Z. Farooq, A.A. Ismail. Successful sugar identification with ATR-FTIR. *Agro FOOD Industry Hi Tech* 2014; 25(1): 36-39.
11. Ionescu, M. *Chemistry and Technology of Polyols for Polyurethanes* 2005; Rapra Technology Ltd.
12. P.S. Sathiskumar, G. Madras. Synthesis, characterization, degradation of biodegradable castor oil based polyesters. *Polymer Degradation and Stability* 2011; 96(9): 1695-1704.
13. D. Yang, J.K. Brett, M.C. Celina. Hydrolysis of poly(ester urethane): In-depth mechanistic pathways through FTIR 2D-COS spectroscopy. *Polymer Degradation and Stability* 2025; 231: 111094.
14. K. Odelius, A. Höglund, S. Kumar, M. Hakkarainen, A.K. Ghosh, N. Bhatnagar, A.C. Albertsson. Porosity and pore size regulate the degradation product profile of polylactide. *Biomacromolecules* 2011; 12(4):1250-1258.

Ethanol-assisted CO_2 hydrogenation to methanol in a trickle-bed reactor

Pattarapol Akeakkharanusorn[1], Kritchart Wongwailikhit[1,2], Rungthiwa Methaapanon[1,2], Apinan Soottitantawat[1,2,*]

[1] Center of Excellence in Particle and Materials Processing Technology, Department of Chemical Engineering, Faculty of Engineering, Chulalongkorn University, Bangkok 10330, Thailand
[2] Bio-Circular-Green-economy Technology & Engineering Center, Department of Chemical Engineering, Faculty of Engineering, Chulalongkorn University, Bangkok 10330, Thailand
[*] Corresponding author: apinan.s@chula.ac.th

ABSTRACT

The hydrogenation of carbon dioxide (CO_2) to methanol is a promising approach for CO_2 utilization, contributing to carbon capture technology and sustainable chemical production. However, conventional methanol synthesis requires high temperatures, which limit equilibrium conversion according to thermodynamics principles. Alcohol-assisted methanol synthesis has emerged as a novel method to enhance methanol production at lower temperatures. In this approach, alcohol is used as a catalytic solvent that modifies reaction pathways. The equilibrium results for ethanol-assisted CO_2 hydrogenation to methanol, with ethanol as the catalytic solvent, were obtained using the Gibbs free energy minimization method in Aspen Plus. The findings indicate that CO_2 conversion and methanol yield increased as more ethanol was added to the reaction. At high ethanol concentrations, ethanol remained in the liquid phase. This study investigated ethanol-assisted CO_2 hydrogenation in a trickle-bed reactor using a commercial $Cu/ZnO/Al_2O_3$ catalyst. CO_2 and H_2 were introduced in gaseous form, while ethanol was supplied as a catalytic solvent in liquid form. The effects of residence time were examined at a temperature of 150°C and a pressure of 30 bar . The findings revealed that CO_2 conversion and methanol yield increased with a lower LHSV, while yield of the ethyl formate, an intermediate, did not change significantly.

Keywords: Methanol; Hydrogenation; CO_2; Alcohol-assisted; Trickle-bed reactor

1. INTRODUCTION

Carbon dioxide (CO_2) is a heat-trapping greenhouse gas that plays a major role in driving global warming and altering the climate. Naturally, CO_2 is released through volcanic eruptions, forest fires, and animal respiration. Since the beginning of the Industrial Revolution, CO_2 emissions have also resulted from human activities, including the burning of fossil fuels (coal, natural gas, and oil) for transportation, electricity, and industry [1, 2]. Therefore, the atmospheric concentration of CO_2 has been rising annually [3].

Carbon Capture, Utilization, and Storage (CCUS) technology has been developed to reduce CO_2 emissions to the atmosphere. This technology consists of three parts. The first part, carbon capture, involves capturing CO_2 either from the stacks of power plants or industrial facilities before it enters the atmosphere, or directly from the air. The second part, carbon utilization, focuses on using the captured CO_2 as a feedstock to produce valuable products, such as methanol, dimethyl carbonate (DMC), and dimethyl ether (DME). The final part, carbon storage, entails storing the captured CO_2 in underground geological formations, such as abandoned oil fields [1, 4]. Converting CO_2 into valuable products is an effective strategy for reducing CO_2 emissions.

Methanol, or methyl alcohol (CH_3OH), is an organic compound and a significant chemical widely used as a feedstock and solvent in the chemical industry. As a feedstock, methanol is utilized on the production of numerous chemicals, such as formaldehyde, methyl tert-butyl ether (MTBE), and acetic acid. On the other hand, as a solvent, methanol is utilized in products such as paints and cleaning agents and serves as a fuel additive. Methanol can be synthesized from a variety of feedstocks, including natural gas, coal, biomass, and CO_2, through hydrogenation reactions. The hydrogenation of CO_2 to methanol (Eq. 1.1) is typically carried out using a $Cu/ZnO/Al_2O_3$ catalyst under high temperatures ranging from 270°C to 300°C and high pressures between 30 bar and 50 bar. The relevant reactions are presented below [5-7].

Hydrogenation of carbon dioxide (CO_2) to methanol:

$$CO_2 + 3\,H_2 \leftrightarrow CH_3OH + H_2O, \quad \Delta H^0_{298K} = -49.8\ \text{kJ mol}^{-1} \qquad (1.1)$$

Reverse water-gas shift (RWGS) reaction:

$$CO_2 + H_2 \leftrightarrow CO + H_2O, \quad \Delta H^0_{298K} = 41.0 \text{ kJ mol}^{-1} \quad (1.2)$$

Hydrogenation of carbon monoxide (CO) to methanol:

$$CO + 2\,H_2 \leftrightarrow CH_3OH, \quad \Delta H^0_{298K} = -90.8 \text{ kJ mol}^{-1} \quad (1.3)$$

There are two major types of catalyst that can be used in these reactions: heterogenous catalyst and homogeneous catalyst. Heterogenous catalysts are known for their high stability and ease of preparation. In this study, the $Cu/ZnO/Al_2O_3$ catalyst was used because it is a commercial heterogeneous catalyst, has high stability, and has been extensively studied [5].

Although the hydrogenation of CO_2 to methanol (Eq. 1.1) traditionally takes place at high temperatures, the equilibrium conversion at these temperatures is still lower than that at low temperatures. According to thermodynamics principles, this reaction is more favorable at low temperatures due to its highly exothermic. Therefore, developing a method for methanol synthesis at lower temperatures is crucial for enhancing the reaction conversion [8]. A novel approach for low-temperature methanol synthesis has been discovered. This method uses syngas mixed with CO_2 as reactants and incorporates alcohol as a catalytic solvent. The technique is called alcohol-assisted methanol synthesis because alcohol changes the reaction pathway and reduces the reaction temperature. Although alcohol is added as a catalytic solvent and is not expected to be consumed in the reaction, side reactions are inevitable [6].

The use of other alcohols was investigated in a batch-scale reactor. Ethanol resulted in the highest methanol yield, while larger alcohol molecules led to a decrease in methanol yield [6]. The reactions related to alcohol-assisted methanol synthesis using ethanol as a catalytic solvent are shown below. Moreover, equilibrium results showed that CO_2 conversion and methanol yield increased as more ethanol was added to the reaction. At high ethanol concentrations, ethanol remained in the liquid phase.

Hydrogenation and esterification of carbon dioxide (CO_2) to ethyl formate:

$$CO_2 + H_2 + C_2H_5OH \rightarrow HCOOC_2H_5 + H_2O \quad (1.4)$$

Hydrogenation of ethyl formate to methanol:

$$HCOOC_2H_5 + 2\,H_2 \rightarrow C_2H_5OH + CH_3OH \quad (1.5)$$

Dehydrogenation of ethanol to ethyl acetate:

$$2\,C_2H_5OH \rightarrow CH_3COOC_2H_5 + 2\,H_2 \quad (1.6)$$

This study investigated alcohol-assisted methanol synthesis in a trickle-bed reactor using a commercial $Cu/ZnO/Al_2O_3$ catalyst with ethanol as a catalytic solvent. Carbon dioxide (CO_2) and hydrogen (H_2) were introduced into the reactor in gaseous form, while ethanol was fed in liquid form. The effects of liquid hourly space velocity (LHSV) on the reaction were investigated.

2. EXPERIMENTAL

2.1 Chemicals

Chemicals that were used in the experiment are shown in Table 1.

Table 1 Chemicals used in the experiment.

Chemical Name and Formula	Grade	Supplier
Carbon dioxide (CO_2)	99.99%	Si Technology
Hydrogen (H_2)	99.99%	Si Technology
Nitrogen (N_2)	99.99%	Si Technology
Methanol (CH_3OH)	99.9%	Fisher Chemical
Ethanol (C_2H_5OH)	99.9%	QReC
Ethyl formate ($HCOOC_2H_5$)	97%	Thermos scientific
Ethyl acetate ($CH_3COOC_2H_5$)	99.9%	Honeywell
Acetonitrile (CH_3CN)	99.7%	RCI Labscan

2.2 Reactor

A trickle-bed reactor is a stainless-steel tube with an outer diameter of 0.5 inches, an inner diameter of 0.9 cm, and a length of 78 cm. A diagram of the reactor used for ethanol-assisted methanol synthesis is shown in Figure 1. The reactor was insulated and heated using a preheater and a two-section heater.

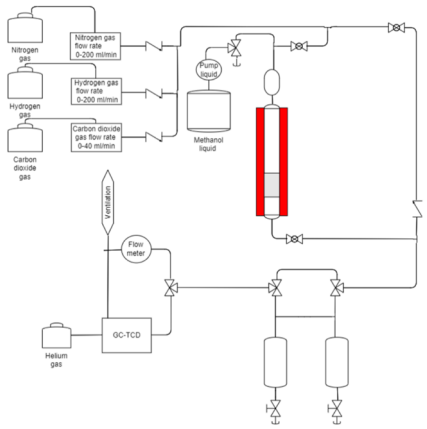

Figure 1 The diagram of the reactor used for ethanol-assisted methanol synthesis.

The temperatures were monitored at four locations and regulated by three temperature controllers. Temperature measurements were taken at the outer surface of the preheater, the outer surface of heater section 1, the outer surface of heater section 2, and the center of the catalyst bed. The pressures were measured at two locations and controlled by a needle valve. Pressure measurements were taken at the reactor inlet and outlet. The flow rate of the gas reactants was

regulated by the gas flow meter, while the liquid ethanol flow rate was controlled by a positive displacement liquid pump. Figure 2 illustrates the preheater, heater, needle valve, gas flow meter, and liquid pump.

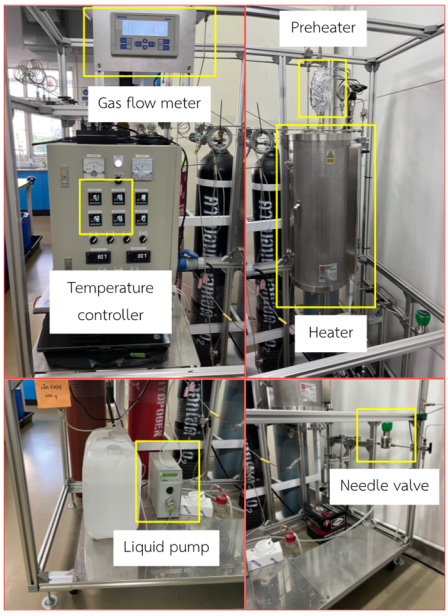

Figure 2 The reactor, preheater, heater, needle valve, gas flow meter, and liquid pump.

2.3 Catalyst preparation

A $Cu/ZnO/Al_2O_3$ catalyst was ground to achieve a particle size within the range of 1.0–1.6 mm. The reactor was loaded with the following components: 0.28 g of quartz wool, 2.15 g of aluminum oxide, 20 g of the $Cu/ZnO/Al_2O_3$ catalyst, and 6.40 g of silica ball. The composition of the $Cu/ZnO/Al_2O_3$ catalyst was 45.0 ± 0.43 wt% CuO, 50.8 ± 0.71 wt% ZnO, and 4.3 ± 1.16 wt% Al_2O_3. The respective heights of the individual components within the reactor are presented in Figure 3.

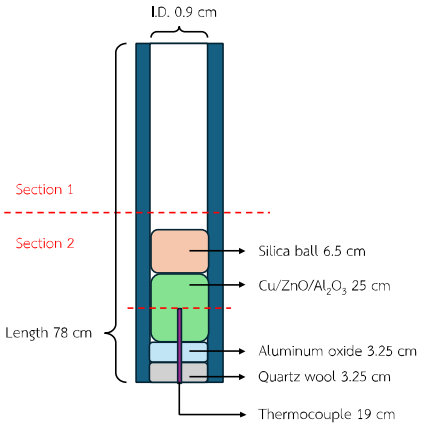

Figure 3 The height of each component.

2.4 Reaction test

The reactor was pressurized to 10 bar using 190 ml/min of N_2 and then heated to 150°C using heaters. The catalyst was reduced with a mixture of 190 ml/min of N_2 and 10 ml/min of H_2 for at least 6 hours. Subsequently, the reactor was pressurized from 10 to 30 bar using only 190 ml/min of N_2. To initiate the reaction, the N_2 was replaced with the desired feed reactants: H_2, CO_2, and liquid ethanol. The reaction was conducted at a temperature of 150°C and a pressure of 30 bar, using 20 g of the $Cu/ZnO/Al_2O_3$ catalyst, a H_2-to-CO_2 molar ratio of 5, and an ethanol-to-CO_2 molar ratio of 4. Gas and liquid effluent from the reactor were analyzed every 3 hours.

The volumetric flow rate of the gas effluent was determined using a bubble flow column, while the total mass of the liquid effluent was measured using an electronic balance. The composition of the gas and liquid effluent was analyzed by gas chromatography (GC) with a thermal conductivity detector (TCD). The reaction results were reported in terms of CO_2 conversion, methanol yield, and methanol selectivity. Details of the gas chromatography system are listed in Table 2.

Table 2 The details of the gas chromatography system.

Detail	Gas analysis	Liquid analysis
Supplier	Agilent Technologies	Agilent Technologies
Column	26ft Hayesep	HP-INNOWax
Carrier gas	Helium (He)	Helium (He)
Injection temperature	-	150°C
Initial oven temperature	40°C	40°C
Final oven temperature	230°C	60°C
Run time	18 min	10 min
Detector type	TCD	TCD
Detector temperature	150°C	150°C

2.5 Equilibrium state calculation

The equilibrium conditions for ethanol-assisted methanol synthesis were determined using the Gibbs free energy minimization method in Aspen Plus software. The SRK (Soave-Redlich-Kwong equation of state) was applied as the thermodynamic model, with REquil reactor conducting the reactions isothermally (at constant pressure and temperature). The reactions are described by Eq. 1.1 to Eq. 1.6. The feed flow rates of H_2, CO_2, and ethanol were set at 3–5 kmol/hr, 1 kmol/hr, and 1–10 kmol/hr, respectively. The simulations were performed at a pressure of 30 bar and temperatures ranging from 130°C to 170°C. The results were presented in terms of CO_2 conversion and methanol yield.

2.6 Investigation of the effects of LHSV

The flow rates of CO_2, H_2, and ethanol were adjusted while maintaining a constant ethanol-to-CO_2 molar ratio of 4 and a constant H_2-to-CO_2 molar ratio of 5. The experiment was conducted at a temperature of 150°C and a pressure of 30 bar. The results were analyzed in terms of the gas hourly space velocity (GHSV) and the liquid hourly space velocity (LHSV).

2.7 Equations and calculation methods

The conversion of CO_2 was calculated using Eq. 3.1, which is based on the total yield of products, including methanol, ethyl formate, and CO. The yields and selectivities of products were determined using Eq. 3.2 and Eq. 3.3, respectively. Additionally, the conversion of ethanol and the yield of ethyl acetate were calculated using Eq. 3.4 and Eq. 3.5, respectively.

$$\text{CO}_2 \text{ conversion (\%)} = \text{Methanol yield} + \text{Ethyl formate yield} + \text{CO yield} \quad (3.1)$$

$$\text{Product}_i \text{ yield (\%)} = \frac{\text{mol of outlet Product}_i}{\text{mol of inlet CO}_2} \times 100\ \% \quad (3.2)$$

$$\text{Product}_i \text{ selectivity (\%)} = \frac{\text{mol of outlet Product}_i}{\text{mol of total outlet product}} \times 100\ \% \quad (3.3)$$

$$\text{Ethanol conversion (\%)} = \text{Ethyl acetate yield} \quad (3.4)$$

$$\text{Ethyl acetate yield (\%)} = \frac{2 \times \text{mol of outlet ethyl acetate}}{\text{mol of inlet ethanol}} \times 100\% \quad (3.5)$$

3. RESULTS AND DISCUSSION

3.1 Equilibrium state calculation

Equilibrium conditions for ethanol-assisted methanol synthesis were determined using Aspen Plus software. The equilibrium results for conditions using H_2-to-CO_2 molar ratios of 3 and 5 are shown in Figure 4 and Figure 5, respectively. The results showed that, without ethanol, increasing the H_2-to-CO_2 molar ratio enhanced the equilibrium conversion of CO_2. This behavior aligns with Le Chatelier's principle, where a higher concentration of H_2, as a reactant, shifts the reaction forward to balance the excess H_2. However, the equilibrium conversion of CO_2 decreased as the temperature increased because exothermic reactions favor lower temperatures, following both Le Chatelier's principle and thermodynamic equilibrium.

In the presence of ethanol, the equilibrium conversion of CO_2 increased as the temperature decreased. This is due to the fact that exothermic reactions are more favorable at low temperatures, as explained by Le Chatelier's principle and thermodynamic equilibrium. Moreover, increasing the ethanol-to-CO_2 molar ratio enhanced the equilibrium conversion of CO_2. This increase in the ethanol-to-CO_2 molar ratio reduced the ethanol vapor fraction, leading to a higher proportion of ethanol in the liquid phase. The presence of more ethanol in the liquid phase could drive the reaction further forward. However, an increase in the H_2-to-CO_2 molar ratio did not directly affect the equilibrium conversion of CO_2 but influenced the ethanol vapor fraction.

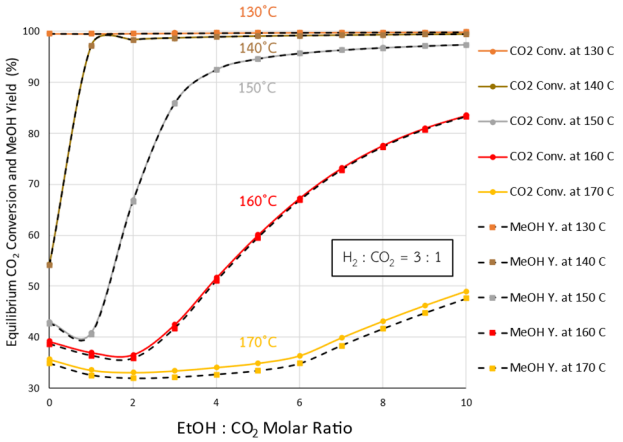

Figure 4 The equilibrium results of ethanol-assisted methanol synthesis using a H_2-to-CO_2 molar ratio of 3 and various ethanol-to-CO_2 molar ratios, at a pressure of 30 bar and different temperatures.

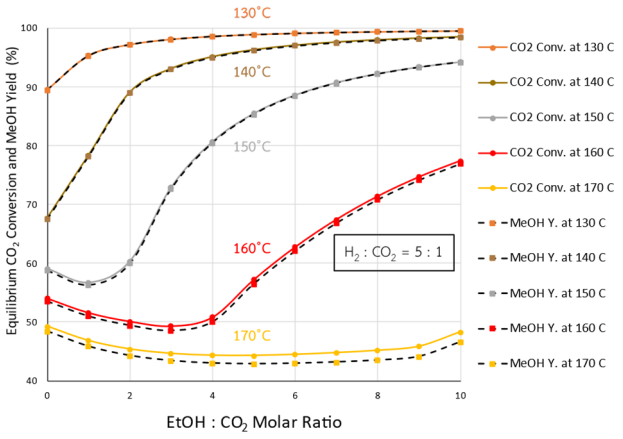

Figure 5 The equilibrium results of ethanol-assisted methanol synthesis using a H_2-to-CO_2 molar ratio of 5 and various ethanol-to-CO_2 molar ratios, at a pressure of 30 bar and different temperatures.

3.2 The effects of LHSV

The flow rates of CO_2, H_2, and ethanol were adjusted while maintaining a constant ethanol-to-CO_2 molar ratio of 4 and a constant H_2-to-CO_2 molar ratio of 5. The experiment was conducted at a temperature of 150°C and a pressure of 30 bar. The results were

analyzed in terms of the gas hourly space velocity (GHSV) and the liquid hourly space velocity (LHSV). Figure 6 illustrates the CO_2 conversion and product yields at various LHSV values. Table 3 and Table 4 show the GHSV under normal and actual conditions corresponding to each LHSV, respectively. The findings revealed that CO_2 conversion, methanol yield, and CO yield increased with a lower LHSV, while the yield of ethyl formate, an intermediate, did not change significantly. Lowering the LHSV increases the residence time of the reactants inside the reactor, allowing them greater opportunity to react and thereby promoting the formation of methanol and CO. Although more ethyl formate was formed, it was further converted into methanol, keeping the ethyl formate yield approximately constant.

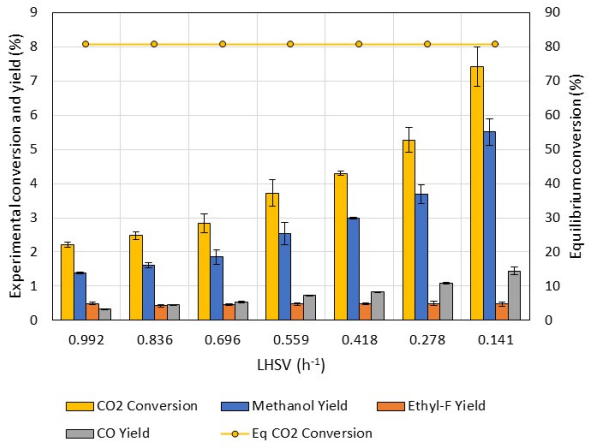

Figure 6 CO_2 conversion and product yields in ethanol-assisted CO_2 hydrogenation to methanol at various LHSV values. Reaction conditions: H_2/CO_2 = 5:1, ethanol/CO_2 = 4:1, pressure = 30 bar, temperature = 150°C.

Table 3 GHSV at normal conditions corresponding to each LHSV.

Type	Value						
LHSV (h^{-1})	0.992	0.836	0.696	0.559	0.418	0.278	0.141
GHSV (h^{-1})	609	513	427	342	257	171	86

Table 4 GHSV at actual conditions corresponding to each LHSV.

Type	Value						
LHSV (h^{-1})	0.112	0.095	0.079	0.063	0.047	0.031	0.016
GHSV (h^{-1})	968	816	679	544	408	272	137

Figure 7 and Figure 8 present the product selectivities at various LHSV values, displayed as a grouped bar chart and a stacked bar chart, respectively. The results indicated that as LHSV decreased, methanol selectivity increased, ethyl formate selectivity decreased, while CO selectivity remained approximately constant. Since ethyl formate can be further converted into methanol, the selectivities of methanol and ethyl formate can be combined, as shown in Figure 8. The findings revealed that the sum of methanol and ethyl formate selectivities, along with the CO selectivity, remained relatively unchanged. This suggests that a decrease in LHSV does not substantially affect the overall reaction pathway but instead enhances the conversion of ethyl formate into methanol

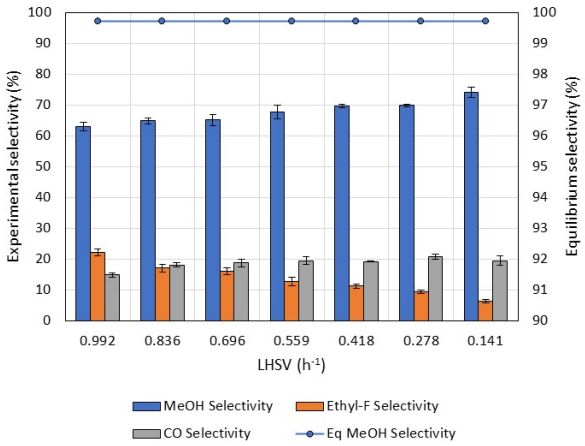

Figure 7 Product selectivities in ethanol-assisted CO_2 hydrogenation to methanol at various LHSV values, presented as a grouped bar chart. Reaction conditions: H_2/CO_2 = 5:1, ethanol/CO_2 = 4:1, pressure = 30 bar, temperature = 150°C.

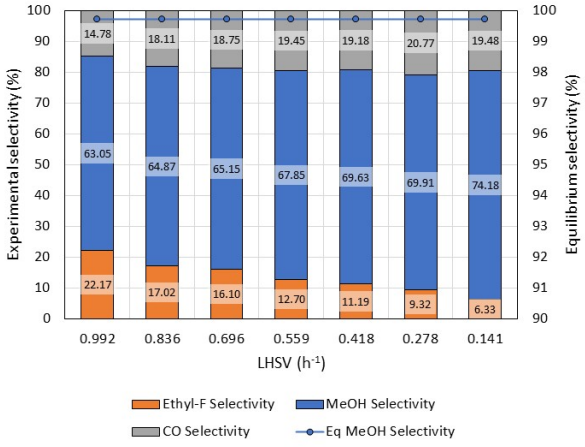

Figure 8 Product selectivities in ethanol-assisted CO_2 hydrogenation to methanol at various LHSV values, presented as a stacked bar chart. Reaction conditions: H_2/CO_2 = 5:1, ethanol/CO_2 = 4:1, pressure = 30 bar, temperature = 150°C.

Figure 12 illustrates the ethanol conversion and ethyl acetate yield at various LHSV values. The results indicated that both ethanol conversion and ethyl acetate yield increased as LHSV decreased. Reducing the LHSV extends the residence time, which promotes the production of ethyl acetate through the side reaction.

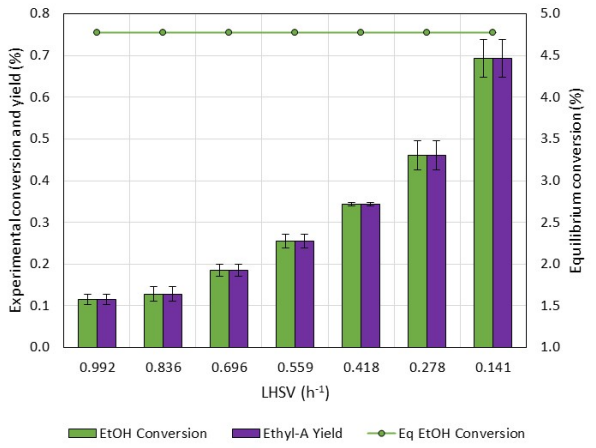

Figure 12 Ethanol conversion and ethyl acetate yield in ethanol-assisted CO2 hydrogenation to methanol at various LHSV values. Reaction conditions: H_2/CO_2 = 5:1, ethanol/CO_2 = 4:1, pressure = 30 bar, temperature = 150°C.

4. CONCLUSION

This study investigated ethanol-assisted methanol synthesis in a trickle-bed reactor, focusing on the effects of liquid hourly space velocity (LHSV) on the reaction. The results showed that CO_2 conversion and methanol yield increased with a lower LHSV, while the yield of ethyl formate, an intermediate, did not change significantly. Lowering the LHSV increases the residence time of the reactants inside the reactor and does not substantially affect the overall reaction pathway but instead enhances the conversion of ethyl formate into methanol. Nevertheless, the reduction in LHSV does not eliminate the formation of byproducts resulting from side reactions.

Based on the findings of this study, it is recommended that further research be conducted to explore the hydrodynamics inside the reactor, as different flow behaviors may yield varying results in terms of reaction rates. Additionally, optimizing the design of the trickle-bed reactor should be considered to help mitigate side reactions and improve the overall selectivity for methanol. Future studies should also include long-term experiments to assess the stability of the catalyst over extended periods, which would provide valuable insights into its practical application. Overall, these suggestions aim to enhance the performance and efficiency of the alcohol-assisted methanol synthesis process, contributing to its potential for large-scale implementation.

ACKNOWLEDGMENTS

We acknowledge the support from Research Cess Fund, Malaysia-Thailand Joint Authority (MTJA) and Center of Excellence in Particle and Materials Processing Technology, Department of Chemical Engineering, Faculty of Engineering, Chulalongkorn University.

REFERENCES

[1] Environmental Protection Agency. (2024). Overview of Greenhouse Gases. Retrieved 24 September 2024 from https://www.epa.gov/ghgemissions/overview-greenhouse-gases

[2] North, M. (2015). Chapter 1 - What is CO2? Thermodynamics, Basic Reactions and Physical Chemistry. In P. Styring, E. A. Quadrelli, & K. Armstrong (Eds.), Carbon Dioxide Utilisation (pp. 3-17). Elsevier.

[3] NASA. (2023). Carbon dioxide concentration. Retrieved 24 September 2024 from https://climate.nasa.gov/vital-signs/carbon-dioxide/?intent=121

[4] International Energy Agency. (2024). Carbon Capture, Utilisation and Storage. Retrieved 24 September 2024 from https://www.iea.org/energy-system/carbon-capture-utilisation-and-storage#how-does-ccus-work

[5] Goeppert, A., Czaun, M., Jones, J.-P., Surya Prakash, G. K., & Olah, G. A. (2014). Recycling of carbon dioxide to methanol and derived products – closing the loop. Chemical Society Reviews, 43(23), 7995-8048.

[6] Meesattham, S., & Kim-Lohsoontorn, P. (2022). Low-temperature alcohol-assisted methanol synthesis from CO2 and H2: The effect of alcohol type. International Journal of Hydrogen Energy, 47(54), 22691-22703.

Sustainable synthesis of monolaurin via glycerol esterification with lauric acid using TPA modified biochar derived from coconut shells

Junyanat Woraphasphaiboon[1], Kanokwan Ngaosuwan[2,*], Suttichai Assabumrungrat[1,3]

[1] Center of Excellence on Catalysis and Catalytic Reaction Engineering, Department of Chemical Engineering, Faculty of Engineering, Chulalongkorn University, Bangkok 10330, Thailand
[2] Chemical Engineering Division, Faculty of Engineering, Rajamangala University of Technology Krungthep, Bangkok 10120, Thailand
[3] Bio-Circular-Green economy Technology and Engineering Center (BCGeTEC), Faculty of Engineering, Chulalongkorn University, Bangkok 10330, Thailand
[*] Corresponding author: kanokwan.n@mail.rmutk.ac.th

ABSTRACT

Monolaurin or glycerol monolaurate is widely used as an emulsifier in food products and dietary supplement. It can be produced via glycerol esterification of lauric acid. The glycerol esterification required acid catalyst to accelerate the reaction rate. Therefore, this research proposed the use of a heterogeneous acid catalyst, tungstophosphoric acid on the biochar derived from coconut shell (TPA/CCS). Biochar was synthesized by pyrolysis of coconut shell under N_2 atmospheric at 600°C for 2 h. Then, 30 wt.% of TPA was loaded on the CCS. The reaction was performed at 150°C, with a glycerol to lauric acid ratio of 3:1 and 3 wt.% of TPA/CSS loading. The highest lauric acid conversion of 83.99% and monolaurin yield of 57.96 % were achieved after 4 h. The high catalytic activity of TPA/CCS could be attributed to its total acidity of 2 mmol/g. This suggested that coconut shell biomass is a promising sustainable and eco-friendly source for production of an effective catalyst for monolaurin production.

Keywords: Monolaurin; Coconut shell biochar; Tungstophosphoric acid (TPA); Lauric acid; Glycerol

1. INTRODUCTION

In recent decades, increasing awareness on environmental issues and the concept of sustainable development have become key impetus, prompting the chemical industry to prioritize more eco-friendly production methods. A process with optimized resource utilization and minimized negative environmental impacts becomes not only an economic necessity in the present era, but also a response to global challenges such as population growth and the rising demand for natural resources. The overexploitation of these resources has intensified sustainability concerns, thereby encouraging industries to explore innovative approaches making effective use of local resources and agricultural waste through green chemistry.

The synthesis of monolaurin occurs through an esterification process. It requires an acid catalyst to improve the reaction rate. Recently, heterogeneous catalysts have gained attention as a promising alternative due to their ease of separation, reusability, and eco-friendly characteristics. Among these, tungstophosphoric acid (TPA) is classified as a heteropoly acid with strong Brønsted acidity and comparable thermal stability. TPA has been studied for its functionalization on various porous materials, such as SBA-15 [1] and Brazil nut shells [2], to utilize in the various catalytic reactions.

Additionally, biochar derived from biomass processing has been emphasized as a promising catalyst support material due to its high specific surface area, adjustable porous structure, and its sustainable natural origin. Various biomass sources, such as acai stone, murumuru kernel shell, corn straw, and rice husk, have been studied for biochar production to be used as supports in esterification processes [3-6].

Coconut shell, a common agricultural waste product in tropical regions including Thailand, represents a high-potential biomass source for conversion into biochar. Utilizing coconut shells not only help to reduce biowaste but also add economic value to this by-product by transforming it into a catalyst support for the synthesis of high-value chemicals.

Although, several biomass-derived biochar materials have been explored as catalyst supports. The research on coconut shell derived biochar supported with tungstophosphoric acid (TPA/CCS) for monolaurin production remains limited.

This research aims to synthesize and characterize a TPA/CCS catalyst derived from coconut shell biochar and evaluate its performance in the production of

monolaurin from glycerol esterification with lauric acid.

2. EXPERIMENTAL

2.1. Materials

Glycerol (99.5%) was procured from Kemaus (Australia), lauric acid (99%) from Bangkok Chemical (Thailand), and tungstophosphoric acid (99%) from Tokyo Chemical Industry (Japan). The coconut shell used in the experiment was purchased from local market in Bangkok, Thailand.

2.1 Preparation of raw material

Coconut shell was utilized as the precursor for biochar synthesis. The raw coconut shell was manually separated from the husk and fibers, and thoroughly washed with deionized (DI) water, and then oven-dried at 110°C for 12 h. Subsequently, the dried coconut shell was ground and sieved to a particle size of 1-2 mm, which was used for the pyrolysis process.

2.2 Synthesis of CCS

The granulated coconut shell was pyrolyzed in a tubular furnace under at 600°C, with a heating rate of 10°C/min, for a duration of 2 h under nitrogen (N_2) atmosphere. After completing the pyrolysis process, the resulting material was ground to a particle size between 40-60 mesh. The resulting sample was labeled as coconut shell biochar (CCS) and stored in a desiccator.

2.3 Synthesis of TPA/CCS

1 g of CCS was placed into a beaker. Then, add 50 mL of deionized (DI) water to the beaker. The mixture was then subjected under ultrasonication for 2 h. After this period, 0.56 g of TPA acid (equivalent to 30 wt.% of TPA) was added and stirred using a magnetic stirrer at room temperature for 1 h. The solution was then filtered, and the solid was oven-dried at 110°C for 12 h. The resulting sample was then carbonized in a muffle furnace at 200°C with a heating rate of 10°C/min for 2 h [2]. This final material of 30 wt.% of TPA loading on coconut shell biochar (TPA/CCS) and stored in a desiccator for subsequent analysis and reaction testing.

2.4 Catalytic performance

The glycerol esterification with lauric acid was carried out in a 250 mL three-neck flask equipped with a condenser placed in a heating mantle with a magnetic stirrer. Glycerol (92.89 g) and lauric acid (67.36 g) corresponded to a glycerol to lauric acid molar ratio of 3:1 were preheated to the reaction temperature of 150°C before being mixed in the three-neck flask and stirred with a Teflon-coated magnetic stirrer at 1,200 rpm. Once the system temperature stabilized at the desired point, 1.5 g of the catalyst was added, and the reaction time was recorded. Samples were collected at specific time intervals over the 4 h reaction period, and both phases of the resulting liquid product were analyzed using a High-Performance Liquid Chromatography (HPLC).

3. RESULTS AND DISCUSSION

3.1 Characterization of the catalyst

The catalyst was analyzed to determine its structural and chemical characteristics. N_2 adsorption-desorption was used to analyze the physical properties of CCS and TPA/CCS catalysts using Brunauer–Emmett–Teller (BET) method to evaluate their specific surface area, pore volume, and average pore diameter. The isotherm and pore size distributions are presented in Figures 1a and 1b, respectively. This behavior corresponds to a Type IV isotherm with hysteresis loop, according to the IUPAC classification [7], suggesting the presence of mesoporous structures (2-50 nm) in both samples [8, 9]. Such a hysteresis loop for both CCS and TPA/CCS were not close under the $P/P_0 < 0.2$, which could be due to the swelling phenomenon occurred in these samples [7]. It is usually observed in solids with a very broad pore size distribution with micro and meso porous structures [10]. As shown in Table 1, the TPA/CCS has a higher specific surface area compared to the CCS, and a slightly increased pore volume.

This observation suggested the significant alterations in the pore structure of the material. The increase in surface area was likely attributed to the formation of micropores and mesopores, or the dispersion of tungsten-based nanoparticles on the CCS surface, leading to enhanced porosity. In addition, the slight increase in total pore volume also supported the incorporation of TPA and its subsequent interaction with the CCS matrix to generate new pore spaces or expanded existing ones, potentially offsetting any pore blockage effects. The formation of these smaller pores, characterized by their inherently high surface area ratio of surface area to volume, could be the primary factor contributing to the overall enhancement in surface area. This increased surface area following TPA incorporation was expected to improve the accessibility of active tungstic acid sites on the TPA/CCS catalyst during catalytic processes [11].

Figure 1c shows the X-ray diffraction (XRD) patterns of the CCS and TPA/CCS. The observed peaks exhibited broad and diffuse peaks at 2θ approximately 20-30°, indicating an amorphous structure. This behavior is commonly observed in biomass derived biochar with non-crystalline structures [2]. Low-intensity peaks were also observed in the 2θ range of 40-50°, corresponding to the (101) plane, which suggesting a low degree of graphitization [12].

Table 1 The table captions should be placed above the table as shown in this example.

Catalyst	Total surface area (m^2/g)	Micropore Area (m^2/g)	External Surface Area (m^2/g)	Total Pore Volume (cm^3/g)	Micropore Volume (cm^3/g)	Average Pore Diameter (nm)
Coconut shell biochar (CCS)	188.44	146.81	41.63	0.11	0.11	3.76
TPA/CCS	270.00	233.79	36.21	0.15	0.109	3.38

The XRD pattern of TPA/CCS also exhibited broad and diffuse peaks, indicating the material remaining largely amorphous. In addition, the TPA species could be uniformly dispersed with interaction of functional groups on surface of CCS [12, 13]. Alternatively, the TPA might be existing in an amorphous state on the surface of the material support.

The catalyst was analyzed to determine its structural and chemical characteristics. Fourier transform infrared (FTIR) analysis is illustrated in Figure 1d. For the coconut shell biochar (CCS), four bands were found at 3759, 1793,1583 and 1105 cm^{-1} corresponding to the stretching vibrations of O-H, C=O, C-O, C=C and C-O groups, respectively [14]. The intensities of bands with O-H and C=O groups were decreased for TPA/CCS which was attributed to the partial replacement of adsorbed water or interactions between TPA and the O–H and C=O groups present on the surface of the CCS [12]. Furthermore, new peaks of TPA/CCS were observed with the expected functional groups of the Keggin structure of TPA (1039 cm^{-1} for P-O and 961 cm^{-1} for $W=O_d$), along with peaks associated with $W\text{-}O_c\text{-}W$ (881 cm^{-1}) and $W\text{-}O_d\text{-}W$ (815 cm^{-1}), which may indicate the presence of TPA on the CCS surface [1].

Scanning electron microscopy (SEM) was employed to reveal the morphology and surface structure of CCS and TPA/CCS catalysts. Figures 2a and 2b show the SEM images of CCS. It indicates the irregular morphology with dispersed pores and a relatively open structure, featuring interconnected channels across compared to TPA/CCS. This texture is characteristics of biochar materials and reflects a rough, porous surface [15]. Considering the SEM images of TPA/CCS catalyst in Figures 2c and 2d, the surface morphology of TPA/CCS catalyst displays a more porosity structure. At a higher magnification (Figure 2d), the surface of TPA/CCS exhibited the multitude of uniformly arranged small pores within the remarkable walls of the multi-pores, indicating the incorporation of TPA onto CCS and leading to a significant. This morphological change suggests an enhancement of surface roughness at the nanoscale, which could improve the accessibility of active sites on the catalyst surface [16, 17].

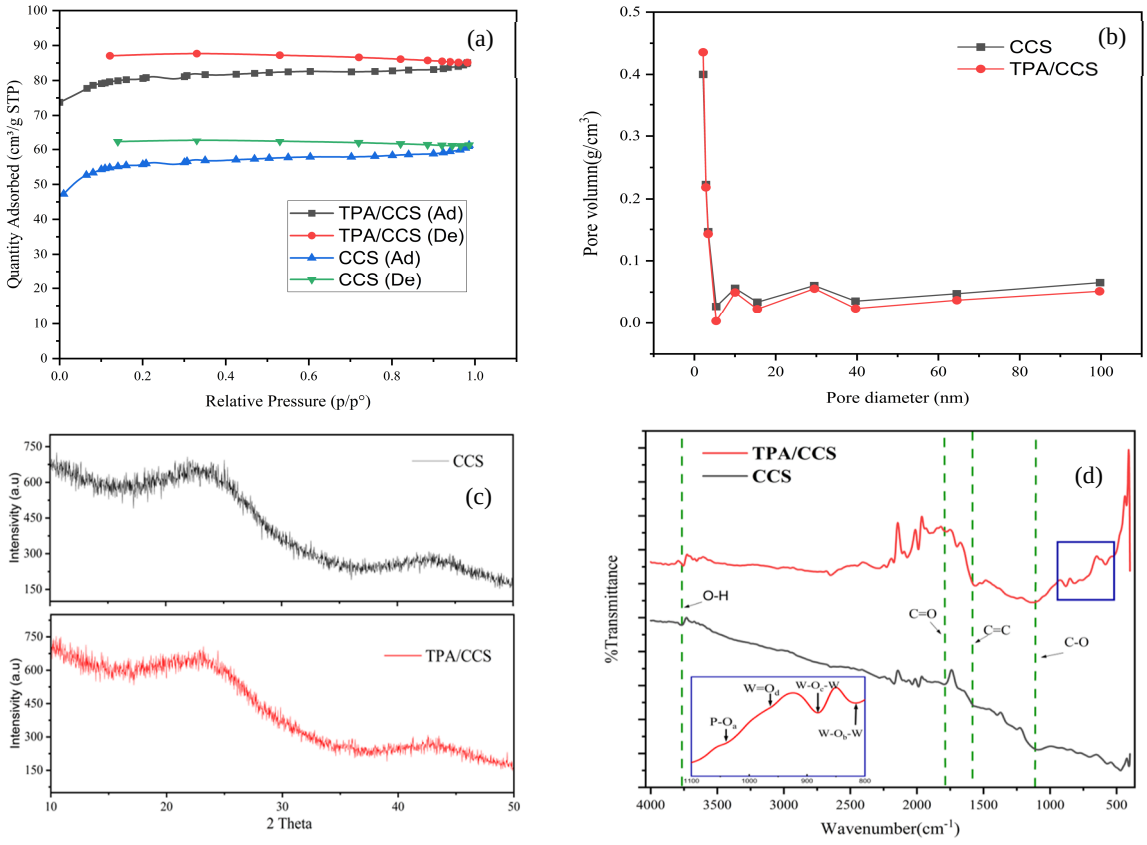

Figure 1 Nitrogen (N_2) adsorption-desorption isotherm profiles: (a) Pore size distribution, (b) XRD pattern, (c) FTIR and (d) for CCS and TPA/CCS.

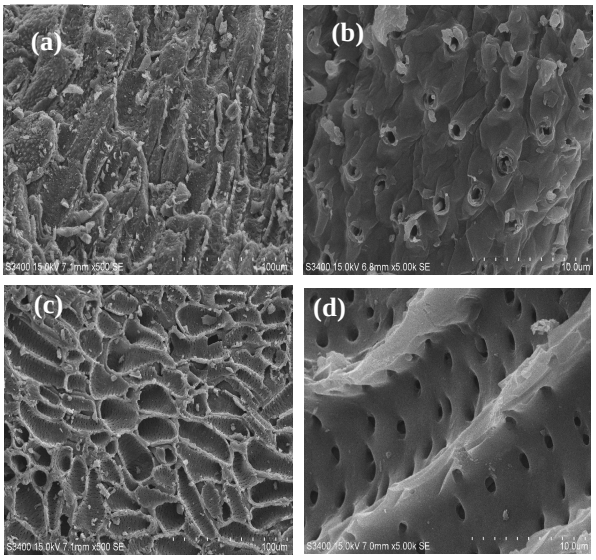

Figure 2 SEM images of CCS (a, b) and TPA/CCS (c, d) at different magnifications.

The strength and quantity of acid sites on the surface of the catalyst were analyzed using the ammonia temperature programmed desorption (NH_3-TPD) technique. The temperature at which ammonia desorption occurs can be used as an effective indicator of the strength of the acid site on the surface [18]. From the NH_3-TPD profile of the TPA/CCS catalyst (Figure 3), three main desorption peaks were observed. First, a small peak observed at approximately 181°C, corresponding to the removal of weakly adsorbed ammonia from acidic functional groups on the CCS surface. The two broader peaks at around 343 and 710°C were associated with moderate and strong acid sites, respectively. The strong acid site desorption at high temperature was likely attributed to the presence of tungsten-based species formed after the interaction of TPA with the CCS surface, which can exhibit strong Brønsted acidity [12, 19].

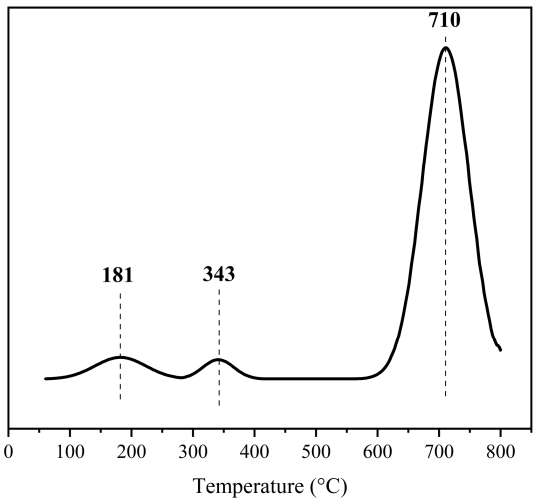

Figure 3 NH_3-TPD spectrum of TPA/CCS catalyst.

For the acidity measurement, the total acidity of the TPA/CCS catalyst was 2 mmol/g, suggesting a significantly high acid site densities, when compared with other catalysts such as PTA/MCM-41 (1.27 mmol/g) and HPW/SBA-15 (1.04 mmol/g) [1, 12, 19]. The TPA/CCS catalyst exhibited a higher total acid site density, which is a crucial factor influencing catalytic efficiency.

3.2 TPA/CCS catalyzed glycerol esterification with lauric acid

TPA/CCS was tested the catalytic activity for glycerol esterification with lauric acid at a temperature of 150°C, a glycerol: lauric acid ratio of 3:1 and catalyst loading of 3wt.%. Lauric acid conversion along the reaction time is illustrated in Figure 4a. The lauric acid conversion increased rapidly during the initial reaction stage and achieved the maximum conversion of lauric acid of was 83.99 % at 4 h. Owing to glycerol esterification is the three consecutive reversible reactions which can produce monolaurin (MO), dilaurin (DO), and trilaurin (TO) with a by-product water at each step. The product selectivity is expressed in Figure 4b. The maximum MO selectivity and MO yield were 75.27 and 57.96 %, respectively at initial reaction stage (0.5 h). When, the reaction time was extended, the MO selectivity tended to slightly decrease. This could be because MO is the first intermediate product which can be further reacted with lauric acid to produce DO and TO at extended reaction time. However, the highest selectivities of DO and TO were observed at 27.75, and 3.23% at 4 h, respectively.

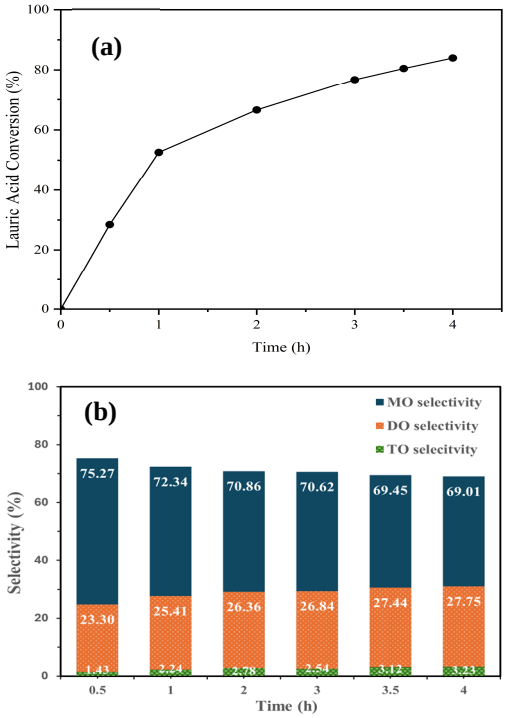

Figure 4 Conversion of lauric acid (a) and products selectivity reaction (b) (mole ratio = 1:3, reaction temperature = 150 °C, reaction time = 4 h and catalyst loading = 3wt.%).

The catalytic performance of TPA/CCS for glycerol esterification with lauric acid in this study was also effective as compared to other acid catalysts. For instance, the magnesium stabilized tungstophosphoric acid impregnated SBA-15 catalyst required a higher temperature of 160 °C, a higher glycerol to lauric acid molar ratio of 4:1, and a longer reaction time of 6 h to achieve lauric acid conversion (78.31%) and MO yield (55.35%) [1]. These results highlight the higher catalytic activity and efficiency of the TPA/CCS catalyst under the investigated conditions for MO synthesis. The ability of TPA/CCS to operate effectively at a lower temperature and with a lower glycerol to lauric acid molar ratio and catalyst loading will be further investigated to achieve high lauric acid conversion and high MO selectivity. The reusability of catalyst will also be performed in the future.

4. CONCLUSION

This research demonstrated the synthesis of TPA supported on coconut shell biochar (TPA/CCS) as an effective catalyst for the synthesis of MO via the glycerol esterification with lauric acid. The TPA/CCS catalyst, with well-dispersed active sites on a porous biochar surface, successfully promoted high lauric acid conversion and MO formation. The suitable operating condition was at a reaction temperature of 150°C, a catalyst loading of 3 wt.% and a glycerol to lauric acid molar ratio of 3:1. Notably, a high lauric acid conversion of 83.99% and a maximum MO yield of approximately 57.96% were achieved at a temperature of 150°C after 4 h. These results indicated a promising catalytic activity and efficiency of TPA/CCS for MO production via glycerol esterification of lauric acid. The ability of TPA/CCS to operate effectively under milder conditions suggests its potential for a more energy-efficient and cost-effective MO production process

ACKNOWLEDGMENTS

This research was funded by the NSRF through the Program Management Unit for Human Resources & Institutional Development, Research, and Innovation (Grant number B05F640085). Appreciation is also extended to the Center of Excellence on Catalysis and Catalytic Reaction Engineering for providing laboratory facilities and technical support.

REFERENCES

1. Ooi, S.Y., et al., Magnesium stabilized 12 tungstophosphoric acid impregnated SBA-15 for selective monolaurin production. *South African Journal of Chemical Engineering*, 2022. **41**: p. 51-64.
2. da Costa, A.A.F., et al., Synthesis of biochar modified with 12-tungstophosphoric acid for the selective conversion of isoeugenol to vanillin. *Arabian Journal of Chemistry*, 2023. **16**(12).
3. Araujo, R.O., et al., Low temperature sulfona-tion of acai stone biomass derived carbons as acid catalysts for esterification reactions. *Energy Conversion and Management*, 2019. **196**: p. 821-830.
4. da Luz Correa, A.P., et al., Preparation of sulfonated carbon-based catalysts from murumuru kernel shell and their performance in the esterification reaction. *RSC Adv*, 2020. **10**(34): p. 20245-20256.
5. Liu, T., et al., Preparation and characterization of biomass carbon-based solid acid catalyst for the esterification of oleic acid with methanol. *Bioresource Technology*, 2013. **133**: p. 618-621.
6. Yadav, G., N. Yadav, and M. Ahmaruzzaman, Microwave-assisted sustainable synthesis of biodiesel on Oryza sativa catalyst derived from agricultural waste by esterification reaction. *Chemical Engineering and Processing - Process Intensification*, 2023. **187**: p. 109327.
7. Thommes, M., et al., Physisorption of gases, with special reference to the evaluation of surface area and pore size distribution (IUPAC Technical Report). *Pure and Applied Chemistry*, 2015. **87**(9-10): p. 1051-1069.
8. Baharum, N.A., et al., Highly efficient removal of diazinon pesticide from aqueous solutions by using coconut shell-modified biochar. *Arabian Journal of Chemistry*, 2020. **13**(7): p. 6106-6121.
9. Huang, X., W. Wang, and X. Liu, $H_3PW_{12}O_{40}$-doped pyromellitic diimide prepared via thermal transformation as an efficient visible-light photocatalyst. *Journal of Materials Science*, 2020. **55**(20): p. 8502-8512.
10. Chang, S.S., et al., Mesoporosity as a new parameter for understanding tension stress generation in trees. *J Exp Bot*, 2009. **60**(11): p. 3023-30.
11. Hosseini, M.S. and M. Masteri-Farahani, Surface Functionalization of Magnetite Nanoparticles with Sulfonic Acid and Heteropoly Acid: Efficient Magnetically Recoverable Solid Acid Catalysts. *Chem Asian J*, 2019. **14**(7): p. 1076-1083.
12. Ning, Y., S. Niu, K. Han, and C. Lu, Catalytic capability of phosphotungstic acid supported on bamboo activated carbon in esterification for biodiesel production with density functional theory. *Biomass and Bioenergy*, 2020. **143**.
13. Bai, J., et al., Fabrication of coconut shell-derived porous carbons for CO_2 adsorption application. *Frontiers of Chemical Science and Engineering*, 2023. **17**(8): p. 1122-1130.
14. Nisa, Z.U., et al., Role of carbonization parameters on surface and microstructural and crystalline properties of mesoporous coconut shell char: Quantitative and structural study. *Journal of Molecular Structure*, 2024. **1300**.

15. Fahruddin, F., et al., Biochar from Coconut Shell Biomass for the Removal of Sulfate and Cadmium Reduction in Acid Mine Drainage Treatment. *Polish Journal of Environmental Studies*, 2024. **33**(5): p. 5627-5634.
16. Wesner, A., et al., Study of supported heteropolyacid catalysts for one-step DME synthesis from CO_2 and H_2. *RSC Advances*, 2025. **15**(1): p. 38-47.
17. M, R., et al., *S*ynthesis and characterisation of a novel silica—CaO/TPA catalyst for biodiesel production. *Biofuels*, 2025: p. 1-9.
18. Glazneva, T.S., N.S. Kotsarenko, and E.A. Paukshtis, Surface acidity and basicity of oxide catalysts: From aqueous suspensions to in situ measurements. *Kinetics and Catalysis*, 2008. **49**(6): p. 859-867.
19. Singh, S. and A. Patel, Mono lacunary phosphotungstate anchored to MCM-41 as recyclable catalyst for biodiesel production via transesterification of waste cooking oil. *Fuel*, 2015. **159**: p. 720-727.

Integration of monoethanolamine-based carbon dioxide absorption and mineralization with calcium chloride

Ratipuk Chung-in[1,2], Rungthiwa Methaapanon[1,2*]

[1] Department of Chemical Engineering, Faculty of Engineering, Chulalongkorn University, Bangkok 10330, Thailand
[2] Center of Excellence in Particle and Material Processing Technology (CEPT), Faculty of Engineering, Chulalongkorn University, Bangkok 10330, Thailand
[*] Corresponding author: rungthiwa.m@chula.ac.th

ABSTRACT

Monoethanolamine (MEA)-based CO_2 absorption has been a technology applied to reduce CO_2 emissions due to its economic feasibility and high CO_2 absorption rate. However, MEA regeneration at high temperatures is still challenging. A potential alternative is to mineralize CO_2 into calcium carbonate ($CaCO_3$) at room temperature, a process that demands low energy and leads to lasting CO_2 storage. In this work, we investigated the simultaneous absorption-mineralization (1 pot) and sequential absorption-mineralization (2 pots), in comparison with direct mineralization with pure water. The highly soluble calcium chloride ($CaCl_2$) was introduced for mineralization. The results showed that MEA content in the solution assisted in maintaining the pH in the appropriate range for mineralization compared to pure water. Absorption-mineralization in 1 pot occurs simultaneously, which keeps CO_2 concentration in the solution at a lower level, while maintaining the higher pH that is more appropriate for mineralization, when compared to the 2-pot setup. In addition, more ionized OH^- ions can shift the reaction into CO_3^{2-} ions and enhance $CaCO_3$ mole yields.

Keywords: CO_2 capture; Mineralization; MEA; $CaCl_2$

1. INTRODUCTION

The chemical absorption process using MEA has been a crucial technology widely applied to reduce CO_2 emissions released from various industries due to its economic feasibility and high CO_2 absorption rate [1]. The reactions for MEA-based CO_2 absorption mainly rely on the Zwitterion mechanism, which is described by Zwitterion intermediate (MEA^+COO^-) formation, Zwitterion deprotonation with contributing base (B), carbamate ($MEACOO^-$) hydrolysis, and bicarbonate (HCO_3^-) deprotonation as follows: equations (1), (2), (3), and (4), respectively, changing as the pH value decreases. [2, 3]

$$CO_2 + MEA \rightleftharpoons MEA^+COO^- \quad (1)$$

$$MEA^+COO^- + B \rightarrow MEACOO^- + BH^+ \quad (2)$$

$$MEACOO^- + H_2O \rightleftharpoons MEA + HCO_3^- \quad (3)$$

$$HCO_3^- + OH^- \rightleftharpoons H_2O + CO_3^{2-} \quad (4)$$

However, the energy requirement during MEA regeneration at high temperatures of 90 – 120 °C is still challenging [4]. This led to finding potential alternatives, such as integrating mineralization with amine-based CO_2 absorption to reduce the energy requirement and increase the stability of CO_2 storage. This approach is to mineralize CO_2 with calcium sources into $CaCO_3$ solid at room temperature, which yields a more thermodynamically stable product compared to CO_2 conversion to other chemicals [5], offers a low-cost requirement, and permanent CO_2 storage [5, 6]. So, the integrated absorption and mineralization processes can offer a lower energy requirement than thermal-based regeneration [7, 8] and a higher $CaCO_3$ yield than mineralization with deionized water [8]. The $CaCO_3$ mineralization reaction between Ca^{2+} and carbonate (CO_3^{2-}) ions is shown in equation (5) [6, 7].

$$Ca^{2+} + CO_3^{2-} \rightleftharpoons CaCO_3 \quad (5)$$

This work used $CaCl_2$, which has a higher solubility and degree of dissociation than other calcium sources [9], as a raw material to mineralize CO_3^{2-} ions into $CaCO_3$ solid. However, free Cl^- ions could extract H^+ from the MEA [10], causing a decrease in pH value and shifting the ion equilibrium toward lower CO_3^{2-} concentration [11]. Therefore, this could lead to a lower $CaCO_3$ rate and yield [12, 13]. Sodium hydroxide (NaOH) was used to adjust the initial pH of the MEA solution [14]. The ionized OH^- ions cause shifting of

species equilibrium toward CO_3^{2-} ions [10]. These could enhance the interaction of Ca^{2+} and CO_3^{2-} ions. In addition, this work also investigated the $CaCO_3$ mole yield obtained from the simultaneous absorption-mineralization (1 pot) and sequential absorption-mineralization (2 pots) processes, compared with direct mineralization with pure water treated initial pH value with NaOH.

2. EXPERIMENTAL

2.1 Material

MEA (99.5%, Grade AR, QRëC™) and $CaCl_2$ (95%, Grade AR, ANaPURE™ Co., Ltd.) were used as an absorbent for CO_2 absorption and a calcium source for $CaCO_3$ mineralization, respectively. CO_2 gas tank (99.5%) was obtained by SI Technology Co., Ltd. NaOH (97%, Grade AR, KemAus™) was used to increase the initial pH value of the MEA solution before the operation. HCl (35.4%, Grade AR, Loba Chemie) was used to measure the amount of CO_2 remaining in the MEA solution via the Chittick apparatus.

2.2 Methods

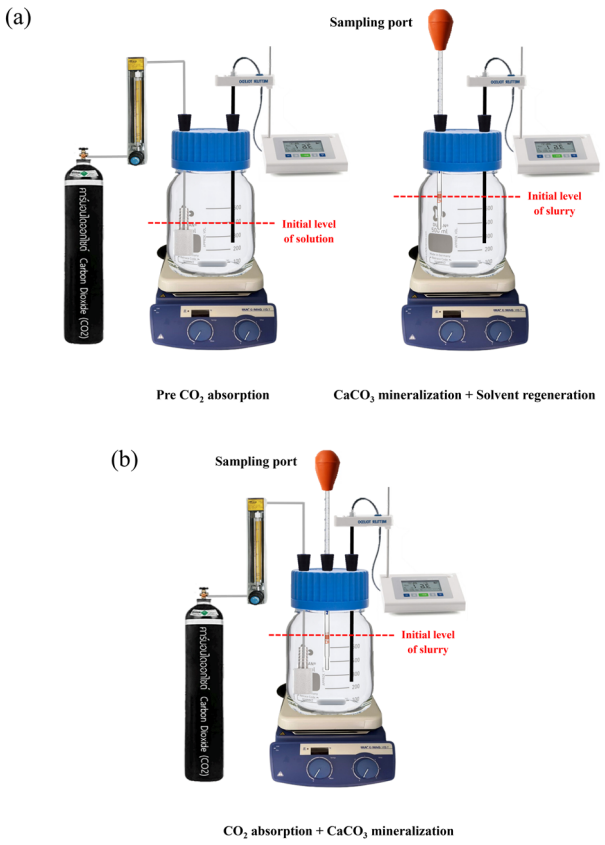

Figure.1 Experimental setup diagrams for (a) sequential absorption and mineralization (2 pots) and (b) simultaneous absorption-mineralization (1 pot).

Each experimental setup was conducted in a 500 ml laboratory bottle at the ambient temperature and pressure. The MEA concentrations were used at 0 and 1 M. The initial pH values increased by adding NaOH before $CaCO_3$ mineralization varied between 7 (final pH of CO_2-saturation MEA solution) and 13 for each experimental setup.

The first setup was 2 pots, which used 2 separate units for the absorption and the mineralization, as shown in Figure.1a. The pure CO_2 gas was bubbled through the solution contained in the laboratory bottle with a flow rate of 45 ml/min to obtain the CO_2-rich solution. The CO_2 bubbling was operated until it reached CO_2 saturation and a constant pH value, and the total amount of CO_2 absorbed in solution was then determined by the Chittick apparatus. The initial pH value of the CO_2-rich solution was adjusted before $CaCO_3$ mineralization. After that, the $CaCl_2$ solution was added to the CO_2-rich solution in a 1:1 mole ratio of the total CO_2 absorbed in the solution. The solvent regeneration/$CaCO_3$ mineralization was operated for 1 hour. The pH value was measured every 1 min during the operation. 10 ml of slurry was extracted every 15 min. The solid portion was separated and dried before analysis.

In a 1-pot setup, absorption occurs along with mineralization within the same unit, as shown in Figure.1b. MEA and $CaCl_2$, together with some NaOH, were pre-loaded into the container. The same quantity of $CaCl_2$ as a 2-pot setup was added. Then, CO_2 absorption and $CaCO_3$ mineralization immediately occurred when the pure CO_2 gas was bubbled through that solution for 1 hour. The pH value measurement and the slurry extraction were carried out in the same way as those in the 2-pot process.

2.3 Characterization

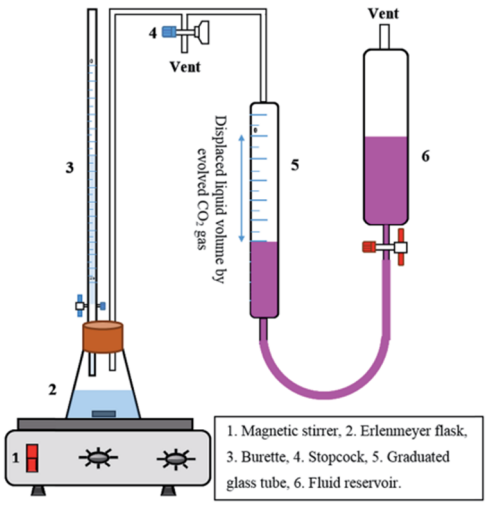

Figure.2 Schematic representation of the Chittick apparatus [15]

The Chittick apparatus (one type of acid titration) was used to find the mole and concentration of CO_2 absorbed in a liquid phase, with the equations shown in (6) and (7), respectively. Titrand consisted of 0.5 ml of

diluted liquid sample and drops of methyl orange indicator. The 1 M HCl solution used as a titrant in the burette is dropped until the titrand changes its color from yellow to red, while the CO_2 gas released from the titrand forces the liquid in the glass tube down. The volume of CO_2 gas is then known. The ambient temperature is measured during titration, while the atmospheric pressure is assumed to be 1000 hPa (1 bar).

The thermogravimetric analyzer (TGA) was employed to verify $CaCO_3$ content in the dry solid powder based on the weight loss with increasing temperature. In the same way, the X-ray diffractometer (XRD) was used to indicate its crystalline phase (Calcite, Aragonite, Vaterite). In addition, the $CaCO_3$ content in total solution at any time and the mole yield were calculated with the equations shown in (8) and (9), respectively. CO_2, $CaCO_3$, and $CaCl_2$ molecular weights are 44.01, 100.0869, and 110.98 g/mol, respectively.

$$\text{mol } CO_2 = \frac{PV}{RT} = \frac{\left(P\ (\text{hPa}) \times \frac{100\ \text{Pa}}{1\ \text{hPa}}\right) \times \left(\left(V_{\text{Displaced liquid by evoluted } CO_2} - V_{\text{Total 1 M HCl used}}\right) \text{ml} \times \frac{1\ \text{m}^3}{10^6\ \text{ml}}\right)}{\left(8.314\ \frac{\text{Pa.m}^3}{\text{mol.K}}\right) \times (T\ (^\circ\text{C}) + 273.15)\ \text{K}} \quad (6)$$

$$CO_2 \text{ concentration } \left(\frac{\text{mol } CO_2}{\text{L of solution}}\right) = \frac{\text{mol } CO_2 \text{ calculated}}{0.5 \text{ ml of liquid used for Chittick} \times \frac{1\ \text{L}}{1000\ \text{ml}}} \quad (7)$$

$$CaCO_3 \text{ content at any time} = \frac{\text{Precipitated solid (g)}}{10 \text{ ml of extracted slurry}} \times \text{Total solution at any time (ml)} \quad (8)$$

$$CaCO_3 \text{ mole yield (\%) at any time} = \frac{\text{Mole of } CaCO_3 \text{ formed at any time}}{\text{Total mole of } CaCl_2 \text{ fed before operation}} \times 100\% \quad (9)$$

3. RESULTS AND DISCUSSION

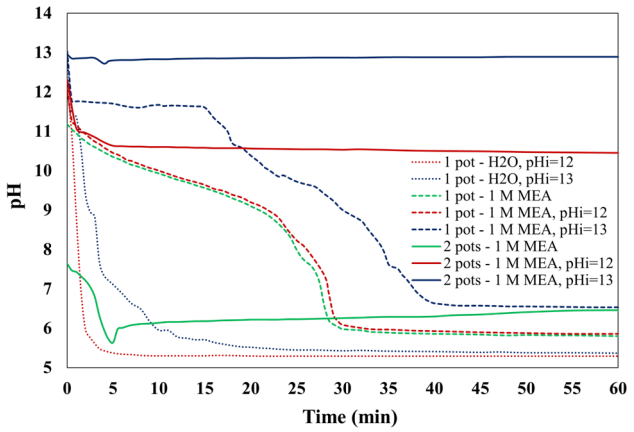

Figure.3 Changes in pH value during $CaCO_3$ mineralization for 1 hour

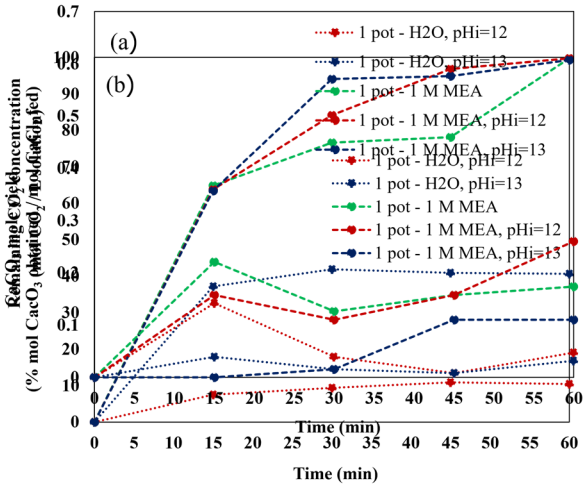

Figure.4 (a) Remaining CO_2 concentration and (b) $CaCO_3$ mole yield changing during the mineralization for 1 hour in the 1-pot process

Generally, pure water (pH = 7-8) at its original pH value results in a much lower CO_2 absorption capacity [16] and low $CaCO_3$ mineralization [8]. Figure. 3 shows that increasing the initial pH of pure water better preserved the pH value of the solution during the absorption and mineralization in the 1-pot process. The remaining CO_2 concentrations in pure water with the initial pH values of 12 and 13 were increased within the first 15 min and gradually decreased later on, as shown in Figure.4a, potentially due to low CO_2 solubility at pH < 5.5 [11, 14, 16]. The $CaCO_3$ mole yields with pure water could only achieve 10% and 40%, respectively, as shown in Figure.4b.

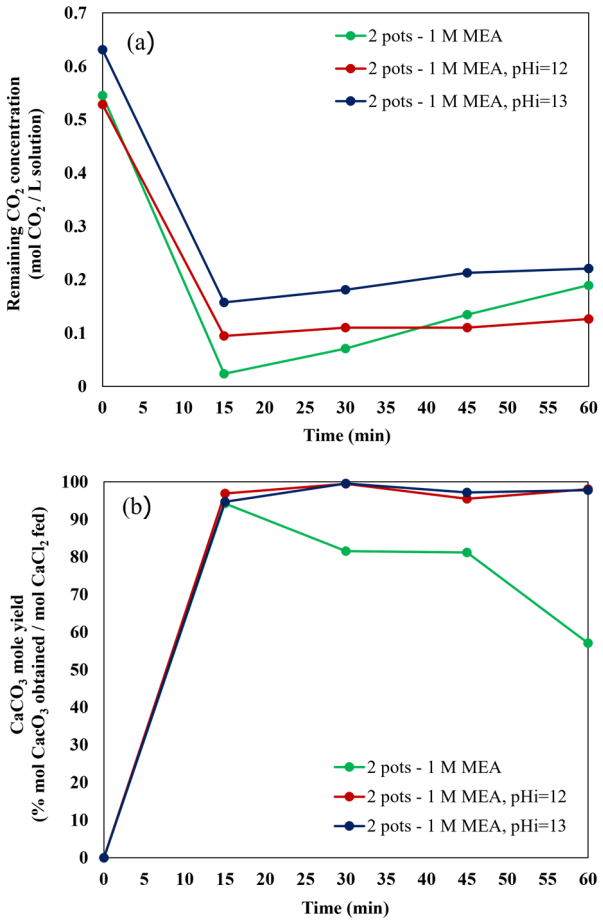

Figure.5 (a) Remaining CO_2 concentration and (b) $CaCO_3$ mole yield changing during the mineralization for 1 hour in the 2-pot process

The 1 M MEA solution was used for absorption and mineralization in the 1-pot process instead of pure water. Figure.3 shows that the pH value was slightly decreased to 5 - 7 during the first 30 min and later remained steady for 30 min because the 1 M MEA solution had higher alkalinity to absorb more CO_2 gas into a high pH-stable carbamate [16] and be hydrolyzed into HCO_3^-/CO_3^{2-} ions as the pH value decreases [17]. The decrease in the initial pH value caused a fast decrease in the remaining CO_2 concentration in the MEA solution within the first 30 min. The remaining CO_2 concentration then gradually increased for all initial pH values, as shown in Figure.4a. In addition, $CaCO_3$ nucleation occurred well at a pH value higher than 8 [12], and following crystal growth was appropriate in the pH value of 6.5 – 9.5 [12, 18], aligned well with the pH conditions during the first 30 min, therefore led to almost complete mineralization. The remaining CO_2 concentrations then decreased. For initial pH values of 12 and 13 in the solution, the $CaCO_3$ mole yields also increased as the initial pH value increased, as shown in Figure.4b.

The 2-pot process was considered using a CO_2-saturated 1 M MEA solution for mineralization. Figure.3 shows that the initial pH value decreased from 7.7 to 6.4. The remaining CO_2 concentration in the liquid readily decreased within the first 15 min and inversely increased between 15 and 60 min as shown in Figure.5a. The $CaCO_3$ mole yield was reduced, coincided with the increase in remaining CO_2 concentration, as shown in Figure.5b. These were caused by the presence of a reverse equilibrium shifting of some $CaCO_3$ into soluble Ca $(HCO_3)_2$ [11, 13]. Conversely, the increase in the initial pH of the CO_2-saturated 1 M MEA solution to 12 and 13, resulting in a decrease in CO_2 concentration in the liquid within the first 15 min and afterward remaining constant at pH values of 10 and 12, respectively. The complete mineralization of Ca into $CaCO_3$ was potentially from more OH^- ions to shift the reaction into CO_3^{2-} ions compared to the 1-pot process.

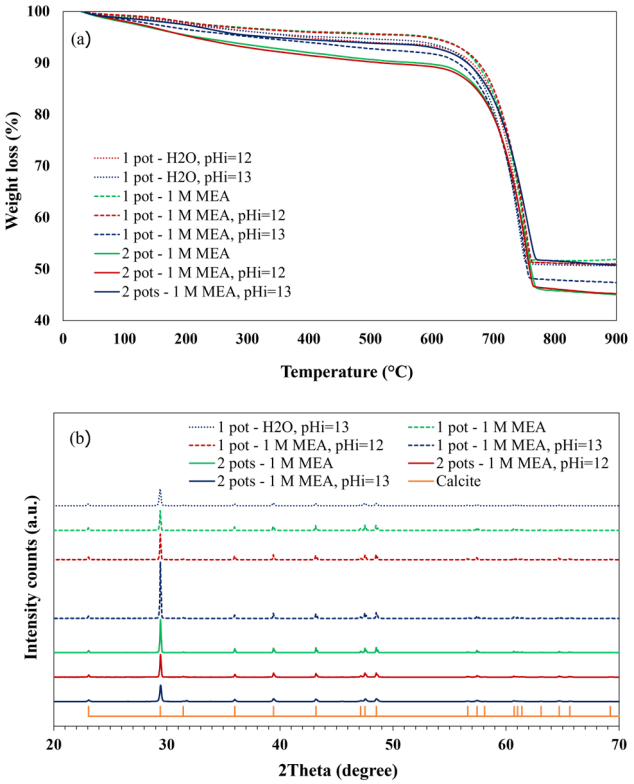

Figure.6 Solid phase characterization for the solid phase obtained from 8 experimental conditions with (a) TGA and (b) XRD analyses

From Figure.6a, the TGA curves of all experimental conditions after 1 hour mineralization showed that the weight loss appeared in the temperature ranges of 500 – 850°C, which corresponds to the decomposition reaction of $CaCO_3$ solid into CO_2 and CaO as gas and solid phases ($1CaCO_3 \rightleftharpoons 1CaO + 1CO_2$) [8], respectively. Because $CaCl_2$ is completely dissolved in the solution, it was not found in the TGA results [9]. XRD diffractograms were shown in Figure.6b, indicating that $CaCO_3$ consisted of only the calcite phase for all experimental conditions, likely because the mineralization temperature was at room temperature of 28°C [6] and the pH value was maintained above 5.5 [12].

4. CONCLUSION

This study investigated the comparison between $CaCO_3$ obtained from the simultaneous absorption-mineralization (1 pot), the sequential absorption-mineralization (2 pots), and direct mineralization with pure water, using $CaCl_2$ as calcium source. MEA content could enhance CO_2 solubility and $CaCO_3$ precipitation more than pure water. The high initial pH of the solution treated before mineralization could also enhance high CO_2 solubility and $CaCO_3$ precipitation. In addition, NaOH contents had the potential to control the decrease in pH value due to H^+ abstraction by Cl^- ions during the mineralization.

ACKNOWLEDGMENTS

This research has received funding support from the NSRF via the Program Management Unit for Human Resources & Institutional Development, Research and Innovation. [Grant number B42G670036] The author also would like to acknowledge the Center of Excellence in Particle and Material Processing Technology (CEPT) and the Department of Chemical Engineering, Faculty of Engineering, Chulalongkorn University, for financial support and equipment to perform the experiments of this work.

REFERENCES

1. Kang, M.-K., et al., Characterization and comparison of the CO2 absorption performance into aqueous, quasi-aqueous and non-aqueous MEA solutions. International Journal of Greenhouse Gas Control, 2017. 63: p. 281-288.
2. Vaidya, P.D. and E.Y. Kenig, CO2-alkanolamine reaction kinetics: a review of recent studies. Chemical Engineering & Technology: Industrial Chemistry-Plant Equipment-Process Engineering-Biotechnology, 2007. 30(11): p. 1467-1474.
3. Lv, B., et al., Mechanisms of CO2 capture into monoethanolamine solution with different CO2 loading during the absorption/desorption processes. Environmental science & technology, 2015. 49(17): p. 10728-10735.
4. Osagie, E., et al., Techno-economic evaluation of the 2-amino-2-methyl-1-propanol (AMP) process for CO2 capture from natural gas combined cycle power plant. International Journal of Greenhouse Gas Control, 2018. 70: p. 45-56.
5. Xie, H., et al., Scientific and engineering progress in CO2 mineralization using industrial waste and natural minerals. Engineering, 2015. 1(1): p. 150-157.
6. Zhang, W., Y. Xu, and Q. Wang, Coupled CO2 absorption and mineralization with low-concentration monoethanolamine. Energy, 2022. 241: p. 122524.
7. Wang, Y., et al., An integrated absorption–mineralization process for CO2 capture and sequestration: reaction mechanism, recycling stability, and energy evaluation. ACS Sustainable Chemistry & Engineering, 2021. 9(49): p. 16577-16587.
8. Yin, T., et al., Regenerable solvents mediate accelerated low temperature CO2 capture and carbon mineralization of ash and nano-scale calcium carbonate formation. Resources, Conservation and Recycling, 2022. 180: p. 106209.
9. Ding, Y., et al., Controllable synthesis of all the anhydrous CaCO3 polymorphs with various morphologies in CaCl2-NH3-CO2 aqueous system. Powder Technology, 2018. 333: p. 410-420.
10. Xie, H.-B., et al., Quantum chemical study on· Cl-initiated atmospheric degradation of monoethanolamine. Environmental science & technology, 2015. 49(22): p. 13246-13255.
11. Han, S.-J., et al., Carbon dioxide capture using calcium hydroxide aqueous solution as the absorbent. Energy & Fuels, 2011. 25(8): p. 3825-3834.
12. Ma, Y., Y. Gao, and Q. Feng, Effects of pH and temperature on CaCO3 crystallization in aqueous solution with water soluble matrix of pearls. Journal of crystal Growth, 2010. 312(21): p. 3165-3170.
13. Xie, H., et al., CO 2 mineralization of natural wollastonite into porous silica and CaCO 3 powders promoted via membrane electrolysis. Environmental Earth Sciences, 2018. 77: p. 1-10.
14. Yoo, M., S.-J. Han, and J.-H. Wee, Carbon dioxide capture capacity of sodium hydroxide aqueous solution. Journal of environmental management, 2013. 114: p. 512-519.
15. Norouzbahari, S., S. Shahhosseini, and A. Ghaemi, Chemical absorption of CO 2 into an aqueous piperazine (PZ) solution: development and validation of a rigorous dynamic rate-based model. RSC advances, 2016. 6(46): p. 40017-40032.
16. Huertas, J.I., et al., CO2 absorbing capacity of MEA. Journal of Chemistry, 2015. 2015(1): p. 965015.
17. Ji, L., et al., Integrated absorption-mineralisation for low-energy CO2 capture and sequestration. Applied energy, 2018. 225: p. 356-366.
18. Chang, R., et al., Calcium carbonate precipitation for CO2 storage and utilization: a review of the carbonate crystallization and polymorphism. Frontiers in Energy Research, 2017. 5: p. 17.

Enhancement of CO_2 capture performance of alcohols on MEA-IL-based biphasic solvents

Rimping Prathumpitak[1], Pattaraporn Kim-Lohsoontorn[1,2,*]

[1] Center of Excellence on Catalysis and Catalytic Reaction Engineering, Department of Chemical Engineering, Faculty of Engineering, Chulalongkorn University, Bangkok 10330, Thailand
[2] Bio-Circular-Green Economy Technology & Engineering Center, BCGeTEC, Faculty of Engineering, Chulalongkorn University, Bangkok 10330, Thailand
[*] Corresponding author: pattaraporn.k@chula.ac.th

ABSTRACT

MEA is commonly used for carbon dioxide (CO_2) capture since it has high reactivity with CO_2; however, amine aqueous solutions still have drawbacks such as high regeneration energy consumption, loss of the reactive amine, and equipment corrosion [1]. In this research, the CO_2 capture using MEA-IL-based was enhanced by incorporating alcohol to form a MEA/[bmim][Tf_2N] /alcohol biphasic system, reducing the stripping volume and regeneration energy consumption [2]. Herein, the CO_2 absorption behavior was analyzed using a CO_2 sensor and the Chittick titration method. The phase separation of MEA/[bmim][Tf_2N] with different types of alcohol (methanol, ethanol, propanol, butanol, pentanol, and hexanol) was investigated. Only the systems containing butanol, pentanol, and hexanol exhibited the phase separation. In addition, the phases of MEA/10%wt [bmim][Tf_2N]/1-hexanol were separated into three phases: upper phase, middle phase, and lower phase while the other alcohol system were separated into two phases, upper and lower phase. The ^{13}C-NMR analysis confirmed that the absorption product occurred, the carbamate of MEA accumulated in lower phase then only this phase was isolated for regeneration. Moreover, the volume of lower phase of the MEA/10%wt [bmim][Tf_2N]/1-hexanol (19.8% of the total volume) was lower than the MEA/10%wt [bmim][Tf_2N]/1-butanol (23.0% of the total volume). Therefore, the MEA/10%wt [bmim][Tf_2N]/1-hexanol biphasic system was expected to enhance the CO_2 capture performance while the reducing regeneration energy consumption.

Keywords: Keyword 1; CO_2 capture 2; Biphasic solve 3; Ionic liquid 4; Nonaqueous absorbents 5; Phase separation

1. INTRODUCTION

The increasing concentration of carbon dioxide (CO_2) in the atmosphere has been identified as a major driver of global climate change, impacting global temperatures, sea levels, and ecological systems [1–3]. Anthropogenic CO_2 emissions, predominantly from industrial activities since the Industrial Revolution, have accelerated these environmental shifts, thereby necessitating the urgent development of effective CO_2 capture and storage (CCS) technologies.

Several CO_2 capture techniques have been proposed and developed, including membrane separation, cryogenic separation, adsorption, chemical looping, and absorption [4]. Among these, chemical absorption using aqueous amine solutions, particularly 30%wt monoethanolamine (MEA), remains the most widely adopted method due to MEA's high reactivity with CO_2 and favorable kinetics [5]. However, conventional MEA-based systems are hindered by significant drawbacks, including high regeneration energy requirements, amine degradation and loss, and severe equipment corrosion [6–8].

Recent advancements suggest that biphasic solvent systems can address these challenges by promoting spontaneous phase separation after CO_2 absorption, thus concentrating CO_2 into a smaller solvent fraction for regeneration. This separation reduces the volume subjected to thermal treatment, minimizing energy consumption, solvent loss, and material corrosion issues [9]. Incorporating alcohol into MEA solutions offers an innovative route to optimize CO_2 absorption behaviors.

In this context, the effects of alcohol addition on the CO_2 capture performance of MEA/[bmim][Tf_2N] biphasic systems was studied, emphasizing how variations in alcohol type and IL concentration influence absorption efficiency, phase behavior, and regeneration performance.

2. EXPERIMENTAL

2.1 Chemical Reagents

The chemical reagents used in this study included monoethanolamine (MEA, 99.0% purity, LOBA CHEMIE PVT. LTD.), 1-butyl-3-methylimidazolium bis(trifluoromethylsulfonyl)imide ([bmim][Tf_2N]), and various alcohols—methanol, ethanol (99.9% purity, Merck), 1-propanol (99.5% purity, Carlo Erba Reagents), 1-butanol (99.5% purity, RCI Labscan), 1-pentanol (99.0% purity, Sigma-Aldrich), and 1-hexanol (98.0% purity, Sigma-Aldrich). Hydrochloric acid (HCl) was used for titration analysis.

2.2 Equipment

The equipment employed included an analytical balance (for precise mass measurements), a hotplate with magnetic stirrer, standard laboratory glassware, and a K33 BLG CO_2 sensor capable of detecting up to 30% CO_2 concentration with integrated RH/T measurement.

2.3 Preparation of Solutions

Biphasic solvents were prepared by mixing designated amounts of MEA, [bmim][Tf_2N], and alcohols in a 20 mL media bottle sealed with a screw cap. The mixture was stirred thoroughly at ambient temperature using a magnetic stirrer to ensure complete homogenization prior to CO_2 absorption experiments. In this study, the alcohol type was varied among methanol, ethanol, 1-propanol, 1-butanol, 1-pentanol, and 1-hexanol, while the ionic liquid species was fixed as [bmim][Tf_2N]. The IL content was varied at 5%wt and 10%wt for butanol systems, and 5%wt, 10%wt, and 12.5%wt for hexanol systems to examine the effect of IL concentration on phase separation and CO_2 capture performance.

2.4 Characterization

After CO_2 absorption, the chemical species of the absorption product was analyzed using ^{13}C-NMR spectroscopy. The spectra were recorded on the BRUKER 500 MHz fourier transform nuclear magnetic resonance spectrometer with DMSO solvent to identify carbamate formation and to investigate phase behavior.

2.5 CO_2 Capture Test

The CO_2 capture performance was evaluated by introducing a mixed gas stream (20% CO_2 and 80% N_2) into the prepared biphasic solvent samples. Each 20 mL sample was placed in a reactor and stirred at 350 rpm. The gas flow rate was maintained at 100 mL/min, and the CO_2 concentration within the reactor was monitored every 5 minutes for a total duration of 3 hours using the CO_2 sensor.

After the absorption test, CO_2 loading was quantified using the Chittick titration method. The amount of absorbed CO_2 was calculated according to the following equation:

$$mol\ CO_2 = \frac{P(V_{gas,fin} - V_{gas,in} - V_{acid})}{RT}$$

$$The\ CO_2 loading = \frac{mol\ CO_2}{volumn\ of\ absorbent}$$

where P is the atmospheric pressure (Pa), $V_{gas,fin}$ is the final volume of gas in the burette (mL), $V_{gas,in}$ is the initial volume of gas in the burette (mL), V_{acid} is the volume of 1 M HCl added (mL), R is the gas constant (8314.46 L Pa mol^{-1} K^{-1}), T is the temperature (K).

3. RESULTS AND DISCUSSION

3.1 Effect of Alcohol Type on CO_2 Loading

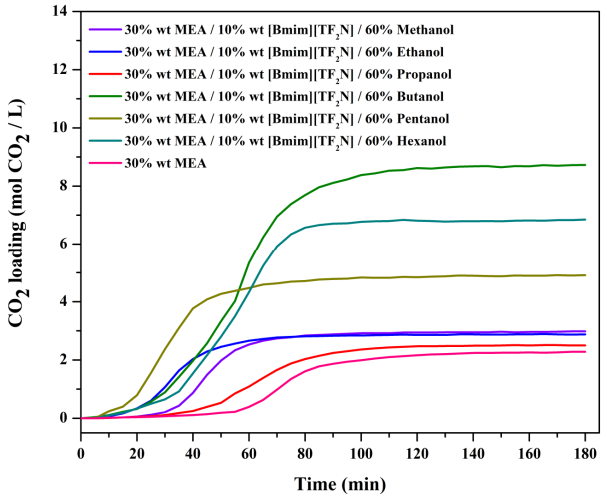

Figure 1 The CO_2 loading of various alcohol types in MEA/[bmim][Tf_2N]/alcohol biphasic systems.

Figure 1 presents the CO_2 loading profiles of various alcohol types incorporated into the 30%wt MEA/10%wt [bmim][Tf_2N]/60%wt alcohol biphasic systems. Among the tested alcohols, butanol exhibited the highest CO_2 loading, followed by hexanol, pentanol, methanol, ethanol, and propanol. The phase separation behavior observed in each alcohol-based system is summarized in Table 1. Short-chain alcohols such as methanol, ethanol, and propanol did not induce phase separation, while longer-chain alcohols including butanol, pentanol, and hexanol exhibited clear biphasic behavior with distinct upper and lower phases. The volume fractions of each phase are also presented.

Table 1 Phase separation behavior and %volume of biphasic systems with different alcohol types.

Alcohol type	Phase separation	%Volume		
		Lower	Middle	Upper
Methanol	No	-	-	-
Ethanol	No	-	-	-
Propanol	No	-	-	-
Butanol	Yes	23.0	-	77.0
Pentanol	Yes	18.2	-	81.8
Hexanol	Yes	19.8	-	80.2
Hexanol (excluding lower phase)	Yes	5.2	18.8	76.0

Interestingly, among these non-phase-separating alcohols, the trend in CO_2 loading follows methanol > ethanol > propanol. This can be explained by considering the balance between solvent viscosity and mass transfer. Although methanol has the highest polarity among the three, it also possesses the lowest viscosity, facilitating faster CO_2 diffusion and enhancing absorption rates. As the molecular size increases from ethanol to propanol, viscosity rises, and mass transfer rates decline, resulting in lower CO_2 loading accordingly.

In contrast, butanol, pentanol, and hexanol systems exhibited clear biphasic behavior, forming distinct upper and lower phases. With pentanol and hexanol, although hydrophobicity increased, the viscosity also became significantly higher, impairing mass transfer rates and slightly decreasing CO_2 loading compared to butanol. This trend indicates an optimal balance between hydrophobicity and viscosity is necessary to maximize CO_2 capture efficiency in biphasic systems.

3.2 Effect of IL Presence and IL/Alcohol Ratio on CO_2 Loading

While MEA provides high reactivity for CO_2 absorption, its limitations, including high regeneration energy and solvent degradation, necessitate further solvent optimization. To address these issues, ionic liquids such as [bmim][Tf_2N] are introduced to promote phase separation and lower regeneration energy. However, the inherent high viscosity of ILs can hinder mass transfer. Incorporating alcohols into the MEA/IL system helps to fine-tune the polarity and density, enhance phase separation, and mitigate viscosity issues. Therefore, varying the IL-to-alcohol ratio was investigated in this study, as it was anticipated that the balance between IL and alcohol content would significantly influence the CO_2 capture performance. By combining MEA, ILs, and alcohols strategically, the system leverages the chemical reactivity of MEA, the phase-splitting ability of ILs, and the viscosity-modifying effect of alcohols, resulting in improved CO_2 capture efficiency.

The effect of ionic liquid concentration on CO_2 capture performance was investigated by varying the IL-to-alcohol volume ratio in hexanol-based biphasic systems (5%wt, 10%wt, and 12.5%wt IL). As shown in Figure 2, the 5%wt IL system exhibited the highest CO_2 loading, followed by the 12.5%wt and 10%wt IL systems. The 5%wt IL system demonstrated a favorable balance between promoting phase separation and maintaining a manageable viscosity, resulting in superior CO_2 absorption efficiency. In contrast, the 10%wt and 12.5%wt IL systems exhibited lower CO_2 loading, which can be attributed to increased viscosity and the hindrance of mass transfer and reactive contact between CO_2 and the MEA phase at higher IL concentrations.

It is noteworthy that when 5%wt IL was incorporated into the MEA/hexanol system, the resulting CO_2 loading was significantly higher compared to the 5%wt IL butanol-based system, which achieved a CO_2 loading of only 5.810 mol CO_2/L. This highlights that not only IL concentration but also the choice of alcohol type critically influences the absorption performance.

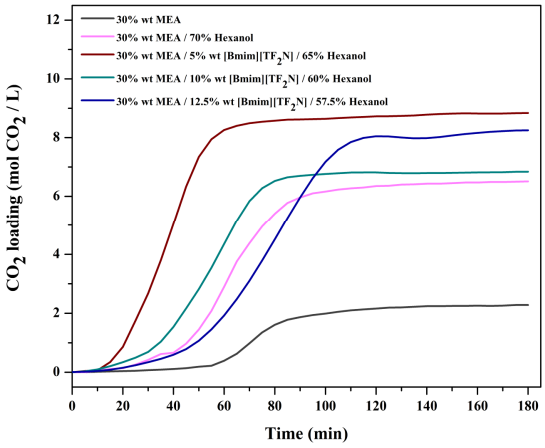

Figure 2 Effect of IL concentration on CO_2 loading in MEA/[bmim][Tf_2N]/hexanol biphasic systems.

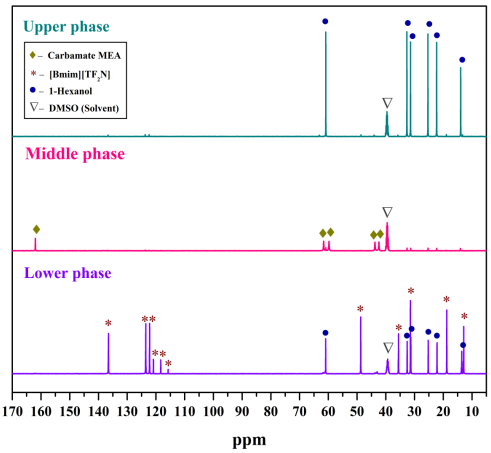

Figure 3 ^{13}C-NMR patterns of three phases in MEA/10%wt-[bmim][Tf_2N]/1-hexanol after CO_2 absorption.

3.3 Volume Fraction of Phases and Its Implication on Regeneration Energy

Beyond the influence of IL concentration and alcohol type on CO_2 loading, the resulting phase separation behavior, particularly the volume distribution between the CO_2-rich lower phase and the upper phase, plays a crucial role in determining the regeneration energy requirement. Therefore, the volume fraction of each phase was further investigated to evaluate its impact on the overall energy efficiency of the biphasic solvent system.

The volume fractions of the upper and lower phases in butanol- and hexanol-based biphasic systems were determined and summarized in Figure 4. The lower phase volume percentages for 5%wt and 10%wt IL systems in butanol were approximately 23.5% and 23.0%, respectively, whereas for hexanol, the lower phases were smaller at 18.8% and 19.8%. (For the MEA/10%wt [bmim][Tf_2N]/1-hexanol system, the lower phase (5.2%) was considered negligible; the middle phase was instead used as the effective lower phase for comparison.) The reduced lower phase volume in hexanol-based systems indicates a concentration of CO_2-rich solvent into a smaller volume, suggesting a lower solvent volume requirement for regeneration. This concentration effect, coupled with reasonably high CO_2 loading, implies a potential for significant energy savings during the stripping process. Recent studies confirm that reducing the volume of rich solvent for regeneration decreases the sensible heat, reaction heat, and vaporization heat contributions to the total regeneration energy, thereby improving overall process efficiency [3]. This aligns with the current findings, where hexanol-based systems, despite slightly lower absolute CO_2 loading compared to butanol-based systems, offer a favorable combination of reduced regeneration volume and sufficient CO_2 concentration, ultimately leading to a lower energy footprint per mole of CO_2 captured.

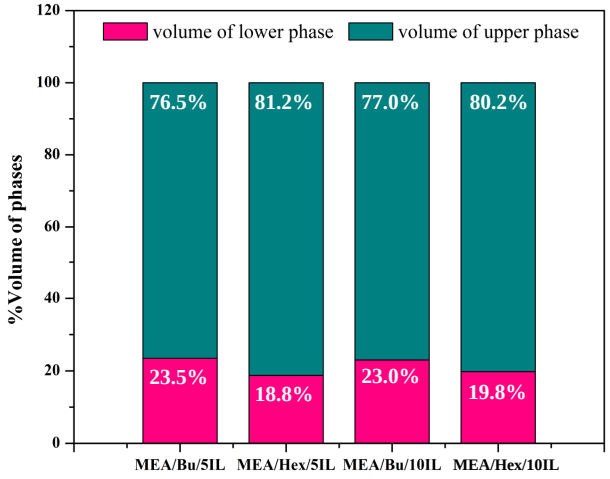

Figure 4 Volume fractions of upper and lower phases for MEA/[bmim][Tf_2N]/1-butanol and MEA/[bmim][Tf_2N]/1-hexanol systems.

3.4 Phase Behavior and NMR Analysis

The phase behavior of the biphasic systems was visually inspected and further validated through ^{13}C-NMR analysis. Notably, the 10%wt and 12.5%wt IL hexanol system demonstrated a unique three-phase separation (upper, middle, and lower phases), as captured in Figure 5. In contrast, 5%wt IL hexanol systems exhibited only two distinct phases.

The ^{13}C-NMR spectra (Figure 3) of the separated phases revealed detailed chemical environments. A characteristic peak for carbamate formation, indicative of chemical CO_2 capture via MEA, was observed at approximately 162 ppm. The lower phase showed signals corresponding primarily to [bmim][Tf_2N] and hexanol, without significant carbamate peaks, confirming the successful isolation of the lower phase from the middle phase. The upper phase exhibited peaks associated mainly with unreacted hexanol and solvent molecules, without detectable carbamate formation. These findings validate that the biphasic separation effectively concentrates CO_2 capture into the lower phase, facilitating a more energy-efficient regeneration process.

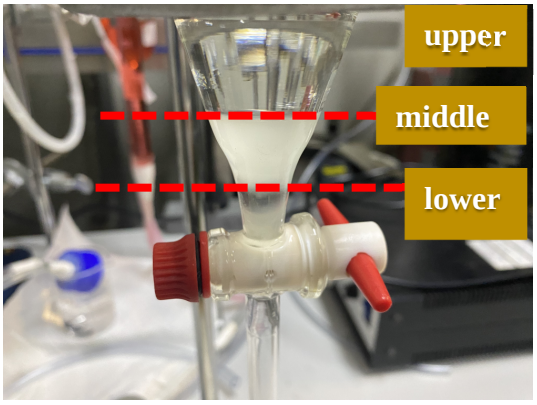

Figure 5 The photograph of phase separation of MEA/10%wt [bmim][Tf_2N]/1-hexanol after standing overnight.

4. CONCLUSION

This study systematically investigated the influence of alcohol type and IL concentration on the CO_2 capture performance in MEA-based biphasic solvent systems. Among the tested alcohols, butanol exhibited the highest CO_2 loading due to its optimal balance between hydrophobicity and viscosity, while hexanol-based systems, despite slightly lower absolute CO_2 loading, achieved superior phase separation and a reduced lower phase volume, favorably impacting regeneration energy requirements. Varying the ratio of IL-alcohol further revealed that an optimized IL concentration was essential to promote phase separation while minimizing viscosity related mass transfer limitations. Notably, the 5%wt IL with hexanol system demonstrated the highest CO_2 loading performance and phase stability.

The findings were further validated through visual observation and ^{13}C-NMR analysis, which confirmed that CO_2 capture occurred in the CO_2-rich lower phase, while the IL-rich and alcohol-rich phases remained largely unreactive. These results underscore the importance of solvent composition tuning to achieve a favorable balance between CO_2 loading capacity, phase separation efficiency, and regeneration energy minimization.

Despite the promising results, certain limitations were identified. Higher IL concentrations were associated with increased solvent viscosity, which can hinder CO_2 absorption kinetics. Future studies should explore the use of alternative ionic liquids with lower viscosities, hybrid solvent formulations, and the optimization of operating conditions to further enhance the performance and applicability of biphasic solvent systems for large-scale CO_2 capture.

ACKNOWLEDGMENTS

This research was funded by Research Cess Fund, Malaysia-Thailand Joint Authority (MTJA) and the NSRF via the Program Management Unit for Human Resources & Institutional Development, Research and Innovation [grant number grant number B16F640164]. Kim-Lohsoontorn also would like to acknowledge Thailand Science research and Innovation Fund Chulalongkorn University (BCG66210021). Prathumpitak would like to acknowledge a scholarship from Department of Chemical Engineering, Chulalongkorn University.

REFERENCES

1. Yang L, Chen J, Ma N, Li X, Huang Z. CO2 absorption enhancement of fluorinated ionic liquids on nonaqueous biphasic absorbents: Experimental and theoretical study. *Carbon Capture Science & Technology* 2023; 9: 100147.
2. Hira U, Kamal A, Tahir J. Chapter 11 - Industrial carbon dioxide capture and utilization. *Green Sustainable Process for Chemical and Environmental Engineering and Science* 2023: 231-278.
3. Zhang W, Wu H, Zhang S, Song J. Physical and Chemical Absorption of CO_2 in Biphasic Solvents. *Ind Eng Chem Res.* 2019;58(30):13570–13578.
4. Yang D, Wang Z, Guo Y, Song J. Nonaqueous Biphasic Solvents for CO_2 Capture: Progress and Perspective. *Chem Eng J.* 2023;452:139438.
5. Jiang K, Zhang X, Wang Z, Yu G, Song J. Advances in Applications of Ionic Liquids for Phase Change CO_2 Capture. *Chem Eng J.* 2022;445:136767.
6. Ritchie H, Roser M. Who has contributed most to global CO_2 emissions? Our World in Data. 2019.
7. Li X, Chen X, Hu Y, Song J. Thermodynamic Study of CO_2 Capture Using Biphasic Systems. *Appl Energy.* 2019;242:302–310.
8. Wu W, Zhang S, Hu Y, Dai S. Advances in Ionic Liquid-Based Solvents for Carbon Capture. *Environ Sci Technol.* 2014;48(10):5996–6002.
9. Ueda K, Saito S, Sugo T. Solubility and Polarity Effects of Alcohols in Solvent Systems. *Polym J.* 2021;53:93–102.
10. Liu Q, Chen X, Hu Y. CO_2 Capture Performance of Nonaqueous Solvents: A Review. *J Ind Eng Chem.* 2024;134:28–50.

Accelerated aging testing of three types of transformer oils in 1 phase distribution transformer

Bowornchai Chareonteraboon[1], Boonyawan Yoosuk[1,*], Sittikorn Lapapong[2], Supakit Chotigo[3], Suthisak Sitthichokchai[1,3], Pathompong Janetaisong[1]

[1] National Energy Technology Center (ENTEC), National Science and Technology Development Agency, Thailand Science Park, Pathum Thani 12120, Thailand
[2] National metals and material Technology Center (MTEC), National Science and Technology Development Agency, Thailand Science Park, Pathum Thani 12120, Thailand
[3] Department of Chemical Engineering, Faculty of Engineering, King Mongkut's University of Technology Thonburi, Bangkok 10140, Thailand
[*] Corresponding author: boonyawan.yoo@entec.co.th

ABSTRACT

EnPAT is a less flammable bio-based transformer oil derived from palm oil developed by National Energy Technology Center (ENTEC). Compared to conventional mineral oil, EnPAT exhibits superior characteristics, including fire point above 300˚C and biodegradable. This study determines the thermal and oxidative degradation of transformer insulation oils of three transformer oils: EnPAT, imported bio bio-based transformer oil, and mineral oil. Using a 6 kVA, 20 kV/220 V transformer as a testing chamber, accelerated aging tests were performed following IEC 60076-7 (2018) standards to simulate 70% expected lifespan of transformer. The duration of testing was 34-46 days. Short-circuit heating was applied to generate hot-spot temperatures ranging between 109.97°C and 113.73°C. Insulation degradation was monitored through dissolved gas analysis (DGA), furan concentration measurements, and the degree of polymerization (DP) of the cellulose-based paper insulation. Results revealed that mineral oil suffered harsh degradation (DP <200; 2-furaldehyde >1,280 ppb), while both EnPAT and imported oil maintained DP values above 400 with furan levels between 250 and 600 ppb, indicating significantly enhanced chemical stability. The estimated degree of polymerization can be determined using 2-furaldehyde concentration with the Chendong equation. The status of degradation as evaluated by the Double Engineering Company. The results confirm that EnPAT provides insulation paper protection comparable to imported bio bio-based transformer oil, as evidenced by DP and 2-Furaldehyde analysis, while exhibiting superior performance over conventional mineral oil.

Keywords: Mineral oil; Bio-based transformer oil; Transformer oil; Degree of polymerization (DP)

1. INTRODUCTION

Mineral oil has been used as both an insulating and cooling fluid in electrical transformers for over a century [1]. Billions of liters of oil are utilized in electrical equipment worldwide, primarily due to its superior technical performance, availability, relatively low cost compared to other insulating materials, and recyclability.

During transformer operation, various forms of wear and degradation can occur within the insulation system. The effects of thermal, electrical, chemical and mechanical stresses, such as voltage spikes and hot zone, are responsible for changes in insulation characteristics. Therefore, monitoring the performance of these devices is essential to ensure safety and prevent costly failures [2].

In recent years, utilities and industries have increasingly recognized the advantages of using natural esters as insulating oils, particularly due to environmental considerations. Issues such as corrosive sulfur in mineral oil and the extended lifespan of insulating paper when using natural ester oils have fueled this interest [3]. Given these factors, natural ester transformer oil has emerged as a viable alternative to mineral oil.

Currently, several internationally recognized natural ester transformer oils are available, including BIOTEMP®, Environtemp FR3®, and MIDEL eN (M&I Materials), which are primarily derived from soybean and rapeseed oils [4].

Thailand is the third largest palm oil producer in the world with around 0.8 million hectares of oil palm

plantations in 2018, an increase of 60% compared to 2009. These plantations produce around 3 million tons of crude palm oil, which is mainly used for edible oil (38%), biodiesel production (37%), exports (11%) and stocks (14%) [5]. However, with Thailand aiming for carbon neutrality by 2050, a move away from petroleum-based energy is expected, which could lead to a decrease in biodiesel consumption and an oversupply of palm oil [6].

Developing alternative palm oil-based products, including natural ester transformer oil, presents a viable solution. In response to this opportunity, the National Energy Technology Center (ENTEC), under the National Science and Technology Development Agency (NSTDA), has developed EnPAT, a bio-based transformer oil with superior properties compared to conventional mineral oil. EnPAT is less flammable, with a flash point exceeding 300°C, and is biodegradable, making it a more sustainable alternative for transformer applications. In this study, accelerated aging tests are performed on single-phase distribution transformers to determine the degradation characteristics of the transformer oil and its effects on the insulation of the transformer, especially the insulating paper. Three types of insulating oils are compared: EnPAT, imported bio bio-based transformer oil, and mineral oil. The research analyzes the physical, chemical and electrical properties of the insulating oils and evaluates their composition before and after the aging process using gas chromatography. In addition, the gas composition after the test is analyzed using dissolved gas analysis (DGA).

2. EXPERIMENTAL

EnPAT oil, mineral oil, and imported bio-based transformer oil were initially evaluated for their physical, chemical, and electrical properties before the experiment. Each type of oil was then filled into a single-phase transformer with a rating of 6 kVA, 20kV/220V. The transformer was connected with a Variac brand voltage regulator to supply electrical power through the high-voltage terminal. A short circuit was applied on the low-voltage winding side to generate a hotspot temperature within the winding, thereby accelerating the aging process. Each transformer was connected three monitoring devices: a thermocouple to measure the top oil temperature, an another thermocouple to measure the ambient temperature surrounding the transformer, and a short-circuit current monitoring device on the low-voltage side. The equipment set up and installation are illustrated in Figure 1.

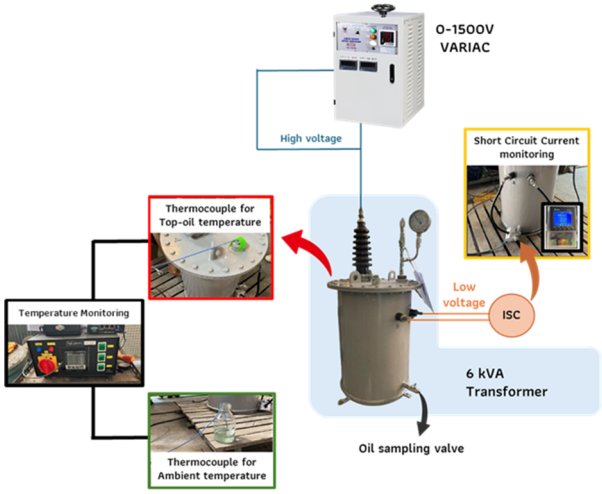

Figure 1 Shows the setup diagram of equipment for aging using a single-phase transformer.

The accelerated aging process was conducted until the transformer reached 70% loss of life in accordance with the IEC60076-7 (2018) standard, with the top oil temperature maintained at 90°C [7]. The test durations for EnPAT, mineral oil, and imported bio bio-based transformer oil were 40, 46, and 34 days, respectively, with hot-spot temperatures recorded at 110.27°C, 109.97°C, and 113.73°C, respectively. Upon completion of the accelerated aging process, the top oil temperature was allowed to decrease to ambient room temperature before measuring the moisture content of the insulating paper. Additionally, the physical, chemical, and electrical properties of the transformer oils were examined, and gas analysis was conducted using a dissolved gas analysis (DGA) device following ASTM D3612 to determine the gas composition in the transformer oil [8]. Furthermore, furan content was determined using high-performance liquid Chromatography (HPLC) according to ASTM D5837 [9]. The degree of polymerization (DP) of 0.18 mm diamond dot insulating paper and 0.5 mm thickness insulating paper placed in the transformers was measured both before and after testing. Additionally, the DP value was estimated using the Chendong equation based on the concentration of 2-furaldehyde. As shown in Table 1, Double Engineering Company evaluated the state of degradation [10].

Chendong equation : $DP = \frac{1.51 - \log_{10}(2 - FAL_{ppm})}{0.0035}$

Table 1 shows the Double Engineering Company's insulating paper condition assessment requirements.

2-FAL (ppb)	Estimated DP	Status
<250	>600	Good condition
>250-1280	400-600	Midlife
>1280	<400	Last third of life

3. RESULTS AND DISCUSSION

As shown in Figure 2, the appearance of the transformer oils before and after the accelerated aging process in actual transformers shows that the color of all three transformer oil types were darker after the aging process. Table 2 exhibited the physical, chemical and electrical properties of the three transformer oils before and after the degradation test and shows that the properties of all three types of transformer oil changed evenly after the test. Comparing mineral oil with two types of bio-based transformer oils, mineral oil showed a smaller increase in acid value and moisture content. However, it showed a significantly greater decrease in dielectric breakdown voltage, indicating a lower water tolerance compared to those bio-based transformer oils. The higher increase in moisture content, the bio-based oils maintained the dielectric breakdown voltage within the acceptable range of IEC 62770 [11], which requires a minimum dielectric breakdown voltage of 35 kV. Based on these results mineral oil does not meet the standard and therefore requires appropriate treatment or disposal. The increased moisture content is primarily due to the oxidation and pyrolysis of insulating paper, which produces water, furan compounds and various organic acids as by-products in the transformer. These reactions lead to a corresponding increase in both the moisture and acid content [12]. In addition, the measured acidity values after accelerated aging show that bio-based transformer oils have higher acidity values than mineral oils. This phenomenon is primarily attributed to the hydrolysis of triglycerides within the molecular structure of the bio-based oils, which leads to the formation of free fatty a cids [13]. This reaction leads to a rapid increase in the acid number of bio-based oils, which can directly effect on the measurement of the tan delta at 90°C. The tan delta value reflects the thermal energy loss due to the vibration of polar molecules; with increasing acidity, the tan delta value increases accordingly. The superior fire safety of both types of bio-based transformer oils, as shown by their PMCC flash points, which are almost twice as high as those of mineral oil.

Figure 2 shows the color properties of EnPAT, imported bio-transformer oil and mineral oil before and after accelerated aging.

Table 2 shows the physical, chemical, and electrical properties of three transformer oil are summarized both before and after accelerated aging.

Property	EnPAT		Imported bio transformer oil		Mineral oil	
	Bef.	After	Bef.	After	Bef.	After
Physical						
Color number	1	1.3	<0.5	1	<0.5	1.1
Flash point CC (°C)	284	-	270	-	152	-
Pour point (°C)	5	5	-21	-19	-49	-53
Viscosity 40°C (mm^2/s)	41.08	40.71	32.62	32.92	8.14	8.72
Electrical						
DBV* (kV)	92	68	83.4	58.7	43.9	24.7
Tan delta @ 90 °C	0.0165	0.1162	0.0042	0.2516	0.0009	0.0665
Chemical						
Water Content (ppm)	33	286	119	334	34	40
Acid number (mg of KOH/g)	0.015	0.24	0.029	0.451	0.009	0.106
Oxidation stability (h)	>100	92	15	12	>100	>100
Dielectric breakdown voltage (DBV*)						

The analysis of Dissolved Gas Analysis (DGA) results in Table 3 that identified methane (CH_4), ethylene (C_2H_4), and acetylene (C_2H_2) as key fault gases indicating the degradation of transformer oil during operation, which can be caused by corona discharge, sparking, arcing, or oil leakage. In addition, the presence of carbon monoxide (CO) and carbon dioxide (CO_2) gases indicates the degradation of the transformer insulation paper. Duval triangle [14] analysis revealed that the EnPAT transformer oil contained CH_4, C_2H_4 and C_2H_2 at 81.6%, 18.4% and 0% respectively, indicating that degradation of the transformer oil occurred at temperatures below 300°C. The values for CO and CO_2 were 2,109 ppm and 66,158 ppm respectively, also representing degradation of the insulating paper. Similarly, the imported bio-transformer oil exhibited gas contents of CH_4, C_2H_4 and C_2H_2 of 89.2%, 10.8% and 0%, respectively, with CO and CO_2 concentrations of 1,495 ppm and 69,666 ppm, respectively, indicating comparable insulation protection performance to the EnPAT oil. In contrast, mineral oil showed that CH_4, C_2H_4 and C_2H_2 values of 78.9%, 21.3% and 0%, respectively, indicating degradation of the transformer oil occurred at 300–700°C. The CO and CO_2 values were significantly higher than bio-transformer oil at 3,376 ppm and 106,624 ppm, indicating greater degradation of the insulating paper compared to bio-based transformer oils, which offer better insulation protection.

Table 3 the results of the analysis of dissolved gasses in three types of transformer oils after the accelerated aging process.

Types of Dissolved Gases	Gas Content in Various Types of Insulating Oil (ppm)		
	EnPAT	Imported bio transformer oil	Mineral oil
H_2	317	319	406
CH_4	40	58	74
C_2H_4	9	7	20
C_2H_2	0	0	0
CO	2,109	1,495	3,376
CO_2	66,158	69,666	106,624

As part of the research in collaboration with EGAT, oil samples were collected for furan analysis. The results are presented in Table 4. Each type of furan compound can serve as an indicator of the cause of transformer insulation degradation. Among them, 2-furfural (2-FAL) is commonly used as the main indicator of paper insulation aging, as it is formed from the hydrolysis of glycosidic bonds in insulating paper (cellulose paper) and directly reflects the degree of paper degradation. Based on the experimental results, EnPAT oil demonstrated the highest effectiveness in protecting paper insulation, followed by imported bio-transformer oil. Mineral oil exhibited the highest concentration of furan compounds, which reaching up to 1,503 ppm, indicating the most severe degradation among the tested transformer oils. Other furan compounds indicate specific abnormal conditions in the insulation system. In particular, a high concentration of 2-furanol (2-FOL) in mineral oil corresponds to its lower moisture absorption capacity compared to imported bio-transformer oil and EnPAT [15]. Regarding 5-hydroxymethylfurfural (5-HMF), which indicates oxidation-induced degradation, the concentration trend is as follows: Imported bio-transformer oil > EnPAT > mineral oil. This corresponds to the oxidation susceptibility of the individual oil types—imported bio-transformer oil, which contains more double bonds, is more prone to oxidation than EnPAT, which is derived from palm oil and exhibits better oxidation resistance than imported bio transformer oil. For 5-methyl-2-furfural (5M2F), an indicator of degradation under high temperatures, the concentration trend is as follows: Mineral oil > Imported bio-transformer oil > EnPAT. This is consistent with the superior thermal stability of ester-based oils (imported bio-transformer oil and EnPAT) compared to mineral oil [15].

Table 4 Concentration of Furan Compounds in Oil After Aging Tests.

Furan types	Furan Content in Various Types of Insulating Oil (ppb)		
	EnPAT	Imported bio transformer oil	Mineral oil
2-FAL (General overheating)	243	572	1,503
2-ACF (Rare causes)	355	1	69
2-FOL (High moisture)	3,135	562	806
5-HMF (Oxidation)	742	1,035	14
5-M2F (High temperature)	9	34	320

The results are shown in Table 5. Paper samples have been collected for the DP (Degree of Polymerization) test and for evaluation using the Chendong equation based on the 2-FAL values. According to the test results, EnPAT oil produced the highest DP value, indicating that paper insulation was more protective. This suggests that paper insulation can be protected by EnPAT transformer oil just as well as by imported bio-transformer oil. Furthermore, the paper insulation condition in the imported bio transformer oil is classified as "Midlife" as per the Double Engineering Company's assessment requirements, whereas it is categorized as "Good condition" in the EnPAT oil. The lowest DP value was found in mineral oil, which was classified as being in the "Last third of life." According to these findings, bio-based transformer oils, especially EnPAT and the imported bio-transformer oil, are consistently effective in maintaining the integrity of paper insulation.

Table 5 Degree of polymerization and 2-furaldehyde concentration in mineral oil, imported transformer oil, and EnPAT after testing.

Oil type	Degree of Polymerization Type of insulation paper		Estimated DP*	2-FAL (ppb)	Status**
	0.18 mm.	0.5 mm.			
Before	976	1,086	-	0	-
EnPAT	915	452	606.97	243	Good condition
Imported bio transformer oil	945	493	500.74	572	Mildlife
Mineral oil	875	356	380.87	1,503	Last third of life

* The DP from the 2-Furaldehyde content using the chendong equation
** Double Engineering Company

4. CONCLUSION

According to this study, EnPAT, a bio-transformer oil that made from palm oil and produced in Thailand, outperforms foreign bio-transformer oils in terms of performance and provides better insulating protection and resistance to degradation than traditional mineral oil. EnPAT exceeded mineral oil in all important performance measurements, retaining a high degree of polymerization (DP >450), low furan content, mild gas generation, and outstanding dielectric strength (>68 kV) during age, according to tests of accelerated aging based on IEC 60076-7 (2018). Bio transformer oils, especially EnPAT, demonstrated superior water tolerance and thermal stability in spite of their increased acidity. These results demonstrate the promise of EnPAT as a locally accessible, secure, and eco-friendly substitute for sustainable transformer applications in Thailand.

ACKNOWLEDGMENTS

The authors gratefully acknowledge the funding support from the National Energy Technology Center (ENTEC), National Science and Technology Development Agency (P2450508 project).

REFERENCES

1. 1. T.O. Rouse. Mineral insulating oil in transformers. IEEE Electrical Insulation Magazine 1998; 14(3): 6-16.
2. M.R. Mohammad, S. Abbospour. Aging study and lifetime estimation of transformer mineral oil. American journal of engineering and applied sciences 2008; 1.4: 384-388.

3. F. Scatiggio, V. Tumiatti, R. Maina, M. Tumiatti, M. Pompili, R. Bartnikas. Corrosive sulfur induced failures in oil-filled electrical power transformers and shunt reactors. IEEE transactions on power delivery 2009; 24(3): 1240-1248.
4. H. Yu, P. Yu, Y. Luo. Renewable low-viscosity dielectrics based on vegetable oil methyl esters. Journal of Electrical Engineering and Technology 201712(2), 820-829.
5. C. Sowcharoensuk, Industry Outlook 2020-2022: Palm Oil Industry, Krungsri, Research. 2020.
6. Department of Alternative Energy Development and Efficiency (DEDE), Ministry of Energy 2014. Energy Balance of Thailand 2014.
7. IEC, 60076-7. Power Transformers Part 7: Loading Guide for Mineral-Oil-Immersed Power Transformers, 2018.
8. ASTM D3612-02. Standard test method for analysis of gases dissolved in electrical insulating oil by gas chromatography. 2017; 22.
9. ASTM D 5837-05, 2005. Standard Test Method for Furanic Compounds in Electrical Insulating Liquids by High-Performance Liquid Chromatography (HPLC). 2015.
10. X. Chendong, C.D. Xue. Monitoring paper insulation aging by measuring furfural contents in oil. In: 7th international symposium on high voltage engineering. 1991. p. 139-142.
11. IEC 62770: 2013. International Electrotechnical Commission. Fluids for electrotechnical applications–Unused natural esters for transformers and similar electrical equipment. 2013.
12. P. Przybylek, Z. Nadolny, H.M. Grzesiak. Bubble effect as a consequence of dielectric losses in cellulose insulation. IEEE Transactions on Dielectrics and Electrical Insulation. 2010; 17(3): 913-919.
13. K. Bandara , C. Ekanayake, T.K. Saha, P.K. Annamalai. Understanding the ageing aspects of natural ester based insulation liquid in power transformer. IEEE Transactions on Dielectrics and Electrical Insulation. 2016; 23(1): 246-257.
14. Z. Shen, F. Wang, Z. Wang, J. Li. A critical review of plant-based insulating fluids for transformer: 30-year development. Renewable and Sustainable Energy Reviews. 2021: 141, 110783.
15. J. Unsworth, F. Mitchell. Degradation of electrical insulating paper monitored with high performance liquid chromatography. IEEE transactions on electrical insulation. 1990: 25(4): 737-746.

Development of fibroin-based solid electrolyte for electrochromic windows

Akarawin Pimarnthisakorn[1,2], Anan Junsukhon[1,2], Pailin Ngaotrakanwiwat[1,3,*]

[1] Department of Chemical Engineering, Faculty of Engineering, Burapha University, Chonburi 20131, Thailand
[2] Research Unit of Developing Technology and Innovation of Alternative Energy for Industries, Burapha University, Chonburi 20131, Thailand
[3] Interdisciplinary Center for Decarbonisation and Green Energy, Faculty of Engineering, Burapha University, Chonburi 20131, Thailand
[*] Corresponding author: pailin@eng.buu.ac.th

ABSTRACT

The electrochromic window is a promising technology for reducing energy consumption related to thermal comfort in glass buildings. However, the leakage of liquid electrolytes in the electrochromic window hinders the application of electrochromic windows. Solid polymer electrolytes have been synthesized to address this issue. The fibroin-based solid electrolyte has been investigated as a potential solution to address environmental concerns and reduce the reliance on petroleum-based solid electrolytes. This study investigated the effects of the electrolyte thickness (7-27 μm) and lithium salt concentration (7.25-21.75 wt%) on ionic conductivity. Consequently, the electrochromic window's optical density and coloration efficiency were examined. Moreover, ATR-FTIR and UV-Vis spectrophotometers were used to characterize the change in the secondary structure of silk fibroin and the light transmission caused by the addition of lithium salt and varying thickness. The results showed that the highest ionic conductivity of 0.4 mS/cm, achieved in the electrolyte containing a 14.5wt% lithium salt with a thickness of 10 ± 1 μm, was 3.3 times lower than that of the liquid electrolyte. Furthermore, the optimal electrolyte was assembled into the electrochromic window consisting of WO_3 and NiO-based electrodes. After the applied potential of -3.0 V, the transmittance of visible and NIR light decreased from 74.15% to 3.20% and from 74.22% to 3.04%, resulting in the coloration efficiency of 124.66 and 126.73 cm^2/C, respectively.

Keywords: Fibroin; Solid electrolyte; Ionic conductivity; Electrochromic window

1. INTRODUCTION

Electrochromism is a phenomenon in which the optical properties of a material change reversibly upon the application of an external voltage. In particular, electrochromic devices are promising technologies for enhancing building energy efficiency due to the selective control of visible and NIR transmission through the window. It typically consists of a transparent conducting oxide layer, an electrochromic layer, an ion transport layer, an ion storage layer, and another transparent conducting oxide layer arranged sequentially. Apart from developing electrochromic materials to enhance the efficiency of electrochromic devices [1,2], the ion transport layer plays a crucial role as an ion source, enabling ion movement between the electrochromic and ion storage layers when a potential is applied to the device.

Polymer electrolytes have been tailored as an ion transport layer for electrochromic devices to replace liquid electrolytes, which suffer from issues such as leakage, volatility, and instability under expansive electrochemical windows. They should exhibit high ionic conductivity (10^{-3}-10^{-7} S/cm) and low electronic conductivity (<10^{-12} S/cm), along with high optical transparency, electrochemical stability over a wide voltage range, good interfacial contact with adjacent layers, and high thermal stability [3]. Among these, the ionic conductivity of the electrolyte serves as a key parameter influenced by factors such as the ion species dissociated from the salt, the lattice energy of the salt, salt concentration, the diffusivity and mobility of the cations, and the amorphous portion and free volume of the polymer matrix [4].

Although many candidate ions are available, lithium ions are widely used due to their small size, which contributes to high ionic conductivity, excellent electrochemical stability, and compatibility with a wide voltage window. Common lithium salts, including $LiPF_6$, $LiBF_4$, LiCl, and $LiClO_4$, are widely used as dopants in polymer electrolytes. However, $LiClO_4$ is relatively more stable against hydrolysis compared to $LiPF_6$ and $LiBF_4$, thus avoiding the formation of HF, which can corrode the electrodes [2,5].

Composite polymer electrolytes (CPEs) are typically formulated by blending a host polymer with an ionic salt and incorporating additives, such as plasticizers, to enhance both ionic conductivity and mechanical properties. A well-known system is based on polyethylene oxide (PEO) blended with lithium perchlorate ($LiClO_4$) and propylene carbonate (PC) as a plasticizer. In this system (PEO–$LiClO_4$–PC), the molar ratio of ethylene oxide (EO) units to Li^+ ions are maintained at EO/Li^+ = 18, with 40 wt% PC, resulting in an ionic conductivity of 0.1 mS/cm at 30 °C [6]. Similarly, poly(methyl methacrylate) (PMMA) has been used to prepare CPEs with PC and $LiClO_4$. The formulation (PMMA: $LiClO_4$: PC = 30:13:57) exhibits an ionic conductivity of 5.64 mS/cm at 80 °C [7].

In recent years, natural polymer-based ion transport layers, such as polysaccharides and proteins, have attracted attention due to their environmental friendliness and compatibility with green electrochromic systems. A polysaccharide-based electrolyte composed of cellulose acetate (CA) blended with 0.8 M $LiClO_4$ in propylene carbonate (PC) at 30 wt% exhibits high ionic conductivity (4.6 mS/cm) and good optical transparency [8]. Fibroin, a protein extracted from silk, possesses a unique hierarchical structure in which protein chains are assembled through noncovalent interactions. It exhibits exceptional mechanical toughness, low density, biocompatibility, and biodegradability [9]. Fibroin has been blended with lithium bis(trifluoromethanesulfonyl)imide (LiTFSI) or lithium tetrafluoroborate ($LiBF_4$), along with glycerol as a plasticizer, yielding ionic conductivities of 1.06×10^{-9} and 1.13×10^{-9} mS/cm, respectively [10]. However, these values fall significantly below the minimum threshold (10^{-4} to 10^{-7} S/cm) required for practical applications in electrochemical devices [9].

The ion transport in amorphous electrolytes, as described by the polymer segment migration model, is affected by the amount of free Li^+ ions, which depends on the dissociation of the lithium salt within the polymer matrix and the mobility of the polymer segments [11]. The low lattice energy of $LiClO_4$ salt and the high dielectric constant of propylene carbonate (PC) facilitate the dissociation of Li^+ ions. At the same time, the modulation of the conformation and proportion of the semi-amorphous structure (α-helix and random coil) and the partially crystalline structure (β-sheet) of fibroin has been carried out through physical and chemical processes [12].

In this work, we prepared a solid electrolyte by blending fibroin with $LiClO_4$ and propylene carbonate (PC) for application in electrochromic devices. This study also investigates the effects of electrolyte thickness and lithium salt concentration on ionic conductivity. A complementary electrochromic device incorporating WO_3-based and NiO-based electrodes were assembled using the prepared solid electrolyte to evaluate the performance of the electrochromic device.

2. EXPERIMENTAL

Silk fibroin (SF) solution was prepared from Bombyx mori cocoons. The cocoons were cut into small pieces and boiled twice in 0.02 M Na_2CO_3 solution for 1 hour to remove sericin. The resulting fibers were rinsed thoroughly with distilled water and dried overnight. The dried SF fibers were dissolved in 9.3 M LiBr solution at 70 °C for 1 hour. The solution was dialyzed against distilled water using a cellulose dialysis membrane with a molecular weight cutoff (MWCO) of 3500 for 2 days. The resulting fibroin solution had a concentration of approximately 4–6 wt%. The SF-based electrolytes were prepared by mixing 1.2 ml of SF solution with PC and $LiClO_4$ with concentrations of 7.25 to 21.75 wt%. The mixture was sonicated using a probe sonicator at a frequency of 10 kHz. The resulting solution was cast onto a Petri dish and left to dry at room temperature for 24 hours.

The ionic conductivity of the electrolytes was measured by assembling a two-electrode electrochemical cell using two ITO-coated glass substrates. Electrochemical impedance spectroscopy (EIS) was conducted over a frequency range of 100 Hz to 1 MHz with an amplitude of 10 mV using a potentiostat (Autolab PGSTAT302N). The bulk resistance (R_{ct}) was determined by fitting the impedance data to an equivalent circuit model. The ionic conductivity (σ) was calculated using the equation $\sigma = l / (R_{ct} \times A)$, where l is the thickness of the electrolyte, R_{ct} is the bulk resistance, and A is the contact area between the electrolyte and electrodes (3x3 cm^2).

The structure of fibroin in the prepared electrolytes was analyzed using attenuated total reflection Fourier transform infrared spectroscopy (ATR-FTIR; Nicolet iS50 FT-IR) in the range of 650–2000 cm^{-1}, with 64 scans at a resolution of 4 cm^{-1}. Deconvolution of peaks in the Amide I region (1580–1720 cm^{-1}) was performed using Origin 2024 software to analyze the secondary structure of fibroin. The fraction of the β-sheet structure, which represents the crystalline domains of fibroin, was calculated as the ratio of the sum of the peak areas at 1616–1621, 1622–1627, 1628–1637, and 1697-1703 cm^{-1} to the total area of the Amide I region [13].

The electrochromic device was assembled by sandwiching the electrolyte between a WO_3-based electrochromic layer and a NiO-based ion storage layer. In-situ optical transmittance spectra were measured in the wavelength range of 200-1100 nm using a UV-Vis spectrophotometer (Agilent Cary 60), while the applied potential was controlled by a potentiostat (AUTOLAB PGSTAT 101).

3. RESULTS AND DISCUSSION

Electrolytes containing 15 wt% $LiClO_4$ were prepared with varying thicknesses ranging from 7 to 27 µm. Figure 1(a) shows the impedance spectra of electrochemical cells assembled with electrolytes of different thicknesses. As the thickness increased from

10 to 27 µm, the bulk resistance (R_{ct}) increased from 2.7 to 7.5 Ω. However, the electrolyte with a thickness of 7 µm exhibited a higher bulk resistance of 3.8 Ω, likely due to poor interfacial contact between the electrolyte and the electrodes.

The corresponding ionic conductivity of the electrolytes is presented in Figure 1(b). A nearly constant ionic conductivity of approximately 0.4 mS/cm was observed for electrolytes with thicknesses ranging from 10 to 27 µm. This phenomenon suggests that the amount of mobile Li^+ ions per unit thickness was consistent across these samples, resulting in similar conductive performance despite the variation in thickness. In contrast, the electrolyte with a thickness of 7 µm exhibited a lower ionic conductivity of 0.2 mS/cm, likely due to poor interfacial contact and surface irregularities that affected ion transport.

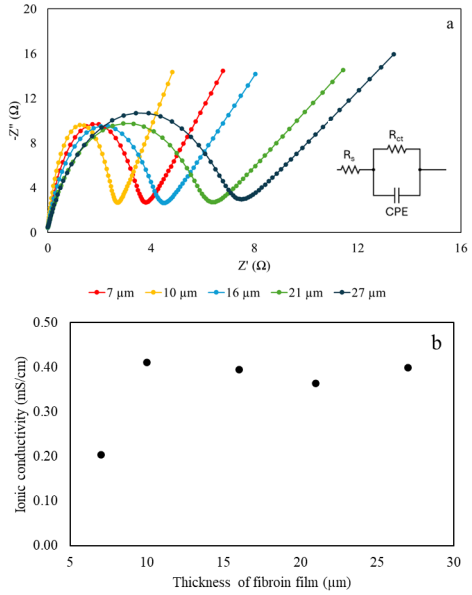

Figure 1 (a) Nyquist plots of SF-based electrolytes with various thicknesses (b) Corresponding ionic conductivity of the electrolytes as a function of thickness.

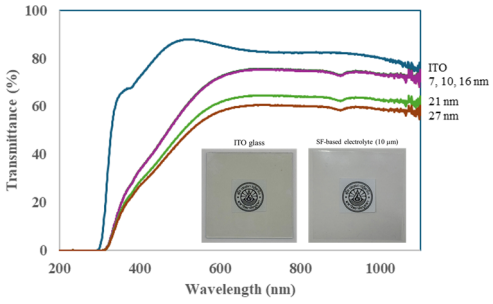

Figure 2 Optical transmittance spectra of SF-based electrolytes as a function of thickness.

Electrolytes suitable for electrochromic devices should exhibit both high ionic conductivity and optical transparency. Therefore, the optical transmittance of the prepared electrolytes was measured, as shown in Figure 2. The electrolytes with thicknesses ranging from 7 to 16 µm appeared transparent and exhibited similar transmittance values of approximately 75%, which is slightly lower than that of bare ITO glass. Although the electrolytes with greater thicknesses (21 and 27 µm) exhibited similar ionic conductivity, the reduction in light transmittance may hinder the optical modulation performance of electrochromic devices.

The performance of electrochromic devices can be evaluated based on their optical modulation and coloration efficiency, as governed by Equations (1) and (2):

$$\text{Optical modulation } (\Delta T) = T_b - T_c \quad (1)$$

$$\text{Coloration efficiency } (CE) = \log (T_b/T_c)/Q \quad (2)$$

where T_b is the transmittance in the bleached state, T_c is the transmittance in the colored state, and Q represents the charge density in the electrochromic devices.

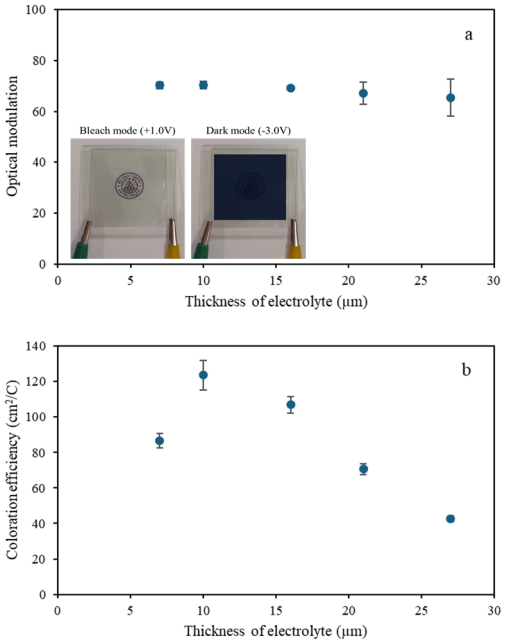

Figure 3 Performance of electrochromic devices with SF-based electrolytes with various thickness: (a) optical modulation (b) coloration efficiency.

The electrochromic device was assembled by sandwiching the SF-based electrolyte between a WO_3-based electrochromic layer and a NiO-based ion storage layer. The working principle involves electrons being injected into the WO_3 layer from an external circuit, resulting in the reduction of WO_3 and the intercalation of Li^+ ions, as shown in Equation (3). As a result, the device changes from a transparent (bleached state) to a dark blue (coloration state), and its transmittance at 630 nm decreases.

$$WO_3 + xLi^+ + xe^- \leftrightarrow Li_xWO_3 \quad (3)$$

Transparent Dark blue

Electrochromic devices assembled with SF-based electrolytes of 7–16 µm thickness exhibited similar optical modulation values of approximately 70% at 630 nm, as shown in Figure 3(a). This phenomenon suggests that the amount of Li^+ ions in the electrolyte was sufficient to intercalate into WO_3 during the coloration process. However, devices using thicker electrolytes (21-27 µm) showed lower optical modulation due to the decreased transmittance of the device in the bleached state, because the thicker electrolytes tend to be opaque, as previously discussed.

Coloration efficiency is defined as the effectiveness of the change in optical transmittance between the bleached state and the colored state per unit of electrons injected into the device. The corresponding coloration efficiencies of devices assembled with SF-based electrolytes of varying thicknesses, ranging from 7 to 27 µm, are shown in Figure 3(b). The device with an electrolyte thickness of 10 µm exhibited the highest coloration efficiency of 124.66 cm^2/C, corresponding to its high optical modulation and low internal resistance. The optimum electrolyte thickness (10 µm) was used to further investigate the effect of Li^+ concentration.

The ionic conductivity of the SF-based electrolyte containing different lithium salt concentrations is presented in Figure 4. An increase in $LiClO_4$ concentration from 7.25 to 14.5 wt% led to a corresponding rise in ionic conductivity, ranging from 0.22 to 0.41 mS/cm. However, a further increase in $LiClO_4$ content from 14.5 to 21.75 wt% resulted in a decrease in ionic conductivity. This observation suggests that ionic conductivity improves with increasing salt concentration, likely due to the greater availability of mobile ions within the polymer matrix. Nevertheless, when the salt concentration exceeds a critical threshold, conductivity tends to decrease due to restricted segmental motion of the polymer chains and ion aggregation [14].

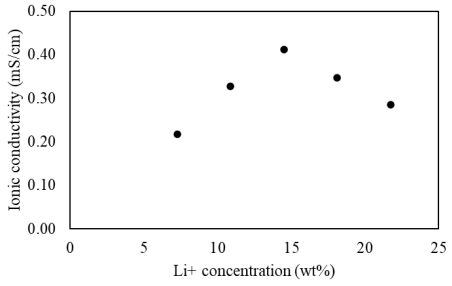

Figure 4 The ionic conductivity of SF based electrolyte with various lithium salt concentrations.

The secondary structure of the SF-based electrolytes was examined to verify the above hypothesis using ATR-FTIR analysis. The FTIR spectra reveal vibrational bands corresponding to Amide I, Amide II, and Amide III groups, as shown in Figure 5. The Amide I region (1585-1722 cm^{-1}) is primarily associated with C=O stretching, C–N stretching, and C–C–N deformation. The Amide II region (1473-1584 cm^{-1}) is attributed to a combination of N–H in-plane bending, C–N stretching, and C–C stretching. The Amide III region (1161-1292 cm^{-1}) involves C–N stretching coupled with N–H deformation modes [15, 16]. Additionally, the peak at 1059 cm^{-1} corresponds to the presence of lithium salt within the fibroin structure [17]. Peaks observed at 1059 and 1776 cm^{-1} also indicate the presence of C–O–C and C=O bonds from propylene carbonate, respectively [18].

The Amide I absorption band is widely used to analyze secondary structures, including β-sheets, random coils, α-helices, turns, and side chains. In particular, β-sheets represent the crystalline structure that can hinder the segmental motion of polymer chains in the electrolyte. Therefore, the β-sheet content in the electrolyte was determined by deconvoluting the corresponding peaks in the Amide I region, as shown in Figure 5(b).

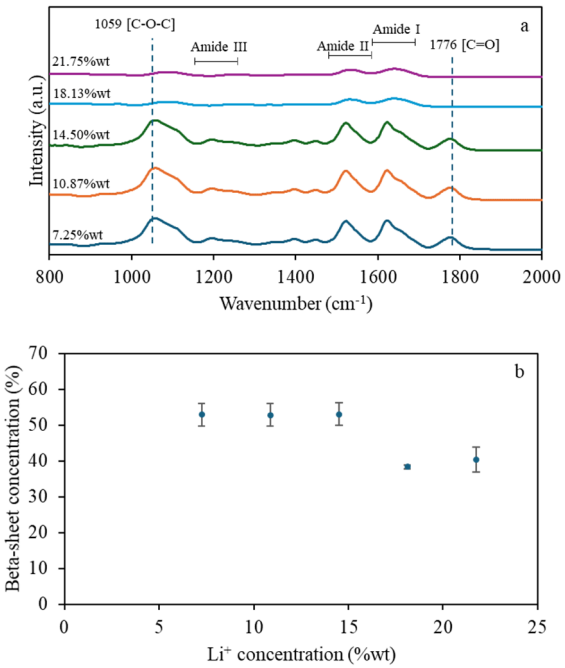

Figure 5 (a) ATR/FTIR spectra and (b) percentage of beta-sheet concentrations of SF-based electrolyte with various lithium salt concentration.

The increase in $LiClO_4$ concentration from 7.25 to 14.5 wt% did not significantly alter the β-sheet content in the electrolyte. However, a further increase from 14.5 to 21.75 wt% resulted in a reduction of β-sheet conformation. Therefore, the increase in ionic conductivity observed between 7.25 and 14.5 wt% $LiClO_4$ can be attributed to the higher concentration of mobile Li^+ ions. At the same time, the β-sheet content remained relatively constant, allowing sufficient segmental motion. Although the β-sheet content decreased as the $LiClO_4$ concentration increased from 14.5 to 21.75 wt%, a decline in ionic conductivity was observed. This phenomenon may be due to strong interactions between the oxygen atoms of the C=O functional groups in propylene carbonate and the Li^+ ions from $LiClO_4$, which could lead to the

aggregation of propylene carbonate molecules and a reduction in the number of mobile Li^+ ions. As a result, the amount of propylene carbonate available to form complexes with fibroin decreased, contributing to a reduction in β-sheet formation. Furthermore, the increased concentration of ClO_4^- anions may weaken intermolecular hydrogen bonding, disrupting β-sheet structures [19]. Furthermore, the disappearance of peaks at 1060 and 1780 cm^{-1}, which correspond to the C–O–C and C=O bonds of propylene carbonate, was observed in the electrolyte containing $LiClO_4$ concentrations ranging from 14.5 to 21.75 wt%.

Therefore, the SF-based electrolyte prepared with a thickness of 10 µm and a $LiClO_4$ concentration of 14.5 wt% exhibited the highest ionic conductivity of 0.41 mS/cm. Although this conductivity is lower than that of a liquid electrolyte containing the same concentration of $LiClO_4$ (1.76 mS/cm), the solid SF-based electrolyte offers advantages such as preventing leakage and bubble formation during operation. Furthermore, the solid SF-based electrolyte is compatible with electrochromic devices and can deliver performance comparable to devices using a liquid electrolyte with the same $LiClO_4$ concentration, as shown in Figure 6.

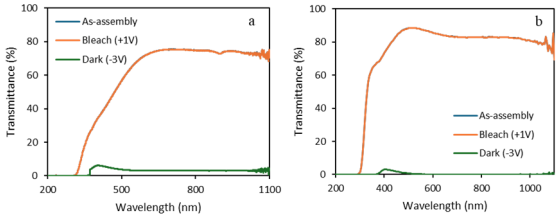

Figure 6 Optical transmittance of electrochromic device using (a) SF-based electrolyte and (b) liquid electrolyte in bleached and colored states.

After applying a potential of -3.0 V, the transmittance of visible light (630 nm) and near-infrared light (930 nm) through the electrochromic device decreased from 74.15% to 3.20% and from 74.22% to 3.04%, respectively, resulting in coloration efficiencies of 124.66 cm^2/C and 126.73 cm^2/C, respectively. In comparison, the device using a liquid electrolyte exhibited transmittance changes from 84.73% to 0.10% for visible light and from 82.76% to 0.04% for NIR, resulting in coloration efficiencies of 344.12 and 384.32 cm^2/C, respectively.

4. CONCLUSION

This work presents a silk fibroin (SF)-based solid electrolyte incorporating $LiClO_4$ for electrochromic applications. The optimal composition, containing 14.5 wt% $LiClO_4$ at a thickness of 10 µm, exhibited the highest ionic conductivity (0.41 mS/cm) and enabled effective optical modulation comparable to that of liquid electrolytes. However, the lower coloration efficiency due to the ionic conductivity of the solid electrolyte is 3.3 times lower than that of the liquid electrolyte.

ACKNOWLEDGMENTS

This work was financially supported by (i) Burapha University, (ii) Thailand Science Research and Innovation (TSRI), and (iii) National Science Research and Innovation Fund (NSRF) (Fundamental Fund: Grant no.26/2565). We would also like to acknowledge the Faculty of Engineering, Burapha University, for the Graduate Research Assistantship (GRA Phase 3) awarded to Mr. Akarawin Pimarnthisakorn. P. N. would also like to thank the financial support provided by the Research and Innovation Administration Division and the Faculty of Engineering, Burapha University.

REFERENCES

[1] V. Rai, R.S. Singh, D. J. Blackwood, D. Zhili. A review on recent advances in electrochromic devices: a material approach. *Advanced Engineering Materials* 2020; 22.8: 2000082.

[2] K. S. Ngai, S. Ramesh, K. Ramesh, J.C. Juan. A review of polymer electrolytes: fundamental, approaches and applications. *Ionics* 2016; 22: 1259-1279.

[3] V.K. Thakur, G. Ding, J. Ma, P.S. Lee, X. Lu. Hybrid materials and polymer electrolytes for electrochromic device applications. *Advanced materials* 2012; 24.30: 4071-4096.

[4] P. Pandurangan. Recent progression and opportunities of polysaccharide assisted bio-electrolyte membranes for rechargeable charge storage and conversion devices. *Electrochem* 2023; 4.2: 212-238.

[5] T.R. Kartha, B.S. Mallik. Revisiting LiClO4 as an electrolyte for Li-ion battery: Effect of aggregation behavior on ion-pairing dynamics and conductance. *Journal of Molecular Liquids* 2020; 302: 112536.

[6] S. DAS, A. GHOSH. Ionic conductivity and dielectric permittivity of PEO-LiClO4 solid polymer electrolyte plasticized with propylene carbonate. *AIP Advances* 2015; 5.2.

[7] C.W. Kuo, W.B. Li, P.R. Chen, J.W. Liao, C.G. Tseng, T.Y. Wu. Effect of plasticizer and lithium salt concentration in PMMA-based composite polymer electrolytes. *International Journal of Electrochemical Science* 2013; 8.4: 5007-5021.

[8] A. Ngamaroonchote, C. Chotsuwan. Performance and reliability of cellulose acetate-based gel electrolyte for electrochromic devices. *Journal of Applied Electrochemistry* 2016; 46: 575-582.

[9] E. Lizundia, D. Kundu. Advances in natural biopolymer-based electrolytes and separators for battery applications. *Advanced Functional Materials* 2021; 31.3: 2005646.

[10] R.F. Pereira, F. Sentanin, A. Pawlicka, M.C. Gonçalves, M.M. Silva, V. de Zea Bermudez. Smart windows prepared from Bombyx mori silk. *ChemElectroChem* 2016; 3.7: 1084-1097.
[11] D. Zhang, X. Meng, W. Hou, W. Hu, J. Mo, T. Yang, M. Li. Solid polymer electrolytes: Ion conduction mechanisms and enhancement strategies. *Nano Res. Energy* 2023; 2.2: e9120050.
[12] N. Johari, L. Moroni, A. Samadikuchaksaraei. Tuning the conformation and mechanical properties of silk fibroin hydrogels. *European Polymer Journal* 2020; 134: 109842.
[13] S. Kaewpirom, S. Boonsang. Influence of alcohol treatments on properties of silk-fibroin-based films for highly optically transparent coating applications. *RSC advances* 2020; 10.27: 15913-15923.
[14] A. Kumar, M.T. Otley, F.A. Alamar, Y. Zhu, B.G. Arden, G.A. Sotzing. Solid-state electrochromic devices: relationship of contrast as a function of device preparation parameters. *Journal of Materials Chemistry C* 2014; 2.14: 2510-2516.
[15] Y. Tamada. New process to form a silk fibroin porous 3-D structure. *Biomacromolecules* 2005; 6.6: 3100-3106.
[16] A. Vasconcelos, G. Freddi, A. Cavaco-Paulo. Biodegradable materials based on silk fibroin and keratin. *Biomacromolecules* 2008; 9.4: 1299-1305.
[17] T.C. Fernandes, H.M. Rodrigues, F.A. Paz, J.F. Sousa, A.J. Valente, M.M. Silva, R.F. Pereira. Highly conducting bombyx mori silk fibroin-based electrolytes incorporating glycerol, dimethyl sulfoxide and [Bmim] PF6. *Journal of The Electrochemical Society* 2020; 167.7: 070551.
[18] Y. Ikezawa, T. Ariga. In situ FTIR spectra at the Cu electrode/propylene carbonate solution interface. *Electrochimica acta* 2007; 52.7: 2710-2715.
[19] S. Gupta, P.K. Varshney. Effect of plasticizer on the conductivity of carboxymethyl cellulose-based solid polymer electrolyte. *Polymer Bulletin* 2019; 76.12: 6169-6178.

Development and characterization of bioplastic from banana peel and chitosan: A sustainable alternative for eco-friendly packaging

Ulia Fitrass[1], Sandhya Babel[1,*]

[1] School of Bio-Chemical Engineering and Technology, Sirindhorn International Institute of Technology, Thammasat University, Pathum Thani 12121, Thailand
[*] Corresponding author: sandhya@siit.tu.ac.th

ABSTRACT

Plastic waste pollution has become a significant environmental challenge, thus development of sustainable and biodegradable alternatives from waste materials are important. This study focuses on the development of bioplastic using banana peel as the primary material, chitosan as a filler, and glycerol from waste cooking oil as a plasticizer. The objective was to enhance the mechanical properties of bioplastic by incorporating chitosan extracted from crustacean shells through a green extraction process, including demineralization with citric acid, deproteinization using bromelain from pineapple peel, and deacetylation with avocado seed extract. Bioplastic films were formulated with 2% chitosan and characterized for tensile strength and modulus young. Results showed that using the waste materials, bioplastic was synthesized successfully. Bioplastic with 0% and 2% chitosan have tensile strength of 0.513 MPa and 0.247 MPa, and Young's modulus of 138 MPa and 49.8 MPa, demonstrating improved flexibility but not strong compared to unmodified banana peel bioplastic. The addition of chitosan contributed to better structural reinforcement, making the material more durable and adaptable for practical applications. This study confirms that bioplastic from banana peel and chitosan have significant potential for biodegradable packaging applications. The findings contribute to the advancement of biopolymer-based materials, supporting global efforts to reduce plastic waste and promote environmentally friendly solutions.

Keywords: Banana Peel; Bioplastic; Chitosan; Mechanical Properties

1. INTRODUCTION

Plastic is a man-made substance which is used globally to a very large extent and has profoundly affected modern society. It has become very common because of such useful qualities such as being light in weight, soft, water-resistant, heat-resistant, resistant to electricity, and easy manufacturing [1]. Plastic waste is producing severe environmental problems because of low degradability. Plastic contributes a major part of municipal solid waste in almost all countries and greatly adds to global environmental problems. The increased buildup and inefficient dumping of plastic waste have exacerbated these problems even more [2]. Open dumping, littering, burning, leakage into nature, and uncontrolled landfilling are the main causes of environmental problems [3]. Global generation of plastic waste reached approximately 400.3 million tons in 2022 [4].

One of the solutions to plastic waste is using bioplastics. Bioplastics are made to be tough when being used but easily degrade and non-toxically harm the environment when thrown away. Degradation in this way is meant to have a smaller environmental footprint, so using bioplastic is a green and eco-friendly solution to reducing plastic pollution. In addition to being biodegradable, most bioplastics are made from renewable feedstocks, e.g., food or agricultural waste, which makes them a sustainable option compared to conventional petroleum-based plastics [5].

Bioplastics are usually modified by the addition of plasticizers in the polymer matrix in order to improve their properties. According to IUPAC, a plasticizer is "a substance or a material added to a plastic to improve its flexibility, workability or distensibility" [6]. Glycerol is a valuable by-product generated during the production of biodiesel from waste cooking oil. It is separated from the biodiesel mixture after the transesterification process, where vegetable or animal fats and oils react with alcohol in the presence of an acid or alkali catalyst [7].

Other than plasticizers, bioplastics development considers waste materials rich in polysaccharides, including chitin. Chitin is the second most abundant polysaccharide in the world, with between six and eight million tons of chitin waste produced every year, the majority of which are being dumped into oceanic and terrestrial ecosystems [8]. The compound is

naturally found in the crustacean shell, fungal cell wall, and insect cuticle [9].

Another biopolymer is chitosan, produced by deacetylation of chitin. Chitosan extraction is generally performed by alkaline treatment at high temperatures, but more environmentally friendly procedures have now been developed, such as microwave and ultrasonic-assisted extraction and low-chemical one-pot procedures. Chitin is composed of a structure of β(1→4)-linked N-acetyl-D-glucosamine, whereas chitosan is composed of β(1→4)-linked units of 2-amino-2-deoxy-D-glucopyranose and 2-acetamido-2-deoxy-D-glucopyranose [10].

In addition to marine and fungal sources, agricultural wastes like banana peels have been found to be a promising raw material for producing bioplastics. Banana peels have sufficient insoluble fibers, i.e., hemicellulose (20.3%), cellulose (18.7%), and lignin (16.8%), along with soluble pectin (15.9%) [11,12]. The presence of cellulose, characterized by its β-1,4 glycosidic linkages and high crystallinity, provides mechanical strength and stability and hence proves to be an ideal basis material for producing bioplastics [13].

Enzymatic processes have also been explored for the extraction of chitin, such as the use of pineapple. Pineapple is a rich source of bromelain, which is a protease enzyme that hydrolyzes cysteine peptide bonds of proteins. The previous study reported that shrimp shell waste upon mixing with crude bromelain underwent efficient deproteinization. The process is a promising, low-cost, and economically significant process for the recovery of chitin [14].

In addition to bromelain from pineapple, recent research also explored the potential use of other fruit enzymes, such as those of avocado, in assisting chitosan processing. Avocado or *Persea americana mill*. is subtropical or tropical fruit from Mexico and Central America that is spread, grown and enjoyed globally. Avocado is one of the *Lauraceae* family from genus Persea, which has more than 150 identified species [15]. Acetogenins are bioactive fatty acid derivatives within avocado tissues. Acetogenins have antibacterial properties that can be used for alternatives to synthetic food additives [16]. Acetogenins are mostly produced in the idioblasts of avocado seed and mesocarp, which have the largest concentrations [17].

The objective in this research is to synthesize and evaluate bioplastics using chitosan from crab shells and banana peels. The bioplastics are plasticized using waste cooking oil to enhance flexibility. The study includes material extraction, film production, and characterization to assess their suitability for eco-friendly packaging applications.

2. EXPERIMENTAL

2.1 Chemicals and Waste Materials

Sodium Hydroxide from Loba Chemie PVT.LTD., Citric Acid from Kemaus, Acetic Acid from Fisher Chemical, sodium metabisulfite ($Na_2S_2O_5$), and crab shell were acquired.

Pineapple peel waste, banana peel waste, and avocado seed waste were collected from the canteen around Sirindhorn International Institute of Technology, Thammasat University, Rangsit Campus, Thailand.

2.2 Preparation of Chitin and Chitosan

Demineralization was done following the method stated by Pohling, 2020 method. Crab shell was weighted 150–200 g and mixed with 119 ml of 50% citric acid is added slowly to the sample and stirred at room temperature. The mixture's pH was observed [18].

Deproteinization used Mohan, 2016 to extract bromelain enzyme. Pineapple peel is blended with deionized water with ratio 1:3 (W/V) and filtered. The pineapple peel extract was centrifuged at 10,000 rpm at 4°C for 10 min to remove insoluble materials. The supernatant from pineapple peel was used as crude extract of bromelain enzyme [19]. The crab shell powder was mixed with extracted crude bromelain solution with ratio 1:10 (W/V) at 53 ℃, pH 7 and put into an incubator for 24 hours. Sample was cleaned with deionized water and heated at 90 ℃ for 10 minutes after finishing the enzymatic reaction for deactivating enzyme. The insoluble fraction was separated from the supernatant using centrifugation at 10,000 rpm for 10 minutes at 28 ℃. The insoluble fraction was crab shell [14].

For deacetylation reaction, dried avocado seeds were first cleaned with deionized water. Avocado seeds were boiled with deionized water in ratio 1:4 and wait until the volume becomes two-thirds from the original and keep for 24 hours. The avocado seed extract was coded ASE. 10 grams of crab shell were soaked with 100 mL ASE and incubated and allowed to interact on a magnetic stirrer and heater until 70 °C and then put into an ultrasonic bath at 70°C for 60 minutes. Crab shell is filtered with filter paper and clean with deionized water.

2.3 Preparation of Plasticizer

Waste cooking oil was filtered. 100 mL of waste cooking oil was heated to 50 °C, after which 50 mL of 96% ethanol premixed with 25 mL of NaOH 2M solution was added, and the mixture was then heated for 60 minutes at 50 °C. The mixture, consisting of glycerol and biodiesel, was left to settle for 24 hours. Afterward, the two layers were separated using a separator funnel, with glycerol forming the bottom layer and biodiesel the top layer.

2.4 Preparation of Banana Peel

The collected banana peels were first rinsed with distilled water, then cut into smaller pieces. Banana peel was weighed 200 gram and soaked in 400 mL sodium metabisulfite ($Na_2S_2O_5$) 0.2 M solution for 45 minutes, which acted as a preservative to inhibit microbial growth throughout the experiment. Additionally, sodium metabisulfite may also extend the biodegradation period of the resulting biofilm. Next, 200 g of banana peel was boiled in 400 ml of distilled water for approximately 30 minutes at 100°C. After decanting the water, the boiled banana peel pieces were dried on filter paper. Once dried, they were placed in a beaker and blended into a uniform paste.

2.5 Bioplastic Synthesis

Banana peel paste weighed 75 gram and combined with 24 grams of glycerol, then stirred and heated for 10 minutes. Separately, 24 mL of a 5% acetic acid solution was added chitosan with varied 0% and 2% from total mass of banana peel, which was mixed using a magnetic stirrer. This chitosan mixture was then gradually incorporated into the heated banana peel paste and glycerol solution. The resulting mixture was heated and stirred for an additional 10 minutes, allowing it to form a gel.

2.6 Bioplastic Characterization

Bioplastic characterization was done using Tinius Olsen H5KT Benchtop based on ASTM D882-00 with speed 5 mm/min to measure tensile strength and young's modulus [20].

3. RESULTS AND DISCUSSION

The first part of the process is demineralization. During this stage, CO_2 release caused foaming, and this was controlled carefully by slowly adding the acid and adjusting the stirring rate to reduce the foam. Foaming was initiated after pH was 2 and continued for approximately 30 minutes before it ceased, with only slight bubbling during the first hour. During this lab-scale experiment, the total addition of citric acid occurred within 2–5 minutes, and foam control was achieved through increased stirring and manual foam dispersal with a spatula. Controlled process allowed the demineralization process to proceed efficiently in spite of the difficulty resulting from CO_2 evolution.

Calcium carbonate was able to react with that first proton found in citric acid at such early stages of reaction. Subsequently, the slow as well as continuous release of protons from dihydrogen citrate ($C_6H_7O_7^-$) and monohydrogen citrate ($C_6H_6O_7^{2-}$) governed the overall process. The gradual release of protons led to a steady decline in the pH of the mixture. This ensured a controlled acidic environment throughout the reaction.

The second step in the process is deproteinization. Extracting chitin from crab shell waste using bromelain from pineapple peels offers a cost-effective and environmentally friendly option to existing chemical methods. Chemical extraction typically utilizes aggressive materials like hydrochloric acid and sodium hydroxide, which work well but endanger safety and environment because of the corrosive nature and toxicity of the residues left behind [14].

Here in this study, naturally occurring bromelain in pineapple peel as an enzyme was used to hydrolyze protein in crab shell under mild conditions (approximately 53 °C and near neutral pH). Such a gentle procedure avoids the use of harmful chemicals and thus makes the method safer as well as environmentally benign. The use of crude enzyme rather than purified one also makes it cost-effective and employs readily available agricultural material.

The final step in the process is deacetylation. Chitin interacts with avocado seed extract to produce chitosan nanofibers from flake chitin and particulate chitosan from crab shell solid waste. Figure 1, as depicted below, indicates a mechanism that explains the process of conversion from chitin to chitosan under a force that comprises physicochemical processes. Degradation of the surrounding protein matrix by heating the chitin ASE mixture frees the trapped chitin fibers.

When exposed, the chitin fibers get influenced by bioactive constituents so-called acetogenins of the extract and undergo deacetylation. In crab shells, re-heating again results in deproteinization followed by dissolution of chitin into the extract, which again gets deacetylated to yield particulate chitosan rather than fibrous material. This suggests a potential acetogenin-mediated deacetylation mechanism, in which nucleophilic -OH groups found in acetogenins are able to catalyze the hydrolysis of acetyl groups found in chitin [21].

Although the mechanism is speculative, it has to be by nucleophilic attack of hydroxyl groups upon the chitin polymer chain. Further work has to be done in order to conclusively characterize the molecular mechanism behind this bio-assisted deacetylation reaction [21].

Synthesis of glycerol from waste cooking oil in this research was conducted with a simple transesterification reaction that converts triglycerides into glycerol and biodiesel with the assistance of a catalyst in the form of a strong base. Ethanol and sodium hydroxide (NaOH) were utilized in the reaction to break ester bonds within triglycerides such that separation of fatty acid esters (biodiesel) from the glycerol backbone could be achieved.

Reaction was conducted under a relatively low temperature (around 50 °C), which made the process low energy and accessible. Upon reaction for one hour, with subsequent 24 hours' settling, two distinct layers were observed: biodiesel at the top and heavier glycerol at the bottom. Successful phase separation indicates the efficiency of transesterification and

further proves the presence of crude glycerol [22]. The picture of synthesized bioplastics can be seen on figure 2.

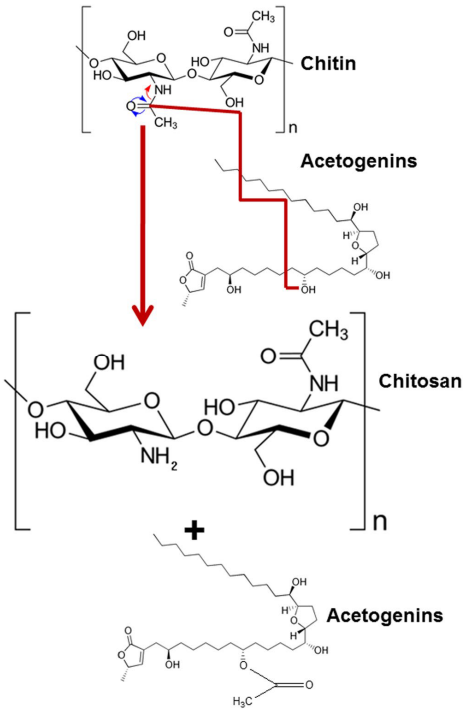

Figure 1 Illustration of the deacetylation reaction steered by the acetogenins in the avocado seed extracts [15].

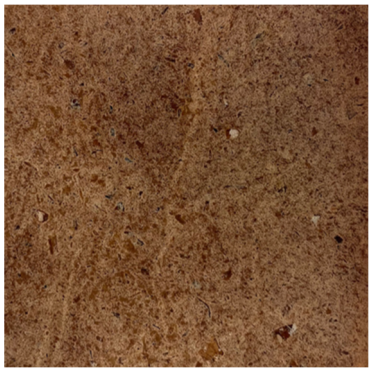

Figure Bioplastic synthesized from banana peel and chitosan 2%

Table 1 The characterization of bioplastic synthesized from banana peel and chitosan.

Bioplastic with Chitosan	Tensile Strength (MPa)	Young's Modulus (MPa)
0%	0.513	138
2%	0.247	49.8

The tensile strength of the film represents the specific strength measured at the maximum force applied before the material breaks or tears. This test determines the amount of force required to reach the breaking point per unit surface area of the film, providing insight into its mechanical durability. The tensile strength of bioplastics from banana peel are presented in Table 1, highlighting the material's ability to withstand tensile stress before failure. Addition of 2% chitosan decreased tensile strength. This indicates that adding chitosan does not lead to a continuous increase in the tensile strength of plastic film. The reduction in tensile strength occurs due to chitosan's linear polymer chain structure, which promotes the formation of a crystalline phase by arranging polymer molecules in an orderly manner [23].

Young's modulus is the ratio of tensile strength to elongation at break, representing the stiffness of a material. A lower Young's modulus value indicates higher elasticity in the bioplastic samples, allowing them to stretch more before breaking. Conversely, a higher Young's modulus value signifies reduced elasticity, meaning the material is more rigid and has a higher tensile strength, making it less flexible and more resistant to deformation. The bioplastic samples with the best elasticity were those with a 2% chitosan addition, exhibiting a Young's modulus of 48.9 MPa. This indicates that the bioplastic with 2% chitosan can maintain a high degree of flexibility while still providing structural integrity. The lower modulus value suggests that these samples could stretch more before breaking, making them more adaptable for applications requiring enhanced elasticity [23].

4. CONCLUSIONS

Chitin was successfully obtained from crab shell through a green enzymatic process with pineapple peel crude bromelain as a reagent, which offers a cleaner and safer alternative than conventional chemical methods. The use of avocado seed extract as a bioactive agent in the deacetylation process also has potential in the conversion of chitin to chitosan.

The application of banana peel as the base matrix and waste cooking oil glycerol as a plasticizer enhances the process sustainability. The mechanical characterization results indicate that chitosan addition influences both tensile strength and flexibility of the resulting bioplastic. While the 2% addition of chitosan reduced tensile strength, it significantly improved elasticity, as evidenced by the decreased Young's modulus.

ACKNOWLEDGMENTS

The first author acknowledges the Excellent Foreign Student (EFS) scholarship awarded by Sirindhorn International Institute of Technology, Thammasat University, Thailand.

REFERENCES

1. González-Fernández, D., Cózar, A., Hanke, G., Viejo, J., Morales-Caselles, C., Bakiu, R., Barceló, D., Bessa, F., Bruge, A., Cabrera, M., Castro-Jiménez, J., Constant, M., Crosti, R., Galletti, Y., Kideys, A. E., Nino, Suaria, G., & Tourgeli, M. Floating macrolitter leaked from Europe into the ocean. *Nature Sustainability* 2021; 4(6), 474–483.
2. Lebreton, L. and Andrady, A. 'Future scenarios of global plastic waste generation and disposal', Palgrave Communications. Springer US 2019; 5(6), pp. 1–11. doi: 10.1057/s41599-018-0212-7.
3. S. Kaza, L. C., Yao, P. B.-T. and Woerden, F. Van. What a Waste 2.0: A Global Snapshot of Solid Waste Management to 2050. Edited by Urban Development Series. Washington, D.C.: World Bank 2018.
4. Statista. Projected plastic waste generation worldwide from 2019 to 2060 (in million metric tons). Statista 2022. Retrieved April 26, 2024, from: https://www.statista.com/statistics/1338839/global-plastic-waste-generation-outlook/
5. Imre B, García L, Puglia D, Vilaplana F. Reactive compatibilization of plant polysaccharides and biobased polymers: Review on current strategies, expectations and reality. Carbohydrate Polymers 2019; 209:20–37.
6. Bocqué, M., Voirin, C., Lapinte, V., Caillol, S., & Robin, J.-J. Petro-Based And Bio-Based Plasticizers: Chemical Structures To Plasticizing Properties. *Journal of Polymer Science* 2015; 52(1), 11–13
7. Singh D, Sharma D, Soni SL, Sharma S, Kumar Sharma P, Jhalani A. A review on feedstocks, production processes, and yield for different generations of biodiesel. *Fuel* 2020; 262,116553.
8. Yan Ning, & Chen Xi. Don't waste seafood waste Turning cast-off shells into nitrogen-rich chemicals would benefit economies and the environment, say Ning Yan and Xi Chen. *Nature* 2015; 524, 155–157.
9. Ismail, M., El-Feky, A., Zaghloul, E., Madkour, F., Elnemr, A., & Ibrahim, H. Extraction of chitosan from Aristeus antennatus shells as a prior for biodegradable plastic production. *Alfarama Journal of Basic & Applied Sciences* 2022; 4(I), 155–170. https://doi.org/10.21608/ajbas.2022.141607.1106
10. Vendruscolo, F., & Ninow, J. L. Apple pomace as a substrate for fungal chitosan production in an airlift bioreactor. *Biocatalysis and Agricultural Biotechnology* 2014; 3, 338–342.
11. Oliveira, T. Í. S., Rosa, M. F., Cavalcante, F. L., Pereira, P. H. F., Moates, G. K., Wellner, N., Mazzetto, S. E., Waldron, K. W., & Azeredo, H. M. C. Optimization of pectin extraction from banana peels with citric acid by using response surface methodology. *Food Chemistry* 2016; 198(5), 113–118.
12. Oberoi, H., Sandhu, S., & Vadlani, P. Statistical optimization of hydrolysis process for banana peels using cellulolytic and pectinolytic enzymes. *Food Bioproducts Processing* 2012; 90, 257–265.
13. Nanda S, Azargohar R, Dalai AK, K. J. An assessment on the sustainability of lignocellulosic biomass for biorefining. *Renewable Sustain Energy Review* 2015; 50, 925–941.
14. Muthaiya, S., Kuruppu Bandara, D. D., Kamani Hewavitharana, I., Sukanya, M., Bolukandura, B. V. T. T., Bandara, L. W. D., & Hewavitharana, K. H. I. K.. Chitin extraction from shrimp shell waste using pineapple crude enzyme. 2022; 198–200.
15. Araújo, Rafael G., Rodriguez-Jasso, R. M., Ruiz, H. A., Govea-Salas, M., Pintado, M. E., & Aguilar, C. N. Process optimization of microwave-assisted extraction of bioactive molecules from avocado seeds. *Industrial Crops and Products* 2020; 154, 112623.
16. Rodríguez-Sánchez, D. G., Pacheco, A., Villarreal-Lara, R., Ramos-González, M. R., Ramos-Parra, P. A., Granados-Principal, S., Garza, R. I. D. de la, García-Rivas, G., & Hernández-Brenes, C. Chemical Profile and Safety Assessment of a Food-Grade Acetogenin-Enriched Antimicrobial Extract from Avocado Seed. *Molecule* 2019; 24(13), 2354.
17. López-Barrera, R. ., & Arrubla-Vélez, J. P. Analysis of phytosterols in seeds of Persea americana miller (var. Lorena) by gas chromatography and high performance liquid chromatography. *Revista Facultad de Ciencias Básicas* 2017; 13(1), 35–41.
18. Pohling, J., Dave, D., Liu, Y., & Trenholm, W. M. and S. Two-step demineralization of shrimp (Pandalus Borealis) shells using citric acid: an environmentally friendly, safe and cost-effective alternative to the traditional approach. *Green Chemistry* 2021; *3*.
19. Mohan, R., Sivakumar, V., Rangasamy, T., & Muralidharan, C. Optimisation of bromelain enzyme extraction from pineapple (Ananas comosus) and application in process industry. American Journal of Biochemistry and Biotechnology 2016; 12(3), 188-195.
20. ASTM International. ASTM D882-00: Standard Test Method for Tensile Properties of Thin Plastic sheeting. ASTM International 2020; 1-12.
21. Gopal, J., Muthu, M., Dhakshanamurthy, T., Kim, K. J., Hasan, N., Kwon, S. J., & Chun, S. Sustainable ecofriendly phytoextract mediated one pot green recovery of chitosan. *Scientific Reports* 2019; 9(1), 1–4.
22. Chilakamarry, C. R., Sakinah, A. M. M., Zularisam, A. W., & Pandey, A. Glycerol waste to value added products and its potential applications. *Systems Microbiology and Biomanufacturing* 2021; 1(4), 378–396.
23. Suryani, Rihayat, T., Fitria, Sariadi, Yunus, M., Hasanah, U., & Safitri, A. (2024). The Impact of Chitosan Incorporation on the Mechanical Characteristics of Biodegradable Packaging based on PLA/PCL Blend. E3S Web of Conferences, 503, 1–11.

Desalination potential using EDTA modified MOF

Nattawut Krasaesueb[1], Suda Ittisupornrat[1,*], Natthawan Prasongthum[2]

[1] Climate Change and Environmental Research Center, Pathum Thani 12120, Thailand
[2] Department of Physics, Faculty of Science, Khon Kaen University, Khon Kaen 40002, Thailand
[*] Corresponding author: suwimolteam@yahoo.com

ABSTRACT

The escalating global water shortage crisis, intensified by climate change, has poses a critical environmental challenge, with seawater intrusion contributing to saline water contamination. Among available desalination methods, adsorption offers advantages such as energy efficiency, low cost, and ease of operation. In this study, an adsorbent was synthesized by incorporating ethylenediaminetetraacetic acid (EDTA) into the pores of Fe-Al-based metal-organic framework MIL-53(Fe, Al). The EDTA-modified MOF was evaluated for its desalination performance in batch experiments, demonstrating over 50% salt removal from water with an initial salinity of 1.1 ppt within 18 hours. This research highlights the potential of MOF-based adsorbents as viable candidates for water desalination, contributing to climate change mitigation.

Keywords: Metal-organic frameworks; Terephthalic acid, Desalination

1. INTRODUCTION

Water scarcity has emerged as a pressing global issue driven by climate change and increasing water demand [1]. Seawater intrusion, exacerbated by rising sea levels and excessive groundwater extraction, significantly contributes to freshwater salinization, threatening drinking water supplies and agricultural productivity [2]. Desalination technologies, including reverse osmosis and thermal distillation, have been widely implemented to address this challenge [3]. However, these conventional techniques are often energy-intensive and expensive, necessitating the development of alternative approaches that are both cost-effective and environmentally sustainable [4].

Adsorption-based desalination has gained attention due to its low energy consumption, operational simplicity, and selective removal capabilities of salts. Metal-organic frameworks (MOFs), known for their high surface area and tunable functionalities, have emerged as promising materials for water purification applications [5]. In particular, functionalized MOFs can be tailored to enhance adsorption capacity and selectivity for salt removal.

This study examines the application of MOF-based adsorbents as a sustainable approach to water desalination, providing a cost-effective and energy-efficient solution that can mitigate the effects of climate change on global water resources.

2. EXPERIMENTAL

2.1 Synthesis of MIL-53(Fe, Al)

MIL-53(Fe, Al) was synthesized by dissolving 1.2948 g of commercially available terephthalic acid (TPA), 0.84 g of $FeCl_3 \cdot 6H_2O$, 1.76 g of $Al(NO_3)_3 \cdot 9H_2O$, and 60 mL of N, N-dimethylformamide (DMF) in a 150 mL beaker. The mixture was stirred using a magnetic stirrer for 30 minutes until a homogeneous solution was achieved. The solution was then transferred to a hydrothermal reactor and heated at 150°C for 10 hours. After cooling to room temperature, the resulting crystals were washed three times with deionized water and centrifuged at 10,000 rpm for 5 minutes per cycle. The crystals were subsequently washed three times with 99% ethanol, centrifuged under the same conditions, soaked in ethanol for 12 hours, and centrifuged again. Finally, the purified crystals were dried in an oven at 100°C for 10 hours, and the dry weight of the synthesized MIL-53(Fe, Al) was recorded [6].

2.2 Functionalization MIL-53(Fe, Al) with EDTA

The synthesized MIL-53(Fe, Al) crystals were activated by heating at 150°C for 12 hours. A 0.05 g portion of the activated crystals was mixed with 0.1 g of ethylenediaminetetraacetic acid (EDTA) in a screw-cap tube, followed by the addition of 25 mL of deionized water. The mixture was heated at 60°C for 24 hours to facilitate the coordination of EDTA with the metal centers within the framework. This post-synthetic modification method is widely employed to enhance the functional groups on the MOF surface, improving adsorption and catalytic performance. After the reaction, the product was washed three times with deionized water and centrifuged at 10,000 rpm for 5 minutes per cycle. The crystals were subsequently washed three times with acetone under the same conditions. Finally, the obtained product was dried at

60°C for 12 hours, and the dry weight of the MIL-53(Fe, Al)-EDTA material was recorded [7].

2.3 Analysis of MOF characterization

The synthesized MIL-53(Fe, Al) adsorbent was characterized to evaluate its morphological, structural, surface, and elemental properties using advanced analytical techniques. The microstructure and surface morphology were examined using a Field Emission Scanning Electron Microscope (FE-SEM, JSM-7800F, JEOL, Japan), while elemental composition was determined using Energy Dispersive X-ray Spectroscopy (EDS, Aztec Energy Standard X-Max 20, Oxford Instruments, UK) attached to the SEM system. To analyze surface characteristics, including specific surface area, pore size distribution, and total pore volume, nitrogen adsorption–desorption isotherms were obtained using a High-Performance Adsorption Analyzer (3Flex, Micromeritics, USA). The specific surface area was calculated using the Brunauer–Emmett–Teller (BET) method within a relative pressure range (P/P_0) of 0–0.30, and pore size distribution was determined from the adsorption branch using the Barrett–Joyner–Halenda (BJH) model. Crystalline structure and phase composition were identified by X-ray diffraction (XRD) analysis performed on a Bruker D8 Advance diffractometer (Germany) using Cu-Kα radiation (λ = 1.5406 Å) operated at 40 kV and 40 mA, with a scanning range of 2θ = 5°–80°. Additional compositional analysis was conducted using X-ray Fluorescence (XRF) spectroscopy to evaluate bulk elemental composition. Furthermore, EDS integrated with the XRD system was utilized to provide complementary analysis of elemental distribution and structural consistency within the synthesized adsorbent

2.4 Salt adsorption test of synthesized MOF crystals

The salt adsorption capacity of the synthesized MIL-53(Fe, Al) with EDTA was evaluated by mixing 0.1 g of MOF-EDTA with a 1000 ppm sodium chloride (NaCl) solution. The mixture was agitated at 150 rpm while maintaining a constant temperature of 25 °C. Measurements of pH, electrical conductivity, and salinity were conducted using appropriate probes (Pro 1030, YSI, USA) were recorded at 0, 12, 18, and 36 hours. For comparison, a 1000 ppm NaCl solution and MIL-53(Fe, Al) without EDTA were tested under the same manner to use as a control to compare adsorption performance of the synthesized adsorbent.

3. RESULTS AND DISCUSSION

3.1 Characterization of MIL-53(Fe, Al)

The synthesized MIL-53(Fe,Al) adsorbent appeared as a light-yellow powder appearance, with no visible contamination from other colors. The powder was relatively coarse, uneven texture and lightweight in apperance (Figure 1a). In contrast, the MIL-53(Fe, Al)-EDTA adsorbent was obtained as a fine, opaque white powder with smaller particle sizes, free from color impurities (Figure 1b).

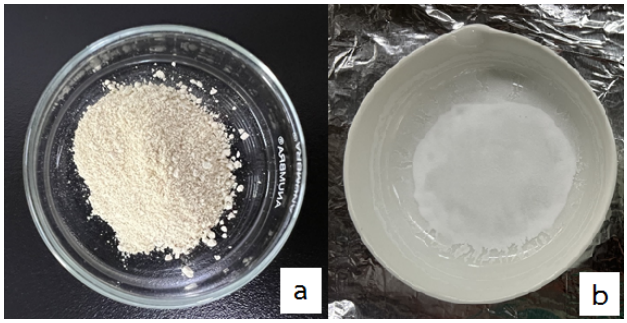

Figure 1 Appearance comparison of (a) MIL-53(Fe,Al) and (b) MIL-53(Fe,Al)-EDTA.

Microstructural characterization of MIL-53(Fe, Al) using SEM revealed irregularly shaped hexagonal crystals with both spherical and elliptical morphologies (Figure 2), with an average particle size of approximately 521 nm. These findings are consistent with the results reported by Chen et al. (2022) [6], indicating that the incorporation of Al influences the crystal structure by increasing the surface area, which may advantageous for enhancing the salt adsorption performance in water treatment.

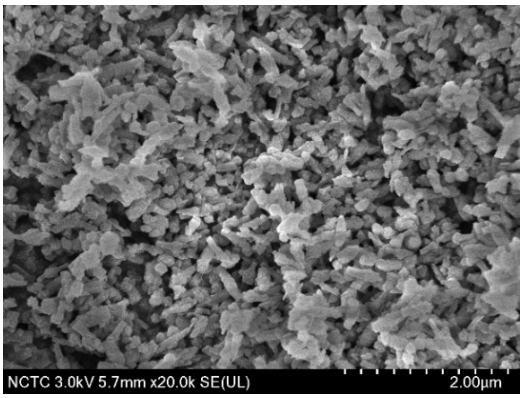

Figure 2 SEM image of synthesized MIL-53(Fe, Al).

The elemental composition of MIL-53(Fe, Al) was determined using EDS, which indicated the presence of carbon (C), oxygen (O), iron (Fe), and aluminum (Al), with respective weight percentages of 82.2%, 15.1%, 1.6%, and 1.2%, as shown in Figure 3. Additionally, the XRD analysis revealed a characteristic diffraction peak at approximately 2θ of 9.3°, corresponding to the presence of Al within the MIL-53 framework, as shown in Figure 4. These complementary results from EDS and XRD confirm the successful incorporation of Fe and Al into the crystal framework of the synthesized MIL-53(Fe, Al).

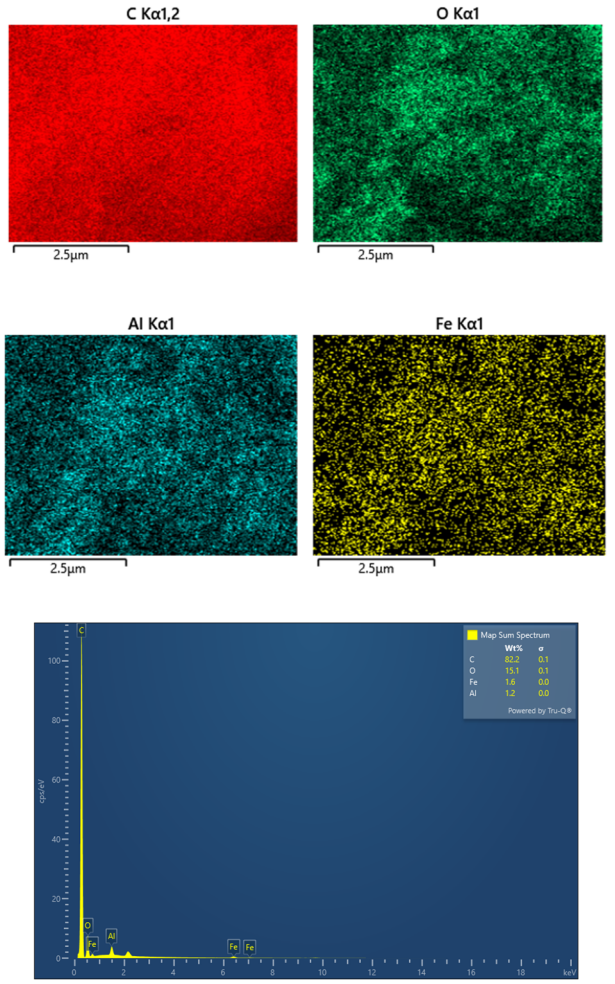

Figure 3 EDS and Mapping images of MIL-53(Fe, Al)

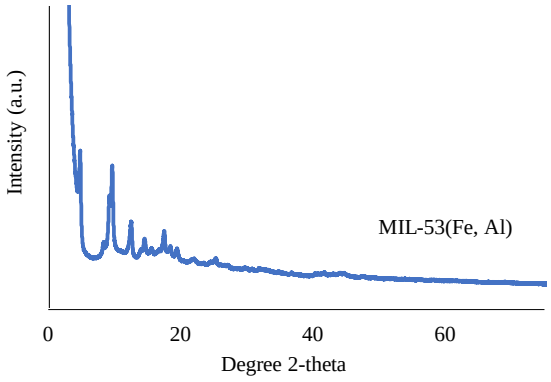

Figure 4 XRD pattern of MIL-53(Fe, Al)

The surface area and porosity of the synthesized MIL-53 (Fe, Al) were analyzed using nitrogen adsorption–desorption measurements. As shown in Figure 5, the nitrogen adsorption-desorption isotherm exhibits a hysteresis loop at relative pressure (P/P_0) close to 1.0, which corresponds to a Type VI isotherm. This behavior indicates the presence of mesopores resulting from interparticle voids of varying sizes. The synthesized MIL-53(Fe, Al) exhibited a significantly higher specific surface area of 834.4 m²/g, a pore volume of 0.711 cm³/g, and an average pore size of 10.4 nm, as summarized in Table 1. These results aligns well with the findings reported by Chen et al. (2022), confirming the structural characteristics conducive to effective adsorption performance [6].

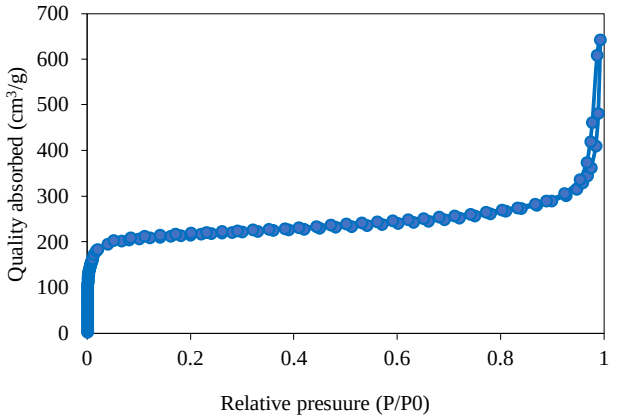

Figure 5 N_2 adsorption-desorption isotherms of MIL-53(Fe,Al).

Table 1. Comparison of the surface area, pore volume, and pore size of MIL-53(Fe,Al) between this study and that reported by Chen et al. (2022).

Type	surface area ($m^2\ g^{-1}$)	pore volume ($cm^3\ g^{-1}$)	pore size (nm)
This study	834.4	0.711	10.4
Chen et al., (2022)	1397.2	1.050	3.01

3.2 Desalination Performance of MIL-53(Fe,Al)-EDTA

The salinity adsorption test indicates that during the initial 12 hours, there was no significant reduction in salinity. However, after the 18 hours, the salinity level of the solution decreased notably from 1.1 ppt to 0.5 ppt. Similarly, the electrical conductivity decreased from 2353 µS/cm to 1073 µS/cm. In contrast, no measurable reduction in salinity or electrical conductivity was observed in unmodified MIL-53 (Fe, Al), indicating that adsorption of NaCl is mainly due to the presence of EDTA functional groups [7]. These findings demonstrate that MIL-53(Fe,Al)-EDTA exhibits considerable desalination efficiency, reducing salinity by 0.6 ppt, which corresponds to a 55% reduction relative to the control, as detailed in Table 2.

Furthermore, previous work by Chen et al. (2022) [6] reported that the bimetallic MIL-53 (Fe,Al) exhibited superior ion-exchange capacity compared to monometallic MIL-53(Fe), due to improved porosity and reduced particle size-factors that contribute to enhanced adsorption performance. The significant decrease in electrical conductivity further supports the

improved ionic capture ability of the synthesized material. Collectively, these results suggest that the synthesized MIL-53(Fe,Al)-EDTA is a promising candidate for water desalination, providing a simple and scalable method to produce high-efficiency adsorbents.

Table 2 Salinity and conductivity measurements at different time intervals for MIL-53 (Fe,Al)-EDTA and without EDTA

Sample	pH				Conductivity (uS/cm)				Salinity (ppt)			
	0 h	12 h	18 h	36 h	0 h	12 h	18 h	36 h	0 h	12 h	18 h	36 h
Control (NaCl)	5.59	5.96	6.35	6.75	1993	1952	1952	2010	1.0	1.0	1.0	1.0
MIL-53(Fe,Al)	4.60	4.61	4.52	4.45	2018	2013	2046	2061	1.0	1.0	1.0	1.0
MIL-53(Fe,Al)-EDTA	3.05	3.02	3.06	3.10	2242	2353	1073	1101	1.1	1.1	0.5	0.5

4. CONCLUSION

This study successfully synthesized and characterized the bimetallic metal-organic framework MIL-53(Fe,Al)-EDTA to evaluate its potential for salt adsorption in water desalination applications. The incorporation of both Fe and Al metal centers into the MOF structure enhanced its structural and textural properties. Characterization by XRD, SEM, EDS, and BET analyses revealed a high specific surface area (834.4 m^2/g), a pore volume (0.711 cm^3/g), mesoporous structure with an average pore diameter of 10.4 nm, which are essential for effective ion diffusion and adsorption.

In the salt adsorption experiments, MIL-53(Fe, Al)-EDTA demonstrated outstanding performance, reducing salinity by 55% and significantly lowering electrical conductivity within 18 hours. These improvements are primarily attributed to the synergistic effects of the Fe and Al centers, which contribute to a stable framework while promoting the formation of mesoporous structures that facilitate ion transport and capture.

Overall, the findings highlight MIL-53(Fe, Al)-EDTA as a promising material for efficient water desalination. Its robust structure, high surface area, and efficient salt adsorption capability makes it a suitable candidate for further development. Future work should focus on evaluating regeneration cycles, assessing long-term performance under practical wastewater conditions, and exploring the integration of this technology into scalable, modular desalination systems for practical applications.

ACKNOWLEDGMENTS

The authors express their sincere gratitude to the Thailand Science Research and Innovation (Grant no. 198397/2024, 204031/2025) for financial support, which made this study possible.

REFERENCES

1. P. H. Gleick. Water, Drought, Climate Change, and Conflict in Syria," Jul. 2014.
2. A. D. Werner. Seawater intrusion processes, investigation and management: Recent advances and future challenges. *Advances in Water Resources*. 2013; 51: 3–26.
3. M. Elimelech and W. A. Phillip. The Future of Seawater Desalination: Energy, Technology, and the Environment. *Science* 2011; 6043: 712–717.
4. M. A. Shannon, P. W. Bohn, M. Elimelech, J. G. Georgiadis, B. J. Mariñas, and A. M. Mayes. Science and technology for water purification in the coming decades. *Nature* 2008; 7185: 301–310.
5. J.-R. Li, R. J. Kuppler, and H.-C. Zhou. Selective gas adsorption and separation in metal–organic frameworks. *Chem. Soc.* 2009; 5: 1477–1504.
6. X. Chen, X. Liu, L. Zhu, X. Tao, and X. Wang. One-step fabrication of novel MIL-53(Fe, Al) for synergistic adsorption-photocatalytic degradation of tetracycline. *Chemosphere* 2022; 291: 133032.
7. C. Ji, H. Yu, J. Lu, Y. Ren, L. Lv, and W. Zhang,. High-Efficiency and Sustainable Desalination Using Thermo-regenerable MOF-808-EDTA: Temperature-Regulated Proton Transfer. *ACS Appl. Mater. Interfaces* 2021; 20: 23833–23842.

Synthesis and scale-up of MOF using PET-derived terephthalic acid

Natthawan Prasongthum[1,*], Chutamat Thongchan[1], Kittiyanee Rattanatairsri[1], Suda Ittisupornrat[2], Nuttawut Krasaesube[2]

[1] Department of Physics, Faculty of Science, Khon Kaen University, Khon Kaen 40002, Thailand
[2] Climate Change and Environmental Research Center, Pathum Thani 12120, Thailand
[*] Corresponding author: natpra@kku.ac.th

ABSTRACT

The growing accumulation of plastic waste has prompted efforts to repurpose it in high-value applications, such as the synthesis of metal-organic frameworks (MOFs), to foster sustainability and waste valorization. This study explores the synthesis and scale-up production of MIL-53 using terephthalic acid derived from PET hydrolysis. The optimized synthesis conditions involved reaction times of 5, 10, and 15 h at 150°C. Structural and morphological characteristics of the synthesized MIL-53(Fe) and MIL-53(Fe, Al) were analyzed via SEM, XRD, and BET. The results demonstrated successful synthesis and scale-up of MIL-53(Fe, Al), maintaining its structural integrity and performance, highlighting its potential for industrial applications like gas separation and desalination.

Keywords: Metal-organic frameworks; Polyethylene terephthalate; Recycling; Terephthalic acid

1. INTRODUCTION

Plastic pollution, particularly from polyethylene terephthalate (PET), poses a significant environmental challenge due to its widespread use and resistance to degradation [1]. To address this, innovative strategies have emerged to upcycle plastic waste into high-value materials, aligning with circular economy principles. Current recycling methods such as mechanical recycling often result in materials with diminished properties, limiting their reuse to lower-value applications [2]. Chemical recycling, specifically hydrolysis of PET, offers a promising alternative by converting plastic waste into fundamental chemical building blocks, including terephthalic acid (TPA) that can serve as a key organic linker in the synthesis of metal-organic frameworks (MOFs) [3].

MOFs are a class of crystalline porous materials formed by the coordination of metal ions or clusters with organic ligands. Their high surface area, tunable pore structure, and chemical versatility have garnered significant attention for applications in gas storage, separation, catalysis, and environmental remediation [4]. Among the extensive MOF family, Materials of Institut Lavoisier (MIL)-53, particularly iron-based MIL-53(Fe), exhibit remarkable structural flexibility and chemical stability, making them suitable for various industrial processes. Recent advancements have further introduced bimetallic MOFs, such as MIL-53(Fe, Al), demonstrating enhanced stability and improved functional properties due to synergistic interactions between different metal centers [5].

Integrating sustainability into MOF synthesis has prompted extensive research into utilizing renewable or waste-derived sources as organic linkers. This approach addresses plastic waste management concerns and simultaneously contributes to developing advanced functional materials with significant industrial potential.

This study focuses on synthesizing MIL-53(Fe) and its bimetallic variant, MIL-53(Fe, Al), utilizing terephthalic acid derived from the hydrolysis of PET waste. The synthesis parameters, specifically examining reaction durations of 5, 10, and 15 h at a consistent temperature of 150°C, was studied to achieve high-quality crystalline MOF structures. To assess the feasibility and scalability of this approach for industrial application, the synthesis process was scaled up, and detailed evaluations of structural and morphological characteristics were performed.

2. EXPERIMENTAL

2.1 Materials

Iron (III) chloride hexahydrate, aluminum nitrate nonahydrate, terephthalic acid (TPA), N,N-dimethylformamide, ethanol, and deionized water were purchased from Sigma-Aldrich. Terephthalic acid (TPA) recovered from PET waste was synthesized following the procedure described in our previous work [6].

2.2 Synthesis of MIL-53(Fe) and MIL-53(Fe, Al)

MIL-53(Fe): $FeCl_3 \cdot 6H_2O$ and TPA were mixed with DMF in a molar ratio of 1:1:100. The mixture was stirred until homogeneous and then transferred into a Teflon-lined stainless steel autoclave. The hydrothermal reaction was conducted at 150 °C for the optimized reaction time. After cooling to room temperature, the resulting product was collected by centrifugation, washed three times with deionized water and ethanol, and dried at 100 °C for 12 h.

MIL-53(Fe,Al): For the bimetallic synthesis, $FeCl_3 \cdot 6H_2O$ and $Al(NO_3)_3 \cdot 9H_2O$ using an Fe:Al molar ratio of 2:3 were dissolved together in DMF, followed by the addition of TPA. The resulting mixture was stirred thoroughly before undergoing hydrothermal treatment at 150 °C for the optimized time. The obtained solid was washed three times with deionized water and ethanol, and dried at 100 °C for 12 h.

MIL-53(Fe,Al) using PET derived TPA: Following optimization, TPA derived from PET hydrolysis was used to synthesize bimetallic MIL-53(Fe,Al) under similar conditions. The product was labeled as MIL-53(Fe, Al)_PET

2.3 Scale-Up Synthesis of MIL-53(Fe, Al)

Following the successful laboratory-scale synthesis, the process was scaled up by a factor of five to assess the feasibility of larger-scale production. Commercial TPA was used as the organic linker, and the optimized synthesis conditions were maintained to evaluate consistency in morphology and crystallinity. After scale-up synthesis, the obtained product was isolated, purified, and dried using the same procedures detailed above. The final product was labeled as MIL-53(Fe, Al)_5T

2.4 Characterization

XRD patterns were recorded using Cu Kα radiation (λ = 1.5406 Å) over a 2θ range of 5°–50° to determine the crystalline structure. Surface morphology was observed using a field-emission SEM. Elemental mapping was performed using an energy dispersive X-ray spectrometer (EDS; Oxford X-MaxN) at a beam voltage of 20.0 kV. Nitrogen adsorption–desorption isotherms at 77 K were used to calculate specific surface areas and pore size distributions.

3. RESULTS AND DISCUSSION

3.1 Synthesis of MIL-53 and MIL-53(Fe, Al) from commercial TPA

Figure 1 presents SEM images of MIL-53(Fe) synthesized at different reaction times (5, 10, and 15 h). At 10 h, uniform hexagonal crystals with an average particle size of 1,595 nm were obtained. Reducing the reaction time to 5 h resulted in a mixture of hexagonal crystals and irregularly shaped particles, leading to lower uniformity and poorer crystal alignment compared to the 10 h sample. Conversely, extending the reaction time to 15 h caused particle agglomeration, resulting in the formation of larger fused crystals. Thus, SEM analysis indicates that 10 h is the optimal reaction time for synthesizing MIL-53(Fe), producing well-faceted and uniform crystals. These findings are consistent with previous reports by Chen et al [7], which demonstrated similar morphologies under comparable synthesis conditions.

MIL-53(Fe, Al) was synthesized using an Fe:Al molar ratio of 2:3 at a synthesis temperature of 100 °C for 10 h. Figure 1(d) shows SEM images of MIL-53(Fe, Al), revealing that the incorporation of Al significantly altered the crystal morphology. The well-defined hexagonal structures observed in MIL-53(Fe, Al) were replaced by irregularly shaped particles, including spherical and elliptical forms. This change indicates that Al doping affects the crystallization process, consistent with the observations reported by Chen et al [7]. Moreover, the average particle size decreased to approximately 521 nm, suggesting that Al incorporation not only modifies the crystal morphology but also contributes to particle size reduction, which is expected to enhance the material's surface area and porosity

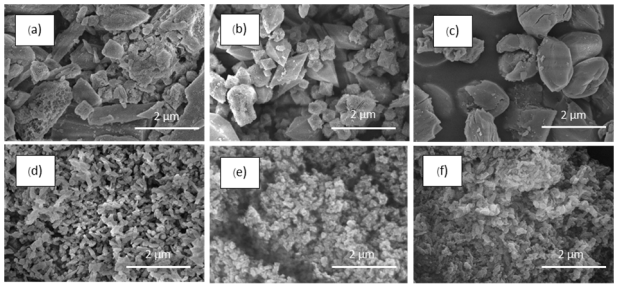

Figure 1 SEM images of MIL-53 (Fe) synthesized at (a) 5 h, (b) 10 h (c) 15 h, (d) MIL-53(Fe,Al), (e) MIL-53(Fe,Al)_PET and (f) MIL-53(Fe,Al)_5T

Figure 2 shows the XRD patterns of MIL-53(Fe) and MIL-53(Fe, Al). The diffraction pattern of MIL-53 (Fe) displays sharp, well-defined peaks at approximately 9.3°, 12.6°, 17.8°, 25.3°, and 27.3°, consistent with previously reported patterns for MIL-53 structures, confirming the formation of a highly crystalline MIL-53(Fe) phase [7]. Upon incorporation of Al, the diffraction peaks in MIL-53(Fe, Al) become broader and less intense, suggesting a reduction in crystallinity and increased structural disorder [7]. This phenomenon aligns well with SEM observations, where the presence of Al led to irregular particle shapes and smaller crystal sizes. The broader peaks imply decreased particle size and crystal imperfections due to the Al substitution into the framework.

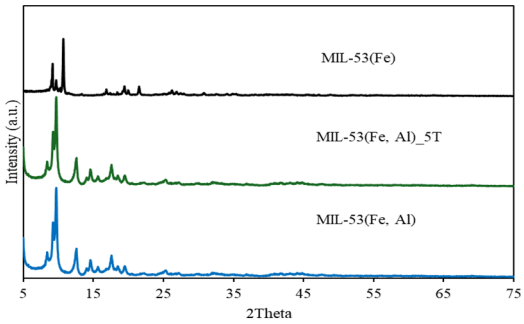

Figure 2 XRD of MIL-53(Fe), MIL-53(Fe,Al) and MIL-53(Fe, AL)_5T

The surface area, pore volume, and pore diameter of MIL-53(Fe, Al) synthesized at 150 °C for 10 h were found to be 834.4 m^2 g^{-1}, 0.711 cm^3 g^{-1}, and 10.4 nm, respectively, as shown in Table 1. Compared to MIL-53(Fe), the incorporation of Al significantly increased the surface area, which is consistent with the SEM observations. The reduction in particle size caused by Al doping resulted in a larger overall surface area, facilitating greater porosity. The surface area increase observed in this study aligns with previous findings by Chen et al [7], where Al incorporation similarly enhanced the surface area of MIL-53 structures. In their report, the surface area of MIL-53(Fe) increased from 39 m^2 g^{-1} to 1,397 m^2 g^{-1} after Al addition. These results confirm that partial substitution of Fe by Al in the MIL-53 framework improves surface area and porosity, making the material more suitable for adsorption-based applications.

Table 1 Surface area, pore volume, and pore diameter of synthesized MIL-53(Fe) and MIL-53(Fe, Al) compared with previous literatures.

Samples	Synthesis Conditions	Surface Area (m^2 g^{-1})	Pore Volume (cm^3 g^{-1})	Pore Diameter (nm)	Reference
MIL-53(Fe)	150 °C, 10 h	46.6	0.117	13.0	This work
MIL-53(Fe, Al)	150 °C, 10 h	834.4	0.711	10.4	This work
MIL-53(Fe)	150 °C, 10 h	39.0	0.070	7.14	[7]
MIL-53(Fe, Al)	150 °C, 10 h	1397.2	1.050	3.01	[7]

Table 2 summarizes the synthesis yield of MIL-53(Fe) and MIL-53(Fe, Al) under different reaction conditions. For MIL-53(Fe), the yield increased with reaction time from 45.51% at 5 h to 53.32% at 10 h, but slightly decreased to 50.10% after 15 h. The increase in yield from 5 to 10 h can be attributed to the more complete nucleation and growth of MIL-53(Fe) crystals during the hydrothermal reaction. At shorter reaction times, incomplete coordination between Fe^{3+} ions and TPA linkers results in lower crystal formation and reduced recovery. Extending the reaction time to 10 h allows more precursors to fully react, leading to improved crystallization and higher yield. However, prolonged reaction times beyond 10 h may lead to framework instability or side reactions, slightly reducing the overall recovery [8]. These findings suggest that a reaction time of 10 h is optimal for maximizing the yield of MIL-53(Fe).

In the case of MIL-53(Fe, Al), a significant improvement in yield was observed. The yield achieved 73.06% after 10 h, demonstrating that the incorporation of Al enhances the crystallization efficiency and product recovery. This improvement can be attributed to the strong coordination ability of Al^{3+} ions with TPA linkers, which stabilizes the framework during synthesis. Additionally, the presence of Al promotes faster nucleation, increases the number of growth sites, and reduces undesirable side reactions such as Fe^{3+} hydrolysis, leading to a higher conversion of reactants into the final crystalline product [1].

3.2 Synthesis of MIL-53(Fe, Al) using PET-Derived TPA

The optimized condition for synthesis MIL-53(Fe,Al)_TPA was applied to evaluate the suitability of PET-derived TPA as a starting material. Figure 1(e) shows the SEM images of MIL-53(Fe, Al)_TPA, showining that morphology predominantly consists of spherical and elliptical particles, closely resembling the structures obtained when using commercial TPA. The average particle size was significantly reduced to approximately 105 nm. The specific surface area, pore volume, and average pore diameter of the scaled-up MIL-53(Fe, Al) were found to be 1,041.9 m^2 g^{-1}, 0.609 cm^3 g^{-1}, and 8.6 nm, respectively. These results confirm that TPA recovered from PET waste can be successfully used for MIL-53(Fe, Al) synthesis without significant changes in particle morphology, demonstrating the feasibility of using waste-derived feedstocks for high-value MOF production.

Table 2 Yield of MIL-53(Fe) and MIL-53(Fe, Al) under different reaction conditions.

Samples	Synthesis Conditions	Yield (%)
MIL-53(Fe)	150 °C, 5 h	45.51
MIL-53(Fe)	150 °C, 10 h	53.32
MIL-53(Fe)	150 °C, 15 h	50.10
MIL-53(Fe, Al)	150 °C, 10 h	73.06
MIL-53(Fe, Al)_5T	150 °C, 10 h	61.61

3.3 Scale-Up Synthesis of MIL-53(Fe, Al)

Figure 1(f) presents SEM images of the scaled-up MIL-53(Fe, Al) sample. The incorporation of Al into the MIL-53(Fe) structure led to a morphological transition from well-defined hexagonal crystals to irregularly shaped particles, including spherical and elliptical forms. This observation is consistent with the SEM analysis performed at the laboratory scale. The introduction of Al was found to influence the crystal growth behavior and resulted in a reduction of particle size. The average particle size of the scaled-up MIL-

53(Fe, Al) crystals was approximately 210 nm. The decrease in particle size is expected to enhance the surface area of the material, which could further improve its performance in adsorption and separation applications.

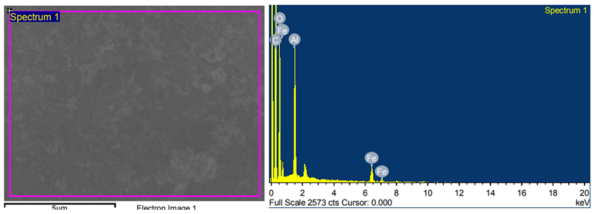

Figure 3 EDS analysis of MIL-53(Fe, AL)_5T.

Figure 3 shows the EDS analysis of MIL-53(Fe, Al)_5T. The results confirm the presence of key elements: carbon (C), oxygen (O), iron (Fe), and aluminum (Al). The elemental weight percentages were determined to be C: 52.7 wt%, O: 34.1 wt%, Fe: 6.5 wt%, and Al: 6.5 wt%. These results validate the successful incorporation of Al into the MIL-53 framework and are consistent with the intended synthesis design.

Figure 2 shows the XRD pattern of the scaled-up MIL-53(Fe, Al) sample. A distinct diffraction peak corresponding to Al incorporation was observed at approximately $2\theta = 9.3°$, confirming the successful integration of Al into the MIL crystal framework. This result is consistent with the XRD analysis of MIL-53(Fe, Al) synthesized at the laboratory scale, further validating that the crystalline structure was maintained during the scale-up process.

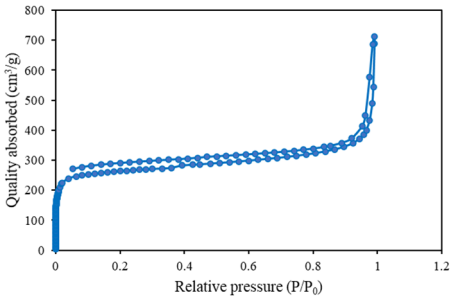

Figure 4 Nitrogen adsorption–desorption isotherms of MIL-53(Fe, Al)_5T.

Figure 4 shows the nitrogen adsorption–desorption isotherms of the scaled-up MIL-53(Fe, Al) sample. The isotherm exhibits a Type VI hysteresis loop at a relative pressure (P/P_0) close to 1.0, indicating the presence of interparticle mesopores formed between non-uniformly sized particles. The specific surface area, pore volume, and average pore diameter of the scaled-up MIL-53(Fe, Al) were found to be 1,015.3 $m^2\ g^{-1}$, 0.714 $cm^3\ g^{-1}$, and 9.0 nm, respectively. These results show that the incorporation of Al significantly increases the surface area, consistent with the observations from the laboratory-scale MIL-53(Fe, Al) samples. The increase in surface area upon Al incorporation further enhances the material's potential for applications requiring high porosity and adsorption capacity.

As seen in Table 2, the scaled-up MIL-53(Fe, Al)_5T sample achieved a yield of 61.61%, which was slightly lower than that of the laboratory-scale synthesis (73.06%), but still represents a satisfactory yield. This result indicates that the scale-up process remains feasible, although minor losses are expected during larger-volume operations.

4. CONCLUSION

In this work, MIL-53(Fe, Al) was successfully synthesized using both commercial and PET-derived terephthalic acid (TPA) under optimized hydrothermal conditions. The incorporation of Al into the MIL-53 framework significantly altered the crystal morphology, reducing the particle size and enhancing the specific surface area compared to pure MIL-53(Fe). The optimized synthesis at 100 °C for 10 h yielded high-quality products, with MIL-53(Fe) achieving a maximum yield of 53.32% and MIL-53(Fe, Al) achieving a significantly higher yield of 73.06% at the laboratory scale. The scaled-up MIL-53(Fe, Al)_5T sample also exhibited a satisfactory yield of 61.61%, demonstrating that larger-scale production is feasible, with only minor losses. Furthermore, the successful synthesis of MIL-53(Fe, Al) using PET-derived TPA without significant changes in morphology or particle size highlights the potential of utilizing waste-derived feedstocks for sustainable and high-value MOF production. Overall, this work demonstrates a promising pathway for sustainable valorization of plastic waste into functional, industrially relevant metal-organic frameworks.

ACKNOWLEDGMENTS

The authors thank to the Thailand Science Research and Innovation (Grant no. 198307/2024, 204301/2025) for the financial support.

REFERENCES

1. G. Férey, C. Mellot-Draznieks, C. Serre, F. Millange. Crystallized frameworks with giant pores: Are there limits to the possible? *Accounts of Chemical Research* 2005; 38(4): 217–225.
2. R. Geyer, J. R. Jambeck, K. L. Law. Production, use, and fate of all plastics ever made. *Science Advances* 2017; 3(7): e1700782.
3. J. Hopewell, R. Dvorak, E. Kosior. Plastics recycling: Challenges and opportunities. *Philosophical Transactions of the Royal Society B: Biological Sciences* 2009; 364(1526): 2115–2126.
4. T. Kundu, B. B. Shah, S. Mukherjee. Bimetallic MIL-53: Enhanced stability and selective gas adsorption behavior. *Microporous and Mesoporous Materials* 2021; 321: 111130.

5. P. H. Q. Pham, D. N. Nguyen, T. H. Le. Upcycling of PET plastic waste to valuable terephthalic acid for MOF synthesis. *Journal of Environmental Chemical Engineering* 2020; 8(5): 104315.
6. N. Prasongthum, N. Khoduangklang, K. Janna, A. Suemanotham, L. Attanatho, P. Reubroycharoen, S. Ittisupornrat, Y. Thanmongkhon. Chemical Recycling of Waste PET into Terephthalic Acid by Alkaline Hydrolysis, *The 33rd Thai Institute of Chemical Engineering and Applied Chemistry International Conference TIChE2024* 2024; Phra Nakhon Si Ayutthaya, Thailand, March 7-8
7. X. Chen, X. Liu, L. Zhu, X. Tao, X. Wang. One-step fabrication of novel MIL-53(Fe, Al) for synergistic adsorption-photocatalytic degradation of tetracycline. *Chemosphere* 2022; 291: 133032.
8. X. Zhao, Y. Wang, D.S. Li, X. Bu, P. Feng. Metal–Organic Frameworks for Separation. *Advanced Materials* 2013; 25(37): 5536–5548.

Effect of co-solvents on the oxidative cleavage of oleic acid under ambient pressure

Chakreeya Santhadklang[1], Panuwat Lawtae[1], Varong Pavarajarn[1,*]

[1] Center of Excellence in Particle and Materials Processing Technology, Department of Chemical Engineering, Faculty of Engineering, Chulalongkorn University, Bangkok 10330, Thailand
[*] Corresponding author: varong.p@chula.ac.th

ABSTRACT

This study investigates the effect of different co-solvents on the oxidative cleavage of oleic acid under ambient pressure using hydrogen peroxide (H_2O_2) as the oxidant and tungsten trioxide (WO_3) as the catalyst. Preliminary experiments under autogenous pressure with tert-butanol identified 100°C as the optimal temperature for maximizing the yields of pelargonic acid (PA) and azelaic acid (AA). To enable ambient-pressure operation, isobutyric acid and ethyl lactate, both with higher boiling points, were evaluated as alternative co-solvents. Reactions were conducted at 80°C and 100°C, and product distributions were analyzed by GC-MS using stearic acid as an internal standard. Although both co-solvents achieved high oleic acid conversion, only isobutyric acid promoted efficient C–C bond cleavage and high yields of PA and AA, reaching 24.87% and 31.47%, respectively, at 100°C with a 98.53% conversion of oleic acid. In contrast, ethyl lactate led to the accumulation of intermediate compounds and limited oxidation efficiency. The protic nature of the co-solvents, while potentially inhibiting electron transfer, improved system homogeneity and solubility. These findings demonstrate that isobutyric acid is a promising co-solvent for oxidative cleavage under ambient pressure, offering a safer, more energy-efficient, and scalable approach for industrial oleochemical production.

Keywords: Oleic acid; Oxidative cleavage; Pelargonic acid (PA); Azelaic acid (AA); Co-solvents

1. INTRODUCTION

Oleic acid, a major unsaturated fatty acid derived from palm oil, serves as a renewable feedstock for the production of valuable chemical intermediates through oxidative cleavage of its carbon–carbon double bond [1, 2]. This reaction yields medium- and short-chain fatty acids, particularly pelargonic acid (PA) and azelaic acid (AA), which are widely applied in industries such as agriculture, cosmetics, and lubricants [3–5]. Efficient utilization of this process is essential for enhancing the value of bio-based resources. However, the significant polarity difference between hydrophobic oleic acid and polar hydrogen peroxide (H_2O_2) leads to mass transfer limitations, which reduce reaction efficiency and must be systematically addressed [6].

Oxidative cleavage of oleic acid using H_2O_2, catalyzed by tungsten-based compounds, is recognized as an effective and environmentally friendly method, offering safety and sustainability advantages over ozone-based processes [7–9]. The reaction pathway leading to the formation of PA and AA is illustrated in Figure 1. Although tungsten catalysts improve reaction kinetics, poor miscibility between oleic acid and H_2O_2 remains a critical barrier, often resulting in lower product yields. The addition of co-solvents is a common strategy to enhance solubility and improve mass transfer between phases [10], with tert-butanol widely adopted due to its compatibility with both reactants [11,12]. However, its low boiling point requires the reaction to be carried out under autogenous pressure, which increases energy consumption and equipment costs. These drawbacks limit the feasibility of large-scale industrial applications and underscore the need for oxidative cleavage processes that can operate efficiently under ambient pressure conditions.

This study focuses on evaluating alternative co-solvents that facilitate the oxidative cleavage of oleic acid using H_2O_2 with tungsten trioxide (WO_3) as the catalyst under ambient pressure. Reactions were conducted at 80°C and 100°C over a 6-hour period. Co-solvents including tert-butanol, isobutyric acid, and ethyl lactate were selected based on solubility, boiling point, and chemical inertness [13,14]. Their performance was assessed by monitoring oleic acid conversion and the yields of PA and AA. Operating under ambient pressure is expected to reduce energy consumption, simplify process operations, and improve safety, offering a more cost-effective and sustainable approach for industrial oleochemical production.

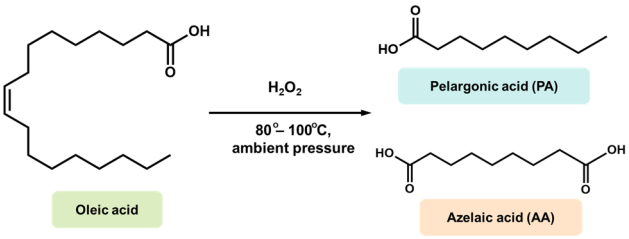

Figure 1 Oxidative cleavage of oleic acid.

2. EXPERIMENTAL

2.1. Materials

Oleic acid (75% w/w, $C_{18}H_{34}O_2$, Commercial Grade) and hydrogen peroxide (30% w/w, H_2O_2, AR Grade) were obtained from ANaPURE. Co-solvents including tert-butyl alcohol ($(CH_3)_3COH$), isobutyric acid ($(CH_3)_2CHCOOH$), and ethyl lactate ($C_5H_{10}O_3$) were used, all of analytical reagent (AR) grade and purchased from Loba Chemie. Tungsten(VI) oxide (WO_3, AR Grade, Loba Chemie) was employed as the catalyst. Silicone oil (Commercial Grade) was used as the heating medium in the oil bath.

For the esterification process, n-hexane (C_6H_{14}), hydrochloric acid (HCl, 37% w/w), and methanol (CH_3OH), all AR Grade (QReC), were utilized along with deionized water.

2.2. Methods

2.2.1. Catalyst preparation

The WO_3 catalyst was evenly spread on a watch glass to ensure uniform heating and dried in a laboratory oven at 100 °C for 24 hours to eliminate moisture prior to use in the reaction.

2.2.2. Oxidative cleavage of oleic acid

Oxidative cleavage reactions were conducted using a molar ratio of oleic acid to hydrogen peroxide to co-solvent of 1:8:20, varying the type of co-solvent (tert-butyl alcohol, isobutyric acid, or ethyl lactate) and the reaction temperature (80°C or 100°C).

Reactions were carried out in a 250 mL three-necked flask equipped with a mechanical stirrer and an oil bath for temperature control, as shown in Figure 2. Once the oleic acid and co-solvent mixture reached the target temperature, hydrogen peroxide was added. The total reaction volume was maintained at 100 mL. The WO_3 catalyst (1 g per 100 mL of reaction mixture) was then introduced, and the system was stirred at 3000 rpm. Each reaction was maintained for 6 hours under ambient pressure.

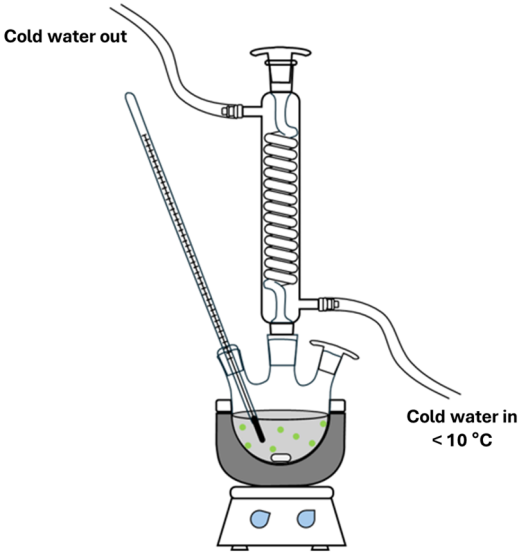

Figure 2 Experimental setup using a three-necked flask.

2.2.3. Catalyst recovery

Upon completion of the reaction, the mixture was centrifuged at 3000 rpm for 5 minutes to separate the precipitated WO_3 catalyst. The catalyst was washed with fresh co-solvent and centrifuged again under identical conditions. The recovered catalyst was dried in an oven at 100°C for 24 hours to remove residual solvent. The clarified reaction mixture was reserved for esterification.

2.2.4. Esterification procedure

Due to the polarity of the reaction products, esterification was required prior to GC-FID and GC-MS analysis, following the method of Ichihara and Fukubayashi [15]. A mixture of 3 mL methanol, 0.6 mL of 9% w/v HCl, and 0.4 mL of the sample was sealed in a reaction vial and heated at 80°C in a water bath for 2 hours. After cooling, 2 mL of hexane and 2 mL of deionized water were added to the mixture to induce phase separation. The system was allowed to equilibrate for 12 hours, after which the upper hexane layer, containing the esterified products, was collected for subsequent GC-FID and GC-MS analysis.

2.3. Sample analysis

2.3.1. GC-FID conditions

Quantitative analysis of pelargonic acid (PA) and azelaic acid (AA) was performed using a GC-FID system equipped with a FAME column (30 m × 0.32 mm × 0.25 µm). Helium was used as the carrier gas at a flow rate of 1.0 mL/min. The detector temperature was set at 260°C with a split ratio of 50:1. The oven temperature was initially set at 60°C and held for 4 minutes, then increased to 80°C at a rate of 30°C/min and held for 3 minutes, followed by an increase to 253°C at a rate of 20°C/min and held for 10 minutes. The injector temperature was programmed from 60°C

to 270°C. The following equations were used for calculations:

$$\text{Mole} = \frac{\text{Area}_{GC(FID)} \times \text{Calibration Curve} \times \text{Final Volume}}{1000} \quad (1)$$

$$\%\text{Conversion} = \frac{\text{Moles}_{\text{initial OA}} - \text{Moles}_{\text{final OA}}}{\text{Moles}_{\text{initial OA}}} \quad (2)$$

$$\%\text{Yield} = \frac{\text{Mole of Product}}{\text{Moles}_{\text{initial OA}} - \text{Moles}_{\text{final OA}}} \quad (3)$$

2.3.2. GC-MS Conditions

Qualitative analysis of PA and AA was conducted using an Agilent 7000C GC-MS Triple Quad system equipped with an HP-5ms column (30 m × 0.25 mm, 0.25 µm). The injection volume was 0.5 µL with a split ratio of 50:1. The oven temperature was initially set at 80°C and held for 2 minutes, then ramped to 280°C at a rate of 20°C/min and held for 6 minutes. Helium was used as the carrier gas at a flow rate of 1.0 mL/min.

3. RESULTS AND DISCUSSION

3.1. Oxidative cleavage of oleic acid under autogenous pressure

The oxidative cleavage of oleic acid was first investigated under autogenous pressure using tert-butanol as a co-solvent across a temperature range of 80–160°C. The reaction follows a pathway involving initial epoxidation of the carbon–carbon double bond, dihydroxylation, and subsequent oxidative cleavage, yielding pelargonic acid (PA) and azelaic acid (AA) as the primary products (Figure 3) [17].

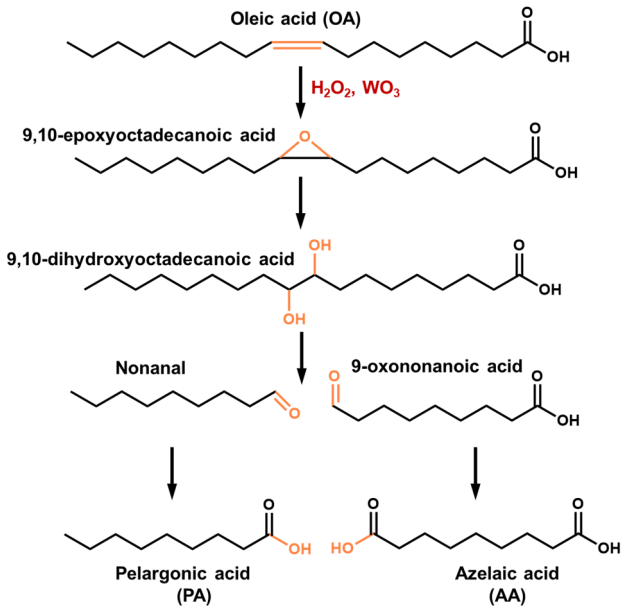

Figure 3 Proposed oxidative cleavage mechanism of oleic acid.

The effect of temperature on product yields is shown in Figure 4. The highest yields of PA and AA were obtained at 100°C. At 80°C, lower yields were observed due to insufficient activation energy for efficient dihydroxylation and C–C bond cleavage. Above 100°C, the yields declined significantly. This decrease is attributed to two main factors. First, GC-MS analysis (Figure 5) revealed increased formation of by-products, indicating more extensive side reactions at elevated temperatures. Second, hydrogen peroxide likely undergoes thermal decomposition above 100°C, reducing the availability of the oxidant and thus limiting cleavage efficiency.

Further insight into temperature effects is provided in Figure 6, which compares product distributions at 80°C and 100°C. At 80°C, a high relative abundance of 9,10-dihydroxyoctadecanoic acid was detected, suggesting that the reaction predominantly proceeds through dihydroxylation without completing the C–C cleavage step [16]. At 100°C, intermediate levels decreased while the yields of PA and AA increased, indicating more complete conversion. These results suggest that although 80°C supports early-stage oxidation, it does not provide sufficient energy to break the carbon–carbon bond between adjacent hydroxyl groups, resulting in limited formation of final products. The greater accumulation of intermediates and oxygenated by-products at 80°C further supports this interpretation.

These findings highlight the importance of temperature control in oxidative cleavage reactions. The need for autogenous pressure arises from tert-butanol's low boiling point (82.4°C), which limits its application at higher temperatures under ambient conditions. Pressurized operation increases energy demand, equipment cost, and safety concerns, making it less attractive for industrial scale-up. Alternative co-solvents with higher boiling points are thus needed to enable ambient-pressure operation.

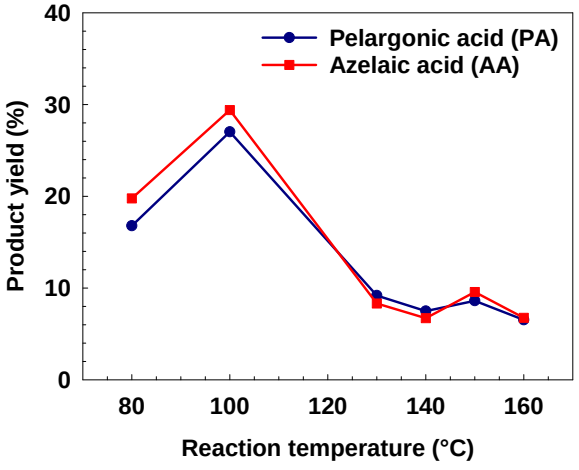

Figure 4 Effect of temperature on PA and AA yields under autogenous pressure.

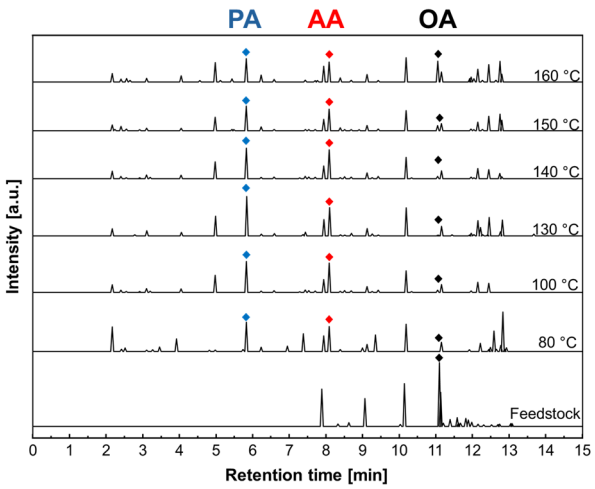

Figure 5. GC-MS analysis of products formed under autogenous pressure with tert-butanol at different reaction temperatures.

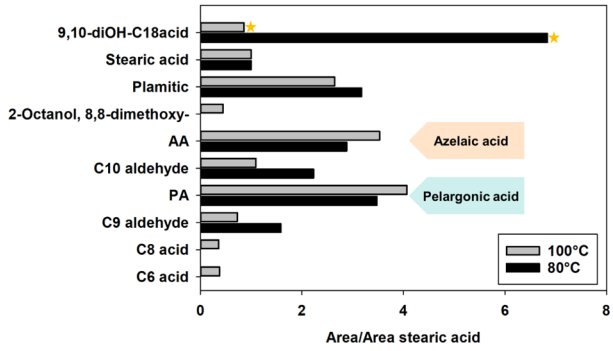

Figure 6 GC-MS comparison of product distributions at 80°C and 100°C under autogenous pressure with tert-butanol.

3.2. Oxidative cleavage of oleic acid under ambient pressure

To avoid pressurized operation, isobutyric acid and ethyl lactate were evaluated as alternative co-solvents to tert-butanol. Both possess boiling points of approximately 153.86°C, allowing reactions to be conducted at elevated temperatures under ambient pressure. Solubility assessments confirmed that these co-solvents are miscible with both aqueous and organic phases, improving system homogeneity. Computational analysis of their highest occupied molecular orbital (HOMO) energy levels indicated relatively wide energy gaps, suggesting low intrinsic reactivity and favorable chemical inertness. All three solvents, including tert-butanol, exhibit protic characteristics, which may stabilize hydrogen peroxide through hydrogen bonding and potentially inhibit its electron transfer reactivity. Nevertheless, the enhanced solubility and improved phase contact provided by the co-solvents are expected to facilitate more efficient oxidative cleavage. The molecular structures of the co-solvents are shown in Figure 7.

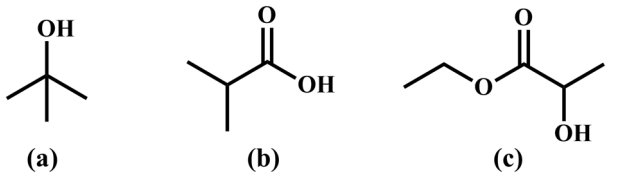

Figure 7 Molecular structures of (a) tert-butanol, (b) isobutyric acid, and (c) ethyl lactate

Reactions were performed at 80°C and 100°C under ambient pressure. Oleic acid conversion is summarized in Table 1. All conditions showed high conversion, although this does not directly reflect product selectivity. GC-MS analysis was conducted to assess product distribution, using stearic acid as an internal standard. Stearic acid, present as an impurity in the oleic acid feedstock, does not undergo oxidative cleavage under the reaction conditions, resulting in a constant concentration throughout the reaction and providing a reliable reference for quantitative analysis.

Table 1 Conversion of oleic acid using different co-solvents under ambient pressure.

Co-solvent	Temperature (°C)	% Conversion
Isobutyric acid	80	90.08
	100	98.53
Ethyl lactate	80	99.74
	100	99.75

GC-MS results with isobutyric acid as the co-solvent are shown in Figure 8. The relative peak areas (normalized to stearic acid) are reported in parentheses. At 80°C, the reaction yielded substantial amounts of 9,10-dihydroxyoctadecanoic acid (4.18), C9 aldehyde (3.14), and 9-oxopelargonic acid (2.75), along with moderate formation of PA (2.18) and AA (1.71). This product profile indicates that while the reaction progresses through early oxidation steps such as dihydroxylation and partial aldehyde formation, C–C bond cleavage remains incomplete at lower temperatures. At 100°C, the yields of PA and AA increased significantly (3.33 and 3.20, respectively), while key intermediates such as C10 aldehyde (1.88) and 9,10-dihydroxyoctadecanoic acid (5.31) remained detectable, consistent with the higher oleic acid conversion observed at 100°C compared to 80°C (98.5% vs 90%). The aldehyde-to-acid transition appears more efficient at the higher temperature, as indicated by the substantial drop in 9-oxopelargonic acid (0.35), suggesting further oxidation to AA. Additionally, the presence of minor dicarboxylic acids such as sebacic acid and caprylic acid at 100°C suggests the occurrence of overoxidation pathways or parallel side reactions.

Figure 9 presents the GC-MS product distribution using ethyl lactate as a co-solvent. At 80°C, the reaction was dominated by 9,10-dihydroxyoctadecanoic acid (16.50), with very low yields of PA (0.23) and AA (0.13). The excessive accumulation of the dihydroxy intermediate, along with high levels of unidentified

products (4.23), indicates limited C–C bond cleavage and significant pathway stalling at the dihydroxylation stage. The oxidant appears poorly utilized under these conditions. At 100°C, the PA yield improved to 1.22 and AA reached 0.80, although 9-oxononanoic acid remained undetected. High levels of 9,10-dihydroxystearic acid (6.52) persisted, indicating diversion toward an unproductive pathway. Overall, ethyl lactate promoted early oxidation but failed to support efficient C–C bond cleavage and final product formation.

The percent yields of PA and AA obtained under ambient pressure were compared with those from autogenous pressure using tert-butanol, as summarized in Table 2. While the highest AA yield was achieved with tert-butanol at 100°C (29.40%), the highest AA yield occurred with isobutyric acid at the same temperature (31.47%). These findings demonstrate that isobutyric acid enables comparable or superior performance under ambient pressure.

In summary, isobutyric acid is more effective than ethyl lactate as a co-solvent for oxidative cleavage under ambient pressure. The optimal reaction temperature is 100°C, providing high conversion and enhanced yields of PA and AA while simplifying process design for industrial applications.

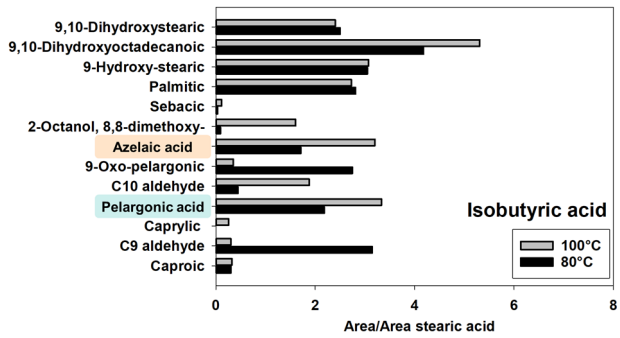

Figure 8 GC-MS product distributions using isobutyric acid at 80°C and 100°C.

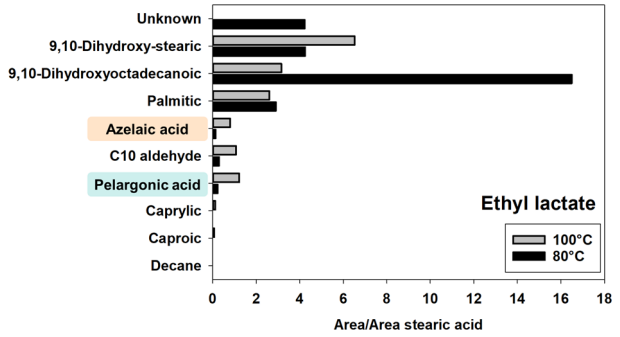

Figure 9 GC-MS product distributions using ethyl lactate at 80°C and 100°C.

Table 2 Product yields of PA and AA under autogenous and ambient pressure

Condition	Co-solvent	Temp. (°C)	%Yield PA	%Yield AA
Autogenous pressure	Tert-butanol	100	27.04	29.40
Ambient pressure	Isobutyric acid	80	20.92	24.07
		100	24.87	31.47
	Ethyl lactate	80	1.73	1.25
		100	9.99	8.64

4. CONCLUSION

This study investigated the oxidative cleavage of oleic acid using hydrogen peroxide with various co-solvents under both autogenous and ambient pressure conditions. The reaction proceeded via epoxidation, dihydroxylation, and subsequent C–C bond cleavage to yield pelargonic acid (PA) and azelaic acid (AA). Under autogenous pressure, tert-butanol provided the highest yields at 100°C; however, further temperature increases led to side reactions and hydrogen peroxide decomposition. To enable ambient-pressure operation, isobutyric acid and ethyl lactate were evaluated as alternative co-solvents. Both supported high oleic acid conversion, but only isobutyric acid promoted efficient bond cleavage and high yields of PA and AA at 100°C. In contrast, ethyl lactate resulted in the accumulation of intermediates and limited oxidative progression. GC-MS analysis confirmed that both temperature and solvent characteristics significantly influence the oxidative pathway, particularly the aldehyde-to-acid transformation. These findings demonstrate that isobutyric acid is a promising co-solvent for ambient-pressure oxidative cleavage, offering comparable or improved performance over tert-butanol and representing a safer and more scalable option for oleochemical production.

ACKNOWLEDGMENTS

This research was financially supported by Patum Vegetable Oil Co., Ltd., whose contribution to the advancement of sustainable oleochemical technology is gratefully acknowledged.

REFERENCES

1. Alhaji, A.M., et al. Palm Oil (Elaeis guineensis): A Journey through Sustainability, Processing, and Utilization. Foods, 2024. 13, DOI: 10.3390/foods13172814.
2. Parker, L., et al. Development and Large-Scale Production of High-Oleic Acid Oil by Fermentation of Microalgae. Fermentation, 2024. 10, DOI: 10.3390/fermentation10110566.
3. Dorado, V., C.I. Herrerías, and J.M. Fraile, Simple metal-free oxidative cleavage of 1,2-diols. Tetrahedron, 2023. 139: p. 133450.

4. Johnson Iii, W.C. and J. Davis, Pelargonic Acid for Weed Control in Organic Vidalia (R) Sweet Onion Production. HortTechnology, 2014. 24: p. 696-701
5. Arshad, T., et al., Structural elucidation and development of azelaic acid loaded mesoporous silica nanoparticles infused gel: Revolutionizing nanodrug delivery for cosmetics and pharmaceuticals. Heliyon, 2024. 10(8): p. e29460.
6. Metzger, J.O. and U. Bornscheuer, Lipids as renewable resources: current state of chemical and biotechnological conversion and diversification. Applied Microbiology and Biotechnology, 2006. 71(1): p. 13-22.
7. Weschler, C.J., Ozone's impact on public health: contributions from indoor exposures to ozone and products of ozone-initiated chemistry. Environ Health Perspect, 2006. 114(10): p. 1489-96.
8. Spannring, P., et al., Transition metal-catalyzed oxidative double bond cleavage of simple and bio-derived alkenes and unsaturated fatty acids. Catalysis Science & Technology, 2014. 4(8): p. 2182-2209.
9. Vondran, J., et al., From tandem to catalysis – organic solvent nanofiltration for catalyst separation in the homogeneously W-catalyzed oxidative cleavage of renewable methyl 9,10-dihydroxystearate††Electronic supplementary information (ESI) available. See DOI: https://doi.org/10.1039/d1cy02317a. Catalysis Science & Technology, 2022. 12(11): p. 3622-3633.
10. Harper, J.B., et al., Non-traditional solvent effects in organic reactions. Physical Chemistry Chemical Physics, 2021. 23(46): p. 26028-26029.
11. Guicheret, B., et al., Aerobic Oxidative Cleavage of Vicinal Diol Fatty Esters by a Supported Ruthenium Hydroxide Catalyst. ACS Sustainable Chemistry & Engineering, 2020. 8(35): p. 13167-13175.
12. Köckritz, A., M. Blumenstein, and A. Martin, Catalytic cleavage of methyl oleate or oleic acid. European Journal of Lipid Science and Technology, 2010. 112(1): p. 58-63.
13. Giannakoudakis, D.A., et al., Additive-free photo-assisted selective partial oxidation at ambient conditions of 5-hydroxymethylfurfural by manganese (IV) oxide nanorods. Applied Catalysis B: Environmental, 2019. 256: p. 117803.
14. Peng, M., et al., Insights into co-solvent roles in oxidative depolymerization of lignin to vanillin and lactic acid. Fuel, 2023. 354: p. 129369.
15. Ichihara, K.i. and Y. Fukubayashi, Preparation of fatty acid methyl esters for gas-liquid chromatography [S]. Journal of lipid research, 2010. 51(3): p. 635-640.
16 A. Kulik, A. Janz, M.-M. Pohl, A. Martin and A. Köckritz, Eur. J. Lipid Sci. Technol., 2012, 114, 1327–1332
17 Gámez, S., E. de la Torre, and E.M. Gaigneaux, Carbon supports for the oxidative cleavage of oleic acid: Influence of textural properties. Molecular Catalysis, 2022. 533.

Demonstration of zeolite A produced from coal ash applied to CO_2 capture process for amine regeneration approach

Punyaporn Khamdaeng[1], Tosporn Phetyim[1], Natthawan Prasongthum[2], Siriporn Tong-on[3], Wanchana Sisuthog[1], Amornrat Suemanotham[1], Lalita Attanatho[1], Apichat Junsod[1] and Yoothana Thanmongkhon[1,*]

[1] Expert Centre of Innovative Clean Energy and Environment, Thailand Institute of Scientific and Technological Research (TISTR), Pathum Thani 12120, Thailand
[2] Faculty of Science, Khon Kaen University, Khon Kaen 40002, Thailand
[3] Expert Centre of Innovative Materials, Thailand Institute of Scientific and Technological Research (TISTR), Pathum Thani 12120, Thailand
[*] Corresponding author: yoothana_t@tistr.or.th

ABSTRACT

The disposal of coal fly ash, a byproduct of coal-fired power plants, presents significant environmental challenges due to its abundance and the costs associated with its removal. However, coal fly ash can be repurposed for more beneficial applications, particularly in the production of construction materials. Additionally, its low price and wide availability make it an attractive resource for other innovative uses. One such application is the synthesis of zeolite A, a high-value material with diverse industrial applications, which can be derived from coal fly ash following circular economy aspects. In this study, zeolite A was synthesized from coal fly ash via a hydrothermal process using a 2-liter electric autoclave at 80°C for 12 hours. The yield of zeolite A was approximately 56-59% by weight. Characterization of the synthesized zeolite revealed its high acidity, a property that can enhance CO_2 release during amine solution regeneration in CO_2 capture processes, 15% by volume of mixed gas. To assess its performance, the prepared zeolite was tested using 5 molar of MEA for regeneration, at 100°C, in a CO_2 capture demonstration unit. The results illustrated that the zeolite A derived from coal fly ash crucially improved CO_2 desorption, indicating its potential to enhance the efficiency of CCUS technologies by reducing about 30% of energy consumption in desorption step compared to no zeolite application. The performance of synthesized zeolite is similar to the commercial one. This study hints that fly ash-derived zeolite A can be an effective and sustainable material for advancing CO_2 mitigation efforts, offering both environmental and economic benefits.

Keywords: CO_2 capture; Coal fly ash; Hydrothermal; Zeolite A; Circular economy

1. INTRODUCTION

Post-combustion carbon capture based on absorption is considered a vital technology for addressing climate change by capturing CO_2 emissions released after the combustion of fossil fuels in power plants. This method involves using solvents to selectively absorb CO_2 from flue gas before it is emitted into the atmosphere. One of the most commonly used amines for CO_2 post-combustion capture is monoethanolamine (MEA), thanks to its low cost, rapid CO_2 absorption rate, and extensive research background.[1] However, a major challenge with this process is the significant energy required for CO_2 removal during solvent regeneration, which typically occurs at high temperatures, around 120-150°C. This step accounts for about 70-80% of the total operational cost of CO_2 capture. Consequently, reducing the heat required for solvent regeneration has become a key consideration when evaluating CO_2 capture methods. To achieve this, the temperature for solvent regeneration should ideally be reduced to 100°C or lower.[2]

Recent studies have suggested that incorporating a solid acid catalyst into the amine regeneration process could be a promising approach to enhancing CO_2 desorption rates at lower temperatures (< 100°C), thereby significantly reducing the energy required for solvent regeneration. Liang et al. explored the addition of Al_2O_3 and HZSM-5 into the regeneration process of 5M MEA at 105°C. Their findings revealed a notable reduction in heat duty, with a 22% decrease for Al_2O_3 and an 18% decrease for HZSM-5. Al_2O_3 facilitated a type of acidity known as Lewis acidity, while HZSM-5 promoted Brønsted acidity. Both types of acids acted as active sites, making the cleavage of the CO_2-amine bond easier.[3] Following these results, various

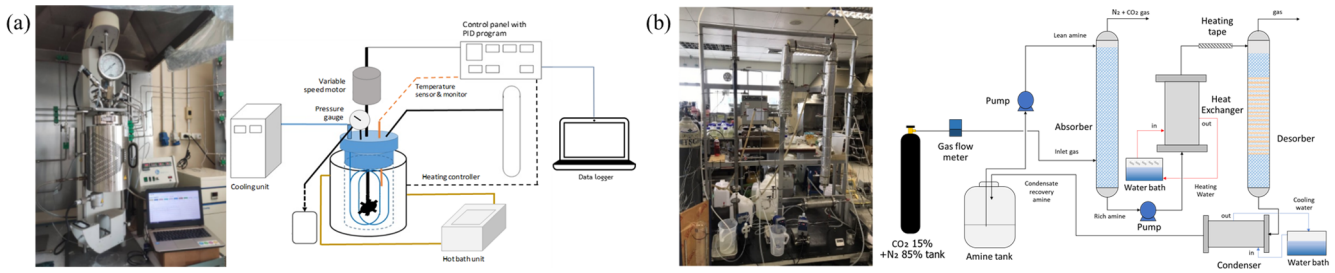

Figure 1 A unit of (a) zeolite synthesis process (b) CO_2 capture process

researchers have examined the catalytic effects of different acid catalysts on CO_2 desorption from MEA solvent, including Hβ, HY, H-mordenite, MCM-41, SO_4^{2-}/ZrO_2 and $Ce(SO_4)_2/ZrO_2$.[4,5] Their studies showed that solid acid catalysts helped lower the operating temperature to between 96°C and 105°C. However, these catalysts still face challenges such as high production costs and limited efficiency in large scale applications. As a result, there is a pressing need for the development of more cost-effective catalysts.

In this study, coal fly ash received from the coal combustion process was utilized as a raw material to synthesize zeolite A and investigate its catalytic effectiveness in the desorption of 5M MEA solvent at 100°C. The catalytic performance was assessed based on the CO_2 desorption rate, the total amount of CO_2 desorbed, and the heat required for regenerating the MEA solvent.

2. EXPERIMENTAL

2.1 Materials

The coal fly ash (CFA) used in this study was kindly provided by BLCP Power Limited (Thailand). Ethanolamine (MEA, ≥99% purity), sodium aluminum oxide ($NaAlO_2$), sodium hydroxide (NaOH, ≥99% purity), 1 N hydrochloric acid (HCl), and methyl orange (used as a titration indicator) were sourced from Sigma Aldrich. Commercial-grade zeolite 4A (Zeolite A_Com) was supplied by Tosoh Corporation, and CO_2 (15 vol% purity) was obtained from Thai Special Gas Co. Ltd.

2.2 Production of zeolite A

Zeolite A was produced from CFA using a fusion process followed by hydrothermal treatment. Firstly, CFA and NaOH, 50 g each, were mixed by a mortar, maintaining a CFA:NaOH mass ratio of 1:1. The mixture was then calcined at 500°C for 1.5 hours to activate the silicon and aluminum components. After calcination, the fused material was ground further, combined with 63 g of $NaAlO_2$, and placed in a batch hydrothermal reactor seen in Figure 1a. Distilled water was added to the solid mixture at a solid-to-liquid mass ratio of 4.5 which was about 734 g. The suspension was stirred by agitator with speed of 300 rpm at room temperature for 30 minutes and then heated up, using electric heater, to 80°C and kept the temperature for 12 hours. Afterward, the product was filtered, washed with distilled water until its pH reached 7, and then dried at 90°C for 16 hours. The final product was named as Zeolite A_CFA.

2.3 Characterization

Both the CFA and the zeolite products were characterized using several analytical techniques. These included X-ray fluorescence spectroscopy (XRF, S8-Tiger Bruker AXS), X-ray diffraction (XRD, SmartLab Rigaku), and scanning electron microscopy (SEM, Hitachi SU-8230). Additionally, the surface properties were analyzed using nitrogen adsorption-desorption with the Brunauer–Emmett–Teller (BET) method (Micromeristics ASAP 2020), and the acid properties were evaluated using NH3-temperature-programmed desorption (NH3-TPD, Bel-Cat B).

2.4 Demonstration of CO_2 capture process

In Figure 1b, the reactor system consists of two packed bed reactors. The first column is referred to as the CO_2 absorber, internally packed with 3 millimeters of glass bead only, using an amine solution, while the second column is called the CO_2 desorber, loaded with glass bead mixed with the produced zeolite A, which releases CO_2 from the amine solution. Both reactors are built from 1-inch diameter stainless steel pipes, each approximately 1.2 meters in length. The thermocouples are installed at various points along the columns, spaced about 20 centimeters apart.

The system is initially filled with MEA solution, 5M, using a pump until all components are completely saturated. The temperature inside the desorber is then raised to 100 °C. Once this temperature is reached, the MEA solution flow rate is regulated according to the experimental setup, with flow rates into and out of the absorber column set at 8 mL/min. A gas mixture containing 15% of CO_2 by volume is introduced to the system at about 5 L/min, regulated by a gas flow controller. Prior to beginning the experiment, the CO_2 concentration in the inlet gas is confirmed using a gas analyzer. The CO_2 capture process is then carried out over a 5-hour period. During this time, MEA solution samples are taken from the outlets of both columns and subjected to titration, using a 1.0 N HCl solution, to determine the CO_2 loadings (Horwitz et al.).[5] Moreover, gas samples are collected from the outlet of each column to analyze the CO_2 content using a gas analyzer.

2.5 Calculations

Catalytic performance was assessed by CO_2 loading, CO_2 desorption rate, cyclic capacity, and heat duty. These parameters were calculated using Eq. (1), (2) and (3), respectively.

$$CO_2 \text{ loading} = \alpha = \frac{n_{CO2}}{n_{amine}} \quad (1)$$

$$\text{Desorption rate} = (\alpha_{rich} - \alpha_{lean}) x\ CV \quad (2)$$

$$\text{Heat duty} = \frac{heat\ input/time}{amount\ CO2/time} = \frac{Electricity\ (kJ)}{nCO2} \quad (3)$$

where, α_{rich} and α_{lean} represent the initial and final amine-CO_2 loading, respectively. C and V refer to amine concentration and amine volume solutions.

3. RESULTS AND DISCUSSION

3.1 Production yields

The detail of production of zeolite A using coal fly ash as feedstock via a hydrothermal process, at 80°C for 12 hours, resulted in the yields of 56-59% by weight seen in Table 1.

Table 1 Details of mass.

run	CFA (g)	NaOH (g)	Mixture after fusion (g)	$NaAlO_2$ (g)	Distilled water (g)	Zeolite A (g)	Yields (%)
1	50.08	50.17	91.59	63.06	734.92	91.49	56.02
2	50.12	50.26	92.30	63.09	735.49	91.67	56.08
3	50.03	50.02	91.54	63.00	733.85	91.01	55.82
4	50.06	50.08	91.63	63.04	734.31	91.72	56.21
5	50.05	50.09	92.93	63.03	734.32	94.41	57.86
6	50.03	50.05	91.31	63.00	733.99	92.08	56.46
7	50.05	50.08	92.40	63.02	734.20	93.08	57.05
8	50.04	50.07	93.23	63.01	734.17	93.83	57.52
9	50.01	50.01	92.45	62.97	733.62	94.93	58.24
10	50.04	50.05	91.62	63.01	734.05	93.21	57.15

Figure 2 shows an overall mass balance of the study. The mass balance for zeolite A produced by the bench scale reactor. When using 50.04 grams of fly ash from a coal-fired power plant, the hydrothermal process provided 93.21 grams of zeolite A.

3.2 Characterization of catalysts

Table 2 presents the chemical compositions of coal fly ash and the obtained zeolite A_CFA. The CFA is primarily composed of SiO_2 (63.36%) and Al_2O_3 (21.92%), with a minor amount of Na_2O (0.33%), resulting in a Si/Al molar ratio of 2.45. Following fusion and hydrothermal synthesis, the Na_2O content significantly increased to 17.6%, suggesting the incorporation of Na^+ ions in the zeolite's extra-framework structure. Besides, the Si/Al molar ratio was reduced to 1.02, which matches the theoretical ratio expected for zeolite A.[6]

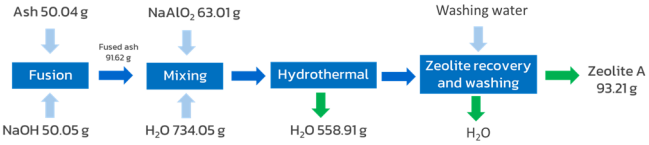

Figure 2 Overall mass balance of zeolite A production.

Table 2 Chemical compositions of CFA and zeolite A.

Composition (wt.%)	CFA	Zeolite A_CFA	Zeolite A_Com
SiO_2	63.36	41.5	43.9
Al_2O_3	21.92	34.3	35.7
Na_2O	0.33	17.6	18.7
Fe_2O_3	5.02	2.27	0.48
CaO	1.00	2.25	0.17
MgO	0.53	0.42	-
K_2O	1.48	0.40	0.16
P_2O_5	0.33	0.56	0.53
TiO_2	1.40	0.53	0.32
MnO	0.05	0.03	-
ZnO	0.02	0.007	0.003
SrO	0.13	0.03	0.001
CuO	0.01	0.05	-
ZrO_2	0.09	-	0.002
SO_3	0.29	0.06	-
Cl	-	-	-
NiO	-	0.007	-
Si/Al molar ratio	2.45	1.02	1.04

Figure 3 displays the XRD pattern of coal fly ash (CFA), showing the presence of amorphous phases, including quartz and mullite. These findings are consistent with the CFA composition reported by Belviso et al. After the synthesis process, the diffraction peaks corresponding to quartz and mullite disappeared, while new peaks appeared that match the reference pattern for zeolite A, as identified by JCPDS No. 01-073-6285.

SEM images in Figure 4(a) show that raw CFA consists mainly of spherical particles averaging 6.3 µm in size. After fusion and hydrothermal treatment, these transformed into smaller cubic crystals (~1.79 µm), confirming the formation of zeolite A as illustrated in Figure 4(b). NaOH facilitated the reaction by dissolving mullite and quartz into silicate and aluminate species, which formed a gel that crystallized into zeolite A during the hydrothermal process.

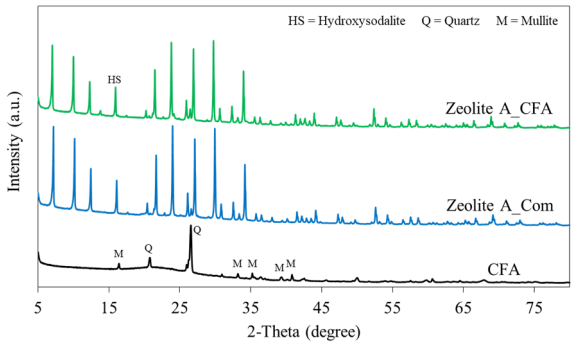

Figure 3 XRD patterns of CFA and Zeolite A.

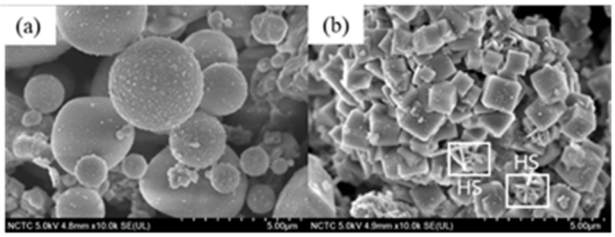

Figure 4 SEM images of (a) CFA and (b) Zeolite A.

Table 3 Properties of CFA and zeolite A.

	BET (m^2/g)	Acidity by strength (mmol/g)		
		Weak	Strong	Total acidity
CFA	5.50	-	-	-
Zeolite A_CFA	23.92	1.298	0.508	1.806

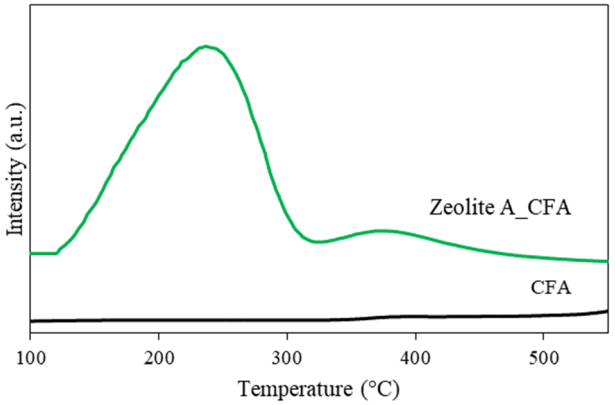

Figure 5 NH_3-TPD images of CFA and Zeolite A.

Table 3 determines the physicochemical properties of CFA and the synthesized zeolite. The surface area increased from 5.50 m^2/g for CFA to 23.92 m^2/g after zeolite formation, corresponding to the morphological changes observed in the SEM analysis.

Due to acid strength plays an essential role in CO_2 desorption. Figure 5 illustrates the NH_3-TPD profiles of CFA and zeolite A. CFA displays no desorption peaks, while zeolite A exhibited two peaks at 200 °C and 400 °C, about, indicating weak and strong acid sites. The total acid site concentration is 1.806 mmol/g.

3.3 Performances of CO_2 capture demonstration unit with zeolite A in the desorber

To achieve a Rich CO_2 loading close to equilibrium, the study of the effect of catalyst addition used an L/G ratio of 1.66 (amine solution flow rate of 8 mL/min), which yielded a Rich CO_2 loading of 0.4873 mol CO_2/mol amine. A comparison was then made between conditions with and without the addition of commercial zeolite (Zeolite_Com) in the desorber to determine the optimal catalyst weight (0, 25, 50, and 75 g). Subsequently, the performance was compared with zeolite synthesized from coal fly ash (Zeolite_CFA).

(1) With commercial zeolite A

- CO_2 loading

This study compares CO_2 loading in a pilot system with and without the addition of zeolite in the desorber column, focusing on the effect of catalyst weight. As shown in Figure 6, adding zeolite increased the Rich CO_2 loading from 0.4837 to 0.5189 mol CO_2/mol amine, while the Lean CO_2 loading decreased from 0.2991 to 0.2726–0.2814 mol CO_2/mol amine. In a cyclic system, lower Lean CO_2 loading indicates freer amine available to react with CO_2, resulting in higher Rich CO_2 loading. Since the reaction between amine and CO_2 is exothermic, temperature measurement in the absorber column can help indicate reaction intensity.

- Cyclic capacity

This study compares the cyclic capacity of a pilot system with and without zeolite catalyst in the desorber column, focusing on the effect of catalyst weight, as shown in Figure 7. Results show that adding zeolite increases cyclic capacity by 20–50%, consistent with CO_2 loading data, since cyclic capacity is the difference between Rich and Lean CO_2 loading. Adding catalyst reduces Lean CO_2 loading, allowing freer amine to react with CO_2, thereby increasing both Rich CO_2 loading and cyclic capacity. The highest cyclic capacity observed was 1.0428 mol CO_2/L solution at 50–75 g of catalyst. These findings align with studies by Sai-Obodai et al. (2022) and Narku-Tetteh et al. (2018), which also reported improved cyclic capacity—up to 60%—with catalyst use.[7,8]

Figure 8 show the CO_2 absorption efficiency over 270 minutes in the pilot system. Adding 25–75 g of zeolite catalyst increased the efficiency from 15.9% (no catalyst) to 20.6–25.2%, consistent with the observed rise in cyclic capacity. These findings align with Afari et al., who reported 20% efficiency using 5M MEA at 85°C, and with Sisang et al. (2017), who found that adding 50 g of HZSM-5 increased CO_2 absorption efficiency by ~15%, and by ~35% with 200 g. Beyond 200 g, further increases in catalyst amount showed no significant effect on efficiency.[9,10]

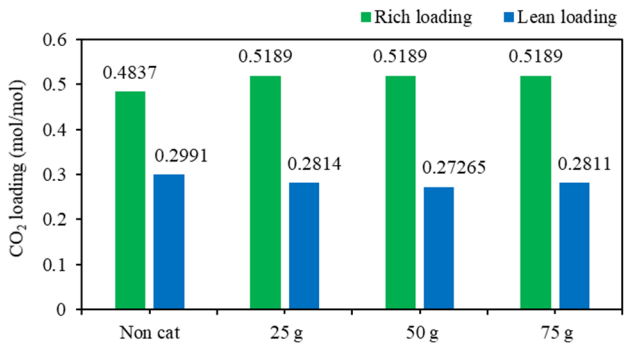

Figure 6 CO_2 loading at various amounts of zeolite

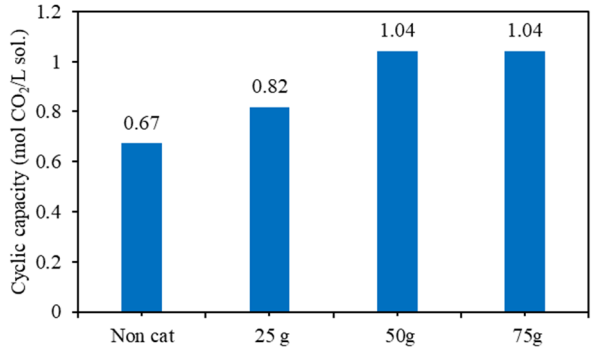

Figure 7 Cyclic capacity at various amounts of zeolite

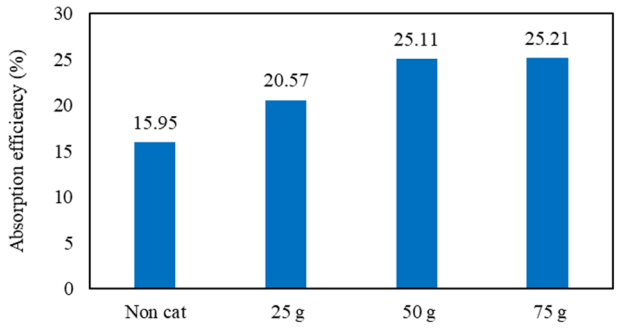

Figure 8 CO_2 absorption efficiency at various amounts of zeolite

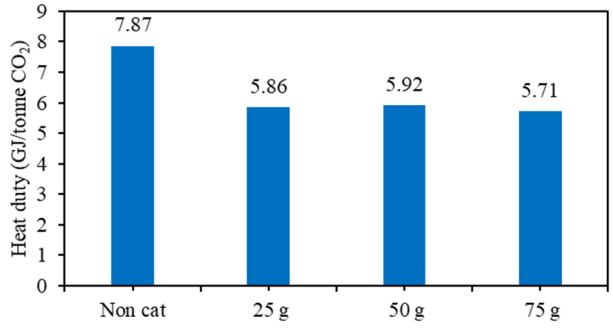

Figure 9 Heat duty at various amounts of zeolite

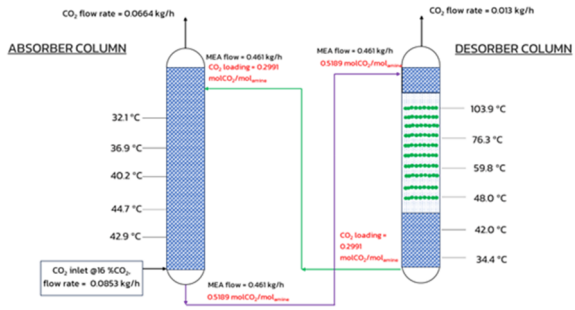

Figure 10 Mass balance of CO_2 capture system using 50 g of zeolite A

- Heat duty

Figure 9 presents the heat duty results over 270 minutes in the pilot system. Adding 50–75 g of zeolite catalyst reduced the heat duty by 25–27% compared to the non-catalyst case, aligning with lab-scale findings. The catalyst promotes the reaction between protons and carbamate ions ($MEACOO^-$), accelerating CO_2 desorption from MEA, as illustrated in Figure 7-8.

- Mass balance of the system

Figure 10 illustrates the mass balance of the CO_2 capture system using 50 g of zeolite over a 270-minute experiment. CO_2 was introduced at 16% concentration and a flow rate of 0.0853 kg/h. It reacted with amine solution (flow rate 0.461 kg/h) entering from the top of the absorber column. As the gas moved upward, CO_2 concentration decreased along the column height due to absorption. The desorber column released CO_2 at a flow rate of 0.0664 kg/h.

(2) With CFA derived-zeolite A

Figures 11–13 present the results of using zeolite synthesized from coal fly ash (Zeolite A_CFA) for CO_2 capture in amine solutions. The addition of Zeolite A_CFA enhanced process performance by increasing cyclic capacity and CO_2 absorption efficiency, while reducing energy consumption (heat duty). These improvements are consistent with those seen using commercial zeolite (Zeolite A_Com). As shown in Figure 13, the heat duty for Zeolite A_CFA and Zeolite A_Com was 5.50 and 5.61 GJ/tonne CO_2, respectively.

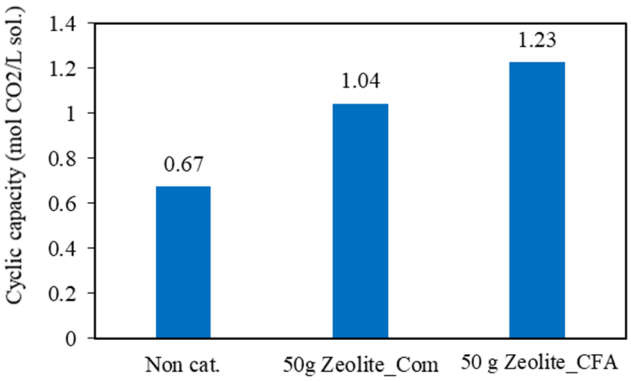

Figure 11 Comparison of the cyclic capacity with and without zeolite A (commercial and derived from coal)

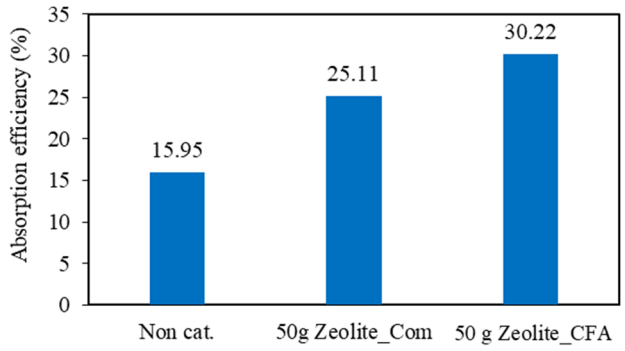

Figure 12 Comparison of CO_2 absorption efficiency with and without zeolite A (commercial and derived from coal)

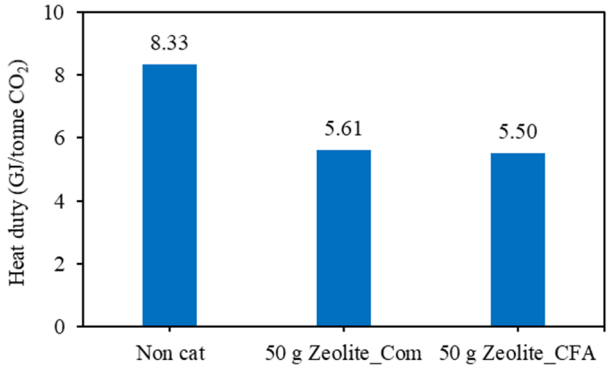

Figure 13 Comparison of the heat duty with and without zeolite A (commercial and derived from coal)

4. CONCLUSION

Zeolite A was generated from coal fly ash and applied as a catalyst in the MEA regeneration of CO_2 capture process. Characterization by XRD and SEM confirmed its crystalline structure, while BET analysis showed a surface area of 23.92 m^2/g. NH_3-TPD analysis revealed a total acid strength of 1.806 mmol/g. When demonstrated in MEA regeneration of pilot scale unit, zeolite A significantly enhanced cyclic capacity and CO_2 absorption efficiency, while reducing energy consumption. Furthermore, the heat duty when applying Zeolite A_CFA and Zeolite A_Com was almost similar.

ACKNOWLEDGMENTS

The authors gratefully acknowledge the financial support provided by the Program Management Unit for Competitiveness Enhancement (PMU-C); Contract No. C04F660071, and BLCP POWER LIMITED.

REFERENCES

1. Appiah, F.A.; Nugloze, D.; SaiObodai, L. S.; Natewong, P.; Idem, R. *ACS Omega*. **2023**, *8*, 9346−9355.
2. Shi, H.; Zheng, L.; Huang, M.; Zuo, Y.; Kang, S.; Huang, Y. Idem, R.; Tontiwachwuthikul, P. *Ind. Eng. Chem. Res.* **2018**, *57*, 11505−11516.
3. Liang, Z.; Idem, R.; Tontiwachwuthikul, P. *AIChE Journal*. **2016**, *62*, 753–765.
4. Prasongthum, N.; Natewong, P.; Reubroycharoen, P; Idem, R. *Energy Fuels* **2019**, *33*, 1334−1343.
5. Horwitz, W.; Senzel, A.; Reynolds, H.; Park, D. *Gaithersburg MD: George Bant.* **1975**.
6. Bairq, Z.A.S.; Gao, H.; Huang, Y.; Zhang, H.; Liang, Z. Appl. Energy. **2019**, *252*, 113440.
7. Sai-Obodaia, L.S.; Appiaha,F.A.; Nuglozea, D.; Idem, R. *Proceeding of GHGT-16*. **2022**.
8. Narku-Tetteh, J.; Afari, D.; Coker, J.; Idem, R. *Energy & Fuels*. **2018**, 32 (9), 9711–9726.
9. Afari, D.; Coker, J.; Narku-Tetteh, J.; Idem, R. *Ind. Eng. Chem. Res.* **2018**, 57, 15824−15839.
10. Srisang, W., Pouryousefi, F.; Osei, P. A.; Decardi-Nelson, B.; Akachuku, A.; Tontiwachwuthikul, P.; Idem, R. *Chem. Eng. Sci*. **2017**, 170, 48-57.

Synthesis of monolaurin through glycerol esterification with lauric acid using 12-tungstophosphoric acid

Kanchisa Chandit[1], Puttiporn Thiamsinsangwon[1,*], Chaiyan Chaiya[1], Rinlada Sirisangsawang[1], Sasiradee Jantasee[1], Weerinda Mens[1]

[1] Department of Chemical and Materials Engineering, Faculty of Engineering, Rajamangala University of Technology Thanyaburi, Pathum Thani 12110, Thailand
[*] Corresponding author: puttiporn_t@rmutt.ac.th

ABSTRACT

Glycerol, a by-product of biodiesel production, can be used as a precursor in producing chemicals such as monolaurin, which is widely used in the food, cosmetic, and pharmaceutical industries. This study focused on the production of monolaurin by esterification of glycerol and lauric acid using 12-tungstophosphoric acid (TPA) as a catalyst. The effects of the operating parameters, such as molar ratio, reaction temperature, and reaction time, were investigated to optimize the production of monolaurin. The results showed that the optimal conditions to produce monolaurin were a molar ratio of 1:4, catalyst loading of 3% of LA, reaction temperature of 150 °C, and reaction time of 90 min, which resulted in a lauric acid conversion of 91.52%. The study confirmed that the molar ratio, reaction time, and temperature significantly affected the efficiency of the glycerolysis reaction.

Keywords: Esterification; Glycerol; Lauric acid; Monolaurin; 12-Tungstophosphoric Acid (TPA)

1. INTRODUCTION

Monolaurin (Glycerol Monolaurate, GML) is a compound produced through the esterification of lauric acid (LA) and glycerol (GL). It exhibits surfactant properties and possesses a broad spectrum of antimicrobial activity. GML has been classified as Generally Recognized as Safe (GRAS) by the U.S. Food and Drug Administration (FDA) and is widely utilized in the food, cosmetic, and healthcare industries [1]. It demonstrates effective antimicrobial activity against bacteria, viruses, and fungi, particularly gram-positive bacteria such as Staphylococcus aureus [2]. In addition, GML inhibit toxin production and biofilm formation, both of which are key factors in the development of chronic infections. Conventionally, the synthesis of GML can be carried out through the esterification between lauric acid and glycerol in the presence of acid catalysts. Previous studies have explored various catalytic systems, including homogeneous acid catalysts and heterogeneous solid catalysts, aiming to enhance reaction efficiency and overcome practical limitations [3]. Among these, 12-tungstophosphoric acid (TPA), a strong heteropoly acid catalyst, has gained substantial attention due to its high acidity, thermal stability, and superior catalytic performance in esterification processes [4]. Furthermore, TPA can function effectively under high-temperature conditions, resulting in fewer by-products and higher yields compared to other catalysts [5]. Cardoso et al. (2008) investigated the catalytic efficiency of 12-tungstophosphoric acid (TPA) in comparison with other acids, including p-toluenesulfonic acid (p-TsOH) and sulfuric acid (H_2SO_4), in the esterification of fatty acids. Their findings revealed that TPA exhibited comparable or even superior catalytic performance and could be reused multiple times without significant loss of activity [6].

Although there have been studies on the synthesis of monoglycerides using various types of catalysts, the application of TPA in the esterification of lauric acid and glycerol remains limited, particularly with regard to the influence of reaction parameters. Therefore, this study aims to evaluate the efficiency of TPA as a catalyst in the esterification reaction between lauric acid and glycerol and to investigate the effects of various reaction parameters, such as reactant molar ratio, catalyst loading and reaction temperature, on lauric acid conversion and monolaurin yield.

2. EXPERIMENTAL

2.1 Chemicals

Glycerin (>99%) was purchased from DAEJUNG, analytical grade lauric acid from Sigma-Aldrich, and 12-tungstophosphoric acid (TPA) from LOBA CHEMIE PVT. LTD. Ethanol (≥99%, analytical grade) was supplied by ACI Labscan, sodium hydroxide pellets (≥97%) were purchased from KemAus, and phenolphthalein was obtained from LabChem.

2.2 Reaction Test

The esterification reaction between glycerol (GL) and lauric acid (LA) was carried out in a 250-ml three-neck flask. Stirring was maintained using magnetic stirrer, while the reaction temperature was controlled by an oil bath and monitored using a thermocouple temperature sensor as shown in Fig. 1. Initially, 52.83 g of lauric acid was added to the reaction flask and heated until completely melted. Simultaneously, glycerol was preheated separately to the designated reaction temperature. After both reactants reached the target temperature, glycerol was added into the reaction flask according to the specified LA:GL molar ratio. Subsequently, the TPA catalyst was introduced into the reaction mixture at a predetermined molar ratio (ranging from 0.5% to 3.0% based on lauric acid). Each experiment was performed twice at temperatures ranging from 110 to 170 °C, maintaining a constant stirring speed of 360 rpm. After the reaction, the mixture was centrifuged to effectively separate the glycerol layer from the synthesized monolaurin product.

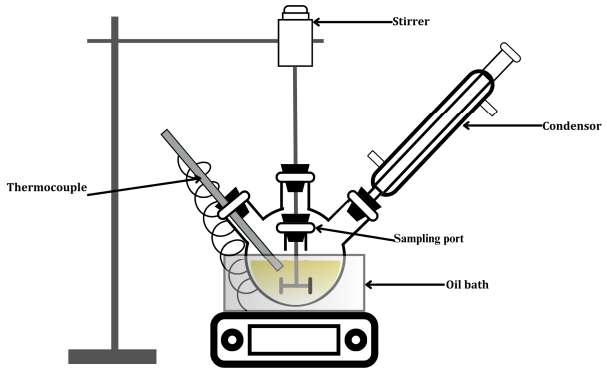

Figure 1 Installation diagram used in monolaurin synthesis.

2.3 Analysis

The conversion of lauric acid was analyzed based on the percentage of free fatty acids (FFA) which showed in (1). The acid-base titration method was used to determine the percentage of free fatty acids. Approximately 0.5 g of sample was placed in a 250 mL Erlenmeyer flask. Then, 25 mL of ethanol was added, mixing with 25 mL of distilled water. After the sample was completely dissolved, 5 drops of phenolphthalein indicator were added. The solution was titrated with 0.1 N sodium hydroxide (NaOH) until a persistent pink endpoint was observed. The volume of NaOH consumed was recorded and used to calculate the percentage of free fatty acids as lauric acid according to the (2)

$$\text{LA conversion (\%)} = \frac{FFA_0 - FFA_t}{FFA_0} x100 \quad (1)$$

$$\text{FFA (\%)} = \frac{\text{V} \times \text{M} \times \text{N} \times 100}{\text{W}} \quad (2)$$

Where:
FFA_0 = The initial concentration of free fatty acid (%)
FFA_t = The concentration of free fatty acid remaining at reaction time (%)
V = Volume of NaOH used in titration (milliliters)
N = NaOH concentration (molars)
M = Molecular mass of lauric acid (200.32 g/mol)
W = Weight of the sample (milligrams)

Each experimental condition was performed in 3 replicates and the results are reported as the mean percentage of FFA. All equipment used was properly calibrated and cleaned to prevent contamination and ensure the accuracy of the analytical results.

3. RESULTS AND DISCUSSION

Fig. 2 shows the effect of varying molar ratios of lauric acid to glycerol (1:2, 1:4, and 1:6) on the synthesis of lauric monoglyceride (GML), investigated under a reaction temperature of 150°C using 1 wt.% TPA catalyst based on lauric acid. The results indicated that increasing the molar ratio of lauric acid (LA) to glycerol (GL) from 1:2 to 1:4 resulted in an enhancement of lauric acid conversion from 40.74% to 43.57%. This improvement can be explained by the increased availability of glycerol molecules, which elevated the frequency of effective collisions between lauric acid and glycerol molecules. Additionally, the higher glycerol concentration provided a stronger driving force for mass transfer, facilitating better diffusion of reactants toward active catalytic sites, thus accelerating the esterification reaction [7].

However, it is noteworthy that further increasing the LA:GL molar ratio to 1:6 resulted in a lower conversion compared to the 1:4 ratio at the same reaction time. This phenomenon can be attributed to excessive glycerol, which increased the reaction mixture viscosity, thereby reducing mixing efficiency and limiting the mass transfer of reactants. Consequently, the diffusion rate decreased, and the access of reactant molecules to active catalytic sites was hindered, leading to lower reaction rates in the early stage [8]. Nevertheless, after extending the reaction time to 60 minutes, lauric acid conversions across all molar ratios became comparable. This result suggests that the reaction system had approached equilibrium conditions, diminishing the influence of different initial reactant molar ratios on the lauric acid conversion at this later reaction stage. This finding is consistent with the report by Hashemizadeh et al., which showed that increasing the molar ratio of LA:GL from 1:4 to 1:6 did not significantly affect the conversion of lauric acid [9] Therefore, the LA:GL molar ratio of 1:4 was selected and used for subsequent experiments.

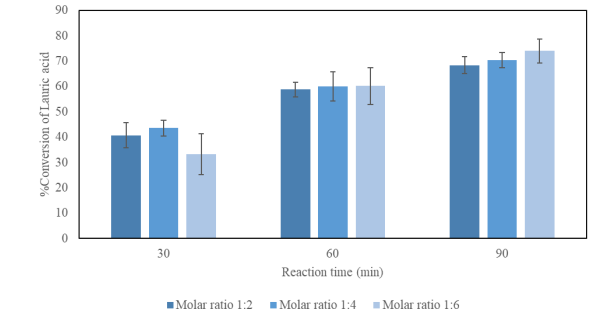

Figure 2 Effect of molar ratio of LA:GL on lauric acid conversion (catalyst loading of 1 wt.% of LA, reaction temperature of 150°C).

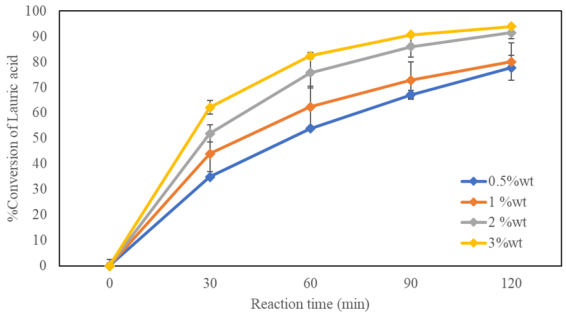

Figure 3 Effect of catalyst loading on lauric acid conversion (LA: GL molar ration of 1:4, reaction temperature of 150°C).

3.2 Effect of catalytic loading on lauric acid conversion

In this study, the effect of TPA catalyst amount on lauric acid conversion in esterification of LA with GL was evaluated, carried out at 150 °C and lauric acid to glycerol molar ratio of 1:4. The experimental results showed that increasing the catalyst amount from 0.5% to 1% by weight of lauric acid resulted in an increase in the conversion of lauric acid from 53.89% to 62.43%. When increasing the catalyst amount from 1% to 2%, the conversion increased to 75.81%, and at 3% by weight, the conversion was 82.47% within 60 min. This increase can be explained by the increase in the number of active sites of the catalyst, which resulted in a more efficient catalysis. However, when considering the increase in conversion value obtained with increasing the amount of catalyst, it was found that increasing from 2% to 3% by weight resulted in an increase in the conversion value of only 6.66%, which is not much increase compared to the previous increase in catalyst amount. In addition, the use of higher catalyst amounts may also result in difficulties in separating GML products from the catalyst.This observation is consistent with the findings reported by A et al., who demonstrated that beyond a certain catalyst concentration, further increases resulted in marginal conversion improvements but caused difficulties in product separation, thus increasing overall production costs [11]. Therefore, the TPA loading of 3 wt.% of LA was selected and used for subsequent experiments.

3.3 Effect of reaction temperature on lauric acid conversion

In this study, lauric monoglyceride (GML) was synthesized using a fixed lauric to glycerol acid molar ratio of 1:4 at TPA catalyst loading t of 3 wt% of LA. The reaction was carried out at various temperatures: 110, 130, 150 and 170°C. As shown in Figure 3, increasing the reaction temperature from 110°C to 130°C significantly enhanced lauric acid conversion from 68.10% to 42.46%. A further increase to 150°C resulted in conversion of 80.61%, and at 170°C, the conversion reached a maximum of 93.23%. The experimental results showed that when the temperature of the esterification reaction between lauric acid and glycerol increased, the conversion rate of lauric acid tended to increase significantly. This was consistent with the principle of chemical kinetics that states that the reaction rate increases with increasing temperature due to the increase in the kinetic energy of the molecules. This gives the opportunity for the lauric acid and glycerol molecules to collide with high enough energy to overcome the activation energy barrier and form ester bonds successfully [12]. In addition, increasing the temperature accelerates the dehydration, which is a by-product of the esterification reaction, causing the reaction equilibrium to shift towards the product according to Le Chatelier's principle [13]. However, caution must be exercised when increasing the reaction temperature, as excessively high temperatures can result inside reactions, such as the degradation of glycerol to acrolein, a substance that is hazardous to health [9].

The synthesis of lauric monoglyceride (GML) at temperatures up to 150 °C yielded a white product, which is the most common color of glycerides. However, at 170°C, the product exhibited a dark cream color. This color change is common issue in esterification reaction between lauric acid and glycerol, especially when using homogeneous acid catalysts such as sulfuric acid (H_2SO_4) or p-toluenesulfonic acid (p-TsOH), which are often carried out under harsh conditions, such as high temperatures and long durations, resulting in side reactions such as dehydration, carbonization or polymerization of glycerol or lauric acid, which cause a dark color [11].

Therefore, the reaction temperature of 150 °C was selected as the optimal condition, as it provides a high lauric acid conversion while maintaining desirable product appearance and quality. The experimental results identified the optimal conditions for monolaurin synthesis as follows: lauric acid to glycerol molar ratio of 1:4, reaction temperature of 150°C, reaction time of 90 min, catalyst concentration of 3 wt.% lauric acid. Under these conditions, the lauric acid conversion was as high as 93.23%, confirming the efficiency of the glycerolysis process using TPA as a catalyst [13].

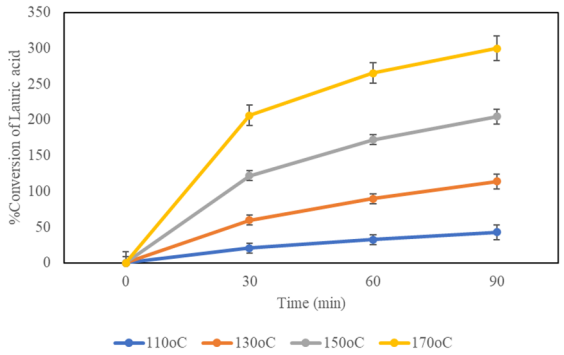

Figure 4 Effect of temperature on lauric acid conversion (LA: GL molar ration of 1:4, catalyst loading of 3 wt.% of LA).

4. CONCLUSION

In this study, monolaurin (GML) was synthesized via the esterification reaction of lauric acid (LA) and glycerol (GL) using 12-tungstophosphoric acid (TPA) as a heteropolyacid catalyst. The effects of key reaction variables, including the molar ratio of LA to GL, catalyst loading, and the reaction temperature, were examined to determine the optimal conditions for GML production. The results showed that increasing the molar ratio of lauric acid to glycerol from 1:2 to 1:6 significantly affected lauric acid conversion during the first 30 min. Meanwhile, increasing the TPA catalyst loading from 0.5% to 3.0% by weight of lauric acid improved re conversion from 53.89% to 82.47%. Additionally, raising the reaction temperature from 110°C to 150°C enhanced the conversion of lauric acid from 62.9% to 84.1% due to increased molecular kinetic energy and efficient removal of water produced during esterification.

Therefore, it can be concluded that suitable conditions for synthesizing GML using TPA as a catalyst were a LA: GL molar ratio of 1:4, a catalyst loading of 3 wt.% of LA, reaction temperature of 150 °C at reaction time of 90 min. Under these optimized conditions, lauric acid conversion reached as high as 89.87%, confirming the effectiveness and suitability of the glycerolysis process catalyzed by TPA for monolaurin production.

ACKNOWLEDGMENTS

This research was supported by the Science, Research and Innovation Promotion Fund, Thailand Science Research and Innovation (TSRI), through Rajamangala University of Technology Thanyaburi (FRB68E07019).

REFERENCES

1. Barker LA, Bakkum BW, Chapman C. The Clinical Use of Monolaurin as a Dietary Supplement: A Review of the Literature. J Chiropr Med. 2019 Dec 1;18(4):305–10.
2. Schlievert PM, Peterson ML. Glycerol monolaurate antibacterial activity in broth and biofilm cultures. PLoS One. 2012 Jul 11;7(7).
3. Zatta L, Ramos P, Wypych F. Acid Activated Montmorillonite as Catalysts in Methyl Esterification Reactions of Lauric Acid [Internet]. Vol. 61, J. Oleo Sci. 2012. Available from: http://mc.manusriptcentral.com/jjocs
4. Hoo PY, Abdullah AZ. Direct synthesis of mesoporous 12-tungstophosphoric acid SBA-15 catalyst for selective esterification of glycerol and lauric acid to monolaurate. Chemical Engineering Journal. 2014 Aug 15;250:274–87.
5. Hoo P, Abdullah AZ. Kinetics Modeling and Mechanism Study for Selective Esterification of Glycerol with Lauric Acid Using 12-Tungstophosphoric Acid Post-Impregnated SBA-15. Ind Eng Chem Res. 2015 Aug 19;54(32):7852–8.
6. Cardoso AL, Augusti R, Da Silva MJ. Investigation on the esterification of fatty acids catalyzed by the H 3PW12O40 heteropolyacid. JAOCS, Journal of the American Oil Chemists' Society. 2008 Jun;85(6):555–60.
7. Neji SB, Chaari A, Galán ML, Frikha F, Bouaziz M. Application of Box-Behnken Design in Production of Monoglyceride with Esterification of Glycerol and Oleic Acid. ACS Omega. 2023 Aug 8;8(31):28813–20.
8. Chanthon N, Ngaosuwan K, Kiatkittipong W, Wongsawaeng D, Mens W, Weeranoppanant N, et al. Intensified modified fruit blender reactor for emulsifier synthesis via glycerol esterification of free fatty acids at mild conditions. Bioresour Technol. 2025 Aug 1;429.
9. Hashemizadeh I, Abdullah AZ. Influence of Process Conditions on Glycerol Esterification Catalyzed by Tetra-N-Butylammonium-Modified Montmorillonite Catalyst [Internet]. 2012. Available from: www.tojsat.net
10. Simsek V, Degirmenci L, Murtezaoglu K. Esterification of Lauric Acid with Glycerol in the Presence of STA/MCM-41 Catalysts. 2017;

11. Nowicki J, Stańczyk D, Drabik J, Mosio-Mosiewski J, Woszczyński P, Warzała M. Synthesis of Fatty Acid Esters of Selected Higher Polyols Over Homogeneous Metallic Catalysts. JAOCS, Journal of the American Oil Chemists' Society. 2016 Jul 1;93(7):973–81.
12. FOGLER SH. Elements of Chemical Reaction Engineering Fifth Edition. 2016.
13. Hamerski F, Corazza ML. LDH-catalyzed esterification of lauric acid with glycerol in solvent-free system. Appl Catal A Gen. 2014 Apr 5;475:242–8.

Development of internally circulating fluidized bed reactor performance for enhancing direct air CO_2 capture

Munyapa Limahksohn[1], Chatiya Tripoonsuk[1], Benjapon Chalermsinsuwan[1,2,3], Pornpote Piumsomboon[1,2,3*]

[1] Department of Chemical Technology, Faculty of Science, Chulalongkorn University, Bangkok 10330, Thailand
[2] Center of Excellence on Petrochemical and Materials Technology, Chulalongkorn University, Bangkok 10330, Thailand
[3] Advanced Computational Fluid Dynamics Research Unit, Chulalongkorn University, Bangkok 10330, Thailand
[*] Corresponding author: pornpote.p@chula.ac.th

ABSTRACT

Climate change, mainly driven by greenhouse gas emissions such as carbon dioxide (CO_2), poses a critical challenge to global environmental stability. CO_2 capture technologies play a vital role in achieving this goal. Recently, several carbon capture technologies have been proposed. Among them, the gaseous-solid adsorption is a promising alternative. In this research, the internally circulating fluidized bed (ICFB) reactor, combining CO_2 adsorption and sorbent regeneration processes in a single unit, was chosen for the direct air CO_2 capture process due to its compact configuration. This study uses alumina as a solid sorbent and focuses on determining the proper operating regeneration conditions to achieve the best performance of the ICFB system. Since CO_2 desorption is endothermic, heating is necessary to improve solid sorbent regeneration and system efficiency. Three key parameters of the process operation were investigated. These are the regeneration temperature, gas velocity, and heater placement in the downer. Results reveal that the ICFB system can operate continuously. Both the downer temperature and heating location consequently have an impact on the overall CO_2 capture performance. Under room-temperature adsorption and desorption, CO_2 concentration initially drops sharply before gradually increasing and stabilizing. With heat-assisted regeneration, CO_2 concentration in the riser remains lower than the inlet concentration by 30% when the system reaches a steady state, improving adsorption performance. However, excessively high regeneration temperatures negatively impact adsorption. The findings highlight the importance of thermal management in the downer and offer practical insights for optimizing ICFB reactor configurations.

Keywords: Internally circulating fluidized bed reactor; Direct air CO_2 capture; CO_2 adsorption; Heat regeneration.

1. INTRODUCTION

In recent years, the escalating levels of global warming, driven by climate change, have been largely attributed to the increasing emissions of greenhouse gases such as carbon dioxide (CO_2). The atmospheric concentration of CO_2 has risen to approximately 410 ppm, primarily due to rapid industrialization and urbanization. Although CO_2 exists in relatively low concentrations in the atmosphere, this increase has significantly disrupted the natural carbon balance, contributing to climate change and causing substantial environmental damage and, in some cases, irreversible losses. To mitigate this critical issue, achieving net-zero CO_2 emissions is essential [1], [2]. One promising approach to reducing atmospheric CO_2 is Carbon Capture, Utilization, and Storage (CCUS). Among the various carbon dioxide removal (CDR) strategies, Direct Air Capture (DAC) has garnered significant attention for its ability to extract CO_2 directly from the ambient air [3].

To remove the CO_2 from the ambient air, the Internally Circulating Fluidized Bed (ICFB) reactor has been selected. The ICFB was designed and operated for atmospheric CO_2 capture. The ICFB offers several advantages over the conventional Circulating Fluidized Bed (CFB) reactor, which has been widely used in industrial applications. A typical CFB system comprises a riser, where gas–solid particle suspension is transported by the fluidizing gas. A cyclone is employed to separate gas and solids. The solids fall into the downer where the fluidized bed is in a bubbling regime and are recirculated through a loop seal into the riser. On the other hand, the ICFB reactor is a simplified and integrated design compared to conventional CFB systems. Unlike traditional setups that require separate

reactor units or external loops, the ICFB reactor is a reactor that is internally divided into two distinct sections, a riser and a downer, by a central draft tube. Solid particles are circulated between the riser and downer by creating a differential in fluidizing velocities and pressure between the two sections. Instead of using an external cyclone for gas–solid separation, the ICFB utilizes a freeboard zone, further streamlining the system. This configuration offers several performance benefits, including a more compact design, lower construction costs, and increased particle residence time, all of which enhance thermal integration and reaction efficiency. However, a known limitation of the ICFB configuration is the potential for gas leakage between sections, which must be carefully managed in system design and operation [4–6].

The Internally Circulating Fluidized Bed (ICFB) reactor could serve as a chemical looping reactor that enables continuous CO_2 adsorption and sorbent regeneration within a single reactor unit. CO_2 capture occurs in the riser section, which functions as the reaction zone, where the exothermic adsorption takes place. The sorption capacity of solid sorbents in this zone is highly dependent on the hydrodynamic behaviour in the riser, with optimal performance achieved under stable and efficient fluidization conditions. In contrast, sorbent regeneration is carried out in the downer section through thermal desorption or depressurization. This process is endothermic and requires sufficient thermal energy for effective CO_2 release and restoration of sorbent capacity. Increasing the regeneration temperature has been shown to enhance desorption efficiency and overall reactor performance [7]. Boonprasop et al. [10] evaluated the performance of hydrothermally treated adsorbents for CO_2 capture under a turbulent fluidized bed (TFB) regime, considering three key parameters: regeneration temperature, regeneration duration, and the number of heat treatment cycles. Their study revealed that both higher regeneration temperatures and longer regeneration times positively affected the CO_2 adsorption capacity of the material. Nevertheless, for practical application in continuous processes, it was found that relatively low regeneration temperatures and short regeneration times were sufficient to maintain stable adsorption performance over multiple cycles. Won et al. [8] identified key performance metrics for evaluating CO_2 capture systems, including CO_2 removal efficiency, dynamic sorption capacity, and regeneration energy. Their findings indicated that higher regeneration temperatures maintained at optimal levels improved both CO_2 removal efficiency and sorption capacity while also reducing the energy required for regeneration, particularly when high CO_2 purity was achieved.

To meet the thermal requirements of regeneration and maintain efficient heat transfer, the use of vertically immersed heat-exchanging tubes within the fluidized bed is recommended. These internal heat-exchanging tubes not only supply intense thermal input but also help to minimize pressure drop, reduce slugging, and stabilize bed height. In a study by Taofeeq et al. [9], a circular arrangement of 30 Plexiglass vertical internal tubes, each with a diameter of 0.0127 m and a height of 1.84 m., was installed, occupying approximately 25% of the bubbling fluidized bed reactor's cross-sectional area. This configuration was designed to simulate high-efficiency internal heat transfer surfaces required for temperature control in strongly endothermic reactions. It was observed that increasing the distance between the distributor plate and the lower end of the internals enhanced bubble frequency and gas holdup. These effects were directly associated with improved convective heat transfer, as enhanced gas–solid interactions facilitated more efficient thermal exchange within the reactor.

Given the continuous circulation loop of the ICFB reactor, achieving a high-efficiency adsorption process requires an optimal balance between adsorption and desorption conditions. Therefore, this study aims to enhance the regeneration performance of the ICFB reactor by identifying the optimal conditions that maintain this balance. To improve thermal regeneration efficiency, vertically immersed heating tubes were incorporated into the reactor design. This work investigates key parameters affecting regeneration performance, including regeneration temperature, gas velocity in the downer section, and the position of the heating tubes. The goal is to determine the most efficient regeneration conditions while ensuring the sorbent maintains a high CO_2 adsorption capacity during continuous operation.

2. EXPERIMENTAL

In this study, the experimental setup comprises an Internally Circulating Fluidized Bed (ICFB) reactor, as illustrated in Fig. 1. The ICFB reactor used in this study was constructed as a two-dimensional (2D) fluidized bed system with a reactor depth of 0.03 m. The total reactor height was 1.8 m. The distributor section is 0.15 m. The design incorporates two primary sections: the riser and the downer. The riser and downer heights are 1 m. The width ratio of the riser to downer is 1:2. The riser and downer functional lengths were approximately 0.1 m and 0.2 m, respectively [11]. This configuration was chosen to enhance gas–solid mixing in the riser, which improves the adsorption performance. In contrast, the downer section supports a dense and stable bubbling fluidized bed, facilitating efficient solid circulation and regeneration. The freeboard zone at the top of the reactor, with a height of approximately 0.8 m and an extended length of 0.5 m from the riser outlet, was designed to accommodate changes in solid particle velocity. The riser is constructed using a transparent material to allow visual observation of fluidization behaviour and hydrodynamics, while the downer is fabricated from a material with high thermal conductivity and equipped

with a sight glass to monitor hydrodynamic changes during the regeneration process. Alumina (Al_2O_3) is used as the solid sorbent, with an initial bed height of 45 cm in both sections.

The operation begins with ambient air supplied by an air compressor (a), which passes through a pressure regulator (b) and a rotameter (c) to control the inlet pressure and flow rate, respectively. The regulated air then enters the wind box (h) and is distributed into both the riser and downer sections at room temperature. In the riser section, the air fluidizes the solid sorbent, initiating a fluidized bed regime where CO_2 from the air is adsorbed onto the surface of the sorbent particles. The unabsorbed gas exits through the upper outlet, while the solid particles are carried to the freeboard zone and subsequently fall into the downer section due to differences in flow velocity. Within the downer section, thermal regeneration of the sorbent occurs. This section is equipped with vertically immersed heating rods, extending along the bed height to approximately 50 cm, to provide the necessary heat for desorption. To prevent flow obstruction, symmetric spacing is maintained between the heaters, as well as between the heaters and the distributor plate. Once the sorbent is regenerated, the particles are recirculated to the riser section by pressure differentials, completing the continuous adsorption–desorption cycle.

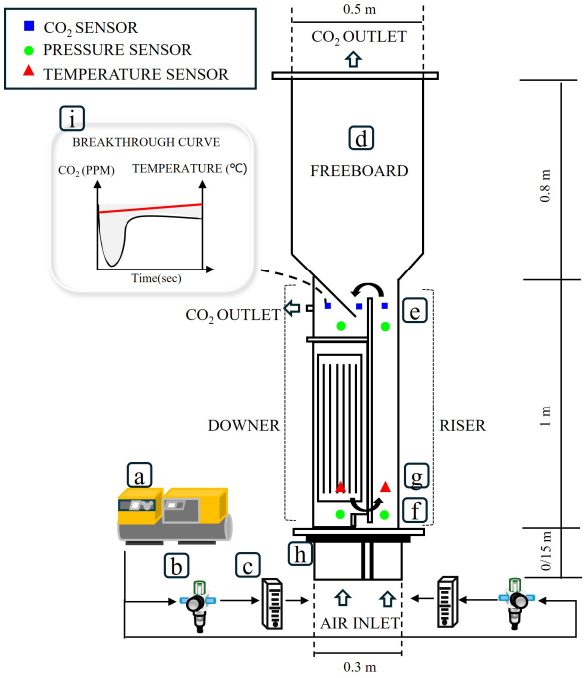

Figure 1 Schematic diagram of an Internally Circulating Fluidized Bed (ICFB) reactor system.

In this study, key operating conditions, including CO_2 concentration, pressure, and temperature, are continuously monitored using CO_2 sensors (e), pressure sensors (f), and temperature sensors (g), respectively, to assess system performance and observe for optimal operating conditions.

Since the efficiency of the regeneration process directly influences the adsorption performance in the riser section, temperature plays a critical role in achieving effective CO_2 capture. To investigate this relationship, data from CO_2 and temperature sensors were recorded and analyzed. Breakthrough curves (Fig. 1.i) were plotted to illustrate the CO_2 concentration profile over time. Initially, the CO_2 concentration is high, followed by a sharp decline as adsorption begins, eventually reaching steady state. This decline indicates active CO_2 adsorption by the solid sorbent. The difference between the initial inlet CO_2 concentration and the steady state concentration, as depicted by the breakthrough curve, was used to calculate the CO_2 removal efficiency. The percentage of CO_2 removal was determined using Eq.(1).

$$\%CO_2\ removal = \left(1 - \frac{C_{steady\ state}}{C_{initial}}\right) \times 100 \qquad (1)$$

where $C_{initial}$ is the CO_2 concentration at the initial condition (ppm) and $C_{steady\ state}$ is the CO_2 concentration at the steady state (ppm).

The experiments were conducted under the conditions outlined in Table 1, with downer gas velocities set at 15 and 20 L/min, corresponding to a bubbling fluidized bed regime. Downer velocity influences gas holdup and bed mixing, which are critical to the regeneration process. Regeneration temperature was controlled using vertically immersed heating tubes set at 80°C and 100°C to determine the effect of temperature on enhancing regeneration and adsorption performance. The heating configuration was also varied by turning all six heating rods on or selectively turning off specific heating rods, particularly those located adjacent to the riser section. This approach aimed to evaluate whether localized heating further from the riser could improve thermal balance and promote heat transfer into the riser zone. Symmetry in heater placement was maintained to ensure consistent temperature distribution. For comparison, additional experiments were conducted at each downer velocity under ambient temperature conditions, with all heaters turned off, to evaluate the adsorption performance in the riser section without active thermal regeneration. The experiment was conducted using a 2^k factorial design, where k represents the three experimental variables: downer gas velocity (A), regeneration temperature (B), and heater position (C), and the results were analysed.

Table 1 The operating variables and their values for conducting the 2^k factorial design

Operating variables		Downer gas velocity	Regeneration temperature	Heater position
Unit		L/min	℃	-
Code of level	-1	15	80	XOOOOX
	1	20	100	OOOOOO

where O is for heater on and X is heater off.

3. RESULTS AND DISCUSSION

3.1 Integration of Regeneration Unit within the ICFB Reactor

The CO_2 breakthrough curve from the ICFB reactor operating without a thermal regeneration process is illustrated in Fig.2.a and serves as the base case. Initially, the CO_2 concentration (blue line) drops sharply from approximately 580 ppm to 240 ppm, indicating strong adsorption performance. However, over time, the concentration gradually increases and stabilizes with the value close to the initial concentration around 3600 seconds. This trend suggests that the adsorbent becomes nearly saturated, significantly reducing its CO_2 capture activity. Simultaneously, the temperature in the riser section (red line) shows a slight increase of 2–3°C, which can be attributed to the exothermic nature of the CO_2 adsorption reaction. After this initial increase, the temperature remains relatively constant at around 30°C. These observations confirm that adsorption is highly effective during the early phase of the cycle but gradually diminishes as the active sites on the sorbent are occupied.

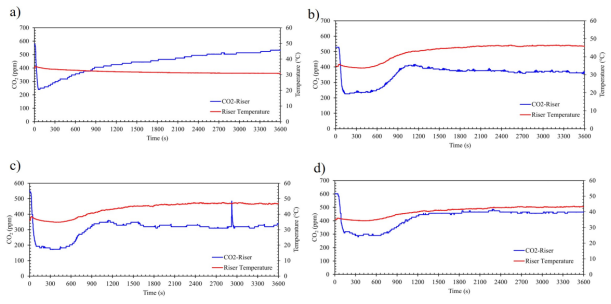

Figure 2 CO_2 breakthrough curves showing trend of CO_2 adsorption performance with no heat regeneration (a), process with heat regeneration (b), process with heat regeneration, process with varied downer velocities (c), heater position change (d).

To observe the effect of thermal regeneration, the CO_2 breakthrough curve in Fig. 2.b represents the performance of the ICFB reactor with heating the downer at 80°C, where all six heating rods were active, and the initial CO_2 concentration remained similar to the base case. In contrast to the case without thermal regeneration, where the CO_2 concentration steadily increased over time, the heat-regenerated system maintained a lower CO_2 concentration for a prolonged period before gradually increasing and stabilizing. This indicates improved adsorption performance during the initial stage of the operation. During the time between 1500 and 3600 seconds, the CO_2 concentration in Fig. 2.b reaches around 400 ppm. It is lower than that observed in the non-regeneration case, suggesting that the system achieved approximately 30% CO_2 removal compared to the initial level, thus enhancing the CO_2 removal capability. Furthermore, the temperature in the riser section (red line) rises to between 40°C and 50°C, reflecting the influence of thermal regeneration in sustaining sorbent activity and improving overall system efficiency.

3.2 Influence of the Downer Gas Velocity

As shown in Fig. 2.c, when the downer gas velocity was increased to 20 L/min and the downer was operated at 80 °C with all heating rods activated, the initial CO_2 concentration dropped significantly compared to when operating at the lower downer velocity case in Fig. 2.b, implying a better adsorption performance. At the steady state, the CO_2 concentration stabilized around 300 ppm, slightly lower than in the lower-velocity case. This corresponds to approximately 32% CO_2 removal from the initial concentration, suggesting that increasing the downer velocity can improve gas–solid contact and enhance the overall adsorption capacity.

3.3 Influence of Heater Position Variation

Fig. 2d shows the process response when the downer gas velocity was maintained at 15 L/min, the downer operated at 80 °C, but with selective heating rods turned off. After running the ICFB until the system reached steady state, the CO_2 concentration stabilized around 450 ppm, which is slightly higher compared to the case where all heaters were activated. The difference between the initial and the steady state CO_2 concentrations corresponds to approximately 23% CO_2 removal. Compared to the case in Fig. 2.b, this indicates a reduction in adsorption performance. Turning off certain heaters reduces the uniformity and intensity of heat distribution within the regeneration zone, leading to incomplete desorption of CO_2 from the sorbent surface. As a result, fewer active sites are available for CO_2 capture during the next adsorption cycle, thereby lowering the overall system efficiency.

3.4 Statistical Analysis (2^3 Factorial Design)

To analyse the effect of each operating parameter on %CO_2 removal, the experiment was conducted with a 2^3 factorial design. The three operating parameters were downer gas velocity (A), regeneration temperature (B), and heater position (C). As shown in Table 2, the highest CO_2 removal was observed in Run 7, which is the combination of a high downer gas velocity, high regeneration temperature, and full heater activation.

This configuration achieved approximately 44% CO_2 removal. In contrast, the lowest CO_2 removal of about 23% was observed with the operating conditions of low downer gas velocity, low regeneration temperature, and partial heater activation. These findings highlight the critical role of thermal input and uniform heat distribution in maintaining effective sorbent regeneration and enhancing CO_2 adsorption performance.

Table 2: Effect of the operating regeneration parameters on the % CO_2 removal

Run	A	B	C	% CO_2 removal
1	-1	-1	1	30.05
2	-1	-1	-1	22.92
3	-1	1	1	26.33
4	-1	1	-1	37.52
5	1	-1	1	36.73
6	1	-1	-1	42.05
7	1	1	1	43.51
8	1	1	-1	30.80

The half-normal probability plot of the estimated effects, presented in Fig. 3, was used to identify the most influential operating parameters and their interactions on the CO_2 removal. In this plot, data points that deviate significantly from the reference line represent statistically significant factors. Among them, factor A (downer gas velocity) and the three-way interaction ABC show the greatest deviation, indicating that they have the most substantial impact on % CO_2 removal. Additionally, the AB interaction (downer gas velocity and regeneration temperature) also demonstrates a moderately significant effect. In contrast, factors B (regeneration temperature), C (heater position), and the two-way interactions AC and BC are located near the reference line, suggesting that their individual contributions are not statistically significant under the tested conditions. The significance of the ABC interaction highlights a complex interplay among all three factors, indicating that their combined influence is critical to system performance. Furthermore, the AB interaction suggests a synergistic effect between downer gas velocity and regeneration temperature, exerting a stronger influence together than an individual variable.

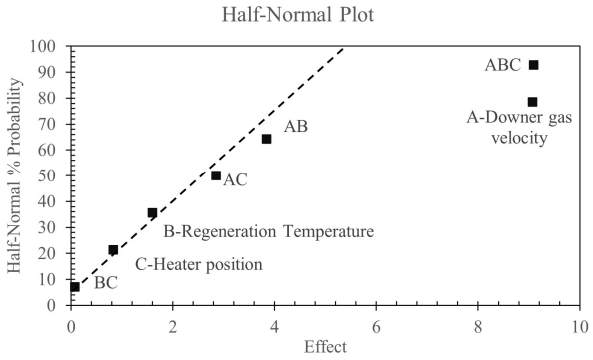

Figure 3. Half-Normal probability plot of the affected parameters

The influence of each factor and the interactions were evaluated through Analysis of Variance (ANOVA), as presented in Table 3. The results indicate that the overall model is statistically significant, with p-values less than 0.0500 identifying significant model terms. In this analysis, factors A (downer gas velocity), AB (interaction between downer gas velocity and regeneration temperature), and ABC (three-way interaction among all variables) were found to be statistically significant. Downer gas velocity (A) emerged as the most dominant factor, evidenced by its lowest p-value and high F-value, suggesting that the gas flow rate through the downer has a substantial effect on adsorption-desorption performance. The AB interaction also demonstrated a statistically meaningful contribution, highlighting the importance of jointly optimizing downer gas velocity and regeneration temperature rather than treating them independently. Conversely, the individual effects of B (regeneration temperature), C (heater position), and the two-way interactions AC and BC were found to have limited or statistically insignificant influence. However, the significant ABC interaction implies that the combined effect of all three parameters produces a synergistic influence greater than the sum of their individual or pairwise contributions. This finding underscores the importance of integrated tuning of downer gas velocity, regeneration temperature, and heater configuration to achieve optimal system performance.

Table 3 ANOVA for selected factorial model.

Source	Sum of Squares	df	Mean Square	F-value	p-value
Model	375.30	4	93.83	42.97	0.0056
A	164.38	1	164.38	75.28	0.0032
AB	29.43	1	29.43	13.48	0.0350
AC	16.33	1	16.33	7.48	0.0717
ABC	165.16	1	165.16	75.64	0.0032
Residual	6.55	3	2.18		
Total	381.85	7			

Figure 4 illustrates the influence of key operating parameters and their interactions on CO_2 removal. Specifically, Fig.4.a presents the relationship between CO_2 removal and downer gas velocity. The plot reveals a positive correlation, indicating that increasing the downer gas velocity from 15 L/min to 20 L/min significantly enhances CO_2 capture performance. At the lower gas velocity, the % CO_2 removal is approximately 28%, whereas at the higher gas velocity, it increases to around 38%. This improvement is attributed to enhanced gas-solid interactions and increased gas holdup, which contribute to better mixing and more uniform temperature distribution within the reactor. Higher downer gas velocities also promote convective heat transfer, which supports more effective thermal regeneration of the sorbent material. As a result, particles are more uniformly regenerated and circulated between the two-reactor zones, leading to improved overall system performance.

Fig.4.b illustrates the interaction between Factor A (Downer gas velocity) and Factor B (Regeneration temperature) on %CO_2 removal. The figure compares the %CO_2 removal at two regeneration temperature levels: high (B^+, blue line) and low (B^-, red line). At the downer gas velocity of 15 L/min, the % CO_2 removal under high regeneration temperature is approximately 31%, compared to 27% under low temperature, indicating that elevated temperatures initially enhance CO_2 capture at lower velocities. However, this trend reverses at a higher downer gas velocity of 20 L/min. Under this condition, the system achieves a CO_2 removal of approximately 40% at low regeneration temperature, compared to 36% at high temperature. This suggests that the combination of high downer gas velocity and low regeneration temperature results in the most effective CO_2 removal. This interaction is attributed to the dynamic between heat transfer, gas-solid contact behaviour. At high downer gas velocities, and sorbent regeneration efficiency, a lower regeneration temperature may create more favourable thermal gradients, enhancing the desorption process and improving sorbent recovery. Consequently, this leads to more efficient CO_2 capture.

The interaction plot from the 2^3 factorial experiment, shown in Fig. 4.c, illustrates the combined effects of three independent variables: Downer Gas Velocity (Factor A), Regeneration Temperature (Factor B), and Heater Position (Factor C) on %CO_2 removal. The influence of downer gas velocity on system performance cannot be isolated; rather, it is significantly affected by both the regeneration temperature and the configuration of heater placement.

Notably, the combination of high downer gas velocity, low regeneration temperature, and less heater operation, specifically turning off those near the wall, results in rather high %CO_2 removal. This can be attributed to several synergistic effects: the increased downer gas velocity enhances particle mixing and circulation, promoting faster regeneration of the spent sorbent and maintaining more active sites for adsorption in the riser section. Operating at a lower regeneration temperature reduces thermal stress on the sorbent, potentially preserving its adsorption capacity over time. Additionally, selectively turning off wall-adjacent heaters promotes a more uniform temperature distribution and efficient regeneration.

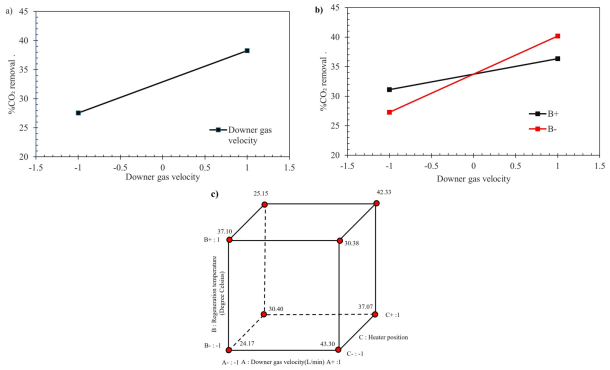

Figure 4 Effect of the operating parameters and their interactions; (a) Downer gas velocity, (b) Downer gas velocity and regeneration temperature, (c) three-way interaction among all variables.

4. CONCLUSION

This study examined the effects of key regeneration parameters, as downer gas velocity, regeneration temperature, and heater placement, on %CO_2 adsorption-desorption in an internally circulating fluidized bed (ICFB) reactor. The integration of vertically immersed internal heating rods significantly enhanced regeneration performance by providing heat sources, promoting desorption, and maintaining favourable thermal conditions within the bed. CO_2 breakthrough curve demonstrated that applying heat regeneration extended the adsorption phase and improved CO_2 removal efficiency at steady state compared to the case without thermal regeneration. An increase in downer gas velocity from 15 to 20 L/min enhanced gas-solid interaction and particle mixing, thereby promoting more effective sorbent regeneration and higher adsorption efficiency. Regeneration temperature exhibited an interactive effect with gas velocity. At lower gas velocities, the higher regeneration temperature enhanced adsorption, while at higher gas velocities, lower regeneration temperatures achieved better results. This is likely due to improved heat distribution and reduced thermal stress on the sorbent material. The heater placement also played a pivotal role; turning off wall-side heaters promoted uniform temperature distribution and prevented localized overheating, which can degrade sorbent activity. Statistical analysis using a 2^3 factorial design confirmed that downer gas velocity and the three-way interaction among velocity, temperature, and heater position (ABC) had the most significant influence on CO_2 removal performance. The optimal operating condition was determined to be a combination of high

downer velocity, low regeneration temperature, and partial heater activation, resulting in approximately 42% CO_2 removal. Although this is slightly lower than the 43% removal achieved with full heater activation and high regeneration temperature, the reduced energy consumption under the optimal condition makes it a more efficient and sustainable option. These findings underscore the importance of optimizing flow dynamics, thermal management, and heater configuration to enhance the performance of ICFB systems.

REFERENCES

1. K. O . Yoro, M.O. Daramola, (2020). CO_2 emission sources, greenhouse gases, and the global warming effect. In *Advances in carbon capture*. Woodhead Publishing.
2. H. Lee, K. Calvin, D. Dasgupta, G. Krinner, A. Mukherji, et al. (2024). Climate change 2023 synthesis report summary for policymakers. *CLIMATE CHANGE 2023 Synthesis Report: Summary for Policymakers*.
3. B.M. Balasubramaniam, P.T. Thierry, S. Lethier, V.Pugnet, P. Llewellyn, A. Rajendran. Process-performance of solid sorbents for Direct Air Capture (DAC) of CO_2 in optimized temperature-vacuum swing adsorption (TVSA) cycles. *Chemical Engineering Journal* 2024;*485*: 149568.
4. D. Thiemsakul, C. Kamsuwan, R. Piemjaiswang, P. Piumsomboon, B. Chalermsinsuwan. Computational fluid dynamics simulation of internally circulating fluidized bed reactor for dry reforming of methane. *Energy Reports* 2022;8; 817-824.
5. H. Gai, P. Yang, Q. Zhang, M. Lin, H. Song, et al .Dual-dense gas-solid circulating fluidized bed reactor. *Fuel* 2023; *337*: 126872.
6. P. Li, X. Yu, F. Liu, T. Wang. Hydrodynamic behaviors of an internally circulating fluidized bed with wide-size-distribution particles for preparing polysilicon granules. *Powder Technology* 2015;*281*: 112-120.
7. S. Boonprasop, B. Chalermsinsuwan, P. Piumsomboon. Effect of operating parameters of potassium carbonate supported on gamma alumina (K_2CO_3/γ-Al_2O_3) on CO_2 capture capacity using depressurized regeneration. *Journal of the Taiwan Institute of Chemical Engineers* 2018;*88*: 215-225.
8. Y. Won, J.Y. Kim, Y.C.Park, C.K. Yi, H.Nam, et al. Post-combustion CO_2 capture process in a circulated fluidized bed reactor using 200 kg potassium-based sorbent: The optimization of regeneration condition. *Energy* 2020; *208*: 118188.
9. H. Taofeeq, M. Al-Dahhan, M. Heat transfer and hydrodynamics in a gas-solid fluidized bed with vertical immersed internals. *International Journal of Heat and Mass Transfer* 2018;*122*: 229-251.
10. S. Boonprasop, B. Chalermsinsuwan, P. Piumsomboon. Effect of the operating parameters on the CO_2 capture capacity of potassium carbonate supported on gamma alumina (K_2CO_3/γ-Al_2O_3) using conventional heat regeneration. *Journal of the Taiwan Institute of Chemical Engineers* 2017; *78*: 282-289.
11. C.Tripoonsuk,, B. Chalermsinsuwan, B., P. Piumsomboon. Computational Fluid Dynamics in ICFB Reactor: Effect of Proportion of Riser and Downer on System Hydrodynamics. *Results in Engineering*, 2025;104187.

Valorization of mung bean seed coat through recovery of bioactive compounds with pharmacological properties using percolation extraction

Suthiwat Srinuch[1], Preuk Tangpromphan[1,2*]

[1] Department of Chemical Engineering, Faculty of Engineering, Kasetsart University, Bangkok 10900, Thailand
[2] Center for High-Value Products from Bioresources: HVPB, Faculty of Engineering, Kasetsart University, Bangkok 10900, Thailand
[*] Corresponding author: preuk.ta@ku.ac.th

ABSTRACT

Mung bean seed coat (MBC) is an agricultural waste from the milling process and is recognized as a source of beneficial bioactive compounds, such as vitexin and iso-vitexin, which have pharmacological properties, including anti-cancer and antioxidant effects. This study aimed to identify the optimal extraction conditions for MBC to achieve the highest yield of MBC extract (vitexin plus iso-vitexin) using the percolation extraction method. The extraction was carried out in a jacketed cylindrical glass column, with MBC packed in the inner tube and water circulating in the outer tube. The extracting solvent was delivered to the packed bed using a syringe pump. Factors investigated included extraction temperatures of 40, 60, and 80 degrees Celsius, and solvent concentrations of 30, 50, and 70 percent v/v acetonitrile. Samples from the extraction columns were analyzed at various time intervals using HPLC. The experimental results showed that the highest total yield, obtained within 15 minutes under conditions of 60°C and 50% v/v acetonitrile, was 190.76 mg of MBC extract per gram of dried MBC. The explanation is that higher temperatures enhanced the solubility of the bioactive compounds in the solvent. The 50% v/v acetonitrile concentration was found to be optimal for the polarity of the target compounds. This finding highlights an effective method for recovering bioactive compounds from MBC in a time-efficient manner. Additionally, the MBC extract obtained was suitable for further purification of vitexin and iso-vitexin.

Keywords: Mung bean seed coat; Extraction; Percolation; Vitexin; Iso-vitexin

1. INTRODUCTION

Mung bean (Vigna radiata L.), commonly known as green gram, is a leguminous plant species from the Fabaceae family that is widely cultivated in Southeast Asia and frequently used in consumer products worldwide [1]. A notable by-product of the mung bean industry is the mung bean seed coat (MBC), which is recognized as a valuable source of total saponins, phenolics, and flavonoids—compounds known for their beneficial pharmacological properties [2]. In light of growing sustainability concerns, the valorization of agricultural and food industry by-products has garnered increasing attention [3].

The primary bioactive compounds in mung bean seed coat are vitexin and iso-vitexin [1, 4], flavonoids known for their diverse pharmacological activities, including antioxidant, anticancer, anti-inflammatory, anti-hyperalgesic, and neuroprotective effects [5]. Consequently, the utilization of mung bean seed coat offers a promising avenue for developing ingredients suitable for nutraceutical and pharmaceutical products.

Various extraction techniques and solvents have been employed to recover bioactive compounds from mung bean seed coat (MBC). For instance, pressurized liquid extraction (PLE) of MBC under optimal conditions—160 °C, 1300 psi, and 50% ethanol—yielded high levels of phenolic and flavonoid compounds with notable antioxidant activity [6]. Another study developed an ultrasound-assisted extraction (UAE) method, optimizing parameters to 37.6% ethanol concentration, a solvent-to-material ratio of 35.1:1, and an extraction time of 46.1 minutes, resulting in superior antioxidant capacity compared to conventional extraction methods [7]. Additionally, a water extract of MBC was shown to significantly enhance insulin sensitivity in insulin-resistant HepG2 cells, attributed to its antioxidant and anti-inflammatory properties [3].

Batch and percolation solid-liquid extraction methods are commonly employed to isolate bioactive compounds from plant materials. Batch extraction involves soaking plant solids in a solvent for a fixed period, ensuring adequate interaction between the solvent and plant matrix. This approach is simple and cost-effective, making it ideal for small-scale applications. However, it typically requires longer

processing times and may yield lower extraction efficiency due to limited solvent diffusion and early saturation. In contrast, percolation extraction operates by continuously passing solvent through a packed bed of plant material, maintaining constant exposure to fresh solvent. This dynamic flow improves mass transfer rates, resulting in higher extraction efficiency and shorter processing durations. Percolation is especially suitable for large-scale processes and the extraction of heat-sensitive compounds, as it can be performed at lower temperatures.

A study by Rodríguez et al. (2018) [8] compared batch and continuous (percolation) extraction methods for obtaining antioxidant compounds from Sterculia apetala seeds. The findings indicated that percolation extraction yielded higher concentrations of phenolic compounds and exhibited greater antioxidant activity compared to batch extraction, underscoring the efficiency of percolation in recovering bioactive constituents.

Therefore, the objective of this study was to determine the optimal extraction conditions for MBC using the percolation technique. Solvent concentration (acetonitrile solution) and extraction temperature were investigated to achieve the highest yield of MBC extract, primarily composed of vitexin and iso-vitexin.

2. EXPERIMENTAL

2.1 Preparation of Mung Bean Seed Coat

Mung bean seed coat was sourced from a local factory in Bangkok. It was thoroughly washed several times with 100% acetonitrile (AR grade, Merck, Germany) to remove surface impurities. The cleaned seed coat was then dried at 65 °C for 24 hours. After drying, the material was ground using a mechanical crusher, and the resulting powder was sieved through screens with mesh sizes of 60, 80, 100, 110, and 130. The fine powder fraction retained between 110–130 mesh was collected, vacuum-sealed, and stored for subsequent extraction.

2.2 Preparation of Extracting Solvent

Acetonitrile solution was selected as the extraction solvent. Acetonitrile (AR grade, Merck, Germany) was mixed with distilled deionized water (18.2 mΩ·cm) at the specified volumetric ratios (% v/v). The resulting solution was filtered through a 0.45-µm nylon membrane and degassed using an ultrasonic sonicator for 30 minutes. It was then transferred into a 50 -mL plastic syringe for use in the extraction step.

2.3 Extraction of Mung Bean Seed Coats

The extraction parameters investigated in this study were extraction temperature (40, 60, and 80 °C) and acetonitrile concentration (30%, 50%, and 70% v/v). The experimental design is presented in **Table 1**. A total of nine experiments were conducted in duplicate.

Table 1 Experimental design for the percolation extraction method of mung bean seed coat (MBC)

Run	Temperature (°C)	Acetonitrile concentration (% v/v)
1	40	30
2	40	50
3	40	70
4	60	30
5	60	50
6	60	70
7	80	30
8	80	50
9	80	70

The percolation extraction apparatus is illustrated in Figure 1. The setup comprises a jacketed vertical cylindrical glass column serving as the extraction unit. A total of 0.5 grams of fine MBC powder was packed into the inner tube, supported by a layer of cotton at the bottom. The extraction temperature was regulated by circulating hot water through the outer jacket, with the water heated using a circulation heater (Cb-15-25e, Heto, Denmark). After preheating the column for 30 minutes, the extracting solvent (acetonitrile solution) was introduced into the column using a syringe pump (Fusion 100 T, Chemyx, United States) at a flow rate of 1 mL/min. The effluent was collected in 2 -mL microtubes at 2-minute intervals for a total duration of 24 minutes, yielding 12 fractions. The obtained samples were subjected to HPLC analysis, and the yield of the MBC extract was calculated using Equation (1).

$$Y_{MBCX} = \frac{(V_{Ef})(C_{Ef})}{m_{DMBC}} \quad (1)$$

Where Y_{MBCX} is the yield of MBC extract (mg MBC extract/g dried MBC) in each tube; V_{Ef} is the volume of the effluent (mL); C_{Ef} is the concentration of MBC extract (g/L) in the effluent; and m_{DMBC} is the weight of dried MBC powder (g). The total yield of MBC extract (Y^{T}_{MBCX}) was calculated as the sum of the yields from all 12 samples, as shown in Equation (2).

$$Y^{T}_{MBCX} = Y^{1}_{MBCX} + Y^{2}_{MBCX} + Y^{3}_{MBCX} + \cdots + Y^{12}_{MBCX} \quad (2)$$

2.4 Preparation of Standard Powder of MBC Extract

The MBC extract powder was prepared using a maceration extraction technique conducted at room temperature. A 50% v/v acetonitrile solution was used as the extracting solvent. One hundred grams of dried MBC powder was placed in a ceramic cylindrical separatory funnel, supported by cotton at the bottom. Then, 150 mL of the extracting solvent was added and allowed to soak for 30 minutes. After the soaking period, the valve was opened to collect the extract. The

procedure was repeated twice, resulting in a solid-to-solvent ratio of 1 g dried MBC to 3 mL solvent. The combined liquid extracts were stored in a freezer at −18 °C overnight to allow precipitation. The resulting slurry was filtered to collect the supernatant, which was subsequently concentrated using a rotary evaporator (IKA RV3, IKA Works GmbH & Co. KG, Germany) operated at 40 °C until a dried MBC extract powder was obtained.

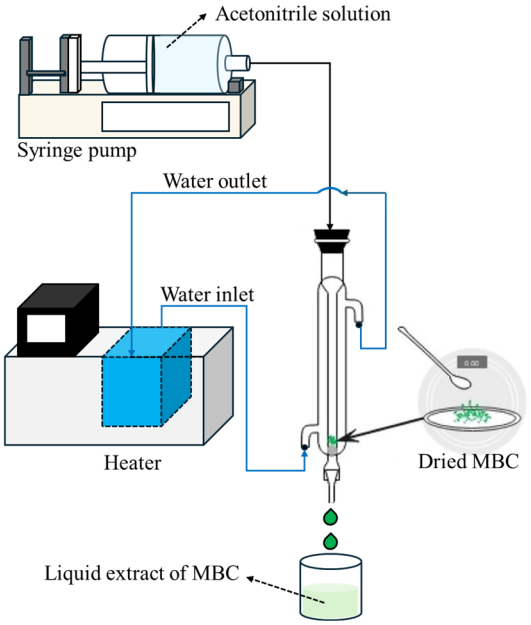

Figure 1 The percolation extraction apparatus for extraction of mung bean seed coat (MBC).

2.5 Analytical Method

High-performance liquid chromatography (HPLC) equipment (Knauer, Germany) was used to determine the concentration of MBC extract in the effluent samples collected from the percolation extraction process. The system consisted of an isocratic pump, autosampler, column oven, and UV detector. The mobile phase was a 15% v/v ethanol solution, prepared by mixing HPLC-grade ethanol (Merck, Darmstadt, Germany) with distilled deionized water, followed by filtration through a 0.45 µm nylon membrane and degassing. The pump flow rate was set at 1 mL/min. A C18 column (ACE Excel, 5 µm, 4.6 × 250 mm) was used and maintained at 53 °C in the column oven. The UV detector was set to a wavelength of 330 nm. Prior to analysis, the effluent samples were filtered through a 0.45 µm nylon syringe filter. The injection volume was 10 µL. The calibration curve for quantification was established using standard solutions of MBC extract powder, prepared by dissolving the powder in 90% v/v ethanol to yield concentrations ranging from 5 to 15 mg/mL.

3. RESULTS AND DISCUSSION

To interpret the results of the percolation extraction via HPLC, a standard powder of MBC extract was required for calibration curve construction. This standard was prepared using maceration with a 50% v/v acetonitrile solution to extract the bioactive compounds from mung bean seed coat, followed by temperature-induced precipitation of the liquid extract at −18 °C to remove impurities, as detailed in Section 2.4. The chromatogram and physical appearance of the MBC extract powder are presented in Figure 2.

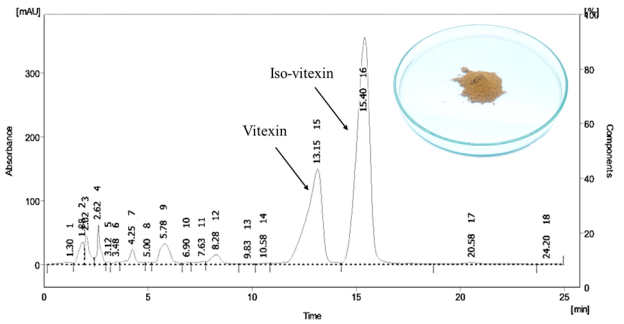

Figure 2 The HPLC chromatogram of the MBC extract powder at a concentration of 5.36 mg/mL. The detail of HPLC analysis is described in section 2.5.

The chromatogram revealed two predominant bioactive compounds in the semi-purified crude extract of MBC. Based on chromatographic profiles reported in the literature [9], these major peaks were identified as vitexin and iso-vitexin. Therefore, by disregarding minor impurity peaks, the MBC extract powder was considered a mixed standard of vitexin and iso-vitexin. This represents a limitation of using crude MBC extract as a standard for HPLC analysis of the extraction samples.

In the percolation extraction of MBC, acetonitrile solution was selected as an alternative to ethanol due to its favorable solvent properties. Based on relative polarity indices—acetonitrile (0.46), ethanol (0.654), and water (1.00) [10]—acetonitrile is less polar than ethanol, making it more suitable for extracting moderately to low-polarity compounds. Given that vitexin and iso-vitexin in the MBC extract are nearly insoluble in water [11], they are likely to exhibit moderate or low polarity. Therefore, acetonitrile is expected to extract these target compounds more effectively than ethanol. Additionally, acetonitrile offers a lower viscosity (0.346 cP) [12] compared to ethanol (1.074 cP) [13], which enhances the flow of the solvent through the packed bed of MBC powder during percolation, improving extraction efficiency.

The plot of the MBC extract yield, calculated using Equation (1), versus time at various acetonitrile concentrations and extraction temperatures is shown in Figure 3, covering all 12 fractions collected over 24 minutes.

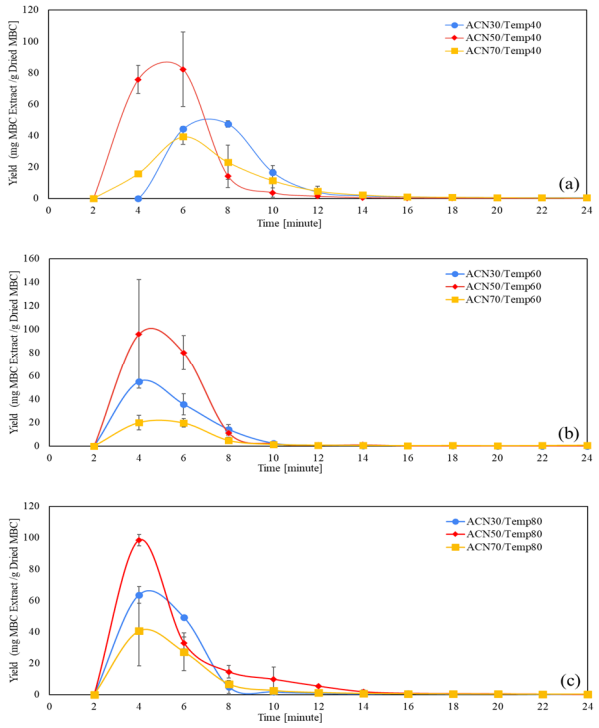

Figure 3 Yield of MBC extract versus extraction time at various acetonitrile concentrations: (a) 40 °C, (b) 60 °C, and (c) 80 °C.

As shown in Figure 3, the yield of MBC extract initially increased with extraction time, reaching a maximum before gradually declining to zero. This trend was consistent across all experimental conditions. The observed pattern can be explained by the percolation dynamics: during the initial stage, acetonitrile diffuses into the solid bed, dissolves the moderately polar compounds, and carries them out into the solvent phase. The solvent effectively leached a large number of bioactive compounds from the top layer of the packed MBC bed. As time progressed, the solvent continued to percolate downward, gradually depleting the extractable compounds from top to bottom. Consequently, the yield decreased over time and eventually reached zero, indicating that the entire packed bed had been exhausted of the target compounds.

Notably, the use of 50% v/v acetonitrile resulted in the highest extract yield, surpassing those obtained with 30% and 70% concentrations. This peak yield occurred consistently around fraction 2 (2–4 minutes) across all extraction temperatures (Figures 3a–3c). These results suggest that 50% v/v acetonitrile is the most suitable solvent concentration for efficiently extracting vitexin and iso-vitexin from MBC, providing a rapid and effective yield.

The plot of the total yield of MBC extract, calculated as the cumulative yield over time (12 fractions) according to Equation (2), is presented in Figure 4. The effects of acetonitrile concentration and extraction temperature were clearly observed. In solid–liquid extraction, the polarity of the solvent must align with that of the target compounds, following the principle of 'like dissolves like,' to achieve high extraction efficiency. At a constant extraction temperature, increasing the acetonitrile concentration from 30% to 50% v/v—effectively reducing the overall polarity of the mixed solvent—resulted in an enhanced yield of MBC extract. However, further increasing the concentration to 70% led to a decrease in yield. This suggests that the polarity of the 50% v/v acetonitrile solution was well-matched with the polarity of vitexin and iso-vitexin, enabling optimal extraction. As shown in Figure 4, the highest total yields were obtained with 50% v/v acetonitrile, reaching 179.06, 190.76, and 165.27 mg MBC extract/g dried MBC at extraction temperatures of 40 °C, 60 °C, and 80 °C, respectively . These findings indicate that the major bioactive compounds in the extract—vitexin and iso-vitexin—are moderately polar in nature.

The effect of extraction temperature was clearly evident when using 50% v/v acetonitrile solution. As shown in Figure 4, increasing the temperature from 40 °C to 60 °C enhanced the total yield of MBC extract from 179.06 to 190.76 mg/g dried MBC. This can be attributed to the fact that higher temperatures generally promote solute solubility and diffusion rates, thereby improving extraction efficiency. However, a further increase to 80 °C resulted in a reduced yield. A possible explanation is that this temperature approaches the boiling point of acetonitrile (81.65 °C) [14], potentially causing solvent evaporation and subsequent loss during extraction. This effect was also observed when using 70% acetonitrile, but it was less pronounced with 30% acetonitrile due to the higher water content and water's higher boiling point. Another likely explanation is the thermal degradation of bioactive compounds at elevated temperatures.

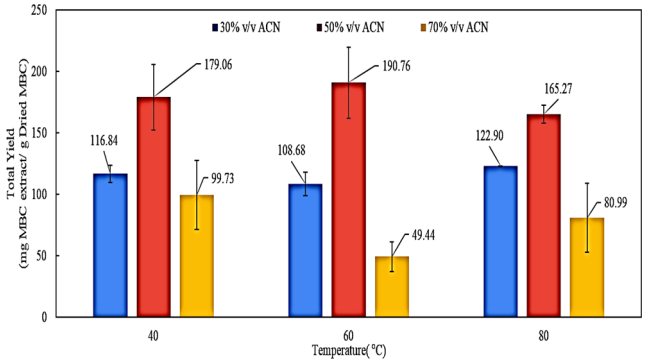

Figure 4 The total yield of MBC extract at varios

It was further noted in Figure 3 that all percolation extraction experiments were completed within 15 minutes, which is significantly shorter than the duration required for batch extraction processes. In batch systems, such as mixing tanks, the extraction is time-consuming due to the need to reach equilibrium—where the solute concentrations in both the solid and liquid phases become constant over time—often resulting in incomplete solute recovery. Additionally, batch processes require a final filtration step to separate

the exhausted solid material from the liquid extract. In contrast, percolation extraction offers several advantages: the continuous flow of solvent through the packed bed promotes efficient, gradient-driven mass transfer and enables effective solute recovery using lower solvent volumes. Moreover, the solute can be almost completely extracted, and the solid material remains stationary in the column, eliminating the need for post-extraction filtration.

The composition of the MBC extract, with emphasis on vitexin and iso-vitexin yields, is presented in Table 2. The percolation extraction process required only 15 minutes, which is comparable to the 10 minutes reported for pressurized liquid extraction (PLE) in the literature. The total yield of MBC extract in this study—defined as the combined content of vitexin and iso-vitexin—was 190.76 mg/g of dried MBC, which is close to the yield reported in the literature (approximately 151.74 mg/g). When considering productivity, calculated as the bioactive compound yield per unit extraction time, the values were also comparable, indicating the high efficiency of the percolation extraction method. The liquid products obtained from this technique can be fully collected and subsequently evaporated to yield MBC extract powder, which is suitable for use as an ingredient in nutraceutical or pharmaceutical products, or as a feedstock for isolating high-purity vitexin and iso-vitexin.

Table 2 Comparison of the MBC extract yields with those reported in the literature.

Source	This work	Literature [6]
Vitexin yield (mg Vitexin/g MBC)	-	130.53
Iso-vitexin yield (mg iso-vitexin/g MBC)	-	21.21
Extraction time (min)	15	10
Total MBC extract yield (mg MBC extract/g MBC)	190.76	151.74
Productivity (mg MBC extract/g MBC·min)	12.72	15.17

4. CONCLUSION

The valorization of mung bean seed coat (MBC), an agricultural byproduct from the milling process, was undertaken due to its potential as a rich source of bioactive compounds, particularly vitexin and iso-vitexin, which exhibit pharmacological activities such as anticancer and antioxidant effects. This study aimed to determine the optimal extraction conditions for maximizing the yield of MBC extract—defined as the combined content of vitexin and iso-vitexin—using the percolation extraction method. The extraction process was conducted in a jacketed cylindrical glass column, where MBC was packed in the inner tube and water was circulated through the outer jacket. The extracting solvent was introduced into the packed bed via a syringe pump. Variables examined included extraction temperatures of 40, 60, and 80 °C, and acetonitrile concentrations of 30%, 50%, and 70% v/v. The highest total yield, 190.76 mg of MBC extract per gram of dried MBC, was achieved within 15 minutes under the conditions of 60 °C and 50% v/v acetonitrile. The enhanced solubility of the bioactive compounds at elevated temperatures, combined with the optimal polarity provided by 50% acetonitrile, accounted for this result. These findings demonstrate that percolation extraction offers a time-efficient and effective method for recovering bioactive compounds from MBC. Furthermore, the resulting extract is suitable for use as a feedstock for the purification of high-purity vitexin and iso-vitexin.

ACKNOWLEDGMENTS

We gratefully acknowledge Prof. Dr. Attasak Jarree for providing the raw materials and essential laboratory equipment. We sincerely thank Miss Sitthima Phurithap for her guidance on the experimental procedures. We also extend our appreciation to the Department of Chemical Engineering, Faculty of Engineering, Kasetsart University, Thailand.

REFERENCES

1. Wang, F., L. Huang, X. Yuan, X. Zhang, L. Guo, C. Xue, and X. Chen, Nutritional, phytochemical and antioxidant properties of 24 mung bean (Vigna radiate L.) genotypes. *Food Production, Processing and Nutrition*, 2021. **3**(1).
2. Gao, J., L. Xie, Y. Peng, M. Li, J. Li, Y. Ni, and X. Wen, Deep Eutectic Solvents as New Extraction Media for Flavonoids in Mung Bean. *Foods*, 2024. **13**(5).
3. Pavasutti, V., C. Sinthuvanich, N. Tayana, S. Kongkiatpaiboon, and S. Sae-tan, Mung bean seed coat water extract restores insulin sensitivity via upregulation of antioxidant defense system and downregulation of inflammation in insulin-resistant HepG2 cells. *NFS Journal*, 2023. **32**.
4. Yu, Y.T., M. Jiang, P.P. Piccaluga, and S. Xie, Progress in the Study of Active Ingredients and Pharmacological Actions of Mung Bean. *BIO Web of Conferences*, 2024. **111**.
5. He, M., J.W. Min, W.L. Kong, X.H. He, J.X. Li, and B.W. Peng, A review on the pharmacological effects of vitexin and isovitexin. *Fitoterapia*, 2016. **115**: p. 74-85.
6. Supasatyankul, B., M. Saisriyoot, U. Klinkesorn, K. Rattanaporn, and S. Sae-Tan, Extraction of Phenolic and Flavonoid Compounds from Mung Bean (Vigna radiata L.) Seed Coat by Pressurized Liquid Extraction. *Molecules*, 2022. **27**(7).

7. Zhou, Y., J. Zheng, R.Y. Gan, T. Zhou, D.P. Xu, and H.B. Li, Optimization of Ultrasound-Assisted Extraction of Antioxidants from the Mung Bean Coat. *Molecules*, 2017. **22**(4).
8. Mosca, F., G.I. Hidalgo, J. Villasante, and M.P. Almajano, Continuous or Batch Solid-Liquid Extraction of Antioxidant Compounds from Seeds of Sterculia apetala Plant and Kinetic Release Study. *Molecules*, 2018. **23**(7).
9. Maneewan, S., P. Tangpromphan, and A. Jaree, Separation of Vitexin and Iso-vitexin from Mung Bean Seed Coats Using a Three-Zone Simulated Moving Bed (SMB). *Waste and Biomass Valorization*, 2021. **12**(12): p. 6601-6618.
10. Christian Reichardt, T.W., *Solvents and Solvent Effects in Organic Chemistry*. 2010: Wiley-VCH Verlag GmbH & Co. KGaA
11. Costa, E.C., P.M.N. Menezes, R.L. de Almeida, F.S. Silva, L.A. de Araujo Ribeiro, J.A. da Silva, A.P. de Oliveira, E.C. da Cruz Araujo, L.A. Rolim, and X.P. Nunes, Inclusion of vitexin in beta-cyclodextrin: preparation, characterization and expectorant/antitussive activities. *Heliyon*, 2020. **6**(12): p. e05461.
12. Mahzbeen Ansari, S.P.S., Viscosities and Densities of Acetonitrile-water systems at 25ºC. *Research Journal of Chemical Sciences*, 2022. **12**: p. 67-69.
13. Haynes, W.M., *CRC Handbook of Chemistry and Physics*. 2011: CRC Press.
14. Joshi, D.R. and N. Adhikari, An Overview on Common Organic Solvents and Their Toxicity. *Journal of Pharmaceutical Research International*, 2019. **28**(3): p. 1-18.

Sustainable ethylene synthesis via photocatalytic conversion of succinic acid over metal-TiO_2 photocatalysts

Suttida Pomsri[1], Worached Laothong[1], Aroonsri Nuchitprasittichai[1], Supunnee Junpirom[1,*]

[1] School of Chemical Engineering, Institute of Engineering, Suranaree University of Technology, Nakhon Ratchasima 30000 Thailand.
[*] Corresponding author: supunnee@sut.ac.th

ABSTRACT

The increasing demand for sustainable chemical production has driven interest in utilizing bio-based feedstocks for valuable chemical synthesis. Succinic acid, a key platform chemical, can be photocatalytically converted into ethylene, an essential monomer for polymer production. This study investigates the photocatalytic conversion of succinic acid using metal-doped TiO_2 photocatalysts (Fe/TiO_2, Pd/TiO_2, Cu/TiO_2, and Ag/TiO_2) under varying reaction conditions. The photocatalysts were synthesized and characterized using X-ray diffraction (XRD) and energy-dispersive spectroscopy (EDS) to confirm their composition and structural properties. Photocatalytic experiments revealed that photocatalyst weight and pH significantly influence ethylene production. Fe/TiO_2 exhibited the highest ethylene yield at pH=3 with a photocatalyst weight of 0.15 g, while Cu/TiO_2 and Ag/TiO_2 peaked at 0.10 g. The findings suggest that metal-doped TiO_2 enhances photocatalytic efficiency, offering a promising route for sustainable ethylene production from succinic acid.

Keywords: Photocatalysis; Succinic acid; Ethylene; Metal-doped TiO_2

1. INTRODUCTION

The increasing demand for sustainable chemical production has driven interest in utilizing bio-based feedstocks for valuable chemical synthesis. Succinic acid, a four-carbon dicarboxylic acid, is a key platform chemical that can be derived from both fossil-based and renewable sources. Traditionally, succinic acid has been produced through petroleum-based processes; however, advancements in biotechnology have enabled its efficient production from biomass sources such as corn, sugarcane, and lignocellulosic waste through microbial fermentation [1, 2]

Succinic acid serves as a crucial intermediate in various chemical transformations and has significant potential for value-added applications [3]. One such application is its photocatalytic conversion into ethylene, a fundamental building block in the polymer industry [4]. Ethylene is conventionally produced from petroleum cracking, contributing to greenhouse gas emissions and environmental concerns [5-9]. The development of sustainable routes for ethylene production from bio-based succinic acid offers an eco-friendly alternative, reducing reliance on fossil fuels [10].

Photocatalysis, particularly using titanium dioxide (TiO_2) based photocatalysts, has gained attention for its ability to drive chemical reactions under mild conditions using solar or ultraviolet (UV) light [11-14]. TiO_2 is widely recognized for its strong oxidative properties, stability, and efficiency in various photocatalytic applications [15]. However, to enhance its photocatalytic performance, metal-doped TiO_2 photocatalysts such as Pd/TiO_2, Fe/TiO_2, Cu/TiO_2, and Ag/TiO_2 have been investigated for improving charge separation and reaction efficiency [16].

This study explores the photocatalytic degradation of succinic acid under different reaction conditions, focusing on the effects of pH and photocatalyst weight on ethylene production. By utilizing bio-derived succinic acid as a precursor, this research highlights a sustainable approach to ethylene synthesis, contributing to the circular economy and reducing dependence on petrochemical processes.

2. EXPERIMENTAL

The materials used in this research include Titanium (IV) n-butoxide (99%, $Ti(C_4H_9O)_4$), Hydrogen peroxide (30%, H_2O_2), Palladium (II) chloride (99%, $PdCl_2$), Copper (II) Nitrate ($CuN_2O_6 \cdot {}_3H_2O$), Iron (III) Sulfate ($Fe_2(SO_4)_3$), Silver Nitrate ($AgNO_3$), Sodium Hydroxide (NaOH).

The metal-doped TiO_2 photocatalyst was prepared from 5 ml of titanium (IV) n-butoxide and 16.67 ml of hydrogen peroxide and mix them in a 500 ml beaker at room temperature. Stir the mixture until homogeneous, which takes about 10 min, and then let it dry for 2 h. Heat the mixture at 100 ◦C for 1.5 h to obtain a yellow precipitate. Then, weigh the dry yellow precipitate. Prepare a 3.5% of metal solution and mix the dry yellow precipitate with metal solution in a crucible. Heat the

mixture at 550 ◦C for 3 h in an air furnace at a 5 ◦C/min heating rate. Finally, the physical properties of the synthesized photocatalyst were analyzed by using an X-ray diffractometer (XRD) and Energy Dispersive Spectroscopy (EDS) [17]. To determine the optimal conditions for ethylene photodegradation, titanium dioxide P25 powder was coated onto plastic pellets and packed into the reactor until full. A 500 mL solution of 0.5 M succinic acid was prepared, along with varying amounts of photocatalyst (0.05 g, 0.1 g, and 0.15 g) in a sealed three-neck flask. The reactants were introduced into the reactor at a flow rate of 30 mL/min until the solution overflowed back into the flask. The reaction was initiated by turning on the light and allowed to proceed for 1 hour. After the reaction, gas samples were collected and analyzed using a Handy Ethylene Gas Detector (WASP-XM).

3. RESULTS AND DISCUSSION

Characterization of photocatalysts by SEM images combined with EDS mapping provides insight into the elemental distribution within the photocatalysts. Figures 1, 2, 3, and 4 correspond to Fe/TiO_2, Pd/TiO_2, Cu/TiO_2, and Ag/TiO_2 photocatalysts, respectively. Figure 1 demonstrates Energy Dispersive X-Ray Spectroscopy (EDS) analysis confirms the presence of metal elements in the photocatalysts. a uniform distribution of Fe, Ti, and O, confirming the successful incorporation of Fe onto the TiO_2 surface. Figure 2 reveals the elemental distribution of Pd/TiO_2, showing that while Ti and O remain evenly dispersed, Pd is concentrated in specific areas, suggesting the aggregation of Pd nanoparticles on the TiO_2 surface. Figure 3 confirms the successful incorporation of Cu onto TiO_2 through its elemental distribution. Finally, Figure 4 illustrates the uniform dispersion of Ag on the TiO_2 surface, indicating successful metal deposition.

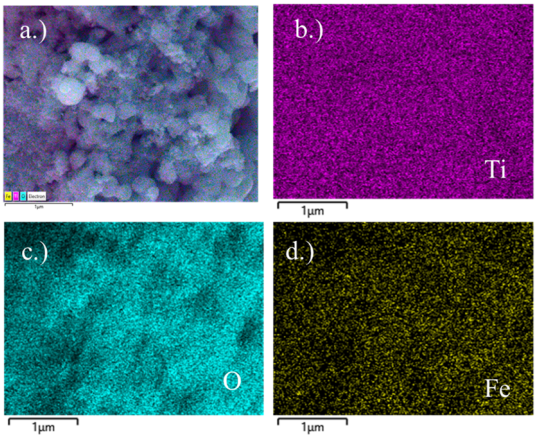

Figure 1 SEM images of Fe/TiO_2 (a) and the elemental dispersion from EDS mapping of (b) Ti, (c) O, (d) Fe.

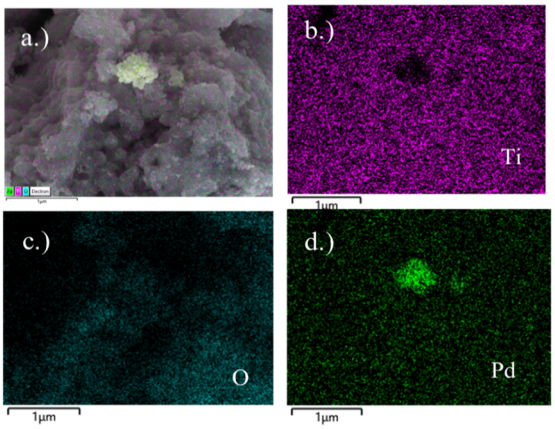

Figure 2 SEM images of Pd/TiO_2 (a) and the elemental dispersion from EDS mapping of (b) Ti, (c) O, (d) Pd.

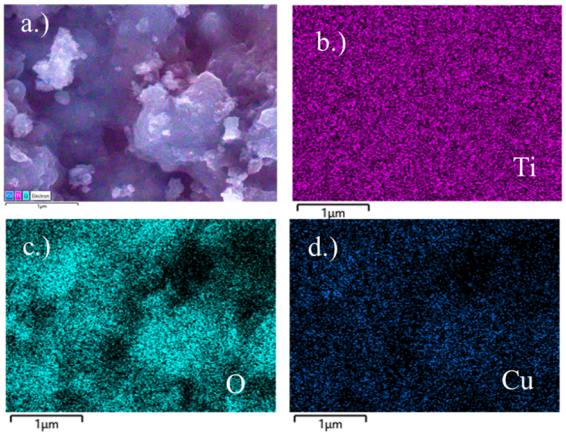

Figure 3 SEM images of Cu/TiO_2 (a) and the elemental dispersion from EDS mapping of (b) Ti, (c) O, (d) Cu.

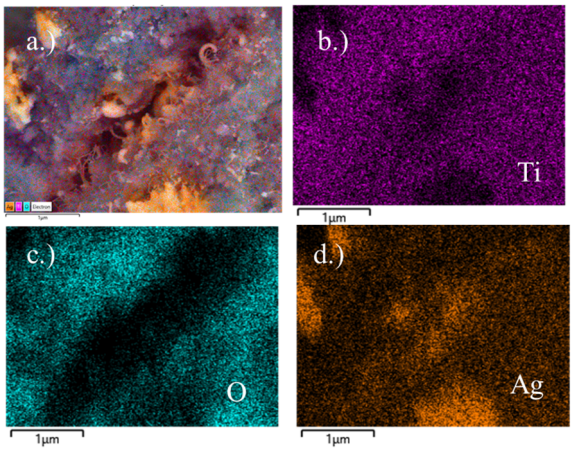

Figure 4 SEM images of Ag/TiO_2 (a) and the elemental dispersion from EDS mapping of (b) Ti, (c) O, (d) Ag.

The XRD patterns of Fe/TiO_2, Pd/TiO_2, Cu/TiO_2, and Ag/TiO_2 confirm the presence of anatase TiO_2 with characteristic peaks at $2\theta = 25°, 37°, 48°$, and 54° [18]. Additional peaks observed in the modified samples suggest the presence of metal or metal oxide phases, indicating successful incorporation of Fe, Pd, Cu, and Ag into the TiO_2 structure, as shown in Figure 5.

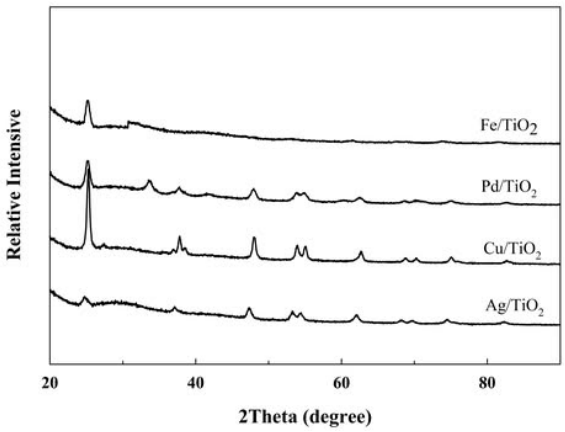

Figure 5 The X-ray diffraction (XRD) patterns for Fe/TiO_2, Pd/TiO_2, Cu/TiO_2, and Ag/TiO_2.

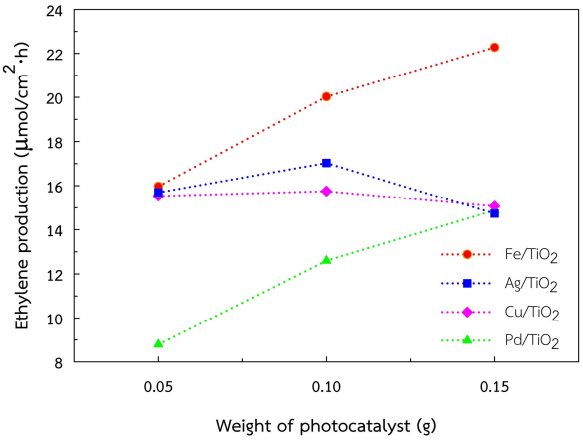

Figure 6 Effect of photocatalyst weight on the photocatalytic reaction over different photocatalysts to produce ethylene at pH=3 (0.5 M succinic acid).

Fig. 6 shows the effect of photocatalyst weight on the photocatalytic reaction of 0.5 M succinic acid over different photocatalysts to produce ethylene at pH=3. At a photocatalyst weight of 0.15 g, ethylene production over Fe/TiO_2 reaches its highest yield and continues to increase steadily with photocatalyst weight, similar to Pd/TiO_2. Meanwhile, Cu/TiO_2 and Ag/TiO_2 peak at 0.10 g before decreasing at 0.15 g. A higher photocatalyst weight means more surface area and active sites available for photocatalytic reactions. In addition, a greater amount of photocatalysts can absorb more photons, generating more electron-hole pairs and increasing the reaction rate [19]. However, an excessive amount of photocatalyst can lead to excessive light scattering and absorption, preventing deeper penetration into the reaction medium. This reduces the number of effective photons reaching all photocatalyst particles.

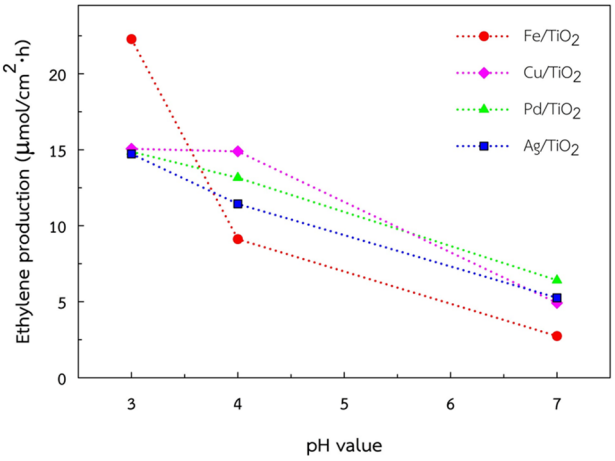

Figure 7 Effect of pH on the photocatalytic reaction over different photocatalysts for ethylene production at a photocatalyst weight of 0.15 g (0.5 M succinic acid).

The effect of pH on the photocatalytic reaction of 0.5 M succinic acid over different photocatalysts for ethylene production at a photocatalyst weight of 0.15 g is shown in Fig. 7. Ethylene production decreases as pH increases for all photocatalysts. Fe/TiO_2 exhibits the highest ethylene production at pH=3 but declines significantly as pH increases. Pd/TiO_2, Cu/TiO_2, and Ag/TiO_2 maintain more stable production between pH=3 and 4, though they also decline at higher pH value. At lower pH, TiO_2 photocatalysts are more effective due to an increased surface charge, which enhances the adsorption of succinic acid [20]. On the contrary, succinic acid exists in its deprotonated form (succinate ions), reducing its interaction with the photocatalyst surface. A higher OH^- concentration may lead to excessive hydroxyl radical formation, promoting side reactions instead of ethylene production [21].

4. CONCLUSION

This study demonstrates the potential of metal-doped TiO_2 photocatalysts for the conversion of succinic acid into ethylene. Structural characterization confirmed the successful incorporation of Fe, Pd, Cu, and Ag into the TiO_2 framework, enhancing photocatalytic performance. The experimental results highlight the importance of photocatalyst weight and pH in optimizing ethylene production. Fe/TiO_2 achieved the highest yield at 0.15 g and pH=3, while Cu/TiO_2 and Ag/TiO_2 exhibited optimal performance at 0.10 g. Excessive photocatalyst loading reduced efficiency due to light scattering, while higher pH levels hindered ethylene production by altering the interaction between succinic acid and the photocatalyst surface. These findings support the development of bio-based ethylene production as a sustainable alternative to conventional petroleum-based methods, contributing to greener chemical synthesis pathways.

ACKNOWLEDGMENTS

This work was supported by (i) University of Technology (SUT), (ii) Thailand Science Research and Innovation (TSRI), and (iii) National Science, Research and Innovation Fund (NSRF). – Grant no. 179280. Suttida Pomsri wishes to express her sincere gratitude to Suranaree University of Technology (SUT) for generously providing a scholarship and financial support for her master's degree studies.

REFERENCES

1. Song H. and Lee S.Y., Production of succinic acid by bacterial fermentation. (2006) Enzyme and Microbial Technology, 352-361.
2. Cukalovic A. and Stevens C., Feasibility of production methods for succinic acid derivatives: A marriage of renewable resources and chemical technology. (2008) Biofuels, Bioproducts and Biorefining, 505-529.
3. Werpy T., Holladay J. and White J., Top Value Added Chemicals From Biomass: I. Results of Screening for Potential Candidates from Sugars and Synthesis Gas. (2004).
4. Shi Q., Li J., Liu Y., et al., Photoelectrocatalytic Valorization of Biomass-Derived Succinic Acid into Ethylene Coupled with Hydrogen Production over an Ultrathin BiOx-Covered TiO2. (2024) ACS Catalysis, 10728-10736.
5. Layritz L., Dolganova I., Finkbeiner M., et al., The potential of direct steam cracker electrification and carbon capture & utilization via oxidative coupling of methane as decarbonization strategies for ethylene production. (2021) Applied Energy, 117049.
6. Amghizar I., Dedeyne J., Brown D., et al., Sustainable innovations in steam cracking: CO2 neutral olefin production. (2020) Reaction Chemistry & Engineering.
7. Wéry F., Geerts M., Vandewalle L.A., et al., Assessing the CO2 emission reduction potential of steam cracking furnace innovations via computational fluid dynamics: From high-emissivity coatings, over coil modifications to firing control. (2023) Chemical Engineering Research and Design, 129-142.
8. Mynko O., Amghizar I., Brown D.J., et al., Reducing CO2 emissions of existing ethylene plants: Evaluation of different revamp strategies to reduce global CO2 emission by 100 million tonnes. (2022) Journal of Cleaner Production, 132127.
9. Salah C., Istrate R., Bjørn A., et al., Environmental Benefits of Circular Ethylene Production from Polymer Waste. (2024) ACS Sustainable Chemistry & Engineering, 13897-13906.
10. Bozell J. and Petersen G., Technology development for the production of biobased products from biorefinery carbohydrates—the US Department of Energy's "Top 10" revisited. (2010) Green Chemistry - GREEN CHEM.
11. Sun Z., Huang X. and Zhang G., TiO2-based catalysts for photothermal catalysis: Mechanisms, materials and applications. (2022) Journal of Cleaner Production, 135156.
12. Nakata K. and Fujishima A., TiO2 photocatalysis: Design and applications. (2012) Journal of Photochemistry and Photobiology C: Photochemistry Reviews, 169-189.
13. Arora I., Chawla H., Chandra A., et al., Advances in the strategies for enhancing the photocatalytic activity of TiO2: Conversion from UV-light active to visible-light active photocatalyst. (2022) Inorganic Chemistry Communications, 109700.
14. Nagaraj K., Radha S., Deepa C.G., et al., Photocatalytic advancements and applications of titanium dioxide (TiO_2): Progress in biomedical, environmental, and energy sustainability. (2025) Next Research, 100180.
15. Schneider J., Matsuoka M., Takeuchi M., et al., Understanding TiO2 Photocatalysis: Mechanisms and Materials. (2014) Chemical Reviews, 9919-9986.
16. Chong M.N., Jin B., Chow C.W.K., et al., Recent developments in photocatalytic water treatment technology: A review. (2010) Water Research, 2997-3027.
17. Rashed M. and Khodari A., Synthesis of pure and palladium doped TiO2 and their applications as modifiers for carbon paste electrode. (2022) Aswan University Journal of Environmental Studies, 267-283.
18. Hanaor D. and Sorrell C., Review of the Anatase to Rutile Phase Transformation. (2011) Journal of Materials Science, 855-874.
19. Yunus N.N., Hamzah F., So'aib M., et al., Effect of Catalyst Loading on Photocatalytic Degradation of Phenol by Using N, S Co-doped TiO 2. (2017) IOP Conference Series: Materials Science and Engineering, 012092.
20. Molea A., Popescu V., Rowson N., et al., Influence of pH on the formulation of TiO2 nano-crystalline powders with high photocatalytic activity. (2014) Powder Technology, 22–28.
21. Nosaka Y. and Nosaka A.Y., Generation and Detection of Reactive Oxygen Species in Photocatalysis. (2017) Chemical Reviews, 11302-11336.

TIChE ENKKU ENGINEERING KHON KAEN UNIVERSITY

The 34th Thai Institution of Chemical Engineering and Applied Chemistry International Conference (TIChE2025)

Organized by

Department of Chemical Engineering
Khon Kaen University

มหาวิทยาลัยอุบลราชธานี

Join us next year in

TIChE2026
UBON RATCHATHANI

By Ubon Ratchathani University